

**2014 IEEE INTERNATIONAL ULTRASONICS SYMPOSIUM**  
**CHICAGO, ILLINOIS, USA**  
**SEPTEMBER 3-6, 2014**



**ABSTRACT BOOK**



**IEEE ULTRASONICS, FERROELECTRICS,  
AND FREQUENCY CONTROL SOCIETY**







## Table of Contents

Welcome from the General Chair .....	1
Conference Venue .....	2
Registration and Fees .....	3
Refund Policy .....	3
Conference Proceedings .....	4
Visa Assistance .....	5
Student Travel Support .....	6
President's Student Reception .....	6
Women in Engineering .....	6
IEEE Event Photography Statement .....	6
IEEE Non-Discrimination Policy .....	6
Conference Reception .....	7
Conference Banquet .....	7
Tours .....	8
Exhibitors list and Booths .....	9
Future Conference .....	12
Conference Organizing Committee .....	13
Short Courses .....	14
Technical Program Committee .....	15
Plenary Speaker .....	20
Clinical Speakers .....	21
Invited Speakers .....	21
Student Paper Competition .....	24
Poster Presentation Guide .....	27
Oral Presentation Guide .....	28
Speaker Ready Room .....	30
Condensed Sessions Program .....	31
Hilton Chicago Hotel Floor Plans .....	33
Sessions Program .....	35
Author Index .....	684

### Oral Sessions, Thursday, September 4, 2014:

Session 1A: MEL: Cardiac Strain Imaging .....	35
Session 2A: MTH: Drug Delivery and Novel Treatment Approaches .....	38
Session 3A: MPA: Photoacoustics I .....	42
Session 4A: Arrays .....	46
Session 5A: General Physical Acoustics 1 .....	50
Session 6A: RF Frontend Devices and Oscillators .....	54
Session 7A: High Frequency Transducers .....	58
Session 1B: MCA: Molecular Imaging .....	61
Session 2B: MEL: Cardiovascular Elasticity Imaging .....	65
Session 3B: MBB: Beamforming I .....	70
Session 4B: Structural Health Monitoring .....	75
Session 5B: Models in Physical Acoustics .....	79
Session 6B: Sensors and Field Characterization .....	83
Session 7B: CMUTs (1) .....	87
Session 1C: MCA: Outlook for Contrast Imaging .....	91
Session 2C: MEL: Elastography: Clinical Applications .....	94
Session 3C: MTC: Low Frequency Tissue Characterization .....	98
Session 4C: Materials Characterization .....	102
Session 5C: Nonlinear Acoustics 1 .....	106
Session 6C: Characterization of Materials .....	109
Session 7C: Micromachined Ultrasound Transducer Modeling .....	113

**Awards Sessions, Thursday, September 4, 2014:**

Session PA:	Student Paper Competition .....	117
-------------	---------------------------------	-----

**Poster Sessions, Thursday, September 4, 2014:**

Session P1A1:	MEL: Shear Wave Imaging Methods 1 .....	131
Session P1A2:	MEL: (Pre-)Clinical Applications of Elasticity Imaging .....	137
Session P1A3:	MCA: Contrast Imaging Applications .....	142
Session P1A4:	MBE: Biological Effects and Dosimetry .....	148
Session P1A5:	MBB: Beamforming I .....	157
Session P1A6:	MSD: Design and Test of Medical Systems & Devices .....	164
Session P1A7:	MPA: Light and Sound I .....	172
Session P1A8:	MIM: Technologies for Enhanced Imaging .....	181
Session P1A9:	MTC: Bone .....	187
Session P1A10:	MTH: Drug Delivery and Stimulation .....	192
Session P1A11:	MSP: Medical Signal Processing .....	198
Session P2A1:	Wave Propagation .....	204
Session P2A2:	Imaging .....	209
Session P2A3:	NDE/ Materials Characterization .....	215
Session P3A1:	Particle Manipulation and Acoustic Tweezing 1 .....	220
Session P3A2:	Nonlinear Acoustics 2 .....	224
Session P4A1:	Innovations for Resonators and Sensors 1 .....	229
Session P4A2:	Acoustic Modeling .....	233
Session P4A3:	Acoustic Sensors 1 .....	235
Session P5A1:	Front End Transducer Electronics .....	240
Session P5A2:	Films and Devices .....	243

**Oral Sessions, Friday, September 5, 2014:**

Session 1D:	MSD: Advanced Multi-Channel and Multi-Modality Systems .....	252
Session 2D:	MBF: Vector Velocity Techniques .....	255
Session 3D:	MPA: Photoacoustics II .....	259
Session 4D:	Nde .....	263
Session 5D:	Particle Manipulation and Acoustic Tweezing 2 .....	267
Session 6D:	Sensors and ID Tags .....	271
Session 7D:	Therapeutic Ultrasound Transducers .....	275
Session 1E:	MCA: Contrast Agents: New Investigations .....	279
Session 2E:	MBF: Novel Flow Techniques .....	283
Session 3E:	MSP: Medical Signal Processing .....	288
Session 4E:	Acoustic Microfluidics .....	292
Session 5E:	Particle Manipulation and Acoustic Tweezing 3 .....	296
Session 6E:	Innovations for Microacoustic Devices .....	300
Session 7E:	Applications of Piezoelectrics .....	304
Session 1F:	MTH: Histotripsy and Lithotripsy .....	307
Session 2F:	MEL: Vascular Strain Imaging .....	310
Session 3F:	MBB: Beamforming II .....	315
Session 4F:	Signal Processing .....	320
Session 6F:	Novel Microacoustic Devices .....	324
Session 7F:	CMUTs (2) .....	327
Session 1G:	MIM: New Developments in Volumetric Ultrasound .....	331
Session 2G:	MTC: High Frequency Tissue Characterization .....	334
Session 3G:	MEL: Elasticity Imaging Methods I .....	338
Session 4G:	Sensing .....	343
Session 7G:	Diagnostic and Imaging Transducers .....	346

**Poster Sessions, Friday, September 5, 2014:**

Session P1B1:	MPA: Light and Sound II .....	350
---------------	-------------------------------	-----

Session P1B2:	MBB: Beamforming II .....	356
Session P1B3:	MBF: Vector Velocity Imaging and Applications .....	363
Session P1B4:	MCA: Contrast Imaging Strategies .....	370
Session P1B5:	MCA: Acoustics and Manipulations .....	377
Session P1B6:	MEL: Mechanical Characterization of the Carotid .....	384
Session P1B7:	MEL: Elastography: Phantoms and Methods .....	391
Session P1B8:	MIM: New Systems for and Applications of Ultrasound Imaging .....	401
Session P1B9:	MTC: Cancer Applications of Tissue Characterization .....	407
Session P1B10:	MSD: Novel Medical Systems & Devices .....	413
Session P1B11:	MTH: Novel Therapeutic Ultrasound Approaches .....	420
Session P2B1:	Signal Processing and NDE Methods .....	427
Session P2B2:	Microfluidics .....	431
Session P2B3:	Transducers .....	435
Session P3B1:	Elastic Wave Propagation .....	438
Session P3B2:	General Physical Acoustics 2 .....	443
Session P4B1:	Innovative Device Concepts .....	448
Session P4B2:	Materials and Propagation .....	452
Session P5B1:	Transducer Materials .....	456
Session P5B2:	Biomedical Diagnosis and Imaging Transducers .....	460

### Oral Sessions, Saturday, September 6, 2014:

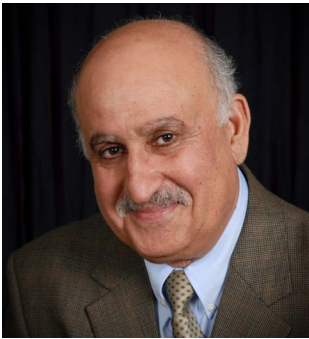
Session 1H:	MIM: Ultrasound Tools to Guide Cardiac Interventions .....	466
Session 2H:	MEL: Elasticity Imaging Methods II .....	470
Session 3H:	MSD: Special Applications of Advanced Ultrasound Systems .....	474
Session 4H:	Wave Propagation .....	479
Session 5H:	Thin-Films 1 .....	483
Session 6H:	Nonlinearity and Tunability .....	486
Session 7H:	Electronic Control and Needle Actuation .....	490
Session 1I:	MCA: Contrast Agents: New Technologies .....	494
Session 2I:	MPA: Photoacoustics III .....	498
Session 3I:	MTH: Blood-Brain Barrier and Sonoporation .....	502
Session 4I:	Transducers .....	506
Session 5I:	Ultrasonic Motors and Multi-Modal Thin Film Transducers .....	509
Session 6I:	Materials for SAW and BAW Applications .....	513
Session 7I:	Piezoelectric Materials .....	516
Session 1J:	MIM: Vascular Imaging .....	519
Session 2J:	MTH: Tumor Treatment and Monitoring .....	523
Session 3J:	MTC: Bone .....	527
Session 4J:	Industrial Applications and Flow Sensing .....	531
Session 5J:	Phononics 1 .....	535
Session 7J:	Photoacoustics and Other Topics .....	539
Session 1K:	MEL: Liver Elasticity Imaging .....	543
Session 2K:	MBB: Beamforming III .....	547
Session 3K:	MBE: Ultrasound Induced Biological Effects .....	552
Session 4K:	Airborne Ultrasound .....	555
Session 5K:	Opto-Acoustics .....	559

### Poster Sessions, Saturday, September 6, 2014:

Session P1C1:	MBB: Beamforming III .....	563
Session P1C2:	MBB: Beamforming IV .....	570
Session P1C3:	MBF: Methods and Applications for Blood Velocity Estimation .....	575
Session P1C4:	MCA: Therapeutics and Physical Properties .....	582
Session P1C5:	MEL: Cardiovascular Elasticity Imaging .....	588
Session P1C6:	MEL: Shear Wave Imaging Methods 2 .....	595
Session P1C7:	MIM: Image Processing and Classification .....	602
Session P1C8:	MTC: Noncancer Applications of Tissue Characterization .....	608
Session P1C9:	MTC: Tissue Characterization Methodology .....	615

Session P1C10:	MTH: Cancer Treatment and Monitoring.....	621
Session P1C11:	MTH: Treatment Monitoring and Novel Applications .....	627
Session P2C1:	Sensing.....	637
Session P2C2:	Ultrasonics and Fluids .....	641
Session P2C3:	Industrial Applications and Energy Harvesting .....	645
Session P3C1:	Ultrasonic Motors .....	649
Session P3C2:	Thin-Films 2.....	654
Session P3C3:	Phononics 2.....	658
Session P4C1:	Acoustic Sensors 2.....	664
Session P4C2:	Innovations for Resonators and Sensors 2 .....	667
Session P5C1:	Micromachined Ultrasonic Transducers.....	670
Session P5C2:	Therapy Transducers .....	679





## Message from the 2014 IEEE Ultrasonics Symposium General Chair

Jafar Saniie, Filmer Endowed Chair Professor  
Department of Electrical and Computer Engineering  
Illinois Institute of Technology, Chicago

The 2014 IEEE International Ultrasonics Symposium - Chicago (September 3-6) serves as a premier venue for bringing researchers and scientists from academia and industry together to share cutting-edge advances in ultrasonics research and inspire new ideas and collaborations between scholars. I would like to acknowledge the dedication and unwavering commitment of the **Organizing Committee** and the **Technical Program Committee** who have put forth a remarkable effort to make this conference a memorable and successful experience.

This year we have received a record number of abstracts and the Technical Program Committee members selected 938 papers for oral and poster presentations. These abstracts cover the five areas of focus for this meeting: Medical Ultrasonics, Sensors, NDE & Industrial Applications, Physical Acoustics, Microacoustics - SAW, FBAR & MEMS, and Transducers & Transducer Materials. The oral presentations include 24 invited papers highlighting emerging technologies or overviews of key areas. The poster presentations include the 20 student poster finalists competing for the Student Paper Awards. In order to accommodate the record number of presentations, the oral sessions are organized into seven parallel tracks over three days. I would like to thank Dr. Jan D'hooge, the Technical Program Committee Chair, who has been leading the organization of the symposium's technical program.

I am particularly pleased that this year the conference will be returning to the vibrant city of Chicago after 26 years. The annual 2014 IEEE International Ultrasonics Symposium will be held at the **Hilton Hotel**, Chicago, Illinois, USA from September 3-6, 2014. The hotel is easily accessed through either public transportation or by car. It is centrally located and **within walking distance** of the following attractions.

- Millennium Park
- Art Institute of Chicago
- Shedd Aquarium
- Field Museum
- Grant Park
- Adler Planetarium
- Buckingham Fountain
- Chicago Theatre District
- Lake Michigan

Arrangements have also been made for a highly popular Chicago tour: **Architecture River Cruise** which spotlights more than 50 architecturally significant sites where participants will discover a new perspective on the city of Chicago. I would like to thank Dr. Erdal Oruklu, Symposium Local Chair, who has been arranging many special activities for our conference attendees.

I sincerely encourage your participation in the conference and look forward to hosting you in the world class city of Chicago.

## CONFERENCE VENUE



### Hilton Hotel Chicago

The IEEE International Ultrasonics Symposium will be held at the beautiful **Hilton Hotel Chicago**. The hotel is easily accessed through public transportation or by car. It is located in the center of downtown adjacent to the majestic Grant Park. The area is central to several local attractions such as the Bean, Buckingham Fountain, and the Jay Pritzker pavilion as well as world renowned architecture such as the Sears Tower, Merchandise Mart, and the Hancock Building.

#### Venue Address:

Hilton Hotel Chicago  
720 South Michigan Avenue  
Chicago, Illinois 60605  
Phone: 1-312-922-4400

To reach the venue by public transit from **O'Hare international airport**: Take a CTA Blue Line train from the O'Hare stop to the LaSalle stop. Upon leaving the LaSalle stop, continue west on Congress Parkway until you reach Michigan Avenue. After taking a right (towards the South), the hotel will be located on the right hand side. This journey will take approximately one hour and cost \$5.

To reach the venue by public transit from **Midway International Airport**: Take an Orange Line train from the Midway stop to the Roosevelt stop. Upon leaving the Roosevelt stop, continue west on Roosevelt Road until you reach Michigan Avenue. After taking a left (towards the North), the hotel will be located on the left hand side. This journey will take approximately 30 minutes and cost \$2.25.

For additional information on public transit, please review [transitchicago.com](http://transitchicago.com) website.

In addition to public transportation, **taxi cabs** are readily available throughout the city. For cab fare information, please refer to the City of Chicago cab fare website:

[https://www.cityofchicago.org/city/en/depts/bacp/supp\\_info/2012\\_passenger\\_information.html](https://www.cityofchicago.org/city/en/depts/bacp/supp_info/2012_passenger_information.html)

## REGISTRATION AND FEES (\$USD)

Registration Type	Before August 3, 2014	After August 3, 2014
IEEE Members*	\$665	\$815
Non-IEEE Members*	\$890	\$1040
Student* (Show valid student ID at conference)	\$250 (IEEE Member) \$400 (Non-IEEE Member)	\$400 (IEEE Member) \$550 (Non-IEEE Member)
Retiree*	\$250	\$400
Life IEEE Member* (Show life member card at conference)	\$250	\$400
One-Day Registration**	\$400	\$400
Short Courses***	\$250 (One Short Course) \$400 (Two Short Courses)	\$350 (One Short Course) \$500 (Two Short Courses)
Short Courses *** (Student with valid student ID) or Retiree	\$150 (One Short Course) \$250 (Two Short Courses)	\$250 (One Short Course) \$400 (Two Short Courses)
Guest**** (Includes reception and breakfasts)	\$150	\$150
Conference Proceedings DVD	\$25	\$25
Banquet	\$90	\$90

\* Registration includes access to all sessions, exhibits, welcome reception, conference program, conference proceedings, plus additional conference handouts. Short courses are not included.

\*\*One Day Registration includes tickets to the Reception (if it coincides with the day of reception) but it does not include tickets to Banquet or Conference Proceedings). The Banquet is optional and is \$90.

\*\*\*Short Course Only Registration does not include access to conference sessions, tickets to the Banquet, Reception, exhibits, and Conference Proceedings

\*\*\*\*Guest registration includes the Thursday night reception and three continental breakfasts on Thursday, September 4rd, Friday, September 5th, and Saturday, September 6th. The Friday banquet is not included in the guest registration. The Banquet is optional and is \$90. Guests are NOT allowed to attend any technical sessions except for the Thursday morning plenary session. Only ages 10 or older need to register.

All registrations include password-controlled internet access to the conference proceedings for a period of one year for downloading the papers

Life Member is defined by IEEE as at least 65-year old and the age plus years of IEEE membership should be equal or greater than 100. Life members should show their IEEE Life Member card or evidence of Life Membership when getting registration materials.

### Refund Policy

General attendees (non-authors) are eligible for a registration refund if the refund is requested in writing prior to August 1, 2014 and will incur a processing fee of \$50. There are no registration refunds after August 1<sup>st</sup>, 2014. Authors who have uploaded their papers are NOT entitled to any refunds.

## **CONFERENCE PROCEEDINGS**

In order for the 2014 IEEE International Ultrasonics Symposium to be published in a timely manner, it is important that authors follow the submission instructions to the best of their ability. Printed proceedings will not be available from the conference but can be ordered directly from the IEEE Shop: Conference Proceedings. Conference attendees will receive the electronic version of the conference contain all the papers presented at the conference as part of their full registration fee.

As the Proceedings is a record of the 2014 IEEE International Ultrasonics Symposium, only those papers which are actually presented and defended at the Symposium by the author during either an oral or a poster session will be accepted for publication in the Proceedings. In the event that an author is unable to personally present the paper, she/he **MUST** be represented in either poster or oral sessions by an individual who is qualified to discuss the technical material in the paper and who will remain in attendance for the full session in which the paper is presented. All the session chairpersons will be recording the presenters attendance, both oral and poster, and sending the results to the Proceedings Editor.

All presenters, both oral and poster, are encouraged to publish in the conference proceedings. Full paper submissions are limited to four (4) single-side pages in the required two-column format. Invited papers can be up to ten (10) pages in length. For all papers: two (2) extra pages may be used at an excess page charge of \$125/page. Payments for excess page charge are part of the paper submission process.

Instructions for the generation of the conference papers can be found at the IEEE Proceedings Author Tools Box at the following website:

[http://www.ieee.org/conferences\\_events/conferences/publishing/templates.html](http://www.ieee.org/conferences_events/conferences/publishing/templates.html). Here you will find Manuscript Templates for Conference Proceedings, IEEE Citation Reference, and IEEE Keyword Guidelines.

Part of the paper submission process involves standard conversion to PDF, and the authors will be given the opportunity to approve the converted files before the completion of the submission process. As part of the submission process, the author will have to indicate that they have read and conformed to the IEEE Proceedings formatting standards. Authors may risk having their paper not included in the proceedings if there is excessive deviations from the IEEE format standards. Our publication schedule will not allow the authors to make changes to their manuscripts after the deadline. If the papers deviate from the standard format they will be removed from publication.

**All paper submissions will be checked by the CrossCheck in order to prevent plagiarism.** CrossCheck compares submitted manuscripts against a very large database of published technical papers. Please note that self-plagiarism will also be checked. Plagiarism in any form is unacceptable and is considered a serious breach of professional conduct.

For authors who are including Multimedia content in their papers, they can find supporting Multimedia Materials instructions at the IEEE Author Digital Tool Box:

<http://www.ieee.org/web/publications/authors/transjnl/index.html>.

While this site provides the Multimedia instructions for the IEEE Transactions and Journals, the instructions are appropriate for our Proceedings. In simple terms, the author needs to make notation in her/his paper as to the multimedia file name so that a link can be added by the editor. During the standard submission process, the author will be requested to upload the multimedia file.



## VISA ASSISTANCE

### Obtaining Visa Application Document (Formal Letter of Invitation)

Visa requirements: The US has updated its visa policies to increase security, so it may take you several months to apply for and receive your visa. For details that apply specifically to your country please go immediately to your nearest US Consulate or Embassy. Review your visa status now to determine if you need a US visa or visa renewal and to find out how to schedule an interview appointment, pay fees, and other vital instructions.

If you need a personal letter of invitation to attend the Conference, please provide the following information (order like stated below):

- salutation (Mrs. / Mr.)
- title (Prof. / Dr. / ...)
- complete name (first, middle, last name)
- complete mailing address (company/institution, street, city, state/province, postal code, country)
- e-mail address
- whether you are author/co-author (including ID# of your contribution)
- whether you have already registered AND paid your registration fee (incl. Invoice #), and any other details that US or your country of residence requires for your visa application

Then, contact the Conference Coordinators by email at:

Erdal Oruklu  
Local Chair, IUS 2014  
[erdal@ece.iit.edu](mailto:erdal@ece.iit.edu)  
Telephone: +1-312-567-8814

### IEEE VISA Guidelines

According to IEEE's guidelines for providing visa letters such formal letters of invitation will only be issued to:

- People the committee knows
- Speakers/Presenters
- Committee members
- Attendees/Exhibitors who have paid their registration fee in full

The Conference cannot contact or intervene with any US Embassy or Consulate office abroad on your behalf so please begin your visa application process as soon as you determine that you want to attend the 2014 IEEE International Ultrasonics Symposium.

## **STUDENT TRAVEL SUPPORT**

Student Travel Support will be available beginning Friday, September 5<sup>th</sup>, 1:00 pm in the registration area. Please have identification and travel receipts available.

## **PRESIDENT'S STUDENT RECEPTION**

Students attending the Conference are invited to attend a complimentary breakfast on Friday, September 5th from 7:00 am to 8:00 am. This is an opportunity for students to network with other students and with the Administrative Committee members of the UFFC Society.

## **WOMEN IN ENGINEERING LUNCHEON**

Women active in the technical areas of the UFFC conference are invited to attend a complimentary lunch and networking event organized by the women in UFFC group on Friday September 5 from 12:00 to 13:00. Elisa Konofagou, Professor of Biomedical Engineering and Radiology at Columbia University, NY, will offer a highlight presentation on securing, pursuing and maintaining an academic career while drawing upon your creative edge and attaining a good work-life balance.

For additional information please contact Dr. Lori Bridal at [lori.bridal@upmc.fr](mailto:lori.bridal@upmc.fr).

## **IEEE EVENT PHOTOGRAPHY STATEMENT**

Attendance at, or participation in this conference constitutes to the use and distribution by IEEE of the attendee's image or voice for informational, publicity, promotional and / or reporting purpose in print or electronic communications media. No flash photography will be used. Video recording by participants and other attendees during any portion of the conference is not allowed without special prior written permission of IEEE. Photographs of PowerPoint or other slides as well as posters are not permitted.

## **IEEE NON-DISCRIMINATION POLICY**

IEEE is committed to the principle that all persons shall have equal access to programs, facilities, services, and employment without regard to personal characteristics not related to ability, performance or qualification as determined by IEEE policy and / or applicable laws.

## CONFERENCE RECEPTION

**Thursday, September 4<sup>th</sup>, 2014**

**Time: 6:00pm-8:00pm**

**Location: Hilton Chicago Hotel, Second floor**

The Conference Reception will be held at the Grand Ballroom.

**Entertainment:**



**The Chicago Jazz Quartet:** This quartet combines some of Chicago's top jazz players into one high powered group. Lead by Chicago Jazz Magazine publisher Mike Jeffers this group includes instrumentalists who have performed at many of Chicago's world famous jazz clubs. Specializing in performing classic standards made famous by such artists as Frank Sinatra, Nat Cole, Ella Fitzgerald, Oscar Peterson and many others, The Chicago Jazz Quartet helps to create the perfect Chicago Jazz atmosphere.

## CONFERENCE BANQUET

**Friday, September 5<sup>th</sup>, 2014**

**Time: 6:30pm-11:00pm**

**Location: Hilton Chicago Hotel, Second floor**

The Conference Banquet will be held at the Grand Ballroom.

**Entertainment:**



**Blooze Brothers:** This high-powered, choreographed, 12-piece show band covers music from the 40's to Top 10, Swing, Motown, Soul, R & B, Classic Rock, Original music from the band, and of course the music and crazy antics of the famous original Blues Brothers. This Chicago favorite cover band will take stage at 8pm.

## TOURS

There is one Chicago tour scheduled during the conference on Saturday, September 6th. Please check the tour option in the conference registration form (online or paper) or contact Local Chair Erdal Oruklu via e-mail [erdal@ece.iit.edu](mailto:erdal@ece.iit.edu).

**Event Date:** Saturday 9/6/2014 **Start Time:** 10:00 am **End Time:** 01:00 pm

### Description: Architecture River Cruise



Chicago Architecture Foundation-certified expert docents interpret the world-class architecture along the Chicago River. Marvel at Chicago's soaring towers while enjoying a 90-minute narrated river cruise. This tour spotlights more than 50 architecturally significant sites where you will discover a new perspective on the city.

**Ticket per person:** \$85

Guests are encouraged to contact [Access Destination Services](#) for other Chicago tours and events including Trolley tour & Skydeck Experience and the Shedd Aquarium:

**Kathryn Kratz, CWEP** | Senior Sales Manager

**ACCESS** Destination Services®

d 312.786.6267 | f 214.716.1064 | c 847.942.1597

27 E. Monroe Street Suite 400 | Chicago, IL 60603

[www.accessdmc.com](http://www.accessdmc.com)

### Description: Trolley Tour and Skydeck Experience



Guests will be picked up from their hotel and transported to the Willis Tower for their Skydeck Experience where they will be able to step outside the tallest building in the western hemisphere and the third tallest in the world. At 1,353 feet in the air, the Ledge's glass boxes extend out 4.3 feet from Skydeck giving guests a unique view of the city.

### Description: Shedd Aquarium




The Total Experience Pass allows your guests to experience everything that Shedd has to offer. Access to all exhibits plus admission to the 4-D Experience and the Shedd's infamous aquatic show that is sure to be the hit of the day! Explore Waters of the World, Caribbean Reef, Amazon Rising, Wild Reef, the Abbott Oceanarium, Polar Play Zone and Jellies special exhibit.









## EXHIBITORS LIST

### Gold Level Exhibitor Information

Logo	Description
	Verasonics has developed revolutionary ultrasound system technology based on real-time software. The system accelerates research, provides unsurpassed control while simplifying data collection and analysis process.

### Exhibitor Information

Logo	Description
	Advanced OEM Solutions (AOS) designs and manufactures customizable Ultrasonic Phased Array and conventional Ultrasonic instruments perfect for research and industrial applications.
	Alpinion Medical Systems believes that technology is only meaningful when it delivers value to health care providers. Guided by this philosophy Alpinion focuses on the development and production of ultrasound including diagnostic ultrasound and advanced piezoelectric and single-crystal transducer technology
	Apex Ultrasound company is one of the leading companies for designing, developing and manufacturing medical ultrasonic transducer and probe products and providing interrelated technical service.
	Cephasonics - Embedded-ultrasound technology and subsystem electronics for B2B health care and industrial applications as well as cutting-edge research can be simply stated: We enable ultrasound.
	EBL Products Inc. provides standard and application specific and industrial piezoceramic transducer elements to researchers as well as manufacturers of piezoelectric transducers according to their terms and specifications
	Electronics & Innovation is a focused and dynamic company fulfilling the market demand for rugged and reliable RF power amplifiers, components and modules. We offer unparalleled service and support with custom designs to meet your specific applications.

	<p>Exelis Acoustic Systems is one of North America's largest manufacturer of piezoceramic materials including components, value added sub-assemblies and transducers for diverse medical imaging, therapy and surgical applications, power ultrasonics for cleaning and welding, oceanographic and oil and gas applications. Exelis has over 60 years of piezomaterials and transducer engineering, design and production experience that has benefitted large and small customers. Exelis offers standard and custom piezoceramic formulations of PZT, PT and PMN-PT materials, FEA and applications assistance for prototype and production volume applications. Exelis is ISO 9001/2008 registered and can provide 100% testing of components</p>
	<p>Hitachi Cable America Inc. (HCA) is an indirect wholly owned subsidiary of Hitachi Metals, Ltd., a global manufacturer of high-grade metal products with customers in the computer, automotive and aerospace industries.</p>
	<p>Imasonic develops and produces ultrasonic transducers for Medical and NDT applications. Using our proprietary Piezocomposite technology, any type of transducer can be designed from single element to Phased Array transducers</p>
	<p>IPPT PAN is a government funded scientific institute conducting research in theoretical and applied mechanics, theory of coupled mechanical and physical fields, theoretical and experimental mechanics of materials and structures, computational methods in mechanics, acoustoelectronics, and ultrasonic medical diagnostics.</p>
	<p>Lecoeur Electronique company is devoted to non-destructive testing, using ultrasounds. We are capable of building your custom-made equipment and we are able to adapt to your technical and budgetary requests.</p>
	<p>We specialise in sensing and monitoring systems that measure physical parameters in the extreme environments of aircraft, space vehicles, power generators, nuclear, oil and gas installations and test laboratories</p>
	<p>Onda has established itself as a global leader in ultrasound measurement instrumentation and services for medical applications. The seasoned team at Onda has extensive knowledge in diagnostic, therapeutic, and physiotherapy ultrasound applications. Markets have also been served outside the medical sector, including wirebonding, non-destructive testing, and cleaning applications</p>
	<p>Polytec is the market leader for non-contact, laser based vibration and velocity measurement instrumentation. Our innovative solutions allow our customers to maintain their own technical leadership across many fields.</p>
	<p>When it comes to measuring ultrasound in the frequency range 40kHz to 50MHz, Precision Acoustics is regarded world-wide as a leading global supplier of products to measure acoustic pressure and intensity. Precision Acoustics offers consultancy, for transducer development and acoustic measurement services to medical, NDT and academic establishments.</p>

	<p>Roth and Rau AG Microsystems provides leading solutions for surface trimming as well as advanced deposition technologies using specialized plasma and ion beam expertise. The equipment and technologies produced by Roth &amp; Rau are used in the photovoltaics, semiconductor, optics, battery, automotive and rail industries</p>
	<p>scia Systems was launched in 2013 and offers advanced ion beam and plasma technologies for the production of microelectronics and precision optical components. In a unique manner the equipment of scia Systems integrate advanced source technologies with innovative sample movement for localized rate and process control.</p>
	<p>SIMetris support ultrasonic product development using our finite element simulation tool NACS. We provide analysis of piezoelectric, vibroacoustic, and magneto-mechanical interactions as well as product optimization.</p>
	<p>Sonic Concepts is the designer, developer and direct marketer of a variety of products which include standard and custom HIFU transducers, custom array transducers, instrumentation, hydrophones and calibration, acoustic lenses, and our transducer design modeling software package, PiezoCAD®.</p>
	<p>S-Sharp is dedicated to providing cutting edge ultrasound solutions to our customers with many years of passion and experiences in ultrasound research and development.</p>
	<p>The goal of TRS Technologies, Inc. is to utilize cutting edge R&amp;D combined with extensive manufacturing knowledge to build and grow lasting and profitable business relationships making us the preferred supplier of high quality, specialty piezoelectrics and dielectrics to OEMs in the medical, sensor, and military markets.</p>
	<p>Ultrasonix diagnostic ultrasound systems are designed to make ultrasound easy to use in more areas of patient care. With high-resolution monitors and excellent image quality, our systems are ideal for point-of-care markets and procedure-driven applications. Analogic Ultrasound designs and manufactures ultrasound systems that are sold to medical practitioners under BK and Ultrasonix brands.</p>
	<p>As a leading structural engineering and applied mechanics consultant, we design and rehabilitate buildings, bridges, and infrastructure and develop advanced analysis software. We also offer special services in vulnerability assessment; risk analysis; forensic, earthquake, wind, and blast engineering; soil/structure interaction; and sustainability.</p>

## FUTURE CONFERENCE



## 2015 IUS

**General Chair**  
Pai-Chi Li  
National Taiwan University,  
Taipei, Taiwan  
[paichi@ntu.edu.tw](mailto:paichi@ntu.edu.tw)

**Technical Program Chair**  
Stanislav Emelianov  
University of Texas, Austin,  
TX, USA

**Finance Chair**  
Mark Schaefer  
Sonic Tech, Inc. Ambler,  
PA, USA

**Short Course Chair**  
Hairong Zheng  
Shenzhen Institute of  
Advanced Technology,  
Chinese Academy of Science,  
Shenzhen, China

**Publication Chair**  
Steve Freear  
University of Leeds  
Leeds, United Kingdom

**Exhibits Chair**  
Tsung-Tsong Wu  
National Taiwan University  
Taipei, Taiwan

**Local Arrangements Chair**  
Che-Chou Shen  
National Taiwan University of  
Science and Technology  
Taipei, Taiwan

**Publicity Chair**  
Ken-Ya Hashimoto  
Chiba University  
Chiba, Japan

**Web Chair**  
Chih-Kuang Yeh  
National Tsing-Hua University  
Hsinchu, Taiwan

The annual 2015 IEEE International Ultrasonics Symposium will be held at [Taipei International Convention Center](#), Taipei, Taiwan, from **October 21-24, 2015**. Oral and poster presentation formats will be used at the symposium. Papers are solicited for this conference describing original work in the field of ultrasonics from the following **subject classifications**:

### Group 1: Medical Ultrasonics

MBB Medical Beamforming and Beam Steering  
MBE Biological Effects & Dosimetry  
MBF Blood Flow Measurement  
MCA Contrast Agents  
MEL Elastography  
MIM Medical Imaging  
MPA Medical Photoacoustics  
MSD System & Device Design  
MSP Medical Signal Processing  
MTC Medical Tissue Characterization  
MTH Therapeutics, Hyperthermia, and Surgery

### Group 2: Sensors, NDE & Industrial Applications

NAF Acoustics Microfluidics  
NAI Acoustic Imaging  
NAM Acoustic Microscopy  
NAS Acoustic Sensors  
NDE General NDE Methods  
NEH Energy Harvesting  
NFM Flow Measurement  
NMC Material & Defect Characterization  
NPA Photoacoustics  
NPC Process Control  
NSP Signal Processing  
NTD Transducers: NDE and Industrial  
NUA Underwater Acoustics  
NWP Wave Propagation

### Group 3: Physical Acoustics

PAT Acoustic Tweezers and Particle Manipulation  
PNL Nonlinear Acoustics  
PGP General Physical Acoustics  
POA Opto-acoustics  
PPN Phononics  
PTF Thin Films  
PMI Magnetic/Electromagnetic Interactions  
PUM Ultrasonic Motors & Actuators

### Group 4: Microacoustics: SAW, FBAR, MEMS

ADA Device Applications  
ADD Device Design  
ADM Device Modeling  
AMP Materials & Propagation  
AMS Microacoustic Sensor Devices & Applications

### Group 5: Transducers & Transducer Materials

TMC Materials Fabrication and Characterization  
TMO Modeling (Analytical & Numerical)  
TFT Thin and Thick Piezoelectric Films  
TMU Micromachined Ultrasonic Transducers  
TMI Biomedical Diagnostic and Imaging Transducers  
TTT Biomedical Therapeutic Transducers  
THF Front-end and Integrated Electronics  
TFI High Frequency Transducers  
TFP Applications of Piezoelectrics & Ferroelectrics

Sponsored by the IEEE Ultrasonics, Ferroelectrics & Frequency Control Society

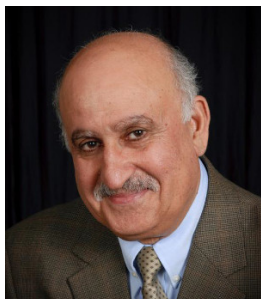


IEEE ULTRASONICS, FERROELECTRICS,  
AND FREQUENCY CONTROL SOCIETY





## CONFERENCE ORGANIZING COMMITTEE



**General Chair:**  
**Jafar Saniie**

Illinois Institute of Technology  
Chicago, IL, USA



**Technical Program Chair:**  
**Jan D'hooge**

Catholic University of Leuven  
Leuven, Belgium



**Finance Chair:**  
**Jacqueline Hines**

Applied Sensor Research and Device  
Corporation  
Maryland, USA



**Local Chair:**  
**Erdal Oruklu**

Illinois Institute of Technology  
Chicago, IL, USA



**Short Course Chair:**  
**Mario Kupnik**

BTU Cottbus  
Germany



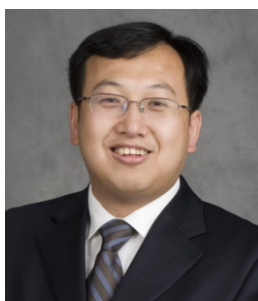
**Exhibits Chair:**  
**Larry Kessler**

Sonoscan Inc.  
Illinois, USA



**Proceedings Chair:**  
**Steve Freear**

University of Leeds  
Leeds, United Kingdom



**Audio-Visual Chair:**  
**Yufeng Lu**

Bradley University  
Peoria, IL, USA



**Web Chair:**  
**Spenser Gilliland**

Illinois Institute of Technology  
Chicago, IL, USA

## **SHORT COURSES**

<b>1A: 8:00am-12:00pm</b> Instructors:	<b>Ultrasound Imaging Systems: from Principles to Implementation</b> Kai Thomenius, Massachusetts Institute of Technology, USA
<b>1B: 8:00am-12:00pm</b> Instructors:	<b>Elasticity Imaging: Methods and Applications</b> Kathy Nightingale and Mark Palmeri, Duke University, USA
<b>1C: 8:00am-12:00pm</b> Instructors:	<b>Acoustic Microfluidics</b> James Friend, Royal Melbourne Institute of Technology, Australia
<b>1D: 8:00am-12:00pm</b> Instructors:	<b>Piezoelectric Ultrasonic Motors</b> Jorg Wallaschek, Gottfried Wilhelm Leibniz Universitat at, Germany and Minoru Kuribayashi Kurosawa, Tokyo Institute of Technology, Japan
<b>1E: 8:00am-12:00pm</b> Instructors:	<b>Radio Frequency Acoustic Resonators in Communications: Fundamentals, Applications and Characterization</b> Ken-ya Hashimoto, Chiba University, Japan
<b>1F: 8:00am-12:00pm</b> Instructors	<b>Piezoelectric Fundamentals - Materials and Transducers</b> Susan Trolier-McKinstry Materials Research Lab, Penn State University, USA and Sandy Cochran Institute for Medical Science and Technology, University of Dundee, UK
<b>2A: 1:00pm-5:00pm</b> Instructors:	<b>Ultrafast Imaging in Biomedical Ultrasound: Principles and Applications</b> Mickael Tanter and Mathias Fink Institut Langevin, ESPCI, France
<b>2B: 1:00pm-5:00pm</b> Instructors:	<b>Ultrasound Vector Velocity Imaging</b> Jorgen Arendt Jensen, Technical University of Denmark, Denmark
<b>2C: 1:00pm-5:00pm</b> Instructors:	<b>Nonlinear Ultrasonic Imaging for NDE: From Laboratory Experiments to R&amp;D of a New Technology</b> Igor Solodov, Institute for Polymer Technology, University of Stuttgart, Germany
<b>2D: 1:00pm-5:00pm</b> Instructors:	<b>Acoustical Imaging; from Acoustic Field Equations to Imaging and Inversion</b> Koen W.A. van Dongen, Delft University of Technology, The Netherlands
<b>2E: 1:00pm-5:00pm</b> Instructors:	<b>A Modern Approach to Modelling and Simulation of Micro-acoustic Devices</b> Alireza Baghai-Wadji, University of Cape Town, South Africa
<b>2F: 1:00pm-5:00pm</b> Instructors	<b>Micromachined Ultrasonic Transducers: PMUTs and CMUTs</b> Firas Sammoura, Masdar Institute of Science and Technology, United Arab Emirates and Amin Nikoozadeh, Stanford University, USA

## TECHNICAL PROGRAM COMMITTEE

### Group 1: Medical Ultrasonics



TPC Vice Chair

Georg Schmitz  
Ruhr-Universität  
Bochum, Germany

### Members

Olivier Basset, CREATIS, France  
Ayache Bouakaz, INSERM, France  
Lori Bridal, University Pierre and Marie Curie, France  
Charles A. Cain, University of Michigan, US  
Jean-Yves Chapelon, INSERM, France  
Paul A. Dayton, University North Carolina/NCSSU, Chapel Hill, US  
Nico de Jong, Erasmus Medical Centre, Rotterdam, The Netherlands  
Chris de Korte, Catholic University of Nijmegen, The Netherlands  
Jan Dhooze, Catholic University of Leuven, Belgium  
Emad Ebbini, University of Minnesota, US  
Stas Emelianov, University of Texas at Austin, US  
Kathy Ferrara, University of California Davis, US  
Stuart Foster, University of Toronto, Canada  
Steven Freear, University of Leeds, UK  
Caterina Gallipi, University of North Carolina, US  
James Greenleaf, Mayo Clinic, US  
Christopher Hall, Philips Research, US  
Peter Hoskins, University of Edinburgh, UK  
John Hossak, University of Virginia, US  
Kullervo Hynnen, University of Toronto, Canada  
Jorgen Arendt Jensen, Technical University Denmark, Denmark  
Hiroshi Kanai, Tohoku University, Japan  
Jeff Ketterling, Riverside Research, US  
Michael Kolios, Ryerson University, Canada  
Elisa Konofagou, Columbia University, US  
Nobuki Kudo, Hokkaido University, Japan  
Pai Chi Li, National Taiwan University, Taiwan  
Jian-yu Lu, University of Toledo, US  
Tom Matula, University of Washington, US  
James G. Miller, Washington University, US  
Kathy Nightingale, Duke University, US  
Svetoslav Nikolov, BK Medical, Denmark  
William D. O'Brien, University of Illinois, US  
Michael Oelze, University of Illinois, US  
Georg Schmitz, Ruhr-Universität Bochum, Germany

Ralf Seip, Philips Research, US  
Mickael Tanter, INSERM, France  
Tom Thomas, Boston Scientific, US  
Kai Thomenius, GE Corporate R&D, US  
Hans Torp, University of Science and Technology, Norway  
Piero Tortoli, University Firenze, Italy  
Ton van der Steen, Erasmus Medical Centre, The Netherlands  
Kendall Waters, Silicon Valley Medical Instruments, US  
Keith Wear, Food and Drug Administration, US  
Wilko G. Wilkening, Siemens Medical Solutions, US  
Hairong Zheng, Shenzhen Institutes of Advanced Technology, China

## **Group 2: Sensors, NDE, and Industrial Applications**



TPC Vice Chair

David Greve  
Carnegie Mellon University  
USA

## **Members**

Robert C. Addison, Rockwell Science Center, USA  
Walter Arnold, Fraunhofer Institute for NDT, Germany  
Michal Bezdek, Endress+Hauser Flowtec AG, Switzerland  
James Blackshire, Air Force Research Laboratory, USA  
Ramazan Demirli, Villanova University, USA  
James Friend, Monash University, Australia  
Eric S. Furgason, Purdue University, USA  
David Greve, Carnegie Mellon University, USA  
Edward Haeggstrom, University of Helsinki, Finland  
Jacqueline Hines, Applied Sensor R&D Corporation, USA  
Patrick Johnston, NASA Langley Research Center, USA  
Fabien J. Josse, Marquette University, USA  
Lawrence W. Kessler, Sonoscan Inc., USA  
Pierre T. Khuri-Yakub, Stanford University, USA  
Mario Kupnik, Brandenburg University of Technology, Germany  
Roman Maev, University of Windsor, Canada  
Kentaro Nakamura, Tokyo Institute of Technology, Japan  
Erdal Oruklu, Illinois Institute of Technology, USA  
Massimo Pappalardo, University di Roma TRE, Italy  
Jafar Saniie, Illinois Institute of Technology, USA  
Gangbing Song, University of Houston, USA  
Bernhard Tittman, Pennsylvania State University, USA  
Jiromaru Tsujino, Kanagawa University, Japan  
John F. Vetelino, University of Maine, USA  
Paul Wilcox, University of Bristol, UK  
William Wright, University College Cork, Ireland  
Donald E. Yuhas, Industrial Measurement Systems, USA

**Group 3: Physical Acoustics**

TPC Vice Chair

Vincent Laude  
Centre National de la Recherche  
Scientifique, France

**Members**

Manabu Aoyagi, Muroran Institute of Technology, Japan  
Arthur Ballato, Clemson University, USA  
Anne Bernassau, University of Glasgow, UK  
Jan Brown, JB Consulting, USA  
Charles Courtney, University of Bath, UK  
Emmanuel Defay, CEA LETI Minatec Campus, France  
Jianke Du, Shanghai Jiaotong University, China  
Tao Han, Ningbo University, China  
Fred Hickernell, Motorola, Inc., USA  
Takefumi Kanda, Okayama University, Japan  
Yoonkee Kim, U.S. Army, USA  
Eun Sok Kim, University of Southern California, USA  
Minoru K. Kurosawa, Tokyo Institute of Technology, Japan  
Amit Lal, Cornell University, USA  
John Larson, Avago Technologies, USA  
Vincent Laude, FEMTO-ST / CNRS, France  
Andreas Mayer, Hochschule Offenburg, Germany  
Roy H. Olsson III, Sandia National Laboratories, USA  
Mihir Patel, Schlumberger-Doll Research,, USA  
Yan Pennec, IEMN / Universite de Lille 1, France  
Susan Schneider, Marquette University, USA  
Bikash Sinha, Schlumberger-Doll Research,, USA  
Takahiko Yanagitani, Nagoya Institute of Technology, Japan  
Koen W.A. Van Dongen, Delft University of Technology, Netherlands  
Jorg Wallaschek, Leibniz Universitat Hannover, Germany  
Ji Wang, Ningbo University, China  
Tsung-Tsong Wu, National Taiwan University, Taiwan  
Yook-Kong Yong, Rutgers University, USA  
Jiun Der Yu, Epson Research & Development Inc., USA

**Group 4: Microacoustics - SAW, FBAR, MEMS**



TPC Vice Chair

Karl Wagner  
TDK Corporation  
Munich, Germany

**Members**

Ben Abbott, Triquint Semiconductor, USA  
Robert Aigner, Triquint Semiconductor, USA  
Ivan Avramov, Institute of Solid State Physics, Bulgaria  
Sylvain Ballandras, freq 'n' sys SAS, France  
Kushal Bhattacharjee, RF Micro Devices, USA  
Sunil Bhawe, Cornell University, USA  
Sergey Biryukov, IFW Dresden, Germany  
Paul Bradley, Avago Technologies, USA  
Jidong Dai, Murata Electronics, Inc., USA  
Omar Elmazria, Universite de Lorraine, France  
Gernot Fattinger, Triquint Semiconductor, USA  
Gerhard Fischerauer, University of Bayreuth, Germany  
Ken-ya Hashimoto, Chiba University, Japan  
Shitang He, IACAS, China  
Chunyun Jian, Ericsson, Canada  
Michio Kadota, Tohoku University, Japan  
Jyrki Kaitila, Avago Technologies, Germany  
Ilia Katardjiev, Uppsala University, Sweden  
Takaharu Kawakatsu, Murata Manufacturing, Japan  
Kimmo Kokkonen, Aalto University, Finland  
Jan Kuypers, Sands 9, Inc., USA  
Don Malocha, University of Central Florida, USA  
Natalya Naumenko, Nat. University of Science & Technology MISIS, Russia  
Hiroyuki Odagawa, Kumamoto National College of Technology, Japan  
Takeo Oita, University of Tokyo, Japan  
Tuomas Pensala, VTT, Finland  
Mauricio Pereira da Cunha, University of Maine, USA  
Maximilian Pitschi, TDK Corporation, Germany  
Leonard Reindl, Albert-Ludwigs-University Freiburg, Germany  
Richard Ruby, Avago Technologies, USA  
Clemens Ruppel, TDK Corporation, Germany  
Marc Solal, Triquint Semiconductor, USA  
Masanori Ueda, Taiyo Yuden, Japan  
Karl Wagner, TDK Corporation, Germany  
Robert Weigel, University of Erlangen-Nuremberg, Germany

Sergei Zhgoon, National Research University, Russia

## Group 5: Transducers and Transducer Materials



TPC Vice Chair

Sandy Cochran  
University of Dundee  
UK

## Members

Sandy Cochran, University of Dundee, UK  
David Cowell, University of Leeds, UK  
Christopher Daft, River Sonic Solutions, USA  
Loriann Davidsen, Philips Healthcare, USA  
Levent Degertekin, Georgia Institute of Technology, USA  
Christine Demore, University of Dundee, UK  
Charles Emery, Ulthera Inc., USA  
Arif Sanli Ergun, TOBB University, Turkey  
Lynn Ewart-Paine, NUWC, USA  
Xiaoning Jiang, North Carolina State University, USA  
Reinhard Lerch, Friedrich-Alexander-Universitat Erlangen-Nuremberg, Germany  
Richard O'Leary, University of Strathclyde, UK  
Omer Oralkan, North Carolina State University, USA  
Wei Ren, Xi'an Jiaotong University, China  
Paul Reynolds, Cliqr, USA  
Yongrae Roh, Kyungpook National University, Korea  
Ahmad Safari, Rutgers University, USA  
Jean-Francois Saillant, Areva, France  
Mark Schafer, Sonic Tech Inc., USA  
Scott Smith, GE Global Research, USA  
Wallace Smith, Office of Naval Research, USA  
Yasuhito Takeuchi, Kagoshima University, Japan  
Susan Trolie-McKinstry, Pennsylvania State University, USA  
Jian Yuan, Philips Shanghai Apex, USA  
Qiming Zhang, Pennsylvania State University, USA  
Shujun Zhang, Pennsylvania State University, USA  
Qifa Zhou, University of Southern California, USA



## PLENARY SPEAKER

*Can Integrated Ultrasound/Photoacoustic Systems Deliver on the Promise of Molecular Medicine?*

**Matthew O'Donnell**, Professor of Bioengineering at University of Washington  
September 4<sup>th</sup>, 2014 Thursday 8:00am – 9:30am, Grand Ballroom, Hilton Chicago



Dr. O'Donnell has worked at General Electric CRD, the University of Michigan, where he was Chair of the BME Department from 1999-2006, and the University of Washington (UW), where he was the Frank and Julie Jungers Dean of Engineering from 2006-2012. He is now Professor of Bioengineering at UW. His most recent research has focused on elasticity imaging, optoacoustic arrays, photoacoustic contrast agents, thermal strain imaging, and catheter-based devices. He is a fellow of the IEEE and AIMBE and is a member of the Washington State Academy of Sciences and the National Academy of Engineering.

### ABSTRACT

For over two decades, microbubble-based contrast agents have been used extensively in biomedical ultrasound. Recent advances in molecular engineering have produced microbubbles targeted to specific molecular biomarkers, especially in the vasculature. Over the same period, parallel advances have been made in the field of photoacoustics in which molecular processes can be directly probed using the mechanism of optical absorption with ultrasonic (US) readout similar to a conventional real-time imaging system. Photoacoustics (PA) brings molecular sensitivity to US imaging for many biomedical applications using nano-scale, bioconjugated contrast agents. In addition, both US and PA agents can potentially be used for molecularly-targeted therapies, opening the possibility for molecular theranostics using integrated US/PA systems.

Although much progress has been made in recent years, there is still not a routine clinical procedure using US/PA for molecular theranostics. If recent advances in molecular engineering and molecular biomarker discovery are to be exploited for real clinical applications, many US/PA technologies must be translated into clinical tools. In this talk, we will explore recent advances in the field and discuss current obstacles to clinical translation. Finally, we will discuss how US/PA molecular theranostic technologies can accelerate the transition to personalized medicine and effective healthcare delivery.



## CLINICAL SPEAKERS

### **1A-1 Strain-derived Cardiac Assessment**

Jan D'hooge, Associate Professor in the Department of Cardiovascular Disease of the Medical Faculty at the Catholic University of Leuven, Belgium  
September 4<sup>th</sup>, 2014 Thursday 10:30am – 11:00am, Grand Ballroom

### **1C-1 Update on Contrast Ultrasound: Diagnostic and Therapeutic Applications**

Steven Feinstein, M.D., Professor of Medicine at Rush University Medical Center, USA  
September 4<sup>th</sup>, 2014 Thursday 3:30pm – 4:00pm, Grand Ballroom

### **1G-1 Three-Dimensional Echocardiography**

Roberto Lang, M.D., Professor of Medicine at the University of Chicago, USA  
September 5<sup>th</sup>, 2014 Friday 3:30pm – 4:00pm, Grand Ballroom

## INVITED SPEAKERS

### **Group 1: Medical Ultrasonics**

#### **1B-5 Ultrasound for Molecular Imaging and Guided Drug Delivery**

Juergen K. Willman, Professor of Radiology at Stanford University, USA  
September 4<sup>th</sup>, Thursday 2:00pm-2:30pm, Grand Ballroom

#### **1D-5 GPU Enabled Ultrasound Imaging Innovations**

Alfred C. H. Yu, Professor of Electrical Engineering at The University of Hong Kong, Hong Kong  
September 5<sup>th</sup>, Friday 9:00am-9:30am, Grand Ballroom

#### **1E-5 Biogenic Nanostructures as Reporters for Ultrasound Imaging**

Mikhail G. Shapiro, Professor of Chemical Engineering at California Institute of Technology, USA  
September 5<sup>th</sup>, Friday 11:30am-12:00pm, Grand Ballroom

#### **1F-1 Histotripsy: Recent Advances**

Charles A. Cain, Professor of Biomedical Engineering at University of Michigan, USA  
September 5<sup>th</sup>, Friday 1:00pm-1:30pm, Grand Ballroom

#### **1H-1 Augmented Trans-esophageal Ultrasound for Guidance of Cardiac Interventions**

Terry Peters, Professor of Biomedical Engineering at Robarts Research Institute, UK  
September 6<sup>th</sup>, Saturday 8:00am-8:30am, Grand Ballroom

#### **1J-1 Optical Coherence Tomography: The Optical Analogue to Ultrasound Imaging**

Stephen A. Boppart, Professor of Engineering at University of Illinois, USA  
September 6<sup>th</sup>, Saturday 1:00pm-1:30pm, Grand Ballroom

**Group 2: Sensors, NDE & Industrial Applications**

**4B-1** Efficient Monitoring and Inspection of Plate-like Structures with Ultrasonic Guided Waves

Jennifer Michaels, Professor of Engineering at Georgia Institute of Technology, USA

September 4<sup>th</sup>, Thursday 1:00pm-1:30pm, Marquette

**4E-1** Interaction of Microbubbles and Microdroplets with Ultrasound

Michel Versluis, Professor Physical and Medical Acoustics Physics of Fluids Group at University of Twente, Netherlands

September 5<sup>th</sup>, Friday 10:30am-11:00am, Marquette

**4G-3** Biosensing using Contactless Quartz Resonators

Hirotsugu Ogi, Professor of Engineering at Osaka University, Japan

September 5<sup>th</sup>, Friday 4:00pm-4:30pm, Marquette

**4I-5** High Temperature Piezoelectric Transducers

Makiko Kobayashi, Professor of Engineering at Kumamoto University, Japan

September 6<sup>th</sup>, Saturday 11:30am-12:00pm, Marquette

**Group 3: Physical Acoustics**

**5C-5** Recent Advances in Nonlinear Modeling of Bulk Acoustic Wave Resonators

David Feld, Dong Shim, Siamak Fouladi, Farhad Bayatpur, AVAGO Technologies, USA

September 4<sup>th</sup>, Thursday 4:30pm-5:00pm, Williford A

**5D-1** Ultrahigh Frequency Ultrasound and Its applications to Cellular Bioengineering

K. Kirk Shung, Professor of Biomedical Engineering at University of Southern California, USA

September 5<sup>th</sup>, Friday 8:00am-8:30am, Williford A

**5H-3** Acoustic Filters Based on Thin Single Crystal LiNbO<sub>3</sub> Films: Status and Prospects

Alexandre Reinhardt, Research Engineer at CEA-Leti, France

September 6<sup>th</sup>, Saturday 8:30am-9:00am, Williford A

**Group 4: Microacoustics: SAW, FBAR, MEMS**

**6C-3** Co-doped AlN Thin Films for Wideband FBAR Applications

Tsuyoshi Yokoyama, Taiyo-Yuden Company, Japan

September 4<sup>th</sup>, Thursday 4:00pm-4:30pm, Williford B

**6F-3** Bulk Acoustic Wave Gyroscope

Farokh Ayazi, Professor of Engineering at Georgia Institute of Technology, USA

September 5<sup>th</sup>, Friday 1:30pm-2:00pm, Williford A

**6I-3** Power Durable Electrode Metallization: Material Choice, Failure Mode, and Characterization

Ryoichi Takayama, Panasonic Corporation, Japan

September 6<sup>th</sup>, Saturday 11:00am-11:30am, Williford B

**Group 5: Transducers & Transducer Materials**

**7A-5** The Evolution and Applications of High Frequency Ultrasound Transducers

Stuart Foster, Professor of Medical Biophysics at Sunnybrook Health Sciences Centre, Canada  
September 4<sup>th</sup>, Thursday 11:30am-12:00pm, Williford C

**7E-3** New Applications of Ultrabiosonics, - Feasibility Studies of Fish Growing by Ultrasonic Stimulation

Yohachi (John) Yamashita, Professor of Engineering at Toyama Prefectural University, Japan  
September 5<sup>th</sup>, Friday 11:00am-11:30am, Williford C

**7I-1** Piezoelectric Ceramics in Ultrasound - 3203HD and Beyond

Gerald Stranford, Thomas Vencill, David Williams, Lillian Gutierrez, and Bruce Johnson, CTS Electronic Components, USA  
September 6<sup>th</sup>, Saturday 10:30am-11:00am, Williford C

## STUDENT PAPER COMPETITION

### Student Paper Competition Chairs:

Group 1 (Ralf Seip), Group 2 (David Greve), Group 3 (Vincent Laude), Group 4 (Karl Wagner), and Group 5 (Sandy Cochran)

### **PA-1** *Comparison of tumor microvasculature assessment via Ultrafast Doppler Tomography and Dynamic Contrast Enhanced Ultrasound*

**Charlie Demene**<sup>1</sup>, Thomas Payen<sup>2</sup>, Alexandre Dizeux<sup>2</sup>, Jean Luc Gennisson<sup>1</sup>, Lori Bridal<sup>2</sup>, Mickaël Tanter<sup>1</sup>

<sup>1</sup>Institut Langevin, ESPCI ParisTech, CNRS UMR7587, Inserm U979, Paris, France,

<sup>2</sup>Laboratoire d'imagerie biomédicale, Université Pierre et Marie Curie, UMR S 1146 / UMR 7371, Paris, France

### **PA-2** *Ultrasound Quantification of Molecular Marker Concentration in Large Blood Vessels*

**Shiying Wang**<sup>1</sup>, F William Mauldin Jr<sup>1</sup>, Alexander L Klibanov<sup>1,2</sup>, John A Hossack<sup>1</sup>

<sup>1</sup>Biomedical Engineering, University of Virginia, Charlottesville, Virginia, USA,

<sup>2</sup>Division of Cardiovascular Medicine, University of Virginia, Charlottesville, Virginia, USA

### **PA-3** *Ultrafast Plane Wave Imaging Based Pulsed Magnetomotive Ultrasound*

**Pei-Hsien Ting**<sup>1</sup>, Yi-Da Kang<sup>2</sup>, San-Yuan Chen<sup>2</sup>, Meng-Lin Li<sup>1,3</sup>

<sup>1</sup>Dept. of Electrical Engineering, National Tsing Hua University, Hsinchu, Taiwan,

<sup>2</sup>Department of Materials Science and Engineering, National Chiao Tung University, Taiwan,

<sup>3</sup>Institute of Photonics Technologies, National Tsing Hua University, Taiwan

### **PA-4** *Ultrafast vaporization dynamics of photoacoustic polymeric microcapsules*

**Guillaume Lajoinie**<sup>1</sup>, Erik Gelderblom<sup>1</sup>, Ceciel Chlon<sup>2</sup>, Marcel Böhmer<sup>2</sup>, Nico De Jong<sup>3</sup>, Wiendelt Steenbergen<sup>4</sup>, Srirang Manohar<sup>4</sup>, Michel Versluis<sup>1</sup>

<sup>1</sup>Physics of Fluids, University of Twente, Netherlands,

<sup>2</sup>Philips Research Laboratories Europe, High Tech Campus, Netherlands,

<sup>3</sup>Biomedical Engineering, Thoraxcenter, Erasmus mc, Netherlands,

<sup>4</sup>Biomedical Photonic Imaging Group, University of Twente, Netherlands

### **PA-5** *Pharmacodynamic analysis for efficient drug delivery through the FUS-induced BBB opening in Non-Human Primates in vivo*

**Gesthimani Samiotaki**<sup>1</sup>, Shih-Ying Wu<sup>1</sup>, Maria Eleni Karakatsani<sup>1</sup>, Matthew Downs<sup>1</sup>, Sachin Jambawalikar<sup>2</sup>, Elisa Konofagou<sup>1,2</sup>

<sup>1</sup>Biomedical Engineering, Columbia University, USA,

<sup>2</sup>Department of Radiology, Columbia University, USA

### **PA-6** *Estimation of arterial wall motion using ultrafast imaging with transverse oscillations*

**Sebastien Salles**<sup>1</sup>, Simon Lai<sup>2</sup>, Damien Garcia<sup>3</sup>, Alfred Yu<sup>2</sup>, Didier Vray<sup>1</sup>, Hervé Liebgott<sup>1</sup>

<sup>1</sup>CNRS UMR 5220, INSERM U1044, Université de Lyon, Insa de Lyon, France,

<sup>2</sup>Biomedical Ultrasound Laboratory, University of Hong Kong, China, People's Republic of,

<sup>3</sup>RUBIC, CRCHUM, University of Montreal, Department of radiology, Canada

**PA-7** *Application of Air-Coupled Ultrasound to Full-Scale Concrete Columns Using Tomography*  
**Hajin Choi**<sup>1</sup>, John S. Popovics<sup>2</sup>

<sup>1</sup>University of Illinois at Urbana-Champaign, Champaign, IL, USA,

<sup>2</sup>Civil and Environmental Engineering, University of Illinois at Urbana-Champaign, Urbana, IL, USA

**PA-8** *Microparticle manipulation and whole blood pre-treatment in surface acoustic wave counterflow devices*

**Marco Travaglini**<sup>1,2</sup>, Richie Shilton<sup>2</sup>, Marco Pagliazzi<sup>1</sup>, Ilaria Tonazzini<sup>1</sup>, Fabio Beltram<sup>1,2</sup>, Marco Cecchini<sup>1</sup>

<sup>1</sup>Laboratorio NEST, Scuola Normale Superiore and Istituto Nanoscienze - CNR, Pisa, Italy,

<sup>2</sup>Center for Nanotechnology Innovation @ NEST, Istituto Italiano di Tecnologia, Pisa, Italy

**PA-9** *Hardware-Software Co-design of 3D Data Compression for Real-Time Ultrasonic Imaging Applications*

**Pramod Govindan**<sup>1</sup>, Jafar Saniie<sup>1</sup>

<sup>1</sup>Electrical and Computer Engineering, Illinois, Institute of Technology, USA

**PA-10** *Cavity modes and optomechanic interactions in phoxonic crystals*

**Said El-Jallal**<sup>1,2</sup>, Mourad Oudich<sup>3</sup>, Yan Pennec<sup>1</sup>, Bahram Djafari-Rouhani<sup>1</sup>, Abdelkader Makhoute<sup>4</sup>, Jordi Gomis-Bresco<sup>5</sup>, Daniel Navarro-Urrios<sup>5</sup>, Alejandro Martínez<sup>6</sup>, Clivia Sotomayor<sup>5,7</sup>

<sup>1</sup>Institut d'Electronique, de Microélectronique et de Nanotechnologie, Université Lille 1, Villeneuve d'Ascq, France,

<sup>2</sup>Physique du Rayonnement et de l'Interaction Laser Matière, Université Moulay Ismail, Meknes, Morocco,

<sup>3</sup>Institut Jean Lamour, Université de Lorraine, Vandoeuvre-lès-Nancy, Nancy, France,

<sup>4</sup>Physique du Rayonnement et de l'Interaction Laser Matière, Université de Moulay Ismail, Meknes, Morocco,

<sup>5</sup>ICN2 - Institut Catala de Nanociencia i Nanotecnologia, Campus UAB, 08193 Bellaterra, Barcelone, Spain,

<sup>6</sup>Nanophotonics Technology Center, Universitat Politècnica de València, Valencia, Spain,

<sup>7</sup>ICREA - Institut Catalana de Recerca i Estudis Avançats, 08010, Barcelone, Spain

**PA-11** *Multiple shear wave roundtrips liquid sensor by c-axis parallel oriented ZnO film/silica glass pipe structure*

**Shoko Hiyama**<sup>1</sup>, Takahiko Yanagitani<sup>2</sup>, Shinji Takayanagi<sup>1</sup>, Yoshiya Kato<sup>1</sup>, Mami Matsukawa<sup>1</sup>

<sup>1</sup>Wave electronics research center, Laboratory of Ultrasonic Electronics, Doshisha University, Kyotanabe, Japan,

<sup>2</sup>Graduate School of Engineering, Nagoya Institute of Technology, Nagoya, Japan

**PA-12** *Non-linear cavitation cloud oscillations in high intensity focused ultrasound*

**Keith Johnston**<sup>1</sup>, Bjoern Gerold<sup>1</sup>, Sandy Cochran<sup>1</sup>, Alfred Cuschieri<sup>1</sup>, Paul Prentice<sup>1</sup>

<sup>1</sup>Institute for Medical Science and Technology, University of Dundee, Dundee, United Kingdom

**PA-13** *Ultrasonic assembly of short fibre reinforced composites*

**Marc-S Scholz**<sup>1</sup>, Bruce W Drinkwater<sup>2</sup>, Richard S Trask<sup>1</sup>

<sup>1</sup>ACCIS, Department of Aerospace Engineering, University of Bristol, Bristol, United Kingdom,

<sup>2</sup>Department of Mechanical Engineering, University of Bristol, Bristol, United Kingdom

**PA-14** *Design of High Q Thin Film Bulk Acoustic Resonator Using Dual-Mode Reflection*

**Ngoc Nguyen**<sup>1</sup>, Agne Johannessen<sup>1</sup>, Ulrik Hanke<sup>1</sup>

<sup>1</sup>Micro and Nano Systems Technology, Buskerud and Vestfold University College, Borre, Vestfold, Norway

**PA-15** *Influence of Dissipated Power Distribution on BAW Resonators' Behavior*

**Andreas Tag**<sup>1</sup>, Dominik Karolewski<sup>2</sup>, Bernhard Bader<sup>3</sup>, Maximilian Pitschi<sup>3</sup>, Robert Weigel<sup>1</sup>, Amelie Hagelauer<sup>1</sup>

<sup>1</sup>Institute for Electronics Engineering, Friedrich-Alexander-Universität Erlangen-Nürnberg, Erlangen, Germany,

<sup>2</sup>IMMS Institut für Mikroelektronik- und Mechatronik-Systeme gemeinnuetzige GmbH, Ilmenau, Germany,

<sup>3</sup>Cellular · Systems, Acoustics, Waves Business Group, TDK Corporation, Munich, Germany

**PA-16** *Chip Scale Reconfigurable Phased- Array Sonic Communication*

**Jason Hoople**<sup>1</sup>, Justin Kuo<sup>2</sup>, Serhan Ardanuç<sup>2</sup>, Amit Lal<sup>2</sup>

<sup>1</sup>Electrical and Computer Engineering, Cornell University, USA,

<sup>2</sup>Cornell University, USA

**PA-17** *Dual frequency transducers for super harmonic intravascular ultrasound imaging*

**Jianguo Ma**<sup>1</sup>, Karl Heath<sup>2</sup>, Yang Li<sup>3</sup>, Paul Dayton<sup>2</sup>, Qifa Zhou<sup>3</sup>, Kirk Shung<sup>3</sup>, Xiaoning Jiang<sup>1</sup>

<sup>1</sup>Mechanical and Aerospace Engineering, North Carolina State University, Raleigh, North Carolina, USA,

<sup>2</sup>UNC/NCSU Joint Department of Biomedical Engineering, University of North Carolina, Chapel Hill, North Carolina, USA,

<sup>3</sup>Department of Biomedical Engineering, University of Southern California, Los Angeles, California, USA

**PA-18** *An Ultrasound-Based Noninvasive Neural Interface to the Retina: Projection Algorithm and Frontend Integrated Circuit Architecture*

**Xun Wu**<sup>1</sup>, Mohit Kumar<sup>1</sup>, Omer Oralkan<sup>1</sup>

<sup>1</sup>Department of Electrical and Computer Engineering, North Carolina State University, Raleigh, North Carolina, USA

**PA-19** *Improved Performance CMUT-on- CMOS Devices Using ALD Hafnium Oxide Insulation Layer*

**Toby Xu**<sup>1</sup>, Coskun Tekes<sup>1</sup>, F. Levent Degertekin<sup>1</sup>

<sup>1</sup>Mechanical Engineering, Georgia Institute of Technology, Atlanta, GA, USA,

**PA-20** *Integration of Pb(Zr,Ti)O<sub>3</sub> (PZT) Thin Films on a Complex Microfluidic System: Toward New Possibilities for Low Consumption Micropumps*

**Pierre-Henri Cazorla**<sup>1</sup>, Olivier Fuchs<sup>1</sup>, Martine Cochet<sup>1</sup>, Sandrine Maubert<sup>1</sup>, Gwenael Le Rhun<sup>1</sup>, Stephane Fanget<sup>1</sup>, Yves Fouillet<sup>1</sup>, Emmanuel Defay<sup>1</sup>

<sup>1</sup>CEA-LETI, Minatec Campus, Grenoble, France



## POSTER PRESENTATION GUIDE

Posters will be on display in the Poster Area located in the **Salon C** (lower level). This year we will have three full day poster sessions. Each poster session is divided into two time slots, as follows:

Mornings: 9:30am to 10:30am  
Afternoons: 2:30pm to 3:30pm

Authors must be present during BOTH TIME SLOTS. Posters must be posted in the morning between 7:30am to 8:00am. They must be removed between 5:00pm to 5:30pm at the end of the day. THEREFORE each poster will be displayed for a full day.

**Student Poster Competition (SPC)** posters will be displayed in **Normandie Lounge** on the Second Floor. In recognition of their accomplishment, SPC posters will be on display for all THREE days of the conference. Student authors are required to be present for all six poster sessions to describe their work. Judges will review the SPC posters on Thursday only.

### Poster Size and Instructions

- One poster board is allocated to each presentation. The recommended poster size is 36 inches high by 48 inches wide (92 cm x 122 cm ).
- Posters must be mounted using tapes/pins provided by the organizing committee.
- Please note that there will be two poster sessions per day, therefore two posters will use the same board in the day, one in the morning and one in the afternoon. For this reason, be considerate and remove your poster in the designated time after your session is over, to allow enough time to the next authors to place their posters.
- Each poster presenter is required to defend his/her poster during the respective poster session slot for the paper to be included in the conference proceedings.
- Simply posting the pages of your written version of the proceedings paper is NOT effective and thus NOT acceptable for your Poster Paper Presentation.
- The title of your poster paper should be done in block letters which are AT LEAST 8 to 10 cm (3 to 4 inches) high.
- All text must be easily readable from a distance of 1 to 2 meters. Make the lettering at least 1 cm high, smaller lettering will not be legible from a distance of 1 to 2 meters.
- All graphs and charts should be AT LEAST 25 X 30 cm (approximately 8.5 x 11 inches) or larger.
- It is a good idea to sequentially number your materials in the poster. This will indicate to the viewer a logical progression through your Poster Paper Presentation.
- Provide an introduction (outline) and a summary or conclusion for your Poster Paper Presentation.
- Prepare your Poster Paper Presentation carefully so that it can be used as the basis to explain and answer questions from the viewers.
- It is helpful to have copies of the written version of your paper available for those viewers who may want to study specifics of your work in more detail.
- Have your business cards available for those who may wish to contact you at a later date.
- Bring along a tablet of blank paper that you may use for a discussion of technical details relating to your poster paper.

## ORAL PRESENTATION GUIDE

### Observing Your Allotted Time

- The total time allotted to each speaker is 15 minutes. You should plan to speak for 12 minutes and leave 3 minutes for questions.
- Invited speakers have twice this time, 30 minutes in total, and they should plan to speak for about 25 min, leaving 5 min. for questions.
- There is NO EXCUSE for using more than your allotted time. Rehearse your presentation several times; projecting slides and doing anything else you would otherwise expect to do at the meeting. It is a discourtesy to your audience, the Session Chair and the other speakers to exceed your allotted time. The Session Chairs are instructed to adhere to the printed schedule for the session. With parallel sessions this is critical to the overall success of the conference.

### Organization of Oral Sessions

- There are seven parallel sessions in the conference and the Technical Program Committee will ensure minimal conflicts of topics between the parallel sessions.
- Audio and Video Equipment Provided at the Conference: The conference will be equipped with a computer video projector and a computer that is connected to the projector for each oral presentation room. Normal audio equipment such as microphones will be provided.
- Software Used in the Conference: The computers are equipped with Windows 7 as well as **Microsoft PowerPoint 2010 (Office 2010)** and **Adobe Acrobat Reader**. The PowerPoint 2010 is the preferred projection software offered at the conference.
- It is strongly recommended to all authors to check their presentation in the Speaker Ready Room for compatibility and proper operation.
- Avoid Font Problems: Since your computer may have sophisticated fonts (such as special equation symbols) that the conference computers do not have, it is suggested that when you save your PowerPoint presentations, use "Save As" from your "File" pull-down menu. When a dialog box pops up, click on the "Tools" menu on that dialog box and select "Save Options". Then, check the option "Embed true type fonts". Click "OK" and then click "Save". This allows you to include the fonts you are using in your presentations to minimize the font incompatibility problems. Otherwise, any fonts that are not recognized by the conference computers would be incomprehensible. In addition to the default ".pptx" file format, we suggest that you also save a copy of your presentations in the ".ppsx" (PowerPoint Show) format for safe (the ".ppsx" version may also include some of the special fonts in your presentations). If you have a full version of Adobe Acrobat, we suggest you also save (or print) your presentations into a ".pdf" format and thus you will be able to use the free Adobe Reader software to present in case nothing else would work.
- Movies or Videos: If you have movies or videos, the best way to present them properly is to use your own laptop computers since the conference computers may not have the Code/Decode (Codec) software that is necessary to play your movies or videos. If you do not wish to bring your own computers, you may have to convert all of your movies and videos to the Moving Picture Experts Group 1 (MPEG1) format to ensure a cross-platform compatibility. In addition, the movie or video files should be placed where the links in your presentations are pointing to. To make it easy, you could place the movies and videos in the same folder as your ".pptx" or ".ppsx" files when you

prepare your presentations and then copy all these files together to a folder or the desktop of the conference computers.

- **USB Thumb Drives:** Nowadays it is convenient to save your PowerPoint presentations in a USB 2.0 thumb drive. The conference computers will be equipped with the USB 2.0 interfaces. However, some USB drives may have security or driver issues that may prevent the drives from being recognized by the conference computers. Please scan your USB drives to remove viruses if there are any before you bring them to the conference.
- **CD or DVD Backup:** You could also save a copy of your presentation on a CD-R, CD-RW, DVD+/-R, or DVD+/-RW as a backup in case your USB thumb drives do not work with the conference computers (such as missing drivers or having security protections). When you use CD or DVD media, you should "close" (not be able to add any more files) them to increase the chance that these media could be read by the conference computers. If you use DirectCD to save your presentations, please make sure they are readable in a computer without DirectCD software installed.
- **VGA Adapters:** The conference computer projectors will be equipped only with a standard 15-pin analog Video Graphic Array (VGA) connector. If you decide to bring your laptop computers that do not have a VGA port, it is your responsibility to bring all necessary video output adapters with you so that your computers can be connected to the projectors (your computer vendors usually sell or ship such converters with your computers). In addition, the highest resolution of the computer projectors is 1024 x 768 pixels and the resolution of your laptop computers may need to be adjusted properly.
- **230V-110V Voltage Converters:** Chicago uses 110V/60Hz as its power standard. If your laptop computers do not work with 110V/60Hz, it is your responsibility to bring all necessary power converters. In addition, please plug the power adapters into the power strips so that your laptop computers will not run out of power during your presentations. Please also notice that the plug of the power adapter of your laptop computer may not necessarily fit with the 110V power strip. In this case, international converters/adaptors may be needed for you to use the power strips.
- **Backup Your Laptop Computers:** We suggest you make a copy of your presentations on a USB thumb drive in case your computers are damaged, lost, or cannot be used for whatever reasons.

### **Good Practices**

- Show no more than 1 slide per minute of speaking time. This means approximately 10-12 slides MAXIMUM for the 12 minutes of presentation at the symposium. Remember, the last three minutes of the presentation are for questions from the audience. It detracts from the quality of the presentation to flash numerous graphs, equations, or tables on the screen in rapid sequence in an effort to squeeze a presentation into its allotted time.
- Make the letters on your slides BIG ENOUGH. Suggested minimum font is 14.
- Put no more than 12 lines of text or 4 curves on any slide.
- Avoid lengthy tabulations of numerical data and limit equations to those for which the terms can be properly defined.
- Your audience needs time to interpret the data that you present. While you are very familiar with the data displayed, the audience is not. Describe the abscissa, coordinates, units and the legend for each curve.
- When you display a curve, tell the audience what they should be looking for in order to grasp the point you are trying to make. The audience will not have time to figure it out for themselves.
- Use repetition in your talk to ensure the facts are understood by the audience.

- In addition to the body of the talk, present an introduction and a summary or conclusion.
- Include only information or data that can be properly explained in the allotted time.
- Repeat any questions that are posed to you.
- If a question requires a lengthy reply, suggest that you and the person asking the question meet after the presentation. Then take the discussion out of the meeting room.

## **SPEAKER READY ROOM**

Speakers' Ready Room, **Room PDR4**, is located on the 3<sup>rd</sup> Floor of the Hilton Chicago Hotel. **Please submit your presentation in person to the Speakers' Ready Room at least 1 ½ hour** before the beginning of session. For the morning sessions please submit power point presentations by the end of the prior day.

**The Speaker ready hours for submitting presentations are:**  
Wednesday-Saturday: 7:00am–5:00pm.

**CONDENSED IUS SESSIONS PROGRAM**

<b>Condensed Program: Wednesday, September 3, 2014</b>						
	<b>Location and Rooms for Short Courses Will be Announced Later</b>					
<b>8:00am-12:00pm</b>	Short Course 1A. Ultrasound Imaging Systems: from Principles to Implementation	Short Course 1B. Elasticity Imaging: Methods and Applications	Short Course 1C. Acoustic Microfluidics	Short Course 1D. Piezoelectric Ultrasonic Motors	Short Course 1E. Radio Frequency Acoustic Resonators in Communications: Fundamentals, Applications and Characterization	Short Course 1F. Piezoelectric Fundamentals - Materials and Transducers
<b>12:00pm-1:00pm</b>	<b>Lunch</b>					
<b>1:00pm-5:00pm</b>	Short Course 2A. Ultrafast Imaging in Biomedical Ultrasound: Principles and Applications	Short Course 2B. Ultrasound Vector Velocity Imaging	Short Course 2C. Nonlinear Ultrasonic Imaging for NDE: From Laboratory Experiments to R&D of a New Technology	Short Course 2D. Acoustical Imaging; from Acoustic Field Equations to Imaging and Inversion	Short Course 2E. A Modern Approach to Modelling and Simulation of Micro-acoustic Devices	Short Course 2F. Micromachined Ultrasonic Transducers: PMUTs and CMUTs

<b>Condensed Program: Thursday, September 4, 2014</b>							
<b>8:00am-9:30am</b>	<b>Opening &amp; Plenary Talk (Grand Ballroom)</b>						
<b>9:30am-10:30am</b>	<b>Poster Session and Refreshments (Salon C)</b>						
	<b>Grand Ballroom</b>	<b>Waldorf</b>	<b>Boulevard</b>	<b>Marquette</b>	<b>Williford A</b>	<b>Williford B</b>	<b>Williford C</b>
<b>10:30am-12:00pm</b>	Session 1A. MEL: Cardiac Strain Imaging	Session 2A. MTH: Drug delivery and novel treatment approaches	Session 3A. MPA: Photoacoustics I	Session 4A. Arrays	Session 5A. General Physical Acoustics I	Session 6A. RF frontend devices and oscillators	Session 7A. High Frequency Transducers
<b>12:00pm-1:00pm</b>	<b>Lunch Break</b>						
<b>1:00pm-2:30pm</b>	Session 1B. MCA: Molecular Imaging	Session 2B. MEL: Cardiovascular Elasticity Imaging	Session 3B. MBB: Beamforming I	Session 4B. Structural Health Monitoring	Session 5B. Models in Physical Acoustics	Session 6B. Sensors and Field Characterization	Session 7B. CMUTs (1)
<b>2:30pm-3:30pm</b>	<b>Poster Session and Refreshments (Salon C)</b>						
<b>3:30pm-5:00pm</b>	Session 1C. MCA: Outlook for Contrast Imaging	Session 2C. MEL: Elastography: Clinical Applications	Session 3C. MTC: Low Frequency Tissue Characterization	Session 4C. Materials Characterization	Session 5C. Nonlinear Acoustics I	Session 6C. Characterization of materials	Session 7C. Micromachined Ultrasound Transducer Modeling
<b>6:00pm- 8:00pm</b>	<b>Reception (Grand Ballroom)</b>						

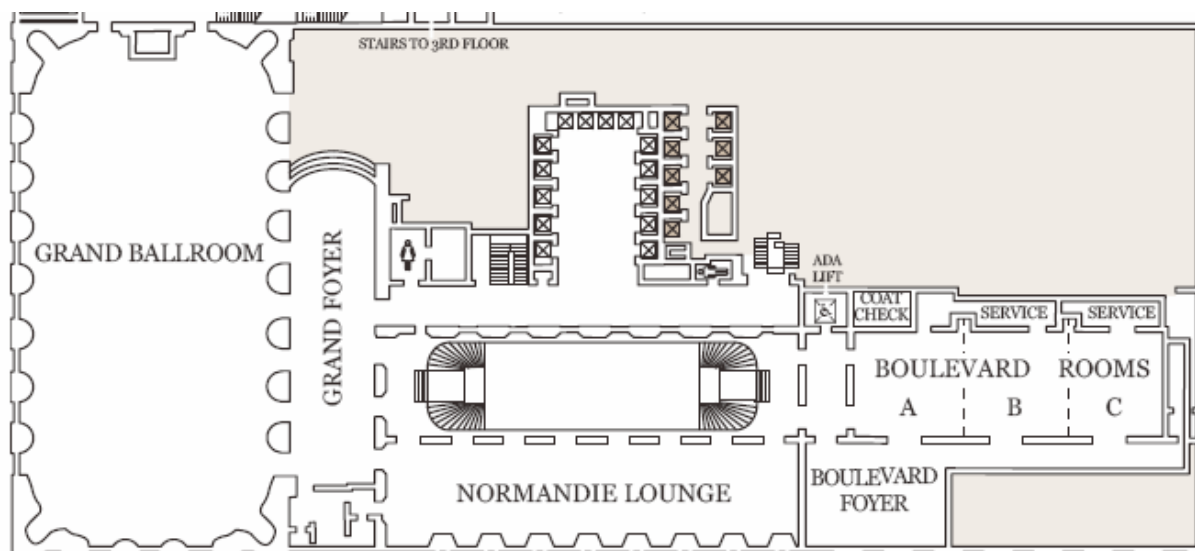
Condensed Program: Friday, September 5, 2014							
	Grand Ballroom	Waldorf	Boulevard	Marquette	Williford A	Williford B	Williford C
8:00am-9:30am	Session 1D. MSD: Advanced Multi-Channel and Multi-Modality Systems	Session 2D. MBF: Vector Velocity Techniques	Session 3D. MPA: Photoacoustics II	Session 4D. NDE	Session 5D. Particle Manipulation and Acoustic Tweezing 2	Session 6D. Sensors and ID tags	Session 7D. Therapeutic Ultrasound Transducers
9:30am-10:30am	Poster Session and Refreshments (Salon C)						
10:30am-12:00pm	Session 1E. MCA: Contrast Agents: New Investigations	Session 2E. MBF: Novel Flow Techniques	Session 3E. MSP: Medical Signal Processing	Session 4E. Acoustic Microfluidics	Session 5E. Particle Manipulation and Acoustic Tweezing 3	Session 6E. Innovations for microacoustic devices	Session 7E. Applications of Piezoelectrics
12:00pm-1:00pm	Lunch Break						
1:00pm-2:30pm	Session 1F. MTH: Histotripsy and Lithotripsy	Session 2F. MEL: Vascular Strain Imaging	Session 3F. MBB: Beamforming II	Session 4F. Signal Processing		Session 6F. Novel microacoustic devices	Session 7F. CMUTs (2)
2:30pm-3:30pm	Poster Session and Refreshments (Salon C)						
3:30pm-5:00pm	Session 1G. MIM: New Developments in Volumetric Ultrasound	Session 2G. MTC: High Frequency Tissue Characterization	Session 3G. MEL: Elasticity Imaging Methods I	Session 4G. Sensing			Session 7G. Diagnostic and Imaging Transducers
6:30pm -11:00pm	Banquet (Grand Ballroom)						

Condensed Program: Saturday, September 6, 2014							
	Grand Ballroom	Waldorf	Boulevard	Marquette	Williford A	Williford B	Williford C
8:00am-9:30am	Session 1H. MIM: Ultrasound Tools to Guide Cardiac Interventions	MEL: Elasticity Imaging Methods II	Session 3H. MSD: Special Applications of Advanced Ultrasound Systems	Session 4H. Wave Propagation	Session 5H. Thin-Films 1	Session 6H. Nonlinearity and Tunability	Session 7H. Electronic Control and Needle Actuation
9:30am-10:30am	Poster Session and Refreshments (Salon C)						
10:30am-12:00pm	Session 1I. MCA: Contrast Agents: New Technologies	Session 2I. MPA: Photoacoustics III	Session 3I. MTH: Blood- brain barrier and sonoporation	Session 4I. Transducers	Session 5I. Ultrasonic Motors and Multi- Modal Thin Film Transducers	Session 6I. Materials for SAW and BAW applications	Session 7I. Piezoelectric Materials
12:00pm-1:00pm	Lunch Break						
1:00pm-2:30pm	Session 1J. MIM: Vascular Imaging	Session 2J. MTH: Tumor treatment and monitoring	Session 3J. MTC: Bone	Session 4J. Industrial Applications and Flow Sensing	Session 5J. Phononics 1		Session 7J. Photoacoustics and other topics
2:30pm-3:30pm	Poster Session and Refreshments (Salon C)						
3:30pm-5:00pm	Session 1K. MEL: Liver Elasticity Imaging	Session 2K. MBB: Beamforming III	Session 3K. MBE: Ultrasound Induced Biological Effects	Session 4K. Airborne Ultrasound	Session 5K. Opto-Acoustics		

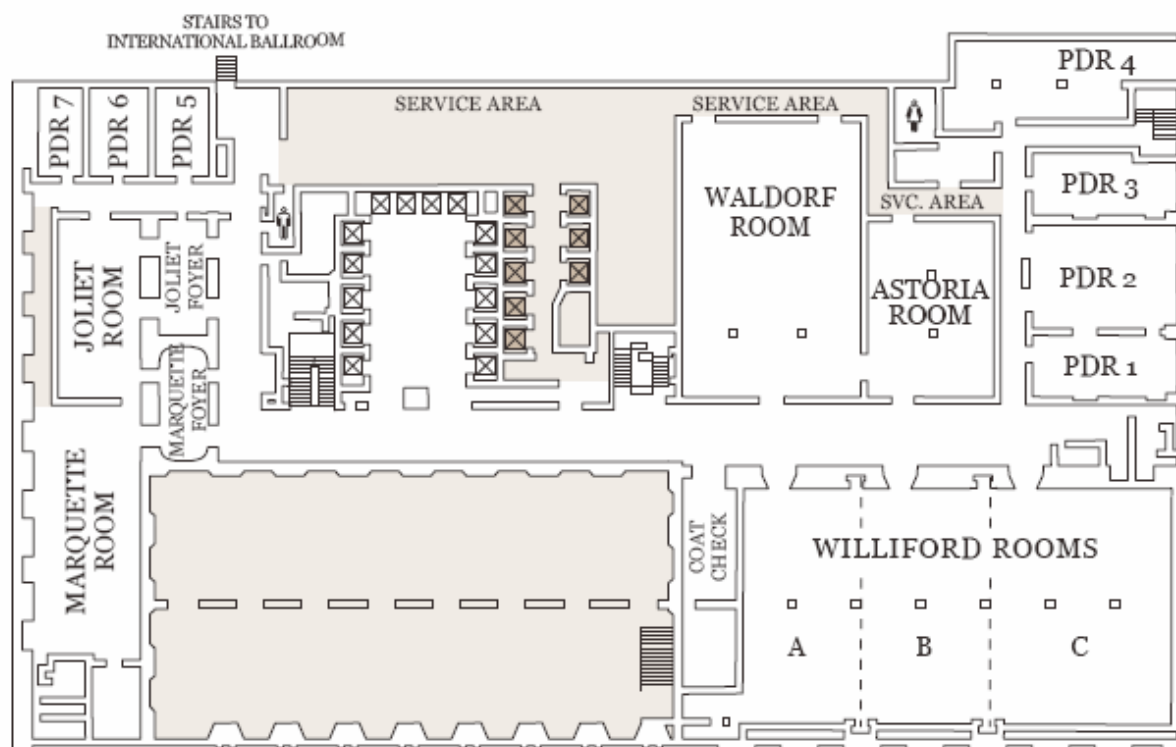


## HILTON CHICAGO HOTEL FLOOR PLANS

### Second floor map: (Oral Sessions, Student Poster Competition)

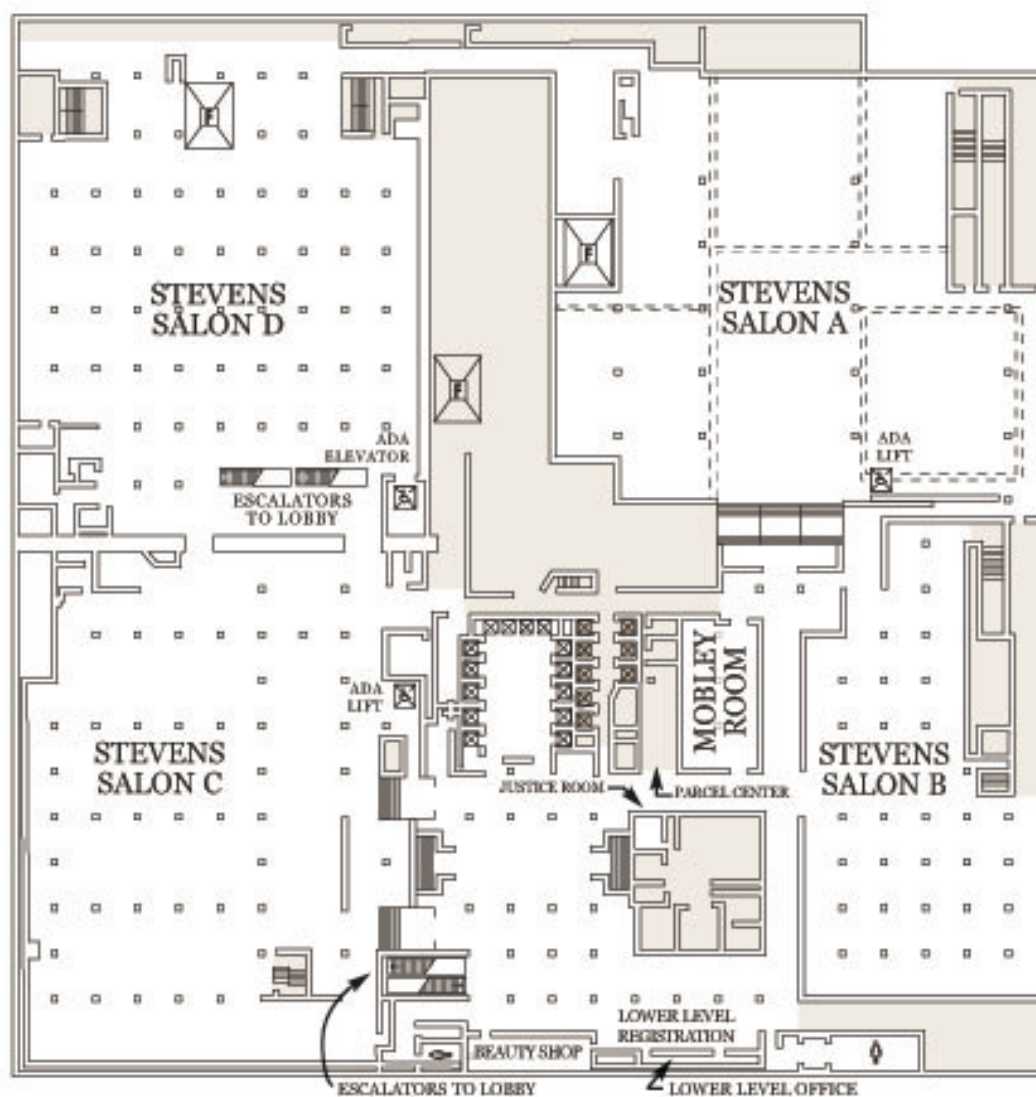


### Third Floor Map: (Oral Sessions)



## HILTON CHICAGO HOTEL FLOOR PLANS

### Salon C Map– Lower Level (Registration, Exhibits, Poster Sessions)



## 1A - MEL: Cardiac Strain Imaging

Grand Ballroom

Thursday, September 4, 2014, 10:30 am - 12:00 pm

Chair: **Georg Schmitz**  
Ruhr-Universität Bochum

1A-1

### 10:30 am Strain-derived Cardiac Assessment

Jan D'hooge<sup>1</sup>, Lieven Herbots<sup>1,2</sup>; <sup>1</sup>Cardiovascular Sciences, University of Leuven, Leuven, Belgium, <sup>2</sup>Cardiology, Jessa Hospital, Hasselt, Belgium

#### Background, Motivation and Objective

The non-invasive assessment of regional cardiac function remains an important goal in clinical cardiology. To this end, visual wall motion scoring remains the method of choice in clinical practice despite the fact that it is known to be subjective and to suffer from high inter-observer variability. Over the past decades, ultrasound methodologies to quantify regional function objectively have been proposed amongst which cardiac velocity, strain and strain rate imaging. Although the original (Doppler-based) technology was angle dependent and labor intensive, later developments could partially overcome these pitfalls and have made these techniques more accessible and practical for clinical routine practice.

#### Statement of Contribution/Methods

After a short overview of the different (commercially available) methodologies, the most important clinical studies showing the added value and potential of these technologies will be reviewed. However, despite these promising publications and the apparent potential of these methodologies, one needs to recognize that they have – to date – not replaced traditional wall motion scoring in most clinical centers. This lecture will therefore end with a critical analysis of the current technology to try to pinpoint bottle necks and pitfalls that hinder true clinical integration.

#### Results/Discussion

1A-2

### 11:00 am Phase rotation in correlation coefficient filtering and multi-pass methods for 3-D speckle tracking in 4-D echocardiography

Emily Wong<sup>1</sup>, Colin Compas<sup>2</sup>, Ben Lin<sup>2</sup>, Albert Sinusas<sup>2</sup>, James Duncan<sup>2</sup>, Matthew O'Donnell<sup>1</sup>; <sup>1</sup>University of Washington, USA, <sup>2</sup>Yale University, USA

#### Background, Motivation and Objective

In 4-D echocardiography (4DE) strain imaging using speckle tracking, large interframe strains can cause significant peak hopping. Conventional correlation filters applied spatially at constant lags are effective for reducing peak hopping in low strain cases, but can degrade the true peak when large strains are present. A tilted method of 3-D filtering can correct for strain-induced incoherence across the correlation function by applying phase rotations in accordance with the local strain distribution prior to filtering. In addition, an iterative or multi-pass process for speckle tracking, using displacement estimates from the previous pass as an initial guess for a subsequent pass, can improve displacement accuracy. We present an approach to reduce peak hopping in 3-D speckle tracking using 3-D tilt filtering and two-pass methods.

#### Statement of Contribution/Methods

4DE data were acquired in an open chest canine at six weeks following surgical coronary occlusion using a commercial 2-D phased array. Initial estimates were obtained using a combined 3-D tracking method, which integrated displacement information from 3-D phase-sensitive correlation-based speckle tracking and 3-D shape tracking in an adaptive manner based on local confidence values. Tilt filtering was applied in first- and second-pass speckle tracking, where the coefficients of the 3-D normalized cross-correlation function were filtered in 3-D space at constant lags, following phase rotation according to the local strain estimate from the combined method. Second-pass tracking was performed with a small search region around the initial estimate (1 x 2 x 1 pixels (lateral x axial x elevational)).

#### Results/Discussion

Tilt filtering reduced peak hopping compared to filtering without phase rotation. The most notable improvements were seen in the transition zones where axial displacements had a high degree of variation along the orthogonal directions. In the transition zones, larger correlation filters without tilting exacerbated peak hopping artifacts, whereas larger tilt filters were able to reduce peak hopping. The lowest peak hopping was seen when both tilt filtering and multi-pass methods were applied. Tilt filtering and two-pass processing will be iteratively integrated into an adaptive 3-D motion tracking method to achieve robust, high-resolution strain quantification from 4DE data.

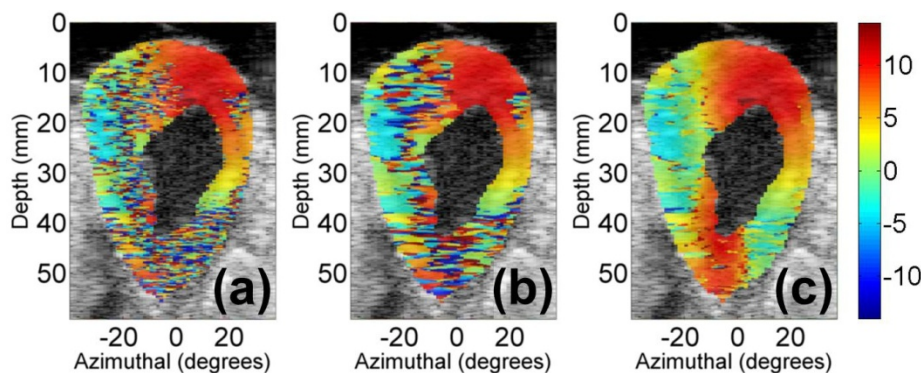


Figure 1. Myocardial axial displacement estimates from 3-D speckle tracking for the first-pass using (a) small (1 x kernel) and (b) large (3 x kernel) filters without phase rotation and (c) second-pass using a large tilt filter (3 x kernel) for a time point in systole.

1A-3

#### 11:15 am Single-Heartbeat Myocardial Elastography in human subjects with Coronary Artery Disease

Julien Grondin<sup>1</sup>, Alok Gambhir<sup>2</sup>, Stanley J. Okrasinski<sup>1</sup>, Ethan Bunting<sup>1</sup>, Elisa E. Konofagou<sup>1,3</sup>; <sup>1</sup>Department of Biomedical Engineering, Columbia University, New York, NY, USA, <sup>2</sup>Department of Medicine, Columbia University, New York, NY, USA, <sup>3</sup>Department of Radiology, Columbia University, New York, NY, USA

##### Background, Motivation and Objective

Myocardial Elastography (ME) is a technique that can image 2-D myocardial strains in vivo. Prior studies have shown that ME can detect abnormal function of coronary artery disease (CAD) patients and identify the territories affected by occluded arteries. However, the previous method required RF frame acquisition using ECG gating with long breath-holding times and/or ECG-gating related artifacts. In this study, the entire field of view was acquired at high temporal resolution during a single heartbeat for CAD patients. The objective of this study was to evaluate the performance of ME in detecting and characterizing abnormal myocardial function in CAD patients using high frame-rate and single-heartbeat data acquisition.

##### Statement of Contribution/Methods

In this study, one normal and seven CAD human subjects were imaged in order to assess the performance of single-heartbeat ME. The patients also underwent coronary angiography and were scanned with ME on the same day as their catheterization procedure. Occlusion superior to 40% measured by angiography was detected in five patients in right coronary artery (RCA), four patients in left circumflex (LCX) and six patients in left anterior descending (LAD). An unfocused transmit sequence was used to acquire transthoracic images in short-axis view using a Verasonics ultrasound system and a P4-2 probe at 2.5 MHz center frequency. Channel data were acquired during 2s at 2000 frames per second and ECG was acquired synchronously. The RF data were reconstructed on a 90° field of view at 20 MHz sampling frequency. Incremental axial and lateral displacements were estimated using normalized 1-D cross-correlation (window size: 5.9 mm, 90% overlap) and then accumulated during systole. Axial and lateral cumulative strains were computed by applying a least-squares estimator using a Savitzky-Golay filter on the axial and lateral cumulative displacements (kernel size: 6.6mm) before converting to radial and circumferential cumulative strains.

##### Results/Discussion

The average radial end-systolic cumulative strain in the normal myocardium was 9.8%, 7.5% and 4.9% in the regions perfused by RCA, LCX and LAD, respectively. The average radial end-systolic cumulative strain in occluded regions in CAD patients were  $-3.6 \pm 5.9\%$  in RCA,  $-2.7 \pm 3.1\%$  in LCX and  $1.0 \pm 2.8\%$  in LAD. The relative variation of strain between the normal and the CAD subjects was 137% in RCA, 136% in LCX and 80% in LAD. These preliminary clinical findings indicate the potential of ME to noninvasively, at high frame rates and within a single heartbeat differentiate CAD-affected from normal left-ventricular myocardium in all regions perfused by coronaries.

This study was supported by the National Institutes of Health (R01EB006042).

1A-4

#### 11:30 am A New Ultrasound Imaging Indicator for Evaluating Vulnerability of Carotid Atherosclerotic Plaques

Lingyun Huang<sup>1</sup>, Xihai Zhao<sup>2</sup>, Manwei Huang<sup>3</sup>, Jianwen Luo<sup>2</sup>; <sup>1</sup>Philips Research China, China, People's Republic of, <sup>2</sup>Department of Biomedical Engineering, Tsinghua University, China, People's Republic of, <sup>3</sup>Ultrasound Department, China Meitan General Hospital, China, People's Republic of

##### Background, Motivation and Objective

Conventional ultrasound imaging techniques as B mode and color flow imaging are widely used in screening carotid atherosclerotic plaques to measure stenosis degree of blood vessel lumen. However, it is lack of vulnerability information of plaques. In this study, we propose a new ultrasound imaging indicator using elasticity imaging technique to evaluate vulnerability of plaques. This indicator will be validated by Magnetic resonance (MR) characterization of vulnerable plaque composition which has been corresponded to histology.

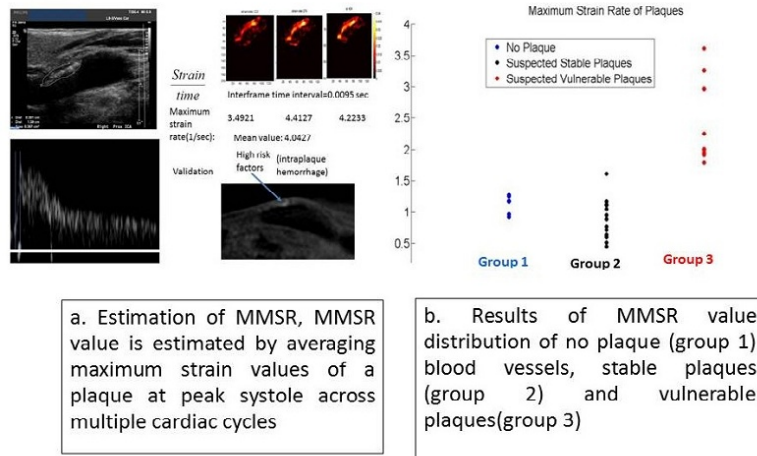
##### Statement of Contribution/Methods

Sequences of ultrasound radiofrequency (RF) data of carotid atherosclerotic plaques were acquired from human subjects using a Philips iU22 ultrasound system with a L9-3 transducer in framerate around 100Hz. The human subject is at supine position and the RF signals were usually acquired in longitudinal view. For a specific plaque, the interframe axial strain of the plaque in one cardiac cycle is estimated using a coarse-to-fine speckle tracking algorithm then normalized by framerate to generate 2D strain rate distribution. The 2D strain rate values of the plaque are then low-pass filtered using a 1mmx1mm kernel. This processing is iterated for several cardiac cycles. Then the strain rate values at peak systolic period of all cardiac cycles are averaged and the maximum mean strain rate (MMSR) is regarded as the vulnerability indicator of this plaque. MR characterization of vulnerable composition is also implemented on the same plaque as ground truth.

### Results/Discussion

MMSR estimation was implemented on 25 plaques or carotid artery sections from 20 human subjects, 5 of which don't have any carotid plaque so that the bifurcation at carotid artery was used for evaluation. As shown in the figure (b), there are significant difference of MMSR values between vulnerable plaques and stable plaques at  $p=0.05$ . It shows the potential and feasibility of MMSR to evaluate vulnerability of plaques and a larger size sample set is being investigated to derive practical classifier of vulnerable and stable plaques.

An ultrasound imaging indicator as MMSR of carotid atherosclerotic plaques is introduced in this study by estimating plaque deformation in multiple cardiac cycles. This indicator is shown to be effective in preliminary studies after validated using MR tissue characterization.



### 1A-5

#### 11:45 am A Pilot Study on AAA Growth vs. Ultrasound Elastography

Tim M. Vonk<sup>1</sup>, V. Lai Nguyen<sup>2,3</sup>, Geert-Willem H. Schurink<sup>2</sup>, Frans N. van de Vosse<sup>1</sup>, Richard G.P. Lopata<sup>1</sup>, <sup>1</sup>Biomedical Engineering, Eindhoven University of Technology, Netherlands, <sup>2</sup>Vascular Surgery, Maastricht University Medical Center, Netherlands, <sup>3</sup>Radiology, Erasmus MC, Netherlands

### Background, Motivation and Objective

Abdominal aortic aneurysms (AAAs) are silent killers and mostly asymptomatic. When rupture occurs, the resulting haemorrhage is fatal in 80-90% of all cases. The current criterion for intervention, the maximum diameter or large growth, do not account for premature rupture. Image-based mechanical characterization of AAAs has been investigated by means of computed tomography or magnetic resonance (MR) imaging based wall stress analysis and MR / ultrasound (US) elastography. In this study, the arterial stiffness was estimated in a group of patients with varying growth rates and followed over time using 2D US elastography. It was investigated whether this technique has the potential to monitor changes in the arterial wall non-invasively.

### Statement of Contribution/Methods

In an ongoing study, 2D RF-data were obtained over a period of four years at 3-5 instances. In this pilot, data were selected of three patients with no growth ( $< 2$  mm), two patients with 5 to 6 mm growth and four patients with significant growth of 5-10 mm between US examinations. 2D RF-data were acquired using a Mylab70 with RF interface (Esaote, NL). The age and maximum diameter of this group was 59 - 81 years and 31 - 58 mm, respectively. The brachial pressure was measured using an arm cuff during the US examination.

Three cardiac cycles were selected in the RF-data and the wall was segmented manually in the reconstructed B-mode image prior to the onset of systole. An RF-based 2D displacement estimation and tracking algorithm was employed to estimate the wall motion. The diameter as a function of time was obtained and converted into distensibility (D) and incremental Young's modulus ( $E_{inc}$ ), assuming axi-symmetry of the aneurysm and by using the brachial pulse pressure. The results from three cardiac cycles were averaged.

### Results/Discussion

Incremental moduli ranging from 1- 8 MPa were found. The distensibility ranged from 2 to 10  $kPa^{-1}$ . The relative change over time in  $E_{inc}$  was -10 to 100% for the patients with no growth, 25% - 125% for the medium group and 75% to 700% for the patients with fast growth. In this group, the distensibility also decreased by a factor of 5. The largest increase in stiffness corresponded to the largest increase in diameter.

These preliminary findings imply that large changes in mechanical properties occur in the aneurysmal wall in periods of considerable growth. In future work, different mechanical parameters need to be investigated, including strain. If the aortic pressure curve was available, more complex material models could be used. Automated segmentation and higher frame rates might decrease the intra-subject variability. Finally, the inclusion of more patients is required to strengthen the evidence found in this study.



## 2A - MTH: Drug Delivery and Novel Treatment Approaches

Waldorf

Thursday, September 4, 2014, 10:30 am - 12:00 pm

Chair: **Cheri Deng**  
University of Michigan, Ann Arbor

2A-1

### 10:30 am Blocking Vascular Rebounds Following Radiation and Microbubble Treatments Using a Dll4 Notch Signalling Antibody.

Ahmed El Kaffas<sup>1,2</sup>, Anoja Giles<sup>1</sup>, Gregory Czarnota<sup>1,2</sup>; <sup>1</sup>Departments of Radiation Oncology and Physical Sciences, Sunnybrook Health Sciences Centre, Canada, <sup>2</sup>Departments of Medical Biophysics and Radiation Oncology, University of Toronto, Canada

#### Background, Motivation and Objective

Ultrasound-stimulated microbubbles (USMB) can be used to radiosensitize endothelial cells. Irradiation of tumours following USMB treatment results in acute vascular shutdown and extensive tumour cell death. However, vascular rebounds have been observed following such treatments, often leading to continued tumour progression. Here, we demonstrate the use of an anti-vascular agent (Dll4-notch signalling blockade) following combined USMB-radiation treatments to prevent vascular rebounds. We use ultrasound to assess the acute and long-term response to treatments.

#### Statement of Contribution/Methods

Tumour xenografts (LS174T) were treated with single 5 Gy radiation doses in conjunction with ultrasound-stimulated microbubbles (USMB), followed by an anti-vascular agent. USMB treatments consisted of a 16-cycles tone burst at 500 kHz center frequency and 570 kPa with a 2.86 cm element diameter ultrasound transducer. The total insonification time was 750 ms over 5 minutes. Definity microbubbles were injected via tail-vein at a volume concentration of 3% v/v. Treatment response was assessed with high-frequency volumetric ultrasound acquired before, during and after treatment using a VEVO770 system and a 30 MHz center frequency transducer. The vascularity index (VI) was used to quantify power Doppler data, while quantitative ultrasound spectroscopy (QUS) parameters were used to monitor tumour response and tissue structural changes. Staining using ISEL and CD31 of tumour sections was used to measure cell death and vascular distributions. Tumour growth delays were used to assess overall tumour response.

#### Results/Discussion

Our results suggest significant tumour response in animals treated with USMB combined with radiation, followed by an anti-vascular maintenance therapy. We found a synergistic growth delay of up to 24 days in tumours receiving triple combination treatments. Tumour growth delays are directly linked to rapid cell death and sustained tumour vascular shutdown, which we confirmed with ultrasound. At 24 hrs following treatment, we noted a VI decrease of up to  $55 \pm 8.6\%$  and  $60 \pm 5.3\%$  for animals treated with radiation followed by the anti-vascular agent only, or combined with USMB, respectively. At 7 days, although the VI had increased by  $\sim 20\%$  in tumours treated with radiation and the anti-vascular agent, tumours receiving the triple combination therapy had a sustained vascular shutdown with a VI of  $51 \pm 4.8\%$ . Quantified cell death paralleled VI results, suggesting that these may be directly linked to overall levels of vascular shutdown. We also observed that the anti-vascular agent alone induced morphological changes in tissue that are potentially reflected in QUS parameters. Overall, results demonstrate the potency of combining radiation and USMB, and suggest a new anti-vascular rebound strategy.

2A-2

### 10:45 am Effect of cavitation on ultrasound and microbubble-mediated gene knockdown in squamous cell carcinoma

Jonathan A. Kopechek<sup>1</sup>, Andrew R. Carson<sup>1</sup>, Xucai Chen<sup>1</sup>, Charles F. McTiernan<sup>1</sup>, Bima Hasjim<sup>1</sup>, Malabika Sen<sup>2</sup>, Jennifer R. Grandis<sup>2</sup>, Flordeliza S. Villanueva<sup>1</sup>; <sup>1</sup>Dept. of Medicine, University of Pittsburgh, Pittsburgh, Pennsylvania, USA, <sup>2</sup>Dept. of Otolaryngology, University of Pittsburgh, Pittsburgh, Pennsylvania, USA

#### Background, Motivation and Objective

A DNA decoy has been shown to knock down STAT3 signaling and inhibit growth of squamous cell carcinoma (SCC) tumors, but a clinically feasible delivery method is lacking. We have developed a cationic lipid microbubble (MB) formulation containing STAT3 decoy nucleic acids for ultrasound (US)-mediated delivery to murine SCC cells and tumors. Whereas it has been widely assumed that inertial cavitation was necessary and sufficient to achieve therapeutic nucleic acid delivery via US-targeted MB destruction (UTMD), systematic investigation of the relationship between effective STAT3 knockdown/tumor growth inhibition and inertial cavitation (IC) dose has not been performed.

#### Statement of Contribution/Methods

For in vivo proof-of-concept, a clinical array transducer was used for image-guided therapy (Philips S3, UltraHarm mode, 1.3 MHz, displayed MI=1.6) in SCC tumor bearing C3H/HeJ mice undergoing UTMD-mediated delivery of i.v. infused MBs loaded with STAT or control (mutant) decoy. The array was positioned such that the tumors were in the near field (10 mm distance, peak rarefactional pressure (PRP) of 0.35-0.70 MPa). Tumor volumes were monitored using 3D US imaging (VisualSonics Vevo 2100). To study acoustic requirements for effective decoy delivery, decoy or control DNA-loaded MBs were infused over 5 min into a suspension of SCC cells expressing STAT-responsive luciferase. During MB infusion, 4-cycle US pulses (1600 Hz PRF) were delivered with a flat Olympus NDT 1 MHz transducer (PRP of 0.2 to 0.7 MPa). Cavitation activity was detected with an Olympus NDT 10 MHz focused transducer and IC dose was calculated by integrating the detected broadband power between 3.25-3.35 MHz.

#### Results/Discussion

UTMD with STAT decoy inhibited murine tumor growth compared to UTMD with control MBs (Fig 1A). In vitro knockdown of STAT decoy-dependent luciferase expression was greatest at 0.4 MPa (Fig 1B), while the IC dose was greatest at 0.7 MPa (4, 20, and 90 arbitrary linear units at 0.2, 0.4, and 0.7 MPa, respectively), suggesting that functional decoy delivery is not determined solely by extent of IC, but that MB persistence and prolonged MB-cell interaction are also important. These data suggest that moderate acoustic pressures above the IC threshold are more effective for decoy delivery than higher pressures, and have implications for optimization of nucleic acid therapeutics via UTMD.



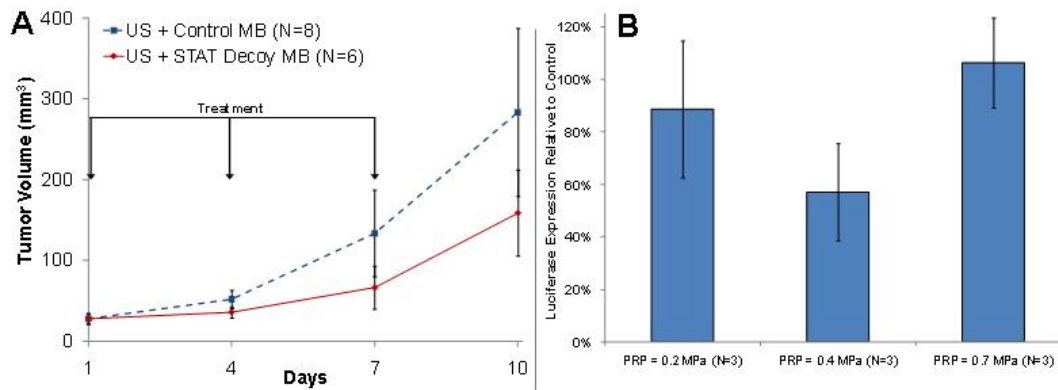


**Figure 1:** (A) Mouse tumor growth rate after UTMD treatment with STAT decoy MBs or control MBs, demonstrating significant growth inhibition with decoy during the treatment period ( $p < 0.05$ ). (B) Luciferase expression after UTMD with STAT decoy relative to UTMD with a scrambled control sequence as a function of acoustic pressure, indicating that the greatest amount of knockdown was detected at a peak rarefactional pressure (PRP) of 0.4 MPa.

## 2A-3

### 11:00 am Neointima reduction with IVUS and rapamycin microbubbles: *in vivo* swine model results

Joseph P. Kilroy<sup>1</sup>, Ali H. Dhanaliwala<sup>1</sup>, Brian R. Wamhoff<sup>2</sup>, Alexander L. Klibanov<sup>1,3</sup>, Douglas K. Bowles<sup>4</sup>, John A. Hossack<sup>1</sup>; <sup>1</sup>Department of Biomedical Engineering, University of Virginia, Charlottesville, Virginia, USA, <sup>2</sup>HemoShear, LLC, Charlottesville, Virginia, USA, <sup>3</sup>Department of Medicine - Cardiovascular Division, University of Virginia, Charlottesville, Virginia, USA, <sup>4</sup>Department of Biomedical Sciences, University of Missouri, Columbia, Missouri, USA

#### Background, Motivation and Objective

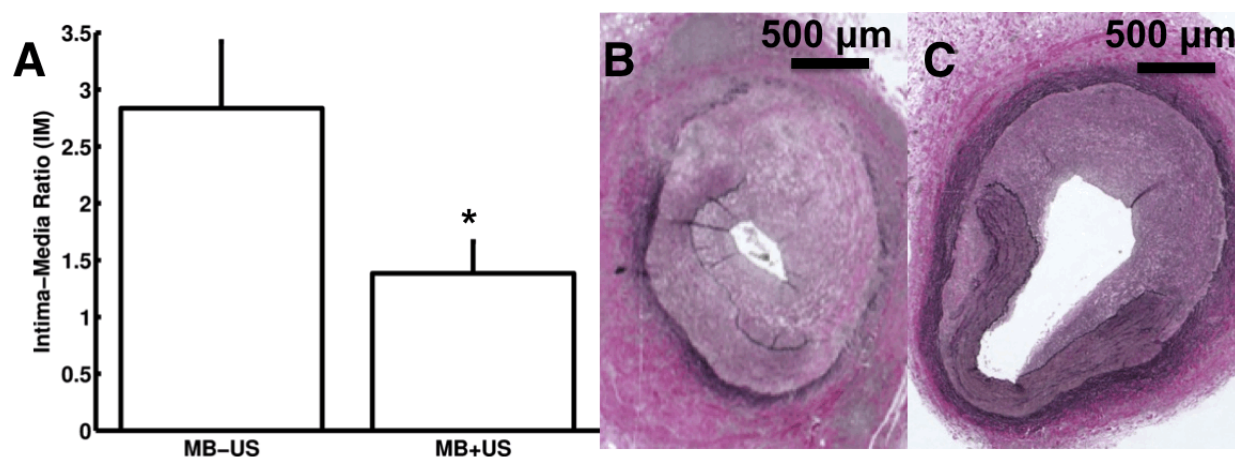
Percutaneous coronary intervention (PCI) is a catheter based intervention in which a balloon is expanded within a narrowed artery in order to restore blood flow. This procedure is associated with trauma to the arterial wall and frequently results in neointimal hyperplasia and consequent restenosis of the artery. Rapamycin is a potent drug that reduces neointima formation, but at high doses induces immunosuppression and slows vessel healing. Localized drug delivery can reduce the systemic dose of rapamycin required to prevent neointima formation by delivering this drug only to the injured artery segment. Current platforms for drug delivery following PCI (i.e. drug eluting stents) offer limited drug choice, dose, and coverage options. We have developed an ultrasound and microbubble enhanced drug delivery system for intravascular drug delivery. Using intravascular ultrasound (IVUS) and rapamycin-loaded microbubbles (RMBs) we have tested this platform as a tool to reduce neointimal hyperplasia in a swine model of balloon injury.

#### Statement of Contribution/Methods

Balloon injury was performed in swine coronary arteries to induce neointima formation. Following balloon injury, a custom IVUS catheter was positioned within the injured artery. RMBs were infused through the catheter while arteries were either treated without ( $n=5$ ) or with ( $n=7$ ) intravascular ultrasound (5 MHz center frequency, 600 kPa PNP, 50% duty cycle). Treated arteries were excised and histology was performed 28 days later. The reduction in intima to media ratio (IM) was measured to determine therapeutic efficacy. All animal experiments were approved by the University of Missouri Animal Care and Use Committee.

#### Results/Discussion

Following ultrasound and RMB treatment, IM decreased by 50% in ultrasound treated vessels (Fig A –  $1.38 \pm 0.28$  vs.  $2.84 \pm 0.59$  vs,  $p=0.034$ ). Artery sections treated with RMBs and ultrasound (Fig C) exhibited less neointima formation than sections treated with RMBs alone (Fig B). This study demonstrates that IVUS and microbubble enhanced rapamycin delivery is a viable method for reducing neointimal hyperplasia following balloon injury. In addition to achieving a level of efficacy comparable to drug eluting stents, IVUS and RMB delivery provides versatility in terms of drug choice, dose, and coverage that drug eluting stents do not offer.



2A-4

**11:15 am High-Speed Fluorescence Imaging of Ultrasound-Triggered Drug Release from Phase-Change Droplets**Tsung-Lun Chang<sup>1</sup>, Shih-Tsung Kang<sup>1</sup>, Chih-Kuang Yeh<sup>1</sup>; <sup>1</sup>Department of Biomedical Engineering and Environmental Sciences, National Tsing Hua University, Taiwan**Background, Motivation and Objective**

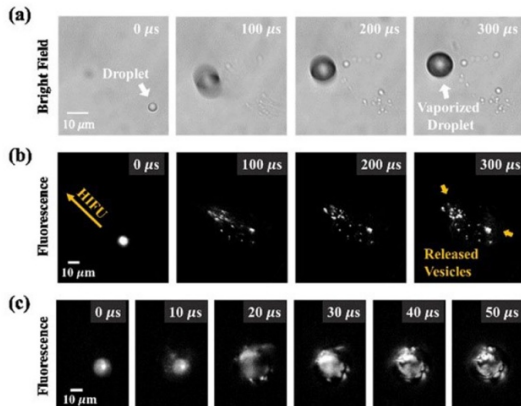
Perfluoropentane (PFP) droplets are promising for drug delivery due to their ability to undergo acoustic droplet vaporization (ADV) under ultrasound excitations. However, no study has investigated the transient dynamics of drug release distribution, since ADV occurs on microsecond scale and drugs are hardly identified in conventional bright field microscopy. Here, we established a high-speed fluorescence imaging system to visualize the drug release process during ADV.

**Statement of Contribution/Methods**

PFP droplets were stabilized by a shell of DSPE and DSPE-PEG2000. DiI (10 mol%) was incorporated into the shell to mimic the lipophilic or hydrophobic drugs. Droplets were immersed in an acousto-optical system that allowed high-speed optical microscopy under ultrasound excitations. A 2-MHz high-intensity focused ultrasound (HIFU) transducer was confocally aligned with the 40X objective to induce ADV by using 3-cycle pulses at acoustic pressures above 7 MPa. A 1210 mW high-power laser (532 nm) was integrated to excite sufficient fluorescence emissions on microsecond scale. Laser beam profile at the optical focus was regulated to be 80  $\mu\text{m}$  (full width at half maximum) with a peak intensity of up to 25 kW/cm<sup>2</sup>. Fluorescence imaging was conducted for PFP droplets with sizes larger than 5  $\mu\text{m}$  at up to 225 kfps.

**Results/Discussion**

The ADV of single droplets produced small vesicles (<2  $\mu\text{m}$ ) that were observable in bright-field imaging on the floor (Fig. 1(a)). In the first 100  $\mu\text{s}$ , the vesicles had a slight tendency to drift in the direction of HIFU transmission. They generally showed fluorescence emissions, indicating the presence of released DiI molecules with lipid residues (Fig. 1(b)). However, a portion of DiI molecules still remained on the surface of ADV-generated bubble, exhibiting a highly mobile fluid phase in the first 40  $\mu\text{s}$  after the onset of ADV (Fig. 1(c)). These suggest that the encapsulated drugs were partially released from host droplets in the form of small vesicles under one short ultra-sound exposure. The effects of droplet size and composition, and ultrasound parameters (e.g., acoustic pressure, pulse duration, and acoustic frequency) on the transient dynamics of ADV-induced drug release were also discussed in this study. This study is anticipated to provide valuable information for the optimization of ADV-based drug delivery.



2A-5

**11:30 am Dual thermal therapeutic method for selective treatment of deep-lying tissue**Heamin Kim<sup>1</sup>, Jin Ho Chang<sup>1,2</sup>; <sup>1</sup>Interdisciplinary Program of Integrated Biotechnology, Sogang University, Seoul, Korea, Republic of, <sup>2</sup>Department of Electronic Engineering, Sogang University, Seoul, Korea, Republic of**Background, Motivation and Objective**

The main drawback of photothermal therapy is the therapeutic depth limited due to the absorption and scattering of laser energy in tissue. Therefore, it is openly impossible to use an optimal laser wavelength for tissue chromophores and photosensitizers to maximally absorb the energy. For example, although the optimal wavelength for melanoma is in between 540 to 570 nm, a relatively long wavelength such as 1064 nm is used in clinical practice, thus causing lowering therapeutic efficacy. In this paper, we propose a dual thermal therapeutic method in which both laser and ultrasound (US) energies are simultaneously transmitted for selective treatment of deep-lying tissue

**Statement of Contribution/Methods**

In the proposed method, the US energy plays a role in increasing the local temperature of the treatment area, but the temperature rise is limited to the threshold level for tissue damage. Under this condition, laser energy is delivered into the treatment area, thus causing the temperature to surpass the threshold for coagulation necrosis only within the tissue chromophores. Since two energies are complementary in elevation of tissue temperature, the therapeutic depth by the laser energy increases under US exposure; its penetration depth also increases in conjunction with US, which is beneficial for photodynamic therapy using photosensitizers. These effects of dual thermal therapy were ascertained using a custom-made tissue mimicking phantom consisting of a front scattering section of 4 mm thickness and a rear absorbing section of 16 mm thickness. US energy was produced using a 1.1 MHz single element transducer with 62.5 mm focal depth and 20 mm central opening. Laser energy was delivered by a Nd:YAG laser system: 1064 nm wavelength, 10 ns pulse length, 10Hz PRF. The laser pulses passed through a hole in the transducer.

**Results/Discussion**

As shown in Fig. 1(a) and (b), the depth of lesion formation was increased by 1.6 mm in the case of simultaneous delivery of both laser energy of 73.5 mJ/cm<sup>2</sup> and US energy (ISPTA) of 200 W/cm<sup>2</sup>, compared with the laser energy alone. Note that no lesion formation was observed when the US energy was used alone. Also, it was ascertained that the US energy allowed more laser fluence to pass through the phantom as shown in Fig. 1(c). The results demonstrate that the proposed therapeutic method can be used for selective treatment of deep-lying tissue

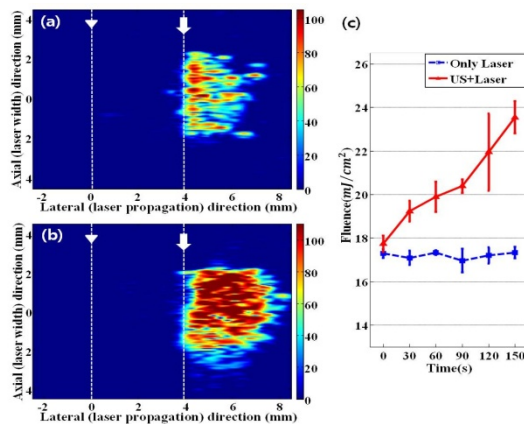


Fig. 1. Lesion formation appeared in the US images in the cases of (a) laser energy of  $73.5 \text{ mJ/cm}^2$  alone and (b) the same laser energy in conjunction with US energy ( $I_{\text{SPFA}}$ ) of  $200 \text{ W/cm}^2$ . The white arrowhead indicates the boundary between the water and the surface of the phantom, and the white arrow is the boundary between the front scattering and the rear absorbing sections. (c) Laser fluence passing through the optical scattering phantom of 10 mm thickness is presented as a function of exposure time.

## 2A-6

### 11:45 am In-vivo HIFU atrial and ventricular ablation and monitoring using a dual-mode high-frequency intracardiac catheter

Wojciech Kwiecinski<sup>1</sup>, Jean Provost<sup>1</sup>, Mathieu Legros<sup>2</sup>, An Nguyen-Dinh<sup>2</sup>, Rémi Dufait<sup>2</sup>, Frédéric Sacher<sup>3</sup>, Rémi Dubois<sup>3</sup>, Mickaël Tanter<sup>1</sup>, Mathieu Pernot<sup>1</sup>; <sup>1</sup>Institut Langevin, ESPCI ParisTech, CNRS UMR7587, INSERM U797, Paris, France, <sup>2</sup>VERMON SA, Tours, France, <sup>3</sup>LIRYC Institute, INSERM 1045, Université de Bordeaux, Bordeaux, France

#### Background, Motivation and Objective

Atrial fibrillation (AF) is the most prevalent heart rhythm disorder. Atrial arrhythmias such as AF can be treated by creating continuous, transmural ablation lines in the heart chambers to isolate or eliminate electrically abnormal regions. However, clinically available systems based on radio-frequency ablation suffer from limited energy penetration depth and the lack of lesion's extent monitoring. In this work, we have developed and validated in vivo a novel non-contact dual-mode ultrasound catheter, which can perform High-Intensity Focused Ultrasound (HIFU), B-mode Imaging and Shear-Wave Elastography (SWE) to create transmural lesions in atria and ventricles and monitor their extent in real-time.

#### Statement of Contribution/Methods

A 64-element intracardiac transducer (6 MHz, 64 elements, 0.2 mm pitch, VERMON, France) mounted on 9F catheter (3-mm diameter) was designed and built for dual mode imaging and therapy. The ultrasonic intracardiac transducer was inserted into the right atrium via the femoral vein under fluoroscopy. It was positioned to target locations in the right atrium (n=2) and in the right ventricle (n=3) under real-time B-mode guidance in two sheep. First, shear waves were generated remotely with the transducer and recorded (8000 frames/s, 5 shear wave generations per sample, 300  $\mu\text{s}$  bursts) with an ultrafast scanner prototype (Supersonic Imagine, France) to map the shear modulus in 2D. This prototype was used to perform both transmit/receive imaging sequences and transmit HIFU high power sequences. HIFU lesions were then induced using the same probe by emitting a focused beam during 2 minutes with a duty cycle of 50%. A second SWE acquisition was performed, the shear modulus maps were processed and the mapping of elasticity ratio between pre and post treatment was compared against gross pathology for validation. The procedure was repeated (up to 5 positions) by electronically steering the HIFU focus laterally and axially to increase the extent of the lesion.

#### Results/Discussion

A total acoustic power of  $3.8 \pm 0.1 \text{ W}$  was measured with an acoustic radiation force balance, which corresponds to an acoustic intensity of  $14.4 \pm 0.2 \text{ W/cm}^2$  at the surface of the probe. Linear and transmural thermal lesion volumes up to  $10 \times 4 \times 3 \text{ mm}^3$  were created in the atrium. Approximately  $3 \times 3 \times 3 \text{ mm}^3$  lesions were created on ventricles' endocardium and epicardium while focusing from the cavity. Ablation was visible on the shear modulus maps but not on B-mode images. The end-diastolic myocardial stiffness was found to increase from  $2.2 \pm 0.7 \text{ kPa}$  to  $13.3 \pm 5.3 \text{ kPa}$  in the ablated regions.

We have demonstrated the feasibility of both thermal ablation and monitoring using the same ultrasonic catheter in vivo. Linear (up to 10-mm long) and transmural lesions were created without moving the probe. This direct therapy/imaging association could lead to a more precise and reliable treatment of atrial fibrillation.

**3A - MPA: Photoacoustics I**

Boulevard

Thursday, September 4, 2014, 10:30 am - 12:00 pm

Chair: **Michael Kolios**  
Ryerson University, Toronto

3A-1

**10:30 am Spatially Adaptive Autofocusing Approach for Automatic Speed of Sound Selection in Photoacoustic Tomography****K Heath Martin**<sup>1</sup>, Richard Lam<sup>2</sup>, Robert Kruger<sup>2</sup>, Paul A Dayton<sup>1</sup>; <sup>1</sup>Joint Dept of Biomedical Engineering, University of North Carolina/North Carolina State University, Chapel Hill, North Carolina, USA, <sup>2</sup>Optosonics, Inc., Oriental, North Carolina, USA**Background, Motivation and Objective**

Previous work in the field of photoacoustic tomography (PAT) has demonstrated the need to appropriately select the speed of sound (SOS) used to reconstruct a 3-dimensional dataset to prevent blurring. An ongoing effort in PAT is to correct for SOS errors associated with imaging materials with inhomogeneous propagation velocities, such as tissue, using a precise and automatic method. The Brenner gradient is an image sharpness metric which has shown previous success in PAT for selecting the SOS that minimizes blurring in whole images automatically. This study further develops the autofocusing approach to calculate SOS maps to adaptively reconstruct PAT images with higher spatial acuity.

**Statement of Contribution/Methods**

Photoacoustic signals were acquired using a 512 element hemispherical transducer array (3.0 mm diameter,  $f_c = 2$  MHz) with a 127 mm radius of curvature. A photoacoustic excitable dot matrix was embedded in a spherical cap gel and imaged through a water bath at 20.6°C. The phantom was illuminated with a tunable laser at 755 nm and the photoacoustic data was recorded at 20 MHz sampling rate. Multiple 3D tomographic volumes of 256 x 256 x 25 mm were reconstructed using a constant SOS for the whole volume (1400–1550,  $\Delta 2.5$  m/s). Maximum intensity projects (MIPs) of the volumes were evaluated using the Brenner gradient to quantify image focus. The SOS producing the maximum focus within a 7 mm search radius for every pixel was stored into the SOS map. Dots ( $n = 11$ ) were selected throughout the field to compute SNR and FWHM for both single velocity and adaptive reconstructions made from SOS maps.

**Results/Discussion**

Adaptive images were highly focused in all regions of the phantom while single SOS reconstructions suffered from heterogeneous blurring. The adaptive autofocusing approach had better mean SNR (172 vs 157, Fig. 1a) and resolution (1.04 vs 1.16 mm, Fig. 1b) in comparison to the best single SOS image, which occur at two different SOS's. The autofocusing, spatially adaptive imaging approach produces images with better SNR and resolution by automatically choosing the best SOS for every pixel location in the MIP.

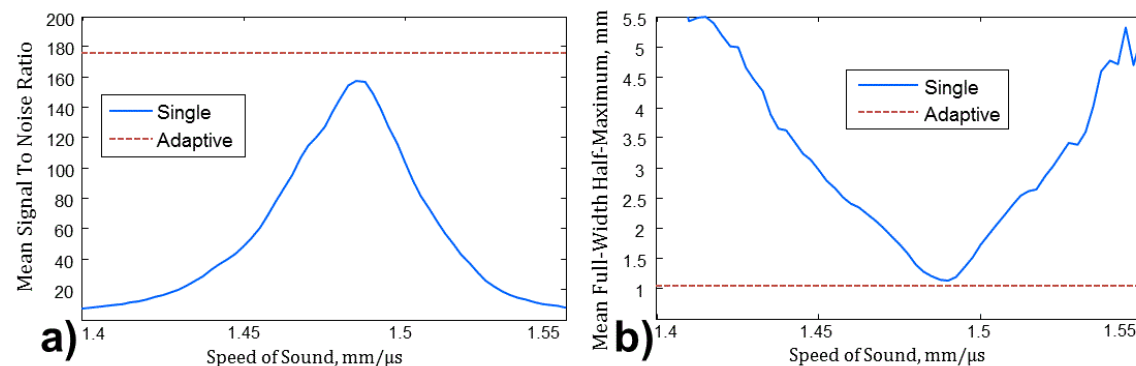


**Figure 1: (a)** Adjusting the speed of sound applied to the entire volume of an image alters the mean SNR of the dot phantom. At 1.485 mm/μs, the single speed of sound has the best SNR (157), but is still lower than when using a spatially adaptive speed of sound map (172). **(b)** Optimally adjusting the speed of sound for single value reconstructions minimizes the mean FWHM to 1.116 mm at 1.490 mm/μs, but is still larger than the mean FWHM of the spatially adaptive image which is 1.038 mm (7.5% decrease)

3A-2

**10:45 am Spectroscopic photoacoustic microscopy in the 1064 - 1300 nm range using a pulsed multi-color source based on stimulated Raman scattering****Takashi Buma**<sup>1</sup>; <sup>1</sup>ECE Department, Union College, USA**Background, Motivation and Objective**

Photoacoustic microscopy (PAM) provides excellent image contrast based on optical absorption. A very common pulsed optical source is a Q-switched Nd:YAG laser. However, the fixed 1064 nm output is not suitable for spectroscopic PAM. We demonstrate a simple approach to increase the number of wavelengths into the 1300 nm range, therefore allowing spectroscopic PAM of lipids. Our approach uses stimulated Raman scattering (SRS) in an optical fiber, where a series of down-shifted frequency components (Stokes lines) are generated by the nonlinear interaction between the propagating laser pulse and glass molecules of the fiber.

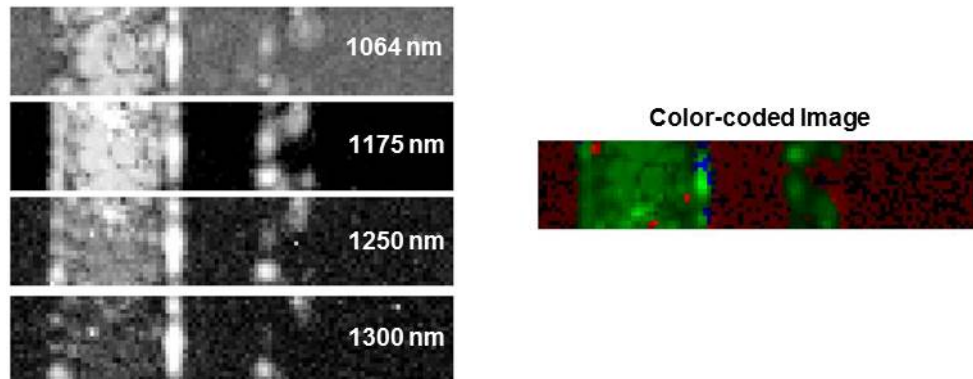
**Statement of Contribution/Methods**

Our Q-switched Nd:YAG microchip laser produces 0.6 ns duration pulses at 1064 nm with 10 μJ of energy at a 7.4 kHz repetition rate. The laser pulses are coupled into a 20 meter long single-mode silica fiber. The multi-color fiber output goes through a dielectric band pass filter, where the selected wavelength is sent to a photoacoustic microscopy system.

The laser is focused into the sample with a 0.16 NA aspheric lens and detection is performed with a 25 MHz spherically focused f/4 transducer. The PAM signal is amplified by 60 dB and averaged 500 times before capture with an 8-bit digitizer board operating at 250 MS/sec. A motorized positioning system raster scans the laser and transducer across the object with a 25  $\mu\text{m}$  step size.

### Results/Discussion

The pulse energies within spectral bands at 1064, 1175, 1250, and 1300 nm are measured to be 250, 135, 125, and 120 nJ, respectively. As a proof of concept, an imaging phantom was made by forming a line pattern with coconut oil (approximately 0.5 mm thickness) on a glass microscope slide. The attached figure shows the single-wavelength PAM images (2.5 x 0.5 mm region) over the same 20 dB logarithmic scale. The line pattern is clearly brightest at 1175 nm, which is consistent with the 1210 nm absorption peak of lipids. The relatively strong signal at 1064 nm suggests that the coconut oil line patterns are not composed of pure lipid, which is not surprising. A major advantage of our technique is the simple arrangement to convert a single-wavelength 1064 nm laser into a multi-color source for spectroscopic PAM in the near-infrared range.



3A-3

### 11:00 am Simulation and experimental detection of radiation-induced acoustic waves from a radiotherapy linear accelerator

Susannah Hickling<sup>1</sup>, Pierre Leger<sup>2</sup>, Issam El Naqa<sup>2</sup>; <sup>1</sup>McGill University, Montreal, Quebec, Canada, <sup>2</sup>McGill University Health Centre, Montreal, Quebec, Canada

#### Background, Motivation and Objective

Analogous to the photoacoustic effect, acoustic waves are induced in objects irradiated with megavoltage (MV) photon beams generated by a clinical linear accelerator (LINAC). The ability to detect such induced acoustic waves (IAWs) has recently been demonstrated, however much about the nature of this phenomenon remains to be understood. This work aims to develop a novel simulation workflow to model IAWs for different LINAC irradiation scenarios. The simulations are then used to optimize the detection of IAWs and verified by experimental measurements.

#### Statement of Contribution/Methods

Computational simulations and corresponding experiments were performed to model and detect the IAWs arising from LINAC irradiation of a lead rod in a water tank. Beam energies of 6 MV and 18 MV, lead rod depths from 5 to 11 cm, and transducer to rod distances ranging from 8 to 16 cm were investigated. To model IAWs, the dose distribution after a pulse of MV irradiation was determined using Monte Carlo simulations. Dose distributions were then converted into initial differential pressure distributions, and transportation of the IAWs in medium was simulated using the MATLAB toolbox k-Wave. Experimentally, IAWs were detected with a single element immersion ultrasound transducer. The transducer output was fed into a commercial preamplifier and a customized analog electronic filter to reduce noise and provide further gain prior to read out on an oscilloscope.

#### Results/Discussion

Based on simulation results, the filter central frequency was tuned to 50 kHz with a 3 dB bandwidth of 20 kHz. This improved the peak signal-to-noise ratio by a factor of four compared to the unfiltered signal. Simulated and experimental results both showed that the amplitude of the IAWs increased by increasing beam energy, decreasing lead rod depth and decreasing lead rod to transducer distance. IAWs for the lead rod at depths of 5 cm and 9 cm demonstrated that the relative amplitude difference between the two depths for the first peak to valley transition is 73% for the simulated signals and 75% for the experimental measurements (Fig. 1). In conclusion, the detection of IAWs was significantly improved by designing a customized filter. Additionally, the simulation platform successfully enabled the prediction of the frequency spectrum and relative amplitudes of IAWs under different irradiation conditions.

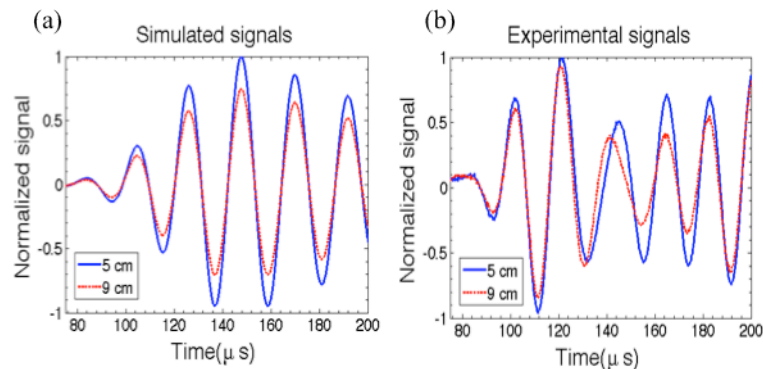


Fig. 1: Simulated (a) and experimental (b) signals for the induced acoustic waves after irradiation of a lead rod placed at depths of 5 cm and 9 cm in a water tank with an 18 MV LINAC beam.



3A-4

**11:15 am Iterative photoacoustic reconstruction in heterogeneous media using the Kaczmarz method**Hans-Martin Schwab<sup>1</sup>, Martin F Beckmann<sup>1</sup>, Georg Schmitz<sup>1</sup>; <sup>1</sup>Medical Engineering, Ruhr-Universität Bochum, Bochum, Germany**Background, Motivation and Objective**

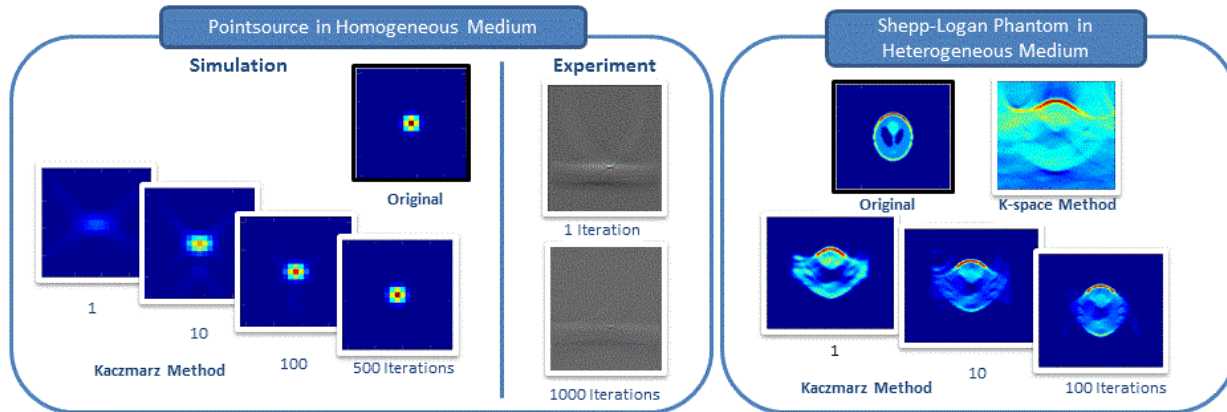
The aim of a photoacoustic image reconstruction is to locate acoustic sources that originate from laser irradiation. Many conventional one-step methods suffer from artifacts caused by simplifications in their derivation. For example, the limited view of most detection systems is usually not considered. Recently, several iterative reconstruction algorithms have been proposed that are able to approximate the original distribution more accurately. Some of them have been shown to reduce the influence of a limited view. However, the efficiency of these algorithms is usually only assessed on a circular detection setup. Also, acoustic medium heterogeneities are often neglected. We propose a new iterative reconstruction algorithm that can be applied to linear array acquisitions and considers known medium heterogeneities. The approach is based on the Kaczmarz method as commonly used in Computed Tomography.

**Statement of Contribution/Methods**

Based on the photoacoustic wave equation for heterogeneous media, we derive an analytical forward and adjoint operator pair. The forward operator is used to determine a residual detection error on the surface based upon an initial source distribution by comparing a simulated measurement with the actual measurement. The adjoint operator maps the residual error onto an adjustment of the source distribution. By employing pseudo spectral finite difference methods to implement the operator pair, we are able to consider heterogeneous media. Based on this algorithm, we can perform a one-step reconstruction that can be improved by applying the algorithm iteratively.

**Results/Discussion**

The image quality improves with an increasing number of iterations for both simulated and experimental data. Reconstruction artifacts are greatly reduced. In a point source simulation, the mean squared error (mse) after one iteration is at 0.59, which resembles the mse using a conventional k-space method (0.60). In the progress of iterations, the value can be decreased to 0.18 within 10 iterations and to 0.003 within 500 iterations. In a simulation with acoustical heterogeneities, the image converges to the actual distribution, while the k-space reconstruction results in a distorted image. Currently, the computationally intensive calculation limits the applicability of the algorithm. This might be overcome soon by the usage of parallel processing.



3A-5

**11:30 am Improved contrast in laser-diode-based photoacoustic images with short-lag spatial coherence beamforming**Muyinatu Lediju Bell<sup>1</sup>, Xiaoyu Guo<sup>1</sup>, Hyun-Jae Kang<sup>1</sup>, Alexis Cheng<sup>1</sup>, Behnoosh Tavakoli<sup>1</sup>, Emad Boctor<sup>1</sup>; <sup>1</sup>Johns Hopkins University, USA**Background, Motivation and Objective**

Pulsed laser diodes enable photoacoustic imaging with lower cost, increased portability, and higher frame rates compared to conventional Q-switched Nd:YAG lasers. However, the main disadvantage of the laser diode is its low peak power, which necessitates averaging thousands of photoacoustic signals to achieve signal-to-noise ratios that are comparable to those produced by an Nd:YAG laser. This averaging process degrades temporal resolution with minimal changes to image contrast. This work is the first to investigate the use of a pulsed laser diode and a short-lag spatial coherence (SLSC) beamformer to display high-contrast photoacoustic images with no signal averaging required.

**Statement of Contribution/Methods**

A phantom containing a 2 mm layer of black-dyed plastisol and a 5 mm layer of bovine liver was attached to the face of an Ultrasonix L14-5W/60 linear array transducer. A diode laser (Model 905D3S3J09, Laser Components, Hudson, NH, USA) was driven with a 100 ns, 7  $\mu$ J, 75 V pulse by a custom-built circuit. The resulting 905 nm wavelength laser beam was air-coupled to an aspherical lens pair, directed in line with the transducer, and focused on the black layer of the phantom. An Ultrasonix data acquisition unit (SonixDAQ, BC, Canada) was utilized to acquire the raw pre-beamformed channel data needed to form 24 single photoacoustic frames.

**Results/Discussion**

The mean contrast in single photoacoustic images (i.e. one frame) was 7 dB with conventional delay-and-sum (DAS) beamforming, compared to 33 dB with SLSC beamforming of the same data. Improvements were achieved because the SLSC beamformer is more sensitive to differences in the spatial coherence of the signal, rather than differences in signal amplitude as in DAS beamforming. The maximum contrast of the DAS image did not increase beyond 7 dB when up to 24 signals were averaged prior to DAS beamforming. In comparison, contrast increased to a maximum of 41 dB when SLSC beamforming was applied to the same averaged signals, yet the appearance of acoustic clutter also increased. If averaging is preferred, the clutter can be reduced by averaging SLSC images rather than RF data. These promising results indicate that coherence-based beamforming of a single frame of photoacoustic data can be used to expand the current limits of image contrast and temporal resolution for real-time clinical applications of photoacoustic imaging with pulsed-laser diodes.

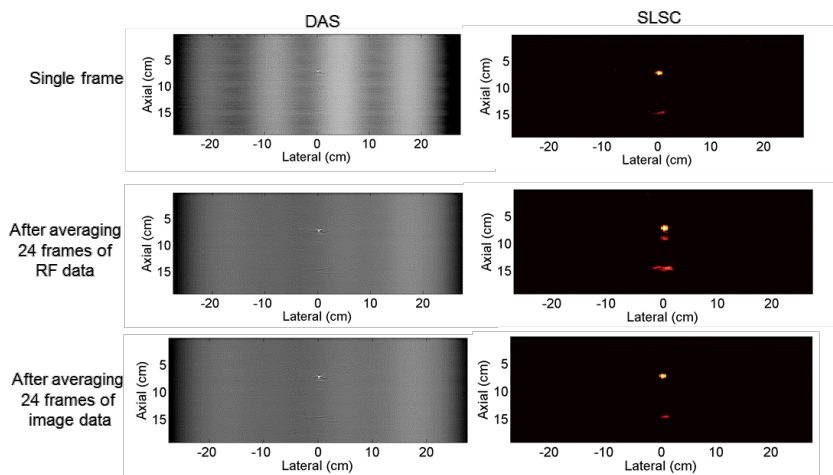


Figure 1: DAS (left) and SLSC (right) images created with a single frame of data (top), after averaging 24 frames of RF data (middle), and after averaging 24 frames of image data (bottom). All images are displayed with 15 dB dynamic range.

### 3A-6

#### 11:45 am Photoacoustic Clutter Reduction Using Short-Lag Spatial Coherence Weighted Imaging

Erwin Alles<sup>1</sup>, Michael Jaeger<sup>2</sup>, Jeffrey C Bamber<sup>1</sup>; <sup>1</sup>The Joint Department of Physics and CRUK Cancer Imaging Centre, The Institute of Cancer Research and the Royal Marsden NHS Foundation Trust, London, United Kingdom, <sup>2</sup>Institute of Applied Physics, University of Bern, Bern, Switzerland

##### Background, Motivation and Objective

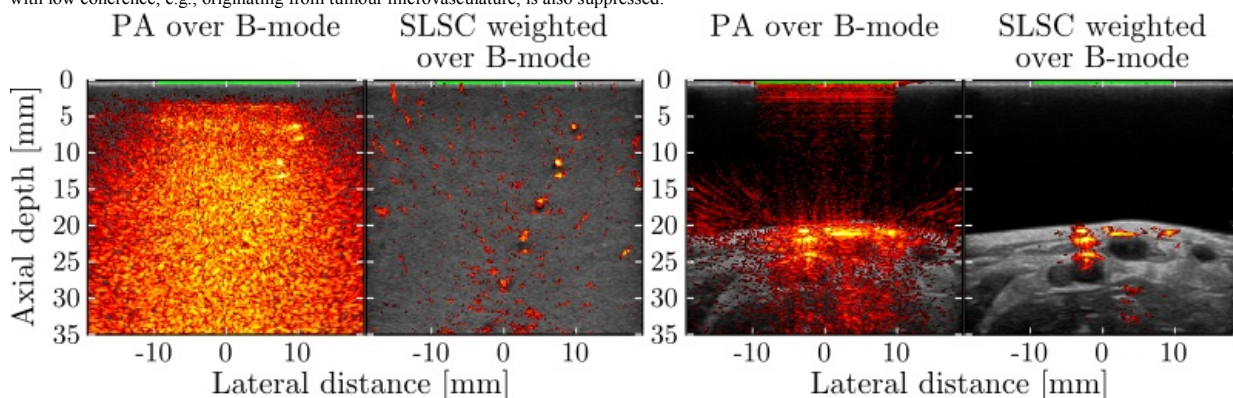
Acoustic emission from optical absorption in locations away from the imaged region may give rise to clutter in photoacoustic (PA) images, either directly or via acoustic scattering. This clutter lowers the contrast by generating additional structure in PA images, which obscures the true signal and limits the image depth. Current clutter reduction methods either treat the clutter as noise, and are therefore ineffective in suppressing clutter that contains structure generated by coherent interference, or require deformation resulting in extended data acquisition and processing times.

##### Statement of Contribution/Methods

Clutter sources will typically be distributed over a larger range of elevational and lateral distances than true sources. Consequently, the coherence between clutter signals recorded by individual transducer elements is potentially lower than that of true signal. Hence, in this work the short-lag spatial coherence (SLSC) metric (Dahl et al, Ultrason Imag 2011) is used as a weighting on PA images in an attempt to suppress clutter.

##### Results/Discussion

Using a system based on a clinical ultrasound scanner (Zonare ultra) and a tuneable pulsed laser, 2D PA images were obtained. On the left of the figure below, images of a phantom (which optically mimicked breast tissue and contained cylindrical absorbing inclusions at depths of 7, 12, 17, 23, 28 and 33 mm) show that without SLSC weighting, only two inclusions are visible through the clutter, whereas SLSC weighting reveals at least four of the inclusions and doubles the image depth. On the right in vivo images of the first author's arm are shown, where the B-mode images show large blood vessels about 5 mm below the skin. Without SLSC weighting, strong artefacts are present above the skin, and unambiguous signal is only observed with confidence between 20 and 26 mm depth. With SLSC weighting, these artefacts are removed and signal (unconfirmed) appears to be revealed at depths up to 35 mm. All PA images are shown on the same logarithmic scale with the same threshold and 40 dB dynamic range. Thus, SLSC weighting can effectively suppress clutter in PA images, without increasing the acquisition time. Further investigation is required to determine how much residual clutter remains and whether real signal with low coherence, e.g., originating from tumour microvasculature, is also suppressed.



## 4A - Arrays

Marquette

Thursday, September 4, 2014, 10:30 am - 12:00 pm

Chair: **David Greve**  
Carnegie Mellon University

4A-1

### 10:30 am Determining Array Element Pitch for NDE Applications

Paul Wilcox<sup>1</sup>; <sup>1</sup>Mechanical Engineering, University of Bristol, Bristol, United Kingdom

#### Background, Motivation and Objective

Despite the widespread use of ultrasonic arrays in NDE applications, there is a lack of quantitative understanding about the effect of inter-element pitch. The number of elements in an array is usually limited by the available channels of the array controller device and/or connectivity, thus the pitch is important because it determines the maximum spatial aperture for an array with limited elements. The “half-wavelength” pitch requirement on spatial-sampling guarantees no grating lobe artefacts; this is often quoted but rarely adhered to. Despite this, NDE practitioners still routinely use spatially under-sampled arrays and obtain perfectly acceptable images. This paper explains why this is, how knowledge of the imaging requirements may be used to obtain the optimum element pitch and how signal-processing may be used to suppress imaging artefacts due to spatial under-sampling.

#### Statement of Contribution/Methods

First, an analytical model of monochromatic, far-field array behavior is developed to qualitatively illustrate the relationship between element pitch and maximum steering angle. This model enables prediction of peak grating lobe amplitude in an image, and the relationship between image structural noise (due to material microstructure) and element pitch. The shortcoming of this model is that it is overly conservative as a quantitative tool for determining array inter-element pitch. This is due to the assumption of monochromatic, far-field operation, whereas virtually all NDE applications use pulse excitation and many also use focusing, the latter implying near-field operation. Both of these effects lead to a smearing out of grating lobe artefacts. To obtain a useful quantitative tool for array design a more complete numerical model is then developed. This model is validated against experimental results, where the effect of element pitch variation is synthesized by digital band-pass filtering of experimental data.

#### Results/Discussion

The basic reasons why spatially under-sampled arrays can be used successfully are because (i) the steering angle of 90° that leads to the half-wavelength criterion is not used in practice and (ii) in general the element width is almost equal to the pitch, so with a larger pitch elements are more directional and provide a natural angular filter on grating lobes. These are both effects that are well-known and predicted qualitatively by the simple analytical model. This paper adds quantitative understanding of the actual element pitch requirements for realistic NDE inspection scenarios. The extension of these findings to both 2D arrays and immersion inspections is discussed.

4A-2

### 10:45 am A Rapid Approach to Speckle Noise Reduction in Ultrasonic Non-Destructive Evaluation Using Matched Filters

Minghui Li<sup>1</sup>, Gordon Hayward<sup>2</sup>; <sup>1</sup>School of Engineering, University of Glasgow, Glasgow, United Kingdom, <sup>2</sup>Alba Ultrasound Ltd, Glasgow, United Kingdom

#### Background, Motivation and Objective

Ultrasound inspection and imaging has received considerable attention from the non-destructive evaluation (NDE) and biomedicine communities in recent years. Due to the intrinsic characteristics, ultrasound images are prone to speckle noise, which is time invariant and coherent to the echo signals from defects in NDE or tissues in medicine. A wide variety of techniques for speckle noise reduction in ultrasound imaging have been investigated and developed, which generally explores either the spatial diversity due to the distribution of transducer elements over an array aperture or the frequency spectrum characteristics of the broadband ultrasonic signals. Those methods are able to reduce the speckle noise and somewhat improve the image contrast; however, one of the major criticisms to these methods is the significant extra computational cost which makes most of them only applicable to offline post processing.

#### Statement of Contribution/Methods

In this paper, we present a rapid technique to reduce the speckle noise in ultrasonic NDE and enhance the image quality using matched filters. It is well known in the literature that the interaction between ultrasonic beams and the insonified medium is a highly nonlinear process, which potentially exhibits distinctive frequency-dependent properties for defects and random reflectors with a degree of randomness. This method implicitly explores the difference between the echoes from legitimate defects and echoes from random reflectors, and uses this distinction in the time and frequency domains to design the template of a filter response, and then utilizes a Genetic Algorithm paradigm to optimize this template with an objective to maximize the signal-to-noise ratio (SNR) of the filter output. Finally, a matched filter using the template of a desired echo from legitimate defects as the response is applied to the received A-scan waveforms.

#### Results/Discussion

Experiments with a 128-element 5MHz transducer array on a mild steel sample are conducted, and the total focusing method (TFM) is used to generate the images. It has been demonstrated that the clutter noise is significantly reduced and the SNR of the image is improved by about 30dB when the optimized matched filter is applied to all of the A-scan waveforms prior to image formation. Due to the fact that the matched filter can be implemented in real-time, the significant performance advantages are obtained with extremely low extra computational cost. This novel method can be applied to ultrasonic array-based imaging systems as well as the conventional single element transducer based non-destructive testing systems.



4A-3

**11:00 am Air-based Synthetic Aperture Sonar Tomography using Compressive Sensing**

Josiah Jideani<sup>1</sup>, Andrew Wilkinson<sup>2</sup>; <sup>1</sup>Material Science and Manufacturing, Council for Scientific and Industrial Research (CSIR), Pretoria, Gauteng, South Africa, <sup>2</sup>Electrical Engineering, University of Cape Town, Cape Town, Western Cape, South Africa

**Background, Motivation and Objective**

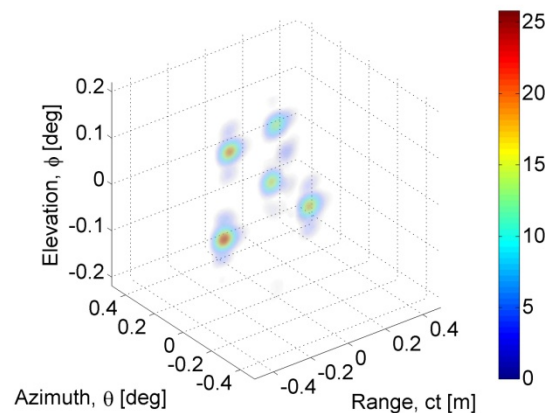
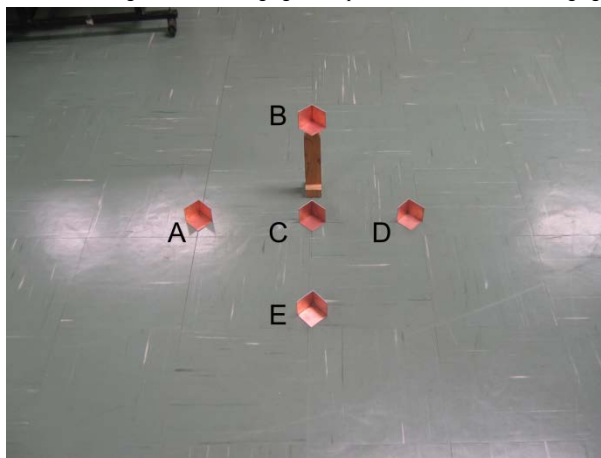
Compressive sensing (CS) also known as compressive sampling is a technique used to reconstruct or recover the full-length of a signal with only a few non-adaptive measurements. This technique has been applied to synthetic aperture radar (SAR) tomography to obtain super-resolution three-dimensional (3D) focusing of SAR data acquired over multiple baselines.

**Statement of Contribution/Methods**

The application of similar reconstruction techniques to the sonar field was the motivation of this work. This paper describes the design and implementation of synthetic aperture sonar (SAS) tomography in air using the compressive sampling technique to obtain 3D focusing of SAS data. In the work, SAS data is acquired over a total of 9 baselines using 9 uniformly spaced ultrasound receiving transducers and 1 ultrasound transmitting transducer that operate at 40kHz. Data acquired from each baseline was range-compressed with a deconvolution filter to compensate for linear system effects. Two-dimensional (2D) SAS image focusing was carried out using the accelerated chirp scaling algorithm. Compressive sampling was applied to the stack of focused 2D SAS images to reconstruct the reflectivity profile of the scene in the elevation direction.

**Results/Discussion**

3D scenes containing corner reflectors and other physical objects were successfully reconstructed using this technique with a super-resolution factor of 3 (Fig. 1). The results confirm that CS is effective in super-resolution tomographic reconstructions provided the baseline span is small compared to the range of imaging. This technique can be used as an alternative high-resolution imaging technique in medical ultrasound imaging, under-water sonar imaging and other various ultrasound imaging applications.



4A-4

**11:15 am Multi-layer Ultrasonic Imaging for Non-destructive Testing Applications**

Nasim Moallemi<sup>1</sup>, Shahram Shahbazpanahi<sup>1</sup>; <sup>1</sup>University of Ontario Institute of Technology, Canada

**Background, Motivation and Objective**

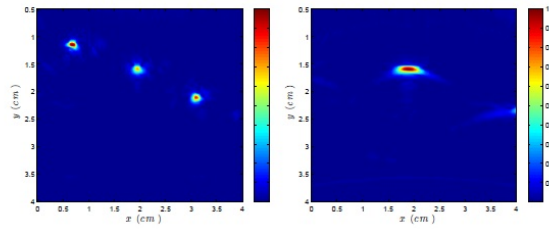
Ultrasonic imaging of a multi-layer medium is a common challenge in seismology, medical diagnoses, and non-destructive testing. One application of multi-layer imaging is ultrasonic immersion test where the material under test and ultrasonic transducers are immersed in water. The main imaging challenge in immersion test (or any multi-layer medium) is that the sound wave propagates with different velocities in different layers, thereby hindering the calculation of the sound travel time for the backscattered received signal. In this paper, we propose a new model for array spatial signature which can be used in any frequency-domain algorithm for imaging multi-layer materials.

**Statement of Contribution/Methods**

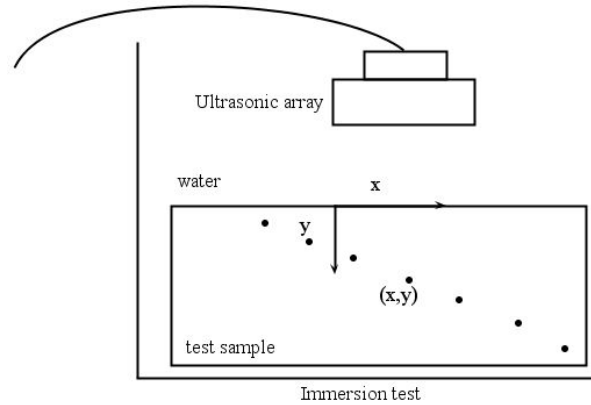
Interfaces between the layers in a multi-layer medium refract the sound wave into the lower layers, thereby playing the role of emitting sources for the lower layers. We model the interfaces between the layers of a multi-layer medium as spatially distributed sources consisting of infinite number of point sources. Then, we use this model to develop a new model for array spatial signature for any point inside a multi-layer medium. This new model can be used in any imaging technique, such as conventional beamforming method, to image a multi-layer medium. Indeed, the conventional beamforming method is used to image a homogeneous medium where the sound velocity is constant in the material under test.

**Results/Discussion**

To evaluate the accuracy of our data model in imaging the second layer of a two-layer medium, we conducted an immersion ultrasonic test (Fig 2.). Using our data model in conventional beamforming method, we obtain an image of the material under immersion test which outperforms the existing methods such as RMS velocity method (Fig 1.).



(a) Conventional beamforming based image using our proposed model for array spatial signature (b) Conventional beamforming based image using the RMS velocity method



4A-5

#### 11:30 am Simulation of Full-Angle Ultrasound Process Tomography with Two-Phase Media Using a Ray-Tracing Technique

Sascha Langener<sup>1</sup>, Thomas Musch<sup>1</sup>, Helmut Erment<sup>1</sup>, Michael Vogt<sup>1</sup>; <sup>1</sup>Dept. of Electrical Engineering and Information Technology, Ruhr-University Bochum, Germany

##### Background, Motivation and Objective

In the field of oil production, the measurement of the volume fractions of the different components of multiphase flows consisting of oil, water, and gas in pipelines is of great interest. Ultrasound tomography allows for a good differentiation of the gaseous phase from the liquid phases along the cross-section of the measurement pipe containing the flow. Echo and transmission measurements are performed using multiple ultrasound transducers, which are positioned along the circumference of the pipe. Depending on the composition of the multiphase flow, the energy and the time- and frequency-domain characteristics of the received signals obtained at the different transducers may strongly vary. Consequently, the proper design of the ultrasound tomography system with regard to the required dynamic range and a suitable signal processing and analysis strategy is challenging.

##### Statement of Contribution/Methods

In this paper, a tool for the simulation of received signals obtained from two-phase media consisting of gaseous inhomogeneities inside a liquid is presented, which has been implemented in order to obtain measurement data under known and well-defined conditions. The developed simulation methodology utilizes ray-tracing for the forward-problem of analytically describing the propagation and reflection of ultrasound waves. Received signals are efficiently calculated in the frequency-domain, and multiple reflections can be included into the simulation by consideration of multiple reflected rays. The proposed technique has been used to analyze various concepts for the extraction of parameters (time of flight, frequency-dependent signal amplitude) and for the reconstruction of images (speed of sound, attenuation, backscattering) containing spatially resolved information about the composition of the two-phase flow. In the framework of solving the inverse problem, the latter is used for volume fractions determination.

##### Results/Discussion

Simulations have been performed with the goal to analyze a process tomography system, which is aimed at measurements using 32 fan-shaped beam transducers (500 kHz center frequency, 88% relative bandwidth, 65° beam angle) in a measurement pipe (53 mm inner diameter) containing oil (1460 m/s speed of sound). In the ray-tracing approach, an angular step width of 0.3° has been used for the emission of waves (2.92 mm wavelength in oil at the center frequency) to guarantee that the spread of the diverging beams along the diameter of the pipe (about 18 wavelengths) is sufficiently small against the wavelength. Configurations with varying number of gaseous inhomogeneities of different shape (point-like, circular, elliptical) and size have been simulated, and the corresponding received signals have been analyzed. For the simulation of a fictitious ideal scenario, only single scattering was considered for simulation, and the actually given conditions have been simulated by including multiple scattering.

4A-6

#### 11:45 am A framework for the optimisation of ultrasonic phased array inspections using statistical forward modelling

Yousif Humeida<sup>1</sup>, Paul D. Wilcox<sup>1</sup>, Michael D. Todd<sup>2</sup>, Bruce W. Drinkwater<sup>1</sup>; <sup>1</sup>University of Bristol, United Kingdom, <sup>2</sup>the University of California, San Diego, USA

##### Background, Motivation and Objective

The use of ultrasonic phased arrays for the non-destructive testing (NDT) of engineering structures has increased rapidly in recent years. NDT inspections are usually designed empirically. This is laborious, time-consuming, and may not result in an optimum approach. Therefore, forward models are usually used to inform and improve the design of inspections. The aim of the current work is to present a framework for the optimisation of ultrasonic array inspection techniques in NDT. The framework utilises both deterministic and statistical forward modelling to simulate the optimisation problem and incorporate inspection uncertainty.

##### Statement of Contribution/Methods

Here we investigate defect detection as our main objective and present a framework to optimise this parameter. As a demonstration, the framework has been used to optimise the detection of planar flaws (i.e. cracks) in aluminium plates using phased arrays contact measurements. Uncertainty in the crack orientation angle was represented using probability distribution functions (PDF). Two imaging algorithms have been considered: plane B-scans and the total focusing method (TFM). The aim was to optimise the design of several parameters (e.g. operating frequency, array size, and element size) by maximising various objective functions. Two objective functions were explored: signal amplitude and signal to noise ratio. In each case, ensembles of 50 cracks with different orientation angles that represent their PDFs were simulated using a deterministic forward model and a Monte Carlo based optimisation approach implemented using a genetic algorithm (GA).

##### Results/Discussion

The optimisation framework has been successfully used to obtain design parameters for the considered inspection problems. Furthermore, a binary hypothesis test was adopted and receiver operating characteristic (ROC) curves were used to compare the performance of the different imaging methods. The figure shows ROC curves for the detection of cracks with normally distributed orientation angles. ROC curves for Plane B-scans and TFM images were calculated for orientation angles with 0° mean and 0, 2, 4, 6, 8, 10, and 15° standard deviation. From the figure, it can be concluded that the TFM provides higher defect detectability than plane B-scan in uncertain inspection environments.

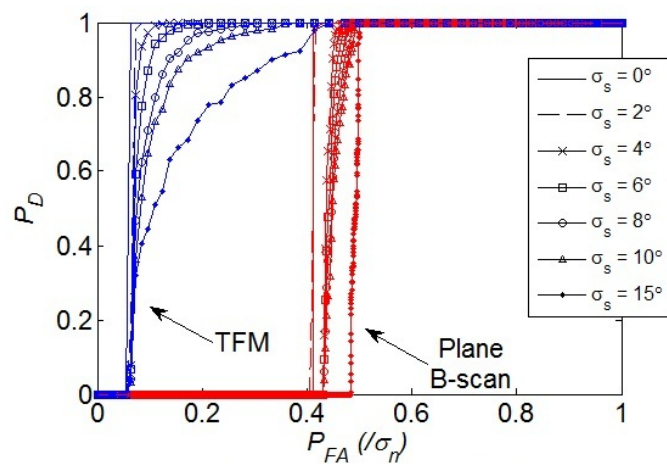


Fig. 1. ROC curves for the optimum design to detect cracks with 0, 2, 4, 6, 8, 10, and 15° standard deviation using plane B-scan and TFM.

## 5A - General Physical Acoustics 1

Williford A

Thursday, September 4, 2014, 10:30 am - 12:00 pm

Chair: **Koen Van Dongen**  
Delft University of Technology

5A-1

### 10:30 am Simple Acoustic Microfluidics Devices using Lamb Waves with Planar Al Electrodes

Amgad Rezk<sup>1</sup>, Leslie Yeo<sup>2</sup>, James Friend<sup>1</sup>; <sup>1</sup>MicroNano Research Facility, RMIT University, Melbourne, Victoria, Australia, <sup>2</sup>School of Environmental and Civil Engineering, RMIT University, Melbourne, Victoria, Australia

#### Background, Motivation and Objective

The fabrication of practical acoustic microfluidics devices suitable for medical diagnostics is predicated upon the availability of inexpensive, easily integrated piezoelectric ultrasonic structures to drive fluid flow, particle manipulation, nebulisation, and all the other functions typical in diagnostics. Much has been made recently of surface acoustic wave (SAW) devices and the potential it presents in overcoming the many problems remaining in microfluidics. Unfortunately, the formation of interdigital electrodes and the lack of control available in manipulating the SAW beyond simple definition of its aperture is not possible. Likewise, simple PZT thickness-mode devices offer insufficient power and excessive heating at frequencies sufficient for microfluidics.

#### Statement of Contribution/Methods

We describe an entirely different approach, using Lamb waves driven by monolithic Al electrodes (Fig 1(a)). We look past the typical electrodes using standard deposition techniques with interdigital structure of a complexity similar to electrodes required for SAW, instead using electrodes formed by loosely attaching Al foil to the bottom surface of a 500- $\mu\text{m}$ , 127.86° Y-rotated, X-propagating cut of lithium niobate (LN). Remarkably, no one has examined the possibility of using bulk Lamb waves to drive microfluidics phenomena. We consider the many acoustic microfluidics phenomena enabled via traditional techniques, from droplet transport to paper diagnostic microfluidics and nebulization.

#### Results/Discussion

Incredibly, loosely attached, monolithic Al foil electrodes are found to provide acoustic energy transmission for microfluidics operation two orders of magnitude more efficient than with Rayleigh wave SAW. The Lamb wave is present at 3.5 MHz as defined by the wafer thickness and is only weakly dependent upon the electrode configuration, even appearing when operating the device with a single coronal pin electrode and floating ground. Higher order Lamb wave modes, to over 160 MHz, exist and are useful in acoustic microfluidics operations. Droplet and particle manipulation, sessile drop microcentrifugation (Fig 1(b,c)), nebulization (Fig 1(d,e)), and paper microfluidics (Fig 1(f,g)) have all been found to be possible at substantially lower powers and with remarkable simplicity facilitated by simply using a bit of Al foil and a piece of LN.

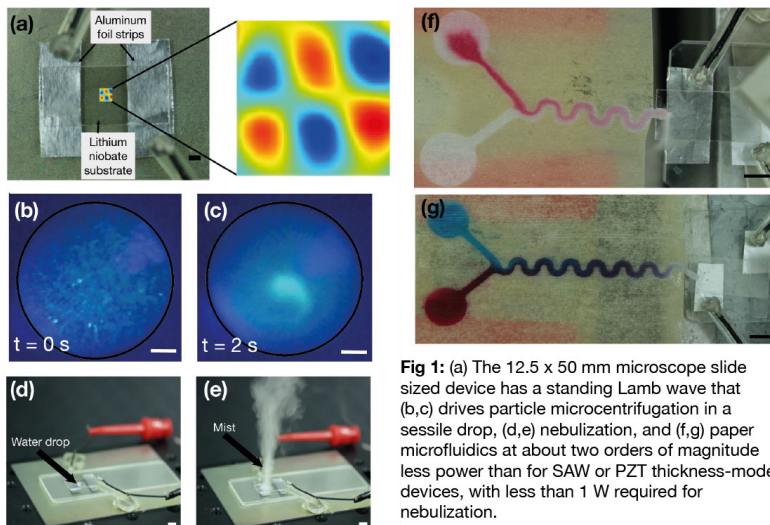


**Fig 1:** (a) The 12.5 x 50 mm microscope slide sized device has a standing Lamb wave that (b,c) drives particle microcentrifugation in a sessile drop, (d,e) nebulization, and (f,g) paper microfluidics at about two orders of magnitude less power than for SAW or PZT thickness-mode devices, with less than 1 W required for nebulization.

5A-2

### 10:45 am Ultrasonically induced dynamics of fluid interfaces in gravity and microgravity environments

Andrei BRYSEV<sup>1</sup>, Pavel SHIRKOVSKIY<sup>2</sup>, Farzam ZOUESHTIAGH<sup>2</sup>, Vladimir PREOBRAZHENSKY<sup>2,3</sup>, Philippe PERNOD<sup>2</sup>; <sup>1</sup>International Laboratory LEMAC/LICS - Wave Research Center, Prokhorov General Physics Institute (RAS), Moscow, Russian Federation, <sup>2</sup>International Laboratory LEMAC/LICS - Institute of Electronics, Microelectronics and Nanotechnology, Villeneuve d'Ascq Cédex, France, <sup>3</sup>Wave Research Center, Prokhorov General Physics Institute (RAS), Russian Federation

#### Background, Motivation and Objective

Hydrodynamic instabilities at fluid interfaces are of special interest for various applications in gravity and microgravity environments. They can be used as alternative techniques for mixing miscible liquids[1]. Here, we experimentally investigate the possibilities of excitation of fluid interfaces by sequential ultrasonic pulses both in the presence and in the absence of gravity.

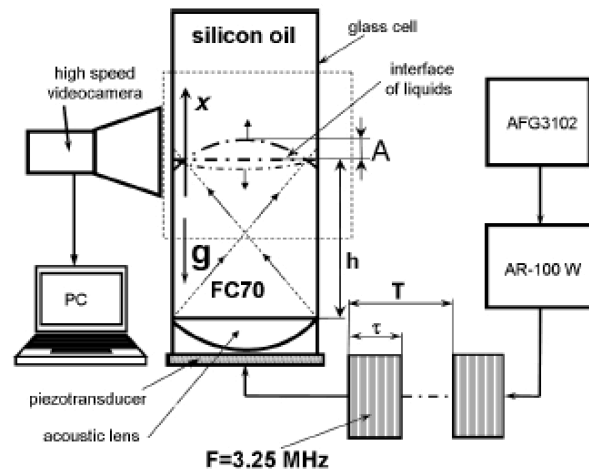
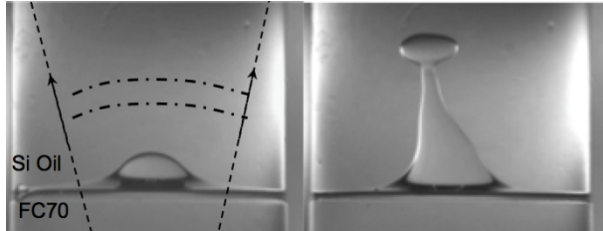
**Statement of Contribution/Methods**

Experiments were carried out on a sealed cylindrical glass cell containing fluorinert FC70 and 1.5cP silicon oil. The excitation of the interface between the two liquids was made by sequences of focused and plane ultrasonic pulses propagating transversely to the interface. The interface dynamics was investigated by means of a high speed video camera and image analysis. Zero-gravity condition was obtained in parabolic flights campagne n°107 of French Space Agency CNES.

**Results/Discussion**

In gravity conditions an effective excitation of gravity-capillary waves due to action of sequences of ultrasonic pulses was achieved for both focused and plane beams. The measured dependencies of the amplitude of interface oscillations on the intensity and energy of the ultrasound pulses indicate the existence of a threshold associated to the boundary conditions of the fluids with the sidewalls. For large ultrasonic intensities, droplets detachment of almost uniform size from the interface was observed. In zero gravity conditions, the absence of stabilizing role of gravity leads to interface destabilization and droplets creation for significantly lower ultrasonic intensities. For both environments creation of monodisperse droplets of one liquid into the other was demonstrated.

[1] S.Amiroudine, F.Zoueshtiagh, R.Narayanan, Phys. Rev. E, Vol. 85, 2012 p. 016326



5A-3

**11:00 am Radiation force-induced cavitation cloud migration in high intensity focused ultrasound**

Bjoern Gerold<sup>1</sup>, Keith Johnston<sup>1</sup>, Paul Prentice<sup>1</sup>; <sup>1</sup>Institute for Medical Science and Technology, University of Dundee, Dundee, United Kingdom

**Background, Motivation and Objective**

Cavitation in focused ultrasound surgery (FUS) is receiving renewed attention as a potential mechanism for targeted drug delivery. Little is known, however, of how cavitation develops during the early stages of a high-intensity focused ultrasound (HIFU) insonation, including the interaction with the field itself. Here, we describe research investigating primary radiation force-induced cloud migration (in degassed water).

**Statement of Contribution/Methods**

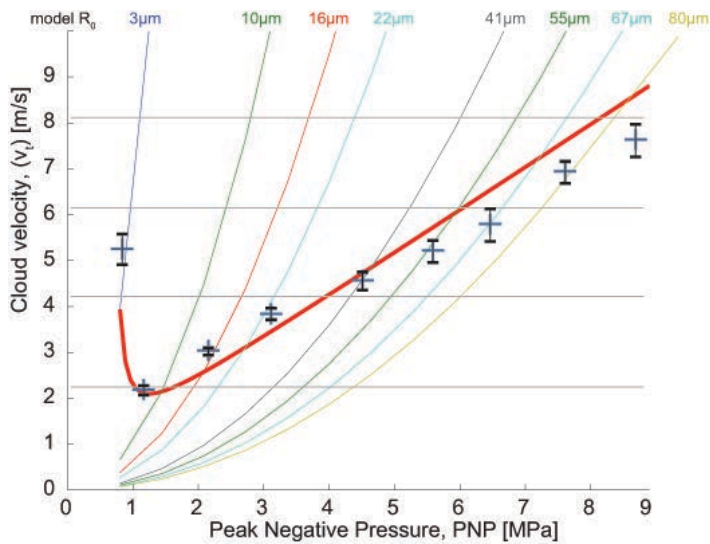
Single cavitation clouds are reproducibly introduced to the focus of a propagating 1.47 MHz HIFU field, via the laser-nucleation technique [1], at peak-negative pressure (PNP) amplitudes from 0.6 – 8.9 MPa. The kinematic response of the clouds over the ensuing 60  $\mu$ s (~ 90 cycles) is observed via high-speed microphotography, at  $500 \times 10^3$  frames per second. A model of radiation-force induced cloud migration is developed, based on a single bubble of equivalent radius approximation ( $R_0$ ).

**Results/Discussion**

Cavitation clouds rapidly develop from nucleation, at a rate and morphology dependent on HIFU intensity. Migration away from the HIFU source at velocities ( $v_t$ ) between 1-10  $\text{ms}^{-1}$ , also dependent on the intensity, is attributable to the primary radiation force of the insonation. Larger clouds at higher intensities migrate more rapidly, although increased drag has a notable retarding effect. Interestingly, the smallest clouds investigated, at PNP = 0.6 MPa, have a much higher translational velocity than anticipated, due to resonant coupling with the primary field. The model demonstrates good agreement with all aspects of the experimental observations. We anticipate these results will have significance for FUS-drug delivery applications, whereby cavitation activity in blood vessels (from microbubbles injected intravascularly, for example), is known to mediate extravasation [2].

1. Gerold et al (2011) Rev. of Sci. Inst. 82(4) 044902.
2. Hernot et al (2008) Adv. Drug Delivery. Rev. 56(9) 1153.

Figure: PNP vs. translation velocity,  $v_t$  (model – red line)  $v_t$  with increasing PNP for single bubbles of  $R_0$  (model - coloured lines) and  $v_t^*$  (experimental - blue crosses).



5A-4

#### 11:15 am Fabrication of an optical lens array using ultraviolet light and ultrasound vibration

Satoki Taniguchi<sup>1,2</sup>, Daisuke Koyama<sup>2,3</sup>, Kentaro Nakamura<sup>4</sup>, Mami Matsukawa<sup>2,3</sup>, <sup>1</sup>Faculty of Life and Medical Sciences, Doshisha University, Kyotanabe, Japan, <sup>2</sup>Wave Electronics Research Center, Doshisha University, Japan, <sup>3</sup>Faculty of Science and Engineering, Doshisha University, Kyotanabe, Japan, <sup>4</sup>Precision and Intelligence Laboratory, Tokyo Institute of Technology, Yokohama, Japan

##### Background, Motivation and Objective

Most of optical microlens arrays are fabricated through etching process and molding system. We proposed the lens array forming technique of ultraviolet curable resin using ultrasound. In our previous report, variable-focus optical lens arrays using acoustic radiation force were investigated [1]. In this report, the fabrication method of optical lens array using ultraviolet light and ultrasound vibration was investigated.

##### Statement of Contribution/Methods

An ultraviolet curable resin film with the thickness of 300  $\mu\text{m}$  was formed on a glass plate ( $50 \times 50 \times 1 \text{ mm}^3$ ). Four PZT transducers ( $10 \times 10 \times 1 \text{ mm}^3$ ) were bonded at the four corners of the glass plate. By exciting the transducers with the amplitude of 12.5 V at the glass plate and four transducers resonance frequency of 92 kHz, the lattice flexural vibration mode can be generated on the glass plate, and the acoustic radiation force acts on the surface of the resin film. The surface profile of the resin film is deformed by the acoustic radiation force and corresponds to the flexural vibration mode; the lens array can be fabricated on the resin film. The lens array was exposed to ultraviolet light with the center wavelength of 365 nm and 0.08 mW/cm<sup>2</sup> under ultrasound irradiation so that the ultraviolet curable film was cured perfectly. The surface profile of the lens array was observed with a confocal laser microscope.

##### Results/Discussion

The change in the frequency characteristics of the admittance and quality factor of the glass plate with respect to time were measured around the resonance frequency of 92 kHz (Figs. 1 (a) and (b)). The quality factor reduced exponentially under ultraviolet light exposure, and the terminal value of the quality factor was 142 and the time constant of resin curing was 9 minutes. These results indicate that the quality factor reduced with the curing of resin film since the cured resin acts as a damper for the vibration of the plate. In the surface profile of the optical lens array exposed to the ultraviolet light for 6 hours (Fig. 1 (c)), the lens pitch was approximately 6.8 mm which corresponded with the half wavelength of the flexural vibration of the plate.

[1]D. Koyama, et al., *Opt. Lett.*, **37**, 5256 (2012).

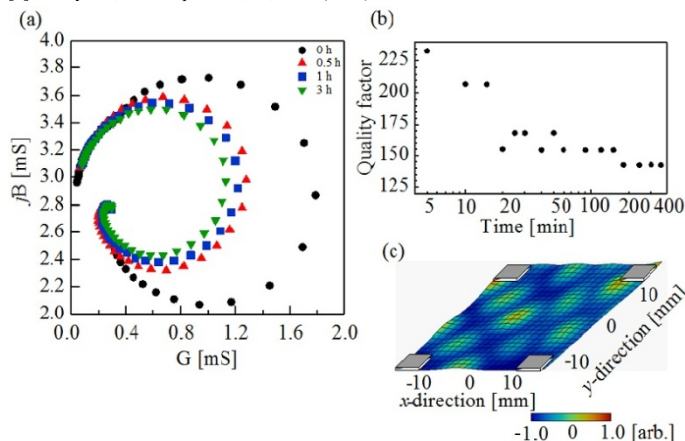


Figure 1 (a) Admittance loops of the lens array at 92 kHz, (b) the change in the quality factor with respect to time, and (c) the surface profile of the lens array exposed to ultraviolet light for 6 hours.



5A-5

**11:30 am Attenuation of ultrasound in heterogeneous media by relaxation processes**Allan Pierce<sup>1</sup>; <sup>1</sup>Retired, East Sandwich, Massachusetts, USA**Background, Motivation and Objective**

While there is extensive data on the attenuation of ultrasound in various types of media, much of it remains to be adequately explained on the basis of fundamental physical principles. The (excess) attenuation of sound in air and in sea water was explained many years ago on the basis of a finite number (two in both cases) of relaxation processes. This attenuation is in addition to the more classical processes of fluid friction and thermal conduction. The present author and colleagues have in recent years been concerned with the propagation of sound in marine sediments, and most recently, in sediments that are composed of mud. In the process of determining the physical causes of the attenuation, their attention was drawn (or redrawn) to the propagation of ultrasound in polycrystalline solid and mammalian tissues. What has emerged is the general idea that one should not think in terms of a finite number of relaxation processes but rather in terms of a continuous distribution of relaxation processes.

**Statement of Contribution/Methods**

The general approach is to formulate a theory of localized molecular (or nanoscale) vibrations that is consistent with the known (possibly only known in a statistical sense) properties of a heterogeneous material. For large molecules, such as protein, these vibrations may be associated with the normal modes of the molecule, considered as a distributed structure. For polycrystalline substances, these vibrations may be the localized vibrations of the separate crystals within grains when there is a change in the external stress field. For mud the localized vibrations occur when adjacent platelets (touching edge to face) are suddenly pulled slightly apart. In each case, quantum mechanical considerations should be taken into account, and the vibrational energy levels are caused to undergo a quantum jump under the influence of the ultrasonic wave. The energy drops down to the original state eventually and there is a relaxation time for this happening.

**Results/Discussion**

This is an ambitious long-term project, and results are still being worked out, and it is hoped that substantial significant results will have been obtained by the time of the presentation in September.

A statistical mechanical theory has been developed with the chief ingredients being joint probability functions for quantum energy gaps and relation times: number within a given relaxational frequency interval and within a given energy level per unit macroscopic volume. The attenuation for any given frequency involves integrals, the integrands of which involve these probability distribution functions. Quantitative estimates based on available data are given for these distribution functions. It is shown, for example, that the often-reported experimental result that attenuation varies linearly with frequency over a broad frequency regime can be explained with a suitable choice for these probability distribution functions.

5A-6

**11:45 am Stress and Temperature Compensated Orientations for Thickness-Shear Languisite Resonators for High Temperature High Pressure Environment**Mihir Patel<sup>1</sup>, Bikash Sinha<sup>1</sup>; <sup>1</sup>Mathematics and Modeling Department, Schlumberger-Doll Research, Cambridge, MA, USA**Background, Motivation and Objective**

Quartz sensors have been widely used in the oil-field services for the past four decades. Recent applications of dual-mode quartz pressure sensors have been possible due to the discovery of stress and temperature compensated crystalline orientations of quartz. Lately, there has been an increasing demand for high precision sensors operating at temperatures as high as 300 degC for geothermal exploration. However, the low transition temperature of quartz limits its application up to about 250 degC. This has led to a growing interest in Languisite (LGS) and its isomorphs. High Q combined with high phase transition temperature makes LGS an excellent candidate for geothermal applications when the operating temperature is greater than 300 degC. However as of now there has been no conclusive study identifying the presence of both stress and temperature compensated crystalline orientation for LGS. The objective of this study is to identify the stress and temperature compensated crystalline orientations for both the fast and slow thickness-shear modes. In addition, we calculate the effects of isotropic stresses in the resonator plane on the Q-factor at 25 and 300 degC for this crystalline orientation.

**Statement of Contribution/Methods**

In this paper we report on an exhaustive study of the variation of the mean force sensitivity and the temperature coefficients in the entire region of the crystalline LGS. A theoretical study was conducted for a 0.5 mm thick circular resonator to calculate the force-frequency and temperature effect on the slow (C-) and the fast (B-) thickness-shear mode using the Sinha-Tiersten perturbation method, and the 3-D Lagrangian finite-element model (FEM). The Q-factor calculation as a function of force and temperature is based on the intrinsic viscosity of LGS.

**Results/Discussion**

We report calculated force-frequency coefficients  $K_f$  ( $\times 10^{-15}$  m.s/N) as a function of the azimuthal angle, which is the angle between the crystalline x-axis of a resonator plate, and the direction of in-plane forces applied to the periphery of the resonator. The C-mode for YX-LGS exhibits mean  $K_f$  value of 0.71 and 1.4, respectively, at 25 and 300 degC. Interestingly, the YX-LGS has a  $Q \times \text{Freq} = 4.48 \times 10^{13}$ , at 25 degC, which is about 2.7 times larger than that of the quartz. Frequency shifts resulting from temperature for YX-LGS is -32 ppm/degC.

Computational results obtained from aforementioned models show an excellent agreement with the available measured data, and have been used to investigate the force- and temperature frequency effect on rotated LGS cuts. The loci of orientations with zero stress and temperature co-efficients of frequency for both the fast and slow thickness-shear mode of vibration for LGS have been identified. We further discuss the design considerations for the development of a high precision pressure sensor based on this orientation for high temperature high pressure applications.

## 6A - RF Frontend Devices and Oszillators

Williford B

Thursday, September 4, 2014, 10:30 am - 12:00 pm

Chair: **Clemens Ruppel**  
TDK Corporation

6A-1

### 10:30 am Co-design of SAW duplexer and LNA in RF transceiver IC for reducing total noise figure in RF front-end of cellular systems

Masafumi Iwaki<sup>1</sup>, Jun Tsutsumi<sup>1</sup>, Masanori Ueda<sup>1</sup>, Yoshio Satoh<sup>1</sup>; <sup>1</sup>MICRODEVICE R&D Dept., TAIYO YUDEN CO.,LTD., Japan

#### Background, Motivation and Objective

There exist increasing demands for reducing a noise figure (NF) in the receiver (Rx) chain of cellular handsets to support the operation of advanced wireless systems such as the carrier aggregation of 4G system. In the circumstances, many efforts have been done to reduce the insertion loss of acoustic duplexers. In some cases, BAW duplexers are used at the sacrifice of production cost.

In this paper, we present a method, which is the co-design of a SAW duplexer and an LNA, as an alternative solution to reduce the total NF in the Rx chain.

#### Statement of Contribution/Methods

In general, an acoustic duplexers and an LNA have been designed to optimize the performances individually. In the circumstances, matching circuits are necessary to match impedance of duplexers and an LNA. However, it is not taking loss of matching circuits into account.

In the proposed method, a SAW duplexer and an LNA are designed on arbitrary impedance to minimize the total NF taking loss of matching circuits into account.

The total NF of the Rx chain is expressed by sum of SAW duplexer loss, matching circuit loss and NF of LNA.

For calculating and minimizing the total NF, we use following procedure.

- (1) First, we decide temporary output impedance of a SAW duplexer.
- (2) Next, we calculate NF of LNA and loss of matching circuits on possible input impedance of LNA.  
(For example, these NF and loss are derived from calculation of equivalent circuits with noise source similar to CMOS noise model conveniently.)
- (3) Then, we calculate sum of SAW duplexer loss and derived NF/loss by step (2), and so, we got total NF of Rx chain on assumed impedance by step (1).
- (4) Finally, we repeat step (1) to (3) changing output impedance of a SAW duplexer, so that we can minimize total loss (NF) of the Rx chain.

In addition, double mode SAW (DMS) has a function of impedance transformation, therefore, we can cover wide range of impedance in step (4) using a SAW duplexer.

#### Results/Discussion

We applied above method to the UMTS Band II SAW Duplexer ( output impedance  $Z : 34 -j 47 \Omega$  ), Common-Source CMOS LNA ( transconductance  $g_m : 80 \text{ mS}$  ) and matching circuits, which include two finite  $Q$  ( 46 ) inductors ( shunt and series inductor ).

As a result, optimized total NF was calculated as 3 dB (SAW duplexer loss is assumed as 2.5 dB).

This NF is approximately 0.3 dB lower than NF, which is calculated on impedance of LNA optimized independently.

In general, the margin of NF in the receiver chain is set at most 3 dB [1]. Therefore, this reduction of total NF have a sufficient impact as to the RF front-end for cellular systems.

[1] H. Holma and A. Toskala, "WCDMA FOR UMTS", New York : J.Wiley & Sons, 2010.

6A-2

### 10:45 am A Fully Matched Quadplexer Based on BAW-SAW Technology for the LTE-A Carrier Aggregation Application

Mingdong LI<sup>1</sup>, Andreas Link<sup>1</sup>, Mohamed El-Hakiki<sup>1</sup>, Tae-young Kim<sup>1</sup>, Danish Kalim<sup>1</sup>, Bert Schumann<sup>2</sup>, Robert Aigner<sup>2</sup>; <sup>1</sup>TruQuint Semiconductor, Munich, Germany, <sup>2</sup>TruQuint Semiconductor, Apopka, USA

#### Background, Motivation and Objective

Over the last years the global mobile data traffic has been increasing dramatically. Carrier Aggregation is one key-enabler of LTE-advanced to meet current and future peak data rates. Therefore, multiplexers having more than two filters are playing more and more an important role in front-end modules for next generation mobile phones. While BAW and SAW technologies allow the necessary high performance acoustic filters for such multiplexers, we need to develop new topology concepts to fulfil the new carrier aggregation requirements. This makes CA multiplexers design more difficult.

The goal of this paper is to present the design and realization of a fully matched CA quadplexer showing a cross-isolation of -55 dB. We use high-Q BAW and SAW filters and discuss different approaches.

#### Statement of Contribution/Methods

In this paper a 3.6 x 2.0 mm<sup>2</sup> B25-B4 quadplexer with carrier aggregation will be presented. We use a hybrid filter technology: B4 is realized in Wafer-Level-Package (WLP) SAW, B25 is realized in WLP BAW. Both WLP processes are in-house technologies from Triquint Semiconductor. A detailed discussion about topology as well as design methods will be done and we will show, not only to get excellent in-band performance (B4 and B25), but also high cross-isolation.

#### Results/Discussion

We discuss several design approaches and show a simulation and measurement comparison. We will see that it is possible to get excellent in-band performance and high cross-isolation at the same time.



11:00 am **Quality Factor Enhancement in Lamb Wave Resonators Utilizing Butterfly-Shaped AlN Plates**Jie Zou<sup>1</sup>, Albert P. Pisano<sup>2</sup>; <sup>1</sup>Department of Mechanical Engineering, University of California, Berkeley, Berkeley, California, USA, <sup>2</sup>Department of Mechanical and Aerospace Engineering, Department of Electrical and Computer Engineering, University of California, San Diego, USA**Background, Motivation and Objective**

Aluminum nitride (AlN) Lamb wave resonators (LWRs) utilizing the lowest symmetric ( $S_0$ ) mode have attracted much interest recently since they have high frequency, low motional impedance, CMOS compatibility and capability of multi-frequency on a single chip. However, the AlN LWR usually shows a quality factor ( $Q$ ) below 2000 so an improvement in the  $Q$  of the AlN LWRs is highly desirable.

**Statement of Contribution/Methods**

There is growing evidence that a large portion of mechanical energy dissipation via the support tether of the LWR, and one effective way of reducing the anchor loss is to design the resonator geometry itself to concentrate the acoustic energy far from the supporting area. By changing the non-reflecting edges from parallel lines to inclined outgoing lines, the displacement field is pushed away from the center in the crosswise direction. To effectively reduce tether loss and without sacrificing the other performance, for the first time, a novel AlN Lamb wave resonator utilizing a butterfly-shaped thin plate is investigated to enhance the  $Q$  in this work.

**Results/Discussion**

Three different designs of AlN LWRs are compared in this work, including butterfly-shaped LWRs with the tether-to-plate angle  $\alpha = 60^\circ$  and  $\alpha = 45^\circ$  and conventional rectangular LWRs. The simulation results based on finite element analysis verify that the use of the butterfly-shaped plates, instead of the conventional rectangular plates, can bring evident reduction in tether vibration that is directly related to the energy dissipated through the supporting tethers, as shown in Figure 1. The measured frequency response for the butterfly-shaped resonator with  $\alpha = 60^\circ$  yields a  $Q$  of 2,433 which represents a  $2.24\times$  increase in  $Q$  over the conventional rectangular resonator, and butterfly-shaped resonator with  $\alpha = 45^\circ$  represents a  $Q$  of 1,779 which represents a  $1.64\times$  increase in  $Q$  (Figure 2). Moreover, the butterfly-shaped AlN plate does not introduce any other spurious mode within a 1.5 GHz frequency band and exhibits smaller motional impedance thanks to the high  $Q$ .

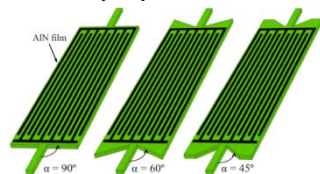


Figure 1(a). Illustration of the conventional rectangular Lamb wave resonator with tether-to-plate angle  $\alpha = 90^\circ$  and the butterfly-shaped resonators with  $\alpha = 60^\circ$  and  $\alpha = 45^\circ$ .

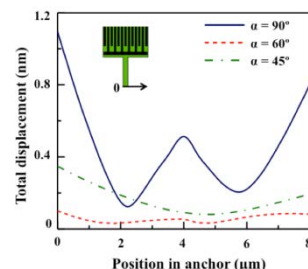


Figure 1(b). COMSOL simulated total displacement at the edges of anchors when the resonators are at resonance of  $S_0$  mode.

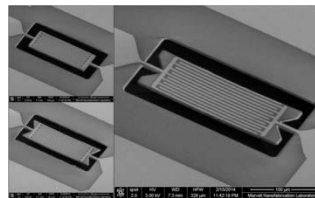


Figure 2(a). SEM images of the fabricated LWRs with  $\alpha = 90^\circ$ ,  $\alpha = 60^\circ$  and  $\alpha = 45^\circ$  with 13 IDT fingers on a 4.4- $\mu\text{m}$ -thick AlN plate.

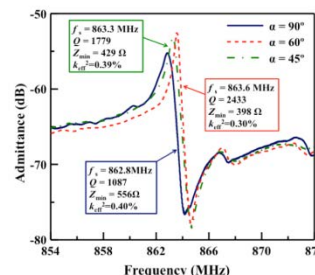


Figure 2(b). The measured frequency responses for the rectangular LWR and butterfly-shaped LWRs with  $\alpha = 60^\circ$  and  $\alpha = 45^\circ$ .

11:15 am **Low Jitter FBAR based chip scale precision oscillator**Suresh Sridaran<sup>1</sup>, Julie Fouquet<sup>1</sup>, Reed Parker<sup>1</sup>, Martha Small<sup>1</sup>, Steve Ortiz<sup>1</sup>, Frank Bi<sup>1</sup>, Stephen R. Gilbert<sup>1</sup>, Lori Callaghan<sup>1</sup>, Rich Ruby<sup>1</sup>; <sup>1</sup>Avago Technologies, USA**Background, Motivation and Objective**

FBAR based oscillators have been shown to offer very good phase noise and low jitter performance [1]. Recently we have integrated the feedback circuitry within the encapsulating lid of the FBAR resonators to allow for a very small package size as compared to state of the art quartz crystal oscillators[2]. The FBAR oscillators in this work operate at 628MHz and achieve low jitter <50fs and good frequency stability <100ppm all while fitting in a small package of 1.1 x 0.9 x 0.25 mm<sup>3</sup>. To achieve the frequency precision required for a reference oscillator, we demonstrate the ability to tune the oscillator over 600ppm to compensate for manufacturing tolerances. These oscillators are suitable for co-integration as reference clocks in high speed communication ICs where size and performance are paramount.

**Statement of Contribution/Methods**

The FBAR resonators employ oxide layer temperature compensation and a stress relieved structure[3] in order to attain frequency stability over temperature and packaging stress. The feedback circuitry in the lid makes use of a Colpitts oscillator design fabricated in 0.6um CMOS technology. The oscillator is designed to drive a balanced load of 100Ohms differentially with a single ended voltage swing of 600mV. To program the frequency of the XO, an eight bit word is input into shift registers which in turn determines the capacitors that are added into the Colpitts circuit to pull the frequency.

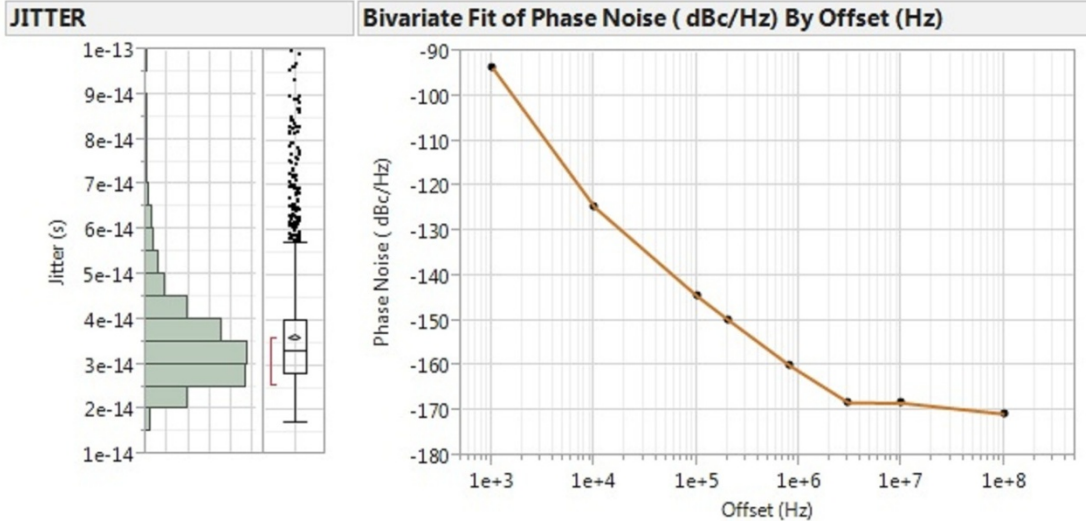
**Results/Discussion**

The measured median jitter (12kHz to 20MHz) for the oscillators with a supply voltage of 3.3V across a wafer is 33fs with a far from carrier phase noise of -168dBc/Hz (Figure). The median current draw from the supply is 16.5mA and the output power measured with a 50Ohm load using a balun is 0dBm. A tuning range of 600ppm is obtained for the 8 bit word which gives a frequency pulling resolution of 2.35ppm per bit.

**References:**

1. Hu, Julie, et al. "A 50ppm 600MHz frequency reference utilizing the series resonance of an FBAR." Radio Frequency Integrated Circuits Symposium (RFIC), 2010.
2. Small, Martha, et al. "Wafer-scale packaging for FBAR-based oscillators." Frequency Control and the European Frequency and Time Forum (FCS), 2011.

3. Ruby, R., et al. "A comparison of FBAR oscillators with standard resonators and stress relieved resonators." European Frequency and Time Forum & International Frequency Control Symposium (EFTF/IFC), 2013.



6A-5

#### 11:30 am Manufacturing and Reliability of Chip-Scale Packaged FBAR Oscillators

Stephen Gilbert<sup>1</sup>, Martha Small<sup>2</sup>, Reed Parker<sup>1</sup>, Lori Callaghan<sup>1</sup>, Steve Ortiz<sup>2</sup>, Frank Bi<sup>2</sup>, Lexie Kekoa<sup>1</sup>, Rich Ruby<sup>1</sup>, Jackie Tan<sup>3</sup>, Norashaz Bin Alias<sup>3</sup>, Gerald Ong<sup>3</sup>, Choon Chowe Chen<sup>3</sup>; <sup>1</sup>Avago Technologies, San Jose, CA, USA, <sup>2</sup>Avago Technologies, Fort Collins, CO, USA, <sup>3</sup>Avago Technologies, Penang, Malaysia

##### Background, Motivation and Objective

Today, millions of FBAR (Film Bulk Acoustic Wave Resonator) Filters and Duplexers are sold into cell phones every year. The filters are hermetically sealed within an all-silicon, chip-scale package which is formed using a wafer-scale bonding process. The base Si wafer contains the high-Q FBAR resonators fabricated using piezoelectric AlN thin films. For filter applications, the primary function of the lid wafer is to provide through-Si vias connecting the FBAR filter to the outside Cu pads. Recently, we have also integrated circuitry within the lid, enabling a host of new applications in markets not necessarily dominated by filtering. Our first targeted application is to integrate oscillator circuitry with a temperature-compensated FBAR resonator. The result is an extremely compact chip-scale oscillator (1mm x 1mm x 0.23mm) suitable for direct package-level integration with a companion ASIC. High native oscillator frequencies have been demonstrated between 500 MHz and 3.5 GHz. The oscillators also possess low random jitter and phase noise over a temperature range from -40 to 125°C. This combination of high native frequency, ultra-low jitter and compatibility with package-level integration can enable superior PLL performance in numerous applications ranging from high speed data links, A/D converters, and base station transceivers.

##### Statement of Contribution/Methods

The goal of the program is to manufacture in high volume a robust and repeatable chip-scale oscillator with superior performance. We present an oscillator design using bipolar circuitry in the lid to create Free Running Oscillators and Voltage Controlled Oscillators operating at native frequencies in excess of 1 GHz. By measuring oscillator output frequency, rather than resonator impedance, we are able to achieve frequency measurement accuracy and precision on the order of 0.2 ppb. This greatly exceeds FBAR capability, and when combined with the large number of oscillators per wafer (>11,000), enables extremely sensitive testing of oscillator performance and reliability over a wide range of conditions.

##### Results/Discussion

We have measured tens of thousands of oscillators at 2.6 GHz and observe mean jitter less than 10 fsec (12 kHz to 20 MHz offset) with many devices running at 8 fsec. The mean phase noise is -158 dBc/Hz at 800 kHz offset and -118 dBc/Hz at 10 kHz offset. The device draws 18 mA at 3.3V, and the phase noise at all frequency offsets remains within 1 dB over the temperature range from -40 to 125°C. Far from carrier noise is set by the power delivered to the resonator. Due to the ability of the resonator to remain linear at high power, far-from-carrier phase noise is as low as -174 dBc/Hz. Tests of chip-scale package hermeticity completed to date indicate that the oscillators behave with the same level of integrity as our standard FBAR filters. The sensitivity to acceleration of these oscillators is better than 0.1 ppB/g. Additional tests of reliability will also be presented.

6A-6

#### 11:45 am Effects of FBAR Resonator Dissipated Power on Discrete Oscillator Phase Noise

Reed Parker<sup>1</sup>, Lori Callaghan<sup>1</sup>, Frank Bi<sup>1</sup>, Steve Ortiz<sup>1</sup>, Frank Ha<sup>1</sup>, Nitesh Kumbhat<sup>1</sup>, Jeff LaTourrette<sup>1</sup>, Mark Unkrich<sup>1</sup>, Choon Chowe Chen<sup>1</sup>, Khang Hoe Gerald Ong<sup>1</sup>; <sup>1</sup>Avago Technologies, Inc., USA

##### Background, Motivation and Objective

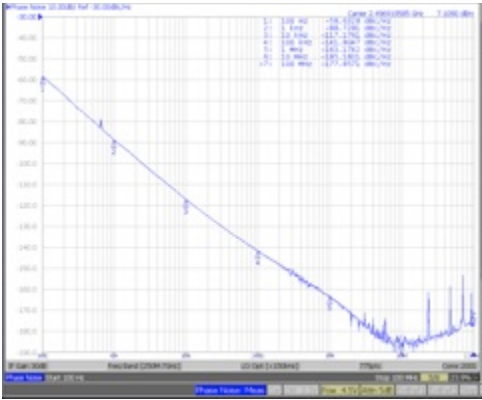
In many piezoelectric resonator based oscillators, the dissipated power in the resonator is limited to 10's of  $\mu$ W because of aging and resonator nonlinearities. One drawback of low power dissipation is far-from-carrier noise floor and jitter are compromised. Some applications, specifically next generation SerDes (Serial-DeSerial) and ADC applications, demand low jitter from the reference clock.

##### Statement of Contribution/Methods

We designed and built a variety of discrete FBAR (using zero drift resonators) based voltage controlled oscillators (VCO's) from 1 GHz to 2.5 GHz with the intent to optimize the jitter of these VCO's. We use discrete bipolar transistors in a Colpitts and Pierce configurations. The dissipated power in the resonators is on the order of 50 mW. Resonators are 2.5  $\mu$ m thick with an electrode area of 27  $\text{K}\mu\text{m}^2$ . These geometries and dissipated power lead to power densities on the order of 700 to 800 GWatts/ $\text{m}^3$ . We have measured several hundred parts based on different designs. Lessons from this effort led to development of an integrated FBAR VCO [see companion paper]. In the companion paper, we discuss performance and reliability data measured on thousands of units.

Results/Discussion

We achieved a noise floor < -180 dBc/hz and jitter as low as 5.5 fs (integrated over 12KHz -20MHz), with median jitter of 7 fs for 2.5 GHz VCOs. (see Fig 1). We hypothesize that the relatively few allowable modes in the acoustic device limit the degradation of the stored energy in the Gibbs free energy calculation. Specifically, the only non-thickness-extensional modes in the FBAR (the S0 and S1 even modes and the A0 and A1 flexure modes) are far from the zero k vector. Hence, the allowable states that encourage entropy are limited. Because of this ability to handle ultra high power densities, integrated FBAR oscillators set best in class jitter, which will have a large impact in high speed systems.



## 7A - High Frequency Transducers

Williford C

Thursday, September 4, 2014, 10:30 am - 12:00 pm

Chair: **Qifa Zhou**  
University of Southern California

7A-1

### 10:30 am Dual Element Needle Transducer for Intravascular Ultrasound Imaging

Sangpil Yoon<sup>1</sup>, Min Gon Kim<sup>1</sup>, Bong Jin Kang<sup>1</sup>, Changhan Yoon<sup>1</sup>, Nestor Cabrera-Munoz<sup>1</sup>, Jay Williams<sup>1</sup>, K. Kirk Shung<sup>1</sup>, Hyung Ham Kim<sup>1</sup>; <sup>1</sup>Biomedical Engineering, University of Southern California, Los Angeles, California, USA

#### Background, Motivation and Objective

We present the design of a dual element needle transducer for intravascular ultrasound imaging. The performance of the developed dual element needle transducer is also demonstrated using a gelatin phantom and *ex vivo* rabbit aorta. Rupture of plaques may cause heart attacks and strokes. The rupture is closely related to the changes of the intimal and medial thickness (IMT) of the arterial wall and the fibrous cap. Hence, the detection and measurement of IMT and the thin fibrous cap have a considerable impact in the early diagnosis of atherosclerosis and cardiovascular-related disease. A dual element needle transducer is able to provide both low and high frequency information such as IMT and thin fibrous cap thickness.

#### Statement of Contribution/Methods

A dual element needle transducer was developed as shown in figure 1(a). The needle diameter is 1.07 mm. The length of the needle transducer is approximately 50 mm. The high frequency element was fabricated with Lithium Niobate (LiNbO<sub>3</sub>) single crystal with a size of 600×600 μm<sup>2</sup>. The low frequency element was made with Lead Magnesium Niobate-Lead Titanate (PMN-PT) single crystal with a diameter of 700 μm. The two elements were focused at 2.5 mm. To test the center frequency and the bandwidth of each element, pulse-echo tests onto quartz were performed. Wire targets of 4 μm and 20 μm diameters were used to measure -6 dB axial and lateral resolutions of high and low frequency elements, respectively. We imaged a phantom, containing 10% gelatin and 0.1% 5 μm and 40 μm diameter silica particles by weight. Rabbit aorta, having an internal diameter of approximately 3 mm, was also imaged.

#### Results/Discussion

The center frequency and bandwidth of the high and low frequency elements were measured as 153 MHz and 53 MHz and 24% and 79%, respectively. Axial and lateral resolutions of the high frequency element were estimated as 18 μm and 30 μm near focus. The low frequency element has axial and lateral resolutions of 28 μm and 110 μm near focus. Images obtained by both elements were overlapped. Overlapped images of a gelatin phantom and rabbit aorta are shown in figures 1(b) and (c). The dual element transducer demonstrates capability to provide both high and low frequency information of the specimen under study.

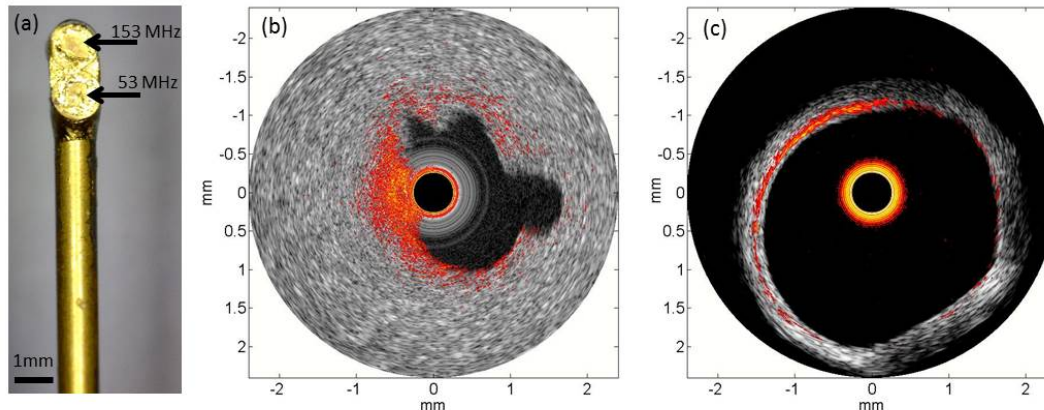


Fig. 1. (a) 153 MHz / 53 MHz dual element needle transducer and overlapped images of (b) gelatin with silica particle phantom and (c) rabbit aorta. In (b) and (c), red and gray parts represent images obtained by a 153 MHz and a 53 MHz elements, respectively.

7A-2

### 10:45 am Development of Focused IVUS Transducer Using PMN-0.33PT Single Crystal

Feifei GUO<sup>1,2</sup>, Cheng LIU<sup>1</sup>, Yaoheng YANG<sup>1</sup>, Yan CHEN<sup>3</sup>, Bin YANG<sup>2</sup>, Jiyan DAI<sup>3</sup>, Lei SUN<sup>1</sup>; <sup>1</sup>Interdisciplinary Division of Biomedical Engineering, Faculty of Engineering, The Hong Kong Polytechnic University, HONG KONG, China, People's Republic of, <sup>2</sup>Department of Physics, Condensed Matter Science and Technology Institute, Harbin Institute of Technology, Harbin, Heilongjiang, China, People's Republic of, <sup>3</sup>Department of Applied Physics, Faculty of Applied Science and Textiles, The Hong Kong Polytechnic University, HONG KONG, China, People's Republic of

#### Background, Motivation and Objective

Intravascular ultrasound (IVUS) is a widely used clinical imaging technique for atherosclerosis detection and diagnosis for its precise wall structure differentiation, lumen dimension evaluation, and composition differentiation. However, commonly used flat single-element IVUS transducer (20MHz-40MHz) cannot provide good lateral resolution (80 μm-300 μm) due to the lack of focusing ability. Until now, three approaches have been adopted in fabricating the focus transducers, such as adding an extra lens, hard pressing and mechanical dimpling techniques. The first two techniques are difficult to be applied to IVUS transducer mainly due to the small size. Mechanical dimpling technique is the approach by which the focusing of transducer is possible in minimal transducer. In this study, we demonstrated the fabrication of focused IVUS transducer using the Morphotropic

Phase Boundary component PMN-0.33PT single crystal by a mechanical dimpling technique. The performance of the focused transducer was demonstrated better than conventional flat transducer.

#### Statement of Contribution/Methods

The (001)-oriented PMN-0.33PT single crystal was used as the active material. The single crystal shows superior properties after poled. Then the single crystal was lapped to the desired thickness and polished on one surface. The Cr/Au electrodes with a thickness of 500 nm were sputtered onto the polished side of the single crystal. A conductive backing material, E-solder 3022, was cured over the polished side of the single crystal and lapped to 2.5 mm. As a focused transducer element, the opposite side of the PMN-PT single crystal was dimpled using a dimple grinder. The focal length was controlled by the radius of the grinding wheel. After that, the single crystal was diced to a proper dimension and housed using Epo-tek 301. An electrical connector was fixed to the conductive backing using a conductive epoxy. An electrode was sputtered across the concave surface and housing with side opening to form the ground plane connection. Acting as the matching and protective layer, Parylene C with a thickness of around 10  $\mu\text{m}$  was used to coat the aperture and the housing by a deposition system. The performance of the focused transducer was tested. Besides, another conventional flat transducer (40 MHz) was fabricated using the same material, backing and matching layers.

#### Results/Discussion

The 40 MHz PMN-PT high-frequency side-looking dimpling focused single-element IVUS transducer is smaller than 3 mm in outer diameter. The -6 dB bandwidth and the average insertion loss are 70% and -20 dB, respectively, which are superior to those of 40 MHz flat transducer (38% and -22 dB). The axial and lateral resolution of the focused transducer are also higher than those of flat transducer. The high-frequency side-looking dimpling focused single-element IVUS transducer gives more detailed microstructure information on vulnerable plaque compared to conventional flat transducer.

### 7A-3

#### 11:00 am Vacuum Deposition of Mass-Spring Matching Layers for High-Frequency Ultrasound Transducers

Jeremy Brown<sup>1</sup>, Srikanta Sharma<sup>2</sup>, Andre Bezanson<sup>1</sup>, Sandy Cochran<sup>2</sup>, Rob Adamson<sup>1</sup>; <sup>1</sup>Biomedical Engineering, Dalhousie University, Canada, <sup>2</sup>Dundee University, United Kingdom

#### Background, Motivation and Objective

We have developed a technique of applying multiple matching layers to high-frequency imaging transducers, by using carefully controlled vacuum deposition alone. This technique uses a thin mass-spring matching layer approach that was previously described in a low-frequency transducer design with epoxied layers [1]. This mass-spring approach is suitable for vacuum deposition in high frequency transducers over the conventional quarter wavelength resonant cavity approach, because thinner layers and more versatile material selection can be used, the difficulty in precisely lapping quarter wavelength matching layers is avoided, the layers are less attenuating, and the layers can be applied to a curved surface.

#### Statement of Contribution/Methods

Two different 3 mm diameter 45 MHz planar lithium niobate transducers and one 45 MHz PMN-32%PT phased array transducer were designed and fabricated using this matching layer approach with copper as the "mass" layer and parylene as the "spring" layer. The first lithium niobate transducer used a single mass-spring matching network and the second lithium niobate transducer used a single mass-spring network, to approximate the first layer in a dual quarter wavelength matching layer system in addition to a conventional quarter wavelength layer as the second matching layer. The PMN-32%PT phased array transducer used a similar matching layer network. These transducers were then compared with identical transducers with no matching layers and the performance improvement was quantified.

#### Results/Discussion

The bandwidth of the lithium niobate transducer with just a single mass-spring layer was measured to be 46 % and the insertion loss was measured to be -21.9 dB. The bandwidth and insertion loss of the lithium niobate transducer with the mass-spring network plus quarter wavelength matching was measured to be 59 % and -18.2 dB respectively. These values were compared to the unmatched transducer, which had a bandwidth and insertion loss of 25 % and -39.5 dB. The bandwidth and insertion loss of the phased array transducer with the mass-spring plus quarter wavelength matching layer combination was measured to be 60 % and 27 dB respectively and this compared to the measured unmatched phased array bandwidth and insertion loss of 28 % and -42 dB. All experimentally measured values were in excellent agreement with theoretical predictions using an in house developed KLM model.

[1] M. Toda, M. Thompson, "Novel Multi-Layer Polymer-Metal Structures for Use in Ultrasonic Transducer Impedance Matching and Backing Absorber Applications, IEEE Trans. on UFFC, Vol. 52, pp. 2818-2827, 2010

### 7A-4

#### 11:15 am Angled and Press-Focused 40 MHz PMN-PT Single Element Transducers for Intravascular Ultrasound Imaging

Hyung Ham Kim<sup>1</sup>, Sangpil Yoon<sup>1</sup>, Nestor Cabrera-Munoz<sup>1</sup>, Jay Williams<sup>1</sup>, Bong Jin Kang<sup>1</sup>, Changhan Yoon<sup>1</sup>, K. Kirk Shung<sup>1</sup>; <sup>1</sup>Department of Biomedical Engineering, University of Southern California, Los Angeles, California, USA

#### Background, Motivation and Objective

High frequency needle transducer with a small aperture size (< 1.0 mm x 1.0 mm) is needed for small vasculature images through an incision hole. The angle of the transducer element with respect to the lumen of vessel provides images of both front and side structures of the specimen. An angled transducer may be used as guidance as well as imaging tool of vessel lumen at the same time. To improve the lateral resolution of images, angled and press-focused transducers were designed and fabricated. In this study, we propose 40 MHz PMN-PT single element needle transducers with angled and press-focused aperture.

#### Statement of Contribution/Methods

We propose "Press & Dice" technique to develop a press-focused needle transducer. Because the element of an angled focused transducer was too small to press-focus, a bigger acoustic stack was made and then press-focused and diced to a desired acoustic stack size. The size of the developed acoustic stack was 0.6 mm x 0.85 mm and it had 45° incident angle with respect to the needle transducer center axis as shown in Figure 1(a). PMN-PT single crystal was chosen for piezoelectric material and double matching layers were used for acoustic matching. Pulse-echo tests were performed to estimate the center frequency and bandwidth of the focused and unfocused transducers. Axial and lateral resolutions of both transducers were measured using 20  $\mu\text{m}$  tungsten wire targets. Ex vivo rabbit aorta was imaged with angled/focused and angled/unfocused needle transducers to compare the performance of two transducers. Rabbit aorta, tied with wire to mimic the blockage of aorta, was also imaged with angled/focused transducer.

#### Results/Discussion

The center frequency and the bandwidth of angled/focused and angled/unfocused transducers were measured as 40 MHz with 52% bandwidth and 31 MHz with 91% bandwidth, respectively. The axial and lateral resolutions were estimated as 45  $\mu\text{m}$  and 200  $\mu\text{m}$  for angled/focused transducer and 26  $\mu\text{m}$  and 309  $\mu\text{m}$  for angled/ unfocused transducer. Rabbit aorta images obtained by angled/focused and angled/unfocused transducers are presented in Figures 1(b) and (c). Aorta sample with blockage and its image obtained by an



angled/focused transducer is also shown in Figures 1(d) and (e). An angled/focused needle transducer shows better lateral resolution than a flat one and may be used for intravascular catheters.

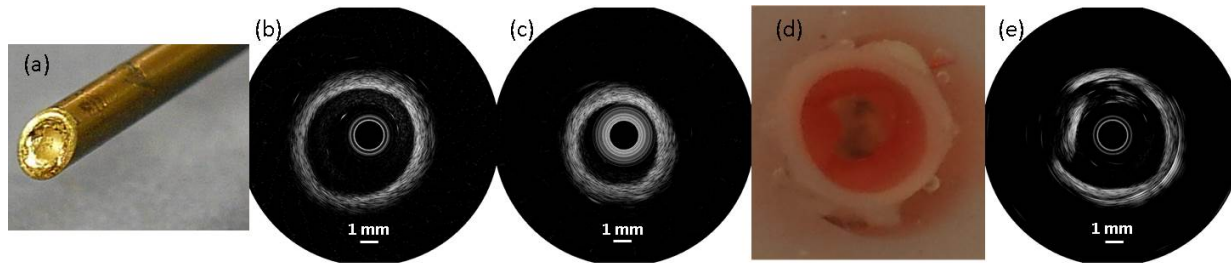


Fig. 1. (a) Angled/focused needle transducer with 40 MHz center frequency. Images of rabbit aorta obtained by using (b) angled/focused and (c) angled/unfocused transducers. Blocked rabbit aorta (d) sample and (e) image obtained with an angled/focused needle transducer.

7A-5

### 11:30 am The Evolution and Applications of High Frequency Ultrasound Transducers

Stuart Foster<sup>1</sup>; <sup>1</sup>Sunnybrook Health Sciences Centre and Dept of Medical Biophysics, University of Toronto, Toronto, Ontario, Canada

#### Background, Motivation and Objective

Transducer technologies sit at the heart of all acoustic visualization applications. Over the past decade, the maximum frequencies of array based devices have risen from about 15 MHz to over 50MHz. Similarly, in intravascular ultrasound imaging, frequencies have risen from 30 to as high as 60 MHz center frequencies. The push to higher frequencies is driven by the need for increased resolution in a diverse range of biological and medical applications. This talk will review the development of high frequency ultrasound transducers and provide context for the current and potential application of these devices.

#### Statement of Contribution/Methods

The evolution of materials, processing, and fabrication methods will be illustrated with concrete examples of array devices based on conventional dice and fill methods and, more recently, using laser micro machining approaches. The development of novel devices such as dual-frequency probes and multi modality transducers will be reviewed. Examples of the latter will include dual frequency devices for angiography and intravascular ultrasound, photoacoustic devices, and combined IVUS-OCT devices. In each of these, specialized configurations of acoustic sensors and optical devices are required to achieve exceptional imaging performance.

#### Results/Discussion

Applications of high frequency transducers are driven both by clinical needs in human applications and by the need for vastly improved in vivo imaging of biological systems used in discovery oriented biomedical research. Examples of applications of high frequency transducers will be drawn from the our activities in the areas of cancer and cardiovascular disease. Further discussion of the special issues related to detection of microbubble and nanoparticle contrast agents will also be included in the discussion.

## 1B - MCA: Molecular Imaging

Grand Ballroom

Thursday, September 4, 2014, 1:00 pm - 2:30 pm

Chair: **Flordeliza Villanueva**  
University of Pittsburgh

1B-1

### 1:00 pm **CD276 Expression in Human Breast Cancer Tissues and Early Detection Evaluation using Ultrasound Molecular Imaging in A Transgenic Mouse Model**

Sunitha Bachawal<sup>1</sup>, Kristin Jensen<sup>1</sup>, Amelie Lutz<sup>1</sup>, Ferdinand Knieling<sup>1</sup>, Katheryne Wilson<sup>1</sup>, Lu Tian<sup>1</sup>, Juergen Willmann<sup>1</sup>; <sup>1</sup>Stanford University, Stanford, CA, USA

#### Background, Motivation and Objective

An ideal molecular imaging target for early cancer detection is differentially expressed in cancer compared to benign pathologies. CD276 (B7-H3) is a member of the B7 molecules involved in T-cell activation; and has been shown to be differentially expressed in breast cancer. Molecularly-targeted contrast enhanced ultrasound (US) is an emerging imaging tool with great potential for improving the diagnostic accuracy of US for earlier cancer detection. For US molecular imaging using micron-sized microbubbles (MB) as contrast agents, imaging targets need to be expressed on the tumor vasculature due to the size of MB. This study evaluates the potential of US molecular imaging using CD276-targeted-MB (MB-CD276) for early breast cancer detection in transgenic mice.

#### Statement of Contribution/Methods

CD276 expression in human breast cancer (n=102, including luminal A, luminal B, Her2 and triple negative subtypes) and benign tissues (n=139, including hyperplasia, atypia, usual ductal hyperplasia, fibroadenoma, adenosis, radical scar etc.) was assessed using immunohistochemical staining. The progression of breast tissue from normal to invasive cancer was examined using US molecular imaging (Vevo2100, VisualSonics) with MB-CD276 (n=160) in a transgenic breast tumor model (FVB/N-Tg(MMTV-PyMT634Mul). Ex vivo CD276 expression was quantified using fluorescence staining.

#### Results/Discussion

CD276 expression was detected on both tumor epithelium and tumor associated vascular endothelium in human breast cancer samples. Expression in breast cancer was significantly higher ( $P < 0.001$ ) compared to normal and benign breast pathologies. There was a significant ( $P < 0.001$ ) increase in CD276-targeted US imaging signal when breast tissue progressed from normal ( $4.5 \pm 0.7$  a.u.) to breast cancer ( $51.9 \pm 5.3$  a.u.) in mice. At a sensitivity of 85%, CD276-targeted US imaging can differentiate benign (normal+hyperplasia) from malignant entities (DCIS+Invasive) with specificity of 93% (AUC of 90.9). Ex vivo expression of CD276 in mouse tissues highly correlated with imaging signal ( $R^2 = 0.76$ ,  $P < 0.001$ ). US imaging allowed the differentiation of benign from malignant diseases with high accuracies. US molecular imaging of tumor angiogenesis using tumor specific endothelial markers in breast cancer may help improve accuracy of US in breast cancer detection in future clinical trials.

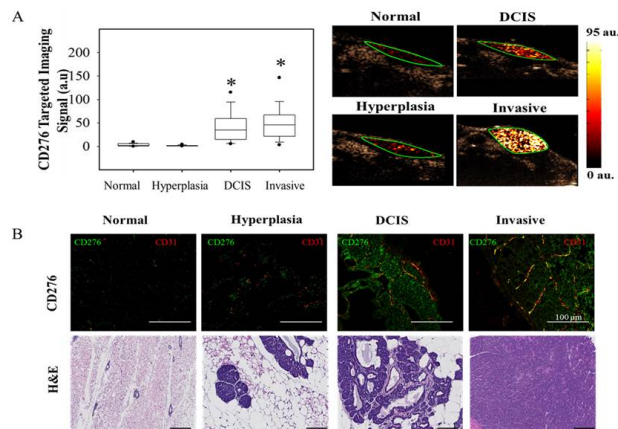


Figure 1: Ultrasound molecular imaging in transgenic mouse model of breast cancer. A) Quantification of the CD276-targeted ultrasound imaging signal and representative ultrasound molecular images obtained using MB<sub>CD276</sub> in corresponding histological subtypes in the transgenic mouse model of breast cancer. B) Representative micrographs of CD276 expression and H&E stains of the various subtypes in this mouse model

1B-2

### 1:15 pm **Feasibility and Reproducibility of Three-dimensional Ultrasound Molecular Imaging of Tumor Angiogenesis using a Clinical Matrix Array Ultrasound Transducer**

Huajun Wang<sup>1</sup>, Osamu Kaneko<sup>1</sup>, Vijay Shamdasan<sup>2</sup>, Lu Tian<sup>3</sup>, Dimitre Hristov<sup>4</sup>, Juergen Willmann<sup>1</sup>; <sup>1</sup>Department of Radiology, Molecular Imaging Program at Stanford, Stanford University, Stanford, USA, <sup>2</sup>Philips Healthcare, Bothell, USA, <sup>3</sup>Department of Health, Research & Policy, Stanford University, Stanford, USA, <sup>4</sup>Department of Radiation Oncology, Stanford University, Stanford, USA

#### Background, Motivation and Objective

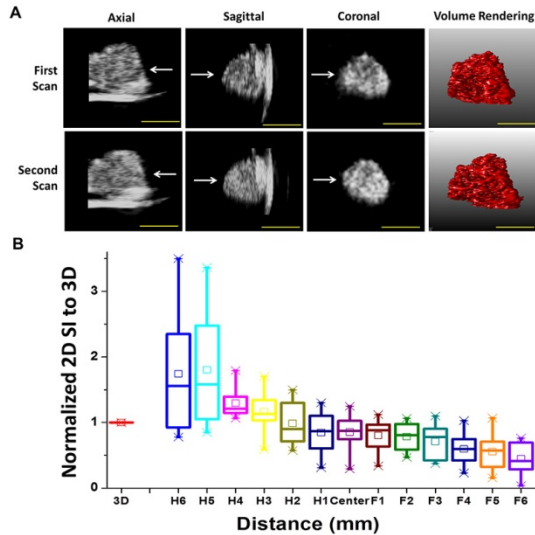
Ultrasound (US) molecular imaging (MI) is a promising technique for non-invasive assessment of various disease processes. However, it is currently limited to two-dimensional (2D) single plane imaging. The purpose of this study was to explore feasibility and reproducibility of three-dimensional (3D) USMI of tumor angiogenesis in mice using a clinical matrix array US transducer.

**Statement of Contribution/Methods**

Subcutaneous human colon cancers were induced in 28 mice. Mice were randomly assigned to 1) control group without any treatment (n=16); 2) an anti-angiogenesis treatment group (n=8; i.v. single dose of bevacizumab at 10mg/kg); and 3) a vehicle group (n=4; saline treatment only). Mice were scanned with a clinical US system and transducer (IU22, Philips; X6-1 transducer) following i.v. injection of a VEGFR2-targeted contrast microbubble (MB<sub>VEGFR2</sub>) or non-targeted control microbubbles (MB<sub>Control</sub>). Group1 mice were scanned twice to assess reproducibility of 3D USMI. Group 2 and 3 mice were scanned before and 24h after treatment. Imaging signal intensity (SI) from reconstructed multiple 1-mm 2D slices vs. 3D volumetric SI was compared. VEGFR2 expression was assessed by immunofluorescence (IF).

**Results/Discussion**

Repeated exams showed that 3D USMI was highly reproducible for both MB<sub>VEGFR2</sub> (ICC=0.92; 95% CI, 0.80-0.97) and MB<sub>Control</sub> (ICC =0.92; 95% CI, 0.78-0.97). SI with MB<sub>VEGFR2</sub> ( $1.2 \times 10^6 \pm 6.2 \times 10^5$ ) was significantly higher ( $P < 0.001$ ) compared to MB<sub>Control</sub> ( $2.1 \times 10^5 \pm 1.9 \times 10^5$ ) in mice of group 1. SI reconstructed from multiple 2D planes differed by 46.8% of their mean value (95% CI: 28-77%), suggesting that the consistency of SI based on different 2D planes is poor. In the treatment group, 3D SI significantly decreased by 66% compared to the non-treated group ( $P=0.01$ ) and correlated with VEGFR2 expression levels on IF. If only the central tumor plane was analyzed for treatment response in 2D, the change in SI was significantly different by average 33% ( $P=0.004$ ) compared to 3D USMI (Fig. 1). In conclusion, 3D USMI is technically feasible and reproducible and shows good correlation with ex vivo VEGFR2 expression. 3D imaging capabilities of US may further expand its future clinical role in molecular imaging of cancer.



1B-3

**1:30 pm Ultrasound Molecular Imaging using P- and E-selectin targeted microbubbles in a murine chronic inflammatory bowel disease model**

Steven Machtaler<sup>1</sup>, Ferdinand Knieling<sup>1</sup>, Thierry Bettinger<sup>2</sup>, Richard Luong<sup>3</sup>, Lu Tian<sup>3</sup>, Huajun Wang<sup>1</sup>, Sunitha Bachawal<sup>1</sup>, John Higgins<sup>3</sup>, Juergen Willmann<sup>1</sup>; <sup>1</sup>Radiology, Stanford University, Stanford, California, USA, <sup>2</sup>Bracco Imaging, Switzerland, <sup>3</sup>Stanford University, USA

**Background, Motivation and Objective**

Inflammatory bowel disease (IBD) is a complex group of chronic diseases (including Crohn's disease and ulcerative colitis) involving changes in mucosal immunity and gastrointestinal physiology that affects approximately 1.4 million people in the USA. As IBD progresses, patients undergo alternating periods of remission and exacerbation resulting in fibrosis, thickening of the colon wall, and inflammation. Ultrasound (US) molecular imaging utilizes micron-sized, gas-filled contrast agents (microbubbles; MBs) that are modified to bind to vascular markers that are up-regulated due to disease or active biological processes. Our goal was to utilize US molecular imaging with MBs targeted to the vascular inflammatory markers P- and E-selectin to quantitatively monitor IBD during periods of quiescence and exacerbation in a clinically relevant, murine model of chronic IBD.

**Statement of Contribution/Methods**

Chronic IBD was induced using three cycles of 4% dextran sodium sulfate in the drinking water of male FVB mice (n = 47, 6-8 weeks). Acute colitis in a subset of mice with chronic colitis (chronic flare, n = 18) was initiated through rectal administration of 1% 2,4,6-trinitrobenzenesulfonic acid. Mice at different stages of IBD were imaged using a small animal ultrasound system (Vevo2100; VisualSonics) following i.v. injection of  $5 \times 10^7$  MB targeted to P- and E-selectin (MB<sub>selectin</sub>) or control microbubbles (MB<sub>control</sub>). In vivo imaging results were correlated with ex vivo immunofluorescence and histology.

**Results/Discussion**

After first validating both chronic IBD and chronic flare phenotypes (Figure 1A), the US molecular imaging signal was obtained. Induction of a chronic flare resulted in an increase in the US molecular imaging signal from  $20.23 \pm 21.23$  arbitrary units (a.u.) at day 0 to  $305.59 \pm 293.75$  a.u. ( $P < 0.01$ ) at day1,  $177.3 \pm 192.3$  a. u. ( $P = 0.02$ ) at day 3, returning to levels similar to control at day 5 (Figure 1B and C). Control microbubbles showed no significant binding at all timepoints. Expression of P- and E- selectin was validated on the colon vasculature (Figure 1D). In conclusion, using a clinically translatable MB targeted to P- and E- selectin, we were able to detect acute inflammation on a chronic background in a clinically relevant murine model of IBD, suggesting that US molecular imaging could accurately describe the inflammatory status of IBD in patients.



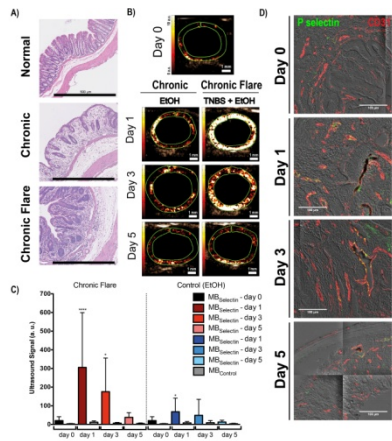


Figure 1: Example of US molecular imaging using MBoselectin in a murine model of chronic IBD. A) H&E staining of normal (left), DSS-induced chronic IBD (middle), and a chronic colon with TNBS-induced acute inflammation (chronic flare, right). B) Representative sonographs of the US molecular imaging signal obtained in chronic colitis after induction of a chronic flare using MBoselectin (right panels) or EIOH control (left panel). C) Quantification of US molecular imaging signal using MBoselectin and MBocontrol. D) Representative micrographs of P-selectin expression in the murine chronic IBD model after induction of a chronic flare (P-selectin = green, CD31 = red).

1B-4

1:45 pm Improved Ultrasound-Mediated Molecular Imaging of Previously Ischemic Mouse Myocardium Using Dual-Targeted Microbubbles and Constant Infusion

Dan Lin<sup>1</sup>, Yikui Tian<sup>1</sup>, Alexander Klibanov<sup>1</sup>, Brent French<sup>1</sup>, John Hossack<sup>1,2</sup>, <sup>1</sup>University of Virginia, USA

Background, Motivation and Objective

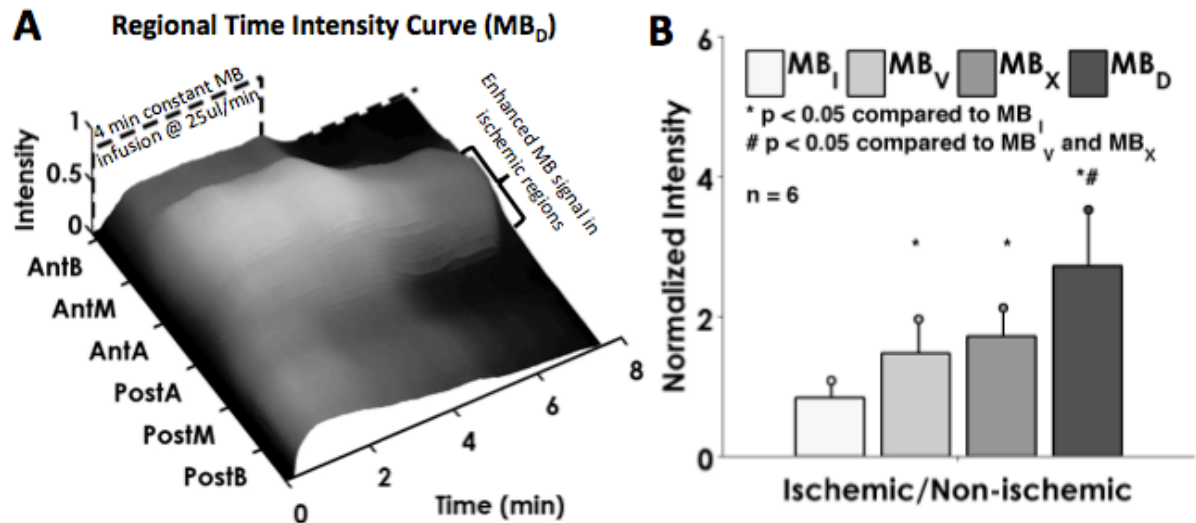
Misdiagnosis of acute coronary syndrome is common in patients with ambiguous symptoms. Molecular imaging using ultrasound microbubbles (MB) has provided the capability to identify previously-ischemic regions of myocardium by molecularly targeting cell adhesion molecules that are displayed on the activated endothelial surface after ischemia/reperfusion injury. Current methods for detection of targeted MB rely on initial bolus injection and waiting for unattached MB to clear out of the circulatory system while targeted MB remain attached in the regions of molecular target upregulation. However, in high blood flow environments, such as those found in the coronary arteries, high shear stress can cause detachment of MB from receptors on the endothelial wall. Furthermore, acoustic shadowing can occur due to MB saturation and regional signal bias using bolus injection. An improved method for targeted MB delivery by constant infusion is presented to remedy acoustic shadowing, and to allow better characterization of MB interaction with activated endothelium.

Statement of Contribution/Methods

Eight male C57BL/6 mice underwent 15-min LAD occlusion followed by 2-hour reperfusion. Immediately after reperfusion, mouse hearts were imaged with a Sequoia 15L8 transducer at 14 MHz. All mice received three of four MB preparations in random order: Sialyl Lewis X MB (MB<sub>X</sub>), anti-VCAM MB (MB<sub>V</sub>), Sialyl Lewis X + anti-VCAM MB (MB<sub>D</sub>), and isotype MB (MB<sub>I</sub>). MB concentrations were approximately 200\*10<sup>6</sup>/mL, and 100  $\mu$ L were infused at a constant rate of 25  $\mu$ L/min via a tail vein catheter. Mouse hearts were excised and stained with TTC/Phthalo blue dye to assess area at risk, and compared to regional time intensity curve (RTIC) retrieved from video data (Panel A).

Results/Discussion

Example RTIC for MB<sub>D</sub> shows enhanced MB signals during and after MB infusion around anterior apical region of the heart (Panel A). In Panel B, normalized intensities are significantly higher for MB<sub>D</sub>, MB<sub>X</sub>, and MB<sub>V</sub>, compared to MB<sub>I</sub> (p<0.05). Furthermore, normalized intensity for MB<sub>D</sub> is higher than both MB<sub>X</sub> and MB<sub>V</sub> (p<0.05). Receiver operating curve analysis using blue dye as the gold standard showed accurate detection of both ischemic and non-ischemic regions using MB<sub>D</sub> (AUC = 0.90), MB<sub>X</sub> (AUC = 0.89), and MB<sub>V</sub> (AUC = 0.97).



1B-5

---

**2:00 pm    Ultrasound for Molecular Imaging and Guided Drug Delivery**

Juergen Willmann<sup>1</sup>; <sup>1</sup>Stanford University, Stanford, CA, USA

**Background, Motivation and Objective**

Molecular imaging provides the ability to measure expression levels of molecules by quantifying imaging signals generated with the help of contrast agents accumulating at sites of molecular target expression. These contrast agents can be directed to bind various molecular targets in vivo, thereby quantifying disease processes at the molecular level. In recent years, the field of molecular imaging has been rapidly expanding to include multi-modality imaging strategies.

Ultrasound imaging is a widely available, inexpensive, and real-time imaging modality that does not expose patients to radiation. It is already the first-line imaging modality for assessment of many diseases in patients. By combining the advantages of ultrasound with the ability to image molecular signatures of diseases, molecular ultrasound has great potential as a highly sensitive and quantitative method that could be used for various clinical applications, including screening for early-stage diseases (such as cancer), further characterization of focal lesions and quantitative monitoring of disease processes at the molecular level. In addition, ultrasound-mediated drug delivery has drawn much research attention in the past few decades and extends the capabilities of ultrasound into the theranostic realms.

The objective of this presentation is to provide an overview on the principles of ultrasound molecular imaging and ultrasound-guided drug delivery strategies, and to highlight current translational efforts to move promising preclinical ultrasound molecular-imaging approaches into clinical applications in patients.

**Statement of Contribution/Methods**

Please note that this is an invited talk

**Results/Discussion**

Please note that this is an invited talk

## 2B - MEL: Cardiovascular Elasticity Imaging

Waldorf

Thursday, September 4, 2014, 1:00 pm - 2:30 pm

Chair: **Jan D'hooge**  
Catholic University of Leuven

2B-1

### 1:00 pm Full 3D ultrafast shear wave imaging

jean-luc gennisson<sup>1</sup>, jean provost<sup>1</sup>, clement papadacci<sup>1</sup>, thomas deffieux<sup>1</sup>, Juan-Esteban Arango Ossa<sup>1</sup>, marion imbault<sup>1</sup>, mathieu pernot<sup>1</sup>, mickael tanter<sup>1</sup>; <sup>1</sup>ESPCI ParisTech CNRS UMR7587 INSERM U979, Institut Langevin, PARIS, France

#### Background, Motivation and Objective

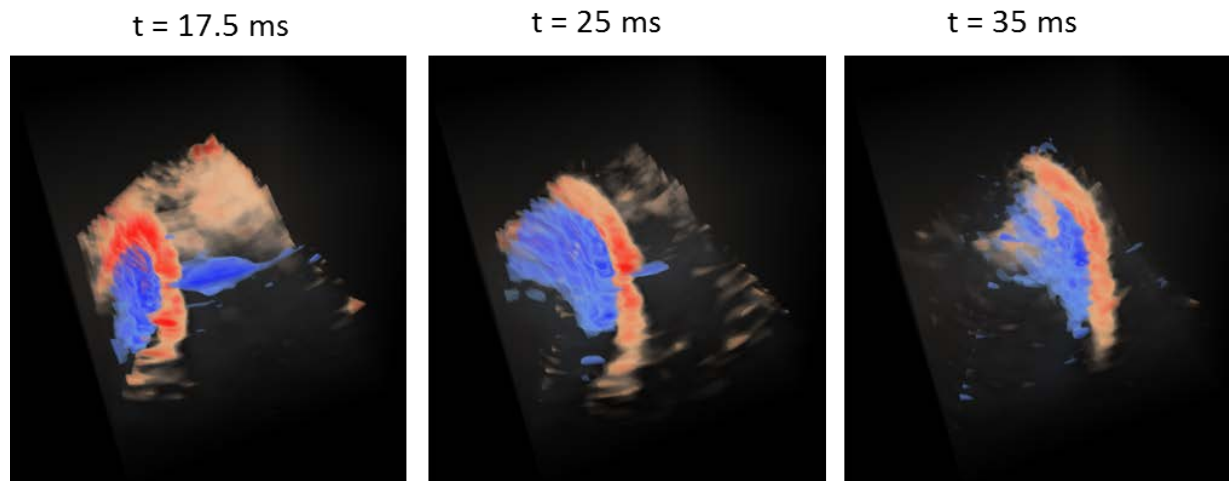
2D shear wave elasticity imaging has been developed within the last ten years and allows mechanical characterization of tissues in order to improve the diagnosis of several pathologies such as breast cancer or liver fibrosis. It is based on ultrafast imaging of shear waves with an ultrafast ultrasound scanner, typically limited to 128 channels and thus to 1D array. Using a full 3D ultrafast ultrasound scanner with a 2D array has many advantages: 3D elastic volume can be reconstructed in a single acquisition in order to limit motion artifacts or track fast changing elastic properties such as in the heart. It allows for better shear wave attenuation and dispersion measurement by either limiting or taking into account the full 3D shear wave diffraction in the volume.

#### Statement of Contribution/Methods

A customized, programmable, 1024-channel ultrasound system was designed to perform 3D ultrafast imaging (3000 volume/s) and shear wave tracking. A 32x32, 3 MHz matrix phased array (Vermon, France), was used to generate shear waves inside the medium using the acoustic radiation force. 3D coherent plane wave compounding was used to perform ultrafast acquisition of the shear wave propagation. Volumetric ultrafast acquisitions were then beamformed in 3D using a conventional sum and delay algorithm. 3D elastic volumes maps were reconstructed using the conventional time-of-flight algorithm based on local multiscale cross correlation of shear wave profiles in the three main directions with directional filters and compounding.

#### Results/Discussion

In figure results are presented at different time steps in an isotropic and homogeneous phantom. The shear wave speed was mapped in the imaging volume (40x40x40 cm<sup>3</sup>) and found to be around 0.8 m/s. Results show that 3D ultrafast shear wave imaging is possible using a single 2D matrix array. With 2D matrix array, 2D plane shear waves were generated using different focusing strategies, with different angles and compared to cylindrical shear waves. Diffraction biases could be estimated in order to retrieve 2D shear attenuation and dispersion measurements leading to a full 3D rheological characterization. Such new full 3D ultrafast ultrasound system has a great potential to help to better understand elastic wave physics and improve shear wave elastography medical device.



2B-2

### 1:15 pm In Vivo Transthoracic Measurement of End-diastolic Left Ventricular Stiffness with Ultrasound Shear Wave Elastography: A Pilot Study

Pengfei Song<sup>1</sup>, Matthew W. Urban<sup>1</sup>, Shigao Chen<sup>1</sup>, Armando Manduca<sup>1</sup>, Heng Zhao<sup>1</sup>, Ivan Z. Nenadic<sup>1</sup>, Sorin V. Pislaru<sup>2</sup>, Cristina Pislaru<sup>1</sup>, James F. Greenleaf<sup>1</sup>; <sup>1</sup>Physiology and Biomedical Engineering, Mayo Clinic College of Medicine, Rochester, Minnesota, USA, <sup>2</sup>Cardiovascular Diseases, Mayo Clinic College of Medicine, Rochester, Minnesota, USA

#### Background, Motivation and Objective

End-diastolic left ventricular (EDLV) stiffness is a strong biomarker of diastolic heart failure (DHF). Ultrasound shear wave elastography (SWE) can provide a quantitative and noninvasive measure of myocardial stiffness, which makes SWE a promising tool for clinical diagnosis of DHF. In practice, however, *in vivo* human heart study with SWE is very challenging due to the difficult imaging situation of the heart. Recently, we proposed a pulse-inversion harmonic imaging (PIHI) approach for shear wave (SW) detection and showed substantial improvement of SW signal quality from the heart. With the long term goal of diagnosing DHF with SWE, a pilot study was conducted in this paper to test the repeatability of measuring EDLV stiffness of healthy subjects with SWE.

**Statement of Contribution/Methods**

A scan sequence with B-mode imaging, interactive SWE and ECG-synchronization capability was developed on the V1 system (Verasonics Inc.) with a cardiac probe P4-2. Both the B-mode and SW detection used PIHI. A multi-zone SW detection method was developed to enhance harmonic excitation and improve SW signal quality. In end-diastole, a reference B-mode image is acquired (~96 ms), immediately followed by a push-detect SWE sequence (~20 ms). Figs. 1(a)-(d) show a typical SW propagation movie mapped on the B-mode image. SW speed (SWS) was estimated using a Radon transform method. Five healthy subjects were recruited and studied on 3 different days.

**Results/Discussion**

The LV posterior wall was imaged from the short-axis view. Multiple SWE trials were obtained for each subject to obtain averaged SWS values of the LV wall. The results are shown in Fig. 1(e). The overall SWS measurements for all subjects are in good agreement to literature values from animal studies. A one-way ANOVA test showed no statistical difference among the SWS across 3 days for Subjects 1 and 4. Student's *t*-tests showed no statistical difference of SWS between day 2 and 3 for Subjects 1 to 4. No SW could be detected from Subject 5 on day 1. The various SWS values for the same subject may be caused by myocardial anisotropy as the scan view and position was not rigorously controlled. The overall success rates of detecting SW for Subjects 1 to 5 are 94%, 83%, 96%, 98%, and 27%, respectively. These results indicate that SWE with PIHI detection is reliable in measuring EDLV stiffness and has great potentials in diagnosing DHF in future studies.

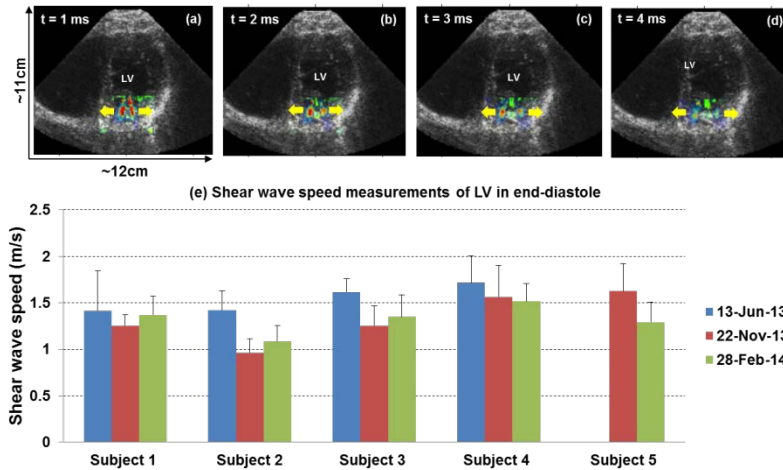


Fig. 1. (a) – (d): Snapshots of the shear wave propagation movie on the posterior LV wall at different time steps. The yellow arrows indicate the shear wave propagation direction. (e): SWS measurements of the LV wall in end-diastole of the five healthy subjects. The error bars represent the standard deviation of SWS measurements from the same day.

2B-3

**1:30 pm Ultrafast Harmonic Compounding for cardiac shear wave imaging**

Mafalda Correia<sup>1</sup>, Simon Chatelin<sup>1</sup>, Clément Papadacci<sup>1</sup>, Jean Provost<sup>1</sup>, Olivier Villemain<sup>1</sup>, Mickael Tanter<sup>1</sup>, Mathieu Pernot<sup>1</sup>; <sup>1</sup>Institut Langevin, ESPCI ParisTech, CNRS UMR 7587, INSERM U979, Université Paris 7, France

**Background, Motivation and Objective**

Shear Wave Imaging (SWI) is a non-invasive technique for myocardial stiffness quantitative mapping. Recently different techniques have been proposed to improve cardiac shear wave motion mapping. Pulse-Inversion Harmonic SWI [P. Song, et al., IEEE TMI, 2013] by limiting reverberation and clutter noise artifacts, at the cost of dividing by half the frame rate, and coherent diverging-wave spatial compounding by increasing signal-to-noise ratio imaging.

In this study, we propose to couple a fully sampled Pulse-Inversion (fs-PI) Harmonic technique to coherent diverging-wave compounding Ultrafast Imaging in an original way that optimizes the imaging frame rate and outperforms both diverging-wave compounding and PI Harmonic Imaging alone.

**Statement of Contribution/Methods**

An Aixplorer system (Supersonic Imagine, France) was used to perform fs-PI harmonic ultrafast SWI acquisitions in vivo transthoracic myocardium in healthy volunteers (N=4) through a parasternal short axis view, using a 2.75-MHz linear phased array probe (Vermon S.A., France). Shear waves were generated during end-diastole on the left-ventricular wall (40-mm to 60-mm depth depending on the volunteer) by focusing ultrasound waves during 300  $\mu$ s (MI < 1.9). One to three coherent diverging-waves were spatially compounded to form harmonic images (3.8-MHz, first-harmonic frequency), at 3205 to 9614 frames/s, depending on the number of diverging waves used.

**Results/Discussion**

Figure 1 presents the shear wave particle velocity signal of fs-PI harmonic acquisitions with (B, C) and without (A) coherent diverging-wave compounding. In most cases, without diverging-wave compounding, no discernible shear wave motion can be detected to measure shear wave speed (cs). For the 4 volunteers, coupling coherent spatial-compounding to fs-PI harmonic technique showed higher consistence for myocardium shear wave motion tracking and end-diastolic cs measurements (1.49  $\pm$  0.26 m/s on the four volunteers). The optimal compounded-waves number at these depth for shear wave motion detection was considered 2 and 3, due to frame rate limitation.

This approach combines spatial-compounding and pulse-inversion harmonic imaging advantages, such as high frame rate acquisitions and imaging artifacts reduction, essential to improve in vivo human transthoracic myocardial SWI for quantitative stiffness mapping.

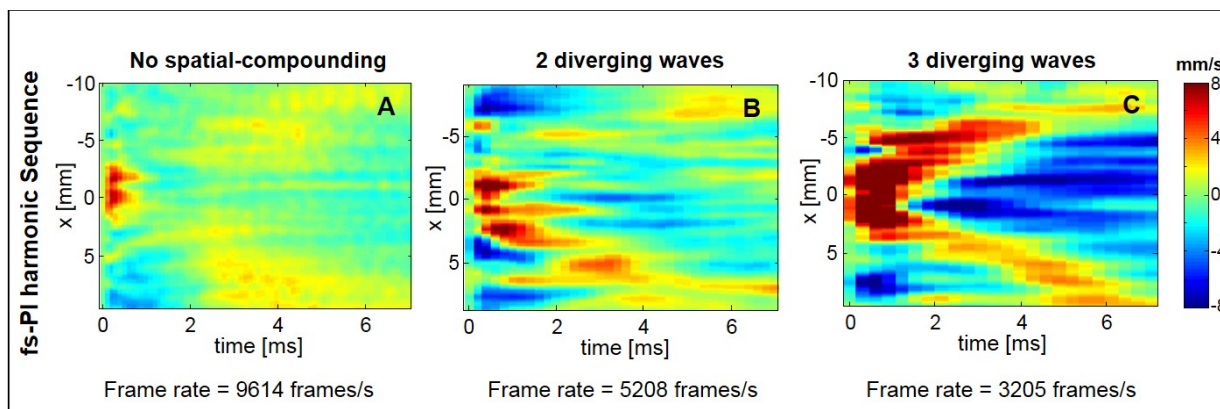


Fig. 1 – Plots of shear wave velocity particles at the focal depth of the push beam (40-mm depth). Comparison of shear wave motion detected by the fully-sampled pulse inversion harmonic (fs-PI) technique (A) as [J. R. Doherty, *et al.*, IEEE T-UFFC, 2013], and fs-PI harmonic coupled to two (B) and three (C) coherent diverging-wave compounding. Shear wave signal was averaged along depth direction.

2B-4

#### 1:45 pm M-mode ARFI Imaging Demonstrates the Effect of Coronary Perfusion on Cardiac Stiffness

Maryam Vejdani-Jahromi<sup>1</sup>, Annette Kiplagat<sup>1</sup>, Gregg Trahey<sup>1</sup>, Patrick Wolf<sup>1</sup>; <sup>1</sup>Biomedical Engineering, Duke University, USA

##### Background, Motivation and Objective

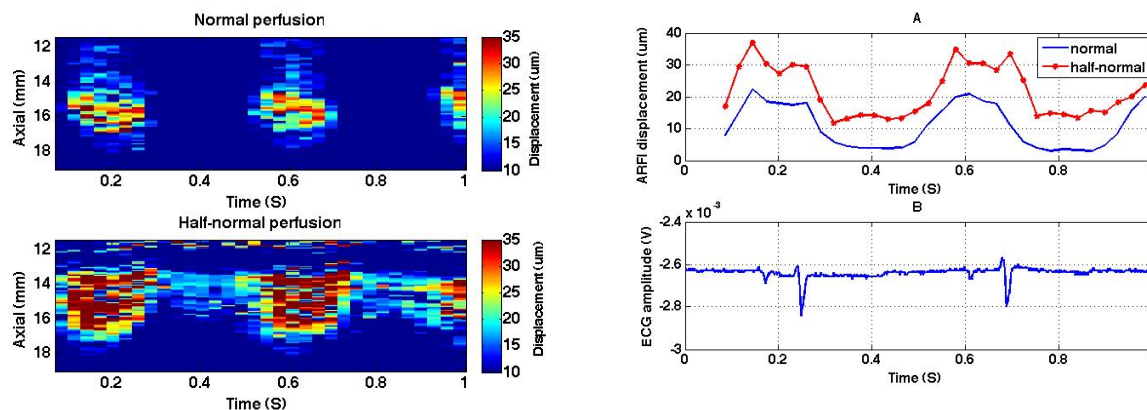
Myocardial stiffness is an important clinical indicator of cardiac function. One of the contributors to stiffness in the heart is the coronary perfusion. The interaction between cardiac tissue and coronary vasculature has been under investigation for several decades using pressure-volume loop measurements. Recently, developments in Elastography methods have enabled researchers to study the mechanical properties of tissues from a distance. Among them, Acoustic Radiation Force Impulse (ARFI) Imaging utilizes an acoustic pulse to push the tissue and ultrasound tracking to measure the resulting displacement. M-mode ARFI was used in this work to investigate the effect of coronary perfusion on cardiac stiffness.

##### Statement of Contribution/Methods

In five isolated Langendorff perfused rabbit hearts, we investigated the effect on myocardial stiffness of a coronary perfusion reduction from normal to half-normal. The acute decrease in coronary perfusion decreases the stiffness of the heart in systole and diastole (Gregg and garden-hose effects respectively).

##### Results/Discussion

Figure 1 shows M-mode ARFI data from a subject before and after the perfusion change. Figure 2 shows the average displacements over 3 mm of cardiac wall through the cardiac cycle before and after the change. As the coronary perfusion was reduced from normal to half-normal, ARFI displacements in systole doubled from  $(9.990 \pm 4.270) \mu\text{m}$  to  $(19.221 \pm 5.610) \mu\text{m}$  ( $p < 0.05$ ). These results are consistent with the Gregg effect explained by researchers using other measurement methods. Despite complicated issues regarding attenuation, anisotropy, and viscoelasticity, ARFI can be used to study the relative changes in cardiac tissue stiffness.





2B-5

**2:00 pm In Vivo Results Comparing ARFI-derived Plaque Stiffness With Composition Determined Using an MRI Gold Standard in Humans**

Joshua Doherty<sup>1</sup>, Jeremy Dahl<sup>1</sup>, Peter Kranz<sup>2</sup>, Nada El Hussein<sup>3</sup>, Hing-Chiu Chang<sup>2</sup>, Nan-kuei Chen<sup>2</sup>, Jason Allen<sup>4</sup>, Gregg Trahey<sup>1,2</sup>; <sup>1</sup>Biomedical Engineering, Duke University, Durham, NC, USA, <sup>2</sup>Radiology, Duke University Medical Center, Durham, NC, USA, <sup>3</sup>Neurology, Duke University Medical Center, Durham, NC, USA, <sup>4</sup>Community and Family Medicine, Duke University Medical Center, Durham, NC, USA

**Background, Motivation and Objective**

Current methods have had limited success in the identification of vulnerable plaques that confer the greatest risk of stroke. Acoustic Radiation Force Impulse (ARFI) imaging has shown promise for its ability to distinguish vulnerable plaques containing lipid pools from otherwise more stable, fibrous and/or calcified plaques and may therefore provide an important diagnostic tool for identifying high-risk patients. To date, however, the method has not been validated *in vivo* in humans.

**Statement of Contribution/Methods**

ARFI derived measures of plaque stiffness were compared with spatially registered composition determined by an MRI gold standard in 5 human subjects. Bmode and ARFI imaging data was implemented on a Siemens S2000 ultrasound scanner with custom, pulse-inversion harmonic sequences. MRI data was acquired on a GE MR750 3.0T scanner according to a standardized multi-contrast weighted protocol. MR PlaqueView (VP Diagnostics) was used to segment the lipid, calcium, and loose matrix components in the MRI data. 3D Slicer was used to render 3D models of the segmented plaque components and register the 2D Bmode image within the 3D MRI volume.

**Results/Discussion**

Figure 1 portrays the spatially registered MRI, Bmode, and ARFI images of a complex heterogeneous plaque in the far wall of one subject. Here, an approx. 0.22 cm<sup>2</sup> MRI identified calcium region (white arrow) in Fig. 1b corresponds to a region of uniformly low displacements (<1  $\mu$ m) in the ARFI image of Fig. 1c. An approx. 0.20 cm<sup>2</sup> MRI identified lipid region (yellow arrow) in Fig. 1b corresponds to a region of increased displacements (>2  $\mu$ m) in the ARFI image of Fig. 1c. ARFI images were spatially and temporally stable across multiple acquisitions acquired at imaging angles of 60°, 90°, and 120° and separated in time approx. 15 min. In total, 3 subjects had a MRI identified lipid region >0.10 cm<sup>2</sup>. The lipid region presented as regions of uniformly increased displacement in 2 subjects, and as a heterogeneous region with small focal regions of increased displacement in 1 subject. Overall, the contrast in displacements of MRI-identified lipid regions compared to surrounding tissues in ARFI was approx. equal to 2. These preliminary results support that ARFI can identify lipid regions in carotid plaques non-invasively, but also indicate that the observed contrast of such regions can be quite small.

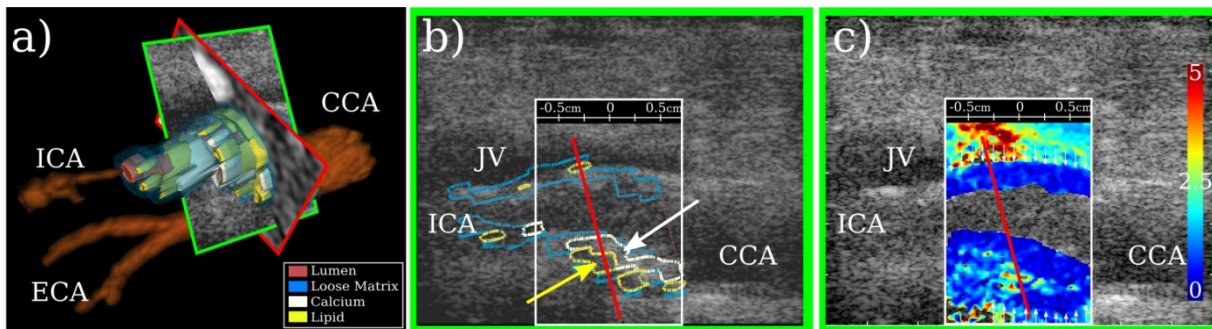


**Figure 1:** a) 3D arterial lumen and 3D segmented plaque model with the spatially registered 2D longitudinal Bmode image (green plane) and 2D transverse MRI TOF image (red plane). b) 2D Bmode image with overlaid contours of the 3D segmented plaque model. c) 2D Bmode image with 2D ARFI image overlay depicting axial displacements in  $\mu$ m.

2B-6

**2:15 pm Carotid plaque assessment using non-invasive shear strain elastography**

Maarten H.G. Heusinkveld<sup>1,2</sup>, Marie-Hélène Roy Cardinal<sup>1</sup>, Yang Ju<sup>1</sup>, Zhao Qin<sup>1</sup>, Richard G.P. Lopata<sup>2</sup>, Gilles Soulez<sup>1</sup>, Guy Cloutier<sup>1</sup>; <sup>1</sup>University of Montreal Hospital, Canada, <sup>2</sup>Eindhoven University of Technology, Netherlands

**Background, Motivation and Objective**

Stroke is a major problem resulting in high mortality and morbidity rates. In 20-25% of all cases, acute stroke underlies rupture of a vulnerable plaque in the carotid artery. Since the rupture of a plaque is related to its mechanical properties, the objective was to evaluate the ability of shear strain non-invasive vascular elastography (NIVE) to characterize carotid plaques *in vivo*. The feasibility of the NIVE algorithm to discriminate between asymptomatic and symptomatic patients, and between stable and vulnerable plaques assessed with magnetic resonance imaging (MRI) criteria, was investigated.

**Statement of Contribution/Methods**

A total of 31 patients with >50% stenosis of the internal carotid artery were recruited. A sub-group of 9 patients had neurological symptoms related to the plaque within 3 months prior to the examination and were considered symptomatic; the remaining 22 patients were asymptomatic. High-resolution MRI images were obtained to assess plaque vulnerability; plaques and internal components were segmented and quantified for lipid, calcium and inflammation contents. Radiofrequency ultrasound (US) data were acquired over multiple cardiac cycles. Carotid plaques were segmented on US images and elastograms were computed with NIVE. The axial, lateral and shear strains were estimated. The absolute shear strain images, i.e., shear magnitude, were threshold to analyze only the 25% highest shear strain values, which were then spatially averaged for each elastogram and plotted over time.

**Results/Discussion**

According to MRI, 7 plaques were identified as vulnerable and 24 as non-vulnerable. Among the non-vulnerable plaques, 12 nevertheless contained inflammation. The analysis of plaque regions experiencing large shear strains showed a statistically significant difference (\*p= 0.046) between symptomatic and asymptomatic patient groups (Max |Shear| in Table 1). Statistically significant differences were also found between the time average shear (Mean |Shear|) of vulnerable versus non-vulnerable plaques without inflammation ( $\dagger$ p=0.036). The Mean |Shear| of non-vulnerable plaques with and without inflammation were also significantly different ( $\ddagger$ p=0.008). The proposed shear measures have the potential to help identifying vulnerable plaques and vulnerable patients.

Table 1: Max |Shear| and Mean |Shear| are respectively the maximal and average value of the time varying absolute axial shear curve over a cardiac cycle. For each patient, both parameters were averaged for all available cardiac cycles. One way analyses of variance were performed to detect significant difference between groups.

Plaque type			
	Symptomatic (N=9)	Asymptomatic (N=22)	
Max  Shear  (%)	1.342 ± 0.281	1.579 ± 0.29*	
Plaque type			
	Vulnerable (N=7)	Non-Vulnerable with inflammation (N=12)	Non-Vulnerable without inflammation (N=12)
Mean  Shear  (%)	0.531 ± 0.122 <sup>†</sup>	0.509 ± 0.15 <sup>†</sup>	0.705 ± 0.152



**3B - MBB: Beamforming I**

Boulevard

Thursday, September 4, 2014, 1:00 pm - 2:30 pm

Chair: **Pai Li**  
National Taiwan University, Taipei

3B-1

**1:00 pm Recursive Fourier-Based High-Frame Rate Imaging**Jian-yu Lu<sup>1</sup>, <sup>1</sup>Bioengineering, The University of Toledo, Toledo, Ohio, USA**Background, Motivation and Objective**

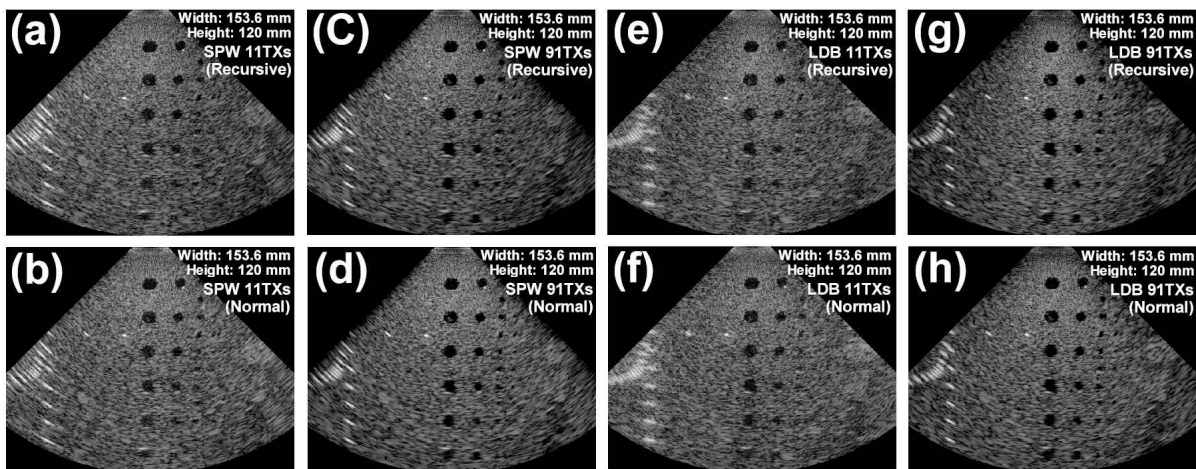
High-frame-rate (HFR) ultrasound imaging is important for elasticity imaging of moving objects, blood flow velocity vector imaging, fast cardiac imaging, strain and strain rate imaging, and functional imaging. Previously, a Fourier-based HFR imaging method that uses a single plane wave, steered plane waves (SPW), steered diverging waves (SDW), or limited diffraction beams (LDB) in transmissions (TXs) has been developed. This method has advantages that Fast Fourier transform can be used in image reconstructions to reduce computations, and when limited-diffraction beams are used in TXs, only one or two high-voltage transmitters are needed to drive all elements of an either 1D or 2D array transducer. Despite the advantages, image frame rate is reduced when multiple TXs are used to reconstruct a frame of image to increase image field of view and to improve image quality.

**Statement of Contribution/Methods**

To achieve the highest image frame rate (reciprocal of one ultrasound round-trip time) for the Fourier-based HFR imaging method when using multiple transmissions per frame, a recursive method (S. I. Nikolov, K. Gammelmark, and J. A. Jensen, Recursive ultrasound imaging, 1999 IEEE Ultrason. Symp. Proc., pp. 1621-1625) is used, where the sub-image obtained from each transmission is recursively added to the reconstructed image. To test the method, a home-made HFR imaging system with a phased array transducer of 128-elements, 2.5-MHz center frequency, 19.2-mm aperture, and 58% -6dB pulse-echo bandwidth was used to acquire data from an ATS539 tissue-mimicking phantom. Images of 90-degree field of view and 120 mm depth were reconstructed with the Fourier-based method.

**Results/Discussion**

Images reconstructed with and without the recursive method at a frame recursive constant of  $c_0=0.5$  (weight between successive frames of images) are shown in the first and second rows of the figure respectively. Images in the 1st and 3rd columns are obtained with 11 TXs per frame and the rest are obtained with 91 TXs per frame. The left and right four images are obtained with the SPW and LDB transmissions respectively. The results show that the quality of images obtained recursively is maintained while achieving a frame rate of 5347 (187  $\mu$ s between TXs). The relatively small  $c_0$  makes the contributions of prior frames of images small (decays as a power of  $c_0$ ), reducing motion artifacts.

**Image Reconstruction with and without Recursion**

3B-2

**1:15 pm Beamforming strategies for plane wave vascular elastography**Prashant Verma<sup>1</sup>, JoHannah Kohl<sup>1</sup>, Steven Huntzicker<sup>1</sup>, Rohit Nayak<sup>1</sup>, Marvin Doyle<sup>1</sup>, <sup>1</sup>Electrical and Computer Engineering, University of Rochester, Rochester, NY, USA**Background, Motivation and Objective**

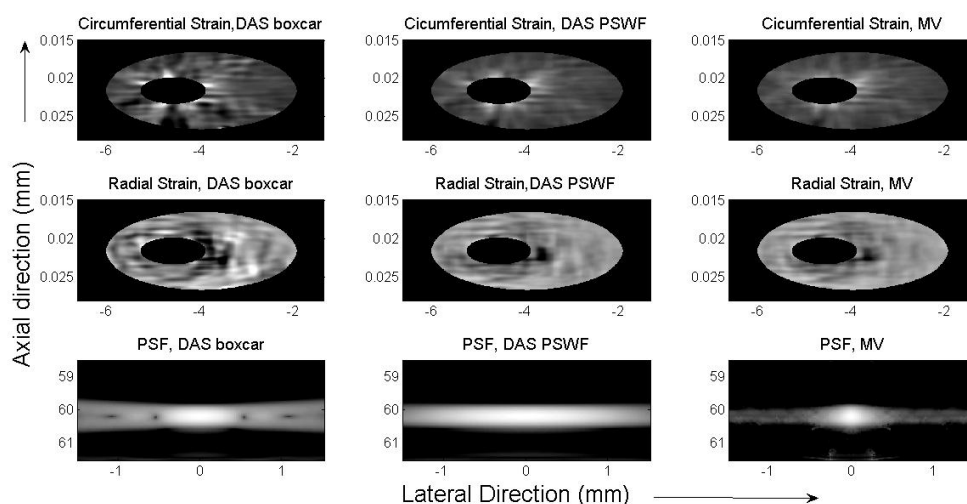
Plane-wave (PW) ultrasound images have narrower main lobe width than conventional imaging which increases the precision of lateral displacement estimates, but side-lobes are considerably higher. We compared the performance of radial and circumferential strain elastograms computed using: a) delay-and-sum (DAS) with boxcar weights, (b) DAS with prolate spheroidal wave functions (PSWF), and (c) minimum variance (MV) beam forming. PSWF has very low sidelobe levels, which makes it an ideal apodization function. Although the minimum variance (MV) approach is computationally more intensive than DAS technique, it promises to improve image quality by suppressing signals originating from off-axis directions.

**Statement of Contribution/Methods**

We used Field II to generate RF data of simulated vessels. The simulated vessels were incompressible ( $\nu \approx 0.495$ ) with Young's moduli of 50 kPa and 12.5 kPa assigned to the vessel wall and plaque, respectively. A uniformly distributed pressure was applied to the inner lumen. The simulated ultrasound system consisted of a linear array of 128 elements (center frequency = 5 MHz), whose pitch and width were 0.0304 mm and 0.279 mm, respectively — these parameters were chosen to represent the L14-5/38 probe used in our experimental study. For the DAS beamforming, we applied apodization functions to the received signals. A sub-array length  $L \leq M/4$  (where M is total number of elements in the array) was used for MV beamforming. Displacements were estimated using a 2D cross-correlation echo tracking method for pre- and post-deformation images. Radial and circumferential strain elastograms were computed in the vessel coordinate system. We used the elastographic contrast-to-noise (CNR) to evaluate the performance of the strain elastograms.

**Results/Discussion**

Radial and circumferential strain elastograms computed with three approaches are shown in top two rows of Fig 1. For [DAS boxcar, DAS PSWF, MV] methods, radial CNR [-3.32, 1.06, 7.04] dB and circumferential CNR [-2.53, 5.82, 8.33] dB was calculated using strain elastograms. Corresponding point spread functions are shown in bottom row of Fig 1. Overall, the best performance (accuracy and CNR) was achieved with the MV method. We conclude that MV beam forming performed sufficiently well to warrant further investigation with vessel phantom and an atherosclerotic rabbit model.

**3B-3****1:30 pm Nonlinear Compressibility and Mass Density Reconstruction under Plane Wave Excitation using Raw Data with Noise**

Markus Hesse<sup>1</sup>, Georg Schmitz<sup>1</sup>, <sup>1</sup>Medical Engineering, Ruhr-Universität Bochum, Bochum, Germany

**Background, Motivation and Objective**

While established linear ultrasound imaging methods solely image tissue features under single scattering, nonlinear diffraction tomographic reconstruction methods have been proposed to reconstruct quantitative maps of various acoustic tissue parameters like compressibility, mass density, speed of sound or attenuation under multiple scattering, e.g. [1]. However, the suggested nonlinear compressibility and mass density reconstruction approach in [1] is just validated numerically for noiseless raw data under cylindrical wave excitation. In terms of future experimental applications, we investigate numerically the method's sensitivity to various noise levels in the raw data under plane wave excitation for a pulse-echo breast imaging application.

**Statement of Contribution/Methods**

Applying a self-created numerical breast phantom with a realistic anatomy, size, and compressibility and mass density distribution, we use an FDTD-code to generate two synthetic pulse-echo raw data sets with 0.1 and 0.2 MHz center frequency under plane wave excitation with 61 angles of incidence in a range of  $90^\circ \pm 30^\circ$ . We subsequently add white Gaussian noise on each detected rf-signal to obtain a mean signal-to-noise ratio (SNR) of about 8, 18, 28 and 38 dB, respectively. Applying the nonlinear approach in [1], we reconstruct the phantom's compressibility and mass density using both sets for pre- and main estimation. Thereby, the corresponding inverse scattering problem is iteratively solved by the Kaczmarz method.

**Results/Discussion**

A statistical error analysis of the calculated reconstructions and exemplary compressibility and mass density reconstructions are illustrated in Figure 1. Nonlinear reconstruction using plane wave excitation yields comparable results for 28 and 38 dB SNR similar to the result achieved in case of noiseless raw data (b). Here, water and all tissue features are correctly located and clearly visible (e), (f). Using raw data with 8 and 18 dB SNR, the image quality is reduced by noise (b-d). The study's reconstruction results demonstrate the approach's robustness to high noise levels under plane wave excitation.

[1] M. C. Hesse, L. Salehi and G. Schmitz, Nonlinear simultaneous reconstruction of inhomogeneous compressibility and mass density distributions in unidirectional pulse-echo ultrasound imaging, *Phys. Med. Biol.*, vol. 58, pp. 6163-6178, 2013.

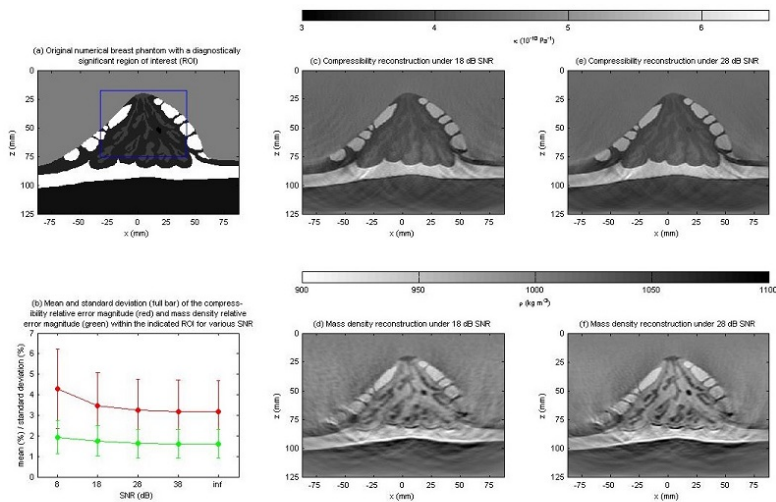


Figure 1: Original breast phantom (a), statistical error analysis (b), and exemplary compressibility and mass density reconstruction images under 18 dB SNR (c, d) and 28 dB SNR (e, f).

### 3B-4

#### 1:45 pm High spatio-temporal resolution imaging of the heart using multi-line transmit beam forming: experimental validation and in-vivo application

Ling Tong<sup>1</sup>, Alessandro Ramalli<sup>2</sup>, Piero Tortoli<sup>2</sup>, Jan D'hooge<sup>1</sup>; <sup>1</sup>Dept. of Cardiovascular Imaging, KU Leuven, Leuven, Belgium, <sup>2</sup>Dept. of Information Engineering, University of Florence, Firenze, Italy

##### Background, Motivation and Objective

Multi-line transmit beam forming (MLT) has recently gained interest in cardiac imaging given its potential to achieve high frame rate without significantly degrading the spatial resolution and signal-to-noise ratio (SNR). We have previously demonstrated by computer simulations that an MLT system should be able to obtain high spatio-temporal resolution images by properly choosing the opening angle between MLT beams and apodization. The purpose of this study was to experimentally verify our simulation findings both in-vitro and in-vivo and to demonstrate that MLT cardiac imaging is feasible.

##### Statement of Contribution/Methods

The ULA-OP system, equipped with a 2.0 MHz phased array, was programmed to interleave MLT and conventional single line transmit (SLT) modes, both covering a 90° sector. To suppress crosstalk artifacts introduced by MLT beams, different apodization schemes were tested on transmit and receive. The performance of MLT and SLT were compared on a home-built wire phantom, a general-purpose tissue mimicking phantom, and on healthy volunteers by quantitatively investigating the spatial resolution and contrast-to-noise ratio (CNR) of the resulting images. Moreover, the 4MLT and SLT cardiac images were shown side-by-side in randomized position to cardiologists (blind to the randomization), who were asked to express their preference for better quality.

##### Results/Discussion

As predicted by simulations, the crosstalk artifacts at distinct MLT opening angles could be reduced below -35dB by using proper apodization schemes. In particular, the images of a 4MLT imaging system with Tukey ( $\alpha = 0.5$ ) apodization showed very similar quality to SLT (spatial resolution: 4MLT = 2.3mm/SLT = 2.3mm, CNR: 4MLT = 0.84/SLT = 0.84). The cardiologists did not express any preference or preferred 4MLT in 4 datasets out of 8. Overall, these results confirmed that the image quality of a 4MLT imaging system with Tukey ( $\alpha = 0.5$ ) apodization was very competitive to SLT while providing a 4 times higher frame rate (Figure a, b, movies will be presented at frame rates: SLT = 23Hz/4MLT = 91Hz). Furthermore, it was demonstrated that MLT can be combined with multi-line acquisition (MLA) to provide images at a 16-fold frame rate without significantly compromising spatial resolution and SNR. This implies that high quality full field-of-view dense 2D images can be obtained at frame rates up to 450 Hz.

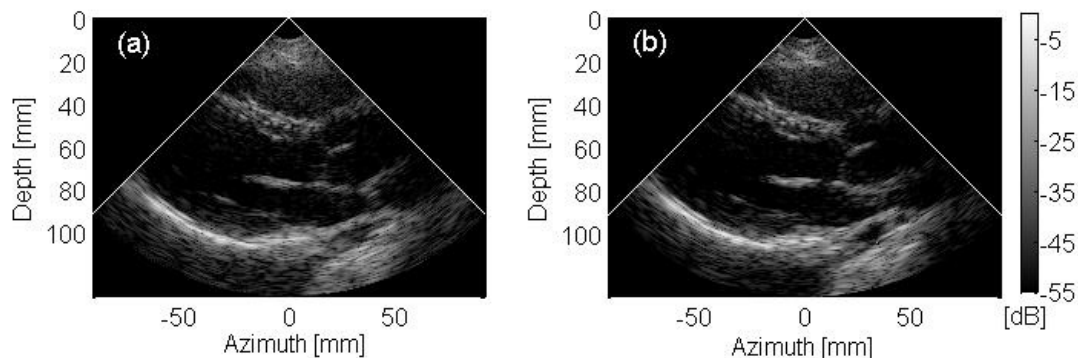


Figure. Cardiac images of healthy volunteers acquired using (a) the conventional single line transmit (SLT) and (b) 4-multi-line transmit (4MLT) beam forming.

3B-5

**2:00 pm Ultrafast echocardiography using full aperture diverging circular beams**Daniel Posada<sup>1</sup>, Guy Cloutier<sup>1</sup>, Damien Garcia<sup>1</sup>; <sup>1</sup>University of Montreal Hospital, Montreal, Canada**Background, Motivation and Objective**

Echocardiography is the most used medical imaging modality to examine the human heart. Applications such as B-mode and color Doppler make possible to image cardiac structures and blood flow in real time. Low temporal resolutions of the conventional single line acquisition (SLA) impede a thorough examination of tissue and blood motions. Alternatively, ultrafast ultrasound employs broadened ultrasound beams to insonify the full region of interest. Dynamic focusing and spatial compounding permit to reconstruct high quality images at very high frame rates. In this study, ultrafast ultrasound is put in practice by using full aperture diverging circular beams (FADCB). The study of this beamforming approach aims to thoroughly analyze this novel imaging modality and to confirm its potential for ultrafast echocardiography.

**Statement of Contribution/Methods**

The FADCB beamforming approach was implemented in the Verasonics scanner using a linear phased array (2.5 MHz, 64 elements). A tissue mimicking Gammex phantom with 0.1 mm nylon threads and 10 mm diameter anechoic cysts was used. Lateral resolution and contrast to noise ratio (CNR) were quantified at 4, 8 and 12 cm depths. Steering angles and the number of compounding images were varied into a large range to find the best configuration. Results were compared to SLA and sub-aperture diverging wave (SDW) beamforming approaches. Finally, *in vivo* ultrasound acquisitions were performed to further prove the clinical feasibility of this beamforming strategy.

**Results/Discussion**

The FADCB and SDW techniques converged to the SLA approach in terms of lateral resolution and CNR. Lateral resolutions obtained with the focused SLA technique were 1, 2.2 and 3.4 mm for 4, 8 and 12 cm depths. The CNR was 9.5 dB at 6 cm depth. Lateral resolution of the FADCB method converged to the same values after compounding 7 images only. Frames rates > 700 fps were attained by compounding 7 consecutive transmits at a PRF of 5 kHz. Comparison with the SDW approach evidenced better off-center quality with FADCB. Ultrafast ultrasound using full aperture diverging circular beams has the potential to provide high-quality echocardiographic images compatible with the clinical needs.

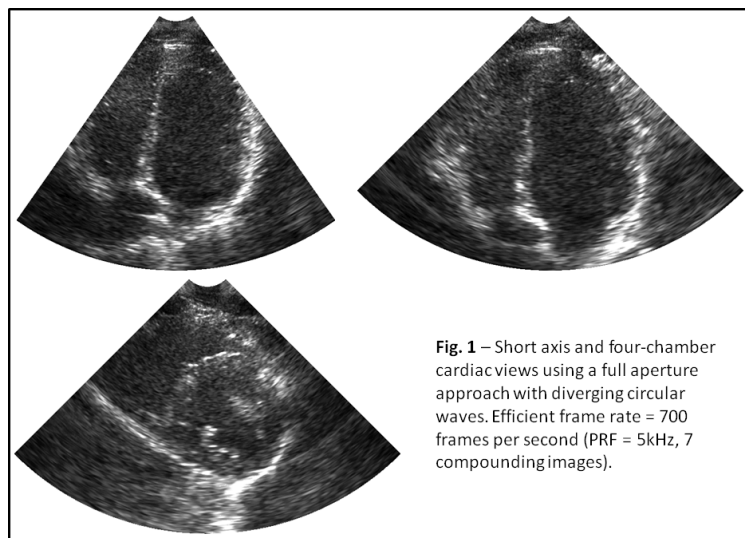


Fig. 1 – Short axis and four-chamber cardiac views using a full aperture approach with diverging circular waves. Efficient frame rate = 700 frames per second (PRF = 5kHz, 7 compounding images).

3B-6

**2:15 pm Ultrasound Fourier Slice Imaging: a novel approach for ultrafast imaging technique**Olivier Bernard<sup>1</sup>, Miaomiao Zhang<sup>1</sup>, François Varray<sup>1</sup>, Jean-Philippe Thiran<sup>2</sup>, Hervé Liebgott<sup>1</sup>, Denis Friboulet<sup>1</sup>; <sup>1</sup>CREATIS; CNRS UMR5220; Inserm U630; University of Lyon; INSA-Lyon; University of Lyon1, Villeurbanne, France, <sup>2</sup>Ecole Polytechnique fédérale de Lausanne (EPFL), Signal Processing Laboratory (LTS5), Switzerland**Background, Motivation and Objective**

Ultrafast imaging based on plane-wave (PW) is an active area of research thanks to its capability of reaching frame rate higher than a thousand of frames per second. Several approaches that have been proposed are based on Fourier-domain reconstruction [Lu et al., IEEE UFFC97], [Garcia et al., IEEE UFFC13]. In these techniques, the Fourier transform of the received echo is projected to the k-space corresponding to the Fourier transform of the object function. For one emitted PW, N lines along the kz axis direction are reconstructed in the k-space. The resulting sampling map is usually not sufficient to reconstruct high quality images. Several steered PW are thus emitted to densify the reconstructed k-space, making the underlying technology more complex. We propose here a new Fourier based method that allows reconstructing high quality ultrasound images using only one emitted PW.

**Statement of Contribution/Methods**

We start from the classical equation modeling the ultrasound image formation process [equ. (12) in Lu et al., IEEE UFFC97]. In the particular case where the emitted field is a PW perpendicular to the probe and the received field is supposed to be a steered PW with angle  $\theta_0$ , we mathematically demonstrate that the temporal Fourier transform of the received signal is equal to a radial line of angle  $\xi_0 = f(\theta_0)$  in the corresponding k-space domain. By simply playing with different delay strategies applied on the received signals, we are thus able, for only one emitted PW, to radially and densely recover the Fourier space of the object and thus reconstruct a high quality ultrasound image.

**Results/Discussion**

Contrast to noise ratio (CNR) has been computed from a numerical phantom of size 2x2cm with an occlusion of 1cm of diameter. CREANUIS simulation software [Varray et al., UMB13] was used to generate the raw signals from the emission of one PW. The resulting data were beamformed using our approach and the one of Garcia and Lu. The obtained CNR were equal to 5.6dB, 6.4dB and 6.9dB (3cm depth) and 4.7dB, 4.8dB and 5.1dB (6cm depth) with Garcia, Lu and our method, respectively. Figure 1 illustrates the behavior the different techniques in the Fourier domain. This result shows the ability of our method in recovering, from one emitted PW, the Fourier space in a dense way compared to the two others approaches.



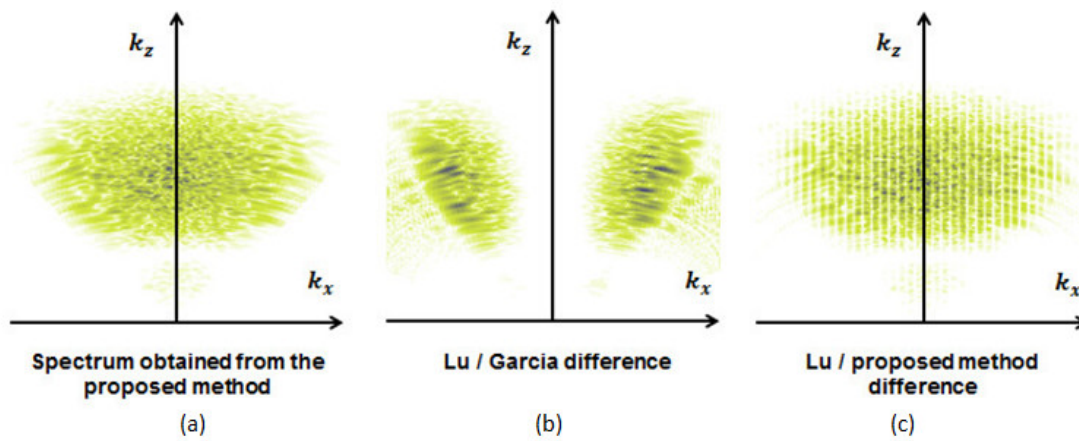


Figure 1: **Spectrum mapping.** (a) Spectral mapping using our method. (b) Absolute differences of Lu's and Garcia's spectra. (c) Absolute differences of Lu's spectrum and the one obtained using our method. The RF signals were simulated using CREANUIS software with randomly distributed scatterers.

## 4B - Structural Health Monitoring

Marquette

Thursday, September 4, 2014, 1:00 pm - 2:30 pm

Chair: **Paul Wilcox**  
University of Bristol

4B-1

### 1:00 pm Efficient Monitoring and Inspection of Plate-like Structures with Ultrasonic Guided Waves

Jennifer Michaels<sup>1</sup>; <sup>1</sup>School of Electrical and Computer Engineering, Georgia Institute of Technology, Atlanta, GA, USA

#### Background, Motivation and Objective

Periodic nondestructive inspections of critical structural components are typically both expensive and time-consuming, contributing to high maintenance costs and undesirable downtime. In situ piezoelectric transducers that both generate and received guided waves are an alternative approach whereby plate-like structures are frequently monitored for changes. The sparse guided wave array (SGWA) is a practical configuration whereby simple, piezoelectric disks are spatially distributed on the structure. The goals are to correlate signal changes with damage (i.e., detection) and characterize detected damage as to its location, size and type (to the extent possible). Closely related is the issue of follow-up inspection for both verification and more complete characterization. The objectives of this work are to evaluate and compare the performance of several sparse guided wave array (SGWA) imaging algorithms for a variety of damage scenarios, and leverage the in situ transducers as sources of guided waves for efficient follow-up inspection via acoustic wavefield imaging (AWI).

#### Statement of Contribution/Methods

Many SGWA imaging algorithms have been proposed, such as delay-and-sum, correlate-and-sum, minimum variance, and maximum likelihood, among others. Most methods work well for single, point sources of damage in simple plates, but tend to degrade in different ways as complexity increases. Here we consider fatigue cracks and impact damage, both simulated and real. Fatigue cracks are highly directional scatterers, whereas impact damage exhibits very complex scattering that is not always point-like; both situations affect imaging performance. Characteristics of the different imaging methods make them more suitable for different damage types, and also can enable some degree of in situ defect characterization. Regardless of the method, the resulting image can be used to define a region of interest for follow-up inspection. Nearby transducers are then used as sources for acquiring AWI data, which is analyzed to first verify detection of a scatterer and then to better locate and characterize it.

#### Results/Discussion

Results are presented for aluminum plates and composite panels with a variety of simulated and real damage types. We show that point-like scatterers such as holes and glued-on masses are typically imaged very effectively, and are also readily detected and localized via AWI. Strongly directional point-like scatterers, such as notches and fatigue cracks, can cause imaging artifacts, but more advanced imaging methods can unambiguously locate them and also approximately characterize their scattering patterns. Distributed and multi-site damage is most difficult to image with a SGWA, but it can be detected and then effectively characterized via AWI. These results demonstrate the advantages of the combined SGWA plus AWI methodology and also illustrate potential issues with using simulated damage for performance assessment.

4B-2

### 1:30 pm Calibration-Free Lamb Wave Source Localization for Structural Health Monitoring

Joel Harley<sup>1</sup>, José M.F. Moura<sup>1</sup>; <sup>1</sup>Department of Electrical and Computer Engineering, Carnegie Mellon University, Pittsburgh, Pennsylvania, USA

#### Background, Motivation and Objective

Guided waves that propagate in plate-like structures, known as Lamb waves, are an attractive tool for nondestructively evaluating the health of civil and aerospace structures. However, Lamb waves are challenging to analyze due to their multimodal and dispersive characteristics, which distort the waves as they propagate through a medium. To localize acoustic sources, researchers often analyze simplified representations of Lamb wave data and/or require calibration data to tune their signal processing methods [1]. In this paper, we present a high resolution source localization method that requires no prior calibration or velocity information about the Lamb waves.

#### Statement of Contribution/Methods

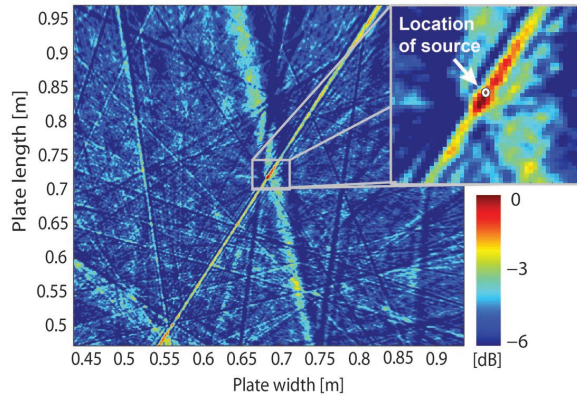
Our prior work has focused on recovering the dispersion curves of Lamb waves, which are known to be sparse in a frequency-wavenumber space, from calibration data [2]. This recovered information is then used to locate acoustic sources [1]. In contrast, the method presented in this paper finds the location where the data is represented by the most statistically sparse frequency-wavenumber representation. That is, we determine the source location by finding the origin from which our data best resembles Lamb waves with arbitrary parameters. We accomplish this by analyzing the kurtosis of the frequency-wavenumber domain at each location under consideration. The kurtosis represents a common statistical measure for detecting non-Gaussian, sparse-like signals.

#### Results/Discussion

We experimentally apply our method to localize an acoustic signature from a PZT transducer on an aluminum plate. Note that this acoustic signature could alternatively originate from an acoustic emission or impact event. Figure 1 illustrates a 0.5 m by 0.5 m image from the plate that is generated using 15 sensors. The largest value in Figure 1 indicates the estimated location of the source. Visually, we see that our method localizes the source accurately and with a high resolution. In our paper, we further discuss our methodology and compare our method with traditional Lamb wave localization techniques.

[1] J. B. Harley and J.M.F. Moura, "Data-driven Matched Field Processing for Lamb Wave Structural Health Monitoring", J. Acoust. Soc. Am., Mar. 2014.

[2] J. B. Harley and J.M.F. Moura, "Sparse recovery of the multimodal and dispersive characteristics of Lamb waves", J. Acoust. Soc. Am., May 2013.



4B-3

#### 1:45 pm Passive flaw detection and localization in thin plate from ambient noise cross-correlation

Lynda Chehami<sup>1,2</sup>, Julien de Rosny<sup>1</sup>, Claire Prada<sup>1</sup>, Emmanuel Moulin<sup>2</sup>; <sup>1</sup>Institut Langevin, ESPCI-CNRS, UMR 7587, Paris, France, <sup>2</sup>IEMN UMR CNRS 8520, Université de Valenciennes et du Hainaut-Cambresis, Valenciennes, France

##### Background, Motivation and Objective

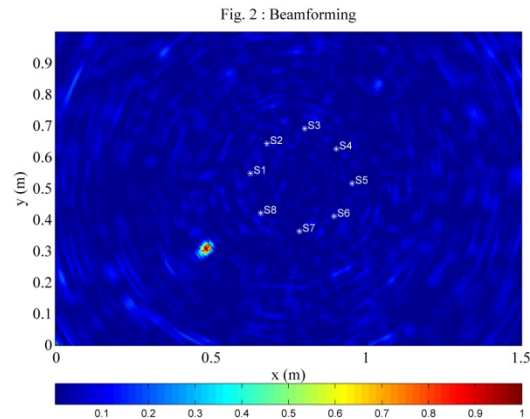
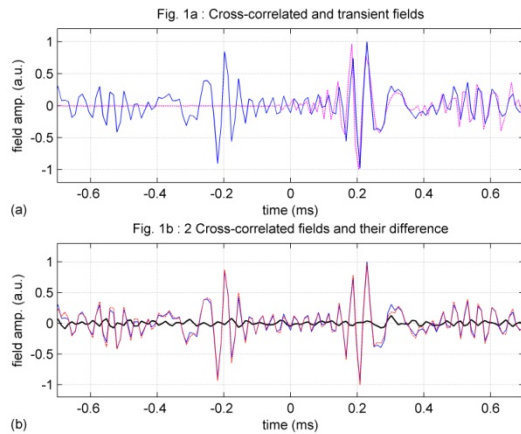
Passive structural health monitoring is an emerging technology. More than 10 years ago, it has been shown that Green's function between two sensors can be passively estimated from the ambient noise cross-correlation. The work presented here is an application of this approach dedicated to detect the occurrence of flaws on thin plates.

##### Statement of Contribution/Methods

The experimental setup consists of a horizontal aluminum plate (150x100x0.3)cm. A network of eight piezoelectric transducers are glued on the surface. A typical source of noise (500Hz to 30KHz) results from friction. Small metallic cylinders are used as defects. During the recording, typically lasting 1 minute, the source of noise is moved over the surface. Before correlation, the recorded signals are whitened. The correlation matrix is built from the 8 by 8 cross-correlated signals. We show that the flaw can be detected from the difference between the correlation matrices measured with and without defect. The differential matrix is beamformed from the transducer positions to localize the flaw.

##### Results/Discussion

In Fig. 1a, a typical result of noise cross-correlation between two channels (blue line) is compared to the transient response directly recorded when one of the two transducers acts as a source (magenta dashed line). The good agreement for positive times confirms the ability to passively retrieve the "Green's function". We observe that the extraction process is reproducible in Fig. 1b where two successive measurements of the correlation without flaw (continuous blue and red dashed lines) and the difference between the two (black line) are plotted. Finally, Fig. 2 displays the result of the beamforming of the differential matrix (white crosses indicate receivers positions). The flaw is successfully localized.



4B-4

#### 2:00 pm Estimation of the Flexural Stiffness of Thin Plates Using a Single Low-Cost Passive Sensor

Erika Svanström<sup>1</sup>, Tugba Özge Onur<sup>2</sup>, Johan E. Carlson<sup>1</sup>; <sup>1</sup>Computer Science, Electrical and Space Engineering, Lulea University of Technology, Sweden, <sup>2</sup>Electrical and Electronics Engineering, Bulent Ecevit University, Turkey

##### Background, Motivation and Objective

The flexural/bending stiffness of thin plates is a function of the Young's modulus and the Poisson's ratio of the plate. From a structural health monitoring point of view it is therefore of interest to develop methods able to track changes in these parameters due to wear and ageing. If a dispersive wave mode can be recorded for known distances between excitation and sensor, the shape of the received wave carries information about the material parameters of interest. The problem is that the recorded signal is affected also by the excitation and the sensor, both of which have unknown transfer functions. This paper demonstrates how this can be overcome by jointly estimating the plate stiffness and the combined effect of the excitation and the sensor.



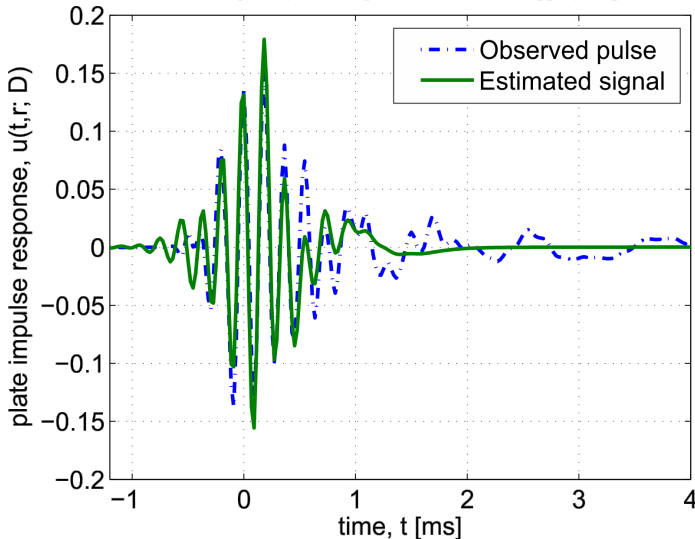
**Statement of Contribution/Methods**

The received signal is modeled as  $u(t, r; D) = h_{\text{er}}(t) * h_{\text{SIR}}(t, r; D) + e(t)$ , where  $h_{\text{er}}(t)$  is the combined impulse response of the excitation and the sensor,  $h_{\text{SIR}}(t, r; D)$  is the spatial impulse response of the plate, parameterized by the unknown plate stiffness  $D$ ,  $r$  is the known distance between the sensor and the excitation, and  $t$  denotes time. The term  $e(t)$  denotes zero mean additive white Gaussian noise with variance  $\sigma^2$ . The problem is that the received signal is a convolution of two unknown quantities. We show that, since  $h_{\text{SIR}}(t, r; D)$  is constrained to be a solution to a wave equation, and that  $h_{\text{er}}(t)$  can be assumed to be subject to some bandwidth and phase constraints, it is possible to separate the two, hence implicitly obtaining an estimate of the plate stiffness.

**Results/Discussion**

The robustness of the algorithm was evaluated in simulations, with a setup mimicking an infinite quartz glass plate with a 2 mm thickness. The simulation results are used to evaluate and discuss sensitivity to noise, initial values of the plate stiffness parameter, etc.

The principle is then verified with experiments on a 2 mm thick quartz glass plate with known density. The figure shows a measured pulse (dashed, blue) and the final modeled pulse (solid, green), after the joint estimation of  $h_{\text{er}}(t)$  and plate stiffness parameter  $D$  has completed. For this example, the final value of  $D$  was found to be 49 Nm, which agrees well with literature values for quartz glass. The pulse was excited by tapping the plate with a sharp object 40 cm away from the sensor.



4B-5

**2:15 pm Generation of ultrasonic edge waves for localised inspection of composite plate stiffeners**

Charles Courtney<sup>1</sup>, Harry Chu<sup>1</sup>; <sup>1</sup>Mechanical Engineering, University of Bath, Bath, United Kingdom

**Background, Motivation and Objective**

Carbon-fibre reinforced composites are increasingly being used in high performance vehicles, in particular aircraft. However their potential advantages in terms of weight reduction have yet to be fully exploited due to the need for conservative design. In-service strains must be restricted to less than the failure strain associated with the smallest detectable defect. Reducing the smallest detectable damage, by developing suitable structural health monitoring methods, allows an increase in allowable strain and hence lighter designs and reduced costs.

Ultrasonic guided waves have studied extensively for inspection of plates, but are limited in their ability to inspect the edges of structures by the complexity of the reflection process. A method of inspecting the edges of structures is desirable as in many applications, including wing panel stiffeners, edges are prone to damage and structurally critical.

**Statement of Contribution/Methods**

The solution proposed is to use permanently attached piezoceramic plates to generate and receive ultrasonic edge waves, which propagate along the edges of thin structures. Figure 1 shows the anticipated configuration. Changes in ultrasonic pulses passed between transducers due to intervening damage indicate the presence of damage and pulse-echo measurements from a single transducer allow location of damage. The localization of the waves allows transmission over substantial distances and simplifies inspection by focussing only on the transmission along the edge.

In order to develop this method it is necessary to generate waves localised at the plate edge without simultaneously generating plate waves propagating in the plate. To this end propagation of edge waves in anisotropic plates are modelled and the resulting dispersion curves used to optimise piezoceramic plate design for transmission of ultrasonic edge waves. Generation, propagation and scattering by impact damage of edge wave are verified experimentally.

**Results/Discussion**

The finite element model developed is used to determine appropriate piezoceramic plate dimensions to generate 200 kHz edge waves in a 3 mm thick CFRP plate. It is then confirmed experimentally that waves localised to the plate edge are preferentially generated and that generation of plate waves cross the plate is minimised. Impact damage to the edge was detected using edge wave transmission.

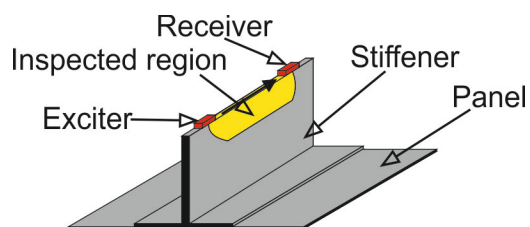


Figure 1: Configuration of detection system using ultrasonic edge waves

## 5B - Models in Physical Acoustics

Williford A

Thursday, September 4, 2014, 1:00 pm - 2:30 pm

Chair: **Andreas Mayer**  
*HS Offenburg - University of Applied Sciences*

5B-1

### 1:00 pm A new Use of the Elastodynamic Reciprocity Theorem

Jan Achenbach<sup>1</sup>, Oluwaseyi Balogun<sup>1</sup>, <sup>1</sup>Northwestern University, USA

#### Background, Motivation and Objective

It appears to be relatively unknown that the reciprocity theorem of elastodynamics can be used to obtain solutions to wave propagation problems. In this talk the theorem, which relates body forces, surface tractions and displacements of two elastodynamic states, State A and State B, in a region V with boundary S, by a volume integral over V and a surface integral over S, will first be shown to yield in a simple way an analytical expression for the amplitude coefficient of surface waves generated by a time-harmonic line load applied to an isotropic homogeneous elastic half-space. This will be achieved by selecting for State A the actual body force and the corresponding radiated surface waves, and for State B a virtual free surface wave. The analogous complete problem is known as Lamb's problem. Lamb obtained the surface waves in a much more complicated manner by the use of the exponential transform technique as contributions from a pole. The simple approach by the reciprocity theorem yields the same result as obtained by Lamb. The reciprocity theorem of elastodynamics is also valid for anisotropic, and inhomogeneous linearly elastic materials.

#### Statement of Contribution/Methods

In this talk we will extend the use of the reciprocity theorem to determine the surface waves generated by a time-harmonic line load on a half-space whose elastic moduli and mass density vary with the distance, z, from its surface.

The following depth profiles are considered:

$$\lambda(z) + 2\mu(z) = (\lambda_0 + 2\mu_0)f(z),$$

$$\mu(z) = \mu_0 g(z),$$

$$\rho(z) = \rho_0 h(z),$$

where  $\lambda_0, \mu_0$  and  $\rho_0$  are constants. The functions  $f(z)$ ,  $g(z)$ , and  $h(z)$  are unity at  $z=0$ .

We consider displacement expressions of the form

$$u(x, z) = iU(z)\exp(ikx - i\omega t)$$

$$w(x, z) = W(z)\exp(ikx - i\omega t)$$

The equations for  $U(z)$  and  $W(z)$  are

$$-k(\lambda + 2\mu)U + \lambda dW/dz + 1/kd/dz(\mu dU/dz) + d/dz(\mu W) = -(\rho\omega^2)/k U$$

$$d/dz[(\lambda + 2\mu)dW/dz] - kd/dz[\lambda U] - k\mu dU/dz - k^2\mu W = -\rho\omega^2 W,$$

The expression for the surface waves radiating from a line load, obtained by the use of the reciprocity theorem, are in terms of an integral I which contains  $U(z)$  and  $W(z)$  and expressions for  $T_x(z)$  and  $T_{xz}(z)$  which are in terms of  $U(z)$  and  $W(z)$ . It is remarkable that to obtain the surface waves for Lamb's problem all that is required are expressions for free surface waves.

For the problem at hand, the coupled system of equations for  $U(z)$  and  $W(z)$  has to be solved for prescribed expressions for  $\lambda(z), \mu(z)$  and  $\rho(z)$ .

In the absence of a method to obtain analytical solutions for  $U(z)$  and  $W(z)$ , we have considered high frequency solutions for  $U(z)$  and  $W(z)$ .

#### Results/Discussion

Figures will show the surface wave velocity computed as a function of  $k$ , in comparison with numerical results. The quantity  $W(0)/2I$  which defines the vertical surface wave displacement at the free surface decreases quite rapidly at small values of  $k$  (long wavelength) to the asymptotic limit at large values of  $k$ .

The final conclusion is that the reciprocity theorem provides a powerful method to determine the surface wave motion generated by an oscillating line load.

5B-2

### 1:15 pm Modeling elastic wave propagation using the k-Wave MATLAB toolbox

Bradley Treeby<sup>1</sup>, Jiri Jaros<sup>2</sup>, Daniel Rohrbach<sup>3</sup>, Ben Cox<sup>1</sup>; <sup>1</sup>Department of Medical Physics and Bioengineering, University College London, London, United Kingdom, <sup>2</sup>Department of Computer Systems, Brno University of Technology, Czech Republic, <sup>3</sup>Lizzi Center for Biomedical Engineering, Riverside Research, New York, NY, USA

#### Background, Motivation and Objective

The simulation of elastic wave propagation has many applications in ultrasonics, including the classification of bone diseases, non-destructive testing, and the design of SAW devices. In biomedical ultrasound in particular, elastic wave models have been used to investigate the propagation of ultrasound in the skull and brain, to optimise the delivery of therapeutic ultrasound through the thoracic cage, and to study the destruction of calculi. However, most existing elastic wave models are based on low-order finite difference (FD)

schemes and thus require large numbers of grid points per wavelength to avoid numerical dispersion. Here, we introduce an accurate and computationally efficient elastic wave model as part of the open-source k-Wave MATLAB toolbox (k-wave.org). The model is designed to be fast, flexible, and easy to use.

#### Statement of Contribution/Methods

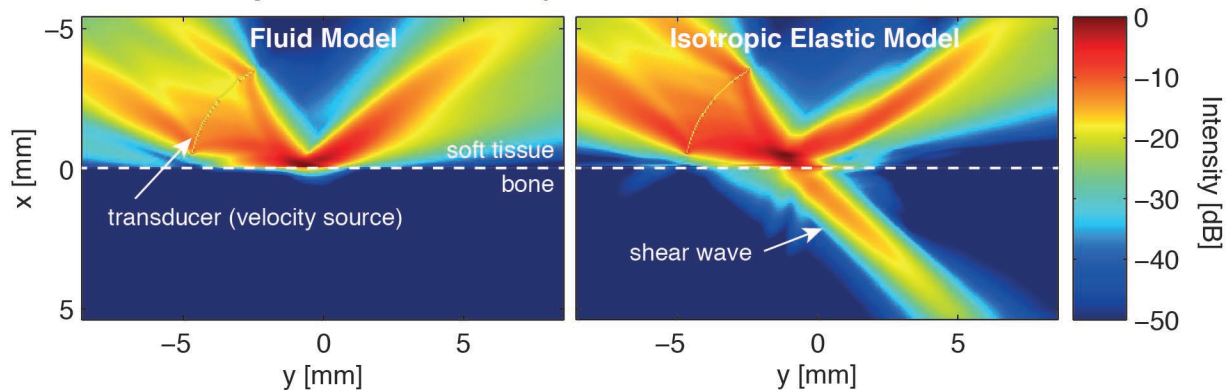
The model is based on two coupled first-order equations describing the stress and particle velocity within the medium. The material parameters are assumed to be heterogeneous and either isotropic or orthotropic with planes of symmetry aligned with the computational grid. For absorbing media, the Kelvin-Voigt model of viscoelasticity is used. The equations are discretised in 2D and 3D using an efficient time-stepping pseudospectral scheme. This uses the Fourier collocation spectral method to compute spatial derivatives and a leapfrog FD scheme to integrate forwards in time.

The model interface is defined analogous to other wave models in the k-Wave toolbox. The simulation functions are called with four input structures that define the computational grid, the distribution of medium parameters, stress and velocity source terms, and the properties and locations of the sensor points used to record the evolution of the wave field over time.

#### Results/Discussion

Model accuracy is validated against canonical cases, including reflection by a homogeneous half-space, scattering by a spherical inclusion, and the absorption of a plane-wave. Several practical examples are also included with the source code, e.g., the heating of a bone layer by a focused transducer (see figure), and ultrasound transmission through an orthotropic femoral cortical bone phantom derived using scanning acoustic microscopy. The model will be released as part of the open-source k-Wave Toolbox, and has a large number of potential uses.

Heating at a bone interface by a focused ultrasound transducer



5B-3

#### 1:30 pm A wave-vector-frequency-domain method for linear/nonlinear wave modeling in heterogeneous media

yun jing<sup>1</sup>; <sup>1</sup>Mechanical Engineering, NC State University, Raleigh, NC, USA

#### Background, Motivation and Objective

Wave-vector-frequency-domain (WVFD) method, also known as the angular spectrum approach (ASA), has traditionally been used to model only homogeneous or layered tissue. This is because this approach was initially developed based on the wave equation for homogeneous media. The WVFD algorithm based on the wave equation for heterogeneous media has not been studied to this date. The objective of this study is to develop and validate a WVFD method for modeling both linear and nonlinear wave propagation in arbitrarily heterogeneous media.

#### Statement of Contribution/Methods

The proposed WVFD algorithm simply considers speed, density, attenuation and nonlinearity variations all in one source term. After applying the x-, y- and t-domain Fourier transform to the wave equation, an implicit analytic solution can be obtained using the Green's function. The implicit analytic solution is an integral equation which can be further solved by a numerical approach.

The proposed WVFD algorithm is versatile in that it is capable of modeling continuous/pulse, linear/nonlinear, forward/backward wave propagation in heterogeneous media. Since the WVFD algorithm operates in the frequency-domain, dispersion and frequency-dependent attenuation can be easily taken into account. Therefore, it is also capable of modeling different tissue following different power laws. This is in general not possible in pseudo-spectral time-domain approaches, i.e., the power law can only be a scalar.

#### Results/Discussion

To validate the algorithm, a plane wave (burst, center frequency at 1 MHz) travels through a cylindrical object (radius at 10 mm) that has a sound speed and density both 5% larger than the background is modeled. Both frequency and time-domain results are compared with the benchmark solutions generated by a k-space time-domain method. Good agreement has been observed. Computationally, the proposed WVFD algorithm is about 4.5 times faster than the k-space method due to the use of a moving time frame.

When modeling a continuous wave, the WVFD can be even more computationally efficient than the k-space method, because it can opt to model only the frequency of interest, therefore significantly speeding up the computation speed by orders of magnitude.

Possible improvement of the algorithm by utilizing Gegenbauer reconstructions and absorption layer will also be discussed.

5B-4

**1:45 pm Acoustic hyperfocusing in solid metamaterials for subwavelength imaging**Badreddine Assouar<sup>1</sup>, Xiaoming Zhou<sup>1</sup>, Mourad Oudich<sup>1</sup>; <sup>1</sup>CNRS - University of Lorraine, France**Background, Motivation and Objective**

Acoustic imaging is an essential tool for medical screening as well as for detecting the structure and composition of matter. The resolution of a conventional acoustic imaging device is limited by the fundamental diffraction limit to half working wavelength [1]. Imaging resolution below this limit requires measuring the evanescent wave with high spatial frequency, which carries information about the object's fine features but vanishes away exponentially from the object in all natural materials. To overcome this limit, several proposals were dealt, these last years, with structured acoustic metamaterials (AMM). The latter have shown, based on their very unique effective properties, the possibility to manipulate the evanescent wave and then contribute to improving imaging resolution [2-3]. AMM with appropriate resonances induced into their constituent building blocks, exhibiting either negative effective mass density or bulk modulus or both have been demonstrated [3]. These unique properties rise from strong coupling of the propagating elastic wave in the hosting medium with the localized resonance in the building blocks.

**Statement of Contribution/Methods**

We present analytical and numerical analyses of a yet unseen lensing paradigm that is based on a solid metamaterial slab in which the wave excitation source is attached. We propose and demonstrate acoustic hyperfocusing induced by surface resonant states of solid metamaterial for sub-diffraction-limited acoustic imaging. The enhancement of evanescent waves across the metamaterial slab produced by their resonant coupling to surface waves is evidenced and quantitatively determined. The effects of metamaterial parameters on surface resonant states, transmission and bandwidth are clearly identified.

**Results/Discussion**

Based on the developed analytical approach, we have found that low shear modulus is a necessary condition for achieving high resolution acoustic hyperfocusing. Based on the concept consisting of a wave source attached to the metamaterial, a high resolution of  $\lambda/28.4$  is obtained with the optimum effective physical parameters, opening then an exciting way to design acoustic metamaterials for ultrasonic focused imaging. We, as well, have numerically investigated the acoustic superfocusing. A complete agreement between analytical and numerical approaches will be showed and discussed.

**References**

1. Y. Cheng et al, APL, 103 (2013) 224104.
2. S. Zhang et al, PRL, 102 (2009) 194301.
3. J. Zhu et al, Nature Physics, 7 (2011) 52.

5B-5

**2:00 pm Elastic switch composed of a 1D phononic crystal with a nonlinear resonator**

Pierre-Yves Guerdier<sup>1,2</sup>, Olivier Bou Matar<sup>1</sup>, Jérôme Vasseur<sup>3</sup>, Pierre Deymier<sup>2</sup>; <sup>1</sup>International Associated Laboratory LEMAC: IEMN, UMR CNRS 8520, PRES Lille Nord de France, École Centrale de Lille, 59652 Villeneuve d'Ascq, France, <sup>2</sup>Department of Materials Science and Engineering, The University of Arizona, Tucson, Arizona, USA, <sup>3</sup>Institut d'Electronique, de Microélectronique et de Nanotechnologie (IEMN, UMR CNRS 8520), PRES Lille Nord de France, 59652 Villeneuve d'Ascq, France

**Background, Motivation and Objective**

Phononic crystals (PnC) are artificial composite materials composed of periodic arrangements of scattering inclusions in a host matrix. Due to their periodic structure, they may behave as perfectly reflecting acoustic mirrors in some frequency ranges named as band gaps.

In optics, a nonlinear photonic crystal, containing a resonating cavity with a nonlinear optical index, capable of performing optimal bistable switching has been described by an analytical model accompanied with numerical experiments (Soljacic 2002).

The purpose of our study is to determine whether we can obtain in elastodynamics similar results with those observed in optics, namely a bistable behavior relatively to the particle velocity, due to nonlinearities of the elastic constants of the material constituting the resonating cavity.

**Statement of Contribution/Methods**

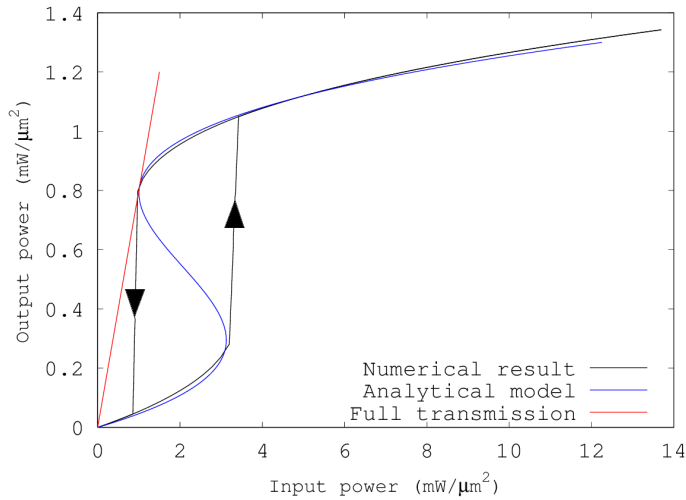
We consider a structure composed of a one-dimensional (1D) PnC containing a nonlinear cavity. We calculate its transmission spectrum using the linear matrix transfer method to determine the resonance frequency and quality factor of the cavity.

Then, we perform a time resolution of the nonlinear propagation of an elastic wave through the structure using a pseudo-spectral method. We compare the transmitted elastic power to the incident elastic power for increasing and decreasing values of the incident power. This relation is nonlinear due to the interaction of the elastic wave with the nonlinear cavity.

**Results/Discussion**

A hysteretic behavior is observed when the incident elastic power is increased and then decreased. This demonstrates without ambiguity the switch behavior in transmission of this structure. Full transmission is reached for a unique point, when the input power is decreased.

We provide a complete analytical interpretation and a theoretical model of the switching phenomenon and we analyze the effects of the different physical and geometrical parameters on the switching capability. We draw conclusions concerning the tunability of PnC through the magnetoacoustic effect.



5B-6

## 2:15 pm Highly Tunable Fabry-Perot resonators and filters using piezoelectric phononic crystals

Bertrand Dubus<sup>1</sup>, Marie-Fraïse Ponge<sup>1</sup>, Jérôme Vasseur<sup>1</sup>, Mai Phamthi<sup>2</sup>, Anne-Christine Hladky<sup>1</sup>; <sup>1</sup>ISEN Department, IEMN UMR 8520 CNRS, Lille, France, <sup>2</sup>Thales Research Technology, Palaiseau, France

### Background, Motivation and Objective

Phononic crystals (PCs) usually defined as artificial composite materials with a periodic structure have received a great deal of attention during the last two decades. Of particular interest is the existence, associated with their periodic structure, of frequency ranges where the propagation of elastic waves is forbidden. In this work, a stack of identical piezoelectric rods with periodical electrical boundary conditions is considered. As a matter of results, the periodicity of this structure results solely from the electrical boundary condition imposed on the electrodes. When electrodes are all connected together, the piezoelectric stack exhibits a band gap that is related to the electric charge located on the electrodes, named electric charge band gap.

### Statement of Contribution/Methods

An analytical model has been developed for calculating dispersion curves of one dimensional PCs containing rods made of a single piezoelectric material and separated with very thin electrodes. When all the electrodes are connected together, a band gap appears that is induced by the electric charges appearing on the electrodes. Its relative width is related to the electromechanical coupling factor of the piezoelectric material (33% in the proposed example). Experiments confirm unambiguously the existence of this band gap. This physical phenomenon is used to design a tunable Fabry-Perot resonator.

### Results/Discussion

A Fabry-Perot resonator is considered, in which the resonant cavity is delimited by two PCs. The PCs are stacks of piezoelectric rods exhibiting an electric charge band gap when the electrodes are connected together. The design of the structure is performed in order to have the resonance and antiresonance frequencies of the Fabry Perot resonator that fall in the electric charge band gap. The cavity/PC boundaries are moved by shifting spatially the electrical connections that produce the electric charge band gap. Thus, the size of the cavity is varied and the resonance of the Fabry-Perot resonator is tuned. In the proposed example, a 35% tuning of the resonance and antiresonance frequencies is obtained while the resonator coupling factor is kept constant around 40%. Experiments are under progress. The design of a filter coupling acoustically two Fabry-Perot resonators is discussed, as well as the electrical control of this coupling in order to reach critical value.



## 6B - Sensors and Field Characterization

Williford B

Thursday, September 4, 2014, 1:00 pm - 2:30 pm

Chair: **Mauricio Pereira da Cunha**  
University of Maine

6B-1

### 1:00 pm Full-Field Characterization of Surface Vibrations in Microacoustic Components by Supercontinuum Laser Stroboscopic White-Light Interferometry

**Lauri Lipiäinen<sup>1</sup>**, Kimmo Kokkonen<sup>1</sup>, Steffen Novotny<sup>2</sup>, Igor Shavrin<sup>2</sup>, Hanne Ludvigsen<sup>2</sup>, Matti Kaivola<sup>1</sup>; <sup>1</sup>Department of Applied Physics, Aalto University School of Science, Espoo, Finland, <sup>2</sup>Department of Micro and Nanosciences, Aalto University School of Electrical Engineering, Espoo, Finland

#### Background, Motivation and Objective

Optical probing techniques have manifested their strength in direct, noncontact measurements of vibration fields in microacoustic components. With a minimum vibration amplitude detection limit of even less than 1 pm, scanning laser interferometry has dominated the characterization of high-frequency microelectromechanical devices, for which the operation frequencies range from 10 MHz up to several GHz and the typical maximum vibration amplitudes are less than 1 nm. Although superior in the low-amplitude detection, these techniques do not typically provide topographic data of the sample surface. Topographic data would be useful to study samples which may have some (semi-)static deformations, e.g., as a function of the drive power or above a certain threshold drive power. These deformations, such as buckling, may lead to nonlinearities in the vibration fields. In this work, we describe a versatile measurement system based on white-light interferometry (WLI) which is capable of simultaneous detection of both the topographic data and surface vibrations down to sub-100 pm amplitudes with frequencies up to GHz range.

#### Statement of Contribution/Methods

WLI is a well established optical technique for noncontact 3D probing of static surface profiles. Also surface vibrations can be studied with such technique, if the light source is pulsed synchronously with the period of the motion. Most of the published results on stroboscopic WLI have been limited to the measurement of low-frequency (<1 MHz), high-amplitude (>100 nm) vibrations. The out-of-plane resolution of the WLI can be further improved by applying a phase-shifting technique, which requires a proper balance of the spectral properties of the light source. Previously, we have presented a LED-based stroboscopic WLI that enables detection of vibration amplitudes of even less than 100 pm by utilizing phase-shifting WLI (PSWLI) with enhanced data analysis. Due to the minimum light pulse width of ~8 ns, however, the frequency range is limited up to tens of MHz.

To extend the frequency range of our PSWLI system up to GHz range, we apply a self-developed supercontinuum (SC) laser source to the instrument, which produces <300 ps light pulses. The spectral properties are tailored to obtain a sub-100 pm minimum detectable amplitude performance. Importantly, the SC source allows freely adjustable repetition rate up to 50 MHz, and can be utilized up to GHz range vibration frequencies by down-converted synchronization scheme.

#### Results/Discussion

We demonstrate the performance of the setup and its applicability to the characterization of electromechanical components up to GHz range. Our results show a minimum detectable vibration amplitude of <100 pm, comparable to that of the reported full-field laser interferometers. Hence, our instrument enables a simultaneous, full-field characterization of the acoustic vibration fields and the topography in a wide variety of microacoustic components.

6B-2

### 1:15 pm Linear and non linear acoustic wave intensity mapping by micro-Brillouin spectroscopy

**Brice Vincent<sup>1</sup>**, Omar elmazria<sup>1</sup>, Keltoouma Aït Aïssa<sup>1</sup>, Didier Rouxel<sup>1</sup>; <sup>1</sup>Institut Jean Lamour, UMR 7198, Université de Lorraine - CNRS, Vandoeuvre les Nancy, France

#### Background, Motivation and Objective

We previously demonstrated for the first time the ability to detect piezoelectrically induced acoustic phonons with Brillouin spectrometer [1]. This experiment allowed us to measure propagation losses of bulk and surface acoustic waves in LiNbO<sub>3</sub> and langasite single crystals [2, 3] as well as in ZnO thin films [4]. This technique is of great interest not only because it is contact-less and non destructive method but also because it gave us direct access to the phonon density. Here, we aimed to demonstrate that the same set-up could be used to determine the acoustic field intensity within SAW-resonators in IDT, reflectors and even outside the active area. This permits to measure the acoustic wave spatial intensity on the device leading thus to experimentally validate the reflectors and IDT design and check if any acoustic leakages occur due to an inappropriate realization or design. Finally thank to the high sensitivity of our technique, detection of harmonic waves generated by acoustic non-linear process was investigated.

#### Statement of Contribution/Methods

Our Brillouin experimental set-up is a classical one, with incoming laser at 532nm and a tandem Sandercock Fabry-Perot. However a microscope is used to focalize and to collect the scattered light from our device. The alignment of the device with the specific scattering geometry of our system is a key point because the acoustic wavevector of the acoustic vibration must coincide with the one detected by our spectrometer.

Experiments were performed using a Y42-X LT SAW resonator operating at 2.45 GHz. In the first step, the S parameters of the device were measured using a network analyser. The packaged resonator was then mounted under microscope for Brillouin spectroscopy and was electrically excited at the chosen frequency and the angle of incidence adjusted to select the acoustic wavevector.

#### Results/Discussion

The induced phonons were detected at 2.47GHz. We observed a very good agreement between the measured spatial distribution and the calculated one. We also showed that some very weak piezo-electrically induced phonons could be detected out of the devices. This sensitivity is of great interest to qualify the efficiency of the Bragg mirrors. Finally with high electric power (25 dBm) applied on our device we detect, out of the device as well as within the IDTs, some harmonic inelastic peaks in our Brillouin spectrum. These peaks seem to be due to acoustic nonlinearity, but some measurements are now under progress to evidence their origin, since they could be also due to a nonlinear detection, where two acoustic phonons could interact with a single photon to give birth to a peak at twice fundamental frequency.

[1] B. Vincent, et al. J. Phys. D: Appl. Phys. 38, 1-5 (2005).

[2] J. K. Krüger, et al. New Journal of Physics 6 (2004) 57.

[3] B. Vincent, et al. IEEE, IUS Proc. 539-542 (2010).

[4] L. Brizoual, et al. Journal of Physics D: Applied Physics, Vol. 10 41 (2008)

The authors thank TDK/Epcos for SAW resonators investigated.

6B-3

### 1:30 pm Evaluation of Viscoelastic Properties of Protein Layers by RAMNE-Q Biosensors

Tomohiro Shagawa<sup>1</sup>, Hirotugu Ogi<sup>1</sup>, Fumihito Kato<sup>1</sup>, Masahiko Hirao<sup>1</sup>; <sup>1</sup>Department of Mechanical Science and Bioengineering, Graduate School of Engineering Science, Osaka University, Toyonaka, Osaka, Japan

#### Background, Motivation and Objective

The quartz crystal microbalance (QCM) biosensor is a mass sensitive biosensor. It detects absorbed mass through the shift in the resonance frequency of the quartz resonator. Thus, a QCM can achieve a real time monitoring of binding reactions without labels. It can also evaluate the viscoelastic properties of adsorbed protein layer.

However, conventional QCM show lower sensitivity than other biosensors with labels. Deterioration of the mass sensitivity is caused by heavy Au electrodes on both surfaces of quartz resonator, which have been needed for applying effective electric field and for immobilizing receptor proteins via the gold-thiol reaction. Increase of inertia resistance due to electrodes significantly decrease the sensitivity. For higher sensitivity, we achieved wireless-electrodeless QCM.

#### Statement of Contribution/Methods

We further developed a resonance acoustic microbalance with naked-embedded quartz (RAMNE-Q) biosensor, where a naked quartz resonator is embedded in a microchannel fabricated in Si wafer by MEMS technology. Figure 1 shows the schematic of RAMNE-Q chip. Both side and surface of the resonator are supported by micro pillars without fixed parts. The thickness of the resonator is about 28  $\mu\text{m}$  (corresponding the fundamental frequency of 58 MHz). The RAMNE-Q chip is installed in a sensor cell that has two flat antennas for generating and detecting the pure shear vibrations of the resonator.

#### Results/Discussion

Figure 2 shows the resonant spectra of the RAMNE-Q biosensor up to the 7th mode with the fundamental resonance frequency of 58 MHz in flowing solution. We simultaneously measured the frequency shifts during binding reactions of antigen-antibody reactions and evaluated the viscoelastic properties of adsorbed protein layers inversely using the Voigt model.

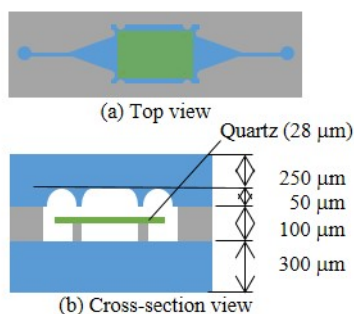


Fig. 1 RAMNE-Q Chip

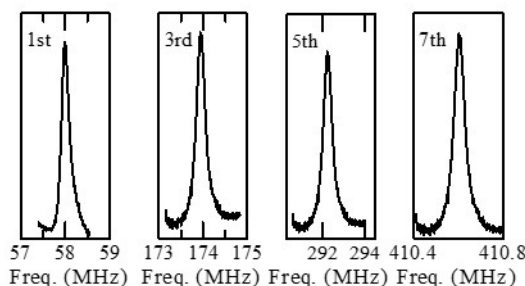


Fig. 2 Measured resonant spectra

6B-4

### 1:45 pm Distinguishing chemicals using CMUT chemical sensor arrays and artificial neural networks

Quintin Stedman<sup>1</sup>, Kwan Kyu Park<sup>2</sup>, Butrus T. Khuri-Yakub<sup>1</sup>; <sup>1</sup>Stanford University, Stanford, California, USA, <sup>2</sup>Hanyang University, Seoul, Korea, Republic of

#### Background, Motivation and Objective

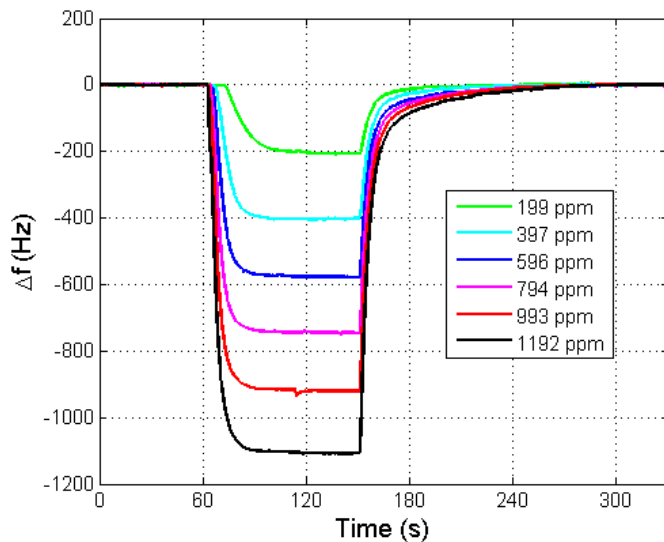
We present results demonstrating the ability of a CMUT chemical sensor array to recognize different chemicals in the gas phase using artificial neural networks. CMUTs can be used as highly-sensitive chemical sensors by monitoring their change in resonant frequency in response to mass-loading (Park, et. al., IUS 2008). Using an array of CMUTs functionalized with different polymers, we can determine the identity and the concentration of a chemical present at low concentrations in a background of nitrogen.

#### Statement of Contribution/Methods

The CMUTs were fabricated using direct wafer-bonding and LOCOS technology. They were functionalized by dissolving polymers in solvents and pipetting the solution onto the top of the CMUT membranes. The devices were placed in an oscillator circuit designed to oscillate at the parallel resonant frequency of the CMUT. The frequency of each oscillator was monitored with a frequency counter as various chemicals were flowed over the device in a carrier gas of nitrogen. The frequency shift of each sensor was scaled and fed into an artificial neural network, which was trained to identify the chemical. The concentration was then determined using linear regression. The neural network performance was cross-validated using data not used to train the network.

#### Results/Discussion

The sensors showed concentration-dependent responses to each chemical. Figure 1 shows the response of a sensor with a poly(4-vinylphenol) functionalization layer to various concentrations of methane. An array of 5 sensors correctly identified analytes as methane, carbon dioxide, water vapor, ethanol vapor, isopropanol vapor or acetone vapor 96% of the time. The system gave the concentration of successfully-identified chemicals with an average accuracy of 20%. Chemicals were successfully identified with concentrations on the order of 100 ppm. The limit of detection of the sensors can be as low as 1 ppm, depending on the sensor and chemical. This suggests that the system could work on much lower concentrations of chemicals than those tested here. The ability of the sensor to detect and distinguish methane suggests applications in natural gas detection for safety purposes.



6B-5

## 2:00 pm Vacuum pressure sensor available beyond atmospheric pressure using leaky attenuation of ball surface acoustic wave sensor

Toshihiro Tsuji<sup>1</sup>, Toru Ozumi<sup>1</sup>, Nobuo Takeda<sup>1</sup>, Tsuneo Ohgi<sup>2</sup>, Takayuki Yanagisawa<sup>2</sup>, Shingo Akao<sup>1,2</sup>, Noritaka Nakaso<sup>2</sup>, Kazushi Yamanaka<sup>1</sup>; <sup>1</sup>Tohoku University, Japan, <sup>2</sup>Toppan Printing Co. Ltd., Japan

### Background, Motivation and Objective

Plasma etching process may be performed in wide pressure range of 0.01 kPa to above atmospheric pressure for the selectivity, dimension control, plasma damage, and throughput [1]. Although the capacitance manometer is commonly used, it is difficult to ensure both the sensitivity to low pressure and the durability to high pressure due to the diaphragm structure. Though the leaky attenuation (LA) was measured in planar surface acoustic wave (SAW) device, the pressure range was limited to 10 kPa to 100 kPa [2]. In this work, the multiple-roundtrip propagation of ball SAW sensor (Fig. 1) [3] is applied to pressure measurement in a much wider range.

### Statement of Contribution/Methods

A langasite (LGS) ball SAW sensor (150 MHz,  $\phi 3.3$  mm) was set in a variable pressure chamber, and multiple-roundtrip waveform was measured. The attenuation  $\alpha$  was calculated by fitting the amplitude decay curve to an exponential function [4]. The extraneous attenuation  $\alpha_p$  was determined by the extrapolation of  $\alpha$  at 0 kPa. Finally, the LA  $\alpha_L$  was obtained by  $\alpha - \alpha_p$ .

### Results/Discussion

An envelope of the waveform measured at 100 kPa  $N_2$  is shown in Fig. 2. Roundtrip signal at 1 m (97 turns) was measured with S/N higher than 20. Fig. 3 shows the logarithmic decay curve at three pressures. As the pressure was increased to 200 kPa, measurement was still possible, indicating the durability above the atmospheric pressure. Fig. 4 shows measured LA as a function of the vacuum pressure, showing the linearity down to 0.01 kPa. The calculation (broken line) by an approximate theory [2] using the density and a SAW velocity of LGS, 5750 kg/m<sup>3</sup> and 2380 m/s, respectively, almost reproduced the experiment. The small difference may be explained by continuous change of SAW velocity along the propagation route. From these results, it was shown that the ball SAW sensor realizes a vacuum sensor available beyond atmospheric pressure.

### References

- [1] Banna et. al., J. Vac. Sci. Technol. A 30 (2012) 040801.
- [2] A. J. Slobodnik Jr., J. Appl. Phys. 43 (1972) 2565.
- [3] Yamanaka et. al., IEEE Trans. Ultrason. Ferroelectr. Freq. Control. 53 (2006) 793.
- [4] Singh et. al., Nanotechnology 18 (2007) 435502-3.

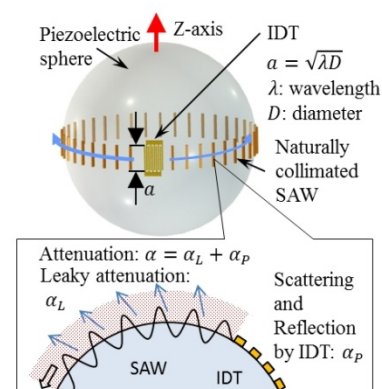


Fig. 1 Schematic illustration of leaky attenuation measurement by ball SAW device.

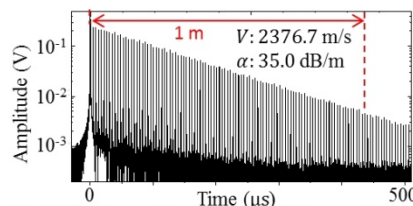


Fig. 2 Envelope of multiple-roundtrip waveform (100 kPa  $N_2$ )

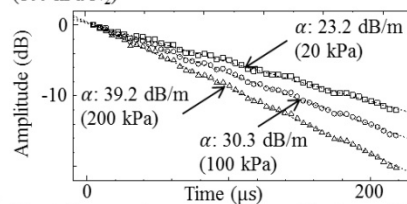


Fig. 3 Pressure dependence of logarithmic amplitude decay curve ( $N_2$ ,  $\square$ : 20 kPa,  $\circ$ : 100 kPa,  $\triangle$ : 200 kPa)

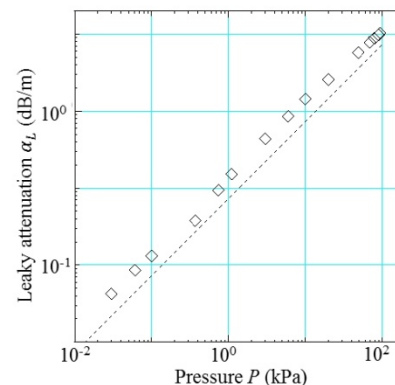


Fig. 4 Pressure dependence of leaky attenuation ( $N_2$ ).  $\diamond$ : measured value, broken line: approximate theory of planar SAW device

6B-6

## 2:15 pm Design of fast and high sensitivity Pirani pressure sensor based on S0 lamb mode measurement of heater temperature

Abdelkrim Talbi<sup>1</sup>, Mohamed Moutaouakil<sup>1</sup>, Jean Claude Gerbedoen<sup>1</sup>, Romain Viard<sup>1</sup>, Thibault Roux Marchand<sup>2</sup>, Frederic Sarry<sup>2</sup>, Olivier Boumatar<sup>1</sup>, Alain Merlen<sup>3</sup>, Omar Elmazria<sup>2</sup>, Philippe Pernod<sup>1</sup>; <sup>1</sup>LLA LEMAC/LICS - IEMN UMR CNRS 8520, ECLille -USTL, PRES Université Lille Nord de France, Cite, France, <sup>2</sup>Université de Lorraine, Institut Jean Lamour, UMR CNRS 7198, France, <sup>3</sup>ONERA, chemin de la lumière 91123, Palaiseau, France., France

### Background, Motivation and Objective

Measuring steady and unsteady pressure is crucial in fluid mechanics, and in any industrial application where pressure monitoring is required such as micro-pumps, or vacuum. High sensitivity, low resolution, and resolved measurements are particularly important characteristics for fluid dynamic, aerodynamic, and acoustic investigations. Nano-Pirani based pressure sensors are relatively easy to elaborate, can be extremely miniaturized and are a potential alternative for diaphragm based pressure sensors near atmospheric pressures. It was previously demonstrated for conventional Pirani sensors, operating in high vacuum, that it is possible to improve their sensitivity using surface acoustic waves as a sensitive mechanism (1). The aim of this work is to increase the sensitivity of nano Pirani sensors, to improve the response time by two order of magnitude (few ms instead of few 100ms) and to extend their application from the high vacuum range to the atmospheric range. A complete model taking into account the thermoelastic coupling in multilayered structures for guided acoustic wave propagation was developed and implemented in Comsol multiphysics enabling to study the NanoPirani sensor with an integrated acoustic wave transduction.

### Statement of Contribution/Methods

First, we performed 3D simulations of a resistive nano-gap Pirani sensor using Comsol Multiphysics by considering both the thermoelastic coupling of materials and the air-gap thermal conductivity variation versus pressure. The optimized design was fabricated and characterized. This permitted to check and to validate the thermal model (2). Secondly, a new design based on a heater element integrated directly with an AlN piezoelectric bridge based S0 lamb wave delay line was elaborated. The transmission, including magnitude and phase, was calculated using FEM analysis. The model takes into account the thermoelastic coupling, the elastic constants temperature dependence and the thermal conductivity pressure dependence of the surrounding air.

### Results/Discussion

For the first device the temperature elevation from each side of pressure transition is close to 40 °C for a driving power close to 10mW. Experimental characterizations under a pressure sweep and using an infrared camera confirm the operating mode with pressure transition close to the atmospheric one. These results agree well with the theoretical model. The response time was estimated to be close to 1ms. For the second device, the temperature elevation is quite similar. The response time is close to 10ms resulting from the increase of the thermal mass inertia. In terms of sensitivity, knowing that the TCF of S0 lamb wave mode is around -25ppm/°C and if we consider an operation frequency close to 1GHz, the sensitivity can reach 10ppm/100Pa. The experimental validation of the last design is in progress.

1)K.J.Singh, O.Elmazria, et al., IEEE Sens., vol.11, no.6, pp.1458,1464, June 2011

2)A.Talbi et al., patent WO 2013008203 A3

## 7B - CMUTs (1)

Williford C

Thursday, September 4, 2014, 1:00 pm - 2:30 pm

Chair: **Levent Degertekin**  
Georgia Institute of Technology

7B-1

### 1:00 pm Bandwidth and Sensitivity Optimization in CMUTs for Airborne Applications

Nikhil Apte<sup>1</sup>, Kwan Kyu Park<sup>2</sup>, Amin Nikoozadeh<sup>1</sup>, Butrus T. Khuri-Yakub<sup>1</sup>; <sup>1</sup>Edward L. Ginzton Laboratory, Stanford University, Stanford, California, USA, <sup>2</sup>Hanyang University, Korea, Republic of

#### Background, Motivation and Objective

CMUTs typically have a wide bandwidth when immersed in a liquid medium like water which makes them quite attractive for applications like medical ultrasound imaging. However, in airborne applications, CMUTs have a very narrow bandwidth. Previously we had proposed CMUTs with the cavity between the plate and the substrate vented to the ambient environment. Such CMUTs have additional damping due to the squeeze film formed behind the CMUT plate. These damped CMUTs have a much enhanced bandwidth, although at the expense of some sensitivity. By carefully engineering the squeeze film, the bandwidth and the sensitivity of such CMUTs can be optimized.

#### Statement of Contribution/Methods

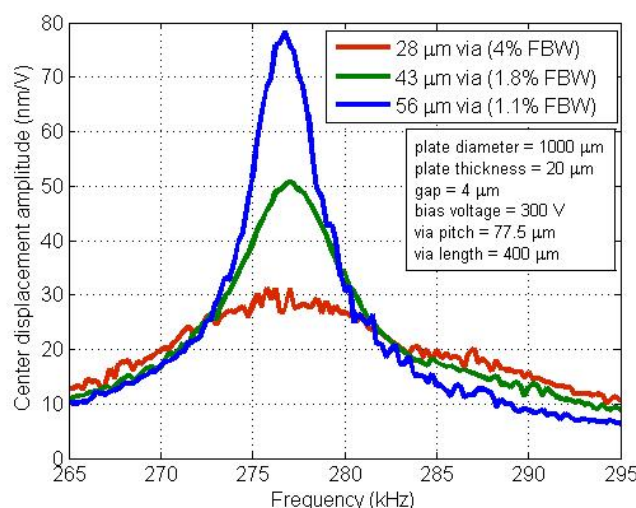
We designed CMUTs such that the cavities are vented through the substrate using through-wafer-vias. The devices were simulated using COMSOL to model the squeeze film behavior. The venting vias were arranged in a hexagonal pattern. Keeping the pitch of the vias the same, the size of the vias was varied. The larger vias reduce the squeeze film effect, but also reduce the sensitivity due to a lower electrode area.

A variety of such CMUTs were fabricated varying the plate radius and plate thickness to get a wide range of frequencies and aperture. The fabricated CMUTs were mounted on pin grid array packages and initially tested under a laser Doppler vibrometer.

#### Results/Discussion

As expected, the devices exhibit a variation in their bandwidth with the size of the venting vias. The device with the smallest vias has a good fractional bandwidth of 4%. The device with the largest vias shows good sensitivity of 78 nm/V, which translates to ~116 dB SPL/V.

We plan to characterize more of these devices, and then utilize the wider bandwidth of these CMUTs for ultrasound imaging experiments in air.



7B-2

### 1:15 pm Rotational Capacitive Micromachined Ultrasonic Transducers

Michael Kuntzman<sup>1</sup>, Neal Hall<sup>1</sup>; <sup>1</sup>Electrical and Computer Engineering, University of Texas at Austin, Austin, TX, USA

#### Background, Motivation and Objective

A rotational capacitive micromachined ultrasonic transducer (RCMUT) for airborne ultrasound applications is presented. The device, shown in Figure 1, is comprised of two conventional cMUTs mechanically coupled via a pivoting beam structure. The pivoting structure is designed to provide high bending stiffness and low rotational stiffness, which reduces common-mode deflection while maintaining sensitivity to pressure gradients between the diaphragms, resulting in a pressure gradient sensor with a dipole response. The diaphragms are vacuum-sealed to reduce thermal-mechanical noise and unwanted air-film dynamics. The coupling structure provides additional resistance to deflection under ambient pressure, allowing larger, more compliant diaphragms than would be possible without the coupling structure. Theoretically, this enables a design path for highly compliant, vacuum-sealed pressure gradient sensors.

**Statement of Contribution/Methods**

The device has multiple modes of vibration. The first mode is excited by the intended  $dp/dx$  measurand, while the second mode responds to common-mode pressure signals. A challenge lays in characterizing the presence of the second mode in the acoustic response. Acoustic and electrostatic characterization will be presented and compared to a finite-element based model.

**Results/Discussion**

Prototype devices have been successfully fabricated and characterized. While the RCMUT is not intended to address every ultrasound application this new device structure may have advantages are (i) targeted ultrasonic acoustic signature recognition with background noise rejection – owing to the directional nature of the response, and (ii) miniature sound source localization systems.

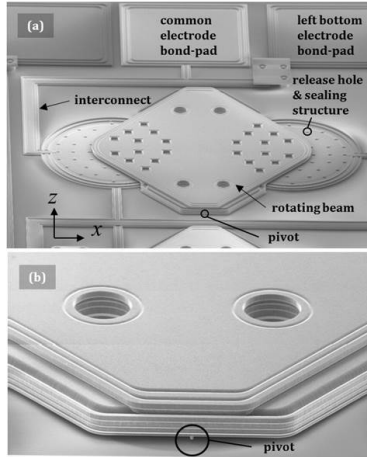


Fig. 1. Labeled SEM of a single RCMUT device,  $510\mu\text{m} \times 390\mu\text{m}$  in size.

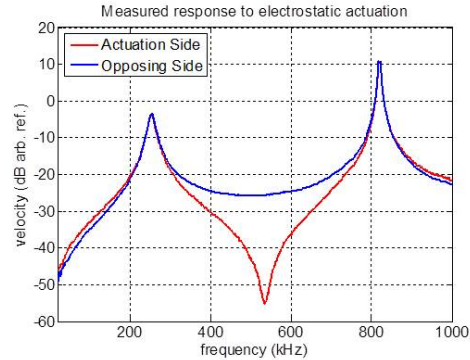


Fig. 2. Measured velocity of the actuated diaphragm (red) and the opposing diaphragm (blue).

7B-3

### 1:30 pm The Influence of Eliminating Fixed Electrode from an Air-Coupled Dual Deflectable Membrane Capacitive Micromachined Ultrasonic Transducer

Tahereh Arzoo Emadi<sup>1</sup>, Douglas Buchanan<sup>1</sup>, <sup>1</sup>Electrical and Computer Engineering, University of Manitoba, Winnipeg, Manitoba, Canada

**Background, Motivation and Objective**

Capacitive micromachined ultrasonic transducers (CMUTs) have been introduced as a promising candidate for non-destructive testing. These transducers offer advantages over their widely used competitor, piezoelectric transducers, e.g. improved bandwidth, temperature independency [1]. A conventional CMUT employs one vibrating membrane suspended over a fixed electrode and operates based on the generation of electrostatic force between its two electrodes. In contrast with a CMUT, a novel configuration of capacitive transducers has been recently developed (M3-CMUT) [2]. This transducer utilizes multiple moving membranes with a fixed electrode and has been shown to benefit from a smaller effective cavity height which improves the power generation capability and sensitivity.

**Statement of Contribution/Methods**

In this work, the further enhancement of the properties of this newly developed M3-CMUT was experimentally investigated by examining the influence of eliminating the fixed electrode. A M3-CMUT was fabricated which included two polysilicon deflectable membranes separated by a 750 nm cavity height, with effective radius of the top membrane of 50  $\mu\text{m}$ . In this configuration, the lower deflectable membrane acted as the ground electrode. In comparison, a CMUT with one deflectable membrane and a fixed electrode was also fabricated using the same fabrication process and with similar dimensions.

**Results/Discussion**

Electrical characterization was conducted using an Agilent Impedance Analyzer 4294A to measure the transducer first natural resonant frequency. DC bias levels of 0-40 V were applied to the transducers top membranes and the resonant frequency shifts were measured using a small ac signal, 50 mV. The lower deflectable membrane in the M3-CMUT and the fixed electrode of CMUT were grounded during the measurements. It was found that the M3-CMUT exhibits a larger resonant frequency shift (69 kHz) for a 20 V DC bias increase compared to the CMUT (41 kHz). This resonant frequency shift arises from the spring softening effect, and is related to the effective cavity height which was found to be smaller for the M3-CMUT due to the displacement of the two flexible membranes. Comparing these results with our previous work [2], where the M3-CMUT cell included a fixed electrode as well, it was observed that the resonant frequency shift has been further enhanced by eliminating the fixed electrode (69 kHz compared to 57 kHz from [2]). Using a parallel plate model, the membrane deflections can be extracted to be 41 and 23 nm for the M3-CMUTs without and with a fixed bottom electrode, respectively. Therefore, it can be seen that eliminating the bottom electrode improves the transducer membrane deflection, which in return improves the transducer properties.

[1] O. Oralkan, et. al., IEEE Trans. Ultrason., Ferroelectr., Freq. Control, 49(11), Nov. 2002.

[2] T. A. Emadi, D. A. Buchanan, IEEE Trans. on Electron Devices, 61(3), Mar. 2014.

7B-4

### 1:45 pm Polymeric capacitive transducers and arrays for gas coupled operation

Richard O'Leary<sup>1</sup>, Gerald Harvey<sup>2</sup>, <sup>1</sup>University of Strathclyde, United Kingdom, <sup>2</sup>Weidlinger Associates, Glasgow, United Kingdom

**Background, Motivation and Objective**

Capacitive ultrasonic transducers comprise a substrate patterned with a regular array of uniformly dimensioned cavities above which a membrane is positioned. Transmission and reception of ultrasound is effected via controlled electrical or mechanical stimulus of the membrane, respectively. Close control of the cavity dimensions can be achieved utilising micromachining in order to create the desired cavity dimensions and spatial distribution, where silicon based materials are common. This paper describes recent progress in a rapid and facile methodology for the creation of capacitive transducer structures based upon micropatterning of polymer substrates.



**Statement of Contribution/Methods**

A 2-d positioning system equipped with a piezoelectric droplet generator is employed to create an array of sessile droplets on the surface of a polystyrene substrate. The droplets act as a positive mask of the desired cavity diameter and spatial distribution. Droplet and hence cavity diameters of 100-1000 $\mu$ m readily achievable. The droplet patterned substrate is exposed to a saturated vapour of toluene which is absorbed by the polystyrene causing swelling of the surface except in the areas where the droplets are positioned. Exposure time, in the range 2-10 minutes, governs the depth of the resultant cavities, with 100-1000nm being typical. After exposure the polystyrene is air-dried and washed with purified water and electroded and packaged with 8 $\mu$ m Kapton membrane to form the capacitive transducer structure.

The PZFlex finite element software has been employed to explore the potential for the use of the micropatterned substrates in the manufacture of capacitive ultrasonic transducers and arrays, in particular the potential reductions in inter-element cross-talk over silicon-based devices.

**Results/Discussion**

Single element and array devices operating in the range 4-600kHz, targeted at air coupled non-destructive evaluation, have been constructed and evaluated experimentally. Transducer bandwidths in excess of 100% were observed with two-way insertion loss of 70dB being typical. Laser vibrometry confirms uniform surface dilation of the excited membrane, in the case of linear array devices inter-element cross talk is minimal and observed to be 21dB.

The methodology affords the independent control of cavity spatial distribution, depth and lateral dimensions with significant potential for the manufacture of capacitive transducers and arrays for a range of applications.

7B-5

**2:00 pm Fabrication and Characterization of Wafer-Bonded cMUT Arrays dedicated to Ultrasound-Image-guided FUS**

Dominique Gross<sup>1</sup>, Caroline Coutier<sup>2</sup>, Mathieu Legros<sup>3</sup>, Marie Perroteau<sup>1</sup>, Dominique Certon<sup>1</sup>; <sup>1</sup>Université François-Rabelais de Tours, GREMAN, UMR-CNRS 7347, Tours, France, <sup>2</sup>CEA, LETI, MINATEC Campus, Grenoble, France, <sup>3</sup>Vernon S.A., Tours, France

**Background, Motivation and Objective**

Besides traditional ultrasonography applications, the cMUT technology demonstrates great advantages for FUS therapeutic purposes: contrary to piezoelectric transducers, great performances can be expected with very low self-heating side effects. Ultrasound-image-guided FUS devices could widely benefit from the strong integration capabilities of cMUTs and the considerable scope of achievable topologies offered by this technology. This paper describes the conception and the characterization of a dual mode cMUT probe incorporating two different kinds of cMUT arrays. The targeted application is the pre-clinical evaluation of liposomal drug release (1-5 MHz) guided with high frequency imaging (20 MHz) [1].

**Statement of Contribution/Methods**

Starting from specifications and requirements in terms of acoustic field for both applications, a dual-probe composed of five arrays was designed: one HF linear array of 64 elements surrounded by four LF cMUT linear arrays of 8 elements. Each array is mechanically ordered so that its points to the investigation depth set at 20 mm. A SOI based wafer-bonding process was chosen for the cMUT fabrication. In order to optimize the manufacturing stage and to get the best possible homogeneity between the different chips, the HF and LF cMUT arrays have been both fabricated on the same wafer and in the same run. A specific process flow (6 levels of masks) was hence developed to implement the two required gap heights.

Optical and electrical measurements were firstly carried out to evaluate classical cMUT parameters: collapse voltage, electrical impedance and the homogeneity of each array. Then, a set of fluid-loading pulsed mode measurements with hydrophone and laser interferometer was done to assess their potential performances: central frequency, bandwidth and sensitivity. For LF arrays, additional characterizations were carried out for 1 hour at 1, 3 and 5 MHz, in CW mode, with operating conditions required for thermal liposome activation (i.e. duty cycle = 50 % and PRF=1 kHz).

**Results/Discussion**

All characterizations show promising results: a good homogeneity, collapse voltages close to the expected ones and very low in-series electrical resistances. The one-way -3 dB relative bandwidths of HF and LF arrays are 100 % and 83 %, with a central frequency of 20 MHz and 10.6 MHz, respectively. The -6 dB elementary directivity of the HF array was measured at 32°. The peak-to-peak pressure amplitude reached with one single element of the LF array was 150 kPa, 450 kPa and 550 kPa at respectively 1, 3 and 5 MHz. Considering the acoustic focusing gain of the probe (between 8 and 25 depending on the frequency), these first measurements of the output pressure amplitude demonstrate that the probe should provide a sufficient acoustic intensity at the ROI for the final applications. Moreover, the first aging tests of LF arrays have been successfully carried out without any loss on the pressure amplitude.

[1] D. Certon *et al.*, submitted to 2014 IEEE IUS

7B-6

**2:15 pm A Novel Method for Measuring Dielectric Charging of CMUT Arrays**

Lawrence Wong<sup>1</sup>, Shuai Na<sup>1</sup>, Albert Chen<sup>1</sup>, John Yeow<sup>1</sup>; <sup>1</sup>University of Waterloo, Canada

**Background, Motivation and Objective**

Dielectric charging can affect the reliability of capacitive micromachined ultrasonic transducers (CMUTs), but it can also be used beneficially for pre-charging of CMUTs (Ho *et al.*, IUS 2012). Controlling dielectric charging becomes more important in CMUT arrays as unevenly charged elements will affect image quality. However, there is no easy way to measure the amount of charge trapped without (1) requiring precise capacitance measurement or causing the device to collapse (capacitance-voltage method) or (2) requiring laboratory equipment (a vibrometer, an impedance analyzer, or a pulse-echo characterisation tank). To measure dielectric charging of CMUT arrays in non-collapsing mode, we propose a method that (1) does not require the measurement of capacitance and does not change the charging state during measurement and (2) can potentially be used in a clinical setting.

**Statement of Contribution/Methods**

In this method, the element to be measured is used to transmit ultrasound while another element, preferably the one next to the transmitting element, is receiving. Sound waves propagate to the receive element through acoustic crosstalk (another potential limitation of CMUTs). In order to measure the built-in bias, or the voltage shift caused by the charges trapped in the transmitting element, two measurements need to be made. The two measurements use the same bias voltage, so that the receive element has the same gain, but require pulsing signals with different DC offsets on the transmit element. The output voltages of the receive element are then recorded. The difference of the two output voltages is caused by the DC offsets, but the magnitude of the difference is related also to the built-in bias of the transmitting element. If the bias voltage is low related to the collapse voltage, the device can be modeled as a linear system. Any built-in bias in the transmitting element can then be calculated by solving the linear equations that relate the output voltages and the input DC offsets.

### Results/Discussion

Using continuous sinusoid waves with different DC offsets, we carried out the experiment and calculated the built-in bias in an element of a 1-D CMUT array. The measured peak-to-peak output voltages are in the order of hundreds of mVs, indicating that acoustic crosstalk is a viable mechanism of ultrasound propagation for this method. The measurement was repeated after the element was intentionally charged, and a change in the built-in bias was detected.

This method can be modified to use single or multi-cycle square pulses (instead of sinusoid signal), thus no additional hardware is required from a standard CMUT array imaging system. The only requirement is that the array must be immersed during the measurement. The proposed method can be useful in real-time calibration of CMUT arrays.

## 1C - MCA: Outlook for Contrast Imaging

Grand Ballroom

Thursday, September 4, 2014, 3:30 pm - 5:00 pm

Chair: **James Miller**  
Washington University, St. Louis

1C-1

### 3:30 pm Update on Contrast Ultrasound: Diagnostic and Therapeutic Applications

Steven Feinstein<sup>1</sup>; <sup>1</sup>Cardiology, Rush University Medical Center, Chicago, USA

#### Background, Motivation and Objective

##### I. Background

Ultrasound contrast agents (UCA's) serve as near perfect acoustic reflectors providing enhanced signal-to-noise ratios within the tissue/blood interface throughout the body.

The current global diagnostic imaging modalities utilize contrast agents to define anatomy and quantify tissue perfusion in nearly every organ of the body.

The unique characteristics of micron-sized, air-filled, microspheres provide unparalleled access to the intrinsic spatial and temporal heterogeneity of tissue perfusion. Today, the use of ultrasound contrast agents today provides a true, volumetric analysis of tissue/organ perfusion.

Importantly, UCA's are defined by these unique parameters:

- (1) Use of non-ionizing, acoustic energy, (2) Unparallel spatial and temporal resolution, (3) Real-time 3D/4D processing,
- (4) well-established user base and (5) accessibility and economy

Coupled with advances in UCA's formulations, the acoustic engineering aspects of hardware and software design are readily apparent in the implementation of sophisticated 3D/4D imaging.

A great deal of credit should be directed at the stalwart efforts of a multitude of clinician/researchers in their efforts to develop and test safe, and efficacious imaging modalities that provided enhanced patient care and novel therapeutic options.

##### II. Clinical applications

In the USA, two FDA UCA's are approved for clinical;

Optison, GE Medical Diagnostics, Princeton, NJ, and, Definity, (Lantheus Medical Imaging, Billerica, MA.). Several additional agents are approved for whole body imaging outside of the USA and include: Sonazoid, Sonovue and Levovist.

##### III. Future therapeutic applications

The current clinical applications of CEUS remain exclusive for diagnostic imaging. However, a sea change in therapeutic applications has occurred. The gas-filled, microspheres that simultaneously act as 'stealth' intravascular indicators, are ideally suited for ultrasound-directed, site-specific, delivery.

The investigators at the University of Bergen, advanced the field following their recent publication describing their ongoing clinical trial for treatment of pancreatic cancer in patients. Ultimately, ultrasound contrast agents may provide the opportunity to dramatically alter both the diagnosis and subsequent treatment of diseases.

Thus, the novel field of non-viral, ultrasound- mediated drug/gene delivery appears to be evolving. Leading scientists throughout the world have demonstrated transduction in a variety of pre-clinical and clinical scenarios, thus allowing one's imagination to speculate on the future of diagnostic and therapeutic uses of CEUS.

#### Statement of Contribution/Methods

#### Results/Discussion

1C-2

### 4:00 pm 4D Harmonic and Subharmonic Contrast-Enhanced Ultrasound for the Characterization of Breast Masses: Update on a Multi-center Prospective Study

John Eisenbrey<sup>1</sup>, Priscilla Machado<sup>1</sup>, Anush Sridharan<sup>1,2</sup>, Haydee Ojeda-Fournier<sup>3</sup>, Annina Wilkes<sup>1</sup>, Alexander Sevrakov<sup>1</sup>, Robert Mattrey<sup>3</sup>, Flemming Forsberg<sup>1</sup>; <sup>1</sup>Department of Radiology, Thomas Jefferson University, USA, <sup>2</sup>Department of Electrical and Computer Engineering, Drexel University, USA, <sup>3</sup>Department of Radiology, University of California, San Diego, USA

#### Background, Motivation and Objective

While mammography has shown high sensitivity in the detection of breast cancer, its low specificity results in a false-positive rate of roughly 80%. Thus, a secondary tool for the characterization of breast masses after mammographic identification would be highly beneficial in reducing the number of unnecessary biopsies. The objective of this ongoing study is to investigate the use of 4D harmonic and subharmonic contrast-enhanced ultrasound for the characterization of breast masses identified by mammography.

#### Statement of Contribution/Methods

This study was approved by Thomas Jefferson University and the University of California's Institutional Review Boards. Patients scheduled for an ultrasound guided biopsy of a mammographically-identified breast mass provided informed consent to undergo a contrast ultrasound study prior to biopsy. All scanning was performed using a modified Logiq 9 scanner with 4D10L mechanically controlled linear array (GE Healthcare, Milwaukee, WI). Experimental software provided 4D pulse inversion harmonic imaging (HI; transmitting 2 cycle pulses at 5 MHz and receiving at 10 MHz) and 4D pulse inversion subharmonic imaging (SHI; transmitting 4 cycle pulses at 5.8 MHz and receiving at 2.9 MHz). As part of the study, patients first underwent 2D B-mode and power Doppler imaging (PDI). Patients then received a 0.25 ml bolus injection of the ultrasound contrast agent Definity (Lantheus Medical Imaging, N. Billerica, MA) through an antecubital catheter during 4D HI of the lesion. After a 30 minute wait, patients received a second contrast injection of 20 µL/kg (up to 1.25 ml) during 4D SHI of the lesion. Finally, patients underwent their ultrasound guided biopsy as part of their clinical standard of care. Cases were then organized in a database for blinded reading by radiologists at each site (2 readers/site plus 1 universal reader). Preliminary evaluations of tissue suppression and the visualization of flow were also evaluated by 2 ultrasound physicists.

**Results/Discussion**

To date, a total of 157 women have been enrolled and 149 have completed the study. Incomplete studies to date have resulted from a failure to gain IV access ( $n = 5$ ), equipment malfunction ( $n = 2$ ), and a previously undisclosed contraindication to the contrast agent ( $n = 1$ ; unstable pulmonary status). 3D volume acquisition rates have ranged from 1.7 Hz (for a  $3.7 \times 1.3 \times 2.0$  cm lesion) to 6.1 Hz (for a  $6 \times 4 \times 6$  mm lesion). SHI has resulted in improved tissue suppression in 146 cases, equal tissue suppression in 2 cases, and inferior tissue suppression in 1 case relative to HI. Malignancy has been confirmed by pathology in 37 cases. The visualization of flow among all lesions (as determined by ultrasound physicists) has been evident in 82 cases on PDI, 8 cases on 4D HI, and 68 cases on 3D SHI. Thus, while the diagnostic value has yet to be determined by the radiologists, initial results indicate that 4D SHI provides improved tissue suppression and visualization of flow in breast masses.

**1C-3****4:15 pm Characterization of Renal Masses with Harmonic and Subharmonic Contrast-Enhanced Ultrasound**

John Eisenbrey<sup>1</sup>, Priscilla Machado<sup>1</sup>, Colette Shaw<sup>1</sup>, Andrej Lyshchik<sup>1</sup>, Costas Lallas<sup>2</sup>, Edouard Trabulsi<sup>2</sup>, Daniel Merton<sup>1</sup>, Traci Fox<sup>3</sup>, Ji-Bin Liu<sup>1</sup>, Daniel Brown<sup>1</sup>, Flemming Forsberg<sup>1</sup>; <sup>1</sup>Department of Radiology, Thomas Jefferson University, USA, <sup>2</sup>Department of Urology, Thomas Jefferson University, USA, <sup>3</sup>Department of Radiological Sciences, Thomas Jefferson University, USA

**Background, Motivation and Objective**

Renal cell carcinoma is typically associated with tumor neovascularity and increased blood flow. Despite concerns related to enhanced axial imaging of patients with renal insufficiency, the current standard for renal mass characterization remains contrast-enhanced CT or MRI. Contrast-enhanced ultrasound (CEUS) relies on encapsulated microbubbles to visualize blood flow and carries no renal-associated contraindications. Additionally several nonlinear contrast specific imaging schemes have been developed to better visualize these microbubbles. The objective of this study was to compare coded harmonic imaging (CHI) to pulse-inversion subharmonic imaging (SHI) in the characterization of renal masses.

**Statement of Contribution/Methods**

Twelve patients with 13 renal masses provided informed consent for an off-label CEUS exam prior to renal mass biopsy and cryoablation. All scanning was performed on a modified Logiq 9 ultrasound scanner with a 4C probe (GE Healthcare, Milwaukee, WI). Following baseline imaging, patients received a 2 ml bolus IV injection of the ultrasound contrast agent Optison (GE Healthcare, Princeton, NJ) and 10 ml flush during simultaneous 2D dual imaging in both grayscale ( $f = 4.0$  MHz) and SHI ( $f_{\text{transmit}} = 2.5$  MHz,  $f_{\text{receive}} = 1.25$  MHz). Following a 15 min wait, patients received a 1 ml contrast injection during imaging with the unit's CHI package ( $f_{\text{transmit}} = 2.0$  MHz,  $f_{\text{receive}} = 4.0$  MHz). A blinded radiologist with experience in CEUS evaluated the heterogeneity, intensity, and wash-in/wash-out kinetics of enhancement in the mass relative to the renal cortex. Additionally, contrast signal time intensity curves (TICs) were constructed from both the renal mass and cortex, fit to a contrast wash-in model, and used to calculate the time to peak, perfusion, maximum intensity, and area under the curve. Finally, the radiologist and TIC findings from each CEUS imaging mode were compared to pathology.

**Results/Discussion**

Biopsy findings showed the 13 renal masses consisted of 9 renal cell carcinomas, 2 areas of benign renal parenchyma, 1 area of renal necrosis, and 1 benign oncocytoma. All masses showed heterogeneous enhancement with both SHI and CHI. Increased enhancement of the mass relative to the renal cortex was observed during the early contrast wash-in phase in 2/9 malignant and 3/4 benign lesions on SHI, and 3/9 malignant and 1/4 benign lesions on CHI. Early contrast wash out in the mass relative to the cortex was observed in 6/9 malignant and 0/4 benign lesions in SHI (sensitivity = 67%, specificity = 100%), and 8/9 malignant and 1/4 benign lesions in CHI (sensitivity = 89%, specificity = 75%). Comparison of the TIC parameters obtained from the renal mass and cortex of malignant lesions showed no statistically significant differences when compared to benign lesions ( $p > 0.2$ ). Thus, visualization of early contrast washout on CHI or SHI appears to be a reliable indicator of renal carcinoma on CEUS; albeit based on a limited sample size.

**1C-4****4:30 pm Plane-wave contrast imaging in transplanted kidney patients**

Matthew Bruce<sup>1</sup>, Kejian Wang<sup>2</sup>, Thomas Frappart<sup>1</sup>, Jean-Michel Correas<sup>2,3</sup>, Thanasis Loupas<sup>1</sup>, Aline Criton<sup>1</sup>, Jeremy Bercoff<sup>4</sup>, Olivier Couture<sup>2</sup>, Mickael Tanter<sup>2</sup>; <sup>1</sup>Supersonic Imagine, Aix en Provence, France, <sup>2</sup>Institut Langevin (ESPCI, CNRS, INSERM, Paris Diderot), Paris, France, <sup>3</sup>Radiology, Necker University Hospital, France

**Background, Motivation and Objective**

Unfocused ultrasound beams enable the imaging of microbubbles hundreds of times faster (kHz) than conventional methods by enabling the reconstruction of an entire plane from a single transmit. Moreover, this approach distributes ultrasound energy to microbubbles in temporally and spatially different manners than focused beams. The advantages of ultrasound contrast pulsing schemes and ultrafast imaging have been explored both in-vitro and in-vivo. The goal of this study is to implement plane-wave contrast sequences on a clinical scanner (Aixplorer, SuperSonic Imagine, France) and investigate its behavior in transplanted kidneys relative to conventional focussed acquisitions.

**Statement of Contribution/Methods**

Renal transplant patients were injected with 1 mL of Sonovue (Bracco, Switzerland). Synthetic plane-wave imaging was combined with contrast pulsing sequences and integrated on the Aixplorer in two different modes. The first mode (single-shot) is a single acquisition of a variable number of frames capable of frame-rates in the kHz range. The second mode is a continuous mode with lower frame rates (~Hz) limited by image reconstruction. Acquisitions consisted of conventional focused, single plane wave, and continuous plane wave acquisitions using a SL10-2 linear probe. All contrast pulsing sequences consisted of changing both phase and amplitude.

**Results/Discussion**

Figure 1a and 1b illustrate conventional focused and single angle plane wave acquisitions respectively in a kidney transplant. Roughly a 10 dB difference in SNR was observed between plane wave and focused images. Figure 1c illustrates differences in temporal variations on the order of milliseconds in differing vasculature. Figure 1d and 1e show conventional focused and continuous plane wave acquisitions in a different kidney transplant. The continuous plane wave acquisition consisted of 11 angles synthetically combined. The SNR was a few dB less than in the focused case (Fig. 1d), however the plane had shifted bringing in regions of microbubbles not previously depleted from scanning in the focalized mode.

The feasibility of imaging of microbubbles using unfocused beams has been demonstrated in transplanted kidneys. The benefits of imaging microbubbles with frame-rates from 100s to kilohertz frame-rates with synthetic plane wave imaging can now be further explored.

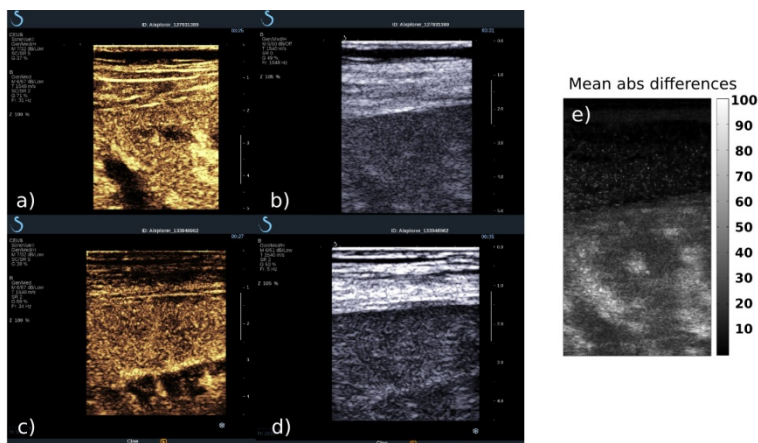


Fig 1: a) Focused contrast image of kidney transplant. b) First plane-wave image of a single-shot acquisition at 1 Khz 6 seconds after a). c) Focused contrast image. d) Eleven angle synthetic plane wave image in real-time mode at 5Hz. e) Mean absolute 3 frame differences over the first 50 frames from the acquisition in b) displayed as a percent of the maximum mean difference.

1C-5

#### 4:45 pm Tumor perfusion and vascular morphology measurements using dynamic contrast-enhanced ultrasound imaging

Kenneth Hoyt<sup>1</sup>, Heidi Umphrey<sup>1</sup>, Mark Lockhart<sup>1</sup>, Michelle Robbin<sup>1</sup>, Andres Forero-Torres<sup>1</sup>; <sup>1</sup>University of Alabama at Birmingham, USA

##### Background, Motivation and Objective

The goal of this study was to investigate the use of quantitative perfusion and vascular morphology measurements derived from dynamic contrast-enhanced ultrasound (DCE-US) images for describing the longitudinal response of breast cancer to neoadjuvant therapy.

##### Statement of Contribution/Methods

Six patients with newly diagnosed operable breast cancer and scheduled to receive neoadjuvant therapy (bevacizumab + letrozole) were enrolled in this pilot study. Patients were scanned before and after microbubble (MB) contrast agent dosing (Definity) using a Philips iU22 US system equipped with an L9-3 transducer before therapy initiation (baseline) and again at weeks 10, 16, 22, and 28. Surrogate measures of tumor perfusion were computed using custom Matlab software. Briefly, tumor tissue region-of-interests (ROIs) were manually segmented from a sequence of DCE-US images and then the mean time-intensity curve describing the history of MB flow was analyzed to compute parametric perfusion measures (e.g., arrival time,  $T_{IN}$ ; time-to-peak enhancement,  $T_{PK}$ ; wash-in rate,  $S_{IN}$ ; wash-out rate,  $S_{OUT}$ ; peak enhancement,  $I_{PK}$ ; area under the curve, AUC). Thereafter, tumor perfusion images were skeletonized using a thinning algorithm and further processed to extract vascular morphology features (e.g., vessel-to-tumor ratio,  $V_R$ ; number of bifurcation,  $N_B$ ; number of vessels,  $N_V$ ; vessel length,  $V_L$ ; vessel tortuosity,  $V_T$ ). All vascular trees were color-coded with spatial parametric perfusion images and overlaid on the DCE-US images to provide a visual description of these tumor features. Statistics (mean  $\pm$  SE) from the tumor encompassing ROI were also generated for each subject and time point.

##### Results/Discussion

Review of imaging results reveals that human breast cancer can exhibit a very pronounced perfusion profile not evident from review of grayscale US images alone. On average, combination therapy produced a progressive change in tumor blood volume (AUC and IPK metrics; 16.0% and 13.7%, respectively) and flow velocity (TPK, WIR and WOR metrics; 70.5%, 39.5%, and 38.1%, respectively) which manifested weeks before any reduction in tumor size was observed. These changes in tumor perfusion were matched by physical changes in the tumor microvascular network. Of note, there was a progressive reduction in the number of vessels (25.8%) and branch points (bifurcations, 46.1%) associated with the breast tumor (and surrounding tissue) along with a marked decrease in vessel tortuosity (21.4%). These changes also corresponded to a slight increase in vessel length (5.6%). Collectively, these changes in vascular architecture suggest that a partial renormalization of tumor vasculature had occurred representing a hallmark feature of antiangiogenic therapy. Review of both imaging and immunohistologic features revealed that all patients had a partial response to treatment with an average residual cancer burden score obtained at surgery of  $3.1 \pm 0.4$ .

## 2C - MEL: Elastography: Clinical Applications

Waldorf

Thursday, September 4, 2014, 3:30 pm - 5:00 pm

Chair: **Mickael Tanter**  
INSERM, Paris

2C-1

### 3:30 pm Intra-operative quantitative measurement of brain tumour stiffness and intracranial pressure assessment using ultrasound shear wave elastography

marion imbault<sup>1</sup>, dorian chauvet<sup>2</sup>, laurent capelle<sup>2</sup>, charlie demené<sup>1</sup>, mathieu mossad<sup>1</sup>, jean-luc gennisson<sup>1</sup>, mickael tanter<sup>1</sup>; <sup>1</sup>ESPCI ParisTech CNRS UMR7587 INSERM U979, Institut Langevin, PARIS, France, <sup>2</sup>Hôpital La Pitié Salpêtrière, Service de Neurochirurgie, paris, France

#### Background, Motivation and Objective

By giving access to tissue stiffness ultrasound Shear Wave Elastography (SWE) is an emerging technology that enable surgical procedure guiding [Chan, Epilepsia, 2014]. Improving quality of brain tumor resection and predict brain swelling are major concerns for neurosurgeons. SWE could be decisive for both of these issues. A clinical study was undertaken, including normal brain and tumors data collected from intraoperative SWE. The aim is to improve shear wave imaging for brain tissue investigation by correlating in vivo stiffness data and histology. At the same time Intracranial Pressure (ICP) was studied, first ex vivo and then during in vivo surgery, to observe brain swelling by using SWE.

#### Statement of Contribution/Methods

Shear waves were generated by using ultrasonic acoustic radiation force (SL10-2 6MHz) and imaged in real-time by an ultrafast ultrasound scanner (Aixplorer, Supersonic Imagine) up to 20 000 frames/s. Shear waves velocity was color coded in m/s or linked to Young's Modulus E (kPa). First, the link between SWE and ICP was experimentally assessed on ex vivo calf's brains (N=6) according to the acoustoelasticity theory. The study was then performed intra-operatively on 62 adult patients presenting brain tumor. While stiffness measurements were systematically compared to histology, stiffness evolution before/after meninges opening and before/after tumor resection gave local information about ICP.

#### Results/Discussion

Histology allows classification of the different types of brain tumor into four main groups: metastases (N=15), meningiomas (N=15), low-grade gliomas (N=16) and high-grade gliomas (N=16). SWE was able to characterize each group of tumor by a mean elasticity value, respectively:  $16.7 \pm 8.3$  kPa,  $32.9 \pm 9.4$  kPa,  $25.2 \pm 5.3$  kPa, and  $10.5 \pm 5.2$  kPa. Statistical analysis using ROC curve analysis shows that SWE could help for diagnosis during tumor resection by distinguishing benign tumors from malignant tumors (AUROC: 0.789,  $p < 0.0001$ ). This technique can also be useful in case of hard tumors to distinguish blood residues from tumors leftover. Moreover stiffness data in peritumoral area could provide decisive information to differentiate normal brain tissue from infiltrated one, especially in low-grade gliomas. Regarding pressure measurements, SWE was first performed in ex vivo brain and E was found to increase (from  $22.3 \pm 12.1$  kPa to  $53.8 \pm 12.8$  kPa, ~58.6% increase) with an increasing pressure from 0 to 80 mmHg. Stiffness variations in peritumoral healthy tissues were recorded in vivo before and after tumor resection (from  $14.7 \pm 9.9$  kPa to  $6.6 \pm 1.6$  kPa, ~55.1% decrease). Such ICP variations highlight the compression of brain tissue by tumors. Both theoretical and experimental link between ICP and SWE enable access to ICP from SWE. This study present great perspective for SWE to ensure full tumor removal and to quantitatively predict brain swelling by using noninvasive ICP measurement.

2C-2

### 3:45 pm Quantitative Ultrasound Spectroscopy and Elastography: Assessing Chemotherapy Response in Breast Cancer Patients by Monitoring Alterations in Tumour Bio-Acoustic and Bio-Mechanical Properties

Ali Sadeghi-Naini<sup>1,2</sup>, Gregory Czarnota<sup>1,2</sup>; <sup>1</sup>Imaging Research | Radiation Oncology, Sunnybrook Health Sciences Centre, Toronto, ON, Canada, <sup>2</sup>Medical Biophysics | Radiation Oncology, University of Toronto, Toronto, ON, Canada

#### Background, Motivation and Objective

No standard cancer treatment works for all patients, with approximately 60% of cancer chemotherapy regimens failing to cure patients. This highlights the necessity for developing a method for the early assessment of tumour response which would facilitate adjustments to standard therapies. Responses to cancer therapies frequently result in early micro-structural changes in tumours which are linked to measurable alterations in tumour bio-acoustic and bio-mechanical properties. Quantifying these in composite provides measures which can potentially be used as early predictors of ultimate tumour response.

#### Statement of Contribution/Methods

This study investigated, for the first time, concurrent alterations in bio-acoustic and bio-mechanical characteristics of locally advanced breast cancer tumours in response to chemotherapy, using quantitative ultrasound (QUS) spectroscopy and elastography. The correlations between microscopic and gross changes in tumour were assessed at different times, and the efficacy of the resulting hybrid ultrasonic biomarkers was evaluated. Breast cancer patients received neoadjuvant chemotherapy and ultrasound (US) data were acquired prior to the start of therapy, and at four times during course of treatment. QUS spectral parameters (mid-band fit and 0-MHz intercept) sensitive to the size and concentration of acoustic scatterers were derived from US data. Strain images were used to probe at tumour stiffness relative to the normal tissue. Patient tumour responses were determined using histopathology analysis on corresponding mastectomy specimens.

#### Results/Discussion

Results indicated statistically significant increases in US backscatter power, linked to decreases in tumour stiffness, in responding patients contrary to non-responders. This was associated with significant increases in QUS parameters, as well as in tumour strain ratio. Mid-band fit and 0-MHz intercept in combination, could predict the ultimate treatment response of patients with a sensitivity/specificity of 80% / 87.5% and 100% / 62.5% at weeks one and four after the start of treatment, respectively. Tumour strain ratio could differentiate between treatment responding and non-responding patients with sensitivity/specificity of 60% / 50% and 80% / 75% at weeks one and four of treatment, respectively. These three parameters in a hybrid profile could separate the two patient populations with sensitivity/specificity of 80% / 75% and 100% / 75% at weeks one and four of treatment, respectively. In addition, significant inverse correlations were observed after four weeks of treatment between changes in tumour echogenicity and alteration in tumour stiffness ( $r = -0.71$ ,  $p = 0.007$ ), whereas no considerable correlation was found at week one. The results imply that these two imaging modalities can be complementary in the context of therapy response monitoring, permitting prediction of patient responses early on during a course of chemotherapy.



## 2C-3

**4:00 pm Comparison of SWS Estimates in *Ex vivo* non-pregnant cervix vs. *In vivo* pregnant cervix**

Lindsey Carlson<sup>1</sup>, Helen Feltovich<sup>1,2</sup>, Mark Palmeri<sup>3</sup>, Alejandro Munoz Del Rio<sup>1</sup>, Timothy Hall<sup>1</sup>; <sup>1</sup>Medical Physics, University of Wisconsin-Madison, Madison, Wisconsin, USA, <sup>2</sup>Maternal Fetal Medicine, Intermountain Healthcare, Provo, Utah, USA, <sup>3</sup>Biomedical Engineering, Duke University Pratt School of Engineering, Durham, North Carolina, USA

**Background, Motivation and Objective**

Throughout pregnancy the cervix begins to soften and it must shorten and dilate (a process referred to as 'ripening') to allow for delivery of the fetus. Error in the timing of this softening may be associated with preterm birth. Currently, there is no objective method to assess changes in the cervix during pregnancy. Our goal is to develop a safe, non-invasive, objective method to assess cervical softness. The aim of our current work is to compare shear wave elasticity measurements in *ex vivo* specimens to *in vivo* measurements in pregnant subjects to determine any confounding factors that may influence shear wave speed (SWS) estimates.

**Statement of Contribution/Methods**

*Ex vivo* hysterectomy specimens (n = 22) were collected from normal non-pregnant women with no cervical pathologies, a subset of which were ripened (n = 13) with misoprostol. *In vivo* female subjects (n = 20) scheduled for induction of labor at term with cervical ripening were recruited. Scanning was performed with a Siemens S2000 Ultrasound system. A 9L4 linear array transducer was used for the *ex vivo* study, and a prototype 128-element catheter probe operated in linear array mode was used for the *in vivo* measurements. Measurements were made at the mid-position along the length of the cervix on the anterior half with the transducer aligned parallel to the endocervical canal. A 5x5mm region of interest was placed mid-way through the thickness of the cervix (about 7mm from the outside of the cervix) and repeat measurements were made. The *ex vivo* measurements were made at room temperature and *in vivo* measurements at body temperature. The SWS were estimated using an iterative Random Sample Consensus (RANSAC) method.

**Results/Discussion**

Previous studies have shown there is large spatial variability in SWS estimates in the non-pregnant cervix and determined an appropriate sampling location. The SWS estimates for anterior mid-location in the *ex vivo* ripened specimens (n = 13) were  $2.40 \pm 0.32$  m/s compared to  $2.21 \pm 0.74$  m/s for the *in vivo* third trimester pregnant cervix (n = 18). Using a two-tailed t-test these were not significantly different at the 0.05 significance level (p = 0.42). This suggests that inducing ripening in a non-pregnant cervix is similar to a 3rd trimester pregnant cervix that is not soft enough for birth. This compares to the SWS estimates of  $3.44 \pm 0.93$  m/s at the anterior mid location for *ex vivo* non-pregnant unripened cervix and  $1.56 \pm 0.43$  m/s for *in vivo* pregnant ripened cervix. Confounding factors such as excitation frequency, temperature, and loading conditions may be important and will be discussed in this analysis. These results suggest there is a large range in SWS values during pregnancy and SWS estimation should be an effective quantitative tool to evaluate cervical compliance with potential for applications to preterm birth.

**Acknowledgements:** This work was supported by NIH grants T32CA009206, R21HD061896, R21HD063031, R01HD072077 and Intermountain Medical and Research Foundation.

## 2C-4

**4:15 pm Sensitivity of 3D ARFI in vivo imaging in Prostate Cancer (PCa) Detection**

Zachary Miller<sup>1</sup>, Mark Palmeri<sup>1</sup>, Tyler Glass<sup>1</sup>, Stephen Rosenzweig<sup>1</sup>, Thomas Polascik<sup>2</sup>, Andrew Buck<sup>3</sup>, John Madden<sup>3</sup>, Kathryn Nightingale<sup>1</sup>; <sup>1</sup>Biomedical Engineering, Duke University, Durham, NC, USA, <sup>2</sup>Department of Surgery, Duke University Medical Center, USA, <sup>3</sup>Department of Pathology, Duke University Medical Center, USA

**Background, Motivation and Objective**

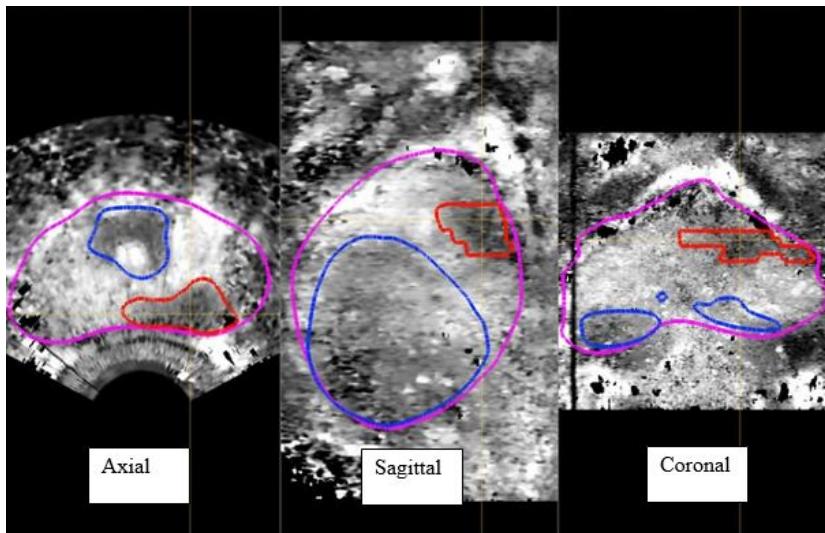
No reliable real-time imaging methods exist for PCa visualization. Instead, urologists rely on systematic sampling biopsy for PCa diagnosis. These methods yield limited information about tumor extent and location which leads to over treatment. The objective of this work was to evaluate the ability of Acoustic Radiation Force Impulse (ARFI) imaging to visualize and identify PCa lesions.

**Statement of Contribution/Methods**

*In vivo* ARFI prostate data were acquired for 22 patients with known PCa using an Acuson ER7B transducer coupled to a Siemens Acuson SC2000 Ultrasound scanner swept through the prostate to generate 3D imaging datasets. ARFI raw data were used to reconstruct ARFI prostate volumes which were imported into 3D Slicer. A reader, blinded to histopathology, identified and segmented ARFI lesions based on their locations, contrast in the peripheral zone, circumscribed boundaries, and smooth texture on all three imaging planes. An example index lesion (capsule outlined in magenta, central gland outlined in blue, index lesion outlined in red) is shown in Fig 1 with these properties. ARFI index and secondary lesion locations were then compared to whole mount histopathology. An ARFI lesion was considered a true positive if any part of the ARFI lesion overlapped with the histopathology lesion, otherwise the lesion was a false negative.

**Results/Discussion**

ARFI imaging identified PCa lesions in a volume-dependent manner with sensitivity values for index and secondary lesions of 0.78 and 0.17, respectively. In a four patient subset with multifocal disease, index lesions were 4 times larger than secondary lesions, with the majority of secondary lesions falling under 0.5 cc, the limit of prostate cancer clinical significance. Further, among the index lesions, ARFI imaging sensitivity for index lesions >5% of the gland volume was 0.87, while ARFI imaging sensitivity for index lesions <5% of the gland volume was 0.62. These results suggest ARFI imaging identifies large, clinically relevant, peripheral zone cancers with high sensitivity.



2C-5

**4:30 pm Comb-Push Ultrasound Shear Elastography of Thyroid: Preliminary In Vivo Human Study**

Mohammad Mehrmohammadi<sup>1</sup>, Max Denis<sup>1</sup>, Pengfei Song<sup>1</sup>, Shigao Chen<sup>1</sup>, Mostafa Fatemi<sup>1</sup>, Azra Alizad<sup>1</sup>; <sup>1</sup>Physiology and Biomedical Engineering, Mayo Clinic, Rochester, MN, USA

**Background, Motivation and Objective**

Conventional ultrasound (US) imaging plays an important role as a standard practice in detection of thyroid nodules. However, low specificity of thyroid US in differentiation between benign and malignant thyroid nodules leads to a large number of unnecessary thyroid biopsies. In clinical practice, an overwhelming majority of thyroid biopsy turn out to be benign. Therefore, there is a need for an additional, complementary, and noninvasive diagnostic tool to provide clinically relevant information about thyroid nodules to reduce the rate of unnecessary biopsies.

**Statement of Contribution/Methods**

The goal of this study is to evaluate the feasibility of utilizing Comb-Push Ultrasound Shear Elastography (CUSE) to measure the stiffness of thyroid nodules and use this information to classify the nodules. CUSE is a fast and robust 2D elasticity imaging in which multiple laterally-spaced simultaneous acoustic radiation force (ARF) beams (resembling teeth of a comb) are utilized to produce multiple shear wave sources (Song, et al., IEEE Trans. Medical Imaging, 31, 1821-1832, 2012). As a result, a 2D full field of view (FOV) elasticity map can be obtained with only one push-detect acquisition. CUSE was implemented on a fully programmable US platform (Verasonics V-1, Verasonics Inc., Redmond, WA) equipped with a linear array transducer L7-4 (Philips Healthcare, Andover, MA). The center frequency for the ARF push beams was set at 4.09 MHz. The ARF pulse duration was set at 600  $\mu$ s. A group of healthy volunteers (n=5) and a group of patients with thyroid abnormalities (n=9, 6 benign and 3 malignant) were included in this study. In case of patients with thyroid nodules, CUSE was performed prior to needle biopsy and the results were compared to those of pathology.

**Results/Discussion**

The measured shear wave speeds in thyroid tissue as well as thyroid nodules were converted to the Young's modulus (E) which indicates tissue stiffness. Our results indicate an increase in measured stiffness of thyroid nodules compared to that of normal thyroid tissue (Fig. 1). This increase was significantly larger in malignant nodules compared to benign. The Young's modulus in normal thyroid tissue, benign, and malignant nodules were found to be  $22.9 \pm 8.6$  kPa,  $79.5 \pm 17.5$  kPa, and  $162.4 \pm 7.6$  kPa, respectively. Results of this study suggest the potential utility of CUSE in differentiating between benign and malignant thyroid nodules.

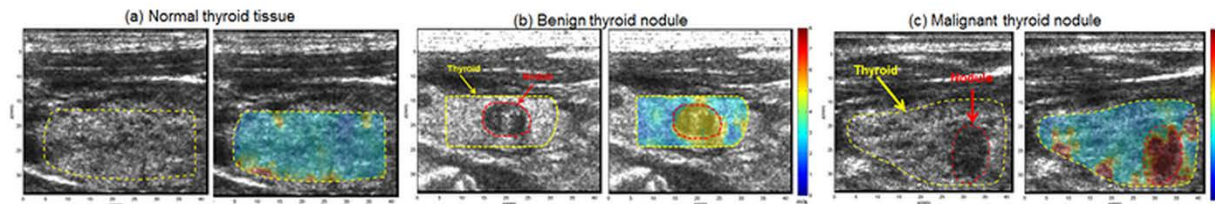


Figure 1: Pairs of US (left) and CUSE (right) shear wave speed map of: (a) normal thyroid tissue, (b) a benign thyroid nodule, and (c) a malignant thyroid nodule (FOV=35 × 42 mm).

2C-6

**4:45 pm Shear wave elastography of ex vivo human corneas using phase-sensitive optical coherence tomography**

Thu-Mai Nguyen<sup>1</sup>, Tuong T. Shen<sup>2</sup>, Shaozhen Song<sup>1,3</sup>, Lei Shi<sup>1</sup>, Zhihong Huang<sup>2</sup>, Ruikang K. Wang<sup>1,2</sup>, Matthew O'Donnell<sup>1</sup>; <sup>1</sup>Department of Bioengineering, University of Washington, Seattle, WA, USA, <sup>2</sup>Department of Ophthalmology, University of Washington, Seattle, WA, USA, <sup>3</sup>School of Engineering, Physics and Mathematics, University of Dundee, Dundee, United Kingdom

**Background, Motivation and Objective**

Assessing the biomechanical properties of the cornea can provide clinically valuable information in addition to structural images for better management of pathologies (e.g. glaucoma) or refractive surgeries. We propose a shear wave elastography (SWE) method based on phase-sensitive optical coherence tomography (PhS-OCT). OCT provides micron scale resolution and a high displacement sensitivity that are ideal for ophthalmic applications. We investigated elasticity variations of excised human corneas with the intraocular pressure (IOP).

### Statement of Contribution/Methods

SWE launches a propagating shear wave in tissues and retrieves tissue elasticity from the shear wave speed. We used a piezoelectric actuator in contact with the cornea to induce kHz-range shear waves. The resulting displacements were tracked using a PhS-OCT system operating in M-B mode at an equivalent frame rate of 45 kHz. The imaging area is 2 mm x 3 mm (depth x lateral) and the pixel size is 4.15  $\mu\text{m}$  x 23.4  $\mu\text{m}$  (depth x lateral). The local shear wave speed is then computed using time-of-flight estimations. We performed experiments on excised human corneas obtained from the eye bank. The corneas were mounted on an artificial anterior chamber allowing the IOP to vary. Elasticity measurements were acquired for IOP ranging from 10 to 40 mmHg. We also performed a lamellar cut on one cornea, similarly to that done clinically for LASIK surgery (myopia correction), and repeated the measurements for different IOP levels.

### Results/Discussion

We obtained significant shear wave speed variations with IOP with a sensitivity < 5 mmHg (see Fig. 1). The repeatability over N=3 repeated measurements was estimated to be < 0.25% of the shear wave speed. The shear wave speed of the cut cornea was estimated to be 17 +/- 2 % lower than that of the intact cornea (mean value and standard deviation over measurements at different IOP from 10 to 40 mmHg). These preliminary studies demonstrate the feasibility of using PhS-OCT to image the elasticity of human corneas. Further studies will focus on enlarging the imaging range to cover the entire 12-mm cornea. Non-contact shear sources will also be investigated for clinical translation.

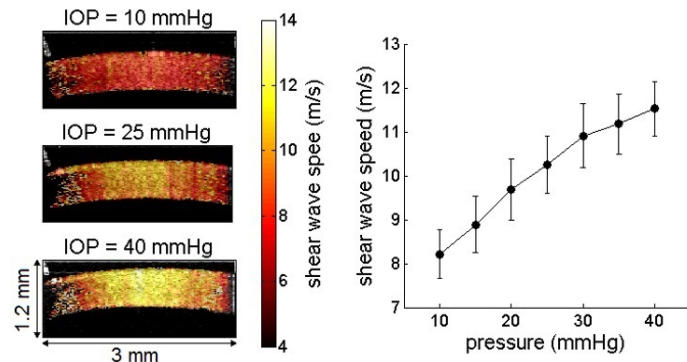


Fig. 1. *Left*: Shear wave speed maps (color scale) of an excised human cornea (31 years old, female donor) at different IOP levels superimposed to the structural image (gray scale). The actuator can be seen in the top left corner. *Right*: Median shear wave speed as a function of IOP. The median value was computed over the central 1-mm of the cornea. The error bars corresponds to the spatial heterogeneity.

### 3C - MTC: Low Frequency Tissue Characterization

Boulevard

Thursday, September 4, 2014, 3:30 pm - 5:00 pm

Chair: **William O'Brien**  
Univ. of Illinois, Urbana-Champaign

3C-1

#### 3:30 pm Characterizing the Pulley Tissues of Trigger Finger with Statistical Parameters of Ultrasonic Backscattering Signals

Yi-Hsun Lin<sup>1</sup>, Tai-Hua Yang<sup>2</sup>, Shyh-Hau Wang<sup>1</sup>, Hsiao-Bai Yang<sup>3</sup>, Fong-Chin Su<sup>2</sup>; <sup>1</sup>Computer Science and Information Engineering, National Cheng Kung University, Taiwan, <sup>2</sup>Biomedical Engineering, National Cheng Kung University, Taiwan, <sup>3</sup>Ton Yen General Hospital, Taiwan

##### Background, Motivation and Objective

Trigger finger is a common disease, which is usually diagnosed by palpating the first annular (A1) pulley of the hand. The accuracy of palpation diagnostics is certainly dependent on physician's experiences. Recently, ultrasound images have been utilized to better assess trigger finger objectively. However, in addition to lacking appropriate resolution to differentiate pulley tissues, those ultrasound scanners used in clinics remain short of providing quantitative ultrasonic properties for the A1 pulley. Therefore, the present study tended to measure signals backscattered from the A1 pulley by a 30 MHz high-frequency ultrasound and to explore tissue characterization using statistical models estimated from the acquired signals.

##### Statement of Contribution/Methods

The *ex vivo* experiments were performed from the normal and diseased A1 pulleys sampled respectively from the cadaver and patients with trigger finger. The excised tissues were immersed in saline solution tank and subsequently scanned at various angles with respect to the fiber orientation of the A1 pulley ranging from 0° to 90°. Statistical parameters, including Nakagami, Weibull, and generalized gamma (GG) models, were estimated from the acquired backscattering signals for quantifying the tissue properties. The histological slices of corresponding tissues were made for results verification.

##### Results/Discussion

Fig. 1(a) demonstrates B-mode images of the normal and diseased A1 pulleys corresponding to the scanning angles of 0° and 90°, respectively. The shape parameters (Nakagami-*m*, Weibull-*b*, and GG-*c*) as a function of scanning angle were shown in Fig. 1(b), where the normal A1 pulley tended to decrease with the increase of scanning angle and those of trigger finger pulley seemed to be less variant. Specifically, the slopes of Nakagami-*m*, Weibull-*b*, and GG-*c* for normal A1 pulleys were  $-2.1 \times 10^{-3} \pm 5.0 \times 10^{-4}$ ,  $-2.8 \times 10^{-3} \pm 6.6 \times 10^{-4}$ , and  $-8.1 \times 10^{-3} \pm 1.7 \times 10^{-3}$ ; whereas those of diseased A1 pulleys were  $-1.5 \times 10^{-4} \pm 4.4 \times 10^{-4}$ ,  $-2.3 \times 10^{-4} \pm 6.3 \times 10^{-4}$ , and  $-1.5 \times 10^{-3} \pm 2.1 \times 10^{-3}$ , respectively. The slopes of shape parameters differed significantly between normal and diseased A1 pulleys indicating that these statistical models could be applied to effectively characterize tissues of different pathological conditions.

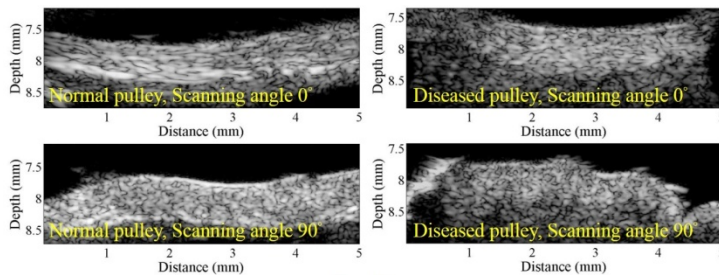


Fig. 1(a)

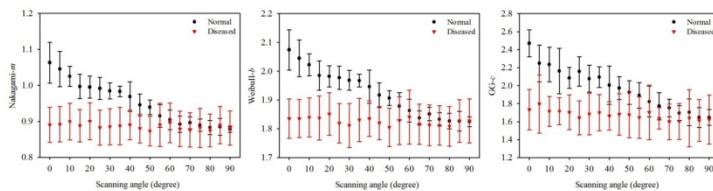


Fig. 1(b)

3C-2

#### 3:45 pm 3D Ultrasound Backscatter Tensor Imaging (BTI): analysis of the full spatial coherence on a 2D matrix array probe

Clement Papadacci<sup>1</sup>, Jean Provost<sup>1</sup>, Jean-Luc Gennisson<sup>1</sup>, Juan-Esteban Arango Ossa<sup>1</sup>, Marion Imbault<sup>1</sup>, Mathias Fink<sup>1</sup>, Mickael Tanter<sup>1</sup>, Mathieu Pernot<sup>1</sup>; <sup>1</sup>Institut Langevin, ESPCI ParisTech, CNRS UMR 7587, INSERM U979, Paris 7, Paris, France

##### Background, Motivation and Objective

The assessment of fiber architecture is of major interest in the progression of myocardial disease. Recently, we have introduced the Ultrasound Backscatter Tensor Imaging (BTI) a technique that use the anisotropy of the spatial coherence of the ultrasound backscattered field to reveal the structure of the myocardium [1]. However, this technique was limited by the need of a mechanical rotation of a 1D probe and was capable to retrieve the fiber orientation only along the rotation axis. The objective of this study was to investigate the spatial coherence in 2D using a matrix array ultrasonic probe and to apply the ultrasound BTI to map the fiber architecture of myocardial sample in a 3D volume.

**Statement of Contribution/Methods**

Acquisitions were performed using a 2D matrix array (3MHz, 32x32 elements, 0.3 mm pitch, Vermon) connected to a customized, programmable, 1024 channel ultrasound system, in an isotropic gel, 3 *ex vivo* bovine muscles and 3 porcine myocardial samples. 121 2D tilted plane waves were transmitted. The RF backscattered signals received by each transducer elements were recorded and coherent compounding of the RF signals received from each plane wave was performed at each point of the volume. The autocorrelation of compounded RF signals received on the elements was performed by pairs to compute the 2D coherence functions (CF) at each point of space. An elliptic fit was used on the 2D CF and the local fiber orientation was derived from the orientation of the major axis. Fractional anisotropy (FA) was calculated using the major axis and the minor axis of the ellipse.

**Results/Discussion**

In the isotropic gel, 2D CF at each point were found to be isotropic ( $FA=0.05\pm0.1$ ) (fig a) whereas in the bovine muscles, CF were found to be anisotropic ( $FA=0.36\pm0.12$ ) with larger coherence along the fibers. In the myocardium, the 2D CF were also found to be anisotropic ( $FA=0.34\pm0.15$ ), and the orientation of the fibers was found to vary transmurally across the myocardial thickness due to the complex fibers distribution (fig b, c). The fiber orientation was successively determined at different locations in space allowing to map fiber orientations over the entire volume. Spatial coherence on 2D matrix probe can thus reveal the micro-structure of soft tissues in 3D. By reducing the number of transmitted plane waves, 3D BTI could be used in real-time for non-invasive mapping of myocardial fibers.

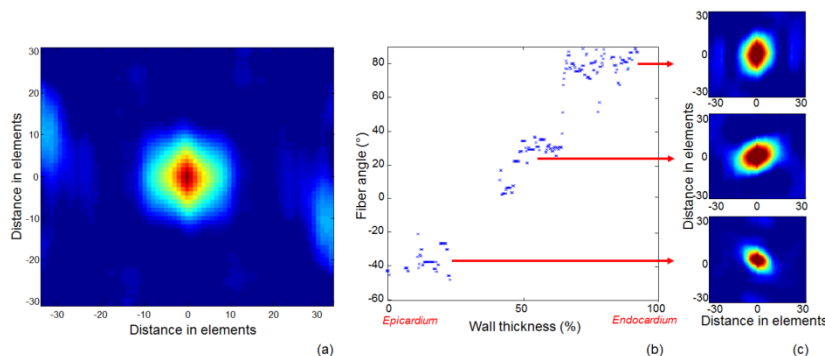


Figure. (a) An example of a 2D coherence function of one point of a volume in the isotropic gel. (b) An example of the fibers orientation variation, on one line of a volume, through the myocardial wall thickness. The associated coherence functions are displayed (c) for three main orientations.

- [1] C. Papadacci, M. Pernot, M. Tanter, and M. Fink, "Towards backscatter tensor imaging (BTI): Analysis of the spatial coherence of ultrasonic speckle in anisotropic soft tissues," in *Ultrasonics Symposium (IUS), 2013 IEEE International*, 2013, pp. 1208–1211.

**3C-3****4:00 pm Acousto-electric speckle pattern in Lorentz force electrical impedance tomography**

Pol Grasland-Mongrain<sup>1</sup>, François Destrempes<sup>1</sup>, Jean-Martial Mari<sup>2</sup>, Rémi Souchon<sup>2</sup>, Stéfan Catheline<sup>2</sup>, Jean-Yves Chapelon<sup>2</sup>, Cyril Lafon<sup>2</sup>, Guy Cloutier<sup>1</sup>; <sup>1</sup>University of Montreal Hospital, Canada, <sup>2</sup>University Claude-Bernard Lyon 1, France

**Background, Motivation and Objective**

Lorentz Force Electrical Impedance Tomography (LFEIT) is a medical imaging technique of the electrical impedance of biological tissues. It is based on transmitting an ultrasound wave in a medium placed in a magnetic field, which induces an electrical current due to Lorentz force. The measurement of this current with electrodes allows producing electrical impedance images with a spatial resolution close to ultrasound (US) imaging. The goal of this study was to assess the existence of an acousto-electric speckle in the LFEIT technique, similar to the US speckle.

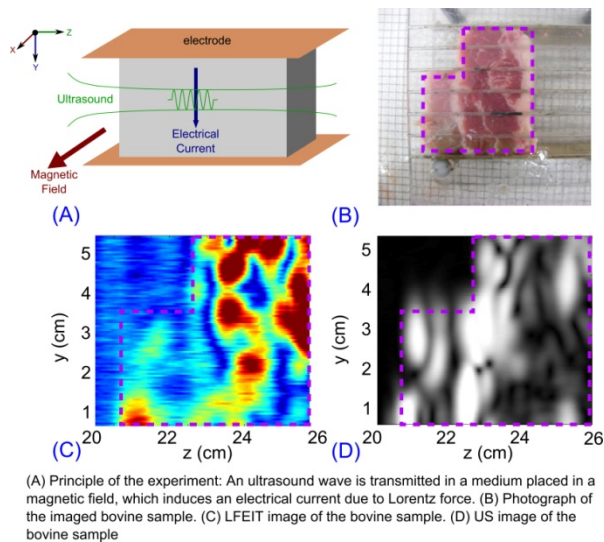
**Statement of Contribution/Methods**

In the first experiment, a 500 kHz transducer generated a 1 MPa peak pressure ultrasound wave in a gelatin phantom placed in a 300 mT magnetic field. The current measured by two electrodes was then compared to the US signal using the same experimental conditions. The gelatin phantom was then replaced by a bovine muscle sample and both LFEIT and US images were produced line by line by moving the transducer perpendicularly to the ultrasound axis.

**Results/Discussion**

The correlation coefficient of the LFEIT and US 1D signals on the gelatin phantom was equal to 0.87, indicating an excellent similarity as suggested by theoretical considerations. The bovine sample presented a speckle pattern on both image types. This suggests the existence of an acousto-electric speckle with spatial characteristics driven by the acoustic parameters but related to electrical impedance inhomogeneities. These electrical impedance inhomogeneities can thus be studied using LFEIT at a scale controlled by the acoustic wavelength instead of the electromagnetic wavelength, which is 5 orders of magnitude larger at a same frequency, and would be prohibitive in the context of biological tissue imaging. Furthermore, electrical impedance inhomogeneities constitute non-redundant extra information to acoustic impedance inhomogeneities observed in US imaging. Consequently, US speckle-based techniques, such as compound imaging, speckle-tracking or quantitative US, could be applied to LFEIT imaging and provide new relevant information on biological tissues.





3C-4

#### 4:15 pm Quantitative Ultrasound Backscatter Parameters in the Human Cervix

Quinton Guerrero<sup>1</sup>, Lindsey Carlson<sup>1</sup>, Helen Feltovich<sup>1,2</sup>, Timothy Hall<sup>1</sup>; <sup>1</sup>Medical Physics Department, University of Wisconsin-Madison, Madison, WI, USA, <sup>2</sup>Maternal Fetal Medicine Department, Intermountain Healthcare, Provo, Utah, USA

##### Background, Motivation and Objective

Attenuation and excess backscattered power loss (eBSPL) have been studied as potential quantitative ultrasound (QUS) parameters for detecting and quantifying cervical change during pregnancy and to assess the risk of preterm birth. Previous studies have demonstrated that collagen in the cervix is aligned and layered, and that the shear wave speed increases along the length of the cervix from the distal to proximal end. This suggests a structural change that might also influence attenuation and backscatter properties in the cervix. This study was designed to investigate the possibility of anisotropic, spatially dependent QUS parameters in ex vivo cervix tissues.

##### Statement of Contribution/Methods

Hysterectomy specimens (N=14) were collected from premenopausal women undergoing hysterectomy for benign reasons. The specimens were bivalved and pinned to sound absorbing rubber and positioned so that the endocervical canal was parallel to the face of the transducer. Samples were scanned along the full length of the cervix with a Siemens Acuson S2000 using the 18L6 linear array. RF frames were collected with beam steering from -40 degrees to +40 degrees in steps of 4 degrees. Reference phantom data was collected for the same angles, and attenuation and eBSPL were calculated using the Reference Phantom Method. Power spectral estimates were calculated using the multitaper method to reduce bias and variance in parameter estimates. The internal and external os of the cervix were used to group QUS parameter estimates among cervix specimens based upon fractional distance along the canal.

##### Results/Discussion

There were differences in the mean attenuation among spatial locations (3.04 dB cm<sup>-1</sup> MHz<sup>-1</sup> vs 2.43 dB cm<sup>-1</sup> MHz<sup>-1</sup> at the distal and proximal ends, respectively). The standard deviation of attenuation showed a decreasing trend along the cervical canal (1.11 dB cm<sup>-1</sup> MHz<sup>-1</sup> vs 0.757 dB cm<sup>-1</sup> MHz<sup>-1</sup> at the distal and proximal ends, respectively). Attenuation estimates also displayed anisotropy at some spatial locations (0.6 dB cm<sup>-1</sup> MHz<sup>-1</sup> average difference between the -40° and +40° estimates at the mid-proximal location). Accounting for the effects of angle of interrogation and spatial location, attenuation estimates showed statistically significant differences between ripening states. (p < 0.001). Findings for eBSPL estimates were in agreement with the attenuation trends.

This work was supported by NIH grants R01HD072077, R21HD061896 and R21HD063031 from the Eunice Kennedy Shriver National Institute of Child Health and Human Development and the Intermountain Medical and Research Foundation. We are also grateful to Siemens Healthcare Ultrasound division for an equipment loan and technical support.

3C-5

#### 4:30 pm Non-Invasive Characterization of Breast Cancer Using Textural Analysis of Ultrasound Spectral Parametric Images

Hadi Tadayyon<sup>1,2</sup>, Ali Sadeghi-Naini<sup>1,2</sup>, Gregory Czarnota<sup>1,2</sup>; <sup>1</sup>Medical Biophysics, University of Toronto, Canada, <sup>2</sup>Physical Sciences and Radiation Oncology, Sunnybrook Health Sciences Centre, Toronto, Canada

##### Background, Motivation and Objective

The identification of tumour histopathological characteristics is an important part of breast cancer diagnosis, prognosis, and treatment planning, but currently requires biopsy as its standard. Here, we investigated a non-invasive quantitative ultrasound method for characterization of breast tumours in terms of their histological grade, by analyzing the textural features of radiofrequency (RF) ultrasound data.

##### Statement of Contribution/Methods

Previous groups have characterized benign versus malignant breast tumours by examining texture-based features extracted from B-mode images. However, B-mode images can vary in terms of imaging parameters, including amplitude gain, focal depth, and time-gain compensation. We have characterized breast tumour histological subtypes by examining texture-based features extracted from calibrated spectral parametric maps computed from 3-D (stacks of 2-D) RF data, which do not depend on instrument settings. Raw ultrasound data from tumours and normal breast tissue from 35 locally advanced breast cancer patients were analyzed as part of this study. Four spectral parameters including mid-band fit, spectral slope, 0-MHz intercept, and scatterer spacing were investigated, and corresponding parametric maps were generated. From these parametric maps, four textural features, including contrast, energy, homogeneity, and correlation were determined as additional potential tumour characterization parameters. Data were examined in regions of surrounding breast tissue and tumour subtypes based on histological grade. Tissue classification was performed using linear discriminant analysis.



**Results/Discussion**

Among the spectral parameters, the mean of the mid-band fit parametric map provided the highest accuracy for discriminating tumours from surrounding breast tissues (85.7%). Furthermore, a higher accuracy was achieved when the combination of all parametric map means and corresponding textural parameters were applied (98.6%). For tumour characterization, whereas the combination of all parametric map means resulted in an accuracy of 54.3%, the combination of all textural parameters alone achieved an accuracy of 85.7% in terms of tumour grade. Furthermore, accuracy of tumour grade classification improved to 91.4% when all the mean and textural parameters were combined. Conclusions: Textural characteristics of quantitative ultrasound spectral parametric maps provided discriminant information about different types of breast tumours. In particular they significantly improved the results of ultrasonic tumour characterization whereas conventional mean values used alone tended to be poorer. As such, this study suggests that texture-based quantitative ultrasound analysis of in-vivo breast tumours can provide complementary diagnostic information about tumour histological characteristics.

3C-6

**4:45 pm Viscoelastic characterization of transverse isotropic tissue mimicking phantoms and muscle**

Sara Aristizabal<sup>1</sup>, Carolina Amador<sup>1</sup>, Bo Qiang<sup>1</sup>, Ivan Z. Nenadic<sup>1</sup>, James F. Greenleaf<sup>1</sup>, Matthew W. Urban<sup>1</sup>; <sup>1</sup>Physiology and Biomedical Engineering, Mayo Clinic College of Medicine, Rochester, Minnesota, USA

**Background, Motivation and Objective**

Ultrasound radiation force-based methods have the ability of estimating the tissue viscoelastic material properties. A limitation of the current methods exists when the estimation of the mechanical properties is performed under the assumption that the tissue is isotropic and homogeneous thus, neglecting the inherent anisotropy nature of tissues. To study the viscoelastic characteristics of this phenomenon in a laboratory setting, we created a transverse isotropic (TI) phantom incorporating fibrous material with preferential orientations embedded in tissue mimicking gelatin, and we studied a sample of ex vivo pork tenderloin in a saline bath at 30°C.

**Statement of Contribution/Methods**

Measurements were made in the phantoms at two gelatin concentrations (8% and 14%) and the pork muscle at different angles by placing each individual phantom and the pork tenderloin on a rotating platform with a rotation range ranging between 0° to 360° in 10° steps. The phantom and excised pork muscle were rotated with respect to the transducer, where 0° and 180° were defined along the fibers, and 90° and 270° were defined across the fibers. Shear waves were generated and measured by a Verasonics ultrasound system equipped with a linear array transducer operating at 4.1 MHz center frequency. The shear wave speed was evaluated from the distribution of particle displacement, which was estimated by a two-dimensional in-phase/quadrature auto-correlation method with spatial and temporal averaging of the compounded echoes from three different angled plane waves detected at an effective frame rate of 4.16 kHz. To estimate the shear elasticity ( $\mu_1$ ) and viscosity ( $\mu_2$ ), a Voigt model was fit to the shear wave dispersion curves of the phase velocity within 100-700 Hz.

**Results/Discussion**

The values for  $\mu_1$  and  $\mu_2$  for the fibrous phantom at both gelatin concentrations and the pork tenderloin are displayed in a polar coordinate system in Figs. 1(a)-(b)-(c), where it is possible to observe that  $\mu_1$  and  $\mu_2$  values for the phantoms and the pork muscle increase as the transducer is placed along the fibers (0°) and decreases as the transducer is placed across the fibers (90°), approximating the profile of an ellipse. This behavior indicates that  $\mu_1$  and  $\mu_2$  are angularly dependent, and exhibit a TI behavior that can be studied using viscoelasticity measurements.

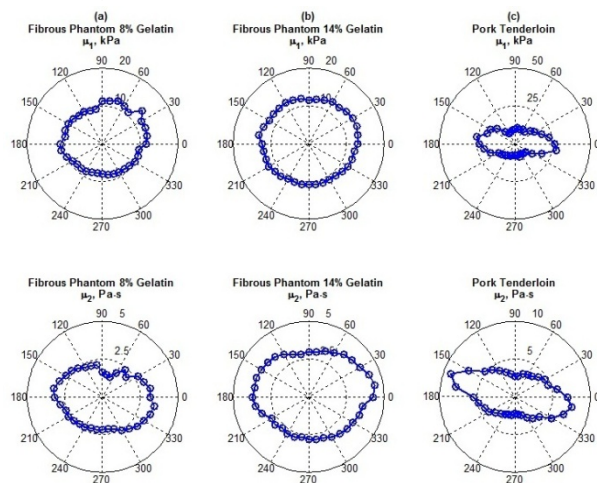


**Figure 1:** Polar plots for the transverse isotropic phantoms and ex vivo pork tenderloin. (a) fibrous phantom at 8% gelatin, (b) fibrous phantom at 14% gelatin, (c) pork tenderloin.

**4C - Materials Characterization**

Marquette

Thursday, September 4, 2014, 3:30 pm - 5:00 pm

Chair: **Edward Haeggstrom**  
University of Helsinki

4C-1

**3:30 pm Effects of Graphite Porosity and Anisotropy on Measurements of Elastic Modulus using Laser Ultrasonics****James B Spicer**<sup>1</sup>, Fan W Zeng<sup>1</sup>, Karen Han<sup>1</sup>, Lauren R Olasov<sup>1</sup>, Nidia C Gallego<sup>2</sup>, Cristian I Contescu<sup>2</sup>; <sup>1</sup>Materials Science and Engineering, The Johns Hopkins University, Baltimore, MD, USA, <sup>2</sup>Materials Science and Technology Division, Oak Ridge National Laboratory, Oak Ridge, TN, USA**Background, Motivation and Objective**

Laser ultrasonic techniques can be used to study the ultrasonic properties of nuclear graphites and can serve as tools in establishing relationships between materials microstructure and the macroscopic stiffnesses of graphite. Variations in graphite porosity can be related directly to overall changes in elastic stiffness while elastic anisotropy can result from processing-induced, preferred grain orientation and from alignment of aspheric pores. Establishing structure-property relationships permits improved ultrasonic sensing of graphite microstructural changes that signal service-related degradation. The focus of this work is on ultrasonic approaches for sensing graphite microstructural changes that might occur as a result of service in nuclear reactors. In particular, porosity changes brought about by oxidation as well as anisotropy variations linked to neutron irradiation are of particular concern.

**Statement of Contribution/Methods**

Elastic stiffnesses for 12 different graphites have been measured and a subset of these has been oxidatively processed to alter pore volume and distribution. Laser ultrasonic measurements were made using a pulsed Nd:YAG laser source and detection was performed using a Michelson-type interferometer. This source-receiver combination provides for non-contacting, highly linear transduction of broadbanded, ultrasonic pulses permitting simultaneous determination of longitudinal and shear stiffnesses. These measurements were used to characterize materials as a function of the ultrasonic mode and frequency as well as assess effects related to propagation direction and polarization. Laser line sources were used to quantify shear wave birefringence. Polarization-dependent moduli were inferred using effective medium descriptions based on elastodynamic Green's functions describing wave propagation in anisotropic materials.

**Results/Discussion**

Measurements show that among the graphites examined, a change in density of 0.26 g/cm<sup>3</sup> (average 1.8 g/cm<sup>3</sup>) results in a change in the longitudinal elastic stiffness of 9.2 GPa (average 11.3 GPa) and 3.2 GPa (average 4.3 GPa) for the shear stiffness. Larger variations in density were produced by controlled oxidation of IG-110 and NBG-18. Materials with nearly uniform, through-thickness oxidation follow trends for stiffness-density established for materials not oxidized. Non-uniform oxidation produces results that differ and these are currently being examined to determine if oxidation layer depth can be inferred. Laser ultrasonic line source models for transversely isotropic materials have been used to interpret ultrasonic measurements made on isostatically molded IG-110 and extruded PCEA. Shear wave birefringence in these materials shows that IG-110 behaves isotropically while PCEA displays texture characteristic of transversely isotropic materials.

4C-2

**3:45 pm Studies on Frequency Selective Iterative Deconvolution Algorithms Applied to Concrete Imaging and Characterization****Alberto Rodríguez**<sup>1</sup>, Sivilainis Linas<sup>2</sup>, Addison Salazar<sup>3</sup>, Luis Vergara<sup>3</sup>, Darius Kybartas<sup>2</sup>, Dobilas Liaukonis<sup>2</sup>; <sup>1</sup>Communications Engineering, Universidad Miguel Hernández, Elche, Alicante, Spain, <sup>2</sup>Signal Processing, Kaunas University of Technology, Kaunas, Lithuania, <sup>3</sup>Institute of Telecommunications and Multimedia Applications, Polytechnical University of Valencia, Valencia, Valencia, Spain**Background, Motivation and Objective**

The aim of our work is to design an automatic method for concrete imaging (sizing and flaw detection) and characterization (measurement of frequency dependent attenuation and phase velocity). Classic time-to-frequency methods as Split Spectrum Processing (SSP) or Wavelets could be used for imaging and/or flaw location, but then information about specimen characteristics will be lost due to the non-linear behavior of these methods. On the other hand, methods for material characterization are neither automatic nor suitable for high dispersive materials because pulses cannot be isolated and/or because high attenuation at higher frequencies.

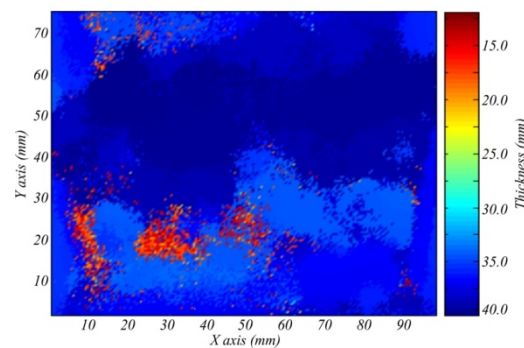
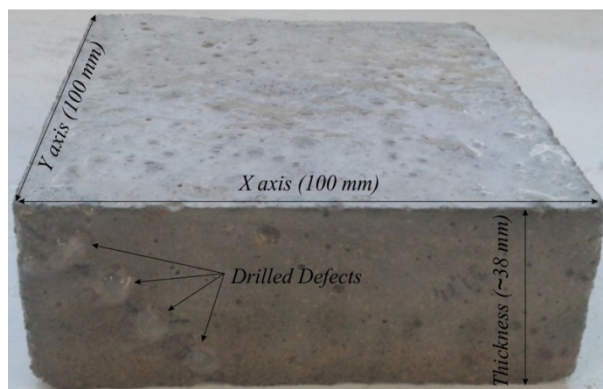
**Statement of Contribution/Methods**

Iterative deconvolution is based on the iterative subtraction of weighted and delayed versions of a reference signal thus obtaining the exact location of the different reflections of the transmitted pulse in the different layers of the material. Then, pulses can be isolated and attenuation and phase velocity can be estimated. Unfortunately, for high dispersive materials inner reflections are strongly affected by dispersion, thus reference subtraction procedure will not be able to track pulse locations.

We have developed a method that combines the filter bank used in SSP to derive a Frequency Selective Iterative Deconvolution (FSID) procedure. Before the deconvolution, both the signal under analysis and the reference signal are filtered using Gaussian filters adapted to estimated time-to-frequency attenuation curves.

**Results/Discussion**

Obtained 2D images of the thickness and inner structure of the specimens are given. We have developed an automatic method for concrete characterization without compromising its detection performance.



4C-3

#### 4:00 pm Numerical and analytical investigation of the influence of porosity on the frequency response of GLARE composite

Istvan Veres<sup>1,2</sup>, Robert A. Smith<sup>2</sup>; <sup>1</sup>Recendt, Linz, Austria, <sup>2</sup>Faculty of Engineering, University of Bristol, Bristol, United Kingdom

##### Background, Motivation and Objective

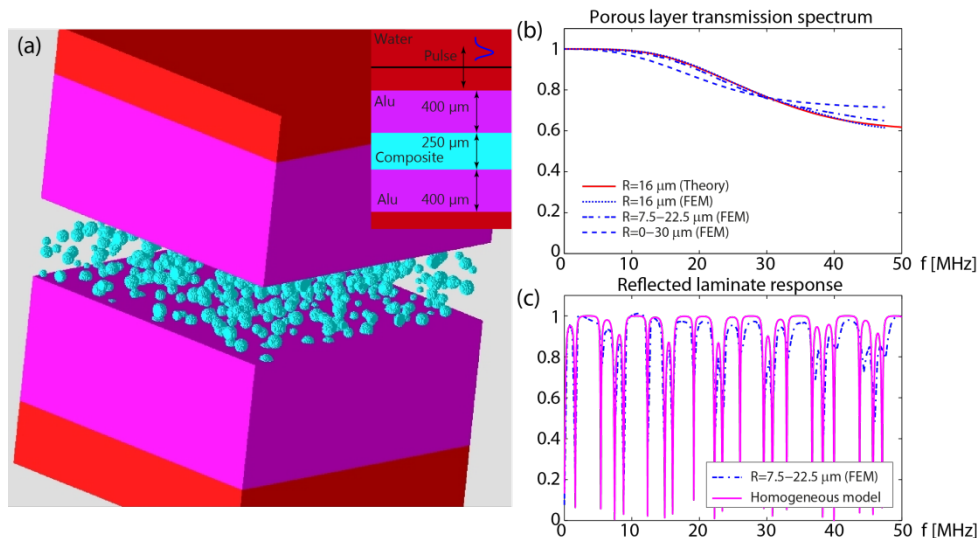
Fiber-metal laminates such as GLARE are composed of alternating glass-fiber composite and aluminum layers. Due to their enhanced fatigue resistance compared with unreinforced metals they are seeing increasing usage on aircraft structures. Composites, however, frequently suffer from air inclusions, or porosity, which reduces the overall strength and performance of the laminate. The evaluation of the bulk-averaged porosity is a state-of-the-art technique but it is hardly applicable for laminates with several layers or to estimate the distribution of the porosity through the depth.

##### Statement of Contribution/Methods

In the presented work analytical models for porosity and their range of validity is investigated by comparing them to numerical (FEM) simulations. Three-dimensional time-domain FEM simulations are carried out to model the scattering of the elastic waves on randomly distributed pores. For the simulations it is assumed that the pores are spherical scatterers and the porosity is limited to the composite material within the layered structure. The analytical model is based on the Foldy approximation, which assumes that multiple scattering can be neglected due to the low void volume fraction ( $\leq 5\%$ ) and the corresponding effective medium properties were calculated.

##### Results/Discussion

Numerical calculations were carried out by assuming identical spherical scatterers with diameters up to  $60\text{ }\mu\text{m}$  and also by assuming different size distributions [Fig.a]. The transmission spectrum of the porous layer [Fig.b] and the reflected laminate response of a GLARE laminate with a single composite layer [Fig.c] were evaluated from the simulations and the results compared to the analytical model. The comparison shows that the frequency-dependent attenuation of the ultrasonic waves is well-estimated by the Foldy approximation within the investigated volume. The results of the numerical simulations also show that the transmission and the frequency dependent attenuation depend on the pore diameter distribution. The reflected laminate response of a single layer GLARE composite is also evaluated from the numerical simulation [Fig.c] which shows that a homogeneous model with effective material properties can be utilized for inverse problems to evaluate the porosity in the composite layer.



4C-4

#### 4:15 pm Response of ultrasound to aluminum alloys sensitization

Gabriela Petculescu<sup>1</sup>, Chukwunonye Chukwunonye<sup>1</sup>; <sup>1</sup>University of Louisiana, USA

##### Background, Motivation and Objective

The sensitization of aluminum alloys used in marine applications is a problem of enormous economical significance for both the private and the defense industries. Mg-rich aluminum alloys (5xxx-series, high-strength and corrosive-resistant) become sensitized when exposed to heat from the sun or from on-board sources. The source of sensitization is

the metastable nature of the phase in which the alloy is produced. Even small amounts of energy are sufficient to make Mg atoms migrate to grain boundaries where they form a corrosive crystalline phase,  $Al_3Mg_2$ . As a result, sensitized aluminum is vulnerable to corrosion, exfoliation, and stress-corrosion cracking. Ultimately, structural failure becomes imminent if the material at high-stress points is sensitized. A large number of ships have already been built from this alloy, benefiting from its properties until sensitization degrades them. The sensitization level of critical structural components is currently evaluated with the NAML T test, a procedure that is destructive, lengthy, and requires large specimens. Since ultrasound is a powerful tool for nondestructive material characterization, it may offer a solution for on-site testing. To this end, the dependence of ultrasonic parameters on sensitization needs to be identified.

#### Statement of Contribution/Methods

Velocity and attenuation for shear and longitudinal waves were measured as a function of sensitization for 5083 and 5456 aluminum alloys with two different methods: Resonant Ultrasound Spectroscopy (RUS) and Pulse Echo (PE). Only the quantities for which the errors were significantly lower than the signal are reported here. The frequency range for RUS was 0.3-1 MHz. For PE, 3.5 MHz and 1 MHz transducers were used for longitudinal and shear excitation, respectively. Sensitization was artificially induced in the laboratory by heating specimens at controlled temperatures (120-183 °C) for given time periods (12-96 h). Measurements were repeated after each heating sequence.

#### Results/Discussion

The changes are reported as percent difference between the as-received and the fully sensitized states. The longitudinal velocity was found to change by 0.5% with error bars within 0.004-0.02%. The shear velocity changed by 1.2% to 1.5% with error bars within 0.01-0.1%. The larger changes were observed for the 5456 alloy, which contains more Mg. The quantity most sensitive to the degree of sensitization in this study was the attenuation coefficient of longitudinal waves,  $\alpha_L$ . The change in  $\alpha_L$  exceeds 20%, with error bars within 1-4%. Despite the larger errors, the trend of the  $\alpha_L$  vs. degree-of-sensitization curve is clear and smooth. The correlation between these three ultrasonic markers offers a new potential nondestructive tool for quantitatively monitoring the sensitization level in Mg-rich aluminum alloys.

#### 4C-5

#### 4:30 pm Nonlinear Resonant Acoustic Detection of Cracks in Multilayer Ceramic Capacitors

Ward Johnson<sup>1</sup>, Sudook Kim<sup>1</sup>, Jaemi Herzberger<sup>2,3</sup>, Grady White<sup>1</sup>; <sup>1</sup>NIST, Boulder, Colorado, USA, <sup>2</sup>GSFC, NASA, Greenbelt, Maryland, USA, <sup>3</sup>University of Maryland, College Park, Maryland, USA

#### Background, Motivation and Objective

Failures of multilayer ceramic capacitors (MLCCs), although rare, are a significant problem in applications such as implantable medical devices and spacecraft where the effects of failure can be catastrophic or replacement is impossible or dangerous. Cost-effective nondestructive methods have not been established for detecting microscale structural flaws that evolve into electrical leakage pathways during service. In this study, we explore the use of nonlinear resonant acoustics for detecting cracks introduced by thermal stress in ferroelectric MLCCs.

#### Statement of Contribution/Methods

Samples in this study were MLCCs with internal noble-metal electrodes interleaved with layers of doped polycrystalline barium titanate. Resonant ultrasonic measurements of an extensional mode near 990 kHz were performed before and after thermal shocks that introduced visible surface-breaking cracks in some samples. The measurements employed internal ferroelectric transduction for both tone-burst excitation and detection of signals during resonant ringdown. Vibrational phase versus time during ringdown was determined from in-phase and out-of-phase components of the signal, relative to the driving sinusoid. Two methods were employed to measure acoustic nonlinearity. In one approach, the power of the driving tone burst was varied and, at each power level, the average resonant frequency during ringdown was determined from a linear fit of phase versus time. In the second approach, the dependence of the resonant frequency on vibrational amplitude was determined from instantaneous derivatives of the phase during a single ringdown.

#### Results/Discussion

Measurements on thirty MLCCs showed systematically greater nonlinearity in samples with treatment-induced cracks visible at the surfaces. Fig. 1 shows the dependence of resonant frequencies on driving voltage before and after heat treatment for two typical MLCCs with and without treatment-induced cracks. Amplitude dependences of frequencies determined from instantaneous phase derivatives during a single ringdown were consistent with those determined with the first method. These results support the conclusion that nonlinear resonant ultrasonic measurements can effectively screen MLCCs for cracks that limit service life.

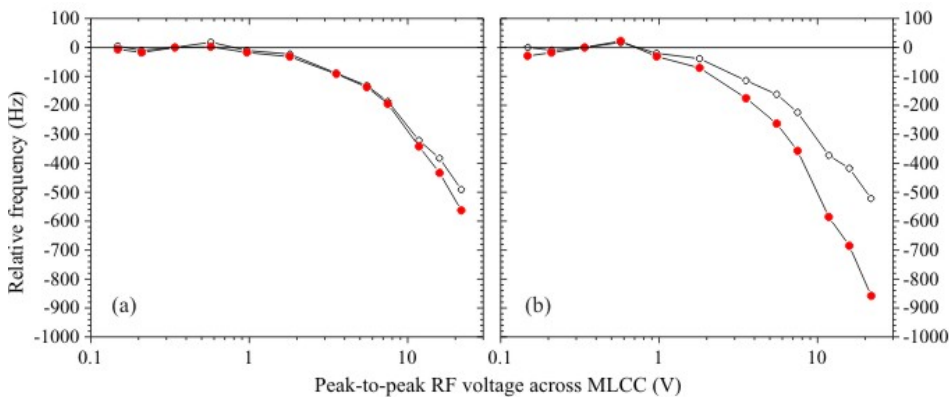


Fig. 1: Relative frequencies of MLCCs without visible cracks (a) and with visible cracks (b) after heat treatment as a function of peak-to-peak driving voltage. The frequency at the third-lowest driving voltage is the reference.  $\circ$ : before heat treatment.  $\bullet$ : after heat treatment.

**4:45 pm Ultrasonic Propagation and Damage Sensing in a Bonded PMC/SiC-Foam**James Blackshire<sup>1</sup>; <sup>1</sup>AFRL/RXCA, Air Force Research Laboratory, Wright-Patterson AFB, Ohio, USA**Background, Motivation and Objective**

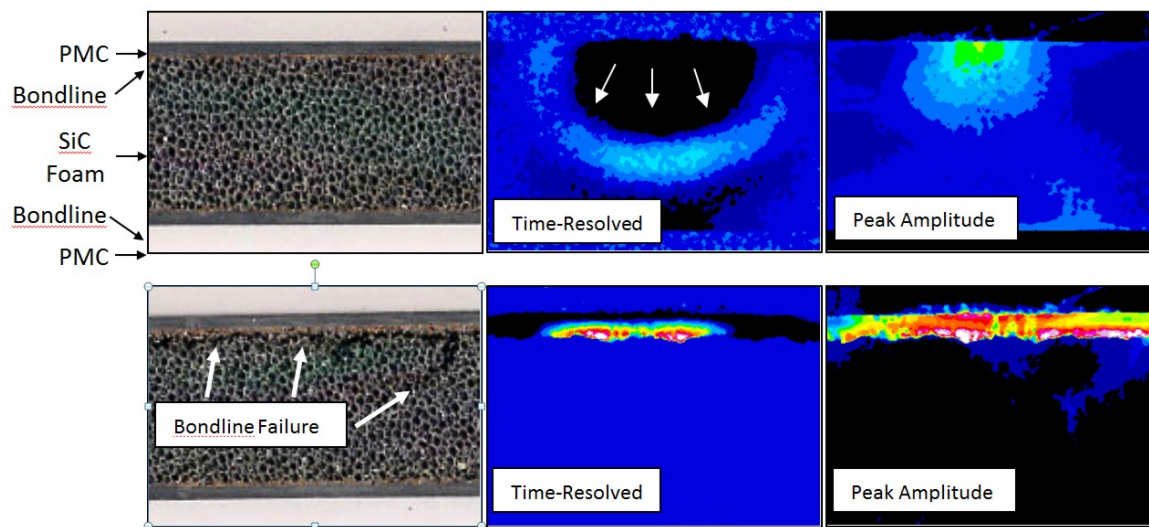
The nondestructive evaluation of hybrid material systems is a challenging problem, where very different materials are often combined to enhance performance. In the present application, the bonline integrity of a sandwich structure is of interest, where two polymer matrix composite (PMC) facesheets are bonded to an insulating silicon carbide (SiC) foam interior.

**Statement of Contribution/Methods**

The propagation of ultrasound within the PMC-SiC Foam sandwich structure was studied using finite element models, contact ultrasound measurements, and scanning laser vibrometry. The material system included two, 2-millimeter thick PMC facesheets bonded to a 12-millimeter thick SiC foam, where the sample had been subjected to a 3-point bend experiment, which generated a localized 45-degree crack in the SiC foam and delamination of the PMC-SiC interface. A direct comparison of ultrasound FEM model predictions was made with scanning vibrometry results, where wave propagation, scattering and localization of energy in the PMC for the damaged case was observed for a 200 kHz pulse waveform.

**Results/Discussion**

Representative scanning laser vibrometry results are presented in the accompanying figure, which depicts a comparison of the undamaged (top) and damaged (bottom) cases. A time-resolved and peak amplitude image is provided for each case, where energy transfer into the SiC foam is observed for the undamaged case, and localization of energy within the PMC layer and near the fracture surfaces is observed for the damaged case.





## 5C - Nonlinear Acoustics 1

Williford A

Thursday, September 4, 2014, 3:30 pm - 5:00 pm

Chair: **John Larson**  
Avago Technologies

5C-1

### 3:30 pm Reduction of frequency deviations in quartz resonators by electric potentials of plate electrodes

Jian Feng Chen<sup>1</sup>, Yook-Kong Yong<sup>1</sup>, Randall Kubena<sup>2</sup>, Deborah Kirby<sup>2</sup>; <sup>1</sup>Civil and Environmental Engineering, Rutgers University, Piscataway, New Jersey, USA, <sup>2</sup>HRL Laboratories, Malibu, CA, USA

#### Background, Motivation and Objective

High precision quartz crystal oscillators are used as frequency sources in systems such as Doppler radars, GPS, satellite and missile applications that require extremely low noise. When the quartz resonators operate on mobile platforms the effects of vibrations/acceleration induce phase noise that is usually greater than all other noise sources combined. The quartz resonators become the most acceleration sensitive component in the frequency sources[1]. While the frequency deviations due to acceleration is well understood to be a nonlinear acoustic phenomenon it is still difficult to lower the frequency deviations to less than  $10^{-10}$  parts per g acceleration. Our objective is to lower the acceleration sensitivity of thickness shear quartz resonators by using the electric potential of one plate electrode for sensing and the setting the electric potential of other plate electrode for reducing acceleration sensitivity.

[1] "The Acceleration Sensitivity of Quartz Crystal Oscillators: A Review", R. L. Filler, IEEE Transactions on Ultrasonics, Ferroelectrics, and Frequency Control, Vol. 35, No. 3 May 1988, pp. 297-305.

#### Statement of Contribution/Methods

Measurements for AT-cut quartz resonators subjected to bending and diametrical forces were compared to a 3-D COMSOL piezoelectric model of the resonator with acceleration sensitivity. The model results compare consistently well with the measured values, hence validating our model for resonators with acceleration sensitivity and providing a means for studying the reduction of acceleration sensitivity by manipulating the electric potentials of plate electrodes. Both frequency deviations and change in electric potentials of the plate electrodes are caused by strains due to vibrations of the quartz resonator. The vibrations are at frequencies that are orders of magnitude lower than the frequency of the quartz oscillator. Hence the electric potentials due to vibrations can be separated from the electric potentials of the oscillator. We manipulate the electric potentials due to vibrations in order to reduce frequency deviations of the resonator.

#### Results/Discussion

Our 3-D COMSOL piezoelectric model of a quartz resonator with acceleration sensitivity validated by measurement results was employed to study the effects of electric potential of plate electrodes on acceleration sensitivity. We found that about 30 mV on the plate electrode was sufficient for cancelling the acceleration effects of 1 g acceleration in the Y-axis (thickness axis) of the resonator. For in-plane acceleration the method was less effective but could still lower the acceleration effects. Since the predominant effect of vibrations was frequency deviations caused by plate bending (acceleration in the thickness direction) the method is effective in minimizing acceleration sensitivity of quartz resonators. This method can be applied to a variety of quartz resonators with different plate geometries and mounting supports.

5C-2

### 3:45 pm Dynamic Nonlinear Probe Utilizing Traveling Multiwave Interaction

Thomas Szabo<sup>1</sup>, Thomas Gallot<sup>2</sup>, Alison Malcolm<sup>2</sup>, Dan Burns<sup>2</sup>, Stephen Brown<sup>2</sup>, Michael Fehler<sup>2</sup>; <sup>1</sup>Biomedical Engineering, Boston University, Boston, MA, USA, <sup>2</sup>Earth Resources Laboratory, Massachusetts Institute of Technology, Cambridge, MA, USA

#### Background, Motivation and Objective

Because conventional methods do not measure the microstructure or pore fluids of rocks, a sensitive enough measurement approach is needed as well as one that can be directed at selected regions of interest. The aim of this study is to utilize the nonlinear interaction of two propagating waves which intersect to characterize induced elastic changes occurring in the rock microstructure at the intersection location. Our experimental technique utilizes a strong shear wave pump that changes (minutely) the elastic properties of the sample and a weaker longitudinal wave probe that senses those changes. Our long term goal is to develop a means of imaging elastic properties of microstructure.

#### Statement of Contribution/Methods

The goal of our experiment is to measure the traveltime delay in a low-amplitude wave (the probe) caused by a high-amplitude wave (the pump). This sort of wave-wave interaction is inherently nonlinear and measuring the magnitude of the travel-time delay can be used to measure the strength of the non-linearity. We use a sample of Berea sandstone which is nearly isotropic, with moderate porosity and permeability. A longitudinal wave is sent along the sample length to a receiver. The pump wave signal is directed perpendicular to the longitudinal wave and is slowly varying compared to that of the probe; therefore, we use a 500 kHz longitudinal probe wave and a 50 kHz shear wave pump. We then vary the delay between the two signals through several periods of the pump wave to observe the induced changes on the probe caused by both directions (i.e.  $\pm x$  of particle motion). Particle velocities are measured on the surface of the sample with the laser vibrometer to calibrate the experiment and estimate the strain with the help of an elastic model.

#### Results/Discussion

Measured changes in time modulation were fitted to a nonlinear Hooke's law function of stress vs. strain,  $\sigma = M(\epsilon + \beta\epsilon^2 + \delta\epsilon^3)$  where  $\sigma$  is stress,  $\epsilon$  is strain,  $M$  is elastic modulus and  $\beta$  and  $\delta$  are nonlinear parameters. Our results for Berea sandstone were  $\beta = -542$  and  $\delta = -3 \times 109$ . By varying the polarization of the shear pump wave relative to the probe direction, we found that the maximum was in the original configuration with the shear displacements aligned with the direction of the longitudinal wave propagation direction and delay effects decreased with angle at other polarizations.

Preliminary imaging results were obtained of WD-40 fluid injected into two sites in a Berea sandstone sample. An image of delay changes was formed by delays back-projected along the beams created with six probe transmitters and six receivers on the opposite side of the sample. This tomographic image, opens up the possibility of imaging the nonlinear parameters of rocks both in the lab, and in the future, in the field.



## 5C-3

**4:00 pm Nonlinear shear wave propagation in water-saturated granular media**

Javier Brum<sup>1</sup>, Jean-Luc Gennisson<sup>1</sup>, Mathias Fink<sup>1</sup>, Mickael Tanter<sup>1</sup>, Xiaoping Jia<sup>1,2</sup>; <sup>1</sup>ESPCI ParisTech CNRS UMR7587 INSERM U979, Institut Langevin, PARIS, France, <sup>2</sup>Universite Paris-Est, Marne la vallee, France

**Background, Motivation and Objective**

Granular materials are ubiquitous in everyday life, ranging from industrial applications to geophysical processes. Static property and dense flow in both dry and water-saturated granular materials strongly depend on the solid frame of particles assembly, resulting from the confining pressure. Elastic wave propagation offers a powerful and sometimes unique probe of this inhomogeneous and fragile contact network. The long-wavelength coherent waves give access to the elastic modulus whereas the short-wavelength scattered waves are sensitive to any rearrangement [Jia PRL 1999]. When the oscillation amplitude is high enough, the elastic waves would not only serve as probe but also as a pump or controlled perturbation to fluidize the jammed granular media [Jia PRE 2011]. Unlike the previous works focusing on the compressional wave [Wildenberg EPL 2013], we here investigate the low-frequency shear wave propagation in very weakly compressed and water saturated glass bead packings. We are interested by the irreversible nonlinear wave-matter interaction as a function of the source amplitude.

**Statement of Contribution/Methods**

Granular media under investigation are composed of 100  $\mu\text{m}$  diameter glass beads confined in a rectangular box with the absorbing walls and free surface. The water-saturate bead packings are only loaded under gravity. A metallic plate fixed to a mechanical vibrator acts as a plane shear wave source [Catheline PRL 2003]. The plate immersed in granular packings is excited by a tone-burst of four cycles centered at a frequency ranging from 100 to 400 Hz. The shear wave propagation is caught at the granular medium surface through an ultrasonic linear array (4 MHz), placed parallel to the direction of propagation and to the medium surface. Thanks to an ultrafast ultrasonic device (Aixplorer, Supersonic Imagine), the out-of-plane displacement field of the low-frequency shear wave is obtained from successive RF ultrasonic signals using a phase conjugation algorithm.

**Results/Discussion**

In this work, three regimes are identified as a function of the source amplitude. In the linear regime, we measure the shear wave velocity of about 20 m/s with a slight dispersion likely due to its comparable wavelength with the packing height. In the weak nonlinear regime, 2nd and 3rd harmonics generation are observed, accompanied by a softening of the shear wave velocity of  $\sim 15\%$ . In the strongly nonlinear regime, the shear wave velocity softening goes up to 50% due to the vibration-induced fluidization. In this regime, the wave-matter interaction becomes irreversible and the important rearrangement of the contact is detected via ultrasonic speckles. Here, we propose an effective medium description to interpret the velocity dispersion and nonlinear behavior. We believe that our acoustic experiments would provide very useful information to monitor immersed granular media such as marine sediments, or in oil prospecting industry.

## 5C-4

**4:15 pm Estimation of Depletion- or Injection-induced Changes in Reservoir Stresses using Time-lapse Sonic Data**

Bikash Sinha<sup>1</sup>, Ergun Simsek<sup>2</sup>; <sup>1</sup>Schlumberger-Doll Research, Cambridge, MA, USA, <sup>2</sup>Department of Electrical and Computer Engineering, The George Washington University, Washington, DC, USA

**Background, Motivation and Objective**

Reservoir depletion and subsequent fluid (water and carbon dioxide) injection for enhanced oil recovery cause changes in the reservoir pressure and formation stresses. Large stress changes can activate pre-existing faults and cap rock fractures, leading to CO<sub>2</sub> leakage. Time-lapse seismic surveys can detect impedance changes on the order of 3% to 9% in CO<sub>2</sub>-saturated rocks that are good indicators of qualitative changes in the reservoir pressure and saturation. A technique to detect small sonic velocity changes related to changes in in-situ stresses and fluid mobility caused by either reservoir depletion or injection would provide reliable estimates essential for maintaining reservoir mechanical integrity and sequestration of injected CO<sub>2</sub>.

**Statement of Contribution/Methods**

A new technique uses time-lapse borehole sonic data acquired in a vertical borehole parallel to the X3-axis to estimate changes in formation stresses caused by reservoir depletion or injection. A pre-production baseline survey acquires sonic data in an open or cased hole along with estimates of reservoir pressure, overburden and minimum horizontal stresses. After years of depletion or injection, a monitor survey acquires sonic data in an observation well. Both sonic datasets are processed to obtain the borehole Stoneley and cross-dipole dispersions. An inversion algorithm inverts the measured Stoneley dispersion to estimate the far-field shear modulus C<sub>66</sub> in the borehole cross-sectional plane. The shear moduli C<sub>44</sub> and C<sub>55</sub> of the two orthogonal borehole axial planes are obtained directly from the low-frequency asymptotes of the two cross-line flexural dispersions. Differences in the three shear moduli from the baseline survey yield the maximum horizontal stress magnitude and an acoustoelastic coefficient using the estimated pore pressure, overburden and minimum horizontal stresses. The three far-field shear moduli in the three orthogonal planes are also obtained from the subsequent monitor survey. An algorithm uses the acoustoelastic coefficient from the baseline survey and the three shear moduli after depletion or injection to estimate of the maximum and minimum horizontal stress magnitudes caused by reservoir pressure changes.

**Results/Discussion**

Using time-lapse sonic data acquired in a reservoir interval before and after production or fluid injection to estimate changes in the reservoir stresses enables monitoring them as a function of change in reservoir pressure to avoid reactivation of an existing fault or introduction of unwanted fractures in the caprock that would result in CO<sub>2</sub> leakage. The estimated maximum and minimum horizontal stresses after depletion or injection together with estimated reservoir pressure can then be used to calculate an injection pressure threshold to avoid fracture creation. They can also be used to determine a reservoir pressure window that will reduce the chances of shear slippage occurring along an existing fault.

## 5C-5

**4:30 pm Recent Advances in Nonlinear Modeling of Bulk Acoustic Wave Resonators**

David Feld<sup>1</sup>, Dong Shim<sup>1</sup>, Siamak Fouladi<sup>1</sup>, Farhad Bayatpur<sup>1</sup>; <sup>1</sup>Wireless Semiconductor Division, AVAGO Technologies, San Jose, CA, USA

**Background, Motivation and Objective**

Microwave acoustic filters operated at high power levels generate nonlinear mixing products necessitating improved nonlinear modeling. The latest communications protocols place strict limits on such mixing products including the generation of inter-modulation distortion products, which desensitize a receiver, as well as second harmonic emissions. We extend the conventional non-linear acoustic theory and practice into the microwave frequency range.

**Statement of Contribution/Methods**

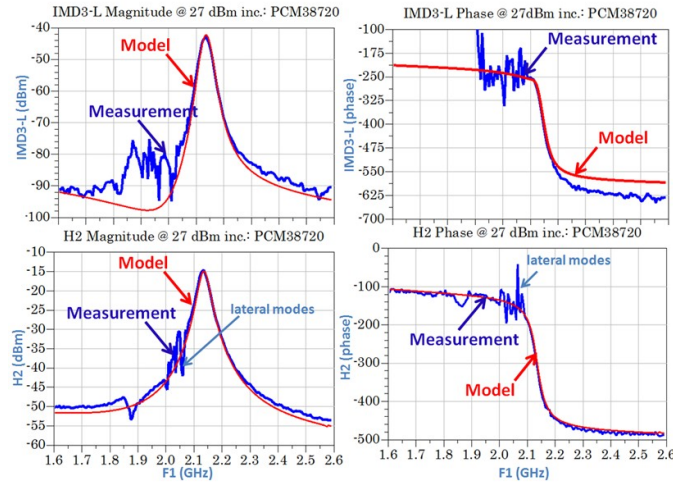
We have developed a methodology for modeling the linear and nonlinear response of a resonator comprised of arbitrary piezoelectric and metal electrode layers and thicknesses. In this work we assume that the piezoelectric film is the dominant nonlinear source. An extended set of piezoelectric constitutive equations containing arbitrary nonlinear terms representing the behavior of the piezoelectric film is mapped into a general purpose nonlinear circuit, which is an extension to Mason's original linear model of a resonator. A

harmonic balance circuit simulator is used to solve this extended set of constitutive equations. We have fitted our model to a set of nonlinear two-tone resonator measurements by identifying four dominant nonlinear terms, by adjusting their corresponding scaling coefficients such that the in- and out-of-band 2nd harmonic emissions and inter-modulation-3 products generated by the model is consistent with our measurements.

### Results/Discussion

Figure 1 shows a plot of the measured and modeled magnitude and phase responses of the 2nd harmonic (H2) and lower sideband intermodulation-3 (IMD3-L) responses of a Molybdenum-AlN-Molybdenum ~2 GHz BAW resonator for a two-tone stimulus. Two +27 dBm incident tones separated by 20 MHz are incident upon the resonator. The frequency axis represents the frequency of the lower tone frequency. In this example, our resonator model employs four constants, two to fit the H2 and IMD3 responses near resonance, and two to fit the responses away from resonance. Near resonance the magnitude and phase response of the model are in superb agreement with the measurements. The resulting model has been verified in two ways: (1) By verifying its validity over a large set of power levels, frequencies, and tone separations, and (2) by verifying its predictive power in simple resonator configurations.

Fig.1



## 6C - Characterization of Materials

Williford B

Thursday, September 4, 2014, 3:30 pm - 5:00 pm

Chair: **Karl Wagner**  
TDK Corporation

6C-1

### 3:30 pm Determination of Full Material Constants of ScAlN Thin Film from Bulk and Leaky Lamb Waves in MEMS-based Samples

Akira Konno<sup>1</sup>, Michio Kadota<sup>1</sup>, Jun-ichi Kushibiki<sup>1</sup>, Yuji Ohashi<sup>1</sup>, Masayoshi Esashi<sup>1</sup>, Yasuo Yamamoto<sup>1,2</sup>, **Shuji Tanaka<sup>1</sup>**; <sup>1</sup>Tohoku University, Japan, <sup>2</sup>DENSO CORPORATION, Japan

#### Background, Motivation and Objective

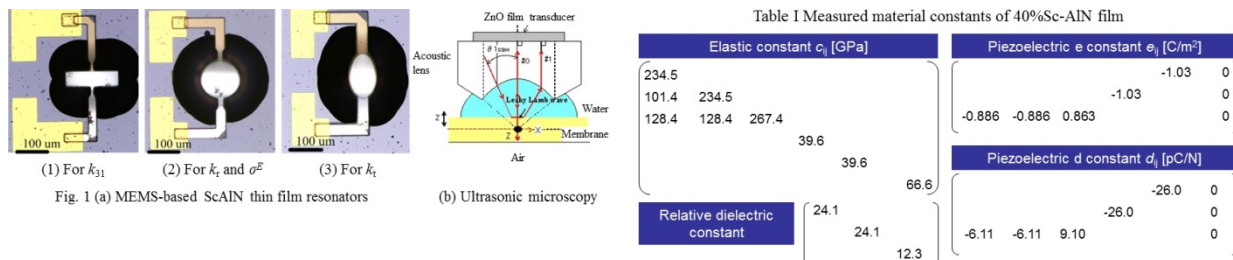
ScAlN is a new piezoelectric material obtained by sputter-deposition as a thin film. Although ScAlN has a higher piezoelectric performance than AlN, its material constants have not been fully measured. The material constants of a bulk crystal are often substituted for those of the thin film, because they can be obtained by measuring the resonance and anti-resonance frequencies of various bulk resonators. However, the full material constants of the material which can be obtained only as a thin film, e.g. ScAlN, are difficult to determine similarly, because limited types of resonator can be fabricated using a thin film. In this study, we first determined the full material constants of a 40%Sc-AlN thin film by a new method using MEMS-based samples.

#### Statement of Contribution/Methods

Several material constants were obtained by measuring the resonance and anti-resonance frequencies of different vibration modes of MEMS-based ScAlN thin film resonators shown in Fig. 1 (a). However, the other material constants are not obtained from the thin film resonators. Therefore, leaky Lamb wave velocity in a ScAlN free membrane sample was measured by ultrasonic microscopy, as shown in Fig. 1 (b). Then, the unknown material constants were parameter-searched based on a theoretical model, as the leaky Lamb wave velocity calculated from the assumed constants agreed with the measured one.

#### Results/Discussion

The full material constants including elastic constants, piezoelectric constants and dielectric constants of the ScAlN thin film were determined, as shown in Table I. The method developed in this study is systematic and applicable to many other piezoelectric thin films.



6C-2

### 3:45 pm A refined method to determine the elastic constants of PVD SiO<sub>2</sub> thin films

Matthias Knapp<sup>1,2</sup>, Philipp Jäger<sup>1</sup>, Werner Ruile<sup>1</sup>, Ingo Bleyl<sup>1</sup>, Leonhard M. Reindl<sup>2</sup>; <sup>1</sup>TDK Corporation, Munich, Germany, <sup>2</sup>Department of Microsystems Engineering IMTEK, University of Freiburg, Freiburg, Germany

#### Background, Motivation and Objective

The improvement of filter performance in recent years has led to a rapid development of layered systems for surface acoustic wave (SAW) filters. Systems with dielectric thin films have the ability to satisfy the requirements for better performance and miniaturization of the devices. Therefore, an accurate knowledge of the properties of the dielectric layer is important to build an appropriate device design. The objective of this work is to establish a method to improve the phase velocity determination for layered systems using differential delay lines. The improvement is shown for a layered system SiO<sub>2</sub>/LiNbO<sub>3</sub>. Material constants of the SiO<sub>2</sub> film deposited by physical vapour deposition (PVD) process were determined.

#### Statement of Contribution/Methods

The phase velocity dispersion of layered structures is evaluated using differential delay lines. The method is described in more detail in a previous publication, where a uniform layer thickness was assumed. PVD layer deposition however, typically shows a varying layer thickness on the wafer. In this work we present a correction method that copes with this problem. It is based on defining a reference thickness to which the impulse responses of the corresponding delay lines have to be shifted. Therefore, signal processing is used. It is shown that the accuracy of this correction method is very high. Thus, it allows the extraction of the elastic constants of the layer. For this purpose, we use finite element simulations and an optimization that fits the calculated phase velocities to the measured ones.

#### Results/Discussion

We built differential delay lines on a LiNbO<sub>3</sub> substrate with two different SiO<sub>2</sub> layer thicknesses deposited by a PVD process. The thickness variation was measured using a profilometer. The phase velocities were extracted from the measurements. The elastic constants were determined by optimization, as described above. It will be shown that the correction method as discussed in this work, yields the elastic constants of the PVD deposited SiO<sub>2</sub> film with high accuracy. The material constants will be shown in the publication.

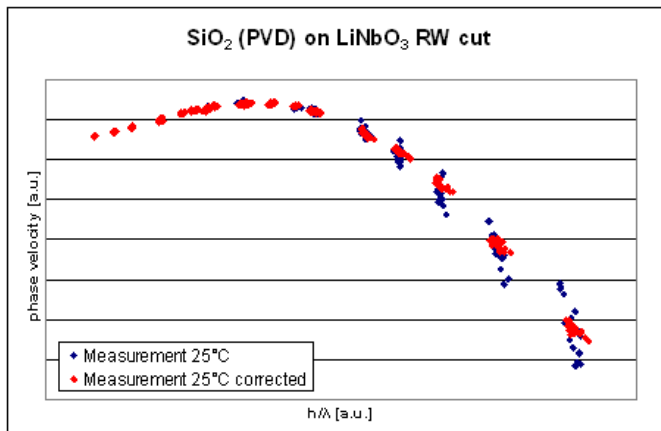


Fig. 1: Phase velocities of a  $\text{SiO}_2/\text{LiNbO}_3$  system. Comparison between uncorrected and corrected data.

6C-3

#### 4:00 pm Highly Piezoelectric co-doped AlN Thin Films for Wideband FBAR applications

Tsuyoshi Yokoyama<sup>1</sup>, Yoshiki Iwazaki<sup>1</sup>, Yosuke Onda<sup>1</sup>, Tokihiro Nishihara<sup>1</sup>, Yuichi Sasajima<sup>1</sup>, Masanori Ueda<sup>1</sup>; <sup>1</sup>Taiyo Yuden Co., Ltd, Japan

##### Background, Motivation and Objective

Aluminum nitride (AlN) thin films have become a standard material for RF bulk acoustic wave (BAW) filters and duplexers in mobile communication systems. Recently, it has been reported that Al substitution by scandium (Sc) allows for a 400% increase of piezoelectric response [1]. Furthermore, several research organizations have confirmed large electromechanical coupling coefficients in Sc-doped AlN based BAW resonators [2]. Therefore, doped AlN thin films have attracted significant interest since there is a possibility to improve the resonance characteristics.

In this study, we report new piezoelectric materials composed of charge-compensated co-doped  $(\text{Mg},\alpha)_x\text{Al}_{1-x}\text{N}$  ( $\alpha = \text{Zr}$  and  $\text{Hf}$ ) that has greatly improved piezoelectric properties based on first-principles calculation and experiments.

[1] M. Akiyama, et al., Adv. Mater., vol. 21, pp. 593-596, 2009

[2] M. Moreira, et al., Vacuum, vol. 86, pp. 23-26, 2011

##### Statement of Contribution/Methods

We have investigated the effect of the doping element into AlN on crystal structure and piezoelectric constants of co-doped AlN based on first principles calculation. Furthermore, we deposited the co-doped AlN thin films using reactive sputtering system and evaluated their lattice constants and piezoelectric constant. Furthermore, thin film bulk acoustic resonators (FBAR) that used co-doped AlN as a piezoelectric thin film were fabricated and were evaluated their resonant characteristics.

##### Results/Discussion

First principles calculation indicated the improvement of piezoelectric performance of co-doped  $(\text{Mg},\alpha)_x\text{Al}_{1-x}\text{N}$  ( $\alpha = \text{Zr}$  and  $\text{Hf}$ ). The X-ray diffraction and transmission electron microscopy (TEM) observation of the fabricated co-doped AlN thin films indicated that the films have c-axis oriented columnar grain growth microstructure similar to that of pure AlN thin film. By increasing the doping concentration, the measured piezoelectric constant  $d_{33}$  of the fabricated co-doped AlN thin films increased, which was almost consistent with the theoretical predictions. The air-gap type FBAR using the  $(\text{Mg}_{0.5}\text{Zr}_{0.5})_{0.13}\text{Al}_{0.87}\text{N}$  and  $(\text{Mg}_{0.5}\text{Hf}_{0.5})_{0.13}\text{Al}_{0.87}\text{N}$  thin films were also fabricated and showed high electromechanical coupling coefficients, that were 8.7% and 10.0%, respectively. The results of this study suggest that co-doped AlN films have potential as a piezoelectric thin film for wideband and high-frequency FBAR applications.

6C-4

#### 4:30 pm Determination Method of Acoustical Physical Constants and Their Temperature Coefficients for Point Group 32 of Trigonal Crystal System

Yuji Ohashi<sup>1</sup>, Mototaka Arakawa<sup>1</sup>, Jun-ichi Kushibiki<sup>1</sup>, Masatoshi Adachi<sup>2</sup>; <sup>1</sup>Tohoku University, Sendai, Japan, <sup>2</sup>Toyama Prefectural University, Toyama, Japan

##### Background, Motivation and Objective

Accurate acoustical physical constants (elastic, piezoelectric, and dielectric constants, and density) and their temperature coefficients are very important to investigate most suitable cut angle of single crystal substrates for designing new piezoelectric devices through numerical calculation. In our previous work [1], we found a problem that some of the constants (especially  $c_{33}^E$  and  $e_{14}$ ) measured by resonance method have significant errors.

In this paper, we propose and demonstrate a method for determining constants and temperature coefficients by a new method using our ultrasonic micro-spectroscopy (UMS) technology combined with the pulse-echo and resonance methods.

##### Statement of Contribution/Methods

Taking  $\text{Ca}_3\text{TaGa}_3\text{Si}_2\text{O}_{14}$  (CTGS) single crystal, point group 32, as a specimen, we prepared 5 substrates for measuring bulk wave velocities. To obtain accurate references of velocities, we measured temperature dependences of velocities around room temperature (20, 23, and 26°C) with the UMS technology. To obtain temperature coefficients of acoustical physical constants in wide temperature range, we also measured the velocities in a range from -30 to 80°C with pulse-echo and resonance methods. We employed the pulse-echo method for measuring propagation modes uncoupled with piezoelectricity such as Y-, Z-, 35.19°Y- and 139.83°Y-propagating longitudinal velocities and Z-prop. shear velocity, and the resonance method for measuring the modes coupled with piezoelectricity such as X-prop. longitudinal velocity and Y- and 35.19°Y-prop. X-polarized shear velocities.

**Results/Discussion**

In results of velocities obtained by the pulse-echo and resonance methods, we observed 3.8% difference at maximum around room temperature as compared with those of the UMS. We determined temperature dependences of elastic and piezoelectric constants from the velocities calibrated with the results of the UMS in which there are no influences of bonding layer, electrodes, spurious modes and so on in principle. The gradients of the constants determined were in good agreement with those for the UMS around room temperature as shown in Fig. 1.

We successfully demonstrated a method of determining accurate constants with their temperature coefficients.

[1] Y. Ohashi, et al., Proc. 2012 IEEE IUS, pp. 2738-2741 (2012).

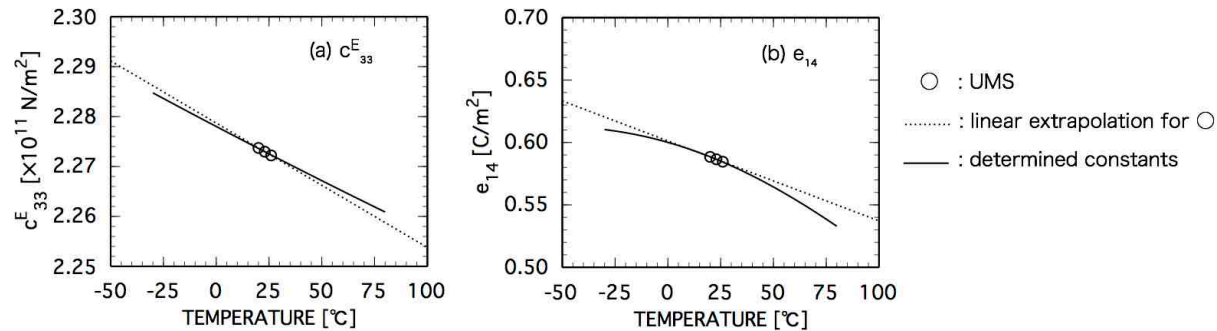


Fig. 1 Temperature dependences of elastic and piezoelectric constants for CTGS single crystal.

6C-5

**4:45 pm A New Method for Fast and Accurate Determination of the Temperature Coefficients of Material Constants up to 700°C. Application to LGS.**

PASCAL NICOLAY<sup>1</sup>, JOCHEN BARDONG<sup>1</sup>, GUDRUN BRÜCKNER<sup>1</sup>; <sup>1</sup>Carinthian Tech Research (CTR AG), Villach, Austria

**Background, Motivation and Objective**

To develop high temperature SAW sensors, accurate sets of material constants and temperature coefficients (TCs) are required. Unfortunately, the determination of accurate TCs requires a lot of investment. In 2013, Nicolay and Aubert suggested to ease the procedure by using a Simulated Annealing optimization algorithm (SA) to fine-tune the TCs. Three SAW Fractional Frequency Curves (FFCs) and SA were used to compute a new set of TCs for Langasite (LGS) and predict with good accuracy the FFC of two other cuts. However, several TC values were not optimized at all. To solve this issue, the use of additional BAW FFCs was suggested. Besides, there was a need for validation of the whole method as a simple and cheap way to determine accurate sets of TCs.

The goal of this work was to tackle these two issues. A solution was found to measure BAW and SAW FFCs simultaneously. Then, the method was used to derive TCs of LGS stiffness constants (TCCs) from a whole new set of FFCs obtained up to 700°C using an innovative and easy-to-use test chamber.

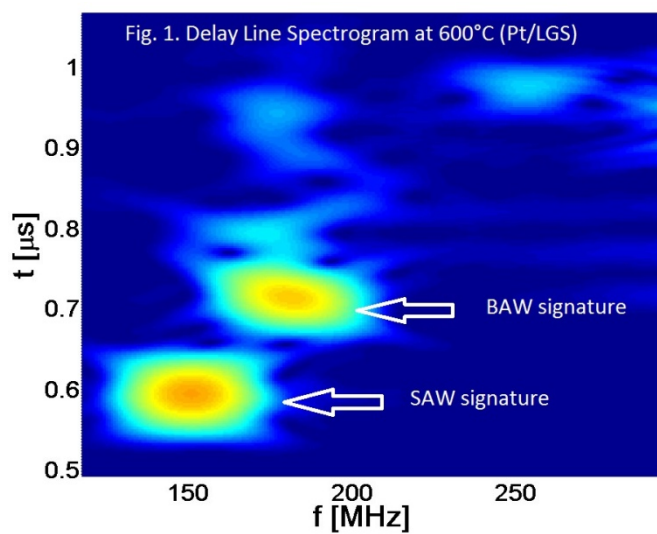
**Statement of Contribution/Methods**

Standard IDTs generate SAW and BAW. The use of polished LGS wafers allowed for measuring simultaneously SAW and BAW signals up to 700°C (Fig. 1). These measurements allowed for determining two of the TCCs which were not optimized in previous work. The method also made it possible to avoid fabricating BAW devices.

Additionally, an easy-to-use test chamber was designed to measure FFCs up to 700°C. The chamber is 20×20×15 cm<sup>3</sup> in size. It is connected to a vacuum pump and comprises a small suspended sample holder, equipped with a resistive heater and connected via feed-through to a Network Analyzer. Each FFC was acquired in less than 30 minutes.

**Results/Discussion**

In total, six LGS orientations were characterized. BAW and SAW FFCs were simultaneously determined up to 700°C then used to derive a new set of optimized TCCs (first and second order) using SA. Especially, new values of TCC11 and TCC33 were obtained. They are discussed in detail in the paper. The new TCCs were used to compute FFCs on two test cuts. A good agreement with experimental data was obtained, which confirms the practical interest of the method. Additionally, error bars were estimated for each TCC. This allows for further comparison with other sets of TCs published in the past. An estimation of the overall costs and time required for the whole procedure is provided at the end of the paper.





## 7C - Micromachined Ultrasound Transducer Modeling

Williford C

Thursday, September 4, 2014, 3:30 pm - 5:00 pm

Chair: **Omer Oralkan**  
North Carolina State University

7C-1

### 3:30 pm Simulation model for CMUT with rapid structure fluid interaction in time domain

Markus Klemm<sup>1</sup>, Anartz Unamuno<sup>1</sup>; <sup>1</sup>Fraunhofer IPMS, Dresden, Germany

#### Background, Motivation and Objective

Acoustic simulation tools are required for CMUT design optimization. A fast solving and accurate model of a CMUT cell including a novel structure-fluid coupling has been developed and supported by measurements.

#### Statement of Contribution/Methods

The bendable plate of the CMUT can be described as a composite plate as in [1]. Embracing all layers into a thicker one with homogenized parameters (Young's modulus, Poisson's ratio, stress) reduces the FEM simulation times as well as avoiding shape related corrections and linearization approximations of reduced order models [2].

Using this approach, a 2D FE model was built in Matlab, capable of simulating any geometry, material stack, and layer dependent initial in-plane stress. The model can be used for static (fig. a) or transient [3] simulations. In addition, the driving and receive side electronic circuitry can be included, providing a complete solution to the system model.

A novel approach to the solid-fluid interaction has been implemented in this model, where every mesh element acts as an acoustic monopole emitting into semi-infinite space. The time and location dependent wave propagation on the surface of the CMUT is merged into a radiation matrix during preprocessing. Solving the equation of continuity on the surface of the CMUT and multiplying it with the radiation matrix provides the sound pressure deviation on the CMUT (fig. b), which is also an input to the solver for the next time step. Expanding the area of sound propagation beyond the border of the emitting cell, and adding more CMUT cell, it is possible to characterize crosstalk effects.

#### Results/Discussion

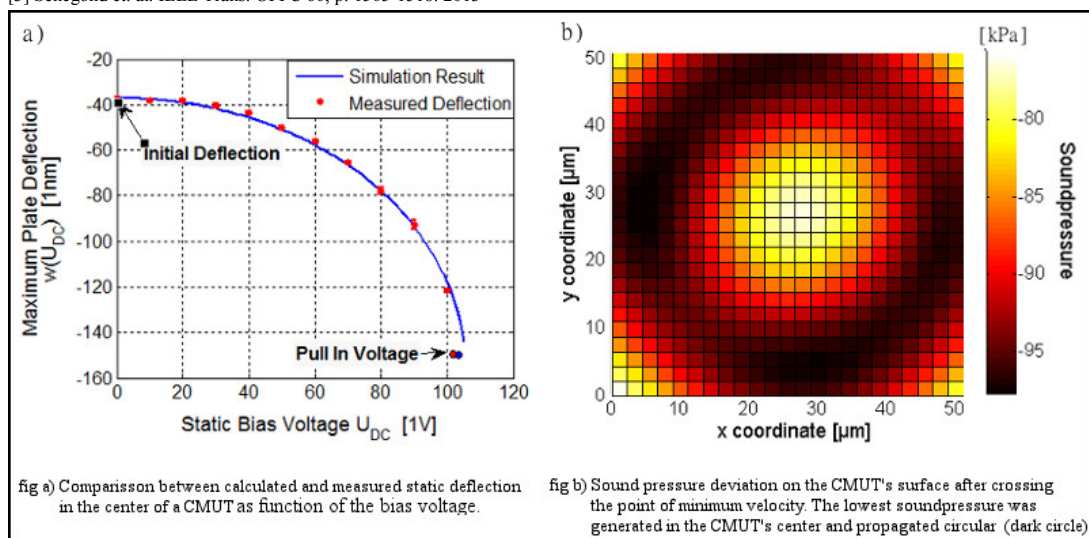
The modeling approach presented here ensures an accurate mechanical and acoustic solution that also contemplates the structure-fluid interaction, avoiding further approximations and time consuming convolution operations.

The model provides pull-in voltages, acoustic and electrical responses as well as sound pressure and velocity deviation on the CMUT's surface, both in send and receive operations. The model has been validated by comparing static and dynamic simulation results in air and water to measurements performed on CMUTs samples built at Fraunhofer IPMS.

[1] Certon et. al. IEEE Trans. UFFC 52, p. 2163-2172. 2012

[2] Ozgurluk et al. IEEE Trans. UFFC 57, p. 969-976. 2010

[3] Senegond et. al. IEEE Trans. UFFC 60, p. 1505-1518. 2013



7C-2

### 3:45 pm Resonances and Nonuniformities in CMUT Elements or Arrays

Abdullah Atalar<sup>1</sup>, Hayrettin Koymen<sup>1</sup>; <sup>1</sup>Electrical and Electronics Engineering, Bilkent University, Ankara, [Please select], Turkey

#### Background, Motivation and Objective

A typical CMUT probe consists of many CMUT cells placed side by side in a compact manner to generate more and directive acoustic power. It was shown that mutual interactions between the cells in such multi-cell configurations play a significant role in the velocity response of the cells [Park, et.al., IEEE IUS 2010, p. 431]. The mutual coupling between two cells through the immersion medium manifests itself as the mutual acoustic impedance between those cells [Senlik, et.al., IEEE Trans. UFFC, vol. 57, p. 969, 2010]. Since an individual CMUT cell has a low acoustic impedance, its response is mainly determined by the total (self and mutual) acoustic impedance imposed on the cell.

### Statement of Contribution/Methods

We show how to model an element or an array of  $n$  CMUT cells immersed in a liquid. We use the small-signal model [Köymen, et al., IEEE Trans. UFFC, v. 59, p.1791, 2012.] of a single cell biased with a DC voltage, the self-radiation impedance of the cell and the mutual radiation impedances created by the neighboring cells. The resulting set of  $n$  linear equations with  $n$  unknowns can be solved to find all cell velocities as a function of the excitation frequency. We are able to find, for example, the response of an array with 16,384 cells in 50 seconds per frequency point.

### Results/Discussion

Simulation results of arrays point out the presence of spurious resonances near the center frequency of individual cells. We show that these resonances, also observed experimentally, are due to Rayleigh-Bloch waves travelling laterally on the CMUT surface-liquid interface. We derive an analytical expression for the dispersion relation of this wave. The highly dispersive Rayleigh-Bloch waves have a phase velocity slower than the sound speed in the liquid and they cannot exist above a cut-off frequency. The spurious resonances occur at frequencies when these waves reflect from the edges of the array and form standing waves similar to that in a Fabry-Pérot resonator. Moderate amounts of loss in the CMUT cell is sufficient to eliminate high order modes, but low order modes remain even in the presence of significant loss, deteriorating the impulse response. The arrays with small size are more prone to this undesired effect, while larger arrays suffer only from low order resonances. It is possible to avoid the resonances altogether by operating above the cut-off frequency. However, the interactions between the cells also cause an unexpected nonuniformity among the cell velocities at frequencies above the cut-off frequency. Those cells, which are on the edge of the element or the array, experience a significantly lower impedance. As a result, the displacement of the cells at the edge is more than the displacement of the cells in the middle. This nonuniformity degrades the point spread function of the CMUT probe. It creates a background radiation level reducing the dynamic range of the system. We propose methods to reduce these effects to improve the performance of CMUT probes.

7C-3

### 4:00 pm An Equivalent Circuit Model for Curved Piezoelectric Micromachined Ultrasonic Transducers with Spherical-shape Diaphragms

Sina Akhbari<sup>1</sup>, Firas Sammoura<sup>1,2</sup>, Liwei Lin<sup>1</sup>; <sup>1</sup>Mechanical Engineering, UC Berkeley, Berkeley, CA, USA, <sup>2</sup>Electrical Engineering and Computer Science, Masdar Institute, Abu Dhabi, Abu Dhabi, United Arab Emirates

### Background, Motivation and Objective

Micromachined ultrasonic transducers are used in medical imaging and gesture recognition. Although pMUTs do not require high input DC voltage and are linear in contrast to cMUTs, they have limited electromechanical coupling factor ( $k_{eff}^2$ ). Curved pMUTs were proposed to have orders of magnitude higher  $k_{eff}^2$  than the state-of-art planar pMUTs. We have investigated curved pMUTs, and verified their superior performance both analytically and experimentally. An equivalent circuit of an ultrasonic transducer is very important for performance prediction, design optimization, and interface with ASIC. The objective of this work is to theoretically develop a circuit model representation of a clamped curved pMUT and determine optimal design parameters at various acoustic loads.

### Statement of Contribution/Methods

The time harmonic deflection equation of a clamped spherical elastic piezoelectric shell cap was analytically solved. The volumetric displacement and electrical charge were determined in terms of the input voltage and acoustic pressure. The lumped element circuit parameters including electrical blocked capacitance, electromechanical transformer ratio, and mechanical admittance were extracted.

### Results/Discussion

Fig. 1(a) shows a 3D schematic of a curved pMUT based on a CMOS-compatible fabrication process. The AlN piezoelectric material, is sandwiched between top and bottom Mo electrodes. Backside DRIE is used to release the diaphragm. Fig. 1(b) shows a 2D schematic of the axisymmetric curved pMUT with clamped boundary condition, in a spherical shell of center O and radius  $R_c$ . Fig. 1(c) shows the equivalent electrical circuit representation of a curved pMUT. Fig. 1(d) illustrates system equations, expressing the volumetric displacement and electric charge in terms of the input voltage and acoustic pressure. The lumped element parameters are explicitly derived. Fig. 1(e, top) shows the volumetric displacement frequency response of a 2- $\mu$ m thick AlN pMUT with 70  $\mu$ m nominal radius and 720  $\mu$ m radius of curvature in air and water, while Fig. 1(e, bottom) shows  $k_{eff}^2$  versus  $R_c$  for both analytical and numerical models. Both models perfectly match in terms of trend and predicted values. The  $k_{eff}^2$  is estimated to max at 3.3%, which shows curved pMUT can potentially reach 60% of the material limit ( $\sim 5.5\%$  for AlN). This is 6x more than the value for conventional AlN pMUT.

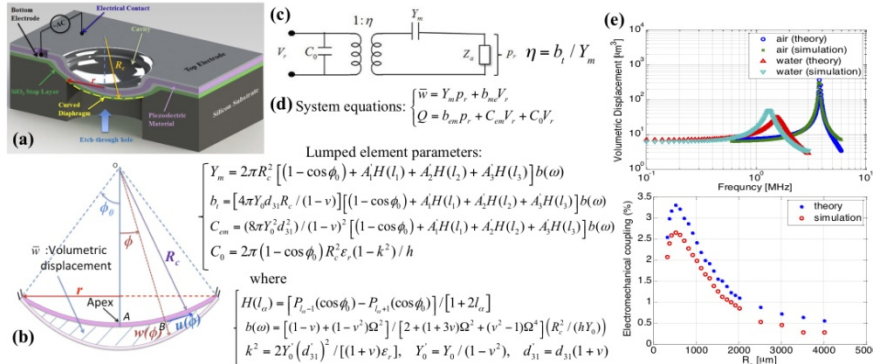


**Figure 1:** (a) 3D schematic of a curved pMUT. (b) 2D schematic of the axisymmetric curved pMUT with clamped boundary conditions, where the radial and tangential displacements at point B with an angular position  $\phi$  from the shell axis are denoted as  $w(\phi)$  and  $u_\phi(\phi)$ , respectively. (c) The representation of the equivalent electrical circuit model for the curved pMUT. (d) System equations, expression the volumetric displacement,  $\bar{w}$ , and the electric charge,  $Q$ , in term of the input voltage,  $V_r$ , and the acoustic pressure,  $P_r$ . Lumped element parameters including the mechanical admittance,  $Y_m$ , electromechanical transduction coefficient,  $b_1$ , induced capacitance due to the mechanical motion,  $C_{em}$ , and blocked capacitance,  $C_o$ , are also derived. (e, Top) The volumetric displacement frequency response, and (e, bottom) shows the effective electromechanical coupling factor for both theoretical model and FEM simulation.

**4:15 pm Multiple Electrode Piezoelectric Micromachined Ultrasound Transducers with enhanced Electromechanical Coupling**Firas Sammoura<sup>1,2</sup>, Liwei Lin<sup>2</sup>; <sup>1</sup>Electrical Engineering and Computer Science, Masdar Institute of Science and Technology, Abu Dhabi, Abu Dhabi, United Arab Emirates, <sup>2</sup>Mechanical Engineering, UC Berkeley, Berkeley, CA, USA**Background, Motivation and Objective**

Ultrasonography is one of the most extensively implemented medical imaging and range sensing techniques. Portable devices for point of care and gesture recognition demand small form factor, acoustically efficient, and high acoustic penetration transducers. A pMUT is attractive due to low-operating voltages, wide bandwidths, and large output acoustic pressure. However, the effective electromechanical coupling factor ( $k_{eff}^2$ ), the ratio of the stored mechanical energy to the input electrical energy, is generally low for pMUTs. The lack of pMUT circuit models limit the estimation of  $k_{eff}^2$  to Finite Element Analysis (FEA). The objectives of this work are: (1) derive an analytical expression for  $k_{eff}^2$  of clamped unimorph circular pMUTs with multiple electrodes, (2) optimize  $k_{eff}^2$  with respect to the ring-shape electrode radii and excitation voltages, and (3) verify model with FEA and published data.

**Statement of Contribution/Methods**

The general expression of  $k_{eff}^2$  is derived explicitly for the first time as a function of the piezoelectric layer properties, the plate dimensions, and the frequency of operation using the plate deflection model we previously developed based on Green's function approach. Numerical techniques were used to optimize  $k_{eff}^2$  using (1) for a 1-, 2-, 3-, and 4-electrode pMUT designs and verified with COMSOL.

**Results/Discussion**

Fig. 1(a) shows the schematical view of a unimorph pMUT plate. The pMUT has a thin top electrode made up of  $m$  circular rings as in Fig. 1(b), where the  $j$ th ring electrode is actuated with a voltage  $V_j$ . Eq. 1 lists the derived expression of  $k_{eff}^2$ . The normalized radii and voltage values that maximize  $k_{eff}^2$  are presented in Fig. 1(c). The electrical input impedances of 1-, 2-, 3-, and 4-electrode pMUT designs in Fig. 1(d, top) are simulated using COMSOL for a prototype pMUT with 5  $\mu$ m-thick poly-Si layer, 2  $\mu$ m-thick PZT layer, and a plate with 135  $\mu$ m radius. Whereas the series resonant frequency ( $f_s$ ) remains constant for the 4 designs as shown in Fig. 1(c), the parallel resonant ( $f_p$ ) increases with the increase in number of top electrodes indicating enhanced coupling. The theoretically predicted  $k_{eff}^2$  matches within 2-13% the simulated values extracted from  $f_s$  and  $f_p$ . Figure 1(d, bottom) shows that the 1-electrode design matches well with experimental data, while the 2-, 3, and 4-electrode designs have 168%, 200%, and 211% larger  $k_{eff}^2$ .

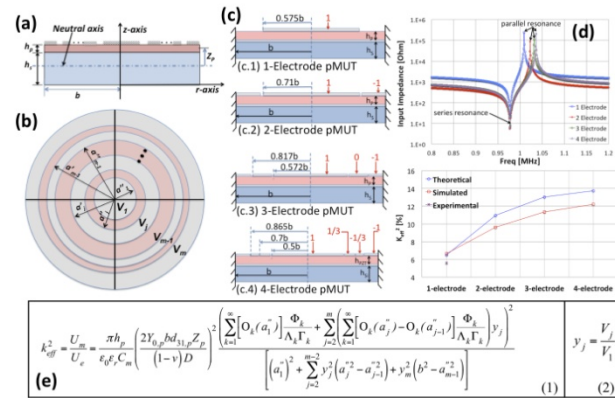


Figure 1: (a) A schematic diagram of a unimorph pMUT plate of radius  $b$  in  $d_{31}$  mode with structural and piezoelectric layers of thicknesses  $h_s$  and  $h_p$  respectively. (b) Top view showing the patterned top electrode with  $m$  circular/ring electrodes. (c) Optimum normalized top electrode radii and excitation voltages for a 1-, 2-, 3-, and 4-electrode pMUT. (d, top) The simulated input impedance showing the respective series and parallel resonances, and (d, bottom) the effective electromechanical coupling factor  $k_{eff}^2$  for a clamped unimorph pMUT with 5  $\mu$ m-thick poly-Si layer and 2  $\mu$ m-thick PZT. The plate radius is 135  $\mu$ m. (e) The general expression of  $k_{eff}^2$  of a multiple-electrode clamped unimorph pMUT

**4:30 pm LUMPED ELEMENT MODELING OF CMUT ARRAYS IN COLLAPSED MODE**Elif Aydogdu<sup>1</sup>, Alper Ozgurkulu<sup>2</sup>, Abdullah Atalar<sup>1</sup>, Hayrettin Koymen<sup>1</sup>; <sup>1</sup>Electrical and Electronics Engineering, Bilkent University, Ankara, Turkey, <sup>2</sup>Electrical Engineering and Computer Sciences, University of California Berkeley, Berkeley, CA, USA**Background, Motivation and Objective**

Lumped element modeling has been used to precisely simulate finite length CMUT arrays, but it was restricted to uncollapsed mode operation [1]. A parametrical lumped element model for collapsed mode operation of single CMUT was obtained in [2]. In this work, this collapsed mode CMUT model is utilized and a CMUT array model for both uncollapsed and collapsed mode operations is obtained.

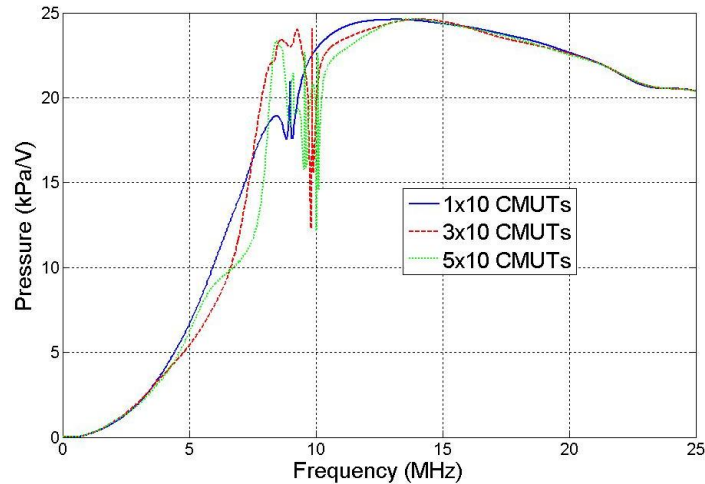
**Statement of Contribution/Methods**

In order to construct an array model, the mutual radiation impedance of the cells should be introduced. In the collapsed mode, the mutual radiation impedance between two CMUT cells is dependent on the contact radii of both cells. We derived the mutual radiation impedance between two CMUTs, one or both of which are in collapsed mode. In the lumped element model, we introduced the mutual radiation impedance between every cell pair, as a function of their instantaneous contact radii.

**Results/Discussion**

Using the lumped element model simulations, we investigated the effect of neighboring cells on the operation of a CMUT array. An element of 1x10 CMUTs is driven with 0.1 V, where the bias voltage is 60 V. We added other elements on both sides of the driven element, and obtained 3x10 and 5x10 arrays, but the side elements are not driven, they are only biased at 60 V. The un-driven neighbors change the frequency response of the center element due to crosstalk. In the figure, the pressure output of 1x10 CMUT array without any neighbors (solid), with two (dashed) and four (dotted) undriven, biased side elements are given. The 9 MHz resonance of 1x10 array arises from the cell interactions, and it shifts to a higher frequency as the neighboring elements are introduced. Additional resonances are observed with the inclusion of the side elements. The model is helpful for understanding how the array resonances arise. We investigate methods for eliminating these resonances. (in water, 1atm, silicon nitride membrane, radius=30  $\mu$ m, cell-to-cell distance=63  $\mu$ m, memb. thick.=1 $\mu$ m, insulator thick.=0.4  $\mu$ m, gap height=0.2  $\mu$ m)

- [1]H. K. Oguz, et.al., IEEE Trans. UFFC, 60, p.1016-1024, 2013.  
 [2]E. Aydogdu, et.al., IEEE Trans. UFFC, 61, p.173-181, 2014.



7C-6

#### 4:45 pm A Computationally Efficient Nonlinear System Model for CMUT Arrays

Sarp Satir<sup>1</sup>, F. Levent Degertekin<sup>1</sup>; <sup>1</sup>Georgia Institute of Technology, USA

##### Background, Motivation and Objective

Accurate and computationally efficient models are essential for designing high performance medical ultrasound transducers. For CMUTs, nonlinearities and large design space in terms of device geometry and array configurations preclude the applicability of simple small signal equivalent circuit models. Especially when CMUTs are driven by large signals to achieve required pressure levels for ultrasound imaging and therapy applications, accurate modeling requires complex and time consuming transient 3D FEA, presenting a significant barrier for researchers interested in evaluating the CMUT technology.

##### Statement of Contribution/Methods

We present a time domain fast nonlinear lumped model that predicts large signal behavior of a CMUT array with arbitrary membrane/electrode geometry in both transmit and receive modes. The model is in MATLAB environment and based on separation of nonlinear electrostatic and linear vibroacoustic CMUT behavior [1]. Model capabilities include selection of arbitrary drive signals and transmit-receive circuitry for individual array elements, enabling accurate modeling of phased arrays of single and multiple electrode CMUTs for harmonic imaging and other ultrasound modalities. Pulse-echo operation, i.e. reflection from a hard wall, is also considered where the incident field source is the image of the CMUT array itself.

##### Results/Discussion

A circular CMUT is modeled, and the results are verified via COMSOL simulations. As an example, response to an incident field is calculated with varying resistive loading. Calculated output currents for short circuit and resistive termination show excellent agreement (Fig.1a). To show the versatility of the method to different scenarios, a dual electrode CMUT is modeled as another case where 2 electrodes are used for transmit with separate circuitry for harmonic reduction investigation. Fig.1b shows that the distortion is suppressed over 20dB when a series resistor is added to each electrode separately. For computational efficiency comparison, a pulse echo simulation is run in the presence of a hard wall. Once the model parameters are calculated, (~30 minutes), the 2 way response for a drive signal configuration is calculated in ~5 seconds. The FEA takes approximately one day using the same computer. The computational efficiency renders the model a versatile tool for rapid CMUT array simulation.

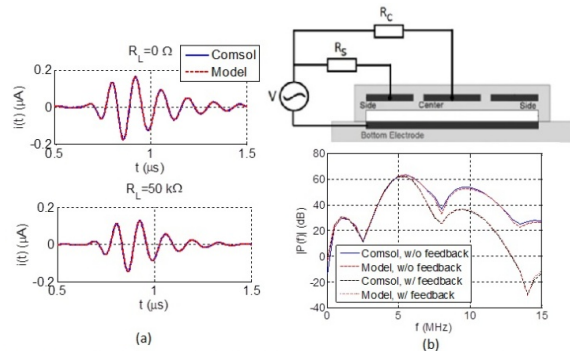


Fig 1 (a) Short circuit and resistive termination output currents in receive mode for plane wave incidence (b) Dual electrode feedback linearization topology and spectra of the transmitted pressure for cases with and without feedback

- [1] S. Satir, J. Zahorian, and F. L. Degertekin, "A large-signal model for CMUT arrays with arbitrary membrane geometry operating in non-collapsed mode," *Ultrasonics, Ferroelectrics and Frequency Control, IEEE Transactions on*, vol. 60, pp. 2426-2439, 2013.



## PA - Student Paper Competition

Normandy

Saturday, September 6, 2014, 8:00 am - 5:00 pm

PA-1

### Comparison of tumor microvasculature assessment via Ultrafast Doppler Tomography and Dynamic Contrast Enhanced Ultrasound

Charlie Demene<sup>1</sup>, Thomas Payen<sup>2</sup>, Alexandre Dizeux<sup>2</sup>, Jean Luc Gennisson<sup>1</sup>, Lori Bridal<sup>2</sup>, Mickaël Tanter<sup>1</sup>; <sup>1</sup>Institut Langevin, ESPCI ParisTech, CNRS UMR7587, Inserm U979, Paris, France, <sup>2</sup>Laboratoire d'imagerie biomédicale, Université Pierre et Marie Curie, UMR S 1146 / UMR 7371, Paris, France

#### Background, Motivation and Objective

Assessing structural organization and dynamics of tumor blood supply is of highest interest since numerous cancer treatments rely on antiangiogenic effects. Dynamic Contrast Enhanced Ultrasound (DCE-US) is widely used in cancer research to extract quantitative parameters reflecting tumor perfusion. However, the underlying vascular structure is not revealed and local spatial fluctuations in DCE parametric maps remain unexplained. The recently introduced Ultrafast Doppler Tomography (UFD-T) has been shown able to reconstruct the 3D vascular network of a rat brain with a 100µm resolution. It is applied here to tumor vasculature imaging and quantitative hemodynamics assessment along with DCE-US to show the complementarity between the techniques.

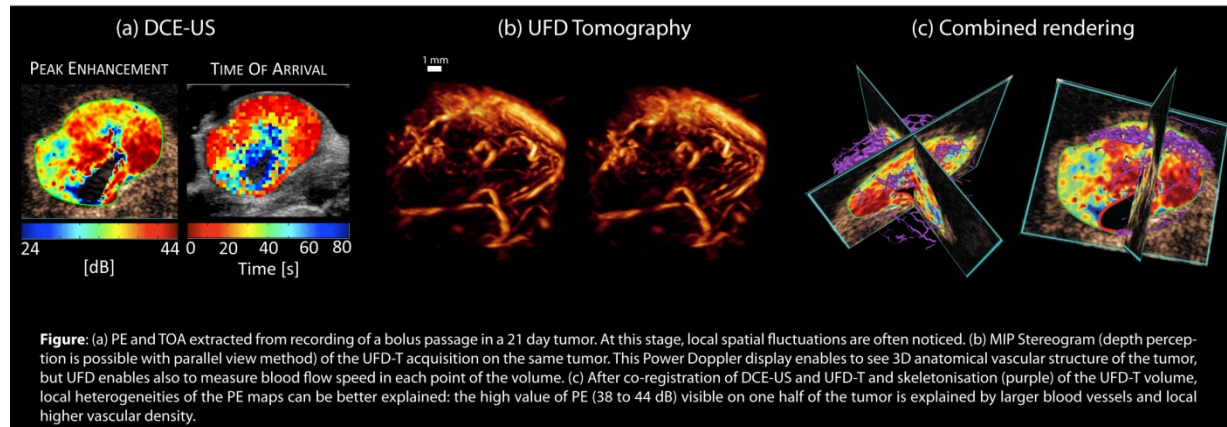
#### Statement of Contribution/Methods

Lewis lung carcinoma (3LL) fragments were subcutaneously implanted in 4, C57BL6 mice imaged at days 9, 15 and 21. UFD-T was performed first : a 15 MHz ultrasound probe (128 elements, 0.08 mm pitch), mounted on a motorized stage with four degrees of freedom was used to acquire 18 (10° apart) swept scans made of 50 slices ( $\Delta$ slice = 200 µm). For each slice a UFD acquisition, consisting of 800 (8 angle compound plane wave emission) frames, is done at a frame rate of 500Hz, then processed to obtain one ultrasensitive Power Doppler image. This dataset was merged in a 10mm wide 3D volume.

DCE-US was then performed in the 0° and 90° planes. A bolus of Sonovue (Bracco Suisse SA) was injected at 1mL/kg and 2mL/min, and microbubble bolus passage was recorded for 60s. Typical perfusion parameters (Peak Enhancement (PE) and Time of Arrival (TOA)) were then extracted from the time-intensity curves and correlated to Ultrafast Doppler vascular estimation.

#### Results/Discussion

UFD-T enabled to reconstruct tumor vascular structure with a 100µm resolution and to measure axial blood flow speed between 0.2 and 2 cm/s. PE maps were calculated from DCE-US acquisition and local signal heterogeneities were shown to be correlated to the repartition of blood vessels: low values of PE indicated local poor blood vessel density. Also TOA gradients can be explained with respect to structural (smaller vessels toward the center of the tumor) and dynamic (blood flow speed measurements) parameters that are revealed by UFD-T.



PA-2

### Ultrasound Quantification of Molecular Marker Concentration in Large Blood Vessels

Shiyang Wang<sup>1</sup>, F William Mauldin Jr<sup>1</sup>, Alexander L Klibanov<sup>1,2</sup>, John A Hossack<sup>1</sup>; <sup>1</sup>Biomedical Engineering, University of Virginia, Charlottesville, Virginia, USA, <sup>2</sup>Division of Cardiovascular Medicine, University of Virginia, Charlottesville, Virginia, USA

#### Background, Motivation and Objective

Current ultrasound molecular imaging techniques have demonstrated efficacy in pre-clinical studies of cancer and cardiovascular disease. These techniques involve the detection of molecular specific bound microbubbles (MBs) through some combination of nonlinear MB detection and elimination of free MBs through waiting periods or low-pass interframe filtering techniques. Non-specific adhesion is typically measured by additional control MB injections. In addition to having prolonged protocols, current limitations include the inability to quantify molecular marker concentration in human tissue environments with highly variable attenuation and imaging path lengths. Consequently, we developed a novel modulated Acoustic Radiation Force (ARF)-based imaging sequence, with the goal of achieving quantitative measurement of molecular marker concentration using a single short imaging protocol (3 min).

#### Statement of Contribution/Methods

Gelatin flow phantom channels ( $\phi = 4$  mm) were constructed to mimic large blood vessels. Targeted and control channels were incubated with streptavidin (1 – 50 µg/mL) and 5% bovine serum albumin (BSA) solution for 12 h, respectively. The surface concentrations of Eu<sup>3+</sup>-labelled streptavidin were measured using dissociation-enhanced time-resolved spectrofluorometry. Biotinylated lipid-perfluorobutane MB ( $\phi \sim 2$  µm) dispersion ( $5 \times 10^5$  /mL) was drawn through the channels (6 – 10 cm/s). The sequence (programmed on

Verasonics scanner) had three components – 10 s of imaging (4.5 MHz, 4 Hz frame rate), 70 s of interspersed imaging and ARF (4.5 MHz, 5 kHz PRF, MI < 0.05), and 100 s of imaging – showing the baseline, rise, and decay of adherent MBs along the bottom wall (Fig a). The residual-to-saturation ratio ( $R$  = residual MB / saturated MB) extracted from the signal magnitude curve was used to quantify molecular marker concentration.

### Results/Discussion

Results demonstrate that  $R$  is linearly related to streptavidin concentration at a range of flow velocities ( $R^2 > 0.94$ , Fig b&c); and within certain bounds, was independent of attenuation and absolute signal magnitude ( $p > 0.13$ ,  $n = 10$ ). The highest detection sensitivity was approximately 900 molecules/ $\mu\text{m}^2$ . In summary, feasibility was demonstrated for a rapid (3 min imaging protocol) quantification of molecular marker concentration in large vessels using the modulated ARF-based sequence.

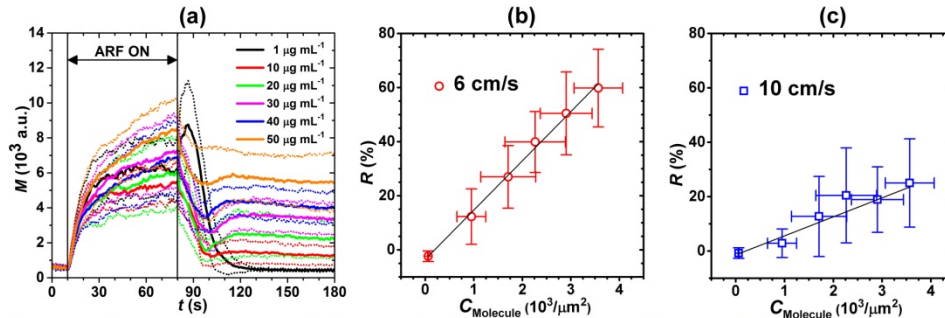


**Figure** (a) Averaged signal magnitude curves for targeted channels at different incubation concentrations of streptavidin solution (1 – 50  $\mu\text{g/mL}$ ). Solid lines indicate the mean values from 10 trials. Dotted lines indicate the corresponding error bars at the range of [mean  $\pm$  standard deviation]. Relationships between the residual-to-saturation ratio ( $R$ ) and corresponding surface concentration of streptavidin at flow velocities of 6 cm/s ( $R^2 = 0.99$ ) (b) and 10 cm/s ( $R^2 = 0.95$ ) (c). Black lines are the weighted linear fits.

### PA-3

#### Ultrafast Plane Wave Imaging Based Pulsed Magnetomotive Ultrasound

Pei-Hsien Ting<sup>1</sup>, Yi-Da Kang<sup>2</sup>, San-Yuan Chen<sup>2</sup>, Meng-Lin Li<sup>1,3</sup>; <sup>1</sup>Dept. of Electrical Engineering, National Tsing Hua University, Hsinchu, Taiwan, <sup>2</sup>Department of Materials Science and Engineering, National Chiao Tung University, Taiwan, <sup>3</sup>Institute of Photonics Technologies, National Tsing Hua University, Taiwan

### Background, Motivation and Objective

Recently, pulsed magnetomotive ultrasound (pMMUS) imaging has been introduced to detect superparamagnetic iron oxide nanoparticles (SPIO) which is not able to be visualized by conventional ultrasound. However, because of the used magnetic short pulse, the reported pMMUS only can use a single-element ultrasound transducer along with mechanical scanning to perform imaging, which significantly limits the imaging frame rates.

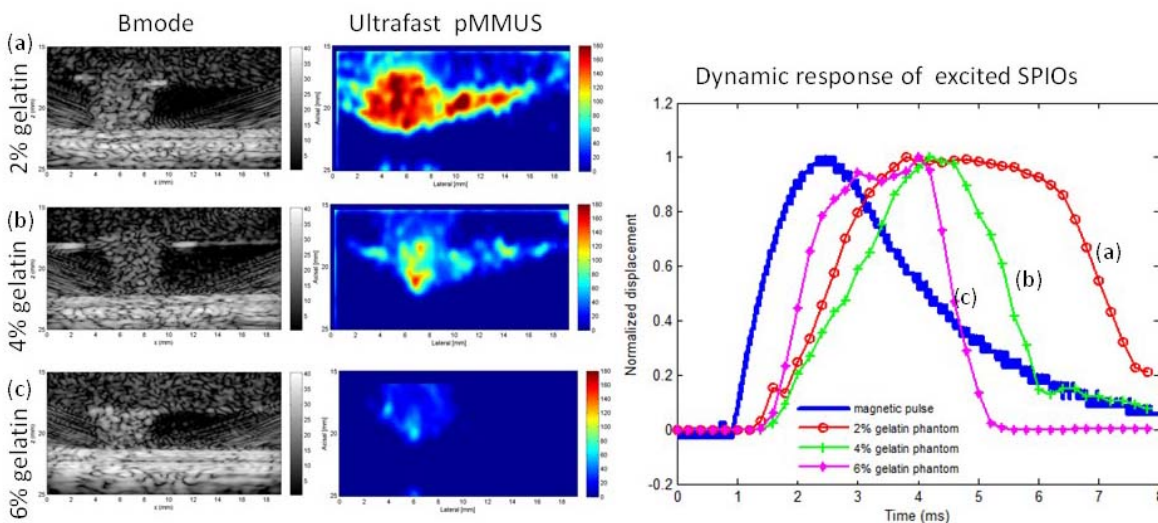
### Statement of Contribution/Methods

To solve this problem, we propose an ultrafast plane wave imaging based pMMUS technique. The ultrafast frame rate of plane wave imaging is fast enough to track the magnetomotion of the excited SPIOs during the period of the magnetic pulse being applied. Therefore, the proposed ultrafast plane wave pMMUS is capable of visualizing the dynamic response of the excited SPIOs, which is highly correlated to tissue characteristics such as viscosity and elasticity, to an externally-applied magnetic pulse. In addition, a new pMMUS motion tracking algorithm based on ultrafast plane wave imaging is developed to reduce the effect of magnetic field inhomogeneity.

### Results/Discussion

In our experiments, ultrafast plane wave imaging with a 5 kHz frame rate was used to implement the pMMUS where the SPIO motion induced by an 8-ms magnetic pulse was tracked. The results showed that there were significant differences between the ultrafast plane wave pMMUS images of the phantoms with and without SPIOs embedded. There was a monotonic increase in displacement with increased concentration of SPIOs. In addition, gelatin phantoms with 2%, 4% and 6% gelatin were used to mimic tissues with different elasticity and viscosity. The dynamic responses of the excited SPIOs in the three types of phantoms were distinguishable (see the figure). Overall, it is demonstrated that the feasibility of our proposed ultrafast plane wave pMMUS imaging technique for the visualization of the magnetomotion and dynamic response of the SPIOs under the excitation of a short magnetic pulse. More studies are required to further improve the magnetomotion tracking algorithm and explore the relationship between the dynamic response of the excited SPIOs and the tissue viscosity and elasticity.





PA-4

### Ultrafast vaporization dynamics of photoacoustic polymeric microcapsules

Guillaume Lajoie<sup>1</sup>, Erik Gelderblom<sup>1</sup>, Ceciel Chlon<sup>2</sup>, Marcel Böhmer<sup>2</sup>, Nico De Jong<sup>3</sup>, Wiendelt Steenberg<sup>4</sup>, Srirang Manohar<sup>4</sup>, Michel Versluis<sup>1</sup>; <sup>1</sup>Physics of Fluids, University of Twente, Netherlands, <sup>2</sup>Philips Research Laboratories Europe, High Tech Campus, Netherlands, <sup>3</sup>Biomedical Engineering, Thoraxcenter, Erasmus mc, Netherlands, <sup>4</sup>Biomedical Photonic Imaging Group, University of Twente, Netherlands

### Background, Motivation and Objective

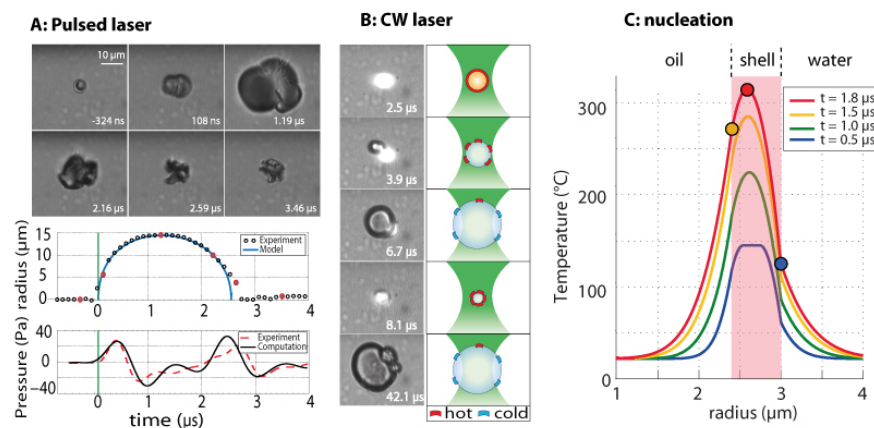
Precision control, both in space and time, of vaporization has many potential applications, ranging from solar energy conversion to microfluidic cell sorting. In particular, laser-induced cavitation was recently shown to have great potential in photoacoustic diagnostic and therapeutic applications [1]. However, the physical mechanisms of vaporization are not well understood, owing primarily to the small length scales and ultrafast time scales involved. Here, we study the nanoseconds vapor bubble dynamics of a photoacoustic agent activated by both pulsed and CW laser excitation. Experimental results are compared to a numerical model revealing the physical mechanisms underlying the photoacoustic effect [2].

### Statement of Contribution/Methods

Oil-filled polymeric microcapsules, formed from ink-jet printed droplets, with a well-controlled radius of 3  $\mu\text{m}$ , incorporate Nile Red dye into the shell to allow laser light absorption. The activation results from the focusing of a pulsed or a CW laser beam through the imaging microscope objective. The Brandaris 128 ultra high-speed camera is then used to record the capsules' response at frame rates up to 15 million frames per second. Simultaneously, a broadband transducer records the photoacoustic signatures. The thermal behavior is modeled using a finite element model and the Rayleigh-Plesset vapor bubble dynamics is solved with an ODE solver, both using Matlab.

### Results/Discussion

Above the threshold laser fluence of 70 mJ/cm<sup>2</sup> the shell disrupts, forming a bubble that grows to a radius of 15  $\mu\text{m}$  in 1  $\mu\text{s}$  (A). The bubble dynamics and the 40 Pa resulting acoustic pressure are well captured by an energy balance model and shows that the event is governed by inertia and not by the phase conversion. Remarkably, CW laser illumination resulted in sustained oscillations of the vapor bubble (B). During expansion the absorbing shell fragments are pushed out of the laser beam and cool down. This leads to condensation followed by inertial entrainment of the fragments back into the beam, thus initiating a new cycle. The nucleation originates from the release of the hot oil core in the superheated water (C). The photoacoustic frequency is directly coupled to the laser intensity and spot size. A high frequency modulation of the laser would have a similar effect and this will open up a wealth of promising opportunities for novel CW photoacoustic modalities.



[1] Wilson, K., Homan, K. & Emelianov, S. Biomedical photoacoustics beyond thermal expansion using triggered nanodroplet vaporization for contrast-enhanced imaging. Nat. Commun. 3, 618 (2012).

[2] Lajoie et al., Ultrafast vaporization dynamics of laser-activated polymeric microcapsules DOI: 10.1038/ncomms4671

# Pharmacodynamic analysis for efficient drug delivery through the FUS-induced BBB opening in Non-Human Primates in vivo

Gesthimani Samiotaki<sup>1</sup>, Shih-Ying Wu<sup>1</sup>, Maria Eleni Karakatsani<sup>1</sup>, Matthew Downs<sup>1</sup>, Sachin Jambawalikar<sup>2</sup>, Elisa Konofagou<sup>1,2</sup>; <sup>1</sup>Biomedical Engineering, Columbia University, USA, <sup>2</sup>Department of Radiology, Columbia University, USA

## Background, Motivation and Objective

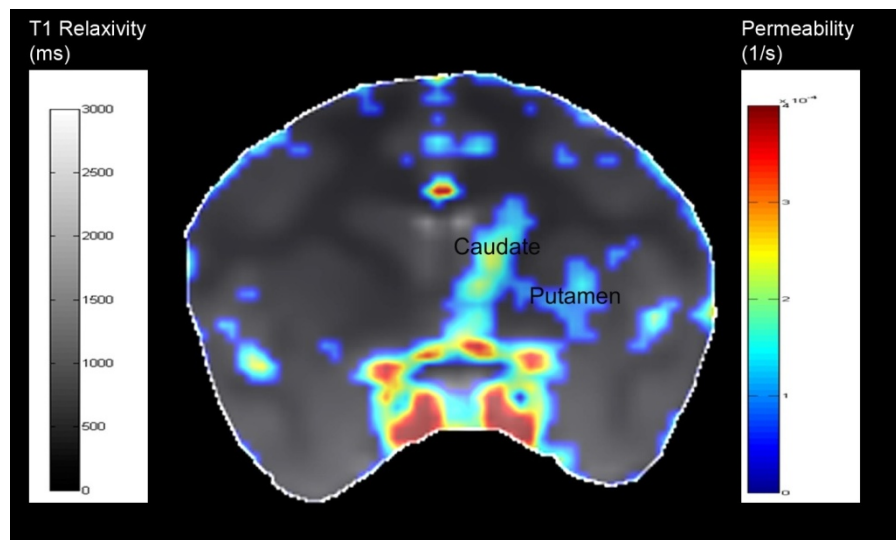
FUS in conjunction with systemically administered microbubbles has been previously shown to open the Blood-Brain Barrier locally, non-invasively and reversibly in non-human primates. However, a trans-BBB pharmacodynamic analysis has not been performed as of yet. The objective of this study was the pharmacodynamic analysis, i.e. permeability and relaxivity mapping, of the NHP brain *in vivo* in order to further investigate the effect of FUS, for safe and efficient drug-delivery.

## Statement of Contribution/Methods

Two brain structures, the caudate (Cau) and the putamen (Pu), were targeted in three rhesus macaques using FUS (Fo: 500 kHz; PRF: 2 Hz; duration: 120 s; PNP: 300-500 kPa) immediately after the IV administration of monodisperse bubbles. In a 3T MR scanner (Philips, USA) five pre-contrast 3D Spoiled Gradient Echo (SPGR) images (TR/TE: 10/4ms, FA: 50-350, res: 1x1x1 mm<sup>3</sup>) were acquired and used for variable flip angle based T1 relaxivity mapping. Subsequently, Dynamic Contrast Enhanced (DCE) imaging was performed, with the acquisition of 90 dynamic T1-weighted 3D repetitions (TR/TE: 4.2/1.7 ms; res: 1x1x2 mm<sup>3</sup>). The data were processed off-line using customized Matlab-based algorithms to generate permeability (K<sub>trans</sub>) maps. The areas of grey (GM) and white matter (WM) and BBB opening were also determined, based upon segmentation of the T1 relaxivity maps since GM and WM have distinctive characteristic relaxivity times. Quantitative permeability changes and the volume of BBB opening (V<sub>BBB</sub>) were measured.

## Results/Discussion

V<sub>BBB</sub> increased from 92±10 mm<sup>3</sup> to 262±34 mm<sup>3</sup> with a FUS pressure change from 300 kPa to 500 kPa. K<sub>trans</sub> was increased from 1.0531 ± 0.0761\*10<sup>-4</sup> s<sup>-1</sup> to 1.863 ± 0.132\*10<sup>-4</sup> s<sup>-1</sup> respectively. When targeting the Pu, an average of 95% of the opening was contained in the GM (T1 relaxivity range: 1001-1400 ms), while in the Cau 87% of the opening occurred in the GM (T1 relaxivity range: 600-1000 ms). No edema or hemorrhage was detected in any of the cases studied. In conclusion, monitoring BBB opening volume and permeability in non-human primates *in vivo* were found to increase significantly with pressure. The gray-to-white-matter ratio undergoing BBB opening varied slightly among the two targeted regions with most opening occurring in the GM. Pharmacodynamic analysis may be proven critical in planning, guidance and prediction of the FUS-enhanced drug delivery.



# Estimation of arterial wall motion using ultrafast imaging with transverse oscillations

Sebastien salles<sup>1</sup>, Simon Lai<sup>2</sup>, Damien Garcia<sup>3</sup>, Alfred Yu<sup>2</sup>, Didier Vray<sup>1</sup>, Hervé Liebgott<sup>1</sup>; <sup>1</sup>CNRS UMR 5220, INSERM U1044, Université de Lyon, Insa de Lyon, France, <sup>2</sup>Biomedical Ultrasound Laboratory, University of Hong Kong, China, People's Republic of, <sup>3</sup>RUBIC, CRCHUM, University of Montreal, Department of radiology, Canada

## Background, Motivation and Objective

Ultrafast ultrasound is a promising imaging modality with several potential clinical applications, such as arterial mechanics assessment, heart motion and blood flow imaging. Ultrafast ultrasound allows one to examine phenomena never analyzed before. However, the detection and measurement of these phenomena still remain challenging because of the difficulty in estimating small displacements, especially in the lateral direction. We thus propose to combine (1) ultrafast ultrasound imaging, (2) transverse oscillations (TO) and (3) a phase-based motion estimator. Our objective was to evaluate the proposed technique for the estimation of arterial wall motion using an *in vitro* phantom.

## Statement of Contribution/Methods

- 1) Plane-wave imaging was implemented on the SonixTouch system (5300 frames/s). Pre-beamformed radio-frequency (RF) data were acquired with the 128-channel Sonix DAQ
- 2) TOs were produced by filtering the beamformed RF signals to ensure an optimal control of the TO parameters.
- 3) Motion vectors were estimated using a phase-based approach: two single quadrant spectra were used to derive two phase images, which were combined to estimate the local displacements between two consecutive images.

Two artery mimicking phantoms were imaged during three consecutive pulsatile cycles: a stenotic and a non-stenotic artery with an inner diameter of 7 mm and a wall thickness of 1 mm. We tracked the proximal and distal arterial walls using our phase-based method, a speckle tracking approach on the B-mode images, and we compared the results with those obtained by a manual tracking.

The absolute mean differences between the estimated and the manually tracked trajectories were calculated for 20 ROI and 5 different frame rates.

### Results/Discussion

5 different frame rates were tested: 5300, 1060, 530, 353 and 256. The axial mean error remained stable around 65/100 pixel with both methods. The lateral mean error was 4.5 (4.6, 5, 5.2, 8, /100 pixel respectively) for our method and 310 (178, 120, 22, 23, /100 pixel) for speckle tracking.

In this phantom study, we have shown that our phase-based technique outperforms speckle tracking in terms of reproducibility and estimation of small radial and longitudinal displacements. Our results tend to show that ultrafast imaging with transverse oscillations is well-adapted to arterial wall motion estimation.

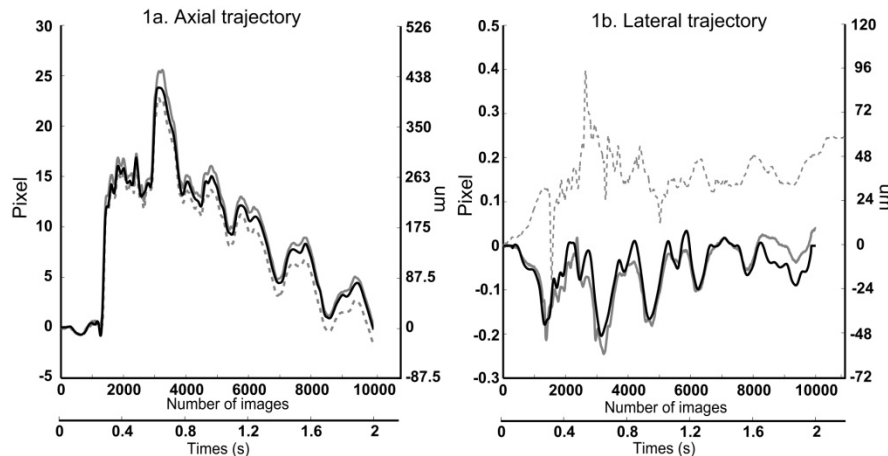


Fig.1: Axial and lateral trajectory estimation at 353 images/s of the non-stenotic artery. Comparison between --- speckle tracking, — our phased-based method and — manual tracking done 1 every 10 images

PA-7

### Application of Air-Coupled Ultrasound to Full-Scale Concrete Columns Using Tomography

Hajin Choi<sup>1</sup>, John S. Popovics<sup>2</sup>; <sup>1</sup>University of Illinois at Urbana-Champaign, Champaign, IL, USA, <sup>2</sup>Civil and Environmental Engineering, University of Illinois at Urbana-Champaign, Urbana, IL, USA

### Background, Motivation and Objective

Internal visualization provides better understanding of damage in materials; however, a large amount of data is required to reconstruct the image. Ultrasonic pulse velocity (UPV) is an efficient method to evaluate concrete. However, the application of conventional UPV is limited with concrete because of required surface preparation and large element size, and this method is labor and time intensive. Another practical problem is large computational effort associated of tomographic algorithm. Although algebraic reconstruction technique is applicable to limited data and diffracted source like ultrasound, it is well known that the algorithm is computationally inefficient compared to filtered back-projection (Radon transform). The structural inspection needs many data and the tomographic process takes a long time. New concept of data measurement and analysis are needed to evaluate full-scale structure in the field.

### Statement of Contribution/Methods

Our newly developed air-coupled ultrasonic measurement system includes electrostatic contactless transmitters and contact accelerometers. Because electrostatic transducers generate much more ultrasonic energy than conventional transducers, it is possible to measure low-noise signals through a full-scale structure without surface preparation. Furthermore, an automated scanning system accurately collects high resolution data within a limited time.

Filtered back-projection is computationally fast, however the algorithm requires data collected sufficient angles. The proposed air-coupled method increases sectional ray coverage so that it is possible to acquire projections from multiple angles. The transform-based algorithm is successfully applied with collected data and interpolation to develop internal image of structure. The speed of computation significantly improves without a significant difference with tomograph quality.

### Results/Discussion

Reconstructed sectional images are stacked vertically in three dimensions. Developed internal visualization shows accurate location of embedded defects inside of a highly reinforced concrete element. The results prove that the proposed ultrasonic method is applicable to full-scale concrete structures. Furthermore, the fast imaging algorithm helps to analyze structural condition in situ.

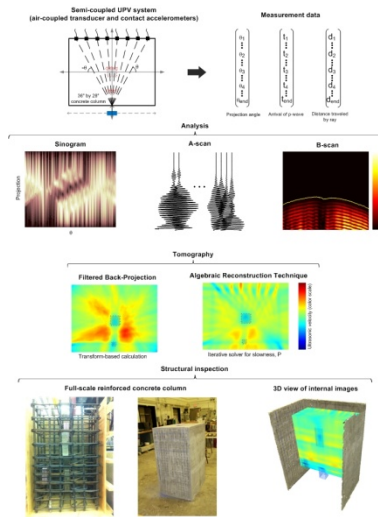


Figure 1. Graphical abstract of air-coupled ultrasonic measurement and tomography

PA-8

### Microparticle manipulation and whole blood pre-treatment in surface acoustic wave counterflow devices

Marco Travaglini<sup>1,2</sup>, Richie Shilton<sup>1</sup>, Marco Pagliuzzi<sup>1</sup>, Ilaria Tonazzini<sup>1</sup>, Fabio Beltram<sup>1,2</sup>, Marco Cecchini<sup>1</sup>, <sup>1</sup>Laboratorio NEST, Scuola Normale Superiore and Istituto Nanoscienze - CNR, Pisa, Italy, <sup>2</sup>Center for Nanotechnology Innovation @ NEST, Istituto Italiano di Tecnologia, Pisa, Italy

#### Background, Motivation and Objective

Surface acoustic wave (SAW) counterflow has been demonstrated to generate efficient integrated fluid pumping in closed microchannels allowing true device portability. Full understanding of the fluid flow and microparticle dynamics during this process is essential in view of point-of-care applications. When SAWs impinge on a fluid, ultrasound waves are refracted into the liquid. These ultrasounds generate a stationary flow, known as acoustic streaming, as well as an acoustic radiation force that acts on suspended microparticles. Here we show that, depending on the microchannel height  $h$  compared with the ultrasound wavelength  $\lambda_f$ , it is possible to switch from an acoustic streaming ( $h \gg \lambda_f$ ) dominated regime to an acoustic radiation force ( $h \leq \lambda_f$ ) dominated regime. We then exploited these two regimes separately for whole blood pre-treatment.

#### Statement of Contribution/Methods

Our experimental devices consisted of two layers bonded together: a 128° YX lithium niobate substrate with a patterned interdigital transducer generating SAWs at 100 MHz and an upper polydimethylsiloxane (PDMS) straight microchannel layer. We fabricated the PDMS layers with microchannel heights ranging from 12.5  $\mu\text{m}$  to 70  $\mu\text{m}$ . We loaded 10  $\mu\text{L}$  of fluid into the device and operated it at fixed surface acoustic wave amplitude. The dynamics of the entire filling process during acoustic counterflow was recorded under a microscope equipped with a fast camera. Particle streamlines were obtained via  $\mu\text{PIV}$  analysis.

#### Results/Discussion

By seeding the fluid with 500 nm particles, we observed that if  $h \leq \lambda_f$  the beads were collected in a two dimensional periodical pattern. This accumulation pattern matches the simulated distribution of semi-nodes in a partially standing ultrasound wave excited in water by SAWs. Conversely, when  $h \gg \lambda_f$  we observed that the particles are dragged into a double vortical pattern which evolves during the initial channel filling. This demonstrates that we can tune the balance between the acoustic radiation force and the acoustic streaming (Stokesian) drag force by simply varying the microchannel height. The transitional height between these two regimes depends on the microparticle size with respect to the set wavelength. We finally investigated the effect of these regimes on whole blood in 14  $\mu\text{m}$  and 70  $\mu\text{m}$  high channels. These represent the extremes where we observed acoustic streaming or particle accumulation with synthetic particles up to 10  $\mu\text{m}$  diameter (like red blood cells). In the 14  $\mu\text{m}$  high channels, we observed that complete plasma separation can be obtained between periodical accumulation lines in proximity of the meniscus. When acoustic streaming dominates, however, we can generate a cell concentration gradient located in the vortical area. Switching between these two regimes is possible by simply tailoring the microchannel geometry, and the associated whole-blood manipulations can be easily integrated as components of handheld point-of-care devices.

PA-9

### Hardware-Software Co-design of 3D Data Compression for Real-Time Ultrasonic Imaging Applications

Pramod Govindan<sup>1</sup>, Jafar Saniie<sup>1</sup>, <sup>1</sup>Electrical and Computer Engineering, Illinois Institute of Technology, USA

#### Background, Motivation and Objective

Many of the ultrasonic NDE and imaging applications require processing of huge amount of data in real-time. Compression of acquired data helps to reduce the storage and to rapidly transmit information to remote locations for further analysis. Signal fidelity, computational speed and resource utilization are the major parameters to be considered while designing the architecture for the compression algorithm. The reconfigurable platform allows analysis of multiple architectures to suit various applications. The objective of this study is to implement discrete wavelet transform (DWT) based ultrasonic data compression algorithm on a reconfigurable ultrasonic system-on-chip hardware platform, with emphasizing high signal fidelity, low resource utilization and high throughput.

#### Statement of Contribution/Methods

The compression algorithm using 3D DWT is implemented on a Xilinx Zynq-7020 all programmable system-on-chip FPGA with an ARM processor. DWT uses multistage sub-band decomposition which can be structured to isolate the high energy sub-bands to provide maximum signal compression with high fidelity. Two different architectures of the compression algorithm are discussed in this study: hardware only design using programmable logic and software only design using ARM processor. Furthermore, the Zynq platform is used to implement the compression algorithm in real-time as a hardware/software co-design, wherein the ultrasonic data acquisition is controlled in hardware, and the compression algorithm is executed in software by ARM processor. DWT mainly requires filtering operations, which involves several multiplications. Multiplication is optimized by using reduced adder graph algorithm; thus the computational speed and the resource usage are improved. Additionally, the lowpass and highpass filters are processed in parallel to further reduce the overall execution time. The software only design is also efficient due to the availability of advanced SIMD (single instruction multiple data) instructions supported by ARM processor, which allows the execution of ultrasonic signal processing algorithms at a very high rate.

**Results/Discussion**

In this study, a volumetric image of 128x128x2048 samples (33 Mbytes) are compressed using 3D DWT. The 3D block of data consisting of several interfering echoes is acquired using a 5 MHz ultrasonic broadband transducer and a steel block specimen with microstructural defects. A 4-level decomposition using Daubechies wavelet basis is performed for the ultrasonic A-scans having 2048 samples. A 2-level decomposition using Haar wavelet basis is performed for the spatial decomposition (128 samples). To reduce the execution time, 16 A-scans are decomposed in parallel. Using this implementation, the volumetric image of 33 Mbytes are compressed to 0.4 Mbytes in less than 0.5 seconds, giving a compression ratio of 95% with a peak SNR of 27 dB, indicating high signal fidelity.

**PA-10****Cavity modes and optomechanic interactions in phoxonic crystals**

Said EL-JALLAL<sup>1,2</sup>, Mourad Oudich<sup>3</sup>, Yan Pennec<sup>1</sup>, Bahram Djafari-Rouhani<sup>1</sup>, Abdelkader Makhoute<sup>4</sup>, Jordi Gomis-Bresco<sup>5</sup>, Daniel Navarro-Urrios<sup>5</sup>, Alejandro Martínez<sup>6</sup>, Clivia Sotomayor<sup>5,7</sup>; <sup>1</sup>Institut d'Electronique, de Microélectronique et de Nanotechnologie, Université Lille 1, Villeneuve d'Ascq, France, <sup>2</sup>Physique du Rayonnement et de l'Interaction Laser Matière, Université Moulay Ismail, Meknes, Morocco, <sup>3</sup>Institut Jean Lamour, Université de Lorraine, Vandoeuvre-lès-Nancy, Nancy, France, <sup>4</sup>Physique du Rayonnement et de l'Interaction Laser Matière, Université de Moulay Ismail, Meknes, Morocco, <sup>5</sup>ICN2 - Institut Català de Nanociència i Nanotecnologia, Campus UAB, 08193 Bellaterra, Barcelona, Spain, <sup>6</sup>Nanophotonics Technology Center, Universitat Politècnica de València, Valencia, Spain, <sup>7</sup>ICREA - Institució Catalana de Recerca i Estudis Avançats, 08010, Barcelona, Spain

**Background, Motivation and Objective**

Phoxonic crystals are periodic structures that can exhibit simultaneously phononic and photonic band gaps (BG). They allow a high confinement of both light and sound in a cavity or a waveguide. This confinement can generate a strong phonon-photon interaction with potential applications in optomechanical (OM) devices, in particular for the modulation of light by acoustic waves. In this paper, we study theoretically the optomechanic interaction in 1D phoxonic crystal constituted by a strip waveguide and show the possibility of strong acousto-optic coupling inside a cavity.

**Statement of Contribution/Methods**

Two mechanisms are considered, the photoelastic (PE) and moving interface (MI) effects. The former is due to a local variation of the dielectric permittivity induced by the acoustic strain inside the materials, whereas the second comes from the variation of the dielectric permittivity in the vicinity of the interfaces due to the motions of the boundaries. The strength of the acousto-optic coupling is evaluated by calculating either the modulation of the photonic frequency by the acoustic mode or the optomechanic coupling rate.

**Results/Discussion**

We have investigated the acousto-optic (AO) interaction in a corrugated phoxonic silicon nanobeam presenting band gaps both for photonic and phononic modes. By creating a well-designed tapered cavity, we were able to create highly confined phononic and photonic defect modes with high quality factor (QF) inside the gap. We have calculated both PE and MI effects and estimate their contributions to the AO coupling. We have obtained a good AO coupling with an acoustic mode outside a gap. However this mode can be pushed into the partial or full BG while increasing the phononic QF and keeping or increasing the AO coupling. The modification of the cavity consists of increasing or decreasing the length of the stubs progressively from the perfect crystal towards the cavity center. The coupling factor is significantly increased when the acoustic mode is pushed inside the full band gap.

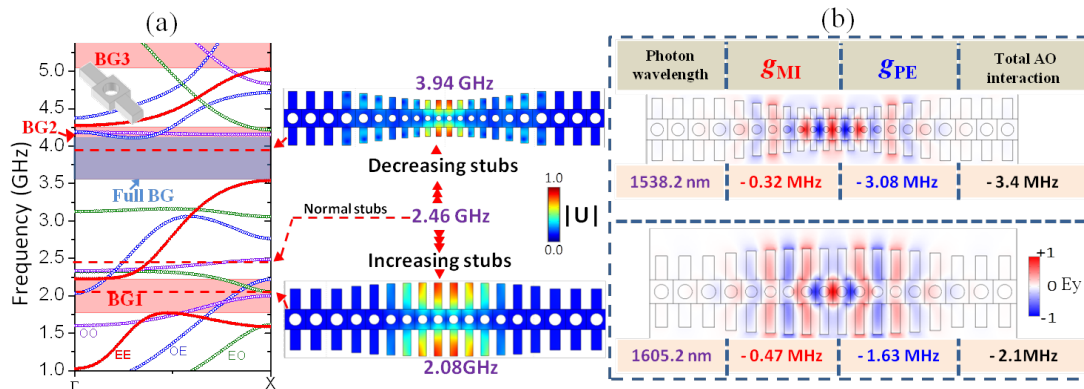


**Figure 1.** (a) Phononic band structure of the perfect nanobeam where the red shaded regions named BG1, BG2 and BG3 are the gaps for the modes which are symmetrical with respect to the symmetry planes of the nanobeam (red branches) and which are the only one that are able to couple with photonic modes and the gray shaded region for the full band gap. (b) AO coupling between the photonic cavity modes and the same phononic mode pushed up inside the full band gap or down inside the partial band gap by decreasing or increasing respectively the length of the stubs. In each figure we give the coupling coefficients  $g_{PE}$  and  $g_{MI}$ .

**PA-11****Multiple shear wave roundtrips liquid sensor by c-axis parallel oriented ZnO film/silica glass pipe structure**

Shoko Hiyama<sup>1</sup>, Takahiko Yanagitani<sup>2</sup>, Shinji Takayanagi<sup>1</sup>, Yoshiya Kato<sup>1</sup>, Mami Matsukawa<sup>1</sup>; <sup>1</sup>Wave electronics research center, Laboratory of Ultrasonic Electronics, Doshisha University, Kyotanabe, Japan, <sup>2</sup>Graduate School of Engineering, Nagoya Institute of Technology, Nagoya, Japan

**Background, Motivation and Objective**

Horizontal shear waves with in-plane displacement can propagate without the energy leakage into liquid, and are suitable for liquid sensors. A high-sensitive device is expected if the long propagation distance can be achieved such as the roundtrip system in the Ball SAW. In previous study, we have demonstrated the excitation of the shear waves using c-axis parallel (11-20) oriented ZnO film [1], which can be fabricated on a glass pipe and curved surface. We consider that the SAW multiple roundtrips also occurs on a glass pipe with small diffraction loss, when the wide aperture (6.6 mm) IDT is used. In this study, to realize a high-sensitive liquid sensor, we fabricated c-axis parallel oriented ZnO film on pipe and the shear wave multiple roundtrips were demonstrated.



# Statement of Contribution/Methods

c-Axis parallel oriented ZnO film was grown on a part of the silica glass pipe by sputtering system [see Fig.1 (a)]. Next, IDT was fabricated on ZnO film so that the electrode fingers are parallel to the pipe axis. The reflection coefficients  $S_{11}$  of IDT were measured with a network analyzer, and the time waveforms were obtained by an inverse Fourier transform. The insertion losses were calculated by the time waveforms. In the same manner, the sensor immersed in pure water was also evaluated.

# Results/Discussion

Fig.1 (a) shows the XRD patterns of ZnO film. Intense ZnO (11-20) peaks, indicating c-axis parallel orientation, were observed at point A and B on glass pipe. The time waveforms of pipe structure immersed and non-immersed in water were shown in Fig.1 (b). A Fourier transform of the first echo showed SH-SAW and bulk wave at the frequencies of 131 MHz and 160-190 MHz, respectively. From these data, twice SH-SAW roundtrips and fifth bulk wave roundtrips were observed. The propagation loss of bulk wave in the sensor immersed in liquid (140 dB/m) is not much smaller than that in non-immersed in liquid (115 dB/m), which implies the shear mode bulk wave. In conclusion, multiple roundtrips of SH-SAW and bulk shear wave can be obtained on pipe structure using c-axis parallel oriented ZnO film. The next step is to measure the viscosity and electric conductivity of the liquid using this sensor.

[1] T. Yanagitani, et al., *TUFFC*, **52**, 3140 (2005).

[2] K. Yamanaka, et al., *APL*, **76**, 2797 (2010).

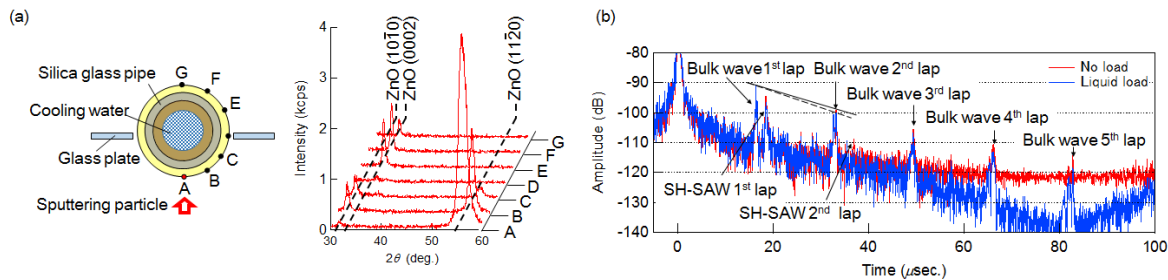


Fig.1 (a) XRD patterns of the ZnO film on the silica glass pipe and (b) time response waveform of pipe structure sensor immersed and non-immersed pure water.

PA-12

# Non-linear cavitation cloud oscillations in high intensity focused ultrasound

Keith Johnston<sup>1</sup>, Bjoern Gerold<sup>1</sup>, Sandy Cochran<sup>1</sup>, Alfred Cuschieri<sup>1</sup>, Paul Prentice<sup>1</sup>; <sup>1</sup>Institute for Medical Science and Technology, University of Dundee, Dundee, United Kingdom

# Background, Motivation and Objective

Cavitation driven by intense ultrasound plays a pivotal role in a range of applications, including acoustic cleaning, sonochemistry and as a potential mechanism for therapeutic ultrasound. Optimisation and refinement of cavitation mediated effects require an improved understanding of cavitation behaviour, particularly during the early, formative, stages of evolution in a given acoustic exposure. Here, we report on high-speed observations of non-linear cloud oscillatory response to propagating high-intensity focused ultrasound (HIFU) insonations, across a range of intensities relevant to therapeutic applications.

# Statement of Contribution/Methods

Single cavitation clouds are reproducibly introduced to the focus of a propagating 254 kHz HIFU field, via the laser-nucleation technique [1], at peak-to-peak pressure amplitudes ( $PA_{pp}$ ) from 0.48-1.22 MPa. Cloud dynamics are recorded via high-speed microphotography at  $1 \times 10^6$  frames per second. Parallel acoustic monitoring is undertaken with a custom-fabricated passive cavitation detector (PCD). By way of analysis, cloud dynamics are compared to a single bubble Rayleigh-Plesset model, subject to equivalent acoustic conditions [2].

# Results/Discussion

Cavitation clouds develop rapidly from nucleation, via component bubble fragmentation, and undergo concerted oscillations from  $t \approx 30 \mu s$ . A dark-pixel counting algorithm is implemented to the high-speed image sequences for analysis of oscillatory behaviour, for clouds at each  $PA_{pp}$  investigated. Distinct regimes of non-linear cloud response are identified via the order of the sub-harmonic frequency (to the fundamental driving) at which the cloud oscillates [2, 3], up to  $nf_0/5$  at 1.22 MPa. Comparison to the single bubble model is favourable for selected values of quiescent radius  $R_0$ , in terms of the period of oscillation, fig. 1, for each intensity. The acoustic emissions collected from the clouds, are also directly correlated to the observed physical dynamics. We anticipate that these observations will have significance to applications for which controlled cavitation activity is desirable.

- Gerold et al (2011) Rev. of Sci. Inst. 82(4) 044902.
- Gerold et al (2013) New J. of Phys. 15 033044.
- Lauterborn and Cramer (1981) Phys. Rev. Lett. 47 1445.



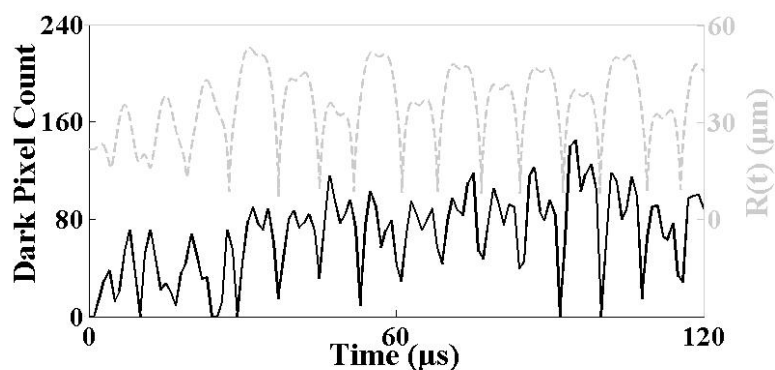


fig. 1, Summed bubble area (black line), representing experimental results of cloud oscillation over time using a dark pixel count algorithm. Rayleigh-Plesset Model (dashed line) represents matching radius time  $R(t)$  curve for a single bubble, selecting  $R_0 = 21.5 \mu\text{m}$ ,  $P(t) = 0.48 \text{ MPa}$ .

PA-13

### Ultrasonic assembly of short fibre reinforced composites

Marc-S Scholz<sup>1</sup>, Bruce W Drinkwater<sup>2</sup>, Richard S Trask<sup>1</sup>; <sup>1</sup>ACCIS, Department of Aerospace Engineering, University of Bristol, Bristol, United Kingdom, <sup>2</sup>Department of Mechanical Engineering, University of Bristol, Bristol, United Kingdom

#### Background, Motivation and Objective

With acoustic tweezers most commonly applied in the biological and life sciences, designs are generally tailored to, and optimised for the aqueous environment. Nevertheless, some reports of ultrasonically arranged particles cast inside various matrix media – including acrylics, agar, epoxy, polyester, and polysiloxane – can be found.

In this study, we aim to develop and optimise a new type of device that allows for the rapid and repeatable fabrication of thin layers of anisotropic short fibre reinforced composite material. Further, a mechanical characterisation of these samples is carried out.

#### Statement of Contribution/Methods

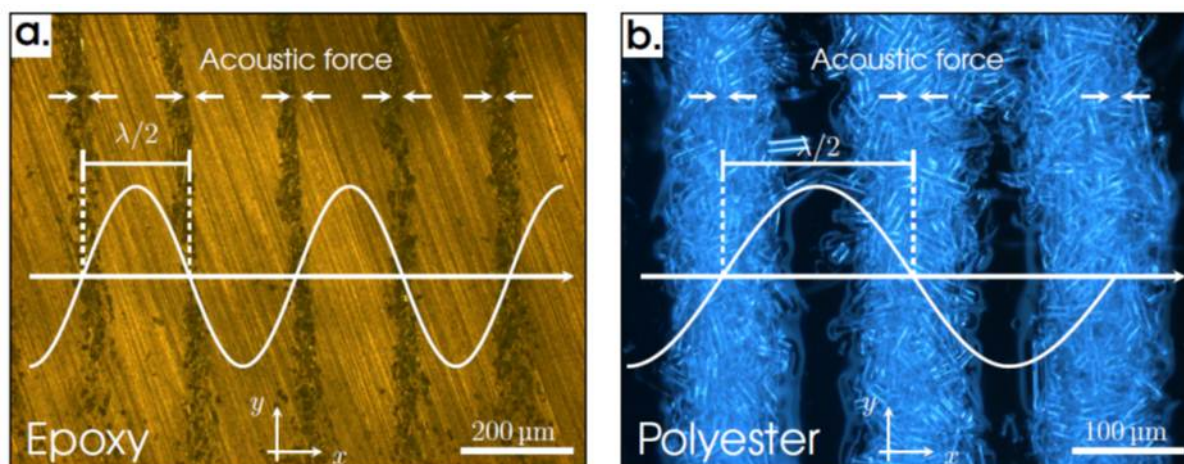
Taking a counter-propagating wave approach, a new type of device was developed to fabricate thin layers of anisotropic material. Both a temperature controlled polymerisation mechanism and a photo-initiator system proved to be suitable for curing. Commercially available, milled glass fibres were used as reinforcement, with a nominal length of  $50 \mu\text{m}$  and approximately  $14 \mu\text{m}$  in diameter. The mechanical response of these ultrasonically formed composites was characterised by mechanical testing.

The effects of various acoustic design parameters were investigated using finite element analysis to both enhance device performance and improve the composite fabrication process. Specifically, the COMSOL Multiphysics package was used to couple together analyses of structural mechanics, piezo-materials, pressure acoustics, and fluid dynamics in a single model. Special attention was paid to the shape and quality of the acoustic standing wave field, the magnitude of the resulting acoustic radiation forces, and the response of fibrous particles to ultrasonic pressure gradients.

#### Results/Discussion

A series of short fibre reinforced composites were manufactured via the above ultrasonic assembly process, using a of the optimised counter-propagating wave device. The test specimens were clearly shown to possess anisotropic mechanical properties, together with a 43% difference in failure stress between principal directions.

The FE optimisation study identified key design parameters to further enhance device performance and improve composite manufacturability. Further, the formation of structurally interesting fibre architectures was explored by studying the possible standing wave patterns in the device's particle manipulation cavity.



### Design of High Q Thin Film Bulk Acoustic Resonator Using Dual-Mode Reflection

Ngoc Nguyen<sup>1</sup>, Agne Johannessen<sup>1</sup>, Ulrik Hanke<sup>1</sup>, <sup>1</sup>Micro and Nano Systems Technology, Buskerud and Vestfold University College, Borre, Vestfold, Norway

#### Background, Motivation and Objective

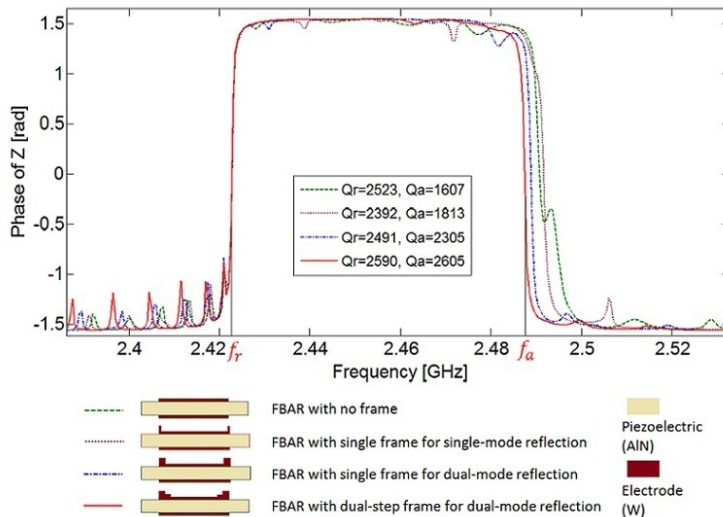
The inevitable propagation of Lamb waves in a traditional thin film bulk acoustic wave resonator (FBAR) leads to the lateral leakage of energy from the active region of the device, and consequently corresponds to a degradation of its quality (Q) factor. The use of a frame on the periphery of a FBAR improves the Q factor potentially providing better filter performance for demanding mobile/wireless communication applications. A single-step frame that can reflect one particular Lamb mode has been introduced in literature. However, a design method for a dual-mode reflection dual-step frame has not yet been published. Based on the idea that the dual-step frame performs as a Bragg reflector, in this work, we propose a procedure to design a dual-step frame with the ability to reflect the two Lamb modes that presumably contribute most to acoustic leakage – the zero and the first order symmetric mode (S0 and S1).

#### Statement of Contribution/Methods

The displacement field of a W/AIN/W stack FBAR is found from 2D Finite Element Simulations (FEM). Then the dispersion diagrams for lateral modes in the active as well as the frame regions are extracted from taking the Fourier transform of the displacement field of the layer stack for the given regions. From this the lateral propagation constants for the S0 and S1 modes at anti-resonance frequency ( $f_a$ ) are obtained for the various regions. Adopting the Diffraction Grating Method (DGM) from optics, a dual-mode reflection single-step frame at  $f_a$  can be achieved when the width of the frame is multiples of a quarter wavelengths for both modes. The mentioned dual-step frame is the combination of these two single-step frames with different step heights.

#### Results/Discussion

The figure shows FEM simulation results for various frame configurations of the FBAR, including the basic FBAR structure without a frame, the one with a single-step frame that can only reflect S1 mode (frame width is a quarter wavelength of S1 mode), and the ones designed for the dual-mode reflection, involving a single-step frame and an advanced dual-step frame. Among all, the FBAR with a dual-step frame provides the highest Q factor. The ripples located at the frequencies near and above  $f_a$  are suppressed, giving a smoother electrical characteristic at these frequencies.



### Influence of Dissipated Power Distribution on BAW Resonators' Behavior

Andreas Tag<sup>1</sup>, Dominik Karolewski<sup>2</sup>, Bernhard Bader<sup>3</sup>, Maximilian Pitschi<sup>3</sup>, Robert Weigel<sup>1</sup>, Amelie Hagelauer<sup>1</sup>, <sup>1</sup>Institute for Electronics Engineering, Friedrich-Alexander-Universität Erlangen-Nürnberg, Erlangen, Germany, <sup>2</sup>IMMS Institut für Mikroelektronik- und Mechatronik-Systeme gemeinnützige GmbH, Ilmenau, Germany, <sup>3</sup>Cellular Systems, Acoustics, Waves Business Group, TDK Corporation, Munich, Germany

#### Background, Motivation and Objective

Bulk Acoustic Wave (BAW) filters and duplexers are often used at high power levels at which the temperature of the device increases due to power dissipation (self-heating) resulting in significant frequency shifts of the transfer function of the device. This behavior needs to be modeled accurately to be able to design devices working appropriately at these power levels.

#### Statement of Contribution/Methods

Simulations with coupled electromagnetic (EM) acoustic thermal 3D finite element methods (FEM) require tremendously high calculation times. The solutions presented in the literature are based on a measured TCF and dissipated power calculated from S-parameters. That means neither the distribution of temperature nor the distribution of the dissipated power are considered. In our previous work, we have shown that the modeling of the frequency shifts caused by the self-heating behavior can be improved by taking the spatial temperature distribution into account. In this work, it will be shown for the first time that the spatial distribution of dissipated power considerably influences the temperature level and temperature distribution. Therefore, it has to be taken into account in order to precisely model the BAW self-heating behavior.

#### Results/Discussion

The acoustic was modeled in one dimension allowing efficient calculation times. EM has been modeled with a 3D FEM simulation program. From the obtained strain distribution along the different layers of the resonator (an example is shown in Fig. 1) the spatial distribution of viscous losses along the different layers was calculated and transferred to the thermal 3D simulation. The remaining main losses (eddy currents, redistribution currents, resistivity losses, and dielectric losses) were applied to the electrodes and piezoelectric layer. The result of the thermal simulation was the spatial temperature distribution. This temperature distribution was used to modify the geometry of the resonator and the materials for the EM and acoustic simulations. Finally, the acoustic and EM simulations were repeated with all the modifications providing the behavior of the resonator at high

power level. By the extension of the modeling approach remarkable improvements in the modeling of the temperature level and in the modeling of the frequency shifts seen in resonator transfer function has been achieved.

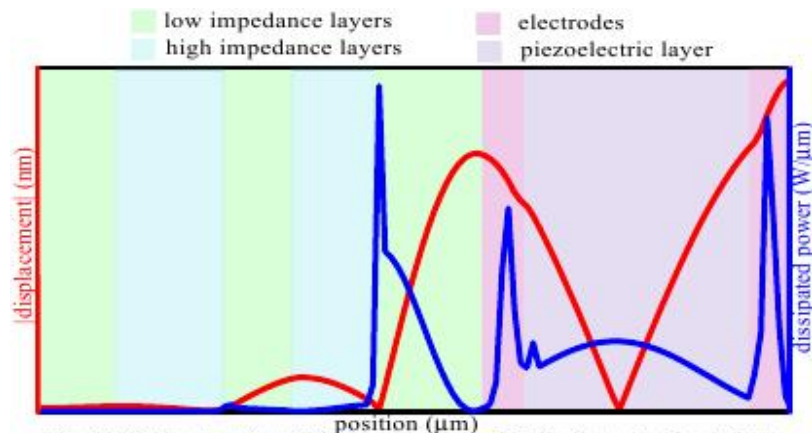


**Fig. 1 Displacement and dissipated power distribution calculated from the displacement across the different layers of a solidly mounted BAW resonator. The substrate is not shown.**

PA-16

### Chip Scale Reconfigurable Phased-Array Sonic Communication

Jason Hoople<sup>1</sup>, Justin Kuo<sup>2</sup>, Serhan Ardanuç<sup>2</sup>, Amit La<sup>2</sup>; <sup>1</sup>Electrical and Computer Engineering, Cornell University, USA, <sup>2</sup>Cornell University, USA

#### Background, Motivation and Objective

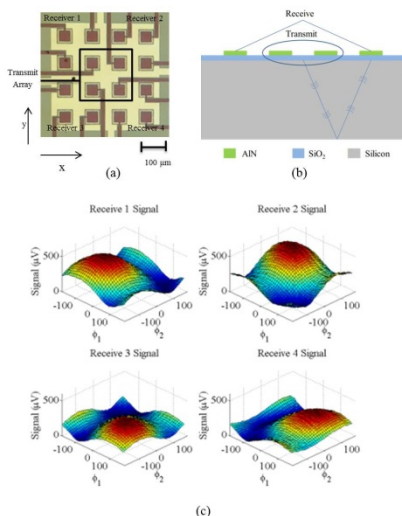
Previously [Hoople et al. "Chip-Scale Sonic Communication Using AlN Transducers" IUS 2013], we reported on the use of thin film aluminum nitride piezoelectric transducers on silicon chips for on-chip ultrasonic communication. This work greatly advances the previous work by using an array of elements, actuated at different phases, forming a sonar beam, to demonstrate directional control of communication channels between four different locations on chip. We envision an additional modality of communication in CMOS 3D stacks with ultrasound using the silicon itself as a communication channel. This would offer reconfigurable interconnects for inter-chip and intra-chip communication and thus open up new vistas for computer architecture and low power computing using ultrasound.

#### Statement of Contribution/Methods

Utilizing Sandia National Lab RF-MEMS process we had 4x4 arrays of aluminum nitride transducers sized 50 μm by 50 μm made on a silicon surface. Utilizing a linear phasing scheme, the inner four elements are driven with pulsed continuous wave RF signals, differing in phase. In the outer ring of the array, four additional transducers are used as receivers (Figure 1a) and measured directly at an oscilloscope. Driving with a 4Vpp signal resulted in 700-μV signals. The measurements match expected signals at the receive channels suffering some from parasitic capacitance in the receive path. The time of arrival of pulses shows that it is bulk waves and not surface waves arriving at the receiver (as illustrated in Figure 1b).

#### Results/Discussion

The inner array was driven with 50 ns of pulsed RF signal at 1 GHz. Each one of the receive pixels is measured after a delay corresponding to the bulk wave propagation time through silicon from top to bottom and back. After the signal is measured a digital amplitude demodulation algorithm is used to measure the signal levels over noise. The phase difference for each element corresponds to two phase shifts, one in the x direction and one in the y direction. Sweeping both phase shifts over the full 360 degrees results in changes in signal levels of the four receive elements. The value of the signal in the four receivers shows that at certain phasing conditions one of the elements has an increased signal while the other three showed decreased levels (Figure 1c). By utilizing a threshold each one of the receive channels can be communicated to selectively.



### Dual frequency transducers for super harmonic intravascular ultrasound imaging

Jianguo Ma<sup>1</sup>, Karl Heath<sup>2</sup>, Yang Li<sup>3</sup>, Paul Dayton<sup>2</sup>, Qifa Zhou<sup>3</sup>, Kirk Shung<sup>3</sup>, Xiaoning Jiang<sup>1</sup>; <sup>1</sup>Mechanical and Aerospace Engineering, North Carolina State University, Raleigh, North Carolina, USA, <sup>2</sup>UNC/NCSSU Joint Department of Biomedical Engineering, University of North Carolina, Chapel Hill, North Carolina, USA, <sup>3</sup>Department of Biomedical Engineering, University of Southern California, Los Angeles, California, USA

#### Background, Motivation and Objective

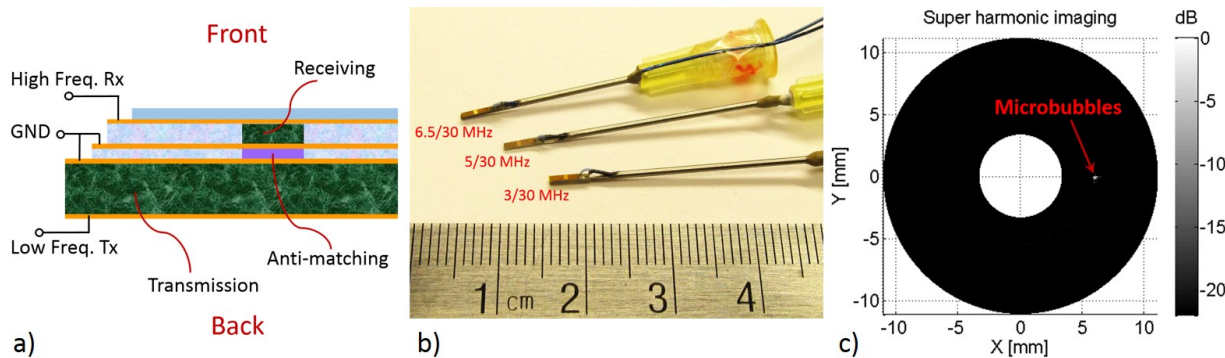
Combining super harmonic ultrasound imaging with intravascular ultrasound (IVUS) imaging is expected promising in vasa vasorum detection and vulnerable plaque assessment. IVUS imaging is effective in plaque and tissue structural detection, but ineffective for imaging microvessels due to their low scattering. Contrast enhanced, super harmonic ultrasound imaging is capable of identifying microvessels by detecting the microbubble super harmonics while suppressing the fundamental and second harmonic noise from tissue. However, combining the two imaging modes into a super harmonic IVUS imaging is challenging because of the spatial and frequency limit. Previously we reported a 6.5 MHz/30 MHz dual frequency transducer for super harmonic IVUS imaging with relatively low (~12 dB) contrast to tissue ratio (CTR). In this paper, we develop dual frequency IVUS transducers with different low frequency transmitters for super harmonic IVUS imaging with enhanced CTR.

#### Statement of Contribution/Methods

Small aperture, dual frequency transducers were designed (Fig. 1 a) for the super harmonic IVUS imaging by separating the transmission and receiving components to cover the interested frequency ranges. Several prototypes were designed with transmission center frequencies at 6.5 MHz, 5 MHz and 3 MHz for imaging comparison. Different active materials for transmitter were also compared between PMN-PT single crystal and 1-3 composite. The receiving element for all transducers was a PMN-PT single crystal receiver with center frequency of 30 MHz. An anti-matching layer was sandwiched between the two active layers to isolate high frequency wave from the low frequency element, without which there would be artifacts in imaging. Super harmonic imaging of microbubbles was tested in both water and a tissue mimic phantom.

#### Results/Discussion

The super harmonic imaging of microbubbles using prototyped transducers (3 x 0.8 x 0.6 mm, Fig. 1 b) was successful (Fig. 1 c). CTR increased from 12 dB to 22 dB by decreasing the transmission frequency. Spatial resolution of the imaging was measured to be less than 0.2 mm in both axial and lateral dimensions, and it was found that higher resolution can be obtained by using the 1-3 composite transmission. These transducers are expected to enable an effective IVUS probe in super harmonic imaging for advanced cardiovascular disease evaluation.



### An Ultrasound-Based Noninvasive Neural Interface to the Retina: Projection Algorithm and Frontend Integrated Circuit Architecture

Xun Wu<sup>1</sup>, Mohit Kumar<sup>1</sup>, Omer Oralkan<sup>1</sup>; <sup>1</sup>Department of Electrical and Computer Engineering, North Carolina State University, Raleigh, North Carolina, USA

#### Background, Motivation and Objective

It has been shown that focused ultrasound creates a neural response in the retina qualitatively similar to visual responses [1]. Ultrasound stimulation has the advantages of noninvasiveness and higher spatiotemporal resolution over electrical stimulation. In this abstract, we report on the algorithm and the frontend integrated circuit (IC) architecture design for an ultrasound-based noninvasive neural interface that will allow real-time image projection onto the retina. The current design is devised for use with a 40-MHz 2D capacitive micromachined ultrasonic transducer (CMUT) array that is under development.

#### Statement of Contribution/Methods

The envisioned system is based on a 2D transducer array with integrated electronics that can be placed in front of the eye to project stimulation patterns onto the retina (Fig. 1a). For a given image, the ultrasound stimulation pattern (USSP), in essence the amplitudes and phases of the excitation signals applied to the elements of the array, is calculated and transmitted wirelessly to the frontend IC.

The Fourier Transform (FT) relationship between the field pattern and the aperture function reveals a straight-forward method to calculate the USSP: take the Inverse FT of the image. Use of inverse Fast Fourier Transform (IFFT) allows real-time computation, an attractive attribute over previously demonstrated iterative algorithms [2].

IFFT results in arbitrary amplitudes and phases. To alleviate the complexity of the frontend IC, we quantize the amplitudes and phases of transducer excitation signals. Our initial analysis showed that setting eight quantization levels for amplitude and phase results in an acceptable projection quality.

A frontend circuit architecture is designed to generate 40-MHz excitation signals of eight equally spaced voltage levels and eight uniformly spaced phases. The eight phases and eight reference levels are generated centrally and routed to each element where a 6-bit register selects the desired amplitude and phase.

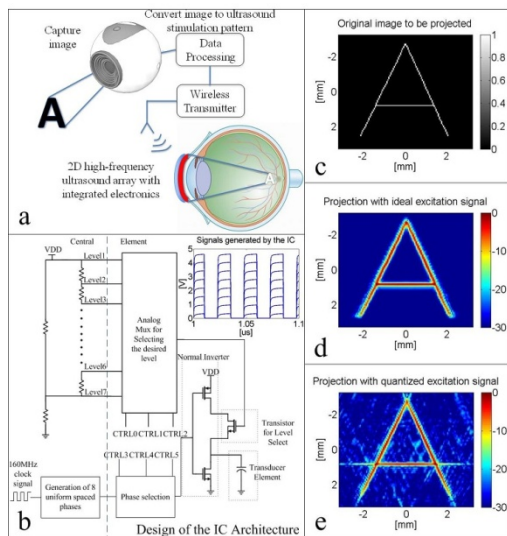
#### Results/Discussion

The system is simulated using Field II for an image pattern of "A" using a 128x128 circularly apodized 2D array with 130-μm element pitch. The rms pressure is calculated on the projection plane. The result shows good conformity to the original image.

[1] M. D. Menz, et al., J. Neurosci. 2013; 33 (10): 4550-60.

[2] Y. Hertzberg, et al., J. Neuroeng. 2010; 7 (5): 056002.





PA-19

### Improved Performance CMUT-on-CMOS Devices Using ALD Hafnium Oxide Insulation Layer

Toby Xu<sup>1</sup>, Coskun Tekes<sup>2</sup>, F. Levent Degertekin<sup>3</sup>; <sup>1</sup>Mechanical Engineering, Georgia Institute of Technology, Atlanta, GA, USA, <sup>2</sup>Mechanical Engineering, Georgia Institute of Technology, Atlanta, Georgia, USA, <sup>3</sup>Mechanical Engineering, Georgia Institute of Technology, Atlanta, GA, USA

#### Background, Motivation and Objective

Higher transmit sensitivity and receive sensitivity at lower bias voltages would be achieved by CMUTs when their structure converges to an ideal parallel plate structure. Using an insulation layer with high relative dielectric constant (high-K) helps achieving this goal with increased capacitance and large electric field in the vacuum gap. The effect of the insulation layer is more pronounced for high frequency, small gap CMUTs. In this paper, we present a simple model for optimal insulation layer properties and significant improvement in both transmit and receive sensitivity by replacing the  $\text{Si}_3\text{N}_4$  insulation layer with high-K  $\text{HfO}_2$  for a low temperature CMUT-on-CMOS process [1].

#### Statement of Contribution/Methods

Two separate wafers with the same 16.5-MHz-4-element design CMUT test devices were fabricated side-by-side with 50-nm gaps, except one with 100-nm  $\text{HfO}_2$  insulation and the other with 200-nm plasma enhanced chemical vapor deposition (PECVD) silicon nitride ( $\text{Si}_3\text{N}_4$ ) insulation. Since the film quality for low temperature PECVD  $\text{Si}_3\text{N}_4$  degrades below 200 nm thickness due to pin-hole effect, high conformity and low temperature atomic layer deposition (ALD) of hafnium oxide ( $\text{HfO}_2$ ) is used to overcome the thickness limitation as well as increased relative dielectric constant. Material characterization shows ALD  $\text{HfO}_2$  deposited at 250°C have a K of 16 and breakdown strength ( $E_{BD}$ ) of 4 MV/cm. Acoustical characterization in TX and RX were performed for both insulation designs CMUT test array. Subsequently, 20-MHz dual-ring CMUT-on-CMOS devices were also fabricated with the 100-nm  $\text{HfO}_2$  insulation. Pulse-echo and imaging experiments in water have been performed with the  $\text{HfO}_2$  CMUT-on-CMOS array.

#### Results/Discussion

Experiments on CMUTs with  $\text{HfO}_2$  and  $\text{Si}_3\text{N}_4$  insulation layers show that transmit sensitivity (Pa/V) is doubled for the same gap device, giving the same maximum output pressure with half the pulse amplitude. The receive sensitivity is also improved by 6dB while reducing collapse voltage by one half. CMUT-on-CMOS integration with  $\text{HfO}_2$  insulation was successful with reduced operating voltages and higher SNR as compared to previous devices. In addition, the receive signal from  $\text{HfO}_2$  insulated CMUT-on-CMOS shows no sign of charging biased at 88% of collapse voltage over a period of 4 hours.

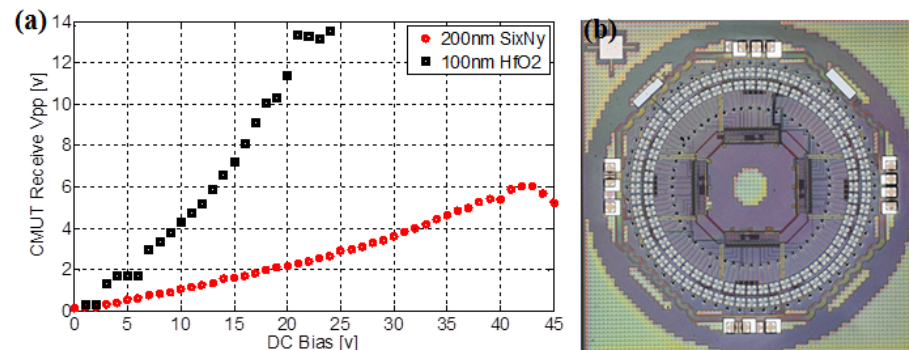


Figure 1: (a) Experimental data comparing the Rx sensitivity of the 2 CMUTs (b) Micrograph of 20 MHz CMUT-on-CMOS 1.4-mm array with 100-nm  $\text{HfO}_2$  isolation and 50-nm gap.

[1] J. Zahorian, M. Hochman, T. Xu, S. Satir, G. Gurun, M. Karaman, F.L. Degertekin, "Monolithic CMUT-on-CMOS integration for intravascular ultrasound applications," *IEEE Transactions on Ultrasonics, Ferroelectrics and Frequency Control*, vol.58, no.12, pp.2659,2667, December 2011.

## Integration of Pb(Zr,Ti)O<sub>3</sub> (PZT) Thin Films on a Complex Microfluidic System: Toward New Possibilities for Low Consumption Micropumps

Pierre-Henri Cazorla<sup>1</sup>, Olivier Fuchs<sup>1</sup>, Martine Cochet<sup>1</sup>, Sandrine Maubert<sup>1</sup>, Gwenael Le Rhun<sup>1</sup>, Stephane Fanget<sup>1</sup>, Yves Fouillet<sup>1</sup>, Emmanuel Defay<sup>1</sup>; <sup>1</sup>CEA-LETI, Minatec Campus, Grenoble, France

### Background, Motivation and Objective

Piezoelectric micropumps have been intensively studied so far and showed many advantages for various microfluidic applications. However the high voltage they request is a major drawback for autonomous systems like implanted devices since they require high consuming amplifiers. The development of PZT thin-films with high mechanical response to low voltage offers very suitable solutions. Some micropumps with piezoelectric thin films have been reported but show low performances mainly since they use passive valves and low efficient piezoelectric material. Here we propose to combine state of the art PZT thin film with active valves to present a highly efficient low voltage micropump.

### Statement of Contribution/Methods

We processed three 50  $\mu\text{m}$  thin membranes above a fluidic pathway etched in silicon as shown figure 1. A 1.5  $\mu\text{m}$  thin sol-gel PZT layer was then deposited on their top. A major breakthrough was to make the sol-gel crystallization step compatible with already processed thin-membranes. The films were investigated electrically and piezoelectrically. Valves and pumps were fully characterized at several actuation frequencies and voltages.

### Results/Discussion

The thin-films have a permittivity of 1100. A 4 $\mu\text{m}$ -deflexion is achieved with a 24 V voltage for a membrane with a 7.5 mm diameter. The valves show no leakage up to 40 mbar pressure. The devices can self-prime and pump air and water. They can yield a 3  $\mu\text{L}/\text{min}$  flow-rate and a 30 mbar pressure for a 1 Hz actuation frequency. A fluidic power of 46 nW is produced for a 0.3 mW electric consumption.

As expected, thanks to a more efficient material and to active valves, the micropump generates higher pressures than other pumps reported with thin-films. One the other hand, devices with bulk piezo materials hardly work below 30 V due to structure's stiffness. Thin-films allow for a drastic voltage reduction, leading to 2.5 fold reduction of the amplifying electronics consumption compared to a 90 V actuated device.

For the first time, a peristaltic micropump actuated by PZT thin film was successfully fabricated. It allows reduction of packaging costs and features low voltage actuation, improving safety and electrical consumption of autonomous devices. Meanwhile it generates flow and pressure well adapted for medical application like drug delivery and could be of crucial help for the development of personalized medicine.



## P1A1 - MEL: Shear Wave Imaging Methods 1

Salon C

Thursday, September 4, 2014, 8:00 am - 5:00 pm

Chair: **James Greenleaf**  
*Mayo Clinic, Rochester*

P1A1-1

### 8:00 am Displacement Underestimation Correction by Shearwave-Induced Displacement Tracking in Viscoelastic Response (VisR) Ultrasound

Mallory R. Setzo<sup>1</sup>, Tomasz J. Czernuszewicz<sup>1</sup>, Caterina M. Gallipoli<sup>1</sup>; <sup>1</sup>Joint Department of Biomedical Engineering, University of North Carolina at Chapel Hill, Chapel Hill, NC, USA

#### Background, Motivation and Objective

We have proposed an imaging technique called Viscoelastic Response (VisR) ultrasound that uses two acoustic radiation force (ARF) impulses for assessing the viscoelastic properties of tissue. Using two successive ARF impulses and monitoring the induced displacements, VisR fits displacements to a mechanical model to measure the relaxation time constant,  $\tau$ . In this method, ARF pulses are generated by the same transducer that is used to track motion. Thus, the displacements are susceptible to shearing decorrelation and underestimation, which will introduce error into our measurement of  $\tau$ . We hypothesize that by tracking displacements outside the region of excitation (ROE), where shearing decorrelation is minimized, we can better estimate displacements and generate  $\tau$  measurements that more closely represent the material.

#### Statement of Contribution/Methods

VisR was performed with a Siemens Antares scanner and VF7-3 linear array with excitation impulses centered at 4.21 MHz with an F/1.5 focal configuration. VisR was implemented using two 300-cycle ARF excitations, separated by 0.6 ms in time. Tracking pulses were centered at 6.15 MHz with a F/1.5 focal configuration. Acoustic displacement measurements were experimentally validated using optical tracking. The optical focus of a microscope fitted with a 10x objective and coupled to a 150 kHz high-speed camera was aligned with the acoustic focus. Acoustic and optical data were acquired in a translucent, gelatin-based, tissue-mimicking phantom. Black polystyrene beads were embedded in the phantom and the phantom was translated such that each of the 3 unique beads was individually positioned at the confocal optical and acoustic foci to serve as markers for optical tracking. Raw rf and optical data were acquired with three repeated measures on each bead. Motion tracking was performed using cross-correlation for both acoustic and optical data sets. The experiment was repeated with the ARF excitations and tracking pulses focused in the same lateral position, and with tracking pulses focused 4.25 mm lateral to the ARF excitations.

#### Results/Discussion

In the ROE, displacements measured acoustically were  $83.9 \pm 20.8\%$  of the optical displacement on average, whereas, acoustic displacements measured 4.25 mm lateral to the ROE were measured to be  $102.0 \pm 24.3\%$  of the optical displacement on average. In the ROE,  $\tau$  was significantly larger when using acoustic displacement estimates ( $1.40 \pm 0.03$  ms) versus optical displacement estimates ( $0.75 \pm 0.07$  ms) ( $p < 0.01$ ). 4.25 mm outside the ROE, however, acoustically- and optically-derived values of  $\tau$  ( $0.76 \pm 0.05$  ms and  $0.75 \pm 0.09$  ms, respectively) were not significantly different ( $p = 0.83$ ) and were consistent with the optically-derived value of  $\tau$  made in the ROE ( $p = 0.94$ ).

These results show that acoustic displacement underestimation impacts VisR derived  $\tau$  measurement, but that this error can be reduced by using shearwave-induced displacement tracked outside the ROE.

P1A1-2

### 8:01 am Recovering Shear Wave Velocity in Boundary Sensitive Media with Two-Dimensional Motion Tracking

Ivan Nenadic<sup>1</sup>, Miguel Bernal<sup>2</sup>, Javier Brum<sup>2</sup>, Jean-Luc Gennisson<sup>2</sup>, Mathieu Pernot<sup>2</sup>, James Greenleaf<sup>1</sup>, Mickael Tanter<sup>2</sup>, Matthew Urban<sup>1</sup>; <sup>1</sup>Mayo Clinic, Rochester, MN, USA, <sup>2</sup>ESPCI ParisTech CNRS UMR7587 INSERM U979, Institut Langevin – Ondes et Images, Paris, France

#### Background, Motivation and Objective

Most shear wave elastography techniques assume that the propagating wave is a pure shear wave, and the shear wave velocity ( $c$ ) is directly related to the shear modulus ( $\mu$ ) via the relationship  $\mu = \rho c^2$ , where  $\rho$  is the density. This relationship holds for bulky organs like the liver and kidneys, where the shear and compressional waves are decoupled. In boundary sensitive organs like the arteries and myocardium, the compressional and shear waves interfere to form guided waves (Lamb waves) which give rise to complicated velocity dispersion diagrams. This requires significant theoretical development and analysis to recover the true shear modulus. We explore the use of applying a curl to two-dimensional shear wave propagation fields to filter out the compressional waves in the geometry of a plate.

#### Statement of Contribution/Methods

In theory, three-dimensional displacement field as a function of time  $u(x,y,z,t)$  completely defines the tissue motion due to a propagating wave. The curl operator can be used to filter out the compressional wave contribution, and the direct inversion of the resulting field can be used to recover the shear wave velocity. In case of a plane wave, one of the directions can be ignored and the tissue motion is defined using two-dimensional (2D) tissue motion. In this study, we explore the use of 2D tissue motion tracking as a function of time to recover the shear wave velocity in the geometry of an elastic plate surrounded by two softer semi-infinite medium. Theory showing the curl of a 2D particle motion in a plate due to a propagating Lamb wave is developed. A finite element model (FEM) of three elastic plates with the shear modulus of 25 kPa, 36 kPa and 49 kPa surrounded by semi-infinite media with the shear modulus of 1 kPa was developed. 2D particle motion due to a harmonic plane shear wave in the frequency range 100–500 Hz was used to obtain the curl field and the direct inversion algorithm was used to obtain shear wave elasticity maps of the plate and the surrounding material. The curl and direct inversion (CDI) based elasticity maps were in excellent agreement with the theoretical FEM values. A mechanical shaker was used to excite plane shear waves in a phantom consisting of a 7 mm 2% agar plate embedded between two semi-infinite 5% gelatin phantoms. Two linear array transducers (SL15-4, 8 MHz) driven by an Aixplorer ultrasound system (Supersonic Imagine, France) were used to track the motion perpendicular and parallel to the excitation axis. The direct inversion of the motion fields after applying the curl was used to recover the shear wave velocity. A 12 x 6 x 4 cm<sup>3</sup> agar cube from the same batch as the plate was made to measure the shear wave velocity for comparison.

#### Results/Discussion

The FEM results confirm the theoretical development. The shear wave velocity in the agar plate using the CDI method was in good agreement with the shear wave velocity measured in the cube phantom. The future work will focus on making measurements with one linear array transducer.

## P1A1-3

## 8:02 am Shear wave vibro magneto acoustography for measuring tissue mimicking phantom elasticity and viscosity

Thiago Almeida<sup>1,2</sup>, Diego Sampaio<sup>1</sup>, Theo Pavan<sup>1</sup>, Antonio Adilton Carneiro<sup>1</sup>; <sup>1</sup>Department of Physics, University of Sao Paulo, Ribeirao Preto, Sao Paulo, Brazil, <sup>2</sup>R&D, FIGLABS Pesquisa e Desenvolvimento S/A, Ribeirao Preto, Sao Paulo, Brazil

## Background, Motivation and Objective

Many methods have been developed to analyze, noninvasively, the viscoelastic properties of soft tissues applying ultrasound-based techniques. Many researches propose to use the shear wave (SW) propagation speed for quantifying the elasticity. However the viscosity is neglected in some methods what can change the estimation of elasticity and important information can be lost. In order to solve quantitatively and demonstrate the values for elasticity and viscosity different methods using multifrequency approach were proposed. A technique called Magneto Motive Ultrasound (MMUS) induces motion within magnetically labeled tissue, and uses ultrasound to detect internal mechanical vibrational response. Applying continuous magnetic field the iron vibration may heat the tissue. Due these thermal constraints, it was proposed the technique pulsed magneto motive ultrasound (p-MMUS) that utilizes pulsed magnetic excitation. The present study proposes a new technique called Shear wave Dispersion Vibro Magneto Acoustography (SDVMA), where a viscoelastic medium labeled with iron oxide nanoparticles is displaced by an external tone burst pulsed magnetic field gradient. The induced motion generates a SW, which is acquired and evaluated through an ultrasound system. The aim of SDVMA is to measure quantitatively the elasticity and viscosity of the medium.

## Statement of Contribution/Methods

For measurement, it was built a phantom containing 6g of gelatin powder (animal hide - Bloom 250) per 100 mL of 18 MΩ.cm deionized water and added 5g of nanoparticles of oxide of iron (Fe<sub>3</sub>O<sub>4</sub> - Nanostructured & Amorphous Materials, Inc.), with 98% purity and particle size ranging from 20 nm to 30 nm, spread homogeneously in the phantom. Using a coil for pulsed excitation of medium and placing a ultrasonic probe (ultrasound system SonixRP – Ultrasonix) in contact with the phantom for measurement of SW, it was collected raw frames data and processed them using Matlab. All frames were processed using a normalized cross-correlation algorithm to evaluate displacement for each depth position. The displacement maps showed SW propagation through the medium. A time of flight, based algorithm was used to quantify the velocity of SW and applying the Voigt model, the viscosity and elasticity were determined. Frequencies between 50Hz and 250 Hz were used, and the results were compared to that obtained through the conventional ultrasound-based transient elastography, where the shear waves were induced by a piston driven by a shaker (Brüel & Kjaer – Type 4810).

## Results/Discussion

The values for elasticity and viscosity were, respectively, 4 kPa e 2,2 Pa.s. These results were consistent to that obtained by the conventional transient elastography, however, in the SDVMA the shear wave frequency shows twice the excitation frequency. This technique demonstrated the possibility to quantify the viscoelastic parameters and the values are closer to the values showed in the literature.

## P1A1-4

## 8:03 am Shear Wave Elastography on the GE LOGIQ E9 with Comb-push Ultrasound Shear Elastography (CUSE) and Time Aligned Sequential Tracking (TAST)

Pengfei Song<sup>1</sup>, Michael Macdonald<sup>2</sup>, Russell Behler<sup>2</sup>, Justin Lanning<sup>2</sup>, Michael Wang<sup>2</sup>, Matthew Urban<sup>1</sup>, Armando Manduca<sup>1</sup>, Heng Zhao<sup>1</sup>, Matthew Callstrom<sup>3</sup>, James Greenleaf<sup>1</sup>, Shigao Chen<sup>1</sup>; <sup>1</sup>Department of Physiology and Biomedical Engineering, Mayo Clinic College of Medicine, Rochester, Minnesota, USA, <sup>2</sup>GE Healthcare, Wauwatosa, Wisconsin, USA, <sup>3</sup>Department of Radiology, Mayo Clinic College of Medicine, Rochester, Minnesota, USA

## Background, Motivation and Objective

Implementation of 2D shear wave elastography on a conventional clinical scanner such as the GE LOGIQ E9 (LE9) that uses hardware beamformers is challenging due to limited pulse repetition frequency (PRF). Software beamformers allow high PRF for shear wave tracking, but are not available on the majority of the clinical scanners including the LE9. To facilitate the translation of shear wave elastography from laboratory to clinic and broaden the spectrum of its applications, this study presents a novel method that uses the CUSE imaging (Song *et al.*, IEEE TMI 32(8), 2013) and the TAST tracking techniques to realize 2D real-time shear wave elastography on the LE9. High quality shear elasticity maps with large field-of-view (FOV) can be obtained from the LE9 in both phantoms and *in vivo* tissues.

## Statement of Contribution/Methods

The shear wave function was tested on the GE 9L-D and the C1-6-D probes. The focused CUSE was used which transmits multiple focused push beams simultaneously at different lateral locations. The TAST technique was developed to track shear waves by sequentially firing multiple tracking lines that can be parallel-beamformed within an imaging zone. Depending on the desired FOV and PRF, the number of imaging zones is adaptively adjusted. The detected shear wave signal is then aligned in time direction to remove the delay caused by the sequential tracking. The directional filter and 2D shear wave speed calculation as used in CUSE are then used to reconstruct 2D shear elasticity maps. Quality control metrics such as correlation coefficient and shear wave energy were used to refine the final displayed maps.

## Results/Discussion

Two CIRS phantoms were studied using the LE9, and the results were compared with the Aixplorer (SuperSonic Imagine, Inc.) and the QIBA phantom study (Hall *et al.*, IUS 2013). Fig. 1(a) shows that the LE9 measurements on both probes are in good agreement to the Aixplorer measurements and the QIBA study results. Fig. 1(b) shows that the LE9 could reconstruct a 2D shear elasticity map of an inclusion with good contrast to the background and sharp boundaries. The measured inclusion stiffness (83.7 kPa) is in good agreement with the nominal value (80 kPa). Figs. 1(c) to (e) show smooth 2D shear elasticity maps obtained by LE9 in real time from *in vivo* biceps, breast, and liver. The measured stiffness values are all in good agreement with values reported in literatures.

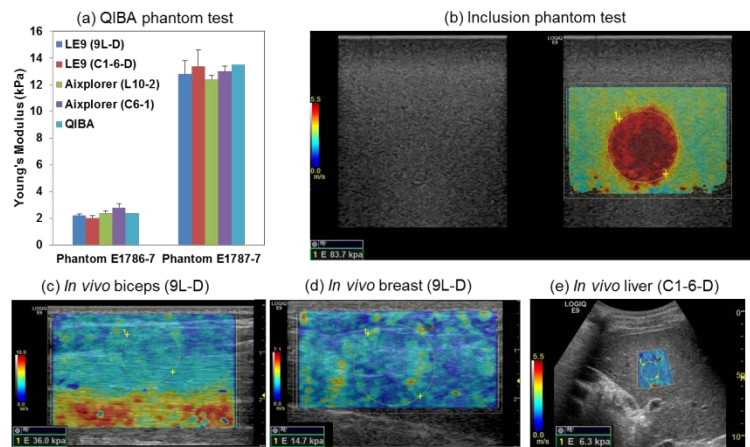


Fig. 1. (a) Young's modulus measurements of the two CIRS phantoms by LE9, Aixplorer, and the QIBA study. (b) 2D shear elasticity map of the inclusion phantom (CIRS 049A, type IV) from LE9. (c) – (e): 2D shear elasticity maps of *in vivo* biceps, breast, and liver obtained from LE9. The dashed circles indicate the region-of-interest (ROI) used for shear elasticity measurements. The measured Young's modulus (E) values are shown on the lower left corners of the images.

## P1A1-5

### 8:04 am Dependence of shear wave spectral content on acoustic radiation force excitation duration and spatial beamwidth

Mark Palmer<sup>1</sup>, Yufeng Deng<sup>1</sup>, Ned Rouze<sup>1</sup>, Manal Abdelmalek<sup>2</sup>, Kathy Nightingale<sup>1</sup>; <sup>1</sup>Biomedical Engineering, Duke University, Durham, NC, USA, <sup>2</sup>Gastroenterology-Hepatology, Duke University Medical Center, Durham, NC, USA

#### Background, Motivation and Objective

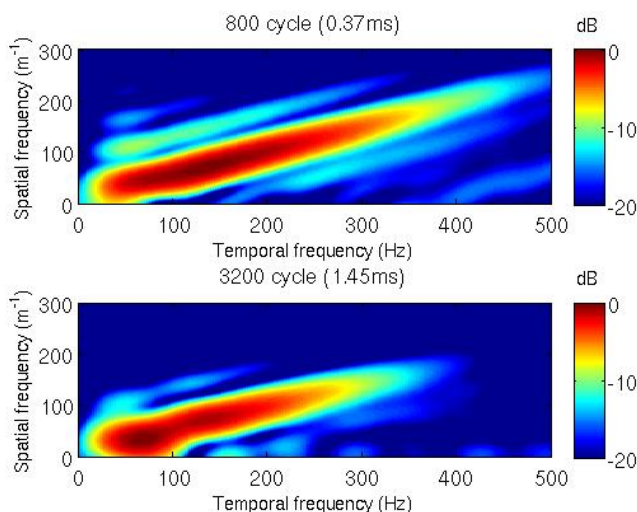
Shear Wave Elasticity Imaging (SWEI) can noninvasively characterize tissue stiffness. There is clinical interest to evaluate liver fibrosis with SWEI instead of liver biopsy. Generating shear waves with adequate displacement is challenging in high BMI patients, requiring changes in the acoustic radiation force (ARF) excitation focusing and duration. The viscoelastic nature of tissue makes shear wave (SW) speeds dependent on their frequency content. The objective of this work is to evaluate the impact of ARF excitation focal configuration and temporal duration on resultant SW spectral content.

#### Statement of Contribution/Methods

Validated Finite Element Method (FEM) simulations were used to generate spatial and temporal displacement and velocity fields for spatially Gaussian-weighted ARF excitations with half-power Gaussian widths ranging from 0.1-0.5 mm in the lateral-elevation plane with negligible axial displacement field gradients in elastic media. Excitation durations were varied from 0.1-1.5 ms. An experimental implementation using a Siemens 4C1 curvilinear transducer on a SC2000 scanner with a focus near 50 mm, F/1.5 focal configuration operating at 2.2 MHz was used to generate SW in a CIRS tissue-mimicking phantom, with excitation durations ranging from 800-3200 cycles (0.37-1.45 ms).

#### Results/Discussion

ARF excitations are "impulsive" if modulating their temporal duration does not affect the resultant SW spectral content (i.e., the tissue's transfer function dictates SW spectral content). Gaussian ARF excitations  $\leq 0.5$  ms were impulsive for the spatial excitation widths analyzed; longer excitations led to SW power spectra center frequency downshifts ( $\leq 50\%$ ) and contraction of the SW bandwidth ( $\leq 25\%$ , evaluated at the -12 dB levels). SWEI experiments demonstrated a SW center frequency downshift from 136.3 Hz to 68.8 Hz ( $-50\%$ ) for an increased excitation duration from 0.37 ms to 1.45 ms ( $+400\%$ ) (Fig 1). The -12 dB upper limit on the SW passband dropped from 443.8 Hz to 341.1 Hz ( $-23\%$ ). Simulations demonstrated a direct correlation between the ARF excitation beamwidth and the SW spectral content, with spatially-anisotropic ARF excitations generating SW spectral content based on a weighted-mean of lateral and elevation beamwidths.



## 8:05 am Dual-frequency Shear Wave Detection for Large Range-of-depth Shear Wave Elastography

Pengfei Song<sup>1</sup>, Heng Zhao<sup>1</sup>, Matthew W. Urban<sup>1</sup>, Armando Manduca<sup>1</sup>, Daniel C. Mellema<sup>1</sup>, James F. Greenleaf<sup>2</sup>, Shigao Chen<sup>1</sup>; <sup>1</sup>Physiology and Biomedical Engineering, Mayo Clinic College of Medicine, Rochester, Minnesota, USA

## Background, Motivation and Objective

Shear wave elastography (SWE) is a promising approach for liver fibrosis staging (LFS). The clinical diagnostic value of SWE, however, is challenged by the high prevalence of obesity in patients who need LFS. While the penetration of shear wave (SW) generation can be substantially improved by using mechanically induced SW, SW detection in obese patients is still challenging due to significant ultrasound attenuation in deep liver and severe clutter noise in shallow liver, both resulting from the thick adipose tissue in the near field. To address this issue, this study presents a dual-frequency SW detection scheme that uses low fundamental frequency signal for SW detection in deep liver to gain penetration, and the second harmonic signal for SW detection in shallow liver to suppress clutter noise.

## Statement of Contribution/Methods

A curved array C5-2v and the V1 system (Verasonics Inc.) were used in this study. Four wide beams ( $f_c = 2.25$  MHz) with different steering angles were designed to cover a 15 x 8 cm (depth x width) FOV with spatial compounding. A wide-band filter was used to receive both fundamental and harmonic signals, which were then separated by a narrow-band FIR filter to calculate SW signal. A piece of pork belly (~2.5 cm) was placed on an elastic phantom (CIRS 040GSE) to mimic adipose tissue from obese patients (Fig. 1(a)). The phantom was placed on a subwoofer which produced 50 Hz continuous SW into the phantom. The detection PRF was 1 kHz.

## Results/Discussion

Fig. 1(a) shows the 2D SW speed map reconstructed from the dual-frequency-detected SW signal – good quality SW speed map could be obtained throughout the large range of depths. The measured SW speed within the ROI is 2.87 m/s (nominal value = 2.89 m/s). Fig. 1(b) shows the SW signal plots from 5 depths calculated from the fundamental and the harmonic signals. The SNR of the SW from fundamental signal is 6.0, 7.8, 5.3, 6.5, and 5.5 dB at the 5 depths, as compared to 9.1, 10, 4.4, -0.31, and -14 dB from the harmonic signal. This corroborates with the plots in Fig. 1(b) which shows that the SW signal quality from harmonics is better than that from the fundamental in depths < 90 mm, and the fundamental outperforms the harmonic signal in depths > 90 mm. These results indicate the proposed dual-frequency SW detection method can gain high SW signal quality throughout a large range of depths in the liver, which is essential for robust LFS of obese patients.

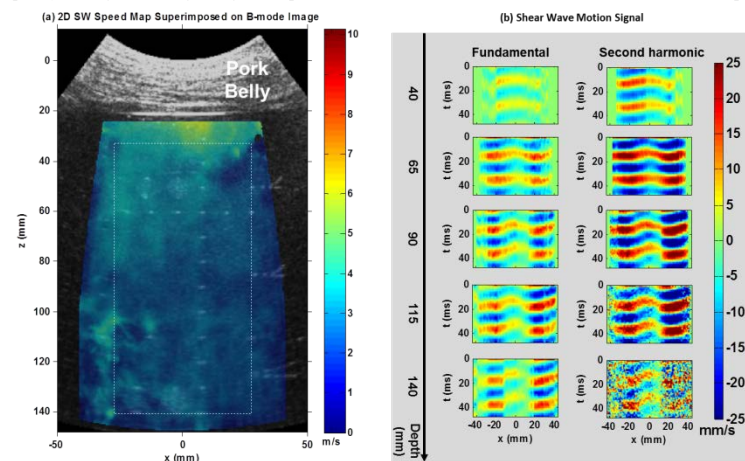


Fig. 1. (a): B-mode image and 2D SW speed map reconstructed by the dual-frequency-detected SW motion signal. The final SW signal was obtained by blending the SW signals from the fundamental and harmonic detections. The white dashed box indicates the region-of-interest (ROI) for SW speed calculation. (b): SW particle velocity signal from 5 depths of the phantom calculated from the fundamental signal and the second harmonic signal. All plots are under the same color scale.

## 8:06 am New shear wave velocity estimation using arrival time differences in orthogonal directions

Sua Bae<sup>1</sup>, Jin Ho Chang<sup>1,2</sup>, Tai-Kyong Song<sup>1</sup>; <sup>1</sup>Electronic Engineering, Sogang University, Seoul, Korea, Republic of, <sup>2</sup>Interdisciplinary Program of Integrated Biotechnology, Sogang University, Korea, Republic of

## Background, Motivation and Objective

Shear wave (SW) elasticity imaging is based on the estimation of shear wave speed (SWS) induced by the radiation force of an ultrasound beam. Although the SW initially propagates in the direction perpendicular to the pushing beam, the SW direction changes because of its refraction occurring during traveling in an inhomogeneous medium. The refraction generally causes the estimation errors of SWS when the speed is measured along the initial propagation direction.

## Statement of Contribution/Methods

In this paper, we propose a novel SWS reconstruction method in which the differences of SW arrival time at two points are measured; the two points are the neighbors of an observation point along the axial or the lateral direction. The arrival time differences are used to calculate both the speed and the direction of SW at the observation point. In the proposed method, a SW velocity vector at every observation point in a 2-D region of interest is estimated and thus its speed can be measured along the propagation direction. Therefore, the estimation errors due to the refraction can be minimized. In addition, the proposed method allows for the reduction of computational cost considerably. The validation study was conducted using a commercial elasticity phantom (CIRS Inc., Norfolk, VA) containing a stiff cylinder. Spatio-temporal SW data were acquired by an ultrasound system (Verasonics Inc., Redmond, WA) with a L7-4 linear transducer (Philips Healthcare, Andover, MA): pushing pulse length of 600-μsec and tracking frame rate of 8-kHz. A 2-D arrival time map (Fig. 1(a)) was obtained by finding a time to peak axial velocity.

## Results/Discussion

Fig. 1(b)-(d) shows the SWS maps reconstructed from the linear regression (LR) method, the level curve (LC) method, and the proposed method. Young's moduli of the stiff cylinder and the background are 45-kPa and 25-kPa. The proposed method yielded the better lesion delineation and lower variance in SWS estimates compared with the conventional methods. The contrast to noise ratios of LR, LC and the proposed method were 23.4, 19.0, and 26.0, respectively, and the contrast errors were 2.0%, 13.4%, and 0.8%, respectively. This result demonstrates that the proposed method can provide a more accurate and uniform SWS map especially in the refractive region. Furthermore, the direction of the wave can be another useful indicator for lesion detection (see Fig. 1(d)).



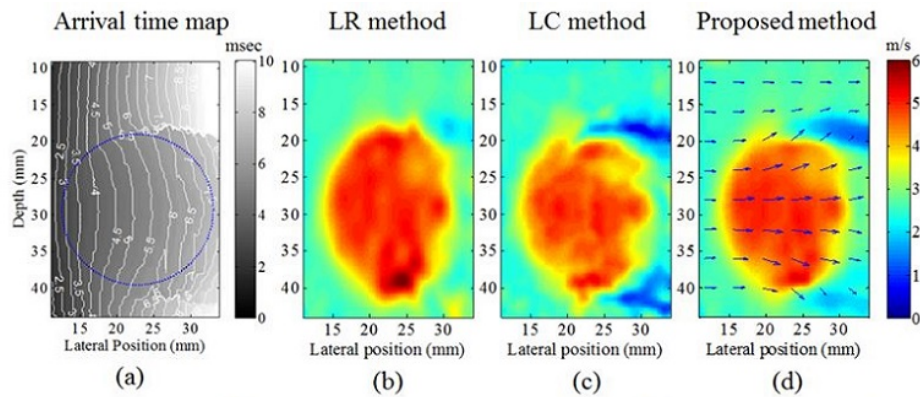


**Figure 1** SW arrival time map (a) and the reconstructed SWS maps using linear regression (b), level curve (c), and the proposed method (d). The blue dotted circle shows the position of the stiff inclusion. Note that the proposed method provides information about SW propagation direction as well as its speed at each point.

P1A1-8

**8:07 am Distinguishing Viscous from Elastic Properties in Viscoelastic Response (VisR) Ultrasound**

Mallory R. Selzo<sup>1</sup>, Caterina M. Gallippi<sup>1</sup>; <sup>1</sup>Joint Department of Biomedical Engineering, University of North Carolina at Chapel Hill, Chapel Hill, NC, USA

**Background, Motivation and Objective**

Viscoelastic Response (VisR) ultrasound is a method for quantitatively assessing the viscoelastic properties of tissue. We have previously demonstrated VisR for characterizing the mechanical properties of gelatin phantoms by fitting displacements to a modified version of the Voigt model, consisting of an inertial component in series with the Voigt model, in order to measure the relaxation time constant,  $\tau$ , given by the ratio of viscosity to elasticity. We hypothesize that by isolating viscosity from elasticity (relative to magnitude of the forcing function) further information about materials can be obtained.

**Statement of Contribution/Methods**

Finite element method (FEM) models of the dynamic response of a viscoelastic media to successive, focused, impulsive acoustic radiation force excitations were solved using LS-DYNA. Field II was used to characterize the three-dimensional acoustic intensity field associated with a VF7-3 linear array transducer. VisR sequences were implemented using two, 70  $\mu$ s ARF excitations administered to the same region of excitation and separated by 0.6 ms in time. VisR imaging was simulated in 6 viscoelastic materials (MAT\_KELVIN-MAXWELL\_VISCOELASTIC) with Young's moduli of 10kPa (materials 1 & 4), 20kPa (materials 2 & 5), or 30kPa (materials 3 & 6) and decay constants ranging from 0.9-10  $\mu$ s. VisR simulated displacement profiles from each material were fit to the modified Voigt model to calculate  $\tau$ , relative elasticity, and relative viscosity.

**Results/Discussion**

The  $\tau$  values, relative elasticity, and relative viscosity are shown in Fig 1. Materials 1-3 are indistinguishable from each other based on their  $\tau$  values alone, however, the relative elasticity and relative viscosity measures of these materials indicate that material 1 has  $\frac{1}{2}$  the stiffness and viscosity of phantom 2, and  $\frac{1}{3}$  the stiffness and viscosity of material 3, consistent with the modeled materials. Similarly,  $\tau$  values of materials 4-6 are the same, whereas, the relative elasticity and relative viscosity indicate that material 4 has the lowest elasticity and viscosity of the 3 materials, and material 6 has the highest.

These data shows that measures of relative elasticity and relative viscosity provide greater differentiation of viscoelastic materials than  $\tau$  measures alone.

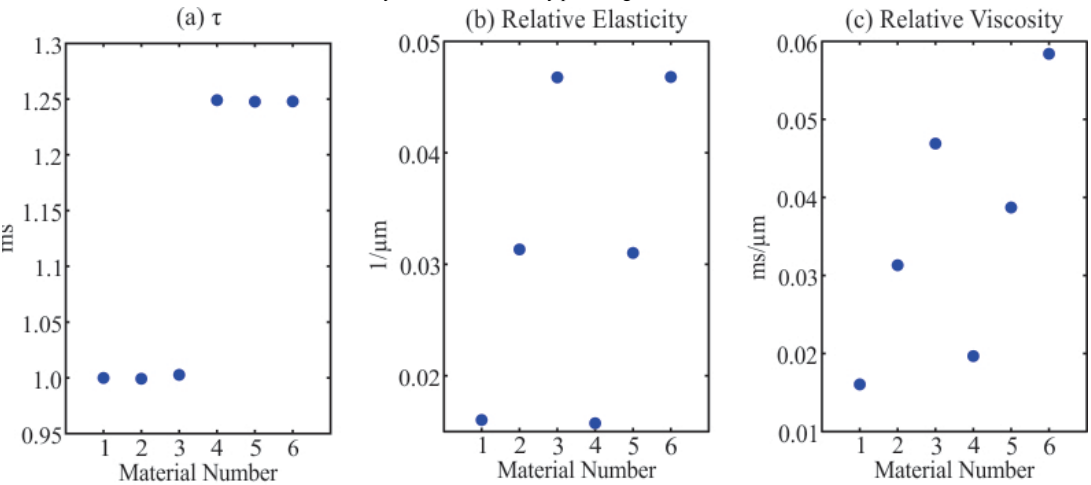


**Figure 1.** (a)  $\tau$ , (b) relative elasticity, and (c) relative viscosity measurements in the six simulated materials

# 8:08 am Shear wave elasticity imaging using inverse filtering and multiple-point shear wave generation

Tomoaki Kitazaki<sup>1</sup>, Kengo Kondo<sup>2</sup>, Makoto Yamakawa<sup>2</sup>, Tsuyoshi Shiina<sup>1</sup>; <sup>1</sup>Graduate School of Medicine, Kyoto University, Kyoto, Japan, <sup>2</sup>Center for the Promotion of Interdisciplinary Education and Research, Kyoto University, Kyoto, Japan

## Background, Motivation and Objective

Estimating shear wave speed enables the quantification of tissue elasticity imaging, but measurement of time-of-flight is based on an assumption about the propagating direction of a shear wave that is highly affected by reflection and refraction and thus might cause an artifact. An alternative shear elasticity estimation approach based on shear wavelength [1] was proposed and applied to passive configurations. We propose a new method for shear wave elasticity imaging, which combines the shear wavelength approach and "active" acoustic pushing configuration, i.e., the multiple shear wave sources induced by acoustic radiation force (ARF). As a result, the method enables shorter acquisition time and more accurate estimation.

## Statement of Contribution/Methods

Shear waves are induced by ARF, recorded by ultrafast imaging, and repeated at multiple pushing points which are sparsely located. Assuming that shear waves obtained by each push point are approximated impulse responses, an inverse filter can be applied to focus a shear wave on an arbitrary point virtually (Fig. 1(a)). By measuring the FWHM of the focal point, it is equivalent to the half-wavelength of the shear wave, and shear wave speed is obtained (Fig. 1(b)). A shear-elasticity image can be obtained by scanning the focal point. The proposed method has the potential to be robust against reflection and refraction because it premises a reverberant field.

## Results/Discussion

The proposed method was validated by phantom experiments. An elasticity phantom with a 10 mm diameter hard inclusion was prepared. Multiple pushing points are sparsely generated, with the density of several points per 1 cm<sup>2</sup>. A Verasonics ultrasound system with a 128-channel linear-array transducer was used to implement our proposed method. The estimated elasticity image clearly visualized the hard inclusion (Fig. 2). It indicated the feasibility of the wavelength estimation by inverse filter using ARF.

The inverse filter can be achieved more efficiently than passive configurations because it can control the shear wave generation and the shear waves induced by the acoustic radiation force impulses are good approximations of the impulse responses of shear wave excitation. Further studies are needed to evaluate the proposed method by comparison with a time-of-flight-based method.

[1] T. Gallot, et al. J. Acoust. Soc. Am. Vol. 131, pp. EL21-27, 2012.

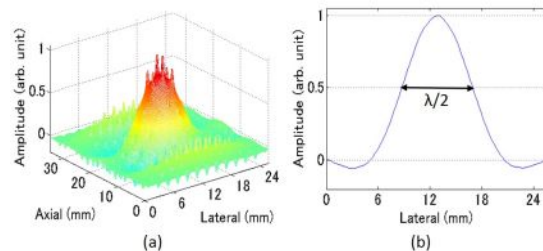


Fig. 1 (a) 2D map and (b) lateral profile of focused share wave.

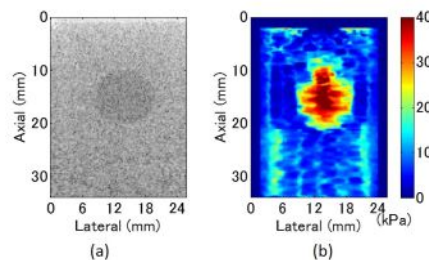


Fig. 2 (a) B-mode and (b) Estimated elasticity image.



## P1A2 - MEL: (Pre-)Clinical Applications of Elasticity Imaging

Salon C

Thursday, September 4, 2014, 8:00 am - 5:00 pm

Chair: **Guy Cloutier**  
University of Montreal Hospital Research Center

### P1A2-1

#### 8:00 am **AdipoScan™ - A novel transient elastography based tool to assess subcutaneous adipose tissue stiffness in morbidly obese patients**

**Magali Sasso**<sup>1</sup>, Meriem Addennour<sup>1,2</sup>, Yuejun Liu<sup>1,2</sup>, Michel Clet<sup>1</sup>, Jean-Luc Bouillot<sup>3</sup>, Gilles Le Naour<sup>4</sup>, Pierre Bedossa<sup>5</sup>, Joan Tordjman<sup>2</sup>, Karine Clément<sup>2</sup>, Véronique Miette<sup>1</sup>; <sup>1</sup>R&D, Echosens, Paris, France, <sup>2</sup>ICAN Institute of Cardiomatobolism and Nutrition, UMR INSERM/UPMC 1166, Pitié Salpêtrière hospital, Paris, France, <sup>3</sup>Department of General, Digestive and Metabolic Surgery, Ambroise Paré Teaching Hospital, Boulogne, France, <sup>4</sup>Department of Anatomic Pathology, Pitié Salpêtrière hospital, Paris, France, <sup>5</sup>Department of Anatomic Pathology, Beaujon hospital, Clichy, France

#### Background, Motivation and Objective

Subcutaneous adipose tissue in human obesity undergoes severe alteration such as fibrosis. It has been shown that this fibrosis is related to metabolic alterations and to less efficiency in losing weight after bariatric surgery (Divoux et al., Diabetes, 2010). Fibrosis also exert a negative impact on adipocytes in part due to mechanical cues. There is currently no non-invasive tool to assess fibrosis in subcutaneous adipose tissue.

Vibration Controlled Transient Elastography (VCTE) using FibroScan® is widely used to assess liver fibrosis in clinical practice. A novel device named AdipoScan™ which is based on VCTE has been developed by Echosens (Paris) so as to assess subcutaneous adipose tissue stiffness.

The objective of this work is: i) to describe the new device AdipoScan™, ii) to show AdipoScan™ results in morbidly obese patients candidates for bariatric surgery.

#### Statement of Contribution/Methods

A new device named AdipoScan™, based on the principle of Vibration Controlled Transient Elastography (VCTE™) has been specifically developed to measure shear wave velocity in subcutaneous adipose tissue. A dedicated probe has been devised to measure this peripheral organ and to limit tissue compression. A dedicated algorithm has been optimized to assess this very heterogeneous organ. This algorithm was validated using Green's functions simulations (homogeneous medium) and on FEM simulations (Comsol Multiphysics) on homogeneous and heterogeneous medium mimicking adipose tissue.

To assess AdipoScan™ performance *in vivo* 74 patients candidate for bariatric surgery were enrolled in the nutrition department of Pitié Salpêtrière hospital (ICAN). AdipoScan™ and Fibroscan® were assessed on patients before surgery. Liver and subcutaneous adipose tissue biopsies were collected from 54 and 32 patients during surgery, respectively and fibrosis (picrosirius red staining) was quantified histologically. Fat and fat-free mass were assessed by DXA before surgery and for 25 patients, 6 months after surgery.

#### Results/Discussion

Adipose tissue stiffness was successfully assessed on all patients. Adipose tissue stiffness is positively correlated to adipose tissue fibrosis ( $p=0.52$ ,  $p=0.002$ ), liver fibrosis ( $p=0.29$ ,  $p=0.006$ ), liver stiffness ( $p=0.28$ ,  $p=0.03$ ), fat-free mass before surgery ( $p=0.30$ ,  $p=0.01$ ) as well as metabolic variables such as fasting glycemia ( $p=0.24$ ,  $p=0.04$ ), insulin ( $p=0.24$ ,  $p=0.04$ ), HDL cholesterol ( $p=-0.36$ ,  $p=0.002$ ), apolipoprotein A1 ( $p=-0.29$ ,  $p=0.02$ ). Furthermore, adipose tissue stiffness assessed before surgery is positively correlated to fat mass loss 6 months after surgery ( $p=0.49$ ,  $p=0.01$ ). Adipose tissue stiffness can be successfully assessed in morbidly obese patients by AdipoScan™. Results show that AdipoScan™ is linked to cardiometabolic risk factors associated with obesity and could be a promising tool to better phenotype morbidly obese patients.

### P1A2-2

#### 8:01 am **Monitoring Radio Frequency Ablation for Liver Tumors with Electrode Displacement Strain Imaging**

**Wenjun Yang**<sup>1</sup>, Marci Alexander<sup>2</sup>, Atul Ingle<sup>1</sup>, Nicholas Rubert<sup>1</sup>, Meghan Lubner<sup>2</sup>, Timothy Ziemlewicz<sup>2</sup>, James Louis Hinshaw<sup>2</sup>, Fred T. Lee Jr.<sup>2</sup>, James A. Zagzebski<sup>1</sup>, Tomy Varghese<sup>1</sup>; <sup>1</sup>Medical Physics, University of Wisconsin-Madison, Madison, WI, USA, <sup>2</sup>Radiology, University of Wisconsin-Madison, Madison, WI, USA

#### Background, Motivation and Objective

Minimally invasive ablative therapies have become important alternatives to surgical treatment of both hepatocellular carcinoma (HCC) and liver metastases, and image guidance and monitoring are essential. Although ultrasound (US) imaging suffers from inadequate contrast between ablated and normal tissue, US based elasticity imaging has shown remarkable ability to depict ablated regions and delineate margins. We are developing novel "electrode displacement elastography," or EDE, a technique that will allow US elastography to monitor shallow to deep liver masses before and after clinical ablation treatments.

#### Statement of Contribution/Methods

We have currently acquired ultrasound radiofrequency data loops on 10 patients who have undergone microwave ablation of their liver tumors. Patients provided informed written consent on a protocol approved by the University of Wisconsin-Madison Institutional Review Board (IRB) prior to the ultrasound and EDE imaging study. The microwave system used was a Neuwave Medical Certus 140 (Madison, WI, USA) operating at 2.45 GHz. A 5 minute MW ablation was typically performed at a 65 W power level. A Siemens S2000 scanner equipped with a curvilinear array transducer (VFX 6C1) pulsed at 4 MHz was used. Electrode displacement was applied manually by the physician, to obtain data before and after the ablation procedure. A multi-seed two-dimensional tracking algorithm, with kernel dimensions of 0.096 mm and 3 A-lines was used to estimate local displacements, on consecutive radiofrequency frames to generate the resulting strain images.

#### Results/Discussion

Strain imaging results obtained using EDE, demonstrate the potential for clear visualization of the ablated region, when compared to the tumor to be ablated before the ablation procedure. Our results on 10 patients include 5 patients with HCC and the remainder with liver metastases. We will present and compare EDE based strain images obtained on human patients with different liver tumors treated at various depths to US B-mode imaging.

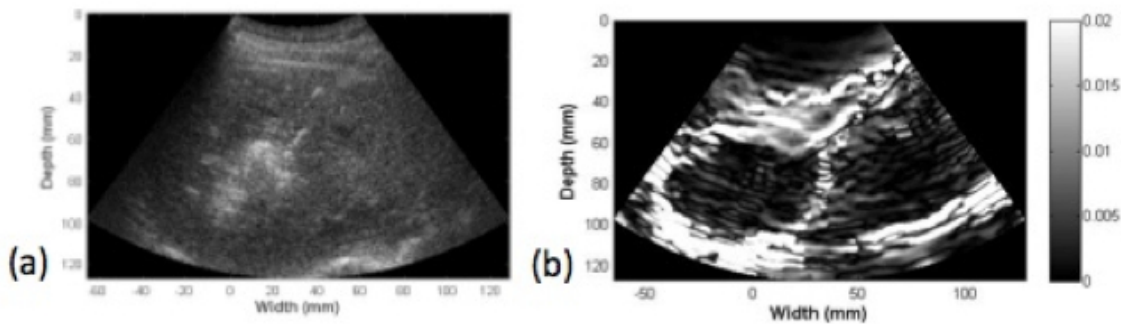


**Figure 1:** Post RF ablation images from a human patient with an ovarian metastases imaged with EDE. The B-mode image (a) shows bubble formation, however the ablated region is not visualized clearly. The decorrelation halo in the strain image (b), delineates the ablated region from the normal background liver.

#### P1A2-3

##### 8:02 am In Vivo Measurements of Bladder Mechanical Properties using Ultrasound Bladder Vibrometry (UBV) Method in Patients and Volunteers

Ivan Nenadic<sup>1</sup>, Mohammad Mehrmohammadi<sup>1</sup>, Matthew Urban<sup>1</sup>, James Greenleaf<sup>2</sup>, Douglas Husmann<sup>2</sup>, Lance Mynderse<sup>1</sup>, Mostafa Fatemi<sup>1</sup>; <sup>1</sup>Mayo Clinic, USA, <sup>2</sup>Mayo Clinic, USA

##### Background, Motivation and Objective

An elastic bladder wall is essential for the bladder storing adequate volumes of urine at low pressures. As the percent of connective tissue in the bladder interstitium increases compared to smooth muscle, the bladder becomes less compliant, resulting in various disorders. Urodynamic studies (UDS) are the clinical gold standard for bladder-compliance assessment, but requires catheterization, and the invasiveness of the procedure carries the risk of infection and discomfort. We have been investigating the use of Ultrasound Bladder Vibrometry (UBV) for noninvasive measurement of bladder mechanical properties. UBV uses acoustic radiation force to induce propagating waves in the bladder wall and the motion is analyzed to evaluate the mechanical properties of the bladder wall. We report on the latest studies in patients and volunteers.

##### Statement of Contribution/Methods

In UDS, the patient's bladder is catheterized and a pressure sensor is inserted into the rectum and the bladder. Saline is infused into the bladder through the catheter using a pump at increments of 50 mL. At each volume, the pressure sensors measure the pressure difference across the bladder wall. UBV measurements of bladder group velocity and elasticity were made concomitantly with the UDS measurements. The bladder wall is identified manually on the B-mode image and targeted for focusing the push beam using the Verasonics V-I system (Verasonics, Redmond, WA) equipped with a curved linear array (C4-2, Philips Healthcare, Bothell, WA) whose center frequency was 2.5 MHz. Impulsive radiation force 400–600  $\mu$ s in length was used to excite mechanical waves in the bladder wall. Plane wave imaging with a three angle coherent compounding was used to track the wave propagation in the bladder wall. Cross-spectral analysis and Fourier-space analysis are used to estimate group velocity and elasticity of the bladder. The measurements of bladder pressure versus volume using UDS, and group velocity and elasticity versus volume using UBV were recorded at each filling volume for later comparison. In UBV measurements in volunteers, the subjects were asked to consume 0.5–1 liter of fluids and allow metabolism to create urine for approximately 45 minutes. The subjects were asked to incrementally empty their bladders and measurements of bladder group velocity and elasticity were made at each increment. A total of 20 patients and volunteers were recruited for the study approved by the Mayo Clinic Institutional Review Board.

##### Results/Discussion

The results show that the group velocity and elasticity in incompressible bladders are significantly higher than in compliant bladders. The comparative studies demonstrate good agreement between the UDS values of pressure and UBV values of group velocity and elasticity ( $R^2 \sim 0.85$ ). In addition, the volunteer studies establish reference values for the bladder group velocity and elasticity as a function of volume in healthy subjects.

#### P1A2-4

##### 8:03 am Stiffness Dynamics of Rabbit's Achilles Tendons Evaluated by Shear Wave Elastography in vivo

Chia-Lun Yeh<sup>1</sup>, Po-Ling Kuo<sup>1</sup>, Pai-Chi Li<sup>1</sup>; <sup>1</sup>National Taiwan University, Taiwan

##### Background, Motivation and Objective

The physiological function of tendon is to withstand the tension generated by muscles during joint movement, thus preventing muscle from damage. The tendon resembles a passive mechanical buffer, while its elasticity property is highly correlated with its functional performance. Recently, shear wave elastography (SWE) has emerged as a promising tool for quantitative stiffness measurements but the applications of SWE to tendons have been limited. The primary challenges are the high speed values of a relatively stiff tissue and the anisotropy. The aim of this study is to evaluate SWE as a diagnostic tool for tendon functionality by monitoring the dynamics at various stretching conditions.

##### Statement of Contribution/Methods

The experiment setup is shown in Fig 1A. A New Zealand white rabbit was anesthetized, with one hind limb skin-shaved and the Achilles tendon imaged by a 5MHz linear transducer connected with a programmable array system (Verasonics Inc, Redmond, WA). Shear waves were generated by using the Supersonic Shear imaging (SSI) technique. The shear wave speed was measured at ankle flexed at 135°, 95°, and 75°, respectively. Shear wave speed was defined as the slope of peak displacement in a shear wave spatial-temporal map (Fig. 1B).

##### Results/Discussion

As depicted in Fig. 1C, the slope of peak displacements against travelling time increased when the ankle angle decreased. The estimated shear wave speeds were 4.4, 7.3 and 12.7 m/s at ankle angle of 135°, 95°, and 75°, respectively, which infers that shear wave speed increases when tendon is stretched. Our results show that the dynamics of tendon elastic properties change during passive stretching and they can be monitored by SWE. In the future, to further evaluate the feasibility of using SWE to differentiate tendon pathological states, a diseased model induced by either physical immobilization or chemical destruction via collagenase enzyme will be performed.

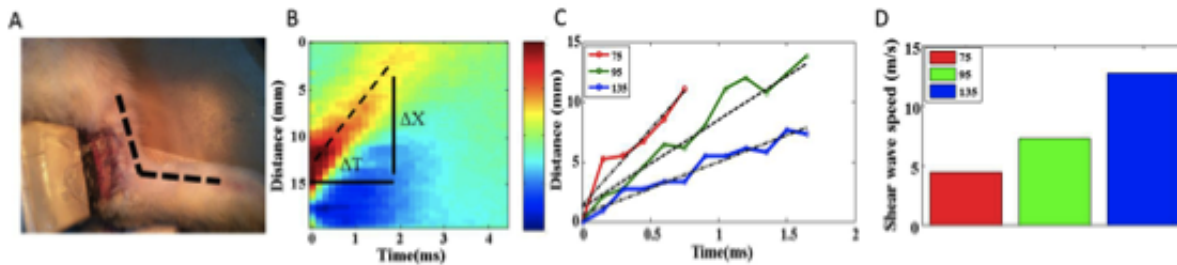


**Figure.1 (A) Experiment setup. (B) A spatial-temporal map of shear wave propagation. (C) Time-to-peak displacement data at different ankle angles. (D) The estimated shear wave speeds corresponding to various ankle angles shown in (C).**

P1A2-5

#### 8:04 am A Microchannel Flow Model of Liver Viscoelasticity

Kevin Parker<sup>1</sup>, <sup>1</sup>Electrical & Computer Engineering, University of Rochester, Rochester, New York, USA

##### Background, Motivation and Objective

A number of advances in elastography have increased our ability to make measurements of viscoelastic properties of tissues. Accordingly, the question is increasingly asked: should our data be fit to a viscoelastic model, and if so which one? Here we focus solely on normal soft tissues and develop a model of behavior based on the flow of viscous fluids through the extensive network of tissue microchannels in response to applied stress. This behavior can be captured in a 2-parameter model, and the model appears to predict the stress-relaxation behavior and the dispersive shear wave behavior of bovine liver specimens and other soft tissues and phantoms over a frequency range of 60 – 400 Hz. The relationship of the microchannel flow model to more traditional models is also examined.

##### Statement of Contribution/Methods

We consider a block of liver tissue, comprised of a fine-scale interlocking of hepatic cells, connective tissue, and a variety of fluid channels including biliary, capillary, and lymphatic. We then consider a small fluid microchannel as a fluid-filled inclusion and derive a characteristic time constant for stress relaxation. Assuming there are multiple microchannels of unequal radius  $r_n$  and therefore unequal flow rates  $Q_n$ , and that each contributes to the stress relaxation at their respective time constant  $\tau_n$ , then the simplest model for this looks like a generalized Maxwell-Weichert model.

In the limit, as we allow a continuous distribution of time constants  $\tau$ ,  $A(\tau)$  is the relaxation spectrum, which can be either discrete or continuous, depending on the particular medium under study (Fung, 1981). Given a material's  $A(\tau)$ , can write the stress relaxation response as  $\sigma_{SR}(t) = \int_0^\infty A(\tau) e^{-t/\tau} d\tau$ . Now consider a specific power law distribution  $A(\tau) = A_0 \tau^{-b}$ ,  $1 < b < 2$ . The power law distribution is naturally occurring in many natural structures including normal and pathological circulatory systems. Substituting and solving yields the solution  $\sigma_{SR}(t) = A_0 t^{1-b} \Gamma[1-b]$  for  $1 < b < 2$ ,  $t > 0$ . We show that this simple expression describes stress relaxation and from this we also derive dispersive shear wave behavior of liver specimens.

##### Results/Discussion

The microchannel model is developed from consideration of the flow of fluids through microvasculature and microchannels in soft tissue. The derivation, along with a power law relaxation spectrum, leads to a 2 parameter model of tissue,  $A_0$  and  $b$ , capable of modeling the frequency domain measurements and the stress relaxation measurements of soft tissues. This resembles a simplified fractional derivative model; however, the microchannel flow model is derived from linear superposition using a relaxation spectrum that is linked to the natural distribution of tissue architecture, specifically fluid channels within the tissue elastic matrix. Supporting examples from shear wave dispersion and stress relaxation in liver tissue specimens are shown to be consistent with the microchannel model.

P1A2-6

#### 8:05 am Comb-Push Ultrasound Shear Elastography (CUSE) Noninvasive Assessment of Pre-biopsy Breast Patients

Max Denis<sup>1</sup>, Mohammad Mehrmohammadi<sup>1</sup>, Azra Alizad<sup>1,2</sup>, Duane Meixner<sup>3</sup>, Penfei Song<sup>1</sup>, Robert Fazio<sup>3</sup>, Shigao Chen<sup>1</sup>, Mostafa Fatemi<sup>1</sup>, <sup>1</sup>Physiology and Biomedical Engineering, Mayo Clinic, Rochester, MN, USA, <sup>2</sup>Internal Medicine, Mayo Clinic, Rochester, Minnesota, USA, <sup>3</sup>Radiology-Diagnostic, Mayo Clinic, Rochester, MN, USA

##### Background, Motivation and Objective

Shear wave elastography techniques provides a noninvasive evaluation of the stiffness of a breast lesion. The rationale for such methods is the fact that the breast lesions are often stiffer than healthy tissue; furthermore, malignant lesions are stiffer than benign lesions. Differentiating benign from malignant can limit the number of biopsies, thus reducing the number of benign breast biopsies diagnose.

##### Statement of Contribution/Methods

In this study, the comb-push ultrasound shear elastography (CUSE) is used to detect and classify breast lesions in pre-biopsy patients. The CUSE imaging technique utilizes a programmable digital ultrasound system (Verasonics, Inc. Redmond, WA, USA) to emit a sequence of laterally spaced acoustic radiation force beams, whereby a shear wave velocity map is reconstructed from the ensuing multiple shear waves generated. Quantitative assessments of measured parameters of the elastic properties of the breast lesion are used to differentiate between benign and malignant breast lesions.

##### Results/Discussion

The results of the CUSE imaging technique from an ongoing clinical study on a group of pre-biopsy breast patients of BI-RADS 3 and above will be presented. The study is performed under a protocol approved by the institutional review board (IRB). All of the patients have undergone ultrasound screening prior to participating in the study. The shear wave velocities in both benign and malignant lesions are compared to their surrounding tissue. To demonstrate, the B-mode ultrasound image a malignant pre-biopsy breast patient is shown in Figure 1a. The region of the lesion is encircled. The CUSE shear wave velocity map is shown in Figure 1b. This figure displays a high shear wave velocity with a mean and standard deviation of  $7.07 \pm 1.18$  m/s in the lesion region. The resultant Young's modulus of 149.95 kPa is indicative of malignancy. In the 29 subset of patients (9 benign and 20 malignant) studied, the mean shear wave velocities were larger in the malignant lesions than in the benign cases. Although, there are some overlap in the mean shear wave velocities between benign and malignant cases creating some false positives. The effects of breast density and probe orientation are examined.

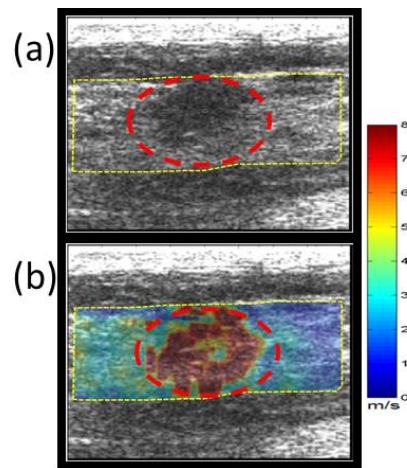


Figure 1. Ultrasound and CUSE shear wave map of a malignant breast tissue.

#### P1A2-7

##### 8:06 am Measurement of Propagation Wave Velocity of Thyroid Induced by Pulsation

Ryo Nagaoka<sup>1</sup>, Kazuto Kobayashi<sup>2</sup>, Shin Yoshizawa<sup>3</sup>, Shin-ichiro Umemura<sup>3</sup>, Yoshifumi Saijo<sup>1</sup>; <sup>1</sup>Graduate School of Biomedical Engineering, Tohoku University, Sendai, Japan, <sup>2</sup>Division of Research and Development, Honda Electronics Co. Ltd., Toyohashi, Japan, <sup>3</sup>Graduate School of Biomedical Engineering, Tohoku University, Sendai, Japan

##### Background, Motivation and Objective

Shear wave Imaging is a technique with ultrasound that estimates tissue stiffness by measuring shear wave induced by Push Beam, which is generated by acoustic radiation force. However, the technique requires Push Beam for a duration of several hundred micron seconds to deform tissue, and a decay of estimate accuracy may be attributed to out-of-focus Push Beam generated by motions of pulsation and heartbeat. In this presentation, the propagation velocity of thyroid was measured by ultrasound spatial compound imaging with a high temporal resolution. In this proposal method, two components of particle velocity can be obtained by using spatial compound imaging, and two kinds of propagation velocity can be also estimated from the propagation appearance of each component.

##### Statement of Contribution/Methods

Verasonic ultrasound scanner (30 MHz, 16 bit, Redmond, WA) and 7.5 MHz UST-5412 Linear Probe (Hitachi Aloka Medical, Ltd.) were used to acquire RF data. Each plane wave was transmitted at 5 different angles, -18, 18, -9, 9, 0, with each time interval of 200 $\mu$ s to acquire echo data for making one spatial compound image. The data of each angle was processed by parallel beamforming, and a spatial compound image was obtained by superposing five B-mode images. Time interval between each spatial compound image is 1 ms. Therefore, the frame rate of the imaging was 1 kfps. A velocity of each angle was calculated by applying a modified 1-D cross-correlation algorithm to the identical echo data obtained by plane wave transmission at each angle. The calculated velocity was separated into two components, which are velocity along lateral direction and velocity along depth. The data for one heartbeat was extracted from the whole data. A measurement area was thyroid of a 22-year-old healthy male at short axis view.

##### Results/Discussion

An appearance of the propagation from the artery to thyroid area induced by pulsation was visualized with high-frame-rate ultrasound imaging. Two regions of interest were set to an area of muscle and that of thyroid respectively, and each propagation velocity, or shear wave velocity, was observed. One was shear wave along lateral direction, and the other was along depth. At the thyroid, the shear wave along depth was  $0.33 \pm 0.23$  m/s at the frequency of 5 Hz, and along lateral direction was  $0.54 \pm 0.15$  m/s at the frequency of 15 Hz. Meanwhile, at the muscle, the shear wave along depth was  $0.46 \pm 0.1$  m/s at the frequency of 5 Hz, and along lateral direction was  $2.09 \pm 0.84$  m/s at the frequency of 15 Hz.

There were obvious difference between the shear waves along lateral direction. It's considered that mechanical properties of tissue can be observed from the propagation. According to our past re-search, the shear wave along muscle fibers was  $7.43 \pm 0.30$  m/s at the frequency of 15 Hz. The muscle fiber direction can be distinguished by the proposal method. These results showed possibility of estimation of tissue stiffness by measuring the shear wave induced by pulsation.

#### P1A2-8

##### 8:07 am Shear Wave Elastography of a Liver Fibrosis Mouse Model Using a High Frequency Ultrasound System with Mechanical Scanning

Chia-Lun Yeh<sup>1</sup>, Bo-Rong Chen<sup>1</sup>, Pai-Chi Li<sup>1</sup>; <sup>1</sup>National Taiwan University, Taiwan

##### Background, Motivation and Objective

Liver fibrosis is one of the most common chronic liver diseases. As the liver fibrosis often involves changes of mechanical properties, shear wave elastography (SWE) can be used for diagnose. Generally, SWE was performed on an array system due to the need for high frame rate imaging. However, for preclinical studies on small animals, a high frequency (> 30MHz) single element transducer with mechanical scanning is often used. It is the goal of this study to develop a high frequency 40MHz SWE platform, which incorporates mechanical scanning for evaluating liver fibrosis on mouse model.

##### Statement of Contribution/Methods

The SWE platform consists of two single element transducers (Fig.1A) in a confocal setup, where one is responsible for inducing acoustic radiation force (push transducer, 20MHz), and the other is used for detecting shear wave propagation (imaging transducer, 40MHz). Two transducers are integrated with an ultrasound preclinical imaging system (Prospect, S-Sharp, New Taipei City, Taiwan) for synchronization and data acquisition. Instead of parallel detection using an array, the single element transducer was positioned at different locations sequentially for displacement measurements.

##### Results/Discussion

Five controls and five carbon tetrachloride-induced diseased mice were used. By analyzing shear wave dispersion and performing curve fitting with Voigt model, the elasticity and viscosity were obtained. The measured mean values of liver elasticity in normal and fibrosis-diseased model are  $2.86 \pm 0.48$  kPa and  $4.9 \pm 1.4$  kPa, while the viscosity are  $1.01 \pm 0.22$

Pa.s and  $1.37 \pm 0.4$  Pa.s, respectively. Results show the control and diseased mice can be distinguished by analyzing its elasticity and viscosity. In summary, SWE was successfully developed on a single element high frequency ultrasound system to evaluate the liver fibrosis in a preclinical animal study.

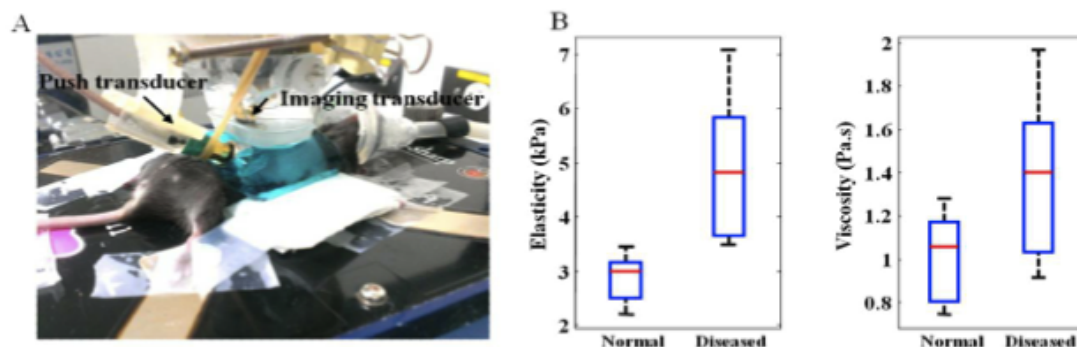


**Figure 1. A. Experiment Setup. B. Boxplot of elasticity and viscosity for control and diseased mice.**

P1A2-9

**8:08 am Ex Vivo mouse skin elasticity properties measurement achieved by laser-induced surface acoustic wave (SAW) method combines phase sensitive optical coherence tomography (PhS-OCT)**

Chunhui Li<sup>1</sup>; <sup>1</sup>University of Dundee, United Kingdom

**Background, Motivation and Objective**

A mechanical property, especially Young's modulus is a useful parameter to assess the physiologic conditions of soft tissues, which can aid the medical diagnosis and clinical disease course tracking. Benefiting from non-invasive, non-destructive and low cost features, laser-induced surface acoustic wave (SAW) method is gaining increasing research interests for the characterisation of tissue elasticity information. This paper evaluates laser-induced SAW as a method that would allow for rapid characterization of the elastic properties of ex vivo mouse skin tissue.

**Statement of Contribution/Methods**

In doing so, we propose a novel approach that utilizes a phase sensitive optical coherence tomography (PhS-OCT) to detect the laser-induced surface acoustic waves (SAW) from the ex vivo mouse skin tissue. A Nd:YAG focused laser line-source is applied to ex vivo mouse skin, and the generated SAW signals are detected by a spectral domain PhS-OCT system. SAW phase velocity dispersion curves are calculated, from which the elasticity of different layers of specimens (dermis and subcutaneous fat layers) is evaluated.

**Results/Discussion**

By analyse the phase velocity of laser-induced SAWs, the mouse skin elastic properties of dermis laser and subcutaneous fat layer can be accurately evaluated: ~150kPa with dermis layer and ~20kPa with subcutaneous layer. For cross validation, a high sensitive force sensor is used to measure the bulk mechanical properties of same samples. We show that the experimental results agree well with those of the different methods and theoretical expectations. In addition, high resolution of ex vivo mouse skin image can be obtained while the measurement of elasticity properties by PhS-OCT system.



# P1A3 - MCA: Contrast Imaging Applications

Salon C

Thursday, September 4, 2014, 8:00 am - 5:00 pm

Chair: **Georg Schmitz**  
Ruhr-Universität Bochum

P1A3-1

## Complementarity of shear wave elastography and dynamic contrast-enhanced ultrasound to discriminate tumor modifications during antiangiogenic and cytotoxic therapy

Alexandre Dizeux<sup>1</sup>, Thomas Payen<sup>1</sup>, Guillaume Barrois<sup>1</sup>, Capucine baldini<sup>1</sup>, Delphine Le Guillou-Buffello<sup>1</sup>, Jean-Luc Gennisson<sup>2</sup>, Mickael Tanter<sup>2</sup>, S. Lori Bridal<sup>1</sup>; <sup>1</sup>Laboratoire d'Imagerie Biomédicale UPMC, CNRS UMR7371, INSERM U1146, France, <sup>2</sup>Institut Langevin ESPCI ParisTech, CNRS UMR7587, INSERM U979, France

### Background, Motivation and Objective

Robust, novel information on tumor microenvironment would improve therapeutic follow-up in oncology. Shear wave elastography (SWE) evaluates Young's modulus (stiffness) based on shear wave velocity. Dynamic contrast-enhanced ultrasound (DCE-US) traces microvascular flow with intravascular microbubbles. Our goal was to evaluate sensitivity and complementarity of these techniques during cytotoxic and antiangiogenic therapies in ectopic, murine tumors.

### Statement of Contribution/Methods

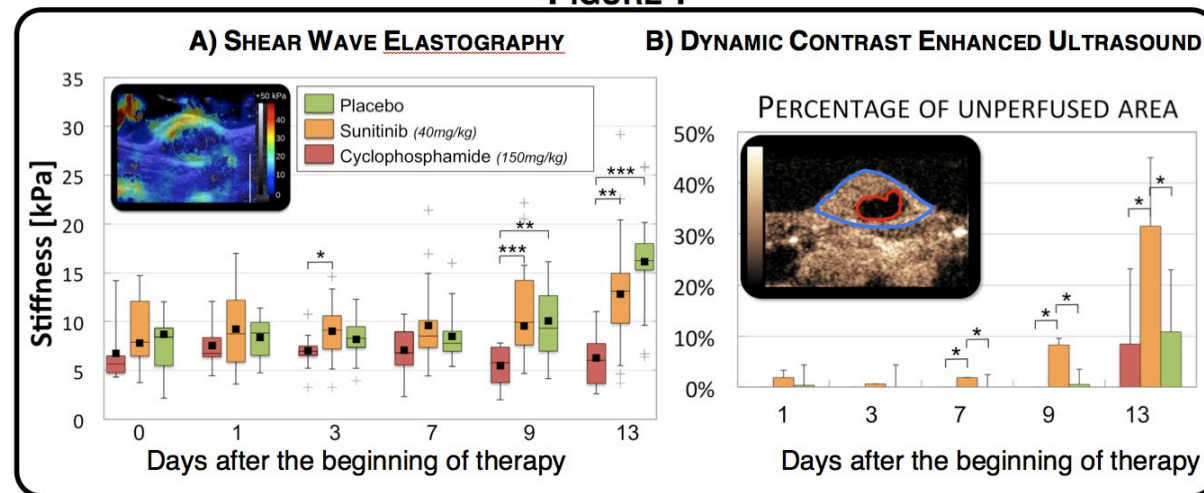
An antiangiogenic agent inhibiting vascularization (sunitinib, N=18), a cytotoxic agent preventing tumor cell duplication (cyclophosphamide, N=14) and placebo (drug-administration vehicle, N=13) were administered in Lewis Lung Carcinomas bearing C57BL6 mice. Six days after implantation, tumors were imaged prior to therapy (Day0) and on Days 1, 3, 7, 9 and 13. Tumor volume was estimated based on B-mode images. Microvascular distribution and flow were assessed with DCE-US data acquired with a Sequoia 512 (Siemens, 7-14 MHz) and a 50-μL bolus of SonoVue. Average stiffness was assessed in six independent elastograms (per day and per mouse) acquired with an Aixplorer system (SuperSonic Imagine, 8MHz). Tumors were harvested and stained to evaluate % necrosis, microvascular density and fibrosis.

### Results/Discussion

Fig. 1 shows (A) mean SWE and boxplot distributions and (B) % unperfused area (mean and standard deviation). Stiffness of sunitinib and placebo groups increase respectively from  $8.7 \pm 3.5$  kPa and  $7.8 \pm 2.8$  kPa (Day 0) to  $13.1 \pm 6.9$  kPa and  $16.1 \pm 6.3$  kPa (Day 13). From Day 9 stiffness was significantly lower in the cytotoxic group than in the other two (Wilcoxon test unpaired). Lower stiffness has previously been associated with changes occurring during cytotoxic therapy such as increased necrosis and decreased fibrosis [1]. At Day 13, unperfused area of sunitinib group reached  $32 \pm 20$  % versus  $8 \pm 15$  % and  $11 \pm 13$  % for cytotoxic and placebo groups, respectively. It was significantly higher in the sunitinib group than the others from Day 7, confirming sensitivity to the antiangiogenic response. The sensitivity of DCE-US to microvascular modifications and SWE to effects of the cytotoxic agent, in this model, underline potential for monitoring complementarity aspects during therapy.

[1] Chamming's, Eur Radiol, 2013

FIGURE 1



P1A3-2

## Ultrasound Molecular Imaging of Pancreatic Cancer Neovasculture Using VEGFR2-Targeted Microbubbles in a Transgenic Mouse Model

Steven Machtaler<sup>1</sup>, Marybeth Pysz<sup>2</sup>, Scott Seeley<sup>2</sup>, John Lee<sup>3</sup>, Teresa Brentnall<sup>4</sup>, Jarrett Rosenberg<sup>5</sup>, Francois Tranquart<sup>6</sup>, Philip Beachy<sup>3</sup>, Juergen Willmann<sup>1</sup>; <sup>1</sup>Radiology, Stanford University, Stanford, California, USA, <sup>2</sup>UCSF, USA, <sup>3</sup>Developmental Biology, Stanford University, USA, <sup>4</sup>University of Washington, USA, <sup>5</sup>Stanford University, USA, <sup>6</sup>Bracco Imaging, Switzerland

### Background, Motivation and Objective

Pancreatic ductal adenocarcinoma (PDAC) is the fourth leading cause of cancer related death, with an average 5 year survival rate of 6%. Over 80% of newly diagnosed patients have non-resectable, advanced disease (median survival, 4 - 6 months), and more than 65% of surgical candidates will develop disease recurrence within 2 years following surgery. Long-term survival following PDAC resection increases with decreasing tumor size, with a 5-year survival time of more than 75% when the primary tumor can be diagnosed with a diameter of less than 1 cm. Our goal was to develop an imaging approach to identify sub-centimeter PDAC lesions in transgenic mice utilizing ultrasound molecular imaging



with clinical-grade microbubbles targeted to one of the key receptors of tumor neoangiogenesis, VEGFR2. The development of an early detection imaging approach for PDAC detection holds great promise for improving the poor prognosis of patients.

#### Statement of Contribution/Methods

Transgenic mice (n = 44; Pdx1-Cre; KRasG12D; Ink4a<sup>-/-</sup>) that spontaneously develop PDAC from age 4 weeks were imaged using a small animal ultrasound system (Vevo2100; VisualSonics), following intravenous injection of  $5 \times 10^7$  clinical grade VEGFR2-MB (BR55, Bracco Suisse SA). The pancreata in wildtype (WT) mice (n = 64) were scanned as controls. Pancreas tissue was analyzed ex vivo by histology (H&E staining) and immunostaining of CD31 (endothelial cell marker) and VEGFR2.

#### Results/Discussion

VEGFR2 targeted ultrasound molecular imaging of PDAC showed significantly higher signal intensities (26.8-fold higher; VEGFR2-targeted ultrasound signal intensity:  $6.7 \pm 8.5$  i.a.u.;  $P < 0.001$ ) in transgenic mice compared with normal, control pancreata of WT mice (signal intensity:  $0.25 \pm 0.25$  i.a.u.). The highest VEGFR2-targeted ultrasound signal intensities were observed in smaller tumors,  $\leq 3$  mm in diameter (30.8-fold higher than control tissue; signal intensity:  $7.7 \pm 9.3$  i.a.u.;  $P < 0.001$ ; Figure 1). Ex vivo quantitative immunofluorescence demonstrated that VEGFR2 expression was significantly higher in pancreatic tumors ( $P < 0.001$ ) compared with normal pancreas. In conclusion, ultrasound molecular imaging with clinical grade VEGFR2-targeted microbubbles allows detection of small foci of PDAC in transgenic mice, and could be further developed for diagnosis and management of patients with PDAC.

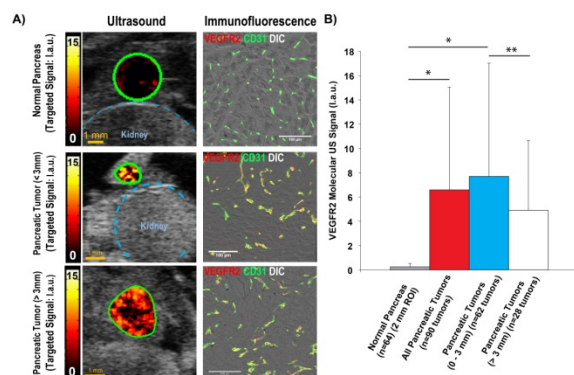


Figure 1. VEGFR2-targeted ultrasound molecular imaging signal observed in small foci of PDAC. (A) Left Panels: Representative VEGFR2-targeted ultrasound imaging signal (green ROI) in normal pancreas (top panel) a very small PDAC tumor (<3 mm; middle panel) and larger tumor (>3 mm; bottom panel) are shown. Scale bar = 1 mm. Right panels: Corresponding confocal micrographs of pancreatic tumors (CD31: green, VEGFR2:red). Scale bar = 100  $\mu$ m. (B) Average VEGFR2-targeted ultrasound molecular imaging signal (linear arbitrary units; i.a.u.) measured in normal pancreas (n=64; gray bar) and all pancreatic tumors (n=90; red bar). Pancreatic tumors were further analyzed by tumor diameter: 0-3 mm (n=62; blue bar) and > 3mm (n=28; white bar). \* represents  $P < 0.001$ , \*\* represents  $P < 0.05$ .

#### P1A3-3

##### Contrast-ultrasound dispersion imaging of cancer neovascularization by mutual-information analysis

Massimo Mischi<sup>1</sup>, Nabil Bouhouch<sup>1</sup>, Libertario Demi<sup>1</sup>, Maarten Kuenen<sup>1</sup>, Arnoud Postema<sup>2</sup>, Jean de la Rosette<sup>2</sup>, Tjalling Tjalkens<sup>1</sup>, Hessel Wijkstra<sup>1,2</sup>; <sup>1</sup>Electrical Engineering, Eindhoven University of Technology, Eindhoven, Netherlands, <sup>2</sup>Urology, Academic Medical Center, University Hospital of Amsterdam, Netherlands

#### Background, Motivation and Objective

Being an established marker for cancer growth, neovascularization is the main target of several approaches for cancer imaging. Recently, analysis of the dispersion kinetics of ultrasound contrast agents (UCAs) has been proposed as a promising approach for localizing neovascularization in prostate cancer. Determined by multipath trajectories through the microvasculature, dispersion enables characterization of the microvascular architecture and, therefore, localization of cancer neovascularization.

Spatiotemporal-similarity analysis of indicator dilution curves (IDCs) measured at each pixel by dynamic contrast-enhanced ultrasound imaging has been proposed to assess the local dispersion kinetics of UCAs. The similarity between neighbor IDCs is analytically related to the dispersion coefficient according to the advection-dispersion equation. Only linear similarity measures, such as temporal correlation or spectral coherence, have been used up until now. Here we propose the use of nonlinear similarity measures by estimation of the statistical dependency between IDCs.

#### Statement of Contribution/Methods

A 2.4-mL SonoVue® (Bracco) bolus is injected intravenously and its passage through the prostate imaged with an iU22 ultrasound scanner (Philips). After data linearization and speckle-size regularization, IDCs are extracted at each pixel and their statistical dependency analyzed. The mutual information with the neighbor pixels, defined according to a specific kernel, is estimated for each pixel. The kernel size ( $3 \times 3$  mm<sup>2</sup>) accounts for the imaging-system resolution and aims at an optimal compromise between diagnostic resolution and noise robustness. An initial validation was performed with 21 measurements in 15 patients referred for radical prostatectomy at the AMC University Hospital of Amsterdam (NL), by comparison with the corresponding histology results on a pixel basis (see Fig. 1).

#### Results/Discussion

Pixel classification using the presented method resulted in sensitivity and specificity equal to 81% and 87%, respectively. The receiver operating characteristic curve area was 0.92. These results outperformed those obtained by linear similarity measures and by any other perfusion measure. These promising results motivate towards further validation with a larger dataset and with other types of cancer with prominent neovascularization.

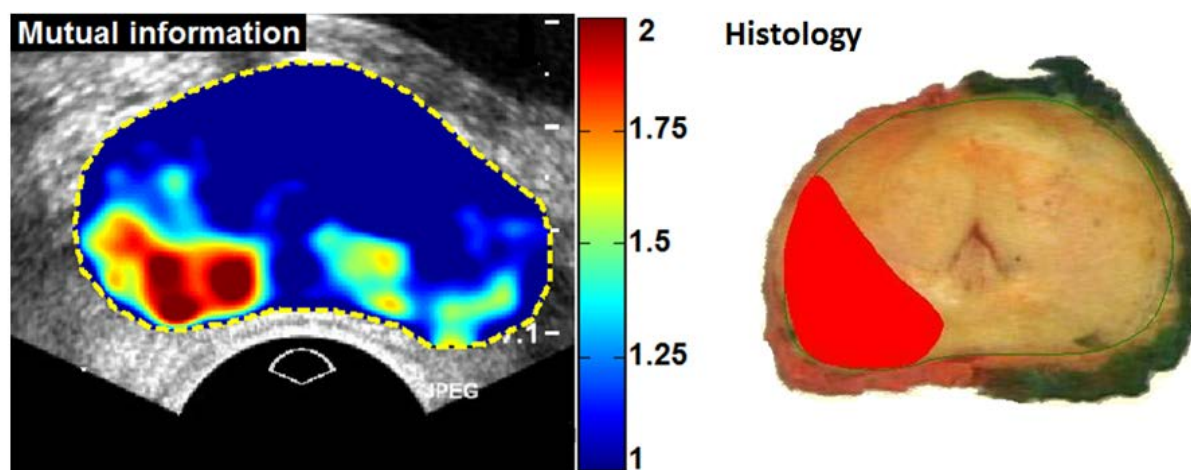


**Figure 1.** Dispersion map by mutual information analysis with corresponding histology result.

P1A3-4

#### Quantification of Tumor Vasculature Using Acoustic Angiography Ultrasound Imaging

Sarah E Shelton<sup>1</sup>, James M Dunleavey<sup>2</sup>, Mike Lee<sup>3</sup>, F Stuart Foster<sup>3</sup>, Andrew C Dudley<sup>2</sup>, Paul A Dayton<sup>1</sup>; <sup>1</sup>BME, UNC-NCSSU, USA, <sup>2</sup>UNC, USA, <sup>3</sup>University of Toronto, Canada

##### Background, Motivation and Objective

Tumor growth requires the recruitment and formation of new blood vessels in a chaotic process known as abnormal angiogenesis. Acoustic angiography is a contrast-enhanced ultrasound imaging technique that produces high resolution images of microvascular structure- providing a novel tool for the study of angiogenesis in vivo. Acoustic angiography utilizes a prototype, dual-frequency transducer to excite microbubbles at low frequency and receive the broadband response at high frequency. The dual-frequency approach produces images with high resolution and superior contrast-to-tissue ratios.

##### Statement of Contribution/Methods

A mouse melanoma cell line (B16F10) was purified into two subpopulations based on the expression of the endothelial cell marker CD31. Based on in vitro studies, it was believed that CD31<sup>+</sup> tumors would be more vascular than their CD31<sup>-</sup> counterparts, and contrast enhanced ultrasound imaging was performed to test this hypothesis on subcutaneous clonal tumors. Matlab was used to analyze the volumetric vascular density, or percent of contrast-containing voxels in the acoustic angiography images.

##### Results/Discussion

Acoustic angiography successfully detected differences in vascular density of the purified melanoma cell lines, with the CD31<sup>+</sup> tumors ( $\mu=72.3\%$ ) showing a statistically significant difference ( $p=0.0025$ ) in vascular density compared to the CD31<sup>-</sup> tumors ( $\mu=47.5\%$ ). Additionally, acoustic angiography proved to be more sensitive to the differences in vascularization than traditional contrast imaging. Further studies will explore at what point in tumor development these differences in vasculature become visible using acoustic angiography.

	$\mu(+)$	$\mu(-)$	P-value	Sensitivity	Effect Size
Volumetric Vascular Density (Acoustic Angiography)	72.3%	47.5%	0.0025	73.2%	1.39
Percent Perfused Voxels (Typical Contrast Imaging)	10.3%	7.7%	0.39	13.1%	0.45
Less Vascular CD31 <sup>-</sup> Tumor      More Vascular CD31 <sup>+</sup> Tumor					

## P1A3-5

**Three-dimensional (3d) parametric maps for visualization of breast lesion vasculature using subharmonic imaging**

Anush Sridharan<sup>1,2</sup>, John Eisenbrey<sup>2</sup>, Priscilla Machado<sup>2</sup>, Kelly Dulin<sup>3</sup>, Samantha Jaffe<sup>3</sup>, Daniel Merton<sup>3</sup>, Haydee Ojeda-Fournier<sup>4</sup>, Robert Mattrey<sup>4</sup>, Kirk Wallace<sup>5</sup>, Carl Chalek<sup>5</sup>, Kai Thomenius<sup>5</sup>, Flemming Forsberg<sup>2</sup>; <sup>1</sup>Drexel University, USA, <sup>2</sup>Thomas Jefferson University, USA, <sup>3</sup>University of Pittsburgh, USA, <sup>4</sup>University of California San Diego, USA, <sup>5</sup>GE Global Research, USA

**Background, Motivation and Objective**

Angiogenesis has been established as an important marker for tumor growth and progression. Current imaging modalities do not have the sensitivity required to visualize breast lesion vascularity in sufficient detail. This study investigated contrast-enhanced 3D subharmonic ultrasound imaging (SHI) to visualize tumor vascularity, evaluate vascular heterogeneity and develop quantitative 3D parametric maps of vascularity in breast lesions

**Statement of Contribution/Methods**

Patients (n = 134) identified with breast lesions on mammography provided informed consent before being scanned using power Doppler imaging (PDI), 3D harmonic imaging (HI) and 3D SHI on a modified Logiq 9 scanner (GE Healthcare, Milwaukee, WI) with a 4D10L probe after injection of a contrast agent (Definity, Lantheus Medical Imaging, N Billerica, MA; dose = 0.25mL for HI & 20µL/kg for SHI). All lesions were subsequently biopsied. A region-of-interest (ROI) corresponding to flow was identified using 4D View (GE Healthcare) and mapped onto the raw slice data to generate a map of the time-intensity curve (TIC) for the lesion volume. Time-points corresponding to baseline, peak intensity and complete washout of contrast were identified to generate vascular heterogeneity plots of the lesion volume. This was subsequently broken down in central and peripheral lesion sections. Finally, 3D parametric volumes were produced for perfusion (PER) and area under the curve (AUC).

**Results/Discussion**

There were a total of 99 benign and 35 malignant lesions. Vascular activity was observed with PDI in 82 lesions (61 benign and 21 malignant). 3D HI showed flow in 8 (5 benign and 3 malignant) lesions, while 3D SHI showed flow in 68 (49 benign and 19 malignant). Analysis of vascular heterogeneity in 3D SHI volumes showed benign lesions to have a significant difference in vascularity between central and peripheral sections ( $1.71 \pm 0.96$  vs.  $1.13 \pm 0.79$ ,  $p < 0.001$ ) whereas malignant lesions showed no significant difference ( $1.66 \pm 1.39$  vs.  $1.24 \pm 1.14$ ,  $p = 0.24$ ), indicative of more vascular coverage, which was validated by the PER and AUC parametric volumes. Our preliminary results suggest that 3D SHI has improved sensitivity to UCA in vascular lesions compared to 3D HI as seen in its ability to detect variations in vascular heterogeneity. Evaluation of vascular heterogeneity combined with parametric volumes could help in the characterization of breast lesions.

## P1A3-6

**Comparing Subharmonic Imaging and Immunohistochemical Markers of Angiogenesis**

Aditi Gupta<sup>1,2</sup>, Mark Forsberg<sup>3</sup>, Kelly Dulin<sup>4</sup>, Samantha Jaffe<sup>4</sup>, Jaydev Dave<sup>1</sup>, Manasi Dahibawkar<sup>1,2</sup>, Valgerdur Halldorsdottir<sup>1,2</sup>, Andrew Marshall<sup>1,2</sup>, Anya Forsberg<sup>5</sup>, Priscilla Machado<sup>1</sup>, Traci Fox<sup>6</sup>, Ji-Bin Liu<sup>1</sup>, Flemming Forsberg<sup>1</sup>; <sup>1</sup>Radiology, Thomas Jefferson University, Philadelphia, PA, USA, <sup>2</sup>School of Biomedical Engineering, Sciences and Health Systems, Drexel University, Philadelphia, PA, USA, <sup>3</sup>Yale University, New Haven, CT, USA, <sup>4</sup>University of Pittsburgh, Pittsburgh, PA, USA, <sup>5</sup>Plymouth Whitmarsh High School, Plymouth Meeting, PA, USA, <sup>6</sup>Radiological Sciences, JSHP, Thomas Jefferson University, Philadelphia, PA, USA

**Background, Motivation and Objective**

Pre-clinical and clinical ultrasound imaging studies into tumor angiogenesis are often conducted with pathological markers as the reference standard. There is, however, no established standard for how to analyze specimen markers. The purpose of this study was therefore, to compare different methods for obtaining tumor neovascularity parameters based on immunohistochemical markers of angiogenesis and compare those to contrast-enhanced subharmonic ultrasound imaging (SHI) in a murine xenograft model.

**Statement of Contribution/Methods**

Twenty-eight athymic, nude, female rats were implanted with  $5 \times 10^6$  breast cancer cells (MDA-MB-231) in the mammary fat pad. The ultrasound contrast agent Definity (Lantheus Medical Imaging, N Billerica, MA) was injected in a tail vein (dose: 36 µl) and pulse-inversion SHI was performed using a modified Sonix RP scanner (Analogic Ultrasound, Richmond, BC, Canada) with an L9-4 linear array (transmitting and receiving frequencies of 8 and 4 MHz, respectively). After the experiments, specimens were sliced corresponding to the imaging planes and stained for endothelial cells (CD31), vascular endothelial growth factor (VEGF), and cyclooxygenase-2 (COX-2). Tumor neovascularity was assessed in 3 different ways using a histomorphometry system based on an SMZ-10A microscope (Nikon, Melville, NJ) at 100x magnification 1) over the entire tumor 2) in small sub-regions of interest (ROIs) and 3) in the tumor periphery (within 2 mm of the margin) and centrally. Results from the specimens and from SHI were compared using a linear regression analysis.

**Results/Discussion**

Of the 28 rats implanted 23 (82 %) exhibited tumor growth and were successfully studied. SHI depicted the tortuous morphology of tumor neovessels and delineated small areas of necrosis. SHI measures of tumor vascularity did not correlate with the immunohistochemical markers when assessed over the entire tumor area or over the small sub-ROIs ( $p > 0.3$ ). However, when the specimens were sub-divided into a central and a peripheral region VEGF was found to correlate with SHI in both areas ( $r = 0.45$  with  $p = 0.032$  and  $r = 0.56$  with  $p = 0.01$ , respectively). The strongest correlation in this breast cancer model was between SHI and COX-2 in the periphery of the tumors ( $r = -0.61$ ;  $p = 0.004$ ). Thus, when comparing quantitative contrast measures of tumor neovascularity to immunohistochemical markers of angiogenesis in xenograft models it appears that sub-ROIs corresponding to the biologically active region (i.e., the tumor periphery) should be used to account for tumor heterogeneity and development.

## P1A3-7

**Tumour Response Evaluation of Concomitant Ultrasound Driven Microbubbles and Radiation in Breast Cancer in vivo**

Priscilla Lai<sup>1,2</sup>, Anoja Giles<sup>1</sup>, William Tran<sup>1</sup>, Azza Al-Mahroukhi<sup>1</sup>, Gregory Czarnota<sup>1,2</sup>; <sup>1</sup>Department of Radiation Oncology, Sunnybrook Health Sciences Centre, Canada, <sup>2</sup>Departments of Medical Biophysics and Radiation Oncology, University of Toronto, Canada

**Background, Motivation and Objective**

There is a growing body of work suggesting that microbubbles have potential therapeutic applications when coupled with ultrasound (US). Specifically, US stimulated microbubbles have been investigated as a form of targeted anti-angiogenic therapy. These agents have been shown to initiate biological effects on the endothelial cells that line the luminal surface of vasculature. Endothelial cells are known to be highly radiosensitive, and account for the majority of cells found in the microvasculature. In order to potentiate the effects of radiation damage, our strategy takes into consideration the endothelial cells' proximity and susceptibility to being targeted, and exploits the endothelial cells' natural radiosensitivity. In the present study, vascular and tumour response to ultrasound-stimulated microbubble and radiation treatment was investigated in vivo to identify effects on vessel endothelium disruption in breast cancer.

## Statement of Contribution/Methods

Mice bearing MDA-MB-231 breast cancer xenografts were exposed to ultrasound after intravenous injection of microbubbles (0% v/v and 3% v/v), and radiation (0 Gy, 2 Gy, and 8 Gy). Mice were sacrificed at 12 hrs and 24 hrs after treatment and the tumours were collected for histopathological analysis. Tumour growth delay was assessed for up to 28 days after treatment.

## Results/Discussion

The results demonstrated synergistic antitumour and antivasular effects when ultrasound stimulated microbubbles were combined with radiation. For the 12 h cohort the average increase in tumour cell death from combining ultrasound microbubble therapy with radiation was 1.3 ( $\pm 0.4$ ) times for 2 Gy dose, and 1.4 ( $\pm 0.4$ ) times for 8 Gy dose ( $P < 0.01$ ). These values were 4.1 ( $\pm 0.7$ ) times and 3.8 ( $\pm 0.7$ ) times for the 2 Gy and 8 Gy treatment groups in the 24 h cohort, respectively ( $P < 0.0001$ ). In addition to enhanced gross tumour death, we observed tumour cell apoptosis, a decrease in tumour vasculature abundance, vascular leakage, a delay in tumour growth and overall tumour disruption. The present study demonstrates adjuvant ultrasound driven microbubbles and radiation treatment as a feasible method of targeted antiangiogenic therapy in breast cancer. The combination of these two therapies demonstrates a supra-additive effect in vivo.

## P1A3-8

### Four-dimensional molecular ultrasound imaging of tumor angiogenesis in a preclinical animal model of prostate cancer

Kenneth Hoyt<sup>1</sup>, Marshall Mahoney<sup>1</sup>, Anna Sorace<sup>1</sup>; <sup>1</sup>University of Alabama at Birmingham, USA

## Background, Motivation and Objective

This study investigated the feasibility of using real-time 4-dimensional (4D) molecular ultrasound (US) imaging for detailing whole tumor angiogenesis in a small animal model of prostate cancer.

## Statement of Contribution/Methods

This imaging study used athymic male nude mice ( $N = 16$ ) that were implanted with PC3 prostate cancer cells and allowed to grow for 6 weeks before being divided into two groups. A streptavidin-coated microbubble (MB) contrast agent (Targestar-SA, Targeson Inc) was conjugated with biotinylated rat IgG antibodies against mouse VEGFR2, p-selectin, and  $\alpha\beta_3$ -integrin or rat IgG control antibody. Either targeted or control MBs were intravenously injected (40 million MBs) in the tail vein. Two min after injection, each animal was imaged for 10 sec using a low-intensity harmonic imaging mode implemented on the portable SONIX Tablet US system (Ultrasonix Medical Corp) equipped with a 4D transducer (5 MHz transmit and 10 MHz receive). At this initial phase, US images depict both bound and systemically flowing MBs. An external unfocused US transducer delivered a 2 sec high-intensity pulse sequence used to destroy (flash) all MBs. Thereafter, low-intensity US imaging was performed again for 20 sec to capture tumor reperfusion. After a 2 h delay to allow MB clearance, animals that received targeted MBs during the first imaging session were reimaged using the control MB and vice versa. Using custom software (Matlab), the mean voxel intensity from manually segmented pre-flash volumes was subtracted from the post-flash volume data. This mean image intensity difference determines the molecular US signal, which represents a surrogate estimate of bound MBs to the targeted angiogenic biomarkers. Also, relative fractional tumor enhancement (FTE) measures were computed as the percentage of voxels above a defined intensity threshold compared to the total number of voxels for the segmented tumor space. Immunohistologic analysis was performed on excised tumor tissue.

## Results/Discussion

Molecular US signals were significantly higher when imaging the tumor angiogenesis targeted MBs versus US imaging of control. Specifically, it was found that molecular US imaging of targeted MBs produced a mean intratumoral enhancement of  $19.5 \pm 2.2$  dB. A significant inverse correlation was found between the molecular US signal and measures of FTE. This suggests that as the spatial distribution of the molecular US signal increases the average intensity of the same reporter signal decreases. This finding is of interest because it could signify that when the neovascularity is inadequate to meet the metabolic demands of the tumor there is a strong angiogenic response as detected using molecular US imaging. This strong angiogenic response is typically found in aggressive cancers and during early stages of tumor growth. Therefore, molecular US imaging may improve US for the early detection of prostate cancer and help distinguish indolent from aggressive disease.

## P1A3-9

### Molecular Imaging of Inflammation with Ultrasound: Feasibility and Reproducibility using a Clinically Translatable Contrast Agent in a Porcine Acute Terminal Ileitis Model

Huaijun Wang<sup>1</sup>, Stephen Felt<sup>2</sup>, Ismayil Guracar<sup>3</sup>, Steven Machtaler<sup>1</sup>, Thierry Bettinger<sup>1</sup>, Richard Luong<sup>2</sup>, Juergen Willmann<sup>1</sup>; <sup>1</sup>Department of Radiology, Molecular Imaging Program at Stanford, Stanford University, Stanford, USA, <sup>2</sup>Department of Comparative Medicine, Stanford University, Stanford, USA, <sup>3</sup>Ultrasound Business Unit, Siemens Healthcare, Mountain View, USA, <sup>4</sup>Bracco Suisse SA, Geneva, Switzerland

## Background, Motivation and Objective

Inflammatory bowel disease (IBD) is a chronic inflammatory disease of the bowel. Monitoring disease activity should be noninvasive and quantitative due to multiple follow-up exams. In this project, we explored feasibility and reproducibility of ultrasound molecular imaging (USMI) using a clinically translatable dual P- and E-selectin-targeted contrast agent (MB<sub>Selectin</sub>) in a large animal model of acute terminal ileitis.

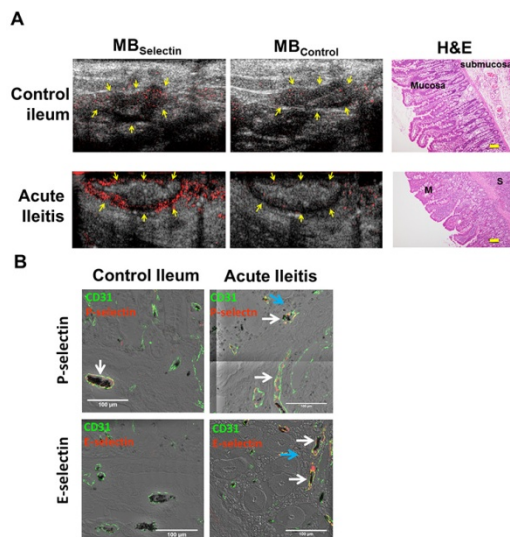
## Statement of Contribution/Methods

An acute terminal ileitis model was established in 17 pigs (ileitis pigs). Ileitis pigs and 3 normal control pigs were examined with USMI using a clinical system (Acuson Sequoia 512, Siemens) following i.v. injection of MB<sub>Selectin</sub> or non-targeted control microbubbles (MB<sub>Control</sub>). Four minutes after injection, images were acquired for 10 sec prior and after a 5-sec high-power destruction pulse. Linearized imaging signal was quantified as intensity ratio (IR), defined as pre-destruction signal intensity divided by post-destruction signal. To test the reproducibility of imaging protocol, scan of the same anatomical locations was repeated twice following both MB<sub>Selectin</sub> and MB<sub>Control</sub>. After imaging, scanned ileum tissues were analyzed ex vivo for both inflammation grade on H&E staining and for expression levels of selectins using immunofluorescence (IF).

## Results/Discussion

USMI was highly reproducible with an intraclass coefficient of 0.88 (95%CI, 0.25-0.99) with MB<sub>Selectin</sub> and of 0.84 (95%CI, 0.24-0.98) with MB<sub>Control</sub>. IR with MB<sub>Selectin</sub> in acute ileitis ( $2.90 \pm 1.09$ ) was significantly higher ( $P < 0.001$ ) than in control ileum ( $1.20 \pm 0.10$ ), and significantly higher ( $P < 0.001$ ) compared to MB<sub>Control</sub> ( $1.22 \pm 0.29$ ) in ileitis. In control ileum, IR was not significantly different ( $P = 0.06$ ) when using MB<sub>Selectin</sub> ( $1.20 \pm 0.10$ ) or MB<sub>Control</sub> ( $1.12 \pm 0.11$ ). Ex vivo analysis showed significantly higher inflammation scores and expression of selectins in acute ileitis compared to control ileum ( $P < 0.05$ , Fig 1). In summary, USMI of inflammation is feasible and reproducible in a porcine ileitis model and correlates well with extent of inflammation on histology. This study lays the foundation for translating USMI to patients with IBD for quantitative and objective assessment of bowel inflammation.





P1A3-10

### Quantitative analysis of the uteroplacental perfusion using contrast enhanced ultrasound imaging

Chloe Arthuis<sup>1,2</sup>, Anthony Novell<sup>1</sup>, Jean-Michel Escoffre<sup>1</sup>, Franck Perrotin<sup>1,2</sup>, Ayache Bouakaz<sup>1</sup>; <sup>1</sup>UMR Inserm U 930, University François Rabelais Tours, France, <sup>2</sup>Department of Obstetrics and Gynecology CHRU Tours, France

#### Background, Motivation and Objective

During pregnancy several complications are associated with the reduced uteroplacental blood flow and are the major cause of maternal and fetal morbidity and mortality. The uteroplacental perfusion is commonly assessed by measuring Doppler resistance index of the uterine and umbilical arteries but their application as screening tools for intrauterine growth restriction, preeclampsia and perinatal death remains controversial. In this context, contrast enhanced ultrasound (CEUS) offers a new opportunity to monitor the uteroplacental circulation and to quantify the intervillous space flow velocity.

#### Statement of Contribution/Methods

Five rats were examined by CEUS on days 14, 17 and 20 of pregnancy. For each rat, a 200 &#61549;1 solution of Vevo Micromarkers was intravenously injected in rat tail. CEUS was performed using a LZ250D probe connected to a Vevo 2100 ultrasound scanner. Data were post-processed using Vevo CQ software and Matlab. Quantitative perfusion parameters during wash-in and wash-out were calculated in 3 compartments: whole placenta, placenta maternal face (PMF), placenta fetal face (PFF) and compared to each other.

#### Results/Discussion

After injection, the contrast agents first appeared in the uterine artery supplying the placenta in blood and in the PFF (Fig. B). Then, the ultrasound signal increased slowly (Fig. C) in the placenta, filling the maternal face. Finally, the signal intensity decreases after few minutes (Fig. D) in the whole placenta. A faster and more intense wash-in was observed in PFF than in PMF. Between day 14 and 20, the peak enhancement increased by a factor 6.1 for both the PFF and PMF ( $p < .01$ ) whereas the whole placenta size increased by a factor 3 ( $p < .01$ ). In the same way, the wash-in rate increased by a factor 18 and 7 for PFF and PMF, respectively ( $p < .01$ ). These results suggest that a rapid expansion of the blood vessels supplying the placenta occurs during the last gestational week. During wash-out, contrast is more persistent in the PMF. At day 20, the fall time was 177s and 56s for PMF and PFF respectively.

Perfusion of the PFF can be distinguished from that of PMF by CEUS in both wash-in and wash-out phase. Noninvasive quantification of placental low velocity microcirculation by CEUS could be useful to manage placental insufficiency in the earlier stage of the pregnancy.

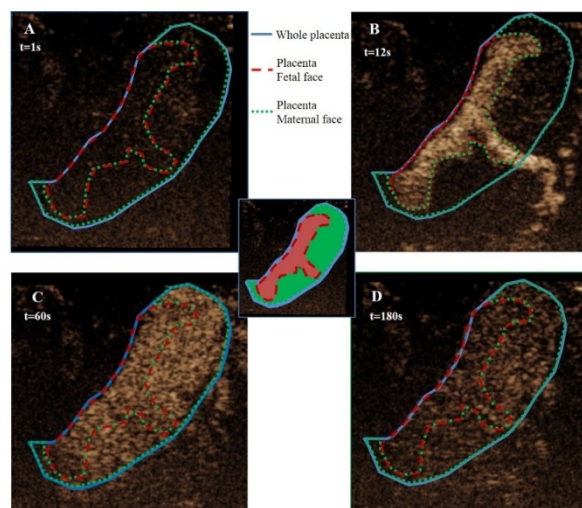


Figure 1. Monitoring of the contrast agents in the uteroplacental unit by CEUS on the 20<sup>th</sup> gestational day

## P1A4 - MBE: Biological Effects and Dosimetry

Salon C

Thursday, September 4, 2014, 8:00 am - 5:00 pm

Chair: **Jørgen Jensen**  
*Technical University Denmark, Kgs. Lyngby*

P1A4-1

### Simulation and Efficient Measurements of Intensities for Complex Imaging Sequences

Jørgen Arendt Jensen<sup>1</sup>, Morten Fischer Rasmussen<sup>1</sup>, Matthias Bo Stuart<sup>1</sup>, Borislav G. Tomov<sup>1</sup>; <sup>1</sup>Dept. of Elec. Eng., Technical University of Denmark, Lyngby, Denmark

#### Background, Motivation and Objective

FDA guided measurements must be conducted before any new imaging sequence can be employed in-vivo. The position of maximum intensity and peak negative pressure values have to be found. For research purposes it can be difficult to predict these, as the advanced imaging sequences often contain a mixture of spherical, plane, and focused emissions with different focal points and pulse lengths. This paper investigates how linear simulation can be used to predict both the magnitude of the intensities as well as the placement of the peak values. The sequence is defined through the normal setup routines for the SARUS scanner and Field II is then used automatically on the sequence to simulate both intensity and MI.

#### Statement of Contribution/Methods

A 3 MHz BK Medical 8820e convex array transducer with  $\lambda$  pitch is connected to the SARUS scanner. The transmit impulse response of one transducer element is measured by placing an Onda HFL-0400 hydrophone (Onda Corporation, Sunnyvale, USA) at the elevation focus of the element. The element is excited by a 20  $\mu$ s white, Gaussian random signal and the cross-correlation between the excitation and hydrophone signals yields the transmit impulse response. This is used in Field II for simulating the pressure fields from the probe. The Onda AIMS III system measures the pressure field for three imaging schemes: a fixed focus, single emission scheme, a duplex vector flow scheme (Duplex sequence), where a 129 emission B-mode sequence is inter-leaved with flow emissions, and finally a vector flow imaging scheme (VFI sequence) with 17 emission directions of 16 emissions followed by a 129 lines B-mode image.

#### Results/Discussion

For the single emission sequence MI was simulated to be 1.42 at (x,y,z)=(0,0,39) mm and measured to 0.81 at (0, 0, 37) mm. The derated  $I_{\text{spita},3}$  was 7.82 mW/cm<sup>2</sup> in simulations at (0, 0, 40) mm and 3.28 mW/cm<sup>2</sup> at (0, 0, 41) mm in the measurements. For the Duplex sequence MI was 0.75 at (0,0,59) mm (simulation) and 0.91 at (0, 0, 56) mm (measurement).  $I_{\text{spita},3}$  was 63.3 mW/cm<sup>2</sup> in simulations at (0, 0, 59) mm and 29.39 mW/cm<sup>2</sup> at (0, 0, 62) mm in the measurements. For the VFI sequence MI was 1.58 (simulation) and 1.32 (measured).  $I_{\text{spita},3}$  was 26.55 mW/cm<sup>2</sup> and 31.87 mW/cm<sup>2</sup>. The overall measured spatial distribution of MI and  $I_{\text{ta}}$  were very similar to the simulated for all sequences. The method can therefore be used for predicting the intensity field of advanced imaging sequences. The measured signals are strongly non-linear for the emitted pressures in the MPa range. Although a linear simulation approach is employed, the measured and simulated intensities are usually within a factor of 2 for both  $I_{\text{spita}}$  and MI. Also the spatial position of both are consistent within 2-3 mm. The simulations cannot replace measurements, but they can give a fairly accurate estimate of the FDA levels and guide where the measurements must be conducted. This can speed up both the measurement process as well as the development cycle for advanced imaging sequences.

P1A4-2

### Suppression of Pressure Measurement Artifacts from Fiber Optic Hydrophones Using Complex Deconvolution of Sensitivity

Keith Wear<sup>1</sup>, Paul Gammell<sup>2</sup>, Subha Maruvada<sup>1</sup>, Yunbo Liu<sup>1</sup>, Gerald Harris<sup>1</sup>; <sup>1</sup>Food and Drug Administration, USA, <sup>2</sup>Gammell Applied Technologies, USA

#### Background, Motivation and Objective

Fiber-optic hydrophones have high spatial resolution (sensitive element size = 10-125 microns), the ability to withstand moderately high intensity therapeutic fields, and the ability to measure temperature as well as pressure. However, their sensitivity (frequency response) can be very nonuniform, which can lead to inconsistent measurements. The objective of this work was to investigate complex deconvolution of sensitivity from fiber-optic hydrophone measurements in order to improve accuracy and precision of acoustic output measurements.

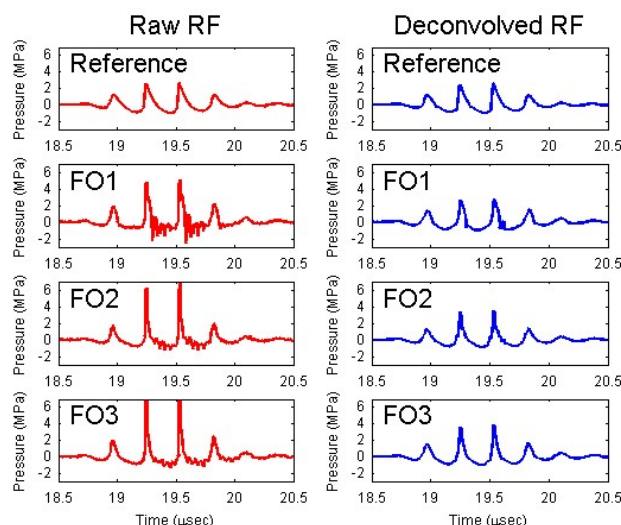
#### Statement of Contribution/Methods

First, a swept-frequency time delay spectrometry system (Wear et al., IEEE Trans UFFC, 58, 2325-2333, 2011) was used to measure magnitude and phase responses of 1) a reference membrane hydrophone with very uniform sensitivity and 2) 6 fiber-optic hydrophones. Measurements were performed using 4 broadband source transducers in order to obtain hydrophone sensitivity from 1 to 40 MHz. Second, the 6 fiber-optic hydrophones and the reference membrane hydrophone were used to measure a 4-cycle, 3.5 MHz pressure waveform that mimicked a pulsed Doppler signal. The voltage waveforms acquired in the second set of experiments were deconvolved with sensitivities measured in the first set of experiments. The effects of deconvolution on measurements of peak compressional pressure (p+), peak rarefactional pressure (p-, which is related to mechanical index), and pulse intensity integral (PII, which is related to thermal index) were measured.

#### Results/Discussion

The figure shows how deconvolution resulted in greater consistency of the fiber-optic hydrophone signals (FO1, FO2, FO3) with the reference waveform. The reference measurements for (p+, p-, PII) in (MPa, MPa, mJ/cm<sup>2</sup>) for the reference membrane hydrophone were (2.4, 1.1, 0.054), with precision better than 10% for all three parameters. The means and standard deviations for the 6 fiber-optic hydrophones were (6.3 +/- 1.1, 2.3 +/- 1.2, 0.122 +/- 0.025) before deconvolution and (3.0 +/- 0.3, 1.2 +/- 0.1, 0.066 +/- 0.010) after deconvolution. Therefore, deconvolution greatly improved agreement between fiber optic hydrophone measurements with uniform reference hydrophone measurements. In conclusion, complex deconvolution greatly improves accuracy and precision of acoustic output measurements with fiber-optic hydrophones.





P1A4-3

### In Vivo Measurement of Temperature Rise in Living Rabbit's Liver Exposed to Ultrasound with Acoustic Radiation Force

Naotaka Nitta<sup>1</sup>, Yasunao Ishiguro<sup>2</sup>, Hideki Sasanuma<sup>2</sup>, Nobuyuki Taniguchi<sup>2</sup>, Iwaki Akiyama<sup>3</sup>; <sup>1</sup>National Institute of Advanced Industrial Science and Technology (AIST), Japan, <sup>2</sup>Jichi Medical University, Japan, <sup>3</sup>Doshisha University, Japan

#### Background, Motivation and Objective

Acoustic radiation force (ARF) has been used for evaluating tissue elasticity, and is generated by longer pulse duration (PD) and higher acoustic pressure than those used in the conventional ultrasound devices. Although the use of ARF produces relatively-high temperature rise in living biological tissue, the thermal effect of ARF is uncertain. In addition, for application to the liver, the thermal effect in combination use of ARF and contrast agents should also be considered. In order to evaluate these effects, we have developed a temperature measurement system using a thermocouple for experiment on living animal. In this study, the temperature rise in living rabbit's liver exposed to ultrasound with ARF was evaluated by using the developed system.

#### Statement of Contribution/Methods

Experimental setup is shown in Fig.1. This experiment was approved by the institutional animal care and use committee. The rabbits under general anesthesia were used and the survival was monitored using an electrocardiograph. The aperture surface of a focused ultrasound transducer (2.5 MHz, focal depth of 25 mm, f-number of 2) was attached to the abdominal skin of rabbit via acoustic coupling jelly. This transducer has a through hole for inserting a thin wire thermocouple ( $\phi 0.15$  mm) with the guide needle into one site of liver. The apex of thermocouple was placed on the focal point inside the liver by adjusting the insertion depth of needle and thermocouple. The transducer was driven and then the temperature data without viscous heating error was recorded at a rate of 10 kS/s and 16 bits. The relation of temperature rise to acoustic outputs around the present regulations of  $I_{\text{spta},3}$  and MI was investigated. Specifically, the ultrasound pulses with PD of 0.3 to 10 ms, MI of 0.7 to 4, PRT of 2 to 10 s were irradiated during 100 to 1000 s. In addition, contrast agent (Sonazoid<sup>TM</sup>) was administered intravenously in a sustained manner at twice the usual dose and the measurement was repeated at another site of liver.

#### Results/Discussion

The relation of maximum temperature rise to  $I_{\text{spta},3}$  was linear. The rates of increase in maximum temperature rise were  $0.35$   $^{\circ}\text{C}/\text{W}/\text{cm}^2$  without contrast agent and  $0.37$   $^{\circ}\text{C}/\text{W}/\text{cm}^2$  with contrast agent. For  $I_{\text{spta},3} < 0.72$   $\text{W}/\text{cm}^2$ , all of the maximum temperature rise was below  $1.5$   $^{\circ}\text{C}$  which WFUMB synopsis (1992) recommends. In future work, the effect of temperature rise on tissue damage will be analyzed.

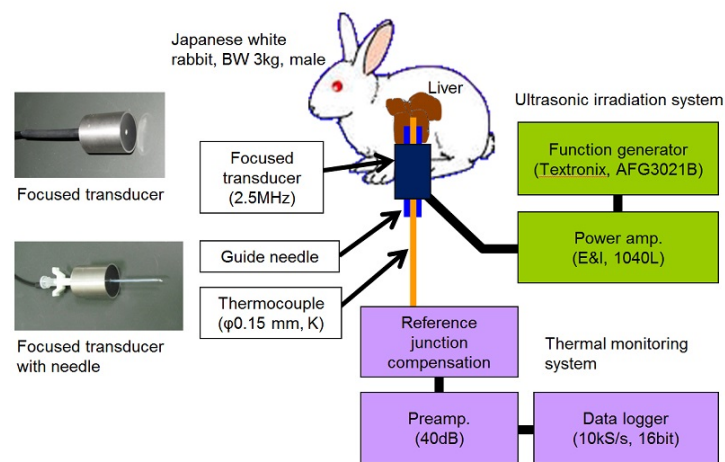


Fig. 1

## Simulation of Temperature Fields in Soft Tissue Caused by Nonlinear Propagation of Ultrasound Pulses

Alexander Doinikov<sup>1</sup>, Anthony Novell<sup>1</sup>, Pierre Calmon<sup>2</sup>, Ayache Bouakaz<sup>1</sup>; <sup>1</sup>INSERM U930, Université François Rabelais, Tours, France, <sup>2</sup>CEA LIST, Saclay, France

### Background, Motivation and Objective

Nonlinear propagation of ultrasound (US) is known to cause increased heating in tissue (D. R. Bacon et al., JASA, vol. 88, pp. 26–34, 1990). This occurs because nonlinear distortions of the US signal in the course of its propagation pump energy into higher harmonics which are absorbed more strongly than the fundamental. This process remains little investigated so far. The aim of our work is to investigate numerically the effect of nonlinear propagation of US pulses on temperature rise in tissue, taking into account that different harmonics of the pulses are absorbed at different absorption coefficients.

### Statement of Contribution/Methods

A code was developed for joint numerical solution of the Westervelt equation (WE), which describes the nonlinear propagation of US pulses, and the bioheat transfer equation (BHTE), which describes temperature rise caused by US. The code carries out a FDTD implementation of WE and BHTE on a 3D Cartesian grid. Waveforms are first calculated that describe the evolution of US pressure at each point of space. Each waveform is then split into harmonic components using Fourier transform and the Butterworth bandpass filter. Thereafter the absorbed US energy is calculated at each spatial point as  $E = E_1 + E_2 + E_3 + \dots$ , where  $E_n$  is the absorbed energy corresponding to the  $n$ th harmonic of the US pulse. It is assumed that  $E_n$  is absorbed at the absorption coefficient  $\alpha(nf)$ , where  $f$  is the center frequency of the pulse.  $E$  is then used in BHTE to calculate temperature rise at each spatial point and for each frequency component. To estimate the effect of nonlinear absorption, comparison to the case of linear absorption is made. This case means that the absorbed energy is calculated without splitting the US pulse into harmonics and the absorption coefficient  $\alpha(f)$  is only used.

### Results/Discussion

Simulations were made for circular and array transducers, for pulses with different durations and for different driving pressures, assuming that US propagates in a tissue-like material. As an example, for a circular transducer with diameter 20 mm, focused at 30 mm, the following results were obtained. Using a 1 MHz, 1 MPa Gaussian pulse as excitation, three pulse durations were tested: 5, 10, and 20 cycles. It was found that the temperature rise doubled when the number of cycles doubled, while excess heating due to nonlinear absorption was 12-13% above that given by linear absorption in all three cases. The dependence of heating on driving pressure amplitude was tested using 1 MHz, 5-cycle Gaussian pulse with peak pressure ranging from 1 MPa to 2 MPa. Exceeding the temperature given by nonlinear absorption over that given by linear absorption was 19% at 1.2 MPa, 28% at 1.4 MPa, 40% at 1.6 MPa, 54% at 1.8 MPa, and 68% at 2 MPa. These results show that proper account of absorption of higher harmonics is important for safe use of US heating. Moreover, the developed code was able to predict temperature increments measured experimentally using a 1 MHz circular transducer.

## Safety of fast cardiac imaging using multiple transmit beams: experimental verification

Alessandro Ramalli<sup>1</sup>, Ling Tong<sup>2,3</sup>, Jianwen Luo<sup>3</sup>, Jan D'hooge<sup>2</sup>, Piero Tortoli<sup>1</sup>; <sup>1</sup>Information Engineering Dept., University of Florence, Firenze, Italy, <sup>2</sup>Dept. of Cardiovascular Sciences, KU Leuven, Leuven, Belgium, <sup>3</sup>Dept. of Biomedical Engineering, Tsinghua University, Beijing, China, People's Republic of

### Background, Motivation and Objective

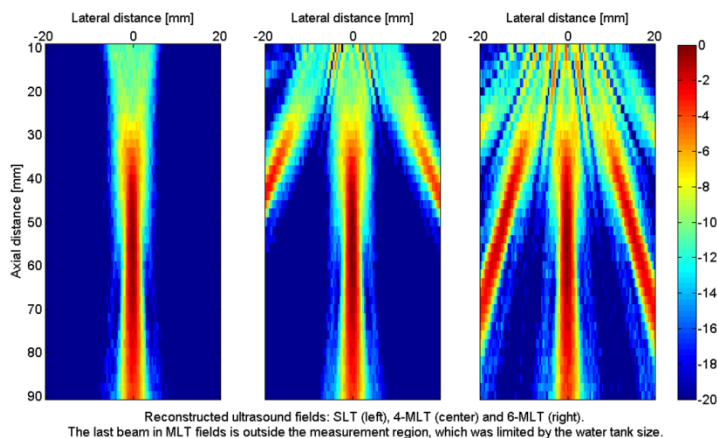
High frame rate (HFR) echocardiography may be of benefit for functional analysis of the heart. It has recently been demonstrated that multiple-line transmit (MLT), i.e. the simultaneous transmission of multiple focused beams into different directions, increases the frame rate without significantly compromising resolution or SNR. In MLT Mode, the excitation pulse applied on a given element is equivalent to the sum of the pulses that would be individually applied to generate single line transmit (SLT) beams along the selected MLT directions. Since a non-standard excitation is involved and an increased number of beams yields an increased energy transfer to the human body, in this paper, the thermal (TI) and mechanical (MI) indexes of MLT are experimentally evaluated and compared with those of SLT.

### Statement of Contribution/Methods

The pressure generated by the phased array probe PA230 (Esaote, Italy) driven by the programmable ULA-OP system, was recorded according to NEMA Std Publication. In all experiments, the excitation signals were limited by the ULA-OP linear amplifiers to the maximum amplitude of 25 Vpp. The measurements were done in a water tank in which a PVDF membrane hydrophone connected to a 25 MSPS digital waveform recorder was immersed. The probe was moved by an automatic positioning system over a 40x80 mm region in steps of 0.4x2 mm in the lateral and axial direction, respectively. The recorded signals were post-processed to reconstruct the ultrasound field and to estimate TI and MI.

### Results/Discussion

TI and MI have been evaluated for SLT, 4-MLT (4 beams) and 6-MLT (6 beams) modes (see figure). ULA-OP was set to produce similar peak pressures in SLT and 4-MLT, according to the strategy recently used (Tong et al., TMI 2014). As expected, the same MI (0.10) was estimated in both cases while the scanned TI for soft tissues (TIS) increased according to the number of beams (0.01 for SLT and 0.03 for 4-MLT at 5 kHz PRF). Lower MI (0.07) and TIS (0.02) values were estimated using the maximum available transmit amplitude in 6-MLT. Therefore, it can be generally stated that the MLT approach does not increase nor influence the risk for mechanical effects. Thermal bio-effects are possible but it might be predicted that MLT modes are safe even for long exposure times, considering the typical peak-to-peak amplitudes used in cardiac imaging (100 Vpp) and assuming a linear behavior.



P1A4-6

#### Ultrasound-Stimulated Microbubble-based Radiation Enhancement Dependence on Endothelial Ceramide Production.

Ahmed El Kaffas<sup>1,2</sup>, Amr Hashim<sup>1</sup>, Anoja Giles<sup>1</sup>, Gregory Czarnota<sup>1,2</sup>; <sup>1</sup>Departments of Radiation Oncology and Physical Sciences, Sunnybrook Health Sciences Centre, Canada, <sup>2</sup>Departments of Medical Biophysics and Radiation Oncology, University of Toronto, Canada

#### Background, Motivation and Objective

Ultrasound-stimulated microbubbles (USMB) are micron-sized (2-12  $\mu\text{m}$ ) spheres, filled with gas or air, and enclosed within a biocompatible shell. These are commonly used as ultrasound contrast agents. We have recently demonstrated that USMB treatments can radiosensitize endothelial cells, resulting in rapid vascular shutdown followed by secondary tumour cell death upon exposure to radiation. Our hypothesis is that USMB-based endothelial membrane perturbations produce ceramide via an ASMase (acid sphingomyelinase) pathway, and act synergistically with radiation to enhance responses to radiation. Here we investigate the role of the ASMase-ceramide pathway on USMB-based endothelial radiosensitization.

#### Statement of Contribution/Methods

Experiments were carried out in wild type (C57BL/6) and ASMase knockout mice, implanted with a fibrosarcoma line (MCA-129). Animals were treated with radiation doses varying from 0-8 Gy alone, or in combination with USMB. In addition, we pre-treated a subset of animals with sphingosine-1-phosphate (SIP) – a chemical ASMase signalling inhibitor. Treatments with USMB consisted of a 16-cycle tone burst at 500 kHz center frequency and 570 kPa using a 2.86 cm element diameter ultrasound transducer. The total insonification time was 750 ms over 5 minutes. Definity bubbles were injected through the tail-vein resulting in a blood volume concentration of 1 % or 3 % (v/v). Treatment response was assessed with Doppler ultrasound acquired at 3, 24 and 72 hrs using a VEO770 system. The vascularity index (VI) was used to quantify power Doppler data. Staining using ISEL, ceramide and CD31 immunohistochemistry of tumour sections was used to complement ultrasound images.

#### Results/Discussion

Wild type tumours treated with a single dose of 8 Gy radiation had a 30 % decrease in the VI by 3 hrs. In contrast, those receiving 8 Gy and USMB resulted in a VI decrease of up to 50 %. Similarly, while 2 Gy alone induced minimal effects on the tumour vasculature, combining it with USMB resulted in up to 40 % decrease in the VI by 24 hrs. Vascular effects were significant ( $p < 0.05$ ) and sustained for up to 72 hrs after combined treatments. These resulted in significant cell death. In contrast to wild type animals, ASMase knockout mice, or wild-type mice receiving SIP, were completely protected from the anti-vascular effects of radiation and USMB. We noted minimal cell death and no vascular shutdown following any of the treatments in those experimental groups. Our results confirm an ASMase-based effect on cell death when endothelial cells are exposed to USMB and radiation. The results suggest a mechanotransduction-like effect that results in endothelial radiosensitization. We also provide evidence of the importance of ceramide in radiation, and confirm blood vessels as regulators of tumour response to therapy.

P1A4-7

#### Sonoporation-induced Heterogeneous Plasma Membrane Potential Depolarization in Hela Cervical Cells

Peng Qin<sup>1</sup>, Ping Cai<sup>1</sup>, Yaxin Hu<sup>2</sup>, Wenjing Zhong<sup>2</sup>, Lifang Jin<sup>3</sup>, Lianfang Du<sup>3</sup>, Alfred C.H. Yu<sup>2</sup>; <sup>1</sup>Department of Instrumentation Science and Engineering, Shanghai Jiaotong University, China, People's Republic of, <sup>2</sup>Medical Engineering Program, The University of Hong Kong, Hong Kong, <sup>3</sup>Department of Ultrasound, Shanghai Jiaotong University Affiliated the First People's Hospital, China, People's Republic of

#### Background, Motivation and Objective

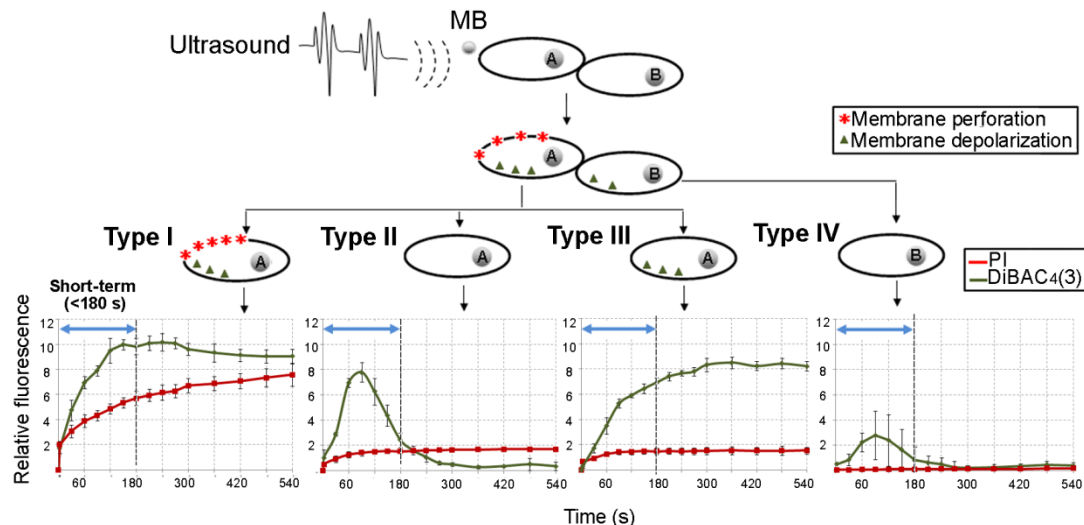
Sonoporation refers to the temporal cell membrane opening caused by ultrasound and microbubbles, resulting in facilitation of the transport of membrane impermeable macromolecular into living cells. Temporal membrane perforation would inevitably disturb anomalous ion fluxes across the membrane and thereby maybe upset the transmembranous potential. There has been validated the correlation of sonoporation with intracellular calcium transients. This research would characterize whether and how sonoporation would affect plasma membrane potential change in living cells.

#### Statement of Contribution/Methods

Our investigation was performed by a customized real-time live cell imaging platform. Hela cervical cancer cells with Sonovue microbubbles (Cell to bubble ratio: 4:3) in Opticell chamber were exposed to 1 MHz ultrasound with 20 cycle pulse duration, 20 Hz pulse repetition frequency, 1 s exposure duration and 0.35 MPa peak negative pressure (pressure profile calibrated by a needle hydrophone). The time-lapse fluorescence images of PI (for tracing sonoporation occurrence) and DiBAC4(3) (for tracking membrane potential change) were concurrently acquired at different time points over 9 min period after exposure. The mean fluorescence intensity of these images was measured by NIS-Elements software to determine the temporal profiles of the intracellular PI uptake level and the dynamics of membrane potential change. After the fluorescence of DiBAC4(3) and PI was acquired, Calcein Blue AM was added to evaluate the relation between different degrees of sonoporated cells and cellular viability.

# Results/Discussion

Results indicate that sonoporation could induce plasma membrane potential depolarization with heterogeneous characteristics, which could be categorized four types. (I) In the irreversibly sonoporated cells, membrane potential was permanent depolarization; (II and III) The membrane potential in the reversibly sonoporated cells was transiently or persistently depolarized; (IV) The unsonoporated cells adjacent to sonoporated ones showed very transient membrane depolarization. These findings validate the relation between the degrees of sonoporation and the heterogeneous plasma membrane depolarization, and would help deeply understand the cellular bioeffects of sonoporation.



P1A4-8

## Evaluation of the effects of clinical diagnostic ultrasound in combination with ultrasound contrast agents on cell stress: Single cell analysis of intracellular phospho-signaling pathways in blood cancer cells and normal blood leukocytes

Spiros Kotopoulos<sup>1,2</sup>, Ragnhild Haugse<sup>3,4</sup>, Maja Mujic<sup>3</sup>, Andre Sulen<sup>3</sup>, Emmet McCormack<sup>3,5</sup>, Odd Helge Gilja<sup>1,6</sup>, Michiel Postema<sup>2</sup>, Bjørn Tore Gjertsen<sup>3,5</sup>; <sup>1</sup>National Center for Ultrasound in Gastroenterology, Haukeland University Hospital, Bergen, Norway; <sup>2</sup>Department of Physics and Technology, University of Bergen, Bergen, Norway; <sup>3</sup>Department of Clinical Science, University of Bergen, Bergen, Norway; <sup>4</sup>Sjukehusapoteka Vest HF, Bergen, Norway; <sup>5</sup>Department of Medicine, Hematology Section, Haukeland University Hospital, Bergen, Norway; <sup>6</sup>Department of Clinical Medicine, University of Bergen, Bergen, Norway

### Background, Motivation and Objective

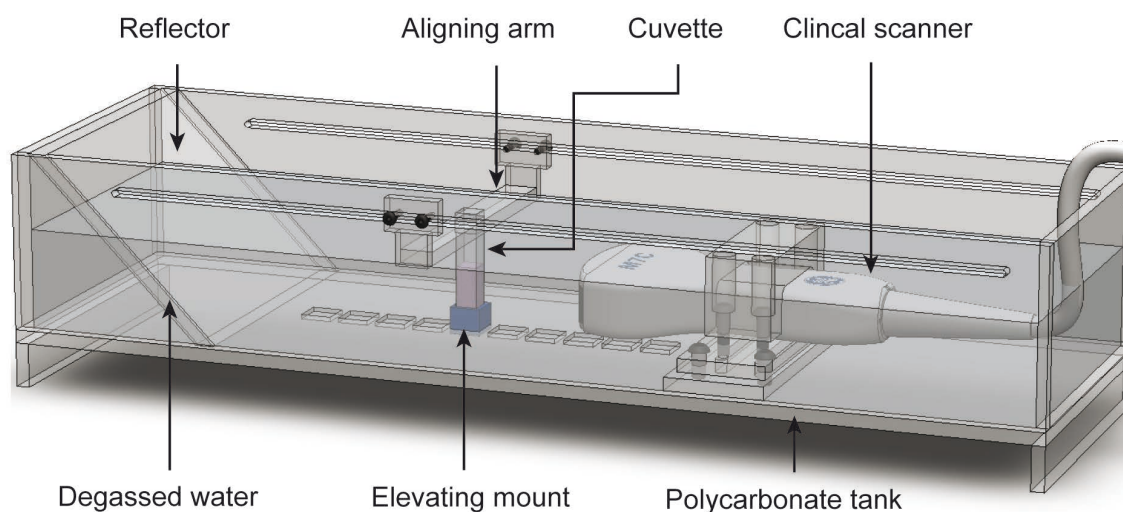
Diagnostic ultrasound is widely used in the clinic and is considered a safe imaging modality with little to no side effects. Currently, the only guidelines for the use on ultrasound are based on the thermal and cavitation effects of ultrasound with or without an ultrasound contrast agent (UCA). With the increased research in ultrasound enhanced drug delivery, understanding the effect of ultrasound on cells is becoming of increased importance. Here we search for an intracellular biomarker of clinical ultrasound.

### Statement of Contribution/Methods

A custom-made setup incorporating a clinical diagnostic ultrasound scanner and disposable cuvette (Fig.1) was used to sonicate a myeloid leukemia cell line (MOLM-13) and normal peripheral blood mononuclear cells (PBMC). SonoVue® ultrasound contrast agent (40µL) was mixed into the 2.5mL cell containing cuvette and continuously homogenized using a magnetic stirrer. An M12L ultrasound probe was used as the ultrasound source and driven by an unmodified Logiq 9 clinical ultrasound scanner. The sound field was calibrated in-situ using a 0.2-mm PVDF hydrophone. The center frequency was determined to be between 5.8 and 6.8 MHz. Acoustic pressures between 0.4 and 1.8 MPa were used. Intracellular signaling was evaluated at multiple time points using different antibodies and multiparameter flow cytometry.

### Results/Discussion

Our results indicate that both the cancer cell line and normal blood cells responded 2 to 6 hours after ultrasound exposure with changed phosphorylation of p38 and ERK1/2; two intracellular signaling enzymes that are frequently phosphorylated during cell stress. Activation was ultrasound contrast agent and acoustic pressure dependent. These signaling pathways are shear stress activated indicating that higher acoustic pressures result in higher shear stresses. In contrast the cancer cells showed a decrease in stress protein p53 signaling when ultrasound contrast agents were added. DNA damage frequently induce p53 activation, hence, the UCA may attenuate the acoustic signal protecting the cell nucleus, whilst forming pores in the cell membrane to allow macromolecular uptake – ideal for ultrasound enhanced drug delivery. In all experimental conditions, the cell viability remained un-altered.



P1A4-9

### Improving DNA Fragmentation Yield by Enhancing Cavitation using Ultrasonically Activated Microbubbles

Sandeep Kasoji<sup>1</sup>, Connor Puett<sup>1</sup>, Sam Pattenden<sup>1</sup>, Jim Tsuruta<sup>1</sup>, William Janzen<sup>1</sup>, Paul A. Dayton<sup>1</sup>; <sup>1</sup>University of North Carolina Chapel Hill, USA

#### Background, Motivation and Objective

Next-generation sequencing is currently used as a diagnostic test to profile changes in the genetic makeup of cancer cells. This technique requires random fragmentation of DNA to specific base pair lengths (300-500bp). DNA fragments outside of this range are misinterpreted by the sequencer. Also, a minimum quantity of DNA is required for the sequencer to offer an accurate analysis. Sonication is one of the current standard methods of fragmenting DNA. Sonication is inexpensive and simple; however it is a slow throughput process and results in broad fragment distributions, yielding only small amounts DNA fragments that can be sequenced. Our preliminary studies have shown that introducing ultrasonically activated microbubbles as a cavitation agent into a sample of DNA prior to sonication, improves fragment size distributions and decreases sonication time.

#### Statement of Contribution/Methods

Lipid-shelled polydispersed microbubbles were fabricated on site with a mean diameter of  $0.9 \pm 0.45 \mu\text{m}$  and a concentration of  $1 \times 10^{10}$  bubbles/mL. DNA samples were prepared in 300  $\mu\text{L}$  thin-walled PCR tubes consisting of 2.5  $\mu\text{g}$  of human genomic DNA suspended in 150  $\mu\text{L}$  of TE buffer solution. 20  $\mu\text{L}$  of microbubble solution were added to each sample prior to sonication. Samples were placed in a floatable raft positioned in the center of an ultrasonic bath (Branson, Danbury, CT) operating at 40kHz with an output of 100W. The ultrasonic bath was actively cooled to 16°C using a refrigerated circulating bath chiller. The raft was continuously rotated at approximately 0.5Hz during the 120 minute sonication period.

#### Results/Discussion

Results showed that the addition of ultrasonically activated microbubbles enhanced fragmentation in the 300-500bp range. Figure 1 displays DNA fragment size distributions of control samples and samples with microbubbles, averaged over five experiments. This data suggests that the presence of microbubbles may significantly improve the efficacy of ultrasound-mediated DNA fragmentation. Our most recent experiments suggest that we will be able to maintain this improved size distribution at sonication times as low as 10 minutes. Further experiments will include optimization of acoustic frequency and power, sonication time, DNA and microbubble volume ratios, pulse sequences, and microbubble size distributions.

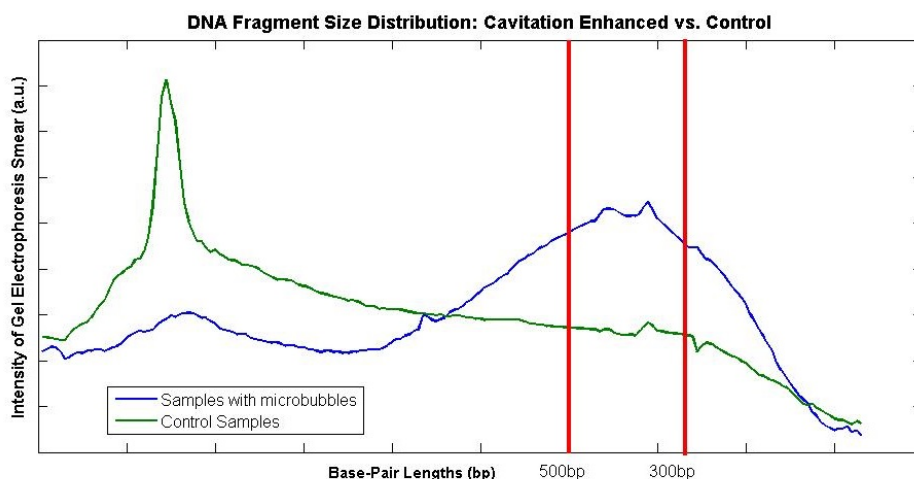


**Figure 1.** DNA fragment size distributions of control samples and samples with microbubbles, averaged over five trials. Samples with bubbles showed increased fragmentation in the 300-500bp range.



## Rapid Localization of Annexin-A1 Phospholipid Binding Proteins at Sonoporation Sites

Wenjing Zhong<sup>1</sup>, Yaxin Hu<sup>1</sup>, Jennifer M. F. Wan<sup>2</sup>, Alfred C. H. Yu<sup>1</sup>; <sup>1</sup>Medical Engineering Program, The University of Hong Kong, Pokfulam, Hong Kong, <sup>2</sup>School of Biological Sciences, The University of Hong Kong, Hong Kong

### Background, Motivation and Objective

The biophysical dynamics happening at the site of sonoporation remain largely unknown as of now. Previous findings of sonoporation mechanisms have mostly focused on either upstream physical events or the influx of Ca<sup>2+</sup> and exogenous molecules, but they have not considered the dynamics of the actual membrane wound itself. Here, we investigate the biologically dynamic nature of sonoporation sites by acquiring a new series of direct observations at a single cell level. We aim to show that, in a sonoporation episode, phospholipid binding proteins residing in the cytoplasm would aggregate at the severed membrane to facilitate wound recovery. Focus will be placed on annexin-A1: a protein with strong binding preference to both phospholipids and Ca<sup>2+</sup>.

### Statement of Contribution/Methods

We first fabricated in-house yellow fluorescent reporter plasmids specific to the annexin-A1 gene. Also, HEK-293 human embryonic kidney cells were cultured and seeded at 1.5e5 cells/ml density inside an enclosed chamber (20x28 mm base; 1 mm height). The annexin-A1 reporter plasmids were then presented to HEK-293 cells via lipotransfection (70% of cells showed fluorescent annexin-A1 expression after 24 h). The plasma membrane was co-labeled using the CellMask dye. Subsequently, Targestar P lipid shelled microbubbles were added at 1:1 cell-bubble ratio to facilitate sonoporation (bubbles were fostered to passively adhere to the plasma membrane through buoyant force). After that, to trigger cavitation which in turn induce sonoporation, the cell chamber was exposed to a 10 cycle, 1 MHz ultrasound pulse that was focused through a cone-shaped waveguide; hydrophone mapping showed that the focal region's peak negative pressure was 0.85 MPa. Over this process, the dynamics of annexin-A1 and plasma membrane were imaged live using confocal microscopy and a 40x oil lens. Mean annexin-A1 fluorescence at different time points was measured using ImageJ; this was done at regions of interest in the cytoplasm and the membrane. From these data, temporal regression trends were derived.

### Results/Discussion

From our cellular cross section images, we observed significant changes in the annexin-A1 distribution upon ultrasound triggered microbubble collapse. Instead of homogeneously spread within the cytoplasm, annexin-A1 was found to translocate to the cell edges immediately upon the onset of sonoporation. Cytoplasmic annexin-A1 fluorescence dropped by 69%, while it increased by one fold at the membrane periphery (N = 15). This trend is temporary in nature, as annexin-A1 distribution gradually returned to its pre-exposure status within 3 min (sonoporation site was found to be resealed on the plasma membrane). To our knowledge, these represent the first ever direct observations on the rapid involvement of phospholipid binding proteins in sonoporation. They serve to demonstrate that the closure of sonoporation sites is biologically dynamic and is not merely based on passive membrane reunion.

## Single-Cell Analysis of Cytochemical Response in Neuroblastoma Cells during Low Intensity Ultrasound Pulsing

Yaxin Hu<sup>1</sup>, Jennifer M. F. Wan<sup>2</sup>, Alfred C. H. Yu<sup>1</sup>; <sup>1</sup>Medical Engineering Program, The University of Hong Kong, Pokfulam, Hong Kong, <sup>2</sup>School of Biological Sciences, The University of Hong Kong, Hong Kong

### Background, Motivation and Objective

While various studies have considered low-intensity pulsed ultrasound (LIPUS) for therapeutic use, the biophysical interactions between LIPUS and living cells have seldom been investigated in a real-time context. Direct observations of cellular dynamics in-situ over the course of LIPUS exposure are particularly lacking. Without unveiling these biophysical interactions, it would be difficult to form a coherent mechanistic explanation to underscore the merit of LIPUS therapy. Hence, in this work, we seek to investigate how cytochemical behavior may be perturbed as a result subjecting cells to LIPUS exposure.

### Statement of Contribution/Methods

Pivotal to our study was the use of an experimental platform with detailed acoustic calibrations and real-time confocal imaging abilities. LIPUS was delivered through a 1 MHz probe that was coupled to a collimator. Using 2 kHz PRF, 1% duty cycle, and 0.85 MPa peak pressure in situ, the applied LIPUS intensity was derived to be equal to 0.24 W/cm<sup>2</sup> (SPTA) and 23.9 W/cm<sup>2</sup> (SPPA) respectively (i.e. below FDA limits). Neuro-2a neuroblastoma cells (with mechanosensitivity kinetics similar to primary cells) were seeded onto custom designed sample holders (with cover glass base) at 1e4 cells/holder density. To examine cytochemical behavior during LIPUS exposure, bright-field imaging was performed using the platform's microscope consecutively track in-situ cellular dynamics over three key periods: 1. 10 min prior to the start of LIPUS exposure, 2. a 10 min LIPUS exposure period, 3. 30 min after the end of LIPUS exposure. To render high-contrast volumetric observations of cell morphology, 3-D confocal scans of membrane and nucleus were also performed (these organelles were fluorescently labeled using CellMask and Hoechst 33342). Acquired images were imported into ImageJ to analyze cell shape and size over time. Time regression was then conducted to gain quantitative insights.

### Results/Discussion

We have observed progressive shrinkage of cellular cross-sectional area (25-45%; N = 7) during LIPUS exposure. The initial shrinkage rate, as quantified through time regression, was between 8% and 14% per minute. Interestingly, this shrinkage was found to be transient. After the end of LIPUS exposure, sonicated cells had recovered at a growth rate of 0.4%-0.9% per minute, and had returned to their pre-exposure size within 30 min. 3-D confocal imaging further revealed: 1. volumetric nature of LIPUS-induced membrane contraction (21%-45% reduction), 2. concomitant decrease in nucleus volume (12%-25% reduction). These findings show that LIPUS, if applied for minutes, would reversibly perturb cellular and subcellular structures. They help to corroborate the prevailing understanding that LIPUS would not pose destructive impact on living cells.

## Lipid Kinetics on the Plasma Membrane During Sonoporation: Correlation with Sonopore Size

Yaxin Hu<sup>1</sup>, Jennifer M. F. Wan<sup>2</sup>, Alfred C. H. Yu<sup>1</sup>; <sup>1</sup>Medical Engineering Program, The University of Hong Kong, Pokfulam, Hong Kong, <sup>2</sup>School of Biological Sciences, The University of Hong Kong, Hong Kong

### Background, Motivation and Objective

As the outermost barrier of the cell, the plasma membrane (PM) protects the cell against influx of extracellular toxic materials and outflow of vital cytoplasmic components. During the sonoporation process, a temporary disruption area (the sonopore) is created on the PM, and the cavitation physics leading to this disruption have been documented. However, the transport phenomena that arise directly and indirectly from the emergence of the sonopore have only been vaguely studied; some reported that enhanced exocytosis and endocytosis would occur, but the associated in situ PM kinetics has not been revealed. Here, we report new evidence on PM transport phenomena evoked by sonoporation through monitoring the PM lipid distribution over the entire cell - both near and away from the sonopore. Our specific objective is to examine the in situ lipid kinetics and surface topography that would arise on the PM during the process of sonoporation.



**Statement of Contribution/Methods**

24hr before the experiment, MRC-5 fetal fibroblasts were seeded into a customized bilayer chamber at a density of 5e4 cells/ml (a total of 3e4 cells in each chamber). The PM of these cells were pre-labeled with CellMask orange dye (reaction took place for 15 min under 37 deg and 5% CO<sub>2</sub> environment; the dye was washed away afterward with HBSS buffer). Subsequently, Targeson microbubbles (MBs) were added to the bilayer chamber at a ratio of one MB per cell. To promote contact of the MBs with cells, the bilayer chamber was flipped over for 15min so that the MBs would naturally float towards the cells. 5 min before exposure, FM 4-64 dye was added to the chamber as a cellular lipid fluorescent tracer. Then, an ultrasound activation pulse (1MHz frequency, 10 us pulse, 0.85 MPa peak neg. pressure) was applied through a conic waveguide to the cell chamber to trigger MB collapse which thereby induce sonoporation. Over this process, lipid distribution on the PM was monitored live with an LSM710 confocal microscopy system (40X oil lens). Images were analyzed using ImageJ to derive quantitative findings on PM lipid kinetics.

**Results/Discussion**

At the sonopore on the punctured PM, rapid increase of CellMask fluorescence was observed within seconds after ultrasound exposure (characteristic time: 4.15s, n=10). This indicates lipid transport to the sonopore is an instant cellular response during sonoporation. In addition, this lipid content increase was co-stained by the influx of FM 4-64, which further showed the docking of cytoplasmic vesicles onto the sonoporated PM. While the PM lipid increase was limited for smaller sonopores (<1um) with faster resealing (characteristic time: 9.41s, n=7), it was significant for large sonopores (>10um; n=10) that failed to repair themselves. Positive correlation was observed between PM lipid increase, sonopore size, resealing outcome, and resealing time. Remarkably, this lipid response led to changes in the surface topography of the cell, introducing striation patterns on the PM.

P1A4-13

**Systematic study on ultrasonically accelerated aggregation phenomenon of amyloid- $\beta$  peptides**

Kichitaro Nakajima<sup>1</sup>, Kentaro No<sup>1</sup>, Hirotsugu Ogi<sup>1</sup>, Hisashi Yagi<sup>2</sup>, Yuji Goto<sup>2</sup>, Masahiko Hirao<sup>1</sup>; <sup>1</sup>Graduate school of Engineering Science, Osaka university, Japan, <sup>2</sup>Institute for Protein Research, Osaka University, Japan

**Background, Motivation and Objective**

Amyloid- $\beta$ (A $\beta$ ) peptides form the needle-like aggregates called amyloid fibrils in vivo, which are deeply related to onset of Alzheimer's disease (AD). The aggregation process of A $\beta$ s normally takes very long time (~60 years in vivo), and this has remained their aggregation mechanism unclear. Acceleration of the aggregation process, therefore, significantly contributes to clarifying the mechanism and then to the drug development of AD.

Then, we focus on ultrasonic-assisted aggregation, the phenomenon that the aggregation of the peptides is drastically accelerated by a high-power ultrasonication. However, its acceleration mechanism is still unclear. We here systematically investigate this phenomenon with various acoustic amplitudes for clarifying the mechanism.

**Statement of Contribution/Methods**

We used A $\beta$ <sub>1-40</sub> peptides and performed ultrasonication for them at pH7.4. As control experiments, we also performed stirring and incubation experiments. The Thioflavin-T (ThT) assay was adopted for monitoring the formation of amyloid fibrils. The morphology of aggregates obtained by ultrasonication and stirring procedure was observed by using AFM and TEM.

The ultrasonic transducer with fundamental frequency of 26 kHz was located in the water bath and several microtubes with the sample solutions were set above the ultrasonic transducer. The degassed water was used to propagate the ultrasonic wave for avoiding bubble generation there, which would significantly attenuate the ultrasonic wave. The acoustic pressures in the microtubes were measured by a handmade PZT probe.

**Results/Discussion**

**Figure 1** shows representative results. From these results, it was revealed that the aggregation can be promoted by ultrasonication and stirring agitations. However, the aggregation process is clearly different. The ThT level of stirred sample rose slightly, soon. In contrast, it significantly rose after a lag time, during which the ThT level remained the baseline. We found that aggregates produced by ultrasonication and stirring agitations are principally composed of amyloid fibrils and amorphous aggregates, respectively, by the TEM observations. The amorphous aggregates produced by stirring were not decomposed with the high-power ultrasonication.

From our vast amounts of experiments, we propose a new aggregation model.

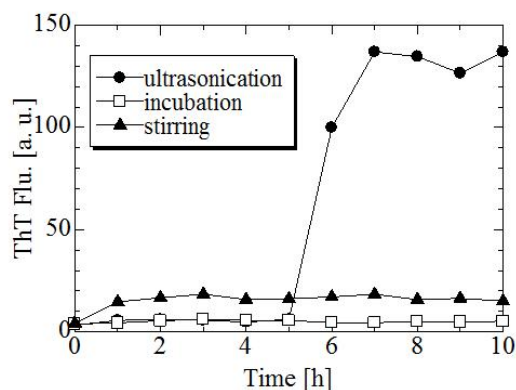


**Figure. 1** Change in the ThT fluorescence intensity in A $\beta$  solutions caused by ultrasonication, stirring and incubation procedures.

## The alteration of protein profile of HepG2 cells during the apoptotic process induced by low intensity pulsed ultrasound

Yi FENG<sup>1</sup>, Lu ZHAO<sup>1</sup>, Mingxi WAN<sup>1</sup>; <sup>1</sup>The Key Laboratory of Biomedical Information Engineering of Ministry of Education, Xi'an city, Shaanxi, China, People's Republic of

### Background, Motivation and Objective

Ultrasound (US) irradiation could induce apoptosis in several carcinoma cells, however, its mechanism has not yet been elucidated. Proteins, dynamically modified and processed at multiple levels during or after US irradiation, always participate in biological processes directly. So it could help us to investigate the mechanism of US induced apoptosis by analyze the alteration of protein profile in US irradiated cells. The objective of the study is to analyze the mechanism of US induced apoptosis by shotgun proteomics.

### Statement of Contribution/Methods

Human hepatocarcinoma HepG2 cells were irradiated by pulsed US (1MHz, PRF=1 kHz, DC=10%) at 0.35MPa for 1 min and then cultured for 12 h before being collected. The morphological alteration of irradiated cells was examined by light and fluorescent microscopy respectively. The percentage of apoptosis cells were examined by flow cytometry with double staining of FITC-labelled Annexin-V/PI. Proteins, extracted from control and US irradiated samples, were separated by sodium dodecyl sulfate polyacrylamide gel electrophoresis (SDS-PAGE), identified by Agilent 1100 HPLC-Chip-MS technology, and then analyzed in GO.

### Results/Discussion

Morphological characteristics of apoptosis cells, such as condensation of nucleus, chromatin margination and formation of apoptosis bodies, were found in US irradiated cells, however few in control cells. The flow cytometry with double staining showed the percentage of apoptosis cells increased more than 15% in US irradiated cells, suggesting apoptosis is induced in irradiated human hepatocarcinoma cells in this study. Several proteins, including apoptosis regulator BAX, HSPs, programmed cell death proteins, p53-inducible protein, voltage-dependent L-type calcium channel subunit beta-4 and BID, are differently expressed in irradiated cells and identified successfully by shotgun proteomics. The GO functional statistical analysis revealed two locations of the proteins are in mitochondrion and endoplasmic reticulum, respectively. It was also revealed that US irradiation induced alteration of protein profile is closely related to several cell processes, such as cell death, cell proliferation. Moreover, GO analysis also showed antioxidation played an important role in US induced apoptosis, suggesting ROS reaction may be one main signal to activate mitochondria.

## Modulation of cartilage metabolism by low-intensity ultrasound via controlled oxidant production

Ke W. Jang<sup>1</sup>, Joseph A. Buckwalter<sup>2</sup>, James A. Martin<sup>1</sup>; <sup>1</sup>Orthopaedics and Rehabilitation, The University of Iowa, Iowa City, Iowa, USA, <sup>2</sup>Veterans Affairs Medical Center, USA

### Background, Motivation and Objective

While low-intensity ultrasound has been shown to be beneficial cartilage repair, the biologic mechanisms underlying this effect remain obscure. Reactive oxygen species (ROS) produced by chondrocyte mitochondria play a critical role in cartilage homeostasis by supporting ATP production via the glycolysis pathway (Martin et al. 2012). ROS couple the production of ATP to mechanical stress, allowing cartilage to adapt to loading (Wolff et al. 2013). Moreover, the lack of ROS and ATP production in cartilage that is not stimulated by mechanical stress leads to atrophy of the tissue. In patients whose joints go unloaded for several weeks or longer, cartilage atrophy is only partially reversible. Further, there is evidence to suggest that atrophy predisposes such individuals to osteoarthritis. Thus, methods for restoring ROS levels and metabolism to unloaded cartilage may have a significant therapeutic impact. Previously we observed that low-intensity ultrasound in cartilage injury stimulated ROS production in chondrocytes (Jang et al. 2013). Therefore, we hypothesized that low-intensity ultrasound can be used for enhancing ROS production in living chondrocytes of intact cartilage, which could modulate chondrocyte energy production, metabolism and matrix synthesis.

### Statement of Contribution/Methods

Manually sawed (2.5 x 2.5 cm<sup>2</sup>) osteochondral explants from mature bovine stifle joints were prepared and cultured in 45% Dulbecco's modified Eagle medium and 45% Ham's F-12 supplemented with 10% fetal bovine serum, 100U/ml penicillin, 100µg/ml streptomycin, and 2.5µg/ml Amphotericin B at 37°C and 5% CO<sub>2</sub> and 5% O<sub>2</sub>. After 48 hours, explants were incubated with or without Hematoporphyrin (HP) (Santa Cruz Biotechnology, Inc.) for 60 minutes and then stimulated with or without low-intensity ultrasound (10W/cm<sup>2</sup>, 50% duty cycle, 1 minute). The cartilage was then stained with 1µM Calcein-AM, a live cell indicator, and 10µM dihydroethidium (DHE), a ROS indicator. Confocal laser scanning microscopy was performed to image ROS production within living chondrocytes in cartilage.

### Results/Discussion

ROS production, measured as the intensity of DHE staining, was 4-fold higher in the ultrasound stimulated group than in the control group. Ultrasound stimulation following 100µM HP treatment increased ROS production by approximately 60% compared to control; however, there was significant chondrocyte mortality, presumably due to ROS overproduction. Our findings indicate that ROS production in living chondrocytes can be induced by low-intensity ultrasound stimulation and suggest that this method could be used to non-invasively modulate chondrocyte energy production, metabolism and matrix synthesis. As such, low-intensity ultrasound may find application in the prevention of cartilage atrophy in immobilized joints.

## P1A5 - MBB: Beamforming I

Salon C

Thursday, September 4, 2014, 8:00 am - 5:00 pm

Chair: **Jian-yu Lu**  
Univ. of Toledo, Toledo

P1A5-1

### Selecting the Number and the Values of the Steering Angles in Coherent Compounded Plane-Wave Imaging and the Effect of that on the Imaging Quality

Zainab Alomari<sup>1</sup>, Sevan Harput<sup>1</sup>, Safer Hyder<sup>1</sup>, Steven Freear<sup>1</sup>; <sup>1</sup>Electronic and Electrical Engineering, University of Leeds, Leeds, United Kingdom

#### Background, Motivation and Objective

Compounded Plane-Wave imaging (CPWI) uses multiple unfocused beams steered with different angles to produce multiple lower-quality images that are compounded to produce a single higher-quality image. The motivation behind this work is to explain the imaging parameters, the criteria by which they are chosen and their effect on imaging quality. The CPWI parameters that are angular step, range and the number of compounded angles should be specified by considering the effect of the tissue type, the imaging depth, the transducer sensitivity and aperture size and the side lobes. These parameters are used in this work to specify the angular range within which the steering is performed.

#### Statement of Contribution/Methods

In order to specify the angular range (AR) of the steered beams, the maximum intensity value received by the field points is plotted with the steering angles at different imaging depths and for different numbers of fixed-size elements using Field II. For each depth, as in fig. 1A, the angle at which the effect of the side lobes starts to occur is considered as the end of the AR.

To evaluate the feasibility of this scheme, L3-8/40EP medical probe with 96 element and -56dB sensitivity is used. To choose the number of compounded angles within the AR, measurements were performed on a wire phantom. Different numbers of steering angles are compounded, and the resulted imaging quality is compared. The imaging quality in terms of the spatial resolution and level of artefacts was improved when increasing the number of the compounded angles up to an optimal number. The optimal number of compounded angles for this scenario was 11, where compounding more angles did not improve the resolution or artefact levels.

#### Results/Discussion

The AR is directly proportional to the aperture size as wider beam is produced, and inversely proportional to the imaging depth, as in fig. 1B. The AR is found from fig. 1A to be  $\pm 10^\circ$  for the 80mm depth. The imaging quality is improved with increasing the number of angles as in fig. 1(C-E). This improvement becomes insignificant when compounding more than 11 angles. As compared to linear imaging at the same level of artefacts, CPWI produces 2.7 times better lateral resolution and more than 7 times higher frame rates.

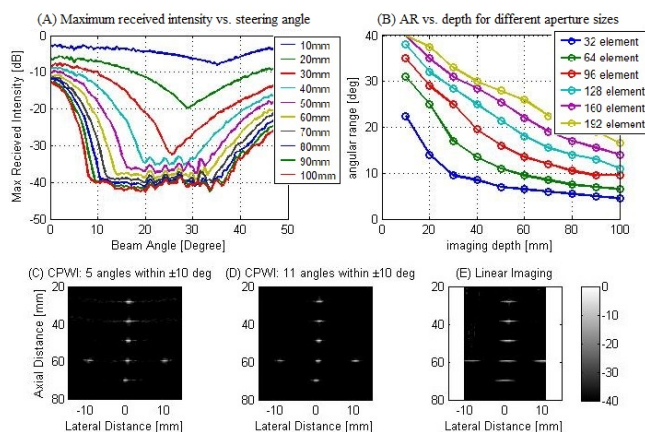


Fig. 1: (A) The change in the maximum received intensity at different depths with the steering angle. (B) The change in the angular range with depth for different aperture sizes. (C-E) wire phantom images using: CPWI with 5 angles, CPWI with 11 angles and Linear Imaging with 24-elements aperture.

P1A5-2

### Fast volumetric cardiac ultrasound: a comparison of different multi-line transmit setups by computer simulation

Alejandra Ortega<sup>1</sup>, Ling Tong<sup>2</sup>, Pedro Santos<sup>1</sup>, Jan D'hooge<sup>1</sup>; <sup>1</sup>Department of Cardiovascular Sciences, KU Leuven, Leuven, Belgium, <sup>2</sup>Department of Biomedical Engineering, Tsinghua University, Beijing, China, People's Republic of

#### Background, Motivation and Objective

It has previously been demonstrated in 2D and 3D that multi-line transmit (MLT) can be used to increase frame rate while preserving image quality. To date, a direct comparison of different MLT implementations for 3D imaging has not been performed. The aim of this study was therefore to determine an optimal trade-off between the amount of parallelization of an MLT system and its SNR.

#### Statement of Contribution/Methods

A 32x32-element 2D phased array (2.5MHz; 50% bandwidth; 1x1cm) focused at 6cm was simulated using a GPU-based implementation of the spatial impulse response method (Simpulse). As MLT is typically combined with multi-line acquisition (MLA), the following setups were tested over a 75°x75° volume: 4MLT-4MLA, 4MLT-16MLA, 9MLT-

4MLA, 9MLT-16MLA, 16MLT-4MLA and 16MLT-16MLA resulting in an increase in frame rate of a factor of 16 to 256. To allow for 16MLA, the transmit beams were broadened. All simulations were done with and without transmit-receive apodization (Tukey  $\alpha=0.5$ ) using dynamic focusing on receive. To reduce cross-talk, as previously shown, the MLT's were positioned in planes along the diagonal of the transducer, and the MLT beams in neighbouring planes were staggered. To quantify the cross-talk, a beam was transmitted along a given MLT direction and the two-way beam profiles for all MLT positions were calculated (including the original transmit direction) in a C-plane at 6.5cm. The energy in the two-way beam profile of the chosen transmit beam was defined as signal while the energy in the remaining two-way beam profiles was considered noise (i.e. cross-talk). This procedure was repeated in each MLT beam direction, and the average SNR per setup was computed.

#### Results/Discussion

The SNR of different setups is given in the Figure. Based on our previous work on 2D MLT, an SNR of -30dB was defined as a cut-off for an acceptable cross-talk level. Given this definition, for 4MLA, 4MLT and 9MLT reached this limit, while apodization suppressed cross-talk so that all the configurations reached the cut-off. Contrarily, none of the 16MLA systems achieved the minimum SNR and apodization had a minimal impact. While the gain in frame rate of a 4MLTx16MLA and a 16MLTx4MLA setup was identical, the latter reached the SNR limit while the former did not. Based on these simulations, a 16MLT-4MLA setup seems to give the highest gain in frame rate while keeping SNR acceptable for B-mode imaging.

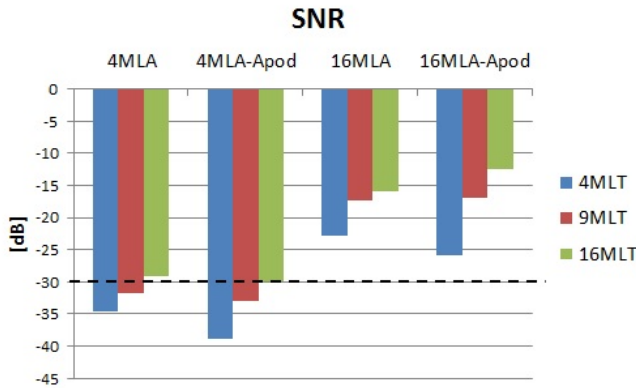


Figure. SNR of the different tested setups: 4MLT-4MLA, 4MLT-16MLA, 9MLT-4MLA, 9MLT-16MLA, 16MLT-4MLA and 16MLT-16MLA. The cut-off SNR was defined as -30dB for an acceptable cross-talk level for B-mode imaging.

#### P1A5-3

##### Safety of Multi-Line Transmit beam forming for fast cardiac imaging – A simulation study

Pedro Santos<sup>1</sup>, Ling Tong<sup>1</sup>, Alejandra Ortega<sup>1</sup>, Eigil Samset<sup>2,3</sup>, Jan D'hooge<sup>1</sup>; <sup>1</sup>Department of Cardiovascular Sciences, KU Leuven, Leuven, Belgium, <sup>2</sup>GE Vingmed Ultrasound AS, Horten, Norway, <sup>3</sup>Center for Cardiological Innovation, Oslo, Norway

#### Background, Motivation and Objective

Multi-Line Transmit (MLT) beam forming (i.e. simultaneously transmitting multiple focused beams) has potential for fast cardiac imaging. However, as the MLT beams spatially overlap close to the transducer, their interference may lead to high acoustic pressures/intensities thereby raising potential safety concerns. To date, few studies have looked into this problem. The aim of this study was thus bi-fold: i) to quantify the acoustic pressures and intensities for MLT beam forming and ii) to propose modifications of the standard MLT beam forming to reduce potential safety issues.

#### Statement of Contribution/Methods

Sound fields of both 2D MLT and conventional 2D Single-Line Transmit (SLT) beam forming were simulated. Their peak acoustic pressure and time averaged intensities (making a plane wave approximation) over a 90° sector (96 transmit lines; 15cm depth) were computed.

Subsequently, two modifications of the standard 4MLT were tested by: i) changing the phases of the transmit pulses corresponding to individual MLT beams with varying combinations; and ii) by introducing small time shifts to the delay lines of MLT beams, while keeping the transmit time for the transmit event.

All the simulations were done in an in-house developed simulator based on the spatial impulse response method (Simpulse) assuming a typical cardiac phased array (64 elements; 18.56x13mm<sup>2</sup>; 290um pitch) transmitting 2.5MHz (50% bandwidth) Gaussian pulse focused at 6 cm. Finally, a Mechanical Index (MI) of 1.0 was used for SLT and the same pressure at the focal point was set for 4MLT.

#### Results/Discussion

The peak acoustic pressure of MLT did not occur in the focal regions but in the proximity of the transducer where the main lobes of the MLT beams overlapped. Compared to SLT, the peak acoustic pressure of 4MLT increased threefold (1.6MPa vs 4.8MPa), while the averaged intensity increased more than 20 times (119 mW.cm<sup>-2</sup> vs 2814 mW.cm<sup>-2</sup>). Both modifications provided a significant decrease in both peak pressure (4.0MPa for phase changes and 2.7MPa for delay shifts) and average intensity (1212 mW.cm<sup>-2</sup> and 736 mW.cm<sup>-2</sup>, respectively) – see Figure.

Overall, this study showed that MLT beam forming may indeed induce safety issues as a result of beam interference, but that these issues could be reduced (if not avoided) by using the proposed modifications. Note that both techniques could be combined for improved performance.

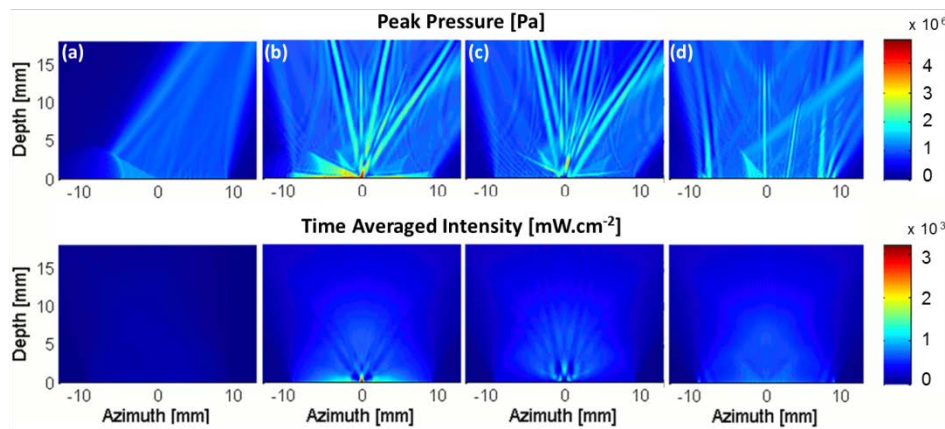


Figure – Sound field (top) and time averaged intensity (bottom) of the tested configurations: (a) SLT, (b) standard 4MLT, (c) best setup for adapted pulse phases [0-180-180-0 degrees] and (d) best setup for the delay shifts [moved towards the end of the transmit event]. Tukey ( $\alpha = 0.5$ ) apodization was applied on transmit for all the 4MLT systems. Please note that all plots are shown in linear scale and just the near field is shown.

P1A5-4

### Speckle Decorrelation of Motion in Ultrasound Fourier Images

Miaomiao Zhang<sup>1</sup>, Hervé Liebgott<sup>1</sup>, François Varray<sup>1</sup>, Denis Friboulet<sup>1</sup>, Olivier Bernard<sup>1</sup>; <sup>1</sup>CREATIS, CNRS UMR5220; Inserm U630; University of Lyon; INSA-Lyon; University of Lyon1, Villeurbanne, France

#### Background, Motivation and Objective

Ultrasound Fourier imaging was firstly proposed by J-Y Lu [Lu et al., IEEE UFFC, 1997] during the 90's to obtain very high frame rate and developed by P. Gueth [Gueth et al., IEEE IUS, 2010] and D. Garcia [Garcia et al., IEEE UFFC, 2013] recently. These methods were evaluated by measuring the static characteristics of the reconstructed image, but no study attempted to evaluate their dynamic behavior, i.e. the influence of this image formation on motion estimation. This study focuses on the speckle decorrelation when various motions are applied to quantify the influence of each method on the accuracy of motion estimation.

#### Statement of Contribution/Methods

The principle of Fourier imaging is summarized as follows. A plane wave is emitted. Back-scattered radio-frequency (RF) signals are measured and Fourier transformed. Then the RF image is remapped in the Fourier domain by interpolating the temporal frequencies. In order to optimize speed, a single horizontal plane wave was used as transmission to reconstruct the images.

In this study, the speckle decorrelation was quantified between two images obtained by applying a motion transformation on the initial image and the scatterers, respectively

#### Results/Discussion

Computer simulations were performed to generate ultrasound raw RF signals beamformed with classical delay and sum (DAS) method, Lu's method, Gueth's and Garcia's method. The simulated tissue was composed of uniformly distributed scatterers in which a translation (lateral and axial) and incompressible deformation were applied. The RF data was simulated by using CREANUIS simulation software [Varray et al., IEEE UFFC, 2011].

Figure 1 shows the speckle decorrelation as a function of depth and motion amplitude for different motion and different imaging methods. Overall, the speckle decorrelation of Fourier imaging methods is close to the conventional DAS method. It can be moreover noted that it is slightly better with axial as well as lateral translation and that it tends to be lower for large deformations. These observations, associated with the fact that the high frame rate of Fourier imaging yields much smaller inter-frame motion, indicate that Fourier based imaging provides a very promising tool for motion estimation.

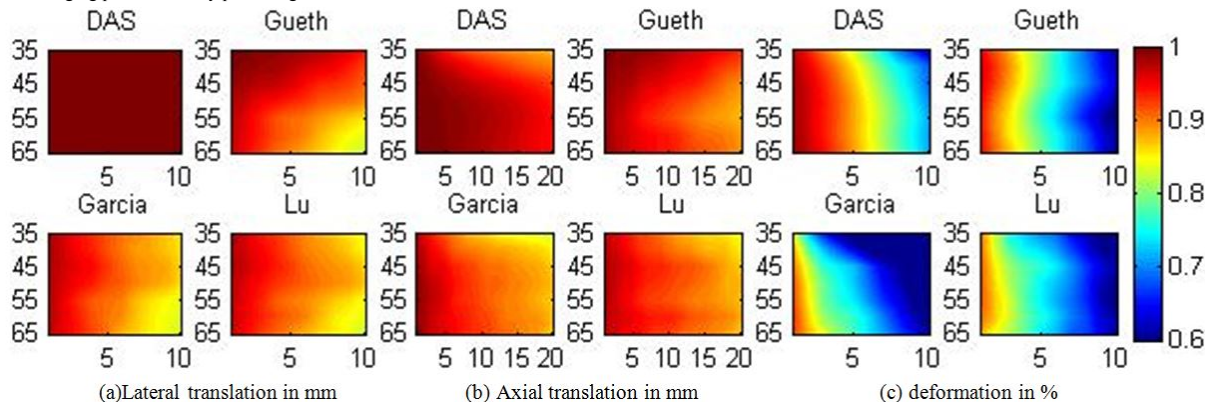


Figure1. Speckle decorrelation of motion, as a function of depth (vertical axis in mm) from the probe and motion amplitude (horizontal axis).



## Blood Flow Visualization with High Speed Ultrasound

Cooper Moore<sup>1</sup>, Zainab Samad<sup>2</sup>, John Castellucci<sup>1</sup>, Joseph Kisslo<sup>2</sup>, Olaf von Ramm<sup>1</sup>; <sup>1</sup>Biomedical Engineering, Duke University, Durham, North Carolina, USA, <sup>2</sup>Division of Cardiovascular Disease, Duke University Medical Center, USA

### Background, Motivation and Objective

A new technique for the real time visualization of blood flow in the heart without injected contrast agent has been developed. This new method of displaying ultrasound images is a non-Doppler, angle independent technique that can be employed in two or three dimensions.

### Statement of Contribution/Methods

By utilizing the parallelism engineered into the Duke University Phased Array Scanner, T5, high frame rate cardiac images (up to 600 per second) were acquired from adult volunteers. To enhance the rapid motion of the heart, a new visualization technique called difference imaging was employed. Difference images were generated in real time by subtracting subsequent scans, two at a time, at the acquisition frame rate. The raw brightness values from sequential frames are subtracted, sample by sample, on a continual basis, to generate difference brightness values. The absolute value of the difference brightness values is then stored. These absolute difference brightness values are then scan converted and displayed as a difference image. The difference images display the change in brightness of each individual sample, effectively acting as a high pass temporal filter. In these images, targets that do not move or change will appear black or dim, while rapidly moving targets will generally appear the brightest.

### Results/Discussion

In all volunteers, difference images provided an increased contrast in moving targets while suppressing any stationary targets in the image. An example high frame rate B-Mode and the accompanying difference image can be seen in Figure 1. This image was taken in late diastole, when the myocardium is stationary but blood is still flowing into the ventricles. As can be seen, the myocardium is suppressed while the rapidly moving blood creates its own contrast in the difference image. When difference images are viewed at reduced playback speed, the complex swirling of the blood in the ventricle during diastole can be clearly visualized, and ejection of blood through the aorta can be seen during systole. This imaging technique holds promise for the real time visualization of coronary arteries using transthoracic ultrasound.

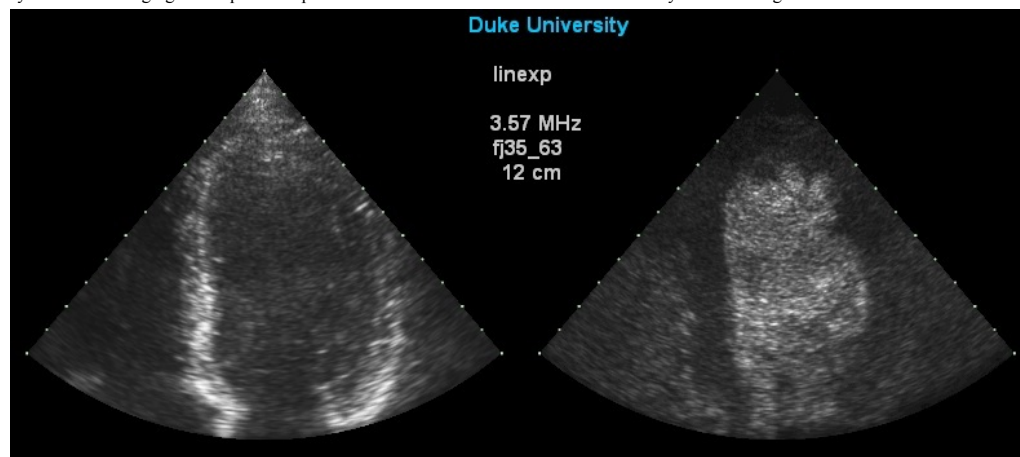


Figure 1: Standard B-Mode (left) and difference image (right) of a 25 y.o. male's heart from an apical view taken during late diastole. Images were acquired at at 361 per second. Note the improved visualization of the blood pool in the difference image.

## In Vivo Synthetic Aperture and Plane Wave High Frame Rate Cardiac Imaging

Matthias Bo Stuart<sup>1</sup>, Andreas Hjelm Brandt<sup>1,2</sup>, Svetoslav Ivanov Nikolov<sup>3</sup>, Michael Bachmann Nielsen<sup>2</sup>, Jørgen Arendt Jensen<sup>1</sup>; <sup>1</sup>Department of Electrical Engineering, Technical University of Denmark, Kgs. Lyngby, Denmark, <sup>2</sup>Radiology, Copenhagen University Hospital, Denmark, <sup>3</sup>BK Medical, Denmark

### Background, Motivation and Objective

Cardiac imaging presents unique challenges with large degrees of tissue motion and long frame-acquisition times. The acquisition time for an image can be reduced by lowering the number of emissions and using parallel beamforming and/or synthetic aperture schemes. This paper compares plane wave (PW) and synthetic aperture (SA) imaging quantitatively on phantom measurements. An in-vivo cardiac scan at 200 frames per second is presented.

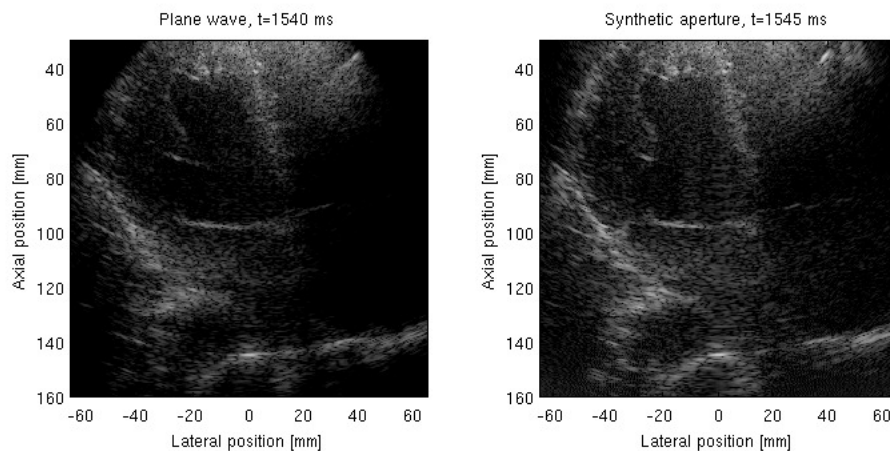
### Statement of Contribution/Methods

A 3.5 MHz 128 element phased array (STv4, Sound Technology Inc., Pennsylvania) is used to create a 90 degrees sector image. All 128 elements are used in both transmit and receive. Both methods use 15 steered emissions with steering angles from -42 to +42 degrees. For synthetic aperture, the virtual source is moved behind the transducer along an arc with a radius of 1 cm. Low-resolution images are made for all emissions in both methods. These are summed coherently to produce high-resolution images. Acquisitions are made using the research scanner SARUS, and validation measurements are made on point targets and tissue mimicking phantoms. The FWHM of a point scatterer and the 20 dB cystic resolution are measured. From scans on a featureless, attenuating tissue mimicking phantom, the SNR is calculated. The pulse repetition frequency is set to 3 kHz giving 200 frames per second. The acquisition of the two frame types is interleaved in a one to one ratio in order to acquire frames at nearly identical locations and time. Hydrophone measurements are made in a water tank (AIMS III, Onda Corporation, California), and the derated peak MI and Ispta.3 are calculated to be 0.44 and 18.6 mW/cm<sup>2</sup> respectively. Both are within respective FDA limits of 1.9 and 430 mW/cm<sup>2</sup> for cardiac imaging. The heart of a healthy, 28 year old male volunteer was scanned by a medical doctor. Four seconds of data was acquired, corresponding to 3-4 heart beats.

### Results/Discussion

The FWHM of a point target at 85 mm depth is 0.8 mm axially and 13 mm laterally for PW and 0.7 mm and 14 mm for SA. The 20 dB cystic resolutions are 51 and 21 mm respectively. PW has on average 1 dB higher SNR than SA across a region covering the range  $x=[-6;6]$  cm and  $z=[2;14]$  cm. The figure shows a single frame of the in-vivo acquisition. The PW image is shown on the left and the SA image on the right. Both images are shown with 60 dB dynamic range. The view shows the left ventricle and part of the mitral valve.





P1A5-7

### Tri-State Hadamard Non-Repeating Interval Codes for Parallel Synthetic Aperture Imaging and SNR Enhancement

Roger Zemp<sup>1</sup>, Tarek Kaddoura<sup>1</sup>; <sup>1</sup>Electrical & Computer Engineering, University of Alberta, Edmonton, Alberta, Canada

#### Background, Motivation and Objective

We propose a set of newly-developed sparse orthogonal codes which we call non-repeating interval codes, which may overcome some limitations of previous codes, and which can be implemented with a tri-state pulser. By simultaneously transmitting a different code from each element of an array and receiving on all available elements we can effectively obtain a full synthetic aperture data set with a single transmit event.

#### Statement of Contribution/Methods

We demonstrate a way to construct non-repeating interval (NRI) codes and illustrate their unique properties and potential applications with simulations and experiments. NRI codes consist of a sequence of  $N$  non-zero bits interlaced with varying numbers of zero bits. For now we restrict non-zero bits to take values of  $(+1, -1)$ . The number of samples between adjacent non-zero bits are called intervals. The intervals between non-zero bits (which we call code bits) are generated using a custom algorithm so that intervals are non-repeating. Codes formed in this way are guaranteed to have out-of-phase cross-correlation and autocorrelation values bounded by a magnitude of 1. We form a set of  $N$  NRI sequences by populating the  $N$  non-zero code bits with Hadamard sequences of length  $N$ , where  $N$  is a power of two. Codes generated in this way are guaranteed to have vanishing zero-lag cross-correlations and height  $N$  zero-lag autocorrelations because of the orthonormality of the Hadamard sequences. Additionally, the sum of the respective autocorrelations is an ideal delta function while the cross-correlations add to vanish. These codes are applied to code-multiplexing for fast parallel synthetic-transmit-receive array imaging and SNR-improvement. We use Field II to model simultaneous transmission of codes from each element of an array and receiving on all available elements. Each receive channel is filtered by cross-correlating with each code-key to recover the transmit-receive signal from each transmitter-receiver element pair then beamforming, however, instead of requiring  $M$  such transmissions (one per element as in traditional synthetic aperture imaging) we only require one.

#### Results/Discussion

We achieve significantly finer spatial resolution and higher contrast-to-noise than previous high-frame rate methods such as flash imaging as evaluated by point-spread and anechoic phantom imaging simulations. Spatial resolution is comparable to synthetic transmit-receive aperture imaging but signal-to-noise is significantly higher because  $M$  elements fire at a time rather than one and there is  $N$  times more energy per transmit waveform than in a single pulse. Signal-to-clutter ratio is worse than with longer synthetic aperture imaging but significantly better than flash imaging.

P1A5-8

### Tissue Harmonic Images obtained with Parallel Transmit Beamforming by means of Orthogonal Frequency Division Multiplexing

Libertario Demi<sup>1</sup>, Jacopo Viti<sup>2</sup>, Gabriele Giannini<sup>2</sup>, Alessandro Ramalli<sup>2</sup>, Piero Tortoli<sup>2</sup>, Massimo Mischi<sup>1</sup>; <sup>1</sup>Lab. of Biomedical Diagnostics, Eindhoven University of Technology, Netherlands,

<sup>2</sup>Information Engineering Dept, Università degli Studi di Firenze, Italy

#### Background, Motivation and Objective

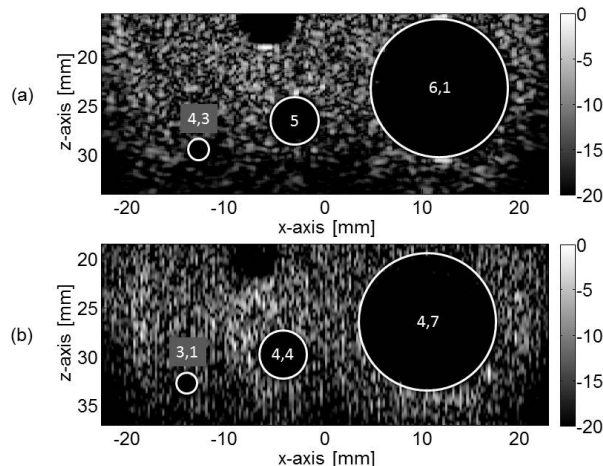
In standard pulse echo ultrasound imaging, the data acquisition rate is limited by the speed of sound. To overcome this drawback, parallel beamforming techniques in transmit (PBT) and in receive mode (PBR) have been proposed. In particular, PBT techniques, based on the transmission of focused beams, are more suitable for harmonic imaging as they are capable of generating stronger harmonics. Recently, orthogonal frequency division multiplexing (OFDM) has been investigated as a means to perform PBT. To date, only numerical studies and experiments in water have been performed, hence neglecting the effect of frequency dependent absorption. Here we present the first tissue harmonic images obtained with PBT by means of OFDM, and evaluate the impact of interbeam interference.

#### Statement of Contribution/Methods

The ULA-OP ultrasound open platform (University of Florence, Italy) is used in combination with the linear array probe LA533 (Esaote Italy). PBT is performed by means of OFDM, hence allocating a portion of the available bandwidth to each beam transmitted in parallel. In receive, appropriate coherent demodulation and low-pass filters are used to discriminate between echoes related to each beam. In particular, three orthogonal frequency bands 1 MHz wide, centered at 4.5, 5.5 and 6.5 MHz, respectively, have been utilized, improving the frame rate by a factor three. The resulting PBT tissue harmonic image is compared to a standard B-mode tissue harmonic image, which is formed using a 3 MHz wide frequency band centered at 5.5 MHz. A homemade agarose tissue mimicking phantom containing cylindrical water filled cavities of different diameters (14 mm, 5 mm, and 2 mm) is used for imaging. Contrast to noise ratio (CNR) and average image brightness inside the cavities have been evaluated to provide an indirect measure of the influence of interbeam interference.

# Results/Discussion

As highlighted in figure, the CNR values obtained for three different cavities are 6.1 dB, 5 dB and 4.3 dB for the standard B-mode, and 4.7 dB, 4.4 dB and 3.1 dB for the PBT image, respectively. The average brightness inside the cavities equals -50 dB, -39 dB and -41 dB for the standard B-mode and -32 dB, -31 dB and -30 dB for the PBT image, respectively. These results are in line with the interbeam interference levels measured in water (Demi *et al.*, UFFC Trans, 60: 2310-2320, 2013), and motivate further in-vivo validation.



Tissue Harmonic Image obtained with (a) standard B-mode and (b) PBT by means of OFDM. Displayed values refer to the measured CNR for each cavity.

## P1A5-9

### Wide-angle tissue Doppler imaging at high frame rate using multi-line transmit beamforming: an in-vivo pilot study

Ling Tong<sup>1,2</sup>, Alessandro Ramalli<sup>3</sup>, Chengwu Huang<sup>2</sup>, Piero Tortoli<sup>3</sup>, Jianwen Luo<sup>2</sup>, Jan D'hooge<sup>1</sup>; <sup>1</sup>Dept. of Cardiovascular Imaging, KU Leuven, Leuven, Belgium, <sup>2</sup>Dept. of Biomedical Engineering, Tsinghua University, Beijing, China, People's Republic of, <sup>3</sup>Dept. of Information Engineering, University of Florence, Firenze, Italy

#### Background, Motivation and Objective

Colour tissue Doppler imaging (TDI) is a well-established methodology to assess local myocardial motion/deformation. Typically, a frame rate of ~200 Hz can be achieved by imaging a narrow sector (~30°, only covering one cardiac wall) at moderate line density, using a dedicated pulse sequence and multi-line acquisition (MLA). However, a wide field of view (FOV) is required in clinical applications to image the whole left ventricle (LV) at high frame rate (HFR). Multi-line transmit (MLT) beamforming has recently been shown capable of providing high quality, full FOV HFR images. The aim of this study was to test the feasibility of MLT for HFR TDI while preserving a wide FOV (90° sector).

#### Statement of Contribution/Methods

To achieve wide FOV TDI, packets of pulses (as in conventional TDI) were simultaneously transmitted into 4 different directions using a 4MLT approach. A 90° sector was thus divided into 4 equally sized subsectors which were simultaneously scanned by corresponding MLT beams. For each transmit direction, the packet size was set to 4 and 4MLA was employed on receive. The 4MLT-4MLA-TDI sequence was implemented on the ULA-OP system yielding a Doppler frame rate of ~90Hz at high line density. Using this setup, the LV of a healthy volunteer was scanned from an apical view and RF-data were acquired and subsequently post-processed using standard RF block matching based on cross-correlation to extract the motion of the whole FOV.

#### Results/Discussion

Unlike normal TDI, the motion of two cardiac walls was simultaneously obtained with a single recording due to the wide FOV enabled by MLT. As an example, two velocity curves at the mid-level of the septal and LV free walls are presented in the Figure. Typical cardiac mechanical events during one cardiac cycle were observed from both curves. Note that the relatively low frame rate in the present study could be increased up to ~430Hz by reducing the packet size and/or the high line density (1.95 vs 0.60 lines/degree in the state-of-the-art systems), which is on-going work. Overall, our preliminary results demonstrate the feasibility of using MLT to achieve wide-angle, HFR TDI and that the MLT beams cross-talk (if any) does not significantly interfere with the motion estimation process. This may be particularly important in clinical applications when determining intra-ventricular time delays (e.g. for cardiac resynchronization therapy).

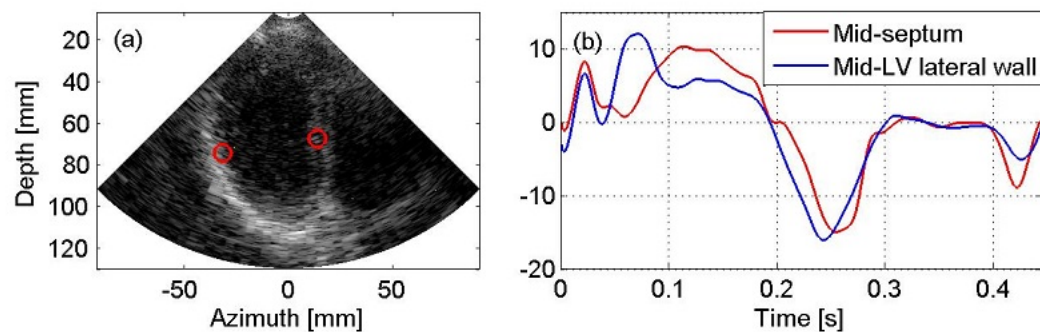


Figure (a) An example B-mode image acquired using 4 multi-line transmit and 4 multi-line acquisition tissue Doppler imaging (4MLT-4MLA-TDI) pulse sequence. The two red circles indicated two regions of interest (ROIs) at the middle level of the septal wall and LV free wall, (b) the velocity curves extracted from the two ROIs.

# P1A6 - MSD: Design and Test of Medical Systems & Devices

Salon C

Thursday, September 4, 2014, 8:00 am - 5:00 pm

Chair: Steven Freear  
University of Leeds

P1A6-1

## A Low-cost High-SNR Ultrasound Imager: Modified Hadamard Synthetic Aperture Imaging (MH-SAI) System with a Sparse Receiving Array

Ping Gong<sup>1</sup>, Michael Kolios<sup>1</sup>, Yuan Xu<sup>1</sup>; <sup>1</sup>Physics, Ryerson University, Toronto, ON, Canada

### Background, Motivation and Objective

Synthetic aperture imaging (SAI) can provide more uniform lateral resolution and reduce shadowing artifacts compared to B-mode imaging. However SAI suffers from a low signal-to-noise ratio (SNR). Hadamard matrix encoded transmission was designed to increase the SNR (Chiao, R.Y. 1997, IEEE, IUS). However, this approach requires driving some array elements with a positive pulse and other elements with the inverted pulse at the same time. This cannot be implemented in most commercial ultrasonic scanners. Therefore, we propose modified Hadamard synthetic aperture imaging (MH-SAI) to increase the SNR which does not require pulse inversion. In this approach, the number of receiving channels can be reduced to lower the system cost without significantly compromising the image quality.

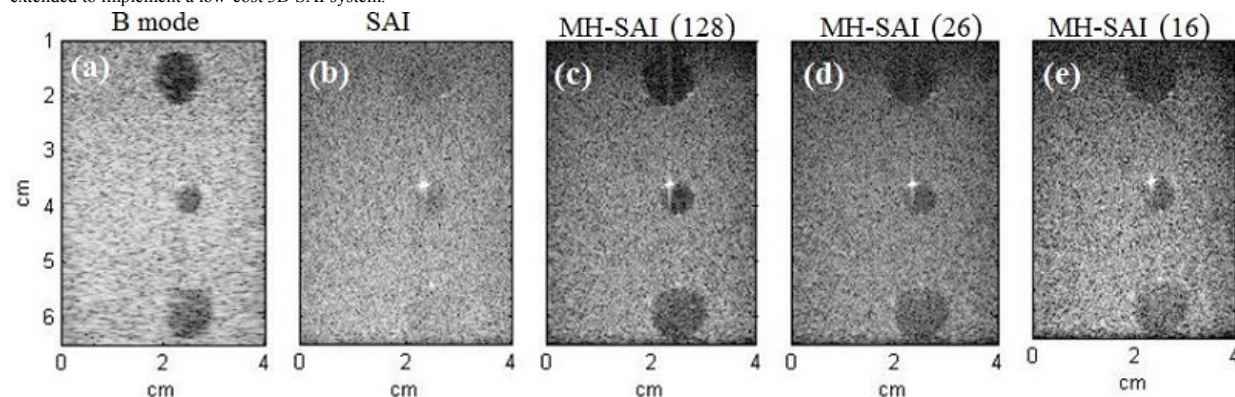
### Statement of Contribution/Methods

In MH-SAI, all the transmission elements in one transmission were grouped into two categories based on the Hadamard encoded transmission design: the elements (group P) driven by positive pulses and the elements (group N) driven by negative/inverted pulses. We first excited group P elements and acquired the signal  $S_{ij}^p$  (the radiofrequency (RF) signal from the  $j^{\text{th}}$  receiver in the  $i^{\text{th}}$  transmission event); then we excited group N elements with the same pulse and acquired the signal  $S_{ij}^n$ . Lastly the RF signal in the Hadamard-encoded transmission was obtained by  $(S_{ij}^p - S_{ij}^n)$ . After decoding, ultrasound images were obtained using the standard image reconstruction method in SAI.

The experimental RF data were acquired using a 128-element 4-cm-wide 5 MHz linear array (L14-5) and a SonixDaq (Ultrasonix, CA) acquisition system. B-mode, standard SAI and MH-SAI images were acquired from a phantom containing three hypo-echoic inclusions. In the MH-SAI image reconstruction, we used 128, 26, and 16 receiving channels emulating a sparse receiving array.

### Results/Discussion

Fig. 1 shows the log envelope images of B mode (a), standard SAI (b), and MH-SAI with 128 (c), 26 (d) and 16 (e) receiving channels. In MH-SAI, both the spatial resolution and the SNR were improved compared with B-mode and standard SAI. High image quality was retained in MH-SAI with sparse receiving channels. MH-SAI can potentially be extended to implement a low-cost 3D SAI system.



P1A6-2

## GPU Acceleration of Acoustic Radiation Force Impulse Imaging System using Scanning-mode

Congzhi Wang<sup>1</sup>, Bo Zeng<sup>1</sup>, Yang Xiao<sup>1</sup>, Weibao Qiu<sup>1</sup>, Hairong Zheng<sup>1</sup>; <sup>1</sup>Shenzhen Institutes of Advanced Technology, Chinese Academy of Sciences, Shenzhen, Guangdong, China, People's Republic of

### Background, Motivation and Objective

Acoustic radiation force impulse (ARFI) system has a more simple hardware architecture than the supersonic shear-wave imaging (SSI) system, which make it easier to be miniaturized for some special clinical practice, such as the emergency treatments in the field first-aid and the donor evaluation for organ transplantation. However, currently ARFI cannot provide 2D stiffness images like SSI can do. To fit this gap, the time-consuming algorithms of ARFI are to be migrated to the graphics processing unit (GPU) for substantial acceleration in this study.

### Statement of Contribution/Methods

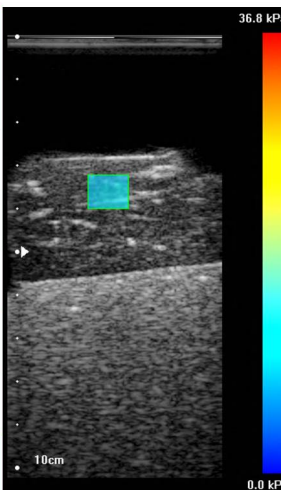
The whole algorithm of ARFI were modified and improved to fit for the parallel computation on GPU: an analytic signal based cross-correlation method was used to assess the tissue displacements, a cyclic reduction (CR) method was used to calculate the cubic spline interpolation, and a time-of-flight (TOF) method based on Radon transformation was used to determine the shear wave velocity. The ratio of the time consumptions of the programs running on CPU and on GPU was calculated using the practical data collected by our self-developed ARFI system. And the system was then tested on the ex vivo pork liver tissue sample.

**Results/Discussion**

Figure 1 (left) shows the execution time of the two programs running on CPU and GPU, dealing with one same data set of 4 tracking locations, 100 frames per location, and 512 data points per frame. For the most time-consuming parts such as cross-correlation, filtering, Radon transformation and cubic spline interpolation, large acceleration ratio has been confirmed between the two programs. The total time listed in the table also includes some additional time consumption when connecting the multi-algorithms, thus it is a little larger than the sum of the above steps. And a quasi-real-time scanning-mode 2D ARFI (s2D-ARFI) imaging system was implemented by the help of GPU acceleration. For a ROI constructed by 100 measurement plots (10x10) and 20mm\*15mm size, the total imaging time including signal processing and displaying is about 25 to 30 seconds. Figure 1 (right) shows an image obtained on the pork liver tissue sample. Although the imaging speed of our s2D-ARFI system is still much slower than SSL, our system can provide an additional choice for quantitatively imaging the tissue stiffness and for further miniaturization.

**Execution time comparison between CPU and GPU****Scanning ARFI image on pork liver (6x4)**

Algorithm steps	Results	Execution Time on CPU (ms)	Execution Time on GPU (ms)	Acceleration ratio
Data transfer		0	14.0	N/A
Cross-correlation		2120.0	50.0	42.4
Filtering		1036.0	4.0	259.0
Radon transformation		1550.0	13.2	117.4
Cubic spline interpolation		1055.0	0.6	1758.3
Total time		5763.0	82.2	70.1


**P1A6-3****Fast Minimum Variance Beamformer for Broad View Ultrasound Imaging Paradigms: A Multi-GPU Approach**

Billy Y. S. Yiu<sup>1</sup>, Alfred C. H. Yu<sup>1</sup>; <sup>1</sup>Medical Engineering Program, The University of Hong Kong, Pokfulam, Hong Kong

**Background, Motivation and Objective**

Broad view imaging methods (e.g. point source emissions, plane wave firings) have recently emerged as new ultrasound imaging paradigms with high frame rate potential. However, because these methods use unfocused transmissions, the resulting image quality is inferior to that of conventional line-based imaging. To circumvent this issue, one can adaptively define the apodization weights during beamforming (done on a pixel-by-pixel basis for each channel-domain data frame) using the minimum variance (MV) method. Such a solution has shown theoretical merit, but its computational cost is inevitably high. In this work, our objective is to design a new high-speed, pixel-based MV beamforming framework for broad view imaging paradigms so as to form entire frames of high resolution images (HRIs) at real-time throughputs.

**Statement of Contribution/Methods**

Our framework makes use of an array of graphics processing units (GPUs) together with parallel computing algorithms. Its general design rule is that each block of computing threads is allocated to perform MV beamforming for one pixel, and multiple thread blocks are executed concurrently to parallelize the operation for different pixels. The real-time feasibility of our framework was demonstrated on a platform equipped with three GTX-590 dual-GPU devices (3,072 computing cores in total). It was used to form HRIs with raw imaging data acquired from a swine eye based on virtual point source emissions (32-element aperture, F-number of -1). Data acquisition was carried out using an L40-8 array and a SonixTouch scanner equipped with SonixDAQ pre-beamformed data sampler (12 MHz freq, 1-cycle pulse, 80 MHz DAQ rate). HRI processing throughput of different aperture sizes was measured by counting the number of HRIs that can be generated over 30 s of operation; process timing was also measured at a per-HRI level. A bivariate benefit analysis was also conducted to form integrative insight between computational performance and image quality gains.

**Results/Discussion**

Our multi-GPU MV beamformer can enhance the quality of HRIs formed using broad view imaging paradigms while satisfying real-time computing constraints. In imaging the swine eye, our framework was able to form in real-time MV-apodized HRIs with: (i) sharper contrast between echogenic and echolucent regions (comparing to classical beamline-based images and HRIs with fixed apodization); (ii) frame sizes with at least  $\lambda/2$  pixel spacing (200x240). In a corneal wound imaging example, both HRI contrast improvement (10.8 dB with respect to HRIs formed with fixed apodization) and real-time computing benefit (>20 fps) may be realized by our GPU-based MV beamformer. These findings show that, using multi-GPU MV beamforming, real-time realization of image quality enhancement can be achieved in broad view imaging.

**P1A6-4****Rapid Prototyping of Real-Time FPGA Beamformers for Synthetic Aperture Imaging Based on High Level Synthesis**

Joao Amaro<sup>1</sup>, Billy Y. S. Yiu<sup>2</sup>, Gabriel Falcão<sup>1</sup>, Marco Gomes<sup>1</sup>, Alfred C. H. Yu<sup>2</sup>; <sup>1</sup>Instituto de Telecomunicacoes, The University of Coimbra, Coimbra, Portugal, <sup>2</sup>Medical Engineering Program, The University of Hong Kong, Pokfulam, Hong Kong

**Background, Motivation and Objective**

As compared to graphics processing units (GPUs), field programmable gate arrays (FPGAs) offer inherent advantage in hardware reconfigurability and low-power consumption budgets. Thus, they can potentially be leveraged to design power-efficient high-speed processing blocks for ultrasound imaging systems. However, to efficiently allocate FPGA computing resources while achieving acceptable run-time performance, extensive hardware design space exploration is required, and this step is labor demanding and is often beyond the technical expertise of academic researchers in ultrasound imaging. In this work, we aim to overcome such a barrier through establishing a new FPGA design framework to facilitate rapid prototyping of advanced ultrasound imaging methods. As a proof of concept, we focused on devising high-speed FPGA beamformer kernels for synthetic aperture (SA) imaging applications.



## Statement of Contribution/Methods

Our solution is founded upon the use of OpenCL-based high level synthesis tools as the design environment, and the Stratix-V FPGA device was used as the computing engine for high-speed SA beamforming and image formation. In this work, OpenCL code kernels were first developed to stage-wise handle the steps of analytic signal conversion, two-way focusing delay calculation, channel-domain data summation, and image compounding to derive high resolution image frames; the processing was done on a pixel by pixel basis. These developed code kernels were then compiled using the Altera SDK high level synthesis tool, and the hardware instructions were sent to the FPGA device. Architectural configurations with different number of compute units (1 or 2), single-instruction multiple-data vector engine widths (1 to 4), and for-loop unroll factors (1 to 32) were evaluated to identify which parallel architectures were more run-time efficient. The tuned FPGA beamformer was then used to compute SA image frames from raw data (i.e. frames of RF channel-domain data obtained from point source firings) acquired from a phantom with an echolucent tube embedded within echogenic tissue, and the resulting processing throughput was measured. For comparison, the same OpenCL code kernel was implemented on an AMD R9 280X GPU. Power consumption measurements were taken on the two beamforming platforms to compare their power efficiency.

## Results/Discussion

For 128-channel raw data sampled at 40 MHz (12 bits), our FPGA beamformer can achieve 38 fps processing throughput at 20 W power consumption (i.e. 1.89 fps/W power efficiency). This is significantly more efficient than the GPU version (0.95 fps/W efficiency). The FPGA beamformer's fabric utilization was ~80% in the most power-efficient design space configuration. These results show that FPGAs, when defined using high level synthesis tools, can be used to develop power-efficient beamformers for SA ultrasound imaging.

## P1A6-5

### Compact Hardware for Real-Time Multi-Line Beamforming

Valentino Meacci<sup>1</sup>, Luca Bassi<sup>1</sup>, **Stefano Ricci<sup>1</sup>**, Enrico Boni<sup>1</sup>, Piero Tortoli<sup>1</sup>, <sup>1</sup>Information Engineering, University of Florence, Firenze, FI, Italy

## Background, Motivation and Objective

Parallel beamforming is increasingly used, since it can deliver imaging frame rates (IFRs) higher than those achievable with standard approaches. Their full implementation (i.e. plane wave imaging) can produce IFRs of several kHz, but real-time operation is hampered by hardware complexity. Powerful GPUs or multiple state-of-the-art FPGAs are typically employed. In direct FPGA implementations, the channel-data are acquired at 50-80 Msps and beamformed at the same rate. Every Pulse Repetition Interval (PRI) N parallel beamformers (BFs) are needed to produce N lines.

In this work, a simple and compact architecture for real-time multi-line beamforming is proposed. A single BF implemented in FPGA works at the maximum frequency,  $F_p$ , permitted by the device, to serially process the same raw channel-data N times during the same PRI.

## Statement of Contribution/Methods

Following the transmission of a defocused beam, M echo samples received by each active element are stored in a FPGA memory buffer. This phase takes  $2D/c$  seconds, i.e. the time needed to the sound to travel, at velocity c, to the maximum depth D and back. Then, N lines are beamformed from the stored data by serializing the operations on the same BF. This operation takes  $N \cdot M / F_p$ . N lines are thus beamformed in the time interval of length  $T_b = 2D/c + N \cdot M / F_p$ .

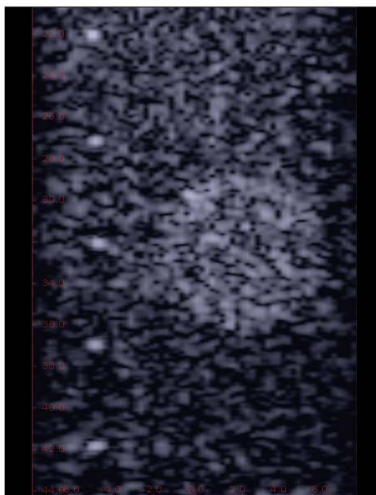
The method was implemented on the Stratix-2 (ALTERA) FPGAs on board the ULAOP research system with  $M = 2048$ ,  $F_p = 200$  Msps,  $D = 50$  mm,  $N = 64$ . Experimental test was made by generating a 64-line image of a B-mode phantom.

## Results/Discussion

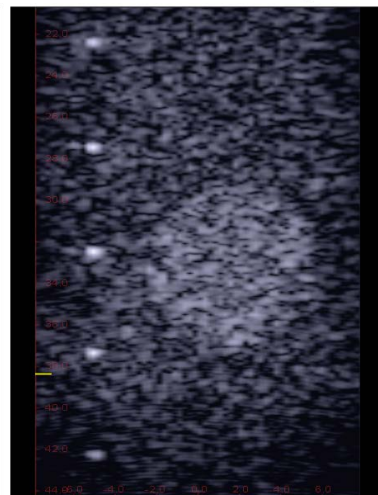
The image reported on the left is obtained by the proposed method at  $IFR = 1200$  Hz. The rate is slightly lower than  $1/T_b$ , due to the unavoidable latencies of the electronics. For comparison, the corresponding image, based on the standard method, is reported on the right. It is obtained at  $IFR = 220$  Hz. As expected, the transmission of defocused beams without compounding, determines lower intensity and contrast.

The proposed method, although does not reach the 64-fold gain on IFR of the full parallel beamformer, allows a 5-fold gain on a Stratix-2 with no hardware complication. A last-generation FPGA, which runs, e.g. at  $F_p = 400$  Msps will generate an 11-fold gain. The proposed method is not limited to B-mode imaging, but can be beneficial in several applications, like, e.g., Color Doppler, where IFR is heavily limited by the multiple transmissions needed.

Real-Time Parallel Beamforming



Conventional Beamforming



P1A6-6

### Design of a Reconfigurable Phase Controller for Focused Ultrasound Therapeutic Device

Minkyung Kim<sup>1</sup>, Hi Yuen Song<sup>1</sup>, Yanghun Lee<sup>2</sup>, Mingyu Cho<sup>2</sup>, Inn-yeal Oh<sup>1</sup>, Chul Soon Park<sup>1</sup>; <sup>1</sup>Department of Electrical Engineering, Korea Advanced Institute of Science and Technology, Daejeon, Korea, Republic of; <sup>2</sup>Samsung Electronics Co., Yongin-si, Gyeonggi-do, Korea, Republic of

#### Background, Motivation and Objective

Non-invasive therapeutic applications with focused ultrasound have allowed the reduction in a risk which causes infection, bleeding and pain. Because the medical devices can transmit acoustic energy to only a specific focal area of biological tissues where constructive interference of ultrasonic waves is generated. The focal point can be changed by applying different time shift (or phase shift) on each element of transducer array depending on a purpose of treatment. Although microprocessor is used for the beamforming technique by generating time delayed signal with high resolution, it has limitations in terms of cost, size, and difficulty to implement as a fully integrated chip. In this study, a reconfigurable phase controller for focused ultrasound therapeutic device is implemented in 0.18  $\mu\text{m}$  CMOS technology.

#### Statement of Contribution/Methods

The proposed phase controller, which varies from  $0^\circ$  to  $360^\circ$  in steps of  $11.25^\circ$ , consists of four parts: a flash-ADC, a resistor-capacitor bank phase shifter, a variable gain amplifier (VGA), and a  $0^\circ/180^\circ$  phase shifter. The flash-ADC with resistor string generates 4-bit control signals depending on the input signal, which control operation of active switches in overall system. The resistor-capacitor bank determines discrete phase shift in the range of  $0^\circ$  to  $180^\circ$ . The VGA amplifies the signal using the variation of the value of feedback resistor to compensate signal degradation caused by RC networks. The  $0^\circ/180^\circ$  phase shifter provides inverting and non-inverting signal paths to cover full range of  $0^\circ$  to  $360^\circ$ .

#### Results/Discussion

Fig. 1 shows the photograph of a fabricated phase controller. The measured and simulated relative phase characteristics are presented in fig. 2. Every 90 mV increase in input voltage makes phase of signal to be changed in intervals of  $11.25^\circ$ . The adaptive phase shifts are selected in this manner and applied to each element of transducer. As a result, ultrasound energy can be concentrated at different focal points as illustrated in fig. 3. Therefore, proposed design with full range of phase shift can be achieved as an active phase controller which has reconfigurable focal depth and is fully integrated in a very small chip with the size of  $1.11 \times 1.993 \text{ mm}^2$ .

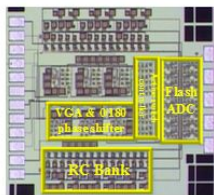


Fig. 1. Photograph of the fabricate chip

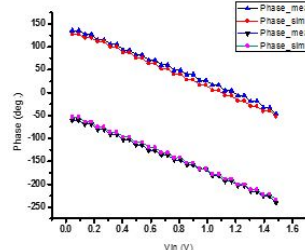


Fig. 2. Comparison of the phase characteristics between simulation and measurement

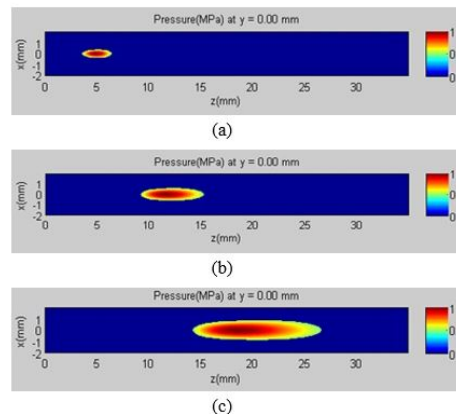


Fig. 3. Normalized acoustic pressure focused at 3 different focal points from the transducer surface: (a) 5mm, (b) 12mm, (c) 20mm

P1A6-7

### High Frame Rate, High Resolution 3D Plane Wave Imaging

Ming Yang<sup>1</sup>, Richard Sampson<sup>2</sup>, Siyuan Wei<sup>1</sup>, Thomas Wenisch<sup>2</sup>, Brian Fowlkes<sup>3</sup>, Oliver Kripfgans<sup>3</sup>, Chaitali Chakrabarti<sup>1</sup>; <sup>1</sup>School of Electrical, Computer and Energy Engineering, Arizona State University, Tempe, Arizona, USA; <sup>2</sup>Department of Electrical Engineering and Computer Science, University of Michigan, Ann Arbor, Michigan, USA; <sup>3</sup>Department of Radiology, University of Michigan, Ann Arbor, Michigan, USA

#### Background, Motivation and Objective

High-frame-rate 3D ultrasound imaging enables many new applications that were previously impossible, such as 3D vector flow imaging and 3D sonoelastography. Plane-wave imaging has the potential to achieve the very high frame rates required for these applications, but suffers from poor lateral resolution and low SNR. In this work, we explore high-frame-rate imaging in the context of the Sonic Millip3De [2] beamforming hardware architecture. Our objective is to improve plane-wave image quality at 2kHz frame rates while remaining within the tight computational and power budget constraints of the Sonic Millip3De platform.

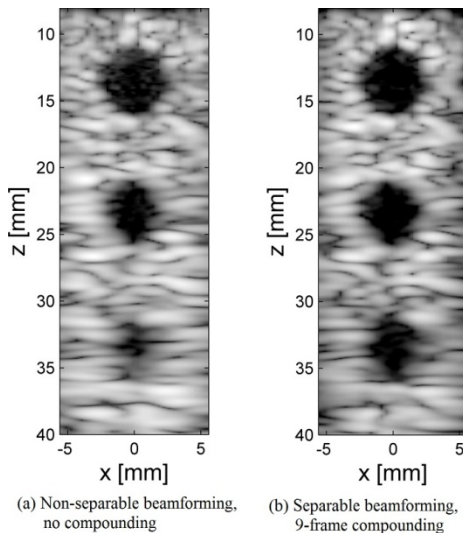
#### Statement of Contribution/Methods

We propose a plane-wave imaging approach that applies coherent image compounding [1] to greatly improve lateral resolution and SNR. We offset the increased computation requirement of compounding by applying separable beamforming to reduce computational complexity. Separable beamforming reduces complexity by decomposing 2D array beamforming into two stages of 1D beamforming. At the heart of this method is a delay decomposition procedure which minimizes RMS phase errors. Separable beamforming achieves 10-20x reduction in computation, creating headroom to compound images over 9 transmits. The resulting system has better image quality and comparable computation throughput requirements as the baseline (non-separable, non-compounded) plane wave system. We describe hardware modifications to the Sonic Millip3De accelerator to facilitate the approach, including additional SRAM arrays and a configurable interconnect to support on-chip compounding and separable beamforming.

#### Results/Discussion

We present image quality analysis using Field II simulations of three 6mm anechoic cysts at depths from 1.3cm to 3.3cm. Compounding helps improve the CNR values of three cysts from 2.6, 1.6, 1.0 to 2.9, 1.9, 1.2, respectively. It also helps improve the SNR by 10dB, relative to the baseline system. Additionally we provide computation complexity analysis to show that our method requires similar compute throughput as the baseline system.

[1] G. Montaldo, M. Tanter, et al. "Coherent plane-wave compounding for very high frame rate ultrasonography and transient elastography," IEEE Transactions on Ultrasonics, Ferroelectrics and Frequency Control, vol.56, no.3, pp.489-506, March 2009



P1A6-8

### A Real-time Streaming DAQ for Ultrasonix Research Scanner

Mateusz Walczak<sup>1</sup>, Marcin Lewandowski<sup>1</sup>, Norbert Zolek<sup>1</sup>; <sup>1</sup>Ultrasonix Department, Institute of Fundamental Technological Research PAS, Warsaw, Poland

#### Background, Motivation and Objective

Access to the raw RF ultrasound signals is required for implementation and testing of the new ultrasound processing methods. A few commercial ultrasound scanners are available with research capabilities. One of them is Ultrasonix SonixTouch (Ultrasonix, Canada) system with SonixDAQ parallel acquisition module providing 128 channels of pre-beamformed data. The SonixDAQ can acquire and store up to 16GB of raw RF data, which can be transferred via USB 2.0 to the PC for further processing. A limited USB data transfer bandwidth prevents implementation of any real-time processing algorithms. Our motivation was an application of a high-speed PCIe interface for real-time streaming and processing of RF data.

#### Statement of Contribution/Methods

RX-DAQ is a 128-channel ultrasound acquisition system designed as an add-on to the Ultrasonix scanner that allows to acquire raw channel data and simultaneously transfer them to the PC in real-time for processing. The RX-DAQ was built on two RX64 acquisition cards and a backplane card. The RX64 card is based on the FPGA Altera Stratix IV, two 2-4GB DDR3 memory modules, and two 32-channel acquisition modules (CSM9132, Cephasonics, USA). Internal RX64 memory buffers and a high-speed PCIe 2.0 x8 interface support real-time streaming of RF data to the CPU memory. Data streaming from the module is performed by the DMA (Direct Memory Access) resulting in high throughput and low CPU load. The backplane card contains a connector (ITT Cannon DL1-156PW), which enables the RX-DAQ to be connected directly to the Ultrasonix scanner (in place of SonixDAQ). A PCIe switch (PLX8632) aggregates two RX64's PCIe 2.0 x8 interfaces into one x16 interface and connects the RX-DAQ to the PC via a PCIe cable. The total bandwidth capacity of that interface is about 6GB/s, which allows for a real-time transfer of the 128 channel data.

#### Results/Discussion

We developed a new 128-channel RF parallel acquisition system, compatible with the Ultrasonix SonixTouch Research scanner, enabling real-time streaming and processing of pre-beamformed data. A demo application implementing Plane Wave Imaging was developed using the Ultrasonix's TEXO API for transmission and RX-DAQ API for acquisition and processing. The reconstruction algorithm was run on the GPU (CUDA/OpenCL), showing the full potential of the system. The RX-DAQ greatly extends the research capabilities of the Ultrasonix Research scanner, especially for emerging applications, such as: synthetic aperture imaging, vector Doppler or elastography.

P1A6-9

### Model-driven Engineering Applied to the Development of Embedded Software for B-mode Ultrasound Imaging Systems - A Case Study

Haroldo J. Onisto<sup>1</sup>, Tiago M. Machado<sup>1</sup>, Ramon C. Fernandes<sup>1</sup>, Johannes D. Medeiros Jr.<sup>1</sup>, Iliezer Tamagno<sup>1</sup>, Tiago C. Dezotti<sup>1</sup>, Jose E. Bertuzzo<sup>1</sup>; <sup>1</sup>Services & Hardware Engineering (DHS), Eldorado Research Institute (ELDORADO), Campinas, São Paulo, Brazil

#### Background, Motivation and Objective

Nowadays, to satisfy the market's desire to produce embedded devices in less time and with different features added to the final product, companies must improve their software development practices in order to become more competitive. Traditional methodologies usually suffer from several limitations: high cost projects, limited architectures, lack of systematic code reuse, among others.

Critical aspects in the design of ultrasound (US) devices are the efficiency of algorithms for beamforming (BF) as well as image and signal processing to get B-mode images, where there are sampling, A-lines and arrays processing, which require intense computational power. Moreover, other difficulties are security reliability and performance constraints imposed by embedded systems, which also involve state machines versus continuous processing complexities and time scales from nano to milliseconds.

In this paper, we present a success case in handling the complexities of this ecosystem. We applied a Model-driven Engineering (MDE) approach in the development project of an Ultrasound Modular Platform for medical research through a consortium of top Brazilian universities led by the University of Campinas in partnership with Eldorado Research Institute, a top Brazilian center in IT and innovation engineering and main developer of this solution.

#### Statement of Contribution/Methods

Our firmware architecture (FA) was designed treating the US problem as a data-flow machine, through which the data undergoes transformation and processing. The MDE aims to raise the level of abstraction and automation to software development.

Hence we segment the FA in three abstraction layers. The lower one denotes the reprogrammable hardware itself as FPGA and DSP. On the middle layer, handwritten codes deal with the communication interface between devices, synchronism signals and I/O requirements to automatically receive generated codes. Finally, the top layer comprises the algorithms for BF, signal and image processing in its highest abstraction via MATLAB®, covering stages from requirement analysis through functional modeling up to automatic generation of Verilog®/VHDL and C/C++ codes.

#### Results/Discussion

The benefits achieved are risk and cost reduction and increased reliability. Early system analysis and model assumption validation reduce risks. After modeling, we adjust and test it for compatibility towards hardware restrictions, adding reliability and only then integrate the codes generated within the hardware. This simple development cycle is cost-effective as it accelerates proofs of concept and increases engineer productivity.

Discussions and initial results of the MDE application are presented through qualitative images both from Field-II and a dataset taken from an Ultrasonix™ device in addition to those generated by our real-time processing platform. We also discuss the use of general timing and the logical programmable resources used.

#### P1A6-10

##### A new powerful system to test ultrasonograph quality

Ladislav Doležal<sup>1</sup>, Jaromír Vachutka<sup>1</sup>, Jiri Mazura<sup>1</sup>; <sup>1</sup>Faculty of Medicine and Dentistry, Palacký University in Olomouc, Olomouc, Czech Republic

#### Background, Motivation and Objective

It is well-known that the use of sonography has increased markedly in the last 50 years. The equipment produced or refurbished must be checked for imaging quality before their expedition. Manufacturers use sophisticated electronic measuring methods to evaluate transmitted/received signals and their digital processing. The imaging quality is checked by use of well-defined test objects, but the methods mostly aren't objective or very accurate. A measurement system to evaluate a comprehensive group of qualitative parameters with high accuracy for the whole imaging system quality assessment using one measuring process only is needed.

A Point Spread Function (PSF) analysis is used to evaluate imaging quality in optics. The IEC 61391-1 standard lists the PSF method as suitable for sonographic imaging quality evaluation. But the method is not used in practice yet.

#### Statement of Contribution/Methods

We designed and tested a PSF tester which measures and numerically expresses 9 important qualitative parameters with good reproducibility in any specified region of the imaged area by one measuring process. The parameters are: received signal amplitude uniformity, lateral resolution (LR), transverse resolution (TR), axial resolution (AR), transverse scan slice profile of the scanned plane, number and position of the foci of the dynamic focussing in the both lateral and transverse planes, ultrasound scan line density and distribution in the scan plane, Time Gain Compensation (TGC) profile in the scan plane, sonogram geometric accuracy. The system will be commercially available soon.

The PSF tester consists of a measuring tank, target positioning system and personal computer, which controls the spherical target position and analyses the data. The measured sonograph scans the spherical target positioned in a measuring tank. An output video signal is analysed by original software. The pixel grey scale distribution in the scanned area is evaluated to obtain the PSF amplitude profile for each point of a specified measuring grid. The PSF Full Width in Half of Maximum (FWHM) value is a key to derive most of the measured parameters. The measurement results are stored as matrix of values for further elaboration and 3D graph results are displayed.

The results were analysed for accuracy and uncertainty and received very good results; e.g. uncertainty of FWHM was 2.18% in lateral and 0.57% in axial direction.

#### Results/Discussion

The method delivers high number of accurate qualitative parameters by use of only one fully automatic measuring process. The results interpretation is performed by our original software. The only disadvantage of the process is time needed for data acquisition from measured area. The time depends on number of measured points (the target positions) and frame rate of the sonograph.

The details of measurement method, samples of results, the uncertainty analysis conclusions and proposals of practice applications will be discussed in our contribution.

#### P1A6-11

##### A Real-time Realization of an Automatic Dynamic Range Adjustment Method on a Smart Mobile Device for Point-of-Care Ultrasound Imaging

Jeeho Kim<sup>1</sup>, Yeonhwa Lee<sup>1</sup>, Yangmo Yoo<sup>1,2</sup>; <sup>1</sup>Electronic Engineering, Sogang University, Seoul, Korea, Republic of, <sup>2</sup>Interdisciplinary Program of Integrated Biotechnology, Sogang University, Korea, Republic of

#### Background, Motivation and Objective

In medical ultrasound imaging, dynamic range (DR) is one of the most essential parameters that affect image quality and feature representation. Previously, the automatic DR adjustment (ADRA) method, in which DR value is adaptively adjusts based on the analysis of reference and input image, was proposed for improved clinical productivity and lowered user dependency. In this paper, the feasibility of a real-time ADRA method running on a smart mobile device with high-performance mobile central processing units (CPUs) and graphics processing units (GPUs) is demonstrated for point-of-care ultrasound imaging where automation of user control is critical.

#### Statement of Contribution/Methods

For real-time realization of the ADRA method on a high-end smartphone (i.e., Galaxy S4, Samsung Electronics Inc., Seoul, Korea), the OpenGL ES cross-platform graphics application processing interface (API) was used. As shown in Fig. 1(a), to accelerate the performance of the mobile GPU embedded in the mobile device, ultrasound core mid and back-end processing tasks, including ADRA, are divided into multiple software pipelines and the load operation for accessing the frame buffer by the mobile CPU is minimized. 200 frames of *in vivo* abdominal data were acquired with a 3.5-MHz convex array transducer from with a commercial ultrasound scanner equipped with a research package (Accuvix V10, Samsung Medison, Seoul, Korea).

#### Results/Discussion

The performance of the real-time ADRA method on the smart phone was evaluated by measuring the contrast-to-noise ratio (CNR) and frame rates. As shown in Fig. 1(b), the ADRA method showed the improved image quality compared to the conventional method (CON) with a fixed 60-dB DR value. The CNR values of the CON and ADRA methods were  $3.35 \pm 0.89$  vs.  $3.89 \pm 0.71$ , respectively. In addition, the frame rates of the CON and ADRA methods were  $74.12 \pm 24.7$  Hz vs.  $60.51 \pm 11.51$  Hz, respectively. These results indicate that the ADRA method can be incorporated in the smartphone-based point-of-care ultrasound imaging system while providing enhanced image quality and lowered user dependency.

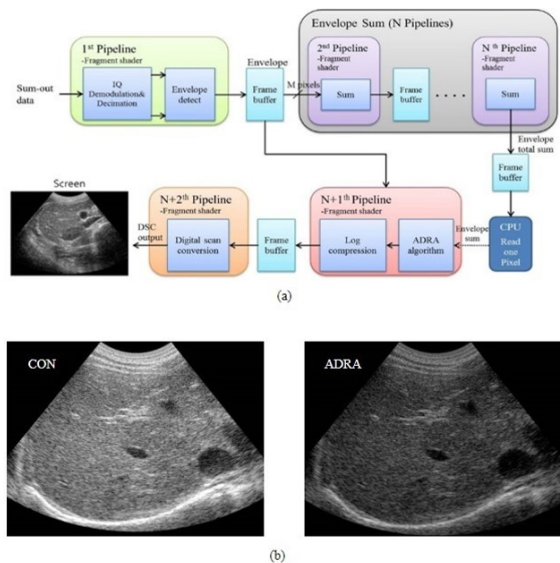


**Figure 1** (a) Block diagram of the implementation of the ADRA method on a smart phone and (b) reconstructed B-mode images with the CON and ADRA methods.

P1A6-12

#### Design of a multiple-rail high-voltage power supply for ultrasound scanners

Enrico Boni<sup>1</sup>, Luca Bassi<sup>1</sup>, Monica Scaringella<sup>1</sup>, Alessandro Ramalli<sup>1</sup>, Piero Tortoli<sup>1</sup>; <sup>1</sup>Dipartimento di Ingegneria dell'Informazione, Università di Firenze, Firenze, Italy

#### Background, Motivation and Objective

Standard ultrasound modes, as implemented in commercial equipment, require to transmit high voltage (HV) signals having amplitudes up to 150 Vpp. HV power supplies typically employ switching circuits that may generate undesired electromagnetic interferences. Further challenging requirements on the power supply circuits are imposed by novel experimental methods that may require programmable amplitudes for consecutive pulse repetition intervals (PRIs). This work presents a 4-rail 200Vpp power supply board for ultrasound systems, able to switch the voltage supply in consecutive PRIs according to a programmable sequence. Multiple control strategies are identified to reduce the switching noise contributions.

#### Statement of Contribution/Methods

The power board was designed to generate, from a 12V DC input, 2 positive and 2 negative HV rails up to 100V and -100V, respectively. Each conversion rail is composed of 8 step-up cells for the positive values, and 8 inverting cells for the negative values. The 4 HV rails can be programmed and monitored either by an UART channel linked to a PC, or by a 1.25Gbit/s LVDS link to the general manager system board. An FPGA (Altera Cyclone IV GX) generates the control signals for each cell and senses the related output voltages and currents to perform a closed loop control system. The flexibility of the FPGA firmware allows the implementation of multiple control strategies in order to achieve a fast voltage rail set-up and to reduce the electromagnetic noise impact on the quality of acquired echo data.

#### Results/Discussion

The board has been realized on a 10x22 cm 10-layer PCB. The tests conducted on the board confirm the ability to generate HVs up to -100V and +100V. A maximum peak current of 10A can be reached to charge the output 400uF capacitance, thus resulting in a peak charging power of 1 kW. The availability of four voltage rails allows switching among the HV amplitudes for each PRI according to a programmable sequence, making the board able to supply the new generation of 5-level pulsers. In typical applications the drop-down of the voltage values (few mV) is recovered in only a few  $\mu$ s. In particular applications where two independent couples of HV values are not sufficient, the rail voltages can be modified at 25V/ms rate.

Three control strategies have been implemented to reduce the effects of the regulator switching noise. The regulation of voltage rails can be suspended during the receiving phase, if sufficient time (typically few  $\mu$ s) to restore the value of the voltage rails is available before the next transmission. The second strategy synchronizes the regulator switching signals with both the PRI and the analog to digital conversion clock, while the third one uses a spread spectrum modulation. The results of measurements of the noise associated to each approach will be presented.

P1A6-13

#### A transcranial device and method for detecting cerebellar brain motion

Sheronica James<sup>1,2</sup>; <sup>1</sup>Department of Chemical and Biomedical Engineering, Cleveland State University, Cleveland, Ohio, USA, <sup>2</sup>Department of Biomedical Engineering, Cleveland Clinic, Lerner Research Institute, Cleveland, Ohio, USA

#### Background, Motivation and Objective

Chiari Type I Malformation is a condition in which the cerebellar tonsils, small lobes on the undersurface of each half of the cerebellum, protrude through the base of the skull and press against the spinal cord. Assessing the motion of these herniated structures and their effects on cerebrospinal fluid dynamics is of significant clinical interest, particularly since the condition has been implicated in the formation of serious secondary disorders affecting the brain and spinal cord, such as hydrocephalus and syringomyelia. While MRI studies have shown no statistically significant differences in tonsillar motion of Chiari Type I patients compared to healthy individuals, surgeons have reported rapid tonsil motion as observed by intraoperative sonography during decompression surgery. However, it remains unclear whether this discrepancy is due to limitations of the MRI technique or decompression facilitating increased movement. Therefore, we aim to test the hypothesis that localized movement of cerebellar tonsils can be assessed non-invasively in the intact skull using ultrasound. Here, an investigation into the use of a novel methodology for transkull imaging in assessing cerebellar tonsil motion is presented.



**Statement of Contribution/Methods**

Two transducers (1MHz, 0.5 inches in diameter) were placed rostrocaudally on the frontal and suboccipital surfaces of a water-filled ex vivo human skull. A sinusoidal pulse was transmitted into the specimen from one transducer, and recorded by the receiving transducer at the opposite surface. Starting at the edge of the foramen magnum, the transducers were rotated between 0° and 60°, with the axis of rotation normal to the sagittal plane of the skull specimen. A tissue phantom was also used to mimic the cerebellar tonsils. Attenuation through the skull and phantom was analyzed.

**Results/Discussion**

It is shown that at a transducer frequency of 1MHz, our through transmission ultrasonic technique allows for substantial energy transmission of up to 8.2%. No signal was observed at the same points in reflection mode. To our knowledge, this level of energy transmission has been achievable only through a very limited temporal acoustic window, which fails in up to 29% of patients in a general population. Results demonstrate the feasibility of using this type of transducer system for a non-invasive pre-surgical assessment of cerebellar tonsil motion without the need for an acoustic window.

# P1A7 - MPA: Light and Sound I

Salon C

Thursday, September 4, 2014, 8:00 am - 5:00 pm

Chair: **Jeffrey Bamber**  
Institute of Cancer Research, Sutton, UK

P1A7-1

## Imaging 3D Cell Culture Systems Using an Optical Resolution Photoacoustic Microscope

Ming-jian Sun<sup>1,2</sup>, Pai-Chi Li<sup>1</sup>, <sup>1</sup>National Taiwan University, Taiwan, <sup>2</sup>Harbin Institute of Technology, China, People's Republic of

### Background, Motivation and Objective

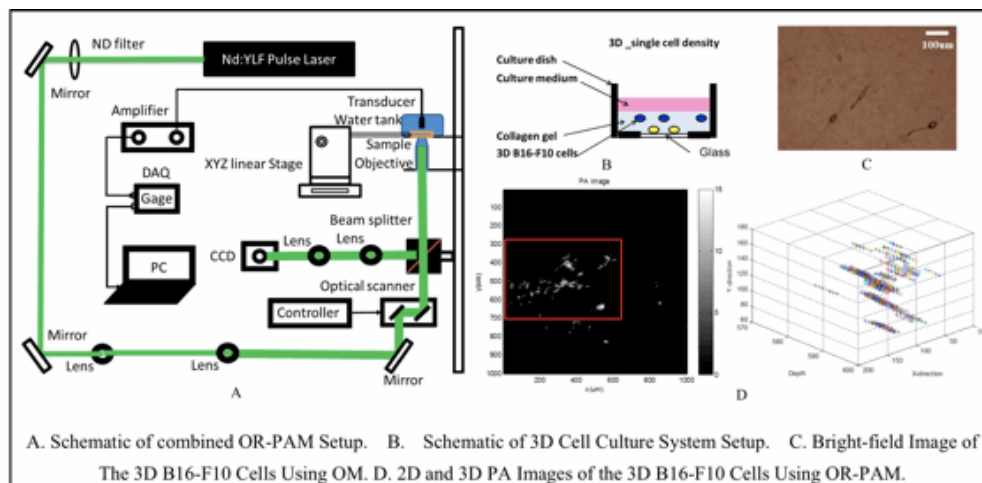
3D cell culture systems (3DCCS) have received wide attention as they provide more realistic anatomy and physiology for biomedical research compared to 2D cell culture systems (2DCCS). However, conventional microscopes used for 2DCCS are apparently not adequate for 3D observations and measurements. In this study, we develop an optical-resolution photo-acoustic microscope (OR-PAM) for 3DCCS, as it offers high spatial resolution with improved penetration (from 100 $\mu$ m to 4cm) without the need for depth scanning.

### Statement of Contribution/Methods

In this study, a combined laser-scanning OR-PAM with an optical microscope (OM) system was developed in transmission mode. Figure A shows a schematic diagram of the combined system. The laser beam is focused on the object by an air-conditioned optical objective and optically scanned with a 2D galvanometer scanner to form optical and photoacoustic images. B16-F10 murine melanoma cells were cultured and imaged (shown in Figure B). With 2D scanning and the depth-resolved detection, the system can provide 3D photoacoustic images.

### Results/Discussion

The proposed OR-PAM achieved a lateral resolution of 0.59 $\mu$ m with a penetration depth of 1mm. With a 3D melanoma cell culture system, optical image using OM in bright-field is shown in Fig. C, 2D/3D photoacoustic images using OR-PAM are shown in Fig. D. In the 2D photoacoustic image, the strongest photoacoustic signal corresponds to where the melanin particle density is greatest, the distribution of the melanin observed closely maps to the photoacoustic images. In the 3D photoacoustic image (Fig. D), the distribution of cells at different layers agrees well with the optical image. Under UV-exposure at different wavelengths, the 2D/3D images show different details corresponding to different absorptions. Thus, it is shown that the OR-PAM is suited for 3DCCS.



P1A7-2

## Image Optimization Method for Joints Photoacoustic Tomography

Jie Yuan<sup>1</sup>, Wenchao Li<sup>1</sup>, Xiaojun Liu<sup>1</sup>, Xueding Wang<sup>2</sup>, Paul Carson<sup>2</sup>, <sup>1</sup>Nanjing University, China, People's Republic of, <sup>2</sup>University of Michigan, USA

### Background, Motivation and Objective

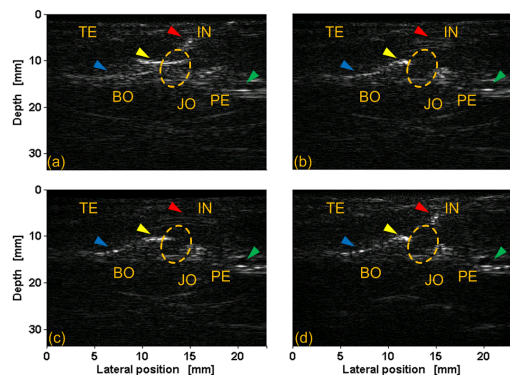
Arthritis and relevant disease are highly prevalent among adults and cause work disability as well as high health-care costs. Early diagnosis and optimized therapies of these disorders are hindered due to the lack of cost-efficient and powerful joint imaging technologies. Photoacoustic tomography (PAT) has emerged as a new biomedical imaging modality and thus attracts more attention among researchers. The distribution of speed of sound (SOS) in biomedical tissue and delay compensation (DC) have significant impact on the image quality of PAT. For a SOS heterogeneous tissue, it is very difficult to determine the accurate values of SOS and DC in the whole PAT reconstruction region. When imaging human peripheral joints, using fixed SOS and DC can only assure that the reconstructed images be focused at a limited depth range, whereas defocus at other depths, which cause severe artifacts and blurring.

**Statement of Contribution/Methods**

We propose a linear DC based reconstruction approach (LDC) to reconstruct the PAT image. By fitting complex relationship between DC and focal depth with a linear function, the whole region of interest (ROI) of PAT can be reconstructed in focus. When the parameters in our proposed LDC method is determined, the PA imaging time complexity of our proposed LDC approach is equivalent to that of traditional delay-and-sum back projection (DNSBP) algorithm.

**Results/Discussion**

Our approach applies fitted linear function to determine the DC along depth so that the whole ROI can be focused and the image quality can be dramatically enhanced. The reconstruction time of a 1024x512 PA image using LDC method only takes about 60 ms which matches the real-time reconstruction requirement of both current scientific research and future clinical try. Two *in vivo* experiments, including one human interphalangeal joint and one human metacarpophalangeal joint, indicate the good performance in optimizing the quality of the reconstructed photoacoustic image.



Reconstructed images of human interphalangeal joint using (a) DNSBP, DC=0.2us (b) DNSBP,

DC=-3.9us (c) DNSBP, DC = -6.1us (d) LDC, DC=-0.8677H+5.3491. TE:tendon, BO:bone, JO: joint,

PE:periosteum, IN:inner structure of tendon

**P1A7-3****In vivo Photoacoustic Oxygen Saturation Imaging Without the Need for Fluence Estimation**

Erwin J Alles<sup>1</sup>, Efthymia Papaevangelou<sup>1</sup>, Jeffrey C Bamber<sup>1</sup>; <sup>1</sup>The Joint Department of Physics and CRUK Cancer Imaging Centre, The Institute of Cancer Research and the Royal Marsden NHS Foundation Trust, London, United Kingdom

**Background, Motivation and Objective**

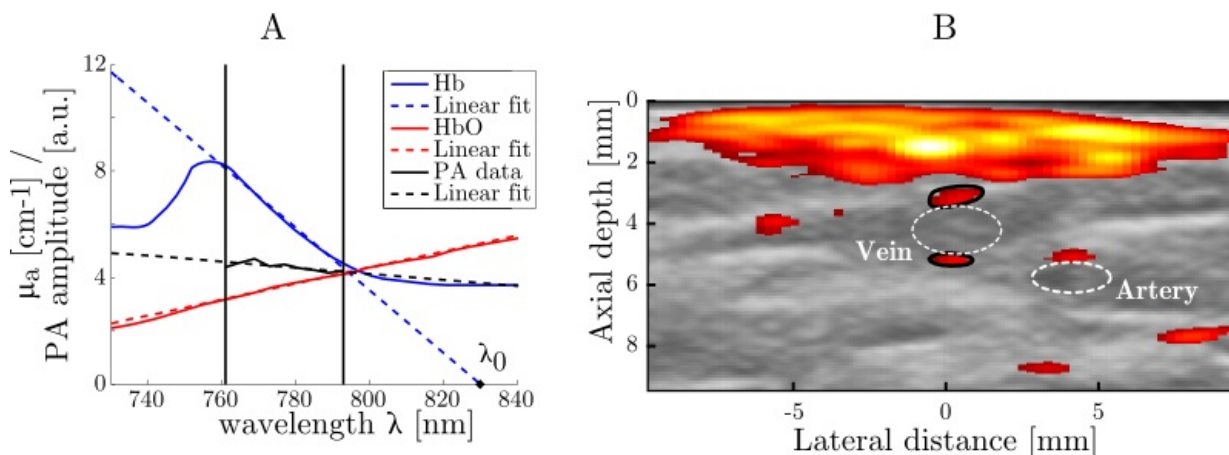
Exploiting the difference between the optical absorption spectra of oxyhaemoglobin (HbO) and deoxyhaemoglobin (Hb), spectroscopic photoacoustics (PA) can be used to image, in vivo and at depth, the blood oxygen saturation level. Current methods of retrieving the concentrations of HbO and Hb, which are then used to compute the oxygen saturation, involve estimating the light fluence at depth, using either models or inversion techniques, and are either potentially inaccurate or computationally expensive.

**Statement of Contribution/Methods**

Here, fluence estimation is circumvented by modelling the absorption spectra of HbO and Hb. If a suitable wavelength range is chosen (here  $761 \leq \lambda \leq 793$  nm), these spectra can to a very good approximation be described by linear functions (fig. A) which can be extrapolated to zero absorption. At the corresponding zero-crossing wavelength  $\lambda_0$ , no PA signal would be generated regardless of the fluence and chromophore concentration, and hence a fluence-insensitive parameter is obtained. Assuming HbO and Hb are the only chromophores present, and that the optical extinction is wavelength-independent, the oxygen saturation is computed from the zero-crossing wavelengths of the data and calibration spectra for HbO and Hb.

**Results/Discussion**

Using a scanner based on a clinical ultrasound scanner (Zonare ultra) and a tuneable pulsed laser, spectroscopic PA images were obtained from the second author's arm. The PA image obtained at a wavelength of 773 nm is shown, overlaid on the corresponding coregistered B-mode image, in fig. B. The average amplitude of the PA signal originating from the vein (evaluated in the regions delineated in black) was computed for each wavelength, and a linear fit of these data was extrapolated to yield a zero-crossing wavelength of 1166 nm. Using absorption spectra for HbO and Hb taken from literature, this was converted to an oxygen saturation of 70%. Similarly, for the artery an oxygen saturation of 97% was found. Both values agree with literature values. While wavelength-independent optical extinction is assumed, small deviations due to scattering and absorption can be corrected for by calibration, and the strong optical scattering in human tissue reduces the influence of local strong absorption. However, in its current form the method does not yield chromophore concentrations.



P1A7-4

### Monitoring and quantification of oxygen saturation in placenta by photoacoustic imaging during rat pregnancy

Chloe Arthuis<sup>1,2</sup>, Anthony Novell<sup>1</sup>, Florian Raes<sup>3</sup>, Stephanie Lerondel<sup>1</sup>, Alain Lepape<sup>3</sup>, Ayache Bouakaz<sup>1</sup>, Franck Perrotin<sup>1,2</sup>; <sup>1</sup>UMR Inserm U 930, University François Rabelais Tours, France, <sup>2</sup>Department of Obstetrics and Gynecology CHRU Tours, France, <sup>3</sup>CNRS – TAAM UPS44, Centre d'Imagerie du Petit Animal, Orleans, France

#### Background, Motivation and Objective

Intrauterine growth restriction complicate 10% of pregnancies and is often associated with impaired placental function and abnormal foetoplacental oxygenation. Recent developments in photoacoustic imaging offer the opportunity to perform non-invasive and real-time measurements of tissue oxygenation. The purpose of this work was to study the uteroplacental oxygenation during rat pregnancy by monitoring and quantifying the oxygen saturation ( $SO_2$ ) in different regions of the placenta.

#### Statement of Contribution/Methods

A total of 9 placentas from 5 rats (Sprague Dawley) were imaged using a LZ250D probe connected to the Vevo LAZR platform. On days 14, 17 and 20 of gestation, the hemoglobin  $SO_2$  was examined by photoacoustic imaging. Placentas were positioned at the optical focus between 10 and 15 mm. Parametric images from estimated  $SO_2$  were displayed by collecting the data at 750 nm and 850 nm. The oxygenation capacity of the placenta was evaluated by maintaining the rats under anesthesia with different oxygenation conditions during the experiment. For each measurement, rats were subjected during 3 min to 100%  $O_2$  inhalation, following by 4 min at 5%  $O_2$  inhalation and finally 4 min at 100%  $O_2$  inhalation to create hypoxia and hyperoxygenation states. Quantitative  $SO_2$  parameters were calculated in 4 regions of interest: skin, mesometrial triangle, placenta maternal face and placenta fetal face.

#### Results/Discussion

$SO_2$  variations and transition velocities between hyperoxygenation and hypoxia states were measured. At day 14 (Fig. 1), the  $SO_2$  variation is lower in placenta (25%) than for skin (68%). Between days 14 and 20, the  $SO_2$  variation remained constant for skin and mesometrial triangle but decreased by approximately 14% in placenta ( $p < 0.05$ ). The slope of hyperoxygenation-hypoxia state transition is higher for skin and mesometrial triangle than for placenta ( $p < 0.01$ ). For placenta, the slope decreased by a factor 3.5 between days 14 and 20 ( $p < 0.001$ ) while it remained constant for the skin and mesometrial triangle. Similar trend was observed for the hypoxia-hyperoxygenation state transition. Even if the placenta is a high perfused organ, these results demonstrate that the placenta has a specific oxygenation which differs from skin or mesometrial triangle. These results suggest that placenta is less sensitive to oxygen variation and acts as an oxygen tank for the foetus.

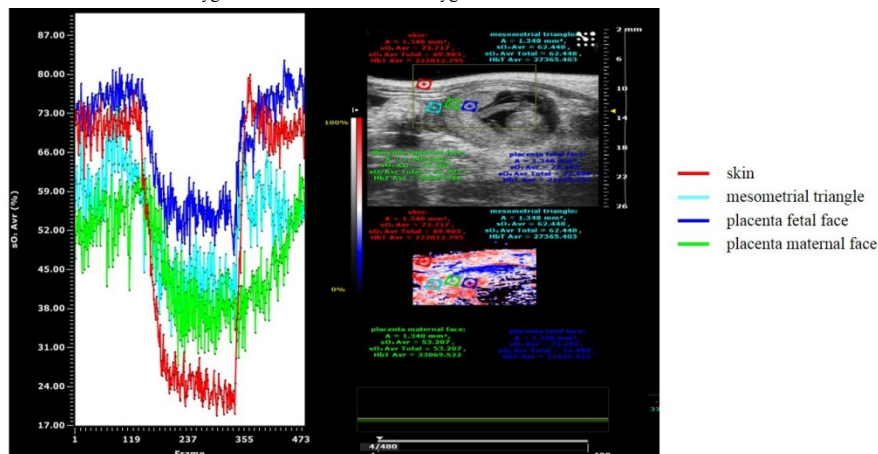


Figure 1: Left panel shows the  $SO_2$  average as a function of the time for skin (red), mesometrial triangle (light blue), placenta fetal face (dark blue) and placenta maternal face (green). B-mode and photoacoustic imaging of hemoglobin oxygen saturation are given in the right panel.

P1A7-5

**Multispectral Photoacoustic Coded Excitation with Low PRF High Power Laser Diodes**Martin F Beckmann<sup>1</sup>, Hans-Martin Schwab<sup>1</sup>, Georg Schmitz<sup>1</sup>; <sup>1</sup>Medical Engineering, Ruhr-Universität Bochum, Bochum, Germany**Background, Motivation and Objective**

Photoacoustic imaging is based on the generation of ultrasound using laser irradiation. Solid state laser systems are commonly employed for this purpose, but pulsed laser diodes can be an attractive alternative. Currently, a photoacoustic handheld probe is developed within the European Union project FULLPHASE and will include multiple wavelengths. In this probe, multiple wavelengths will be available simultaneously. This can be exploited for increasing the signal to noise ratio of acquired images by generating images containing all wavelengths ("fused" images) at the loss of spectral information [1]. Here, we show that applying a multispectral code instead of a simple fusion of the wavelengths, allows to generate both a high SNR fused image and separate wavelength images simultaneously.

**Statement of Contribution/Methods**

In a system of two laser diodes (650 nm, 905 nm), orthogonal Golay codes [2] were applied. These provide perfect separation of the wavelengths. In contrast to the previous photoacoustic coded excitation (PACE) applications, the pulse repetition rate of the diodes was kept low enough to avoid aliasing. This allowed the reuse of the acquisitions to obtain a fused image at high SNR and use the same acquisitions for separate wavelength images by decoding the Golay codes. A phantom consisting of two absorbers, one absorbing primarily one of the wavelengths, the other absorbing both, was used to demonstrate the separation. The performance of the codes was compared to separate acquisition of single wavelengths, obtaining only fused images, and acquiring both fused and single wavelength images after each other. For the comparison, it was assumed that the total applicable energy is limited due to laser safety constraints.

**Results/Discussion**

If only single wavelength data or only fused data is desired, the code will neither outperform the single wavelength acquisitions nor the fused image acquisition. If, however, both types of data are desired, for example, to use the fused image as a background for the spectroscopic single wavelength data it is beneficial to apply a code instead of using separate acquisitions. Using a code, it is possible to trade reductions in single wavelength's SNR for fused data's SNR. For the two wavelengths used in the experiments, it was possible to improve the fused data's SNR by a factor of about 1.5 while the SNR of the single wavelengths is reduced by a similar factor, which corresponds well to the theory. For three wavelengths, calculations show that the improvements for the fused data exceed the reduction of single wavelengths by a ratio of 4:3.

[1]P. Hajireza et al.: "Multifocus optical-resolution photoacoustic microscopy using stimulated Raman scattering and chromatic aberration", Optics Letters, 38, 2013, pp 2711-3

[2]M. Mienkina et al.: "Multispectral photoacoustic coded excitation imaging using unipolar orthogonal Golay codes", Optics Express, 18, 2010, pp 9076-87

P1A7-6

**Simultaneous measurement of erythrocyte aggregation and oxygen saturation under *in vitro* pulsatile blood flow by high-frequency photoacoustics**Tae-Hoon Bok<sup>1</sup>, Eno Hysi<sup>1</sup>, Michael Kolios<sup>1</sup>; <sup>1</sup>Physics, Ryerson University, Toronto, Ontario, Canada**Background, Motivation and Objective**

The main role of erythrocytes is oxygen delivery to body tissues via blood flow. Erythrocytes become aggregated when flowing blood is exposed to stasis or very low shear rate conditions due to various pathologies such as deep vein thrombosis or diabetes. Erythrocyte aggregation (EA) is known to alter blood viscosity which affects blood flow dynamics, vascular resistance and tissue perfusion. The relation between oxygen transport and EA may provide a new biomarker. In this paper, high-frequency photoacoustic (PA) imaging is proposed to simultaneously measure EA and oxygen saturation ( $sO_2$ ).

**Statement of Contribution/Methods**

All experiments were conducted using whole blood units from healthy volunteers (Canadian Blood Services). The pulsatile blood flow was generated within a 2 mm diameter vessel and was adjusted using a peristaltic pump (MasterFlex, Cole-Parmer, Canada). The beat rates were 30, 60, and 90 bpm, and the minimal/maximal velocities at each beat rate were 3/20, 7/32, and 8/39 cm/s, respectively. PA images of flowing blood were acquired at a frame rate of 20 Hz by a PA imaging system (Vevo LAZR, VisualSonics, Canada) equipped with a 40 MHz linear-array probe and an a pulsed laser operating at 680/850 nm. EA was estimated by the PA amplitude. The  $sO_2$  was computed by the ratio of oxygenated hemoglobin to total hemoglobin concentrations assessed at two optical wavelengths.

**Results/Discussion**

For all optical wavelengths, the mean PA amplitude inside the region of interest cyclically varied at intervals corresponding to the beat rate (Fig. 1). The vessel diameter also cyclically varied at the same time interval, but the phase of its variation was reversed compared to the PA amplitude variations. This was expected that as the blood velocity decreased, the shear rate in the radial direction also decreased, resulting in increased EA. This increases the absorber (aggregate) size thus enhancing the PA amplitude. When the velocity is increased, the aforementioned process is reversed, resulting in decreased EA and PA amplitude. The cyclic variation in  $sO_2$  was evident for the highest beat rate, and differences in the mean PA amplitude at 680 and 850 nm was detected for all beat rates. This indicates that  $sO_2$  was varying while blood was flowing with the different beat rates. The temporal variation in  $sO_2$  can be correlated to EA, since it has been reported that oxygen release is inhibited by EA.



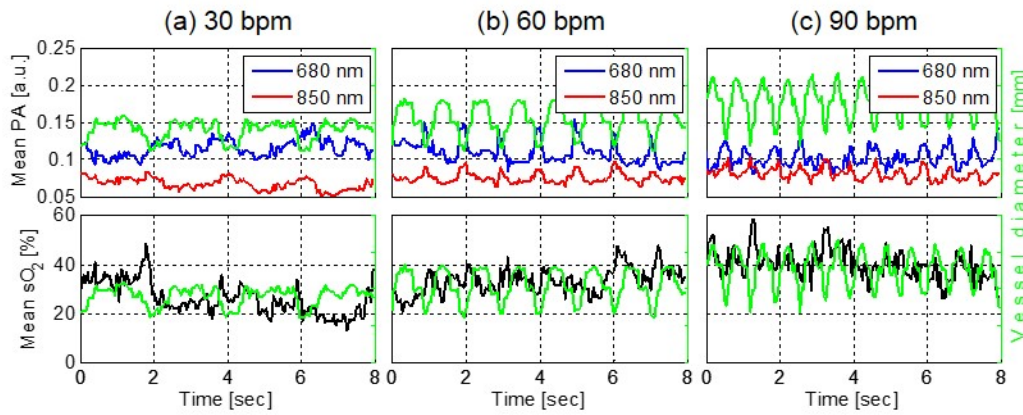


Figure 1. The temporal variation in photoacoustic amplitude (upper), oxygen saturation (lower), and vessel diameter under pulsatile flow of three beat rates 30 (a), 60 (b), and 90 (c) bpm.

P1A7-7

#### Enhancement of photoacoustic imaging quality by using cMUT technology: experimental study

Maëva Vallet<sup>1</sup>, François Varray<sup>1</sup>, Mohammad Azizian Kalkhoran<sup>1</sup>, Jérôme Boutet<sup>2</sup>, Didier Vray<sup>1</sup>; <sup>1</sup>Université de Lyon, CREATIS ; CNRS UMR5220 ; Inserm U1044 ; INSA-Lyon ; Université Lyon 1, France, <sup>2</sup>CEA-LETI, MINATEC, Grenoble Cedex 9, France

#### Background, Motivation and Objective

Photoacoustic (PA) signals are known to be wideband thanks to their N-shape. Yet, ultrasound (US) transducers commonly used for PA imaging use piezoelectric technology (PZT) and hence present a limited bandwidth in reception. Thus, the signal can not be fully acquired and is filtered by the receiver. Capacitive micromachined ultrasonic transducer (cMUT) technology has emerged as an alternative to conventional PZT transducers in the field of medical imaging. Among the interesting properties offered by this technology, a theoretically infinite bandwidth in reception may be reached. In this work the interest of cMUT larger bandwidth for PA imaging is studied by comparing it to a classical PZT US probe.

#### Statement of Contribution/Methods

A cMUT and a PZT linear US probes, each with 128 elements, have been compared. PA acquisitions have been made on several homemade bimodal phantoms whose properties are well-known. For each phantom, acquisitions have been realized with both probes in the same configuration and at several energy levels. Averaging has been made over thirty images. The probes central frequencies and fractional bandwidths are calculated from the backscattered signal of a punctual optical absorber. A second phantom with a spherical inclusion containing optical absorbers is imaged. These acquisitions are used to evaluate several criteria to compare the two linear probes: signal-to-noise ratio (SNR), contrast-to-noise ratio (CNR), and the maximal amplitude of PA signals.

#### Results/Discussion

The cMUT probe presents indeed a larger fractional bandwidth in reception than the piezoelectric probe: 80% for the PZT probe and 140% for the cMUT probe. Moreover, as shown in the figure, the SNR and CNR are enhanced by at least 6dB. Furthermore, the sensitivity of the cMUT probe is higher and it receives 3 to 4 times more energy than the PZT probe. Hence, the targeted absorbers are better imaged. In conclusion, this work showcases the potential of cMUT technology for PA imaging through quantitative as well as qualitative parameters.

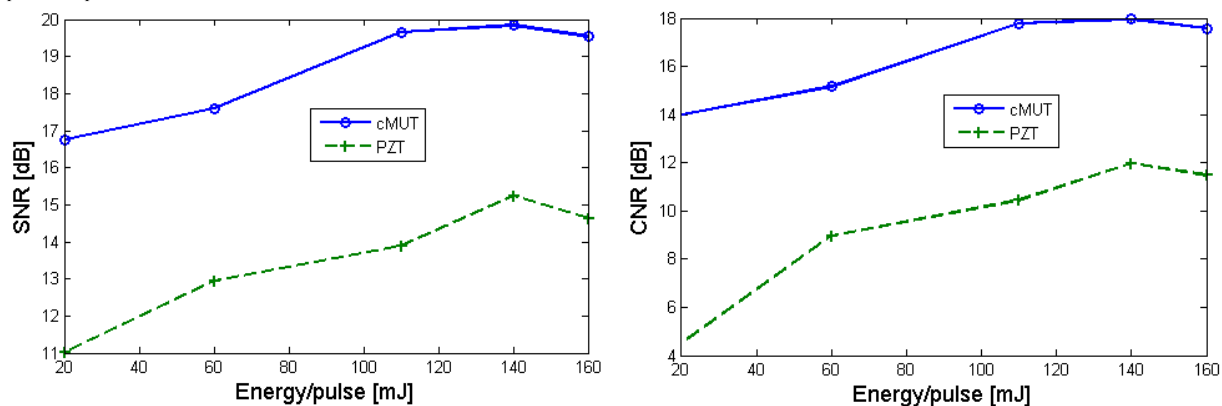


Figure: Evolution of the SNR and CNR of PA images acquired *in vitro* at different excitation energies.

P1A7-8

**Photoacoustic - Acoustic Radiation Force Impulse (PA-ARFI) Microscopy**

Bong Jin Kang<sup>1</sup>, Jae Youn Hwang<sup>2</sup>, Changyang Lee<sup>1</sup>, Hyung Ham Kim<sup>1</sup>, Jinhyoung Park<sup>1</sup>, Qifa Zhou<sup>1</sup>, K. Kirk Shung<sup>1</sup>; <sup>1</sup>Department of Biomedical Engineering, University of Southern California, USA, <sup>2</sup>Department of Information and Communication Engineering, Daegu Gyeongbuk Institute of Science & Technology, Korea, Republic of

**Background, Motivation and Objective**

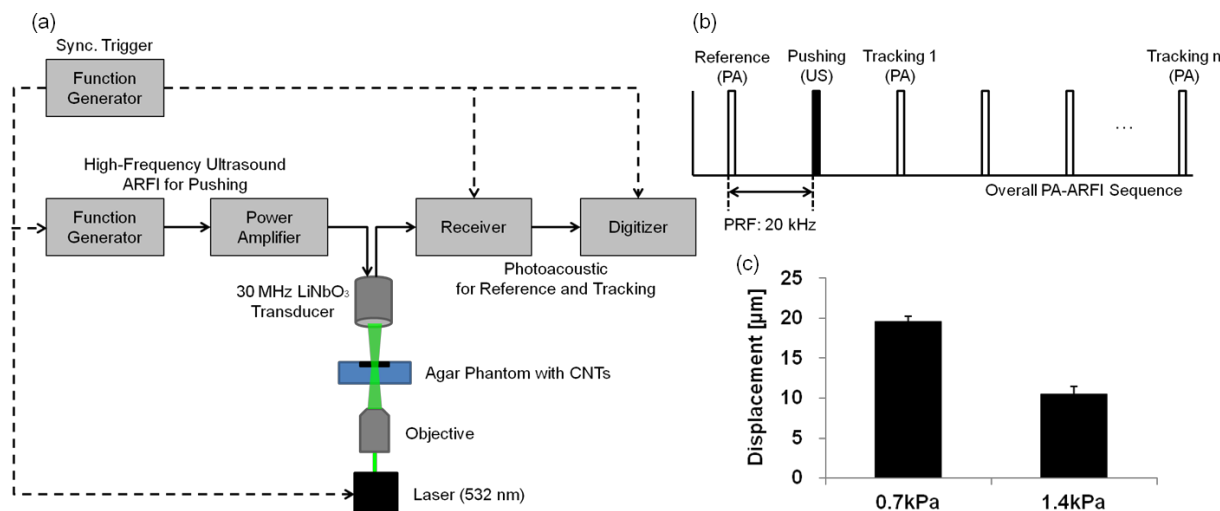
Acoustic radiation force impulse (ARFI) imaging has been used to illustrate the elastic properties of tissues. In this method, focused ultrasound is used to apply the radiation force and the resulted tissue displacements are measured by detecting ultrasound echo signals. However, for ARFI imaging of cells, displacement measurement will be challenging since cells have a dimension in the order of tens of micrometer and have acoustic properties similar to water. In this paper, ARFI microscopy based on photoacoustic signal detection for assessing the mechanical properties of cells is reported.

**Statement of Contribution/Methods**

Figure (a) shows the experimental setup for PA-ARFI microscopy. A pulsed laser (532 nm) was used for excitation of a target and a 30 MHz lithium niobate single element transducer was used to both generate acoustic radiation force and detect photoacoustic signals. Principle of PA-ARFI microscopy is similar to that of a typical ARFI imaging except a laser is used to generate photoacoustic signals for reference and tracking sequences as shown in Figure (b). Two agar phantoms (0.7 and 1.4 kPa) contains a layer of carbon nanotubes were prepared. Carbon nanotubes, which can be attached to cell membrane, were used as a contrast agent to produce photoacoustic signals. The displacements of carbon nanotubes by acoustic radiation force were measured by detecting photoacoustic signals with a pulse repetition frequency (PRF) of 20 kHz.

**Results/Discussion**

Figure (c) shows the phantom experiment results using PA-ARFI microscopy. The displacements of CNTs in each agar phantom were 19.5  $\mu\text{m}$  (Young's modulus: 0.7 kPa) and 10.5  $\mu\text{m}$  (Young's modulus: 1.4 kPa) when an input voltage of the transducer was 50 Vpp with a burst of 5000 cycles. The displacement of CNT in agar phantom with Young's modulus of 0.7 kPa was about two-times higher than that in agar phantom with Young's modulus of 1.4 kPa. These results demonstrate PA-ARFI microscopy would be a useful tool for the measurement of mechanical properties and could be used to assess mechanical properties of cells.



P1A7-9

**Assessment of HIFU-induced tissue damage using multi-wavelength photoacoustic imaging**

Joshua Gray<sup>1,2</sup>, Nicholas Dana<sup>3</sup>, Florian Maier<sup>1</sup>, Oguzhan Ege<sup>1</sup>, Trevor Mitcham<sup>1</sup>, Jason Stafford<sup>1,2</sup>, Stanislav Emelianov<sup>1,3</sup>, Richard Bouchard<sup>1,2</sup>; <sup>1</sup>Department of Imaging Physics, University of Texas MD Anderson Cancer Center, USA, <sup>2</sup>University of Texas Graduate School of Biomedical Sciences, USA, <sup>3</sup>Department of Biomedical Engineering, University of Texas Austin, USA

**Background, Motivation and Objective**

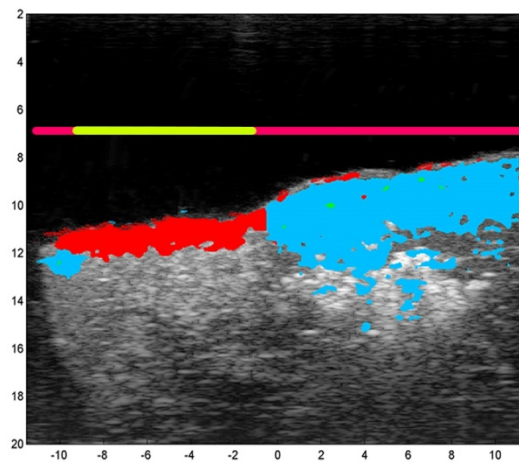
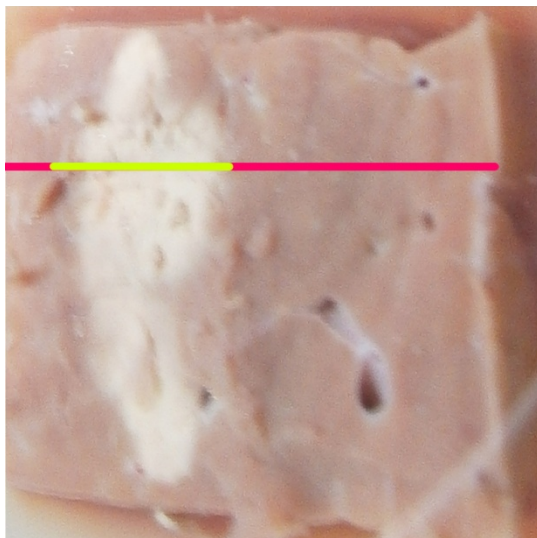
High-intensity focused ultrasound (HIFU) thermal ablation therapies can provide non-invasive treatment to a wide variety of tissues while minimizing damage to non-targeted regions. Unfortunately, HIFU ablation lacks the intrinsic imaging techniques needed to assess lesion characteristics, and thus it is typically combined with magnetic resonance (MR) imaging for clinical applications. Multi-wavelength photoacoustic (PA) imaging could provide an inexpensive alternative (i.e., order-of-magnitude less cost) to current MR temperature imaging (MRTI) guidance techniques and may be well suited to HIFU guidance for specific organs (e.g., prostate). In this study, we demonstrate the feasibility of using combined PA and ultrasound (PA-US) imaging to characterize HIFU tissue damage.

**Statement of Contribution/Methods**

Tissue samples were acquired from fresh bovine cardiac, liver, and skeletal neck muscle tissue and embedded into an agar phantom. Ablations were performed using an ExAblate 2000 system (InSightec Inc., Tirat Carmel, Israel). In each tissue sample, multiple ablation regions were sonicated for 20 seconds at a power of 131W. Following HIFU ablation, combined US and multi-wavelength PA imaging in the NIR spectrum (680-970 nm) was performed using a Vevo LAZR imaging system (FUJIFILM VisualSonics Inc., Toronto, Canada); the PA-US imaging field of view was chosen so that ablated and non-ablated tissue regions were imaged simultaneously. The observed PA spectra were then correlated to reference spectra to generate a tissue characterization map identifying ablated and non-ablated regions.

**Results/Discussion**

In all tissues tested, multi-wavelength PA imaging was able to successfully distinguish adjacent ablated (red) and non-ablated (cyan) regions and predict lesion boundaries to sub-millimeter precision. The provided image offers an overhead photograph (left) of an ablated (yellow bar) region in a liver sample and a PA-US image (right) providing an orthogonal view through the sample. These results demonstrate that combined PA-US imaging has the potential to accurately assess HIFU ablation size and location and thus could be developed into a powerful modality for guiding HIFU therapies in clinical settings at significantly lower costs.



P1A7-10

### All-optical photoacoustic imaging and detection of early-stage dental caries

Ashwin Sampathkumar<sup>1</sup>, David Hughes<sup>2</sup>, Christopher Longbottom<sup>3</sup>, Katherine Kirk<sup>2</sup>; <sup>1</sup>Biomedical Engineering, Riverside Research, New York City, New York, USA, <sup>2</sup>School of Engineering, University of the West of Scotland, Paisley, United Kingdom, <sup>3</sup>Dental Innovation and Translation Centre, London, United Kingdom

#### Background, Motivation and Objective

Dental caries are one of the most common oral diseases in the world. Current detection methods, such as dental explorer and X-ray radiography, suffer from poor sensitivity and specificity at the earliest (and reversible) stages of the disease because of the small lesion size (< 100 microns). We used a fine-resolution, ultra-broadband (1 GHz) all-optical photoacoustic imaging system (AOPAI) to image and detect early stages of tooth decay. The AOPAI system provides a non-contact, non-invasive and non-ionizing means of detecting early-stage dental caries.

#### Statement of Contribution/Methods

Ex-vivo teeth exhibiting early-stage, white-spot lesions were imaged using the AOPAI. A 3 x 3 mm<sup>2</sup> region from an early-stage lesion and a healthy enamel region were imaged at 10 microns resolution. Photoacoustic (PA) signals were generated in the tooth using a 532-nm pulsed laser and the light-induced, broadband ultrasound signal was detected at the surface of the tooth with an optical path-stabilized Michelson interferometer operating at 532 nm. The measured time-domain signal was spatially resolved and back-projected to form 2D and 3D maps of the lesion using k-wave reconstruction methods.

#### Results/Discussion

Representative RF data collected from areas of healthy and diseased enamel are shown in Fig. 1a. The graph clearly indicates the larger PA response generated by the lesion compared to the healthy enamel. Time reversal reconstructions of the PA scans quantitatively depict the depth of the lesion (Figs. 1 b and d). The depth of the lesion in the PA image (Fig. 1 d) was 0.4 mm compared to 0.38 mm in the histological image (Fig. 1c). The thickness of the enamel was 0.6 mm in the PA image compared to 0.84 in the histological image. The slight mismatches in the measured dimensions were attributed to the very small amplitude of the propagating ultrasound wavelet, high attenuation in the dental tissue, inhomogeneous sound velocity through the lesion, and the choice of viewing aperture of the reconstruction method. Furthermore, 3D PA reconstruction of the scan region (Fig. 1e) indicated a sub-surface lesion at a depth of 0.6 mm in addition to the surface lesion. These results suggest that our all-optical photoacoustic imaging method is well suited for rapid clinical assessment of early-stage dental caries.

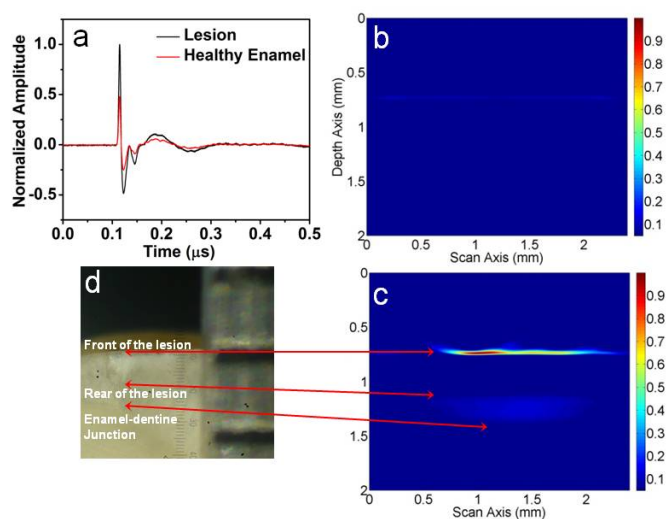


**Figure 1** (a) Representative PA curves for lesion and healthy enamel. (b) PA image of a healthy enamel. (c) PA image of a early stage lesion (d) Histology image of a diseased tooth (e) 3D PA reconstruction of a region showing a sub-surface lesion beneath a surface lesion.

P1A7-11

**Multi-modal acousto-optic/ultrasound imaging of ex vivo liver tumors at 790 nm by wavefront adaptive holography**

jean-baptiste laudereau<sup>1</sup>, Emilie Benoit a la guillaume<sup>1</sup>, vincent servois<sup>2</sup>, Pascale Mariani<sup>2</sup>, Alexander Grabar<sup>3</sup>, mickael tanter<sup>1</sup>, jean-luc gennissou<sup>1</sup>, francois ramaz<sup>1</sup>; <sup>1</sup>ESPCI ParisTech CNRS UMR7587 INSERM U979, Institut Langevin, PARIS, France, <sup>2</sup>Institut Curie, France, <sup>3</sup>Institute of Solid State Physics and Chemistry, Uzhgorod, Ukraine

**Background, Motivation and Objective**

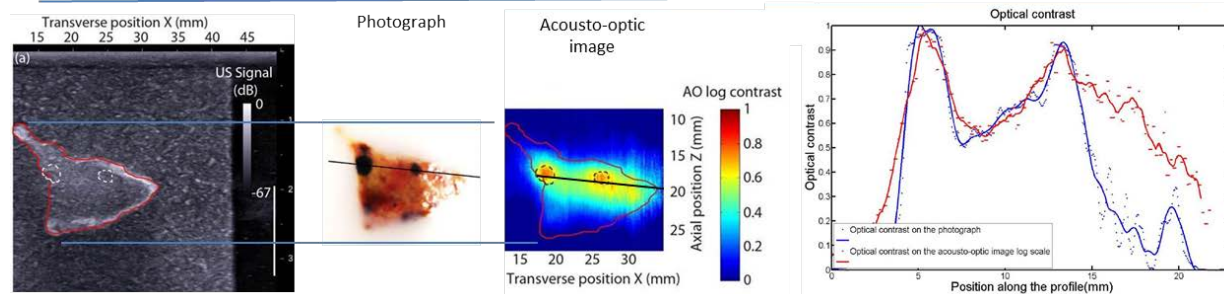
Ultrasound is the most widely used intra-operative imaging technique. However, in some cases such as uveal melanoma liver metastases which is one of the most common ocular tumor, ultrasound are difficult to handle due to poor contrast. As those tumors are usually highly pigmented due to melanin deposits, optical contrast may be complementary to ultrasound diagnosis. In order to increase ultrasound sensitivity this way, an acousto-optic technique was developed to map the local optical properties of tissues.

**Statement of Contribution/Methods**

Acousto-optic imaging is a light-ultrasound coupling technique that uses the optical sidebands created by acousto-optic effect to map the local light intensity inside a medium. It takes advantage of the ballistic propagation of ultrasound in biological tissues to access optical contrast with a millimeter resolution. Thanks to photorefractive crystals, we developed a system based on wavefront adaptive holography that works at 790 nm and allows us to measure acousto-optic signal on a photodiode with a significant SNR. This setup was coupled to a commercial ultrasound scanner (Aixplorer, Supersonic Imagine, France) driving a linear array (SL15-4, 8 MHz) and providing ultrasound images and acousto-optic ultrasound sequences ( $f/d = 1$  at 20 mm depth). The transmitted scattered light interferes on the SPS crystal (1 cm<sup>2</sup> surface, 7 mm thick) with a reference beam, thus filtering the frequency-shifted photons (tagged-photons). At last acousto-optic signals were acquired thanks to a photodiode (Thorlabs PDA36A-EC). A cohort of human biopsy samples with about 5 mm large uveal melanoma metastases were embedded within a scattering matrix mimicking biological tissues and tested. The whole volume of each biopsy (~5 to 10 mm thick) was scanned by fixing the ultrasonic probe on a step by step motor.

**Results/Discussion**

Due to its working at an appropriate wavelength range inside the optical therapeutic window, such a technique is particularly well-suited for biological applications. With such a technique, optical contrast revealed the presence of melanoma metastases while acoustical contrast was not significant. Correlation with the photograph taken after cutting the gel in two pieces was in good accordance. It shows the potential of acousto-optic imaging technique to be in vivo a complementary tool to improve physician diagnosis in ultrasound.



P1A7-12

**Focusing the light within the scattering media for photoacoustic tomography in a limited-view-angle tomography setting**

Hiroshi Abe<sup>1,2</sup>, Tsuyoshi Shiina<sup>1</sup>; <sup>1</sup>Graduate school of medicine, Kyoto University, Kyoto, Japan, <sup>2</sup>R&D Headquarters, Med. Imaging Project, Canon Inc., Tokyo, Japan

**Background, Motivation and Objective**

Photoacoustic imaging can provide biological tissue information such as blood vessel structure, plaque, or chromophores. However, when transducer arrays detect photoacoustic signals in a limited-view-angle tomography setting, we cannot truly depict the biological tissue. In particular, biological tissue positioned vertically across the transducer array line cannot be imaged with sufficient quality because each adjacent small absorber emits photoacoustic signals that cancel out, and only edge-line signals can reach the transducer.

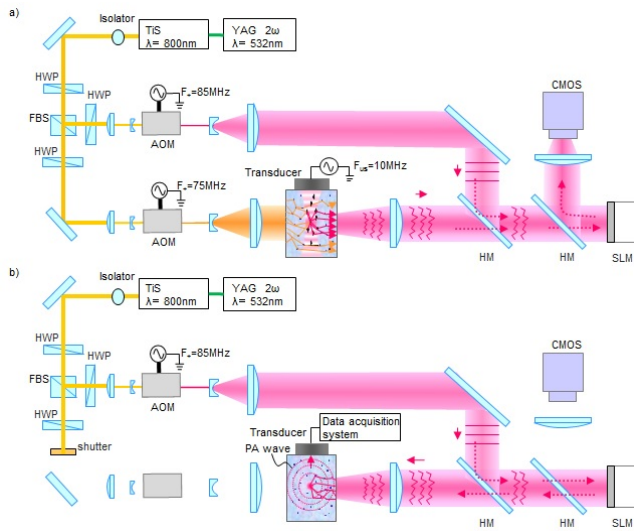
**Statement of Contribution/Methods**

In recent years, scattering light control using ultrasound modulation has been studied in various imaging fields. This control was applied for photoacoustic imaging to focus light in the scattering media in a limited-view-angle setting. We used a carbon wire embedded in gel-based tissue-mimicking phantom to verify the focusing light control. A confined region of the scattered 800nm TiS pulse laser (40mJ/pulse, 10Hz) light in the phantom is frequency-shifted by a focused 10MHz ultrasound pulse. Both the frequency-shifted light through the phantom and the non-shifted light are collected. Then interference fringe at a spatial light modulator (SLM) surface is captured by a high speed CMOS camera through the beam-splitter light path to record the phase map (Fig1a). After calculating the frequency-shifted light phase map, the phase map are projected onto the SLM and reference light throw at SLM and then is returned to the ultrasound modulation location in the phantom as a time reversal focusing light (phase-conjugate light) (Fig1b).

**Results/Discussion**

The focusing time reversal light causes a local photoacoustic effect, then the emitted photoacoustic signal can be detected by the transducer as a point spread. This point-spread signal can be detected in any absorber orientation with respect to the transducer. In this report, we demonstrate a connected carbon wire image in a limited-view-angle tomography setting at a depth of several centimeters. We believe that the photoacoustic tomography with scattered light control is a promising technique for a limited-view-angle tomography setting.





P1A7-13

### Compressive-Sensing Like Grating-Lobe Suppressed Image Reconstruction for Photoacoustic Linear Array imaging

Chien-Hao Chiu<sup>1</sup>, Meng-Lin Li<sup>1,2</sup>; <sup>1</sup>Dept. of Electrical Engineering, National Tsing Hua University, Hsinchu, Taiwan, <sup>2</sup>Institute of Photonics Technologies, National Tsing Hua University, Taiwan

#### Background, Motivation and Objective

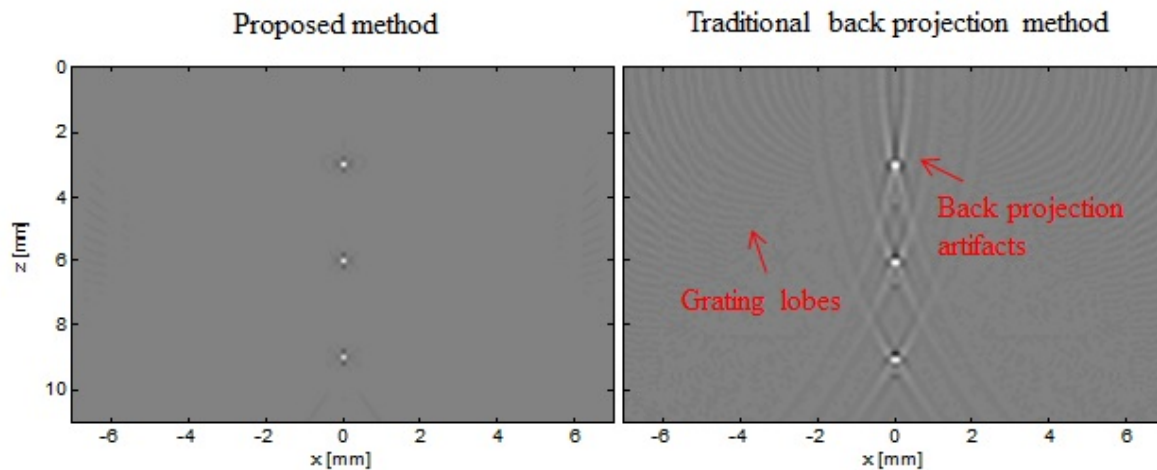
To avoid large grating lobes, using a small element-to-element pitch of ultrasound array transducers for photoacoustic (PA) imaging is necessary. Such constraint introduces higher system cost and complexity, especially when greater than 20-MHz high-frequency arrays are used. As a result, to reduce fabrication difficulties and obtain better signal sensitivity in PA imaging, ultrasound linear array transducers are commonly used in practice instead of phased arrays. However, the field-of-view (FOV) is limited to the full aperture size because linear arrays do not have the ability to steer PA receive beams without the introduction of large grating lobes. In addition, strong PA signals are commonly generated in the near field in the back-ward mode where grating-lobe clutters can even hamper the image contrast seriously. Therefore, developing a grating-lobe suppressed image reconstruction method for back-ward mode PA linear array imaging is valuable.

#### Statement of Contribution/Methods

In this study, we proposed a novel compressed-sensing-like grating-lobe suppressed image reconstruction method for PA linear array imaging. To overcome the tradeoff between FOV and grating lobe clutters introduced by using a linear array, compressive sensing concept (CS) is adopted here to reduce the grating lobes. The CS theory relies on an important principle: sparsity. Fortunately, unlike ultrasound imaging, PA imaging is speckle-free; therefore, in the spatial domain, PA images directly results in a sparse representation. In consequence, a sparsity constraint minimizing the L1 norm of energy deposition can be introduced to the conventional reconstruction method. By adopting such a constraint and using the nonlinear recovery algorithm based on convex optimization, PA linear array imaging can be reconstructed with grating lobe clutters greatly suppressed.

#### Results/Discussion

Simulation results demonstrated that the proposed method can reduce the grating lobes caused by using a linear array with large FOV. In the meantime, compared with the image reconstructed by the traditional back-projection method, the image reconstructed by the proposed method has fewer artifacts.





## P1A8 - MIM: Technologies for Enhanced Imaging

Salon C

Thursday, September 4, 2014, 8:00 am - 5:00 pm

Chair: **Lasse Lovstakken**  
Norwegian University of Science and Technology

P1A8-1

### Orthogonal Golay Pair for Range Side Lobe Elimination in Harmonic Imaging

Che-Chou Shen<sup>1</sup>, Jun-Kai Peng<sup>1</sup>, Chi Wu<sup>1</sup>, <sup>1</sup>National Taiwan University of Science and Technology, Taiwan

#### Background, Motivation and Objective

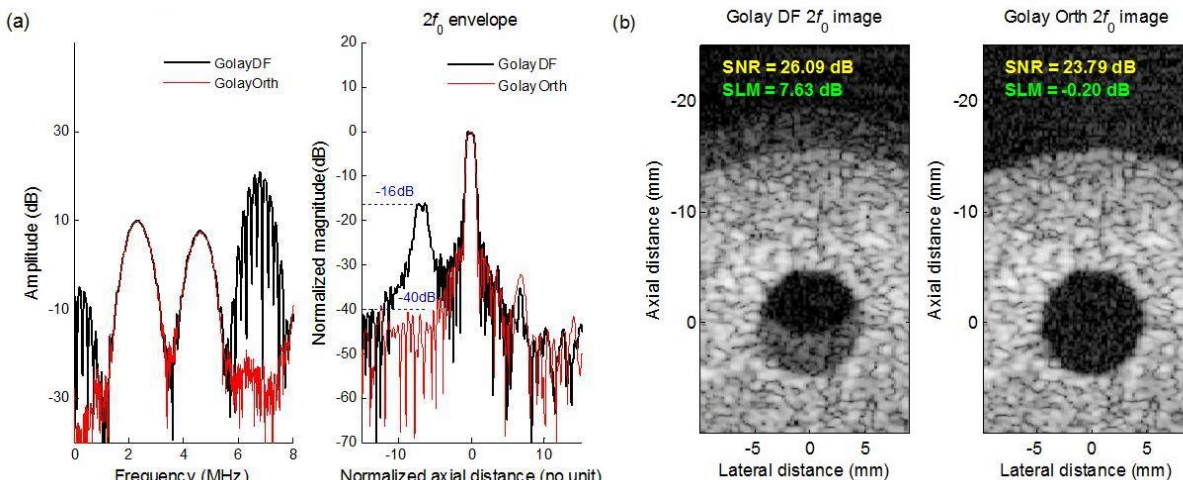
Coded excitation is a well-known solution to boost the signal-to-noise ratio (SNR) in ultrasound imaging. Particularly, it can incorporate with the harmonic imaging to alleviate the low SNR limitation. Nonetheless, in dual-frequency (DF) harmonic imaging where the second harmonic signal at second harmonic ( $2f_0$ ) frequency and the inter-modulation harmonic signal at fundamental ( $f_0$ ) frequency are simultaneously utilized for detection, the spectral crosstalk from the neighboring bands (i.e.  $DC$  and  $3f_0$ ) often produces image degradation in the decoding process. In this work, the orthogonal Golay code is proposed to eliminate the unwanted spectral interference in DF harmonic imaging without loss of frame rate.

#### Statement of Contribution/Methods

When the received harmonic signals are correctly Golay-coded as  $A=[1 \ -1]$  and  $B=[-1 \ 1]$  at both ( $f_0$ ) and ( $2f_0$ ) frequencies, erroneous coding of the  $DC$  and  $f_0$  crosstalk as  $[1 \ 1]$  will produce range side lobes after pulse compression. By the exchange of decoding filtering of the A and B codes, the orthogonal Golay will output zero for the signal (i.e.,  $A(n)*B(-n)+B(n)*A(-n)=0$ ) and keep the crosstalk the same. Therefore, the output of exchanged filtering can be subtracted from that of the original filtering to completely remove the spectral crosstalk. Note that the proposed scheme does not require any addition transmit events to achieve the cancellation and can be readily implemented in the decoding process.

#### Results/Discussion

The signal spectra from hydrophone measurements in Fig. (a) demonstrate that the  $DC$  and  $3f_0$  crosstalk can be completely removed by the proposed decoding scheme. The harmonic signal envelopes verify a reduction of peak range side lobe level (RSL) from  $-16$ dB to  $-40$ dB. Corresponding B-mode harmonic images in Fig.(b) also indicate that the orthogonal Golay code effectively suppresses the side lobe artifacts to the noise level. However, the SNR will be slightly reduced by about 2 dB in the proposed decoding.



P1A8-2

### An Interleaved Data Acquisition to Reduce Common Noise in Coronary Doppler Vibrometry

Daeheon Lee<sup>1</sup>, Jongin Park<sup>1</sup>, Jeesu Kim<sup>1</sup>, Sungjoo Yoo<sup>1</sup>, Hong-June Park<sup>1</sup>, Jin S. Lee<sup>2</sup>, Jong-Seon Park<sup>3</sup>, Ung Kim<sup>3</sup>, <sup>1</sup>Department of Electrical Engineering, Pohang University of Science and Technology, Korea, Republic of; <sup>2</sup>Department of Creative IT Excellence Engineering, Pohang University of Science and Technology, Korea, Republic of; <sup>3</sup>Division of Cardiology, Yeungnam University Medical Center, Korea, Republic of

#### Background, Motivation and Objective

The Coronary Doppler Vibrometry (CDV) is a non-invasive ultrasonic diagnosis method to detect vibrations on a heart wall caused by stenosis in the coronary artery. However, in previous studies, CDV has a crucial problem that the heart wall can show high-frequency motion, which we call common noise, mostly due to the blood flow in the atrium and ventricle. To remove this noise, we performed a differential signal acquisition. First, we obtained ultrasound data at two heart wall segments by transmitting pulses in an interleaved way. Then, we calculated common noise and obtained the differential signal by subtracting the common noise from the signal obtained at each segment. The differential signal acquisition can improve the signal quality of vibration due to stenosis.

#### Statement of Contribution/Methods

We recruited 13 subjects from the hospital; four are normal subjects and nine are known as coronary artery stenosis patients. To configure the interleaved data acquisition technique, we used Verasonics ultrasound system. The Doppler PRF of system was 2400 Hz and each frame rate was 1200 fps at two focusing positions. After data acquisition, we beamformed the data and calculated wall velocity. To characterize the vibration, we generated the velocity spectrogram of heart wall by using short-time Fourier Transform. Then,

we obtained common signal from the two interleaved data. Then, in order to remove common noise, we subtracted the common noise from the original signal. After that, we estimated the vibration power by integrating the spectrogram intensity between 300 and 600 Hz in the early diastole period. We judged that, in the case of patients, the difference of vibration power intensities in two adjacent segments is larger than in the normal subject cases. Fig. 1 illustrates the analysis.

### Results/Discussion

The total diagnosis time including data acquisition is less than 20 minutes per subject which is competitive compared with one hour in the existing focused mode method. We obtained a sensitivity of 83% and a specificity of 80% in the right coronary artery (RCA) cases and a sensitivity of 100% and a specificity of 83% in the left anterior descending (LAD) cases. We can conclude that there was a significant difference between normal and abnormal subjects. However, there are several limitations such as remaining noise and diagnostic difficulty in setting the range gate.

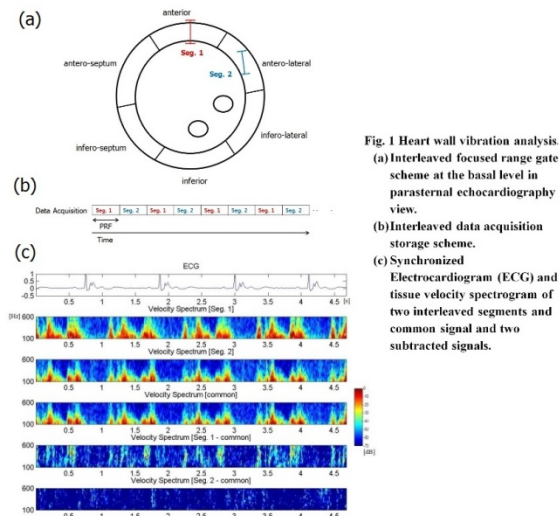


**Fig. 1 Heart wall vibration analysis.**  
(a) Interleaved focused range gate scheme at the basal level in parasternal echocardiography view.  
(b) Interleaved data acquisition storage scheme.  
(c) Synchronized Electrocardiogram (ECG) and tissue velocity spectrogram of two interleaved segments and common signal and two subtracted signals.

P1A8-3

### Small calcification depiction in ultrasonography using frequency domain interferometry

Hirofumi Taki<sup>1</sup>, Guillaume Haiat<sup>2</sup>, Makoto Yamakawa<sup>3</sup>, Tsuyoshi Shiina<sup>4</sup>, Toru Sato<sup>1</sup>; <sup>1</sup>Graduate School of Informatics, Kyoto University, Kyoto, Japan, <sup>2</sup>Faculte des Sciences et Technologie, Universite Paris-Est Creteil Val de Marne, Paris, France, <sup>3</sup>Advanced Biomedical Engineering Research Unit, Kyoto University, Kyoto, Japan, <sup>4</sup>Graduate School of Medicine, Kyoto University, Kyoto, Japan

### Background, Motivation and Objective

In breast cancer screening, mammography plays a major role. Mammography depicts small calcifications that accompany breast cancers; however, it is not effective in young women with rich mammary glands. In contrast, the existence of mammary glands causes little effect to the imaging performance of ultrasonography (US), whereas US has insufficient ability in depicting small calcifications. The purpose of our work is to improve the performance of US in depicting small calcifications.

### Statement of Contribution/Methods

In this study, we employ the imaging method based on frequency domain interferometry (FDI). The proposed FDI imaging method selectively depicts small calcifications, because the method suppresses the contribution of echoes when their waveforms are different from the waveform of a small calcification echo. To investigate the performance of the proposed method, we applied the method to the raw data of a calcification phantom acquired by a commercial US device. A calcification phantom consisted of a gelatin block and a 0.2 mm spherical glass bead embedded at the depth of 19 mm. We added white noise to the acquired raw data of the calcification phantom, where the signal-to-noise ratio after the noise addition was 0 dB.

### Results/Discussion

Fig. 1 shows the B-mode image of a gelatin block with a 0.2 mm spherical glass bead. In the B-mode image there was no indication that a 0.2 mm glass bead existed. In contrast, the FDI imaging method succeeded to depict the 0.2 mm glass bead, as shown in Fig. 2. This result shows that the proposed FDI imaging method has the potential to depict 0.2 mm small calcifications that are not depicted in the conventional B-mode images. This study indicates that the FDI imaging method has high potential to improve the performance of US in depicting small calcifications.

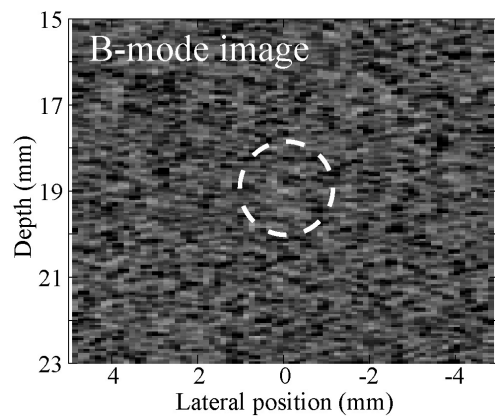


Fig. 1 B-mode image of a 0.2 mm glass bead with the addition of white noise, where the signal-to-noise ratio is 0 dB. The glass bead is located at the center of the broken circle.

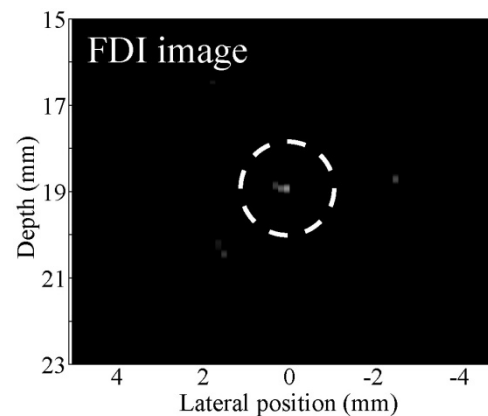


Fig. 2 FDI image of a 0.2 mm glass bead with the addition of white noise, where the signal-to-noise ratio is 0 dB. The glass bead is located at the center of the broken circle.

P1A8-4

#### Improved FL-IVUS Imaging with Low Voltage Single-chip CMUT-on-CMOS Array Using Temporally Coded Excitation

Coskun Tekes<sup>1</sup>, Toby Xu<sup>1</sup>, F. Levent Degertekin<sup>1</sup>; <sup>1</sup>Mechanical Engineering, Georgia Institute of Tech, Atlanta, Georgia, USA

##### Background, Motivation and Objective

Synthetic phased array based high frequency imaging devices on catheter probes suffer from low SNR and limited penetration due to small active transducer area and frequency-dependent tissue attenuation. Although using signal averaging improves the SNR, it increases data collection time which degrades real time imaging performance. Temporally coded pulses emit high energy to the imaging medium and enhance SNR, using a suitable decoding procedure, without compromising frame rate. We previously demonstrated the volumetric imaging performance of a single-chip forward looking CMUT-on-CMOS system [1]. In this study, we describe the implementation of temporal coding excitation in our single-chip system with reduced DC voltage levels and present the imaging results.

##### Statement of Contribution/Methods

The fabricated single-chip CMUT-on-CMOS dual ring array system has 56 and 48 elements in transmit and receive, respectively. The 1.5-mm CMUT array operates at 20 MHz with a FBW of 50%, and has only 40 V collapse voltage with 50 nm gap. To implement coded excitation, we used an FPGA to produce coded pulse control sequence for the on-chip pulser circuit. A 2-cycle 13-bit Barker code was generated to encode a rectangular unipolar pulse waveform. 24-ns pulse width was chosen for maximum energy transfer to the system. Due to the limitation of internal pulsers, a 25-V pulse amplitude was used to produce the encoded excitation signal. The received signals were decoded by using spectrum inversion filtering.

##### Results/Discussion

The imaging experiments were performed using a pig artery phantom immersed in water (Fig 1.). For comparison, pulse-echo data was collected from the same target using both single pulse and coded pulse excitation. The reconstructed 2D cross-sectional images using coded excitation produces 9 dB improvement in image SNR compared to single pulse excitation without any frame rate degradation. The side walls of the pig artery can be easily seen up to 8 mm depth.

The imaging results show that temporal coding excitation can be effectively implemented on CMUT-on-CMOS systems to significantly increase image SNR and penetration depth without compromising frame rate. This SNR improvement can be used to decrease the number of firings for increasing imaging speed, and hence reduce motion artifacts.

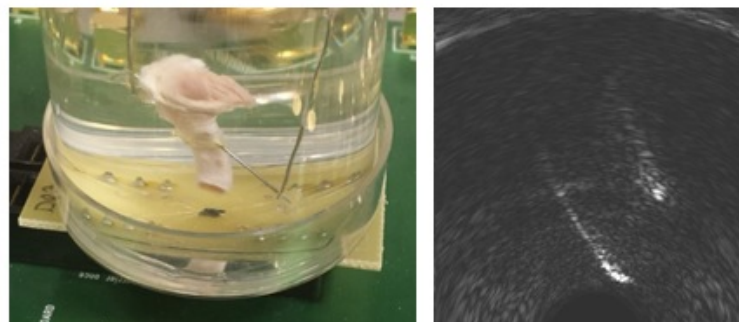


Figure 1. (left) Experimental setup for pig artery, (right) 2D cross-sectional image of pig artery using coded pulse excitation.

[1] G. Gurun, C. Tekes, J. Zahorian, T. Xu, S. Satir, M. Karaman, J. Hasler, F.L. Degertekin, "Single-Chip CMUT-on-CMOS Front-End System for Real-Time Volumetric IVUS and ICE Imaging", IEEE Transactions on, Ultrasonic, Ferroelectrics and Frequency Control, Vol. 61, No. 2, February 2014.

# Focal Liver Pathology Imaging combining Synthetic Aperture Sequential Beamforming and Tissue Harmonic Imaging

Andreas Hjelm Brandt<sup>1,2</sup>, Martin Christian Hemmsen<sup>2</sup>, Peter Møller Hansen<sup>1</sup>, Theis Lange<sup>3</sup>, Michael Bachmann Nielsen<sup>1</sup>, Jørgen Arendt Jensen<sup>2</sup>; <sup>1</sup>Radiology, Copenhagen University Hospital, Denmark, <sup>2</sup>Center for Fast Ultrasound Imaging, Technical University of Denmark, Denmark, <sup>3</sup>Biostatistics, University of Copenhagen, Denmark

## Background, Motivation and Objective

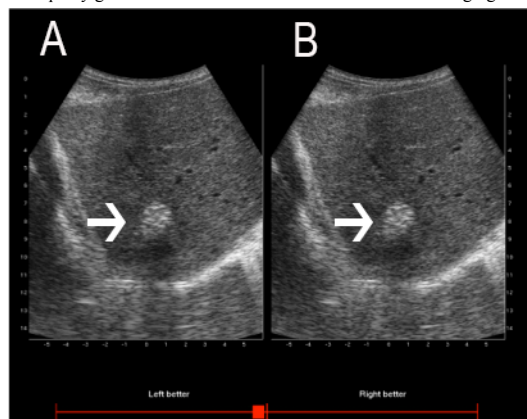
In medical ultrasound Dynamic Received Focus (DRF) is often combined with Tissue Harmonic Imaging (THI) to achieve higher resolution and improved contrast. A previous comparison study between Synthetic Aperture Sequential Beamforming (SASB) and DRF showed equally good image quality for clinical imaging. Derived from this the clinical feasibility of combining Synthetic Aperture Sequential Beamforming (SASB) and THI are considered in this study. Patients with focal liver pathology were scanned to set a clinical condition where medical ultrasound is widely performed. The objective of the study was to compare image quality of sequences generated by SASB-THI with sequences generated by DRF-THI.

## Statement of Contribution/Methods

A BK medical UltraView 800 ultrasound scanner equipped with a research interface and an abdominal 3.5 MHz 3.5CL192-3ML convex array transducer was connected to a stand alone PC. SASB-THI and DRF-THI scan sequences were recorded interleaved and processed offline. Nineteen patients diagnosed with focal liver pathology were scanned. A total of 114 sequences were recorded and evaluated by five radiologists. The evaluators were blinded to the technique. Each sequence was shown twice with different left-right positioning resulting in 1140 evaluations. The program Image Quality Assessment Program (IQap) and a Visual Analog Scale (VAS) were applied for the evaluation. The figure shows IQap screenshot and VAS at the bottom. For guidance SASB-THI is indicated by A, DRF-THI by B and the white arrows are pointing at the focal liver pathology. By dragging the bar to one side the evaluators could specify which technique they preferred. The scale ranges from -50 to 50, where positive values favoured SASB-THI. Wilcoxon signed-rank test was applied for statistical analysis.

## Results/Discussion

SASB-THI and DRF-THI was evaluated alike in 49% of the evaluations, 28% favoured SASB-THI and 23% favoured DRF-THI. The average rating was 0.70 (CI: -0.80 to 2.19). In the statistical analysis, where the hypothesis of no differences between the techniques was tested yielded a p-value of p=0.64, indicating no preference to any technique. The general notice from the evaluators was very little difference between the techniques and no observation of motion artefacts. This study demonstrates that SASB-THI and DRF-THI are equally good and SASB-THI can be used for clinical imaging.



# On the feasibility of speckle reduction in echocardiography using strain compounding

Yuxin Guo<sup>1</sup>, Wei-Ning Lee<sup>1</sup>; <sup>1</sup>EEE, HKU, Hong Kong

## Background, Motivation and Objective

Speckle reduction has been studied extensively to improve the ultrasound image quality. Strain compounding, proposed by Li and Chen (IEEE TUFFC 2002), has been demonstrated capable of reducing speckle noise in superficial tissues through combining a series of partially re-correlated B-mode images of the tissue under externally applied quasi-static deformation.

In this study, the feasibility of strain compounding for echocardiography was studied. Not only did the prerequisite deformation stem from the natural contraction of the heart, but computational efficiency could also remain using the strain estimates yielded from cardiac strain imaging. The resultant reduction of speckle noise is expected to improve the performance of automated-segmentation for the volume measurement of heart chambers.

## Statement of Contribution/Methods

2D B-mode images of the normal human heart in a four chamber view were acquired by a GE Vivid E9 system at a frame rate of 33 fps. The average heart rate was 60 bpm. For each set of five consecutive images with the third one as the reference frame, standard block matching with normalized cross correlation was performed for heart motion estimation, followed by correction. Each set of five re-correlated consecutive images were thereafter compounded.

## Results/Discussion

An example of the original and compounded images at early systole is shown in Fig. 1. ROIs were chosen in the interatrial septum and the cavity as indicated in the red and blue boxes, respectively, for the calculation of SNR and CNR. The compounded image exhibited higher SNR and CNR (5.91, 3.81) than the original image (4.81, 3.07) but comparable values (6.08, 3.61) obtained from the Speckle Reducing Anisotropic Diffusion method.

Moreover, average improvement of SNR and CNR from interatrial and interventricular septa and the right ventricular wall were found to be (77%, 81%), (35%, 46%) and (29%, 40%) at mid, end of systole and end of diastole.

The preliminary results have demonstrated the feasibility of strain compounding in speckle reduction in echocardiography. The observed variation of the SNR and CNR improvement over one cardiac cycle was possibly due to different strain rates at different cardiac phases. To achieve consistent performance, determining the number of frames to be compounded is being investigated. Local SNR and CNR improvements throughout the heart will also be examined.



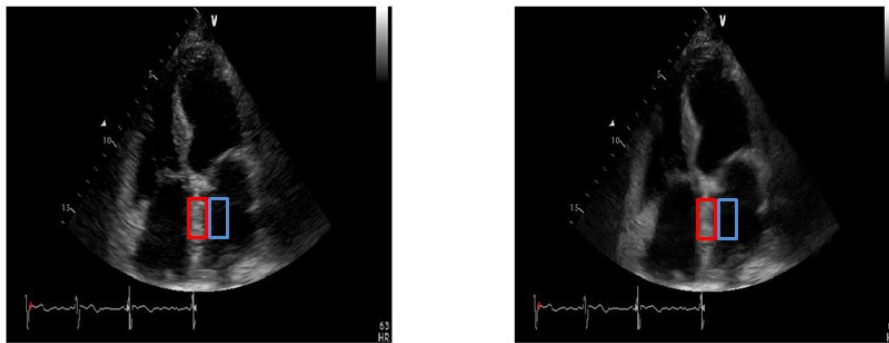


Figure 1 original ultrasound (left) and compounded images (right) of the human heart in an apical four-chamber view at early systole.

P1A8-7

#### A New Feature-enhanced Speckle Reduction Method based on Multiscale Analysis and Synthesis for Ultrasound B-mode Imaging

Jinbum Kang<sup>1</sup>, Yangmo Yoo<sup>1,2</sup>; <sup>1</sup>Electronic Engineering, Sogang University, Seoul, Korea, Republic of, <sup>2</sup>Interdisciplinary Program of Integrated Biotechnology, Sogang University, Seoul, Korea, Republic of

#### Background, Motivation and Objective

Effective speckle reduction in ultrasound B-mode imaging is important for improving image quality and the accuracy in image analysis. While multiscale analysis-based speckle reduction methods such as Laplacian pyramid nonlinear diffusion (LPND) and nonlinear multiscale wavelet diffusion (NMWD) showed enhanced speckle reduction, they suffer from excessive blurring and artificial appearance. In this paper, a new feature-enhanced speckle reduction (FESR) method based on multiscale analysis and feature enhancement filtering is presented for ultrasound B-mode imaging.

#### Statement of Contribution/Methods

In the proposed FESR method, an edge-sensitive noise reduction and feature enhancement filtering method is applied with multiscale analysis and synthesis. To separate true clinical features (e.g., boundaries of lesions) from noise, the sub-band images from a Laplacian pyramid model are firstly generated. Then, a robust anisotropic diffusion process is applied to suppress the identified noise and the extracted features are selectively emphasized by appropriate edge, coherence and contrast enhancement filtering from fine to coarse scales. The performance of the proposed FESR method was compared with the LPND and NMWD methods by measuring speckle signal-to-noise ratio (SSNR) and contrast-to-noise ratio (CNR). *In vivo* abdominal images were captured with a commercial ultrasound system from the liver area of a volunteer, and the captured images were transferred to an external PC for processing.

#### Results/Discussion

Figure 1 shows the original B-mode image and the processed images from three speckle reduction methods. Under visual assessments, the proposed FESR method in Fig. 1(d) clearly depicts boundaries of hepatic vessels and a gall bladder while substantially reducing speckle in the parenchymal region, compared to other two methods. The SSNR and CNR values were measured for 30 consecutive frames. With the FESR method, the mean SSNR value and the mean CNR value are significantly higher compared to the LPND and NMWD methods, i.e.,  $8.06 \pm 0.74$  vs.  $5.69 \pm 0.48$ ,  $7.14 \pm 0.93$  and  $6.89 \pm 0.68$  vs.  $5.08 \pm 0.33$ ,  $6.01 \pm 0.53$ , respectively. These preliminary results demonstrates that the proposed FESR method can improve the image quality of ultrasound B-mode imaging by enhancing the visualization of borders and boundaries of lesions while effectively suppressing speckle.

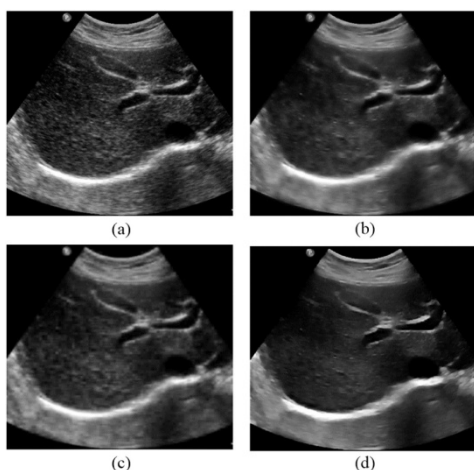


Figure 1. Ultrasound *in-vivo* abdominal liver image and its filtered results. (a) Conventional noisy image. (b)-(d) Image filtered by LPND, NMWD and FESR, respectively.



# Multiscale Nonlocal Means method for Ultrasound despeckling

Lars Hofsoy Breivik<sup>1</sup>, Sten Roar Snare<sup>1</sup>, Hani Nozari Mirarkolaei<sup>1</sup>, Erik Normann Steen<sup>2</sup>, Anne H Schistad Solberg<sup>1</sup>; <sup>1</sup>Department of Informatics, University of Oslo, Oslo, Norway, <sup>2</sup>GE Vingmed Ultrasound, Norway

## Background, Motivation and Objective

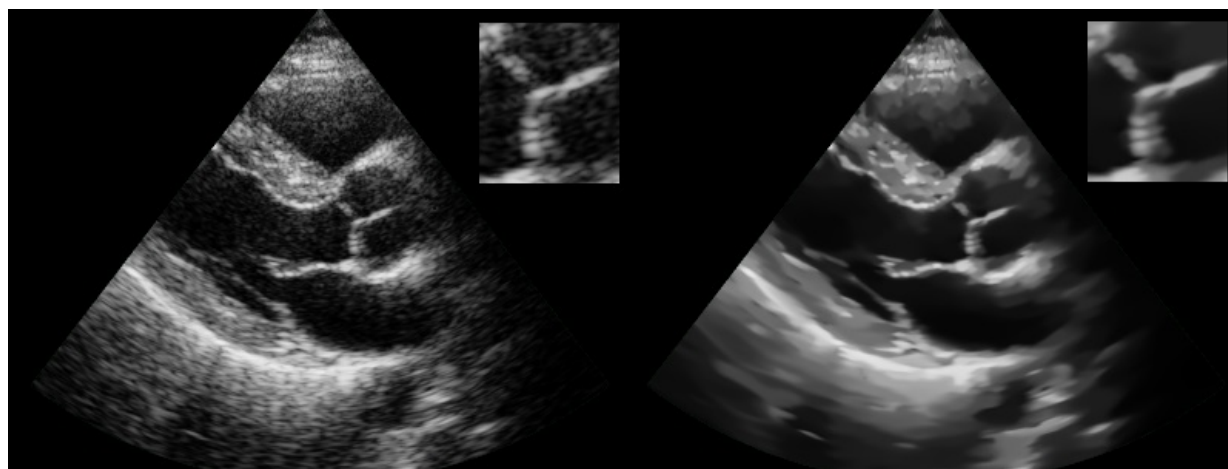
Speckle noise is inherent in ultrasound (US) images and the main source of image degradation, causing reduced contrast and separability of anatomical structures. In this paper we propose a real-time multiscale despeckling filter based on the recently proposed nonlocal means (NLM) filter. We identify two major limitations of the classical NLM filter for ultrasound despeckling: Computational complexity and inability to distinguish speckle structure from signal. To simultaneously solve these two problems we propose an ultrasound tailored multiscale NLM filter.

## Statement of Contribution/Methods

The classical NLM filter restores image pixels by a weighted averaging scheme where weights are determined by pixel neighborhood similarities in large search windows. Our proposed despeckling method applies a cascade of NLM filters from fine to coarse scale. With each new scale, the applied NLM filter is increasingly selective (structure preserving), and the size of its search window is increased. The number of samples examined per scale is constant, such that only sampling stride increases. The filter has been tested using an optimized OpenCL GPU implementation. It is applied to the US image prior to scan conversion to allow a more uniform filter response and better adaption to the point spread function of the imaging system.

## Results/Discussion

Our filter achieves consistent real-time frame rates above 60 frames per second on a mid-range GPU on real ultrasound images. Our results, as seen in the figure, show that areas of fully formed speckle (FFS) are effectively smoothed while structured anatomical details are preserved. FFS regions are increasingly smoothed through the scales, reducing the bias introduced by local spatial correlation in the speckle. In structured areas, the increasing selectivity of the filtering at higher scales limits the smoothing across edges and even small structured features. When compared to 5 other recent despeckling filters, including diffusion and NLM based approaches, our method performed comparably or favorably according to the Structural Similarity Index (SSIM), the Ultrasound Despeckling Assessment Index (USDAI) and the Peak Signal-to-Noise Ratio (PSNR) on Field 2 simulated images.



## P1A9 - MTC: Bone

Salon C

Thursday, September 4, 2014, 8:00 am - 5:00 pm

Chair: **Keith Wear**  
Food and Drug Administration, Silver Spring

P1A9-1

### Finite-Difference Time-Domain Analysis of Ultrasound Backscattering in Cancellous Bone

Atsushi Hosokawa<sup>1</sup>; <sup>1</sup>Department of Electrical and Computer Engineering, Akashi National College of Technology, Akashi, Japan

#### Background, Motivation and Objective

Ultrasound backscatter measurements in bone have been attempted as a quantitative ultrasound technique for clinical assessment of bone quality because of their easy applicability to various skeletal sites. However, the backscatter measurements are not yet established because the mechanisms are not sufficiently clarified. In this study, the backscattered waves from various depths of cancellous bone were analyzed, using finite-difference time-domain (FDTD) simulations with microcomputed tomographic ( $\mu$ CT) models of bovine cancellous bone.

#### Statement of Contribution/Methods

In the FDTD simulation model, an ultrasound pulse wave was transmitted toward the front surface of cancellous bone from a circular concave transmitter/receiver in water. An artificial absorbing boundary was set at the back surface opposite to the ultrasound transmission so that the ultrasound wave could not be reflected (or could be absorbed). Therefore, in the case of the cancellous bone thickness of  $d_1$ , the reflected wave,  $p_1$ , from the front surface and the backscattered waves,  $p_2$ , inside the bone between 0 and  $d_1$  can be received. In the case of the thickness of  $d_2$  ( $>d_1$ ), in addition to  $p_2$  and  $p_3$ , the backscattered waves,  $p_4$ , inside the bone between  $d_1$  and  $d_2$ . Only  $p_4$  can be extracted by subtracting the simulated result for the received signal in the case of  $d_1$  from the simulated result in the case of  $d_2$ .

#### Results/Discussion

For 18  $\mu$ CT cancellous bone models with main trabecular orientation parallel to the ultrasound transmission, the backscattered waves inside cancellous bone between 0.5 and 1.5 mm, between 1.5 and 2.5 mm, and between 2.5 and 3.5 mm were simulated when the focal point of the transmitter/receiver was 2.5 mm inside the bone. The peak-to-peak amplitudes of the backscattered waves are shown in Fig. 1 as a function of the porosity. The backscattered wave amplitude from the bone depth of 0.5–1.5 mm was slightly correlated with the porosity ( $R^2 = 0.06$ ), which is considered to be because the reflected wave from the bone surface could greatly affect. On the other hand, the correlations of the backscattered wave amplitudes from the bone depths of 1.5–2.5 mm and 2.5–3.5 mm ( $R^2 = 0.49$  and 0.39, respectively) were moderate, which means that the backscattered waves from the deep depth could reflect the bone density.

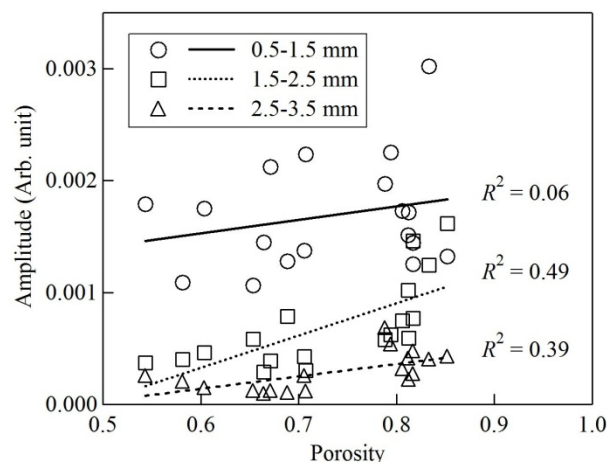


Fig. 1 Amplitudes of backscattered waves from various depths of cancellous bone as a function of porosity.

P1A9-2

### Obstructing Propagation of Interfering Modes Improves Detection of Guided Waves in Coated Bone Models

Vantte Kilappa<sup>1</sup>, Petro Moilanen<sup>1</sup>, Ari Salmi<sup>2</sup>, Zuomin Zhao<sup>3</sup>, Risto Myllylä<sup>3</sup>, Edward Haeggström<sup>2</sup>, Jussi Timonen<sup>1</sup>; <sup>1</sup>Department of Physics, University of Jyväskylä, Jyväskylä, Finland, <sup>2</sup>Department of Physics, University of Helsinki, Helsinki, Finland, <sup>3</sup>Department of Electrical Engineering, University of Oulu, Oulu, Finland

#### Background, Motivation and Objective

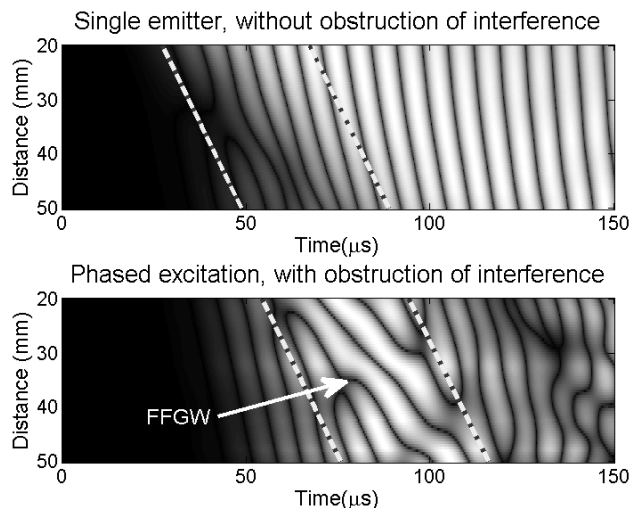
Interference due to wave propagation in soft tissue that covers the bone is a major challenge to *in vivo* assessment of the fundamental flexural guided wave (FFGW) in bone. We have previously shown that a tailored excitation by a phased array (six emitters), operating at a low ultrasound frequency (50 kHz), permits a 10-15 dB improvement in the signal-to-interference ratio (SIR) compared to using only one transducer. To further improve SIR we here obstructed the propagation in soft tissue of interfering modes by locally deforming the coating by external mechanical compression.

# Statement of Contribution/Methods

We report on a new method for improving bone measurements. The effect of obstructing the propagation in soft tissue of interfering modes was modeled by 2D finite-element transient domain (FETD) simulations in a fluid-coated (7 mm) solid plate (3 mm), so as to mimic the soft tissue that covers the bone. A single emitter or a 6-element phased array excited ultrasound pulses at 50 kHz (with a -6dB bandwidth of 30 kHz) on the surface of the coating, and a receiver array was placed on the surface, 20-50 mm apart from the last emitter. Localized deformation of the coating was modeled by a 5 mm wide and 0-7 mm deep notch, centered between the emitting and receiving array.

# Results/Discussion

The localized deformation of the coating increased the SIR of FFGW by  $20 \pm 3$  dB. In particular, a 50% deformation of the coating thickness was effective and only a small improvement of SIR was achieved by further compression. Combining phased excitation with a 50% deformation of soft tissue resulted in a  $30 \pm 3$  dB SIR gain, and enabled a clear identification of the FFGW wave packet (Fig. 1, bottom panel). It was impossible to distinguish FFGW from the interference by a conventional measurement (Fig. 1, top panel). These results thus suggest that obstructing the propagation of interfering modes is important for improving the detection of FFGW in *in vivo* measurements.



P1A9-3

# Ultrasonic wave propagation in the distal end of adult human radius model

Takuma Hachiken<sup>1</sup>, Yuka Matsuura<sup>1</sup>, Fuminori Fujita<sup>1</sup>, Isao Mano<sup>1</sup>, Toshiho Hata<sup>1</sup>, Yoshiaki Nagatani<sup>2</sup>, Mami Matsukawa<sup>1</sup>; <sup>1</sup>Wave electronics research center, Laboratory of ultrasonic electronics, Doshisha university, Kyotanabe, Japan, <sup>2</sup>Kobe city college of technology, Department of Electronics, Japan

# Background, Motivation and Objective

Longitudinal wave in cancellous bone is separated into fast and slow wave. The fast wave propagates mainly along trabeculae, and the slow wave propagates mainly in bone marrow [Hosokawa J.A.S.A, (1997)]. The propagation behavior in *in vivo* bone is complicated because bone has a complex structure. In this study, we studied the propagation behavior in an adult human radius bone model.

# Statement of Contribution/Methods

Referring to CT images of *in vivo* adult male human radius, we fabricated a human radius model using bovine bone. The model is composed of a cancellous bone and a cortical bone layer (sample A). We also fabricated the sample of the cortical bone layer only, in which the air is filled (sample B). Ultrasonic pulse measurements were performed using a focus PVDF transmitter (Custom made, Toray) and a hand-made flat PVDF receiver. A single sinusoidal pulse at 1 MHz was sent from the transmitter. By changing the incident angle  $\theta$  of wave to the specimen from -20 to 20 degrees (0 degree was the direction from a palm to a back of the hand, unclockwise was plus), ultrasonic wave, which passed through the specimen, was observed.

# Results/Discussion

In sample A, observed wave included fast wave, slow wave and circumferential wave. Whereas in sample B, the longitudinal wave can only propagate circumferentially along the cortical bone. By comparing observed waveforms, we checked the effects of circumferential wave on the fast and slow waves. First, when incident angle was higher than 12 degrees, circumferential waves were always overlapped. However, when incident angle was lower than 10 degrees, the fast wave never overlapped with the circumferential one. In addition, at any angles, slow wave did not overlap the circumferential wave. According to the above results, we confirmed that in adult human radius model, two-wave phenomenon can be observed clearly without the influence of circumferential wave, when incident angle is from -20 to 10 degrees.

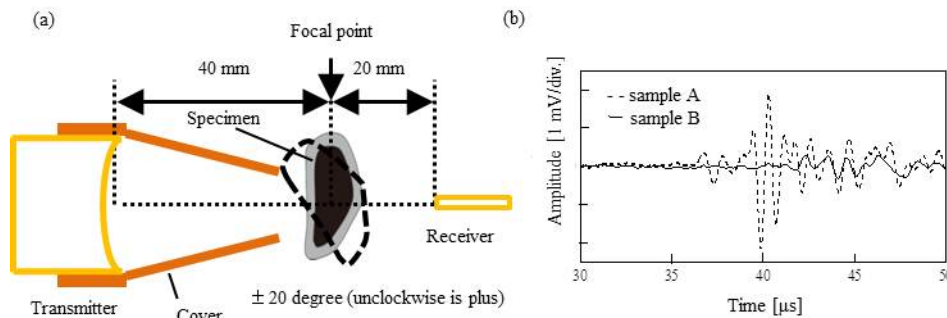


Fig. 1 (a) The layout of transducers and specimen and (b) the observed waveform (angle is 0 degree).

P1A9-4

#### Estimation of cortical thickness and axial bulk longitudinal velocity from axial transmission measurements on ex vivo tibiae

Jean-Gabriel Minonzio<sup>1</sup>, Melanie Dauschies<sup>2</sup>, Simon Bernard<sup>1</sup>, Johannes Schneider<sup>3</sup>, Reinhard Barkmann<sup>2</sup>, Quentin Grimal<sup>1</sup>, Kay Raum<sup>3</sup>, Claus-Christian Giller<sup>2</sup>, **Pascal Laugier<sup>1</sup>**; <sup>1</sup>Laboratoire d'Imagerie Biomédicale, Sorbonne Universités, UPMC Univ Paris 06, INSERM, CNRS, Paris, France, <sup>2</sup>Diagnostic Radiology Quantitative ultrasound, Christian-Albrechts-Universität zu Kiel, Kiel, Germany, <sup>3</sup>Julius Wolff Institute for Biomechanics and Musculoskeletal Regeneration, Charité Universitätsmedizin Berlin, Berlin, Germany

#### Background, Motivation and Objective

Reported axial transmission (AT) measurements at the tibia essentially consisted in measuring the time-of-flight of the first arriving signal (FAS). The FAS offers the advantage of a straightforward signal analysis, but it has the disadvantage that individual bone properties such as cortical thickness and stiffness cannot be simultaneously inferred from a single FAS measurement [1]. A new AT approach in which the dispersion curves of guided modes excited in the cortical shell of the radius has been described by our group [2]. In this study, the measurement protocol has been adapted to measure the tibia. We assess the reliability of this new approach to measure both the cortical thickness (Ct.Th) and the axial compression bulk wave velocity ( $V_L$ ). The trueness of estimates is quantitatively evaluated.

#### Statement of Contribution/Methods

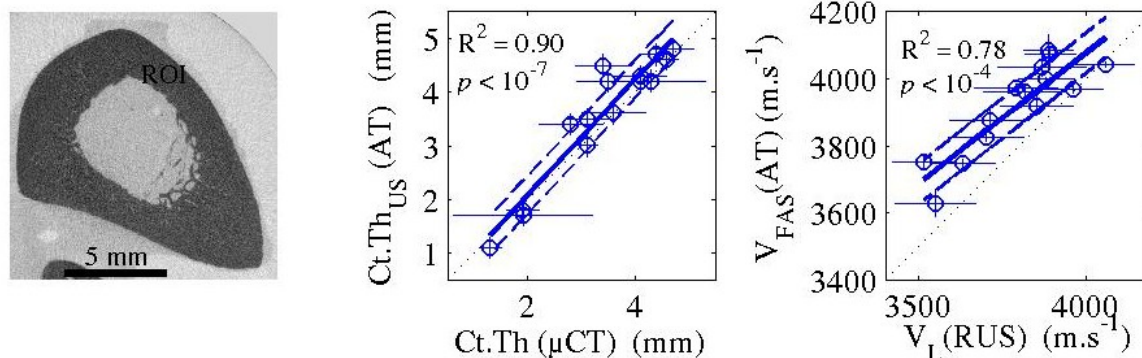
19 ex vivo human tibiae have been measured with a 1 MHz axial transmission transducer array. The full time response of the waveforms recorded on the receivers allows measurements of (i) the FAS velocity ( $V_{FAS}$ ) and (ii) the dispersion curves of the guided modes propagating in the cortical layer (ROI in left figure). From these dispersion curves, Ct.Th<sub>US</sub> is estimated by fitting experimental data to a model of 2D-transverse isotropic free plate of constant elasticity and adjustable thickness.  $V_{FAS}$  and Ct.Th<sub>US</sub> are compared with reference values obtained on small site matched harvested specimens (~4\*3\*2 mm<sup>3</sup>) using resonant ultrasound spectroscopy (RUS) [3] and micro-computed tomography (Scanco vivaCT40, voxel 38 μm), respectively.

#### Results/Discussion

The results show a good agreement between Ct.Th<sub>US</sub> and Ct.Th ( $R^2 = 0.90$ ,  $p < 10^{-7}$ , RMSE = 0.35 mm, central figure) with no bias and between  $V_{FAS}$  and  $V_L$  ( $R^2 = 0.78$ ,  $p < 10^{-4}$ , RMSE = 60 m.s<sup>-1</sup>, right figure). For  $V_L$ , we note a small bias (overestimation by ~100 m.s<sup>-1</sup>) which may be due to several causes including a slight misorientation of the probe for AT measurements or inaccurate site matching. This study opens perspectives towards a multi parametric enhanced assessment of cortical bone mechanical status.

#### References

- [1] E. Bossey, M. Talmant, F. Peyrin, L. Akrou, P. Cloetens, and P. Laugier, J. Bone Mineral Res. **19**, 1548-1556 (2004)
- [2] J. G. Minonzio, J. Foiret, M. Talmant, and P. Laugier, J. Acoust. Soc. Am. **130**, 3574-3582 (2011)
- [3] S. Bernard, Q. Grimal, and P. Laugier, J. Mech. Behavior Biomed. Mat. **18**, 12-19 (2013)



## Clinical Ultrasonic Assessment at the 1/3 Radius

Jonathan Kaufman<sup>1,2</sup>, Emily Stein<sup>3</sup>, Gangming Luo<sup>1</sup>, Fernando Rosette<sup>3</sup>, Zvi Schechner<sup>1</sup>, Mariana Bucovsky<sup>3</sup>, Elizabeth Shane<sup>3</sup>, Robert Siffert<sup>2</sup>; <sup>1</sup>CyberLogic, Inc., New York, NY, USA, <sup>2</sup>Orthopedics, The Mount Sinai School of Medicine, New York, NY, USA, <sup>3</sup>Medicine, Columbia University College of Physicians and Surgeons, New York, NY, USA

### Background, Motivation and Objective

Osteoporosis is a major public health problem. Worldwide, osteoporosis causes more than 8.9 million fractures annually which are associated with a high degree of morbidity and mortality. It is estimated that osteoporosis affects 200 million women - of which approximately 30 percent are less than 70 years old. Presently the gold standard for bone assessment uses dual-energy x-ray absorptiometry (DXA) to obtain an estimate of an individual's bone mineral density (BMD). However, because patients must typically be referred to specialists for DXA, many individuals at high risk of fracture are not diagnosed. Indeed, osteoporosis remains one of the world's most under-diagnosed diseases. For example, in the U.S. it is estimated that only about 20% of individuals at increased risk of fracture have been identified. Therefore, the primary objective of this research is to develop an ionizing radiation-free tabletop ultrasound device that estimates the BMD of the 1/3 radius. This device is designed to be used in primary care settings and to assess bone loss in individuals who may otherwise not have their BMD measured. Early detection is crucial to initiating therapeutic interventions as this is the optimal way to prevent a fragility fracture.

### Statement of Contribution/Methods

A bone sonometer (*UltraScan 650*, CyberLogic, NY, NY, USA) has been used in a clinical study to evaluate its ability to estimate BMD at the 1/3 radius. Seventy-eight adult subjects were recruited for this study under an IRB approved protocol and informed consent was received from each participant. The non-dominant arm of each study subject was measured in thru-transmission and two *net time delay* (NTD) parameters,  $NTD_{CW}$  and  $NTD_{DW}$ , were obtained. These parameters are defined by  $NTD_{DW} = \tau_{SW} - \tau_{DW}$  and  $NTD_{CW} = \tau_{SW} - \tau_{CW}$ , where  $\tau_{DW}$ ,  $\tau_{CW}$ , and  $\tau_{SW}$  are the time-delays associated with 3 distinct ultrasound propagation pathways through the forearm. An ultrasound-based estimate,  $BMD_{US}$ , of the 1/3 radius BMD was computed as  $BMD_{US} = a \cdot \{NTD_{CW} \cdot NTD_{DW}\}^{1/2} + b$ . In this equation,  $a$  and  $b$  are regression coefficients obtained by the method of least squares. Each subject was also measured with DXA (QDR 4500, Hologic, USA) to obtain an estimate,  $BMD_{DXA}$ , of their 1/3 radius BMD. Finally, an ultrasound reproducibility study was carried out on three additional subjects each with 15 independent measurements, and the percent coefficient of variation (%CV) was evaluated.

### Results/Discussion

For these clinical data, there was high correlation ( $r = 0.93$ ,  $P < 0.001$ ) between  $BMD_{DXA}$  and  $BMD_{US}$ . The regression coefficients were  $a=0.19$  and  $b=0.28$ . The %CV was found to be 2.1%. Therefore a new device, the *UltraScan 650*, has been shown to be able to accurately estimate BMD at the 1/3 radius. Its ease of use and lack of ionizing radiation provides a basis by which to expand ultrasonic assessment to the primary care setting. This will in turn lead to a reduction in the incidence of osteoporotic fractures through timely therapeutic interventions.

## Ex vivo measurement of guided waves in human radius: Experimental and simulated results

Bruno Fain<sup>1</sup>, Jean-Gabriel Minonzio<sup>1</sup>, Emmanuel Bossy<sup>2</sup>, Maryline Talmant<sup>1</sup>, Pascal Laugier<sup>1</sup>; <sup>1</sup>Laboratoire d'Imagerie Biomédicale, Sorbonne Universités, UPMC Univ Paris 06, INSERM, CNRS, Paris, France, <sup>2</sup>Institut Langevin, ESPCI ParisTech, CNRS UMR 7587, Paris, France

### Background, Motivation and Objective

Novel approaches in quantitative ultrasound (QUS), known as axial transmission techniques, are currently explored to measure the guided waves propagating axially in the cortical shell of long bones. The identification of the different modes and the measurement of their frequency-dependent velocity should lead to an estimation of the bone geometrical and anisotropic elastic properties. To measure the guided wave dispersion curves in the  $(f, k)$  space, referred to as the *Norm* function, an experimental setup associated with a specific multi-transmitter /multi-receiver probe and singular value decomposition based signal processing has been used [1].

### Statement of Contribution/Methods

Ex vivo experimental measurements performed on 10 human radius were compared to FDTD simulations achieved with SimSonic software [2]. Site matched 2D binary maps (spatial step: 10  $\mu m$ ) were extracted from realistic 3D datasets obtained by X-ray high resolution computed tomography (Scanco XtremeCT - voxel size:  $(82 \mu m)^3$ ). Estimated guided waves were compared with the theoretical guided modes of a 2D transverse isotropic free plate model.

### Results/Discussion

An example of 2-D numerical cortical bone model used for FDTD simulation (size 46 x 2.5 mm) is shown on figure 1 (top). Corresponding experimental (left) and simulated (right) *Norm* functions are shown at the bottom. The theoretical modes of a 2D transverse isotropic free plate model, with a thickness equal to 1.1 mm, are also plotted (white lines). Apart A0 mode, which is strongly influenced by the wave propagation in the surrounding medium, two guided modes are experimentally measured: S0 (0.5-1MHz) and A1 (0.8-1.8 MHz). Similar results are observed for the ten measured radius.

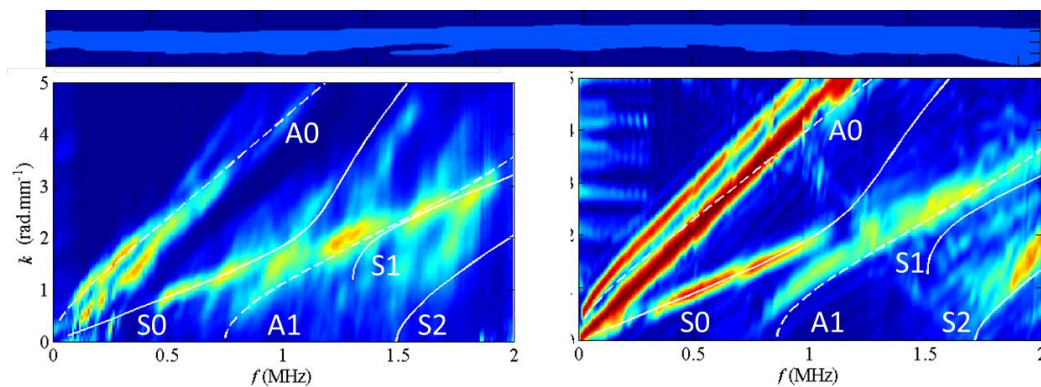
A reasonable agreement is evidenced between simulations and experimental data, which suggests the validity of the waveguide assumption despite the irregular geometry of cortical bones.

The authors acknowledge Azalée for financial support, Mrs. A. Nzie Ngapout and Dr. C. Chappard for assisting in HRpQCT data acquisition and image processing.

### References

- [1] J. G. Minonzio, J. Foiret, M. Talmant, and P. Laugier, J. Acoust. Soc. Am. **130**, 3574–3582 (2011).
- [2] E. Bossy, M. Talmant, and P. Laugier, J. Acoust. Soc. Am. **115**, 2314-2324 (2004).





P1A9-7

### Ultrasonic Wave-field Reconstruction of Bone Fractures: Numerical Modelling and In-vitro Studies

Tho N.H.T. Tran<sup>1</sup>, Kim-Cuong T. Nguyen<sup>1,2</sup>, Mauricio D. Sacchi<sup>3</sup>, Edmond Lou<sup>4</sup>, Lawrence H. Le<sup>1,3</sup>; <sup>1</sup>Department of Radiology & Diagnostic Imaging, University of Alberta, Edmonton, Alberta, Canada, <sup>2</sup>Department of Biomedical Engineering, Ho Chi Minh City University of Technology, Vietnam, <sup>3</sup>Department of Physics, University of Alberta, Edmonton, Alberta, Canada, <sup>4</sup>Department of Surgery, University of Alberta, Edmonton, Alberta, Canada

#### Background, Motivation and Objective

In recent years, interest of using ultrasound to diagnose bone fractures and monitor fracture healing has been increasing. Compared to other diagnostic imaging modalities, such as X-ray and CT, ultrasound does not involve ionizing radiation, which is beneficial to pediatric patients because their bony tissues are still in proliferation and more susceptible to the harmful X-rays. Conventional ultrasound scanners are not optimally designed to image hard tissues such as bone. Post-acquisition inversion/imaging algorithms are necessarily developed to reconstruct the geometrical characteristics of the cortical layer. In this work, we applied the split-step Fourier imaging (SSFI) method to image long bone fractures using simulated and in-vitro data sets.

#### Statement of Contribution/Methods

We applied the SSFI method to reconstruct internal bone structure using the pulse-echo (zero-offset) time-distance data acquired on the sample's surface. The method requires an estimated slowness model, which is approximated by a depth-dependent term and a first-order spatially-varying perturbation. Since the recorded wave-fields are generated by the underlying scatterers or reflectors, imaging those reflectors can be accomplished by reversing the propagation path of the wave-fields or propagating backwards in time the wave-fields to the source of scatterers. Simulated data sets were used to validate the method. We used a stratified cortical bone model with water to mimic the overlying soft tissue and underlying marrow. The thickness of the soft tissue, cortical bone, and marrow layers were 6 mm, 7 mm, and 7 mm respectively. The model had a 3-mm-wide 45° inclined crack. The in-vitro data were acquired using a 2.25-MHz 64-element Tomoscan Focus LT™ phased array system. The sample used was a bovine tibia with 6 mm thick overlying soft-tissue-mimicking layer. The 3 mm wide irregularly-shaped fracture was manually created to mimic comminuted type of fractures.

#### Results/Discussion

The reconstructed images show proper mapping of the cortical layer and fracture. The cortical thickness was reasonably determined with less than 10% error. The result also demonstrates reasonable bone images even though the input slowness model was crude, indicating the robustness of the proposed method. The split-step imaging method is a promising technique to map the recorded time-distance data to depth-distance images, which provide better bone/fracture geometry information. The method extends the application of conventional medical ultrasound to study bone tissue and has the potential to be developed for clinical application.

P1A9-8

### Characterization of transcranial ultrasonic passage in the Göttingen minipig

Amit Mulgaonkar<sup>1,2</sup>, Meghedi Babakhanian<sup>1,2</sup>, Martin Culjat<sup>1,3</sup>, Bryan Nowroozi<sup>1,2</sup>, William Melega<sup>4</sup>, Warren Grundfest<sup>2,3</sup>; <sup>1</sup>Center for Advanced Surgical and Interventional Technology (CASIT), University of California, Los Angeles (UCLA), Los Angeles, California, USA, <sup>2</sup>Biomedical Engineering, University of California, Los Angeles (UCLA), Los Angeles, California, USA, <sup>3</sup>Surgery, University of California, Los Angeles (UCLA), Los Angeles, California, USA, <sup>4</sup>Department of Molecular and Medical Pharmacology, University of California, Los Angeles (UCLA), Los Angeles, California, USA

#### Background, Motivation and Objective

There is continuing interest in targeted transcranial stimulation of deep brain structures using techniques such as Low Intensity Focused Ultrasound (LIFU). As the brain of the gyrencephalic Göttingen minipig more closely resembles the human brain in anatomy, growth, and development compared to the brains of more commonly used small laboratory animals, a minipig model for studies on transcranial ultrasonic neurostimulation has been proposed. Accurate transcranial targeting and dosage of acoustic energy onto target neural structure requires quantification of the acoustic effect the skull has on the ultrasound wave. The objective of this work is to assess the effect of transcranial passage, both in terms of attenuation and orientation of an incident acoustic wave, in the minipig.

#### Statement of Contribution/Methods

The large impedance mismatch between the regions of the skull bone that must be transited to deliver the acoustic energy to the brain results in a significant reduction of the effective acoustic energy at the target site, relative to what is generated by the transducer outside of the skull. Furthermore, the curved shape of the skull can induce lensing effects, potentially skewing the focus of the beam. A series of theoretical and ex-vivo ultrasound studies on the skull were conducted to address these issues. A simplified transmission model of the transit of an acoustic wave across a thin section of bone was considered to provide a theoretical baseline for attenuative effects. Ex-vivo samples of the lower skull lamina of the Göttingen minipig were acquired and their acoustic transmission properties measured using standard techniques in a water-tank scanning acoustic measurement system. These measurements were compared to those taken from intact Göttingen minipig skulls using a custom stereotactic measurement apparatus, also mounted in a water tank.

#### Results/Discussion

Based on the theoretical calculations of reflection at the bone interface, an acoustic loss on the order of 5 dB was expected from the transit through the lower lamina of the minipig skull. However, water tank measurements of transmission through the lower lamina sample revealed high, and highly variable acoustic loss greater than 11 dB, with the results indicative of a likely shift in beam orientation relative to its free-water axis. The spatial point of acoustic focus was found to be highly sensitive to the targeting paradigm used. Precision measurements of the acoustic transit of the stereotactically addressed intact-skulls resulted in a consistently measured acoustic loss of 8.5 dB from the skull transition, corresponding to an intensity transmission coefficient of  $0.1298 \pm 0.00990$ . Negligible spatial shift in the acoustic focus was observed. These results indicate that the Göttingen minipig may be suitable for studies of targeted transcranial neuromodulation due to the predictable acoustic transmission measured from the intact skull.

# P1A10 - MTH: Drug Delivery and Stimulation

Salon C

Thursday, September 4, 2014, 8:00 am - 5:00 pm

Chair: **Tom Matula**  
Univ. of Washington, Seattle

P1A10-1

## Serum influence on in-vitro Gene Delivery using Microbubble-Assisted Ultrasound

Aya Zeghimi<sup>1</sup>, Anthony Novell<sup>1,2</sup>, Rose-Anne Thepault<sup>1</sup>, Ayache Bouakaz<sup>1</sup>, **Jean-Michel Escoffre**<sup>1,3</sup>, <sup>1</sup>UMR Inserm U 930 Imagerie & Cerveau, Université François Rabelais, Tours, France, France, <sup>2</sup>Joint Department of Biomedical Engineering, The University of North Carolina and North Carolina State University, Chapel Hill, NC 27599, USA, USA, <sup>3</sup>Imaging Division, University Medical Center Utrecht, Utrecht, Netherlands, Netherlands

### Background, Motivation and Objective

Plasmid DNA (pDNA) is attractive molecule for gene therapy. Safe and efficient pDNA delivery is required to enhance its intra-tissue bioavailability. Among non-viral methods, sonoporation has become a promising method for in-vitro and in-vivo pDNA delivery. The efficiency of these methods is generally limited by the presence of serum. The aim of this study was to evaluate the influence of serum on in-vitro pDNA delivery using sonoporation.

### Statement of Contribution/Methods

The effects of a range of serum concentrations (0-50%) on efficiency of in-vitro pDNA delivery by sonoporation were determined on U-87 MG cells. The cell suspension ( $5 \times 10^5$  cells in 1.5 mL) was placed in a plastic cuvette containing 7.1  $\mu$ L of SonoVue microbubbles (MB:cell, 5:1) and 7.5  $\mu$ g pDNA (for transfection evaluation) or 100  $\mu$ M propidium iodide (for membrane permeabilization rate). The cell suspension was exposed to 1 MHz US waves for 30 s with a pulse repetition of 100  $\mu$ s using 40 cycles/pulse. The peak negative pressure was 400 kPa. The transfection level and membrane permeabilization rate were measured by flow cytometry and the cell viability was evaluated using MTT assay, 48 h later. The serum influence on pDNA topology and microbubble destruction was also assessed.

### Results/Discussion

As shown in Fig. 1, pDNA delivery in the absence of serum induced a transfection level of  $21 \pm 3$  %. The presence of 1% serum resulted in a significant enhancement in the transfection level compared with that obtained in the absence of serum achieving an optimal level of  $33 \pm 2$  %. However, the transfection level significantly decreased from  $29 \pm 3$  % to  $5 \pm 1$  % when the serum concentration increased from 5% to 50%. The increment in transfection level with low serum concentration (from 0% to 1%) also correlated with a significant increase in cell viability ( $64 \pm 9$  % vs  $88 \pm 8$  %). The decrease in transfection level observed with the increasing serum concentration from 5% to 50% was not associated with a loss of cell viability or with decreases in MB destruction or in membrane permeabilization. This decrease in transfection level was positively correlated to the serum DNase-mediated decrease in the proportion of supercoiled pDNA while sonoporation has no impact on pDNA topology. In conclusion, serum influences the efficiency of in-vitro pDNA delivery by sonoporation through change in pDNA topology.

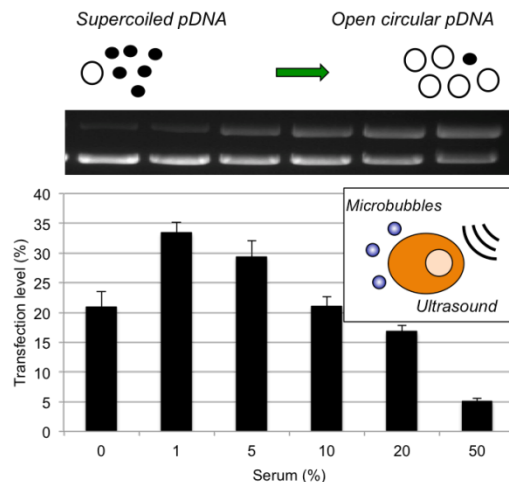


Figure 1: Serum influence on in-vitro gene delivery using microbubble-assisted ultrasound

P1A10-2

## Development of an ultrasound-sensitive antimicrobial platform for reducing infection after spinal stabilization surgery

Flemming Forsberg<sup>1</sup>, **John Eisenbrey**<sup>1</sup>, Keith Fitzgerald<sup>2</sup>, Alex Sevit<sup>3</sup>, Steven Kurtz<sup>3</sup>, Chris Kepler<sup>2</sup>, Noreen Hickock<sup>2</sup>, <sup>1</sup>Department of Radiology, Thomas Jefferson University, USA, <sup>2</sup>Department of Orthopaedic Surgery, Thomas Jefferson University, USA, <sup>3</sup>School of Biomedical Engineering, Science & Health Systems, Drexel University, USA

### Background, Motivation and Objective

Infection arises in 1-6% of elective and up to 25% of trauma cases of spinal fusion surgery. Consequences of infection are devastating and include prolonged hospital admission during infection eradication, replacement of the surgical hardware, and significant morbidity and mortality. Current strategies of prophylaxis involve packing the surgical site with free antibiotic, but this is short lived in the presence of aseptic drains. An antibiotic-loaded implant that could be noninvasively triggered 3-5 days post surgery and provide immediate and complete drug release would prolong prophylaxis, and eradicate residual infection with a supra-therapeutic dose of antibiotic. Hence, the objective of this study is to develop an ultrasound-sensitive antimicrobial implant for reducing infection after spinal surgery.

**Statement of Contribution/Methods**

Porous polyether ether ketone (PEEK; kind gift of Invibio, Lancashire, United Kingdom) samples were fabricated in 1 cm<sup>3</sup> blocks for this study (the future geometry will be c-shaped clips that attach to spinal hardware). Methylene blue (MeB; 0.5 ml in saline) was injected into the porous PEEK via 24 gauge syringe and allowed to dry overnight. PEEK samples were then coated with 1.5 grams of 70 kDa poly-lactic acid (PLA; Lakeshore Biomaterials, Birmingham, AL) dissolved in 30 ml of chloroform followed by solvent evaporation. This fabrication process resulted in air/MeB-filled channels within the PEEK, covered by a layer of PLA. To determine the effect of ultrasound on release kinetics, PEEK blocks were placed in 200 ml of saline within a 500 ml beaker. Ultrasound triggering of the experimental group was performed for 30 minutes using an Ultrasonics RP scanner with L4-9 probe (Analogic Corp, Peabody MA) transmitting at 5 MHz and 100% acoustic output. Saline was then sampled over an 8 day period to determine the MeB concentration over time and compared to the unisonated control.

**Results/Discussion**

No immediate release of MeB was observed after suspension of the loaded PEEK blocks, demonstrating complete coating. During ultrasound insonation, small gas bubbles were observed leaving the PEEK block, indicating rupture of the PLA coating and penetration of saline into the porous channels. Solution from the non-isonated control group showed a 26% increase in MeB concentration 2 days after suspension, and then remained stable the following 6 days. Solution from the insonated (experimental group) showed a 757% increase in MeB concentration relative to baseline levels over an 8 day period, with the largest increase occurring over days 3-5 (with a 539% increase in MeB concentration). Preliminary results demonstrate the feasibility of using drug-loaded porous PEEK as an implantable material for delayed, ultrasound-triggered antibiotic release. Future studies on the incorporation of vancomycin, and in vivo release are planned.

**P1A10-3****Ultrasound-mediated gene delivery by using folic acid-modified cationic microbubbles**

En-ling Chang<sup>1</sup>, Chien-Yu Ting<sup>1</sup>, Chih-Kuang Yeh<sup>1</sup>; <sup>1</sup>Department of Biomedical Engineering and Environmental Sciences, National Tsing Hua University, Taiwan

**Background, Motivation and Objective**

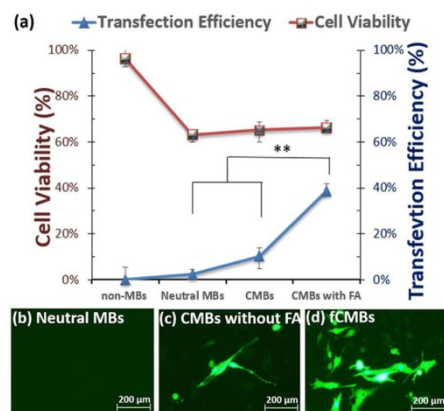
Glioblastoma multiforme (GBM) is a malignant brain tumor with poor prognosis and high recurrence rate despite traditional chemotherapy. Ultrasound-targeted microbubbles destruction (UTMD) has been approved to achieve local blood-brain barrier disruption (BBBD), enhancing therapeutic agents into the brain. Besides, UTMD has been employed to deliver tumor-killing gene. Recently, folate receptor (FR) has been found to be overexpressed in GBM which benefits tumor-specific targeting therapy. In this study, we fabricated cationic microbubbles with folic acid (fCMBs) simultaneously to achieve targeting, and nonviral ultrasound gene transfection in C6 glioma cells (a major precursor cell of brain tumor).

**Statement of Contribution/Methods**

The fCMBs were composed of DSPC, DPPC, DSPE-PEG2K, cationic DPTAP, and DSPE-PEG2K-amino-FA. DSPE-PEG2K-amino-FA was synthesized via intermediate reactant of 1-Ethyl-3-(3-dimethylaminopropyl) carbodiimide. Green fluorescent protein (pCMV-GFP) was utilized as reporter gene for transfecting into FR-positive C6 cells. Non-focused ultrasound (3 MHz, 1.1 MPa, 10 % duty-cycle, and 60 sec) was used to enhance gene delivery after fCMBs (5 µg pCMV-GFP/ 6×10<sup>7</sup> MBs) targeting onto C6 cells. MBs targeted efficiency, gene expression and cell viability were assessed using optical microscopy, cell counting assay and MTT assay, respectively.

**Results/Discussion**

The fCMBs had a mean diameter and concentration of  $1.09 \pm 0.21$  µm and  $(33.61 \pm 5.38) \times 10^9$  MBs/mL. The pCMV-GFP was successfully bound onto the shell of fCMBs, lowering the surface charge from +30.5 to +17.1 mV. Owing to FR-ligand binding, the targeting efficiency of MBs was increased. Gene transfection efficiency under fCMBs was 3.74 and 4.77 folds higher than those under CMBs without FA and neutral MBs, respectively (Fig. a-d). Besides, there was no significant difference in cell viability among fCMBs, CMBs without FA and neutral MBs ( $63.53 \pm 2.51\%$ , Fig. a). In this study, improvement of gene transfection using CMBs with FA in C6 glioma cells under UTMD was confirmed. Future work includes applying this targeting gene transfection system on in vivo GBM model with BBBD for brain tumor therapy.

**P1A10-4****Ultrasonic monitoring of skeletal muscle response to electrical stimulation of peripheral nerve**

Andy Huang<sup>1</sup>, Yuu Ono<sup>1</sup>; <sup>1</sup>Carleton University, Ottawa, Ontario, Canada

**Background, Motivation and Objective**

Peripheral nerve stimulation (PNS) is used for regional anesthesia to estimate the distance between the needle tip and target nerve and to adjust the dose of anesthetic drug based on the muscle twitches invoked by PNS. The visual observation of the muscle twitches is often subjective and cannot provide quantitative information of muscle response or detect small twitches. Ultrasonic methods are capable of performing non-invasive and quantitative real-time measurements of internal tissue displacements. However, conventional ultrasound probes are bulky, and difficult to attain the consistent and stable contact between the probing surface and the patient body having movement. In addition, the weight of the probe may impede the muscle contraction, which results in inaccurate estimation of the tissue displacement caused by PNS. In this study, the capability of a flexible and wearable ultrasonic sensor was investigated for monitoring muscle response to PNS.

## Statement of Contribution/Methods

A flexible, lightweight ultrasonic sensor was constructed using a piezoelectric PVDF film. It had an active ultrasonic area (electrode size) of 20 mm by 20 mm. The total thickness and the weight of the sensor developed were 0.2 mm and less than 1 g, respectively. Therefore, this sensor can be attached onto a curved and deformable body surface without restricting the underlying tissue motion. The ultrasonic sensor was attached to the left palm of a subject over the abductor pollicis brevis to monitor the muscle response to PNS. Involuntary muscle twitches were invoked by PNS using a contact electrode with a hemispherical tip of 1-mm radius, instead of a needle electrode. The electrode tip contacted to the wrist 7 cm away from the ultrasonic sensor. The pulse repetition frequency and square wave width of PNS were set 1 Hz and 0.5 ms, respectively. To investigate the measurement sensitivity of tissue displacement, the PNS current was changed from 2 mA to 3 mA with 0.2 mA step in this experiment. Ultrasonic signals reflected from the trapezium bone were acquired in M-mode. The internal tissue displacement was obtained using a phase tracking method. The displacement value for each PNS current was calculated by the average of 6 twitches over 6 seconds.

## Results/Discussion

The muscle twitches corresponding to the PNS frequency of 1 Hz were visually observed with the PNS currents at 2.4 mA and above, but not 2.2 mA and below. The subject still felt the electrical stimulation at 2.2 mA but not at 2.0 mA. The almost constant tissue displacement of 0.67 mm was measured with a PNS current from 2.6 mA to 3 mA with the proposed ultrasonic method. The measured displacement value decreased to 0.4 mm at 2.4 mA, which is 40 % less than those obtained at 2.6 to 3mA. The displacement values were not obtained at 2.2 mA and below with the experimental configuration employed in this study. It was verified that the proposed ultrasonic method could provide quantitative estimation of muscle response to PNS.

## P1A10-5

### ULTRASOUND STIMULATION OF INSULIN RELEASE FROM PANCREATIC BETA CELLS

Ivan Suarez<sup>1</sup>, Aleksandar Jeremic<sup>2</sup>, Vesna Zderic<sup>1</sup>; <sup>1</sup>Department of Electrical and Computer Engineering, The George Washington University, Washington, District of Columbia, USA, <sup>2</sup>Department of Biological Sciences, The George Washington University, Washington, District of Columbia, USA

## Background, Motivation and Objective

Type 2 diabetes mellitus is a complex metabolic disease that has reached epidemic proportions. Controlling type 2 diabetes is often difficult. Many patients are poorly compliant with lifestyle change recommendations, and pharmacological management routinely requires complex therapy with multiple medications, and loses its effectiveness over time. Thus, new modes of therapy are needed that will target directly the underlying causes of abnormal glucose metabolism. The objective of this study is to explore a novel, non-pharmacological approach that utilizes the application of ultrasound energy to augment insulin release from pancreatic beta cells.

## Statement of Contribution/Methods

Our experiments focus on determination of effectiveness and safety of ultrasound application in stimulation of insulin release from pancreatic beta cells. ELISA insulin release assay was used to determine and quantify the effects of ultrasound on insulin release in cultured beta cells. Effects of ultrasound on cell viability were assessed by employing MTT, Caspase-3, LDH release and Annexin-apoptotic cytotoxic assays. Ultrasound exposure was generated using a commercial ultrasound device (Sonicator 740, Mettler Electronics) and a planar ultrasound transducer with center frequency of 1 MHz and intensity of 0.8 W/cm<sup>2</sup> was used to treat the cells for 5 minutes. Insulin has been shown to be released in a calcium-dependent manner in response to changes in blood sugar levels. Furthermore, it has been reported that calcium signaling can stimulate insulin transcription, as well as beta cell proliferation. Therefore, we are also looking to evaluate extracellular calcium influx as a potential mechanism for enhanced ultrasound-induced insulin release. Calcium transients were thus measured and quantified by ratiometric calcium-imaging assay.

## Results/Discussion

Our preliminary data indicated that application of therapeutic ultrasound may lead to increase of insulin secretion from beta cells while maintaining cell viability. ELISA results showed a 25% increase in insulin release from beta cells after ultrasound exposure for 5 minutes. Cell viability was not significantly affected during and for up to one hour after treatment. Effects of ultrasound on beta cell function are currently being studied for a wide range of ultrasound parameters as to find the exposure inducing optimized insulin release from beta cells. Insulin release and cell viability results will be correlated as a function of temperature increase and cavitation activity, as well as extracellular calcium influx. If shown successful our approach may eventually lead to new methods in the treatment of diabetes and other secretory diseases. Our future studies will focus on application of ultrasound to the pancreas in an in vivo animal model to determine whether it would be possible to stimulate beta cells without stimulating other endocrine and exocrine cells of the pancreas.

## P1A10-6

### Active induction of microbubbles in flow at T-form bifurcation through acoustic focal points with phase variation

Kohji Masuda<sup>1</sup>, Naoto Hosaka<sup>1</sup>, Ren Koda<sup>1</sup>, Shinya Miyazawa<sup>1</sup>, Takashi Mochizuki<sup>1</sup>; <sup>1</sup>Tokyo Univ. of A&T, Japan

## Background, Motivation and Objective

To contribute therapeutic applications using microbubbles with ultrasound, e.g. local enhancement in HIFU therapy or drug delivery, we have reported the method to produce three-dimensional acoustic force field to prevent the diffusion of microbubbles in blood flow. However, there was a limitation in induction rate at a bifurcation of artificial blood vessel because the acoustic field was stable. In this research we examined an active induction of microbubbles at a T-form bifurcation, which is difficult to control the course of microbubbles, by considering phase variation of acoustic field.

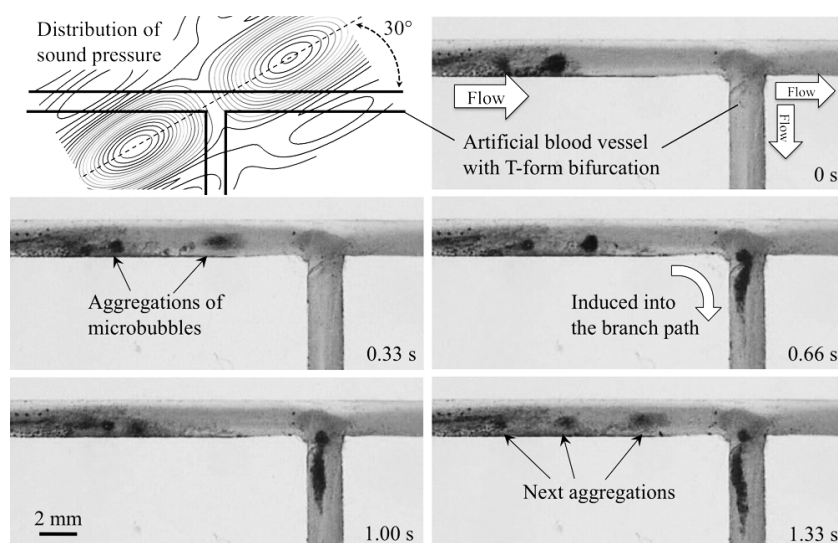
## Statement of Contribution/Methods

We used a flat matrix array transducer including 64 PZT elements, which was specially developed to produce a continuous wave. We prepared an artificial blood vessel with T-form bifurcation made of Poly(ethylene glycol) Monomethacrylate (PEGMA) with the inner diameter of 2 mm. We produced an acoustic field of two focal points over the bifurcation, where the distance between the two peak points was 12 mm, maximum sound pressure in each peak was 200 kPa-pp, and the phase difference of them was 180 degree (opposite phase).

## Results/Discussion

Figure shows the transition of microbubbles behavior at the bifurcation when microbubbles suspension (average diameter of 4 μm, density of 2.35 μl/ml) entered from left with inflow velocity of 40 mm/s. In 0 s, microbubble aggregation was formed near the left peak point because primary Bjerknes force, which is produced in the direction of the gradient of acoustic field, propelled microbubbles against flow resistance. In 0.33 s, a grown aggregation was released to enter the bifurcation, where the right peak produced another primary Bjerknes force to prevent from entering the right branch path. Meanwhile, because no force was produced to prevent from entering the lower branch path, the aggregation was induced into the lower path in 0.66 s. Similarly other aggregations were produced and induced into lower path successively.

Here it must be noted that the above-mentioned induction was not confirmed when the phase between two peaks was same because they were merged together to form greater one peak. In conclusion, we have confirmed to induce microbubbles in flow using T-form bifurcation through acoustic focal points with phase variation, which is going to be applied to more complicated shape of blood vessel.



P1A10-7

### Molecular-Targeted Nanorods for the Localised Destruction of Cancer Cells

James McLaughlan<sup>1</sup>, Sevan Harput<sup>1</sup>, David Cowell<sup>1</sup>, Steven Freear<sup>1,2</sup>, <sup>1</sup>School of Electronic and Electrical Engineering, University of Leeds, Leeds, West Yorkshire, United Kingdom

#### Background, Motivation and Objective

Nanorods are used to improve the signal-to-noise ratio of the thermoelastic emissions from tissue and can be functionalised with molecular-targeting ligands to be specifically targeted to cancer cells, for both imaging and therapeutic applications. By simultaneously illuminating these nanorods whilst they are under tension from an ultrasound field, localised inertial cavitation is generated at significantly lower laser fluence and pressure thresholds than for either of these mechanisms alone. The broadband acoustic emission generated with an inertial collapse can be detected, where it has been shown that the magnitude of these emissions are over an order of magnitude greater than thermoelastic emissions alone and thus have a greater depth penetration. As the inertial collapse is driven by the peak pressure of the ultrasound field it can be sufficiently violent to result in the localised destruction of cancer cells. The aim of this study is to investigate the formation and activity of nanorod nucleated inertial cavitation for the detection and destruction of colorectal cancer cells *in vitro*.

#### Statement of Contribution/Methods

HCT116 colorectal cancer cells were cultured in a flow cell and a concentration of  $1 \times 10^9$  nanorods/ml was flown through. A 1.1 MHz high intensity focused ultrasound (HIFU) transducer was synchronised with a tuneable 5 ns pulse laser, such that the third rarefaction of a 5-cycle burst was co-incident with a single laser pulse (850 nm,  $15.3 \text{ mJ/cm}^2$ ) in the flow-cell. Broadband emissions were detected with a 15 MHz focused transducer (Fig 1a) and a computer controlled 3D positioning system was used to raster-scan the confocally aligned transducers, over the flow-cell. The nucleation threshold was established by varying the peak negative pressure from 0-1 MPa.

#### Results/Discussion

Fig.1(b) shows the raster-scans of a flow cell at different pressure levels with and without a laser pulse (Lon and Loff), where the white dotted line approximately indicates the channel. Broadband emissions from inertial cavitation were 30 dB greater than photoacoustic emissions. Fig.1(c) demonstrates that the formation of inertial cavitation is highly controllable and the magnitude of emissions increases with increasing acoustic pressure. Thus this technique could be a used for identifying then destroying cancerous cells by controlling the ultrasound exposure.

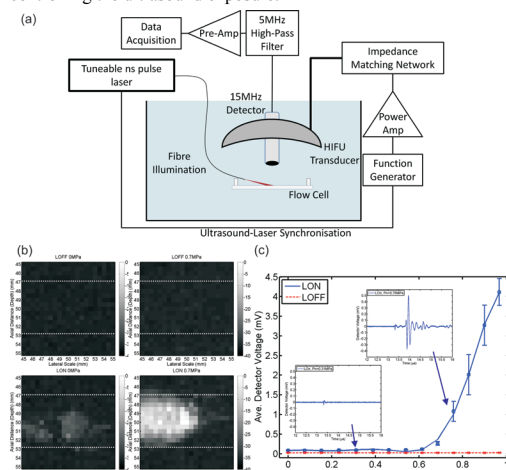


Fig. 1(a) shows a schematic of the experimental set-up. (b) raster-scan images of the flow cell with (top-left) laser off, HIFU off, (top-right) laser off, HIFU on, (bottom-left) laser on, HIFU off and (bottom-right) laser on, HIFU on. The white dotted line indicates the approximate position of the nanorod filled channel. (c) Average peak detector voltage detected for increasing peak negative pressure for a fixed laser fluence.



P1A10-8

# Inhalation Delivery of Surface Acoustic Wave-Nebulised Monoclonal Antibodies, siRNA, and Stem Cells for Treatment of Lung Disease

Leslie Yeo<sup>1</sup>, James Friend<sup>2</sup>; <sup>1</sup>School of Environmental and Civil Engineering, RMIT University, Melbourne, Victoria, Australia, <sup>2</sup>MicroNano Research Facility, RMIT University, Melbourne, Victoria, Australia

## Background, Motivation and Objective

Treatment of lung disease would be far more attractive via pulmonary delivery than intravenous and oral delivery methods if it were not for the difficulty in forming liquid droplet aerosols with low dispersity and appropriately sized for delivery to the small airways and alveoli. Dry particle formulations would be ideal but for the cost and time required in their development. Numerous methods of nebulization, including the use of ultrasound with meshes, orifices, and so forth have been examined, but these nearly universally cause destruction of the biomolecules, produce polydisperse mists inappropriate for inhalation, and certainly are very effective at lysis of cells. Stem cell delivery is only an option via intravenous injection, with less than 1% uptake into the tissues of the lung.

## Statement of Contribution/Methods

A novel approach is presented here, employing a handheld, radio frequency surface acoustic wave nebulizer that produces <5µm droplets from an open fluid meniscus formed by an aqueous suspension of antibodies, siRNA, or pDNA, depending on the target application. We use laser diffraction, next-generation impactor equipment, *in vitro* cell work with cancer cell lines and stem cells, and *in vivo* small and large animal trials to examine the potential of surface acoustic wave nebulization in pulmonary drug and cell delivery. We also employ substantial physical analysis to understand the nebulization process and use this knowledge to improve the nebulizer performance and avoid damage of sensitive biomolecules and cells through the nebulization process.

## Results/Discussion

Monoclonal antibodies raised against EGFR have been shown in *in vitro* work to effectively suppress its activity in A431 cells, pDNA-based vaccines against H1N1 Solomon Islands influenza have been shown---for the first time---to exhibit *in vivo* systemic immune response in mice and sheep, and siRNA+PEI/lipofectamine has been shown to exhibit effective transfection and knockdown *in vitro* in 293T cells. Finally, we have successfully nebulised stem cells into 10µm droplets and found upon their collection that they retain their proliferation and differentiation characteristics, their immunophenotypic profile via flow cytometry, and their genetic expression via qPCR despite the nebulisation process.

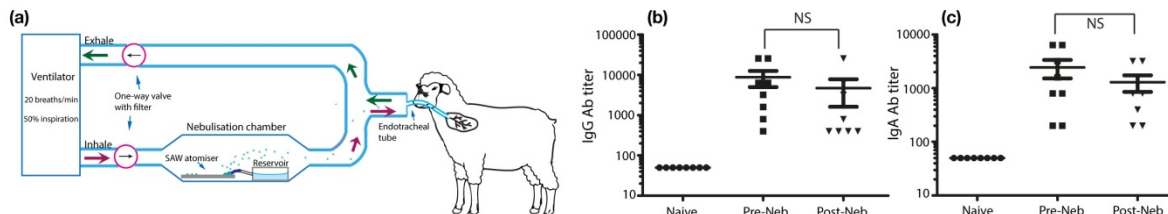


**Fig: (a)** Nebulisation in sheep for pulmonary delivery of H1N1 Solomon Islands pDNA for immunization, indicating (b,c) effective systemic immune system response. Hemagglutination inhibition and other supporting evidence to be provided at the presentation.

P1A10-9

# Ultrasound-Stimulated Microbubble Effects on Cell Membrane Damage: UDP glycosyltransferase 8 (UGT8) Involvement *in vitro* and *in vivo*

Azza Al-Mahrouki<sup>1,2</sup>, Anoja Giles<sup>1,2</sup>, Amr Hashim<sup>1,2</sup>, Hyunjung Christina Kim<sup>1,2</sup>, Ahmad El-Falou<sup>1,2</sup>, Gregory Czarnota<sup>1,2</sup>; <sup>1</sup>Department of Radiation Oncology and Imaging Research, Sunnybrook Health Sciences Centre, Toronto, ON, Canada, <sup>2</sup>Physical Sciences, Sunnybrook Health Sciences Centre, Toronto, ON, Canada

## Background, Motivation and Objective

We have recently demonstrated that the use of ultrasound (US) stimulated microbubbles (MB) in cancer therapy is a new approach to sensitize cells to radiation (XRT), however the molecular determinants are yet to be identified. In this study we have investigated the effect of down regulating UGT8 on the microbubble effects in a prostate cancer tumor line (PC3). UGT8 is an enzyme involved in ceramide metabolism.

## Statement of Contribution/Methods

Stably transfected PC3 cells with a shRNA construct against *UGT8* and the generated xenograft tumors were treated with radiation, US/MB, or a combination of radiation and US/MB. Both ceramide and UGT8 labeling were used to evaluate treatments outcome in cells. Tumor xenografts (PC3, UGT8-silenced PC3, and UGT8-upregulated PC3) were treated with 8Gy, US/MB or US/MB+8Gy. Ultrasound treatments consisted of a 16-cycle tone burst at a center frequency of 500 kHz and a pressure of 570 kPa. The total insonification time was 750 ms over 5 minutes resulting in a duty cycle of 0.25%. Definity microbubbles were used at a concentration of 3% v/v, administered via tail-vein immediately before ultrasound treatment. The outcome was evaluated with high frequency ultrasound acquired before, and 24 hours after treatment using a VEVO770 system and a 25 MHz center frequency transducer. The vascularity index was used to quantify power Doppler data, while quantitative ultrasound spectroscopy parameters were used to assess tumor response and tissue structural changes. Staining using H&E, TUNEL and Trichrome of tumor sections was used to measure and correlate cell death following treatments to ultrasound parameters.

## Results/Discussion

UGT8 down regulated cells exhibited an increased sensitivity to microbubble effects. Specifically, an increase in the immuno-labeling of ceramide was observed in the cells where UGT8 was down-regulated as opposed to the cells where UGT8 was not regulated or was up-regulated. Clonogenic assays have revealed a decreased level of cellular survival with the down-regulation of UGT8. Histopathology demonstrated more cellular damage in tumors with down-regulated UGT8 when compared to tumors with up-regulated UGT8. Additionally, when investigating the effect of the treatment on the vasculature of tumors using power Doppler imaging, a greater reduction in the vascular index was observed in UGT8-down-regulated specimens. In conclusion, microbubble effects appear to be modulated by cellular lipid metabolism effects linked to increase in cell death induced by ultrasound-stimulated microbubble effects.

## P1A10-10

**Ultrasound-enhanced Delivery of Ophthalmic Drugs into the Eye**

Marjan Nabili<sup>1</sup>, Aditi Shenoy<sup>1</sup>, Shawn Chawla<sup>1</sup>, Sankaranarayanan Mahesh<sup>2</sup>, Ji Liu<sup>2</sup>, Craig Geist<sup>2</sup>, Vesna Zderic<sup>1</sup>; <sup>1</sup>Department of Electrical and Computer Engineering, The George Washington University, USA, <sup>2</sup>Department of Ophthalmology, The George Washington University, USA

**Background, Motivation and Objective**

Topical administration of drugs through cornea, for treatment of ocular inflammations and infections, is the preferred method for drug delivery. Our research work focused on applying ultrasound for increasing corneal permeability for ophthalmic drugs while generating minor changes in the eye tissues.

**Statement of Contribution/Methods**

The *in vitro* study was designed using New Zealand rabbit corneas in standard diffusion cell set-up, to investigate corneal permeability of dexamethasone sodium phosphate. Ultrasound application at frequencies of 400 kHz - 1 MHz, intensities of 0.3 - 1.0 W/cm<sup>2</sup> for 5 min was studied. Using the most effective parameters used *in vitro* study; the *in vivo* study was designed to investigate effects of ultrasound on corneal permeability. Tested ultrasound frequencies were 400 kHz and 600 kHz, at intensity of 0.8 W/cm<sup>2</sup>, applied for 5 min. Drug concentration in aqueous humor, collected from ultrasound and sham-treated samples, was determined using chromatography methods. Histology slides were used to examine structural changes in the cornea. Modeling studies were performed using a finite element modeling software (PZFlex) to further understand the temperature changes during ultrasound application (frequencies of 400 kHz - 1 MHz and intensities of 0.3 - 1.0 W/cm<sup>2</sup>) and establish safety of the proposed application.

**Results/Discussion**

Our *in vitro* results showed that corneal permeability increased by 2.0 times ( $p < 0.01$ ) at 400 kHz and 1.5 times ( $p < 0.01$ ) at frequency of 600 kHz and intensity of 0.8 W/cm<sup>2</sup> as compared to sham-treated samples. Increase in corneal permeability was 1.4 - 2.1 ( $p < 0.05$ ) times at other parameter combinations. For *in vivo* study, increase in drug concentration in aqueous humor samples was 2.8 times ( $p < 0.05$ ) at frequency of 400 kHz and 2.4 times ( $p < 0.01$ ) using 600 kHz ultrasound frequency, as compared to sham-treated samples. Histological analysis showed some structural changes which were limited to epithelial layer, with no changes to stroma and endothelium, at different applied ultrasound parameters combinations. Epithelium damages were minimal in *in vivo* samples as compared to *in vitro* cases at the same parameter combinations. The temperature was determined to be 37.7°C and 38.0°C on the cornea surface, 38.5°C and 39.5°C in the lens, and no change in back of the eye (base temperature of 37°C) at frequency of 400 kHz and 600 kHz respectively at 0.8 W/cm<sup>2</sup> intensity (parameters used *in vivo*). The maximal temperature of 40°C in cornea, 43°C in lens, and 39°C in back of the eye was observed using 1 MHz frequency and 1.0 W/cm<sup>2</sup> intensity.

**Conclusion**

Ultrasound parameters used in *in vivo* study, that resulted in up to 2-3 times increase in the corneal permeability, did not have a major effect on temperature increase in sensitive eye tissues (such as lens and cornea). Ultrasound has a potential to provide effective and safe method for ocular drug delivery in treatment of eye diseases.

## P1A10-11

**New Drug Delivery System with Acousto-Chemical Manipulation of Drug Distribution**

Ken-ichi Kawabata<sup>1</sup>, Takashi Maruoka<sup>2</sup>, Rei Asami<sup>1</sup>, Reiko Ashida<sup>3</sup>; <sup>1</sup>Medical Systems Research Department, Central Research Laboratory, Hitachi, Ltd., Kokubunji, Tokyo, Japan, <sup>2</sup>Medical Systems Research Department, Central Research Laboratory, Hitachi, Ltd., Kokubunji, Tokyo, Japan, <sup>3</sup>Department of Hepatobiliary and Pancreatic Oncology, Osaka Medical Center for Cancer and Cardiovascular diseases, Japan

**Background, Motivation and Objective**

Mechanical effects of ultrasound have potentials for drug delivery system (DDS). Histotripsy is supposed to be the most controllable way to induce the mechanical effects. Histotripsy uses extremely high intensity pulsed ultrasound. A method which reduces acoustic intensity for histotripsy would lead to a scaling down of the transducer size and increased targetability in deep tissues in the body. Previously, we proposed to use liquid droplets with superheated perfluorocarbons for the reducing. It was found that such droplets can induce controlled ultrasonic mechanical effects with acoustic intensity of several kW/cm<sup>2</sup> *ex vivo*. In this study, we further investigated if such droplet-induced mechanical effects can be utilized to manipulate the distribution of locally injected drugs, for a new DDS with ultrasound.

**Statement of Contribution/Methods**

Perfluorocarbon droplets (PCND) were prepared as emulsions by an extruder method with mixtures of perfluoropentane / perfluorohexane and an aqueous phospholipid suspension. Polyacrylamide gels with aqueous regions filled with PCND and sham drug (black ink) were used as tissue mimicking phantom with locally injected PCND and drug. In the phantom, 0.5 ml aliquots of emulsions containing ca. 0.1 mg of perfluorocarbons and 0.05 ml of drug were fulfilled and they were exposed to pulses of focused ultrasound at 1 MHz in a water tank. Typical acoustic conditions were as follows: pulse intensity = 2.5 kW/cm<sup>2</sup>, duration = 300 cycles, repetition frequency = 0.5 kHz, exposure time = 30 sec.

**Results/Discussion**

Exposing focused ultrasound pulse to the phantom was found to cause the traveling of the drug toward the transducer. The traveling speed was about 0.4 mm/s in the focal zone and significant traveling was not observed when the traveling reached at the boundary of the focal zone. Shifting of the focus during the exposure with a proper timing resulted in an enlarged drug traveling while maintaining traveling speed. Those results suggested that the spatial distribution of locally injected drugs can be manipulated by the pulsed ultrasound when the drug is injected with PCND. As a control experiment, the effect of Sonazoid®, a commercially available microbubble contrast agent was investigated. No drug traveling was observed by using Sonazoid® at a bubble concentration 20 times higher than that used in the PCND experiments. Pressure resistance properties of PCND and Sonazoid® might be related to the absence of the drug traveling phenomena with Sonazoid®. Since PCND-injected regions as well as cavitating regions are visualized by ultrasound imaging, our method can serve a highly controllable DDS modality for locally injected drugs. Our approach would be applicable for the treatment of deep-seated and hypovascular tumors such as pancreatic cancer.

# P1A11 - MSP: Medical Signal Processing

Salon C

Thursday, September 4, 2014, 8:00 am - 5:00 pm

Chair: **Svetoslav Nikolov**  
BK Medical, Herlev

P1A11-1

## Realtime automatic detection of heart failure in echocardiography

**Sigurd Storve**<sup>1</sup>, Jahn Frederik Grue<sup>1</sup>, Håvard Dalen<sup>2</sup>, Bjørn Olav Haugen<sup>3</sup>, Hans Torp<sup>1</sup>; <sup>1</sup>Department of Circulation and Medical Imaging, Norwegian University of Science and Technology, Trondheim, Sor-Trøndelag, Norway, <sup>2</sup>Levanger Hospital, Nord-Trøndelag Health Trust, Levanger, Norway, <sup>3</sup>Department of cardiology, St.Olav University Hospital, Norway

### Background, Motivation and Objective

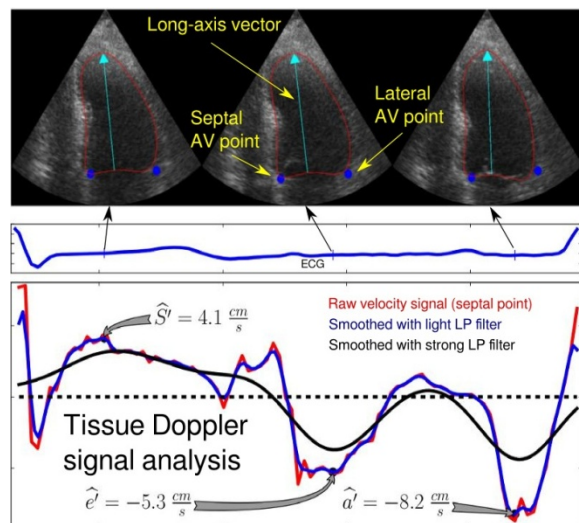
Assessment of heart function by echocardiography is challenging for non-experts. In a patient with dyspnea, assessment of mitral annular excursion (MAE) and velocities are important for the diagnosis of heart failure. By automatic measurement of these parameters, a preliminary diagnosis could be performed by the non-expert.

### Statement of Contribution/Methods

We propose an automatic algorithm to localize the mitral annular points, in the apical tissue Doppler image, and estimate MAE, as well as the three peak velocities S', e' and a'. A deformable left ventricle model fitted onto the ultrasound B-mode frames estimates the long-axis vector and the septal and lateral annular points. The tracking of the annular points results in a position and velocity signal that is analyzed at the end of each cardiac cycle. The algorithm is implemented as a C++ application that can operate both on stored DICOM loops and in realtime on streamed rawdata from the ultrasound scanner, using an in-house protocol. The peak velocities are estimated using a three-peak model shown in the figure, which also demonstrates the segmentation and the tracked annular points' position at the three peaks. The estimation accuracy was evaluated on 78 recordings from HUNT, a Norwegian health study consisting of healthy subjects. Classification based on the estimated septal MAE value was tested in 46 patients, where 21 of them had reduced LV function, i.e. MAE < 10 mm using manual measurement. All ground-truth values were supplied by an expert using M-mode for excursion and color tissue Doppler for the velocities. Results on a larger dataset of approximately 200 patient recordings and 200 recordings from the health study will be presented at the conference.

### Results/Discussion

The estimation error (mean ± SD) for the septal (lateral) excursion was  $-3.1 \pm 19\%$  ( $-8.8 \pm 24\%$ ). For the peak velocities the corresponding errors are: S':  $-14 \pm 12\%$  ( $-14 \pm 18\%$ ), e':  $-2.4 \pm 17\%$  ( $-0.7 \pm 20\%$ ), a':  $-5.0 \pm 16\%$  ( $4.8 \pm 26\%$ ). Classification of MAE was correct in 42 of the 46 patients. The incorrect classifications were one false positive and three false negatives. Future work will investigate multivariate classification using excursion and peak velocities from both septal and lateral points.



P1A11-2

## Compressive Sensing-based multidimensional Doppler signal analysis for fetal activity monitoring

Adrian Basarab<sup>1</sup>, Céline Quinsac<sup>1</sup>, Jean-Marc Girault<sup>2</sup>, **Denis Kouamé**<sup>1</sup>; <sup>1</sup>IRIT, UMR CNRS 5505, University of Toulouse, Toulouse, France, <sup>2</sup>Inserm U930, University of Tours, Tours, France

### Background, Motivation and Objective

Fetal activity monitoring is an important part of monitoring at-risk pregnancies and labor.

Fetal activity parameters (FAP) consist of fetal heart rate (FHR), fetal movements (FM) rate, fetal tone and fetal breathing (FB) movement. FAP monitoring is to date an open challenge because, first, the estimation of FAP is highly time consuming and thus cannot be used routinely. Second, part of FAP such as FM estimation is sometimes subjective (mothers are asked to count the felt movements) [e.g. Stacey '11] and inaccurate. For this purpose, we developed a 2MHz pulsed wave ultrasound Doppler system, consisting of 12 transducers with 5 adjustable gates. The Doppler signals were sampled at 1KHz, [Kribeche '07]. It has been shown that this system is very accurate [Ribes '11]. However, its counterpart is the huge number of signals necessary to estimate the FAP. For instance, each millisecond, there are 120 complex Doppler samples. In order to reduced the volume of the data during acquisition and accelerate the FAP estimation rate, we propose to investigate the utility of compressive sensing (CS).

**Statement of Contribution/Methods**

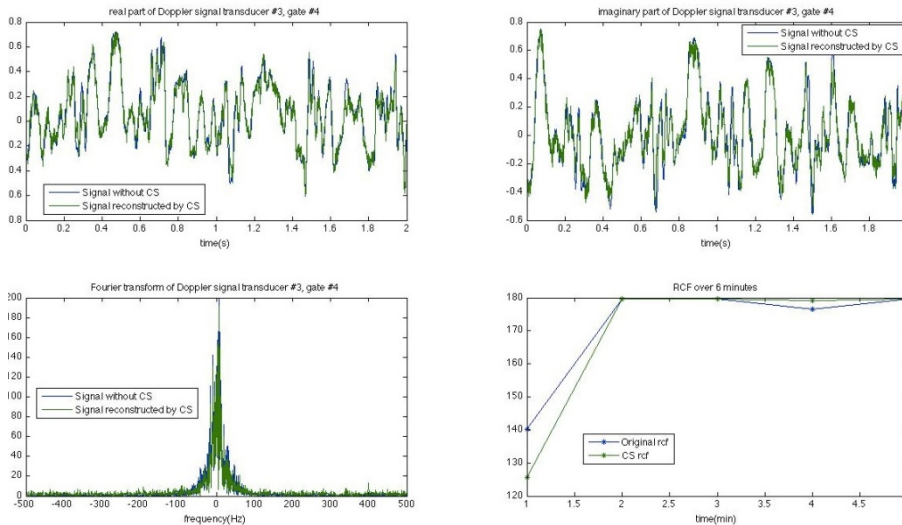
The main idea here is that the FAP are available in the frequency domain. For instance FHR, FM or FB can be estimated using Fourier analysis of the Doppler signal.

CS in US imaging consists in taking a small number of spatial or time samples at random locations as incoherent linear combinations of the original Fourier transform signals [Liebgott '12]. The reconstruction of the signals is then performed via  $l_1$ -norm minimization. Following CS methodology, our measurements consist of few samples taken randomly from the initial data. The original signal can then, either be recovered using an inverse Fourier

transform or as in our case, be processed in Fourier domain. Doing so we can reduce the number of samples required to reconstruct the US Doppler signals. Note that CS is different from classical compression since here one doesn't need to acquire the whole signal, but only few samples.

**Results/Discussion**

The results of our method allowed a reconstruction of US Doppler signal and estimate FAP from as little as 30% of time samples. We compare the reconstructed signal using CS vs the signal obtained without CS and related FAP (we only show here FHR). The result show very small difference in terms of RMSE (less than 10%).



P1A11-3

**Beamforming with sparse prior in ultrasound medical imaging**

Teodora Szasz<sup>1</sup>, Adrian Basarab<sup>1</sup>, Denis Kouamé<sup>2</sup>; <sup>1</sup>IRIT, UMR CNRS 5505, University of Toulouse, France

**Background, Motivation and Objective**

Beamforming (BF) plays a major role in medical ultrasound (US) imaging. The classical delay-and-sum (DAS) BF is fast and yet widely used in practice, but suffers from low resolution and contrast. To beamform the signal ( $s_i(t)$  from eq. (1)), a fixed set of weights,  $w_k$ , is applied to the dynamically focused raw data,  $y_k^{(i)}(t)$ .

A promising alternative is the standard Minimum-Variance (MV) BF [Asl, IEEE US'09] that adaptively calculates  $w_k$  from the raw data, but that requires high computational costs due to the covariance matrix calculation and inversion.

Our study is motivated by the recent advances of sparse priors in US image reconstruction, especially in compressive sampling (CS) [Liebgott, IEEE US'12]. Our objective is to evaluate the interest of sparse representation in the BF process, based on the Bayesian Information Criterion (BIC) [Stoica, IEEE SPM'04].

**Statement of Contribution/Methods**

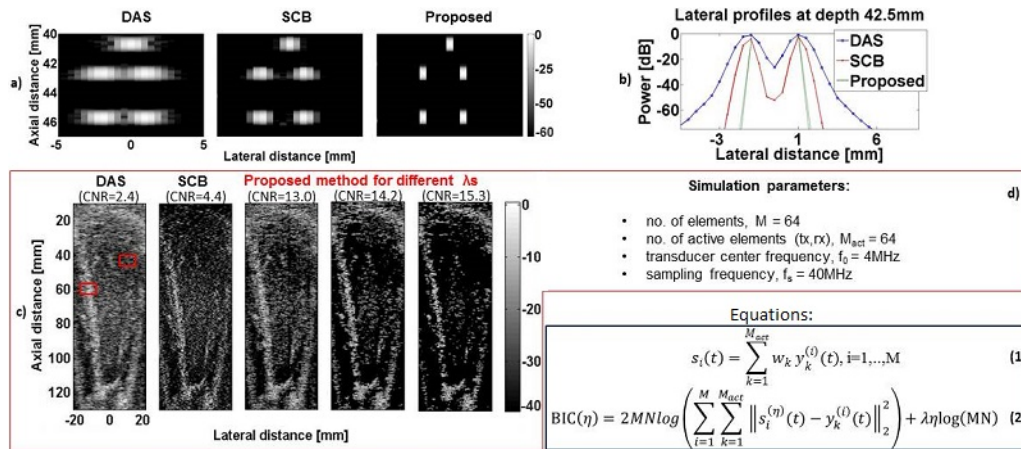
With the proposed method, the BF signal ( $s_i^{(n)}(t)$  from eq. (2)) is modeled as a sum of pulses with unknown shapes and amplitudes, received from a limited number ( $\eta$ ) of point-like sources whose positions are also unknown [Wagner, IEEE TSP'12]. Based on this modelisation, we propose a novel approach that iteratively estimates  $\eta$  by minimizing a cost function representing a tradeoff (imposed by the penalty-term  $\lambda$ ) between data attachment and the sparsity of the beamformed RF image.

Note that all the RF lines are addressed simultaneously in BIC expression. At each iteration, one additional source is picked, guided by the power of the DAS image, which was pre-calculated. The algorithm stops when the BIC value is increasing.

**Results/Discussion**

The first FieldII simulation (figures a) and b)) considers 5 individual scatterers. In this case, our method, based on a sparse assumption of sources, perfectly detects them. The second (figure c)), more realistic, represents a cardiac image (the amplitudes of the scatterers were related to the grey levels of an apical view in vivo image, as suggested in [Alessandrini, IEEE ICIP'12]). Three results obtained with our BF scheme, for different values of  $\lambda$ , are compared to DAS and MV. They clearly demonstrate that, in terms of contrast-to-noise ratio (CNR), our method achieves a significant improvement over DAS and MV.

An innovative perspective of this work is to combine the proposed BF with CS, both being based on sparse prior, which can provide more reliable results.



P1A11-4

### A Two Dimensional Sub-Sample Estimator Based on Zero Phase Crossing in Ultrasound

Fei Zheng<sup>1</sup>, Emad Ebbini<sup>1</sup>, <sup>1</sup>Electrical and Computer Engineering, University of Minnesota, Twin Cities, Minneapolis, MINNESOTA, USA

#### Background, Motivation and Objective

Displacement estimation in ultrasound is a common yet important task for various applications, including tissue/blood motion estimation, elastography imaging and temperature estimation. It is usually achieved using speckle tracking. Accuracy of displacement estimation in the lateral direction is primarily limited by the sparse pitch in ultrasound. Due to the discrete nature of window-based cross correlation, interpolation in the lateral direction is necessary in order to achieve a subsample estimation accuracy. An accurate and continuous subsample displacement estimator is critically important for applications where multidimensional strain computations are necessary.

#### Statement of Contribution/Methods

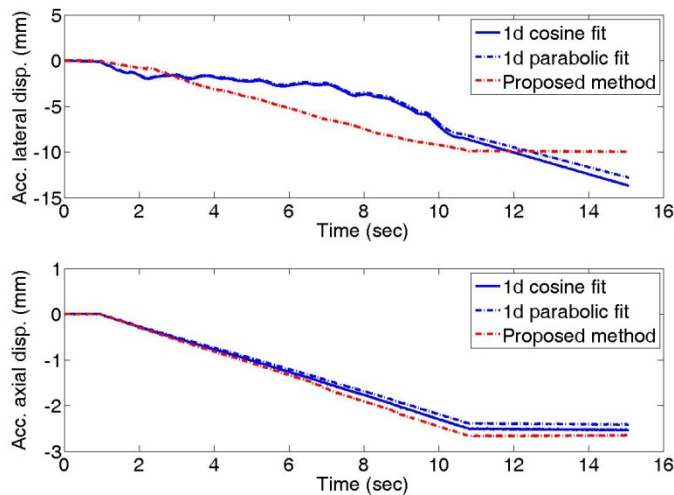
A zero phase crossing method is presented based on two dimensional complex normalized cross correlations (NCCs). Due to the fact that there is no analytic signal in the lateral direction, the phase of complex cross correlation is not necessarily linear. However, the subsample of maximum magnitude of complex correlation still lies on the zero phase line. Therefore, subsample displacement can be estimated by finding the zero phase crossing. Under the two dimensional scenario, displacement can be estimated by the intersection point of two zero phase lines, one from Hilbert transformation in the axial direction and the other one from Hilbert transformation in the lateral direction.

The proposed 2D zero-phase crossing algorithm was compared to the following subsample estimators in terms of bias and standard deviation:

- 1) Parabolic fitting to normalized cross correlation (PF),
- 2) Cosine fitting to normalized cross correlation (CF).

#### Results/Discussion

Fig. 1 shows one example of accumulated displacement in the lateral direction (top) and the axial direction (bottom) from one experiment where the tissue-mimicking phantom was moved laterally and axially using a servomotor. All methods performed well in estimating the axial displacement. However, only the proposed method faithfully reproduced the linear lateral motion without distortion. The discrepancy is a result of the lateral interpolation of the RF lines. These experimental results are consistent with simulation results on RF lines generated using Field II for the same range of motion. The simulation results show that the new method exhibits smaller bias and deviation in both axial and lateral directions.





P1A11-5

**Fast characterization of the fast and slow ultrasound waves in cancellous bone using frequency domain interferometry**

Hirofumi Taki<sup>1</sup>, Yoshiki Nagatani<sup>2</sup>, Mami Matsukawa<sup>3</sup>, Katsunori Mizuno<sup>4</sup>, Toru Sato<sup>1</sup>; <sup>1</sup>Graduate School of Informatics, Kyoto University, Kyoto, Japan, <sup>2</sup>Department of Electronics, Kobe City College of Technology, Kobe, Japan, <sup>3</sup>Graduate School of Engineering, Doshisha University, Kyotanabe, Japan, <sup>4</sup>Institute of Industrial Science, the University of Tokyo, Tokyo, Japan

**Background, Motivation and Objective**

Several researchers have reported on the fast and slow longitudinal wave propagation of ultrasound in cancellous bone. The fast and accurate characterization of the fast and slow waves may enable a real-time ultrasound measurement of bone properties, e.g. porosity. In this study, we proposed a fast signal processing method to characterize the fast and slow waves based on frequency domain interferometry (FDI).

**Statement of Contribution/Methods**

The FDI imaging technique has been proposed to acquire real-time high-range-resolution ultrasound images. It suppresses the contribution of interferences subject to a constant response of a desired signal. The proposed method applies the FDI imaging technique to the received signal, where various simulated signals are employed as the desired signals. The proposed method chooses the candidates for the fast and slow waves from the simulated signals by using the FDI intensity profile. We use a linear least squares method to select the fast and slow waves from the candidates.

**Results/Discussion**

We applied the proposed method to the ultrasound data acquired in a through-transmission experiment using bovine bone specimens, where their thicknesses were from 6 mm to 15 mm. Fig. 1 shows the fast and slow waves estimated by the proposed method for the experimental data of a 6 mm bone specimen. Fig. 2 shows the residual intensity after the subtraction process of the estimated fast and slow waves, normalized by the whole intensity of the experimental data. The calculation time for a single experimental data was 4.5 s when a Desktop PC with a single CPU was used. This result indicates the high potential of the proposed method to achieve the short-time characterization of fast and slow waves in a cancellous bone for the measurement of bone properties.

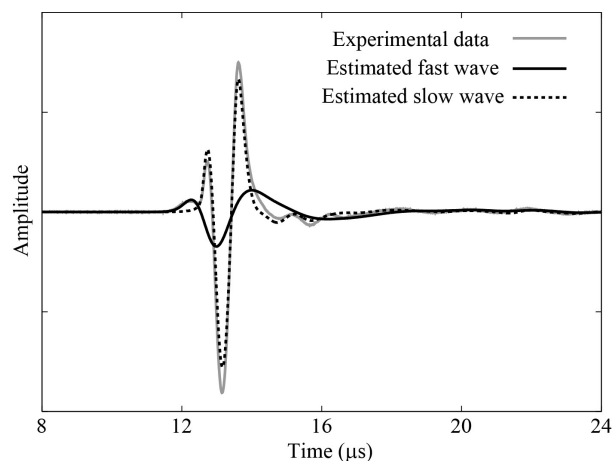


Fig. 1 Fast and slow waves estimated by the proposed method for the experimental data of a 6 mm bone specimen.

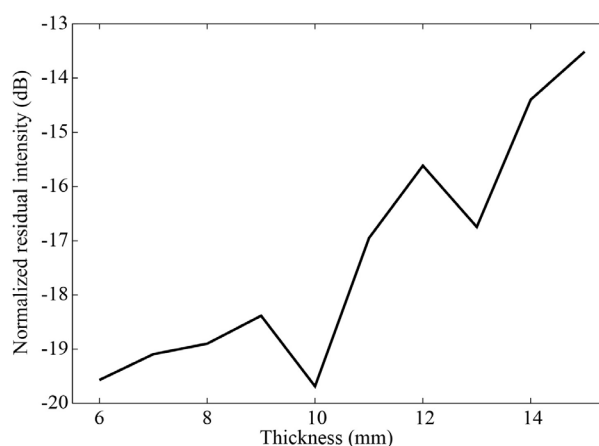


Fig. 2 Residual intensity after the subtraction of the estimated fast and slow waves, normalized by the whole intensity of the experimental data.

P1A11-6

**Automatic tracking of the tongue deformation in ultrasound image for diagnosing sleep apnea**

Yi-Shiuan Lu<sup>1</sup>, Cho-Chiang Shih<sup>2</sup>, Jeng-Wen Chen<sup>3</sup>, Chun-Hsiang Chang<sup>3</sup>, Chih-Chung Huang<sup>2</sup>; <sup>1</sup>Department of Electrical Engineering, Fu Jen Catholic University, Taiwan, <sup>2</sup>Department of Biomedical Engineering, National Cheng Kung University, Taiwan, <sup>3</sup>Cardinal Tien Hospital, Taiwan

**Background, Motivation and Objective**

Sleep disordered breathing defined as the patient who has recurrent collapse of upper airway during sleeping. Some serious cases may cause complete block of upper airway and lead to suffocation or even death during sleeping. Many studies have demonstrated that the deformation of tongue plays an important role in sleep apnea. Ultrasound examination is a useful medical tool which can be used to provide a real-time monitor and detection in clinical diagnosis. Therefore, the purpose of this study is to develop a novel automatic extraction and tracking method for detecting the deformation of tongue from patients who suffer the sleep apnea. The tongue deformation was obtained quantitatively for demonstrating the level of sleep apnea.

**Statement of Contribution/Methods**

In the study, totally 39 subjects (including sleep disordered breath in 19 subjects) were examined by a 6 MHz ultrasound array system, as shown in Fig. 1(a). All the subjects were required to perform Mueller Maneuver for causing the temporal collapsibility of the tongue base, as shown in Fig. 1 (b). The contours of air-mucosa interface during the state of Eupneic to Mueller were tracked by an adaptive snake algorithm. In this approach, the initial positions of the contour can be automatically generated for an optimized contour. The optimized contour was used as the initial position for the optimization of the next frame, and the process continues until all the images were performed. Subsequently, the variations of length and area between skin to tongue base (STB) during the different states were measured for demonstrating the deformation of tongue.

**Results/Discussion**

Fig. 1 (c) shows the detected area of STB. The total areas of STB for subjects with and without sleep apnea had no statistical difference, as shown in Fig. 1 (d). In order to represent the deformation of tongue, the STB was separated into eight parts from R1 to R8 by snake algorithm, as shown in Fig. 1(e). Under the state of Eupneic, the lengths of STB (R1 to R8) exhibited no significant difference ( $p > 0.05$ ) between the subjects with and without sleep apnea. However, the lengths of STB for R6, R7, and R8 had significant differences ( $p < 0.05$ ) between two groups under the state of Mueller, as shown in Fig. 1 (f). This information can help physicians to choose the best treatment method for helping sleep-disordered breathing patients to improve symptoms.

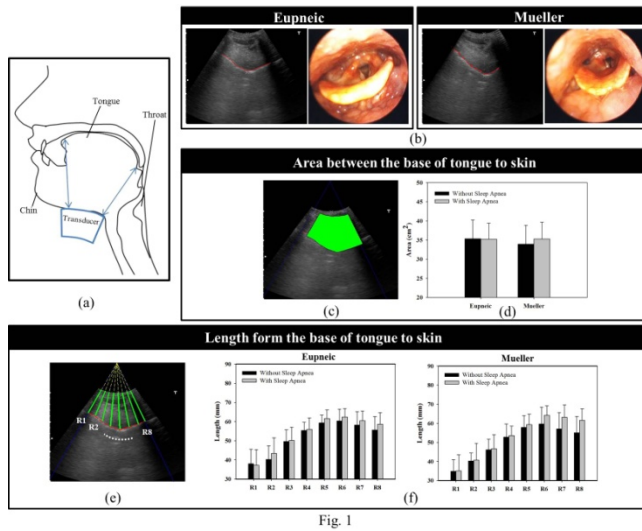


Fig. 1

P1A11-7

### Compensation Method of Frequency Dependent Attenuation for Tissue Harmonic Imaging

Takuya Hiraoka<sup>1</sup>, Norio Tagawa<sup>1</sup>, Kan Okubo<sup>1</sup>, Yihsin Ho<sup>1</sup>, Iwaki Akiyama<sup>2</sup>; <sup>1</sup>Graduate School of System Design, Tokyo Metropolitan University, Tokyo, Japan, <sup>2</sup>Department of Biomedical Information, Doshisha University, Kyoto, Japan

#### Background, Motivation and Objective

Applying the pulse compression technique (PCT) to tissue harmonic imaging (THI) improves the SNR of deep internal imaging with keeping the high resolution characteristics of THI. However, high-frequency echo is strongly affected by frequency dependent attenuation (FDA), which makes exact pulse compression impossible and causes the image blur. We already proposed an FDA compensation method [1] in which the transmitted pulse whose echo becomes desired FM chirp after distorted by FDA is generated using adaptive transmitting and receiving for obtaining a reference. In this study, we extend this method for THI in a natural way.

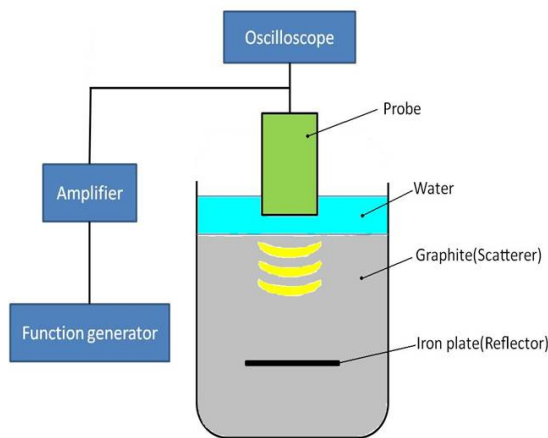
#### Statement of Contribution/Methods

We define the mapping from the fundamental component to the second harmonic component in the frequency domain as  $F_2 = H_{conv}(F_1)$ , and also the inverse mapping as  $F_1 = H_{inv}(F_2)$ . We suppose that an arbitrary FM chirp signal  $f_1(t)$  is applied to the transducer and the echo signal  $g_1(t)$  corresponding to the fundamental echo is received. Using an ideal FM chirp signal  $c_1(t)$ , which has a rectangular spectrum with a suitable window function, the distortion function in the second harmonic domain is defined as  $R_2 = C_2/G_2$ .  $C_1$  is a frequency domain representation of  $c_1(t)$  and  $C_2 = H_{conv}(C_1)$ .  $G_2$  is the second harmonic echo in a frequency domain for transmission  $f_1(t)$ . Hence,  $S_1 = H_{inv}(R_2 H_{conv}(F_1))$  is a signal compensated for the transducer's property. After performing it, by recursively using  $S_1 = H_{inv}(|R_2| H_{conv}(F_1))$ , FDA compensation can be performed. In actual application, curve fitting is adopted to stably compute  $|R_2|$ . The FDA compensation has to be done repetitively, if necessary.

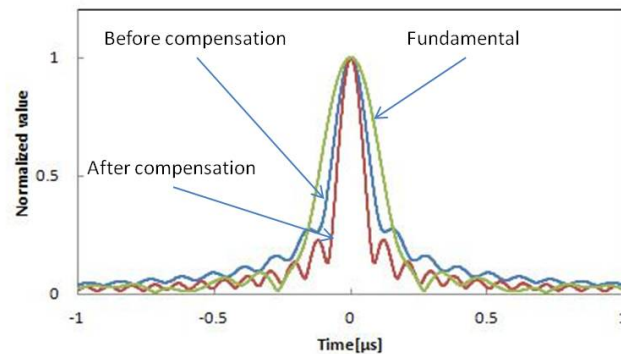
#### Results/Discussion

We performed simple experiments using a standard transducer with a fixed focusing. Experimental setup is shown in the left figure. An iron plate was used as a reflector. Transmitted FM chirp pulse has a center frequency of 7.5MHz, a band-width of 3MHz, a pulse-width of 10us. A Hanning window is used as an apodization. The right figure shows the envelopes before and after applying the method expanded for THI. The envelope of the fundamental echo obtained simultaneously is also shown. It is noted that for the fundamental echo the method in [1] gives a slightly good result. From the results, we confirmed that the proposed method is accommodated to THI and is effective.

[1] H. Hiraoka, et al., IEEE Int. Ultrasonics Symp., pp.914-917, July, 2013.



Experimental setup



Envelopes of compressed echo

**Design of Huffman Sequences with Limited Bandwidth**

Shreyank Gupta<sup>1</sup>, Michael Zapf<sup>1</sup>, Herbert Krauß<sup>2</sup>, Nicole Ruiter<sup>1</sup>; <sup>1</sup>Institute for Data Processing and Electronics, Karlsruhe Institute of Technology, Germany, <sup>2</sup>Electrical engineering, Hochschule Darmstadt, University of Applied Sciences, Germany

**Background, Motivation and Objective**

A 3D Ultrasound Computer Tomography (USCT) system for early detection of breast cancer was developed at KIT. Coded excitation (CE) is used for emission in order to send more energy while maintaining the bandwidth. Currently chirps are used as CE and matched filtering is applied. The resulting separability of single reflections is mainly limited by the system bandwidth due to sidelobe artifacts.

The literature suggests Huffman sequences (HS) as CEs with the property of suppressed side lobes (defined as ratio of main lobe to peak side lobe) yet lower SNR. Ackroyd suggested in 1972 a method for generating efficient HS in the Z domain in full bandwidth. The objective of this work was to develop HS with limited bandwidth and evaluate them on the example of USCT (see table 1).

**Statement of Contribution/Methods**

Following Ackroyd's approach the HS was generated with full bandwidth. Then it was filtered via a rectangular filter of limited bandwidth. This result in poor performance as the energy of the HS is 73% smaller compared to the filtered Chirp. Energy was defined as  $E = \sum_{n=1}^{n=N} (|x(n)|^2)$  where  $|x(n)|$  represents the absolute amplitude per sample and N is the total length in samples. Our proposed method allocates the zeros in the Z domain to a lower and upper frequency defined by the system bandwidth. The resulting samples in the frequency space are irregularly sampled. Then they are interpolated which allows to adapt to the requested HS length and sample frequency. The HS is then transformed into the time domain.

**Results/Discussion**

The standard USCT Chirp was used as ground truth for evaluation of the HS. The amplitudes of the sequences were normalized to one. The Chirp was found to result in the highest energy (E) (see table 1) whereas the proposed bandlimited HS show two times higher sidelobe suppression in MSR while compromising only 7% in energy, see Table 1.

The proposed approach for HS generation with limited bandwidth shows significant sidelobe suppression compared to chirps. In contrast to Ackroyd's approach this method allows an arbitrary number of zeros independent of the sampling frequency. This additional parameter allows optimizing the performance of the HS further, which is currently ongoing research.

CE parameters for evaluation:		Sequences in limited bandwidth	Energy of the sequence (E)	Main lobe to peak side lobe ratio (MSR)	Main lobe energy relative to total energy (ME)
Bandwidth:	1.7 MHz	Chirp	31.75	1.37	44.56%
Center frequency:	2.5 MHz	Huffman sequence	8.42	2.55	43.75%
Sampling frequency:	10 MHz	Huffman sequence filtering approach			
Length:	128µs	Huffman sequence	26.10	2.56	54.08%

Table 1

# P2A1 - Wave Propagation

Salon C

Thursday, September 4, 2014, 8:00 am - 5:00 pm

Chair: **David Greve**  
Carnegie Mellon University

P2A1-1

## Temperature distribution of Piezoelectric Transformer with Heat Couple Component Using Finite Element Method

Weiwei Shao<sup>1</sup>, Zhile Han<sup>1</sup>, Yongjia Xiang<sup>1</sup>, Peiyang Li<sup>1</sup>, Yaoyao Cui<sup>1</sup>; <sup>1</sup>Suzhou Institute of Biomedical Engineering and Technology (SIBET), Chinese Academy of Sciences (CAS), China, People's Republic of

### Background, Motivation and Objective

Piezoelectric transformers (PTs) are proposed to adjust the state of an electric power supply through piezoelectric direct and converse effects and vibration propagation. During the operation of PTs, the internal heats due to dielectric, piezoelectric, and mechanical losses are generated, which result in the temperature rise of PTs and change the characteristics of device. Especially for high-power devices, while the temperature reaches to a limit value, it will decrease of piezoelectric material properties and increases of the internal losses, then leading to an unstable status of the electromechanical conversion. To solve the heat problem of PTs, in our previous work, a heat transfer structure(HTS) was designed to decrease the temperature rise. The experimental results showed that with a temperature increase of less than 10 °C and an efficiency of 90.8%, the sample PT had a maximum output power density of 135 W/cm<sup>3</sup> at 90.1 kHz, which was more than two times larger than the one without HTS. A heat couple component (HCC), which serves as the core element of HTS, is in contact with the PT body as the transition between PT and external heat sink. The HCC has great potential to influence heat dissipation of HTS. Therefore, it is necessary to establish a three-dimensional analysis for obtaining the influence of HCC to PT's temperature distribution.

### Statement of Contribution/Methods

Mechanical vibration losses, dielectric losses and friction heat were considered as the heat source of PT with HCC and calculated using three-dimensional finite element method. The calculated results of the transformer without(shown in fig.1) and with HCC are verified by experimental results. It shows that the presented method for the temperature field distribution of PT's with HCC is feasible.

### Results/Discussion

In this paper, the three-dimensional finite element analysis were used to calculate the temperature field distribution for PTs with HCC. The HCC depresses temperature gradient of PT and improves piezoelectric material utilization rate effectively. In order to verify the correctness of the calculation method, the PT without and with HCC was simulated and compared with the experimental results. The deficiency from the HCC also will be considered and studied.

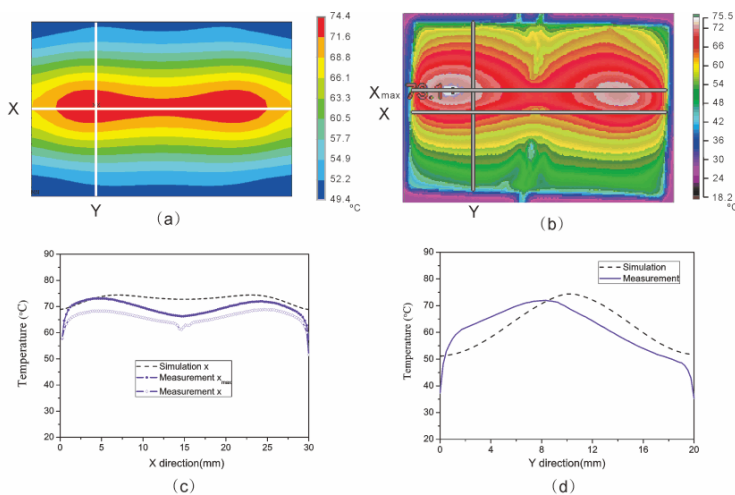


Fig. 1 Temperature distribution of PT sample; (a) Calculated temperature distribution. (b) Measured temperature distribution.

P2A1-2

## The study of broadband acoustic metamaterials in air

Stefano Laureti<sup>1,2</sup>, Marco Ricci<sup>2</sup>, David Arthur Hutchins<sup>1</sup>, Lee Andrew John Davis<sup>1</sup>; <sup>1</sup>School of Engineering, University of Warwick, Coventry, United Kingdom, <sup>2</sup>Polo scientifico e didattico di Terni, Università degli Studi di Perugia, Terni, Italy

### Background, Motivation and Objective

Metamaterial are materials that exhibit exotics properties that cannot be found usually in nature. In recent years, several types of acoustic metamaterials have been proposed. Although phenomena such as acoustic focusing [1] and superlensing have been described, there is still a need to achieve broadband operation for practical applications. In addition, broadband operation would allow the use of signal processing techniques such as pulse compression, widely used in air-coupled nondestructive evaluation, for example.

**Statement of Contribution/Methods**

Starting from previous studies about transmission of acoustic waves through isolated sub-wavelength holes [3,4], we have analyzed both numerically and experimentally the behavior of different structures operating in air at ultrasonic frequencies. We then explored the possibility of using chirp and optimized multi-tone signals as excitation into a structure that operated across a range of frequencies.

**Results/Discussion**

3D printing was used to manufacture samples with one and two paired sub-wavelength square holes, whose filtering properties were then characterized by using a broadband transducer and a chirp excitation signal. Further samples of metamaterial were also investigated, including a regular and pseudo-noise grid of square sub-wavelength holes. Fig. 1(a) shows a sketch of the one of the sample realized (dimension in mm), while Fig. 1(b) shows a picture of the experimental set-up used in air.

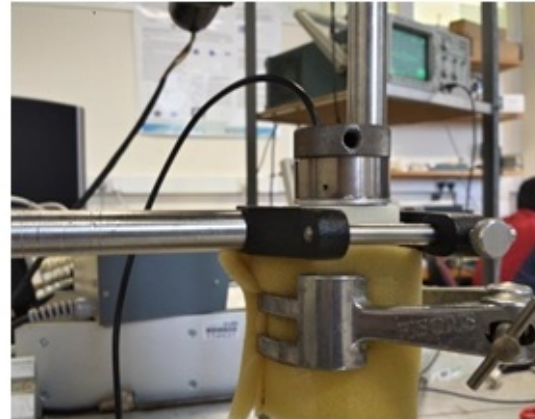
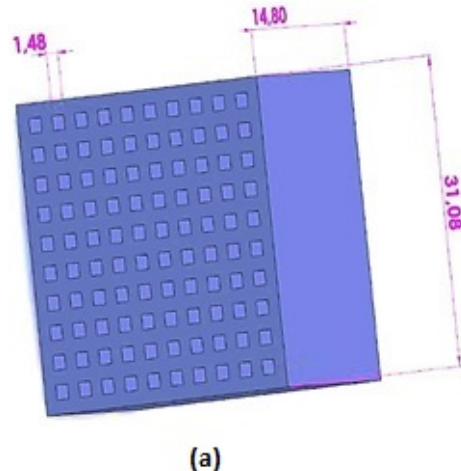
We conclude that it is possible to manufacture broad bandwidth acoustic metamaterials that exhibit interesting properties when used at ultrasonic frequencies in air.

[1] J. H. Page, Zhengyou Liu, M. L. Cowan, C.T. Chan and S. Y. P. Sheng, *Physical Review Letters*, 93(2), 2004.

[2] M. Ambati, N. Fang, C. Sun and X. Zhang, *Physical Review B* 75, 195447, 2007.

[3] H. Estrada et al, *Phys. Rev. Lett.* 101, 084302 (2008).

[4] J.J. Park, et al., *Phys. Rev. Lett.* 110, 244302, (2013)



P2A1-3

**Time-causal material modeling in the simulation of guided waves in circular viscoelastic waveguides**

Fabian Bause<sup>1</sup>, Hauke Gravenkamp<sup>2</sup>, **Andreas Schröder<sup>1</sup>**, Jens Rautenberg<sup>1</sup>, Bernd Henning<sup>1</sup>; <sup>1</sup>Measurement Engineering Group, University of Paderborn, Paderborn, Germany, <sup>2</sup>Federal Institute for Materials Research and Testing, Berlin, Germany

**Background, Motivation and Objective**

(Ultrasonic) Material properties are the fundament of modern engineering e.g. regarding computer aided design or structural health monitoring. While material characterization approaches in the quasi-static domain are mostly standardized, the identification of ultrasonic material characteristics is in general much more complex and has not been standardized yet. There exist several approaches for ultrasonic material characterization, whereas the latest mostly focus on waveguide based inverse problems.

In this contribution, we present an efficient approach for the transient and time-causal modeling of guided waves in viscoelastic cylindrical waveguides. This model is part of the nonlinear inverse problem considering material characterization based on transient measurements through polymeric circular waveguide samples.

**Statement of Contribution/Methods**

For the description of linear viscoelasticity, we use the fractional Zener model. Based on the spectral decomposition of the elasticity matrix as proposed by Theocaris, we generalize the one-dimensional analysis of the material model into three dimensions and discuss appropriate simplifications to reduce the amount of unknowns for the material description. Then, we propose a decomposition approach that considers the real valued frequency dependence of the viscoelastic moduli and the real valued frequency dependence of their attenuation separately. The Scaled Boundary Finite Element Method is used for the efficient computation of the phase velocity dispersion and the modal wave fields given a frequency dependent but real valued viscoelasticity matrix. Utilizing the modal expansion approach, the transmitting and receiving transducer are taken into account to compute the modal amplitudes. Combining these modal amplitudes, the phase velocity dispersion and re-introducing the viscoelastic attenuation results in a transfer function of the viscoelastic waveguide including excitation and receiving conditions.

**Results/Discussion**

Preliminary simulation results of the proposed algorithm are in a good agreement with measurements. Regarding efficiency, the runtime of the simulations vary between 1 s and approx. 10 s, depending on the number of waveguide modes. Based on measurements, we discuss the applicability of the simulation model to represent the physical reality. Furthermore, we present first results of the inverse material characterization approach.



## Stress Measurement with Ultrasonic LFM LCR Wave :Theoretical Verification and Numerical Simulation

Han ZHANG<sup>1</sup>, <sup>1</sup>Institute of Acoustics, Chinese Academy of Sciences, Beijing, China, People's Republic of

### Background, Motivation and Objective

The critically refracted longitudinal (LCR) wave has been applied to measure stress in the researches and applications of NDT&E, due to its sensitivity to the stress. However, LCR wave is still lack in both traveling distance and time accuracy for stress measurement. Aimed to solve these issues, the linear frequency modulated (LFM) ultrasonic signal is applied in this paper to improve the ultrasonic stress measurement with LCR wave in isotropic materials.

### Statement of Contribution/Methods

Based on acoustoelasticity theory, velocity change of LCR wave caused by stress can be transformed to time delay estimation of ultrasonic wave propagation. According to the definition of the LFM signal, its frequency change should keep a constant-slope relation with its time delay all the time. So, its significant advantages of the controllable time duration and scanning bandwidth will be beneficial in the stress measurement, especially in solving the two issues mentioned at least.

Moreover, the pulse compression of the received signals is able to improve the signal noise ratio (SNR) of echoes, and is not sensitive to the Doppler effect caused by the loading process during measurement.

### Results/Discussion

- 1) This paper gives out the explicit expression about the relation of the stress change and the frequency change of ultrasonic LCR wave.
- 2) The further derivation on the basis of this method obtains the specific functions of the range and accuracy for stress measurement, including key factors like the signal linearity, SNR and the Doppler frequency shift fd.
- 3) To verify the efficiency of the systematically theoretical results above, a specific model is set up using the finite element method. A LFM LCR wave with the time-bandwidth product of 33, under the parameters of PMMA wedges angled 27.4 and mounted on a plate of Steel 45# by a set of distances, shows the improvement in energy and resolution simultaneously, compared with conventional signals. The SNR reaches 3.2 times to the spiky pulse form with the same peak value of the input excitation.
- 4) Distorted LFM LCR wave will bring a huge mistake into measurement. With the help of the excitation optimization to suppress the distortion of LFM signal, the linearity can be provided.
- 5) Caused by measuring loads, fd is always a puzzled factor in the real applications. But the numerical simulation of this method shows the fd influence can be avoided very well, which thanks to the characteristics of LFM signal.

Above all, this method is verified to be useful in the ultrasonic stress measurement with a longer distance and higher accuracy. And it will benefit for the future works of structural healthy monitoring in isotropy materials and structures.

[Supported by NSFC No.11374325]

## Generalization of the k-space Method for Elastic Wave Propagation in Heterogeneous Anisotropic Media

Kamyar Firouzi<sup>1</sup>, Amin Nikoozadeh<sup>2</sup>, Butrus T. Khuri-Yakub<sup>2</sup>, <sup>1</sup>Mechanical Engineering, Stanford University, Stanford, California, USA, <sup>2</sup>Electrical Engineering, Stanford University, Stanford, California, USA

### Background, Motivation and Objective

Elastic wave propagation in inhomogeneous anisotropic media has widespread applications in many different areas of science and technology including seismology, geophysics and soil mechanics, non-destructive testing, design of sensors and transducers and biomedical ultrasound. Therefore, efficient and accurate numerical methods are of great importance. The dominant conventional numerical methods such as finite elements or finite-differences are cumbersome and slow as they require many points per wavelength for a satisfactory accuracy. They may also exhibit a poor performance for problems in heterogeneous media. Moreover, in order to control the dispersion error, the time-steps should be taken very small. Therefore, explicit time integration is preferred over implicit ones. However, the classical explicit schemes are all conditionally stable and sensitive to dispersion error. We present a k-space pseudospectral method which is designed to address these problems: (1) It uses spectral basis instead of polynomials to approximate the solution in space, hence it shows spectral accuracy for the spatial derivatives. (2) It can be implemented using the fast Fourier transform algorithm, hence it is fast. (3) The integration scheme is unconditionally stable and can be parameterized to minimize the dispersion error. (4) It handles propagation in heterogeneous media very efficiently.

### Statement of Contribution/Methods

We generalize the theory of the k-space methods to the case of elastic wave propagation in heterogeneous anisotropic media. The k-space operator is derived in the spatially continuous form using the displacement formalism of elastodynamics. The k-space scheme is then discretized in space using a Fourier collocation spectral method. This leads to an efficient numerical algorithm, where the time advancement can be performed in order of N operations, where N is the number of unknowns. We provide in-detail analysis of the method, more precisely we prove the method is consistent and convergent, and also provide the error estimates. We prove that the proposed method is temporally exact for homogeneous media, unconditionally stable for heterogeneous media, and also allows larger time steps without loss of accuracy. It also achieves an improved accuracy in time compared to the classical pseudo-spectral methods.

### Results/Discussion

We validate the algorithm against canonical model problems of elastodynamics. Benchmark simulations are also provided to show the efficacy of the method compared to the existing ones. Different applications of the algorithm are also motivated.

## Application of SLM-generated patterns for laser-ultrasound in f-λ space

Clemens Grünsteidl<sup>1</sup>, Istvan Veres<sup>1</sup>, Thomas Berer<sup>1</sup>, Peter Burgholzer<sup>1</sup>, <sup>1</sup>Research Center for Non Destructive Testing, Linz, Austria

### Background, Motivation and Objective

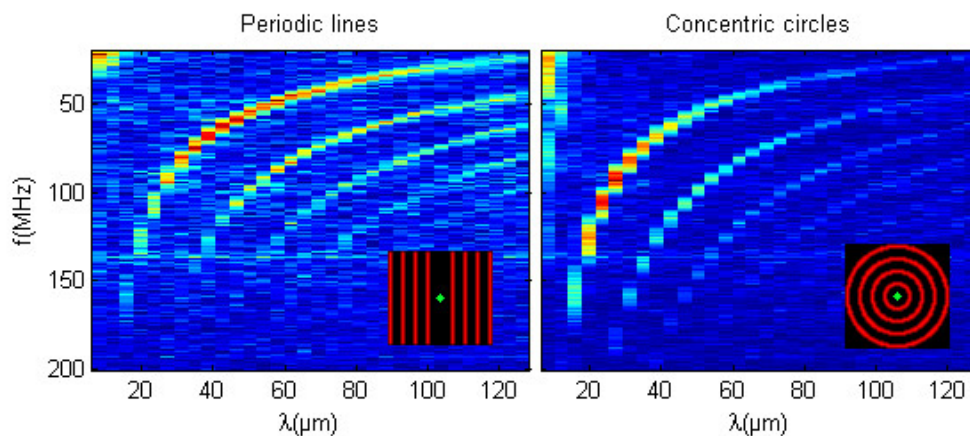
Spatial Light Modulators (SLMs) allow to image arbitrary excitation patterns for laser ultrasound (LUS) on a sample surface. This enables to excite waves with a particular wavelength by interfering elastic waves originating from equidistant sources. In conventional LUS, in contrast, excitation light is focussed to a spot or line, leading to emission of broadband acoustic waves. By combining SLM with intensity modulated lasers, single wavelength and single frequency LUS is realized. Our system uses high sensitivity lock-in detection for surface acoustic waves (SAWs) and plate waves. The setup will be used to detect the zero group velocity point in Lamb wave dispersions.

**Statement of Contribution/Methods**

Excitation of SAWs with complex patterns, such as concentric circles and arcs, leads to increased sensitivity compared to previous reports on generation with periodic lines. This technique, however, requires a more accurate control of the micro-scale patterns. A 3D moving pinhole technique was developed to scan the intensity of the patterns and to verify their alignment relative to the detection laser spot. To overcome the spatial resolution limit of the SLM and to scale the patterns continuously we designed a system of tunable lenses made of electro-active polymers.

**Results/Discussion**

The SLM imaging optics and the image field have been experimentally characterized and the overall performance of the ultrasound generation process was improved. We compared SAW velocity dispersion measurements from periodic lines and concentric circles. Due to acoustic focusing, the signal-to-noise ratio in  $f$ - $\lambda$  scans achieved with concentric circles was improved compared to those achieved with lines. A higher number of lines or circles resulted in sharper interference peaks; however, the number of lines is limited by the size of the imaging field. The rapid change of dispersion relations for short wavelengths (see measurements in Fig.) results in fewer data points for frequencies  $>100$  MHz. Thus, a zoom optic was implemented to allow to scale the excitation patterns in arbitrary steps, leading to an arbitrary resolution, temporally and spatially.



P2A1-7

**Accurate Finite Element Model of Equiaxed Coarse-grained Engineering Material for Ultrasonic Inspection**

Bo Xiao<sup>1</sup>, Richard O'Leary<sup>2</sup>, Anthony Gachagan<sup>2</sup>, Wenqi Li<sup>3</sup>, Timothy Burnett<sup>4</sup>; <sup>1</sup>Electronic and Electrical Engineering, University of Strathclyde, Glasgow, United Kingdom, <sup>2</sup>University of Strathclyde, United Kingdom, <sup>3</sup>University of Nottingham, United Kingdom, <sup>4</sup>University of Manchester, United Kingdom

**Background, Motivation and Objective**

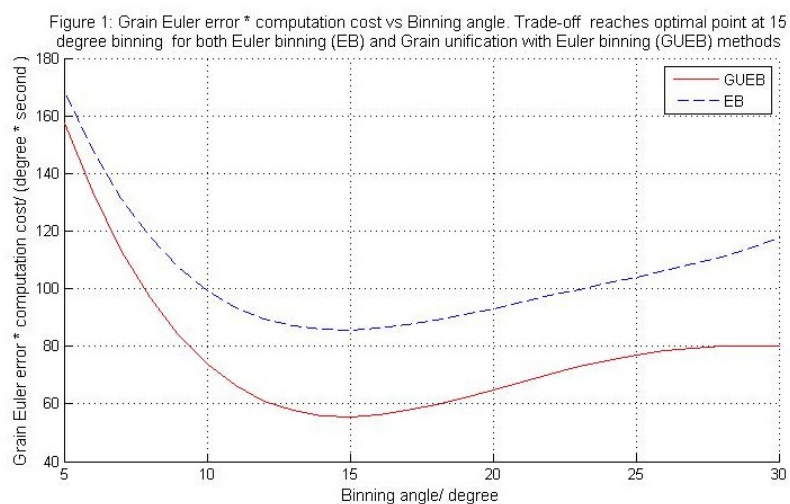
Anisotropic and inhomogeneous materials are used widely in many industrial sectors. Accurate modelling of wave propagation in such materials will facilitate the optimization of ultrasonic inspection and associated signal processing algorithms. Most existing relevant research focuses on modelling analysis of coarse-grained materials, e.g., austenitic welds, which are strongly textured and usually characterized by columnar grains. Creating model of such materials is relatively straightforward due to the presence of several ( $<10$ ) dominant crystallographic orientations in the material map. However, modelling of coarse-grained material with equiaxed grain distribution is challenging as excessive randomly oriented grains necessitate extra processing of the microstructural information before inputting to a finite element (FE) model. This paper concentrates on analysis and processing of orientation space and microstructure in order to maximise computational efficiency whilst maintaining appropriate accuracy of the constructed model.

**Statement of Contribution/Methods**

Spatially Resolved Acoustic Spectroscopy (SRAS) and Electron Backscattered Diffraction (EBSD) have been employed to characterise a sample of Inconel 617 with an equiaxed grain structure. The material maps generated by both techniques are compared and show a good agreement. In order to create cost-effective FE models of the sample, two processing methods are proposed: rigid Euler space binning and Euler space binning following unification of spatially indexed grains.

**Results/Discussion**

The parametric studies show that the trade-off between model accuracy, particularly the relationship between grain orientation accuracy and computational cost will be optimized if grains are unified using a misorientation parameter of 10 degree per Euler phase prior to segmenting Euler space with a  $15^\circ \times 15^\circ \times 15^\circ$  bin, shown as Figure 1. The FE models are used to create images from a 32-channel linear array; this is compared to experimental equivalents for validation purposes. Microstructure variations across array width are simulated by randomly adding Gaussian noise to the FE models. The minor difference of results prove the constructed FE models are validated for this specific Inconel 617 sample, highlighting potential of the proposed treatment methods for application on other equiaxed materials.



## P2A2 - Imaging

Salon C

Thursday, September 4, 2014, 8:00 am - 5:00 pm

Chair: **Robert Addison**  
Rockwell Science Center

### P2A2-1

#### Resonant acoustic nonlinearity of defects for nonlinear and thermosonic imaging and NDE

Igor Solodov<sup>1</sup>; <sup>1</sup>University of Stuttgart, Stuttgart, Germany

##### Background, Motivation and Objective

Elastic wave-defect interaction is a background of ultrasonic nondestructive evaluation (NDE) of materials and industrial components. The efficiency of the interaction becomes particularly crucial for power-dependent techniques such as nonlinear ultrasonic and thermosonic NDE. In both cases, an increase in efficiency is achieved by choosing the wave frequency equal to one of the resonance frequencies of the specimen provided that the defect is outside the nodal areas of the standing wave pattern.

##### Statement of Contribution/Methods

In this paper, the effect of Local Defect Resonance (LDR) [1] is applied for enhancement of efficiency of nonlinear ultrasonic and thermosonic imaging of defects. Unlike the resonance of the whole specimen, the LDR naturally provides an efficient energy pumping from the wave directly to the defect. For simulated and realistic defects in various materials, the LDR-induced local increase in the vibration amplitude averages (20-40 dB). The use of LDR, which strongly intensifies local vibrations, is found beneficial for dramatic enhancement of both nonlinear and thermosonic responses of defects.

##### Results/Discussion

As the local vibration amplitude increases, the LDR-"amplifier" exhibits transition to nonlinear regime with an efficient generation of nonlinear frequency components solely in the defects area. The concept of the defect as a nonlinear oscillator brings about new dynamic and frequency scenarios characteristic of parametric oscillations. The experiments confirm unconventional nonlinear dynamics of simulated and realistic defects subject to LDR. It features threshold transition to resonant nonlinear modes of unstable nonlinear vibrations. The modes observed include sub- and superharmonic resonances with anomalously efficient generation of the higher harmonics and subharmonics. A modified version of the superharmonic resonance (combination frequency resonance) is used to enhance the efficiency of frequency mixing mode of nonlinear NDE.

The nonlinear LDR suggests a unique opportunity to generate the higher frequency components directly in the defect area and thus to enhance local heating of the defect selectively. Unlike traditional thermosonic experiments, the LDR-thermography requires substantially lower acoustic power to activate defects. This makes it possible to use conventional ultrasonic instrumentation in ultrasonic LDR-thermography and even to proceed to remote thermosonic imaging by using air-coupled ultrasonic excitation.

[1]. Solodov, I., Bai, J., Bekgulyan, S. and Busse, G. A Local Defect Resonance to Enhance Acoustic Wave-Defect Interaction in Ultrasonic Nondestructive Testing. Applied Physics Letters, 99, 211911 (2011).

### P2A2-2

#### Iterative Photoacoustic Image Reconstruction Based on Calculating Optimum Acoustic Sound-Speed Distribution Using B-mode Images

Bing Cong<sup>1</sup>, Kengo Kondo<sup>1</sup>, Makoto Yamakawa<sup>1</sup>, Tsuyoshi Shiina<sup>1</sup>; <sup>1</sup>Kyoto University, Japan

##### Background, Motivation and Objective

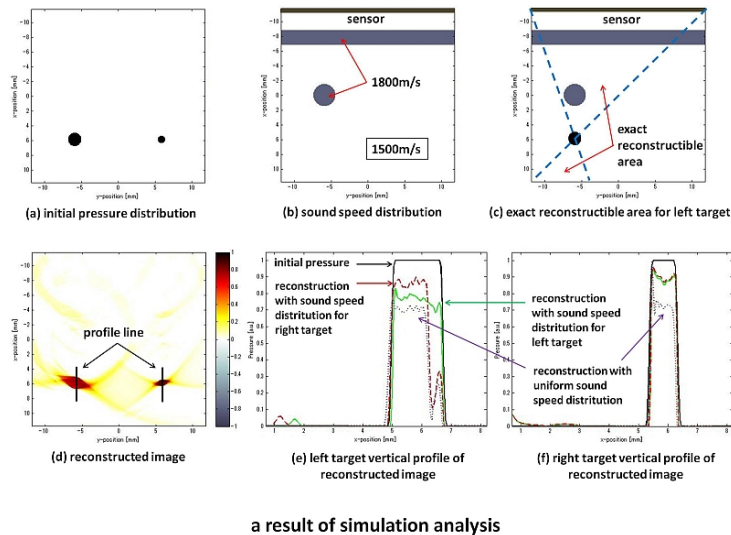
Most photoacoustic reconstruction algorithms are based on the assumption that the sound-speed distribution is homogeneous. In practice, the variations between sound speeds in human tissues can be as great as 10%. The uniform sound-speed assumption causes both blurring of features and depth position errors, and reduces contrast in the reconstructed images. This study develops a method for compensating sound-speed distribution based on B-mode images and reconstruction with an optimized sound-speed distribution to improve the quality of reconstructed images.

##### Statement of Contribution/Methods

First, we assign the B-mode image to a sound-speed distribution. We then set the values for areas of the sound-speed distribution. The specified sound-speed distribution can be used as a time-reversal reconstruction algorithm to reconstruct the image. The previous procedure should be executed iteratively unless the maximum of contrast or sharpness, similarity, i.e. of the reconstructed image as quantified by a mathematic function achieved. For limited-view photoacoustic, the area that can be exactly reconstructed depends on the sensor geometry but not the reconstruction algorithm. According to this principle, we only need to focus on the sound-speed distribution of the exact reconstructible area to rapidly estimate the optimized sound-speed distribution. We demonstrate the effectiveness of the proposed method by numerical simulations and phantom experiments.

##### Results/Discussion

Figure (a) shows the initial pressure distribution; Fig. (b), the sound-speed distribution; and Fig. (c), the exact reconstructible area for the left target. Figure (d) presents an image reconstructed using the sound-speed distribution for the left target. The improved target position and contrast compared to reconstruction with uniform sound-speed can be numerically confirmed in Figs. (e) and (f). The vertical profile of the right target also shows that a similar quality reconstructed image can be achieved by using the sound-speed distribution for either target because the circle area of sound-speed distribution is out of the exact reconstructible area of right target. Optimum sound-speed distribution estimation requires prior information such as B-mode images, and the iterative reconstruction procedure increases computing time. We will address these issues in our future work.



P2A2-3

### 3D Synthetic Aperture Imaging Using a Water-Jet Coupled Large-Aperture Single Transducer

Johan E. Carlsson<sup>1</sup>, Miguel Castaño Arranz<sup>2</sup>, Matti Rantatalo<sup>2</sup>, Robert Risberg<sup>3</sup>, Miles Weston<sup>4</sup>; <sup>1</sup>Computer Science, Electrical and Space Engineering, Lulea University of Technology, Sweden, <sup>2</sup>Civil, Environmental and Natural Resources Engineering, Lulea University of Technology, Sweden, <sup>3</sup>Creo Dynamics AB, Linköping, Sweden, <sup>4</sup>TWI Technology Centre Wales, Port Talbot, United Kingdom

#### Background, Motivation and Objective

There are several approaches for ultrasonic imaging of metal structures, depending on the geometry, accessibility, etc. For small structures, arrays can be used which are coupled directly to the surface. For plate-like structures or other wave-guides, other wave modes can be used to localize defects over longer ranges. In other applications, where the surface is too rough to accomplish good coupling with a contact transducer, or when the sample can not be immersed in a water tank, water jet coupling has been used. In a typical setup, the transducer is a non-focused transducer with a diameter in the range of 1/4" – 1/2". The resulting sound lobe is fairly narrow, which limits the applicability of standard ultrasonic imaging techniques such as synthetic aperture focusing (SAFT), which typically requires a wide sound beam to be transmitted into the sample. Making the transducer smaller will result in a wider beam, but then the transmitted energy is reduced. Since there are significant losses involved when transmitting from water into a metal sample, this makes it unsuitable. Using array probes with water jet coupling requires large water supplies, which is not suitable for field applications.

#### Statement of Contribution/Methods

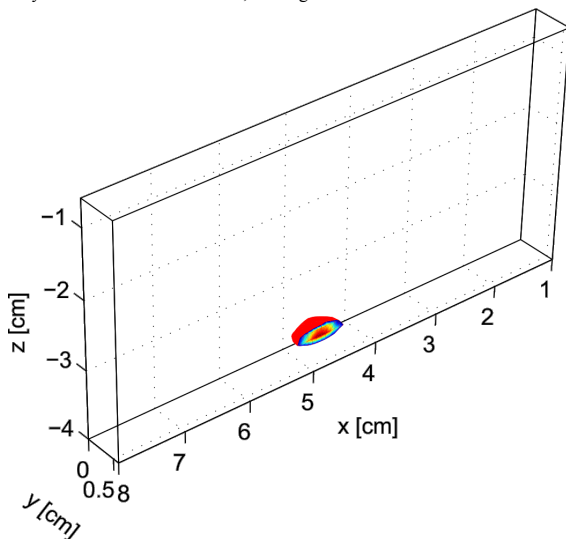
In this paper we present a technique that uses a transducer that focuses the sound at the surface of the sample, thus generating a diverging sound field within the sample. By focusing the sound field, the water jet probe can be built with a small nozzle opening, limiting the water consumption to only 1-2 liters/minute.

The probe is used to scan the surface of the sample in a way that enables a 3D SAFT algorithm to be applied, providing a volume image. We also show how the SAFT algorithm is adapted to compensate for the dual layer (water and sample) propagation.

#### Results/Discussion

The figure shows the result of imaging a block of aluminum with a flat-bottomed hole of diameter 3.2 mm. Approximately half of the top surface of the hole is visible in the figure. The probe was positioned at the top of the sample and measurements were made in a 100 by 6.5 mm grid, with a spacing of 1 mm, corresponding to approximately 0.4 wavelengths.

We demonstrated a water jet coupling system in combination with a focused transducer suitable for imaging using SAFT algorithms. The system operates at 2.5 MHz and uses only 1-2 liters of water/minutes, making usable in field tests.





P2A2-4

**Characterization of the spatio-temporal response of optical fiber sensors to incident spherical waves**

Istvan Veres<sup>1</sup>, Amir Rosenthal<sup>2</sup>, Peter Burgholzer<sup>1,3</sup>, Georg Wissmeyer<sup>2</sup>, Vasilis Ntziachristos<sup>2</sup>, Thomas Berer<sup>1,3</sup>, <sup>1</sup>Recendt, Linz, Austria, <sup>2</sup>Institute for Biological and Medical Imaging (IBMI), Technical University of Munich and Helmholtz Center Munich, Neuherberg, Germany, <sup>3</sup>Christian Doppler Laboratory for Photoacoustic Imaging and Laser Ultrasonics, Linz, Austria

**Background, Motivation and Objective**

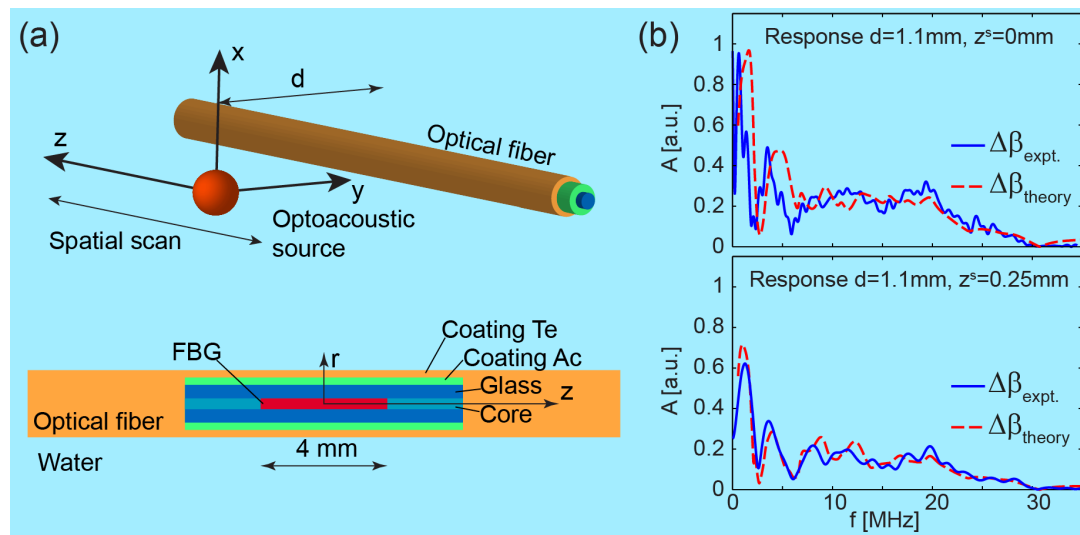
Optical fiber-based sensing of ultrasound is a well-established alternative technique to classical ultrasound detection, with e.g. hydrophones, and regularly used to detect waves up to tens of megahertz. The measurement principle is based on the changes of the refractive index in the optical fiber core due to mechanical stresses/strains. Recently, optical fibers found their application in biomedicine to detect photoacoustically generated ultrasonic waves in tissue. In photoacoustic imaging the imaged object is naturally represented by a finite sum of point-like acoustic sources, and the resulting wavefront may be described by a finite sum of spherical waves. Therefore, knowledge of the response of the sensor to point sources allows enhancing the reconstruction process by incorporation of this information, e.g., in a model-based inversion algorithm.

**Statement of Contribution/Methods**

The aim of the presented work is to evaluate the frequency response of a coated optical fiber to an incident spherical wave. To this end, first a fundamental solution to the scattering of plane waves from a layered cylinder is obtained by using the transfer matrix method for cylindrical geometries. Then the incident spherical wave is described in cylindrical coordinates by using an integral representation which allows the evaluation of the acoustically induced strains using the fundamental solution. Finally, the response of the optical fiber is calculated as the integrated phase shift of the propagating light due to the acousto-optical coupling.

**Results/Discussion**

Experimentally measured responses of a double layered optical fiber are compared to theoretically calculated acoustic responses. A pi-shifted fiber Bragg grating sensor with spatially varying sensitivity was used to detect acoustic waves from a photo-acoustic source [Fig.(a)]. The results [Fig.(b)] show that the response of the fiber is a combination of the change in the length of the sensor and the variation of the refractive index in the core. Longitudinal guided waves are responsible for the first effect which leads to two major peaks at low frequencies (10MHz). For higher frequencies the second effect dominates the response as the result of transverse resonances of the cross-section of the fiber. The experimental and analytical results show a reasonable agreement.



P2A2-5

**Non-recursive Synthetic Aperture Imaging for Multilayered Media with Irregular Boundary**

Shiwei Wu<sup>1</sup>, Jianxin Meng<sup>1</sup>, <sup>1</sup>Zhejiang University, Hangzhou, Zhejiang, China, People's Republic of

**Background, Motivation and Objective**

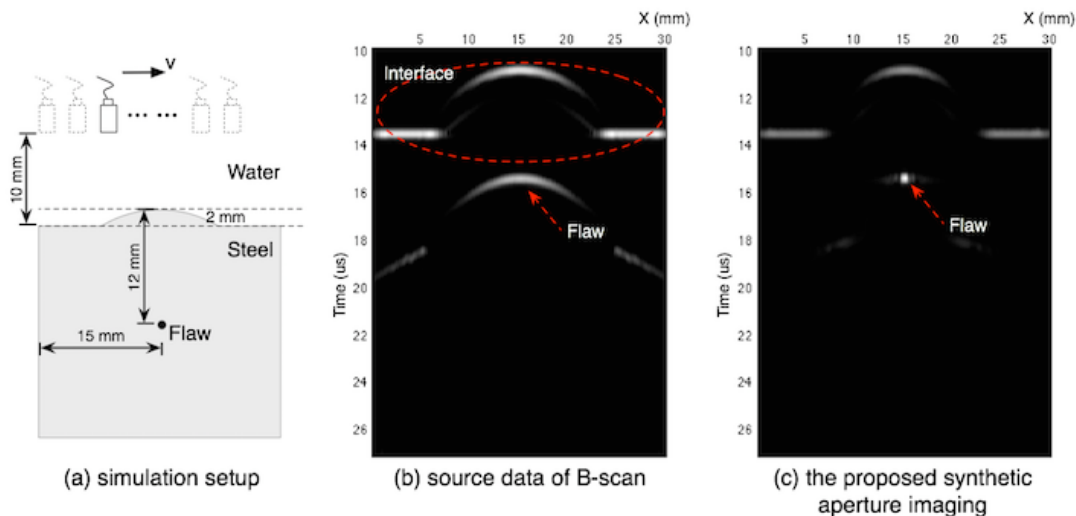
The synthetic aperture focusing technique (SAFT) is used for detection and sizing of material discontinuities (flaws) because of its significantly improved lateral resolution of monostatic imaging systems. The technique has been well studied for contact testing of single homogenous objects, but the efforts to research on multilayered media are relatively insufficient, which has in turn prevented a widespread use of SAFT in ultrasonic nondestructive testing (UNDT). In this paper, a new non-recursive synthetic aperture imaging algorithm for UNDT is proposed to alleviate the situation.

**Statement of Contribution/Methods**

The derivation of the algorithm is inspired by theory of nonstationary linear filtering to reformulate the Stolt  $f$ - $k$  migration as a nonstationary filter which can be extended to imaging of multilayered objects by root-mean-square velocity.

**Results/Discussion**

It is demonstrated that the proposed imaging technique is fine adapted to media with constant velocity, or velocity variations only in depth, which has the same accuracy as phase shift migration (PSM). Moreover, compared with a number of recent algorithms based on PSM, the new algorithm can be made suitable for imaging of irregularly multilayered media with both vertical and lateral velocity variations without recursive procedure. And the experiments also show that the proposed imaging technique is capable of obtaining the focused imaging of flaws in multilayered media with irregular boundary.



P2A2-6

#### Background, Motivation and Objective

Acoustic systems such as side-scan sonar, echosounders, and multi-beam sonar, have been used to measure aquatic plants. Chunhui et al. (J. Marine Acoust. Soc. Jpn., 2013) were the first to apply high-resolution acoustic video camera to an aquatic plant survey in a shallow lake and obtained high quality acoustic image of submerged aquatic plants. However, an acoustic image processing using high-resolution image has not been fully exploited for aquatic plant surveys, especially for precise counting, individual species classification and mapping. In this study, we used high-resolution acoustic imaging sonar and applied the fine acoustic image processing (e.g. counting and classification) for quantification of aquatic plants habitat to maintain and improve the aquatic environments.

#### Statement of Contribution/Methods

The standard DIDSON (Sound Metrics, Bellevue, WA, USA) with a 3° concentrator lens, motion sensor (OS-5000US, Ocean Server Technology, Massachusetts, USA), and DGPS (A100, Hemisphere, Alberta, Canada) were used in this experiment. The field experiments were carried out at two lakes. After the experiments, some acoustic image processing techniques were conducted. As one of the processing, the classification and 3-D mapping of aquatic plants based on spectrum analysis with DoG (Difference of Gaussian) filtering and difference of intensity as following the acoustic image processing algorithm developed for this study.

#### Results/Discussion

We applied the proposed acoustic image processing to high-resolution acoustic image (resolution: 5 mm ~ 2 cm) and 3-D mapping of submerged aquatic plants as shown in Fig. 1. The distribution of three types of aquatic plants including two endangered species was visualized and quantified the water depth and volume of them. *Chara globularis* was distributed at shallow area (1 - 3 m), *Elodea nuttallii* was mainly middle area, and *Nitella flexilis* was deep area (5 - 7 m) but competing with *Elodea nuttallii*. Thus, this measurement system, based on high-resolution acoustic imaging, can be useful for assessing the status of lakes and the distribution of aquatic plants.

P2A2-7

#### Wide 3D Ultrasound Palmprint for Biometric Recognition

Antonio Iula<sup>1</sup>, Gabriel Hine<sup>1</sup>, <sup>1</sup>University of Basilicata, Italy

#### Background, Motivation and Objective

Ultrasound imaging has been experimented in biometric applications mainly for fingerprint and palmprint recognition.

Classical palmprint recognition is based on the acquisition of a 2D image of the palm. A 3D palmprint recognition technique has been explored as well. It is based on structured-light imaging and allows to extract the features by taking account of the palm curvature.

Recently, the authors have proposed an ultrasound technique for extracting 3D palmprints. The proposed approach is able to provide both the 3D profile of the human palm, as it was done in recent works, and, furthermore, 3D information (under skin) of the main traits of the human palmprint.

A drawback of the proposed method relies in the small Volume Of Interest (VOI) acquired, which is limited by the aperture of the array (less than 40 mm). In this way, the base of the fingers, usually used as reference points in the matching procedure, cannot be included.

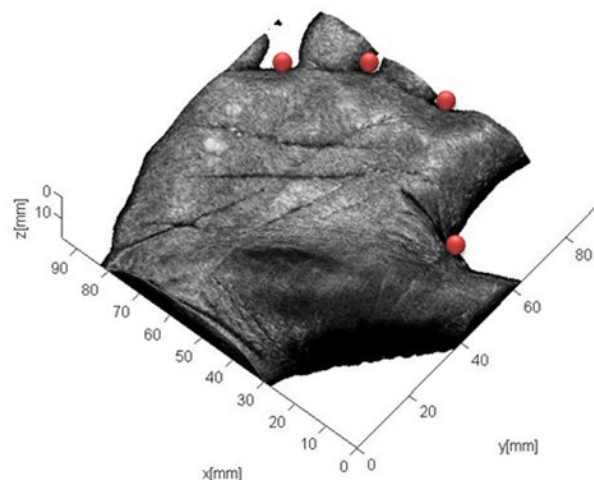
#### Statement of Contribution/Methods

To overcome this drawback, an improved method able to acquire a VOI interest that includes the base of the fingers is presented in this work. A 3D image of the human palm is acquired by exploiting the Ultrasound Advanced Open Platform (ULA-OP) as ultrasound imaging system and a commercial high frequency linear array, which is moved in the elevation direction by an automated scanning system based on a numeric controlled pantograph.

The VOI is acquired through three linear parallel scans. The adjacent scans are partially overlapped to guarantee an effective continuity. To make the acquisition process very fast (less than 30 s), the whole VOI is acquired in a single record; the overlapped volumes are then realigned offline and fused using a convex combination, which weights follow a raised cosine law.

#### Results/Discussion

Several palmprints have been acquired (see one example in the figure); the improvements achieved with the proposed technique in the biometric recognition process are highlighted and discussed.



P2A2-8

### A novel method of evaluating surface properties of tempered glasses by the ultrasonic microspectroscopy technology

Mototaka Arakawa<sup>1</sup>, Jun-ichi Kushibiki<sup>1</sup>, Yuji Ohashi<sup>1</sup>, Kuniko Kawaguchi<sup>1</sup>, Nobuo Takeda<sup>1</sup>; <sup>1</sup>Electrical Engineering, Tohoku University, Sendai, Japan

#### Background, Motivation and Objective

Tempered glasses are processed to increase resistance to break by introducing surface compressive stress. Thinner and more reliable tempered glasses are required for cover glasses of cell phones and personal digital assistants. And, highly reliable evaluation methods of surface compressional stress (CS) and depth of the layer (DOL) of tempered glasses are also required.

We have studied the development of the ultrasonic microspectroscopy (UMS) technology and the application to material characterization. Line-focus-beam ultrasonic material characterization (LFB-UMC) system is able to measure propagation characteristics (velocity and attenuation) of leaky surface acoustic waves (LSAWs), excited and propagated on the water-loaded specimen surface.

In this paper, we discussed a method of evaluating tempered glasses by the UMS technology.

#### Statement of Contribution/Methods

Five aluminosilicate glass (Gorilla glasses (Corning Inc.)) substrates were prepared for the specimens. Four specimens were chemically strengthened by immersing in a bath containing  $\text{KNO}_3$  at  $425^\circ\text{C}$  for 0.5 h, 1 h, 3 h, and 8 h. One specimen was not processed, and used as reference.

Leaky acoustic wave (LAW) velocities were measured by the LFB-UMC system at  $f = 225$  MHz. Velocities of LSAW and leaky surface skimming compressional wave (LSSCW) were obtained according to the analytical procedure of  $V(z)$  curve. CS and DOL of specimens were measured by an optical method measuring light propagation in the strengthened layers.

#### Results/Discussion

LSAW and LSSCW velocities of tempered specimens were larger than those of the unprocessed specimen caused by CS. Figure 1 shows the relationships among LSAW velocities, LSSCW velocities, and DOL. The wavelengths of LSAW and LSSCW at 225 MHz for Gorilla glasses were  $14\ \mu\text{m}$  and  $26\ \mu\text{m}$ , respectively. Linear relationships were observed for DOL and velocities of LSAW and LSSCW in the ranges of the wavelength. We also detected the distribution of CS in the depth direction by measuring frequency dependencies of LSAW and LSSCW velocities. The resolutions of DOL by LSAW and LSSCW velocity measurements were  $0.12\ \mu\text{m}$  and  $0.52\ \mu\text{m}$ , respectively.

This ultrasonic method is extremely useful for evaluation of glass production processes and quality control of tempered glasses.

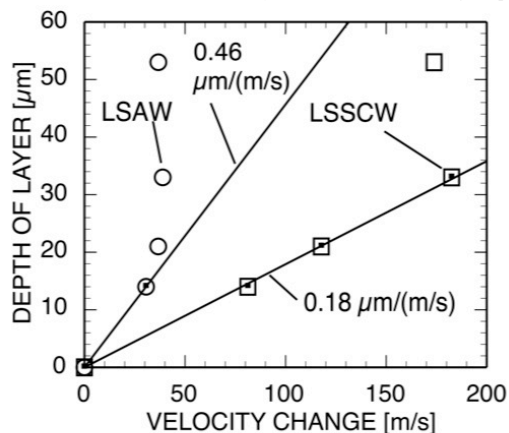


Fig. 1. Relationships between velocity changes of LSAW and LSSCW and depth of layer for Gorilla glasses.

# Non-contact measurement of ultrasonic propagation characteristics in human tissues using pass-through airborne ultrasound

Shinnosuke Hirata<sup>1</sup>, Lalita Haritaipan<sup>1</sup>, Kotaro Hoshiba<sup>1</sup>, Hiroyuki Hachiya<sup>1</sup>, Nobuo Niimi<sup>2</sup>; <sup>1</sup>Tokyo Institute of Technology, Japan, <sup>2</sup>NIPPON SIGMAX CO.,LTD., Japan

## Background, Motivation and Objective

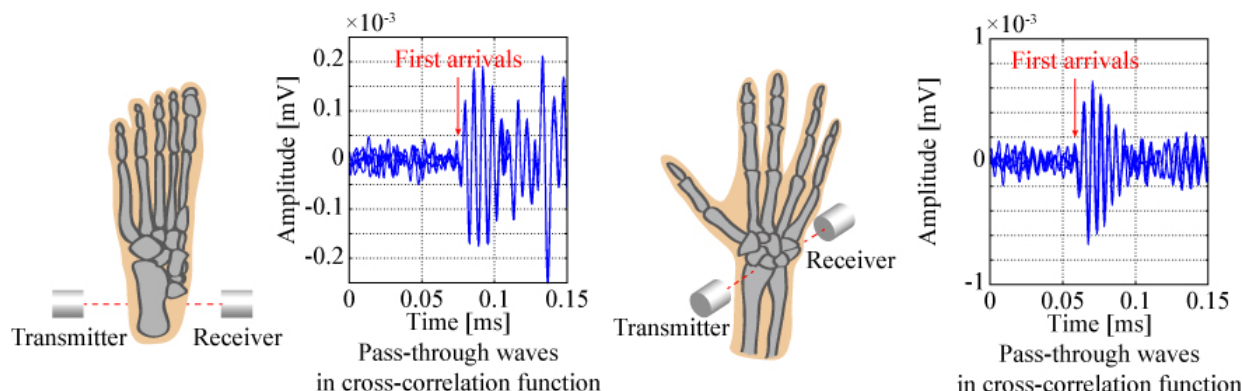
Quantitative ultrasound, which is a quantitative diagnosis method of osteoporosis from propagation characteristics of ultrasound, is studied and applied in clinical practice. In typical ultrasonic bone assessment, ultrasonic transducers are brought into contact with tissue surfaces through water or an ultrasonic gel to effectively propagate ultrasound in human tissues. We have been proposed non-contact measurement of ultrasonic propagation characteristics using airborne ultrasound. Airborne ultrasound which passed through human tissues is extremely attenuated due to large reflections at boundaries between air and tissues. In previous work, therefore, pass-through waves in heels could be detected by pulse compression using 18th-order M-sequence. Propagation speeds in heels could not be estimated, however, because TOFs of pass-through waves could not be determined from their wave forms.

## Statement of Contribution/Methods

TOFs of pass-through waves can be determined from their wave fronts. Therefore, fronts of pass-through waves are clarified in this paper. First, wideband transducers are employed to narrow the pulse width and increase the amplitude of the wave front. Then, the wave form in 1 digit of M-sequence is modified from a sine wave to a square wave for compensation the impulse response of transducers. Furthermore, the order of M-sequence is increased to 19th order. Propagation speeds in the heel and the wrist were estimated in 4-times experiments.

## Results/Discussion

Experimental configurations and detected pass-through waves in the heel and the wrist are illustrated in the figure. TOFs were determined from zero-cross points in averaged pass-through waves. In case widths of the heel and the wrist are and 51.8 and 39.1 mm, estimated propagation speeds are 1567 and 1549 m/s, respectively. The TOF of pass-through airborne ultrasound could be determined by improvement of the S/N and the resolution of the wave front. However, shapes of a heel and a wrist are not uniform. Furthermore, boundaries between air and them are not sufficiently flat as compared with the radius of ultrasonic beam. Therefore, lengths of propagation passes in a heel and a wrist have to be also determined with high accuracy.



## P2A3 - NDE/ Materials Characterization

Salon C

Thursday, September 4, 2014, 8:00 am - 5:00 pm

Chair: **Donald Yuhas**  
Industrial Measurement Systems

P2A3 -1

### Celerity and thickness measurements by ultrasound in protons exchange membranes

**Julien Fortineau**<sup>1</sup>, François Vander Meulen<sup>1</sup>, Laurianne Blanc<sup>1</sup>, Janick Bigarré<sup>2</sup>, Jérôme Fortineau<sup>3</sup>, Guy Feuillard<sup>3</sup>; <sup>1</sup>GREMAN UMR 7347, Université François Rabelais de Tours, Blois, France, <sup>2</sup>CEA, DAM, Monts, France, <sup>3</sup>GREMAN UMR 7347, INSA Centre Val de Loire, Blois, France

#### Background, Motivation and Objective

Protons Exchange Membrane Fuel Cell is a promising green electrochemical energy conversion system to produce heat (hot water) and electricity. The heart of the fuel cell is the protonic polymeric membrane that allows protons conductivity between the two sides of the cell. Typically the thickness of this membrane is 25  $\mu\text{m}$ . Its performances are highly dependents on the hydration rate. The ultrasonic technique has demonstrated its ability to assess the water content in polymer materials [1]. The objective of this work is to develop a high frequency characterization setup to monitor the hydration rate in these protonic membranes thanks to ultrasonic celerity and swelling measurements.

#### Statement of Contribution/Methods

Measurements are made using an insertion substitution method in transmission with two 50 MHz wide band. The ultrasonic celerity and the thickness of the membrane are unknown. They are determined from the time delay between the reference and the transmitted signals and from frequency analysis. Indeed, the ratio between the reference and transmitted spectra shows resonances due to the different echoes in the layer.

This setup was tested on a crystalline silicon (111) sample with a thickness close to three wavelengths at 50 MHz. The thickness is close to the nominal value and the celerity is found in good agreement with literature (maximum error 2 %). Repeatability of this method was checked by measurements on a cellulose acetate film (about two wavelengths thick at 50 MHz). The standard deviation is less than 2 % for both for the velocity and the thickness.

#### Results/Discussion

25  $\mu\text{m}$  thick NAFION® membranes were characterized in the dry and fully hydrated state. To avoid hydration during the measurement, the reference fluid was a low viscosity paraffin oil. The measurements on the dry NAFION® membrane give a celerity of 1240 m/s and a thickness of 22  $\mu\text{m}$ . To our knowledge, this is the first reported ultrasonic celerity measurements in this material. The measured thickness is 12 % lower than the nominal value. This discrepancy can be explained by the very thin thickness of the membrane compared to the wave length (close to one wavelength).

Measurements on hydrated membranes show an increased velocity of 10 – 15 % and an increased thickness about 15 %. This latter has to be compared to the typical swelling of 10 % in NAFION.

In conclusion, a specific setup has been successfully used to evaluate the swelling and the celerity of thin protons exchange membranes. Future work will focus on the real time monitoring of these properties to study the dynamic hydration process.

[1] J. Fortineau, F. Vander Meulen, L. Haumesser, G. Feuillard, S. Barré and O. Bou Matar "Evaluation of the moisture content in phenolic resin via acoustic measurements", Journal of applied physics 100, 074911, 2006.

P2A3 -2

### Fundamental Study on Guided Wave Testing of Cylindrical Bars Embedded in Soil

**Masanari Shoji**<sup>1</sup>, Yasuhiro Higashi<sup>1</sup>; <sup>1</sup>NTT Energy and Environment Systems Laboratories, Nippon Telegraph and Telephone Corporation, Japan

#### Background, Motivation and Objective

Ultrasonic guided wave NDE is a prospective approach for inspecting a long length of bar or pipe. However, for a structure embedded in a solid medium, the properties of guided wave propagation have not been sufficiently investigated and the guided wave NDE technologies have not been adequately established. Thus far, those properties and/or technologies have been investigated mainly for bars surrounded by grout and epoxy to carry out ultrasonic testing of architectural structures, but have scarcely been examined for bars embedded in soil. In this work, basic technologies of guided wave testing of long, small-diameter (2-m-long and 13-mm-diameter) cylindrical steel bars embedded in soil have been experimentally examined by using piezoelectric probes attached to the side of the bars.

#### Statement of Contribution/Methods

On the basis of theoretical attenuation dispersion curves of longitudinal  $L(0,n)$  modes in cylindrical steel bars surrounded by soil [1], 60-kHz and 120-kHz  $L(0,1)$  modes were chosen as guided waves for a pulse echo technique because of their low attenuation. Then, 60-kHz and 120-kHz shear wave normal probes were prepared as prototype probes attached to the side of the bars. It is shown that the  $L(0,1)$  mode can be selectively generated by appropriate phase control of voltages applied to the probes. Measurements were conducted using a double probe technique.

#### Results/Discussion

Figure 1 shows the pulse echo result of a 13-mm-diameter cylindrical steel bar embedded vertically to the ground with an underground depth of two meters, measured by means of the 60-kHz  $L(0,1)$  mode. The bar was embedded more than one year before the experiment. The measurement was carried out using probes attached to the side of the bar protruding above ground. The signal-to-noise ratio of the first reflection signal from the bottom end surface was estimated to be more than 30 dB for both 60-kHz and 120-kHz  $L(0,1)$  modes. The attenuation of the propagation in the underground part was approximately 5 dB/m and 8 dB/m for the 60-kHz and 120-kHz  $L(0,1)$  modes, respectively, which is consistent with the attenuation dispersion curve obtained by calculation. The results indicate sufficient potential for guided wave testing of long (at least a few meters) small-diameter cylindrical bars embedded in soil.

[1] M. Shoji and T. Sawada, in proceedings of IUS, Joint UFFC, EFTF and PFM Symposium, pp. 170-173, 2013.



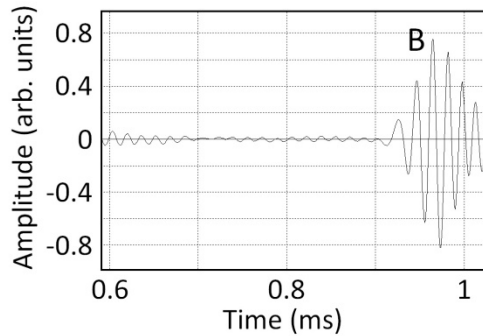


Fig. 1. Pulse echo result of a 13-mm-diameter cylindrical steel bar embedded vertically to the ground with an underground depth of 2 m, measured by means of 60-kHz L(0,1) mode. B indicates the first reflection signal from the bottom end surface of the bar.

P2A3 -3

#### Application of one-bit time reversal technique to mechanical strain monitoring in plates

Alan Kubrusly<sup>1</sup>, Nicolas Perez<sup>2</sup>, Julio Cesar Adamowski<sup>3</sup>, Timoteo Francisco Oliveira<sup>3</sup>, Arthur Braga<sup>1</sup>, Jean Pierre von der Weid<sup>1</sup>; <sup>1</sup>Pontifical Catholic University of Rio de Janeiro, Brazil, <sup>2</sup>Polo Agroalimentario Agroindustrial de Paysandú, Universidad de La Republica, Uruguay, <sup>3</sup>Department of Mechatronic and Mechanical Systems Engineering, University of Sao Paulo, Brazil

#### Background, Motivation and Objective

Ultrasonic guided waves in mechanical structures, such as plates or bars, are dependent on the strain or stress states of the medium. This characteristic was already used to measure the stress condition in plates for single mode Lamb waves by observing the time of flight shift. In a plate, each propagating mode presents a different phase dependence on strain. Thus, if many modes are excited in a specimen, it is hard to interpret the signal changes meaning. The time reversal technique acts as a dispersion compensator, allowing time re-compression for the guided waves, and has already been used by our group to measure strain variation in a plate structure. The one-bit variation of time reversal sets the amplitude of the exciting signal to  $\pm 1$  depending on the sign of the signal received. It is simpler to implement, as only a voltage switch is required instead of a full analog synthesizer used in the normal technique. Using this implementation, the focus gain is maximized, but the whole signal shape depends on the system. The setup consists of a pair of piezoelectric transducers bonded in the extremities of an aluminum plate. When the plate is subjected to traction, time reversal is performed, the mismatch between the impulse response at initial and strained levels causes loss in the focusing quality. The strain can be evaluated by measuring either the time of flight shift or the amplitude decrease.

#### Statement of Contribution/Methods

In this work, we used the one-bit time reversal setup especially aiming to use the changes in the focus amplitude rather than time of flight. Amplitude sensitivity is simpler to use due to the high sampling rate necessary for sensing the time shift. To enlarge the number of excited modes, three different 2-2 piezocomposite transducers pairs at 500, 1000 and 2250 kHz were especially designed. These transducers have lower impedance and wider frequency band than single ceramic transducers. With a richer spectrum response, more modes collaborate on the focusing processes and the stress induced mismatch is more relevant, increasing the sensitivity of the focus amplitude. One-bit and normal time reversal results were compared for all transducers configurations.

#### Results/Discussion

The strain sensor was tested in laboratory for longitudinal strain up to 150  $\mu$ -strains. All transducers presented higher amplitude sensitivity than mono-element transducers used in previous work, up to about 2.5 times. The time reversal energy efficiency was proposed as a spectrum figure of merit and obeys the sensitivity behavior. The one-bit time reversal variation provided good focused signal for all experiments. Moreover, every configuration showed a higher sensitivity than its normal time reversal version, at least 5% depending on the transducer. The one-bit technique reveals an important enhancement for the method; it holds the natural advantage of being simpler and the benefit of higher sensitivity on the measurand.

P2A3 -4

#### Modal analysis of leakage-induced acoustic vibrations in different directions for leak detection and location in fluid-filled pipelines

Shuaiyong Li<sup>1</sup>, Yumei Wen<sup>1</sup>, Ping Li<sup>1</sup>, Jin Yang<sup>1</sup>, Jing Wen<sup>1</sup>; <sup>1</sup>College of Optoelectronic Engineering, Chongqing University, China, People's Republic of

#### Background, Motivation and Objective

The acoustic emission technique (AE) as one of real-time and in-service nondestructive examination methods has received considerable attention for leak detection in fluid-filled pipelines. In the conventional leak location surveys using AE technique, the most widely used methods are based on the correlation technique, whose prerequisite is that the leakage-induced acoustic vibrations propagate along the pipelines over a significant distance as a single non-dispersive mode. In practice, the acoustic vibrations possess multi-modal, attenuation, dispersive natures, and thus the requirement is not satisfied, which brings a great challenge for leak detection in pipelines.

#### Statement of Contribution/Methods

In this work, the dispersive behaviors, modal distributions of acoustic vibrations in different directions in the gas pipelines are analyzed using guided wave theory of hollow cylinders, considering acoustic impedance mismatch between the pipe wall and the in-pipe gas.

#### Results/Discussion

From the cross-correlation of two spatially separately collected acoustic vibrations on either sides of a leak in different directions as shown in Fig.1, it can be seen that there are two peaks in radial and circumferential directions respectively representing torsional and dispersive flexural modes, only one obvious peak in axial direction representing non-dispersive longitudinal mode in low-frequency range, which convinces the theoretical predictions. Figure 2 gives attenuation rates of acoustic vibrations in different directions. These facts show that, at information acquisition stage, exclusively picking up the axial vibration is significant for improving leak detection in pipelines.

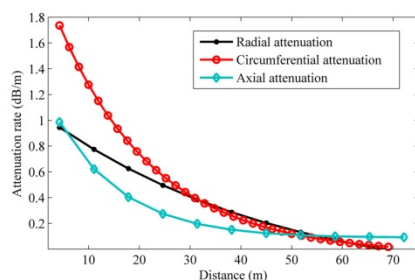


Fig. 2. Attenuation rates of the gas-leakage acoustic vibrations of various directions

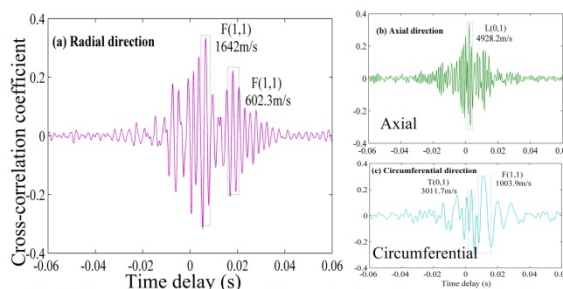


Fig.1. The cross-correlation time delay estimations for acoustic vibrations in different directions

P2A3 -5

#### Wood characterization using the power spectral density and phase velocity of ultrasonic signals

Ozana Maria de Andrade Maia<sup>1</sup>, Fabio Kurt Schneider<sup>2</sup>, Joaquim Miguel Maia<sup>2</sup>, Susete do Rocio Chiarello Penteadó<sup>3</sup>, <sup>1</sup>CPGEI/UTFPR, Federal University of Technology - Paraná, Curitiba, Paraná, Brazil, <sup>2</sup>DAELN/CPGEI/UTFPR, Federal University of Technology - Paraná, Curitiba, Paraná, Brazil, <sup>3</sup>EMBRAPA, Brazilian Agricultural Research Corporation, Colombo, Paraná, Brazil

#### Background, Motivation and Objective

The application of non-destructive testing (NDT) in the analysis of trees in forest plantations permits the evaluation of the wood quality, the internal defects in development or pest attack and its characterization for application as solid wood and its products. These techniques have been constantly improved with the use of computers, electronics and agricultural control levels in order to provide tools to the specialists in integrated management. The ultrasound has been used in agriculture as NDT to determine the elasticity modulus of juvenile and mature wood of pinus and other species. This study aimed to the evaluation of new techniques for characterization of wood using parameters such as the power spectral density (PSD) and phase velocity of ultrasonic signals propagating in wood.

#### Statement of Contribution/Methods

The tests were performed using a pair of ultrasonic transducers with central frequency of 50 kHz (083-067-038, GE) which were connected to an ultrasonic pulser/receiver (5077PR, Olympus). The transmitting transducer was coupled to the samples of pinus using ultrasound gel and excited with negative pulses of short duration (5  $\mu$ s) and high amplitude (-400 V) to generate longitudinal and shear waves. The ultrasound signals that propagated through the samples were received by the receiving transducer, amplified (20 to 40 dB), acquired in a digital scope (MSO4104B, Tektronix) and then transferred to a microcomputer. The tests have been done with 10 reference samples (healthy) and 10 damaged by wood wasps, with small holes in the bark. The transducers were placed on the samples in the axial, radial and inclined modes.

#### Results/Discussion

The data were processed using the Matlab (Mathworks Inc.) to determine the power spectral density (PSD), the root mean square deviation index (RMSDdB) and the phase velocity between the reference and damaged samples. The RMSDdB calculated between the PSD of the reference and the damaged samples were generally higher for samples with higher degree of damage, however, in some cases, they were lower due to the presence of wood knots (Fig. 1a). The phase velocities were calculated in the frequency range 1-200 kHz and generally show higher values for the reference samples. The group velocities were also calculated and the results were in the range 1200-3000 m/s, indicating that these parameters can be used to characterize wood.

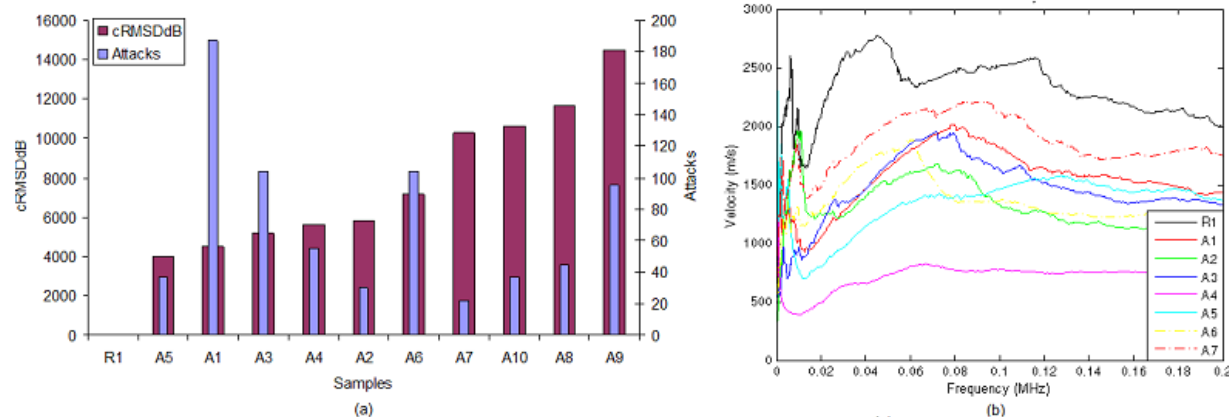


Figure 1. (a) Root mean square deviation (cRMSDdB) of the power spectral density of reference (R1) and damaged samples (A1 to A10); (b) phase velocity of reference (R1) and damaged samples (A1 to A7).

P2A3 -6

#### Methodology for the 3-Dimensional Model-Assisted Evaluation of Polycrystalline Materials

Darius Johnson<sup>1</sup>, James Blackshire<sup>1</sup>, <sup>1</sup>AFRL/RXCA, Air Force Research Laboratory, Wright-Patterson AFB, Ohio, USA

#### Background, Motivation and Objective

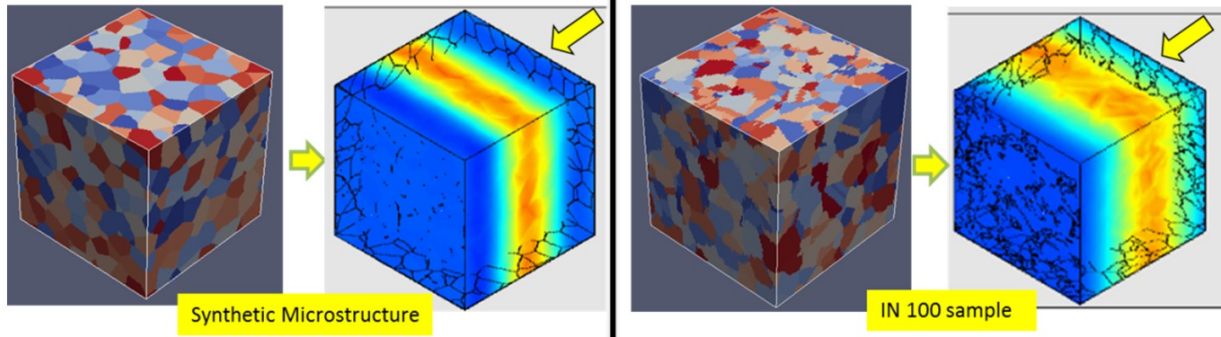
The quantitative nondestructive evaluation of tailored microstructures is becoming an increasingly important topic. In aerospace engine materials, NDE methods are needed to characterize polycrystalline grain information related to mean grain sizes, grain size distributions, and misorientation states. In the present research effort, model-assisted ultrasound methods are being developed to study fully 3-dimensional elastic wave propagation and scattering interactions with synthetic and realistic microstructures in nickel superalloy materials.

#### Statement of Contribution/Methods

A methodology for integrating synthetic and realistic 3-dimensional microstructure states into ultrasonic finite element models has been developed. The methodology utilizes a recently developed software platform called DREAM3D, which provides a means for generating, analyzing, and archiving 3-dimensional microstructure volumes. In the present effort, custom Matlab code was developed to synergistically connect the DREAM3D environment with PZFLEX ultrasound FEM modeling software. The resulting software capability provides a means for accurately representing the full 3-dimensional crystallographic stiffness matrix values in complex polycrystalline systems, where ultrasonic sensing models are being used to understand time-resolved, backscatter phenomenon for enhanced microstructure characterization in aerospace materials.

#### Results/Discussion

Preliminary 3-dimensional modeling results are provided in the figure below, where longitudinal ultrasonic waves propagating along the positive x-axis are depicted for a synthetically generated nickel alloy material (left), and a realistic Inconel 100 microstructure (right). The elastic wave energy is depicted at the approximate mid-point of each virtual sample during the model run, where perturbations of the advancing wavefront and scattering from individual grains can be observed.



P2A3 -7

#### High-performance Nondestructive Inspection Method for High-attenuation Billet: Ultrasonic Computerized Tomography Using Time-of-flight

Yoko Norose<sup>1</sup>, Koichi Mizutani<sup>1</sup>, Naoto Wakatsuki<sup>1</sup>, Tadashi Ebihara<sup>1</sup>; <sup>1</sup>University of Tsukuba, Japan

#### Background, Motivation and Objective

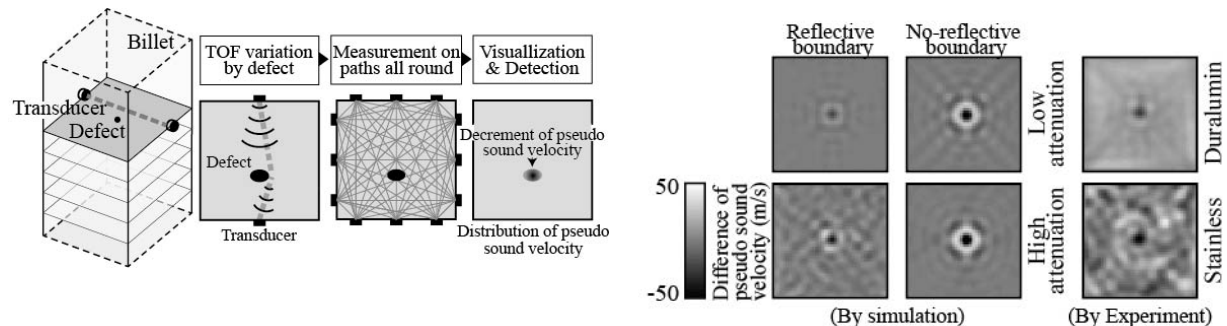
A pulse echo method is generally employed for a defect detection inside a billet. However, the pulse echo method cannot detect the defect inside a high-attenuation billet, such as cast stainless steel. We had proposed ultrasonic computerized tomography (CT) method using time-of-flights (TOFs) as a defect detection method. In this method, because the transmitted waves instead of echoes are used for the measurement of TOFs, the received signal can be stably obtained, and multiple signals are obtained by single transmission. Hence, this method is suitable for a high-attenuation billet. In this study, we considered the applicability of this method to the high-attenuation billet.

#### Statement of Contribution/Methods

In this method, the TOF variation, which is caused by diffraction and scattering of the signal, is measured at first, as shown in the left figure. Then, the defect is reconstructed by CT method using TOF variations. In this method, the ability of detection is not directly determined by the received signal level. Therefore, we confirmed the ability of defect detection inside the high-attenuation billet, and evaluated the effect of the attenuation rate to the CT image.

#### Results/Discussion

From the simulation and the experiment, we obtained the interesting result that when the attenuation was high, the visualized defect was vivid in the CT image as shown in the right figure. It was found that this reason was that the effect of the reflected wave on the billet surface decreased and TOF measurement error decreased. However, when the attenuation rate is high, the signal-to-noise ratio becomes low and the artifacts in the CT image increase. As a result, it was indicated that the CT method using TOF could apply to detect defect inside the high-attenuation billet under the condition of the certain SNR.



P2A3 -8

#### Characterization of Natural Fibre-Reinforced Composites with Advanced Ultrasonic Techniques

Inna Seviaryna<sup>1</sup>, Elena Maeva<sup>1</sup>, Jimi Tjong<sup>2</sup>; <sup>1</sup>Physics Department, University of Windsor, Canada, <sup>2</sup>Ford Motor Company, Canada

#### Background, Motivation and Objective

Increasing request for improving vehicle energy efficiency and environmental concern has forced the automotive industry to develop new lightweight bio-based composite materials. The natural fibre reinforcement has several advantages over synthetic ones such as lower cost, wide availability, and biodegradability. Most of NDE methods in automotive industry are adjusted to the evaluation of synthetic fibre composites and should be adapted to this change of materials.

The objective of this research is to establish the correlation between acoustic characteristics, the composition of natural fibre-reinforced composites (NFRC) and its performance, as well as to develop the approach for ultrasonic visualization of major composite defects such as non-uniform fibre distribution, voids, cracks and impacts.

#### Statement of Contribution/Methods

The important viscoelastic properties of novel NFRC were examined through a combination of experimental and theoretical approaches. The classical ultrasonic pulse-echo technique was applied for qualitative estimation and quantitative measurements of basic viscoelastic parameters of polypropylene-based composites filled with microfibers. The series of samples with different fibre content was produced and tested in order to study the correlation between composition and macroscopic characteristics. Special attention was paid to the effect of the processing variables on the performance of the NFRC. The experiments were conducted based on a custom designed ultrasonic system in a wide frequency range (1-25 MHz). Anisotropy measurements provided information about preferential fibre orientation which appears during extrusion process.

High frequency ultrasonic imaging was applied to examine the major types of NFRC defects. B- and C-scans acquired with high-resolution acoustic microscope reveals distribution of fibers in polymer matrix. Statistical analysis of these images allows estimation of fiber-matrix bonding.

#### Results/Discussion

The obtained results justify the feasibility of using the ultrasonic technique for evaluation of the fibre content and homogeneity of fibre distribution. It was found that the attenuation and sound velocity are the most convenient and useful parameters for the estimation of fibre content in the composites. Their frequency dependencies in range of 1-25 MHz are in good correlation with the model prediction. Finally, this study provides a solid basis for the development of technology for ultrasonic in-process monitoring of material formation. It should provide quick feedback in optimizing the technological regime settings to produce composites with the required mechanical performance.

This Project was funded by Automotive Partnership Canada NSERC.

P2A3 -9

#### Guided Waves in Material Characterization for 3D-printed Parts

Chao-Kuo Chan<sup>1</sup>, Che-Hua Yang<sup>1</sup>; <sup>1</sup>Department of Mechanical Engineering, National Taipei University of Technology, Taiwan

#### Background, Motivation and Objective

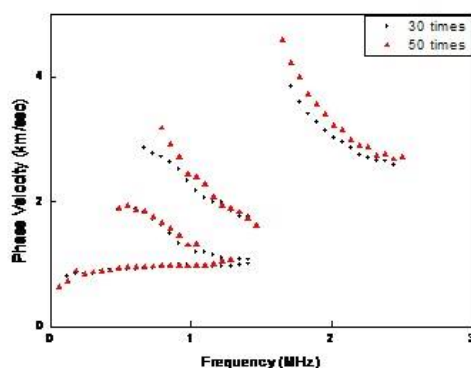
Additive manufacture (AM), or so-called 3D printing, has been treated as a revolutionary manufacturing technology. Not limited to pure geometrical formation, 3D printed objects are now replacing critical parts made by traditional machining technologies in the form of metals or ceramics. Usually these parts have critical load-supporting function which demands stable mechanical properties. Different from traditional manufacture, AM parts are built with a layer-by-layer manner. Material properties such as tensile strength and elastic modulus can vary widely and cause problems in critical applications. This paper focuses on characterizing mechanical properties of AM parts with different UV light exposure times.

#### Statement of Contribution/Methods

Acrylic plastic samples prepared by a 3D printer (Project 3510SD) are prepared in the format of plates with a thickness of 1.0 mm. The process uses UV light exposures to solidify powder in liquid form layer by layer. With the same thickness of 1.0mm, however, these samples are prepared with different exposures of 15, 25, 30, 40 and 50 times, respectively. Mechanical properties of these plate samples are measured with a laser ultrasound technique for dispersion curves, then followed by an inversion algorithm to explore the effects of exposure time.

#### Results/Discussion

Dispersion curves for two AM manufactured plates with 30 and 50 exposures are shown in the figure. Higher phase velocities are observed for the AM sample with a higher 50 exposures. Further with the inversion procedure, elastic moduli are calculated from their measured dispersion curves. The AM prepared plate with 15 exposures is found to have a Young's modulus of 3,639 MPa, 3,704 for the exposure of 25, 3,901 for 30, and 4,081 for 40, respectively. In other words, the AM manufactured parts get harder as the number of exposure increases. This results imply an uneven distribution of elastic modulus (or hardness) across the layers along that different times of exposure are naturally experienced in this type of AM. This paper will further explore this uneven distribution and present this method in characterizing AM parts. Results of this study will be useful in the development of 3D printing technology towards replacing traditional manufacture technology.



# P3A1 - Particle Manipulation and Acoustic Tweezing 1

Salon C

Thursday, September 4, 2014, 8:00 am - 5:00 pm

Chair: **Anne Bernassau**  
University of Glasgow

P3A1-1

## Influence of Nonlinear Effects on the Acoustic Levitation of Small Spheres

Tiago Ramos<sup>1</sup>, Marco Andrade<sup>2</sup>, Julio Adamowski<sup>1</sup>; <sup>1</sup>Mechanical Engineering, University of Sao Paulo, Sao Paulo, Brazil, <sup>2</sup>Institute of Physics, University of Sao Paulo, Sao Paulo, Brazil

### Background, Motivation and Objective

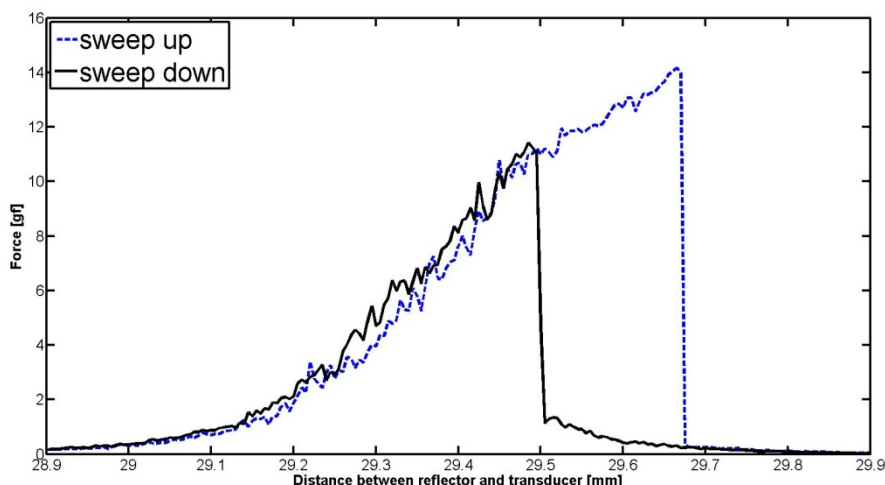
A widely used approach to design acoustic levitators consists in simulating the pressure field with linear numerical models and then to apply the Gor'kov theory to calculate the potential of the acoustic radiation that acts on a small sphere. This method predicts the radiation force with a reasonable accuracy for low amplitude pressure. For high amplitude pressure there are nonlinear effects, not predicted by this model. The objective of this work is to investigate the influence of these nonlinear effects on the acoustic levitation of small spheres.

### Statement of Contribution/Methods

The nonlinear effects that occur in a single-axis acoustic levitator consisting of a 20.3 kHz Langevin transducer and a concave reflector are experimentally investigated. The nonlinear characterization of the levitator is performed by applying an electronic balance to measure the acoustic radiation force that acts on the reflector as a function of the separation distance between the transducer and the reflector. Moreover, small spheres of different materials are levitated and a high speed camera is used to obtain the position of the levitated sphere as a function of time for different levitator parameters.

### Results/Discussion

The measurement of the acoustic radiation force on the reflector shows that the force-distance curve becomes asymmetric when the pressure amplitude is increased. For high pressure amplitudes, the curve becomes so distorted, that a jump phenomenon occurs, in which a small increment of the separation distance produces a sudden decrease of the acoustic radiation force. It was also verified by using the high speed camera that the levitated sphere can fall into the reflector when the jump phenomenon occurs. The jump phenomenon and the hysteresis effect can be observed in the figure.



P3A1-2

## Acoustic filtering of particles in a flow regime

Kristoffer Johansen<sup>1</sup>, Spiros Kotopoulos<sup>1,2</sup>, Michiel Postema<sup>1</sup>; <sup>1</sup>Department of physics and technology, University of Bergen, Bergen, Norway, <sup>2</sup>National Center for Ultrasound in Gastroenterology, Haukeland University Hospital, Bergen, Norway

### Background, Motivation and Objective

Hydroelectric power is a clean source of energy. However, a vast majority of hydroelectric power plants are affected by the damage induced by  $\mu$ -sized particles, e.g., silt, in the water. The damage done by these particles is twofold, a) high velocity impact creates  $\mu$ -sized pits on turbine blades, and b) these particles also act as nuclei for cavitation. Both the  $\mu$ -sized pits and cavitation cause surface damage and even failure of turbine blades. The filters commonly used reduce the water flow, thus reducing power generated while requiring continuous maintenance. We explore the use of ultrasonic primary radiation force to filter the particles without drastically reducing the water flow velocity.

### Statement of Contribution/Methods

Simulations were performed at frequencies from 100 - 600 kHz to evaluate the acoustic pressure necessary to force  $\mu$ -sized particles to a pipe wall in high-flow situations. Primary radiation force on a sphere was computed in a low viscous fluid for a plane progressive wave. We study the condition  $a, \lambda \ll \delta$ . Where  $a$  is the radius,  $\lambda$  is the wavelength and  $\delta$  is the viscous penetration depth. A large diameter flow chamber with an optical window was fabricated to observe the behavior of  $\mu$ -sized particles under sonication. The incoming



and outgoing flow rates were measured using variable area flow meters. A high-speed camera mounted to a microscope was used to observe the particles. The chamber was designed to allow for interchangeable ultrasound transducers. The particle concentration was measured before and after filtration using a hemocytometer.

### Results/Discussion

Simulations indicate that at high flow rates, with a 100 kHz, 16 kPa traveling plane wave, the particles should be radiated from transducer to the far wall of a 1-inch water pipe. The higher the center transmit frequency is, the stronger the primary radiation force. Hence, the particles should clear the water pipe at a faster rate. This is because the primary radiation force is proportional to  $ka^3$ . Where  $k$  is the wavenumber and  $a$  is the radius. Figure 1, shows the effect of frequency on the radiation distance of a 200  $\mu\text{m}$  silt particle. Our simulations are compared to the experimental mode.

The first experiments confirm that the higher the center frequency and/or acoustic pressure, the larger the primary radiation force. This causes further particle translation distances, at higher flow rates.

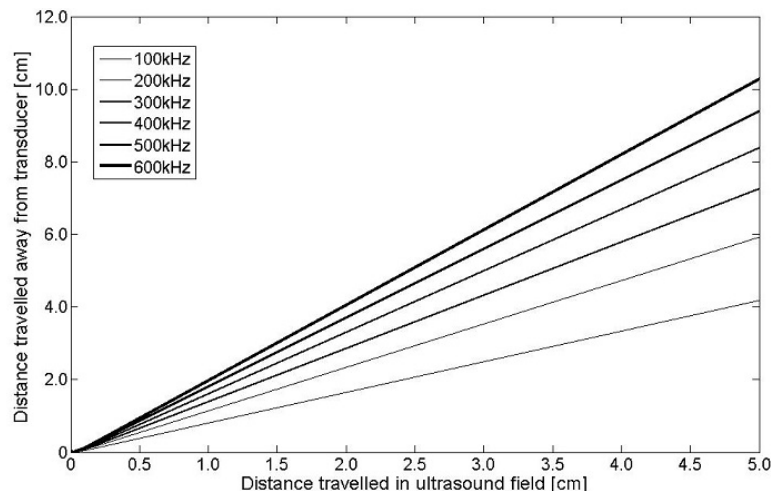


Figure 1: Distance travelled by particle from face of transducer. Pressure is 16kPa, frequencies 100-600 kHz and radius of particle is 100 $\mu\text{m}$ .

P3A1-3

### FPGA Embedded Systems for Ultrasound Particle Manipulation with Sonotweezers

Han Wang<sup>1</sup>, Yongqiang Qiu<sup>1</sup>, Christine Demore<sup>1</sup>, Sandy Cochran<sup>1</sup>; <sup>1</sup>Institute for Medical Science and Technology, University of Dundee, United Kingdom

#### Background, Motivation and Objective

Recent research in acoustic tweezing has mainly focused on the behaviour of devices for specific applications and the fundamental theories of the forces exerted on the target particles. However, compared to optical tweezers, there have been only limited reports about developments and applications of acoustic tweezers at the system level. This paper reports the results of the development of a low-cost, low power consumption, fully programmable and bench top size electronic system for research applications of "Sonotweezer" devices.

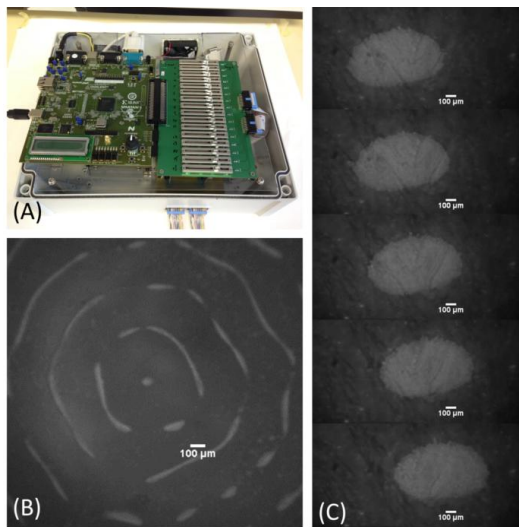
#### Statement of Contribution/Methods

The electronic system is designed to provide 16 channels of independently controlled signals in the form of continuous waves with approximately sinusoidal characteristics. For each channel, the signal frequency, phase and amplitude can be controlled individually. The system incorporates both programmable digital electronics and bespoke analogue electronics, in a form that can be easily expanded to deal with a higher channel count.

A customized FPGA soft core is designed to generate 16 channels of independent digital signals with frequencies and phases which can be adjusted in real time from a PC within the MATLAB (Mathworks, Cambridge, UK) environment. Bespoke analogue electronics were constructed in two parts, for signal conditioning and amplification. The signal conditioning stage is designed to provide an arbitrary amplitude attenuated signal from CMOS logic signals generated from the digital stage. The 16-channel analogue amplifier array was designed for direct amplification of the attenuated digital signal for transducer actuation.

#### Results/Discussion

The electronics have been used successfully to demonstrate the capability to manipulate microparticle clusters for different array-based ultrasonic manipulation devices. In Figure 1 below (A) is a photograph of the 16-channel Sonotweezer control system; (B) is the acoustic field formed in the shape of concentric circles illustrated by the trapping of 10  $\mu\text{m}$  polystyrene microspheres with a 16-element ring array Sonotweezer; (C) is a demonstration of a cluster of 10  $\mu\text{m}$  polystyrene microspheres manipulated by a 1-D linear array Sonotweezer. Further improvements of the system will emerge from work on diverse applications as well as enhanced packaging of the IP core and user friendly interface development.



P3A1-4

### Micropatterning based on single-beam acoustic trapping

Changhan Yoon<sup>1</sup>, Bongjin Kang<sup>1</sup>, Changyang Lee<sup>1</sup>, Hyung Ham Kim<sup>1</sup>, K. Kirk Shung<sup>1</sup>; <sup>1</sup>Biomedical engineering, University of Southern California, USA

#### Background, Motivation and Objective

Micropatterning of cells and microparticles is of particular importance in many biological applications including cell biology studies, biosensors and tissue engineering. Among various methods (e.g., optical tweezers, magnetic tweezers, and microstamping), acoustic tweezers have several advantages in miniaturization, low power consumption, and technical simplicity. In this paper, we report the feasibility of micropatterning with a single-beam acoustic tweezer (MSAT) using a high-frequency array transducer.

#### Statement of Contribution/Methods

In MSAT, a sparse array (SA), where an array with fewer elements than the required condition (e.g.,  $\lambda$  and  $\lambda/2$  element space for linear array and phased array, where  $\lambda$  is the wavelength) is utilized in transmission, is applied to separate the microparticles into desired patterns. The grating lobe at focal depth without steering in the SA method occurs at  $mF/Sd$  ( $m$ =integer), where  $F$  is the focal depth,  $S$  is the sparse factor, and  $d$  is the element pitch; thus the location of grating lobe can be adjusted by changing the sparse factor (i.e.,  $S$ ), with a given array transducer. To assess the feasibility of this approach, a 30 MHz high-frequency linear array with a 50  $\mu$ m azimuth pitch was utilized. The array was driven by a FPGA based 64-channel ultrasound imaging system. A 200-cycles of 30 MHz sinusoidal burst was transmitted to a depth of 2.6 mm at pulse repetition period of 1 ms or a duty factor of 0.67. Polystyrene microparticles with a mean diameter of 50  $\mu$ m were utilized as the targets. The array transducer was mounted on an inverted microscope (Olympus lx70) and the images were recorded using a high-sensitive CCD camera (ORCA-Flash2.8, Hamamatsu, Japan).

#### Results/Discussion

The accompanied figure shows microparticles (indicated with red arrows) trapped using the SA method with (a)  $S=2$  (SA10) and (b)  $S=3$  (SA100), respectively. As can be seen, two particles were simultaneously captured at the locations of the main lobe and grating lobe. The first locations of grating lobe (i.e.,  $F/Sd$ ) was computed to be 860  $\mu$ m and 650  $\mu$ m away from the main lobe for SA10 and SA100, respectively, which were consistent with the results from the experiment. These results indicate that the proposed method hold promise as a useful tool for various biological applications, one of which is to interrogate cell to cell interaction.

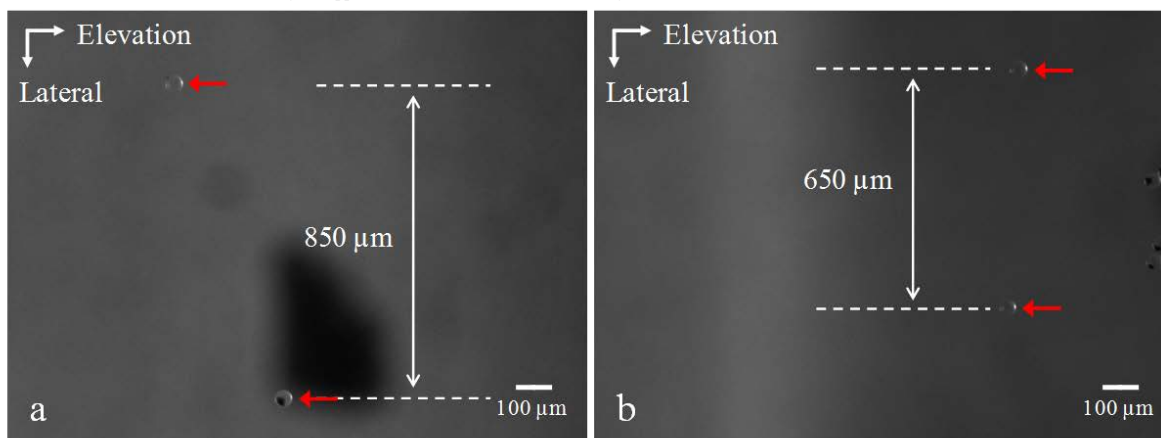


Fig. Micropatterning of particles using the sparse array with (a)  $S = 2$  and (b)  $S = 3$

**Temperature-dependent Displacement Modulation at Acoustic Trap**

Jungwoo Lee<sup>1</sup>, Jae Youn Hwang<sup>2</sup>; <sup>1</sup>Kwangwoon University, Korea, Republic of, <sup>2</sup>Daegu Gyeongsang Institute of Science and Technology, Korea, Republic of

**Background, Motivation and Objective**

In this work, an experimental study is carried out to investigate the quantitative relation between temperature and laterally displaced distance (or displacement) of lipid microdroplets with a two-dimensional acoustic trapping technique. A 20/40 MHz LiNbO<sub>3</sub> dual element transducer is utilized to establish the trap formation and to measure the sound speed inside a trapped droplet at the same time. 40 MHz trapping ultrasound is generated from the inner circular element, while 20 MHz sensing beam from the outer ring element. Since the acoustic radiation force is inversely proportional to the temperature-dependent sound speed in propagating media, the displacement indicating how strongly the trap can be formed is also linked with the temperature change. The results are presented to suggest that the acoustic trapping mechanism may further be altered by controlling the temperature level near the trap, rather than by modifying the trapping system parameters such as resonance frequency or input voltage amplitude of transducers.

**Statement of Contribution/Methods**

The transducer moves over the focal plane, as targeting a particular droplet from the bottom with 40 MHz ultrasound. After the 40 MHz acoustic trap is set up at the focus, a monitoring camera attached to a microscope determines the lateral displacement of the trapped droplet with an imaging analysis software. 20 MHz sensing beam then simultaneously interrogates the droplet to measure the sound speed within it. The whole experimental procedure is repeated 10 times at a given temperature for obtaining statistical data. Both lateral displacement and sound speed are measured as a function of temperature near the acoustic trap.

**Results/Discussion**

The displacement of a migrating droplet is measured every 1 degree C, as the temperature varies from 25 degree C to 30 degree C. The excitation parameters for the transducer are summarized as follows; Pulse repetition frequency = 1 kHz, Input voltage amplitude to the transducer = 16 V. The average displacement is found from 145 micrometers to 156 micrometers over the given temperature range. The average sound speed inside the droplet decreases as the temperature rises, for example, 1440 m/s at 25 degree C and 1429 m/s at 30 degree C.

The experimental results show that a temperature rise inducing a reduced sound speed within a trapped droplet leads to its increased displacement. As the temperature elevates near the trap, the force applied on the droplet tends to increase because the acoustic force is inversely proportional to the sound speed. In previous studies regarding the fat tissue characterization, a similar inverse relation between the temperature and the sound speed has already been reported. Therefore, the results suggest that this acoustic force-based method can also be used as a non-invasive manipulation tool in thermally unstable environment by precisely adjusting the trapping strength corresponding to the temperature variation near the trap.

## P3A2 - Nonlinear Acoustics 2

Salon C

Thursday, September 4, 2014, 8:00 am - 5:00 pm

Chair: **David Feld**  
AVAGO Technologies

P3A2-1

### Evolution of Nonlinear Acoustics during Creep in Welded Joint for High Cr Ferritic Heat Resisting Steels

Toshihiro Ohtani<sup>1</sup>, Yuki Kusanagi<sup>2</sup>, Yutaka Ishi<sup>2</sup>, Masaaki Tabuchi<sup>3</sup>, Hiromichi Hongo<sup>3</sup>, Masahiko Hirao<sup>4</sup>; <sup>1</sup>Mechanical Engineering, Shonan Institute of Technology, Fujisawa, Japan, <sup>2</sup>Graduate School of Engineering, Shonan Institute of Technology, Fujisawa, Japan, <sup>3</sup>National Institute for Material Science, Tsukuba, Japan, <sup>4</sup>Graduate school of engineering science, Osaka University, Toyonaka, Japan

#### Background, Motivation and Objective

Creep lives of high Cr ferritic heat resisting steel weldments decreased due to Type IV damage and fracture, which occurs as result of formation and growth of creep voids and crack on grain boundaries in fine-grained heat affected zone (HAZ). This damage and cracks initiated and progressed inside  $\square$  rather than the surface. We studied the evolutions of the acoustic nonlinearities with the nonlinear resonant ultrasound spectroscopy (NRUS), and non-collinear wave mixing technique throughout the creep life in welded joint for High Cr ferritic heat resisting steels with an electromagnetic acoustic transducer (EMAT).

#### Statement of Contribution/Methods

The material used was a 25-mm-thick ASME Gr.91 and GR. 122 steel plate. Using this plate as base metal, a welded joint with a double U-groove was made employing gas tungsten arc (GTA) welding. The creep and creep interruption tests employed with L-welded joint. The creep tests were conducted at 873 K and 90 MPa for Gr.91 100 MPa for Gr.122, where a typical Type IV failure was observed, and the tests were interrupted at approximately 0.2, 0.5, 0.7, 0.8, and 0.9 of rupture life ( $t_r=8853$  h) for Gr.91 and 0.46, 0.82, 0.92, 0.96, 0.98 of rupture life ( $t_r=16340$  h). From these crept L-welded joint specimens, plate specimens with 3.5 mm thick were cut and brought down.

To measure acoustic nonlinearity around fine grained-HAZ, we used a bulk-shear-wave EMAT. We used a nonlinear acoustic phenomenon (SNAP) manufactured by RITEC. While changing the driving voltage of SNAP into ten phases from 10 % to 100%, we measured the shift of the resonant frequency ( $\Delta f$ ). We defined the nonlinearity with NRUS as  $\Delta f/f_0$  ( $f_0$ : resonance frequency at lowest drive).

In non-collinear wave mixing technique, we placed on two EMATs to sandwich the specimen. An EMAT is for the transmission, and the other for a transmission and reception for shear wave to the thickness direction. Two EMAT generated different resonant frequencies  $f_1$ ,  $f_2$ , and an EMAT measured maximum amplitude  $A_3$  at the difference resonant frequency;  $f_3=f_1-f_2$ . We measured maximum amplitudes,  $A_1$ ,  $A_2$ ,  $A_3$  at each frequency,  $f_1$ ,  $f_2$ ,  $f_3$ . In addition, we measured the attenuation coefficients at resonant frequencies.

#### Results/Discussion

We show the relationships between two nonlinear acoustic parameters, relative velocity and attenuation coefficient and life fraction,  $t/t_r$  near fine-grained HAZ for GR. 122 during creep. In non-collinear wave technique, we used fifth and eighth resonant mode and measured third resonant mode. Two nonlinear acoustic parameters, attenuation decreased from start of creep to  $t/t_r=0.4$ . After that, they rapidly increased to  $t/t_r=90\%$ . Creep voids initiated from 46% of life, and do not change very much. From 90% of the life they increased rapidly to the rupture. The changes of two nonlinear acoustic parameters, attenuation caused by the microstructural change related creep void initiation and growth.

P3A2-2

### Measurement of Convergence Ultrasound in Cone-like Bubble Structure Using Light Deflection Method

Takanobu Kuroyama<sup>1</sup>, Koichi Mizutani<sup>2</sup>, Naoto Wakatsuki<sup>2</sup>, Takeshi Ohbuchi<sup>3</sup>; <sup>1</sup>Graduate School of Systems and Information Engineering, University of Tsukuba, Tsukuba, Ibaraki, Japan, <sup>2</sup>Faculty of Engineering, University of Tsukuba, Tsukuba, Ibaraki, Japan, <sup>3</sup>Department of Applied Physics, National Defense Academy, Yokosuka, Kanagawa, Japan

#### Background, Motivation and Objective

It is important to measure the ultrasound in the medium containing the optical scatterers, such as converging ultrasound in cone-like bubble structure (CBS) forming under the horn of sonicator, to evaluate the acoustic phenomenon. In this paper, we focus on the light deflection method, which is relatively robust against the scatters, and apply the technique to measure the ultrasound in CBS to demonstrate the viability of the light deflection method for measurement of ultrasound in water containing scattering mediums.

#### Statement of Contribution/Methods

Figure 1(a) shows the experimental setup of the proposed method. A CBS is formed under the horn of a bolt-clamped Langevin type transducer (BLT) in a glass cell filled by water. A laser beam enters the glass cell and the centroid of the outgoing laser beam from the cell is measured by using a position-sensitive detector (PSD). The deflection amplitude of the laser beam is proportional to the gradient of the projection of acoustic pressure along z-axis, here, the acoustic pressure can be evaluated from the deflection angle of the laser beam measured by the PSD. The laser beam is scattered by the acoustic cavitation but the scattered light distributes axisymmetrically around the laser beam axis and the acoustic cavitation does not affect the measurement of the laser beam centroid.

#### Results/Discussion

Figures 1(b) - 1(c) show the obtained results from the experiment. This result was agreed with the general theory of the CBS and the viability of the proposed method was established. We consider the light diffraction method has advantages in comparison with hydrophone measurement because of its nondestructive characteristics. We concluded that the method is appropriate for measurement of high intensity ultrasound generating acoustic cavitation which sometimes harm physical probes (e. g. hydrophone) because it can measure the ultrasound with no contact.

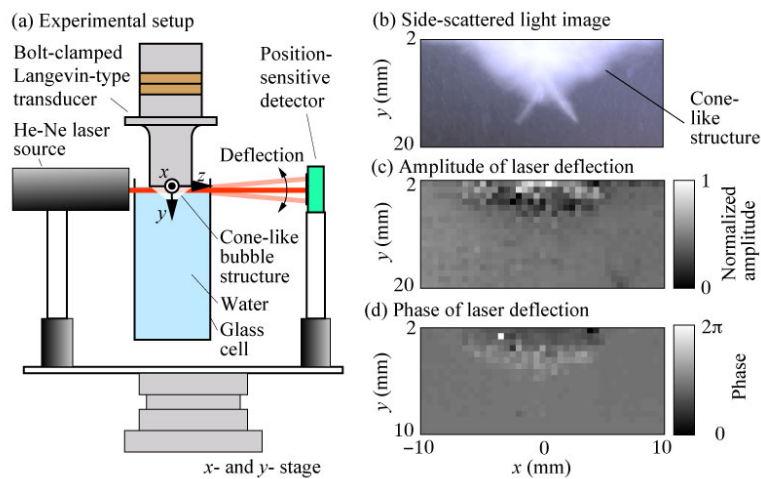


Fig. 1 Experimental setup and result (a) Measurement system (b) Side-scattered light image of CBS (c) Deflection amplitude and (d) Deflection phase.

### P3A2-3

#### Shear elastic properties of 1-D model granular unconsolidated media

Natalia Shirgina<sup>1</sup>, Alexandr Korobov<sup>2</sup>; <sup>1</sup>Physics Department, M.V. Lomonosov Moscow State University, Moscow, Russian Federation

#### Background, Motivation and Objective

Studies of elastic properties of granular unconsolidated media (GUM) are of interest to modern acoustics due to their importance for a wide range of industries, from geophysics, seismology to industrial bulk materials. 1-D chains of elastic balls are often used for laboratory studies of elastic properties of GUM [1-4]. Most of the works focuses on the propagation of longitudinal elastic waves in such modeling media. Study of shear properties GUM is paid much less attention.

#### Statement of Contribution/Methods

To study the elastic shear properties of GUM, we have developed a technique and experimental setup. We used a model chain consisting of 30 steel balls with a diameter  $d = 9$  mm, placed in a plexiglas tube. Linear and nonlinear shear elastic properties of GUM were studied using torsional waves. For generating and registration of received torsional elastic waves in the frequency range (3-10) kHz, we have developed the original transmitter and receiver, which were placed at opposite ends of the tube with balls. Controlled external static pressure was applied to the system on one end of tube.

#### Results/Discussion

The experimentally measured values of the velocity of torsional waves allowed us to calculate the dependence of the shear modulus  $\mu$  in GUM on the external pressure. Measuring the velocity of torsional waves was carried by the impulse method. Dependence of the shear modulus on the external pressure had hysteresis at reversing of the pressure changes. The magnitude of the shear modulus increased by approximately 40% when the pressure changing in the interval (3.7-98.7) kPa. At these pressures, the deformation in the contact of the balls remained elastic. Nonlinear shear elastic properties of GUM were studied by spectral method by measuring of the efficiency of generation of the 2nd and 3rd shear elastic harmonics. Experimental measurements of the amplitudes of 1st, 2nd, 3rd shear elastic harmonics at different values of external static pressure allowed us to explore the nonlinear dependence of the elastic parameters of the 2nd and 3rd order in the GUM on the external static pressure. We discovered an anomalous behavior of nonlinear elastic parameters of the 2nd and 3rd order of the external preload. Nonmonotonic dependence of the nonlinear parameters of the external pressure is explained us structural phase transitions within the chain [4]. The experimental results are analyzed using the Hertz-Mindlin theory. This study was supported by the Russian Foundation for Basic Research (project no. 14-02-31195), the Federal Program of Support for Leading Scientific Schools (project no. NSH-283.2014.2).

- [1] Nesterenko V.F et al. Physical Review Letters, 95, 158702 (2005)
- [2] Hladky-Hennion A.-C. et al. Journal of Appl.Phys. 98, 054909 (2005)
- [3] V. Tournat et al. Physical Revue E 70, 056603 (2004)
- [4] A. I. Korobov et al. Acoust. Physics, Vol. 56, No. 4, pp. 446-452 (2010)

### P3A2-4

#### Temperature Dependence of Harmonics Generated by Nonlinear Ultrasound Beam Propagation in Water: A Simulation Study

Borna Maraghechi<sup>1</sup>, Mojtaba H. Hasani<sup>2</sup>, Michael C. Kolios<sup>1</sup>, Jahan Tavakkoli<sup>1</sup>; <sup>1</sup>Physics, Ryerson University, Toronto, Ontario, Canada, <sup>2</sup>Biomedical Engineering, Amirkabir University of Technology, Tehran, Iran

#### Background, Motivation and Objective

Thermal therapy is a type of cancer treatment in which the tissue temperature is increased to levels where controlled cancer cells killing can be achieved. A major limitation of thermal therapies is the lack of a simple and robust non-invasive and real-time temperature monitoring technique.

In order to noninvasively estimate the tissue temperature using ultrasound, a temperature sensitive acoustic parameter is required. The temperature could be estimated by knowing the temperature dependence of that parameter and tracking changes in the parameter during heating. The main objective of this study is to investigate and understand the temperature dependence of acoustic harmonics generated by nonlinear ultrasound beam propagation in water.

#### Statement of Contribution/Methods

Nonlinear ultrasound beam simulations were performed using a time-domain numerical solution of a modified Khoklov-Zabolotskaya-Kuznetsov (KZK) nonlinear wave equation in which temperature dependence of the medium parameters were included. Nonlinear propagation of a 30-cycle pulse in water with source pressure amplitude of 0.35 MPa from a flat circular transducer of 22 mm diameter was simulated. The center frequency of the excitation pulse was increased from 1 to 5 MHz. Simulation of an ideal progressive plane wave using the Burgers' wave equation was also performed for comparison.



The values of sound speed, medium's density, absorption coefficient and B/A as a function of temperature were obtained from the literature. These temperature dependent parameters were used as an input to the simulation codes. The change in the first, second and third harmonics at the axial distance from the transducer where the last pressure maximum occurs was analysed as the water temperature increased from 20°C to 60°C.

#### Results/Discussion

The results demonstrate that a minimum in the value of the harmonics occurs within the temperature range of 35°C to 50°C at transmit frequencies lower than approximately 3 MHz. However, for higher transmit frequencies, the harmonics increase with temperature monotonically. It is concluded that temperature estimation based on changes in the harmonics is feasible with transmit frequencies higher than 3 MHz. The large changes in the harmonics as a function of temperature indicate that this could potentially be a promising basis for ultrasound-based thermometry.

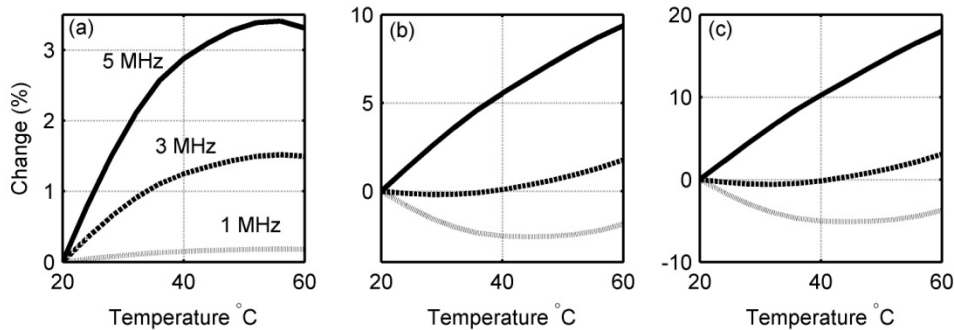


**Figure 1:** Change in (a) the fundamental frequency, (b) the second (c) and the third harmonics as a function of temperature in water with respect to the initial temperature.

P3A2-5

#### Influence of pulse polarity to nonlinear ultrasonic wave propagation

Darius Kybartas<sup>1</sup>, Dobilas Liaukonis<sup>1</sup>, Linas Svilainis<sup>1</sup>, Andrius Chaziachmetovas<sup>1</sup>; <sup>1</sup>Electronics Engineering Department, Kaunas University of Technology, Kaunas, Lithuania

#### Background, Motivation and Objective

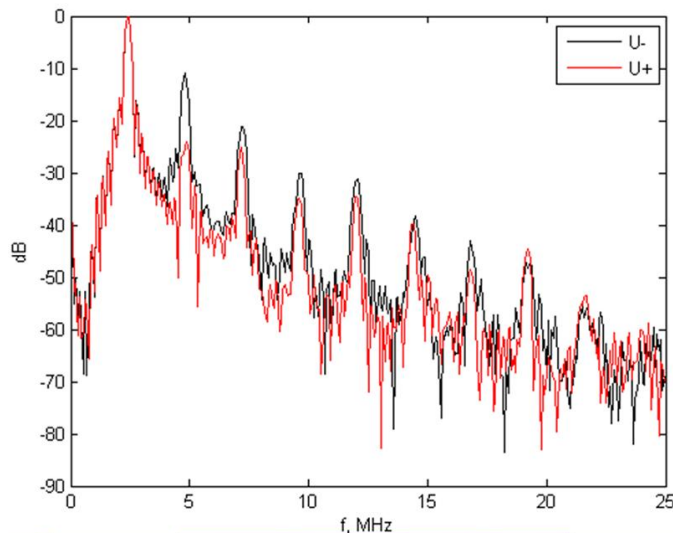
Nonlinear effects in propagation of ultrasonic (US) pulses are wide used for diagnostic purposes. Non-uniform distortion of positive and negative pulses causes higher harmonics in wave after some propagation in media. Such distortions are observable when pressure is higher than (100-400) kPa. Second and other harmonics are used for improve of resolution of echoscopic images. Many modern US pulsers are based on electronic swithes such as FETs. The simplest design of excitation of transducer use unipolar switch and matching transformer. In preliminar study we found that polarity of excitation pulses has influence to shape of US pulse in water. There is a need to evaluate this phenomenon using different pulse parameters such as polarity, frequency and amplitude. The aim of investigation is to compare pressure of fundamental and higher harmonics under different excitation parameters and to find out origin of different distortion of US signal under positive and negative excitation.

#### Statement of Contribution/Methods

Nonlinear propagation of ultrasonic pulses in water was investigated using focused 2-7 MHz and 4-20 MHz transducers and wideband 1-20 MHz Onda hydrophone placed on 3D scanner. Data acquisition was performed using LeCroy HRO66Zi scope. An influence of possible effects to the pressure and spectral characteristics was studied in order to verify all hypotheses. Transducer was excited by 50-150 V single frequency bursts in range 1.6-3.4 MHz. Influence of possible polarization of piezoceramic was simulated by bias voltage applied. Pulse polarity was changed using positive and negative excitation voltage switches or reversing polarity in special transformer. Influence of propagation distance was analysed.

#### Results/Discussion

The main difference in spectra of nonlinear US pulses is in magnitude of even harmonics. Pulse polarity can change level of second harmonic by 5-15 dB. Increase of harmonics is followed by decrease in level of fundamental frequency. This effect is caused by propagation effects because it doesn't depend on bias and excitation voltages and on type of transducer or hydrophone. It exists at all distances where second harmonic in aquired signal can be observed. Analysis over frequency range shows that influence of polarity of excitation pulses to the pressure of second harmonic can be opposite in lower frequencies 1.6-2.2 MHz.



P3A2-6

### Bifurcation Structure of Nonlinear Modal Coupling in Quartz Crystal Resonator Exhibiting Internal Resonance

Christopher Kirkendall<sup>1</sup>, Jae Kwon<sup>1</sup>; <sup>1</sup>University of Missouri-Columbia, USA

#### Background, Motivation and Objective

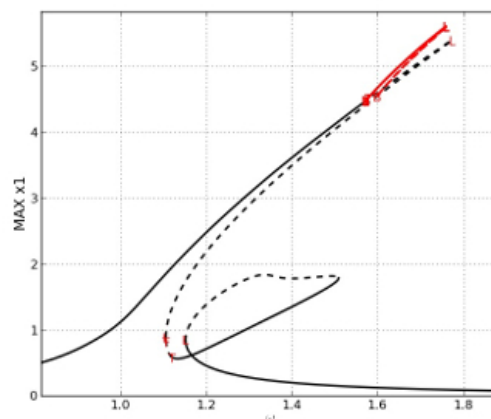
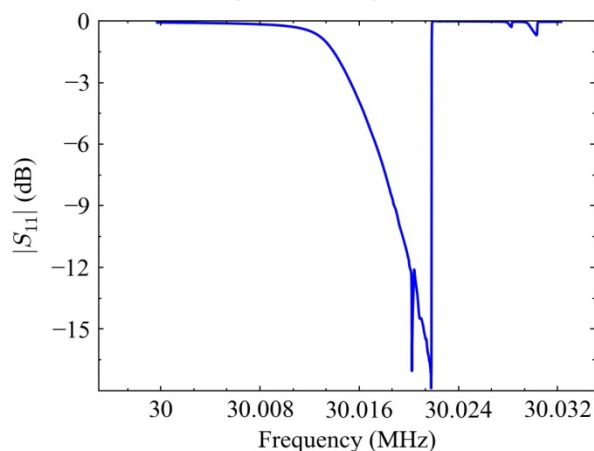
Nonlinear resonance has been receiving much attention due to its high potential to enhance performance metrics in sensors, oscillators and other devices. However, the complex dynamics of resonators operating in the nonlinear regime—such as the bifurcation structure, modal coupling, and internal resonance—are still underexplored. Although hysteresis in the frequency response has been applied to enhance sensitivity (as a bifurcation amplifier), extensive research is needed to exploit the potential of nonlinear resonance. Thus, here we experimentally and theoretically explore the use of a Duffing resonator to achieve internal resonance via coupling of multiple eigenmodes to the externally excited mode.

#### Statement of Contribution/Methods

The nonlinear resonator was implemented with a piezoelectric quartz crystal (Laptech Precision Inc. model XL1191-30.0M). After driving the device into the nonlinear regime, we adjusted the driving force and frequency to achieve internal resonance at 30.02 MHz (Fig. 1). To model the bifurcation structure, we simulated two coupled Duffing equations with the continuation software AUTO (Fig. 2). We were able to show the existence of both quasiperiodic and phase locked motion, depending on the choice of parameters.

#### Results/Discussion

Figure 2 shows that near the frequency of internal resonance a torus bifurcation occurs in which the stable limit cycle destabilizes and generates an invariant two-dimensional torus in the phase space of the system. This enables the choice between quasiperiodic or phase locked motion. Also, multiple zones of hysteresis were observed due to the internally resonant mode. By controlling phase locking the phase noise of the resonator can be reduced.



P3A2-7

### Comparison between two different full-wave methods for the computation of nonlinear ultrasound fields in inhomogeneous and attenuating tissue

Bradley Treeby<sup>1</sup>, Libertario Demi<sup>2</sup>, Martin Verweij<sup>3</sup>; <sup>1</sup>Dept. of Medical Physics and Bioengineering, University College London, London, United Kingdom, <sup>2</sup>Lab. of Biomedical Diagnostics, Eindhoven University of Technology, Eindhoven, Netherlands, <sup>3</sup>Lab. of Acoustical Wavefield Imaging, Delft University of Technology, Delft, Netherlands

#### Background, Motivation and Objective

Nonlinear propagation is important in many diagnostic and therapeutic applications of medical ultrasound. Harmonic imaging uses the reflections of higher harmonics to improve resolution and decrease near-field artifacts, as compared to fundamental imaging. High intensity focused ultrasound (HIFU) benefits from higher harmonics, which increase the heat deposition during tumor ablation. The design of equipment and protocols for these nonlinear modalities is facilitated by the simulation of the nonlinear wave field. Many simulation tools have been developed over the years, but often these cannot deal with tissue inhomogeneity, power law losses, or steered beams. Recently, two full wave simulation methods for nonlinear ultrasound have been developed that are able to deal with these realistic features. Both methods lack a priori assumptions about the direction and shape of the wave field. Those methods are known as k-Wave and the Iterative Nonlinear Contrast Source method (INCS). This paper assesses the accuracy of both methods by comparing their results.

#### Statement of Contribution/Methods

k-Wave (a pseudospectral time domain method) and INCS (an integral equation method) are quite different in nature, but have in common that the only approximation involves the replacement of continuous space-time by a discrete grid. It seems justified to think that for similar media and transducer excitations, both methods should yield the same nonlinear wave field. To verify this assumption, two test configurations have been defined. The corresponding nonlinear wavefields have been simulated by both k-Wave and INCS, and the results are compared spatially and spectrally (harmonics-wise).

#### Results/Discussion

The first test configuration was homogenous, with a speed of sound of 1483 m/s, a density of mass of 1000 kg/m<sup>3</sup>, a coefficient of nonlinearity of 3.48, and power law loss with exponent 1.5 and a magnitude of 0.75 dB/cm at 1 MHz. A square piston excited a three-cycle Gaussian-modulated tone burst with a center frequency of 1 MHz and a source pressure of 750 kPa. The results obtained with k-Wave and INCS were in excellent agreement, with a maximum local difference of only 0.8 dB. The second configuration was inhomogeneous, with a hollow cylinder (speed of sound equal to 1540 m/s) and a solid sphere (parameter of nonlinearity equal to 1) being contrasting objects that were put in the way of the radiated beam. Again, the results matched excellently, with maximum local differences of 0.8 dB occurring mainly outside the distorted beam.

The comparisons between k-Wave and INCS show that both methods yield highly similar results. Because both methods are quite different, it is improbable that both methods suffer from the same systematic error. Hence it is established that both methods are correct and highly accurate, and may be used to generate accuracy benchmarks.

## Nonlinear reflection of elastic waves from the boundary of solids

Natalia Shirgina<sup>1</sup>, Aleksey Kokshaitski<sup>2</sup>, Alexandr Korobov<sup>1</sup>; <sup>1</sup>Physics Department, M.V. Lomonosov Moscow State University, Russian Federation, <sup>2</sup>M.V. Lomonosov Moscow State University, Russian Federation

### Background, Motivation and Objective

A number of studies have shown that the boundary of solids has a strong elastic nonlinearity. This nonlinearity is called non-classical (structural) nonlinearity. Structural nonlinearity can be several orders of magnitude greater than the elastic nonlinearity associated with the crystal lattice anharmonicity in solids. Therefore, investigation of the interaction of elastic waves at the solid can be applied to the diagnosis of different types of discontinuities: microcracks, delamination in products made of composite materials.

### Statement of Contribution/Methods

We investigated experimentally reflection of monochromatic elastic waves of finite amplitude on the boundary of two flat metal surfaces. We placed different interface layers between the surfaces: a) flat rough metal surfaces, b) rough surfaces with the metal foil with a thickness of 10 microns between them, c) one-dimensional layer of steel balls with a diameter of 4 mm between rough metal surfaces, and d) layer of steel balls with foil (thickness of 10 microns) between the balls and one of the surfaces. Piezoceramic transducer was attached to one of the surfaces; harmonic signal with a frequency of 2.5 MHz was supplied to the transducer from automated ultrasonic transceiving complex. Controlled static pressure was applied to the interface. For all these cases we measured amplitude of the 1st and 2nd elastic harmonics reflected from the interface layer. Changes in the external static force held in the range of  $0 < P < 800$  kPa, whereby deformation between contacts of the balls and metal surfaces remained elastic.

### Results/Discussion

For the case of two rough metal surfaces amplitude of the reflected 2nd harmonic increased, amplitude of the 1st reflected harmonic decreased. This is due to the fact that the rough surfaces contact with micro protrusions of varying heights. Each individual micro protrusion is the source of Hertz elastic nonlinearity. Number of contacts between the surfaces grows with increasing compression, elastic nonlinearity increase on the border, the transmission coefficient of the first harmonic elastic wave across the border increases. When there is a one-dimensional layer of steel balls between the surfaces, the amplitude of the reflected 1st elastic harmonics decreases smoothly with rising the pressure, but amplitude of the reflected 2nd harmonics has a maximum when the pressure is about 400 kPa. In the case when the thin aluminum foil is placed between the surfaces, it is "smoothes" roughness between the surfaces, and the above-mentioned effects are significantly reduced. Reflectance of the 1st harmonic of the layer balls and nonlinear elastic parameter of the 2nd order are theoretically calculated. The experimental results are analyzed using the theory of Hertz contact nonlinearity. This study was supported by the Russian Foundation for Basic Research (project no. 14-02-31195), the Federal Program of Support for Leading Scientific Schools (project no. NSh-283.2014.2).

## P4A1 - Innovations for Resonators and Sensors 1

Salon C

Thursday, September 4, 2014, 8:00 am - 5:00 pm

Chair: **Robert Aigner**  
Triquint Semiconductor

P4A1-1

### The influence of Acoustic Reflectors on the Temperature Coefficient of Frequency of Solidly Mounted Resonators

Mario DeMiguel-Ramos<sup>1</sup>, Girish Rughoobur<sup>2</sup>, Jimena Olivares<sup>1</sup>, Luis García-Gancedo<sup>2</sup>, Teona Mirea<sup>1</sup>, Marta Clement<sup>1</sup>, Enrique Iborra<sup>1</sup>, Andrew J. Flewitt<sup>2</sup>; <sup>1</sup>GMME-CEMDATIC-ETSIT, Universidad Politécnica de Madrid, Spain, <sup>2</sup>University of Cambridge, United Kingdom

#### Background, Motivation and Objective

Perturbations in the behavior of electronic devices due to temperature changes are a major concern for designers. Acoustic resonators experience shifts in their resonant frequency, which entails a serious drawback for the application of such devices in filters and sensors. Particularly, resonators based on aluminum nitride (AlN) piezoelectric films exhibit temperature coefficients of frequency (TCF) as high as -25 ppm/°C, which is a large value for some applications. A solution to reduce the TCF in film bulk acoustic resonators (FBAR) is the addition of SiO<sub>2</sub> layers, which act to lower the TCF of the whole structure thanks to their positive TCF. As a counterbalance, the weight added to the structure worsens the overall performance of the resonators. As for the temperature performance of solidly mounted resonators (SMR) based on AlN, the influence of the different layers that compose the acoustic reflector on the TCF of the whole structure is frequently neglected. In this communication, we present an analysis of the influence of the high and low acoustic impedance layers on the TCF of the resonators as a function of their nature, thickness and position in the acoustic reflector. The analysis includes simulations of the electrical behavior using Mason's model as well as finite element analysis (FEA) using COMSOL and fabrication and measurements on actual devices. Possible procedures to minimize the TCF are suggested and experimentally carried out.

#### Statement of Contribution/Methods

SMRs have been designed, simulated and fabricated to investigate the variations of the TCF with the acoustic reflector parameters such as materials and their thicknesses. The different layers under study were SiO<sub>2</sub> as low impedance layer, and Mo, W, or Ta<sub>2</sub>O<sub>5</sub> as high impedance layers. The behavior of symmetric reflectors composed of  $\lambda/4$ -thick layers was first investigated. Afterwards, the thickness of the low impedance layer closer to the piezoelectric stack was increased to evaluate the changes in the TCF. The same operation was repeated for the uppermost high impedance layer. SMRs containing AlN tilted films (24°) were used, in order to excite both longitudinal and shear resonances. Their electrical response as a function of the frequency up to 10 GHz was assessed for temperature dependence in the range from 25°C to 100°C.

#### Results/Discussion

The TCF of the shear and longitudinal resonant modes have been measured in SMRs with SiO<sub>2</sub>/Mo, SiO<sub>2</sub>/W, and SiO<sub>2</sub>/Ta<sub>2</sub>O<sub>5</sub> acoustic reflectors. The TCF of all the resonant modes can be modified by changing the materials of the mirrors but also by changing the thicknesses of the different layers. The position of the layers in the acoustic reflector can also affect the TCF. This effect is due to the influence of all the components of the SMR in the resonant frequency of each mode. A careful design of the stacks, including geometries and materials, allows reduction of the TCF of the devices.

P4A1-2

### High volume production system for piezoelectric multi-material depositions

Michael Gutkin<sup>1</sup>, Sergey Mishin<sup>1</sup>; <sup>1</sup>Advanced Modular Systems, Goleta, CA, USA

#### Background, Motivation and Objective

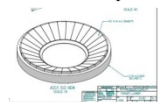
Previous studies demonstrate a considerable increase in kt<sub>2</sub> as a function of Sc content of the film [2], [3], [5], [6]. Unfortunately, when higher concentration of Sc or a third material such as Er is used, composite targets are very difficult to manufacture.

#### Statement of Contribution/Methods

In this paper, we present system for depositing piezoelectric films with multiple target materials using a standard production system that is used in high volume production of Aluminum Nitride films. This system uses standard dual conical magnetron with AC deposition source [1]. Targets are cut into multiple pieces as shown in Figure 1. Films containing various concentrations Scandium (Sc) and Erbium (Er) in AlSc(x)Er(y)N films have been demonstrated using different number of Sc and Er pieces relative to the number of the Al pieces. Coupling coefficient (kt<sub>2</sub>) was measured across the wafer and wafer to wafer as a function Sc and Er content in the target.

#### Results/Discussion

We were able to control kt<sub>2</sub> across wafer and wafer-to-wafer by adjusting magnetic fields in our magnetron, rotating wafer during deposition as well as adjusting concentration of Sc and Er in sputtering targets.



## Carbon Nanotubes Forests as Top Electrode for AlN-Based Electroacoustic Resonators

Teona Mirea<sup>1</sup>, Jimena Olivares<sup>1</sup>, Santiago Esconjauregui<sup>2</sup>, Mario DeMiguel-Ramos<sup>1</sup>, Marta Clement<sup>1</sup>, Jesús Sangrador<sup>1</sup>, Enrique Iborra<sup>1</sup>; <sup>1</sup>GMME-CEMDATIC-ETSIT, Universidad Politécnica de Madrid, Madrid, Spain, <sup>2</sup>University of Cambridge, United Kingdom

### Background, Motivation and Objective

Owing to their outstanding properties, carbon nanotubes (CNTs), in their single- or multi-walled form, are currently used or likely to find applications in microelectronics. For example, CNTs could be used to fill interconnecting vias between different metallization levels of devices. Dense CNT forests or composites are used as sensing layers in gas sensors. Multi-walled CNT (MWCNTs) forests directly grown on insulating materials can be integrated into devices as conductive layers. They are usually deposited by the decomposition of light hydrocarbons, such as CH<sub>4</sub> or C<sub>2</sub>H<sub>2</sub>, diluted in reducing gases like H<sub>2</sub> or NH<sub>3</sub>. For enhancing hydrocarbon decomposition, catalyst nanoparticles are previously formed on the substrate by annealing a very thin metal layer. Typical catalytic materials are Fe, Ni, Co, and their alloys, sometimes together with other metals, such as Ti or Al, to favor the formation of the nanoparticles.

Specific applications require CNT forests to be patterned, e.g. by lift-off. To act as electrode, CNT forests must show a sheet resistance as low as possible. This particular property is hardly controlled, since the transverse electric conductivity through the CNT forest strongly depends on the area density of the tubes; the denser the forest, the lower its sheet resistance. To be used as top electrode in bulk acoustic wave resonators, three critical characteristics of the CNT forests have to be carefully considered: their weight, their sheet resistance, and the actual effective area of the piezoelectric capacitor. In this communication we assess their influence on the performance of BAW resonators by varying the type of CNT forest (number of walls and defects), the thickness of the forest, and its area density.

### Statement of Contribution/Methods

AlN-based solidly mounted resonators with Ir bottom electrodes and Mo/SiO<sub>2</sub> acoustic reflectors were fabricated. MWCNT forests were grown on top of the AlN films under different conditions to obtain top electrodes of different characteristics. The electrical impedance as a function of the frequency was measured and assessed using Mason's model. Series resistance, electromechanical coupling factor and quality factor were chosen as figures of merit to evaluate the suitability of the CNT forest as top electrode.

### Results/Discussion

One of the most interesting results is the weak influence of the CNT top electrodes on the electrical characteristics of the resonators. Their very low mass density (tenths of gr/cm<sup>3</sup>) and high propagation velocity allows using layers as thick as 40 μm without significantly worsening the resonator characteristics or shifting the resonant frequency by a considerable amount. The series resistance appears to be strongly dependent on the surface density of tubes, which also affects the electrical static capacitance by a factor of ten in some cases. Further reduction of the sheet resistance can be achieved by growing denser forests.

## Langatate and langasite microacoustic gyro sensors

Gobong Choi<sup>1</sup>, Yook-Kong Yong<sup>1</sup>; <sup>1</sup>Civil and Environmental Engineering, Rutgers University, Piscataway, New Jersey, USA

### Background, Motivation and Objective

The characteristics of gyro sensors made of the langasite family of crystals are compared with the quartz crystal since they belong to the same trigonal crystal class 32. The characteristics of a vibratory gyroscope are a function of mass density, its piezoelectric properties and modes of vibration. The mass density and electromechanical coupling factor of langasite and langatate are significantly higher than quartz crystal. Langasite and langatate have mass density of 5.75 g/cm<sup>3</sup> and 6.13 g/cm<sup>3</sup>, respectively, compared with 2.65 g/cm<sup>3</sup> for quartz. The electromechanical coupling constant of langasite and langatate is 2.26 and 2.86 times higher than those for quartz. In this paper, we study microacoustic gyro sensors of each material and thereby confirm that langasite and langatate microacoustic gyroscopes are more desirable for high precision equipment.

### Statement of Contribution/Methods

Measurements for a gyro sensor using double-ended tuning fork quartz resonator [1] were first compared with our COMSOL model results. Our model results were found to compare well with the measurements. Thus having validated our models, we set out to model microacoustic gyro sensors made of langasite and langatate respectively and compare their gyro characteristics with similar sensors made of quartz. Modal analyses were performed to obtain the optimal geometry and frequency response analyses were used to simulate the Coriolis effect on each gyro sensor.

[1] "Experimental Study of Gyro Sensor Using Double-Ended Tuning Fork Quartz Resonator", K. Sato, A. Ono, Y. Tomikawa, Proceedings of the 2004 IEEE International Frequency Control Symposium, Montreal, Canada, 2004, pp 573-578

### Results/Discussion

Comparison of measurement results for a gyro sensor using double-ended tuning fork quartz resonator were found to be consistent with those of our COMSOL model results. They compare well. The langasite and langatate gyroscopes were found to be more sensitive since the langasite and langatate have a significantly higher mass density and a higher electromechanical coupling factor constant than quartz, see figure 1. The sensitivity of the quartz, langasite, and langatate gyroscope were 0.0172V/deg./sec, 0.042V/deg./sec, and 0.0705V/deg./sec, respectively. Therefore langasite and langatate are promising materials for gyro-sensors.



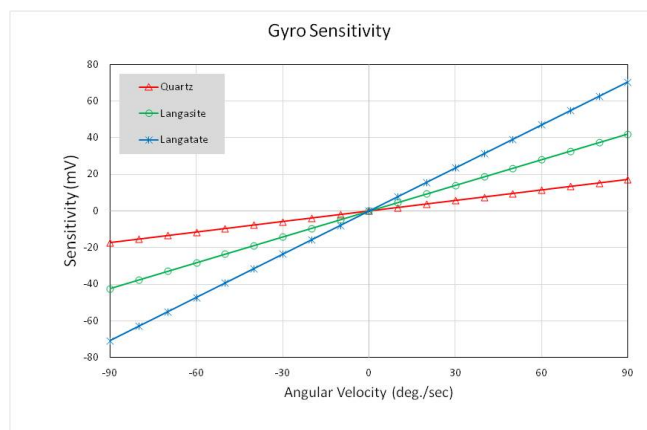


Figure 1: Comparison of the sensitivity of gyro sensors made of quartz, langasite and langatate, respectively.

P4A1-5

#### ZnO/AlN Stacked BAW Resonators with Double Resonance

Mario DeMiguel-Ramos<sup>1</sup>, Girish Rughoobur<sup>2</sup>, **Marta Clement<sup>1</sup>**, Jimena Olivares<sup>1</sup>, Teona Mirea<sup>1</sup>, Andrew J. Flewitt<sup>3</sup>, Enrique Iborra<sup>1</sup>; <sup>1</sup>GMME-CEMDATIC-ETSIT, Universidad Politécnica de Madrid, Spain, <sup>2</sup>University of Cambridge, United Kingdom, <sup>3</sup>University of Cambridge, Spain

#### Background, Motivation and Objective

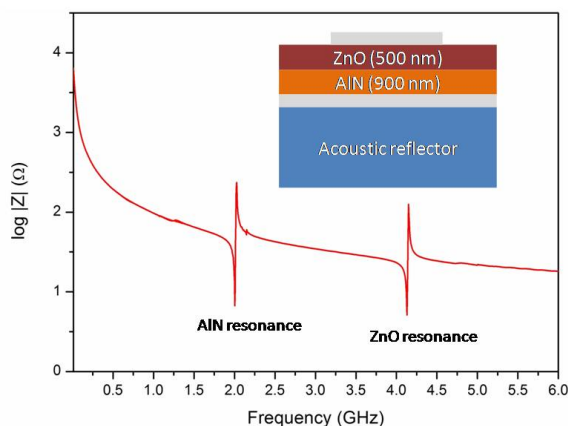
During the last decade, bulk acoustic wave resonators have raised an increasing interest among the industrial and scientific community. Their applications in mobile communications as multiplexers and filters and as gravimetric sensors for gases and biological agents are widely extended. Researchers usually choose between AlN and ZnO as the piezoelectric material for the devices, depending on the applications and the operation frequency. The combination of AlN and ZnO piezoelectric films in one device is not common in BAW resonators, although some tests have been made using one of them as seed layer for the other. In this communication we propose a method to fabricate stacked ZnO/AlN BAW resonators that exhibit a double longitudinal resonance, with potential applications in simultaneous measurement of different physical magnitudes, such as mass and temperature.

#### Statement of Contribution/Methods

AlN thin films were sputtered at 400°C in an UHV system on top of acoustic reflectors of alternating layers of Mo and porous SiO<sub>2</sub> with  $\lambda/4$  thicknesses. ZnO films were then deposited at room temperature. XRD and FTIR measurements were used to assess the crystal quality of the stack. Finally, BAW resonators were fabricated and their frequency response assessed. The results were fitted using the Mason model to obtain actual values of the  $k^2$  and the Q-factor of the piezoelectric layers.

#### Results/Discussion

We fabricated BAW solidly mounted resonators with piezoelectric stacks of ZnO on AlN. These devices show a clear longitudinal dual response (see figure), with two resonances between 1.5 GHz and 5 GHz; the low-frequency resonance is produced in the AlN layer and the high-frequency one in the ZnO. XRD and FT-IR measurements show that stacking the materials does not worsen the quality of the ZnO film. We achieved devices with a  $k^2$  up to 6% and a Q over 500 for both resonances; these values high enough for most of the sensing applications. ZnO resonance is enhanced thanks to the AlN layer underneath. We also present FEA simulations of the devices that substantiate the experimental results.



# Equivalent Parameters for Microwave HBAR based on Al/AlN/Mo/(100) Diamond Piezoelectric Layered Structure

Boris Sorokin<sup>1,2</sup>, Vladimir Blank<sup>1</sup>, Gennadiy Kvashnin<sup>1</sup>, Alexander Volkov<sup>1</sup>, Vitaliy Bormashov<sup>1</sup>, Mikhail Kuznetsov<sup>1</sup>, **Arseniy Telichko<sup>1,2</sup>**, Georgy Gordeev<sup>1,2</sup>, Sergey Burkov<sup>3</sup>; <sup>1</sup>Technological Institute for Superhard and Novel Carbon Materials, Troitsk, Moscow, Russian Federation, <sup>2</sup>Moscow Institute of Physics and Technology, Dolgoprudny, Moscow Region, Russian Federation, <sup>3</sup>Siberian Federal University, Krasnoyarsk, Russian Federation

## Background, Motivation and Objective

Diamond is the hardest material with the highest bulk and surface acoustic wave velocities, high thermal conductivity, etc. Now polycrystalline diamond films have been widely used as a material for SAW devices. The High-overtone Bulk Acoustic Resonator (HBAR) is a prospective acoustoelectronic device with properties mainly determined by the substrate.

Objective of this paper consists of obtaining the equivalent scheme and calculating of diamond-based HBAR's equivalent parameters by the experimental data.

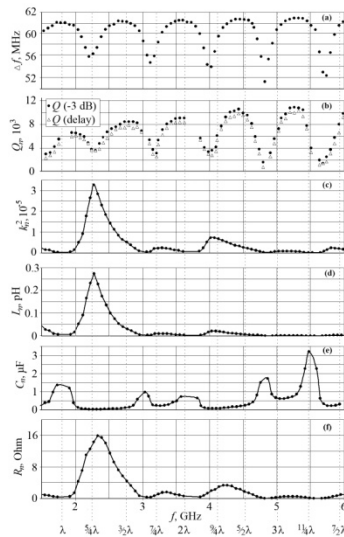
## Statement of Contribution/Methods

As a substrate material the (100) plates of diamond single crystal type IIa grown by HPHT method at TISNCM (Russia) have been used. Fabrication of Al/AlN/Mo/(100) diamond piezoelectric layered structures was produced by AJA ORION 8 magnetron rf sputtering equipment. For more details see [1]. Substrate faces of synthetic diamond were prepared with  $< 5^\circ$  deviation from [100] crystalline direction, and were polished to obtain the roughness  $R_a < 10 \text{ nm}/100 \text{ }\mu\text{m}$ . Two samples of the "Al/AlN/Mo/(100) diamond" layered structure (#1 and #2)) have been prepared. Microwave acoustic properties, such as  $n$ -th overtone resonant frequencies  $f_n$ , frequency difference  $\Delta f$  between two nearest overtones, and quality factor  $Q_n$  were tested by M-150 Multipurpose Probing System and E5071C Network Analyzer at room temperature.

## Results/Discussion

Using the experimental data on frequency dependences of reflectance coefficient  $S_{11}$ , frequencies  $f_n$  and  $Q_n$  factors were measured. All experimental results were of good accordance with the proposed equivalent scheme. Frequency dependences of experimental data (a, b) and equivalent parameters (c – f) for the HBAR #1 are represented on Fig. 1. Periodical variation of  $\Delta f$  and  $Q_n$  was observed. Minimal values of  $\Delta f(f)$  and  $Q_n(f)$  are in accordance with the  $\sim(m/4)\times\lambda$  point locus, where  $m = 1, 3, 5, \dots$ , and  $\lambda$  is the wave length of the longitudinal acoustic wave excited in the AlN film. It can be explained by the peculiarities of piezoelectric transducer's loading as a sequence of the hard acoustic contact on diamond substrate and by relation between acoustic impedances of piezoelectric film and substrate. The frequency ranges with higher  $Q$  have more important significance of a practical sense only. Calculated equivalent parameters will be useful for advanced HBAR design.

[1] B.P. Sorokin et al. Appl. Phys. Lett. V. 102. P. 113507 (2013).



## P4A2 - Acoustic Modeling

Salon C

Thursday, September 4, 2014, 8:00 am - 5:00 pm

Chair: **Maximilian Pitschi**  
TDK Corporation

### P4A2-1

#### A Novel Ab-initio Finite Difference-based Method for Convenient Implementation of the Mass-loading Effect in Micro-acoustic Devices

Ireka Ikenna E.<sup>1</sup>, Mebratu Fenta Wakeni<sup>2</sup>, **Alireza Baghai-Wadji**<sup>3</sup>; <sup>1</sup>Department of Mathematics and Applied Mathematics Mathematics, University of Cape Town, Rondebosch, Western Cape, South Africa, <sup>2</sup>Centre for Research in Computational and Applied Mechanics, University of Cape Town, Rondebosch, Western Cape, South Africa, <sup>3</sup>Electrical Engineering, University of Cape Town, Rondebosch, Western Cape, South Africa

#### Background, Motivation and Objective

Accurate and fast implementation of the mass-loading effect in non-periodic structures continues to be a challenging undertaking in micro-acoustic devices. Existing works, nearly exclusively, apply the (Finite Element Method) FEM/ (Boundary Element Method) BEM hybrid technique to periodic structures. Application of the FEM/BEM to non-periodic structures is excessively time consuming and leads to comparatively inaccurate results. On the other hand the BEM/BEM monolithic technique, while being impressively accurate, is extraordinarily cumbersome to formulate, and computationally very expensive to handle realistic device models, as the present authors have discussed elsewhere.

#### Statement of Contribution/Methods

This work presents a novel technique based on the (Finite Difference Frequency Domain) FDFD/BEM hybrid formulation. The breakthrough result consists of an easy-to-implement formulation of the edge-effects to an arbitrary accuracy and the complete elimination of the corner points from the analysis. These distinguished properties render the implementation of the mass-loading effect amenable to realistic models and parallel computing at the same time. Based on the tables provided for the partial derivatives, the effort for developing the code is negligible: existing software can easily be augmented to account for the mass-loading effect.

#### Results/Discussion

Numerical results are thoroughly tested by an independently developed FEM-based package. Excellent results with predictable figures of accuracy have been achieved. This comprehensive contribution concludes with a discussion of conservative FDFD implementation of the mass-loading effect to account for arbitrarily-shaped electrode geometries.

### P4A2-2

#### Full Analysis of the Mixed Matrix parameters for a SAW Transducer Having Aperiodic Multi-Electrode Cells

**Pascal Ventura**<sup>1</sup>, Pierre Dufilié<sup>2</sup>, Frédéric Hecht<sup>3</sup>; <sup>1</sup>Laboratoire LEM3, Université de Lorraine, Metz, France, <sup>2</sup>Phonon Corporation, Connecticut, USA, <sup>3</sup>Laboratoire Jacques Louis Lions, Université Pierre et Marie Curie, Paris, France

#### Background, Motivation and Objective

Low loss SAW filters sometimes require a structure with a complex geometry in order to improve the electro-acoustic response (coupling coefficient, reflection coefficient, static capacitance).

In the case of complex electro-acoustic cells (like Hanma-Hunsinger cells), it is necessary to obtain the COM parameters from the analysis of the entire multi-electrode electro-acoustic cell. Typically the analysis is made for the cell in an infinite periodic array of identical cells using periodic boundary conditions.

For each COM parameter, like the reflectivity or the piezoelectric coupling, the amplitude and the phase need to be known with a good accuracy in order to obtain good SAW filter designs.

#### Statement of Contribution/Methods

At the 2013 IEEE Ultrasonics Symposium, an original coupled Finite Element Model / Boundary Integral Equation (FEM/BIE) was presented which computes the harmonic admittance of an infinite array of aperiodic multi-electrode cells.

In this paper, we will focus on extracting accurate mixed matrix parameters of Hanma-Hunsinger electro-acoustic cells especially for the absolute reflection and transduction phases.

#### Results/Discussion

Numerical data will be given for various electro-acoustic cells including Hanma-Hunsinger cells for various substrate materials and orientations.

Applications in the design of SAW filters are shown.

### P4A2-3

#### A Lateral Modes Model for Membrane BAW Resonators

**Eduard Rocas**<sup>1</sup>, Carlos Collado<sup>1</sup>, Jordi Mateu<sup>1,2</sup>, Jordi Verdu<sup>1</sup>, Alberto Hueltes<sup>1</sup>, Robert Aigner<sup>3</sup>; <sup>1</sup>Universitat Politècnica de Catalunya (UPC), Spain, <sup>2</sup>Centre Tecnològic de Telecomunicacions de Catalunya (CTTC), Spain, <sup>3</sup>TriQuint Semiconductor, USA

#### Background, Motivation and Objective

The finite dimensions of BAW resonators cause Lamb waves to laterally propagate, creating visible resonant modes in the in-band response of BAW filters, thus degrading its performance. The 3D nature of these lateral modes makes it inherently complex to predict their resonance frequency, so that previous circuit modeling efforts in literature are based

on phenomenological lumped models fitted to pre-computed FEM solutions. These previous modeling approaches lead to circuit implementations with many parallel RLC branches, one for each mode, added to the BVD model, thus becoming dimension-specific models not able for prediction.

On the other hand, the border ring solution, to diminish the lateral modes, degrades the effective coupling coefficient and produces its own resonant mode, which is strongly coupled to the main mode, and changes its resonance frequency abruptly with its width. An ambitious objective to this regard, would be having a circuit model able to predict the effect of the lateral modes and the border ring on the electrical response of BAW resonators. A first step towards this is proposing a model with no border ring to shed light on the nature of lateral modes; a circuit model capable of predicting the resonance frequency of all modes for any dimensions, with the right coupling to the thickness mode.

## Statement of Contribution/Methods

The method here used for the lateral modes model makes use of the analogy between acoustic plate waves and electromagnetic waveguides; the transverse resonance method, which allows treating both in-plane spatial directions independently, is the method of choice. Propagating modes are defined in the transverse direction, which sets their cut-off frequency according to the lateral and thickness dimensions, as well as phase velocity and mode order. These modes are then allowed to propagate in the other in-plane direction by implementing a transmission line circuit for each propagating mode, so that each transverse mode will show its harmonic resonances in the other direction. These transmission lines make use of the dispersive phase constant, with the cut-off frequency obtained from the transverse analysis, to model the Lamb waves.

Finally, separation of spatial variables is used to solve for the coupling; the strength of the mode will be the result of coupling in all directions independently, so that each transmission line is coupled to the BVD model by use of a factor dependent on the thickness direction coupling and the transverse direction coupling. With this, the total strength of the propagating mode will be set by the transmission line conditions.

## Results/Discussion

A lateral modes circuit model for membrane BAW resonators has been proposed and validated with FEM simulations. The model allows to predict the electrical response of square-shaped and rectangular resonators, with no limitation on dimensions. Future work should be done on extending the current work to SMR resonators including a border ring.

## P4A2-4

### Fast Full-FEM Computation of COM Parameters. Application to Multilayered SAW Structures.

Kirill Shaposhnikov<sup>1</sup>, Manfred Kaltenbacher<sup>1</sup>, Pascal Nicolay<sup>2</sup>; <sup>1</sup>Institute of Mechanics and Mechatronics, Vienna University of Technology, Vienna, Austria, <sup>2</sup>Carinthian Tech Research (CTR AG), Villach, Austria

## Background, Motivation and Objective

Accurate and fast simulation tools are needed to design future Surface Acoustic Wave (SAW) devices, based on increasingly complex material structures. Notably, there is a need for accurate simulation of multilayered structures combined with heavy electrodes, for SAW filters and SAW sensors. Most of the tools used today for this purpose involve the simulation of a semi-infinite unit cell with periodic boundary conditions, the derivation of the Harmonic Admittance (HA) and the extraction of the Coupling-of-Modes (COM) parameters to be used later for simulation of SAW devices. The most widely used solution to compute the HA relies on a combination of finite and boundary element methods (FEM/BEM). However, full-FEM is also an option, especially in the case of multilayered structures. Indeed, FEM remains easy to use in that case, while FEM/BEM becomes increasingly complicated due to the initial computation of sophisticated Green's functions. Unfortunately, full-FEM computation is usually time-consuming and requires tremendous computing power. Additionally, an adequate solution is required to get rid of spurious non-physical reflections on the cell lower boundary.

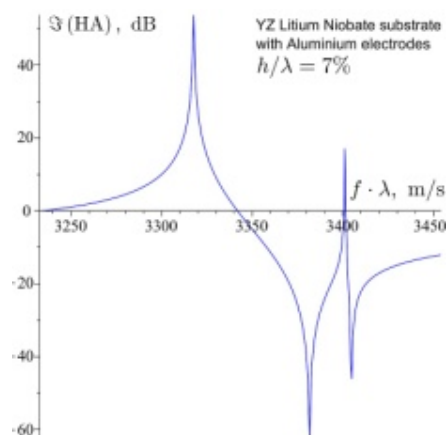
In this work, we present a full-FEM tool devised to perform accurate and fast simulations of complex SAW structures. A perfectly matched layer (PML) was incorporated into the model to successfully suppress spurious reflections.

## Statement of Contribution/Methods

A FEM-model with PML for a unit cell was implemented within fast and accurate software tool CFS++ (Coupled Field Simulation). The model allows for simulating one- and multilayered substrates with periodic structures of massive electrodes on the top. The influence of PML parameters on SAW and leaky SAW solutions was investigated. The HA is obtained from calculated charge distributions on electrode surfaces. This provides the necessary information for the extraction of COM parameters.

## Results/Discussion

Numerical results obtained for different SAW piezoelectric materials (see attached Fig.) were compared with those obtained using a proprietary FEM/BEM tool developed by IMTEK/CTR AG. The computation time is comparable for one-layer piezoelectric substrates. For multilayered substrates, the computation time with full-FEM is several times faster. The observed difference in the COM parameters extracted using full-FEM and FEM/BEM is within 2%.



## P4A3 - Acoustic Sensors 1

Salon C

Thursday, September 4, 2014, 8:00 am - 5:00 pm

Chair: **Omar Elmazria**  
*Université de Lorraine*

P4A3-1

### Choice of quartz cut for sensitive wireless SAW temperature sensor

Alexander Shvetsov<sup>1</sup>, **Sergei Zhgoon**<sup>1</sup>, Ivan Antsev<sup>2</sup>, Sergei Bogoslovsky<sup>2</sup>, Gennadiy Sapozhnikov<sup>2</sup>, Konstantin Trokhimets<sup>2</sup>, Mikhail Derkach<sup>2</sup>; <sup>1</sup>National Research University MPEI, Moscow, Russian Federation, <sup>2</sup>Radar-mms, Russian Federation

#### Background, Motivation and Objective

Sensors for very accurate wireless temperature measurements are required in several important applications. SAW resonators are established candidates for such applications. In wireless systems, a resonator sensor element needs a paired reference element in order to reduce the error related to electromagnetic wave propagation between antennas. The aim is to find materials with good resonator properties and with the largest difference between temperature responses of resonators in a pair (a pair on a single substrate is preferable).

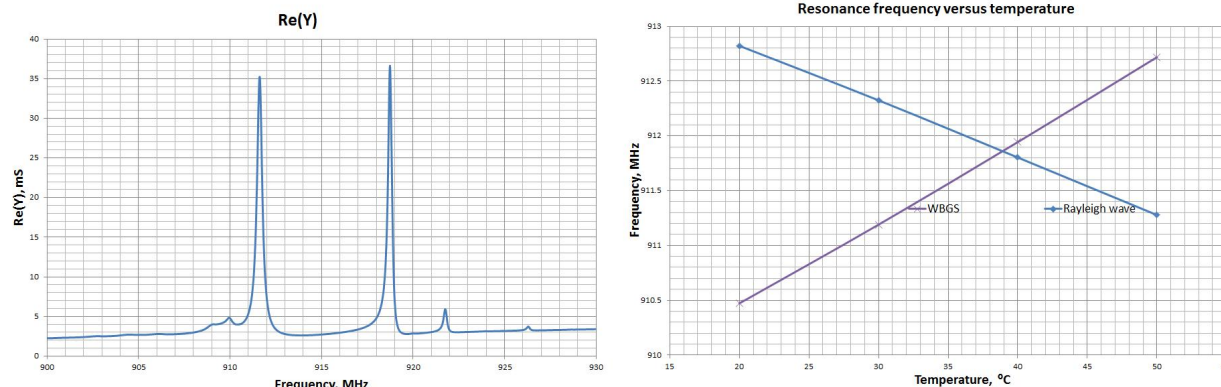
#### Statement of Contribution/Methods

Several materials and their cuts were analyzed before choosing quartz as a promising candidate. We have identified several cuts of quartz having useful properties with TCF difference up to 140 ppm/°C for a pair of resonators on a single substrate. As a rule, placing of such resonators on a single substrate requires rotation by up to 90° relative to each other thus increasing the die size. The limited range of cuts presents a unique opportunity to place both resonators along the X+90° direction with one resonator using BGS waves (with electrodes placed along X axis) and the other one (with electrodes inclined by about ±10° to X axis) using Rayleigh waves. These cuts are close to the 70°Y-cut where high TCF difference is reached together with acceptable characteristics of resonators.

#### Results/Discussion

Resonators were designed for all useful cuts (including the 70°Y-cut) and tested. The use of different periods in reflectors and IDT together with individual choice of gaps between reflectors and IDT allowed obtaining low spurious content in resonator responses. The quality factors reached values up to 4000 at central frequencies around 915 MHz for both BGS and Rayleigh types of waves. The measured difference of TCF is about 138 ppm/°C on 70°Y-cut that is close to the calculated value. The size of the die containing a pair of such resonators is very compact.

The left figure below shows the frequency response example of a resonator pair connected in parallel. Equal values of resonator conductance are achievable for both BGS and Rayleigh types of waves (the left resonance is related to BGS wave). The figure on the right illustrates the resonance frequencies temperature behavior of another pair of resonators for Al metal thickness to wavelength ratio of 2.55% for Rayleigh wave and of 2.25% for BGS wave.



P4A3-2

### Online real-time monitoring method of methanol concentration for direct methanol fuel cell using shear horizontal surface acoustic wave

Jun Kondoh<sup>1</sup>, Takuya Nozawa<sup>1</sup>; <sup>1</sup>Shizuoka University, Japan

#### Background, Motivation and Objective

Online real-time measurements of liquid properties are important for sensors. A shear horizontal surface acoustic wave (SH-SAW) sensor can detect liquid properties. As detection principle of the SH-SAW sensor is relative measurement, the SH-SAW sensor needs reference liquid to measure liquid properties. Normally, temperature of the reference liquid is set the same with sample liquid. This is one of difficulties to apply the SH-SAW sensor for online real-time monitoring system. When the SH-SAW sensor is inserted into the liquid flow tube, it is difficult to measure reference liquid. In this paper, we discuss the determination method of methanol (MeOH) concentration for a direct methanol fuel cell (DMFC).

#### Statement of Contribution/Methods

The 155MHz SH-SAW sensor is fabricated on 36YX-LiTaO<sub>3</sub>. The sensor is inserted in the flow tube of the DMFC. Phase and amplitude of the sensor and temperature of liquid are measured. As the sensor responses for MeOH solution agree with the theory, the theory is used for the concentration estimation. From the measurement, phase and amplitude changed at x°C are obtained. When we determine the liquid properties, we need phase and amplitude of the reference liquid at the same temperature. In case of the online real-time measurements, however, measurement of the reference water is impossible. Therefore, phase and amplitude of water at x °C are estimated using the theory. From differences between measured and estimated values at x °C, liquid properties are obtained. For calculation of the theoretical values at x deg. C, we assume nonconductive water at 20 °C. Also, before measurements of MeOH concentration, water at 20 °C is measured using the SH-SAW sensor. This measurement is performed only one-time after the sensor is



developed. From the following equation,  $\{(\text{measured sample at } x^\circ\text{C}) - (\text{measured water at } 20^\circ\text{C})\} - \{(\text{calculated water at } x^\circ\text{C based on } 20^\circ\text{C})\}$ , differences between measured and estimated values at  $x^\circ\text{C}$  are obtained. Then, the MeOH concentration is estimated.

#### Results/Discussion

The fuel in the DMFC is measured and MeOH concentration is estimated. However, the measured results of the fuel are complex and modification of the estimation method is needed. After temperature of the fuel is saturated, drift of the sensor responses must be reduced. From the longtime measurement, a sensor drift is approximated by a linear function. The theory is modified on the basis of comparison the expected results of 3 wt% MeOH using the theory with the experimental results. The results of the fuel measurements indicate that the conductivity cannot be ignored. From the theory for the attenuation change, effective conductivity is estimated. By modifying of the estimated methods, reasonable concentration of MeOH of the fuel is obtained. The change of concentration corresponds to the operation voltage of pump which connects to MeOH tank. When concentration decreases, pump is operated and vice versa.

#### P4A3-3

##### Design and characterisation of a combined pressure, temperature, ID sensor for harsh environment

Alfred Binder<sup>1</sup>, Jochen Bardong<sup>1</sup>, Gudrun Bruckner<sup>1</sup>; <sup>1</sup>CTR Carinthian Tech Research AG, Austria

#### Background, Motivation and Objective

Wireless pressure and temperature monitoring has been investigated and developed up to a very good technical maturity [1]. For the deployment in industrial environment a new SAW pressure/temperature/ID sensor concept has been established capable of stable operation in hot environment. This paper investigates the SAW design, mechanical aspects of packaging and full characterization of pressure drift and sensitivity for 20°C to 180°C.

#### Statement of Contribution/Methods

A delay line on YZ cut Lithium Niobate was chosen as sensitive element for pressure and temperature sensing. The unique sensor identification was realized using a pulse-position code. The crystal is mechanically supported by 3 pins and stressed by one centre pin, which directly transfers the deflection of a membrane to the crystal. The tensile and transverse stresses on the propagation path have been simulated and the geometrical position of the support pins was optimized to reduce the impact of mechanical tolerances on the strain distribution compared to previous designs [2].

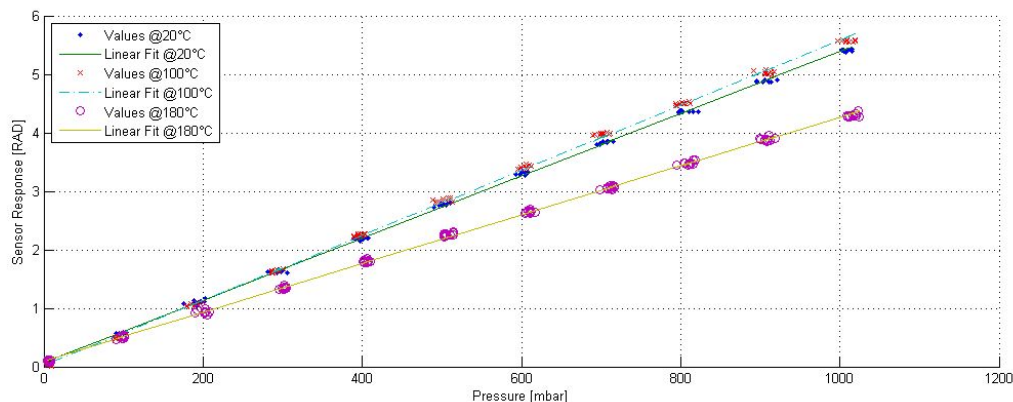
#### Results/Discussion

The pressure reading is evaluated by phase analysis. The pressure sensitivity of the sensor follows a linear relationship and results in 5.3 rad/bar at 20 °C (Fig.). The temperature and pressure readings are not completely independent. The sensitivity rises slightly until a turning point between 80 °C and 100°C at 5.6rad/bar and decreases to 4.2 rad/bar at 180 °C. This effect was adjusted by the use of temperature information. The strain induced temperature effect can be up to 0.3 °C, but nevertheless allows an overall accuracy of  $\pm 2^\circ\text{C}$  within the operation range. The offset drift of the pressure signal stays within 0.3 rad from 20 °C to 180 °C.

A wireless combined pressure/temperature sensor for elevated operation temperatures up to 180°C has been demonstrated. The unique identification of the sensor in combination with the temperature information is used for automatic compensation of drift. Further investigation will focus on performance stability of small production series in pilot applications.

[1] B. Dixon, et. al., "A second generation in-car tire pressure monitoring system based on wireless passive SAW sensors," IEEE Int. Freq. Control Symposium 2006

[2] A. Binder, et. al., "Wireless Surface Acoustic Wave Pressure and Temperature Sensor With Unique Identification Based on LiNbO<sub>3</sub>," IEEE SENSORS JOURNAL, 2013



#### P4A3-4

##### Dual Rayleigh and Love surface acoustic wave structures based on ZnO thin film for Microfluidic applications

Frederic Sarry<sup>1</sup>, Thibaut Roux-Marchand<sup>1</sup>, Denis Beyssens<sup>1</sup>, Omar Elmazria<sup>1</sup>; <sup>1</sup>Universite de Lorraine, IJL UMR7198 CNRS, Vandœuvre-les-Nancy, France

#### Background, Motivation and Objective

Lab-on-a chip (LOC) is one of the most important microsystems with promising applications in point of care (POC) testing. POC testings are defined as tests designed to be used at or near the site where the patient is located, that do not require permanent dedicated space, and that are performed outside the physical facilities of the clinical laboratories. Such an approach will not replace clinical laboratories but this should give a first response within less time and no scientists.

In order to realize chemical analysis, it is essential to manipulate small quantities of biofluids, immobilize probe molecules on the surface of a biosensor and/or react with the target molecules for the detection.

The aim of this study is to propose a microfluidic system able to interact efficiently with microdroplet coupled with a sensitive unit on the same substrate.

**Statement of Contribution/Methods**

SAW devices have found applications in microfluidics and LOC. Rayleigh-SAW/Liquid interaction induces acoustic streaming, which can be used for mixing, heating, droplet motion and atomization. Love-SAW can be used as biochemical sensors with high sensitivity. These two possibilities (sensing and actuating) are key components for LOC. The SAW device investigated here is based on an AT-quartz substrate with a ZnO thin layer deposited on the top. Two pairs of gold IDTs were patterned on the substrate in cross configuration leading to generate and to detect acoustic wave in AT-X and AT-X+90 directions. Gold was chosen for its biocompatibility and inertness. 1.4  $\mu\text{m}$  thick ZnO layer was deposited by RF magnetron sputtering using optimized sputtering parameters. The film thickness was theoretically determined to simultaneously minimize the temperature coefficient of frequency, enhance the coupling factor and maximize the mass sensitivity. The realized structure can generate both pure Rayleigh and Love modes.

**Results/Discussion**

The designed structure was fabricated and characterized. As expected, the observed responses present two functional frequencies:  $f_R=125.5\text{MHz}$  and  $f_L=163.90\text{MHz}$ . The R-SAW was successfully tested alone for efficiently mixing. Indeed, various powers, 250mW up to 4W at  $f_R$ , were applied to the IDT and the acoustic interaction in the microdroplet was clearly observed using infrared thermography. Note that when L-SAW structure is used instead of R-SAW, no interaction was observed. To avoid undesirable effect of RF heating on the sensor (L-SAW), we measure the central frequency of the L-SAW when various power were applied on the R-SAW without microdroplet. Any effect was observed. However, the L-SAW shows a non-linear frequency shift of 260kHz for a microdroplet viscosity variation of 760mPa.s.

We have now to demonstrate its efficiency with the well-known biomolecular binding systems such as biotin-streptavidin and deoxyribonucleic acid (DNA) hybridization for testing cell immobilization and removal.

**P4A3-5****A single-chip biosensing platform integrating FBAR sensor with digital microfluidic device**

Mengjun Zhang<sup>1</sup>, Weiwei Cui<sup>1</sup>, Ji Liang<sup>1</sup>, Daihua Zhang<sup>1</sup>, Wei Pang<sup>1</sup>, Hao Zhang<sup>1</sup>; <sup>1</sup>Tianjin University, Tianjin, China, People's Republic of

**Background, Motivation and Objective**

Although digital microfluidics has shown great potential in a wide range of applications, a true lab-on-a-chip with integrated powerful biochemical sensors is still lacking. To address this need, a fully integrated platform combining thin film bulk acoustic wave resonator (FBAR) sensor and electrowetting-on-dielectric (EWOD) is introduced. The EWOD module is for automatic droplet manipulation and the FBAR sensor module is for sample detection. The platform promises an ideal candidate for a true lab-on-a-chip with profound impacts in chemistry, biology and medicine.

**Statement of Contribution/Methods**

In this paper, the device configuration, fabrication process, and ability demonstrations are described. The piezoelectric layer of the FBAR sensor and the dielectric layer of the EWOD share the same aluminum nitride (AlN) thin film, which is a key feature to realize the full integration. In terms of detection protocols, two sensing modes, i.e. dry sensing mode and wet sensing mode, are proposed. Droplet transportation, comparison of the two sensing modes, and  $\text{Hg}^{2+}$  detection experiments are conducted to characterize the actuation ability, limit of detection (LOD), and detection ability of the integrated platform, respectively.

**Results/Discussion**

The droplet manipulated by the EWOD can be placed on the FBAR sensor accurately and reliably. Experimental results of the mode comparison demonstrate that the integrated platform can suppress the noise floor by more than an order of magnitude, compared to conventional FBAR sensors. A  $\text{Hg}^{2+}$  droplet of  $10^{-7}\text{M}$  is transported by the EWOD module and detected by the FBAR sensor module with the dry sensing mode, and a resonant frequency shift of 28 KHz is monitored, which corresponds to a relative resonant frequency shift of 13 ppm.

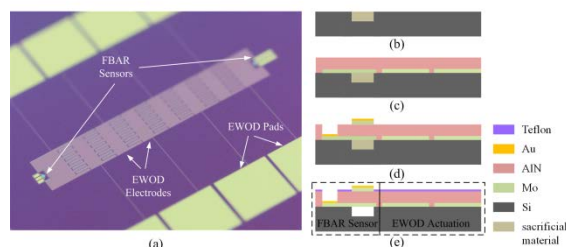


Fig. 1. (a) Photo of the fabricated device. (b)-(e) Brief fabrication process of the integrated platform.

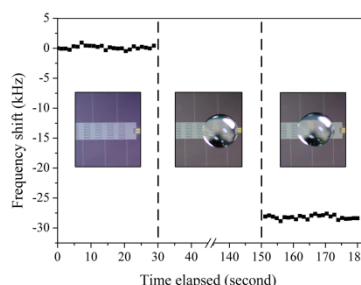


Fig. 2. Real-time recording of resonant frequency in  $\text{Hg}^{2+}$  detection experiment. In stage I, the FBAR sensor works in air; in stage II, a  $\text{Hg}^{2+}$  droplet of  $10^{-7}\text{M}$  is loaded on the sensor by EWOD; in stage III, the droplet is moved off the sensor by EWOD. A 28 kHz frequency shift of the dry sensing mode is recorded.

**P4A3-6****AlN solidly mounted resonators for high temperature applications**

Teona Mirea<sup>1</sup>, Mario DeMiguel-Ramos<sup>1</sup>, Ventsislav Yantchev<sup>2</sup>, Marta Clement<sup>1</sup>, Jimena Olivares<sup>1</sup>, Enrique Iborra<sup>1</sup>, Ilia Katardjiev<sup>2</sup>; <sup>1</sup>GMME CEMDATIC, Universidad Politécnica de Madrid, Madrid, Spain, <sup>2</sup>Uppsala University, Sweden

**Background, Motivation and Objective**

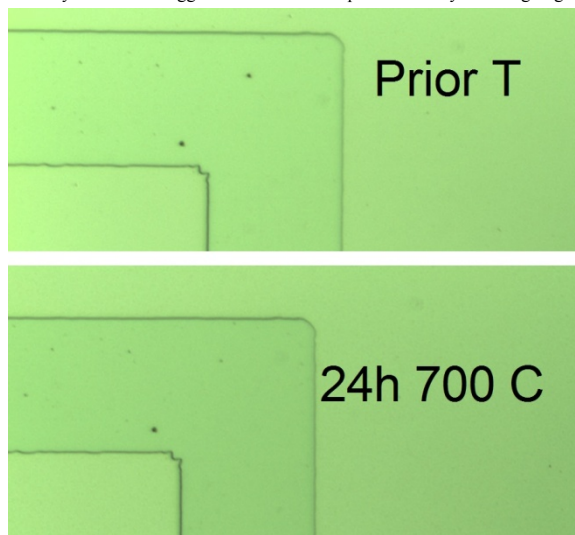
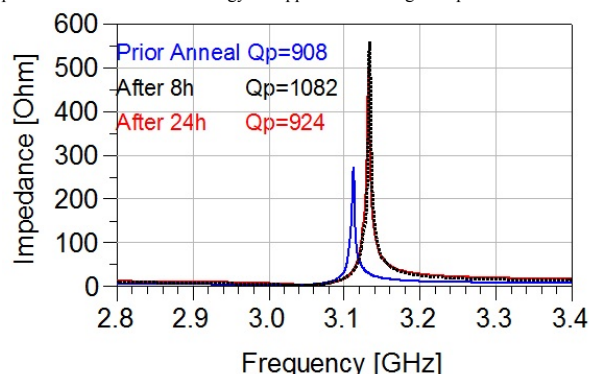
High temperature resonators have been extensively developed during the last decade. One of the most explored approach is that of a Langasite SAW resonators with Pt and Ir electrodes. One disadvantage of the latter is related to the topology of the SAW transducers. Namely they are constructed by long and narrow electrode strips which are subjected to destructive agglomeration at high temperatures. On the other hand AlN solidly mounted bulk resonators (SMR) are mechanically rigid structures with electromechanical coupling of 6%. Further, the electrodes are large and can be designed relatively thick at the expense of the electromechanical coupling. Last but not the least AlN is a chemically stable piezoelectric compound at high temperatures provided that the resonator is passivated.

**Statement of Contribution/Methods**

Here two types of SMRs are annealed at about 700°C. Both types consist of 629 nm Mo/ 535nm SiO<sub>2</sub> Bragg reflector with bottom 130nm Ir electrode on which 1.1  $\mu\text{m}$  AlN is deposited. The top electrodes are 130nm Mo and Ir, respectively. The annealing was performed under vacuum condition with radiative resistive heater. The time duration of each annealing cycle was 8h until a cumulative time of 24h was reached.

# Results/Discussion

After the first annealing cycle an overall improvement of device performance was achieved for both types. Subsequently slight Q degradation was observed. Inspection with optical microscope has shown no agglomeration effects. SEM images of the Bragg reflectors prior and after annealing will be further shown. These first experiments show the potential of the SMR technology for applications at high temperatures. Further work on fully dielectric Bragg mirror and suitable passivation layers is ongoing.



P4A3-7

## Label-free Detection of Protein Released during Platelet Activation by CNT-Enhanced Love Mode SAW Sensors

Huiyan Wu<sup>1</sup>, Guangyi Zhao<sup>2</sup>, Hongfei Zu<sup>1</sup>, James H-C Wang<sup>2</sup>, Qing-Ming Wang<sup>1</sup>; <sup>1</sup>Mechanical Engineering and Materials Science, University of Pittsburgh, USA, <sup>2</sup>MechanoBiology Laboratory, Department of Orthopaedic Surgery, University of Pittsburgh, USA

### Background, Motivation and Objective

Shear-Horizontal Surface Acoustic Wave (SH-SAW, Love Mode) devices are promising for bio-sensor applications in liquid medium. Due to the lack of proper bio-interface, most studies by far neglected their innovative applications as cell-based sensors. Carbon nanotube (CNT) has been proven potential of non-specific protein adsorption, as well as co-immobilization of ligands, which induces specificity in protein binding on nanotube surface. In this study, a novel CNT-embedded bilayer structure was used as the wave-guiding layer for cell-based Love mode SAW devices, and applied to non-specific (label-free) detection of protein released from platelet non-selective activation.

### Statement of Contribution/Methods

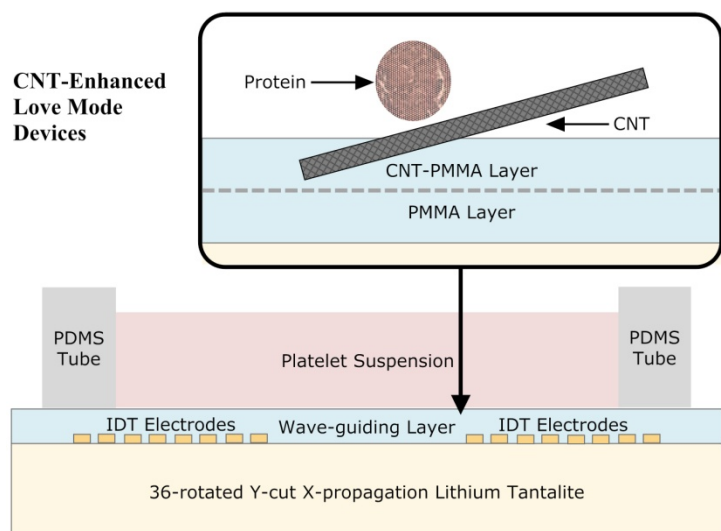
Love mode SAW devices were fabricated using 36° YX-LiTaO<sub>3</sub> crystals. Pure PMMA was pre-coated on these electrodes using spinning and baking procedures. Subsequently, CNT-embedded PMMA was spin coated on the surface as both the wave-guiding layer and bio-interface layer. After bilayer coating, one rectangular tube of poly(dimethylsiloxane) was used to form the well-like structure for platelet activation.

Rat blood mixed with anticoagulant was centrifuged to obtain the platelet-rich plasma (PRP) in the supernant. Platelets were suspended at various concentrations in Tyrode's albumin buffer containing 0.02 U/mL apyrase.

Platelet suspension of different concentrations (400  $\mu$ L) and CaCl<sub>2</sub> solution (200  $\mu$ L) were added into wells successively and maintained in an incubator at 37°C with 5% CO<sub>2</sub> for 2 hr, in order to activate these platelets and then allow released protein cover the entire well bottom. During this process, S<sub>21</sub> of Love mode sensors were monitored every min. After removing the platelet suspension, all devices were washed with distilled deionized (DD) water and dried with air. S<sub>21</sub> of Love mode devices with empty wells and protein coatings were recorded, respectively.

### Results/Discussion

The resonance frequency shifts of CNT-enhanced Love mode devices were significantly increased compared with single-layer devices. The relationship of resonance frequency shift and platelet concentration was not strictly linear but showed small variations. Both mass sensitivity and stability were improved in detecting protein released by activated platelets, indicating the potential of CNT-enhanced Love mode devices for future cell-based applications.



## P5A1 - Front End Transducer Electronics

Salon C

Thursday, September 4, 2014, 8:00 am - 5:00 pm

Chair: **David Cowell**  
University of Leeds

P5A1-1

### An Integrated Beamforming Driver for CMUT based Ultrasound Catheter Ablation System

Hasan Yetik<sup>1</sup>, Arif Sanli Ergun<sup>1</sup>, Ayhan Bozkurt<sup>2</sup>; <sup>1</sup>Faculty of Engineering, TOBB University of Economics and Technology, Ankara, Turkey, <sup>2</sup>Faculty of Engineering and Natural Sciences, Sabanci University, Istanbul, Turkey

#### Background, Motivation and Objective

In CMUT based ultrasound catheter ablation systems, transducer arrays and their drivers are to be kept as small as possible due to size restrictions, while maintaining a reasonable number of channels for proper beamforming. In addition, these systems should be highly integrated with minimal power consumption for flexibility and functionality. Despite the size restrictions on these systems, such problems can be overcome by ASICs. In this work, we present a simple 8 channel high-frequency, high-voltage driver, together with its beamforming and control circuitry designed with AMS's H35 high voltage process.

#### Statement of Contribution/Methods

Linear beamforming consists of time or phase shifted sinusoidal waves with varying envelopes. Since HIFU applications use monotonous sine wave excitation, a simple and effective beamforming approach that involves delayed sine wave synthesis, can be utilized. This is done by constructing a 32 state ring counter which activates one sine-weighted current sinking MOSFET at a time. The MOSFETs are arranged in an inverting amplifier configuration and their W/L ratio is chosen by its corresponding sample on a sine wave. Using serial control circuitry, starting phase data is loaded to the counter to produce phase shifted signals. Number of MOSFETs is selected based on the phase resolution needed. The frequency of operation is determined by the clock frequency of the counter and the number of samples. The design is made using Cadence Design Environment.

#### Results/Discussion

The proposed circuit is shown in Fig. 1. In the simulation environment (performed by Spectre) we achieved 36.25 Vpp voltage swing at 10 MHz, 8.74% THD, and phase resolution of 11.25°, assuming a CMUT model of 20pF capacitor in parallel with 8kΩ resistor. The maximum output frequency is determined by the switching times of the high voltage MOSFETs, so the voltage swing decreases as the frequency increases. At 15 MHz, the voltage swing drops to 30 Vpp. The circuit produces fixed amplitude sine waves, so the power output is adjusted by applying the clock in bursts. At 10MHz per channel dissipated and delivered power are 56mW and 316mW, respectively. Although these results will vary with a more realistic CMUT model, they are promising for an effective integrated HIFU driver circuit.

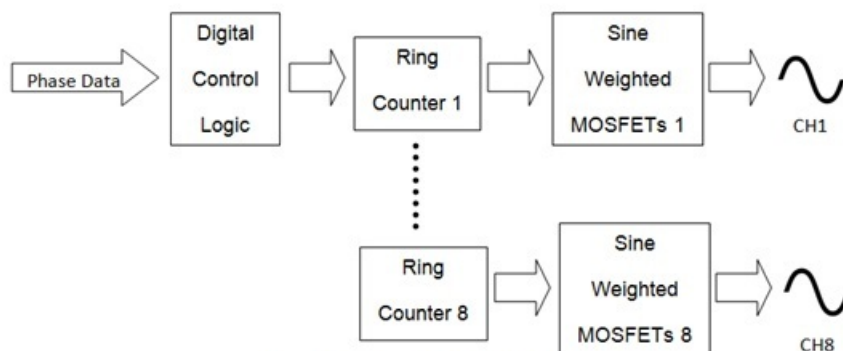


Fig. 1 Circuit Block Diagram

P5A1-2

### Design of a Driver IC for an Ultrasound Catheter Ablation System

Ayhan Bozkurt<sup>1</sup>, Omid Farhanieh<sup>1</sup>, Rupak Bardhan Roy<sup>1</sup>, Arif Ergun<sup>2</sup>; <sup>1</sup>Electronics Engineering, Sabanci University, Tuzla, Istanbul, Turkey, <sup>2</sup>TOBB University of Economics and Technology, Ankara, Turkey

#### Background, Motivation and Objective

High Intensity Focused Ultrasound (HIFU) is generally administered externally, or through body orifices such as the esophagus, the urethra, the uterus, or the rectum. The devices used in conventional treatment are not suitable to be used in endoscopic interventions or in intravascular catheterization due to their dimensions. In this work, we present the design of an integrated circuit for driving a CMUT therapy array of 2 mm diameter. The proposed device would be small to fit through key holes in endoscopic treatment or through vessels.

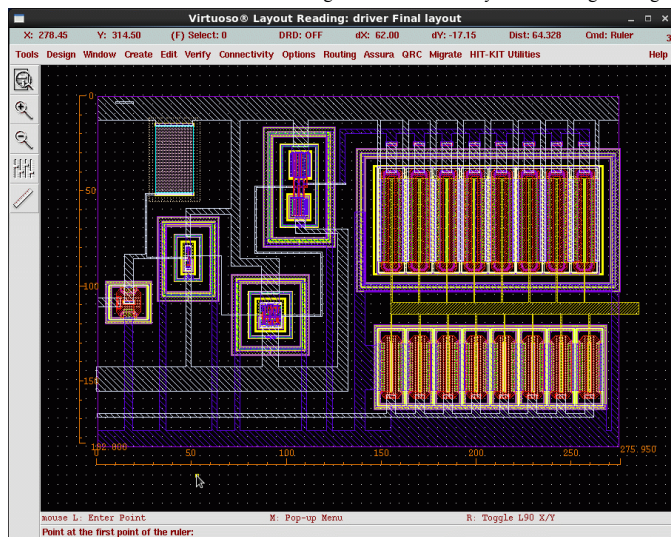
#### Statement of Contribution/Methods

The excitation signals to drive a catheter based HIFU system may be carried through individual cables along the catheter. Another solution is to locally generate the phased signal by the use of an application specific integrated circuit (ASIC) which may reduce cable count and increase phase accuracy. The proposed ASIC is composed of (1) an 8 channel drive signal generator, (2) 8 high voltage drivers, and (3) a PLL for the local generation of a high frequency tunable master clock signal based on a low frequency reference.



### Results/Discussion

Each channel of the digital phased signal generator is based on presettable counters dividing a master clock signal at 160 MHz, providing a phase resolution of  $11.25^\circ$  with  $180^\circ$  out of phase signals for driving the NMOS and PMOS sections of a high-voltage CMOS push-pull stage. The duty cycle of each drive voltage can be adjusted in 6.25% steps for apodization. Each driver channel has an area of  $100\mu\text{m} \times 210\mu\text{m}$ . The PLL, which is based on a ring oscillator VCO provides a tuning range of 100-220 MHz. The circuit has less than 100  $\mu\text{s}$  settling time, -100 dBc/Hz phase noise at 1 MHz offset,  $58^\circ$  phase margin, 5 MHz reference frequency, and consumes less than 2.6 mW power. The high voltage driver comprises NMOS and PMOS drivers of width 400 and 700  $\mu\text{m}$ , respectively, and will be capable of driving an 8 element concentric ring array in CMUT technology with a load of 20 pF per channel at 10 MHz. The power consumption for a purely capacitive load would be 500 mW. Each driver section occupies a die area of  $180\mu\text{m} \times 275\mu\text{m}$ . The total die area is less than 2 mm<sup>2</sup>. The IC is designed in austriamicrosystems h35 high-voltage CMOS technology.



P5A1-3

### Design of Frequency-Division Multiplexing Front-End Receiver Electronics for CMUT-on-CMOS Based Intracardiac Echocardiography

M Wasequr Rashid<sup>1</sup>, Coskun Tekes<sup>2</sup>, Maysam Ghovanloo<sup>1</sup>, F Levent Degertekin<sup>2</sup>; <sup>1</sup>School of Electrical & Computer Engineering, Georgia Institute of Technology, Atlanta, Georgia, USA, <sup>2</sup>G.W. Woodruff School of Mechanical Engineering, Georgia Institute of Technology, Atlanta, USA

### Background, Motivation and Objective

Designing Intracardiac Echocardiography (ICE) imaging catheters using 2D arrays with large number of elements is extremely challenging with standard interconnect and transducers technology. Using microbeamformers inside the catheter reduces the number of cables; however it requires complex front-end electronics which consumes considerable amount of real estate. By using the CMUT-on-CMOS technology, one can efficiently optimize the 2D transducer array to use less number of active elements and further reduce the number of cables by combining multiple channels on a single output cable. Reducing the number of cables with integrated electronics may provide a flexible catheter which can be used for 3D ICE imaging under MRI as well as X-Ray. In this study, we explore the design of the CMOS receiver circuit which implements a Frequency Division Multiplexing (FDM) scheme to achieve reduced number of output channels.

### Statement of Contribution/Methods

A circuit was custom designed to multiplex the output of 8 CMUT array elements with center frequency 7MHz and 80% fractional bandwidth for ICE application. Parallel readout of 8 CMUT signals over single RF transmission line during each firing was achieved by implementing on chip analog FDM. The IC was designed in .35 $\mu\text{m}$  4M2P TSMC process with supply voltage of 3.3V. The block diagram of the system is shown in Fig 1. The CMUT signals were first amplified using low noise transimpedance amplifier (TIA). The signals were then frequency up shifted to different frequencies using on-chip mixer using the orthogonal carrier signals of 40 MHz, 80 MHz, 120 MHz and 160 MHz. The 4 orthogonal carrier signals were also generated on-chip from 2 external clock signals of 240MHz and 320MHz. The up-converted signals were combined and sent out via driver circuit.

### Results/Discussion

The FDM modulation was simulated in Cadence environment using Spectre circuit simulation tool. The layout of the IC was completed. Post layout simulation was performed. Fig 2 shows the modulation scheme and amplitude spectrum of the FDM output signal from post layout simulation. Detailed design of the circuit and experimental results obtained from the fabricated IC chips will be presented in the paper.

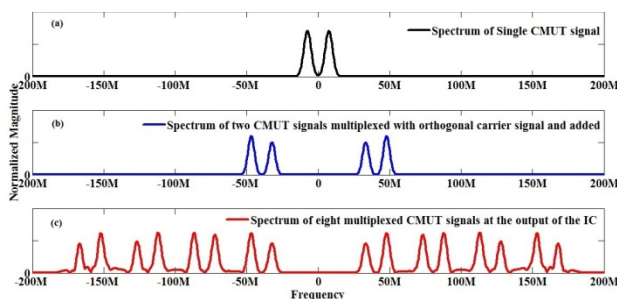


**Figure2:** (a) Spectrum of a single CMUT signal (b) Spectrum of two CMUT signal multiplexed with orthogonal carrier signal and added together (c) Spectrum of the 8 combined CMUT signals at the output of the IC

<sup>1</sup>Gurun, G.; Tekes, C.; Zahorian, J.; Xu, T.; Satir, S.; Karaman, M.; Hasler, J.; Degertekin, F.L., "Single-chip CMUT-on-CMOS front-end system for real-time volumetric IVUS and ICE imaging." *Ultrasonics, Ferroelectrics and Frequency Control, IEEE Transactions on*, vol.61, no. 2, pp.239-250, February 2014

## Optimized Thermal Design for ASICs-embedded Clinical Ultrasound Probes Using Phase-change Materials

## Background, Motivation and Objective

### Statement of Contribution/Methods

In an experiment, at first, ASIC-embedded prototype probes were filled with PCM having 310 Kelvin of phase transition temperature ( $T_{tr}$ ), or silicone compound. Secondly, temperature on the probe surface was measured during running the probe in the air with a few wattage of heat flow for more than 30 minutes.

## Results/Discussion

Duration time [sec]	PCM Temperature [K]	Silicone compound Temperature [K]
0	0.0	0.0
600	5.5	8.0
1200	10.0	14.0
1800	11.5	17.0
2400	12.0	-
3000	12.2	-
3600	12.5	-

**Fig. 1 Measurement of the Lens surface temperature**

## P5A2 - Films and Devices

Salon C

Thursday, September 4, 2014, 8:00 am - 5:00 pm

Chair: **David Cowell**  
University of Leeds

P5A2-1

### ULTRASONIC MICROMOTOR CONTROL USING SELF-ACTUATED MICRO-STRUCTURES

Sarvani Piratla<sup>1</sup>, Amit Lal<sup>2</sup>; <sup>1</sup>Cornell University, Ithaca, New York, USA, <sup>2</sup>Cornell University, USA

#### Background, Motivation and Objective

This paper presents for the first time, minimal or non-contact control of an ultrasonic micromotor using self-actuated micro-structures, placed at a micro-gap separation to the rotor. An ultrasonic micromotor fabricated using MUMPS process and driven by the piezoelectric PZT plate bonded to the motor operates at a drive voltage of 4 – 10 Vpp in the frequency range of 100 kHz to 5 MHz as shown in [1][2]. A thermal actuator driven gripper placed close to the rotor as a brake. An external voltage supplied to thermal actuator varied the rotor-gripper gap, and achieved the control of rotor speed [2]. In this abstract, we show the control of the motor rotation with minimal or zero-contact using micro-structures without additional supply of power.

#### Statement of Contribution/Methods

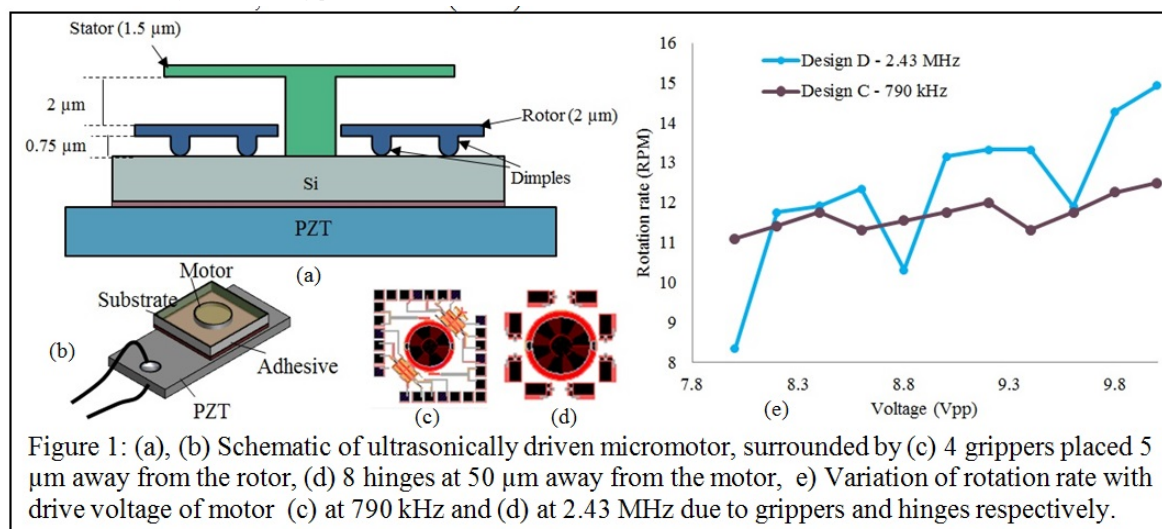
A non-contact method of controlling the motor with as little physical contact as possible increases the reliability and life time of the motor. To achieve this, two motors are surrounded by distinct micro-structures as shown in Figure 1(c) and (d). The former is surrounded by 4 grippers placed 5  $\mu\text{m}$  away from the rotor; the latter motor is surrounded by 8 hinges at 50  $\mu\text{m}$  away from the rotor.

#### Results/Discussion

At the actuation frequencies, the motors rotated at 5 – 15 RPM. In the absence of the grippers/hinges, the rotation rate of the motor increases linearly with drive voltage in this speed range. The grippers/hinges at an end are anchored to the Si substrate. As the substrate is bonded to the PZT plate, during the motor actuation, the grippers and the hinges vibrate at the PZT drive frequency and have sinusoidal vibration displacement whose amplitude increases with drive voltage. The gripper touches the rotor during vibration acting as a brake, and the hinge vibration dampens surrounding air speeds resulting in reduction of rotation rate of the motors as shown in Figure 1(e). The hinge has larger surface area and translated to significant change of rotation rate as compared to the gripper design. At frequencies with speeds in the range of 100 – 300 RPM, there is no noticeable change of speed due to gripper vibration.

#### References:

1. S. Piratla, A. Lal, "Resonant Stator Actuation of Gear Coupled Ultrasonic Motors", Transducers 2011, Beijing, pp. 2450-2453.
2. S. Piratla, M. Pandey, A. Lal, "Nanogap Ultrasonic Actuator for Non-Contact Control of Levitated Inertial Sensor Rotor", Hilton Head'12 (2012): 82-85.



P5A2-2

### A New Piezoelectric Motor using d14 Actuator

Yung Ting<sup>1</sup>, Chih Hao Lin<sup>1</sup>, Hao Ping Lin<sup>1</sup>; <sup>1</sup>Mechanical Engineering, Chung Yuan Christian University, Chung Li, Taiwan

#### Background, Motivation and Objective

A new piezoelectric motor using d14 actuator is developed. As compared to the piezoelectric motor using d15 actuator, the proposed d14 type is of good characteristics of providing higher torque and speed. Moreover, increasing the thickness along the poling direction is required in order to enhance the output speed and force while using d15 actuator.

# Statement of Contribution/Methods

Using proposed d14 actuator, increase of the length perpendicular to the contact plane can improve the performance without the need of applying large poling and driving voltage like d15 actuator. Also, different from our previous study, larger speed is gained by using lower vibration frequency while choosing the corresponding mode in particular.

# Results/Discussion

With applying voltage of  $\pm 150V$ , the d14 actuator made of PZT-8 is able to generate about  $4.4\mu m$  and  $1.9\mu m$  for vertical and transverse amplitude respectively. Analytical simulation by using ANSYS is in comparison with the experiment results. Both results show with a good agreement. An example of rotation speed can reach about 60rpm and maximum torque about 0.00329Nm is presented.

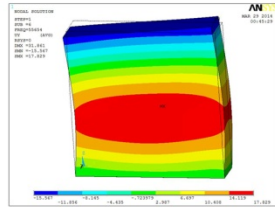


Fig. 1. Modal shape of d14 @55kHz

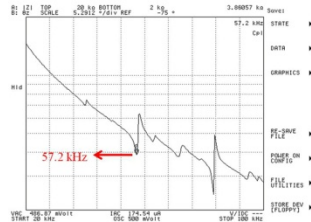


Fig. 2. Resonance frequency by impedance analyzer

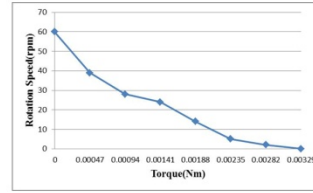


Fig. 3. Rotation speed vs torque

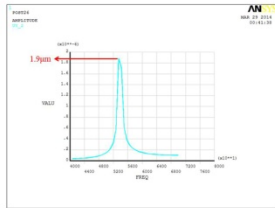


Fig. 4. Transverse displacement (ANSYS)

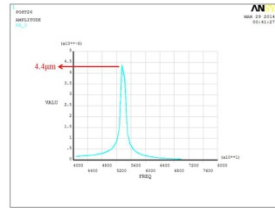


Fig. 5. Vertical displacement (ANSYS)

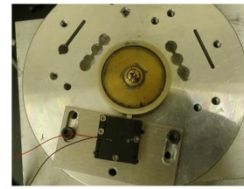


Fig. 6. Photo of d14 motor for rotation

## P5A2-3

## Performance Evaluation of PVDF Single-Element Transducers with Different Backing Materials for Photoacoustic Microscopy

Jun Su Lee<sup>1</sup>, Jin Ho Chang<sup>1,2</sup>; <sup>1</sup>Department of Electronic Engineering, Sogang University, Seoul, Korea, Republic of; <sup>2</sup>Interdisciplinary Program of Integrated Biotechnology, Sogang University, Seoul, Korea, Republic of

## Background, Motivation and Objective

Ultrasound transducers for photoacoustic microscopy (PAM) should have high operating frequency, broad bandwidth and high signal reception efficiency. Polyvinylidene fluoride (PVDF) is a suitable material for this purpose. To take full advantage of this material, the selection of backing material is crucial because it influences the center frequency and bandwidth of the transducer. Therefore, we experimentally investigated to find the most suitable backing material among EPO-TEK 301, E-Solder 3022, and RTV.

## Statement of Contribution/Methods

Three single element transducers were fabricated with PVDF and each backing material. The material properties are summarized in Table 1. The aperture size and focal depth were 5 mm in diameter and 6 mm, which are suitable for PAM. By pulse-echo test, the center frequency and the -6dB bandwidth of each transducer were ascertained. For this, a commercial UT340 pulse/receiver system was used to excite the transducer and to receive the echo reflected from a stainless reflector placed at the focal depth.

## Results/Discussion

Figure 1 shows the pulse-echo responses and the frequency spectra of the transducers. The transducer with RTV had the highest center frequency and bandwidth, but it had the lowest signal magnitude because the energy propagating toward the backing block is as high as the front medium. In contrast, E-Solder allowed the PVDF to resonate in the quarter wave mode due to its relatively high acoustic impedance, thus severely lowering both the center frequency and bandwidth. Consequently, EPO-TEK is the most suitable backing material for a PAM transducer because the large portion of the energy propagated toward the front medium and the PVDF resonated in the half wave mode, thus providing the highest signal magnitude and the reasonable bandwidth.

Table 1

Material	Property	Value
PVDF	Longitudinal wave velocity (m/s)	1400
	Density (g/cm <sup>3</sup> )	1800
	Acoustic impedance (MRayls)	2.52
RTV	Acoustic impedance (MRayls)	1.32
	Attenuation	4.08/(1MHz • cm)
EPO-TEK 301	Acoustic impedance (MRayls)	3.08
	Attenuation	13.5/(30MHz • mm)
E-SOLDER 3022	Acoustic impedance (MRayls)	5.92
	Attenuation	110/(30MHz • mm)

Table 1. Material properties of the PVDF film with a 9 $\mu$ m thickness and backing materials.

Figure 1

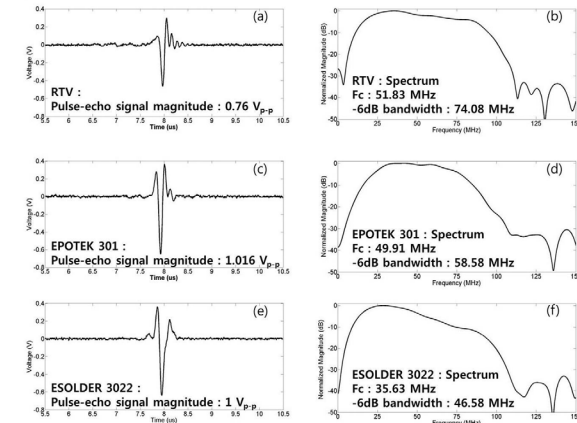


Figure 1. Pulse-echo response and frequency spectra of the fabricated transducers.

P5A2-4

### High Frequency Transducer Based on Hydrothermal PZT Film for Ultrasound Imaging and Trapping

benpeng zhu<sup>1,2</sup>, Ying Li<sup>2</sup>, Yang Li<sup>2</sup>, Michihisa Shiiba<sup>3</sup>, Shimichi Takeuchi<sup>3</sup>, qifa zhou<sup>2</sup>, Koping Shung<sup>2</sup>; <sup>1</sup>Huazhong University of Science and Technology, Wuhan, China, People's Republic of, <sup>2</sup>Department of Biomedical Engineering and NIH Transducer Resource Center, University of Southern Cali, USA, <sup>3</sup>Medical Engineering Course, Graduate School of Engineering, Toin University of Yokohama, Yokohama 225, Japan

#### Background, Motivation and Objective

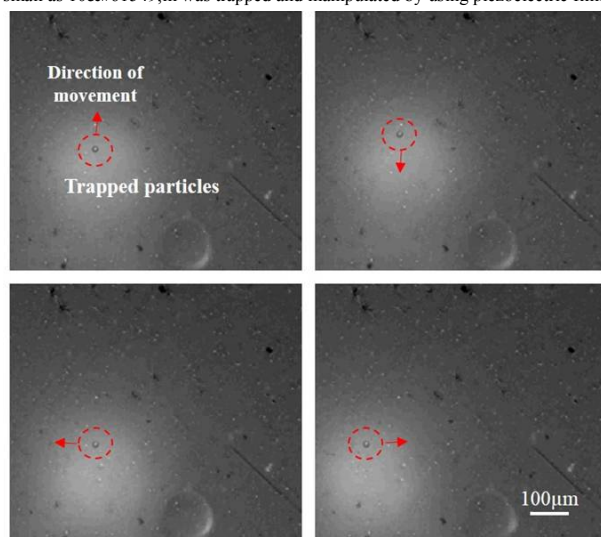
With the advance of high frequency ultrasound transducer, high frequency imaging and acoustic microparticle trapping become possible. Higher operational frequency is beneficial for better resolution of imaging as well as smaller particle manipulation. The size of trapped microparticle is related with the central frequency of transducer, consequently dependence on the thickness of piezoelectric element. Therefore, it is vital to prepare the piezoelectric element of a thickness on the order of only a few micrometers with high accuracy. Because of the difficulty and time consuming of lapping down for bulk piezoelectric materials, piezoelectric thick film may be a cost effective choice. In this work, self-separated hydrothermal PZT thick films with excellent properties have been achieved. Therefore, it is worthy and interesting to investigate high frequency transducer based on such film for high frequency imaging and micro beam trapping applications.

#### Statement of Contribution/Methods

In this study, we present the fabrication process of high frequency transducers using self-separated hydrothermal PZT thick films. One of transducers was applied to obtain the ultrasound imaging from rabbit eye ball. Meanwhile, it also could service as a single beam acoustic tweezers to trap 10 &micro;m polystyrene. It suggests that PZT thick films could be a useful material to fabricate the transducer for both imaging and trapping applications.

#### Results/Discussion

Based on self-separated hydrothermal PZT thick films, ultrasound transducers with the operational frequencies in the range of 50-100MHz were successfully fabricated. A focused 50MHz single element high frequency transducer with f-number around 1 was obtained with press-focusing technology. Without any matching layer, the transducer had a bandwidth at -6dB of 41%. An imaging of rabbit eye ball was achieved using homemade ultrasound backscatter microscopy (UBM) system. The microparticle with the diameter as small as 10&micro;m was trapped and manipulated by using piezoelectric film transducer.



P5A2-5

### A Novel Wireless Power Transmission Scheme Based on Ultrasonic Phased Array Transducers

Jinying Zhang<sup>1</sup>, Gang Han<sup>1</sup>, Xi Ning<sup>1</sup>, Shuming Chen<sup>1</sup>; <sup>1</sup>National University of Defense Technology, China, People's Republic of

#### Background, Motivation and Objective

Last decade has seen an enormous increase in the number and variety of medical devices implanted into the body for monitoring or therapeutic purposes. These devices require electrical energy for their operation. In recent years, some interesting methods for intrabody electrical energy sources have been reported, such as biological fuel cells that consume inter-cellular glucose, and the biomechanical energy created by the movement of internal organs. However, with these techniques, only an average power below 1 mW can be generated. A wireless mechanism is capable of transferring power up to 10 W based on the penetration of electromagnetic energy through the tissue. But it suffers from low power transfer efficiency and electromagnetic radiation hazard. Presently, for the power range of tens of mW, ultrasonic transcutaneous energy transfer (UTET) may be a preferable technology due to its power transfer efficiency, compactness and electromagnetic immunity.

#### Statement of Contribution/Methods

The reported UTET device used a uniform piezoelectric transmitter which benefits from the self natural focusing zone and simplicity of realization. However, beyond the self natural focusing zone, the intensity of acoustic wave decreases rapidly. This paper proposes a UTET device in which the energy is transmitted via ultrasonic waves generated by piezoelectric phased array transducers. The phased array scheme helps to increase the power transfer efficiency in a relatively long zone and correspondingly reduce the size of intrabody piezoelectric receiver.

#### Results/Discussion

A finite element method (COMSOL Multiphysics) is applied to investigate the properties of the phased array UTET for optimized design. The source is continuous sine wave with frequency of 1 MHz and amplitude of 1 V. Two linear arrays, 32-element and 64-element, are simulated and compared. Their acoustic field distribution is obtained with no focusing (uniform phase) and phased focusing at 3 cm, 5 cm, 7 cm, 10 cm, 15 cm and 20 cm, respectively. The lateral and vertical pressure distribution in tissue is quantitatively presented. The voltage of the receiver is calculated when the piezoelectric receiver is 4 mm wide. At the axial depth of 10 cm, the received voltage is improved by almost three times for the 64-element phased array compared to uniform element of the same aperture. The results indicate that the proposed approach is a promising candidate in power transmission field.



P5A2-6

# Effect of pre-deposition rf plasma etching on wafer surface morphology and crystal orientation of piezoelectric AlN thin films

Valeriy Felmetger<sup>1</sup>, Mikhail Mikhov<sup>1</sup>, Pavel Laptev<sup>1</sup>; <sup>1</sup>PVD, OEM Group Incorporated, Gilbert, AZ, USA

## Background, Motivation and Objective

A maximal piezoelectric response can be achieved in polycrystalline aluminum nitride (AlN) thin films when they exhibit a columnar microstructure with the majority of the grains precisely oriented in the (0002) crystallographic direction perpendicular to the substrate surface. Film nucleation stage plays a determinant role in the formation of the preferred orientation; therefore AlN films deposited on smooth and highly textured bottom electrodes evince better crystalline quality. For this reason, non-reactive rf plasma etching is widely used in the device fabrication process for a pre-deposition wafer treatment. In this work, we investigate how etching in Ar plasma modifies the substrate surface morphology with the goal to better understand the physical mechanisms leading to considerable improvement of the preferred orientation in the bottom metal electrodes as well as in the subsequently deposited AlN thin films as a result of plasma etching.

## Statement of Contribution/Methods

A multi-module Endeavor-AT sputter tool equipped with a planarized capacitively coupled rf plasma source and dual-target S-gun magnetron was employed for the wafer etching as well as the deposition of 100-nm thick Al bottom electrodes and 500-nm thick AlN films on nominally unheated 6" Si (100) wafers. To ensure formation of highly (111) textured Al electrodes with smooth surface, the PVD process involved wafer etching at 70-300 W rf power, reactive magnetron sputtering of a 20-30 nm thick AlN seed layer enhancing the oriented crystallization of the electrode film, and Al deposition at low Ar pressure.

## Results/Discussion

The crystallographic texture in Al films, deposited over the AlN seed layer on an unetched wafer, was not well developed; however wafer etching at even low rf power enabled growth of highly (111) oriented films. Moreover, the seed layer's orientation efficiency enhanced with increasing the rf power to 300 W and resulted in further narrowing the Al (111) rocking curves.

AFM and XRD data have shown that crystal orientation of both the electrode and AlN films can be considerably improved when the substrate micro roughness is reduced from an ordinary level of a few nm to atomic level (RMS as low as about 0.2-0.3 nm). In this case, the seed layer consists of small (nano-scale), equal-sized grains with clearly elicited c-axis texture promoting an oriented growth of the electrode film.

Thus, the most perfectly crystallized film stacks of Al and AlN were obtained in this work using rf plasma etching process optimized to create an atomically smooth, epi-ready Si surface morphology that enables superior AlN seed layer nucleation conditions. X-ray rocking curves around the Al (111) and AlN (0002) diffraction peaks exhibited extremely low FWHM values of 0.68° and 1.05°, respectively. These results exceed, to our knowledge, previously published results on crystal orientation of polycrystalline AlN and Al thin films sputter deposited on nominally unheated substrates.

P5A2-7

# Preparation of (K, Na)NbO<sub>3</sub>-CaTiO<sub>3</sub> Film by RF Magnetron Sputtering

Shinsuke Ikeuchi<sup>1</sup>, Toshimaro Yoneda<sup>1</sup>, Yoshitaka Matsuki<sup>1</sup>, Naoyuki Endo<sup>1</sup>, Yutaka Takeshima<sup>1</sup>, Hideya Horiuchi<sup>1</sup>, Yutaka Kishimoto<sup>1</sup>, Kansho Yamamoto<sup>1</sup>, Katsumi Fujimoto<sup>1</sup>; <sup>1</sup>Murata Manufacturing Co., Ltd., Nagaokakyō-shi, Kyoto, Japan

## Background, Motivation and Objective

(K, Na)NbO<sub>3</sub> (KNN) film is well-studied as a good candidate to substitute for Pb(Zr, Ti)O<sub>3</sub> film for applications to Micro Electro Mechanical Systems (MEMS). In addition, CaTiO<sub>3</sub>-added KNN (KNN-CT) ceramics are well-studied for their good piezoelectric properties by polymorphic phase transition between orthorhombic system and tetragonal system near room temperature. In this study, we developed a new KNN films by adding CaTiO<sub>3</sub>.

## Statement of Contribution/Methods

KNN-CT films were prepared on Si substrates by RF magnetron sputtering.

Regarding piezoelectric constant, because of the difficulty of measuring Young's modulus in film state, instead of conventional  $d_{31}$ , the representation of  $e_{31}^* = d_{31}/s_{11,p}$  (where,  $s_{11,p}$  is elastic compliance of the films) were employed and calculated from tip displacement of Pt/Ti/KNN-CT/Pt/Ti/SiO<sub>2</sub>/Si unimorph cantilevers.

## Results/Discussion

KNN-CT films with the target composition  $n > 0$  in  $(1-n)(K_{1-x}Na_x)NbO_3-nCaTiO_3$  ( $x=0.473-0.487$ ) exhibited  $|e_{31}^*| > 6.0C/m^2$ , whereas  $n=0$  exhibited  $|e_{31}^*| < 5.0C/m^2$  (Fig.1). The (002) peak angle of pseudocubic perovskite films increased with increasing  $n$  (Fig.2). From these results, we conclude that CaTiO<sub>3</sub> are successfully substituted as part of KNN and the piezoelectric constant increases by effect of CaTiO<sub>3</sub>.

Moreover, the highest  $|e_{31}^*| = 11.7C/m^2$  was observed with  $x=0.587$ ,  $n=0.040$  after post-annealing.

These KNN-CT films have not been optimized but exhibited one of highest piezoelectric properties for lead free piezoelectric films.

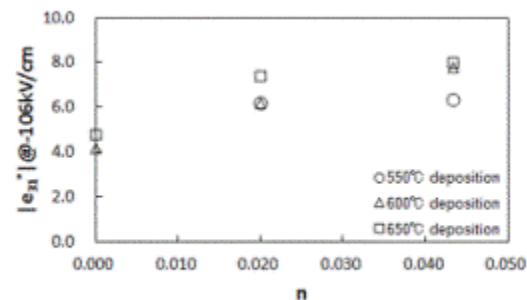


Fig. 1 Variation of  $|e_{31}^*|$  with the composition  $n$ .

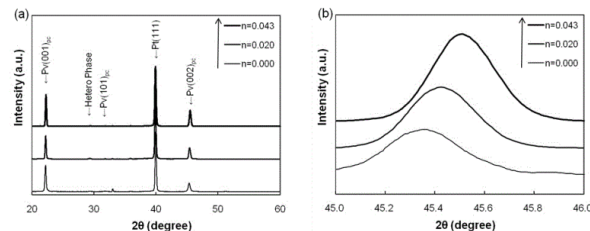


Fig. 2 Diffraction pattern of the KNN-CT films. (a)  $2\theta=20\sim60^\circ$ . (b)  $2\theta=45\sim46^\circ$ .

P5A2-8

**PVDF Cylindrical Film Device Influenced by Axial Film length**Minoru Toda<sup>1</sup>; <sup>1</sup>Measurement Specialties Inc, Lawrenceville, NJ, USA**Background, Motivation and Objective**

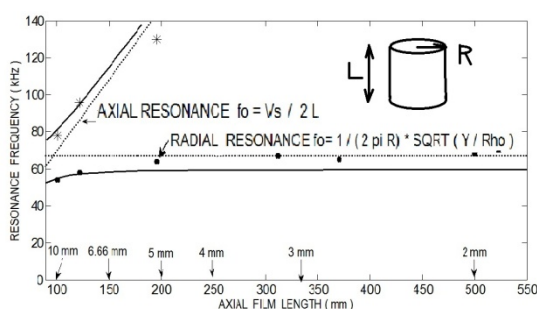
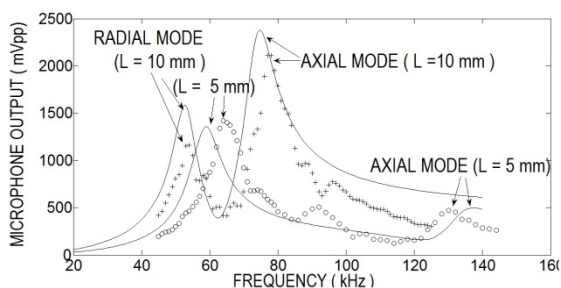
Cylindrical PVDF air transducers have been used in pen or stylus based digitizer systems for many years. These devices are applied for note taking, hand writing for OCR, and drawing or other graphical input. The two operating modes are known (propagations in the radial or axial direction). The axial propagation mode produces a point acoustic source at the tip of the pen. In this work features of cylindrical PVDF film transducers were investigated.

**Statement of Contribution/Methods**

This paper investigates the influence of the film length  $L$  on the resonant behavior and directivity of cylindrical PVDF transducers. Novel behavior is reported showing the existence of a strong high frequency radial mode resonance ( $f = 1.3$  to  $2.0 \times f_0$  at  $L > \lambda$ ) in addition to the breathing mode resonance at  $f_0$ . Directivity testing shows that the axial acoustic radiation is a maximum when  $L = \lambda/2$ . Additionally it is determined that the radial acoustic radiation strength is increased by the addition of a protective cage around the cylindrical PVDF.

**Results/Discussion**

A radial-axial coupled mode theory was developed for cylindrical PVDF transducers and the observed higher frequency radial mode was explained by the coupling to axial mode. It is known that the radial displacement is caused by  $d_{31}$  and axial displacement by  $d_{32}$  ( $\ll d_{31}$ ). The newly reported coupling mechanism results from axial mode excitation causing a higher frequency radial mode through Poisson's ratio behavior. Directivities of cylindrical and ring radiators were calculated and the results agreed with observed directivity patterns. The protection cage effect was explained by better impedance matching to radiation impedance in air. Fig. 1 shows double peaks of radial and axial modes. Fig. 2 is peak frequencies vs  $L$ .



P5A2-9

**PVDF copolymer transducers used to evaluate microparticle suspensions**Sanat Wagle<sup>1</sup>, Adit Decharat<sup>1</sup>, Michael Wegener<sup>2</sup>, Frank Melandso<sup>1</sup>; <sup>1</sup>Department of Physics and Technology, Norway, <sup>2</sup>Sensors and Actuators, Fraunhofer Institute for Applied Polymer Research, Germany**Background, Motivation and Objective**

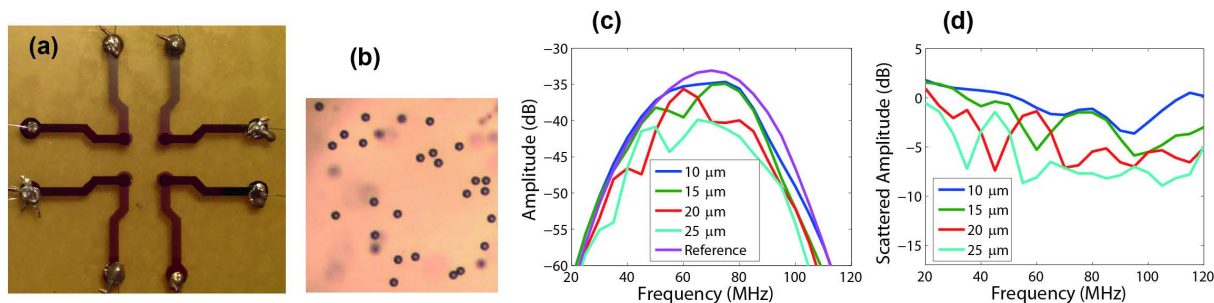
High frequency ultrasound has previously been used to evaluate particle sizes and concentrations in liquid suspensions/emulsions [R. Weser, S. Wockel, B. Wessely and U. Hemple, *Ultrasonics* 53, 706–716, 2013], and to detect changes in cells or tissues suspended in solutions [R.E. Baddour and M.C. Kolios, *Proc. IEEE Ultrasonics Symposium* 3, 1672 – 1674, 2005]. For many cases, the acoustic attenuation spectrum and back scattering amplitude can be used as important evaluation parameters. However, weak scattering from the particles and close acoustic mismatch impose some implications on the analysis [Weser et al.].

**Statement of Contribution/Methods**

The aim of the current work is to investigate the ability of using polymer transducers to detect and evaluate microparticles. The experimental investigation was conducted using transducers made from the copolymer poly(vinylidene fluoride – trifluoroethylene) [P(VDF-TrFE)]. These transducers with a central frequency ranging from 65 to 80 MHz were produced from the fluid phase, directly on top of a polyetherimide (Utem) backing in panels containing 4 circular apertures with 1 mm diameter each as shown in Fig. (a). Each transducer panel was coupled to a number of small solution volumes with various particle diameters (ranging from 5 to 25  $\mu$ m) and concentration (see the optical image in Fig. (b) for an example). The circular apertures were then driven in sequential order by a wide-band pulse, and the backscattered signals were analysed and compared to analytical and numerical models in order to identify size and concentration signatures.

**Results/Discussion**

The FFT spectra of the microparticle solutions together with a reference spectrum without particles are shown in Fig. (c). Scattered responses in terms of the difference between the one obtained from micro particles and the reference FFT are shown in Fig. (d). It has been found that both the back scattering amplitudes and spectra are quite sensitive to both the particles sizes and the solution concentrations. The suggested polymer transducers also offer large flexibility with respect to transducer frequency scaling and physical size, making them attractive as lab-on-a-chip detectors/analyzers for microparticles.



P5A2-10

### Durability Test and Observation on Non-Linear Distortion in Output Waveform of Anti-Cavitation Hydrophone in High Intensity Ultrasound

Nagaya Okada<sup>1</sup>, Michihisa Shiiba<sup>2</sup>, Takeyoshi Uchida<sup>3</sup>, Masahiro Yoshioka<sup>4</sup>, Minoru K. Kurosawa<sup>4</sup>, Shinichi Takeuchi<sup>2</sup>, <sup>1</sup>Research and Development Div., HONDA ELECTRONICS CO., LTD., Japan, <sup>2</sup>Department of Clinical Engineering, Faculty of Biomedical Engineering, Toin University of Yokohama, Japan, <sup>3</sup>National Metrology Institute of Japan (NMIJ), National Institute of Advanced Industrial Science and Technology (AIST), Japan, <sup>4</sup>Interdisciplinary Graduate School of Science and Engineering, Tokyo Institute of Technology, Japan

#### Background, Motivation and Objective

Recently, ultrasound applications with the assistance of high-intensity ultrasound pulse are used increasingly in medical systems. It is necessary to measure the intensity distributions to ensure low-risk treatment. However, conventional pointed hydrophones are unable to use as measuring equipments, as they are damaged by means of the very high pressure and inertial cavitation. We have developed pointed anti-cavitation hydrophone by the deposition of a hydrothermally synthesized lead zirconate titanate (PZT) thick film on the reverse surface of Ti plate. The deposited film is protected from acoustic cavitation by the Ti plate. This hydrophone was prevented from damage at a high pressure field (15 MPa) at a focal point of a concave transducer driven CW with input power to the sound source up to 50 W[1]. However, a non-linear distortion in output waveform of the hydrophone was not observed because of sensitivity reducing at high frequency range. Accordingly, this study is aimed at durability against inertial cavitation and observation on non-linear distortion in output waveform of the anti-cavitation hydrophone.

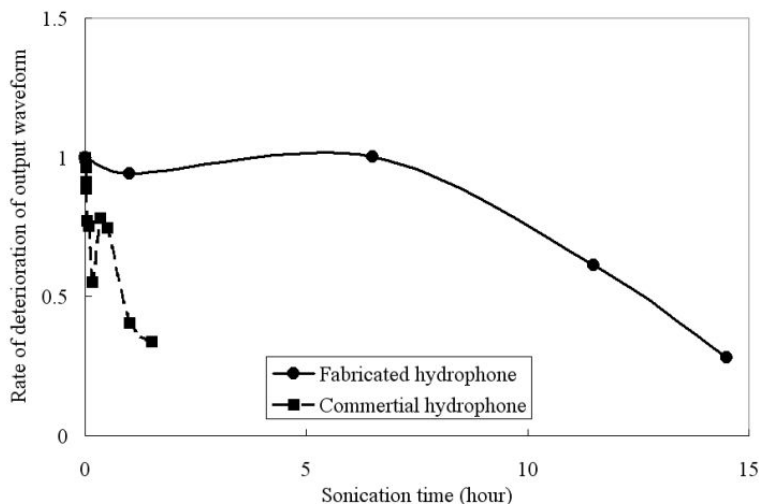
#### Statement of Contribution/Methods

The durability test of our anti-cavitation hydrophone was performed using ultrasound cleaner (22.5 kHz, 48 W) which had the effects of cavitation remarkably. The sound pressure at about 300 mm from surface of the commercial ultrasound probes (Harisonic, 1 MHz to 10 MHz) were investigated to demonstrate non-linear distortion in waveform as compared with the commercial hydrophone.

#### Results/Discussion

As the result of durability test, the electrode (Ti plate) of our anti-cavitation hydrophone was not damaged after continuous 10 hours sonication, which had 10-fold longer lifetime by the commercial hydrophone in figure. However, epoxy resin seal surrounding the edge of Ti front plate was removed from the tip of the hydrophone after sonication of ultrasound cleaner. A robust extracting electrode structure as well as robust Ti electrode was important. As a consequence of the nonlinear observation, the output distortion of the anti-cavitation hydrophone characterized by an adjusting specific acoustic impedance of backing material was compatible with the commercial hydrophone in the frequency ranges from 2.5 MHz to 5.0 MHz.

[1]: N. Okada et al., Proc. IEEE Joint UFFC, EFTF and PFM Symp., pp. 1121-1124, 2013.



P5A2-11

**Electronic Radial Scanning Echoendoscope Probe with High Resolution**

Jue PENG<sup>1</sup>, Xiaojian PENG<sup>1</sup>, Hu TANG<sup>1</sup>, Tianfu WANG<sup>1</sup>, Siping CHEN<sup>1</sup>; <sup>1</sup>Department of Biomedical Engineering, Guangdong Key Laboratory for Biomedical Measurements & Imaging, National-Regional Key Technology Engineering Laboratory for Medical Ultrasound, Shenzhen University, Shenzhen, Guangdong, China, People's Republic of

**Background, Motivation and Objective**

EUS is performed with radial imaging perpendicular to the endoscope shaft, and lateral imaging parallel to the shaft and biopsy channel. Radial imaging is preferred for some diagnostic and staging purpose because of ease of use as well as the production of a full 360 degree field of view. In this paper, a EUS probe integrating an 8 MHz radial electrical scanning transducer and a 5 million pixels CMOS camera module is presented.

**Statement of Contribution/Methods**

The radial electrical scanning echoendoscope arrays operating at 8 MHz, with 64 elements and the external diameter less than 10 mm have been fabricated. We used multiple layers of welding wire combined with a poured backing layer to form isolated electrical connections. Aiming at the shortcoming of the existing products, we firstly proposed the idea of auto focus and image stabilization, the main research work include: FPCB design, integration of autofocus and image stabilization motor. On the other hand, a high frequency 64-elements convex 0.7Pb(Mg1/3Nb2/3)O3-0.3PbTiO3 (PMN-PT) single crystal array is also integrated into the compact package for ultrasonic radial scanning.

**Results/Discussion**

The high resolution electronic radial scanning echoendoscope probe with dual functions has been developed as shown in Fig. 1. The high-definition optical vision of over 5 million pixels can be achieved by the forward looking miniature camera modules with auto focus function. The measured center frequency and -6 dB fractional bandwidth of the radial electrical scanning arrays were 8 MHz and 85%, respectively. A two-way insertion loss of -64 dB was obtained at the average center frequency. We also carried out a sound field simulation and measured the actual transmitting (one-way) sound field data by using a hydrophone. According to the specific needs, 360 degree radial view arrays can also be achieved with the same method.



P5A2-12

**Dual-concentric transducer with phase apodization for wide depth of field of high-frequency ultrasound imaging**

Jong Seob Jeong<sup>1</sup>, Sung Min Kim<sup>1</sup>; <sup>1</sup>Medical Biotechnology, Dongguk University, Seoul, Korea, Republic of

**Background, Motivation and Objective**

In general, the length of the depth of field (DOF) is related to the quality of ultrasound B-mode image because the high-performance focusing can be accomplished within the DOF. Typically, under the fixed frequency and aperture size, the length of the DOF can be extended by increasing the focal depth while the intensity at focal point is reduced. This phenomenon is more severe at high frequency ultrasound imaging due to a short wavelength. In this study, we present a dual-concentric transducer combined with phase apodization resulting in the extended DOF maintaining intensity within the DOF range. The performance of the proposed method was numerically demonstrated by Field-II program based on 40 MHz point target and cyst imaging.

**Statement of Contribution/Methods**

A simulated transducer consists of a disc- and an annular-type element with a confocal point. The center frequency of each element is 40 MHz and the overall aperture size is 3 mm. The diameter of the inner element is 2.1 mm considering intensity of each element. Each element in the transducer is connected to two signals with 0° and 180° phases, and all elements are activated simultaneously. The focal point is 6 mm resulting in F-number (focal depth/aperture size) = 2.

**Results/Discussion**

The simulation results showed that two focal zones were simultaneously generated in the axial direction (Figure 1(a)). The total -6 dB axial beamwidths (sum of two DOFs for the near- and the far-lobe) were 1.4 mm which was 40 % longer than the single element transducer (1 mm). Figure 1(b) and (c) display the point target simulation results for a conventional single element and a dual-concentric transducer, respectively. A slightly low intensity part at the focal point in Figure 1(c) was removed by employing a compound scheme, i.e., combination of a single element and a dual-concentric transducer with phase apodization mode (Figure 1(d)). Through this simulation, we found that the signal to noise ratio of the near-/far-field region of the proposed method was higher than the single element transducer as shown in Figure 1. Our preliminary simulation results show that the DOF can be increased by using a dual-concentric transducer with phase apodization. Thus, if the target movement is not fast, the proposed method may be a potential method to improve the quality of the high frequency imaging.

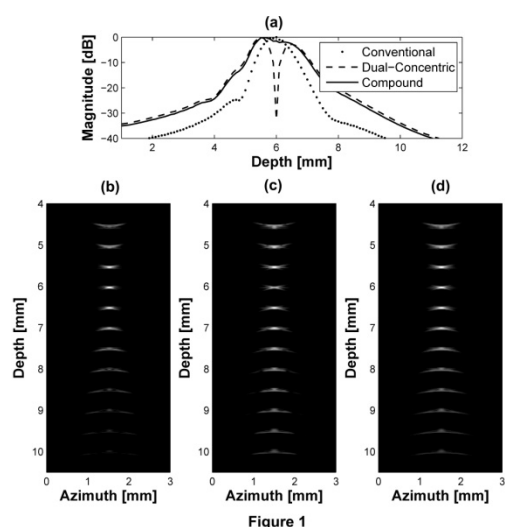


Figure 1

P5A2-13

### Pulse Pressure Sensor Based on Flexible Piezoelectric PZT Thick-Film Composite Device

Rongjie Liang<sup>1</sup>, Qing-Ming Wang<sup>1</sup>; <sup>1</sup>Mechanical Engineering and Materials Science, University of Pittsburgh, USA

#### Background, Motivation and Objective

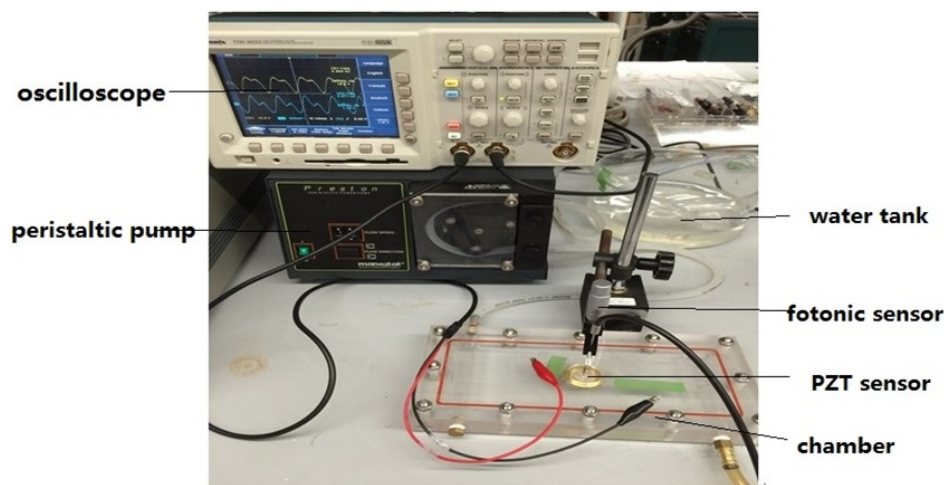
Piezoelectric devices have been used for dynamic pressure sensing and other electromechanical applications. Highly sensitive and flexible piezoelectric sensors are preferred for pressure monitoring in biomedical diagnostics. Flexible piezoelectric pulse pressure sensors based on PVDF, and AlN or ZnO thin films have already been investigated. Compared with above materials, PZT ceramic has much higher dielectric permittivity and larger piezoelectric coefficients, but its stiff and brittle characters make it unfeasible for flexible piezoelectric sensors. Recent development in the fabrication of thick-film PZT ceramic with thickness down to 10  $\mu\text{m}$  using tape-casting processing makes it possible for the design and fabrication of flexible piezoelectric composite sensors. In this study, we investigated the response of thick-film PZT composite sensors for pulse pressure monitoring, mimicking the diagnostic test of human blood pulse pressures.

#### Statement of Contribution/Methods

The circular PZT thick film unimorph was used in this study as pressure sensor. The sensor structure consists of a PZT layer bonded to a thin metal or polymer substrate layer. A flow chamber with one sensor mounting port, one inlet and one outlet port was formed. A peristaltic pump was used to generate pulse flow with different dynamic pressures. During measurement process, pulsed flow entered the chamber through the inlet port, passed the flow channel, providing a pulse pressure onto the piezoelectric PZT sensor. The PZT device is deformed, generating charge on the PZT surfaces and thus the open-circuit voltage can be measured. In order to enhance the flexibility of the sensor, polyimide film was used as substrate layer for thinner PZT film (less than 20  $\mu\text{m}$  in thickness). Compared with PZT thick film sensor with metal substrate, this type can be deformed larger with low pressure loading, resulting in high sensitive monitoring for human blood pulse pressure.

#### Results/Discussion

The output voltage data of sensor under different pulse pressure was recorded. Theoretically, these sensors would have a linear voltage- pressure relationship within a pressure range, while the experimental results exhibit small variations which may result from the turbulent flow wave and other parasitic factors. The sensitivity of these sensors can be improved by optimal design of the pressure sensor and the test setup.





P5A2-14

**Multi-mode Langevin transducers for  $\pi$ -shaped ultrasonic motor with multi-degree of freedom.**Takaaki Ishii<sup>1</sup>, Seiya Mochizuki<sup>1</sup>, Tsuyoshi Shimizu<sup>1</sup>; <sup>1</sup>Mechatronics, University of Yamanashi, Kofu, Yamanashi, Japan**Background, Motivation and Objective**

The motors with multi-degree of freedom are strongly needed in robotics and other applications. We had proposed the  $\pi$ -shaped ultrasonic motor with multi-degree of freedom using four multilayered piezoelectric actuators (Fig. 1). It has several advantages such as simple structure and small in size, however, the adhesive degradation and high cost of multilayered actuators are the next subjects. In this report, bolt-clamped Langevin transducer with segmented electrodes is designed and fabricated to excite not only longitudinal vibration mode but also bending vibration modes (Fig. 2). The disadvantages are overcome by using this transducer. The diameter of the transducer is 15 mm (Fig. 3). The structure, driving principle and application of the transducer are discussed.

**Statement of Contribution/Methods**

The electrode of PZT element used for this transducer is segmented into four as shown in figure 2. Longitudinal vibration mode can be excited by applying in phase voltage to all of the segmented four electrodes. Bending vibration mode can be excited by applying out of phase voltage to the diagonal electrodes. The four multilayered piezoelectric transducers can be replaced by the two multi-mode Langevin transducers. These transducers are bolted to the elastic body made of duralumin (Fig. 4). The  $\pi$ -shaped ultrasonic motor with multi-degree of freedom using multi-mode Langevin transducers is successfully obtained.

**Results/Discussion**

The operation of the prototype  $\pi$ -shaped motor was successfully confirmed for the first time. The detailed motor characteristics are the future work.

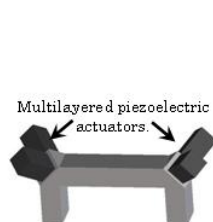


Fig. 1 Schematic illustration of the  $\pi$ -shaped ultrasonic motor with four multilayered piezoelectric actuators.

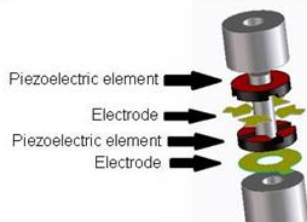


Fig. 2 Schematic illustration of the proposed Langevin transducer with novel structure.



Fig. 3 Picture of the proposed Langevin transducer.

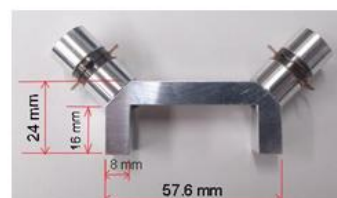


Fig. 4 Picture of the  $\pi$ -shaped ultrasonic motor with multi-mode Langevin transducers.

P5A2-15

**Fabrication and Characteristics of Inversion Layer LiNbO<sub>3</sub> for High Frequency Ultrasound Transducers**

Zhitian Zhang<sup>1</sup>, Chao Zhang<sup>2</sup>, Jin Chen<sup>3</sup>, Qifa Zhou<sup>4</sup>; <sup>1</sup>Research Institute of Tsinghua Univ., China, People's Republic of, <sup>2</sup>Research Institute of Tsinghua University, China, People's Republic of, <sup>3</sup>Tsinghua University, China, People's Republic of, <sup>4</sup>University of Southern California, USA

**Background, Motivation and Objective**

High frequency broadband ultrasonic transducers are required for high resolution imaging. Recently, it's reported that the inversion layer transducers with even harmonic frequencies can increase the bandwidth of the transducers and presented good performance for broad bandwidth transducer design. Previous studies have found that the ratio of inversion layer in LiNbO<sub>3</sub> plate depends on the process conditions, such as heating temperature and time. However, the fabrication and characteristics of the LiNbO<sub>3</sub> inversion layer have not been studied systematically, so that it is hard to get the appropriate inversion layer materials for transducers. In this paper, we studied the relationship between the ratio of LiNbO<sub>3</sub> inversion layer plate and its thickness, process conditions. The impedance characteristics of these inversion layer devices are also studied.

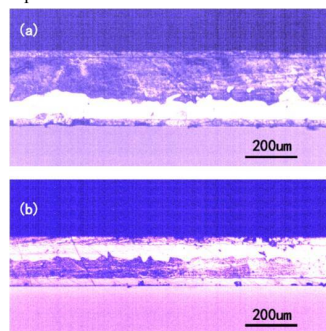
**Statement of Contribution/Methods**

Several lithium niobate plates with the thickness of 0.1mm, 0.2mm, 0.3mm, 0.4mm and 0.5mm are fabricated. The heating temperature and time for each thickness plate vary from 1100 to 1140 degrees Celsius and 2 to 20 hours. After the heating process, the domain structures in the cross section along the thickness direction of these plates are observed by the optical microscope after etching process. The resonance impedances of these devices are characterized and compared. Fig.1 shows the etched cross section of the planar inversion layer plate with different thickness of 0.3mm and 0.2mm which have been annealed for 15 hours at 1120 degrees Celsius.

**Results/Discussion**

For the 0.3mm thickness plate in Fig. 1(a), the inversion layer boundary of the two major domains doesn't reach the median plane of the plate. The boundary is uneven and small isolated domains can be seen near it. For the 0.2mm thickness plate in Fig. 1(b), the inversion layer reaches the median plane but is still ragged.

This study shown that the ratio of inversion layer plates depend on the thickness, heating temperature and time of the plate. Systematic analysis will be presented. The resonant impedance characteristics of these inversion layer devices will also be analyzed.





## Results/Discussion

We have demonstrated a modular approach, which at the prototype stage began with a single 64-channel (3:1 mux to 192-element) unit, and was scaled up to a system with thousands of channels in a matter of a few months. This flexibility and performance optimized development resources, which could be focusing on the final product features without significant re-engineering of the initial prototype approach. Beyond the hardware capabilities, other factors that came into play during the scale up process included image quality and software scalability. Because of the stability of the hardware platform in terms of clock jitter, image quality was maintained as the channel count and transducer/beamformer complexity grew. Further, a flexible application program interface (API) that was also scalable became a key factor in maintaining the development schedule. Detailed system “tuning” became the final factor in achieving the requisite clinical performance. Example images from the system during its development from prototype to successful clinical trials will be shown, showing a range of system configurations and channel counts.

## 1D-3

### 8:30 am Tri-modality Ultrasound Imaging System: Design and Phantom Experiment Results

Man Nguyen<sup>1</sup>, Jaesok Yu<sup>1,2</sup>, Xuan Ding<sup>1,2</sup>, Daewoo Park<sup>1</sup>, Francois Yu<sup>1</sup>, Kang Kim<sup>1,2</sup>; <sup>1</sup>Center for Ultrasound Molecular Imaging and Therapeutics & Heart and Vascular Institute, University of Pittsburgh Medical Center, Pittsburgh, Pennsylvania, USA, <sup>2</sup>Bioengineering, University of Pittsburgh, Pennsylvania, USA

## Background, Motivation and Objective

Recent developments of ultrasound imaging technologies allow assessing tissue changes in morphology, composition, functional and mechanical properties. These include shear wave imaging (SWI) – providing mechanical properties, thermal strain imaging (TSI) - detecting lipids, and photoacoustic imaging (PAI) – providing structural and functional information based on optical absorption contrast. The co-registered integrated images of these modalities can provide more complete characterization of diseases, such as atherosclerosis and liver steatosis, for improved diagnosis accuracy and yield. This study presents the realization and evaluation of the first noninvasive hybrid ultrasound imaging system that incorporates SWI, TSI, and PAI.

## Statement of Contribution/Methods

A commercial ultrasound open platform (Verasonics) with L7-4 transducer was used to integrate the three imaging modalities. The pulse/imaging sequences were designed for 1) synchronizing the laser (OpoTek) and acquiring RF data for PAI, 2) generating a push-pulse sequence (8 pushes, 1.5 mm axially apart) followed by IQ beamformed data collection at a rate of 8 kHz for SWI, and 3) adaptive heating beam sequence (11 mm axial x 9 mm lateral heated area) with pre- and post-heating IQ beamformed data. One-way delay-and-sum beamforming was used to reconstruct PAI images from 128-channel data. Helmholtz inversion equation was applied to reconstruct shear modulus from displacements estimated by 1D Kasai tracking. Thermal strains were estimated using 2D phase-sensitive speckle tracking. A gelatin phantom, consisting of 5 mm diameter rubber inclusion and 2.5 mm diameter gelatin inclusion mixed with 0.5 uM indocyanine green (ICG), were used to evaluate the system.

## Results/Discussion

The system successfully provides co-registered images from 3 modalities shown in Fig. 1. In TSI (B), a rubber inclusion was detected in thermal strain image with +0.143% strain from gelatin background with -0.035% strain. In PAI (C), photoacoustic signals from ICG dyed inclusion was approximately 15 dB higher than those from background. Finally, SWI (D) successfully identified the stiff inclusion from the gelatin background with average shear moduli of 0.67 kPa and 0.20 kPa, respectively. Further improvements include implementation of a robust shear modulus reconstruction for SWI and larger heated area for TSI.

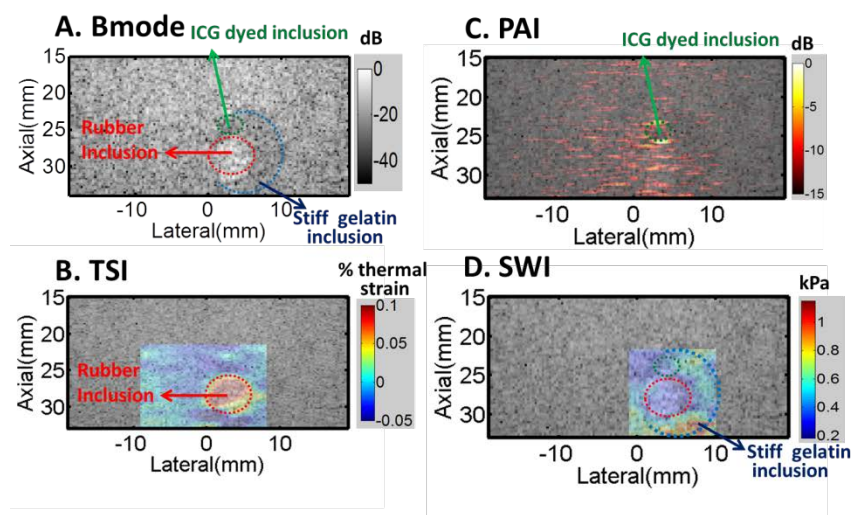


**Fig. 1. Auto-co-registered images obtained from the tri-modality imaging system.**  
A) B-mode  
B) Overlaid thermal strain – Bmode  
C) Photoacoustic  
D) Overlaid shear modulus - Bmode

## 1D-4

### 8:45 am Ultrasound pre-clinical Platform for Diagnosis and Targeted Therapy

Dominique Certon<sup>1</sup>, Mathieu Legros<sup>2</sup>, Dominique Gross<sup>1</sup>, Philippe Vince<sup>3</sup>, Fabrice Gens<sup>3</sup>, Jean-Marc Grégoire<sup>4</sup>, Caroline Coutier<sup>4</sup>, Anthony Novell<sup>4</sup>, Ayache Bouakaz<sup>4</sup>; <sup>1</sup>Université François-Rabelais de Tours, GREMAN, UMR-CNRS 7347, Tours, France, <sup>2</sup>Vernon S.A., Tours, France, <sup>3</sup>Université François-Rabelais de Tours, CETU Althais Technologies, Tours, France, <sup>4</sup>Université François-Rabelais de Tours, Inserm, Imagerie et Cerveau UMR U930, Tours, France, <sup>5</sup>CEA, LETI, MINATEC Campus, Grenoble, France

## Background, Motivation and Objective

Among all targeted drug delivery systems, combining nanocarriers / activation source with a dedicated imaging modality, thermo-sensitive liposomes activated with ultrasound (US) are a very promising approach. In addition, the combination of this delivery system with microbubble mediated sonoporation increases further therapeutic efficiency. Today, despite numerous encouraging results, elaboration of more accurate treatment protocols, with *in vivo* – preclinical validation, is still required. To meet this demand, our group has undertaken the development of a full US platform for diagnosis and targeted therapy dedicated to the preclinical validation of image-guided (20 MHz) / ultrasound-triggered (1-5 MHz) local drug delivery protocols, combined with sonoporation and thermosensitive nanocarriers.

### Statement of Contribution/Methods

The diagnosis/therapy platform is composed of a dual-mode probe [1] constituted of low frequency four 8-elements arrays for therapy located on a semi-cylinder in order to focus US at a distance of 20 mm and a 64-elements high frequency array for imaging. The wafer-bonded cMUT technology [1] was retained to simplify the final packaging and integration step. Note that LF electronic matching circuits and HF preamplifiers are integrated in the probe head.

The heart of the electronic system is a PC-based control and digitization unit associated with an analog electronic module dedicated to high resolution coded US scanning and LF power beamforming. To ensure real-time imaging with dynamic focusing the digitization unit aggregates 16 synchronous 14 bits A/Ds with four Virtex5 FPGA computing cores, and 8-lane PCI Express interface that provide over 1 GB/s to the host. Finally, an IHM software allows the user choosing LF sequences (amplitude, frequency, duty cycle) and monitoring treatment with the help of HF US images.

### Results/Discussion

In order to assess that the performances of the platform match well with specifications, advanced electro-acoustic tests were carried out (see cMUT characterizations in [1]). HF elements were driven with bi-polar signal (20 MHz, 100 Vpp). All received pulse-echo signals were similar, showing a good homogeneity: the mean center frequency was 17 MHz, the -6 dB fractional bandwidth was 80 %, and the SNR was 50 dB. For the LF function, focusing tests were carried out with a CW at 1 MHz (30 Vpp, duty-cycle 50 %, 1 kHz). The electronic matching integrated in the head of the probe allows obtaining at the end of the connection cable 100 Vpp. Maximum peak-to-peak pressure amplitude of 1.5 MPa was measured. From 3D pressure field cartography, the volume defined at -3 dB was assessed to  $5 \times 5 \times 5 \text{ mm}^3$ , which agrees with typical size of tumor developed for preclinical validation.

All electro-acoustics tests were successfully achieved with regards of expected performances, heating and HF preclinical imaging tests are now currently in progress.

[1] D. Gross *et al.*, submitted to 2014 IEEE IUS

### 1D-5

---

#### 9:00 am GPU Enabled Ultrasound Imaging Innovations

Alfred C. H. Yu<sup>1</sup>, Billy Y. S. Yiu<sup>1</sup>, Adrian J. Y. Chee<sup>1</sup>; <sup>1</sup>Medical Engineering Program, The University of Hong Kong, Pokfulam, Hong Kong

#### Background, Motivation and Objective

As a rapidly maturing class of many-core parallel computing hardware, graphics processing unit (GPU) has enjoyed a surge of interest in the medical ultrasound community in recent years. In particular, the software-level programmability of GPUs has significantly lowered the entry barrier for ultrasound imaging researchers (who might not be parallel computing specialists) to pursue fast realization of novel imaging algorithms that have known theoretical potential but whose real-time feasibility has yet to be demonstrated because of their high computational complexity. This presentation will give an overview of how GPUs have emerged as a new computing workhorse in realizing various ultrasound imaging innovations.

#### Statement of Contribution/Methods

The practical merit of GPUs in ultrasound imaging will be demonstrated through various case examples that range from beamforming to flow visualization. First, we will present how GPUs can enable fast execution of beamforming operations in broad-view ultrasound imaging based on point-source transmissions or plane wave excitation. Coverage will include both the conventional delay-and-sum approach and the more recent adaptive apodization method based on minimum variance optimization. Algorithmic parallelization considerations and power consumption issues will be described, and their practical efficacy will be demonstrated through bivariate analysis that includes image quality metric. Next, we will highlight the feasibility of leveraging GPUs for a range of advanced flow imaging innovations. These new solutions essentially require high-speed processing in the slow-time domain, including Doppler frequency and power estimation, vector estimation, and eigen-based clutter filtering.

#### Results/Discussion

Using the state-of-art GPU technology, it is readily possible to achieve >1,000 fps processing throughput. Also, this performance can be readily scaled by simply hosting more GPU devices on the same platform, as long as the associated power demand is met. With the use of GPUs, we can anticipate that the pace of translating various ultrasound imaging innovations from theory toward practice can be bolstered and accelerated. These will be important to expand the current role of ultrasound imaging in clinical diagnostics.



## 2D - MBF: Vector Velocity Techniques

Waldorf

Friday, September 5, 2014, 8:00 am - 9:30 am

Chair: **Hans Torp**  
Univ. of Science and Technology, Trondheim

2D-1

### 8:00 am Vector Projectile Imaging (VPI): A New Tool for Dynamic Visualization of Complex Flow Fields

Billy Y. S. Yiu<sup>1</sup>, Alfred C. H. Yu<sup>1</sup>; <sup>1</sup>Medical Engineering Program, The University of Hong Kong, Pokfulam, Hong Kong

#### Background, Motivation and Objective

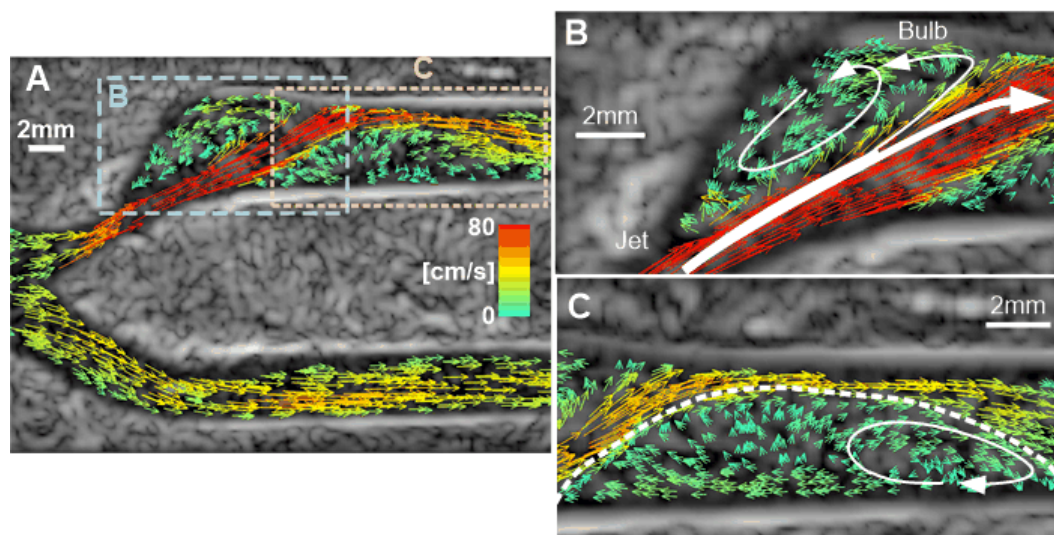
Using ultrasound to visualize complex flow is known to be challenging. Two practical vascular flow conditions must be accounted for: (i) at a given time instant, flow speed and direction (i.e. the flow vector) may vary spatially in tortuous vessels; (ii) over a cardiac cycle, flow would deviate temporally due to pulsatile behavior. Hitherto, it has been difficult to use color flow imaging to visualize these flow patterns intuitively. Here, we have developed a new technique called vector projectile imaging (VPI) that can dynamically render complex flow dynamics over an imaging view at millisecond time resolution.

#### Statement of Contribution/Methods

VPI is founded upon three principles: (i) high-frame-rate broad-view data acquisition (steered plane wave firings); (ii) flow vector estimation derived from multi-angle Doppler analysis (with data regularization and least-squares fitting); (iii) dynamic visualization of color-encoded vector projectiles (flow speckles displayed as adjunct). For proof of concept, VPI has been implemented on a research scanner with SonixTouch transmit core, SonixDAQ pre-beamform data acquisition tool, and a GPU processor (for flow processing). A configuration with three Tx angles (−10, 0, +10 deg) and three Rx angles (−10, 0, +10 deg) was realized (10 kHz PRF; 5 MHz freq; 3-cycle pulses). Its performance was first assessed on a multi-vessel phantom with three tubes of differing depths (1.5, 4, 6 cm), angles (−10, 0, 10 deg), and sizes (2.2, 4.4, 6.3 mm diameter; 2.5 ml/s steady flow rate). VPI cineloops were then generated on anthropomorphic flow models of stenosed carotid bifurcation (fabricated via lost-core casting; PVA as tissue mimic).

#### Results/Discussion

In the multi-vessel calibration test, VPI showed that it can consistently derive flow vector estimates that resembled the theoretical profile. Moreover, in a bifurcation with 50% eccentric stenosis at the internal carotid artery (ICA) inlet, VPI vividly highlighted the flow jet emerging from the stenosis site and its trajectory (Fig A) (time resolution: 2.4 ms). Also, it enabled time-resolved observation of multiple flow disturbance zones in the ICA (Figs B & C). These results show that VPI can achieve time-resolved vector visualization of multi-directional and spatiotemporally varying flow patterns within curvy vasculature under pulsatile flow conditions.



2D-2

### 8:15 am In-vivo Convex Array Vector Flow Imaging

Jørgen Arendt Jensen<sup>1</sup>, Andreas Brandt<sup>2</sup>, Michael Bachmann Nielsen<sup>2</sup>; <sup>1</sup>Dept. of Elec. Eng., Technical University of Denmark, Lyngby, Denmark, <sup>2</sup>Department of Radiology, Rigshospitalet, Copenhagen University Hospital, Copenhagen, Denmark

#### Background, Motivation and Objective

Transverse oscillation vector flow imaging (VFI) can be used for visualizing the complex flow in the human circulation without angle compensation to yield the correct velocity magnitude. Currently it is restricted to peripheral vessels due to the employment of linear array probes. The field of view in VFI can be increased by using convex array transducers and this paper presents the first in-vivo VFI scans obtained from the abdomen of human volunteers.

#### Statement of Contribution/Methods

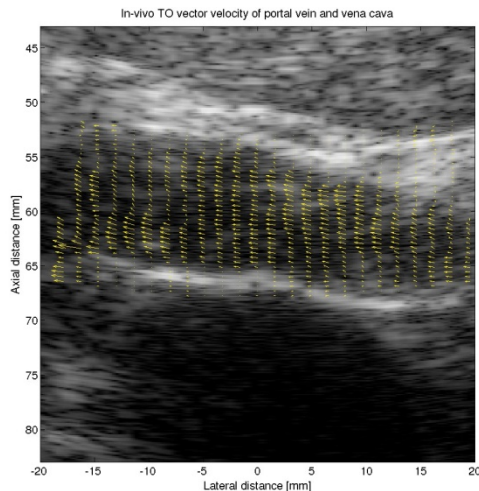
A 3 MHz BK Medical 8820e (Herlev, Denmark) 192 elements convex array probe is used with the SARUS scanner. A sequence with a 129 lines B-mode image is followed by a VFI sequence in 17 directions with 32 emissions in each direction. The B-mode image is focused at a depth of 42 mm with an F# of 2 and a Hanning apodization in transmit. The



VFI emissions are focused at 105 mm with a F# of 5 and uses 64 transmit elements with Hanning apodization. Four elements are skipped between each VFI direction. All 192 channels were sampled at a frequency of 35 MHz. The receive apodization consisted of two 32 element wide peaks separated by 96 elements between peaks. This gave a TO wavelength of 2.17 mm at 60 mm in a Field II simulation that yielded a residual left side energy below -20 dB. The pulse repetition frequency was set to 5 kHz, and the intensity and MI were measured with the Acoustic Intensity Measurement System AIMS III (Onda, Sunnyvale, California, USA). The derated Ispta.3 was 79.7 mW/m<sup>2</sup> and MI was 1.32, which are within FDA limits for abdominal scans. The left liver lobe of a 28 years healthy volunteer was scanned with a view of the left portal vein and vena cava inferior. at a frame rate of 7.4 Hz. Thirty frames were acquired giving 4 seconds of data amounting to 14.2 Gbytes. For this volunteer the duration corresponded to roughly 3 heartbeats.

## Results/Discussion

One still frame from the video sequence is shown in the figure. A zoom on the portal vein between depths of 55 to 68 mm was made. Vena cava inferior is situated below the vein. The yellow arrows indicate the velocity direction and magnitude in the portal vein. A consistent motion from right to left and along the vessel boundaries can be seen. Several other scans on two volunteers show similar patterns. This demonstrates the methods ability to measure a lateral velocity in-vivo as a function of time and depth for a convex array image using only 64 active receive elements.



## 2D-3

### 8:30 am 3-D Ultrafast Doppler Imaging In Vivo

Jean Provost<sup>1</sup>, Clement Papadacci<sup>1</sup>, Charlie Demene<sup>1</sup>, Olivier Villemain<sup>1</sup>, Juan-Esteban Arango Ossa<sup>1</sup>, Marion Imbault<sup>1</sup>, Jean-Luc Gennisson<sup>1</sup>, Mickael Tanter<sup>1</sup>, Mathieu Pernot<sup>1</sup>; <sup>1</sup>Institut Langevin, ESPCI ParisTech, INSERM U979, CNRS UMR7587, Université Paris 7, Paris, France

## Background, Motivation and Objective

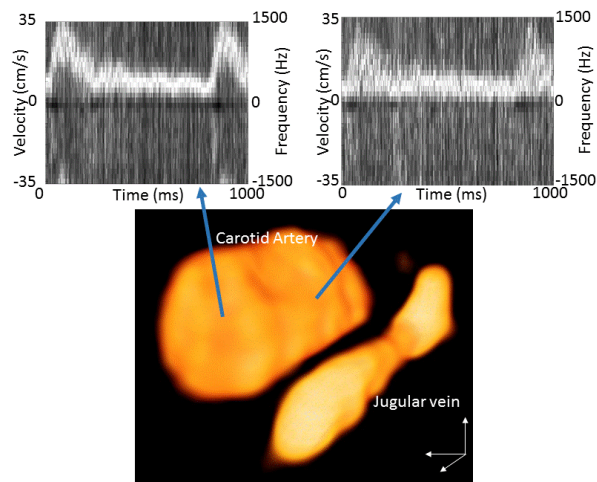
Ultrafast Doppler Imaging was recently introduced as a technique to quantify blood flow in an entire 2-D field of view, expanding the field of application of ultrasound imaging to the highly sensitive anatomical and functional mapping of blood vessels. 2-D imaging, however, has important limitations for real-time mapping of complex 3D vasculatures, e.g in tumor growth monitoring or brain vasculature mapping for functional studies. In this study, we developed 3-D Ultrafast Doppler Imaging, a technique that can produce thousands of ultrasound volumes per second, based on three-dimensional tilted plane wave emissions, and demonstrated its clinical feasibility in human subjects in vivo.

## Statement of Contribution/Methods

A customized, programmable, 1024-channel ultrasound system was designed to perform 3-D Ultrafast Imaging. Using a 32X32, 3-MHz matrix phased array (Vernon, France), volumes were beamformed by coherently compounding successive emissions from several plane waves tilted in 2D. In receive, a conventional delay-and-sum 3-D beamforming was applied on the 1024 elements of the array. The relationship between angle pitch, number of plane waves and the corresponding trade-offs between resolution, contrast and SNR were quantified on an imaging phantom (ATS, 551). The carotid arteries of two subjects were imaged at 3000 volumes/s during one second. The 3000 frames were high pass filtered in order to generate Power Doppler, Pulsed-Wave Doppler, and Color Flow Imaging volumes using a single acquisition.

## Results/Discussion

A configuration of 3 emission tilted plane waves was chosen to optimize the frame rate and the contrast. Figure 1 shows how both the jugular vein and the carotid artery of a healthy subject can be depicted in a 3-D space using a Power Doppler map obtained using three sources at infinity. Additionally, since the entire volume was acquired 3000 times per second during an entire cardiac cycle, the Pulsed-Wave Doppler spectrum for each individual voxel could be depicted, along with Color Flow Imaging. This study demonstrates that 3-D Ultrafast Imaging can be used to quantitatively map flow at high frame rates in an entire 3-D field of view in humans in vivo.



2D-4

**8:45 am Robust angle-independent blood velocity estimation based on multi-angle speckle tracking and vector-Doppler**

Solveig Fadnes<sup>1</sup>, Ingvild Kinn Ekroll<sup>1</sup>, Siri Ann Nytnes<sup>1,2</sup>, Hans Torp<sup>1</sup>, Lasse Lovstakken<sup>1</sup>; <sup>1</sup>MI Lab and Department of Circulation and Medical Imaging, Norwegian University of Science and Technology, Trondheim, Norway; <sup>2</sup>Department of Pediatrics, St. Olav's University Hospital, Trondheim, Norway

**Background, Motivation and Objective**

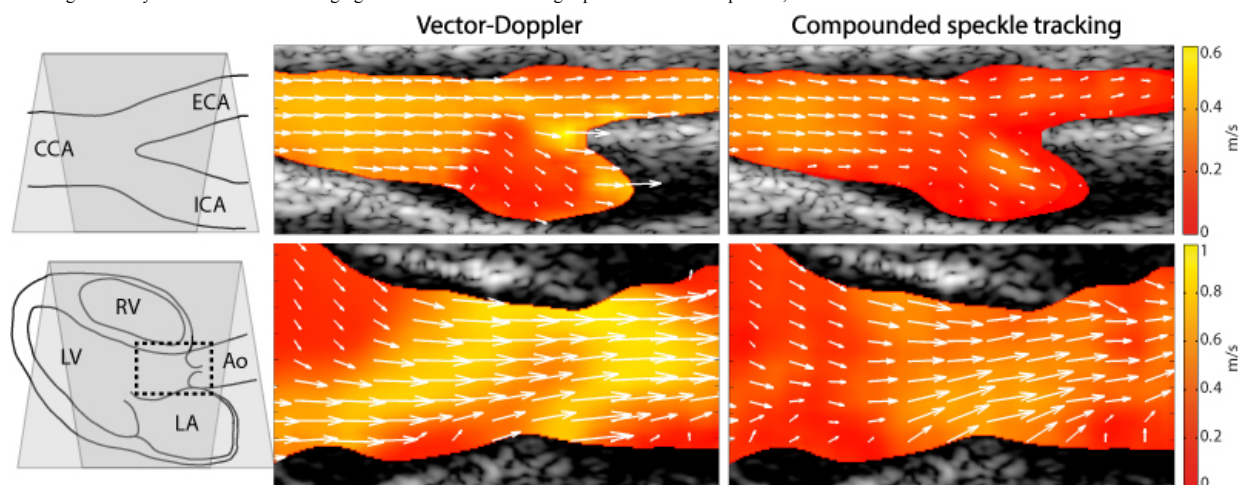
Two-dimensional blood velocity estimation based on speckle tracking (ST) or vector-Doppler (VD) has shown potential for solving the angle-dependency limitation in ultrasound Doppler imaging. Clutter filtering is, however, still required and currently leads to drop-outs and biased velocity estimates for near-perpendicular beam-to-flow angles and/or low flow velocities. In result, these approaches are not truly angle-independent which may limit the final clinical applicability. In this work we investigate if multi-angle plane wave imaging where unfocused pulses at different steering angles may be used to ensure that a minimum blood velocity is measurable for any blood flow angle.

**Statement of Contribution/Methods**

A dual-angle plane wave imaging sequence steered at  $\pm 10$  deg. was utilized to compare ST and VD for 2-D velocity estimation. As only a single scan angle is required for ST, a second oppositely steered scan can be used to increase robustness. Simulations of a rotating phantom were used to compare the statistical performance of the single-angle ST, compounding ST and VD estimator for all beam-to-flow angles and a span of velocities (0-20 cm/s). Further, *in vivo* images from a healthy carotid artery and a neonatal heart were used to investigate the potential benefit of multi-angle imaging.

**Results/Discussion**

In a challenging region in the filter transition band, simulations revealed a relative bias and RMS error for the absolute velocity estimates to be 22% and 4 cm/s for the single-angle ST, 10% and 2 cm/s for compounding ST, and 37% and 6 cm/s for VD. While VD suffered from large overestimation, ST provided consistent velocity estimates for approximately all beam-to-flow angles, but with significantly increased variance for perpendicular flow (low SNR). These observations were confirmed *in vivo* for flow in a carotid artery bifurcation and the left ventricular outflow tract of a neonate (see figure), where the most consistent blood flow depiction was observed for the compounded ST estimates throughout the cardiac cycle. Increased robustness may be achieved for both VD and ST by adding additional scan angles at the expense of a reduced Doppler PRF. However, dual-angle ST may be of benefit in the imaging of conditions where a large span of velocities is present, such as in stenotic arteries and some cardiac abnormalities.



## 9:00 am Intraventricular Blood Flow Vector and Streamline Imaging Using High Frame Rate Cardiac Ultrasound

Hiroki Takahashi<sup>1</sup>, Hideyuki Hasegawa<sup>1</sup>, Hiroshi Kanai<sup>1</sup>; <sup>1</sup>Tohoku University, Sendai, Miyagi, Japan

## Background, Motivation and Objective

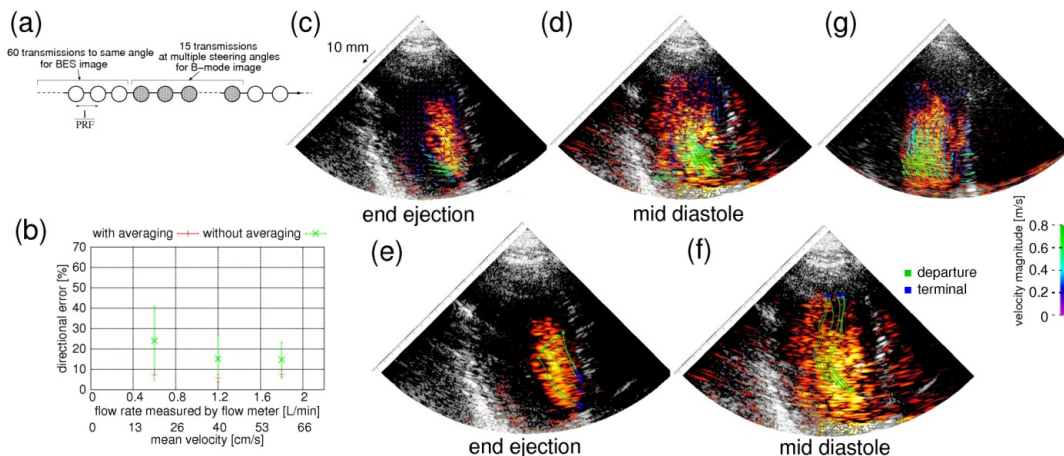
We have studied imaging of blood echo speckle (BES) in the heart with high frame rate echocardiography (HFR-EC), which visualize qualitative blood flow pattern and vector flow velocity without any contrast agents [H. Takahashi, et. al., 2013 IEEE Ultrason Symp Proc]. In the present study, we proposed a method for robust vector estimate using motions of BESs with speckle tracking (ST) technique. The feasibility of the proposed method for blood flow streamline imaging was examined.

## Statement of Contribution/Methods

BESs, which were enhanced by high-pass-filtered echo signals, were obtained at a very HFR of 6 kHz using one diverging beam (DB) from a virtual point source placed at 50 mm behind the probe surface (i.e., snapshot). In the present study, 241 focused receiving beams were created for each transmission. A two dimensional correlation function (2D-CF) between two consecutive frames was temporally averaged for 12 times (frames) to obtain stable estimate of blood flow vectors; and the averaged 2D-CF was up-sampled. Streamlines were determined by the 4th-order Runge-Kutta method using estimated flow vectors. To obtain B-mode with better image quality, 15 plane wave emissions with angular intervals of 6 degrees and compounding were interleaved every 60 transmissions for BES imaging as shown in Fig. (a).

## Results/Discussion

Figure (b) shows directional errors in velocity vectors estimated by ST from the direction of a tubular flow of 56 degree under steady flow of blood mimicking fluid in a tissue mimicking phantom. As shown in Fig. (b), the error was reduced by ST with averaged 2D-CFs. Figures (c)-(f) show BES images (hot-scale) with flow velocity vectors and streamlines overlaid on B-mode images (gray-scale) in late ejection and mid diastole in transthoracic measurement of a 27-year-old healthy male. The fluxes flowing into and out of cardiac cavity were visualized by flow vectors and streamlines. Figure (g) shows the BES image with B-mode image obtained by the HFR-EC with a coherent factor preserving speckled-echoes [Hasegawa and Kanai, IEEE Trans. UFFC, 2012] in diastole using single DB. The improved HFR-EC shows the number of transmissions for B-mode imaging in the proposed method can be decreased using coherent factor. Intraventricular blood flow vector and streamline imaging was possible using BESs without contrast agents.



## 9:15 am Blood velocity measurement in healthy and diseased carotid arteries by vector Doppler techniques

Matteo Lenge<sup>1</sup>, Daniele Righi<sup>2</sup>, Stefano Ricci<sup>1</sup>, Hervé Liebgott<sup>3</sup>, Piero Tortoli<sup>1</sup>; <sup>1</sup>Information Engineering, Università di Firenze, Firenze, Italy, <sup>2</sup>Heart and vessels, AOU Careggi, Firenze, Italy, <sup>3</sup>CREATIS, Université Lyon 1, Lyon, France

## Background, Motivation and Objective

Vector Doppler (VD) methods are increasingly attractive for the capability of providing angle-independent blood velocity measurements. This may be particularly important in carotid artery peak systolic velocity (PSV) measurements, which are widely used for stenosis assessment. Although several VD techniques have been proposed and validated in vitro, there are few reports on their extensive clinical application. In this study, two VD techniques recently introduced by our lab have been applied to the measurement of PSVs in 22 common carotid arteries (CCAs) and 15 internal carotid arteries (ICAs) of healthy volunteers and of patients with different degrees of stenosis.

## Statement of Contribution/Methods

The Angle tracking [DOI: 10.1016/j.ultrasmedbio.2009.11.004] and the Multigate [DOI: 10.1109/ULTSYM.2013.0164] VD techniques, using the transmission of focused beams and plane waves, respectively, have been implemented in the ULA-OP research system. In both cases, ULA-OP shows in real time the temporal profile of the velocity magnitude in a sample volume which the operator can locate in the B-mode image. The average PSV calculated over the last 5 cardiac cycles is presented as well.

The protocol used for all subjects, besides the application of the two VD techniques by ULA-OP, included the "reference" PSV measurement provided by a commercial echograph. In this case, the peak spectral Doppler frequencies were directly converted to PSVs by the Doppler equation, assuming a flow direction parallel to the vessel walls. An expert sonographer aimed at keeping the same sample volume location (i.e. 2 cm proximal to the bifurcation apex for the CCA and in the point of maximum velocity for the ICA) in all measurements.

## Results/Discussion

The PSVs measured in 22 healthy CCAs by the two VD techniques were very close to each other (according to Bland-Altman [B-A]: average difference: 3.2%, limits of agreement:  $\pm 8.5\%$ ). These values were significantly lower than those obtained by the reference method. Application of B-A to the data of any of the two VD techniques and of the reference method provided a 20-25% average difference with  $\pm 15.4\%$  limits of agreement. In the 15 ICAs, B-A shows even better matching between the vector techniques (average difference 0.4%) with wider range of agreement ( $\pm 13.5\%$ ). The ICA VD velocities were 37% lower than those obtained by the standard method. The range of PSVs measured in 5 stenotic ICAs was 86-115 cm/s with VD, and 110-201 cm/s with the reference method.

The high measurement correlation obtained with the two VD techniques, strengthens their suitability to perform accurate PSV measurements in carotid arteries. The angle independency of VD measurements is of particular value and encourages their thorough clinical application, especially considering that the possible angle uncertainties doubly affect the peak Doppler frequencies (i.e., through the intrinsic spectral broadening, too), increasing the spread of measured PSVs.

## 3D - MPA: Photoacoustics II

Boulevard

Friday, September 5, 2014, 8:00 am - 9:30 am

Chair: **Paul Dayton**  
Univ. North Carolina/NCSU, Chapel Hill

3D-1

### 8:00 am Enhancement of photoacoustic signal using a novel light illumination improvement device: *in vivo* animal study

Jaesok Yu<sup>1,2</sup>, Youngsoo Jung<sup>3</sup>, Jeeun Kang<sup>4</sup>, Sang Goo Lee<sup>5</sup>, Jin Ho Chang<sup>4,6</sup>, Jung-Kun Lee<sup>3</sup>, Kang Kim<sup>1,2</sup>; <sup>1</sup>Center for Ultrasound Molecular Imaging and Therapeutics & Heart and Vascular Institute, University of Pittsburgh and University of Pittsburgh Medical Center (UPMC), Pittsburgh, PA, USA, <sup>2</sup>Bioengineering, University of Pittsburgh, USA, <sup>3</sup>Mechanical Engineering and Materials Science, University of Pittsburgh, USA, <sup>4</sup>Electronic Engineering, Sogang University, Korea, Republic of, <sup>5</sup>IBULE PHOTONICS, Korea, Republic of, <sup>6</sup>Sogang Institute of Advanced Technology, Korea, Republic of

#### Background, Motivation and Objective

A large portion of near infrared (NIR) laser energy is lost at the skin surfaces by reflection, for example 30% of the incident energy reflects off with incident angle of 20°. Retrieving the reflected light and redirecting it onto the skin surfaces will increase the effective excitation energy, resulting in an increased photoacoustic (PA) signal for the same light source without increasing power. Furthermore, the light catcher protects the operator from the exposure of the scattered light, allowing a safe free-hand scanning. In this study, we fabricated a light illumination improvement device, called light catcher, and integrated it into a compact high frequency ultrasound transducer. Using a mouse cancer model, *in vivo* feasibility of the light catcher for PA imaging was demonstrated.

#### Statement of Contribution/Methods

A concave-shape light catcher (D: 25.4mm; H: 15mm) was manufactured with 3D printing technology using water resistant materials. The inner surface of the light catcher was coated with silver, providing a high reflectivity (>95%) at NIR, using low-temperature coating technique. The light catcher assembled with optical fiber bundles was then integrated into a custom-made high frequency array transducer ( $f_c=15\text{MHz}$ , 128 elements, 100um pitch, 14.2mm width) made of single crystal PZN/PT-polymer composites for small animal imaging, which is connected to a commercial ultrasound scanner. A high power, 5 ns-long pulsed Nd:YAG laser tuned at 800nm was used as PA light source.

PA signal intensity and SNR were compared between with and without using the light catcher. For *in vitro* study, a polyethylene tube (ID:280 $\mu\text{m}$ ) filled with indocyanine green (ICG) was embedded in a chicken breast at 10mm depth. For *in vivo* feasibility, SCC-7 carcinoma cells were introduced into a mice. At day 7, ICG was locally injected into the tumor for imaging.

#### Results/Discussion

When using the light catcher, PA signal intensity was increased by 32.0% (59.2 $\pm$ 24.5 vs 78.2 $\pm$ 21.0) and 27.8% (45.8 $\pm$ 7.7 vs 58.6 $\pm$ 9.7) and corresponding SNR was enhanced by 2.3dB (33.2dB vs 35.5dB) and 2.8dB (25.2dB vs 28.0dB) compared to without the light catcher for *in vitro* and *in vivo* study, respectively as shown in Figure 1. In this study, we demonstrated *in vivo* feasibility of the light illumination enhancement device for PA imaging. This device might allow deep tissue PA imaging with improved SNR using the same laser power.

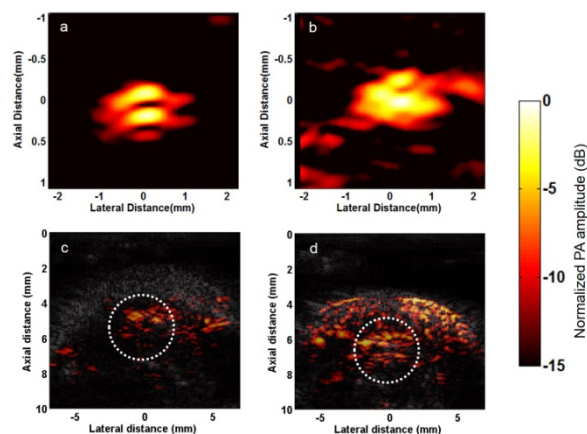


**Figure 1** *In vitro* PA images of a polyethylene tube filled with ICG, embedded in chicken breast a) without b) with the light catcher. *In vivo* PA images of mouse tumor with local injection of ICG c) without d) with the light catcher. The dashed circle indicates the area of ICG injection.

3D-2

### 8:15 am An adaptive-interferometric sensor for all-optical photoacoustic microscopy

Parag V. Chitnis<sup>1</sup>, Harriet Lloyd<sup>2</sup>, Ronald H. Silverman<sup>2</sup>; <sup>1</sup>F. L. Lizzi Center for Biomedical Engineering, Riverside Research, New York, NY, USA, <sup>2</sup>Edward S. Harkness Eye Institute, Columbia University Medical Center, New York, NY, USA

#### Background, Motivation and Objective

Conventional photoacoustic (PA) microscopy involves detection of optically induced thermo-elastic waves using ultrasound transducers. This approach requires acoustic coupling and spatial resolution is limited by the focusing properties of the transducer. We present an all-optical microscopy approach that involves detection of PA-induced surface displacements using an adaptive, two-wave mixing interferometer.

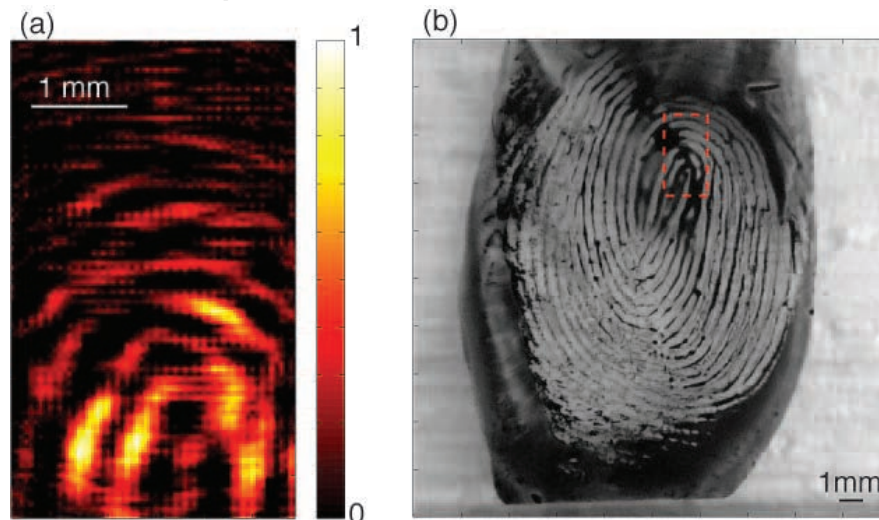


# Statement of Contribution/Methods

The interferometer consisted of a 532-nm, CW laser and a Bismuth Silicon Oxide photorefractive crystal (PRC) that was 5x5x5 mm<sup>3</sup>. The laser beam was expanded to 3 mm and split into two paths using a combination of a half-wave plate, two polarizing beam splitters and a quarter-wave plate. One path was the reference beam that passed directly through the PRC. The other was the signal beam that was focused at the surface through a 100-X, infinity-corrected objective and returned to the PRC, where it interfered with the reference beam to produce intensity modulations that were correlated with surface displacements. The PRC produced a dynamic holographic grating that adapted the wave front of the reference beam to that of the signal beam for optimal interference. A GHz-bandwidth photoreceiver, a low-noise, 20-dB amplifier, and a 12-bit digitizer were employed for time-resolved detection of the surface-displacement signals. The probe was tested by detecting displacements produced on the surface of an impulse excited, 9-μm PVDF film. In combination with a 5-ns, 532-nm pump laser, the interferometric probe was employed for imaging an ink fingerprint on a glass slide. The signal beam was focused at a reflective cover slip that was separated from the fingerprint by 6 mm of acoustic-coupling gel. A 3X5 mm<sup>2</sup> area of the coverslip was raster scanned with 100-μm steps and surface-displacement signals at each location were averaged 20 times. A time-reversal image-reconstruction algorithm produced a PA image of the fingerprint.

# Results/Discussion

The interferometric probe detected sub-nm surface-displacement pulses of the PVDF film at a center frequency of 50 MHz and bandwidth of 70%, which was consistent with the impulse response of a 9-μm film. The reconstructed image of the fingerprint was comparable to its photograph (Fig 1), which demonstrated the ability of the system to resolve micron-scale features at a depth that exceeded 5 mm.



3D-3

# 8:30 am Label-free ultrasound and spectroscopic photoacoustic imaging for the identification of metastatic lymph nodes

Geoffrey Luke<sup>1,2</sup>, Stanislav Emelianov<sup>1,2</sup>; <sup>1</sup>Biomedical Engineering, The University of Texas at Austin, Austin, Texas, USA, <sup>2</sup>Electrical and Computer Engineering, The University of Texas at Austin, Texas, USA

# Background, Motivation and Objective

A critical step after the detection of a primary tumor is to determine the extent to which it has spread. Many tumors initially invade regional lymph nodes en route to distant sites. The current standard of care for detecting this spread is an invasive procedure known as the sentinel lymph node biopsy. Because it is associated with relatively high rates of morbidity, a noninvasive method to detect metastatic lymph nodes could spare thousands of patients from lymphedema and nerve damage. We have developed a method to detect lymph node metastases by measuring the tissue oxygenation throughout the node with spectroscopic photoacoustic imaging.

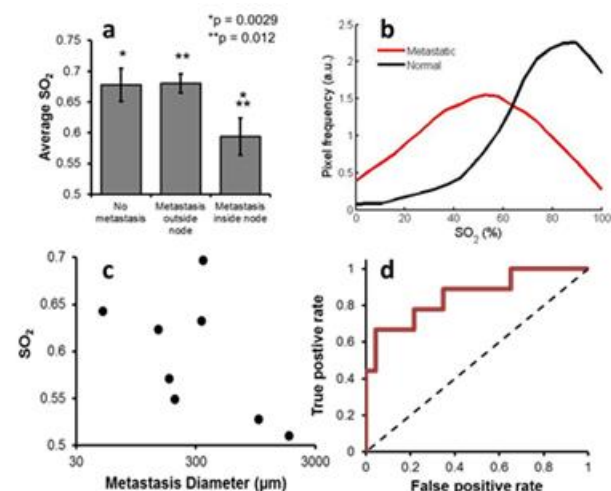
# Statement of Contribution/Methods

We demonstrated our method on an orthotopic metastatic mouse model of oral cancer. Two weeks after inoculation of luciferase-labeled FaDu cells in the tongue of nude mice, metastases developed in 82% of mice. Three-dimensional ultrasound and spectroscopic photoacoustic images of the cervical lymph nodes were acquired using a Vevo LAZR system with a 40-MHz linear array transducer. Photoacoustic images from ten optical wavelengths spanning 680 nm to 860 nm were used for spectroscopic analysis. A linear least squares spectral unmixing algorithm was used to measure the oxygenation of the tissue within each lymph node (as segmented from the ultrasound images).

# Results/Discussion

Analysis of 31 nodes from 15 mice found that lymph nodes harboring metastases showed a marked decrease in the oxygenation throughout the entire node (panel a). In fact, this effect was detectable even when the metastatic colony only inhabited 1% of the entire lymph node volume. Interestingly, the functional changes were present throughout the lymph node (panel b). Furthermore, the tissue oxygenation was inversely related to the size of the metastasis (panel c). Overall, these results present a promising new method for noninvasively detecting the presence of lymph node micrometastases without injections or surgical intervention with high sensitivity and specificity (panel d).





3D-4

**8:45 am Molecular Imaging of Hemoglobin and Lipid Content in Breast Cancer with Multivariate Spectroscopic Photoacoustic Imaging**Katheryne Wilson<sup>1</sup>, Sunitha Bachawal<sup>1</sup>, Lu Tian<sup>2</sup>, Juergen Willmann<sup>1</sup>; <sup>1</sup>Radiology, Stanford University, Palo Alto, California, USA, <sup>2</sup>Health Research and Policy, Stanford University, Palo Alto, California, USA**Background, Motivation and Objective**

An estimated 232,670 cases of breast cancer, the second deadliest in women, will be diagnosed in 2014 in the USA. However, if detected early, typically through mammography and ultrasound (US), mortality decreases by one-fifth. For women with a genetic risk for breast cancer, routine screening begins at an early age even though mammography is notoriously insensitive (30-48% detection) in younger women due to the presence of high density breast tissue, resulting in delayed detection and worse prognosis. Although B-mode US increases detection rate, the positive predictive value is low. Photoacoustic imaging can add molecular information by imaging tissue chromophores. In this study, we explored the potential of spectroscopic photoacoustic (sPA) imaging for quantification of tissue oxygen saturation ( $sO_2$ ), hemoglobin content, and lipid content in order to differentiate among varying breast histologies in a transgenic mouse model of breast cancer development.

**Statement of Contribution/Methods**

To assess the ability of multivariate sPA imaging to aid in detection and diagnosis of breast cancer development a transgenic mouse model for breast cancer development (FVB/N Tg(MMTV/PyMT634Mul) was used to assess tissue characteristics in four breast histologies (normal, hyperplasia, ductal carcinoma in situ (DCIS), and invasive carcinoma). Mammary glands of female mice at varying ages (4-10 weeks) were imaged using the VisualSonics Vevo LAZR, collecting combined ultrasound and photoacoustic data (10 mJ/cm<sup>2</sup> fluence, 700-860 nm, 10 nm increments) using a 25 MHz transducer. Using an in-house spectroscopic data analysis algorithm, the average  $sO_2$ , hemoglobin levels, and lipid content of each gland were calculated. Glands were excised and stained with H&E for histological diagnosis.

**Results/Discussion**

In total, 251 mammary glands were imaged, analyzed, and classified into four histological diagnoses: normal (n=82), hyperplasia (n=14), DCIS (n=96), and invasive carcinoma (n=61). Based on sPA imaging, the oxygen saturation of hyperplasia (50.6%), DCIS (43.0%), and invasive carcinoma (46.2%) significantly increased compared to normal glands (35.5%,  $P < 0.0001$ ), while both total hemoglobin ( $P < 0.01$ ), and lipid content ( $P < 0.0008$ ) significantly decreased with advancing histology. Spectroscopic analysis based on a linear least squares resulted in coefficients of determination ( $R^2$ )  $> 0.96$ , indicating a high degree of model fit. In differentiating normal and hyperplasia from DCIS and invasive breast carcinoma, multiparametric imaging of oxygen saturation, lipid content, and raw photoacoustic signal at 750 nm provided an AUC value of 0.770. Our results suggest that sPA imaging in a transgenic mouse model of breast cancer development is feasible and allows detection of differences in concentration of tissue chromophores among different histologies in a transgenic mouse model of breast cancer development.

3D-5

**9:00 am Magnetomotive photoacoustic/ultrasound imaging using coded magnetic excitation**Chen-wei Wei<sup>1</sup>, Bastien Arnal<sup>1</sup>, Junwei Li<sup>1</sup>, Xiaohu Gao<sup>1</sup>, Matthew O'Donnell<sup>1</sup>; <sup>1</sup>University of Washington, Seattle, Washington, USA**Background, Motivation and Objective**

In previous work, we have shown that magnetomotive photoacoustic (mmPA) imaging can enhance the specificity compared to conventional PA imaging, with background suppression of 2-3 orders. In this study, we propose an advanced generation of mmPA with both PA and ultrasound (US)-based displacement estimates using multi-cycle, narrowband magnetic excitation. With thresholding based on the coherence of the displacement profile with the excitation signal (instead of displacement magnitude), targeted objects with magnetically-induced movement can be isolated from static background or tissue moving incoherently.

**Statement of Contribution/Methods**

HeLa cells (5,000 cells) targeted with magnetic nanoparticle-polymer core-shell particles were fixed in a polyvinyl-alcohol gel and sandwiched between porcine liver tissue to serve as the imaging target. An electromagnet delivers 5-cycle magnetic pulses over the frequency range from 0.5 – 40 Hz and a magnitude of about 0.12 Tesla at a 6-mm distance. Laser pulses at 800 nm illuminates the target at a 20-Hz repetition rate and a fluence of 14 mJ/cm<sup>2</sup>. For mmPA, a linear US array (9 MHz) connected to a Verasonics scanner acquires 440 PA frames while 5-cycle 0.5-Hz magnetic pulses are applied. For US-based displacements, the magnetic excitation increases up to 40-Hz, and the scanner performs ultrafast pulse-echo imaging (1,000 frame/s). Speckle tracking correlates displacements with the magnetic excitation signal to obtain an image mask, which is applied to the original images to reject background signals.

**Results/Discussion**

Fig. 1a shows the conventional PA image (center region, hot scale) integrated with US image (gray scale) of the targeted cells in the phantom. The contrast between the cells and the tissue is -19 dB, indicating that it's impossible to identify the target region. Applying the mask from US-based displacement estimation eliminates background and the contrast

increases to 55 dB (Fig. 1b), with maximal displacement  $< 2 \mu\text{m}$  (Fig. 1c). While US imaging has a higher sensitivity due to a better signal-to-noise ratio, PA-based displacement estimation provides superior specificity since the targeted cells act as both PA and moving sources. Combining PA- and US-based displacement estimations for mmPA with coded magnetic excitation provides a highly sensitive and specific diagnostic tool robust to physiological motion.

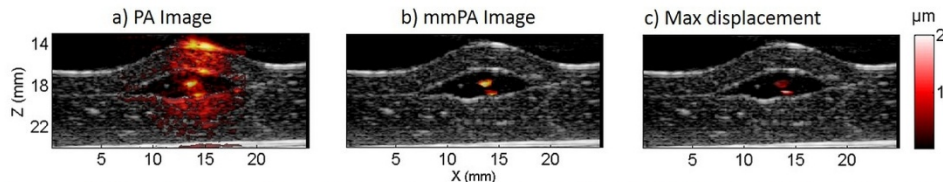


Fig. 1. mmPA using US based displacement measurements. a) PA image. b) mmPA image obtained with a 20 Hz magnetic excitation. c) Maximum displacements.

3D-6

### 9:15 am Longitudinal monitoring of oxygen saturation with photoacoustic imaging: An early, functional indicator of the in vivo efficacy of thermosensitive liposome treatments

Eno Hysi<sup>1</sup>, Jonathan P. May<sup>2</sup>, Lauren Wirtzfeld<sup>1</sup>, Elijus Undzys<sup>2</sup>, Shyh-Dar Li<sup>2,3</sup>, Michael C. Kolios<sup>1</sup>; <sup>1</sup>Physics, Ryerson University, Toronto, Ontario, Canada, <sup>2</sup>Drug Delivery and Formulation Group, Drug Discovery Platform, Ontario Institute for Cancer Research, Toronto, Ontario, Canada, <sup>3</sup>Leslie Dan Faculty of Pharmacy, University of Toronto, Toronto, Ontario, Canada

#### Background, Motivation and Objective

Tumor vasculature has been long thought to play a critical role in providing oxygen to growing tumors. A modality with the non-invasive ability to monitor structural and functional changes longitudinally is highly desirable. We propose using photoacoustic imaging (PAI) to monitor early (hours) and late (days) in-vivo functional changes in tumors treated with a unique thermosensitive liposome (TSL) design by assessing oxygen saturation ( $\text{SO}_2$ ) as an indicator of therapeutic effect.

#### Statement of Contribution/Methods

A TSL called Heat activated cytoToxic (HaT) was designed to deliver doxorubicin (DOX) at mild hyperthermic temperatures ( $42^\circ\text{C}$ ). Its therapeutic effect was tested in 5 BALB/c mice and compared to 2 heated control mice (saline) in EMT-6 tumors subcutaneously grown in the mouse footpad.

Animals were imaged with the Vevo LAZR ultrasound (US) and PA imaging device (Fujifilm VisualSonics, Canada) before treatment (Pre) and 30m/2h/5h/24h/7d post treatment. Co-registered 3D US/PA imaging was performed using a 40 MHz linear array probe coupled to optical fibers (750/850 nm, 30 mJ pulse energy). US images were used to anatomically segment 21 2D tumor regions of interest (ROI).  $\text{SO}_2$  maps based on the PA signal amplitude were computed at every pixel within the ROI. For every frame, the  $\text{SO}_2$  pixel distribution (histogram) and its mode were computed, averaged across all animals and monitored longitudinally.

#### Results/Discussion

As the HaT-DOX treatment progressed, the  $\text{SO}_2$  inside the tumors significantly changed (Fig. 1a) dropping sharply as early as 30m post treatment. The  $\text{SO}_2$  histograms (Fig. 1b) show a clear decrease in oxygenation from pre-treatment levels. The 30%  $\text{SO}_2$  decrease (Fig. 1d) can be attributed to tumor hemorrhage caused by endothelial cell destruction as a result of the rapid and localized increased DOX delivery. Control animals (Fig. 1c) exhibited no significant changes. By 24h,  $\text{SO}_2$  levels for HaT-DOX approached pre-treatment levels and increased by 25% by 7d. Even though the tumor volume of control animals increased 200% in 7d and the  $\text{SO}_2$  appears to increase, no significant changes were observed. HaT-DOX efficacy was highest (i.e. 50% tumor regression) when the tumors exhibited  $> 30\%$  drop in  $\text{SO}_2$  30m post treatment. Such observed variations in tumor oxygenation demonstrate the ability of PAI to assess vascular changes as early predictors of treatment outcome.

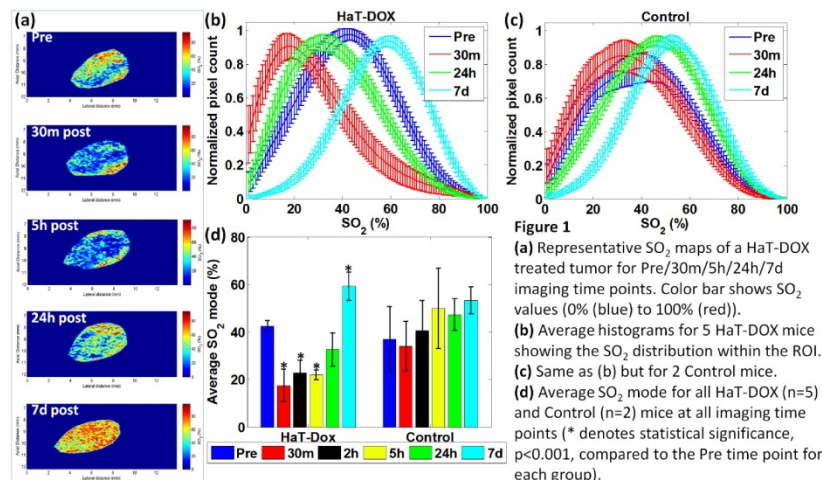


Figure 1  
(a) Representative  $\text{SO}_2$  maps of a HaT-DOX treated tumor for Pre/30m/5h/24h/7d imaging time points. Color bar shows  $\text{SO}_2$  values (0% (blue) to 100% (red)).  
(b) Average histograms for 5 HaT-DOX mice showing the  $\text{SO}_2$  distribution within the ROI.  
(c) Same as (b) but for 2 Control mice.  
(d) Average  $\text{SO}_2$  mode for all HaT-DOX ( $n=5$ ) and Control ( $n=2$ ) mice at all imaging time points (\* denotes statistical significance,  $p<0.001$ , compared to the Pre time point for each group).

**4D - Nde**

Marquette

Friday, September 5, 2014, 8:00 am - 9:30 am

Chair: **James Blackshire**  
Air Force Research Laboratory

4D-1

**8:00 am Monitoring corrosion in plates based on wideband dispersion reversal of Lamb waves: a simulation study**Kailiang Xu<sup>1,2</sup>, Dean Ta<sup>1</sup>, Mingxi Deng<sup>3</sup>, Pascal Laugier<sup>2</sup>, Weiqi Wang<sup>1</sup>; <sup>1</sup>Department of Electronic Engineering, Fudan University, Shanghai, China, People's Republic of, <sup>2</sup>Laboratoire d'Imagerie Biomedicale, Sorbonne Universités, UPMC Univ Paris 06, INSERM, CNRS, Paris, France, <sup>3</sup>Department of Physics, Logistics Engineering University, Chongqing, China, People's Republic of**Background, Motivation and Objective**

Ultrasonic Lamb waves can be used to monitor corrosion and other damages in plate-like structures. However, the dispersion of guided waves always causes waveform temporal spreading and amplitude weakening. While self-focus guided signals can be successfully excited using time reversal, completely removing the mode ambiguity and achieving pure pulse compression remain challenging because of multiple modes existence and mode conversion. This study investigates the use of a novel wideband dispersion reversal (WDR) method to selectively excite a pure mode with the aim to quantify mode conversion and ultimately characterize the corrosion status of steel plates.

**Statement of Contribution/Methods**

Two-dimension finite-difference time-domain (2D-FDTD) simulations were performed using a custom-made software to analyze the propagation of fundamental symmetrical S0 and anti-symmetrical A0 Lamb modes in a 1-mm-thick steel plate over a length of 300 mm. Corrosion region of 100 mm in length and corrosion depth varying from 0.2 mm to 0.8 mm were simulated in the wave path. The WDR A0 signal, calculated from the dispersion function, was time reversed and launched to selectively excite a single A0 pulse. The WDR A0 excitation was centered at 150 kHz with a bandwidth of 300 kHz. The corrosion status was assessed by evaluating the amount of mode conversion reflected by the amplitude and pulse duration of A0 and S0 modes.

**Results/Discussion**

Simulations show that in intact steel plate, a pure A0 mode with short pulse duration of 20  $\mu$ s can be selectively excited using the proposed WDR approach. Without S0 mode overlap, the self-focused A0 pulse presents a good performance to suppress the mode dispersion and environment noise, which inherently simplifies the signal processing, such as mode separation and dispersion compensation. In the corrosive plates, mainly affected by surface discontinuity and thickness decrease, the WDR A0 mode gradually loses energy in mode conversion and spreads in time domain. In the plate with 80% corrosion, the A0 pulse duration extends to 45  $\mu$ s with a 70% amplitude attenuation. In contrast, S0 mode gradually gains energy from mode conversion, when the corrosion degree increases.

In the present work, *a priori* knowledge of the guided dispersion was utilized to synthesize the corresponding WDR excitations, which is able to selectively excite a self-compensated pure mode pulse. The mode ambiguity resulting from multimode dispersion and mode conversion can thus be overcome by the proposed WDR method. The application of WDR technology is capable of enhancing the effectiveness of the classical time reversal procedure in corrosion evaluation and structural health monitoring.

4D-2

**8:15 am Ultrasonic flexural wave responses to debonding at the cement-formation interface of a cased borehole**Xiao He<sup>1</sup>, Hao Chen<sup>1</sup>, Xiuming Wang<sup>1</sup>; <sup>1</sup>State Key Laboratory of Acoustics, Institute of Acoustics, Chinese Academy of Sciences, Beijing, China, People's Republic of**Background, Motivation and Objective**

Cement bond quality is a crucial factor for productivity and security of an oil/gas wellbore. Debonding appeared at the interface between the formation and the cement sheath is hard to be detected using the conventional sonic evaluation methods. Previous studies revealed that the properties of leaky Lamb waves are sensitive to the mechanical features of the concealed interfaces in multilayered structures. In this article, we present the ultrasonic wavefields in a radially-layered cased hole and then reveal the leaky flexural-mode responses to debonding at the outer interface of the cement annulus.

**Statement of Contribution/Methods**

To excite and record Lamb waves of the flexural modes, an inclined pitch-catch sonic system is arranged inside the steel casing. The central frequency of the transducers is 250 kHz. The synthetic wavefields in the layered media are simulated by a finite difference method. Two kinds of models are considered: (a) the cased hole is well bonded; and (b) debonding appears at the cement-formation interface. We also investigate the variation of the flexural wave features with geometrical and physical parameters of the debonding defects according to the numerical simulation results.

**Results/Discussion**

It is found that two groups of flexural waves are prominent in the wavefields. They are the primary wave propagating all along the casing and the secondary mode, which is generated by reflection echoes from the formation. Fig. 1 illustrates a comparison of simulated snapshots of ultrasonic wavefields in a cased borehole at the same moment (150  $\mu$ s). It is revealed that once a fluid-filled channel (denoted by the double white lines in the figure) appears at the cement-formation interface, the energy of the secondary wave will be greatly enhanced compared to that in a well bonded borehole. Furthermore, the amplitudes and arrival times of the secondary waves have definite correlations with the acoustic impedances and thicknesses of the debonding channels, respectively. Hence it is possible to effectively evaluate bond quality at the cement-formation interface by extracting properties of the secondary flexural waves.

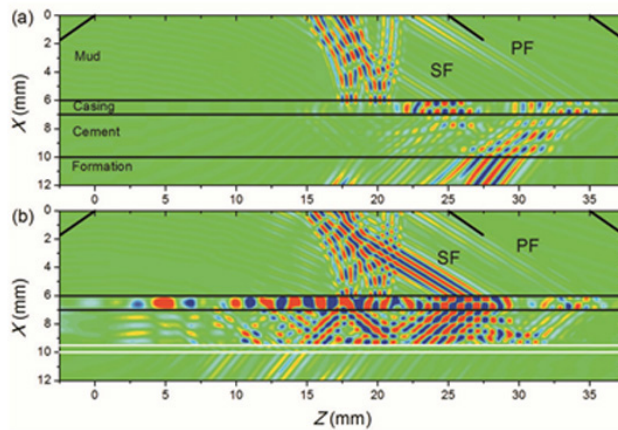


Fig 1. Snapshots of primary flexural (PF) and secondary flexural (SF) waves for the cases of (a) well bonded, and (b) debonding at the cement-formation interface.

4D-3

### 8:30 am Ultrasonic Detection of the Alkali-Silica Reaction in Concrete

Peng Gong<sup>1</sup>, Mark Patton<sup>1,2</sup>, David Greve<sup>3</sup>, Joel Harley<sup>4</sup>, Warren Junker<sup>5</sup>, Irving Oppenheim<sup>1</sup>, Chang Liu<sup>1</sup>; <sup>1</sup>Department of Civil and Environmental Engineering, Carnegie Mellon University, Pittsburgh, PA, USA, <sup>2</sup>Mark Patton Ltd., Murrysville, PA, USA, <sup>3</sup>Department of Electrical and Computer Engineering, Carnegie Mellon University, PA, USA, <sup>4</sup>Department of Electrical and Computer Engineering, Carnegie Mellon University, Pittsburgh, PA, USA, <sup>5</sup>W. Junker Consulting, Pittsburgh, USA

#### Background, Motivation and Objective

Degradation of concrete structures can occur if the concrete contains certain aggregates that react with alkali species in the presence of water, resulting in expansion and cracking of the concrete. Detection of the alkali-silica reaction (ASR) is important for assessing the integrity of concrete structures.

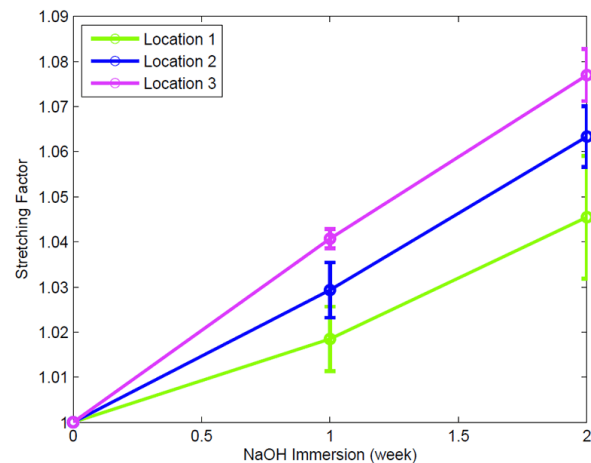
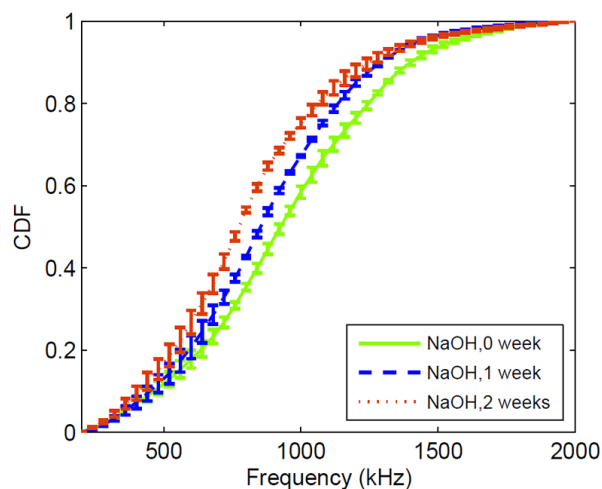
#### Statement of Contribution/Methods

Concrete specimens  $1 \times 1 \times 11.25$  inch and  $4 \times 2 \times 11.25$  inch in size were fabricated using a moderately reactive aggregate. Pitch-catch transient measurements were performed using 1 MHz ultrasonic transducers driven by a RITEC RPR-4000 high power pulser and responses acquired with a National Instruments data acquisition system.

We have explored the detection of ASR damage using two different analysis methods for the analysis of recorded ultrasonic transients. In the first method, which we refer to as the ultrasonic passband method, conventional ultrasonic transducers are used to measure the frequency-dependent attenuation in the 200 kHz- 2.0 MHz frequency range. Exposure to NaOH at 80 °C caused a progressive increase in attenuation at higher frequencies. The cumulative distribution function computed from the frequency-dependent attenuation is particularly revealing of the onset of the reaction. In the second (time-stretching) method, we determine the time stretching factor that provides the best correlation between the transient signals before and after exposure to NaOH. The stretching factor increases monotonically with alkali exposure.

#### Results/Discussion

Two different analysis methods based on ultrasonic pitch-catch transient measurements provide a clear indication of the damage from ASR. Changes in frequency-dependent attenuation can be measured even when resonant transducers are used.





## 4D-4

**8:45 am A new fiber-optic fast laser ultrasound scanner for efficient nondestructive evaluation of aircraft composites**

Ivan Pelivanov<sup>1,2</sup>, Takashi Buma<sup>3</sup>, Jinjun Xia<sup>1</sup>, Matthew O'Donnell<sup>1</sup>; <sup>1</sup>Bioengineering, University of Washington, Seattle, Washington, USA, <sup>2</sup>Moscow State University, Moscow, Russian Federation, <sup>3</sup>Union College, Schenectady, NY, USA

**Background, Motivation and Objective**

Laser ultrasonic inspection with full optical generation and detection of ultrasound represents an attractive, non-contact method to evaluate composite materials. Current systems, however, use laser interferometers with relatively low sensitivity compared to contact piezoelectric detection. These devices are also difficult to adjust, very expensive, and strongly influenced by environmental noise. Here we demonstrate that most of these drawbacks can be eliminated with a new generation of compact, inexpensive fiber lasers, new developments in fiber telecommunication optics, and an optimally designed balanced probe beam detection scheme.

**Statement of Contribution/Methods**

We have designed and built an all-optical pump-probe system for non-contact nondestructive evaluation (NDE) which combines a high repetition rate ( $> 1$  kHz) fiber laser for the generation of ultrasound signals and a Sagnac-based balanced fiber interferometer for ultrasonic pressure detection from the test material surface.

We have demonstrated that B-scan imaging on composite materials can be done in a single shot regime, acquiring each A-line for one laser pulse with a linear scanning speed limited primarily by the scan speed of the translation stage. The ultra-wide frequency band of the interferometer (ultrasound detection from 1 MHz to 10 MHz) enables axial resolution better than 150  $\mu\text{m}$  in B-scans. Large defects, as well as individual layers of the composite structure itself, are clearly visible at high scan rates.

**Results/Discussion**

Fig.1 presents results from a one-dimensional scan of a 19 ply carbon-fiber-reinforced-polymer (CFRP) composite plate (3.5 mm thick) with a very thin tape inclusion embedded in the structure. Each A-line corresponds to one laser shot, i.e. with no averaging. All layers of the composite structure are clearly seen as well as the artificial inclusion (in the round circle).

Given the possibility of a high-resolution, high-speed, compact, and cost-effective laser ultrasonics system based on this technology, NDE of composite structures can be greatly improved not only during manufacturing, but also in the field.

We thank Dick Bossi, Jeff Kollgaard, Bill Motzer, and Jill Bingham at the Boeing Company for help with nearly every aspect of this project, and especially for supplying composite samples.

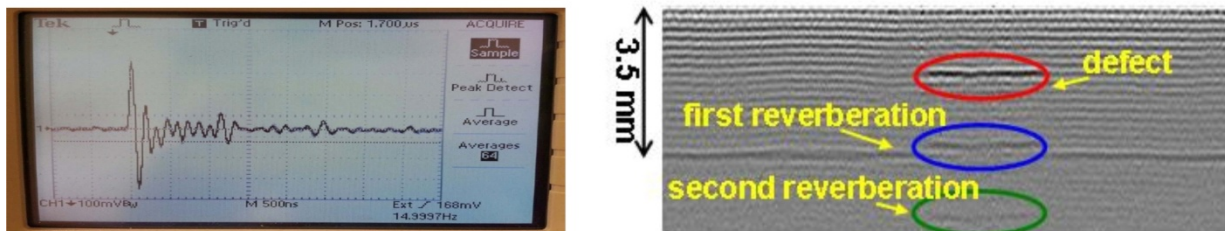


Fig.1. Typical radio frequency (RF) A-Scan (left) and RF B-Scan (right) of the 19 ply (3.5 mm) graphite-epoxy composite acquired with a single shot per A-line. Scanning distance is 30 mm.

## 4D-5

**9:00 am Estimation of consolidation profiles for archaeological ceramics using ultrasonic signature**

Addisson Salazar<sup>1</sup>, Gonzalo Safont<sup>1</sup>, Alberto Rodríguez<sup>2</sup>, Luis Vergara<sup>1</sup>; <sup>1</sup>Institute of Telecommunications and Multimedia Applications, Universitat Politècnica de València, Spain, <sup>2</sup>Communications Engineering, Universidad Miguel Hernández, Elche, Spain

**Background, Motivation and Objective**

The objective of this work is a method to estimate consolidation profiles for archaeological ceramic characterization. The consolidation process consists in injecting a material in the ceramic to preserve it from damage. The proposed method is based on through-transmission ultrasonic inspection that is in general, less costly and the experiments are easier to perform, than the currently used techniques applied in archaeometry. Thus, the consolidation profiles show the evolution of several features extracted from ultrasonic signals measured from pieces with a varying grade of consolidation (using different consolidation products and methods and kinds of ceramics). Considering the profiles obtained from a training database, an automatic recommendation of consolidation method and product can be obtained for new ceramic pieces.

**Statement of Contribution/Methods**

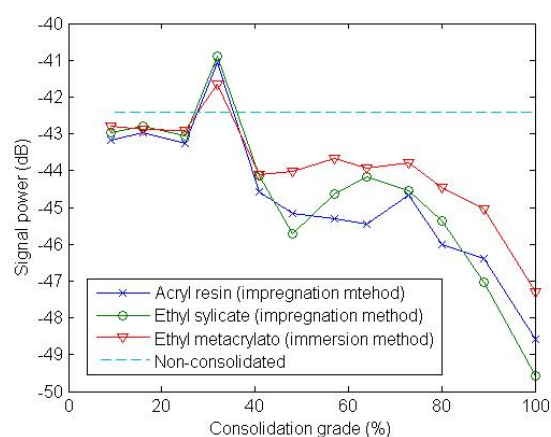
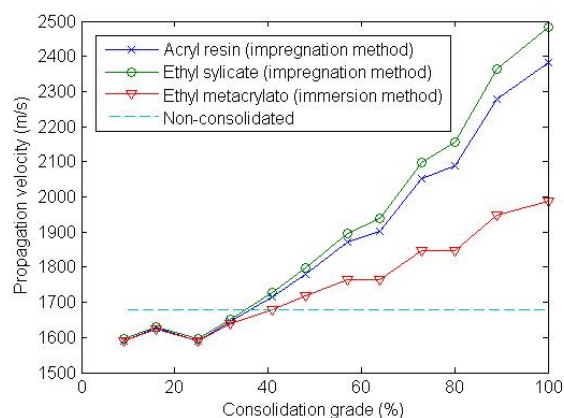
There are relatively few references of the applications of ultrasounds in archaeology that can be roughly organized into the following: imaging, cleaning, flaw detection, and material characterization. Recently, we introduced the ultrasounds for chronological classification of ceramics, but there are no references of a study for obtaining consolidation profiles such as the proposed in this work.

We have considered a linear time variant system approach for modeling the ultrasound-through transmission experiment. Thus, from the perspective of global material characterization into a finite number of classes, we have employed some features that form an ultrasonic signature of the consolidation behavior, e.g., propagation velocity, signal power, and centroid frequency.

**Results/Discussion**

We have demonstrated the suitability of the proposed method for an extensive number of simulated and experimental signals.





4D-6

**9:15 am Microwave-Induced Thermoacoustic Tomography Experimental Study and Hybrid FDTD Modeling**Ryan Jacobs<sup>1</sup>, Xiaoye Chen<sup>1</sup>, Yiming Deng<sup>1</sup>, Mark Golkowski<sup>1</sup>; <sup>1</sup>Electrical Engineering, University of Colorado Denver, Denver, CO, USA**Background, Motivation and Objective**

Ultrasonography is widely used in medical practice as a low-cost alternative and supplement to magnetic resonance imaging (MRI). Although ultrasonography has relatively high image resolution (depending on the ultrasonic wavelength at diagnostic frequencies), it suffers from low image contrast of soft tissues. Microwave-Induced Thermoacoustic Tomography (MI-TAT) is a noninvasive hybrid modality which improves contrast by using thermoelastic wave generation induced by microwave absorption. Samples are irradiated with sub-microsecond electromagnetic pulses inducing acoustic waves in the sample that are then detected with an unfocused transducer. The advantage of this hybrid modality is the ability to take advantage of the microwave absorption coefficients which provide high contrast in tissue samples. This in combination with the superior spatial resolution of ultrasound waves is important to providing a low-cost alternative to MRI and early breast cancer detection methods.

**Statement of Contribution/Methods**

Preliminary research on MI-TAT has been conducted by our group over the past several years; most recently a hybrid finite-difference-time-domain (FDTD) model was developed and validated [1]. In this paper we present an experimental setup that combines both microwave induced ultrasonic wave generation with ultrasonography. We utilize a microwave power supply with 2 kW peak power, 1 microsecond pulse length that radiates at 2.4 GHz and a pulse repetition rate of up to 20 kHz. The sample is contained in an RF shielded safflower oil tank. Acoustic signals are observed using an Olympus 5800PR pulse receiver system.

**Results/Discussion**

The experimental setup is used on samples ranging from tissue phantoms to concrete samples. The concrete samples are used to assess thermoacoustic imaging capabilities for nondestructive testing of structures and/or materials characterization, while the biological phantoms assess the technique for medical applications, including breast cancer. Averaging over several thousand 1-D waveforms for a given position, produced in under a second due to the 20 kHz repetition rate, allows for compensating the relatively low 2 kW peak power compared to other published works. The results show promise for a low cost, non-ionizing imaging system cheaper than MRI and with superior resolution and contrast to pure ultrasound or microwave approaches.

[1] Y. Deng, and M. Golkowski, Innovative biomagnetic imaging sensors for breast cancer: A model-based study, J. Appl. Phys., vol. 111, 2012, pp. 07B323.

## 5D - Particle Manipulation and Acoustic Tweezing 2

Williford A

Friday, September 5, 2014, 8:00 am - 9:30 am

Chair: **Charles Courtney**  
University of Bath

5D-1

### 8:00 am Ultrahigh Frequency Ultrasound and Its applications to Cellular Bioengineering

K. Kirk Shung<sup>1</sup>; <sup>1</sup>Department of Biomedical Engineering, University of Southern California, Los Angeles, CA, USA

#### Background, Motivation and Objective

Although acoustic microscopy at ultrahigh ultrasound frequency (100 MHz – 1 GHz) has been used in non-destructive evaluation of materials and biomedical imaging for decades, its applications in biology and medicine have remained to be limited. The primary reasons are (1) high cost and (2) few advantages over optical microscopy. Biomedical applications of ultrasound at these frequencies other than imaging however have been mostly overlooked. At UHF frequencies, the width of an ultrasound beam is of only a few microns, approaching the dimensions of many cells, hence it may be called “ultrasound microbeam”. Ultrasound microbeam may have many applications in cellular bioengineering. Acoustic tweezer, and acoustic cell sorter are just two examples.

#### Statement of Contribution/Methods

Both sensitive UHF single element transducers and driving and receiving electronics must be developed for the further advance of ultrasound microbeam. Traditionally piezoelectric materials like ZnO and PVDF have been used for UHF transducer fabrication. These materials although possesses a desirable low dielectric constant for single element transducers, have a very serious shortcoming, a very low electromechanical coupling coefficient. In order to improve the performance of UHF transducers, a variety of piezoelectric thin films including PZT and KNN-LSO have been developed and evaluated. Transducers at frequencies as high as 200 MHz have been prepared from these materials, yielding a bandwidth of 30-60%. They have been successfully used for applications in cell-sorting and trapping.

#### Results/Discussion

Preliminary experimental results have been obtained to demonstrate potential cellular applications of ultrasound microbeam. Efforts are now underway to utilize ultrasound microbeam in interrogating intercellular interactions e.g., quantitating intercellular forces and in estimating cellular elasticity and in studying mechanotransduction.

5D-2

### 8:30 am Ultrasonic assembly of short fibre reinforced composites

Marc-S Scholz<sup>1</sup>, Bruce W Drinkwater<sup>2</sup>, Richard S Trask<sup>1</sup>; <sup>1</sup>ACCIS, Department of Aerospace Engineering, University of Bristol, Bristol, United Kingdom, <sup>2</sup>Department of Mechanical Engineering, University of Bristol, Bristol, United Kingdom

#### Background, Motivation and Objective

With acoustic tweezers most commonly applied in the biological and life sciences, designs are generally tailored to, and optimised for the aqueous environment. Nevertheless, some reports of ultrasonically arranged particles cast inside various matrix media – including acrylics, agar, epoxy, polyester, and polysiloxane – can be found.

In this study, we aim to develop and optimise a new type of device that allows for the rapid and repeatable fabrication of thin layers of anisotropic short fibre reinforced composite material. Further, a mechanical characterisation of these samples is carried out.

#### Statement of Contribution/Methods

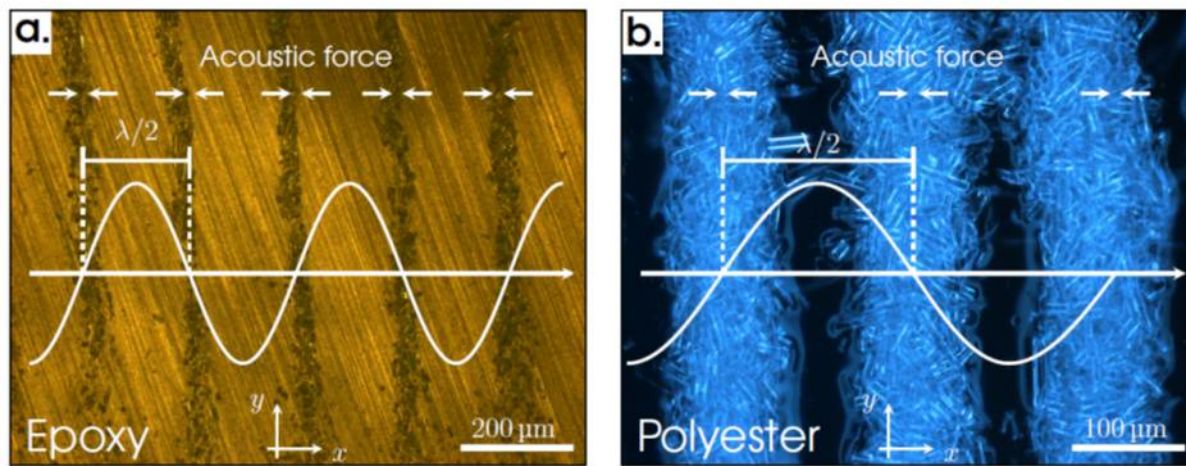
Taking a counter-propagating wave approach, a new type of device was developed to fabricate thin layers of anisotropic material. Both a temperature controlled polymerisation mechanism and a photo-initiator system proved to be suitable for curing. Commercially available, milled glass fibres were used as reinforcement, with a nominal length of 50 µm and approximately 14 µm in diameter. The mechanical response of these ultrasonically formed composites was characterised by mechanical testing.

The effects of various acoustic design parameters were investigated using finite element analysis to both enhance device performance and improve the composite fabrication process. Specifically, the COMSOL Multiphysics package was used to couple together analyses of structural mechanics, piezo-materials, pressure acoustics, and fluid dynamics in a single model. Special attention was paid to the shape and quality of the acoustic standing wave field, the magnitude of the resulting acoustic radiation forces, and the response of fibrous particles to ultrasonic pressure gradients.

#### Results/Discussion

A series of short fibre reinforced composites were manufactured via the above ultrasonic assembly process, using a of the optimised counter-propagating wave device. The test specimens were clearly shown to possess anisotropic mechanical properties, together with a 43% difference in failure stress between principal directions.

The FE optimisation study identified key design parameters to further enhance device performance and improve composite manufacturability. Further, the formation of structurally interesting fibre architectures was explored by studying the possible standing wave patterns in the device's particle manipulation cavity.



5D-3

# 8:45 am Non-linear cavitation cloud oscillations in high intensity focused ultrasound

Keith Johnston<sup>1</sup>, Bjoern Gerold<sup>1</sup>, Sandy Cochran<sup>1</sup>, Alfred Cuschieri<sup>1</sup>, Paul Prentice<sup>1</sup>; <sup>1</sup>Institute for Medical Science and Technology, University of Dundee, Dundee, United Kingdom

## Background, Motivation and Objective

Cavitation driven by intense ultrasound plays a pivotal role in a range of applications, including acoustic cleaning, sonochemistry and as a potential mechanism for therapeutic ultrasound. Optimisation and refinement of cavitation mediated effects require an improved understanding of cavitation behaviour, particularly during the early, formative, stages of evolution in a given acoustic exposure. Here, we report on high-speed observations of non-linear cloud oscillatory response to propagating high-intensity focused ultrasound (HIFU) insonations, across a range of intensities relevant to therapeutic applications.

## Statement of Contribution/Methods

Single cavitation clouds are reproducibly introduced to the focus of a propagating 254 kHz HIFU field, via the laser-nucleation technique [1], at peak-to-peak pressure amplitudes ( $PA_{pp}$ ) from 0.48-1.22 MPa. Cloud dynamics are recorded via high-speed microphotography at  $1 \times 10^6$  frames per second. Parallel acoustic monitoring is undertaken with a custom-fabricated passive cavitation detector (PCD). By way of analysis, cloud dynamics are compared to a single bubble Rayleigh-Plesset model, subject to equivalent acoustic conditions [2].

## Results/Discussion

Cavitation clouds develop rapidly from nucleation, via component bubble fragmentation, and undergo concerted oscillations from  $t \approx 30 \mu s$ . A dark-pixel counting algorithm is implemented to the high-speed image sequences for analysis of oscillatory behaviour, for clouds at each  $PA_{pp}$  investigated. Distinct regimes of non-linear cloud response are identified via the order of the sub-harmonic frequency (to the fundamental driving) at which the cloud oscillates [2, 3], up to  $n f_0/5$  at 1.22 MPa. Comparison to the single bubble model is favourable for selected values of quiescent radius  $R_0$ , in terms of the period of oscillation, fig. 1, for each intensity. The acoustic emissions collected from the clouds, are also directly correlated to the observed physical dynamics. We anticipate that these observations will have significance to applications for which controlled cavitation activity is desirable.

1. Gerold et al (2011) Rev. of Sci. Inst. 82(4) 044902.
2. Gerold et al (2013) New J. of Phys. 15 033044.
3. Lauterborn and Cramer (1981) Phys. Rev. Lett. 47 1445.

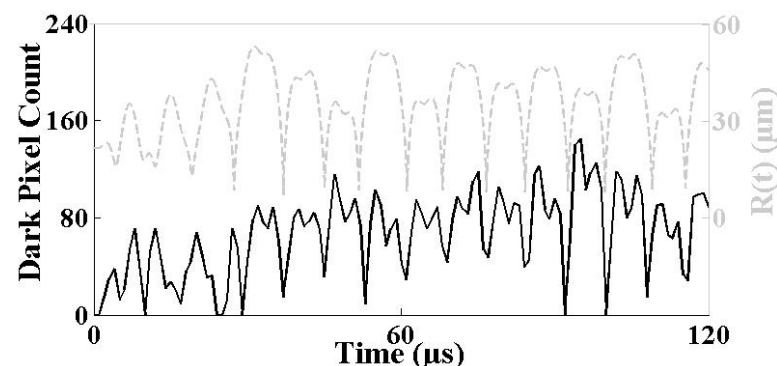


fig. 1, Summed bubble area (black line), representing experimental results of cloud oscillation over time using a dark pixel count algorithm. Rayleigh-Plesset Model (dashed line) represents matching radius time  $R(t)$  curve for a single bubble, selecting  $R_0 = 21.5 \mu m$ ,  $P(t) = 0.48 MPa$ .

## 5D-4

9:00 am **Controlled Live-cell Subcellular Mechanical Modulation by Acoustic Tweezing Cytometry**

Di Chen<sup>1</sup>, Yubing Sun<sup>2</sup>, Yising Hsiao<sup>1</sup>, Madhu Gudur<sup>1</sup>, Ziqi Wu<sup>1</sup>, Jianping Fu<sup>1,2</sup>, Cheri Deng<sup>1</sup>; <sup>1</sup>Department of Biomedical Engineering, University of Michigan, Ann Arbor, Michigan, USA, <sup>2</sup>Department of Mechanical Engineering, University of Michigan, Ann Arbor, Michigan, USA

**Background, Motivation and Objective**

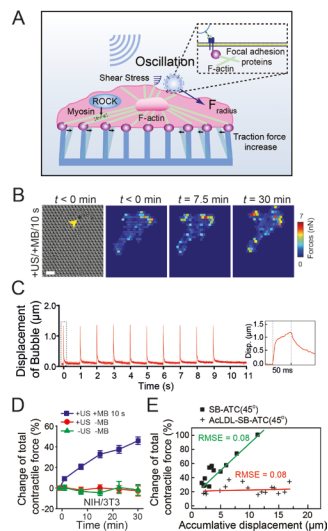
Mechanical stimulation is critical in controlling many important functions of mammalian cells, including cell contractility, gene expression, and even stem cell differentiation. Progress in mechanobiology relies on the availability of effective tools that can apply controllable mechanical forces with a subcellular precision to a large number of live cells for both scientific investigation and translational applications.

**Statement of Contribution/Methods**

We have developed a novel acoustic tweezing cytometry (ATC) utilizing ultrasound-excitable microbubbles targeted to cells capable of generating spatiotemporally controlled subcellular mechanical forces to live single cells. We have demonstrated that by exciting functionalized lipid microbubbles attached to cell integrins with appropriate ultrasound pulses, we can apply subcellular mechanical forces to mechanosensitive cells such as NIH/3T3 fibroblasts. We quantified the contractility of the cells exposed to ATC utilizing an elastomeric micropost array as subcellular live-cell force sensors. The in situ bubble activities during ATC were recorded by high-speed imaging system. A customized algorithm was developed to track the size and displacement of the bubbles to investigate its potential correlation with the cell cytoskeleton (CSK) contractile force response.

**Results/Discussion**

The total CSK contractility of NIH/3T3 fibroblasts with integrin-bound microbubbles increased up to  $148.5\% \pm 3.6\%$  30 min after exposed to ATC. The displacement profile of a bubble during ATC was obtained using our bubble tracking algorithm with a resolution of 50 nm. The overall CSK contractile force increase was positively correlated with the accumulative displacement of an integrin-bound microbubble, suggesting the important role of the microbubble-integrin-CSK in regulating cellular contractile force responses. ATC application to excite acetylated low density lipoprotein (AcLDL)-bound microbubble generated much less contractile force increase, indicating the contractile force increase requires connection to the integrin-focal adhesion-CSK. Our results demonstrated for the first time that ATC technique could enable controlled application of subcellular biomechanical stimuli to live single cells, which may provide a new and powerful technique for cell mechanics and mechanobiology studies.



## 5D-5

9:15 am **Cancer Cell Mechanotransduction Study using Acoustic Tweezers: Fibronectin-Integrin Binding Induced Calcium Elevation in Breast Cancer Cells**

Jae Youn Hwang<sup>1</sup>, Chi Woo Yoon<sup>2</sup>, Hae Gyun Lim<sup>2</sup>, Jinman Park<sup>1</sup>, Jungwoo Lee<sup>3</sup>, K. Kirk Shung<sup>2</sup>; <sup>1</sup>Information and Communication Engineering, Daegu Gyeongbuk Institute of Science & Technology, Korea, Republic of, <sup>2</sup>Biomedical Engineering, University of Southern California, USA, <sup>3</sup>Electrical Engineering, Kwangju University, Korea, Republic of

**Background, Motivation and Objective**

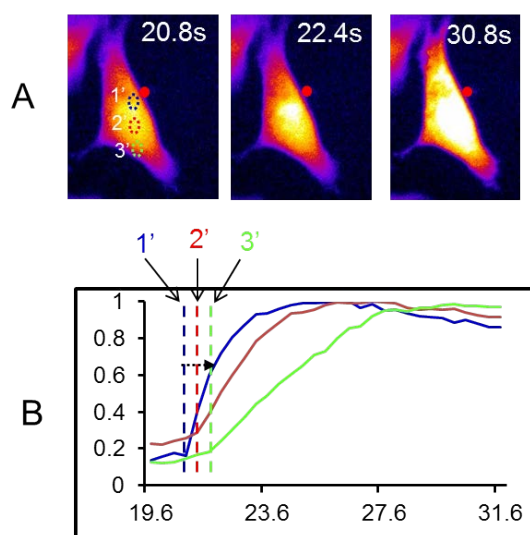
In this study, acoustic tweezers with a 193 MHz single-element LiNbO<sub>3</sub> ultrasound transducer was employed to study mechanotransduction of breast cancer SKBR-3 cells. We particularly investigated the effects of fibronectin on intracellular calcium signaling in the SKBR-3 cells using the acoustic tweezers. The fibronectin, which is recognized by integrins, has a crucial role in cell adhesion, migration, proliferation, and invasion. Therefore, the elucidation of the fibronectin-integrin binding induced intracellular signaling would provide important clues for better understanding of mechanotransduction of breast cancer cells associated to migration, proliferation, and etc. In this study, a single 5 μm microbead coated with fibronectin was trapped by the acoustic tweezers and then attached to cell membrane. Meanwhile, intracellular calcium elevations were monitored.

**Statement of Contribution/Methods**

The 193 MHz single-element LiNbO<sub>3</sub> ultrasound transducer was fabricated with the procedures previously described to trap a 5 μm microbead. The focal length and aperture diameter of the transducer were 0.75 mm and 0.65 mm, respectively (f-number=1.15). Microbeads were coated with fibronectin, trapped at beam focus, and then attached to the cell membrane by manipulating x-y motorized stages incorporated with the transducer. Intracellular calcium changes were meanwhile monitored via performing fluorescence imaging of Fluo-4 AM staining cells using an epi-fluorescence microscope.

**Results/Discussion**

We experimentally demonstrated that the acoustic tweezers was useful for the mechanotransduction study of breast cancer cells. A single 5 μm microbead coated with fibronectin was successfully trapped by using the acoustic tweezers. The results showed that the trapped microbead coated with fibronectin significantly induced intracellular calcium elevation in the SKBR-3 cells, but not the microbead without fibronectin coating. Also, it was found that the calcium propagation over the cell was first initiated around the area where the microbead contacted, suggesting that intracellular calcium elevation due to fibronectin-integrin binding was likely to be caused by ion channel opening. Altogether, the results showed the potential of the acoustic tweezers for mechanotransduction study of breast cancer cells.





## 6D - Sensors and ID Tags

Williford B

Friday, September 5, 2014, 8:00 am - 9:30 am

Chair: **Don Malocha**  
University of Central Florida

6D-1

### 8:00 am Technological process and resonator design optimization of Ir/LGS High Temperature SAW Devices

Sergey Sakharov<sup>1</sup>, Alexey Zabelin<sup>1</sup>, Andrey Medvedev<sup>1</sup>, Oleg Buzanov<sup>1</sup>, Dmitry Roshchupkin<sup>2</sup>, Serguei Kondratiev<sup>1</sup>, Alexander Shvetsov<sup>3</sup>, Sergei Zhgoon<sup>3</sup>; <sup>1</sup>JSC Fomos-Materials, Moscow, Russian Federation, <sup>2</sup>Institute of Microelectronics Technology and High-Purity Materials Russian Academy of Sciences, Russian Federation, <sup>3</sup>National Research University "Moscow Power Engineering Institute", Russian Federation

#### Background, Motivation and Objective

Ir metallization has been established as a promising candidate for high temperature SAW devices based on LGS. Useful cuts for temperature sensing applications have been reported. However device production and stability are still a challenge. We report on successful approaches in the preparation technology and on the design of one-port resonators for use on different cuts of LGS.

#### Statement of Contribution/Methods

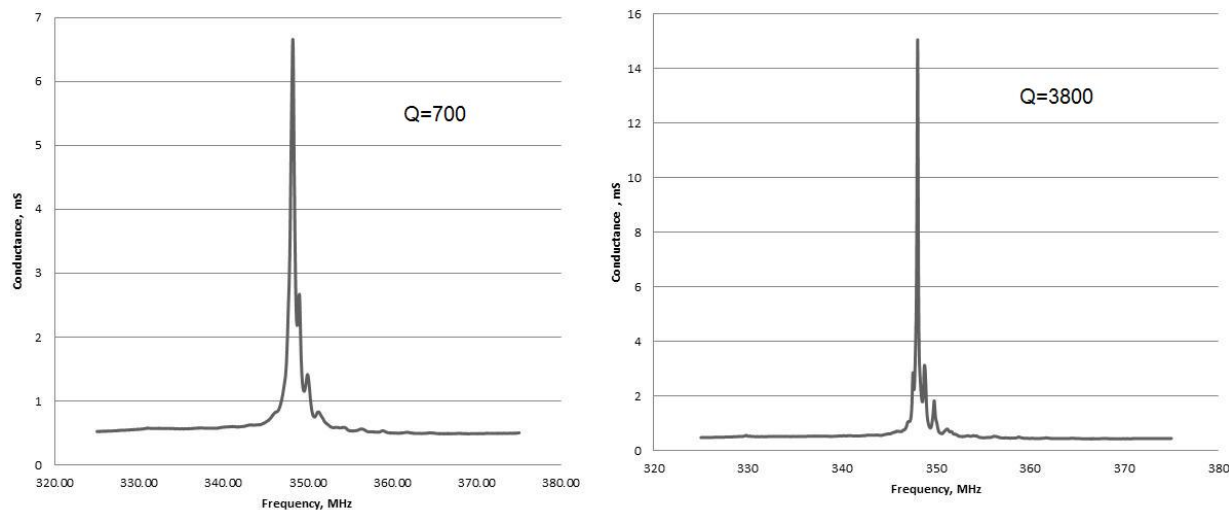
SAW resonators were designed in a way to obtain a single resonance peak for different orientations of LGS wafers and different angles of SAW propagation. Photolithography was adopted together with ion beam etching for electrode patterning. The Ir thin film (0.3 microns thick) was deposited by magnetron sputtering without additional adhesion layers at different temperatures and the film was annealed either before or after electrode patterning in different conditions.

#### Results/Discussion

The resistivity of magnetron sputtered Ir films drops noticeably after annealing. However, this process requires special care in order to avoid delaminating of the film due to developing high stress during such procedures. We have annealed the substrates with Ir films in different regimes and in different gas/vacuum conditions. The results of these studies have shown that annealing in air up to about 550°C decreases the Ir film resistivity 1.5-2 times (up to 1.3 Ohm per square). With increasing annealing temperature above 600°C, the resistivity of Ir film begins to grow, because we reach the temperature when Ir oxides start to form on the film surface. Further temperature rise in air up to 1000°C leads to Ir film degradation.

Vacuum annealing did not show much improvement in comparison to open air annealing. Magnetron sputtered thin Ir films have somewhat porous structure allowing oxygen to diffuse from the substrate surface through Ir films. Vacuum annealing changes noticeably Ir film properties. The results of these studies will be presented. Surface morphology has lower level of roughness with air annealing. Many resonator structures were prepared in different conditions and tested. Examples of the resonator structures show very promising properties, such as low conductance and high Q-factor.

Resonator response: as prepared – left, after annealing at 500°C for 60 min. – right. Drastic improvement in conductance and in Q factor at resonance frequency was obtained.



6D-2

### 8:15 am Wireless Harsh Environment SAW Array System for Power Plant Application

Mauricio Pereira da Cunha<sup>1</sup>, Robert Lad<sup>1</sup>, Thomas Pollard<sup>2</sup>, Donald McCann<sup>2</sup>, Eric McCarthy<sup>2</sup>, Peter Prata<sup>3</sup>, Richard Kelley<sup>3</sup>; <sup>1</sup>Lab. for Surface Science and Tech. (LASST), University of Maine, Orono, Maine, USA, <sup>2</sup>Environetix Technologies Corp., Orono, Maine, USA, <sup>3</sup>Penobscot Energy Recovery Co., Orrington, Maine, USA

#### Background, Motivation and Objective

Power plants are among the industry sectors which can benefit from improvements in harsh environment technologies aimed at monitoring fuel burning, reaction processes, and equipment integrity for safety. Better temperature control in fuel burning, for instance, translates into better efficiency in power generation and less equipment maintenance, thus reduced costs, improved operational safety, and less pollution. In waste-to-energy power plant boilers, temperature ranges from 300°C to 1200°C, and highly energetic erosive and

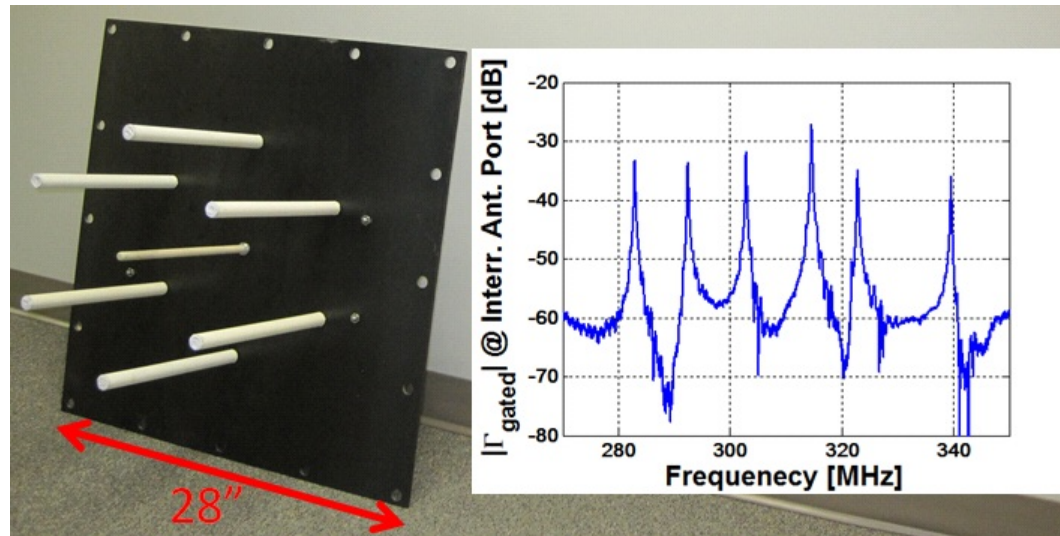
corrosive compounds are present. Wireless temperature monitoring within the plant boiler can provide much needed flexible and reliable identification of ash blockage locations, thus leading to localized cleaning, no need to shut down the entire operation, better maintenance scheduling, and improvement of plant efficiency. The University of Maine and Environetix Technologies Corp. have teamed up with the Penobscot Energy Recovery Company (PERC) with the objective of monitoring the temperature within the operational boiler of a municipal solid waste (MSW) power plant using an array of wireless surface acoustic wave (SAW) devices.

## Statement of Contribution/Methods

In this work, Environetix and UMaine tested in an operating waste-to-energy PERC boiler environment diverse materials including steel, Inconel, alumina, platinum, yttria-stabilized zirconia, and different types of sealants, together with langasite SAW devices. Out of this study, packaging materials and procedures were identified in order to satisfy wireless SAW device operation in such harsh environments.

## Results/Discussion

The results of the tests performed in the MSW burning environment revealed that the direct exposure of the SAW devices, antennas, and most of the packaging materials destroys them within hours or days. Alumina, however, showed good resilience, thus was employed in the packaging. A wireless array of 6 alumina-based packaged sensors, operating around 300 MHz, each with an integrated antenna and SAW sensor, and interrogated by one common interrogation antenna, was fabricated (see Fig.; wireless interrogation of the six SAW devices) and is now under test in the PERC power plant. The resulting door fixture has been installed in the PERC solid waste power plant for *in situ* real-time wireless temperature monitoring over power plant operation.



6D-3

## 8:30 am Correlation between the microstructure of AlN films and the performances of AlN/Sapphire-based SAW devices in wide temperature range

Keltouma Ait Aïssa<sup>1</sup>, **omar elmazria<sup>1</sup>**, Pacal Boulet<sup>1</sup>, Thierry Aubert<sup>2</sup>; <sup>1</sup>Institut Jean Lamour, UMR 7198, Université de Lorraine - CNRS, Vandoeuvre les Nancy, France, <sup>2</sup>Laboratoire SYMME, Université de Savoie, Annecy, France

## Background, Motivation and Objective

Our previous works have shown that AlN/Sapphire is a promising solution as piezoelectric structure for high temperature (HT) [1] and high frequency [2] SAW applications under low-oxygen environments. In situ measurements of S parameters have shown that the insertion losses (IL) are fairly constant between 20°C and 1050°C with variations below 3 dB (Fig. 1). However a remarkable phenomenon, consisting in the decrease of IL, was observed between 600 and 800°C. The present work aims at explaining this phenomenon by investigating the evolution of the structural properties of the AlN film and the Ir electrodes during the high-temperature exposure.

## Statement of Contribution/Methods

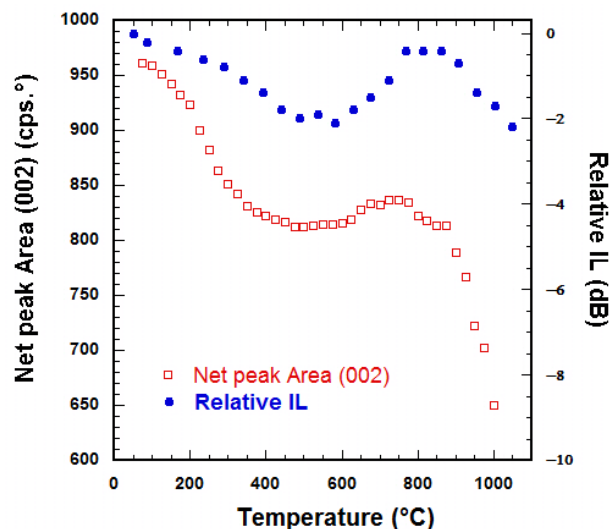
Ir/AlN/Sapphire SAW delay lines, identical to those investigated in ref [1], have been progressively heated up to 1000°C under a pressure of 2.10-2 mbar. The temperature profile was identical to the one used in ref [1]. The microstructure of the AlN film and Ir electrodes was examined by in situ X-ray diffraction (XRD) on a 4 circles X-ray diffractometer equipped with a Dome Hot Stage DHS 1100. Post-annealing measurements of the electrical conductivity of the Ir electrodes have been also conducted.

## Results/Discussion

In situ XRD measurements reveal that the AlN film remains c-oriented even at high temperature. Moreover, one can observe that the evolution of the crystalline quality of the film (net area of (002) peak) with temperature follows similar trends as the evolution of IL (fig. 1). In particular, the improvement of the AlN crystalline quality between 600 and 800°C could explain the IL decrease in the same temperature range. This phenomenon could also be related to the observed recrystallization of the Ir electrodes around 600°C, which results in a diminution of their electrical resistivity (measured at room temperature). Ongoing in situ XRD measurements are conducted to understand completely the physical origin of the evolution of the AlN crystalline quality with temperature. The determination of the correlation between the microstructure of the AlN film and the SAW device performances in a wide range of temperature is crucial to achieve reliable SAW sensors for high temperature applications.

[1] T. Aubert, J. Bardong, et al., J. Appl. Phys., 114, 014505 (2013)

[2] E. Blampain, O. Elmazria, et al., Proc. IEEE IUS., 1084 (2013)



6D-4

**8:45 am Lamb-wave resonator for microphone application**

Johanna Meltaus<sup>1</sup>, Brandon Harrington<sup>2</sup>, Markku Ylilampi<sup>1</sup>, James Dekker<sup>1</sup>, Tommi Riekkinen<sup>1</sup>, Pekka Rantakari<sup>1</sup>, Arto Nurmela<sup>1</sup>, Eric Lautenschlager<sup>2</sup>, Tuomas Pensala<sup>1</sup>; <sup>1</sup>VTT Technical Research Centre of Finland, Espoo, Finland, <sup>2</sup>Knowles Electronics, Itasca, Illinois, USA

**Background, Motivation and Objective**

Microphones based on Si or poly-Si membranes with capacitive read-out are reaching the limits of scalability. Higher dynamic range is required for many applications, but voltage output is already close to the compression limit. An alternative solution could be to use a piezoelectric thin-film membrane supporting Lamb plate waves as a microphone element. This approach would potentially provide a high dynamic range with the additional advantage of having frequency as the read-out parameter, instead of voltage. Also, the narrow gap behind the diaphragm with the associated viscous noise could be abandoned. Here we study the pressure sensitivity of frequency of AlN thin-film resonators on a poly-Si membrane sublayer. The poly-Si sublayer was selected because it is commonly used in the current MEMS microphone processes.

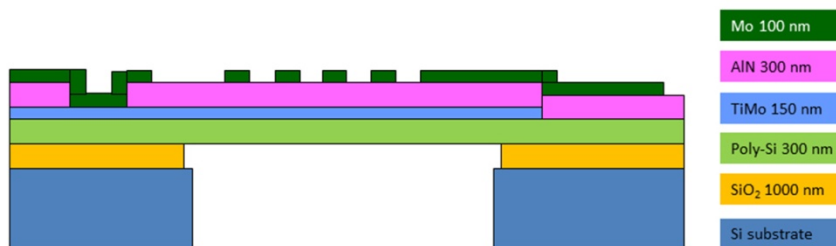
**Statement of Contribution/Methods**

The studied resonators operate on the S0-mode Lamb wave. The resonators were fabricated on a 300-nm poly-Si sublayer and consisted of a 300-nm AlN piezoelectric layer between Mo electrodes. Membrane shape was a square with side length of 532  $\mu\text{m}$ . Resonator structure was an interdigital transducer with reflectors on both sides, operating at 800 MHz. The pressure sensitivity of the devices was measured by probing them on-wafer and applying a pressure differential over the diaphragm. The frequency shift as a function of pressure was extracted from the S-parameter response measured at several pressures ranging from 0.2 Pa to 10 Pa, and the pressure sensitivity of frequency was determined. Experimental results were compared to FEM (Comsol Multiphysics) simulations.

**Results/Discussion**

The simulated pressure sensitivity at 1 Pa for a poly-Si / AlN membrane resonator was 0.05 ppm/Pa. Median sensitivity from measurement results was 0.5 ppm/Pa at 1 Pa, which for operation frequency of 800 MHz translates to 400 Hz shift / Pa. However, measurement uncertainty below 1 Pa was large. Residual tensile stress in the thin-film stack was approximately 300 MPa. Minimizing the stress should further improve the pressure sensitivity.

The poly-Si / AlN membrane showed a detectable frequency shift at the pressure difference of 1 Pa. However, sensitivity closer to 2 ppm/Pa would be required for practical microphone applications. With minimized residual stress, optimal materials and modified membrane design, the pressure sensitivity can be improved.



6D-5

**9:00 am SAW Tags for the 6 GHz range and SAW devices for 2-5 GHz range produced with nano-imprint-lithography**

Victor Plessky<sup>1</sup>, Zachary Davis<sup>2</sup>, Marc Lamothe<sup>3</sup>, Sergey Suchkov<sup>4</sup>; <sup>1</sup>GVR Trade SA, Switzerland, <sup>2</sup>Center for Micro & Nanotechn., DTI, Denmark, <sup>3</sup>FEMTO-ST, France, <sup>4</sup>Saratov State University, Russian Federation

**Background, Motivation and Objective**

At the last IEEE Ultrason. Symp.(2013) we have shown theoretically [1] the feasibility of 6 GHz SAW-tags with acceptable performance. In this paper we report experimental results for this device. We have also used the Nano-Imprint-Lithography (NIL) for manufacturing a few different SAW test devices operating at the 2-5 GHz frequency range – delay lines (DL), reflective DL and sensors. The frequencies higher 3 GHz, although inaccessible for optical lithography, represent great interest for many applications. NIL technology has a potential of cheap mass-production tool for SAW devices in this range.

## Statement of Contribution/Methods

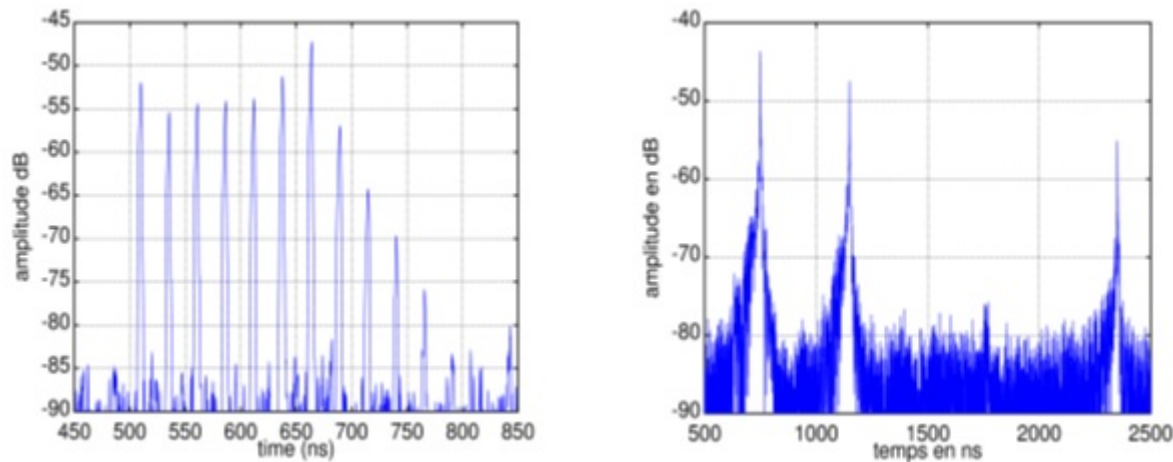
We have fabricated 6 GHz SAW-tag devices using E-beam lithography on a 4-inch LiNbO<sub>3</sub> 128° cut substrate. Then e-beam writing is performed using a state-of-the-art, JEOL JBX-9500 and sequentially developed using a standard wet development method. Finally, 50 nm of Al is deposited and lift-off is performed, leaving the Al in the desired SAW ID-tag pattern. The NIL process consists of imprinting using a Imrio100 J-FIL process followed by a tailored dry development process and finally metallization and lift-off. Ultra-Wide-Band (UWB) reflective delay lines suitable for SAW sensor operation in 2 GHz-3 GHz range have been manufactured.

## Results/Discussion

Figure 1 below shows performance of the 6 GHz SAW-tag and Fig.2 shows the measured reflective delay line sensor responses in time domain. The 6GHz devices have such attractive features as small size (0.9 x 2.0 mm<sup>2</sup>), loss level comparable with that of devices operating in 2.45 GHz ISM band, large information capacity.

This work was supported by EU project EUROSTARS E! 6785 – NILSAW.

[1] SVESHNIKOV, B. V., Et Al, "FEASIBILITY OF SAW TAGS IN THE 6 GHZ FREQUENCY BAND", 2013 IEEE ULTRASONICS SYMP., 2013, JULY, (PP. 1408-1411).



6D-6

## 9:15 am Analysis of Inter-Sensor Interference for Wireless SAW Sensors

James Humphries<sup>1</sup>, Mark Gallagher<sup>1</sup>, Donald Malocha<sup>1</sup>, <sup>1</sup>Department of Electrical Engineering and Computer Science, University of Central Florida, Orlando, FL, USA

## Background, Motivation and Objective

This paper will present a theoretical development of the effects of inter-sensor interference that is applicable to surface acoustic wave (SAW) sensors. There have been a number of papers suggesting that the number of possible multi-sensors simultaneously interrogated can be greater than 10, 100, or 1000. Theoretically and with ideal codes and sensors, this can be obtained. However, large numbers of functional realizable SAW sensors cannot be operated simultaneously in a manner that guarantees coding orthogonality due to manufacturing tolerances and to the variations due to temperature and/or other stimulus. For large numbers of simultaneously received sensor devices, it would require overlap of several (or many) sensors' time responses and this can cause interactions affecting the sensor accuracy and precision. Moreover, the effects of band limit filtering cause multiple time convolutions, causing time spreading and further overlap of sensor information.

## Statement of Contribution/Methods

An approach will be presented to statistically estimate the interference effect of multi-sensors depending on their degree of orthogonality and the number of interacting sensors. The mathematical approach is complete in that it takes into account the complete system and parameters, and can be easily understood using superposition and fundamental communication theory principles. The theoretical model is developed; simulations and predictions will be presented for typical orthogonal frequency control (OFC) SAW sensors using the frequency correlator extraction approach previously published. This approach uses matched filtering and correlation to use all data points to separate signals and minimize noise. Simulations are used to compare the statistical predictions of the effective inter-sensor interference. The analysis also shows how pseudo-orthogonality or minimization of code interference may be possible. The predictions are then used to estimate the effective stationary or near-stationary noise from multiple interfering sensors and will be compared to theory. Finally, this effective noise can be related to the signal to noise ratio that affects the precision of the sensor information.

## Results/Discussion

Considering the effects of inter-sensor interference provides valuable insight for wireless sensor network design. This analysis offers an approach to obtain a realizable quantity of wireless sensors being interrogated simultaneously with minimum inter-sensor interference. Although the results will be shown for OFC SAW devices, discussion will show the principles can be applied to any sensors.

## 7D - Therapeutic Ultrasound Transducers

Williford C

Friday, September 5, 2014, 8:00 am - 9:30 am

Chair: **Sandy Cochran**  
University of Dundee

7D-1

### 8:00 am Single Archimedean Spiral Close Packed Phased Array HIFU

Kyle Morrison<sup>1</sup>, George Keilman<sup>1</sup>, Peter Kaczowski<sup>2</sup>; <sup>1</sup>Sonic Concepts, Inc., Bothell, Washington, USA, <sup>2</sup>Verasonics, Inc., Redmond, Washington, USA

#### Background, Motivation and Objective

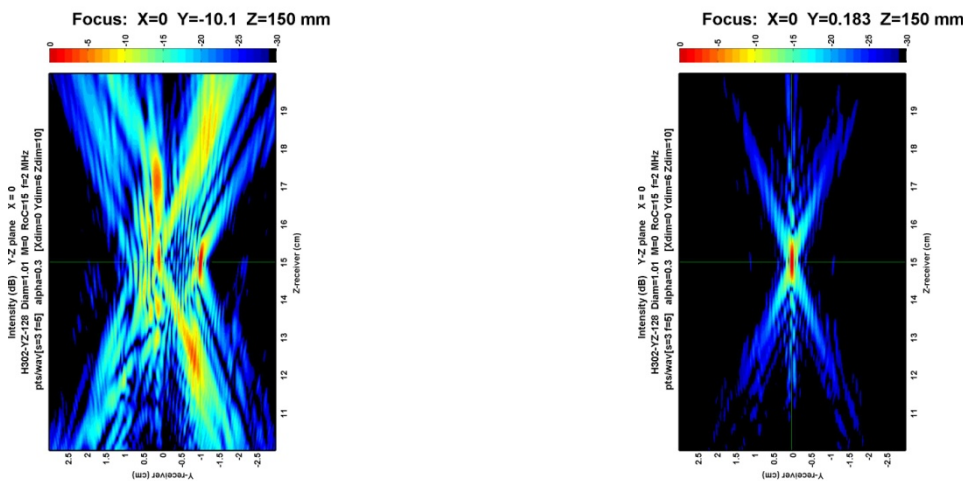
This presentation describes a series of high intensity focused ultrasound (HIFU) phased array transducers with a single Archimedean spiral close packed element arrangement on a spherical surface extending from the central axis outward. Simulation and measurement reveal the spiral element arrangement reduces grating side lobes while maximizing power density at the focus.

#### Statement of Contribution/Methods

Several configurations of the single Archimedean spiral have been characterized under different frequencies and number of elements using  $n \times 128$  elements, where  $n = 1$  thru 16, between 1 and 5 MHz. Elements are sized to fully fill the available space, constrained by a 15.0 cm O.D. x 4.4 cm I.D.  $f/1.0$  aperture surface. Two configurations have been built and tested to verify the grating lobes with simulation. All configurations use a similar transducer geometry and provide an operating band of  $\pm 20\%$  down -3 dB one-way about the transducer's resonant frequency and at least 80% transmit efficiency.

#### Results/Discussion

Tests in a free field closely resemble simulation showing the grating lobes are well below the level of the main lobe while within the transducer's steering range using the single Archimedean spiral. Further analysis is presented on the grating lobe reduction versus the ratio of element diameter to wavelength across several simulated configurations and two measured configurations. Simulation configurations range from 2.6 mm (2,048 elements) to 10.5 mm (128 elements) and 1 to 5 MHz. Measured configurations range from 6.6 mm (384 elements) to 10.5 mm and 1.7 to 2.7 MHz in a free field.



7D-2

### 8:15 am Design of a Minimally Invasive Low-Frequency Microtransducer for Ultrasonic Neuromodulation

Amit Mulgaonkar<sup>1,2</sup>, Rahul Singh<sup>2,3</sup>, George Saddik<sup>2,4</sup>, Ashkan Maccabi<sup>1,5</sup>, William Melega<sup>6</sup>, Martin Culjat<sup>1,2</sup>, Warren Grundfest<sup>2,3</sup>; <sup>1</sup>Center for Advanced Surgical and Interventional Technology, University of California, Los Angeles (UCLA), USA, <sup>2</sup>Bioengineering, University of California, Los Angeles (UCLA), USA, <sup>3</sup>Surgery, University of California, Los Angeles (UCLA), USA, <sup>4</sup>Center for Advanced Surgical and Interventional Technology, University of California, Los Angeles (UCLA), United States Minor Outlying Islands, <sup>5</sup>Electrical Engineering, University of California, Los Angeles (UCLA), USA, <sup>6</sup>Molecular and Medical Pharmacology, UCLA, USA

#### Background, Motivation and Objective

Much of the promise for the emerging clinical applications of low intensity focused ultrasound (LIFU) neuromodulation lies in its potential to be implemented noninvasively. However, there remain unresolved issues with this approach, namely, the challenge of accurately targeting and focusing known quantities of ultrasonic energy on specific neural structures from outside the skull. The ability to deliver ultrasound directly to target neural structures from within the brain would eliminate many of the complications of transcranial targeting by eliminating the acoustically lossy transcranial transition and simplifying the acoustic transmission path. However, no commercial or research probes are available that met the dual requirements of both small diameter, and low frequency robust sonication necessary for invasive ultrasonic neurostimulation. The objective of this work was to produce a low frequency microtransducer with a tight, confined acoustic beam pattern suitable for direct implantation within the brain of a small animal under stereotactic guidance.



# Statement of Contribution/Methods

A number of different transducer designs were considered, and transducer microfabrication techniques developed. As proof of concept, a matched pair of two transducers with the piezoelectric element mounted external to a support structure were produced for invasive targeted neural sonication, as well as a proof of concept of a transducer with a piezoelectric element mounted inside a glass micro capillary tube. Electrical and acoustic measurements of the transducers were performed to assess their performance and functionality, and an experimental validation trial was conducted to develop and validate techniques necessary for assessment of invasive neurostimulation.

# Results/Discussion

Probes with a diameter ranging between 1.2 - 1.8 mm, operating at a fundamental frequency around 600 kHz were produced. The resulting radiation pattern of these probes was found to be tight and spatially confined, with low lateral energy spread and a measured Full Width Half Max (FWHM) intensity profile of approximately 3.5 mm wide by 5 mm tall. Successful probe implantation in the rat model was demonstrated as a proof of concept. This work has demonstrated the feasibility of constructing mm-scale low-frequency microtransducers and subsequently implanting them within the brain in vivo studies of invasive ultrasonic neuromodulation. First of their kind microtransducers were designed and fabricated that were capable of generating low-frequency ultrasound with a confined beam pattern.

7D-3

## 8:30 am Partial hemispherical element of array transducer for second-harmonic superimposition

Shin-ichiro Umemura<sup>1</sup>, Kenji Otsu<sup>1</sup>, Shin Yoshizawa<sup>1</sup>, <sup>1</sup>Tohoku University, Japan

# Background, Motivation and Objective

Second-harmonic superimposition has been reported to be significantly effective not only at inception of cavitation but also at the formation of cavitation cloud, both of which are the key processes of ultrasonic treatment utilizing cavitation [1]. However, a conventional thickness-mode transducer cannot naturally generate the second harmonic as well as the odd harmonics. It needs to depend on a specially designed matching layer to do so. Recently, a novel array transducer element utilizing the corsonance between a hemispherical piezoceramic shell and a water sphere has been proposed to generate high-power ultrasound at a relatively low drive voltage [2]. Because the mechanism of resonance is completely different from the conventional thickness-mode transducer, this type of transducer may have potential to generate the second harmonic when its geometrical configuration is properly modified.

[1] S. Yoshizawa et al., J. Acoust. Soc. Am., vol. 130, 1515-20, 2013.

[2] K. Otsu, Kenji et al., Jap. J. Appl. Phys., vol 51, 07GF24, 2012.

# Statement of Contribution/Methods

The behavior of the proposed transducer with a partial hemispherical shell, as shown in Fig. 1, was simulated using a finite element code, PZFlex. The frequency dependence of its electrical impedance was examined by varying the angular diameter of the partial hemisphere, and its lowest and second lowest resonance frequencies were tracked.

# Results/Discussion

As shown in Fig. 2, the second lowest resonance frequency increased as the angular diameter decreased while the fundamental resonance frequency stayed approximately the same at a constant diameter of the partial hemisphere. It was approximately as twice as the fundamental frequency at an angular diameter of 130 deg. The frequency dependence of its electrical impedance, as plotted in Fig. 3, shows that the partial hemispherical transducer element is suitable not only to generate the second but also third harmonic at the particular angular diameter. The output acoustic power was significantly high at the second harmonic as well as fundamental frequency at reasonable drive voltages. Furthermore, the focal ultrasonic field generated by an array transducer consisting of hundreds of the proposed transducer elements will also be numerically simulated and discussed in the presentation.

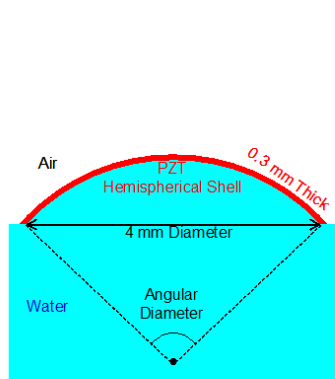


Fig. 1 Geometry of hemispherical transducer element.

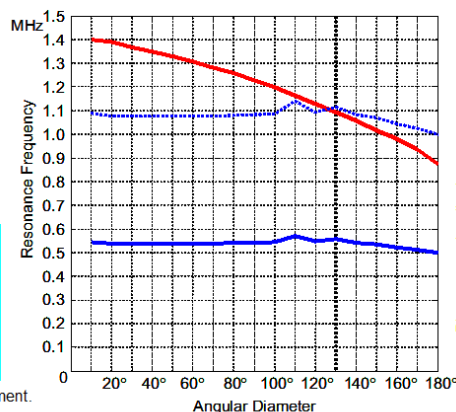


Fig. 2 Angular diameter dependence of resonance frequency.

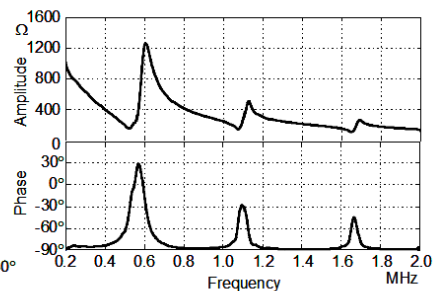


Fig. 3 Electrical impedance at angular diameter of 130°.

7D-4

## 8:45 am Piezoelectric and Electromechanical Properties of Hard Lead-free Bi0.5Na0.5TiO3-based Ceramics

Elaheh Taghaddos<sup>1</sup>, Mehdi Hejazi<sup>1</sup>, Ahmad Safari<sup>1</sup>, <sup>1</sup>Material science and Engineering, Rutgers University, Piscataway, NJ, USA

# Background, Motivation and Objective

The objective of this research was to develop hard lead-free Bi0.5Na0.5TiO3 (BNT) based piezoceramics with high mechanical quality factor (Qm) and low dielectric loss. The high power performance of the ceramics was evaluated by constant vibration velocity method. It was shown that these lead-free ceramics are potential replacement for lead-based ceramics such as PZT4 and PZT8 in high power applications.

# Statement of Contribution/Methods

BNT-based ceramics prepared by mixed oxide route were doped with different amounts of Mn as an acceptor dopant. The electromechanical and dielectric properties were measured by an impedance analyzer. For high power measurements, the impedance frequency sweep, temperature rise, and input power were measured as a function of vibration velocity. A single element ultrasonic transducer was built by hard BNT-based ceramic and acoustic characterization was carried out by water tank method.

**Results/Discussion**

Significant enhancement of mechanical quality factor  $Q_m$  and vibration velocity was achieved by Mn-doping. The lowest mechanical and dielectric losses were obtained in 1.5 mol.% Mn-doped ceramics with a planar  $Q_m$  of about 970 and  $\tan\delta$  of 0.89%. Mn-doping, remarkably suppressed heat generation and resonance frequency shift under high drive condition. The maximum vibration velocity was increased from 0.28 m.s<sup>-1</sup> in undoped ceramic to 0.6 m.s<sup>-1</sup> in 1.5 mol.% Mn-doped composition. Furthermore, single element high-intensity focus ultrasound (HIFU), with center frequency of 5-8 MHz were developed with .15 mol% Mn-doped ceramic. The result of this study displayed the superior high power performance of Mn-doped BNT-based piezoelectric compare to their lead-based counterparts such as PZT4 and PZT8 ceramics.

**7D-5****9:00 am Frequency Optimization in High Intensity Focused Ultrasound**

Hasan Yetik<sup>1</sup>, Cemre Ariyurek<sup>2</sup>, Ayhan Bozkurt<sup>3</sup>, Arif Ergun<sup>1</sup>, <sup>1</sup>TOBB University of Economics and Technology, Turkey, <sup>2</sup>Bilkent University, Turkey, <sup>3</sup>Sabanci University, Turkey

**Background, Motivation and Objective**

In high intensity focused ultrasound (HIFU) the choice of transducer frequency depends on the target depth and tissue type. At high frequencies attenuation does not permit enough acoustical power to be transmitted to the target whereas at low frequencies the transmitted power is not absorbed efficiently. Hence, there exists an optimum frequency at which the power deposited at the target is maximum. The relation between optimum frequency and target depth can be found as shown in [1] which was also verified using finite element simulations [2]. Our objective is to verify this relation experimentally using magnetic resonance (MR) thermometry.

**Statement of Contribution/Methods**

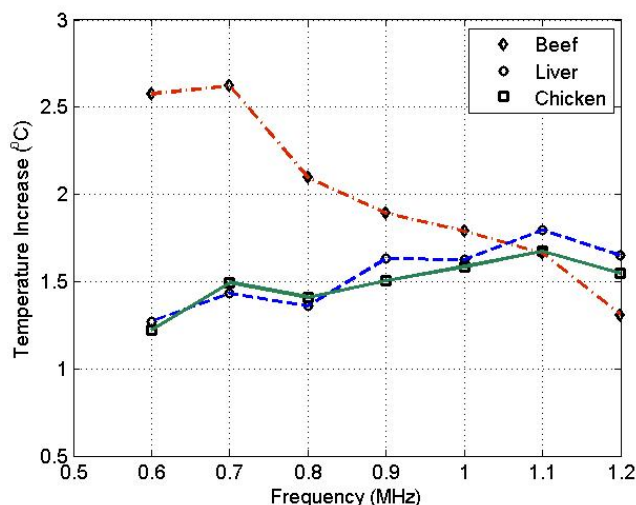
Power absorption is proportional to both absorption coefficient  $\alpha$  which is approximately proportional to frequency, and the acoustic intensity  $I(z)$  which is also a function of absorption coefficient. Analytical calculations [1] show that the product of optimum frequency and target depth is constant and equal to  $1/(2\alpha_a)$  where  $\alpha_a$  is the frequency independent attenuation coefficient. Hence, for a target depth of  $z$ , the optimum frequency is  $f_{opt} = 1/(2\alpha_a z)$ .

In this work we used an MR compatible fixed focus transducer (focus at 50 mm,  $F/\# = 1$ ) centered at 1 MHz. We used lean cow muscle along fibers, cow liver and chicken breast as samples. We applied 2 Watt CW signal for 4 minutes and measured the temperature increase at the focus using MR thermometry. We repeated the experiment at several frequency points while keeping the acoustic power constant.

**Results/Discussion**

Given that  $\alpha_a = 1.38 \times 10^{-7}$  Np/(Hz-cm) for muscle along fibers and  $0.94 \times 10^{-7}$  Np/(Hz-cm) for liver, the optimum frequency at 5 cm is expected to be at 0.72 MHz and 1.06 MHz, respectively. MR thermometry results for these two cases along with chicken breast sample are plotted in Fig. 1. Although the measurements are limited by the bandwidth of the transducer and inaccurate calibration at low frequencies, the results strongly support the analytic relation reported in [1].

1. AS Ergun, "Analytical and Numerical Calculations of Optimum Design Frequency for Focused Ultrasound Therapy and Acoustic Radiation Force," Ultrasonics vol 51 pp 786-794, 2011
2. A Bozkurt, RB Roy, AS Ergun, "Optimization of Operating Frequency of Acoustic Transducers for Obtaining Maximum Temperature in HIFU Based Therapeutic Ablation", IEEE Int Ultrasonics Symp Oct 2012

**7D-6****9:15 am Rapid Prototyping Fabrication of Focused Ultrasound Transducers**

Yohan Kim<sup>1</sup>, Adam Maxwell<sup>2</sup>, Timothy Hall<sup>1</sup>, Zhen Xu<sup>1</sup>, Kuang-Wei Lin<sup>1</sup>, Charles Cain<sup>1</sup>, <sup>1</sup>Biomedical Engineering, University of Michigan, Ann Arbor, MI, USA, <sup>2</sup>Center for Industrial and Medical Ultrasound, Applied Physics Laboratory, University of Washington, Seattle, WA, USA

**Background, Motivation and Objective**

The majority of ultrasound therapy transducers in use for research or clinical applications are currently constructed using traditional manufacturing methods, which are typically complex and costly. Rapid prototyping (RP) fabrication methods have found wide adoption in a variety of industrial and medical fields over the years, providing substantial advantages in fabrication time and costs. We present a new method for the fabrication of customized high intensity focused ultrasound transducers for pulsed operation using RP technology.

# Statement of Contribution/Methods

As an example with which to demonstrate the method, a modular transducer array system was designed consisting of 32 focused 50.8 mm element modules distributed in a 300 mm hemispherical scaffold with a geometric focus of 150 mm. Individual element focusing was achieved by the use of flat piezoceramics coupled to elliptical lenses. With the exception of the ceramic elements, the entire structure of the array, including the lenses and the hemispherical scaffold was designed in-house and fabricated through a stereolithography apparatus (SLA) using a photopolymer resin. The elements were bonded to the lenses through a quarter-wave tungsten-epoxy matching layer, in order to optimize acoustic transmission under short sonication pulses.

# Results/Discussion

Individual modules showed a high degree of electroacoustic consistency, with an electrical impedance mean and standard deviation of  $109 \pm 10.2 \Omega$  for the 32 elements at 500 kHz. Once mounted on the array scaffold, time-of-flight measurements for individually pulsed modules showed that all pulses arrived at the focus within a 350 ns range, indicating good element alignment. Focal pressure profiles of the transducer also showed close agreement with simulated results, with measured -6 dB focal beamwidths of  $1.9 \times 4.0$  mm ( $1.9 \times 3.9$  mm simulated) in the transversal and axial directions respectively. The transducer can theoretically reach maximum focal P- pressures in excess of 100 MPa using pulses of 1.5 cycles. Total material expenses associated with the fabrication of the transducer were approximately 5000 USD (as of 2011). The versatility and low fabrication costs afforded by RP methods may be beneficial in the development of complex transducer geometries suitable for a variety of research and clinical applications.

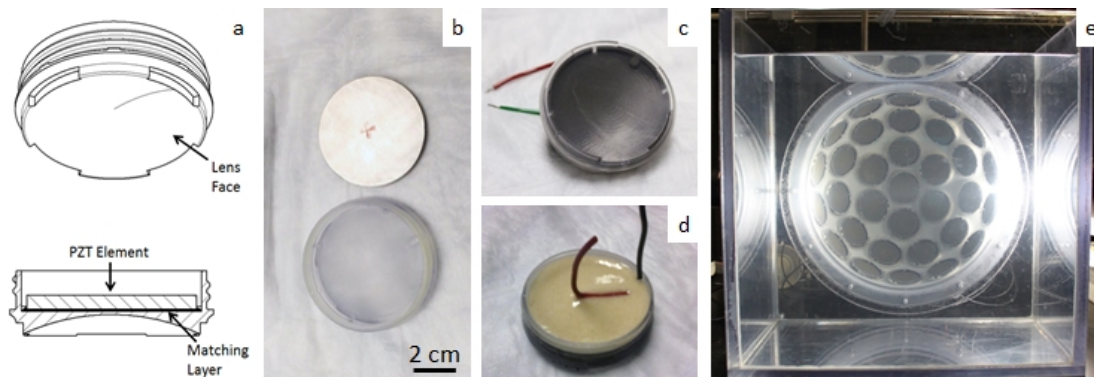


**Figure 1.** CAD schematic of an individual housing module showing element construction details (a). Picture of a single 50.8 mm diameter PZT disc with an empty housing module (b). Frontal view of a single assembled module with matching layer compound applied between the PZT disc and the lens (c). Application of urethane compound to seal the backside of the element (d). Fully populated transducer array mounted on the side of a water tank (e).

## 1E - MCA: Contrast Agents: New Investigations

Grand Ballroom

Friday, September 5, 2014, 10:30 am - 12:00 pm

Chair: **Juergen Willmann**  
Stanford University

1E-1

### 10:30 am Unraveling lipid-coating movements of oscillating microbubbles - a fluorescence high-speed optical study

Klazina Kooiman<sup>1,2</sup>, Flordeliza S. Villanueva<sup>1</sup>, Bin Qin<sup>1</sup>, Tom van Rooij<sup>3</sup>, Frits Mastik<sup>3</sup>, Alexander L. Klibanov<sup>4</sup>, Nico de Jong<sup>2,3</sup>, Xucai Chen<sup>1</sup>; <sup>1</sup>Center for Ultrasound Molecular Imaging and Therapeutics, University of Pittsburgh Medical Center, Pittsburgh, PA, USA, <sup>2</sup>Interuniversity Cardiology Institute of the Netherlands, Utrecht, Netherlands, <sup>3</sup>Biomedical Engineering, Erasmus MC, Rotterdam, Netherlands, <sup>4</sup>Cardiovascular Division, University of Virginia, Charlottesville, USA

#### Background, Motivation and Objective

In an ultrasound (US) field, microbubbles (MB) oscillate. Acoustic behavior of MB has been widely studied, which have led to several mathematical models [1]. The Marmottant model [2] incorporates lipid coating behavior, such as buckling and rupture. However, this has never been shown experimentally as optical high-speed imaging to resolve MB oscillations in the MHz range could only be performed in bright field (BF), thereby only visualizing the gas core. This research studies the lipid movement in the MB coating by fluorescence (FL) high-speed imaging.

#### Statement of Contribution/Methods

MB with a DSPC/DSPE-PEG(2000)-PDP coating (molar ratio 4:1) and C<sub>4</sub>F<sub>10</sub> gas core were made with a Vialmix, after which FL Oregon Green 488-maleimide was conjugated. MB were insonified at 1 MHz (10 or 15-cycle sine wave burst) at 50-300 peak negative acoustic pressure (P<sub>-</sub>). FL (using a 488 nm laser) and BF recordings were obtained at ~5 million frames/s with the UPMC Cam [3].

#### Results/Discussion

FL recordings revealed a variety of MB coating behaviors. At 50 kPa, for MB with a homogeneous FL coating before US (n=14) we observed homogeneous FL during oscillation (Fig A; 50%), "hot spots" (focal areas of increased FL) only during compression (Fig B; 29%), or hot spots during oscillation that persisted after US (Fig C; 21%), suggesting lipids can move on the order of a micron within one acoustic cycle, thereby reaching speeds on the order of 1 m/s. These coating characteristics were not evident from the BF recordings (see Fig). For MB with hot spots before US (n=29), the hot spots persisted or intensified (Fig D). Occurrence of hot spots during US could be due to buckling, hypothesized to correlate with compression only behavior. However, we did not find such correlation. At higher P<sub>-</sub>, we also observed other phenomena: formation of a tail (Fig E) that was not evident in BF, or a non-continuous lipid coating during the expansion phase (Fig F; MB diameter 29% smaller after US), suggesting a ruptured coating correlating with deflation. In conclusion, this study reveals for the first time ultra-fast lipid movements in the MB coating during US.

Ref: [1] Faez et al, IEEE Trans UFFC 60:7, 2013; [2] Marmottant et al, J Acoust Soc Am 118:3499, 2005; [3] Chen et al, Rev Sci Instrum 84:063701, 2013.

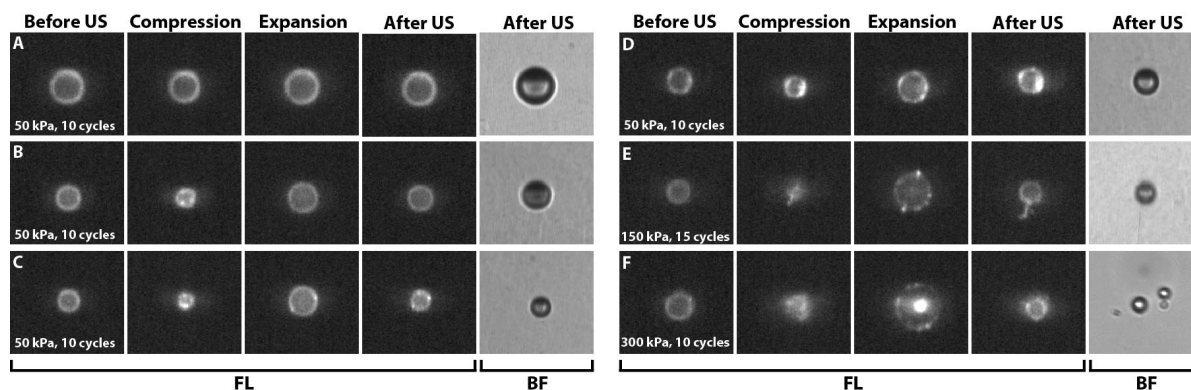


Fig. Selected frames from FL and BF high-speed recordings (~5 million frames per second). MB were insonified with a single burst at 1 MHz. Note that the MB seem larger in BF, which has also been reported by E. Gelderblom (PhD thesis, Ultra-high speed fluorescence imaging, University of Twente, Enschede, the Netherlands, 2012).

Funding from ICIN, the Center for Ultrasound Molecular Imaging and Therapeutics, UPMC, the Center for Translational Molecular Medicine and the Dutch Heart Foundation (PARISK) is gratefully acknowledged.

1E-2

### 10:45 am Influence of binding on the vibrational responses of targeted lipid-coated microbubbles

Tom van Rooij<sup>1</sup>, Antonius F.W. van der Steen<sup>1,2</sup>, Nico de Jong<sup>1,2</sup>, Klazina Kooiman<sup>1</sup>; <sup>1</sup>Department of Biomedical Engineering, Thoraxcenter, Erasmus MC, Rotterdam, Netherlands, <sup>2</sup>Laboratory of Acoustical Wavefield Imaging, Faculty of Applied Sciences, Technical University Delft, Delft, Netherlands

#### Background, Motivation and Objective

Microbubbles (MB) have been used in ultrasound imaging for the last decades and are promising for molecular imaging. MB for molecular imaging are targeted to disease-specific biomarkers and the main challenge is to acoustically distinguish free MB from MB bound to their target. In this study we used the Brändaris 128 high-speed camera [1] to compare the responses to ultrasound of two types of lipid-coated MB in their free and bound state with the aim to acoustically discriminate them.

**Statement of Contribution/Methods**

Two types (DSPC and DPPC) of MB (mol %: DSPC or DPPC 59.4; PEG-40 stearate 35.7; DSPE-PEG(2000) 4.1, DSPE-PEG(2000)-biotin 0.8) with a  $C_4F_{10}$  gas core were made by sonication [2]. MB floated against an OptiCell wall (free MB) or adhered to the biomarker streptavidin which was covalently bound to a polyester membrane (bound MB). MB dynamics were recorded at 15 Mfps using the Brandaris 128 high-speed camera. We used single ultrasound bursts (8-10 cycles) at 30 and 50 kPa. The frequency was swept from 1-4 MHz.

**Results/Discussion**

We investigated 15 DSPC and 14 DPPC free MB, and 10 DSPC and 11 DPPC bound MB. Shrinkage was larger for DPPC than for DSPC MB in both conditions, indicating higher stability for DSPC. Moreover, for bound MB the stability of both types increased. This can be explained by the lower relative oscillations we found for bound MB (Fig. A), as also reported by Overvelde et al [3]. We found similar resonance frequencies for DSPC and DPPC, whether they were free or bound, in contrast to others [3]. More free DPPC than DSPC MB responded at the subharmonic and the second harmonic frequency [4], which did not change upon binding. Interestingly, the relative oscillations at the second harmonic frequency were higher for bound MB (median: DSPC=0.03, DPPC=0.03) than for free MB (DSPC=0.01, DPPC=0.02), see Fig. B.

In conclusion, **bound** DSPC and DPPC MB were more stable, had 1.8x lower relative oscillations, and had 2x higher relative oscillations at the second harmonic frequency than the **free** MB. We found no differences between bound DSPC and bound DPPC MB. The almost two times higher relative oscillations of free MB may provide opportunities to acoustically discriminate them from bound MB.

[1] Chin et al, Rev Sci Instrum 2003; [2] Klivanov et al, Invest Radiol 2004; [3] Overvelde et al, Ultrasound Med Biol 2011; [4] van Rooij et al, IEEE Proceedings 2013; [5] van Neer et al, IEEE TUFFC, 2010.

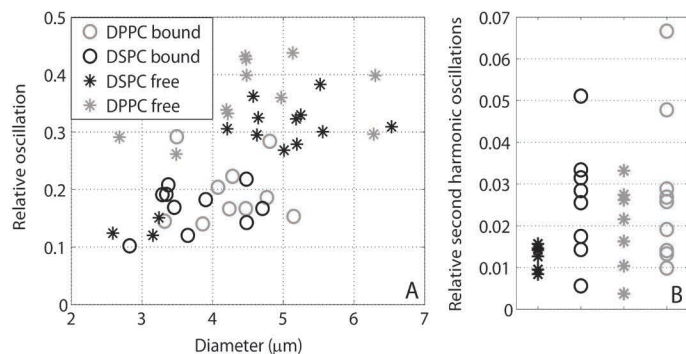


Fig. **A**) Relative oscillations obtained from the diameter-time curves  $(D_{\max} - D_{\min}) / D_0$ , with  $D_{\max}$  the maximum diameter,  $D_{\min}$  the minimum diameter, and  $D_0$  the resting diameter. **B**) The relative oscillations at the second harmonic frequency were obtained from the amplitude of the peak at the second harmonic frequency in the Fourier spectrum divided by  $D_0$ . These relative oscillations result in acoustical pressures above the clinical detection limit of 1 Pa [4,5].

This work is supported by NanoNextNL, a micro and nanotechnology consortium of the Government of the Netherlands and 130 partners.

1E-3

### 11:00 am In Vivo Quantification of Image Enhancement and Circulation Kinetics for Phase Change Perfluorocarbon Agents Using Custom Pulse Sequences

Paul S. Sheeran<sup>1</sup>, Juan D. Rojas<sup>1</sup>, Connor Puett<sup>1</sup>, Gloria Nyankima<sup>1</sup>, Jordan Hjelmquist<sup>2</sup>, Paul A. Dayton<sup>1</sup>; <sup>1</sup>Joint Department of Biomedical Engineering, University of North Carolina at Chapel Hill and North Carolina State University, USA, <sup>2</sup>Department of Biomedical Engineering, North Carolina State University, USA

**Background, Motivation and Objective**

Several studies have explored the potential of phase-change contrast agents (PCCAs) that vaporize into microbubbles for ultrasound imaging. With typical formulations, high pressures are required to vaporize droplets small enough to form microbubbles 1-5 micrometers in diameter, but recent studies have demonstrated droplets composed of volatile perfluorocarbons (PFC) such as decafluorobutane and octafluoropropane to reduce the vaporization pressures. Additionally, PCCAs require unique pulse sequences to maximize diagnostic information that are not available in conventional scanners. In this study, we use a customizable ultrasound system to demonstrate *in-vivo* activation and imaging of PCCAs, and to explore contrast generation, wash-out kinetics, and circulation profiles of droplet made with DFB and OFP.

**Statement of Contribution/Methods**

PCCAs composed of DFB and OFP were prepared using a previously developed 'microbubble condensation' method, and were intravenously administered to Fischer 344 rats. Activation and imaging of PCCAs in the kidney was accomplished using a custom image-activate-image sequence in which the imaging consisted of angularly-compounded plane-wave pulse inversion at low pressures (1 cycle, 5MHz), and vaporization was achieved by delivering a series of high pressure (2 cycle, 5MHz), electronically steered focused pulses to a predetermined region of interest. The pulses were spaced laterally by half of the lateral FWHM, and axially by five times the axial FWHM. All imaging and activation was achieved with the Verasonics research platform using an ATL L12-5 linear transducer.

**Results/Discussion**

Results demonstrate the feasibility of PCCAs diagnostic imaging using a custom pulse sequence. DFB droplets showed a maximum contrast enhancement of  $9.0 \pm 2.7$  dB 1 min after injection, and circulation half-life of  $9.8 \pm 1.7$  min ( $N = 5$ ). In the same animals, the more volatile OFP droplets showed a contrast enhancement of  $17.1 \pm 2.0$  dB and half-life of  $2.2 \pm 2.0$  min (Fig. 1). Although OFP provided a larger area of contrast, DFB and OFP displayed similar wash-out characteristics after activation. No instances of breathing irregularities or death were observed. The results suggest that PCCA-specific imaging sequences can be used to evaluate the *in-vivo* impact of changes in droplet formulation in order to develop PCCAs tuned for specific applications.



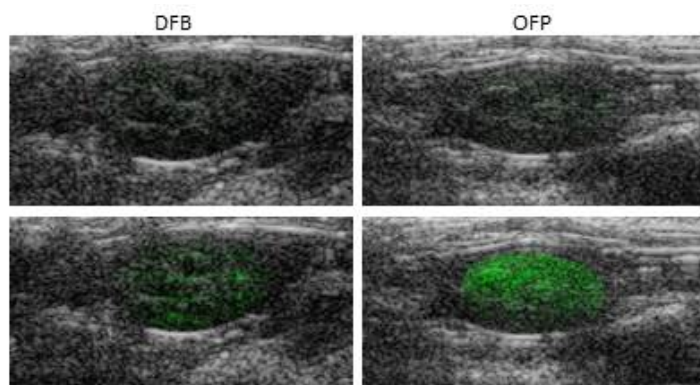


**Figure 1.** Overlays of contrast-specific pixel intensity (green) and B-mode (grey) ultrasound scans of the rat kidney. (Top) Before injection, no contrast is produced following the activation pulse. (Bottom) One minute after injection, activation pulses produce high contrast within the kidney ROI.

1E-4

#### 11:15 am Condensation Properties of Perfluorobutane Microbubbles

Paul Mountford<sup>1</sup>, Shashank Sirsi<sup>1</sup>, Mark Borden<sup>1</sup>, <sup>1</sup>Mechanical Engineering, University of Colorado, Boulder, Colorado, USA

##### Background, Motivation and Objective

Phase-change emulsions are being researched as agents for biomedical imaging and therapeutic applications. These emulsions take advantage of the volume change associated with vaporizing a liquid nano-scale drop into a micron-scale bubble for the purpose of enhanced circulation and possible extravasation. A new phase-change emulsion developed by Sheeran et al.[1] consists of condensing pre-formed gaseous microbubbles into liquid nanodrops through dropping microbubble temperature and increasing hydrostatic pressure. Little is known about microbubble shell and core behavior during compression and condensation.

##### Statement of Contribution/Methods

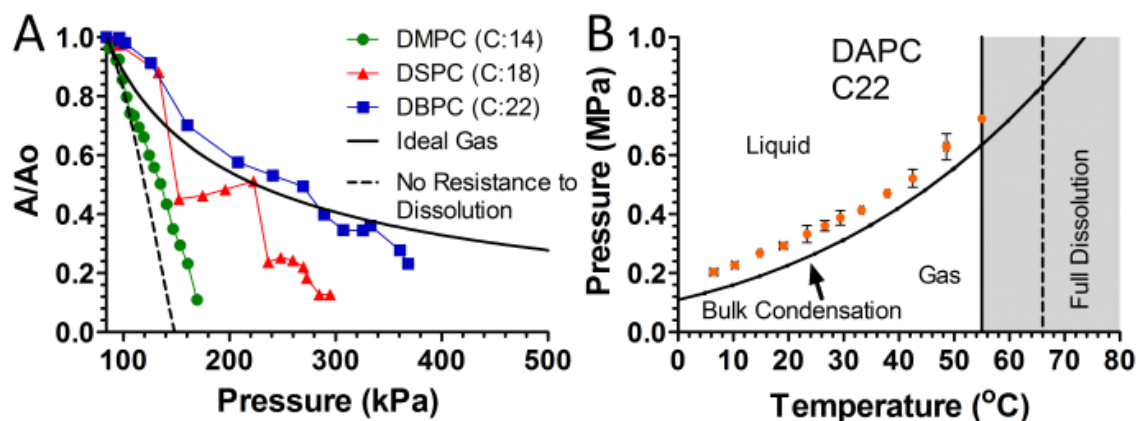
In this investigation we addressed the effect of changing lipid acyl chain length for 4-5  $\mu\text{m}$  diameter size-selected microbubbles and observed the impact it had on compression and condensation behavior. Bright field microscopy was used with a custom chamber having temperature and pressure control to track the size and onset of condensation for individual perfluorobutane microbubbles being subjected to a constant rate of pressurization. Light scattering was used to measure the resulting microbubble condensed droplet size distribution. The resulting experimental data was used to construct temperature-pressure phase diagrams for lipid-coated microbubbles, which we expect will aid in the materials selection of optimal microbubble condensed droplets for various biomedical and industrial applications

##### Results/Discussion

When observing microbubble compression it was seen that the microbubble shell undergoes deformation through multiple stages of wrinkling and collapse prior to condensation. Defining the reduced temperature as the temperature of the solution over the phase transition temperature of the dominant lipid, it was seen that the shell resisted compression at colder reduced temperatures (Fig.1A) and that longer acyl chain lipids resisted compression more at the same reduced temperatures. It was also observed that the microbubble shell reduced internal core pressure resulting in higher needed pressure for condensation (Fig.1B).

##### Reference:

(1) Sheeran, P. S.; Luo, S.; Dayton, P. A.; Matsunaga, T. O. Formulation and Acoustic Studies of a New Phase-Shift Agent for Diagnostic and Therapeutic Ultrasound. *Langmuir* 2011, 27, 10412–10420.



## 11:30 am Biogenic Nanostructures as Reporters for Ultrasound Imaging

Mikhail Shapiro<sup>1</sup>; <sup>1</sup>Chemical Engineering, California Institute of Technology, Pasadena, CA, USA

### Background, Motivation and Objective

Despite providing excellent resolution, sensitivity and convenience compared to other imaging modalities, ultrasound is currently limited in many molecular imaging applications by a lack of suitable nanoscale reporters. The basic physics of conventional “microbubble” contrast agents, which dictates sizes larger than one micron and half-lives shorter than a few hours, limits their use as labels of specific cells and tissues outside the bloodstream. We are developing a new class of reporters for ultrasound based on genetically encoded gas nanostructures from buoyant bacteria and archaea. These inherently stable nanoscale reporters overcome some of the main limitations of microbubbles, and raise the possibility of ultrasound contrast agents engineered and delivered to cells at the genetic level.

### Statement of Contribution/Methods

Gas vesicles (GVs) are gas-filled protein-shelled compartments typically 50-500 nm in size that exclude water and are permeable to gas. They are biosynthesized by photosynthetic cyanobacteria and halobacteria as a means to regulate buoyancy and thereby migrate to optimal aqueous depths for access to light and nutrients. GV from different species have different shapes and sizes. Like microbubbles, GV are gas-containing structures, but they exhibit different physics: they are smaller, the gas inside them is at equilibrium with the aqueous environment, they are inherently stable, and their shell is relatively inelastic. We recently demonstrated the first use of GV as ultrasound contrast agents.

### Results/Discussion

Our results show that sub-nanomolar concentrations of GV produce robust ultrasound contrast at frequencies of 5-17 MHz. Contrast mechanisms include linear scattering, attenuation and harmonics, enabling enhanced detection. GV contrast is readily observed in vitro and in vivo. Furthermore, differences in genetically-determined critical collapse pressures among GV from different species enables multiplexed imaging through a serial in situ collapse paradigm. In addition, we show that clustering- dependent contrast enhancement permits the use of GV as molecular biosensors and reporters of cellular integrity. These results highlight the potential of this new class of reporters to support unique modes of molecular imaging, and raise the intriguing prospect of genetically engineered and targeted reporters for ultrasound. In this talk, I will review our initial experiences and the current state of the development of GV as nanoscale imaging reporters for ultrasound.

Background reading: Shapiro\*, Goodwill, Neogy, Yin, Foster, Schaffer, Conolly. Nature Nanotechnology (2014) DOI: 0.1038/nnano.2014.32.

## 2E - MBF: Novel Flow Techniques

Waldorf

Friday, September 5, 2014, 10:30 am - 12:00 pm

Chair: **Jørgen Jensen**  
Technical University Denmark, Kgs. Lyngby

2E-1

### 10:30 am Comparison of tumor microvasculature assessment via Ultrafast Doppler Tomography and Dynamic Contrast Enhanced Ultrasound

Charlie Demene<sup>1</sup>, Thomas Payen<sup>2</sup>, Alexandre Dizeux<sup>2</sup>, Jean Luc Gennisson<sup>1</sup>, Lori Bridal<sup>2</sup>, Mickaël Tanter<sup>1,2</sup>; <sup>1</sup>Institut Langevin, ESPCI ParisTech, CNRS UMR7587, Inserm U979, Paris, France, <sup>2</sup>Laboratoire d'imagerie biomédicale, Université Pierre et Marie Curie, UMR S 1146 / UMR 7371, Paris, France

#### Background, Motivation and Objective

Assessing structural organization and dynamics of tumor blood supply is of highest interest since numerous cancer treatments rely on antiangiogenic effects. Dynamic Contrast Enhanced Ultrasound (DCE-US) is widely used in cancer research to extract quantitative parameters reflecting tumor perfusion. However, the underlying vascular structure is not revealed and local spatial fluctuations in DCE parametric maps remain unexplained. The recently introduced Ultrafast Doppler Tomography (UFD-T) has been shown able to reconstruct the 3D vascular network of a rat brain with a 100µm resolution. It is applied here to tumor vasculature imaging and quantitative hemodynamics assessment along with DCE-US to show the complementarity between the techniques.

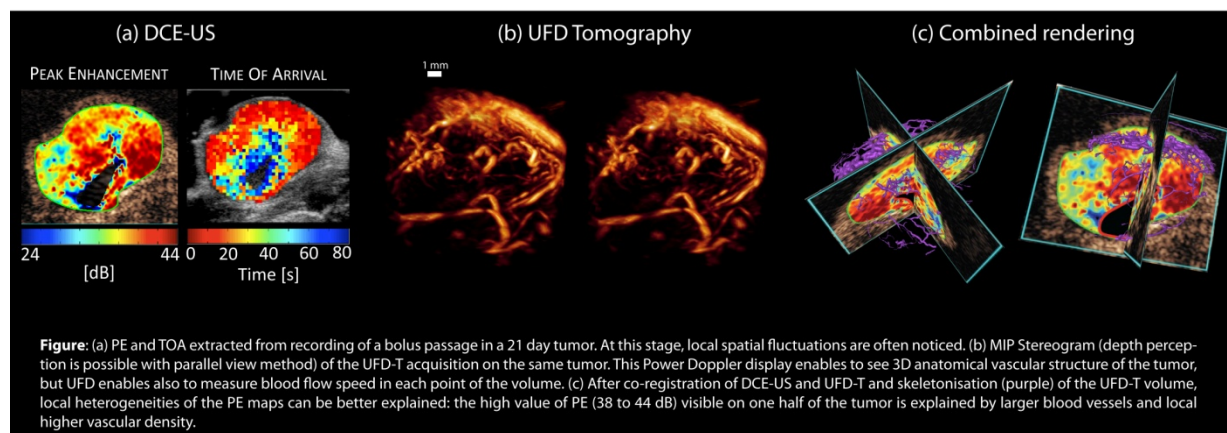
#### Statement of Contribution/Methods

Lewis lung carcinoma (3LL) fragments were subcutaneously implanted in 4, C57BL6 mice imaged at days 9, 15 and 21. UFD-T was performed first : a 15 MHz ultrasound probe (128 elements, 0.08 mm pitch), mounted on a motorized stage with four degrees of freedom was used to acquire 18 (10° apart) swept scans made of 50 slices (Δslice = 200 µm). For each slice a UFD acquisition, consisting of 800 (8 angle compound plane wave emission) frames, is done at a frame rate of 500Hz, then processed to obtain one ultrasensitive Power Doppler image. This dataset was merged in a 10mm wide 3D volume.

DCE-US was then performed in the 0° and 90° planes. A bolus of Sonovue (Bracco Suisse SA) was injected at 1mL/kg and 2mL/min, and microbubble bolus passage was recorded for 60s. Typical perfusion parameters (Peak Enhancement (PE) and Time of Arrival (TOA)) were then extracted from the time-intensity curves and correlated to Ultrafast Doppler vascular estimation.

#### Results/Discussion

UFD-T enabled to reconstruct tumor vascular structure with a 100µm resolution and to measure axial blood flow speed between 0.2 and 2 cm/s. PE maps were calculated from DCE-US acquisition and local signal heterogeneities were shown to be correlated to the repartition of blood vessels: low values of PE indicated local poor blood vessel density. Also TOA gradients can be explained with respect to structural (smaller vessels toward the center of the tumor) and dynamic (blood flow speed measurements) parameters that are revealed by UFD-T.



2E-2

### 10:45 am Ultrasound Microangiography of the Metacarpophalangeal Joint using Ultrafast Doppler

David Maresca<sup>1</sup>, Mathieu Pernot<sup>1</sup>, Mickaël Tanter<sup>1,2</sup>; <sup>1</sup>Institut Langevin, ESPCI ParisTech, CNRS UMR 7587, INSERM U979, France

#### Background, Motivation and Objective

Rheumatoid arthritis (RA) is a common autoimmune disease associated with chronic inflammation, referred to as synovitis, and ultimately joint destruction. It is acknowledged that ultrasound Power Doppler imaging can reveal subclinical synovitis [Grassi W, Filippucci E: Rheumatoid arthritis: diagnosis of RA. Nature Reviews Rheumatology 2013] but the quantification of inflammation stages is currently limited by the coarse resolution of conventional Doppler imaging. Here we show that ultrafast Doppler imaging [Tanter M, Fink M: Ultrafast Imaging in Biomedical Ultrasound. IEEE transactions on UFFC 2014] characterizes metacarpophalangeal joint microvasculature with an unprecedented accuracy, making it a promising microangiography method for the early diagnosis of RA.

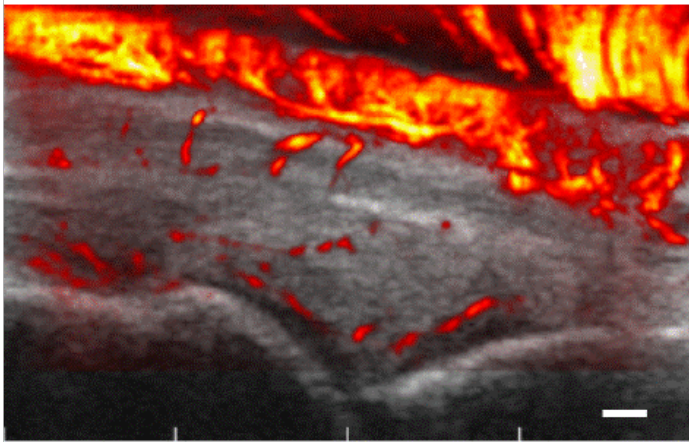
#### Statement of Contribution/Methods

We made use of a 15 MHz probe (256 elements linear array, 0.125 mm pitch) connected to a programmable ultrafast ultrasound scanner (Aixplorer, Supersonic Imagine, France). We insonified the metacarpophalangeal joint of 13 healthy volunteers with a dedicated ultrafast Doppler imaging sequence consisting of 41 plane wave transmissions at a pulse

repetition frequency of 20 kHz during one second. The received ultrasound data were beamformed and digitally filtered to get rid of tissue clutter. Power Doppler maps were computed and overlaid on co-registered Bmode images of the joint anatomy (see Figure).

### Results/Discussion

Ultrafast Doppler imaging allowed for the detection of healthy metacarpophalangeal joint microvasculature, which is invisible in conventional Power Doppler imaging. We imaged microvascular blood flow in 12 out of 13 healthy joints, with Doppler signal to noise ratios of the order of 5 dB. In addition, we computed for each individual a functional capillary density (defined as the length of perfused capillaries in mm per tissue area in mm<sup>2</sup>) and obtained values of the order of  $0.6 \pm 0.1$  mm capillary/mm<sup>2</sup> tissue. The method, which can be readily implemented on ultrafast ultrasound scanners, shows strong potential for the early diagnosis of RA and has the advantage of being fully noninvasive. A group of RA patients with different stages of inflammation will be investigated next.



**Ultrafast Doppler imaging of the metacarpophalangeal joint of a healthy volunteer. The scalebar represents 1 mm.**

2E-3

### 11:00 am Flow Detection based on the Spatial Coherence of Backscattered Echoes

You Li<sup>1</sup>, Jeremy Dahl<sup>1</sup>,<sup>1</sup>Biomedical Engineering, Duke University, Durham, NC, USA

#### Background, Motivation and Objective

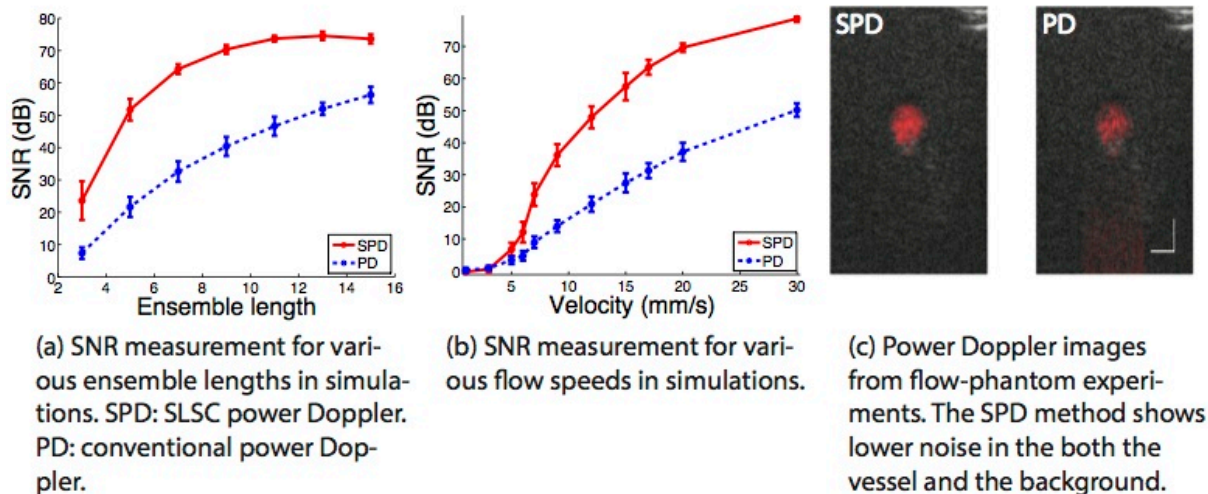
Power Doppler imaging is a common method for flow detection in various organs. Compared to color Doppler imaging, power Doppler imaging can provide higher sensitivity with slow flow detection at the expense of direction information. However, it requires a large ensemble to achieve high SNR, limiting the frame rate to a few frames per second, and may suffer from two major noise sources: thermal noise and reverberation clutter. These two noise sources may degrade the quality of the power Doppler image and limit the detection of slow flow. In order to circumvent these two limitations, we have developed a coherent flow imaging technique.

#### Statement of Contribution/Methods

This coherent flow imaging technique utilizes power Doppler techniques with the short-lag spatial coherence imaging method, which produces the spatial coherence of backscattered echoes. Because this technique is based on the spatial coherence, spatially incoherent signals such as thermal noise and reverberation clutter can be suppressed. Therefore, the limit of detection is no longer determined by the power of the noise. This enables Doppler imaging with smaller ensemble lengths and higher frame rates. A lower detection limit of flow velocity can also be achieved. The performance of this method is demonstrated with Field II simulations, and phantom experiments and in-vivo studies on a Verasonics scanner. The results were compared with conventional power Doppler techniques.

#### Results/Discussion

Simulations showed that coherent flow imaging yielded a 15-25 dB increase of contrast over conventional power Doppler imaging, particularly when thermal noise is high. Due to this improvement, the coherence flow method requires smaller ensemble lengths (Fig. (a)), potentially improving frame rate by a factor of 2. Also, simulations with flow speed varying from 1 mm/s to 30 mm/s demonstrated that the method had a limit of detection ~30% lower than that of the power Doppler (Fig. (b)). Experimental studies with a 6-mm diameter flow phantom confirmed the superiority of the coherent flow method, detecting flow with a velocity ~30% below limit of power Doppler with lower noise (Fig. (c)). Application of the coherent flow imaging to in vivo thyroid demonstrated greater sensitivity to blood flow of small arteries compared to conventional power Doppler imaging.



2E-4

**11:15 am Improved Wall Shear Rate Method for Robust Measurements**

Stefano Ricci<sup>1</sup>, Abigail Swillens<sup>2</sup>, Alessandro Ramalli<sup>1</sup>, Magnus Cinthio<sup>3</sup>, Patrick Segers<sup>2</sup>, Piero Tortoli<sup>1</sup>; <sup>1</sup>Information Engineering, University of Florence, Florence, Italy, <sup>2</sup>IBiTech-bioMMeda, Gent University, Belgium, <sup>3</sup>Biomedical Engineering, Lund University, Lund, Sweden

**Background, Motivation and Objective**

Wall Shear Rate (WSR), being related to the frictional force that the blood exerts on the arterial wall, has the potential to be a prognostic marker of vascular pathology. WSR can be obtained by assessing the blood velocity variation in the radial direction near the wall. However, in such a region, the echo-signal is masked by clutter, and the velocity profile needs to be restored. Moreover to assess the accuracy of a WSR measuring method, a gold standard WSR is necessary.

In this work we propose an improved velocity reconstruction method for WSR measurement based on a two-step interpolation process. The method is verified through realistic multiphysics simulations and *in-vivo* investigations.

**Statement of Contribution/Methods**

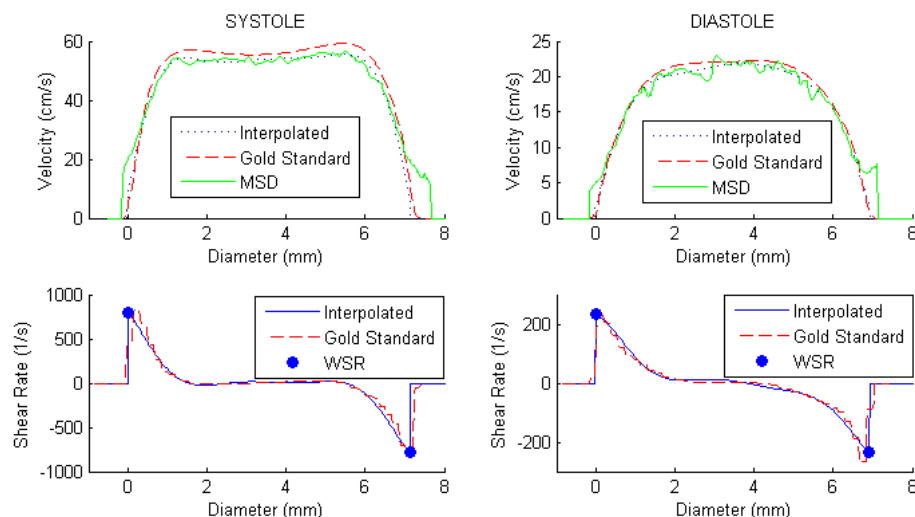
WSR-algorithm: B-mode images and multigate spectral Doppler (MSD) profiles are simultaneously reconstructed from the raw echo data. The wall positions estimated from the B-mode image are superimposed to the profile. The flow profile in the regions close the walls is replaced by a linear interpolation. The resulting profile, i.e. the central section of the MSD profile with the interpolated component on each side, is fitted through a polynomial function. The WSR is selected as the maximum of the derivative of this fitting function, evaluated in the proximity of the wall.

Validation: The accuracy was assessed by analyzing several frames generated by FIELD II simulations in a patient-specific carotid bifurcation in which the flow/wall scatterers were moved according to fluid-structure interaction (FSI) simulations. Moreover, the method was tested by scanning 10 healthy volunteers and 10 patients with cardiovascular diseases through the ULA-OP system.

**Results/Discussion**

The simulations showed that the two-step interpolation method is able to reconstruct the velocity with a 5% RMS error and to estimate the WSR with an accuracy of -10.5%. The sample frames reported in figure, taken during systole (left) and diastole (right), compare the profiles obtained by: MSD from raw FIELD II data (where clutter is visible), interpolated through the proposed method (where clutter is removed), and gold standard (FSI data). The shear rate, i.e. the derivative of the interpolated profile, and the gold standard are shown as well. Filled circles represent the measured WSR. *In-vivo* measurements (range 500 - 1400 1/s) confirm the method suitability for clinic applications.





2E-5

### 11:30 am In vivo Evaluation of An Objective Method to Select Power Doppler Wall Filter Cut-Off Frequency for Microvascular Quantification

Mai Elfarnawany<sup>1,2</sup>, Matthew R. Lowerison<sup>2,3</sup>, M. Nicole Hague<sup>2,4</sup>, Ann F. Chambers<sup>3,4</sup>, James C. Lacefield<sup>2,3</sup>; <sup>1</sup>Biomedical Engineering Graduate Program, Western University, Canada, <sup>2</sup>Robarts Research Institute, Western University, Canada, <sup>3</sup>Department of Medical Biophysics, Western University, Canada, <sup>4</sup>London Regional Cancer Program, London, ON, Canada

#### Background, Motivation and Objective

Operator-dependent settings such as the wall filter cut-off frequency control the incidence of artifacts in Doppler images and limit the reliability of comparisons of Doppler vascular indices across longitudinal studies. To address this problem, we developed the wall filter selection curve (WFSC) method to objectively select the cut-off frequency. Selection curves are constructed by plotting the color pixel density as function of the filter cut-off and exhibit characteristic intervals within which the cut-off is automatically selected. In previous studies, the WFSC method improved vascular quantification accuracy in multiple-vessel flow phantoms. We report here the first evaluation of the WFSC method in a tumor model.

#### Statement of Contribution/Methods

3-D quadrature demodulated power Doppler data were acquired at 40 MHz from murine xenograft breast cancer tumors over a six-week study. The WFSC method was applied in each image plane to select a cut-off frequency for an IIR wall filter. Images reconstructed using the WFSC method were compared to images processed using a fixed cut-off frequency equal to the mean of the WFSC-selected cut-offs for that volume. Longitudinal variations in the WFSC-selected cut-offs were also analyzed.

#### Results/Discussion

Consistent with our flow-phantom data, selection curves for tumor images exhibited one or more characteristic intervals corresponding to the number of distinct distributions of Doppler signal power (Fig. 1(a) and 1(b)). 3-D images processed using the WFSC method depicted additional vascular structures compared to volumes processed using a fixed cut-off frequency (Fig. 1(c) and 1(d)). The mean WFSC-selected cut-off showed small but significant variation among images acquired at different time points from each tumor (preliminary results using 3 animals x 3 time points, ANOVA,  $p < 0.05$ ), which demonstrates the relevance of adjusting the cut-off frequency to match changing flow conditions. The WFSC method selects among 100 candidate cut-offs for each image plane in the time needed to manually compare images reconstructed using five different fixed cut-offs. Therefore, the WFSC method can facilitate acquisition of reliable, quantitative Doppler images by inexperienced or time-sensitive operators.

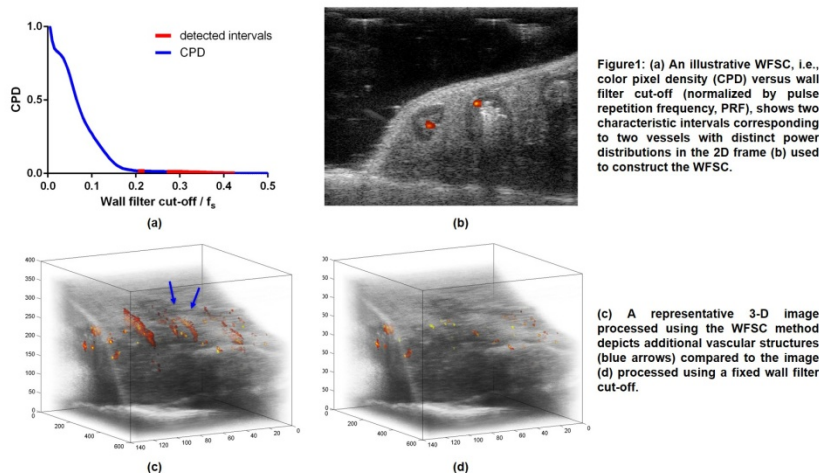


Figure1: (a) An illustrative WFSC, i.e., color pixel density (CPD) versus wall filter cut-off (normalized by pulse repetition frequency, PRF), shows two characteristic intervals corresponding to two vessels with distinct power distributions in the 2D frame (b) used to construct the WFSC.

(c) A representative 3-D image processed using the WFSC method depicts additional vascular structures (blue arrows) compared to the image (d) processed using a fixed wall filter cut-off.

**11:45 am 2D Flow Imaging in Rat Carotid Bifurcation Using Automatic Image Segmentation and Micro Ultrasonic Particle Image Velocimetry**

Ming Qian<sup>1,2</sup>, Lili Niu<sup>1</sup>, Qifa Zhou<sup>2</sup>, K. Kirk Shung<sup>2</sup>, Hairong Zheng<sup>1</sup>; <sup>1</sup>Paul C. Lauterbur Research Center for Biomedical Imaging, Shenzhen Institutes of Advanced Technology, Chinese Academy of Sciences, Shenzhen, Guangdong, China, People's Republic of; <sup>2</sup>NIH Ultrasonic Transducer Resource Center and Department of Biomedical Engineering, University of Southern California, Los Angeles, California, USA

**Background, Motivation and Objective**

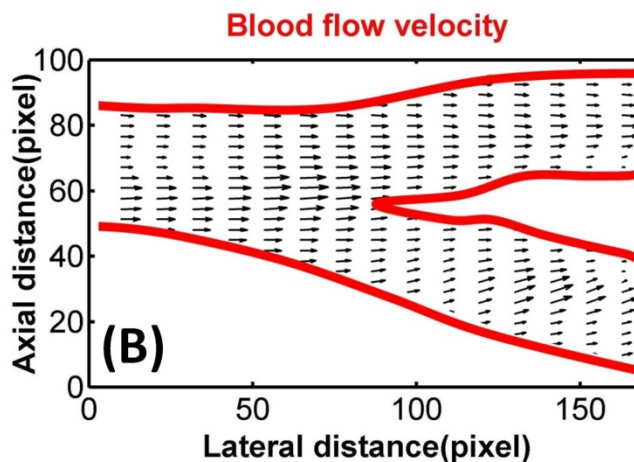
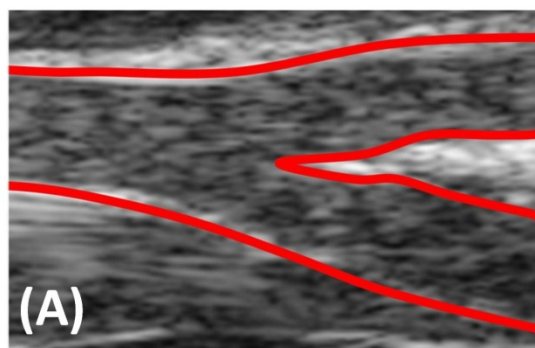
It is often difficult to characterize blood flow in rat carotid bifurcation artery (CBA) due to sophisticated artery structure, small artery size, and fast moving blood. By combining high-frequency ultrasound and optical particle image velocimetry (PIV), micro echo PIV (MicroEPIV) is suitable for such application with high spatial resolution and fast imaging speed. Since CBA has irregular geometry in an ultrasound image, accurate determination of the blood region (BR) is necessary before PIV processing, so as to ensure accurate measurements of near-wall flow velocity. Here, ultrasound contrast images were automatically segmented based on a level set method and MicroEPIV was used for imaging blood flow in CBA of a living rat.

**Statement of Contribution/Methods**

The rat was anesthetized with isoflurane gas to maintain heartbeat at 300beats/min, and was put on a heating pad to keep its body temperature around 37°C. A proper dose of ultrasound contrast microbubbles (UCMs, SonoVue, Italian Bracco Company) was injected via caudal vein to achieve a bubble concentration of  $1\sim5\times10^5$  bubbles/ml in the blood. Image sequence of CBA was acquired with a Vevo2100 (VisualSonics, Canada) equipped with a 30MHz linear array probe. A sequence of ultrasound images were acquired at imaging speed of 300 frames/sec. UCMs in BR moved much faster than vessel walls and tissue and caused larger grayscale variation in BR in two sequential frames, and initial contour of the BR can be generated based on such variations. This initial contour converged to the boundaries of the BR based on a level set model. BRs in two consecutive frames were subjected to a cross-correlation-based PIV algorithm, and flow velocity map was obtained.

**Results/Discussion**

Fig. A shows a typical computer-obtained delineations (in red) superimposed on a rat CBA's B-mode image. This automatic segmentation was favorably compared to two radiologists' hand-outlined boundaries, and good agreement was found between these two methods. Fig. B shows the blood flow velocity vector map at peak systole. The peak velocity in the map was at the carotid common artery region, and the value was 65 cm/s. The peak velocity against time was compared with ultrasonic pulse wave Doppler and a good agreement was found, with deviations below 5%. In sum, the combination of automatic image segmentation and MicroEPIV enables better imaging of blood flows in rat CBA.



## 3E - MSP: Medical Signal Processing

Boulevard

Friday, September 5, 2014, 10:30 am - 12:00 pm

Chair: **Svetoslav Nikolov**  
BK Medical, Herlev

3E-1

### 10:30 am New performance metrics for ultrasound pulse compression systems

Sevan Haput<sup>1</sup>, James McLaughlan<sup>1</sup>, David M. J. Cowell<sup>1</sup>, Steven Freear<sup>1</sup>; <sup>1</sup>School of Electronic and Electrical Engineering, University of Leeds, Leeds, United Kingdom

#### Background, Motivation and Objective

In medical ultrasound, B-mode images are log-compressed and displayed with a grayscale map, typically on a 40-60 dB dynamic range. The image formation process is the same for an ultrasound pulse compression system using coded excitation. Metrics, such as *full width at half maximum (FWHM)*, *peak sidelobe level (PSL)* and *integrated sidelobe level (ISL)*, used to evaluate pulse compression systems were adopted from radar and communications. These metrics are utilized to evaluate the performance of an auto-correlation function, which is the ideal case. In ultrasound imaging, frequency and depth dependent attenuation, dispersion, harmonic generation and limited transducer bandwidth create a more complicated case far from the ideal.

#### Statement of Contribution/Methods

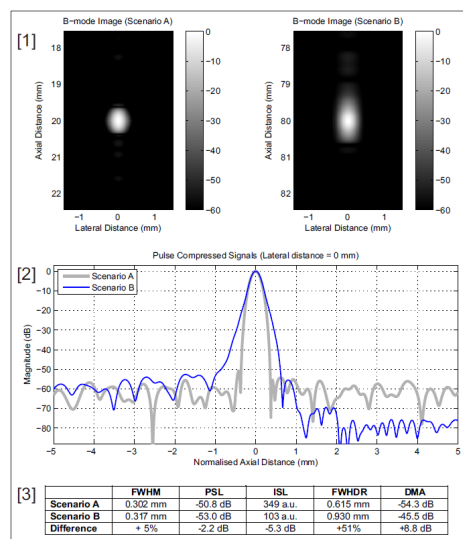
This study proposes two new performance evaluation metrics for ultrasound imaging: *full width at half dynamic range (FWHDR)* and *doubled mainlobe level (DML)*. The *DML* corresponds to the level where the projection of point spread function's (PSF) area at half dynamic range is doubled, which is equivalent to  $\sqrt{2} \times FWHDR$ . The *DML* reflects a combination of mainlobe widening and sidelobe behaviour.

Two B-mode images, as shown in Figure (1), were acquired in an attenuating medium ( $\alpha = 0.54$  dB.MHz.cm) using a 5 MHz chirp excitation from a point scatterer located at **A)** 2 cm with a broadband array and **B)** 8 cm with a narrowband array resulting in a loss of signal bandwidth.

#### Results/Discussion

When central lines of both images are compared visually and quantitatively as given in Figure (2) and (3), the *FWHM* shows a negligible difference. Scenario **B** performs 2.2 and 5.3 dB better than **A** in terms of *PSL* and *ISL*, respectively. However, the B-mode images relating to these scenarios do not support the quantitative results achieved by these metrics. When *FWHDR* was used to measure the axial width, there was a difference of 51% between these two cases. By using the *DML* the performance of scenario **A** is evaluated as 8.8 dB better than **B**.

The existing metrics are critical for the efficient design of a pulse compression system. However, to evaluate B-mode image quality, metrics based on dynamic range and PSF are necessary. These new metrics are especially important for applications like superharmonic imaging with chirps, where the final signal is a summation of higher-order harmonics with an imponderable mainlobe and sidelobe behaviour.



3E-2

### 10:45 am High-Resolution Blood Flow Imaging Directly Through the Skull

Aryaz Baradaran<sup>1,2</sup>, Jeffrey Sadler<sup>3</sup>, Jason R. B. Taylor<sup>2</sup>, Roman Gr. Maev<sup>2,3</sup>; <sup>1</sup>Electrical and Computer Engineering, University of Windsor, Ontario, Canada, <sup>2</sup>Institute for Diagnostic Imaging Research, University of Windsor, Windsor, Canada, <sup>3</sup>Department of Physics, University of Windsor, Windsor, Canada

#### Background, Motivation and Objective

Ultrasonic blood flow imaging and diagnosis of injuries under the skull remains a challenging problem since in most emergency cases, such as a battlefield or ambulance, there is no MRI or CT scanner. Existing blood flow imaging techniques are difficult to employ due to the thickness of the skull and acoustic properties. We introduce an efficient technique to extract blood flow features and verify it on a laboratory scale.

**Statement of Contribution/Methods**

The array is a medical-grade 128-element 2.25 MHz phased-array, driven in a linear pattern focused approximately at the blood flow region. For each point in the region of interest, scanning is repeated 15 times with a 0.5 ms delay. We first construct three bundles of consecutive A-scans as  $\{A_1, A_2, A_3\}$ ,  $\{A_7, A_8, A_9\}$ ,  $\{A_{13}, A_{14}, A_{15}\}$ . Moving features of the middle A-scan in each bundle are initially determined from its neighbor scans where the results are denoted by  $M^2_{1,3}$ ,  $M^8_{7,9}$ ,  $M^{14}_{13,15}$ , respectively. The vector  $[M^2_{1,3}, M^8_{7,9}, M^{14}_{13,15}]$  is decomposed into low- and high-resonance components via a dual-Q-factor resonance based transform. Subbands of the two components are first denoised and then reconstructed with an inverse transformation. The obtained signal is smoothed via the fast-smoothing technique, which recursively implements shift and multiply type smoothing. To extract the desired features, we designed a highpass FIR digital filter where the passband edge frequency and ripple size can be tuned for the array used in experiments. A single A-scan per position is constructed from the indices of the maximum absolute value among its processed moving feature vectors. The same procedure is applied to the rest of A-scans in the scanning area. From these A-scans, B-scans of the flowing region are created. The main contributions of the proposed technique are: 1) extracting high-resolution blood flow images beneath the skull; 2) being fully automated; 3) its efficiency for real-world application, as few A-scans are required.

**Results/Discussion**

Experiments were carried out using custom skull phantoms with realistic acoustic properties, including a diploe layer and undulating inner surface. Vessel analogues were modeled with thin-walled Tygon tubing of varying diameter bound in a tissue-mimicking solid. The results indicate a significant improvement over recent techniques in the literature, including our previous method.



Fig.1. (a) Custom made phantom used in our previous work; (b) Structure of the skull in these phantoms (top to bottom: outer, middle, and inner layers, respectively); (c) Additionally, a more realistic phantom has been used in this paper (left: perspective view; right: inner view with the brain and vessels); (d) Scanner and the experiment setup; (e) The best result obtained using our previous work; (f) Proposed method.

3E-3

**11:00 am Dynamic Ultrasound Imaging of Cervical Spine Intervertebral Discs**

Mingxin Zheng<sup>1,2</sup>, Aidin Masoudi<sup>2</sup>, Daniel Buckland<sup>2,3</sup>, Brian Stemper<sup>4</sup>, Narayan Yoganandan<sup>4</sup>, Thomas Szabo<sup>1</sup>, Brian Snyder<sup>2,5</sup>; <sup>1</sup>Boston University, Boston, MA, USA, <sup>2</sup>Beth Israel Deaconess Medical Center - Harvard Medical School, Boston, MA, USA, <sup>3</sup>Massachusetts Institute of Technology, Cambridge, MA, USA, <sup>4</sup>Medical College of Wisconsin, Milwaukee, WI, USA, <sup>5</sup>Children's Hospital Boston, Boston, MA, USA

**Background, Motivation and Objective**

The diagnoses of C-spine injury and degenerative intervertebral disc (IVD) disease are challenging because these conditions are more evident under dynamic loading conditions. This measurement requirement rules out CT and MRI for evaluation of C-spine kinematics in work environments. Ultrasound (US) imaging, though more usually applied to soft tissue imaging, can be used to track the movement of vertebrae and IVDs under dynamic conditions. The aim of this study was to validate the ability of portable ultrasound to accurately track movement of vertebrae body and measure IVD deformation *ex-vivo*.

**Statement of Contribution/Methods**

Cadaveric human cervical C6-7 functional spinal units (FSU) were submerged in 0.9% saline at 37°C to replicate physiological conditions. Each FSU was subjected to sinusoidal compressive/distractive loads (90N @1-8Hz) and imaged by US (4 MHz linear array @ 50 frames/s). The vertebrae were modeled as rigid bodies, attributing the motion of the FSU to deformation of the IVD. Regions of interest (ROI) corresponding to distinct bony vertebral landmarks were specified by the user on the initial B-mode image and subsequently tracked automatically using a block matching operation on the radio frequency (RF) US image data generated during dynamic loading. We developed a normalized precise, error-correcting, cross correlation tracking algorithm with parabola fitting for subsample motion. The dynamic motion of the FSU derived using this US algorithm was compared to direct measurements using a linear variable differential transformer (LVDT).

**Results/Discussion**

C6-7 IVD deformation derived from US using the RF algorithm accounted for ~92% of the variation in IVD motion compared to that measured directly using the LVDT for frequencies ≤6Hz and 77% of the variability at 8Hz ( $R^2=0.77$ ). This establishes the feasibility of using clinical US to measure in real time the dynamic IVD deformation in response to applied loads. This will allow the non-invasive assessment of the mechanical compliance of human cervical spine FSU. As treatments to reconstitute degenerated IVD become available, quantitative analysis of IVD mechanics will be necessary to determine which patients will be appropriate for these treatments and to monitor their response.

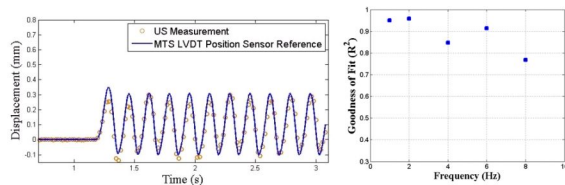


Figure 1. Representative C6-7 IVD deformation deduced by RF compared to deformation measured directly by in-line LVDT for applied -90N to +90N sinusoidal force @ 6Hz. Blue line is LVDT displacement measurements and red circles are displacements deduced from US. The coefficient of determination for US vs. LVDT measurements of IVD deformation plotted as function of applied frequency on the right

### 3E-4

#### 11:15 am Improved Detection of Kidney Stones Using an Optimized Doppler Imaging Sequence

Bryan Cunitz<sup>1</sup>, Barbrina Dunmire<sup>1</sup>, Marla Paun<sup>1</sup>, Oleg Sapozhnikov<sup>1</sup>, John Kuciewicz<sup>1</sup>, Ryan Hsi<sup>2</sup>, Franklin Lee<sup>2</sup>, Matthew Sorensen<sup>2</sup>, Jonathan Harper<sup>2</sup>, Michael Bailey<sup>1</sup>; <sup>1</sup>Applied Physics Lab, University of Washington, Seattle, WA, USA, <sup>2</sup>Dept. of Urology, University of Washington School of Medicine, Seattle, WA, USA

##### Background, Motivation and Objective

The imaging standard in the management of nephrolithiasis, or kidney stones, is computed tomography (CT), not ultrasound. This is primarily due to ultrasound's broad range of sensitivity (20% - 80%) and specificity (70% - 100%) in the detection of stones. Previous work has shown that kidney stones imaged under color-flow Doppler ultrasound appear to "twinkle". That is to say, there is a rapidly changing Doppler velocity measurement on the stone's location. Recent investigations suggest the source of this artifact is micron sized bubbles in the cracks of the stone. Under this hypothesis, we have developed an ultrasound algorithm optimized to enhance the bubble signature to improve the detection of stones compared with B-mode.

##### Statement of Contribution/Methods

A Verasonics Ultrasound engine with an HDI P4-2 and C5-2 imaging probe was used. The algorithm was tuned/optimized using an in-vitro phantom by maximizing the power of the twinkling artifact on the stone while suppressing motion artifact. B-mode and stone mode (S-mode) were compared on 6 ( $\leq 1$  mm) stones pushed into a tissue phantom and in a clinical study with 9 patients/27 stones (mean size  $4.4 \pm 3.3$  mm). The patients were scanned for kidney stones and the RF data of the detected stones was saved for further algorithm optimization.

##### Results/Discussion

In vitro results showed improved detection of S-mode over B-mode in detecting stones  $\leq 1$  mm (Fig. 1). For the clinical study, the custom stone detection algorithm had a sensitivity of 80%, specificity of 89.6%, positive predictive value of 76.2%, and negative predictive value of 91.5%. The algorithm eliminated two false positives identified with B-mode alone. False positives are important because they can lead to unnecessary surgery. These results show that an algorithm tuned to stone specific signatures, such as small bubbles on hard structures, rather than developed for soft tissue differentiation, can improve the detection of kidney stones. The improved detection algorithms also show the potential for reduced user variability and automation. This work was supported by NIH DK43881 and DK092197, and NSBRI through NASA NCC 9-58.

### 3E-5

#### 11:30 am Ultrafast Plane Wave Imaging Based Pulsed Magnetomotive Ultrasound

Pei-Hsien Ting<sup>1</sup>, Yi-Da Kang<sup>2</sup>, San-Yuan Chen<sup>2</sup>, Meng-Lin Li<sup>1,3</sup>; <sup>1</sup>Dept. of Electrical Engineering, National Tsing Hua University, Hsinchu, Taiwan, <sup>2</sup>Department of Materials Science and Engineering, National Chiao Tung University, Taiwan, <sup>3</sup>Institute of Photonics Technologies, National Tsing Hua University, Taiwan

##### Background, Motivation and Objective

Recently, pulsed magnetomotive ultrasound (pMMUS) imaging has been introduced to detect superparamagnetic iron oxide nanoparticles (SPIO) which is not able to be visualized by conventional ultrasound. However, because of the used magnetic short pulse, the reported pMMUS only can use a single-element ultrasound transducer along with mechanical scanning to perform imaging, which significantly limits the imaging frame rates.

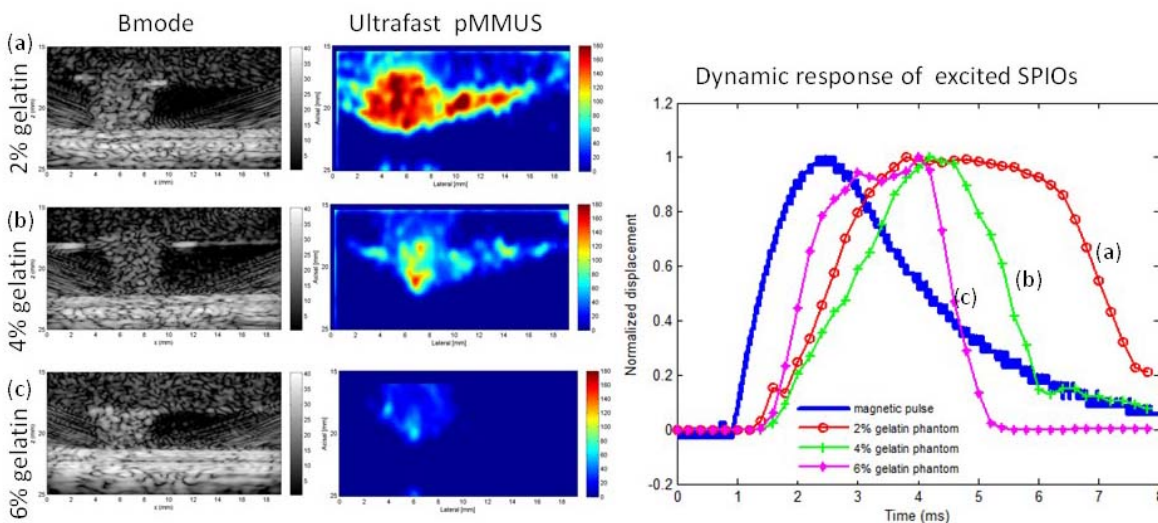
##### Statement of Contribution/Methods

To solve this problem, we propose an ultrafast plane wave imaging based pMMUS technique. The ultrafast frame rate of plane wave imaging is fast enough to track the magneto-motion of the excited SPIOs during the period of the magnetic pulse being applied. Therefore, the proposed ultrafast plane wave pMMUS is capable of visualizing the dynamic response of the excited SPIOs, which is highly correlated to tissue characteristics such as viscosity and elasticity, to an externally-applied magnetic pulse. In addition, a new pMMUS motion tracking algorithm based on ultrafast plane wave imaging is developed to reduce the effect of magnetic field inhomogeneity.

##### Results/Discussion

In our experiments, ultrafast plane wave imaging with a 5 kHz frame rate was used to implement the pMMUS where the SPIO motion induced by an 8-ms magnetic pulse was tracked. The results showed that there were significant differences between the ultrafast plane wave pMMUS images of the phantoms with and without SPIOs embedded. There was a monotonic increase in displacement with increased concentration of SPIOs. In addition, gelatin phantoms with 2%, 4% and 6% gelatin were used to mimic tissues with different elasticity and viscosity. The dynamic responses of the excited SPIOs in the three types of phantoms were distinguishable (see the figure). Overall, it is demonstrated that the feasibility of our proposed ultrafast plane wave pMMUS imaging technique for the visualization of the magneto-motion and dynamic response of the SPIOs under the excitation of a short magnetic pulse. More studies are required to further improve the magneto-motion tracking algorithm and explore the relationship between the dynamic response of the excited SPIOs and the tissue viscosity and elasticity.





3E-6

### 11:45 am Automatic measurement of biparietal diameter with a portable ultrasound device

**Naiad Hossain Khan<sup>1</sup>**, Eva Tegnander<sup>2,3</sup>, Johan Morten Dreier<sup>2</sup>, Sturla Eik-Nes<sup>2,3</sup>, Hans Torp<sup>1</sup>, Gabriel Kiss<sup>1</sup>, <sup>1</sup>ISB, MI Lab and Department of Circulation and Medical Imaging, NTNU, Trondheim, Norway, <sup>2</sup>National Center for Fetal Medicine (NCFM), St. Olavs Hospital, Trondheim, Norway, <sup>3</sup>Department of Laboratory Medicine, Children's and Women's Health (LBK), NTNU, Trondheim, Norway

#### Background, Motivation and Objective

Knowledge of the exact gestational age and expected day of delivery is essential for providing optimal medical surveillance. Fetal biparietal diameter (BPD) computed by ultrasound has been shown to correlate well with gestational age (before week 22) or it can be used for detecting growth abnormalities, later in the pregnancy. We have been developing a portable ultrasound scanner (the Umoja scanner) that can be used by midwives in LMIC countries with limited ultrasound and technological expertise. The aim of this work was to develop a technique for automatized computation of BPD which can run on tablet devices.

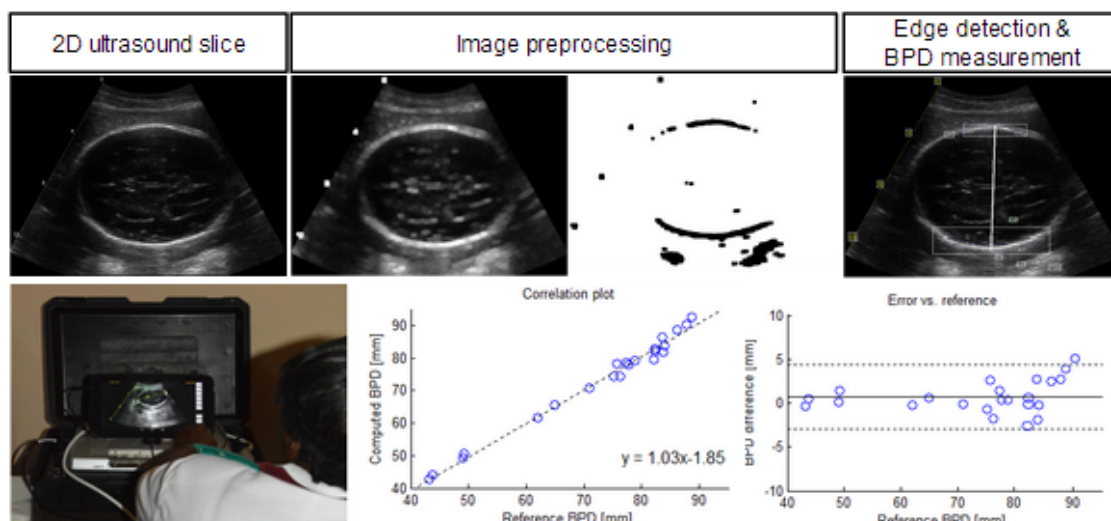
#### Statement of Contribution/Methods

An ultrasound image containing a contour of a fetal head is recorded with the prototype scanner. The image is preprocessed: converted to grayscale, gain adjusted, smoothed, dilated/eroded and finally binary thresholded. The potential contour candidates and their Cartesian coordinates are identified by applying the Canny edge detector. Region candidates for the measurement are found by connected component analysis on the edge detection result. A line connecting the two most distant edges across the skull is computed. The original grayscale values along this line are used to identify the top and the bottom edge points which are used for measuring the BPD value. All image processing is performed using OpenCV (Open source Computer Vision), which is optimized for tablet devices.

#### Results/Discussion

27 ultrasound images suitable for BPD measurement were acquired by an experienced midwife and 9 student midwives with limited or no prior ultrasound experience, on 8 different fetuses from 18 to 34 weeks. Both manual (experienced midwife) and automatic BPD measurements were computed. The correlation plot and the error versus reference plot are shown in figure 1, the mean error $\pm$ 1.96\*STD was  $0.72\pm 3.62$  [mm], while the correlation coefficient was  $R=0.9932$ . The automatic measurement failed in 4 cases.

The overall computation time on a Nexus 10 tablet was 3.47 seconds, therefore our tool is suited for a portable device with limited computation power. The agreement of the proposed algorithm with the reference measurements is comparable to the interobserver agreement for BPD (2.9mm from literature study). Testing of the method on an extended dataset, including fetuses at different gestational ages is ongoing.



## 4E - Acoustic Microfluidics

Marquette

Friday, September 5, 2014, 10:30 am - 12:00 pm

Chair: **Pierre Khuri-Yakub**  
Stanford University

4E-1

### 10:30 am Interaction of Microbubbles and Microdroplets with Ultrasound

Michel Versluis<sup>1</sup>; <sup>1</sup>MIRA Institute for Biomedical Technology and Technical Medicine, MESA+ Institute for Nanotechnology, Physics of Fluids Group, University of Twente, Enschede, Netherlands

#### Background, Motivation and Objective

Bubbles and droplets are important for a large variety of medical, microfluidic and nanotechnology applications in acoustics. Stabilized microbubbles are used as contrast agents for ultrasound imaging and therapy. In lab-on-a-chip technology transient bubbles act as actuators, mixers, and valves. Piezo-driven inkjet printing excels in fast, reliable and accurate microdroplet deposition for IC prints, 3D engineered tissues and food products. Bubble-driven high-speed jet sprays assist in the cleaning of surfaces and monodisperse aerosols for pulmonary drug delivery are produced using surface acoustic wave atomization. Key to all these applications is precise acoustic control of the interaction of ultrasound with the bubbles and droplets. The challenge here is the combined microscopic length scales and ultrashort time scales associated with the mechanisms controlling the bubble and droplet formation and activation processes.

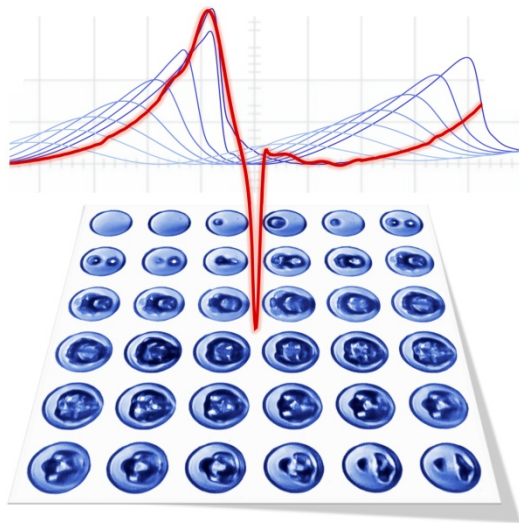
#### Statement of Contribution/Methods

The perfect example of how droplets, bubbles and ultrasound interact is the use of acoustically sensitive emulsion microdroplets. The physical mechanisms underlying the acoustic activation of these phase-change emulsions into vapor bubbles, termed acoustic droplet vaporization, have not been well understood. The droplets have a very high activation threshold, its frequency dependence does not comply with homogeneous nucleation theory and focusing spots have been observed while the wavelength is at least an order larger than the droplet size.

#### Results/Discussion

Here we show that acoustic droplet vaporization is initiated by a combination of two effects: highly nonlinear distortion of the acoustic wave before it hits the droplet, and focusing of the distorted wave by the droplet itself [1]. At high excitation pressures, nonlinear distortion causes significant superharmonics with wavelengths of the order of the droplet radius. The proposed model is validated with experimental data captured with an ultra high-speed camera taken at 20 million frames per second pinpointing the exact locations of the nucleation spots. Moreover, the presented mechanism explains the hitherto counterintuitive dependence of the nucleation threshold on the ultrasound frequency.

[1] O Shpak, M Verweij, HJ Vos, N de Jong, D Lohse, and M Versluis, PNAS 111, 1697–1702 (2014).



4E-2

### 11:00 am Ultrasound-induced vaporization of perfluorocarbon for efficient mixing in microfluidic channels

Marine Bezagu<sup>1,2</sup>, Fabrice Monti<sup>1</sup>, Stelios Arseniyadis<sup>2</sup>, Olivier Couture<sup>3</sup>, Mickael Tanter<sup>3</sup>, Janine Cossy<sup>2</sup>, Patrick Tabeling<sup>1</sup>; <sup>1</sup>MMN (ESPCI, CNRS, UPMC), Paris, France, <sup>2</sup>LCO (ESPCI, CNRS, UPMC), Paris, France, <sup>3</sup>Institut Langevin (ESPCI, CNRS, INSERM), Paris, France

#### Background, Motivation and Objective

Mixing two liquids in microfluidic devices remains a challenging operation. Passive mixers are robust albeit poorly flexible. In opposition, active mixers are usually more difficult to implement but have proven greater efficacy. In this context, we propose to take advantage of the concomitant use of ultrasound and perfluorocarbon (PFC), the latter benefiting from its non-miscibility with most fluids and its low boiling point, to induce mixing in microfluidic channels. Indeed, we envisioned that the vaporization of the PFC phase at the focus of a transducer would lead to a remote, fast and particularly efficient mixing of adjacent fluids with no geometry constraints. By taking advantage of the non-miscibility properties, such mixer would be compatible with both hydrophilic and hydrophobic microfluidic systems while the PFC phase could be easily recycled at the end of the run.

**Statement of Contribution/Methods**

The demonstration was achieved by concomitantly injecting a PFC stream and two adjacent phases of the same nature, travelling side by side in a microfluidic channel (Figure 1a) and by locally focusing a 2.25 MHz transducer. One of the external flows (either hydrophobic or hydrophilic) was stained with a fluorescent dye while the other one was injected pure, the PFC layer serving as a central separation. Consequently, prior to the ultrasound trigger, the two phases to be mixed appeared white and black, respectively (see Figure 1b). A series of ultrasound pulses (30 cycles every 1 ms, 12.3 MPa PNP) was emitted while a camera (35 fps) mounted on a fluorescent microscope recorded the mixing evolution. Optimum mixing was attained when the fluorescence of the mixed fluids reached an average intensity.

**Results/Discussion**

When the ultrasound were active within the microfluidic channel, less than 10 ms were necessary to switch from a laminar flow situation to a transient vaporization and mixing zone (red box, Figure 1c), after which a spontaneous separation of the mixed fluids from PFC occurs. High mixing efficacy was reached, as illustrated by the low mixing index values between 0.2 and zero (Figure 1d). We believe that such ultrasound-triggered mixing using PFC vaporization properties will lead to a new generation of switchable, extremely fast, and highly versatile mixers easily incorporable in microfluidic chips.

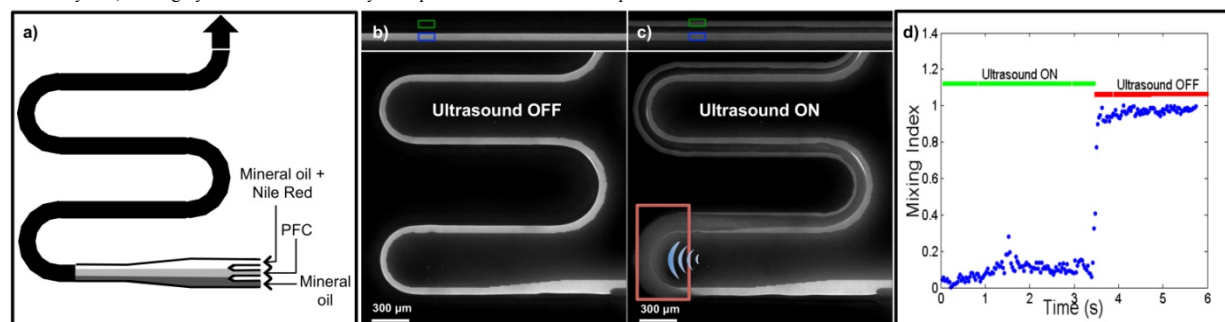


**Figure 1.** Scheme of injected fluids in the microfluidic channel (a), and microscope images of the channel with (c) or without (b) ultrasound-induced vaporization of PFC, mixing efficacy (d)

4E-3

**11:15 am Formation and Double Reversal of Micron to Submicron Thin Fluid Films using Surface Acoustic Waves**

Amgad Rezk<sup>1</sup>, Ofer Manor<sup>2</sup>, Leslie Yeo<sup>3</sup>, **James Friend<sup>1</sup>**; <sup>1</sup>MicroNano Research Facility, RMIT University, Melbourne, Victoria, Australia, <sup>2</sup>Chemical Engineering, Technion, Israel, <sup>3</sup>School of Environmental and Civil Engineering, RMIT University, Melbourne, Victoria, Australia

**Background, Motivation and Objective**

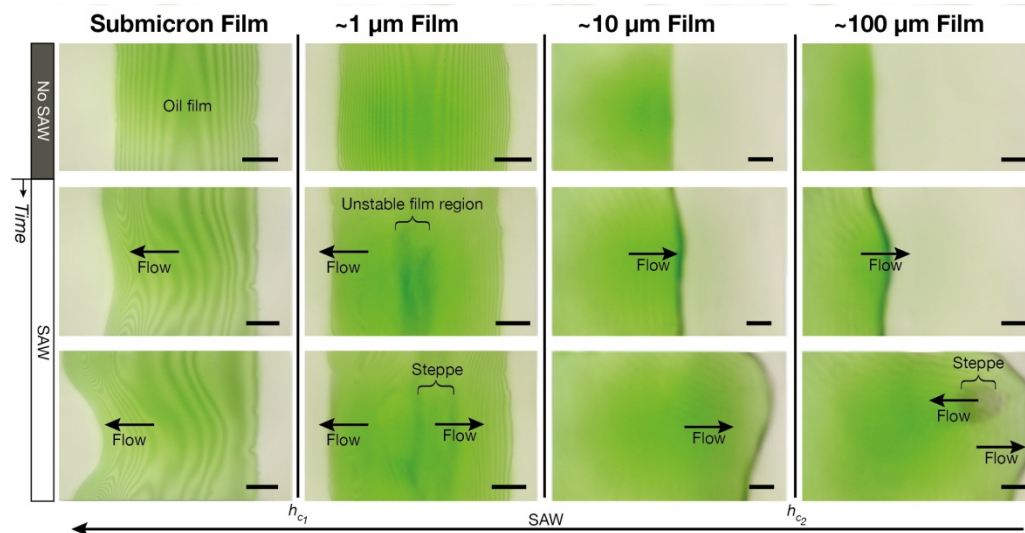
Surface acoustic wave (SAW) devices promise to overcome a broad variety of problems in microfluidics in manipulating fluids and suspended objects. One application is the formation and manipulation of thin fluid films for defining cell culture films, paint and acoustic "doctor blade" green state ceramic material deposition, and leveling photoresist. Curiously, it is possible to form and drive the rapid flow of thin fluid films using SAW, with the fluid depth defined into discrete values in turn dependent upon the wavelength of the SAW. But the phenomena is extraordinarily complex, with opposing flows, sudden fluid height changes, and rapid and perplexing surface wetting behavior.

**Statement of Contribution/Methods**

We systematically deposit wetting fluids of controlled depth using fountain pen lithography, set across the aperture of a 127.68° Y-rotated, X-propagating lithium niobate (LN) device carrying a simple, 30 MHz Rayleigh SAW propagating across the LN substrate without reflection. We used Hertzian fringes with monochromatic light and a high-speed camera to measure the thickness distribution of the thin film over time, and examined the propagation of the film's edges and bulk flow while changing the fluid's properties and the amplitude of the SAW as measured using scanning laser Doppler microvibrometry. We constructed a film flow model based on asymptotic matching techniques.

**Results/Discussion**

For sufficiently thin (submicron) films of depth less than the viscous penetration length, the acoustic waves do not penetrate into the fluid, and so there is no acoustic radiation pressure on the fluid interface. Films of this depth flow in the SAW direction via convective drift at ~1 mm/s, and remain stable over long propagation distances. Films of intermediate depth, ~10 µm, propagate in opposition to the SAW at a similar velocity as the submicron films, driven by acoustic radiation pressure now present from entry of sound into the fluid of the film. The acoustic radiation pressure also discretizes the film height to specific values until the film becomes "thick", where attenuation of the sound in the film can give rise to Eckart streaming sufficient to drive rapid flow of the film with the SAW once again, at 100 mm/s or more. The analytical model helps us collapse the data and thoroughly explain what is going on, indicating the underlying complexity of acoustic streaming.



4E-4

#### 11:30 am Ultra High Frequency Surface Acoustic Wave Driven Microfluidics

Marco Travaglini<sup>1,2</sup>, Richie Shilton<sup>2</sup>, Fabio Beltram<sup>1,2</sup>, Marco Cecchini<sup>1</sup>; <sup>1</sup>Laboratorio NEST, Scuola Normale Superiore and Istituto Nanoscienze - CNR, Pisa, Italy, <sup>2</sup>Center for Nanotechnology Innovation @NEST, Istituto Italiano di Tecnologia, Pisa, Italy

##### Background, Motivation and Objective

Surface acoustic wave (SAW) microfluidics is a promising technology for lab-on-a-chip devices owing to efficient fluid actuation capabilities in handheld devices, such as microfluidic mixing and particle manipulation. The minimum accessible volumes of digital microfluidic droplet reactors are typically in the microliter range, and this lower limit represents one of the issues of these types of devices. Within SAW microfluidics, this limitation can be related to the typical device operating frequencies being in the very high frequency (VHF) range. We therefore investigated decreasing these limits by operating devices in the ultra high frequency (UHF) range [Shilton et al. *Adv Mat*, doi:10.1002/adma.201400091 (2014)]. We demonstrated how the different acoustic length scales associated with varying the SAW operating frequency affects the acoustic streaming. We show here that efficient acoustic streaming and mixing can be carried out by exploiting 1.1 GHz devices with 1 nL reactors, significantly reducing the minimum reactor volumes previously possible in digital microfluidics.

##### Statement of Contribution/Methods

SAW microfluidic devices were fabricated by patterning straight-fingered interdigital transducers onto 128° YX lithium niobate substrates with operating frequencies in the range of 50 – 1100 MHz. We set the operating SAW amplitude of each device to 100 pm by calibration with a laser Doppler vibrometer. Finally, we placed the device under a microscope equipped with a fast camera. To study the fluid flow, deionized water seeded with 500 nm particles was dispensed into a hydrophilic well formed by patterned surface silanes. A coverslip with 385 μm spacers was placed on top of the 1 μL drops to improve the visualization. Microfluidic mixing was demonstrated with the same setup by initial segregation of fluid-particles regions.

##### Results/Discussion

We observed that as the volume is reduced to the order of nanoliters the flow dynamics in the drops exhibit a transition from vortical acoustic streaming to ring pattern accumulation at a critical diameter related to the SAW frequency in the VHF range. We demonstrated that this transition can be understood in terms of the ratio between the drops diameter  $d$  and the SAW damping length in water  $x_d$ . When  $x_d \ll d$ , a sufficient pressure gradient is established in the drops to initiate acoustic streaming rather than standing wave patterns. Additionally, we demonstrated that the acoustic streaming pattern depends on the ratio between the drops thickness  $h$  and the attenuation length of ultrasound transmitted in water  $x_f$ . As  $x_f$  becomes smaller than  $h$ , we observed that the flow becomes strongly three dimensional and the vortical pattern, typically extended over an entire droplet, compresses towards the front and a single rolling motion appears in the rear area. We lastly demonstrated that by exploiting 1.1 GHz SAW, the mixing time in nanoliter order droplets is two orders of magnitude faster than by diffusion alone.

4E-5

#### 11:45 am Microparticle manipulation and whole blood pre-treatment in surface acoustic wave counterflow devices

Marco Travaglini<sup>1,2</sup>, Richie Shilton<sup>2</sup>, Marco Pagliuzzi<sup>1</sup>, Ilaria Tonazzini<sup>1</sup>, Fabio Beltram<sup>1,2</sup>, Marco Cecchini<sup>1</sup>; <sup>1</sup>Laboratorio NEST, Scuola Normale Superiore and Istituto Nanoscienze - CNR, Pisa, Italy, <sup>2</sup>Center for Nanotechnology Innovation @NEST, Istituto Italiano di Tecnologia, Pisa, Italy

##### Background, Motivation and Objective

Surface acoustic wave (SAW) counterflow has been demonstrated to generate efficient integrated fluid pumping in closed microchannels allowing true device portability. Full understanding of the fluid flow and microparticle dynamics during this process is essential in view of point-of-care applications. When SAWs impinge on a fluid, ultrasound waves are refracted into the liquid. These ultrasounds generate a stationary flow, known as acoustic streaming, as well as an acoustic radiation force that acts on suspended microparticles. Here we show that, depending on the microchannel height  $h$  compared with the ultrasound wavelength  $\lambda_f$ , it is possible to switch from an acoustic streaming ( $h \gg \lambda_f$ ) dominated regime to an acoustic radiation force ( $h \leq \lambda_f$ ) dominated regime. We then exploited these two regimes separately for whole blood pre-treatment.

##### Statement of Contribution/Methods

Our experimental devices consisted of two layers bonded together: a 128° YX lithium niobate substrate with a patterned interdigital transducer generating SAWs at 100 MHz and an upper polydimethylsiloxane (PDMS) straight microchannel layer. We fabricated the PDMS layers with microchannel heights ranging from 12.5 μm to 70 μm. We loaded 10 μL of fluid into the device and operated it at fixed surface acoustic wave amplitude. The dynamics of the entire filling process during acoustic counterflow was recorded under a microscope equipped with a fast camera. Particle streamlines were obtained via  $\mu$ PIV analysis.

**Results/Discussion**

By seeding the fluid with 500 nm particles, we observed that if  $h \leq \lambda_f$  the beads were collected in a two dimensional periodical pattern. This accumulation pattern matches the simulated distribution of semi-nodes in a partially standing ultrasound wave excited in water by SAWs. Conversely, when  $h \gg \lambda_f$  we observed that the particles are dragged into a double vortical pattern which evolves during the initial channel filling. This demonstrates that we can tune the balance between the acoustic radiation force and the acoustic streaming (Stokesian) drag force by simply varying the microchannel height. The transitional height between these two regimes depends on the microparticle size with respect to the set wavelength. We finally investigated the effect of these regimes on whole blood in 14  $\mu\text{m}$  and 70  $\mu\text{m}$  high channels. These represent the extremes where we observed acoustic streaming or particle accumulation with synthetic particles up to 10  $\mu\text{m}$  diameter (like red blood cells). In the 14  $\mu\text{m}$  high channels, we observed that complete plasma separation can be obtained between periodical accumulation lines in proximity of the meniscus. When acoustic streaming dominates, however, we can generate a cell concentration gradient located in the vortical area. Switching between these two regimes is possible by simply tailoring the microchannel geometry, and the associated whole-blood manipulations can be easily integrated as components of handheld point-of-care devices.



## 5E - Particle Manipulation and Acoustic Tweezing 3

Williford A

Friday, September 5, 2014, 10:30 am - 12:00 pm

Chair: **K. Kirk Shung**  
University of Southern California

5E-1

### 10:30 am Quantification of the capabilities of a circular array acoustic tweezer

Charles Courtney<sup>1</sup>, Christine Demore<sup>2</sup>, Hongxiao Wu<sup>2</sup>, Paul Wilcox<sup>3</sup>, Sandy Cochran<sup>2</sup>, Bruce Drinkwater<sup>3</sup>; <sup>1</sup>Mechanical Engineering, University of Bath, Bath, United Kingdom, <sup>2</sup>Institute for Medical Science and Technology (IMSaT), University of Dundee, Dundee, United Kingdom, <sup>3</sup>Mechanical Engineering, University of Bristol, Bristol, United Kingdom

#### Background, Motivation and Objective

The ability to trap and manipulate objects on the micrometre scale has attracted interest in the biosciences and for micro-fabrication. While optical tweezers are well established, analogous systems using ultrasound are in their relative infancy. However, the use of ultrasonic manipulation offers the ability to work with larger objects than optical systems, including agglomerates of biological cells.

One approach to acoustic tweezing, developed by the authors, uses a circular ultrasonic array to generate an ultrasonic standing wave in a fluid filled chamber. By appropriately designing the ultrasound, field particles can be trapped and manipulated. Independent manipulation of up to 3 microparticles with diameters in the range of 10-90  $\mu\text{m}$  has been demonstrated using a 64-element array. This work quantifies the capabilities of such devices in terms of forces applied and the effects of interference between traps.

#### Statement of Contribution/Methods

A circular ultrasonic array was constructed with 64 elements around a ring of diameter 10.98 mm and height 1.63 mm. This array acts as the perimeter of a fluid filled chamber sealed at the top and bottom with glass coverslips to allow easy optical access. Microparticles are manipulated in the chamber, supported against gravity by a layer of agar or an ultrasonic levitation stage operating perpendicular to the plane of the array. Bessel-function-shaped fields are generated by the array and allow trapping and manipulation of particles. Superpositions of Bessel-function-shaped fields allow multiple particles to be trapped and higher order Bessel functions allow trap radii to be increased.

The ultrasonic fields in the chamber are modelled using a Huygens's model to predict the effects of interference and a finite element model to predict the element behaviour and the effects of reflections and resonances within the chamber. The field shape is experimentally measured using a Schlieren imaging system and a hydrophone provides a direct measurement of the amplitude of the field. Forces are measured by tracking the movement of particles of various sizes under the influence of the field and fitting to the equation of motion for a particle under the influence of the acoustic field and Stokes drag.

#### Results/Discussion

Modelled pressure fields for a single trap are presented and verified experimentally by Schlieren imaging and hydrophone measurements. The forces applied by these fields are measured experimentally. Forces of up to 2 nN (on a 90  $\mu\text{m}$  particle) are observed. The models are used to predict the effects of interference and determine the variation in trapping forces as a result of interference between traps. This is then verified experimentally. The model is used to optimise the excitation applied to improve trap consistency in the presence for multiple traps.

5E-2

### 10:45 am Solid particle transverse trapping at the focus of 1.5-MHz vortex beam radiated by 12-sector ultrasonic array

Oleg Sapozhnikov<sup>1,2</sup>, Adam Maxwell<sup>1,3</sup>, Wayne Kreider<sup>1</sup>, Michael Bailey<sup>1</sup>; <sup>1</sup>Center for Industrial and Medical Ultrasound, University of Washington, Seattle, WA, USA, <sup>2</sup>Department of Acoustics, Physics Faculty, Moscow State University, Moscow, Russian Federation, <sup>3</sup>Department of Urology, University of Washington School of Medicine, Seattle, USA

#### Background, Motivation and Objective

Similar to optical tweezers, it has been shown that acoustic trapping can be achieved by tightly focused ultrasound when the acoustic impedance of a particle and surrounding liquid is nearly matched, and the particle size is greater than a wavelength (Li *et al.*, Acoustics Today, 2013). These conditions cannot always be satisfied in practice. For instance, in our recent studies it was shown that acoustic radiation force can effectively move kidney stones that are on the order of a wavelength with poor acoustic matching. The present talk reports on theoretical and experimental studies on a method for acoustic trapping under such conditions.

#### Statement of Contribution/Methods

The proposed method of trapping uses a focused beam that has a donut-shaped pressure distribution at the focal plane, with zero intensity at the beam axis. Such a beam can create a potential well that traps an on-axis target particle in transverse directions. To create the desired ultrasound beam, a 1.5-MHz focused transducer has been developed that consists of 12 sectors with electrical control of the amplitude and phase applied to each element. The phase delay applied increases linearly with each adjacent sector, with a limiting condition that the total shift around the circumference is an integer multiple of  $2\pi$ , and the integer controls the beam diameter. Theory describing these effects was based on a recently developed analytical approach for calculating the acoustic radiation force of an arbitrary beam on spheres (Sapozhnikov & Bailey, JASA, 2013). Experiments were conducted to test the performance of the transducer using spherical target beads made of different materials with diameters of several millimeters. To prevent axial motion, target beads were positioned on a flat gel in a degassed water bath, along with the transducer.

#### Results/Discussion

Theoretical modeling predicted transverse trapping at the vortex beam focal plane, with a force dependent on the incremental phase shift between elements, frequency, particle size and material. Experimentally, holographic reconstruction of the transducer surface velocity distribution confirmed the operation of each transducer sector element as designed. Experiments with target beads confirmed that the beads can be trapped and controllably translated along the gel surface in any direction transverse to the beam. The trapping effect was disrupted at increased transducer powers, possibly by generation of acoustic streaming. In conclusion, a method was proposed for transverse acoustic trapping of solid particles with a vortex beam generated by a sector-element transducer. It was shown both theoretically and experimentally that the transducer was able to effectively trap and shift solid mm-sized particles with MHz ultrasound beams. Work supported by RFBR 14-02-00426, NIH EB16118, DK43881, DK92197, and DK07779, and NSBRI through NASA NCC 9-58.

5E-3

**11:00 am Two-dimensional noncontact transportation of small objects in air using flexural vibration of a plate**

Ryota Kashima<sup>1,2</sup>, Daisuke Koyama<sup>2,3</sup>, Mami Matsukawa<sup>2,3</sup>; <sup>1</sup>Faculty of Life and Medical Sciences, Doshisha University, Japan, <sup>2</sup>Wave Electronics Research Center, Doshisha University, Japan, <sup>3</sup>Faculty of Science and Engineering, Doshisha University, Japan

**Background, Motivation and Objective**

In production lines in medical field, the small products such as tablets and capsules will be cracked or scratched under the transportation by the conveyor belt. Our group has been investigating the noncontact ultrasonic transportation technique of small objects over long distances using a flexural vibrating plate and reflector. The ultrasound manipulation technique enables precise positioning for small objects without contact by using the acoustic standing-wave field. This report investigates ultrasound manipulation in two dimensions.

**Statement of Contribution/Methods**

The vibrator consists of an aluminum plate ( $170 \times 170 \times 1$  mm<sup>3</sup>), and four bolt-clamped Langevin transducers with a step horn. The vibration mode of the plate and the positions where the transducers were attached were determined by finite element analysis. A reflector was installed parallel to the vibrator with a distance of approximately 6 mm to generate an acoustic standing wave in air between them. Small objects can be levitated at the nodal points. By changing the phase deference between the input voltages to the transducers, the acoustic standing wave can be moved horizontally and the trapped small object is transported without contact.

**Results/Discussion**

The lattice flexural vibration mode with the wavelength of 29 mm was excited in the plate at 24.8 kHz when the transducers were attached at the position of 12 mm from plate edge. By controlling the phase difference between two pairs of the transducers, the nodal lines of the flexural vibration of the plate and the acoustic standing wave in air could be shifted in the same direction, which enabled the manipulation of the small particles in x- and y-directions (Fig. 1). When the phase difference was changed from 0 to 720 degrees, the moving distance of small particles was approximately 27.3 mm, which corresponds with the wavelength of flexural vibration on the aluminum plate.

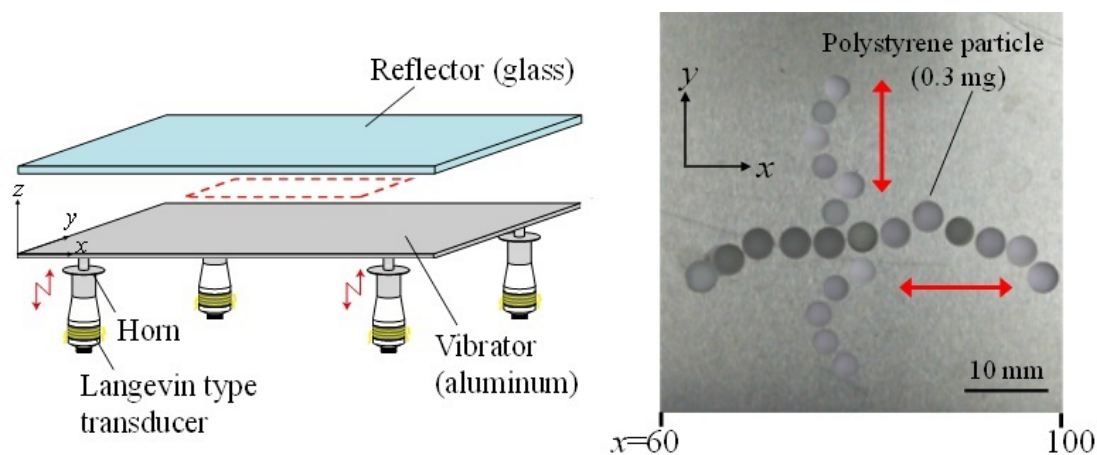


Fig. 1 Noncontact transportation of a polystyrene particle in two dimensions.

5E-4

**11:15 am Two-dimensional Acoustic Manipulation of Microbubbles Using Mechanical Focus Control of Ultrasound Beam**

Taichi Osaki<sup>1</sup>, Kazuhito Inoue<sup>2</sup>, Takashi Azuma<sup>2</sup>, Mitsuhiro Ichihana<sup>3</sup>, Shu Takagi<sup>2</sup>, Yoichiro Matsumoto<sup>2</sup>; <sup>1</sup>The University of Tokyo, Tokyo, Japan, <sup>2</sup>The University of Tokyo, Japan, <sup>3</sup>Sophia University, Japan

**Background, Motivation and Objective**

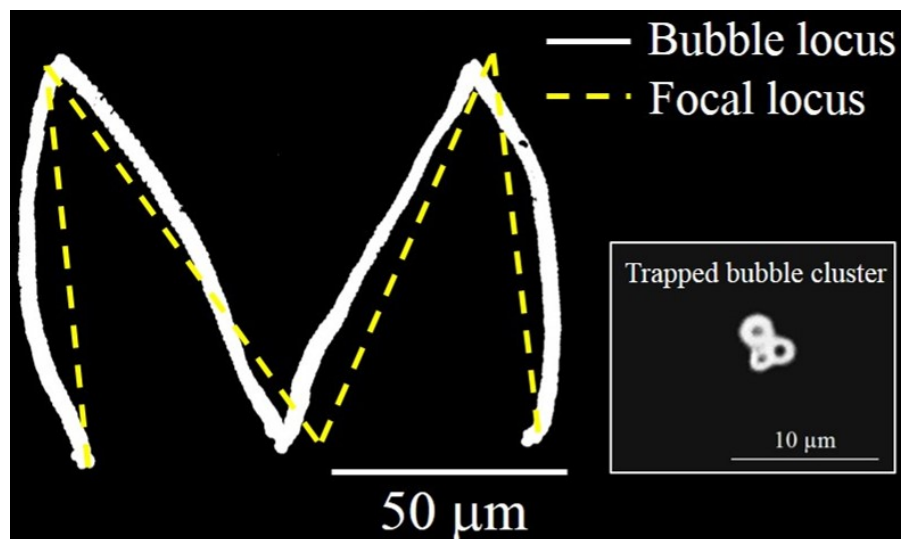
The use of acoustic tweezers for contactless manipulation of microbubbles (MBs) is expected to contribute to the mechanism investigation on the drug delivery system using MBs a drug carrier or a gene-transfection enhancer. In particular, it may be possible to achieve selective accumulation of MBs on target cells or a positional control of relative position of cells and MBs. However, the techniques developed so far are based on the use of standing waves, and are lacking in flexibility and precision. In the present study, a novel MB manipulation tool using a focused ultrasound beam was developed, and its accuracy was evaluated.

**Statement of Contribution/Methods**

Bubbles in an ultrasound field are subjected to the primary Bjerknes force, which is an acoustic radiation force given by the product of the bubble volume and the pressure gradient. In a standing wave field, this force causes bubbles smaller than the resonant size to be driven to antinodes. In the proposed method, MBs are trapped at an antinode and manipulated by moving the antinode. A focused ultrasound beam is produced using a concave transducer, and is used to trap and move a cluster of Sonazoid<sup>TM</sup> MBs.

**Results/Discussion**

The proposed method was evaluated by attempting to move a cluster of 3 MBs along an M-shaped path with a total width of 100  $\mu$ m, as shown in Fig. 1. The dashed line shows the path traced by the focused beam, and the solid line shows the path actually followed by the MB cluster. Although the width of the focused beam was about 500  $\mu$ m, this trapping motion was demonstrated in a smaller area than this. Thus, the pressure gradient near the beam center was effective at trapping the MBs. For a single MB, the measured speed profile along the path was consistent with that calculated using the equation of motion under the primary Bjerknes force. The maximum estimated trapping force was about 6 pN, which is comparable to that exerted by an optical tweezers. The above results clearly demonstrate that the proposed method can be used for flexible and accurate manipulation of MBs.



5E-5

### 11:30 am Experimentation and Simulation of Levitating Water Droplets Formed By Mist Particles In the Acoustic Field

Kamlesh Suthar<sup>1</sup>, Stephen Lomperski<sup>2</sup>, Chris J. Benmore<sup>3</sup>, Anthony Tamalonis<sup>4</sup>, Richard Weber<sup>4</sup>, Patric Den Hartog<sup>1</sup>, <sup>1</sup>Advanced Photon Source, Argonne National Laboratory, Lemont, IL, USA, <sup>2</sup>Nuclear Engineering, Argonne National Laboratory, Lemont, IL, USA, <sup>3</sup>X-Ray Science Division, Advanced Photon Source, Argonne National Laboratory, Lemont, IL, USA, <sup>4</sup>R&D, Materials Development, Inc., Evanston, IL, USA

#### Background, Motivation and Objective

An acoustic levitator provides a containerless and contaminant free space for creating high-purity amorphous drugs by quick drying process. At the midpoint of each node of standing waves in the acoustic levitator, liquid gather into droplets (see Figure 1). It is important to investigate the velocity field around levitating droplets in order to understand a drying process.

#### Statement of Contribution/Methods

An acoustic levitator has been successfully employed at the Advanced Photon Source for In-situ high-energy x-ray diffraction measurements via particles suspended in an acoustic field. It is demonstrated that acoustic levitation can be utilized to mimic the spray drying amorphization process under controlled conditions. It is important to understand the physics behind levitation and the flow field around levitating liquid droplet to enhance the drying process of pharmaceuticals and food products.

#### Results/Discussion

This paper presents experimental results to map the flow field in an acoustic field using Particle Imaging Velocimetry and high-speed infrared imaging. Finite element analysis is also employed to simulate the required experimental conditions. The finite element results of acoustically levitated droplets from an ultrasonic wave operating at 22KHz are compared and presented. The simulation results are in good agreement with the experiment.

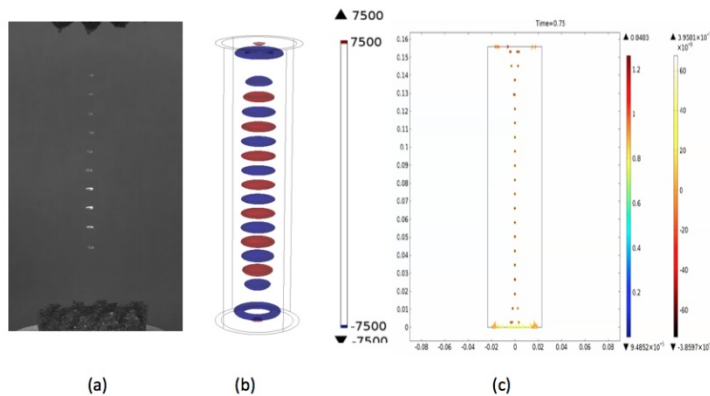


**Figure 1:** (a) Levitating water droplet in the acoustic field with 22KHz frequency (b) Finite Element simulation of standing wave of pressure field (in Pa) of the acoustic field (c) FEM simulation results of levitating water droplets after 0.75sec of sprinkling water mist. Left color bar represent velocity (m/s) and right color bar represent force field (in N).

5E-6

**11:45 am Reconfigurable Acoustic Metamaterials: From Random to Periodic**Mihai Caleap<sup>1</sup>, Bruce Drinkwater<sup>1</sup>; <sup>1</sup>University of Bristol, United Kingdom**Background, Motivation and Objective**

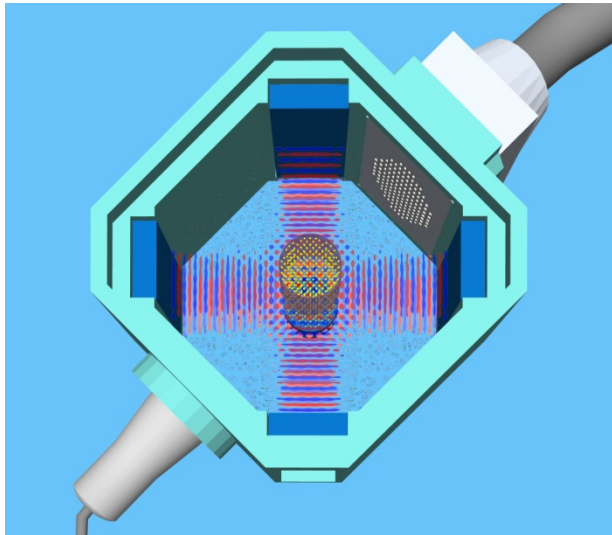
Acoustic metamaterials have the potential to form the basis for a new generation of acoustic devices: examples include super-thin absorbers, reflectors or cloaking for sound insulation and hyper-lenses to provide incredibly high imaging resolution. Photonic and phononic crystals are periodic metamaterials typically created from multiple elementary repeating cells. They exhibit a well-known series of band-pass and band-stop frequencies that have attracted significant attention for use as filters and absorbers. The frequencies of the band-gaps in phononic crystals can be tuned by changing the lattice geometry and the width of the gaps depends on the contrast between the densities and sound velocities of the component materials. Most of the work to date has not involved any reconfigurability, for example, two-dimensional (2D) phononic crystals with a periodicity millimetre order and above have been assembled manually and used to explore their basic properties. Colloids represent a particularly attractive option as they are known to self-assemble into simple three-dimensional (3D) crystalline structures. However, whilst the choice of particle shape, size, volume fraction, etc. allows the colloidal crystal to be tuned, they do not facilitate real-time reconfigurability and so cannot be used in an active mode.

**Statement of Contribution/Methods**

Here we describe a new class of metamaterial that is reconfigurable in real-time and demonstrate its ability to rapidly alter its frequency filtering characteristics. Our reconfigurable acoustic metamaterial is made up of micrometre-sized polystyrene spheres suspended in controllable patterns within a fluid and held in place with acoustic radiation forces. The acoustic radiation force is governed by a potential energy landscape, determined by an applied high amplitude acoustic standing wave field, in which particles move swiftly to energy minima.

**Results/Discussion**

We use five ultrasonic sources to form an energy landscape that resembles a crystal lattice. This creates a colloidal crystal with spheres arranged in a simple orthorhombic lattice in which the acoustic wavelength can be used to control the lattice spacing. When illuminated with acoustic waves, the new metamaterial is shown to exhibit a complex distribution of band-pass and band-stop frequencies in-line with simulation, which can be adjusted in real time.



**6E - Innovations for Microacoustic Devices**

Williford B

Friday, September 5, 2014, 10:30 am - 12:00 pm

Chair: **Gernot Fattinger**  
*Triquint Semiconductor***6E-1****10:30 am Plate Modes in LiTaO<sub>3</sub> for Application in Wide Band Resonator Filters with Improved Temperature Characteristics**Natalya Naumenko<sup>1</sup>; <sup>1</sup>Acousto-Optical Research Center, National University of Science and Technology "MISIS", Moscow, Russian Federation**Background, Motivation and Objective**

Plate modes propagating in thin LiNbO<sub>3</sub> (LN) have been recently successfully utilized in high frequency and ultra wide band resonators for tunable filters [1]. In LiTaO<sub>3</sub> (LT) plate modes are less investigated, though in addition to high coupling, up to 20%, and velocities exceeding 10,000 m/s they can provide low or zero TCF [2]. Fabrication of thin LN and LT plates with parallel faces for high-frequency devices is a challenge today, but the advantages of employing such modes and simplicity of their excitation with common IDTs may be a strong reason for fast development of technologies. The paper is aimed at rigorous numerical investigation of zero- and higher-order plate modes propagating under periodic Al grating in rotated Y-cuts of LT and finding optimal orientations, in which one of the modes shows high coupling and low or zero TCF combined, if possible, with high velocity.

**Statement of Contribution/Methods**

Effective velocities, coupling and TCF of plate modes propagating under Al grating were calculated as functions of LT thickness and cut angle using numerical technique SDA-FEM-SDA, which has been previously applied to investigation of Lamb waves in AlN [3] and demonstrates excellent agreement of the simulated plate mode characteristics in LN with experimental data reported in [1]. The method provides accurate simulation for LT plates with and without Al film of finite thickness at the bottom and takes into account geometrical parameters of the grating (IDT).

**Results/Discussion**

The velocities and coupling of three zero-order modes and three first-order modes were simulated as functions of cut angle in rotated Y-cuts of LT. Orientations with maximum coupling were found for the zero-order shear-horizontal (SH0), the first-order quasi-antisymmetric (qA1) and the first-order SH1 modes. 36°YX was investigated as an example of SH0-mode cut with maximum coupling  $k^2=19\%$  and TCF at resonance varying between -13 and +20 ppm/°C, dependent on LT thickness. In this cut, the spectrum of plate modes was investigated in wide range of LT thicknesses. The mode qA1 shows high coupling around 120°YX cut:  $k^2$  exceeding 13% can be combined with velocity about 18,000 m/s, zero TCF at resonance and suppressed spurious mode if plate thicknesses and geometry of the grating are properly optimized. SH1 mode demonstrates high  $k^2>13\%$  only if Al film is added at the bottom of a plate. The effect of bottom electrode is illustrated by changes in the dispersion curve of the grating and varying structure of the analyzed mode when bottom electrode is added. The sensitivity of plate mode characteristics to variation of geometrical parameters of a resonator is also discussed.

- [1] M.Kadota, M.Esashi, S.Tanaka, Y.Kuratani, and T.Kimura, Proc. 2013 Joint IEEE UFFC, EFTF and PFM Symposium, pp.1680-1683.  
[2] H.Fujiwara, D.Yamazaki and K.Nakamura, Proc. 2005 IEEE Ultrasonics Symposium, pp.1864-1867.  
[3] N.Naumenko, Proc. 2013 Joint IEEE UFFC, EFTF and PFM Symposium, pp. 243-246.

**6E-2****10:45 am Complete Bandgap SAW Phononic Resonant Topologies**Ventsislav Yantchev<sup>1</sup>; <sup>1</sup>Engineering Sciences, Uppsala University, Uppsala, Sweden**Background, Motivation and Objective**

2D composite surface phononic gratings with hexagonal symmetry are proposed for the design of SAW resonators. The proposed structures have the advantage of being compatible with the planar SAW technology, while exhibiting a complete frequency bandgap. Three distinct types SAW phononic resonant transducers are here invented and their operation confirmed both analytically and experimentally. The proposed research paves the way for subsequent implementation of the phononic bandgap technology in high performance micro-acoustic RF SAW components.

**Statement of Contribution/Methods**

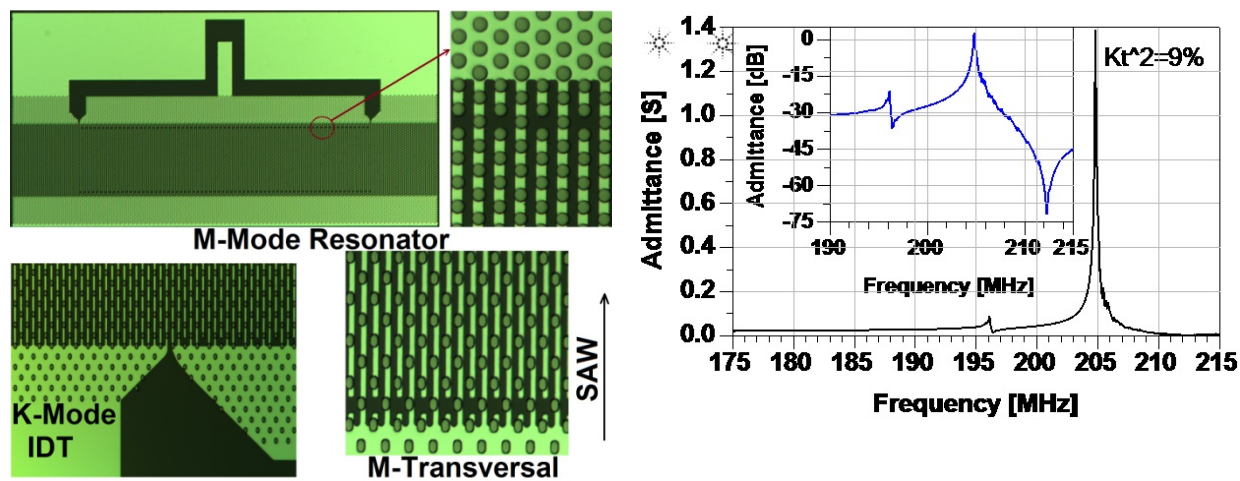
Initially finite element analysis (FEA) have been used to study the propagation and excitation characteristics of three types phononic grating structures formed on to a 128° Y-cut LiNbO<sub>3</sub> substrate. All of them consisted of periodic Al strips on which a hexagonal array of W heavy masses is superimposed. Three types of resonant test structures are subsequently designed, fabricated and measured in a prove of principle study.

**Results/Discussion**

The 200MHz resonant test structures are fabricated by low resolution photo-lithography on to a 128° Y-cut LiNbO<sub>3</sub>. Distance between W masses was chosen to be  $a=10\mu\text{m}$ , while the Al grating pitch was either  $\sqrt{3}a/2$  or  $a/2$  for the different resonant topologies. The thicknesses of the W and Al layers have been 700nm and 400nm, respectively. Resonances corresponding to the lower and upper edges of the phononic bandgap has been measured proving thus operation in the vicinity of complete phononic bandgap.

Figure 1. Shows the three distinct type of phononic resonant test structures operating at the M and K points of the Brillouin zone, respectively. Figure 2 shows the measured response of a one-port phononic M-mode resonator.





6E-3

### 11:00 am Chip Scale Reconfigurable Phased-Array Sonic Communication

Jason Hoople<sup>1</sup>, Justin Kuo<sup>2</sup>, Serhan Ardanuç<sup>2</sup>, Amit Lal<sup>2</sup>; <sup>1</sup>Electrical and Computer Engineering, Cornell University, USA, <sup>2</sup>Cornell University, USA

#### Background, Motivation and Objective

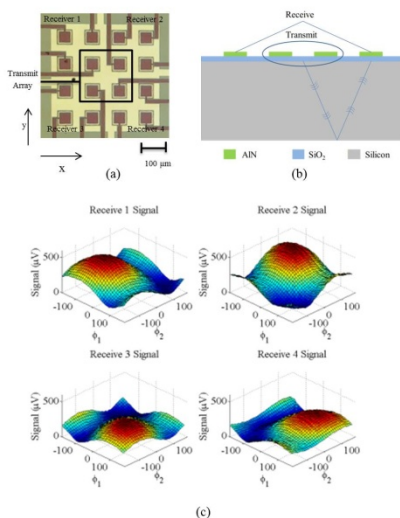
Previously [Hoople et al. "Chip-Scale Sonic Communication Using AlN Transducers" IUS 2013], we reported on the use of thin film aluminum nitride piezoelectric transducers on silicon chips for on-chip ultrasonic communication. This work greatly advances the previous work by using an array of elements, actuated at different phases, forming a sonar beam, to demonstrate directional control of communication channels between four different locations on chip. We envision an additional modality of communication in CMOS 3D stacks with ultrasound using the silicon itself as a communication channel. This would offer reconfigurable interconnects for inter-chip and intra-chip communication and thus open up new vistas for computer architecture and low power computing using ultrasound.

#### Statement of Contribution/Methods

Utilizing Sandia National Lab RF-MEMS process we had 4x4 arrays of aluminum nitride transducers sized 50  $\mu\text{m}$  by 50  $\mu\text{m}$  made on a silicon surface. Utilizing a linear phasing scheme, the inner four elements are driven with pulsed continuous wave RF signals, differing in phase. In the outer ring of the array, four additional transducers are used as receivers (Figure 1a) and measured directly at an oscilloscope. Driving with a 4V<sub>pp</sub> signal resulted in 700- $\mu\text{V}$  signals. The measurements match expected signals at the receive channels suffering some from parasitic capacitance in the receive path. The time of arrival of pulses shows that it is bulk waves and not surface waves arriving at the receiver (as illustrated in Figure 1b).

#### Results/Discussion

The inner array was driven with 50 ns of pulsed RF signal at 1 GHz. Each one of the receive pixels is measured after a delay corresponding to the bulk wave propagation time through silicon from top to bottom and back. After the signal is measured a digital amplitude demodulation algorithm is used to measure the signal levels over noise. The phase difference for each element corresponds to two phase shifts, one in the x direction and one in the y direction. Sweeping both phase shifts over the full 360 degrees results in changes in signal levels of the four receive elements. The value of the signal in the four receivers shows that at certain phasing conditions one of the elements has an increased signal while the other three showed decreased levels (Figure 1c). By utilizing a threshold each one of the receive channels can be communicated to selectively.



# 11:15 am Towards Ultrasonic Through-Silicon Vias (UTSV)

Justin Kuo<sup>1</sup>, Jason Hoople<sup>1</sup>, Serhan Ardanuç<sup>1</sup>, Amit Lal<sup>1</sup>; <sup>1</sup>School of Electrical and Computer Engineering, Cornell University, Ithaca, NY, USA

## Background, Motivation and Objective

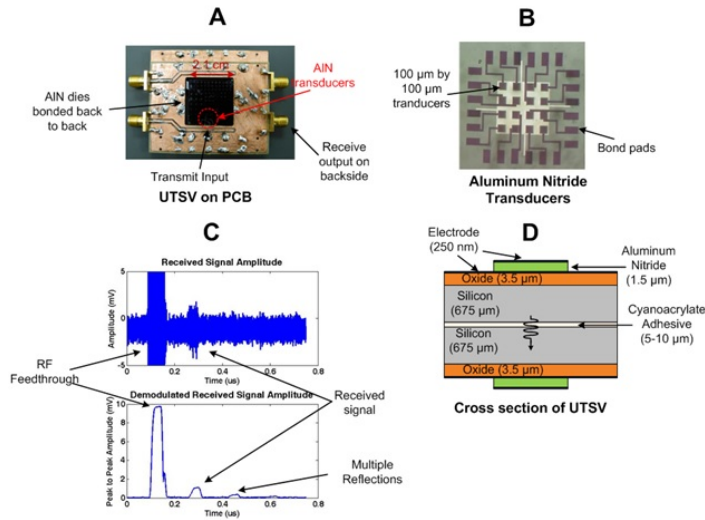
Traditionally, 3D interconnects between stacked silicon chips in 3D integrated circuits (3DICs) have been realized with through-silicon vias (TSVs). These require special processing requiring through wafer etching and metal filling which add to the cost and can lead to lower reliability due to thermal expansion mismatches. In this paper, we present a novel interconnect for 3DICs – an ultrasonic TSV implemented with piezoelectric aluminum nitride thin film transducers on silicon. Whereas TSVs require a physical via through the entire thickness of a wafer, the ultrasonic TSV works by propagating signals from one aluminum nitride transducer to another with bulk acoustic waves through the silicon wafer. This technology is thus inherently wireless and thereby has the potential to simplify processing in 3DIC manufacturing and integration and increase TSV density.

## Statement of Contribution/Methods

The aluminum nitride transducers were fabricated on a double side polished silicon wafer with Sandia National Lab RF MEMS process (Fig 1A, 1B). The TSVs were implemented by bonding two chips back to back with an acoustically thin layer of cyanoacrylate adhesive and using 100 micron by 100 micron sized transducers as the transmit and receive elements, as shown in the cross section in Fig. 1D. To mitigate possible misalignment issues, multiple transducers were used on the receive side to pick up the signal, while a single transducer was used on the transmit side.

## Results/Discussion

The transmit AlN transducer was actuated with a 4 Vpp RF pulse at 900 MHz, with high third harmonic content, and with pulse widths as low as 10 ns resulting in data bandwidths of 100 MHz. Due to the third harmonic frequency residing close to the resonance frequency of the transducers, the receive signal has a higher amplitude at that frequency, as opposed to at the fundamental frequency of the actuation signal. The RF feedthrough can eventually be eliminated by shielding the transmit pixel and electronics. Demodulation of the received signal, as well as a power spectral density measurement to verify harmonic content, was performed in MATLAB. For a 50ns wide RF pulse, the demodulated amplitude at the third harmonic was approximately 1 mVpp for a 50 Ohm load, without amplification, as shown in Fig. 1C. This result paves the way for CMOS integrated UTSV architectures for future 3D stacked circuits.



# 11:30 am UV Direct Write Metal Enhanced Redox (MER) Domain Engineering for Realization of Surface Acoustic Devices on Lithium Niobate

Didit Yudistira<sup>1</sup>, Andreas Boes<sup>1</sup>, Amgad Rezk<sup>2</sup>, Leslie Yeo<sup>3</sup>, James Friend<sup>2,3</sup>, Arnan Mitchell<sup>1</sup>; <sup>1</sup>School of Electrical and Computer Engineering, RMIT University, Melbourne, Victoria, Australia, <sup>2</sup>Micro/Nanophysics Research Laboratory, RMIT University, Melbourne, Melbourne, Victoria, Australia, <sup>3</sup>The Melbourne Centre for Nanofabrication, Clayton, Victoria, Australia

## Background, Motivation and Objective

The ability to integrate surface acoustic waves (SAWs) into microdevices have opened a new frontier in a wide range of fields. Typically, the SAW is generated using interdigital electrodes deposited on piezoelectric substrate such as lithium niobate (LiNbO<sub>3</sub>). While they have found broad acceptance, high fabrication resolution in the metal film's structure is required, particularly in the finger electrode structure, which can be difficult to fabricate, and subject to substantial damage when used for high power applications. An alternate means of generating and detecting the SAWs is through the use of a piezoelectric acoustic superlattice (ASL), achieved on Z-cut LiNbO<sub>3</sub> using the electric field poling method. However, for applications where concentrated SAW energy is required, for example in microfluidic actuation, the substrate of choice is 128° YX-cut LiNbO<sub>3</sub>, as it possesses an optimal coupling constant and also suppresses parasitic bulk waves. Unfortunately, it is not possible to create an ASL on 128° YX-cut LiNbO<sub>3</sub> using electric field poling, as the polar axis is not aligned to a vertical axis of the wafer.

## Statement of Contribution/Methods

In this paper, we present a new and highly versatile domain patterning method—UV direct write Metal Enhanced Redox (MER)—that we show to be effective for the patterning of piezoelectric ASL structures on 128° YX-cut LiNbO<sub>3</sub>. This new technique achieves domain engineering by energizing a thin film of chrome on the surface of the LiNbO<sub>3</sub> crystal using a focused UV beam in a dry nitrogen atmosphere. The energized chrome drives a redox process and the subsequent movement of defect ions causes domain inversion beneath the irradiated regions. To demonstrate the utility of this technique, we fabricated an ASL structure and employed it as a SAW transducer. The functionality of this device was then validated through a brief demonstration of microfluidic actuation.

## Results/Discussion

UV direct MER enables the fabrication of practical piezoelectric acoustic superlattice structures on 128° YX-cut LiNbO<sub>3</sub>, the most widely used crystal cut for surface acoustic wave applications. For example, UV direct write MER was used to form an acoustic superlattice 128° YX structure that in turn enabled the generation of surface acoustic waves of sufficient strength to develop fluid flow within a droplet of water, demonstrating its potential in practical microfluidic manipulation. This is the first demonstration of a UV direct write surface acoustic wave transducer reported to date, made possible only due to the unique qualities of the MER domain engineering process.

6E-6

11:45 am Design of High Q Thin Film Bulk Acoustic Resonator Using Dual-Mode Reflection

Ngoc Nguyen<sup>1</sup>, Agne Johannessen<sup>1</sup>, Ulrik Hanke<sup>1</sup>; <sup>1</sup>Micro and Nano Systems Technology, Buskerud and Vestfold University College, Borre, Vestfold, Norway

Background, Motivation and Objective

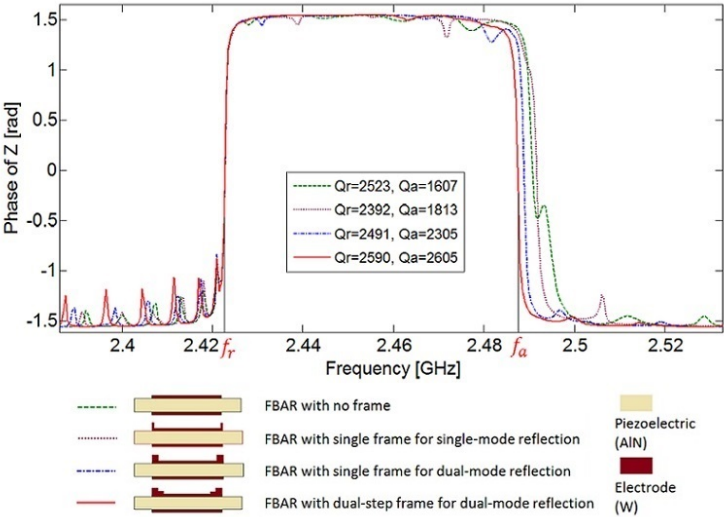
The inevitable propagation of Lamb waves in a traditional thin film bulk acoustic wave resonator (FBAR) leads to the lateral leakage of energy from the active region of the device, and consequently corresponds to a degradation of its quality (Q) factor. The use of a frame on the periphery of a FBAR improves the Q factor potentially providing better filter performance for demanding mobile/wireless communication applications. A single-step frame that can reflect one particular Lamb mode has been introduced in literature. However, a design method for a dual-mode reflection dual-step frame has not yet been published. Based on the idea that the dual-step frame performs as a Bragg reflector, in this work, we propose a procedure to design a dual-step frame with the ability to reflect the two Lamb modes that presumably contribute most to acoustic leakage – the zero and the first order symmetric mode (S0 and S1).

Statement of Contribution/Methods

The displacement field of a W/AIN/W stack FBAR is found from 2D Finite Element Simulations (FEM). Then the dispersion diagrams for lateral modes in the active as well as the frame regions are extracted from taking the Fourier transform of the displacement field of the layer stack for the given regions. From this the lateral propagation constants for the S0 and S1 modes at anti-resonance frequency ( $f_a$ ) are obtained for the various regions. Adopting the Diffraction Grating Method (DGM) from optics, a dual-mode reflection single-step frame at  $f_a$  can be achieved when the width of the frame is multiples of a quarter wavelengths for both modes. The mentioned dual-step frame is the combination of these two single-step frames with different step heights.

Results/Discussion

The figure shows FEM simulation results for various frame configurations of the FBAR, including the basic FBAR structure without a frame, the one with a single-step frame that can only reflect S1 mode (frame width is a quarter wavelength of S1 mode), and the ones designed for the dual-mode reflection, involving a single-step frame and an advanced dual-step frame. Among all, the FBAR with a dual-step frame provides the highest Q factor. The ripples located at the frequencies near and above  $f_a$  are suppressed, giving a smoother electrical characteristic at these frequencies.



FRIDAY ORAL

## 7E - Applications of Piezoelectrics

Williford C

Friday, September 5, 2014, 10:30 am - 12:00 pm

Chair: **Xiaoning Jiang**  
North Carolina State University

7E-1

**10:30 am Integration of Pb(Zr,Ti)O<sub>3</sub> (PZT) Thin Films on a Complex Microfluidic System: Toward New Possibilities for Low Consumption Micropumps**  
Pierre-Henri Cazorla<sup>1</sup>, Olivier Fuchs<sup>1</sup>, Martine Cochet<sup>1</sup>, Sandrine Maubert<sup>1</sup>, Gwenaél Le Rhun<sup>1</sup>, Stéphane Fanget<sup>1</sup>, Yves Fouillet<sup>1</sup>, Emmanuel Defay<sup>1</sup>; <sup>1</sup>CEA-LETI, Minatec Campus, Grenoble, France

### Background, Motivation and Objective

Piezoelectric micropumps have been intensively studied so far and showed many advantages for various microfluidic applications. However the high voltage they request is a major drawback for autonomous systems like implanted devices since they require high consuming amplifiers. The development of PZT thin-films with high mechanical response to low voltage offers very suitable solutions. Some micropumps with piezoelectric thin films have been reported but show low performances mainly since they use passive valves and low efficient piezoelectric material. Here we propose to combine state of the art PZT thin film with active valves to present a highly efficient low voltage micropump.

### Statement of Contribution/Methods

We processed three 50 µm thin membranes above a fluidic pathway etched in silicon as shown figure 1. A 1.5 µm thin sol-gel PZT layer was then deposited on their top. A major breakthrough was to make the sol-gel crystallization step compatible with already processed thin-membranes. The films were investigated electrically and piezoelectrically. Valves and pumps were fully characterized at several actuation frequencies and voltages.

### Results/Discussion

The thin-films have a permittivity of 1100. A 4µm-deflexion is achieved with a 24 V voltage for a membrane with a 7.5 mm diameter. The valves show no leakage up to 40 mbar pressure. The devices can self-prime and pump air and water. They can yield a 3 µL/min flow-rate and a 30 mbar pressure for a 1 Hz actuation frequency. A fluidic power of 46 nW is produced for a 0.3 mW electric consumption.

As expected, thanks to a more efficient material and to active valves, the micropump generates higher pressures than other pumps reported with thin-films. One the other hand, devices with bulk piezo materials hardly work below 30 V due to structure's stiffness. Thin-films allow for a drastic voltage reduction, leading to 2.5 fold reduction of the amplifying electronics consumption compared to a 90 V actuated device.

For the first time, a peristaltic micropump actuated by PZT thin film was successfully fabricated. It allows reduction of packaging costs and features low voltage actuation, improving safety and electrical consumption of autonomous devices. Meanwhile it generates flow and pressure well adapted for medical application like drug delivery and could be of crucial help for the development of personalized medicine.

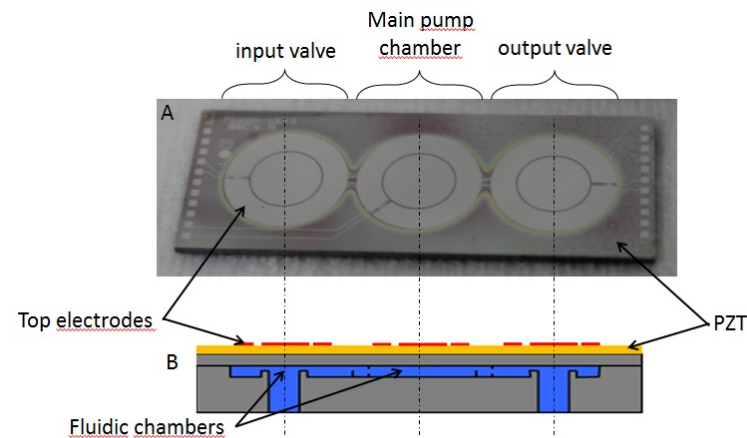


**Figure 1 : A) Picture of the micropump after processing B) Schematic of the micropump (not on scale)**

7E-2

**10:45 am Numerical Simulation and Performance Evaluation of Droplet Particle Formation by Using A New Approach of Ultrasonic Atomization**  
Yung Ting<sup>1</sup>, Amelia Sugondo<sup>1</sup>, Makajia Madoka<sup>1</sup>; <sup>1</sup>Mechanical Engineering, Chung Yuan Christian University, Chung Li, Taiwan

### Background, Motivation and Objective

Atomization processes have been applied in many fields, such as industrial, medical, agricultural, pharmaceutical and etc. Ultrasonic atomization is rapidly developed since its process offers more advantages than conventional atomization process. Many researches have been doing to develop the ultrasonic atomization theory. Unfortunately, the whole theory of ultrasonic atomization and guidelines design of new model have not yet satisfied since this process is a lot of complexity.

**Statement of Contribution/Methods**

A proposed bending tube for atomization consists of a tube and piezoelectric actuators implemented around the tube that is able to vibrate and generate radial vibration. Since first vibration mode of the both sides fixed structure is chosen; the vibration shape is obtained with the highest amplitude in the middle of the tube, in which a small hole is designed. The fluid inside the tube will flow out from the hole and stay on the surface of the tube for atomization. Due to many advantages that offered by CFD, VOF model of ANSYS FLUENT 12.0 is used to simulate the proposed design in this study. Part of the design includes a number of water are placed on the surface in simulation. The main focus is to investigate the possibility of generating droplets resultant from the curvature vibration and the effect of droplets distribution in ultrasonic atomization process. A regular model of the flat plate with longitudinal vibration was utilized to compare with the proposed bending tube. Several tube lengths and ultrasonic frequency are simulated to study the atomization phenomena because to vary geometrical and operational parameters in numerical treatment are less effort compares to experiment.

**Results/Discussion**

User Defined Function (UDF) that compiles with the Volume of Fluid (VOF) in ANSYS FLUENT 12.0 was applied to perform ultrasonic atomization processes in 2D model. It is found that the maximum amplitude less than 5.5  $\mu\text{m}$  with 100 kHz frequency and less than 6  $\mu\text{m}$  with 70 kHz frequency, for example, the liquid surface merely establishes standing capillary waves, which cannot make atomization. However, while maximum vibration is assumed to be 7.5  $\mu\text{m}$ , occurs in the middle of the arc length, and slightly decreases to zero at both ends. In the flat plate, atomization happens along almost all the vibrating surface.

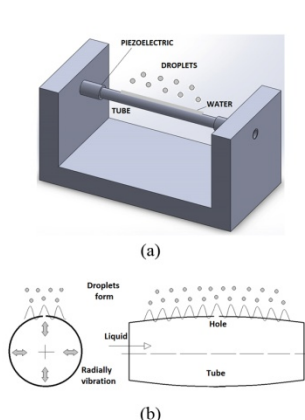


Fig. 1. (a) Structure of bending tube and (b) the generated curvature shape with radial vibration

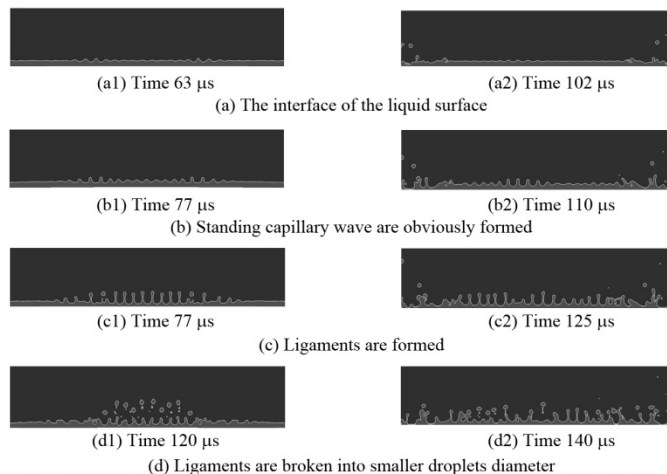


Fig. 2. Deformation of the atomization process of bending tube (a1-a4) and flat plate (b1-b4) at frequency 70 kHz

**7E-3****11:00 am New Applications of Ultrabiosonics, - Feasibility Studies of Fish Growing by Ultrasonic Stimulation**

Yohachi (John) Yamashita<sup>1</sup>, Hiroki Sugiura<sup>1</sup>, Tomoaki Karaki<sup>1</sup>, Hiroki Iwanaga<sup>2</sup>, Zuo-Guang Ye<sup>3</sup>; <sup>1</sup>Intelligent Systems Design Engineering, Toyama Prefectural University, Imizushi, Toyama, Japan, <sup>2</sup>Horioka Aquaculture Association, Japan, <sup>3</sup>Department of Chemistry and 4D LABS, Simon Fraser University, Canada

**Background, Motivation and Objective**

Duarte found in 1987 that low intensity pulse ultrasound (LIPUS) stimulation for 20 minutes every day is an effective way for the treatment of bone fracture. The mechanism of the LIPUS stimulation was related to the induced piezoelectricity of collagen and apatite,  $(\text{Ca}_{10}(\text{PO}_4)_6(\text{OH})_2)$ , in the bone, which was referred to ultrabiosonics. Nowadays, many orthopedic doctors know that the LIPUS stimulation is very effective for new bone growth.

The present feasibility study is aimed at exploring new applications of the ultrabiosonics by utilizing the LIPUS stimulation to change immune and/or circulation system of the aquaculture fishes so as to allow fish to obtain high survival rate, thereby increasing food production.

**Statement of Contribution/Methods**

A combination of sonic and the LIPUS stimulation (SLIPUS) was applied to the surface of the aquaculture tank containing takifugu rubripes and Japanese flounders. The effects have been investigated for 13 weeks using SLIPUS of 92 Hz and 1 MHz.

**Results/Discussion**

The survival rates of SLIPUS-stimulated group and the reference group were found to be 50% and 0% for takifugu, and 100% and 30% for Japanese flounders, respectively. It is suggested that the SLIPUS stimulation could improve the immune and/or circulation system so as to allow the fish to obtain vital force.

In addition, new concept of ultrabiosonics medicine which is based on the combination of western medicine and oriental medicine will be introduced.

This work contributes to the development new applications of ultrasonics and piezoelectricity in ultrabiosonics and biotechnology, and could lead to a new technology to solve the world food shortage issue in the future.

**7E-4****11:30 am Nucleic Acid Extraction using a Rapid, Chemical Free, Ultrasonic Technique for Point-of-Care Diagnostics**

Darren W. Branch<sup>1</sup>, Gennifer T. Smith<sup>1</sup>, Erika C. Vreeland<sup>1</sup>, David Alland<sup>2</sup>, Robert Blakemore<sup>2</sup>; <sup>1</sup>Biosensors and Nanomaterials Department, Sandia National Laboratories, Albuquerque, New Mexico, USA, <sup>2</sup>Department of Medicine, Rutgers University Medical School, Newark, NJ, USA

**Background, Motivation and Objective**

Most biosensors in today's market and in research and development require a critical sample preparation procedure prior to analysis of cellular contents such as nucleic acids or proteins. Technology is needed to release those cellular contents in a format compatible with sealed nano/microfluidic and point-of-care (POC) devices. To solve this problem, our approach uses ultrasonic waves that rapidly disrupt cellular membranes without chemical treatment, thereby releasing the intracellular material without damage or undesirable physical or chemical inhibitors.



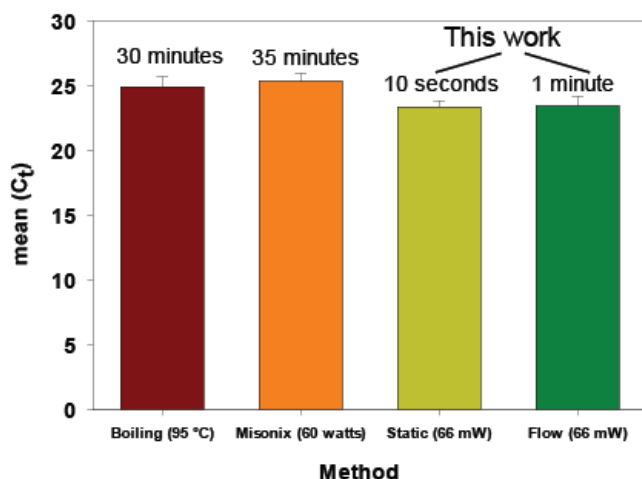
# Statement of Contribution/Methods

Recent work to develop cost-effective diagnostics to detect and treat *Mycobacterium tuberculosis* (MTB) demonstrates that gaining rapid access to the nucleic acid content (e.g. lysis) is the limiting factor. Ultrasonic methods can effectively release nucleic acids from MTB and difficult to lyse biological agents without introducing chemicals that interfere with genetic detection methods such as Polymerase Chain Reaction (PCR). This work develops a miniature ultrasonic array suitable for scaling-up to 96-well format plates. The transducer array was fabricated using 36° YX lithium niobate transducers which coupled ultrasonic waves into disposable plastic cartridges for nucleic acid extraction. The transducers limit the amount of heat, minimizing thermal damage to the biological samples. Using disposable plastic cartridges, raw samples were captured using a single filter clean-up prior to ultrasonic lysis and PCR detection.

# Results/Discussion

This work demonstrates efficient ultrasonic lysis of MTB in a disposable microfluidic device. The transducer array operated at 68 MHz, producing a wavelength of 22  $\mu\text{m}$  in fluid, which is very similar to the size of biological cells and required far less power (50-100mW) for lysis with minimal sample heating ( $\Delta T < 6^\circ\text{C}$ ). The return loss at 68 MHz was -18 dB with a bandwidth (BW) of 3.6 MHz. MTB samples were exposed to ultrasonic waves using either a static-fill lysis or flow-through lysis approach. Release of nucleic acid was measured using PCR to determine the cycle threshold ( $C_t$ ) – the number of cycles required for fluorescent signal to exceed background levels. Results demonstrate that nearly all the nucleic acid was released from MTB in one minute or less using 66 mW of input power with a similar efficiency to boiling at 95°C for 30 minutes.

Figure 1. Releasing Nucleic Acid from *Mycobacterium Tuberculosis* (MTB). (Lower  $C_t$  is better, N=10).



7E-5

# 11:45 am Nuclear Radiation Tolerance of Aluminum Nitride

Bernhard Tittmann<sup>1</sup>, David Parks<sup>2,3</sup>, <sup>1</sup>Engineering Science & Mechanics, Penn State University, University Park, Pennsylvania, USA, <sup>2</sup>Navico Americas, Tulsa, Oklahoma, USA, <sup>3</sup>Pennsylvania State University, Oklahoma, USA

# Background, Motivation and Objective

Currently, ultrasonic non-destructive evaluation (NDE) is employed periodically on reactor components, but online monitoring has not been implemented. The need for continuous online monitoring is becoming all the more important with the need for reactor license extension, the development of small and medium reactors (SMRs) and the next generation nuclear power plants. Additionally, ultrasound is an attractive NDE methodology in that it allows inspection in optically opaque materials. Further applications may be found in materials research reactors where ultrasonic NDE can be used for in-situ analysis of radiation effects on novel radiation hard materials currently being developed. The objective of this work is the analysis of radiation tolerance of candidate piezoelectric material and in parallel experiments during radiation.

# Statement of Contribution/Methods

For practical use in harsh radiation environments, we pose selection criteria for piezoelectric materials for NDE and material characterization. The radiation tolerance prediction method herein consists of a three pronged approach considering depoling, amorphization and unstable atomic species. Using these criteria, piezoelectric Aluminum Nitride is shown to be an excellent candidate. AlN is found to be resistant to amorphization by virtue of its Wurtzite structured common to hard piezoelectrics. Moreover, the very high transition temperature renders this material immune to thermal spike damage. It is also clear that the transmutation reaction  $^{14}\text{N}(n,p)^{14}\text{C}$  is generating a fraction of a dpa at 1021n/cm<sup>2</sup> and insignificant doping. A single crystal AlN element (4.8 mm in diameter and 0.45 mm thick) resonant at 13.4 MHz, was coupled to an aluminum cylinder via mechanical pressure. Aluminum foil was used as an acoustic coupler between the aluminum cylinder and the AlN element, allowing for strong, clear A-scan data to be obtained. The AlN element was loaded, on the side opposite the aluminum cylinder, with a sintered carbon/carbon composite to reduce ringing and improve the signal clarity.

# Results/Discussion

We demonstrated the tolerance of single crystal piezoelectric aluminum nitride after a fast and thermal neutron fluence of 1.85X10<sup>18</sup> n/cm<sup>2</sup> and 5.8X10<sup>18</sup> n/cm<sup>2</sup>, respectively, and a gamma dose of 26.8 MGy. The radiation hardness of AlN is most evident from the unaltered piezoelectric coefficient d<sub>33</sub>, which measured 5.5 pC/N after a fast and thermal neutron exposure in a nuclear reactor core for over 120 MWhrs in agreement with the published literature value. The results offer potential for improving reactor safety and furthering the understanding of radiation effects on materials by enabling structural health monitoring and NDE in spite of the high levels of radiation and high temperatures known to destroy typical commercial ultrasonic transducers.

## 1F - MTH: Histotripsy and Lithotripsy

Grand Ballroom

Friday, September 5, 2014, 1:00 pm - 2:30 pm

Chair: **Zhen Xu**  
*University of Michigan, Ann Arbor*

1F-1

### 1:00 pm Histotripsy: Recent Advances

Charles Cain<sup>1</sup>; <sup>1</sup>Univ. of Michigan, Ann Arbor, Ann Arbor, Michigan, USA

#### Background, Motivation and Objective

test

#### Statement of Contribution/Methods

#### Results/Discussion

1F-2

### 1:30 pm Synthesis of Near Monopolar Ultrasound Pulses Using a Frequency-Compounding Transducer

Kuang-Wei Lin<sup>1</sup>, Timothy L. Hall<sup>1</sup>, Robert J. McGough<sup>2</sup>, Zhen Xu<sup>1</sup>, Charles A. Cain<sup>1</sup>; <sup>1</sup>University of Michigan, USA, <sup>2</sup>Michigan State University, USA

#### Background, Motivation and Objective

In histotripsy, a cavitation-based ultrasound therapy, short acoustic pulses (< 3 cycles) can produce precise tissue ablation wherein lesion formation only occurs when the applied peak negative pressure exceeds an intrinsic threshold of the medium. This paper investigates a frequency compounding technique to synthesize extremely short, nearly "monopolar" (half-cycle) ultrasound pulses. Monopolar pulses with a dominant negative phase can inhibit shock scattering during histotripsy, leading to more predictable lesion formation using the intrinsic threshold mechanism, while greatly reducing any constructive interference, and potential "hot-spots," elsewhere.

#### Statement of Contribution/Methods

A custom transducer [Fig. 1(A)] composed of 23 individual relatively-broadband piezoceramic elements with various resonant frequencies (0.5, 1, 1.5, 2, and 3 MHz) was used. Each frequency component of the transducer was capable of generating 1.5-cycle pulses with only one high amplitude negative half-cycle using a custom 23-channel high voltage pulser [Fig. 1(B)]. By varying time delays of individual frequency components to allow their principal negative peaks to arrive at the focus of the transducer constructively, destructive interference occurs elsewhere in time and space, resulting in a monopolar pulse approximation with a dominant negative phase. By inverting the excitation pulses to individual elements, monopolar pulses with a dominant positive phase can also be generated.

#### Results/Discussion

Hydrophone measurement demonstrated that near monopolar pulses were synthesized using this frequency compounding approach [Fig. 1(C)]. The ratio of P- to P+ was 4.68 for the negative monopolar pulse, while the ratio of P+ to P- for the positive monopolar pulse was 4.74. Experiments in RBC phantoms indicated that negative monopolar pulses were able to produce very precise histotripsy-type lesions using the intrinsic threshold mechanism [Fig 1(D)], while neither lesions nor bubble clouds were generated using positive monopolar pulses. Moreover, these monopolar pulses could have many potential benefits in ultrasound imaging, including axial resolution improvement, speckle reduction, and contrast enhancement in pulse inversion imaging.

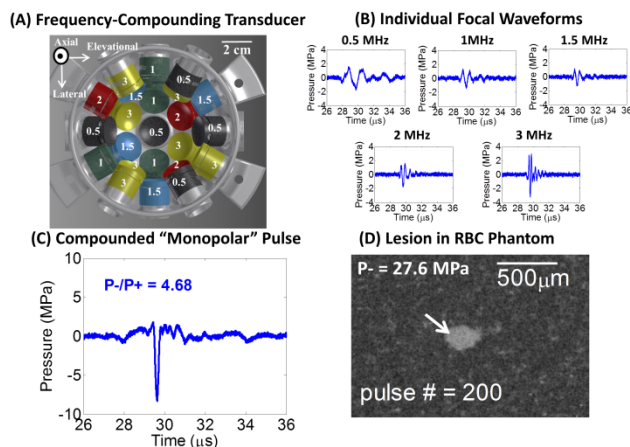


**Figure 1** (A) The frequency-compounding transducer composed of elements with various resonant frequencies (color-coded, with numbers indicating their frequencies in MHz). (B) Focal acoustic waveforms for individual frequency components. (C) The resulting "monopolar" (half-cycle) pulse. (D) A lesion generated in the RBC phantom using 200 frequency-compounded negative "monopolar" pulses.

**1:45 pm Liquefaction of Large Volume Clots Using Histotripsy and Precise Lesion Generation Through the Skull**

Jonathan Sukovich<sup>1</sup>, Yohan Kim<sup>1</sup>, Aditya Pandey<sup>2</sup>, Hitinder Gurm<sup>3</sup>, Charles Cain<sup>1</sup>, Zhen Xu<sup>1,4</sup>, <sup>1</sup>Biomedical Engineering, University of Michigan, Ann Arbor, Michigan, USA, <sup>2</sup>Neurosurgery, University of Michigan, Ann Arbor, Michigan, USA, <sup>3</sup>Internal Medicine, University of Michigan, Ann Arbor, Michigan, USA, <sup>4</sup>Pediatrics, University of Michigan, Ann Arbor, Michigan, USA

**Background, Motivation and Objective**

Hemorrhagic stroke can lead to the formation of large clots (>60mL) in the brain, which can cause direct and indirect brain injury due to increasing intracranial pressure. Current treatment options include surgery and medication, both with high mortality and morbidity rate. To improve treatment, researchers are exploring minimally invasive methods, and MRgFUS therapy has shown particular promise. Using MR guidance, HIFU was used to liquefy clots through the skull in pigs and human cadaver, and a catheter was used to drain the resulting fluid. However, the treatment rate was slower than desirable (3 hours to drain ≤40 mL clot). This study seeks to demonstrate the feasibility of using histotripsy to swiftly liquefy large volume ex vivo clots, and to evaluate the spatial precision achievable by histotripsy applied through the skull.

**Statement of Contribution/Methods**

Histotripsy pulses were delivered using a custom 500 kHz, 256-element phased array transducer. First, to determine the feasibility of using histotripsy to quickly liquefy large clots, ex vivo clots (78mL) made with whole bovine blood were treated using 2-cycle pulses with peak negative pressures of 30 MPa. The array was focused in parallel to 4 independent treatment sites throughout a 40cm<sup>3</sup> spherical region within the clot with a density of 120 steering locations/cm<sup>3</sup>. With a 1.67 ms delay between steering sites (i.e. 600Hz PRF), and a total of 50-200 pulses per location, total treatment times ranged from 1.5 to 6 minutes. After treatment, a catheter was inserted into the clot to drain the liquefied volume for measurement. Second, to evaluate the accuracy of applying histotripsy through the skull, treatment was applied to agarose phantoms embedded with red-blood-cells (RBC) through an excised human skull. The therapy focus was steered electronically (with aberration correction) and the resulting cavitation bubbles and lesions were imaged via high-speed camera. Lastly, to determine the feasibility of using histotripsy to liquefy large clots through the excised human skull, a 78 mL ex vivo clot was treated through the skull. The transducer was fired to one focus at a time instead of four as in the first experiment, with the other parameters the same.

**Results/Discussion**

First, histotripsy was used to liquefy large clots (>40mL) in under 2 minutes using 50 pulses per location, and the liquefied volume was drained via catheter. Second, through an excised human skull, the focal region was steered electronically over a 2 cm range, and discrete lesions (2 x 2 x 4 mm) were formed in the RBC phantoms with minimal damage generated at the periphery. Finally, 30 mL of clot was liquefied in under 30 minutes through the skull. These data demonstrate the potential of using histotripsy for fast liquefaction of large clots in treatment of hemorrhage stroke. More work is needed for further optimization, safety investigation, and in vivo feasibility.

**2:00 pm Ultrasonic Propulsion of Kidney Stones: Preliminary Results from Human Feasibility Study**

Michael Bailey<sup>1,2</sup>, Bryan Cunitz<sup>1</sup>, Barbrina Dunmire<sup>1</sup>, Marla Paun<sup>1</sup>, Franklin Lee<sup>2</sup>, Susan Ross<sup>2</sup>, James Lingeman<sup>3</sup>, Michael Coburn<sup>4</sup>, Hunter Wessells<sup>2</sup>, Mathew Sorensen<sup>2,5</sup>, Jonathan Harper<sup>2</sup>, <sup>1</sup>CIMU, Applied Physics Laboratory, University of Washington, Seattle, WA, USA, <sup>2</sup>Department of Urology, University of Washington, Seattle, WA, USA, <sup>3</sup>Department of Urology, Indiana University School of Medicine, Indianapolis, IN, USA, <sup>4</sup>Department of Urology, Baylor College of Medicine, Houston, TX, USA, <sup>5</sup>Division of Urology, Puget Sound Veteran Affairs Medical Center, Seattle, WA, USA

**Background, Motivation and Objective**

One in 11 Americans has experienced kidney stones with a 50% recurrence rate within 5 years. Among other applications, ultrasonic propulsion (UP) offers a potential method to expel small stones or residual fragments before they require further surgery. Reported here are the preliminary findings from the first investigational use of UP in humans.

**Statement of Contribution/Methods**

The device uses a Verasonics ultrasound engine and a Philips HDI C5-2 probe to generate uninterrupted real-time B-mode imaging and apply targeted "push" pulses on demand. Push pulses are 50 ms and have an ISPPA<sub>3</sub> ≈ 64 W/cm<sup>2</sup> at 90 Vp with an effective focal width of 4.5mm. There are three arms of the study: de novo stones, post-lithotripsy fragments, and the preoperative setting. A pain questionnaire is completed immediately prior to and following the study. A maximum of 40 push attempts are administered at 50 or 90 Vp excitation. Movement is classified based on extent (Table 1). Patients are followed for 90 days and receive a clinical ultrasound exam after 4 weeks. Stone motion is graded during the treatment and confirmed during a review of the saved B-mode video.

**Results/Discussion**

Six subjects have been enrolled and undergone UP to date. None of the subjects reported pain associated with the treatment. Subjects did report a mild warming of the skin with a 90 Vp excitation; no sensation was reported with a 50 Vp excitation. A summary of movement results is provided in Table 1. One subject in the post-lithotripsy arm passed two small stones immediately following treatment, corresponding to the two stones displaced from the interpolar region. Two subjects reported passage of multiple small fragments on days 1 and 2 post treatment. In three subjects, ultrasonic propulsion identified a collection of stones previously characterized as a single stone on x-ray and ultrasound. Subjects who did not have significant movement were in the de novo arm. There have been no treatment related adverse events reported with mean follow-up of 3 weeks. This is the first report on the successful repositioning of kidney stones in humans using ultrasound. Treatment was therapeutic in two subjects and provided diagnostic information in three. Trial supported by NSBRI through NASA NCC 9-58. Research and development supported by NIH DK043881 and DK092197.

Table 1: Ultrasonic Propulsion of Kidney Stones – Preliminary Results

Study Arm	Patient #	Number of stones	Stone size (mm)	Motion Grading*								Total # Pushes
				1		2		3		U		
				n	%	n	%	n	%	n	%	
De- Novo Stones	1	3	2 - 3	20	75%	5	19%	0		2	7%	27
	2	5	2 - 3	17	44%	16	41%	0		2	5%	39
	3	2	3	21	91%	1	4%	0		1	4%	23
Post-Lithotripsy	4	2	2	9	24%	23	62%	5	13%	0		37
	5	5	2 - 3	17	42%	21	53%	2	5%	0		40
	6	Multiple	< 2	21	53%	14	35%	4	10%	1	2%	40

\*1: no motion; 2: movement with rollback or stone jiggle; 3: movement to new location; U: unintentional push.

All subjects treated with a combination of 50 V and 90 V output.

1F-5

**2:15 pm In vivo evaluation of cavitation activity and hemorrhagic kidney injury caused by burst wave lithotripsy**

Wayne Kreider<sup>1</sup>, Adam Maxwell<sup>1,2</sup>, Bryan Cunitz<sup>1</sup>, Yak-Nam Wang<sup>1</sup>, Ryan Hsi<sup>2</sup>, Franklin Lee<sup>2</sup>, Mathew Sorensen<sup>2</sup>, Jonathan Harper<sup>2</sup>, Vera Khokhlova<sup>1,3</sup>, Oleg Sapozhnikov<sup>1,3</sup>, Bret Connors<sup>4</sup>, Andrew Evan<sup>4</sup>, Michael Bailey<sup>1</sup>; <sup>1</sup>CIMU, Applied Physics Laboratory, University of Washington, Seattle, WA, USA, <sup>2</sup>Department of Urology, University of Washington School of Medicine, Seattle, WA, USA, <sup>3</sup>Department of Acoustics, Physics Faculty, Moscow State University, Moscow, Russian Federation, <sup>4</sup>Department of Anatomy and Cell Biology, Indiana University School of Medicine, Indianapolis, IN, USA

**Background, Motivation and Objective**

Shock wave lithotripsy (SWL) is a noninvasive treatment for kidney stones that has been in clinical use for over 30 years. SWL utilizes high-amplitude shocks to break stones into passable fragments, but produces relatively poor stone-free rates in patients. A new noninvasive treatment approach for kidney stones has been proposed that relies on short bursts of sub-megahertz ultrasound: burst wave lithotripsy (BWL). Although BWL uses much lower pressure amplitudes than SWL, pulses are delivered more rapidly so that energy is delivered to the stones and tissue at higher rates. This effort aims to assess the potential for BWL to cause renal injury.

**Statement of Contribution/Methods**

BWL treatments at 170 kHz were applied *in vivo* to kidneys from six pigs (55-60 kg) for durations up to 25 minutes. Treatment exposures comprised bursts of 10 cycles of ultrasound at a burst repetition rate of either 40 Hz or 200 Hz, with peak focal pressures from 4.9–6.5 MPa. Each exposure targeted either the upper or lower pole of a given kidney. Treated kidneys were perfusion-fixed and evaluated for injury by either gross examination or by an image-based method for quantitation of hemorrhagic lesion volume. During exposures, a P7-4 imaging probe was mounted inline with the therapy transducer to provide real-time B-mode images of the treatment site. Given that injury in SWL is typically associated with cavitation, B-mode images were monitored during each exposure to identify echogenic regions that presumably represent bubble activity.

**Results/Discussion**

Echogenic regions identified in B-mode images consistently started in the collecting space and spread back toward the transducer. Upon gross examination of treated kidneys, the persistence of echogenic regions throughout a treatment was observed to correlate with hemorrhagic injury at corresponding treatment sites. Subsequently, 9 BWL exposures were applied to 6 different kidneys from 4 pigs; during these exposures, the pressure level was reduced if echogenicity was observed. In these exposures, the threshold for the onset of echogenicity was always higher than 4.9 MPa and typically lower than 5.5 MPa. In two kidneys for which injury quantitation was performed, the hemorrhagic lesion volume was estimated to be less than 0.1% of functional renal volume. During the same *in vivo* experiments, equivalent exposures (5.5 MPa, 40 Hz PRF) were applied to several 5–10 mm stones implanted in pig bladders. With exposures ranging from 10.4–23 minutes, comminution into passable fragments was achieved for 2 struvite stones and 1 calcium oxalate monohydrate stone. These results suggest that if echogenicity is avoided, BWL exposures at 170 kHz induce negligible kidney injury at pressures that can break stones. Work supported by NIH 2T32 DK007779-11A1, R01EB007643, P01DK043881, R01DK092197, and NSBRI through NASA NCC 9-58.

## 2F - MEL: Vascular Strain Imaging

Waldorf

Friday, September 5, 2014, 1:00 pm - 2:30 pm

Chair: **Chris de Korte**  
Radboudumc

2F-1

### 1:00 pm Determining the Stability of Murine Abdominal Aortic Aneurysms with Pulse Wave Imaging

Sacha Nandlall<sup>1</sup>, Monica Goldklang<sup>2</sup>, Aubrey Kalashian<sup>1</sup>, Nida Dangra<sup>1</sup>, Jeanine D'Armiento<sup>2</sup>, Elisa Konofagou<sup>1,3</sup>; <sup>1</sup>Biomedical Engineering, Columbia University, New York, NY, USA, <sup>2</sup>Medicine, Columbia University, New York, NY, USA, <sup>3</sup>Radiology, Columbia University, New York, NY, USA

#### Background, Motivation and Objective

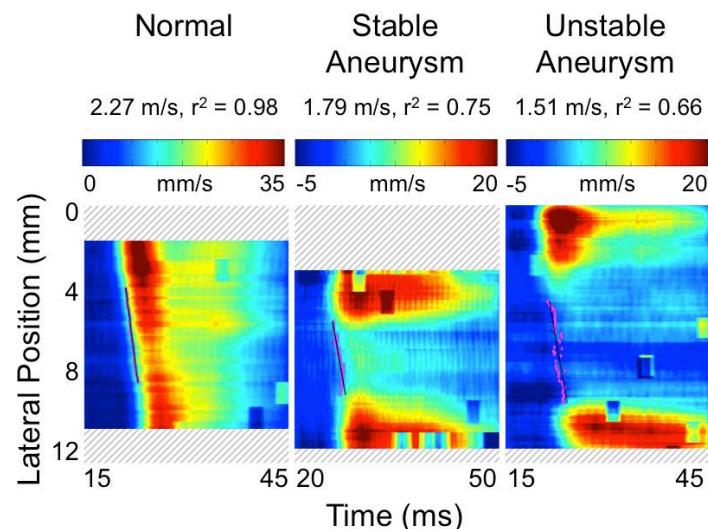
The Abdominal Aortic Aneurysm (AAA) is a silent and often deadly vascular disease. The leading cause of AAA-induced death is rapid internal hemorrhaging following a sudden rupture of the vessel wall, usually within the sac of the aneurysm. This study aims at assessing the capability of Pulse Wave Imaging (PWI) to predict the stability of murine AAAs. PWI is a non-invasive technique for tracking the propagation of pulse waves along the wall of the aorta at high spatial and temporal resolutions. Pulse Wave Velocity (PWV) is a well-established marker of wall stiffness, which is closely related to the likelihood of rupture.

#### Statement of Contribution/Methods

An AAA model was generated by infusing eighteen (N = 18) ApoE/TIMP-1 knockout mice with angiotensin II, delivered at a constant flow rate via subcutaneously implanted osmotic pumps. AAAs were deemed to be unstable if they had ruptured within 30 days of infusion, and stable otherwise. The suprarenal sections of the abdominal aortas were imaged every 2-3 days after implantation using a Visualsonics Vevo 770 imager with axial and lateral resolutions of 62 and 115  $\mu$ m, respectively. Pulse wave propagation was estimated and imaged at an effective frame rate of 8 kHz by using retrospective ECG gating. The displacements induced by the pulse waves were estimated by performing 1-D cross-correlation on the radiofrequency echo signals. PWVs and their associated coefficients of determination ( $r^2$ ) were obtained by performing linear regressions on the 50% upstroke markers in the resulting spatiotemporal displacement maps (see Fig. 1).

#### Results/Discussion

Fig. 1 illustrates representative examples of pulse wave propagation in a normal aorta (left), a stable AAA (middle), and an unstable AAA (right). Overall, in normal aortas (n = 100 acquisitions in N = 18 mice), the pulse waves propagated at constant velocities ( $2.8 \pm 0.9$  m/s,  $r^2 = 0.89 \pm 0.11$ ). In stable AAAs (n = 17, N = 7), both PWV and  $r^2$  decreased ( $1.8 \pm 0.7$  m/s,  $r^2 = 0.77 \pm 0.10$ ), while in unstable AAAs (n = 13, N = 4), PWV and  $r^2$  were the lowest of all ( $1.3 \pm 0.5$  m/s,  $r^2 = 0.51 \pm 0.27$ ). These findings show that PWI can be used to distinguish normal murine aortas from AAAs, as well as differentiate AAAs that will eventually rupture from AAAs that do not. Hence, PWI could potentially be used to assess the stability of human aneurysms by providing information that is complementary to B-mode-based anatomical information.



2F-2

### 1:15 pm Stiffness mapping in murine atherosclerotic and aneurysmal aortas using Pulse Wave Imaging (PWI) in vivo

Iason Zacharias Apostolakis<sup>1</sup>, Sacha D. Nandlall<sup>1</sup>, Elisa E. Konofagou<sup>1</sup>; <sup>1</sup>Columbia University, USA

#### Background, Motivation and Objective

Atherosclerosis and abdominal aortic aneurysms (AAAs) are two of the main causes of overall morbidity and mortality in Western populations. Both of these diseases are known to change the mechanical properties of the arterial wall. Pulse Wave Imaging (PWI) is a noninvasive technique developed by our group to measure the mechanical properties of the aortic wall in the absence or presence of pathology *in vivo*. This study aims at optimizing this technique to map aortic wall stiffness at high spatial resolution along the arterial wall.

#### Statement of Contribution/Methods

ApoE knockout mice (n=12) were fed an atherogenic high-fat diet for 30 weeks. AAAs were modeled by infusing ApoE/TIMP-1 knockout mice (n=9) with angiotensin II for 30 days. The mouse aortas were imaged with a Visualsonics Vevo 770 high resolution imager at a frame rate of 8 kHz using ECG gating. The displacements induced by the pulse



waves were estimated by performing 1D cross-correlation on the radiofrequency signals. The aortic walls were segmented semi-automatically from the B-mode images and the wall velocities were depicted over time to generate spatiotemporal profiles of the pulse propagation. The local Pulse Wave Velocities (PWVs) and associated coefficients of determination ( $r^2$ ) were calculated by performing linear regressions on the 50% upstroke markers of the pulse-wave-induced displacements, with a 50% window overlap across the imaged aortic wall. Following PWV mapping, stiffness was also estimated using the Moens-Korteweg equation.

### Results/Discussion

Figure 1 shows generated PWV and stiffness maps. In atherosclerotic aortas, the mean sub-regional PWV was found to increase significantly ( $p < 0.01$ ) from  $2.61 \pm 0.54$  m/s in normal aortas to  $3.99 \pm 1.07$  m/s, while the respective regional Young's modulus values averaged  $23.27 \pm 8.14$  kPa in normal aortas and  $68.92 \pm 40.71$  kPa in the high-fat aortas ( $p < 0.01$ ). In aneurysmal aortas, a decrease in both the mean sub-regional PWVs ( $2.04 \pm 0.62$  m/s,  $p < 0.05$ ) and the average regional Young's modulus ( $21.95 \pm 11.56$  kPa) was observed. The mean of the piecewise  $r^2$  values was also shown to differentiate normal aortas from both the high-fat ( $p < 0.01$ ) and the aneurysmal aortas ( $p < 0.01$ ). In conclusion, PWI-based stiffness mapping along the abdominal aortic wall could provide new information for localizing atherosclerotic plaque or aneurysms and characterizing their stiffness.

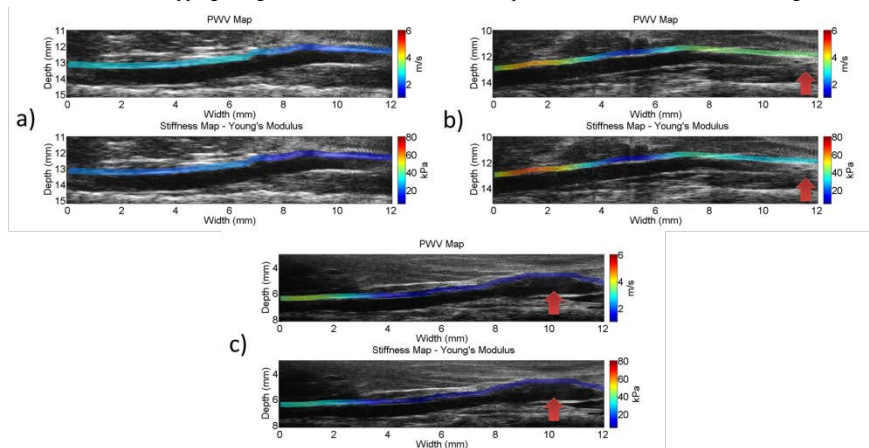


**Figure 1: Pulse Wave and stiffness maps for the case of (a) a normal aorta (b) an aorta of a mouse after 30 weeks of high fat diet (c) an aneurysmal aorta. In the diseased cases red arrows indicate the position of the b) atherosclerotic and c) aneurysm pathology.**

2F-3

### 1:30 pm High-resolution harmonic motion imaging (HR-HMI) for tissue biomechanical property characterization

Teng Ma<sup>1,2</sup>, Xuejun Qian<sup>3</sup>, Chi Tat Chiu<sup>1,2</sup>, Yao-sheng Tung<sup>1,2</sup>, Qifa Zhou<sup>1</sup>, K. Kirk Shung<sup>1,2</sup>; <sup>1</sup>Department of Biomedical Engineering, University of Southern California, USA, <sup>2</sup>NIH Resource Center on Medical Ultrasonic Transducer Technology, University of Southern California, USA, <sup>3</sup>Department of Electrical Engineering, University of Southern California, USA

#### Background, Motivation and Objective

Many acoustic radiation force (ARF) based imaging techniques have been developed to remotely access elastic properties of tissues. Among which, harmonic motion imaging (HMI) has shown promise in imaging HIFU-generated thermal ablation lesions by evaluating peak-to-peak amplitude of vibrating tissue under dynamic amplitude-modulated (AM) acoustic excitation. However, due to lower operating frequencies of transducers, its spatial resolution is insufficient for revealing stiffness distribution on small scale applications, such as cancerous tumor margin detection and atherosclerotic plaque characterization. Though recently developed high-resolution (HR) resonant ARF optical coherence elastography opens a new window for HMI by using mechanical resonant frequency as an additional contrast to identify tissues of different types, it suffers from a shallow depth penetration. The aim of this study is to develop a HR-HMI method for detecting localized vibration on a small scale.

#### Statement of Contribution/Methods

The block diagram of the system was shown in Fig. (a). A 4MHz ring transducer was used to generate the 100Hz AM excitation to vibrate tissue, and a 40MHz needle transducer was confocally aligned with ring transducer for tracking the displacement during 1D mechanical scanning. The 2D displacement map was calculated based on 1D cross-correlation algorithm. Left-right and up-down agar phantoms (0.5% and 1.5% in concentration) were constructed for HMI to validate the system. Finally, the system was tested on a section of human cadaver coronary artery.

#### Results/Discussion

B-mode and HR-HMI images of the soft part of phantom (0.5%, left) and hard part of the phantom (1.5%, right) are displayed in Fig.1(c) and (d). The vibrational displacement at different depths highlighted in Fig.1 (d) is shown in Fig.1 (b) with a maximum peak-to-peak displacement of 14μm and 5μm for soft and hard parts of the phantom, respectively. Similarly, the B-mode image and HR-HMI image of upper portion (0.5%-soft) and lower portion (1.5%-hard) are displayed in Fig.1 (e) and (f). The results demonstrate the feasibility of HR-HMI for detecting stiffness distribution in the axial and lateral direction. Finally, the coronary artery images [Fig.1 (g) and (h)] show that HR-HMI is capable of characterizing different layers of coronary artery wall and identifying atherosclerotic plaque.

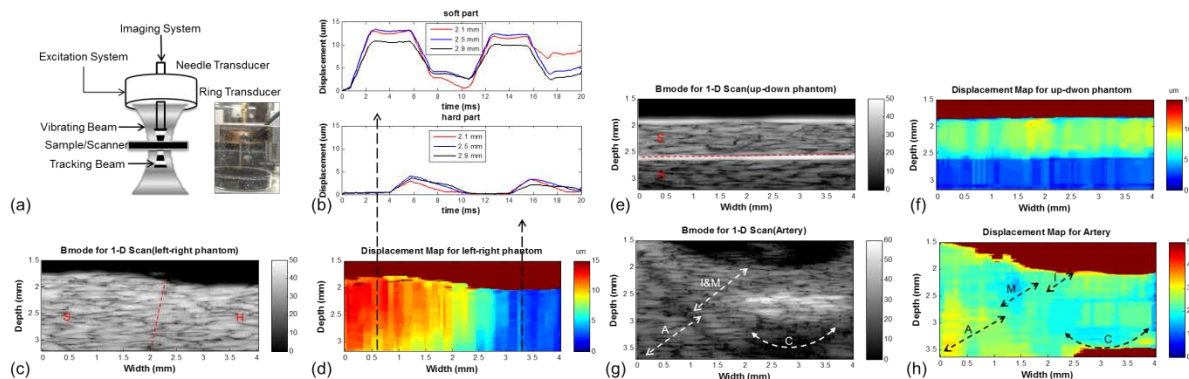


Figure.1 (a): Block diagram of HR-HMI system and actual set-up image of ring transducer and needle transducer. (b): Displacement amplitude at different depth indicated by the two lateral location in (c). (c): B-mode image of left-right agar phantom, S: soft part 0.5% concentration, H: hard part 1.5% concentration, dashed line: actual transition of soft and hard part. (d): Displacement map of left-right phantom. (e): B-mode image of up-down phantom. (f): Displacement map of up-down phantom. (g): B-mode image of coronary artery segment, I: intima layer, M: media layer, A: adventitia layer, C: calcified plaque. (h): Displacement map of coronary artery segment.

2F-4

# 1:45 pm A sequential Bayesian based method for tracking and strain palpography estimation of arteries in intravascular ultrasound images

Nicolas Widynski<sup>1</sup>, Jonathan Porée<sup>1</sup>, Marie-Hélène Roy Cardinal<sup>1</sup>, Jacques Ohayon<sup>2</sup>, Guy Cloutier<sup>1</sup>, Damien Garcia<sup>1</sup>; <sup>1</sup>University of Montreal Hospital, Montreal, QC, Canada, <sup>2</sup>Laboratory TIMC, DyCTIM, CNRS UMR5525, Joseph Fourier University, La Tronche, France

## Background, Motivation and Objective

Recent studies revealed that modeled peak circumferential stress, occurring in the fibrous cap of a diseased artery, could be a major indicator of plaque vulnerability. Ultrasound palpography has been introduced as a surrogate to elastography for highlighting fibrous cap stress, by means of quantifying the strain distribution induced by the intraluminal pressure. State-of-the-art literature indicates that quantifying the strain map requires two steps: 1) the detection of the vessel wall inner contour, and, 2) the estimation of the radial strain along it. The proposed model jointly estimates the contour of the vessel wall and the strain by including mechanical a priori. This leads to a constraint problem that drives the segmentation while ensuring palpography consistency. The method outputs tangential contour strains, which are related to the stress distribution in the fibrous cap.

## Statement of Contribution/Methods

A tracking method is proposed to extract both the inner contour of the vessel wall and the tangential strain distribution along it. This estimation is carried out by a non parametric sequential Bayesian method. The Bayesian modeling holds three ingredients: the prior, which is given by a manually defined segmentation of the contour wall on the first image; the transition, which is assumed to follow a Markovian random walk; and the likelihood, which is a non parametric measure of the difference of intensity distributions between the blood and the vascular wall. The underlying Bayesian posterior distribution is approximated using a sequential Monte Carlo approach.

## Results/Discussion

The proposed method was evaluated on a sequence of an atherosclerotic pig carotid artery acquired with a 20 MHz IVUS transducer operating at 30 frames per second (200 B-mode images). Figure 1 depicts the segmentation in the whole temporal sequence (left), and the results obtained at a particular frame (right). The plaque is illustrated by a red arrow. Cumulative tangential deformations along the contour of the vascular wall are also mapped, exhibiting a singular signature of the plaque. The errors between manual segmentation of the lumen boundary and detected contours were quantified by a Hausdorff distance of  $0.17 \pm 0.04$  mm; a Jaccard coefficient of  $0.95 \pm 0.01$ ; and a Dice coefficient of  $0.98 \pm 0.005$ .

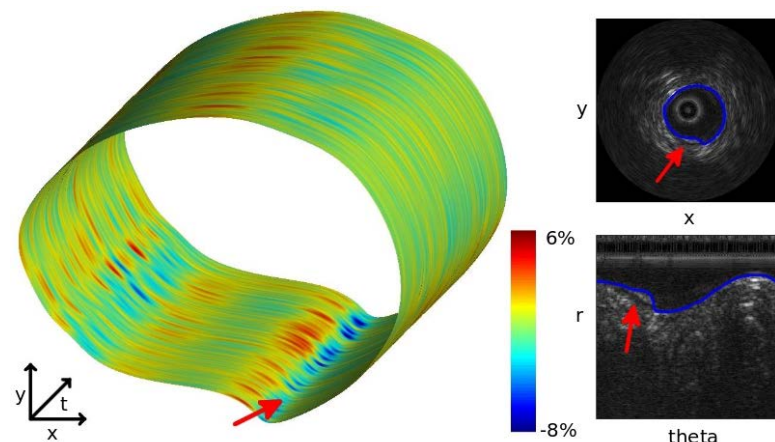


**Fig. 1** - Pig artery in vivo experiment. (Left) Contours (without catheter motions) extracted on the whole sequence. Colors represent the tangential deformations. (Right) Results obtained on a single image. The plaque is illustrated by a red arrow.

2F-5

**2:00 pm Semi-3D strain imaging of an atherosclerotic carotid artery by multi cross-sectional radial strain estimations using simulated multi angle plane wave ultrasound**

Stein Fekkes<sup>1</sup>, Abigail E.S. Swillens<sup>2</sup>, Hendrik H.G. Hansen<sup>1</sup>, Anne E.C.M. Saris<sup>1</sup>, Maartje M. Nillesen<sup>1</sup>, Patrick Segers<sup>2</sup>, Chris L. de Korte<sup>1</sup>; <sup>1</sup>Medical Ultrasound Imaging Center, Department of Radiology and Nuclear Medicine, Radboud University Medical Center, Nijmegen, Netherlands, <sup>2</sup>Department of Electronics and Information Systems, Ghent University, Ghent, Belgium

**Background, Motivation and Objective**

Three-dimensional vascular strain estimation is crucial for detection of vulnerable plaque locations in the carotid artery. This study introduces a semi-3D radial strain imaging method which is tested in a 3D model of an atherosclerotic carotid artery.

**Statement of Contribution/Methods**

A 3D finite element model of a patient-specific, pulsating atherosclerotic carotid artery (pulse pressure 60 mmHg) was generated with Abaqus. Radiofrequency (RF) data were simulated in Field II by moving point scatterers (~vessel wall) according to the calculated deformation patterns (ground truth). RF element data were simulated for a linear array transducer ( $f_c = 9$  MHz, pitch = 198  $\mu$ m, 192 elements) that transmitted plane waves at 3 sequentially alternating angles (+20°, 0°, -20°) at a pulse repetition frequency of 12 kHz. Simulations with 25 ms inter-frame time were performed for 25 equally spaced (0.5 mm) transversal positions of the internal carotid artery containing fatty and calcified areas. After delay-and-sum beamforming, inter-frame axial displacements were estimated using a coarse-to-fine normalized cross-correlation method. The 0° axial displacement was used as vertical displacement component. Projection of the +20° and -20° axial displacements yielded the horizontal displacement component. Tracking was performed to accumulate displacements for each transversal position. A polar grid and the lumen center were defined in the end-diastolic frame of each transversal position and used to convert the tracked axial and lateral displacements to radial displacements. Least squares strain estimation was performed to acquire accumulated radial strain. Strains derived from the model dynamics and estimated strains were compared by the Root Mean Squared Error (RMSE).

**Results/Discussion**

Good agreement between the ground truth and the estimated radial strain was observed for all volumes over the entire pressure cycle. Figure 1 shows the cumulative strains at max. pressure difference revealing a ~10% strain region corresponding to a fatty region and a ~2% strain region corresponding to a calcified region. The RMSE between the ground truth and estimated strain was 1.7% at the maximum systolic pressure. These results prove the feasibility of 3D carotid strain imaging although this is only the first step.

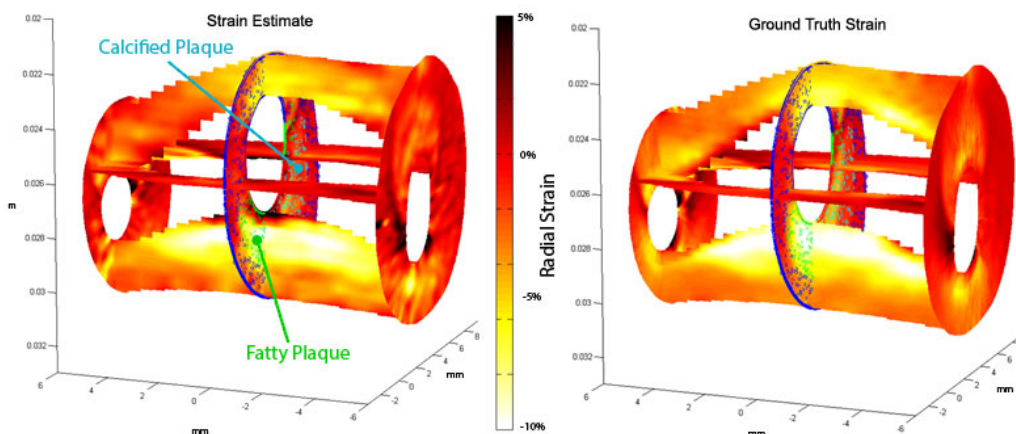


Figure 1: semi-3D strain imaging of a atherosclerotic carotid artery at the maximum systolic pressure indicating correspondence between high strain regions and fatty plaque location (green scatterers = fatty, cyan scatterers = calcified, blue scatterers = healthy tissue). For clarification only 3 of 25 transversal slices are shown.

2F-6

**2:15 pm In vivo Radial and Longitudinal Carotid Artery Plaque Strain Estimation via Ultrasound-Based Speckle Tracking**

Erik Widman<sup>1</sup>, Kenneth Caidahl<sup>2</sup>, Jan D'hooge<sup>3</sup>, Matilda Larsson<sup>1</sup>; <sup>1</sup>Department of Medical Imaging, KTH Royal Institute of Technology, Stockholm, Sweden, <sup>2</sup>Department of Molecular Medicine and Surgery, Karolinska Institute, Stockholm, Sweden, <sup>3</sup>Cardiovascular Imaging & Dynamics, Department of Cardiovascular Sciences, KU Leuven, Leuven, Belgium

**Background, Motivation and Objective**

Carotid Artery (CA) plaque characterization is critical for the prevention of ischemic events. In clinical practice, ultrasound (US) based methods for plaque characterization are limited to visual assessment of morphological and echogenic properties. Since plaque stiffness has shown to correlate with plaque vulnerability, quantification of plaque strain throughout the cardiac cycle would be useful. Previously, we have developed and validated a 2D speckle tracking (ST) algorithm to evaluate plaque stiffness by measuring strain in CA plaque phantoms in vitro. The objective of this study was to demonstrate the feasibility of in vivo plaque strain measurements in atherosclerotic plaque patients, with the hypothesis that echolucent plaques with a large lipid or intraplaque hemorrhage core would exhibit larger strain compared to more echogenic fibrous plaques.

**Statement of Contribution/Methods**

Long-axis US cine-loops were collected in the CA from 7 patients ( $77 \pm 6$  years) on a GE Vivid E9 US machine at 10 MHz, 3.5 cm depth, 42 Hz, with two focal points on the arterial walls. Prior to ST analysis, the cine-loops were visually analyzed and scored using 4 different measures by two experienced physiologists. The plaques were scored: 1) heterogeneous versus homogeneous; 2) smooth versus rough surface; 3) on the Gray-Weale (G-W) scale; 4) based on their Gray Scale Median pixel value. The cine-loops were analyzed by the in-house ST algorithm (kernel size  $4 \times 2 \lambda$ ) with a region of interest placed in the plaque. The Pulse-Pressure (PP) adjusted peak negative radial and peak positive longitudinal strain from two cardiac cycles was averaged for each plaque and compared to the plaques G-W score.

**Results/Discussion**

Fig. 1a shows a sample echolucent plaque located in the CA bulb. Corresponding sample radial (blue) and longitudinal (red) strain curves are shown in Fig. 1b. The absolute value of PP adjusted means and standard deviations for radial (blue) and longitudinal (red) strain for in vivo plaques sorted by G-W classification (1, 2 correspond to echolucent plaques and 3 corresponds to echogenic plaque) can be seen in Fig. 1c. The results show increased radial and longitudinal strain in echolucent plaques compared to echogenic plaques indicating the possibility of characterizing plaque vulnerability based on strain.

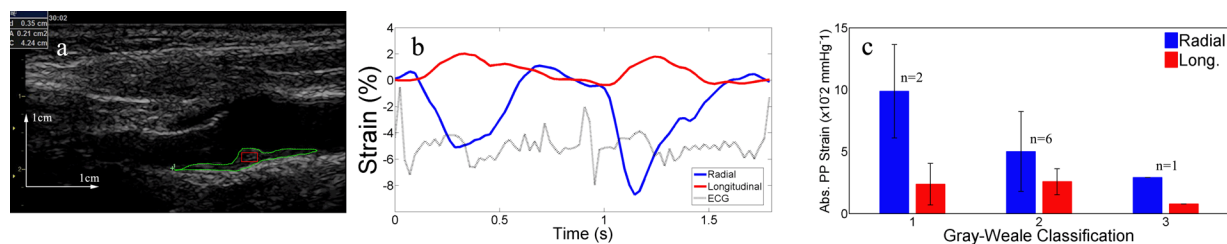


Fig 1 a) *In vivo* B-mode ultrasound image of an echolucent plaque located in the left carotid artery bulb of a 78 year-old man. The green line is the physicians' outline of the plaque and the regions of interest for speckle tracking analysis are shown in red. b) Corresponding radial (blue) and longitudinal (red) strain for 2 cardiac cycles. The patient's ECG curve is displayed for reference as a black dotted line. c) The absolute value of Pulse-Pressure (PP) adjusted means and standard deviations for radial (blue) and longitudinal (red) strain for *in vivo* plaques sorted by Gray-Weale classification.



### 3F - MBB: Beamforming II

Boulevard

Friday, September 5, 2014, 1:00 pm - 2:30 pm

Chair: **Herve LIEBGOTT**  
*Universite de Lyon*

3F-1

#### 1:00 pm An Adapted Beamforming Free from Crystalline Lens Phase Aberration for Ocular Ultrasonography – In-vitro Results with a 20 MHz Linear Array

Tony Matéo<sup>1</sup>, Yassine Mofid<sup>1</sup>, Jean-Marc Grégoire<sup>1</sup>, Frédéric Ossant<sup>1,2</sup>; <sup>1</sup>Université François-Rabelais de Tours, Inserm, Imagerie et Cerveau UMR U930, Tours, France, <sup>2</sup>CHRU de Tours, Tours, France

##### Background, Motivation and Objective

In ophthalmic ultrasonography the crystalline lens is known to be the main source of phase aberration as ultrasound (US) propagate about 10% faster than in the surrounding intra-ocular medium. Consequently, it causes significant decrease in both spatial and contrast resolution together with distortion effects on axial B-scans. It impairs diagnosis of retinal detachment, vitreous status, extent of disorders such as proliferative retinopathy, and ocular tumors differentiation on the posterior coat.

In view of the next coming of US arrays in ophthalmologic practice, where the effects of aberration are likely to be more severe due to larger aperture, the need for beamforming (BF) strategies adapted to the eye appears essential.

##### Statement of Contribution/Methods

Assuming the intraocular medium consists of two homogeneous media (crystalline lens + aqueous and vitreous humors), a bending ray tracing approach based on Fermat's principle has been developed to enable the fast calculation of focusing delays that compensate for the lens phase aberrations, including refraction effects, for much kind of US array. An eye-adapted BF based on this method was implemented in both emission and reception on a custom US scanner, the ECODERM, working with a 20MHz linear array. It required the detection of the actual contour of the lens, deduced from conventional delay-and-sum BF.

To quantify its performance, the adapted BF was tested in-vitro by imaging a wire phantom through an eye phantom consisting of a synthetic gelatin lens anatomically set up in an appropriate liquid (turpentine) to approach the in-vivo velocity ratio. The synthetic lens shape corresponded to that of an adult human crystalline lens in unaccommodated state. Both image quality and fidelity from the adapted BF were compared to conventional BF, in relation to that in homogeneous medium (Reference).

##### Results/Discussion

In-vitro quantitative study showed 2-fold improvement of the lateral resolution, greater sensitivity (SNR higher from 21dB) especially at retina depth and 90% reduction of the mean spatial error (from 758  $\mu$ m to 76  $\mu$ m) with adapted BF compared to conventional BF. Compared to Reference, lateral resolution was only 39% lower with adapted BF.

In addition, B-scans from adapted BF exhibited the lens with a contour in much greater agreement with its actual shape than conventional BF, which is promising for US phakometry.

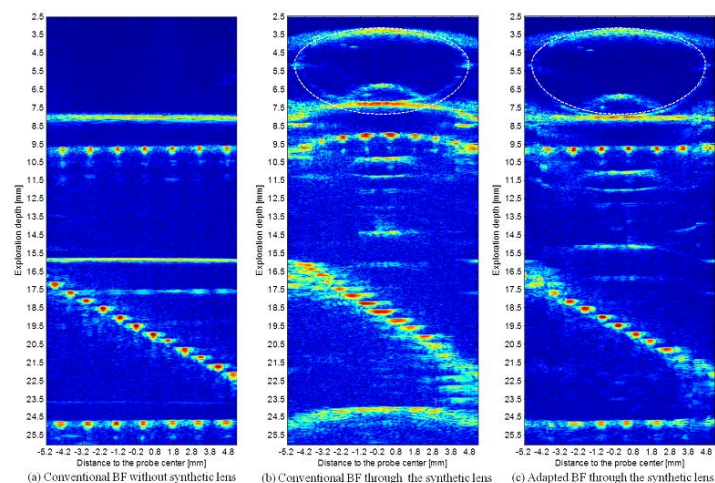


Fig. 1. B-scans of the wire phantom (2 horizontal and one tilted plate) in pure turpentine with conventional BF (a) for Reference, in presence of the synthetic lens with conventional BF (b) and with adapted BF (c). Detected contour from conventional BF of the synthetic lens with unaccommodated shape is superimposed with white dashed line on (b) and (c).

3F-2

#### 1:15 pm Full aberration correction in echo ultrasound after detecting aberrators spatially resolved via transmit beam steering

Michael Jaeger<sup>1</sup>, Martin Frenz<sup>1</sup>; <sup>1</sup>University of Bern, Switzerland

##### Background, Motivation and Objective

Phase aberrations of the acoustic wave front, caused by spatial variations of the speed of sound (SOS) inside tissue, are a main limiting factor to the diagnostic power of medical ultrasound. Previous research focused on the compensation for a fixed phase delay screen in front of the array probe. This model can account for inhomogeneous superficial tissue, however, significant variations of SOS are also found inside the body. We present a novel approach where full and automatic aberration correction (AC) can be achieved in the presence of a two-dimensionally varying SOS.

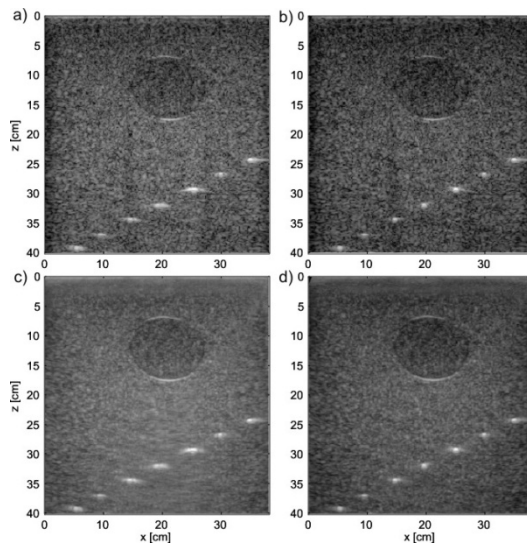


# Statement of Contribution/Methods

For this purpose, a sequence of reconstructed pulse-echo in-phase quadrature (IQ) data is obtained using different transmit steering angles. The inhomogeneous SOS is reflected in the transmit angle dependent phase of local echoes behind the aberrating structures. Correlation based tracking of the local IQ phase results in an estimation of the propagation-angle dependent aberrating delays independent of any assumption on the spatial distribution of SOS. In a second step, this information is employed to correct the arrival phases as a function of receive angle during receive beamforming, to achieve aberration-free diffraction-limited lateral resolution.

# Results/Discussion

In phantom experiments we have demonstrated accurate AC in presence of an inclusion with 1% contrast relative to the background SOS. B-mode ultrasound assuming a constant SOS shows significant lateral blurring of point like reflectors below that inclusion, along with an increased side lobe level (multiple dot structure) (Fig. a). AC results in equal lateral resolution of those reflectors independent on lateral position and side lobes are reduced (Fig. b). In addition, perfect registration of b-mode images obtained with different transmit steering angles is demonstrated as a result of AC, visualised by the homogeneous resolution of the diffuse speckle background after spatial compounding (SC) (Fig. d). In comparison, significant blurring of background speckle is observed in SC without AC owing to the misregistration of different steering angles (Fig. c). Our real-time capable technique is promising to strongly improve diagnostic ultrasound in deep tissues where prior knowledge on SOS is not available, such as in the case of liver imaging with an unknown spatial distribution of fatty infiltration.



3F-3

# 1:30 pm Acoustic Signal Modeling for Direct *in vivo* Assessment of Off-Axis and Reverberation Clutter Energy in the Liver

Brett Byram<sup>1</sup>, Kazuyuki Dei<sup>1</sup>, Douglas Dumont<sup>1</sup>, <sup>1</sup>Biomedical Engineering, Vanderbilt University, Nashville, TN, USA

# Background, Motivation and Objective

Recent work by us and others implies that reverberation may be a significant source of ultrasonic image degradation. However, there is still no method for precisely quantifying *in vivo* levels of reverberation for arbitrary clinical scenarios. Existing algorithms are designed to suppress clutter indiscriminately, so distinct causes of clutter cannot be differentiated. To solve this, we present a model-based approach for quantifying levels of *in vivo* reverberation and off-axis scattering. The model is an improvement on our previous work and is validated against simulations and applied to channel data of the liver from 5 patients.

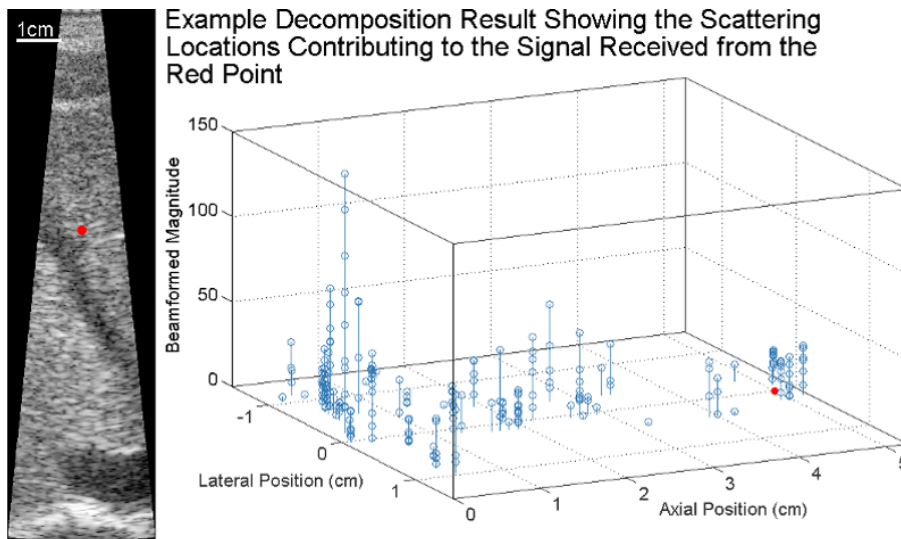
# Statement of Contribution/Methods

We made three improvements to our previous model. First, we better accounted for broadband ultrasound pulses. Second, we modeled exact arrival time delays instead of using the Fresnel approximation. Third, we modeled the necessary axial windowing of the channel data.

For validation, we estimated model error using Field II with a custom extension to simulate reverberation. The model was further validated with Field II by simulating a signal of 4 loci of 15 scatterers arriving from the receive focus and three off-axis and reverberative clutter sites. Twenty-five scattering realizations were evaluated. The model was fit to the data using least squares regression with Elastic Net regularization (ENR). ENR mixes L1 and L2 constraints for sparsity while enabling correlated model components. ENR parameters were systematically assessed, and we chose a  $\lambda$  of .1394 and L1/L2 mixing of .999. For the *in vivo* study, we used 56 data sets from 5 patients using a Siemens S2000. For the *in vivo* data, we consider the signal from a 5cm depth and defined energy originating 0 to 4 cm deep as reverberation, energy within 2 mm of the focus as the desired signal, and all other energy as off-axis scattering. We report the two beamformed clutter signals relative to the signal of interest. All parameters were consistent between Field II and *in vivo* data.

# Results/Discussion

The model compared to Field II shows average error over the model space of  $-16.4 \pm 2.8$  dB. For the diffuse scattering validation, the model assigns  $97.8 \pm 3.4\%$  of the power to within 5 mm of the 4 loci. For the *in vivo* study, relative off-axis power was  $-11.5 \pm 19.4$  dB, while relative multipath power was  $5.7 \pm 12.5$  dB. For our data, reverberation is the dominant mechanism of image degradation.



3F-4

#### 1:45 pm Sparse sampling and alternative methods for efficient spatial coherence estimation

Dongwon Hyun<sup>1</sup>, Gregg Trahey<sup>1</sup>, Jeremy Dahl<sup>1</sup>; <sup>1</sup>Duke University, Durham, NC, USA

##### Background, Motivation and Objective

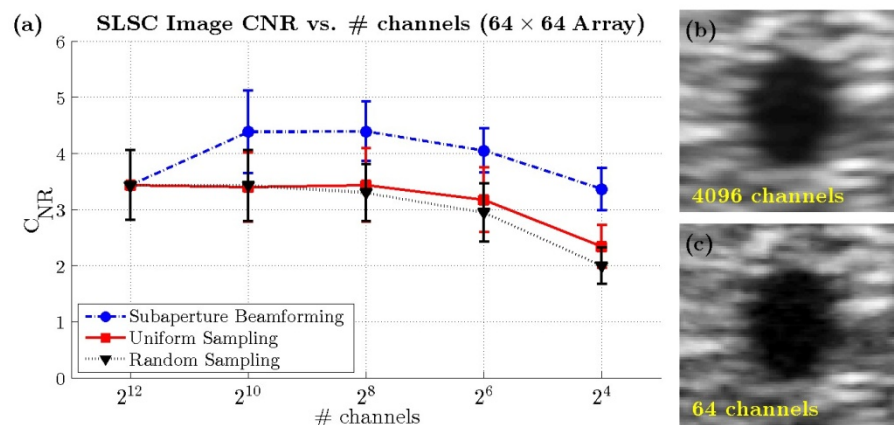
Short-lag spatial coherence (SLSC) is an ultrasound imaging technique that forms images based on the level of spatial coherence within the backscatter rather than its magnitude, as is done in traditional B-mode. SLSC imaging has been shown to be less susceptible to high-amplitude incoherent clutter (e.g., from near-field reverberations) compared to B-mode. However, the SLSC algorithm is far more computationally expensive. Reducing the computational cost is critical to imaging with SLSC at real-time frame rates, and can be accomplished by either reducing the number of computed normalized cross-correlations (NCCs) or by using alternative methods of coherence computation. We investigate several methods, including subaperture beamforming (SAB) and sparse sampling, and assess the effects of each approach in simulation and phantom studies on both 1D and 2D arrays.

##### Statement of Contribution/Methods

A 192 element 1D linear array and a 64x64 2D phased array were simulated with Field II. Each array was used to image a hypoechoic spherical lesion, and imaging performance was quantified using lesion contrast-to-noise ratio (CNR). Realistic imaging conditions were simulated with 12dB channel signal-to-noise ratio (cSNR) on the 1D array and 0dB cSNR on the 2D array. The number of NCCs was reduced by using either SAB or by utilizing a small subset of the receive signals. Signal subsets were created by sampling the aperture uniformly, randomly, or at its center.

##### Results/Discussion

SLSC imaging was remarkably robust to reduced sampling of the aperture on both the 1D and 2D arrays. The 1D array demonstrated a 10% loss in CNR of a -20dB lesion (from 4.5 to 4) when using just 32 elements of 192, spread either uniformly or randomly across the aperture. The 2D array was even more robust, with a CNR drop from 3.4 to 3.2 of an anechoic lesion when using 64 elements of 4096, corresponding to 1.6% of the aperture. Furthermore, SAB showed an improvement in CNR on the 2D array, likely due to the increased cSNR. These results show that sparse sampling of the NCCs is sufficient to generate high quality SLSC images. Additionally, use of other coherence metrics with lower computational cost (e.g., sum-absolute-difference) were found to generate similar images. Because the computation time scales roughly by the square of the number of signals, these results are promising for the development of real-time SLSC imaging.



(a) The measured CNRs of SLSC images of an anechoic lesion are plotted as a function of channel count for several computationally efficient methods. High quality SLSC images are formed even when reducing the number of channels significantly using different schemes. (b) An SLSC image was formed using all 4096 channels. (c) An SLSC image was formed using just 64 channels distributed uniformly across the aperture.

3F-5

## 2:00 pm Phase Coherence Factor with Sub-Aperture Beamforming

Hideyuki Hasegawa<sup>1</sup>, Hiroshi Kanai<sup>2</sup>; <sup>1</sup>Graduate School of Biomedical Engineering, Tohoku University, Japan, <sup>2</sup>Graduate School of Engineering, Tohoku University, Japan

### Background, Motivation and Objective

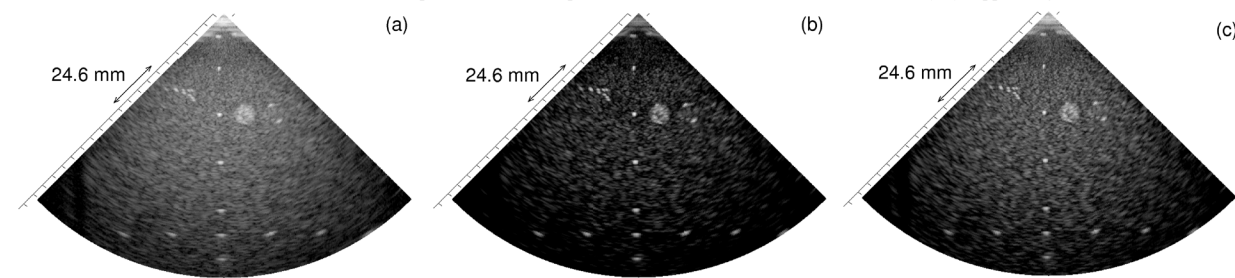
High-frame-rate echocardiography using unfocused transmit beams and parallel receive beamforming is a promising method for evaluation of cardiac function, such as imaging of rapid propagation of the heart wall vibration. In this technique, high temporal resolution is realized at the expense of spatial resolution and contrast. The phase coherence factor has been developed to improve spatial resolution and contrast in ultrasonography. It evaluates the variance in phases of echo signals received by individual transducer elements after delay compensation as in the conventional delay and sum beamforming process. However, the phase coherence factor suppresses speckle echoes because phases of speckle echoes fluctuate due to their mutual interference.

### Statement of Contribution/Methods

In the present study, total receiving aperture was divided into several sub-apertures, and conventional delay and sum beamforming was performed with respect to each sub-aperture to suppress echoes from scatterers except for that from a focal point. After sub-aperture beamforming, the phase coherence factor was obtained from beamformed RF signals from respective sub-apertures. By means of this procedure, undesirable echoes, which can interfere with the echo from a focal point, can be suppressed by sub-aperture beamforming, and the degradation of the phase coherence factor due to phase fluctuation caused by such interference can be avoided.

### Results/Discussion

Effects of sub-aperture beamforming were evaluated using a phantom. By sub-aperture beamforming, the average intensity of speckle echoes from a diffuse scattering medium was significantly higher (-39.9 dB, Fig. (c)) than that obtained without sub-aperture beamforming (-48.7 dB, Fig. (b)). As for spatial resolution, the width at half maximum of the lateral echo amplitude profile obtained without the phase coherence factor was 1.06 mm (Fig. (a)). Using the phase coherence factor, spatial resolution was improved significantly, and sub-aperture beamforming achieved a better spatial resolution of 0.75 mm than that of 0.78 mm obtained without sub-aperture beamforming. Using sub-aperture beamforming in estimation of coherence factor, better visualization of speckle echoes and spatial resolution could be realized simultaneously by suppressing out-of-focus echoes.



3F-6

## 2:15 pm Robust Ultrasonic Reverberation Clutter Suppression Using Multi-Apodization with Cross-correlation

Junseob Shin<sup>1</sup>, Yu Chen<sup>1</sup>, Jesse Yen<sup>1</sup>; <sup>1</sup>Biomedical Engineering, University of Southern California, Los Angeles, CA, USA

### Background, Motivation and Objective

Previously, we have introduced a beamforming technique called Dual Apodization with Cross-correlation (DAX), which utilizes two distinct receive apodizations to intentionally introduce grating lobes that allow for clutter signal suppression. Our results from a tissue-mimicking phantom demonstrated its utility in suppressing clutter due to off-axis scatterers and phase aberration effects. However, its effectiveness would likely diminish in the presence of near-field reverberation clutter as they often dominate over the grating lobe signals, resulting in an unreliable weighting matrix. In this work, we propose a modified version of DAX, called Multi-Apodization with Cross-correlation (MAX), which benefits from added phase diversity for increased robustness in reverberation clutter suppression.

### Statement of Contribution/Methods

Field II simulations of a point target at a depth of 70 mm were performed. Imaging parameters were chosen to model a 64-element ATL P4-2 phased array with center frequency of 2.5MHz, 50% bandwidth, azimuthal element pitch of 320  $\mu$ m. For experimental evaluation, RF data were acquired using a Verasonics system from a custom sponge phantom having a 4cm-diameter hole. To mimic the near-field reverberation clutter artifacts, a 1cm-thick copper wire mesh was placed at the surface of the transducer. Data sets were acquired with and without the copper wire mesh for comparison. For MAX, every possible permutation between 2 groups of 4 independent receive apodizations yielded a total of 16 cross-correlation coefficients. For each pixel, the coefficient that maximizes the performance in terms of contrast, contrast-to-noise ratio (CNR), and speckle SNR, was chosen. Initial results for echocardiography were also obtained to demonstrate feasibility *in-vivo*.

### Results/Discussion

The beamplots show the differences between DAX and MAX (Fig 1a). While the grating lobe locations remain unchanged when compared to DAX, MAX shows higher grating lobe level. MAX was shown to be highly robust, yielding CNR improvements of 130% and 252% without and with reverberation artifacts from the copper wire mesh, respectively (Figs 1b & 1c). MAX also achieved a CNR improvement of 88% over DAS from *in-vivo* echocardiography (Fig 1d). In all cases, MAX outperformed DAX in terms of CNR and its utility becomes more pronounced with high levels of reverberation clutter.

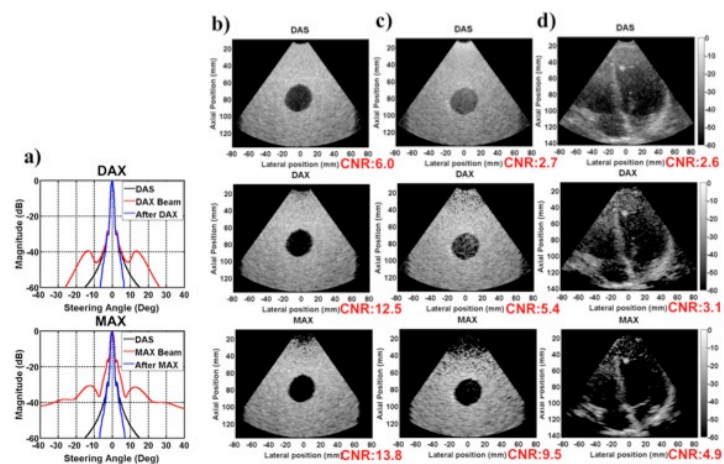


Fig 1. Comparison between DAS, DAX, and MAX with a) simulated beamplots, b) sponge phantom without a copper wire mesh, c) sponge phantom with a copper wire mesh, and d) in-vivo echocardiography (end-diastole) from an apical 4-chamber view.

## 4F - Signal Processing

Marquette

Friday, September 5, 2014, 1:00 pm - 2:30 pm

Chair: **Erdal Oruklu**  
*Illinois Institute of Technology*

4F-1

### 1:00 pm Low-rate ultrasonic communication axially along a cylindrical pipe via transverse waves

Soumya Chakraborty<sup>1</sup>, Kyle Wilt<sup>2</sup>, Gary Saulnier<sup>1</sup>, Robert Litman<sup>2</sup>, Henry Scarton<sup>2</sup>; <sup>1</sup>Electrical Engineering, Rensselaer Polytechnic Institute, USA, <sup>2</sup>Mechanical, Aerospace, and Nuclear Engineering, Rensselaer Polytechnic Institute, USA

#### Background, Motivation and Objective

Acoustic-electric channels have been introduced in the recent past to send power and data through metallic barriers. The majority of work to date has dealt with the use of a reverberant acoustic-electric channel formed through a single and relatively thin mechanical barrier. Multi-layered acoustic-electric channels, as well as those formed along a structure, which are highly attenuative and non-reverberant, could have potential applications in aerospace, nuclear, and oil industries, among others. This work considers data transmission along the length of a cylindrical pipe both when in air and filled and immersed in water.

#### Statement of Contribution/Methods

The channel is formed by epoxying steel wedges with attached ultrasonic transducers on the exterior of a 5.2 m long steel pipe with a separation of 4.8 m. The open-ended pipe is placed into a water-filled trough for immersed experiments. The transducers are shear-mode plates which are epoxied to the wedges, producing transverse waves in the wedges and pipe wall, where the wave displacement is oriented in the circumferential direction of the pipe (transverse polarization). The channel response is measured using a vector network analyzer and it is found that the channel attenuation varies considerably with small changes in frequency. To combat the effects of this frequency selectivity, and address the power constraints, simple modulation schemes using non-coherent demodulation methods are employed for data transmission, including Chirp-On-Off keying (C-OOK). The chirp waveform is a frequency modulated wave whose frequency increases linearly over the bit-interval, where the chip's spectrum is specified a-priori (10 kHz in this case). The wideband nature of the chirp waveform provides resilience against nulls in the channel response while making it possible to implement a simple non-coherent transceiver. The test data link is assembled using an arbitrary waveform signal generator to generate the chirp signal that is applied to the transmit transducer, a demodulator circuit consisting of a ceramic filter and logarithmic amplifier followed by a computer controlled digitizer to capture the signal from the receive transducer, with final processing and bit-decoding done via the computer.

#### Results/Discussion

Successful data transmission is achieved across the 4.8 m length of pipe (in air and water) for a data rate of 100 bps using a few milliwatts of transmit power. The power required for comparable operation is greater when the channel is immersed in water due to the additional attenuation introduced by energy loss into the water. The modulation scheme is found to be similar in performance to the theoretical non-coherent OOK system using a single tone for the flat channel case. Monte-Carlo simulation results are presented along with the experimental results to establish the bit-error-rate performance of the setup for various signal-to-noise values using the measured physical channel response.

4F-2

### 1:15 pm Signal optimization of PSK modulated gold-sequences for narrow band transducers

Andreas Schröder<sup>1</sup>, Bernd Henning<sup>1</sup>; <sup>1</sup>Measurement Engineering Group, University of Paderborn, Paderborn, NRW, Germany

#### Background, Motivation and Objective

Code division multiple access (CDMA) can be used to minimize crosstalk between air ultrasound distance sensors. For the transmission of different code sequences using such narrow band systems (ultrasonic transducers) an appropriate modulation process is necessary. Typical modulations are phase shift keying (PSK) or frequency shift keying (FSK). A critical point is the orthogonality of electrical received signals, which can be described by the cross correlation of the signals. For a non-synchronized system, every possible time shift between the signals generated with different code sequences has to be taken into account. The maximum of the normalized cross correlation is used as evaluation criterion, which depends on the limited transducer bandwidth and the limited symbol length. The maximum of all cross correlations, which are calculated based on all possible modulated signals generated out of one code family, is used to rate the signal family. So the weakest signal is used to evaluate the whole family.

#### Statement of Contribution/Methods

Simulations show that the cross correlation of signals generated out of different code sequences of a gold code family vary from sequence to sequence and depend on the carrier frequency for a band pass system. There are code sequences with a small and some with a large maximum of the cross correlation. By shifting the carrier frequency the large maxima of the cross correlation can be reduced. Thus it is not necessary to reduce the number of code sequences to improve the whole set of modulated signals generated with the gold code family. Thereby it is important to consider the signal energy as an important property when determining the optimal frequency shift. Otherwise an optimization would propose a high frequency shift, which leads to a small cross correlation but with quit small signal energy.

#### Results/Discussion

Numerical simulations using Butterworth van Dyke models of air ultrasound transducers show an optimal carrier frequency shift for PSK modulated gold sequences depending on the symbol length. Thereby the cross correlation of the weakest signal of the code family can be decreased by 30%. This is used to reduce the symbol length, which leads to a smaller blind zone of air ultrasound distance sensors.



4F-3

**1:30 pm Echo Identification by Singular Value Decomposition of Cross Wigner-Ville Distribution**Chi-Hang Kwan<sup>1</sup>, Anthony N. Sinclair<sup>1</sup>; <sup>1</sup>Mechanical & Industrial Engineering, University of Toronto, Toronto, Ontario, Canada**Background, Motivation and Objective**

Although the Cross Wigner-Ville Distribution (XWVD) has previously been applied to estimate instantaneous frequency and separate overlapping echoes, to our knowledge it has not been analyzed with Singular Value Decomposition (SVD).

SVD exploits the oscillatory nature of XWVD to facilitate the identification of heavily overlapped ultrasound pulses. Compared to previous methods, this novel echo identification technique is non-iterative and only requires knowledge of the approximate bandwidth of the echoes. This flexibility allows the method to separate both symmetric and asymmetric pulses. In addition, noise filtering and echo identification are performed synergistically.

**Statement of Contribution/Methods**

XWVD is computed by performing the Fourier Transform of the instantaneous auto-correlation between the experimental signal and a reference for a series of time shifts. XWVD is in general complex valued and oscillatory in nature. These oscillation periods are inversely proportional to the time and frequency difference between the reference and experimental signals.

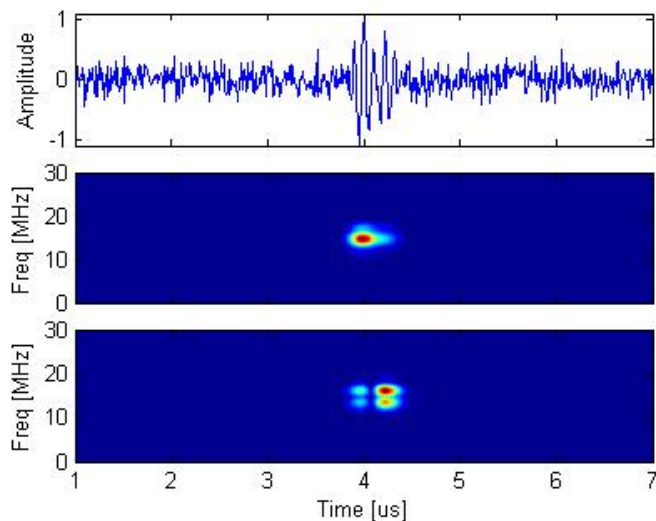
These characteristics of XWVD make it ideally suited for analysis by SVD. SVD decomposes a matrix into the sum of Rank 1 matrices. Since components with similar frequency supports but different oscillation periods cannot be represented by a single Rank 1 matrix, SVD can separate XWVD components that overlap significantly in time. The echo identification algorithm of this work is summarized below:

1. Compute the XWVD using the optimal reference signal
2. Compute the SVD of the complex valued XWVD
3. Determine the number of Rank 1 matrices used to identify the echoes
4. Analyze the chosen Rank 1 matrices to identify the number of echoes
5. Estimate the location and magnitude of each identified echo

**Results/Discussion**

The top plot of Figure 1 shows two 50% overlapped synthetic asymmetric pulses at a SNR of 8 dB. The bottom two plots show the amplitude of the first two Rank 1 matrices computed from the SVD of XWVD.

Using a weighted average estimation algorithm, the time locations of the echo peaks are determined to be at 3.99 and 4.23  $\mu$ s. This is close to the actual values of 4.00 and 4.22  $\mu$ s. In summary, SVD of XWVD is a non-iterative method that is capable of separating overlapping pulses in a high noise environment.



4F-4

**1:45 pm Anisotropic diffusion filter for robust timing of ultrasound echoes**Yunlu Jia<sup>1</sup>, Mikhail Skliar<sup>1</sup>; <sup>1</sup>University of Utah, USA**Background, Motivation and Objective**

Accurate and robust timing of ultrasound echoes is important in many applications. Of particular interest to us is the measurement of the speed of sound in solid dissipative materials. In this case, standard timing techniques based on zero-crossing or peak signal values in time domain give unsatisfactory timing accuracy. For these materials, techniques that use cross-correlation between waveforms perform better but are still affected by waveform broadening caused by preferential attenuation of higher frequencies in broad-band signals. The envelope methods present an attractive alternative with several advantages. For example, the peak energy of the signal is a convenient reference point to measure its time of flight (TOF). However, the timing results are still affected by the artifacts and measurement noises, as illustrated in Fig. 1II, which shows that envelopes of two echoes acquired at identical conditions, but having different locations of envelope peaks.

## Statement of Contribution/Methods

We developed a new timing method that used anisotropic diffusion to stabilize the peak location of a signal's envelope. This method utilizes favorable de-noising properties of nonlinear diffusion to iteratively enhance the envelope of an echo and improve the accuracy in measurements of its TOF.

## Results/Discussion

The developed method was experimentally validated and compared with the alternatives. An US pulse was created by piezoelectric transducer (5MHz central frequency) excited by a square wave. The signal propagated through an alumina waveguide and the TOF of an echo reflected from its distal end was measured. Fig. II shows the measured echo, its envelope (Fig. 1IA), and the envelope's transformation after anisotropic diffusion was applied (panels B through E correspond to 100, 500, 1000 and 1500 iterative applications of anisotropic diffusion operator). The red triangles mark the peak values of the envelopes after filtering. With an increased number of iterations, the position of the peak value stabilizes and becomes less sensitive to the measurement noises and shape distortions. Figure 1II shows two waveforms collected at identical conditions, but having envelopes with different peak positions (green marks). After filtering, the peak values coincide and provide robust and consistent reference for timing the echoes.

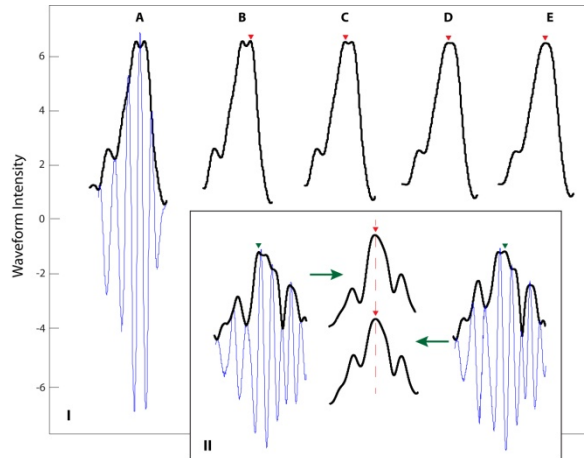


Figure 1: (I) The envelope of the original waveform (in blue) is shown in A. Anisotropic diffusion was applied 100, 500, 1000 and 1500 times to obtain panels B through E; red marks indicate peak values. (II) Two echoes collected at identical conditions but different times have different peak envelope positions (green marks). After using anisotropic diffusion, the peak values coincide (red arrows).

4F-5

## 2:00 pm Second generation ultrasound sensing in micro drones

Tobias Dahl<sup>1</sup>, Butrus (Pierre) T. Khuri-Yakub<sup>2</sup>, Sverre Holm<sup>3</sup>; <sup>1</sup>ICT, SINTEF, Oslo, Norway, <sup>2</sup>E.L. Ginzton Laboratory, Stanford University, Stanford, USA, <sup>3</sup>Department of Informatics, University of Oslo, Oslo, Norway

## Background, Motivation and Objective

Micro unmanned aerial vehicles, or drones, have become popular for search and rescue operations, law enforcement, journalism, and in the consumer markets both indoors and outdoors. Presently, ultrasound sensors are used only for altitude measurements for automatic landing at ranges up to 10 m. We want to study the potential of a second generation miniature ultrasound sensors, for imaging and positioning purposes. Their small wavelength and potential for high resolution, low power and low weight are exploited. Challenges include sensitivity to noise from propellers and the environment.

## Statement of Contribution/Methods

We have identified three technologies: 1) Synthetic aperture (SA) imaging 2) Room shape estimation 3) Swarm positioning. 1) and 2) can be done from a single drone or from a coordinated swarm using 3) with ultrasound used also for relative positioning of the individual drones.

SA imaging (1) benefits from the accomplishments of SA sonar, where techniques have been developed to overcome the slow speed of sound relative to radar (SAR). The key is to use an ultrasound receiver array rather than a single element. Recent developments in CMUTs have made this feasible.

Room shape estimation (2) may be accomplished by listening to own echoes and estimate ranges to the main reflecting surfaces. More sensors and larger distance between them is a beneficial, so the use of multiple drones is preferable.

Swarm positioning (3) can be done by measuring distance between drones timing ultrasound pulses relative to radio. This is known from indoor positioning systems. CMUT arrays mounted both vertically and horizontally can be used to reject noise and increase range by scanning in space.

## Results/Discussion

A calculation for a SA system shows the potential. A sensor with 30 degs beamwidth (aperture of  $2\lambda$ ) has a footprint of 5 m at a range of 10 m. This is the maximal size of the SA. If all data can be coherently integrated, the SA resolution will be half the aperture size, or 9 mm at 40 kHz. The two-way travel time is almost 60 ms, and as the sensor can only be moved half its length per ping, this results in a speed of only 0.15 m/s. A receiver array will increase the mapping rate by the number of elements, so 6-7 elements will allow for a more acceptable 1 m/s. An array will also allow swarm micro navigation.

The other two approaches, room size estimation and swarm positioning, are further developed in the paper.

**2:15 pm Hardware-Software Co-design of 3D Data Compression for Real-Time Ultrasonic Imaging Applications**Pramod Govindan<sup>1</sup>, Jafar Saniie<sup>1</sup>; <sup>1</sup>*Electrical and Computer Engineering, Illinois Institute of Technology, USA***Background, Motivation and Objective**

Many of the ultrasonic NDE and imaging applications require processing of huge amount of data in real-time. Compression of acquired data helps to reduce the storage and to rapidly transmit information to remote locations for further analysis. Signal fidelity, computational speed and resource utilization are the major parameters to be considered while designing the architecture for the compression algorithm. The reconfigurable platform allows analysis of multiple architectures to suit various applications. The objective of this study is to implement discrete wavelet transform (DWT) based ultrasonic data compression algorithm on a reconfigurable ultrasonic system-on-chip hardware platform, with emphasizing high signal fidelity, low resource utilization and high throughput.

**Statement of Contribution/Methods**

The compression algorithm using 3D DWT is implemented on a Xilinx Zynq-7020 all programmable system-on-chip FPGA with an ARM processor. DWT uses multistage sub-band decomposition which can be structured to isolate the high energy sub-bands to provide maximum signal compression with high fidelity. Two different architectures of the compression algorithm are discussed in this study: hardware only design using programmable logic and software only design using ARM processor. Furthermore, the Zynq platform is used to implement the compression algorithm in real-time as a hardware/software co-design, wherein the ultrasonic data acquisition is controlled in hardware, and the compression algorithm is executed in software by ARM processor. DWT mainly requires filtering operations, which involves several multiplications. Multiplication is optimized by using reduced adder graph algorithm; thus the computational speed and the resource usage are improved. Additionally, the lowpass and highpass filters are processed in parallel to further reduce the overall execution time. The software only design is also efficient due to the availability of advanced SIMD (single instruction multiple data) instructions supported by ARM processor, which allows the execution of ultrasonic signal processing algorithms at a very high rate.

**Results/Discussion**

In this study, a volumetric image of 128x128x2048 samples (33 Mbytes) are compressed using 3D DWT. The 3D block of data consisting of several interfering echoes is acquired using a 5 MHz ultrasonic broadband transducer and a steel block specimen with microstructural defects. A 4-level decomposition using Daubechies wavelet basis is performed for the ultrasonic A-scans having 2048 samples. A 2-level decomposition using Haar wavelet basis is performed for the spatial decomposition (128 samples). To reduce the execution time, 16 A-scans are decomposed in parallel. Using this implementation, the volumetric image of 33 Mbytes are compressed to 0.4 Mbytes in less than 0.5 seconds, giving a compression ratio of 95% with a peak SNR of 27 dB, indicating high signal fidelity.

## 6F - Novel Microacoustic Devices

Williford B

Friday, September 5, 2014, 1:00 pm - 2:30 pm

Chair: **Sunil Bhawe**  
Cornell University

6F-1

### 1:00 pm Study of Shear Horizontal Wave MEMS resonators based on X-cut Lithium Niobate thin film

Songbin Gong<sup>1</sup>, Gianluca Piazza<sup>2</sup>; <sup>1</sup>Department of Electrical and Computer Engineering, University of Illinois Urbana Champaign, Urbana, Illinois, USA, <sup>2</sup>Department of Electrical and Computer Engineering, Carnegie Mellon University, Pittsburgh, Pennsylvania, USA

#### Background, Motivation and Objective

For next generation RF front ends, chip-scale wide-band multiple-frequency solutions are highly sought-after for adaptive frequency-agile functionalities. Piezoelectric micro-resonators, particularly MEMS resonators based on transferred LN thin film of various cuts, hold strong potentials to deliver the performance required. S0 mode laterally vibrating resonators (LVRs) have recently been demonstrated with high electromechanical coupling coefficient ( $kt_2$ ) and quality factor ( $Q$ ) simultaneously, resulting in an unprecedented FoM. However, monolithic wideband filtering platforms that can cover entire RF spectrum remain a great challenge considering the dependence of wave dispersion on  $h/\lambda$  and the frequency sensitive nature of spurious mode suppression techniques. It is likely multiple acoustic modes need to be leveraged for different frequency ranges based on their wave propagation characteristics. Shear horizontal mode (SH0) vibrations, with high  $kt_2$  and lower acoustic velocity in X-cut LN, can be favorably utilized for duplexing lower RF bands. This work aims to theoretically study SH0 mode devices and experimentally verify their performance at 350MHz.

#### Statement of Contribution/Methods

The electromechanical coupling is modeled versus a variety of design parameters, including device orientation, film thickness, aspect ratio, and electrode configuration. Multiple designs were fabricated based on a previously demo'd process. The measured performance is compared with theory to verify the optimum device design at the center frequency of 350 MHz. In operation, the device (Fig.1) is excited into shear horizontal vibrations, and its center frequency is determined collectively by the aforementioned parameters. The impact of the device orientation in X cut plane on  $kt_2$  and  $Q$  has been experimental identified. The maximum  $kt_2$  of 14.5% is observed at an orientation of 20 degree to -Y, with maximum  $Q$  of 510.

#### Results/Discussion

The LN resonators were modeled with COMSOL and an equivalent circuit model. The circuit simulation and measurement show excellent agreement. A spurious-free response was demonstrated with an optimum design at 20° to -Y. The shown mode shape (Fig.1(b)) confirms SH0 mode vibrations and a phase velocity of 4260 m/s. The extracted  $kt_2$  for the tested orientations matches the simulation very well.

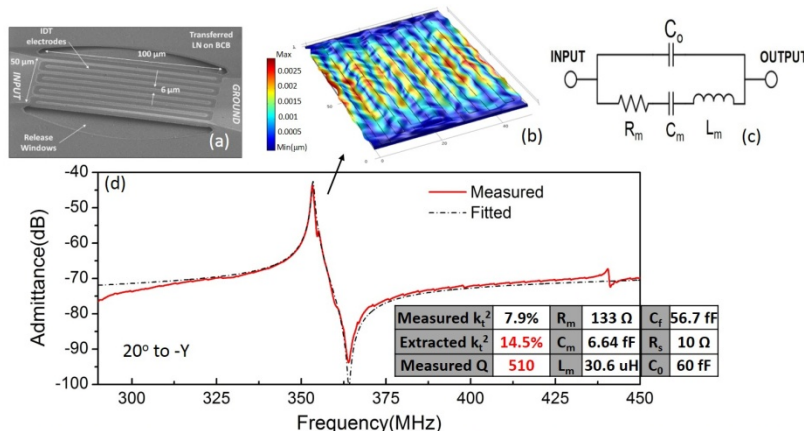


Fig.1(a) SEM of the fabricated LN resonator with an orientation of 20° to -Y in X-cut plane, (b) the identified SH0 displacement mode shape at the resonance (c) equivalent circuit model of the SH0 LN resonator, and (d) the measured and fitted admittance response of a designed LN resonator. Both the designed and extracted parameters are listed in the inset.

6F-2

### 1:15 pm Suppressing Fine-Frequency Modes in Aluminum Nitride Microresonators

Darren W. Branch<sup>1</sup>, Roy H. Olsson<sup>2</sup>; <sup>1</sup>Biosensors and Nanomaterials Department, Sandia National Laboratories, Albuquerque, New Mexico, USA, <sup>2</sup>Advanced MEMS Department, Sandia National Laboratories, Albuquerque, NM, USA

#### Background, Motivation and Objective

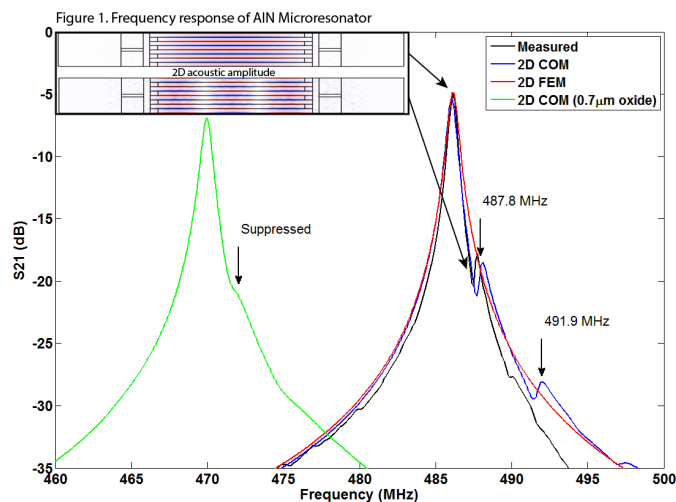
Eliminating spurious modes in Aluminum Nitride (AlN) microresonators improves their insertion loss and quality factor by reducing acoustic energy leakage. Spurious modes that result from transverse wave propagation, termed fine-frequency modes, leak energy and propagate in the electrical bussing and appear near the primary resonance. Although these modes can be predicted using three-dimensional (3D) finite element methods (FEM) for devices with very short acoustic length (e.g.  $N=2$ ), 3D FEM is very slow and memory intensive compared a two-dimensional (2D) simulation. A fast 2D coupling-of-modes (COM) model was developed to predict, identify and implement strategies to suppress the fine-frequency modes.

**Statement of Contribution/Methods**

Though scalar potential theory is commonly applied to determine the conditions to confine transverse modes within the transducer region, it does not address 2D variation or directly compute the electrical response. AIN microresonators can be divided into multiple domains in 2D, each with their own velocity: transducer ( $v_t$ ), electrical bussing ( $v_{e1}$ ,  $v_{e2}$ ), and free regions ( $v_f$ ). Acoustic confinement occurs when:  $v_t < v_{e1} \approx v_{e2} < v_f$ , that is the fine-frequency modes are suppressed from trapping acoustic energy in the transducer. This work applies the 2D-COM method across the entire structure which is valid since the transverse wavenumber is much less than the normal wavenumber  $|k_y| \ll k_x$ . A separate 2D FEM model was used to calculate the COM parameters in the various domains for the 2D COM model.

**Results/Discussion**

An AIN microresonator with  $N = 8$  fingers ( $\lambda = 16 \mu\text{m}$ ) was simulated using the 2D COM model. The transducer used all four COM parameters, where the electrical buss had no reflectivity and the free domains lacked reflectivity and capacitance. The 2D COM model predicted a spurious mode at 487.8 MHz and a second at 491.9 MHz, where the latter was more damped in the measured data. The amplitude profile of these modes is shown in the inset of Figure 1. Spurious mode suppression was achieved by depositing  $0.7 \mu\text{m}$  of silicon dioxide in the transducer domain which reduced the phase velocity, shifting the resonance to 470 MHz. The increased insertion loss is due to reduction in strain from the silicon dioxide film. The computational time was 1.5 seconds/frequency point.



6F-3

**1:30 pm Bulk Acoustic Wave Gyroscope**

Farokh Ayazi<sup>1,2</sup>; <sup>1</sup>Georgia Institute of Technology, Atlanta, GA, USA, <sup>2</sup>Qualtré Inc., Marlborough, MA, USA

**Background, Motivation and Objective**

The motion of an object in space can be mapped through the use of an inertial measurement unit (IMU), which comprises of a three-axis accelerometer and a three-axis gyroscope. Accelerometers measure linear motion (axial acceleration) while gyroscopes measure rotation (angular velocity). The gyroscope resolution and drift have been the bottleneck in achieving accurate and extended periods of navigation using silicon IMU chips. High-Q bulk acoustic wave (BAW) modes of a silicon disk or an annulus resonator can be used to sense rotation around all three axes. If two of these modes have identical frequencies and are coupled through Coriolis effect, the sensitivity of the gyroscope is amplified by the Q-factor of the modes, which can reach hundreds of thousands on-chip. The high frequency BAW gyroscopes offer many advantages over low frequency tuning-fork and ring structures including improved shock resistance, reduced vibration sensitivity, large dynamic range and large open-loop bandwidth. The nano-gap capacitive transducers implemented using the HARPSSTM process enable system-on-chip (SOC) integration of all IMU components using a foundry-compatible monolithic process.

Single-chip wafer-level-packaged silicon BAW IMUs have been implemented and their response have been fully demonstrated. Individual gyroscopes have been interfaced with a self-sufficient ASIC utilized to capture the angular rate response of the yaw and pitch-and-roll sensors. Both the disk yaw gyroscope, and the annulus pitch-and-roll sensors yielded high-Q excitation and sense modes with inherently low frequency splits, tunable to 0 Hz. Similarly, nanogap capacitive accelerometers have been characterized to measure the acceleration response along all three axes.

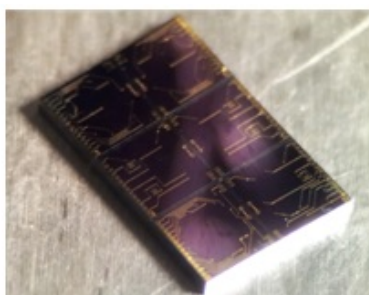
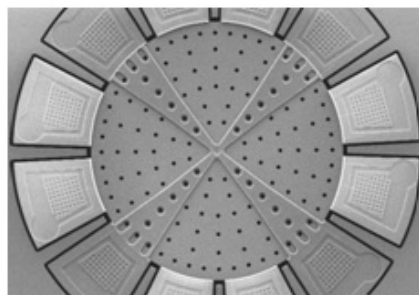
**Statement of Contribution/Methods****Results/Discussion**

Figure 1: (left) SEM view of a silicon bulk acoustic wave (BAW) gyroscope, (right)  $4 \times 6 \times 0.9 \text{ mm}^3$  WLP MEMS BAW IMU die.



2:00 pm INVESTIGATION OF QUALITY FACTOR FOR HIGH COUPLING AND HIGH FREQUENCY LATERALLY VIBRATING LN on SiO<sub>2</sub> MICRORESONATORS

Lisha Shi<sup>1</sup>, Gianluca Piazza<sup>1</sup>; <sup>1</sup>Electrical and Computer Engineering, Carnegie Mellon University, Pittsburgh, Pennsylvania, USA

Background, Motivation and Objective

Laterally Vibrating Resonators (LVRs) based on Y-cut Ion-Sliced Lithium Niobate (LN) thin films on silicon dioxide (SiO<sub>2</sub>) (Fig. 1) have shown great potentials for enabling a new wide bandwidth, reconfigurable, and temperature stable RF filtering platform. Despite the promising features, there is no understanding of what affects the quality factor ( $Q$ ) of these devices. This paper investigates, for the first time, the dependence of  $Q$  of LN LVRs on different device characteristics and the environment.

Statement of Contribution/Methods

Devices operating between 100 MHz and 1.5 GHz were designed and fabricated to explore the dependence of  $Q$  on: (i) electrode coverage and location, (ii) air damping, (iii) frequency, (iv) vibration mode, and (v) temperature.

To study the impact of electrode coverage and location on  $Q$ , segmented electrodes (Fig. 1) were introduced. The parameters of LVRs under study are listed in Table I. To determine the impact of temperature and pressure on  $Q$ , the LVRs were tested from 10 to 298 K at 5.3e-5Torr and 298 to 368 K under ambient air.

Results/Discussion

We studied how  $Q$  is impacted by: electrode coverage and location: for S0 mode vibrations 70% increase in  $Q$  is recorded when segmented electrodes are used. Furthermore, placing the electrodes over regions with reduced stress enables a higher  $Q$ . These results show that interfacial losses play a dominant role. air damping: at 298 K, the  $Q$  of resonators vibrating in the A0 mode from 100 to 550MHz increases at low pressure. The increment drops from 57.5% to 2% with frequency. For resonators vibrating in the S0 mode from 450MHz to 1.5GHz,  $Q$ 's improvement changes from 8.3% to 0% with frequency. We conclude that air damping plays a role in setting the  $Q$  of flexural-like A0 modes, but has a secondary impact for S0 mode. It is interesting to note that the impact of air damping weakens with frequency. temperature: most of the tested resonators exhibited a parabola-like trend for  $Q$  vs. temperature from 10 to 298 K. From 298 to 368 K, the  $Q$  of most resonators exhibited a rather constant behavior with fluctuations  $\leq 20\%$  of the average value. Finally, it is important to note that this is the first demonstration of LN LVRs with resonant frequency higher than 750 MHz. The LN on SiO<sub>2</sub> LVRs of this work exhibited high  $Q$  in air  $> 1,100$  at 870 MHz, and 650 at 1 GHz, hence extending the range of applicability of this technology.

Variable	Type a 10, 20	Type b 10, 20	Type c 10, 20
Top electrode finger number	4	6	6
Electrode pitch [ $\mu\text{m}$ ]	1 1.5	4	2 3 4 6
Metal strip width [ $\mu\text{m}$ ]	40, 80	40, 80	1 1.5 2 3
Electrode aperture [ $\mu\text{m}$ ]	50	67	50
Electrode coverage[%]	100	100	100
Top Al electrode thickness[nm]	100	100	100

**Table 1.** Characteristic geometrical parameters of the main LN/SiO<sub>2</sub> LVRs studied in this work. **Type a** refers to devices with segmented electrodes. Metal strip width refers to the size of a single electrode forming the pair. **Type b** and **c** corresponds to the devices of traditional design.

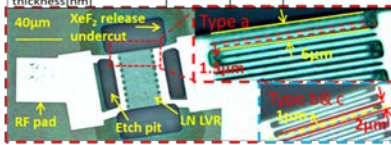


**Figure 1.** (left) Optical image of a fabricated LN/SiO<sub>2</sub> LVR with segmented fingers (type a). The zoomed-in image shows the period of the segmented interdigitated fingers of 6  $\mu\text{m}$  and the size of each metal strip (1.5  $\mu\text{m}$ ). The length of each finger is 40  $\mu\text{m}$ . (right bottom) This inset is a zoomed-in view of the electrode layout for type b & c designs. In this case the metal strip is 1  $\mu\text{m}$  wide and the pitch is 2  $\mu\text{m}$ .

2:15 pm Piezoelectric MEMS Gyroscope with Sputtered PZT Film

Tsuyoshi Takemoto<sup>1</sup>, Hiroaki Minami<sup>1</sup>, Glen Fox<sup>2</sup>; <sup>1</sup>Silicon Sensing Products Ltd, Amagasaki, Hyogo, Japan, <sup>2</sup>Fox Materials Consulting, LLC, Colorado Springs, CO, CO, USA

Background, Motivation and Objective

Within the past few years, the vibrating gyroscope has emerged from PZT-MEMS development to result in manufacturable products. This paper presents a detailed description of the design, fabrication and operation of a novel thin film PZT-MEMS gyroscope, Pinpoint®, that uses the converse piezoelectric effect to drive the vibration of a MEMS ring structure and uses the direct effect for sensing.

Statement of Contribution/Methods

Compared with other gyroscope designs the PZT-based PinPoint® has a reduced device size and a low power consumption of  $<16$  mW with a 2.7V to 3.6V operating voltage. The MEMS portion of the device consists of a Si ring supported by 8 pairs of equally spaced legs. The PZT actuator and sensing elements are deposited onto the top surface of the Si ring by using RF magnetron sputtering. The PZT film has a thickness of 3  $\mu\text{m}$  and exhibits a columnar microstructure with {100} crystallographic texture. A bottom electrode consisting of Pt and Ti adhesion layer is deposited before the PZT and a subsequently a Ti adhesion layer and Au top electrode is deposited. The PZT elements show a typical piezoelectric coefficient of  $d_{31} \geq 160$  pm/V. Both the actuator and sensor elements are split on either side of the Si ring neutral axis to produce differential transducers.

Results/Discussion

The size of PinPoint® as a packaged component is 5.7mm x 4.8mm x 1.2mm. The width of the resonating ring is 48 $\mu\text{m}$  and it was designed to give an operating typical frequency of 22 kHz. The variation of the transverse piezoelectric coefficient,  $d_{31}$ , is less than 2% when measured during reliability tests operating for 8,000 hours at +125°C. PinPoint® device stability meets reliability specifications for automotive use. SSSL's PinPoint® piezoelectric MEMS gyros have been supplied to global markets for automotive, industrial and commercial applications. A description of the device design, functionality and performance will be presented. In addition, a description of Silicon Sensing Products' PZT-MEMS foundry services, which are based on an extension of the PZT-MEMS gyroscope process flow, will be presented to make device developers aware of the novel manufacturing services that are available.

## 7F - CMUTs (2)

Williford C

Friday, September 5, 2014, 1:00 pm - 2:30 pm

Chair: **Richard O'Leary**  
University of Strathclyde

7F-1

### 1:00 pm CMUT-in-CMOS 2D Arrays with Advanced Multiplexing and Time-Gain Control

David Lemmerhirt<sup>1</sup>, Amir Borna<sup>1</sup>, Sushma Alvar<sup>1,2</sup>, Collin Rich<sup>1</sup>, Oliver Kripfgans<sup>2</sup>; <sup>1</sup>Sonetics Ultrasound, Inc., Ann Arbor, MI, USA, <sup>2</sup>Basic Radiological Sciences Division, University of Michigan Medical School, USA

#### Background, Motivation and Objective

CMUT-in-CMOS technology uses the metal & dielectric layers of CMOS circuitry to manufacture transducer arrays with electronics integrated directly on the same substrate. Compared to mating transducers to chips or building up elements over circuit wafers, this approach offers simple/robust manufacturing in high-volume foundries at low enough cost for portable imagers, patch transducers, and even disposable devices. Past work integrated CMUTs with pre-amps, static multiplexers, and logic. The current work is motivated by the need to more rapidly read out large, dense arrays for high-frame-rate imaging and volume flow. The objective is to demonstrate CMUT-in-CMOS 2D arrays with low-noise amplification (LNA), time-gain control (TGC), and high-speed dynamic multiplexing to deliver real-time signals from all elements using a reduced output channel count.

#### Statement of Contribution/Methods

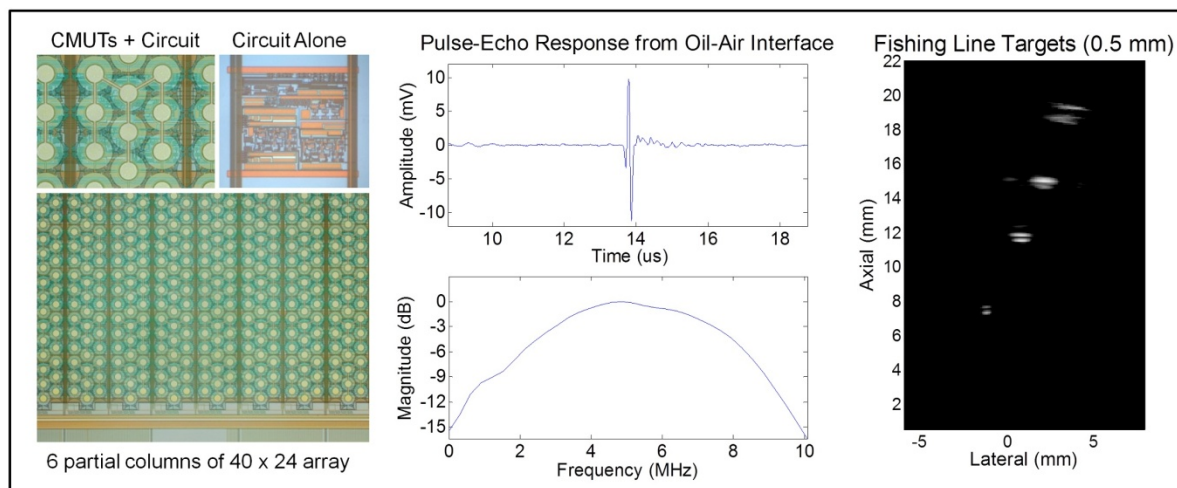
A fully-populated 960-element 2D array is reported, with each element coupled to a single-ended signal path with a charge-amp LNA and linear-in-dB TGC (~28dB, 3-bit ctrl), giving an overall gain of 135 dB. Local analog switches with control logic provide distributed 16:1 dynamic multiplexing. All stages are biased by local V<sub>th</sub>-ref current sources with selective shutdown to save power when a channel is not active. The LNA & gain stages employ a novel ac-coupled, pseudo-open-loop topology designed for low-power/noise with sufficient bandwidth for real-time IQ-sampled multiplexing (5 MHz, 100% BW, 16 Ch requires > 160 MSPS). The 40 x 24 array (162  $\mu$ m pitch) was fabricated in 0.35  $\mu$ m CMOS (4M2P), with CMUTs formed in the top 3 metal/glass layers, and circuits directly beneath. The only post-CMOS steps are wet-etching and dielectric deposition to release & seal the membranes, and dry-etching to open bondpads. For hydrophone and pulse-echo testing, chips were mounted in pin-grid packages on a PCB with high-speed logic, HV pulsers, and gain. Preliminary wire-target images were obtained (see below), and 3D imaging/flow measurements are forthcoming.

#### Results/Discussion

The measured CMUT center frequency is 5.0 MHz, with >100% BW. The RX sensitivity is 33.6 mV/kPa, giving a competitive noise-equivalent pressure of 3.3 mPa/rHz. On-chip TGC provides 29.2 dB of compression, with a linear slope of 4.5 dB per bit.

This highly-integrated array highlights the benefits of producing CMUTs in CMOS.

FRIDAY ORAL



7F-2

### 1:15 pm Improved Performance CMUT-on-CMOS Devices Using ALD Hafnium Oxide Insulation Layer

Toby Xu<sup>1</sup>, Coskun Tekes<sup>2</sup>, F. Levent Degertekin<sup>3</sup>; <sup>1</sup>Mechanical Engineering, Georgia Institute of Technology, Atlanta, GA, USA, <sup>2</sup>Mechanical Engineering, Georgia Institute of Technology, Atlanta, Georgia, USA, <sup>3</sup>Mechanical Engineering, Georgia Institute of Technology, Atlanta, GA, USA

#### Background, Motivation and Objective

Higher transmit sensitivity and receive sensitivity at lower bias voltages would be achieved by CMUTs when their structure converges to an ideal parallel plate structure. Using an insulation layer with high relative dielectric constant (high-K) helps achieving this goal with increased capacitance and large electric field in the vacuum gap. The effect of the insulation layer is more pronounced for high frequency, small gap CMUTs. In this paper, we present a simple model for optimal insulation layer properties and significant improvement in both transmit and receive sensitivity by replacing the Si<sub>3</sub>N<sub>4</sub> insulation layer with high-K HfO<sub>2</sub> for a low temperature CMUT-on-CMOS process [1].

# Statement of Contribution/Methods

Two separate wafers with the same 16.5-MHz-4-element design CMUT test devices were fabricated side-by-side with 50-nm gaps, except one with 100-nm HfO<sub>2</sub> insulation and the other with 200-nm plasma enhanced chemical vapor deposition (PECVD) silicon nitride (Si<sub>3</sub>N<sub>4</sub>) insulation. Since the film quality for low temperature PECVD Si<sub>3</sub>N<sub>4</sub> degrades below 200 nm thickness due to pin-hole effect, high conformity and low temperature atomic layer deposition (ALD) of hafnium oxide (HfO<sub>2</sub>) is used to overcome the thickness limitation as well as increased relative dielectric constant. Material characterization shows ALD HfO<sub>2</sub> deposited at 250°C have a K of 16 and breakdown strength (E<sub>BD</sub>) of 4 MV/cm. Acoustical characterization in TX and RX were performed for both insulation designs CMUT test array. Subsequently, 20-MHz dual-ring CMUT-on-CMOS devices were also fabricated with the 100-nm HfO<sub>2</sub> insulation. Pulse-echo and imaging experiments in water have been performed with the HfO<sub>2</sub> CMUT-on-CMOS array.

# Results/Discussion

Experiments on CMUTs with HfO<sub>2</sub> and Si<sub>3</sub>N<sub>4</sub> insulation layers show that transmit sensitivity (Pa/V) is doubled for the same gap device, giving the same maximum output pressure with half the pulse amplitude. The receive sensitivity is also improved by 6dB while reducing collapse voltage by one half. CMUT-on-CMOS integration with HfO<sub>2</sub> insulation was successful with reduced operating voltages and higher SNR as compared to previous devices. In addition, the receive signal from HfO<sub>2</sub> insulated CMUT-on-CMOS shows no sign of charging biased at 88% of collapse voltage over a period of 4 hours.

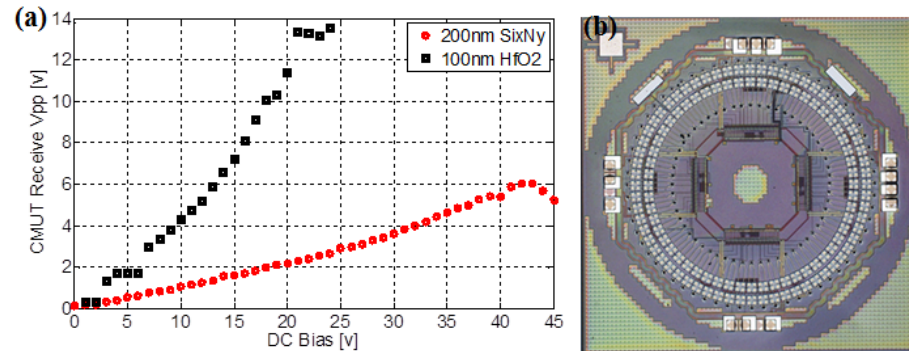


Figure 1: (a) Experimental data comparing the Rx sensitivity of the 2 CMUTs (b) Micrograph of 20 MHz CMUT-on-CMOS 1.4-mm array with 100-nm HfO<sub>2</sub> isolation and 50-nm gap.

[1] J. Zahorian, M. Hochman, T. Xu, S. Satir, G. Gurun, M. Karaman, F.L. Degertekin, "Monolithic CMUT-on-CMOS integration for intravascular ultrasound applications," *IEEE Transactions on Ultrasonics, Ferroelectrics and Frequency Control*, vol.58, no.12, pp.2659,2667, December 2011.

7F-3

# 1:30 pm Non-Flexural Parallel Piston Movement across CMUT with Substrate-Embedded Springs

Byung Chul Lee<sup>1</sup>, Amin Nikoozadeh<sup>1</sup>, Kwan Kyu Park<sup>2</sup>, Butrus (Pierre) T. Khuri-Yakub<sup>1</sup>,<sup>1</sup>Stanford University, USA, <sup>2</sup>Hanyang University, Korea, Republic of

# Background, Motivation and Objective

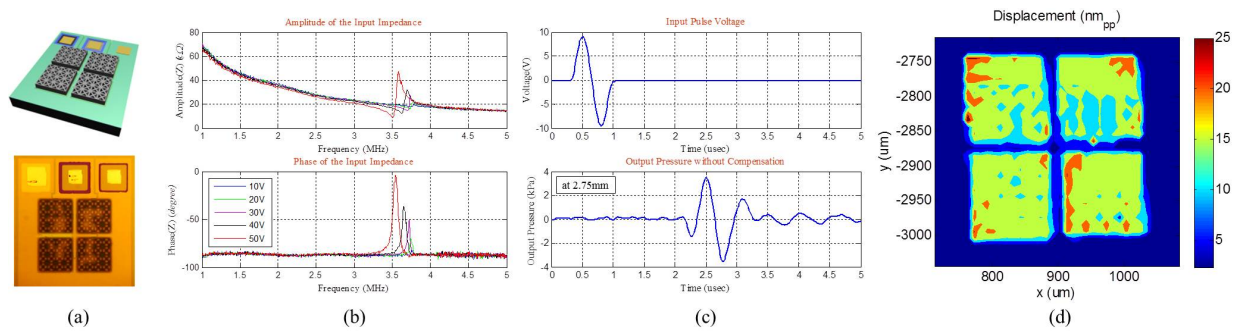
A CMUT with substrate-embedded springs, called post-CMUT (PCMUT), has been developed that improves the transducer performance over the classical CMUT architecture by increasing the average volume displacement as well as fill factor (A. Nikoozadeh et al, IUS 2010). 3-D finite element analysis (FEA) was used to comprehensively simulate the device performance as well as demonstrate non-flexural parallel piston movement across the active moving plate (B.C. Lee et al, IUS 2011). We have also reported on fabrication of second-generation PCMUT (B.C. Lee et al, IUS 2013). In this paper, we report on an improved fabrication method and experimental results for recently fabricated PCMUTs.

# Statement of Contribution/Methods

In our previous work reported in 2013, we successfully fabricated our second-generation PCMUT devices by using three critical steps: deep reactive ion etching (DRIE) of springs, wafer bonding of two silicon-on-insulator (SOI) wafers, and wafer polishing. However, due to the thin, brittle 250-nm Si layer, the process yield was less than 10%. For our recently fabricated PCMUTs, we added a vacuum cleaning procedure for the patterned substrate wafer in the bonding process as well as kept the 150 nm buried oxide (BOX) layer on top of the 250-nm Si layer; these steps improved the process yield to 21%. From these fabricated PCMUT devices, we measured electrical input impedance with an impedance analyzer (4294A, Agilent Technologies, Inc.), output pressure with a hydrophone (HGL-0200, ONDA Corp.), and plate displacement with a laser Doppler vibrometer (OFV-511, Polytec GmbH).

# Results/Discussion

A fabricated PCMUT with a truss pattern in the plate is shown in figure 1(a). This PCMUT with 9 Si post springs and reduced mass from the truss plate resonates at around 3.5 MHz in air (figure 1(b)), which matches well with the FEA results. Hydrophone measurement shows a peak-to-peak pressure of 7.0 kPa at 2.75 mm distance in immersion (figure 1(c)), corresponding to a normalized pressure of 11.5 kPa/V at the face of the transducer. The LDV measurement confirms a non-flexural plate displacement with a peak-to-peak value of 15 nm across the whole truss plate (figure 1(d)); this displacement measurement is in good agreement with the hydrophone measurement. Additional testing of the devices from this wafer is ongoing as well as finishing another wafer with a further improved yield.



7F-4

**1:45 pm A Vacuum-sealed Rotational Capacitive Micromachined Ultrasonic Transducer (RCMUT)**Donghwan Kim<sup>1</sup>, Michael Kuntzman<sup>1</sup>, Neal Hall<sup>1,2</sup>; <sup>1</sup>Electrical and Computer Engineering, The University of Texas at Austin, Austin, Tx, USA**Background, Motivation and Objective**

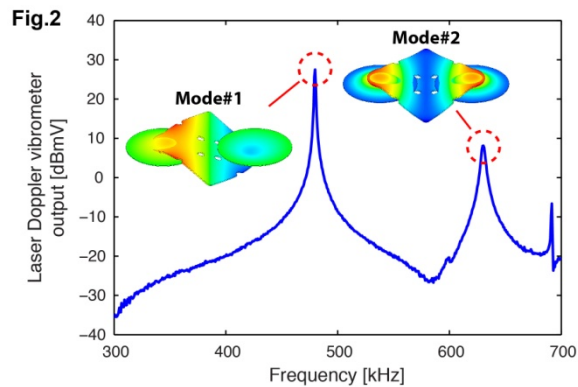
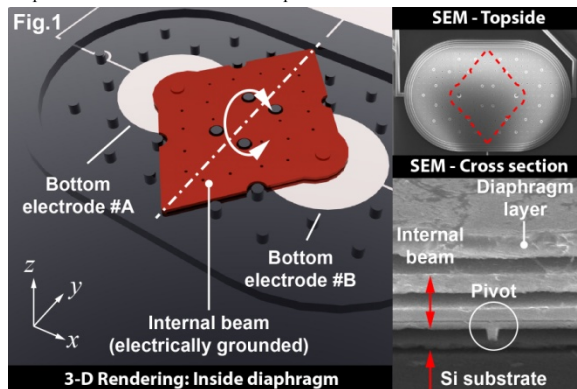
We present an unconventional CMUT in which a vacuum-sealed cavity beneath a diaphragm layer is comprised of an internal beam that pivots and has a first rocking or rotational vibration mode and a second flapping mode of vibration. It is anticipated that the unique structure may find application in biologically-inspired ultrasound sensors that simultaneously detect omnidirectional sound pressure and pressure gradient as shown by Miles [Miles et al., 1995]. The transducer is capable of transmit and receive operation using either first or second modes of vibration. Use of the first rocking mode may be useful in applications where it is desirable to radiate ultrasound in-plane along the surface of a die.

**Statement of Contribution/Methods**

The rotational CMUT presented in Fig. 1 has a pivoting beam sealed under vacuum in the cavity formed between the substrate and the diaphragm layer. Two pistons are formed in the diaphragm layer. The pivoting beam couples the two diaphragms to create a first “rocking” and second “flapping” vibration mode. Vacuum sealing the back-cavity eliminates squeeze-film damping that would otherwise cause excessive damping and/or stiffness. This paper presents (i) scanning electron micrographs (SEMs) of successfully sealed prototypes, (ii) dynamic frequency response measurements, and (iii) pitch-catch measurements using laterally generated ultrasound in air at 480 kHz.

**Results/Discussion**

The insets of Fig. 1 are SEMs images of a fabricated prototype and the rotating beam residing in the vacuum-sealed cavity. Fig. 2 summarizes frequency response measurements in air using laser Doppler vibrometry to measure the vibration of a piston at one far end of the beam in response to electrostatic actuation. The insets in Fig. 2 highlight the mode shape of vibration at each resonance peak.



7F-5

**2:00 pm Row-Column Addressed 2-D CMUT Arrays with Integrated Apodization**Thomas Lehrmann Christiansen<sup>1</sup>, Morten Fischer Rasmussen<sup>2</sup>, Jørgen Arendt Jensen<sup>2</sup>, Erik Vilain Thomsen<sup>1</sup>; <sup>1</sup>Department of Micro- and Nanotechnology, Technical University of Denmark, Kgs. Lyngby, Denmark, <sup>2</sup>Department of Electrical Engineering, Technical University of Denmark, Kgs. Lyngby, Denmark**Background, Motivation and Objective**

The number of transmit and receive channels needed to perform real-time 3-D ultrasonic imaging can be greatly reduced if row-column addressed 2-D transducer arrays are used. However, the significant element length and the lack of an acoustic lens result in edge waves, which compromise the image quality. These edge waves cannot be removed using conventional electronic apodization due to the lack of electronic control along the length of the elements. If row-column addressed arrays are to achieve a satisfactory image quality, it is therefore essential that the apodization can be integrated in the transducer itself. Our objective is twofold: to demonstrate how an apodization can be integrated into a CMUT array by varying the number of cells along the length of the elements and to demonstrate that the integrated apodization effectively dampens the edge waves.

**Statement of Contribution/Methods**

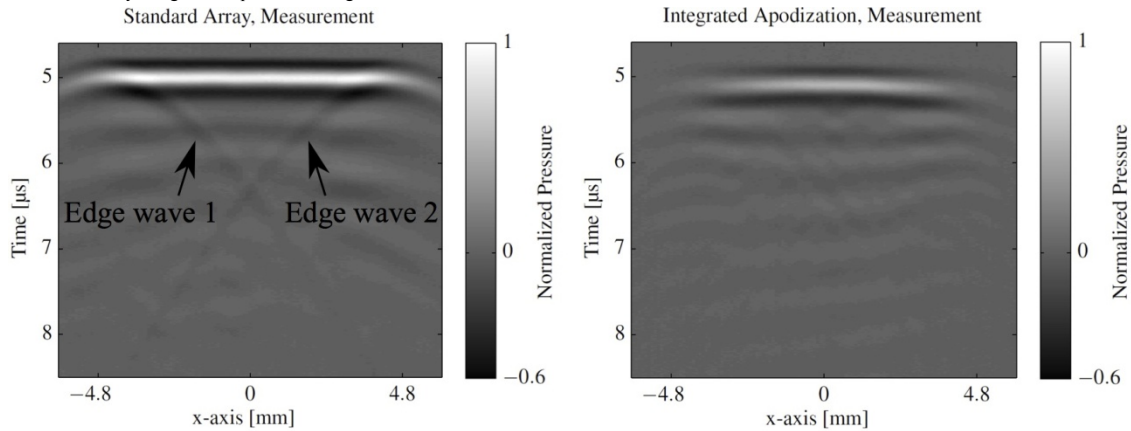
Two 32x32 row-column addressed CMUT arrays have been fabricated using wafer bonding. Both arrays have a side length of 9.6 mm and a pitch of 300  $\mu\text{m}$ . Each individual circular CMUT cell has a diameter of 72  $\mu\text{m}$  and is comprised of a 2  $\mu\text{m}$  silicon plate with 200 nm aluminum on top. The gap is defined by a 200 nm thick insulation oxide and a 200 nm vacuum gap. The first array contains 9216 CMUT cells, 3 along the width and 96 along the length of each element. The second array is apodized by varying the number of cells according to a circular symmetric Hann function with nine discrete levels, which is optimized through Field II simulations. For both arrays, the transmitted sound field across



the center of the array is measured in oil with a hydrophone placed 1 mm, 5 mm, and 10 mm, respectively, from the array. All elements are excited simultaneously using a DC bias voltage of 40 V (80 % of the pull-in voltage) and a 1 cycle 3 MHz AC excitation burst of 30 Vpp.

### Results/Discussion

The emitted field from the non-apodized array measured at a depth of 5 mm (left figure) shows two edge waves arriving after the main wave. The measured field from the apodized array at the same depth (right figure, same scaling as left figure) contains no visible edge waves. The energy of the measured edge waves is reduced by 46 %. The corresponding simulated value is 94 %. This demonstrates that apodization can indeed be integrated in the construction of row-column addressed ultrasonic transducer arrays, and that it effectively mitigates the problem of edge waves.



7F-6

### 2:15 pm Fabrication of Anodically Bonded Capacitive Micromachined Ultrasonic Transducers with Vacuum-Sealed Cavities

F. Yalcin Yamaner<sup>1</sup>, Xiao Zhang<sup>1</sup>, Omer Oralkan<sup>1</sup>,<sup>1</sup>Department of Electrical and Computer Engineering, North Carolina State University, Raleigh, NC, USA

#### Background, Motivation and Objective

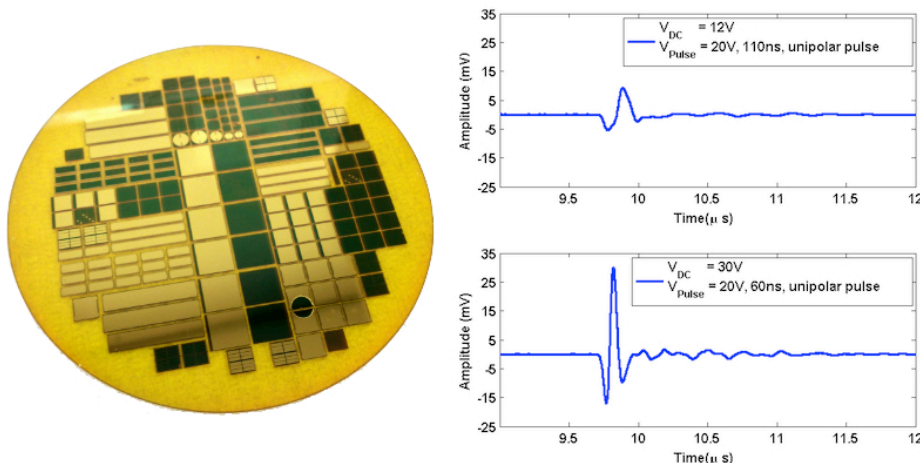
Capacitive micromachined ultrasonic transducers (CMUTs) have demonstrated great promise for next-generation ultrasound technology. Wafer-bonding technology particularly simplifies the fabrication of CMUTs by eliminating the requirement for a sacrificial layer and increases control over device parameters. Anodic bonding has many advantages over other bonding methods such as low temperature compatibility, high bond strength, high tolerance to particle contamination and surface roughness, and cost savings. Furthermore, the glass substrates lower the parasitic capacitance and improve reliability. The major drawback is the trapped gas inside the cavities, which occurs during bonding. Earlier CMUT fabrication efforts using anodic bonding failed to demonstrate a vacuum-sealed cavity. In this study, we developed a fabrication scheme to overcome this issue and demonstrated vacuum backed CMUTs using anodic bonding. This new approach also simplifies the overall fabrication process for CMUTs.

#### Statement of Contribution/Methods

We demonstrated a CMUT fabrication process with three lithography steps. A vibrating plate is formed by bonding the device layer of an SOI wafer on top of submicron cavities defined on a borosilicate glass wafer. The cavities and the bottom electrodes are created on the borosilicate glass wafer with a single lithography step. The recessed bottom metal layer over the glass surface allows bonding the plate directly on glass posts and therefore helps reduce the parasitic capacitance and improve the breakdown reliability. A surface roughness of 0.8nm is achieved in the cavity using wet chemical etching. A 200nm PECVD silicon nitride layer deposited on the 2μm device layer of the SOI wafer prior to bonding serves as the insulation layer to prevent shorting after pull-in. The trapped gas inside the cavities is evacuated after anodic bonding by reactive ion etching. The 150nm cavities are then sealed with PECVD silicon nitride.

### Results/Discussion

We measured the atmospheric deflection of the plates after fabrication, which proves the vacuum inside the cavities. Impedance and hydrophone measurements were performed both in conventional (3.9 MHz) and collapse (6.7 MHz) modes (Fig.1). Bonding on posts with widths as small as 2μm was successfully demonstrated using anodic bonding which is difficult to achieve with other wafer bonding methods.





## 1G - MIM: New Developments in Volumetric Ultrasound

Grand Ballroom

Friday, September 5, 2014, 3:30 pm - 5:00 pm

Chair: **James Miller**  
Washington University, St. Louis

### 1G-1

#### 3:30 pm Three Dimensional Echocardiography Comes of Age: Promises and perspective

Roberto Lang<sup>1</sup>; <sup>1</sup>Roberto Lang, Wilmette, IL, USA

##### Background, Motivation and Objective

Significant advances in 3-dimensional echocardiography (3DE) technology have ushered its use into clinical practice.

The recent advent of real-time 3DE using matrix array transthoracic and transesophageal transducers has resulted in improved image spatial resolution, and therefore, enhanced visualization of the pathomorphological features of the left ventricle and cardiac valves compared with previously used sparse array transducers. It has enabled an unparalleled real-time visualization of valves and subvalvular anatomic features from a single volume acquisition without the need for offline reconstruction. On-cart or offline post-processing using commercially available and custom 3-dimensional analysis software allows the quantification of multiple parameters, such as left ventricular volumes, orifice areas, prolapse height and volume in mitral valve disease, area of the left ventricular function, and tricuspid annular geometry. In this talk, I will discuss the incremental role of 3DE in evaluating valvular anatomic features, volumetric quantification, pre-surgical planning, intraprocedural guidance, and post-procedural assessment of valvular heart disease

##### Statement of Contribution/Methods

##### Results/Discussion

### 1G-2

#### 4:00 pm 3-D Ultrafast Imaging of the Heart In Vivo

Jean Provost<sup>1</sup>, Clement Papadacci<sup>1</sup>, Olivier Villemain<sup>1</sup>, Juan-Esteban Arango Ossa<sup>1</sup>, Marion Imbault<sup>1</sup>, Jean-Luc Gennisson<sup>1</sup>, Mickael Tanter<sup>1</sup>, Mathieu Pernot<sup>1</sup>; <sup>1</sup>Institut Langevin, ESPCI Paris Tech, INSERM U979, CNRS UMR7587, Université Paris 7, France

##### Background, Motivation and Objective

Heart failure (HF) is the leading cause of hospitalization in patients above 65 years old. 2-D Ultrafast imaging of the heart has recently been shown to provide new promising contrast sources for the monitoring of HF in real-time, such as the Young's Modulus and the electromechanical activation. However, the limited acoustic window available in echocardiography prevents the imaging of regions that could contain, for example, a pacing lead or infarcted tissue. In this study, we performed ultrafast imaging in 3D at very high frame rates (>1000 volumes/s) with coherent compounding of spherical emissions, using a 2-D matrix array, and we show the clinical feasibility of tracking motion and deformation in 3D in the human heart in vivo.

##### Statement of Contribution/Methods

A customized, programmable, 1024-channel ultrasound system was designed to perform 3-D Ultrafast Imaging. Using a 32X32, 3-MHz matrix phased array (Vermon, France), volumes were beamformed by coherently compounding successive emissions from virtual sources organized in arrays located behind the probe. In receive, a conventional delay-and-sum beamforming was applied in the 3D volume on the 1024 elements of the array. The number and the position of virtual sources as well as the number of elements of the virtual arrays were optimized for cardiac applications in a resolution (ATS, 551) and a heart-mimicking phantoms (CIRS, 067). Finally in vivo validation was performed in 3 healthy volunteers: an entire heart cycle was acquired at ultrafast frame rates (3000 volumes at 3000 volumes/s) in the apical view using 1, 2 and 3 virtual sources. Tissue motion and deformation were mapped in the entire heart in a single acquisition and validated against 2-D imaging.

##### Results/Discussion

From 1 to 3 diverging waves, ultrafast frame rates were achieved at large depth (from 3000 to 1000 volumes/s for a depth of 12 cm). The phantom study revealed that a large contrast improvement occurred when coherent compounding was performed. An increase of  $3.8 \pm 0.5$  dB on the beamformed IQ data was found when two diverging waves was used instead of one. When the number of diverging waves was increased the improvement was smaller but still significant ( $4.6 \pm 0.7$  dB from 1 to 3 diverging waves). A resolution improvement was also observed when 3 sources were used instead of one. The position of virtual sources were also optimized to image a large field of view ( $60^\circ \times 60^\circ$  sector size) and a virtual array of  $16 \times 16$  elements was found to be a good trade-off between contrast and resolution. Finally, tissue motion and strain estimation were obtained in three healthy volunteers in a full 3D field of view over an entire cardiac cycle and a significant enhancement of the image quality was noticed when 3 sources were used instead of 1. This study demonstrates that 3-D ultrasound imaging of the heart at thousands of volumes/s can be performed for the complete evaluation of the function of the myocardium in humans in vivo.

**4:15 pm Elastic registration vs. block matching for quantification of cardiac function with 3D ultrasound: initial results of a direct comparison in silico based on a new evaluation pipeline**

Martino Alessandrini<sup>1</sup>, Brecht Heyde<sup>1</sup>, Szymon Cygan<sup>1,2</sup>, Maxime Sermesant<sup>3</sup>, Hervé Delingette<sup>3</sup>, Olivier Bernard<sup>4</sup>, Mathieu De Craene<sup>5</sup>, Jan D'hooge<sup>1</sup>; <sup>1</sup>Medical Imaging Research Center, KU Leuven, Leuven, Belgium, <sup>2</sup>Politechnika Warszawska, Instytut Metrologii i Inżynierii Biomedycznej Wydział Mechatroniki, Warsaw, Poland, <sup>3</sup>Asclepius Res. Project, INRIA, SOPHIA ANTIPOLIS Cedex, France, <sup>4</sup>Université de Lyon, CREATIS, CNRS UMR5220, INSERM U1044, Université Lyon 1, INSA-LYON, France, Villeurbanne, France, <sup>5</sup>Medisys, Philips Research Paris, Paris, France

**Background, Motivation and Objective**

Cardiac strain quantification from 3D ultrasound is an active area of research. Commercially available solutions are mainly based on block-matching (BM) while techniques based on elastic registration (E-Reg) have also been proven feasible and potentially more accurate than BM although still confined to the research arena and less extensively tested. Surprisingly, a thorough and reproducible comparison between these two solutions is to date still missing likely – in part – due to the lack of a solid benchmarking framework. Recently, we have proposed such a framework by combining an advanced electro-mechanical model of the heart with state-of-the-art ultrasound simulation methodologies to achieve ultra-realistic synthetic data sets [DeCraene *et al.*, ISBI2014]. The aim of this study was therefore to benchmark state-of-the-art BM and E-Reg algorithms using this framework.

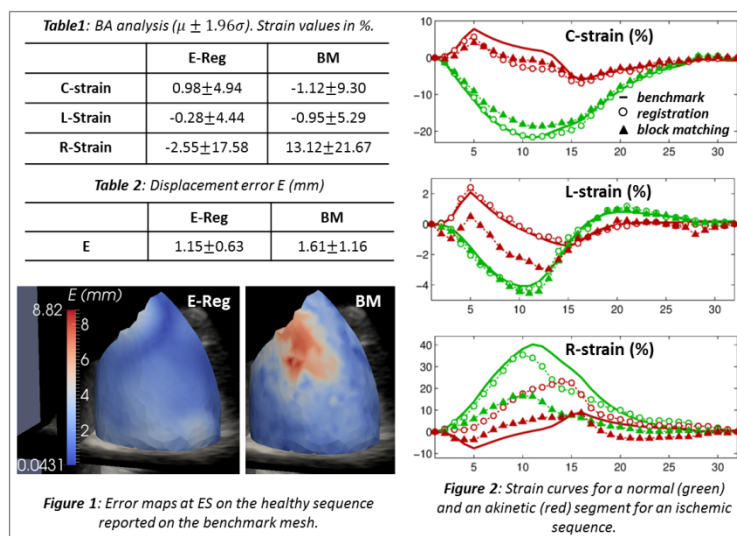
**Statement of Contribution/Methods**

Five ultra-realistic synthetic sequences were generated using our simulation framework: one healthy case and 4 ischemic ones. As such, scan-converted voxel data (voxel size =  $0.6 \times 0.8 \times 0.5 \text{ mm}^3$ ) at a frame rate of 30Hz were available as well as the ground truth motion and strain derived from the tetrahedral mesh used in the finite element model. BM employed a block-size of  $23 \times 23 \times 23 \text{ pixel}^3$ , a search region of  $17 \times 17 \times 17 \text{ pixel}^3$ , an interpolation factor of 8 for sub-pixel accuracy and normalized cross-correlation as similarity measure. No regularization was used. The E-Reg technique employed an anatomical grid topology to parameterize the displacement field as recently proposed in [Heyde *et al.*, FIMH2013]. For both algorithms parameters were tuned by minimizing the average displacement error on the healthy sequence.

To compare both methodologies, we measured the error  $E$  in estimating the displacement at end systole (ES) averaged over the LV myocardium. For strain accuracy we used Bland-Altman (BA) analysis for the 3 components (radial, longitudinal and circumferential) at ES.

**Results/Discussion**

E-Reg returned on average smaller  $E$  and smoother error maps (cf. Fig 1). This allowed for a more accurate strain computation. Qualitatively, C-strain accuracy seemed sufficient for both methods to detect akinetic segments (cf. Fig 2). For BM this was less evident for L-strain while both methods performed poorly for R-strain. Values found are summarized in Tab. 1 and 2.

**4:30 pm Semi-automatic left-atrial segmentation from volumetric ultrasound using B-spline explicit active surfaces**

Nuno Almeida<sup>1</sup>, Daniel Barbosa<sup>2</sup>, Brecht Heyde<sup>1</sup>, Razvan Olimpiu Mada<sup>3</sup>, Denis Friboulet<sup>4</sup>, Olivier Bernard<sup>4</sup>, Eigil Samset<sup>5,6</sup>, Jan D'hooge<sup>1</sup>; <sup>1</sup>Lab. on Cardiovascular Imaging and Dynamics, KU Leuven, Leuven, Belgium, <sup>2</sup>Life and Health Sciences Research Institute (ICVS), Universidade do Minho, Braga, Portugal, <sup>3</sup>Dept. of Cardiovascular Sciences, KU Leuven, Leuven, Belgium, <sup>4</sup>CREATIS, CNRS UMR5220, Inserm U630, Université Lyon 1, INSA-Lyon, France, <sup>5</sup>GE Vingmed Ultrasound AS, Horten, Norway, <sup>6</sup>Center for Cardiological Innovation (CCI), Oslo, Norway

**Background, Motivation and Objective**

Segmentation of the left atrium (LA) of the heart allows quantification of LA volume dynamics which can give insight into LA function. However, very little attention has been given to LA segmentation from 3D ultrasound (US), most efforts being focused on the segmentation of the left ventricle (LV). The B-spline explicit active surfaces (BEAS) framework has been shown to be a very robust and efficient methodology to perform LV segmentation. The aim of this study was to adapt the BEAS framework to allow for semi-automatic LA segmentation.

**Statement of Contribution/Methods**

BEAS is an active contour-based approach in which the contour is explicitly represented as a sum of B-splines. In the original formulation of BEAS, resolution and smoothness were intrinsically coupled. We chose to uncouple these two parameters for the current application. The workflow of the LA segmentation can be described by the following steps: 1) The user initializes the algorithm by selecting LA end-diastolic (ED) and end-systole (ES) frames. At ED and ES, 5 landmarks are indicated (4 points at the mitral valve (MV), 1 at the roof) to which a truncated ellipsoid is fit; 2) The surface is then evolved using BEAS, keeping the MV plane fixed at each frame. For each subsequent frame, the segmentation from the previous frame is used as initialization, while interpolating the MV plane position between ED and ES.

This framework was tested on 20 apical 3D US sequences, acquired with a GE Vivid E9. The resulting segmentations at ED and ES were compared against manual contours by calculating: 1) mean absolute distances (MAD), 2) Dice coefficients and 3) correlations and Bland-Altman statistics of the derived LA functional parameters.

### Results/Discussion

The MAD was  $1.52 \pm 0.23$  mm and  $1.97 \pm 0.30$  mm for the atrial ES and ED frames respectively, while the respective Dice coefficients were  $0.86 \pm 0.02$  and  $0.85 \pm 0.04$ . These results suggest that the accuracy can be clinically relevant. The derived functional parameters showed a good correlation:  $R = \{0.97, 0.98, 0.84, 0.89\}$ , for LA maximum and minimum volumes, ejection fraction (EF) and expansion index (EI), respectively. Bland-Altman analysis showed good limits of agreement (Figure 1). A significant bias was observed, although it cancelled out when deriving EF and EI.

We showed that the modified BEAS framework is capable of accurate semi-automatic LA segmentation in 3D transthoracic US.

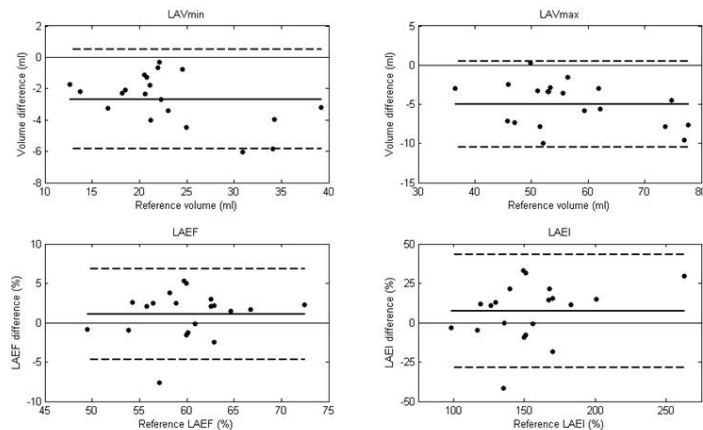


**Figure 1** - Bland-Altman plots for the derived LA functional parameters: LA minimum volume (LAVmin), LA maximum volume (LAVmax), LA ejection fraction (LAEF) and LA expansion index (LAEI). Solid line – bias (\*,  $p$ -value < 0.05); Dashed line – limits of agreement ( $\mu \pm 1.96\sigma$ ).

1G-5

### 4:45 pm Three-dimensional Contrast-ultrasound Dispersion Imaging for Prostate Cancer Localization, a Feasibility Study

Stefan Schalk<sup>1</sup>, Libertario Demi<sup>1</sup>, Martijn Smeenge<sup>2</sup>, Jean de la Rosette<sup>2</sup>, Hessel Wijkstra<sup>1,2</sup>, Massimo Mischi<sup>1</sup>; <sup>1</sup>Eindhoven University of Technology, Netherlands, <sup>2</sup>Academic Medical Center (AMC) Amsterdam, Netherlands

#### Background, Motivation and Objective

Prostate cancer (PCa) is the type of cancer with the highest incidence in Western countries. To date, reliable tools for PCa localization are lacking. Recently, contrast-ultrasound dispersion imaging (CUDI) by spatiotemporal analysis performed on transrectal dynamic contrast-enhanced ultrasound (TDCE-US) has been proposed as a promising option for PCa localization. This technique evaluates the spatial similarity between indicator dilution curves in a ring-shaped kernel and its center pixel. Until now, CUDI has been performed in 2D only. Hence, each imaged plane requires a separate bolus injection, motion compensation is limited, and out-of-plane contrast flow cannot be observed. 3D TDCE-US can potentially solve the aforementioned issues, permitting the analysis of the entire prostate with a single bolus injection. In this work, we implement a full 4D spatiotemporal similarity analysis and evaluate its feasibility to perform 3D CUDI.

#### Statement of Contribution/Methods

A Logiq E9 scanner (GE Healthcare) with an IC5-9 and RIC5-9 probe was used to perform TDCE-US in 2D and 3D, respectively. The speckle size was estimated in vitro for both probes, giving an indication of the spatial resolution of the imaging system. Three 2D and 3D prostate scans were performed in two patients at a frame rate of 7.4 and 0.26-0.34 Hz, respectively. The speckle size estimates were used to compensate for the anisotropy and depth-dependency of the resolution prior to CUDI analysis. To perform full 3D CUDI, the ring-shaped kernel was replaced by a shell-shaped one, and the analysis parameters were reconfigured. Results from 2D and 3D CUDI were compared with each other in the corresponding planes and with the results from 12-core systematic biopsies.

#### Results/Discussion

The speckle size in the axial direction was 0.5 mm for both 2D and 3D. In the lateral direction, the respective speckle size was 0.4 and 0.6 mm at 1 cm and 0.9 and 1.8 mm at 5 cm distance from the probe. The speckle size in the elevational direction was similar to that in the lateral direction for 3D. Figure 1 gives an example of CUDI in one plane along with the biopsy results. The 2D and 3D dispersion maps and the biopsy results showed good agreement. The characteristics of the 3D recordings and the obtained dispersion maps confirmed the feasibility of 3D CUDI and its ability to localize PCa, encouraging an extension of this study to a larger dataset.

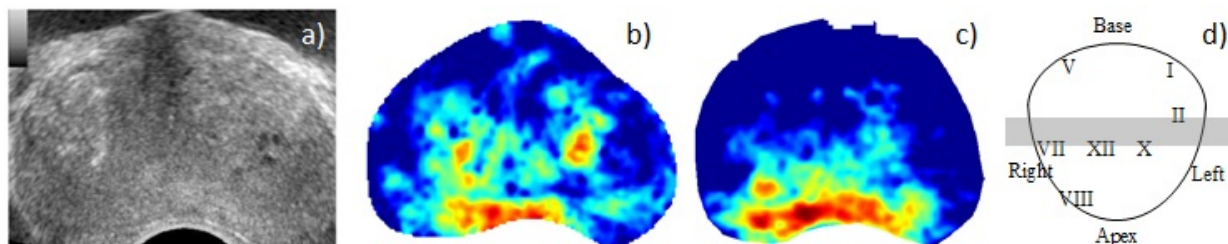


**Figure 1: Comparison between 2D and 3D CUDI by spatiotemporal analysis for corresponding planes.**  
a) B-mode, b) 2D and c) 3D CUDI by spatiotemporal analysis. d) Coronal image with biopsy results: the Roman numerals indicate positive biopsies (Gleason 4+3 in 10-50% of the tissue). The grey area shows the estimated location of the analyzed plane.

## 2G - MTC: High Frequency Tissue Characterization

Waldorf

Friday, September 5, 2014, 3:30 pm - 5:00 pm

Chair: **Timothy Hall**  
University of Wisconsin, Madison

2G-1

### 3:30 pm Quantitative ultrasound analyses of cell starvation in HT-29 pellets

Elizabeth S. L. Berndt<sup>1</sup>, Lauren A. Wirtzfeld<sup>1</sup>, Michael C. Kolios<sup>1</sup>; <sup>1</sup>Department of Physics, Ryerson University, Toronto, Ontario, Canada

#### Background, Motivation and Objective

Noninvasive detection and monitoring of sub-cellular changes in cancer cells and tumors offers the potential to provide feedback on dynamic changes not readily detectable by gross volumetric changes. There are known changes in quantitative ultrasound backscatter parameters due to apoptotic cell death, however the use of anti-angiogenesis agents and vascular disruptors cause cellular changes in structure due to cellular starvation, which has not been extensively studied. This project aims to quantify ultrasound changes as cells undergo starvation using a cell pellet model. Cell pellets are homogenous within and between samples, therefore two samples are imaged over the course of the experiment, and identical samples are used for histological confirmation at each time point. Structural changes cells undergo as they decay in an uncontrolled manner differ from the rigorous defined path of apoptosis and will have a different signature in quantitative ultrasound parameters estimated.

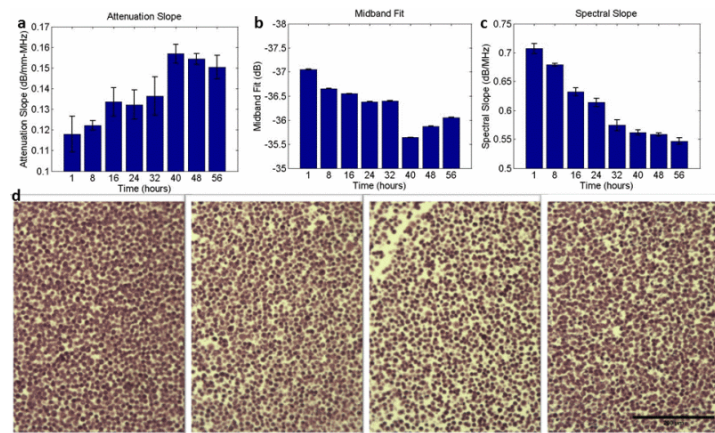
#### Statement of Contribution/Methods

HT-29 human colorectal carcinoma cells (ATCC, HTB-38) were centrifuged at 200xG for 10 minutes to form two pellets a custom polished steel holder for ultrasound acquisition and seven pellets in flat bottom tubes for histology. Pellets were maintained in PBS at room temperature over the course of the 56 hour experiment. At each of the seven imaging time points the PBS of one pellet for histology was exchanged with formalin.

Raw RF data was acquired from pellets in the holder at eight hour intervals, using a VisualSonics Vevo770 with a nominal 55 MHz centered frequency transducer with a 420 MHz sample frequency. Reference data was acquired from an empty well to allow for attenuation estimation and to calculate spectral parameters and backscatter coefficient.

#### Results/Discussion

ANOVA on attenuation, spectral slope and midband fit (Figure 1a-c) all show statistical significance for time. Attenuation and midband fit show opposite trends, both with inflections at 40 hours, while spectral slope shows a constant decrease through the 56 hours. Histology (Figure 1d) indicates structural changes occur in the pellets, with a visible decrease in cellular density from 1 to 40 hours, and then an increased density at 48 hours. Together, the results suggest a significant change in cell morphology around 40 hours that results in a change in parametric trends at this time point.



a) Attenuation slope estimates, b) midband fit estimates and c) spectral slope estimates from two cell pellets in PBS. Data shows average and standard deviation of 12 slices, of 100 pulse-echo lines from each of the two pellets. d) H&E stained histology samples at time points of 1, 32, 40 and 48 hours show a decrease in cellular density to 40 hours with a slight increase again at 48 hours. Scale bar is 200 μm.

2G-2

### 3:45 pm Ultrasound-Based Diagnostic Assay of Cancer Cell Invasiveness

Andrew Weitz<sup>1</sup>, Nan Sook Lee<sup>1</sup>, Jae Youn Hwang<sup>2</sup>, Robert Chow<sup>1</sup>, K. Kirk Shung<sup>1</sup>; <sup>1</sup>University of Southern California, Los Angeles, CA, USA, <sup>2</sup>Daegu Gyeongbuk Institute of Science & Technology, Daegu, Korea, Republic of

#### Background, Motivation and Objective

We reported previously that high-frequency ultrasound (200 MHz) can be used to distinguish invasive versus noninvasive breast cancer cells. We found that stimulation triggers calcium influx in the MDA-MB-231 cell line (invasive), while causing little to no response in the MCF-7 cell line (noninvasive). In this study, we investigated the effect of lower-frequency stimulation and determined the likely mechanism of calcium influx. This work supports our goal of developing an assay that can rapidly assess invasiveness of biopsied tumors, thus informing treatment plans for cancer patients.



**Statement of Contribution/Methods**

MDA-MB-231 and MCF-7 cells were plated on separate 35-mm Petri dishes, incubated with the cell-permeant calcium dye Fluo-4 AM (1  $\mu$ M) for 30 minutes, and then washed and immersed in external buffer solution. The dishes were placed on an inverted microscope stage and positioned at the focus of a LiNbO<sub>3</sub> transducer (3 MHz or 38 MHz). Cells were stimulated with ultrasound while imaging calcium dye fluorescence at low magnification (4x). To determine the mechanism of calcium influx, MDA-MB-231 cells were stimulated in the presence of pharmacological blockers (each applied separately). We tested the Ca<sup>2+</sup> channel blocker CdCl<sub>2</sub> (20  $\mu$ M), the Na<sup>+</sup> channel blocker TTX (1  $\mu$ M), the BK<sub>Ca</sub> channel inhibitor iberiotoxin (100 nM), and the transient receptor potential (TRP) channel inhibitor 2-APB (100  $\mu$ M).

**Results/Discussion**

Both 3-MHz and 38-MHz stimulation evoked strong calcium responses in MDA-MB-231 cells, but not in MCF-7 cells. In most cases, MDA-MB-231 stimulation evoked a calcium wave that emanated outward from the transducer focus. This wave was not eliminated when stimulating cells seeded on a Mylar membrane, indicating that it arose from cell-to-cell signaling rather than from ultrasonic surface waves. Of the four channel blockers we tested (CdCl<sub>2</sub>, TTX, iberiotoxin, and 2-APB), only 2-APB had an effect. Application of 2-APB abolished all calcium responses within minutes, many of which were restored upon washout. This suggests that calcium influx is triggered by acoustic activation of TRP channels, which are known to be mechanosensitive. Consistent with this result, increased TRP channel expression has been found to correlate with tumor invasion in several cancer types. Therefore, our method may have applications beyond breast cancer alone.

**2G-3****4:00 pm Fine-resolution maps of acoustic properties at 250 MHz of fresh samples and unstained fixed 12  $\mu$ m thin sections from cancerous human lymph nodes.**

Daniel Rohrbach<sup>1</sup>, Emi Saegusa-Beecroft<sup>2</sup>, Eugene Yanagihara<sup>3</sup>, Junji Machi<sup>2</sup>, Ernest J. Feleppa<sup>1</sup>, Jonathan Mamou<sup>1</sup>; <sup>1</sup>Lizzi Center for Biomedical Engineering, Riverside Research, New York, NY, USA, <sup>2</sup>Department of General Surgery, University of Hawaii and Kuakini Medical Center, Honolulu, HI, USA, <sup>3</sup>Department of Pathology, Kuakini Medical Center, Honolulu, HI, USA

**Background, Motivation and Objective**

Quantitative acoustic microscopy (QAM) at 250 MHz permits measuring the acoustic properties, such as speed of sound (SOS), attenuation (A) and acoustic impedance (Z), of tissue microstructure with a spatial resolution of 7  $\mu$ m. Although high frequency QAM has been shown to be a suitable tool for measuring the acoustic properties of liver samples, no such data exists for sentinel lymph nodes.

**Statement of Contribution/Methods**

QAM was performed on ten fixed and two fresh lymph-node samples. 12- $\mu$ m sections of deparaffinized, fixed tissue and fresh half nodes were scanned using a custom-built acoustic microscope that incorporated an F-1.16, 250-MHz transducer with a 160-MHz bandwidth and 7- $\mu$ m lateral beamwidth to acquire reflected signals from the tissue and a substrate in intimate contact with the tissue. The signals were digitized at 2.5 GHz with 12-bit accuracy using an oscilloscope, and 2D QAM maps of SOS (Fig. 1a), A (Fig. 1b), and Z were generated using custom-developed signal processing algorithms. Scanned samples then were stained using hematoxylin and eosin (HE) (Fig. 1c) and imaged by light microscopy.

**Results/Discussion**

The spatial resolution and contrast of QAM maps were sufficient to distinguish among tissue regions consisting of lymphocytes, fat cells, and fibrous tissue (Fig. 1). Average properties for lymphocyte-dominated tissue were  $1552.6 \pm 30$  m/s for SOS,  $9.53 \pm 3.6$  dB/MHz/cm for A, and  $1.58 \pm 0.08$  Mrayl for Z. For the sample of Fig. 1, we found a significant increase ( $p < 0.05$ , ANOVA) of  $69.0 \pm 0.5$  m/s for SOS and  $1.2 \pm 0.1$  dB/MHz/cm for A in fibrous connective tissue compared to lymphocyte-dominated tissue. The study demonstrates that fine-resolution maps of acoustic properties of lymph nodes can be assessed at 250 MHz. The data will serve as a basis for developing new lymph-node-specific ultrasound-scattering models that are expected to improve current quantitative ultrasound approaches for detecting metastatic regions in freshly-excised sentinel lymph nodes from breast-cancer patients. NIH Grant R21EB016117.

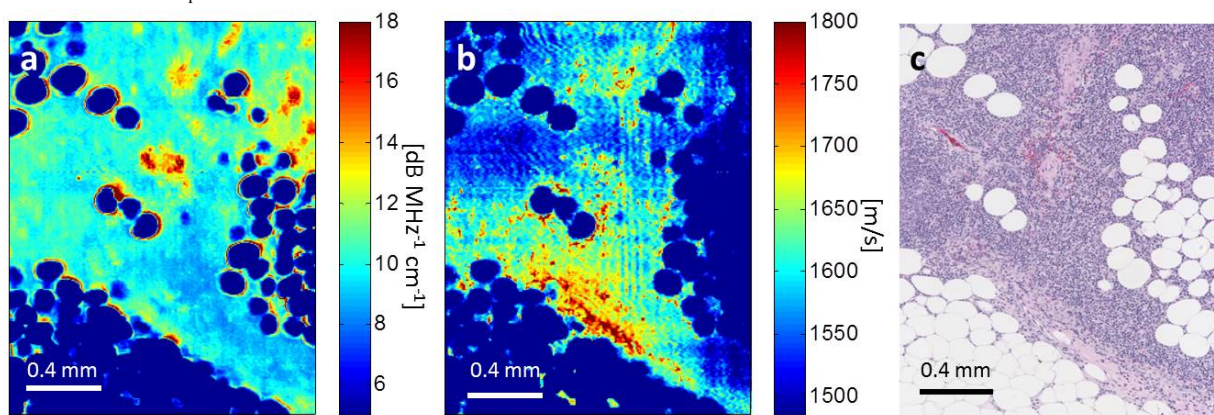


Figure 1: Site-matched maps of (a) A, (b) SOS and (c) HE-stained microscopy show different contrast for different tissue types such as fat cells (circular spots of 110  $\mu$ m diameter), fibrous connective tissue with fewer lymphocytes (f) and lymphocyte-dominated (darker areas in c).

**2G-4****4:15 pm Structure Factor Model for understanding the ultrasonic scattering from concentrated cell pellet biophantoms**

Emilie Franceschini<sup>1</sup>, Régine Guillermin<sup>1</sup>, Franck Tourniaire<sup>1</sup>, Jean-François Landrier<sup>2</sup>; <sup>1</sup>Laboratoire de Mécanique et d'Acoustique LMA CNRS, Aix-Marseille Université, Centrale Marseille, France, <sup>2</sup>Nutrition, Obésité et Risque Thrombotique, UMR INSERM 1062/INRA 1260, Aix-Marseille Université, France

**Background, Motivation and Objective**

Quantitative Ultrasound techniques for determining the tissue microstructure rely on theoretical scattering models to fit the BackScatter Coefficient (BSC) from biological tissues to an estimated BSC using an appropriate model. The models adapted to densely packed cells in tumors are the Structure Factor model (SFM) and the Particle Model (PM, i.e. the low-frequency limit of the SFM), which are generally used in blood characterization. The aim of this work was to use the SFM and the PM to go further in the understanding of the measured BSCs from simple tumor models (i.e. cell pellet biophantoms).

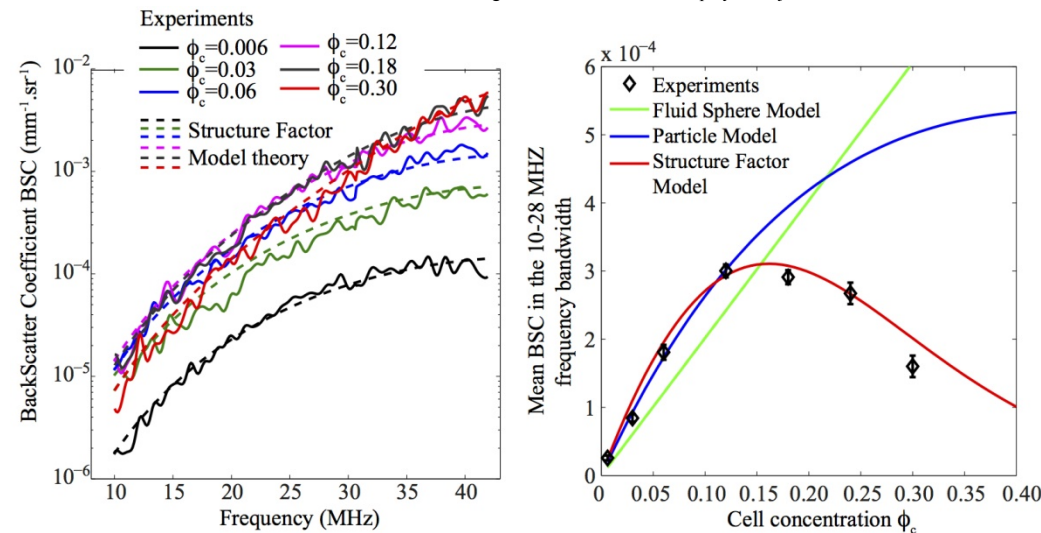


# Statement of Contribution/Methods

Ultrasonic backscatter measurements were performed at frequencies ranging from 10 to 42 MHz on biophantoms. These biophantoms consisted of human leukemia K562 cells trapped in a mixture of plasma and thrombin with different cell concentrations ranging from 0.006 to 0.30. A parameter estimation procedure was developed in order to estimate the scatterer size and relative impedance contrast that could explain the measured BSC from all the studied cell concentrations using three scattering models: the SFM, the PM and the classical Fluid-Filled Sphere Model (FFSM) (that does not account for dense medium) for polydisperse scatterer size distribution. This procedure was applied to our BSC data from K562 cell pellet biophantoms in the 10-42 MHz frequency bandwidth and to the BSC data from Chinese Hamster Ovary (CHO) cell pellet biophantoms in the 26-105 MHz frequency bandwidth given in [Han et al., J. Acoust. Soc. Am. 130, 2011]. The scatterer sizes estimated using our parameter estimation procedure were compared to the true cellular features to identify the scattering sites.

# Results/Discussion

The results obtained with the K562 cells (in the 10-42 MHz frequency bandwidth) and with the CHO cells (in the 26-56 MHz frequency bandwidth) revealed that the FFSM and PM are insufficient to model the complex behavior of the BSC and that the polydisperse SFM is the model that better explains the behavior of BSC. The impedance and size estimated with the polydisperse SFM are satisfactory: the relative impedance contrast estimates seem to be in a reasonable range of values and the fluid sphere radii match the true whole cell radii for both K562 and CHO cell studies. This finding shows that the whole cell plays a major role in the BSC behavior for the K562 and CHO cells studied.



2G-5

## 4:30 pm Effective scatterer size estimates in HT-29 spheroids at 55 MHz and 80 MHz

Lauren A. Wirtzfeld<sup>1</sup>, Elizabeth S. L. Berndt<sup>1</sup>, Michael C. Kolios<sup>1</sup>; <sup>1</sup>Department of Physics, Ryerson University, Toronto, Ontario, Canada

## Background, Motivation and Objective

In-vitro cancer research is often limited by unrealistic two-dimensional geometry. Changes in cell signaling, growth, interaction, and many other parameters differ in a more natural three dimensional configuration. Spheroids offer a simple, self-constructed model of 3D arrangement on the size scales (200-600  $\mu$ m) amenable to probing with high-frequency ultrasound (55-80 MHz). Previous studies have observed qualitative contrast between spheroid rims and cores. This study applies quantitative analyses to determine sub-wavelength changes in cellular structure and cellular spatial arrangement in HT-29 spheroids as a function of original seeding numbers and location (core vs rim) using high-frequency ultrasound (55 and 80 MHz).

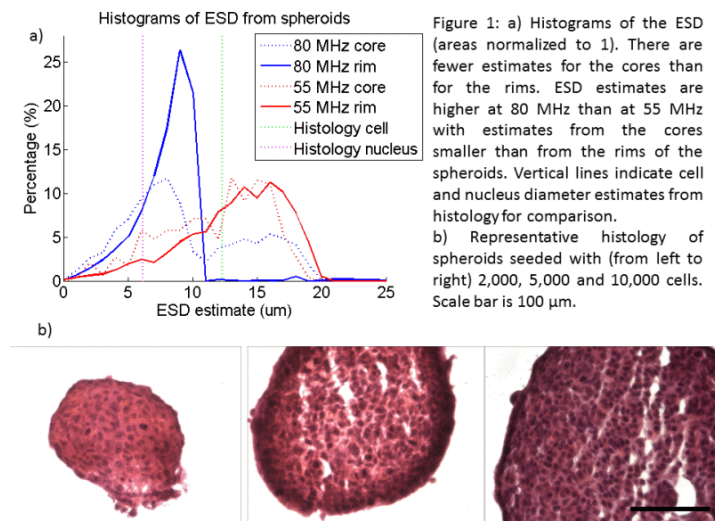
## Statement of Contribution/Methods

Spheroids were produced by hanging drops seeded with 2,000 to 10,000 HT-29 human colorectal adenocarcinoma cells. On day four, spheroids were imaged with a VisualSonics Vevo770 system and a Kibero SASAM using a 55 MHz and 80 MHz transducer, respectively. Several planes of raw RF data were collected from both systems through each spheroid. Offline, the spheroids and their cores were manually segmented. Individual regions (5x5 wavelengths in size) were analyzed to calculate the spectral slope, midband fit and effective scatter diameter (ESD).

## Results/Discussion

ANOVA analysis shows statistically significant differences ( $p < 0.05$ ) in the midband fit, spectral slope and effective scatter diameter (ESD) estimates for frequency and location. The distinct separation in ESD values (Figure 1a) between the 55 MHz ( $12.8 \pm 0.4 \mu$ m) and the 80 MHz ( $7.0 \pm 0.6 \mu$ m) suggests sensitivity to different scatterers. Cellular and nuclear diameters estimates from histology (Figure 1b) are  $12.27 \pm 0.17 \mu$ m and  $6.13 \pm 0.17 \mu$ m respectively, which agree well with the estimated ESD from the 55 MHz and 80 MHz transducers.

The demonstrated sensitivity of high-frequency ultrasound to spectral parameter changes in spheroids, suggest that this model can be used to evaluate changes observed due to cell viability and in response to drug treatments. The apparent change in sensitivity to different scatterer sizes, which correlate well with the cellular and nuclear size, offers the ability to monitor changes to different cell structures.



2G-6

#### 4:45 pm Impact of microscale properties measured by 50-MHz acoustic microscopy on mesoscale elastic and ultimate mechanical cortical bone properties

Adeline Bourignon<sup>1</sup>, Annette Sitzer<sup>2</sup>, Aritra Chababarty<sup>1</sup>, Kerstin Rohde<sup>3</sup>, Peter Varga<sup>1</sup>, Robert Wendlandt<sup>2</sup>, **Kay Raum<sup>1</sup>**; <sup>1</sup>Julius Wolff Institute, Charité-Universitätsmedizin Berlin, Berlin, Germany, <sup>2</sup>Labor für Biomechanik, Universitätsklinikum Schleswig Holstein, Lübeck, Schleswig Holstein, Germany, <sup>3</sup>Klinik für Diagnostische Radiologie, Universitätsklinikum Schleswig Holstein, Kiel, Schleswig Holstein, Germany

##### Background, Motivation and Objective

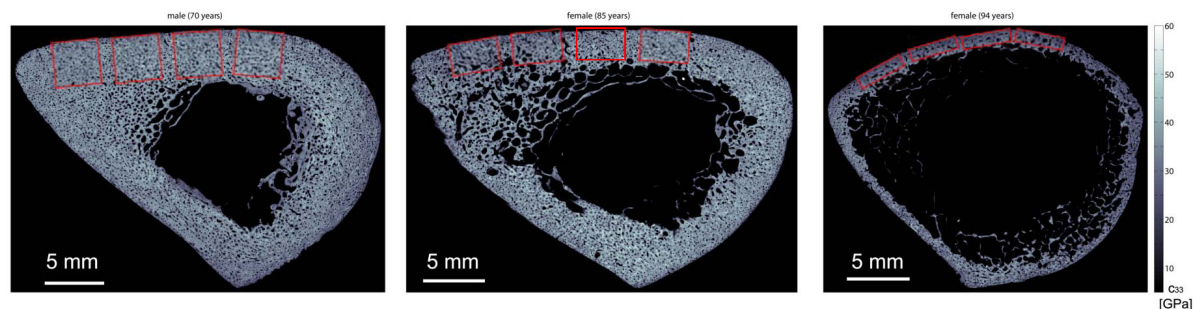
Cortical bone strength is determined by multiple factors in addition to tissue mineralization. Among them, changes in cortical porosity and elastic properties of the extracellular bone matrix have been suggested to be related to fracture risk. The objective of this study was to assess matrix stiffness and porous structure by means of 50-MHz acoustic microscopy (lateral resolution: 25  $\mu\text{m}$ , Fig. 1) of native samples obtained from the tibia mid-shaft in a representative sample cohort and to compare these properties to elastic and ultimate properties in cuboidal samples assessed by means of mechanical testing.

##### Statement of Contribution/Methods

Mid-diaphyseal tibia samples were obtained from 19 human donors (age range: 69-94 yrs). 25-mm thick cross-sections were prepared using a diamond band saw. One polished section surface was then scanned in temperature controlled saline at 50 MHz. The confocal reflection amplitude at each scan point was converted to an apparent stiffness coefficient  $c_{33}$ . After binarization and selection of the regions evaluated by mechanical testing, the mean stiffness, average pore size, porosity and number of large resorption lacunae (N.R.L) were evaluated in each ROI. Thereafter, up to four cuboidal blocks were cut from each sample and forwarded to mechanical investigations. The cuboidal samples ( $n=48$ ) were tested under moist conditions for Young's modulus and ultimate compressive strength using a material testing machine. After preconditioning (three times, strain rate:  $.05 \text{ min}^{-1}$ ) testing was conducted until mechanical failure occurred.

##### Results/Discussion

$c_{33}$  ranged from 22.4 GPa to 46.9 GPa (CV: 19%). Cortical porosity and pore density varied between 3.5% and 34% (CV: 52.7%), and  $9.2 \text{ mm}^{-2}$  and  $37.8 \text{ mm}^{-2}$ , respectively. Young's Modulus and ultimate strength could be measured in 37 of 48 samples and the values ranged from 8.6 GPa to 19.6 GPa (CV: 18.7%) and 117.1 MPa to 201.6 MPa (CV: 14.7%), respectively. Young's modulus and ultimate strength were significantly correlated ( $R=.72$ ) and both properties were associated with N.R.L ( $-.55 < R < -.52$ ), but not with the matrix stiffness. These findings underline the diagnostic values of resorption lacunae and the compound Young's modulus for the prediction of bone strength.



## 3G - MEL: Elasticity Imaging Methods I

Boulevard

Friday, September 5, 2014, 3:30 pm - 5:00 pm

Chair: **Kathy Nightingale**  
Duke University, Durham

3G-1

### 3:30 pm Induced tissue displacement in magnetomotive ultrasound imaging - simulations and experiments

Tomas Jansson<sup>1,2</sup>, Maria Evertsson<sup>3</sup>, Esayas Atile<sup>3</sup>, Roger Andersson<sup>3</sup>, Sarah Fredriksson<sup>4</sup>, Hans W Persson<sup>3</sup>, Ingrid Svensson<sup>3</sup>, Magnus Cinthio<sup>3</sup>; <sup>1</sup>Clinical Sciences Lund, Biomedical Engineering, Lund University, Lund, Sweden, <sup>2</sup>Medical Services, Skåne University Hospital, Lund, Sweden, <sup>3</sup>Biomedical Engineering, Faculty of Engineering LTH at Lund University, Lund, Sweden, <sup>4</sup>Geccodots AB, Lund, Sweden

#### Background, Motivation and Objective

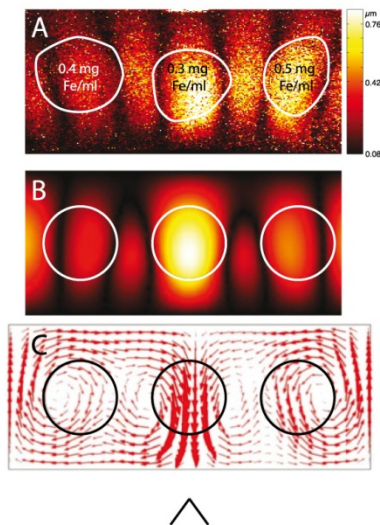
Magnetomotive ultrasound (MMUS) imaging is a method that enables the use of superparamagnetic iron oxide nanoparticles (SPIO NP) as an ultrasound contrast agent. This is achieved by virtue of a time-varying external magnetic field whereby NPs are set in motion. Ultrasound can be used to detect the motion as NPs move also their immediate surrounding. We have in previous studies noted an induced displacement occurring laterally outside nanoparticle-laden regions, but also found that it has opposite phase, and can thus be filtered out. It has been suggested that the opposed motion is a result of a diamagnetic response of tissue or material free from iron oxide NPs, while we hypothesize that it is caused by mechanical coupling from movement of SPIO NP laden regions. This study aims to compare experimental data to a simulation of generated displacements in response to a magnetic field.

#### Statement of Contribution/Methods

The situation was modeled in COMSOL as identical to the experimental: a solenoid with a cone-shaped iron core placed under a 25x10x10mm PVA phantom with 5mm diameter inserts of added SPIO-NP at 0.4, 0.3, and 0.5 mg Fe/ml concentrations, contained in a rigid walled container. The location of the iron core tip is indicated in panel C. First the magnetic field extending from the iron core tip was simulated. From this the force on the magnetic material was calculated, and then input as a body load applied to the NP-laden areas by magnitudes corresponding to NP concentrations. Properties of the simulated phantom material were set as the experimental in terms of Young's and bulk moduli, Poisson's ratio, and density. Boundaries were modeled as fixed, with a slip condition tangentially to the surface.

#### Results/Discussion

Panel A shows the experimental MMUS image, while panel B is the simulation (cut to show same field of view as panel A). Color is scaled according to the absolute value of the vertical displacement. Movement in-between inserts can be seen, of opposed direction. Panel C shows both displacement magnitude and direction as arrows, with trajectories that explain the opposed motion as a result of mechanical coupling. The tilt of the NP areas in panel A reflects attraction to the tip, while in the simulation lateral forces dominate. We suggest that this is due to the simulated slip condition at the boundary, which in reality presumably is a combination of slip and non-slip due to friction.



3G-2

### 3:45 pm Shear Wave Arrival Time Estimates Correlate with Local Speckle Pattern

Stephen McAleavey<sup>1</sup>, Laurentius Osapoetra<sup>2</sup>, Jonathan Langdon<sup>1</sup>; <sup>1</sup>Biomedical Engineering, University of Rochester, Rochester, New York, USA, <sup>2</sup>Physics, University of Rochester, Rochester, New York, USA

#### Background, Motivation and Objective

Ultrasound speckle tracking is used in a wide variety of shear wave elastography (SWE) techniques. The displacements involved in ARFI SWE are small, the echo correlation high, and the shear wavelengths are comparable to the ultrasound beamwidth used to track them. Quantitative SWE techniques estimate the velocity of these shear waves by tracking tissue motion at one or more locations. These shear wave arrival time estimates are known to be noisy even at high echo SNR.

We hypothesize that the observed arrival time variations are largely due to the underlying speckle pattern, and call the effect *speckle bias*. The amplitude of the tracked echo is a combination of the spatial sensitivity function of the imaging system and the particular scatterer interference pattern. For a particular arrangement of scatterers the result can be a

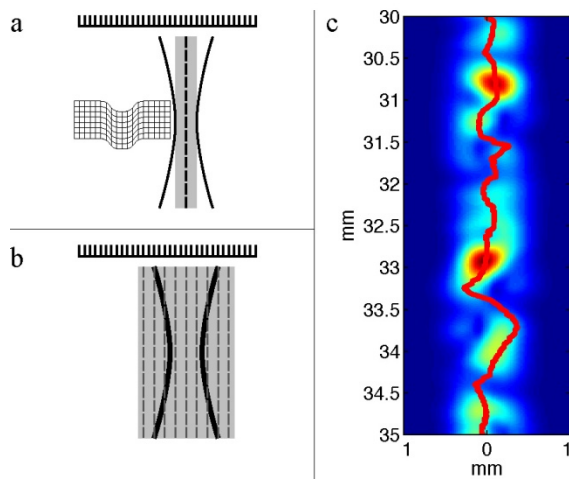
total echo signal that arises from a location off the tracking beam axis. The motion tracked will correspond to this off-axis point, resulting in a biased estimate of the shear wave arrival time.

#### Statement of Contribution/Methods

We demonstrate a strong correlation between the shear wave arrival time estimate and the local speckle pattern. Field II was used to simulate imaging of both diffuse and point targets subject to shear wave motion. A 5.3 MHz linear array with transmit apertures of  $f/2-8$  and receive apertures of  $f/2-4$  was modeled, with a range of shear wave amplitudes (5-20  $\mu\text{m}$ ) and profiles simulated. Shear waves in phantoms were imaged with a Siemens VF7-3 transducer. Tracking (a) was performed by normalized cross correlation with RF window lengths of 1-10 $\lambda$ . The local speckle pattern was determined through swept-receive-aperture imaging of the transmit beam (b).

#### Results/Discussion

Arrival time bias is strongly ( $r=0.6$ ) correlated with the location of the lateral peak of the swept-receive speckle pattern as illustrated in the figure, wherein the estimated shear wave arrival time scaled by the shear wave speed is plotted over the weighted swept receive speckle pattern (c). Our results suggest that high echo correlation does not equate to an accurate shear wave arrival time estimate, and that echo correlation is weakly related to arrival time accuracy. The arrival time bias at a given location is stable for the range of shear wave amplitudes considered, with a variation  $1/10^{\text{th}}$  that produced by different speckle realizations tracked along a given a-line.



3G-3

#### 4:00 pm Shear wave generation with steered ultrasound push beams

Alireza Nabavizadeh<sup>1,2</sup>, Pengfei Song<sup>2</sup>, Shigao Chen<sup>2</sup>, James F. Greenleaf<sup>2</sup>, Matthew W. Urban<sup>2</sup>; <sup>1</sup>University of Minnesota-Rochester, USA, <sup>2</sup>Mayo Clinic College of Medicine, USA

#### Background, Motivation and Objective

The objective of the steered push beam (SPB) method is to create multiple foci generated by the interference of different ultrasound push beams to create shear waves. SPB can produce more shear wave sources which can improve SNR, and push beam depth-of-field.

#### Statement of Contribution/Methods

In the SPB method, we divide the array transducer aperture into segments of  $N_s$  elements. Each segment uses an unfocused beam that can be steered with a positive or negative angle. Through this framework we came up with two new beamforming configurations generally called a deterministic configuration (DC) where the angles are manually assigned by the user and a randomized configuration (RC) where the sign and the angle are randomly assigned. For the randomized configuration, we can fix the angle and vary the sign randomly or vary the sign and angle randomly. We performed simulations in Field II to design the DC arrangements and to determine RC optimal arrangements. We implemented these configurations on the Verasonics V-1 system, and tested them in a homogeneous phantom with a shear wave speed (SWS) of  $c = 1.55$  m/s and phantoms with spherical and cylindrical inclusions. We implemented unfocused and focused Comb-push Ultrasound Shear Elastography (UCUSE and FCUSE) to compare with the SPB results. Maps of SWS were calculated using CUSE processing techniques (Song et al., IEEE TMI: 31:1821-1832, 2012).

#### Results/Discussion

Figs. 1(a)-(c) show the acoustic intensity simulated with Field II for UCUSE and one DC and RC configuration, respectively. The experimental SWS maps generated by these configurations in the homogeneous phantom are shown in Figs. 1(d)-(f). Means and standard deviations of the SWS for a region-of-interest in the middle of the image were evaluated. Figs. 1(g)-(i) show the SWS maps from the configurations for a cylindrical inclusion with diameter of 10.4 mm. Means and standard deviations of the SWS of the background and inclusion were evaluated and used to calculate the contrast-to-noise ratio (CNR) for each image. The SWS map results show that SPB generates images with similar or improved CNR compared to the CUSE implementations. The range of depth from the DC configuration (Figs. 1(e) and 1(h)) can also be improved compared to UCUSE.

The SPB results demonstrate that uniformity and depth-of-field for SWS maps compare equivalently or better to those achieved with CUSE implementations.



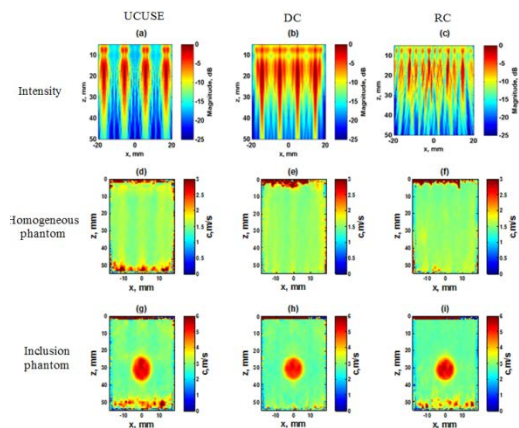


Fig. 1. Simulated intensity field for (a) UCUSE, (b) DC, and (c) RC. Shear wave speed map for homogeneous phantom for (d) UCUSE,  $c = 1.49 \pm 0.07$  m/s, (e) DC,  $c = 1.47 \pm 0.04$  m/s, and (f) RC,  $c = 1.48 \pm 0.05$  m/s. Shear wave speed maps for the inclusion phantom for (g) UCUSE, CNR = 18.52, (h) DC, CNR = 23.07, and (i) RC, CNR = 45.99.

3G-4

#### 4:15 pm Shear wave elastography method combining phase-sensitive optical coherence tomography and coded acoustic radiation force

Thu-Mai Nguyen<sup>1</sup>, Shaozhong Song<sup>1,2</sup>, Bastien Arna<sup>1</sup>, Emily Y Wong<sup>1</sup>, Ruikang K. Wang<sup>1,3</sup>, Matthew O'Donnell<sup>1</sup>, <sup>1</sup>Department of Bioengineering, University of Washington, Seattle, WA, USA, <sup>2</sup>School of Engineering, Physics and Mathematics, University of Dundee, Dundee, United Kingdom, <sup>3</sup>Department of Ophthalmology, University of Washington, Seattle, WA, USA

##### Background, Motivation and Objective

Optical coherence tomography (OCT) offers micron scale resolution that is ideal for characterizing ocular tissues. Shear wave elastography (SWE) can provide valuable information by assessing tissue biomechanics from the speed of shear waves propagating through tissue. Non-contact shear sources are preferable for clinical purposes. Thus, we implemented SWE by combining OCT for detection and acoustic radiation force (ARF) as a remote shear source. To increase the signal-to-noise ratio (SNR) of detected shear waves, we also used a pulse compression method in which the instantaneous peak energy is spread over long emissions and the detected signal is digitally compressed into a short pulse to increase both SNR and spatio-temporal resolution.

##### Statement of Contribution/Methods

A single-element focused transducer (frequency 7.5 MHz) was used to apply maximum pressures of 1 to 3 MPa in a gelatin phantom. The transducer was driven by a 3-ms long coded excitation where the amplitude was modulated by a linear-swept frequency square wave (from 1 to 7 kHz, 50% duty cycle). It yielded linear-swept frequency shear waves. Phase-sensitive OCT was used to track and record the resulting axial displacements at an equivalent frame rate of 45 kHz across an imaging area of 3 mm x 2 mm (lateral x axial). The displacements were then digitally compressed using an inverse filtering method as described in [1]. The SNR was compared to that obtained with a "standard excitation" (100-μs pulse). The local shear wave speed was computed using a time-of-flight algorithm.

##### Results/Discussion

We obtained displacements of a few tens of microns. At a pressure of 3 MPa, a standard excitation has a 7.4 dB SNR whereas the pulse compression (see Fig. 1) has a 22.6 dB SNR. A pressure of 1 MPa does not yield a detectable shear wave with a standard excitation (-2.3 dB SNR) while pulse compression gives a 18.4 dB SNR. As expected, the shear wave speed of a 15%-gelatin phantom was estimated to be  $6.2 \pm 1.3$  m/s. We demonstrated the feasibility of combining ARF and OCT to perform elastography with low acoustic pressures using pulse compression. In future work, we will optimize the transducer and the pulse compression parameters for clinical implementation.

[1] Nguyen et al. "Shear wave pulse compression for dynamic elastography using phase-sensitive optical coherence tomography" J. of Biomed. Opt. 19(1), 016013, 2014.

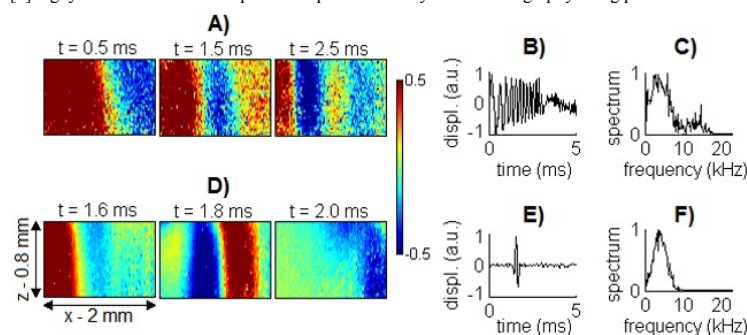


Fig. 1. Displacements in a 15%-gelatin phantom obtained at a pressure of 3 MPa with a coded excitation before (A-C) and after (D-F) pulse compression. (A,D): snapshots of the shear wave propagation at three time steps. The normalized amplitude of the displacements is coded in color scale, x and z are respectively the lateral and axial coordinates. (B,E): normalized temporal profile at one location. (C,F): normalized spectrum at one location. The SNRs are respectively 12.2 dB and 22.6 dB before and after compression.



## 3G-5

## 4:30 pm Shear wave elastography by Lorentz force: ex-vivo experiment and computer simulation

Pol Grasland-Mongrain<sup>1</sup>, Rémi Souchon<sup>1</sup>, Florian Cartellier<sup>1</sup>, Ali Zorgani<sup>1</sup>, Jean-Yves Chapelon<sup>1</sup>, Cyril Lafon<sup>1</sup>, Stefan Catheline<sup>1</sup>; <sup>1</sup>LabTAU, INSERM u1032, Lyon, France

## Background, Motivation and Objective

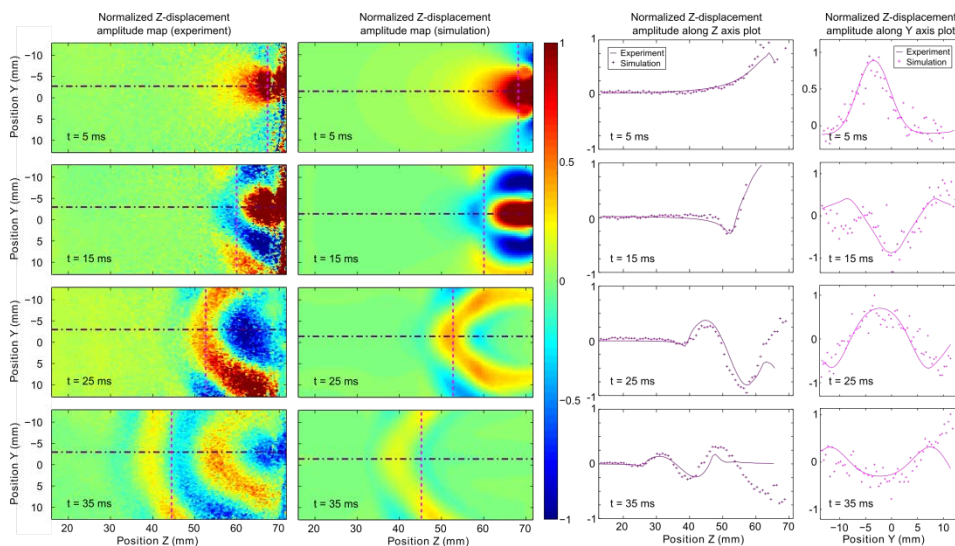
Shear wave elastography is a medical imaging technique where the propagation of a movement as a shear wave is observed to find a tissue elasticity. Most of techniques are using manual compression or acoustic radiation force to create the initial movement. This shear wave can also be induced by applying an electrical current and a magnetic field, leading to a "shear wave elastography by Lorentz force" technique. In this study we compare the experimental results on a gelatin phantom with a computer simulation, and then we apply the technique on an ex-vivo liver sample.

## Statement of Contribution/Methods

In the experiments, a 80 V, 100 Hz electrical signal is applied by two electrodes in a sample placed in a 300 mT magnetic field. The sample is either a gelatin phantom with an electrical conductivity of 1 S/m, close to the human soft tissue conductivity, or a swine liver sample unfrozen in a 1% salt solution. An ultrasonic probe is acquiring an image in ultrafast mode at 1000 images per second with a Verasonics scanner. Movement of the sample is measured with a speckle-tracking technique based on correlations between each ultrasound image. The results on the gelatin phantom are compared with a computer simulation based on the solving of Green functions, which calculates the propagation of a movement in an infinite medium.

## Results/Discussion

Results show a very good agreement between the experimental and simulation results. Main differences are probably due to the infinite medium hypothesis in the computer simulation. Shear waves are also visible in the experiment on the liver sample, which lead to a shear modulus of  $2.0 \pm 0.6$  kPa, a value in excellent agreement with the literature.



## 3G-6

4:45 pm Assessment of the Nonlinear Elastic Properties of Soft Tissues *in vivo* by using Supersonic Shearwave Imaging Technique

Miguel Bernal<sup>1</sup>, Mathieu Couade<sup>2</sup>, Foucauld Chamming's<sup>3</sup>, Jeremy Bercoff<sup>2</sup>, Jean-Luc Gennisson<sup>1</sup>, Mickael Tanter<sup>1</sup>; <sup>1</sup>ESPCI ParisTech, CNRS UMR7587, INSERM U979, Institut Langevin – Ondes et Images, Paris, France, <sup>2</sup>SuperSonic Imagine, France, <sup>3</sup>Radiology Department, Université Paris Descartes Sorbonne Paris Cité, Hôpital Européen Georges Pompidou, Paris, France

## Background, Motivation and Objective

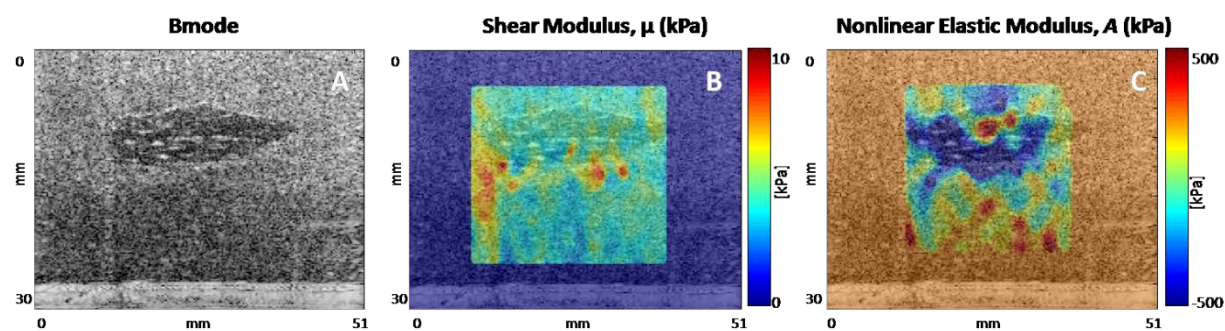
Nonlinear elasticity is a parameter that could better help characterization of soft tissues. Previous studies using mechanical tests showed that nonlinear response was useful in the differentiation of benign and cancerous tissues. Unfortunately, these tests can only be done *ex vivo*, therefore, the development of real time imaging technique for the visualization of soft tissues nonlinear elasticity would be of great interest for medical diagnosis.

## Statement of Contribution/Methods

In this work we present a new, real time imaging technique of nonlinear elastic properties based on acoustoelasticity theory. This theory was developed in the case of soft tissues and is based on the development of the strain energy as defined by Landau. The nonlinear shear parameter  $A$ , is found from the change in shear wave speed  $V_s$  as a function of the stress applied ( $\sigma$ ) on tissues, according to:  $\rho^*V_s^2 = \mu - \rho^*A/12\mu$ , where  $\rho$  is the density and  $\mu$  is the stress-free shear modulus. The technique was implemented on an Aixplorer system driving an 8 MHz probe. It consists on generating deformations in the medium while shear wave velocity maps and strain measurements are performed by ultrafast acquisition, simultaneously. Combining these two parameters at multiples steps of deformation allows us to retrieve the stress field within the tissue and deduce a map of the nonlinear parameter  $A$ .

## Results/Discussion

Calibration of the system was done on pork-liver and gelatin phantoms. The concentration of gelatin was set to match the elastic properties of liver, making this last one almost invisible in stress-free elasticity images. Mean values of shear moduli were found to be similar in the liver ( $1.8 \pm 0.4$  kPa) and in the gelatin ( $1.4 \pm 0.1$  kPa); while  $A$  significantly differs between the two tissues,  $A_L = -540 \pm 111$  kPa and  $A_G = -61 \pm 60$  kPa. The figure shows results for Bmode,  $\mu$  and  $A$ . A clinical study on breast tissue is currently underway. A cohort of 30 patients is currently being scanned with different types of lesions. Five women have been scanned at this point and promising results showed that values of  $A$  significantly deviate between lesions and healthy tissues. As an example on patient #1 (abscess),  $\mu$  and  $A$  were found to be respectively inside the lesion:  $9.8 \pm 3.1$  kPa and  $-343 \pm 171$  kPa and outside the lesion:  $8.5 \pm 5.8$  kPa and  $7.4 \pm 8.0$  kPa. Therefore, this technique can be used as a complementary tool for breast cancer diagnosis.



The figure shows the corresponding B mode (Panel A), Shear modulus (Panel B) and Nonlinear elastic parameter  $A$  (Panel C) images for a liver phantom embedded in gelatin.

## 4G - Sensing

Marquette

Friday, September 5, 2014, 3:30 pm - 5:00 pm

Chair: **John Vetelino**  
University of Maine

4G-1

### 3:30 pm A Novel MEMS Gas Sensor Based on Ultrasonic Resonance Cavity

Panu Koppinen<sup>1</sup>, Teuvo Sillanpää<sup>1</sup>, Anu Kärkkäinen<sup>1</sup>, Jaakko Saarilahti<sup>1</sup>, Heikki Seppä<sup>1</sup>; <sup>1</sup>VTT Technical Research Centre of Finland, VTT, Finland

#### Background, Motivation and Objective

Measuring gas concentrations with high resolution is important for a wide variety of applications for example in healthcare, in ventilation control and in process industry. There is an increasing demand for low-cost and low-power applications, where it would be beneficial to measure gas concentrations in battery operated systems. Also, e.g. personal health care applications would benefit of low-cost sensors, since this would justify disposal of the sensors after use.

Typically gas sensors are based on optical absorption properties of the gas composition, change of electrical properties such as resistance or capacitance of a sensor, change in thermal conductivity or e.g. change in the mechanical resonance frequency (mass) of a MEMS resonator with functional coating or on mass spectrometry. However, many of these solution are expensive, complicated or will saturate over time. In this paper, we demonstrate a novel low-cost and low-power MEMS sensor concept based on ultrasonic resonance cavity, we call this sensor UltraGas.

#### Statement of Contribution/Methods

UltraGas sensor consist of a capacitive micromachined ultrasonic transducer (CMUT), which is embedded into an acoustic resonance cavity with a rigid termination. The mechanical impedance  $Z_0$  of the resonance cavity depends on the length of the cavity  $l$  and the composition/concentration of the gas. The changes in the gas composition/concentration can be measured simply by measuring the electrical impedance of the cavity coupled transducer.

#### Results/Discussion

We have demonstrated a proof of concept of a novel MEMS gas sensor based on an ultrasonic transducer embedded to an acoustic cavity. The initial experiments show a clear shift of the resonance frequency of the sensor as a function of CO<sub>2</sub> gas concentration.

The sensor shows a linear response of the frequency to the concentration, linear fit to the data yields a slope of 0.072 Hz/ppm. With our simple readout electronics the measured noise level was about 0.8 – 1 Hz, which corresponds to the resolution of 10 – 20 ppm. The current resolution is competitive with existing commercially available technologies. The major advantages of the UltraGas sensor are low cost, low power consumption, and small size.

4G-2

### 3:45 pm Microacoustic in-liquid sensors based on thin AlN films: A comparative study

Teona Mirea<sup>1</sup>, Enrique Iborra<sup>1</sup>, Ventsislav Yantchev<sup>2</sup>; <sup>1</sup>GMME-CEMDATIC-ETSIT, Universidad Politécnica de Madrid, Spain, <sup>2</sup>Uppsala University, Sweden

#### Background, Motivation and Objective

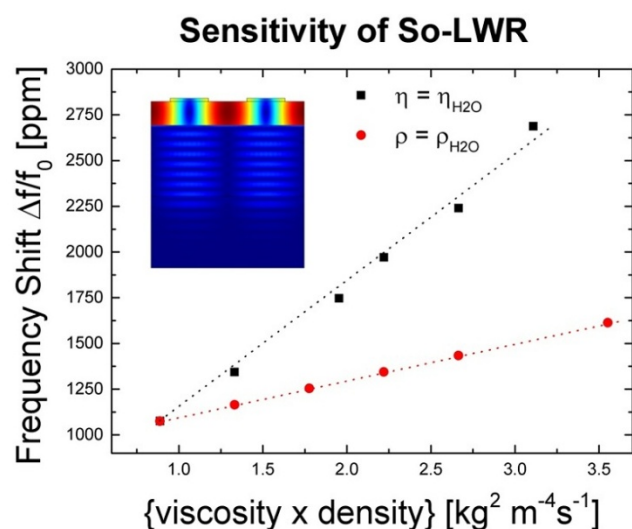
The current needs of the society for prevention of medical diseases have boosted the biosensors market the last years. Microacoustic resonators based on AlN thin films have demonstrated to be promising candidates for in-liquid and biosensing applications. Their IC compatibility allows a multiplexed detection while employing a mature AlN technology. The most explored devices are the shear Film Bulk Acoustic Resonators (SH-FBAR) and the S0 mode Lamb Wave Resonators (S0-LWR). They demonstrate retained performances in liquid, while employing different sensing mechanisms. SH-FBARs, similarly to classical QCM, sense the liquid through the decaying tail of the shear displacement, while in S0-LWRs a small portion of the energy is coupled to the liquid bulk. Here we study the sensitivity features in liquid of both resonators. For clarity, SH-FBAR and S0-LWR are considered at the same frequency (900 MHz). This allows us to study them operating at comparable noise floors, primary determined by the liquid losses.

#### Statement of Contribution/Methods

A new model was developed, using finite element analysis, to study the behavior in liquid environments of both types of resonators. The model was initially approved on SH-FBAR by comparing with the available data from the literature. Subsequently, the model was applied to study the sensing mechanism of the S0-LWR. Specific sensor design rules are deduced.

#### Results/Discussion

The results show that SH-FBARs, although quasi shear, behave as pure shear resonators, thus sensing in a non-specific manner changes in density and viscosity of the liquid, with frequency shifts proportional to the square root of the density viscosity product. On the contrary, S0-LWRs demonstrate different sensitivities to density and viscosity and their frequency shifts are linearly dependent to the latters. Besides, S0-LWRs can also sense changes in the dielectric permittivity of the liquid through the variation of the coupling coefficient. These results allow us to consider orthogonal sensing scenarios in which we can combine SH-FBARs and S0-LWRs, to separately detect changes in viscosity and density, or to combine two S0-LWRs to detect separately mechanical and electrical changes of the liquid. The proposed scenarios provide access to a more specific information of the liquid properties. These scenarios can be further applied to biosensor applications.



4G-3

**4:00 pm Biosensing using contactless quartz resonators**Hirotugu Ogi<sup>1</sup>; <sup>1</sup>Osaka University, Japan**Background, Motivation and Objective**

The quartz crystal microbalance (QCM) biosensor is a label-free biosensor, which is expected to be used in diagnosis and drug development processes. It is a mass-sensitive biosensor, and its mass sensitivity can be significantly improved by removing electrodes and wires attached on the quartz surfaces. We established a noncontacting method for measuring intended vibrations of naked quartz oscillators by antennas through electromagnetic waves, achieving high-sensitive detection of proteins with resonators thinner than 10 μm. The high transparency of the electrodeless quartz also allows its integration into any optical-microscopy techniques. The wireless-electrodeless QCM biosensor can be an important tool for life-science studies.

**Statement of Contribution/Methods**

Naked quartz crystals with different thicknesses were located inside the microchannel, where analyte solutions flow. The generation and detection antennas were located outside the flow channel. The electromagnetic field from the generation antenna excites vibrations of the quartz resonators, which were detected by the detection antenna, allowing the measurements of their resonance frequencies. Thus, a multichannel detection is made possible. A MEMS technique was also used to fabricate the wireless-electrodeless QCM biosensors. Integration of the contactless QCM biosensor into a total-internal-reflection-fluorescence microscopy was successfully achieved. This new measurement tool was used for real-time monitoring of aggregation process of Alzheimer-disease peptides.

**Results/Discussion**

The contactless QCM biosensors allowed high sensitive detection of various biomarkers and accurate measurement of binding affinities between biomolecules. The fundamental resonance frequency of the shear vibration of quartz resonator exceeds 500 MHz.

4G-4

**4:30 pm Self-Sensing Ultrasound Transducer for Cavitation Detection**

Peter Bornmann<sup>1</sup>, Tobias Hemsel<sup>1</sup>, Walter Sextro<sup>1</sup>, Gianluca Memoli<sup>2</sup>, Mark Hodnett<sup>2</sup>, Bajram Zeqiri<sup>2</sup>; <sup>1</sup>Chair of Mechatronics and Dynamics, University of Paderborn, Paderborn, Germany, <sup>2</sup>National Physical Laboratory, Teddington, United Kingdom

**Background, Motivation and Objective**

Ultrasound is established as versatile tool for enhancing various chemical and biotechnological processes. In many cases, the beneficial effect of ultrasound can be ascribed to ultrasound-induced cavitation. To decide whether cavitation is beneficial for a process or not, to optimize the sonic exposure and to monitor cavitation activity throughout the process it is necessary to detect and quantify cavitation during operation.

In situ measurements of the cavitation activity can be carried out by evaluation of the acoustic emission picked up by pressure sensors in the liquid.

However, in some applications it is impossible to insert a sensor in the liquid due to disturbance of the sound field, contamination or due to harsh environments often employed in sonochemistry. Such processes demand alternative measurement methods.

**Statement of Contribution/Methods**

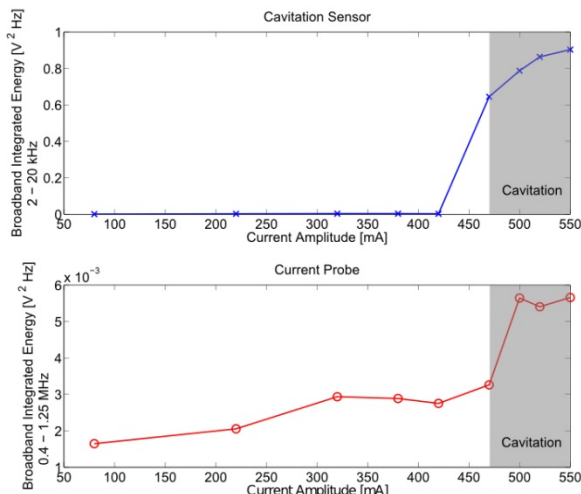
To avoid the need to deploy cavitation sensors within liquids under harsh conditions, electrical signals from the ultrasound generating transducer itself are being studied concerning their applicability for cavitation monitoring. This will considerably simplify the measurement setup and might be applied to various existing ultrasound systems with low effort.

The applicability of these electrical signals for cavitation monitoring was assessed through comparative measurements with a cavitation sensor designed by NPL. Derived measurement data was used to extract indicators correlating with cavitation onset. These indicators were compared with regard to their cavitation detection sensitivity. Furthermore, the influence of the transducer design on obtainable signals will be discussed to evaluate the versatility of this method.

**Results/Discussion**

The measurements demonstrate that indicators for cavitation onset from the current signal of the transducer can be correlated with sensor data. As an example, the broadband integrated energy obtained for a 28 kHz transducer, depicted in Fig. 1, shows a distinct increase as cavitation sets in. Further measurements have shown that the indicators must be

carefully chosen as they might be affected by the characteristics of the transducer. Once characterized, the self-sensing transducer will be a useful tool for cavitation monitoring in otherwise inaccessible liquids or for applications where it is sufficient to know only whether the liquid is cavitating or not.



4G-5

#### 4:45 pm High temperature ultrasonic technique for monitoring of the properties of plastic melts during manufacturing process

Liudas Mazeika<sup>1</sup>, Rymantas Kazys<sup>1</sup>, Reimondas Sliteris<sup>1</sup>, Alfonsas Vladisauskas<sup>1</sup>, Egidijus Zukauskas<sup>1</sup>, Regina Rekuviene<sup>1</sup>; <sup>1</sup>K.Barsausko Ultrasound Institute, Kaunas University of technology, Lithuania

##### Background, Motivation and Objective

Different plastic materials are widely used in various areas of industry not only due to the mechanical properties, but also due to relatively easy and adaptive manufacturing technologies based on extrusion and injection of melted plastics. The quality control of these technologies requires measurement of multiple interrelated parameters such as the pressure, temperature, extrusion speed and etc. However those parameters do not determine completely properties of the melt itself, what is especially important when blends, filling are used. On the other hand there are known ultrasonic evaluation techniques which exploit the parameters of the waves transmitted through the material under investigation. The measurement should be carried out at high temperatures and pressures. Additional problems are caused by the requirement that the measurements under in situ should be carried out through a relatively narrow access standard port. So, the objective of the work presented was to develop ultrasonic measurements techniques suitable for the monitoring of the properties of the melted plastics at high temperatures during manufacturing process.

##### Statement of Contribution/Methods

In order to solve this challenging task a novel ultrasonic technique based on application of waveguides has been developed. The waveguides enable to reduce temperature from the melt temperature down to the temperature suitable for piezoelectric transducers. The geometry of the waveguide was optimized using a finite element modelling. Optimization enabled to reduce trails in the signals caused by multiple reflections inside the waveguide. The most important part of the waveguide is the tip with a special matching layer which is used for estimation of the melt density. The density was evaluated exploiting the known acoustic impedance of the matching layer, the parameters of the signals reflected by the tip and the ultrasound velocity in the melt. The developed technique was calibrated and verified under the laboratory conditions using different liquids with known densities.

##### Results/Discussion

The performance of the proposed technique was demonstrated under in situ conditions by monitoring the properties of a melted polypropylene under different operation conditions of the extruder. The measurements were carried out in the temperatures range from 180°C up to 250°C. It was shown that any changes of the material properties caused by temperature or variation of the content of the blend can be easily observed in the measurement results. The developed technique is suitable for monitoring of relatively small density variations during manufacturing process.



## 7G - Diagnostic and Imaging Transducers

Williford C

Friday, September 5, 2014, 3:30 pm - 5:00 pm

Chair: **Scott Smith**  
GE Global Research

7G-1

### 3:30 pm 20 MHz/40 MHz Dual-layer Micromachined Composite Transducer for Tissue Harmonic Imaging

Sibo Li<sup>1</sup>, Jian Tian<sup>2</sup>, Pengdi Han<sup>2</sup>, Xiaoning Jiang<sup>1</sup>; <sup>1</sup>Mechanical and Aerospace Engineering, North Carolina State University, Raleigh, NC, USA, <sup>2</sup>HC Materials Corporation, Bolingbrook, Illinois, USA

#### Background, Motivation and Objective

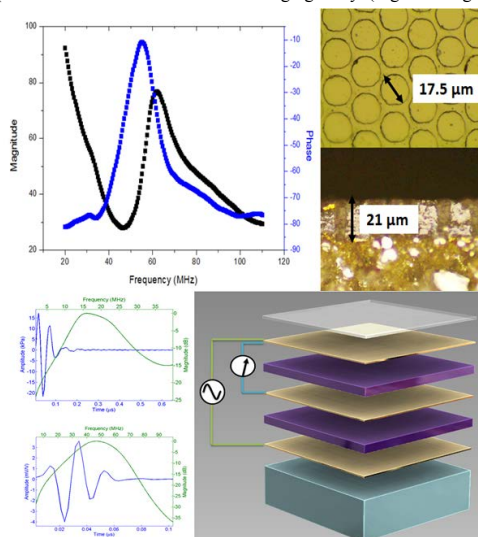
Broadband ultrasound imaging including tissue harmonic imaging has been widely studied in imaging for cardiology, bladder and other fluid-filled or cyst structures. The technique usually captures acoustic information from the frequency higher than that of transmission waves. Compared to the conventional pulse-echo imaging method, the broadband imaging possesses advantages in contrast resolution enhancement, artifacts reduction, and good signal-to-noise ratio. However, those benefits require broadband ultrasound transducers (>100%) and high sensitivity, which are hardly available. PMN-PT 1-3 composite has been increasingly used in medical imaging transducers due to its low impedance, high piezoelectric coefficients and high electromechanical coupling coefficients (kt). In this paper, a micromachined PMN-PT 1-3 composite based dual frequency dual layer transducer was designed, fabricated and characterized for tissue harmonic imaging.

#### Statement of Contribution/Methods

The dual frequency PMN-PT 1-3 composite transducer was designed with 20 MHz transmission and 40 MHz receiving. A KLM model was performed for the transducer design. PMN-PT 1-3 composite was design and fabricated using micromachined technique at HC Materials Corp. Selected properties including the resonance, dielectric constant, dielectric loss and kt were measured to characterize the composite. Two active layers were stacked in series, and electrically connected in parallel. The transducer works in two modes. In the first mode, transmitting at 20 MHz, both layers are excited at the same time; and in the second mode, only the front layer is active serving as a receiver at 40 MHz. In this way, the transducer can be used to transmit fundamental waves and receive harmonic echoes.

#### Results/Discussion

Micromachined 1-3 composite with thickness of 21  $\mu\text{m}$  was fabricated and characterized, showing the resonance of 40 MHz and kt of 72%. From the KLM model for a dual layer configuration, the initial results showed that this dual layer transducer can transmit at 20 MHz and receive at 40 MHz, where the 40 MHz receiving response shows a -6dB fractional bandwidth of 70% and sensitivity of 4 mV/V, and the 20 MHz transmitting sensitivity is 20 KPa/V. All above transmitting and receiving performances hold great potential in broadband ultrasound imaging study. (Figure: Image of 1-3 composite and transducer assembly)



7G-2

### 3:45 pm Design and Fabrication of a High-Frequency Phased Array with Sparse Vernier Array Element Spacing for Grating Lobe Suppression

Andre Bezanson<sup>1</sup>, Jeremy Brown<sup>1</sup>; <sup>1</sup>Biomedical Engineering, Dalhousie University, Halifax, Nova Scotia, Canada

#### Background, Motivation and Objective

Modern developments in high resolution ultrasound imaging have seen a push towards smaller and higher frequency transducer arrays. In miniature endoscopic forward looking arrays, the packaging and interconnect constitutes a significant fraction of the transducer volume. This can limit the total number of interconnections when designing for a specific endoscopic form factor. In previous work we developed a 64-element 45-MHz phased array transducer with  $1\lambda$  pitch packaged into a miniaturized endoscopic form factor. As a result of the relatively large pitch the array generated unacceptable grating lobe artifacts at large steering angles. Although we were able to adequately suppress these grating lobes with an unconventional phase coherence weighting function, it required a significant amount of signal processing which increasing complexity and reducing frame rate. In this work we investigate the simulation, design, and fabrication of a phased array of equal aperture but with 128 elements at  $1/2\lambda$  spacing. Although 128 elements are present, only 64 elements are connected in the form of a sparse Vernier array for the purpose of grating lobe suppression and reduction of interconnect size.

**Statement of Contribution/Methods**

In a sparse Vernier array design transmit and receive elements are spaced at different element pitches to allow for a reduction in grating lobes despite the low element count. To optimize design parameters impulse response simulations were run and a design was established that showed a peak grating lobe level reduction from approximately -30 dB for a 64 element array with  $1\lambda$  pitch at a steering angle of  $30^\circ$  to -50 dB for the sparse Vernier array design with 42 transmit elements and 32 receive elements. In the Vernier design there are 128 elements at  $1/2\lambda$  pitch with every third element being used for transmit and every fourth element being used for receive.

The array was fabricated using high-resolution positive photolithography and wet etching on a substrate of PZT-5H coated with a  $1\ \mu\text{m}$  layer of copper. The element pitch was defined at  $19\ \mu\text{m}$  ( $1/2\lambda$ ) and the sample was lapped to  $47\ \mu\text{m}$  to achieve an operating frequency of 45 MHz. A copper ground electrode was evaporated onto the sample over the active area of the array and 17  $\mu\text{m}$  wirebonds were used to connect the array elements on the front surface of the array to a flexible circuit interconnect oriented in-line with the forward looking beam. Lastly, matching layers were vacuum deposited to the front face of the transducer and an elevation lens was applied.

**Results/Discussion**

The electrical impedance was measured to be  $135\ \Omega$  on resonance with a variance of  $5.8\ \Omega$  between elements. Needle hydrophone measurements were performed on individual array elements and the one-way directivity was measured to be  $29^\circ$  which was an improvement over the  $24^\circ$  directivity measured with the  $1\lambda$  pitch array. Beam profile and sensitivity measurements are currently ongoing using an in-house developed high frequency phased array beamformer.

7G-3

**4:00 pm Dual frequency transducers for super harmonic intravascular ultrasound imaging**

Jianguo Ma<sup>1</sup>, Karl Heath<sup>2</sup>, Yang Li<sup>3</sup>, Paul Dayton<sup>2</sup>, Qifa Zhou<sup>3</sup>, Kirk Shung<sup>3</sup>, Xiaoning Jiang<sup>1</sup>; <sup>1</sup>Mechanical and Aerospace Engineering, North Carolina State University, Raleigh, North Carolina, USA, <sup>2</sup>UNC/NCSSU Joint Department of Biomedical Engineering, University of North Carolina, Chapel Hill, North Carolina, USA, <sup>3</sup>Department of Biomedical Engineering, University of Southern California, Los Angeles, California, USA

**Background, Motivation and Objective**

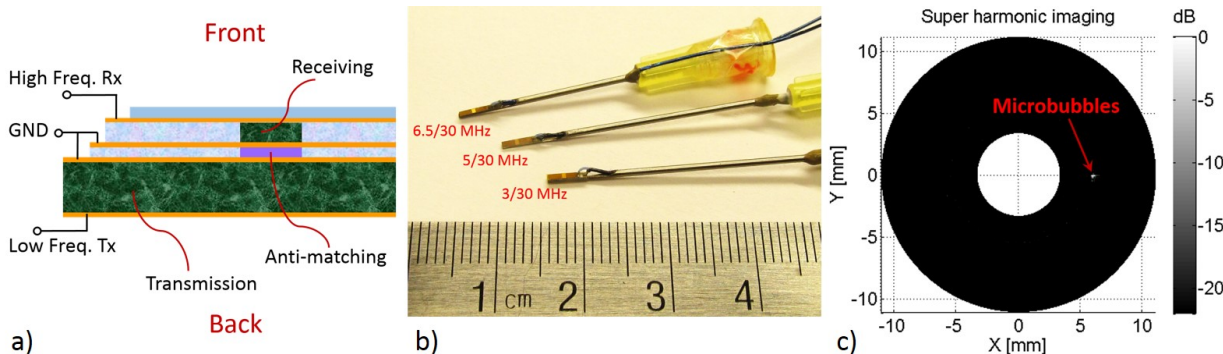
Combining super harmonic ultrasound imaging with intravascular ultrasound (IVUS) imaging is expected promising in vasa vasorum detection and vulnerable plaque assessment. IVUS imaging is effective in plaque and tissue structural detection, but ineffective for imaging microvessels due to their low scattering. Contrast enhanced, super harmonic ultrasound imaging is capable of identifying microvessels by detecting the microbubble super harmonics while suppressing the fundamental and second harmonic noise from tissue. However, combining the two imaging modes into a super harmonic IVUS imaging is challenging because of the spatial and frequency limit. Previously we reported a 6.5 MHz/30 MHz dual frequency transducer for super harmonic IVUS imaging with relatively low ( $\sim 12$  dB) contrast to tissue ratio (CTR). In this paper, we develop dual frequency IVUS transducers with different low frequency transmitters for super harmonic IVUS imaging with enhanced CTR.

**Statement of Contribution/Methods**

Small aperture, dual frequency transducers were designed (Fig. 1 a) for the super harmonic IVUS imaging by separating the transmission and receiving components to cover the interested frequency ranges. Several prototypes were designed with transmission center frequencies at 6.5 MHz, 5 MHz and 3 MHz for imaging comparison. Different active materials for transmitter were also compared between PMN-PT single crystal and 1-3 composite. The receiving element for all transducers was a PMN-PT single crystal receiver with center frequency of 30 MHz. An anti-matching layer was sandwiched between the two active layers to isolate high frequency wave from the low frequency element, without which there would be artifacts in imaging. Super harmonic imaging of microbubbles was tested in both water and a tissue mimic phantom.

**Results/Discussion**

The super harmonic imaging of microbubbles using prototyped transducers ( $3 \times 0.8 \times 0.6\ \text{mm}$ , Fig. 1 b) was successful (Fig. 1 c). CTR increased from 12 dB to 22 dB by decreasing the transmission frequency. Spatial resolution of the imaging was measured to be less than 0.2 mm in both axial and lateral dimensions, and it was found that higher resolution can be obtained by using the 1-3 composite transmission. These transducers are expected to enable an effective IVUS probe in super harmonic imaging for advanced cardiovascular disease evaluation.



7G-4

**4:15 pm Development of Transmitters in Dual-Frequency Transducers for Interventional Contrast Enhanced Imaging**

Jinwook Kim<sup>1</sup>, Sibbo Li<sup>1</sup>, Xiaoning Jiang<sup>1</sup>; <sup>1</sup>Mechanical and Aerospace Engineering, North Carolina State University, Raleigh, North Carolina, USA

**Background, Motivation and Objective**

Dual-frequency contrast-enhanced ultrasound imaging, or super-harmonic imaging, is capable of high resolution imaging of blood vessels filled with microbubbles. In super harmonic imaging, microbubbles are excited by low frequency acoustic waves (a few MHz) with high negative pressure and short ringing near the resonant frequency of microbubbles; the high frequency ( $> 15$  MHz) nonlinear echoes from microbubbles are received by a high frequency receiver. However, due to the spatial and frequency limitation in many interventional ultrasound imaging probes, conventional transmitter design with a thick lossy backing layer for a short ringing at a low frequency is not practical. Therefore, a new design concept considering optimal matching, backing, and isolation layer as well as the active layer is required for the dual-frequency ultrasound enabled super harmonic imaging.

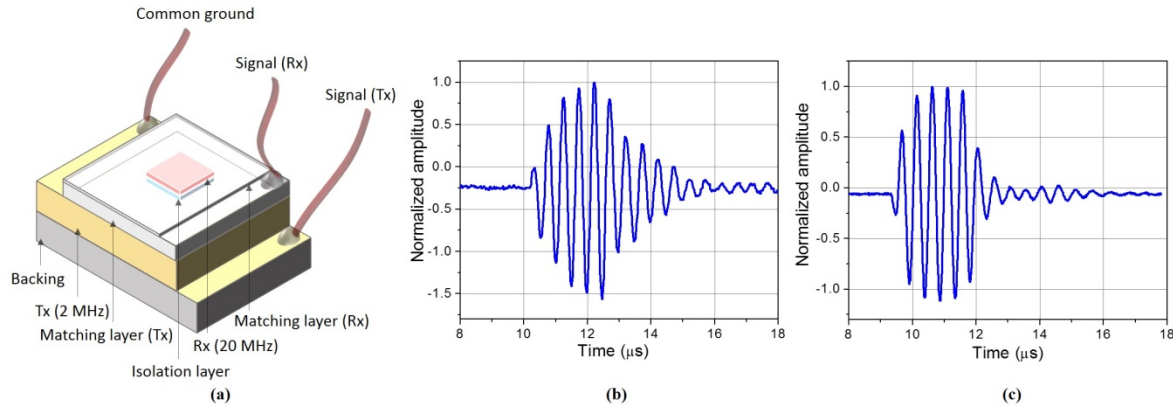
**Statement of Contribution/Methods**

The contribution of this work is to design small aperture dual-frequency transducers using 1-3 composite transmitters for super harmonic imaging with high resolution and high contrast-to-tissue ratio (CTR). Dual frequency transducers consisting of a 2 MHz transmitter and a 20 MHz receiver was designed, as shown in Fig. 1(a). The basic design involved

a PMN-PT single crystal plate as a transmitter. In the composite design a 1-3 piezoelectric composite was adopted as the transmitter. For both designs, 20 MHz PZT ceramic high frequency receivers were utilized. The prototyped transducers were characterized to obtain their pulse-echo response, transmitting sensitivity, and beam profiles.

### Results/Discussion

The transmitting waveform of prototyped dual frequency transducers was shown in Figure 1(b) and (c) for the basic design and composite design, respectively. A much shorter waveform was obtained from the composite design than from the basic design under a 2 MHz 5-cycle burst excitation; the composite design showed a -6 dB ringing down time of 0.16  $\mu$ s, whereas the basic design showed that of 0.94  $\mu$ s. Negative pressure amplitude of 0.75 MPa was achieved by applying 100 Vpp voltage, with the calculated mechanical index (MI) of 0.54, which is enough to oscillate or fragment microbubbles for a wideband ultrasound scattering. The improved transmitting performance of the composite design is promising for super harmonic imaging with high CTR.



7G-5

### 4:30 pm Design and Simulation of a High-Frequency Ring-Shaped Linear array for Capsule Ultrasound Endoscopy

Holly Lay<sup>1</sup>, Vipin Seetohul<sup>1</sup>, Benjamin Cox<sup>1</sup>, Christine Demore<sup>1</sup>, Sandy Cochran<sup>1</sup>; <sup>1</sup>University of Dundee, United Kingdom

#### Background, Motivation and Objective

Current research into endoscopy and colonoscopy has significantly advanced visualization of the gastro-intestinal tract (GIT). The Sonopill project seeks to combine the imaging capabilities of endoscopic ultrasound with the full GIT transit of capsule endoscopy through the development of a capsule capable of ultrasonic imaging of the GIT, focussing on the small intestine. However, due to the small internal volume of the proposed capsule and the need to transmit received data wirelessly, the Sonopill system is limited both in data bandwidth and power. This paper presents a MATLAB-based simulation to allow testing of transducer topologies and imaging methodologies to achieve optimum results within the physical limitations of the system.

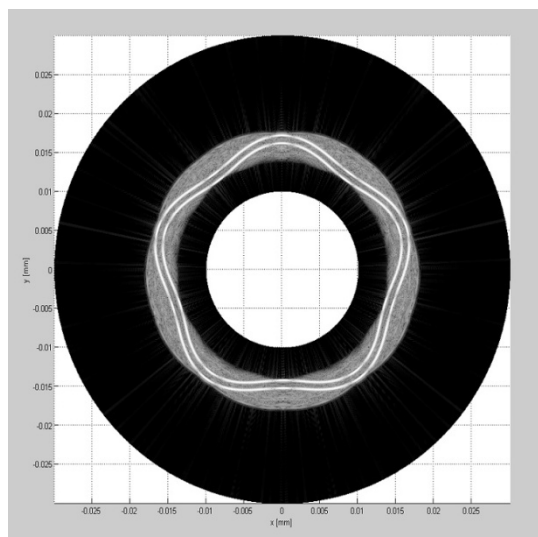
#### Statement of Contribution/Methods

To allow rapid evaluation of possible transducer configurations and circuit elements, a hybrid MATLAB simulation was created, incorporating both KLM circuit elements for analog analysis and digitizing and beamforming elements to render a final grey-scale image for imaging quality analysis. This was used in conjunction with a theoretical acoustic propagation model to image ideal point scatterers.

The proposed transducers consist of a single, unfocused 5 mm radius transmit ring separated into eight segments for impedance control, and a 512 element receive linear array curved into a matching ring. Because of the high element count and pad limitations on the intended electronics, the design requires the use of 34 integrated 16:1 multiplexers which will be bonded directly to the connecting flex circuit before the ASIC. Simulating the loading effects of these multiplexers as well as the proposed transducer configuration was critical to the analysis of the design.

### Results/Discussion

The MATLAB model was used to simulate a standard pulser transmitting over a 2.5 m cable to a 0.25 mm x 8 mm x 85  $\mu$ m PZT5H transmit transducer with a calculated centre frequency of 25 MHz. This was then used to calculate the theoretical reflections from 720 perfect point targets arranged to approximate a two-layer gut wall. These reflections were input into a receive KLM model representing an array of 512 60  $\mu$ m x 1 mm x 85  $\mu$ m PZT5H transducers connected to 34 multiplexer models. The resulting B-scan can be seen in Figure 1. This B-scan displays the distinction between the gut walls necessary for clinical diagnosis.



7G-6

#### 4:45 pm 15-20MHz Single Element Ultrasound Transducers in a Needle for Neurological Applications

Yun Jiang<sup>1,2</sup>, Carl Meggs<sup>1,2</sup>, Daniel Rodriguez Sanmartin<sup>2</sup>, Zhen Qiu<sup>3</sup>, Rachael McPhillips<sup>3</sup>, Christine D  mor  <sup>3</sup>, Sandy Cochran<sup>3</sup>, Graeme Casey<sup>3</sup>, Syed Mahboob<sup>3</sup>, Sam Eljamel<sup>3</sup>, Giuseppe Schiavone<sup>3</sup>, Marc Desmulliez<sup>4</sup>, Tim Button<sup>1,2</sup>, <sup>1</sup>University of Birmingham, Birmingham, United Kingdom, <sup>2</sup>Applied Functional Materials Ltd., Birmingham, United Kingdom, <sup>3</sup>University of Dundee, Dundee, United Kingdom, <sup>4</sup>Heriot-Watt University, Edinburgh, United Kingdom

#### Background, Motivation and Objective

Neurosurgical intervention is required for a broad range of medical conditions related to the brain, such as tumours and haematomas. Localisation of the intracranial target has predominately relied on preoperative images acquired from computed tomography and magnetic resonance imaging for decades. However, shifting and deforming of the brain tissues occur in the course of surgery in response to physical and physiological phenomena, and therefore preoperative image-guided navigation becomes inaccurate and unreliable. For the real-time visualisation of tissue in the brain, we report the use of a needle capable of minimally-invasive and high resolution ultrasound imaging. The incorporation of the single element transducers looking forward and sideways within the needles enables the neurosurgeon to obtain intraoperatively real-time image guided information about the intricate brain structures that lie in the path of the needle on the way to the target site of interest.

#### Statement of Contribution/Methods

As an alternative to conventionally used dice-and-fill methods, a micro-moulding approach combining viscous polymer processing and lost polymer mould techniques has been applied for the fabrication of 1-3 piezocomposites used as the active materials in single element devices. Issues related to the restricted volume in the needle with an inner diameter of 1.8 mm for the transducer packaging have been overcome by cast-in-place tungsten epoxy backings as well as optimised electrical connections. The functionality of the needles has been demonstrated using pulse-echo testing. Preclinical demonstration of the needles has been carried out by real-time imaging various animal and human brain tissues and subsequently comparing the acquired information with those from MRI before and after needle insertion.

#### Results/Discussion

Homogeneous and dense PZT pillars with lateral dimensions of ~20  $\mu\text{m}$  and aspect ratios of ~7 have been produced. Impedance spectra and pulse-echo responses of the needles carrying integrated and miniature transducers have demonstrated their operating frequencies at 15-20 MHz. Acoustic images obtained from both of the forward and sideways facing devices have proved their imaging capability and suggested their potential uses in neurological applications including image-guided and minimally invasive surgery and functional neurosurgery.



Finished forward facing single element ultrasound transducer in a needle.

## P1B1 - MPA: Light and Sound II

Salon C

Friday, September 5, 2014, 8:00 am - 5:00 pm

Chair: **Pai Li**  
National Taiwan University, Taipei

P1B1-1

### Diagnostic Imaging of Molecular-Targeted Nanorods Simultaneously Exposed to Light and Sound

James McLaughlan<sup>1</sup>, David Cowell<sup>1</sup>, Zubair Kakakhe<sup>1</sup>, Sevan Harput<sup>1</sup>, Steven Freear<sup>1</sup>; <sup>1</sup>School of Electronic and Electrical Engineering, University of Leeds, Leeds, West Yorkshire, United Kingdom

#### Background, Motivation and Objective

Light-absorbing nanoparticles can be used to improve the signal-to-noise ratio of the thermoelastic emissions from tissue that are used in photoacoustic tomography (PAT) and microscopy (PAM). Nanorods can be functionalised with molecular-targeting ligands in order to specifically target cancerous cells for both imaging and therapy. It has been shown that simultaneously illuminating nanorods whilst they are under tension from an ultrasound field, results in the formation of localised inertial cavitation at significantly lower laser fluence and pressure thresholds than for either of these mechanisms alone. The ability to nucleate inertial cavitation from nanorods at lower thresholds allows for increased tissue penetration for this technique. This study aims to demonstrate the formation and activity of inertial cavitation from nanorods, through the combination of a diagnostic ultrasound system and nanosecond pulsed laser, which could be used for both imaging and therapeutic applications.

#### Statement of Contribution/Methods

A linear medical probe (L3-8/40EP, Prosonic) was connected to a 96-channel Ultrasound Array Research Platform (UARP) that was synchronised with a tuneable 5 ns pulse laser (Surelite, Continuum). This system was used to image a nanorod-doped tissue-mimicking phantom (Fig 1a). The laser pulse (850 nm, 20.4 mJ/cm<sup>2</sup>) was synchronised to each A-line generated by the linear array, during the formation of a single B-mode frame and coupled into the phantom with an optical fibre. Each pulse was timed to be co-incident in the target region with the second rarefaction of a 3-cycle 4 MHz ultrasound pulse, which had a mechanical index of 1.2.

#### Results/Discussion

Fig 1(b) shows two B-mode frames of the phantom with (left) and without (right) the laser pulse. Fig 1(c) shows the emitted spectra from the interaction region of the laser pulse and focal peak of each A-line (dashed box). Broadband emissions from nanorod-nucleated inertial cavitation were observed in this region, at approximately 33 mm only when the laser pulse was present. Conversely, in the absence of ultrasound no emissions are generated. This demonstrates that a diagnostic ultrasound system combined with a pulse laser could be used for imaging of molecular-targeted nanorods, and the controllable generation of inertial cavitation can also be used to selectively destroy cancer cells.

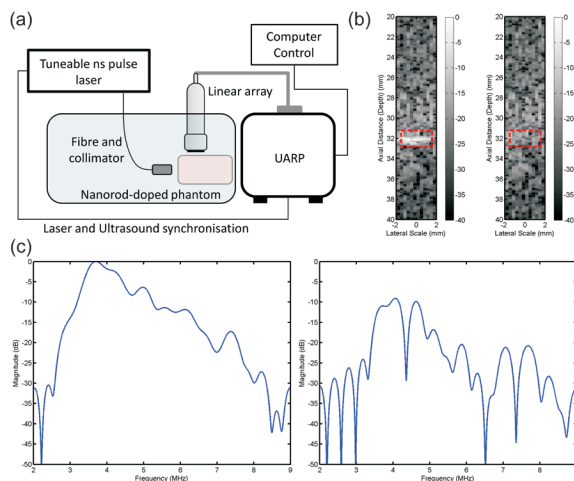


Fig. 1(a) A schematic of the experimental set-up. (b) Two B-mode images acquired with (left) laser on and (right) laser off. (c) The measured emitted spectra from the highlighted region (dashed red box) along the central A-line.

P1B1-2

### In vitro study of PLGA/PFC particles loaded with gold nanoparticles as theranostic agents for photoacoustic imaging and cancer therapy

Yan Wang<sup>1</sup>, Eric Strohm<sup>1</sup>, Yang Sun<sup>2</sup>, Yuanyi Zheng<sup>2</sup>, Zhigang Wang<sup>2</sup>, Michael Kolios<sup>1</sup>; <sup>1</sup>Physics, Ryerson University, Toronto, Ontario, Canada, <sup>2</sup>Institute of Ultrasound Imaging, Second Affiliated Hospital, Chongqing Medical University, Chongqing, China, People's Republic of

#### Background, Motivation and Objective

Phase-change contrast agents have been developed for photoacoustic (PA) imaging and therapy. They consist of a perfluorocarbon (PFC) liquid and silica-coated gold nanoparticles (NPs) stabilized by a Poly Lactide-co-Glycolic Acid (PLGA) polymer. PLGA is an approved biocompatible and biodegradable material for clinical applications. Silica-coated gold nanoparticles can absorb in the visible and near-infrared wavelengths with excellent stability under laser irradiation. In this study, PLGA/PFC particles loaded with NPs were characterized using PA methods. The cytotoxicity of these particles was examined before and after the vaporization using a MCF7 human breast cancer cell line.



**Statement of Contribution/Methods**

PLGA particles 2 to 10  $\mu\text{m}$  in diameter loaded with perfluorohexane (PFH) liquid and 35nm diameter GNPs with a 20nm silica shell were synthesized using a double emulsion method. Using an acoustic microscope (Kibero, GmbH) and a 532 nm pulsed laser, the PA signal intensity and vaporization threshold were recorded as a function of particle size using a 375 MHz transducer. PLGA particles were then incubated with MCF7 cells for 24 hours, internalization was confirmed using confocal fluorescence microscopy. The cytotoxicity of the PLGA particles in cells was examined using the MTT assay. The nuclear stain propidium iodide (PI) was used as an indicator of membrane integrity and cell viability after vaporization.

**Results/Discussion**

The PA signal intensity increased as the laser energy increased prior to vaporization (Fig. 1A). The laser-induced vaporization threshold decreased with increasing particle size (Fig. 1B), and was 670, 330 and 145 nJ for 2, 5, 10  $\mu\text{m}$ -sized PLGA particles, respectively. Viability of cells incubated with PLGA particles was similar to a control using the MTT assay test. Upon laser irradiation, PLGA particles within the cell were vaporized and bubbles formed. In most cases, the bubble remained trapped within the cell, slowly expanding (Fig. 1C). PI fluorescence was not observed indicating intact membrane integrity. However the bubble exerted pressure within the cell, and it slowly retracted (white arrows, Fig. 1C). In other cases, membrane integrity was lost upon bubble formation (Fig. 1D). Some cells eventually lifted off the substrate. The PLGA particles have shown potential as theranostic agents for PA imaging and cancer therapy.

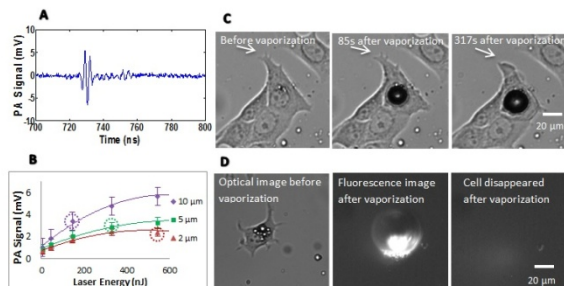


**Fig 1** Photoacoustic signal of single PLGA particle obtained before vaporization (Fig 1A), as functions of laser energy and particle size (Fig 1B). Threshold energies indicate by the dish circles (Fig 1B).

Vaporization effects inside the cells show in Fig 1C and 1D. The cell slowly retracted during vaporization indicated by the white arrows (Fig 1C). Vaporization causes membrane disintegration and nucleus fluorescence due to the PI stain. When the cell is not attached to other cells, it is lifted off the substrate by the bubble (Fig 1D).

P1B1-3

**Photo-thermal responsive nanocluster as photoacoustic contrast agents**

Soon Joon Yoon<sup>1,2</sup>, Yun-Sheng Chen<sup>1,2</sup>, Stanislav Emelianov<sup>1,2</sup>; <sup>1</sup>Department of Electrical and Computer Engineering, The University of Texas at Austin, Austin, TEXAS, USA, <sup>2</sup>Department of Biomedical Engineering, The University of Texas at Austin, Austin, TEXAS, USA

**Background, Motivation and Objective**

For the molecular photoacoustic (PA) imaging, nano-sized contrast agents are generally essential for targeting specific molecule and providing superior contrast and sensitivity. In this paper, we present thermo-responsive metallic nanoparticles loaded nanoclusters designed for enhancing contrast in PA imaging. The nanoclusters remain in a swollen stage when temperature is below low critical solution temperature (LCST), but they shrink if the temperature exceeds LCST. Reports indicate that the different forms of nanoclusters amplify PA signal due to the thermal interaction between individual nanoparticles. Therefore, these nanoclusters provide the amplified PA signal when they are in the shrunken state. These swelling/shrinking process is reversible and the size of these nanoclusters can be controlled by external trigger, therefore, the nanoclusters can provide enhanced contrast for PA imaging.

**Statement of Contribution/Methods**

The poly-N-isopropylacrylamide (PNIPAM) nanocarrier was synthesized and Au nanorods (NRs) and CuS nanoparticles were loaded in the nanocarriers. The size of the nanocluster is 700 nm in diameter and it decrease to 350 nm when temperature is above 32°C. The PA signal from Au NR-PNIPAM nanoclusters and CuS-PNIPAM nanoclusters were measured at various temperature points and compared with their individual nanoparticles. The blood vessel phantoms containing Au NR-PNIPAM nanoclusters and individual gold nanorods were imaged by a PA system. During the experiment, the temperature was changed by a temperature-controlled circulator. To demonstrate the signal enhancement from the nanoclusters in a tissue environment, the CuS loaded PNIPAM nanoclusters were injected into porcine tissue and heated by a 1064 nm continuous wave laser.

**Results/Discussion**

The results show drastic increase in PA signal was observed from the nanoclusters compared to their individual nanoparticles when the temperature is above LCST. From the vessel phantoms, the PA images can clearly differentiate the gold nanorod loaded nanoclusters from the individual nanoparticles by comparing the signal before and after the heating the phantom. The signal from CuS-PNIPAM nanoclusters also can be identified from the individual CuS nanoparticles in the porcine tissue. These results show that the nanoclusters are promising candidate for PA contrast agents

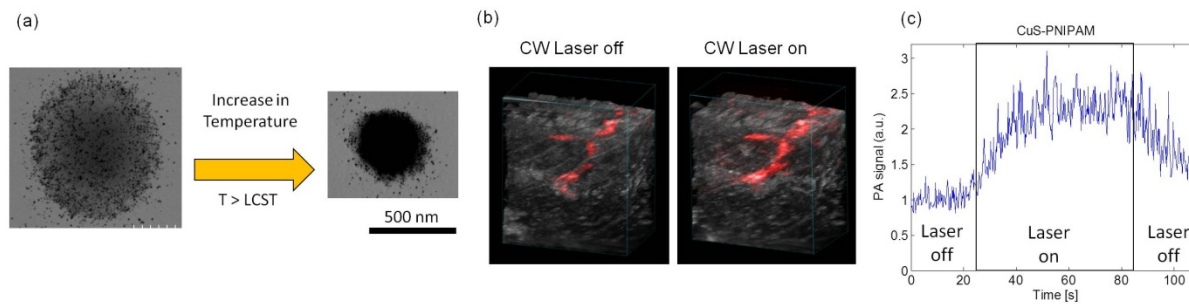


Figure 1. (a) TEM images of CuS loaded nanocluster when  $T < LCST$  (left) and  $T > LCST$  (right). (b) The PA images of gold nanorods loaded PNIPAM nanocluster when the temperature is below (left) and above (right) LCST. (c) The PA images and signal from CuS loaded nanocluster injected porcine tissue before after the CW laser irradiation.

P1B1-4

### Assessing storage-induced red blood cell lesions using photoacoustic measurements of oxygen saturation and the frequency content of photoacoustic signals

Eno Hysi<sup>1</sup>, Eric M. Strohm<sup>1</sup>, Elizabeth S. L. Berndt<sup>1</sup>, Jason P. Acker<sup>2</sup>, Michael C. Kolios<sup>1</sup>; <sup>1</sup>Physics, Ryerson University, Toronto, Ontario, Canada, <sup>2</sup>Canadian Blood Services, Edmonton, AB, Canada

#### Background, Motivation and Objective

Assessing the safety of stored blood is one of the most pressing issues in transfusion medicine. Storage-induced morphological changes (lesions) of red blood cells (RBCs) may adversely affect patient health during transfusions. Currently, no modalities are capable of assessing changes in RBC structure and simultaneously measure their oxygen carrying capacity. We propose using photoacoustic (PA) imaging for estimating oxygen saturation ( $sO_2$ ) and the frequency content of the PA signals to assess the structural changes of RBCs during blood storage.

#### Statement of Contribution/Methods

Blood donated to the Canadian Blood Services was stored and sampled over 35 days. Optical and PA microscopy were used to assess RBC morphology while PA imaging was performed weekly to measure  $sO_2$  on 1 ml whole blood samples.

PA  $sO_2$  estimations were made using the Vevo LAZR PA imaging device (Fujifilm VisualSonics, Canada). A 40 MHz linear array probe coupled with optical fibers illuminating at 750 and 850 nm (30 mJ pulse energy) was used to calculate average  $sO_2$  estimates and PA spectra as a function of storage time.

PA microscopy of single RBC lesions was performed using a 375 MHz transducer coupled with a pulsed 532 nm laser (< 100 nJ per pulse; Kibero, Germany). Storage lesions were created by changing suspending medium osmolality and normal, spherocytic and echinocytic RBCs were characterized using the PA power spectrum.

#### Results/Discussion

RBCs exhibited significant morphological changes during storage (Fig. 1a). By day 21, spherocytic and echinocytic RBCs become apparent and increased in number with storage time. These morphological changes correlate with the decrease (50%) in the oxygen carrying capacity of RBCs as shown by the  $sO_2$  of day 21 (Fig. 1b). By day 35, abnormal RBCs dominate, and the measured  $sO_2$  was 10%.

PA power spectra can be used to quantify morphological changes. As storage time increases to 35 days, the spectral amplitude and minima location for the RBC solutions (Fig. 1c) drops by 10 dB and 40 MHz, respectively. For single RBCs (Fig. 1d), the flat spectrum of normal cells differs significantly from echinocytes and spherocytes, with a 20 dB and 30 dB decrease at 375 MHz, respectively. These results suggest that PA imaging and spectroscopy has potential to monitor storage induced RBC lesions and quantify their functionality by estimating  $sO_2$ , a crucial parameter for blood transfusions.

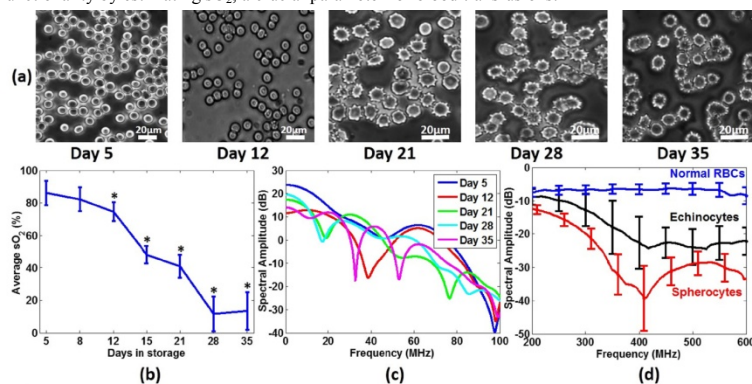


Figure 1

- (a) Representative optical microscopy images as a function of storage time.
- (b) Average oxygen saturation ( $sO_2$ ) as a function of storage time. Error bars represent standard deviation of 50 PA signals and the \* denotes statistically significant differences compared ( $p < 0.05$ ) compared to day 5.
- (c) PA power spectra from the Vevo LAZR as a function of storage time.
- (d) PA power spectra from the PA microscope for an average of 21 single RBCs.

P1B1-5

**Optically driven oscillations of nanoparticle-coated microbubbles**Jacob Dove<sup>1</sup>, Mark Borden<sup>1</sup>, Todd Murray<sup>1</sup>; <sup>1</sup>Mechanical Engineering, University of Colorado Boulder, Boulder, CO, USA**Background, Motivation and Objective**

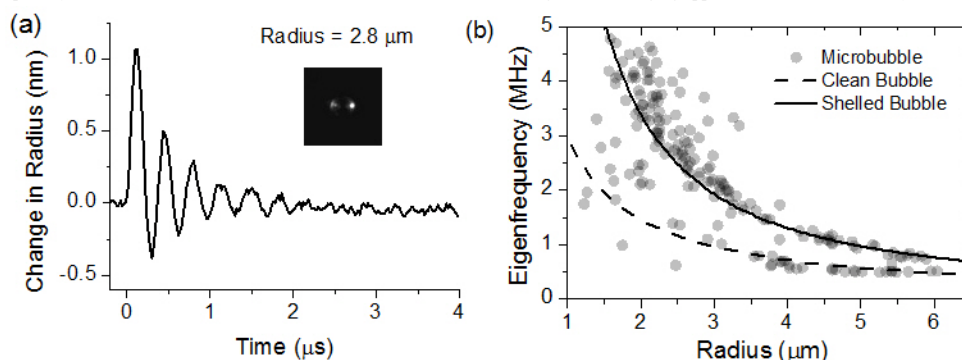
Medical imaging contrast agents have improved the ability to detect and treat diseased tissue. Specifically, two such contrast agents are nanoparticles and microbubbles. Nanoparticles offer enhanced photoacoustic contrast due to their strong optical absorption, while microbubbles increase ultrasound contrast through efficient scattering around resonance. Recently, it was demonstrated that coating gold nanoparticles around a microbubble lead to enhancements in both the photoacoustic and ultrasound response. The objective of this study was to examine the photoacoustic response from individual gold nanoparticle-coated microbubbles.

**Statement of Contribution/Methods**

In this study, the ability to optically excite and detect microbubble oscillations is demonstrated. Nanoparticles were coated to the surface of a lipid encapsulated microbubble via a biotin-avidin conjugation scheme. A modified optical microscope was developed to interface with individual nanoparticle-loaded microbubbles. Here, a single bubble was excited with a pulsed laser and the bubble wall radius was tracked using light scattering. The eigenfrequency and radial displacement were characterized for bubbles in the 1-6  $\mu\text{m}$  range and compared to theory.

**Results/Discussion**

The response from a single bubble to pulsed laser illumination is shown in Fig. 1(a). The laser pulse was incident at  $t=0$  at which point the bubble initially expanded to the maximum radius and then exhibited damped harmonic oscillations back to the resting radius. Eigenfrequencies for 194 bubbles are shown in Fig. 1(b). These were determined by extracting the resonant frequency and damping ratio from the respective time-domain response. The solid line is the theoretical eigenfrequency for a shelled bubble with a shell elasticity of 0.74 N/m and the dashed line is for a "clean" or unshelled bubble. The majority of the measured bubbles respond with an eigenfrequency close to that of a shelled bubble. In addition, the maximum radial displacement was found to increase with decreasing radius which is expected for a photothermally driven bubble. In conclusion, the ability to optically drive a bubble into resonance was demonstrated and is advantageous for imaging applications or the basic study of microbubble physics.



P1B1-6

**Ultrafast vaporization dynamics of photoacoustic polymeric microcapsules**Guillaume Lajoie<sup>1</sup>, Erik Gelderblom<sup>1</sup>, Ceciel Chlon<sup>2</sup>, Marcel Böhrer<sup>2</sup>, Nico De Jong<sup>3</sup>, Wiendelt Steenbergen<sup>4</sup>, Srirang Manohar<sup>4</sup>, Michel Versluis<sup>1</sup>; <sup>1</sup>Physics of Fluids, University of Twente, Netherlands, <sup>2</sup>Philips Research Laboratories Europe, High Tech Campus, Netherlands, <sup>3</sup>Biomedical Engineering, Thoraxcenter, Erasmus mc, Netherlands, <sup>4</sup>Biomedical Photonic Imaging Group, University of Twente, Netherlands**Background, Motivation and Objective**

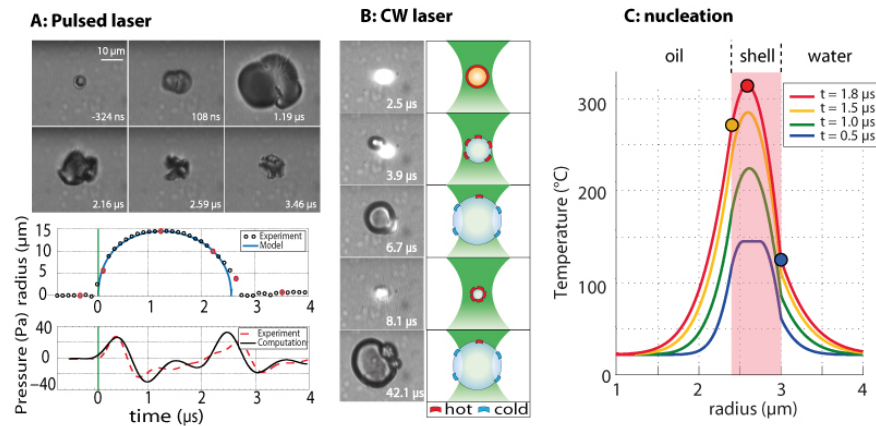
Precision control, both in space and time, of vaporization has many potential applications, ranging from solar energy conversion to microfluidic cell sorting. In particular, laser-induced cavitation was recently shown to have great potential in photoacoustic diagnostic and therapeutic applications [1]. However, the physical mechanisms of vaporization are not well understood, owing primarily to the small length scales and ultrafast time scales involved. Here, we study the nanoseconds vapor bubble dynamics of a photoacoustic agent activated by both pulsed and CW laser excitation. Experimental results are compared to a numerical model revealing the physical mechanisms underlying the photoacoustic effect [2].

**Statement of Contribution/Methods**

Oil-filled polymeric microcapsules, formed from ink-jet printed droplets, with a well-controlled radius of 3  $\mu\text{m}$ , incorporate Nile Red dye into the shell to allow laser light absorption. The activation results from the focusing of a pulsed or a CW laser beam through the imaging microscope objective. The Brandaris 128 ultra high-speed camera is then used to record the capsules' response at frame rates up to 15 million frames per second. Simultaneously, a broadband transducer records the photoacoustic signatures. The thermal behavior is modeled using a finite element model and the Rayleigh-Plesset vapor bubble dynamics is solved with an ODE solver, both using Matlab.

**Results/Discussion**

Above the threshold laser fluence of 70 mJ/cm<sup>2</sup> the shell disrupts, forming a bubble that grows to a radius of 15  $\mu\text{m}$  in 1  $\mu\text{s}$  (A). The bubble dynamics and the 40 Pa resulting acoustic pressure are well captured by an energy balance model and shows that the event is governed by inertia and not by the phase conversion. Remarkably, CW laser illumination resulted in sustained oscillations of the vapor bubble (B). During expansion the absorbing shell fragments are pushed out of the laser beam and cool down. This leads to condensation followed by inertial entrainment of the fragments back into the beam, thus initiating a new cycle. The nucleation originates from the release of the hot oil core in the superheated water (C). The photoacoustic frequency is directly coupled to the laser intensity and spot size. A high frequency modulation of the laser would have a similar effect and this will open up a wealth of promising opportunities for novel CW photoacoustic modalities.



- [1] Wilson, K., Homan, K. & Emelianov, S. Biomedical photoacoustics beyond thermal expansion using triggered nanodroplet vaporization for contrast-enhanced imaging. Nat. Commun. 3, 618 (2012).  
 [2] Lajoinie et al., Ultrafast vapourization dynamics of laser-activated polymeric microcapsules DOI: 10.1038/ncomms4671

P1B1-7

### Enhanced Plasmonic Photothermal Therapy with Synergistic Sonoporation of Gold Nanodroplets

Shu-Wei Liu<sup>1</sup>, Pai-Chi Li<sup>1</sup>,<sup>1</sup>National Taiwan University, Taiwan

#### Background, Motivation and Objective

Plasmonic photothermal therapy (PTT) with gold nanorods (AuNRs) as an efficient photoabsorbing agent has been pro-posed in preclinical research. A critical task in PPTT is the delivery of AuNRs into the cells. In our previous research , we had AuNRs encapsulated in microbubbles (AuMBs) to leverage the targeting capabilities of microbubbles (MBs) and the cavitation effects for sonoporation when the MBs are destructed to release the AuNRs. In the current study, we propose to use gold nanodroplets (AuNDs) for further improvement of AuNR delivery. The hypothesis is that stronger cavitation ef-fects can be expected during the liquid-to-gas phase change of AuNDs. In addition, as the phase change can be induced by ultrasound and/or laser, the synergistic effects of the two mechanisms will also be explored.

#### Statement of Contribution/Methods

AuNDs and AuMBs were prepared with the applications of ultrasound and/or laser. Differential inertial cavitation dose (dICD) was measured to quantify cavitation. The sonoporation effects were assessed by measuring destruction ratio, opti-cal density (OD) and cell viability of AuNDs and AuMBs under different conditions. Animal tests were also performed to evaluate the heating capabilities.

#### Results/Discussion

In both in vitro and in vivo studies using AuNDs, the temperature can reach to 50°C in 3 minutes, which is adequate for photothermal therapy (Fig 1). It is also evident that the heating capability of AuNDs is higher than that of AuMBs. The destruction ratio of AuNDs under ultrasound in combination with laser is 45%, which is higher than the 35% of AuMBs. It is also higher than those when only ultrasound or laser is applied. Furthermore, the OD value of AuNDs is 1.5 times higher than that of AuMBs. Viability of tumor cells without AuNDs but with the application of both ultrasound and laser is 96%. Finally, the tumor size decreases with photothermal therapy using AuNDs. Combing ultrasound and laser to perform AuNDs sonoporation can enhance the delivery of AuNRs and thus photothermal therapy. Because of higher stability and cavitation dose, AuNDs can release more AuNRs into the tumor. Moreover, uti-lizing both ultrasound and laser decreases vaporization threshold and cavitation threshold of AuNDs.

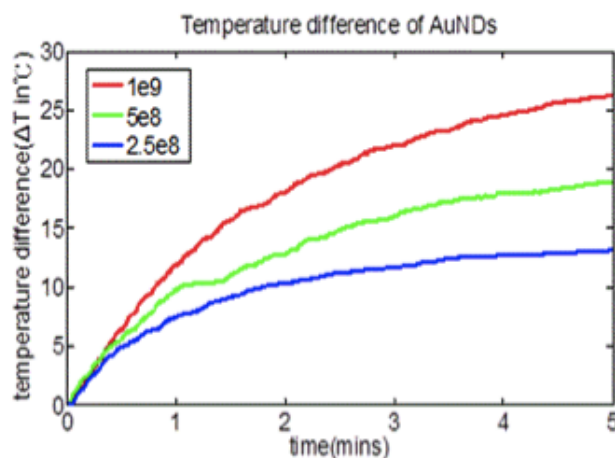


Figure 1. Temperature increase under three difference AuNR concentrations.

P1B1-8

**Thermoacoustic Contrast of Prostate Cancer due to Heating by Very High Frequency Irradiation**

Sarah Patch<sup>1</sup>, David Hull<sup>2</sup>, Stephanie Griep<sup>3</sup>, Majorca Thomas<sup>4</sup>, Kenneth Jacobsohn<sup>4</sup>, William See<sup>4</sup>; <sup>1</sup>Physics, UW-Milwaukee, Milwaukee, Wisconsin, USA, <sup>2</sup>Bostwick Laboratories, USA, <sup>3</sup>University of Southern California, USA, <sup>4</sup>Urology, Medical College of Wisconsin, Milwaukee, WI, USA

**Background, Motivation and Objective**

Prostate cancer is a good application for thermoacoustic imaging for several reasons. Mechanical properties of healthy and cancerous prostate tissue are well matched, so the assumption of constant sound speed is accurate. Measurements represent integrals of the thermoacoustic source term over spheres centered at the transducer focus. Signal production by very high frequency irradiation is proportional to ionic content, and ionic content of prostatic fluids produced by healthy tissue in the peripheral zone are approximately three times higher than in blood and plasma whereas cancer suppress ionic content of prostatic fluid. Signal strength is expected to decrease with extent of cancerous involvement.

**Statement of Contribution/Methods**

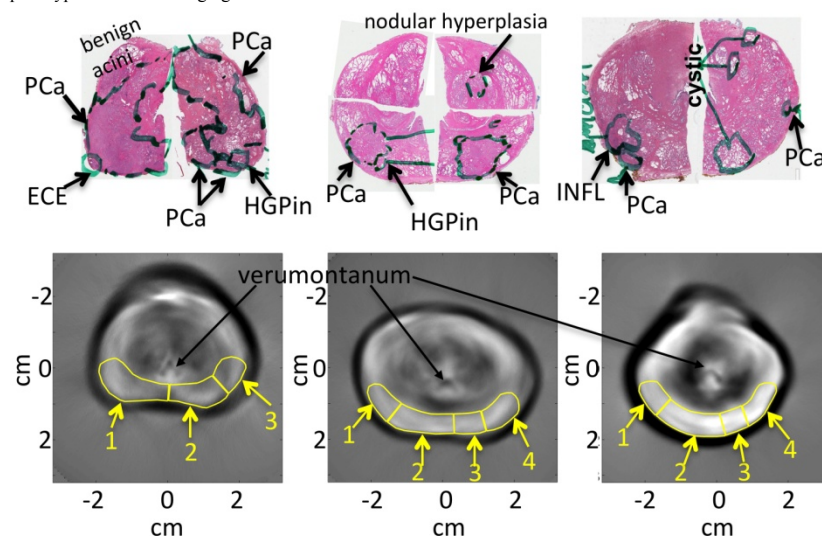
To test this hypothesis we imaged fresh human prostate specimens ex vivo and compared to the gold standard, histology. Specimens were scanned immediately after radical prostatectomy performed as part of normal care.

Irradiation pulses with carrier frequency 108 MHz ensured excellent electromagnetic depth penetration. 700 ns pulses with power exceeding 20 kW propagated 20-25 mJ into a benchtop imaging system. 2.25 MHz focused single element transducers (Olympus V306) with 0.5" diameter and 0.8" focus received the thermoacoustic pulses, which were amplified by 54 dB and signal averaged 64 times before recording to disc. Spatial encoding was performed in step-and-shoot mode, with 1.8-degree rotations between views and 3 mm translation between acquisition slices. Approximately 20 slices were acquired per specimen. Reconstruction was performed by filtered backprojection after extensive preprocessing.

**Results/Discussion**

Reconstructions revealed some common features: the verumontanum and urethra are frequently visualized. Histology slides were digitized for comparison to select cases. The peripheral zone was subdivided into regions of interest corresponding to tissue type as annotated on histology slides. Mean reconstruction values in cancer-free regions were four times greater than in regions with a high percentage of cancer.

If these results can be corroborated in a larger study, and results continue to support the hypothesis that the contrast mechanism is sensitive to cancer, development of a clinical prototype for in vivo imaging will be warranted.





## P1B2 - MBB: Beamforming II

Salon C

Friday, September 5, 2014, 8:00 am - 5:00 pm

Chair: **John Hossack**  
Univ. of Virginia, Charlottesville

P1B2-1

### Suppression of aberration in deeper region US images using multi-look adaptive beamforming

Teichiro Ikeda<sup>1</sup>, Shinta Takano<sup>1</sup>, Hiroshi Masuzawa<sup>1</sup>, <sup>1</sup>Hitachi Ltd., Japan

#### Background, Motivation and Objective

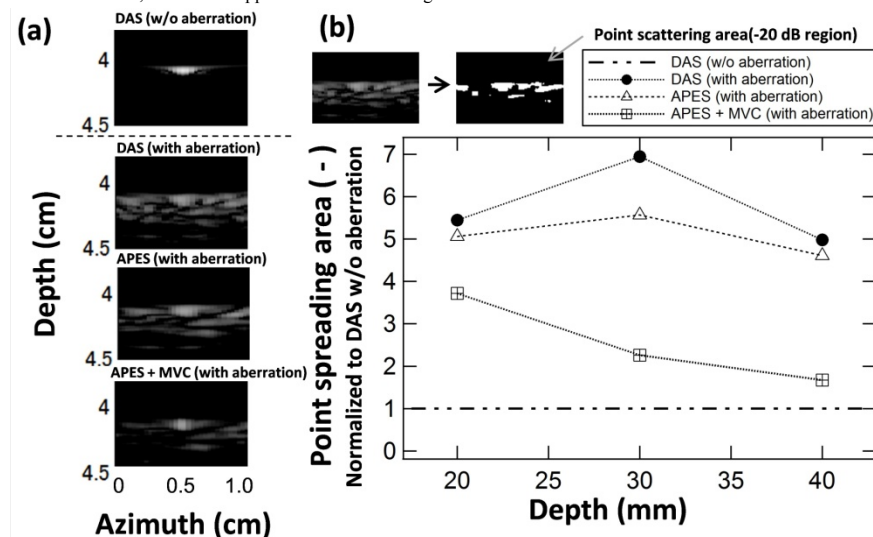
Wave aberration by the structure of organs and tissues in the human body is a cause of the poorer resolution in the deeper regions of diagnostic ultrasound images. Multi-look techniques, such as spatial compounding and synthetic aperture, are useful to suppress the unwanted aberration with the improved coherence by compounding the signals of multi-transmission events. Here, we propose a different approach for multi-look techniques using just a single transmission event with the help of adaptive beamforming.

#### Statement of Contribution/Methods

The method uses delay and sum (DAS) output, which is constructed from one transmission event. Adaptive weights are calculated for several virtually oriented mode vector directions. Then we obtain compounded output by summing the weighted signals. Because the directions are slightly away from the transmit axis, the output is expected to yield reduced multi-path signals that do not come directly from the axis of dynamic focusing. To validate the method, the wave aberration in an inhomogeneous medium is modeled. Ultrasound pulses were calculated that propagate through spatially dispersed aberrators with different speeds of sound to the surrounding medium. The aberrated RF data was then processed by the offline beamforming programs. We chose an amplitude and phase estimation (APES) method for the adaptive algorithms because of its inherent robust response to the arrival directions. We compared B-mode images for different beamformers: DAS, APES, and APES with mode vector compounding (MVC).

#### Results/Discussion

Under the wave aberration, the point-source image is significantly blurred and segmented (Fig.1(a)). Though DAS and APES neither recover nor compensate for the scattered images, APES with MVC significantly reduces the aberrated signal peripheral the point scatter. The effect is very prominent in the deep region of the image (Fig.1(b)). The point-spreading-area is comparable to that of DAS without aberration at 40-mm-depth. These results suggest the influence of spatial correlation of the aberrated wave is suppressed by the compounding of mode directions. In the case of APES with MVC, the spatial resolution is not degraded because of the strong sidelobe reduction by the adaptive weights itself. With this method, aberration suppression within the single transmission events without the tradeoff of the resolution is promising.



P1B2-2

### Phantom and *In vivo* Evaluation of Sound Speed Estimation Methods: Preliminary Results

Sooah Cho<sup>1</sup>, Jeeun Kang<sup>1</sup>, Yangmo Yoo<sup>1,2</sup>, <sup>1</sup>Electronic Engineering, Sogang University, Seoul, Korea, Republic of, <sup>2</sup>Interdisciplinary Program of Integrated Biotechnology, Sogang University, Korea, Republic of

#### Background, Motivation and Objective

Sound speed is one of the most essential parameters that affect image quality in ultrasound B-mode imaging since it is directly used for computing transmit and receive focusing delays. The constant sound speed corresponding to soft tissues (e.g., 1540 m/s) is typically used, but its performance degrades because of the disparity in sound speed between soft tissue and fatty layers. Various sound speed estimation (SSE) methods were previously proposed, but these methods have not been extensively evaluated. In this paper, five different SSE methods were evaluated with tissue mimicking phantom and *in vivo* breast studies.

#### Statement of Contribution/Methods

The five SSE methods, i.e., coherent factor (CF), minimum average phase variance (MAPV), minimum average sum of the absolute difference (MASAD), focus quality spectra (FQS) and edge conspicuity using modified nonlinear anisotropic diffusion (MNAD), were implemented on MATLAB (Mathworks Inc., Natick, MA, USA). For quantitative

evaluation, pre-beamformed radio-frequency (RF) data were acquired from a tissue mimicking phantom (ATS549, ATS Laboratories Inc., Bridgeport, CT, USA) with the mean sound speed of 1450 m/s and from a patient with breast lesions by a 7.5-MHz linear array transducer connected to the ultrasound research platform (SonixTouch, Ultrasonix, Vancouver, BC, Canada).

### Results/Discussion

Fig. 1(a) shows the reconstructed B-mode image with a white box as region-of-interest (ROI), and the object function values from the CF, MAPV, MASAD, FQS and MNAD methods are plotted against varying sound speeds in Fig. 1(b). The five SSE methods show the comparable performance with the tissue mimicking phantom (i.e.,  $1450 \pm 25$  m/s). The reconstructed B-mode image for the *in vivo* breast data is displayed in Fig. 1(c) where four ROIs are indicated as a white box. As shown in Fig. 1(d), the CF and FQS methods show the lower errors, but, unlike the phantom study, the MAPV, MASAD and MNAD methods have difficulty in estimating the optimal sound speed in image quality (i.e., 1530 m/s) i.e.,  $25.0 \pm 12.9$  and  $20.0 \pm 8.2$  vs.  $72.5 \pm 45.0$ ,  $72.5 \pm 41.9$ ,  $52.5 \pm 28.7$ , respectively. These results indicate that the previously-proposed CF and FQS methods can robustly determine the optimal sound speed for the phantom and heterogeneous soft tissues (e.g., breast). The further evaluation with a large amount of breast *in vivo* data is under investigation.

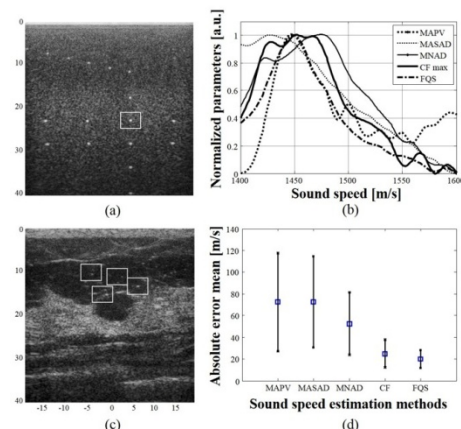


Figure 1. (a) The reconstructed B-mode image from the phantom, (b) the object function values against varying sound speeds, (c) the reconstructed B-mode image from the *in vivo* breast data, and (d) the absolute error in sound speed estimation for the five SSE methods. The ROIs are indicated as a white box.

### P1B2-3

#### Improved Lateral Resolution and Contrast in Ultrasound Imaging Using a Sidelobe Masking Technique

Alessandro Stuart Savoia<sup>1</sup>, Giulia Matrone<sup>2</sup>, Alessandro Ramalli<sup>3</sup>, Enrico Boni<sup>3</sup>, Giosuè Caliano<sup>1</sup>, Giovanni Magenes<sup>2</sup>, Piero Tortoli<sup>3</sup>; <sup>1</sup>Dipartimento di Ingegneria, Università degli Studi Roma Tre, Roma, Italy, <sup>2</sup>Dipartimento di Ingegneria Industriale e dell'Informazione, Università degli Studi di Pavia, Pavia, Italy, <sup>3</sup>Dipartimento di Ingegneria dell'Informazione, Università degli Studi di Firenze, Firenze, Italy

### Background, Motivation and Objective

The lateral resolution of an ultrasound image generated using delay-and-sum beamforming is limited by the aperture size and by the operating frequency. Increasing such parameters produces a narrower beam with lower side lobes at the expense of the depth of field and the penetration capability.

In this paper, we propose a method to improve the lateral resolution and the contrast of ultrasound images, based on the cancellation of the sole contribution due to the sidelobes, thus maintaining the original depth of field and penetration capability.

### Statement of Contribution/Methods

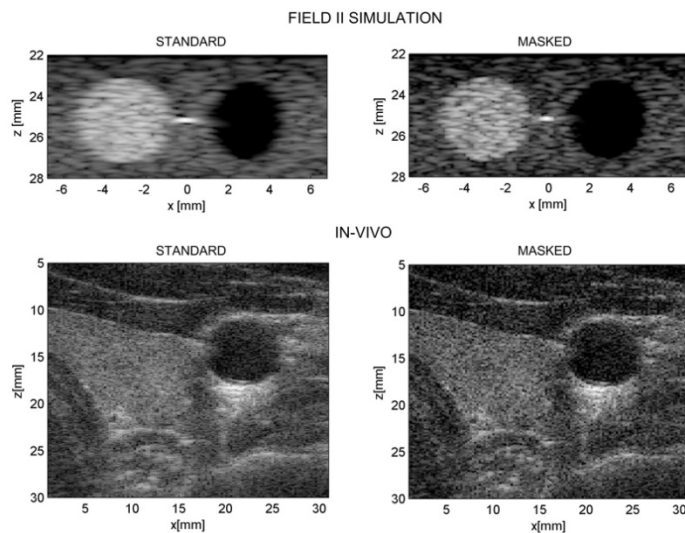
In the new approach, each scan line is obtained by compounding the signals reconstructed by two emissions. For the first one, typical aperture and apodization profile are adopted. In the second emission, the same aperture is used, but the sign of the apodization profile is inverted over the second half of the aperture. The same approach is applied in receive. In this way, the second beam has a main lobe with near-zero amplitude and its sidelobes are close to those of the first beam. The RF echo-signals corresponding to the two emissions are demodulated and successively subtracted in order to reduce the sidelobes contribution and to improve the lateral resolution. The resulting signal is finally log-compressed and scan converted.

The described method was applied to a 7 MHz B-mode linear imaging case. Beampatterns and Point Spread Functions were calculated using Field II. A synthetic phantom, including a point scatterer and two hyperechoic and anechoic cysts, was generated and linearly scanned.

Finally, the proposed technique was implemented on the ULA-OP research platform and *in-vivo* images of a carotid artery were obtained with a 7 MHz linear probe.

### Results/Discussion

The simulated two-way -6 dB beamwidths for the standard and the new approach are respectively 650  $\mu$ m and 350  $\mu$ m. The simulation and experimental imaging results show a significant improvement of both detail and contrast resolutions (see figure). Since two transmissions are necessary to form each scan line, the frame rate is halved as compared to standard pulse-echo imaging.



P1B2-4

### Adaptive Beamforming for Thermal Strain Imaging Using a Single Ultrasound Linear Array

Man Nguyen<sup>1</sup>, Xuan Ding<sup>1,2</sup>, Francois Yu<sup>1</sup>, Kang Kim<sup>1,2</sup>, <sup>1</sup>Center for Ultrasound Molecular Imaging and Therapeutics & Heart and Vascular Institute, University of Pittsburgh Medical Center, Pittsburgh, Pennsylvania, USA, <sup>2</sup>Bioengineering, University of Pittsburgh, Pennsylvania, USA

#### Background, Motivation and Objective

Ultrasound-induced thermal strain imaging (TSI) using separate heating and imaging transducers, while successfully identifies lipids in atherosclerosis plaques, has 1) limited field of view due to narrow heating beams and 2) bulky setup that limits in-vivo operation. This study proposes and evaluates a new design for heating beams to be implemented in the same imaging transducer with improved efficiency and heating areas. This beamforming (BF) technique may also be adopted in acoustic radiation force imaging for a higher frame rate.

#### Statement of Contribution/Methods

A single transducer (L7-4) connected to a commercial ultrasound platform (Verasonics) was used to both induce and image thermal strain, using a new adaptive BF. This BF technique involves dividing the 128-element transducer into sub-apertures of 30-45 elements, each with a separate delay profile, and implementing magnitude apodization to broaden the main beams. Each transmit beam has 7 foci evenly spaced at 25 mm depth. These foci were generated by a 4-foci transmit beam intervened with a 3-foci transmit beam. The heating beams were first simulated with Field II. The pressure fields were then measured in a water tank using a hydrophone (Onda). An FE-based 3-D heating simulation (Comsol) was conducted based on bio-heat transfer equation and the simulated pressure. The heating beam was applied on a gelatin phantom (mimicking water-bearing tissue) with a rubber inclusion (mimicking lipid-bearing tissue). The temperature rise was recorded using a thermocouple (Thermoworks). 2D phase-sensitive speckle tracking was used to estimate thermal strain.

#### Results/Discussion

Field II simulation (A) and hydrophone measurements (B) were comparable. Temperature rise at 25 mm depth was measured to be 0.44, 0.30, and 0.37°C/sec at 0 mm, 1 mm, and 2 mm away from the transducer center line in lateral direction, respectively (D). The effective heating area was found to be about 0.9 cm lateral x 1.1 cm axial, based on temperature measurements, which compared well with FE simulation (C) as well as the displacement (E) and thermal strain images (F). The average strains were +0.033 % in rubber inclusion, and -0.037 % in gelatin background. Further improvements include an increased duty cycle (currently 1.8%) for a higher rate of temperature rise, and optimizing sub-aperture size and foci spacing for more uniform and broader beam.

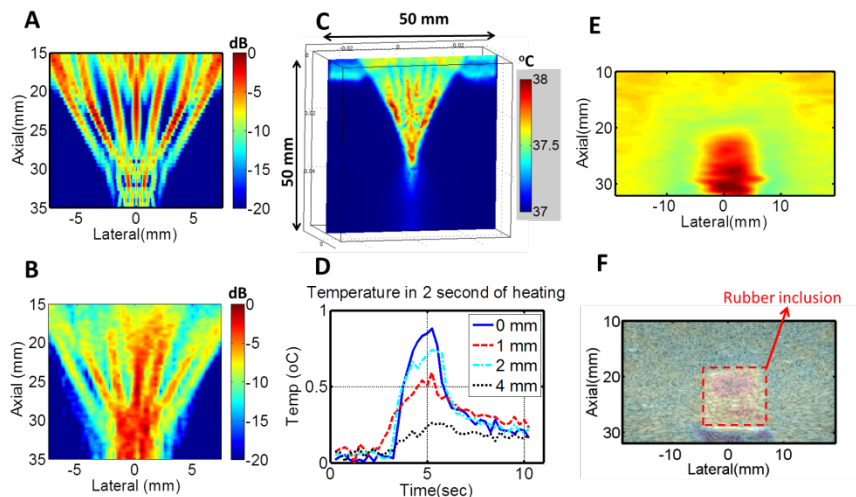


**Fig.1.** Multi-foci beamforming with improved heating area and efficiency.  
A) Field II simulation  
B) Pressure field measurements  
C) Comsol thermal simulation  
D) Temperature measurements at focal depth  
E) Displacement  
F) Overlaid thermal strain and B-mode

P1B2-5

**Robust Adaptive Beamforming for Artifact Suppression in Gastrointestinal Ultrasonography**

Brian Tracey<sup>1</sup>, Dominique Penninck<sup>2</sup>, David Lemmerhirt<sup>3</sup>, Joseph Polak<sup>4</sup>; <sup>1</sup>Electrical and Computer Engineering, Tufts University, Medford, Ma, USA, <sup>2</sup>Department of Clinical Sciences, Cummings School of Veterinary Medicine, Tufts University, North Grafton, MA, USA, <sup>3</sup>Sonetics Ultrasound, Inc, Ann Arbor, MI, USA, <sup>4</sup>Department of Radiology, Tufts University School of Medicine, Boston, MA, USA

**Background, Motivation and Objective**

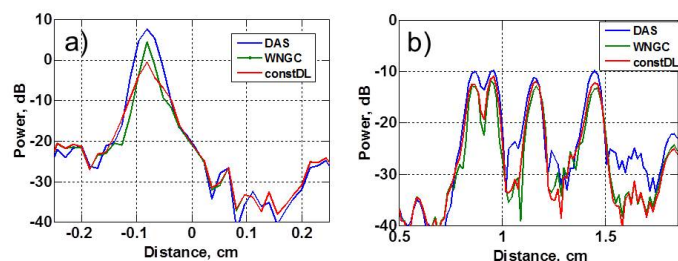
Reverberation artifacts are well-known to degrade the quality of ultrasound images. In gastrointestinal (GI) ultrasound, reverberation artifacts caused by intraluminal gas obscure details of the intestinal wall and any deeper structures, and are a main reason that ultrasound is used infrequently for imaging the GI tract in humans. We hypothesize that adaptive beamforming (ABF), which estimates and suppresses interfering signals, should be well suited to suppressing the reverberation caused by isolated bubbles in the bowel lumen. A key issue in ABF is controlling the aggressiveness of adaptation via diagonal loading so the beamformer is robust to calibration errors. In this context, we explore the potential benefits of applying a White Noise Gain Constraint (WNGC) to Minimum Variance Distortionless Response (MVDR) algorithms. WNGC has been widely applied in sonar, but to our knowledge has not been previously applied to medical ultrasound.

**Statement of Contribution/Methods**

We collected element-level RF data on a Verasonics ultrasound system (courtesy of U. Michigan) using a 5 MHz linear array. We evaluated scenarios including wire phantoms, cyst phantoms, and animal (pig) data. Animal data were reviewed to identify examples where reverberation artifacts might have the greatest potential clinical impact. All images were reconstructed using standard delay-and-sum (DAS) methods, MVDR-WNGC, and MVDR methods published previously in the ultrasound literature (denoted 'constDL' in the plots below), which apply a load which is a fixed fraction of the energy in the estimated covariance matrix.

**Results/Discussion**

Preliminary experimental results using wire phantoms show that the MVDR-WNGC approach can reduce self-nulling of strong targets by ~4 dB when compared to more commonly used MVDR variants (line plot seen in subfigure a) and improve the null depth between closely spaced wire targets by ~3 dB (subfigure b). These gains are accomplished because WNGC adjusts the diagonal load as needed to limit adaptivity, giving high loading on strong targets and zero diagonal loading for locations between closely spaced targets. This improvement is achieved with minimal additional computational load. While much work remains, initial results suggest that the proposed approach may prove useful in improving the quality of ultrasound derived images of the GI tract.



P1B2-6

**Understanding Contrast Improvements from Capon Beamforming**

Ole Marius Hoel Rindal<sup>1</sup>, Jon Petter Åsen<sup>2</sup>, Sverre Holm<sup>1</sup>, Andreas Austeng<sup>1</sup>; <sup>1</sup>Department of Informatics, University of Oslo, Oslo, Norway, <sup>2</sup>Squarehead Technology AS, Norway

**Background, Motivation and Objective**

It is common to state that Capon beamforming applied to ultrasound images increases both contrast and resolution. However, the increased contrast is mainly a result of the increased resolution giving sharper edges in e.g. a cyst. Recently it has also been shown that lateral oversampling is needed to achieve lateral shift-invariance between image frames when using Capon beamforming (Åsen et al IEEE UFFC 2014). This is also essential for single frame scenarios, and especially when considering contrast. This work aims at understanding the contrast improvements obtained with Capon beamforming, and how to image point scatterers and speckle without loss of information.

**Statement of Contribution/Methods**

We have simulated a 196 element linear probe with center frequency at 7.5 MHz in Field II. Speckle statistics from conventional and Capon beamforming are investigated with emphasis on the lateral oversampling factor needed to avoid loss in information when imaging speckle with Capon beamforming. Cylindrical cysts with different radii were included in the simulations and the contrast was investigated by calculating the CNR (contrast-to-noise ratio) between regions of different sizes inside the cyst and a region of speckle.

We have also simulated brighter inclusions together with dark cysts and discussed how this influences the dynamic range and how the different beamformers influence the visibility of the inclusions. We demonstrate that Capon beamforming gives sharper edges and examine the beampatterns for the different beamformers at the edge of the cyst to explain why Capon beamforming produces sharper edges.

## Results/Discussion

We show that lateral oversampling is needed when using the Capon beamformer, but the factor of oversampling is smaller when imaging speckle than point scatterers. If the Nyquist requirement for beam spacing is used for Capon beamforming a point scatterer placed between two beams has a 40 dB lower amplitude than a point scatterer directly on the beam.

We demonstrate that Capon beamforming does not increase the contrast in general. The same contrast as Capon is achieved with DAS with Hamming apodization, but Capon improves the edges and thus gives better contrast for smaller cysts. Compared to non-weighted DAS, a cyst with 2.5 mm radius has 33 % better CNR for the Capon beamformer with  $K=5$  temporal averaging and  $L=32$  subarray averaging, when the CNR calculation is based on a circular region with radius of 1.25 mm in the center of the cyst. The CNR for DAS with Hamming apodization is actually 1 % better for the same region compared to the Capon beamformer. When the radius of the area from which the CNR is calculated is increased and approaches the radius of the cyst, the Capon beamformer gives higher CNR compared to the DAS beamformers i.e. Capon beamforming provides contrast improvements near edges because of the improved lateral resolution.

P1B2-7

## Imaging with Large Coherent Apertures: Ex vivo Studies

Marko Jakovljevic<sup>1</sup>, Gregg Trahey<sup>1</sup>, <sup>1</sup>Biomedical Engineering, Duke University, Durham, NC, USA

## Background, Motivation and Objective

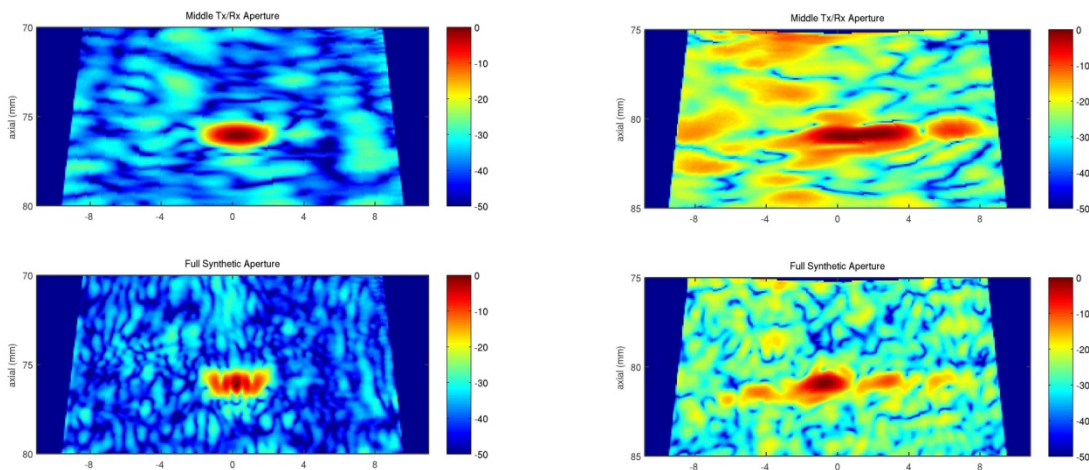
As ultrasound scanner manufacturers continue to develop larger arrays with higher element counts, the extent to which such increases (in effective aperture size) will be followed by improvements in the image quality in the presence of acoustic noise remains unclear. To systematically address this questions we use large synthetic aperture data sets collected with the fully sampled matrix array in an ex vivo setting to quantify the improvements in lateral resolution as a function of aperture size.

## Statement of Contribution/Methods

We acquired the full synthetic aperture data (synthetic transmit and synthetic receive) of a point target phantom using a Siemens 4z1c matrix arrays on a Siemens SC2000 ultrasound scanner. Using a translation/rotation stage setup the data was collected at 5 partially overlapping lateral positions of the array and summed coherently to extend the size of the physical aperture and generate a large virtual aperture. The point target was imaged through a long slab of porcine ribs and connective tissue. A control data set without the ribs/connective tissue in the acoustic path was acquired as well. Control simulations in FIELD II were also run to determine the improvement in image quality under ideal imaging conditions.

## Results/Discussion

Figure on the left side shows sample images of the point target reconstructed from a control data set. Top image is reconstructed from the data acquired at a single transducer position while the bottom image is reconstructed from the data collected at three non-overlapping aperture positions. As the size of the synthetic aperture increases from 19 mm to 57 mm, the measured width of the point target (at -6 dB) reduces from 2 mm to 0.5 mm which is in agreement with the simulation results (1.8 and 0.47 mm for a single and combined aperture positions respectively). Figure on the right side shows similar point target images but reconstructed from the data acquired through the ribs and connective tissue. In the presence of acoustic noise, the width of the measured point target is increased and overall image quality is degraded. Under noisy conditions, increasing the synthetic aperture reduces measured point target size from 4.7 mm to 1.8 mm.



P1B2-8

## A novel method for sound velocity estimation in pulse-echo ultrasound imaging

Piotr Karwat<sup>1</sup>, <sup>1</sup>Institute of Fundamental Technological Research, Polish Academy of Sciences, Warsaw, Poland

## Background, Motivation and Objective

The sound velocity in human soft tissue varies from approx. 1450 m/s in fat to over 1600 m/s in muscles. In standard ultrasound imaging the exact sound velocity in tissue is unknown and therefore, for the purpose of image reconstruction, it is assumed to be uniform and equal to 1540 m/s. This obviously leads to phase aberrations in the reconstructed images. Until now, the known solutions to this issue provided the optimal value of the sound velocity in the whole imaged area or, to address the layered structure of the tissue - in a few layers, which is still far from expectations.

Our objective was to develop a novel method which would provide the spatial distribution of the sound velocity in the pulse-echo ultrasound. This would potentially lead to a substantial reduction of the aberrations in the standard ultrasound imaging. Moreover, it would possibly improve the performance of some image enhancement algorithms such as those basing on the phase coherence of the reconstructed data.



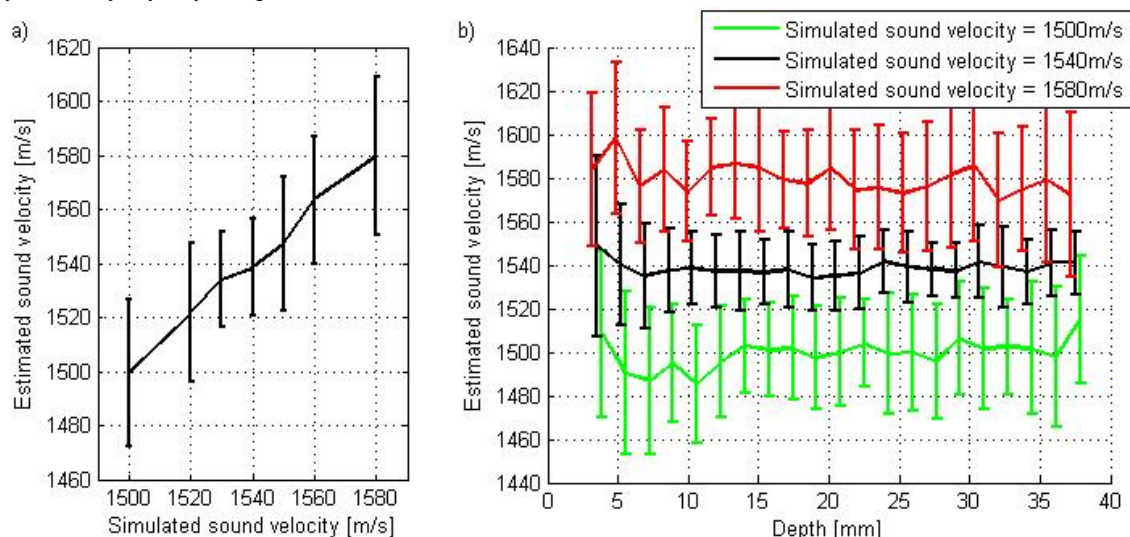
### Statement of Contribution/Methods

The proposed solution exploits the fact that a change in the transmit angle in aberrated images is accompanied by speckles migration. The intensity of this phenomenon depends on the severity of the phase aberrations and can therefore be used for estimation of the aberration source i.e. error in the local sound velocity.

The introduced method involves a speckle tracking over subsequent low resolution images obtained through synthetic transmit aperture technique. The resulting speckle migration trails are the basis for a new sound velocity estimator which can be used for reconstruction of aberration-corrected images. The presented estimator was calibrated based on numerical simulations and then verified with use of data obtained from both: simulations and examinations of tissue phantoms.

### Results/Discussion

The preliminary study shows that the introduced sound velocity estimator generates results which correlate well with the values set in simulations (fig. a). The results, however, suffer from high variance and need spatial averaging. The method in its current state can therefore provide reliable sound velocity estimates in a form of in-depth profiles (fig. b) rather than two-dimensional maps. It is nevertheless a brand new technique and there are still many improvements to be made such as optimization of the transmission scheme or spatial and frequency compounding.



P1B2-9

### A Phantom Study on Temporal and Subband Minimum Variance Adaptive Beamforming

Konstantinos Diamantis<sup>1</sup>, Iben Høffort Voxen<sup>2,3</sup>, Alan Greenaway<sup>1</sup>, Tom Anderson<sup>4</sup>, Jørgen Arendt Jensen<sup>2</sup>, Vassilis Sboros<sup>1</sup>, <sup>1</sup>School of Engineering and Physical Sciences, Heriot-Watt University, Edinburgh, United Kingdom, <sup>2</sup>Center for Fast Ultrasound Imaging, Dept. of Electrical Engineering, Technical University of Denmark, Lyngby, Denmark, <sup>3</sup>Greenwood Engineering, Brøndby, Denmark, <sup>4</sup>Medical Physics, Centre for Cardiovascular Science, University of Edinburgh, Edinburgh, United Kingdom

### Background, Motivation and Objective

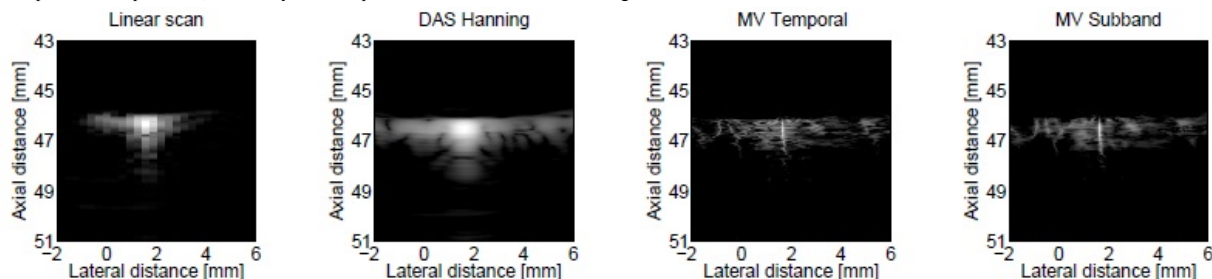
Past simulation studies have shown that Minimum Variance (MV) adaptive beamforming yields higher resolution compared with the conventional Delay-and-Sum (DAS) beamformer that is widely used in ultrasound imaging. The purpose of this work is to verify and compare temporal and subband implementations of the adaptive method experimentally. This is accomplished by displaying wire phantom measurements, obtained by the research ultrasound scanner SARUS and a linear array.

### Statement of Contribution/Methods

The MV beamformer calculates a set of data-dependent apodization weights with the objective to preserve the signal from the focus point while minimizing contributions from other points. The calculation requires the estimation of the sample covariance matrix that can be done either in the time domain directly from the data or in frequency domain where division of data into frequency subbands precedes; increasing the complexity of this implementation. A 7 MHz 192 element linear array with a pitch of 0.21 mm was used to scan a wire phantom in which wires are separated by 1 cm. 128 elements are used in transmit with a Hanning window and an  $F\# = 2$ , while all elements are used in receive. Data from 129 emissions are acquired from all elements with SARUS and MV beamformers are applied to data from one emission. Beamformed responses of a single wire target are shown in the Figure with a 60 dB dynamic range. Emission 70 was selected so that aperture center is above the target. For the same emission, response from DAS beamformer using fixed Hanning weights is included for comparison. A B-mode image from beamformation toolbox BFT3 with Hanning receive apodization and dynamic receive focusing is also displayed. Lateral Full-Width-Half-Max (FWHM) and Peak Sidelobe Level (PSL) are used for performance evaluation.

### Results/Discussion

FWHM measured at the depth of 46.6 mm, is 0.03 mm (0.14 $\lambda$ ) for both adaptive methods while values for Hanning weights and linear scan are 0.74 and 0.46 mm respectively. Between the MV beamformers a 3 dB difference in PSL is noticed in favor of the subband approach (-38 and -41 dB), whereas values from conventional are not lower than -33 dB. This slight improvement in the case of the subband implementation comes at the expense of increased computational load; 2.7 TFlops per image are required in contrast to 81 GFlops of the temporal one, when only 1.5 GFlops are needed in DAS beamforming.



## Experimental Demonstration of Passive Acoustic Mapping in the Human Skull Cavity using CT-based Aberration Corrections

Ryan Jones<sup>1,2</sup>, Meaghan O'Reilly<sup>2</sup>, Kullervo Hynynen<sup>1,2</sup>; <sup>1</sup>Medical Biophysics, University of Toronto, Toronto, Ontario, Canada, <sup>2</sup>Physical Sciences Platform, Sunnybrook Research Institute, Toronto, Ontario, Canada

### Background, Motivation and Objective

The adoption of passive imaging techniques to spatially map cavitation activity over time may be useful for monitoring bubble-mediated ultrasound therapies in the brain. However, if not properly accounted for, the strong aberrations introduced to ultrasound waves as they pass through the skull bone can lead to image distortions and artifacts upon reconstruction. It has previously been shown that the skull's acoustical properties can be obtained from CT scans of the head, and that numerical models can be employed to achieve noninvasive focusing on transmit using large-aperture phased array transducers [1]. In a recent simulation study, we demonstrated that similar principles can also be applied during beamforming on receive, allowing for passive acoustic imaging over a large region within the skull cavity [2]. The objective of the current study was to provide validation of the proposed transcranial imaging technique through benchtop and *in vivo* experiments.

### Statement of Contribution/Methods

A sparse hemispherical receiver array (30 cm diam.) consisting of 128 piezoceramic discs (2.5 mm diam., 612 kHz center frequency) was used to passively listen through an *ex vivo* human skullcap to emissions from a 1 mm, 516 kHz narrow-band source. The raw RF waveforms were captured and passive beamforming was performed offline to reconstruct spatial maps of the source activity. Measurements were taken at various locations within the skull cavity, by moving the source around the field using a 3D positioning system. Spatial registration of the skull was determined by measuring the location of multiple landmarks on the inner and outer skull surfaces that were easily identifiable in CT image data of the same specimen. A previously described full wave ultrasound propagation model [3] was used to calculate the receiver delays required to correct for the distortions caused by the skull bone. The images reconstructed using the noninvasive CT-based correction technique were compared with those without aberration correction and with an invasive hydrophone-based aberration correction technique. Preliminary *in vivo* testing of the method was performed in a rat model.

### Results/Discussion

In general, the CT-based skull correction technique provides a substantial improvement in image quality over the case where no aberration correction is performed. Using data from 5 source locations inside the skull cavity within 2 cm of the array's geometric focus, the -3 dB lateral (axial) main lobe beamwidth was reduced from  $1.92 \pm 0.14$  mm ( $4.5 \pm 1.2$  mm) to  $1.79 \pm 0.08$  mm ( $3.4 \pm 0.3$  mm) when the noninvasive technique was used. The peak sidelobe ratio of the reconstructed images was also improved, reducing from  $0.65 \pm 0.13$  without corrections to  $0.22 \pm 0.03$  through the use of CT-based corrections. Similar improvements in image quality were observed *in vivo*.

[1] Clement & Hynynen, *PMB*. 2002; **47**:1219-36

[2] Jones, O'Reilly & Hynynen, *PMB*. 2013; **58**:4981-5005

[3] Connor & Hynynen, *PMB*. 2002; **47**:1911-28

## P1B3 - MBF: Vector Velocity Imaging and Applications

Salon C

Friday, September 5, 2014, 8:00 am - 5:00 pm

Chair: **Damien Garcia**  
CRCHUM - Research Centre, University of Montreal Hospital

P1B3-1

### 3-D *in vivo* velocity estimation in two planes

Simon Holbek<sup>1</sup>, Michael Johannes Pihl<sup>1</sup>, Caroline Ewertsen<sup>2</sup>, Michael Bachmann Nielsen<sup>2</sup>, Jørgen Arendt Jensen<sup>1</sup>; <sup>1</sup>Department of Electrical Engineering, Center for Fast Ultrasound Imaging, Lyngby, Denmark, <sup>2</sup>Department of Radiology, Rigshospitalet Copenhagen University Hospital, Copenhagen, Denmark

#### Background, Motivation and Objective

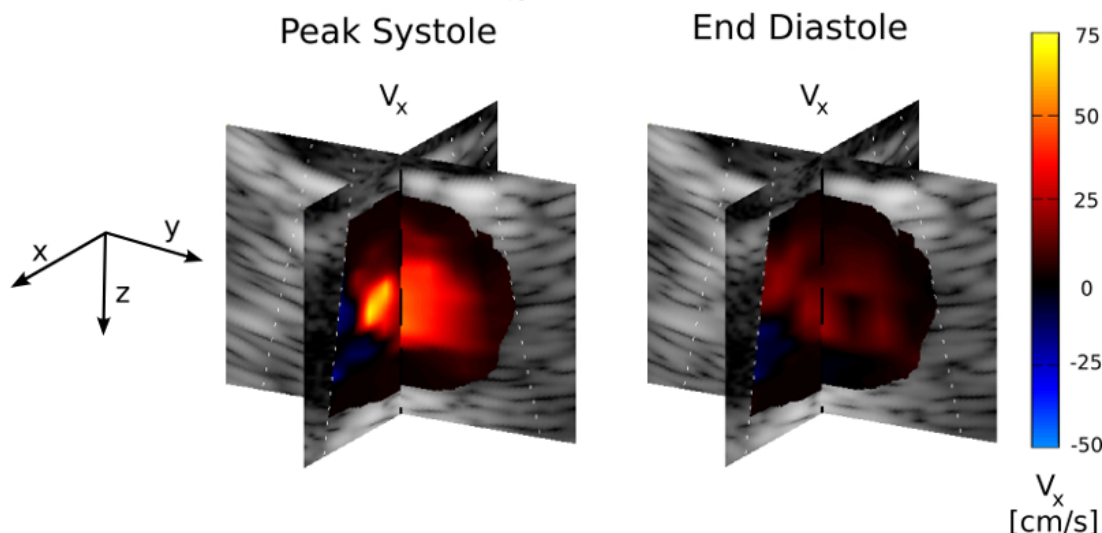
3-D velocity vectors can provide additional flow information applicable for diagnosing cardiovascular diseases e.g. by estimating the out-of-plane velocity component. A 3-D version of the Transverse Oscillation (TO) method has previously been used to obtain this information in a carotid flow phantom with constant flow. This paper presents the first *in vivo* measurements of the 3-D velocity vector flow obtained over 3-4 cardiac cycles. It is the first imaging modality scheme that provides real-time 3-D vector velocity information simultaneously for two crossing planes.

#### Statement of Contribution/Methods

At 13 Hz, 45 frames were acquired with a complex interleaved sequence composed of 768 emissions (128 B-mode and 32x10 flow). Intensity measurements of the complex emission sequence were conducted with an acoustic intensity measurement system, AIMS III (Onda, Sunnyvale, California, USA). The derated value for MI was 1.50, and the pulse repetition frequency was scaled to 9.9 kHz to obtain  $Ispta.3 = 720 \text{ mW/cm}^2$  in compliance with the FDA limits. In collaboration with an experienced radiologist, the *in vivo* measurements were conducted on the right common carotid artery of a 32 year old healthy male volunteer. Data were acquired using a Vermon 3.5 MHz 32x32 element 2-D phased array transducer (Vermon S.A., Tours, France) and the experimental ultrasound scanner SARUS. When acquiring the *in vivo* data, the transducer was oriented to obtain a cross sectional (ZY) and a longitudinal (ZX) plane in which the three velocity vectors  $v_x$ ,  $v_y$  and  $v_z$  are estimated.

#### Results/Discussion

The figure shows  $v_x$  as it provides the main contribution to  $\|v\|$  due to the transducer orientation. At peak systole (PS) the mean velocities ( $v_x$ ;  $v_y$ ;  $v_z$ ) [cm/s] in the ZX-plane are estimated to (5.8; -0.1; 0.9) and (13.4; -1.5; 1.1) in the ZY-plane, with maximum  $v_x$  of 67.7 and 49.4 cm/s respectively. At end diastole the mean velocities in the ZX-plane are estimated to (2.9; -0.1; 0.5) and (3.2; 1.6; 0.8) in the ZY-plane, with maximum  $v_x$  of 17.9 and 19.6 cm/s respectively. The maximum velocities for  $v_x$  are consistent with a value of 74 cm/s measured with spectral Doppler at PS. Inconsistencies between the estimated velocities of the two planes can be explained by their difference in spatial position. The result shows that real-time 3-D velocity vector flow in two crossing planes for the first time has been obtained in an *in vivo* study.



P1B3-2

### A multi-angle plane wave imaging approach improves volume flow estimation: simulation study in the murine arterial system

Abigail Swillens<sup>1</sup>, Darya Shcherbakova<sup>1</sup>, Ingvald Kinn Ekroll<sup>2</sup>, Bram Trachet<sup>1</sup>, Lasse Lovstakken<sup>2</sup>, Patrick Segers<sup>1</sup>; <sup>1</sup>IBiTech-bioMMeda, Ghent University, Ghent, Belgium, <sup>2</sup>Department of Circulation and Medical Imaging, NTNU, Norway

#### Background, Motivation and Objective

High-resolution ultrasound (US) blood flow imaging in mice might increase our understanding on the origin and progression of cardiovascular diseases in mouse models. Current small animal systems are equipped with traditional 1D flow imaging techniques, suffering from insufficient spatial/temporal resolution to accurately resolve in-vivo flow fields. Instead of imaging, one often resorts to 'computational fluid dynamics' (CFD), allowing determination of hemodynamic parameters like wall shear stress, particle residence time, ... where US currently lacks precision to do so. However, one of CFD's restrictions is the need for hemodynamic conditions (flow/pressure) to be imposed at the boundaries of the flow domain, typically derived from in-vivo 1D Doppler measurements.

Aim of our study is to demonstrate the potential of multi-angle plane wave imaging for 2D vector flow visualization in mice, serving a 2-fold purpose:

1. Improving accuracy of CFD by providing better boundary conditions

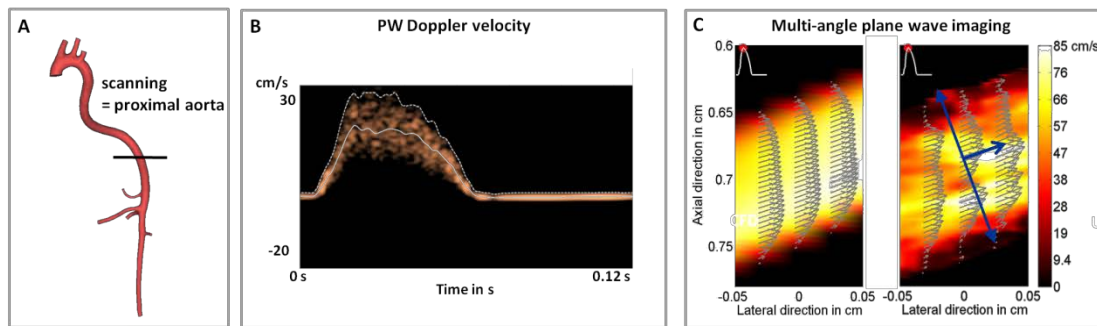
## 2. Assessing feasibility of direct, in-vivo hemodynamical imaging

### Statement of Contribution/Methods

Field II simulations were performed by modeling a probe for murine cardiovascular imaging (VEVO 2100, Visualsonics). Point scatterers representing aortic blood flow were moved according to CFD flow fields in a 3D mouse aorta, reconstructed from  $\mu$ CT-scans (fig.1A). This allowed comparing simulated US flow estimates with a ground truth (CFD). A high frame-rate scanning sequence was ensured via emission of plane waves (PRF = 50 kHz) and receiving 200 beams in parallel. 2D vector flow was obtained by triangulating Doppler estimates from 2 angles ( $\pm 10^\circ$ ). Volume flow was derived by averaging the 2D velocity profile, assuming a circular cross-section (blue line in fig.1C). Results were compared with the outcome of traditional PW Doppler.

### Results/Discussion

Fig.1B shows the simulated PW Doppler for a 0.15 mm sample volume in the proximal aorta. The vector flow image in fig.1C shows the corresponding 2D velocity info at peak systole, though in a larger 1x2 mm region. Volume flow was underestimated compared to the CFD ground truth, both by PWD and the vector flow approach. However, the mean bias improved from 25% to 16% when using 2D velocity vector info. The underestimation could be attributed to a skewed velocity profile in the aorta, demonstrating the need for 3D vascular imaging modalities.



## P1B3-3

### In Vivo Evaluation of an Angle Independent Flow Rate Estimator

Jonas Jensen<sup>1</sup>, Jacob Bjerring Olesen<sup>1</sup>, Peter Møller Hansen<sup>2</sup>, Michael Bachmann Nielsen<sup>2</sup>, Jørgen Arendt Jensen<sup>1</sup>; <sup>1</sup>Center for Fast Ultrasound Imaging, Dept. of Elec. Eng., Technical University of Denmark, Kgs. Lyngby, Denmark, <sup>2</sup>Department of Radiology, Rigshospitalet, Copenhagen University Hospital, Copenhagen, Denmark

### Background, Motivation and Objective

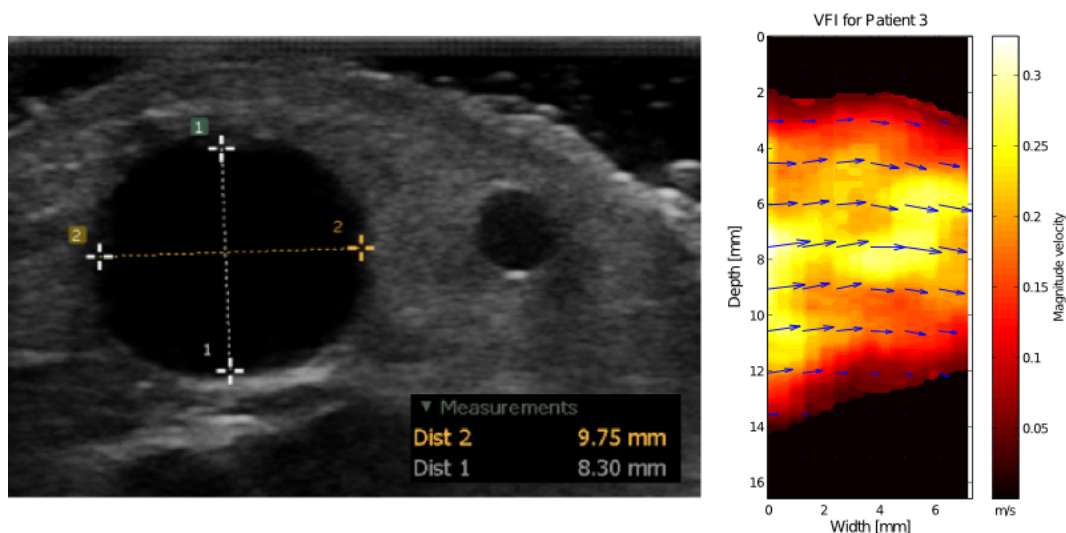
Angle independent flow rate estimation is achievable by integrating the velocity field acquired with the transverse oscillation approach. The flow rate estimator assumes axisymmetric flow, a circular cross-sectional area of the vessel, and that the ultrasound beam intersects the middle of the vessel. Clinical application of the technique, however, requires an understanding of the degree to which these assumptions affect the accuracy of the estimator. The purpose is to study the effects of vessel ellipticity and beam intersection on flow rate estimation using simulations. Furthermore, the extents to which the assumptions are met in a practical scanning situation are investigated *in vivo*.

### Statement of Contribution/Methods

Womersley's model for pulsatile flow was used to simulate velocity profiles and to calculate the true and estimated flow rate. This was accomplished for situations of elliptical vessels and in the case of the ultrasound beam being off-axis. In an evaluation, 20 patients with arteriovenous fistulas for hemodialysis were scanned just prior to dialysis. An UltraView 800 ultrasound scanner (BK Medical, Denmark) with a 9 MHz linear array transducer was used to obtain Vector Flow Imaging (VFI) sequences of a superficial part of the fistulas. The flow rate was calculated by integrating the velocity profile over a cross-sectional area of the fistula. To study ellipticity, cross-sectional diameters of a fistula were measured on B-mode scans by rotating the scan plane 90 degrees. Beam-vessel intersection was determined by comparing diameters on B-mode scans with the actual width of a velocity profile estimated by blood-tissue discrimination.

### Results/Discussion

Flow rate through an elliptic cross-section is proportional to the flow rate through a circular cross-section with a factor equal to the ellipticity. The major axis of the fistulas was on average 7 % larger than the minor axis, so ellipticity should be taken into account. The ultrasound beam was on average  $1.5 \pm 0.8$  mm off-axis, corresponding to  $28.5 \pm 11.3$  % of the major semiaxis of a fistula, and this could result in 15 % underestimated flow rate according to the simulation. Therefore, it is recommended to use cross-sectional B-mode scans as guidance for beam-vessel intersection. An example of a fistula B-mode scan (cross-sectional plane) and VFI (longitudinally) is shown in the figure.



P1B3-4

### 2D Tracking Doppler for Cardiac Jet Flow Velocity Estimation

Jørgen Avdal<sup>1</sup>, Lasse Løvstakken<sup>2</sup>, Solveig Fadnes<sup>1</sup>, Ingvild Ekroll<sup>2,3</sup>, Hans Torp<sup>2</sup>; <sup>1</sup>MI Lab and Dept. of Circulation and Medical Imaging, Norwegian University of Science and Technology, Norway, <sup>2</sup>Dept. of Circulation and Medical Imaging, NTNU, Norway, <sup>3</sup>St. Olavs Hospital, Norway

#### Background, Motivation and Objective

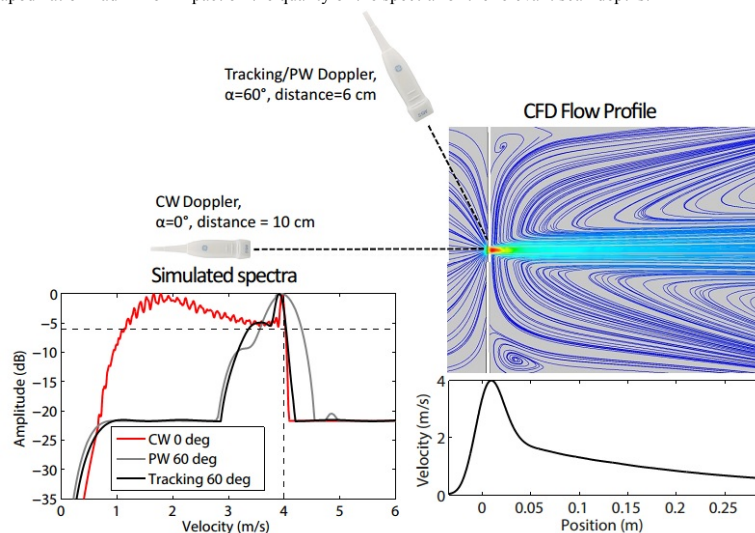
The maximal velocity of jet flow through an insufficient heart valve gives important information on the pressure gradient, and is usually measured by continuous wave Doppler. With this method, correct estimation of the maximal velocity relies on a small ( $<20^\circ$ ) beam-to-flow angle. Angle correction is not recommended due to difficulties in estimating the correct flow angle, and increasing transit-time effect. 2D tracking Doppler (Fredriksen et al 2013) is a recently proposed method which has been shown to produce robust estimates of the true velocities even at high (50-80 deg) beam-to-flow angles. The method reduces transit-time broadening by summation of the signal along the trajectory of the blood scatterers. Choosing the wrong tracking angle decreases the transit-time and leads to spectral broadening, an effect which may be utilized for angle correction. The method has been successfully demonstrated in vivo for carotid stenosis with a linear array. In this study we will investigate the use of the tracking Doppler technique with a phased array probe for cardiac use.

#### Statement of Contribution/Methods

Plane wave transmissions were used in combination with parallel beams on receive. Due to diffraction effects, transmit apodization using a Tukey window was used to obtain a more homogeneous field in the depth range of interest (5-10 cm). The Computational Fluid Dynamics (CFD) software ANSYS Fluent was used to simulate a jet from a 5 mm opening with different maximal velocities. Using the resulting velocity fields, the received signals were simulated using Field II, for CW Doppler with flow angle  $0^\circ$ , and PW Doppler with multiple receive beams with flow angle  $60^\circ$  (see figure). The scan sequence has been implemented on a modified GE scanner, and in vitro and in vivo results will be presented.

#### Results/Discussion

The figure shows an example with CFD simulation of a jet with maximal velocity 4 m/s, and corresponding power spectra for CW-, conventional PW-, and tracking Doppler. Using a -6dB threshold, the maximal velocity overestimation is less than 1% for CW and tracking Doppler and 8% for PW Doppler. Additionally, it was found that transmit apodization had minor impact on the quality of the spectra for the relevant scan depths.





# Spatially Adaptive Pulse Repetition Frequency in Synthetic Aperture Vector Flow Imaging

Carlos A. Villagomez Hoyos<sup>1</sup>, Matthias Bo Stuart<sup>1</sup>, Jorgen Arendt Jensen<sup>1</sup>; <sup>1</sup>Department of Electrical Engineering, Technical University of Denmark, Denmark

## Background, Motivation and Objective

In current ultrasound systems the range of detectable velocities is susceptible to the selected pulse repetition frequency (PRF). The PRF selection affects the entire flow mapping region. Whenever a region with large differences in velocity magnitude is mapped, a trade-off is made between selecting a high PRF for visualizing high velocity blood flow or a low PRF for low velocity flow.

In this work, a spatially-independent PRF is synthesized and adaptively selected for every estimation point. Previous work has shown the ability of synthetic aperture (SA) to provide continuous data, thereby allowing a lower PRF to be synthesized without affecting the system actual PRF.

## Statement of Contribution/Methods

A 7 MHz BK Medical 8670(Herlev, Denmark) 128 element linear array transducer is used with the SARUS scanner. A sequence with 8 defocused emissions, equally distributed at the center of the aperture, is emitted with a system PRF of 5 kHz. A 2-cycle sinusoidal pulse with 64 elements are used in transmit, while all 128 elements are used in receive. All 128 channels were sampled at a frequency of 35 MHz.

Measurements are made in a transverse vessel phantom with an internal diameter of 7.2 mm. A pump circulates blood-mimicking fluid within a closed loop circuit with constant flow. Two measurements with estimated peak velocities of 0.04 m/s and 0.4 m/s are acquired for 0.24 seconds each.

Flow velocity estimation is done by beamforming directionally along the vessel, echo-cancelling, and averaging 16 cross-correlations. Several pulse repetition frequencies are synthesized, from system PRF to PRF/7, by selecting a different set of signals to be cross-correlated. The selection of the synthesized PRF is done adaptively for each estimation point by selecting the estimation with the lowest standard deviation.

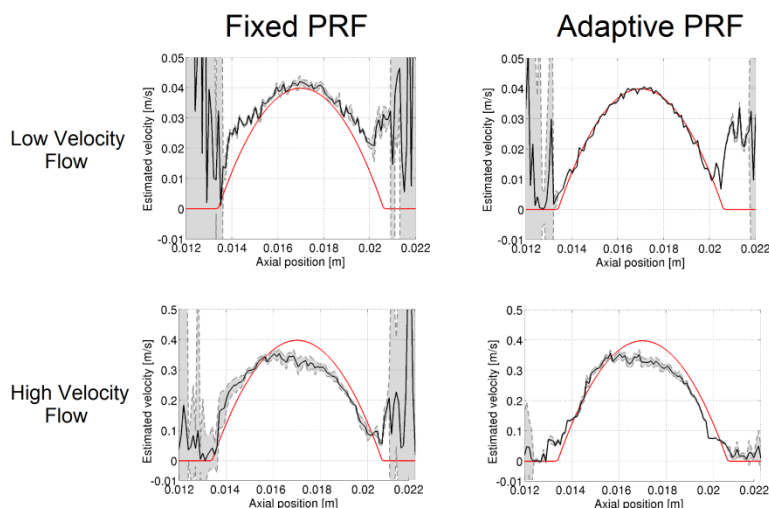
## Results/Discussion

Cross-sectional flow profiles are shown in the figure. Velocities are estimated from the same data set using the adaptive method and compared to the fixed system 5kHz PRF estimation.

For the low velocity flow, the bias and std. dev. are -0.77% and 0.31% respectively for the adaptive method and 7.08% and 1.83% for the fixed PRF.

For high velocity flow, they are -4.78% and 1.47% for adaptive and -3.45% and 2.61% for the fixed PRF.

Improvements in flow detection is possible, when optimal PRF is synthesized.



# Does large beam-steered angle velocity compounding using plane wave transmission improve blood vector velocity estimation in a 3D carotid artery flow field?

Anne E.C.M. Saris<sup>1</sup>, Hendrik H.G. Hansen<sup>1</sup>, Stein Fekkes<sup>1</sup>, Maartje M. Nillesen<sup>1</sup>, Marcel C.M. Rutten<sup>2</sup>, Chris L. de Korte<sup>1</sup>; <sup>1</sup>Medical Ultrasound Imaging Center, Department of Radiology and Nuclear Medicine, Radboud University Medical Center, Nijmegen, Netherlands, <sup>2</sup>Cardiovascular Biomechanics, Department of BioMedical Engineering, Eindhoven University of Technology, Eindhoven, Netherlands

## Background, Motivation and Objective

Quantification of complex flow patterns with variations in blood flow direction throughout an image plane and strong fluctuations over the cardiac cycle, requires dedicated transmission schemes. Plane wave imaging enables assessment of the entire velocity field (2D/3D) at frames rates up to 10 kHz. This study compares the performance of 0° and compound 2D vector velocity estimation using angled plane wave transmissions, a method originally developed for vascular strain imaging.

## Statement of Contribution/Methods

Fluid-structure interaction modeling was used to generate realistic 3D flow velocity fields inside a curved carotid artery, over a full cardiac cycle. Field II was used to simulate ultrasound radiofrequency element data for a linear array transducer ( $f_c = 9$  MHz, pitch = 198  $\mu$ m, 192 elements), using the 3D velocity field as input. The transducer emitted plane waves at a PRF of 2 kHz at either 0° angle only, or at sequentially changing angles of 20°, 0°, and -20°. RF data were beamformed in the direction of the steered plane waves by delay-and-sum beamforming. The 0° data were additionally beamformed at angles of +20° and -20°. Band-limited noise was added to obtain a signal-to-noise ratio of 13 dB. Displacements were estimated iteratively using a 2D normalized cross correlation-based method, rendering the velocity by multiplication with the frame rate.

The horizontal velocity components were determined in 3 ways: 1) directly from the 0° acquisitions (PW0), or by compounding of the axial velocity components obtained from 2) the 0° data beamformed at +20° and -20° (PW0<sub>C</sub>), or 3) the +20° and -20° multi-angle acquisition (PW<sub>C</sub>). The vertical velocity was determined from the 0° angle, albeit at a 3x lower frame rate for PW<sub>C</sub>. The performance of the 3 methods was compared by calculating the root mean squared error (RMSE) between estimated and true horizontal and vertical velocity components.

### Results/Discussion

Figure 1 shows that PW0 and PW0<sub>C</sub> provided accurate velocity estimates, with similar RMSEs. PW<sub>C</sub> showed significantly higher RMSEs probably caused by the reduced frame rate and the presence of severe grating lobes. Opposed to vascular strain imaging, large inter-frame displacements and gradients in the velocity field occur for this application. Optimization of transducer, frame rate and compound angles might however make compounding beneficial for this application as well.

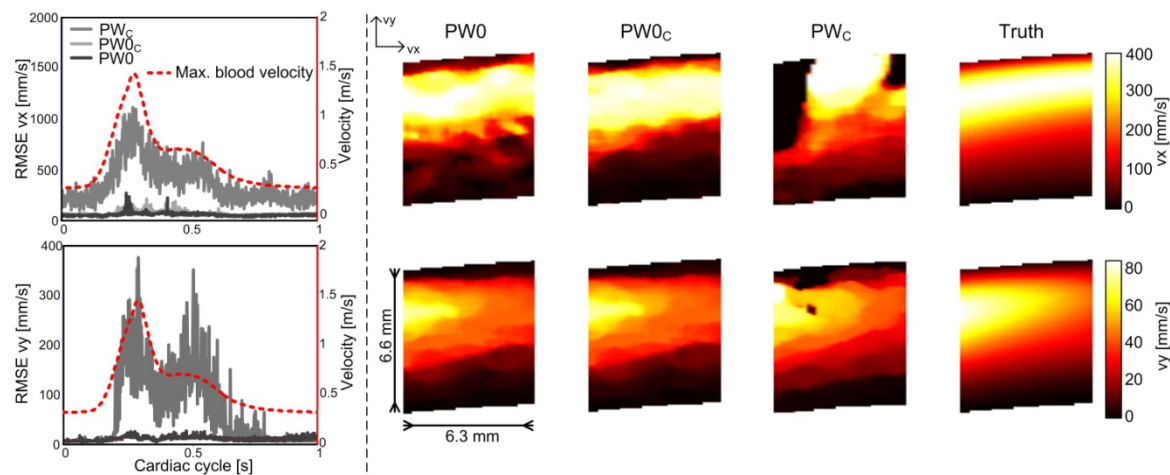


Figure 1. Left: RMSE for horizontal (vx) and vertical (vy) velocity components, over the cardiac cycle, for the 3 different methods. Right: Illustrative frame in diastolic phase, showing horizontal and vertical velocity estimates and ground truth.

### P1B3-7

#### On the Accuracy of Coherent Compounding Doppler Imaging

Ingvald K. Ekroll<sup>1,2</sup>, Marco Voormolen<sup>1</sup>, Øyvind Standal<sup>1</sup>, Jochen Rau<sup>1</sup>, Hans Torp<sup>1</sup>, Lasse Lovstakken<sup>1</sup>; <sup>1</sup>Dept. Circulation and Medical Imaging, Norwegian University of Science and Technology, Trondheim, Norway; <sup>2</sup>St. Olavs University Hospital, Trondheim, Norway

### Background, Motivation and Objective

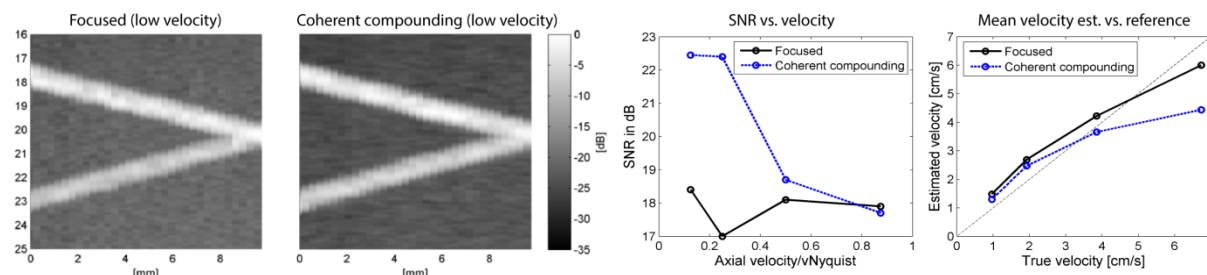
Coherent plane-wave compounding Doppler (CCD) has shown great potential for improved imaging of small blood vessels, achieving dynamic transmit focusing and improved SNR, as well as a high ensemble size for improved clutter filtering. The technique, however, relies on (near) stationary image objects which inherently is not the case when imaging blood flow. In this work we investigate the influence of blood scatterer movement on the signal-to-noise (SNR) and mean velocity estimator accuracy for CCD compared to conventional focused imaging.

### Statement of Contribution/Methods

Simulations of moving point target ensembles (Field II) and in vitro experiments were setup to mimic flows with varying velocities. The in vitro setup was a custom flow rig with two crossing wall-less channels (0.7mm diameter) set at 75 degree beam-to-flow angles (see figure). The flow was driven at average fluid velocities of 4 to 26 cm/s, and the Nyquist velocity was set above the maximum axial velocity (PRF=1kHz). A research system (Ultrasonix Touch with DAQ) was setup to subsequently acquire channel data for coherent compounding (15 tx angles) and conventional focused imaging (f-number=2.5). The same acquisition setup and processing was used for all examples (f0 = 5MHz, firing PRF = 15kHz, tx-voltage = 50V, ensemble size = 45 & 160, clutter filter cut-off = 4.4 mm/s).

### Results/Discussion

Results showed that increasing flow velocities caused a gradual decrease in SNR for CCD imaging, with a reduction of about 5dB measured in vitro when approaching the Nyquist limit (see figure, middle panel). In power-Doppler imaging this limit is often breached, and a higher loss of SNR is to be expected. Interestingly, the in vitro experiments showed an increasing bias for higher velocities using CCD compared to focused imaging, amounting to approximately 15 - 40% difference at 0.5 - 0.9x the Nyquist velocity (see figure, rightmost panel). In-depth simulations revealed that the lateral flow velocity component was the dominating origin for this effect, causing skewed Doppler spectra for CCD and thus biased mean velocity estimates. The potential implications of this effect will be further investigated.



# Robust Speckle Tracking using a Non-Rigid Point Set Registration Algorithm

Nicolas Widynski<sup>1</sup>, Damien Garcia<sup>1</sup>; <sup>1</sup>University of Montreal Hospital, Montréal, Québec, Canada

## Background, Motivation and Objective

Analysis of both myocardial and intracardiac flow motions by ultrasound imaging are of major interest for the assessment of the heart function. A variety of methods have been proposed to estimate heart motions. Among them, multiscale optical flow and particle image velocimetry (PIV) methods are the most popular, but also have well-known limitations: the former is sensitive to intensity variations and inefficient to track large displacements, the latter biases the estimation toward integer values which is problematic especially when the motion is slow. The objective of this study was to propose a novel speckle tracking method, which is not subject to the aforementioned limiting cases.

## Statement of Contribution/Methods

Speckle tracking was turned into a non-rigid point set registration problem. Points of set corresponded to bright speckle cells and thus were used as markers for the tracking. The methodology pipeline was divided into three steps. First, speckle cells were mathematically defined by exploiting their structural and geometric properties (size, shape, and topology). They were then retrieved using a contrast-invariant morphological tree approach. Finally, they were registered using a point set registration algorithm. Our methodology presents promising characteristics compared to state-of-the-art literature: no window artifacts (detection is performed on connected components of pixels), sub-pixel resolution (point sets are defined as centroids of speckle cells), non-rigid transformations, robustness to changes in attenuation / shadowing (the detection is invariant by contrast) and to a large range of amplitude displacements.

## Results/Discussion

Experiments were conducted on: 1) a 10 cm-diameter disc phantom spinning at 1 to 50 rpm using ultrafast imaging (circular waves, 11-angle compounding, 100 fps after compounding) with a 2.5 MHz probe; 2) the same setup with the phantom spinning at 1 to 30 rpm using focused imaging (25 fps); 3) an *in vivo* pig heart using a linear 2.5 MHz probe. Results (see Fig. 1) showed that our approach outperforms the state-of-the-art multiscale smoothed PIV method by obtaining stable results over the whole range of angular velocities (mean angle error  $\sim 15^\circ$ , mean amplitude error  $\sim 20\%$  of the max amplitude, for both ultrafast and focused imaging). Perspective works include *in vivo* experiments on human hearts.

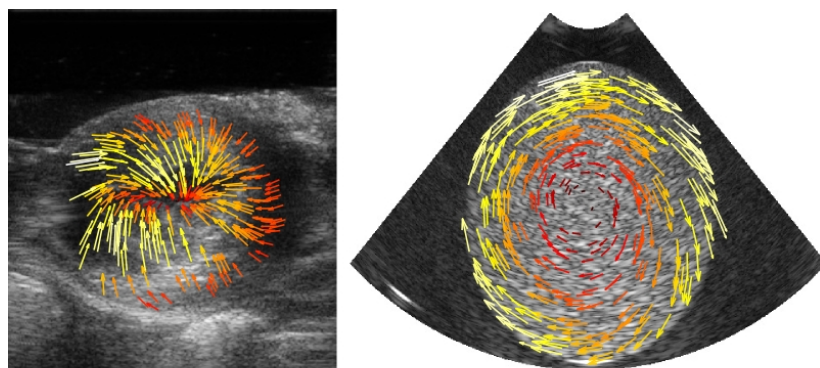


**Fig. 1** - Left: Pig heart *in vivo* experiment. Estimated flow occurred in the diastole phase of the cardiac cycle. Right: Flow estimated on a 10 cm spinning disc phantom by circular wave insonifications at 30 rpm. Color intensities range from black to white, corresponding to the amplitude displacement.

# Analysis of Angle Compounding on a Fast Color Doppler Imaging: Phantom Study

Hyohee Kim<sup>1</sup>, Sunmi Yeo<sup>1</sup>, Yeokyeong Yoon<sup>1</sup>, Yangmo Yoo<sup>1,2</sup>; <sup>1</sup>Electronic Engineering, Sogang University, Seoul, Korea, Republic of; <sup>2</sup>Interdisciplinary Program of Integrated Biotechnology, Sogang University, Seoul, Korea, Republic of

## Background, Motivation and Objective

Fast color Doppler imaging (CDI) based on plane wave excitation and angle compounding is useful for evaluating vascular diseases with high frame rates. Due to limited spatial resolution from plane wave excitation, the image quality of CDI is substantially degraded. To enhance the spatial resolution, angle compounding, in which several tiled plane waves are excited and coherently summed together during receive beamforming, can be used. However, the effect of angle compounding on fast CDI has not been extensively analyzed. In this paper, the analysis of angle compounding on fast CDI with phantom studies is presented.

## Statement of Contribution/Methods

To evaluate the effect of the angle compounding, in this paper, the recently-proposed sliding angle compounding (SAC) method is adopted. In SAC, the angle compounding is updated as each new angle compounding is acquired. The pre-beamformed radio-frequency (RF) data were captured by using a L7-4 linear array transducer connected to the research platform (Vantage, Verasonics Inc., Redmond, WA, USA) from a tissue mimicking flow phantom (Gammex 1425A LE, Gammex Inc., Middleton, WI, USA). The pulse-repetition frequency of 2 kHz and four different sets of compounding angles (i.e., 3, 6, 8 and 12) were used for generating a color Doppler image.

## Results/Discussion

The color Doppler images with plane wave excitation and SAC for 3, 6, 8 and 12 angle sets are shown in Fig. 1(a). As shown in the first image of Fig. 1(a), when 3 angle excitations and corresponding SAC are applied, the blocky artifacts are clearly shown in the vessel region. These artifacts are decreased as the number of angles for plane wave excitation increases. With 12 angle excitation, it is difficult to identify the blocky artifacts as shown in the last image of Fig. 1(a). The parabolic flow profiles at the 64th scanline with a parabolic are displayed in Fig. 1(b), which is consistent with the visual assessments in Fig. 1(a). The measured root mean square errors (RMSEs) for three angle sets (3, 6, and 8) by assuming the 12 angle set as the reference are 0.0124, 0.0107 and 0.0082, respectively. These results indicate that the proper selection of the number of angles in fast color Doppler imaging is important for improving spatial resolution while reducing the blocky artifacts. The evaluation of the fast color Doppler imaging with *in vivo* carotid data is under investigation.

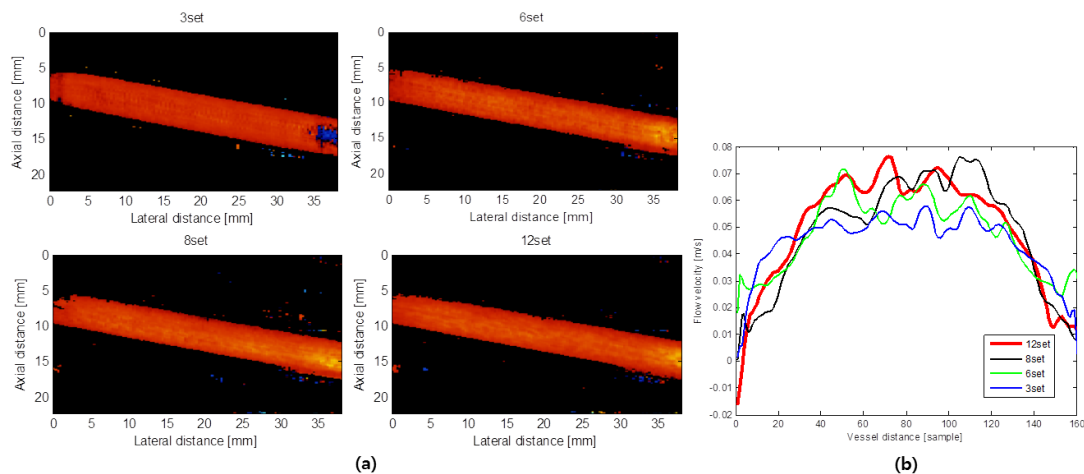


Figure 1. (a) Color Doppler images with plane wave excitation and SAC for 3, 6, 8 and 12 angle sets and (b) the flow profile at the 64th scanline

P1B3-10

### Plane Wave Ultrasound Imaging Velocimetry

Chee Hau Leow<sup>1</sup>, Robert J. Eckersley<sup>2</sup>, Meng-Xing Tang<sup>1</sup>; <sup>1</sup>Department of Bioengineering, Imperial College London, United Kingdom, <sup>2</sup>Department of Biomedical Engineering, King's College London, United Kingdom

#### Background, Motivation and Objective

Ultrasound Imaging Velocimetry (UIV), which uses microbubbles as tracking particles, has shown promising results in evaluating flow, both in vitro and in-vivo [1]. However, the application of UIV has been limited by low temporal resolution and measurement error associated with conventional scanning beamformed ultrasound imaging systems [2]. In this work, a more accurate flow measurement technique which makes use of a fast plane wave imaging system in conjunction with UIV methods is developed.

#### Statement of Contribution/Methods

Using a Verasonics ultrasound system, contrast images of a fully developed laminar flow in a 6mm diameter latex tube using both conventional and plane wave pulse inversion techniques were acquired. A temporal resolution of 60 frames per second (fps) was attained when using conventional focus wave technique while 555 fps was obtained with a plane wave imaging approach. Measurements of both a slow flow with peak velocity of 28cm/s and a fast flow with peak velocity of 47cm/s were analysed using an established UIV algorithm.

#### Results/Discussion

The figure shows the displacement vectors acquired using both conventional UIV (a) and (b) and plane wave UIV (c) and (d), under slow and fast flow conditions. Using conventional ultrasound, the slow flow condition (a) shows 18% overestimation due to beam sweeping, similar to [2], while (b) shows the loss of correlation under fast flow condition. By comparison the plane wave approach to UIV shows higher accuracy measurements and the potential to measure fast flow.

[1] F. Zhang et al., "In Vitro and Preliminary In Vivo Validation of Echo Particle Image Velocimetry in Carotid Vascular Imaging," *Ultrasound Med. Biol.*, vol. 37, no. 3, pp. 450–464, Mar. 2011.

[2] B. Zhou et al., "Ultrasound Imaging Velocimetry: Effect of Beam Sweeping on Velocity Estimation," *Ultrasound Med. Biol.*, vol. 39, no. 9, pp. 1672–1681, Sep. 2013.

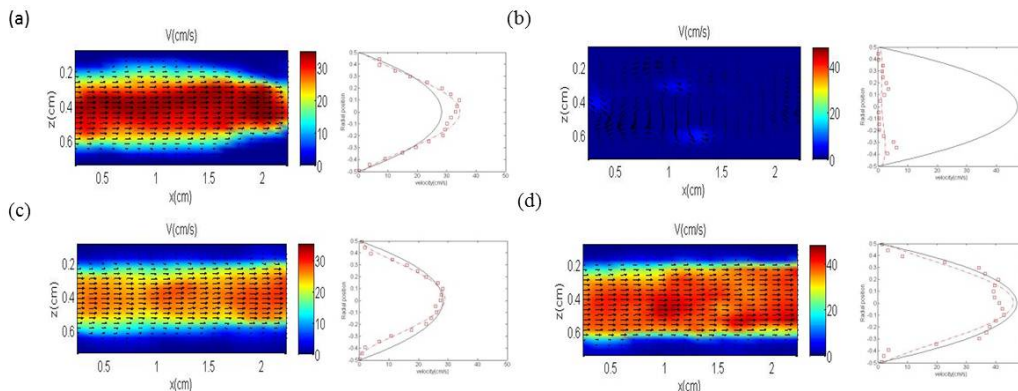


Figure: (a) Slow flow measurement using conventional ultrasound technique. (b) Fast flow measurement using conventional ultrasound technique. (c) Slow flow measurement using plane wave imaging technique. (d) Fast flow measurement using plane wave imaging technique. Notes: Vector images are averaged with 5 images and estimated using the same windows size; Flow profiles are taken from the centre of its corresponded vector image and the black line represent the analytical flow profile.



# P1B4 - MCA: Contrast Imaging Strategies

Salon C

Friday, September 5, 2014, 8:00 am - 5:00 pm

Chair: **Wilko Wilkening**  
Siemens Medical Solutions, Mountain View

P1B4-1

## Adapting amplitude modulation to plane-wave non-linear Doppler imaging

Charles Tremblay-Darveau<sup>1</sup>, Ross Williams<sup>2</sup>, Laurent Milot<sup>1,2</sup>, Matthew Bruce<sup>3</sup>, Peter Burns<sup>1,2</sup>, <sup>1</sup>University of Toronto, Canada, <sup>2</sup>Sunnybrook Health Sciences Centre, Canada, <sup>3</sup>Supersonic Imagine, France

### Background, Motivation and Objective

High frame-rate plane-wave ultrasound allows one to combine Doppler and contrast-enhanced imaging without compromising the ensemble length, thus maintaining SNR and flow sensitivity. We have shown in previous work [1] that pulse inversion Doppler (PID) [2] adds vessel hemodynamic data to microbubble perfusion imaging in real time. However, our ability to differentiate perfusion from the hyperechoic tissue signal is still limited by the contrast-to-tissue ratio (CTR). One way to improve the CTR is to use a Doppler sequence based on amplitude modulation (AM), which compares the echoes from driving pulses of different amplitudes. In this work, we show that although phase is not modulated, AM-Doppler (AMD) is feasible by using an appropriate renormalization of a Doppler vector. We also demonstrate that AM performs considerably better than PI as the acoustic pressure is decreased below 200kPa.

### Statement of Contribution/Methods

An AMD vector is acquired by repeatedly insonating the Definity microbubbles (Lantheus Medical Imaging Inc., MA,) with full and half amplitude (1/2) pulses at a pulse repetition frequency of 1-8kHz using an Aixplorer scanner (Supersonic Imagine, Aix-en-Provence, France). The received echo is then multiplied by 2 for (1/2) pulses. The linear and non-linear signal are centered around 0Hz and the Nyquist frequency, respectively. The Doppler profile from flowing microbubbles was compared to that of flowing linear scatterers (cornstarch) using both PID and AMD. The CTR was measured as a function of acoustic pressure. Perfusion of a rabbit kidney was imaged with AMD and PID.

### Results/Discussion

Both AMD and PID enabled segmentation of microbubbles from moving linear scatterers (Fig. 1a), but AM improved the CTR by ~19dB through a higher non-linear microbubble signal (10 dB) and a better tissue cancellation (-9 dB). The improved echogenicity of Definity with AM resulted from the non-linear fundamental, with only a small component at the second harmonics. In-vivo results also show a better CTR for AM (Fig. 1b) versus PI (Fig. 1c). This work opens the path to new trade-off opportunities in contrast-enhanced Doppler.

[1] C. Tremblay-Darveau et al., IEEE ULTSYM (2012), p.1315-1318

[2] D. Hope Simpson et al., IEEE Trans. Ultrason., Ferroelect., Freq. Contr. (2001), vol. 48 (6), p.1483-1494

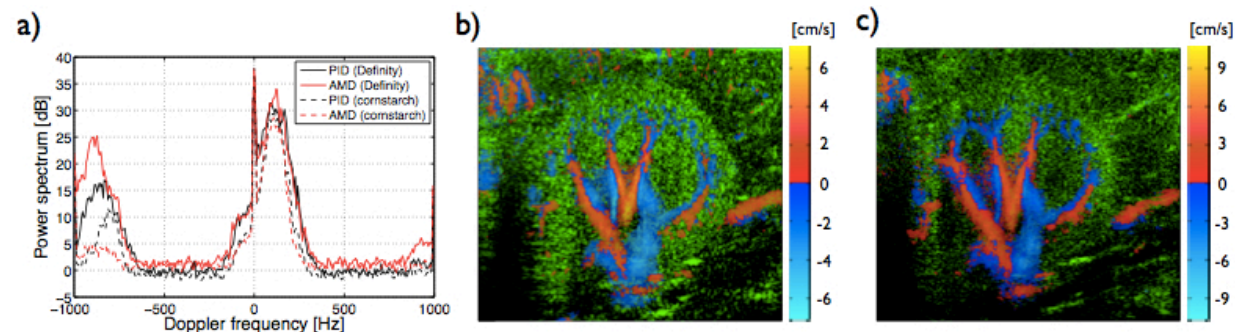


Figure 1: a) PID (black) vs AMD (red) for flowing microbubbles (solid) and linear scatterers (dash). b) AMD and c) PID colour Doppler of an in-vivo Rabbit kidney with a 160Hz frame rate at 4.5MHz centre frequency. The green colormap (normalized to the same dynamic range) corresponds to the AM/PI contrast-enhanced signal.

P1B4-2

## Contrast Enhanced Ultrasound Imaging using Adaptive Third-order Volterra Filter

JUAN DU<sup>1</sup>, Dalong Liu<sup>1</sup>, Emad Ebbini<sup>1</sup>, <sup>1</sup>University of Minnesota, Minneapolis, Minnesota, USA

### Background, Motivation and Objective

We have previously demonstrated the ability of the post-beamforming Volterra filter (VF) to separate linear and nonlinear echo components in contrast-enhanced ultrasound (CEUS) application, including imaging tumor perfusion in vivo. Compared to pulse inversion, the quadratic and cubic components from a 3rd-order VF (ThOVF) produce the same or higher level of contrast without sacrificing bandwidth or frame rate. However, CEUS imaging of small vessels with high level of sensitivity and specificity remains a challenge using clinical probes. Imaging such fine structures with highly focused beams may improve the specificity and sensitivity of CEUS in some applications.

### Statement of Contribution/Methods

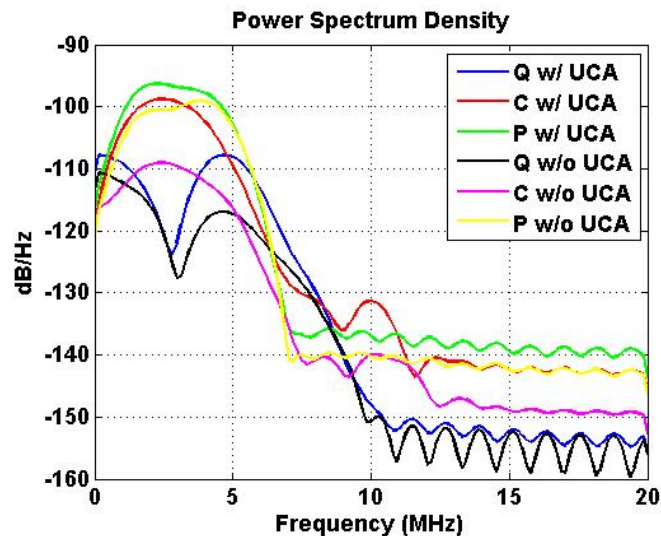
We have used a concave 64-element, 3.5-MHz array (40-mm roc) in cross sectional imaging a 200-μm cellulose tube (Spectrum Laboratories, Inc.) embedded in a tissue-mimicking phantom. An infusion syringe pump (KD Scientific) was used to pump a saline solution with small concentration of Targestar P (Targeson) or cellulose linear scatterers through the cellulose tube. Pulse inversion data was acquired using positive and negative transmit pulses for each image line. An adaptive 3rd order VF was applied to the



beamformed data to separate the linear, quadratic, and cubic signal components. Pulse inversion data was also obtained by summing the echoes due to the positive and negative transmit pulses. The quadratic and cubic components from the ThOVF were compared to the corresponding PI component with and without the UCA.

#### Results/Discussion

Fig. 1 shows the PSDs of the quadratic and cubic components of the ThOVF and the PI signal with and without UCA. All three signals show enhancement due to the presence of UCA in different frequency bands. For instance, the quadratic component shows enhancement in both the 2nd harmonic regime and low frequency. Similarly, the cubic component shows increased components in the fundamental band and in the 3rd harmonic band. The PI shows enhancement in the fundamental and 2nd harmonic bands. However, the quadratic and cubic components show higher levels of enhancement compared to approximately for PI. Specifically, the enhancement level is 9 dB, 10 dB and 4 dB for quadratic, cubic and PI components respectively. The results also demonstrate the advantages of localized UCA imaging using a highly focused transducer compared to a standard diagnostic probe.



P1B4-3

#### Spatiotemporal Denoising and Compression of Contrast-Enhanced Ultrasound Movies

Avinoam Bar Zion<sup>1</sup>, Charles Tremblay-Darveau<sup>2</sup>, Melissa Yin<sup>3</sup>, F. Stuart Foster<sup>2,3</sup>, Dan Adam<sup>1</sup>; <sup>1</sup>Department of Biomedical Engineering, Technion – Israel Institute of Technology, Haifa, Israel, <sup>2</sup>Department of Medical Biophysics, University of Toronto, Toronto, Ontario, Canada, <sup>3</sup>Sunnybrook Health Sciences Centre, Toronto, Ontario, Canada

#### Background, Motivation and Objective

Dynamic contrast-enhanced ultrasound (d-CEUS) is a promising modality used for the evaluation of tissue perfusion in various diseases and treatments. However, speckle noise, an inherent characteristic of d-CEUS cines and ultrasound images in general, reduces the contrast of these scans and limits their diagnostic value. Due to the fast-changing spatial distribution of microbubbles inside the vasculature, the noise in consecutive d-CEUS images is independent, simplifying its removal. Therefore, time-intensity curve (TIC) estimation is reformulated in this work as a spatiotemporal denoising problem. This problem is solved in the framework of wavelet denoising, without assuming a flow model or defining *a priori* the signal's degree of smoothness. Another objective of this study is the compression of these scans using the sparse representation of TICs in wavelet bases, facilitating the handling of high frame-rate scans.

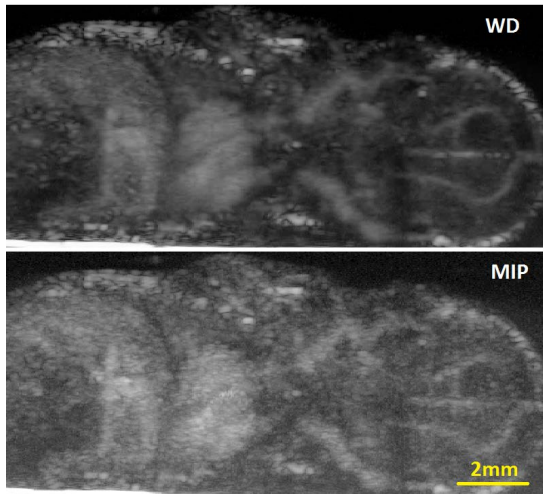
#### Statement of Contribution/Methods

In this work, a multiplicative model for the formation of speckled images was adopted. A pre-processing step was used for the removal of low value outliers from the log-transformed d-CEUS signals, enabling the use of wavelet denoising methods optimized for Gaussian white noise. Wavelet denoising was compared against MIP, temporal compounding and log-normal model fitting, in a series of *in-vitro* and *in-vivo* experiments. Scans from two mouse models were processed: mouse embryos (E17.5, n=8) and human xenograft hind-limb tumors (LS174T n=6, PC3 n=6). All these scans were performed using the Vevo<sup>®</sup>2100 scanner and MicroMarker<sup>™</sup> contrast agent.

#### Results/Discussion

Dynamic phantom experiments demonstrated improved estimation of single pixel time-intensity curves using wavelet denoising, when compared to log-normal model fitting ( $r = 0.74$  vs.  $r = 0.69$ ). In the *in-vivo* tests, the proposed approach resulted in improved noise removal (Fig 1, top), reflected by a significantly lower value of the spatial coefficient of variation in homogenous regions ( $C_v = 0.21$  vs.  $C_v = 0.34$ ), when compared to MIP (Fig 1, bottom). In addition, the denoised signal was highly compressible, represented using ~5% of the wavelet coefficients. In conclusion, the proposed approach successfully enhances the visualization of blood vessels while enabling high-resolution analysis of flow dynamics and compression of relevant denoised data.

# Mouse Embryo d-CEUS: Wavelet Denoising Vs. MIP



P1B4-4

## Contrast Detection Efficacy for Plane vs. Focused Wave Transmission

Jacopo Viti<sup>1,2</sup>, Francesco Guidi<sup>2</sup>, Hendrik J. Vos<sup>1</sup>, Nico de Jong<sup>1</sup>, Piero Tortoli<sup>2</sup>; <sup>1</sup>Biomedical Engineering, Erasmus Medical Centre, Rotterdam, Netherlands, <sup>2</sup>Information Engineering, Universita' degli Studi di Firenze, Firenze, Italy

### Background, Motivation and Objective

Plane-wave transmission with high number (N) of compounding angles has been suggested as a means to produce good quality images at pressure levels that do not destroy ultrasound contrast agents (UCA). In this paper, a programmable research platform is used to compare the contrast to tissue ratio (CTR) obtainable by focused (F) and plane wave (PW) power modulation (PM) imaging at pressure levels below 140 kPa. In particular, the influence of N on the CTR is investigated.

### Statement of Contribution/Methods

An agar-based tissue-mimicking material (TMM) was molded in a phantom containing a 5 mm diameter wall-less vessel, in which BR-14 UCA (Bracco Medical Imaging, Switzerland) with 1:2000 dilution was forced to flow at 10 cm/s.

The ULA-OP system was used with a linear array probe LA332 (Esaote, Italy) to perform F-PM and PW-PM contrast imaging. 4-cycle, Gaussian weighted pulses at 3.5 MHz were transmitted. In F-PM, the transmission (TX) was focused on the UCA; in PW-PM a programmable N was used (range: 1-64), covering a total angle of 13 degrees. The same peak-negative pressure (PNP) at the agent's location was maintained for both methods, in a pressure range that avoids destruction. The frame rate was in all cases fixed at 21 frames/s, as determined by the 3-pulse F-PM sequence (50/100/50% TX amplitude) complete 64-lines scan at 4 kHz PRF.

For each method, the raw RF data were processed offline to produce 64-line B-Mode images. Two same-sized regions of interest (ROIs) were selected in the images, covering the UCA and a piece of TMM, respectively. The CTR was calculated as the ratio of mean power measured in the two ROIs.

### Results/Discussion

The CTR measured in different experimental conditions is reported in Table 1. F-PM typically shows a CTR 3-5 dB higher than single-angle PW-PM. Compounding significantly improves the CTR. Especially at low TX power, major improvements are obtained by a limited n. of angles. Even at N=9, which is sufficient to guarantee good resolution, as will be shown by experimental images, the CTR increases by 6.5-7.8 dB and PW-PM outperforms F-PM.

To conclude, preliminary data indicate that PW-PM can be more sensitive than F-PM when performing low-pressure detection of UCA. Moreover a few compounding angles (in the range of 10) are sufficient to guarantee good performance in terms of resolution and CTR, thus making high frame rate contrast imaging actually feasible.

	CTR (dB)		
	140 kPa PNP	112 kPa PNP	70 kPa PNP
F-PM	24.1	21.3	19.8
PW-PM 1-angle (N=1)	19.0	17.4	16.2
PW-PM 9-angles (N=9)	26.1	25.1	22.7
PW-PM 63-angles (N=63)	28.1	28.5	27.1

P1B4-5

## Evaluation of Bias Voltage Modulation sequence for nonlinear contrast agent imaging using a cMUT array

Anthony Novell<sup>1,2</sup>, Mathieu Legros<sup>3</sup>, Jean-Marc Gregoire<sup>1</sup>, Paul Dayton<sup>2</sup>, Ayache Bouakaz<sup>1</sup>; <sup>1</sup>UMR Inserm U930, Université François-Rabelais de Tours, France, <sup>2</sup>Department of Biomedical Engineering, The University of North Carolina, Chapel Hill, NC, USA, <sup>3</sup>Vermont SA, Tours, France

### Background, Motivation and Objective

Over the past few years, Capacitive Micromachined Ultrasonic Transducers (cMUTs) have emerged as a promising alternative to traditional piezoelectric transducers. One notable advantage of cMUTs is their wide frequency bandwidth, however, their use in nonlinear imaging approaches such as those used to detect contrast agents have been challenging due

to their intrinsic nonlinear behavior. In this context, a new contrast imaging sequence, called bias voltage modulation (BVM), was specifically developed for contrast agent detection.

#### Statement of Contribution/Methods

A multi-pulse scheme was designed in which three successive pulses were transmitted with different amplitudes. The amplitude variation was only applied on the bias voltage ( $V_{dc}$ ) modulation which was varied for the three transmitted pulses (called  $P_1$ ,  $P_2$ ,  $P_3$ ) with an amplification factor of 1, 2 and 3. The amplitude of excitation voltage ( $V_{ac}$ ) remained exactly the same. All received tissue echoes from the transmitted fundamental frequency ( $f_0$ ) component and harmonics ( $2f_0$ ) arising from nonlinearities in the cMUT were cancelled by the following operation:  $E_3 + 3E_1 - 3E_2$  where  $E_i$  is the backscattered signal from  $P_i$ . In-vitro validation was performed using a 64-element cMUT probe centered at 5 MHz (99% bandwidth at -3dB) and connected to an open scanner using a mechanical index of 0.32.  $V_{dc}$  was fixed at 20 V, 40 V and 60 V according to the transmitted pulse while  $V_{ac}$  was set to 40 V<sub>peak</sub>. Images of a flow phantom setup containing SonoVue microbubbles were recorded. The efficiency of BVM sequence was compared to 2nd harmonic imaging (2H) and amplitude modulation (AM).

#### Results/Discussion

Experimental results show that a complete cancellation of the nonlinear signal from the source was reached when the BVM sequence is implemented. After processing, the backscattered signal from a linear reflector is reduced by 30 dB and 15 dB at  $f_0$  and  $2f_0$  components, respectively. The approach allows the preservation of nonlinear response from microbubbles at  $f_0$ ,  $2f_0$  and  $3f_0$  due to the wide frequency bandwidth of the cMUT probe. In comparison to 2H and AM imaging modes, BVM sequence induces an increase of the contrast to tissue ratio of 17.4 dB and 6.1 dB, respectively. These results reveal that the cMUT intrinsic nonlinearity can be addressed, thus expanding the potential of this transducer technology for nonlinear contrast agent detection.

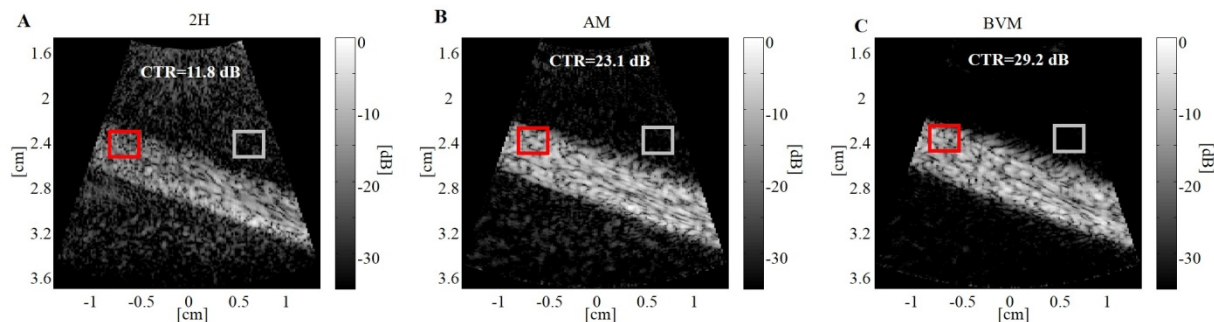


**Figure 1.** In-vitro images of a flow phantom containing a diluted solution of SonoVue. Imaging resulting from 2<sup>nd</sup> harmonic, amplitude modulation and bias voltage modulation are displayed in panel A, B and C, respectively. Each image is displayed with 35 dB dynamic range.

#### P1B4-6

##### Detection of early therapeutic response with dynamic contrast enhanced ultrasound (DCE-US) using a perfusion clustering algorithm

Guillaume Barrois<sup>1</sup>, Alain Coron<sup>1</sup>, Lori S. Bridal<sup>1</sup>; <sup>1</sup>Laboratoire d'Imagerie Biomédicale UPMC, CNRS UMR7371, INSERM U1146, PARIS, France

#### Background, Motivation and Objective

DCE-US has been applied in clinical and pre-clinical studies, to monitor microvascular tumoral response to antiangiogenic therapies. Flow quantification in DCE-US 2D+t is generally done by averaging the signal in large regions of analysis and then fitting parametric models to the obtained echo-power (EP) versus time curves. This approach leads to a loss of spatial information concerning the microvascular flow distribution throughout the tumor. This work adapts a clustering method developed previously for evaluation of contrast-enhanced computed tomography [1] to DCE-US data and tests its sensitivity to antiangiogenic modifications in a pre-clinical tumor model.

#### Statement of Contribution/Methods

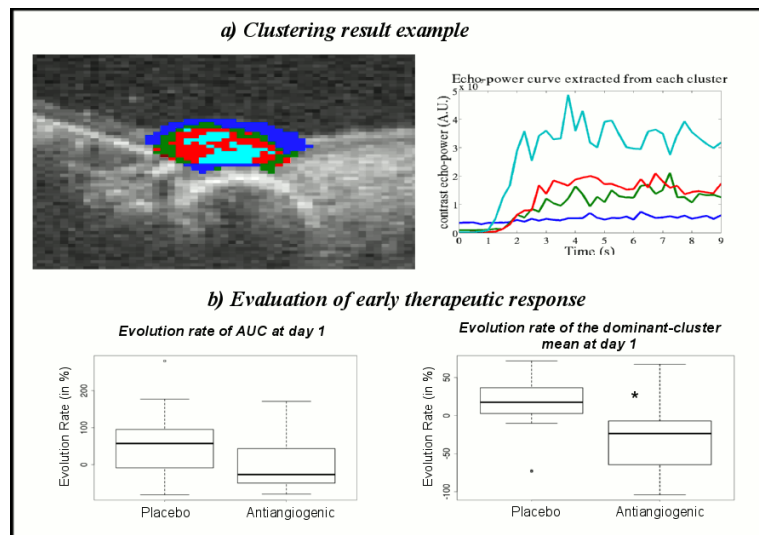
Pancreatic adenocarcinomas were induced by subcutaneous injection of cells in 21 mice. DCE-US sequences (20s) were acquired before and one-day after administration of therapy. Eight mice received antiangiogenic therapy. Thirteen others received a placebo.

The clustering algorithm regroups pixels based on the statistical similarity of the signal versus time curves dynamics. To accelerate clustering, sequences were downsampled by a factor of 3. The EP vs time curve for each 3 x 3 pixels region underwent logarithmic transformation to comply with the algorithm's assumptions. Clusters were identified throughout a region of interest delimiting the whole tumor. The mean EP value between 0 and 20s was computed for each cluster and the highest value was retained. For each tumor, the EP versus time curves were also extracted from whole-tumor regions of interest. These curves were fit to a lognormal model and the area under the curve (AUC) extracted. Results indicating the % change at day 1 relative to baseline for the dominant-cluster mean flow and the full-tumor AUC are compared.

#### Results/Discussion

For the evolution of AUC, the difference between Placebo and treated group was not significant. The evolution of the dominant-cluster mean flow, however, was significantly lower for the group receiving antiangiogenic therapy ( $p < 0.05$ ). This shows the potential interest of the method for more sensitive monitoring of antiangiogenic modifications with potential toward development of sensitive mapping of the heterogeneous microvascular remodeling.

[1] – Yves Rozenhole et al. : «DynClust: Denoising and clustering for dynamical image sequence (2D or 3D)+T», R-package available on CRAN.



P1B4-7

### New reference-free, simultaneous motion-correction and quantification in dynamic contrast-enhanced ultrasound

Guillaume Barrois<sup>1</sup>, Lori S. Bridal<sup>1</sup>, Alain Coron<sup>1</sup>; <sup>1</sup>Laboratoire d'Imagerie Biomédicale UPMC, CNRS UMR7371, INSERM U1146, PARIS, France

#### Background, Motivation and Objective

Analysis of 2D+t, dynamic contrast-enhanced ultrasound sequences to assess microvascular flow can be complicated by motion, and thus, often must be preceded by image registration. Common registration strategies rely on operator-selection of a reference image, against which other images in the sequence are re-aligned. If the choice made does not well-represent features, registration accuracy is undermined. In turn, regions selected for flow assessment will be poorly tracked, leading to errors in the estimation of the echo-power (EP) vs. time curve. We propose an automatic method to combine motion-correction and flow-quantification (M/Q) in a single algorithm, thereby, eliminating operator-dependent choice of a reference image.

#### Statement of Contribution/Methods

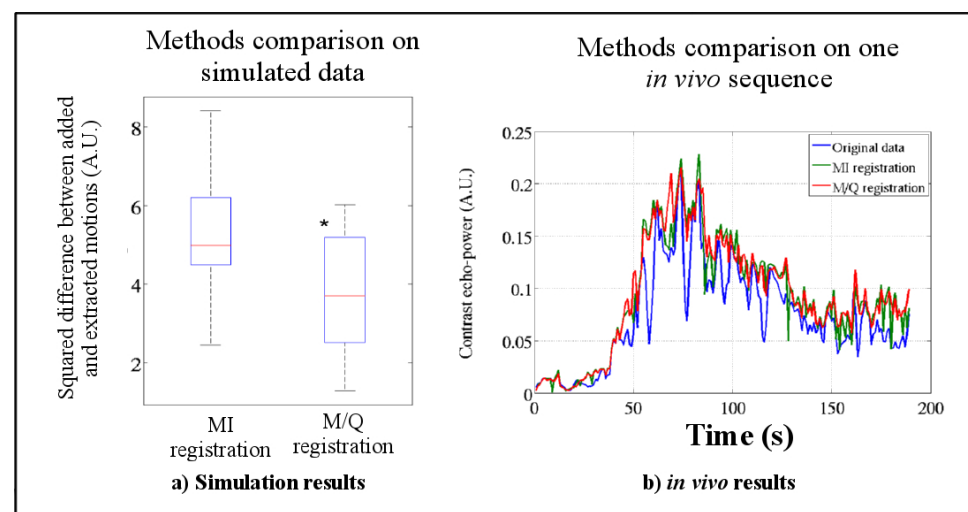
First, a parametric curve is fit (MM metric described in [1]) to the EP vs. time curve from each 3x3 pixel region of the initial sequence. The original sequence is then registered with respect to a smoothed sequence extracted from the parametric fits based on minimization of the MM metric. These steps are repeated iteratively until convergence. A final registration is performed to remove persistent, low-amplitude motion artifacts against the sequence smoothed in the temporal dimension.

The new method was compared to registration using mutual information (MI) to a reference image selected by an expert. For this, 27 sequences were simulated with known motion. Performance was assessed quantitatively based on the squared difference between the estimated motion and the added known motion. Motion compensation was also compared qualitatively for 12 sets of motion-artefacted, patient data, based on visual comparison of the EP vs. time curves in selected ROIs.

#### Results/Discussion

Fig. 1 a) squared difference between the estimated motion and the true motion for the simulated data set was significantly lower for M/Q ( $p < 0.05$ ). Fig. 1 b) EP vs. time curves from a tumoral region in patient data: before and after registration. M/Q handles large variations due to breathing motion better than MI. A central originality is that flow quantification and motion estimation are done in a single optimization process. This improved registration should, in turn, provide more robust quantification of perfusion parameters in the presence of motion.

[1] - Barrois et al. (2013). A multiplicative model for improving... *IEEE Trans. on UFFC*



P1B4-8

**Transcranial functional ultrasound using ultrafast Doppler with microbubbles**

Claudia Errico<sup>1</sup>, Bruno-Felix Osmanski<sup>1</sup>, Sophie Pezet<sup>2</sup>, Olivier Couture<sup>1</sup>, Zsolt Lenkei<sup>2</sup>, Mickael Tanter<sup>1</sup>; <sup>1</sup>Institut Langevin (ESPCI, CNRS, INSERM, Paris Diderot), Paris, France, <sup>2</sup>Laboratoire de Neurobiologie (ESPCI, CNRS UMR 7637), France

**Background, Motivation and Objective**

Functional Ultrasound (fUS) has been validated as a novel imaging technique capable of measuring the brain activity through the neurovascular coupling with a high spatio-temporal resolution (1ms, 100µm). It relies on the high sensitivity ultrafast Doppler based on plane wave imaging. However, due to the attenuation of the skull, this method requires a cranial window (thinning skull or craniotomy) which is a highly invasive surgical procedure. In this work, we propose to perform transcranial fUS by enhancing the blood signal with contrast agents.

**Statement of Contribution/Methods**

In-vivo experiments were performed on 4 rats following two different imaging protocols: half-thinned skull (A) and full transcranial (B) imaging. fUS and activations were achieved without contrast agent and following an injection of 200µL of microbubbles (2\*10<sup>7</sup> SonoVue /ml). In-vivo activations of the brain were performed using 5 electrical stimulations (5s) of the sciatic nerve with an on/off pattern. The activation was performed 1min after the injection of microbubbles and the acquisition lasted 150 s. The fUS sequence consisted in insonifying the brain at 500Hz using a compounded sequence of 9 tilted plane waves (PRF=4500Hz) with a 15MHz probe (128 elements) connected to an ultrafast scanner (SSI, France). The signal coming from the tissue was removed by using a high-pass filter with a cut-off frequency of 75Hz.

**Results/Discussion**

Vascular maps are shown on the grayscale background of figure 1. The activated areas, shown as color overlays, are extracted by correlating the increase in the cerebral blood volume with the targeted electrical stimulation pattern. Strong activation in the corresponding sensory-motor cortex could be observed under the thin skull window (fig 1A, correlation coefficient ( $\rho$ ) =0.6±0.2). However, because of high attenuation due to the skull, the activation could not be observed without microbubbles transcranially (fig 1B). With the addition of microbubbles, activation could be observed without the skull (fig 1C,  $\rho$ =0.40±0.06), but also when the cortex is observed through the skull (fig 1D,  $\rho$ =0.35±0.07).

This experiment has demonstrated that functional ultrasound can be performed transcranially when microbubbles are injected in rats. These results pave the way to human functional ultrasound.

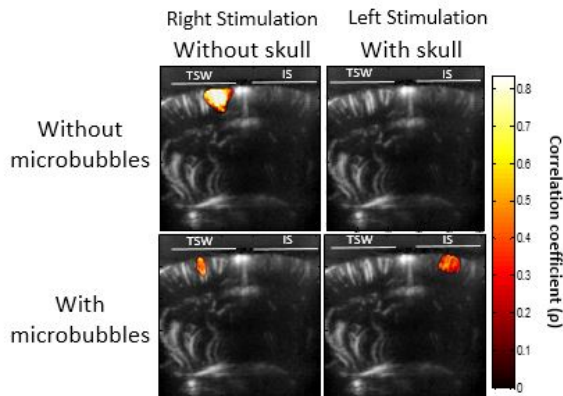


Fig 1: Activation of the contralateral sensory-motor cortex is observed under the unilateral thinned-skull window (TSW) after electric stimulation of the right sciatic nerve with or without injection of a vascular contrast agent (inert gas microbubbles). Whereas, under the intact skull (IS) after activation of the left sciatic nerve, the cortical activation could only be detected with the injection of microbubbles (IS side after left sciatic nerve stimulation).

P1B4-9

**Ultrasound Contrast Plane Wave Imaging with Higher CTR based on Bubble Wavelet Transform**

Diya Wang<sup>1</sup>, Xuan Yang<sup>1</sup>, Jinjin Wan<sup>1</sup>, Bowen Jing<sup>1</sup>, Mingxi Wan<sup>1</sup>; <sup>1</sup>Department of Biomedical Engineering, Xi'an Jiaotong University, Xi'an, Shaanxi, China, People's Republic of

**Background, Motivation and Objective**

Although ultrasound contrast plane wave imaging (UCPI) can avoid the repeated disruption and capture the transient spatial distribution of microbubbles (MBs), it is still limited by lower contrast-to-tissue ratio (CTR) and SNR due to its scan mode and lower negative peak pressure. The purpose of this paper was to improve the CTR of UCPI by pulse inversion MB wavelet transform imaging (PIWI) and enhance the SNR of time-intensity-curve (TIC) by detrended fluctuation analysis (DFA).

**Statement of Contribution/Methods**

First, a pair of MB wavelets was constructed by MB scattering echoes predicted by modified Herring equation driven by two inverted plane waves. Next, the original echoes from such plane waves were performed by MB wavelet correlation analysis. Then, such echoes replaced by the maximal wavelet correlation coefficients were summed to distinguish echoes of MBs and tissues. Finally, the fluctuations of TIC and CTR curves caused by plane wave scan mode were removed by DFA in order to evaluate perfusion.

**Results/Discussion**

The results from perfusion experiments of vessel-bone phantom indicated that UCPI had the advantages of lower disruption, longer lifetime of MBs, and could capture transient reperfusion distribution of MBs in vessel. CTR of UCPI using PIWI was increased by 10.7-16.8 dB over UCPI and 9.0-15.2 dB over line-by-line focus imaging. Besides that, the disturbance of guided wave from bone surface was also restrained and spatial resolution of UCPI was improved by PIWI with the lowest disruption ratio 0.156. Moreover, the fluctuations of TIC and CTR were obviously removed by DFA with quality of fitting up to 0.88. In summary, these methods could contribute to UCPI and perfusion evaluation by allowing the continuous monitoring of the accumulation of MBs with higher CTR and SNR.



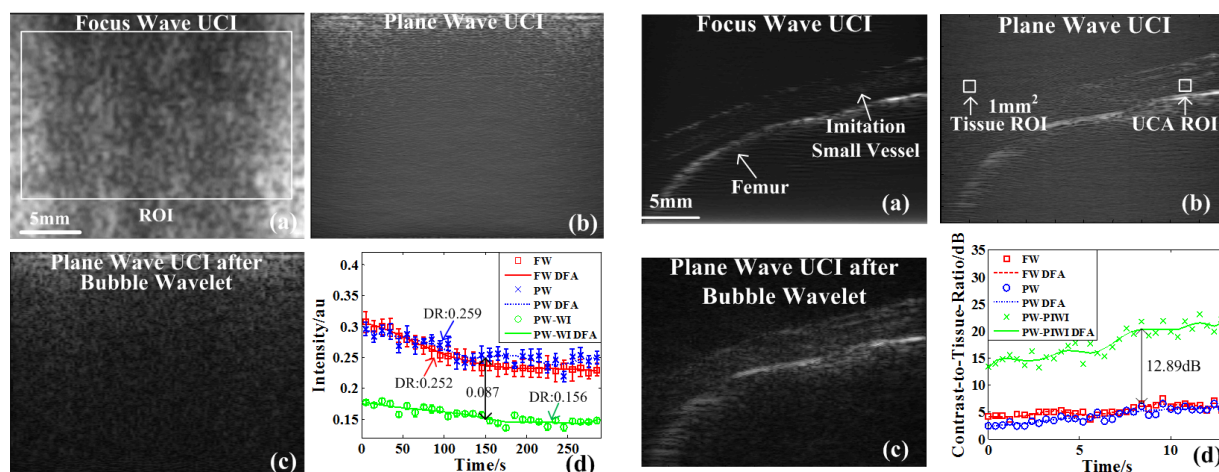


**Fig.1** The lifetime and disruption ratio (DR) detection of MBs at line-by-line focus wave (a), plane wave (b) and result of PIWI (c) in 150 s, whose TICs and results of DFA are shown in (d).

**Fig.2** The MBs perfusion of vessel-bone phantom at line-by-line focus wave (a), plane wave (b) and result of PIWI (c) in 8.4 s, whose CTR curves and results of DFA are shown in (d).

P1B4-10

### Three-Dimensional Ultrasound Imaging of Rat Brain Vasculature Using a Human-Scale Sparse Hemispherical Array

Meaghan O'Reilly<sup>1</sup>, Kullervo Hynynen<sup>1,2</sup>, <sup>1</sup>Sunnybrook Research Institute, Toronto, Ontario, Canada, <sup>2</sup>University of Toronto, Canada

#### Background, Motivation and Objective

The ability to image small vascular structures in the brain could greatly enhance our understanding of brain function and disease. However, the need to image deep tissue structures, and through the skull bone, necessitates the use of low ultrasound frequencies and limits imaging resolution. We have previously shown on the benchtop that we can image tubing of approximately 250  $\mu\text{m}$  diameter through an *ex vivo* human skull, using a hemispherical sparse array operating at 306 kHz and a passive beamforming method [1]. By applying super-resolution methods we were further able to image well beyond the diffraction limit [1]. Here we investigate these methods for imaging rat brain vasculature.

#### Statement of Contribution/Methods

Male Wistar rats (150-400 g) were used in this study. The hair was removed from the heads and the animals were coupled to the ultrasound array via a waterbath. The ultrasound array was as described in [1]. In brief, 128 receive elements (2.54 mm diameter,  $f_c=612$  kHz) were sparsely distributed over the aperture of a 306 kHz, 30 cm diameter hemispherical therapy array [2]. A subset of 128 transmit elements was excited using 5 cycle bursts at a repetition rate of 100 Hz. The transmit focus was scanned over the whole brain (approx.  $15 \times 20 \times 10$  mm<sup>3</sup>) in 1 mm steps. The signals at the receivers were captured using a multichannel receiver at a sampling rate of 10 MHz. Next a solution of microbubbles (Definity, Lantheus Medical Imaging) was injected via the tail vein and the imaging sequence was repeated. Various concentration of microbubbles, and both continuous infusions and boluses, were investigated. MR imaging was performed on a 1.5 T MRI before and after treatments to confirm the ultrasound scan area and assess the integrity of the Blood-Brain barrier (BBB) following the ultrasound imaging. The captured data was post-processed in Matlab. Data acquired without the bubbles in circulation were subtracted from the subsequent sonifications in order to suppress signals from static objects. Images were reconstructed using a passive beamforming technique. Super-resolution techniques were applied to images acquired at low bubble concentrations to further improve image resolution.

#### Results/Discussion

The resulting images were compared with micro-CT data sets of rat brain vasculature. Preliminary results show that structures such as the rat internal carotid and Circle of Willis (approx. 200  $\mu\text{m}$  diameter) can be imaged. Application of the super-resolution techniques greatly improved the image quality. MR imaging showed no damage to the BBB or tissue as a result of the ultrasound imaging. Continued studies will assess the ability of this method, and various post-processing techniques, to resolve even smaller vascular structures.

[1] O'Reilly and Hynynen, Medical Physics (2013), [2] Song and Hynynen, IEEE TBME (2010)

## P1B5 - MCA: Acoustics and Manipulations

Salon C

Friday, September 5, 2014, 8:00 am - 5:00 pm

Chair: **Michel Versluis**  
*Physics of Fluids Group, University of Twente*

P1B5-1

### Optimization of ultrasound contrast agent for high frequency ultrasound molecular imaging using subharmonic oscillation

**Verya Daeichin**<sup>1</sup>, Klazina Kooiman<sup>1</sup>, Ilya Skachkov<sup>1</sup>, Johan G. Bosch<sup>1</sup>, Antonius van der Steen<sup>1,2</sup>, Nico de Jong<sup>1,2</sup>; <sup>1</sup>Biomedical Engineering, Thorax Center, Erasmus MC, Rotterdam, Netherlands; <sup>2</sup>Technical University Delft, Netherlands

#### Background, Motivation and Objective

Ultrasound molecular imaging visualizes disease biomarkers using targeted ultrasound contrast agents (t-UCA). t-UCA are functionalized with specific ligands bound to their coated shells [1]. Different lipids result in UCA with different acoustic behavior [2]. In this study, SH response of MicroMarker UCA and four homemade UCA with different lipid coatings were compared in-vitro with array-based micro-ultrasound system (Vevo 2100).

#### Statement of Contribution/Methods

UCA with a C4F<sub>10</sub> gas core were made with DSPC (bubble A and C) or DPPC (bubble B and D) as main lipid by sonication (bubble A and B) or Vialmix (bubble C and D), resulting in different size distribution (Fig. 1). We transmitted long bursts (20-cycle, 30 MHz, 10% power, MS250 probe) with pulse inversion sequence for optimized SH imaging [3]. The effect of the UCA concentration on SH imaging was tested using two concentrations: 8.0×10<sup>6</sup> and 4.0×10<sup>5</sup> bubbles per milliliter. Three regions of interests (ROI) were selected within UCA area: before focus (15 mm), at focus (18 mm), and after focus (21 mm). 200 RF lines were averaged in frequency domain for analysis of UCA responses at fundamental (30 MHz) and SH (15 MHz) frequencies within each ROI.

#### Results/Discussion

Fig. 1 shows SH images at high and low UCA concentrations and corresponding spectra for the three ROIs. For A, B and D type UCA, attenuation effect is dominant at high concentration. MicroMarker and C type UCA had the highest and most homogeneous SH response throughout entire UCA area at high concentration. Although nonlinear fundamental responses of MicroMarker dropped 10 dB in ROIs below and above focus, SH amplitude stayed constant in all three ROIs. SH amplitude of MicroMarker dropped about 11 dB when UCA concentration was reduced by factor of 20. For this low concentration, SH amplitude of B type UCA was 10 dB higher than that for MicroMarker and was homogeneous throughout UCA area.

We showed that for 30 MHz transmit frequency, at low concentration of UCA, DPPC bubbles have higher SH responses than DSPC ones and at high concentration, smaller bubbles (MicroMarker and C) produce the most homogeneous SH responses. Our results suggest a high concentration of MicroMarker or C type UCA for SH imaging.

In conclusion, for molecular imaging applications where UCA concentration is low, our DPPC bubble produced by sonication (B) is a good choice for SH imaging.

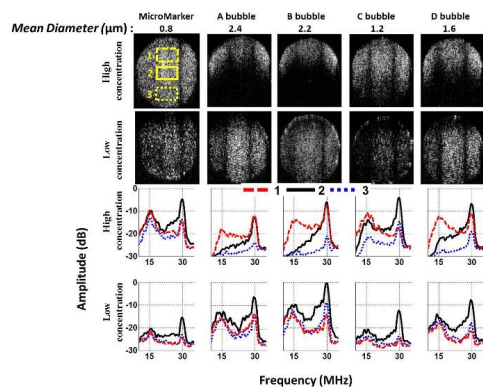


Figure 1. Subharmonic images of MicroMarker UCA and homemade A, B, C and D type UCA at high (8.0×10<sup>6</sup> microbubbles/ml) and low (4.0×10<sup>5</sup> microbubbles/ml) concentrations (top panel) and the corresponding spectra of each region of interest at three depths for each image (bottom panel).

*This research was supported by the Center for Translational Molecular Medicine and the Netherlands Heart Foundation (PARISK).*

[1] Klibanov, Med Biol Eng Comput 47:875, 2009.

[2] Van Rooij et al., IEEE Proceedings 2013.

[3] Daeichin et al., IEEE Proceedings 2013.

P1B5-2

### Optimization of Contrast-to-tissue Ratio and Role of Bubble Destruction in Dual-Frequency Contrast-Specific “Acoustic Angiography” Imaging

**Brooks Lindsey**<sup>1,2</sup>, Juan Rojas<sup>1,2</sup>, Sarah Shelton<sup>1,2</sup>, Heath Martin<sup>1,2</sup>, Paul Dayton<sup>1,2</sup>; <sup>1</sup>Biomedical Engineering, University of North Carolina, Chapel Hill, North Carolina, USA; <sup>2</sup>Biomedical Engineering, North Carolina State University, Raleigh, USA

#### Background, Motivation and Objective

Recently, dual frequency transducers have enabled high spatial resolution and high-contrast imaging of microvasculature with minimal tissue artifacts by transmitting at a low frequency and receiving broadband superharmonic echoes from microbubble contrast agents. This technique has previously distinguished between healthy and cancerous

microvasculature in a rodent fibrosarcoma model. In this work, we examine the imaging parameters for optimizing contrast-to-tissue ratio (CTR) for dual-frequency imaging and the relationship between bubble destruction and broadband harmonic signal production.

#### Statement of Contribution/Methods

Confocal piston transducers were used in a water bath setup to measure the signal-to-noise ratio (SNR), CTR, and axial resolution for microbubble superharmonic signals at transmit frequencies from 1.5 - 8 MHz and receiving frequencies from 7.5 - 25 MHz. CTR and resolution were also investigated as a function of peak negative pressure (0.2 - 2 MPa), microbubble concentration (0.01% - 1.0%), and microbubble diameter (1 - 4  $\mu$ m).

As part of this study, the mechanism of superharmonic signal production was investigated through simultaneous optical-acoustic single bubble measurements at a common focus while transmitting 5 successive single-cycle pulses. Transmit frequency (1.75 - 3.75 MHz), peak negative pressure (100 - 500 kPa), and bubble diameter (1-4  $\mu$ m) were varied independently. Acoustic signals were recorded using a 10 MHz transducer. Frequency-pressure optimizations and bubble destruction were then assessed in 2 rodents within the frequency limitations of our dual-frequency imaging transducer (3.5-4.5 MHz, 0.7-1.3 MPa) at two frame rates (4 and 7 Hz) and peak negative pressures 500-1300 kPa.

#### Results/Discussion

CTR is maximized (25.5 dB) at the lowest transmit frequencies but maintains a broad peak within the 1.5-3.5 MHz range. At these frequencies, CTR is optimized when receiving at a center frequency of 10 - 15 MHz. A 4  $\mu$ m-diameter microbubble population yielded ~5 dB higher CTR than a 1  $\mu$ m population.

For  $n=250$  single bubbles, three primary categories of bubble behavior were observed optically: 1) no change in bubble diameter, 2) bubble shrinking (dissolution), and 3) immediate bubble destruction (fragmentation). Matched acoustic data indicate that superharmonic signals having the broadest bandwidth and highest energy are produced when bubbles are broken. In the dissolution case, a weaker superharmonic signal is produced having an amplitude approximately 25% of the signal when bubbles break. Similar regimes were observed in vivo: Increasing frame rate from 4 to 7 Hz decreased mean steady-state image brightness by 27.0% at 1000 kPa and 28.8% at 1300 kPa. These results suggest that bubble diameter, transmit frequency, peak negative pressure, and frame rate must be selected in light of the intended application, accounting for attenuation and local perfusion rate in the region of interest.

#### P1B5-3

#### Ultrasound Imaging from Vaporization Signals Emitted by Phase Change Contrast Agents

Christopher Arena<sup>1</sup>, Anthony Novell<sup>1</sup>, Paul Sheeran<sup>1</sup>, Connor Puett<sup>1</sup>, Linsey Phillips<sup>1</sup>, Paul Dayton<sup>1</sup>; <sup>1</sup>Joint Department of Biomedical Engineering, University of North Carolina - North Carolina State University, USA

#### Background, Motivation and Objective

Phase change contrast agents (PCCAs) exhibit a unique acoustic signature during the transition from a liquid filled nanodroplet to a gas filled microbubble [1]. Here, we demonstrate that this event can be used to generate an ultrasound image, and that the signal can be separated from that of a conventional microbubble. This presents a new opportunity to monitor PCCA activation in both diagnostic and therapeutic applications.

#### Statement of Contribution/Methods

A 'pulse high, listen low' scheme was implemented to isolate vaporization signals. Specifically, a confocal, dual-frequency transducer was used to transmit a 2 cycle, Gaussian enveloped sinusoid at 8 MHz from the inner element and passively receive at 1 MHz from the outer element. A microcellulose tube (350  $\mu$ m diameter) was placed in heated (37°C) degassed water at the focus and angled at 15° to reduce wall reflections. PCCAs were generated by condensing microbubbles with an octafluoropropane gas core according to established techniques, and a concentration of 0.3% was continuously infused at 50  $\mu$ l/min. LabVIEW was used to raster the transducer in the elevational (4 mm, 121  $\mu$ m steps) and lateral (3 mm, 125  $\mu$ m steps) dimensions. Signals were filtered (100 kHz to 3 MHz pass band) and amplified (32 dB) prior to A/D conversion. Five acquisitions were made per location, and images were created using a custom MATLAB script that filtered the data (500 kHz to 900 kHz pass band) and used the highest energy signal within a 30  $\mu$ s window as the representative pixel value at each location.

#### Results/Discussion

At low pressures, vaporization signals from PCCAs were of significantly higher energy than signals emitted from the equivalent microbubble formulation. When a peak negative pressure (PNP) of 242 kPa was transmitted the contrast to noise ratio (CNR) was 16 dB for PCCAs, 0.7 dB for microbubbles, and 0 dB for a water control. As the PNP was increased to 445 kPa, these values changed to 18.5 dB, 16.9 dB, and -0.1 dB, respectively. Additionally, with increasing pressure the apparent diameter of the tube increased from 0.71 mm at 242 kPa to 1.15 mm at 445 kPa. Thus, the lateral resolution decreased with increasing pressure, due to the fact that the focal zone capable of inducing vaporization expanded. Future work will explore the limits of resolution axially, which we hypothesize is dictated by the initial size of the PCCAs.

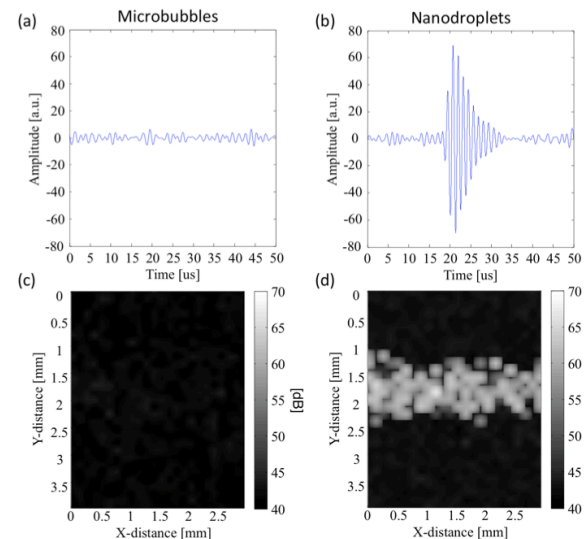


Figure: Example of raw radiofrequency data at a PNP of 242 kPa for (a) microbubble oscillation and (b) nanodroplet vaporization. The corresponding images formed from (c) microbubble and (d) nanodroplet signals. The cellulose tube is visible on the image formed from nanodroplet signals. Data was obtained using a transducer with high (transmit, 8 MHz) and low (receive, 1 MHz) frequency confocal elements.

[1]: P. S. Sheeran, T. O. Matsunaga, and P. A. Dayton, 'Phase Change Events of Volatile Liquid Perfluorocarbon Contrast Agents Produce Unique Acoustic Signatures', *Phys Med Biol*, 59 (2014), 379-401.

## P1B5-4

**Detecting and quantifying activation of perfluorocarbon based phase-change contrast agents using ultrasound**

Sinan Li<sup>1</sup>, Shengtao Lin<sup>1</sup>, Terry O. Matsunaga<sup>2</sup>, James J. Choi<sup>1</sup>, Robert J. Eckersley<sup>3</sup>, Meng-Xing Tang<sup>1</sup>; <sup>1</sup>Department of Bioengineering, Imperial College London, United Kingdom, <sup>2</sup>Department of Radiology Research, University of Arizona, USA, <sup>3</sup>Biomedical Department, King's College, United Kingdom

**Background, Motivation and Objective**

One limitation of microbubble mediated ultrasound techniques is that microbubble contrast agents are typically a few microns in size, preventing their permeability and therefore restricting the scope of applications to endovascular space. Recently, development of phase-change contrast agents (PCCAs) makes ex-vasculature applications possible. PCCAs are initially produced on the scale of a few hundreds of nanometres by condensing microbubbles into droplets. These droplets can then be activated (vaporised) to microbubbles by an ultrasound pulse. PCCAs offer a unique opportunity for imaging and therapeutic ultrasound applications beyond endothelial wall. We report a method to detect and quantify PCCAs activation acoustically. The aim is to develop a practical tool for monitoring and evaluating droplet activities in-vivo.

**Statement of Contribution/Methods**

Perfluorocarbon based PCCAs [1] are used in this study. We aligned two focused ultrasound transducers - one transmitting 10 MHz pulses to activate PCCAs and a second receiving with a 3.5 MHz central frequency to passively detect interrogation echoes from the microtube both pre and post activation. Optical microscopy was used to observe droplet vaporisation. The focus of the microscope coincides with the foci of the two acoustic transducers allowing cross-validation.

Activation of PCCAs of various concentrations in a micro-tube was facilitated by a 10 cycle ultrasound pulse with a mechanical index of 1.7. Before and after the activation pulse, two interrogation pulses with lower pressure (MI<0.3) were sent to investigate changes in acoustic properties due to vaporisation. Any differences, pre and post activation, were quantified. Corresponding measurements were made in both water and water-bubble mixtures as controls.

**Results/Discussion**

Optical views of PCCAs before and after activation are shown in Fig1(a), and the differences in acoustic measurements between the two interrogation pulses are shown in Fig1(b). Compared with control measurements, PCCA activation generated a significant difference between two interrogation pulse echoes. The amplitude of the 'difference signal' at fundamental frequency showed good sensitivity and correlation to the independently measured droplet concentration and the corresponding optical observations.

[1] Sheeran, P.S., et al., Langmuir, 2011. 27(17): p. 10412.

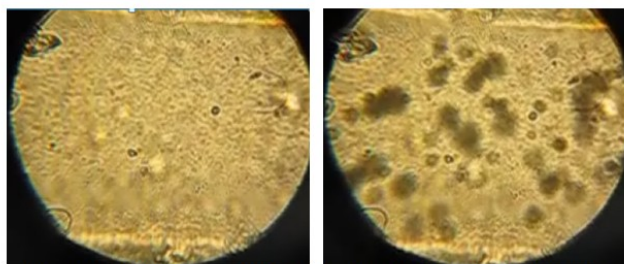


Figure 1(a) Pictures of PCCAs before (left) and after (right) ultrasound activation pulse; the black shadows in right are the bubbles vaporised from PCCAs. The diameter of scope is around 180  $\mu\text{m}$ .

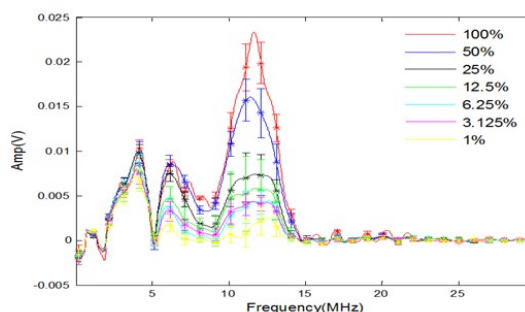


Figure 1(b) Subtraction of spectra of two interrogation pulses echo for droplet emulsions with various concentrations

## P1B5-5

**Imaging laser activated microbubble recondensation kinetics using high frame rate ultrasound**

Alexander Hannah<sup>1</sup>, Geoffrey Luke<sup>2</sup>, Stanislav Emelianov<sup>1</sup>; <sup>1</sup>Biomedical Engineering, The University of Texas at Austin, Austin, TX, USA, <sup>2</sup>Electrical and Computer Engineering, The University of Texas at Austin, Austin, TX, USA

**Background, Motivation and Objective**

Ultrasound and photoacoustic contrast agents can be used to improve image contrast and probe the tissue for valuable diagnostic information. Specifically, light-activated liquid perfluorocarbon nanodroplets amplify photoacoustic signal through vaporization and enhance ultrasound contrast through bubble formation. High boiling point nanodroplets consisting of a perfluorohexane (boiling point = 56°C) core undergo repeatable vaporization/recondensation cycles in response to pulsed laser irradiation. We used high frame rate ultrasound imaging to demonstrate the recondensation kinetics of perfluorohexane nanodroplets. Specifically, recondensation kinetics was investigated in relationship to tissue stiffness – a functional indicator of disease.

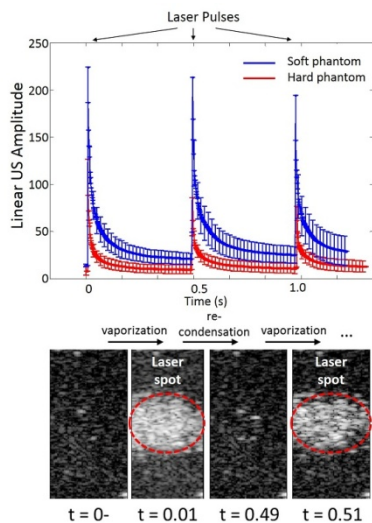
**Statement of Contribution/Methods**

Perfluorohexane photoacoustic nanodroplets were made by adding fluorinated gold nanorods to a solution of 0.3 mL perfluorohexane, 1.5 mL water, and 0.5 mL of 1% Zonyl FSO fluorosurfactant, followed by sonication to form nanodroplets. The particles were diluted 1000x and added to each of two polyacrylamide phantoms, made with varying concentrations of acrylamide to control stiffness. A Polaris Nd:YAG laser irradiated the phantoms to induce droplet vaporization, and the samples were imaged using a Vevo ultrasound imaging system at 580 frames/second to observe droplet vaporization and recondensation.

**Results/Discussion**

Increased phantom stiffness resulted in lower ultrasound intensity immediately following each laser pulse and quicker decay of the ultrasound signal. This indicates that elevated stiffness hinders stable bubble formation and hastens recondensation. These differences in bubble formation and recondensation kinetics can be quantified and may be used to map the intracellular and extracellular stiffness in tissue with high resolution in order to identify tumor formation and growth.





P1B5-6

### Forming acoustic attraction force to concentrate microbubbles in flow using a matrix array transducer

Naoto Hosaka<sup>1</sup>, Shinya Miyazawa<sup>1</sup>, Toi Sawaguchi<sup>1</sup>, Ren Koda<sup>1</sup>, Shinya Onogi<sup>1</sup>, Takashi Mochizuki<sup>1</sup>, Kohji Masuda<sup>1</sup>; <sup>1</sup>Tokyo Univ. of A&T, Japan

#### Background, Motivation and Objective

To improve the feasibility of local treatment using microbubbles with ultrasound *e.g.* HIFU therapy or drug delivery, because of the diffusion of *in vivo* microbubbles, we have reported the method of controlling the movement of microbubbles. However, it was difficult to attract microbubbles in flow using a single sound source because primary Bjerknes force acts to propel microbubbles along the direction of propagation. Thus, we report our challenge to concentrate microbubbles in flow by forming acoustic attraction force □Which was realized by setting symmetrical focal points with opposite phase using

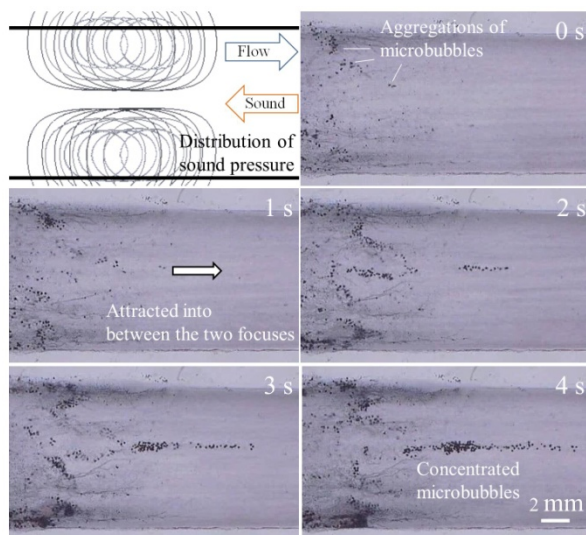
#### Statement of Contribution/Methods

A flat matrix array transducer includes 64 PZT elements, which was newly developed to produce a continuous wave. We designed an acoustic field, which had two focal points in the same time and their positions were repeatedly changed with the interval of 100 ms. The two focal points kept the distance of 8 mm and located along the center line of the channel symmetrically. Five positions were prepared for each cycle with interval distance of 1 mm, where sound pressure in each peak was 200 kPa-pp and the phase difference between them was 180 degree (opposite phase).

#### Results/Discussion

We prepared a thin channel made of Poly(ethylene glycol) monomethacrylate (PEGMA). Figure shows the behavior of microbubbles in the channel under the irradiation of the designed acoustic field. Microbubbles suspension (average diameter of 4  $\mu\text{m}$ , density of 2.35  $\mu\text{l/ml}$ ) entered from left with flow velocity of 10 mm/s. In 0 s, microbubble aggregations can be confirmed to enter the acoustic field. In 1-2 s, aggregations began to concentrate through the symmetrical focal points. After 3 s, streamline of aggregations was clearly confirmed along the center of the channel. Here it must be noted that the above-mentioned concentration was not confirmed when there was no phase difference (same phase) between two symmetrical points.

In conclusion, we have confirmed to concentrate aggregations in flow by forming acoustic attraction force using a matrix array transducer. We are going to apply the acoustic field to more complicated shape of blood vessel.





P1B5-7

**Acoustic monitoring of single freely-floating microbubble dynamics coupled with optical sizing**Ying Luan<sup>1</sup>, Guillaume Renaud<sup>1</sup>, Jason L. Raymond<sup>1</sup>, Tim Segers<sup>2</sup>, Robert Beurskens<sup>1</sup>, Tom Kokhuis<sup>1</sup>, Guillaume Lajoine<sup>2</sup>, Antonius F.W. van der Steen<sup>1,3</sup>, Michel Versluis<sup>2</sup>, Nico de Jong<sup>1,3</sup>,  
<sup>1</sup>Erasmus Medical Center, Rotterdam, Netherlands, <sup>2</sup>University of Twente, Netherlands, <sup>3</sup>Delft University of Technology, Netherlands**Background, Motivation and Objective**

The acoustic nonlinear responses of ultrasound contrast agent microbubbles (MBs) are of great interest for both diagnostic (e.g. contrast-enhanced imaging) and therapeutic (e.g., drug delivery) applications. Previously, optical and acoustical methods were developed to characterize single MBs [1-3]. Here we describe a new technique to optically size and acoustically measure the dynamical response of single freely-floating MBs simultaneously. A flow-focusing device was used to generate a bubble train, and the radial dynamics of single MBs was monitored using a high frequency probing wave while driving the bubble at a low frequency modulation wave [1].

**Statement of Contribution/Methods**

Figure 1a shows the setup of the optical and acoustic systems with co-located focal regions. Bubbles with a spacing of  $\sim 300 \mu\text{m}$  were injected into the focused ultrasound field established using a 30 MHz probing wave (200 kPa peak amplitude) and a 1 MHz modulation sine wave (50 kPa peak amplitude). The scattered signal from a single DSPC-based MB was collected by a 30 MHz receive transducer, which triggers a high-speed optical camera to capture the very same MB. The MB size was obtained from the bright-field image. The radial strain at 1 MHz ( $\epsilon_r$ ) was derived from the bubble echo [1].

**Results/Discussion**

The radial strain of 72 single MBs having a radius of  $1.5 \mu\text{m}$  to  $4.6 \mu\text{m}$  as sized optically was measured. Figure 1b shows the plot of radial strain ( $\epsilon_r$ ) as a function of the MB radius with a linear fit to the Lorentzian function as a simplified and first approach [2]. The maximum response ( $\epsilon_r \approx 35\%$ ) can be found for MBs with a radius near  $3.4 \mu\text{m}$ , corresponding to the resonant radius of a bubble driven at large amplitude oscillations at a frequency of 1 MHz. This result agrees with earlier observations obtained for MBs floating against a membrane [2,3]. This technique enabled for the first time simultaneous optical and acoustical characterization of single freely-floating microbubbles.

[1] Renaud et al. Applied Physics Letter, 2012. 100 (10).

[2] van der Meer et al. J Acoust Soc Am, 2007. 121(1).

[3] Overvelde et al. Ultrasound Med Biol, 2010. 36 (12).

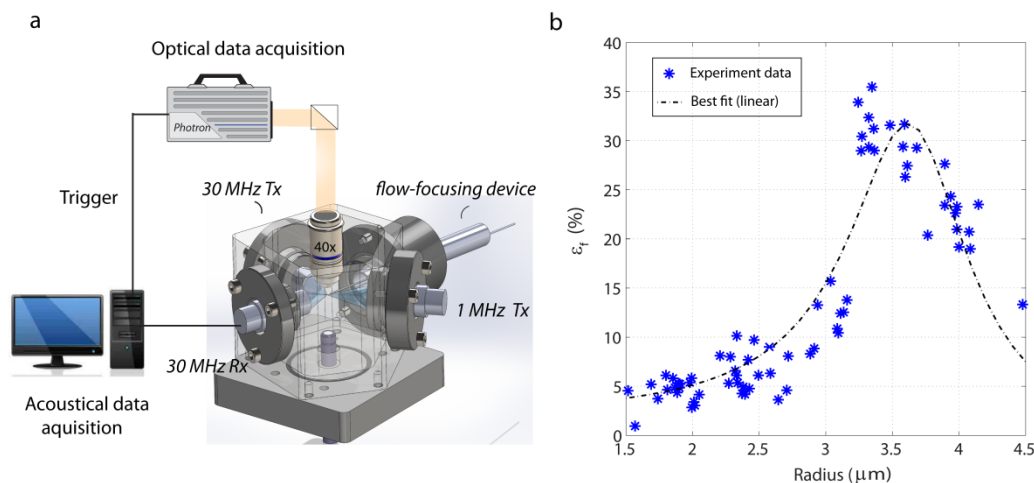


Figure 1. a) The schematic plot of the setup and b) the dynamic radial strain ( $\epsilon_r$ ) versus the resting radius for 72 MBs.

P1B5-8

**Effects of Ultrasound Parameters on the Acoustic Characteristics of Phase-Change Droplets**Wei-Pu Kao<sup>1</sup>, Shih-Tsung Kang<sup>1</sup>, Chih-Kuang Yeh<sup>1</sup>, <sup>1</sup>Department of Biomedical Engineering and Environmental Sciences, National Tsing Hua University, Taiwan**Background, Motivation and Objective**

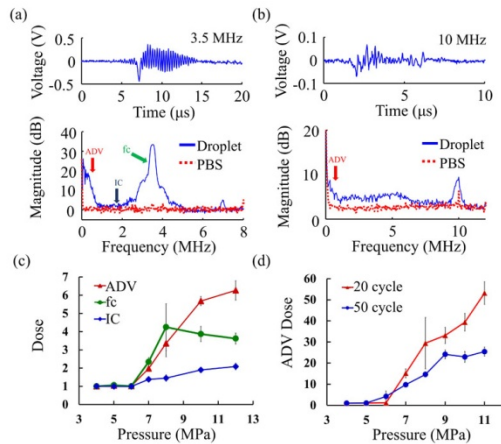
Phase-change droplets (PCDs) can be vaporized into bubbles by ultrasound (acoustic droplet vaporization, ADV) as promising diagnostic and therapeutic agents. The substantial volume expansion during the droplet-to-bubble transition with duration of a few microseconds may produce low-frequency shock wave, serving as the acoustic characteristics for monitoring and control of ADV. However, few studies explored the preferable conditions for producing the acoustic characteristics of ADV. In this study we investigated the influence of ultrasound parameters including acoustic frequency, pulse duration, and pressure upon producing low-frequency shock wave from ADV process.

**Statement of Contribution/Methods**

PCDs were fabricated with DSPC, DSPE-PEG2000, and perfluoropentane under intense sonication. A vessel phantom with a 1-mm diameter was immersed in degassed  $37^\circ\text{C}$  water for infusion of diluted droplets. The infused droplets were exposed to 3.5- and 10-MHz high-intensity focused ultrasound (HIFU) hanning window weighted pulses with pulse durations from 10 to 50 cycles at varying pressures from 4 to 11 MPa for ADV initiation. A 0.5-MHz transducer and a 2.25-MHz (for 3.5-MHz HIFU) or 5-MHz (for 10-MHz HIFU) transducer were confocally-arranged with the HIFU transducers for passive detection of low-frequency shock wave, wideband emissions (inertial cavitation, IC), and linear backscattered echoes (i.e., center frequency,  $f_c$ ). The three dose indicators were calculated with the area under curve based on the frequency spectra.

**Results/Discussion**

The low frequency shock wave (below 1 MHz) was present for the case of ADV at the beginning of the acquired signal under exposures on 3.5- and 10-MHz HIFU pulses with a duration of 50 cycles at 7 MPa (Fig. 1(a) and (b)). For 3.5 MHz HIFU, the intensity of the low frequency shock wave presented more pronounced positive dependence with acoustic pressure, as compared with other two dose indicators, suggesting its higher sensitivity for monitoring the extent of ADV (Fig. 1(c)). Shortening pulse duration from 50 to 20 cycles effectively enhanced the dose of the low-frequency shock wave by up to 105%. These results suggest that varying pulse duration and acoustic pressure (not including acoustic frequency) have great impacts on the producing low-frequency shock wave. This allows the optimization of this signal for practical in vivo use.



P1B5-9

### Sorted ultrasound contrast agents boost the scattering to attenuation ratio: modeling and experiments

Tim Segers<sup>1</sup>, Maarten Kok<sup>1</sup>, Nico de Jong<sup>2</sup>, Michel Versluis<sup>1</sup>; <sup>1</sup>Physics of Fluids, University of Twente, Enschede, Netherlands, <sup>2</sup>Biomedical Engineering, Erasmus Medical Center, Rotterdam, Netherlands

#### Background, Motivation and Objective

An ultrasound contrast agent (UCA) suspension contains encapsulated microbubbles with radii ranging from 1 to 10 μm. Clinical ultrasound systems typically operate at a single frequency, therefore only a small fraction of the bubbles will resonate to the driving ultrasound pulse. Thus, the sensitivity of diagnostic imaging and molecular imaging with targeted microbubbles can be improved by narrowing down the size distribution. Increased sensitivity by the use of monodisperse contrast agents was already predicted, and here it is shown experimentally for the first time. We characterized acoustically narrow size distribution bubble populations obtained by microfluidic and acoustic sorting of a polydisperse commercial contrast agent. The responses of the enriched bubble suspensions were compared to the response of the native agent by their scattering-to-attenuation ratios (STAR).

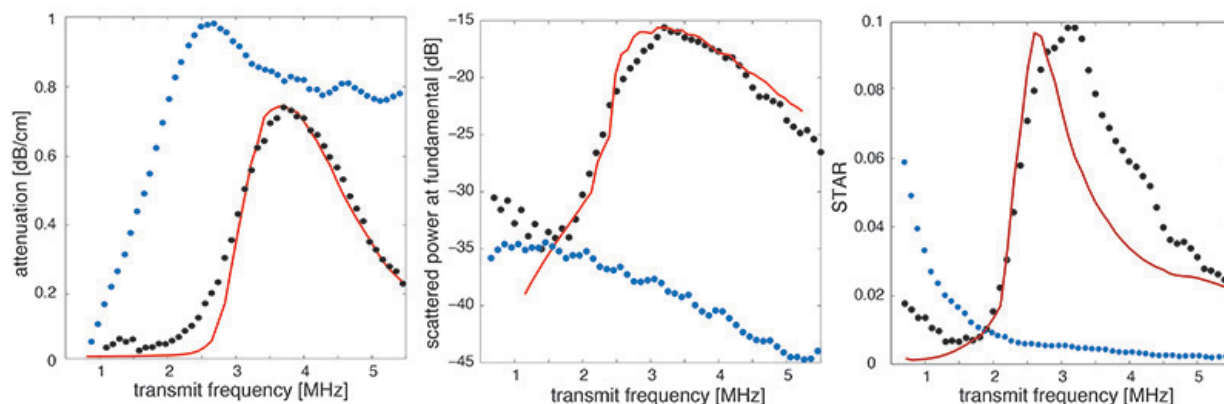
#### Statement of Contribution/Methods

Acoustic scattering and attenuation were measured simultaneously in the frequency range from 0.7 MHz to 5.5 MHz at acoustic peak negative pressures of 10, 25, 50 and 100 kPa with a setup comprising three ultrasound transducers. The modeling is based on a Rayleigh-Plesset type equation accounting for buckling and rupture of the viscoelastic bubble shell. The modeled local pressure and frequency-dependent volume pulsations of all bubble sizes in the suspension are modeled through summation from which the scattered pressure and attenuation are calculated. Inclusion of the position-dependent acoustic pressure in the 1.5 x 1.5 cm<sup>2</sup> sample holder turned out to be essential for an accurate description of the nonlinear bubble response within the monodisperse suspension.

#### Results/Discussion

We find a maximum STAR of 0.16 for acoustically enriched contrast and a STAR of 0.11 for PFF sorted agent as compared to a STAR value of 0.01 for the native agent. Moreover, excellent agreement was found between the modeled and the measured scattering and attenuation curves. The characterization procedures provide valuable insight in an optimized bubble response obtained from contrast enrichment strategies in addition to fundamental insight in bubble shell parameters. Moreover, it opens up the perspective for a quantitative evaluation of myocardial perfusion using a significantly higher UCA concentration without the drawback of increased attenuation.

- measured acoustically sorted contrast at 10 kPa
- modelled sorted contrast at 10 kPa
- measured native contrast at 10 kPa



**High throughput production of uniformly-sized fluorocarbon emulsions for ultrasonic therapy using a silicon-based microfluidic system**Mario Fabiilli<sup>1</sup>, Justin Silpe<sup>1</sup>, Collin Rush<sup>1</sup>, Oliver Kripfgans<sup>1</sup>; <sup>1</sup>Radiology, University of Michigan, Ann Arbor, MI, USA**Background, Motivation and Objective**

Sonosensitive particles are common in both diagnostic and therapeutic ultrasound applications. Conventional production methods, such as high-speed mixing and sonication, are simple and fast; yields of  $\sim 10^{10}$  particles, which are required for many applications, are generated in minute timeframes. However, these methods yield polydisperse distributions that are less than ideal as only a subset of the population is acoustically-responsive and physiologically-optimized. Highly uniform particles can be generated using microfluidic-based techniques, but these methods are typically impractical in terms of production scalability, requiring hours to produce  $10^{10}$  particles. We developed a microfluidic system, capable of producing uniformly distributed emulsions, with realistic production rates.

**Statement of Contribution/Methods**

Devices were designed with 2,500 parallel microchannel junctions. Fabrication was carried out with a dual-sided and two-layer photomask approach for deep reactive ion etching. This combination allowed for tolerances in critical dimension  $< 250$  nm and mask uniformity  $< 125$  nm. Y- and T-junctions were established with combinations of 4 and 6  $\mu\text{m}$  exit channels. Three input ports are supported per device – ultimately enabling the production of double emulsions. For these experiments, single emulsions (i.e. fluorocarbon in water) were formed. The outer phase consisted of a normal saline solution with 1% (w/v) Pluronic F-68 and 1% (w/v) bovine serum albumin. The inner phase consisted of methoxy-nonafluorobutane ( $\text{C}_4\text{F}_9\text{OCH}_3$ , HFE-7100, 3M, boiling point:  $61^\circ\text{C}$ ). Inner and outer flow rates were varied from 0.05-0.4 mL/min and 8-16 mL/min, respectively. Resulting emulsions were sized using a Coulter counter, yielding similar results as microscopy. Emulsions were characterized by their coefficient of variance (CV), which is the standard deviation of the distribution divided by the mean droplet diameter.

**Results/Discussion**

The mean droplet diameter and CV were inversely related to the flow ratio, defined as the outer phase flow rate divided by the inner phase flow rate. The most uniform distribution was obtained at a flow ratio of 320, which yielded a mean droplet diameter of 5.2  $\mu\text{m}$  and a CV of 17.5%. CVs of 70-90% are typical for emulsions produced using conventional methods such as high-speed shaking. Production rates as high as  $8 \times 10^6$  droplets/sec were obtained, meaning that  $10^9$  to  $10^{10}$  droplets could be produced in 2-20 minutes. Overall, our results demonstrate the potential of generating uniform emulsions at rates feasible for scale-up use in ultrasound experiments.

## P1B6 - MEL: Mechanical Characterization of the Carotid

Salon C

Friday, September 5, 2014, 8:00 am - 5:00 pm

Chair: **Richard Lopata**  
Eindhoven University of Technology

P1B6-1

### In vivo characterization of atherosclerotic plaque of human carotid arteries with histopathological correlation using acoustic radiation force impulse (ARFI) ultrasound

**Tomasz Czernuszewicz**<sup>1</sup>, Jonathon Homeister<sup>2</sup>, Melissa Caghey<sup>3</sup>, Mark Farber<sup>4</sup>, Joseph Fulton<sup>4</sup>, Peter Ford<sup>4</sup>, William Marston<sup>4</sup>, Raghuvver Vallabhaneni<sup>4</sup>, Timothy Nichols<sup>2,3</sup>, Caterina Gallippi<sup>1,5</sup>, <sup>1</sup>Joint Department of Biomedical Engineering, University of North Carolina/North Carolina State University, Chapel Hill, NC, USA, <sup>2</sup>Department of Pathology and Laboratory Medicine, University of North Carolina, Chapel Hill, NC, USA, <sup>3</sup>Department of Medicine, University of North Carolina, Chapel Hill, NC, USA, <sup>4</sup>Department of Surgery, University of North Carolina, Chapel Hill, NC, USA, <sup>5</sup>Department of Electrical and Computer Engineering, North Carolina State University, Raleigh, NC, USA

#### Background, Motivation and Objective

Stroke is one of the leading causes of death and long-term disability in the US. The vast majority of strokes are related to ischemia secondary to atheroembolism originating from unstable plaques located in neck vasculature. Specifically, plaques that are composed of mechanically-soft lipid/necrotic regions covered by thin fibrous caps are the most vulnerable to rupture. Atherosclerotic plaque characterization with ARFI has recently been developed using phantoms and atherosclerotic pigs, but has yet to be validated in vivo in humans. We present initial results from an ongoing clinical trial investigating in vivo ARFI imaging of human carotid plaque with spatially-matched histopathology.

#### Statement of Contribution/Methods

Patients undergoing clinically-indicated carotid endarterectomy (CEA) were recruited from UNC Hospitals and imaged with ARFI implemented on a Siemens Acuson Antares with modifiable beam sequencing and a VF7-3 linear array. ARFI excitation pulses were 300 cycles at 4.21 MHz (F/1.5), while tracking pulses were 2 cycles at 6.15 MHz. Imaging was performed pre-operatively by focusing on the carotid bifurcation. After surgery, the extracted specimen was sectioned according to noted arterial geometry for spatial registration to the ultrasound imaging plane. The sections were stained with H&E, combined Masson's elastin, and Von Kossa for calcium, and compared to parametric 2D ARFI images of peak displacement (PD). Data is presented from six patients.

#### Results/Discussion

In two asymptomatic patients with predominantly calcified plaques, ARFI PDs were small ( $2.1 \pm 1.5 \mu\text{m}$  and  $1.8 \pm 0.8 \mu\text{m}$  respectively) suggesting large amounts of stiff tissue. In three patients, all symptomatic, plaques were composed of a mixture of small and large necrotic cores, mild intra-plaque hemorrhage, small focal calcifications, and fibrosis. ARFI PDs in regions corresponding to either necrotic core or intra-plaque hemorrhage were observed to be increased by 2 or 3-fold compared to surrounding fibrotic tissue, ranging as high as  $19.9 \mu\text{m}$  in one case. Fibrous cap thickness was estimated with <10% error in caps larger than 0.8 mm. In a sixth patient, also symptomatic, an ulcerated plaque with extensive organized thrombus was observed. ARFI displacements in regions corresponding to thrombus were small ( $\sim 1\text{-}2 \mu\text{m}$ ), similar to that in the fibrotic/calcified plaques. The results of this study indicate that areas of relatively large displacement by ARFI imaging correlate with lipid/necrotic cores and/or inflammation, which may confer an increased chance of plaque rupture and future ischemic event. Interestingly, in the ulcerated plaque with organized thrombus, ARFI-induced displacements were relatively small, suggesting stiffer and more stable plaque. Discrimination of organized thrombus from other stiff atherosclerotic features may be improved by more advanced imaging techniques that evaluate both viscous and elastic properties of plaque.

P1B6-2

### In Vitro Elastography of Porcine Carotid Arteries, a validation study.

**Renate W. Boekhoven**<sup>1</sup>, Martijn F.J. Blatter<sup>1</sup>, Rens M.J.M. de Vries<sup>1</sup>, Frans N. van de Vosse<sup>1</sup>, Richard G.P. Lopata<sup>1</sup>, <sup>1</sup>Eindhoven University of Technology, Netherlands

#### Background, Motivation and Objective

Reliable non-invasive assessment of mechanical properties of the arterial wall, either healthy or diseased, is of great importance for patient specific diagnosis in the field of vascular disease. Vascular elastography is a promising tool to assess these mechanical properties. Validation of these techniques should preferably imply a similar stress-strain range. Therefore, in this study, the most controllable and realistic approach of mechanical testing of arteries in vitro, inflation testing, is compared to the gold standard of mechanical testing, bi-axial testing.

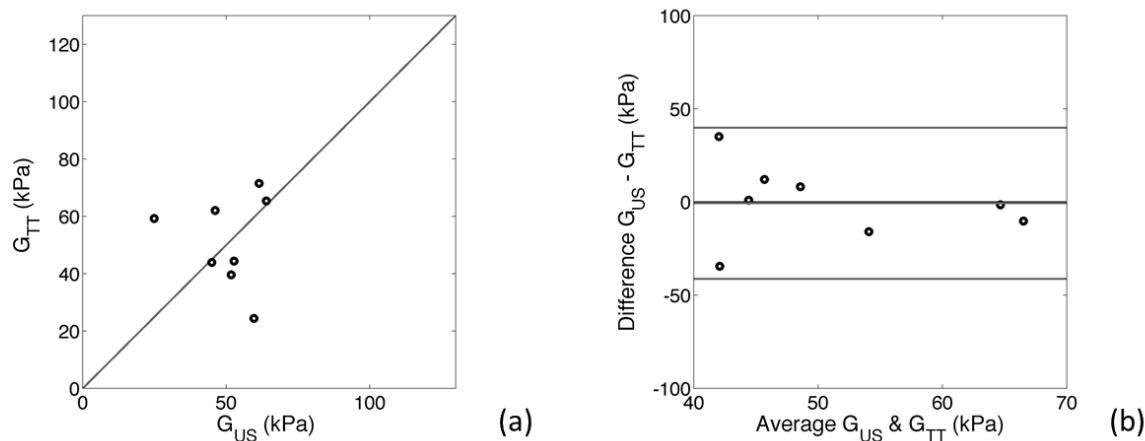
#### Statement of Contribution/Methods

Vascular elastography is applied to porcine carotid arteries (n=8). The arteries were stretched to their in vivo length ( $\lambda_e=1.6$ ), were surrounded and perfused with PBS and dynamically pressurized (0 - 120 mmHg), in a circulation mock loop (van den Broek et al. 2011) at 38.5°C. Longitudinal RF-data were acquired with a MyLab70 scanner (Esaote, NL). Local deformations were estimated using a 2D coarse-to-fine strain algorithm (Lopata et al. 2009). For comparison, bi-axial tensile experiments (CellScale, CA) were performed on two samples from each artery (7 by 7 mm, n=16). Samples were stretched to a fixed length ( $\lambda_e = 1.6$ ), and stretched in steps of 5% in circumferential direction up to 40%. Displacements were assessed with Labjoy©. Finally, a Neo-Hookean model was used to estimate the shear modulus (G) of the carotid arteries for both experiments, assuming isotropy, linear elasticity and incompressibility.

#### Results/Discussion

Pressure, diameter and wall thickness change were used to estimate  $G_{US}$ , while for  $G_{TT}$  estimation, force and displacements were used and the initial wall thickness at  $\lambda_e = 1.6$  (from inflation). In Figure 1, the estimated shear moduli of both experiments were compared. Results show good correspondence between the two techniques (Fig. 1a), with a shear modulus of  $G_{US} = 51 \pm 13 \text{ kPa}$  and  $G_{TT} = 51 \pm 20 \text{ kPa}$ , for ultrasound and tensile testing, respectively. Bland-Altman analysis revealed little bias ( $G_{US} - G_{TT} = 1 \pm 20 \text{ kPa}$ , Fig. 1b).

In conclusion, vascular elastography was validated in healthy porcine carotid arteries by comparing controlled, inflation experiments with bi-axial tensile testing. In future work, these data will be used as input to compare several hyperelastic models, which will describe the mechanical behaviour of the arteries more realistically.



P1B6-3

### Non-invasive strain imaging on normotensive and hypertensive patients, an in vivo pilot

Renate W. Boekhoven<sup>1</sup>, Louise Marais<sup>2</sup>, Marcel C.M. Rutten<sup>1</sup>, Frans N. van de Vosse<sup>1</sup>, Pierre Boutouyrie<sup>3</sup>, Richard G.P. Lopata<sup>1</sup>; <sup>1</sup>Eindhoven University of Technology, Netherlands, <sup>2</sup>Université Paris-Est, France, <sup>3</sup>Hôpital Européen Georges Pompidou, France

#### Background, Motivation and Objective

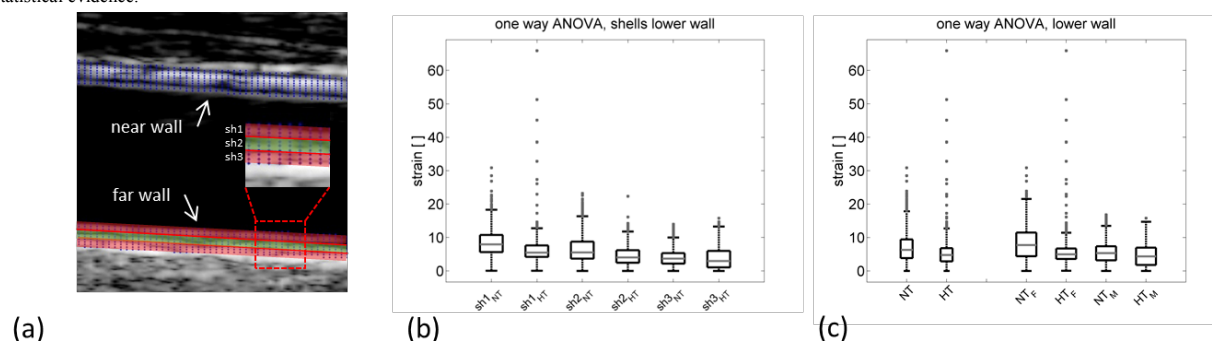
Literature shows that arterial stiffness is related to age and degrees in atherosclerosis. It has been hypothesized that there is no difference between normotensive (NT) and hypertensive (HT) patients of same sex and age. This was demonstrated in a previous study by analysing pressure-diameter curve data and estimating the incremental Young's modulus (Bussy et al. 2000). In this study, 2D strain imaging was used to investigate possible differences in carotid stiffness by quantifying the response to pressure, i.e., strain, in a group of NT and HT subjects, matched for both age and sex.

#### Statement of Contribution/Methods

Radio-frequency data of the carotid were acquired in ten NT and ten HT patients, with a mean age of  $52 \pm 11$ , using the Mylab 70 (Esaote, NL). Brachial pressure was obtained using a cuff during the ultrasound exam. A 2D strain imaging algorithm was applied to the RF-data (Lopata et al. 2009). Radial strains in the far wall data were estimated over the entire cardiac cycle. On average, a region of 40 (out of 127) RF-lines was used, which was divided into three layers (sh1-3, Fig. 1a). In a controlled, ex vivo experiment, two porcine carotid arteries were pressurized and strains were analysed for the average mean arterial pressures and pulse pressures as was found in the NT and HT patients.

#### Results/Discussion

One-way ANOVA indicates significant lower strains in the HT groups, within all three shells ( $sh1_{NT} = 7.9\% \pm 5.1\%$ ,  $sh1_{HT} = 5.5\% \pm 3.4\%$ ,  $sh2_{NT} = 5.6\% \pm 5.1\%$ ,  $sh2_{HT} = 4.1\% \pm 3.7\%$ ,  $sh3_{NT} = 3.7\% \pm 3.1\%$ ,  $sh3_{HT} = 3.0\% \pm 4.9\%$ , Fig. 1b). The same difference was found in the HT group when comparing strains throughout the vessel wall ( $NT = 6.3\% \pm 5.6\%$ ;  $HT = 4.8\% \pm 3.9\%$ , Fig. 1c). Furthermore, when matching age and sex, again the strains were significantly lower in HT patients for both sexes (Fig. 1c). The lower strain can be explained by the higher mean arterial pressure and non-linear behaviour of the vascular tissue. At higher strains, and equal pulse pressure, the total strain will be lower, which was corroborated in the ex vivo experiment. Hence, these results, both ex vivo and in the patient population, confirm the hypothesis that the stiffness in HT patients is not higher compared to NT patients. This pilot study also shows that it is definitely relevant to conduct a large scale, multi-centre, patient population study to provide thorough statistical evidence.



P1B6-4

### Direct estimation of carotid artery wall strain parameters using autocorrelation of high frame rate ultrasound images

Yasaman Adibi<sup>1</sup>, Afshin Divani<sup>1</sup>, Emad Ebbini<sup>1</sup>; <sup>1</sup>University of Minnesota, Minneapolis, Minnesota, USA

#### Background, Motivation and Objective

Elastography is a well-developed method for measuring mechanical properties of biological tissues. Achieving high accuracy in elastography may lead to significant developments in diagnosis and treatment of cancerous tumors, atherosclerosis, etc. Existing techniques utilize speckle tracking-based methods to estimate displacement of tissue. Gradient of displacement in different directions produces estimates of the strain parameters. Due to low frame rates and noise amplification by gradient operation, the estimated strain parameters may have low accuracy, especially when gradients are based on lateral shifts.



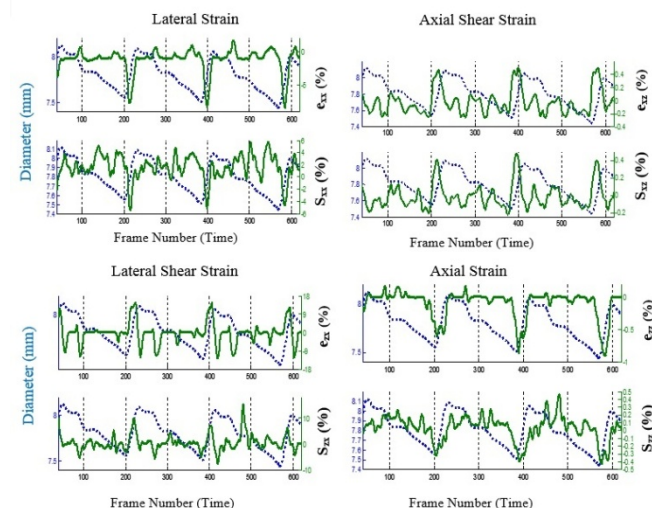
# Statement of Contribution/Methods

We propose a new method of directly estimating normal and shear strain parameters from the 2D complex correlation. It is shown that normal and shear strains can be estimated as parameters of an affine transformation between the 2D correlation functions at subsequent frames. Estimation of strains in tissue is based on local properties of 2D autocorrelation function of the speckle region undergoing deformation. Proposed method is applied to in-vivo and in-vitro data. Measurements have been obtained at the walls of common carotid artery of a healthy subject. Additionally, the method has been used to find strain parameters of a data set from an elastography phantom compress-release experiment result<sup>1</sup>.

1: [http://ultrasonics.bioen.illinois.edu/data\\_phantom.asp](http://ultrasonics.bioen.illinois.edu/data_phantom.asp)

# Results/Discussion

In vivo results from Carotid arteries of healthy human subjects show consistency over heart cycles. Figure (1) is a comparison between strain parameters computed by spatial gradient of 2D displacements and new direct method over three heart cycles (in each set, upper curve represents direct method parameter and lower curve represents gradient based parameter). Observations reveal that strain parameters have a positive slope during systole (rising part of diameter (blue) curves) which counts for the pressure wave driving blood flow in arteries. They ultimately subside to initial value before the beginning of next heart cycle (mostly during diastole and heart relaxation. The two methods generally agree when the displacement estimates are suited for differentiation (e.g.  $S_{xx}$ ) while the affine transformation method appears to be superior when the displacement estimate is noisy (e.g.  $S_{xx}$ ).



P1B6-5

## Performance evaluation of compounding and directional beamforming techniques for carotid strain imaging using plane wave transmissions

Hendrik H.G. Hansen<sup>1</sup>, Matthias B. Stuart<sup>2</sup>, Carlos A. Villagomez Hoyos<sup>2</sup>, Jørgen Arendt Jensen<sup>2</sup>, Chris L. de Korte<sup>1</sup>; <sup>1</sup>Medical Ultrasound Imaging Center, Department of Radiology and Nuclear Medicine, Radboud University Medical Center, Netherlands, <sup>2</sup>Center for Fast Ultrasound Imaging, Department of Electrical Engineering, Technical University of Denmark, Denmark

## Background, Motivation and Objective

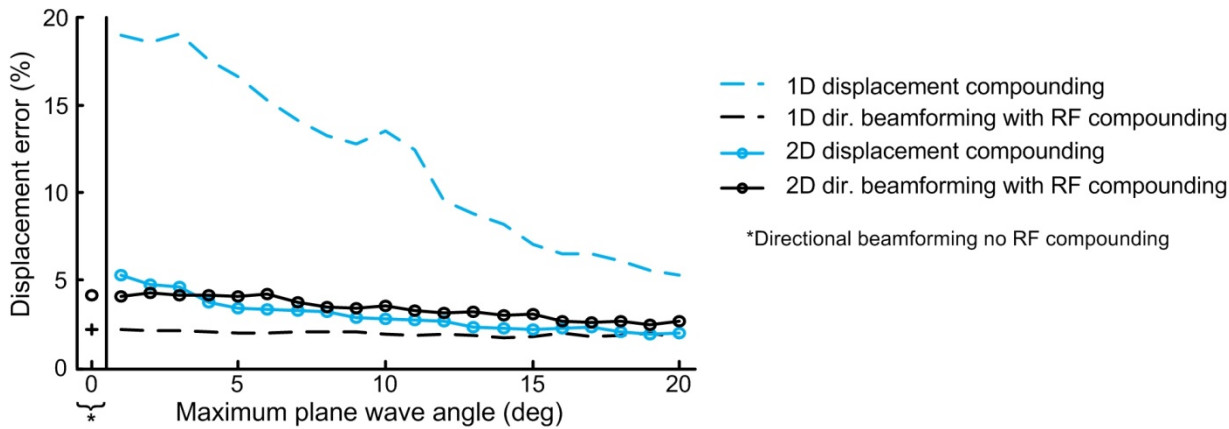
Carotid strain imaging in 3D is not possible with conventional focused imaging, because the frame rate is too low. Plane wave ultrasound provides sufficiently high frame rates, albeit at the cost of off-axis resolution. Multiple techniques have been developed to cope with the low off-axis resolution when performing 2D (and in future 3D) motion estimation: cross correlation with directional beamforming (with or without RF (coherent) compounding) and displacement compounding. This study compares the precision of these techniques using simulations of a pulsating artery

## Statement of Contribution/Methods

Ultrasound RF element data of a homogeneous artery (Young's modulus 170 kPa) with a concentric lumen (radius 3.5 mm, wall thickness 1.5 mm) were simulated for a linear array transducer ( $f_c = 9$  MHz, pitch = 198  $\mu$ m, 192 elements) that transmitted plane waves at 3 sequentially alternating angles ( $0^\circ$ ,  $+0^\circ$ ,  $-0^\circ$ ) at a PRF of 2 kHz using Field II. The vessel was deformed according to a carotid pressure curve of a 75 year old man. Simulations were repeated for  $\theta$  ranging from  $1^\circ$  to  $20^\circ$  with increments of  $1^\circ$ . Displacements were estimated for frame intervals of 1/15th s, tracked, and cumulated from diastole to systole using either displacement compounding, or directional beamforming optionally enhanced by RF compounding. For both techniques delay-and-sum beamforming followed by 1D or 2D normalized cross-correlation and parabolic interpolation was performed to estimate the displacements. For displacement compounding, beamforming was performed in the direction of the steered plane waves after which projection of the angular displacements yielded the angle and magnitude of the displacement. For directional beamforming, lines were beamformed in the direction of motion and summed for all transmission angles. To compare the precision of the techniques as a function of the maximum plane wave angle, the mean relative error of the estimated displacements was determined with respect to the analytical solution.

## Results/Discussion

1D directional beamforming with RF compounding and 2D displacement compounding with  $\geq 18^\circ$  performed equally and best with an error of  $\sim 2\%$ . However, displacement compounding requires no assumptions regarding the motion direction and, therefore, seems the best option for plane wave carotid strain imaging. The mean error of the estimated motion direction was  $1.5^\circ$ .



P1B6-6

Feasibility of Shear Wave Elastography for Plaque Characterization – An experimental study using Mechanical testing

Erik Widman<sup>1</sup>, Elira Maksuti<sup>1</sup>, David Larsson<sup>1</sup>, Kenneth Caidah<sup>2</sup>, Matthew W Urban<sup>3</sup>, Anna Bjällmark<sup>1</sup>, Matilda Larsson<sup>1</sup>; <sup>1</sup>Department of Medical Engineering, KTH Royal Institute of Technology, Sweden, <sup>2</sup>Department of Molecular Medicine and Surgery, Karolinska Institutet, Sweden, <sup>3</sup>Department of Physiology and Biomedical Engineering, Mayo Clinic Coll, USA

Background, Motivation and Objective

Carotid artery (CA) plaque characterization is critical for the prevention of ischemic events. Plaque stiffness has been suggested for plaque characterization because elastic properties of plaques have shown to correlate with plaque vulnerability. Shear wave elastography (SWE) has previously been applied in arterial applications but assessment in plaques is challenging, due to geometry and inhomogeneity causing complex wave propagation. The aim of this study was to test the feasibility of SWE plaque characterization in an in vitro setup using mechanical testing as a reference.

Statement of Contribution/Methods

Two CA phantoms (length: 100 mm, wall thickness: 3 mm, inner diameter: 6 mm, 10% PVA) were constructed with a soft plaque inclusion (phantom walls/plaques: 1/3 freeze-thaw cycles). The phantoms were placed in a fixture submerged in water with the plaques located in the anterior phantom wall. Radiation force generation and plane-wave imaging (8 kHz) was performed in the plaque and wall using an Aixplorer system (Supersonic Imagine). The axial particle velocity of the propagating waves was tracked using a 2D auto-correlation approach (Figs. 1 a-b). Fourier analysis was applied to calculate phase velocity ( $c_T$ ) as a function of frequency. Shear modulus,  $\mu$ , for the wall and plaque was obtained by fitting the  $c_T$  curve to a thin plate model. Moreover, the shear moduli of the plaques were calculated from the group velocity ( $c_g$ ), derived based on a Radon transform method. The shear modulus from SWE was then compared with shear modulus obtained from axial tensile displacement testing.

Results/Discussion

SWE estimations based on both group and phase velocity detected lower shear moduli in the soft plaque inclusions than in the stiffer wall (Fig. 1c). A good agreement in wall shear modulus was found between SWE and mechanical testing, whereas plaque shear modulus was largely overestimated by SWE when based on phase velocity. When using group velocity, a smaller discrepancy between SWE and mechanical testing was obtained. These results indicate that the plate model might not be valid in plaques and that estimation based on group velocity might be more accurate. A better estimation would probably be achieved by optimizing the technique for this specific application and developing a wave propagation model adapted for plaques. Moreover, studies are needed to test SWE in plaques in vivo.

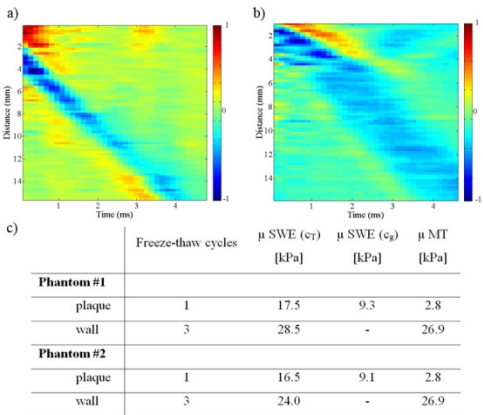


Fig. 1 Normalized axial velocity map of shear wave propagation in a phantom vessel wall (a) and in a soft plaque inclusion (b). c) Shear modulus ( $\mu$ ) of vessel wall and soft plaque inclusion estimated by shear wave elastography (SWE) from phase velocity ( $c_T$ ) and group velocity ( $c_g$ ) and mechanical testing (MT).

FRIDAY POSTER

# Evaluation of pulse wave at back and forth of the carotid bifurcation by PZT transducer

Takuya Odahara<sup>1</sup>, Mami Matsukawa<sup>1</sup>, Masashi Saito<sup>2</sup>, Takaaki Asada<sup>2</sup>; <sup>1</sup>Wave Electronics Research Center, Doshisha University, Kyotanabe, Japan, <sup>2</sup>Murata Manufacturing Co., Ltd., Japan

## Background, Motivation and Objective

Pulse wave evaluation is suitable for screening arteriosclerosis. Pulse wave is composed of two displacement waveforms: incident and reflected waves. Because the attenuation of the reflected wave during propagation changes due to viscoelastic properties of the artery, we have proposed a method to extract the reflected wave from the pulse wave at the left common carotid artery. There was a good correlation between the age and the maximum amplitude of the reflected wave ( $R^2=0.65$ ). The common carotid artery branches into two types of carotid arteries: the internal carotid artery supplies blood to the brain and the external carotid artery supplies blood to the face and scalp. These carotid arteries differ in their composition. In this study, to check the characteristics of the reflected wave in detail, we focus on the reflected wave obtained at back and forth of the carotid bifurcation.

## Statement of Contribution/Methods

We first measured pulse wave and blood flow velocity at the left common carotid artery and the left internal carotid artery. A piezoelectric sensor (MA40E7R, Murata Manufacturing Co., Ltd) was used to measure the pulse waves. The blood flow velocity waves were measured using an ultrasonic Doppler system (Prosound  $\alpha$ , Hitachi Aloka Medical, Ltd.). The reflected waves were estimated from the pulse and blood flow velocity waveforms measured at the same points [1]. 7 male subjects in their 20s were measured.

## Results/Discussion

We compared the pulse waves and blood flow velocity at the left common carotid artery with those at the left internal carotid artery. The pulse and blood flow velocity waveforms changed depending on the measurement positions. However, the amplitudes of estimated reflected waves stayed similar. Fig. 1 shows the correlation between the maximum amplitudes of reflected waves measured at the left common carotid artery with those measured at the left internal carotid artery ( $R^2=0.83$ ). These data indicate that the evaluation technique using the reflected wave is possibly independent of the measurement positions in the carotid artery. Therefore, this method is considered to be user-friendly and good for screening use.

[1] M. Saito *et al.*, IEEE, TUFFC. (2012) vol. 59, pp. 2411-2419

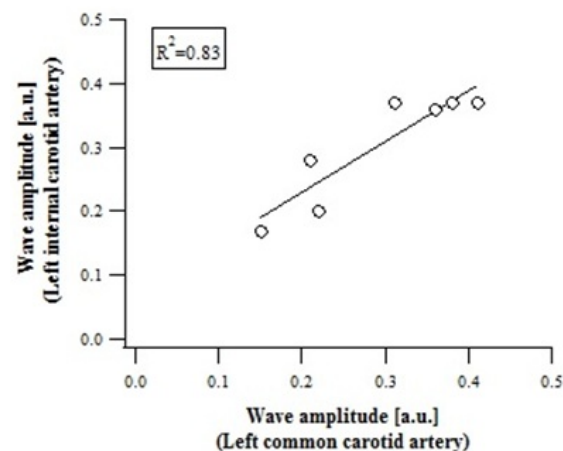


Fig. 1 The maximum amplitudes of reflected waves.

# Effects of Key Parameters on the Accuracy and Precision of Local Pulse Wave Velocity Measurement

Chengwu Huang<sup>1,2</sup>, Tianling Ren<sup>3,4</sup>, Jianwen Luo<sup>1,2</sup>; <sup>1</sup>Department of Biomedical Engineering, School of Medicine, Tsinghua University, Beijing, China, People's Republic of, <sup>2</sup>Center for Biomedical Imaging Research, Tsinghua University, Beijing, China, People's Republic of, <sup>3</sup>Institute of Microelectronics, Tsinghua University, Beijing, China, People's Republic of, <sup>4</sup>Tsinghua National Laboratory for Information Science and Technology (TNList), Tsinghua University, Beijing, China, People's Republic of

## Background, Motivation and Objective

The predictive value of pulse wave velocity (PWV) for various cardiovascular diseases has been demonstrated by many studies. By means of ultrasound-based pulse wave imaging (PWI), local PWV, instead of global PWV as in conventional methods, can be measured noninvasively (Luo et al, IEEE TUFFC 2012). To date, the accuracy and precision of PWV has not been fully investigated and several key parameters (i.e. frame rate, line density, image width and PWV) are shown to play an important but still unclear role on the performance of PWV measurement. Thus, the aim of this study is to systemically assess the effects of parameters on the performance of PWV measurement with computer simulations and in vivo experiments.

## Statement of Contribution/Methods

In simulations, by applying different time delays on the pre-obtained pulse waveform based on specific PWI parameters, the pulse wave propagation along arterial phantom was simulated and the ultrasound RF signals were generated from a convolutional image formation model. The in vivo RF signals were acquired from the common carotid artery of a healthy subject by means of plane wave-based ultrafast imaging with a frame rate of ~15 kHz (SonixDAQ, Ultrasonix). Different values of frame rate were achieved by decimation of the frames while line density and image width were determined by the number and spacing of beamformed scan lines. PWI technique was applied to both the simulated and in vivo RF signals to estimate the PWV at different values of frame rate, line density, image width and PWV.

## Results/Discussion

PWVs can be correctly estimated when the frame rate is higher than a certain value, below which the estimated PWVs become inaccurate. Considering the interference of reflected waves, the minimum frame rate required for PWV estimation in vivo (about 400 Hz) is higher than that in simulations (about 168 Hz). As shown in Fig. 1, the standard deviation of PWV estimation decreases with the line density and image width, in both simulations and in vivo experiments, indicating a better performance with a larger line density and image width. A higher value of PWV is found to deteriorate the PWV estimation in the simulations. Overall, a larger number of line density and image width with a sufficiently high frame rate is preferred. Our quantitative findings can provide important guidelines for optimization of parameters in ultrasound-based local PWV measurement.

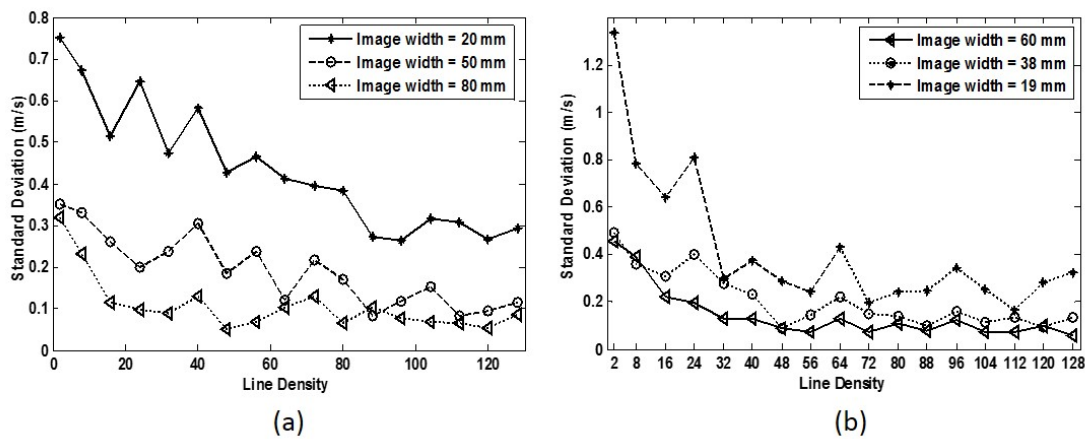


Figure 1. Standard deviation of estimated PWVs as a function of line density and image width. (a) Computer simulation, frame rate = 1000Hz, PWV = 5 m/s. (b) *In vivo* experiments, frame rate = 750Hz.

P1B6-9

#### In vivo detection of atherosclerotic plaques using Pulse Wave Imaging-based peak displacement maps and wave arrival isochrones

Ronny Li<sup>1</sup>, Jason Apostolakis<sup>1</sup>, Prathyush Narayanan<sup>1</sup>, James McKinsey<sup>2</sup>, Elisa Konofagou<sup>1,3</sup>, <sup>1</sup>Department of Biomedical Engineering, Columbia University, New York, NY, USA, <sup>2</sup>Division of Vascular Surgery, Columbia University, New York, NY, USA, <sup>3</sup>Department of Radiology, Columbia University, New York, NY, USA

#### Background, Motivation and Objective

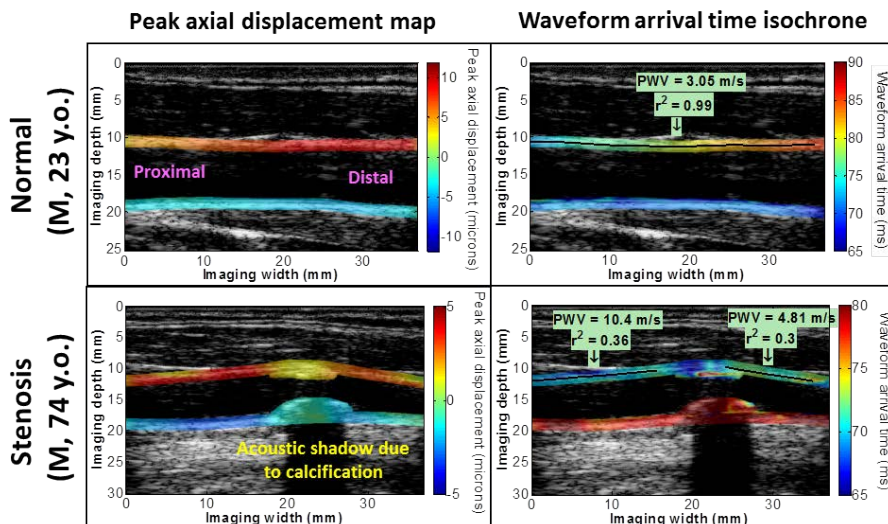
Postmortem studies linking atherosclerotic plaque morphology and composition to acute cardiovascular events have motivated efforts to develop imaging methods for interrogating plaques *in vivo*. Our group has demonstrated the capability of ultrasonic Pulse Wave Imaging (PWI) to map the pulse wave-induced displacements in the arterial walls, allowing for measurement of the local pulse wave velocity (PWV) and propagation uniformity ( $r^2$ ). In this paper, peak displacement maps and wave arrival isochrones derived from PWI are introduced as additional quantitative information to aid in plaque detection and characterization.

#### Statement of Contribution/Methods

Five stenotic carotid arteries were scanned in the longitudinal view using a SonixTOUCH system (Ultrasonix Medical Corp., Burnaby, Canada) and a 10 MHz linear array transducer at 505 FPS. The inter-frame axial displacements in the ROI containing the arterial walls and plaque regions were estimated offline using a 1-D cross-correlation-based motion estimation method on the RF signals with a 1.2 mm window size a 95% overlap. Peak displacements at each pixel in the ROI were computed over one cardiac cycle. Isochrones were computed by obtaining the displacement waveform at each pixel in the ROI and identifying the absolute time point at which the 50% upstroke is reached (i.e. wave arrival time). PWV and  $r^2$  were estimated in the normal segments of each artery via linear regression of the wave arrival times along the anterior wall.

#### Results/Discussion

Compared to the relatively uniform displacements in the normal carotid artery seen in the figure, both calcified plaque cases included in this study (one of them shown in the figure) exhibited a 60-80% decrease in peak displacement within the plaque regions compared to the normal segments, confirming the increased stiffness of calcified plaques. In the other cases, greater peak displacement was observed in the atherosclerotic areas, indicating softer plaques due to higher lipid content. Around the plaque regions in all stenosis cases, phenomenon such as variations in PWV, reduced  $r^2$ , and wave spreading were observed based on the isochrones (see figure). The findings from this preliminary study demonstrate the potential of PWI to detect and characterize atherosclerotic plaques *in vivo* using complementary information from the peak displacement map and wave arrival time isochrone.



# Non-invasive vascular modulography: An inverse problem method for imaging the local elasticity of atherosclerotic carotid plaques

Jonathan Porée<sup>1</sup>, Damien Garcia<sup>1</sup>, Boris Chayer<sup>1</sup>, Gilles Soulez<sup>1</sup>, Jacques Ohayon<sup>2</sup>, Guy Cloutier<sup>1</sup>; <sup>1</sup>University of Montreal Hospital, Canada, <sup>2</sup>Joseph Fourier University of Grenoble, France

## Background, Motivation and Objective

Recent studies revealed that quantifying mechanical properties of atherosclerotic plaques may help preventing strokes. Non-invasive vascular elastography (NIVE) in superficial carotid arteries was shown to have the potential to assess such properties and to discriminate plaque components (e.g., fibrosis, lipid and calcium) through elastograms (i.e., spatial strain distribution). The elasticity and morphology of the vessel wall, however, cannot be assessed directly from those maps since the stress distribution remains unknown. Several studies have been performed to reconstruct a Young's modulus map (i.e., a modulogram) from strain maps in intravascular ultrasound. To our knowledge, those techniques have not yet been extended to non-invasive vascular ultrasound.

## Statement of Contribution/Methods

In this study, we describe an unsupervised inverse problem for elasticity mapping (non invasive vascular modulography), which is capable of reconstructing a heterogeneous Young's modulus distribution of a plaque. Elastograms were computed from ultrasound compounded plane wave images using the Lagrangian speckle model estimator (LSME). Von Mises strains were then compensated for radial decay and used as a criterion for the segmentation of mechanical heterogeneities. This approach was then combined with an optimization procedure to highlight modulograms of atherosclerotic carotid plaques.

## Results/Discussion

In vivo carotid plaque morphologies were segmented from MRI sequences and used to model their mechanical behavior with finite element analysis. Those models were used to simulate realistic ultrasound sequences. Figure 1 shows an example of a carotid plaque segmented in MRI (panel a) along with the simulated B-mode image (panel b). The estimated von Mises strains compensated for strain decay are compared with the ground truth (center panels). The modulogram obtained from the estimated strain field using the proposed approach is also compared with the expected modulogram (panels e and f). Young's moduli of calcium (5000 kPa), lipid (10 kPa) and fibrosis (600 kPa) were estimated with relative errors of 41 %, 130 % and 3 %, respectively. Considering high contrasts in elasticity moduli, plaque components could be clearly identified even when considering those estimation errors.

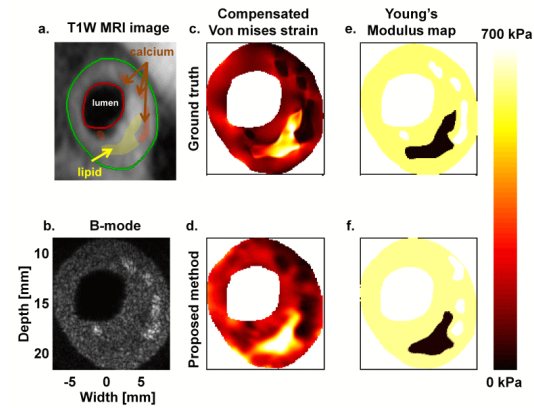


Figure 1: Realistic carotid plaque geometry extracted from multi-contrast MRI carotid sequences (T1W, T2W & PDW) (1.a shows the T1W sequence), simulated ultrasound B-mode image (1.b) and corresponding elastograms (decay compensated Von mises strain) computed from the finite element model (1.c ground truth) and from simulated ultrasound data using our estimator (LSME) (1.d). Expected (1.e) and estimated (1.f) Young's modulus maps using the proposed method are also compared.



## P1B7 - MEL: Elastography: Phantoms and Methods

Salon C

Friday, September 5, 2014, 8:00 am - 5:00 pm

Chair: **Piero Tortoli**  
Università di Firenze

P1B7-1

### C-plane Reconstructions from Sheaf Acquisition for Ultrasound Electrode Vibration Elastography

Atul Ingle<sup>1</sup>, Tomy Varghese<sup>1</sup>; <sup>1</sup>University of Wisconsin-Madison, USA

#### Background, Motivation and Objective

Electrode vibration shear wave elastography can be used for monitoring liver ablation procedures to estimate the size of the ablation based on local shear wave velocities. In this method, the ablation needle is vibrated using a pulse actuation to create a shear wave which travels away from the needle; the ablation needle acts as a line source for the shear wavefront. Shear wave imaging has thus far been limited to single imaging planes due to the widespread use of 1D array transducers and computational challenges associated with real time 3D processing. In this work, the method is extended to reconstruct C-plane views of the ablation by acquiring data over multiple intersecting imaging planes, also known as a sheaf acquisition. This can be a valuable tool for quickly generating transverse plane and 3D views of the ablated region and better assist clinicians in deciding treatment steps.

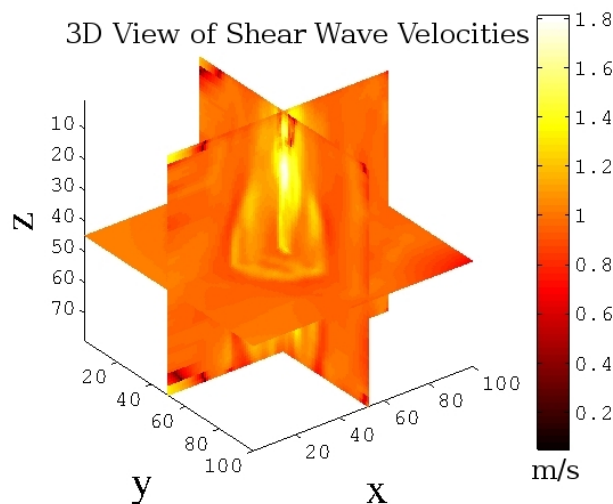
#### Statement of Contribution/Methods

Radiofrequency ultrasound echo data is acquired over multiple imaging planes by rotating a linear array transducer around the ablation needle. For each fixed imaging plane, the needle is vibrated to produce a shear wavefront which is tracked using the time-to-peak method to obtain shear wave velocity map on the image plane. This is repeated to reconstruct shear wave velocity images for different imaging planes that form a sheaf and share a common axis of intersection aligned with the needle. The C-planes are then reconstructed by solving a penalized least squares regression problem which approximates a smooth surface on a fine grid of points on each C-plane. The optimization is formulated such that it can be solved quickly even for large grid sizes. A 3D view can be generated by displaying a stack of reconstructed C-planes.

#### Results/Discussion

Validation of the algorithm using data acquired on a tissue mimicking phantom suggests that it is possible to reconstruct ellipsoidal inclusions with as few as six equiangular imaging planes. Shear wave velocity values in the stack of C-planes were within 20% of measurements obtained from a commercial shear wave imaging system and a contrast of around 4 dB between the stiff inclusion and soft background. Moreover, the algorithm is general enough to accommodate a variety of nonuniform sampling schemes and can also be used to generate 3D maps of other quantities of interest such as strain.

(Supported in part by NIH grant R01-CA112192-06.)



P1B7-2

### Bayesian Estimation of Small Displacements using a Robust Prior Scheme

Douglas Dumont<sup>1</sup>, Mark Palmeri<sup>2</sup>, Stephanie Eyerly<sup>2</sup>, Patrick Wolf<sup>2</sup>, Brett Byram<sup>1</sup>; <sup>1</sup>Biomedical Engineering, Vanderbilt University, Nashville, Tennessee, USA, <sup>2</sup>Biomedical Engineering, Duke University, Durham, North Carolina, USA

#### Background, Motivation and Objective

Precise displacement estimation can be a challenging task in acoustic radiation force impulse (ARFI) imaging and shear wave elasticity imaging (SWEI), where signal decorrelation degrades the ability of a normalized cross-correlation (NCC) estimator to characterize the tissue response.

Previously, we showed that Bayes' Theorem can be used to incorporate knowledge of adjacent displacements to reduce the local estimate's mean-square error (MSE). Here, we describe a likelihood function that is related to our previous work but can be implemented more efficiently and accounts for noise and signal decorrelation in the data. We combine this with a generalized-Gaussian Markov random field prior scheme to improve all estimates in a manner that is robust to initial conditions.

# Statement of Contribution/Methods

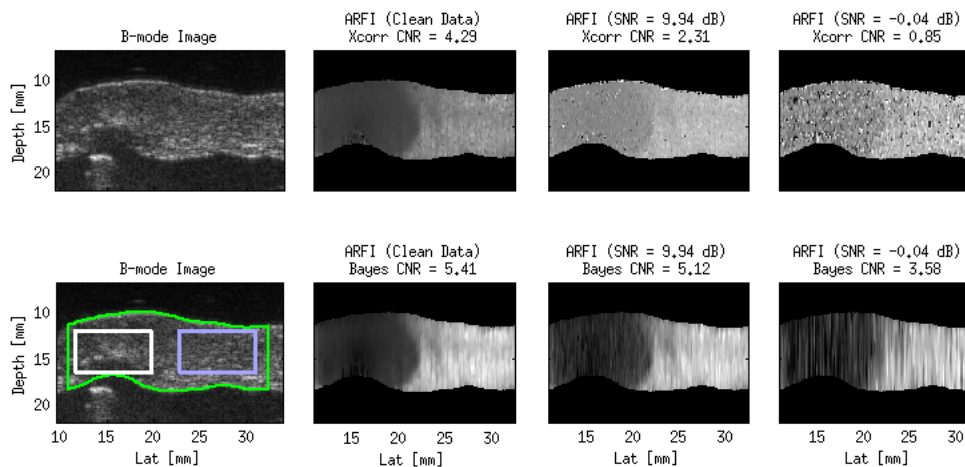
Estimator (BSE) performance was evaluated in a simulation modeling the response of a 8.5 kPa phantom to a radiation-force impulse with varying noise (10, 20, and 40 dB SNR, 100 realizations). Bias, variance, and MSE were calculated and compared to the results obtained when using NCC. *In vivo* feasibility was evaluated by evaluating lesion contrast-to-noise ratios (CNR) in post-ablation ARFI displacement data.

# Results/Discussion

The results suggest that appropriately weighting the prior information is crucial for reducing MSE. Estimates obtained using overly-wide priors show little improvement while estimates obtained using overly-narrow priors have worse MSE when compared to NCC. However, our results show that there is a range of prior widths---about an order of magnitude---where significant improvement can be realized. For example, the MSE at the location of the peak displacement ( $20.3 \pm 0.5$  mm, 20 dB SNR) can be reduced from  $17.9 \pm 9.9 \mu\text{m}^2$  to  $3.9 \pm 0.5 \mu\text{m}^2$  when using BSE.

Figure 1 shows ARFI images of an ablation lesion corrupted with additive noise. The top row shows the results obtained with NCC, while the bottom row shows the results obtained with BSE, the boxes used to calculate CNR and the contour used to mask non-tissue data. The images are shown using the full dynamic range to avoid image saturation.

The results demonstrate the reduction in variance and the improvement in CNR that can be achieved by BSE. Given the improved noise-performance, BSE could be useful for ARFI or SWEI measurements in decorrelation-prone environments, such as at-depth or in rapidly-moving tissues.



P1B7-3

## Experimental optimization of the elevational focus for radiation force applications

Bastien Arnal<sup>1</sup>, Thu-Mai Nguyen<sup>1</sup>, Matthew O'Donnell<sup>1</sup>, <sup>1</sup>Bioengineering, University of Washington, Seattle, WA, USA

## Background, Motivation and Objective

Dynamic elastography techniques based on radiation force require an ultrasound field to be focused during hundreds of microseconds. Many previous studies have relied on focused single element transducers or 1-D ultrasound arrays to generate the radiation force. As shear waves are often observed in a plane, the importance of the focal width in the elevational direction has often been neglected because spherical elements are usually designed for HIFU and linear arrays for imaging. The source geometry determines diffraction effects, as well as shear wave amplitude and spectrum. We propose a tunable approach to modify existing transducers using toric lenses to extend the focus in one direction. The motivation is to understand the role of the elevational focus in radiation force applications.

## Statement of Contribution/Methods

A toric lens geometry has been calculated using PDMS. All lenses were designed to stick directly to a spherical transducer surface with a minimum thickness of 200  $\mu\text{m}$ . The resulting fields were simulated using Field II. Several lenses were designed with a tunable focal size in the elevational direction. Molds were built using a CNC mill. Lenses were then manufactured and the resulting fields from a focused transducer (7.5 MHz,  $f\#1.5$ ,  $f=35$  mm) were measured using a hydrophone. Shear wave elastography experiments were then carried out using a Verasonics system and an ultrasound array (9 MHz) in a 5%-gelatin phantom at the same imaging location with and without lens.

## Results/Discussion

With very low attenuation due to absorption, the optimal lens induced a reasonable loss in pressure at the focus (-7.7 dB) due mainly to diffraction. Experiments showed an increase of the shear wave amplitude by at least a factor of 2 at the same pressure with a two-fold decrease in diffraction losses. The optimal focal width in the elevational direction was found to be close to the wavelength of the shear wave in the medium, leading to a directional shear wave. We demonstrated an approach to optimize transducers fields for radiation force applications. With the advent of 2D dimensional arrays for 3D shear wave elastography, this approach can be used to optimize toric focusing laws to maximize the radiation force amplitude for a given application. Modeling the dependency of the amplitude with elevational focal width is currently under investigation.

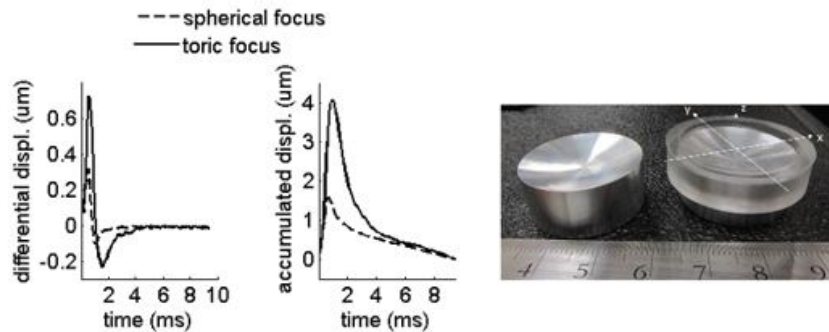


Fig. 1. Axial displacement amplitude (left: differential displacements recorded at 10 kHz, center: cumulative displacements) obtained without lens (dash line) and with a toric lens (solid line) at a peak pressure of 3 MPa in a 5%-gelatin phantom. Right: picture of the mold and the lens.

P1B7-4

#### Measurement of both elastic and optical properties using an ultrasound modulated optical imaging system

Yi Cheng<sup>1</sup>, Sinan Li<sup>1</sup>, Robert J. Eckersley<sup>2</sup>, Daniel S. Elson<sup>3</sup>, Meng-Xing Tang<sup>1</sup>; <sup>1</sup>Department of Bioengineering, Imperial College London, United Kingdom, <sup>2</sup>Department of Biomedical Engineering, King's College London, United Kingdom, <sup>3</sup>Institute of Global Health Innovation and Department of Surgery and Cancer, Imperial College London, United Kingdom

#### Background, Motivation and Objective

Optical and mechanical properties of soft tissue are important indices of early tumour detection. A number of imaging techniques have been developed to measure either elastic or optical properties of tissue. Here we develop and evaluate a dual mode system that measures both optical and mechanical properties by combining ultrasound modulated optical tomography (UOT) [1] and shear wave laser speckle contrast analysis [2].

#### Statement of Contribution/Methods

As shown in Fig. 1a, a tissue mimicking phantom was exposed simultaneously to a 532 nm CW laser and a 5 MHz focused ultrasound transducer which was stimulated by a 2 ms burst. A CCD camera was used to detect scattered light in a reflection geometry. UOT signals were obtained by detecting the light modulated by the ultrasound burst and associated acoustic radiation forces (ARF) immediately after US exposure, while the elasticity was quantified via the shear wave speed which was calculated by finding the delay in the time-of-flight ( $\Delta T$ ) between two time-resolved shear wave signals originating from two ultrasound excitation positions. There were two cylindrical inclusions buried in the phantom - a mechanical inclusion with higher stiffness and an optical inclusion with higher absorption coefficient (white and black circles respectively in Fig. 1a). The phantom was scanned from left to right with 1 mm step size.

#### Results/Discussion

In Fig. 1b, inclusions are identifiable through the UOT signal, and the shear wave tracking provides complementary quantified elasticity measurement. This is the first time that optical properties and quantitative elasticity were measured simultaneously at depth of tissue mimicking phantom. In addition, the detection was in the reflection geometry, which makes the set-up more accessible in practical applications.

[1] Li R, Song L, Elson DS, Tang M-X. Optics Letters 2010; 35(15):2633.

[2] Cheng Y, Li S, Elson DS, Tang M-X. Journal of Biomedical Optics 2013; 18(12):121511

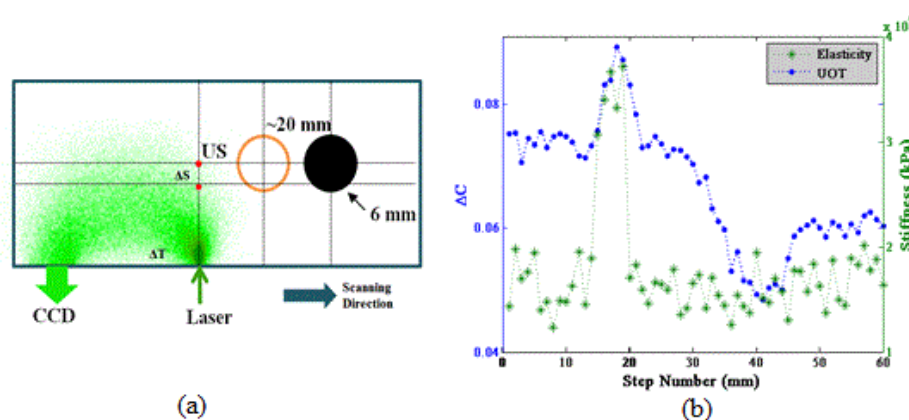


Figure 1(a) Top view of experimental setup. (b) Dual-mode scanning result.

# Shear Modulus Imaging Based on Full-Field Laser Speckle Contrast Analysis for Improved Spatial Resolution

Pei-Yu Chao<sup>1</sup>, Pai-Chi Li<sup>1</sup>; <sup>1</sup>National Taiwan University, Taiwan

## Background, Motivation and Objective

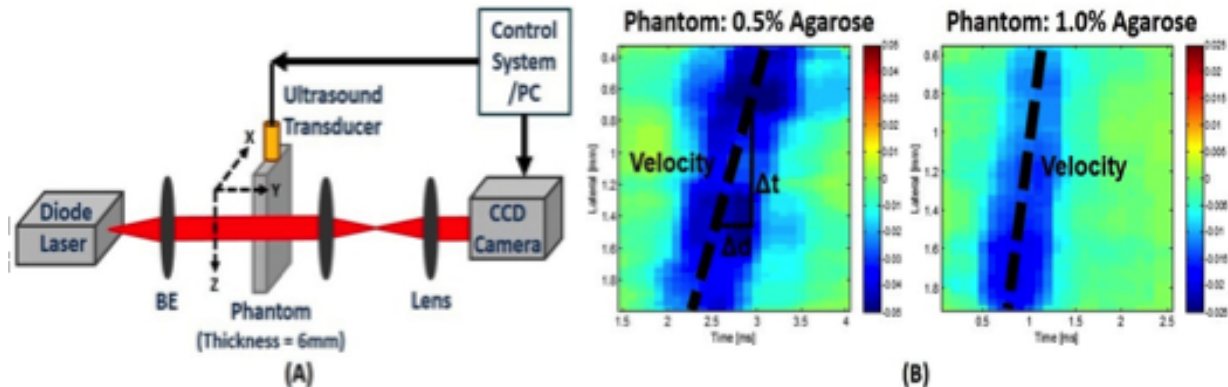
Matrix mechanics plays an important role in cell development. Studies have shown that the physical interactions between cancer cells and microenvironment is one of the key factor in cancer cell invasion. A local quantitative shear modulus map of cell microenvironment, hence, may provide valuable information for cancer research. The spatial resolution of a shear modulus map is dependent on sensitivity of the imaging system, i.e., the ability of detecting small SW displacement, which is related to the wavelength of the probing signal. In this regard, conventional ultrasound detection of shear wave (SW) propagation may not be adequate due to insufficient sensitivity. Laser speckle contrast imaging (LSCI) is a tool that has been used for imaging blood flow dynamics with spatial resolution in tens of micron and sensitivity in tens of nanometers. Hence, it may be suitable for detecting SW in a cell culture system in dimension of  $10 \times 10 \times 5 \text{ mm}^3$ . We hypothesize that LSCI is able to provide a shear modulus map with higher spatial resolution for matrix mechanics analysis.

## Statement of Contribution/Methods

The application of acoustic radiation force induces SW propagation and local particle displacement, which causes the laser speckle pattern to fluctuate. The intensity fluctuation is integrated by a camera, and is shown as local blurring in the raw image. The spatial blurring is measured and defined by the speckle contrast  $K = \sigma_s / I$ , where  $\sigma_s$  and  $I$  are the standard deviation and mean intensity of pixel values in a small image region. A two-dimensional SW velocity map is calculated by computing speckle contrast at each point in the image using a spatial kernel of  $450 \times 450 \mu\text{m}^2$ .

## Results/Discussion

The system setup is shown in Fig. 1-A, and spatial-temporal SW propagation map for two homogeneous agar phantoms (0.5% and 1.0% concentration) are shown in Fig. 1-B. The SW velocity, which is deduced by calculating the slope of the spatial-temporal maps, is 2.61m/s and 4.37m/s for 0.5% and 1.0% agar phantom, respectively. The deviation from the values recorded in the literature is 6.5% and 13.1%. The spatial resolution is approximately  $450 \mu\text{m}$  for softer materials, which can be improved by utilizing a shorter camera exposure time. A heterogeneous study will be presented in the full report.



**1-A. Experiment Setup. 1-B. Spatial-temporal SW propagation map of two homogeneous phantoms.**

# Two-way strain estimation quality assessment approach for tumor detection using free-hand strain imaging: Experimental study

Saefer Hyder<sup>1</sup>, Sevan Harput<sup>1</sup>, Zainab Alomari<sup>1</sup>, Steven Freear<sup>1</sup>; <sup>1</sup>School of Electrical and Electronic Engineering, University of Leeds, Leeds, United Kingdom

## Background, Motivation and Objective

Free-hand strain imaging has been in research focus for detecting stiffer tissue lesions surrounded by soft background. Little attention has been rendered to quantitative reliability assessment of elastograms. In this work, a two-way quantitative assessment approach is proposed using strain contrast-noise-ratio (CNRs), and correlation coefficient. Using only one of the metric to select optimal elastogram is often misleading. The objective is to propose a free-hand strain imaging solution which is accurate and reliable for tumor detection.

## Statement of Contribution/Methods

An agar-gelatin tissue-mimicking phantom with an inclusion three times stiffer than background was prepared as shown in fig1a. Phantom was compressed up to 4% with increment of 0.22% using a medical probe. A Gaussian pulse with 6 dB bandwidth of 5 MHz was used for excitation with a custom-built ultrasound array research platform (UARP). Strain estimation was performed by a normalized cross-correlation algorithm with adaptive temporal stretching.

## Results/Discussion

Normalized values of CNRs are computed between region-1 and region-2 and between region-3 and region-2, and then averaged. The noise masking technique detects portions of elastogram where correlation coefficient falls below 0.7, calculates the noisy area in percentage, and masks the noisy portions of an elastogram with white colour as shown in fig1b. CNRs measures target contrast with background, and noise masking technique helps to discard noisy elastograms. For CNRS, threshold of -3dB is set and within 1.76% to 2.86% strain, CNRs was found above the threshold level, as shown in fig2. Finally, using noise-masked area metric, it was found that, 1.76% strain elastogram has least noise masked portion within the -3 dB CNRs window.

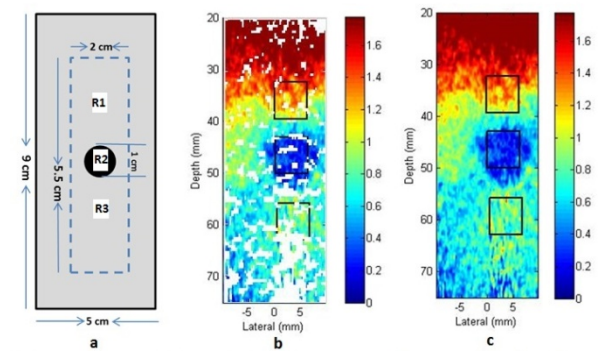


Fig1: a) Phantom geometry with imaging plane dimensions b) Noise-masked elastogram c) Final selected elastogram

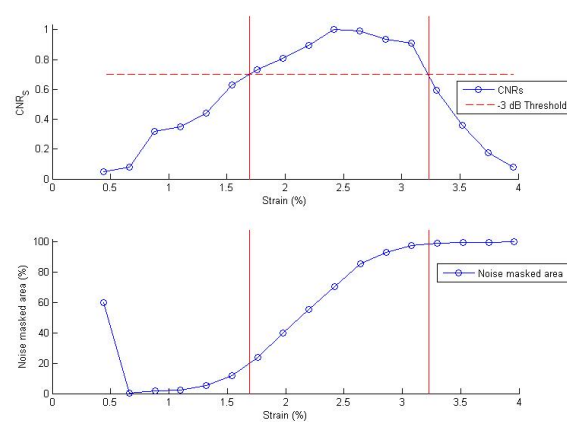


Fig2: above) CNRs vs strain plot below) Noise masked area vs strain plot

P1B7-7

### Anisotropic polyvinyl alcohol hydrogel phantom for shear wave elastography in fibrous biological soft tissue

Simon Chatelin<sup>1</sup>, Miguel Bernal<sup>1</sup>, Clément Papadacci<sup>1</sup>, Jean-Luc Gennisson<sup>1</sup>, Mickael Tanter<sup>1</sup>, Mathieu Pernot<sup>1</sup>, <sup>1</sup>Institut Langevin - ESPCI ParisTech, INSERM Paris U979 - CNRS UMR 7587, Paris, France

#### Background, Motivation and Objective

Shear wave elastography can provide quantitative measurement of soft tissues viscoelastic properties based on the measurement of shear wave speed in the medium. Muscular and cerebral tissues are composed of fibers which induce a strong anisotropic effect on the mechanical behavior. Currently, these tissues cannot be accurately represented by existing elastography phantoms and there is an urgent need of developing new anisotropic tissue mimicking phantoms. In the present study we propose an original multimodality imaging characterization of a transverse isotropic (TI) polyvinyl alcohol (PVA) cryogel.

#### Statement of Contribution/Methods

The mechanical anisotropy is induced in the PVA hydrogel by stretching the physical crosslinks of the polymeric chains while undergoing freezing cycling [1]. Multiple properties of these phantoms were investigated using a variety of techniques at different scale. The mechanical (dynamic and static) properties were studied using Supersonic Shearwave Imaging (SSI) technique [2] and Full-Field Optical Coherence Tomography (FFOCT) strain imaging. The optical and ultrasonic spatial coherence properties were measured by FFOCT volumetric imaging [3] and Backscatter Tensor Imaging (BTI) [4], respectively. The results in the anisotropic phantom were compared with an isotropic PVA hydrogel undergoing similar imaging protocols.

#### Results/Discussion

Results showing anisotropy for BTI, SSI, FFOCT (strain and volumetric) images are presented in figures A to D respectively. Correlation of mechanical and optical properties demonstrates the complementarity of these techniques for the study of anisotropy on a multi-scale range. At the same time, the phantom shows properties mimicking the mechanical and optical anisotropy of the biological fibrous tissues, such as cardiac, muscular or tendinous structures. The results suggest that this type of phantom (TI) could be used in the development of techniques and equipment to study anisotropy, such as the design of new ultrasound probes for cardiac and musculoskeletal application.

1 Millon et al, J of Biomed Mat Res Part B, 2006

2 Bercoff et al, IEEE UFFC, 2004

3 Nahas et al, BOE, 2013

4 Papadacci et al, IEEE TUF, 2014

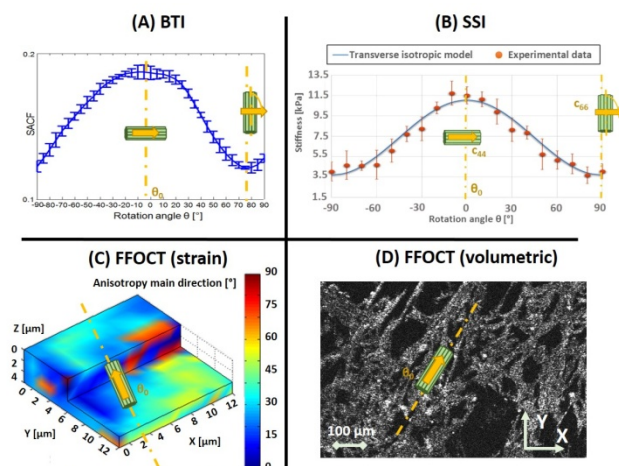


Figure. (A): Spatially Averaged Coherence Factor (SACF) variations as a function of rotation angle from BTI; (B): Shear wave speed variations from SSI; (C): anisotropy main directions from FFOCT strain imaging; (D): FFOCT volumetric images.



### Simulations of Tendon Mechanical Properties by ABAQUS: Comparison with Results from Elasticity Imaging

Tang-Ting Chu<sup>1</sup>, Chia-Lun Yeh<sup>1</sup>, Pai-Chi Li<sup>1,2</sup>, **Po-Ling Kuo<sup>1,2</sup>**, <sup>1</sup>Graduate Institute of Biomedical Electronics and Bioinformatics, National Taiwan University, Taipei, Taiwan, <sup>2</sup>Department of electrical engineering, National Taiwan University, Taipei, Taiwan

#### Background, Motivation and Objective

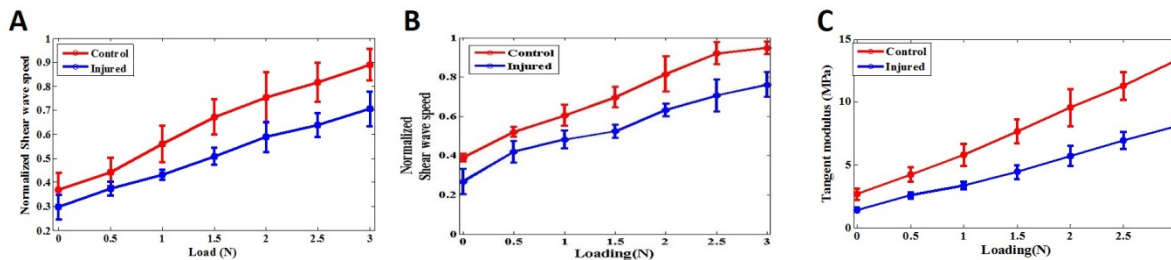
Tendons play a key role in maintaining the efficiency of human kinetics. Shear wave elasticity imaging is a promising clinical tool to non-invasively assess tendon functionalities. Due to the complex architecture and mechanical behaviors of tendons, a numerical approach is of great need to delineate the changes of shear wave speeds when tendons are subject to various loads. Hence the main objective of this research is to develop a quantitative framework to enhance the diagnostic potential of shear wave elasticity imaging in tendon disorders.

#### Statement of Contribution/Methods

A finite element model of tendon was built using ABAQUS/CAE. The tendon was modeled as a cylinder, with the length of 50 mm and the radius of 14.64 mm. The model consisted of 128800 hexagonal C3D8R elements and 136566 nodes. We defined a normal tendon as control and the material properties of control/injured tendons at different loads were adapted from experimental results. Shear waves were simulated in the model and the Explicit method was chosen to analyze wave propagation. Shear wave speeds at various loads matching the experimental conditions were estimated.

#### Results/Discussion

The simulated shear wave speeds both in control and injured tendons increased in proportion to increasing loads (Figure 1A). The shear wave speed in control tendon was higher than that in injured one at the same load, which is well consistent with our experimental results (Figure 1B). To facilitate data comparison, the wave speeds in both figures were rescaled by normalizing with their maximum. Also, the shear wave group velocity is highly correlated with tangent modulus of the tendon along the longitudinal axis (Figure 1C). These results suggest that shear wave elasticity imaging is of great potential in evaluating tendon functionalities clinically.



### 3D Cell Mechanobiology Study using Shear Wave Elasticity Imaging

Chun-Ting Li<sup>1</sup>, Chin-Hsiung Tsai<sup>1</sup>, Pai-Chi Li<sup>1,2</sup>, **Po-Ling Kuo<sup>1,2</sup>**, <sup>1</sup>Graduate Institute of Biomedical Electronics and Bioinformatics, National Taiwan University, Taipei, Taiwan, <sup>2</sup>Department of electrical engineering, National Taiwan University, Taipei, Taiwan

#### Background, Motivation and Objective

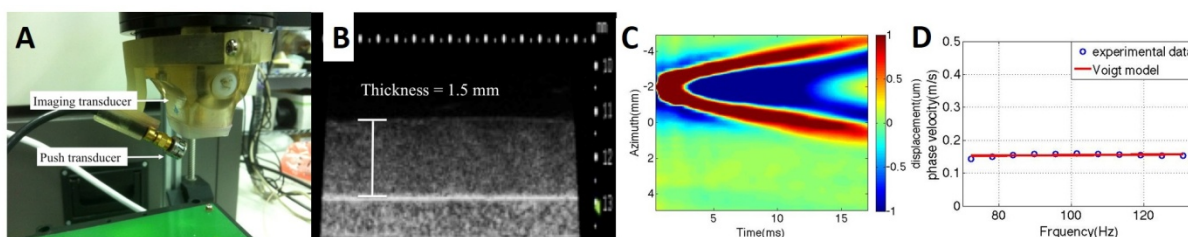
Extracellular matrix (ECM) stiffness plays a crucial role in cell mechanobiology. Culturing cells in 3D better recapitulates the in vivo conditions. However, there are few platforms allowing measurements of the dynamics of 3D ECM stiffness resulting from cell remodeling. Ultrasound shear wave elasticity imaging (SWEI) is a promising tool to evaluate the spatiotemporal change of ECM stiffness. Therefore the aim of this study is to evaluate the feasibility of quantifying changes of ECM stiffness in a 3D cell culturing system using SWEI.

#### Statement of Contribution/Methods

We developed a collagen-based 3D cell culture complex suitable for SWEI. The cell-culturing complex was mounted to a SWEI system consisting of a 20 MHz push transducer for shear wave (SW) generation and a 40 MHz imaging transducer motorized by a mechanical scanner (Fig. 1A). The change of complex thickness resulting from cell remodeling was determined by B-mode images (Fig. 1B). A spatiotemporal map of matrix displacement resulting from SW propagation (Fig. 1C) was generated and converted into a k-space map by 2D discrete fast Fourier transform. The SW speed,  $v$ , was derived from  $v=2fk/k$ , in which  $f$  and  $k$  represent frequency and wavenumber corresponding to individual peaks in the k-space. The dispersion curve, defined as the function of SW speeds with respect to frequencies, was fitted by viscoelastic models to estimate the shear moduli (Fig. 1D).

#### Results/Discussion

Selective cell lines including lung and hepatic cancer, fibroblast, and myoblast were tested with our 3D system. We found that most of the calculated dispersion curves fitted well by the Voigt model. The cultured cells actively remodeled the ECM with significant contraction of matrix, with that a higher degree of matrix contraction corresponded to a larger shear modulus. Inhibition of cell contraction released the matrix shrinkage and decreased matrix stiffness. Numerical analysis revealed that the relationship between the matrix contraction and the shear modulus followed a power law. Our preliminary results suggest that cell contraction plays a primary role in the stiffening of solid tumors and SWEI plus the 3D system as a valuable tool for cell mechanobiology.



P1B7-10

### Elastographic characterization of two viscoelastic phantoms using three techniques: Shear Wave Induced Resonance Elastography, Transient Elastography and Supersonic Shear Imaging

Caroline Chartier<sup>1</sup>, Mélouka Elkateb<sup>1</sup>, Anis Hadj Henni<sup>2</sup>, Cédric Schmitt<sup>2</sup>, Cécile Bastard<sup>3</sup>, Véronique Mietté<sup>3</sup>, Frédéric Ossant<sup>1,4</sup>; <sup>1</sup>Université François-Rabelais de Tours, Inserm, Imagerie et Cerveau UMR U930, Tours, France, <sup>2</sup>Rheolution Inc, Montréal, Québec, Canada, <sup>3</sup>Echosens company, Paris, France, <sup>4</sup>CHRU de Tours, Tours, France

#### Background, Motivation and Objective

Elastography methods are used to characterize mechanical properties of soft tissues. In this context, different types of phantoms are produced with a defined Young's modulus (E) for in vitro validation. However, it is necessary to verify experimentally its mechanical parameters, already measured at low frequencies for SEBS phantoms [1]. The aim of this work is to compare E measurement using three elastographic techniques and to analyze measurement dispersion for different elasticity values for two kinds of phantoms.

#### Statement of Contribution/Methods

Two sets of three gradual stiffness phantoms are produced. The first set was a SEBS copolymer-in-oil. Three polymer percents were used to obtain three stiffness soft to hard (5.37%, 8.39%, 10.33%), with 1% silica (Si) scatterers. The second set was a new phantom material called Plastileurre®. This material allows an easier manufacturing especially for higher stiffness values. Plastileurre® is available in several mixable liquid preparations: Softener (S1), Soft (S2) and Standard (S3). We used three combinations: 50/50 S1-S2, 100% S2, 50/50 S2-S3, with 1% Si.

E values were estimated by three techniques: 1D Transient Elastography (TE), Shear Wave Induced Resonance Elastography (SWIRE - Rheospectris™ device), and Supersonic Shear Imaging (SSI - Aixplorer®). In TE, wavefront velocity and then E are estimated through the depth (1D) while SSI estimates an E in 2D. Otherwise, SWIRE estimates an E in function of frequency in a specific slice volume sample. Elasticity median values are estimated at 400Hz for TE and SWIRE techniques.

#### Results/Discussion

The three techniques show a good sensitivity to estimate different stiffness values. TE and SSI results were obtained with a dispersion increasing from 2kPa for softer media (SEBS) to 50kPa for harder media (Plastileurre®). The last one seems to have a greater heterogeneity; this assumption could be validated by improving the Plastileurre® phantom manufacturing. In contrast, values dispersion (0.5 to 4kPa) with SWIRE was low and steady for both phantoms. Finally, each technique has different characteristic measurements, leading to small deviations of the measured values of E. Pending further measurements, assigning a range of elasticity values at a specific frequency using several techniques rather a single one could be more representative to characterize a viscoelastic medium.

[1] J. Oudry et al, "Copolymer-in-oil phantom materials for elastography", 2009

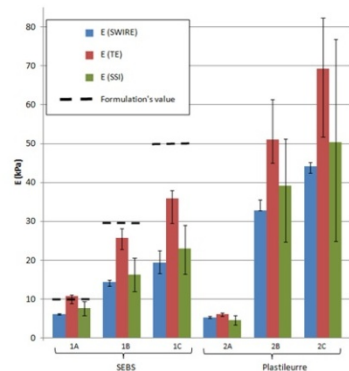


Figure 1: TE, SWIRE and SSI techniques used to estimate Young's modulus dispersion for SEBS and Plastileurre® phantoms for different hardness values.

P1B7-11

### Characterization of transverse isotropy in tissue mimicking phantoms under static stress

Matthew Urban<sup>1</sup>, Randall Kinnick<sup>1</sup>, Xiaoming Zhang<sup>1</sup>, James Greenleaf<sup>2</sup>; <sup>1</sup>Mayo Clinic College of Medicine, Rochester, MN, USA

#### Background, Motivation and Objective

Tissues such as skeletal muscle and kidneys have well-defined structure that affects the measurements of mechanical properties. As an approach to characterize the material properties of these tissues, different groups have assumed that they are transversely isotropic (TI) and measure the shear wave speed as it varies with angle with respect to the structural architecture of the organ. To refine measurements in these organs, it is desirable to have tissue mimicking phantoms that exhibit similar anisotropic characteristics. Some approaches involve embedding fibers into a material matrix. However, if a homogeneous solid is under compression due to a static stress, an acoustoelastic effect can manifest which makes the measured wave speeds change with the compression stress. We propose to exploit this characteristic to demonstrate that stressed tissue mimicking phantoms can be characterized as a TI material.

#### Statement of Contribution/Methods

We tested two gelatin phantoms made with different concentrations of gelatin (9%, 11%). Stress was applied by pouring water into a container centered on top of a plate on top of the phantom. The stress was varied from 318-2670 Pa. A linear array transducer and a V-I Verasonics system (Verasonics, Inc., Redmond, WA) were used to induce and measure shear waves in the phantoms. The shear wave motion was measured using a compound plane wave imaging technique and applying autocorrelation to the received in-phase/quadrature data. The shear wave speed,  $c$ , was estimated using a Radon transform method. The transducer was mounted on a rotating stage so measurements were made every  $10^\circ$  over a range of  $0-360^\circ$ , where the compression is applied along  $0-180^\circ$  direction. The shear moduli were estimated by applying  $\mu = \rho c^2$ , where  $\rho$  is the mass density. A TI model was fit to the data (Wang, *et al.*, IEEE Trans. Med. Imaging. 32:1671-84. 2013) and the fractional anisotropy (FA) was evaluated (Lee, *et al.*, Phys. Med. Biol. 57:5075-95. 2012).

# Results/Discussion

Figures 1(a)-(d) show the shear moduli varying with angle (blue open circles) and the solid lines are the TI model fit. The FA in Fig. 1(e) varies over a range of 0.22-0.55 and 0.05-0.33 for the gelatin phantoms with 9% and 11% concentrations, respectively. This approach can be used to explore many configurations of transverse isotropy with the same phantom, simply by applying stress to the tissue mimicking phantom.

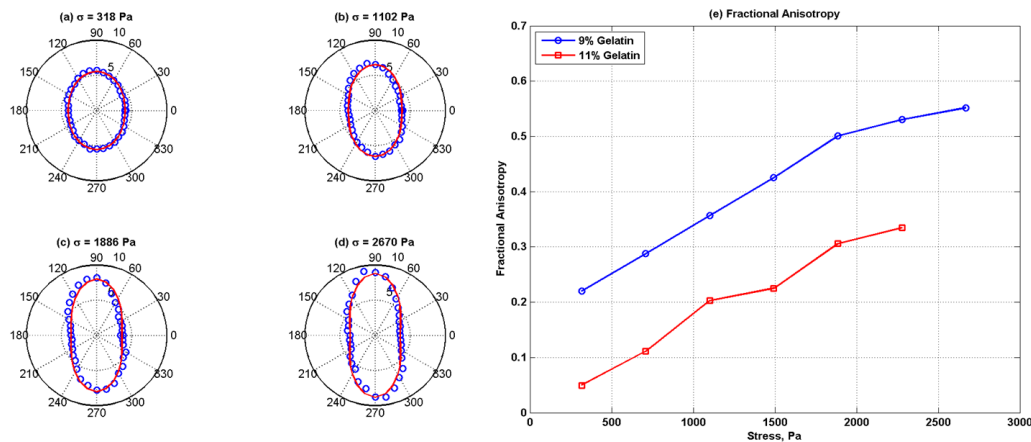


Figure 1. Polar plots of shear modulus measured at different stress levels in 9% gelatin phantom and evaluation of fractional anisotropy. In (a)-(d), the measured data are the open blue circles and the red lines are the model fit for a transverse isotropic material. (a)  $\sigma = 318$  Pa, (b)  $\sigma = 1102$  Pa, (c)  $\sigma = 1886$  Pa, (d)  $\sigma = 2670$  Pa, (e) fractional anisotropy of 9% and 11% gelatin phantoms.

## P1B7-12

### 1D high resolution transient elastography: an optimized elastographic tool for a viscoelastic characterization of thin heterogeneous tissues - a preliminary study

Yassine MOFID<sup>1</sup>, Caroline Chartier<sup>1</sup>, Mélouka El Kateb<sup>1</sup>, Cécile Bastard<sup>2</sup>, Stéphane Audière<sup>2</sup>, Véronique Miette<sup>2</sup>, Valérie Tauveron<sup>3</sup>, Anabel Maruani<sup>1,3</sup>, Frédéric Ossant<sup>1,3</sup>, <sup>1</sup>Université François-Rabelais de Tours, Inserm, Imagerie et Cerveau UMR U930, Tours, France, <sup>2</sup>Echosens company, Paris France., Paris, France, <sup>3</sup>CHRU de Tours, Tours, France, tours, France

#### Background, Motivation and Objective

Transient elastography (TE) is a parametric technique used to quantify Young's modulus (E) by estimating the shear wave (SW) velocity (Vs) in a homogeneous and elastic medium. In fact, TE has been successfully integrated in the Fibroscan® [1] for hepatic fibrosis diagnosis. In this work, we present a preliminary study using a new development in TE dedicated to 1D high resolution (HR) estimation of E in thin, heterogeneous and viscoelastic tissues such as the skin.

[1] www.echosens.com

#### Statement of Contribution/Methods

A HR elastography prototype was used to generate a SW using a mechanical vibration system coupled to 15MHz high frequency (HF) ultrasound (US) transducer. A 400Hz pulse was generated by the transducer's surface and SW was tracked through 15mm depth using 50kHz ultrafast scanning. For a maximum estimation of  $E=300$ kPa ( $V_s \sim 10$ m/s), the SW velocity could be followed each 0.2mm. A HR elastogram (axial resolution = 25 $\mu$ m) was performed using our algorithm based on calculating local minima/maxima displacements in US signals [2]. A frequency analysis was applied for local depths (0.2mm kernel; 50 $\mu$ m shift) to calculate Vs in function of frequency [10 to 800Hz]. Then, a Kelvin-Voigt rheological fit was applied to estimate local E. Finally, E in function of depth E(z) was obtained as a 1D quantitative information.

[2] Y. Mofid et al. "Axial displacement tracking in transient elastography using neighboring local minima maxima in radio frequency signals" IUS 2013 IEEE.

#### Results/Discussion

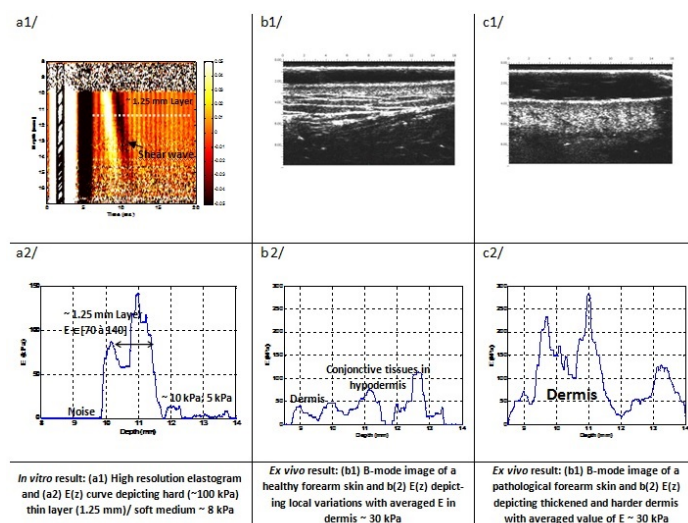
Figure shows the potential of HR TE through three typical results.

In vitro results on multi-layers phantom show the HR elastogram (a1) and E(z) curve depicting a hard thin (~1.25 mm and averages E ~ 100kPa) layer mimicking dermis (a2).

Ex vivo results in a healthy human forearm skin with important heterogeneity especially in the hypodermis (b1). E(z) well described the E variation through thickness (E ~ 30kPa in 1mm dermis) (b2).

Ex vivo results in a pathological forearm skin in the same subject allowed only investigation in the dermis at 15MHz US frequency since the pathological dermis thickened to reach 2.5mm (c1). The averaged E in dermis was higher: 150kPa (c2).

In conclusion, The HR TE shows a good performance to estimate an accurate 1D estimation in vitro and ex vivo results promise a sensitive tool to characterize mechanical properties through human skin thickness for cosmetology and dermatology.



P1B7-13

### Building A Virtual Breast Ultrasound Phantom Lab Using Open Source Software

Yu Wang<sup>1</sup>, Emily Helminen<sup>1</sup>, Jingfeng Jiang<sup>1</sup>; <sup>1</sup>Michigan Tech Univ, Houghton, Michigan, USA

#### Background, Motivation and Objective

Elastography is being used to augment in vivo characterization of breast lesions. Results from early clinical trials indicated that there was a lack of confidence in image interpretation (Gong et al, Breast Cancer Res Treat, 2011). Such confidence can only be gained through rigorous imaging tests using complex, heterogeneous but known media. Our objective of this study is to build a virtual breast phantom lab in the public domain that can be used for rigorous imaging testing of this kind.

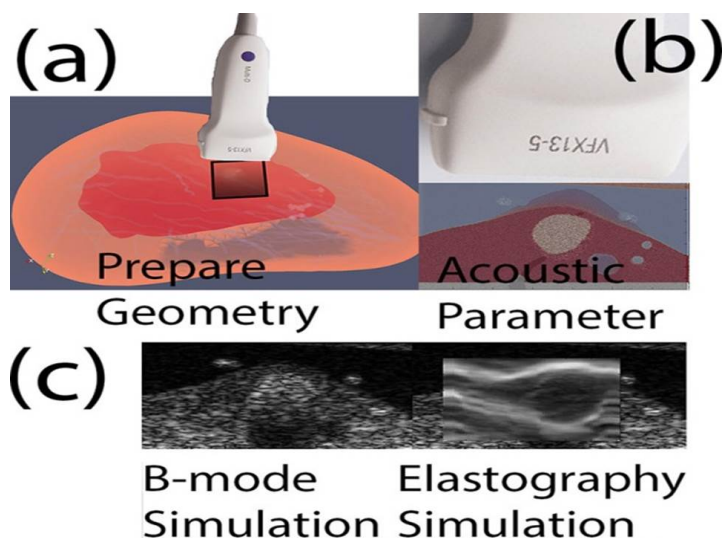
#### Statement of Contribution/Methods

Main thrust of this work is to streamline biomedical ultrasound simulations by leveraging existing open source software packages including K-wave or Field II, VTK, FEBio and Tetgen. The integration of these four open source packages was based on a simple message-passing scheme to facilitate its use among imaging scientists. Firstly, a virtual breast model containing complex geometries was created using VTK and meshed to unstructured grids (Tetgen). Secondly, the unstructured meshes can be converted to rectilinear grids using an in-house program derived from VTK. This step enables assignment of acoustic parameters such as density and speed-of-sound (SOS) in complex phantoms for K-wave and Field II. Thirdly, ultrasound simulations were readily performed by either K-wave or Field II. Tissue deformation for quasi-static elastography applications can be applied using FEBio.

#### Results/Discussion

As shown in the figure, a complex and heterogeneous phantom (a) was built based on the Visible Human Project data. Flexibility provided by the proposed virtual infrastructure enabled us to select a volume of interest (b) where heterogeneous acoustic impedance maps can be assigned. A complex B-mode image (c) realistically represents the underlying complex but known medium. A pair of pre- and post-deformation echo fields led to a strain image (d). The simulated strain image showed complex patterns that were normally seen in freehand data (e.g. Hall et al, UMB, 2003).

The proposed virtual software infrastructure utilizes open source software as a shared resource and therefore can be tailored to meet specific research needs by potential users. Hopefully, this open source approach will accelerate development of ultrasound imaging methods including elastography.



## In vitro Study of Shear Wave Velocity Dependency on Heart-Motion Induced Tissue Compression

Hideki Yoshikawa<sup>1</sup>, Ken-ichi Kawabata<sup>1</sup>, Kunio Hashiba<sup>2</sup>; <sup>1</sup>Central Research Laboratory, Hitachi, LTD., Tokyo, Japan, <sup>2</sup>Hitachi Aloka Medical, Ltd., Tokyo, Japan

## Background, Motivation and Objective

Ultrasound shear wave elastography (SWE) has great potential in diagnosing liver diseases such as fibrosis. In SWE, shear wave velocity ( $V_s$ ) is used as a measure of tissue elasticity. In measuring  $V_s$ , tissue compressions are considered to be major error sources. Typically,  $V_s$  measurements in the left liver lobe are thought to be too inaccurate because of tissue compression due to heart-beat[1]. In this study, the dependence of shear wave velocity on tissue compression is quantitatively studied to understand the dominant factors of errors in  $V_s$  in the left liver.

## Statement of Contribution/Methods

A tissue mimicking phantom (A: 2.4 m/s, B: 1.7 m/s) was set between an ultrasound pulse wave transducer and diagnostic probe (Fig. 1). A shear wave was generated by acoustic radiation force with the transducer, and the  $V_s$  was measured by detecting tissue displacement with the probe. The phantom was uniaxially compressed along the y-axis statically. With this setup, the shear wave velocities under statically compressed conditions were measured with various strain ratios from 0 to 29%.

## Results/Discussion

The dependence of shear wave velocity on strain ratio is shown in Fig. 2. The vertical axis shows velocity dispersion (VD) defined as  $dV_s/V_0$ , which shows the rate of change in  $V_s$  from a value  $V_0$  obtained without compression. The VD value changed linearly with the increasing strain ratio and reached 26% at a strain ratio of 29%. Further, we found that the tendency of VD on the increasing strain ratio differed depending on the direction between wave propagation and compression. VD increased and decreased with the increasing strain ratio when the direction was parallel (A(X) and B(X)) and perpendicular (A(Y) and B(Y)), respectively. This anisotropic phenomenon could be clearly visualized in a C-plane (Fig. 3). The acousto-elasticity theory indicates that, for solid materials in non-destructive inspection, VD is a linear function of the compression ratio. Our results suggest that the theory is also applicable to tissue mimicking phantoms and possibly further to biological tissues. Using the obtained results, we confirmed compression is one dominant factor of SWE errors in the left liver. We will perform further studies such as measurements with transient compression to understand the significance of tissue compression in liver left lobes.

[1] T. Toshima et al.: J. Gastroenterol, 46 (2011) 705.

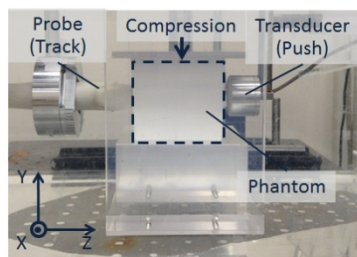


Fig. 1 Experimental setup

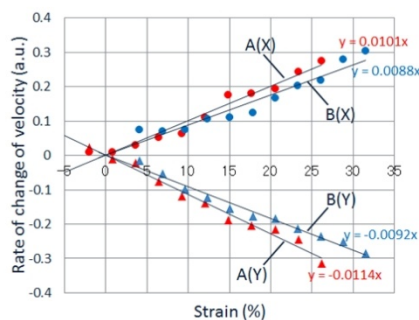


Fig. 2 Dependence of shear wave velocity on strain (red: A, blue: B)

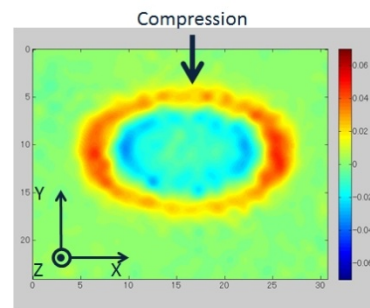


Fig. 3 Displacement distribution of shear wave in compressed media



## P1B8 - MIM: New Systems for and Applications of Ultrasound Imaging

Salon C

Friday, September 5, 2014, 8:00 am - 5:00 pm

Chair: **Jeremy Dahl**  
Duke University

P1B8-1

### Gastric emptying evaluation using magneto-acoustic transducer.

Alexandre Colello Bruno<sup>1</sup>, Oswaldo Baffa<sup>1</sup>, Antonio Carneiro<sup>2</sup>; <sup>1</sup>Department of Physics, University of Sao Paulo, Ribeirão Preto, SP, Brazil, <sup>2</sup>Department of Physics, University of Sao Paulo, Ribeirão Preto, São Paulo, Brazil

#### Background, Motivation and Objective

Gastrointestinal (GI) motor activities consist of an intricate group of functions that are essential for life, and malfunction of GI transit or contractility are common. Gastric emptying reflects a diversity of important physiological functions. Alternating Current Biosusceptometry (ACB) is an inexpensive, radiation-free and noninvasive method to evaluate gastric emptying but its responses depends on the spatial distribution of the magnetizing sample around the magnetic sensor and doesn't have anatomical information. The magneto-acoustic (MA) transducer which combines ACB and ultrasound transducer improved susceptometric measurements potential, namely the spatial localization of the magnetized source. This study monitored relative stomach emptying in rats using the hybrid transducer and check ultrasound and ACB system complementarity.

#### Statement of Contribution/Methods

Male Wistar rats (300g) were used individually in the study. We injected (gavage) yogurt mixed with ferrite particles (diameter 37 - 70  $\mu\text{m}$ ) at concentration of 10%, in rats' stomach before experiment. An ultrasonic transducer microconvex (Ultrasonix) was placed in the center of an ACB. This Hybrid transducer was placed on rat's abdominal during experiments. Susceptometric signal was acquired during 20 minute and ultrasound images each 10 minute. The magnetic excitation frequency (from ACB) was maintained at 35 Hz and susceptometric signal sample rate was 0.5 Hz. We used MatLab (Mathworks, Inc.) to analyze all raw signals and Ultrasonix RP to make images along this study. The power Doppler (PwD) ultrasound data were saved and post processed to get area of region marked with magnetic particles in the gastric system. In a second experiment, we scanned the gastric region labeled to generate a volumetric image.

#### Results/Discussion

We evaluated the relative stomach emptying using PwD images and susceptometric signal with MA transducer. PwD maps highlighted the movement of magnetic particles (due magnetic force from ACB excitation coils) on B mode images which showed rats' stomach location with anatomic information. The susceptometric signals variation was consistent with published studies about rats' stomach emptying and ACB. The ACB mean relative signal decay was  $4.6 \pm 0.1\%$  and mean relative PwD area decreased was  $4.5 \pm 0.2\%$  after acquisition period due stomach emptying. However, this results diverged a little more ( $\approx 0.5\%$ ) when stomach shape was bigger and the meal was more spread. The spatial distribution was more sensitive to PwD than ACB. The PwD volumetric image provided stomach wall details which may enable to detect abnormalities noninvasively. Ultrasound image increased ACB spatial resolution even as add anatomy information.

P1B8-2

### Dependence of ultrasound decorrelation on urine scatter particle concentration for a non-invasive diagnosis of bladder outlet obstruction.

Muhammad Arif<sup>1</sup>, Tim Idzenga<sup>2</sup>, Ron van Mastrigt<sup>1</sup>, Chris L. de Korte<sup>2</sup>; <sup>1</sup>Erasmus Medical Center, Rotterdam, Netherlands, <sup>2</sup>Radboud UMC Nijmegen, Netherlands

#### Background, Motivation and Objective

Bladder outlet obstruction (BOO) is a common disease in elderly men. A correct diagnosis currently requires invasive techniques. Decorrelation of ultrasound (US) signals developed to estimate blood flow velocity, has been proposed as a non-invasive method for diagnosing BOO. However, unlike in blood, the particle concentrations in urine may vary between patients and with time, which can affect the decorrelation. Therefore in this study we investigated the dependence of US decorrelation on the urine particle concentration.

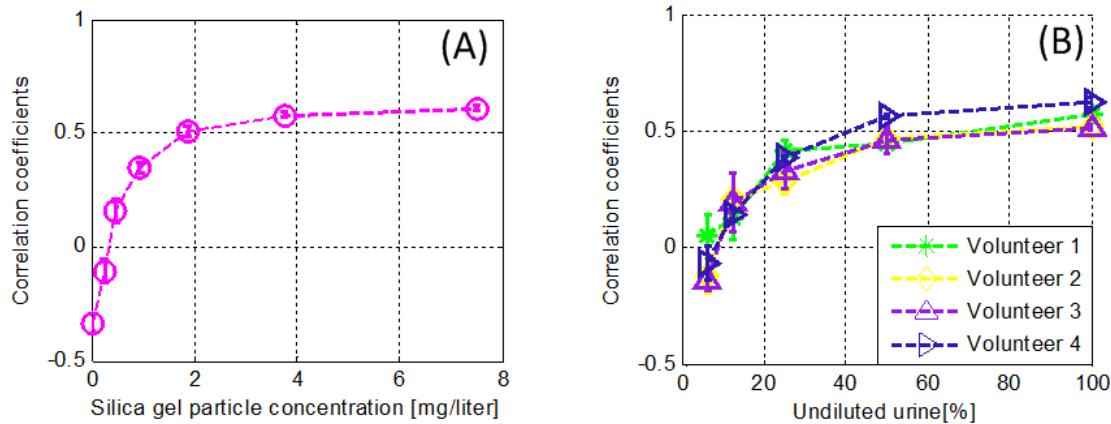
#### Statement of Contribution/Methods

A tissue mimicking urethra model was infused with stepwise diluted morning urine samples from 4 healthy volunteers and 6 aqueous solutions containing increasing concentrations of silica gel particles. We acquired 10 subsequent radiofrequency (RF) data sets for each solution using a BK-Medical, Pro Focus UltraView 2202 ultrasound system at a Pulse Repetition Frequency of 5 kHz. The correlation coefficients between each two RF-data sets were calculated. The average of the correlation values was taken and plotted as a function of particle concentration.

#### Results/Discussion

Both in urine and in the silica gel particle solutions the average correlation between sequential RF signals decreased exponentially with decreasing concentration. Also the correlation curves derived from the urine samples of the volunteers displayed a very similar behavior to those of the silica particle solutions.

The correlation coefficients at 100% urine concentration from most of the volunteers corresponded with the high silica particle concentrations and change very little down to a 50% dilution. This suggests that undiluted urine is suitable for decorrelation based estimation of flow velocity and for diagnosing BOO from US decorrelation without correcting for differences in particle concentration.



The average correlation values corresponding to (A) aqueous solutions with different silica gel particle concentration and (B) urine solutions, where 100% represents undiluted urine.

P1B8-3

### Estimation of Needle Tip Location using Ultrasound Image Processing and Hypoechoic Markers

Ian McSweeney<sup>1</sup>, Brian Murphy<sup>1</sup>, William Wright<sup>1</sup>; <sup>1</sup>Electrical and Electronic Engineering, University College Cork, Cork, Cork, Ireland

#### Background, Motivation and Objective

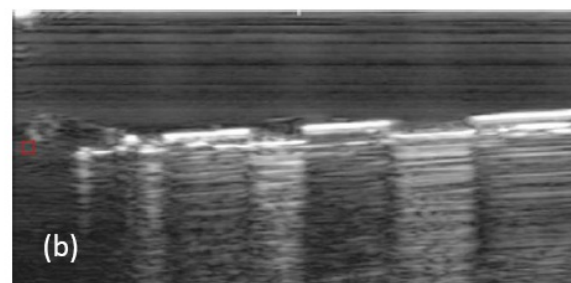
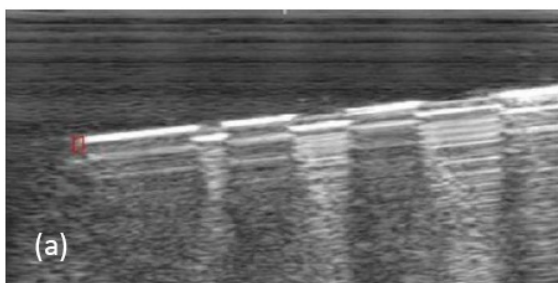
Ultrasound guidance is a common method used in procedures such as regional nerve blocks and biopsies. Accurate determination of the location of the needle tip is critical in many such procedures. Visual graduations on the needle may give an external estimate of the depth of the needle tip, but the tip itself may be difficult to find in the ultrasound image even with in-plane imaging. The needle tip echo may also be occluded by other hyperechoic regions in the image. The objective of the current work was to develop a simple technique to accurately estimate the location of the needle tip in an ultrasound image, using a set of hypoechoic reference markings on the shaft of the needle with image processing to improve accuracy and minimize error.

#### Statement of Contribution/Methods

A unique set of discrete hypoechoic markings was made along the shaft of a 14-gauge (1.6 mm nominal outer diameter) needle to provide a number of needle location reference points in the ultrasound image. Ultrasound scans were obtained of the needle in agar- and gelatin-based tissue mimicking phantoms using an 8.0 MHz linear array. The resulting images were cropped and binarized using an intensity filter before morphological operations were applied to isolate the needle echo in the image. A straight line was fitted to the top edge of the needle echo and up to three adjacent reference markings were found along this line. These were then used to estimate the actual position of the tip in the image.

#### Results/Discussion

Example in-plane ultrasound images are shown below, with the needle tip location overlaid in red, (a) where the end of the needle is visible in the image and (b) where the end of the needle is occluded and the tip location has been estimated from the number and spacing of the hypoechoic markers on the shaft of the needle. The red box bounding the tip location also includes the margin of error in the tip locations shown. The accuracy of the location is affected by the resolution of the ultrasound image and the probe frequency. Redundancy in the number of markings used increased the robustness of the technique.



P1B8-4

### Needle visibility for deep punctures with curved arrays

Stefanie Dencks<sup>1</sup>, Georg Schmitz<sup>2</sup>; <sup>1</sup>Medical Engineering, Ruhr-Universität Bochum, Germany

#### Background, Motivation and Objective

With the increasing number of punctures in deep tissues the problem of poor needle visibility in ultrasound images is aggravated: the insertion angle of the needle  $\beta$  becomes larger and, thus, the angle of incidence  $\alpha$  increases. Additionally, for deep punctures often curved arrays are used where  $\alpha$  is varying.

Unexpectedly, sometimes the needle becomes visible in image sectors with large angles of incidence. We hypothesize this to be caused by exciting resonance modes of the needle under oblique incidence. We validate our hypothesis and investigate the angle dependency of resonant scattering. The results could be used to optimize imaging modes for deep needle visibility.

**Statement of Contribution/Methods**

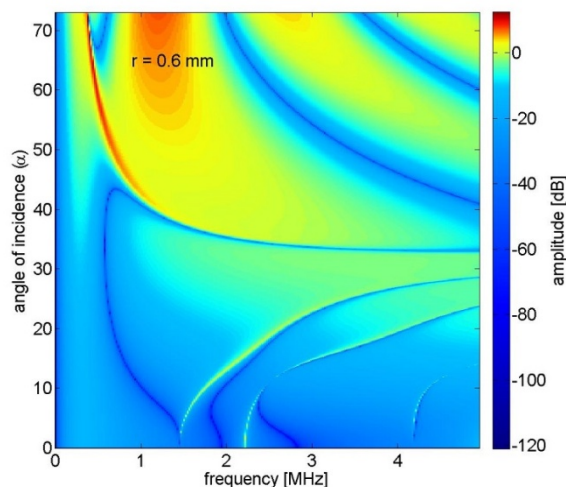
First, we calculated the theoretical resonance behavior of the needle: the needle was modelled as a steel cylinder with typical radius for puncture needles (0.6 mm). Assuming a field of view of  $56^\circ$  (Ultrasonix transducer array C5-2/60) and an insertion angle  $\beta$  of  $45^\circ$ , the angle of incidence  $\alpha$  ranges between  $17^\circ$  and  $73^\circ$ . The frequency was varied between 0 MHz and 5 MHz.

Furthermore, measurements were performed with a Sonix Touch ultrasound scanner; the C5-2/60 curved array was driven with 2.5 MHz center frequency. The insertion angle  $\beta$  was varied between  $30^\circ$  and  $60^\circ$  in steps of  $5^\circ$ . For each angle the depth of the needle was varied between 5 and 15 cm in increments of 2 cm.

**Results/Discussion**

In figure 1 the cylinder resonances at oblique incidence are plotted over the ultrasound frequency and  $\alpha$ . The dynamic range of the resonance spectrum is about 130 dB. E.g. for a frequency of 2.5 MHz sharp negative peaks up to  $-90$  dB are to be expected, but also positive resonances for  $\alpha \approx 19^\circ$  ( $-1$  dB), for  $\alpha \approx 35$  to  $46^\circ$  (about 0 dB), and for  $\alpha > 69^\circ$  ( $> 0$  dB). The measurements confirmed that the needle visibility depends on the angle of incidence of the ultrasound beam and is in agreement with the predicted resonance behavior.

If resonance modes can be used to improve needle imaging, steeper insertion angles  $\beta$  and thus puncture techniques for deeper tissues are possible.



P1B8-5

**Ultrasound Based Muscle Kinematics Measurement with Tracklet Stitching**

Paul Otto<sup>1</sup>, Frances Gavelli<sup>2</sup>, Hyun Soo Im<sup>2</sup>, Siddhartha Sikdar<sup>3</sup>; <sup>1</sup>Electrical and Computer Engineering, George Mason University, Fairfax, Virginia, USA, <sup>2</sup>National Institutes of Health, Bethesda, Maryland, USA, <sup>3</sup>Bioengineering, George Mason University, Fairfax, Virginia, USA

**Background, Motivation and Objective**

This study develops and validates a robust ultrasound (US) tissue tracking algorithm for measuring muscle dynamics that can serve as an outcome measure for movement disorders while providing insight into musculoskeletal injury and subsequent adaptation. The technique can be applied to a wide variety of muscles by overcoming the limitations of previously published methods that require visualization of complete muscle fascicles, and be performed in an office-based setting using B-mode imagery from commercially-available equipment.

**Statement of Contribution/Methods**

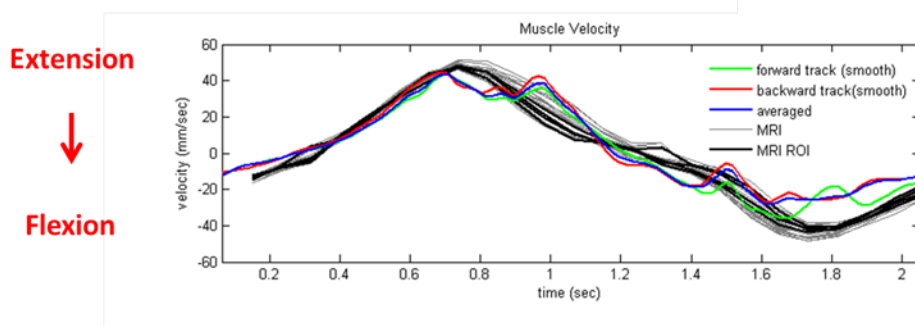
The tracking algorithm identifies dense sets of features to be tracked over time moving forward and backward in time. These feature sets are divided into short time series, spatially related neighborhoods known as tracklets. The tracklet's temporal length is limited due to speckle decorrelation, however partially overlapping tracklets are stitched together to create a quantifiable final trajectory for the motion across different regions of the muscle.

The algorithm was validated by comparing US results against cine phase contrast (CPC) magnetic resonance imaging (MRI) for the muscle velocities of the rectus femoris. Subjects performed cyclic knee flexion and extension, in time to a metronome while CPC and US anatomic and velocity data were independently collected. US B-mode image sequences were obtained with an Ultrasonix SonixTouch US system and a 5-14 MHz linear array transducer.

**Results/Discussion**

The figure shows a strong qualitative comparison between MRI region based velocity estimates (black) and US muscle velocities for the forward and backward tracks (green, red) along with their weighted average (blue). Quantitatively the average rectus femoris velocity was calculated for the US data and found over 12 cycles to be  $19.94 \pm 4.78$  mm/sec during extension and  $20.13 \pm 7.34$  mm/sec during flexion. Over 4 spatial locations in the rectus femoris the MRI's single cycle measured velocities of  $22.5 \pm 0.6$  mm/sec during extension and  $21.6 \pm 0.6$  mm/sec during flexion. Additional subjects are being examined for US and MRI agreement.

Acknowledgment: This work was supported in part by Grant Number 0953652 from the National Science Foundation and by the Intramural Research Program of the National Institutes of Health Clinical Center, Bethesda, MD, USA.



P1B8-6

### Ultrasound Strain Rate Imaging of Individual Muscle Motor Units

Max Heger<sup>1</sup>, Oyvind Stavaht<sup>2</sup>, Hans Torp<sup>3</sup>; <sup>1</sup>Information Technology, Mathematics and Electrical Engineering, Norwegian University of Science and Technology, Horten, Norway, <sup>2</sup>Information Technology, Mathematics and Electrical Engineering, Norwegian University of Science and Technology, Trondheim, Norway, <sup>3</sup>Department of Circulation and Medical Imaging, Norwegian University of Science and Technology, Trondheim, Norway

### Background, Motivation and Objective

Skeletal muscle is organized in motor units, each comprising a motor neuron and all its connected muscle fibres. The arrival of an action potential (a neural "impulse") causes the fibers to contract – they exhibit a twitch. This study aimed for the spatiotemporal detection of individual twitches, which may allow for a more explicit study of muscle physiology and more dexterous prosthesis control.

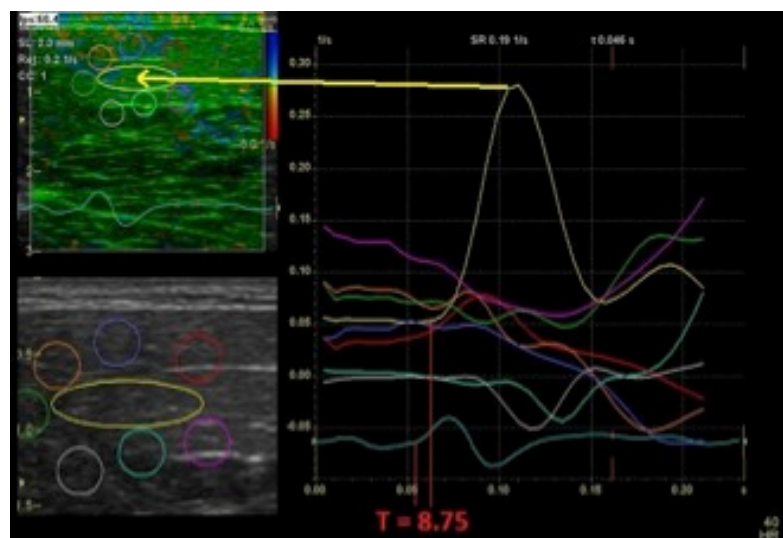
### Statement of Contribution/Methods

We used a GE-Vingmed Vivid E9 ultrasound scanner and an ML6-15 linear probe in a clamped and fixed position over the biceps, giving images perpendicular to muscle fibers. The scans were executed by using "Strain rate"-mode in the test option "msc TVI" with a frequency of 15MHz, which results in a frame rate between 120 and 220 FPS, depending on depth. Recordings of tiny voluntary isometric muscle contractions were made, with ECG electrodes placed on each side of the probe to detect the associated motor unit action potentials (MUAPs).

### Results/Discussion

The recordings were analyzed using the scanners quantitative analysis (Q-analysis) tool for measuring strain rates inside elliptical regions of interest (ROIs). Figure 1 shows an image containing eight ROIs. The figure includes b-mode images with and without strain rate measurements, respectively, and a graph showing the mean strain rate of the ROIs marked in the strain rate image. The turquoise graph at the lower right shows a single MUAP recorded simultaneously with the ultrasound data. The yellow strain rate graph shows what is believed to be the mechanical contraction associated with this single MUAP. The time delay from MUAP onset to twitch onset (approx. 8.75ms) and the spatial extent of the contracting region supports this claim. To our best knowledge, this is the first ultrasound image of a single motor unit twitch.

The results show that it is possible to image the mechanical response of a contracting muscle caused by a single motor unit by using ultrasonic strain rate imaging. This technique could thus be a future supplement to electromyography in certain applications.



P1B8-7

**High frequency ultrasound imaging of dental acid erosion in-vitro**

David Hughes<sup>1</sup>, Steven Stewart<sup>1</sup>, David Hutson<sup>1</sup>, Christopher Longbottom<sup>2</sup>, Katherine Kirk<sup>1</sup>; <sup>1</sup>Centre for Advanced Technology, University of the West of Scotland, Paisley, United Kingdom, <sup>2</sup>Dental Innovation and Translation Centre, Kings College London, London, United Kingdom

**Background, Motivation and Objective**

Acid erosion is the irreversible loss of dental material through dissolution of the enamel in acidic environments. It is an increasing problem with the change in dietary habits around the world. Accurate and reliable measurements are hard to come by due to the lack of a stable reference point in the tooth and as such there is no diagnostic device available for the early detection and quantification of dental erosion. Ultrasound has previously been demonstrated as a non-invasive tool for measuring the thickness of enamel, with resolution being the main limit in the technique. This study investigates the use of high frequency ultrasound (110 MHz) to monitor the small changes in thickness of enamel during acid erosion to assess the potential of the technique in the laboratory compared to other, destructive, laboratory methods.

**Statement of Contribution/Methods**

Time lapse b-mode images of a tooth undergoing acid erosion are recorded using a custom unfocused single element 110MHz Lithium Niobate transducer operating in pulse-echo mode providing 0.5mm and 30  $\mu$ m of spatial and axial resolution in enamel ( $v=6500$ m/s) respectively. Teeth, collected for clinical reasons with patient consent, are embedded in epoxy, with a window allowing a small exposed area of enamel to be eroded by an acidic agent (150 mMol Hydrochloric Acid). The sample is continually mechanically scanned by the transducer, providing an ultrasound image every minute for one hour. Data is analysed and the rate of erosion measured from the thickness of the enamel layer over time.

**Results/Discussion**

The set of b-mode images are analysed to choose a set of A-scan time-points such that the enamel surface and underlying dentine are easily resolved and identified, as shown in Figure 1A and B. Each time-point is used to measure the enamel thickness to the dentine, and depth of enamel from the artificial epoxy layer, over time to produce a graph of the erosion depth, as shown in Figure 1C. The gradient of this graph is then used to calculate the rates of erosion and are found to be  $1.7 \pm 0.24 \mu\text{m}/\text{min}$  for the stable epoxy layer, and  $1.42 \pm 0.34 \mu\text{m}/\text{min}$  for the internal dentine reference point, showing good agreement with each other. The values measured here are found to be slightly lower than that in the literature, and this is assumed to be due to variations in velocity of sound in enamel as the material becomes eroded.

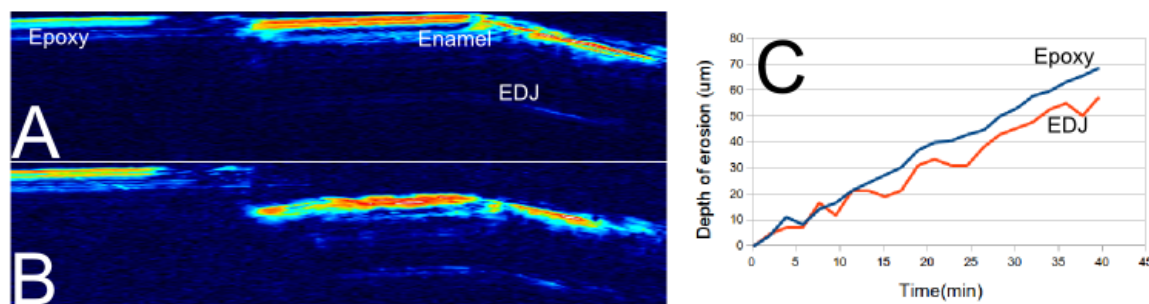


**Figure 1.** Ultrasonic B-mode images of tooth encased in epoxy at initial (A) and final (B) time point of the erosion experiment. The enamel is clearly resolved against the enamel dentine junction (EDJ) allowing for the rate of erosion (C) to be measured with this internal reference point, and verified against the external epoxy showing good agreement.

P1B8-8

**Fast Detection of Breast Position for 3D USCT**

Bo Qin<sup>1</sup>, Michael Zapf<sup>1</sup>, Ernst Kretzek<sup>1</sup>, Xiaochuan Ma<sup>2</sup>, Nicole Ruiter<sup>1</sup>; <sup>1</sup>Karlsruhe Institute of Technology, Germany, <sup>2</sup>Institute of Acoustics, Chinese Academy of Science, China, People's Republic of

**Background, Motivation and Objective**

A 3D Ultrasound Computer Tomography (USCT) system for early detection of breast cancer is developed at KIT. It uses a 3D synthetic aperture focusing technique (SAFT) to reconstruct 3D images, which requires a large amount of data and calculation. USCT is designed as offline imaging method. As a semi-ellipsoidal aperture surrounding the breast is used, the breast should be located centrally in a hemispherical volume, i.e. Depth of Field (DOF), to reconstruct optimal images. Thus the position information of the breast is needed to reposition patients before a measurement starts. A method was developed for fast breast positioning.

**Statement of Contribution/Methods**

Reflections from the skin can be used to produce images to estimate the position of breasts. This information is only a small part of the complete data, which can be extracted by time and energy.

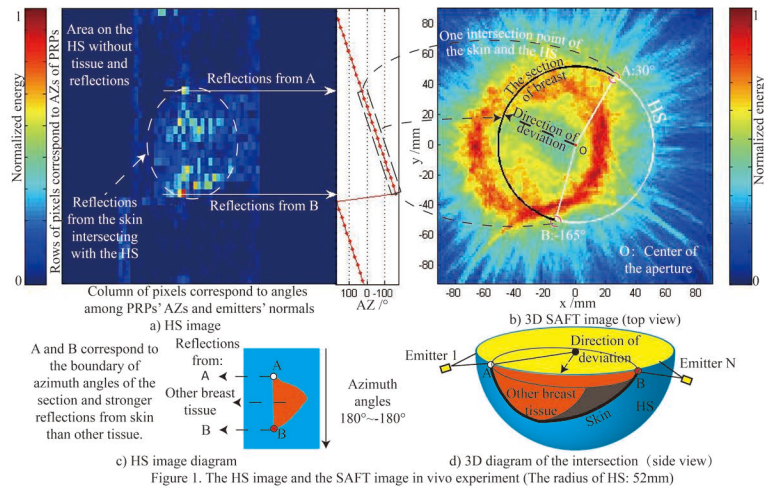
The DOF's boundary is a hemispherical shell (HS) (Figure 1 d). For each combination of emitter and receiver, the position of a reflecting point (PRP) on the HS with the shortest reflection path is calculated. The earliest travel-time of reflections corresponding to PRPs is used to extract data. HS images (Figure 1 a, c) are produced by drawing this data over the azimuth angles (AZ) of the PRPs.

If a breast is partly outside the HS, a part of the skin and the HS intersect. This intersection has a horizontal start and end point (A, B in Figure 1) which correspond to more significant reflectivity from skin than other tissue. Currently they are detected using an energy threshold. These two intersection points indicate two horizontal angles of edge direction in which the breast is dislocated. The midrange of these two angles is assumed as the AZ of the breast position error. If the breast is centrally located, the HS image has a low energy compared to skin's reflection. The radius of HS can be changed to fit breasts of different sizes.

**Results/Discussion**

The approach's performance was evaluated with the data of seven patients. A simplified SAFT imaging using a low number of A-scans (Figure 1 b) was used as ground-truth for comparison, with manual extraction of the AZ of the position error. The difference between achieved AZs from both methods is calculated. The described method had a mean error of  $3.6^\circ$ , a standard deviation of  $\pm 2.7^\circ$  and a median error of  $5.2^\circ$ . It results in a speed-up factor of 10.6 with only 3.4 kB of data compared to 65 MB for a basic SAFT image.





P1B8-9

### The spatio-temporal variation of rat carotid artery bifurcation by ultrasound imaging

Chang-zhu Jin<sup>1</sup>, Kweon-Ho Nam<sup>1</sup>, Dong-Gu Paeng<sup>1</sup>; <sup>1</sup>Ocean System Engineering, Jeju National University, Jeju si, Jeju do, Korea, Republic of

#### Background, Motivation and Objective

The evaluation of arterial wall motion and hemodynamics contributes to early diagnosis of carotid atherosclerosis. The low wall shear stress in arteries was known to be related to develop atherosclerosis. Ultrasound imaging with high temporal resolution provides real time observation of anatomy structure. Reconstruction of three-dimensional (3-D) geometry with temporal variation was not only helps us to know the 3-D behavior of arteries but also provides reliable geometry for numerical simulation to evaluate the wall shear stress distribution.

#### Statement of Contribution/Methods

In present study, the 3D data set of carotid artery bifurcation (CAB) in three rat subjects was acquired using a high spatiotemporal resolution ultrasound imaging system, Vevo 770, with linear mechanical scanning. Total of 31 slices of cross-section image were stored for each subject. A star algorithm was implemented to radially scan the lumen area based on a pre-tracked seed point in polar coordinate. The boundary of lumen was segmented using a dynamic threshold filter with polynomial fitting. The manual segmentation was processed by two operators separately based on the same protocol for comparison.

#### Results/Discussion

Finally, 3-D geometries of CAB during one cardiac cycle were constructed based on segmented lumen boundaries. The 3-D variation of CAB was observed by overlapping the geometries on peak systolic and diastolic phase. The 3-D asymmetric variation was observed both in manual-based geometry and semi-automatic based geometry. Both geometries were in agreements, and two manual-based geometries also confirm this asymmetrical variation phenomenon. This asymmetrical variation in 3-D could improve our understanding of arterial behavior and also provide reliable references for numerical simulation of hemodynamics.

(This work was supported by the MSIP (Ministry of Science, ICT & Future Planning), Korea, under the C-ITRC (Convergence Information Technology Research Center) support program (NIPA-2013-H0401-13-1007) supervised by the NIPA (National IT Industry Promotion Agency).)

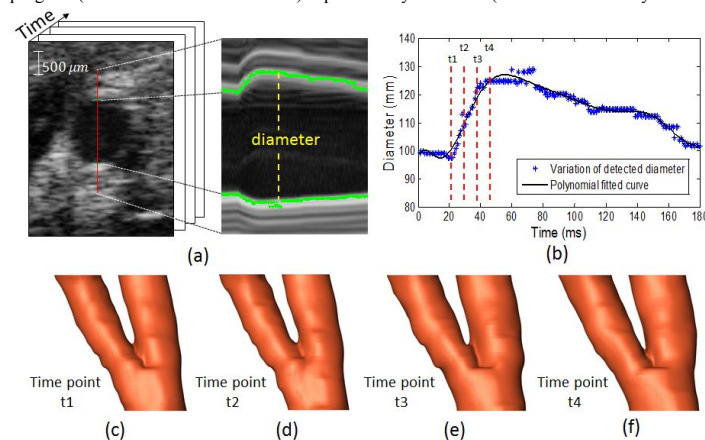


**Fig. 1.** (a) Extraction of M-mode image from B-mode to track diameter variation. (b) Diameter variation of common carotid artery during one cardiac cycle. (c)(d)(e)(f) Illustration of constructed three dimensional geometry of carotid artery bifurcation on four time points during artery expansion phase.

## P1B9 - MTC: Cancer Applications of Tissue Characterization

Salon C

Friday, September 5, 2014, 8:00 am - 5:00 pm

Chair: **Michael Kolios**  
Ryerson University, Toronto

P1B9-1

### Cell Death Detection in Locally Advanced Breast Cancer Using Quantitative Ultrasound and Diffuse Optical Spectroscopy

WILLIAM TYLER TRAN<sup>1,2</sup>, Christina Kim<sup>1</sup>, GREGORY J CZARNO<sup>1,2</sup>; <sup>1</sup>RADIATION ONCOLOGY, SUNNYSIDE HEALTH SCIENCES CENTRE, Canada, <sup>2</sup>PHYSICAL SCIENCES, SUNNYSIDE HEALTH SCIENCES CENTRE, Canada

#### Background, Motivation and Objective

Background: Cell death is characterized by several subtypes including: apoptosis, oncosis, and necrosis and the monitoring of cell death plays an important role in being able to adapt chemotherapy treatment strategies for personalized medicine. In the present study, we use quantitative ultrasound (QUS) and diffuse optical spectroscopy (DOS) to characterize tumour cell-death response to chemotherapy in locally advanced breast cancer (LABC). Breast cancer monitoring using QUS was used to probe tumour parenchyma for cellular responses due to cell death whereas DOS was used to study coincident metabolic changes in breast cancer patients.

Motivations and Objective: The present study aims to identify QUS and DOS parameters to gain predictive insight to treatment response.

#### Statement of Contribution/Methods

Women (n=10) with diagnosed LABC who were undergoing neoadjuvant anthracycline and taxane chemotherapy were studied. Five women were clinically classified as non-responders and five as responders from post-mastectomy pathology reports. Women were imaged using QUS and DOS at weeks 0, 1, 4, 8 and months later, pre-operatively. Parameters from QUS were investigated (mid-band fit, 0-MHz intercept and the spectral slope) in regards to response correlation with DOS. DOS parameters studied included oxyhemoglobin (HbO<sub>2</sub>), deoxyhemoglobin (Hb), total hemoglobin (HbT), O<sub>2</sub> saturation (STO<sub>2</sub>), O<sub>2</sub> desaturation (ST), lipids, water, scattering amplitude (SA), scattering power (SP) and total optical index (TOI).

#### Results/Discussion

Results revealed that QUS parameters changed with clinical responsiveness. There was a significant increase ( $p < 0.05$ ) in the US backscatter signals with changes in the mid-band fit ( $+6.0 \text{ dBr} \pm 2.0$ ), and the 0-MHz intercept ( $+6.8 \pm 2.0 \text{ dBr}$ ), at week 4 of treatment. The spectral slope was invariant ( $+0.2 \pm 1.3 \text{ dBr}$ ). DOS parameters showed a whole breast post-inflammatory flare resulting from necrotic cell death in responding patients. At week 4, responding and non-responding patients showed a significant difference for the following tumour-specific parameters ( $p < 0.05$ ): Hb ( $\Delta\text{Hb}_{\text{responder}} = 0.5 \pm 0.1 \text{ [SEM]}$ ),  $\Delta\text{Hb}_{\text{non-responder}} = 0.8 \pm 0.1$ ; HbO<sub>2</sub> ( $\Delta\text{HbO}_{2\text{responder}} = 0.5 \pm 0.1$ ,  $\Delta\text{HbO}_{2\text{nonresponder}} = 0.9 \pm 0.1$ ); SA ( $\Delta\text{SA}_{\text{responder}} = 0.4 \pm 0.1$ ,  $\Delta\text{SA}_{\text{nonresponder}} = 1.0 \pm 0.1$ ) ( $p < 0.01$ ); and TOI ( $\Delta\text{TOI}_{\text{responder}} = 0.5 \pm 0.1$ ,  $\Delta\text{TOI}_{\text{nonresponder}} = 0.9 \pm 0.1$ ).

QUS parameters were able to identify cell death and DOS parameters showed metabolic markers for cell death. Cell death measurements from QUS/DOS correlated to clinical pathological responders and non-responders. In summary QUS and DOS can be used in tandem to identify cell death in chemotherapy treatment response.

P1B9-2

### Statistics of envelope of Ultrasonic Backscatter from Basal Cell Carcinoma and Actinic Keratosis lesions

Jerzy Litniewski<sup>1</sup>, Hanna Piotrkowska-Wroblewska<sup>1</sup>, Elzbieta Szymanska<sup>2</sup>, Andrzej Nowicki<sup>1</sup>; <sup>1</sup>Ultrasound, Institute of Fundamental Technological Research, Warsaw, Poland, <sup>2</sup>Dermatology Clinic, CSK MSWiA Hospital, Warsaw, Poland

#### Background, Motivation and Objective

Basal cell carcinoma is the most common cutaneous malignancy, what is 80% of all skin cancer cases. The quantitative ultrasound can provide information potentially helpful in its diagnosing. The goal of this study was to find a quantitative measure of skin tissue backscattering properties that could be used for differentiation of the changes of tissue structure caused by Basal Cell Carcinoma (BCC) and precancerous lesions - Actinic Keratosis (AK). The study presents the results concerning the statistical properties of ultrasonic echoes scattered in cancer lesions and attenuation coefficient values determined from the backscatter.

#### Statement of Contribution/Methods

The patients with diagnosis of the basal cell carcinoma and precancerous lesions underwent examination. The ultrasonic data (RF echoes) were obtained in vivo from pathological and healthy regions reference of the skin using high frequency scanner operating at 30MHz. Prior to determination of the attenuation coefficient all RF signals were compensated for focusing and time gain compensation, and additionally also for attenuation when the statistical properties were considered. Four statistical distributions of echoes' envelopes were examined; Rayleigh, Nakagami, K and homodyned K. Shape parameters were determined for each distribution and for each data-set: BCC and healthy, and AK and healthy.

The statistical analysis was performed using Statistica software to assess a significance of differentiation of BCC and AK cases from a normal one basing on attenuation coefficient, Rayleigh SNR, and Nakagami, K and homodyned K shape parameters. Three non-parametric statistical tests, Wald-Wolfowitz, 2-series Kolmogorow-Smirnow and U Mann-Whitney were performed.

#### Results/Discussion

All three tests confirmed the statistical significance of results, differentiating AK groups from healthy one (for attenuation coefficient), BCC group from healthy one (for attenuation coefficient) and BCC from healthy one (for SNR and all shape parameters). No statistical significance was found for differentiation the AK group and healthy one using echo statistical features. However, application of both - statistical parameters and attenuation coefficient enables distinguishing basal cell carcinoma lesions from precancerous lesions or healthy skin.

P1B9-3

## Quantitative Ultrasound Monitoring of Tumour Cell Death Response in Locally-Advanced Breast Cancer Patients Using A Multiparameter Approach

Lakshmanan Sannachi<sup>1,2</sup>, Hadi Tadayyon<sup>1,2</sup>, Ali Sadeghi-Naini<sup>1,2</sup>, Gregory Czarnota<sup>1,2</sup>; <sup>1</sup>Department of Radiation Oncology and Imaging Research - Physical Sciences, Sunnybrook Health Sciences Centre, Canada, <sup>2</sup>Departments of Radiation Oncology and Medical Biophysics, Univeristy of Toronto, Toronto, ON, Canada

### Background, Motivation and Objective

Currently, no clinical imaging modality is used to detect locally-advanced breast cancer (LABC) response to neoadjuvant chemotherapy within days after treatment. Imaging techniques based on analysis of ultrasonic backscatter have been successfully used to characterize different types of tissue. The goal of this study was to monitor changes in breast tumours during chemotherapy in order to distinguish between treatment responding and non-responding patients using quantitative ultrasound.

### Statement of Contribution/Methods

Tumour responses of breast cancer patients (n=25) to chemotherapy were examined using quantitative ultrasound. A clinical US scanner operating with a 5 MHz linear array transducer (bandwidth: 3.6 – 6.6 MHz) was used to collect RF data from patients. Patients were classified as responders or non-responders based on their ultimate clinical and pathological response. Ultrasound spectral parameters such as midband fit (MBF), spectral slope (SS), spectral 0-MHz intercept (SI), apparent integrated backscatter (AIB) and backscatter parameters, such as scatterer diameter (ASD) and acoustic concentration (AAC), were estimated from tumours prior to treatment onset and at four times during chemotherapy (weeks 1, 4, 8 and prior to surgery). Patients were followed clinically after treatment with a mean period of 31 ± 11 months for recurrence-free survival.

### Results/Discussion

Results demonstrated that all the ultrasound parameters except SS and ASD increased with time in clinically treatment responding patients. Among all parameters, AAC dominated in reflecting the tumour response and the value increased substantially in responders as early as 1 week after treatment initiation and attained a maximum increase of 7 dB/cm<sup>2</sup> at week 8. Non-responders did not show any significant changes in all parameters over treatment times. The best prediction of treatment response was achieved using the combination of ASD and AAC or the combination of MBF and SI at week 4 (100% sensitivity and 100% specificity). At week 1, therapy response was predicted using the combination of ASD and AAC with 79% sensitivity, 75% specificity and 78% accuracy and with less sensitivity using the combination of MBF and SI with 68% sensitivity, 75% specificity and 70% accuracy. The survival of responding patients determined based on ultrasound parameters was higher than non-responding patients. In conclusion, the results demonstrate that the backscatter parameters derived from ultrasound backscatter are more sensitive in quantifying histological changes in tumours than spectral parameters during treatment. It has a capacity in distinguishing treatment responders and non-responders as early as 1 week from the start of treatment. This is important for the customization therapies for non-responding patients early after treatment initiation and can potentially increase their survival rate.

P1B9-4

## Quantitative Ultrasound Characterization of Genetically Modified Prostate Cancer Responses to Ultrasound-stimulated Microbubbles and Radiation

Lakshmanan Sannachi<sup>1,2</sup>, Azza Al-Mahrouki<sup>1,2</sup>, Gregory Czarnota<sup>1,2</sup>; <sup>1</sup>Department of Radiation Oncology and Imaging Research - Physical Sciences, Sunnybrook Health Sciences Centre, Toronto, ON, Canada, <sup>2</sup>Departments of Radiation Oncology and Medical Biophysics, Univeristy of Toronto, Toronto, ON, Canada

### Background, Motivation and Objective

In a previous study, we identified an up-regulation of UDP glycosyltransferase 8 (UGT8) gene in endothelial cells treated with ultrasound (US) activated microbubbles (MB) therapy. This UGT8 enzyme is known to modify ceramide which signals for apoptosis. We also investigated the effect of down regulating *UGT8* on the sensitization of prostate cancer cell line (PC3) to bubbles and radiation therapies *in vitro* and observed more cell death where *UGT8* was down-regulated as oppose to the cells where *UGT8* was up-regulated. Here, we have characterized genetically modified PC3 tumours and their response to bubbles and radiation therapies in mouse models using quantitative ultrasound (QUS) methods.

### Statement of Contribution/Methods

Three types of genetically modified PC3 tumours including sham control, *UGT8* up-regulated and *UGT8* down-regulated were xenografted in mice and then treated with US/MB, 8Gy radiation, or a combination of US/MB and radiation. Specimens were examined using quantitative ultrasound with a centre frequency 25 MHz (bandwidth range: 16 – 32 MHz). Ultrasound parameters such as midband fit (MBF), spectral slope (SS), 0-MHz intercept (SI), scatterer spacing (SAS), scatter diameter (ASD) and acoustic concentration (AAC) were estimated inside the tumours before treatments and 24 hours later. The spherical Gaussian model (SGM) and fluid-filled sphere model (FFSM) were used to estimate backscatter parameters, ASD and AAC and estimates were compared with changes in histology with treatment.

### Results/Discussion

SGM did not fit with measured data as well as FFSM. Estimated ASDs were 28.4 ± 1.23 µm, 27.6 ± 1.13 µm and 26.4 ± 1.82 µm with the FFSM for sham control, *UGT8* up-regulated and down-regulated PC3 tumours respectively. All acoustic parameters calculated from *UGT8* down-regulated tumour were significantly different from sham control and up regulated tumour types. However, linear discriminant analysis suggested a favorable classification and a promising separability of genetically modified tumour types using combinations of ASD and AAC. The ASD estimates from the FFSM were close to the size of cells calculated from histology sections. This suggests modelling the total cell as a fluid-filled sphere and not just considering the nucleus is important to scattering. Analysis of cell death from histology revealed a consistent increase in cell death after 24 hours in sham control and down-regulated tumours with combined treatment. Detectable cell death was even higher in down-regulated tumours than sham control specimens. All ultrasound amplitude parameters, MBF, SI and AAC increased with cell death and followed the similar trends obtained from histological analyses. In conclusion, the results obtained in this research demonstrate FFSM based estimates of backscatter parameters can potentially be used to differentiate genetically modified tumour types and detecting their responses to bubbles and radiation therapies.

P1B9-5

## Quantitative Ultrasound Characterization of Tumour Cell Death: Ultrasound-Stimulated Microbubbles for Radiation Enhancement

Christina Kim<sup>1</sup>, Azza Al-Mahrouki<sup>1</sup>, Alborz Gorjizadeh<sup>2</sup>, Ali Sadeghi-Naini<sup>1</sup>, Raffi Karshafian<sup>3</sup>, Gregory Czarnota<sup>1</sup>; <sup>1</sup>Sunnybrook Health Sciences Centre, Toronto, Ontario, Canada, <sup>2</sup>University of Toronto, Canada, <sup>3</sup>Ryerson University, Canada

### Background, Motivation and Objective

In the past quantitative ultrasound imaging has demonstrated use for detecting cellular changes within tumours. The objective of this study was to evaluate the efficacy of this modality in characterizing cell death caused by radiation treatments enhanced by therapeutic ultrasound. This investigation focuses on developing a novel technique that incorporates dual-purpose ultrasound: a radiosensitizing agent as well as an imaging based non-invasive substitution for biopsy.

**Statement of Contribution/Methods**

High frequency ultrasound (25 MHz) was used to monitor tumour responses caused by ultrasound-stimulated microbubbles followed by radiation. Human prostate xenografts in severe combined immunodeficiency (SCID) mice were administered 8, 80, or 1000  $\mu\text{L/kg}$  of microbubbles stimulated with 250, 570, or 750 kPa of ultrasound, and exposed to 2 or 8 Gy of radiation. Tumours were imaged prior to treatment and 24 hours after treatment.

**Results/Discussion**

Results of quantitative ultrasound exhibited changes that paralleled those with histology validating the sensitivity as a non-invasive monitoring methodology. With increasing exposure of ultrasound treatments spectral analysis of treatment results revealed overall increases in backscatter intensity and parameters linked to the number of cell-death related scatterers. The increase in backscatter intensity when compared to the control ranged from  $1.9 \pm 1.6$  dB for the clinically-recommended imaging dose of microbubbles (8  $\mu\text{L/kg}$ , 250 kPa, 2 Gy) to  $7.0 \pm 4.1$  dB for the most intense treatment condition (1000  $\mu\text{L/kg}$ , 750 kPa, 8 Gy). Similarly, in situ end-labeling (ISEL) staining, ceramide, and cyclophilin A staining indicated increases in cell disruption led by DNA fragmentation, ceramide-mediated apoptosis, and cell permeabilization, respectively.

In conclusion, results demonstrated that quantitative ultrasound is capable of determining a wide range of tumour responses that even tumours treated with low to high radiation-enhancer (microbubble) doses could be differentiated. This preliminary investigation presents a significant groundwork for developing a clinical application that benefits patients by offering both non-invasive tissue characterization, simultaneously with ultrasound-mediated microbubble radiosensitization.

**P1B9-6****Evaluation of Hyperthermia Induced Breast Tumor Cell Apoptosis in Mice by Ultrasonic Spectrum Analysis in vivo**

Guofeng Li<sup>1,2</sup>, Weibao Qiu<sup>1</sup>, Mingbin Zheng<sup>3</sup>, Congzhi Wang<sup>1</sup>, Qunfang Zhou<sup>1</sup>, Yingjuan He<sup>1</sup>, Fei Yan<sup>1</sup>, Yang Xiao<sup>1</sup>, Hairong Zheng<sup>1</sup>; <sup>1</sup>Paul C. Lauterbur Research Center for Biomedical Imaging, Shenzhen Institutes of Advanced Technology, Chinese Academy of Sciences, Shenzhen, China, People's Republic of, <sup>2</sup>Guangdong Medical College, China, People's Republic of, <sup>3</sup>Shenzhen Institutes of Advanced Technology, Chinese Academy of Sciences, China, People's Republic of

**Background, Motivation and Objective**

Ultrasonic spectrum analysis is a promising technique to delineate tissue microstructures. It can support non-invasive and real time imaging method to evaluate the cell apoptosis by different tumor therapy. However, the relationship between ultrasound spectral parameters and cells apoptosis variation distribution inside breast tumor have been rarely studied. This work investigates the breast tumor cell apoptosis in mice induced by hyperthermia with high frequency ultrasonic spectrum analysis method.

**Statement of Contribution/Methods**

16 BALB/c mice, 6 weeks old, 20g(+/-25%) in weight were used. Each mouse was injected 100 $\mu\text{L}$ ,  $2.5 \times 10^6$  cells/mL 4T1 cell. 12 mice had borne mammary carcinoma successfully after 10 days. A commercial high frequency ultrasound imaging system (Visualsonics, Vevo2100) was used in this experiment, which supports raw radio frequency (RF) ultrasound data acquisition. 4 mice were used as control group, and the other 8 mice were applied hyperthermia therapy by 808nm, 5W laser radiation for 120 seconds. B-mode imaging scan was taken at 0 hours, 12 hours, 24 hours and 48 hours time points after hyperthermia therapy, respectively. Power spectral parameters, e.g. slopes, intercepts, and mid-band fits within ROI were calculated offline base on the acquired RF data. Spectral parameters were carried out by moving window, followed by FFT, calibration, and linear-regression approximation. 4 ROIs located at different depth were evaluated with spectral parameters. Hematoxylin and Eosin (H&E) stain and TUNEL assay were used to identify tissue structure and cell apoptosis on tumor section.

**Results/Discussion**

Figure(a-c) showed the B-mode image, H&E stain image, and TUNEL assay image obtained from mice at 48 hours after therapy. ROIs were marked by four yellow rectangles in figure (a). H&E stain (b) showed that tissue in the center of tumor section was flabby or necrosis, while TUNEL assay (c) indicated more cells apoptosis happened around the edge of tumor tissue in contrast with the center position. Spectral slopes curve shown in (d) demonstrated that the slopes varied more in the outer region than the inner region. It was consistent with the quantity distribution of apoptosis cells. Slopes parameters were sensitive to differentiate cells apoptosis from necrosis in early stage in vivo. Intercepts (e) showed similar appearance.

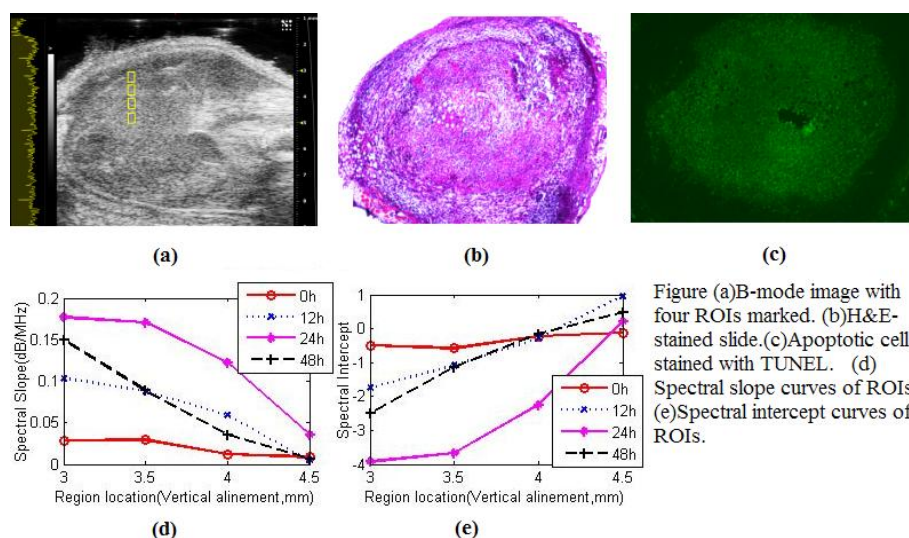


Figure (a) B-mode image with four ROIs marked. (b) H&E-stained slide. (c) Apoptotic cells stained with TUNEL. (d) Spectral slope curves of ROIs. (e) Spectral intercept curves of ROIs.



### Texton-Based Method in Clinical Cancer Response Monitoring

Mehrdad Gangeh<sup>1,2</sup>, Hadi Tadayyon<sup>1,2</sup>, Lakshmanan Sannachi<sup>1,2</sup>, Ali Sadeghi-Naini<sup>1,2</sup>, William Tran<sup>1,2</sup>, Gregory Czarnota<sup>1,2</sup>; <sup>1</sup>Departments of Medical Biophysics and Radiation Oncology, University of Toronto, Toronto, Ontario, Canada, <sup>2</sup>Department of Radiation Oncology and Physical Sciences, Sunnybrook Health Sciences Centre, and Sunnybrook Research Institute, Toronto, Ontario, Canada

#### Background, Motivation and Objective

Assessing the efficacy of cancer treatments on subjects in preclinical and clinical treatments is presently limited; results may not be available to the clinician for typically months. This can lead to ineffective cancer treatments continued needlessly as no faster feedback mechanisms have yet reached broad biomedical adoption. Quantitative ultrasound (QUS) methods provide a promising alternative framework that can non-invasively, inexpensively and quickly assess tumour response to cancer treatments using standard ultrasound equipment. Due to heterogeneous responses developed in tumours as a result of treatment, texture methods can potentially characterize these responses and assist to quantify the assessment of cancer response monitoring. In this research, texton-based methods as the state-of-the-art technique for texture analysis was used to model (as features) locally advanced breast cancer (LABC) responses to chemotherapy.

#### Statement of Contribution/Methods

Sixty Patients with locally advanced breast cancer (LABC) who received neoadjuvant chemotherapy treatments were imaged before and at 4 times during treatment, i.e., weeks 1, 4, 8, and months later pre-operatively. The images were acquired using a Sonix RP ultrasound machine at the central frequency of ~7 MHz. Mid-band fit and 0-MHz intercept parametric maps were computed by deploying quantitative ultrasound spectroscopy techniques. The patients were grouped into good and poorly responding based on their ultimate clinical and pathological response to treatment. By extracting 500 random patches of size 5×5 from parametric maps and by using k-means, a dictionary of textons was constructed. Subsequently, histogram of textons was computed for each parametric map as the model/feature set to represent the pre- and post-treatment images for each patient at a specific time frame after treatment. The distance between these features for each subject was used as a criterion of the effectiveness of the treatment, which was ultimately submitted to a nearest mean classifier to classify the patients to responding or non-responding in a leave-one-subject-out manner.

#### Results/Discussion

The classification of patients with LABC (for the first 10 patients) to responding and non-responding using the proposed texton-based system achieved an accuracy of  $60 \pm 0.00\%$  and  $76.67 \pm 3.51\%$ , area under curve (AUC) of 58.75 and 78.61, sensitivity of 75% and 100%, and specificity of 50% and 66.67% after 4 and 8 weeks of treatment, respectively. In this study, texture methods based on texton-based approach was proposed, for the first time, to quantify the assessment of LABC response to chemotherapy. The proposed system achieves a promising accuracy and sensitivity 8 weeks after treatment initiation. This would permit clinicians to receive feedback and switch to alternate treatments far earlier, in a step towards the goals of personalized medicine.

### Ultra-High Frequency Acoustic Impedance Imaging of Cancer Cells

Muhammad Fadhel<sup>1</sup>, Elizabeth Berndt<sup>1</sup>, Eric Strohm<sup>1</sup>, Michael Kolios<sup>1</sup>; <sup>1</sup>Ryerson University, Toronto, ON-Ontario, Canada

#### Background, Motivation and Objective

The acoustic impedance map (AIM) of a cell can be used to gain insight into its microstructure and physiological state. Information about the cell's microstructure can be acquired from the variation in AIM, and these variations can be used in identifying the dominant ultrasound scattering source in cells. Furthermore, the cell's physiological state can be inferred from acoustic impedance values as many physiological changes in the cell are linked to alterations in the mechanical properties. The objective of this work is to develop an acoustic impedance imaging method to measure AIMs of cancer cells and correlate them to the cell's microstructures and morphological changes.

#### Statement of Contribution/Methods

Fluorescence microscopy was used to image MCF7 cells marked with CellTracker Orange and Hoechst for staining cytoplasm and nucleus, respectively. These cellular compartments are hypothesized scattering sources and therefore targets for variations in acoustic impedance. A single element 375MHz center frequency transducer (SASAM) was used to generate the AIMs of inverted MCF7 cells on a plastic substrate (Fig. 1a). Fluorescence images of the cell's cytoplasm and nucleus were used to correlate the variations in the AIMs to cell structure. The acoustic impedance images were post-processed to segment the cell from the background then measure its average acoustic impedance values. The average acoustic impedance of 20 single-live, 10 clustered-live and 7 clustered-fixed MCF7 cells were measured and compared.

#### Results/Discussion

Fluorescent (Fig. 1b) and acoustic impedance (Fig. 1c) images suggest that the acoustic impedance of the nucleus is similar to the surrounding cytoplasm due to the lack of significant variations in acoustic impedance values within the cell (Fig. 1c). The highest acoustic impedance variation occurred between the cytoplasm and the background. Physiological differences between cells can be assessed by measuring the average AIMs of cell/cluster. For single-live, clustered-live and clustered-fixed cancer cells, the average acoustic impedance values were found to be  $1.60 \pm 0.01$  MRayl,  $1.61 \pm 0.02$  MRayl and  $1.55 \pm 0.02$  MRayl. This work demonstrates, for the first time, the use of acoustic impedance imaging on live cells. This work also provides insights into ultrasound scattering of biological tissues for the purpose of tissue characterization.

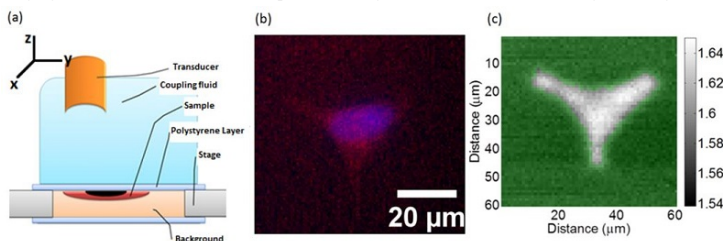


Fig. 1: (a) Schematic setup of the acoustic microscopy technique used to obtain acoustic impedance images. (b) Representative fluorescent image of MCF7 cell stained with CellTracker Orange (red) and Hoechst (blue). (c) Acoustic impedance image of the same cell shown in Fig. 1b. The green transparent overlay represents the eliminated pixels to calculate the average acoustic impedance values.



P1B9-9

**Evaluation of classification strategies using quantitative ultrasound markers and a thyroid cancer rodent model**

Maria Luisa Montero<sup>1</sup>, Omar Zenteno<sup>2</sup>, Benjamin Castaneda<sup>2</sup>, Michael Oelze<sup>3</sup>, **Roberto Lavarello<sup>2</sup>**; <sup>1</sup>Departamento de Ciencias, Pontificia Universidad Católica del Perú, San Miguel, Lima, Peru, <sup>2</sup>Departamento de Ingeniería, Pontificia Universidad Católica del Perú, San Miguel, Lima, Peru, <sup>3</sup>Department of Electrical and Computer Engineering, University of Illinois at Urbana-Champaign, Urbana, Illinois, USA

**Background, Motivation and Objective**

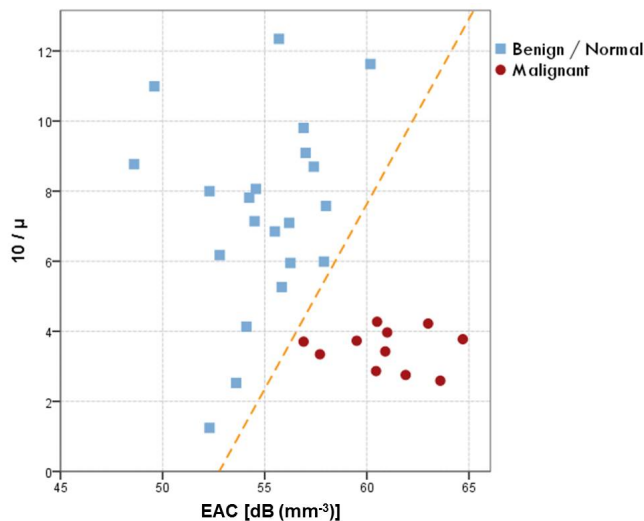
Parameters derived using quantitative ultrasound (QUS) techniques have been studied in the past for tissue characterization tasks. Recently, studies have reported that significant differences were observed in the values of QUS parameters derived from a thyroid cancer rodent model between normal/benign and malignant tissues. In this study, the performance of multi-parametric classification for the differentiation of thyroid cancer in this rodent model has been evaluated.

**Statement of Contribution/Methods**

The experimental database consisted of 32 mice having different predispositions to developing thyroid abnormalities. The histopathologic evaluation indicated that 11 of them developed thyroid cancer (six with papillary carcinoma and five with follicular variant papillary carcinoma), six developed benign tumors (c-cell adenoma) and 15 did not develop any thyroid abnormalities. Backscattered data was obtained from excised thyroid tissues using a 40 MHz, f/3 single element transducer. Five QUS parameters were derived from the ultrasound data: two from backscatter coefficients (i.e., the effective scatterer diameter (ESD) and effective acoustic concentration (EAC)), two from envelope statistics (i.e., the  $\mu$  and  $k$  parameters), and one from ultrasound attenuation (i.e., attenuation coefficient slope). A two-class classification between normal/benign and malignant cases was performed using linear discriminant analysis with both one- and two-dimensional feature spaces. The performance of the classifiers was evaluated in terms of their sensitivity and specificity values using a leave-one-out approach.

**Results/Discussion**

When using a one-dimensional feature space, the sensitivity and specificity of the classification were 100% and 81% for the ESD, 81.8% and 85.7% for the EAC, 63.6% and 61.9% for the attenuation coefficient slope, 81.8% and 71.4% for the  $k$  parameter, and 81.8% and 85.7% for the  $\mu$  parameter. When using a two-dimensional feature space, it was found that the combination of EAC and  $1/\mu$  resulted in both a sensitivity and specificity of 100%. The scatter plot corresponding to this feature space is shown in Fig. 1. Although further studies in human subjects are required to assess the clinical implications of these observations, the results of this study suggest that multi-parametric QUS may prove valuable for the diagnosis of thyroid cancer.



P1B9-10

**Alterations in Ultrasound Scattering Following Thermal Ablation in Ex Vivo Bovine Liver**

Nicholas Rubert<sup>1</sup>, Tomy Varghese<sup>1,2</sup>; <sup>1</sup>Medical Physics, University of Wisconsin-Madison, Madison, Wisconsin, USA, <sup>2</sup>Electrical and Computer Engineering, University of Wisconsin-Madison, Madison, WI, USA

**Background, Motivation and Objective**

The spatial arrangement of acoustic scatterers within liver tissue has frequently been modeled as pseudo-periodic. Generally, pseudo-periodic scatterers are assumed to be gamma distributed in one dimension, and these scatterers are characterized by their mean scatterer spacing (MSS). Pathological changes to the liver, such as cirrhosis, have been hypothesized to result in changes to MSS due to structural changes in the liver. Thermal ablation is a minimally invasive cancer treatment which has been rapidly gaining clinical acceptance, and this treatment also results in structural changes to the liver. It is well known that thermal ablation increases the acoustic attenuation and shear or Young's modulus of tissue. However, relatively few results have been reported regarding changes in MSS following thermal ablation.

**Statement of Contribution/Methods**

In this study, we estimated MSS in ex vivo bovine liver by detecting local maxima in spectral coherence functions calculated using Thomson's multi-taper method. We examined a large number of uncorrelated regions of interest recorded from five normal bovine livers (~300 images from each animal). We also examined a large number of ROI's from five bovine livers following thermal coagulation. All bovine livers were obtained from a commercial meat production facility immediately following animal sacrifice and imaged within 12 hours. Thermal coagulation was induced by heating liver in saline baths at 80° C for 45 minutes.

**Results/Discussion**

In the normal, unheated liver an MSS of approximately 1.5 mm was found. Following thermal ablation, we found an MSS of approximately 0.5 mm in thermally coagulated tissue. Frequently, studies estimating MSS in liver tissue provide an MSS estimate regardless of the pathological state of tissue. Authors rarely present what their MSS estimation algorithm would produce if it were applied to tissue which is better modeled as a collection of uniformly, randomly distributed scatterers lacking periodicity. In this study, we

found that thermal coagulation results in a loss of periodicity. The MSS of 0.5 mm corresponds to the value that a spectral coherence-based MSS algorithm would produce if presented with a signal that was uniform, random noise.

Work supported by NIH–NCI grants R01CA112192-S103, R01CA112192-05, and T32 CA09206-32.

P1B9-11

---

### Measuring Tumour Heterogeneity using Quantitative Ultrasound Acoustic Texture as a Biomarker of Chemotherapy Response

Ali Sadeghi-Naini<sup>1,2</sup>, Michael Kolios<sup>3,4</sup>, Gregory Czarnota<sup>1,2</sup>; <sup>1</sup>Imaging Research | Radiation Oncology, Sunnybrook Health Sciences Centre, Toronto, ON, Canada, <sup>2</sup>Medical Biophysics | Radiation Oncology, University of Toronto, Toronto, ON, Canada, <sup>3</sup>Physics, Ryerson University, Toronto, ON, Canada, <sup>4</sup>Medical Biophysics, University of Toronto, Toronto, ON, Canada

#### Background, Motivation and Objective

The development of cancer therapy response in tumours is a gradual process and intrinsically inhomogeneous. Quantitative ultrasound (QUS) spectral parametric maps (mid-band fit, 0-MHz intercept and spectral slope) have been demonstrated to be capable of visualizing distributions of acoustic scatterer size and concentration within tissue. We posit that quantifying levels of alterations in spatial heterogeneity of QUS spectral parametric maps is potentially expected to provide early and accurate insights into the ultimate response of a tumour to treatment.

#### Statement of Contribution/Methods

Preclinical and clinical studies were carried out in order to investigate the efficacy of alterations in acoustic texture as early surrogate of ultimate response to chemotherapy. Textural analysis methods were applied on QUS spectral parametric maps in order to characterize levels of heterogeneity in tissue micro-structures. Preclinical mouse models of xenografted human breast tumours were treated with chemotherapy and ultrasound data were acquired at different times after exposure. Standard histology analyses were performed on tumour sections after imaging to detect cell-death effects. In a corresponding clinical study, locally advanced breast cancer patients received neo-adjuvant chemotherapy and data collection consisted of acquiring tumour ultrasound images and radio-frequency data prior to treatment onset and at 4 times during treatment. Histopathology examinations were performed on mastectomy specimens using three-dimensional whole-mount technique in order to determine ultimate pathologic response.

#### Results/Discussion

Pre-clinical results indicated that QUS-based textural biomarkers are more sensitive to development of cell death, compared to mean values of spectral parametric maps, and were able to detect alterations in tumour microstructure with a higher level of correlation to histologic cell death. In the clinical study, statistically significant differences were obtained between treatment responding and non-responding patients at weeks one and four after chemotherapy initiation, using textural and spectral biomarkers, respectively ( $p < 0.05$ ). Obtained results suggested that alterations in the textural properties (homogeneity, contrast) of QUS spectral parametric maps become apparent at early stages of treatment, and later result in detectable changes in the mean values of these maps. Results of discriminant analysis, however, implied that spectral biomarkers can provide further information, when combined with their textural biomarker counterparts, for treatment response monitoring (with sensitivity and specificity of up to 100%,  $p < 0.001$ ). These QUS biomarkers, in a combination, may be applied for early prediction of ultimate treatment response in patients undergoing cancer-targeting therapies, facilitating the decision of switching to a more effective therapy for treatment-refractory patients.

## P1B10 - MSD: Novel Medical Systems & Devices

Salon C

Friday, September 5, 2014, 8:00 am - 5:00 pm

Chair: **Hervé Liebgott**  
CREATIS

P1B10-1

### A System for Real-Time Intravascular Ultrasound and Photoacoustic Imaging

Don VanderLaan<sup>1</sup>, Andrei Karpouk<sup>1</sup>, Doug Yeager<sup>1</sup>, Stanislav Emelianov<sup>1</sup>; <sup>1</sup>Biomedical Engineering, University of Texas at Austin, Austin, Texas, USA

#### Background, Motivation and Objective

Combined intravascular ultrasound (IVUS) and intravascular photoacoustic (IVPA) imaging has shown promise for identifying anatomical and compositional features of plaques. Clinical translation of this multi-modality imaging technology necessitates real-time operation. We present development and implementation of a real-time IVUS/IVPA system which addresses major hurdles – high data throughput and computational complexity requisite for real-time visualization, synchronization with appropriate high pulse-repetition-frequency lasers, and intricate mechanical assembly for transmission of high-bandwidth RF signals across the rotating frame – while maintaining a central path for laser-light delivery.

#### Statement of Contribution/Methods

The PXIe platform was chosen to implement system control and synchronization, data acquisition, signal/image processing and display, along with user interface. Custom software runs on an embedded PXIe controller, synchronizes all hardware, and pipelines the image generation process from acquisition through final rendering. Figure 1 illustrates the process. A Panametrics 5910PR was employed for pulse-echo IVUS, while receiving PA transients interleaved between US echoes. Baseband digitization occurs at 200 MSamples/s with 12 bit sample depth. A hollow electrical rotary joint, brushless servo motor, and 8192-line encoder permit indefinite and smooth catheter rotation with an uninterrupted return path for receiving ultrasound echoes.

#### Results/Discussion

Preliminary results were obtained at 30 frames per second using a 40 MHz IVUS catheter to image a carbon fiber target. For real-time imaging at 512 lines per frame, the required acquisition, processing, and live display of 15360 RF traces per second was achieved. For 8mm radial depth of view, each trace is 2000 samples long. Acquisition rates as high as 25000 traces per second are possible.

In conclusion, our system yields similar image quality to previous IVUS/IVPA implementations, but at clinically relevant frame rates.

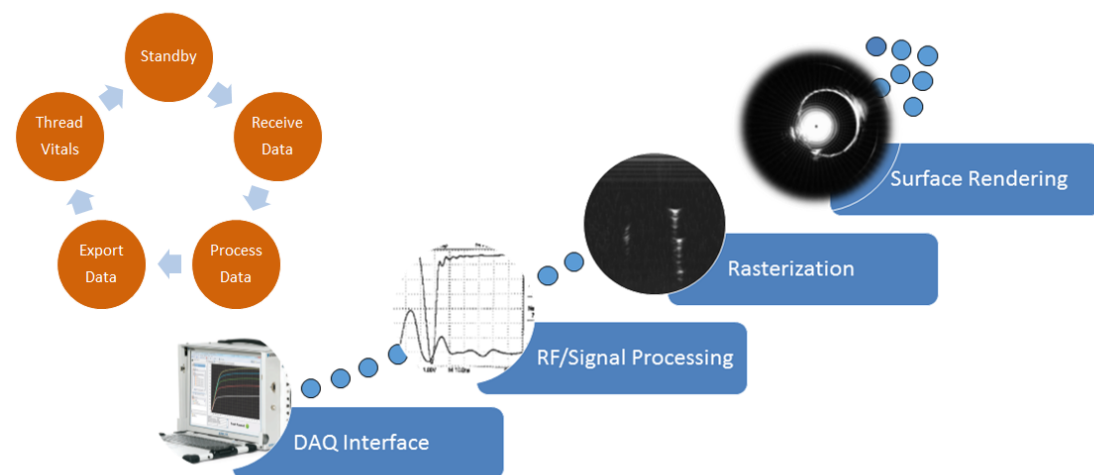


Figure 1 – Basic implementation. Each component in the data pipeline (seen on right), functions internally (left)

P1B10-2

### A CMUT-based Finger-mounted 3D Ultrasound Probe

Albert I.H. Chen<sup>1</sup>, Lawrence L.P. Wong<sup>1</sup>, John T.W. Yeow<sup>1</sup>; <sup>1</sup>Systems Design Engineering, University of Waterloo, Waterloo, ON, Canada

#### Background, Motivation and Objective

Capacitive Micromachined Ultrasonic Transducers (CMUTs) offer superior bandwidth and ease of electronics interfacing over traditional piezo-based transducers. They can also be precisely fabricated into high-density arrays at low cost for high frequency applications. CMUT developments are more common in intravascular/intracardiac ultrasound imaging applications where a 1D array is typically used. Meanwhile, developing 2D array-based systems for 3D imaging is overall more challenging due to the complexity in addressing the transducer elements. As a result, some methods of simplification are necessary to reduce the number of leads to the transducers. Here, we present a CMUT-based probe, which has a simplified element addressing scheme, designed to be mounted at the tip of a finger for 3D imaging. A potential application is ultrasound palpation where tactile sensing can be coupled with 3D ultrasonic imaging.

### Statement of Contribution/Methods

Our team has previously fabricated row-column (RC) addressing-based 2D CMUTs. The RC scheme results in a significant reduction in electrical leads at a reasonable cost in imaging quality. Using a  $32 \times 32$  elements RC CMUT array, a finger-mounted ultrasound probe is designed and manufactured with the aim of helping physicians to perform imaging and palpation simultaneously. The RC CMUT array is wire-bonded to flexible circuit board on each of the four sides. Epoxy is added to minimize exposed wires and to provide device structural rigidity. The flexible circuit allow the transducer to be facing away from the fingertip while including edge connectors that can connect to the front-end circuit placed at the back of the hand. The front-end circuit includes two pairs of 16-channel pulser and 16-channel receive circuit boards, which are designed to be compact and modular. The CMUT array aperture is  $4.8\text{mm} \times 4.8\text{mm}$  and operates at a center frequency of 5.9MHz. Simulation of the RC transducer array is performed to show some scanning parameters of the aperture. Variation in aperture definition is also simulated to show how various frequency settings or aperture sizes would affect image quality and scanning volume. Noise characterization, pulse-echo experiments, and target imaging are conducted to demonstrate the functionality of the prototype. A custom-built fast ultrasound imager based on the PXI platform is used to control the finger-mounted probe and display images.

### Results/Discussion

The simulation and experiment show that the scanning volume is limited by the aperture size. The calculated resolution is approximately 1.3mm in lateral direction while the scanning height and width is 4.5mm by 4.5mm at 20mm in depth. The designed prototype can be fitted over a finger and be used for scanning a small targeted volume. The front-end electronics are also designed so that the device can be attached to the back of the hand for a more portable experience.

### P1B10-3

#### A compact and reconfigurable 8-channel Ultrasound Evaluation System for experimental research

Amauri Asséf<sup>1</sup>, Joaquim Maia<sup>2</sup>, Vera Button<sup>3</sup>, Eduardo Costa<sup>3</sup>; <sup>1</sup>DAELT/CPGEI, UTFPR, Curitiba, Brazil, <sup>2</sup>DAELN/CPGEI, UTFPR, Curitiba, Brazil, <sup>3</sup>DEB/FEEC/CEB, UNICAMP, Campinas, Brazil

### Background, Motivation and Objective

Although new ultrasound (US) signal processing techniques can be designed and evaluated from simulations tools, the experimental test of novel transmission (Tx) and reception (Rx) strategies may require the development of dedicated electronic systems for research purposes. In this paper we present a compact and reconfigurable 8-channel FPGA-based US platform for generating arbitrary waveforms and direct access to raw radiofrequency (RF) data using high-level commercial modules and integrated circuits.

### Statement of Contribution/Methods

The novel Ultrasound Evaluation System (UES) consists of three main boards: a digital transceiver control FPGA-based board; an arbitrary waveform generator (AWG) board; and an analog front-end (AFE) board. For maximum flexibility, an Altera Cyclone III FPGA Development Board has been used to implement the Tx controlling algorithms for custom excitation waveforms and programmable pulse sequences. The FPGA board can be connected by USB port to a host computer for easy user control of Tx and Rx parameters during pulse-echo experiments and fast raw RF data transfer. It also controls the eight-channel deserializer Rx segment, which captures the low-voltage differential signaling (LVDS) data outputs from the AFE board. The proprietary AWG board includes a set of eight high-speed US beamformer source drivers using Supertex ICs MD2131 and conventional T/R switches for overload protection. In order to simplify the connection to the FPGA board, we choose the commercial AFE5805EVM evaluation tool as the AFE module. The board uses an eight-channel fully integrated US AFE receiver AFE5805 (Texas Instruments Inc., USA), including a low-noise amplifier (LNA), variable gain amplifier (VGA), low-pass filter (LPF) and a 12-bit ADC with LVDS outputs and operating frequency of up to 50MHz.

### Results/Discussion

Fig. 1 shows the developed UES. To ensure signal integrity, special Samtec 50-Ohm RF cables were used to connect the AWG to the AFE board. Although the limited number of channels, the proposed low-cost platform provides flexibility, portability and an easy way to develop and validate a large class of US experimental investigations. The further works include optimization of user interface for conducting new Tx and Rx methods for US research and teaching.

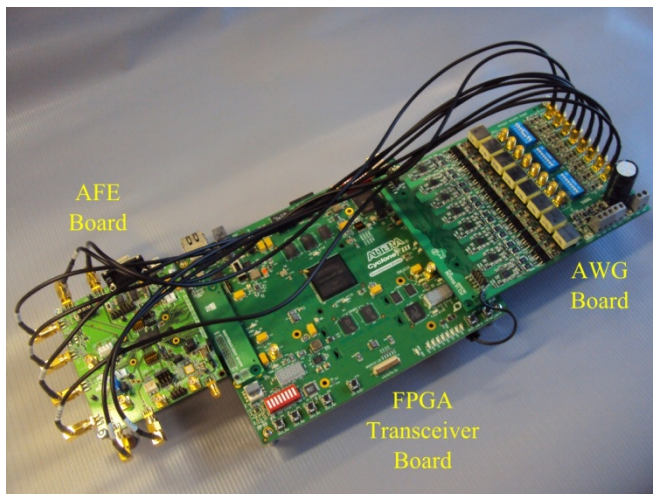


Figure 1. Photo of the Ultrasound Evaluation System.

### P1B10-4

#### Toward a high performance hand-held volumetric ultrasound imaging system

Carlos Julián Martín-Arguedas<sup>1</sup>, David Romero-Laorden<sup>2</sup>, Oscar Martínez-Graullera<sup>2</sup>, César Gutiérrez Fernández<sup>1</sup>, Ana Jiménez Martín<sup>1</sup>; <sup>1</sup>Universidad de Alcalá, Spain, <sup>2</sup>Consejo Superior de Investigaciones Científicas, Spain

### Background, Motivation and Objective

In recent years there has been an important research work in the design of volumetric ultrasound imaging equipment for medical applications. However, the development of such systems is severely limited by some technical constraints not satisfactorily solved yet. Thus, due to the high number of transducers used, these systems require a large number of

transmit and receive channels that must work in parallel. Moreover, due to the high volume of data to be acquired, a high bandwidth and processing power are demanded. This supposes an increment in the complexity, size and power consumption of the equipments, raising their price and limiting their use in hand-held and low-cost applications.

#### Statement of Contribution/Methods

While there are already many studies that attempt to solve each of these handicaps separately, here we propose a new volumetric ultrasound imaging system that addresses them globally, solving efficiently these technical constraints by means of a simple architecture with high performance. Thanks to the use of synthetic aperture techniques for data acquisition and GPGPU techniques for processing and beamforming, we achieve a volumetric ultrasound imaging system capable to obtain high quality images in real-time using very few resources.

We propose an acquisition system based on the  $2^2R$ -SAFT technique, which uses only one element in emission and subapertures with  $2 \times 2$  elements in reception. With this simple configuration we can reduce drastically the number of electronic channels, while avoiding the appearance of grating lobes in the beampattern, which is a common problem in other synthetic aperture techniques. Once the acquisition sequence concludes, a total of  $(2\sqrt{N}-1)^2$  signals (where  $N$  is the number of elements of the array) are stored in memory and they should be beamformed. Until recently, this was a huge volume of data that prevented to conform the images in real-time. However, thanks to GPGPU techniques, where graphics processors of conventional PCs or laptops are used for massive parallel computations, this limitation can be easily overcome to this day. Thus, once all acquired signals are stored in GPU memory, beamforming is applied in a post-processing stage, focusing every point in the image and correcting emission and reception simultaneously, obtaining in this manner a high quality image.

#### Results/Discussion

The imaging system described here demonstrates the advantages of merging synthetic aperture techniques with GPU beamformers for volumetric ultrasound imaging. The reduction of the hardware complexity, the high data acquisition rate, and the exceptional frame rate achieved with this architecture allow us to attain a small and compact equipment, able to represent high quality images in realtime, making it suitable to be used in applications where constraints on size, power consumption and cost are crucial.

#### P1B10-5

##### A New Smart Probe System for a Tablet PC-based Point-of-Care Ultrasound Imaging System: Feasibility Study

Yeongnam Lee<sup>1</sup>, Jeun Kang<sup>1</sup>, Sunmi Yeo<sup>1</sup>, Jaemin Lee<sup>1</sup>, Gi-Duck Kim<sup>2</sup>, Yangmo Yoo<sup>1,3</sup>, Tai-Kyong Song<sup>1</sup>; <sup>1</sup>Electronic Engineering, Sogang University, Seoul, Korea, Republic of; <sup>2</sup>Sogang Institute of Advanced Technology, Sogang University, Seoul, Korea, Republic of; <sup>3</sup>Interdisciplinary Program of Integrated Biotechnology, Sogang University, Seoul, Korea, Republic of

#### Background, Motivation and Objective

There is a growing interest in a smart ultrasound probe system wirelessly connected to a mobile device (e.g., smartphone and tablet PC) for point-of-care ultrasound imaging due to its enhanced accessibility. In this paper, the feasibility of a smart ultrasound probe system, in which transmit and receive modules along with a digital receive beamformer are embedded, is demonstrated.

#### Statement of Contribution/Methods

Figure 1(a) shows the block diagram of the new smart probe system connected to the external tablet PC. In the smart probe, two eight-channel high-voltage pulsers with transmit/receive switch (MAX14808, Maxim Integrated, San Jose, CA, USA) and two analog-to-digital converter (AFE5808, Texas Instruments, Dallas, TX, USA) are embedded. The transmit/receive beamforming and mid processing blocks are implemented on a single low-cost field programmable gate array chip (Spartan 6 LX150, Xilinx Inc., San Jose, CA, USA). As shown in Figs. 1(a) and 1(b), the complex base-band data after quadrature demodulation are transferred to the commercial tablet PC (ATIV Smart PC, Samsung Electronics, Seoul, Korea) via the USB 3.0 interface. The tablet PC handles ultrasound back-end processing (i.e., envelope detection, log compression, image filtering, and digital scanline conversion) and image display with graphical user interface (GUI). To evaluate the performance of the proposed smart probe system, the phantom study with a commercial linear array probe (L5-13IS, Samsung Medison, Seoul, Korea) and a phantom (ATS539, ATS Laboratories, Inc., Bridgeport, CT, USA), was conducted.

#### Results/Discussion

Figure 1(c) shows the ultrasound B-mode image captured from the custom-built point-of-care ultrasound imaging system with the smart probe connected to the tablet PC. The developed smart probe system with the size of  $150 \text{ mm} \times 50 \text{ mm} \times 10 \text{ mm}$ , the weight of 100 g and total power consumption of 7 W can support 32-channel dynamic receive beamforming with an extended aperture technique while providing the frame rates of 11 Hz for the 4-cm imaging depth with 128 scanlines. These results indicate that the developed smart probe system connected to a general tablet PC can support point-of-care ultrasound imaging. The further evaluation of the developed system, wireless communication, is under investigation.

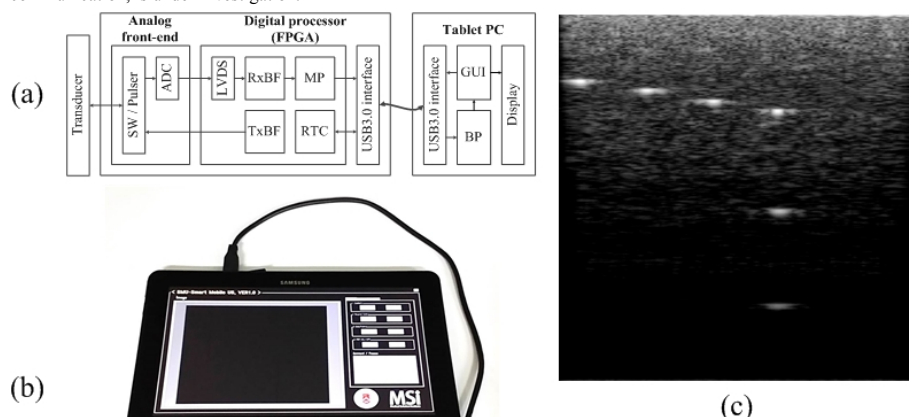


Figure 1. (a) Block diagram of the developed smart probe connected to an external tablet PC, (b) picture of the developed smart probe system and the tablet PC, and (c) ultrasound B-mode image captured from the developed system.



# A New Automated Breast Ultrasound System with Dual Wide Field-of-View Imaging

Jaeyoung Son<sup>1</sup>, Jongho Park<sup>1</sup>, Hyunjae Song<sup>1</sup>, Jin Ho Chang<sup>1,2</sup>, Tai-Kyong Song<sup>1</sup>, Yangmo Yoo<sup>1,2</sup>; <sup>1</sup>Electronic Engineering, Sogang University, Seoul, Korea, Republic of, <sup>2</sup>Interdisciplinary Program of Integrated Biotechnology, Sogang University, Korea, Republic of

## Background, Motivation and Objective

Breast ultrasound imaging is useful for observing the mass according to the desired locations and differentiating the shape of consistency of the mass during breast cancer screening, but its performance is highly dependent on the examiners' skill and has a poor reproducibility. Recently-introduced automated breast ultrasound (ABUS) systems have a potential to decrease user dependency due to its automated scanning protocols. However, the current ABUS system suffers from the limited field-of-view (FOV) and the long scanning time. In this paper, a new automated breast ultrasound system with dual wide FOV imaging is proposed.

## Statement of Contribution/Methods

To improve the FOV and the scanning time, in the newly-developed ABUS system, as shown in Fig. 1(a), ultrasound volume scanning is conducted while compressing breast between two plates, similar to mammography. This new ABUS system concurrently supports two 1024-element wide FOV linear array transducers in Fig. 1(b) so that two imaging planes can be acquired to reduce the volume scanning time. To enable the dual wide FOV imaging, as shown in Figs. 1(b) and 1(c), the custom-built ABUS system has four transmit (Tx)/Receive (Rx) boards and two 1024-to-128 high-voltage multiplexing board that support 128-channel Tx/Rx beamforming simultaneously. The beamformed radio-frequency (RF) data are sent to an external PC for mid and back-end processing running on high-performance graphic processing units (GPUs) using CUDA, via the PCI express 2.0 interface.

## Results/Discussion

Figure 1(d) shows the ultrasound B-mode images generated by multi-planar reconstruction during volume scanning after placing raw meat between two plates. The developed ABUS system can acquire a 3D breast volume set with 20 cm (width), 25 cm (length), 8 cm (length) within 20 seconds. As demonstrated in Fig. 1(d), two image planes are concurrently captured during the scanning with dual wide FOV imaging. The further evaluation of the developed ABUS system including pre-clinical studies is under investigation. These results indicate that the proposed dual wide FOV-based ABUS system can enhance the FOV and the volume scanning time for improving clinical productivity of breast ultrasound imaging.

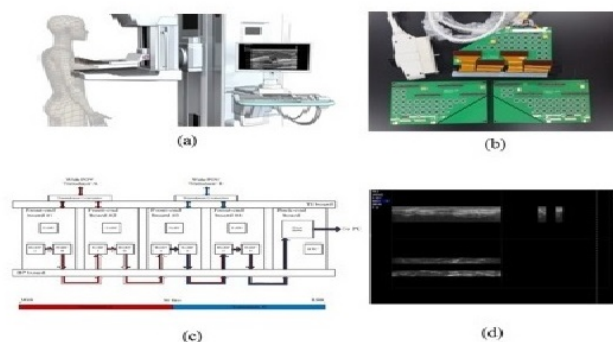


**Figure 1.** (a) Conceptual drawing of an automated breast ultrasound imaging (ABUS) system with dual wide field-of-view imaging, (b) dual wide field-of-view ultrasound transducers, (c) system block diagram of the developed ABUS system, and (d) example ultrasound images with multi-planar reconstruction.

# A Programmable Ultrasound Platform for Multi-gate Doppler Measurement

Weibao Qiu<sup>1</sup>, Zongying Ye<sup>1</sup>, Liyang Chi<sup>1</sup>, Peitian Mu<sup>1</sup>, Guofeng Li<sup>1</sup>, Congzhi Wang<sup>1</sup>, Yang Xiao<sup>1</sup>, Ming Qian<sup>1</sup>, Lei Sun<sup>2</sup>, Hairong Zheng<sup>1</sup>; <sup>1</sup>Paul C. Lauterbur Research Center for Biomedical Imaging, Shenzhen Institutes of Advanced Technology, Chinese Academy of Sciences, Shenzhen, China, People's Republic of, <sup>2</sup>Interdisciplinary Division of Biomedical Engineering, The Hong Kong Polytechnic University, Hong Kong

## Background, Motivation and Objective

Many cardiovascular diseases such as hypertension, thrombosis, and atherosclerosis are the notorious troubles to human people. The development of endothelial dysfunction and atherosclerosis produces measurable alterations in pulse wave velocity, velocity profiles, and wall shear stress. As a noninvasive visualization method, Doppler ultrasound has been widely applied to measure blood flow patterns. This paper presents a programmable platform with high frequency ultrasound ability, which can provide high resolution flow measurement. The imaging tests were conducted to demonstrate the performance of the programmable platform.

## Statement of Contribution/Methods

A programmable imaging platform with digital multigate pulsed wave (PW) Doppler algorithm was proposed for flow measurement and wall motion estimation. Hilbert transform based quadrature demodulation method was employed to facilitate the multigate PW Doppler acquisition. A programmable field programmable gate array (FPGA) was employed to control pulse excitation and echo data acquisition. Bipolar pulse scheme was used with adjustable center frequency, as well as the number of the pulses. All the electronics were soldered in one printed circuit board (PCB) for compactness. It supports wide range (2-80MHz) ultrasound PW Doppler imaging.

## Results/Discussion

The prototype of the programmable imaging platform is shown in Fig. 1(a). The platform is a 12 layers PCB design incorporating high speed pulse generator, low-noise frontend electronics, high speed analog-to-digital converter (12bit, 250MSPS), and high speed FPGA (Processor for programmable imaging algorithms). Fig. 1(b) describes the obtained multigate sonogram of fluid inside the vessel phantom with different interrogation depths. A 35MHz LiNbO<sub>3</sub> transducer was employed in this measurement. The interrogation depths were from 5.4mm to 9.9mm with about 0.4mm step. The waveform profiles were visualized by the proposed imaging platform.

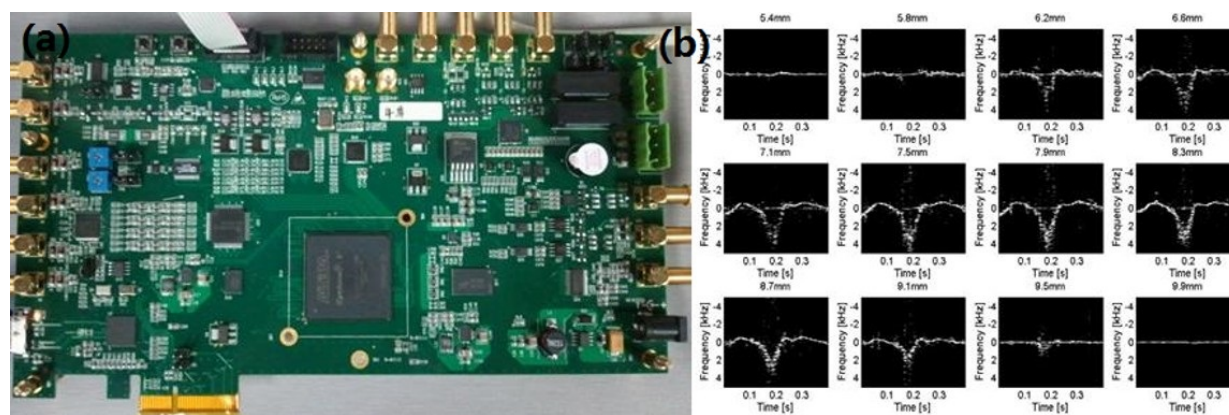


Fig.1. (a) The proposed programmable imaging platform. (b) Multigate PW Doppler imaging of flowing fluid with multiple interrogation gates.

P1B10-8

### Magnetically-powered Implantable Doppler Blood Flow Meter

Sai Chun Tang<sup>1</sup>, David Vilkomerson<sup>2</sup>, Tom Chilipka<sup>2</sup>; <sup>1</sup>Radiology, Harvard Medical School, Brigham and Women's Hospital, Boston, MA, USA, <sup>2</sup>DVX LLC, Princeton, NJ, USA

#### Background, Motivation and Objective

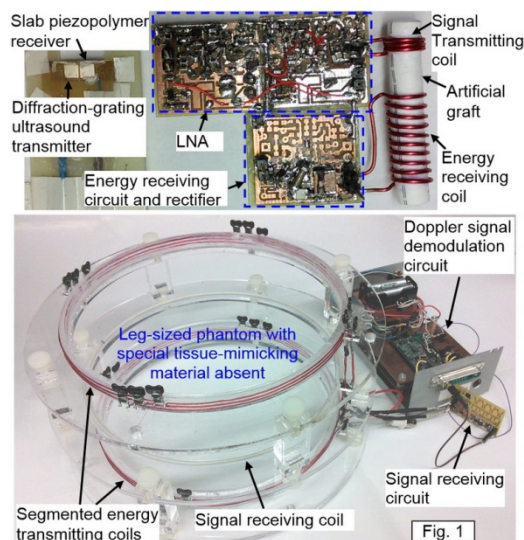
Artificial vascular grafts are used in patients with impaired circulation in the legs. The graft provides a bypass around narrowed arteries that cause poor circulation. However, thrombosis often occurs in the graft and leads to amputation. If the graft could be examined periodically by measuring the blood flow, the regions of stenosis could be fixed and graft failure and limb amputation prevented. Here we demonstrate an implantable Doppler blood-flow measuring device (shown in Fig.1) that is wirelessly powered from outside the body and transmits blood velocity waveforms from within the body.

#### Statement of Contribution/Methods

The blood flow sensor is flexible and wrapped around a 7-mm artificial graft. It consists of a piezopolymer diffraction-grating ultrasound transmitter and a slab piezopolymer receiver to detect Doppler-backscattered ultrasound from moving blood in the graft. The Doppler signal is amplified by a low-noise-amplifier (LNA) and wirelessly transmitted out to an external receiver. Both the sensor and its driving circuit are powered wirelessly by magnetic coupling by a 10-turn 7-mm diameter energy receiving coil wrapped around the graft. A 6-turn 20.6-cm diameter energy transmitting coil in a Helmholtz-coil-configuration is designed to wrap around the leg and generate a uniform magnetic field. A novel coil segmentation technique is applied to significantly reduce the required transmitting coil voltage, from 480Vpp to less than 10Vpp. Thus, device safety is increased and manufacturing cost reduced as there is no high-voltage needed. Since the magnetic field is uniform over a large volume inside the leg, the receiving coil can be located deep in the leg and precise coil alignment is not required, leading to increased freedom in graft placement by this method.

#### Results/Discussion

In the implanted circuit, the LNA and the 30MHz transducer driver consume a power of 62.7mW. The transmitting coil is excited by a 6.78MHz current of 0.43Arms. The required coil voltage is 3.1Vrms. The Doppler signal was transmitted out from a 3-turn 7-mm coil to a 1-turn 20-cm external receiving coil designed to wrap around the leg. An external receiving circuit was implemented to demodulate the Doppler signal to the blood velocity waveform. We expect to report the use of such a device in animals at the time of the Meeting.



# Development of A Crossed-Coupled Power MOSFET-based Protection Circuit for High Frequency Ultrasound Systems

Hojong Choi<sup>1</sup>, Kirk K. Shung<sup>1</sup>; <sup>1</sup>NIH Ultrasonic Transducer Resource Center and Biomedical Engineering, University of Southern California, Los Angeles, CA, USA

## Background, Motivation and Objective

Analog ultrasound transceivers with protection circuits play a critical role in determining high frequency ultrasound system performance because the parasitic impedance caused by interconnections of the analog transceiver and cable loading can affect the transducer's sensitivity and bandwidth. Therefore, performance enhancement of the protection circuit is of crucial importance for high frequency transducers with low sensitivity. We developed a novel crossed-coupled power MOSFET-based protection circuit in order to increase the sensitivity of high frequency transducers.

## Statement of Contribution/Methods

The crossed-coupled protection circuit (expander and limiter) was implemented on a printed circuit board. The performance of the proposed protection circuit was compared with a commercial diode-based expander and limiter (DEX-3 and DL-1, Matec). Measured data is summarized in Table I. The pulse-echo measurement with a single element 60 MHz LiNbO<sub>3</sub> transducer was also performed to compare the sensitivity of the developed protection circuit with the diode-based protection circuit.

## Results/Discussion

For the pulse echo measurement, the sensitivity of the echo signals using our crossed-coupled power MOSFET-based protection circuit increased by 7.8 times compared to that of the commercial diode-based protection circuit. These results demonstrate that the protection circuit described herein can improve the sensitivity of high frequency transducers. This effort represents the first step to constructing complete analog ultrasound front-end systems.

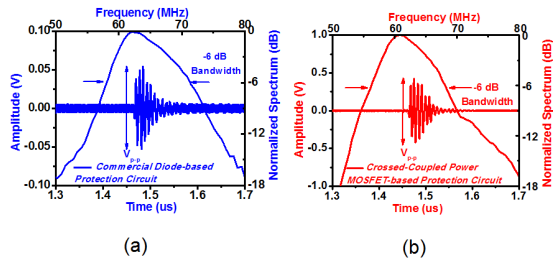


Fig. 1: Comparison of the sensitivity data of the echo signals measured using (a) a commercial diode-based protection circuit (blue line) and (b) our crossed-coupled power MOSFET-based protection circuit (red line).

Table 1: Comparison of the crossed-coupled power MOSFET-based with commercial diode-based protection circuit.

	Cross-coupled power MOSFET-based expander	Commercial diode-based expander	Cross-coupled power MOSFET-based limiter	Commercial diode-based limiter
Insertion loss	-0.9 dB	-1.5 dB	-0.8 dB	-7.5 dB
Recovery time	-----	-----	111 ns	109 ns

\* The insertion loss of the expanders was measured using a 60 MHz 70 V<sub>pp</sub> single cycle pulse.

\*The insertion loss of the limiters was measured using 60 MHz 0.1 V<sub>pp</sub> sine waveform.

\*Recovery time of the expanders was measured using a 60 MHz 70V<sub>pp</sub> three cycle pulse.

# High frequency GaN-based pulse generator with active T/R switch circuit

Enrico Boni<sup>1</sup>, Andrea Cellai<sup>2</sup>, Luca Bassi<sup>1</sup>; <sup>1</sup>Dipartimento di Ingegneria dell'Informazione, Università di Firenze, Firenze, Italy, <sup>2</sup>X-Phase s.r.l., Sesto Fiorentino, Italy

## Background, Motivation and Objective

High frequency ultrasound systems capable of high spatial resolution are commonly used for small biological structures imaging and non-destructive testing. For transducers operating at 50MHz central frequency excitation pulses with amplitude of several tens of Volts and 100V/ns slew rate are needed. Different solutions have been proposed to isolate the receive Low Noise Amplifier (LNA) from the transmission signal (T/R switch). The active solutions include biased bridges and high voltage switches. Forward biased bridges poorly perform when blocking high slew rate signals, mainly because of the junction capacitance and the minority carrier life time. High voltage switches present good blocking performance, but they can inject a charge whenever they are commutated, sending a bump signal to the transducer. This paper proposes a high frequency transmit (TX) circuit with a T/R switch capable of overcoming such limitations.

## Statement of Contribution/Methods

A compact high frequency negative pulse generator with an active T/R switch has been designed. The TX section is based on a Gallium Nitride (GaN) FET. The GaN device has very low gate charge and thus enables a high switching speed. The driving circuit has been carefully optimized both for components and layout in order to achieve a clean negative pulse with sharp edges and no ringing. The output impedance of the TX section has been kept near 50Ohm, to avoid multiple reflections on the probe cable.

The active T/R switch is a variation of the forward biased bridge circuit. Here, the bridge can be either forward biased or reverse biased by a digital control signal. When the bridge is forward biased, it exhibits a low impedance path between the transducer connector and the LNA circuit. When the bridge is reverse biased only the small junction capacitance of the diodes contributes to the path toward the LNA. The circuit has been designed to perform a smooth transition between the two states, to keep a negligible signal injection due to the T/R commutation phase.

## Results/Discussion

The circuit has been implemented on a six layer PCB and tested. The board area is less than 4 square centimeters. The TX section is able to generate up to 82V negative pulses on 50Ohm loads. The fall and the rise times are 1.8ns and 3.5ns respectively. No ringing nor overshoot are overlapped to the transmitted waveform. The pulse width can be as short as 6.5ns. The output impedance is 330Ohm during the pulse emission (GaN FET switched on) and 550Ohm when receiving. The T/R switch has a receiving bandwidth of more than 80MHz when switched on, while the TX signal feedthrough to the LNA is limited to 1Vpp when switched off. The T/R commutation signal injection to the probe is limited to 50mV over 400ns, but it spans a bandwidth narrower than 2 MHz. This circuit has been developed for application in a high resolution biometric system.

P1B10-11

**Handheld Device for Diagnostics of Pulmonary and Abdominal Pathologies by Multifunctional Analysis of Acoustic Percussion Signals**Eugene Malyarenko<sup>1</sup>, Mircea Pantea<sup>2</sup>, Fedar Seviaryn<sup>2</sup>, Roman Maev<sup>2</sup>; <sup>1</sup>Tessonics Corp., Birmingham, MI, USA, <sup>2</sup>Institute for Diagnostic Imaging Research, Windsor, ON, Canada**Background, Motivation and Objective**

Traditional medical percussion has been successfully used for the diagnosis of various conditions related to the thoracic and abdominal cavities of the human body. With the advent of modern imaging techniques offering more precise and objective methods of physical diagnostics, the percussion-based approach has lost some of its former importance. One of the main drawbacks of the classical percussion is its subjectivity, the reliance on the experience, training and acoustical aptitude of the physician.

Taking advantage of the digital techniques for the generation and analysis of acoustic signals, objective methods of diagnostics can be developed based on percussion principles. The goal is not to displace or compete with the imaging techniques but to provide an alternate method, which combines the objectivity with portability of percussion.

**Statement of Contribution/Methods**

In this work, we present a method - Objective Percussion Technology (OPT) - as well as its implementation in a handheld device. The initial goal of the development is the rapid detection of pneumothorax in the field, but the OPT can be extended to other areas of diagnostics, such as fluid and gas detection in intra-pleural and intra-peritoneal spaces or even monitoring of gas and motility in abdominal cavity.

The OPT takes advantage of the relative simplicity and low cost of the traditional percussion method and eliminates its dependence on the subjective factors.

To achieve these goals and to realize unbiased diagnostics of pulmonary trauma or disease, we take an approach of automated generation and analysis of acoustic percussion signals. In this approach, the patient's body is tapped with an electromechanical percussion head activated by a calibrated excitation signal, which can be adjusted to the necessities and whose parameters (intensity, spectral band) can be reproduced identically. The response of the body to this percussion input is captured with a sensor, converted into a digital signal, and analyzed. The parameters of received acoustic signals are used to differentiate between the responses produced by various abnormalities.

**Results/Discussion**

Studies on phantoms, in volunteers, and in animal models have indicated that several time domain and spectral parameters can be used for classification and recognition of percussion signals. The maximum frequency and the quality factor of the spectral peak(s) are the most intuitive parameters to use for automatic classification. They were used to successfully detect a 50 - 400 ml pneumothorax in the animal model.

The signals produced and collected by the device show significantly improved signal-to-noise ratio, are more reproducible and less operator-dependent than traditional manual percussion signals. High operational stability is a major advancement towards completely objective acoustic diagnostics by percussion.

# P1B11 - MTH: Novel Therapeutic Ultrasound Approaches

Salon C

Friday, September 5, 2014, 8:00 am - 5:00 pm

Chair: **Shin-ichiro Umemura**  
Tohoku University

P1B11-1

## Histotripsy Lesion Formation Using an Ultrasound Imaging Transducer Enabled by a Low-Frequency Pump Transducer

Kuang-Wei Lin<sup>1</sup>, Timothy L. Hall<sup>1</sup>, Zhen Xu<sup>1</sup>, Charles A. Cain<sup>1</sup>; <sup>1</sup>University of Michigan, USA

### Background, Motivation and Objective

When histotripsy therapy is applied using pulses shorter than 2 cycles, the generation of energetic dense bubble clouds only depends on where the peak negative pressure ( $P_-$ ) exceeds an intrinsic threshold of a medium. Additionally, our previous study showed that a sub-threshold low-frequency pump pulse can enable a sub-threshold high-frequency probe pulse to exceed the intrinsic threshold, thus generating lesion-producing dense bubble clouds (dual-beam histotripsy). This paper investigates the feasibility of using an imaging transducer to provide the high-frequency probe pulse in this dual-beam histotripsy approach. The advantages of this approach include 1) lesions can be steered by the steering of the imaging transducer, which can be performed by the built-in beamformer of a programmable ultrasound imaging system, and 2) the imaging transducer can also provide imaging feedback when it is used in conjunction with the ultrasound imaging system.

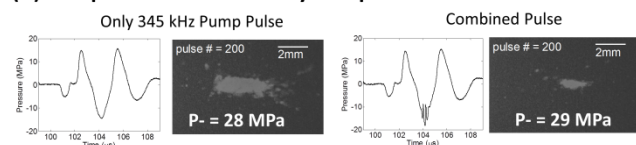
### Statement of Contribution/Methods

An ATL L7-4 imaging transducer, controlled and pulsed by a Verasonics V-1 Data Acquisition System, was used to generate the high-frequency probe pulses. The low-frequency pump pulses were generated by a 20-element 345 kHz array transducer, driven by a custom high voltage pulser. These dual-beam histotripsy pulses were applied to red-blood-cell (RBC) tissue-mimicking phantoms at a pulse repetition frequency of 1 Hz, and optical imaging was used to visualize bubble clouds and lesions generated in the RBC phantoms.

### Results/Discussion

The results showed that dense bubble clouds (and resulting lesions) were generated when the  $P_-$  of the sub-threshold pump and probe pulses combined constructively to exceed the intrinsic threshold. The average size of the smallest reproducible lesions using the imaging probe pulse enabled by the sub-threshold pump pulse was  $0.7 \times 1.7$  mm while that using the supra-threshold pump pulse alone was  $1.4 \times 3.7$  mm [Fig. 1(A)]. When the imaging transducer was steered laterally, bubble clouds and lesions were steered correspondingly until the combined  $P_-$  no longer exceeded the intrinsic threshold [Fig. 1(B)]. This dual-beam histotripsy approach using an imaging transducer can be applicable in several applications, e.g., prostatic tissue ablation (transperineal application of low-frequency pulse + high frequency pulses using a transrectal imaging transducer).

### (A) Comparison Between Only Pump Pulse and Combined Pulse



### (B) Lesion Steering Using the Steering of Imaging Transducer

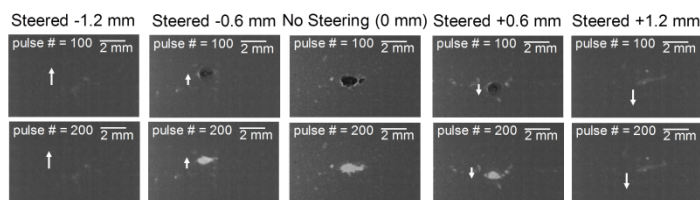


Fig. 1 (A) Comparison between the 345 kHz pump pulse and combined pulse (345 kHz + 5 MHz). Focal acoustic waveforms at a pressure level lower than the one used in RBC phantom experiments are shown in the left. Generated lesions in RBC phantoms are shown in the right with applied pressure level indicated. (B) Lesion steering using the steering of the 5 MHz imaging transducer in the combined pulse case (a combined  $P_-$  of 29 MPa). Bubble cloud images are shown in the upper row, while lesion images are shown in the lower row.

P1B11-2

## Closed-loop Multiple-focus Lesion Formation Control Using Dual Mode Ultrasound Arrays

Dalong Liu<sup>1</sup>, Alyona Haritonova<sup>2</sup>, Emad Ebbini<sup>1</sup>; <sup>1</sup>Electrical and Computer Engineering, University of Minnesota, Minneapolis, Minnesota, USA, <sup>2</sup>Biomedical Engineering, University of Minnesota, Minneapolis, Minnesota, USA

### Background, Motivation and Objective

Bubble activity during the high intensity focused ultrasound (HIFU) application could create overexposed and distorted lesions due to the increase in acoustic absorption. This process, however, can be utilized to drastically reduce the lesion formation time if the bubble activity at the HIFU focus can be reliably monitored and controlled. We have previously demonstrated the real-time closed-loop control of lesion formation using an FPGA-controlled single-element dual-mode transducer (DMUT). Precise volumetric lesions were formed in bovine heart tissue by raster scanning the HIFU focus on a predefined trajectory. The volumetric lesion formation rate could be increased by using a dual-mode ultrasound array (DMUA) to generate multiple-focus heating patterns with closed-loop control based on monitoring bubble activity at the different foci.



### Statement of Contribution/Methods

We present the results from an ultrasound-guided focused ultrasound platform designed to perform real-time monitoring and control of lesion formation using multiple-focus patterns. A DMUA is used for both lesion formation and bubble activity monitoring with high frame rate single transmit focus (STF) imaging. The beam sequencing is designed to maintain spatial and temporal synchronization between therapy and imaging pulse, this ensures optimum STF imaging performance during the respective therapy application for reliable bubble activity detection.

The DMUA is driven by a custom designed 32-channel arbitrary waveform generator and linear power amplifier. Use of arbitrary waveform and linear output allows optimum synthesis of multiple-focus pattern with minimum pre-focal artifacts. The beamformed RF data has been shown to be very sensitive to cavitation activity in response to HIFU in a variety of modes, e.g., boiling cavitation. This mode is characterized by sudden increase in echogenicity that could occur within milliseconds of the HIFU application. The real-time STF beamforming and the signal processing chain are implemented on a multi-GPU platform which support frame rates in excess of 500 fps for image formation and pattern control.

### Results/Discussion

Results from a series of experiments in bovine cardiac tissue demonstrate the robustness and increased volumetric lesion formation rate with close-loop control and multiple-focus pattern for a range of clinically-relevant exposures.

The multiple-focusing capability of the phased array, combined with bubble activity detection and control, has been shown to produce precisely controlled lesions with no evidence of overexposure even when fast raster scan (5s between consecutive shots) of volumetric HIFU lesions is attempted. The same size lesion would otherwise require significantly longer duration using lower intensity shot, long inter-lesion cooling time and single-focus scanning. In addition, closed-loop control results in well-behaved volumetric lesions with minimal pre focal damage.

P1B11-3

### Transcranial Focusing and HIFU beam Localization with Dual-Mode Ultrasound Arrays

Alyona Haritonova<sup>1</sup>, Dalong Liu<sup>2</sup>, Mahdi Bayat<sup>2</sup>, Emad Ebbini<sup>2</sup>; <sup>1</sup>Department of Biomedical Engineering, University of Minnesota, Minneapolis, MN, USA, <sup>2</sup>Department of Electrical and Computer Engineering, University of Minnesota, Minneapolis, MN, USA

### Background, Motivation and Objective

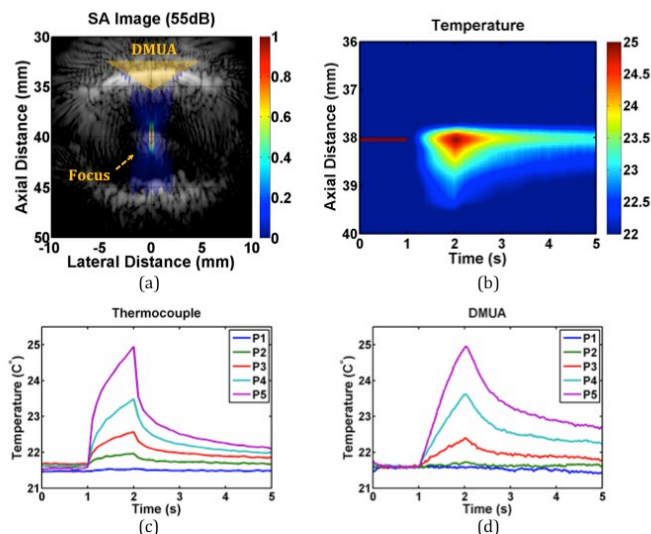
Focused ultrasound (FUS) has been proposed for a variety of transcranial applications, including neuromodulation, tumor ablation, blood brain barrier opening. A flurry of activity in recent years have generated encouraging results demonstrating its feasibility in these and other applications. To date, monitoring of FUS beams have been primarily accomplished using MR guidance, where both MR thermography and elastography have been used. With the use of dual-mode ultrasound array (DMUA) systems with real-time imaging capability, it is possible to localize sub-therapeutic and therapeutic transcranial FUS (tFUS) beams using ultrasound.

### Statement of Contribution/Methods

We have designed and implemented a 64-channel DMUA system with real-time GPU-based beamformer capable of supporting single transmit focus (STF) imaging at frame rates in excess of 500 fps. A 3.5-MHz, concave (40-mm roc), 32-element DMUA transducer was used to produce sub therapeutic tFUS while simultaneously imaging a decapitated head of a Copenhagen rat. A 150-um needle thermocouple was placed at the center of the brain to measure the tFUS induced temperature. DMUA imaging was used to localize the T/C needle and place the tFUS beam near the T/C junction. A number of sub-therapeutic tFUS beams with varying power were then generated while T/C measurements were recorded synchronously with the STF frames. Speckle tracking of echo data from the tFUS beam location within the brain was used to produce transcranial images of temperature change. We have also characterized the distortion to the array psf due to the skull using images of a 50-um wire at the center of the brain.

### Results/Discussion

The figure shows a transcranial DMUA image of the brain with an overlay of the expected tFUS location (a). A spatio-temporal map of the temperature change obtained using our ultrasound thermography (UST) method is shown in (b). The lower panels show the T/C measurements for various power settings (c) and the estimated temperature change using transcranial STF echo data (d). The T/C baseline temperature was added to the UST estimates of temperature change. The T/C data exhibit some self-heating artifact which was not removed, but the correspondence between the measured and estimated temperature is clear. More importantly, estimate of the axial extent of the tFUS based on UST is consistent with the (distorted) tFUS beam.



# Design of high intensity focused ultrasound systems for therapeutic applications utilizing shock wave exposures

Vera Khokhlova<sup>1,2</sup>, Adam Maxwell<sup>3</sup>, Petr Yuldashev<sup>1</sup>, Pavel Rosnitskiy<sup>1</sup>, Wayne Kreider<sup>4</sup>, Oleg Sapozhnikov<sup>1,2</sup>, Michael Bailey<sup>4</sup>; <sup>1</sup>Physics Faculty, Moscow State University, Moscow, Russian Federation, <sup>2</sup>Center for Industrial and Medical Ultrasound, University of Washington, Seattle, WA, USA, <sup>3</sup>Department of Medicine/Urology, University of Washington, Seattle, WA, USA, <sup>4</sup>Center for Industrial and Medical Ultrasound, University of Washington, USA

## Background, Motivation and Objective

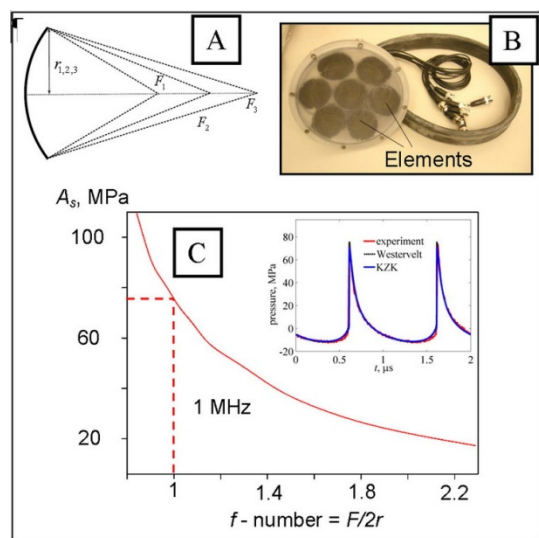
High intensity focused ultrasound (HIFU) is currently emerging into many clinical applications. Certain therapeutic modalities, for example, histotripsy, rely on formation of high amplitude shocks at the focus. These shocks, caused by nonlinear propagation effects, start to develop at different focal pressure levels depending on the frequency and geometry of the HIFU transducer. Certain values of the peak negative pressure, another critical parameter for HIFU therapies, correspond to this shock-forming condition. The goal of this work was to develop a method to determine parameters of the transducers that would provide certain shock amplitudes and corresponding peak negative pressures at the focus.

## Statement of Contribution/Methods

The hypothesis was that pressure level for shocks to form is mainly determined by an f-number of the transducer (Fig.1a). Transducers of lower f-number,  $F/2r$ , generate fields with a shorter focal lobe as compared to those with higher f-number. Formation of shocks within a short length of the focal lobe requires high acoustic pressures leading to high values of the shock amplitudes. Simulations based on the KZK equation were carried out to test the hypothesis and to determine characteristic shock amplitude for transducers of different f-numbers. Geometrical parameters and power output of the transducer were approximated in the KZK simulations using the equivalent single element model. The results were compared to the measurements and simulations based on the Westervelt equation for a 1 MHz array transducer developed for boiling histotripsy applications (Fig.1b).

## Results/Discussion

The results of modeling show the dependence of the shock amplitude versus f-number. For 1 MHz and f-number of 1 corresponding to the developed array source, the results of simulations determine the shock amplitude of 75 MPa and peak negative pressure of 14 MPa for 360 W power output, which compare very well to the measured values (Fig.1c). It is shown that for typical HIFU transducers of 1 – 3 MHz frequencies, the f-number to generate 65-75 MPa shocks is also close to one. Higher amplitude shocks will be formed for lower f-number transducers. [Work supported by NIH (T32 DK007779, R01 EB007643, P01 DK043881), RFBR 13-02-0018, and NSBRI through NCC 9-58].



# Development of the Algorithm for HIFU focus Visualization

Daeseung Kim<sup>1</sup>, Myungdeok Kim<sup>1</sup>, Kookjin Kang<sup>1</sup>, Keonho Son<sup>1</sup>; <sup>1</sup>New Business Department, ALPINION MEDICAL SYSTEMS, Korea, Republic of

## Background, Motivation and Objective

The ultrasound waves emitted from the HIFU transducer propagate through water and various tissue layers to a focus of the internal body. During propagation the multiple refractions and reflections occur due to in-homogeneity nature of the tissues. These cause the aberration of the focal location. Therefore, in the view of safety for the HIFU treatment it is important to know where the focus is formed. In this study, the method of synchronization control between a HIFU and an imaging devices was proposed for the focus visualization. And in order to get the clear focus image, the signal processing with the harmonics of the transmitted HIFU pulses was introduced.

## Statement of Contribution/Methods

The convex imaging probe is installed at the center of the phased-array HIFU transducer. The time delays for the imaging probe as well as the HIFU array-elements are calculated along the focus location. The time delay for the imaging probe is used as the starting time of the imagint device to receive the echo signals after HIFU exposure starts. The HIFU array elements send a short-pulse train of 1 MHz and the imaging probe starts to receive the echo-signal in sequence according to the delays. In this manner, the IQ data were obtained using the ultrasound research platform, ECUBE 12R of ALPINION Medical Systems. At this stage, the focus is not clear due to the random distribution of the scatters with non-uniform intensity. Through the FFT of the IQ data the spatial distribution of the amplitudes at the fundamental and the harmonic frequencies are extracted. The amplitudes at the harmonic frequencies are divided by the amplitude at the fundamental frequency. And then the divided results are displayed on the B-mode ultrasound images. This algorithm was tested in ex-vivo and in-vivo.

## Results/Discussion

The algorithm was tested at a bovine leg tissue and a uterine myoma of a Korean woman. The visualized focus was displaced a little from the intended focus location. It seems that the difference between the assumed sound velocity of the imaging device and the real sound velocity yields the aberration of the focal location. And when the focus visualization was failed the HIFU lesion was not generated well. The algorithm was verified through the in-vivo and ex-vivo experiment. It is confirmed that the algorithm can provide the precise information of the focus location in a simple manner.

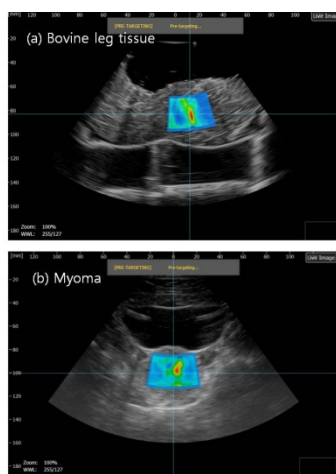


Fig. 1 Visualized HIFU focus in ex-vivo and in in-vivo. Red spot indicates the focus obtained through the developed algorithm. The blue cross-line indicates the targeted location.

P1B11-6

### Characterization of acoustic droplet vaporization and inertial cavitation thresholds in acoustically-responsive tissue scaffolds

Alexander Moncion<sup>1</sup>, Oliver Kripfgans<sup>1</sup>, J. Brian Fowlkes<sup>1</sup>, Paul Carson<sup>1</sup>, Mario Fabiilli<sup>1</sup>; <sup>1</sup>University of Michigan, Ann Arbor, Michigan, USA

#### Background, Motivation and Objective

Hydrogel scaffolds are used in regenerative medicine as an adhesive substrate for cells and growth factor (GF) delivery. Non-invasive, spatio-temporal control of GF release could greatly improve cell viability within a scaffold, thus furthering the clinical translation of scaffold-based tissue regeneration. Our group recently developed acoustically-responsive scaffolds (ARS) by doping hydrogels with a sonosensitive emulsion. Controlled release of GF, encapsulated within the emulsion, was triggered by focused ultrasound. This work investigates two acoustic mechanisms - acoustic droplet vaporization (ADV) and inertial cavitation (IC) - involved in the release of GF from ARSs.

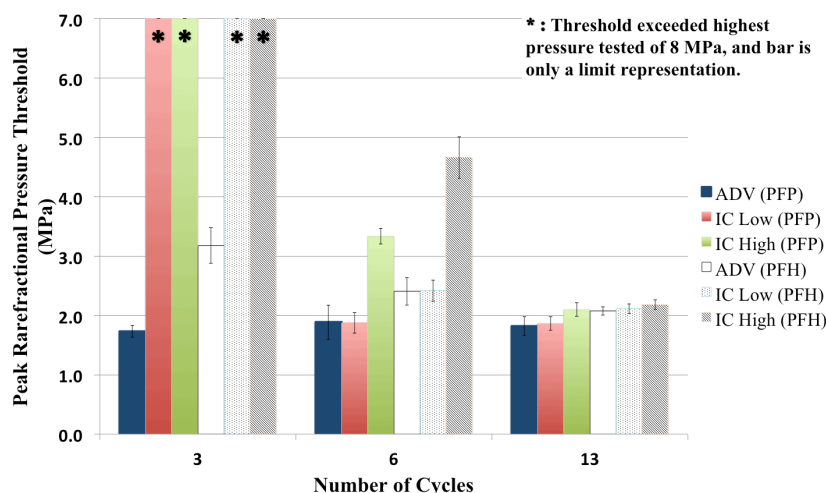
#### Statement of Contribution/Methods

Lipid-shelled, sonosensitive emulsions were made using either perfluoropentane (PFP) or perfluorohexane (PFH) (mean diameter: 1.8-2.1  $\mu\text{m}$ ). ARS were cast in OptiCells by adding the emulsions to 5 mg/mL fibrin gels at 1%(v/v) (i.e. 8.33 x 10<sup>8</sup> droplets/mL). A 2.5 MHz single-element transducer ( $t/\# = 0.8$  10 Hz PRF; cycles: 3, 6 or 13) was used to generate ADV/IC. ADV was detected in the scaffold using B-mode ultrasound (10 MHz linear array). The ADV threshold occurred at the lowest acoustic pressure where an increase in echogenicity was observed. IC was passively detected by digitizing RF segments collected by a broadband hydrophone (1-10 MHz). Two IC thresholds were measured: IC<sub>L</sub> and IC<sub>H</sub>. IC<sub>L</sub> was the lowest acoustic pressure at which IC was detected and IC<sub>H</sub> was the pressure at which all RF signals contain IC. Differences between threshold values was considered significant for  $p < 0.05$ .

#### Results/Discussion

At 3 cycles, ADV occurred at a lower pressure threshold than IC<sub>L</sub> whereas at 6 and 13 cycles, ADV and IC<sub>L</sub> thresholds were similar. The ADV threshold of the PFP emulsion was lower than the PFH emulsion at 3 and 6 cycles. ADV and IC thresholds can be modulated by altering the composition of the sonosensitive emulsion or by adjusting the number of acoustic cycles. At 6 and 13 cycles, ADV and IC<sub>L</sub> occur at similar pressure. Due to the large molecular size of GFs, release in the absence of IC may decrease the likelihood that GF bioactivity is reduced. Furthermore, the distinct ADV thresholds for PFP and PFH emulsions could enable controlled release of multiple GFs within a single ARS.

#### ADV/IC Threshold for PFP and PFH



P1B11-7

## High Intensity Focused Ultrasound applied to the placental unit: Preliminary results of an in-vivo study in monkeys

David Melodelima<sup>1</sup>, Jonathan Caloone<sup>1,2</sup>, Cyril Huissoud<sup>2,3</sup>, Jérémy Vincenot<sup>1</sup>, Anthony Kocot<sup>1</sup>, Jean-Yves Chapelon<sup>1</sup>; <sup>1</sup>LabTAU - INSERM U1032, France, <sup>2</sup>Maternité de la Croix Rousse - Hospices Civils de Lyon, France, <sup>3</sup>INSERM U846, France

### Background, Motivation and Objective

Demonstrate the feasibility of high intensity focused ultrasound (HIFU) to treat extracorporally the placental unit using a toroidal-shaped transducer with possible application to the treatment of the twin-to-twin transfusion syndrome using a monkey pregnant model.

### Statement of Contribution/Methods

A toroidal HIFU transducer working at 2.5 MHz and composed of 32 ring-shaped emitters was used. An ultrasound probe working at 7.5 MHz was placed in the center of the HIFU transducer. The imaging plane was aligned with the HIFU acoustic axis. The acoustic parameters used during HIFU exposures were selected according to preliminary simulations taking into account the attenuation coefficient of placentas, measured previously. Ex vivo experiments were then performed. An animal abdominal wall simulated the maternal wall was used and placed at the top of placenta. Single and juxtaposition of HIFU lesions were created. A monkey pregnant for a gestational age of 63 days, was then included and exposed to the HIFU treatment determine from previous ex vivo trials. A single HIFU lesion was performed after maternal anesthesia, and monitoring of maternal and fetal parameters such as subcutaneous and amniotic fluid temperature, maternal and fetal heart rate. These parameters were recorded continuously during the treatment. The resulting HIFU lesion was studied on sonogram, macroscopically and microscopically.

### Results/Discussion

Attenuation coefficients of 12 human placentas were measured in vitro and ranged from 0.07 to 0.10 Np.cm-1.MHz-1 according to the gestational age (17 to 40 weeks). Thirty-three human placentas (from 17 to 40 weeks) were included and exposed to HIFU. 25 single HIFU lesions were obtained, with an average diameter and depth of 7.1±3.2 mm, and 8.2±3.1mm respectively. Eight placentas were used for juxtaposing 6 HIFU lesions. The average diameter of these HIFU lesions was 23±5 mm and the average depth was 11±5 mm. The average thickness of the abdominal wall was 10.5±1.8 mm. No lesions or damage were observed in intervening tissues. In-vivo, a single HIFU lesion has been created in the placenta with a diameter of 10 mm and a depth of 5 mm. No lesions or damage were observed in intervening tissues not in the fetus. These findings were confirmed by histological analyses. Ultrasound examination revealed a hyperechoic HIFU lesion in the placenta. The diameter and the depth of the HIFU lesion measured in ultrasound images were 10.0 and 4.4 mm respectively. During the HIFU exposure, no significant variation of maternal and fetal parameters was observed. The subcutaneous and intra-amniotic fluid temperature were 25°C (24.9-26) and 34°C(33.4-34.5) respectively. The fetal heart rate was 124 (122-125).

This study demonstrates the feasibility, the reproducibility, the harmlessness and the effectiveness of HIFU applied to the placental unit within an in vivo model using a toroidal transducer.

P1B11-8

## Integrated ultrasound thermometry and multiphysics modeling for RF ablation monitoring: ex vivo studies on bovine liver tissue

Shriram Sethuraman<sup>1</sup>, Ajay Anand<sup>1</sup>, Jun Bo Li<sup>2</sup>; <sup>1</sup>Philips Research North America, Briarcliff Manor, New York, USA, <sup>2</sup>Philips Research China, Shanghai, China, People's Republic of

### Background, Motivation and Objective

Radiofrequency ablation (RFA) is one of the minimally invasive ablative therapies that can be used to treat hepatic tumors. Lack of techniques to accurately monitor ablation volume cause variability in treatment and could possibly lead to high local tumor recurrence rates. Current monitoring techniques either rely on sparse temperature sampling from a few sensors on the RFA device or indirect inference of the ablative zone on an ultrasound image. Such methods are sub-optimal and do not estimate the extent of the lesion. Ultrasound thermometry has the potential to monitor ablations. However, drawback of the approach is its applicability only in sub-ablative temperatures. To overcome this limitation we integrate a thermal model with ultrasound thermometry to extend the applicability to ablative temperatures.

### Statement of Contribution/Methods

In this work, we test and demonstrate the feasibility of our approach ex vivo on fresh bovine liver tissue. The method involves a two-stage approach. First, low power heating is performed using the RFA electrode to raise the temperature of the sample by 5 – 10°C. This sub-ablative temperature rise is measured using ultrasound thermometry in a plane away from the ablation electrode. The ultrasound temperature estimates are generated using the ultrasound RF data acquired during heating from a Philips iE-33 ultrasound scanner and Philips L9-3 probe. Temperature distribution in the tissue is also obtained from a multiphysics model (COMSOL) customized for the ablation device geometry and boundary conditions for various candidate tissue thermal conductivity values. The electrical power output from the RFA device is used as a known input in the coupled electrical and heat transfer simulation. A least square minimization is performed between the ultrasound thermometry data and temperature profiles from the model to estimate the unknown local tissue thermal and electrical conductivities. Thus, the multiphysics model adapts to the local in-situ conditions. Second, a high power heating is performed to create the lesion. Using the tissue parameters estimated in stage 1, ablation parameters used in stage 2, and apriori literature values for the temperature dependence of electrical parameters, the model is executed to predict the ablation volume. Finally, the ablation size is compared with gross pathology.

### Results/Discussion

The thermal and electrical conductivity estimated using our approach for N=5 samples are 0.59±0.07 W/m°C and 0.20±0.02 S/m respectively. Further, the lateral and axial lesion widths are 14.6±2.3 mm and 30.6±1.1 mm respectively and compare well with gross pathology estimates of 12.5±1.8 mm and 25.5±1.5mm. In ex vivo conditions devoid of blood perfusion effects, we have demonstrated the successful integration of the multiphysics model with the experimentally measured ultrasound backscatter data and the feasibility of the approach to monitor ablations.

P1B11-9

## Healing Tissue Response with ITU (Intense Therapy Ultrasound) in Musculoskeletal Tissue, Feasibility Study

Michael H. Slayton<sup>1</sup>, Jennifer Kehlet Barton<sup>2</sup>; <sup>1</sup>Guided Therapy Systems, Mesa, Arizona, USA, <sup>2</sup>University of Arizona, Tucson, Arizona, USA

### Background, Motivation and Objective

ITU effectively creates thermal injury zones inside soft tissue, initiating a tissue repair cascade in the skin, promoting collagen generation. It may be feasible to promote a robust healing response in musculoskeletal tissue accelerating healing from injury. The objective of the study is to establish feasibility of generating healing response via ITU thermal injuries in live rabbit Achilles tendon model.

### Statement of Contribution/Methods

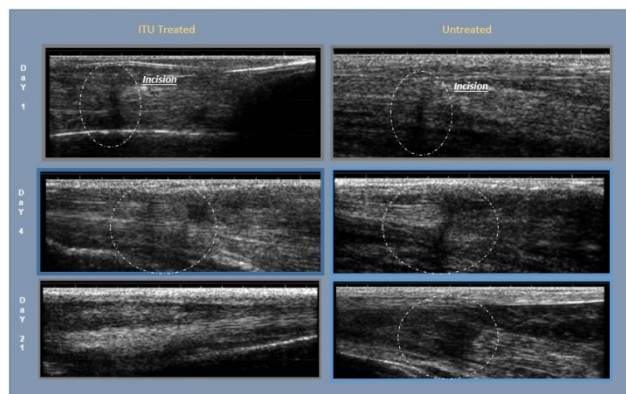
The rabbit studies were performed under protocol approved by IACUC, University of Arizona. Anesthetized animals were imaged with conventional ultrasound (Spark, Ardent Sound). The Achilles tendon of one limb was exposed and partially transected, the other tendon exposed only and served as an operative control. 24 hours post-surgery Achilles tendons were treated with ITU (Gen 2, GTS). One set of 2 rabbits, 4 tendons represented 4 groups (cut or not, treated or not). At time points of 4, 14 and 21 days post-treatment the

tendons were explanted and subjected to PCR to examine growth factors, cytokine and collagen gene expression. At time points 14 and 21 days tendons were mechanically tested to measure stress-strain curves and rupture strength. Five sets of rabbits (20 tendons) were sacrificed: 1 at 4 days, 2 each at 14 days and 21 days. At all time points the limbs were ultrasonically imaged and recorded.

### Results/Discussion

Results of PCR showed significant increase of the growth factors (TGF- $\beta$ 1), inflammation related interleukin-1 beta (IL1 $\beta$ ) and expected reduction and increase respectively between collagen type 1 and collagen type 2. Ultrasound images showed complete tendons' recovery at time points of 21 days when treated with ITU. Mechanical testing for stress-strain and rupture showed no compromise in ITU treated tendons vs. control: uncut/untreated tendons. In conclusion, feasibility of initiating a healing cascade in musculoskeletal tissue in live animal model was demonstrated utilizing ITU.

Right Achilles Tendon Post Surgery, Incision Site Circled



### P1B11-10

#### Improving sonoporative cellular drug-delivery with microbubble size

Kang-Ho Song<sup>1</sup>, Alexander Fan<sup>1</sup>, Tammy Trudeau<sup>2</sup>, Arthur Gutierrez-Hartmann<sup>2</sup>, Mark Borden<sup>1</sup>; <sup>1</sup>Mechanical Engineering, University of Colorado at Boulder, USA, <sup>2</sup>Department of Medicine, Biochemistry & Molecular Genetic, University of Colorado at Denver, USA

#### Background, Motivation and Objective

While viral therapeutics promise a highly efficient means of transfecting cells, safety concerns have pushed interest towards less efficient non-viral therapeutics. *In vitro* studies have demonstrated that mechanically-porative transfection methods, such as electroporation and microbubble-assisted sonoporation (MAS), offer superior transfection rates in previously difficult-to-transfect cells. While current use of electroporation is limited to *in vitro* applications, there have been a handful of translational studies examining the performance of MAS *in vivo*. While MAS offers a high level of spatial and temporal control over treatment regimes, further improvements to transfection efficiency are desirable for therapeutic applications. In this study, we improve MAS drug delivery to suspended cells by utilizing size-isolated microbubbles (SIMB) to lengthen microbubble persistence and the sonoporative treatment window, resulting in increased cellular drug delivery and microbubble persistence under ultrasonic stimulation.

#### Statement of Contribution/Methods

**Microbubble generation:** Microbubbles filled with perfluorobutane gas and encapsulated with DSPC and DSPE-PEG2000 lipid monolayers were generated by sonication. Differential centrifugation was used to obtain microbubbles with diameters of 2- $\mu$ m, 4- $\mu$ m and 6- $\mu$ m (Feshitan 2009). Samples were sized utilizing an Accusizer and Multisizer 3.

**Microbubble-assisted sonoporation:** Microbubbles were mixed with model drug, FITC-Dextran, or reporter gene (EGFP), in HeLa cell suspensions at fixed concentrations (1E6, 1E7, 5E7, 1E8, 1E9 /mL) and volume in a custom polystyrene sonoporation cartridge. The cartridge was immersed and subject to ultrasound from a therapeutic transducer. Samples were washed and anti-fluorescein (Invitrogen) added to reduce background fluorescence. Sample sizes were n=3.

Data acquisition and analysis: An Accuri C6 flow cytometer was utilized to detect treated and damaged cells.

#### Results/Discussion

Significant differences in sonoporation efficiency were found at all concentrations of microbubbles, with larger microbubbles providing greater FITC-Dextran uptake. Microbubble longevity under sonoporative stress is also seen to increase with microbubble size. The results suggest that significant improvements can be made to MAS performance by altering microbubble size for specific applications. In general, larger sized microbubbles demonstrate significant drug delivery potential, but risk irreversibly permeabilizing cells. Potential applications include the transformation of immune cells, in which a high (>100ug/mL) concentration of plasmid may be required to effect transfection utilizing other methods such as electroporation. Implications for future *in vivo* study include more efficient delivery of drug payloads, as well as improved treatment efficacy with dilute microbubble concentrations.

### P1B11-11

#### In-vitro stimulation of cells of the musculoskeletal system with Focused Low-Intensity Pulsed Ultrasound (FLIPUS): control over the physical output and analyses of cellular responses

Josefine Albers<sup>1</sup>, Aritra Chakraborty<sup>1</sup>, Thomas Ambrosi<sup>1</sup>, Anke Kadow-Romacker<sup>1</sup>, Kay Raum<sup>1</sup>, Regina Puts<sup>1</sup>; <sup>1</sup>Berlin-Brandenburg School for Regenerative Therapies, Julius Wolff Institute, Charite, Berlin, Germany

#### Background, Motivation and Objective

Low-Intensity Pulsed Ultrasound (LIPUS) is an alternative non-invasive treatment for fresh fractures, delayed- and non-union bones. However, significant inconsistency is associated with the reported clinical and experimental data, concealing the mechanism behind accelerated bone-regeneration. This discrepancy is caused by the lack of introduction of acoustic dose, which results in poor reproducibility of set-ups. These issues can be addressed by using focused LIPUS (FLIPUS), which allows more robust "acoustic dose" definition and an "acoustic dose – observed effect" correlation in an *in-vitro* setting. Our major objective is (i) to analyze the effect of FLIPUS on differentiation, proliferation and



migration of murine pre-osteoblasts MC3T3-E1 and rat mesenchymal stem cells (rMSCs); (ii) to examine signaling cascades, regulating the observed effects, i.e., Smad and non-Smad Bone Morphogenetic Proteins (BMP) pathways; and (iii) to evaluate the possible synergistic effects when FLIPUS and BMP-2 are applied together.

### Statement of Contribution/Methods

MC3T3-E1 cells and rMSCs were stimulated with FLIPUS in a 24-well plate, positioned in a sealed chamber supplied with 5% CO<sub>2</sub> humidified air and submerged in a 37 °C temperature-controlled water-bath. This treatment was performed through the well bottom with the diverging far field positioned at the cell layer. All relevant sound field parameters were measured and adjusted to provide an optimal and even sound transmission without standing wave effects, as follows: 3.6 MHz frequency, 100 Hz PRF with 20% duty cycle, and intensity (ISPTA) 20.9 mW.

### Results/Discussion

On the 5th day of stimulating rMSCs, FLIPUS up-regulated mRNA expression of the osteogenic markers osteocalcin (OC), osteopontin (OPN), Runx2, collagen-1, E11, and dentin matrix protein-1. Under reduced nutrient supply, rMSCs showed higher proliferation rate on day 3 and 4 when stimulated, as well as enhanced expression of OPN, OC and Runx2. Preliminary results also showed enhanced proliferation of MC3T3-E1 within 5 days of stimulation. Increased expressions of c-jun (an early response gene) and cyclooxygenase-2 (a rate-limiting enzyme in the production of prostaglandin-2) were observed 30 min post-FLIPUS-exposure. Both genes are associated with bone regeneration. When BMP-2 and FLIPUS were applied simultaneously, FLIPUS induced enhanced phosphorylation of receptor-associated Smad1/5/8 (signaling proteins downstream from BMP receptors) in both MC3T3-E1 and rMSCs. The contribution of FLIPUS to this synergistic co-action is to be further evaluated. In summary, our FLIPUS dose enhances proliferation and differentiation of MC3T3-E1 preosteoblasts and rMSCs, while Smad signaling appears to regulate the synergistic effect of FLIPUS and BMP-2 treatment. The focused field allows localized application of the same dose under in-vivo conditions.

## P2B1 - Signal Processing and NDE Methods

Salon C

Friday, September 5, 2014, 8:00 am - 5:00 pm

Chair: **Erdal Oruklu**  
*Illinois Institute of Technology*

P2B1-1

### Resolution Limit of Overlapping Ultrasound Chirplet Echoes via Hypotheses Testing

Ramazan Demiri<sup>1</sup>, Jafar Saniie<sup>2</sup>; <sup>1</sup>Department of Radiology, University of Pennsylvania Medical School, Philadelphia, PA, USA, <sup>2</sup>Illinois Institute of Technology, Chicago, IL, USA

#### Background, Motivation and Objective

The axial resolution capability of an ultrasonic pulse-echo imaging system is known to depend on the bandwidth of the propagating pulse. However, the exact resolution limit, the minimum spacing between two reflectors that a given ultrasound imaging system can resolve, has been lacking. In particular, for a known transducer bandwidth, noise level, excitation frequency, and the speed of sound in the medium, it is desirable to know the exact axial resolution limit. Such a limit is useful for assessing the performance of high-resolution algorithms such as model-based estimation or compressed sensing based deconvolution methods.

#### Statement of Contribution/Methods

In this paper we derive the resolution limit in terms of propagating pulse characteristics and measurement conditions. To analyze resolution capacity in terms of imaging parameters we consider two closely spaced overlapping echoes that obey the Gaussian Chirplet (GC) model. GC provides an excellent representation of an ultrasound echo with six parameters, bandwidth, time-of-arrival, center frequency, chirp rate, phase and amplitude. First, the resolution limit is defined as the limit above which two overlapping echoes can be discriminated by the observer. The limit is derived based on a formulation that the observer have to make a decision between two hypotheses, one of which is only one echo is observed and the other one is two overlapping echoes are observed. The resolution limit is derived by minimizing the minimum probability of error in making decisions between these two hypotheses. This resolution limit depends on the, the echo spectral parameters (bandwidth, chirp rate, center frequency), noise level, as well as the relative strength of the two closely spaced reflectors with respect to each other and a desired resolution success rate (RSR).

#### Results/Discussion

The resolution limit provides valuable insights into ultrasonic axial resolution problem. It indicates that echoes with high bandwidth and high chirp rates are easier to resolve. This implies that using broadband chirp type excitations would improve the resolution capability. Furthermore, it is easier to resolve echoes with comparable strengths. This implies that weak targets in the vicinity of strong ones may be missed.

We performed Monte-Carlo (MC) simulations in varying noise level to validate the resolution limit under typical imaging conditions in water using a 5 MHz center frequency transducer. For a given resolution limit, SNR, and known GC parameters, the desired RSR is attained when we performed empirical detection over 1000 MC trials. The detection problem is defined as deciding whether one or two echoes are present. RSR is defined as the number of successful detections of the number of echoes over the total number of trials. Finally we tested a compressed sensing (CS) method if it can attain the RL. It is observed that CS can attain the resolution limit for high SNR levels. These results are confirmed with experimental studies.

P2B1-2

### Dynamically Reconfigurable Analog Front-End for Ultrasonic Imaging Applications

Vidya Vasudevan<sup>1</sup>, Pramod Govindan<sup>1</sup>, Jafar Saniie<sup>1</sup>; <sup>1</sup>Electrical and Computer Engineering, Illinois Institute of Technology, USA

#### Background, Motivation and Objective

Ultrasonic systems, applied in the field of Medical Imaging and Non-Destructive Testing, have evolved from the trolley-based units to more portable, hand-held devices. These systems are built to suit a specific application or aim at specific target material. In order to make these systems portable and adaptable to the testing environment, we focus on building a more flexible and programmable hardware. We present a fully configurable Analog Front-End (AFE) which possesses the capability for dynamic re-configuration by using Xilinx Zynq SoC for real-time control, data acquisition and signal analysis. The flexibility built into the AFE allows for various beamforming and signal conditioning requirements. This arrangement enables the back-end processor to support various signal processing algorithms.

#### Statement of Contribution/Methods

A Reconfigurable AFE is built to optimize the High Voltage (HV) Pulser/Receiver for ultrasonic systems. Our system comprises of a pulser, conditioning block and a back-end processor. The hardware is built with Texas Instruments (TI) LM96550 HV Pulser, LM96530 Transmit/Receive (T/R) Switch, and LM96570 Beamformer over TX-SDK-V2 EVM. This AFE has the capability to beamform specific pulse train sequences on each of the 8-channels. The configurable excitation sequence for the ultrasonic transducer array can be a bit pattern of 4 to 64 bits at 62.5 KHz to 80 MHz with a programmable delay up to 102.4μs. Signal conditioning of the captured echo data are controlled through the embedded software. Controlled amplification and noise filtering of the raw analog data is carried out through VCA8500 EVM which incorporates a Low Noise Pre-amplifier and a Variable Gain Amplifier. Together they provide a maximum gain of 50 dB through the receiver. Analog Devices analog-to-digital converter (ADC) AD9467 is used for data acquisition at 250 MSPS through the Native FMC (FPGA Mezzanine Card) unit. This 16-bit ADC converts the 20 KHz to 20MHz echo information at 250 MSPS resulting in a throughput of 500 MB/s for a 250 MHz clock. Any modifications in the data capture logic can be carried out by selectively programming the AFE for each transducer. The post-processing of ultrasonic signals is executed on the ARM core of the Zynq SoC. This system can be controlled locally by a computing device or remotely via internet.

#### Results/Discussion

The system developed in this study is capable of executing typical ultrasonic signal processing algorithms in real-time. Reconfigurable AFE presents great possibilities by virtue of dynamic real-time control over the components on the data capture path. This offers performance enhancements by supporting varied applications involving material characterizations, NDE experimentation and imaging. The adaptability offered through a robust processing device in this system sets it apart and the capability of analyzing and processing real-time high speed data is a great improvement over the existing systems.

## NDE applications of compressed sensing, signal decomposition and echo estimation

Yufeng Lu<sup>1</sup>, Ramazan Demiri<sup>2</sup>, Jafar Saniie<sup>3</sup>; <sup>1</sup>Electrical and Computer Engineering, Bradley University, USA, <sup>2</sup>Department of Radiology, Perelman School of Medicine, University of Pennsylvania, USA, <sup>3</sup>Electrical and Computer Engineering, Illinois Institute of Technology, USA

### Background, Motivation and Objective

Recent progress in compressed sensing (CS) shows that low-rate sampling schemes with 20–30 times lower than the Nyquist rate can be used to reconstruct medical ultrasound images with high fidelity. This paper aims to connect the existing model-based restoration algorithms with the CS framework. In ultrasonic NDE applications, the pattern of ultrasonic echo signal reveals important physical information such as the location, size and orientation of defects, as well as attenuation and dispersion characteristics of the propagation path. In this study, the interest particularly lies in ultrasonic echo parameter estimation and signal decomposition algorithms using the CS framework.

### Statement of Contribution/Methods

In this investigation, CS framework is closely incorporated into ultrasound signal decomposition. The CS is used to exploit the sparsity of ultrasound echo signals and thereby significantly reduce the sampling rate. Furthermore, the time-of-arrivals (TOAs) of dominant echoes are estimated with the sparse sampling. The estimated TOAs along with a priori information of the transducers are used for signal decomposition on the incomplete ultrasonic data. Gaussian Chirplet (GC), a commonly used echo model, is adopted to describe a broad range of ultrasonic echo signals: narrowband or broadband, dispersive or non-dispersive. Parameters of GC echoes such as TOAs, center frequency, bandwidth, chirp rate and phase are estimated for pattern recognition and defect characterization. The efficiency of characterizing echoes and the accuracy of estimating echo parameters are also examined.

### Results/Discussion

For an experimental study, ultrasound microstructure scattering signals are acquired from a steel block with embedded defects using a 5 MHz broadband transducer. Additionally, benchmark data from different types of flaws such as a flat-bottom-hole, side-drilled hole and disk-shape cracks are utilized to demonstrate the effectiveness of the CS based decomposition algorithm. The result shows that the proposed algorithm provides a low-rate sampling scheme with an efficient estimation of TOAs for the subsequent signal decomposition. With the support of the CS framework, the signal decomposition has a narrower search range for parameter estimation. Conventional signal decomposition algorithms such as chirplet signal decomposition and fractional Fourier transform are used for a comparative study. The new technique not only successfully characterizes defects in complex materials but also shows higher computation efficiency in parameter estimation. The decomposition results and estimated parameters confirm the robustness and effectiveness of the proposed technique. The study has a broad range of applications in signal analysis including sparse representation, parameter estimation, and defect detection.

## Adaptive filtering and Fractional Fourier transform for ultrasonic signal processing and flaw detection

Yufeng Lu<sup>1</sup>, Jafar Saniie<sup>2</sup>; <sup>1</sup>Electrical and Computer Engineering, Bradley University, USA, <sup>2</sup>Electrical and Computer Engineering, Illinois Institute of Technology, USA

### Background, Motivation and Objective

Ultrasonic NDE signals often contain highly overlapped echoes from random scattered grains and irregular boundaries along the propagation path. The high density echoes from grains make it difficult to extract the desired information for defect characterization. Additionally, the dispersive echoes from irregular boundaries make it further challenging to analyze the non-stationary ultrasonic signals. Therefore, a signal processing technique which can greatly reduce the grain noise is highly sought-after. In this study, an adaptive filtering algorithm using Fractional Fourier transform (FrFT) is proposed for ultrasonic NDE signal processing.

### Statement of Contribution/Methods

Chirplets are type of signals commonly encountered in ultrasonic NDE applications. The chirp rate of a chirplet describes the dispersive level of an ultrasonic echo. As a generalized Fourier transform, the FrFT has been utilized to analyze non-stationary ultrasonic signals for echo decomposition and parameter estimation. FrFT rotates the spectrum of ultrasonic signals with an arbitrary angle in the time-frequency domain. In this investigation, the application of FrFT for adaptive filtering of ultrasonic signals is explored. In particular, the FrFT is introduced as a transformation tool to prepare ultrasonic signals for adaptive processing for flaw detection. The transform order of FrFT is chosen to match the chirp rate of the signal. It allows for a more compact support and reduces the non-stationarity of signals. Furthermore, a normalized least mean square (NLMS) algorithm is used for adaptive filtering on the transformed signals. The convergence and complexity of the algorithm are also discussed.

### Results/Discussion

In order to evaluate the performance of the algorithm, various experimental ultrasonic data sets are acquired from a large grained specimen with embedded defects. A 5MHz broadband transducer is utilized for data acquisition. The proposed algorithm is applied to discriminate defects in presence of high grain scattering noise. The experimental study shows that the algorithm greatly reduces grain noise and improves the signal-to-noise ratio by about 12 dB. Consequently, the algorithm identifies defects in complex materials successfully. Compared with conventional adaptive filtering, the proposed technique shows a fast convergence with the support of Fractional Fourier transform. This type of study can have a broad range of applications in interference cancellation, signal classification and flaw detection.

## FPGA Hardware Acceleration Using OpenCL for Ultrasonic Imaging Applications

Spenser Gilliland<sup>1</sup>, Jafar Saniie<sup>1</sup>; <sup>1</sup>Electrical and Computer Engineering, Illinois Institute of Technology, USA

### Background, Motivation and Objective

The objective of this study is to design and evaluate the hardware accelerators created by the OpenCL toolkit for ultrasonic signal processing and imaging applications. The OpenCL toolkit enables hardware/software co-design using the industry standard OpenCL API that is commonly used in General Purpose Graphics Processing Unit (GPGPU) applications. OpenCL based hardware accelerators allow rapid system development while meeting the real-time processing requirements for practical ultrasonic applications. In our ultrasonic applications, we are using OpenCL to accelerate applications with sampling rates exceeding 100 MHz which generate massive amounts of data for processing.

### Statement of Contribution/Methods

In this study, three ultrasonic signal processing algorithms (i.e., parametric echo estimation, frequency diverse flaw detection, and joint time-frequency distribution) are evaluated with the objective of optimizing the computational efficiency, utilizing the OpenCL toolkit on the Zynq 7020 All Programmable SoC (System-on-Chip). The Zynq consists an ARM dual-core processing unit with an FPGA fabric, which makes it ideal for ultrasonic signal processing applications. The FPGA fabric provides a significant enhancement to the software execution capabilities. Additionally, due to the wide adoption of OpenCL toolkit in GPGPU computing, it is convenient to develop code and prototype on common GPUs from Nvidia and AMD. These OpenCL based hardware accelerators have been integrated into a Reconfigurable Ultrasonic System-on-Chip (RUSH) platform, thus allowing support for hardware/software co-design.

**Results/Discussion**

Three ultrasonic signal processing algorithms mentioned above are implemented in software using ARM processor and also in OpenCL on the RUSH platform and the computational performance is analyzed. The ARM processor executes a real-time frequency-diverse ultrasonic flaw detection application with a repetition rate of 1000 measurements/sec using split-spectrum processing (SSP) in about 250 ms for 2048 samples. The implementation of parametric echo estimation using the chirplet signal decomposition (CSD) algorithm on the ARM processor estimates 100 echoes per second. Furthermore, time-frequency distributions including Wigner-Ville distribution (WVD) and short-time Fourier transform (STFT) require a computation time of less than 2015 ms for 2048 points on the ARM processor. However, our study proves that, the Zynq All Programmable SoC with the OpenCL toolkit improves the performance of these three applications at least by an order of magnitude while allowing portability between GPGPU and FPGA platforms. The performance improvement of moving to OpenCL clearly demonstrates the advantages of using portable platforms for ultrasonic imaging and signal processing applications.

P2B1-6

**Spatial Optimal Filter for Ultrasound Based Imaging of Vehicle Environments**

Alexander Urban<sup>1</sup>, Sergio Flores Contreras<sup>2</sup>, Martin Vossiek<sup>2</sup>; <sup>1</sup>Volkswagen, Germany, <sup>2</sup>Institute of Microwaves and Photonics, University of Erlangen-Nuremberg, Germany

**Background, Motivation and Objective**

Recent approaches for ultrasonic imaging of environments in air rely on complex systems which use large amounts of sensors to elaborate the image. Our objective is to generate detailed images with a simple setup using few sensors and a-priori generated ultrasonic reflection patterns to filter objects from measured echo signals.

**Statement of Contribution/Methods**

We address the problem of ultrasonic imaging in air by means of a 1-D array with 4 US sensors and a spatial optimal filter (SOF) for detecting specific objects from which an image may be derived. The advantages of this combination of 1-D array with the SOF is that objects may be detected using few sensors and few computational operations which enables real-time applications. The resulting 2-D image is a representation of the scene composed of objects having the characteristics for which the filter was specified. In our case two filters are specified, thus an environment is composed of walls and point reflectors. This is especially suitable for monitoring indoor environments.

**Results/Discussion**

Filtering walls out from a set of echoes with the SOF and the used array setup required 10 operations for each point in a parameter space which contains all parameter pairs (angle and distance to origin) that could describe a wall. Only two parameters are needed to describe a wall using the Hesse Normal form in a 2-D image, namely a distance and an angle. Fig. 1 was generated using the described sensor array. It shows (left) the parameter space after filtering the 10 non redundant echo paths resulting from imaging with 4 sensors. To the right is the generated image composed of 2 walls. The process of filtering lines using the SOF is similar to that of finding lines in a pixel image using the Hough transform. Yet, the SOF requires fewer steps to get to the image.

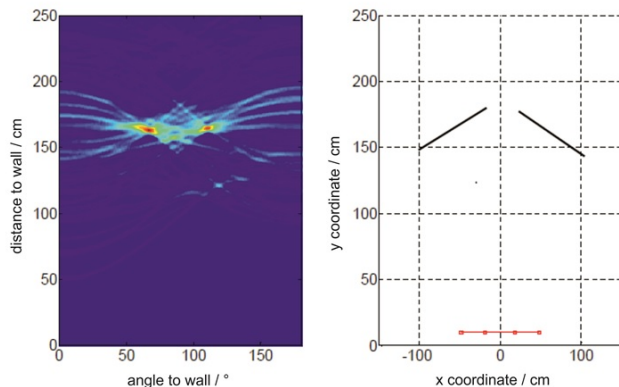


Figure 1: Example of the reconstruction of a scene using a 4 element array and the SOF. Left: The parameter space after applying the spatial optimal filter for detecting walls. Right: Reconstructed image of the scene (black) and sensor array (red).

P2B1-7

**Contextual use of pulse-compression and post processing to improve Ultrasonic Non Destructive Testing of high diffusing materials.**

Lee Davis<sup>1</sup>, Stefano Laureti<sup>1,2</sup>, Marco Ricci<sup>2</sup>, Pietro Burrascano<sup>2</sup>, David Hutchins<sup>1</sup>; <sup>1</sup>School of Engineering, University of Warwick, Coventry, United Kingdom, <sup>2</sup>Dipartimento di Ingegneria, Università di Perugia, Terni, Italy

**Background, Motivation and Objective**

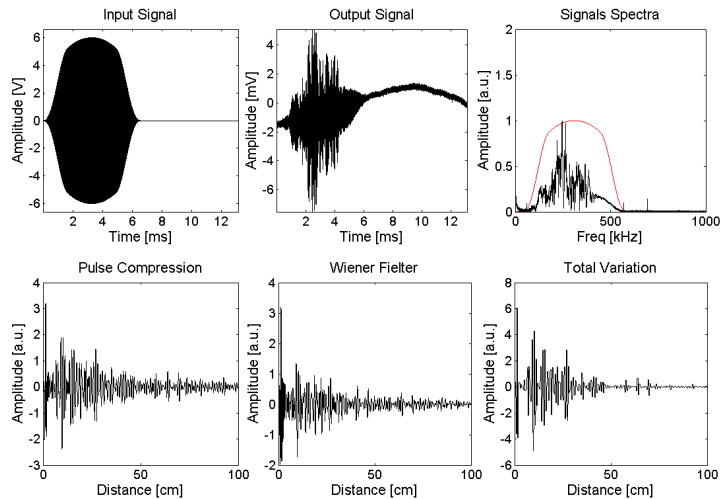
Ultrasonic Non Destructive Testing of high diffusing and attenuating material is quite challenging due to the low value of the Signal to Noise Ratio achievable and due to the pile-up of multiple small reflections caused by the coarse grain of the structures. A lot of efforts have been devoted to reduce the "so-called" speckle noise, in particular for diagnostic ultrasounds, and it has been found that the use of advanced post-processing techniques allows the enhancement of the SNR and of the inspection capability. Similar issues can be found in inspecting thick building materials and concrete. In many cases, their integrity is of utmost importance for the safety of structures, but it is quite challenging to have the capability of detecting inner defects by ultrasonic inspection. To tackle the problem of enhancing the SNR while improving the resolution, we contextually exploit pulse compression and various post processing techniques.

**Statement of Contribution/Methods**

The research has compared different combinations of pulse-compression techniques with post-processing algorithms. In particular, both Chirp signals and Golay sequences have been used in combination with L2- and L1-based deconvolution algorithms and with Wavelet denoising [H. Chen et al., Measurement 43, 570-585, (2010); J.L. S. Emeterio, et. al, Ultrasonics Symposium (IUS), 2009 IEEE International, 1992-1995; T. Goldstein, S. Osher. SIAM Journal on Imaging Sciences 2.2, 323-343, (2009)]. These combinations help in performing a set of measurements in highly attenuating material, using a low excitation voltage level, and hence will be of interest industrially.

# Results/Discussion

The effects of post processing on impulse responses, retrieved after pulse compression, is shown in Fig.1 for a highly-scattering building material. The input and the output signals and their respective spectrum amplitudes (red=input, black=output) are presented in the upper row, while the bottom row reports the impulse responses retrieved by using Pulse Compression, Pulse Compression with a Wiener Filter, and Pulse Compression and Total Variation respectively. It can be seen that by using the Total Variation deconvolution results in a significant amount of denoising. Such techniques can be applied to a wide range of highly scattering media.



P2B1-8

## Auto-adjustment of Image Produced by Multi-transducer Ultrasonic System

Aryaz Baradarani<sup>1</sup>, Roman Maev<sup>1</sup>, Fedar Severin<sup>1</sup>, Jason Taylor<sup>1</sup>, Serge Zhelnakov<sup>1</sup>; <sup>1</sup>Institute for Diagnostics Imaging Research, Windsor, Ontario, Canada

### Background, Motivation and Objective

The acoustic microscopy is characterized by relatively long scanning time, which is required for motion of the transducer over the entire scanning area. This time may be reduced by using of a multi-channel acoustical system. It has several identical transducers arranged as an array and mounted on mechanical scanner so each transducer scans a fracture of the total area. The resulting image is formed as combination of acquired partial data sets. The mechanical instability of the scanner, difference in parameters of individual transducers causes misalignment of the image fractures. This distortion may be partially compensated by introduction of constant or dynamical signal leveling and data shift procedures. However, reduction of random instability component requires more advanced algorithms including autoadjustment of processing parameters.

### Statement of Contribution/Methods

The described procedure was implemented into the prototype of ultrasonic fingerprint reading system. The specialized cylindrical scanner provides helical spiral lens trajectory which eliminates repeatable acceleration, reduces vibration and allows constant data flow on maximal rate. It is equipped with array of four spherically focused 50 MHz acoustic lens operating in pulse-echo mode. Each transducer is connected to separate channel including pulser, receiver and digitizer. The output 3D data volume contains interlaced B-scans coming from each channel. Afterward data processing includes pre-determined procedures of constant layer shift in order to compensate transducer displacement, phase shift and amplitude leveling for compensation of variation in transducer characteristics. Analysis of statistical parameters of individual scans allows adaptive eliminating of the axial misalignment and mechanical vibrations. Further 2D correlation of overlapping partial C-scans will realize an interpolative adjustment which essentially improves the output image.

Implementation of this adaptive algorithm into data processing sequence allows to significantly reduce misreading due to hardware noise and finger motion during scanning. The system provides a high quality acoustic image of the fingerprint including different levels of information: fingerprint pattern, sweat porous locations, internal dermis structures. These additional features can essentially facilitate fingerprint based identification.

### Results/Discussion

The developed principles and algorithm implementations allows improved quality, stability and reliability of acoustical data obtained with the mechanical scanner, accommodating several transducers. General principles developed during this work can be applied to other configurations of advanced ultrasonic systems designed for various biomedical and NDE applications. The data processing algorithm, developed for a specific biometric task, can be adapted for the compensation of mechanical imperfections of the other devices.



## P2B2 - Microfluidics

Salon C

Friday, September 5, 2014, 8:00 am - 5:00 pm

Chair: **Lawrence Kessler**  
Sonoscan Inc.

P2B2-1

### Single nano particle collecting by using ultrasonic humidifier

Jungsoo Kim<sup>1</sup>, Minkun Bae<sup>2</sup>, Moojoon Kim<sup>2</sup>, Kanglyeol Ha<sup>2</sup>, Mincheol Chu<sup>3</sup>; <sup>1</sup>Media Engineering, Tongmyong University, Korea, Republic of, <sup>2</sup>Pukyong National University, Korea, Republic of, <sup>3</sup>Korea Research Institute of Standards and Science, Korea, Republic of

#### Background, Motivation and Objective

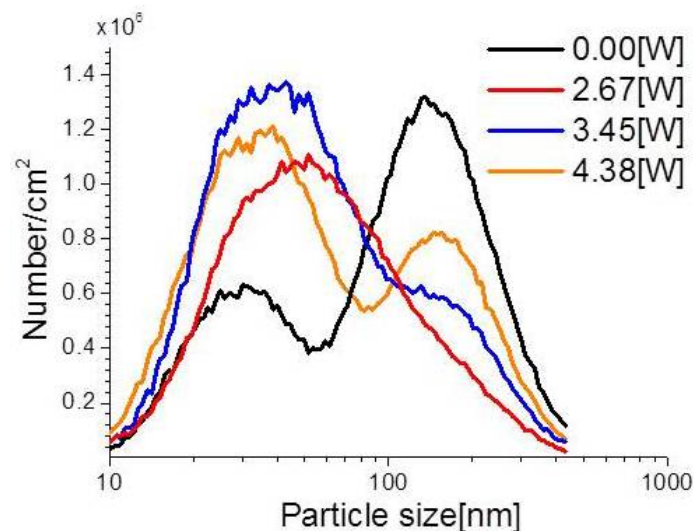
It is very important to obtain the single nano particle state for practical application of nano technology. Dispersion of nano particles is generally not easy, and agglomerated states with a few particles are found even in the dispersed suspension. This agglomeration veils the unique properties of nano particles and has disturbed their practical use. In this study, a separation method for single nano particle is suggested by using ultrasonic humidifier.

#### Statement of Contribution/Methods

The ultrasonic humidifier, which scatters the droplets to the air by ultrasonic energy from the water, can control the droplet size by its driving power and frequency. When the ultrasonic humidifier scatters the nano particle suspension into the air, the agglomerated particles cannot be drowned into the droplets because of their size and mass. Therefore, the separated single nano particles or the particles smaller than a certain size can be recollected by controlling the driving power. In this work, the suspension of TiO<sub>2</sub> was scattered by the ultrasonic humidifier and its particles were recollected. Then the particle size distribution was measured.

#### Results/Discussion

Figure 1 shows that the particle size distributions of recollected particles were different depending on the driving acoustic power. The particle distribution of original state (0.0 W) shows the maximum peak at around 200 nm even though the size of single particle is 30 nm. The figure shows the peak decreased as the acoustic power of the humidifier increased. It means that the agglomerated particles cannot be included in the droplets when the driving acoustic power is not enough. Especially, in the case of 2.67 W, the size distribution has only one peak at around single particle size. From these results, the single particles can be separated with the suggested method.



P2B2-2

### Microparticle separation using a PMMA channel at an oblique angle to a SAW field

Erin Dauson<sup>1</sup>, David Greve<sup>2</sup>, Irving Oppenheim<sup>1</sup>, Kelvin Gregory<sup>1</sup>; <sup>1</sup>Civil and Environmental Engineering, Carnegie Mellon University, Pittsburgh, Pennsylvania, USA, <sup>2</sup>Electrical and Computer Engineering, Carnegie Mellon University, Pittsburgh, Pennsylvania, USA

#### Background, Motivation and Objective

Concentration of particles in acoustic standing waves is well known. Other researchers have built SAW devices to sort microparticles using two opposing transducers to create standing waves in a parallel microfluidic channel. The acoustic force on microparticles is proportional to the volume of the particles, while the drag force is proportional to the radius of the microparticles. Consequently, larger particles migrate towards acoustic nodes faster than smaller particles. We have investigated particles flowing in channels at an oblique angle relative to the SAW field. By applying the drag force and the acoustic force to the particles at an angle, depending on the water velocity, larger particles migrate towards one side of the channel faster than smaller particles, enabling particle separation in a continuous flow system without dilution from sheath flow.

#### Statement of Contribution/Methods

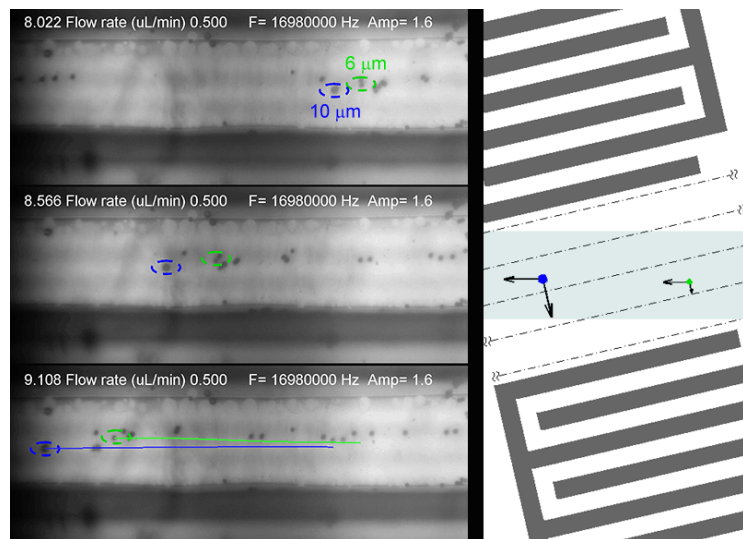
A parallel pair of interdigitated transducers (IDTs) with 20 finger pairs and 50  $\mu$ m finger width and spacing was fabricated on a 0.5 mm thick Y-cut LiNbO<sub>3</sub> substrate. A PMMA channel with fluid width 254  $\mu$ m and depth  $\sim$ 100  $\mu$ m was fabricated by micromachining, and bonded between the IDTs at a 13° angle from parallel. 10  $\mu$ m and 6  $\mu$ m diameter

particles, suspended in water, were driven through the channel with a flow rate near 0.5  $\mu\text{L}/\text{min}$  while the IDTs were excited near 16.98 MHz. The motion of the particles in the water was observed and recorded through a microscope.

## Results/Discussion

As the amplitude of the exciting frequency varied the comparative behavior of the two different particle sizes changed. At low amplitude all particles migrate towards node lines, but larger particles are driven slightly towards one side of the channel, so most 10  $\mu\text{m}$  particles align in one node line, while 6  $\mu\text{m}$  particles remain distributed between node lines. At slightly higher amplitude, many 10  $\mu\text{m}$  particles collect at the intersections of node lines and the channel wall while many smaller particles continue to flow through the channel. At higher amplitude, all particles collect at the intersections of node lines and the channel wall.

By appropriately choosing excitation frequency, amplitude, water velocity, and channel angle, we are able to drive particles of different sizes to different paths, and thus enable particle separation.



P2B2-3

## Temperature uniformity of microdroplet heated by buried surface acoustic wave device

Thibaut ROUX-MARCHAND<sup>1</sup>, Frédéric Sarry<sup>1</sup>, Denis beyssen<sup>1</sup>, Omar Elmazria<sup>1</sup>; <sup>1</sup>Université de Lorraine, IJL UMR7198 CNRS, VANDOEUVRE les NANCY, France

### Background, Motivation and Objective

Rayleigh Surface Acoustic Waves (R-SAW), which are widely used as analog filters, are nowadays employed in microfluidic applications. R-SAWs, which present an elliptical displacement, become a leaky-SAW when they encounter droplet loaded on the wave path. A longitudinal wave is then radiated into the liquid and induces, according to the wave's power and frequency, an internal streaming, droplet's heating, motion of droplet and atomization.

Using the R-SAW technique, biological reaction such as DNA amplification by PCR and hybridization should be performed. In recent work we have shown that R-SAWs don't affect the PCR biological species. More, we have shown that R-SAWs can heat the microdroplets up to the needed maximum PCR temperature with viscous liquids. Last year, we studied the uniformity of the microdroplet temperature which is very important for lot of biological and chemical reactions, particularly the PCR.

Now, we present a new study with an original microfluidic device in order to improve the temperature uniformity of microdroplet heated by R-SAW.

### Statement of Contribution/Methods

There are different techniques for temperature measurements available, contact as well as non-contact methods. For R-SAW PCR devices, only non-contact methods like infrared thermography may be used so as to not interfere with the reaction. Our approach is to record the temperature of a microdroplet heated by the new R-SAW device with an infrared camera.

The new device consists to put the microdroplet directly on the transducer. For that, it has to be covered by an insulating layer to avoid short circuit with liquid. A thin film of silicon dioxide is thus sputtered on the transducer. Before that, the transducer is performed by sputtering and lithography on 128°Y-X lithium niobate substrate.

The microdroplet temperature value and its uniformity, expressed by the temperature standard deviation, are then studied as a function of the power injected to IdTs.

### Results/Discussion

First of all, we have studied the effect of the insulating thin film. This layer has little impact regarding the generation of R-SAW. In fact, the central frequency of the R-SAW device shifts by 100kHz and the insertion losses are reduced by 0.5dB.

Concerning the microdroplet temperature, the uniformity is improved with the new device. Indeed, there are many reasons for that. Firstly, the acoustic streaming generated within droplet is not the same that with classical device. Here, we observe four vortices (two with classical device) which allow to propagate the heating by forced convection leading to a better temperature uniformity. Secondly, the droplet being on the transducer, the self-heating of the transducer increases the microdroplet average temperature and improves also the temperature uniformity.

Thus, to develop a future lab on chip assisted by R-SAW with a microdroplet heater function, the microdroplet should be move on the transducer in order to have the best temperature uniformity.

## P2B2-4

**Development of a microfluidic device with integrated high frequency ultrasound probe for particle characterization**

Eric Strohm<sup>1</sup>, Byeong-Ui Moon<sup>2</sup>, Dae Kun Hwang<sup>3</sup>, Scott Tsai<sup>2</sup>, Michael Kolios<sup>1</sup>; <sup>1</sup>Department of Physics, Ryerson University, Toronto, Ontario, Canada, <sup>2</sup>Department of Mechanical and Industrial Engineering, Ryerson University, Toronto, Ontario, Canada, <sup>3</sup>Department of Chemical Engineering, Ryerson University, Toronto, Ontario, Canada

**Background, Motivation and Objective**

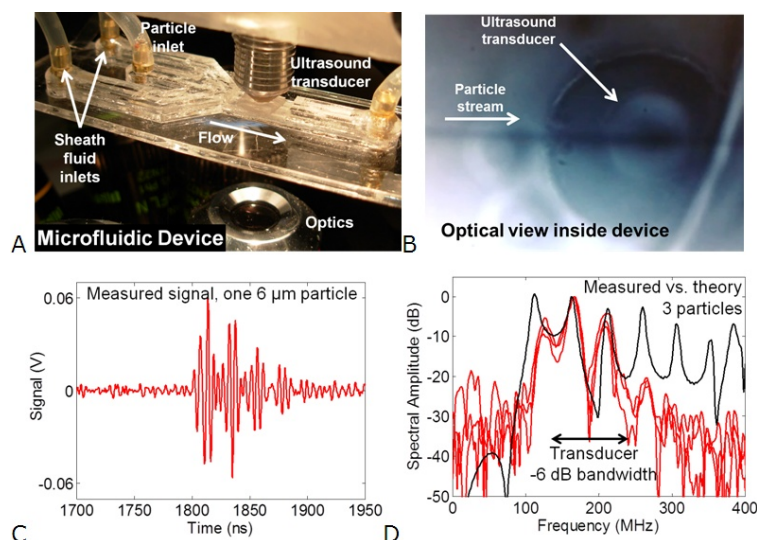
A microfluidic device incorporating a 200 MHz ultrasound (US) probe has been developed to rapidly characterize micron-sized particles. When the US wavelength is similar to the particle size, the scattered wave depends strongly on the particle size, and the ratio of the sound speed and density between the particle and surrounding fluid, respectively. If the sound speed and density of a particle are known, the size can be deduced by comparing unique features in the power spectrum to theoretical predictions or previously measured data. A new method of characterizing particles using sound waves is introduced, with applications towards classifying biological cells.

**Statement of Contribution/Methods**

A microfluidic device was designed and built using layers of bonded acrylic with lasercut channels (fig. 1A). A solution of 6 and 10  $\mu\text{m}$  polystyrene microspheres were hydrodynamically focused into a narrow stream. Black ink was added to aid visual contrast. An optical microscope was used to align a single element 200 MHz transducer in the device, and to view the particle stream (fig. 1B). Flow rates between 0.1-0.5 mL/min were used, and the stream was insonified using a pulse repetition rate of 1-125 kHz. The US backscatter from particles in the stream were sampled at 2.5 GS/s, and then the power spectrum calculated. The results were compared to theoretical predictions (Faran analytical model).

**Results/Discussion**

Signals from single particles flowing past the target area were recorded (fig. 1C). Stream widths as narrow as 15  $\mu\text{m}$  were obtained by varying the flow rates. Using the known particle size (6 or 10  $\mu\text{m}$ ), sound speed (2350 m/s) and density (1050 kg/m<sup>3</sup>), the analytical Faran model was solved and compared to measurements. For the 6  $\mu\text{m}$  particles, the average standard deviation between measurements was 2.0 MHz, and 3.2 MHz between measurement and theory (fig. 1D). Similar results were found for the 10  $\mu\text{m}$  particles but with different spectral peak locations. The unique spectral patterns were used to identify whether the particle was 6 or 10  $\mu\text{m}$ . These results show for the first time, a microfluidic device with an integrated US probe for the rapid characterization of flowing particles. An application is the classification of biological cells, particularly blood samples which contain a heterogeneous mixture of cell types.



## P2B2-5

**Fabrication, operation and evaluation of microfluidic device**

Brian Reinhardt<sup>1</sup>, Feng Guo<sup>2</sup>, Jun Huang<sup>2</sup>, Bernhard Tittmann<sup>3</sup>; <sup>1</sup>ESM, Penn State University, University Park, USA, <sup>2</sup>Penn State University, USA, <sup>3</sup>Engineering Science and Mechanics, Pennsylvania State University, USA

**Background, Motivation and Objective**

Microfluidic devices are having a large impact in the medical industry providing robust, reliable, and inexpensive solutions to problems such as cell patterning, trapping, sorting, separation and so on. These devices utilize nonlinear properties of standing surface acoustic waves (SSAW) to impart acoustic radiation forces which vary depending on the size, density, and shape of the target. Accurate control of the targets requires reliable predictions of the surface acoustics wave amplitudes. The objective of this work is the fabrication, operation and evaluation of a SSAW device including the measurement and modeling of the displacement amplitudes in order to optimize control of the particle interaction with the streaming forces.

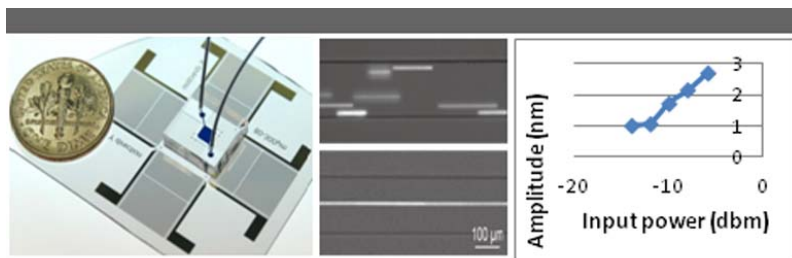
**Statement of Contribution/Methods**

A SSAW device was fabricated by the standard lift-off process. The device was designed with a wavelength of 300  $\mu\text{m}$ . A function generator (Agilent N5181) and an amplifier (ENI 325LA) were used to generate traveling SAW or standing SAW by applying a RF signal with powers from 1dbm to 10 dbm, and a frequency from 13 to 14 Mhz. The electrical signal applied to two inter-digitized electrodes converges to mechanical vibration on the lithium niobate substrate. A laser Doppler vibrometer was used to measure the out-of-plane surface displacement amplitudes. A 50nm gold layer was deposited onto the surface of the device to increase reflectivity for higher signal-to-noise ratio.

**Results/Discussion**

A two dimensional map was generated from raster scanning the SSAW device. The three part figure shows on the far left a photo of the device. In the middle is shown a two part image showing cell focusing by the SSAW: TOP-Without acoustic manipulation, cells (HeLa cells) were randomly distributed along the flow. BOTTOM With presence of a SSAW field, cells were focused in the center of the channel which is the center of the pressure node of the SSAW). The image on the right gives the SAW amplitude as measured

by the laser interferometer as a function of input power. These experimental results demonstrate that SSAW can be employed to control biological samples. The paper will also give results from modeling the displacements amplitudes.



## P2B3 - Transducers

Salon C

Friday, September 5, 2014, 8:00 am - 5:00 pm

Chair: **Donald Yuhas**  
Industrial Measurement Systems

### P2B3-1

#### Transverse Horizontal Ultrasonic Transducers Made from Piezoelectric Fiber Composites

**Ching-Chung Yin**<sup>1</sup>, Wei-Che Tsai<sup>2</sup>, Jing-Shi Chen<sup>2</sup>, Shih-Ming Hsu<sup>2</sup>; <sup>1</sup>Department of Mechanical Engineering, National Chiao Tung University, Hsinchu, Taiwan, <sup>2</sup>National Chiao Tung University, Taiwan

#### Background, Motivation and Objective

The piezoelectric fiber composite (PFC) comprises a periodic linear array of piezoelectric fibers surrounded by a matrix resin and sandwiched between two flexible polymer sheets. Transverse horizontal (TH) waves localized between the periodic structures are studied theoretically and experimentally in an effort to develop a novel TH wave transducer. The wave motion vibrates along the axis of fiber and propagates perpendicular to the fibers.

#### Statement of Contribution/Methods

A periodic finite-element approach has been used to determine dispersion relations of the fundamental symmetric and anti-symmetric transverse horizontal modes. The transverse horizontal ultrasonic transducer is made from a piezoelectric fiber composite with distributed electrodes on its surfaces. The poling direction in each piezoelectric fiber is inverted. The surface electrode pattern has a form of sinusoidal wave along the direction of wave propagation. The thickness shear deformation is actuated in this transducer as an alternate voltage is applied to the surface electrode.

#### Results/Discussion

The symmetric modes of TH waves propagate in PFC with constant phase velocity in the range of lower frequency and longer wavelength. Piezoelectric fiber has distinctly different mechanical and electrical properties from the surrounding resin. The high mass density fibers play a more significant role on the frequency characteristics of both symmetric and anti-symmetric TH waves. The fibers have notable influence on the formation of symmetric and anti-symmetric TH waves. The inertia effect from the embedded piezoelectric fibers causes the frequency spectra to be dispersive as frequency increases. The same influence also happens to the fundamental anti-symmetric modes. The latter modes are dispersive and occur in the frequency range higher than the fundamental symmetric modes. The TH wave devices have two frequency bands for a single electrode layout. Symmetric modes can be generated below 1.5 MHz and anti-symmetric modes can be transmitted in the frequency range higher than 4 MHz. This device has been adhered on the top surface of a host plate to transmit and receive TH plate wave. Its low-voltage drive capability and performance as a plate wave transducer have been assessed.

### P2B3-2

#### A Reciprocity-Based Method to Determine Hydrophone Complex Sensitivity and Tested at Frequencies from 1 to 7 MHz

**Everande Oliveira**<sup>1</sup>, Rodrigo Costa-Felix<sup>1</sup>, João Machado<sup>2</sup>; <sup>1</sup>Division of Scientific and Industrial Metrology, National Institute of Metrology, Quality and Technology, Duque de Caxias, Brazil, <sup>2</sup>Biomedical Engineering Program, Federal University of Rio de Janeiro, Rio de Janeiro, Brazil

#### Background, Motivation and Objective

Ultrasound hydrophone calibration comprises its sensitivity determination, i.e., its voltage response to a dynamic pressure incident on its active element. Among different methods, the self-reciprocity one is absolute, traditional, long time validated and well known among ultrasound technicians, and has been standardized by International Electrotechnical Commission for calibration of the hydrophone sensitivity magnitude. Competing methods claim the merit of determining the hydrophone sensitivity phase as well, although they are mainly comparison methods, i.e., a calibrated transducer is needed to implement procedure. Self-reciprocity is the basis for the method considered in the present work, which was already tested for magnitude and phase calibration of hydrophone sensitivity at 3 MHz. The hydrophone, previously calibrated at NPL (National Physical Laboratory, UK), sensitivity magnitudes resulted from NPL and the present method were statistically identical, considering an expanded uncertainty with coverage probability of 95 %. This result encouraged further tests of the method and the hydrophone complex sensitivity was determined at frequencies from 1 to 7 MHz.

#### Statement of Contribution/Methods

This work contributes with an upgrade of a method, recently disclosed and used to determine ultrasonic transducer complex transfer function, in order to add the calibration of hydrophone phase sensitivity. The disclosed method uses an auxiliary transducer and a flat reflector immersed in a water tank and allows calculating the on-axis pressure waveform, given the excitation signal and the propagation medium properties. The upgrade considers replacing the reflector by the hydrophone aligned with the auxiliary transducer axis of symmetry. The pressure waveform at the exact spot of the hydrophone is calculated and used together with the hydrophone output voltage waveform to determine its complex sensitivity. The method was tested at frequencies of 1, 2, 3, 4, 5, 6 and 7.0 MHz using two similarly manufactured PVDF membrane hydrophones, with 0.4 mm of active element diameter, previously calibrated in magnitude by NPL. Corresponding auxiliary transducers, with 12.7 mm or 25.4 mm of active element diameter, were excited with a 20-cycles burst signal with repetition frequency of 100 Hz.

#### Results/Discussion

Considering an expanded uncertainty with coverage probability of 95 %, the magnitude sensitivity results from NPL and the present method are statistically equal as well as the phase sensitivities of the two hydrophones, at all the seven frequencies and for both hydrophones. The results achieved in this work are metrological acceptable, with inter-laboratorial agreement within the declared uncertainties in magnitude sensitivity (less than 7.4 %) and intra-laboratorial agreement in sensitivity phase calibration, with uncertainty of less than 15 degrees.

Acknowledgments: to CAPES, CNPq and FAPERJ for the financial support.



## New Tonpilz Type Ultrasonic Vector Sensor for Underwater Applications

Yongrae Roh<sup>1</sup>, Youngsub Lim<sup>1</sup>; <sup>1</sup>*School of Mechanical Engineering, Kyungpook National University, Daegu, Daegu, Korea, Republic of*

### Background, Motivation and Objective

Typical piezoceramic transducers for underwater applications detect acoustic pressure, a scalar quantity, and convert this pressure into a proportional output voltage. These scalar sensors have no directional sensitivity. Localization of acoustic sources is usually done with sensor arrays that utilize such techniques as time-difference-of-arrival estimation and beam forming. However, these techniques require a large number of sensors and the detection system becomes complicated. In this work, we propose a new Tonpilz type underwater sensor which is sensitive to both the magnitude and the direction of an acoustic wave, and is accordingly referred to as an acoustic vector sensor. Feasibility of this structural design is confirmed through finite element analyses (FEA) as well as fabrication and characterization of an experimental prototype of the vector sensor.

### Statement of Contribution/Methods

The Tonpilz vector sensor was composed of a piezoceramic ring stack between a head mass and a tail mass. The piezoceramic ring was divided into four radial segments, each segment polarized alternately to its neighbors. An acoustic pressure wave coming from outside causes positive or negative signed electric voltage signals in the piezoceramic segments in accordance with their polarization directions. For instance, suppose that the four piezoceramic segments a, b, c, and d have electric voltages  $V_a$ ,  $V_b$ ,  $V_c$ , and  $V_d$  in response to an incoming pressure wave. The segments a and c have their polarization direction upward while the segments b and d have their polarization direction downward. With this configuration,  $V_a+V_d$  is positive and  $V_b+V_c$  is negative when the acoustic source is located at the azimuthal angle from  $0^\circ$  to  $180^\circ$ . On the other hand,  $V_c+V_d$  is positive and  $V_a+V_b$  is negative when the acoustic source is located at the azimuthal angle from  $0^\circ$  to  $90^\circ$ . With these combinations, we can easily determine the quadrant the acoustic source is located in. Further, depending on the azimuthal angle inside each quadrant, the magnitude of the paired voltage increases or decreases in the form of trigonometric functions. In this manner, the exact direction of the incoming wave can be determined with a single unit of the Tonpilz type vector sensor.

### Results/Discussion

Feasibility of this vector sensor was confirmed through the FEA. Through the FEA, the detailed structure of the Tonpilz transducer was also determined. An experimental prototype of the Tonpilz vector sensor was fabricated to have the structure as designed in the FEA. Performance of the prototype was measured in a water tank, and the measurement results showed excellent agreement with the design, which confirmed the validity of the design. The directional information of an acoustic target is very important in the field of underwater detection. The new vector sensor having the structure of a Tonpilz transducer can discriminate as a single unit both the magnitude and the direction of an incoming acoustic wave.

## New Wideband Tonpilz Transducer with a Voided Head Mass

Yongrae Roh<sup>1</sup>, Hyunki Kim<sup>1</sup>; <sup>1</sup>*School of Mechanical Engineering, Kyungpook National University, Daegu, Daegu, Korea, Republic of*

### Background, Motivation and Objective

Typically, a Tonpilz transducer is composed of a head mass and a tail mass connected by a drive section while being pre-stressed by a high strength rod. Applying an electrical voltage to the drive section induces an extensional displacement along the length of the transducer. A typical Tonpilz transducer is suitable for generating high power ultrasonic waves. However, when a wide frequency bandwidth is also required, the conventional structure frequently fails to meet the requirement. In this paper, a new Tonpilz structure has been developed to achieve the wide bandwidth as well as the high power by designing a voided head mass.

### Statement of Contribution/Methods

The first step of widening the bandwidth is to achieve the dual-mode operation of the head mass. The first flapping mode of the head mass is coupled to the typical longitudinal mode to attain the wide bandwidth. The flapping mode frequency ( $f_r$ ) is proportional to the head mass thickness. A wider bandwidth requires a higher  $f_r$ , which in turn leads to a larger head mass thickness. However, the larger thickness results in a heavier head mass, which in turn decreases the bandwidth since the mechanical quality factor is proportional to the weight of the head mass. Hence, in this work, a cavity was inserted inside the head mass, by which the thickness was allowed to extend over a wider range without much increasing the head mass weight. On the other hand, the mechanical quality factor of a Tonpilz transducer is given by  $Q_m \sim M_h/R_r$ , where  $M_h$  and  $R_r$  are the head mass weight and the radiation resistance, respectively. Based on this expression, there are two options to lower the quality factor: increasing the radius of the head mass for high radiation resistance or decreasing the weight of the head mass. Since a large head mass radius may cause problems in using the transducers in an array form, the latter option is preferred. Here, again, insertion of a cavity inside the head mass can evidently reduce the weight of the head mass. Insertion of the cavity does not touch the radiation resistance.

### Results/Discussion

Based on the concept, the optimal structure of the invented head mass was determined by the finite element method and genetic algorithm. Once the head mass geometry was determined, the tail mass structure was also optimized to match the new head mass. Following the design results, a prototype of the transducer was manufactured and characterized through measurements in a water tank. The measured transmitting voltage response (TVR) spectrum showed good agreement with the design results, which confirmed validity of the design. The measured spectrum showed that the Tonpilz transducer with the voided head mass had the -3dB frequency bandwidth of 88%, which is much larger than that of conventional Tonpilz transducers. TVR of the new transducer was 156 dB which is equivalent to that of typical Tonpilz transducers. These results verified the efficacy of the new voided head mass in widening the frequency bandwidth of the Tonpilz transducer.

## Optical Characterization of Surface Displacement Fields of High-Frequency Transducers

Ashwin Sampathkumar<sup>1</sup>, Jonathan Mamou<sup>1</sup>, Jeffrey Ketterling<sup>1</sup>; <sup>1</sup>*F.L. Lizzi Center for Biomedical Engineering, Riverside Research, New York City, New York, USA*

### Background, Motivation and Objective

Optical interferometric techniques have been used to measure the surface displacement of transducers to predict the radiated acoustic pressure field. Transducer-surface vibration frequently is considered to be uniform, which may be incorrect because of transducer structure, fabrication inhomogeneities and surface conditions. Therefore, measurement of surface-displacement amplitude and phase can provide valuable information for transducer calibration as well as for sound-field modeling. We have developed a GHz bandwidth, fine-resolution ( $0.5 \mu\text{m}$ ), optical interferometer to map the displacement and pressure fields of high-frequency transducers beyond the limits of conventional hydrophones and laser vibrometers.

### Statement of Contribution/Methods

Several transducers, including a 40-MHz annular array, a 100-MHz,  $\text{ZnO}$ , focused transducer, and a 75-MHz focused transducer were characterized. The transducers were excited with an impulse, and the surface vibrations were detected using a Michelson interferometer. The surface of the transducer was raster scanned to map the 2D displacement

amplitude and phase distributions. A high numerical aperture ( $NA = 0.55$ ) optical lens was used to detect the vibrations from a  $0.5\text{-}\mu\text{m}$  spot at each scan location at  $100\text{ }\mu\text{m}$  step size.

### Results/Discussion

Fig. 1a shows the transducer surface response in air and a reference pulse-echo signal measured on a glass plate in water. Fig. 1b shows the corresponding 6-dB bandwidths of 30 and 50 MHz for operation in air and water respectively. The narrower bandwidth with a bimodal response measured optically was attributed to the strong acoustic-impedance mismatch at the transducer surface-to-air interface. Loading the transducer with a thin water film of 2 mm provided comparable results to the measured pulse-echo signal in water. A  $3.2 \times 2.7\text{ mm}$  surface scan produced the 2D surface displacement amplitude and phase maps shown in Figs. 1c and 1d) respectively. A peak surface displacement of 2.8-nm was measured. The phase map showed no appreciable variation in phase over the surface of the active element indicating uniform motion of the transducer. We observed a minimum surface-displacement detection sensitivity of  $100\text{ fm/Hz}^{1/2}$ . Hence, the interferometric system can non-destructively evaluate and calibrate high-frequency transducers and can provide valuable information for modeling the response.

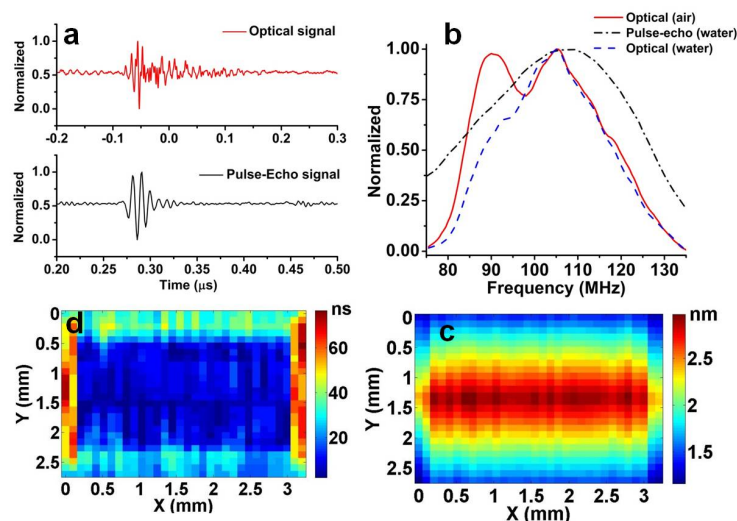


**Figure 1.**(a) Response of the 100-MHz transducer measured in air, and water loaded conditions (optical) as well as reference glass plate measurement in water (pulse-echo). (b) Corresponding transducer bandwidth in air and water (c) 2D surface displacement and (d) phase map of the transducer.

## P3B1 - Elastic Wave Propagation

Salon C

Friday, September 5, 2014, 8:00 am - 5:00 pm

Chair: **Bikash Sinha**  
Schlumberger-Doll Research,

P3B1-1

### Effects of viscous liquid on SH wave propagation in layered viscoelastic/piezoelectric structures

Jing Cui<sup>1</sup>, Jianke Du<sup>1</sup>, Ji Wang<sup>1</sup>, <sup>1</sup>Ningbo University, China, People's Republic of

#### Background, Motivation and Objective

It is well known that SH waves in the piezoelectric materials are extensively used in sensors and transducers. The layered structures, for example, a thin film bonded on the piezoelectric substrate, are currently adopted to achieve high performance for these devices. The analysis of the dispersion relation at nonslip boundary conditions between the coating thin layer and the resonator surface can give the expressions for the phase velocity shift and the damping coefficient of the resonator. The application of shear acoustic wave devices to chemical and biological sensing has recently received much attention since these waves are very sensitive to mass loading on the device's surface. After coated with a receptive layer, the SH-SAW sensors are widely used for detecting compounds in gases or liquids. The properties of receptive layers often show viscoelasticity after absorbing some components, which should be considered in practical biosensors or chemical sensors.

#### Statement of Contribution/Methods

We investigate the effects of the viscous nonconductive liquid on SH wave propagation in a layered viscoelastic/piezoelectric structure. The interface between the viscoelastic layer and the piezoelectric substrate is perfect. The dispersion relations are obtained for electrically shorted and open cases, respectively. The effects of the viscous coefficient of the liquid are figured and presented. We choose two different liquids (alcohol and glycerol) in calculation. The effects of the liquid on wave properties are obtained and presented.

#### Results/Discussion

We analyze the effects of the mass density and the viscous coefficient of the liquid to the phase velocity. Figure 1 shows the relation between the phase velocity and the viscous coefficient of the liquid with different mass density for electrically shorted and open cases, respectively. The phase velocity decreases with the increase of viscous coefficient and density of the liquid. Figure 2 shows the phase velocity versus wave number for the first mode with different liquid. We can find the phase velocity decreases with the increase of the wave number. Figure 3 is presented to show the attenuation versus wave frequency with different liquid. We can see that the attenuation increases with the increase of the frequency.

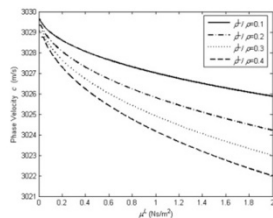


Fig.1

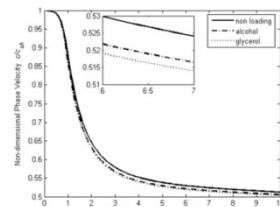


Fig.2

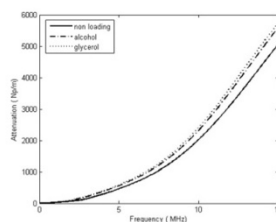


Fig.3

P3B1-2

### Design and Performance Evaluation of Phased Parametric Array for the Detection of Geological Conditions Ahead of Drill Bit

Xiumei Zhang<sup>1</sup>, Weijun Lin<sup>1</sup>, Xiuming Wang<sup>1</sup>, <sup>1</sup>State key laboratory of Acoustics, Institute of Acoustics, Chinese Academy of Sciences, China, People's Republic of

#### Background, Motivation and Objective

The detection of reflectors ahead of drill bit in oil drilling well is vital in ensuring the safety production and realizing well geosteering. In order to achieve the objective, a phased parametric array is designed and the performance is evaluated by simulating wave propagation in a drilling well with reflectors ahead of the drill bit. Specially, interactions of acoustic wave among the borehole, the formation and the reflector are revealed in detail.

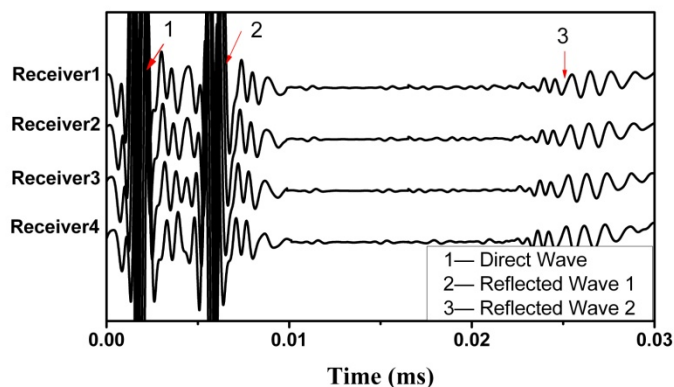
#### Statement of Contribution/Methods

According to self-demodulation effect of sound field excited by parametric array and phased array method, a phased parametric array with particular parameters is designed by taking into account conditions in the drilling well. The designed parametric array is generated by using modulated primary wave with 4 elements and 0.2m spacing, where the frequencies of the primary wave and the balanced modulation wave are about 10.0kHz and 0.5kHz, respectively. The angle between the main lobe and the central axis of the drilling hole is about 30°. Supposing that acoustic signals are emitted from the parametric array in the borehole, wave propagation of the signals in the drilling hole underground

are investigated by using 3-D finite difference method in cylindrical coordinates, where the propagation mechanism of waves in the borehole, the formation surrounded and the reflectors ahead of the drill bit are studied in detail by analyzing the synthetic data.

#### Results/Discussion

Typical filtered waveforms gathered by array receivers in the drilling hole are shown in Fig.1. It is clear that three wave components can be obtained, including direct wave traveling from the source to the receiver, reflected wave 1 generated at the bottom of the borehole, and reflected wave 2 generated from the reflector ahead of the drill bit. The geological information of the reflector such as the distance from the bit derived from the waveforms agrees well with the numerical model. The results in the study indicate that a properly designed phased parametric array has the potential to be used in detecting geological conditions ahead of the drill bit.



P3B1-3

#### The matrix of resonators with a lateral electric field on a single piezoelectric plate

Irina Borodina<sup>1</sup>, Boris Zaitsev<sup>1</sup>, Andrey Teplykh<sup>1</sup>, Iren Kuznetsova<sup>2</sup>; <sup>1</sup>Saratov Branch, Institute of Radio Engineering and Electronics of RAS, Saratov, Russian Federation, <sup>2</sup>Institute of Radio Engineering and Electronics of RAS, Moscow, Russian Federation

#### Background, Motivation and Objective

At present the problem of the development of acoustic gas analyzers based on matrix of gas sensors placed on the single plate is extremely important. Each sensor consists of piezoelectric resonator and gas sensitive film and selectively reacts to specific gas or vapor. The most interest is excited by the piezoelectric resonators with lateral electric field because their electrodes are set on the same side of the piezoelectric plate. This allows the spatial separation of resonators and films by their location on different sides of plate. But the main problem of the development of such resonators is the suppression of the spurious oscillations which worsen resonant properties of resonators and lead to the strong acoustic coupling between them when they are set on the single plate. The way of the solving such problem is presented in this work.

#### Statement of Contribution/Methods

The matrix of two resonators which were placed on the plate of X-cut lithium niobate with thickness 0.5 mm was investigated. The electrodes have the rectangular shape with dimensions of 5×10 mm and gap between them of 2 mm. The lateral electric field of each resonator was directed along crystallographic axis Y. For the suppression of spurious oscillations the sources of which were mainly Lamb waves the space around each resonator was covered by special absorbing layer with thickness of 0.2 mm. The electrodes were partly also covered by absorbing layer. Each resonator was connected to the meter of S parameters E5071C (Agilent). We measured the frequency dependencies of parameters S11 and S22 of each resonator which allowed to determine the frequency dependencies of the real and imaginary parts of electrical impedance/admittance of each resonator and to find the frequencies and Q-factors of series and parallel resonances. Then we have measured the frequency dependency of parameter S12, which characterize the degree of the acoustic coupling between resonators.

#### Results/Discussion

The measurements have shown that the stable resonances occur on the longitudinal acoustic wave propagating along axis X in the space between electrodes. The frequencies of series and parallel resonances practically did not depend on the width of absorbing layer on electrodes and were equal 6.47 and 6.56 MHz, respectively. The values of Q-factor depended on pointed layer width and lay in ranges 1000-13000 and 1200-2500, respectively. It was also shown that the maximum value of parameter S12 of order 50 dB corresponds to the frequency of series resonance. It means that the resonators under study are practically uncoupled. So the absorbing coating ensures not only high quality of the resonance of each resonator but also a total their acoustic uncoupling. It is obviously that this way allows making matrix with various numbers of resonators.

The work is supported by the Grants RFBR 12-02-01057, 13-08-00678.

P3B1-4

#### New approach to ultrasonic absorption in subgrain-free Cd<sub>0.2</sub>Hg<sub>0.8</sub>Te crystals

Yaroslav Oliikh<sup>1</sup>, Oleg Oliikh<sup>2</sup>, Igor Lysyuk<sup>1</sup>; <sup>1</sup>Institute of Semiconductor Physics, National Acad. of Sci. of Ukraine, Kyiv, Ukraine, <sup>2</sup>Faculty of Physics, Taras Shevchenko National University of Kyiv, Kyiv, Ukraine

#### Background, Motivation and Objective

The photosensitive CdHgTe crystals remain a material for IR radiation detectors. The acoustically stimulated reconstruction of point defects was found to result changes of photoelectric properties of this material. But the mechanism of the ultrasonic wave and crystal interaction was unknown. This work was aimed at the experimental study of the temperature dependences of the ultrasonic absorption in subgrain-free CdHgTe crystals and at the search of adequate models for the description of the acousto-dislocation interaction.

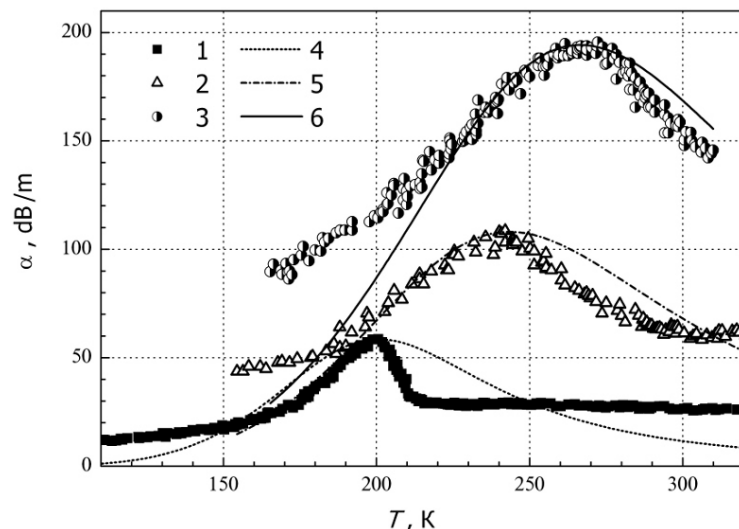
# Statement of Contribution/Methods

The monocrystalline bulk  $\text{Cd}_{0.2}\text{Hg}_{0.8}\text{Te}$  specimens  $10 \times 6 \times 2.5 \text{ mm}^3$  in size and oriented in the directions [100] and [110] were used. The pulse-echo method was used for measuring of the longitudinal bulk acoustic wave absorption coefficient  $\alpha$ .

# Results/Discussion

For the first time the temperature dependence of ultrasonic absorption was studied experimentally in the frequency range  $10 \div 55 \text{ MHz}$  and the temperature interval  $150 \div 300 \text{ K}$ . The maximum value of absorption coefficient was found to increase and to shift toward higher temperatures with grows of the ultrasonic frequency. The obtained data were analyzed within the classical Granato-Lucke model and the dislocation segment length ( $3.5 \times 10^{-6} \text{ m}$ ) and vibrations characteristic frequency ( $9 \times 10^8 \text{ rad/s}$ ) were estimated. However, was shown that the temperature dependence of  $\alpha$  may be explained by using the Brailsford model only. This model considered ultrasonic absorption as a result of the motion of thermally activated dislocation kinks. The characteristic parameters of this model were determined. Namely, the frequency coefficient and kink diffusion activation energy is equal to  $6 \times 10^9 \text{ Hz}$  and the  $0.11 \text{ eV}$  respectively. Also the dislocation density ( $\approx 2 \times 10^{10} \text{ m}^{-2}$ ) was evaluated. This value is close to another one ( $\approx 0.7 \times 10^{10} \text{ m}^{-2}$ ), obtained by the selective etching method. Thus the features of an ultrasonic absorption in  $\text{CdHgTe}$  crystals with high dislocation density deal with motion of dislocation kinks and are described by the Brailsford model sufficiently.

Fig. Experimental (1-3) and calculated within Brailsford model (4-6) temperature dependences of the absorption coefficient for longitudinal ultrasonic waves with frequency 11.2 (1 and 4), 34.8 (2 and 5), and 55.4 (3 and 6) MHz.



P3B1-5

# The influence of electrical boundary conditions close to free surface of piezoelectric lateral electric field excited resonators on their characteristics

Boris Zaitsev<sup>1</sup>, Alexander Shikhabudinov<sup>1</sup>, Andrey Teplykh<sup>1</sup>, Irina Borodina<sup>1</sup>, Iren Kuznetsova<sup>2</sup>; <sup>1</sup>Saratov Branch, Institute of Radio Engineering and Electronics of RAS, Saratov, Russian Federation, <sup>2</sup>Institute of Radio Engineering and Electronics of RAS, Moscow, Russian Federation

# Background, Motivation and Objective

At present a great interest is stimulated by piezoelectric lateral electric field excited resonators. The electrodes of such resonators are set on the same side of piezoelectric plate and electric field is present not only in the plate but outside of one. Therefore the liquid sensors based on such resonators are characterized by higher sensitivity compared to resonators with longitudinal field. It is apparent that change of electrical boundary conditions not far from the free surface of resonator can lead to significant change its characteristics. The present paper is devoted to the experimental investigation of characteristics of series and parallel resonances of lateral electric field excited resonator at approaching to its free surface the dielectric plate with various permittivity and with arbitrary surface conductance.

# Statement of Contribution/Methods

We investigated the piezoelectric lateral electric field excited resonator based on the plate of lithium niobate of X-cut with thickness of 0.5 mm. Two aluminum electrodes of rectangular form with dimensions  $5 \times 10 \text{ mm}$  and with gap between them of 2 mm were deposited on one side of the plate. For suppression of spurious Lamb waves the area around resonator and part of electrodes were covered by the special absorbing layer with thickness of 0.2 mm. The dielectric plate was placed nearby the free surface of resonator and the gap between the plate and resonator could be changed with the help of special micrometer device. We measured the frequency dependencies of real and imaginary parts of electrical impedance/admittance of such resonator by means of LCR meter. We determined the dependencies of resonant frequency and Q-factor on the value of the pointed gap for series and parallel resonances at various values of plate permittivity and surface conductance of plate surface.

# Results/Discussion

Experiments have shown that the frequency of the parallel resonance increases with the increase of the gap between resonator and plate and achieves saturation. At that if the surface conductance is equal zero the range of the change in frequency increases with the increase of permittivity. For example, for the plate of alumina the frequency of parallel resonance is unambiguously determined by the value of gap in the range 0-2.5 mm. With increasing the surface conductance of the layer on the plate surface this range decreases and for well conducting layer is equal 0-0.3 mm. The frequency of the series resonance does not depend on value of gap but is determined by the temperature. So these results show the possibility of the development of the displacement controller with temperature compensation for monitoring of the deformations and crack opening of various constructions and also for noncontact measuring the surface conductance of thin layers.

The work is supported by the Grants RFBR 12-02-01057 ÷ 13-08-00678.



P3B1-6

**A Calculation and Validation of Electrical Resistance of Quartz Crystal Resonators with Structural Viscosity**

Ji Wang<sup>1</sup>, Hui Chen<sup>1</sup>, Julian Shen<sup>2</sup>, Shi-Yung Pao<sup>2</sup>, Min-Chiang Chao<sup>2</sup>, Tingfeng Ma<sup>1</sup>, Jianke Du<sup>1</sup>; <sup>1</sup>Piezoelectric Device Laboratory, Ningbo University, Ningbo, Zhejiang, China, People's Republic of; <sup>2</sup>TXC (Ningbo) Corporation, Beilun, Ningbo, Zhejiang, China, People's Republic of

**Background, Motivation and Objective**

Among many important parameters of a resonator, what we can obtain with the linear theory of vibrations of piezoelectric plates are actually limited and almost irrelevant to the key variables we are more concerned about because the electrical resistance and quality factor, two key parameters in the performance and specifications, cannot be determined without considering the viscosity of resonators. The inclusion of viscosity as energy dissipation mechanism requires analysis of high frequency vibrations with complex coefficients and solutions. Our efforts on estimating electrical resistance with material viscosity started with the inclusion of viscosity of quartz crystal, but found the effect is actually negligible.

**Statement of Contribution/Methods**

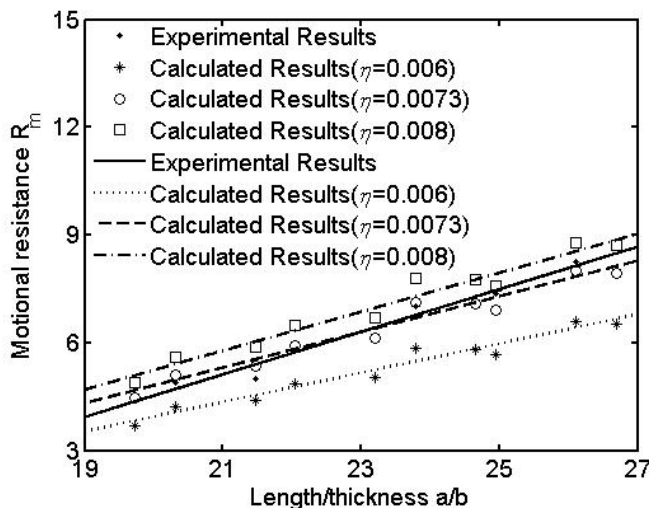
By examining the structure of a typical quartz crystal resonator, it is reasonable to assume that major viscosity is from the electrodes and fabrication process, because it is the most important addition to pure quartz crystal. Of course, we also expect some contributions from mountings particularly if it is not ideally designed. As an alternative attempt, we inserted an equivalent viscosity  $\eta$  in the elastic constants of quartz crystal under electroded area in the form of

$$C_{pq} = c_{pq} + i\eta, p, q = 1, 2, 3, 4, 5, 6,$$

to have complex elastic constants and  $c_{pq}$  are elastic constants of quartz crystal. Then we carry out the analysis of vibrations with couplings of flexural, thickness-shear, and face-shear modes for solutions of frequency and displacements as complex variables. The electrical properties of the resonator are calculated with the procedure shown in an earlier study.

**Results/Discussion**

With our formulation of electrical resistance, we obtained the relation between electrical resistance and resonator properties such as the length/thickness as shown below with assumed equivalent viscosity. Then through controlled measurements of test samples prepared for this study, we made the comparison of calculated and measured resistances. It is clear that with these samples, the calculated resistance followed the trend of actual measurement. For a detailed comparison, we use a series of equivalent viscosity for optimal fit to the measurement. We found that with  $\eta = 0.0073$  we obtained a better prediction of resistance.



P3B1-7

**Reflection of elastic waves from a randomly rough surface**

Alexei Maznev<sup>1</sup>; <sup>1</sup>Department of Chemistry, MIT, Cambridge, USA

**Background, Motivation and Objective**

Boundary scattering of phonons has a profound effect on thermal transport in nanostructures. The model of perfectly diffuse scattering proposed by Casimir is widely used to analyze thermal conductivity in thin films and nanowires. However, surfaces tend to become specular for long wavelengths or at grazing incidence angles, and the specularity parameter is often invoked to explain discrepancies between the diffuse scattering model and the experimental data. Despite extensive literature on wave scattering from rough surfaces, a comprehensive analysis of phonon scattering by a randomly rough surface appears to be still lacking. Researches typically rely on a simple analytic formula, often ascribed to Ziman, that relates specularity to roughness. In this report, we will show that Ziman's equation is only valid in the Kirchhoff approximation that assumes the correlation length of surface roughness to be much greater than the acoustic wavelength. Furthermore, we will present a perturbation analysis of acoustic wave scattering by a randomly rough surface of an isotropic elastic half-space that accounts for scattering into bulk transverse and longitudinal waves as well as into Rayleigh surface waves.

**Statement of Contribution/Methods**

A perturbation approach (see F. Gilbert and L. Knopoff, J. Geophys. Res. 65, 3437 (1960)) is used to analyze scattering of longitudinal and transverse acoustic waves normally incident on a weakly rough surface. The total power of diffusely scattered waves is calculated using surface Green's functions of an isotropic elastic half-space. The method naturally separates the contributions of bulk waves and Rayleigh surface waves. Limiting cases of large and small roughness correlation length are analyzed analytically, while the general case results are obtained numerically.

**Results/Discussion**

In the limiting case when the correlation length is much greater than the acoustic wavelength, diffusely scattered power (for an incident power of unity) is given by  $4\eta^2 k^2$ , where  $\eta$  is the RMS roughness and  $k$  is the acoustic wavenumber, which is in agreement with the well-known Kirchhoff approximation result. In the opposite limiting case of small correlation lengths, the scattered power is found to be proportional to  $\eta^4 k^4 L^2$ , where  $L$  is the correlation length, with the fourth power dependence on frequency, as expected for

deeply sub-wavelength scatterers. Numerical calculations of the scattered power vs.  $L$  for a Gaussian correlation function of surface roughness connect these limiting cases and reveal a maximum of the scattered power at an intermediate  $L$  value. The results indicate that analyzing phonon scattering from rough surfaces with the Kirchhoff approximation formula is a reasonable approach at  $kL > 1$  but becomes inadequate at small correlation lengths.

P3B1-8

## The influence of uniaxial pressure on the elastic waves propagation in piezoelectric layered structures langasite/fused silica

Sergei Burkov<sup>1</sup>, Olga Zolotova<sup>2</sup>, Pavel Turchin<sup>1,3</sup>; <sup>1</sup>Condensed Matter Physics Department, Siberian Federal University, Krasnoyarsk, Russian Federation, <sup>2</sup>Siberian State Aerospace University, Krasnoyarsk, Russian Federation, <sup>3</sup>Kirensky Institute of Physics, Krasnoyarsk, Russian Federation

### Background, Motivation and Objective

Investigation of the influence of external static fields, especially the external uniaxial stress on elastic waves characteristics in crystals, has recently attracted the attention of developers in connection with the expansion of the application of acousto-electronic devices. For example, changes in the crystal material properties under the influence of a uniform mechanical pressure were used to stabilize the resonator frequency, in particular for temperature compensating the resonator frequency drift on the basis of quartz and langasite crystals. In this paper we investigate the dispersion characteristics of elastic waves under static mechanical stresses in structure layer the crystal langasite on the substrate fused silica. A comparative analysis of the effect of static deformation on the piezoelectric layer from the substrate and under effect of mechanical stress to the layer provides.

### Statement of Contribution/Methods

The study is based on a previously developed theory of elastic waves propagation in piezoelectric crystals under finite static actions. The motion equations and boundary conditions under the influence of external mechanical pressure recorded to analyze the dispersion characteristics of elastic waves.

### Results/Discussion

Based on the equations describing the elastic waves propagation in a layered piezoelectric structure, were calculated the dispersion characteristics of the modes of the elastic Rayleigh and Love waves (phase velocity, electromechanical coupling coefficient, coefficients controllability) layered structure "La<sub>3</sub>Ga<sub>5</sub>SiO<sub>14</sub> / fused silica" in different variants of the application of uniaxial mechanical pressure. The analysis of changes in the dispersion characteristics of elastic waves due to the lower effective symmetry of the piezoelectric structure and modifying its effective material constants was performed. Cases of static deformation of the piezoelectric layer when pressure is applied to the substrate as well as application of mechanical impact to the layer itself are considered. It is noted that the control coefficients of the elastic waves phase velocities, depending on the type of impact may vary by more than an order. The results may be useful in the development of controlled acousto-electronic SAW devices.

P3B1-9

## Comparative Study of Lithium Niobate Crystal Cuts for use as High Voltage Acoustic Wave Sensors

Nishant Patel<sup>1,2</sup>, Darren Branch<sup>1</sup>, Edl Schamiloglu<sup>2</sup>, Stefan Cular<sup>1</sup>; <sup>1</sup>Sandia National Laboratories, USA, <sup>2</sup>University of New Mexico, USA

### Background, Motivation and Objective

Though measuring high voltages (HV) in excess of 10 kV is routinely performed using a voltage divider connected to a voltmeter or digitizer, the divider introduces significant loading on the voltage source, often resulting in measurement errors. In contrast, piezoelectric approaches offer distinct advantages for HV measurements compared to voltage dividers due to their high electric field breakdown voltage, wide frequency bandwidth, small form factor, and error reduction.

### Statement of Contribution/Methods

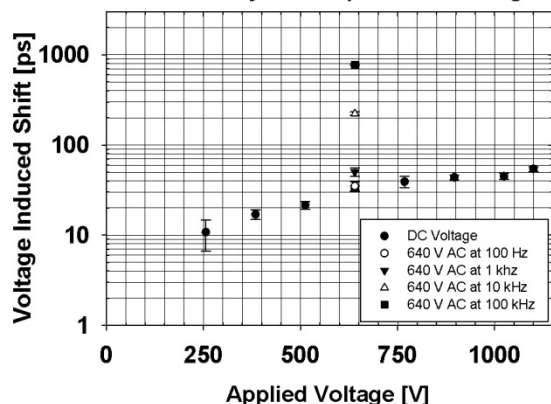
Acoustic waves were propagated through two crystal orientations (X-cut and 36° Y-cut) of LiNbO<sub>3</sub> (Lithium Niobate) as a method to measure high voltages directly. The wave propagation modes were computed for both cuts and measured to determine their voltage responses. The propagation delay time of an acoustic wave traveling in the crystal was used to measure the applied voltage. The acoustic wave propagation time was recorded using a time interval counter and digital oscilloscope.

### Results/Discussion

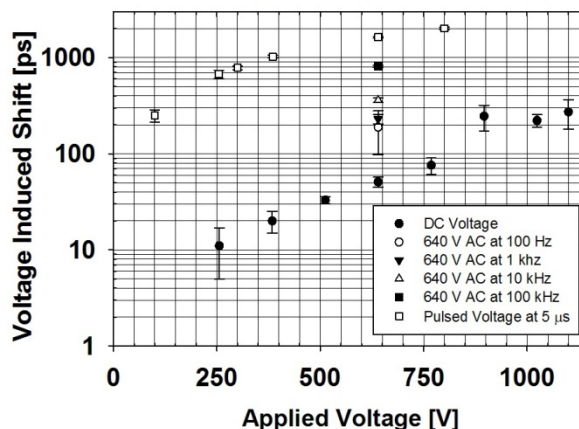
X-cut LiNbO<sub>3</sub> results show the propagation time scale quadratically with DC and AC voltages. The measured shift from DC voltages was 10-270 ps, and 190-810 ps for AC voltage at 640 V up to 100 kHz. For 5  $\mu$ s single pulses from 100-800 V, a shift of 250 ps-2 ns was observed and the response scaled linearly with voltage.

36°-Y cut LiNbO<sub>3</sub> results show the propagation time scaled linearly for DC voltages and quadratically for AC voltages using the same test conditions mentioned above. The measured shift from DC voltages was 11-54 ps and 35-775 ps for AC voltages. The differences seen between the two cuts suggest that frequency variation and the crystal's mode propagation affect the response to applied voltage. This work describes preliminary findings for the development of a high voltage sensor.

36° Y Cut Crystal Response vs. Voltage



0° X Cut Crystal Response vs. Voltage



## P3B2 - General Physical Acoustics 2

Salon C

Friday, September 5, 2014, 8:00 am - 5:00 pm

Chair: **Mihir Patel**  
Schlumberger-Doll Research,

P3B2-1

### Ultrasonic studies of onion-like carbons/polydimethylsiloxane composites

Vytautas Samulionis<sup>1</sup>, Jan Macutkevicius<sup>1</sup>, Juras Banys<sup>1</sup>, Jaroslavas Belovickis<sup>1</sup>, Olga Shenderova<sup>2</sup>; <sup>1</sup>Physics Faculty, Vilnius University, Vilnius, Lithuania, <sup>2</sup>International Technology Center, USA

#### Background, Motivation and Objective

The integration of nanoparticles into a polymer matrix allows both properties from nanoparticles material and polymer to be combined, thus resulting in advanced polymer nanocomposites. In particular, additional nanoscale fillers such as carbon nanotubes or onion-like carbons, can be used to reinforce polymer matrices. Composite materials made of polymers with functional nanofillers can become a perspective alternative for conventionally used materials in industry and science. Ultrasonic waves as non-destructive testing technique is usually used for determination of elastic properties of polymers and polymer composites [1]. This method allows to obtain information about vibrating particles of a media and how it is influenced by addition of another material in the host lattice of polymer. Ultrasonic spectroscopy allows to observe and evaluate relaxation processes that govern their ultrasonic behaviour and to depict variation of these processes because of the change of the nanofiller concentration.

#### Statement of Contribution/Methods

In this contribution we present the temperature measurements of longitudinal ultrasonic velocity and attenuation in polydimethylsiloxane (PDMS) polymer composites with onion-like carbons (OLCs). The temperature dependencies of longitudinal ultrasonic velocity and attenuation, of these PDMS-OLS nanocomposites have been studied in wide temperature range including glass transitions. Ultrasonic measurements were carried out using automatic computer controlled pulse-echo ultrasonic system. The system have large dynamic range and large input ultrasonic power, therefore the large ultrasonic attenuation values could be measured.

#### Results/Discussion

In investigated PDMS-OLS composites ultrasonic studies revealed large ultrasonic attenuation maxima - of the order of  $\alpha \approx 20 - 25 \text{ cm}^{-1}$  at 10 MHz frequency - which appeared above the glass transition temperature  $T_g \approx 150 \text{ K}$  of the PDMS polymer matrix. It was shown that the shape and position of these attenuation peaks was influenced by the presence of OLSs nanoparticles similarly to our former observations in polyurea/inorganic  $\text{MoS}_2$  nanotubes [2]. The increase of ultrasonic velocity because of reinforcement of composites also was observed. The significant increase of ultrasonic attenuation with OLS concentration was observed at room temperature and such behavior can be attributed to ultrasonic - OLS interaction in polymer matrix.

*Acknowledgement:* This research is funded by the European Social Fund under the Global Grant measure.

[1] V. Samulionis, J. Banys, A. Sanchez-Ferrer and R. Mezzenga, Ultrasonic Characterization of Dynamic Elastic Properties of Polymer Composites with Inorganic Nanotubes, *Sensors & Transducers* **12**, 66 (2011).

[2] V. Samulionis, S. Svirkas, J. Banys, A. Sanchez-Ferrer, S. Jegu Chin and T. McNally, Ultrasonic properties of composites of polymers and inorganic nanoparticles. *Phys. Status Solidi A* **210**, 2348 (2013).

P3B2-2

### Acoustics of a finite-aperture Laguerre-Gaussian vortex beam

Farid G. Mitri<sup>1</sup>; <sup>1</sup>Chevron Area 52 Technology, Santa Fe, New Mexico, USA

#### Background, Motivation and Objective

Acoustical vortex beams are potentially useful for transporting and rotating particles and larger objects in applications involving acoustical tweezers, container-less processing, acoustic levitation and other areas. Numerical predictions, modelling the interaction of vortex beams with a particle, are necessary for understanding the underlying physics and the induced phenomena, such as the scattering, radiation force and radiation torque that occur during this process. Previous works considered the cases of infinite vortex beams, however, considering the fact that practically every acoustic transducer produces a beam of finite geometry, it is necessary to devise a method which enables the modelling of the incident pressure field taking into account the diffraction effects from the finite source. The objective is to provide partial-wave series expansions for the pressure field of a finite Laguerre-Gaussian vortex beam (chosen as an example) in spherical coordinates, which can be used to model the arbitrary scattering, radiation force and torque on a sphere placed randomly in the beam's field.

#### Statement of Contribution/Methods

The method is based on the Rayleigh-Sommerfeld surface integral as well as the addition theorem for the Legendre and spherical wave functions. With this method, partial-wave series expansions are derived for the incident and scattered pressure fields from a sphere, which makes it possible to rigorously model the scattering, radiation force and torque on a sphere placed arbitrarily in the beam's path. Numerical simulations illustrate the analysis for the scattering, radiation force and torque on a viscous sphere with emphasis on the dimensionless frequency, the beam waist and the order (or topological charge) of the beam.

#### Results/Discussion

The applications of the proposed method illustrated here concern a viscous sphere placed arbitrarily in the field of a Laguerre-Gaussian beam of arbitrary integer order  $m$ . The resulting predictions for the acoustic scattering, radiation force and radiation torque show the possibility to trap, pull back and rotate a sphere in the field of an acoustic Laguerre-Gaussian beam. The generalized equations involving the scattering asymmetry and valid in non-viscous fluids, are so general that they do not require the object to be a sphere nor to be centered on the axis of wave propagation of the incident beam.

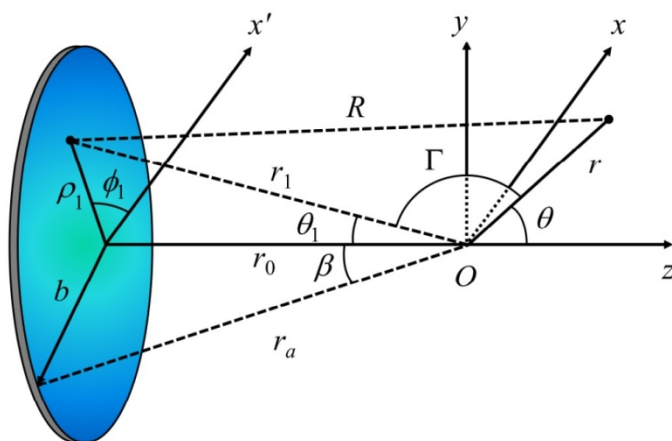


Figure 1 Geometry of the problem used in the derivation of the incident acoustic fields of finite vortex beams.

P3B2-3

### Density and viscosity of liquids determination using an Inverse Method for Love wave propagation

Piotr Kielczyński<sup>1</sup>, Marek Szalewski<sup>1</sup>, Andrzej Balcerzak<sup>1</sup>, Krzysztof Wieja<sup>1</sup>,<sup>1</sup>Institute of Fundamental Technological Research, Polish Academy of Sciences, Warsaw, Poland

#### Background, Motivation and Objective

Determination of the density and viscosity of liquids is very important in monitoring the technological parameters of liquids during the course of technological processes in the chemical, food and petroleum industry as well as in geophysics. Simultaneous on-line measurements of density and viscosity of process liquids are necessary for quality control and for productivity enhancing. Traditional mechanical methods of such measurements are cumbersome and time consuming. Therefore, due to their inherent limitations, these methods cannot be applied on-line to determine the density and viscosity of process liquids. To date, liquid viscosity and density were measured simultaneously using ultrasonic dual element sensors or special sensors. These sensors are highly complex and are applicable only in laboratory conditions.

#### Statement of Contribution/Methods

Love waves sensors are ideally suited to investigate the physical parameters of liquids. In this paper, an inverse method (established by the authors) that allows to determine simultaneously the density and viscosity of liquids is presented. This method employs the measured dispersion curves of phase velocity and attenuation of Love waves (from 1 to 5 MHz) that propagate in a layered elastic wave waveguide covered on its surface by a viscous liquid. The inverse problem was formulated and solved as a minimization problem. The objective function that depends on material parameters of the waveguide, the frequency, experimental data (phase velocity and attenuation) and unknown liquid density and viscosity, has been constructed. To minimize the objective function, Nelder-Mead optimization procedure was employed. The proposed Love wave sensor for measuring liquid density and viscosity is easy to fabricate, robust and can operate in harsh environment.

#### Results/Discussion

Numerical calculations were performed for the following waveguide structure: Cu surface layer on steel substrate, loaded on its surface with a viscous (Newtonian) liquid. Minimization of the considered objective function enabled determination of optimum values of liquid density and viscosity simultaneously. These optimum values of liquid density and viscosity constitute the solution of the inverse problem. Inverse problem solution enables simultaneous determination of both the density and viscosity of a viscous liquid with good accuracy (of the order of 5%). Inverse method, developed by the authors, is superior in relation to the existing so far ultrasonic methods for the simultaneous determination of liquid density and viscosity. Our method is relatively simple and uses only one miniaturized sensing element. The results obtained are novel and original and can be of high relevance in industrial applications, for monitoring parameters of liquids during the course of technological processes.

P3B2-4

### Ultrasonic evaluation of thermodynamic parameters of liquids under high pressure

Piotr Kielczyński<sup>1</sup>, Marek Szalewski<sup>1</sup>, Andrzej Balcerzak<sup>1</sup>, Krzysztof Wieja<sup>1</sup>, Aleksander Rostocki<sup>2</sup>, Ryszard Siegoczyński<sup>2</sup>,<sup>1</sup>Institute of Fundamental Technological Research, Polish Academy of Sciences, Warsaw, Poland, <sup>2</sup>Institute of Physics, Warsaw University of Technology, Poland

#### Background, Motivation and Objective

In many technological processes (e.g. in the chemical, petrochemical, food and plastics industry) processed liquids are subjected to high pressures and temperatures. Therefore, knowledge of their thermodynamic properties is essential for the understanding, design and control of the technological processes. Knowledge of high-pressure thermodynamic properties of fuels and biofuels is also indispensable due to the increasing operating pressures in modern fuel injection systems. Direct evaluation of thermodynamic parameters of liquids under high pressure, using conventional methods, is very difficult. Therefore, these methods are useless in industrial conditions, particularly in on-line control of the technological parameters of liquids. Ultrasonic methods (e.g., sound speed measurements) due to their simplicity and accuracy are suitable for this purpose.

#### Statement of Contribution/Methods

The sound velocity is closely related with numerous thermodynamic properties of liquids. In this work ultrasonic velocity and density measurements (performed by the authors) in diacylglycerol (DAG) oil over a range of pressures and temperatures have been employed. DAG oil is very ubiquitous fat in foodstuffs. The time-of-flight of ultrasonic wave pulses was measured using cross-correlation method. The values of the density of DAG oil under high pressure were evaluated by measuring changes in the volume of the pressurized DAG oil sample. On the basis of experimental results (the sound velocity and liquid density versus pressure and temperature) the thermal expansion coefficient, specific heat capacity at constant pressure, isothermal and adiabatic compressibility were calculated. Measurements were performed in the pressure range from atmospheric pressure up to 300 MPa and for temperatures from 20 °C to 50 °C, ( $f = 5$  MHz).

**Results/Discussion**

The results of this work confirm that a number of important thermodynamic parameters of the liquid can be established from measurement of the sound velocity and density isotherms as a function of pressure. These results can be utilized in numerical modeling and optimization of new methods of high-pressure food processing and conservation. Presented in the paper ultrasonic method can also be applied in the petroleum industry in designing efficient oil production processes. Moreover, it can provide important information for designers to model the fuel injection systems for diesel engines. Sound velocity and density measurements can be applied for evaluation of high-pressure thermodynamic properties of various other liquids, such as: lubricants, drilling fluids or polymers. The results obtained are novel and original. To date, similar measurements of the thermodynamic properties of liquids have not been performed in such a wide range of pressures.

**P3B2-5****Quantifying Errors in the Numerical Simulation of Transcranial Ultrasound**

James Robertson<sup>1</sup>, Ben Cox<sup>1</sup>, Bradley Treeby<sup>1</sup>; <sup>1</sup>Medical Physics and Bioengineering, University College London, London, United Kingdom

**Background, Motivation and Objective**

Recently there has been a renewed interest in the transcranial transmission of ultrasound for HIFU ablation, and for novel therapies such as opening the blood-brain barrier and neurostimulation. To correct for aberrations caused by the skull, multi-element arrays are often used in conjunction with a numerical model of ultrasound propagation to select optimal values for the amplitude and phase of each transducer element. In the large-scale, highly heterogeneous simulations required, numerical errors can accumulate which may significantly affect the accuracy of the delivered therapy. The objective of this work was to investigate the different sources of error and quantify their practical significance and relative impact, as well as the suitability of different numerical schemes for these simulations.

**Statement of Contribution/Methods**

A taxonomy of errors arising from transcranial ultrasound simulations was established. Those caused by the discretisation of the simulated domain were then considered in detail. These were numerically evaluated using a 2-4 finite difference time domain (FDTD) model, and leapfrog and k-space corrected pseudospectral time domain (PSTD) models. The errors were examined at different numbers of grid points per wavelength (PPW), and criteria for minimising the errors were established.

Four sources of error were considered: numerical dispersion, reflection errors, staircasing, and the perfectly matched layer (PML). Dispersion error was measured by propagating broadband pulses through homogeneous media, and was quantified for bone and soft tissue per unit distance. Reflection error due to the representation of impedance step-changes within numerical schemes was isolated using normally incident plane waves, while angled-plane and spherical waves showed the effect of discretisation of curved and angled surfaces. Finally, the response of a split-field PML for different incidence angles was examined.

**Results/Discussion**

For a CFL of 0.05, to restrict position errors due to dispersion to < 1mm following 25cm propagation, the FDTD model required 10 PPW, while the PSTD models required only 3 PPW. The k-space corrected model showed the best performance for large simulations, and increasing the CFL increased dispersion due to time-stepping in all models.

For a normally incident plane wave, to restrict reflection-transmission errors to < 3%, the FDTD model required 6 PPW, while the PSTD models required 5 PPW. Error was shown to be independent of time step. The effects of staircasing and angled reflection were also quantified, and a new model to explain the impact of step changes for spectral models was proposed. For a PML of 10 grid points reflected waves were reduced by > 60 dB.

Numerical dispersion is considered the most significant source of error, particularly when considering the path lengths traversed in transcranial ultrasound. The established criteria can be used to quantify and minimise the different numerical errors.

**P3B2-6****Optic and Acoustic detection of laser-induced optical breakdown in DDFP**

Yi FENG<sup>1</sup>, Dui QIN<sup>1</sup>, Chenxiang MA<sup>1</sup>, Yujin ZONG<sup>1</sup>, Mingxi WAN<sup>1</sup>; <sup>1</sup>The Key Laboratory of Biomedical Information Engineering of Ministry of Education, China, People's Republic of

**Background, Motivation and Objective**

Laser induced optical breakdown (LIOB) in water has been investigated widely. Several patterns of laser induced cavitation bubble are involved. However, LIOB in water needs relatively high laser intensity and extremely short pulse length in femtosecond. In the study, low intensity laser was utilized in the LIOB in dodecafluoropentane (DDFP), and then the optic and acoustic detection were performed to reveal the characteristics of bubble dynamics and acoustic signal.

**Statement of Contribution/Methods**

LIOB was realized in the confocal system of laser, acoustic detection and microscopic imaging. A single pulse laser of 521nm-wavelength, with a 5ns pulse width and average power of 50  $\mu$ J, is employed in the experiment after being focused on 200  $\mu$ m cellulose tube by 40 $\times$ , 0.8 numerical aperture objective lens. High speed camera was used to acquire the images during LIOB, bubble formation and collapse. Passive acoustic detection (PCD) was performed by 10 MHz transducer connected via an amplifier to an NI card data acquisition system. The spectrum analysis and time-frequency analysis were performed to show the characteristics of LIOB in DDFP.

**Results/Discussion**

Comparing to LIOB in water, focused laser at lower intensity could also induce optical breakdown in DDFP liquid. Three patterns were observed. In the relatively low temperature (less than 18°C), the LIOB bubble grew rapidly in less than tens of microseconds, and then shrank relative slowly until collapsed gently for about several milliseconds. In the relatively high temperature (normally higher than 18°C), the LIOB bubble grew slowly without shrinking process, until the volume reached to its maximum and didn't grow anymore. In the cases above, temperature may be the reason causes the difference. In some cases (normally in temperature higher than 24°C), multi LIOB bubbles were produced, and the multi bubbles shrank and collapsed gently with different life time corresponding to their maximum radius. In acoustic detection, significant RF signal were recorded by PCD when LIOB occurred. The main peak corresponding to the shock wave from the rapid expansion of plasma to form LIOB had the amplitude of 0.64 V. Its spectrum analysis and time-frequency analysis revealed LIOB happened in the duration of 3 $\mu$ s, and the spectrum of LIOB signal was mainly distributed between 0-12 MHz, with peaks near 2 MHz, 4 MHz, 7 MHz respectively. These characteristics of LIOB bubble in DDFP gives information for analyzing LIOB, suggesting acoustically monitored LIOB has potential as an important tool in diagnosis and treatment *in vivo*.



P3B2-7

## Numerical Study of the Acoustic Streaming and Mean Excess Pressure Produced in a Small Gap between a Vibrating Surface and a Thin Boundary

Arturo Santillan<sup>1</sup>; <sup>1</sup>Department of Technology and Innovation, University of Southern Denmark, Odense M, Denmark

### Background, Motivation and Objective

The development of high-intensity ultrasonic sources has widely increased the investigation of nonlinear ultrasonic phenomena such as acoustic streaming and radiation pressure. As a consequence, new potential applications of ultrasonic waves have been studied. Of particular interest is the use of acoustic streaming to pump gases or liquids without the need of rotating elements.

Acoustic streaming appears mainly as a result of the interaction of sound waves with boundaries. It has been reported in the literature that the net movement of fluid can be increased if the space between a rigid wall and a vibrating surface is made very small.

In this paper, a circular plane piston located horizontally and immersed in water is considered. A rigid pipe is assumed to be placed vertically with its lower end very closed to the surface of the vibrating surface. The general objective of the work has been to investigate the acoustic streaming produced in the gap between the piston and the lower end of the pipe, and to study the associated spatial distribution of the mean excess pressure in the fluid.

### Statement of Contribution/Methods

The numerical simulations are implemented by using the classical finite-difference time-domain (FDTD) algorithm. To simplify the problem, heat conduction and temperature effects are not taken into account. In addition, an axial symmetric configuration is considered, for which the numerical method is formulated using cylindrical coordinates. Non-linear terms of the fundamental equations of acoustics are included in the numerical algorithm.

The work contributes to further understand nonlinear effects produced by acoustic waves of high intensity and the associated physical mechanisms. In this particular case, the acoustic streaming and mean excess pressure.

### Results/Discussion

It is shown that the FDTD method can be used to simulate the evolution in time of the studied phenomena. The obtained values of the acoustic variables include the time-independent quantities. As a result, the time average of the particle velocity gives the acoustic streaming, and the time average of the calculated sound pressure gives the mean Eulerian excess pressure. In addition, the method provides a clear picture of the physical mechanisms involved.

The effects of the size of the piston, the amplitude of its oscillations, and the inner radius of the cylinder on the net flow of mass and the spatial distribution of the mean excess pressure are studied.

P3B2-8

## Analytical theory of thickness acoustic resonances in liquid drop on solid substrate

Anna V. Begar<sup>1</sup>, Ilya A. Nedospasov<sup>1</sup>, Vladimir G. Mozhaev<sup>1</sup>; <sup>1</sup>Faculty of Physics, Lomonosov Moscow State University, Moscow, Russian Federation

### Background, Motivation and Objective

The knowledge of acoustic resonances in a liquid drop lying on a solid substrate is important for the purposes of drop weighting and liquid parameter determination, as well as for understanding complex processes in laboratories-on-chips with acoustic drive. Until now, the measured drop resonances have been interpreted using only numerical modeling for the real drop geometry or primitive formulae for the resonances of plane-parallel liquid layer. The objectives of this study are to develop an analytical theory of the discussed resonances with account of wave field localization in the vicinity of the drop central axis and to estimate the capillary-nonlinearity effect on the drop resonances.

### Statement of Contribution/Methods

Three different methods are used to construct approximate solutions to the linear problem: (i) the parabolic equation method, (ii) the Wilson approach (1974) popular in the theory of plano-convex crystal resonators (it is modified by us to include into equation of motion an additional term proportional to the drop-thickness gradient), (iii) the spheroidal approximation for the upper part of the drop surface. The effect of nonlinearity is studied using the perturbation theory based on the complex reciprocity relation (Auld, 1973).

### Results/Discussion

It is found that all three mentioned methods give the same formula for the resonance frequencies and the same Hermite-Gaussian and Laguerre-Gaussian eigenmodes if the ratio between the drop thickness and diameter is a small parameter. The exact relation between the surface curvature and the drop profile gives quadratic and cubic nonlinearities. Both of them produce the effect of self-action for the resonant drop vibration. However, the quadratic nonlinearity has an indirect effect which occurs due to double interaction with generation of second harmonic and static component at the intermediate stage. This static component is responsible for a jump-like reconstruction of the drop thickness and shape that produces jumps between adjacent large-amplitude modes of the drop vibration. Thus, the liquid drop on the solid substrate be considered as a nonlinear acoustic analog of laser resonators in which the vibrations move the reflective mirror and change its shape.

P3B2-9

## Improvement of the time-reversal focalization through a multiple scattering medium by using a coherent wave compounding technique

Nicolas Benech<sup>1</sup>, Yamil Abraham<sup>1</sup>, Diego Carrasco<sup>1</sup>, Carlos Negreira<sup>1</sup>; <sup>1</sup>Laboratorio de Acústica Ultrasonora, Instituto de Física, Facultad de Ciencias, Montevideo, Uruguay

### Background, Motivation and Objective

Time-reversal of acoustic waves in a multiple scattering medium can be viewed as a correlation technique. From this point of view, the spatial resolution depends on the correlation length of the scattered field [A. Derode et al, Phys. Rev. E, 64, 036606]. The field is expressed as the sum of the coherent and the incoherent contribution. The spatial correlation of the coherent contribution is infinite and its spatial resolution is poor. On the other side, the spatial correlation of the incoherent contribution is of the order of a wavelength. The weight of each contribution to the scattered field depends on the thickness L of the scattering region. If L is greater than some times the elastic mean free path, the field is dominated by the incoherent contribution. If L is much lower than that, the field is dominated by the coherent contribution. In intermediate situations, the spatial resolution will be a combination of both terms giving an intermediate spatial resolution. Here, we use a combination of time-reversal and coherent wave compounding [G. Montaldo et al, IEEE Trans. Ultras. Ferroelec. Freq. Control, 56, 489-506], to improve the spatial resolution in the last condition considered.

### Statement of Contribution/Methods

The coherent wave compounding consists in replace the standard cylindrical delay law by illuminating the medium with several plane waves at different angles of emission. The experimental setup is as follows. A small transducer (2,25 MHz) emits a sound pulse that crosses a multiple scattering medium of randomly positioned parallel copper rods set perpendicular to the sound beam. The total depth of the scattering medium is 35 mm and the rod density is 0.14 mm<sup>-2</sup>. The wave is recorded in the opposite side of the scattering medium by a 32 elements, 25 mm length linear array. Each channel acquires a coda signal due to the multiple scattered pulse. A delay law is applied to each channel of the array as

a way to select plane waves coming from a specific direction. Changing the delay law is equivalent to change the incoming direction. We used 15 different reception angles to ensure the incoming directions are independent each other.

### Results/Discussion

When the signal for a particular direction is reemitted into the medium by the array, a focal spot is achieved around the position of the small transducer (now acting as a receiver). In the experimental situation considered here, the resolution is broader than the wavelength and side lobes are observed. However, when the signals from all the incoming directions are reemitted into the medium, the spatial resolution achieves values comparable to a larger-depth medium. In addition, the side lobes decrease. The use of plane waves with different angles of emission adds information to the system about different components of the wave vector. This extra information reduces the spatial correlation length compared with a single plane emission. Therefore the compounding technique makes the field behave as "more incoherent".

### P3B2-10

#### High Frequency Scattering Measurements of a Live Single Cell

Changyang Lee<sup>1</sup>, Hayong Jung<sup>1</sup>, Kwok Ho Lam<sup>2</sup>, ChangHan Yoon<sup>1</sup>, K. Kirk Shung<sup>1</sup>; <sup>1</sup>Department of Biomedical Engineering, University of Southern California, USA, <sup>2</sup>Department of Electrical Engineering, The Hong Kong Polytechnic University, Hong Kong

### Background, Motivation and Objective

Micro-particle separation and sorting techniques have been employed in such biomedical applications as cancer diagnosis and study of cell gene expression. Fluorescence Activated Cell Sorter (FACS) using light scattering with flow cytometry has been popular for these applications due to its high throughput and accurate sorting performance. However, FACS is bulky and complicated and needs well trained users for pre-treatment of a sample. MEMS technology has been investigated to overcome these drawbacks. High frequency ultrasound microbeam combined with micro-fluidics channel has been reported as one of alternatives. Its feasibility as a single cell sorter has been demonstrated. This paper reports experimental results from scattering measurements carried out on live single cells at a frequency of 86 MHz. The capability to accurately measure scattering from cells is crucial if ultrasound scattering is to be used as the sensing mechanism as well in a cell sorter. These results show that it is possible to characterize cells, in this case two different live cells, namely leukemia cells (K562 cells) and red blood cells (RBCs), from scattering.

### Statement of Contribution/Methods

A highly focused 86 MHz single element transducer of f-number 0.75 was fabricated for single cell scattering or sensing experiments. The transducer was positioned perpendicular to agar phantom surface at the focal point. K562 cells and RBCs were placed on the top of an agar substrate which has acoustic impedance similar to water in a mixed solution of alsever's solution and phosphate-buffered saline. The experimental schematic is shown in figure 1(a).

### Results/Discussion

A focused transducer was driven with a sinusoidal single cycle signal at the resonance frequency. When a single live cell on the substrate surface was moved to the focus of ultrasound beam, echo signals were collected and analyzed with a microscope and oscilloscope. The integrated backscatter of the two different types of cells and the agar surface is  $-89.39 \pm 2.44$  dB,  $-89.00 \pm 1.19$  dB, and  $-92.32 \pm 1.12$  dB respectively.

These results demonstrate the feasibility of ultrasonic scattering a sensing mechanism in the development of ultrasonic cell sorters.

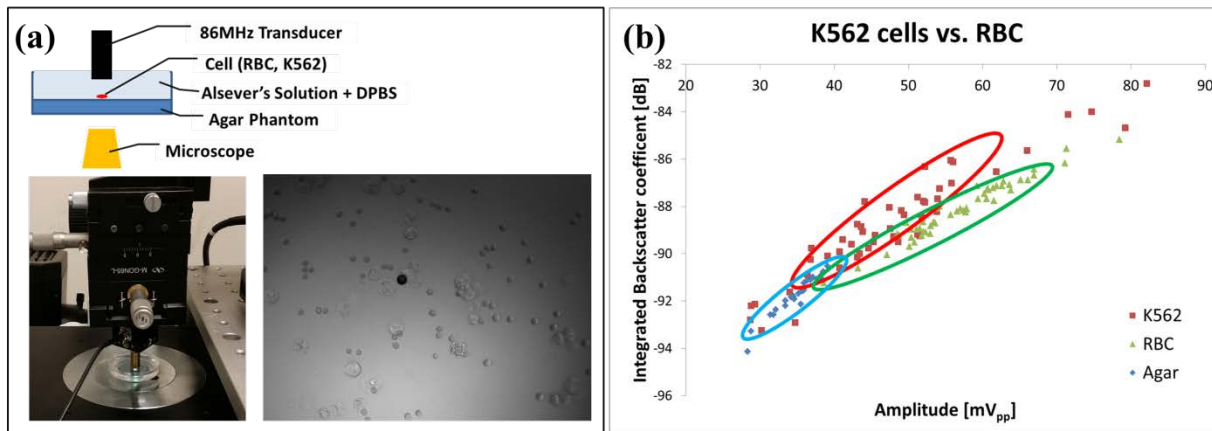


Figure 1. (a) Experimental Schematic (b) Integrated Backscatter coefficient and echo amplitude of K562 and RBCs

## P4B1 - Innovative Device Concepts

Salon C

Friday, September 5, 2014, 8:00 am - 5:00 pm

Chair: **Marc Solal**  
*Triquint Semiconductor*

P4B1-1

### Second-Harmonic Suppression in DART-SFIT devices

Gunter Martin<sup>1</sup>, Eduard Chilla<sup>2</sup>, Hagen Schmidt<sup>1</sup>; <sup>1</sup>IFW Dresden, Germany, <sup>2</sup>Vectron International GmbH, Germany

#### Background, Motivation and Objective

It is known that the 2nd harmonic is suppressed by interdigital solid finger structures. However, it can occur in structures with different finger and/or gap widths. For instance, important SPUDT cell types (DART, EWC) yield large 2nd harmonic levels. In contrast, Hunsinger cell types do not generate 2nd harmonic. The existence of 2nd harmonic reduces the stopband rejection within the stopband above passband. The passband of 2nd harmonic is an especially serious problem because it is located nearer to passband of 1st harmonic than the 3rd harmonic. The goal is to reduce the level of 2nd harmonic in SFIT devices using DART cells by design tools. Of course, the tools can be applied in SPUDT designs as well.

#### Statement of Contribution/Methods

One-track and two-track solutions of DART-SFIT filters are presented. For suppressing 2nd harmonic one-track SFITs are divided into partial SFITs. The gaps between them are widened by a half of one DART cell length and opposite finger polarities of the partial SFITs surrounding the gap considered are adjusted. As a result, the contributions of all partial SFITs superimpose constructively. In contrast, the contributions of partial SFITs to 2nd harmonic are suppressed by destructive interference. The influence of the method on the 2nd harmonic level is studied for partial SFITs serially or connected in parallel. Two-track solutions of SFITs are composed of two sub-SFITs arranged in acoustically parallel tracks. For suppressing 2nd harmonic the sub-SFITs are shifted to each other by a half of minimum DART cell length. To ensure the 2nd harmonic suppression for all DART cell lengths a slight slope of one of sub SFITs is required. Moreover, the sub-SFITs of one SFIT have opposite finger polarities. Additionally, they can be designed including partial SFITs and widened gaps between them corresponding to one-track DART-SFIT filters.

#### Results/Discussion

In the most cases the SFIT devices were analyzed by means of known channel model neglecting diffraction. Some combinations of widened gap numbers of 1st and 2nd SFIT called 2/1, 2/3 and 2/7 gaps were analyzed in the case of one-track SFIT filters. An improved analysis taking diffraction into account was performed as well. Test layouts of the cases no widened gaps, 2/1, 2/3 and 2/7 widened gaps were implemented and S21 was measured. As an experimental result, the combination 2/3 gaps yields the lowest level of 2nd harmonic in agreement to diffraction analysis. We obtain approximately 10 dB additional 2nd harmonic suppression in comparison with the case of no widened gaps. The analysis of comparable two-track solutions according to the channel model yields lower 2nd harmonic levels than the one-track solutions. Admittedly, the two-track designs need larger areas on the wafer for the same bandwidth and the same finger slopes.

P4B1-2

### Improved SAW Slanted Array Compressor Structure for Achieving > 20,000 Time-Bandwidth Product

Pierre Dufile<sup>1</sup>, Clement Valerio<sup>1</sup>, Tom Martin<sup>1</sup>; <sup>1</sup>Phonon Corporation, Simsbury, Connecticut, USA

#### Background, Motivation and Objective

Many of today's radar systems rely on digital processing for pulse compression. The future of SAW pulse compression systems depends on achieving superior performances over all-digital solutions. SAW-based pulse compression systems can consume less power and have higher dynamic range than all-digital systems, properties important for portable and long-range radars.

The future market for SAW dispersive devices depends on development of larger time-bandwidth (BT) product device structures. Currently a BT of 10,000 is achievable, with a goal of achieving > 20,000 in a single SAW device.

#### Statement of Contribution/Methods

The SAW structure which achieves the largest %BW is the Slanted Array Compressor (SAC) on a LiNbO<sub>3</sub> substrate. The structure consists of two slanted aperiodic transducers with balanced microstrip bus bars and refraction-correcting acoustic lenses. It may also include a metallic shield/phase correction region between the two transducers.

By using a different number of strips-per-wavelength for each transducer (eg 3 and 4 strips/ $\lambda$ ) it is possible to increase the spurious-free %BW to greater than 100%. This eliminates the mechanical reflections when 2 strips/ $\lambda$  transducers are used. The acoustic impedances are increased by using series-connected transducer channels.

The new structure eliminates the refraction-correcting acoustic lenses by compensating for refraction in the transducer strip region. This approach simplifies device analysis and reduces the sensitivity of insertion loss to temperature. The metallic shield/phase correction region can also be removed by including a compensated digital exciter in the system.

#### Results/Discussion

Measurements on a dispersive filter having a BT of 15,000 will be presented. Near-ideal performance of 1.8ns 3dB compressed pulse with 30dB close in sidelobes is achieved in a pulse compression system using a compensated digital exciter. The achieved pulse gain through the filter is close to 0dB.

P4B1-3

**140MHz narrowband MEMS filters based on aluminum nitride Lamb wave resonators**Ji Liang<sup>1</sup>, Hongxiang Zhang<sup>1</sup>, Hao Zhang<sup>1</sup>, Daihua Zhang<sup>1</sup>, Wei Pang<sup>1</sup>; <sup>1</sup>Tianjin University, Tianjin, China, People's Republic of**Background, Motivation and Objective**

Recent decades have seen the increased demand for microwave band-pass filters for advanced wireless communication systems. With miniaturized sizes and perfect compatibility with CMOS, aluminum nitride (AlN) Lamb wave resonators (LWRs) are a promising solution for future single-chip multi-band wireless communications. However, so far, LWR filter research has not been fully developed and its poor functionality and large impedance prevent it from being applicable. This work presents the design and fabrication of a 140MHz high-performance ladder-type LWR filter, which is perfectly matched to a 50  $\Omega$  system, demonstrating its great potential for intermediate frequency (IF) band applications.

**Statement of Contribution/Methods**

This work reports the design and fabrication of a LWR narrowband filter compatible to a 50  $\Omega$  system for the first time. According to a guideline for designing LWRs with high figure of merit (FOM), a 140MHz LWR with a pitch of 35  $\mu\text{m}$ , an aperture of 400  $\mu\text{m}$  and 6 interdigital fingers is designed. Consisted of such well functionalized resonators, a 6-stage ladder type filter is achieved. A fabrication process compatible to IC is employed and the filter is tested by a pair of GSG probes. On the basis of the extracted S parameters, an LC network is designed to match the filter to 50  $\Omega$  systems.

**Results/Discussion**

As shown in Fig. 1(a), the MEMS LWR filter occupies an area of only 1500  $\mu\text{m} \times 1150 \mu\text{m}$ , much less than the commercial SAW filters. Connected with an LC network ( $L=112\text{nH}$ ,  $C=8.75\text{pF}$ ), as shown in Fig. 1(b), the final filter shows a return loss exceeding -10dB in the pass band, which means a perfect match to 50  $\Omega$  systems. It roll-offs sharply (with a shape factor of 3.2 at 50dB) and has an insertion loss as low as -4.8 dB and a rejection of -50 dB.

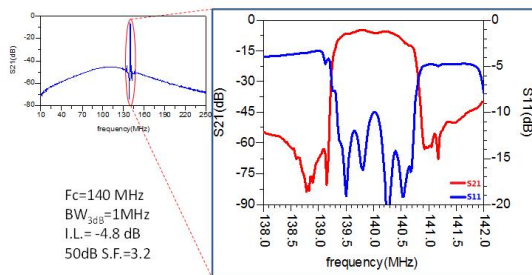


Fig. 2 The measured electrical response of the filter combined with the LC network, matching to 50  $\Omega$  terminations.

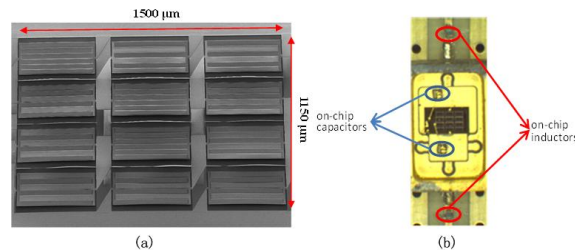


Fig. 1 (a) The SEM image of a 6-stage ladder type LWR filter.  
(b) The micrograph of the filter combined with on-chip LC components

P4B1-4

**Q-enhancement with electrode materials in the FBAR for timing devices**Motoaki Hara<sup>1</sup>, Hiroki Kuwano<sup>1</sup>; <sup>1</sup>Department of Nanomechanics, Tohoku University, Sendai, Japan**Background, Motivation and Objective**

Thin film bulk acoustic resonators (FBAR) are essential for RF systems. It is widely accepted as a key part of duplexers or RF filters. The FBAR also recently draw attention as a timing device such as FBAR-based voltage controlled oscillators (VCOs) or wake-up-circuits for wireless sensor nodes.

For the timing applications, theoretical analysis of  $Q$  is crucial rather than analysis of  $k_{eff}^2$ . It has been reported that  $k_{eff}^2$  is enhanced using electrodes with high acoustic impedance  $Z_a$  and appropriate thickness. This effect is explained as matching of strain distribution for electric field in the piezoelectric film. Similarly, it has been known that  $Q$  factor can be enhanced by the electrode. But, the mechanism was not clear.

**Statement of Contribution/Methods**

Calculation program based on Mason's model was developed in this study (Fig.1 (a)). The  $Q$  is interacted readily by many parameters, such as resonant frequency  $f_r$  or characteristic impedance  $Z_0$ . In our flow,  $f_r$  and  $Z_0$  were kept constant against the conventional FEM simulations. So influences of them were cancelled. We can clearly analyze the mechanism of  $Q$  enhancement with this program.

**Results/Discussion**

Figure 1 (b) shows calculated  $Q$  for various electrodes and attenuation constant  $\alpha$ , which is an imaginary part of a wave number. From these figures, it was grasped that  $\alpha$  must be smaller than a specific value  $\alpha_{th}$  to enhance the  $Q$ . As shown in Table I, the  $\alpha$  has linear relation for nonlinear coefficient  $\eta$  on Hook's law. The threshold  $\eta$  calculated from that equation indicates positive correlation to  $Z_a$ . This trend shows the  $Q$  can be insensitive for the acoustic loss in the electrodes by using high  $Z_a$  electrodes, and is well agreed with previous experimental works reported by other researchers.

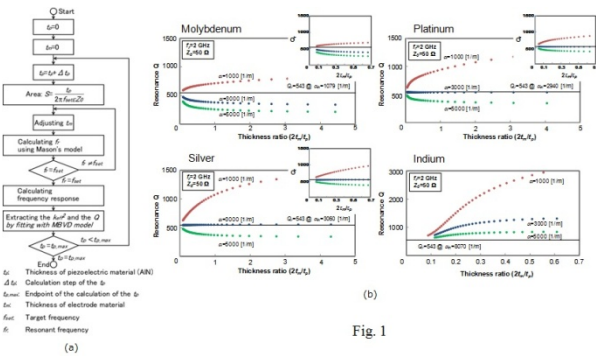


Table I				
Material	$\alpha_{\text{eff}} [1/\text{m}]$	$Z_s [\text{M}\Omega]$	$v_s [\text{m/s}]$	$\eta_s = \frac{1}{4\pi^2} \frac{Z_s^2}{f^2} \alpha_{\text{eff}} [\text{Ns/m}^2]$
Tungsten	2168	100.5	5224	0.075
Platinum	2940	81.4	3662	0.045
Molybdenum	1079	63.4	6660	0.042
Silver	3060	39.2	3741	0.021
Aluminum	1621	17.4	6451	0.015
Indium	8070	10.4	1423	0.022

P4B1-5

Balanced Wideband Fan-Shaped Three-Transducer Saw Filters With Reduced Insertion Loss And Improved Frequency Response

Sergei Doberstein<sup>1</sup>, <sup>1</sup>ONIIP, Omsk, Russian Federation

Background, Motivation and Objective

For obtaining the frequency responses of the SAW filters with the high rectangularity, large fractional bandwidth, low passband ripples and medium insertion loss the tapered (fan-shaped) SPUDTs are used [1]. But sufficiently large insertion losses of 9-10 dB limit the application of these filters.

Statement of Contribution/Methods

This paper presents the new balanced SAW filters using fan-shaped interdigital transducers (IDTs) with the reduced insertion loss, a fractional bandwidth of 10-24% in a frequency range >100 MHz on 128°YX LiNbO<sub>3</sub>. The three-transducer structure containing one input fan-shaped IDT and two output fan-shaped IDTs with the split electrodes is used in these filters. Theoretically the insertion losses of the three-transducer structure are 3 dB under full matching with the loads and the internal reflections from the split electrodes of the IDT are zero. Moreover, a passband ripple of the fan-shaped three-transducer structure is controlled by the inclination angle of the electrodes and inclination of the output IDTs [2]. A shape factor of the frequency response is determined by the number of the electrode pairs in the fan-shaped IDTs with the specified fractional bandwidth. An optimization of the mentioned parameters allows to obtain the improved shape of the filters with a large range of the fractional bandwidths under the low insertion loss and reduced passband ripple in comparison with the known methods [3]. The balanced operation of the filters is made by a symmetrical connection of the input IDT and output IDTs to the loads. Matching filters with the loads is provided by the LC-elements. To simplify matching and obtain a flat shape the frequency response in the passband a series connection of the output fan-shaped IDTs is employed. The withdrawal weighting is used for increasing the selectivity of the filters. The constructional and topological optimization of the SAW filters is provided with a computer simulation using an equivalent circuit model on the base of the admittance and mixed matrices.

Results/Discussion

The 128, 255, 305 MHz samples of the SAW filters have shown 3-dB bandwidth of 14-61 MHz, insertion loss of 5.5-7 dB, passband ripple of less than 2 dB, shape factor of 1.28-1.5, stopband attenuation over 40 dB in a matched system. The samples were housed in the 7x5x1.6 mm and 5x5x1.35 mm SMD packages and could operate in balanced/unbalanced 50-Ω system. Our new balanced wideband fan-shaped three-transducer SAW filters with the reduced insertion loss and improved frequency response will find a wide use as IF filters in the telecommunication equipment.

- [1] L. Solie, Proc. IEEE Ultrasonics Symposium, 1998, pp. 27-37.
- [2] M. Tsukamoto, J. Appl. Phys., V.50, N°5, 1979, pp. 3146-3152.
- [3] S. Doberstein, Proc. 20th EFTF, 2006, pp. 54-57.

P4B1-6

Ultrawide-Band Ladder Filter using SH<sub>0</sub> Mode Plate Wave in LiNbO<sub>3</sub> Plate

Michio Kadota<sup>1</sup>, Shuji Tanaka<sup>2</sup>, Yasuhiro Kuratani<sup>3</sup>, Tetsuya Kimura<sup>4</sup>, <sup>1</sup>Microsystem Integration Center, Tohoku University, Sendai, Miyagi prefecture, Japan, <sup>2</sup>Graduate School of Engineering, Tohoku University, Sendai, Miyagi prefecture, Japan, <sup>3</sup>New Technology & Products Department Group, Murata Manufacturing Co., Ltd., Yasu, Shiga prefecture, Japan, <sup>4</sup>New Technology & Products Department Group, Murata Mfg. Co. Ltd., Yasu, Shiga prefecture, Japan

Background, Motivation and Objective

Currently, cognitive radio using TV white space of digital TV (DTV) channels is receiving a lot of attention. One of the key devices of a cognitive radio system is a tunable filter capable of changing a frequency and a bandwidth. The required filtering is possible by combining an ultrawide-band filter covering all DTV channels (470 to 710 MHz) and a tunable band rejection filters. In this study, the ultrawide-band filter has been developed using a 0-th shear horizontal (SH<sub>0</sub>) mode plate wave in an ultrathin LiNbO<sub>3</sub> plate.

Statement of Contribution/Methods

SH<sub>0</sub> mode plate wave resonators consisting of an interdigital transducer of 6.2 μm and 7.75 μm in wavelength were fabricated on a 0.5 μm thick 30°YX-LiNbO<sub>3</sub> plate supported with a Si wafer, and an ultrawide bandwidth (BW) of 22% was demonstrated. A T-type ladder filter was constructed from the resonators monolithically on the ultrathin LiNbO<sub>3</sub> plate.

Results/Discussion

Fig. 1 shows the frequency characteristic of the ladder filter, which was numerically synthesized from the measured characteristics of the three resonators, as shown in the inset. The filter has an ultrawide bandwidth (20 dB BW of 37%), but the frequency and impedance of the filter slightly mismatch with the DTV band. Also, large ripples are found in the passband. Thus, the frequency and impedance of each resonator were numerically adjusted, and the frequency characteristic shown in Fig. 2 was obtained. A low minimum insertion loss of 0.5 dB and an ultrawide 20 dB BW (40%) of 240 MHz, which fully covers the DTV channels, are confirmed. The feasibility of such an ultrawideband ladder filter with a low insertion loss was proved for the first time. The combination of this wideband filter and a tunable band rejection filters enables a tunable filter with a large rejection of the outside of DTV band.



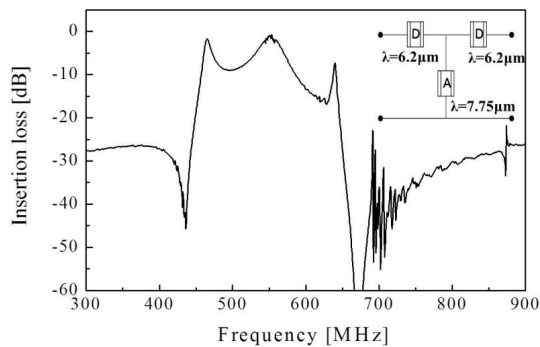


Fig. 1 Frequency characteristic of T-type ladder filter composed three resonators with  $\lambda$  of IDT=6.2 and 7.75  $\mu\text{m}$

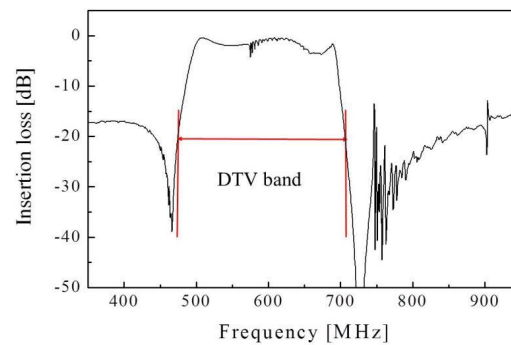


Fig. 2 Frequency characteristic after adjusting resonators' frequencies and impedances

P4B1-7

#### Tunable Transversal and Resonator Filters Using the Variable Velocity Inter-Digital Transducers with the Variable Capacitors

Kazuhiko Yamanouchi<sup>1</sup>, Hiroyuki Odagawa<sup>2</sup>, Ikuya Iwa<sup>2</sup>, <sup>1</sup>Tohoku University, Research Institute of Elect. comm., Japan, <sup>2</sup>Kumamoto National College of Technology, Japan

##### Background, Motivation and Objective

Surface acoustic waves (SAWs) have been applied in various electronic devices, eg., different kinds of filters, stable high frequency oscillators, VCO, real time signal processing devices, convolvers and correlators used in spread spectrum communication systems. Especially, SAW devices are the key devices for the mobile communication systems. In order to obtain the high performance of Surface Acoustic Wave (SAW) devices, it is very important for the tunable interdigital transducer (IDT) and IDT resonators to be made by the IDT with variable capacitance and gap control IDT between the IDT and the short electrodes.

##### Statement of Contribution/Methods

Many types of variable delay lines (1,2) and tunable resonator filters using variable capacitors (3).

- (1) The propagation velocities are changed by control of the gap between the shorted electrodes and the piezoelectric surfaces.
- (2) The propagation velocities are changed by the control of the depletion layers of the ZnO/semiconductor substrates.
- (3) The resonant frequency changes are caused by the connected parallel and series variable capacitors to IDT. Therefore the propagation velocities of SAW on the resonance are the shorted SAW velocities and coupling factors are reduced by the series and parallel capacitors. The resonant and anti-resonant frequency responses are poor and ranges of the center frequency are not wide.

In this paper, the new configuration of tunable interdigital transducers and resonators using the one of IDT connected alternately to the only variable capacitance (impedance) or one of IDTs connected alternately with the series connection to the variable capacitors through the sending and receiving electrode, or the gap control between the shorted electrode and IDT.

Propagation SAW velocities on the excitation and receiving IDT are changed by the change of the impedance connected to IDT without the connection to the sending and receiving electrodes or gap control between the shorted electrode and IDT.

The propagation velocities change from the shorted velocities by zero impedance to open velocities by the large impedance. The center frequency of IDT and resonant frequency of IDT are changed by propagation velocities caused by the IDT connected to the variable capacitors.

Also the tunable resonators are obtained by using the IDT reflector with variable capacitors or the IDT reflector with the gap control of shorted electrode and IDT surface.

These IDT are applied for the tunable filters, sensors, temperature compensation devices, signal processing devices and VCO. etc.

##### Results/Discussion

The theoretical results showed the tunable unidirectional filters with the directivity around 6dB and zero insertion loss, and tunable resonators. The center frequency changes were 2% and 13% for using 128° YX LiNbO<sub>3</sub> with  $k^2=0.055$  and SiO<sub>2</sub>/YX-LiNbO<sub>3</sub> with  $k^2=0.3$ , respectively. We will show the experimental results.

P4B1-8

#### Three-Dimensional Electric Charge Distribution on Finitely-thick Bus-bars in Micro-acoustic Devices

Alireza Baghai-Wadji<sup>1</sup>, <sup>1</sup>Electrical Engineering, University of Cape Town, Rondebosch, Western Cape, South Africa

##### Background, Motivation and Objective

The author's original work for three dimensional charge distributions in micro-acoustic devices - dating back to 1986 - has been manifestly extended to include finitely-thick bus-bars. The work has been initiated to investigate the electric charge localization and field enhancement at the electrode/bus-bar junctions depending on the thickness of the metallization in submicron geometries.

##### Statement of Contribution/Methods

An easy-to-follow recipe for the construction of relevant Green's functions has been provided. Universal Functions for setting up system matrices in the Method-of-Moments implementations have been constructed. Universal functions (moments of Green's functions) turn out to be extraordinarily smooth and thus easy to compute. Four additional features stand out in the paper: (i) The Green's function for finite-size substrates has also been constructed. (ii) Furthermore, Green's functions for including the metallic package have been derived. (iii) In addition Green's functions for electrodes imbedded in dielectrics have been constructed. (iv) Finally, the Multi-level Multi-pole Method has been introduced, for the first time, in the micro-acoustic device modelling literature, to significantly accelerate computations and ensure O(N) or O(NlogN) computational complexity.

##### Results/Discussion

The developed package promises to set a new standard for three dimensional accelerated computing of electric field distributions in micro-acoustics. The paper concludes with a discussion on including higher-order quasi static terms, for further enhancing the accuracy of the method.

## P4B2 - Materials and Propagation

Salon C

Friday, September 5, 2014, 8:00 am - 5:00 pm

Chair: **Jyrki Kaitila**  
Avago Technologies

P4B2-1

### Investigation of Platinum Based Periodic Gratings on Languisite for High Temperature SAW Applications

Guðrún Bruckner<sup>1</sup>, Nicolay Pascal<sup>1</sup>, Jochen Bardong<sup>1</sup>, <sup>1</sup>Sensor Development, CTR AG, Villach, Austria

#### Background, Motivation and Objective

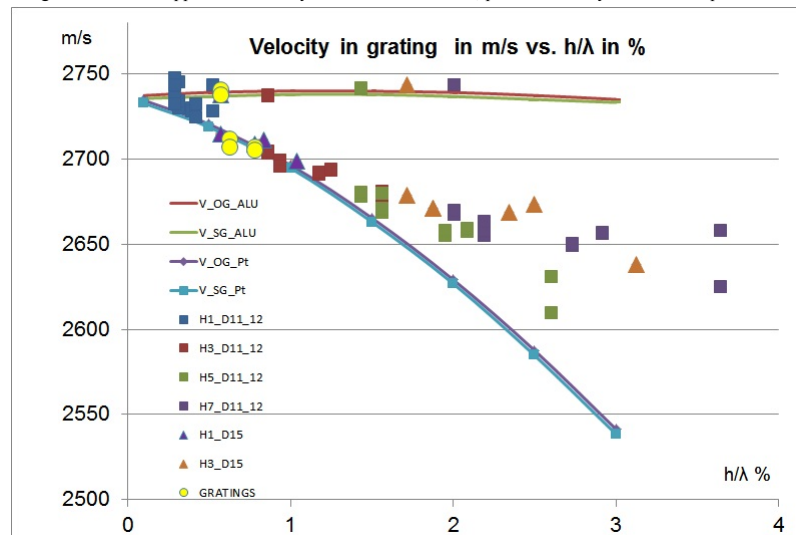
Languisite (LGS) is a successful substrate material for high temperature SAW applications. Next to the substrate properties the behavior of the wave inside the gratings of the electrodes or reflectors is a key parameter for any design of SAW devices. The properties of high temperature stable electrodes, which are generally made of heavy materials like Pt, Ir or Rh are not easily accessible by simulation. For a reliable simulation the material parameters of the thin metal layers used for SAW electrodes have to be accurately known. This is not always the case, as their exact parameters differ from the well-known bulk values and can in addition vary with the method of fabrication. We therefore have done an intensive study, combining experiment and simulation to provide reliable design parameters for Pt based electrodes on LGS.

#### Statement of Contribution/Methods

We have chosen LGS with Euler angles (0°, 138.5°, 26.6°) and investigated the propagation velocity and reflectivity of Rayleigh waves in periodic gratings experimentally as a function of  $h/\lambda$  (metallization thickness/ wavelength). We used delay line designs with free propagation paths as well as open and shorted gratings to assess the velocity inside the grating and the reflection coefficient. The chosen designs allow measuring the position and width of the stop band directly for both types of gratings. To change the ratio of  $h/\lambda$  the design frequency and the height of the metallization were altered in several production runs. The wavelength was varied from 1.7  $\mu\text{m}$  to 19.2  $\mu\text{m}$  corresponding to a frequency range of ~140 MHz to 970 MHz. We fabricated devices with Pt electrode metallizations between 50 nm and 110 nm to cover a region of  $h/\lambda$  from 0.3 to 3%, while Al electrodes with 60 nm thickness were used for comparison.

#### Results/Discussion

The stop band analysis of delay lines with long gratings allowed us to obtain the velocity and reflectivity inside open and shorted gratings. Some examples of the experimental results are given in the figure below, where the velocity is plotted versus  $h/\lambda$  for Pt (blue-violet) and Al (green-red) gratings. A comparison of the experiments with simulation using three different approaches namely FEM simulation, pure FEM analysis and COM parameter analysis is given in the paper.



P4B2-2

### Theoretical and experimental investigation of Lamb wave characteristics in AlN/TiN/NCD composite membrane.

Ali Soltani<sup>1</sup>, Abdelkrim talbi<sup>2</sup>, Abdallah Bassam<sup>3</sup>, Vincent Mortet<sup>4</sup>, Jean Claude De Jaeger<sup>1</sup>, Philippe Pernod<sup>2</sup>, <sup>1</sup>HEMN-UMR CNRS 8520, PRES Université Lille Nord de France, France, France, <sup>2</sup>LIA LICS-IEMN UMR CNRS 8520, ECLille, PRES Université Lille Nord de France, France, France, <sup>3</sup>Atomic Energy Commission Syrian, BP 6091, Damascus, Syrian Arab Republic, Syrian Arab Republic, <sup>4</sup>Physics, Academy of Sciences, CZ-18221 Prague, Czech Republic, Czech Republic

#### Background, Motivation and Objective

During the last decade, a great interest was carried on the development of electro-acoustic devices based on AlN piezoelectric thin films including resonators and filters for applications ranging from telecommunication and sensing fields, thanks to their high acoustic wave velocity, good electromechanical coupling coefficient, wide band gap and resistant to severe environmental conditions and can be integrated with high power devices operating in super high frequency range. Nano-crystalline diamond (NCD) have been proven to be suitable for Nano-electro-mechanical systems (NEMS) thanks to some interesting properties such as low mechanical loss, high acoustic wave velocity and high hardness. We have demonstrated previously that it is possible to synthesize a metallic buffer layer based on titanium nitride TiN (111) prior to the deposition of low stress and highly oriented (002) AlN thin film. We have, recently, investigated theoretically the fundamental quasi symmetric lamb wave mode S0 propagating along AlN/TiN/NCD composite membrane. The structure enables to achieve operation frequency in the SHF range with electromechanical coupling coefficient higher than 5%. In this study, we confirm both theoretically and experimentally the effectiveness of the AlN/TiN/NCD composite membrane for operation in SHF domain.

**Statement of Contribution/Methods**

First, TiN thin films are deposited on NCD/Si substrate by sputtering followed by an annealing under vacuum. This permits to reduce drastically the intrinsic stress and to improve the TiN crystal orientation and favors (111). In the second time, highly oriented AlN thin films are deposited by sputtering at low temperature on TiN/Nanocrystalline diamond(NCD)/Si substrate. IDTs were then fabricated using optical lithography, and the AlN/TiN/NCD membrane was then released using Silicon deep trench etching based on Bosch process. FEM analysis of the structure were performed using Comsol multiphysics.

**Results/Discussion**

Figure 1 shows transmission responses of different acoustic wave devices. Sample 1 (S1) was performed AlN/TiN membrane (green). Sample 2 (S2) was performed on AlN/TiN/NCD membrane (blue). We can see clearly the contribution of the NCD resulting on the operation frequency increase. Complete characterization of the device including TCF, electromechanical coupling coefficient are in progress.

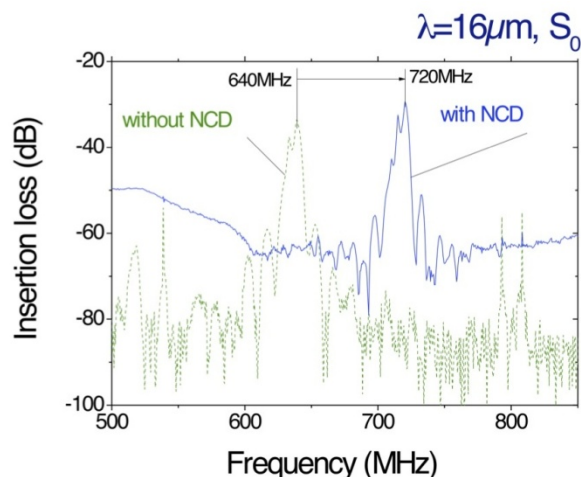


Fig.1: Insertion loss of devices made on AlN/TiN and AlN/TiN/NCD composite membranes

P4B2-3

**Simulation for viscoelastic effects of SH-SAW biosensor**

Mikihiro Goto<sup>1,2</sup>, Hiromi Yatsuda<sup>1,3</sup>, Jun Kondoh<sup>2</sup>; <sup>1</sup>Japan Radio Co., Ltd., Japan, <sup>2</sup>Graduate School of Science and Technology, Shizuoka University, Japan, <sup>3</sup>OJ-Bio Ltd., United Kingdom

**Background, Motivation and Objective**

Recently, an innovation platform for the detection and identification of the infectious agents that can be used by the patients has been required. There are various important requirements for the sensor platform, such as portable, cost per test, maximum achievable sensitivity and specificity, ease of use and so on. The authors have developed the shear horizontal surface acoustic wave (SH-SAW) based biosensor on quartz which propagation area covered with a gold film [1]. However, there are only few papers on the numerical analysis of SH-SAW biosensors. Numerical analysis of SH-SAW biosensors must be one of important factors for the commercialization of SH-SAW biosensors. In the analysis of the bio-reactions with mass loading, the sensitivities of SH-SAW biosensors are too small to confirm the experimental results [2]. In the analysis of the bio-reactions with viscosity sensitivity, the absolute values of velocity and attenuation changes of SH-SAWs agreed with the experiments [3]. However for the experiment of a model immunoassay using human serum albumin (HSA) detections, the velocity and attenuation changes did not agree with the calculated results [1]. Therefore we analyze the bio-reactions as viscoelastic sensitivity of SH-SAW biosensors using a numerical calculation method.

**Statement of Contribution/Methods**

In order to evaluate propagation analysis of SH-SAW biosensors on quartz, we have studied influence of viscoelasticity by the numerical calculation method. The numerical calculation method which was proposed by Campbell and Jones has been generally used to obtain SAW propagation characteristics. In this paper, a numerical calculation method for propagation characteristics, which was a modified Campbell and Jones method involving influence of viscoelasticity was applied to quartz. The SH displacement at the surface drives shear fluid movement by viscosity and viscoelasticity coupling, which eventually results in additional increment of the propagation loss. Analysis of the bio reactions with viscoelastic sensitivity of SH-SAW biosensors were discussed using the calculated velocities and attenuations of the SH-SAW.

**Results/Discussion**

We have compared the calculated results with the experimental results for the SH-SAW biosensor that structure of liquid/viscoelastic/gold-film/36Y-90X quartz. Delay-line type SH-SAW sensors on quartz with center frequency of 250MHz were evaluated. In order to evaluate viscoelastic sensitivities, a model immunoassay based upon HSA detection was used for experiments [1]. The velocity and amplitude changes of the SH-SAWs were increment in antigen antibody reactions as theoretically expected. Very good agreements between theoretical and experimental results were obtained.

**[References]**

- [1] M. Goto, et al., Proc. IEEE Ultrasonics Symp., 2010 p.736.
- [2] M. Goto, et al., Jpn. J. Appl. Phys., vol. 52, 07HD10, 2013.
- [3] M. Goto, et al., Proc. IEEE Ultrasonics Symp., 2012 p. 2110.

## Surface acoustic wave scattering by substrate edges

Alexander Darinskii<sup>1</sup>, Manfred Weihnacht<sup>2,3</sup>, Hagen Schmidt<sup>2</sup>; <sup>1</sup>Institute of Crystallography RAS, Russian Federation, <sup>2</sup>IFW Dresden, Dresden, Germany, <sup>3</sup>InnoXacs, Dippoldiswalde, Germany

### Background, Motivation and Objective

Substrate edges are natural obstacles preventing the propagation of surface acoustic waves (SAW). Investigations of the SAW scattering by edges of anisotropic substrates are practically lacking. It is notable that the SAW scattering is not studied completely even for isotropic substrates despite a considerable number of publications on this problem. Our work numerically studies the SAW scattering by edges of piezoelectric substrates formed by two mutually orthogonal faces (in other words, the SAW scattering in 90-degree piezoelectric wedges).

### Statement of Contribution/Methods

A substrate occupies the quarter space  $X, Z \geq 0$ . An incident harmonic SAW propagates along the surface  $Z=0$  towards face  $X=0$  and is scattered at edge  $X=Z=0$ . The ultimate task is to determine the reflection coefficient  $R$  and the transmission coefficient  $T$ , that is, in practice, the amplitude and the phase of the SAW travelling backward on surface  $Z=0$  (reflected wave) and the same characteristics of the SAW generated at face  $X=0$  (transmitted wave). The scattered wave field is computed by means of 2D-FEM. A perfectly matched layer (PML) is used in simulations. The coefficients  $R$  and  $T$  are obtained with the help of the spatial Fourier transform of the scattered field on faces  $Z=0$  and  $X=0$ , respectively. When scattered, the SAW also generates bulk modes but finding their characteristics is out of the scope of our work.

### Results/Discussion

Dependences of  $R$  and  $T$  on different parameters describing the conditions of scattering are computed and analyzed. Among them is the dependence of these coefficients on the ratio of the radius  $r$  of the fillet at the edge to the wavelength  $\lambda$  of the incident SAW. The computations are performed for 128YX and YZ LiNbO<sub>3</sub> as well as for ST-X SiO<sub>2</sub>, with the listed orientations specifying the geometry of the propagation of the incident SAW. In particular, it is found that in the case of the normal incidence on the rounded edge the magnitude of  $R$  first increases with  $r/\lambda$ , reaches a maximum at  $r/\lambda$  values lying in the range 0.3-0.5 (depending on the substrate), and then decreases towards zero. The magnitude of  $T$  first decreases, reaches a minimum at  $r/\lambda$  values lying in the range 0.3-0.5, and then increases up to a certain value around which it slightly oscillates as  $r/\lambda$  increases. It is also shown that coefficients  $R$  can differ strongly for the reciprocal directions of the normal incidence in anisotropic substrates. The same holds true for coefficients  $T$ . An example is YZ LiNbO<sub>3</sub> (we compare the scattering of SAW propagating parallel and antiparallel to the 3-fold axis of LiNbO<sub>3</sub>). However, it is proved that there are 4 classes of orientations at which the SAW is scattered identically for reciprocal directions. For instance, this is the case for 128YX LiNbO<sub>3</sub> and ST-X SiO<sub>2</sub>. Summing up, our results about specific features of the SAW scattering at substrate edges broaden one's knowledge in the field of SAW propagation in anisotropic media and are useful for practical applications as well.

## Investigation of UHF attenuation of synthetic IIa type diamond single crystal

Arseniy Telichko<sup>1,2</sup>, Boris Sorokin<sup>1,2</sup>, Gennadiy Kvashnin<sup>1</sup>, Georgy Gordeev<sup>1,2</sup>; <sup>1</sup>Technological Institute for Superhard and Novel Carbon Materials, Moscow Troitsk, Russian Federation, <sup>2</sup>Moscow Institute of Physics and Technology, Dolgoprudny, Moscow Region, Russian Federation

### Background, Motivation and Objective

Development of modern acoustoelectronic devices up to microwave frequencies proposes application of certain materials with low acoustic attenuation. For example such devices as High-overtone Bulk Acoustic Resonators (HBAR) can operate at frequencies up to 20 GHz. Now there is a limited number of appropriate materials as IAG, sapphire, etc. For this purpose synthetic diamond is a prospective material due to high acoustic velocities, thermal conductivity, etc. But experimental hypersonic attenuation of diamond is still unknown. Objective of this paper is the estimation of acoustic attenuation of synthetic diamond single crystal by the data on HBAR's  $Q$  factor.

### Statement of Contribution/Methods

It is well known that total attenuation at high frequencies depends on phonon-phonon scattering attenuation, roughness of a substrate, depth of damage subsurface layer, etc. Internal phonon-phonon attenuation in diamond single crystal was calculated in terms of Akhiezer theory of sound attenuation. Attenuation dependence vs diamond's Gruniesen parameter  $\gamma$  was studied. Resonant properties and  $Q$  factors frequency dependences were experimentally studied for "Al/AlN/Mo/(100) diamond" piezoelectric layered structures. Its fabrication was produced by AJA ORION 8 magnetron rf sputtering equipment [1]. Diamond substrate faces were polished up to the roughness  $R_a < 10$  nm/100  $\mu$ m controlled by AFM method. Our recent investigations have shown that depth of diamond damage layer is less than 30 nm. This result was confirmed by 3-30 eV electron backscattering diffraction and clear Kikuchi lines observation. Frequency dependence of quality factor  $Q$  was studied by M-150 Multipurpose Probing System and E5071C Network Analyzer from 1 up to 20 GHz at room temperature. The best quality parameter  $Q \times f = 10.2 \times 10^4$  GHz has been obtained.

### Results/Discussion

Akhiezer's attenuation theory predicts squared frequency relationship and as a result the  $Q \times f$  product must be constant. Using our HBAR's experimental data on  $Q$  factor for diamond substrate one can easily calculate the value of acoustic attenuation  $\alpha = (0.025 \dots 0.03)$  dB/(GHz<sup>2</sup>×cm) and  $Q \times f = (8 \dots 10) \times 10^4$  GHz.

Estimation of diamond acoustic attenuation by  $\gamma = 0.74$  obtained from the data on heat capacity measurement and taken at room temperature gives us the lowest value of  $\alpha \sim 0.006$  dB/(GHz<sup>2</sup>×cm) and  $Q \times f = 4.5 \times 10^5$  GHz. This value can be treated as an estimation of theoretical limit of diamond's hypersonic acoustic attenuation. Discrepancy between theoretical estimation and experimental data can be explained mainly by uncertainty of AlN film influence. An additional error will be associated with the unknown longitudinal mode Gruniesen constant which derivation will be of great interest in a future by means of acoustic experiment.

Already obtained results show that synthetic diamond has a lowest acoustic attenuation at microwave frequencies between known materials.

[1] B.P. Sorokin et al. Appl. Phys. Lett. V. 102. P. 113507 (2013).

## Optimization of Aperture in SAW and STW Resonators on Langasite

Natalya Naumenko<sup>1</sup>; <sup>1</sup>Acousto-Optical Research Center, National University of Science and Technology "MISIS", Moscow, Russian Federation

### Background, Motivation and Objective

Langasite (LGS) found wide application in sensors operating in harsh environment due to its ability to stand high temperatures and existence of orientations with zero TCF for SAW and quasi-bulk SH waves (STW). The choice of orientation depends on specific requirements to the substrate material but it is often made between commercially available temperature compensated SAW cut with Euler angles (0, 138.5, 26.7), STW cut (0, 22, 90) and symmetric YX-cut. Strong acoustic anisotropy of LGS determines high sensitivity of resonator characteristics to electrode material, thickness and other geometrical parameters of a grating. In the reported resonators the aperture  $W$  of the grating is usually about 40-50 wavelength because at lower values spurious modes appear. In this paper, a numerical technique developed for simulation of admittance of a finite-aperture resonator is applied to three LGS orientations to optimize the resonator aperture.

**Statement of Contribution/Methods**

The admittance of a finite-aperture resonator is built by SAWs or STWs propagating along the grating and at oblique angles. Each obliquely propagating wave generates frequency response in the grating. Integration of such responses over finite range of angles, with weighting function dependent on the aperture, yields the admittance with spurious modes, which grow with decreasing aperture. Such analysis takes into account the dependence of resonant and anti-resonant frequencies on oblique angle but ignores the waveguiding effect, which can be minimized, e.g. in piston mode structures. The spurious modes manifest themselves as ripples in the admittance function. The transverse anisotropy, i.e. the slowness surface referred to a grating with specified geometrical parameters, determines the frequencies of ripples. Minimum acceptable aperture of the grating depends on orientation and parameters of the grating.

**Results/Discussion**

Admittances of resonators with apertures 20-100 wavelengths and Pt grating,  $h/2p=1-2\%$ , were simulated on three LGS cuts as substrate materials. STW cut of LGS was found as most sensitive to decreasing of resonator aperture when  $h/2p$  is about 1%: some ripples were observed even at  $W/2p=200$ . These ripples occur below resonance and inside the stopband because of the strong interaction between STW and Rayleigh SAW typical for this cut[1]. The aperture can be reduced to  $W/2p=35$  if electrode thickness increases to 2%. In YX-cut of LGS degradation is expected between resonance and anti-resonance when  $W/2p<40$ , which is explained by the strong transverse anisotropy combined with negative reflection coefficient and cannot be suppressed by variation of electrode thickness. In the optimal SAW cut of LGS with  $W/2p<40$  there are ripples around the stopband, which can be minimized by variation of electrode thickness or duty factor. This analysis can be helpful in optimization of resonator size.

[1] N. F. Naumenko, IEEE Transactions UFFC, 2012, vol. 59, no. 11, pp.2515-2521.



## P5B1 - Transducer Materials

Salon C

Friday, September 5, 2014, 8:00 am - 5:00 pm

Chair: **Paul Reynolds**  
Consulting

P5B1-1

### Adhesive-free dual layer piezoelectric PVDF copolymer transducers used with sender and receiver separation

Sanat Wagle<sup>1</sup>, Adit Decharat<sup>1</sup>, Frank Melandsø<sup>1</sup>; <sup>1</sup>Department of Physics and Technology, The University of Tromsø, Tromsø, Tromsø, Norway

#### Background, Motivation and Objective

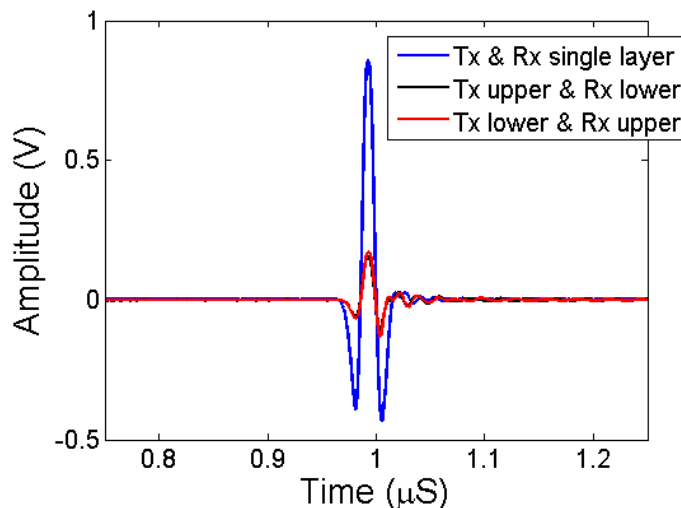
Ultrasonic transducers made from polymers [e.g. polyvinylidene fluoride (PVDF) and its copolymer poly(vinylidene fluoride – trifluoroethylene) P(VDF-TrFE)] are known to yield both higher attenuation and lower piezoelectric coupling factors than comparable ceramic transducers. It is to some extent, possible to increase the transducer efficiency by using two or more piezoelectric layer with embedded electrodes [e.g. A. Decharat, S. Wagle and F. Melandsø, Proc.- Ultrasonic Symposium 2013, p. 471]. A multi-layer transducer design also enable separate sender (TX) and receiver (RX) layers that can be electrical shielded to reduce the capacitive induced currents (CIC) during pulse firing, or to facilitate continuous wave (CW) applications for example in Doppler imaging.

#### Statement of Contribution/Methods

In the current work, we have both experimentally and through FEM modeling, investigated adhesive free dual-layer P(VDF-TrFE) transducer used in TX and RX modus i.e. sending the signal from one layer and receiving by the another layer. The results have then been compared to single layer transducers, i.e. sending and receiving the signal from same layer. To characterize the transducer experimentally, the acoustic backscattering from the backing-air interface is performed. The ultra-wideband pulse (UWB) various pulse width and CW mode were used to excite the transducer.

#### Results/Discussion

By using the dual layer transducer in the sender and receiver mode, we are able to reduce CIC significantly as shown in Fig. 1. The amplitude of the acoustical responses and frequency spectrum from the backscattering measurements were also compared for different excitation modus. The simulated results obtained by COMSOL showed good agreements with the experimental results.



P5B1-2

### Graded Piezocomposite for the Construction of Air-Coupled Ultrasound Transducer

David Costa<sup>1</sup>, Luis Segura<sup>2</sup>, Francisco Espinosa<sup>2</sup>, Flávio Buiocchi<sup>1</sup>; <sup>1</sup>Mechatronics Engineering, University of Sao Paulo, Brazil, <sup>2</sup>Center for Applied Acoustics and Non-Destructive Evaluation, CSIC, Madrid, Spain, Spain

#### Background, Motivation and Objective

In some cases of ultrasound nondestructive evaluation, the use of a coupling agent can damage the object being inspected, thus requiring the use of an air-coupled ultrasound transducer. This article presents a specific configuration of a graded piezocomposite of central frequency of 820 kHz to be used for constructing a transducer capable of emitting in air. The goal is to get a piezocomposite with a higher with bandwidth when compared to a type 1-3 piezocomposite of the same electromechanical coupling factor. With a higher bandwidth the graded piezocomposite emits more energy in a wider frequency range. Both piezocomposites were constructed and used for the construction of ultrasonic transducers for emission in air, and the following parameters were analyzed: displacement of the front surface of the transducers for the frequency range of 0.5 to 1 MHz, impulse response and impedance curve.

#### Statement of Contribution/Methods

Two transducers were built with 1-MHz Pz27 ceramics using the dice and fill technique. One transducer was made of a 1-3 piezocomposite and the other one was made of graded piezocomposite. The matching layers were composed of an epoxy layer and a porous cellulose membrane layer. Transducers were excited in the pulse-echo mode. The impulsive

impulse response was acquired by an oscilloscope and the impedance curve by an impedance analyzer. A laser interferometer was used to measure the displacement on the surface of the transducer as a function of frequency in order to better understand the increased bandwidth

#### Results/Discussion

The graded piezocomposite transducer presented a bandwidth of 13% and the 1-3 piezocomposite transducer presented a bandwidth of 8.4%. The bandwidth of the graded transducer was 55% higher than the type 1-3 transducer. Therefore the graded piezocomposite is the most suitable for the construction of a piezoelectric transducer for emission in air.

#### P5B1-3

##### Growth and Piezo-/Ferroelectric Properties of $\text{Pb}(\text{Mg}_{1/3}\text{Nb}_{2/3})\text{O}_3\text{-PbTiO}_3\text{-Bi}(\text{Zn}_{1/2}\text{Ti}_{1/2})\text{O}_3$ Ternary Single Crystals

Reagan Belan<sup>1</sup>, Hamel Tailor<sup>2</sup>, Zuo-Guang Ye<sup>3</sup>; <sup>1</sup>Chemistry, Simon Fraser University, Burnaby, British Columbia, Canada, <sup>2</sup>Simon Fraser University, Canada, <sup>3</sup>Chemistry, Simon Fraser University, Canada

#### Background, Motivation and Objective

Single crystals of relaxor-based perovskite solid solutions, namely  $\text{Pb}(\text{Mg}_{1/3}\text{Nb}_{2/3})\text{O}_3\text{-PbTiO}_3$  [PMN-PT] and  $\text{Pb}(\text{Zn}_{1/3}\text{Nb}_{2/3})\text{O}_3\text{-PbTiO}_3$  [PZN-PT], show extraordinary piezoelectric performance, enabling them to be the leading choice of materials for the next generation of electromechanical transducers in a broad range of applications<sup>1</sup>. However, these materials suffer from some drawbacks, in particular, a low Curie temperature ( $T_C$ ) and a low coercive field ( $E_c$ ), limiting their usefulness in high temperature and field applications. In order to overcome these shortages,  $\text{Bi}(\text{Zn}_{1/2}\text{Ti}_{1/2})\text{O}_3$  [BZT] was added to 'harden' the PMN-PT system and the ternary solid solution system of  $\text{Pb}(\text{Mg}_{1/3}\text{Nb}_{2/3})\text{O}_3\text{-PbTiO}_3\text{-Bi}(\text{Zn}_{1/2}\text{Ti}_{1/2})\text{O}_3$  [PMN-PT-BZT] was prepared in our laboratory in the form of ceramics and single crystals<sup>2,3</sup>.

In this work, we report the growth of the single crystals of this ternary solid solution by the high temperature solution (flux) method using a mixture of  $\text{PbO}$  and  $\text{H}_2\text{BO}_3$  as flux. By varying both the temperature profile of the growth and the nominal composition of charge, large and good-quality multinucleated crystals of PMN-PT-BZT were obtained. The domain structure and phase transitions of the PMN-PT-BZT crystals are characterized by polarized light microscopy (PLM). The chemical compositions of the grown crystals are determined by XPS analysis. The dielectric and ferroelectric properties of the crystals are investigated, with a thorough analysis of the relaxation behaviour. It is found that the ternary single crystals exhibit enhanced piezoelectric performance compared to their ceramic counterparts.

This work is supported by the Office of Naval Research (Grants No. N00014-11-1-0552 and N00014-12-1-1045) and the Natural Science and Engineering Research Council of Canada.

1Z.-G. Ye, Mater. Res. Soc. Bull., Vol. 34, No. 4, pp. 277-283 (2009).

2H. N. Tailor, A. A. Bokov, Z.-G. Ye, Ferroelectrics, 405, 67-75 (2010).

3R. Belan, H. N. Tailor, X. Long, A. A. Bokov and Z.-G. Ye, J. Cryst. Growth, 318, 839-845 (2011)

#### Statement of Contribution/Methods

#### Results/Discussion

#### P5B1-4

##### Preparation, structure and properties of potentially high- $T_C$ ferroelectric complex perovskite solid solutions based on $\text{Bi}(\text{Zn}_{2/3}\text{Nb}_{1/3})\text{O}_3$

Alisa Paterson<sup>1</sup>, Hoi Ting Wong<sup>1</sup>, Zuo-Guang Ye<sup>1</sup>; <sup>1</sup>Department of Chemistry and 4D Labs, Simon Fraser University, Burnaby, BC, Canada

#### Background, Motivation and Objective

Piezoelectric and ferroelectric materials form an important class of inorganic functional materials that may be used as sensors and actuators. The Curie temperature ( $T_C$ ) is an important parameter of these materials. Therefore, there is a great interest in developing new materials systems that possess a higher  $T_C$  in order to increase the operating range for potential applications. Solid solution systems based on the  $\text{Bi}(\text{Zn}_{2/3}\text{Nb}_{1/3})\text{O}_3$  end-member are studied in this work because of their potential to exhibit extremely large polarization and high  $T_C$ .

#### Statement of Contribution/Methods

Polycrystalline  $(1-x)\text{PbTiO}_3\text{-xBi}(\text{Zn}_{2/3}\text{Nb}_{1/3})\text{O}_3$  (PT-BZN) and  $(1-x)\text{BaTiO}_3\text{-xBi}(\text{Zn}_{2/3}\text{Nb}_{1/3})\text{O}_3$  (BT-BZN) solid solutions are prepared in the form of ceramics via a solid state reaction and sintering process. These systems are studied by x-ray diffraction and dielectric measurements. Detailed structural refinements are performed to reveal the trends in lattice parameters, cation displacements, and bond lengths/angles as a function of BZN concentrations to reveal the effects of the couple substitutions of  $\text{Bi}^{3+} \rightarrow \text{Pb}^{2+}$  on the A-site and  $(\text{Zn}_{2/3}\text{Nb}_{1/3})^{3+} \rightarrow \text{Ti}^{4+}$  on the B-site.

#### Results/Discussion

The PT-BZN solid solution is found to adopt a tetragonal structure, up to the solubility limit of  $x = 0.30$ . An increase in the structural asymmetry is observed with the increase of BZN concentration, which is accompanied by an increase in the  $T_C$  of the material. On the other hand, the BT-BZN solid solution possesses a mixture of rhombohedral and tetragonal phases, and the increase in the concentration of BZN causes a decrease in the  $T_C$  of this solid solution. Therefore, the PT-BZN solid solution is proved to be a high- $T_C$  ferroelectric material potentially useful for applications as electromechanical sensors and actuators.

#### P5B1-5

##### Lead-Free BNT based piezoelectric films for high-frequency ultrasonic transducer applications

Jinyan Zhao<sup>1</sup>, Xinwei Yan<sup>1</sup>, Wei Ren<sup>1</sup>, Qifa Zhou<sup>2</sup>, K. Kirk Shung<sup>2</sup>; <sup>1</sup>Xi'an Jiaotong University, Xi'an 710049, China, People's Republic of, <sup>2</sup>University of Southern California, Los Angeles, CA, USA

#### Background, Motivation and Objective

Lead-based materials, such as  $\text{Pb}(\text{Zr,Ti})\text{O}_3$  and  $\text{Pb}(\text{Mg}_{1/3}\text{Nb}_{2/3})\text{O}_3\text{-PbTiO}_3$  have been extensively used in various piezoelectric applications. In recent years, concerning the ecological impacts from high Pb concentration in lead-based materials, lead-free materials have attracted much attention from researchers.

## Statement of Contribution/Methods

In this work, lead-free  $(1-x)(\text{Bi}_{0.5}\text{Na}_{0.5})\text{TiO}_3$ - $x\text{BaTiO}_3$  (BNT- $x\text{BT}$ )/ $\text{Bi}_{0.5}\text{Na}_{0.5}\text{TiO}_3$  (BNT) 0-3 composite ferroelectric thick films have been fabricated at low-temperature using a modified composite sol-gel technique. In this process, the BNT- $x\text{BT}$  ( $x=0, 0.05, 0.06, 0.07$ ) ferroelectric powders were suspended in the BNT precursor solution to form a uniform slurry which was spin-coated on (111) Pt/ $\text{TiO}_2$ / $\text{SiO}_2$ /Si substrates and then annealed at 700°C. Repeated layering and vacuum infiltration were used during the deposition process to produce dense composite thick films without any cracking.

## Results/Discussion

Influence of the composition of the ferroelectric powders and the thickness of films on the structures and electrical properties of (BNT- $x\text{BT}$ )/BNT composite thickfilms has been investigated. X-ray diffraction analysis indicates that all the thick composite films exhibit a pure perovskite structure. The dielectric permittivity and remnant polarizations increase with thickness, while the leakage current densities shows nearly independent of the thickness. Moreover, the dielectric and ferroelectric properties of the thick films are found to be strongly dependent on the composition of the ferroelectric powders. 8  $\mu\text{m}$ -thick BNT-0.06BT/BNT thick film exhibits the maximum relative permittivity of 1079 and 3  $\mu\text{m}$ -thick BNT-0.06BT/BNT thick film exhibits the maximum  $P_r$  of 21.6  $\mu\text{C}/\text{cm}^2$ . The results indicate that the (BNT- $x\text{BT}$ )/BNT 0-3 composite thick films are promising lead-free piezoelectric materials for the ultrasonic transducer applications.

## P5B1-6

### Pulse Monitoring by Sol-Gel Composite Flexible Piezoelectric Sensors

Takahiro Ikari<sup>1</sup>, Shugo Kurose<sup>1</sup>, Tomohiko Igasaki<sup>1</sup>, Makiko Kobayashi<sup>1</sup>, <sup>1</sup>Kumamoto University, Japan

## Background, Motivation and Objective

In order to maintain quality of life, it is preferable to establish low cost home health monitoring system and development of highly sensitive sensors with noise canceling system was desired. Pulse information could contain many information even though it was much less stressful compared with electrocardiogram. In the past, authors developed ☐ ghealth monitoring chair with kept resting. However, PVDF sensors were too flexible so that ringing effect might not be ignorable and it would resulted in not perfect match with electrocardiogram. ~~It was successfully operated when the subjects wore polyvinylidene fluoride~~

## Statement of Contribution/Methods

Piezoelectric films made by sol-gel composite itself was flexible and it could be integrated onto various substrate easily. Therefore, lead zirconate titanate (PZT)/PZT sol-gel composite films were fabricated onto stainless steel, aluminum, and gold foil substrates with different thickness. PZT/PZT was chosen as sol-gel composite because it had high sensitivity and fabrication facility. Stainless steel was chosen as high stiffness constant material, and aluminum and gold was selected as low stiffness constant materials. Gold was preferable since it had higher melting point than aluminum and for sol-gel composite fabrication, high enough firing temperature such as 650°C was preferable, though aluminum substrates with different thickness were used more because of low cost.

## Results/Discussion

First, piezoelectric constant  $d_{33}$  was measured by Piezo  $d_{33}$  meter supplied by Institute of Acoustics Chinese Academy of Sciences. As a results, for thickness of sol-gel composite, higher thickness showed higher  $d_{33}$  values though maximum thickness was 120 $\mu\text{m}$ . Further research was required to find optimized thickness. For substrate, higher thickness and stainless steel showed highest piezoelectric constant values. Piezo  $d_{33}$  meter applied vibration to the sample with clamping so that force could applied efficiently to piezoelectric film. Pulse monitoring results showed similar tendency; 120 $\mu\text{m}$  thick PZT/PZT onto 80 $\mu\text{m}$  thick stainless steel substrates could measure the pulse, on contrary, the other samples was difficult to find the pulse even though they were sensitive for postural disturbance. Further investigation will be carried out concerning noise canceling.

## P5B1-7

### Feasibility of lead-free piezoceramic based power ultrasonic transducers

Andrew Mathieson<sup>1</sup>, Dominick DeAngelis<sup>2</sup>, <sup>1</sup>School of Engineering, University of Glasgow, United Kingdom, <sup>2</sup>Mechanical Engineering, Ultrasonics Group, Kulicke & Soffa Industries, USA

## Background, Motivation and Objective

Lead-based piezoceramics are currently the most widely used transduction material in power ultrasonic applications and although lead can cause serious health and environmental damage, lead-based piezoceramics are exempt from the EU directive Restriction of Hazardous Substances (RoHS) due to a lack of a genuine substitute or replacement. However, these exemptions are reviewed every four years which allows for the possibility that this could be revoked in the future. With other regions of the world also adopting similar legislation, lead-free piezoceramics may provide an alternative. These have existed since the 1960s, and while they have not previously been suitable for power ultrasonic transducers, the latest generation of lead-free piezoceramics may have the potential to be utilized in these applications. This study reports on power ultrasonic devices that incorporate lead-free piezoceramics and discusses the limitations that presently impede the viability lead-free based devices.

## Statement of Contribution/Methods

A lead-free piezoceramic material is investigated as both a single element and as a number of elements incorporated in a commercial unidbody transducer. The transducers, which is used in the semiconductor wire bonding process and which normally contains PZT8, are experimentally characterized to assess their impedance, electro-mechanical coupling factor and response time, while their thermal characteristics are investigated under operational conditions. Their resonant and non-resonant behaviors are also examined to investigate their actuation and sensing capabilities which are compared with current PZT8 based devices.

## Results/Discussion

The mechanical quality factor (QM) and coupling coefficient (k) of the lead-free piezoceramic elements (QM:~103 and k:~0.1141) was found to be significantly lower than the corresponding PZT8 elements (QM:~820 and k:~0.4188). This, as expected, has an adverse effect on the performance of the lead-free piezoceramic based transducers. Nevertheless, design and fabrication considerations; such as preloading limits which ensure mechanical integrity, material property stability and the prevention of depolarization, and the thermal characteristics of the lead-free piezoceramic when driven at operational drive conditions are reported on as they are also capable of significantly influencing the behavior and performance of a transducer. Finally, the wire bonds generated by both lead-free and PZT8-based transducers are assessed to give a practical measurement of how the lead-free piezoceramic based transducers directly compare while in situ in the wire bonding process to the PZT8-based transducers.

P5B1-8

### Transparent glass windowed ultrasound transducers

Torstein Yddal<sup>1,2</sup>, Spiros Kotopoulos<sup>1,2</sup>, Odd Helge Gilja<sup>2,3</sup>, Sandy Cochran<sup>4</sup>, Michiel Postema<sup>1</sup>; <sup>1</sup>Institute of Physics and Technology, University of Bergen, Bergen, Norway, <sup>2</sup>National Center for Ultrasound in Gastroenterology, Haukeland University Hospital, Bergen, Norway, <sup>3</sup>Department of Clinical Medicine, University of Bergen, Bergen, Norway, <sup>4</sup>Institute for Medical science and Technology, University of Dundee, Dundee, United Kingdom

#### Background, Motivation and Objective

Optical measurements are a cornerstone of today's technology, they are widely used for measuring speed, distance, chemical analysis and more. Optical equipment draws great advantages from modern micro-electronics knowledge, making it extremely compact. A limitation with optical equipment is that it can often be fragile, and needs an optically clear window. Some environments makes this difficult to obtain and sustain, an example is measurements in oil pipes where crude oil will attach to the measurement window. We have therefore created a glass ultrasound transducer, capable of both protecting optical equipment and cleaning the window, whilst maintaining all typical ultrasound field characteristics.

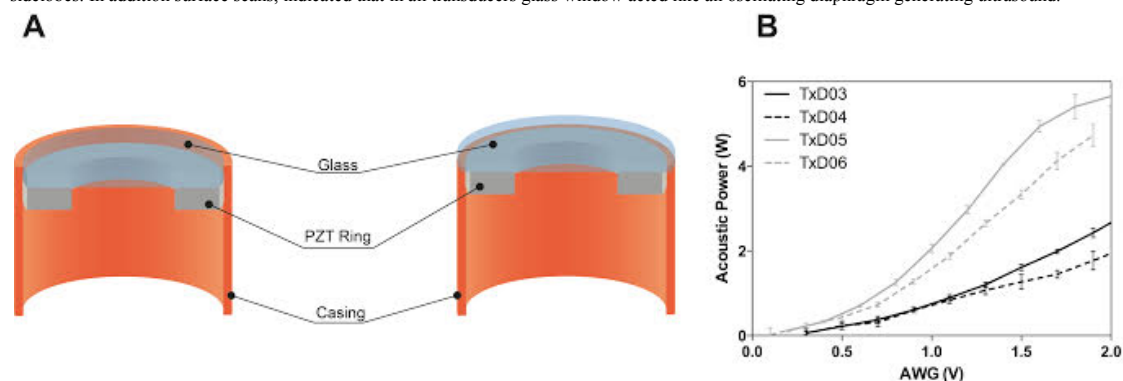
#### Statement of Contribution/Methods

The glass windowed ultrasound transducers were fabricated using 5-mm thick PZT-26 rings. Two to four mm glass discs were used to form the optical window. Two construction designs were evaluated. The PZT-26 ring was epoxied to a glass disc inside a metal cylinder casing, leaving a large transparent window in the center of the transducer (c.f. Fig. 1A). The transducers were driven by a 53-dB linear RF power amplifier during the characterisation procedure. The acoustic power output was measured using a radiation force balance and the acoustic propagation pattern was characterised using a 3D scanning tank combined with a 0.2- $\mu$ m needle hydrophone. Electrical impedance was measured to find the resonant modes and frequencies.

#### Results/Discussion

The completed ultrasound transducers had an average acoustic bandwidth (-6dB) of 56%. With an electrical reflection coefficient at the respective center frequencies of the transducers ranging from 0.9% to 18.9% depending on the transducer design. Figure 1B shows the acoustic power output as a function of waveform generator voltage. The reduced power output may be due to the mismatch of acoustic impedances between PZT, glass, and water.

The field scans showed that the acoustic propagation pattern was very similar to traditional ultrasound transducers, yes the different constructions affected the focal distance and sidelobes. In addition surface scans, indicated that in all transducers glass window acted like an oscillating diaphragm generating ultrasound.



P5B1-9

### An induced state with dominant shear vibration mode originated from domain reconfiguration in [001] PMN-PT single crystals

Yaoyao Zhang<sup>1</sup>, Philip Garland<sup>2</sup>, Robert Adamson<sup>1</sup>, Jeremy Brown<sup>1</sup>; <sup>1</sup>School of Biomedical Engineering, Dalhousie University, Halifax, Nova Scotia, Canada, <sup>2</sup>Department of Mechanical Engineering, University of New Brunswick, Fredericton, New Brunswick, Canada

#### Background, Motivation and Objective

Garland et al. [1] previously observed a low-frequency vibration mode (LVM) in the impedance spectrum of PMN-0.32PT and PMN-0.33PT, which has an approximate 25-30% resonance frequency drop relative to the normal thickness longitudinal mode and becomes dominant in high frequency wafers[1]. There have been relatively few discussions about this mode and no clear explanation about its origin has been reached. In the current work, we examined more closely the relation between crystal structure and the LVM, quantified the crystal/domain structural changes related to this mode, and extended the potential application of this mode in the manufacturing of high-frequency transducers.

[1] P. P. Garland, R. B. A. Adamson, and J. A. Brown, "Discovery of Microscopic Tetragonal Crystal Structure of < 001 > Oriented PMN-PT after Quenching from a Poled State," 2012 IEEE

#### Statement of Contribution/Methods

By quenching or applying a proper negative bias, an induced state can be formed with the dominant LVM (defined as LVM state). PMN-PT prepared in this way is metastable and will remain in the LVM state until a voltage exceeding the coercive field of 2 kV/cm is applied or the temperature is increased to close to Trt. The phase and domain structures under both of the two states were observed by polarization microscopy, and the transformation of the two states were determined by impedance and dielectric measurement at different temperatures.

#### Results/Discussion

The LVM state displays a macroscopic orthorhombic symmetry (mm2) with a mean polarization vector along the [110] orientation as evidenced by the measurement of transverse vibration modes in samples cut at different orientations in the (001) plane. The structural differences between the LVM state and the poled state can be entirely explained by differences in ferroelectric domain structure rather than phase structure. The domain structure with (110) domain walls was found to be formed in the tetragonal phase during heating, and can be frozen by the rapidly quenching even as the microscopic phase within each domain changes to rhombohedral symmetry on cooling through the Trt. The possible causes in formation of this domain structure are based on the compatibility of polarizations and domain walls, and were corroborated with polarization microscope observations. The [110] polarization component associated with the LVM state originates from the domain structure with well-organized (110) domain walls. Because the LVM and poled states exhibit very different mechanical and acoustic properties, such a processing approach may have applications in the engineering of kerfless ultrasound transducer arrays to obtain better directivity. We have fabricated several 45 MHz arrays with an induced LVM between elements and directivity, sensitivity, and beam profile measurements are ongoing.

## P5B2 - Biomedical Diagnosis and Imaging Transducers

Salon C

Friday, September 5, 2014, 8:00 am - 5:00 pm

Chair: **Paul Reynolds**  
Consulting

P5B2-1

### 256-element density-tapered spiral matrices for ultrasound phased imaging

Alessandro Ramalli<sup>1</sup>, Piero Tortoli<sup>1</sup>, <sup>1</sup>Information Engineering Dept., University of Florence, Firenze, Italy

#### Background, Motivation and Objective

The increasing interest in 3D ultrasound imaging is pushing the development of 2D probes with a challenging number (N) of active elements. The most popular approach in order to contain N is the sparse array technique. Here the design of the array layout requires complex optimization algorithms which are typically constrained by a limited number of steering conditions. Ungridded extensions of the sparse array technique seem to offer improved performance by adding a further degree of freedom in the optimization process. In this paper, it is proposed to design the layout of large circular arrays with limited N according to Fermat spiral seeds with spatial density modulation. This deterministic, aperiodic and balanced positioning procedure aims at guaranteeing uniform performance over a wide range of steering angles.

#### Statement of Contribution/Methods

The element position is defined by radial distance and circular angle. The Fermat spiral law for radial distance has been modified so that the spatial density of elements is adapted to a desired tapering window. To evaluate the performance of probes having only 256 elements, the corresponding 3D one-way fields have been simulated by Field II. 105 probes have been considered by modifying aperture diameter (40 $\lambda$ , 60 $\lambda$ , 80 $\lambda$ ), element size (0.5 $\lambda$ , 0.7 $\lambda$ , 1.0 $\lambda$ , 1.2 $\lambda$ , 1.5 $\lambda$ ) and density tapering (7 windows). The focal distance was fixed at 120 $\lambda$  while for each probe 25 steering angles were simulated, i.e. the combinations of 5 uniformly spaced angles between 0° and 32° in both elevation and azimuth planes. The probe performance was evaluated in terms of grating-lobe-level (GLL), sensitivity, lateral resolution, depth of field (DoF) and side- to main-lobe energy ratio (SMER). Such parameters were also compared to those obtained with dense arrays showing the same characteristics in terms of element size and aperture diameter. In the latter arrays the number of elements varied between 468 and 11897, according to the aperture to element size ratio.

#### Results/Discussion

Full matrices and the 256-element spiral probes feature equivalent resolution and DoF. As expected, in spiral probes the mean values of GLL and SMER are typically higher but the corresponding standard deviations are lower, confirming more uniform performance at all steering angles. A good performance trade-off was found in the 60 $\lambda$  spiral probe with 1.0 $\lambda$  elements and Blackman density tapering window. In this configuration, the number of elements is reduced by an 8.3 factor (i.e. 256 vs 2136). The GLL is -16 $\pm$ 2.5 dB (vs 20 $\pm$ 5 dB for the full matrix), the lateral resolution is 6.0 $\lambda$ , the DoF is 120 $\lambda$ , the sensitivity remains in a 5 dB range while the average SMER is -29 dB. It should be underlined that the spatial density tapering, like apodization, increases the DoF and reduces the SMER, but, unlike apodization, it increases the probe sensitivity. In the aforementioned example, it is increased by 3 dB instead of being reduced of 11 dB.

P5B2-2

### Detection of Elastic Guided Waves Using an Axial Transmission Method: Performance Comparison Between PZT and cMUT Technologies

Jean-Gabriel Minonzio<sup>1</sup>, Audren Boulmé<sup>2</sup>, Mathieu Legros<sup>3</sup>, Philippe Vince<sup>4</sup>, Pascal Laugier<sup>1</sup>, Dominique Certon<sup>2</sup>, <sup>1</sup>Laboratoire d'Imagerie Biomédicale, UMR CNRS 7371 - INSERM U1146 - UPMC, Paris, France, <sup>2</sup>Université François-Rabelais de Tours, GREMAN, UMR-CNRS 7347, Tours, France, <sup>3</sup>Vernon S.A., Tours, France, <sup>4</sup>Université François-Rabelais de Tours, CETU Althais Technologies, Tours, France

#### Background, Motivation and Objective

Recent experiments have shown that cortical bone behaves like an elastic waveguide supporting the propagation of several guided modes, depending on the waveguide thickness and elasticity. This therefore offers new perspectives for quantitative assessment of fracture risk-related bone characteristics. The cMUT large frequency bandwidth compared to the PZT is expected to reach important improvements for cortical bone assessment. In a previous paper [1] the potential of cMUT technology to detect and measure elastic guided waves, using an axial transmission technique, was demonstrated. The work reported here is an extension of our previous developments and investigates more thoroughly the comparison between the cMUT and PZT technologies.

#### Statement of Contribution/Methods

Two probes with the same geometrical characteristics were designed and packaged, with PZT and cMUT technologies respectively. Detailed description of their topology is given in [1]. The two probes were designed to work at 1 MHz with the highest frequency bandwidth possible.

A specific home-made beamformer dedicated to axial transmission measurements was developed by our group, allowing the real-time detection of guided waves, following the singular value decomposition-based method presented in [2]. The custom-made electronic device (emitter-receiver) was found to be suitable for driving both PZT and cMUT probes.

#### Results/Discussion

The comparison between the two technologies was first carried out on 2 mm-thick plates made of non-absorbing (copper) or absorbing (a bone mimicking) material. The main observations were:

- for the same signal magnitudes (2 mV without gain) the cMUT noise level was 10 dB larger than the PZT one while its frequency bandwidth was wider; 5 MHz and 1.5 MHz at -3 dB, respectively,
- the guided mode wavenumber values were the same with the two probes and in agreement with a free plate model.

Finally, measurements were performed on a bone mimicking tube (outer radius: 10 mm; thickness: 2 mm). An unexpected result was observed: when the cMUT probe is in contact with the tube, only cMUTs belonging to the contact surface collect ultrasound, the others act like "passive-capacitances", and so as additional noise sources. The SNR of the final dispersion curve diagram was hence better for the PZT probe.

As a partial conclusion, at this step of our development, the tested cMUT probe prototype offers very nice prospects to investigate and model guided waves in non-homogeneous plate shape devices (for example, complex material or variable thickness guides). For tube shape waveguides, other prototypes are being studied with a total height smaller and more adapted to the typical range of radius dimension.



- [1] A. Boulmé *et al.*, IEEE-UFFC, **61**, 710-723 (2014)  
 [2] J.G. Minonzio *et al.*, JASA, **130**, 3574-3582 (2011)

**P5B2-3****An array transmitter for contrast enhanced intravascular ultrasound imaging**

Zhuochen Wang<sup>1</sup>, Jianguo Ma<sup>1</sup>, Karl Martin<sup>2</sup>, Paul Dayton<sup>2</sup>, Xiaoning Jiang<sup>1</sup>; <sup>1</sup>Department of Mechanical & Aerospace Engineering, North Carolina State University, Raleigh, NC, USA, <sup>2</sup>Joint Department of Biomedical Engineering, University of North Carolina and NC State University, Chapel Hill, NC, USA

**Background, Motivation and Objective**

Conventional intravascular ultrasound (IVUS) transducers with frequency of 20 MHz-60 MHz are not optimized for imaging with micro-bubble contrast agents due to the less effective micro-bubble excitation at high frequencies. However, recent study suggests that contrast ultrasound for molecular imaging or vasa vasorum assessment can be promising in identification of vulnerable plaque. Our group reported an initial success last year in developing a dual frequency IVUS transducer (6.5 MHz/30 MHz) for contrast enhanced IVUS imaging. In this paper, a low frequency transmitting array was developed to excite micro-bubbles more effectively. The contrast signal is received by a high frequency receiver. The goal is to obtain contrast enhanced IVUS imaging with high contrast to noise ratio (CNR) and high resolution more easily.

**Statement of Contribution/Methods**

This IVUS transmitting array consists of 8 PMN-PT elements, and the aperture of each element is 5 mm by 0.37 mm. The center frequency of this array is 2.25 MHz. The prototyped transmitting array was characterized by measuring the acoustic pressure profile using a hydrophone. The contrast tests will be performed by detecting high frequency echo of the nonlinear response from micro-bubbles in a micro-tube with diameter of 0.2 mm using high frequency receivers. Several transducers with central frequency of 20 MHz, 25 MHz and 30 MHz are used as receivers for comparison.

**Results/Discussion**

Initial test shows that this transmitting array can be used to transmit acoustic waves with pressure >3 MPa at 100 V excitation, which is much higher than our previous 6.5 MHz transducer and enough to induce non-linear response from micro-bubbles. Our study also shows that 2.25 MHz is more efficient to excite micro-bubbles. The receivers with different central frequency are used to find out the optimum receiving frequency for contrast imaging. The details of contrast imaging using the prototyped cylindrical transmitting array will be reported in the full paper.

**P5B2-4****A bi-frequency 7.5MHz/15MHz co-linear array**

Zhuochen Wang<sup>1</sup>, Sibol Li<sup>1</sup>, Ruibin Liu<sup>2</sup>, Xuegang Geng<sup>2</sup>, Xiaoning Jiang<sup>1</sup>; <sup>1</sup>Department of Mechanical & Aerospace Engineering, North Carolina State University, Raleigh, NC, USA, <sup>2</sup>Blatek, Inc., State College, PA, USA

**Background, Motivation and Objective**

Ultrasound imaging with high resolution and large field of depth is important in disease diagnosis, surgery guidance and post-surgery assessment. There is always a tradeoff between the resolution and depth of field in ultrasound imaging. Conventional ultrasound works at a particular frequency, with -6 dB fractional bandwidth of < 100%, limiting the resolution or field of depth in many ultrasound imaging cases. In this paper, a bi-frequency co-linear array covering a frequency range of 5 MHz-20 MHz was developed to meet the requirements of resolution and depth of field for a broad range of ultrasound imaging applications.

**Statement of Contribution/Methods**

A 7.5 MHz/15 MHz bi-frequency co-linear array was designed and fabricated. This co-linear array consists of two piezoelectric 1-3 composite layers with the same thickness and the same aperture, together with the matching, backing and flex circuit layers. The pitch of this array for both of top and bottom layers is 0.132 mm. The width of each element is 0.112 mm and the length is 4 mm. This co-linear array was designed to operate at two different modes. One is the high frequency mode (15 MHz), with the top piezoelectric layer as the active layer. In the other mode, two piezoelectric layers are activated electrically parallel at a lower frequency (7.5 MHz). The prototyped 31-element co-linear array was characterized electrically and acoustically, followed by the phantom imaging of sectorial scan (S-scan) using the Verasonics system.

**Results/Discussion**

This array was characterized element by element. The capacitance of each element is about 117 pF  $\pm$  3.23 pF and dielectric loss is about 0.018  $\pm$  0.0016. The center frequency of dual layer mode is about 7.9 MHz  $\pm$  0.99 MHz. The resonant frequency of single layer mode is 19.7 MHz  $\pm$  0.56 MHz. Axial and lateral resolution was measured with imaging of a commercial wire phantom. For the low frequency mode, axial resolution is better than 1 mm and lateral resolution is better than 2 mm. The high frequency mode will be tested with a new Verasonics system later. Beamforming and phantom imaging via Verasonics system will be reported in the full paper.

**P5B2-5****Development of a wearable ultrasonic sensor and method for continuous monitoring of mechanical properties of planter soft tissue for diabetic patients**

Bruno Trindade<sup>1,2</sup>, Yuu Ono<sup>1</sup>, Edward Lemaire<sup>2</sup>; <sup>1</sup>Department of Systems and Computer Engineering, Carleton University, Ottawa, ON, Canada, <sup>2</sup>Centre for Rehabilitation Research and Development, University of Ottawa, Ottawa, ON, Canada

**Background, Motivation and Objective**

Diabetes is a chronic disease in which the body cannot efficiently produce or use insulin. One of the long-term complications of diabetes is peripheral neuropathy, where insensitive nerves can lead to serious foot ulcerations. Studies have shown that the mechanical properties of plantar soft tissues change with diabetes. Ultrasound methods could be used to measure planter tissue thickness and mechanical properties, as a quantitative assessment tool. Diabetic shoes or orthoses are often custom-designed for each person to prevent foot injury during daily activities. The objective of this study was to develop ultrasonic method and sensors that can be embedded into footwear, in order to continuously monitor the mechanical properties of planter soft tissue during physical activities in real-time.

**Statement of Contribution/Methods**

Our previous work has demonstrated that a wearable and flexible ultrasonic sensor made of a piezoelectric PVDF film was capable of measuring the thicknesses of soft tissue layers and their changes. In order to investigate and improve the sensor performance, numerical simulations using the Mason's equivalent circuit model were conducted. The simulation results showed that the thicknesses of the polyimide insulation/protection and silicone adhesive layers used for the sensor construction affected the ultrasonic performance of the sensor due to internal reflections of ultrasound within these layers. Therefore, in the new sensor design, the protection layer was eliminated in the probing

(bottom electrode) side. Since the probing side is electrically grounded, there is no risk of electric shock to a person. In addition, the sensor's top side was electrically shielded with an aluminum foil to reduce environmental electrical noises.

### Results/Discussion

An ultrasonic sensor was constructed using a 110  $\mu\text{m}$  thick PVDF film. Its electrode size was 23 mm by 23 mm. The total thickness of the sensor was 344  $\mu\text{m}$ . Ultrasonic noises due to the internal reflections within the sensor were no longer observed with the new design. A preliminary experiment to measure the planter thickness was performed using the developed sensor. The sensor was attached onto a person's left heel. A force was applied on the heel using the person's own weight. This force was applied only on the heel area at the sensor by placing a cylindrical Plexiglas spacer, having the diameter of 27 mm and height of 10 mm, between the sensor and a balance plate. The force was measured by the plate and the pressure values at the heel were calculated. The ultrasonic signals reflected from the heel bone were acquired using the developed sensor with an M-mode frame rate of 200 Hz. Tissue thicknesses were obtained by the time-of-flight method using cross-correlation. It was successfully measured that the planter tissue thickness at the heel decreased from 14.3 mm to 8.5 mm with the pressure change from 0 to 122 kPa.

### P5B2-6

#### Crossed Array Transducer for Real-Time 3D Imaging

Andrew Joyce<sup>1</sup>, Geoff Lockwood<sup>1</sup>; <sup>1</sup>Physics, Queen's University, Kingston, ON, Canada

### Background, Motivation and Objective

Three-dimensional medical ultrasound imaging is increasingly finding new applications in diagnostic protocols. However, implementation of three-dimensional ultrasound systems remains difficult due to the high element counts required and limitations on acquisition times from the time-of-flight constraints in tissue. The objective of this research was to construct a crossed array transducer, as proposed in our previous publication [1]. The array uses two orthogonally oriented, one-dimensional arrays to focus on intersecting cross-sectional planes on transmit and on receive. This strategy allows volumetric imaging with resolution and acquisition rates that are comparable with conventional two-dimensional systems. In this paper we detail the design and implementation of a crossed array transducer using a novel piezocomposite material, an acoustically integrated interconnection scheme, and the supporting transmit electronics to excite and beamform the crossed array transducer. The transducer is characterized through its transmit radiation pattern, demonstrating performance consistent with the design objectives.

### Statement of Contribution/Methods

A 5MHz two-dimensional crossed array transducer has been built using a 50mm diameter 1-3 piezocomposite substrate. The composite has a 36% volume fraction, with 45 $\mu\text{m}$  pillars and 30 $\mu\text{m}$  kerfs, finished to a final thickness of 360 $\mu\text{m}$ . It employs a radially variable polarization scheme to alleviate edge artifacts that would otherwise be introduced due to the large aperture. The orthogonal array structures, each composed of 288 elements with  $\lambda/2$  spacing, are formed on either side of the substrate using a flexible circuit bonded to the face of the composite with the array pattern defined by the circuit board copper. The flexible circuit also serves as a matching layer in the acoustic stack and provides breakout and connection to the micro-coax cabling. An RTV-11 lens is incorporated to defocus the transmission and reception, alleviating the influence of near field effects on the radiation pattern. 288 pulse channels have been implemented to perform transmit beamforming accurate to 5ns while exciting each array element with a bipolar 200Vpp pulse. Critical to the receive performance, each pulse channel provides 2 $\Omega$  impedance to ground between transmissions to present a low-impedance receive channel.

### Results/Discussion

The transducer has been mounted onto a motion controller and the transmit radiation pattern characterized in a water tank. The profile demonstrates effective insonation of an entire cross-sectional plane consistent with the design objectives. Measured at  $f/2$ , the wavefront displays a -3dB beam spread of 36° along the defocused axis and confinement of 1mm in the beamformed axis.

[1] C. Démore, A. W. Joyce, K. Wall, and G. R. Lockwood, "Real-time volume imaging using a crossed electrode array," *IEEE Trans. Ultrason. Ferroelectr. Freq. Control*, vol. 56, no. 6, pp. 1252–1261, June 2009.

### P5B2-7

#### Fabrication and Characterization of a 20 MHz Microlinear Phased Array Transducer for Intervention Guidance

Chi Tat Chiu<sup>1</sup>, Jay A. Williams<sup>1</sup>, Bong Jin Kang<sup>1</sup>, Theodore Abraham<sup>2</sup>, K. Kirk Shung<sup>1</sup>, Hyung Ham Kim<sup>1</sup>; <sup>1</sup>Department of Biomedical Engineering, University of Southern California, Los Angeles, CA, USA, <sup>2</sup>InnoScion LLC, Baltimore, MD, USA

### Background, Motivation and Objective

Interventional procedures such as biopsy have been widely carried out in clinics for both diagnostic and therapeutic purposes of many different kinds of diseases, including cancer and cardiovascular disease. Ultrasound has been commonly used for the guidance of the interventional devices inside the patients' bodies. However, the image quality and penetration depth are limited currently as the ultrasound transducer is placed at the body surface. Therefore the aim of this project is to develop a miniature phased array transducer that can be placed next to the tip of the interventional device, so as to give a clear and simultaneous visualization of the interventional process for improving both efficiency and safety.

### Statement of Contribution/Methods

A 48-element, 20 MHz phased array has been fabricated and placed inside a needle housing with 4mm outer diameter. The 2-2 composite was made from a C-92H (Fuji Ceramics Corp., Japan) wafer by dice-and-fill method with a half-wavelength pitch for grating lobe suppression. The first matching layer was 2-3  $\mu\text{m}$  silver particles loaded epoxy and the second matching layer was Parylene. A flex circuit was bonded to the back of the composite followed by the epoxy backing block. An adaptor board was used for routing between the flex circuit and the imaging system. Pulse-echo measurements and phantom imaging were performed for performance evaluation.

### Results/Discussion

The pulse-echo testing results show a center frequency of 18.5 MHz with a bandwidth of 61%. The axial and lateral resolutions are 80  $\mu\text{m}$  and 210  $\mu\text{m}$  respectively at the focus (6 mm) from the wire phantom image. Images of a cow liver with a needle inserted were also obtained, and the needle trace was clearly visualized. The performance of the proposed phased array transducer was acceptable to be used for intervention guidance.

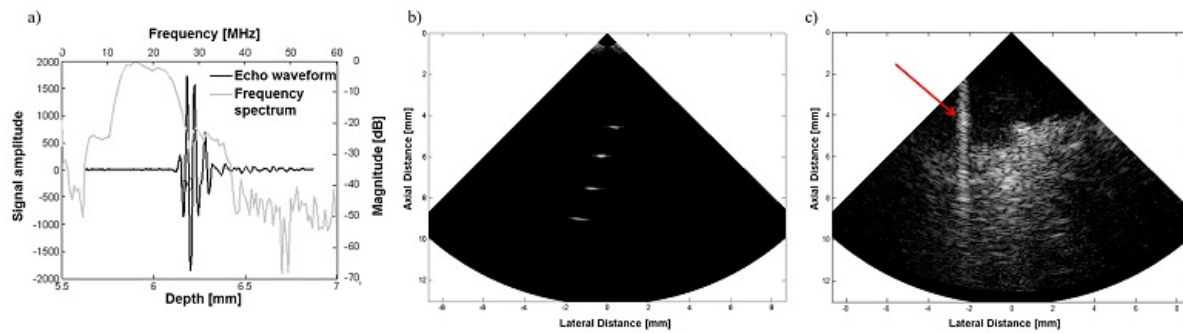


Figure 1. (a) Pulse-echo measurement results of a 20 MHz phased array, (b) image of 20  $\mu$ m tungsten wire phantom, (c) image of the needle trace (as indicated by the red arrow) in the cow liver.

P5B2-8

### Realistic acoustic simulation of 2D probe elements in simulated annealing sparse array optimization

Emmanuel Roux<sup>1,2</sup>, Bakary Diarra<sup>1</sup>, Marc Robini<sup>1</sup>, Christian Cachard<sup>1</sup>, Piero Tortoli<sup>2</sup>, Hervé Liebgott<sup>1</sup>, <sup>1</sup>CREATIS, Université de Lyon; CNRS UMR 5220 INSERM U1044; Université Claude Bernard Lyon 1; INSA-Lyon, France, <sup>2</sup>Information Engineering Dept, Università degli Studi di Firenze, Italy

#### Background, Motivation and Objective

The optimization of 2D sparse array ultrasound probes is frequently based on the simulated annealing algorithm. The cost function controlling the optimization process is directly related to the probe radiating pattern (RP) through the measurement of the main lobe width and the sidelobes level. However, most proposed approaches compute the RP by considering the active elements as punctual omnidirectional acoustic radiators. This analytical model reduces the computation time but does not take into account the transducer elements characteristics. In this work, we investigate the benefits of integrating a realistic pressure field computation within the optimization process of a 2D non-grid sparse array probe. A short computation time is achieved by updating only the modified element contribution to the full RP.

#### Statement of Contribution/Methods

Let us consider a 3.5 MHz sparse array probe made of 256 rectangular elements with short side size equal to  $a = \lambda/2$ . The integration of a realistic pressure field in the optimization process was made using FIELD II simulation software which allows the size, orientation or even the shape of the elements as new degrees of freedom in the optimization process. At each step of the optimization a single element is randomly translated by  $\pm a$  mm and randomly apodized by  $w_i = [0.1-1.0]$ . Because of this change, the RP and the cost function have to be updated. Since the full RP simulation repeated at each step would take too much time, in our method a full simulation is done only at the beginning of the algorithm. Afterwards, the RP is updated by replacing only the contribution of the modified element.

#### Results/Discussion

The new technique was tested for optimizing a 256 rectangular elements 2D sparse array probe. The size of the elements was set to  $a = \lambda/2 = 0.22$  mm on the x-axis and  $b = \lambda(1+\sqrt{5})/4 = 0.36$  mm on the y-axis. With our MATLAB implementation on a i7-3740QM 2.7GHz CPU machine, the initial RP was computed in 8 seconds. The  $180 \times 180 = 32400$  RP measurement points were equally spaced on the half sphere of radius 70 mm centered on the probe. At each step the RP was updated, on average, in 0.9 seconds. Fig 1 shows the RPs of two probes having elements with the same size and position but perpendicular orientations. While with the omnidirectional model the RP would have been the same for the two layouts, this example illustrates the importance of having a realistic simulation tool.

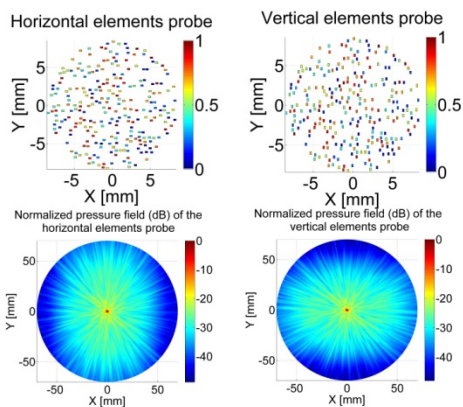


Fig 1 horizontal (left) and vertical (right) orientations of the rectangular elements of the probe  
top: footprints of the 256 elements  
bottom: RP at 70 mm

P5B2-9

### Improvement of Driving Efficiency of Ultrasonic Motor by Improvement of Vibration Configuration

Shogo Kumamoto<sup>1</sup>, Kenjiro Takemura<sup>1</sup>, Kyohei Hosoda<sup>1</sup>, <sup>1</sup>Keio Univ, Japan

#### Background, Motivation and Objective

Ultrasonic motors are the frictionally driven motor in which the vibration energy of stator is converted to the kinetic energy of rotor via friction force between stator/rotor. It has superior features such as high torque at low speed etc. However, the problem is the wear between stator/rotor which decreases the efficiency. Hence we propose a novel method to reduce the wear and improve the efficiency.

# Statement of Contribution/Methods

Since the contact points on the stator draw elliptic trajectory when driving ultrasonic motors, the relative speed of the points against the rotor varies even when the rotor speed is constant. This relative speed variation causes the wear between stator/rotor. So, we propose a method to modify the time history of this relative speed to become a square wave, i.e., when a contact point is in contact with the rotor, the stator speed may become almost equal to the rotor speed resulting in reducing the wear. We will superimpose high-frequency component to the driving signal to modify the trajectory of each contact point. In order to verify the proposed method, we have conducted numerical analysis. In the numerical analysis, the rotor is modeled with discrete spring-mass system. The elasticity of the rotor in tangential/normal directions is expressed by springs with spring coefficient of  $k_x$  and  $k_y$ , respectively. The output force and efficiency of the motor are calculated from the spring force and frictional force. The  $k_x/k_y$  is set to 0.1, 1 and 10.

# Results/Discussion

Figure1 and Figure2 shows the relation between normalized thrust ( $F_x/F_y$ ) and efficiency. It is obvious that with the small  $F_x/F_y$ , the efficiency becomes close to 1. Comparing Figure1 and Figure2, only small difference appears in the case of  $k_x/k_y = 0.1$  and 1, however, in the case of  $k_x/k_y = 10$ , the efficiency is improved by 27%.

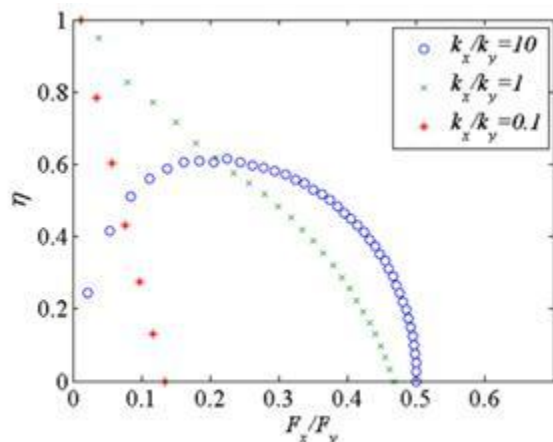


Figure. 1 General ultrasonic motor

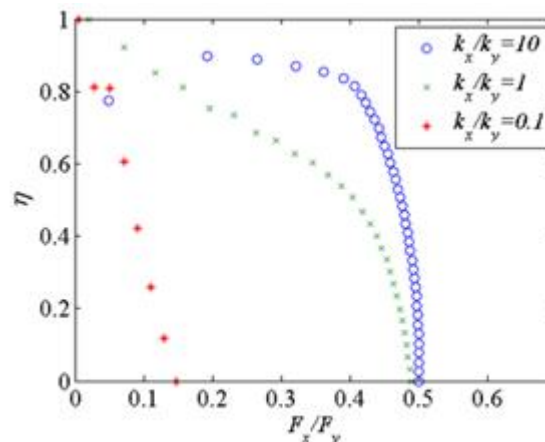


Figure. 2 proposed ultrasonic motor

P5B2-10

# Analysis of transmitter-receiver designs for a miniature matrix TEE probe

Shreyas Raghunathan<sup>1</sup>, Sandra Blaak<sup>2</sup>, Deep Bera<sup>3</sup>, Chao Chen<sup>4</sup>, Michiel Pertijs<sup>4</sup>, Johan Bosch<sup>3</sup>, Nico de Jong<sup>1,3</sup>, Martin Verweij<sup>1</sup>; <sup>1</sup>Lab. Of Acoustic Wavefield Imaging, Delft University of Technology, Delft, Netherlands, <sup>2</sup>Oldelft Ultrasound, Delft, Netherlands, <sup>3</sup>Dept. of Biomedical Engineering, Erasmus MC, Rotterdam, Netherlands, <sup>4</sup>Electronic Instrumentation Laboratory, Delft University of Technology, Delft, Netherlands

# Background, Motivation and Objective

We propose and evaluate different transducer designs for a miniature three-dimensional (3D) transesophageal (TEE) probe (head volume  $\approx 1$  cm<sup>3</sup>) that would be suitable for use in neonates or for prolonged transnasal use in adults.

# Statement of Contribution/Methods

Within the available aperture of 25mm<sup>2</sup>, an array of 33x33 elements was analysed. The frequency was chosen near 5 MHz for a penetration depth of 12-15 cm. To limit the number of cables, the array is mounted on an application-specific integrated circuit (ASIC) for local data reduction by microbeamforming. We focus on partitioned designs, in which a minority of transmit elements is directly wired out and the majority of receive elements connect to a limited number of receive cables via the ASIC, implemented in dense low-voltage technology. The designs are evaluated based on the pressure and beam width of the transmitted field, and the resolution, grating lobes and side lobes of the received field.

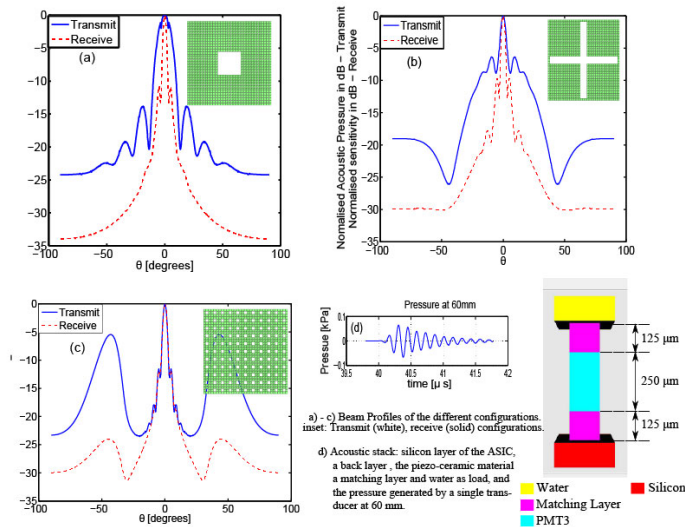
The acoustic stack (Fig 1d) was optimized using the FEM modelling software PZFlex. Further, different configurations for the transmitter and receiver were simulated with FieldII to obtain their corresponding beam profiles: a central transmitter (Fig 1a), a cross transmitter (Fig 1b) and a staggered transmitter configuration (Fig. 1c)

# Results/Discussion

The pressure generated at the surface of a single optimized transducer element (resonance frequency 5.3 MHz) was estimated to be 25 kPa/V. A 9x9 central transmit array (as shown in Fig. 1a) generated a peak to peak pressure of 125 kPa for an excitation voltage of 50Vpp at a depth of 60 mm. The design involving this central transmitter (fig 1a) benefits from a larger opening angle of 11.4 degrees (-3dB points) in comparison to about 3 degrees with the other two designs. In addition, the design in Fig 1c is unsuitable due to the presence of grating lobes. Side lobes appear in the receiver's beam profile for all of the proposed designs +5 and -5 degrees, with their heights around -10dB.

The comparison between various configurations for partitioned transmit-receive designs for a matrix transducer indicate the advantages of a central transmitter over a cross transmitter and a staggered transmitter configuration.





P5B2-11

### Rigorous Analytical Analysis of Resonant Euler-Bernoulli Beams with Constant Thickness and Polynomial Width

Roman Beigelbeck<sup>1</sup>, Michael Schneider<sup>2</sup>, Michael Stifter<sup>1</sup>, Thomas Voglhuber-Brunnmaier<sup>1,3</sup>, Franz Keplinger<sup>2</sup>, Ulrich Schmid<sup>2</sup>, Bernhard Jakoby<sup>3</sup>; <sup>1</sup>Center for Integrated Sensor Systems, Danube University Krems, Wiener Neustadt, Austria, <sup>2</sup>Institute of Sensor and Actuator Systems, Vienna University of Technology, Vienna, Austria, <sup>3</sup>Institute for Microelectronics and Microsystems, Johannes Kepler University Linz, Linz, Austria

#### Background, Motivation and Objective

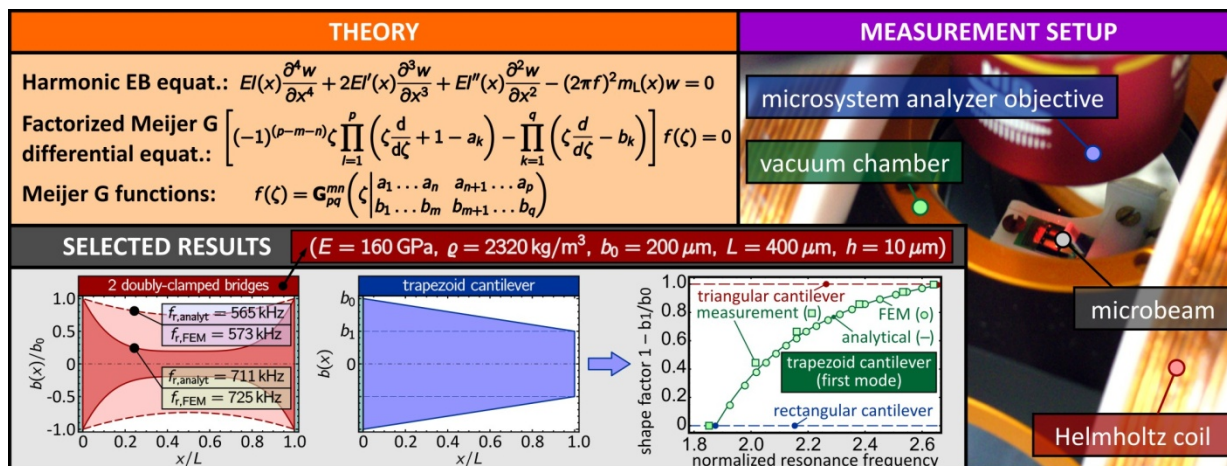
The operation of many ultrasonic transducers relies on resonant flexural vibrations of non-uniform Euler-Bernoulli (EB) beams. Accurate design of such devices requires detailed knowledge of the beams' resonance characteristics, where the governing theory was enunciated more than a quarter-century ago. Since then, many approximate and computational models for a variety of beam shapes as well as some exact solutions for a few particular geometries have been reported. Wherever feasible, analytical solutions are preferred as it is difficult to draw general conclusions using only numerical methods. However, no all-embracing exact closed-form solutions for EB beams are known hitherto. In this contribution, we study the vibration characteristics of a very general class of EB beams with in  $x$ -direction varying stiffness  $EI(x)$  and mass per unit length  $m_L(x)$  but constant  $EI(x)/m_L(x)$  -ratio analytically and present novel exact solutions in order to bridge the gap between known results.

#### Statement of Contribution/Methods

We apply the EB theory to beams with a constant thickness  $h$  and a polynomially varying width  $b(x)$ . Next, the arising fourth order differential equation with non-constant coefficients is factorized by a sophisticated non-linear transformation into a Meijer G differential equation. Afterwards, its general solution can be written in terms of four linearly independent Meijer G functions which can be efficiently computed. At this point, this closed-form solution is independent of the clamping conditions and is therefore valid for arbitrary beam types like cantilevers or bridges. Finally, straightforward fitting of four boundary conditions yields characteristic equations for natural frequencies  $f_i$  and mode shapes up to any order.

#### Results/Discussion

Our solution allows analytically studying of a comprehensive class of flexural beam vibration problems which has not been possible hitherto and has thus high potential in modern vibration tailoring. We validate our method by finite element simulations and measurements carried out on cantilevers and bridges with varying widths  $b(x)$  (e.g. trapezoid and quadratic), where the specimens are fabricated by silicon micromachining. During the experiments, the beams are placed in a vacuum chamber, excited to vibrations by Lorentz forces and measured by Laser Doppler vibrometry to obtain their transverse deflection  $w(x)$ .





# 1H - MIM: Ultrasound Tools to Guide Cardiac Interventions

Grand Ballroom

Saturday, September 6, 2014, 8:00 am - 9:30 am

Chair: **John Hossack**  
Univ. of Virginia, Charlottesville

1H-1

## 8:00 am Augmented Trans-esophageal Ultrasound for Guidance of Cardiac Interventions

Terry Peters<sup>1</sup>; <sup>1</sup>Robarts Research Institute, Canada

### Background, Motivation and Objective

Traditional surgical approaches for repairing diseased mitral valves (MVs) have relied on placing the patient on cardiopulmonary bypass (on pump), stopping the heart and accessing the arrested heart directly. However, because this approach has the potential for adverse neurological, vascular, and immunological consequences, less invasive beating heart alternatives are desirable.

Emerging beating heart techniques have been developed to offer high-risk patients MV repair using ultrasound guidance alone without stopping the heart. One such approach involves accessing the mitral valve via the apex of the heart, and effecting the repair while it is still beating

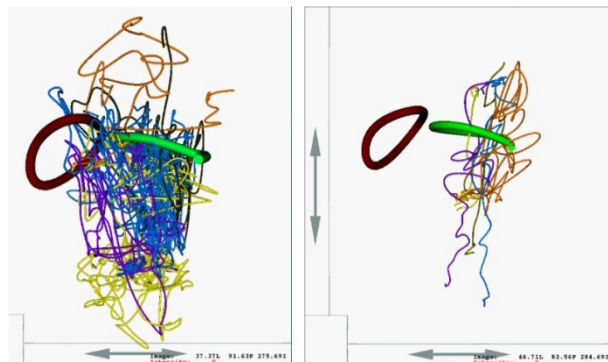
### Statement of Contribution/Methods

This procedure is usually performed under the guidance of simultaneous bi-plane Ultrasound, with occasional reference to a real-time 3D image to confirm positioning. 3D US is not used throughout the procedure due to its lower resolution relative to the bi-plane 2D images, its restricted field of view, and the excessive heat generated within the trans-esophageal probe. However, even under these conditions the procedure can be lengthy, and the probe can potentially enter into danger zones within the left ventricle.

To address these issues we have developed an "augmented-virtuality" system that adds minimally to the surgical workflow, while greatly facilitating the navigation procedure. In and animal study involving experienced cardiac surgeons using this system, We demonstrate a reduction in navigation time by a factor of 5, and in the trajectory path length by a similar amount. We also identified that the number of potential "danger-zone" incursions was in one case reduced by a factor of 40.

### Results/Discussion

This study highlights the fact that while ultrasound is increasingly becoming the imaging modality to guide minimally-invasive procedures, US imaging alone may not always be sufficient for successful completion of the procedure. While registration of pre-operative datasets has often been proposed as a solution, this approach can lead to cognitive overload on the part of the surgeon. Our augmented Virtuality approach provides a low cost alternative to enhance the navigation stage of a procedures, leaving the US image as the primary means of finally positioning the instrument on target, once the navigation step has been successfully completed.



Left: Tool trajectories from 5 surgeons using US guidance alone. Right: Trajectories from the same surgeons using AV guidance. Target is mitral-valve annulus in green

1H-2

## 8:30 am Segmentation of multiple heart cavities in wide-view fused 3D transesophageal echocardiograms

Alexander Haak<sup>1</sup>, Harriet Mulder<sup>2</sup>, Ben Ren<sup>3</sup>, Gonzalo Vegas-Sanchez-Ferrero<sup>4</sup>, Gerard van Burken<sup>5</sup>, Marijn van Stralen<sup>2</sup>, Antonius van der Steen<sup>5</sup>, Josien Pluim<sup>2</sup>, Theo van Walsum<sup>6</sup>, Johan Bosch<sup>5</sup>; <sup>1</sup>Erasmus MC, Rotterdam, Netherlands, <sup>2</sup>Image Sciences Institute, University Medical Center Utrecht, Netherlands, <sup>3</sup>Cardiology, Erasmus MC, Netherlands, <sup>4</sup>Image Processing Laboratory, Valladolid University, Spain, <sup>5</sup>Erasmus MC, Netherlands, <sup>6</sup>Medical Informatics & Radiology, Erasmus MC, Netherlands

### Background, Motivation and Objective

Three-dimensional transesophageal echocardiography (3D TEE) is an excellent modality for real-time visualization of the heart and monitoring of interventions. However, 3D TEE segmentation is still a challenging task due to the complex anatomy, typical ultrasound artifacts, and the limited field of view. To improve the segmentation accuracy of the left atrium we created wide-view TEE images by fusing several individual recordings.

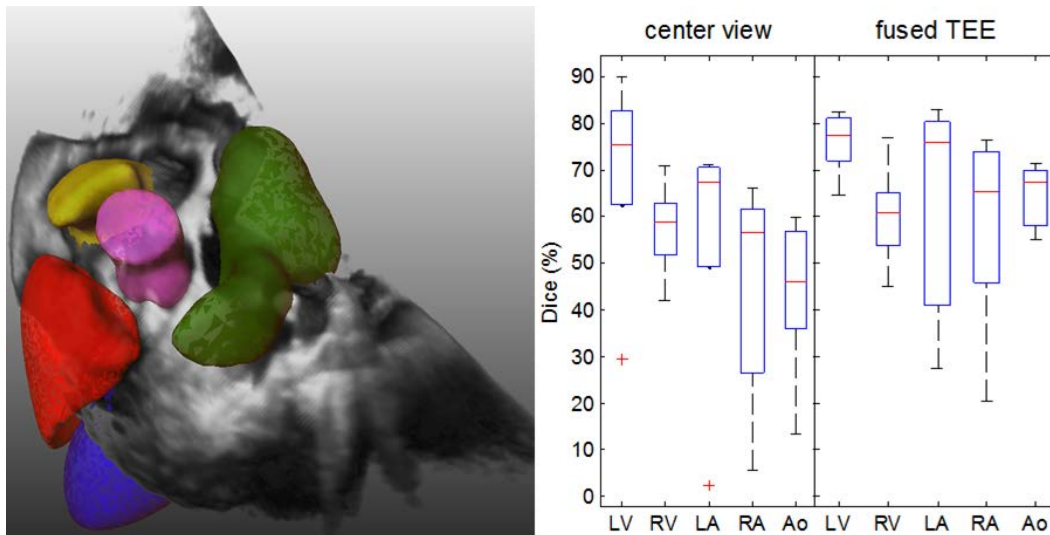
**Statement of Contribution/Methods**

For five patients, four individual 3D TEE volumes were acquired (Philips X7-2t) by manipulating (e.g. rotating) the TEE probe head in the esophagus. CTA images were also acquired in these patients and segmented automatically by an atlas-based method, which served as ground truth (GT). The TEE volumes were manually registered by aligning them first with the CTA volume and afterwards with each other. The individual TEE sets were fused using a maximum intensity projection. Five cavities, containing left and right ventricle, left and right atrium and aorta (LV, LA, RV, LA, Ao) were segmented (fig. left) using a three stage segmentation scheme using an active shape model (ASM) and tissue probability maps estimated by a two class Gamma mixture model. The multi-cavity shape model was generated by Principal Component Analysis from a large database of segmented CTA images. The ASM stages involved a rigid transform fitting of the model, a shape updating stage for the total model and a refinement stage for each individual cavity model.

The Dice coefficients for the individual cavities between the TEE segmentations and the GT CTA segmentations were computed (fig. right). We compared the quality of the segmentation results on the fused TEE sets with those using only the central single TEE view.

**Results/Discussion**

There was a considerable improvement of the Dice coefficients for the fused data sets. The median increase of the Dice coefficients was 2, 3, 12, 10, and 13 percent points for LV, RV, LA, RA, and Ao respectively. These results show that image fusion significantly improves the segmentation of the cavities close to the TEE probe head (LA, RA, and Ao).

**1H-3****8:45 am Augmented reality based tools for echocardiographic acquisitions**

Gabriel Kiss<sup>1</sup>, Sigurd Storve<sup>1</sup>, Bjørn Olav Haugen<sup>1</sup>, Hans Torp<sup>1</sup>; <sup>1</sup>MI Lab and Department of Circulation and Medical Imaging, ISB, NTNU, Trondheim, Norway

**Background, Motivation and Objective**

It is envisioned that tablet based ultrasound systems will be targeting non-expert users in the near future. However ultrasound is operator dependent and requires an extensive training process. The aim of this work is to provide visual guidance during scanning and as such improve the understanding of the anatomy that is currently being imaged.

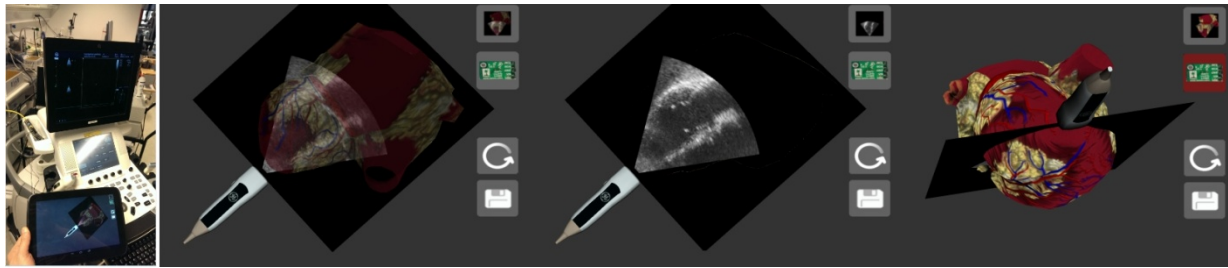
**Statement of Contribution/Methods**

A highly descriptive anatomical mesh model of the heart is adapted and deformed to the patient, based on data acquired in real-time. The non-linear deformation of the mesh is derived from a set of anatomic landmarks, which are identified and then tracked throughout the cardiac cycle by using Real-time Contour Tracking Library (RCTL). The same landmarks were identified manually on the anatomic heart model and both a rigid alignment matrix and an elastic deformation simulating the movement of the mitral plane have been computed. An inertial measurement unit (IMU, Pololu, MinIMU-9) has been attached to the probe and is used to track its orientation. A custom plugin that receives as input 3D volumes and generates as output the landmarks together with a corresponding 2D slice was implemented on an ultrasound scanner (GE Vivid E9). The data is sent via a local wireless connection to a general purpose Android tablet (Nexus 10, Samsung). The IMU information is also sent to the tablet and synchronized with the echo data. The final step is image compositing whereby all elements are placed in a virtual 3D scene and displayed on the device. This was implemented on the tablet in OpenGL SL to obtain real-time performance.

**Results/Discussion**

Cardiac acquisitions were taken on two healthy volunteers from the apical window, without ECG triggering. The depth and angle of the ultrasound sector were adjusted such that the entire left ventricle was covered. Figure 1 shows the system setup and typical renderings obtained with our prototype. Depending on scanner settings between 6 and 10 frames per second were achievable.

The developed tool presents the user a highly informative visualization, furthermore it can be used for teaching purposes as the compounded visualization allows for a faster correlation between the ultrasound image and the cardiac anatomy during live scanning. Using the IMU device allows for more accurate probe movement tracking and to visualize its influence on the acquired image.



1H-4

#### 9:00 am Identification and Optimization of Response to Cardiac Resynchronization Therapy using Electromechanical Wave Imaging

Ethan Bunting<sup>1</sup>, Litsa Lambrakos<sup>2</sup>, Elisa Konofagou<sup>1,3</sup>; <sup>1</sup>Department of Biomedical Engineering, Columbia University, New York, New York, USA, <sup>2</sup>Division of Cardiology, Columbia University, New York, New York, USA, <sup>3</sup>Department of Radiology, Columbia University, New York, New York, USA

##### Background, Motivation and Objective

Although cardiac resynchronization therapy (CRT) has been shown to improve symptoms and decrease mortality in large populations of mid-to-late stage heart failure (HF) patients, a relatively high percentage of patients (30–40%) do not derive any benefit from CRT and are considered non-responders. Therefore, there is increasing interest among cardiologists to discover new criteria for patient selection other than the ECG parameters currently used. Recently, patient-specific optimization of CRT has been discussed, which is made possible by using multipolar pacing leads in the left ventricle (LV). Electromechanical wave imaging (EWI) is a novel technique that is able to map the electromechanical wave, i.e. the transient mechanical strains that occur in response to electrical activation. The electromechanical wave can be visualized at a high temporal (2000 Hz) and spatial (< 1 mm) resolution, and has been shown to closely correlate with the electrical activation sequence. EWI has previously been shown capable of imaging the electromechanical activation sequence in sinus rhythm in mice, canines, and humans. In human subjects undergoing CRT, EWI has also been shown capable of identifying right ventricular (RV) pacing compared to LV pacing.

##### Statement of Contribution/Methods

EWI was performed in eight HF patients (including four non-responders) with implanted CRT devices and in three normal subjects. HF patients were scanned in their native rhythm without CRT and using their preprogrammed CRT settings. Additionally, three patients with multipolar LV leads were scanned using several different pacing vectors. Axial inter-frame displacements were estimated at high precision using 1-D cross-correlation of RF signals acquired in transthoracic four-chamber views with a Verasonics system and a 2.5 MHz phased-array probe. Strains were computed using a least-squares strain estimation technique. Electromechanical activation times, defined by the sharp transition from near-zero to negative strain, were presented in the form of isochronal maps for each pacing protocol. Lateral wall activation times (LWAT) were computed by calculating the average of EWI activation times in the left ventricular lateral wall.

##### Results/Discussion

EWI was shown capable of distinguishing normal subjects from HF patients by mapping delayed LV electromechanical activation in HF patients. LWAT for HF patients in native rhythm was found to be significantly higher (139.0±32.2 ms) compared to normal subjects (81.7±23.5). Furthermore, unlike CRT non-responders, CRT responders showed a significant decrease in LWAT when CRT was initiated. EWI was also able to detect a difference in electromechanical activation arising from the different pacing vectors initiated by the multipolar LV lead in 3 patients. These results indicate that EWI may be used as an adjunct tool in the clinical routine to monitor CRT treatment and identify optimal LV pacing vectors from multipolar leads.

1H-5

#### 9:15 am Ultrasound current source density imaging of the electrocardiogram in live rabbit hearts

Yexian Qin<sup>1</sup>, Qian Li<sup>2</sup>, Pier Ingram<sup>1</sup>, Russell Witte<sup>1,2</sup>; <sup>1</sup>Medical Imaging, University of Arizona, Tucson, Arizona, USA, <sup>2</sup>College of Optical Sciences, University of Arizona, Tucson, Arizona, USA

##### Background, Motivation and Objective

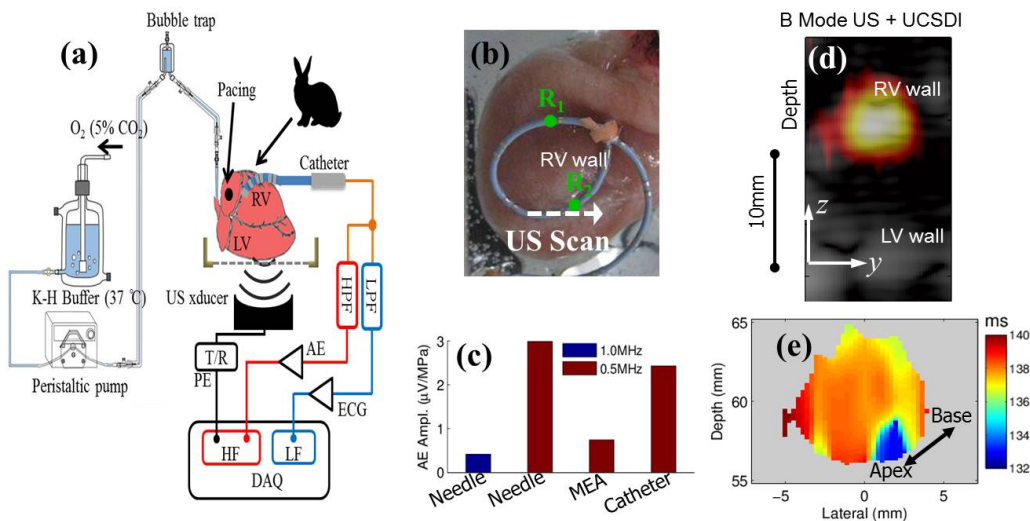
Ultrasound current source density imaging (UCSDI), based on the acoustoelectric (AE) effect, is a noninvasive method for mapping electric current fields in 4D (space + time). This technique potentially overcomes limitations (e.g., poor spatial resolution, time consuming, prone to registration errors) of conventional mapping procedures used during treatment of arrhythmias or epilepsy. However, the AE signal associated with biocurrents in the heart and brain is very weak. To optimize the sensitivity of UCSDI for mapping the electrocardiogram (ECG), we examined the effects of the electrode configuration and the ultrasound frequency on the AE signal.

##### Statement of Contribution/Methods

Four hearts were excised from white New Zealand rabbits and kept alive for several hours using a Langendorff system (Fig. 1a). 2,3-Butanedione monoxime solution was added to the perfusion buffer to suppress the mechanical contractions. Two stimulating electrodes were placed on the right atrium for pacing the heart. Recording electrodes from clinical catheter were placed on the surface of right ventricle (RV) (Fig. 1b). An ultrasound transducer was focused on the wall of the ventricle and scanned across the heart. At each scan position, pulse echo and AE traces were collected every 0.5 ms during each cardiac cycle. The amplitude of the AE signal was compared for each recording configuration. The peak time of the ECG<sub>AE</sub> signals was used to generate a cardiac activation map.

##### Results/Discussion

Fig. 1 (c) depicts the AE sensitivity at two different ultrasound frequencies and three different recording configurations: intramuscular needle, epicardial (planar array), and epicardial (catheter). The results indicate that the needle electrodes and catheter at 0.5 MHz transducer yielded the best sensitivity. Fig. 1 (d) displays B mode UCSDI (colors) superimposed with the simultaneously measured PE image (gray). The scan region and direction are marked in Fig. 1 (b). A strong AE signal was observed near the recording electrode in the ventricle wall. Fig. 1(e) presents the ECG<sub>AE</sub> activation map of the same B-mode cross-section in Fig. 1 (d). The image illustrates proper activation from base to apex with a mean conduction velocity of 1.31 m/s, which is consistent with atrial pacing. The results demonstrated the potential of UCSDI for rapid, noninvasive volume mapping of electrical propagation in the heart.



## 2H - MEL: Elasticity Imaging Methods II

Waldorf

Saturday, September 6, 2014, 8:00 am - 9:30 am

Chair: **Caterina Gallippi**  
University of North Carolina, Chapel Hill

2H-1

### 8:00 am Micro-Elasticity ( $\hat{\mu}$ -E): Contrast, CNR, and Resolution of Acoustic Radiation Force Impulse Imaging and Single- and Multiple Track Location Shear Wave Elasticity Imaging for Visualizing Small Targets.

Peter Hollender<sup>1</sup>, Stephen Rosenzweig<sup>1</sup>, Kathy Nightingale<sup>1</sup>, Gregg Trahey<sup>1,2</sup>; <sup>1</sup>Biomedical Engineering, Duke University, Durham, North Carolina, USA, <sup>2</sup>Radiology, Duke University, Durham, North Carolina, USA

#### Background, Motivation and Objective

A number of elasticity imaging techniques have been developed in recent years that combine focused Acoustic Radiation Force to generate shear displacements in tissue with high frame rate ultrasound to monitor and characterize the induced mechanical response. Acoustic Radiation Force Impulse (ARFI) images the magnitude of induced displacements, while Shear Wave Elasticity Imaging (SWEI) images the local propagation velocity of the generated shear waves. Traditional SWEI images are made by comparing motion measured at multiple offset tracking locations (MTL) from a single push. Recently, the use of multiple offset push locations and a single tracking location (STL) to create STL-SWEI images has been demonstrated to suppress speckle bias noise. STL-SWEI may be able to image significantly smaller targets than MTL-SWEI, with improved CNR. This work compares the three imaging modalities in a controlled phantom experiment.

#### Statement of Contribution/Methods

Six highly-sampled (0.15 mm push and track beam spacing) matched ARFI, STL-SWEI and MTL-SWEI images were acquired in an elasticity phantom at each combination of five sizes and four elasticities for 20 cylindrical targets. Contrast, contrast-to-noise ratio (CNR), and both lateral and axial edge resolution were computed in each image with different levels of spatial filtering.

#### Results/Discussion

All modalities show visualization of the large, high contrast lesions, with ARFI and STL-SWEI showing best resolution of the small, low contrast lesions. ARFI demonstrated the highest resolution, while STL-SWEI had the best CNR. While STL-SWEI and ARFI images have a longer minimum acquisition time than MTL-SWEI, their improved resolution and CNR makes them good candidates for visualization and characterization of small targets.

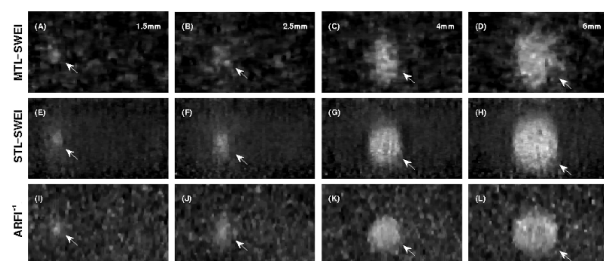


Figure 1: MTL-SWEI (top row), STL-SWEI (middle row) and inverse ARFI (bottom row) images of  $G = 9.33$  kPa cylindrical inclusions of four different sizes. STL-SWEI has the least background noise, and ARFI and STL-SWEI have better edge resolution than MTL-SWEI.

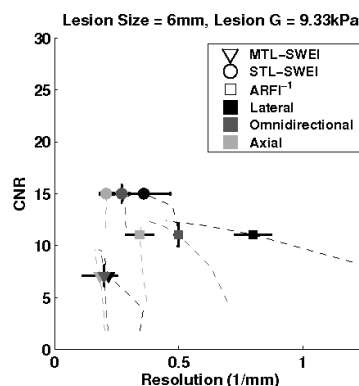


Figure 2: CNR - resolution tradeoff for the three imaging modalities. The dotted line shows the change in the mean associated with varying degrees of spatial filtering. ARFI shows the highest resolution, while STL-SWEI has the best CNR.

2H-2

### 8:15 am High Frame Rate Ultrasound Displacement Vector Imaging

Pieter Kruizinga<sup>1</sup>, Frits Mastik<sup>1</sup>, Johannes G Bosch<sup>1</sup>, Nico de Jong<sup>1,2</sup>, Gijs van Soest<sup>1</sup>, Antonius FW van der Steen<sup>1,3</sup>; <sup>1</sup>Thorax Center, Erasmus MC, Netherlands, <sup>2</sup>Delft University of Technology, Delft, Netherlands, <sup>3</sup>Shenzhen Institutes of Advanced Technology, Chinese Academy of Sciences, Shenzhen, China, People's Republic of

#### Background, Motivation and Objective

The tissue displacement vector obtained with high frame rate (HFR) imaging may provide valuable diagnostic information. Measuring 2D displacements caused by rapid dynamic processes, such as arterial pulse waves or shear waves, requires inter-frame displacement precision in the  $\mu$ m range. Conventional vector estimation techniques do not satisfy this criterion. In this paper we describe a new robust technique for estimating the 2D displacement vector with the required precision. We provide an exact solution for a moving scatterer using non-beamformed array data. Echoes reflected from a moving scatterer will cause unique delays along the elements of an array. For each pair of elements the solution for the new scatterer position is exact. By averaging many pair-wise estimates we find a robust estimation of the new scatterer location and thereby the displacement vector.



### Statement of Contribution/Methods

We validated our method experimentally with nine isolated rotating scatterers (1mm diameter metal rods) in water. We applied HFR plane wave imaging with 3.1 kHz frame rate. The ultrasonic plane waves (2 cycle, 8 MHz) were transmitted using a 128 element (4-9 MHz, -6dB bandwidth) linear array (Vermon). The array was interfaced with a 128 channel programmable ultrasound system using 12 bits, 80 MHz sampling (Lecoeur Electronique). The rods were rotated for a period of 0.7 sec covering 90° rotation. Sample specific delays were computed by subtracting the phase of the analytical signals prior to beamforming. We estimated a displacement vector with the new algorithm for each reconstructed image and each image pixel above a -10dB envelope threshold.

### Results/Discussion

Figure 1(a) shows a B-mode frame acquired during this scan with the frame-to-frame displacement vectors in colour overlay. The superimposed vectors were computed using the average displacement values of the neighbouring pixels. Figure 1(b) and (c) shows the scan average displacement values for the x and z direction respectively. For an isolated scatterer we can estimate the displacement in the x and z direction with a position standard deviation of  $\pm 50\text{nm}$  ( $\# = 1$ ). Further research is now directed towards in-vivo tissue displacement vector estimation in the carotid artery. The overall aim is to improve the 2D elastographic assessment of lesions within diseased carotid arteries.

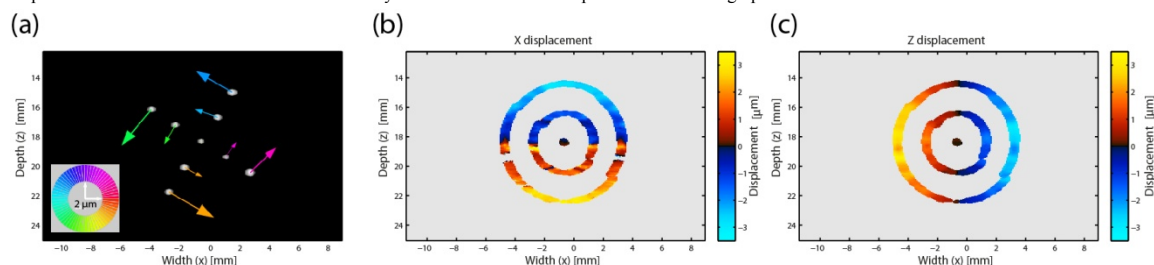


Figure 1: a) B-mode high frame rate image of nine rotating rods in water. The superimposed coloured vectors are computed with the new displacement estimation algorithm. Subfigures (b) and (c) are average projections of the displacement values found for all the rods in the x and z direction respectively.

## 2H-3

### 8:30 am Two Frequencies Push-Pull Differential Imaging

Andrzej Nowicki<sup>1</sup>, Michal Byra<sup>1</sup>, Jerzy Litniewski<sup>1</sup>, Janusz Wójcik<sup>1</sup>; <sup>1</sup>Ultrasound Department, Institute of Fundamental Technological Research, Polish Academy of Sciences, Warsaw, Poland

### Background, Motivation and Objective

In a reflection based US imaging the different stiffness regions in the homogenous tissue are not easily resolved. We are proposing a novel approach called Two Frequencies Push-Pull Differential Imaging (PPDI) to differentiate regions with different elastic properties by probing the tissue simultaneously using combination of two pulses differing in frequency and pressure.

### Statement of Contribution/Methods

PPDI is based on additional compression and rarefaction of the scanning tissue. Two pulses are transmitted along each scanning line. First with the high frequency probing pulse superimposed on the low frequency pulse, starting with positive slope, so propagating on the maximum compression resulting in maximum displacement. On the second transmission the low frequency pulse is inverted, so the imaging pulse coincides now with the maximum of the rarefaction. It means that in both sequences the tissue under examination is slightly modified in terms of its material constants affecting the local acoustic impedance and scattering properties.

Although the local tissue displacements are considered small, even at high pressures, on the order of a few  $\mu\text{m}/\text{MPa}$ , well below the threshold of detection by ultrasound, the gradients of displacements are large enough. Thus the differentiating of the material properties can be based on an examination of the backscattered echoes from the spatially variable impedance profile caused by the pressure wave.

The novel imaging system consists of two transducers; an imaging spherical transducer with operating frequency of 7MHz placed in the opening of a concave transducer with lower operating frequency of 1.1MHz. The pressure distribution of the combined pulse was measured using a needle hydrophone. A mechanical scanning was performed over a homogeneous tissue mimicking phantom. After processing including subtraction of the echoes from two subsequent transmissions, the differential images were reconstructed.

### Results/Discussion

Fig. 1 shows images obtained using standard technique and the PPDI with ROI where beam from the low frequency/high pressure transducer was focused. Comparison of probing pulses results in change of the image in ROI. It is clear that adding low frequency pulsing improve the detectability of tissue with modified stiffness - hardly visible speckles in a standard image are clearly shown after PPDI processing.

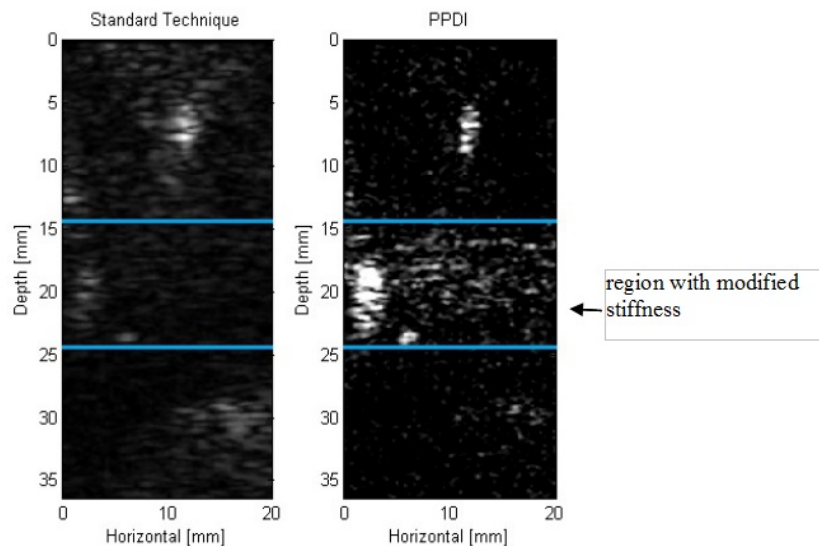


Fig 1. Standard imaging (left) and PPDI (right).

2H-4

#### 8:45 am Strain Estimator based on Analytical Phase Tracking

Lili Yuan<sup>1</sup>, Peder C Pedersen<sup>1</sup>, <sup>1</sup>ECE, Worcester Polytechnic Institute, Worcester, MA, USA

##### Background, Motivation and Objective

This paper presents an analytical phase tracking (APT) method for strain determination, suitable for imaging elastic properties of biological tissues. Most current strain methods are correlation based and as such are usually slow, suffer from limited resolution and are error prone for large displacements. The APT method achieves its advantages of faster processing, higher axial resolution and less susceptibility to large displacement errors by operating simultaneously across all RF lines.

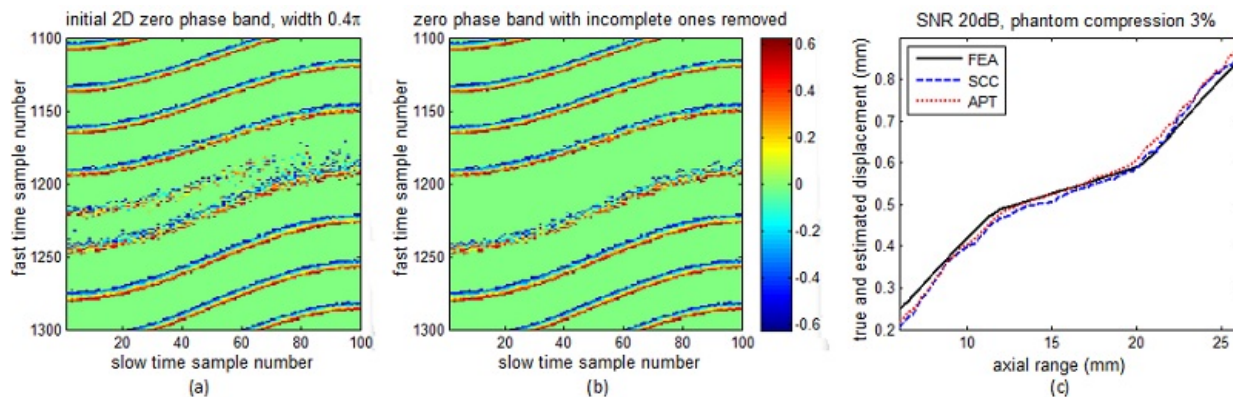
##### Statement of Contribution/Methods

The APT method involves 4 steps: 1) based on acquired RF signals, produce analytical amplitude and wrapped phase matrices as a function of axial range (fast time) and the applied force (slow time); 2) create zero phase bands across the phase matrix by retaining only phase values in a small range, e.g.  $\pm 0.2\pi$  (Fig. (a)); 3) track zero phase bands across the phase matrix to obtain the fast time shifts of the zero phase bands between pre- and peak-compression; 4) convert the time shifts to displacement versus range with one sample per wavelength resolution and calculate strain.

While most of the zero phase bands are continuous across the slow time dimension of the phase matrix, abnormalities occur in the form of discontinuities, bifurcations or mergers, correlated with low analytical signal amplitudes. This is remedied as follows: 1) apply an amplitude threshold filter to the zero phase bands, eliminating bifurcating or merging phase bands; 2) remove discontinuous phase bands using connected component labeling, leaving only the complete phase bands (Fig. (b)). Figure (c) displays three displacement curves: A reference curve determined by Finite Element Analysis (FEA); estimation based on standard time domain cross correlation (SCC); estimation based on APT.

##### Results/Discussion

Simulations and experiments on inhomogeneous phantoms were performed with inclusion of various stiffness contrasts and sizes. Both results indicate that APT estimates tissue displacement roughly 20 times faster than SCC with comparable or better accuracy. Specifically, at compression level 3% and 6% with SNR 20 dB, statistical simulation assessment demonstrates average strain error of 10% for CCL versus 18% for SCC. Estimated displacement and strain curves using APT from 5 phantom experiments also show good agreement with true value from FEA simulations.



2H-5

**9:00 am Analyzing the impact of increasing Mechanical Index (MI) and energy deposition on shear wave speed (SWS) reconstruction in human liver**Yufeng Deng<sup>1</sup>, Mark Palmeri<sup>1</sup>, Ned Rouze<sup>1</sup>, Stephen Rosenzweig<sup>1</sup>, Manal Abdelmalek<sup>2</sup>, Kathy Nightingale<sup>1</sup>; <sup>1</sup>Biomedical Engineering, Duke University, Durham, NC, USA, <sup>2</sup>Gastroenterology-Hepatology, Duke University Medical Center, Durham, NC, USA**Background, Motivation and Objective**

Liver fibrosis occurs in most types of chronic liver diseases. Shear wave elasticity imaging (SWEI) has recently been introduced commercially and is finding success in the staging of liver fibrosis. However, technical failure and unreliable measurement rates for liver stiffness have been reported to increase both with elevated patient Body Mass Index (BMI, a measure of obesity) and in the presence of significant hepatic fibrosis. This work evaluates hepatic SWEI measurement success as a function of push pulse energy using 2 MI values (1.7 and 2.5) over a range of pulse durations. The goal is to quantify the effect of increasing pulse energy on measurement success, and to determine if there is clinical benefit in exceeding the current FDA guideline of MI 1.9 in the context of SWEI.

**Statement of Contribution/Methods**

Group SWS was measured using a 4C1 transducer and modified Siemens SC2000 ultrasound scanner from patients evaluated for known or potential liver diseases. Each measurement consisted of 8 SWEI excitations, each with different push energy configurations. Four of 8 excitations had an MI of 1.7, and through increased excitation voltage, the other four had an MI of 2.5. Pairs of MI 1.7 and 2.5 sequences had matched scanner energy (E) by adjusting the pulse duration. The push pulse duration ranged from 157  $\mu$ s - 1ms, and the Isppa.3 values ranged from 608 - 1073 W/cm<sup>2</sup>. Pulse-inversion harmonic tracking was used for all sequences, and the push had a fixed F/1.5 focus near 50 mm axially. Eight repeated measurements were performed in each patient, and the order of the 8 excitations within each measurement was randomized to avoid systematic errors. SWS was reconstructed using the RANSAC algorithm applied to arrival times of the peak particle velocities. Acquisitions with less than 50% inliers in the RANSAC algorithm were considered unsuccessful and were rejected.

**Results/Discussion**

Data have been collected in 9 patients to date under an ongoing IRB approved protocol. Preliminary results indicate that the rate of successful SWS reconstructions increases with increasing push energy, and that a threshold exists in each patient such that successful reconstructions are readily achieved when push energies exceed the threshold. In addition, the threshold varies with each patient, with the lowest to date being E=32mJ, (SWS=1.5 m/s, BMI= 27), and increasing in patients with increased liver stiffness (SWS=2.3 m/s, BMI=34, E=64mJ) or high BMI (SWS=2.3m/s, BMI=39, E=125mJ). In one patient, measurements failed for all energy levels (BMI=56).

Sequences at the same energy level had similar performance using either MI 1.7 or 2.5, indicating that there is minimal difference in nonlinear force enhancement between the two MIs. This is consistent with hydrophone measurements of the push waveform, indicating similar harmonic content in both waveforms (2.4% increase in the energy content of the 1st harmonic comparing MI 2.5 to 1.7).

2H-6

**9:15 am Shear waves generated with magnetomotive force on an embedded sphere**Matthew Urban<sup>1</sup>, Randall Kinnick<sup>1</sup>, Mohammad Mehrmohammadi<sup>1</sup>, James Greenleaf<sup>1</sup>; <sup>1</sup>Mayo Clinic College of Medicine, Rochester, MN, USA**Background, Motivation and Objective**

The characterization of the material properties of tissue and tissue mimicking materials has been an important area of study to develop methods for elasticity imaging. Many methods utilize acoustic radiation force to produce shear waves and to extract elastic or viscoelastic properties of the medium by measuring the propagation of the shear waves within the medium. However, the push beam geometry used to generate the shear waves can induce motion that may cause bias for conventional processing methods. Towards the aim of characterizing a medium with a simpler excitation distribution, we propose the use of magnetomotive force on an embedded metallic sphere to generate shear waves. The shear wave motion can be compared with an analytic Green's function for a spherical source.

**Statement of Contribution/Methods**

A gelatin phantom with an embedded steel sphere of 2 mm diameter was placed above an electromagnet with diameter of 101.6 mm. A dc voltage was applied for 20 ms to drag the sphere and the motion after the cessation of the excitation pulse was measured. A linear array transducer used compound plane wave imaging with a frame rate of 3.8 kHz to measure the shear wave motion. A Green's function formulation (Bercoff, et al., IEEE Trans. Ultrason. Ferroelectr. Freq. Control. 51: 1523-36. 2004) was used to compare with the motion induced in the experimental setting. The motion from the simulation and experiment was temporally filtered with a bandpass filter using a passband of 100-700 Hz.

**Results/Discussion**

Figure 1(a) shows the image of the shear wave displacement after the cessation ( $t \geq 20$  ms) of the magnetomotive force from the Green's function simulation for a medium with a shear elasticity of 2.56 kPa and shear viscosity of 1.5 Pa·s. Figure 1(b) shows the imaging of the shear wave displacement from the experimental. Figures 1(c)-(d) show displacement profiles of the shear wave motion separated by 2.4 mm in the x-direction. The agreement between the Green's function simulation and experimental results is very good. Magnetomotive-generated shear waves provide a unique tool to characterize material properties without the complications of an acoustic radiation force push beam.

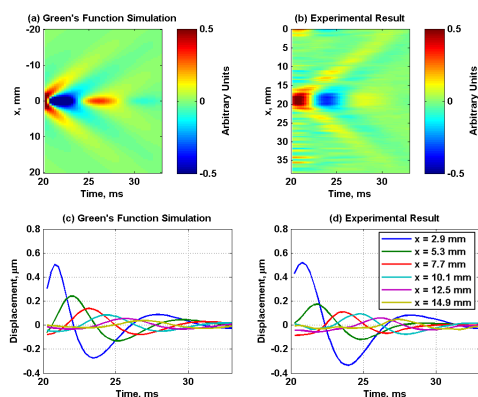


Figure 1. Comparison of Green's function simulation and experimental result for shear waves generated using magnetomotive force. (a) Green's function simulation for medium with shear elasticity of 2.56 kPa and shear viscosity of 1.50 Pa·s, (b) experimental result, (c) displacement profiles from Green's function simulation, (d) displacement profiles from experiment.

### 3H - MSD: Special Applications of Advanced Ultrasound Systems

Boulevard

Saturday, September 6, 2014, 8:00 am - 9:30 am

Chair: **Alfred Yu**  
The University of Hong Kong

3H-1

#### 8:00 am Multiparametric Characterization of a Single Cell by an Ultrasound and Optical Combined Microscope

Yoshifumi Saijo<sup>1</sup>, Koki Yoshida<sup>1</sup>, Joe Shikama<sup>1</sup>, Ryo Nagaoka<sup>1</sup>, Mototaka Arakawa<sup>1</sup>, Kazuto Kobayashi<sup>2</sup>; <sup>1</sup>Graduate School of Biomedical Engineering, Tohoku University, Sendai, Japan, <sup>2</sup>Division of Research and Development, Honda Electronics Co. Ltd., Toyohashi, Japan

##### Background, Motivation and Objective

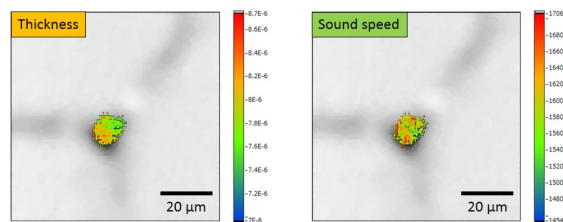
Biomechanics of the cell has been gathering much attention because it affects the pathological status in atherosclerosis and cancer. Various methods for measuring biomechanics have been developed but easy, continuous, non-invasive and quantitative method is still desired. Quantitative acoustic microscopy specially designed for cell observation will clarify cellular biomechanics because acoustic parameters provide information of mechanical properties. In the present study, an ultrasound and optical combined microscope system for characterization of a single cell with multiple ultrasound parameters was developed.

##### Statement of Contribution/Methods

The transducer was made of thin film ZnO and sapphire lens and the central frequency was 375 MHz. The transducer was mechanically scanned by a two-dimensional piezoelectric actuator and the controller with the precision of 1 nm. Ultrasound data were transferred to a PC through a digitizer unit with the sampling rate of 8 GHz. The scan area was 80 x 80 micron with up to 200 x 200 sampling points and the resolution was enough to visualize a single cell. An inverted optical microscope was installed in the system and simultaneous observation of the cells cultured in the petri-dish was available. The ultrasound parameters such as attenuation, sound speed and acoustic impedance were obtained by analysis of the interference occurred by two reflections from the cell surface and the interface between the cell and the substrate. Two-dimensional mapping of the multiple ultrasound parameters as well as the thickness and density at each measuring point in the cell was realized by the system.

##### Results/Discussion

3T3-L1 fibroblast cell was observed just after taking out from a CO<sub>2</sub> incubator. Figure shows the morphology of the cell with the pseudopod like shape. The thickness and sound speed distribution of the cell are shown by the color scale. The average thickness and sound speed was 7.9 micron and 1602 m/s, respectively. The same cell was observed after 30 minutes left in the room temperature. The morphology changed to spherical shape and the average thickness and sound speed changed to 16.0 micron and 1558 m/s, respectively. The total measurement time was 1 min and that was enough to observe static cells. The ultrasound and optical combined microscope system may contribute to understand the cellular biomechanics.



3H-2

#### 8:15 am A Co-registered Open System for Acoustic Angiography and High-Resolution B-Mode Imaging

Yang Li<sup>1</sup>, Jianguo Ma<sup>2</sup>, Karl Martin<sup>3</sup>, Hojong Choi<sup>1</sup>, Paul Dayton<sup>3</sup>, Xiaoning Jiang<sup>2</sup>, K.Kirk Shung<sup>1</sup>, Qifa Zhou<sup>1</sup>; <sup>1</sup>NIH Ultrasonic Transducer Resource Center and Department of Biomedical Engineering, University of Southern California, Los Angeles, CA, USA, <sup>2</sup>Department of Mechanical and Aerospace Engineering, North Carolina State University, Raleigh, NC, USA, <sup>3</sup>Joint Department of Biomedical Engineering, University of North Carolina/North Carolina State University, Chapel Hill, NC, USA

##### Background, Motivation and Objective

Acoustic angiography is a high-resolution imaging modality for small vascular structure. It utilizes the nonlinear backscatter of ultrasound contrast microbubbles (UCMs) to delineate blood vessels. UCMs used commercially are between 1-5µm, which has a resonant frequency below 5 MHz. In acoustic angiography, where UCMs are insonified with high rarefactional pressures, high-order harmonics (>25 MHz) become more evident and can be utilized to produce high-resolution images ideal for detecting small vascular structures. Tissue B-mode image can be acquired at the same frequency band to provide high-resolution anatomical reference. Here, we develop a co-registered open system platform which can support both acoustic angiography and B-mode imaging.

##### Statement of Contribution/Methods

Figure 1A shows the system structure and experimental setup. A digital T/R switch controls the system to work in either contrast-enhanced mode (low-frequency transmit, high-frequency receive) or B-mode (high-frequency transmit/receive). Bipolar pulses or a single frequency burst can be generated through an ultrafast pulser to provide high voltage output for B-mode or to elicit the nonlinear microbubble behavior for contrast-enhanced mode, respectively. The returned echo signal is digitized by a 12-bit 200MHz ADC. The

system is controlled by a field-programmable gate array (FPGA), which makes it flexible to program and capable of many on-board signal processing and stimulation modes. The system can be synchronized to a rotational motor through PC.

### Results/Discussion

Figure 1B shows the contrast-enhanced image we collected. A dual-frequency confocal transducer probe was used, transmitting at 5MHz and receiving at 30MHz. UCMs with a mean size of  $0.88\ \mu\text{m}$  were injected continuously (5mL/hr) into the ultrasound-transparent tube (200  $\mu\text{m}$  diameter) that was buried in a tissue mimic phantom. The tube was not exactly transverse to the image plane and may be bent, resulting in multiple light spots in the image; a contrast-to-tissue ratio of 22dB was obtained. The fundamental frequency noise from tissue phantom and water-filled tube (control group) was successfully suppressed. The system is shown to be capable of acoustic angiography and B-mode (not shown) imaging.

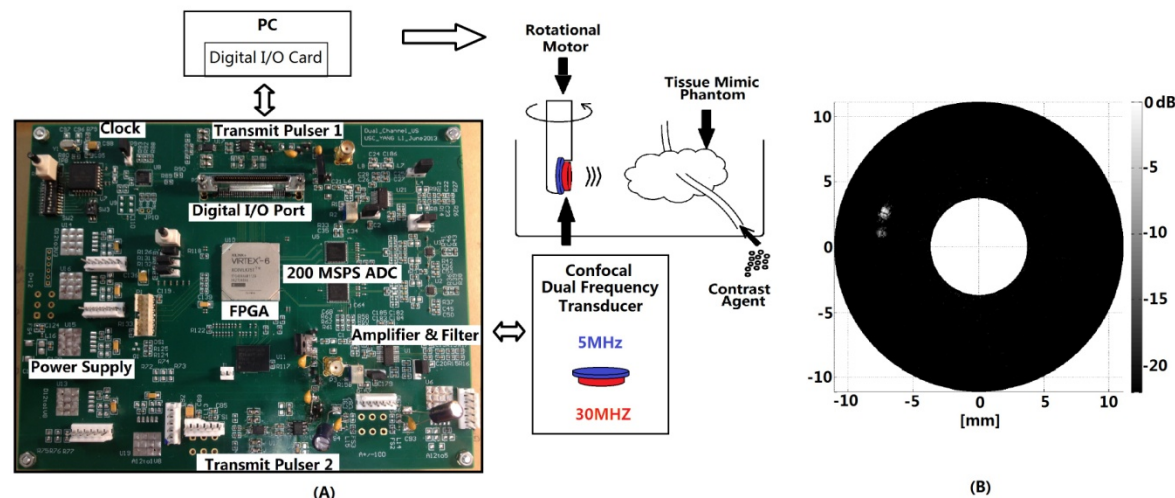


Figure 1: A. System structure and experimental setup; B. Image of microbubbles inside tissue mimic phantom.

3H-3

### 8:30 am Towards Wireless Capsule Endoscopic Ultrasound (WCEU)

John Lee<sup>1</sup>, Carl Schoellhammer<sup>1</sup>, Giovanni Traverso<sup>1,2</sup>, Daniel Blankschtein<sup>1</sup>, Robert Langer<sup>1</sup>, Kai Thomenius<sup>1</sup>, Duane Boning<sup>1</sup>, Brian Anthony<sup>1</sup>; <sup>1</sup>Massachusetts Institute of Technology, Cambridge, MA, USA, <sup>2</sup>Division of Gastroenterology, Massachusetts General Hospital, Harvard Medical School, Boston, MA, USA

#### Background, Motivation and Objective

Imaging of the small bowel (SB) is challenging due to its long length and winding path. Wireless Capsule Endoscopy (WCE) provides convenient access to the SB, but lacks ultrasound imaging capabilities necessary for accurate diagnosis. Wireless capsule endoscopic ultrasound (WCEU) combines benefits of WCE and ultrasound imaging. This work has two goals: (1) evaluate transducer designs appropriate for WCEU in regards to image quality, system complexity and cost; and (2) investigate whether the SB can produce sufficient contact to ensure acoustic coupling necessary for ultrasound imaging.

#### Statement of Contribution/Methods

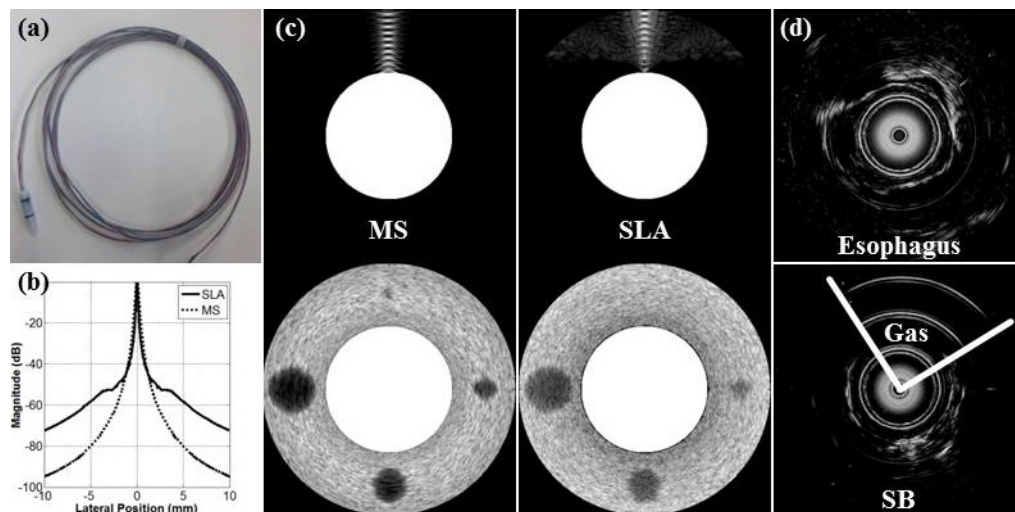
Mechanical-scanned (MS) and side-looking array (SLA) are evaluated. MS is implemented with a focused disc transducer and a motor; SLA uses TX and RX focusing with fixed F-numbers. Simulations of point and cyst phantoms were done using Field II. The MS tethered capsule developed for imaging feasibility study shown in Fig. 1(a) consists of a 10 MHz transducer and a micro stepper motor with a 4 m long tether. *Ex vivo* pig tissue imaging was done to evaluate image quality. *In vivo* pig esophagus, stomach and SB imaging were performed using the tethered capsule.

#### Results/Discussion

Simulation results are shown in Fig. 1(b) and (c). MS performs better for both point and cyst imaging. SLA suffers in the near zone due to small number of active elements and in the far zone due to large side lobes caused by the curvature of the capsule. Despite the motor, MS has much simpler system compared to SLA, which requires a very large number of elements ( $> 400$  for 10 mm diameter at  $\lambda/2$  spacing), multiplexing, parallel channel front-end and beamforming. MS power can suffer due to the motor, but SLA power suffers from significantly more complex signal chain. With current transducer technology, cost for SLA is prohibitively high to be a disposable device.

*In vivo* images are shown in Fig. 1(d). Full circumferential coverage was difficult to maintain due to partial contact with the capsule. Peristalsis can potentially produce better coupling, but its effect could not be adequately examined due to reduced activity under anesthesia. With current technology, MS shows better performance overall. *In vivo* imaging shows promising results although the effect of peristalsis and resulting coverage need to be further investigated.





3H-4

#### 8:45 am Head motion tracking for functional MRI using an air ultrasound array

Qi Wang<sup>1</sup>, Mark Howell<sup>1</sup>, Sheronica James<sup>1</sup>, Gregory Clement<sup>1</sup>; <sup>1</sup>Cleveland Clinic, USA

##### Background, Motivation and Objective

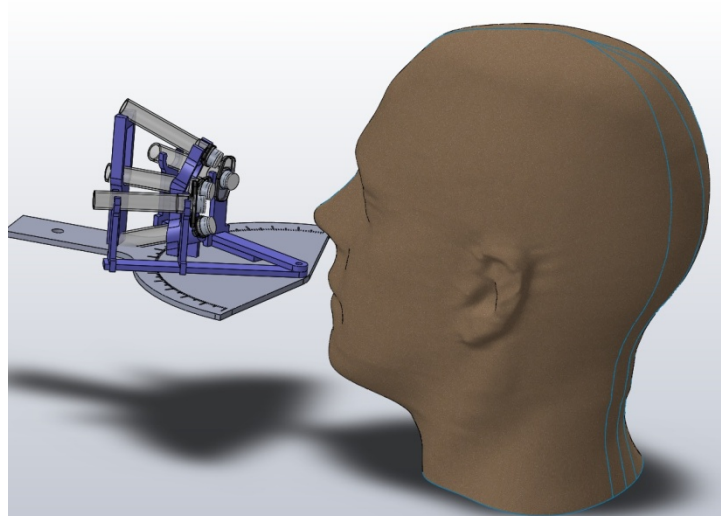
Patient motion is known to be a major cause of image artifact during magnetic resonance imaging (MRI). Especially in functional MRI (fMRI), head motion can corrupt signals from brain activity, and deviations of under a millimeter can accumulate nonlinearly, rendering the fMRI technique altogether incapable of brain imaging. It is apparent that the addition of a real time MR-compatible motion tracking system could provide critical information that, if combined with MR-motion correction techniques, could result in more reliable imaging.

##### Statement of Contribution/Methods

Here an MR-compatible air ultrasound transducer array was developed, with the goal of quantifying fMRI-relevant motions of under 0.5 mm. The array was designed to track nose position so that, by approximating head movement as a rigid body rotation about the second cervical vertebra (C2), the position of the entire head could be estimated. The array consisted of 5 planar air transducers (400 kHz, 1-cm-diameter) whose axes were oriented to coincide at the tip of the nose, approximately 6 cm in front of the array. One transducer, working as a transmitter, was situated in the array center and aligned approximately parallel with the tip of the nose. The remaining 4 elements were situated left, right, above and below the transmitter, all relative to the head position. After verifying MR-compatibility and optimizing element spacing, preliminary bench top measurements were made using a plastic head phantom affixed to a rotational motor. By analyzing the phase shift in back-scattered acoustic signals, the angle of head "shaking" or "nodding," were estimated; motions that correspond to the most commonly observed movements during fMRI.

##### Results/Discussion

In five measurements over a range of one degree rotation, predicted angles were found to agree within 85% of the actual head position. Finally, we verified the device on a human volunteer. Overall results demonstrated the ability of the array to identify sub-millimeter (0.2 mm) head motion, thereby allowing estimation of head rotation angles as small as 0.10. This method, applied as feedback into existing MR-motion correction algorithms, may lead to a practical approach to more robust fMRI imaging.



## 3H-5

**9:00 am MEMS-Based Silicon Ultrasonic Twin-Nozzle Nebulizer for Inhalation Drug Delivery\***

R. W. Mao<sup>1</sup>, S. K. Lin<sup>1</sup>, S. C. Tsai<sup>2</sup>, M. Brenner<sup>3</sup>, S. Mahon<sup>4</sup>, G. Boss<sup>5</sup>, G. Smaldone<sup>6</sup>, Chen Tsai<sup>1</sup>; <sup>1</sup>Electrical Eng & Computer Science, University of California, Irvine, Irvine, CA, USA, <sup>2</sup>Chemical Eng and Materials Science, University of California, Irvine, Irvine, CA, USA, <sup>3</sup>Division of Pulmonary and Critical Care Medicine, University of California, Irvine, Irvine, CA, USA, <sup>4</sup>Beckman Laser Institute and Medical Clinics, Univ. of California, Irvine, USA, <sup>5</sup>Medicine, Univ. of California, San Diego, CA, USA, <sup>6</sup>Medicine, Pulmonary/Critical Care Div, State Univ. of New York at Stony Brook, NY, USA

**Background, Motivation and Objective**

The innovation and potential applications of megahertz (MHz) MEMS-based multiple-Fourier horn ultrasonic nozzles that utilize temporal instability of Faraday waves for ejection of monodisperse micro droplets were highlighted in a new ground-breaking journal most recently [1]. In fact, the resulting ultrasonic device module using a single nozzle was used successfully to nebulize a number of common pulmonary drugs [1,2]. Controlability of particle (aerosol) size range (2 to 6µm) and much narrower size distribution achieved by the new device will improve targeting of treatment within the respiratory tract and improve delivery efficiency. Clearly, the treatment time can be shortened by increasing the aerosol output rate. Short treatment time is a critical requirement in situations such as massive cyanide poisoning [3]. An array of nozzles can be utilized for this purpose. Furthermore, nozzle arrays with individual nozzles operating at identical or different frequency will provide the unique capability for production and mixing of medicinal aerosols of the same or different medicines at identical or different aerosol sizes. Note that such strategy is essential in order to avoid instability of mixed drug solutions prior to aerosolization. Thus, our objective is to realize such a twin-nozzle array and demonstrate its unique capability via nebulization of the same or different drug solutions in-vitro towards ultimate inhalation drug delivery to human lung.

**Statement of Contribution/Methods**

Here we report the realization of a versatile twin-nozzle array at 1-2 MHz operation frequency and successful aerosolization of  $\gamma$ - interferon, cobinamide, and magnesium thiosulfate drug solutions via separate nozzles of the array. The drug solutions were transported separately via silica tubes to the individual end faces of the twin-nozzle for aerosolization. Experiments were carried out using either the same drug solution or combination of the drug solutions at varying concentrations, flow rates, and operation frequency.

**Results/Discussion**

Encouraging results have been obtained. For example, using a single 2MHz nozzle at 100µL/min flow rate, a single vial (100µg/0.5mL) of  $\gamma$ - interferon required aerosolization for 5 min. but required <2 min. using the twin-nozzle each at 150µL/min flow rate. Also, using the 2 MHz twin-nozzle simultaneous aerosolization of 1.0 M thiosulfate solution at 250µL/min flow rate and 100 mM cobinamide solution at 200µL/min flow rate has been accomplished. Continuous aerosolization for 7 min. delivered 430mg thiosulfate and 152mg cobinamide - sufficient antidote dosages for effective detoxification of cyanide poisoning. The findings of further in-vitro experiments using the same and combination of the drug solutions will also be presented.

[1] TECHNOLOGY, 2, 75-81, 2014. [2] Proc. of IEEE Int. Ultras. Symp., 1190-1192, 2013. [3] *ibid*, 1632-1634, 2012.

\* Supported by Army/NIH U54-NS063718 and AMRMC W81XWH-12-2-0114, USA.

## 3H-6

**9:15 am An Ultrasonic Micro-Scanner for Thickness Assessment of the Vestibular Jawbone: In-Vitro Accuracy Evaluation**

Daniel Habor<sup>1</sup>, Thorsten Vollborn<sup>1</sup>, Fabrice Chuembou<sup>1</sup>, Klaus Radermacher<sup>1</sup>, Katharina Degen<sup>2</sup>, Juliana Marotti<sup>2</sup>, Stefan Wolfart<sup>2</sup>, Stefan Heger<sup>1,3</sup>; <sup>1</sup>Chair of Medical Engineering, Helmholtz Institute for Biomedical Engineering, RWTH Aachen University, Aachen, Germany, <sup>2</sup>Department of Prosthodontics and Biomaterials, Medical Faculty, RWTH Aachen University, Aachen, Germany, <sup>3</sup>Institute for Biomedical Engineering, Mannheim University of Applied Science, Germany

**Background, Motivation and Objective**

Progressive peri-implant bone loss may lead to implant failure. Conventionally, the vestibular jawbone thickness (VJT) is monitored via cone beam computed tomography. Ionizing radiation and artifacts due to metallic implants, as well as superstructures, are major drawbacks of x-ray-based imaging techniques. As a non-invasive and patient-friendly alternative, high frequency ultrasonic (HFUS) micro-scanning can be used to assess the jawbone surface. In this study, we present a HFUS scanner and algorithm for assessing the jawbone thickness which is based on a priori information of the superstructure surface and which does not require ultrasound penetration of the jawbone.

**Statement of Contribution/Methods**

Four implants were inserted into bovine ribs. Prior to mounting the polymer superstructures, the position and orientation of the implant relative to the superstructure surface was determined based on optical 3-D scans. Subsequently, porcine gingiva samples were attached to the ribs. The specimens were fixed in a water basin filled with isotonic saline solution. Ultrasound data was acquired with a HFUS micro-scanner (center frequency: > 50 MHz, relative bandwidth: > 70%, aperture 4 mm, focus 8 mm) designed for intra-oral use supporting highly dynamic accurate positioning in micrometer-resolution. Within this study, the ultrasound trigger spacing was set to 39 µm. Bone and superstructure surfaces were segmented out of the ultrasound data and converted to polygon meshes. These meshes were matched to an a priori acquired 3-D model of the superstructure. Finally, the vestibular jawbone thickness was calculated from the matched 3-D model. For evaluation of the proposed ultrasonic technique all specimens were cut into slices (thickness approx. 1 mm), examined using a stereo-microscope and compared to the calculated bone thickness.

**Results/Discussion**

The overall error of ultrasound based bone thickness determination was 38±99µm (max: 260µm, min: -240µm) which is in good agreement to clinical requirements and which outperforms conventional x-ray based cone beam computed tomography.

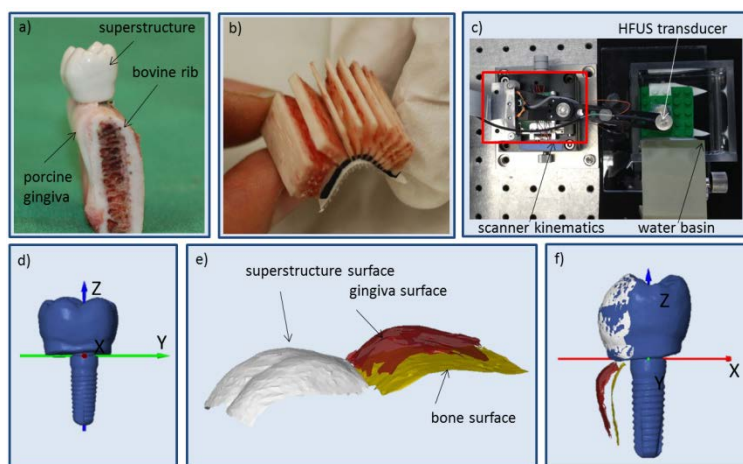


Figure 1: a) specimen, b) sliced specimen for microscope examination, c) HFUS micro-scanner and measurement setup, d) a priori 3-D model, e) example of polygon meshes generated from ultrasound data, f) a priori 3-D model matched with ultrasound based polygon meshes

## 4H - Wave Propagation

Marquette

Saturday, September 6, 2014, 8:00 am - 9:30 am

Chair: **Bernhard Tittman**  
*Pennsylvania State University*

4H-1

### 8:00 am Optical Visualization of Ultrasonic Pulses in the Total Internal Reflection Ultrasonic Sensor

Alexander Yurchenko<sup>1</sup>, Polishko Oleksandr<sup>1</sup>, Pilgun Yuri<sup>1</sup>, Eugene Smirnov<sup>1</sup>; <sup>1</sup>Quantum Radiophysics, Taras Shevchenko National University of Kyiv, Kiev, Ukraine

#### Background, Motivation and Objective

A Total Internal Reflection Ultrasonic Sensor (TIRUS), recently reported in [1], operates as a two-port device whose insertion loss (IL) is affected by a defect beneath the surface of a tested object. The IL measured proved to be by 7-8 dB greater than the estimated ones. Possible reasons for that can be a difference between real and calculated paths of ultrasonic pulses in the sensor body, which is a strongly anisotropic TeO<sub>2</sub> crystal, or conversion of acoustic modes at the crystal boundaries. The objective of this study is to visualize propagation and reflection of a shear wave (SW) pulses to reveal their actual behavior in the crystal that can lead to these effects.

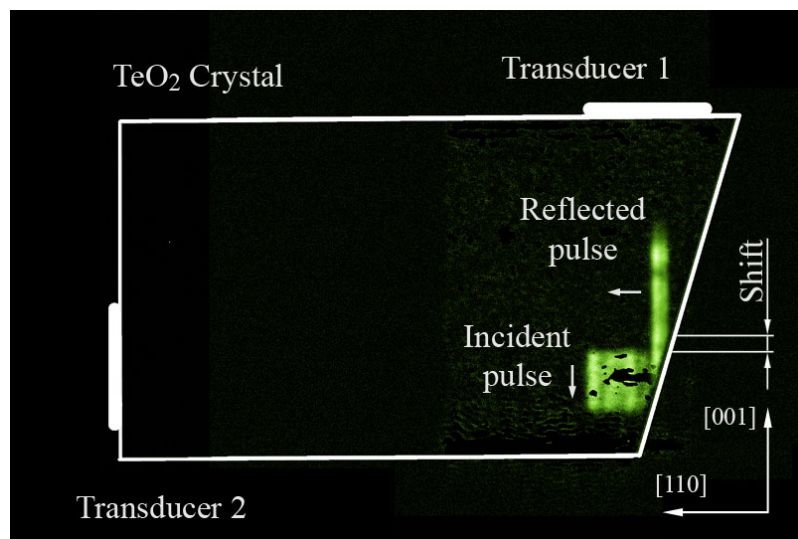
#### Statement of Contribution/Methods

A 1  $\mu$ s pulse of 27 MHz SW radiated by transducer 1 from the crystal face (001) propagates into the [001] direction and then reflects from a tilted face into the [110] direction towards transducer 2 (Fig. 1). It is visualized in its plane of incidence that should make it "invisible" for optical methods because of the zero value of the effective photo-elastic constant. Despite that, it proved to be observable in practice by means of an acousto-optic technique using spatial filtration of the diffracted light beams. Those are filtered in the focal plane of a lens placed behind the crystal and then are collected by the lens of a low-noise CCD camera recording optical images of observed ultrasonic beams.

#### Results/Discussion

Images of observed SW and extraneous longitudinal (LW) waves radiated by either the side or top transducer were recorded in experiments. An unexpected occurrence of a satellite ultrasonic pulse due to a mismatched size of the radiating top transducer was discovered. It was produced because of its re-excitation by a SW pulse reflected from the bottom of the crystal. No conversion of the SW at reflection from the tilted free surface of the crystal was visualized. At the same time, a backward shift was observed (Fig. 1) of an ultrasonic beam that might be a manifestation of the acoustic Goos-Hanchen effect. The effects observed show the behavior of ultrasonic beams in the crystal is more complicated than is usually assumed and should be taken into account while designing the TIRUS.

1. A. Yurchenko, V. Danilov, Yu. Pilgun, E. Smirnov, "Detection of a Subsurface Flaw with the Total Internal Reflection Ultrasonic Sensor," 2013 IUS Proceedings, pp. 190-193.



4H-2

### 8:15 am THREE-DIMENSIONAL MODELING OF LAMB WAVE PROPAGATION INDUCED BY PIEZOELECTRIC TRANSDUCERS

Kamyar Firouzi<sup>1</sup>, Amin Nikoozadeh<sup>2</sup>, Butrus T. Khuri-Yakub<sup>3</sup>; <sup>1</sup>Mechanical Engineering, Stanford University, STANFORD, California, USA, <sup>2</sup>Electrical Engineering, Stanford University, Stanford, California, USA, <sup>3</sup>Electrical Engineering, Stanford University, STANFORD, California, USA

#### Background, Motivation and Objective

During the last decade, there have been emerging ultrasound technologies relying on dispersive propagation of Lamb waves inside thin and bounded plates. Depending on the frequency of the operation and the thickness of the plate, various Lamb modes, from the low frequency flexural waves to higher ones such as Rayleigh waves, can be used in structural monitoring for the purpose of defect/inclusion localization, measurement of material properties, temperature monitoring, etc. Sensing is commonly done via piezoelectric transducers mounted on the edges of the plate. Lamb waves are multi-mode, dispersive, and have a very complicated nature. Hence, a proper design of the piezoelectric transducers, in order to excite the desired modes, can be very challenging and often standard analytical design methodologies of piezoelectric sensors fail to give the actual three-

dimensional behavior. This may lead to a poor design and performance. It is, thus, important to understand/analyze/model the multi-modal behavior of piezoelectric resonators when used for selective excitation of Lamb waves. We present mathematical modeling and full three-dimensional finite element analysis of the piezoelectrically induced Lamb wave propagation inside thin plates. This involves interaction between the piezoelectric transducers and the waves propagating inside the plate, and also the interaction between the waves and the possible inclusions.

## Statement of Contribution/Methods

The problem, in its nature, is multi-physics involving acoustic, elastic, and piezoelectric waves. The domain of the problem is decomposed into subdomains each of which governed by a different physics. The coupling is essentially at the interface between the subdomains. We first explain the underlying physics in each subdomain, and then couple them by enforcing the compatible interface conditions. We consider two different scenarios: (1) Uniform plate, where the waves excited by the piezoelectric transducer propagate inside the plate with stress-free boundary conditions both on the top and bottom faces and (2) Plate with an inclusion, where an acoustic inclusion is placed in contact with the top face of the plate. We also discuss how the electronic circuit can be coupled with the model. This makes it possible to have the inputs and outputs of the model as the actual voltage of a pulse generator.

## Results/Discussion

The prototype is a 4"x6" aluminum plate with two piezoelectric transducers attached to two opposite edges. One is excited by a short voltage pulse, hence creates multi-mode Lamb waves inside the plate, which is picked up by the other transducer on the opposite edge. We investigate the effect of different piezoelectric polarizations in transmit and receive, different transducers design, and different frequencies of operation. We validate the numerical results through comparison with the experimental results.

4H-3

## 8:30 am Propagation behaviors of wedge waves interacting with defects along wedge tips

Che-Hua Yang<sup>1</sup>, Pei-Yuan Lo<sup>2</sup>; <sup>1</sup>Department of Mechanical Engineering, National Taipei University of Technology, Taipei, Taiwan, <sup>2</sup>National Taipei University of Technology, Taiwan

## Background, Motivation and Objective

Some blade-like structures, such as machine tool blades, are subject to the risk of having defect which may further cause a degradation of the structure's functions. It is therefore important to inspect the defect and mostly wanted in a remote and nondestructive way. Anti-symmetric flexural (ASF) modes are guided acoustic waves propagating along the tip of a wedge with the energy tightly confined near the wedge. Propagation behaviors of ASF modes along wedge tips render a possibility to inspect the existence and characteristics of a defect along a wedge-like structure. Also, physical significance for the ASF mode interacting with a defect is also of great interest.

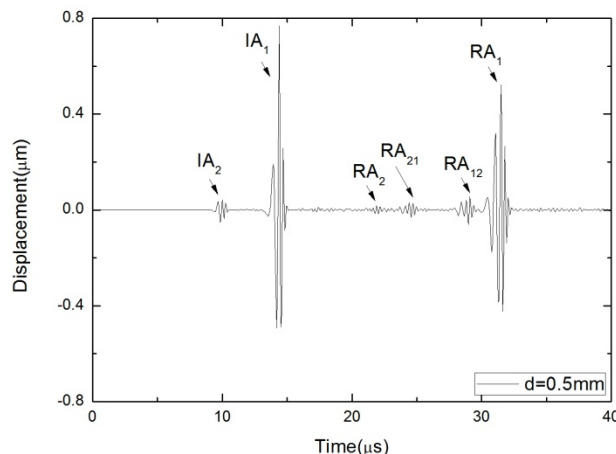
## Statement of Contribution/Methods

Numerical simulations based on finite element method (FEM) and experimental measurements using a laser ultrasound technique (LUT) are employed to characterize ASF modes propagation along a 40° wedge tip with rectangular defects. Reflection coefficient (RC) and transmission coefficient (TC) for the first (A1) and second (A2) ASF modes are characterized for rectangular defects with a width of 1.0 mm and depths (d) ranging from 0.2 mm to 0.8 mm.

## Results/Discussion

With an impulse excitation on the wedge tip, the first and second ASF modes (IA1 and IA2) are simultaneously detected. The reflected signal contains reflected A1 (RA1), reflected A2 (RA2) modes, and mode-converted modes as RA21 and RA12. The RA21 mode is a mode-converted A2 mode upon the incidence of the IA1 mode interacting with the defect. RA12 is the reflected A2 mode upon the incidence of the IA1 mode. For the A1 mode, RC starts at 0.35 for d=0.2 mm and increases up to d=0.75 at d=0.8 mm; TC decreases from 0.2 to 0.1. For the mode-conversion efficiency, RA21 starts at 0.11 for d=0.2 and increases up to 0.39 for d=0.8 mm. Very surprisingly, the RA12 is found to be much smaller than the RA21 at least for an order of magnitude; it goes from 0.0 to 0.015.

In conclusion, interaction behaviors of ASF modes with rectangular defects of various depths ranging from 0.2  $\lambda$  to 0.8  $\lambda$  are investigated. RC and TC as a function of the defect size are characterized. On the other hand mode conversions from higher-ordered to lower ordered ASF modes and those on the reversed way are explored and characterized. Mode-conversion for the high-to-low type is found to have efficiency higher than those for the low-to-high type with an order of magnitude larger.





## 4H-4

**8:45 am Visualization of Time-Evolving Wavefront Advance in Polycrystalline Materials**James Blackshire<sup>1</sup>; <sup>1</sup>AFRL/RXCA, Air Force Research Laboratory, Wright-Patterson AFB, Ohio, USA**Background, Motivation and Objective**

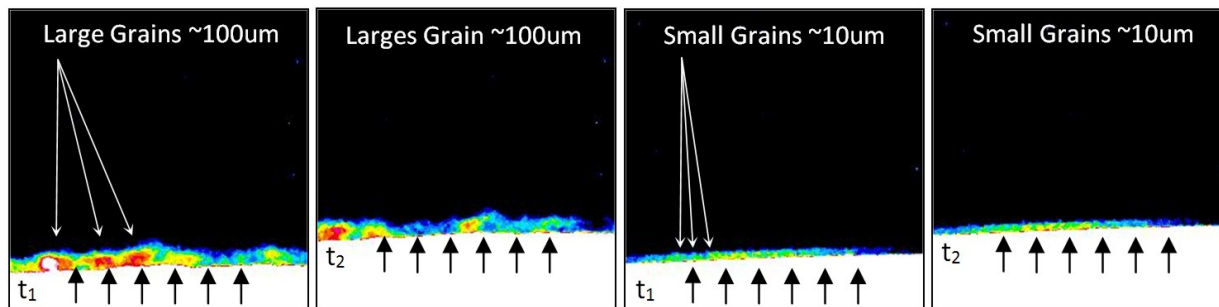
The nondestructive quantification of grain feature information in polycrystalline aerospace materials is an important area of recent research, where information related to mean grain size, grain size distribution, and crystallographic orientation is needed for engineering analysis and material state awareness evaluations.

**Statement of Contribution/Methods**

In the present effort, the interaction of ultrasonic surface waves (SAW) with a dual-microstructure nickel polycrystalline material is studied, where an innovative wavefront imaging method is utilized to study the time-evolving advance of the primary wavefront through grain features. The method involves a time-gated analysis of scanning laser vibrometry signal content, where the advance of the wavefront through individual grains is observed and analyzed with respect to orientation-dependent crystallographic slowness.

**Results/Discussion**

Representative scanning laser vibrometry results are presented in the accompanying figure, which depict the interaction of a 5MHz, 1-cycle SAW with large grain features (left images), and small grain features (right) at two separate times (t<sub>1</sub> and t<sub>2</sub>). The primary wavefront advance can be seen to flow or translate through individual grain features as phase delay/advances in localized grains, which is attributed to the crystallographic slowness within each grain relative to the forward propagating direction.



## 4H-5

**9:00 am Guided Ultrasonic Waves in Steel Pipe with Welded Bend with Defect**Jin Jack Tan<sup>1</sup>, Anthony Guo<sup>1</sup>, Xin Wang<sup>1</sup>, Jee-Hou Ho<sup>2</sup>; <sup>1</sup>Monash University Malaysia, Malaysia, <sup>2</sup>University of Nottingham Malaysia Campus, Malaysia**Background, Motivation and Objective**

There is an interest in propagating guided ultrasonic wave past a bend in pipes as such region may not be physically accessible for inspection purposes. Most bends are also welded together and disperse guided wave strongly, making defect detection beyond pipe bend difficult. Therefore, there is motivation to inspect the guided wave behaviour due to different pipe features, namely a bend, a welded bend and a welded bend with defect near the weld. The results will serve to improve the understanding on the effects of these features in propagating guided wave in pipes.

**Statement of Contribution/Methods**

The study is carried out numerically where three propagating modes, i.e. the longitudinal L(0,2), torsional T(0,1) and flexural F(1,1) modes are used. The finite element model is built to allow high accuracy. The time steps are discretised such that there are 16 nodes in one period of the investigated frequency and the spatial element sizes are discretised such that there are at least 16 nodes in one wavelength corresponding to the interested modes. To understand the effect of the bend, excitation of guided wave on two pipes of same length are carried out where one pipe involves a bend with the other perfectly straight. The transmission of the guided wave and the mode conversion at the pipe bend are studied. The model is then extended to include welds (one before and one after the bend), which are accurately modelled with its anisotropy and scattering effect considered. The model is further extended by including artificial thin cuts of variable circumferential extents just after the weld, an area where detection is often difficult. The effects of weld and cut are studied by monitoring the reflections of the guided waves at the excitation points.

**Results/Discussion**

It is found out that pipe bend has reduced the transmission of guided waves. The non-dispersive torsional T(0,1) mode has the highest transmission coefficient where mode conversion at the bend is minimal. L(0,2) transmits with limited but noticeable mode conversions while F(1,1) has poor transmission as unwanted F(1,3) mode is also excited. By studying the displacement-time response graph, welds reflect distinctive wave packets. Small defects, however, are not detectable as they do not reflect stronger than the weld and the reflection packet is too close with the weld to be separated. Moderately-sized cuts are confidently detected by both torsional T(0,1) and longitudinal L(0,2) modes as the reflection waves have higher magnitude than the weld reflection. T(0,1) mode is preferable due to its lower mode conversion where converted higher order modes are consistently only half as strong as the higher order reflections in L(0,2) mode. F(1,1) modes are not suitable for defect detection but show properties that promise further studies.

## 4H-6

**9:15 am Modeling Guided waves propagating in Bones with a Multilayer Model**Ming-Yen Lee<sup>1</sup>, Che-Hua Yang<sup>1</sup>; <sup>1</sup>Department of Mechanical Engineering, National Taipei University of technology, Taiwan**Background, Motivation and Objective**

Osteoporosis is A popular disease. A reduction in the cortical bone thickness or cancellous bone density is the reason for osteoporosis. Human bone is covered by soft tissue in the body. There is only research for the bones of osteoporosis now, but discussion without the soft tissue. This paper focus on simulation the soft tissue by water, with phantom to establish the multilayer structures, to verify the guided waves propagation behaviors and theory.

# Statement of Contribution/Methods

The method is divided into two categories: experimental and theoretical. A theoretical model based on recursive asymptotic stiffness matrix (RASM) method with multilayered include soft tissue, cortical, and cancellous parts. Effects of soft tissue layer on the influence of dispersion relation are theoretically modeled. Experiment based on a laser ultrasound technology (LUT) to measure the dispersion relation. Specimens are using bi-layers bone immersing in the water, it can simulate the soft tissue layer. By using experiment data and theory data to prove the RASM. Addition the soft tissue layer, change the cortical bone thickness and cancellous density to observe the mode in the dispersion.

# Results/Discussion

Fig 1 shows the effect of soft tissue, the phase velocity of liquid soft tissue is slow than the solid phantom bone, A0 mode is offset to the low frequency part. Theoretical data and experiment data agree well in the low frequency regime. Fig 2 shows the effect of soft tissue thickness variation. For the first three guided modes, A0, S0, A, the effects of the soft tissue thickness can be clearly observed. Other important parameters such as the reduction in cortical bone thickness and increase in the porosity of cancellous bone are discussed in this paper.

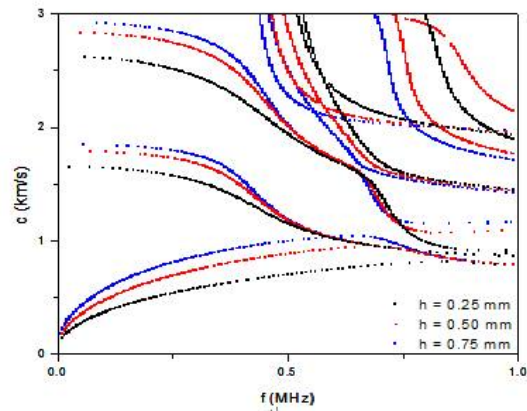


Fig 2

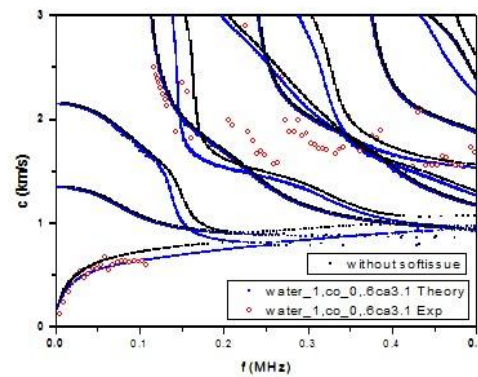


Fig 1

## 5H - Thin-Films 1

Williford A

Saturday, September 6, 2014, 8:00 am - 9:30 am

Chair: **Yook-Kong Yong**  
Rutgers University

5H-1

### 8:00 am Multiple shear wave roundtrips liquid sensor by c-axis parallel oriented ZnO film/silica glass pipe structure

Shoko Hiyama<sup>1</sup>, Takahiko Yanagitani<sup>2</sup>, Shinji Takayanagi<sup>1</sup>, Yoshiya Kato<sup>1</sup>, Mami Matsukawa<sup>1</sup>; <sup>1</sup>Wave electronics research center, Laboratory of Ultrasonic Electronics, Doshisha University, Kyotanabe, Japan, <sup>2</sup>Graduate School of Engineering, Nagoya Institute of Technology, Nagoya, Japan

#### Background, Motivation and Objective

Horizontal shear waves with in-plane displacement can propagate without the energy leakage into liquid, and are suitable for liquid sensors. A high-sensitive device is expected if the long propagation distance can be achieved such as the roundtrip system in the Ball SAW. In previous study, we have demonstrated the excitation of the shear waves using c-axis parallel (11-20) oriented ZnO film [1], which can be fabricated on a glass pipe and curved surface. We consider that the SAW multiple roundtrips also occurs on a glass pipe with small diffraction loss, when the wide aperture (6.6 mm) IDT is used. In this study, to realize a high-sensitive liquid sensor, we fabricated c-axis parallel oriented ZnO film on pipe and the shear wave multiple roundtrips were demonstrated.

#### Statement of Contribution/Methods

c-Axis parallel oriented ZnO film was grown on a part of the silica glass pipe by sputtering system [see Fig.1 (a)]. Next, IDT was fabricated on ZnO film so that the electrode fingers are parallel to the pipe axis. The reflection coefficients  $S_{11}$  of IDT were measured with a network analyzer, and the time waveforms were obtained by an inverse Fourier transform. The insertion losses were calculated by the time waveforms. In the same manner, the sensor immersed in pure water was also evaluated.

#### Results/Discussion

Fig.1 (a) shows the XRD patterns of ZnO film. Intense ZnO (11-20) peaks, indicating c-axis parallel orientation, were observed at point A and B on glass pipe. The time waveforms of pipe structure immersed and non-immersed in water were shown in Fig.1 (b). A Fourier transform of the first echo showed SH-SAW and bulk wave at the frequencies of 131 MHz and 160-190 MHz, respectively. From these data, twice SH-SAW roundtrips and fifth bulk wave roundtrips were observed. The propagation loss of bulk wave in the sensor immersed in liquid (140 dB/m) is not much smaller than that in non-immersed in liquid (115 dB/m), which implies the shear mode bulk wave. In conclusion, multiple roundtrips of SH-SAW and bulk shear wave can be obtained on pipe structure using c-axis parallel oriented ZnO film. The next step is to measure the viscosity and electric conductivity of the liquid using this sensor.

[1] T. Yanagitani, et al., *TUFFC.*, **52**, 3140 (2005).

[2] K. Yamanaka, et al., *APL.*, **76**, 2797 (2010).

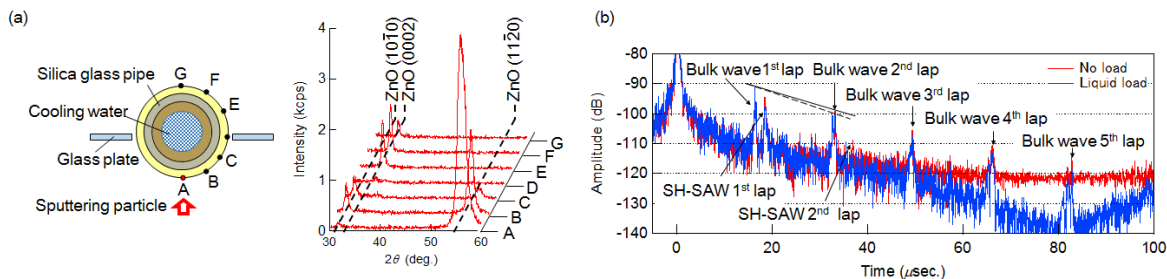


Fig.1 (a) XRD patterns of the ZnO film on the silica glass pipe and (b) time response waveform of pipe structure sensor immersed and non-immersed pure water.

5H-2

### 8:15 am Effect of process parameters on structure and piezoelectric properties of AlN and $\text{Al}_x\text{Sc}_{1-x}\text{N}$ films deposited by pulsed magnetron sputtering

Stephan Barth<sup>1</sup>, Hagen Bartzsch<sup>1</sup>, Daniel Gloess<sup>1</sup>, Peter Frach<sup>1</sup>, Olaf Zywitzki<sup>1</sup>, Thomas Herzog<sup>2</sup>, Susan Walter<sup>2</sup>, Henning Heuer<sup>2</sup>; <sup>1</sup>Fraunhofer Institute for Electron Beam and Plasma Technology (FEP), Dresden, Germany, <sup>2</sup>Fraunhofer Institute for Ceramic Technologies and Systems, Materials Diagnostics (IKTS-MD), Dresden, Germany

#### Background, Motivation and Objective

The paper will report on the deposition and characterization of piezoelectric AlN and  $\text{Al}_x\text{Sc}_{1-x}\text{N}$  films. Potential applications of the films are in ultrasonic microscopy, energy harvesting and SAW/BAW filters. Special focus will be on the characterization of the influences of sputter parameters on the structure and the piezoelectric properties of  $\text{Al}_x\text{Sc}_{1-x}\text{N}$ .

#### Statement of Contribution/Methods

The depositions were done by reactive pulse magnetron sputtering using the Double Ring Magnetron DRM 400 sputter source. This type of magnetron combines two concentric discharges from metallic targets in order to deposit uniform films on substrates with a diameter of up to 200 mm. In the case of AlN depositions, pure Al targets were used.  $\text{Al}_x\text{Sc}_{1-x}\text{N}$  was deposited by reactive co-sputtering of an Al and Sc target. Argon and Nitrogen were used as inert and reactive gas, respectively. Using the DRM 400, the pulse mode of the pulse magnetron sputtering process can be changed between unipolar and bipolar, resulting in different plasma properties. Using the mixed unipolar and bipolar mode, the time slices of both pulse modes can be adjusted at a time scale smaller than 1 ms. This is much shorter than the time necessary for the deposition of 1 monolayer. Thus, the film properties can be freely adjusted between those resulting from both pure pulse modes.

The films were characterized regarding piezoelectric coefficient  $d_{33}$ , pulse echo measurements, film stress, chemical composition, structure and morphology. The used analytical methods include FE-SEM and EDS, X-ray diffraction (XRD), nano-indentation and glow discharge optical emission spectroscopy (GD-OES).

## Results/Discussion

The piezoelectric coefficient  $d_{33}$  of AlN films was up to 9 pm/V on silicon substrates. X-ray diffraction (XRD) revealed highly textured AlN films with no visible peaks besides those of the (001) orientation. XRD rocking curves show very good alignment of the c-axis perpendicular to the surface and a FWHM of between 2° and 4°. Film stress of AlN ranges from -2 GPa to +0.2 GPa and strongly depends on film thickness, deposition pressure and pulse mode.

By scandium doping of the film,  $d_{33}$  could be raised to up to 30 pm/V. The measured stress values were similar to those of pure AlN films. The characterization by FE-SEM investigations shows that the columnar crystallites of the  $\text{AlAl}_x\text{Sc}_{1-x}\text{N}$  films are smaller and contain more lattice defects as the AlN films. The drastic improved piezoelectric behavior of the  $\text{Al}_x\text{Sc}_{1-x}\text{N}$  film in comparison to the AlN films can be mainly explained by higher polarity of the c-axis and the lower Young's modulus.

## 5H-3

### 8:30 am Acoustic Filters Based on Thin Single Crystal $\text{LiNbO}_3$ Films: Status and Prospects

Alexandre Reinhardt<sup>1</sup>, Lamine Benaissa<sup>1</sup>, Jean-Baptiste David<sup>1</sup>, Emmanuel Defay<sup>1,2</sup>; <sup>1</sup>CEA, Leti, Minatec Campus, Grenoble, France

#### Background, Motivation and Objective

With the crowding of the frequency spectrum and the increase in data rates, filters manufacturers face new challenges related to improving filter rejection or proposing frequency agile solutions. In this context, the transfer of thin films of Lithium Niobate (LNO) seems a promising technique to answer the limitations faced by conventional filter technologies. This technique has been proposed more than a decade ago as a way to increase the operation frequency of Surface Acoustic Wave (SAW) filters while improving their temperature behavior [1]. In the context of Bulk Acoustic Wave (BAW) filters, it should allow designers to benefit from the advantages brought by the choice of crystalline orientation, from larger electromechanical coupling factors and from a low loss material.

#### Statement of Contribution/Methods

We first review the techniques proposed to transfer a thin LNO film onto a host substrate. We position the various bonding and thinning techniques with respect to targeted applications. Additionally, through realizations, we demonstrate the expected benefits of single crystal LNO films: SAW devices with large propagation velocity and reduced temperature dependence; High overtone Bulk Acoustic Resonators (HBAR) based on a LNO/LNO structures with quality factors close to 40,000 [2] or BAW resonators with electromechanical coupling factors close to 45 % [3].

## Results/Discussion

Eventually, we discuss the use of LNO in tunable BAW filters with two possible mechanisms: first the addition of tunable passive elements in LNO-based filter [4], and second the use of composite resonators obtained by stacking two LNO films [5]. Through numerical examples, we will focus on the second option and demonstrate its capability to address filters capable of being tuned across LTE bands 2 and 9 for example, demonstrating over 130 MHz tuning range in the 1.9 GHz region while maintaining 60 MHz bandwidth. The technological challenges raised by such a promising solution will be finally listed, giving an orientation for future developments in the years to come.

[1] T. Pastureauud *et al.*, *High-Frequency surface acoustic waves excited on thin-oriented  $\text{LiNbO}_3$  single-crystal layers transferred onto silicon*, IEEE Trans. Ultrason. Ferroelec. and Freq. Contr. 54, p. 870, 2007.

[2] M. Pijolat *et al.*, *Large  $Q_f$  product for HBAR using Smart Cut reported  $\text{LiNbO}_3$  on  $\text{LiNbO}_3$  substrate*, Proceedings of the 2008 IEEE International Ultrasonics Symposium.

[3] M. Pijolat *et al.*, *Large electromechanical coupling factor film bulk acoustic resonator with X-cut  $\text{LiNbO}_3$  layer transfer*, Applied Physics Letters vol. 95, 182106 (2009).

[4] M. Inaba *et al.*, *A widely tunable filter configuration composed of high Q RF resonators and variable capacitors*, 2013 European Conference on Microwave Integrated Circuits (2013).

[5] A. Reinhardt *et al.*, *Tunable composite piezoelectric resonators: a possible "Holy Grail" of RF filters?* IEEE International Microwave Symposium Digest (2012).

## 5H-4

### 9:00 am Investigation of ferroelastic domain relaxation of PZT thin-film in the GHz range using Picosecond Acoustics

Arnaud Devos<sup>1,2</sup>, Fabrice Casset<sup>3</sup>, Sabrina Sadtler<sup>2</sup>, Arnaud LeLouarn<sup>2</sup>, Gwenael Le Rhun<sup>3</sup>, Christel Dieppedale<sup>3</sup>, Patrick Emery<sup>2</sup>, Stéphane Fanget<sup>3</sup>, Emmanuel Defay<sup>3</sup>; <sup>1</sup>IEMN CNRS, Lille, France, <sup>2</sup>MENAPIC, Lille, France, <sup>3</sup>CEA-LETI, France

#### Background, Motivation and Objective

$\text{Pb}(\text{Zr}_{0.52}, \text{Ti}_{0.48})\text{O}_3$  (PZT) thin-films are good candidates for actuator applications such as RF MEMS[1], loudspeakers[2] or haptic interfaces[3] thanks to its high piezoelectric coefficients[4]. For a predictive MEMS design, the accurate knowledge of the mechanical properties of the materials at submicron scale is required especially because thin films behavior can exhibit significant changes with respect to bulk. In ferroelectric material, polarization regions are separated by wall domains which can move, relax and impact the material properties. When the material is solicited in the Gigahertz range, wall domains move, vibrate and react to acoustic waves. But beyond a threshold frequency, wall domains relax, what affects elastic, piezoelectric and dielectric properties of ferroelectric materials. To experimentally evidence such threshold (estimated to be close to 10GHz for PZT), one needs to excite the material with acoustic waves below and above this frequency.

#### Statement of Contribution/Methods

The Picosecond Acoustic (PA) technique is able to measure accurately the Young modulus and the Poisson ratio of thin-films from acoustic velocity measurement. This is a full optical setup that offers the opportunity to implement a sonar at nanoscale[5]. Acoustic pulses with frequency up to several 100 GHz result from the optical absorption of femtosecond laser pulses.

In this work we propose an alternative way to use the PA technique to study the dependence of the sound velocity of PZT versus acoustic frequency. The method is first based on a specific design of the sample that is used to control the central frequency of the acoustic pulse emitted by the laser from a few GHz to several 100 GHz. Secondly, for detecting the low frequency pulses, a dedicated optical detection is needed since the usually used photo-elastic mechanism is then inefficient. An interferometric detection is implemented on the setup, which gives the opportunity to measure the surface displacement at very low frequency.

## Results/Discussion

We first confirm the performances of the setup over the wide range of frequencies. Besides, PZT longitudinal acoustic velocity decreases of about 10% between low and high frequencies. This observation is in line with ferroelastic domain wall relaxation occurring in the 10-40GHz range.

#### REFERENCES

- [1]. M. Cuffe *et al.*, Proc. MEMS Conference, 212 (2010).
- [2]. R. Dejaeger *et al.* Proc. Eurosensors Conference, 184 (2012).
- [3]. F. Casset *et al.* Proc. Transducers Conference, 2733 (2013).
- [4]. M. Cuffe *et al.* Proc. IEEE Ultrasonics Symposium, 1948 (2011).

[5]. A. Devos, Ultrasonics 2014, DOI 10.1016/j.ultras.2014.02.009.

5H-5

# 9:15 am Second overtone mode polarization inverted resonator consisting of (001)/(00-1) PbTiO<sub>3</sub> thin film

Takahiko Yanagitani<sup>1</sup>, Katsuyoshi Katada<sup>1</sup>, Masashi Suzuki<sup>1</sup>, Kiyotaka Wasa<sup>2</sup>; <sup>1</sup>Nagoya Institute of Technology, Japan, <sup>2</sup>Kyoto University, Japan

## Background, Motivation and Objective

Tunable BAW resonator filter have attracted attention in recent years. One possible way of achieving a large tunability is to use the overtone mode resonance in polarization inverted multilayer [1]. Usual single layer resonator operates at fundamental mode whereas the double layer resonator with opposite polarization operates at second overtone mode. Polarization inverted ferroelectric multilayer structure make it possible to switch operation modes using DC bias voltage. However, experimental studies of these structures have not been reported. We experimentally demonstrated second overtone thickness extensional mode excitation in (001)/(00-1) polarization inverted PbTiO<sub>3</sub> film resonator structures.

[1] S.Gevorgian, and A.Vorobiev, IEEE TUFFC, 60, 795, (2013).

## Statement of Contribution/Methods

PbTiO<sub>3</sub> epitaxial films were grown on La-doped conductive (001) SrTiO<sub>3</sub> substrate by RF magnetron sputtering with powder target. The 13 V (420 kV/cm) was applied to a part of first PbTiO<sub>3</sub> layer (310 nm) to invert polarization direction. Next, second layer of PbTiO<sub>3</sub> (375 nm) was grown to obtain polarization inverted double layer resonator.

## Results/Discussion

The  $k_t$  before and after the polarization treatment was estimated to be 0.53 and 0.44 from resonator conversion loss, respectively. Polarization directions (sign) of films were determined by a press test [3]. The conversion loss [2] was measured at the region where the polarization treatment was performed at first layer and where that was not performed. As shown in Fig. 1 (a), 1st thickness extensional mode resonance was observed at 1.3 GHz in the region where polarization direction of the first and second layer is same. In contrast, as shown in Fig. 1 (b), 2nd mode resonance excitation was clearly observed at 3.6 GHz and 1st mode resonance at 1.2 GHz was suppressed in the region where polarization direction of the first and second layer is opposite. Experimental curve shows good agreement with theoretical curve simulated by Mason's model considering polarization inverted structure [4]. Electrically switchable overtone mode resonator filter is expected in the future by inserting conductive SrTiO<sub>3</sub> layer between the polarization inverted double layers.

[2] T. Yanagitani and M. Kiuchi, JAP. 102, 044115 (2007).

[3] J. F. Rosenbaum, Bulk acoustic wave theory and devices, p.136.

[4] T. Yanagitani, et al. IEEE TUFFC 58, 1062 (2011).

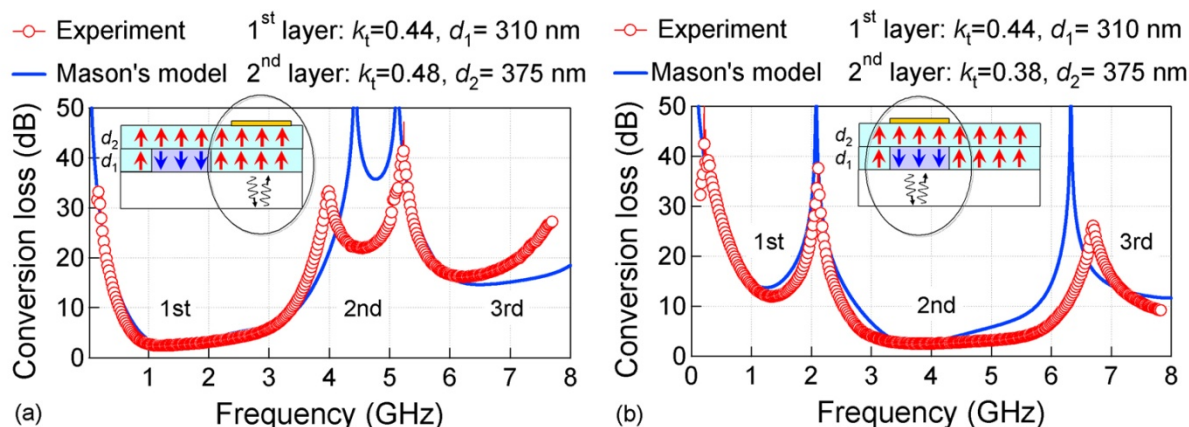


Fig. 1 The conversion loss measured (a) at the region where the polarization treatment was not performed at first layer: Au/epitaxial (001)/(001) PbTiO<sub>3</sub>/SrTiO<sub>3</sub> and (b) at the region where polarization treatment was performed: Au/ epitaxial (001)/(00-1) PbTiO<sub>3</sub>/SrTiO<sub>3</sub>.



## 6H - Nonlinearity and Tunability

Williford B

Saturday, September 6, 2014, 8:00 am - 9:30 am

Chair: **Jan Kuypers**  
*Sand 9, Inc.*

6H-1

### 8:00 am Effective Suppression Method for 2nd nonlinear signals of SAW Devices

Ryo Nakagawa<sup>1</sup>, Haruki Kyoya<sup>1</sup>, Hiroshi Shimizu<sup>1</sup>, Takashi Kihara<sup>1</sup>; <sup>1</sup>Murata Manufacturing Co., Ltd., Nagaokakyo, Kyoto, Japan

#### Background, Motivation and Objective

The requirements of high linearity performance of SAW duplexers have been getting strong in recent years. This is because receiver sensitivity is deteriorated by their nonlinearities significantly.

In this work, we focus on the 2nd nonlinearity of SAW devices. First, the generation mechanism of nonlinearity on a 42°Y-X LiTaO<sub>3</sub> substrate is discussed. And next, based on the discussion, the effective IDT design for suppression of 2nd nonlinear signals of SAW devices is proposed.

#### Statement of Contribution/Methods

As the occurrence factor of 2nd nonlinear signals, we considered the possibility of the crystalline asymmetry properties of 42°Y-X LiTaO<sub>3</sub> that is caused by the lean of polarization axis. According to this assumption, the crystalline asymmetry should be canceled in some way to suppress the 2nd nonlinear signals of SAW duplexers. To realize this cancelation, we invented novel IDT design as shown in Fig. 1. Specifically, an IDT is equally divided in two and they are connected in parallel. In addition, the divided IDTs are allocated so that they are symmetric about the wave propagation axis. In this structure, all nonlinear signals caused by the crystalline asymmetry are canceled electrically.

#### Results/Discussion

To estimate the effect of the new design, we fabricated a one-port resonator on a 42°Y-X LiTaO<sub>3</sub> substrate. As the measurement result, it was verified that both 2nd harmonic and IMD of the fabricated resonator are dramatically improved. As one instance, the measurement result of 2nd harmonics is shown in Fig. 2. The signal level is improved about 15dB at the maximum, and the peak level is improved more than 10dB. From these results, it was proved that the main factor of 2nd nonlinearity of SAW devices is the crystalline asymmetry properties.

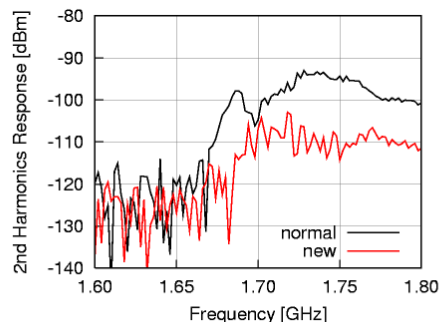


Fig. 2. Measurement result of 2nd harmonic response

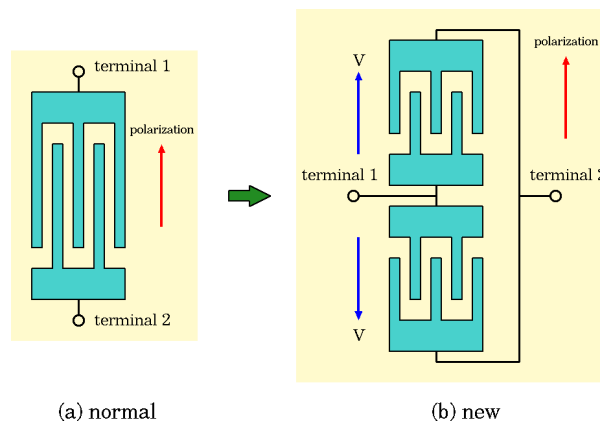


Fig. 1. Proposed structure.

6H-2

### 8:15 am Application of a rigorous nonlinear P-matrix method to the simulation of third order intermodulation in test devices and duplexers

Markus Mayer<sup>1</sup>, Werner Ruile<sup>1</sup>, Andreas Mayer<sup>2</sup>, Elena Mayer<sup>2</sup>, John Johnson<sup>1</sup>, Juergen Kiwitt<sup>1</sup>, Romeo Jr San Jose<sup>3</sup>, Ingo Bleyl<sup>1</sup>, Karl Wagner<sup>1</sup>; <sup>1</sup>TDK corporation, Germany, <sup>2</sup>Hochschule Offenburg, Germany, <sup>3</sup>TDK corporation, Singapore

#### Background, Motivation and Objective

With increasing number of simultaneously active frequency bands and continuing miniaturization nonlinear effects may lead to spurious signals at receiving ports. Simulation of these nonlinear effects allows to identify critical devices in the individual filters and to test countermeasures.

Recently we presented COM and P-matrix formalisms which describe third order nonlinear effects of propagating waves by a single frequency independent constant. In this way nonlinearities of the elastic, piezoelectric and dielectric constants are treated. This method allows the calculation of IMD3 and triple beat in SAW filters.

#### Statement of Contribution/Methods

In this work we extend our approach by taking into account the metallization in more detail. We apply our new method to a variety of devices on lithium tantalate (YX1)/42: For duplexers the analysis of IMD3 of the constituting resonators and coupled mode filters allows the optimization of the total nonlinear filter performance.

Special attention in the simulation receives here the inclusion of the electro-magnetic environment.

**Results/Discussion**

Successful reduction of IMD3 in duplexers using the analysis of contributions of single SAW devices is presented. A good agreement of IMD3 measurement and simulation of original and optimized devices is demonstrated.

6H-3

**8:30 am Origin of IMD2 Signal Generation in Surface Acoustic Wave Devices**

Ken-ya Hashimoto<sup>1</sup>; <sup>1</sup>Dept. EEE, Chiba University, Chiba, Japan

**Background, Motivation and Objective**

The carrier aggregation requests RF duplexers to suppress the intermodulation distortion (IMD) ultimately. It is known that second-order IMD (IMD2) signals generated in surface acoustic wave (SAW) devices are not detectable by the interdigital transducer (IDT) due to its structural symmetry. But IMD2 generated signals are electrically detectable in real SAW devices on rotated Y-cut LiNbO<sub>3</sub> and LiTaO<sub>3</sub> substrates.

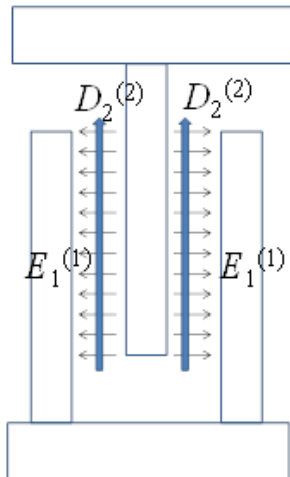
**Statement of Contribution/Methods**

This paper describes origin of the IMD2 generation in SAW devices. Namely, (a) the applied electrical input generates linear electric fields  $E_1^{(1)}$  and  $E_3^{(1)}$ , and (b) the non-linear electric flux  $D_2^{(2)}$  is generated and detected as the voltage difference between bus-bars (See Fig. 1). For the  $D_2^{(2)}$  generation by this mechanism, second-order non-linear permittivity elements  $\epsilon_{211}^{(2)}$  and/or  $\epsilon_{233}^{(2)}$  must be non-zero. Since  $\epsilon_{ijk}^{(2)}$  is the rank three tensor and possesses the same symmetry relation as the linear piezoelectric constant  $e_{ijk}$ ,  $\epsilon_{211}^{(2)}$  and/or  $\epsilon_{233}^{(2)}$  are zero for Z-cut 6mm substrates such as ScAlN but they are non-zero for rotated Y-cut LiNbO<sub>3</sub> and LiTaO<sub>3</sub> substrates with the 3m symmetry.

**Results/Discussion**

The above-mentioned discussion indicate that (a) the IMD2 is not detectable in ScAlN SAW devices, (b) the IMD2 can be cancelled by parallel-connecting two identical SAW resonators with sign inversion, and (c) the frequency dependence of the IMD2 output is similar to that of the IDT impedance. Experiments confirmed these expectations.

The electrostriction also has a potential to generate IMD2 signals in real SAW devices. Further discussions will also be given on this mechanism.



6H-4

**8:45 am Bandwidth-tunable Filter Consisting of SAW Resonators and BaSrTiO<sub>3</sub> Varactors Directly Fabricated on a LiTaO<sub>3</sub> Wafer**

Tetsuya Kimura<sup>1</sup>, Hideaki Kobayashi<sup>1</sup>, Yutaka Kishimoto<sup>1</sup>, Hideyuki Kato<sup>1</sup>, Mao Inaba<sup>2</sup>, Ken-ya Hashimoto<sup>2</sup>, Takeshi Matsumura<sup>3</sup>, Hideki Hirano<sup>4</sup>, Michio Kadota<sup>4</sup>, Masayoshi Esashi<sup>4</sup>, Shuji Tanaka<sup>4</sup>; <sup>1</sup>Murata Manufacturing Co., Ltd., Japan, <sup>2</sup>Graduate School of Engineering, Chiba University, Japan, <sup>3</sup>National Institute of Information and Communications Technology, Japan, <sup>4</sup>Microsystem Integration Center, Tohoku University, Japan

**Background, Motivation and Objective**

An up-conversion type RF front-end has been proposed for TV white space applications known as IEEE802.11af, and bandwidth-tunable filters are required in the system. In another paper to be presented in this Symposium, the authors report fabrication of a bandwidth-tunable filter by integration of Barium Strontium Titanate (BST) varactors and SAW devices on a LiTaO<sub>3</sub> wafer, where a newly developed laser-assisted technique is applied to transfer a BST film deposited on a Si wafer to the LiTaO<sub>3</sub> wafer.

**Statement of Contribution/Methods**

This paper describes fabrication of BST varactors directly deposited on a LiTaO<sub>3</sub> wafer with relatively low Curie temperature of 610°C and development of the bandwidth-tunable filter. The BST thin film, which is promising as a small varactor, requires high deposition temperature (>600°C) in order to obtain good performances. Thus special cares must be paid to the BST deposition not to cause performance deterioration in SAW resonators.

Figure 1 shows the developed fabrication process. First, a BST film was sputter-deposited on the LiTaO<sub>3</sub> wafer (#1), and BST varactors were fabricated (#2-#3). Then SAW filters with Al-IDTs (interdigital transducers) and NiCr resistor were carefully fabricated on it (#4-#6).

**Results/Discussion**

A prototyped bandwidth-tunable filter consisting of BST varactors, NiCr resistors and SAW resonators on a LiTaO<sub>3</sub> wafer was successfully realized for the first time using our newly developed direct fabrication process. Figure 2 shows the developed filter which contains 10 pieces of varactors, resistors and resonators, respectively. No damage was observed in the filter. The center frequency of the filter was 1GHz, and the 3dB bandwidth was electrically tuned from 4.5MHz to 9.6MHz over a DC supply voltage from 0V to 10V.

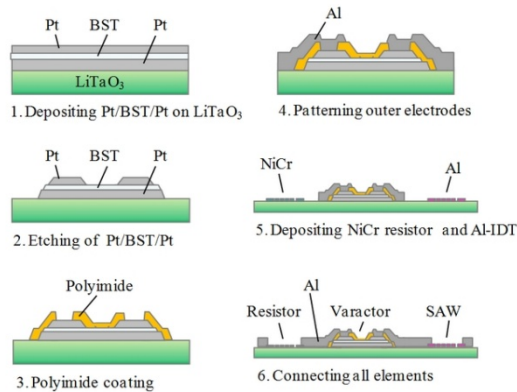


Figure.1 Full-wafer process for the tunable bandwidth filter.

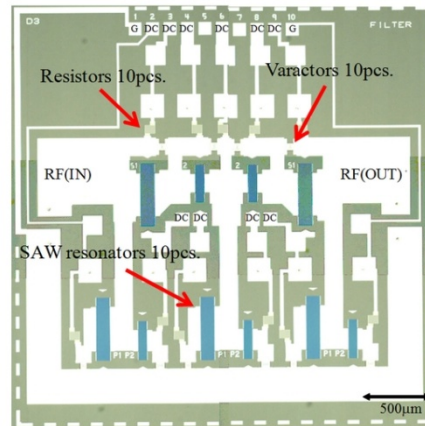


Figure.2 A developed tunable bandwidth filter.

6H-5

### 9:00 am Reconfigurable Mode of Vibration in AlN MEMS Resonators Using Phase Change Materials

Gwendolyn Hummel<sup>1</sup>, Yu Hui<sup>1</sup>, Matteo Rinaldi<sup>1</sup>; <sup>1</sup>Electrical and Computer Engineering, Northeastern University, Boston, MA, USA

#### Background, Motivation and Objective

High performance Aluminum Nitride (AlN) piezoelectric MEMS resonators, oscillators, and filters operating in a wide range of frequencies (100MHz-10GHz) have been demonstrated. Nevertheless, due to the very limited tuning capability, this technology has not fully satisfied the growing demand of the single-chip reconfigurable timing solutions for multi-band wireless communication. This paper presents the first demonstration of a new approach to dynamic reconfiguration of the mode of vibration in AlN piezoelectric MEMS resonators using phase change material (PCM) based switchable electrodes. This innovative design solution enables effective ON/OFF switching of the acoustic resonance ( $\sim 14$  dB impedance variation at resonance,  $C_{ON}/C_{OFF} \sim 4X$ ), and reconfiguration of the device electromechanical coupling ( $k_t^2: 0 - 0.33\%$ ), electrical capacitance ( $C_0: 0 - 496$  fF), and operating frequency ( $f_1 \sim 257$  MHz,  $f_2 \sim 378$  MHz). Such unique reconfiguration capabilities can potentially lead to the implementation of filter architectures (exclusively based on AlN/PCM high performance resonators and capacitors) whose frequency, order, bandwidth, and roll-off can be dynamically reconfigured.

#### Statement of Contribution/Methods

The device prototype was fabricated using a 6 mask process. Miniaturized ( $5 \times 5 \mu m^2$ )  $Ge_{50}Te_{50}$  vias were employed as low loss ( $R_{ON} \sim 10 \Omega$ ), high dynamic range ( $ON/OFF$  ratio  $\sim 10^6$ ), and low OFF capacitance ( $95$  fF) ohmic switches to connect the metal lines forming the device interdigital electrode to the electrical terminals of the resonator through a  $SiO_2$  insulating layer. Reconfiguration was achieved by applying voltage pulses to each individual PCM via (direct heating) to switch the electrical connection of the metal lines forming the electrodes ON/OFF.

#### Results/Discussion

The device was reconfigured to operate in 3 different states corresponding to various combinations of the fingers forming the device interdigital electrode (Fig. 1): *OFF*, all the PCM vias in the OFF state; *State 1*, 2 vias in the ON state, one connected to each terminal, to excite a 257MHz mode of vibration in the AlN micro-plate; *State 2*, 3 PCM vias are in the ON state, two connected to one terminal and one to the opposite terminal, to excite a 378MHz mode of vibration in the AlN micro-plate. Finally, all the PCM vias were returned to the OFF state (*OFF 2*), demonstrating reversible switching behavior.

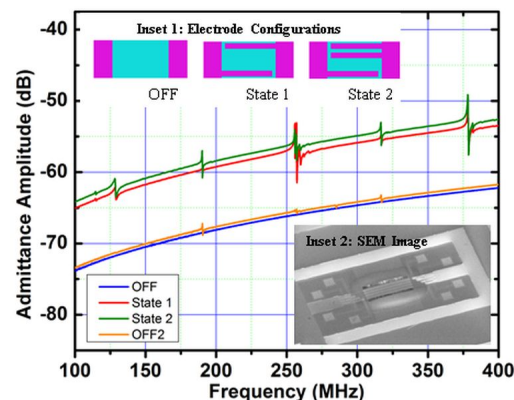


Figure 1: Measured admittance of the resonator in the different states. Insets 1 and 2 show the electrode configuration for each state and an SEM image of the device, respectively.

**9:15 am Bandwidth-tunable SAW Filter Based on Wafer-level Transfer-integration of BaSrTiO<sub>3</sub> Film for Wireless LAN System using TV White Space**

Hideki Hirano<sup>1</sup>, Tetsuo Samoto<sup>1</sup>, Tetsuya Kimura<sup>2</sup>, Masahiro Inaba<sup>3</sup>, Ken-ya Hashimoto<sup>3</sup>, Takeshi Matsumura<sup>4</sup>, Kousuke Hikichi<sup>1</sup>, Michio Kadota<sup>1</sup>, Masayoshi Esashi<sup>1</sup>, Shuji Tanaka<sup>1</sup>; <sup>1</sup>Tohoku University, Japan, <sup>2</sup>Murata Manufacturing Co. LTD, Japan, <sup>3</sup>Chiba University, Japan, <sup>4</sup>National Institute of Information and Communication Technology, Japan

**Background, Motivation and Objective**

A tunable filter is a key device for the RF front-end of cognitive wireless LAN system using TV white space. Frequency tuning is possible by varactors connected to SAW resonators. Ferroelectric (e.g. BaSrTiO<sub>3</sub>, BST) varactors are preferable for this use in terms of small footprint and high tuning ratio. In another paper to be presented in this symposium, the authors report a bandwidth-tunable filter based on the direct deposition of BST on a LiTaO<sub>3</sub> substrate at low temperature. This paper describes, as another approach, use of new technology to transfer BST films from a sapphire substrate to a LiTaO<sub>3</sub> substrate, on which SAW resonators are fabricated in advance.

**Statement of Contribution/Methods**

A key process of the BST transfer technology is the pre-irradiation of laser to metal/BST/metal structures from the backside of the sapphire substrate. Fig. 1 shows the fabrication process. First, a Au/Pt/BST/Pt film was sputter-deposited on the sapphire substrate at 650°C and patterned (#1-#2). The Pt layer under BST was irradiated by laser through the sapphire substrate (#3). The BST-on-sapphire substrate was bonded to a LiTaO<sub>3</sub> substrate by plasma-assisted Au-Au bonding at 150°C (#4), and then separated at BST/Pt interface near sapphire (#5). Finally, the tunable filter was completed by wiring the SAW resonators and the transferred BST varactors (#6).

**Results/Discussion**

Perfect BST transfer was achieved after intensive process optimization, and the tunable filter with 10 resonators and 10 varactors was completed. Voltage tuning of the passband was demonstrated, as shown in Fig. 2. The 3dB bandwidth at the center frequency of 1.050GHz was tuned between 3.50MHz and 5.50MHz, as designed. The prototyped tunable filter was actually installed in a cognitive wireless LAN demo system and worked successfully.

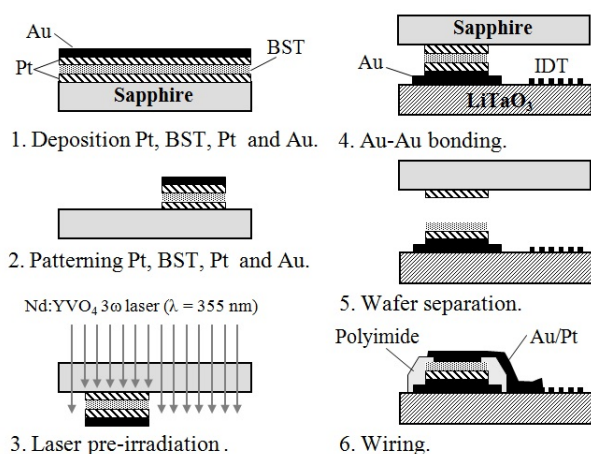


Figure 1 Fabrication process of bandwidth tunable filter.

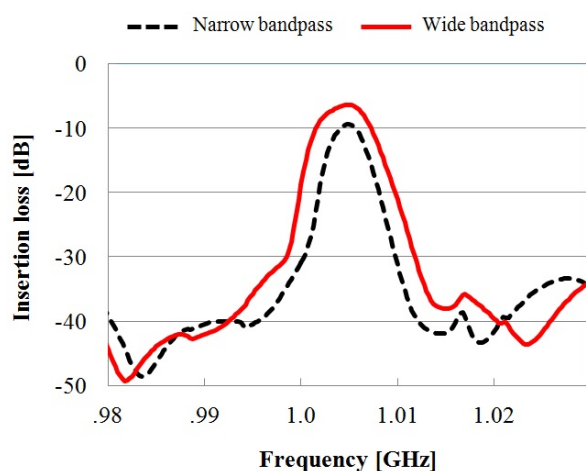


Figure 2 Passband characteristics.

## 7H - Electronic Control and Needle Actuation

Williford C

Saturday, September 6, 2014, 8:00 am - 9:30 am

Chair: **Mark Schafer**  
Sonic Tech Inc.

7H-1

### 8:00 am Non-linear Harmonic Reduction Pulse Width Modulation (HRPWM) for the Arbitrary Control of Transducer-integrated Switched Excitation Electronics

David Cowell<sup>1</sup>, Peter Smith<sup>1</sup>, James McLaughlan<sup>1</sup>, Sevan Harput<sup>1</sup>, Steven Freear<sup>1</sup>; <sup>1</sup>School of Electronic and Electrical Engineering, University of Leeds, Leeds, United Kingdom

#### Background, Motivation and Objective

Improvements in electronics and transducer fabrication now provide the ultrasound (US) system designer an opportunity to integrate front-end electronics directly into the transducer body, thus overcoming practical limitations on transducer cabling. This is possible through miniaturized, high current, high voltage, high efficiency switched excitation integrated circuits.

The US system designer desires excitation amplitude control for waveform shaping (temporal) and array apodisation (spatial), frequency control for coded excitation and minimal excitation harmonics for harmonic imaging.

It has previously been shown that switched mode excitation affords all these benefits. However, the resulting waveform contains significant harmonics that are detrimental to the performance of US modalities including tissue harmonic, harmonic contrast and super-harmonic imaging. We present a novel, non-linear modulation technique that allows simultaneous amplitude and frequency control whilst suppressing all harmonics below the 5th.

#### Statement of Contribution/Methods

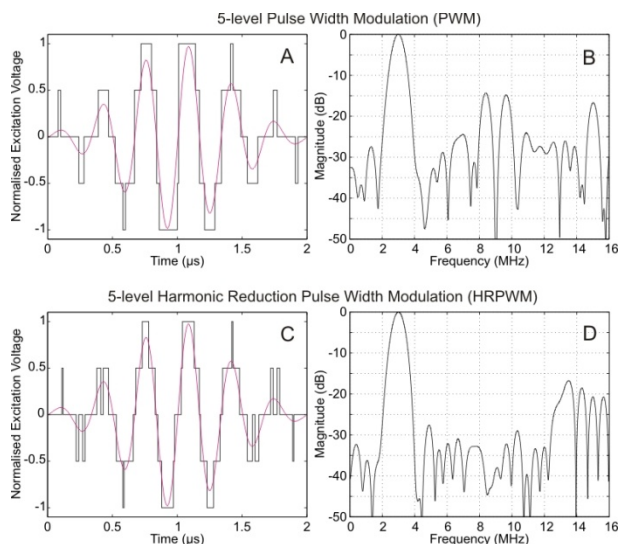
In a switched mode excitation the output waveform is determined by the phase threshold or transition/commutation point where the output voltage switches between each voltage level. This work establishes a non-linear mathematical relationship between the phase of switching angles  $[\theta_1, \theta_2]$  relative to power at the fundamental and harmonic components for a quinary (5-level)  $[\pm V, \pm V/2, \text{GND}]$  switched excitation system, and is termed Harmonic Reduction Pulse Width Modulation (HRPWM).

HRPWM navigates the  $\theta_1$ - $\theta_2$  plane such that the fundamental power and frequency can be instantaneously varied whilst maintaining complete suppression of the 2nd, 3rd and 4th harmonics.

#### Results/Discussion

Fig A shows 5-level PWM excitation of a Gaussian windowed 3 MHz, 6 cycle tone, with -20 dB fundamental BW of 2-4 MHz. The spectrum (Fig B) shows a 3rd harmonic (6-12 MHz) of -15 dB. The proposed HRPWM (Fig C) shows individual pulses replaced by double pulses and adjustments in pulse duration and timing to achieve harmonic suppression. The spectrum (Fig D) shows an average 3rd harmonic of -30 dB, a suppression of 15 dB.

HRPWM allows amplitude and frequency modulation and arbitrary excitation waveforms with suppressed 2nd to 4th harmonics using solid state integrated circuits suitable for embedding within the transducer.





## 7H-2

**8:15 am Customized Modular Multichannel Electronics for Ultrasound-mediated Targeted Drug Delivery with a Geodesic Piezocrystal Phased Array**Zhen Qiu<sup>1</sup>, Roderick Habeshaw<sup>1</sup>, Dave Lines<sup>2</sup>, Sandy Cochran<sup>1</sup>; <sup>1</sup>IMSaT, University of Dundee, United Kingdom, <sup>2</sup>Diagnostic Sonar Ltd, United Kingdom**Background, Motivation and Objective**

Ultrasound-mediated targeted drug delivery (UmTDD) has the potential to enhance the chemotherapeutic treatment of cancer by allowing increased drug doses preferentially at the location of the tumor. Although gaining increasing interest over the past few years, research into UmTDD system configurations has been hindered by the limited availability and high cost of experimental ultrasound array sources and suitable experimental driving electronics. In the work reported here, a geodesic phased array with 96 individual elements was fabricated in-house, using piezocrystal PMN-PT material. This was connected to programmable multi-channel electronics based on PXI / FlexRIO hardware (NI, Houston, TX, USA) modified to provide appropriate ultrasound intensities.

**Statement of Contribution/Methods**

Binary PMN-PT piezocrystal composites were diced into 24 triangular plates to form a spherical, faceted array inspired by the geodesic dome structure, taking into account that the thermal sensitivity and crystalline structure of the PMN-PT make the alternative thermoforming undesirable. Each triangular composite plate was further divided into four smaller triangles to increase the number of individual elements to 96, operating at 1 MHz. A modular instrumentation system (FI Toolbox, Diagnostic Sonar Ltd, UK) was used to drive the array. Based on its original development in non-destructive testing (NDT) application, the system configuration, in both hardware and software, was modified to match UmTDD requirements.

**Results/Discussion**

With modifications to reduce internal power and heat dissipation, the system is able to drive the array transducer with pulse-width modulated square waves in continuous wave (CW) mode. The transmission and reception boards in the FI Toolbox are stackable to increase the number of channels but the available test system had 32 channels for CW driving configuration. The 96 elements of the array were therefore interconnected in 32 groups of three, in a 2D segmented annular configuration, to match the instrumentation channel count. The phase is controlled and adjusted in 11.25° increments for each channel. Residual aberration of the array elements caused by minor geometric positioning errors was estimated and corrected using 1-D cross-correlation on the received RF signals from point reflectors. Our results show that modular electronics offer a valuable prototyping route for UmTDD systems and that good focusing at 70 +/- 5 mm along the axis and limited steering of the ultrasound beam, +/- 2.5 mm off the axis, can be achieved with the geodesic array geometry, with side lobes's intensity less than -12dB. Larger numbers of elements and alternative array designs will be explored in future.

## 7H-3

**8:30 am Automatic frequency tracking system for needle actuating device**Lin Gui<sup>1</sup>, Xiaojia Xie<sup>1</sup>, Yang Kuang<sup>1</sup>, Sandy Cochran<sup>2</sup>, Zhihong Huang<sup>1</sup>; <sup>1</sup>School of Engineering, Physics and Mathematics, University of Dundee, Dundee, Scotland, United Kingdom, <sup>2</sup>Institute for Medical Science and Technology (IMSaT), University of Dundee, Dundee, Scotland, United Kingdom**Background, Motivation and Objective**

A needle actuating device we developed previously has shown promising results in improving the visibility of percutaneous needles under ultrasound imaging. It uses a piezoelectric transducer to actuate a standard percutaneous needle. The longitudinally vibrating needle can be clearly visualised as a coloured line under colour Doppler imaging. However, when the needle is inserted into biological tissue, the resonant frequency of the needle actuating device varies because of the external loads. Manual adjusting of the excitation frequency is required to keep the needle visible, which is particularly tricky when the needle is advancing. This paper presents an automatic frequency tracking system which has the ability to automatically track the resonant frequency shift and adjust the excitation frequency accordingly. The effectiveness of this system in improving the performance of the needle actuating device is studied.

**Statement of Contribution/Methods**

The automatic frequency tracking system was designed as an embedded system controlled by a micro control unit (MCU). The voltage across and the current through the needle actuating device was sampled. Their phase difference was measured by a phase comparator and fed back to the MCU. The MCU adjusted the frequency output of the signal output module according to a PID controller so that the phase difference between voltage and current kept at zero value. Consequently, the resonance of the needle actuating device was maintained.

The needle actuating device was driven by the frequency tracking system and inserted into ex vivo porcine tissue at 3 cm with needle-beam angle of 30°. The colour Doppler imaging of the needle was recorded by SonixTablet (Ultrasonics, Richmond, Canada) with a 5 MHz linear ultrasound imaging probe.

**Results/Discussion**

The frequency tracking system developed was able to track the resonant frequency of ultrasonic transducers in the frequency range of 10 to 200 kHz with maximum output power of 100W. It maintained the resonance of the needle actuating device successfully during the whole needle insertion procedure. The needle thus was always visualised without tuning the excitation frequency manually. This enables the real time monitoring of the needle position as shown in Fig. 1.

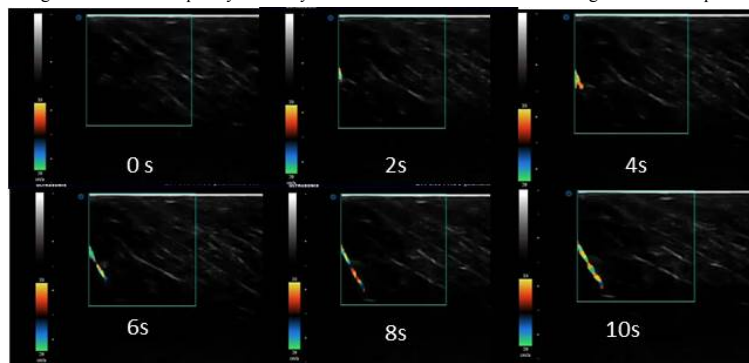


Fig.1 Doppler ultrasound imaging of the needle actuating device during needle insertion into porcine tissue at 3 cm: the needle entered into the visual field of the imaging probe at 2s and reached the desired depth at 10s.

7H-4

# 8:45 am Characterization of Langevin transducers incorporating Mn-doped piezocrystal material

Andrew Mathieson<sup>1</sup>, Muhammad Sadiq<sup>2</sup>, Sandy Cochran<sup>2</sup>, Margaret Lucas<sup>1</sup>; <sup>1</sup>School of Engineering, University of Glasgow, United Kingdom, <sup>2</sup>Institute for Medical Science and Technology, University of Dundee, United Kingdom

## Background, Motivation and Objective

Recent developments of third generation relaxor-PT piezoelectric single crystals, Mn:PIN-PMN-PT, herald significant potential benefits to high power ultrasonic devices due to their ability to possess a high electro-mechanical coupling coefficient while exhibiting low mechanical losses and increased temperature and field stability. This study reports the experimental characterization of two power ultrasonic transducers, one based on Mn:PIN-PMN-PT and one based on PZT4. The results demonstrate the feasibility of incorporating the piezocrystal material and illustrate the influence, as compared with piezoceramic, on the vibrational behavior of the device.

## Statement of Contribution/Methods

The two transducers are tuned, using finite element analysis (FEA) models validated through experimental modal analysis (EMA), to operate in a longitudinal mode at 28 kHz and contain piezoelectric rings which are geometrically identical. Performance indicators, QM, keff and QE, are calculated from impedance sweeps, while dynamic behaviors are characterized through harmonic sweeps close to the tuned frequency. The transducers are also driven under operational conditions to determine and compare the maximum amplitude of vibration achieved for each transducer and the heat generated in the two piezoelectric materials.

## Results/Discussion

It is shown that meaningful validation of FEA models with EMA relies on measurement of the material properties, rather than reliance on manufacturer data, Table 1. This is achieved through using combined ultrasonic and resonant techniques that also allow for characterization of the piezoelectric material under the elevated temperatures and pressures typical of operational conditions of high power ultrasonic transducers.

Nonlinear vibrational behaviors exhibited by piezoceramic materials can have a detrimental effect on the performance of high power ultrasonic devices, but the influence of Mn-doped piezocrystal is unknown. The nonlinear responses of the two transducers are characterized. Common behaviors and differences are identified, providing design guidance for controlling the response of devices incorporating Mn-doped piezocrystal material in the transducer.

Table 1

Parameter of Mn:PIN-PT	Measured	Manufacturer data
Coupling coefficient, $k_t$	0.54	0.54
Frequency constant, $N_t$	1912	1911
Stiffness constant, $c_{33}^D$ (N/m <sup>2</sup> )	1.59E11	1.59E11
Stiffness constant, $c_{33}^E$ (N/m <sup>2</sup> )	1.13E11	1.13E11
Dielectric constant, $\epsilon_{r33}^T$	3185	3427
Dielectric constant, $\epsilon_{r33}^S$	677	595
Piezoelectric constant, $e_{33}$ (C/m <sup>2</sup> )	22.5	-
Quality factor, $Q_M$	~700	-

7H-5

# 9:00 am Performance Optimization of Ultrasonic Needle Actuating Device for Insertion Operation into Tissue Mimics

Xiaochun Liao<sup>1</sup>, Yang Kuang<sup>1</sup>, George Corner<sup>2</sup>, Sandy Cochran<sup>3</sup>, Zhihong Huang<sup>1</sup>; <sup>1</sup>School of Engineering, Physics and Mathematics, University of Dundee, Dundee, Scotland, United Kingdom, <sup>2</sup>Department of Medical Physics, Ninewells Hospital and Medical School, Dundee, Scotland, United Kingdom, <sup>3</sup>Institute for Medical Science and Technology, University of Dundee, Dundee, Scotland, United Kingdom

## Background, Motivation and Objective

An ultrasonic needle actuating device we developed previously demonstrated the ability to reduce the penetration force during needle insertion and consequently to increase the targeting accuracy and minimize local tissue damage. These advantages are important in minimally invasive percutaneous procedures such as cancer biopsy and regional anesthesia. The device consisted of a Langevin piezoelectric transducer, which clamped a standard needle at the needle shaft and actuated it to oscillate longitudinally. The achieved force reduction was found to be proportional to the vibration amplitude at the needle tip. In practice, the actuated needle interacted with peripheral tissue with external loads.

The present paper aims to identify the effect of the external load on the needle vibration amplitude, optimize the vibration performance through numerical analysis with different needle clamping positions and dimensions, and confirm improved performance of the needle actuating device on penetration force reduction with experiments.

## Statement of Contribution/Methods

The needle performance was examined by measuring the needle tip vibration amplitude with a laser vibrometer (OFV-534 / 2570, Polytec Ltd, Herts, UK), when the needle was inserted through *ex vivo* porcine tissue at different depths with a constant driving voltage.

The performance optimization was carried out with the finite element analysis package ABAQUS (6.12-1, Dassault Systeme, Paris, France). Modal analyses were performed to match the resonance of the transducer and the needle by adjusting the clamping positions and constraints. Three needles (G20 hollow, G22 solid, G22 hollow) were selected to investigate the effects of needle dimensions and external load on the vibration amplitude through steady state analyses with a fixed pre-loading condition at the transducer's resonant frequency of 22.0 KHz.

To verify the numerical results, trials were carried out with the three different needles inserted into tissue mimics with frequency tracking to achieve stable performance. The force response variation with the insertion depth was recorded by a commercial material testing machine (H5KS, Tinius Olsen, Surrey, UK).

#### Results/Discussion

Results from laser vibrometry indicated that the vibration amplitude of the needle tip could reduce by 55% with deep insertion to 50 mm. Numerical analysis for better vibration performance revealed higher needle tip vibration amplitude for the G20 hollow needle as - G20 hollow: 11.66  $\mu\text{m}$ , G22 solid: 11.28  $\mu\text{m}$ , G22 hollow: 7.56  $\mu\text{m}$ - under a 0.1 N load on the needle's bevel surface with a driving voltage of 55 V. Trials on tissue mimics confirmed better performance of the G20 hollow needle, with penetration force reduced by 60% up to 50 mm depth, compared with a 35% reduction for the G22 hollow needle.

The results demonstrate a feasible method to analyze and optimize the mechanical performance of an ultrasonic needle actuating device for high power medical applications.

#### 7H-6

#### 9:15 am Enhanced US-Guided Needle Intervention through Ultrasound Actuation of a Standard Needle

Muhammad Sadiq<sup>1</sup>, Xiaochun Liao<sup>1</sup>, Lin Shengtao<sup>1</sup>, Sandy Cochran<sup>1</sup>, Zhihong Huang<sup>1</sup>; <sup>1</sup>University of Dundee, Dundee, United Kingdom

#### Background, Motivation and Objective

In ultrasound (US)-guided percutaneous needle procedures, there are universal problems of poor visibility and deflection of needle tip, especially in dense tissues and at steep insertion angles. These can have serious consequences, including nerve damage, internal bleeding and need of repeat biopsy. This paper reports a pre-clinical prototype of an ultrasound needle actuating device initially developed based on piezoceramic (PZT4) to enhance visibility under Doppler ultrasound and reduce deflection of standard needles. The requirement of this device for low spatial volume, high performance actuation has also led us to investigate the potential of Generation III relaxor-PT piezocrystals (Mn:PIN-PMN-PT) because of their high piezoelectric properties, low mechanical losses and increased temperature and field stability.

#### Statement of Contribution/Methods

Based on the structure of the Langevin transducer, the device design was realised considering the typical needs of the end users, in this case experienced clinicians. Comprehensive data for both PZT4 piezoceramic and Mn:PIN-PMN-PT piezocrystals (from Ferroperm SA, Kvistgaard, Denmark and TRS Technologies Inc., PA, USA, respectively) were obtained experimentally and utilized for virtual prototyping (PZFlex, Weidlinger Associates, CA, USA) allowing detailed design while ensuring the longitudinal operating mode in the needle. For PZT4,  $d_{33} \geq 250 \text{ m/V}$  and  $Q_M \geq 500$  while for Mn:PIN-PMN-PT,  $d_{33} \geq 1000$  and  $Q_M \geq 700$ .

Complete characterization of both PZT4 and Mn:PIN-PMN-PT based devices were then carried out to measure and compare the performance parameters, including  $k_{eff}$ ,  $Q_M$ , and displacement amplitude at the tip of the needle. Furthermore, to assess the device's feasibility in clinical practice, pre-clinical trials were carried out on ex-vivo animal tissues and Thiel embalmed cadavers.

#### Results/Discussion

The proposed device actuates standard needles in the low ultrasound frequency range, 20 - 40 kHz, with displacement amplitude  $\geq 5 \mu\text{m}$  leading to three clinical benefits: (a) enhanced tip visibility under 2D color Doppler US imaging, (b) reduced tip deflection and (c) better tissue penetration through action similar to ultrasonic cutting. Efficiency was observed particularly at angles steeper than  $45^\circ$  and depths  $\geq 3 \text{ cm}$ , feat that is difficult to achieve conventionally. Although both PZT4 and Mn:PIN-PMN-PT based devices are effective, the common behaviors and differences between the two devices were identified. Its low cost suggests PZT4 as the better choice at present, but the performance benefits of Mn:PIN-MN-PT cannot be ignored.

# 1I - MCA: Contrast Agents: New Technologies

Grand Ballroom

Saturday, September 6, 2014, 10:30 am - 12:00 pm

Chair: **Ayache Bouakaz**  
INSERM, Tours

1I-1

## 10:30 am In Vivo Acoustic Single Bubble Tracking at Super-Resolution

Kirsten Christensen-Jeffries<sup>1</sup>, Richard J Browning<sup>1</sup>, Meng Xing Tang<sup>2</sup>, Christopher Dunsby<sup>3,4</sup>, Robert J Eckersley<sup>1</sup>; <sup>1</sup>Biomedical Engineering Department, Division of Imaging Sciences, Kings College London, London, United Kingdom, <sup>2</sup>Department of Bioengineering, Imperial College London, London, United Kingdom, <sup>3</sup>Department of Physics, Imperial College London, London, United Kingdom, <sup>4</sup>Centre for Histopathology, Imperial College London, London, United Kingdom

### Background, Motivation and Objective

Changes in blood flow in the micro-circulation are of clinical importance in the study of a number of disease processes such as cancer and diabetes. Imaging of blood flow using ultrasound (US) has been possible through the use of techniques such as color Doppler imaging, however micro-vascular flow has not been adequately imaged by current techniques due to limitations of resolution and/or attenuation. Improving resolution in US requires the use of high frequency waves, which are strongly attenuated making imaging beyond a few millimeters impossible.

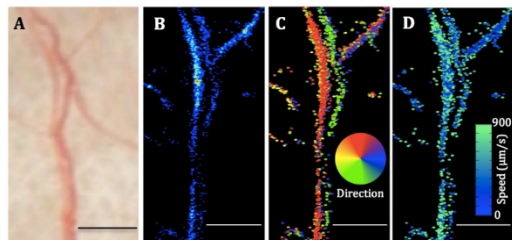
In previous work, we demonstrated a super-resolution technique which overcomes the diffraction limit by localizing spatially isolated microbubble signals for US imaging at depths of up to 7 cm *in vitro*. By adapting this technique to track individual bubble flow profiles through the vasculature, flow information can be imaged at depth at a significantly enhanced resolution, which improves vascular information for the diagnosis and management of a wide range of diseases.

### Statement of Contribution/Methods

We present a method of imaging blood flow velocity at super-resolution through the implementation of a single bubble tracking technique using a standard clinical US system *in vivo*. Microbubbles flowing at low concentration within micro-vessels can be localized by calculating the center of mass of each spatially isolated signal. Through the subsequent tracking of many of these microbubble signals across a series of image frames using a cross correlation identification algorithm, a color-encoded flow velocity image of the vascular structure can be attained at super-resolution. Here, we present the use of this method to image micro-vessel flow in the ear of a live, CD1 female mouse *in vivo*.

### Results/Discussion

Results in the figure show an optical image of the ear vasculature in (A), and the corresponding super-resolution image of the ear vasculature in (B). Flow direction can be distinguished over 360°, as shown in (C). Blood velocity is displayed as a bubble speed color map in (D). This enhances vascular information through the identification and separation of arteries and veins.



1I-2

## 10:45 am Super-resolution ultrasound imaging with “blinking” microbubbles

Geoffrey Luke<sup>1,2</sup>, Alexander Hannah<sup>1</sup>, Stanislav Emelianov<sup>1,2</sup>; <sup>1</sup>Biomedical Engineering, The University of Texas at Austin, Austin, Texas, USA, <sup>2</sup>Electrical and Computer Engineering, The University of Texas at Austin, Austin, Texas, USA

### Background, Motivation and Objective

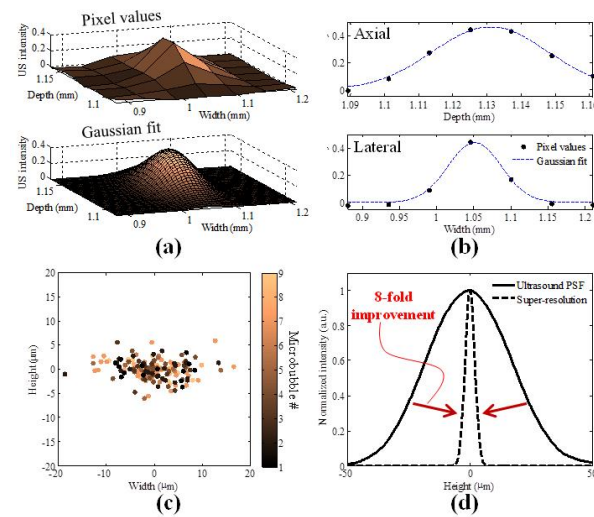
Despite the power and versatility of ultrasound to image soft tissue, its spatial resolution is fundamentally limited by the characteristics of the acoustic wave and transducer, typically to be on the order of 100  $\mu\text{m}$ . However, the ability to visualize the many biological structures which are on the scale of nanometers to tens of micrometers could open new avenues in biology and medicine. We have developed a technique to exceed the resolution limit in ultrasound imaging. Our method is based on detecting the stochastic condensation of transient laser-activated microbubbles (LAMBs) with high frame rate ultrasound imaging.

### Statement of Contribution/Methods

The LAMBs are synthesized in their stable nanodroplet form, consisting of a perfluorohexane core, a Zonyl fluorosurfactant shell, and encapsulated gold nanorods. The LAMBs are vaporized using a pulsed nanosecond laser, and the resulting microbubbles have a lifetime on the order of 10-100 ms before recondensing into their native droplet state due to the lower background temperature. Because each LAMB undergoes condensation at a random time after the initial trigger, high frame rate ultrasound imaging can be used to visualize the “blinking” off of a sparse subset of LAMBs between successive frames (panel A). After fitting a two-dimensional Gaussian function to the image (panels A-B), its peak denotes the precise location of the LAMB. This process is repeated for each condensation event, and repeatable vaporization enables multiple measurements of the location each LAMB.

### Results/Discussion

Analysis of 9 LAMBs (panel C) over 40 laser pulses shows that the location of individual LAMBs can be estimated to within 5-10  $\mu\text{m}$ . This is an 8-fold improvement in axial and lateral resolution over conventional b-mode imaging (panel D). These results pave the way for imaging at the micro-scale deep in tissue. Furthermore, by adding molecular targeting, complex biological environments could be characterized with excellent resolution.



11-3

### 11:00 am Theoretical and experimental resolution limit of Sono-Activated Ultrasound Localization Microscopy (SAULM)

Yann Desailly<sup>1</sup>, Juliette Pierre<sup>1</sup>, Olivier Couture<sup>1</sup>, Mickael Tanter<sup>1,2</sup>, <sup>1</sup>Institut Langevin, ESPCI ParisTech, CNRS, INSERM, Paris VII university, Paris, France

#### Background, Motivation and Objective

Ultrasound contrast agents observed in-vivo with an ultrafast scanner (up to 20 000 frames per second), display a stochastic behavior which results in punctual acoustic echoes coming from individual microbubbles. Since these sources are isolated, they do not abide to classical diffraction limit, a principle that is the basis of sono-activated ultrasound localization microscopy (SAULM). We previously showed experimentally that SAULM can resolve two vessels closer than  $\lambda/4$  [Desailly et al., 2013]. However, higher resolutions are theoretically achievable. This study demonstrates that the experimental resolution of SAULM can be predicted through theoretical and numerical modelling.

#### Statement of Contribution/Methods

Experimentally, the resolution limit of SAULM is determined by injecting high concentrations of microbubbles within a single vessel phantom in PDMS that is 20 times smaller than the wavelength. Superlocalization is performed with a 256 channels ultrafast scanner equipped with a matrix probe at 1.75 MHz. Distinct events from microbubbles are obtained by performing high frame-rate (beyond 1 kHz) differential imaging. The resolution is measured as the FWHM of the channel, converted to variance. Theoretically, the localization's variance is determined by the precision of the fit of a single echo to its point spread function, which is represented by a hyperbola in the element-by-element radio-frequency matrix. The spatial accuracy is hence determined by the time accuracy  $\sigma_t$  of the fit of a time-of-flight model of the echo.

### Results/Discussion

We can thus extrapolate the coordinates of the localized source with a variance shown in equation 1 ( $n$  is the number of parallel reception channels and  $\Gamma^{-1}$  an asymptotic 3-by-3 matrix function of the geometry and sensibility of the transducer matrix and the location  $(x_0, y_0, z_0)$  of the source). As shown in figure 1d, the resolution of SAULM predicted by the numerical simulations and the analytical model was close to the experimental measurements. At 3 cm, a resolution of 60  $\mu\text{m}$  ( $\lambda/14$ ) could be obtained. Because it is not limited by diffraction, the resolution of SAULM depends on new parameters such as the SNR, the time sampling of the RF signal and the number of elements. Understanding these new limits can help optimize SAULM to yield new super-resolved images which bypass the classical tradeoff between attenuation and resolution.

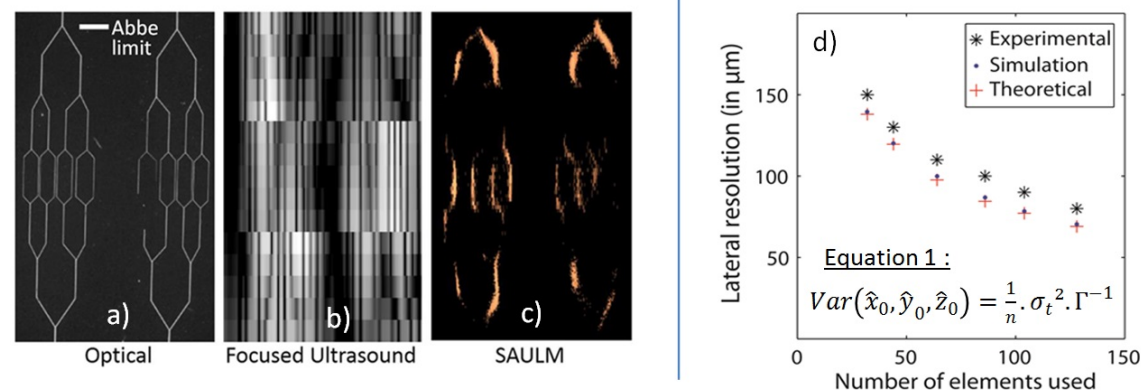


**Figure 1:** On the left panel, a circulatory network observed with fluorescence microscopy (a), focused ultrasound (b) and SAULM (c); on the right panel, the dependency of the lateral resolution in SAULM on  $n$  - the number of reception transducers (d)



# 11:15 am Ultrasound Quantification of Molecular Marker Concentration in Large Blood Vessels

Shiying Wang<sup>1</sup>, F William Mauldin Jr<sup>1</sup>, Alexander L Klibanov<sup>1,2</sup>, John A Hossack<sup>1</sup>; <sup>1</sup>Biomedical Engineering, University of Virginia, Charlottesville, Virginia, USA, <sup>2</sup>Division of Cardiovascular Medicine, University of Virginia, Charlottesville, Virginia, USA

## Background, Motivation and Objective

Current ultrasound molecular imaging techniques have demonstrated efficacy in pre-clinical studies of cancer and cardiovascular disease. These techniques involve the detection of molecular specific bound microbubbles (MBs) through some combination of nonlinear MB detection and elimination of free MBs through waiting periods or low-pass interframe filtering techniques. Non-specific adhesion is typically measured by additional control MB injections. In addition to having prolonged protocols, current limitations include the inability to quantify molecular marker concentration in human tissue environments with highly variable attenuation and imaging path lengths. Consequently, we developed a novel modulated Acoustic Radiation Force (ARF)-based imaging sequence, with the goal of achieving quantitative measurement of molecular marker concentration using a single short imaging protocol (3 min).

## Statement of Contribution/Methods

Gelatin flow phantom channels ( $\phi = 4$  mm) were constructed to mimic large blood vessels. Targeted and control channels were incubated with streptavidin ( $1 - 50 \mu\text{g/mL}$ ) and 5% bovine serum albumin (BSA) solution for 12 h, respectively. The surface concentrations of Eu<sup>3+</sup>-labelled streptavidin were measured using dissociation-enhanced time-resolved spectrofluorometry. Biotinylated lipid-perfluorobutane MB ( $\phi \sim 2 \mu\text{m}$ ) dispersion ( $5 \times 10^5 / \text{mL}$ ) was drawn through the channels ( $6 - 10$  cm/s). The sequence (programmed on Verasonics scanner) had three components – 10 s of imaging (4.5 MHz, 4 Hz frame rate), 70 s of interspersed imaging and ARF (4.5 MHz, 5 kHz PRF, MI < 0.05), and 100 s of imaging – showing the baseline, rise, and decay of adherent MBs along the bottom wall (Fig a). The residual-to-saturation ratio ( $R = \text{residual MB} / \text{saturated MB}$ ) extracted from the signal magnitude curve was used to quantify molecular marker concentration.

## Results/Discussion

Results demonstrate that  $R$  is linearly related to streptavidin concentration at a range of flow velocities ( $R^2 > 0.94$ , Fig b&c); and within certain bounds, was independent of attenuation and absolute signal magnitude ( $p > 0.13$ ,  $n = 10$ ). The highest detection sensitivity was approximately 900 molecules/ $\mu\text{m}^2$ . In summary, feasibility was demonstrated for a rapid (3 min imaging protocol) quantification of molecular marker concentration in large vessels using the modulated ARF-based sequence.

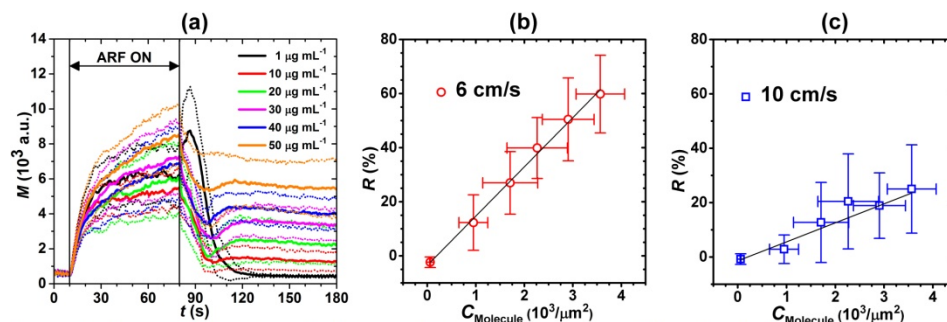


**Figure** (a) Averaged signal magnitude curves for targeted channels at different incubation concentrations of streptavidin solution ( $1 - 50 \mu\text{g/mL}$ ). Solid lines indicate the mean values from 10 trials. Dotted lines indicate the corresponding error bars at the range of  $[\text{mean} \pm \text{standard deviation}]$ . Relationships between the residual-to-saturation ratio ( $R$ ) and corresponding surface concentration of streptavidin at flow velocities of 6 cm/s ( $R^2 = 0.99$ ) (b) and 10 cm/s ( $R^2 = 0.95$ ) (c). Black lines are the weighted linear fits.

# 11:30 am StemBells: a novel stem cell delivery platform using microbubbles and acoustic radiation force

Tom Kokhuis<sup>1,2</sup>, Ilya Skachkov<sup>1</sup>, Benno Naeijens<sup>2,3</sup>, Lynda Juffermans<sup>2,4</sup>, Otto Kamp<sup>2,5</sup>, Antonius van der Steen<sup>1,2</sup>, Michel Versluis<sup>6,7</sup>, Nico de Jong<sup>1,2</sup>; <sup>1</sup>Biomedical Engineering, Erasmus Medical Center, Rotterdam, Netherlands, <sup>2</sup>Netherlands Heart Institute, ICIN, Utrecht, Netherlands, <sup>3</sup>Pathology, VU Medical Center, Amsterdam, Netherlands, <sup>4</sup>Physiology, VU Medical Center, Amsterdam, Netherlands, <sup>5</sup>Cardiology, VU Medical Center, Amsterdam, Netherlands, <sup>6</sup>Physics of Fluids Group, University of Twente, Enschede, Netherlands, <sup>7</sup>Institute of Biomedical Technology and Technical Medicine, MIRA, Enschede, Netherlands

## Background, Motivation and Objective

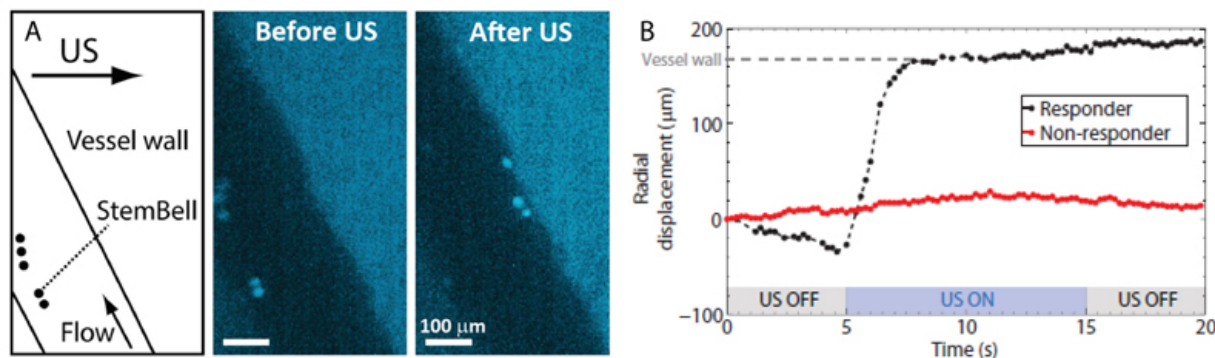
Cardiac regenerative therapy is currently hampered by the low number of stem cells that are delivered at the site of infarction [1]. To improve the homing of stem cells, we are currently investigating a novel delivery platform in which stem cells are conjugated with targeted microbubbles (tMBs), creating echogenic complexes dubbed StemBells. In this study we investigated the feasibility of manipulating the position of StemBells within the blood vessels of a chicken embryo ( $150 - 400 \mu\text{m}$  in diameter) using acoustic radiation force (ARF). Translational dynamics were measured for different saturation grades (i.e. bare stem cells, unsaturated StemBells with  $< 5$  tMBs/cell and saturated StemBells with  $> 30$  tMBs/cell) and peak acoustic pressures ( $P_- = 200$  kPa and  $P_- = 450$  kPa).

## Statement of Contribution/Methods

Stem cells were cultured in platelet lysate enriched medium. Next, cells were fluorescently labeled (Hoechst), trypsinized, washed and mixed with CD90-targeted microbubbles for 30 min under continuous rotation at room temperature to create StemBells. The mixing ratios (stem cell : tMBs) used to get unsaturated and saturated StemBells were 1:10 and 1:200 respectively. For the experiment, the embryo (5 days old) was taken out of the eggshell, transferred to a cup and embedded in a heated water bath which was connected to a microscope equipped with a color camera. The water tank was also holding the 1 MHz ultrasound (US) transducer. Samples were infused into one of the vitelline veins upstream from the optical field of view. The radial displacement of the fluorescent stem cells following acoustic forcing (1 MHz,  $P_- = 200$  kPa or  $P_- = 450$  kPa, 10 seconds, 10% duty cycle) was studied using intravital time-lapse fluorescence microscopy.

**Results/Discussion**

Bare stem cells ( $n = 21$ ) or unsaturated StemBells ( $n = 11$ ) did not respond to US application. However, saturated StemBells ( $n = 12$ ) could be propelled toward and arrested at the vessel wall (see panel A). The mean translational velocities measured are  $61 \mu\text{m/s}$  and  $177 \mu\text{m/s}$  for  $P_- = 200 \text{ kPa}$  and  $P_- = 450 \text{ kPa}$  respectively. Panel B shows a typical radial displacement-time curve of a saturated StemBell in response to US (200 kPa, black); the curve of a non-responding bare stem cell (red) is also shown. The StemBell-technique offers potential to increase the homing of stem cells to their target tissue in a well-controlled and minimally invasive manner.

**References**

[1] Hofmann et al. *Circulation* 111:17 (2005)

This work was supported by the Dutch Technology Foundation STW

11-6

### 11:45 am In vivo acoustic contrast enhancement via simultaneous production and injection of microfluidic-produced microbubbles

Ali Dhanaliwala<sup>1</sup>, Adam Dixon<sup>2</sup>, Dan Lin<sup>1</sup>, Alexander Klibanov<sup>1</sup>, John Hossack<sup>1</sup>; <sup>1</sup>University of Virginia, USA, <sup>2</sup>Biomedical Engineering, University of Virginia, USA

**Background, Motivation and Objective**

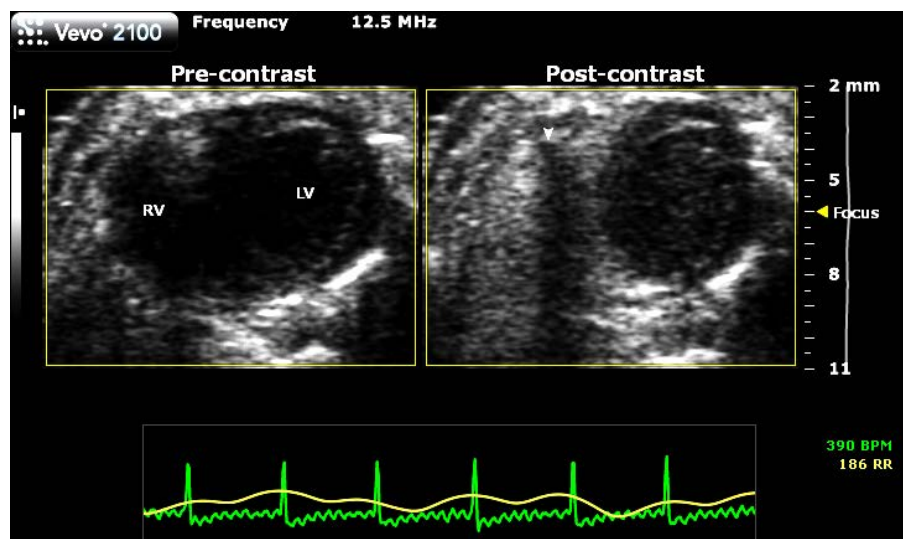
Microfluidic production of microbubbles for ultrasound contrast has, to date, focused on producing stable microbubbles to facilitate useful shelf storage and long circulation times. Instead, in this work, we exploit the small size of microfluidic devices leading to the potential to produce microbubbles directly within the vasculature. By situating microbubble production near the site of use, the microbubble circulation stability requirement can be relaxed as the microbubbles need only need to survive for a few seconds. Furthermore, intentionally producing short-lived microbubbles enables the consideration of larger diameter microbubbles as rapid dissolution can be relied upon to reduce the risk of gas emboli. Towards this goal, we investigated whether a microfluidic device producing microbubbles could produce adequate acoustic contrast when directly connected through a tail vein catheter placed in vivo in a mouse.

**Statement of Contribution/Methods**

A flow-focusing microfluidic device (FFMD) was used to produce microbubbles nitrogen gas microbubbles in a 3% bovine serum albumin (BSA) 10% dextrose aqueous solution. The microbubbles were injected into C57 Bl/6 mice via a tail vein catheter directly connected to the FFMD output. A short-axis image of the mouse heart was acquired with a high frequency small animal scanner. Microbubble diameter and production rate were determined optically with a high speed camera connected to an inverted microscope.

**Results/Discussion**

In total, 18 imaging sessions were conducted. The median microbubble diameter was  $14 \mu\text{m}$ . The median production rate was 400,000 microbubble/s. Microbubbles were observed in both the right and left ventricles; however, the image intensity in the left ventricle was on average 18% lower than the intensity measured in the right ventricle (Fig 1: RV - right ventricle; LV - left ventricle; arrowhead - sternal artifact). All mice survived the procedure with no obvious respiratory or cardiac issues. Overall, we demonstrated that microfluidic produced microbubbles directly injected into the vasculature are safe and capable of providing adequate image contrast.



## 2I - MPA: Photoacoustics III

Waldorf

Saturday, September 6, 2014, 10:30 am - 12:00 pm

Chair: **Stanislav Emelianov**  
Univ. of Texas at Austin, Austin

2I-1

### 10:30 am Two-wavelength identification of lipid in atherosclerotic plaques by intravascular photoacoustic imaging at 1.7 $\mu\text{m}$

Min Wu<sup>1</sup>, Gijs van Soest<sup>1</sup>, Krista Jansen<sup>1,2</sup>, Antonius F. W. van der Steen<sup>1,2</sup>; <sup>1</sup>Department of Biomedical Engineering, Thorax Center, Erasmus University Medical Center, Netherlands, <sup>2</sup>Interuniversity Cardiology Institute of the Netherlands, Netherlands

#### Background, Motivation and Objective

The rupture of the vulnerable atherosclerotic plaques is the major contributor to the acute cardiac events sudden cardiac deaths. Lipid content in atherosclerotic plaques is an important marker for lesion detection and may provide additional information on the disease physiology. Intravascular photoacoustic imaging (IVPA) is a promising new tool to detect lipids in atherosclerotic coronary lesions on the basis of the optical absorption contrast between different tissue types. Lipids are highly effective absorbers at wavelengths near 1720 nm due to the first overtone of the C-H bonds which are abundant in lipids. There is spectroscopic contrast between different lipid species; in vivo imaging however does not allow for extensive scans. In this study we investigated the possibility to detect lipids in the vessel wall, and distinguish plaque lipids from adipose tissue, using only two wavelengths in the 1.7  $\mu\text{m}$  spectral range.

#### Statement of Contribution/Methods

The spectra of atherosclerotic plaque lipids (dominated by cholesterol and several cholesteryl esters) and human peri-adventitial fat were measured in the wavelength range from 1660 to 1760 nm. Spectral differences between plaque lipids and adipose tissue were small, and required a careful wavelength selection for distinction. Using the relative difference between the IVPA signal strengths at 1718 and 1734 nm wavelengths, cholesterol species and fatty acids could be successfully detected and distinguished. Based on the statistical analysis of hundreds of spectra, we determined the difference threshold. The method was tested on IVPA images of a PVA vessel mimicking phantom and human coronary arteries ex-vivo.

#### Results/Discussion

The lipid identification results of a human coronary artery agrees well with the histology data showing that IVPA can detect all the lipids (plaque lipids and peri-adventitial fat) and positively identify atherosclerotic plaque lipids with only two wavelengths of 1718 and 1734 nm. In the artery specimen, 85% lipid pixels were accurately classified. Our study may suggest a new avenue for the fast data acquisition of in-vivo IVPA application.

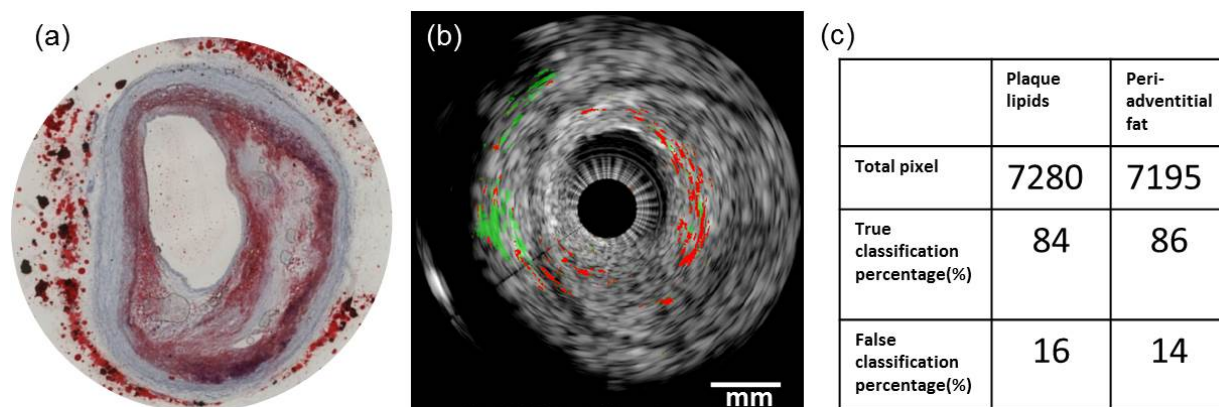


Figure. Ex-vivo lipid identification result of a human coronary artery (human LAD, male, 80 years old). (a) Lipid identification with 1718&1734 nm. Plaque lipid is in red and peri-adventitial fat is in green. (c) Lipid histology stain (Oil Red O). (d) Table with true/false classification results in this cross section.

2I-2

### 10:45 am Integrated Catheter for Real-Time Intravascular Ultrasound and Photoacoustic Imaging

Andrei Karpouk<sup>1</sup>, Don VanderLaan<sup>1</sup>, Doug Yeager<sup>1</sup>, Stanislav Emelianov<sup>1</sup>; <sup>1</sup>Biomedical Engineering, University of Texas at Austin, Austin, Texas, USA

#### Background, Motivation and Objective

The hallmark of cardiovascular disease is the development of atherosclerotic plaques within the arterial walls. The reliable detection and differentiation of rupture-prone plaques features have been recently demonstrated using combined intravascular ultrasound (IVUS) and intravascular photoacoustic (IVPA) imaging performed at 1720 nm. While several designs of integrated IVUS/IVPA imaging catheters demonstrated both ex vivo and in vivo have been reported, clinical implementation of the technology requires development of small, flexible and safe imaging catheters capable of real-time imaging.

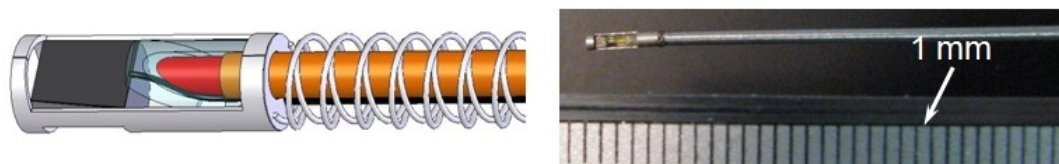
#### Statement of Contribution/Methods

The diagram and microphotograph of the distal end of a 1-mm diameter integrated IVUS/IVPA catheter capable of real-time imaging are shown in the figure below. This prototype consists of a single-element ultrasound transducer connected to a 200- $\mu\text{m}$ -thick co-axial cable and light delivery system aligned to ensure maximal overlap of emitted ultrasound

and light beams within the arterial wall. An optical fiber with a core diameter of 300  $\mu\text{m}$  was polished at a 30° angle with respect to its longitudinal axis and covered by a sealed glass pipe to enable total internal reflection effect at the fiber's tip. A torque cable with outer/inner diameters of 1/0.6 mm was finished by a custom designed 5-mm-long and 1-mm-diam fixture on the distal end. The proximal end was finished by 30-mm-long pipe connected to a motor with encoder and slipping rings. The catheter is suitable for operation with custom real-time (30 frames/second) imaging system, comprising a processor unit, pulser/receiver, and up to 10 KHz pulse repetition frequency (PRF) laser.

### Results/Discussion

An integrated catheter capable of combined IVUS/IVPA imaging in real-time has been presented. In real-time experiments, IVUS images can be reconstructed from 256 A-lines. The real time IVPA imaging at 1720 nm with such parameters requires laser PRF of  $\sim 7.7$  kHz which is not available using off the shelf lasers. Possible solutions such as reducing the A-lines number in IVPA images, decreasing frame/second number, alternative types of light sources, etc. are discussed. Overall, the experimental results suggest that the developed integrated IVUS/IVPA imaging catheter is suitable for real-time, combined IVUS/IVPA imaging of atherosclerosis.



Schematic diagram (left) and microphotograph (right)  
of the integrated IVUS/IVPA catheter designed for real-time imaging

2I-3

### 11:00 am Photoacoustic imaging of the carotid artery

Pieter Kruizinga<sup>1</sup>, Geert Springeling<sup>1</sup>, Jan Lukas Robertus<sup>2</sup>, Aad van der Lugt<sup>3</sup>, Nico de Jong<sup>1,4</sup>, Antonius FW van der Steen<sup>1,5</sup>, Gijs van Soest<sup>1</sup>; <sup>1</sup>Thorax Center, Erasmus MC, Netherlands, <sup>2</sup>Department of Pathology, Erasmus MC, Netherlands, <sup>3</sup>Department of Radiology, Erasmus MC, Netherlands, <sup>4</sup>Delft University of Technology, Netherlands, <sup>5</sup>Shenzhen Institutes of Advanced Technology, Chinese Academy of Sciences, China, People's Republic of

### Background, Motivation and Objective

The human carotid artery (CA) is one of the main arteries of interest to cardiovascular research. The biological constituents that make up the artery wall including diseased lesions (plaques) within are important parameters for the clinical evaluation of the carotid artery. Photoacoustic (PA) imaging could potentially be used to image the relevant biological plaque constituents. In this study we evaluate a multimodality imaging device for ultrasound (US) and PA carotid imaging and show experimental proof that photoacoustic imaging can reveal the relevant constituents of the carotid artery plaque.

### Statement of Contribution/Methods

We propose to image the carotid artery by means of internal illumination (via the throat) and external (neck side) ultrasound detection. For this purpose we built a PA - US carotid imaging system comprising a small 1 mm diameter side-firing optical probe coupled to a wavelength tuneable pulsed laser (Opotek). For PA signal acquisition and US imaging we used a conventional linear ultrasound array (ATL L12-5 50mm) interfaced with an open ultrasound system (Verasonics). We mimicked the neck imaging situation with a scattering agar phantom that allowed for a transmission geometry. A diseased common carotid artery was positioned in a water holding cavity in-between the illumination probe and the transducer. We obtained PA images from the wavelengths 1130 nm up to 1250nm with 5nm spacing and with a pulse energy of 2.5mJ. The resulting PA images were cross-correlated with reference spectra for tissue identification.

### Results/Discussion

In Fig. 1(left) we show an US image of a post-mortem human carotid artery mounted in a neck phantom with superimposed the result of the PA spectral unmixing for the tissue types: water, collagen, plaque lipids and peri-adventitial fat. Histology (right side) confirms the presence of a lipid plaque (red frame; Oil Red O stain), and general morphology (H&E and RF stains) in the red section and a healthy artery wall in the green section. The results provide proof that PA imaging can be used to image the relevant plaque constituents. Extensive evaluation of in vitro results and initial human in vivo recordings of a healthy volunteer will be shown.

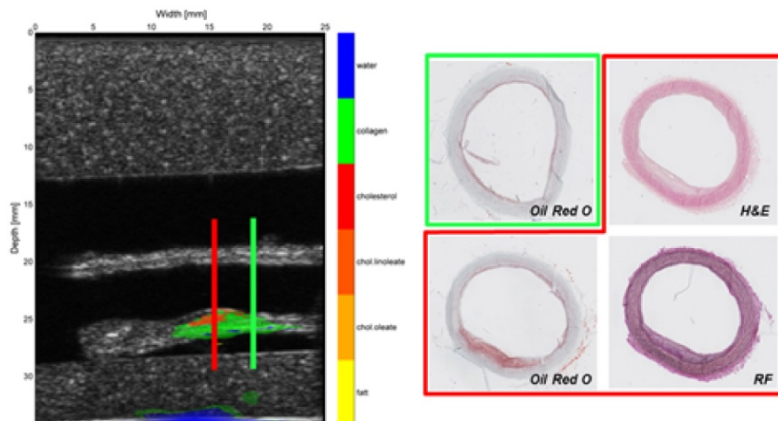


Figure 1: Left panel: ultrasound image of carotid artery embedded in neck phantom with superimposed photoacoustic signals that are spectrally unmixed for the tissue types: water, collagen, plaque lipids and peri-adventitial fat. Right panel: corresponding histology, showing presence of lipid droplets in the plaque (red frame; Oil Red O stain), and general morphology (H&E and RF stains). There is no intimal lipid 3 mm downstream (green frame).



11:15 am **Ultrahigh Resolution Photoacoustic Microscopy and Endomicroscopy**

Ruimin Liu<sup>1</sup>, Xiaosong Bai<sup>1</sup>, Xiaojing Gong<sup>1</sup>, Wei Song<sup>1</sup>, **Liang Song<sup>1,2</sup>**; <sup>1</sup>*Institute of Biomedical and Health Engineering, Shenzhen Institutes of Advanced Technology, Chinese Academy of Sciences, China, People's Republic of*; <sup>2</sup>*Beijing Center for Mathematics and Information Interdisciplinary Sciences (BCMIS), China, People's Republic of*

**Background, Motivation and Objective**

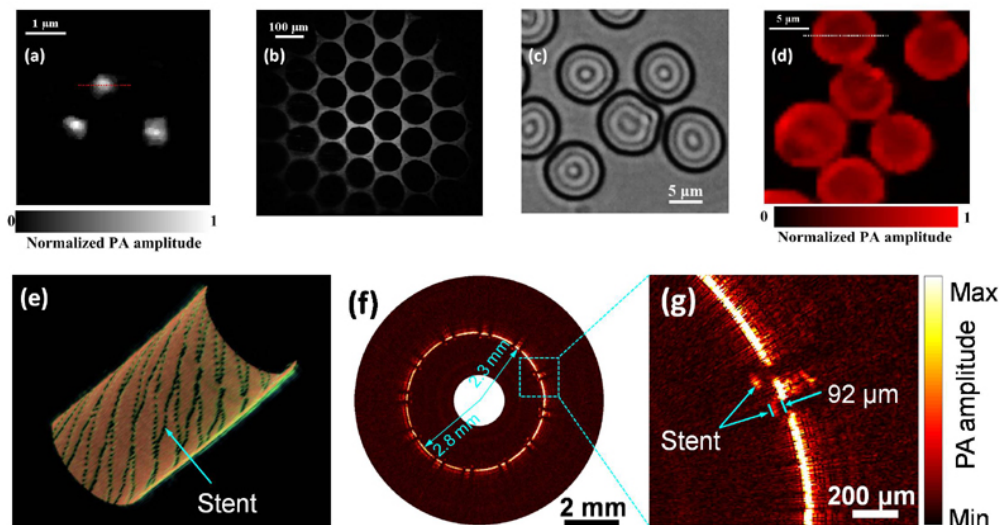
Optical-resolution photoacoustic imaging (OR-PAI) provides in vivo label-free imaging of intrinsic tissue chromophores, including hemoglobin, melanin and lipids, with optical-diffraction limited spatial resolution. It has found broad biomedical applications in tumor angiogenesis study, functional vascular imaging, and ophthalmic imaging. In this report, we present two novel OR-PAI technologies that may further broaden the scopes of these biomedical applications: (1) in vivo reflection-mode ultrahigh resolution photoacoustic microscopy (UH-PAM) offering a spatial resolution as fine as 320 nm; (2) intravascular photoacoustic endomicroscopy (IV-PAEM) with a spatial resolution of 19.6 micrometers, ~10-fold better over that of conventional intravascular photoacoustics and ultrasound.

**Statement of Contribution/Methods**

(1) In order to achieve UH-PAM in reflection mode, we developed a novel acoustic-optical beam-combining method using a water-immersion optical objective in conjunction with a miniature 40-MHz ultrasonic transducer; (2) to realize optical resolution in IV-PAEM, a series of miniature optical and ultrasonic components were designed and engineered to achieve focused photoacoustic excitation within a 1 mm diameter catheter.

**Results/Discussion**

(1) Representative images of carbon nanoparticles (to determine the spatial resolution) (a), copper grids (to determine the field of view) (b), red blood cells (RBCs) (d), and microvasculature in vivo were acquired with UH-PAM. Individual RBCs in vivo were clearly imaged and identified. To our knowledge, the 320-nm resolution in our UH-PAM represents the finest spatial resolution achieved hitherto in reflection-mode PAM, which may open up new avenues for both technology improvement and in vivo biomedical applications; (2) with IV-PAEM, the visualization of stent implantation (e-g) at unprecedented high resolution and contrast were demonstrated, its potential for identifying atherosclerotic plaque composition was also shown.

11:30 am **Clinically translatable ultrasound/photoacoustic imaging for real-time needle biopsy guidance**

Chen-wei Wei<sup>1</sup>, Thu-Mai Nguyen<sup>1</sup>, Jinjun Xia<sup>1</sup>, Bastien Arnal<sup>1</sup>, Ivan Pelivanov<sup>1,2</sup>, Matthew O'Donnell<sup>1</sup>; <sup>1</sup>*University of Washington, Seattle, Washington, USA*; <sup>2</sup>*International Laser Center, Moscow State University, Moscow, Russian Federation*

**Background, Motivation and Objective**

Ultrasound (US) needle tracking with a real-time, portable imaging system is common for biopsies and therapeutic injections. However, image quality is directly related to the needle orientation relative to the scan direction since the primary signal is the specular reflection from the surface. In many cases, proper orientation is problematic and tracking precision is lost because of poor US contrast and additional artifacts. In contrast, the strong photoacoustic (PA) signal from a needle is relatively independent of light orientation. Unfortunately, a bulky, slow (10s of Hz) laser is usually required for sufficient pulse energy at centimeters depth inside the body, hindering PA integration into a real-time US scanner. We employ a compact, low-cost, low pulse energy (1 mJ/pulse) laser that can operate at 10s of kHz to construct an integrated US/PA system with frame rates higher than 30 Hz.

**Statement of Contribution/Methods**

A semiconductor fiber laser (HM 40W G3.1, SPI, South Hampton, UK) delivered 1064-nm laser pulses with a 1.6-mm diameter beam, resulting in a fluence of 66 mJ/cm<sup>2</sup>. A linear US array (AT8L12-5 50 mm, BroadSound, Taiwan) interfaced with an US scanner (Verasonics, Redmond, WA) received both PA and US pulse-echo signals. To provide SNR comparable to conventional PA signals (i.e. with bulky lasers), a scanning approach with a rotating galvo mirror was used by combining multiple laser shots covering a large scan region to form an integrated image. Multiple pulse-echo US focused beams were formed between laser firings. With a laser repetition rate of 924 Hz, 14 single-shot PA frames and 84 US beams are formed during one mirror cycle, leading to an integrated PA/US image at a 33 Hz frame rate. An 18-gauge needle, a typical size for biopsy, moving at 4 mm/s inside a tissue-mimicking gelatin phantom (absorption coefficient of 0.2 cm<sup>-1</sup> and reduced scattering coefficient of 3.6 cm<sup>-1</sup>) was imaged.

**Results/Discussion**

Integrated US/PA images at different time points show the needle moving in the phantom (Fig. 1). A contaminated region was observed at the phantom surface. Clearly, the PA image displays the needle at higher contrast (> 30 dB) than the US image, even at a depth of ~9 mm where light energy has largely decayed, demonstrating the potential of the current scanning system for real-time needle guidance. An improved frame rate of 100 Hz is envisioned with an upgraded US system.



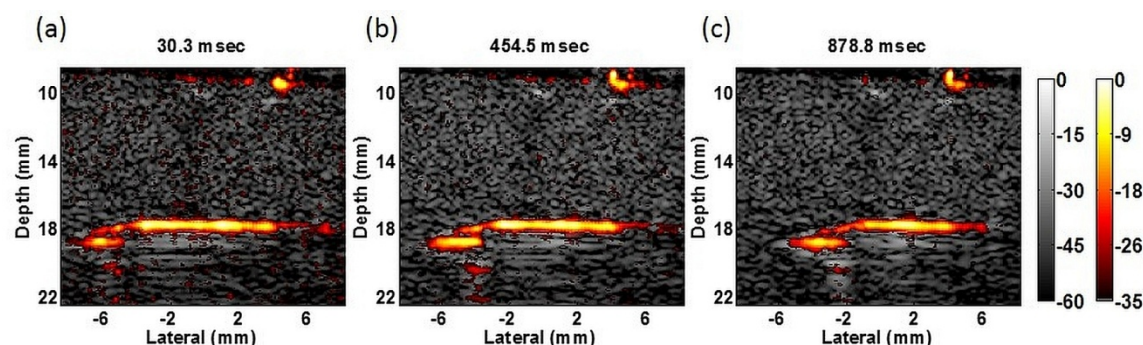


Fig. 1. Integrated US/PA images of an 18-gauge needle moving from left to right at 4 mm/s in a gelatin phantom. The PA amplitude contrast of the needle to the background is more than 30 dB. Images were acquired at 33 Hz, corresponding to the scan rate of a 1.6-mm beam over a 1-cm region laterally. A dirt spot was seen at the phantom surface.

21-6

#### 11:45 am Non-contact Photoacoustic Characterization of Retinal Vasculature for Assessing Brain Injuries

Ashwin Sampathkumar<sup>1</sup>, Ronald Silverman<sup>2</sup>; <sup>1</sup>F.L. Lizzi Center for Biomedical Engineering, Riverside Research, New York City, New York, USA, <sup>2</sup>Department of Ophthalmology, Columbia University Medical Center, New York City, New York, USA

##### Background, Motivation and Objective

Retinal hemorrhages and vascular abnormalities can be considered to be manifestations of head trauma. Ensuring accurate and complete diagnosis of the trauma requires a quantitative description of the hemorrhages. A conventional photoacoustic (PA) microscope (PAM) can provide molecular information at ample sensing depths. However, standard PAM approaches are limited by transducer bandwidth, spatial resolution, and the requirement for a coupling medium. To overcome these limitations, we have developed an optical, interferometry-based PAM to evaluate the retinal tissue at sub-micron resolution remotely with ultra-broadband bandwidth (GHz).

##### Statement of Contribution/Methods

To demonstrate feasibility, ex-vivo porcine ocular-tissue samples retaining choroidal blood vessels were imaged using an all-optical PAM. A region containing three blood vessels in the choroid was raster scanned in steps of 20  $\mu\text{m}$  over an area of 1 x 0.3 mm<sup>2</sup> to produce a fine-resolution, 3D, PA image. PA signals were generated in the tissue using a 532-nm pulsed laser and PA-induced broadband ultrasound was detected at the surface of the blood vessels using an optical interferometer operating at 532 nm. K-space reconstruction methods were employed to reconstruct the PA images. A tunable, pulsed laser was employed to perform multispectral PA imaging of the vasculature to demonstrate the feasibility of measuring blood volume, oxygen concentration and lipid content. PA data were obtained from a line scan of 5 mm, in steps of 50  $\mu\text{m}$  over the wavelength range of 680 to 950 nm.

##### Results/Discussion

A representative PA signal collected from a 0.5- $\mu\text{m}$  spot on the blood vessel is shown in Fig. 1a. A 3D, PA image of the choroidal blood vessels (Fig. 1b) was generated. Time-reversal PA reconstruction of the cross-sectional planes (Fig. 1c) was used to obtain quantitative data on the wall thickness, lumen diameter, and constituents of the blood vessels. The average diameter of the vessels was found to be 250  $\pm$  25  $\mu\text{m}$  with a wall thickness of 20  $\pm$   $\mu\text{m}$ . Figure 1d presents multispectral PA data from a single cross-section; the data depict the molecular signature of deoxy- (760 nm), and oxy- (840 nm) hemoglobin and their isobestic characteristics (800 nm) in the vessels. Hence, all-optical PAM is well suited for imaging and characterizing retinal vasculature.

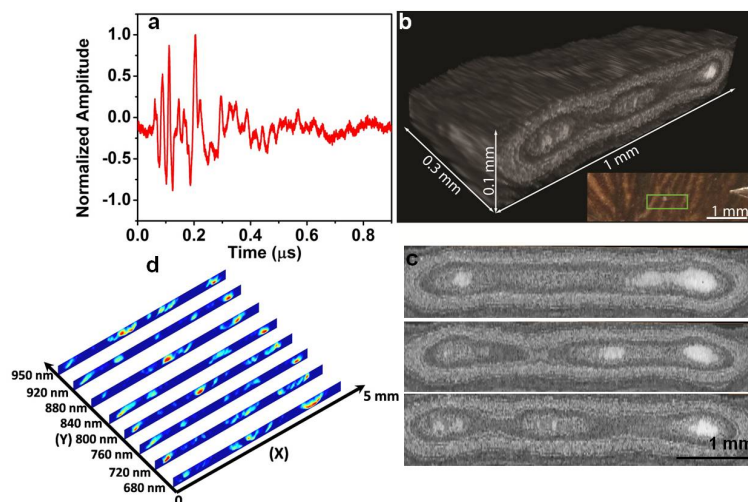


Figure 1 (a) Representative PA curve for choroid vasculature. (b) 3D PA image of choroid vasculature, (inset) optical image depicting the scan region. (c) Select cross-sectional PA images of choroidal vessels. (d) Multi-spectral, cross-sectional PA images of choroidal vessels (optical wavelength: 680 – 950 nm)

## 3I - MTH: Blood-Brain Barrier and Sonoporation

Boulevard

Saturday, September 6, 2014, 10:30 am - 12:00 pm

Chair: **Kullervo Hynynen**  
Univ. of Toronto, Toronto

3I-1

### 10:30 am Focused ultrasound-mediated blood-brain barrier opening for treatment of Alzheimer's disease.

Alison Burgess<sup>1</sup>, Sonam Dubey<sup>1,2</sup>, Isabelle Aubert<sup>1,2</sup>, Kullervo Hynynen<sup>1,2</sup>; <sup>1</sup>Sunnybrook Research Institute, Canada, <sup>2</sup>University of Toronto, Canada

#### Background, Motivation and Objective

Focused ultrasound (FUS)-mediated opening of the blood-brain barrier (BBB) has been used as an effective method for antibody delivery to the brain in mouse models of Alzheimer's disease leading to reduced amyloid-beta peptide pathology. It has been demonstrated that FUS alone, in the absence of exogenous drug delivery, can also reduce amyloid pathology. In this study, we determine whether the reductions in pathology by FUS-mediated BBB opening with and without antibody delivery, is correlated to changes in cognitive function. FUS-mediated improvements in cognition would support the use of FUS as a strategy for the treatment of Alzheimer's disease.

#### Statement of Contribution/Methods

We used 8-month-old transgenic (Tg) mice that exhibit behavioral deficits and amyloid pathology as well as the non-transgenic littermates. At 7 months of age, the mice began weekly MRI-guided FUS treatments to temporarily open the BBB in the hippocampus. In addition to untreated Tg and non-Tg controls, the treated mice were split into two groups: i) FUS + anti-amyloid antibodies or ii) FUS alone. After 3 repeated treatments, the mice were evaluated using the Y-maze with novel arm. Post-mortem histology was used to evaluate the pathology after treatment.

#### Results/Discussion

In the Y-maze with novel arm, non-Tg mice spend significantly more time exploring the novel arm than the untreated Tg mice indicating that the Tg mice have impaired spatial memory of the novel arm. Following treatment with FUS, Tg mice performed as well as the non-Tg mice suggesting that FUS can improve cognition in a mouse model of Alzheimer's disease. After 3 weekly FUS treatments, we did not detect any significant difference between the performance of Tg mice treated with FUS and the Tg mice treated with FUS + anti-amyloid antibodies. These data suggest that repeated FUS treatments to temporarily open the BBB promotes endogenous mechanisms of repair which can reduce pathology and improve cognitive function.

3I-2

### 10:45 am Effect of drug injection protocol on delivery of liposomal doxorubicin to the brain using ultrasound mediated blood brain barrier disruption

Muna Aryal<sup>1,2</sup>, Yong-Zhi Zhang<sup>1</sup>, Nathan McDannold<sup>1</sup>; <sup>1</sup>Radiology, Harvard Medical School, Boston, MA, USA, <sup>2</sup>Physics, Boston College, Chestnut Hill, MA, USA

#### Background, Motivation and Objective

Focused ultrasound (FUS) combined with microbubbles has been used to disrupt blood brain barrier (BBB) in a non-invasive, repeatable, and targeted manner to deliver wide range of therapeutics and imaging agents to the brain. Previous studies in rats have shown that FUS-mediated BBB disruption (FUS-BBBD) can enhance the delivery of liposomal doxorubicin (DOX) to the brain and improve survival in tumor models. Here we compared DOX delivery for cases when the agent was administered before and after FUS-BBBD.

#### Statement of Contribution/Methods

FUS-BBBD was induced in volumes by sonicating nine overlapping brain targets in 3x3 grid (0.69 MHz; 0.55 MPa; 10 ms bursts at 1 Hz for 60s) in rats. Each sonication was combined with an IV injection of Definity (10µl/kg). DOX was injected either before (n=5; group 1) or 10 min after (n=4; group 2) FUS-BBBD. Volumes in both brain hemispheres were sonicated in group 1. For the first volume, the total DOX dose (5.67 mg/kg) was administered in 9 fractions, one before each sonication. We used this scheme previously in rat tumor studies. For the second volume, since DOX has a long plasma half-life (2-3 days), we assumed the entire dose was present in circulation before sonication. Only one hemisphere was sonicated in group 2. Sonication time was ~30 min for the 9 targets. FUS-BBBD was confirmed with contrast-enhanced MRI. Four hours after sonication, the rats were sacrificed, sonicated and control samples were collected, and DOX concentrations were measured with a fluorometer.

#### Results/Discussion

DOX concentrations for the fractional and full dose injections in group 1 were 4164±446 and 4264±501 ng/g, respectively; they were not significantly different (p>0.05). In contrast, the concentration when DOX was administered 10 minute after sonication was 2651±280 ng/g, a 38% reduction which was significantly (p<0.05) less than both schemes in group 1.

While a high DOX concentration was achieved in both groups, this work demonstrates that FUS is more effective if we inject the agent before sonication rather than afterwards. This finding may simply be due to partial BBB restoration in group 2. It might also reflect transient effects occurring during sonication that can enhance transport DOX across the vasculature beyond what passively leaks out after BBBD. It may also be possible that the ultrasound exposures break the ~100 nm liposomes and release its contents. Different results may be possible for smaller drugs, or for those with short plasma half-lives.

3I-3

### 11:00 am Pharmacodynamic analysis for efficient drug delivery through the FUS-induced BBB opening in Non-Human Primates in vivo

Gesthimani Samiotaki<sup>1</sup>, Shih-Ying Wu<sup>1</sup>, Maria Eleni Karakatsani<sup>1</sup>, Matthew Downs<sup>1</sup>, Sachin Jambawalikar<sup>2</sup>, Elisa Konofagou<sup>1,2</sup>; <sup>1</sup>Biomedical Engineering, Columbia University, USA, <sup>2</sup>Department of Radiology, Columbia University, USA

#### Background, Motivation and Objective

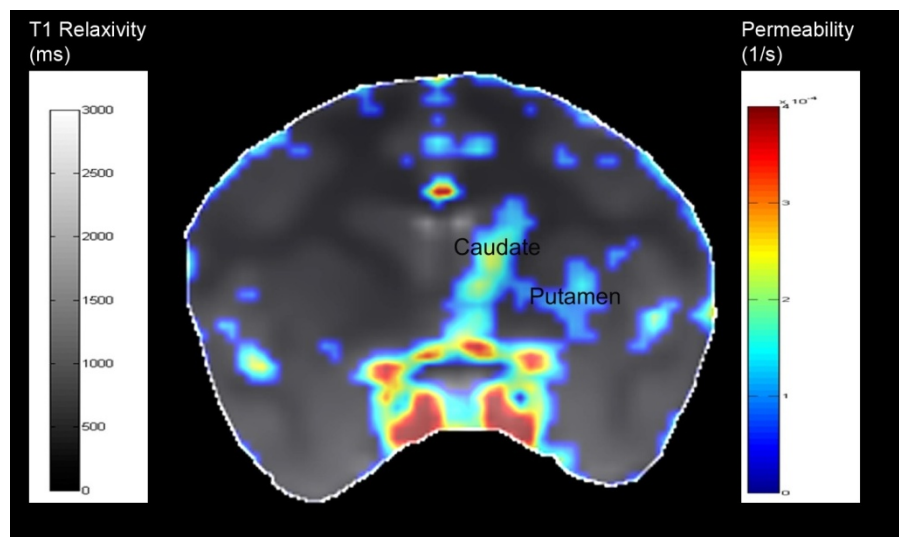
FUS in conjunction with systemically administered microbubbles has been previously shown to open the Blood-Brain Barrier locally, non-invasively and reversibly in non-human primates. However, a trans-BBB pharmacodynamic analysis has not been performed as of yet. The objective of this study was the pharmacodynamic analysis, i.e. permeability and relaxivity mapping, of the NHP brain *in vivo* in order to further investigate the effect of FUS, for safe and efficient drug-delivery.

**Statement of Contribution/Methods**

Two brain structures, the caudate (Cau) and the putamen (Pu), were targeted in three rhesus macaques using FUS (Fo: 500 kHz; PRF: 2 Hz; duration: 120 s; PNP: 300-500 kPa) immediately after the IV administration of monodisperse bubbles. In a 3T MR scanner (Philips, USA) five pre-contrast 3D Spoiled Gradient Echo (SPGR) images (TR/TE: 10/4ms, FA: 50-350, res: 1x1x1 mm<sup>3</sup>) were acquired and used for variable flip angle based T1 relaxivity mapping. Subsequently, Dynamic Contrast Enhanced (DCE) imaging was performed, with the acquisition of 90 dynamic T1-weighted 3D repetitions (TR/TE: 4.2/1.7 ms; res 1x1x2 mm<sup>3</sup>). The data were processed off-line using customized Matlab-based algorithms to generate permeability (K<sub>trans</sub>) maps. The areas of grey (GM) and white matter (WM) and BBB opening were also determined, based upon segmentation of the T1 relaxivity maps since GM and WM have distinctive characteristic relaxivity times. Quantitative permeability changes and the volume of BBB opening (V<sub>BBB</sub>) were measured.

**Results/Discussion**

V<sub>BBB</sub> increased from 92±10 mm<sup>3</sup> to 262±34 mm<sup>3</sup> with a FUS pressure change from 300 kPa to 500 kPa. K<sub>trans</sub> was increased from  $1.0531 \pm 0.0761 \times 10^{-4} \text{ s}^{-1}$  to  $1.863 \pm 0.132 \times 10^{-4} \text{ s}^{-1}$  respectively. When targeting the Pu, an average of 95% of the opening was contained in the GM (T1 relaxivity range: 1001-1400 ms), while in the Cau 87% of the opening occurred in the GM (T1 relaxivity range: 600-1000 ms). No edema or hemorrhage was detected in any of the cases studied. In conclusion, monitoring BBB opening volume and permeability in non-human primates in vivo were found to increase significantly with pressure. The gray-to-white-matter ratio undergoing BBB opening varied slightly among the two targeted regions with most opening occurring in the GM. Pharmacodynamic analysis may be proven critical in planning, guidance and prediction of the FUS-enhanced drug delivery.



31-4

**11:15 am Focused Ultrasound-Induced Blood-Brain Barrier Opening In Non-Human Primates With Transcranial Cavitation Detection In Vivo**

Shih-Ying Wu<sup>1</sup>, Carlos Sierra Sanchez<sup>1</sup>, Matthew Downs<sup>1,2</sup>, Amanda Buch<sup>2</sup>, Gesthimani Samiotaki<sup>1</sup>, Vincent Ferrera<sup>2</sup>, Elisa Konofagou<sup>1,3</sup>; <sup>1</sup>Biomedical Engineering, Columbia University, USA, <sup>2</sup>Neuroscience, Columbia University, USA, <sup>3</sup>Radiology, Columbia University, USA

**Background, Motivation and Objective**

Focused ultrasound (FUS) with microbubbles has shown great promise in assisting brain drug delivery by noninvasively and locally opening the blood-brain barrier (BBB). Real-time monitoring of the treatment with transcranial passive cavitation detection (PCD) is critical to assess efficacy and safety without requiring online MRI. The objective of this study is to investigate the consistency of PCD monitoring and opening threshold during BBB opening at different regions and across non-human primates of different ages and weights.

**Statement of Contribution/Methods**

The experiments were performed in three rhesus macaques (7-19 years old, 6-11 kg) with pre-planned targeting at the subcortical structures including caudate nucleus and putamen. During the experiment, in-house microbubbles (lipid-shell and monodisperse with a median diameter of 4-5  $\mu\text{m}$ ) were injected intravenously at the beginning of sonication (frequency: 0.5 MHz, peak negative pressure: 200-600 kPa, pulse length: 10 ms), with a confocal hydrophone serving as a passive cavitation detector to real-time monitor the PCD signals. After sonication, pre- and post-contrast enhanced 3D T1-weighted, 3D T2-weighted, and susceptibility weighted MRI were used to confirm the opening and potential damage. The harmonic, ultraharmonic, and broadband signals within 1-5 MHz were separately filtered for quantifying the stable cavitation dose (SCD) and inertial cavitation dose (ICD), which were used to correlate the opening volume quantified from MR images. A total of 15, 30, and 10 sonications were performed at the caudate nucleus, putamen, and thalamus, respectively.

**Results/Discussion**

The opening volume increased with pressure, while the opening threshold of pressure varied between separate animals, which was 250 kPa, 300 kPa, and 350 kPa was required for NHP 1, 2, and 3, respectively. BBB opening occurred in both the gray and white matter. For assessment of the BBB opening outcome with the SCDh, it was found that the success rate and opening volume were correlated with the SCDh and thus could be estimated. The SCDh could be used to predict if the opening was successful or not; the success rate was found to be 75% and 100% when the SCDh reached 200 and 500 mV\*s, respectively. The SCDh showed linear correlation with the opening volume, with slopes varying among animals (0.75, 0.54, and 0.33 for NHP 1, 2, and 3, respectively) and no significant difference observed between targeting to different subcortical structures.

PCD monitoring of the BBB opening was shown capable of predicting and characterizing the BBB opening (success rate and opening volume) using the SCDh. In addition, the BBB opening pressure threshold and the SCDh-opening volume relationship was found to vary among animals, warranting planning and monitoring as essential in ensuring BBB opening at safe pressures.



### 11:30 am Sonoporation: From the lab to human clinical trials.

Spiros Kotopoulos<sup>1,2</sup>, Georg Dimcevski<sup>1</sup>, Bjørn Tore Gjertsen<sup>3</sup>, Odd Helge Gilja<sup>1,3</sup>, Emmet McCormack<sup>3</sup>, Michiel Postema<sup>2</sup>; <sup>1</sup>National Center for Ultrasound in Gastroenterology, Haukeland University Hospital, Bergen, Norway, <sup>2</sup>Department of Physics and Technology, University of Bergen, Bergen, Norway, <sup>3</sup>Department of Clinical Science, University of Bergen, Bergen, Norway

#### Background, Motivation and Objective

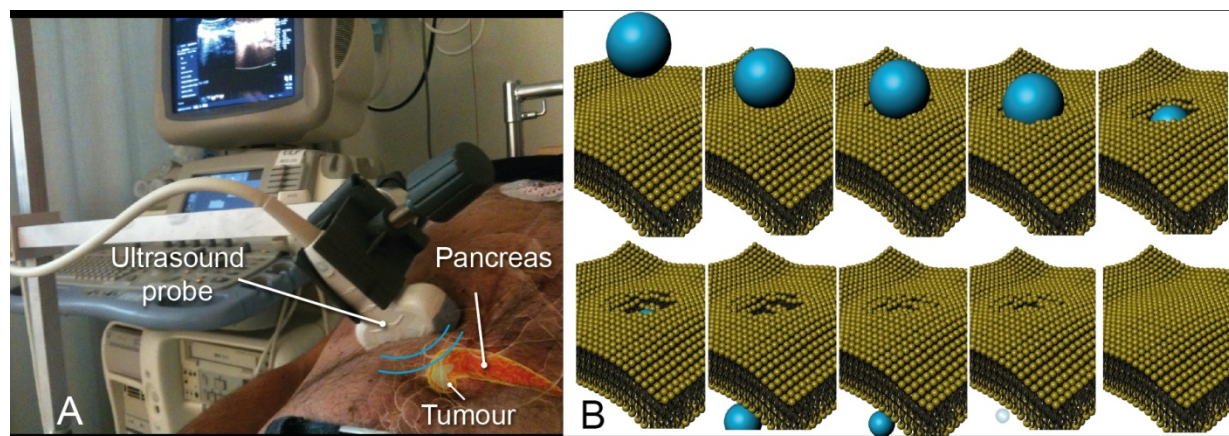
One of the major barriers in effective drug delivery is the cell membrane; it acts as wall choosing what to allow in and out of the cell. For this reason, sonoporation, the formation of pores in cell membranes, due to ultrasound or ultrasound and microbubbles has been gaining interest for its potential as a therapeutic modality. By forming pores in the cell membranes we can effectively bypass this barrier resulting in highly efficient targeted drug delivery. In our work we explore the phenomenon of sonoporation, from the lab bench all the way to the world first clinical trials.

#### Statement of Contribution/Methods

The phenomenon of sonoporation for use in drug and gene delivery was explored using clinically approved ultrasound conditions ( $MI < 0.2$ ,  $ISPTA < 1W/cm^2$ ) at low frequencies (1-MHz) using commercially available microbubbles (Definity®, SonoVue®, MicroMarker™). In-vitro work was performed using cervical cancer cells, seeded into OptiCells®. Pre-clinical experiments were performed on orthotopic pancreatic adenocarcinoma mice models. Clinical trials were performed on patients with pancreatic adenocarcinoma using a clinical diagnostic ultrasound machine allowing for simultaneous visualisation and treatment of the tumour (Fig. 1A).

#### Results/Discussion

In-vitro work showed that we could force microbubbles into cells (Fig. 1B), on demand, with no effect on proliferation or cell death (Fig. 1B). Based on these acoustic conditions, pre-clinical mice experiments indicated that combining sonoporation with a standard chemotherapeutic could drastically inhibit primary tumour growth and delay metastatic spread. Finally, human clinical trials showed that sonoporation also inhibits primary tumour growth and in some cases even reduce the tumour size; in addition the patients healthy period was effectively doubled.



### 11:45 am Involvement of cytoskeleton in sonoporation and drug delivery

Aya ZEGHIMI<sup>1</sup>, Jean-Michel ESCOFFRE<sup>1,2</sup>, Ayache BOUAKAZ<sup>1</sup>; <sup>1</sup>Université François-Rabelais de Tours, Inserm, Imagerie et Cerveau UMR U930, Tours, France, Tours, France, <sup>2</sup>Imaging Division, UMC Utrecht, Utrecht, The Netherlands, Utrecht, Netherlands

#### Background, Motivation and Objective

The mechanisms by which sonoporation increases the native plasma membrane permeability are still unknown but various hypotheses have been suggested including pore formation and endocytosis. We have shown recently that caveolae-mediated endocytosis plays a major role during sonoporation. Besides, it is also known that endocytosis implies the involvement of cytoskeleton. Thus, the aims of this study are to investigate the effect of sonoporation on cytoskeleton and to identify the role of this cellular scaffolding.

#### Statement of Contribution/Methods

Adherent U-87 MG cells were sonicated at 1MHz, 1 W/cm<sup>2</sup>, 20% duty cycle for 60 s, in the presence of BR14 microbubbles (5 microbubbles/cell). SYTOX Green was used to assess the membrane permeabilization, by flow cytometry. The cells were incubated with phalloidin-TRITC to stain actin microfilaments and tubulin antibody Alexa Fluor 555 to stain tubulin. The ultrastructural changes of plasma membrane were monitored by scanning electron microscopy (SEM). To inhibit the polymerization of actin and tubulin cytoskeleton, the cells were treated with 50 uM cytochalasin D (cytoD) and 10 uM nocodazole (Noco), respectively.

#### Results/Discussion

Immunofluorescence results show alteration of actin and tubulin cytoskeleton, immediately after sonoporation while control cells present a typical cytoskeleton with polygonal shape. The punctiform staining testifies the depolymerization of actin microfilaments and microtubules (Figure 1). However, the disorganization of the cytoskeleton network is reversible since 60 min post-sonoporation, only few cells show a tubulin (8%) and actin (25%) cytoskeleton disruption. Moreover based on SEM images of the cell membrane morphology, the treatment of the cells with both cytoD and Noco induced a strong decrease in the number of permeation structures:  $98.5 \pm 0.2\%$  and  $96 \pm 0.6\%$ , respectively. In addition, flow cytometry results showed that cytoD and Noco lead to a decrease in the membrane permeabilization rate: 58% and 87%, respectively.

In conclusion, this study demonstrates the transient alteration of actin and tubulin cytoskeleton following sonoporation. It suggests that cytoskeleton plays a role during sonoporation, as cytoskeleton inhibitors provoke a decrease in the cell permeabilization rate. Its implication could occur during both the entry and transport of endocytosed molecules.

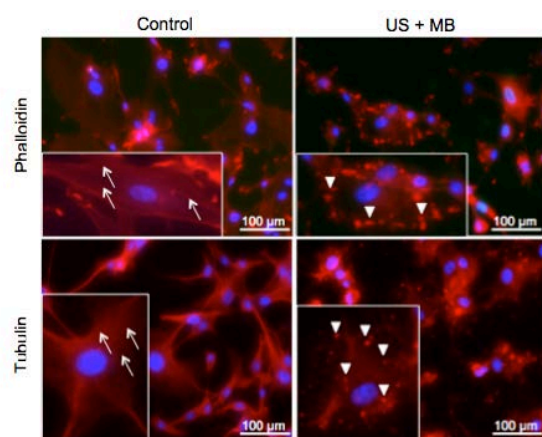


**Figure 1 :** Immunofluorescence images depict the effect of sonoporation on actin and tubulin cytoskeleton of the U-87 MG cells. White arrows show the actin microfilaments and microtubules for control cells, while arrowhead show disorganized cytoskeleton in insonified cells.



## 4I - Transducers

Marquette

Saturday, September 6, 2014, 10:30 am - 12:00 pm

Chair: **Kentaro Nakamura**  
*Tokyo Institute of Technology*

4I-1

### 10:30 am Phased Array Inspection at Elevated Temperatures

Mohammad Hassan Marvasti<sup>1</sup>, Anthony N. Sinclair<sup>1</sup>; <sup>1</sup>Mechanical and Industrial Engineering, University of Toronto, Canada

#### Background, Motivation and Objective

Interruption of plant operation can be avoided if NDT inspections are performed on-line at operating temperatures; this may be up to several hundred degrees Celsius in a petrochemical or electric power generating plant. However, there are operational temperature limits of the phased array transducers and associated plastic wedges for angled-beam inspections; in addition, there is a gap in terms of approved, appropriate high temperature inspection techniques.

This paper describes an ultrasonic phased array system for planar wave inspections of test pieces such as pipe welds at elevated temperatures up to 350oC. Wedges are built from plastics resistant to high temperature degradation, and equipped with a cooling jacket around the arrays. Inside the wedge, thermal gradients lead to variations in the temperature-dependent wave velocity and skewing of the wave direction; this invalidates conventional calculation of individual array element delay times that are based on a homogeneous propagation medium. We develop a numerical model to describe wave propagation in the presence of thermal gradients, and an algorithm to calculate delay times for the array elements.

#### Statement of Contribution/Methods

Temperature profile inside a wedge mounted on a hot test piece with convective cooling is first modeled using finite element software and validated experimentally. The link between temperature and velocity is obtained by measuring ultrasonic compression wave velocities of wedge materials over a wide temperature range. The arced path of waves propagating across thermal gradients in the wedge is then modeled by a 2D discretized solution of the wave equation for a non-homogenous medium. The result is used to modify the phased array focal law to obtain the required delays for individual arrays elements.

#### Results/Discussion

Numerical modeling of inspections on test pieces at 150oC demonstrates that application of conventional array focal laws can lead to incorrect phase delays on array elements of up to 60% of the wave period. This would lead to major distortion of the desired beam profile, and very poor imaging resolution. It is noted that the phase error would increase sharply with temperature. Experimental verification of our new algorithm indicates that the phase error on individual elements is reduced by over 95%. The magnitude of the remaining error is within the expected error range due to uncertainties in the modeled temperature profile of the wedge and timing resolution limitations of the phased array instrument.

4I-2

### 10:45 am Design of an Electromagnetic Acoustic Transducer for in-line inspection

Miguel Freitas<sup>1</sup>, Jean Pierre von der Weid<sup>1</sup>, Thomas Grimsley<sup>2</sup>; <sup>1</sup>CPTI/CETUC, PUC-Rio, Rio de Janeiro, Brazil, <sup>2</sup>Ritec Inc, Warwick, RI, USA

#### Background, Motivation and Objective

Ultrasound inspection has long been an industry standard in terms of reliability and accuracy for integrity assessment of oil and gas pipelines. However, piezoelectric transducers require a coupling liquid to be used, a major limitation for dry, gas filled, pipeline inspection. This requirement led some major service providers to start offering Electromagnetic Acoustic Transducer (EMAT) based solutions, focusing on crack detection (Stress Corrosion Cracking - SCC) and coating disbondment analysis. The motivation for such specificity is twofold: the easiness of producing superficial shear waves with EMAT and the reduced number of transducers required.

This work presents a bulk-wave EMAT transducer with integrated driver and amplifier, optimized for high performance and low power consumption. These are characteristics of uttermost importance to create a battery-powered system with hundreds of sensors for corrosion inspection.

#### Statement of Contribution/Methods

EMAT coupling is orders of magnitude less energy efficient than liquid-coupled piezoelectric. The feasibility of a multi-channel battery-powered system relies on aggressively optimizing different aspects of the project: (1) the use of wear resistant materials with low signal attenuation, (2) keeping high currents confined within the transducer to lower cabling losses, (3) gating the integrated pre-amplifier so that time-multiplexed transducers waste no energy between acquisitions, (4) design of a curved transducer to match the internal pipe surface and reduce the coil lift-off.

#### Results/Discussion

Results are presented showing the contribution from each of the employed methods. A combination of titanium foil and ceramic ball bearings prevented the wearing of the probe while leaving the coil with a lift-off of 0.2mm. Gated pre-amplifier reduced the receiver's power consumption to a duty-cycle of 15%. Properly matching the integrated driver to the coil's complex impedance provided ~6 dB gain, while curved transducer surface accounted for another 4 dB improvement. The most SNR-efficient frequency range obtained in a real pipe made of API 5L X60 steel was determined to be 2-3 MHz, achieving a SNR of 30 dB for the first echo in the less corroded areas. Total energy required from the power supply per shot is adjustable between 2 and 11 mJ. The paper further demonstrates the feasibility of a multichannel inspection system given the volume and battery constraints for typical in-line tools.

4I-3

**11:00 am A Robust Air Coupled Ultrasonic Piezoelectric- Carbon Fiber Reinforced Polymer (CFRP) Sensor for Mobile Robot Navigation**Sergio Flores Contreras<sup>1</sup>, Martin Vossiek<sup>1</sup>; <sup>1</sup>Institute of Microwaves and Photonics, University of Erlangen-Nuremberg, Erlangen, Germany**Background, Motivation and Objective**

Ultrasonic sensors are used for robot navigation for a long time. Mobile robot navigation requires air-coupled transducers with a good reading range and a radiation beam pattern that allows for a good angular resolution. In addition the sensors should be small and robust. For air-coupled ultrasonic sensors it is beneficial to use transducers vibrating in a flexural mode to accomplish large displacements. Mobile robots are very often equipped with electrostatic transducers. By activating a membrane with a large aperture a good reading range and narrow radiation pattern is obtained. However, electrostatic transducers are rather big and the membrane can easily be damaged mechanically. Hence this transducer type is not well suited for outdoor or industrial use. Another type of air-coupled ultrasonic sensors are so called "unimorph" transducers. A typical simple and robust version is e.g. made of a single piezoelectric plate bonded to a metallic element. However, this sensor type is not well matched to air and a good reading range and beam pattern is not easy to achieve.

**Statement of Contribution/Methods**

We present an air coupled ultrasonic sensor, which is simple in design, very robust and compact. The sensor is built in a unimorph configuration, but instead of using metal, the piezoelectric disc is attached to a carbon fiber reinforced polymer (CFRP) plate. Due to the low phase velocity in CFRP a rather small transducer can exhibit a narrow beam pattern that is well suited for our intended robot application. Another advantage of CFRP is that the acoustic impedance of this material is much better matched to air than metal. Since the robustness of CFRP and metal is comparable the new sensor type in general is well suited for air-coupled ultrasound in industrial and outdoor applications.

**Results/Discussion**

The resonant structure of the fabricated sensor was designed for operation around 65 kHz. The bandwidth of the transducer is 5.2 kHz, which is rather good for a sensor operated at resonance and lead to a pulse-width and radial resolution of around 35 cm. The diameter of the CFRP aperture is 15.5 mm. This aperture leads to a 6dB beam width of  $\pm 20^\circ$  which allows for an angular resolution well suited for robot navigation. If the transducer is driven with an electrical average pulse power of 3.5 W a good signal to noise ratio for typical indoor objects is achieved in a reading range of around 5 m."

The very good performance of the designed sensor is illustrated by measurements of the transducer characteristics and by measurements where the sensor is applied for mobile robot navigation. The measurement results prove that CFRP is a very interesting material for building air-coupled ultrasonic unimorph sensors and that this robust new sensor type is especially suited for robot applications and for industrial and outdoor use.

4I-4

**11:15 am Numerical simulations of a cross-dipole transducer for acoustic well logging**Yuyu Dai<sup>1</sup>, Penglai Xin<sup>1</sup>, Zhengbo Wang<sup>1</sup>, Hongbin He<sup>1</sup>, Xiuming Wang<sup>1</sup>; <sup>1</sup>Institute of Acoustics, Chinese Academy of Sciences, China, People's Republic of**Background, Motivation and Objective**

The cross-dipole transducer is the vital portion of the array-sonic-well-logging instrument. It excites flexural waves in the borehole, and it can be used to measure shear wave velocities and anisotropy parameters of formations. For practical purposes, broadband transducers are often required, because of the wide range of acoustic impedances of different formations. In this paper, numerical analyses of the transducer based on the trilaminar-bender-bars have been carried out, in order to design a broadband cross-dipole transducer with its operating frequency in the range of 0.5-5 kHz.

**Statement of Contribution/Methods**

A cross-dipole transducer design scheme based on trilaminar bender bars has been developed. Trilaminar bender bars can realize effective radiation at low frequencies with a small size, which is suitable for designing the well logging transducer. Two bender bars with different sizes have been applied to form the cross-dipole array. There are four resonances exhibit in this structure, so that to broaden the bandwidth. The Finite Element Method (FEM) has been used to simulate the modes of vibration, input electrical admittance, directivity pattern, transmitting voltage responses of the array transducer in the air and in the silicon oil, respectively (see Figs.1a and 1b). Moreover, influences of both the mutual impedance of bender bars and the vibration of the mounting framework have been taken into considerations for accurate simulations.

**Results/Discussion**

Fig.1 shows the input electrical admittances of the transducer in the air (c) and in the oil (d), respectively. It is concluded that (1) there are four resonance peaks in operating range, they are contributed by the 1st and 3rd flexural vibration of the long (1 and 3) and short (2 and 4) bender bars, respectively; (2) cooperating by these resonances, transducer is able to achieve broadband transmitting in the range of 0.5-5kHz. .

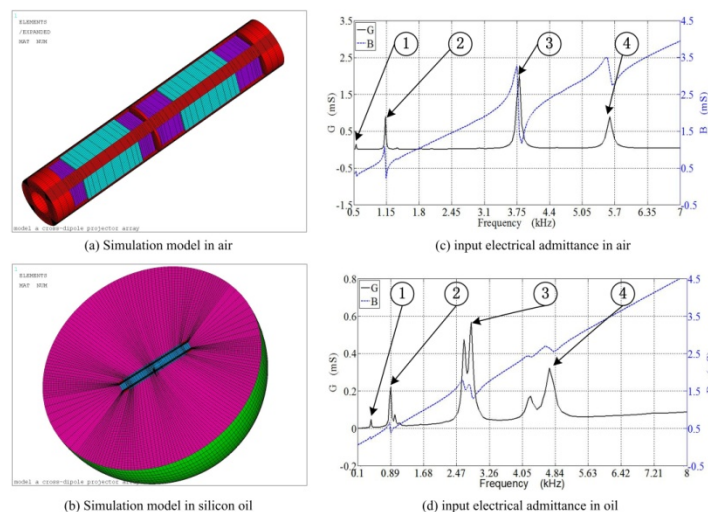


Fig. 1 simulation models and results in air and in silicon oil

**11:30 am High temperature piezoelectric transducers**

Makiko Kobayashi<sup>1</sup>; <sup>1</sup>Graduate School of Science and Technology, Kumamoto University, Kumamoto, Japan

**Background, Motivation and Objective**

Ultrasonic monitoring at high temperature has gained importance with economic globalization. For safety assurance, ultrasonic inspection was effective because of sub-surface monitoring ability and material property sensitivity. In order to increase safety assurance, it was ideal to increase monitoring frequency, though it was difficult to maintain safety assurance and the international competitiveness unless ultrasonic monitoring could carry out at elevated temperature. Piezoelectric transducers were generally used for ultrasonic testing though it was challenging to use them at high temperature by following reasons; couplant was necessarily in order to transmit ultrasound energy from piezoelectric transducers and it was hard to find high temperature couplant for long term. Backing material was also used for piezoelectric transducers and it caused problems at high temperature.

**Statement of Contribution/Methods**

We found that piezoelectric transducers made by sol-gel composite film was suitable for high temperature ultrasonic transducer applications. Sol-gel composite film was made by sol-gel solution and bulk ceramics powder and it was invented in order to fabricate thick film. By this method, it was possible to fabricate more than 100 $\mu$ m thick film, though this thick film was porous and it was considered as undesired characteristics. However those porous piezoelectric films showed several advantages. First, it had broadband characteristic without backing material. Second, sol-gel composite piezoelectric transducers did not require couplant. Third, it was facile to adapt complex geometry, including spherical convex surface, and it could be even flexible if the substrate was flexible such as thin metal. In addition, it had high thermal/physical shock resistance. Because of those advantages, piezoelectric transducers made by sol-gel composite film was expected for industrial applications.

**Results/Discussion**

In order to increase sensitivity and operation temperatures, several sol-gel composite materials have been investigated. At this moment, sol-gel composite material made by lead titanate (PT) bulk powder and lead zirconate titanate (PZT) sol-gel solution demonstrated highest sensitivity up to 300°C, though poling was more difficult than PZT/PZT. For higher temperature applications, other materials such as bismuth titanate (BiT/PZT) and calcium bismuth titanate (CBT/PZT) became preferable. Sol-gel composite transducers were currently applied for kettle inspection of zinc galvanization. Sol-gel composite piezoelectric film was fabricated onto steel delay line and it could serve as high temperature immersion ultrasonic transducer inside molten zinc at 450°C without cooling system and it reduced inspection time and transportation cost drastically. Guaranteed measurement accuracy was  $\pm 1.5$ mm.

## 5I - Ultrasonic Motors and Multi-Modal Thin Film Transducers

Williford A

Saturday, September 6, 2014, 10:30 am - 12:00 pm

Chair: **Jörg Wallaschek**  
*Leibniz Universität Hannover*

5I-1

### 10:30 am Evaluation of a Novel Reflector in a Surface Acoustic Wave Motor

Deqing Kong<sup>1</sup>, Minoru Kuribayashi Kurosawa<sup>1</sup>, <sup>1</sup>Tokyo Institute of Technology, Yokohama, Japan

#### Background, Motivation and Objective

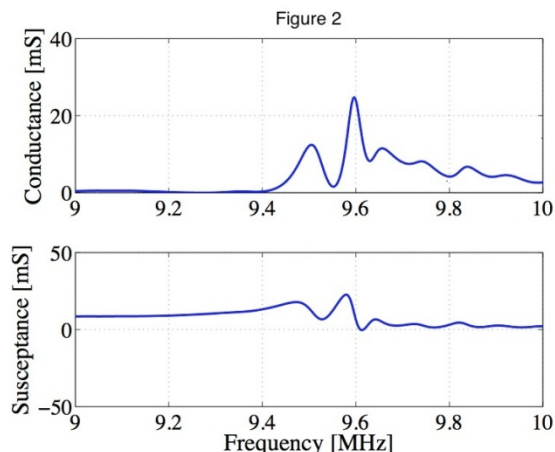
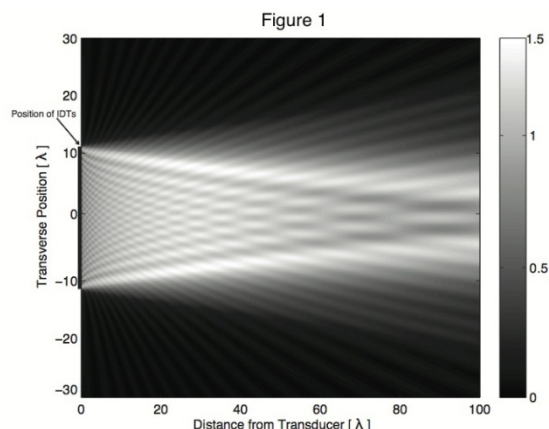
Interdigital transducers (IDTs) of a surface acoustic wave (SAW) motor is made of two unidirectional interdigital transducers (U-IDTs) including a driving IDTs (D-IDTs) and a reflector (R-IDTs) at both end ports of a substrate. In the previous research, recycle efficiency only reached 70% because of the wave leakage of the substrate and others. The aim of this research is to improve the recycle efficiency in the SAW motor with the aid of a novel R-IDTs.

#### Statement of Contribution/Methods

Actually, wave leakage is the major contributor to the power loss of the SAW motor. In pervious experiments, 5.8% wave leakage was found behind the U-IDTs even though the reflection coefficient of R-IDTs reached close to 1. Additionally, wave became wider than the aperture of IDTs as it propagates, as shown in Fig. 1. Using the acoustic field analysis, 2.7% wave leaked laterally in the rectangular area of double wavelength times 11 mm width. In this paper, the number of strip electrodes pairs of R-IDTs increases from 32 to 42 while remaining the reflection coefficient close to 1. In addition, the aperture width of R-IDTs is expanded from 9 mm to 11 mm. It should be noted that the gap between D-IDTs and R-IDTs must be adjusted from 878  $\mu\text{m}$  to 812.5  $\mu\text{m}$ . In short, a novel design of R-IDTs was investigated, when D-IDTs remained.

#### Results/Discussion

Based on the improved cross field model, the conductance of U-IDTs using the novel R-IDTs was up to 16.9 mS from 12.5 mS at 9.61 MHz, while the susceptance remained 0 mS, as shown in Fig. 2. The novel design of the substrate was fabricated using basic MEMS process. To evaluate the recycle efficiency, several experiments including wave vibration were conducted to compare with the simulation results.



5I-2

### 10:45 am Performance of Micro Ultrasonic Motor using One Cubic Millimeter Stator

Tomoaki Mashimo<sup>1</sup>, <sup>1</sup>Toyohashi University of Technology, Toyohashi, Aichi, Japan

#### Background, Motivation and Objective

Piezoelectric ultrasonic motors are well-known as the most prominent micromotors for actuating miniature devices that can help minimally invasive diagnoses and treatments, such as endoscopes and catheters. They have two advantages for miniaturization: (1) high energy densities with high torques at low speeds without a gear and (2) simple structures using simple components. In front line of ultrasonic motor miniaturization, prototypes using a few millimeter stators have succeeded in generating rotation.

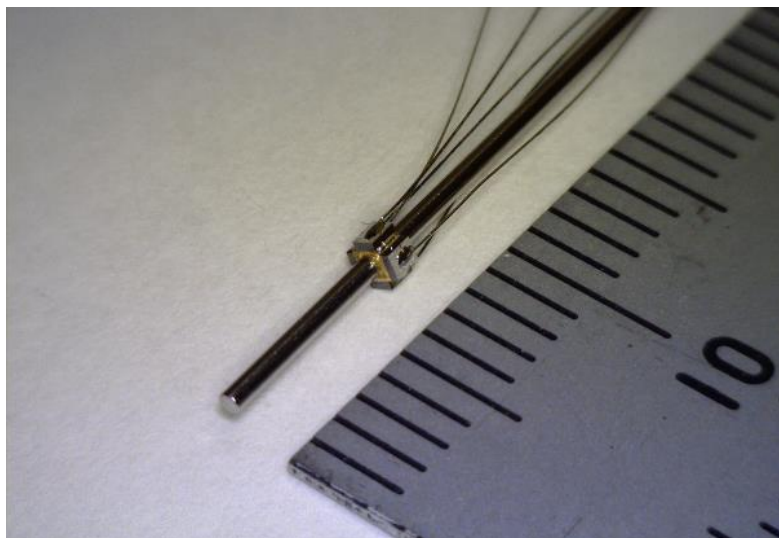
#### Statement of Contribution/Methods

We build a prototype micro ultrasonic motor consisting of a cubic stator with a volume of approximately one cubic millimeter. An advantage of this motor is the use of a vibration mode that generates three waves around the circumference of the hole in the stator. This mode, independent of the length of the stator, can generate a certain magnitude of vibration amplitude, even if the size is reduced to as little as 1 mm. Also, the simple structure of the motor makes the size miniaturized without using any special machining process. In this study, we build and demonstrate the performance of a prototype micro ultrasonic motor. Figure shows the prototype motor: one cubic millimeter stator with four piezoelectric elements at sides and the rotor inserted into the through-hole of the stator. When voltages are applied to the piezoelectric elements, the stator generates travelling wave and spins the rotor.

#### Results/Discussion

In experiments, we measure the transient response of the angular velocity and the torque as the performance of the prototype. At the applied voltages of 98 Vp-p and 935 kHz, the angular velocity reaches a steady-state at approximately 20 ms and the peak is about 2000 rpm. The motor torque of approximately 1  $\mu\text{Nm}$  is computed from the product of the

moment of inertia and its angular acceleration. This torque value is useful for rotating tiny things, because calendar rings in watches has been practically rotated by torque of 2  $\mu\text{Nm}$ . Another important aspect of motor is the stability of rotation: We discuss how to eliminate an instable behavior of the angular velocity by adjusting the mechanism between the stator and rotor.



51-3

### 11:00 am Ultrasonic Motor for sample spinning of solid-state nuclear magnetic resonance spectrometer in high magnetic field

Daisuke Yamaguchi<sup>1</sup>, Dai Takeda<sup>1</sup>, Takefumi Kanda<sup>1</sup>, Koichi Suzumori<sup>1</sup>; <sup>1</sup>Graduate School of Natural Science and Technology, Okayama University, Okayama, Okayama, Japan

#### Background, Motivation and Objective

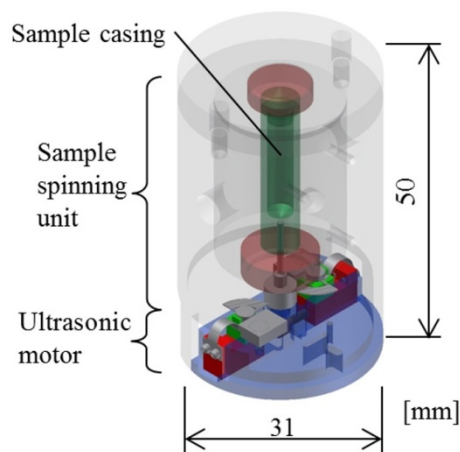
A solid-state high-resolution nuclear magnetic resonance (solid-state NMR) analysis is one of an important application in organic chemistry, molecular technics, and many other fields. Samples of solid-state NMR analysis are required to spin accurately at high speed in a high magnetic field. Our objective is achieving an ultrasonic motor that can be used in solid-state NMR spectrometer. In this study, an ultrasonic motor that can be rotated in high magnetic field was fabricated and evaluated. Additionally, the motor was applied to a sample spinning system of the spectrometer.

#### Statement of Contribution/Methods

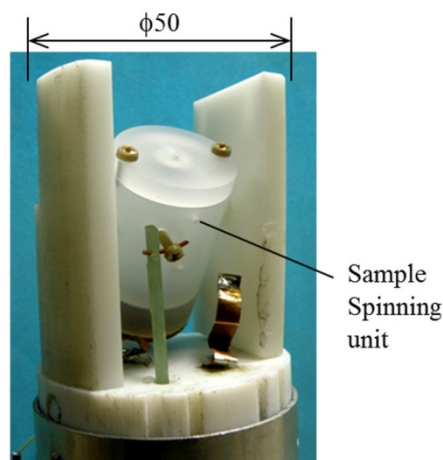
To mount the motor in small sample space, a low-profile ultrasonic motor was designed and fabricated. The motor has two sector-shaped transducers that are fabricated by bonding a base plate with two lead zirconate titanate (PZT) plates. The thickness of the transducer is less than 0.6 mm. The motor is made of materials that have low magnetic permeability. The diameter and height of the motor including sample casing is 31 and 50 mm, respectively. Additionally, the motor was applied to the solid-state NMR analysis. In solid-state NMR analysis, the axis of the sample spinning is angled at 54.7 degree from a magnetic field direction.

#### Results/Discussion

The motor was evaluated in a superconducting magnet. The rotation speed of the motor was 1200 rpm at 9.4 T when the motor was driven using a PI control system. The noise of the rotation was small enough for using NMR analysis. The solid-state NMR analysis was conducted at 9.4 T. The solid sample material was glycine. The rotation speed was controlled at 1080 rpm by using PI control. We have succeeded in measuring the chemical shift of carboxyl. This result shows the ultrasonic motor can be used for the sample spinning system of a solid-state NMR spectrometer.



(b) Structure of ultrasonic motor



(a) Tip of NMR Probe with motor



**11:15 am Theoretical and experimental study of layered SAW magnetic Sensor**

Meriem ELHOSNI<sup>1</sup>, Omar Elmazria<sup>1</sup>, Sébastien Petit-watlot<sup>1</sup>, Laurent Bouvot<sup>1</sup>, Michel Hehn<sup>1</sup>, Abdelkrim Talbi<sup>2</sup>, Nicolas Tiercelin<sup>2</sup>, Vladimir Preobrazhensky<sup>2</sup>, Philippe Pernod<sup>2</sup>, Olivier Boumatar<sup>2</sup>; <sup>1</sup>Institut Jean Lamour, UMR 7198, Université de Lorraine - CNRS, Vandoeuvre les Nancy, France, <sup>2</sup>LIA LEMAC/LICS - IEMN UMR CNRS 8520, ECLille - USTL, PRES Université Lille Nord de France, Villeneuve d'Ascq, France

**Background, Motivation and Objective**

SAW-based sensors have been developed for different applications including industrial, medical and automotive ones. When the wireless and the battery-less are a requirement for the aimed application, SAW sensors show a real advantage versus existing ones. Demand for small, sensitive, accurate and wireless magnetic sensor record an important increase. Accurate modeling of SAW magnetic sensors including magnetostrictive materials requires to take into account the coupling between electrical, magnetic, mechanical, and acoustic domains. The aim of this work is to implement a full model using the Comsol multiphysics software, leading to the study of both SAW structures, resonators and delay lines. The model accuracy will be validated experimentally.

**Statement of Contribution/Methods**

A general finite element method (FEM) of two-dimensional piezo-magnetic devices is used. In the magnetostrictive thin film, a coupling between the AC/DC module and the structural mechanics module was implemented by adding appropriate terms to the subdomain variables for the strain and the magnetic fields. The coupled equations for the mechanical and magnetic systems allowing the determination of the dependence between the elastic constants and the applied magnetic field are detailed in Ref [1],

A heterostructure Ni/ZnO/IDT/LN-Y128 SAW delay line was fabricated using conventional photolithography and two mask levels. The S21 frequency response was measured using a network analyzer at different steps of fabrication (IDT/LN, ZnO/IDT/LN, Ni/ZnO/IDT/LN) and compared to the simulated results. The final and packaged structure was then characterized under magnetic field. Three directions of the magnetic field were considered X, Y and Z where X is parallel to the direction of the acoustic wave propagation.

**Results/Discussion**

The methodology was first validated using a SAW resonator based on a Quartz substrate and Nickel IDTs. The variation of the resonance frequency, the quality factor and the electromechanical coupling coefficient were investigated versus the magnetic field intensity and its direction and compared to the experimental results published by Kadota [2]. The methodology was then considered to predict the sensor magnetic sensitivity of others structures. We studied theoretically and experimentally a SAW delay line based on Ni/ZnO/IDT/LN-Y128 layered structure. The latter structure shows a moderate sensitivity of 65 ppm/100mT when the fundamental SAW is considered (158 MHz) and 200 ppm/100mT when considering the third pseudo-harmonic (460 MHz). When the Al<sub>2</sub>O<sub>3</sub> was used as an insulator instead of ZnO, the sensitivity was enhanced by a factor 15 using a comparable operating frequency while a sensitivity of 12000 ppm/100mT is obtained when considering the device operating at 2.45 GHz.

[1] O. Boumatar et al, J. Appl. Phys. 111, 054901 (2012)

[2] M. Kadota et al, J. Appl. Phys. 51, 07GC21 (2012)

**11:30 am RF bias induced polarity inversion of ScAlN film for overtone mode BAW resonator**

Masashi Suzuki<sup>1</sup>, Takahiko Yanagitani<sup>1</sup>; <sup>1</sup>Nagoya Institute of Technology, Japan

**Background, Motivation and Objective**

Polarity-inverted multilayer structure resonator is suitable for high frequency or high power operation. In IUS 2012, we reported that negative ion beam from oxide ingot on the target induces polarity inversion in the ScAlN films. In this study, we investigated the mechanism of the polarity inversion of c-axis oriented AlN and ScAlN films due to ion beam irradiation. In addition, by using this method, the second overtone mode excitation in bilayer polarity inverted ScAlN film resonator was demonstrated.

[1] M. Suzuki, T. Yanagitani, and H. Odagawa, in Proc, 2012 IUS.

**Statement of Contribution/Methods**

c-Axis oriented AlN and ScAlN films were grown on (0001) Ti films (rocking curve FWHM = 4.0-4.8°) / silica glass substrate by anode RF bias sputtering deposition. The substrate was set on an anode with magnetron circuit. The degree of ion beam irradiation to the substrate was adjusted by the RF (14 MHz) bias power of 0-1.50 W. The polarity of these films were determined by a press test using an oscilloscope probe.

To obtain bilayer polarity inverted FBAR, ScAlN film with RF bias was grown on usual ScAlN film.

**Results/Discussion**

As shown in Fig. 1 (a), when the compressive stress was applied, a negative response, indicating Al-polarity, were observed in usual AlN film, whereas a positive response, indicating N-polarity, were observed in the AlN film with 0.50 W RF bias. Similarly, a negative response, indicating Al-polarity, appeared in usual ScAlN film, and a positive response, indicating N-polarity, appeared in the ScAlN films with 0-0.75 W RF bias. However, a negative response, indicating Al-polarity, appeared in ScAlN film with 1.00-1.50 W RF bias. These results demonstrated that the polarity of ScAlN and AlN film was inverted by enhancing ion beam irradiation. This polarity inversion may result from ion beam tolerant anisotropy between N-polar and Al-polar crystal planes.

As shown in Fig. 1 (b), the 1st and 3rd mode resonance was excited around 1.0 GHz and 3.4 GHz in the monolayer FBAR. On the other hand, the 1st and 3rd mode resonance around 1.0 GHz and 3.2 GHz was suppressed, whereas the 2nd mode resonance was excited around 2.0 GHz in the bilayer FBAR whose total thickness is same as monolayer FBAR. From these results, the polarity of upper and bottom layer in the bilayer film were completely inverted with each other.

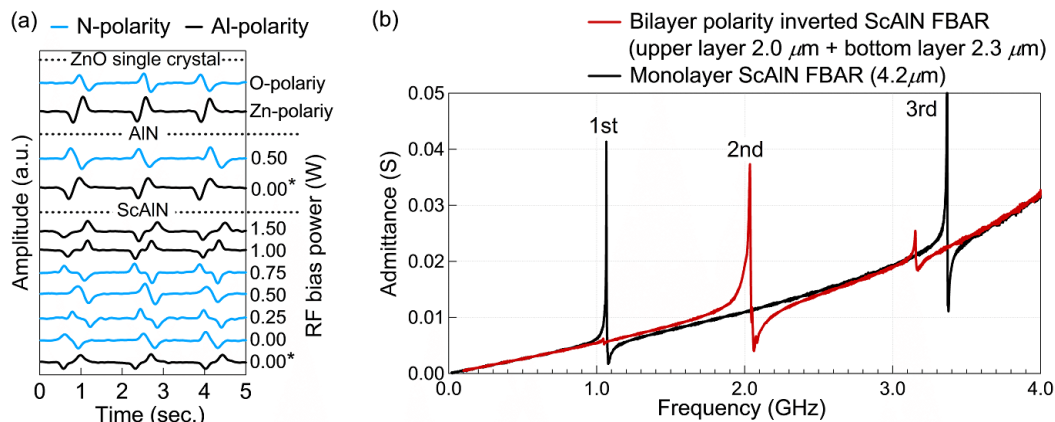


Fig. 1 (a) Piezoelectric response of ScAlN, AlN films, and ZnO single crystal plate measured by a press test.

\* shows usual AlN and ScAlN films.

(b) Frequency characteristic of admittance of bilayer polarity inverted ScAlN FBAR and monolayer ScAlN FBAR.

51-6

#### 11:45 am Air-backed optoacoustic transmitter

Tae-hwa Lee<sup>1</sup>, Cheng Zhang<sup>2</sup>, Qiaochu Li<sup>2</sup>, Hyoung Won Baac<sup>3</sup>, Jong G. Ok<sup>1</sup>, L. Jay Guo<sup>1,2</sup>; <sup>1</sup>Mechanical Engineering, University of Michigan, Ann Arbor, Michigan, USA, <sup>2</sup>Electrical Engineering and Computer Science, University of Michigan, Ann Arbor, Michigan, USA, <sup>3</sup>School of Electronic and Electrical Engineering, Sungkyunkwan University, Suwon, Korea, Republic of

#### Background, Motivation and Objective

Unipolar acoustic wave is advantageous for high resolution imaging and detection due to its high frequency characteristic. However it is difficult to achieve the unipolar waveform using with traditional piezoelectric transducers. Here, we demonstrate unipolar acoustic wave form using an optoacoustic approach by directly exposing the absorbing layers of photoacoustic transmitters to air (i.e., an air-backed optoacoustic transmitter), which simultaneously increases signal amplitudes by employing an acoustic matching layer on the air-side.

#### Statement of Contribution/Methods

We use a carbon-nanotube (CNT)-polymer composite as an optoacoustic transmitter. PDMS film as an acoustic matching layer is coated on the air-side of the CNT composite (Fig. 1), substituting for typical hard backing substrates. Acoustic signals are calculated and compared with those measured by a broadband acoustic detector (micro-ring).

#### Results/Discussion

Acoustic signal amplitude is significantly changed with the thickness of the PDMS matching layer due to interference effect (Fig. 2). Without a matching layer ( $d=0$ ), the air-backed transmitter generates the bipolar acoustic signal(near-field) an order of magnitude lower than that of the rigid boundary (hard backing). As increasing the thickness ( $d$ ), signal amplitudes increase, reaching up to half of the amplitude of the hard boundary. Such thickness dependency arises from the interference effect of optoacoustic waves in presence of the pressure-releasing boundary (air/PDMS boundary). The more detailed analysis of the results will be presented in the conference. This work renders the air-backed optoacoustic transmitter feasible for practical applications, e.g., high-resolution medical imaging.

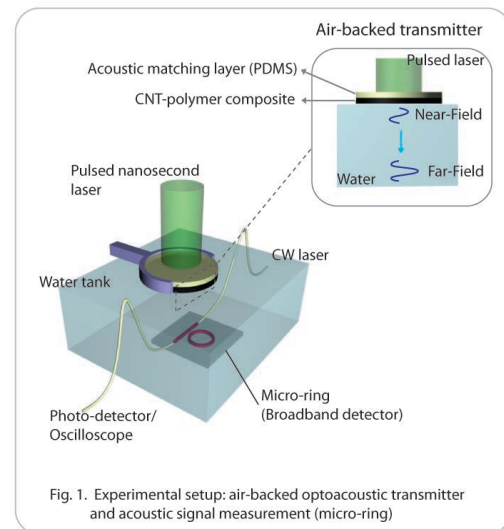


Fig. 1. Experimental setup: air-backed optoacoustic transmitter and acoustic signal measurement (micro-ring)

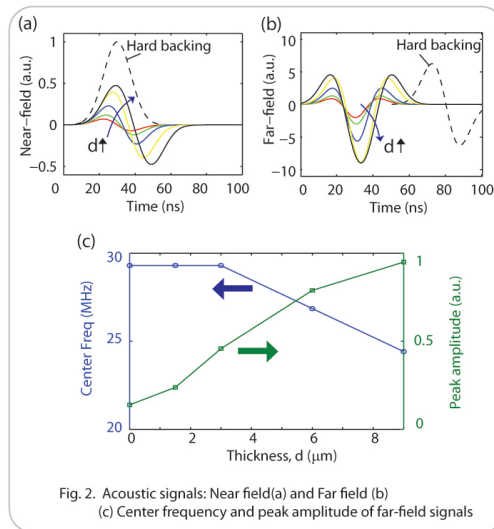


Fig. 2. Acoustic signals: Near field(a) and Far field (b) (c) Center frequency and peak amplitude of far-field signals

## 6I - Materials for SAW and BAW Applications

Williford B

Saturday, September 6, 2014, 10:30 am - 12:00 pm

Chair: **Masanori Ueda**  
*Taiyo Yuden*

6I-1

### 10:30 am CTGS material parameters obtained by versatile SAW measurements

Sergey Biryukov<sup>1</sup>, **Hagen Schmidt**<sup>1</sup>, Andrey Sotnikov<sup>1,2</sup>, Manfred Weihnacht<sup>1</sup>, Sergey Sakharov<sup>3</sup>, Oleg Buzanov<sup>3</sup>; <sup>1</sup>IFW Dresden, Dresden, Germany, <sup>2</sup>Ioffe Physical-Technical Institute, St. Petersburg, Russian Federation, <sup>3</sup>JSC Fomos-Materials, Moscow, Russian Federation

#### Background, Motivation and Objective

To our knowledge, for the promising single crystal material  $\text{Ca}_3\text{TaGa}_3\text{Si}_2\text{O}_{14}$  (CTGS) there exist at least three different sets of material parameters extracted from bulk acoustic wave measurement. But these sets give discrepancies between calculated and measured SAW velocities which is unacceptable for the design of modern high-tech SAW devices [1]. Measurement of SAW phase velocities with widely varied propagation angle on differently oriented samples can yield accurate and consistent data. The objective of this work is to determine reliable CTGS material parameters by such kind of velocity measurement and related extraction.

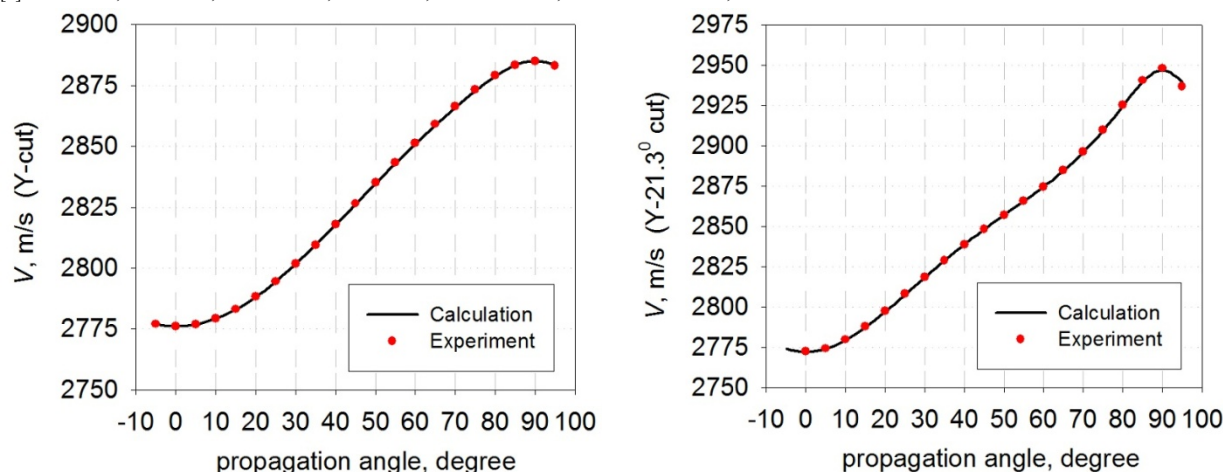
#### Statement of Contribution/Methods

Our high accuracy measurement method for SAW phase velocities realizes laser-pulse excitation and piezoelectric probing without use of interdigital transducers. Hereby a variation of the propagation angle can be simply implemented. The extraction of material parameters is based on minimization of the discrepancy between experimental and calculated SAW velocities which has been done for many propagation angles on different crystal cuts by variation of material parameter values. Along with previous CTGS cuts [1] new high quality samples with new cuts were used. Finally, the best-fitting material parameter set was achieved by starting from the material data found in our recent work [1].

#### Results/Discussion

A new full set of CTGS material parameters has been extracted. This set exhibits an excellent agreement between measured and calculated SAW velocities for differently oriented samples. Two examples are shown below for SAW velocity  $V$  on the metallized surface of CTGS Y-cut and Y-21.3° cut as function of propagation angle.

[1] A. Sotnikov, H. Schmidt, M. Weihnacht, O. Buzanov, and S. Sakharov, Proc. 2013 IEEE IUS, 1688-1691.



6I-2

### 10:45 am Temperature coefficients of fluorine-doped amorphous-SiO<sub>2</sub> thin films measured by picosecond ultrasonics

Akira Nagakubo<sup>1</sup>, Satoru Matsuda<sup>2</sup>, Hirotsugu Ogi<sup>1</sup>, Masahiko Hirao<sup>1</sup>; <sup>1</sup>Engineering Science, Osaka University, Toyonaka-City, Japan, <sup>2</sup>Taiyo Yuden Co., LTD, Japan

#### Background, Motivation and Objective

Sound velocities and temperature coefficient (TCV) of thin films are important parameters of FBAR and SAW filters because they govern resonant frequencies and their temperature behaviors. To make sound velocity insensitive to temperature, amorphous-SiO<sub>2</sub> films have been widely used as temperature-compensate materials because their elastic constants show positive temperature coefficients around room temperature. Recently, it has been revealed that TCV of a SiO<sub>2</sub> film can be controlled by doping some other materials. However, it is difficult to directly measure the acoustic properties of thin films using conventional ultrasonic methods, which has prevented accurate evaluation. Although many researchers have reported acoustic properties of amorphous-SiO<sub>2</sub> bulk specimens in a wide temperature and frequency range, thin films should show different properties from bulk specimens. Therefore, direct measurements of the sound velocity and its temperature dependence of amorphous-SiO<sub>2</sub> thin films are necessary.

#### Statement of Contribution/Methods

We developed optics for low-temperature picosecond ultrasonic measurements using a specimen holder in a cryostat. Fluorine-doped SiO<sub>2</sub> are deposited on Si substrates. Their film thicknesses are 2-4 micrometers. To discuss the difference between thin-film and bulk specimen, we also measure a bulk specimen. Because SiO<sub>2</sub> is transparent for visible light, we deposited a 10-nm Al thin film as a transducer. 800-nm wavelength pump light is absorbed in the Al film and generates a sharp strain pulse in the SiO<sub>2</sub> film. Time-delayed probe light pulse, whose wavelength is converted into 400 nm by a second harmonic generator crystal, is normally applied to the specimen and back-scattered by the strain pulse through a photo-elastic effect. We can observe the backscattering light which satisfies Bragg's condition. The observed signal shows an oscillation, which is called Brillouin oscillation.

## Results/Discussion

Firstly, we measured non-fluorine-doped specimens. TCV of the bulk specimen is in relatively good agreement with reported TCVs of bulk specimens measured by conventional ultrasonic methods. Although the difference of sound velocity of our bulk and thin-film specimens is less than 0.5% at room temperature, TCV of thin film is significantly smaller than that of bulk specimen by a factor of 0.6, indicating that we cannot use bulk values for acoustic properties of a thin film. Secondly, we measured sound velocities of fluorine-doped amorphous-SiO<sub>2</sub> thin films. Sound velocity decreased and TCV increased with fluorine content ratio. The tendency is the same as reported properties of bulk fluorine-doped SiO<sub>2</sub>, but sound velocity and TCV of thin film exhibit larger fluorine dependence than those of reported bulk values. TCV of fluorine-doped thin film increased by approximately 140%. These results highly insist that reported bulk values cannot be used for thin film devices, and our results contribute to many device design.

6I-3

## 11:00 am Power Durable Electrode Metallization: Material Choice, Failure Mode, and Characterization

Ryoichi Takayama<sup>1</sup>, Hidekazu Nakanishi<sup>1</sup>, Ken-ya Hashimoto<sup>2</sup>; <sup>1</sup>Automotive & Industrial Systems Company, Panasonic Corporation, Kadoma, Japan, <sup>2</sup>Dept. Electrical and Electronic Engineering, Chiba University, Chiba, Japan

### Background, Motivation and Objective

Surface Acoustic Wave (SAW) duplexers have become increasingly popular, and now they have become key devices for modern mobile communication terminals. Conventionally, SAW filters are limited to use under the low power signal because of their poor power durability. Therefore, it is essential to improve the power durability of SAW filters to apply them to antenna duplexers. Up to today, the improvement of power durability of SAW filters have been mainly accomplished by a filter design and a material of electrodes. In their many cases, the evaluation of power durability has been discussed only in term of estimated lifetime which has been extrapolated from some measured lifetimes under either input power levels or ambient temperatures. In this paper, I review the power durable electrodes metallization technology of SAW filters with Al-alloy electrodes from the standpoint of their dependence on each of a temperature and an input power, and try to understand them systematically.

### Statement of Contribution/Methods

To examine the dependence of power durability on a temperature and an input power, the Eyring model was adopted when we estimated a life time. The evaluation method was revised to keep the independence of two acceleration factors of deterioration, temperature and input power, as possible. The ladder type SAW filters with 4-layered Al-alloy/Ti/Al-alloy/Ti electrodes were employed. Concerning Al-alloys, ternary Al-alloys containing both a Cu which segregated on Al grain boundary and another element which formed a solid solution with Al were used. These metal films were formed with sputtering method.

## Results/Discussion

We were able to get the data with small variation by the tests which were performed according to the devised methods. The evaluation results show that an enhancement of power durability level owing to the electrode material or its structure related to the change of the dependency of lifetime on the acceleration factors of the deterioration. With the recent trend of component miniaturization and with the development of modularization, the usage environment of SAW duplexers, including chip size and package type, has changed a great deal. These evaluation results say that it is important to take into account of actual use conditions in order to evaluate and improve a power durability of SAW duplexers in mobile terminal.

6I-4

## 11:30 am Characterization of Elastic Properties of SiO<sub>2</sub> Thin Films by Ultrasonic Microscopy

Kensuke Sakamoto<sup>1</sup>, Satoshi Suzuki<sup>1</sup>, Tatsuya Omori<sup>1</sup>, Ken-ya Hashimoto<sup>1</sup>, Jun-ichi Kushibiki<sup>1,2</sup>, Satoru Matsuda<sup>3</sup>; <sup>1</sup>Graduate School of Engineering, Chiba University, Chiba, Japan, <sup>2</sup>Tohoku University, Sendai, Japan, <sup>3</sup>Microdevice R&D Department, Taiyo Yuden Ltd., Akashi, Japan

### Background, Motivation and Objective

SiO<sub>2</sub> films are often used in high performance surface acoustic wave (SAW) devices for their temperature compensation. Since acoustic properties of SiO<sub>2</sub> films considerably vary with the deposition apparatus and conditions, proper means are highly demanded for their direct evaluation. Two of the authors (SM and KH) pointed out that elastic properties and their temperature coefficients of SiO<sub>2</sub> films are closely related to the FTIR spectra.

### Statement of Contribution/Methods

This paper describes characterization of elastic properties of SiO<sub>2</sub> films by the Line-Focus-Beam (LFB) ultrasonic microscopy.

SiO<sub>2</sub> films with 1 μm thickness were deposited on Si(001) substrates by sputtering or CVD with two different deposition conditions each, and the water-loaded SAW velocity *V* on these samples was measured by the LFB system.

## Results/Discussion

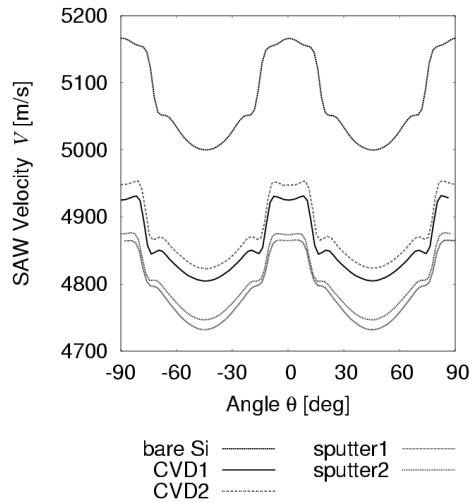
Fig. 1 shows measured *V* as a function of the SAW propagation angle  $\theta$ . It is seen that amount of the *V* decrease changes significantly with the deposition apparatus and conditions. The *V* decrease in CVD samples is smaller than that in sputtered samples, and change in the deposition condition also causes the *V* variation. This reflects large variation of elastic properties because the film thickness is much smaller than the SAW wavelength (~22 μm).

The figure also indicates large variation of *V* with  $\theta$ , which is caused by the anisotropy of the Si (001) substrate, and the  $\theta$  dependence varied with the films.

Then elastic constants of SiO<sub>2</sub> films were estimated by fitting the measured  $\theta$  dependence of *V* with that obtained by the full-wave simulation. The result indicated that variation of elastic constants of several tens of percents is necessary to explain such large *V* variation. In addition, the measured  $\theta$  dependence could not be explained when SiO<sub>2</sub> films were assumed to be isotropic. Namely, elastic properties normal to the surface seems to be significantly different from those along the surface. This anisotropy might be induced during the deposition.

It should be noted that for the bare Si substrate, the measured  $\theta$  dependence can be explained well by the simulation.

[1] S.Matsuda, M.Hara, M.Miura, T.Matsuda, M.Ueda, Y.Satoh, and K.Hashimoto, "Correlation Between Temperature Coefficient of Elasticity and Fourier Transform Infrared Spectra of Silicon Dioxide Films for Surface Acoustic Wave Devices," IEEE Trans. UFFC, **58**, 8 (2011) pp.1684-1687.



6I-5

### 11:45 am Sezawa mode SAW with high electromechanical coupling at the boundary of polarization-inverted (000-1)/(0001) ZnO, AlN and ScAlN films

Shinji Takayanagi<sup>1</sup>, Takahiko Yanagitani<sup>2</sup>, Mami Matsukawa<sup>1</sup>; <sup>1</sup>Faculty of Science and Engineering, Doshisha University, Kyotanabe, Japan, <sup>2</sup>Graduate School of Engineering, Nagoya Institute of Technology, Nagoya, Japan

#### Background, Motivation and Objective

c-Axis oriented ZnO and AlN films are widely used for SAW filters and acoustic resonators. ZnO and AlN crystals have piezoelectric polarization in the c-axis direction. Piezoelectric constants of (0001) oriented film are opposite in sign to those of (000-1) oriented film. In previous study, we fabricated polarization-inverted (000-1)/(0001) ZnO [1], AlN and ScAlN [2] films on silica glass substrates, as shown in Fig. 1(a). Second overtone mode resonance was observed in the BAW resonator using polarization-inverted film [1, 2]. However, the SAW propagation characteristics have never been reported. In this study, the electromechanical coupling coefficients  $K^2$  of SAWs in polarization-inverted film were calculated. We found the high  $K^2$  value in the second mode Rayleigh SAW (Sezawa mode SAW) at the boundary of polarization-inverted film.

#### Statement of Contribution/Methods

We theoretically analyzed the  $K^2$  values of SAWs in three structures of polarization-inverted ZnO/silica glass, AlN/diamond and  $\text{Sc}_{0.3}\text{Al}_{0.7}\text{N}$ /diamond. Due to the three boundaries at the film surface, polarization-inverted-film interface and film/substrate interface, twelve configurations of IDTs or metal layers can be considered, as shown in Fig. 1(b). The  $K^2$  values were calculated as functions of normalized film thickness  $H/\lambda$  and thickness ratio  $r$ , where  $H$  is whole thickness of polarization-inverted film and  $r$  ( $0 \leq r \leq 1$ ) is the ratio of bottom-(0001)-layer thickness to  $H$  [see Fig. 1(a)].

#### Results/Discussion

High  $K^2$  values were obtained in the Sezawa mode SAW in structure B. Figs. 1(c) and (d) show contour plots of the calculated  $K^2$  values of the Sezawa mode SAW in structure B-IV of polarization-inverted ZnO/silica glass and  $\text{Sc}_{0.3}\text{Al}_{0.7}\text{N}$ /diamond, respectively. Maximum  $K^2$  value was found to be 6.6 % at  $H/\lambda = 0.83$  and  $r = 0.51$  in Fig. 1(c). This  $K^2$  value is higher than that in conventional (0001) oriented ZnO/silica glass in both Rayleigh SAW (3.0 %) and Sezawa mode SAW (1.2 %). Maximum  $K^2$  values were also obtained in structure B-IV at  $r$  of about 0.5 in the case of polarization-inverted AlN/diamond (3.6 %) and  $\text{Sc}_{0.3}\text{Al}_{0.7}\text{N}$ /diamond (4.4 %). In conclusion, Sezawa mode SAW excitations with high electromechanical coupling were demonstrated at the boundary of polarization-inverted films.

[1] R. Hashimoto, et al., presented at *IEEE IUS 2013*, IUS3-H-6 (2013).

[2] M. Suzuki, et al., *Proc. IEEE IUS 2012*, 1922 (2012).

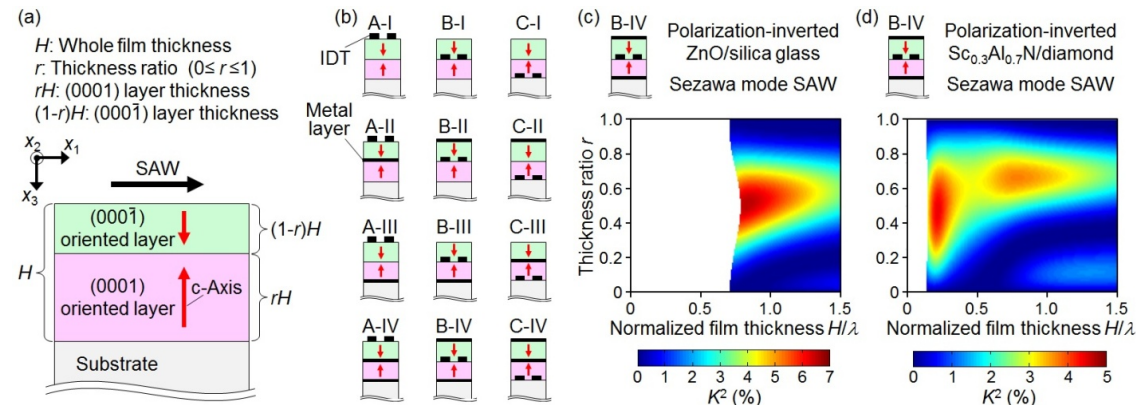


Fig. 1 (a) Schematic image of polarization inverted film/substrate structure, (b) cross sections of the twelve configurations used in the calculations of the  $K^2$  values, and contour plots of the calculated  $K^2$  values of the second mode (Sezawa mode) SAW in the B-IV type configuration of polarization-inverted (c) ZnO/silica glass and (d)  $\text{Sc}_{0.3}\text{Al}_{0.7}\text{N}$ /diamond.



## 7I - Piezoelectric Materials

Williford C

Saturday, September 6, 2014, 10:30 am - 12:00 pm

Chair: **Wei Ren**  
*Xi'an Jiaotong University*

7I-1

### 10:30 am Piezoelectric Ceramics in Ultrasound – 3203HD and Beyond

Gerald Stranford<sup>1</sup>, Thomas Vencill<sup>1</sup>, David Williams<sup>1</sup>, Bruce Johnson<sup>1</sup>, Lillian Gutierrez<sup>1</sup>; <sup>1</sup>CTS Electronic Components, Albuquerque, NM, USA

#### Background, Motivation and Objective

3203HD, a piezoelectric ceramic material, was developed in the 1980's to meet the requirements of medical ultrasound. This high dielectric constant, high electromechanical coupling coefficient material, which is known for its consistency and reproducibility, became the reference material for medical ultrasonic imaging and is still used in many transducers today. However, material requirements for ultrasonic imaging have evolved over the past twenty five years leading to the need for new materials. In particular there has been a demand for higher dielectric constant materials and materials that offer good mechanical strength and performance at dimensions less than 50 microns. The property trade-offs that occur as the dielectric constant is increased will be discussed along with the effect of smaller dimensions on the piezoelectric properties.

#### Statement of Contribution/Methods

- The effect on other piezoelectric properties as the dielectric constant is enhanced was determined by modifying an existing composition to achieve a range of dielectric constants.
- The effect of machining damage on the piezoelectric properties was measured by comparing the properties of wafers thinner than 150 microns with the bulk material properties. A similar approach was also used to determine the effect of rail width in 2-2 composites on the composite properties.

#### Results/Discussion

Optimization of a particular property within a family of PZT materials typically causes other properties to decrease. For example, increasing the dielectric constant generally causes the Curie point to decrease and aging rates to increase. Such relationships make it challenging to enhance the performance within a particular material class.

Reducing wafer thickness or reducing rail width in 2-2 composites results in lower dielectric constants than predicted based on bulk material properties. A model is presented that correlates the property degradation with machining damage, assuming that the damage layer is constant.

7I-2

### 11:00 am Lead-free piezoelectric materials and composites for high frequency medical ultrasound transducer applications

Tanikan Thongchai<sup>1</sup>, Yun Jiang<sup>1</sup>, Yang Bai<sup>1</sup>, Carl Meggs<sup>1</sup>, Ales Matousek<sup>2</sup>, Pavel Tofel<sup>2</sup>, Hana Hughes<sup>2</sup>, Tim Button<sup>1,2</sup>; <sup>1</sup>School of Metallurgy and Materials, University of Birmingham, Birmingham, United Kingdom, <sup>2</sup>CEITEC – Central European Institute of Technology, Brno, Czech Republic

#### Background, Motivation and Objective

Lead-free ceramics based on the (BaCa)(TiZr)O<sub>3</sub> system (BCTZ) have been reported to exhibit properties comparable to PZT, and are thus being considered as replacement materials for some applications. This paper reports an investigation of the interdependence of synthesis, processing and sintering conditions on the physical, structural, microstructural and functional properties of piezoelectric compositions in the BCZT system. Standard solid-state powder synthesis routes have been used and test samples have been fabricated in bulk and composite forms to allow material properties to be compared. Novel micromoulding techniques have been used to prepare composites suitable for application in medical ultrasound images applications >15MHz that can be directly compared to PZT analogues.

#### Statement of Contribution/Methods

A range of four compositions across the Ba(Zr<sub>0.2</sub>Ti<sub>0.8</sub>)O<sub>3</sub>–(Ba<sub>0.7</sub>Ca<sub>0.3</sub>)TiO<sub>3</sub> (BZT-BCT) pseudo phase diagram were prepared from BaCO<sub>3</sub>, CaCO<sub>3</sub>, ZrO<sub>2</sub> and TiO<sub>2</sub> precursors by calcination at 1100°C for 4 hours. Bulk samples were fabricated by uniaxial pressing and sintered at temperatures from 1450-1500°C for 4 hours. 1-3 composite structures were produced to net shape using gel casting methods. A gelling system based on the polymerization of a water-based epoxy resin, hardener and dispersant was developed achieving solids loadings of up to 50 volume % in a well-dispersed slurry which could be cast into polymer moulds. Following drying and demoulding, samples were sintered using the same conditions as for the bulk materials, backfilled with polymer, lapped to thickness, electroded and poled.

#### Results/Discussion

All sintered samples exhibited perovskite-related XRD patterns indicative of the rhombohedral and tetragonal phases expected according to the phase diagram. Densities ranging from 89.5-96.2% of theoretical density were achieved for the bulk samples with grain sizes increasing from ~20 µm for samples sintered at 1450°C to ~30 µm for samples sintered at 1500°C, the effect being independent of composition. d<sub>33</sub> values for the different compositions range from 100-450 pC/N and are broadly in line with what would be expected from the phase diagrams. However, even for a single composition, the d<sub>33</sub> value was shown to be extremely sensitive to processing conditions and exhibit a similar wide range in values. Selected compositions were used to fabricate composites with centre frequencies in the range 15-30MHz. Their properties will be discussed in the context of those of the corresponding bulk materials and their suitability for medical ultrasound transducer applications.

7I-3

### 11:15 am Highly c-Axis Oriented Monocrystalline Pb(Zr, Ti)O<sub>3</sub> Based Thin Film on Si Wafer by Sputter Deposition with Fast Cooling Process

Hiroaki Hanzawa<sup>1</sup>, Shinya Yoshida<sup>1</sup>, Kiyotaka Wasa<sup>2</sup>, Shuji Tanaka<sup>1</sup>; <sup>1</sup>Tohoku University, Sendai, Miyagi, Japan, <sup>2</sup>Yokohama City University, Yokohama, Kanagawa, Japan

#### Background, Motivation and Objective

For high performance MEMS sensors, e.g. gyroscope, large piezoelectricity for driving a sensing structure and low dielectric constant for efficient charge-to-voltage conversion are necessary. However, large piezoelectricity and low dielectric constant are normally incompatible with each other for conventional piezoelectric materials. Recently, c-axis oriented

monocrystalline  $\text{Pb}(\text{Zr}, \text{Ti})\text{O}_3$  (PZT)-based films on MgO crystal was demonstrated to have the compatibility. But, such films on Si were not reported because a large mismatch of thermal expansion between PZT and Si induces *a*-axis orientation.

#### Statement of Contribution/Methods

In this study, we first obtained *c*-axis oriented PZT-based films on Si by sputter deposition with fast cooling. A  $\text{Pb}(\text{Zr}_{0.5}, \text{Ti}_{0.5})\text{O}_3$ -based film was epitaxially grown on a (100) Si wafer covered with  $\text{SrRuO}_3/\text{La}_{0.5}\text{Sr}_{0.5}\text{CoO}_3/\text{CeO}_2$ /yttria-stabilized zirconia as buffer layers by sputtering at 600°C. Just after deposition, the wafer was force-cooled by blowing cool air over the surface. The average cooling rate from 600°C to 300°C measured ca. -180°C/min.

#### Results/Discussion

X-ray diffraction analysis of fast- and slow-cooled films (Fig. 1(a)) demonstrated that the fast cooling dramatically enhanced *c*-axis orientation, and *c*-domain ratio reached 95% (Fig. 1(b)). Transmission electron microscopy (Fig. 2) confirmed perfect epitaxial growth without dislocation lines or grains. A 1- $\mu\text{m}$ -thick  $\text{Pb}(\text{Mn}_{1/3}, \text{Nb}_{2/3})\text{O}_3$ -doped PZT film prepared by this method exhibited a large piezoelectric constant,  $e_{31,f}$  of -13.6 C/m<sup>2</sup> and a remarkably small dielectric constant,  $\epsilon_r$  of 170. As a result, the figure of merit for gyroscope ( $(e_{31,f})^2/\epsilon_r\epsilon_0$ ) reached 120 GPa, which is more than double of the best reported value on Si. This achievement has a great impact on piezoelectric MEMS.

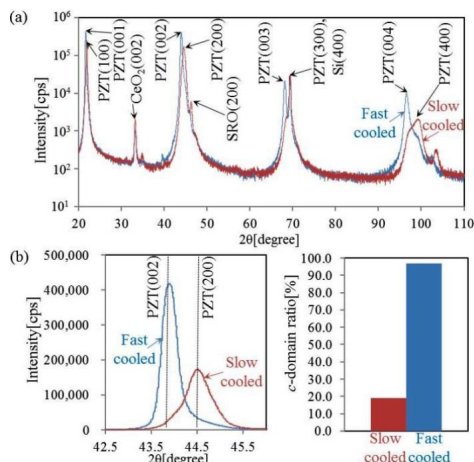


Figure 1. (a) X-ray diffraction spectra of 1.1- $\mu\text{m}$ -thick PZT films treated with fast and slow cooling. (b) *c*-domain ratio quantification from the peak intensity ratio between PZT (200) and PZT (002) in each film.

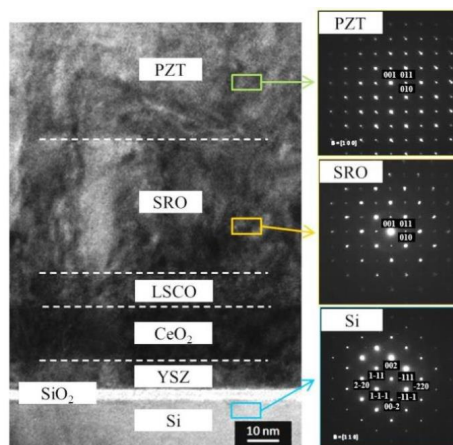


Figure 2. (Left) Cross-sectional transmission electron microscope image near the interface between PZT and SRO. (Right) Electron diffraction images of PZT, SRO and Si along the [100] zone axis. (SRO:  $\text{SrRuO}_3$ , LSCO:  $\text{La}_{0.5}\text{Sr}_{0.5}\text{CoO}_3$ , YSZ: yttria-stabilized zirconia)

71-4

#### 11:30 am Growth and Characterization of $\text{Pb}(\text{Zr}_{1-x}\text{Ti}_x)\text{O}_3$ Single Crystals

Zuo-Guang Ye<sup>1,2</sup>, Yujun Xie<sup>1</sup>, Bixia Wang<sup>1</sup>, Alexei Bokov<sup>1</sup>, Nan Zhang<sup>1</sup>, Wei Ren<sup>2</sup>; <sup>1</sup>Simon Fraser University, Canada, <sup>2</sup>Xi'an Jiaotong University, China, People's Republic of

#### Background, Motivation and Objective

Lead zirconate-titanate solid solution,  $\text{PbZr}_{1-x}\text{Ti}_x\text{O}_3$  (PZT), has been studied extensively over the past decades for both industrial applications and fundamental research, but almost exclusively in the forms of ceramics and thin films because of the difficulties encountered in the growth of PZT single crystals. On the other hand, it is of particular interest to grow large single crystals of PZT, which are not only necessary for thorough characterization of the anisotropic properties of this prototype ferroelectric solid solution system, but are also expected to exhibit superior piezo- and ferroelectric performance over the PZT ceramics, and a higher depoling temperature (*T<sub>d</sub>*) and higher coercive field (*E<sub>c</sub>*) (than the relaxor-based PMN-PT and PZN-PT single crystals), which are required for a broader range of applications in electromechanical transducers. The objective of this work is to synthesize the PZT single crystals and to characterize their domain structures, phase transitions and micro polar structures in order to understand the structure-property relations.

#### Statement of Contribution/Methods

In this paper, we present our successful growth of  $\text{PbZr}_{1-x}\text{Ti}_x\text{O}_3$  single crystals with a wide composition range across the morphotropic phase boundary (MPB) ( $0.20 \leq x \leq 0.65$ ) by a top-seeded solution growth (TSSG) technique. The systematic characterization of the grown PZT single crystals by a variety of techniques, such as dielectric and piezo-/ferroelectric measurements, polarized light microscopy, piezoresponse force microscopy and aberration-corrected transmission electron microscopy, has allowed us to discover a series of new physical phenomena in this important family of piezo-materials.

#### Results/Discussion

The crystal growth conditions are optimized in terms of chemical, thermodynamic and kinetic parameters. The growth temperature is found to be a key factor for controlling the composition of the grown crystals. PZT crystals with composition from  $x = 0.42$  to  $x = 0.47$  show characteristic ferroelectric-to-ferroelectric phase transitions due to the presence of a curved MPB. The crystals of MPB composition,  $x = 0.46$ , are found to exhibit the best properties, with a piezoelectric coefficient  $d_{33} = 1223$  pC/N, an electromechanical coupling factor  $k_{33} = 0.8$ , a coercive field  $E_c = 7$  kV/cm and a high Curie temperature  $T_c = 386$  °C, potentially useful for high temperature and high power electromechanical transducer applications.

The studies of the local polar domain structure and properties of PZT crystals reveal the formation of nanodomain state in PZT, which is discussed in the framework of the random-field theory and relaxor ferroelectricity. The atomic structure of PZT crystals with  $x=0.42$  is imaged by TEM. The accurate Pb displacements and their directions are determined on the  $\langle 110 \rangle$  monoclinic mirror plane. The orientation and distribution of local polarizations indicate a mixture of rhombohedral, tetragonal and monoclinic local symmetry.

### 11:45 am Growth of Piezoelectric Single Crystal for Medical Ultrasound Applications

Jian Tian<sup>1</sup>, Pengdi Han<sup>1</sup>; <sup>1</sup>H.C. Materials Corporation, Bolingbrook, Illinois, USA

#### Background, Motivation and Objective

Significant progresses have been made in the development of piezoelectric single crystals in the past decade. Binary lead magnesium niobate-lead titanate (PMN-PT) crystal has been commercialized in medical ultrasound imaging since 2004 and the application of piezoelectric crystals in medical ultrasound has become increasingly popular. To meet the crystal demand and transducer requirements, crystal growth has evolved to produce larger diameter, longer boules with more uniform and improved properties. In this presentation, development of piezoelectric crystal growth, property characterization and improvement, and crystal application will be discussed.

#### Statement of Contribution/Methods

PMN-PT single crystal has been the mainstream piezoelectric crystal materials for medical ultrasound imaging transducers. In recent years, ternary piezoelectric single crystals lead indium niobate-lead magnesium niobate-lead titanate (PIN-PMN-PT) showed improved electrical and thermal properties while maintaining excellent dielectric and piezoelectric properties like PMN-PT. Such improvements are advantages for transducers where a high drive and/or better temperature rating are needed. Preliminary tests on some higher frequency medical ultrasound imaging applications have demonstrated the advantages of PIN-PMN-PT single crystals over PMN-PT. Crystal growth behavior and composition-property relationships of both the binary PMN-PT the ternary PIN-PMN-PT crystals will be presented.

Bridgman growth technique is used to grow the PMN-PT based piezoelectric single crystals. Currently single crystals with boule diameter of 3"-4" are grown routinely in production. For medical ultrasound application, in-plane property homogeneity is critical for transducer performance. Since d33 mode is used for ultrasound imaging and PMN-PT based crystals have the best d33 property in <001> direction, it is preferable to grow the piezoelectric crystal along the <001> crystallographic direction to obtain the optimal in-plane property uniformity. In the meanwhile, improved growth technique is under development to produce crystals with reduced variation in composition/property along the growth direction.

#### Results/Discussion

PMN-PT crystal is excellent for general purpose ultrasound imaging. PIN-PMN-PT crystals offer advantages for higher frequency medical ultrasound imaging applications. <001> crystal growth has been proven the most effective way to control composition/property uniformity within a crystal wafer. Improved growth technique will further improve the property homogeneity along the crystal growth direction.

## 1J - MIM: Vascular Imaging

Grand Ballroom

Saturday, September 6, 2014, 1:00 pm - 2:30 pm

Chair: **Ton van der Steen**  
Erasmus Medical Centre, Rotterdam

1J-1

### 1:00 pm Optical Coherence Tomography: The Optical Analogue to Ultrasound Imaging

Stephen Boppart<sup>1</sup>; <sup>1</sup>Departments of Electrical and Computer Engineering, Bioengineering, and Medicine, University of Illinois at Urbana-Champaign, Urbana, IL, USA

#### Background, Motivation and Objective

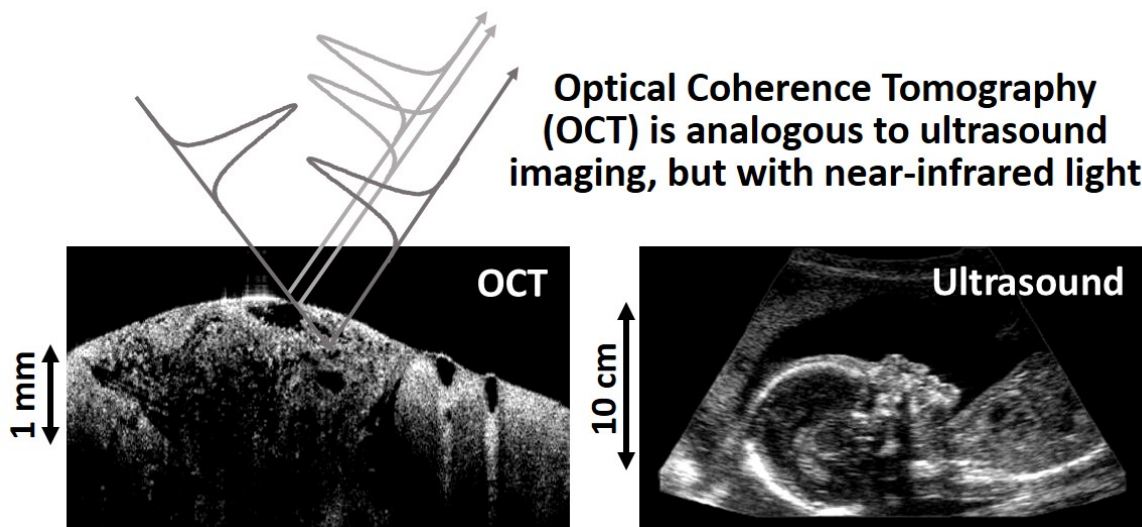
Optical coherence tomography (OCT) is a high-resolution, real-time, biomedical imaging modality that can generate cross-sectional and three-dimensional images of tissue based on intrinsic differences in optical scattering or refractive indices of biological structures. OCT is frequently described as the optical analogue to ultrasound, since reflections of near-infrared light are detected rather than sound. OCT has made significant contributions to ophthalmology and is now the gold-standard for retinal imaging. OCT continues to rapidly expand into other fields including cardiology, gastroenterology, and oncology, to name a few.

#### Statement of Contribution/Methods

OCT can use a variety of optical interferometers including superluminescent diodes, ultrafast lasers, or wavelength-swept lasers. Because of the high speed of light, compared to the speed of sound, low-coherence optical interferometry is used to spatially localize signals on the nano-to-micro scale, and depth-resolve reflections from within tissue. OCT is commonly performed using a spectral-domain system where a spectrometer simultaneously captures reflected signals from all depths along the beam path. By transversely scanning a focused beam across tissue and assembling adjacent depth scans (A-scans), a B-mode OCT image is generated. Coherence gating effectively rejects multiply-scattered light, enabling imaging depths up to several millimeters in highly-scattering tissue, beyond the limits of confocal or multiphoton microscopy. Virtually any tissue site can be accessed for OCT using beam delivery systems such as microscopes, hand-held probes, fiber-optic catheters/endoscopes, or optical needles.

#### Results/Discussion

OCT fills a niche in biomedical imaging between high-resolution lab-based microscopy and the cross-sectional radiological imaging modalities such as x-ray CT, MRI, and PET. OCT offers higher resolution than clinical ultrasound and provides different tissue contrast, but at more limited imaging depths. Recent developments in optical coherence elastography and computational wavefront engineering share related principles with ultrasound techniques. This presentation will review the principles, technology, and applications of OCT, and include areas that could mutually benefit from collaborative investigations between the OCT and ultrasound research communities.



1J-2

### 1:30 pm Improved diagnostic accuracy of human coronary atherosclerosis by using a fully integrated intravascular ultrasound and optical coherence tomography (IVUS-OCT) system

Teng Ma<sup>1,2</sup>, Jiawen Li<sup>3</sup>, Dilbahar Mohar<sup>4</sup>, Adrian Correa<sup>5</sup>, Pranav M. Patel<sup>4</sup>, K. Kirk Shung<sup>1</sup>, Zhongping Chen<sup>3</sup>, Qifa Zhou<sup>1</sup>; <sup>1</sup>Department of Biomedical Engineering, University of Southern California, USA, <sup>2</sup>NIH Resource Center on Medical Ultrasonic Transducer Technology, University of Southern California, USA, <sup>3</sup>Department of Biomedical Engineering and Beckman Laser Institute and Medical clinic, University of California, Irvine, USA, <sup>4</sup>Division of Cardiology School of Medicine, University of California, Irvine, USA, <sup>5</sup>Department of Pathology Keck School of Medicine, University of Southern California, USA

#### Background, Motivation and Objective

Intravascular ultrasound (IVUS) and optical coherence tomography (OCT) are the only two clinically used imaging modalities to provide real-time cross-sectional visualization of human coronary artery morphology. An integrated IVUS-OCT system is hypothesized to improve atherosclerosis characterization by capitalizing the advantage of sufficient imaging depth of IVUS and the high resolution of OCT. To date, the combined use IVUS and OCT imaging has not been investigated in sufficient detail to assess its diagnostic accuracy for identifying atherosclerotic plaques. The aim of this study is to establish objective criteria of using integrated IVUS-OCT system for atherosclerotic plaque characterization in preclinical study.

# Statement of Contribution/Methods

A fully-integrated IVUS-OCT imaging system and 3.6F catheter was developed for simultaneous IVUS-OCT imaging of 175 coronary artery sites with 241 regions of interests (ROI) from 20 cadavers. Each ROI was classified as calcified, fibrotic and lipid-rich by experienced pathologist (Dr. Correa) based on histology results as the "gold-standard". All IVUS-OCT, OCT-only and IVUS-only diagnosis were performed in random order by two skilled interventional cardiologists (Dr. Patel and Dr. Mohar), blinded to histology. The sensitivity and specificity of IVUS-OCT, OCT-only and IVUS-only diagnosis were calculated compare the predictive ability of three modalities. Interobserver variability, intraobserver variability, and the degree of agreement of histopathology vs imaging-based diagnosis by cardiologists were quantified by Cohen's  $\kappa$  test.

# Results/Discussion

As shown in Fig.1 (e), IVUS-OCT had significantly higher sensitivity for characterizing lipid-rich plaque than IVUS and higher sensitivity for identifying calcified plaque than OCT. IVUS-OCT also had obviously higher specificity for characterizing fibrotic plaque than IVUS only and OCT only ([Fig.1 (f)]). The overall agreement between IVUS-OCT vs histology diagnoses ( $\kappa=0.96$ ) was excellent, which was also higher than the overall agreement between IVUS vs histology diagnoses ( $\kappa=0.89$ ) and OCT vs histology diagnoses ( $\kappa=0.92$ ). Representative IVUS-OCT image pairs and histology of coronary artery segments with a lipid-rich plaque were shown in Fig.1 (a-d) to demonstrate the diagnosis criteria of IVUS-OCT for lipid-rich plaque

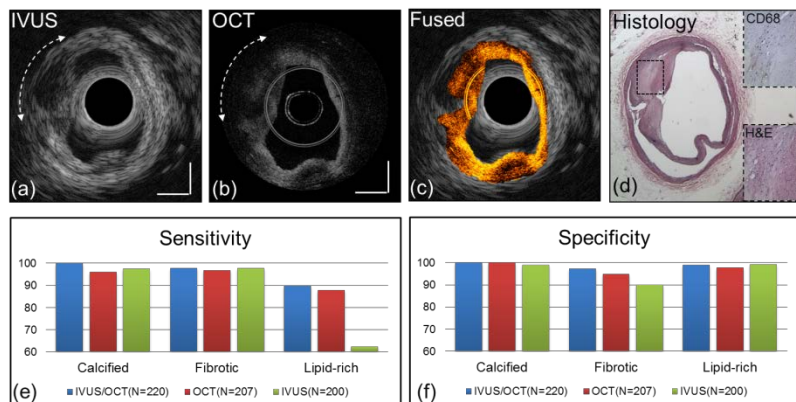


Figure1. (a): IVUS image: whole artery structure and low echo-signal at arrow region. (b): OCT image: high resolution lumen boundary and diffused signal-poor arrow region. (c) Fused IVUS-OCT image. (d): Corresponding H&E histology. Top right: high magnified CD68 stain of box region confirms foam cells. Bottom right: high magnified H&E image of box region. Note: original images of (a-d) were published in JACC 2014. (e): Sensitivity results. (f): Specificity results. Image bar: 1mm.

1J-3

# 1:45 pm Fast 3-D Reconstruction of the Carotid Artery Bifurcation Based on Real-time 2-D Segmentation

Daniel H. Iversen<sup>1</sup>, Sigurd Storve<sup>1</sup>, Torbjørn Dahl<sup>1,2</sup>, Hans Torp<sup>1</sup>, Lasse Lovstakken<sup>1</sup>; <sup>1</sup>Dept. Circulation and Medical Imaging, Norwegian University of Science and Technology, Trondheim, Norway; <sup>2</sup>St. Olavs University Hospital, Trondheim, Norway

# Background, Motivation and Objective

For detection and grading of plaques in the carotid artery, 3-D imaging of the plaque geometry and extent is considered clinically useful. Further, plaque volume measurements have been proposed as a potential risk factor for future ischemic events. However, due to the current non-availability of real-time matrix array transducers for vascular applications, 3-D imaging is currently not readily available for bedside diagnosis.

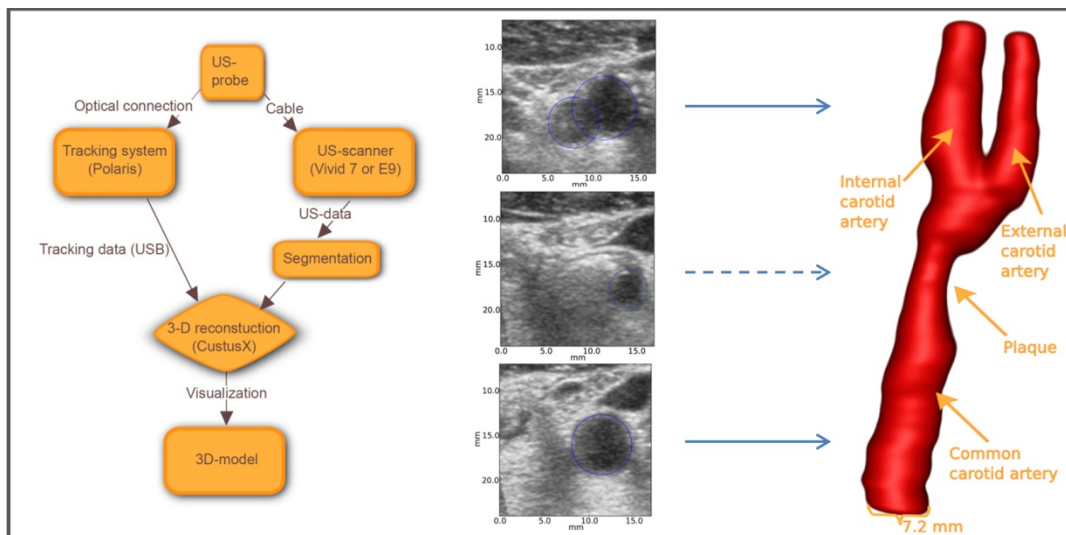
# Statement of Contribution/Methods

We describe a method for on-the-fly 3-D reconstruction of the carotid artery based on real-time automatic segmentation of the vessel lumen in 2-D cross-sectional B-mode images. The position and orientation of each image plane was registered by an accurate optical position sensor system (Polaris, NDI), and segmented images were combined to a 3-D model of the carotid artery lumen (see figure). The automatic segmentation was based on a Kalman filter approach (RCTL, Orderud2008) where edge-detection (local movement) and 2-D block matching (global movement) served as input measurements, and a deformable circular model served as a regularizing prior in space and time. Regularization was needed to increase robustness in presence of reverberation noise. Initially two seed points are placed in the external and internal artery, and two separate segmentation models run in parallel, where the union is chosen as the total vessel lumen when eventually overlapping in the carotid bifurcation.

# Results/Discussion

The parameters in the automatic segmentation algorithm were tuned on a test data set consisting of five carotids (healthy volunteers and patients), and further evaluated on N=5 patients with suspected carotid plaques from the hospital polyclinic. Results from the automatic segmentation were compared to manual segmentation done by two expert evaluators. The resulting average disagreement (modified Hausdorff distance) was 0.64 and 0.96 mm respectively, compared to an inter-observer disagreement of 0.84 mm. For hypochoic plaques and for imaging under very noisy conditions the method may require manual corrections, but as the total segmentation and reconstruction time is done within a minute, these corrections can be done bedside. The fast and relatively accurate reconstruction of 3-D carotid models may be suited for bedside 3-D visualization and volume estimation of moderate to large plaques.





1J-4

## 2:00 pm Fully Automated Carotid Plaque Segmentation in Combined B-mode and Contrast Enhanced Ultrasound

Zeynettin Akkus<sup>1</sup>, Diego D.B. Carvalho<sup>2</sup>, Stijn C.H. van den Oord<sup>3</sup>, Arend F.L. Schinkel<sup>1</sup>, Nico de Jong<sup>1,4</sup>, Wiro J. Niessen<sup>2,4</sup>, Antonius F.W. van der Steen<sup>1,4</sup>, Stefan Klein<sup>2</sup>, Johan G. Bosch<sup>1</sup>,  
<sup>1</sup>Biomedical Engineering Department, ErasmusMC, Rotterdam, Netherlands, <sup>2</sup>Biomedical Imaging Group Rotterdam, Depts. of Medical Informatics & Radiology, ErasmusMC, Rotterdam, Netherlands, <sup>3</sup>Department of Cardiology, Thoraxcenter, ErasmusMC, Rotterdam, Netherlands, <sup>4</sup>Imaging Science and Technology, Faculty of Applied Sciences, Delft University of Technology, Delft, Netherlands

### Background, Motivation and Objective

Segmentation of carotid plaques in standard B-mode ultrasound is challenging due to irregular lumen shapes, noise, artifacts, and plaque echolucency. To overcome these challenges, we propose a novel carotid plaque segmentation method which exploits the benefits of simultaneously acquired B-mode ultrasound (BMUS) and contrast enhanced ultrasound (CEUS).

### Statement of Contribution/Methods

We first estimate the anatomical motion from the BMUS image sequence, using nonrigid intensity-based image registration, and apply to BMUS and CEUS image sequences for motion compensation. We average the motion-compensated image sequences to obtain single BMUS&CEUS images with improved signal-to-noise ratio, which serve as 'epitome' images. We apply vessel detection to distinguish single and multiple branches in the CEUS epitome. The lumen-intima layer is segmented from the epitomes by a joint-histogram classification approach, followed by a 1D dynamic programming procedure. Then, the media-adventitia layer is segmented by using dual (2D) dynamic programming (DDP) (Fig.1). As media-adventitia layer and adventitial wall are almost parallel to each other, DDP is used to find two almost parallel and smooth lines by combining their costs. For validation, the lumen-intima and media-adventitia layers of 13 carotid arteries with atherosclerotic plaques were manually segmented by two observers and compared to the automated results. The average of the two manual segmentations was considered as ground-truth.

### Results/Discussion

For the lumen-intima layer, average ( $\pm$  std. dev.) root-mean-square-error was  $283 \pm 123 \mu\text{m}$ . The inter-observer variability was  $261 \pm 128 \mu\text{m}$ . For the media-adventitia layer, average root-mean-square-error was  $334 \pm 170 \mu\text{m}$ . The inter-observer variability was  $225 \pm 130 \mu\text{m}$ .

The differences between automated and ground-truth contours are in the same order as those between two observers. In conclusion, we present an accurate, robust, and novel fully automated plaque segmentation method in combined BMUS&CEUS images. To the best of our knowledge, this is the first study to exploit the combination of BMUS&CEUS to solve the segmentation challenges for carotid plaques.

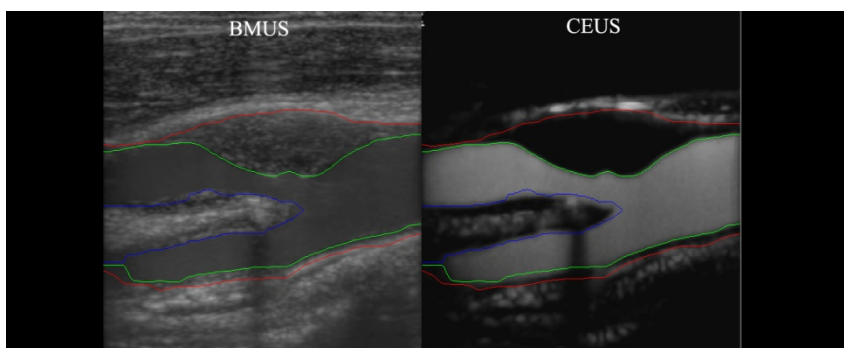


Figure 1: An example of the lumen-intima and media-adventitia layer segmentation of a bifurcated carotid. Images shown are the BMUS and CEUS epitomes.

This research was supported by the Center for Translational Molecular Medicine and the Netherlands Heart Foundation (PARISK).

## 2:15 pm Estimation of arterial wall motion using ultrafast imaging with transverse oscillations

Sebastien salles<sup>1</sup>, Simon Lai<sup>2</sup>, Damien Garcia<sup>3</sup>, Alfred Yu<sup>2</sup>, Didier Vray<sup>1</sup>, Hervé Liebgott<sup>1</sup>; <sup>1</sup>CNRS UMR 5220, INSERM U1044, Université de Lyon, Insa de Lyon, France, <sup>2</sup>Biomedical Ultrasound Laboratory, University of Hong Kong, China, People's Republic of, <sup>3</sup>RUBIC, CRCHUM, University of Montreal, Department of radiology, Canada

### Background, Motivation and Objective

Ultrafast ultrasound is a promising imaging modality with several potential clinical applications, such as arterial mechanics assessment, heart motion and blood flow imaging. Ultrafast ultrasound allows one to examine phenomena never analyzed before. However, the detection and measurement of these phenomena still remain challenging because of the difficulty in estimating small displacements, especially in the lateral direction. We thus propose to combine (1) ultrafast ultrasound imaging, (2) transverse oscillations (TO) and (3) a phase-based motion estimator. Our objective was to evaluate the proposed technique for the estimation of arterial wall motion using an in vitro phantom.

### Statement of Contribution/Methods

- 1) Plane-wave imaging was implemented on the SonixTouch system (5300 frames/s). Pre-beamformed radio-frequency (RF) data were acquired with the 128-channel Sonix DAQ
- 2) TOs were produced by filtering the beamformed RF signals to ensure an optimal control of the TO parameters.
- 3) Motion vectors were estimated using a phase-based approach: two single quadrant spectra were used to derive two phase images, which were combined to estimate the local displacements between two consecutive images.

Two artery mimicking phantoms were imaged during three consecutive pulsatile cycles: a stenotic and a non-stenotic artery with an inner diameter of 7 mm and a wall thickness of 1 mm. We tracked the proximal and distal arterial walls using our phase-based method, a speckle tracking approach on the B-mode images, and we compared the results with those obtained by a manual tracking.

The absolute mean differences between the estimated and the manually tracked trajectories were calculated for 20 ROI and 5 different frame rates.

### Results/Discussion

5 different frame rates were tested: 5300, 1060, 530, 353 and 256. The axial mean error remained stable around 65/100 pixel with both methods. The lateral mean error was 4.5 (4.6, 5, 5.2, 8, /100 pixel respectively) for our method and 310 (178, 120, 22, 23, /100 pixel) for speckle tracking.

In this phantom study, we have shown that our phase-based technique outperforms speckle tracking in terms of reproducibility and estimation of small radial and longitudinal displacements. Our results tend to show that ultrafast imaging with transverse oscillations is well-adapted to arterial wall motion estimation.

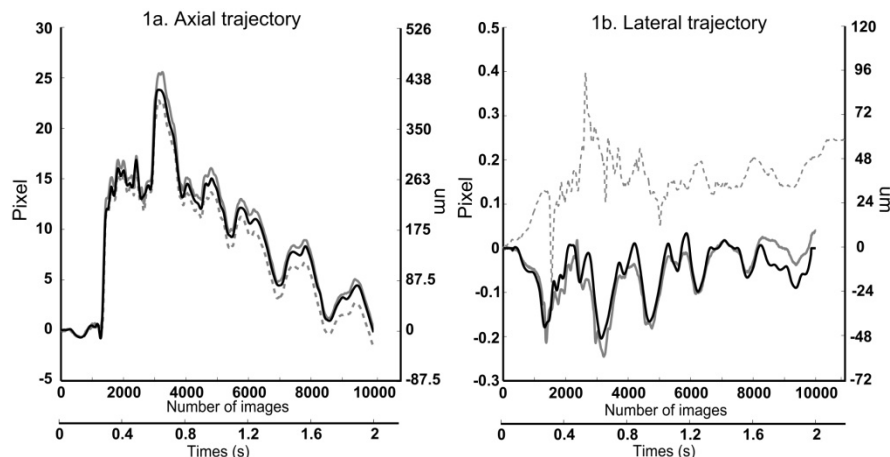


Fig.1: Axial and lateral trajectory estimation at 353 images/s of the non-stenotic artery. Comparison between --- speckle tracking, — our phased-based method and — manual tracking done 1 every 10 images

## 2J - MTH: Tumor Treatment and Monitoring

Waldorf

Saturday, September 6, 2014, 1:00 pm - 2:30 pm

Chair: **Elisa Konofagou**  
Columbia University, New York

2J-1

### 1:00 pm Intra-operative toroidal HIFU transducer for liver metastases and pancreatic tumors treatment: System development, in vivo studies and clinical evaluation.

David Melodelima<sup>1,2</sup>, Jeremy Vincenot<sup>1</sup>, Yao Chen<sup>2</sup>, Aurelien Dupre<sup>2</sup>, Anthony Kocot<sup>1</sup>, Michel Rivoire<sup>2</sup>, Jean-Yves Chapelon<sup>1</sup>; <sup>1</sup>LabTAU - INSERM U1032, France, <sup>2</sup>Centre Leon Berard, France

#### Background, Motivation and Objective

An ultrasound device that uses a toroidal HIFU transducer guided by ultrasound imaging was evaluated in vivo and clinically for the treatment of pancreatic tumors and colorectal liver metastases during an open procedure. Here we report in vivo results obtained in 24 pigs for the treatment of the pancreas and clinical results obtained in 22 patients for the treatment of liver metastases.

#### Statement of Contribution/Methods

The transducer has a toroidal shape with a diameter of 70 mm and is divided into 32 ring-shaped emitters of 86 mm<sup>2</sup> each. The radius of curvature is 70 mm to enable treatment of the deepest regions of the liver. The operating frequency was 2.5 MHz. A 7.5 MHz ultrasound imaging probe was placed in the center of the device to guide the treatment. The imaging plane was aligned with the HIFU focal zone.

In vivo evaluation of a pancreatic treatment was performed in 24 pigs with treatments performed in the tail and the isthmus of the pancreas. Evaluation of the efficacy, safety and tolerance was performed at 8 and 30 days after treatment.

Clinical evaluation of the device was performed in 22 patients with liver metastases after informed consent and scheduled for elective surgical resection of their metastases. HIFU lesions were created in metastases of less than 2 cm in diameter and just before the planned liver resection.

#### Results/Discussion

Using electronic focusing it was possible to ablate roughly spherical volumes of up to 20 cm<sup>3</sup>, average diameter: 4.5±0.2 cm. Treatment time was 6 minutes, without any mechanical displacement of the HIFU device. All HIFU lesions were homogeneous.

Pancreatic parenchyma destruction using an intra-operative HIFU device was feasible, safe and effective. Importantly, we demonstrated the feasibility of the treatment in the isthmus of the pancreas with complete ablation around the mesenteric artery and without any complication. HIFU lesions through such large vessels (up to 5 mm) being feasible, treatment of inoperable pancreatic tumors located in the isthmus should be possible.

Treatment of liver metastases with safety margins was feasible. The demarcation between ablated and non-ablated tissue as well as with the treated tumor was apparent in ultrasound images as a hypoechoic boundary and a central hyperechoic zone. The dimensions measured on ultrasound imaging were correlated ( $r=0.92$ ) with dimensions measured during histological analysis. This device is capable of achieving selective ablation of predefined liver metastases. Ultrasound imaging evidence of complete ablation of the target region can be taken to infer histological success.

2J-2

### 1:15 pm Inertial cavitation at low, simultaneous ultrasound and light intensities using nanoemulsion bead coated with gold nanospheres: application to sonothrombolysis.

Bastien Arnal<sup>1</sup>, Camilo Perez<sup>1,2</sup>, Chen-Wei Wei<sup>1</sup>, Jinjun Xia<sup>1</sup>, Michael Lombardo<sup>3</sup>, Ivan Pelivanov<sup>1,4</sup>, Thomas J. Matula<sup>1,2</sup>, Lilo D. Pozzo<sup>3</sup>, Matthew O'Donnell<sup>1</sup>; <sup>1</sup>Bioengineering, University of Washington, Seattle, WA, USA, <sup>2</sup>CIMU, Applied Physics Lab, University of Washington, Seattle, WA, USA, <sup>3</sup>Chemical engineering, University of Washington, Seattle, WA, USA, <sup>4</sup>Moscow State University, Russian Federation

#### Background, Motivation and Objective

Targeted inertial cavitation can be achieved using perfluorocarbon droplets. Shell coated nano-droplets (lipid or polymer) require high acoustic pressure for vaporization due to increased encapsulation stability. A combination of light and focused ultrasound (US), however, can reduce this threshold. A nano-emulsion composed of a perfluorohexane core (56 °C boiling point) stabilized in water by amphiphilic gold nanospheres has been synthesized and characterized. It combines the advantage of an US contrast agent and a broadened absorption spectrum due to plasmonic coupling of densely packed gold nanospheres (12 nm diameter around the droplet) with an overall low toxicity. This work aims to show the benefits of using this agent with a combination of light and sound to reduce vaporization exposure parameters.

#### Statement of Contribution/Methods

The theranostic agent was placed into a container, transparent to both light and US. The sample was placed into a tank filled with ultrapure, degassed water and positioned at the focus of a low-frequency focused transducer. A pulsed laser (750 nm, 10-ns pulses) was also focused on the sample (beam diameter = 6 mm). An in-house PVDF receiver acted as a wideband passive cavitation detector (Bandwidth = 30 MHz). An automated platform was developed to record signals from the receiver while sweeping both the fluence from 0.2 mJ/cm<sup>2</sup> to 85 mJ/cm<sup>2</sup> using a filter wheel (FW103, Thorlabs) and the US peak negative pressure from 0.3 to 8.1 MPa. For each parameter, 200 recordings of broadband noise from potential bubbles were analyzed to calculate the cavitation probability.

#### Results/Discussion

While the beads did not induce cavitation at a peak negative pressure (P-) of 8 MPa alone, the addition of a low fluence (2.4 mJ/cm<sup>2</sup>) greatly reduced the cavitation threshold to less than 1 MPa (P-) (cf Fig 1.). The US pressure and laser fluence used here, both under safety limits, potentially enable applications within tissue (~1 cm depth using 25 mJ/cm<sup>2</sup> at the skin surface). Compared to gold nanospheres alone, the laser fluence inducing the same effect at 1 MPa was 10 times lower because of the perfluorohexane nanoemulsion. Using our parameter scan results (Fig 1.), we are currently exploring in vitro thrombolysis treatment of fibrin clots at intensities well within diagnostic levels.

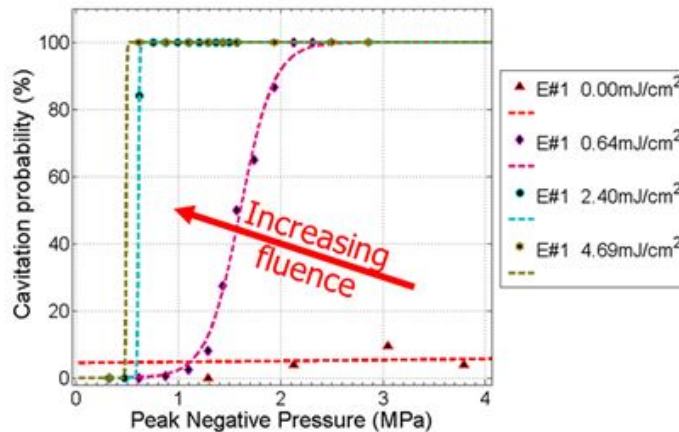


Fig 1 Cavitation probabilities over a wide parameter sweep of laser fluence and pressure. Significant cavitation was not observed without laser up to 8.1 MPa. The addition of pulsed light radiation of small intensity reduced considerably the cavitation threshold to less than 2 MPa.

2J-3

### 1:30 pm Differential Effects of Nanodroplets and Microbubbles on Tumor Vascularity Following Focused Ultrasound: An Acoustic Angiography Study

Linsey Phillips<sup>1</sup>, K. Heath Martin<sup>1</sup>, Ryan Gessner<sup>1</sup>, Paul A. Dayton<sup>1</sup>; <sup>1</sup>Joint Dept. of Biomedical Engineering, University of North Carolina at Chapel Hill and North Carolina State University, USA

#### Background, Motivation and Objective

MR-guided high intensity focused ultrasound (HIFU) surgery is currently under pre-clinical (U.S., Europe) and clinical (China, Europe) evaluation for the treatment of many types of solid tumors. As a result of HIFU, blood perfusion of the tissue is diminished, but the effect's magnitude is dependent on the intensity of the HIFU. The combination of ultrasound contrast agents and ultrasound are known to cause a variety of cellular and tissue-level effects including capillary hemorrhage at relatively low pressures, and thermal ablation at high pressures. The effects of acoustically active agents on vascular perfusion of tumors after moderate focused ultrasound (FUS) has not been well characterized. We hypothesized that microbubbles (MB) and nanodroplets (ND) would both reduce vascularity inside tumors. The goal of this study was to volumetrically evaluate immediate and chronic changes in tumor vasculature following FUS therapy with MB or ND.

#### Statement of Contribution/Methods

Microbubbles and nanodroplets were prepared in house. All studies were institutional animal care and use committee approved. Rats bearing flank fibrosarcoma tumors were injected with  $1.5 \times 10^9$  microbubbles ( $n=3$ ), nanodroplets ( $n=3$ ), or control/no-injection ( $n=3$ ) during targeted FUS. The FUS transducer was centered over the tumors and targeted a 5mm x 5mm area for 2.5 minutes (1 MHz, 2 MPa, 10% duty cycle, 1 Hz PRF). A dual-frequency US transducer enabled acquisition of contrast-enhanced, acoustic angiographic volumes of the tumors before, 15 minutes after, and 72 hours after the application of FUS.

#### Results/Discussion

No significant changes in tumor perfusion were observed when FUS was applied with nanodroplet or control injections. Although not statistically significant from the MB or control groups, the nanodroplets did reduce the growth rate of the tumor the most (nearly 40%). MBs with FUS resulted in a  $66.2 \pm 15.2\%$  ( $p < 0.05$ ) reduction in perfused tumor volume. These results suggest that FUS, when combined with microbubbles, can dramatically remodel tumor vasculature networks even at the low pressure used in this study. The reduction was achieved at only 125 W/cm<sup>2</sup>. Even at 1% of clinical levels, this low amount of energy combined with MB or ND could potentially enhance the safety of HIFU therapy.

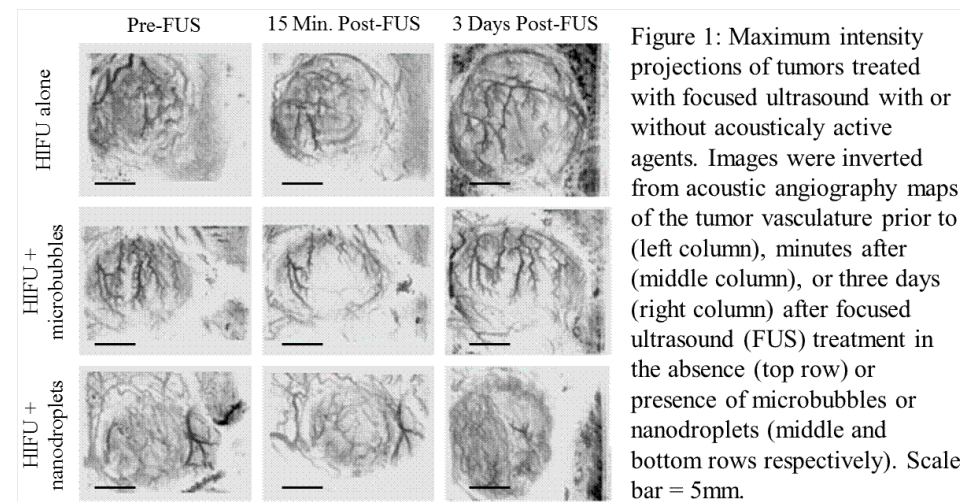


Figure 1: Maximum intensity projections of tumors treated with focused ultrasound with or without acoustically active agents. Images were inverted from acoustic angiography maps of the tumor vasculature prior to (left column), minutes after (middle column), or three days (right column) after focused ultrasound (FUS) treatment in the absence (top row) or presence of microbubbles or nanodroplets (middle and bottom rows respectively). Scale bar = 5mm.

## 2J-4

**1:45 pm Laser-activated PLGA theranostic agents for cancer therapy in vivo**

Yang Sun<sup>1</sup>, Yan Wang<sup>2</sup>, Chengcheng Nui<sup>1</sup>, Eric Strohm<sup>2</sup>, Yuanyi Zheng<sup>1</sup>, Haitao Ran<sup>1</sup>, Dong Wang<sup>1</sup>, Rongzhong Huang<sup>1</sup>, Yuping Gong<sup>1</sup>, Di Zhou<sup>1</sup>, Zhigang Wang<sup>1</sup>, **Michael Kolios<sup>2</sup>**; <sup>1</sup>*Institute of Ultrasound Imaging, Department of Ultrasound, The Second Affiliated Hospital of Chongqing Medical University, Chongqing, China, People's Republic of*; <sup>2</sup>*Department of Physics, Ryerson University, Toronto, Ontario, Canada*

**Background, Motivation and Objective**

Poly(Lactide-co-Glycolic Acid) (PLGA) particles encapsulating a perfluorocarbon (PFC) liquid core have been developed as theranostic agents. PLGA is an FDA-approved biocompatible material, while PFC liquids are chemically and biologically inert. The PLGA shell contains optically absorbing gold nanoparticles (NPs); upon irradiation with the appropriate laser energy, the PFC liquid undergoes a phase change from liquid to gas, rupturing the shell and causing damage to surrounding cells. In comparison to conventional PFC emulsions that use a liquid shell, the biocompatible PLGA shell provides stability to spontaneous vaporization, the surface can be functionalized and NPs/dyes can be incorporated into the shell. The effectiveness of the PLGA particles for cancer therapy was examined in vivo using rabbits with lymph node metastasis.

**Statement of Contribution/Methods**

Gold NPs, PFC liquid and the fluorescent dye DiI were incorporated into 1-6  $\mu$ m diameter PLGA particles using a double emulsion evaporation method. The NPs and DiI were contained within the PLGA shell, while the PFC was located within the core. New Zealand rabbits were inoculated with a VX2 tumor cell line (squamous carcinoma). After three weeks of tumor growth, three treatments were performed at two-day intervals. The treatment was performed on three groups of five rabbits each, one group with the PLGA/DiI-NPs, and two controls: one using saline injection only, the other using PLGA particles without NPs or DiI. For each treatment, the PLGA particles were injected into the rabbit foot pad. After 30 minutes, B-mode and contrast-enhanced ultrasound imaging (12 MHz), and blood perfusion maps were recorded around the lymph nodes. Then the area was irradiated with a 532 nm laser (140 mJ) for one minute. After the three treatments, the rabbits were sacrificed and the lymph nodes harvested. Tissue sections were examined using histology (H&E) stains and electron microscopy (TEM).

**Results/Discussion**

Ultrasound imaging showed decreased blood perfusion and necrosis was visible within the lymph nodes treated with PLGA/DiI-NPs, but not in the two controls. The tumors showed a decrease in the growth volume rate compared to the two controls (40% vs. 70%,  $p < 0.05$ ). Significant cellular damage was observed in the H&E stains, and TEM imaging showed fragmented cellular and nuclear membranes. Red blood cells were also observed in the images, which indicates rupturing of the blood vessels. These effects were not observed in the two control experiments. No weight changes or adverse effects were observed during the seven day treatment. These observations indicate that vaporization of the PLGA particles induce damage within the irradiated area, limiting tumor growth. The treatment effectiveness could be further increased by incorporating chemotherapeutic drugs within the particle and targeting ligands on the shell for better targeting and controlled release during irradiation.

## 2J-5

**2:00 pm In vivo pancreatic tumor detection and high-intensity focused ultrasound ablation monitoring using harmonic motion imaging technique**

**Hong Chen<sup>1</sup>**, Yang Han<sup>1</sup>, Carmine Palermo<sup>2</sup>, Kenneth Olive<sup>2</sup>, Elia Konofagou<sup>1,3</sup>; <sup>1</sup>*Biomedical Engineering, Columbia University, USA*; <sup>2</sup>*Herbert Irving Comprehensive Cancer Center, Columbia University, USA*; <sup>3</sup>*Department of Radiology, Columbia University, USA*

**Background, Motivation and Objective**

The clinical application of high-intensity focused ultrasound (HIFU) in pancreatic tumor ablation is hampered by the lack of a reliable treatment monitoring technique. Harmonic motion imaging (HMI) uses periodic acoustic radiation force generated by amplitude-modulated focused ultrasound (FUS) to induce a localized oscillatory tissue motion, the amplitude of which is directly related to the underlying tissue stiffness. The FUS can be operated to induce thermal ablation, which allows the system to generate thermal lesions while performing treatment monitoring using HMI. The objective of the current study was to evaluate the feasibility of HMI in pancreatic tumor (1) imaging and (2) HIFU treatment monitoring.

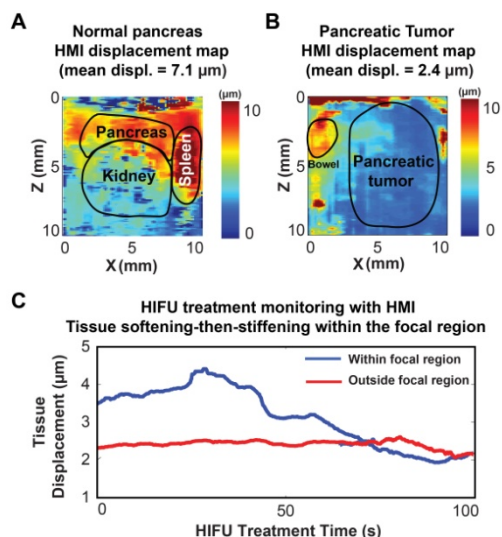
**Statement of Contribution/Methods**

A transgenic mouse model of pancreatic cancer and wild-type mice were used. A FUS transducer generated periodic radiation force, which induced a tissue motion at 50 Hz within the targeted region. The axial tissue displacement amplitude was estimated using 1D cross-correlation of acquired RF signals. (1) For pancreatic tumor imaging, FUS was operated to generate radiation force without causing ablation. 2D HMI displacement maps for transgenic mice ( $n=3$ ) and wild-type mice ( $n=3$ ) were generated by raster-scanning of selected regions. (2) For HIFU monitoring (transgenic mice  $n=7$ ), FUS was used to induce thermal ablation and tissue motion at the same time, allowing HMI monitoring without interrupting tissue ablation. The HMI displacements of the targeted tumor regions were imaged before, during and after HIFU ablation. All pancreases were excised immediately after sonication for histological evaluation.

**Results/Discussion**

HMI was shown capable of both in vivo pancreatic tumor imaging and HIFU ablation monitoring. (1) For imaging pancreas, it generated 2D displacement maps of both the normal pancreas (Figure A) and the pancreatic tumor (Figure B), showing a high HMI displacement contrast between normal and malignant tissue (average displacement ratio of 2.8). (2) For HIFU ablation monitoring, it displayed consistent HMI displacement decrease after HIFU ablation with a mean reduction rate of 38.1% (Figure C), indicating tissue stiffening within the targeted tumor region. H&E staining of the excised tumors confirmed that the decrease in the displacement amplitude was correlated with lesion formation.





2J-6

## 2:15 pm DETECTION OF HIFU LESION USING PASSIVE ELASTOGRAPHY : A PRELIMINARY STUDY ON PORCINE PANCREAS

ali zorgani<sup>1</sup>, Jérémy Vincenot<sup>1</sup>, Anthony Kocot<sup>1</sup>, Paul Leduc<sup>2</sup>, Yao chen<sup>3</sup>, Rémi Souchon<sup>1</sup>, Stefan Catheline<sup>1</sup>, David Melodelima<sup>1</sup>; <sup>1</sup>UMR 1032 INSERM, Lyon, France, <sup>2</sup>Lyon UNICANCER, Lyon, France, <sup>3</sup>Lyon UNICANCER, France

### Background, Motivation and Objective

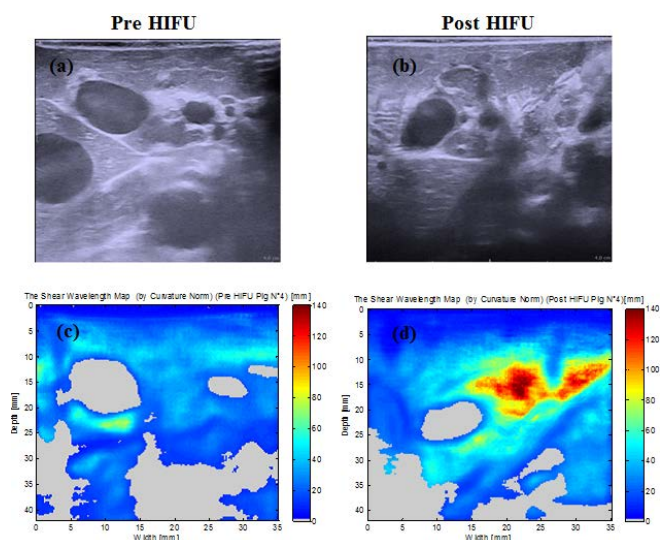
HIFU lesion in porcine pancreas with ultrasound B-Mode imaging is not satisfactory. Otherwise shear wave elasticity imaging techniques have proved its ability to locally retrieve the tissue elasticity by tracking the shear wave generated by an external source. In recent works, physiological shear waves naturally produced by muscles activity, heart beating, blood network pulsatility have shown to be efficient for elasticity tomography. Furthermore, these physiological shear wave elastography techniques are fully compatible with standard ultrasound scanners working at a typical imaging frame rate of 25Hz. The aim of this study was to use passive elastography in vivo in pigs to characterize HIFU lesions created in the pancreas.

### Statement of Contribution/Methods

The animal experiments were carried out on six healthy porcine. HIFU ablations were created in 160 seconds using a toroidal transducer developed for intra-operative treatments. The general idea is to use a diffuse shear wave field and cross-correlation or time reversal. Due to heart beating and mesenteric vessels pulsatility, the displacement field is measured inside the sample at a 25Hz frame rate using a 12 MHz ultrasonic array and a standard ultrasound scanner (Hoak B&K). In a second step, one displacement line at (xo,zo) is selected and correlated to the others. This can be interpreted as a virtual time reversal experiment. Thus, shear waves will virtually focalize at (xo,zo). By measuring the vibration amplitude, which is directly linked to the tissue elasticity and unaffected by the temporal under sampling of the displacement field, a relative elasticity image is constructed before and after HIFU treatment. For experimental reasons passive elastography experiments were successfully carried on only two pigs.

### Results/Discussion

Homogeneous HIFU ablations were created in the pancreas with an average diameter of 4.5±0.2 cm (average volume 20 cm<sup>3</sup>). The elasticity images of the pancreas are represented before the HIFU in Fig. 1(b), and after the HIFU lesion Fig. 1(d). The obtained relative elasticity contrast allows to clearly observing the effect of the HIFU treatment and evaluating the lesion size compared the B-mode image (Fig 1.a and 1.b) Although these results are preliminary they demonstrate in vivo evidence that the use of passive elastography can detect HIFU lesions in the pancreas not visible in sonograms.



## 3J - MTC: Bone

Boulevard

Saturday, September 6, 2014, 1:00 pm - 2:30 pm

Chair: **Pascal Laugier**  
Université Pierre et Marie Curie, Paris

3J-1

### 1:00 pm Anisotropic elasticity of human tibial cortical bone measured by resonant ultrasound spectroscopy

Simon Bernard<sup>1</sup>, Johannes Schneider<sup>2</sup>, Robert Wendlandt<sup>3</sup>, Quentin Grimal<sup>1</sup>, Kay Raum<sup>2</sup>, Peter Varga<sup>2</sup>, Pascal Laugier<sup>1</sup>; <sup>1</sup>Laboratoire d'Imagerie Biomédicale, Sorbonne Universités, UPMC Univ Paris 06, INSERM, CNRS, Paris, France, <sup>2</sup>Julius Wolff Institute for Biomechanics and Musculoskeletal Regeneration, Charité Universitätsmedizin, Berlin, Germany, <sup>3</sup>Labor für Biomechanik, Universitätsklinikum Schleswig Holstein, Luebeck, Germany

#### Background, Motivation and Objective

Elasticity measurement combined with microstructure and tissue properties assessment can help to understand pathological variations of bone functional properties and guide diagnosis strategies. Resonant ultrasound spectroscopy (RUS) uses the vibration spectrum of a mm-sized sample to estimate elasticity, based on a comparison of measured and model-predicted resonant frequencies. Contrary to mechanical tests, RUS is well adapted to the measurement of cortical bone elasticity (Bernard et al. 2013) because: i) bone is anisotropic; ii) samples are at most a few mm thick. While a RUS experiment is relatively straightforward, the post-processing (solving an inverse problem) is elaborate and relies on finding the optimal pairing of measured and predicted frequencies. In this paper, we introduce a method to automatize this task. We show that RUS is suited to the evaluation of stiffness tensors of large collections of specimens by non-expert users. An ancillary objective is to compare Young's modulus obtained by RUS and quasi-static mechanical testing.

#### Statement of Contribution/Methods

Two to four rectangular parallelepiped specimens (typical size 2x3x4 mm<sup>3</sup>) were prepared from 19 human tibial diaphyseal cross-sections (donors ages 70-94). RUS vibration spectra were obtained for a total of 59 specimens in a frequency band (typically 150-500 kHz) containing the first ~30 expected resonant modes. The spectra were fitted to Lorentzian lineshapes to retrieve the resonant frequencies. The latter are inputs of an inverse problem that consists in determining 5 stiffness coefficients (transverse isotropy) together with the optimal pairing of measured and predicted frequencies. The problem is solved without user interaction in a Bayesian framework using an a priori knowledge of cortical bone properties from a previous study on human femur bone. The Young's modulus was then measured in compression for all specimens but a few which were too small.

#### Results/Discussion

The stiffness tensor was successfully obtained for 52 specimens. For 7 specimens the method did not achieve a sufficiently good fit between measured and model predicted frequencies, possibly due to an insufficient quality of specimen geometry. Stiffness coefficients measured with RUS are (in GPa): C11=14.8 ± 3.4, C33=26.8 ± 3.9, C13=7.9 ± 1.6, C44=5.6 ± 0.9, C66=3.8 ± 0.7. The acoustical Young's modulus Ea, obtained from the stiffness tensor, correlates to the mechanical modulus E (n=44, R<sup>2</sup>=0.45, p<1e-3) but shows a significant bias (Ea=20.9 ± 3.2; E=13.9 ± 3.8). These findings are in agreement with a previous study (Grimal et al. 2009) and may be due to bone viscoelasticity and difference in loading speed between ultrasound and mechanical testing. The elasticity database obtained in this study for human tibia, a clinically relevant site for in vivo assessment of bone, is unique. RUS successfully assessed elastic anisotropy of human tibial cortical bone despite the small thickness of the cortex.

3J-2

### 1:15 pm Ultrasonic guided mode conversion using axial transmission for fracture evaluation in long bones: a tubular phantom study

Shixiao Hu<sup>1</sup>, Kailiang Xu<sup>1,2</sup>, Dean Ta<sup>1</sup>, Jean-Gabriel Minonzio<sup>2</sup>, Pascal Laugier<sup>2</sup>, Weiqi Wang<sup>1</sup>; <sup>1</sup>Department of Electronic Engineering, Fudan University, Shanghai, China, People's Republic of, <sup>2</sup>Laboratoire d'Imagerie Biomédicale, Sorbonne Universités, UPMC Univ Paris 06, INSERM, CNRS, Paris, France

#### Background, Motivation and Objective

While the potential of cortical bone characterization using ultrasonic guided waves has recently emerged, several challenging issues remain to be addressed such as multimode dispersion and mode overlapping. On top of that, mode conversion occurring when guided waves interact with a defect seriously complicates the interpretation of guided signals measured in fractured long bone. The present work is an extension of our previous analysis of the conversion of Lamb waves in fractured plate-like bone phantoms to fractured tube-like bone phantoms. We aim ultimately at defining sensitive ultrasonic indicators for long bone fracture evaluation.

#### Statement of Contribution/Methods

Axial transmission experiments were performed in acrylic pipes, with wall thickness of 1.8 mm, 2.5 mm and 3.0 mm and outer radius of 10 mm. To simulate different fracture status, artificial notches were circumferentially sawed on the phantom pipes with varying fracture depth from 0% to 80% of the thickness. In parallel to the experiments, 3-D finite-difference time-domain simulations were performed by a custom-made code Simsonic. To suppress the high-order mode and simplify the signal interpretation, a narrowband low-frequency signal was used as excitation. Group velocities and energy percentages of the originally-transmitted modes and newly-converted modes were quantitatively determined for fracture characterization.

#### Results/Discussion

We found a good agreement between simulations and experiments. Using a narrowband (-3 dB bandwidth of 40 kHz) 100 kHz excitation, only two originally-transmitted modes, L(0,1) and L(0,2), can be measured in the intact acrylic phantoms. However, the surface discontinuity (notch) generates new wave-packets propagating between the originally-transmitted L(0,1) and L(0,2) modes through mode conversion. The energy percentages of the originally-transmitted modes monotonically decline from 100% to 40% with the notch-depth increasing. On the other hand, the mode conversion caused by the notch-deepening greatly enhances the energy percentages of the converted modes, from 0% to 60%. The monotonic variation of the mode energy highly correlates with the mode conversion degree, which is capable of revealing the severity of the surface discontinuity in the acrylic tubes.

Both simulations and experiments demonstrate that longitudinal mode conversion theory can be used to interpret the guided waves propagation in fractured tubes. The transmission energy percentages are good indicators to assess the mode conversion degree and further can be employed to evaluate the severity of the surface discontinuity. Further studies will be carried out to confirm whether the methodology may also contribute to the ultrasonic evaluation and healing monitoring of fractured long bones.

### 1:30 pm Temporal Evolution of Fast and Slow Waves During Propagation Through Bovine Cancellous Bone In Vitro

Keith Wear<sup>1</sup>, Yoshiaki Nagatani<sup>2</sup>, Katsunori Mizuno<sup>3</sup>, Mami Matsukawa<sup>4</sup>; <sup>1</sup>Center for Devices and Radiological Health, US Food and Drug Administration, USA, <sup>2</sup>Kobe City College of Technology, Japan, <sup>3</sup>University of Tokyo, Japan, <sup>4</sup>Doshisha University, Japan

#### Background, Motivation and Objective

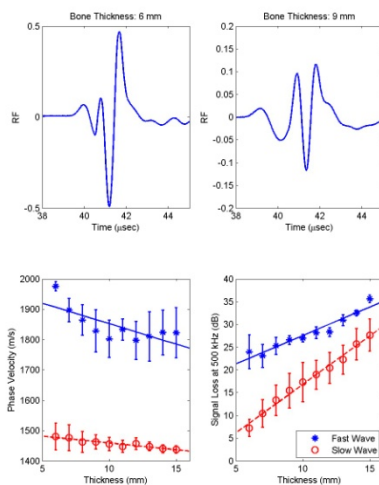
Through-transmission measurements in porous media such as cancellous bone in vitro often reveal two longitudinal waves ("fast" and "slow" waves). The velocities and amplitudes of fast and slow waves are related to bone microstructure and composition, and therefore may provide diagnostic information related to fracture-risk. One commercial system provides diagnostic measurements based on properties of fast and slow waves in the wrist (Otani et al., Jap. J. Appl. Phys., 48, 07GK05-1 - 07GK05-5, 2009; Breban et al., Bone, 46, 1620-1625, 2010).

#### Statement of Contribution/Methods

In order to gain insight regarding evolution of fast and slow waves as they propagate through bone, signal loss and phase velocity at 500 kHz for fast and slow waves were measured as a function of propagation depth in 3 bovine cancellous bone samples. After initial through-transmission measurement of each 15-mm thick bone sample, 1 mm of thickness was filed away. Then each 14-mm bone sample was measured. As in (Nagatani et al., Ultrasonics, 48, 607-612, 2008), an alternation of ultrasound measurement and 1-mm filing continued until a set of measurements for thicknesses ranging from 15 to 6 mm, in 1 mm increments, was obtained for each of the 3 bovine cancellous bone samples. The top panels of the figure show a lower-amplitude, lower-frequency fast wave that precedes but overlaps a higher-amplitude, higher frequency slow wave. Fast and slow wave properties were estimated using the modified least-squares Prony's method with curve fitting (MLSP+CF) (Wear, J. Acoust. Soc. Am., 133, 2490-2501, 2013).

#### Results/Discussion

Mean phase velocities at 500 kHz decreased by  $14 \pm 4$  m/s per mm (mean  $\pm$  standard error) (fast wave) and  $5 \pm 1$  m/s per mm (slow wave). Mean signal losses at 500 kHz increased by  $1.3 \pm 0.1$  dB per mm (fast wave) and  $2.1 \pm 0.1$  dB per mm (slow wave). Decreases in phase velocity with bone sample thickness may be due to increasingly complicated propagation paths with depth. The linear relationship between signal loss at 500 kHz and bone sample thickness is consistent with an attenuation coefficient that is independent of sample thickness.



### 1:45 pm Polarity of piezoelectric properties in bone induced by ultrasound irradiation

Hiroko Tsuneda<sup>1</sup>, Isao Mano<sup>1</sup>, Elena Hernandez<sup>1</sup>, Katsunori Mizuno<sup>2</sup>, Takahiko Yanagitani<sup>3</sup>, Shinji Takayanagi<sup>1</sup>, Mami Matsukawa<sup>1</sup>; <sup>1</sup>Wave electronics research center, Laboratory of ultrasonic electronics, Doshisha University, Japan, <sup>2</sup>Inst. Industrial Science, The University of Tokyo, Japan, <sup>3</sup>Nagoya Institute of Technology, Japan

#### Background, Motivation and Objective

Fukada has reported that mechanical stress at low frequencies induces electrical potentials in bone [1]. However, there are few studies on the high frequency stress induced electrical potentials in bone, although the piezoelectric phenomenon can be a key to understand the bone fracture healing mechanism by the low intensity pulse ultrasound technique. To evaluate the stress induced electrical potentials in bone in the MHz range, we have fabricated bone transducers, and obtained output signals induced by ultrasound irradiation [2]. In this study, we investigated the polarity of piezoelectric properties in bone in the MHz range.

#### Statement of Contribution/Methods

We prepared circular plate cortical bone samples (diameter; 10.0 mm, thickness; 0.70-1.00mm) from the mid shaft of right bovine femur. The normal direction of these plates were equal to the bone axis. Using these plates as piezoelectric materials, we fabricated two types of bone transducers as can be seen in Fig.1: (type A) transducer surface was proximal part and (Type B) transducer surface was distal part. In the ultrasonic immersion experiments, a PVDF focused transducer (custom-made by Toray) was used as a transmitter and a handmade bone transducer was used as a receiver. A function generator (33250A; Agilent Technologies) applied a square pulse to the transmitter. Ultrasound was transmitted at the initial rise and last decrease of the pulse. The transmitted ultrasound pressure was about 10 kPa<sub>peak-peak</sub>.

#### Results/Discussion

All type A transducers showed clear initial rise for the positive ultrasound pressure, whereas type B showed initial decrease. For the negative pressure both transducers showed opposite changes. Received pulse widths of bone transducers were 1-2 μs, showing relationship between the bone sample thickness and pulse width. These data show the existence of polarization in the piezoelectric properties in bone, which is considered to result from the collagen fibers [1]. The polarization properties can give us further information of the bone piezoelectric characteristics.

[1] E. Fukada, et al., *Journal of the Physical Society of Japan*, **12**, 1158-62 (1957).

[2] M. Okino et al., *Appl. Phys. Lett.* **103**, 103701 (2013).

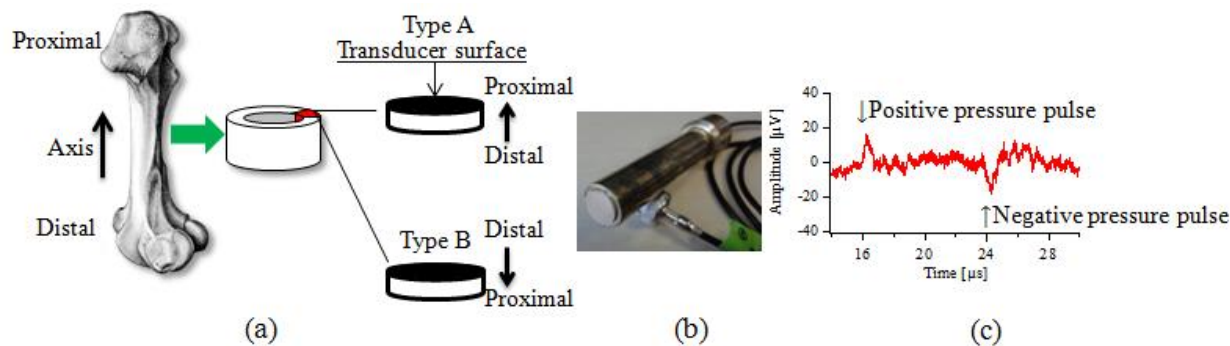


Fig. 1. (a) Fabrication process of bone plate samples, (b) Bone ultrasound transducer and (c) Output of bone transducer (Type A) by ultrasound pulse irradiation.

3J-5

#### 2:00 pm In vivo measurements of guided wave at the forearm

Quentin Vallet<sup>1</sup>, Jean-Gabriel Minonzio<sup>1</sup>, Christine Chappard<sup>2</sup>, Maryline Talmant<sup>1</sup>, Pascal Laugier<sup>1</sup>; <sup>1</sup>Laboratoire d'Imagerie Biomédicale, Sorbonne Universités, UPMC Univ Paris 06, INSERM, CNRS, Paris, France, <sup>2</sup>B2OA, UMR CNRS7052, University Denis Diderot, PRES Sorbonne Paris Cité, Paris, France

##### Background, Motivation and Objective

Because of the recognized importance of cortical bone in osteoporotic fracture risk, efforts have been made to improve its measurement. A step forward towards the ultrasonic characterization of cortical bone has been made recently with reports showing that cortical bone behaves as a waveguide (WG) for ultrasound [1]. Measurements of the guided modes dispersion relationships, together with appropriate waveguide modeling have the potential for providing estimates of strength-related factors such as stiffness (which is largely determined by cortical porosity) and cortical thickness (Ct.Th). The present work presents the first in vivo ultrasound-based estimate of Ct.Th<sub>US</sub> from axial transmission guided waves measurement in healthy subjects.

##### Statement of Contribution/Methods

Cortical bone is readily accessible for measurements at the radius using the axial transmission (AT). A 1-MHz bi-directional multi-element probe, comprising two groups of 5 transmitters each placed at each side of a group of 24 receivers was used. The bi-directional approach allows the automatic compensation of the bias introduced on the dispersion curves when the thickness of the soft tissue varies in the direction of propagation [2]. The full time response of the WG for all possible pairs of transmitter-receiver is recorded and then processed using a 2-D time-space Fourier transform and a singular value decomposition-based denoising step [3]. The guided waves spectrum is used to estimate Ct.Th<sub>US</sub>, based on a comparison of measured and model-predicted dispersion curves. The post-processing relies on finding the optimal pairing of measured and predicted dispersion curves from a free transverse isotropic 2-D plate model, assuming a constant elasticity.

Nine healthy subjects (24-58 years old) were included in this pilot study. High resolution X-ray peripheral computed tomography (Scanco XtremeCT - voxel size : (82 μm)<sup>3</sup>) was used to measure the bone mineral density (BMD) and the actual thickness (Ct.Th<sub>ref</sub>) in all the subjects.

##### Results/Discussion

A1, S2 and A3 guided modes were identified in all the subjects. The use of a plate model with constant elasticity was in agreement with the almost constant BMD values ranging between 1043 and 1084 (mg.cm<sup>-3</sup>). Results showed a good agreement between Ct.Th<sub>US</sub> (3.6 ± 0.3 mm) and Ct.Th<sub>ref</sub> (3.6 ± 0.3 mm) with a R<sup>2</sup> = 0.7 (RMSE = 0.15 mm, p < 0.005). The results indicate that guided waves might become a new method for the in vivo estimation of bone strength factors to enhance prediction of fracture risk.

The authors acknowledge Azalée for financial support.

[1]Foiret et al., IUS Prague July 2013

[2]Moreau et al., JASA. **135**, EL15-EL21 (2014)

[3]Minonzio et al., JASA. **130**, 3574-3582 (2011)

3J-6

#### 2:15 pm Evaluation of anisotropy in cortical bone by micro-Brillouin scattering

Yuki Imoto<sup>1</sup>, Mami Matsukawa<sup>1</sup>, Ryo Tubota<sup>1</sup>; <sup>1</sup>Wave Electronics Research Center, Doshisha University, Kyotanabe, Kyoto, Japan

##### Background, Motivation and Objective

Bone is mainly composed of collagen and minerals such as hydroxyapatite (HAp). In order to evaluate bone strength, it is important to know not only bone mineral density (BMD) but also bone quality such as microstructure and anisotropy. However, there are just a few studies on the anisotropic elasticity characterization of bone by the ultrasonic wave velocity measurements. So, in this study, we have investigated the velocity anisotropy in the minute area of cortical bone using a micro-Brillouin scattering technique (μ-BR). Especially, we focused on the effect of collagen on the velocity anisotropy.

##### Statement of Contribution/Methods

The mid-shaft of a 30 month-old bovine femur was cut into 2 plate specimens (10 mm×5 mm) obtained from lateral and posterior parts. The plates were perpendicular to the bone-axis or radial direction. The specimens thickness was about 70 μm. Longitudinal wave velocities in GHz range were measured by μ-BR using a tandem Fabry-Perot interferometer (JRS) and the reflection induced scattering geometry, with a solid-state laser (λ=532 nm, spectra Physics). An optical microscope system enabled the measurement in a small area (diameter: 10 μm), which was smaller than the microstructure scale of the bovine bone. After the first measurements, HAp was decalcified using the ethylenediaminetetraacetic acid (EDTA). The specimens were placed in EDTA for 5 days and were washed by running water for 24 hours. The wave velocities in decalcified specimens were then measured.

# Results/Discussion

Fig. 1 shows the velocity anisotropy in the posterior part of cortical bone before and after decalcification. Before decalcification, the anisotropy (difference between maximum and minimum velocity/maximum velocity) was around 4%. After decalcification, the wave velocities decreased and the anisotropy increased up to 12% or more. In addition, the maximum velocities were always found near the bone-axis direction which was the direction of collagen alignment. The specimen obtained from the lateral part also showed similar changes. Because there were no HAp crystallites after decalcification, the anisotropic character seems to depend on the collagen. Thus, the strong contribution of collagen to the elastic properties in the small part of bone was confirmed.

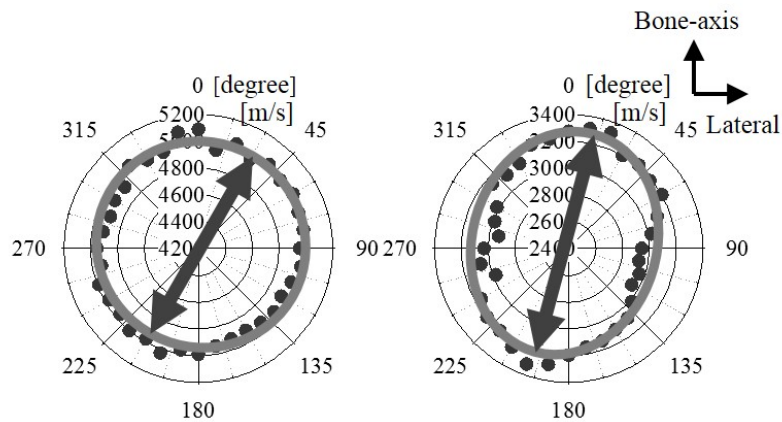


Fig. 1 Velocity anisotropy in the posterior cortical bone.  
(a) before decalcification, (b) after decalcification.



## 4J - Industrial Applications and Flow Sensing

Marquette

Saturday, September 6, 2014, 1:00 pm - 2:30 pm

Chair: **James Friend**  
 RMIT University

4J-1

### 1:00 pm Numerical Analysis of Transducer Installation Effect on Ultrasonic Gas Flowmeter

Longhui Qin<sup>1</sup>, Zhuoyuan Tang<sup>1</sup>, Liang Hu<sup>1</sup>, Xin Fu<sup>1</sup>; <sup>1</sup>State Key Laboratory of Fluid Power Transmission and Control, Zhejiang University, Hangzhou, China, People's Republic of

#### Background, Motivation and Objective

Ultrasonic flowmeter based on transit time difference has been widely used to measure gas flow rate. Special attention should be paid to transducer installation effect as the flow disturbed by the transducer will greatly affect the transit time determination and accordingly reduce metering accuracy. This paper presents a numerical method to analyze the disturb effects based on CFD, which can give valuable guides for transducer installations.

#### Statement of Contribution/Methods

Simulation based on finite-element method was implemented to determine the flow distribution and then calculate average axis velocity on the measuring path of the transducers. The relative error between the calculated velocities when transducer installed whether or not was defined to formulate the installation effect. Different conditions were computed: i) transducers were installed in recess or protrusion positions on different chords; ii) the upstream was configured as straight pipe with no bend, single bend or double bends out-of-plane; iii) the input velocity upstream varied from 0.1 m/s to 20 m/s.

#### Results/Discussion

Huge numbers of results were obtained by above numerical tests. Table 1 lists results when flow velocity is 10 m/s. Generally, the recess installation influences measurement accuracy more seriously. As we can find from the simulated flow field, the reason is negative velocity exists on the transducer top-side in recess installation while behind the transducers in protrusion installation. Suggestions about better transducer installations and a modified weighting factor method to improve the incredible error were also given in the paper.

Table 1. Transducer installation effects when flow velocity is 10 m/s

Pipe Config.	Chord	Stand. velocity (m/s)	Recess installation		Protrusion installation	
			Velocity (m/s)	Error (%)	Velocity (m/s)	Error (%)
No bend	1	8.65	6.12	-29.25	6.62	-23.47
	2	10.10	9.34	-7.53	10.53	4.26
	3	10.55	10.12	-4.08	10.92	3.51
	4	10.12	9.33	-7.81	10.53	4.05
	5	8.62	6.14	-28.77	6.65	-22.85
Single bend	1	7.57	6.83	-9.78	6.79	-10.30
	2	9.64	9.07	-5.91	9.95	3.22
	3	10.32	9.68	-6.20	10.25	-0.68
	4	10.25	9.33	-8.98	8.11	-20.88
	5	10.72	7.90	-26.31	10.29	-4.01
Double bend	1	9.91	7.34	-25.93	7.37	-25.63
	2	11.03	9.03	-18.13	9.91	-10.15
	3	9.67	9.76	0.93	10.42	7.76
	4	9.77	8.99	-7.98	8.76	-10.34
	5	9.04	7.34	-18.81	10.28	13.72

4J-2

### 1:15 pm A Discontinuous Galerkin Approach for the Numerical Simulation of Transit-Time Ultrasonic Flowmeters

Adrian Luca<sup>1,2</sup>, Régis Marchiano<sup>2</sup>, Jean-Camille Chassaing<sup>2</sup>, Julien Porté<sup>1</sup>; <sup>1</sup>Ultraflux, Éragny, France, <sup>2</sup>Institut Jean le Rond d'Alembert (UPMC-CNRS, UMR 7190), Paris, France

#### Background, Motivation and Objective

The most popular method used in ultrasonic flow measurement is based on the transit-time principle. This approach is robust, efficient and it can be employed without damaging the pipe or stopping the process. Nevertheless, accuracy issues may occur when dealing with low-pressure gas, high-velocity gas flow or highly-turbulent flows. The aim of this work is the development of a numerical solver able to simulate the propagation of ultrasonic waves inside such ultrasonic flow measurement systems.

#### Statement of Contribution/Methods

An ultrasonic flowmeter implies the propagation of high frequency ultrasonic waves on nearly one hundred wavelengths through multiple fluid/solid interfaces. The physical model of this problem is described by two sets of equations, the elastic wave equations (EWE) for the solid medium and the linearized Euler's equations (LEE) for the fluid medium, coupled at interfaces by continuity rules. The simulation of this model requires a numerical method which can take into account complex geometries and minimizes the numerical attenuation as well as the numerical dispersion. For this purpose, a discontinuous Galerkin (DG) formulation has been chosen. It is a high-order method, whose accuracy can be adjusted by changing the order of the polynomials used to approximate the solution. Another advantage of this method is that it can be massively parallelized. In the current work, most of the computational stages of the simulation code are done on GPU (Graphical Processing Unit).

#### Results/Discussion

In the first part of this work, we present the analytical validation of the simulation code. Several test cases are performed in order to validate the code for both separated and coupled fluid-solid media. The second part of this work is focused on the numerical simulation of an ultrasonic flowmeter in clamp-on configuration (Fig. 1) for different types of flow profiles. By processing the signals obtained during the simulation we find an accurate flow rate. Results show that solving the coupled EWE - LEE problem using a GPU based DG method leads to a powerful tool for the simulation of complex configurations in the domain of ultrasonic flow measurement.

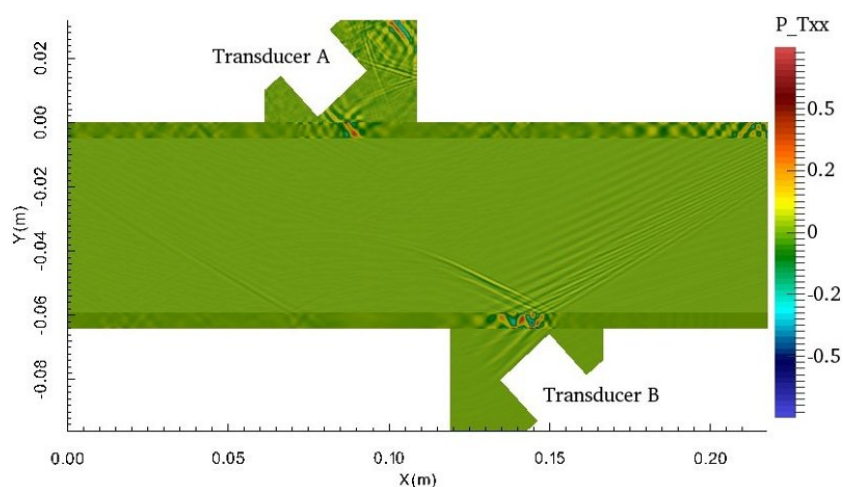


Fig. 1: Acoustic waves propagating from Transducer A to Transducer B into an ultrasonic flow measurement system in clamp-on configuration.

4J-3

### 1:30 pm Towards the Measurement of Local Particle Mass Fractions in Magnetite Suspensions

Jan Stener<sup>1</sup>, Johan E. Carlson<sup>2</sup>, Anders Sand<sup>1</sup>, Bertil Pålsson<sup>1</sup>; <sup>1</sup>Civil, Environmental and Natural Resources Engineering, Lulea University of Technology, Sweden, <sup>2</sup>Computer Science, Electrical and Space Engineering, Lulea University of Technology, Sweden

#### Background, Motivation and Objective

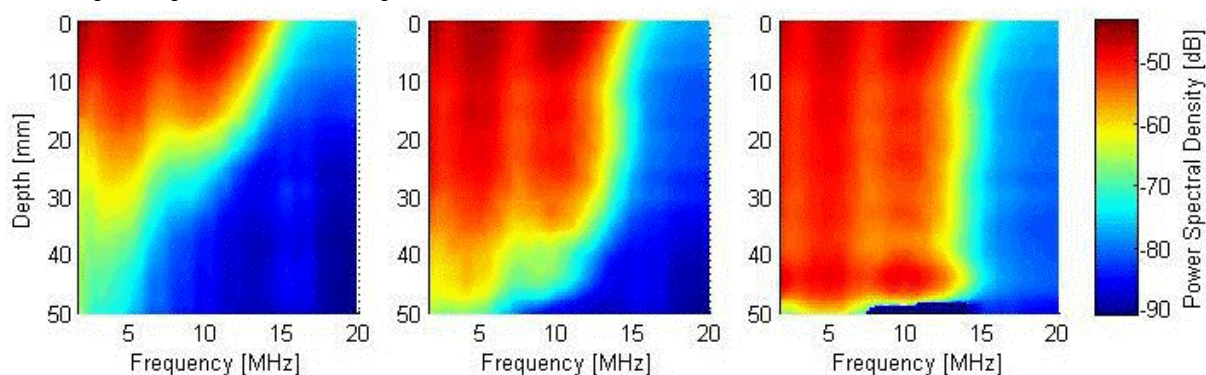
In the mining industry, magnetite particles are transported in suspensions with water through different stages of the process. In some of these stages, it is of interest to monitor both the concentration and particle velocity over a cross-section of the flow, e.g. in order to develop models for efficient control of the unit processes. High particle concentration makes development of flow measurement techniques challenging. An additional challenge is that the flow is often only accessible from one side, which limits the selection of applicable techniques even further. Previous work by the authors focused on using pulse-echo ultrasonic for flow velocity profile measurements. In the current work the same equipment is used to study local solids concentration variations, which is also highly interesting.

#### Statement of Contribution/Methods

Ultrasound pulses are transmitted into the suspension, and the resulting backscatter is treated as random signals carrying information about the suspension. The statistics of the signal vary with mass fraction, particle size distribution, particle density, etc. In this paper, it is shown that the Power Spectral Density (PSD) of the signal is significantly affected by the mass fraction solids. By implementing a short-time (windowed) PSD it is possible to study how the frequency information of the signal varies with depth through the suspension. As a proof of concept a sedimentation process is studied.

#### Results/Discussion

For demonstration, a magnetite suspension carrying 9 wt% particles (2 vol%, mean particle size 34  $\mu\text{m}$ ) is pumped through a closed rectangular channel. When the pump is stopped, pulse-echo ultrasound (with a center frequency of 5 MHz) is used to monitor the sedimentation process. Three snapshots of the sedimentation process are shown in the figure, with the start of the sedimentation to the left, and with a time of 3.7 s between the images. It is clear that the short-time PSD is a good indicator of local mass fraction variations. High local signal attenuation indicates high local solids concentration.



4J-4

### 1:45 pm Sonocrystallization under various frequencies and powers

Judy Lee<sup>1</sup>; <sup>1</sup>Chemical and Biomolecular Engineering, The University of Melbourne, Australia

#### Background, Motivation and Objective

Antisolvent crystallisation is a common and convenient method used by the pharmaceutical industry. However, this approach suffers from broad particle size distribution and variable nucleation rate. Ultrasound has shown to alleviate these problems, but the mechanism is still contentious. Most studies use 20 kHz ultrasonic horns, which suffers from

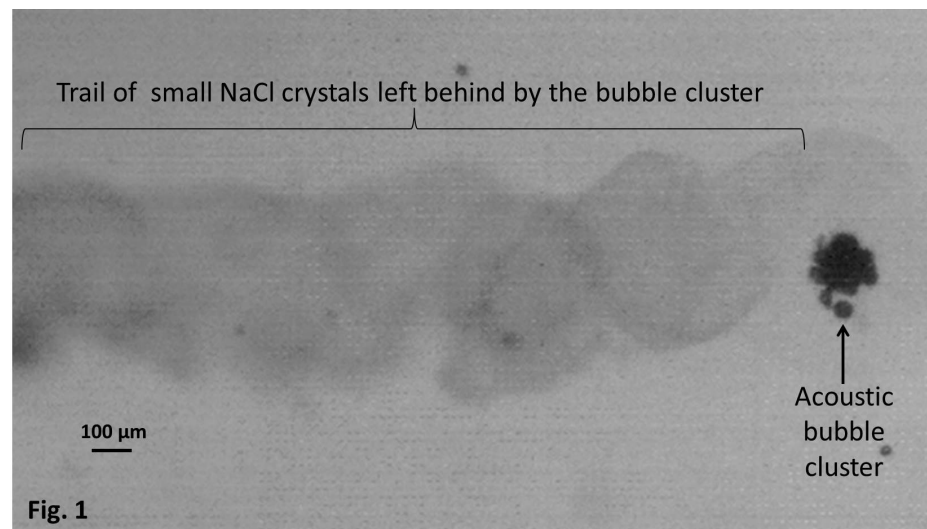
localised cavitation and surface erosion. Reports on the effect of high frequency plate transducers on crystallisation processes, which can offer broader spatial distribution of cavitation activity, are limited. This study aims to examine sonocrystallisation under different frequencies and powers, and model the data with classical nucleation theory.

#### Statement of Contribution/Methods

Crystallisation of sodium chloride (NaCl) in ethanol under frequencies 22 kHz - 1.08 MHz and various powers were conducted, and the crystal size produced measured. To determine the nucleation rate, induction time was measured by turbidity method. The data was fitted with the classical nucleation theory to obtain the additional energy from sonication. Images of sonocrystallisation were also captured.

#### Results/Discussion

The crystal size distribution under various frequencies and powers show an optimum frequency at 98 kHz, with a minimum crystal size of  $7.2 \pm 0.1 \mu\text{m}$  at a power of 8 W. For frequencies 647 kHz and 1 MHz, the power needs to overcome a threshold before any size reduction is observed. This threshold was found to coincide with the threshold for sonoluminescence. Fig. 1 shows a cluster of acoustic bubbles initiating sonocrystallisation by increasing nucleation time and hence decreasing induction time. This additional free energy was quantified and found to increase from  $1.20 \times 10^8 \text{ J/m}^3$  to  $1.74 \times 10^8 \text{ J/m}^3$  as the sonication power was increased from 2 W to 15 W.



4J-5

#### 2:00 pm Investigation on using two types of sonoreactors for Kraft lignin fractionation

Eric Loranger<sup>1</sup>, Guillaume Milot<sup>1</sup>, Claude Daneault<sup>1</sup>; <sup>1</sup>Lignocellulosic Materials Research Centre (CRML), Université du Québec à Trois-Rivières (UQTR), Trois-Rivières, Québec, Canada

#### Background, Motivation and Objective

As the traditional market of many pulp and paper industry is steadily declining, new products from wood are needed. Research with biomass from the forest is more and more oriented toward making energy (pyrolysis, gasification, etc.) or making new synthesis molecules that will enable more sustainable industries than those based on fossil fuel. Wood is mainly composed of cellulose, hemicellulose and lignin. As lignin is the second most abundant polymer on earth (cellulose is the first), many studies are oriented toward her utilisation. Lignin is rich in many carbon based polymer, phenolic groups, alcohol groups but the highly 3 dimensional structure prohibit easy usage of this material. In order to promote lignin usage, we are investigating fractionation through ultrasonic cavitation in the two flow-through sonoreactor developed by our research group. Thus the objective of this work is to study the ultrasound fractionation efficiency on Kraft lignin and to determine the best operation conditions.

#### Statement of Contribution/Methods

Kraft lignin was produced by precipitation with the addition of sulfuric acid in Kraft black liquor the properly dried. A small quantity was then re-solubilized in water at pH 12. The solution was then recirculated in one of the two sonoreactors developed by our research group. One sonoreactor is equipped with 2 banks of 12 transducers (2000 W) and is able to produce ultrasound at different frequency (40, 68 and 170 kHz). The other sonoreactor is limited at 1000W but various transducers configuration can be explored (face to face, orthogonal and star pattern) as he equipped of 4 banks of 3 transducers. The sonication time was kept at one hour and temperature controlled between 25 and 35°C. As all variables were explored, the impact of ultrasound on lignin was measured by FTIR spectroscopy on dried sample.

#### Results/Discussion

From the FTIR spectrum, we can easily show that ultrasound at all frequencies modify the chemical structure of the lignin. For a given power, more effect is shown at low (40 kHz) than high (170 kHz) frequency. These results are suggesting that mechanical cavitation is dominantly affecting lignin over the radical species produced at high frequency. As more power his applied, more effect is found. For the variable transducer configuration reactor, the star pattern is more efficient, thus reinforcing our hypothesis on mechanical cavitation. Ultrasound are able to modify the chemical structure of lignin and may potentially help reduced the molecular weight.

4J-6

#### 2:15 pm Ultrasonic welding of electronic parts and devices using a long and thin complex vibration welding tip

Jiromaru Tsujino<sup>1,2</sup>, Eiichi Sugimoto<sup>3</sup>; <sup>1</sup>Kanagawa University, Yokohama, Kanagawa, Japan, <sup>2</sup>Asahi EMS Co. Ltd, Yokohama, Kanagawa, Japan, <sup>3</sup>Asahi EMS Co. Ltd, Tokyo, Japan

#### Background, Motivation and Objective

Ultrasonic welding have been applied to join various fields including electronic parts and devices but could not been applied for deep and narrow parts positioned at long distance from the vibration system. Usually, electric resistance welding was used to weld such part, but there are possible defect caused by sparked metal particles radiated from welding position. To overcome the defect and make possible to join such deep area, ultrasonic complex vibration system using small diameter long welding tip were developed. Using

ultrasonic complex vibration with circular to elliptical vibration locus, required vibration amplitude, and static pressure decreased significantly due to inducing two-dimensional vibration stress compared with conventional linear vibration.

## Statement of Contribution/Methods

27 kHz and 19.5 kHz ultrasonic complex vibration systems using 2.0- and 3.0-mm-diameter, 75- to 120-mm-length welding tip were developed for joining deep and narrow welding part. Welding tip materials used were hard metal and tungsten rods which have large density and stiffness and are effective for reducing vibration attenuation along the welding tip. Node numbers required for hard metal welding tip are 5 to 6 and 6 to 7 for 19.5 kHz and 27 kHz 3.0-mm-diameter, 90-mm-length welding tip. The welding tip was installed a longitudinal to torsional complex vibration converter with diagonal slit part. Fig. 1 shows 19.5 kHz and 27 kHz ultrasonic complex vibration systems with 2.0- and 3.0-mm-diameter hard metal welding tips. Fig. 2 shows 19.5 kHz elliptical vibration locus. Fig. 3 shows welding condition of copper terminal. Transverse vibration distribution along a 27 kHz 3.0-mm-diameter, 82-mm-length welding tip is shown in Fig. 4. Node number along the tip is 5.

## Results/Discussion

Using developed 19.5 and 27 kHz ultrasonic complex vibration welding systems with 2.0- or 3.0-mm-diameter, 70- to 100-mm-length welding tips, various specimens including aluminum, copper, nickel coated copper electrode and terminal and steel or nickel coated steel which used for container of electronic part such as film capacitors were successfully welded with weld strength near to material strength. Weld strength of 0.5-mm-thick copper terminal was over 100 N using a 3.0-mm-diameter welding tip. The developed complex vibration systems will be effectively applied various electronic devices.

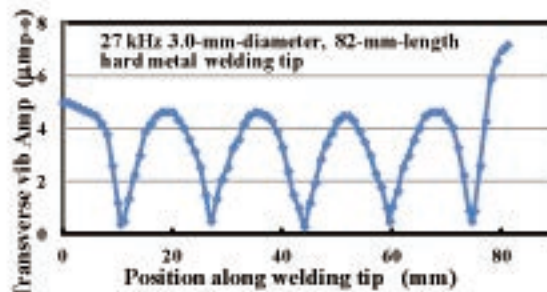
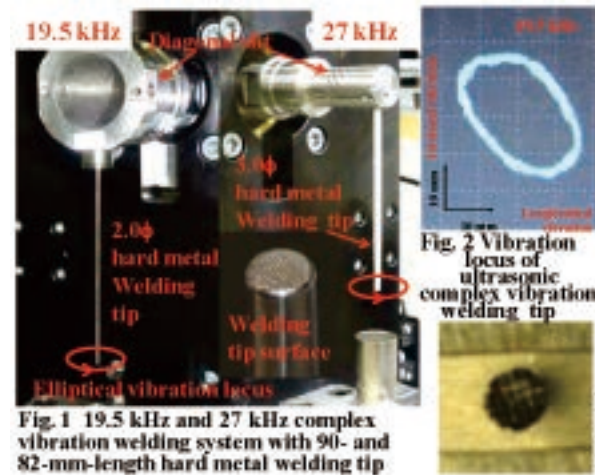


Fig. 3 Welded condition of 0.3-mm-thick nickel plated copper specimen using 2.0-mm-diameter welding tip



## 5J - Phononics 1

Williford A

Saturday, September 6, 2014, 1:00 pm - 2:30 pm

Chair: **Yan Pennec**  
IEMN / Université de Lille 1

5J-1

### 1:00 pm Monolithic surface phonon polariton phononic crystals

**Didit Yudistira**<sup>1</sup>, **Andreas Boes**<sup>1,2</sup>, **Bahram Rouhani**<sup>3</sup>, **Yan Pennec**<sup>3</sup>, **Leslie Yeo**<sup>4</sup>, **Arman Mitchell**<sup>1,2</sup>, **James Friend**<sup>4</sup>; <sup>1</sup>*School of Electrical and Computer Engineering, RMIT University, Melbourne, Victoria, Australia*, <sup>2</sup>*RC Centre of Excellence for Ultrahigh bandwidth Devices and Optical Systems, Australia*, <sup>3</sup>*Institut d'Electronique, de Micro electronique et de Nanotechnologie, UMR CNRS 8520, Villeneuve d'Ascq Cedex, France*, <sup>4</sup>*Micro/Nanophysics Research Laboratory, RMIT University, Melbourne, Melbourne, Victoria, Australia*

#### Background, Motivation and Objective

Recently, we have shown that an oriented surface acoustic wave (SAW) bandgap may be formed using one-dimensional (1D) periodic domain inversion through phonon polariton coupling between the electromagnetic wave and acoustic phonons. In contrast with previously demonstrated band gap structures formed using topographical modulation, the phonon-polariton band gap can be achieved by simply reversing the sign of the piezoelectric tensor without impacting the density and the elasticity. The existence of a SAW bandgap via the 1D periodic domain inversion suggests complete SAW bandgaps may exist in the 2D case in much the same way as conventional linear optical gratings have been extended to photonic crystals. In fact, 2D periodic domain inversion itself has been used in optics, where it is known as a 2D nonlinear photonic crystal, and useful for nonlinear frequency conversion applications. The presence of SAW phononic bandgap and the ability to perform nonlinear optical processes in one platform could open a pathway for exploration of entirely new phenomena in a nonlinear photon-phonon interaction. The structure is fully monolithic, is mechanically and electromagnetically homogenous and is topographically flat enabling direct access to the PC structure providing unique opportunities for emerging applications in optomechanical crystals and microfluidics.

#### Statement of Contribution/Methods

To investigate the existence of a SAW bandgap, we compute the surface acoustic band structure of an infinite periodic honeycomb lattice using finite element analysis (FEA). We fabricate the surface phonon polariton PC on 500- $\mu\text{m}$ -thick Z-cut lithium niobate using the electric field poling technique. The fabricated phononic crystal is subsequently characterized using a SAW delay line, a pair standard interdigital transducers with 20 finger pairs. We compare the measured and the calculated transmission for surface phonons propagating over the phonon polariton phononic crystals.

#### Results/Discussion

We have experimentally and theoretically shown what we believe to be the first demonstration of the existence of a complete SAW bandgap in a novel surface phonon polariton phononic crystals formed using a periodic arrangement of domain inversions on a Z-cut lithium niobate crystal. The bandgap is formed through the phonon polariton coupling that exists about twice the Bragg bandgap at the  $\Gamma$  point. The two most paramount advantages offered by the proposed phononic crystals are firstly that, it physically remains a uniform material, hence fully monolithic. Secondly, the structure can be easily formed through electrical poling, which has been significantly refined in the last decade owing to advances in the developments in novel photonic application. We thus envisage that these structures will enable a new generation of phononic crystal devices.

5J-2

### 1:15 pm Beam Path of Flexural Lamb Waves within Phononic Crystals-Based Acoustic Lenses

**Jinfeng Zhao**<sup>1</sup>, **Bernard Bonello**<sup>1</sup>, **Rémi Marchal**<sup>1</sup>, **Olga Boyko**<sup>1</sup>; <sup>1</sup>*INSP (box 840), University Pierre et Marie Curie, Paris, France*

#### Background, Motivation and Objective

In the gradient-index (GRIN) phononic crystals (PCs), the equal frequency contours (EFCs) of the constitutive PCs may slightly deviate from being circular, giving rise to the broadening of the focus area. In most of the works devoted to these systems so far, this anisotropy is overlooked and the GRIN PCs are generally supposed to have an effective index which reflects the anisotropy of the system only along the main directions in the first Brillouin zone. In contrast, in this work we have considered the anisotropy along any direction in the first Brillouin zone, and we have made an accurate analysis of the effects induced by the anisotropy of the EFCs.

#### Statement of Contribution/Methods

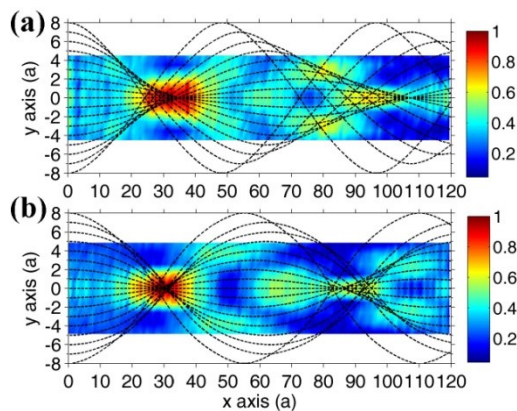
We have considered GRIN PCs formed by piercing air holes through a silicon plate. The refractive index is settled by modulating either the diameter of air holes or their spacing along the transverse direction. For both systems, a space dependent formula is proposed to fit the EFCs with an excellent accuracy within a broad frequency range. This allows in turn to calculate the wave number at any position within the GRIN PCs. Noticing that the tangent of ray trajectory is parallel to the direction of group velocity, each ray trajectory are then computed. Numerical simulations were performed using a finite element method. From the experimental side, we used a laser-based experimental setup to measure the normal displacement over a large area on the sample.

#### Results/Discussion

An excellent agreement between numerical simulations and experimental data is found. In addition, the ray trajectories derived from our model well explain the broadening at the focus (Fig. 1). We found the full width at half maximum at the first focus along y-axis to be respectively  $0.71\lambda$  and  $0.64\lambda$  in the system with variable holes diameter and in the system with variable spacing between the holes.

**Fig. 1.** Experimental maximum of the out-of-plane displacement  $u_z$  in a GRIN PC by modifying diameter (a) or spacing (b) of air holes. Dash lines are for the computed ray trajectories.





5J-3

### 1:30 pm Active control of a piezoelectric phononic crystal using electrical impedance

Sid Ali Mansoura<sup>1</sup>, Pierre Maréchal<sup>1</sup>, Bruno Morvan<sup>1</sup>, Anne-Christine Hladky-Hennion<sup>2</sup>, Bertrand Dubus<sup>2</sup>; <sup>1</sup>Laboratoire Ondes et Milieux Complexes, University of Le Havre, Le Havre, France, <sup>2</sup>Groupe Acoustique, IEMN Lille, Lille, France

#### Background, Motivation and Objective

Phononic crystals (PC) have a wide range of applications (wave guiding, acoustic isolation, frequency filtering...). These applications are however limited due to a lack of frequency tunability of the PC which is fixed by the geometrical and physical properties of the constituent elements of the PC. In this study we propose to include piezoelectric materials in PC in order to achieve an active control of the propagation of ultrasonic waves. Thus, not only the acoustic impedance contrast and the thickness to wavelength ratio allow to design the stop bands and pass bands in the dispersion curves, but also electric boundary conditions are a critical parameter. We want to analyse the effect of different types of electric boundary conditions (capacitance, inductance,...) connected to the active elements.

#### Statement of Contribution/Methods

We consider a one dimensional PC based on a stack of piezoelectric and passive layers. We assume that an electrical impedance load is connected to each piezoelectric layer. Using the fundamental equations of piezoelectricity, a theoretical model is proposed to calculate the electrical impedance of one layer within a finite PC. Only longitudinal waves propagation (thickness modes) through the PC is taken into account and the lateral dimensions of the plates are assumed to be much larger than their thickness. Experimentally, a finite periodic structure based on a Pz26/PMMA elementary stack is studied in the MHz frequency range. Different types of external electrical load (inductance, capacitance,...) are investigated.

#### Results/Discussion

The measure of the impedance across a range of frequencies shows some significant changes with respect to the nature of the electrical impedance load connected to the piezoelectric layers. The electrical impedance of an active layer depends on the position of the layer within the PC and is affected by the electrical boundary conditions. These changes can be related to changes in the band structure of the piezoelectric PC. Indeed the transmission through piezoelectric PC presents significant variation depending on the electric boundary conditions. For example, an inductive load leads to new stop bands or pass bands in the dispersion curves of the ultrasonic waves. Experimental and theoretical results are compared in good agreement.

5J-4

### 1:45 pm Interaction of surface acoustic waves with a monolayer of microspheres

Nicholas Boechler<sup>1,2</sup>, Jeffrey K. Eliason<sup>3</sup>, Anshuman Kumar<sup>1</sup>, Tian Gan<sup>1</sup>, Alexei A. Maznev<sup>3</sup>, Keith A. Nelson<sup>3</sup>, Nicholas Fang<sup>1</sup>; <sup>1</sup>Department of Mechanical Engineering, MIT, Cambridge, USA, <sup>2</sup>Department of Mechanical Engineering, University of Washington, Seattle, USA, <sup>3</sup>Department of Chemistry, MIT, Cambridge, USA

#### Background, Motivation and Objective

Interaction of propagating acoustic modes with local mechanical resonances is a rapidly developing area of research that recently yielded a new subfield described as “locally resonant metamaterials”. The interaction of surface acoustic waves (SAWs) with oscillators on the surface has been considered theoretically (see e.g. E. A. Garova et al., Phys. Rev. B 59 13291 (1999)), but has not been hitherto observed experimentally. In this work, we study the propagation of SAWs on a substrate covered with a monolayer of microspheres forming a two-dimensional “granular crystal”. A microsphere adhered to a substrate acts as a “mass-on-a-spring” oscillator, whereby the Hertzian elastic contact presents the spring. The stiffness of the contact and, consequently, the frequency of the contact resonance, is determined by the adhesion force pulling the microsphere towards the substrate. The objective of the study is to investigate the interaction of SAWs with the contact resonance of the microspheres (preliminary results have been reported in N. Boechler et al., Phys. Rev. Lett. 111, 036103 (2013)).

#### Statement of Contribution/Methods

Monolayers of 1  $\mu\text{m}$  and 500 nm silica microspheres were formed on glass substrates coated with a 200 nm thick aluminum layer by a convective self-assembly technique. A laser-based transient grating technique was used to generate and detect SAWs. The technique involves crossing two short optical pulses on the sample which interfere to create a sinusoidal interference pattern. Absorption of the laser light by the thin metal layer leads to a rapid thermal expansion, which launches counter-propagating SAWs with wavelength equal to the period of the interference pattern. The detection of SAWs was performed via diffraction of a probe laser beam. By changing the crossing angle we varied the acoustic wavelength from 7 to 50  $\mu\text{m}$ .

#### Results/Discussion

The measured SAW dispersion curves reveal “avoided crossing” behavior as a result of the hybridization of the contact resonance of the microspheres at a frequency of  $\sim 200\text{MHz}$  with the SAWs in the substrate. The measured dispersion is matched to an analytical model with the contact stiffness as the only fitting parameter. The measured contact resonance frequency is compared with estimates based on the Derjaguin-Muller-Toporov contact model. The effect of varying the particle size, substrate material and surface treatment will be discussed. The study opens the door for a new class of locally resonant metamaterials based on the contact resonance of microparticles, with potential applications ranging from studying adhesion and contact mechanics to linear and nonlinear SAW devices.

5J-5

**2:00 pm Ultrasonic Screening Based on the Interaction of Resonant Cavities**Aliyasir El Ayouch<sup>1</sup>, Mahmoud Addouche<sup>1</sup>, Philippe Lasaygues<sup>2</sup>, Abdelkrim Khelif<sup>1</sup>; <sup>1</sup>MN2S, Femto-ST, Besançon, France, <sup>2</sup>LMA, Marseille, France**Background, Motivation and Objective**

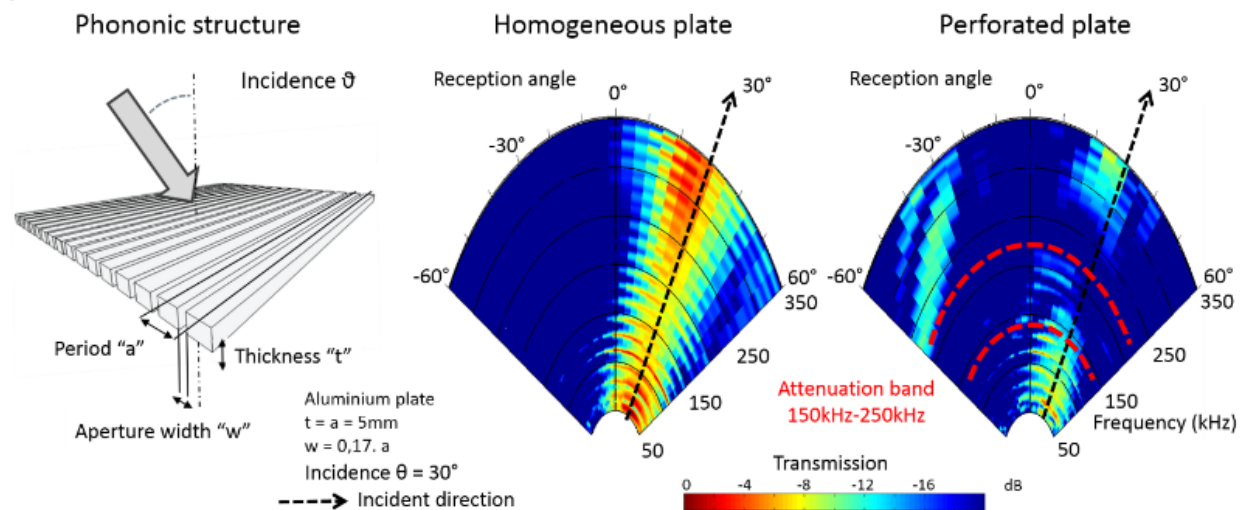
This study deals with the acoustic screening of a perforated phononic plate. Key to this screening is the use of local resonances, which can give the system the ability of blocking the propagation of an acoustic wave. Some recently designed structures with periodic distribution of local resonators have been developed to this purpose. They fall within the category of acoustical metamaterials that are artificial structures having unintuitive behaviors.

**Statement of Contribution/Methods**

This phononic plate is constituted of subwavelength slits array in an aluminium plate immersed in water. The slits array act as Fabry-Perot acoustic resonators that can interact with each other, mainly through the fluid-solid coupling. This can lead to an improved attenuation frequency band by generating resonances and antiresonances phenomena. We performed the experimental realization of this study by an omnidirectional transmission characterization. Indeed, this screening is studied from a directional point of view by changing the incident angle and considering the directional properties of the transmission. Finally, in order to reveal the mechanism that underpin such a behavior, we use the finite element method (FEM) to calculate the transmission spectra and represent the pressure field.

**Results/Discussion**

We show that fluid-solid interaction leads to resonances-antiresonances phenomena that can be mainly shifted by changing geometrical features. The confrontation of simulation results with the experimental measurements are in good accordance. Therefore, at normal incidence, the composition between these antiresonance frequencies permits to reach an attenuation of 20 dB, with a relative bandwidth of 15%, at a center frequency of 170 kHz. As can be seen in the figure, this attenuation is maintained at different incidence angles, until reaching a first order of diffraction. The frequency localization of the first diffraction order fits well with analytical calculation. The coupling between Fabry-Perot resonators permits to reach a better attenuation than the classical "mass law".



5J-6

**2:15 pm Airborne sound transmission loss analysis through acoustic metamaterial plate**MOURAD OUDICH<sup>1</sup>, Badreddine Assouar<sup>1</sup>, Xiaoming Zhou<sup>1</sup>; <sup>1</sup>Institut Jean Lamour, UMR CNRS 7198, University of Lorraine, Vandoeuvre-lès-Nancy, France, Metropolitan**Background, Motivation and Objective**

Acoustic metamaterials (AMM) are artificial composite structures which exhibit unusual physical properties for acoustic/elastic wave propagation [1]. These engineered materials are designed to perform anomalous behavior for wave propagation to seek some unique properties such as negative refraction. Many appealing applications were developed last decade to evidence the promising properties of such artificial materials such as: super-focusing, cloaking and low frequency sound mitigation [2,3]. In this work we report on the analysis of the airborne sound transmission loss (STL) through a thin metamaterial plate. We provide a complete theoretical study of the airborne STL and confronted it to the structure-borne dispersion of a metamaterial plate.

**Statement of Contribution/Methods**

We have developed a specific numerical method to investigate the STL performances of a plate-type acoustic metamaterial with an airborne sound excitation. The AMM is made of soft rubber stubs squarely arranged in a thin aluminum plate [4], and the STL is calculated at low frequency range [100Hz to 3kHz] for an incoming incident sound pressure wave. The approach is based on finite element method and gives the STL for all angles of incident waves impinging the metamaterial plate. This approach allows the assessment of the metamaterial performances in an environment close to the reality where acoustic waves come from different directions.

**Results/Discussion**

Numerical calculations were performed over different types of metamaterial plates (Fig. 1.a) for different incident angles. A typical example is presented in figure 1.b where the airborne STL is calculated for an oblique incident sound pressure (right panel) and compared to the band structure for structure-borne dispersion of the system (left panel). The increase of STL is evidenced around the resonant frequencies and a high value of about 90dB is found at 2kHz which also corresponds to the structure-borne gap for the out-of-plane modes of the metamaterial plate.

**References**

- [1] Z. Liu et al. Science 289, 1734 (2000)
- [2] K. Imamura et al. Phys. Rev. B 70, 174308 (2004)

[3] M. Farhat et al. Phys. Rev. Lett. 101, 134501 (2008)

[4] M. Oudich et al, New J. Phys. 12, 083049 (2010)

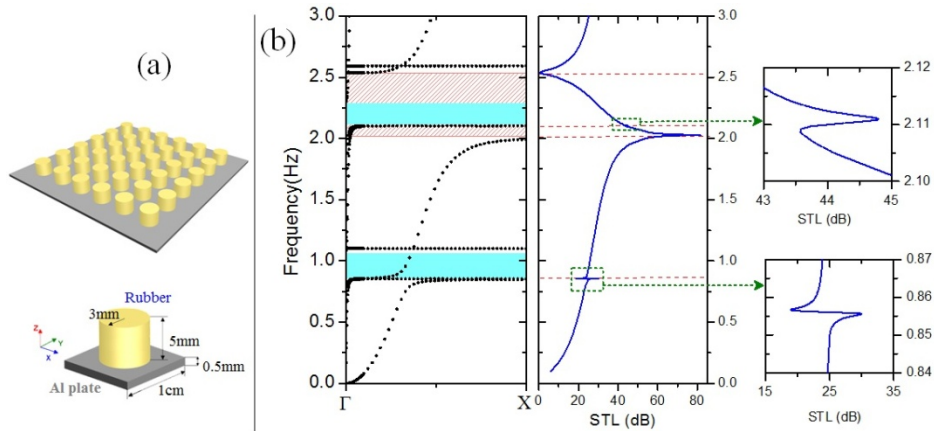


**Figure 1.** (a) AMM structure made of cylindrical rubber stubs on aluminum plate. (b) (left panel) Band structure of the stubbed AMM plate in  $\Gamma X$  where cyan colored and red dashed regions indicate gaps for the modes with dominant in-plane polarization and those with out-of plane dominant displacement respectively. (Right panels) Sound transmission loss for an 45° oblique incident wave through the AMM plate.

## 7J - Photoacoustics and Other Topics

Williford C

Saturday, September 6, 2014, 1:00 pm - 2:30 pm

Chair: **Jian Yuan**  
Philips Shanghai Apex

7J-1

### 1:00 pm Microsphere resonator for optoacoustic detection of high frequency ultrasound

Takashi Buma<sup>1</sup>; <sup>1</sup>ECE, Union College, Schenectady, NY, USA

#### Background, Motivation and Objective

Optical techniques offer a promising approach to realizing high frequency ultrasound imaging arrays. Exceptional pressure sensitivity has been demonstrated with high Q-factor optical resonators, such as polymer microring devices. However, excessive bend loss restricts the microring diameter to roughly 50  $\mu\text{m}$  or larger. This poses a problem for high frequency array applications.

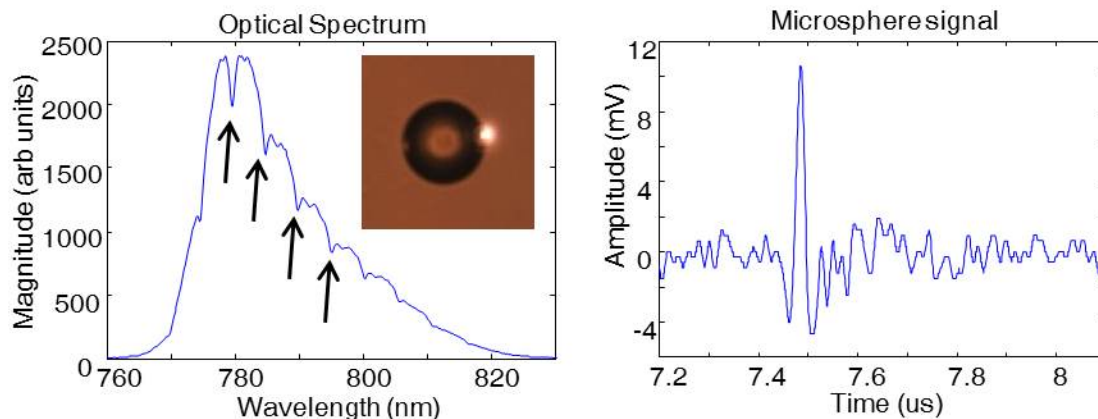
We are exploring an alternative optoacoustic sensor based on a microsphere resonator. Optical whispering gallery modes (WGMs) circulate within the microsphere surface via total internal reflection. Q-factors over 10,000 are possible with microspheres less than 50  $\mu\text{m}$  in diameter.

#### Statement of Contribution/Methods

For proof of concept, we use a prism coupling technique to excite WGM resonances in a 25  $\mu\text{m}$  diameter polystyrene microsphere. The microsphere is placed on the surface of an equilateral prism made from a UV-curable polyurethane. The microsphere was encapsulated within an approximately 50  $\mu\text{m}$  cured layer of polydimethylsiloxane (PDMS). Light is focused into the prism with a 10X 0.25 NA microscope objective. The incident angle is approximately 70 degrees in order to excite WGM resonances. Ultrasound excitation is provided by a 25 MHz unfocused transducer with ultrasound coupling gel. The light reflected from the prism-microsphere interface is detected with a silicon avalanche photodiode and digitized (64 averages) with a 200 MHz 8-bit digital oscilloscope.

#### Results/Discussion

The attached figure shows an optical micrograph of the 25  $\mu\text{m}$  diameter microsphere supporting a WGM resonance. As expected for a 25  $\mu\text{m}$  diameter polystyrene microsphere, the optical resonance dips are separated by approximately 5 nm. The Q-factor is about 800. Optoacoustic performance was evaluated by illuminating the microsphere with a temperature controlled Fabry-Perot AlGaAs diode laser tuned to a wavelength of 780 nm. The optoacoustic data has a peak frequency of 22 MHz and -6 dB bandwidth of 15 MHz. Based on single-shot measurements, the noise equivalent pressure (NEP) of the microsphere detector is 15 kPa over a 50 MHz bandwidth. The Q-factor of our microsphere resonator can be improved by at least an order of magnitude by optimizing the separation between the microsphere and coupling prism. We believe these encouraging results suggest the potential of microsphere resonators for optoacoustic detection.



7J-2

### 1:15 pm Piezoelectric Micromachined Ultrasound Array Transducer with 31 Channels for Photoacoustic Imaging

Hongmin Ahn<sup>1</sup>, Kyoungun Been<sup>1</sup>, Min Sung<sup>1</sup>, Wonkyu Moon<sup>1</sup>; <sup>1</sup>Mechanical Engineering, POSTECH, Pohang, Gyeongsangbuk, Korea, Republic of

#### Background, Motivation and Objective

Photoacoustic imaging (PAI) is a non-invasive medical imaging technique that has been studied by many groups because of its inherent advantages. Not only does PAI have highly scalable spatial resolution, but it can also overcome the penetration depth limits of optical imaging. Furthermore, PAI can provide functional imaging due to its optical absorption contrast. While various studies have examined PAI, fewer have examined the transducers for PAI systems, despite the fact that they are an important component. Therefore, we studied a transducer for it.

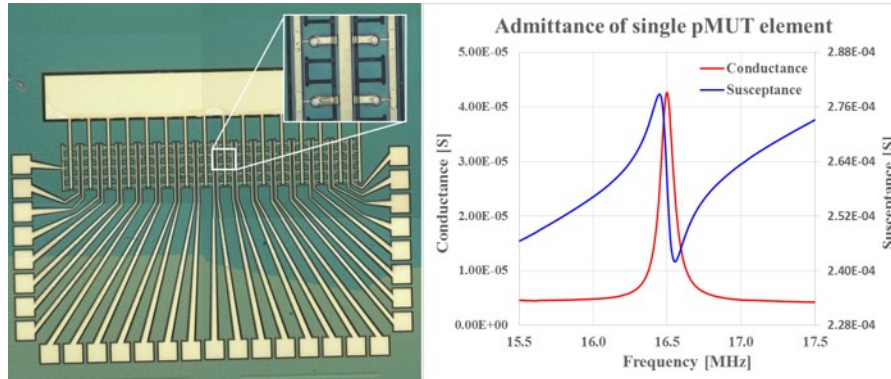
A piezoelectric micromachined ultrasound transducer (pMUT) was selected as the PAI transducer. pMUTs are useful in arrays, and the design can be optimized to alter the receiving sensitivity and power efficiency. Therefore, the use of pMUTs has been considered for transducer arrays in medical ultrasonic imaging systems. However, pMUT arrays for medical imaging have limits in terms of bandwidth, directivity, and receiving sensitivity. The design and fabrication of a pMUT array that can overcome these limits is presented here.

# Statement of Contribution/Methods

A pMUT array was designed for PAI using a lumped parameter model (LPM). Many PAI systems have been applied in water because of the improved impedance matching. Consequently, each element of the pMUT array was designed to have a resonant frequency of 10 MHz in water (16.8 MHz in air). The pMUT array was also designed to have 31 channels considering a beam formation with wide bandwidths. A pMUT array including 155 elements ( $5 \times 31$  array) was bulk micromachined in silicon substrate. The LPM of the pMUT was compared with the commercial FEM package COMSOL Multiphysics. The admittance and surface displacement of the fabricated pMUT were measured.

# Results/Discussion

The admittance of a single pMUT element measured using an impedance analyzer revealed that the resonant frequency was about 16.5 MHz in air, which was close to the value of the LPM (16.8 MHz). However, the surface displacement of the pMUT elements measured using a laser vibrometer showed that the resonant frequency was in the range 15.5–18.5 MHz, depending on the region. It might be attributable to uniformity problems in the micromachining process. This is a problem that must be resolved to achieve high-quality PAI. However, the experimental results demonstrated the potential of a pMUT array for an array probe in a PAI system.



7J-3

# 1:30 pm Waveguide optical micromachined ultrasound transducer (WOMUT) for high frequency ultrasound detection

Mohammad Amin Tadayon<sup>1</sup>, Martha-Elizabeth Baylor<sup>2</sup>, Shai Ashkenazi<sup>1</sup>; <sup>1</sup>Biomedical Engineering, University of Minnesota, Minneapolis, Minnesota, USA, <sup>2</sup>Physics and Astronomy, Carleton College, Northfield, Minnesota, USA

# Background, Motivation and Objective

Piezoelectric ultrasound transduction is currently the leading technology in imaging devices. However, it falls short in meeting the size, frequency, and sensitivity requirements for high resolution, high-frequency imaging devices. Optical sensing and generation of ultrasound has been proposed and studied as an alternative technology for implementing sub-millimeter size arrays with element size down to 10  $\mu\text{m}$ .

# Statement of Contribution/Methods

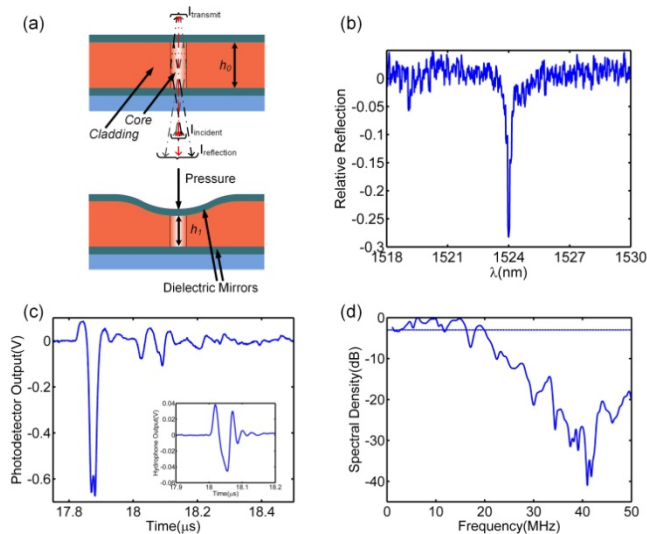
Here, we introduce a new method to increase the sensitivity of an optical ultrasound receiver by utilizing a waveguide between the mirrors of the Fabry-Perot resonator. This approach eliminates diffraction loss from the cavity and therefore the finesse is only limited by mirror loss and absorption. Recently, we have reported our measurements of high finesse (695) and quality factor (59000) in a waveguide Fabry-Perot film resonator of 100  $\mu\text{m}$  thickness. Here we describe the implementation of this method for the design of a thin film ultrasound detector.

# Results/Discussion

By applying this method (Fig. a), we have achieved noise equivalent pressure of 178 Pa over a bandwidth of 30 MHz or 0.03 Pa/ $\sqrt{\text{Hz}}$  which is 20 folds better than the sensitivity of our previous non-waveguide detector. The relative reflected light intensity is recorded using an optical power meter and the results are presented in Fig. b. The finesse of the waveguide Fabry-Perot resonator is approximately 200 which is about 5 times higher than the measured non-waveguide area on the same wafer. The free spectral range of this device is about 31 nm.

The response of the device (Fig. c) shows an initial oscillation that is of high-amplitude with short-period, followed by a smaller amplitude oscillation. The former can be attributed to the direct arrival of a pressure pulse from the transducer. The oscillation following the main dip in the received signal is due to the back reflection from the bottom side of 500  $\mu\text{m}$  Borofloat wafer (reflection traveling time = 183 ns, corresponding frequency = 5.46 MHz). The main signal consists of two minima separated 12 ns from each other. This signal shape can be due to the internal reflection of the ultrasound pulse in the cavity. The frequency spectrum of the recorded signal from the photodetector is presented in Fig. d.





7J-4

#### 1:45 pm Development of a High Temperature Transducer Backing Element with Porous Ceramics

Mohammad Hossein Amini<sup>1</sup>, Thomas Coyle<sup>2</sup>, Anthony Sinclair<sup>1</sup>; <sup>1</sup>Mechanical & Industrial Dept, University of Toronto, Toronto, Outside US, Canada, <sup>2</sup>Material Science and Engineering Department, University of Toronto, Toronto, Outside US, Canada

##### Background, Motivation and Objective

An ultrasonic transducer's backing element is made of an acoustically attenuative material that dampens the vibration of the piezoelement. This broadens the bandwidth of the signal and improves the timing resolution of echo pulses. Epoxy-based backing materials are favored for room-temperature testing conditions, but will degrade at temperatures of the order of 200-300 °C. We present a new application of porous ceramics as a thermally stable backing element. Acoustic impedance and attenuation of the porous medium can be tailored for compatibility with a specific high-temperature piezoelectric element, through control of the fractional porosity and pore size.

##### Statement of Contribution/Methods

X-cut gallium phosphate (GaPO<sub>4</sub>) was selected as the piezoelectric element for a 3 MHz high-temperature transducer with a 3dB bandwidth of 95-100%; piezoelectric properties of GaPO<sub>4</sub> are stable up to 970°C. An optimized value of acoustic impedance of 11-13 MRayls for the backing element was estimated using a KLM transducer model, to yield the required bandwidth. To minimize any spurious pulses in the transmitted signal, a minimum attenuation coefficient of ~1dB/mm is required.

The ceramic backing material was a silicate mineral ceramic known as mullite. The proximity of the thermal expansion coefficients of mullite and GaPO<sub>4</sub> will help to minimize interfacial thermal stresses during temperature cycling of the transducer. To model the wave propagation in porous media with a random set of spherical voids, we followed the Effective Field Method work of Kanaun et al. The resulting dispersion equation is applicable at all pore radius-to-wavelength ratios, and a wide range of volume fraction of inclusions. This model showed that a porosity of 25% with pore radius of 200 μm would yield the desired ultrasonic properties.

To generate pores in a ceramic matrix, mullite powder was mixed with polyethylene (PE) polymer microspheres as the pore forming agent. The powder was then isostatically pressed and sintered. The polymer particles are burned out during the sintering process, leaving behind closed (i.e. unconnected) pores.

##### Results/Discussion

Various mullite samples with a range of porosities and pore sizes were manufactured and evaluated, to confirm the predicted ultrasonic attenuation and impedance results. Immersion ultrasonic testing was used to measure the acoustic impedance and attenuation of the porous samples. Test results confirmed the model predictions that 25% porosity with pore radius of 100μm yields the required ultrasonic properties.

The design procedure can be employed in designing the backing element for ultrasonic transducers covering a wide range of frequencies and bandwidths; a one-dimensional model of the system was found to be an adequate guide to selecting the optimal porosity and pore size in the design process.

7J-5

#### 2:00 pm Design and prototyping of dual layer linear arrays

Tung Manh<sup>1</sup>, Lars Hoff<sup>1</sup>, Tonni F. Johansen<sup>2,3</sup>; <sup>1</sup>Department of Micro and Nano Systems Technology, Buskerud and Vestfold University College, Norway, <sup>2</sup>Department of Circulation and Medical Imaging, Norwegian University of Science and Technology, Norway, <sup>3</sup>Department of Acoustics, SINTEF ICT, Norway

##### Background, Motivation and Objective

A wide bandwidth, flexible transducer that can operate at different frequency bands is a strong desire for a variety of applications, such as harmonic imaging or imaging in different frequency bands and at different depth ranges. A multiplexing configuration where a dual layer transducer has one piezocomposite layer on top of the other is a tempting solution. Electrical excitation can be applied to the back layer alone to excite the high frequency (HF) band, whereas both piezocomposite layers can be electrically connected in parallel to perform imaging in the low frequency (LF) band. Single element transducers with two stacked piezoelectric composite layers have been studied previously [1]. In this work we study linear arrays with stacked piezocomposite layers, both by simulations and by fabricating and characterizing real arrays.

##### Statement of Contribution/Methods

The arrays were designed with 300 μm element pitch and 60 μm kerf width. The active layers were 2-2 connectivity composites, containing 60% PZT filled with Spurr's epoxy, having acoustic impedance 17.6 MRayl. Two acoustic matching layers were added, the inner layer is a 2-2 composite with acoustic impedance 6.9 MRayl and the outer is an epoxy with acoustic impedance 2.4 MRayl. Light backing with acoustic impedance 6.5 MRayl was used. Two matching strategies were tested: An LF version when the two active layers worked in parallel, at centre frequency 2.5 MHz, and an HF version when using only the rear active layer, at centre frequency 5 MHz. A one dimensional Mason model and COMSOL simulations were used to model the performance of the arrays. Prototypes of both the LF and HF versions of the dual transducer arrays were fabricated and tested by measuring electrical impedance and acoustic pulse-echo. The measured results were compared with the simulations.

# Results/Discussion

Electrical impedances measured on the fabricated arrays show fair agreement with the simulations. However, the measured phases of the electrical impedance indicate higher attenuation in the fundamental frequency band and lower loss in the third harmonic band. Acoustic pulse-echo measurements on the LF version transducers showed that the width of the fundamental passband is in accordance with the simulations, though the measured sensitivity is about 5 dB below the simulated one. The measured sensitivity at the third harmonic band is about 8 dB higher than predicted from the simulations. The differences can be attributed to the lack of good attenuation parameters and imperfections in the fabrication process. However, the measured results demonstrate the feasibility of fabricating versatile arrays based on this stacked dual active layer configuration.

# References

[1] J. A. Hossack and B. A. Auld, "Improving the characteristics of a transducer using multiple piezoelectric layers," *Ultrasonics, Ferroelectrics and Frequency Control*, IEEE Transactions on, vol. 40, pp. 131-139, 1993.

7J-6

## 2:15 pm Sol-Gel Composite Film Fabrication by Paint Stencil Printing

Tsukasa Kaneko<sup>1</sup>, Kazuki Iwata<sup>1</sup>, Makiko Kobayashi<sup>1</sup>; <sup>1</sup>Kumamoto University, Japan

# Background, Motivation and Objective

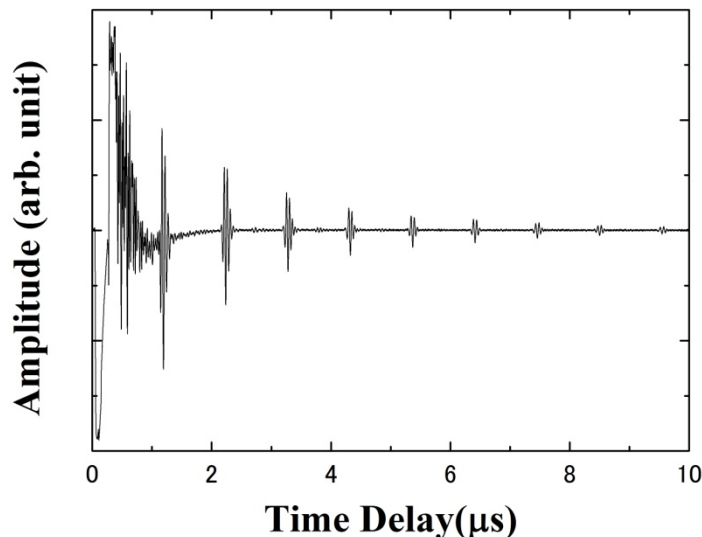
Sol-gel composite films were found to be suitable for industrial ultrasonic transducer applications because of high temperature durability, no necessity of couplant nor backing materials, and curved surface applicability and industrial realization could be accelerated if fabrication cost became lower. Sol-gel composite film fabrication required at least two fabrication process; coating and heating. Spray coating and spin coating was mainly used for sol-gel composite film fabrication coating process, though coating process and heating process must be repeated until desired thickness to obtain operation frequency was achieved. If thickness limitation by one coating process increased, fabrication time could be reduced so that it would be more suitable for industrial applications.

# Statement of Contribution/Methods

It was expected that thickness limitation could be enlarged when paint stencil printing was used. Stencil printing was similar coating process to screen printing using stencil mask and squeegee except for mesh was also required for screen printing. Since suitable viscosity for paint stencil printing was higher than those of spray coating and spin coating so that sol-gel solution could be more condensed. As a result, internal stress during heating process would be reduced and then crack possibility of sol-gel composite films would be suppressed by stencil printing.

# Results/Discussion

Several sol-gel composite films such as lead zirconate titanate (PZT)/PZT, bismuth titanate (BiT)/PZT and lead titanate (PT)/PZT were fabricated onto flat and curved surfaces by stencil printing. Over 100µm thick films were successfully fabricated by one coating process so that total fabrication time could be drastically reduced. Ultrasonic performance was comparable with those by spray coating. BiT/PZT films were integrated onto a steel pipe with around 40mm diameter. Those films showed and reasonable signal strength and signal to noise ratio after three time thermal cycle as shown in Fig. 1 so that it was expected to have high enough adhesion strength with the substrate. On-site fabrication without furnace was also tried using dryer and gas torch and that sample also demonstrated comparable ultrasonic performance.



# 1K - MEL: Liver Elasticity Imaging

Grand Ballroom

Saturday, September 6, 2014, 3:30 pm - 5:00 pm

Chair: **Hairong Zheng**  
*Shenzhen Institutes of Advanced Technology, Shenzhen*

1K-1

## 3:30 pm Liver Elasticity Imaging Using External Vibration Multi-directional Ultrasound Shearwave Elastography (EVMUSE)

Heng Zhao<sup>1</sup>, Pengfei Song<sup>1</sup>, Duane D. Meixner<sup>2</sup>, Randall R. Kinnick<sup>1</sup>, Matthew R. Callstrom<sup>2</sup>, William Sanchez<sup>2</sup>, Matthew W. Urban<sup>1</sup>, Armando Manduca<sup>1</sup>, James F. Greenleaf<sup>4</sup>, Shigao Chen<sup>1</sup>;  
<sup>1</sup>Physiology & Biomedical Engineering, Mayo Clinic College of Medicine, USA, <sup>2</sup>Radiology, Mayo Clinic College of Medicine, USA, <sup>3</sup>Gastroenterology & Hepatology, Mayo Clinic College of Medicine, USA

### Background, Motivation and Objective

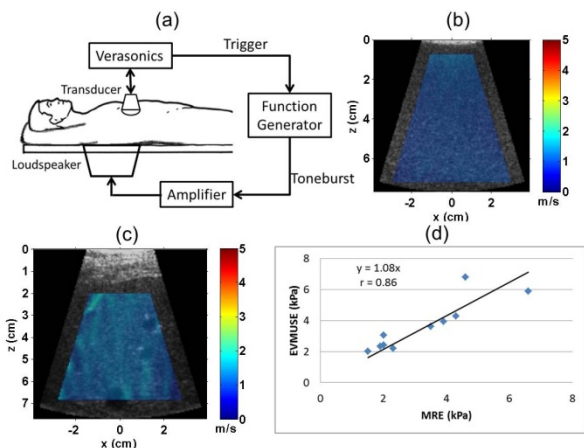
Shear wave speed ( $c_s$ ) can be used to assess tissue elasticity, which is associated with tissue health. Ultrasound shear wave elastography techniques based on measuring the  $c_s$  of the shear waves induced by acoustic radiation force are becoming promising alternatives to biopsy in liver fibrosis staging. However, shear waves generated by such methods are typically very weak. Therefore, penetration may become problematic, especially for overweight or obese patients. To improve penetration, we present a new method called External Vibration Multi-directional Ultrasound Shearwave Elastography (EVMUSE) for liver elasticity imaging.

### Statement of Contribution/Methods

External vibration from a loudspeaker was used to generate a multi-directional shear wave field. A directional filter was then applied to separate the complex shear wave field into 8 shear wave fields propagating in 8 different directions. A two-dimensional (2D)  $c_s$  map was reconstructed from each of the 8 shear wave fields based on 1D cross-correlation in  $x$  and  $z$ , and spatial weighted averaging. By compounding these individual  $c_s$  maps based on the shear wave energy, a final 2D  $c_s$  map was constructed. The method was validated using two homogeneous tissue-mimicking phantoms calibrated by Supersonic Imagine (SSI) Aixplorer. Ten patients undergoing liver Magnetic Resonance Elastography (MRE) were also studied with EVMUSE to compare results between the two methods.

### Results/Discussion

Five EVMUSE measurements were taken for each phantom at 5 random locations. The measured  $c_s$  averaged over 5 measurements were  $1.18 \pm 0.04$  m/s and  $2.08 \pm 0.05$  m/s for Phantom 1 and 2, respectively, compared to  $1.18 \pm 0.01$  m/s and  $2.04 \pm 0.01$  m/s, respectively from the same measurements using the SSI. For the patient study, 15 measurements were taken for each patient through 3 different intercostal spaces, and a median value was calculated from liver regions down to 7 cm deep for each patient. To compare with MRE,  $c_s$  results of EVMUSE were converted to shear modulus, and the Pearson product-moment correlation coefficient between MRE and EVMUSE results was 0.86 (95% confidence interval: 0.71-0.98) with  $p < 0.001$ , indicating the correlation was significant. Phantom and *in vivo* results indicate EVMUSE has the potential of non-invasive staging of liver fibrosis in obese patients.



(a) Illustration of the experimental setup; (b) EVMUSE result from a homogeneous phantom. The measured  $c_s$  using EVMUSE was  $1.18 \pm 0.04$  m/s as compared to  $1.18 \pm 0.01$  m/s using SSI; (c) Representative EVMUSE result from a patient ( $1.48 \pm 0.07$  m/s within the colored image region); (d) Correlation between EVMUSE and MRE.

1K-2

## 3:45 pm A new portable probe for real-time ultrasound elastic tensor imaging in fibrous tissues

Simon Chatelin<sup>1</sup>, Mafalda Correia<sup>1</sup>, Jean-Luc Gennisson<sup>1</sup>, Mickael Tanter<sup>1</sup>, Mathieu Pernot<sup>1</sup>; <sup>1</sup>Institut Langevin - ESPCI ParisTech, INSERM Paris U979 - CNRS UMR 7587, Paris, France

### Background, Motivation and Objective

Non-invasive real-time evaluation of viscoelastic properties with supersonic shear wave imaging (SSI) [1] remains a big challenge in fibrous tissues such as skeletal muscles, brain or myocardium. Their anisotropic structure induces a dependence of the shear wave speed with fibers orientation. We introduced the Ultrasound Elastic Tensor Imaging technique [2] that can derive the complete elastic tensor from several SSI acquisitions (as low as 5) performed at different probe orientations. However, this method could not be used in real-time because the probe was rotated mechanically. The aim of this study is to develop a novel tool dedicated to fibrous tissue measurement by local real-time evaluation of the anisotropic stiffness tensor in unique acquisition.

# Statement of Contribution/Methods

A 9 elements transducer was designed to generate remotely a shear wave using the acoustic radiation force and simultaneously probe the displacement field induced along 8 different directions. This design was validated using a combined 3D numerical simulation of the ultrasound field and of the shear wave propagation. The numerical simulation of the shear wave propagation in anisotropic medium was implemented based on the 3D transverse isotropic (TI) viscoelastic Green's formalism. The transducer was built and experimentally validated. 8 channels transmit-receive programmable electronics was used to acquire the shear wave propagation at high frame rate (8.8 kHz) simultaneously along the 8 directions of propagation. This approach is evaluated on a TI hydrogel, in vivo biceps and cardiac left ventricle wall.

# Results/Discussion

The numerical simulations demonstrated the possibility to measure the displacement field simultaneously along 8 different directions of shear wave propagation and to derive the complete elastic tensor with no a priori knowledge on the fiber orientation (A). The transducer was successfully validated on a TI hydrogel with known elastic constants (1.9 to 3.3 m/s). The same measurement was performed successfully using a single acquisition in vivo on skeletal muscles and on the myocardium in end-diastole (B). Fiber orientation, transverse ( $0.9 \pm 0.1$  m/s) and parallel ( $1.6 \pm 0.2$  m/s) shear modulus were derived at each depth. This new probe allows quantifying the elastic properties of the myocardium and shows potential for the early diagnosis of cardiomyopathies.

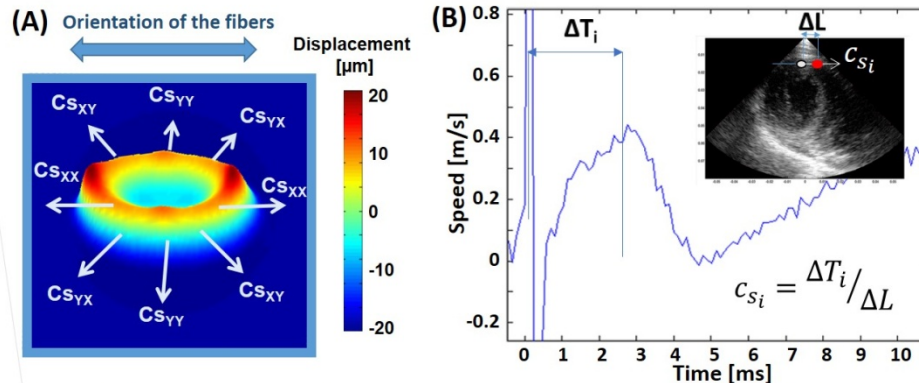


**Figure.** (A): Numerical simulation of shear wave propagation in fibrous tissue; (B) Local displacement of the cardiac tissue measured *in vivo* for an *i*-direction. The  $\Delta t_i$  delay from the push to the focalized region gives an estimation of the shear wave speed  $c_{si}$  for this direction.

[1] Bercoff *et al.*, IEEE UFFC, 2004 [2] Lee *et al.*, Physics in Medicine and Biology, 2012

1K-3

# 4:00 pm Detection of Steatosis through Shear Speed Dispersion

Christopher Barry<sup>1</sup>, Christopher Hazard<sup>2</sup>, Gang Cheng<sup>3</sup>, Zaeyoo Hah<sup>4</sup>, Kuang-Hsiang Chuang<sup>1</sup>, Alexander Partin<sup>1</sup>, Robert Mooney<sup>5</sup>, Wenqing Cao<sup>5</sup>, Deborah Rubens<sup>6</sup>, Kevin Parker<sup>4</sup>, <sup>1</sup>Surgery, University of Rochester Medical Center, USA, <sup>2</sup>GE Global Research, USA, <sup>3</sup>GE Global Research, China, People's Republic of, <sup>4</sup>Electrical & Computer Engineering, University of Rochester, Rochester, New York, USA, <sup>5</sup>Pathology & Laboratory Medicine, University of Rochester Medical Center, USA, <sup>6</sup>Radiology, University of Rochester Medical Center, USA

# Background, Motivation and Objective

We aim at detecting early stage liver steatosis by measuring shear speed dispersion over the frequency range of 60 – 260 Hz. Lean and early-stage steatotic rat livers were chosen for the preliminary experiments.

# Statement of Contribution/Methods

Five Zucker Diabetic Fatty (ZDF-*Lep<sup>fa/fa</sup>*) rats and 5 lean ZDF (ZDF-*Lep<sup>+/+</sup>*) controls were chosen for the experiments. For *ex vivo* studies, histologic examination of percentage hepatic steatosis was performed by a single, experienced pathologist using H & E stained tissue sections. Triglyceride (TG, a representative of fat concentration) assay was performed and reported as mg TG/mg liver. The rest of the liver was suspended in a gelatin phantom for CrW (crawling wave) scanning.

The liver-gelatin phantom was studied at  $17.5 \pm 1^\circ\text{C}$  with GE LOGIQ E9 system which was modified for this experiment. The measurements were performed at least at 6 shear wave frequencies in the range of 60 – 260 Hz. The acquired data were further analyzed to extract shear speed values at each frequencies and the linear regression produced the speed dispersion.

# Results/Discussion

Triglyceride levels for the lean rat livers showed below 5 mgTG/g liver while fat livers showed 16 – 25 mgTG/g liver. Histologic exam showed no macrosteatosis and 0-5% microsteatosis in the lean group and 5-20% microsteatosis in the fatty liver group. Crawling wave analysis showed noticeable difference between the lean and the fat groups. The group analysis produced the speed dispersion of  $1.1 \times 10^{-4}$  m/s/Hz with 95% confidence level ( $-1.4 \times 10^{-3}$ ,  $1.6 \times 10^{-3}$ ) for lean group and  $3.3 \times 10^{-3}$  ( $1.6 \times 10^{-3}$ ,  $4.8 \times 10^{-3}$ ) for fat group, respectively. The shear wave speed at 150 Hz was found to be 3.24 (3.14, 3.34) m/s for lean and 3.18 (3.09, 3.28) m/s for fat groups, respectively.

The group analysis results between the lean and fat group is promising and indicate the feasibility of using the shear speed dispersion for the detection of early stage steatosis. Future study will include increasing the numbers of test livers, the fine gradation of steatosis, and conducting *in vivo* experiments.

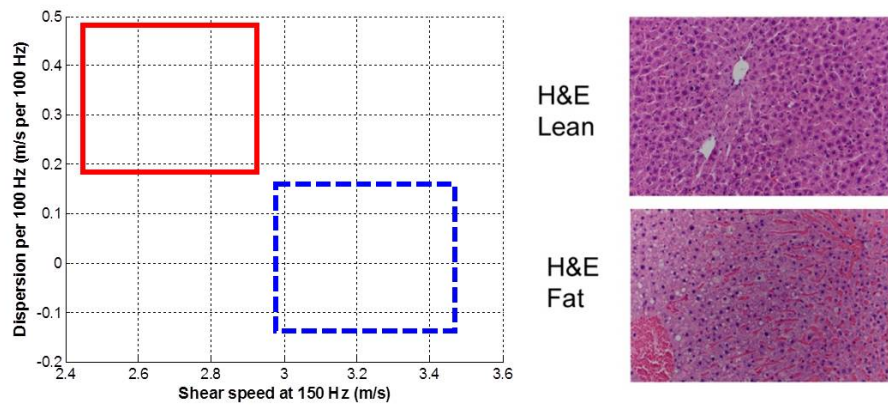


Figure 1: Left: Group analysis of 5 obese rat livers with average 5% macrosteatosis and 14% microsteatosis (red, solid) and 5 lean controls (blue, dashed). Increased dispersion and decreased shear speed is demonstrated in the fatty liver rats. Right: Shows representative histology.

1K-4

#### 4:15 pm Use of a Radon-like summation algorithm to estimate viscoelastic model parameters from shear wave propagation following impulsive excitation in *in vivo* human liver

Ned Rouze<sup>1</sup>, Mark Palmeri<sup>1</sup>, Kathryn Nightingale<sup>1</sup>; <sup>1</sup>Biomedical Engineering, Duke University, Durham, North Carolina, USA

##### Background, Motivation and Objective

Commercially-available shear wave imaging systems measure group shear wave speed and often report stiffness parameters applying purely elastic material models. Soft tissues, however, are viscoelastic, and higher-order material models are necessary to characterize the dispersion associated with broadband shear waves. Often, the frequency-dependent phase velocity is measured and parameterized in terms of Voigt or linear dispersion models with a small number of parameters. The objective of this work is to evaluate a method for estimating viscoelastic model parameters using a Radon-like summation algorithm without the need to measure the phase velocity at discrete frequencies.

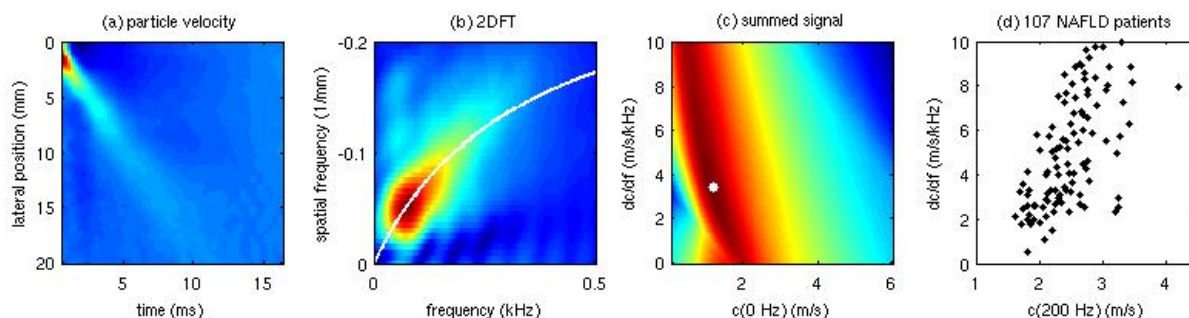
##### Statement of Contribution/Methods

The method described here estimates viscoelastic model parameters by calculating the 2D Fourier transform (2DFT) of the shear wave propagation signal and performing Radon-like summations of the 2DFT signal along paths with the spatial and temporal frequencies related by the model under consideration. This calculation is performed for a range of parameters in the solution space, and the optimal solution is identified by the coordinate of the greatest sum.

##### Results/Discussion

The figure shows particle velocity as a function of position and time (a) and the corresponding 2DFT (b) for shear wave propagation following an impulsive excitation in human liver. The summation signal (c) shows the results obtained by summing along paths described by a linear dispersion model using frequencies  $0 < f < 500$  Hz. The best fit slope and intercept are indicated by the white point on (c) and by the white line on (b).

The Radon-like summation method described here has three distinct advantages compared to methods that estimate model parameters from phase velocity data at discrete frequencies; (1) the summation is automatically weighted by the relative signal energy in the Fourier domain, (2) by considering individual solutions as a whole, the fitting is robust to gross outlier data that is often present in low SNR data such as obtained *in vivo*, and (3) potential sources of bias in frequency-dependent phase velocity data are reduced by considering only solutions allowed by the model under investigation. This algorithm was applied to a cohort of 107 fatty liver patients (d), and the results indicate that dispersion slopes of  $1 - 10$  m/s/kHz, and mid-band fits of  $1.5 - 4$  m/s occur in their livers.





## 4:30 pm Application of Attenuation Measuring Ultrasound Shearwave Elastography in 8 Post-Transplant Liver Patients

Ivan Nenadic<sup>1</sup>, Matthew Urban<sup>1</sup>, Heng Zhao<sup>1</sup>, William Sanchez<sup>2</sup>, Paige Morgan<sup>1</sup>, James Greenleaf<sup>1</sup>, Shigao Chen<sup>1</sup>; <sup>1</sup>Mayo Clinic, USA

### Background, Motivation and Objective

Palpation is an important part of a medical exam during which mechanical properties of a tissue are evaluated by manual compression in an effort to assess changes in tissue elasticity and viscosity. Shear wave ultrasound elastography techniques mimic manual palpation by exciting shear waves in the tissue and measuring the shear wave velocity to assess tissue elasticity. Attempts have been made to quantify tissue viscosity by measuring shear wave velocity at several frequencies and using various rheological models to inversely solve for the viscoelastic parameters. The necessity for rheological models stems from the inability to quantify both the shear wave velocity and attenuation independently. We have developed Attenuation Measuring Ultrasound Shearwave Elastography (AMUSE) technique for measuring shear wave velocity and attenuation without a rheological model. This technique was applied to 8 liver transplant patients and the results were compared to the biopsy findings.

### Statement of Contribution/Methods

In AMUSE, a two-dimensional (2D) Fourier Transform of the tissue motion yields the k-space whose coordinates are the frequency (f) and the wave number (k). The shear wave velocity (c) at the given frequency is equal to  $f_0/k_0$ , where  $f_0$  and  $k_0$  are the coordinates of the peak at the given frequency. The shear wave attenuation is calculated using  $\alpha = (\pi/\sqrt{3}) \times \text{FWHM}$ , where FWHM is the full-width at half maximum of the peak along the wave number axis. Measurements of shear wave velocity and attenuation were made at 100 Hz and 200 Hz in 8 patients with transplanted livers that were being evaluated for potential acute cellular rejection, and the results were compared to clinical diagnoses made by liver biopsy in a blind study.

### Results/Discussion

At 100 Hz, the mean and standard deviation for the shear wave velocity and attenuation for patients without acute rejection were  $c = 1.57 \pm 0.04$  m/s and  $\alpha = 124.27 \pm 8.14$  Np/m, and for patients with acute rejection were  $c = 2.54 \pm 0.38$  m/s and  $\alpha = 96.14 \pm 7.52$  Np/m. At 200 Hz, the mean and standard deviation for the shear wave velocity and attenuation for patients without acute rejection were  $c = 1.69 \pm 0.08$  m/s and  $\alpha = 157.17 \pm 15.66$  Np/m, and for patients with acute rejection were  $c = 2.93 \pm 0.52$  m/s and  $\alpha = 113.87 \pm 15.90$  Np/m. The Hotelling trace criterion assessing the ability of parameters to differentiate between groups was 4.15 for the velocity, 4.29 for the attenuation, and 14.76 for velocity and attenuation combined at 100 Hz. At 200 Hz, the Hotelling trace criterion was 3.62 for the velocity, 2.51 for the attenuation, and 9.72 for velocity and attenuation. The data presented in this study suggests that using both the shear wave velocity and attenuation improves the ability to differentiate between two groups of patients.

## 4:45 pm Single Tracking Location Viscosity Estimation by Maximum Likelihood Estimation

Jonathan Langdon<sup>1</sup>, Stephen McAleavey<sup>1</sup>; <sup>1</sup>Biomedical Engineering, University of Rochester, Rochester, New York, USA

### Background, Motivation and Objective

Single Tracking Location Viscosity Estimation (STL-VE) is a method for determining the shear modulus and shear viscosity of tissue using impulsive shearwave excitations generated by Acoustic Radiation Force (ARF). While the variation of shear viscosity with disease state is unclear, the simultaneous measurement of shear viscosity and shear modulus is necessary to accurately measure shear modulus. Importantly, since the ARF excitations are broadband, the estimation problem cannot be reduced to a mono-frequency problem without sacrificing much of the excitation energy. Additionally, cross-correlation based estimation methods are not applicable in viscoelastic systems because such methods assume shift-invariance. Therefore, shift-variant techniques that simultaneously measure shear modulus and shear viscosity are being pursued. STL-VE is one such method. We previously introduced STL-VE as a frequency domain nonlinear least squares problem (STL-VE NLLS). Our objective in this work is to improve the accuracy of the STL-VE method by treating it as a maximum likelihood estimation problem.

### Statement of Contribution/Methods

Here we contribute a significantly revised implementation of STL-VE using a maximum likelihood estimation (STL-VE MLE) based algorithm. The estimator is derived from a general viscoelastic model of the STL-VE problem. The resulting estimator is then recast in the form of an iterative Gauss-Newton solver. We implement the algorithm using Graphics Processing Units (GPUs) and the OpenCL programming language for real-time processing. The software is then validated using data from a Kelvin-Voigt based Finite Difference Time Domain (FDTD) simulation with particle velocity estimates corrupted by added white Gaussian noise (AWGN). The resulting estimates are compared to those achieved using the STL-VE NLLS. Finally, the algorithm is adapted for imaging using a Tikhonov regularization scheme, and is demonstrated with tissue data acquired with a Siemens Antares Ultrasound System.

### Results/Discussion

Simulation results comparing STL-VE NLLS and STL-VE MLE demonstrate the improved accuracy of the MLE method with noisy shearwave particle velocity measurements. For example, in a simulation using a material with a 2 kPa shear modulus and 1.0 Pa.s shear viscosity, the NLLS yielded an estimated viscosity of  $0.96 \pm 0.06$  Pa.s for 1% AWGN and  $0.24 \pm 0.26$  Pa.s for 5% AWGN. The MLE method yielded  $1.01 \pm 0.02$  Pa.s for 1% AWGN and  $1.01 \pm 0.13$  Pa.s for 5% AWGN. Similar results are seen for other combinations of shear modulus and viscosity. These results suggest that the MLE method is robust against measurement bias introduced by the presence of noise. This is important in the setting of imaging because the amount of data needed to suppress noise and eliminate bias in the NLLS case limits the imaging resolution. We demonstrate this by comparing STL-VE MLE and NLLS images of tissue mimicking phantoms and excised porcine liver.

## 2K - MBB: Beamforming III

Waldorf

Saturday, September 6, 2014, 3:30 pm - 5:00 pm

Chair: **Steven Freear**  
University of Leeds

2K-1

### 3:30 pm Clinical feasibility of computed ultrasound tomography in echo mode (CUTE)

Michael Jaeger<sup>1</sup>, Martin Frenz<sup>1</sup>; <sup>1</sup>University of Bern, Switzerland

#### Background, Motivation and Objective

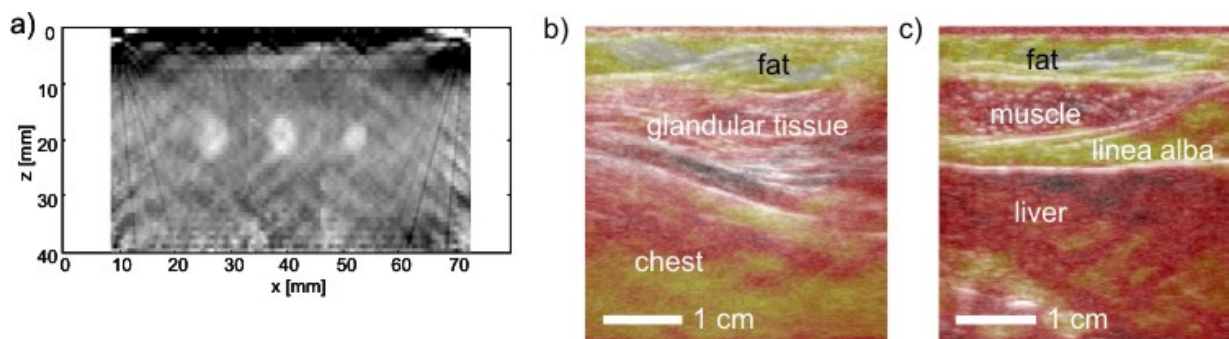
Local speed of sound (SOS) is a promising diagnostic marker because it depends on both composition and structure of human tissue. Computed ultrasound tomography in echo mode (CUTE) is a recently developed technique that allows imaging SOS spatially resolved based on the changing pulse-echo phase with changing angle of ultrasound transmission. Phantom results have shown spatial resolution and contrast suitable for diagnosis integrated with conventional b-mode ultrasonography (Fig. a: CUTE image of gelatine phantom containing three inclusions with 0.6% contrast relative to the background SOS). However clinical CUTE is still challenging owing to adverse influences such as clutter, strong variations of echo level, motion artefacts and ultrasound refraction. We present techniques of how to solve these problems towards a first successful application of CUTE in human volunteers.

#### Statement of Contribution/Methods

Our approach towards clinical CUTE includes 1) Mitigation of echo phase tracking errors that are caused by the rotating point-spread-function around strong echoes when changing the transmission angle. 2) Improvement of phase tracking of deep echoes by aberration correction of deep tissue regions based on the reconstructed SOS of superficial tissue. 3) Mitigation of multiple reflections between tissue layers based on a dark-field imaging approach that reduces specular reflections. 4) Implementation of motion compensation.

#### Results/Discussion

As a result, first CUTE images of human volunteers are able to consistently distinguish the subcutaneous fat layer from the underlying tissue in the abdomen (Fig. b) and the breast (Fig. c) with good contrast and axial resolution (CUTE images superposed in colour scale onto greyscale b-mode ultrasound for comparison to anatomy). The ability to resolve parallel layered tissue is confirmed by simulations and indicates that absolute SOS can be measured in addition to providing pure contrast, enabling quantitative characterisation of tissue composition. The performance of CUTE is further analysed and optimised based on phantoms made of different tissues.



2K-2

### 3:45 pm 192-element 1.5D phased array with elliptic footprint

Svetoslav Nikolov<sup>1</sup>, Jens Munk Hansen<sup>1</sup>, Henrik Jensen<sup>1</sup>, Dean McHenry<sup>2</sup>, Christopher Beers<sup>2</sup>; <sup>1</sup>RD Applications and Technologies, BK Medical Aps, Herlev, Denmark, <sup>2</sup>Sound Technology, State College, PA, USA

#### Background, Motivation and Objective

More than one third of adults and 17% of youths were obese in 2009-2010 in the US. The scan depth for a person with a waist of 130 cm in circumference is more than 30 cm. More than 3% of ultrasound studies are limited by bad image quality at large depths.

The objective of this work was to design a transducer that will produce an image whose quality at a depth of 30 cm is comparable to the quality of an image at 20 cm acquired with a state-of-the-art curved linear array.

#### Statement of Contribution/Methods

Image quality can be quantified by penetration depth, detail resolution, and contrast resolution. An existing transducer, 8820e, by BK Medical was used as a baseline for comparison of the new design.

43 dB increase in signal-to-noise ratio (SNR) is needed to increase scan depth from 20 to 30 cm. The transducer-related factors that increase the penetration are: (a) lower frequency; (b) higher number of active channels; (c) larger element size; (d) focusing in elevation.

We investigated 22 different designs in simulation: 10 curved, 6 linear, and 6 phased arrays. We varied curvature, pitch, element height and elevation focus. A 1.5D phased array was designed using the experience from the 22 designs. The middle row has 128 elements and the outer rows have 64 elements, giving an elliptical footprint of the probe and allowing for a scanner with 192 channels to use all elements all the time.

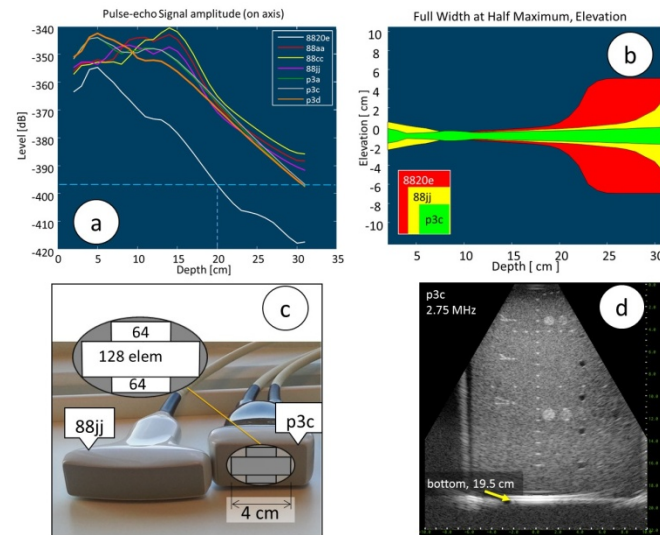
Prototypes for 2 of the designs were built and experimentally investigated (Fig 1c).

## Results/Discussion

Point spread functions (PSF) for depths 0 to 30 cm were simulated in Field II in 0.5 cm steps. All of the 22 designs have amplitude at 30 cm larger than the signal level from 8820e at depth of 20cm (Fig 1a).

Based on PSF we chose two candidate designs: a curved linear array 88jj (415 $\mu$ m pitch, 20 mm height, 192 elements, 152 mm radius of curvature); and a 1.5D phased array p3c (308  $\mu$ m pitch, 28 mm height, 128 elements mid row + 64 element in outer rows).

Fig 1b shows the beam shape in elevation of 8820e, 88jj and p3c. Fig 1c shows the built prototypes. The p3c prototype (3 x 192 elements, outer rows connected) allowed us to connect any 192 elements to a 192-channel system. The scan geometry is expanded sector which allows a large field of view needed for abdominal scans. Evaluations on phantoms (Fig 1d) and in-vivo show that the performance of p3c is comparable to that of 88jj at depths from 15 to 25 cm, and to 8820e at depths 0 to 15 cm.



2K-3

## 4:00 pm A Dicing-free Transducer Based on Beamforming by Spatial Matched Filtering

Yuling Chen<sup>1</sup>, Jesse Yen<sup>1</sup>, <sup>1</sup>Biomedical Engineering, University of Southern California, Los Angeles, CA, USA

### Background, Motivation and Objective

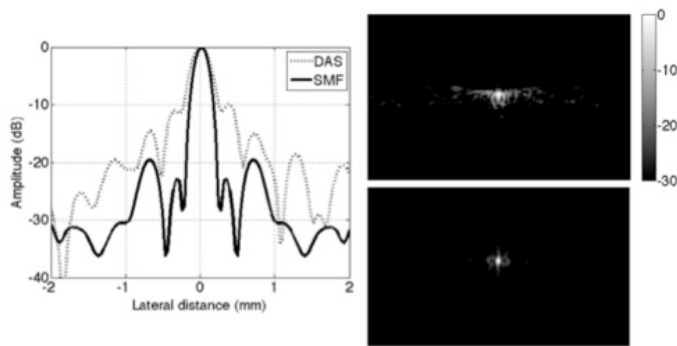
Kerfs between elements of an array transducer are typically created by dicing to prevent electrical and mechanical coupling. Unfortunately, the dicing procedure can be challenging in terms of cost, yield and limitations on fine-scale dimensions for high frequency arrays. A transducer built based on un-diced piezoelectric materials is clearly easier to fabricate. However, the image quality of such transducers is degraded because the ultrasonic beams are not focused as well as in arrays. Spatially matched filtering (SMF) echo signals is an advanced beamforming technique that focuses transmit and receive beams dynamically throughout field of view. We present our work on designing and fabricating a 7 MHz, dicing-free transducer that can provide comparable image quality to array transducers by employing SMF beamforming.

### Statement of Contribution/Methods

The proposed transducer has separate layers for transmit and receive. A 10 mm  $\times$  20 mm piece of un-diced PZT-5H ceramic, served as transmitter, was bonded onto an 8 MRayls backing, and emitted unfocused plane waves during imaging. A layer of P(VDF-TrFE) copolymer was then bonded on top of the PZT for reception. The receive layer was an array whose elements were defined by patterned traces of a flexible circuit. No dicing was required throughout the fabrication procedure. Though dynamic focusing can be obtained by the receive array with delay-and-sum (DAS) beamforming, transmit focusing is not available because plane waves are emitted. SMF beamforming was implemented to compensate the degradation of image quality caused by the loss of transmit focusing. A prototype was built and interfaced with a Verasonics data acquisition system for collecting data. We acquired data of a phantom containing a single wire at 25 mm depth. Beam patterns and B-mode images were generated and compared between DAS and SMF.

### Results/Discussion

We designed a 7 MHz, dicing-free transducer and successfully developed a prototype. SMF beamforming was applied to compensate the loss of transmit focusing. Measured beamplots show that SMF provides a -6 dB beamwidth of 0.25 mm and a side lobe level of below -20 dB, which are superior to those of DAS (0.35 mm and -10 dB respectively). Preliminary B-mode images of a single wire phantom were also presented. Future work includes imaging scattering phantoms and eventually in-vivo targets using the dicing-free transducer.



2K-4

#### 4:15 pm Delay-encoded Transmission in Synthetic Aperture Imaging (DE-SAI)

Ping Gong<sup>1</sup>, Arash Moghimi<sup>1</sup>, Michael Kolios<sup>1</sup>, Yuan Xu<sup>1</sup>; <sup>1</sup>Physics, Ryerson University, Toronto, ON, Canada

##### Background, Motivation and Objective

It is desirable to improve the signal-to-noise-ratio (SNR) of radiofrequency (RF) signals in synthetic aperture imaging (SAI). Hadamard matrix encoded transmission was designed to increase the SNR (Chiao, R.Y. 1997, IEEE, IUS). However, this approach requires driving some array elements with a positive pulse and other elements with the inverted pulse at the same time. This cannot be implemented in most commercial ultrasonic scanners. Therefore we propose delay-encoded synthetic aperture imaging (DE-SAI) to encode the transmission in some array elements with half-period delay, rather than with reversing the polarity, to increase SNR. This approach can be implemented in many commercial scanners.

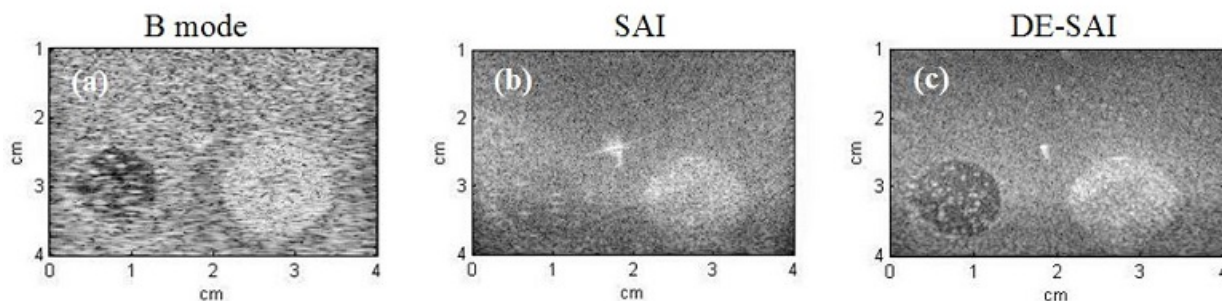
##### Statement of Contribution/Methods

The transmission protocol is similar to the Hadamard encoding protocol except that DE-SAI replaces inverted transmission pulses with positive pulses delayed by half period of the central frequency of the probe. Elements were delayed according to a 128 by 128 encoding matrix  $A$ . It stands for 128 active transmit elements in each excitation and 128 transmission events to acquire one complete data set for one image. Equivalent signals to the standard SAI were obtained by decoding the signals in DE-SAI in the frequency domain. Then ultrasound images were obtained using the standard image reconstruction method in SAI.

The experimental RF data were acquired using a 128-element 4-cm-wide 5 MHz linear array (L14-5) and a SonixDaq (Ultrasonix, CA) acquisition system. RF data were acquired in the B-mode, standard SAI and DE-SAI from a 4\*4 cm<sup>2</sup> tissue mimicking phantom which contained two 1.2-cm-diameter inclusions (left: hypo, right: hyper echoic) and two 0.05-cm-diameter wire inclusions at 1.5 cm and 2.4 cm depth. The beamformed signals were displayed as log-envelope images. The data acquisition time is the same as the standard SAI.

##### Results/Discussion

Fig. 1 shows the reconstructed images of B-mode (a), standard SAI (b) and DE-SAI (c). The lateral resolution (as assessed by the FWHM of the wire) of DE-SAI is improved by 52% and 68% and the SNR of the wire at 2.4 cm depth is increased by 2.4 and 1.3 times, compared with the B mode and the standard SAI, respectively. In conclusion, we proposed and implemented a delay-encoded transmission algorithm that improved the spatial resolution and SNR in SAI.



2K-5

#### 4:30 pm An Improved 3D Ultrasound Computer Tomography System

Hartmut Gemmeke<sup>1</sup>, Michael Zapf<sup>1</sup>, Torsten Hopp<sup>1</sup>, Nicole Ruiter<sup>1</sup>; <sup>1</sup>IPE, KIT, Eggenstein-Leopoldshafen, Germany

##### Background, Motivation and Objective

At the University Hospital Jena we carried out a pilot study with our 3D Ultrasound computer Tomography system for breast imaging. We used MRI as ground truth for comparison, see Fig.: MRI subtraction image with tumor (left) and USCT reflectivity image (right) with high speed of sound (sos) at approximately the same position. Transmission tomography imaging 3D speed-of-sound and attenuation might be a unique tool for identifying tumors. However our current device was optimized for reflection tomography. Therefore we simulated and analyzed the physical limits for transmission tomography and started to develop and build an improved device, overcoming the current limitations in resolution of transmission and increasing the contrast in reflection tomography.

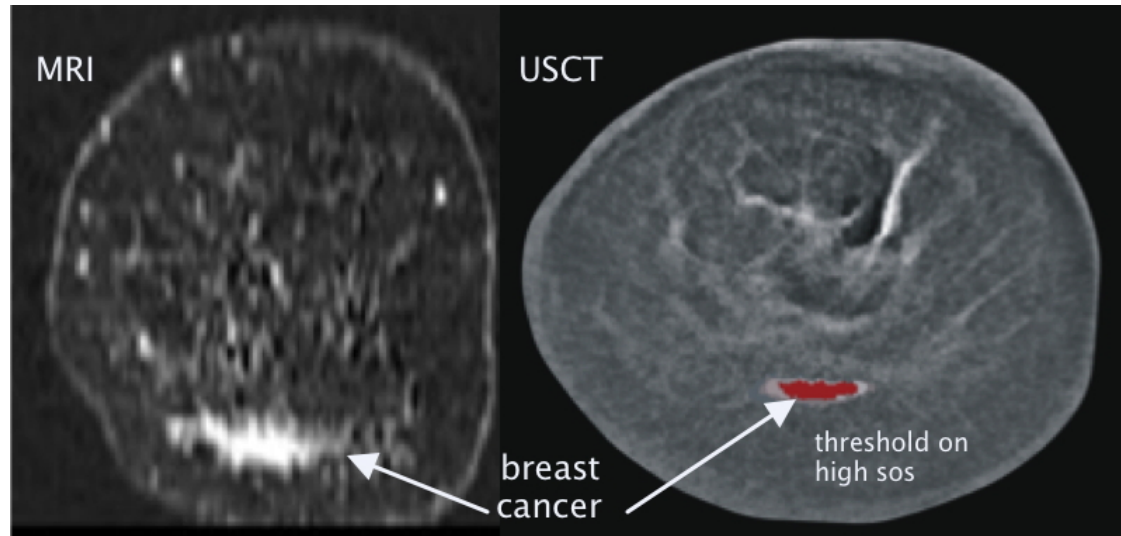
# Statement of Contribution/Methods

1. Two methods are introduced to minimize the grating lobes for reflection imaging:
  - a. Acquiring more A-scans per minute ( $>10^7$ ).
  - b. Random distribution of transducers over the aperture. The developed algorithm yields an optimized distribution for given input parameters.
2. The current opening angle of the transducer and the aperture limit the possible resolution and illumination homogeneity of the breast. An increase of the diameter of the aperture from 260 to 350 mm and of the opening angle from  $38^\circ$  to  $60^\circ$  can overcome these problems.
3. We are improving transmission tomography by a more precise forward model of the ultrasound propagation using the paraxial approximation, a homogeneous distribution of the transducers and a larger aperture.

# Results/Discussion

We enhance the contrast in the reflection tomography by minimizing the grating lobes. The simulations gave an improvement by a factor 6.8. Up to 80% of the device surface could be covered with transducer arrays. Randomness was obtained by random distribution of the transducer in each transducer array and the rotation of the arrays to each other. The contrast of the transmission tomography could be improved by a factor 4 and the visibility of the entire breast is now significantly increased.

Finally with the optimized aperture we obtain a large number of A-scans ( $>10^7$ ) without an increase of measuring time (1 to 2 min). We need only about 1 to 3 rotations and may eliminate lifts of the transducer holder. We are now able to reduce complexity, costs and data acquisition time.



2K-6

## 4:45 pm Algebraic Reconstruction Considering Curved Ray For ultrasound Tomography with Ring Array to Integrate HIFU Therapeutic System

Hirofumi Nakamura<sup>1</sup>, Haruka Imoto<sup>1</sup>, Takashi Azuma<sup>1</sup>, Satoshi Tamano<sup>2</sup>, Kiyoshi Yoshinaka<sup>3</sup>, Akira Sasaki<sup>1</sup>, Shu Takagi<sup>1</sup>, Shin-ichiro Umemura<sup>2</sup>, Yoichi Matsumoto<sup>1</sup>; <sup>1</sup>The University of Tokyo, Japan, <sup>2</sup>Tohoku University, Japan, <sup>3</sup>Advanced Industrial Science and Technology, Japan

# Background, Motivation and Objective

Our objective is to develop an ultrasound treatment and diagnosis integrated system for breast cancer. Ultrasound Computed Tomography (UCT) in imaging and High Intensity Focused Ultrasound (HIFU) in therapy was integrated to achieve ideal treatment system. Profiles of sound speed and attenuation obtained by UCT has informative parameters to correct deformed HIFU beam caused by tissue inhomogeneity. UCT has also many potentials to monitor tissue change during HIFU treatment.

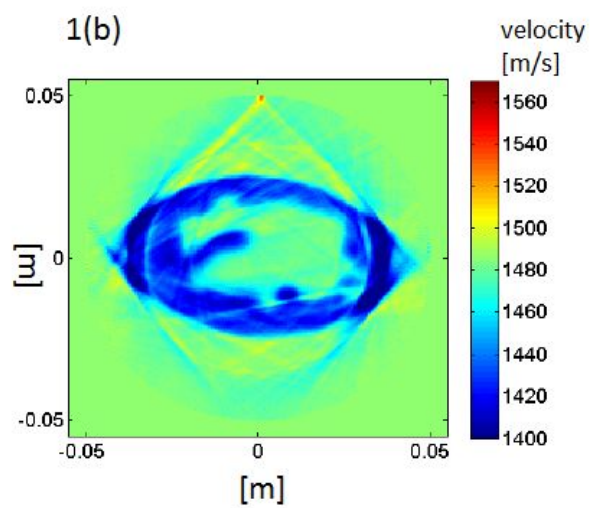
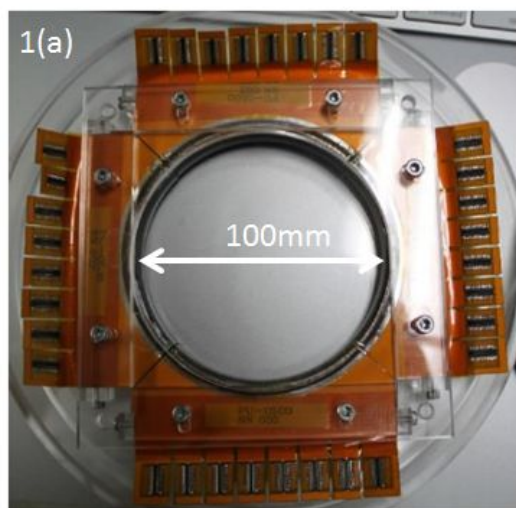
# Statement of Contribution/Methods

An imaging system using a 1024-element ring-array transducer with diameter of 100 mm as shown in Fig. 1a was fabricated and connected to Verasonics imaging system with 256 channels via a self-made multiplexer connecting 1024 to 256 and. To estimate time of flight (TOF), cross correlation was employed to obtained RF data. Before experiment, two different reconstruction algorithms were applied to the simulation TOF data. Firstly, an iterative Simultaneous Algebraic Reconstruction Technique (SART) reconstruction methods with an assumption of straight path was computed. After that, SART with curved path estimated from the local gradient of sound speed was computed. In this forward problem solver, a projection data was calculated from a temporal sound speed profile. In iteration process, the temporal sound speed profile was updated to reduce the difference between temporal and actual projection. Urethane gel phantoms were used as an imaging object for experiments.

# Results/Discussion

In the results of SART with straight path, estimated size errors were proportional to sound speed difference. When its speed difference was equal to speed difference between fat and normal tissue, the size error was 20%. On the other hand, in the results of SART with curved path, estimated size errors were not depend on the sound speed difference, and its values were under 5 %. This algorithm was employed to experimental data as shown in Fig. 1b. A complicated structure including fat and normal tissue in typical human breast was emulated in this gel phantom on the basis of a clinical MRI data. Estimated sound speed in fat and water area were consistent with each actual sound speed. Estimated structure shape was also consistent with the shape of a silicone from to make this phantom. These results clearly demonstrated practical usefulness of our prototype UCT system.





## 3K - MBE: Ultrasound Induced Biological Effects

Boulevard

Saturday, September 6, 2014, 3:30 pm - 5:00 pm

Chair: **Jean-Yves Chapelon**  
INSERM, Lyon

3K-1

### 3:30 pm Sonoporation Induced Persistent Disruption of Balance between Filamentary and Globular Actin Cytoskeleton

Xian Chen<sup>1</sup>, Ruen Shan Leow<sup>1</sup>, Jennifer M. F. Wan<sup>2</sup>, Alfred C. H. Yu<sup>1</sup>; <sup>1</sup>Medical Engineering Program, The University of Hong Kong, Pokfulam, Hong Kong, <sup>2</sup>School of Biological Sciences, The University of Hong Kong, Hong Kong

#### Background, Motivation and Objective

Previously, we have shown that, at a single-cell level, sonoporation would disrupt the actin cytoskeleton adjacent to the perforation site. This has practical implications because the actin network is well recognized as an important subcellular scaffold that provides mechanical support to the cell. If actin disruption persists over time, the functional activeness of the actin machinery would be hampered. As such, this work has sought to characterize the downstream distribution of post-sonoporation actin contents.

#### Statement of Contribution/Methods

We have made use of an acoustically coupled confocal microscopy platform with calibrated ultrasound pressure fields (0.45 MPa peak negative pressure in-situ, 1 MHz frequency, 30-cycle pulse period). A novel cassette-shaped cell chamber was also designed to enable in-situ registration of cell position and pre-exposure microbubble location. It housed a 0.13mm-thick glass cover slip, in which a numerated line grid with 1x1 mm boxes was impressed onto its bottom surface using heat transfer printing. ZR-75-30 breast cancer cells were seeded onto the cell chamber, and VEGFR-targeted microbubbles (1-4  $\mu$ m diameter) were added to foster site-specific induction of sonoporation (only cells with single microbubble binding were used for experiments). Sytox-Orange was added as the sonoporation tracer. After registering the pre-exposure cell-microbubble location (via bright-field imaging), ultrasound was applied to trigger sonoporation, and the cells were re-incubated for 1 h. A live-dead stain (Calcein-AM-Blue + Sytox-Red) was then added to discern between viable and non-viable sonoporated cells. Then, two physical forms of actin were analyzed: (i) filamentary actin (F-actin), and (ii) globular actin (G-actin). They were stained respectively with phalloidin-FITC and DNase I. Their fluorescence were imaged and measured via confocal microscopy, and their ratio was calculated to estimate the post-sonoporation balance between F-actin and G-actin. For comparison, sham exposure and positive control (cyto-D chemical induction of actin depolymerization) experiments were also conducted.

#### Results/Discussion

Sonoporated cells exhibited reduction in F-actin (on avg. 32.2% lower than that for sham control; N = 50) and concomitant increase in G-actin (2.6 times higher). These in turn resulted in a mean increase in G:F-actin ratio by 3.7 fold comparing to sham exposure. Such trend was similar to that for cells which underwent cyto-D treatment. Over this process, cell viability may remain unaffected. The morphology of viable sonoporated cells also differ from sham control which appeared as stretched, and it was not the same as that of non-viable sonoporated cells which showed irregular budding. These results show that the range of biological consequences that can be instigated by the physical action of sonoporation should not be underplayed. Persistent perturbation of actin cytoskeleton would indeed occur.

3K-2

### 3:45 pm Cavitation characterization in the safety assessment of FUS-enhanced blood-brain barrier opening

Tao Sun<sup>1</sup>, Shutao Wang<sup>1</sup>, Camilo Acosta<sup>1</sup>, Elisa Konofagou<sup>1,2</sup>; <sup>1</sup>Biomedical Engineering, Columbia University, USA, <sup>2</sup>Radiology, Columbia University, USA

#### Background, Motivation and Objective

Applying focused ultrasound (FUS) with systemic administration of microbubbles has been confirmed to transiently induce localized and reversible blood-brain barrier (BBB) opening for drug delivery to the brain parenchyma. However, safety, and real-time monitoring thereof, remains one of the key elements to be established prior to clinical translation of this technique. The objective of this study is to investigate the relationship between the safety assessment after BBB opening and the bubble behavior during FUS exposure. Our hypothesis is that stable cavitation plays a more important role in predicting damage at lower pressures while inertial cavitation dominates the likelihood of damage once a certain pressure threshold is exceeded.

#### Statement of Contribution/Methods

In this study, in-house-manufactured microbubbles (4 – 5  $\mu$ m in diameter) and a single element FUS transducer (center frequency 1.5 MHz) were utilized to induce BBB opening. A 10-MHz pulse-echo transducer was used as a passive cavitation detector during sonications. The right hippocampus was targeted in forty-five mice for this study. The stable and inertial cavitation signals were monitored during sonication. A 9.4-T MRI system was used to assess potential edema, brain tissue permeability and BBB opening. Pre-contrast T2-weighted, contrast-enhance dynamic and T1-weighted MR scans were performed immediately after sonication on day 0, day 1 and day 6. The volumes of contrast enhancement and diffusion rates of the contrast agent were quantified as indicators for the induced BBB opening. All the mice were sacrificed for H&E histological evaluations to determine if there was any neurovascular damage in the brain.

#### Results/Discussion

Harmonic emissions were found to reach a plateau beyond 450 kPa, while the ultraharmonic components underwent a 10-dB sharp increase from 300 to 450 kPa and then increased linearly ( $r^2 = 0.93$ ) between 450 to 900 kPa. Broadband emissions also showed a linear increase ( $r^2 = 0.94$ ) in the same frequency range. The percentages of reversible opening (BBB closed before Day 6) were 100%, 28.6%, 40%, 0% and 33% at 300, 450, 600, 750 and 900 kPa, respectively. With these same parameters, 0%, 28.6%, 40%, 100% and 66% of the cases exhibited edema on Day 6. Interestingly, we confirmed that edema would not fully form until 24h post sonication ( $P < 0.05$ , within the 750 - 900 kPa range). The findings of this study strongly indicated that stable cavitation was deemed more reliable at assessing the likelihood of safe opening when the pressure was below 600 kPa. Once the pressure was increased beyond 750 kPa, peak inertial cavitation power amplitude became a better indicator of predicting edema.

## 3K-3

**4:00 pm Targeting Endothelial Cells In Cancer Therapy Using Ultrasound Activated Microbubbles**

Azza Al-Mahrouki<sup>1,2</sup>, Emily Wong<sup>1,2</sup>, Gregory Czarnota<sup>1,2</sup>, <sup>1</sup>Department of Radiation Oncology and Imaging Research, Sunnybrook Health Sciences Centre, Toronto, Ontario, Canada, <sup>2</sup>Physical Sciences, Sunnybrook Health Sciences Centre, Toronto, ON, Canada

**Background, Motivation and Objective**

Microbubble-enhanced ultrasound cancer therapy target endothelial cells lining tumor vasculatures where tumor cell death is known to be secondary to the demise of endothelial cells. Here, we investigated the optimization of the ultrasound-stimulated microbubble treatments and the molecular mechanisms involved in their interaction with endothelial cells.

**Statement of Contribution/Methods**

Human umbilical vein endothelial cells were used as an *in vitro* model, treated in suspension with ultrasound-stimulated microbubbles (MB), radiation (XRT), or a combination of MB+XRT. Ultrasound treatments consisted of a 16-cycles tone burst at 500 kHz center frequency and a pressure of 570 kPa. Cell effects were monitored at 0, 3, 6, and 24 hours after treatment. Investigating the effect of timing of the combined treatment was also done with a 0, 3, 6, and 24 hours interval between treatments. Modulators of cell death signaling were also used in experiments including ceramide, fumonisins B1, monensin, and sphingosine-1-phosphate (S1P). Experimental outcomes were evaluated using histological, TUNEL, clonogenic, immuno-fluorescence, electron microscopy, and endothelial cell blood-vessel-like tube forming assays.

**Results/Discussion**

Fewer cells survived 24 hours after treatment for the MB+XRT condition compared to either the control ( $P<0.0011$ ) or to the single treatment of XRT ( $P<0.0043$ ). Optimal time interval for the combined condition of MB+XRT was 0 hour, which resulted in significant low level of survival ( $P<0.0011$ ) as well as significant less number of formed branches compared to the control ( $P<0.0001$ ). Incubating cells with exogenous ceramide resulted in a decrease in cell survival by about 50% compare to the control group and cells failed to form tubes, while the use of the other modulators (such as fumonisins B1, monensin, or S1P) resulted in different degrees of functional cellular recovery. Cellular survival, when using the different modulators, was similar to that of the control group with the lowest for the combined treatment of MB+XRT with  $P<0.05$  for the groups treated with the different modulators. The functional ability to form tubes was however only reduced in the MB+XRT condition in the control group ( $P<0.0001$ ), the ceramide treated group ( $P<0.0031$ ), and the S1P treated group ( $P<0.0286$ ), but was not affected in either the fumonisins B1 treated group (blocks *de novo* synthesis of ceramide), or in the monensin treated group (blocks acid sphingomyelinase). This validates the idea that ceramide signaling is a key element in cell death initiation under the bubbles treatment conditions.

## 3K-4

**4:15 pm Shockwave Lithotripsy with Renoprotective Pause is Associated with Renovascular Vasoconstriction in Humans**

Michael Bailey<sup>1,2</sup>, Franklin Lee<sup>2</sup>, Ryan Hsi<sup>2</sup>, Marla Paun<sup>1</sup>, Barbrina Dunmire<sup>1</sup>, Ziyue Liu<sup>3</sup>, Jonathan Harper<sup>2</sup>, Mathew Sorensen<sup>2,4</sup>, <sup>1</sup>CIMU, Applied Physics Laboratory, University of Washington, Seattle, WA, USA, <sup>2</sup>Department of Urology, University of Washington, Seattle, WA, USA, <sup>3</sup>Department of Biostatistics, Indiana University School of Medicine, Indianapolis, IN, USA, <sup>4</sup>Division of Urology, Puget Sound Veteran Affairs Medical Center, Seattle, WA, USA

**Background, Motivation and Objective**

During shockwave lithotripsy (SWL), pre-treatment with low-energy shocks followed by a pause mitigates renal injury in an animal model. The pause is associated with an increase in resistive index (RI) measured on ultrasound, suggesting that renal vasoconstriction plays a role in protecting the kidney from injury. The purpose of our study was to investigate whether this association is observed in humans.

**Statement of Contribution/Methods**

Patients were prospectively recruited from two hospitals. All underwent SWL of renal stones with a Dornier Compact S lithotripter at 1 Hz, and all received an initial 250 shocks at the lowest power setting followed by a 2 minute pause. Treatment power was then ramped up while maintaining the 1 Hz shock frequency. The rate at which the power was increased, and the total shocks delivered were at the discretion of the operating surgeon. An intralobar artery was imaged by ultrasound (HDI-5000, P4-2 probe). RI measurements were taken from the same artery at baseline after induction, during the pause at 250 shocks, after 750 shocks, after 1500 shocks, and at the end of the procedure. A linear mixed-effects model was used to compare RIs at the different time points and to account for age, gender, laterality, and body mass index (BMI).

**Results/Discussion**

Fifteen patients (4 female, 11 male) were enrolled with a mean age of  $61 \pm 15$  years and average BMI of  $29 \pm 5$  kg/m<sup>2</sup>. Average stone size was  $10.4 \pm 7.7$  mm with an average treatment time of  $45 \pm 9.7$  min. Average RI pretreatment, after 250 shocks, after 750 shocks, after 1500 shocks, and post-treatment was  $0.68 \pm 0.06$ ,  $0.71 \pm 0.07$ ,  $0.73 \pm 0.06$ ,  $0.75 \pm 0.07$  and  $0.75 \pm 0.06$ , respectively. RI was found to be significantly higher after 250 shocks compared to pre-treatment ( $p=0.04$ ). The RI remained significantly elevated for the length of treatment. RI was not found to correlate with age, gender, BMI, or treatment side. In summary, the human group treated with SWL plus the pause had elevated RI during SWL. Previous animal studies tested for RI rise with SWL minus the pause, with SWL plus the pause, with just pretreatment and the pause, and with sham treatments. Only the animal group treated with SWL plus the pause showed a rise in RI during the treatment time, and that group had negligible injury following SWL compared with injury to 4% of the functional renal volume without the pause. The current work supports use of the pause in humans. Also, monitoring for a rise in RI during SWL is possible and may provide real-time feedback as to when the kidney is protected. Work supported by NIH DK043881 and DK092197 and NSBRI through NASA NCC 9-58.

## 3K-5

**4:30 pm Non-invasive cardiac stimulation by MRI-guided focused ultrasound: a feasibility study on isolated beating pig heart**

Fabrice Marquet<sup>1</sup>, Pierre Bour<sup>1</sup>, Sana Amraoui<sup>1</sup>, Fanny Vaillant<sup>1</sup>, Rémi Dubois<sup>1</sup>, Bruno Quesson<sup>1</sup>, <sup>1</sup>Université de Bordeaux, INSERM U1045, IHU LIRYC, France

**Background, Motivation and Objective**

Heart failure (HF) affects 23 million people worldwide (10% of all in-hospital admissions), leading to death within 5 years of 50% of patients with severe HF (stages 3-4 NYHA). In Cardiac resynchronization therapy (CRT), electrical stimuli are delivered through implanted leads into the myocardium to coordinate the contraction of the heart. Different factors may influence the likelihood of response to CRT, but appropriate left ventricle lead placement is an important determinant of the success and functional benefit of CRT. We propose to use MRI-guided focused ultrasound (MRI-FUS) to precisely control the location of the excitation site (MRI) and to stimulate the heart without contact (FUS), allowing a non-invasive evaluation of the tissue response to local stimuli, with the objective of optimizing CRT lead positioning. The feasibility of this approach was validated on ex vivo isolated beating hearts from pigs.

**Statement of Contribution/Methods**

Experiments (N=5) were performed on a MRI-FUS platform combining a 1.5T MRI (Siemens Avanto, Germany) and a focused ultrasound device (Image Guided Therapy, France, 256 elements, 13/13 cm aperture/focal, operating at 1 MHz). Each heart was perfused ex vivo (Langendorff blood-perfusion) in near physiological conditions and positioned on top of the MRI-FUS platform. MR images were recorded to select the location of the stimulation site and to adjust beam focusing characteristics (mechanical positioning and electronic beam steering). Local cardiac electrograms were continuously recorded by two MR-compatible catheters (4 electrodes/catheter) inserted into the left ventricle and right

atrium and connected to a clinical electrophysiology recording system (Bard Inc., New Jersey, USA) thru dedicated filters specifically designed for the MR environment. Histological analysis (macroscopic inspection and Haematoxylin Erythrosine Saffron staining) was performed to assess for potential damages induced during stimulation.

### Results/Discussion

Several stimulation sites in the left ventricle were tested with various FUS protocols (single pulse/sequence of pulses with adjustable delay for pacing) using peak positive pressures of ultrasound ranging from 2 MPa to 4 MPa and individual pulse length ranging from 0.1 ms to 6 ms. Ventricular extra systoles (N=30), ventricular tachycardia (N=5) and mechanical pacing (N=4) were attested by EP recordings for pressure higher than 2.5 MPa at focus and for pulse length ranging from 2 ms to 6 ms. Histological study did not revealed presence of damages. This study demonstrates the capability of remotely stimulating different heart regions without any harmful side effect, while offering a precise location of the stimulation site (millimetric range) by combining MRI and FUS.

Such approach could prove as a major step in translating this technology to clinical applications.

This study was supported by ANR TecSan TACIT and IHU LIRYC.

### 3K-6

#### 4:45 pm Study of factors affecting drug delivery when using low intensity ultrasound

Sophie Tardoski<sup>1,2</sup>, Evelyne Gineyts<sup>2</sup>, Anthony Kocot<sup>1</sup>, Philippe Cl  zardin<sup>2</sup>, David Melodelima<sup>1</sup>; <sup>1</sup>INSERM UMR1032, France, <sup>2</sup>INSERM UMR1033, France

### Background, Motivation and Objective

Ultrasound energy can produce both mechanical and thermal effects in biological tissues. Mechanical effects of US mainly include non-inertial and inertial cavitation, radiation force and acoustic streaming. A radiation force and the resulting radiation pressure exist if sound absorption or an acoustic impedance mismatch is present within the acoustic path. Low-intensity ultrasound can be delivered in pulse mode to create radiation force effects and acoustic streaming or in continuous mode to create hyperthermia. In this study, we examined the feasibility of delivering drugs in tumor cells by low intensity ultrasound. We present in vitro evidence that pulsed ultrasound (LIPUS) creating mechanical effects or continuous ultrasound (C-US) producing mild hyperthermia lead to the penetration of drugs into tumor cells.

### Statement of Contribution/Methods

Sonications were generated with flat air-backed transducers at a resonance frequency of 2.9 MHz for C-US and 1.2 MHz for LIPUS. C-US was used to induce and maintain a temperature increase of 5  C to create mild hyperthermia. This was achieved by adjusting the acoustic power between 8 and 13 W as a function of time and temperature. Mechanical effects were created using LIPUS. Pulse length was 200   s at 40 mW/cm<sup>2</sup> (SATA) and repeated every 1 ms. Both treatments (C-US and LIPUS) lasted 30 minutes. Breast human cancer cells MCF-7 were treated with zoledronic acid (ZOL) alone or in combination with C-US or LIPUS. An evaluation of the effect of acoustic power on cell viability and ZOL penetration was also conducted. An hydrophone was used to measure if cavitation occurred during treatments. A surrogate marker (IPP) of zoledronic acid penetration was measured by mass spectrometry.

### Results/Discussion

No cavitation was detected when C-US or LIPUS were applied to tumor cells. A controlled temperature increase, up to 40  C, was created with C-US. No temperature increase was observed when using LIPUS. In the C-US group we observed that the drug penetrates in higher quantity as a function of acoustic power. The accumulation of IPP was 2000 pmol/mg for 13 and 8 acoustic watts against 1000 pmol/mg for 6 acoustic watts. If the acoustic power is increased (with the same exposure time) a significant decrease of drug penetration was observed as well as a blockage of cells proliferation. Accumulation of IPP of less than 300 pmol/mg was measured when acoustic powers superior to 14 watts were used. Interestingly, the use of LIPUS also induces a significant accumulation of IPP 3-fold more than ZOL alone, meaning that such mechanical effects are sufficient to enhance the penetration of drugs into cells. Proliferation of cells was not affected by LIPUS or C-US. The amounts of IPP found in C-US are more important than in LIPUS suggesting that the association of both mechanical effects and mild hyperthermia are more effective to enhance drug delivery into tumor cells than mechanical stimulation alone.

## 4K - Airborne Ultrasound

Marquette

Saturday, September 6, 2014, 3:30 pm - 5:00 pm

Chair: **Mario Kupnik**  
Brandenburg University of Technology

4K-1

### 3:30 pm Application of Air-Coupled Ultrasound to Full-Scale Concrete Columns Using Tomography

Hajin Choi<sup>1</sup>, John S. Popovics<sup>2</sup>; <sup>1</sup>University of Illinois at Urbana-Champaign, Champaign, IL, USA, <sup>2</sup>Civil and Environmental Engineering, University of Illinois at Urbana-Champaign, Urbana, IL, USA

#### Background, Motivation and Objective

Internal visualization provides better understanding of damage in materials; however, a large amount of data is required to reconstruct the image. Ultrasonic pulse velocity (UPV) is an efficient method to evaluate concrete. However, the application of conventional UPV is limited with concrete because of required surface preparation and large element size, and this method is labor and time intensive. Another practical problem is large computational effort associated of tomographic algorithm. Although algebraic reconstruction technique is applicable to limited data and diffracted source like ultrasound, it is well known that the algorithm is computationally inefficient compared to filtered back-projection (Radon transform). The structural inspection needs many data and the tomographic process takes a long time. New concept of data measurement and analysis are needed to evaluate full-scale structure in the field.

#### Statement of Contribution/Methods

Our newly developed air-coupled ultrasonic measurement system includes electrostatic contactless transmitters and contact accelerometers. Because electrostatic transducers generate much more ultrasonic energy than conventional transducers, it is possible to measure low-noise signals through a full-scale structure without surface preparation. Furthermore, an automated scanning system accurately collects high resolution data within a limited time.

Filtered back-projection is computationally fast, however the algorithm requires data collected sufficient angles. The proposed air-coupled method increases sectional ray coverage so that it is possible to acquire projections from multiple angles. The transform-based algorithm is successfully applied with collected data and interpolation to develop internal image of structure. The speed of computation significantly improves without a significant difference with tomograph quality.

#### Results/Discussion

Reconstructed sectional images are stacked vertically in three dimensions. Developed internal visualization shows accurate location of embedded defects inside of a highly reinforced concrete element. The results prove that the proposed ultrasonic method is applicable to full-scale concrete structures. Furthermore, the fast imaging algorithm helps to analyze structural condition in situ.

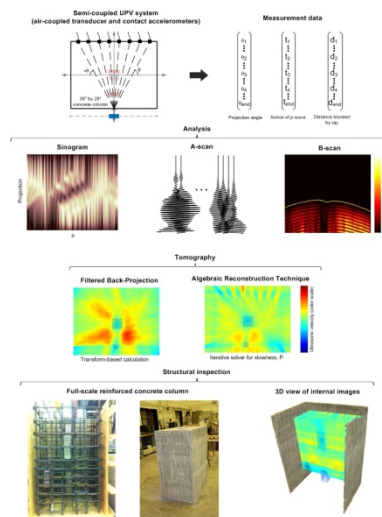


Figure 1. Graphical abstract of air-coupled ultrasonic measurement and tomography

4K-2

### 3:45 pm Fully contactless ultrasonic system to characterized concrete structure with guided wave approach and energy attenuation

Suyun Ham<sup>1</sup>, John S. Popovics<sup>1</sup>; <sup>1</sup>civil engineering, University of Illinois at Urbana Champaign, Urbana, Illinois, USA

#### Background, Motivation and Objective

Ultrasonic techniques provide an effective non-destructive evaluation (NDE) method to monitor concrete structures, but the need to perform rapid and accurate interpretation assessment requires evaluation of hundreds, or even thousands, of measurement data.

#### Statement of Contribution/Methods

Use of a fully contactless ultrasonic system can save time and labor through rapid implementation, and can enable automated and controlled data acquisition for example through robotic scanning. The fully contactless ultrasonic system consists of both air-coupled electrostatic transducer and air-coupled MEMS sensor. This paper describes our efforts to

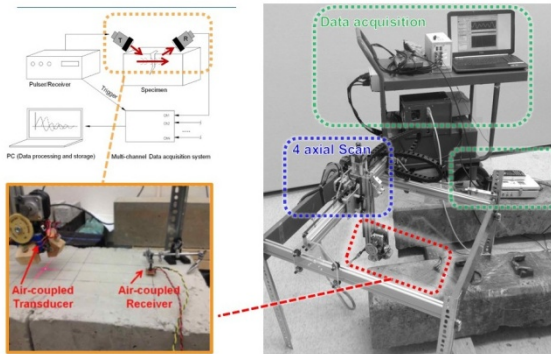


develop contactless surface wave system for NDE of concrete in structures. The developed contactless sensors, controlled scanning system with mobile apparatus and employed signal processing scheme are described. Our fully contactless system is used for detecting delaminations with guided wave approach and characterizing the level of microcracked concrete with energy attenuation. The concrete delamination are interpreted in terms of guided plate wave (Lamb wave) theory carried out on full-scale concrete slabs.

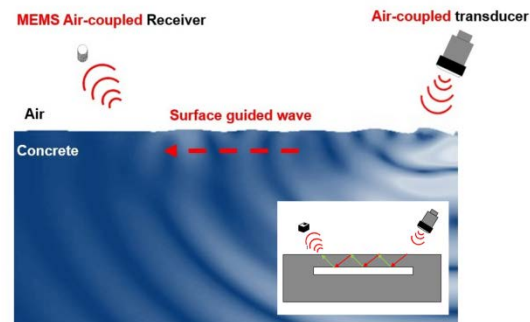
## Results/Discussion

They are formed by coupled longitudinal and transverse wave motion and include an infinite number of individual symmetrical (S) and anti-symmetrical (A) solution modes. Each Lamb mode has a distinct phase velocity, which unlike the body and surface waves, is dispersive (i.e. is a function of frequency). Also, energy loss (attenuation) is a good indicator of distributed cracks in concrete. Therefore, our ultrasonic system showed a sensitive detector of delamination and level of microcracking in concrete providing many consistent data.

### Fully contactless scanning system



### Fully contactless ultrasonic technique



4K-3

## 4:00 pm Air-Coupled Flexural Electrodynamic Acoustic Transducers

Tobias Johan Robert Eriksson<sup>1</sup>, Michael Laws<sup>1</sup>, Sivaram Nishal Ramadas<sup>2</sup>, Steve Dixon<sup>1</sup>; <sup>1</sup>Department of Physics, University of Warwick, Coventry, United Kingdom, <sup>2</sup>Elster NV/SA, Essen, Belgium

## Background, Motivation and Objective

Flexural transducers use the bending modes in a plate or membrane to produce sound. Piezoelectrically actuated flexural transducers can produce large amplitude vibrations for relatively low excitation voltages and have good acoustic coupling to low impedance load media, for both generation and detection of ultrasonic waves. In this work, the use of electrodynamic forces generated by current carrying coils is investigated, as an alternative excitation method for generating ultrasound by flexural vibrations. Using an excitation coil instead of a piezoelectric element has some notable advantages, including the following: the coil can easily be customised to predominantly generate specific modes of vibration, it's cheaper and easier to manufacture, and there is no problem of the active element debonding/depolarising over time.

## Statement of Contribution/Methods

Analytical models for vibrations in thin, circular plates were used to predict mode frequencies and shapes generated by metal caps used in the flexural Electrodynamic Acoustic Transducer (EDAT) assembly. Finite Element Modelling (FEM) was also used to study the flexural transducer behaviour in detail. Prototype transducers were then constructed using two aluminium cap designs - one simple disc (approx. 11 mm diameter and 0.5 mm thick front face) and another ring shaped (approx. 40 mm outer diameter, 3 mm inner diameter and 0.5 mm thick front face). Inside each cap, a pancake coil was placed close to the vibrating face and a standard EMAT (Electromagnetic Acoustic Transducer) pulser/receiver was used to drive the prototype transducers. Laser interferometer and microphone measurements were used to study the transduction behaviour of these devices. The frequency spectrum of the flexural EDATs were also compared to that obtained from the same transducer caps, excited thermoelastically by a Nd:YAG laser.

## Results/Discussion

Extensive modelling (both analytical & FEM) was carried out to study the characteristic behaviour of a flexural EDAT design. The performance of the prototype flexural EDAT (two cap designs and pan cake coil arrangements) was presented. The displacement measurements from the prototype devices revealed a frequency spectrum with narrowband (~3 kHz FWHM) modal frequency peaks, and a dominant fundamental mode at ~50 kHz. The effects of device behaviour as a function of coil density, both in transmit and reception mode is also reported. Comparison analysis of flexural EDAT device performance against piezoelectric devices (both conventional thickness mode and flexural designs) is also presented. Results to date indicate that flexural EDAT could be an interesting alternative to piezoelectric devices for air-coupled application.

4K-4

## 4:15 pm Ultrasonic Wireless Communication in Air using OFDM-OOK Modulation

Wentao Jiang<sup>1</sup>, William Wright<sup>1</sup>; <sup>1</sup>Electrical and Electronic Engineering, University College Cork, Cork, Ireland

## Background, Motivation and Objective

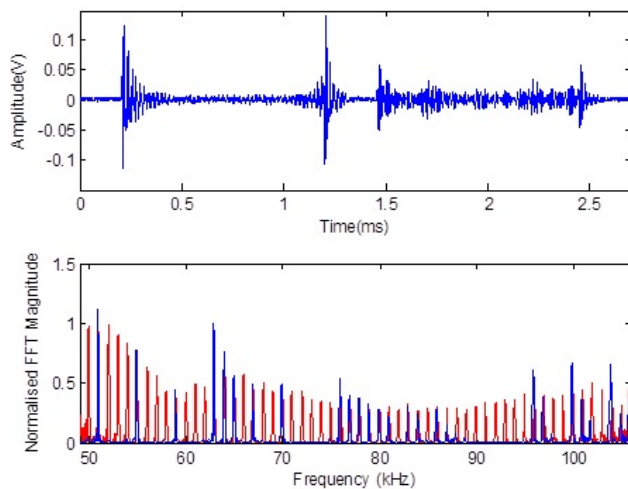
Ultrasound may be used for short-range wireless communication in air as an alternative to radio frequency (RF) based solutions. It has several advantages over RF in that ultrasonic transmissions are unregulated and interference free from most electronic devices. Ultrasonic signals in air also provide good privacy as they are difficult to intercept through solid barriers, thus increasing network security in an indoor environment. Previous work has achieved ultrasonic communication via single-channel modulation schemes using prototype broad-band air-coupled ultrasonic transducers to produce data transfer rates of up to 83 kbps over limited ranges. The aim of this work is to investigate parallel-channel modulation methods that can achieve the highest data rate possible with sufficient reliability over longer distances for ultrasonic wireless communication.

## Statement of Contribution/Methods

A pair of commercially available Senscomp 600 series air-coupled capacitive ultrasonic transducers was used in the implementation of an indoor wireless ultrasonic data communication system. The transducers have a centre frequency of 50 kHz with a nominal 100% bandwidth. A multi-carrier modulation scheme OFDM-OOK (Orthogonal Frequency Division Multiplexing – On-Off Keying) was implemented successfully allowing up to 56 sub-channels to be transmitted simultaneously over short distances. The OFDM system also coped well with the interfering effects of multi-path, which makes it an effective system for ultrasonic communication robust to reflected waves. Wireless synchronization was also achieved by ultrasonic means, instead of a hardwired link as used in previous work.

### Results/Discussion

A system data rate of up to 56 kbps was achieved using the OFDM-OOK modulation, which can transmit multiple narrow-band signals in parallel with excellent spectrum efficiency. System performance metrics including Signal-to-Noise Ratio (SNR) and Bit Error Rate (BER) were analysed and compared across the parallel channels. Error-free transmission over distances of 2 metres was achieved at 56 kbps and 1 kHz channel spacing, and 6 metres at 32 kbps with 2 kHz channel spacing. The spectral efficiencies were 0.93 bps/Hz and 0.53 bps/Hz respectively. Typical received signals (reference then data) and frequency spectra (overlaid) are shown.



### 4K-5

#### 4:30 pm Feasibility of pulse-echo thickness measurements in air with a laterally displaced receiver

Grunde Waag<sup>1,2</sup>, Petter Norli<sup>2</sup>, Lars Hoff<sup>3</sup>; <sup>1</sup>Department of Maritime Technology and Innovation, Buskerud and Vestfold University College, Norway, <sup>2</sup>Halfwave AS, Høvik, Norway, <sup>3</sup>Department of Micro and Nano Systems Technology, Buskerud and Vestfold University College, Norway

### Background, Motivation and Objective

Air-coupled ultrasound offers an attractive method for measuring the thickness of steel plates and pipes. Avoiding the coupling medium enables an easier measurement procedure, at the cost of a reduced signal level.

The authors have previously demonstrated the feasibility of thickness measurements of steel plates in air, using half-wave resonances in a through-transmission setup. The aim of this study is to extend the method to enable single-sided measurements in air, which is preferred in most practical applications.

Compared to through-transmission measurements, the strong specular echo from the air-steel interface introduces an extra challenge, as it is orders of magnitude higher than the resonant signal from within the steel plate. The ringing of the transducer from this echo masks the resonant signal. The aim of this paper is to investigate the effect of displacing the receiver from the acoustical axis to remedy this problem.

### Statement of Contribution/Methods

An analytical model for transmission and reflection of sound from a steel plate immersed in a fluid has been developed. Results from the model are compared to laboratory through-transmission measurements in a water tank, where a hydrophone was moved on the back side of the plate, laterally away from the acoustical axis. The excitation signal consisted of sinc pulses containing energy in the frequency range 0.1 - 2 MHz.

After the model had been justified by the water measurements, it was used to assess the feasibility of single-sided thickness measurements, for the steel plate in air.

### Results/Discussion

The measured through-transmitted signal shows a main lobe and two sidelobes within the measurement region, in decent accordance with the analytical solution. The mean square error in energy between the analytical solution and the measurements is below 30%.

In the analytical model the specular reflection is observed to drop 1.1 dB/mm moving away from the acoustical axis, whereas the through transmitted signal is observed to drop at a rate of 0.1 dB/mm. The model further predicts that the ratio of the resonant tail to the specular echo is -72 dB. This means that at about 80 mm the energy in the resonant signal is comparable to the energy in the specular echo. The resonant signal energy has dropped 8 dB at this distance.

The SNR in the through-transmission measurements of the steel plate in air was measured to be about 10 dB. Displacing the receiver 80 mm laterally will reduce the SNR by 8 dB. Hence, the SNR in the resonant tail signal is predicted to be about 2 dB in pulse-echo measurement in air. The SNR can be improved by e.g. increasing the area of the receiver or transmitter. This indicates the feasibility of single-sided thickness measurements of steel plates in air, provided the receiving transducer is laterally offset from the acoustic axis of the transmitter.

#### 4:45 pm Non-contact thermoacoustic imaging based on laser and microwave vibrometry

Yexian Qin<sup>1</sup>, Pier Ingram<sup>1</sup>, Xiong Wang<sup>2</sup>, Tao Qin<sup>2</sup>, Hao Xin<sup>2</sup>, Russell Witte<sup>1,3</sup>; <sup>1</sup>Medical Imaging, University of Arizona, Tucson, Arizona, USA, <sup>2</sup>Electrical and Computer Engineering, University of Arizona, Tucson, Arizona, USA, <sup>3</sup>College of Optical Sciences, University of Arizona, Tucson, Arizona, USA

##### Background, Motivation and Objective

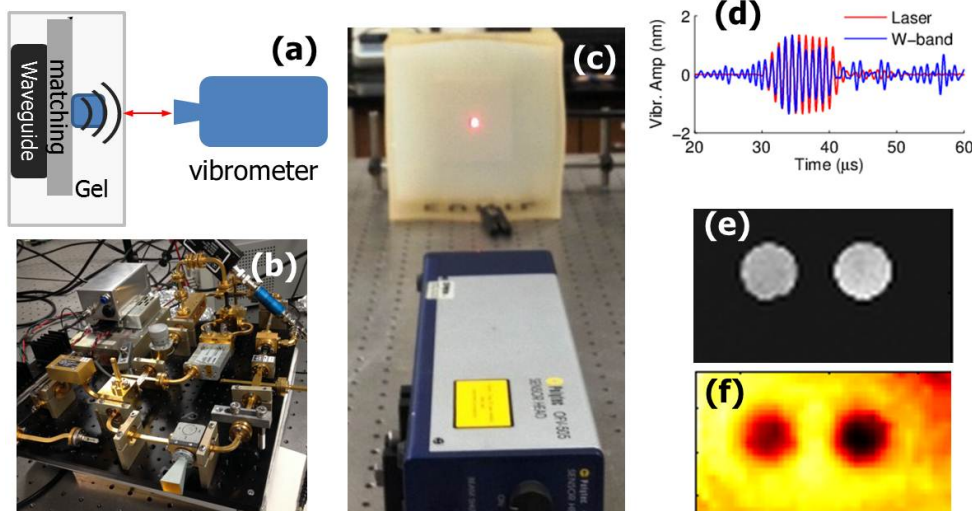
Microwave-induced thermoacoustic imaging (TAI) exploits the high resolution of ultrasound imaging and high contrast of microwave imaging. It has been investigated as a new imaging technique for a wide range of applications, such as cancer imaging, brain imaging, and foreign object detection. In conventional TAI, the TA signal is detected using ultrasound transducers in contact with the sample for acoustic coupling. This requirement limits the application of TAI in many situations, including high temperature samples, rough surface, and samples in motion. The goal of this work is to demonstrate a non-contact approach for detecting the TA signal using two types of vibrometers: a laser vibrometer and a W-band microwave vibrometer and estimate their sensitivity.

##### Statement of Contribution/Methods

Microwave pulses (3 GHz, 4 kW peak power, 4  $\mu$ s pulse width) were delivered through an oil-filled waveguide and matching layer into an absorbing sample (Fig.1a), producing TA signals. The targets were RDX samples (Rexolite 1422 disk) embedded in Agarose™ gel, a medium with high loss at 3 GHz. A calibrated laser vibrometer (Polytec OFV-505, Fig.1c) and a custom 94 GHz W-Band microwave vibrometer (Fig.1b) were each used to detect the TA vibration at the surface of the gel.

##### Results/Discussion

To first determine the sensitivity of the W-band vibrometer, a 1MHz flat ultrasound transducer was embedded in the gel to generate acoustic signals. Fig.1 (d) displays the measured surface vibration using the two vibrometers. The laser and W-band vibrometers can detect 1.3 nm vibration with a SNR of 41 dB and 18 dB, respectively. Fig.1 (e) and (f) display the pulse echo image (gray) and TA image (color) of the two Rexolite disks. The TA image was acquired using the laser vibrometer with a standoff distance of 60 cm. The peak vibration for this image is  $\sim$ 400 pm. The phantoms appear dark in the TA image since the Rexolite has much less microwave absorption than the surrounding gel. The results demonstrate the non-contact imaging technique based on a laser or W-band vibrometer is capable of detecting TA signals. Although the laser vibrometer exhibited better sensitivity, the w-band vibrometer is potentially less sensitive to the surface roughness of the sample. Noncontact TA imaging may have applications ranging from standoff detection of embedded foreign objects to detection of traumatic brain injuries.



## 5K - Opto-Acoustics

Williford A

Saturday, September 6, 2014, 3:30 pm - 5:00 pm

Chair: **Vincent Laude**  
FEMTO-ST / CNRS

5K-1

### 3:30 pm Attenuation of high-order sub-THz thickness resonances in thin Si membranes

Alexei Maznev<sup>1</sup>, Felix Hofmann<sup>2</sup>, John Cuffé<sup>3</sup>, Jeffrey K. Eliason<sup>1</sup>, Keith A. Nelson<sup>1</sup>; <sup>1</sup>Department of Chemistry, MIT, Cambridge, USA, <sup>2</sup>Department of Engineering Science, University of Oxford, Oxford, United Kingdom, <sup>3</sup>Department of Mechanical Engineering, MIT, Cambridge, USA

#### Background, Motivation and Objective

Thickness resonances of suspended thin films are widely used in acoustoelectronic devices such as thin film resonators typically operating at frequencies up to a few GHz. With femtosecond lasers, it is now possible to excite and probe thickness resonances of ultrathin membranes in the sub-THz range. While the frequency of thickness resonances can be readily obtained from the speed of sound and the film thickness, the attenuation in the sub-THz range has not been explored until the recent work by Cuffé et al., Phys. Rev. Lett. 110, 095503 (2013), where lifetimes of fundamental thickness resonances of ultrathin Si membranes were reported. In this study, we investigate lifetimes of high-order thickness resonances of Si membranes at ~0.27 THz and their dependence on the membrane thickness and surface roughness.

#### Statement of Contribution/Methods

Femtosecond pump-probe technique was used to excite and probe longitudinal acoustic pulses in suspended single crystal Si membranes with thickness ranging from 0.4 to 15  $\mu\text{m}$ . Due to the preferential sensitivity of the probe to the Brillouin frequency corresponding to the probe wavelength 387 nm, the signal is comprised of acoustic wavepackets with frequency centered at ~270 GHz. A Fourier transform of the signal reveals high-order thickness resonant modes of the membrane. The acoustic phonon lifetime is determined from the amplitude ratio of two wavepackets separated by a round trip.

#### Results/Discussion

The thickest 15  $\mu\text{m}$  sample yielded a Q-factor of 2300 which presents a lower bound for the intrinsic material Q. Such a high Q-factor at 270 GHz at room temperature indicates the existence of a local maximum of the material Q in the sub-THz range arising due to the transition from the Akhiezer relaxation to three-phonon scattering mechanism of phonon dissipation. Phonon lifetimes in thinner samples (0.37 – 1.7  $\mu\text{m}$ ) were found to be controlled by the boundary scattering. The measured surface specularly was correlated with surface roughness measured by atomic force microscopy and compared with theoretical models describing scattering of acoustic waves by a randomly rough surface.

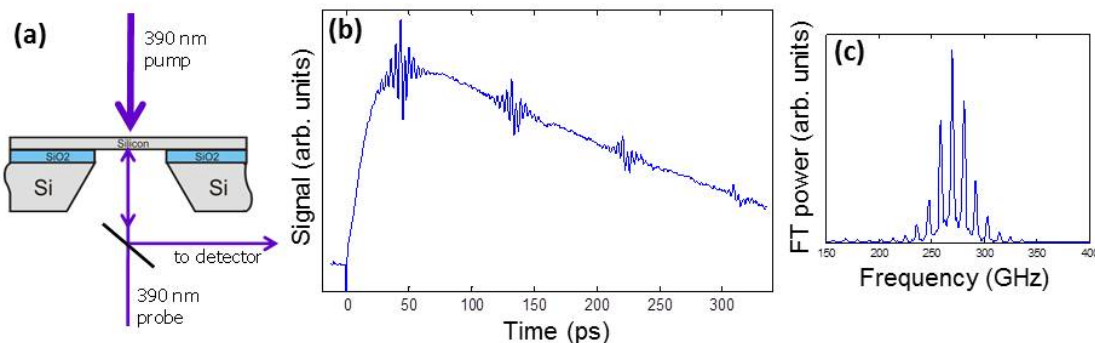


Figure 1. (a) Schematic of the measurement; (b) signal from the 370 nm-thick membrane; (c) spectrum of the acoustic oscillations shown in (b).

5K-2

### 3:45 pm Cavity modes and optomechanic interactions in phoxonic crystals

Said EL-JALLAL<sup>1,2</sup>, Mourad Oudich<sup>3</sup>, Yan Pennec<sup>4</sup>, Bahram Djafari-Rouhani<sup>1</sup>, Abdelkader Makhoute<sup>4</sup>, Jordi Gomis-Bresco<sup>5</sup>, Daniel Navarro-Urrios<sup>5</sup>, Alejandro Martínez<sup>6</sup>, Clivia Sotomayor<sup>5,7</sup>; <sup>1</sup>Institut d'Electronique, de Microélectronique et de Nanotechnologie, Université Lille 1, Villeneuve d'Ascq, France, <sup>2</sup>Physique du Rayonnement et de l'Interaction Laser Matière, Université Moulay Ismail, Meknes, Morocco, <sup>3</sup>Institut Jean Lamour, Université de Lorraine, Vandoeuvre-lès-Nancy, Nancy, France, <sup>4</sup>Physique du Rayonnement et de l'Interaction Laser Matière, Université de Moulay Ismail, Meknes, Morocco, <sup>5</sup>ICN2 - Institut Català de Nanociència i Nanotecnologia, Campus UAB, 08193 Bellaterra, Barcelona, Spain, <sup>6</sup>Nanophotonics Technology Center, Universitat Politècnica de València, Valencia, Spain, <sup>7</sup>ICREA - Institutio Catalana de Recerca i Estudis Avançats, 08010, Barcelona, Spain

#### Background, Motivation and Objective

Phoxonic crystals are periodic structures that can exhibit simultaneously phononic and photonic band gaps (BG). They allow a high confinement of both light and sound in a cavity or a waveguide. This confinement can generate a strong phonon-photon interaction with potential applications in optomechanical (OM) devices, in particular for the modulation of light by acoustic waves. In this paper, we study theoretically the optomechanic interaction in 1D phoxonic crystal constituted by a strip waveguide and show the possibility of strong acousto-optic coupling inside a cavity.

#### Statement of Contribution/Methods

Two mechanisms are considered, the photoelastic (PE) and moving interface (MI) effects. The former is due to a local variation of the dielectric permittivity induced by the acoustic strain inside the materials, whereas the second comes from the variation of the dielectric permittivity in the vicinity of the interfaces due to the motions of the boundaries. The strength of the acousto-optic coupling is evaluated by calculating either the modulation of the photonic frequency by the acoustic mode or the optomechanic coupling rate.

# Results/Discussion

We have investigated the acousto-optic (AO) interaction in a corrugated phoxonic silicon nanobeam presenting band gaps both for photonic and phononic modes. By creating a well-designed tapered cavity, we were able to create highly confined phononic and photonic defect modes with high quality factor (QF) inside the gap. We have calculated both PE and MI effects and estimate their contributions to the AO coupling. We have obtained a good AO coupling with an acoustic mode outside a gap. However this mode can be pushed into the partial or full BG while increasing the phononic QF and keeping or increasing the AO coupling. The modification of the cavity consists of increasing or decreasing the length of the stubs progressively from the perfect crystal towards the cavity center. The coupling factor is significantly increased when the acoustic mode is pushed inside the full band gap.

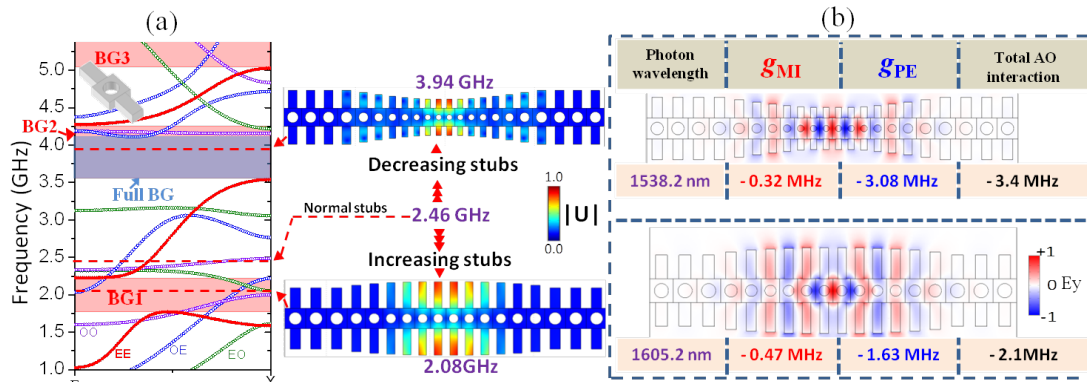


**Figure 1.** (a) Phononic band structure of the perfect nanobeam where the red shaded regions named BG1, BG2 and BG3 are the gaps for the modes which are symmetrical with respect to the symmetry planes of the nanobeam (red branches) and which are the only one that are able to couple with photonic modes and the gray shaded region for the full band gap. (b) AO coupling between the photonic cavity modes and the same phononic mode pushed up inside the full band gap or down inside the partial band gap by decreasing or increasing respectively the length of the stubs. In each figure we give the coupling coefficients  $g_{PE}$  and  $g_{MI}$ .

5K-3

## 4:00 pm Acoustic Pulses at Crystal Wedges Studied by Laser Ultrasonics

Alexey M. Lomonosov<sup>1,2</sup>, Pavel D. Pupyrev<sup>1,3</sup>, Peter Hess<sup>2</sup>, **Andreas P. Mayer<sup>3</sup>**; <sup>1</sup>General Physics Institute, Moscow, Russian Federation, <sup>2</sup>University of Heidelberg, Heidelberg, Germany, <sup>3</sup>HS Offenburg - University of Applied Sciences, Gengenbach, Germany

### Background, Motivation and Objective

Laser ultrasonics is an efficient method for non-destructive evaluation involving guided acoustic waves. It has also been used successfully to investigate the properties of such waves that are guided at surfaces and edges. Acoustic edge or wedge waves (WW) are less well-known than surface acoustic waves, but have attractive features like the absence of diffraction and their low speed. With the help of laser ultrasonics, strong effects of anisotropy on wedge waves were revealed, including the existence of leaky wedge waves in numerous propagation geometries in silicon crystals. In this contribution, we focus on the existence of fully edge-localized guided waves in various orientations of rectangular edges in crystals and on the shapes of laser-generated edge-localized acoustic pulses. These pulse shapes must be known for the analysis of pulse distortions due to defects or nonlinearity, for example.

### Statement of Contribution/Methods

Acoustic pulses were generated near the apex of silicon wedges having various orientations with respect to the cubic axes and wedge angles. In addition to thermo-elastic excitation by focusing a pulsed laser on a line normal to the apex, a laser-operated transducer was applied that exerts a pressure pulse on one of the wedge faces.

The pulses were detected by probe-beam deflection at various distances from the source and from the apex line. Their shapes were compared with results of calculations based on an expansion of the displacement field in a double series of Laguerre functions modeling the two excitation mechanisms.

### Results/Discussion

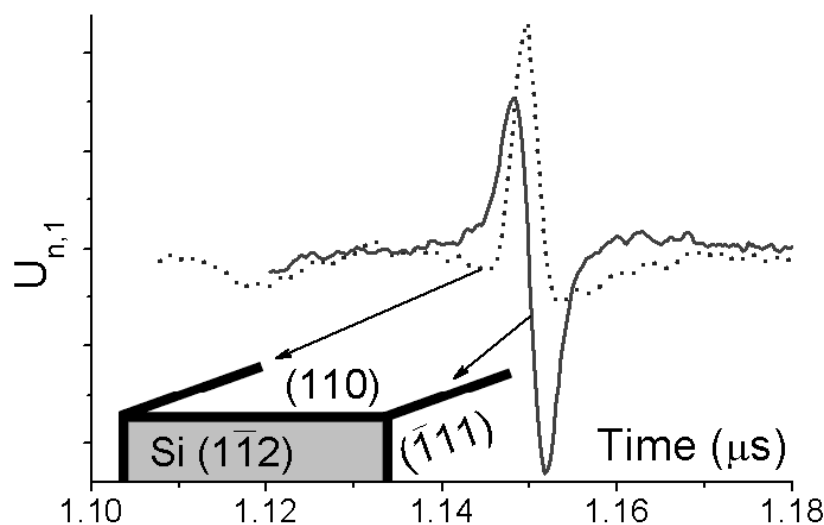
Good agreement between experiment and theory was obtained for pulse shapes and speeds, and pronounced effects of anisotropy have been found in the properties of WWs. They include a dependence of the thermo-elastically generated pulse shapes on the propagation direction, which is due to the same lack of symmetry exploited by natural uni-directional transducers.

The existence and the degree of tip-localization of guided acoustic waves at rectangular edges in silicon is discussed in view of recent rigorous theoretical results for WWs in isotropic media obtained by Kamotzki, Savorokhin and Nazarov.

This work has been supported by Deutsche Forschungsgemeinschaft (Grant No. Ma 1074/11).

Figure: Laser-generated WW pulse shapes in the thermo-elastic regime, measured surface slope  $U_{n,1}$  as a function of time.





5K-4

#### 4:15 pm Acousto-optical modulator based on elastic energy trapping in high aspect ratio interdigital transducers

Sarah Benchabane<sup>1</sup>, Ludovic Socie<sup>1</sup>, Luca Furfaro<sup>1</sup>, Vincent Laude<sup>1,2</sup>, <sup>1</sup>FEMTO-ST, Besançon, France

##### Background, Motivation and Objective

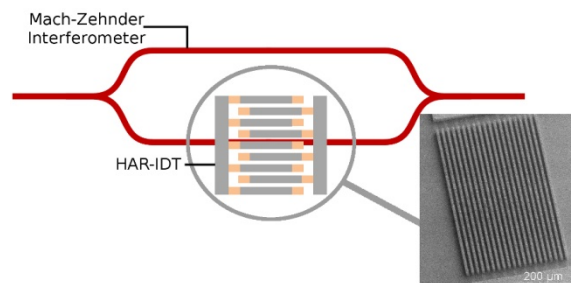
Acousto-optics (AO) is a well established concept, widely used in applied photonics for the control of the propagation of light beams. Surface acoustic waves have been for long considered as the privileged way of modulating light in monolithic integrated optical devices due to their intrinsic confinement at the substrate surface. The increasing demand for compact, low-power photonic devices however calls for the development of more efficient AO modulators. A very promising direction lies in a better use of the available acoustic energy. This can be obtained through a tighter confinement of the elastic strain at the vicinity of the optical guided modes.

##### Statement of Contribution/Methods

We propose an AO intensity modulator exploiting the elastic energy trapping capabilities of an interdigital transducer with high aspect ratio electrodes (HAR IDTs). The device relies on an integrated Mach-Zehnder interferometer (MZI) consisting of optical waveguides obtained by annealed proton-exchange of an X-cut lithium niobate substrate. The acoustic modulation is applied through an 18-μm pitch HAR IDT on a single arm of the interferometer in a transverse configuration. The device was optically characterized in a butt-coupling configuration and the output signal monitored in both the time and frequency domains. The influence of the acoustic modulation on the channeled spectrum of the MZI was also investigated.

##### Results/Discussion

A strong slowing down of the acoustic wave velocity along with a tight confinement of the elastic displacement field in the electrodes is observed for the modes lying well below the sound cone, resulting in a wave velocity of 1200 m/s for the slowest mode. A leaky surface wave is also excited at about 145 MHz. A modulation of the output optical signal is observed for each of the IDT resonance frequencies. The measured acousto-optical modulation amplitude is currently limited (15% for a confined mode, 5% for the leaky SAW) but can be increased by adjusting the MZI operating point which is not optimal in the present configuration. More unexpectedly, measurements performed at zero-frequency with an optical spectrum analyzer revealed a wavelength shift of the interferometer channeled spectrum reflecting a static modulation of the optical signal. This effect is directly linked to the electro-acoustic response of the HAR IDT and results in a shift as high as 20 nm at 145 MHz.



5K-5

#### 4:30 pm Dynamic control of optically generated ultrasound fields using binary amplitude holograms

Michael Brown<sup>1</sup>, Thomas Allen<sup>1</sup>, Ben Cox<sup>1</sup>, Bradley Treeby<sup>1,2</sup>, <sup>1</sup>Medical Physics and Bioengineering, University College London, London, United Kingdom

##### Background, Motivation and Objective

Piezoelectric transducers are vital for all areas of biomedical ultrasound, but they have several shortcomings. In particular, piezoelectric materials are resonant, with each transducer constrained to a limited bandwidth and centre frequency based on its manufactured properties. Laser generated ultrasound (LGUS) is a promising alternative modality in which a thin strongly absorbing layer emits ultrasound following optical irradiation. This allows broadband pulses with bandwidths of 100's of MHz. There is also the exciting possibility of using optoacoustic holography to generate arbitrarily shaped ultrasound fields and to tune the centre frequency of the ultrasound pulse. This works by patterning the absorber or the incident light field to control the acoustic field.

The goal of this work was to numerically and experimentally investigate if amplitude holography with a patterned absorber can be used to focus broadband LGUS waves produced by a pulsed laser.

#### Statement of Contribution/Methods

An algorithm was written to compute binary amplitude holograms from a desired source frequency and set of focal points.

Simulations concentrated on single focal point holograms or zone plates. The convergence in focal point volume of the acoustic pulse with greater numbers of discrete laser pulses applied at the hologram frequency was investigated. The focal spot sizes achieved using discrete laser pulses were also compared to using a sinusoidal source. The size of the focal spot was calculated from the number of voxels in which the maximum pressure exceeded half the overall maximum.

Initial experiments to test simulation results were carried out. A zone plate was fabricated using photolithography to create a patterned mirror over a highly absorbing nanocomposite material. A Litron Nano L 200-15 was used to excite the absorber with two narrowly spaced pulses. The resulting pressure field was recorded using a membrane hydrophone and a stepping motor rig.

#### Results/Discussion

Simulation results demonstrated two laser pulses can resolve the hologram focal point. This was validated experimentally. The number of pulses for the field to converge was related to the time taken for waves from the edge of the hologram to reach the focus.

The pulsed source was found to achieve smaller foci than the sinusoidal source. Lateral resolutions could be smaller than the diffraction limit of the pulsing frequency due to higher frequencies in the pulse constructively interfering at the focal point. This means that high lateral resolutions could be achieved without needing to design or pulse the hologram at a high frequency. This could have applications for high frequency 2D transducers.

This work shows that optoacoustic holography can be used to focus broadband LGUS sources using a binary amplitude mask and a pulsed laser. This will allow for flexible adaptation of the focus and frequency of LGUS pulses with important applications ranging from high frequency imaging to acoustic tweezers.

5K-6

#### 4:45 pm Controlled generation of micro-bubble at solid surface by focused nanosecond pressure pulse

Tae-hwa Lee<sup>1</sup>, Hyoung Won Baac<sup>2</sup>, Jong G. Ok<sup>1</sup>, Hong Seok Youn<sup>3</sup>, L. Jay Guo<sup>1,3</sup>; <sup>1</sup>Mechanical engineering, University of Michigan, Ann Arbor, Michigan, USA, <sup>2</sup>School of Electronic and Electrical Engineering, Sungkyunkwan University, Suwon, Korea, Republic of, <sup>3</sup>Electrical Engineering and Computer Science, University of Michigan, Ann Arbor, Michigan, USA

#### Background, Motivation and Objective

Acoustically generated micro-bubble at solid surface is of paramount importance in applications such as selective surface treatment and controlled permeation of biological samples. However, surface heterogeneity (e.g., micro-sized nucleation sites) poses some challenges in controlling bubble, leading to uncontrolled heterogeneous bubbles. Here, we demonstrate controlled single micro-bubble rather insensitive to surface quality as a result of small focused acoustic spot and high-amplitude negative pressure (~50 MPa) due to acoustic interference.

#### Statement of Contribution/Methods

We use a carbon-nanotube (CNT)-polymer composite as an optoacoustic transmitter. Acoustic interference from impedance mismatched boundary is simulated. Bubble nucleation process is visualized by laser flash shadowgraphy. To study effect of surface heterogeneity on bubble nucleation, we conduct a control experiment by using two different surfaces: a smooth glass substrate and a glass substrate patterned with micro-hole array.

#### Results/Discussion

Figure 1a shows peak negative pressure field near the glass surface, normalized to the maximum peak negative pressure (without the surface). Acoustic wave is highly localized near the surface due to constructive interference of the incident and reflected waves. The interfered peak pressure is much greater than peak pressure without the surface (vertical direction in Fig. 1b, horizontal direction in Fig. 1c). The interfered pressure almost doubled (~50 MPa), leading to micro-bubble nucleation (shadowgraph images in Fig. 2a). Lastly, single micro-bubble generation is rather immune to surface heterogeneity, especially micro-nucleation sites. Our method could offer a new approach to be universally applicable for selective modification of surfaces.

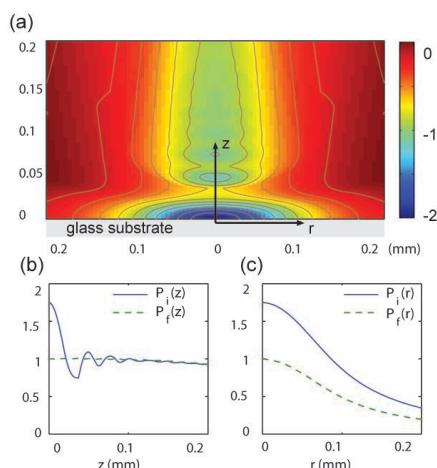


Fig. 1. Acoustic interference of focused acoustic wave  
(a) Peak negative pressure field near the glass surface.  
Peak pressure distributions in vertical (b) and horizontal (c) directions

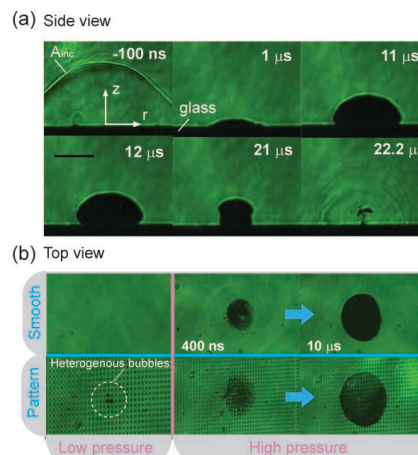


Fig. 2. Shadowgraph images of bubble nucleation on the glass surface.  
(a) side view (b) top view (smooth, patterned surfaces)

## P1C1 - MBB: Beamforming III

Salon C

Saturday, September 6, 2014, 8:00 am - 5:00 pm

Chair: **Roberto Lavarello**  
Pontificia Universidad Católica del Perú

P1C1-1

### A New Nonlinear Zone-based Beamforming Method for Point-of-Care Ultrasound Imaging

Pilsu Kim<sup>1</sup>, Jeeun Kang<sup>1</sup>, Jaemin Lee<sup>1</sup>, Gi-Duck Kim<sup>2</sup>, Yangmo Yoo<sup>1,3</sup>, Tai-kyong Song<sup>1</sup>; <sup>1</sup>Electronic Engineering, Sogang University, Seoul, Korea, Republic of, <sup>2</sup>Sogang Institute of Advanced Technology, Sogang University, Seoul, Korea, Republic of, <sup>3</sup>Interdisciplinary Program of Integrated Biotechnology, Sogang University, Seoul, Korea, Republic of

#### Background, Motivation and Objective

It is important for reducing the hardware complexity of an ultrasound dynamic receive beamformer for point-of-care ultrasound imaging systems. While the previously-proposed linear zone-based beamforming (ZBF-LI) method that piecewisely interpolates receive focusing delays between predetermined zones can substantially lower the complexity, it degrades image quality in the near field. In this paper, a new nonlinear zone-based beamforming (ZBF-NLI) method, which can considerably decrease focusing delay errors in the near field while reducing the hardware complexity, is proposed.

#### Statement of Contribution/Methods

In the proposed ZBF-NLI method, the optimal length of each zone is dynamically determined to limit the delay error below the allowance error (i.e., 0.25 for  $16f_0$  focusing delay resolution at  $4f_0$  sampling). The ZBF-NLI method was implemented on the low-cost FPGA chip (Spartan 6, Xilinx Inc., CA, USA) that was embedded in the custom-built portable US imaging system as shown in Fig. 1. To evaluate the proposed ZBF-NLI method, the Field II simulation was conducted by considering the system specification of the portable US imaging system (i.e., 7.5-MHz linear array with 40-MHz sampling). The peak signal-to-noise ratio (PSNR) was measured for the conventional dynamic receive focusing (CON) and the linear and nonlinear zone-based focusing methods (i.e., ZBF-LI, ZBF-NLI) while varying the allowance error from 0.25 to 1.0.

#### Results/Discussion

Figure 2(a) shows the number of zones and the corresponding memory size over the varying allowance error for the ZBF-LI and ZBF-NLI methods. As shown in Fig. 2, the proposed ZBF-NLI method provides the fewer zones for each allowance error than that of the ZBF-LI method (e.g., 136 vs. 2048 zones for 0.25). Figure 2(b) shows the US images from the respective methods where the same number of zones (i.e., 136) is used. The proposed ZBF-NLI method shows the more comparable image quality with the CON method than ZBF-LI method, which is consistent with the PSNR (i.e., 13.7 dB vs. 21.4 dB for ZBF-LI and ZBF-NLI). Also, the proposed ZBF-NLI method only requires 6.9% of memory (i.e., 4.4 KB) needed in the ZBF-LI method. These results indicate that the proposed ZBF-NLI method can improve image quality in the zone-based focusing method while substantially lowering the hardware complexity (i.e., memory size) for point-of-care ultrasound imaging.

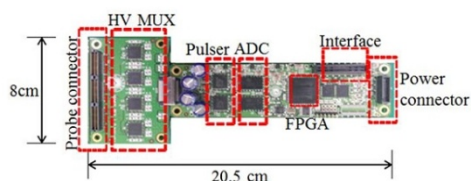


Figure 1. The portable US imaging system whose size is 8 cm and 20.5 cm for width and length, respectively. The developed ZBF-NLI component is implemented in the low-cost FPGA (Spartan 6 LX150, Xilinx Inc., CA, USA)

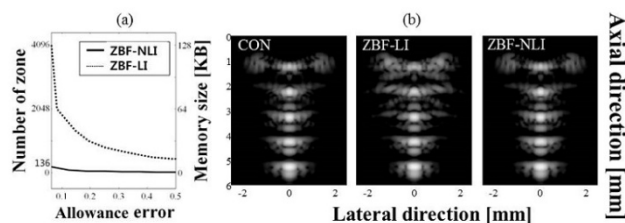


Figure 2. (a) The number of zone and corresponding memory size for the varying allowance error for the respective methods. (b) US images reconstructed by CON (reference), ZBF-LI, and ZBF-NLI methods, respectively.

P1C1-2

### Implementation of synthetic aperture imaging on a hand-held device

Martin Christian Hemmsen<sup>1</sup>, Thomas Kjeldsen<sup>2</sup>, Lee Lassen<sup>2</sup>, Borislav G. Tomov<sup>1</sup>, Jesper Mosegaard<sup>2</sup>, Jørgen Arendt Jensen<sup>1</sup>; <sup>1</sup>Center for Fast Ultrasound Imaging, Dept. of Elec. Eng., Technical University of Denmark, Kgs. Lyngby, Denmark, <sup>2</sup>Computer Graphics Lab, Alexandra Institute, Aarhus, Denmark

#### Background, Motivation and Objective

Conventional ultrasound imaging techniques rely on the use of multi-element transducers, where the analog signals from all elements are wired independently to the processing unit. The large number of signals is contributing to a high image quality, but comes with the cost of an expensive and fragile cable with difficulties to control infection risk. Synthetic Aperture Sequential Beamforming (SASB) is a technique that produces image quality comparable to dynamical receive focusing, but requires much lower data bandwidth between the probe and processing unit. It is hypothesised that the low data bandwidth requirement makes it possible to substitute the analog communication link with wireless technology standards. The objective of this work is to evaluate if modern mobile devices such as the LG Nexus 5 have the bandwidth and processing power to receive a Wi-Fi transmitted ultrasound data set and generate images in real-time.

# Statement of Contribution/Methods

Implementation of the SASB imaging technique requires integration of a simple fixed focus beamformer in the transducer handle. The beamformed data is transferred as a single stream to the main processing unit, and the final image is created by refocusing the fixed focus scan lines. In this work two LG Nexus 5 are used to emulate a setup consisting of a wireless transducer and a hand-held medical ultrasound device. Using a pre-recorded data set, the data throughput and processing performance are evaluated. The data throughput is evaluated using the wireless 802.11ac technology and Wi-Fi Direct (peer-to-peer connection without requiring a wireless access point) as well as Basic Wi-Fi (network based on the presence of a wireless access points). The processing performance is evaluated by implementing the refocusing of the fixed focused scan lines using (the high performance compute framework) OpenGL ES 3.0 on the Android 4.4.2 environment. The signal processing is validated with a Matlab implementation and consists of upsampling, beamforming of 269 image lines with each 1472 complex samples, amplitude detection, log-compression, and scan-conversion to an image of 1080x1080 pixels.

# Results/Discussion

Performance evaluations were carried out for a 3 seconds long pre-recorded data set consisting of 48 frames of each 269 lines x 1472 complex samples (1.58 MB pr. frame). The measured data throughput for Direct Wi-Fi is 7.3 MB/s equivalent to 4.6 frames/s and 4.3 MB/s equivalent to 2.7 frames/s using Basic Wi-Fi. Benchmarking of the signal processing showed a total processing time of 18.9 ms (53 frames/s) which is faster than the acquisition time (62.5 ms). The result of the benchmarking show that current high-end mobile devices do provide sufficient processing power for high-quality real-time imaging.

Evaluation of the data throughput showed that additional data bandwidth is required to achieve the needed bandwidth of 24 MB/s for a shorter data transfer time than acquisition time.

## P1C1-3

### Synthetic Aperture Sequential Beamforming implemented on multi-core platforms

Thomas Kjeldsen<sup>1</sup>, Esben Jern<sup>2</sup>, Lee Lassen<sup>1</sup>, Jesper Mosegaard<sup>1</sup>, Martin Christian Hemmsen<sup>2</sup>, Borislav G. Tomov<sup>2</sup>, Jørgen Arendt Jensen<sup>2</sup>; <sup>1</sup>Computer Graphics Lab, Alexandra Instituttet, Aarhus N, Denmark, <sup>2</sup>Center for Fast Ultrasound Imaging, Dept. of Elec. Eng., Technical University of Denmark, Kgs. Lyngby, Denmark

# Background, Motivation and Objective

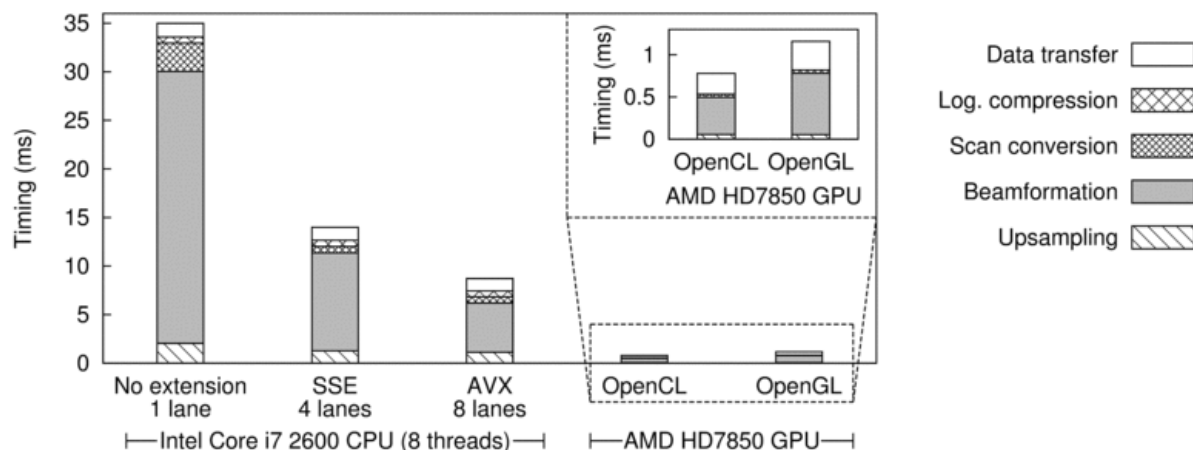
Medical ultrasound imaging systems are traditionally implemented using dedicated hardware for the beamformer. With the recent development in consumer level parallel processors, such as multi-core CPUs and graphics processing units (GPUs), it is advantageous to move the beamformer to software for improved flexibility and cost reduction. Synthetic Aperture Sequential Beamforming (SASB) is a beamforming technique that has recently been evaluated in a clinical trial. The evaluation showed that the image quality was comparable to conventional dynamic receive beamforming. This paper presents the first real-time SASB implementations utilizing modern multi-core platforms.

# Statement of Contribution/Methods

The basic idea in SASB is to use two separate beamformers. The first beamformer creates fixed focused scan lines. The final image is created in the second beamformer by refocusing these scan lines. A BK Medical UltraView 800 scanner was programmed to transfer fixed-focused scan lines to a PC. Image sequences were acquired at 16 Hz using a STI 3ML 3.5CLA192 convex transducer, and consisted of 269 emissions sampled at 20 MHz, creating 1472 complex samples per emission over the 14.6 cm of scan depth (1.58 MB/frame). All second stage processing algorithms were specifically designed for efficient utilization of the underlying hardware. The implementations targeting the CPU utilized multi-threading and instruction extensions. OpenCL and OpenGL high-level parallel languages were used for the GPU. The resolution of the final image was 512x512 pixels.

# Results/Discussion

Benchmarking of the second stage processing was performed using an Intel Core i7 2600 CPU (4 cores/8 threads) and an AMD HD7850 GPU. CPU timings were measured with  $\mu$ s-precision, and vendor-provided profiling tools were used to time the GPU implementations. All CPU benchmarks used 8 threads, and modern instruction extensions, SSE and AVX, were utilized for concurrent operations on 4 or 8 single-precision elements. The figure shows the timings per frame for the individual processing steps. The fastest CPU and GPU implementations use only 14% and 1.3% of the real-time budget of 62 ms/frame (16 fps), respectively. Hence, it is possible to lower the hardware specification, introduce image post processing steps or increase the output image size and still achieve real-time performance.



## P1C1-4

### A novel beamforming method for wireless ultrasound smart probe

MooHo Bae<sup>1</sup>, Nam Ouk Kim<sup>1</sup>, Sung-Bae Park<sup>2</sup>, Sung-Jae Kwon<sup>3</sup>; <sup>1</sup>Hallym University, Korea, Republic of, <sup>2</sup>Alpinion Medical Systems, Korea, Republic of, <sup>3</sup>Daejin University, Korea, Republic of

# Background, Motivation and Objective

Recently, in the field of medical ultrasound systems, the wireless smart probe is attracting attention. This probe has a constraint that all or part of the system beamformer should be integrated within the probe handle to reduce the data transmission rate. In this case, we should minimize the space and power dissipation of the integrated beamformer. In this paper, we propose a novel beamforming (BF) method which combines subaperture BF with phase rotation, digital BF, and synthetic aperture sequential BF (SASB; see J. Kortbek et al., IUS 2008) altogether in order to design a probe that meets these constraints effectively and is affordably implementable.

### Statement of Contribution/Methods

The method we adopt here is a 2-stage BF method in which the full aperture is divided into several subapertures, and the delays between signals in adjacent channels in a subaperture are approximately compensated with analog phase rotators, because the time delay can be approximated by phase rotation to save chip area and power consumption using a viable fabrication and/or design technology. Then these signals in a subaperture are added together. These added signals are digitized, and digital BF is performed.

For a linear probe, at small depths, there is a large difference in focusing delay between adjacent channels. The phase rotation BF in this situation results in large sidelobe levels because the signal envelopes cannot be aligned.

The 2-stage BF we have employed has tolerable phase rotation approximation errors in the middle depth region, and we can fairly well approximate the fixed point receive BF in the first step of the SASB. Thus, sidelobe reduction at small depths can be accomplished by combining the 2-stage BF method with SASB.

### Results/Discussion

The efficacy of the proposed method is verified with the Field II simulation. A linear probe with 7 MHz, 128 elements, and 0.3 mm pitch is modeled, and we assumed that four elements comprise a subaperture, and that the system can handle signals from a total of 16 subapertures. The Tx focal point is placed at a depth of 40 mm. Targets are placed at intervals of 5 mm from a depth of 5 mm to 70 mm.

Shown in Fig. 1 are images and lateral beam patterns reconstructed from 2-stage phase rotate & digital BF, and 2-stage BF combined with SASB. These results clearly show the efficacy of our proposed method.

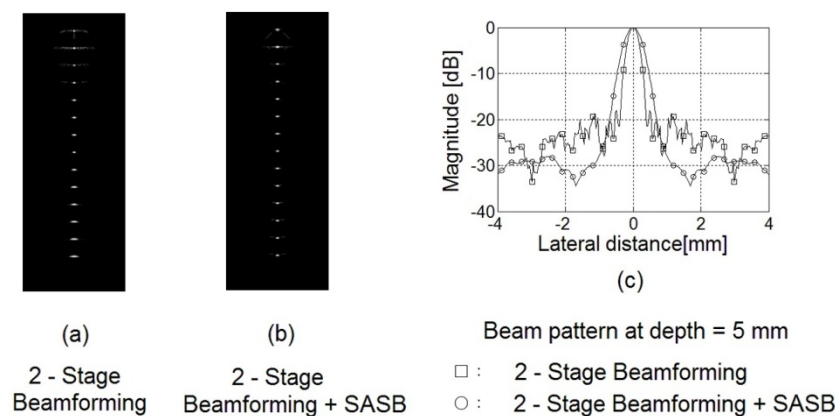


Fig 1

P1C1-5

### Optimization of free-moving elements in 2D ultrasound sparse arrays

Bakary Diarra<sup>1</sup>, Marc Robini<sup>1</sup>, Emmanuel Roux<sup>1,2</sup>, Piero Tortoli<sup>2</sup>, Hervé Liebgott<sup>1</sup>, Christian Cachard<sup>1</sup>; <sup>1</sup>CREATIS, Université de Lyon ; CNRS UMR 5220 ; INSERM U1044 ; Université Lyon 1 ; INSA Lyon, Villeurbanne, France, <sup>2</sup>Information Dept., Università degli Studi di Firenze, Florence, Italy

### Background, Motivation and Objective

In 3D ultrasound imaging, 2D sparse array design is useful to cope with the limited number of channels available in current scanners. The recently proposed non-grid sparse array technique (IEEE TBME, doi:10.1109/TBME.2013.2267742), in which the elements are not aligned on a regular grid, substantially reduces the number of necessary elements while maintaining low sidelobe level (SLL) and acceptable energy loss. In this approach, called simple apodization-based method (SABM), the possible element positions are fixed and their apodization weights are optimized using a sparsity promoting penalty. Consequently, the solution space is not entirely explored, as the algorithm does not allow to change the element positions during the optimization process. The method proposed here introduces this additional degree of freedom to further improve the beam properties.

### Statement of Contribution/Methods

In the new “moving-elements” approach, the number of active elements is fixed and a simulated annealing procedure optimizes both their apodization weights and positions to satisfy the constraints in terms of SLL and main lobe width. The performance obtained by this free placement strategy is compared to that of SABM via Field II simulations of the optimized arrays. The central frequency (3.5 MHz), footprint (17x17 mm<sup>2</sup>) and number of elements (256 of 4/5  $\lambda$  width each) are the same in both cases.

### Results/Discussion

The optimization of positions and apodization weights of the 256 elements (activated from an initial 64x64 dense array) has been tested for different steering angles. Fig.1 shows the beam profiles obtained (a) without steering and (b) with a 45° steering angle. The improvements in terms of grating- and side-lobes obtained with the moving-elements method are clearly visible: the lobes are reduced by about 6 dB. For the 45° steering angle (Fig 1.b), the highest SLL is -44 dB for SABM and -50 dB for the moving-elements method, and the -6 dB main lobe width is 2.8° for SABM and 2.3° for the proposed approach. Furthermore, the energy level is increased by about 8 dB with the new method because of the well-balanced placement and apodization of the elements. Similar results obtained at different steering angles confirm the moving-elements method's validity and its efficiency in terms of beam profile improvement.



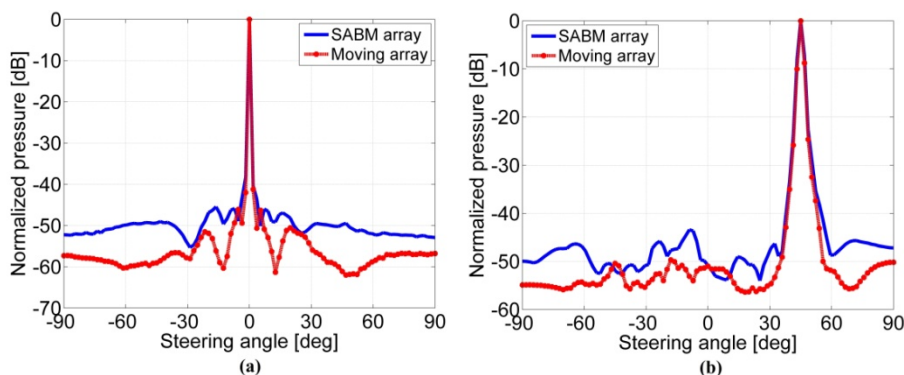


Fig. 1 : beam profiles of the reference SABM array and the moving-elements array obtained with a scatterer placed (a) on the array axis ( $0^\circ, 0^\circ$ ) and (b) out of axis ( $45^\circ, 45^\circ$ ).

P1C1-6

### Beamforming techniques for ultrasound microcalcification detection

Sheng-Wen Huang<sup>1</sup>, Jean-Luc Robert<sup>1</sup>, Emil Radulescu<sup>1</sup>, Francois Vignon<sup>1</sup>, Ramon Erkamp<sup>1</sup>; <sup>1</sup>Philips Research North America, USA

#### Background, Motivation and Objective

Mammography's success in breast cancer screening can be mostly attributed to its capability to image microcalcifications. In dense breast tissue, however, mammography shows poor performance. On the contrary, though ultrasound is a proven adjunct to mammography, especially in dense breast tissue, its sensitivity to microcalcifications is usually poor. To enable early ultrasound-based cancer detection in dense breast, the sensitivity has to be improved. In [1], Robert et al. developed a beamforming technique to address this issue.

#### Statement of Contribution/Methods

Here we report different beamforming techniques for imaging microcalcifications. The strategy is to involve channel-data-based parameters that favor point/sub-resolution targets, which microcalcifications resemble acoustically. Figure 1 shows an algorithm applied to in vivo data collected from a female volunteer using an HDI-5000 scanner and a linear probe (L12-5). Coherence factor and dominance of the first eigenvalue of covariance matrices are used to derive a likelihood map for microcalcification, which is then thresholded to obtain a binary microcalcification map.

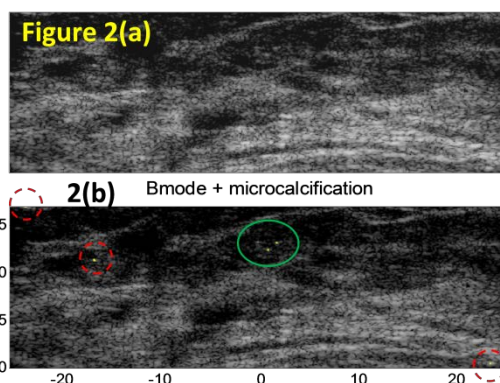
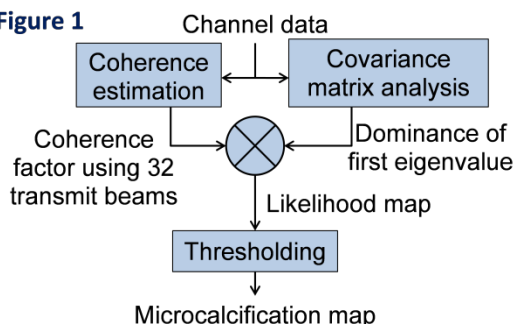
#### Results/Discussion

Figures 2(a) and 2(b) display the B-mode images without and with the microcalcification map overlaid. The yellow spots indicate detected microcalcifications. Three confirmed microcalcifications highlighted by the green circle were successfully detected. The yellow spots in the red dashed circles might be false positives. The exact sensitivity/specificity needs further evaluation, but the initial results show promise of the algorithm for microcalcification detection.

Results based on breast-mimicking phantoms will also be presented at the conference.

[1] J.-R. Robert et al., JASA, vol. 119, pp. 3848-3859 (2006).

Figure 1



P1C1-7

### Broad-Band, Large Delay Range, High Precision, and Variable Analog Delay Lines for a High-Frequency Phased Array Beamformer

Katherine Latham<sup>1</sup>, Craig Arthur<sup>2</sup>, Jeremy Brown<sup>1</sup>; <sup>1</sup>Biomedical Engineering, Dalhousie University, Canada, <sup>2</sup>Capital Health, Nova Scotia, Canada

#### Background, Motivation and Objective

Developing a suitable receive beamformer for high-frequency phased array transducers is extremely costly and very challenging to accomplish in the digital domain when using a conventional approach of recording the individual A-lines for each individual element and steering angle. This is due to the high sampling rates, large amount of parallel data throughput, up-sampling, and large lookup tables required. A much simpler approach to receive beamforming for phased arrays is to use broadband variable RF delay lines on

receive such that the beamforming delays are implemented before the channels are digitized. If the receive beamforming delays are implemented in the analog domain, then the channels can also be summed in the analog domain requiring only one channel to be digitized. This dramatically cuts down on the cost and complexity of the beamformer.

#### Statement of Contribution/Methods

We have successfully developed a prototype RF delay line that meets the required bandwidth, delay accuracy, and delay range requirements for a previously developed 64 channel endoscopic phased array prototype. Each delay line is based on a planar PMN-32%PT pulse-echo transducer situated in a water bath, reflecting off a polished brass reflector. The pulse-echo transducers are mounted on an individual in-house fabricated piezoelectric bimorphs, which are 'simply' supported. Each pulse echo transducer is connected to an individual array element in the phased array, and each bimorph actuator is connected to a variable high voltage signal controlled by an FPGA and parallel digital to analog converters. This causes the bimorph actuation and in turn the variable delays for the pulse echo transducers.

#### Results/Discussion

Each pulse echo transducer was fabricated from the same PMN-PT wafer and a dual matching layer was applied to the front face. The transducers were designed to be 1.2mm in diameter to provide a natural focus at the location of the brass reflector so that it minimizes degradation due to alignment. The experimentally measured centre frequency and bandwidth for the transducers was 40 MHz and 60 % respectively. The pulse echo insertion loss without considering water attenuation was measured to be -20.8 dB, therefore one single low-noise amplifier with 20 dB gain was required for each delay line to have zero insertion loss. The signal-to-noise ratio was only decreased by 1.1dB with this amplifier in place. The total delay range measured by adjusting the bimorph voltage by +/-65V was greater than 1 $\mu$ s, and the accuracy/repeatability of the pulse delay was approximately 1ns. To date 16 channels of individually controlled parallel delays have been fabricated and the fabrication/testing of a full 64 channel system is ongoing.

#### P1C1-8

##### Interpolation methods for economical pulse-echo signal synthesis

Pedro Nariyoshi<sup>1</sup>, Robert J. McGough<sup>1</sup>, <sup>1</sup>Electrical and Computer Engineering, Michigan State University, East Lansing, Michigan, USA

#### Background, Motivation and Objective

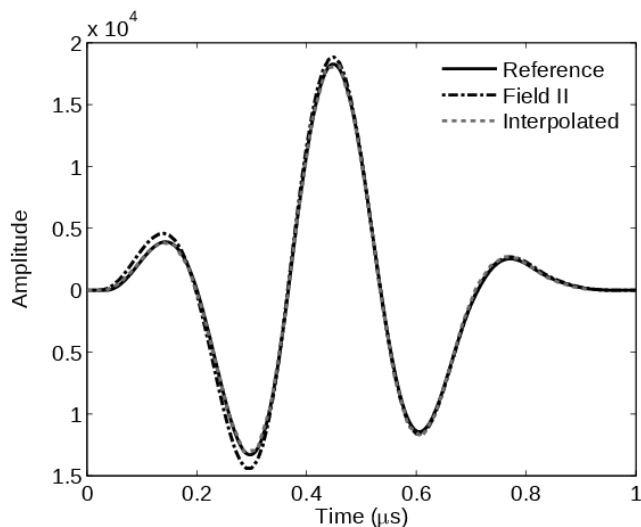
Models for pulse-echo simulations use a distribution of point scatterers to generate realistic computer phantoms. In these simulations, the contribution from an individual transducer element evaluated at a single scatterer produces the same signal on each A-line with different time delays and amplitude scale factors. Instead of re-calculating the pressure signals for each A-line, a much more efficient approach delays and scales the pressure signals before superposing the contributions from different transducer elements to obtain each simulated A-line.

#### Statement of Contribution/Methods

To delay these signals, appropriate interpolation schemes are necessary. New routines that are under development in FOCUS (<http://www.egr.msu.edu/~fultras-web>) implement cubic-splines using the exact arrival and edge times. The non-uniform sampling in the first and last sample allow better representation of the start and end of the signal where the slope is discontinuous. Cubic splines avoid Runge's phenomenon found in polynomial interpolators. Simulations are performed using 64 element sub-apertures in a linear array consisting of 192 rectangular elements that are 5mm high and 0.5133mm wide with 0.1mm center to center spacing. The simulation is evaluated for a computer phantom with 100,000 scatterers. The center frequency of the excitation is 3MHz. The intermediate signals from the transmit and receive apertures and the pulse-echo signals are shown for each simulation step and compared to a reference signal evaluated at 5GHz. The same configuration is used in Field II (<http://field-ii.dk>) to compare the computation time and accuracy.

#### Results/Discussion

The figure below shows a pulse-echo signal evaluated at 30MHz for a single transducer element and a single scatterer that demonstrates excellent agreement between the 5GHz reference and the 30MHz FOCUS result. Small differences in the Field II result obtained at 100MHz are also evident. To achieve 1% RMS error, FOCUS requires a sampling frequency of 30MHz, where Field II requires a sampling frequency of 180MHz and a factor of six increase in computation time to reach the same error. The results show that cubic splines provide an efficient and accurate way to represent signals for B-mode imaging simulations in FOCUS. [This work is supported in part by NIH Grant R01 EB012079]



# Pulse-Echo Ultrasound Imaging Using Compressed Sensing and the Fast Multipole Method

Martin Schiffer<sup>1</sup>, Georg Schmitz<sup>1</sup>; <sup>1</sup>Medical Engineering, Ruhr-Universität Bochum, Bochum, Germany

## Background, Motivation and Objective

Modern concepts for fast image acquisition, e.g. coherent plane wave (PW) compounding or synthetic aperture focusing (SA), are based on physical models that mainly account for the waves' times-of-flight. The usage of realistic physical models allowing for power-law absorption, dispersion, and inhomogeneous mechanical material parameters significantly improves image quality [1] but also increases hardware demands.

In this study, we extended our concept for pulse-echo ultrasound imaging (UI) based on compressed sensing (CS) / sparse recovery (SR) [1] by the fast multipole method (FMM) to drastically reduce memory consumption and computational costs. Our goal was to benefit from realistic physical models while reducing hardware demands.

## Statement of Contribution/Methods

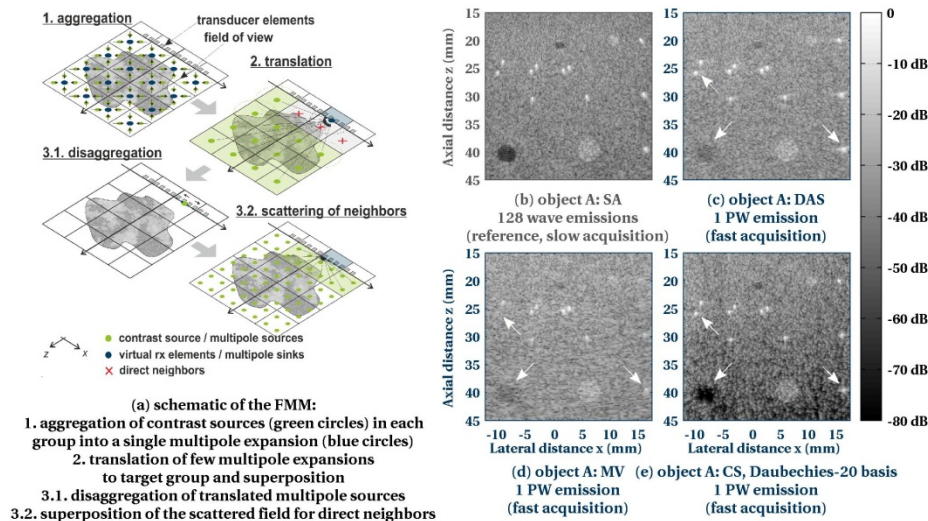
We formulated a linear inverse scattering problem (ISP) to recover spatial fluctuations in compressibility in a specified field of view from measurements of the scattered sound. The governing wave equation accounted for power-law absorption and dispersion based on a time causal model. Its associated Green's function was expanded into a multipole representation to enable the efficient numerical treatment of distant scatterers by the FMM (cf. (a)). We adopted a CS / SR strategy to regularize the ill-posed ISP, i.e. we ensured incoherent measurements and assumed that there exists a sparse representation of the fluctuations in compressibility in a known basis.

For the FMM's assessment, we acquired pulse-echo measurement data from a commercial tissue phantom (A). Recovered images were compared to those generated by SA, delay-and-sum (DAS), and minimum variance (MV) algorithms.

## Results/Discussion

In comparison to the standard matrix-vector product, the FMM reduced the memory consumption and the number of floating point operations for a single broadband wave emission by 98 % to 2 GiB and by 25 %, respectively. The proposed CS-based concept improved image quality in terms of lateral -6 dB-widths and image contrast (cf. (b)-(e)), while the FMM enabled its efficient implementation. The concept could be beneficial in applications that crucially depend on short acquisition times, e.g. cardiac UI and flow UI.

[1] M. F. Schiffer and G. Schmitz, "Compensating the Combined Effects of Absorption and Dispersion in Plane Wave Pulse-Echo Ultrasound Imaging Using Sparse Recovery", Proc. IEEE IUS, 2013, pp. 573-576



# Improving Performance of GPU-based Software Beamforming using Transform-based Channel Data Compression

U-Wai Lok<sup>1</sup>, Pai-Chi Li<sup>1</sup>; <sup>1</sup>National Taiwan University, Taiwan

## Background, Motivation and Objective

The massive data transfer of ultrasound channel data between the analog frontend and the digital backend becomes a critical limitation for a real-time GPU-based software beamformer. Our previous study proposed a real-time lossless compression/decompression algorithm to truncate unnecessary bits of ultrasound data and achieved a compression ratio of 1.7. Since the compression ability of the previous compression method depends on the largest signal within a batch, if the location of the largest signal within a batch can be identified and suppressed, higher compression ratio can be achieved. In this study, we propose Fast Walsh Transform (FWT) in combination with lossless compression to further improve the compression performance.

## Statement of Contribution/Methods

With FWT, the largest signal after transforming a batch of amplitude data is located at the first basis. Since the location of the largest signal is identified, the largest signal can be stored separately. This process is equivalent to suppressing the largest transformed signal within a batch data while maintaining the completeness of this signal (can be recovered by extracting the required bits). The compression ratio can thus be increased. FWT is used due to the low complexity of transformation/inverse transformation process performed by the butterfly architecture. Note that only the magnitude is compressed but the phase data is unchanged and quantized with 6 bits. Block diagrams of the proposed encoder and decoder are shown in Fig. A and B. The algorithm is implemented on a real-time array system (Prodigy, S-Sharp, Taiwan) as shown in Fig. C.

## Results/Discussion

The compression ratio improves to 2.13 with the proposed method. Hence, the bandwidth requirement from hardware front end to CPU can be reduced. At the software backend, the processing time of transferring a compressed frame data from CPU to GPU with the parallel decoder and inverse FWT requires about 7.8 ms. Nearly 1 ms improvement can be achieved as compared with transferring uncompressed baseband data. Results are summarized in Fig. D. Due to compression, data transfer rate between the front end and the

backend becomes less demanding. Furthermore, although additional time is needed to decompression, the overall processing time for each frame is also reduced due to the reduction in data transfer time.

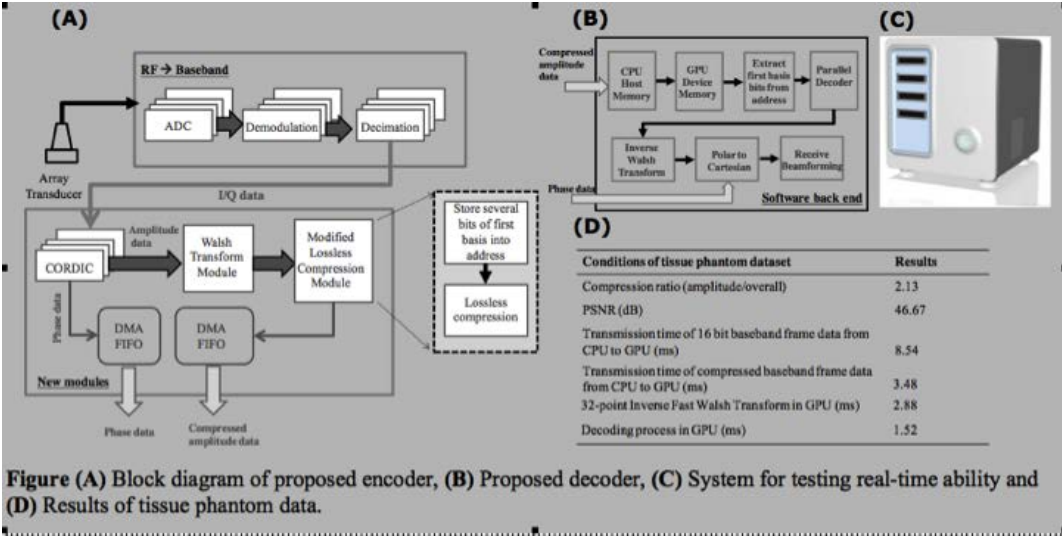


Figure (A) Block diagram of proposed encoder, (B) Proposed decoder, (C) System for testing real-time ability and (D) Results of tissue phantom data.

## P1C2 - MBB: Beamforming IV

Salon C

Saturday, September 6, 2014, 8:00 am - 5:00 pm

Chair: **Kai Thomenius**  
MIT

P1C2-1

### 2D Localization Of Specular Reflections Using Ultrasound

Raja Sekhar Bandaru<sup>1</sup>, Anders Sornes<sup>1</sup>, Jan D'hooge<sup>2</sup>, Eigil Samset<sup>1,3</sup>; <sup>1</sup>GE Vingmed Ultrasound, Oslo, Norway, <sup>2</sup>Cardio-vascular Imaging & Dynamics, KU Leuven, Leuven, Belgium, <sup>3</sup>Department of Informatics, University of Oslo, Oslo, Norway

#### Background, Motivation and Objective

Minimally-invasive catheter-based interventions are performed using image-guidance, typically X-ray fluoroscopy. X-ray provides an excellent visualization, but both patient and physician are exposed to significant amount of radiation. We present a novel method to locate and track a metallic device in real time using 2D (2 Dimensional) ultrasound. The objective of this method is to detect metallic objects (e.g. needle, catheter or guide wire) from ultrasound channel data by analyzing specular reflected pulses.

#### Statement of Contribution/Methods

Reflected echoes from smooth surfaces are focused with a clear peak received on one element, unlike diffuse echoes which are more evenly scattered across the transducer elements as shown in Figure 1.

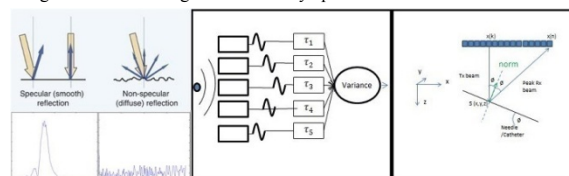
Test data was acquired by imaging a phantom (container with foam, water and a wire) as shown in Figure 2 and Vivid E9 with an 11L linear probe (GE, Horten, Norway). The maximum amplitude (normalized by the mean) and normalized variance across the elements were found to be large for echoes from each point on the specular reflecting objects. These values were small for diffused back scattering from the surrounding foam.

#### Results/Discussion

Guide wire was detected by beamforming with delay-and-variance and applying vesselness filter as shown in Figure 1. Normal vectors of wire were calculated by considering Snell's law using transmit beam's origin and orientation, depth of specular reflector and location of receive element with highest peak value as shown in Figure 1. The unwanted specular echoes from non-wire objects could be filtered using a Frangi Vesselness filter.

The location of a guide wire, along with its normal vectors, could successfully be detected and represented in all test data (Figure 2).

Range of detectable angles is limited by aperture size.



Echo amplitude received across transducer elements (left), beam forming with variance method (middle), and Snell's law to find orientation of a point on wire (right).

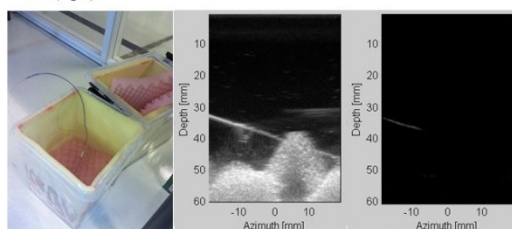
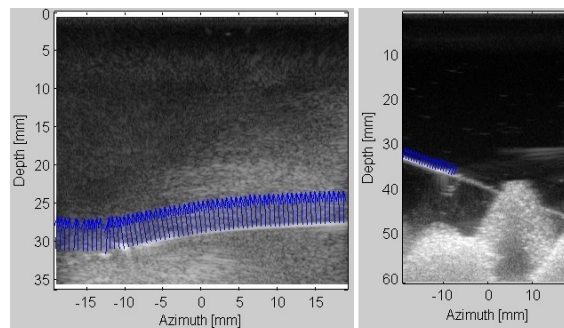


Figure1: Phantom (left), Normal beam formed (B-mode) image with a catheter wire (middle), Beamformed with delay-and-variance and filtered with Frangi Vesselness filter (right)



	Mean difference	Standard deviation
Data1 (curved wire) (left)	1.4°	2.4°
Data2 (curved wire)	-1.57°	1.43°
Data3 (straight) (right)	0.8°	1.68°
Data4 (curved wire)	0.52°	1.2°

Figure 2: B-mode images with detected normal vectors (top), validation of results with 4 different data sets: Mean and standard deviation of angular difference between detected normal vectors (by Snell's law) and normal vectors to a curve fitted through the center line of the guide wire (bottom)

P1C2-2

### Bi-static passive mapping of the field distribution of single element transducer in agar phantom

Trong Nguyen<sup>1</sup>, Michael Oelze<sup>1</sup>, Minh Do<sup>1</sup>; <sup>1</sup>Electrical and Computer Engineering, University of Illinois at Urbana Champaign, Urbana, Illinois, USA

#### Background, Motivation and Objective

High intensity focused ultrasound (HIFU) can provide a means of noninvasive ablation or hyperthermia of tissues such as tumors. Real-time monitoring of the progression of the field distribution of the HIFU transducer during treatment is important for localizing the intersection of the beam with the tissue. By continuously visualizing the HIFU field in a tissue, better positioning of the HIFU beam for therapy can be obtained during treatment. To visualize the HIFU field in a tissue, a passive listening technique was employed using beam forming approaches and a linear array system co-aligned with the HIFU source. The passive array made use of the weakly scattered signal from the medium to reconstruct the field pattern of the HIFU field in the medium.

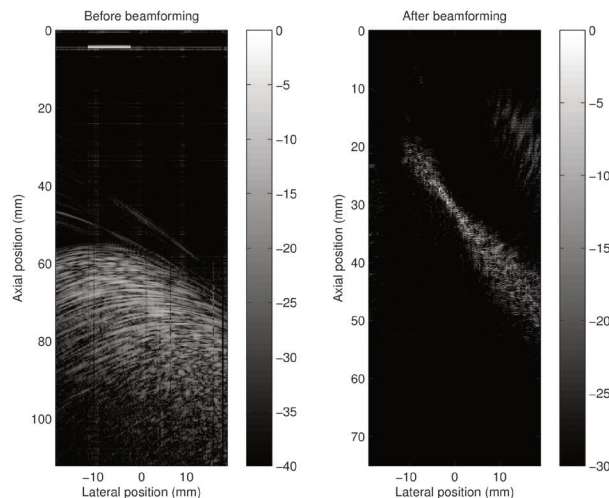


### Statement of Contribution/Methods

The focus of a 6-MHz single-element transducer ( $f/2$ ) was aligned perpendicular to the field of view from a linear array (14L5) operated by a SonixRP system equipped with a SonixDAQ. A homogeneous tissue-mimicking phantom made of agar containing glass beads was placed at the focus between the 6-MHz source and the linear array. The 6-MHz source was excited with a pulse and the field scattered from the phantom was received by each element of the linear array. Beamforming techniques were used to focus the received field of the linear array around the focal region of the 6-MHz source. The intensity field pattern of the 6-MHz source was reconstructed from the scattered field. Next, a wire target was placed in the field and the intensity field pattern was reconstructed by moving the wire throughout the focal region. The intensity pattern from the phantom was compared to the nominal field characteristics of the 6-MHz source and to the field characterized by a wire.

### Results/Discussion

The figure shows an image (left) of the received scattered field from the phantom and (right) the reconstructed intensity field pattern after beam formation. The beam width at the focus of the reconstructed intensity field pattern was estimated to be 1.76 mm. The nominal estimate of the beam width was approximately 0.5 mm (-3 dB) and the beam width as estimated from the wire target field mapping was 0.53 mm. These results suggest that the proposed passive reconstruction technique successfully visualized the field from a focused source in a weakly scattering medium and may therefore be useful as a method for real-time monitoring of HIFU.



P1C2-3

### Simulation of fast and realistic nonlinear radio-frequency ultrasound images using a pseudo-acoustic strategy

François Varray<sup>1</sup>, Hervé Liebgott<sup>1</sup>, Christian Cachard<sup>1</sup>, Didier Vray<sup>1</sup>; <sup>1</sup>Université de Lyon, CREATIS ; CNRS UMR5220 ; Inserm U1044 ; INSA-Lyon ; Université Lyon 1, Villeurbanne, France

### Background, Motivation and Objective

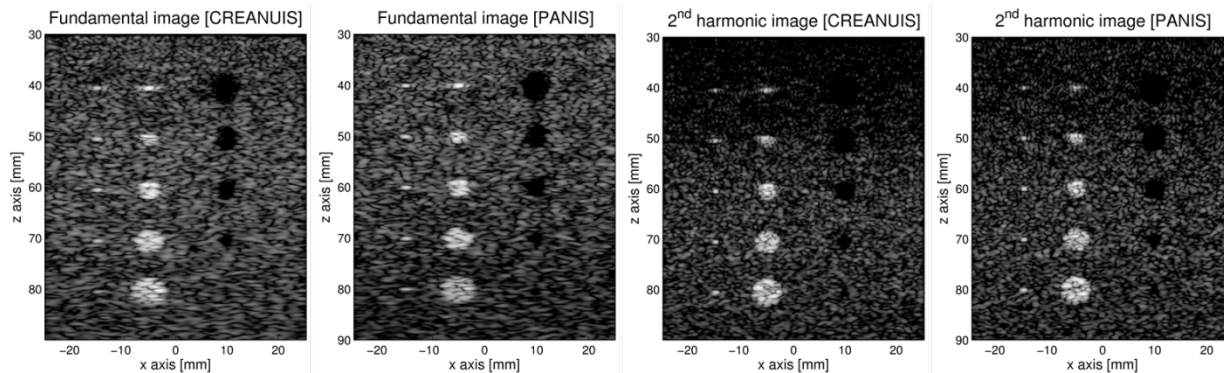
Acquisition and processing of nonlinear ultrasound (US) wave are considered to improve image resolution and to exhibit the nonlinear properties of living tissues. However, few simulators fully simulate such nonlinear effects and the resulting nonlinear B-mode images, whereas such a tool would be of great interest for the ultrasound community. Recently, a full acoustic simulation tool, Creanuis [Varray et al., UMB 2013], has been proposed and provides realistic nonlinear radio-frequency US images. However, the computation time is not comparable with the fastest simulation tools based on convolution strategy (Cole, Fusk, Creasimus), but based on linear US wave propagation. In this work, we proposed a pseudo-acoustic nonlinear image simulation (PANIS) based on convolution strategy including both linear and nonlinear propagation models.

### Statement of Contribution/Methods

To handle such objective, a convolution strategy is used and consists to convolve the scatter map with a nonlinear and depth-variant PSF. This simulates the dependence of the PSF (point spread function) of the imaging system as function of depth and also the nonlinear behavior of the imaged media. Firstly, the simulation of  $N$  punctual scatters placed on the central axis is conducted with Creanuis and  $N$  corresponding PSF are extracted. Then, the convolution is conducted between each PSF and the desired scattering medium. At this step,  $N$  nonlinear images are generated and the final PANIS image is obtained by merging the different elementary images calculated at the various depths. The obtained PANIS image is thus nonlinear and the corresponding PSF depth dependent.

### Results/Discussion

The simulation of such images is much faster than those calculated with other approaches. Using 6 elementary PSF (1 each centimeters) and 100 000 scatters in the cyst phantom, the final simulation is conducted in less than 20 s in comparison of 33 mn with Creanuis. The obtained images are presented and both produced images are extremely similar. The mean absolute difference between Creanuis and PANIS image are 2.5% and 2.0% for the fundamental and second-harmonic, respectively. The resulting images contain nonlinear information. Note that specific apodization in transmission and reception, varying impulse response of the transducer and all the settings that can be selected in Creanuis can also be modified using PANIS.



Obtained images with Creanuis and PANIS for the fundamental and second-harmonic images. A 40 dB dynamic range has been set on each images.

P1C2-4

### Nonlinear Reconstruction of the Speed of Sound in Soft Tissues: A Comparison between the Simulation Results Applying Kaczmarz and Contrast Source Inversion Methods

Leili Salehi<sup>1</sup>, Georg Schmitz<sup>2</sup>; <sup>1</sup>Medical Engineering, Ruhr-Universität Bochum, Bochum, Germany

#### Background, Motivation and Objective

Reconstruction methods for nonlinear ultrasound diffraction tomography retrieve material parameters accounting for multiple scattering. Such an algorithm based on the Kaczmarz method (K-M) reconstructs the spatially varying speed of sound (SoS), equivalent to a spatially varying compressibility, in the time domain [1]. The Contrast Source Inversion method (CSI-M) reconstructs the SoS from the refractive index of an inhomogeneous object in a known background in the frequency domain [2]. Here, we compare the reconstruction results for the SoS applying both methods to the same object in the same medium.

#### Statement of Contribution/Methods

A pseudo spectral time domain simulation is performed for the forward propagation in a solution space of 48 mm × 48 mm full of water with perfectly matched layers on the borders. Here, we used simulated measurement data obtained from a simulated phantom. 36 point transducers for transmit and receive are distributed on a circle around the object with varying compressibility and constant density of 1074 kg/m<sup>3</sup>. The object is insonified with pulse excitation ( $f_0 = 1$  MHz, BW = 850 kHz) using all transducers, consecutively. Scattered pressures are recorded and used to reconstruct the SoS changes.

In K-M, the adjoint operator for the Fréchet derivative of the wave propagation's nonlinear operator for compressibility changes is calculated. However, the forward and backward problems have to be solved in each iteration.

In CSI-M, the forward propagation is performed once to calculate the incident field. In each iteration, having the incident and scattered fields for 10 frequencies (220-1700 kHz) the unknown contrast is updated in the object domain by conjugate gradient steps to minimize a proper cost function without requiring the solution of the full forward problem.

#### Results/Discussion

Fig. 1 shows the SoS maps of the phantom (a), the reconstruction with K-M (b) and the reconstruction with CSI-M (c). Corresponding errors of (b,c), are displayed in (d,e), respectively. As indicated in Fig. 1, both methods reconstruct the SoS with the same precision; however, K-M needs more iterations (Mean Fractional Errors after 36, 180, and 360 iterations are 64.7%, 19.1%, and 10.5%) in comparison to CSI-M (13.8%, 11.4%, and 11.2%) to converge. Each iteration takes about 114 sec for both methods. Additional simulations show that K-M is more robust for higher contrasts.

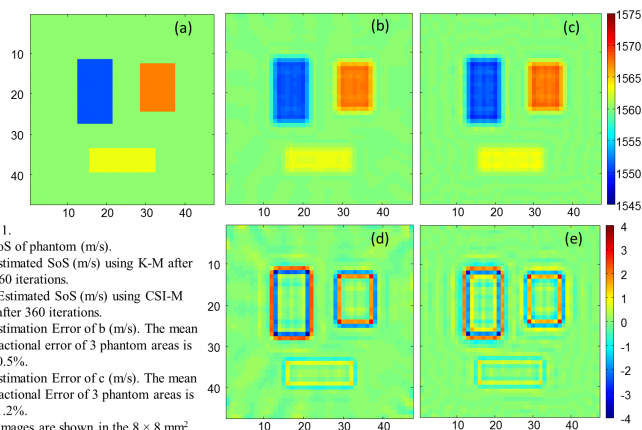


Fig. 1.

a) SoS of phantom (m/s).

b) Estimated SoS (m/s) using K-M after 360 iterations.

c) Estimated SoS (m/s) using CSI-M after 360 iterations.

d) Estimation Error of (b) (m/s). The mean fractional error of 3 phantom areas is 10.5%.

e) Estimation Error of (c) (m/s). The mean fractional error of 3 phantom areas is 11.2%.

All images are shown in the 8 × 8 mm<sup>2</sup> object domain.

[1] L. Salehi and G. Schmitz, "Nonlinear reconstruction of compressibility and density variations using the Kaczmarz method," 2012 IEEE Int. Ultrason. Symp., pp. 386–389, Oct. 2012.

[2] P. Van Den Berg and R. Kleinman, "A contrast source inversion method," Inverse Probl., vol. 13, pp. 1607–1620, 1997.

## P1C2-5

**Finite difference implementation of power law attenuation in the Khokhlov – Zabolotskaya – Kuznetsov (KZK) equation for continuous-wave nonlinear ultrasound simulations in FOCUS**Xiaofeng Zhao<sup>1</sup>, Robert J. McGough<sup>1</sup>; <sup>1</sup>Electrical and Computer Engineering, Michigan State University, East Lansing, Michigan, USA**Background, Motivation and Objective**

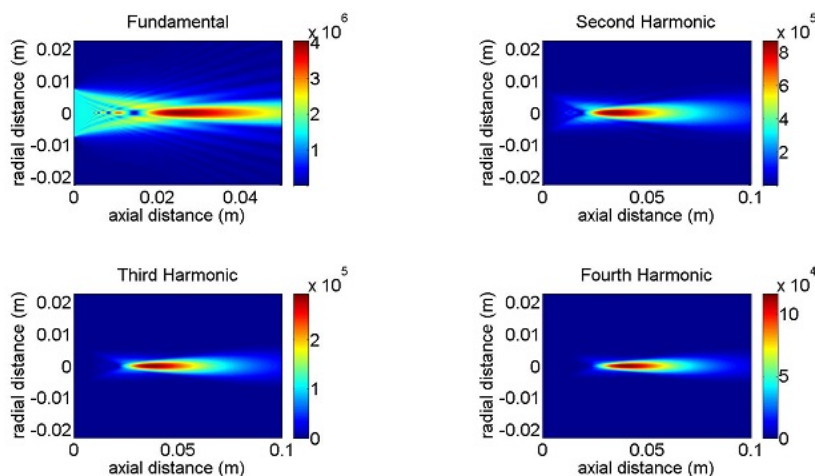
The Khokhlov – Zabolotskaya – Kuznetsov (KZK) equation is a nonlinear wave equation with a viscous loss term that describes frequency-squared attenuation. However, for soft tissues, ultrasound attenuation follows a power law with an exponent between 1 and 1.5. A modified version of the KZK equation is needed for continuous-wave simulations of nonlinear ultrasound propagation that experience power law attenuation in soft tissue.

**Statement of Contribution/Methods**

Routines that combine nonlinear effects with power law attenuation are presently under development for FOCUS, the 'fast object-oriented C++ ultrasound simulator.' The implementation generally follows the approach employed in the Bergen finite difference code [Berntsen, Proceedings of the 12th ISNA, 1990], where the corresponding FOCUS routine is written in C++ instead of Fortran and the viscous attenuation is replaced by power law attenuation. The FOCUS routine simulates pressure fields generated by a spherically focused transducer with an aperture radius of 7.5 mm and a radius of curvature equal to 60 mm. The peak pressure on the surface of the transducer is 1.5 MPa, and the frequency of the fundamental is equal to 1 MHz. The parameters of the medium include the nonlinearity parameter  $\beta = 3.5$ , the attenuation constant  $\alpha_0 = 0.7$  Np/cm/MHz<sup>2</sup>, and the power law exponent  $\gamma = 1.5$ .

**Results/Discussion**

Simulation results are evaluated for continuous-wave excitations in both linear lossy media and nonlinear lossy media. For simulations of linear ultrasound propagation in power law media, the results obtained from the modified KZK model with power law attenuation are compared to FOCUS simulations with the fast nearfield method. The results are consistent in the farfield of the paraxial region for transducers with larger f-numbers, but significant differences are observed elsewhere. Nonlinear pressure fields are also computed for different harmonics. The pressure fields computed for the first four harmonics are shown in the figure below. Additional related simulation results will be presented, and implementation issues will also be discussed [This work was supported in part by NIH Grant R01 EB012079].



## P1C2-6

**A Multi-threaded Version of Field II**Jørgen Arendt Jensen<sup>1</sup>; <sup>1</sup>Dept. of Elec. Eng., Technical University of Denmark, Lyngby, Denmark**Background, Motivation and Objective**

Field II has been used in numerous investigations of advanced imaging techniques. The initial versions of the Field programs were developed in 1990 on the Apollo DN3000 workstation with a calculation speed of 72 kFLOPS and very limited RAM. Modern processors have access to Gbytes of RAM and can yield around 10-100 GFLOPS. This made it possible to use Field II in Monte Carlo simulations of very large parameter studies for e.g. 3-D imaging, vector velocity imaging, and other applications. The studies, however, often take a significant amount of CPU time. The purpose of this work is to develop a multi-threaded version of Field II, which uses all the benefits of modern CPUs to reduce computation time.

**Statement of Contribution/Methods**

The old workstations only contained one CPU, and RAM access was fast compared to the time for executing floating point operations. Current CPUs hold multiple computing cores, and the RAM access time is large compared to the time for one floating point calculation. They also house generous caches for speeding up data access. A multi-threaded version of Field II was written with dynamic partition of the calculation. The memory allocation routines were rewritten to minimize the number of dynamic allocations and to make pre-allocations possible for each thread. This ensures that the simulation job can be automatically partitioned and the interdependence between threads minimized.

**Results/Discussion**

The new code has been compared to Field II version 3.22, October 27, 2013 (latest freeware version). A 64 element 5 MHz focused array transducer with 4 mathematical rectangular elements per physical element was simulated. The electronic focus was at 60 mm and the elevation focus at 40 mm. One million point scatterers randomly distributed in a plane of 20 x 50 mm (width x depth) with a random Gaussian amplitude were simulated using the command calc\_scatt. Dual Intel(R) Xeon(R) CPU E5-2630 2.60 GHz CPUs were used under Ubuntu Linux and Matlab version 2013b. Each CPU holds 6 cores with hyper-threading corresponding to a total of 24 hyper-threading cores. The averaged simulation time for 10 realizations for the old version was 108.7 s. A single thread run for the new version took 46.7 s; a speed-up of 2.3. Employing all 24 cores gave a simulation time of 4.1 s for the one million scatterers corresponding to a speedup factor of 26.5 times or 11.5 relative to the single threaded run. The speed-up in general depend on the transducer, scatterers and simulation, and it varies across applications between 13 and 30. A significant speed-up of Field II has been attained by employing pre-allocation, reuse of memory in the cache, and multi-threaded execution. The program is fully compatible with older versions and only a single command for setting the number of threads to use has

been added. The division of labor is automatically handled by the program. For a phantom with 100,000 scatterers, it is now possible to simulate a full 128 line image in around 53 seconds with full precision.

## P1C2-7

### Beamforming designs for breast sonography

Nghia Nguyen<sup>1</sup>, Craig Abbey<sup>2,3</sup>, Michael Insana<sup>4</sup>; <sup>1</sup>ECE, University of Illinois at Urbana-Champaign, Urbana, Illinois, USA, <sup>2</sup>Psychology, University of California at Santa Barbara, Santa Barbara, California, USA, <sup>3</sup>Psychology, University of California, Santa Barbara, California, USA, <sup>4</sup>Bioengineering, University of Illinois at Urbana-Champaign, Urbana, Illinois, USA

#### Background, Motivation and Objective

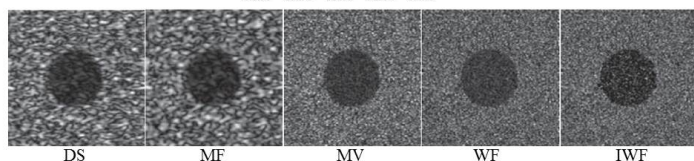
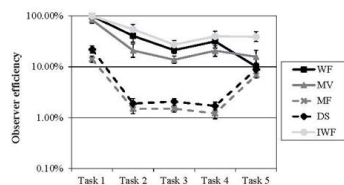
The goal of task-based Bayesian beamformer design is to optimize performance for visualizing the entire range of patient features essential for diagnosis, not just one feature. Patient information is represented statistically within a log-likelihood function that describes the ideal observer (IO) strategy for beamforming. However, only approximations to the IO strategy can be realized in practice. We show how various approximations give rise to the family of beamformers found in the literature today.

#### Statement of Contribution/Methods

The objective of Bayesian beamformer design is to diagonalize a form of the echo-data covariance matrix. Approximations to the diagonalization procedure yield the many types of beamformers now under consideration, including classic approaches that minimize variance and the mean-squared error. We show how the IO strategy results in delay and sum (DS), matched filtering (MF), linear constrained minimum variance (MV), and Wiener filtered (WF) beamformers, and that all but the DS assume stationary echo statistics equivalent to low-contrast features. Iterative approaches to WF beamformer (IWF) can include high-contrast features at the cost of a factor of five in computational load.

#### Results/Discussion

We explored beamformer performance using simulated lesion data for breast sonography from the BIRADS lexicon. Comparing task-dependent information before and after receive-channel compression, we estimated the ideal-observer efficiency  $\epsilon$  for five large-area and boundary features. An example of beamformer effects on a simple circular lesion and the efficiency for the five tasks are shown below. Clearly information transfer efficiency is highly task dependent. Those best able to decorrelate echo data while preserving lesion feature contrast are more efficient at transferring task information into the B-mode image. Trade-offs among diagnostic performance and computation time (frame rate) for five beamformers are evaluated under this single approach to design.



## P1C3 - MBF: Methods and Applications for Blood Velocity Estimation

Salon C

Saturday, September 6, 2014, 8:00 am - 5:00 pm

Chair: **Abigail Swillens**  
Ghent University

P1C3-1

### Design of Atherosclerotic Artery Phantoms with Modulated Vessel Thickness and Regional Stiffness Variations

Adrian J. Y. Chee<sup>1</sup>, Simon S. M. Lai<sup>1</sup>, C. K. Ho<sup>1</sup>, Alexander K. K. Poon<sup>1</sup>, Billy Y. S. Yiu<sup>1</sup>, Alfred C. H. Yu<sup>1</sup>; <sup>1</sup>Medical Engineering Program, The University of Hong Kong, Pokfulam, Hong Kong

#### Background, Motivation and Objective

Flow phantoms are well-regarded as essential tools in vascular ultrasound. For these devices to operate in similar conditions as those in vivo, two key features should be included: (i) anatomically relevant vessel geometry, and (ii) compliant vessel mimicking material. While earlier studies have shown that 3D printing can fabricate flow phantoms with compliant vessels, the elastic properties of the vessel mimic cannot be tuned due to inherent material properties of photopolymers. Thus, it is difficult to develop phantoms with controllable mechanical properties. In this study, we seek to devise a new framework that can facilitate the design of flow phantoms whose vessels exhibit regional stiffness variations and modulated thickness.

#### Statement of Contribution/Methods

Our framework has been devised to fabricate atherosclerotic artery models with various pathologically relevant mechanical behavior and morphologies, including regional wall stiffening, diffusive plaque, stenotic narrowing, and plaque ulceration. It first used computer aided design software to generate: 1) a negative outer mold of the vessel (9 mm diameter), and 2) various inner cores (7 mm baseline diameter) with structural modulation patterns. After fabricating them, the inner core was mounted within the negative outer mold, and the resulting cavity between them was injected with a polyvinyl alcohol (PVA) gel solution to form the vessel wall. Wall stiffness was manipulated by varying the number of PVA freeze-thaw cycles (1 to 5) and PVA concentration (5%, 10%, 15%). Regional variations in wall stiffness was achieved by, in between freeze-thaw cycles, selectively excising the intended vessel segments and refilling the resulting void with fresh PVA solution. To measure the vessel properties, uniaxial load tests (Instron) were conducted to estimate Young's modulus. Acoustic speed and attenuation values were also derived via insertion-loss measurements. To assess whether the vessels would distend in a way similar to that of human arteries, the phantom was connected to a pulsatile pump (carotid pulse; 1.2 Hz rate), and gated M-mode imaging was conducted (SonixTouch; 5 MHz freq., 500 Hz PRF, 1 cycle pulse). Vessel distension waveforms were then derived, and pulse wave velocity was estimated.

#### Results/Discussion

The elastic modulus of our vessel wall material was found to range between 30-170 kPa, and millimeter-range segments of local stiffness variations were successfully realized. As a demonstration, we fabricated stenosed common carotid artery phantoms with 1.5mm wall thickness. The stenosed region (10mm length; 50% narrowing) had an elastic modulus of 100kPa, while that for the rest of the vessel was 70kPa. M-mode estimation results show that the change in pulse wave velocity was synchronized with the ratio of stiffness between stenosed and non-stenosed regions. These phantoms can be used to investigate new arterial imaging methods, such as lateral wall motion estimation.

P1C3-2

### An Analytical Model of the Doppler Spectrum for Peak Blood Velocity Detection

Stefano Ricci<sup>1</sup>; <sup>1</sup>Information Engineering, University of Florence, Florence, Italy

#### Background, Motivation and Objective

The peak blood velocity is a parameter of high medical interest. It is typically measured by locating, on the Doppler spectrum, the frequency  $f_M$  which corresponds to a given threshold,  $Th$ . The peak velocity,  $V_M$ , is obtained by converting  $f_M$  through the Doppler equation. The accuracy of the final estimate strongly relies on the choice of  $Th$ . Specific mathematical models, like doi: 10.1109/TUFFC.2013.2798, can be employed to assess the  $Th$  to be used in a specific set-up, but an analytical and parametric expression of  $Th$  is still missing.

In this work an extension of the aforementioned model is proposed and an analytical formula for  $Th$  is calculated. The model efficacy is checked through peak velocity measurements based on Field II simulations.

#### Statement of Contribution/Methods

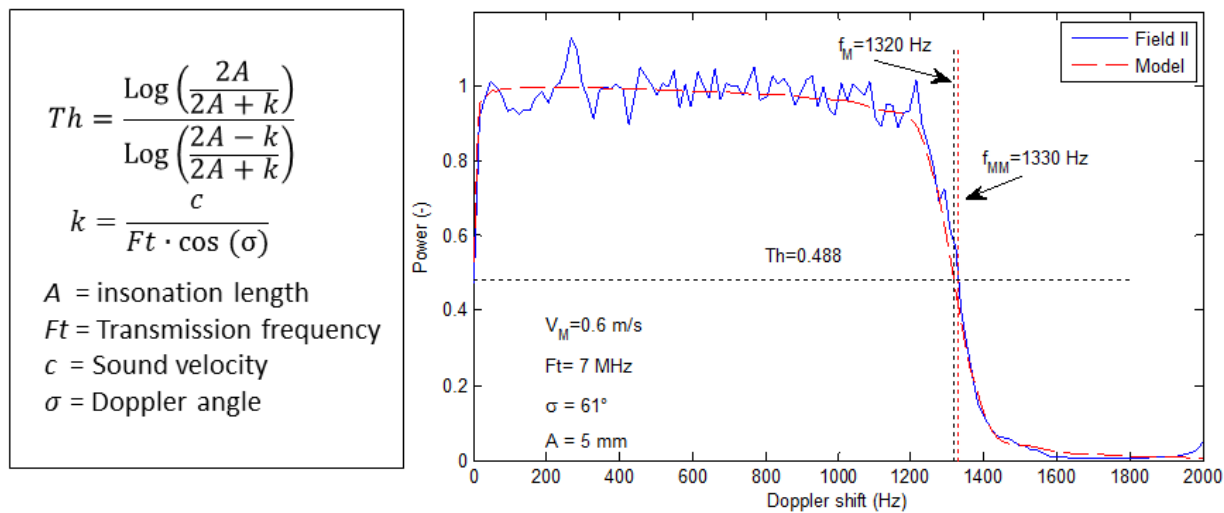
The model: The new analytical model is build following the same approach as described in doi: 10.1109/TUFFC.2013.2798. The investigating sample volume covers the whole lateral extension of the vessel of interest and extends longitudinally for the length  $A$ . A flow runs in the vessel with a parabolic profile and peak velocity  $V_M$ . The analytical Doppler spectrum, and thus  $Th$ , are obtained by integrating the frequency contributions of all the scatterers crossing the illuminated region.

Validation: Several Doppler spectra are calculated by the model and compared to corresponding spectra generated by Field II. The peak velocities measured by applying the  $Th$  originated by the new model are compared to the corresponding velocities from Field II simulations. 20 experiments were carried out with  $V_M$  between 0.2-1 m/s, insonation length  $A$  in the range 1-10 mm, transmission frequency  $F_t$  between 3-9 MHz.

#### Results/Discussion

The proposed analytical expression of  $Th$  is reported in the figure, on the left, as a function of insonation length  $A$ , Doppler angle  $\sigma$ , transmission frequency  $F_t$ . On the right, an example of predicted spectrum obtained with  $V_M = 0.6$  m/s,  $F_t = 7$  MHz,  $\sigma = 61^\circ$ , is compared to that generated by Field II. The corresponding  $Th = 0.488$  is reported by the horizontal dotted line. The vertical lines represent the frequency  $f_M$  corresponding to  $V_M$  and the frequency  $f_{MM}$  located on the measured spectrum by the threshold  $Th$ . In this example the error is 0.8%. The accuracy achieved in the 20 peak velocity measurements by applying the proposed  $Th$  was  $+1.2$  cm/s with 1.5 cm/s standard deviation.





P1C3-3

### An Improved Method of Determining Peak Blood Velocity

Stefano Ricci<sup>1</sup>, David Vilkomerson<sup>2</sup>, Riccardo Matera<sup>1</sup>, Piero Tortoli<sup>1</sup>; <sup>1</sup>Information Engineering, University of Florence, Firenze, FI, Italy; <sup>2</sup>DVX LLC, Princeton, NJ., USA

#### Background, Motivation and Objective

The peak blood velocity is used in important diagnostic applications, e.g. stenosis evaluation. The peak velocity is typically assessed by locating the highest frequency detectable from noise in the Doppler spectrum, or by applying a heuristic threshold. The selected frequency is then converted to velocity by the Doppler equation. This procedure contains multiple potential sources of error: the frequency selection is sensitive to noise and affected by spectral broadening, and the velocity conversion is affected by the Doppler angle uncertainty. The result is an inaccurate estimate.

In this work we propose a new method that removes the errors due to both the frequency selection and the Doppler angle ambiguity, thus providing peak velocity measurements with improved accuracy.

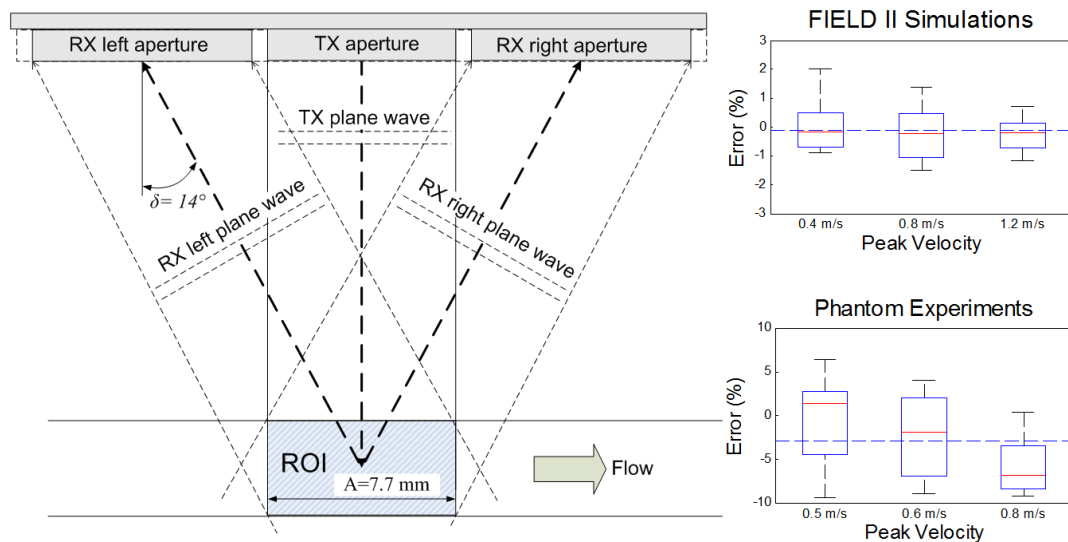
#### Statement of Contribution/Methods

A linear array is placed longitudinally above the vessel of interest (see figure, left). A central aperture transmits a defocused wave. Two receiving apertures, symmetrically placed on the array at angles  $\pm \delta$  receive the backscattered echoes. No focusing is applied. This geometry produces a large sample volume which covers the whole vessel diameter for a length of  $A$ . The frequencies  $f_l, f_r$  are located at the half point of the Doppler spectrum slope received from the left and right aperture, respectively. As predicted by the recent mathematical model (doi: 10.1109/TUFFC.2013.2798) those frequencies correspond to the peak velocity. No broadening compensation is needed. Peak velocity and direction are finally obtained by the triangulation of  $f_l$  and  $f_r$ .

The method has been tested on Field II with 32 measurements at peak velocities of 0.4, 0.8, 1.2 m/s, pipe diameters of 4, 6, 8 mm, angles between probe surface and flow  $0^\circ$ - $30^\circ$ . The ULAOP system was used in 60 experiments on a phantom where a blood mimicking fluid flowed in 4 mm pipe. Steady flows with 0.5-0.8 m/s peak velocities, angles  $0^\circ$ - $30^\circ$  were tested.

#### Results/Discussion

The figure, on the right, reports the measured error distribution. A mean underestimation of -0.13 % and -2.8 % (dashed lines) was obtained in simulations (top) and phantom tests (bottom), respectively. The proposed method is non-heuristic, independent of noise level and spectral broadening, and angle-corrected. Because of the very large sample volume, the probe is easily positioned, speeding the examination as well as making it more accurate.



P1C3-4

### Stress phase angle depicts differences in hemodynamics due to change in arterial stiffness

Liu Jia<sup>1</sup>, Niu Lili<sup>2</sup>, Xu Lisheng<sup>3</sup>, Qin Qianli<sup>1</sup>, Qian Ming<sup>2</sup>, Zheng Hairong<sup>2</sup>; <sup>1</sup>Sino-Dutch Biomedical and Information Engineering School, Northeastern University, Shenyang, China, People's Republic of; <sup>2</sup>Paul C. Lauterbur Research Center for Biomedical Imaging, Shenzhen Institutes of Advanced Technology, Chinese Academy of Sciences, Shenzhen, China, People's Republic of

#### Background, Motivation and Objective

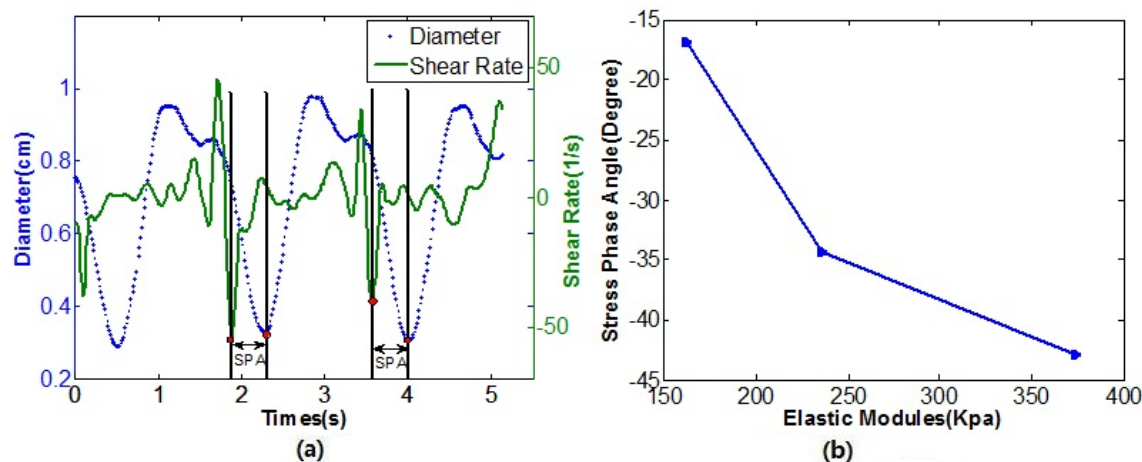
The endothelial cells (ECs) lining a blood vessel wall are exposed to both the wall shear stress (WSS) of blood flow and the circumferential strain (CS) of pulsing artery wall motion. Studies at the cellular level have indicated that concomitant WSS and CS affect EC biochemical response modulated by the temporal phase angle between WSS and CS (stress phase angle, SPA). SPA is highly negative at sites that are prone to atherosclerosis and suggest that SPA plays an important role in atherogenesis. However, it was not experimentally validated. Therefore, this study investigated the changes of SPA of arterial phantoms with different stiffness to better understand the role of SPA in predicting early atherosclerosis.

#### Statement of Contribution/Methods

Three different stiffness arterial phantoms (elastic modules: 162.45, 235.68, 374.24kpa), made from polyvinyl alcohol cryogel, were imaged by a L14-5W/60 linear array transducer (10 MHz) connected to an ultrasound imaging system (Sonix RP; Ultrasonix Medical Corporation, Canada). A sequence of 2-D ultrasound B-mode images were acquired at a frame rate of 141 Hz using 128 ultrasound beams with a focal depth of 16 mm and field of view of 25 mm (depth) by 20.8 mm (width). Pulsatile flow, which simulates the ventricular action of the heart, was produced from a pulsatile pump (Model 55-3305; Harvard Apparatus, USA) at a heart rate of 30 beats/min. The SPA of each phantom was calculated by the 2D non-invasive ultrasonic method described in detail (Niu L et al. Clin Physiol Funct I, 2012, 32(4): 323-329).

#### Results/Discussion

Figure 1(a) shows the arterial diameter and shear rate profiles as a function of time for the first phantom. Figure 1(b) shows the SPAs of different stiffness arterial phantoms. The SPA were  $-16.9^\circ$ ,  $-34.3^\circ$  and  $-42.9^\circ$  for three different stiffness phantoms, respectively. Our results indicated that the 2D non-invasive ultrasonic method can be used to calculate the SPA and the SPA is highly negative with the increases of stiffness, which suggests that SPA may play a role in localization of atherosclerosis.



# A compound speckle model for vascular complexity quantification in nonlinear contrast-enhanced ultrasonography

Matthew R. Lowerison<sup>1,2</sup>, M. Nicole Hague<sup>1,3</sup>, Ann F. Chambers<sup>2,3</sup>, James C. Lacefield<sup>1,2</sup>; <sup>1</sup>Robarts Research Institute, Canada, <sup>2</sup>Medical Biophysics, Western University, Canada, <sup>3</sup>London Regional Cancer Program, Canada

## Background, Motivation and Objective

Conventional analyses of wash-in kinetics in contrast-enhanced ultrasonography (CEUS) rely on point estimates of contrast signal intensity that do not account for additional information available from first-order speckle statistics. In particular, structural differences in tumor microcirculation should lead to heterogeneous contrast enhancement within a region of interest. A method to characterize those heterogeneities would provide a useful tool for tumor vascular characterization.

## Statement of Contribution/Methods

Our method models contrast speckle as a compound distribution of exponential probability density functions (PDFs) with gamma-distributed weightings that yields a two-parameter Type-II Pareto distribution. The PDF of the weights of the exponential terms, which characterizes the heterogeneity of the speckle pattern, is determined from maximum-likelihood estimates of the two Pareto parameters (scale and shape). The model was applied to amplitude-modulated nonlinear CEUS images acquired at 18 MHz from a murine orthotopic xenograft breast cancer model using a VisualSonics Vevo 2100 system.

## Results/Discussion

The compound PDF exhibited close agreement to the intensity histogram over the entire duration of the wash-in datasets. The time-dependent discrepancy of the weighting function, which describes the change in the compound PDF from baseline during contrast wash in and is a surrogate measure of the perfused vascular volume fraction, conformed to theoretical monoexponential indicator-dilution curves more closely than conventional signal-intensity time series. Segmentations of surrounding dermal tissues and feeding arterioles demonstrate the ability of the weighting function to distinguish between different scattering environments. The proposed compound PDF was able to quantify heterogeneities in contrast speckle from our xenograft model and may provide a useful metric for vascular characterization in tumors.

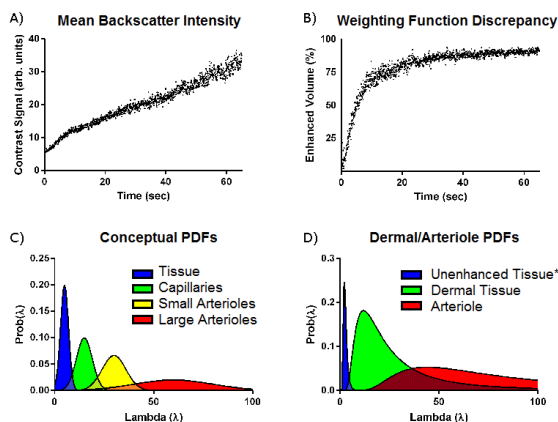


Figure 1: Representative wash-in curves showing A) conventional analysis and B) weighting function discrepancy. C) A conceptual weighting function for different scattering environments. D) Experimental weighting functions (\* scaled for visibility).

# Perfusion Signal Processing for Optimal Detection Performance

Craig Abbey<sup>1</sup>, MinWoo Kim<sup>2</sup>, Michael Insana<sup>2</sup>; <sup>1</sup>UC Santa Barbara, USA, <sup>2</sup>University of Illinois Urbana-Champaign, USA

## Background, Motivation and Objective

There is considerable interest in developing high-resolution power-Doppler imaging to assess dynamic scattering that lacks the coherence necessary for color-flow Doppler methods. These methods have applications in evaluating the vascularity of cancerous lesions as well as micro-vasculature associated some auto-immune disorders.

The power-Doppler signal at a given point in a scan line is determined from the observed RF value over a series of repeated pulse-echo acquisitions. The standard approach is to apply a wall-filter to remove the contributions from static scatterers, and compute the resulting signal power as the perfusion signal. This process neglects any temporal structure in the RF correlations as well as additional information in neighboring axial samples. We contend that an alternative measure of perfusion based on statistical properties of the RF signal can be used to detect smaller and more subtle regions of perfusion.

The objective of this study is to demonstrate the degree to which incorporating additional statistical properties of the perfusion signal can improve power-Doppler imaging. We evaluate this question at the level of a simulated ultrasound system detecting a small region of scatterer diffusion against a stationary scattering background.

## Statement of Contribution/Methods

The analytical contribution of the work is the derivation of an optimal perfusion detector tuned to the correlation structure of the power-Doppler signal. We use this to compare the statistically optimal detector to detection performance of the standard wall-filtered intensity as proof-of-principle for the incorporation of signal statistics into perfusion imaging. The results were verified in a flow and perfusion phantom.

## Results/Discussion

We model the tissue by a dominant static scattering component with a small region (0.2mm diameter) where a weak diffusion component is to be detected. When present, this component contributes a small exponential decay in correlations over the time window of the perfusion scan. The statistically optimal detector is given by a quadratic form involving the difference of inverse covariance matrices of the signal with and without diffusion. The standard approach involving wall filters can also be written as quadratic form, but with a different central matrix. In both cases, larger values indicate a greater likelihood of a diffusion component.

We find a modest but significant ( $p < 0.001$ ) improvement in detecting against a static background (AUC = 0.873 compared to 0.862) when the optimal detector is used. This difference increases in the presence of a small amount of background decorrelation (AUC = 0.734 compared to 0.671).

Our approach provides a theoretical framework for understanding and optimizing performance of power-Doppler imaging specifically for contrast-free perfusion imaging.

### P1C3-7

#### Non-invasive Estimation of Pressure Gradients in Pulsatile Flow using Ultrasound

Jacob Bjerring Olesen<sup>1</sup>, Marie Sand Traberg<sup>1</sup>, Michael Johannes Pihl<sup>1</sup>, Jørgen Arendt Jensen<sup>1</sup>; <sup>1</sup>Center for Fast Ultrasound Imaging, Dept. of Elec. Eng., Kgs. Lyngby, Denmark

##### Background, Motivation and Objective

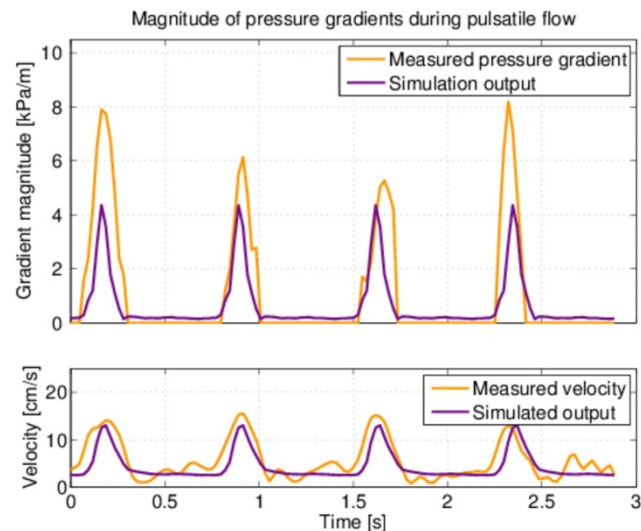
Currently, measurement of pressure gradients are performed using catheters inserted into an artery and threaded to the region of interest. Although this procedure is reported reliable, it remains an invasive procedure that exposes the patients to risk of infection. Also, the measured pressure will be affected by the catheter itself. This paper demonstrates a non-invasive alternative for estimating pressure gradients using vector velocity ultrasound data. Previously, we presented a study on estimating pressure gradients in a constant flow environment, the objective of this work is to show pressure gradients during pulsatile flow.

##### Statement of Contribution/Methods

The proposed method relies on vector velocity fields acquired from ultrasound data. 2-D flow data were acquired at 26 fps using an UltraView 800 ultrasound scanner (BK Medical, Denmark). Pressure gradients were calculated from the measured velocity fields using the Navier-Stokes equation assuming blood is an incompressible Newtonian fluid. The velocity fields were measured for pulsatile flow on a carotid bifurcation phantom (Shelley Medical Imaging Technologies, Canada) with a 70% constriction. A 9 MHz BK8670 linear transducer was used in performing the scans. The calculated pressure gradients were compared to a finite element simulation of the flow model. The geometry of the simulation model was reproduced using MRI scans of the phantom, thereby providing identical flow domains in measurement and simulation. The MRI scans were performed at the Dept. of Diagnostic Radiology, Rigshospitalet, Denmark, using a 3 Tesla scanner (Magnetom Trio Siemens, Germany).

##### Results/Discussion

The figure shows the magnitude of the estimated and simulated pressure gradients during pulsating flow. The plotted data are acquired upstream to the centre of the constriction. The peak pressure gradients are estimated with a standard deviation of 35% and a bias of 56% relative to the simulated peak gradient. Pressure gradients estimated between the pulses have been suppressed as the level of estimator noise during non-flow periods increased dramatically. This resulted in unrealistic high pressure estimates. The result demonstrates that pressure gradients in a pulsatile environment are achievable from non-invasive data obtained using an ultrasound scanner already approved for clinical use.



### P1C3-8

#### Optimal Method of Intraventricular Pressure-Difference Imaging for Vector Flow Mapping

Tomohiko Tanaka<sup>1</sup>, Takashi Okada<sup>2</sup>; <sup>1</sup>Hitachi Ltd., Japan, <sup>2</sup>Hitachi Aloka Medical Ltd., Japan

##### Background, Motivation and Objective

Since pressure difference (PD) in the left ventricle (LV) closely relates to blood-flow motions such as early filling, it can be a clinically useful index for diagnosing cardiac functions, where PD is calculated from flow velocity in the LV. Recently developed techniques for flow visualization, such as vector flow mapping (VFM), will provide multi-dimensional PD in the LV. Regarding the governing equations for calculating PD, a few conventional choices, such as the Navier-Stokes equation (NSE) and the pressure Poisson equation (PPE), are available. However, their characteristics when VFM data are used have not been sufficiently investigated. In the present study, NSE, PPE and a proposed equation were compared to determine the optimal method for VFM-based PD imaging (PDI).

##### Statement of Contribution/Methods

An ultrasound scanner, ProSound  $\alpha 10$  (Hitachi Aloka Medical) obtained VFM data inside a pulsated LV phantom (Fig. (a)) [1] developed by our research group, and vector fields were calculated using DAS-RS1 analysis software (Hitachi Aloka Medical). Three equations, PPE, NSE and the proposed VFM-specialized equation (VSE), were used to calculate PDI. Note that the calculation cost for NSE is higher than that for PPE by a factor of 8 ( $2^3$ ), because the size of the system of equations for NSE in vector form is twice that for PPE in scalar form. On the basis of the VFM characteristics, VSE is derived from NSE to be scalar "Poisson-type" to reduce the cost and also to be physically identical to NSE.

[1] Tanaka et al. IEEE IUS (2012)

##### Results/Discussion

Figs. 1(b-d) show PDI results obtained in early diastole by (b) PPE, (c) NSE and (d) VSE. Upper and bottom parts in each figure are apex and base, respectively. The PDIs obtained by NSE and VSE show "suction in early filling", that is, higher pressure in the base than that in the apex, while the PDI obtained by PPE does not show this trend. This observation is due to a violation of mass conservation (MsC) imposed on PPE. Note that VFM does not satisfy 2D-MsC due to vector-correction in the VFM calculation, although

it uses a 2D-MsC assumption. While only momentum conservation (MmC) is imposed on NSE, both MmC and MsC are imposed on PPE in the calculation domain. The PDI obtained by PPE was thus degraded compared with that obtained by NSE. The three methods are compared in Fig. (e). It can be concluded that VSE is optimal for VFM-based PDI in terms of validity and cost.

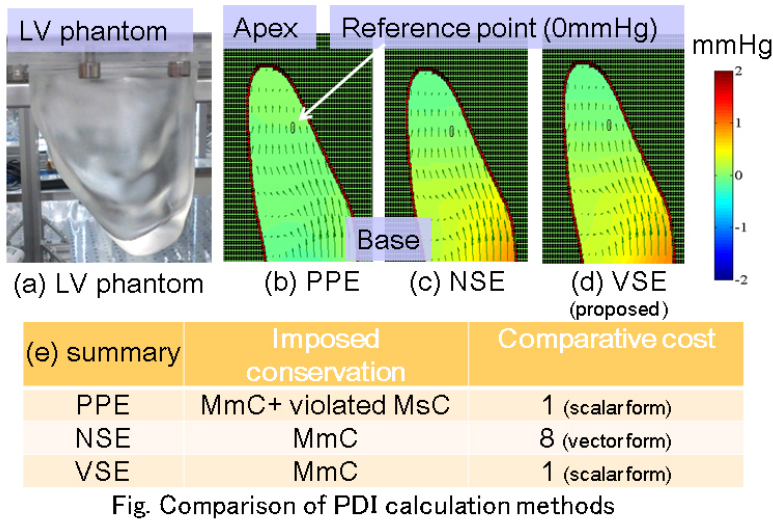


Fig. Comparison of PDI calculation methods

P1C3-9

Staggered multiple-PRF ultrafast color Doppler

Daniel Posada<sup>1</sup>, Boris Chayer<sup>1</sup>, Guy Cloutier<sup>1</sup>, Damien Garcia<sup>1</sup>; <sup>1</sup>University of Montreal Hospital, Montreal, Canada

Background, Motivation and Objective

Color Doppler is an established pulsed ultrasound technique to visualise blood flow in patients. In color Doppler, aliasing occurs whenever the flow speed exceeds the maximum unambiguous (Nyquist) velocity. Such Nyquist velocity is proportional to the pulse repetition frequency (PRF): either the maximal image depth or the Nyquist velocity can be increased at the expense of the other. Aliasing is thus a typical constraint in Doppler echocardiography. In addition, conventional color Doppler also exhibits a low frame rate (~15-20 fps for cardiac applications) due to the sequential focused beam emission. In this study, we propose to use ultrafast color Doppler (with diverging circular beams) with a staggered multiple-PRF scheme to solve the ambiguity Doppler dilemma and obtain non-aliased Doppler velocities at very high frame rates.

Statement of Contribution/Methods

The multiple-PRF scheme for ultrafast color Doppler was tested in two *in vitro* models. 1) A spinning tissue-mimicking disc (PVA cryogel, diameter 10 cm) was rotated at 60 to 270 RPM. 2) A free water jet with scattering particles was created by a 10 cm-deep orifice plate with flow rates ranging from 1 to 3 L/min. The two set-ups were insonified with a phased array transducer (2.5 MHz, 64 elements) using the V-1 Verasonic scanner. Diverging circular beams insonified the full region of interest at every single transmit. A staggered dual- or tri-PRF (2.67, 2 and 1.77 kHz) sequence was used to delay transmits. The RF signals were beamformed using dynamic focusing. After signal demodulation, the 2-D autocorrelator provided Doppler velocity estimates. The Nyquist velocity was extended (up to six-fold) using the full information provided by the dual- or tri-PRF velocity data.

Results/Discussion

Dealiased (unambiguous) velocity estimates obtained by ultrafast color Doppler were compared against ground truth values. The NRMSE ranged between 8.2% (at 94 cm.s<sup>-1</sup>) and 4.8% (at 140 cm.s<sup>-1</sup>), showing an accurate agreement for the spinning disc set up. A significant correlation (r<sup>2</sup> = 0.97) was also obtained between the estimated and theoretical maximal jet velocities in the free jet set up. Staggered multiple-PRF ultrafast color Doppler has the potential to provide high quality Doppler velocities at very high frame rates in a range much beyond that dictated by the sampling criterion.

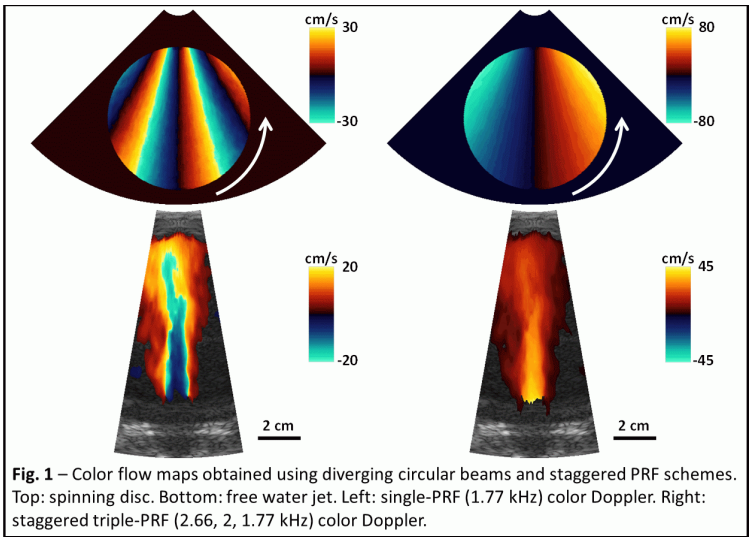


Fig. 1 – Color flow maps obtained using diverging circular beams and staggered PRF schemes. Top: spinning disc. Bottom: free water jet. Left: single-PRF (1.77 kHz) color Doppler. Right: staggered triple-PRF (2.66, 2, 1.77 kHz) color Doppler.



## P1C3-10

**Microvascular Blood Flow in the Thyroid: Preliminary Results with a Novel Imaging Technique**

Flemming Forsberg<sup>1</sup>, Priscilla Machado<sup>1</sup>, Sharon Segal<sup>1</sup>, Yoko Okamura<sup>2</sup>, Gilles Guenette<sup>3</sup>, Cynthia Rapp<sup>2</sup>, Andrej Lyshchik<sup>1</sup>; <sup>1</sup>Radiology, Thomas Jefferson University, Philadelphia, PA, USA, <sup>2</sup>Toshiba America Medical Systems, USA, <sup>3</sup>Toshiba Medical Research Institute USA, Inc., USA

**Background, Motivation and Objective**

In clinical practice, ultrasound (US) imaging - including color and power Doppler imaging (CDI and PDI, respectively) - is the primary method for the assessment of the thyroid. Nodules in the thyroid are common and present in 13 to 76 % of US evaluations; although only 4 to 15 % are malignant. A better understanding of thyroid nodule vascularity might be clinically helpful and the purpose of this study was thus to determine the flow imaging capabilities of a new prototype US image processing technique (SMI; Toshiba Medical Systems, Tokyo, Japan) for the depiction of microvascular flow in normal thyroid tissue and thyroid nodules compared to standard CDI and PDI.

**Statement of Contribution/Methods**

SMI is a novel, microvascular flow imaging mode implemented on the Aplio 500 US system (Toshiba). By analyzing clutter motion and using a new adaptive algorithm to identify and remove tissue motion SMI is designed to improve the visualization of microvascular (i.e., slower velocity) blood flow. SMI depicts this information as a color overlay image or as a monochrome map of flow. Ten healthy volunteers and 22 patients, with 25 thyroid nodules, scheduled for an US guided fine needle aspiration were enrolled in this prospective study, which was approved by the Institutional Review Board of Thomas Jefferson University. Subjects underwent a thyroid US examination consisting of grayscale US, CDI and PDI followed by color and monochrome SMI. In the volunteers, pulsed Doppler guided by the 4 flow modes determined the lowest velocity measurable within the normal thyroid microvasculature and results were compared using a one-way ANOVA. For the patient data, 2 radiologists independently analyzed digital clips of the nodules scoring overall flow detection, vessel branching details and noise on a subjective scale of 1 (worst) to 10 (best). Scores were compared (on a per nodule basis) using a non-parametric Wilcoxon signed rank test.

**Results/Discussion**

In the volunteers color and monochrome SMI captured microvasculature with lower velocities (as low as 1.5 cm/s) than CDI and PDI ( $2.2 \pm 0.35$  and  $2.1 \pm 0.32$  cm/s vs.  $2.6 \pm 0.44$  and  $2.8 \pm 0.77$  cm/s;  $p < 0.012$ ). For all 25 nodules both readers found that color and monochrome SMI showed microvascular flow with significantly higher image scores and provided better depiction of the vessel branching details compared to CDI and PDI ( $p < 0.0001$ ). Clutter noise was significantly higher in the monochrome SMI mode than in the other modes, including the color SMI mode ( $p < 0.001$ ). Consequently, while the diagnostic value has yet to be determined by the radiologists, initial results indicate that SMI can depict more detailed peri- and intra-nodular thyroid microvascular flow than CDI and PDI.

## P1C4 - MCA: Therapeutics and Physical Properties

Salon C

Saturday, September 6, 2014, 8:00 am - 5:00 pm

Chair: **Lori Bridal**  
Univ. Pierre and Marie Curie, Paris

P1C4-1

### Increasing nanoparticles delivery and accumulation in a mouse breast tumor model using microbubbles

Josquin Foiret<sup>1</sup>, Hua Zang<sup>1</sup>, Lisa Mahakian<sup>1</sup>, Sarah Tam<sup>1</sup>, Chun-Yen Lai<sup>1</sup>, Katherine W. Ferrara<sup>1,2</sup>; <sup>1</sup>Department of Biomedical Engineering, University of California, Davis, CA, USA

#### Background, Motivation and Objective

Previous studies performed in our lab have shown that ultrasound driven microbubbles (MB) change the permeability of tumor blood vessels in a mouse model of cancer, enhancing the accumulation of nanoparticles. Therefore, here, we study the accumulation of nanoparticles resulting from the combined effects of ultrasound and MB using alternative imaging methods. To this end, ultrasound parameters (including frequency, pressure and duty cycle) are varied to efficiently generate the desired bioeffects in a mouse model of breast cancer.

#### Statement of Contribution/Methods

All studies were approved by the UC Davis Institutional Animal Committee on Use and Care. Neu deletion mutant (NDL) breast tumors were implanted in the mammary fat pads of 9 mice. Non-targeted house made lipid-shelled MB (median diameter: 1.3  $\mu$ m) were activated and diluted to a concentration of  $6.6 \times 10^8$  MB/mL. MB were continuously injected in the mouse tail vein using a syringe pump at a rate of 30  $\mu$ L/min (injection dose: 150  $\mu$ L per mouse). At the same time, insonation of one tumor was accomplished with a modified Siemens Antares Ultrasound System (Siemens Health Care Inc., Ultrasound Division, CA) driving a custom dual-frequency array probe [1]. This system was used to generate ultrasound bursts of 1.2 MPa at 1.5 MHz (100 cycles at a PRF of 5 kHz) for 2 s of each 17 s for a treatment time of 5 minutes. Liposomes (HSPC:chol:DSPE-PEG2k (56:39:5); diameter:  $109 \pm 29$  nm), encapsulating a near infrared dye (SIDA, Em/Ex = 754/789 nm), were synthesized and injected immediately before ultrasound treatment (injection dose: 1 mg lipid per mouse). Mice were sacrificed after the treatment at 1 (N = 3) and 2 hours (N = 6) after insonation and tumors were harvested for immediate fluorescence imaging on an IVIS Spectrum (Perkin Elmer, MA), and for histology.

#### Results/Discussion

The increase of the average fluorescence intensity on 1 and 2 hour ex vivo images was  $52 \pm 21$  % and  $31 \pm 20$  % in ultrasound-treated tumors as compared to contra-lateral tumors. Histological studies confirmed the enhanced permeability by demonstrating that red cells had extravasated in the ultrasound-treated tumors. Further experiments to quantify accumulation with respect to the injected dose using radiolabelled nanoparticles are currently underway.

[1] D. E. Kruse *et al.*, IEEE TBE, 57(1), 2010.

P1C4-2

### Oxygen-Filled Surfactant Microbubbles for Overcoming Tumor Hypoxia-Associated Radiotherapy Resistance

Lorenzo Albala<sup>1</sup>, John Eisenbrey<sup>2</sup>, Flemming Forsberg<sup>2</sup>, Patrick O'Kane<sup>2</sup>, Margaret Wheatley<sup>1</sup>; <sup>1</sup>School of Biomedical Engineering, Science and Health Systems, Drexel University, Philadelphia, PA, USA, <sup>2</sup>Department of Radiology, Thomas Jefferson University, Philadelphia, PA, USA

#### Background, Motivation and Objective

Angiogenesis in tumors falls short of cellular oxygen demand, resulting in a chronically hypoxic microenvironment. Studies have shown this deficit results in cellular resistance to irradiation, which limits the efficacy of radiation therapy. The objective of this study was to develop a surfactant-based, oxygen-filled microbubble for delivering oxygen to tumors. These microbubbles could be noninvasively triggered within the tumor environment via focused ultrasound to elevate oxygen levels immediately prior to radiation therapy, thereby increasing tumor response and limiting recurrence.

#### Statement of Contribution/Methods

The ultrasound contrast agent (UCA) SE61 was fabricated by sonicating a mixture of non-ionic surfactants and entrapping perfluorocarbon gas. After freeze-drying to remove water and perfluorocarbon gas, the SE61 vials were sealed under vacuum, and subsequently filled with oxygen gas. These agents were then resuspended in DI water immediately prior to use. Echogenicity and stability testing of oxygen-filled UCA was done via a cumulative dose response (0 -1080  $\mu$ L/l) and half-life evaluation (280  $\mu$ L/l) in a custom acrylic vessel in a tank filled with deionized water. UCA was insonated using a single element 5 MHz transducer (Panametrics, Waltham, MA) at a pulse repetition frequency of 100 Hz and peak negative pressure amplitude of 0.45 MPa. Flow phantom evaluation of the oxygen-filled UCA was also performed in a model 524 phantom (ATS Laboratories, Bridgeport, CT) with scanning performed using a Logiq 9 ultrasound scanner operating in coded harmonic imaging mode with a 9L or 4C probe (GE Healthcare, Milwaukee, WI).

#### Results/Discussion

Preliminary studies have shown that oxygen-filled SE61 provides  $16.9 \pm 1.0$  dB of enhancement at a dose of 880  $\mu$ L/l. This agent was also found to be sensitive to insonation, with an in vitro half-life of approximately 15 minutes. Images were also obtained in a flow phantom using a commercial ultrasound scanner, with noticeable enhancement up to 15 minutes post-injection. An example is shown in Figure 1. Follow-up experiments will further test this UCA as an oxygen-delivery vehicle. However, initial findings indicate SE61 microbubbles provide a stable yet ultrasound-sensitive oxygen carrier and may be useful in overcoming hypoxia-associated tumor radiotherapy resistance.

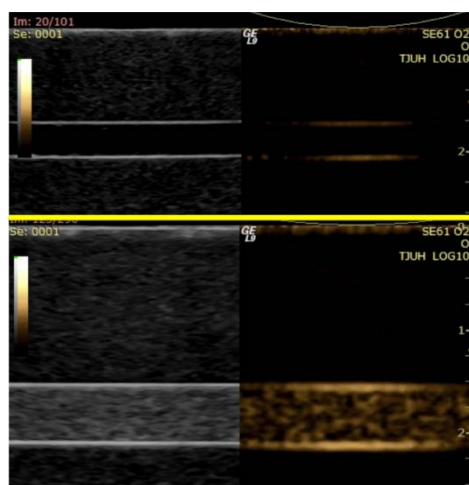


Figure 1: B-mode (left) and coded harmonic (right) images of a flow phantom using the 9L probe at 6 MHz during baseline (top series) and 3 minutes after bolus injection of 1 mL of oxygen-filled SE61 (bottom series)

#### P1C4-3

##### Ultrasound based dosimetry for radiotherapy: in-vitro proof of principle

Erik Verboven<sup>1</sup>, Emiliano D'Agostino<sup>2</sup>, Jan D'hooge<sup>3</sup>, Helge Pfeiffer<sup>4</sup>, Koen Van Den Abeele<sup>1</sup>; <sup>1</sup>Physics, KU Leuven Kulak, Kortrijk, Belgium, <sup>2</sup>DoseVue NV, Hasselt, Belgium, <sup>3</sup>Cardiovascular Sciences, KU Leuven, Leuven, Belgium, <sup>4</sup>Metallurgy and Materials Engineering, KU Leuven, Leuven, Belgium

##### Background, Motivation and Objective

Advances in radiotherapeutic treatments and the ability to detect accidents due to equipment mishandling or malfunctioning require the development of on-line in-vivo dosimetry systems. Here, we propose to use ultrasound contrast agents (UCA's) as a possible candidate for such a system. It is hypothesized that irradiation of UCA's will modify their visco-elastic and/or their geometric properties and consequently their ultrasonic response. The aim of this study is to provide a proof of principle in-vitro.

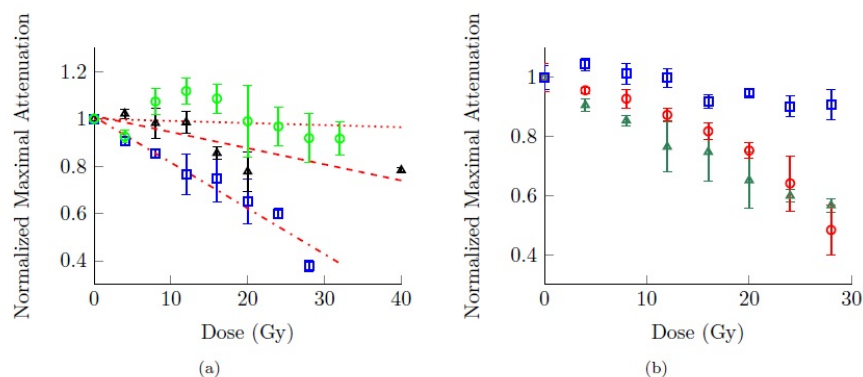
##### Statement of Contribution/Methods

In this study several commercially available lipid-shelled UCA samples (MicroMarker®, SonoVue® and Targestar-P®) were investigated. The agents were characterized with a through-transmission set-up. Phase velocity and attenuation dispersions in the range of 500 kHz to 20 MHz as well as nonlinear coefficient dispersions in the range of 500 kHz to 10 MHz were determined. Subsequently, agents from the same batch were subjected to cumulative ionizing radiation doses up to 40 Gy with a dose rate of 5 Gy/min delivered by a Linac accelerator at the academic hospital UZ Brussels, with dose fractions of 4 Gy. After each irradiation fraction, part of the microbubble solution was extracted to determine the ultrasonic dispersion relations. The entire procedure was carried out within 2 hours, and to account for diffusion and other effects, measurements on control batches were taken at the same time points as the irradiated ones.

##### Results/Discussion

Although the agents were not yet optimized for radiation sensitivity, Targestar-P showed a noticeable dose dependency of the magnitude of the jump in phase velocity and amplitude of the attenuation at resonance (see figure). The other agents under investigation did not show a clear dependency.

These results indicate that the ultrasonic readout of UCA's can be correlated with the ionizing radiation dose delivered to the agents. This supports the concept of using ultrasound and UCA's as a potential tool for in vivo dosimetry.



a) Dose dependence of the maximal attenuation for several UCA's: MicroMarker (circles), SonoVUE (triangles) and Targestar-P (squares). Red lines are linear fits through the measurements. Errorbars are standard deviations resulting from three ultrasonic measurements. b) Dose dependence of different vials of Targestar-P (circles and triangles) compared to control (squares - measured without radiation at the same time points).

# Regulating Nonlinear Properties of Lipid-Coated Microbubbles Using Polymer Network Scaffolds for Ultrasound Drug Delivery Applications

Shih-Tsung Kang<sup>1</sup>, Jian-Liang Lin<sup>1</sup>, Chung-Hsin Wang<sup>1</sup>, Chih-Kuang Yeh<sup>1</sup>; <sup>1</sup>Department of Biomedical Engineering and Environmental Sciences, National Tsing Hua University, Hsinchu, Taiwan

## Background, Motivation and Objective

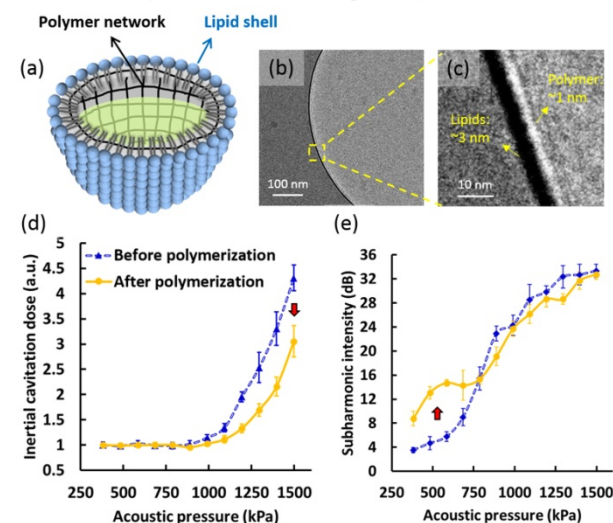
The nonlinear properties of MBs, including stable and inertial cavitation, can enhance tissue permeability and increase drug delivery efficacy. However, the inertial cavitation involves rapid fragmentation and collapse of MBs, having high risk to injure biological tissues. We developed lipid-polymer composite MBs that allow the regulation of these nonlinear properties, making them more preferable for ultrasound (US) drug delivery.

## Statement of Contribution/Methods

A polymer network was added in the inner shell of lipid MBs composed of DSPC and DSPE-PEG2000 (Fig. 1(a)). The network served as a flexible scaffold to stabilize the lipids, rendering MBs more resistant to disruption whereas maintaining their ability to resonate under US excitation. Lipids, monomers (butyl methacrylate), and crosslinkers (ethylene glycol dimethacrylate) were mixed in a vial filled with C3F8 gas. MBs formed after agitation, followed by polymerization for 2 h initiated under increased temperature. Different transmission electron microscopy (TEM) techniques were used to confirm the presence of the hybrid lipid-polymer shell structure. US attenuation measurements were performed in the frequency range of 3–40 MHz to determine their resonance frequencies, at which the degrees of stable and inertial cavitation were tested at pressures of 200–1500 kPa, and quantified at the peak and within periphery of the subharmonic component, respectively.

## Results/Discussion

MBs had a mean size of ~1.8 µm. Cryo-TEM showed the shell of a single MB with an outer lipid layer and an inner polymer layer with thickness of ~3 nm and ~1 nm, respectively (Fig. 1(b) and (c)). TEM showed the integrity of the polymer structure with negative staining even after removal of the lipids. No significant difference in the resonance frequencies of 10–15 MHz was observed before and after the polymerization process. However, the subharmonic intensity at 5 MHz was increased by up to 9 dB at below 800 kPa and the inertial cavitation dose was decreased by up to 30% at above 1000 kPa (Fig. 1(d) and (e)). The lipid-polymer structure has high potential to lower the US pressure required to achieve the comparable effectiveness for use of MBs in diagnostic and therapeutic applications, providing higher safety in clinical use. Research is underway to validate the in vivo feasibility (e.g., blood brain barrier disruption or gene delivery).



# Evaluation of Microbubble Vascular Disrupting Agents and Radiation in Bladder Cancer Using Quantitative Ultrasound

WILLIAM TYLER TRAN<sup>1</sup>, ALBORZ GORJIZADEH<sup>2</sup>, GREGORY J CZARNOTA<sup>2,3</sup>; <sup>1</sup>SUNNYBROOK HEALTH SCIENCES CENTRE, Canada, <sup>2</sup>PHYSICAL SCIENCES, SUNNYBROOK HEALTH SCIENCES CENTRE, Canada, <sup>3</sup>RADIATION ONCOLOGY, SUNNYBROOK HEALTH SCIENCES CENTRE, Canada

## Background, Motivation and Objective

Background: Quantitative ultrasound (QUS) can be an effective tool to monitor tumour-cell response to anti-cancer agents. Quantitative ultrasound and immunohistochemical analysis were used to monitor the synergistic interaction of ultrasound-stimulated microbubbles and radiation to treat human bladder cancer xenografts tumours in vivo.

Motivations and Objective: The objective of the study was to evaluate if ultrasound-driven microbubbles and radiation would effectively increase tumour cell death in bladder cancer in vivo. The present study investigated if QUS could be used to evaluate treatment response to an anti-vascular agent and radiation.

## Statement of Contribution/Methods

Methods: Tumours were exposed to 9 treatment conditions consisting of different concentrations of ultrasound-stimulated microbubbles (no, low, high) combined with single fractionated doses of radiation (0 Gy, 2 Gy, 8 Gy). Ultrasound data collection was performed using high-frequency (30 MHz) ultrasound.

## Results/Discussion

Results: Quantitative ultrasound analysis using the midband fit and 0-MHz intercept parameters revealed increases in ultrasound backscatter intensity with treatments. Treatment effects were measured using QUS 24 hours after treatment and revealed a  $4.75 \pm 0.37$  (SEM) dBr increase in the midband fit and a  $7.24 \pm 0.31$  (SEM) dBr increase in the 0-MHz intercept ( $p < 0.05$ ). Histological data revealed increasing amounts of cell death from combined treatments using ultrasound-stimulated microbubbles and radiation. Histological data were mirrored by changes in quantitative ultrasound parameters.

Discussion and Conclusions: The results demonstrate the feasibility of using quantitative ultrasound to monitor treatment responses in an in vivo bladder cancer xenograft model. The present study also demonstrated that bladder cancer tumours are susceptible to radiation enhancement from ultrasound-mediated microbubbles.

## P1C4-6

**Dynamics of Volatile Phase-Change Contrast Agents: Theoretical Model and Experimental Measurements**

Alexander Doinikov<sup>1</sup>, Paul Sheeran<sup>2</sup>, Ayache Bouakaz<sup>1</sup>, Paul Dayton<sup>2</sup>; <sup>1</sup>INSERM U930, Université François Rabelais, Tours, France, <sup>2</sup>Joint Department of Biomedical Engineering, University of North Carolina and North Carolina State University, Chapel Hill, NC, USA

**Background, Motivation and Objective**

Interest in perfluorocarbon (PFC) phase-change contrast agents (PCCAs) is motivated by the fact that they can be triggered to transition from the liquid state to the gas state by an externally applied acoustic pulse. This property opens up new approaches to ultrasound (US) imaging and therapy. Insight into the physics of this process is vital for effective use of PCCAs and for anticipating bioeffects. Our paper reports on (i) the development of a new theoretical model that describes the conversion of a PFC droplet into a vapor bubble and subsequent bubble evolution and (ii) the validation of this model by comparison with in vitro experimental data. The proposed model has been specifically developed to explain the complex behavior which is demonstrated by volatile PFC droplets experimentally but has not been well-described theoretically so far.

**Statement of Contribution/Methods**

The developed theoretical model describes the following processes: the growth of a vapor bubble, triggered by an US pulse, inside a PFC droplet until the droplet is completely converted into the bubble, the over-expansion of the vapor bubble and subsequent damped oscillations of the bubble until settling to a final diameter. The derivation of the model is based on rigorous mathematical consideration of the above processes. The developed model is used to simulate numerically the evolution of decafluorobutane (DFB) and octafluoropropane (OFP) microdroplets of different sizes. Simulated curves are fit to ultra-high-speed video microscopy data of droplet vaporization in vitro.

**Results/Discussion**

It is shown that agreement between simulated and measured curves can be attained by varying three model parameters: evaporation rate, viscosity and surface tension of the host liquid surrounding the droplet. The first parameter is used to fit the process of vaporization and over-expansion and the other two parameters are used to fit the damped oscillation of the vapor bubble. The values of other model parameters were set to correspond to the material properties of gaseous and liquid PFC. Investigations were made for DFB and OFP droplets with diameters in the range 2 – 7 micrometers. It has been found that the developed theoretical model is capable of reproducing the behavior of PCCAs observed in experiments. Differences between simulated and measured curves suggest that experimentally the surface of bubbles contains the remains of the initial lipid shell of PFC droplets. Therefore one has to vary the viscosity and the surface tension of the host liquid in simulations to achieve agreement with experimental curves describing the oscillatory part of the bubble evolution.

## P1C4-7

**Modelling rheological shear with finite elements for non-spherical microbubble modes**

Gaël Y. V. Léauté<sup>1</sup>, James McLaughlan<sup>1</sup>, Sevan Harput<sup>1</sup>, David Cowell<sup>1</sup>, Steven Freear<sup>1</sup>; <sup>1</sup>School of Electronic and Electrical Engineering, University of Leeds, Leeds, West Yorkshire, United Kingdom

**Background, Motivation and Objective**

Common clinical ultrasound contrast agents are microbubbles encapsulated with a monolayer of amphiphilic molecules such as phospholipids or fatty acids. The interaction of the molecules at the interface with the adjacent gas and liquid phases in the presence of acoustic pressure results in bending moments and shear forces in the coating (Figure 1). In this study, a novel three-dimensional finite element model (FEM) is developed to model the rheological properties of the amphiphilic molecules. The aim of the study is to model the non-spherical deformations at low acoustical insonation pressures to understand the mechanism contributing to the presence of shell modes and its effect on sonoporation.

**Statement of Contribution/Methods**

The amphiphilic molecules at the interface are modeled as a viscoelastic material with the generalized Maxwell model in Comsol Multiphysics<sup>TM</sup>. The rheological parameter is the relaxation time  $\lambda_s$  which parameterizes the relaxation of the shear modulus. Sequences of 100 images were acquired with a high-speed Shimadzu HPV-1 camera at 1 million frames per second with a flash lamp. The camera was coupled to an inverted Nikon Ti-E microscope with a 40x magnification. In house produced lipid coated microbubbles of 2 to 10  $\mu\text{m}$  radii were driven by a 0.5MHz ultrasound transducer at a peak negative pressure of approximately 100kPa with a 30 cycle pulse length.

**Results/Discussion**

Optical data was compared to simulated microbubble shape deformation (Figure 2). The FEM accurately models oscillation modes exhibited by lipid coated microbubbles. The study emphasize the importance of the shear stress mechanism for modeling the microbubble shape modes. The three-dimensional FEM was able to compute the shape modes which is not possible with models of lower dimensions. Thus this model could lead to a greater understanding of micro-streaming due to shell modes that could be applied to sonoporation applications.

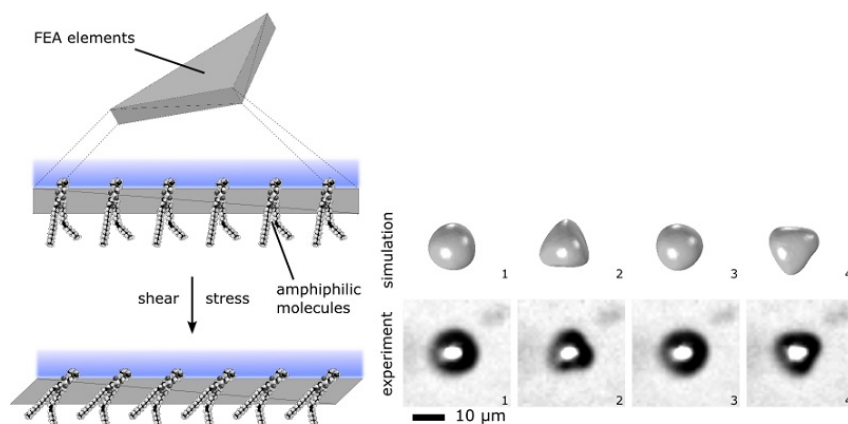


Figure 1: FEA elements are able to model the shear deformation necessary for non-spherical deformation of the microbubble.

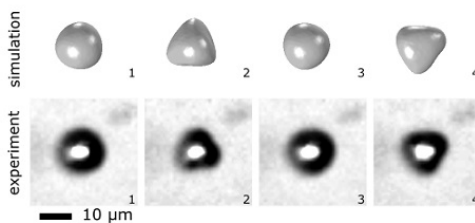


Figure 2: Comparison in time-domain of simulated (top) and experimental (bottom) non-spherical oscillations of a 6 $\mu\text{m}$  radii microbubble.



P1C4-8

### Lattice of nonlinear coupled oscillators: an acousto-mechanical analogy of gas microbubble

Jennifer Chaline<sup>1</sup>, Ayache Bouakaz<sup>1</sup>, Victor Sanchez-Morcillo<sup>2</sup>, Noé Jiménez<sup>2</sup>, Serge Dos Santos<sup>1,3</sup>, <sup>1</sup>Université François-Rabelais de Tours, Inserm, Imagerie et Cerveau UMR U930, Tours, France, <sup>2</sup>IGIC, Universidad Politécnica de Valencia, Grao de Gandia, Spain, <sup>3</sup>INSA Centre Val de Loire, Campus Blois, Blois, France

#### Background, Motivation and Objective

Under specific ultrasound (US) excitation, contrast microbubbles undergo nonlinear oscillations. Considering the size and the complexity of the phenomenon, expensive and complex experiments and/or simulations are required. To overcome this, the use of an analogy has been proposed and validated numerically [1, 2]. When subjected to US, microbubbles present a fairly complex dynamics of which some aspects can be described by a lattice of nonlinearly coupled oscillators. In this study, the oscillatory behavior of a microbubble is investigated through this acousto-mechanical system of coupled pendula parametrically excited by a vertical force. The aim of this work is to understand the dynamics of a single microbubble, to subsequently study it in experimental and clinical conditions for both imaging and therapy.

#### Statement of Contribution/Methods

The setup consists of a circular ring with a diameter  $d=0.3\text{m}$ , on which 54 pendula are fixed with nylon strings forming a “V” shape with the vertical axis. The coupling is obtained by overlapping the strings and fixing them with nodes. The influence of the coupling has been optimized experimentally in order to fit as close as possible to the microbubble. The excitation system consists of a loudspeaker driven by an arbitrary waveform generator through an audio amplifier. The sinusoidal excitation varies from  $f_{\text{exc}}=1\text{Hz}$ - $5\text{Hz}$  with amplitudes varying from  $A=0.5\text{Vpp}$  to  $4\text{Vpp}$  corresponding to a vertical displacement of  $2\text{mm}$  to  $8\text{mm}$ .

#### Results/Discussion

Experiments show surface modes up to  $n=20$  with an unstable mode for  $n=0$  are developed. For  $n=1$ , the displacement of the center of mass is observed. Modes oscillating at subharmonics of the parametric excitation are observed for amplitudes varying from  $A=0.5\text{Vpp}$  to  $A=2.5\text{Vpp}$  and an excitation frequency equal to twice the natural frequency of the simple pendulum. Graphics representations show that for a given excitation frequency, the amplitude of the excitation has no effect on the appearance of specific vibration mode. These results are in agreement with simulations and are similar to those obtained from gas for microbubbles.

[1] J. Chaline et al., 2013 Joint UFFC, EFTF and PFM Symposium, pp. 329-332

[2] V. Sanchez-Morcillo et al., Localized Excitations in Nonlinear Complex Systems, Springer International Publishing Switzerland Vol. 7, pp.251-262, 2014

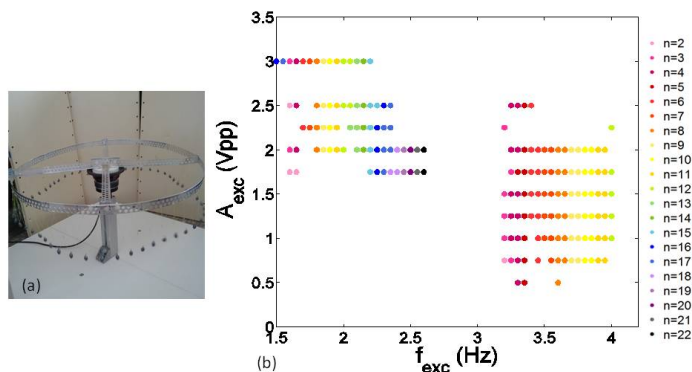


**Figure:**  
a- experimental setup of the pendula ring  
b- Phase diagram: appearance of vibration modes versus the excitation frequency and amplitude

P1C4-9

### Estimation of microbubble resonance frequency from lipid intermolecular forces

Mark Borden<sup>1</sup>, <sup>1</sup>Mechanical Engineering, University of Colorado, Boulder, Colorado, USA

#### Background, Motivation and Objective

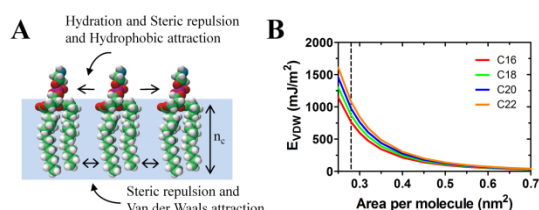
Microbubbles coated and stabilized by phospholipid monolayers are used clinically as ultrasound contrast agents and in research for molecular imaging and targeted drug delivery. Recent research efforts have elucidated the effect of the lipid shell on microbubble acoustic properties, but the models remain largely phenomenological and fail to capture the molecular nature of the lipid coating. It is therefore desirable to bridge the knowledge gap between lipid composition and microbubble shell mechanics. The objective of this study was to estimate the microbubble resonance frequency from the lipid intermolecular forces.

#### Statement of Contribution/Methods

The problem is first approached by considering the balance of intermolecular forces when the microbubble is at rest. The investigation then moves to molecular processes associated with very small amplitude surface dilation and compression.

#### Results/Discussion

The optimal area per molecule as a function of lipid acyl chain length was determined by minimizing the chemical potential of the lipid molecules at the gas/liquid interface. The van der Waals pair potentials between methylene groups were summed to determine the cohesive energy, which in turn was used to predict the surface elasticity for small dilations or contractions of the monolayer. The surface elasticity was fed into de Jong's modified Rayleigh-Plesset equation to determine the natural frequency for small amplitude oscillations, which is compared to experimental observations of optically driven microbubbles. It is concluded that lipid acyl chain length has a large effect on monolayer cohesion and corresponding shell mechanical and transport properties. The discussion includes the impact of lipid intermolecular forces on microbubble stability and resonance.



P1C4-10

### Non-linear behavior of gas vesicle nano-structures at high ultrasound frequencies

Emmanuel Cherin<sup>1</sup>, Ray Bourdeau<sup>2</sup>, Melissa Yin<sup>1</sup>, Mikhail Shapiro<sup>2</sup>, F. Stuart Foster<sup>1</sup>; <sup>1</sup>Imaging Research, Sunnybrook Research Institute, Toronto, Ontario, Canada, <sup>2</sup>Division of Chemistry and Chemical Engineering, California Institute of Technology, Pasadena, California, USA

#### Background, Motivation and Objective

Gas vesicles (GVs) are gas-filled nano-structures generated by species of archaea and bacteria as a means to regulate buoyancy. Though very similar in structure to microbubble ultrasound contrast agents (UCA), GV's exhibit major differences in size (smaller), shape (anisotropic), shell composition (protein), elastic properties (stiffer) and porosity to gas (permeable). Their size could potentially allow them to exit the intravascular space into solid tumors, benefiting from the enhanced permeability and retention properties of these tissues. Their potential as UCAs, however, will depend in part on their acoustic nonlinear behavior. In this preliminary study, we establish and characterize the non-linear acoustic behavior of haloarchaeal GV's in the frequency range of 12.5 - 27.5 MHz

#### Statement of Contribution/Methods

The acoustic behavior of GV's from *Halobacterium* NRC-1, and their collapse pressure, were investigated in vitro with a Vevo770 imaging system (VisualSonics, Toronto, Canada), at 12.5, 20 and 27.5 MHz (6 cycle pulses), with pressures ranging from 0.19 to over 1 MPa. GV's were embedded in Agar phantoms by mixing 250  $\mu$ L of OD 2.0 solutions of GV's with a 750  $\mu$ L of 1% (w/w) Agar solution at 40°C. The mixture solidified in a 0.4(W) x 0.7 (D) x 4 (L) cm<sup>3</sup> cast. The phantom was scanned along the width direction with the focus of the probe positioned at 3.5 mm below the surface. Ten successive frames were collected at different positions for each frequency and amplitude and signal digitized. A ROI corresponding to -1dB focal zone was selected, in which the average power spectrum was computed, corrected for the background noise and transducer receive sensitivity. Fundamental (FU) and second harmonic (SH) powers were estimated as the average of the power spectrum over a 30% bandwidth (rel. to the fundamental frequency F0) centered on F0 and 2F0, respectively, and analyzed as a function of transmit pressure (measured in water), frequency, and frame number.

#### Results/Discussion

At all frequencies, SH was detected (1dB above noise) at a pressure of around 190 kPa. At these pressures, in the first frame, the ratios SH/FU were -10.2, -10.6 and -7.6 dB at 12.5, 20 and 27.5 MHz respectively. These ratios increase up to -3.8, -6, -3.5 dB at 373 kPa (12.5 MHz), 324 kPa (20 MHz) and 348 kPa (27.5 MHz). Under 400 kPa, FU and SH stay constant over 10 frames at all frequencies. Above 418 kPa (12.5 MHz), 458 kPa (20 MHz) and 400 kPa (27.5 MHz), FU and SH decrease between successive frames, more rapidly as pressure increases, strongly indicating detectable collapse.

GV's exhibit a strong second harmonic when exposed to fundamental in the 12.5 to 27.5 MHz range, and an apparent (not corrected for attenuation in the phantom) collapse pressure of around 400-450 kPa, both relatively independent of frequency, potentially allowing the use of existing nonlinear imaging schemes implemented in existing technology.

## P1C5 - MEL: Cardiovascular Elasticity Imaging

Salon C

Saturday, September 6, 2014, 8:00 am - 5:00 pm

Chair: **Brett Byram**  
Vanderbilt University

P1C5-1

### RF-based motion estimation using non-rigid image registration techniques: in-silico and in-vivo feasibility

Brecht Heyde<sup>1</sup>, Martino Alessandrini<sup>1</sup>, Ling Tong<sup>2</sup>, Jan D'hooge<sup>1,3</sup>; <sup>1</sup>Lab on Cardiovascular Imaging and Dynamics, KU Leuven, Leuven, Belgium, <sup>2</sup>Center for Biomedical Imaging Research, Tsinghua University, Beijing, China, People's Republic of, <sup>3</sup>Medical Imaging Lab, Norwegian Institute for Science & Technology, Trondheim, Norway

#### Background, Motivation and Objective

Ultrasound (US) motion/deformation estimation techniques can roughly be divided in block matching (BM) and non-rigid image registration (NRIR). From a data processing perspective, motion can be extracted from the radiofrequency (RF) signals, from their envelope, or from the B-mode data (after subsampling and scanconversion). For small displacements, RF-based BM is known to outperform B-mode tracking. However, BM typically requires an a-posteriori regularization step and a least-squares fitting to obtain robust strain maps.

NRIR on the other hand incorporates prior information during the motion estimation process and allows computing the strain analytically. However, NRIR has typically been applied on B-mode data. The aim of this study was therefore to test whether RF-based NRIR is feasible and whether it would outperform B-mode NRIR.

#### Statement of Contribution/Methods

Synthetic 2D RF images of a phantom (60 x 60 mm) containing a soft mid-layer were simulated (3.4 MHz, 75° sector). The phantom was fixed at the bottom and underwent an inter frame axial compression of 0.25%. In order to assess the spatial resolution of NRIR, the thickness of the soft layer was reduced from 20 mm to 2 mm (in 2 mm steps), and its stiffness was decreased to obtain a range of axial strain values (0.5% to 1.5%, in 0.25% steps). For each of these stiffness-thickness combinations, a pair of RF images was simulated from which the envelope and B-mode images were generated. This process was repeated 3 times to account for the stochastic nature of the RF data.

A previously developed NRIR technique based on a B-spline free-form deformation model was used to compute axial strain between the RF, envelope and B-mode image pairs. The resulting strain values were classified as background or inclusion using the average reference strain difference between the soft layer and its surroundings as a cutoff. The softer inclusion was considered found when the sensitivity and specificity were both larger than 0.8.

Finally, the performance of the RF-based NRIR technique was evaluated in-vivo by tracking the septum of a healthy volunteer (2.0 MHz, 90° sector, 138 Hz frame rate).

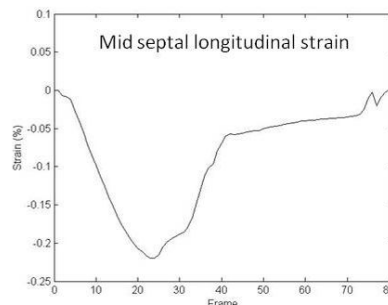
#### Results/Discussion

RF tracking was better at identifying smaller and more subtle inclusions compared to envelope tracking, and was superior to B-mode tracking (Fig 1A). In-vivo, RF tracking at high frame rate produced physiological strain curves (Fig 1B).

#### A. Phantom with soft inclusion

Minimum detectable inclusion		
Tracking	Size [mm]	Strain difference [%]
RF	10	0.25
Envelope	12	0.25
B-mode	14	1

#### B. Clinical dataset



P1C5-2

### Feasibility of 3D-Myocardial Elastography using a 2D array in an Experimental Phantom

Stanley Okrasinski<sup>1</sup>, Julien Grondin<sup>1</sup>, Elisa Konofagou<sup>1,2</sup>

<sup>1</sup>Biomedical Engineering, Columbia University, New York, New York, USA, <sup>2</sup>Radiology, Columbia University, USA

#### Background, Motivation and Objective

Myocardial Elastography (ME) is a high-precision, ultrasound-based 2D imaging modality for estimating myocardial deformation, and has been previously validated against sonomicrometry to provide accurate identification of ischemia at various levels of stenosis in humans and canines. While ME is capable of providing information in 2-D imaging planes, a more complete analysis of cardiac deformation would consider strain across the whole myocardium. In this study, a custom 2D matrix array is used in order to estimate 3D displacements and strains in a polyacrylamide phantom.

#### Statement of Contribution/Methods

A polyacrylamide phantom was constructed, and three deformation schemes were applied: 1% axial only, 1% lateral only, and 1% elevational strain only, while all three strain components were estimated in each case. The phantom was imaged

throughout the entire deformation. A custom, 2D matrix array probe (Sonic Concepts, Inc., Bothell, WA) was used in this study to image the phantom. This probe has a total of 256 elements in a 16x16 element grid with 0.8x0.8 mm element size, 0.1 mm kerf, and 2.5 MHz central frequency. The transducer was used in conjunction with a Verasonics scanner (Verasonics, Inc., Redmond, WA). A custom diverging beam sequence with a virtual focus placed behind the transducer face was implemented on the Verasonics in order to interrogate the entire field of view in a single transmit sequence. Element data were acquired, and reconstructed in a pixel-wise fashion. Inter-frame axial, lateral, and elevational displacements were estimated at a 500 Hz motion-estimation rate and at a 2000 Hz motion-sampling rate using normalized cross-correlation (window size: 4.6 mm, 90% overlap). Axial, lateral, and elevational Lagrangian strains were estimated using a least-squares estimator (window size: 10.7 mm).

### Results/Discussion

After the axial deformation, the axial, lateral, and elevation strains were imaged and estimated at  $0.9 \pm 1\%$ ,  $0.1 \pm 3\%$ , and  $0.2 \pm 3\%$ , respectively. After the lateral deformation, the axial, lateral, and elevation strains were imaged and estimated at  $0.1 \pm 1\%$ ,  $0.8 \pm 3\%$ , and  $0.3 \pm 3\%$ , respectively. After the elevational deformation, the axial, lateral, and elevation strains were imaged and estimated at  $0.1 \pm 1\%$ ,  $0.2 \pm 3\%$ , and  $0.8 \pm 3\%$ , respectively. As a result, the axial strain estimate was found to provide the best accuracy (root-mean squared error (RMSE): 0.17), while the lateral and elevational strain estimates were found to have comparable but lower accuracy (RMSE: 0.30 and 0.41). In this study, initial feasibility of axial, lateral, and elevational strain imaging in a polyacrylamide phantom was shown using a 2D matrix transducer and high frame rate imaging.

### P1C5-3

#### Electromechanical Wave Imaging of Atrial Arrhythmias using Frequency Analysis Processing Techniques: Validation in vivo.

Alexandre Costet<sup>1</sup>, Ethan Bunting<sup>1</sup>, Julien Grondin<sup>1</sup>, Stanley Okrasinski<sup>1</sup>, Alok Gambhir<sup>1,2</sup>, Elisa Konofagou<sup>1</sup>; <sup>1</sup>Biomedical Engineering, Columbia University, New York, New York, USA, <sup>2</sup>Medicine-Cardiology, Columbia University, New York, New York, USA

#### Background, Motivation and Objective

Atrial fibrillation is the most common arrhythmia in the US. Electromechanical Wave Imaging (EWI) is a direct imaging technique that can map the transmural electromechanical activation in all four chambers in vivo. Because some arrhythmias, such as AF, are chaotic, standard EWI processing techniques cannot be applied to their studies. As a result, frequency analysis of the transient, incremental strains upon which EWI relies was investigated. In this study, we validate EWI frequency analysis for the noninvasive characterization of atrial arrhythmia in vivo.

#### Statement of Contribution/Methods

A Verasonics system (Verasonics, Redmond, WA) with a 2.5-MHz phased array was used to perform EWI in five open-chest canines (n=5) during pacing from the left atrial appendage (LAA) at rates ranging from 120 to 400 beats per minute (cycle length from 150 to 400 ms). An unfocused beam sequence at 2000 frames/s in the standard apical and parasternal views was used and axial incremental displacements and strains were estimated using RF-based cross-correlation with a window size of 9.2mm and a window shift of 0.385 mm, and a least-square kernel size of 5.0 mm, respectively. The atrial myocardium was segmented and frequency analysis of the corresponding incremental axial strain curves was performed using a modified Goertzel algorithm. Dominant frequencies were extracted and converted to cycle lengths. Finally, histograms and maps of the cycle lengths in the atria were generated.

#### Results/Discussion

Good agreement between the LAA pacing rate and the cycle length estimated with the EWI frequency analysis method can be seen in Figure 1, showing excellent correspondence (slope=1.01) and correlation ( $R^2 = 0.96$ ). Cycle length maps show cycle lengths similar to the pacing rate evenly distributed across the atria.

This preliminary validation study showed that novel frequency based processing of EWI images can provide the accurate rate of as well as map the activation in the atria during tachycardia. Since cycle lengths maps derived from EWI can also provide regional information on the rate of electromechanical activation of the atria, these findings indicate the potential of EWI in characterizing disorganized arrhythmias such as atrial fibrillation. Ongoing studies include clinical validation in patients undergoing RF ablation. Supported in part by NIH funding (R01EB006042 & R01HL094410)

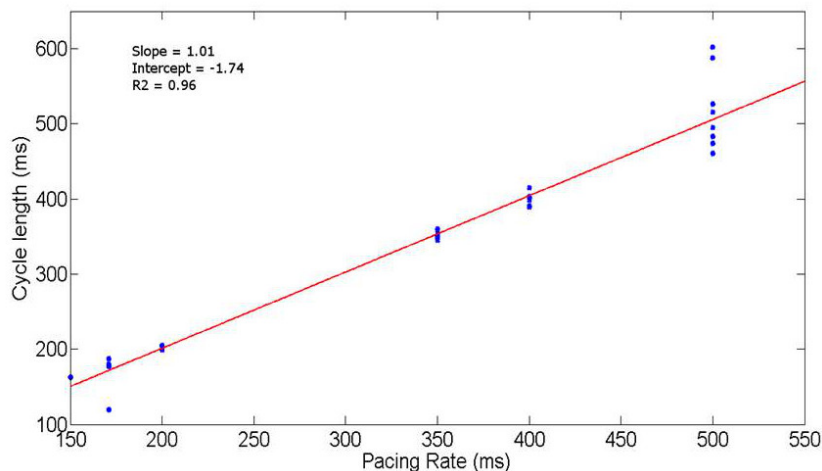


Figure 1: EWI-detected cycle length versus LAA pacing rate

## P1C5-4

### Acoustic radiation force (ARF) generation with a novel dual-frequency intravascular transducer

Tomasz Czernuszewicz<sup>1</sup>, Zhuochen Wang<sup>2</sup>, Jianguo Ma<sup>2</sup>, Xiaoning Jiang<sup>2</sup>, Caterina Gallippi<sup>1,3</sup>; <sup>1</sup>Joint Department of Biomedical Engineering, University of North Carolina/North Carolina State University, Chapel Hill, NC, USA, <sup>2</sup>Department of Mechanical and Aerospace Engineering, North Carolina State University, Raleigh, NC, USA, <sup>3</sup>Department of Electrical and Computer Engineering, North Carolina State University, Raleigh, NC, USA

#### Background, Motivation and Objective

Atherosclerosis and coronary artery disease remain the leading cause of death in the US. Coronary plaque is visualized with intravascular ultrasound (IVUS) and is typically implemented with high center frequencies (>30 MHz) for superior spatial resolution. Coronary plaque characterization may be improved by implementing elasticity imaging techniques such as acoustic radiation force impulse (ARFI) imaging on IVUS transducers. In this work we propose to extend ARFI imaging to the coronary vasculature with a novel, dual-frequency small-aperture transducer design that includes a low-frequency “pushing” element and a high-frequency tracking element.

#### Statement of Contribution/Methods

A 35 MHz transducer (0.6 mm x 0.6 mm) was integrated into a 6.5 MHz transducer (0.6 mm x 3 mm). Both transducers were fabricated from single crystal PMN-PT and mounted on a 20 gauge needle tip. A needle hydrophone placed in a water bath was used to characterize the acoustic output of both the low and high frequency elements. To test acoustic output, the high frequency element was driven with an Olympus pulser/receiver (5900PR, Panametrics Inc.), while the low-frequency element was driven with a function generator and radiofrequency amplifier in order to generate adequate intensities to produce radiation force. ARF-induced motion from the low frequency element was quantified using optical tracking methods in a translucent phantom (~7 kPa) containing embedded graphite microparticles. The motion of the graphite particles was captured with a high speed camera (150 kHz framerate) coupled to a 10x microscope, and quantified using 2D normalized cross correlation. Ten repeated ARF excitations (6.5 MHz) were captured at 300, 600, and 900 cycles and compared to baseline to confirm displacement. Optical displacement profiles were filtered with a 5th order, 1 kHz low-pass Butterworth to remove high frequency noise, and mean peak displacement was measured.

#### Results/Discussion

The acoustic output pressure of the 6.5 MHz transducer was measured to range between -1.87 and +2.14 MPa when driven by a 250 Vpp waveform. In the pulse-echo test, the 35 MHz probe bandwidth was measured to be 52.1%. In the optical experiments, the mean ( $\pm$  standard deviation) peak displacement for 300, 600, and 900 cycle ARF bursts was  $0.23 \pm 0.14 \mu\text{m}$ ,  $0.37 \pm 0.14$ , and  $0.51 \pm 0.14 \mu\text{m}$ , respectively. To predict whether these displacements would be measureable using acoustic motion tracking, the Cramer-Rao Lower Bound was computed for a 35 MHz probe. Using a 1.5 $\lambda$  kernel, and assuming 30 dB SNR and correlation coefficient of 0.995, the jitter magnitude is expected to be  $0.22 \mu\text{m}$ . The results of this study show that ARF generation is feasible on a small-aperture transducer.

## P1C5-5

### A dedicated guided-search displacement algorithm for cardiovascular strain imaging

Niels J. Petterson<sup>1</sup>, Frans N. van de Vosse<sup>1</sup>, Richard G.P. Lopata<sup>1</sup>; <sup>1</sup>Biomedical Engineering, Eindhoven University of Technology, Netherlands

#### Background, Motivation and Objective

In recent years, numerous methods for 2D strain imaging have been introduced, all with varying outcome, precision and robustness. Traditionally, an exhaustive search is performed, often using a priori knowledge or an iterative, multi-level (ML) approach to improve strain quality when frame rate is low or deformation is large. More recently, Chen et al. introduced a guided-search algorithm (GS) that significantly increased robustness against discontinuities and de-correlation. The application of such an algorithm is not trivial for cardiovascular applications where large multi-directional translation, deformation and complex geometry are present. In this study, the GS algorithm is adapted for cardiovascular applications (CGS) and compared to existing methods (ML and GS).

#### Statement of Contribution/Methods

The guided search was implemented according to Chen et al. Next, a sophisticated seeding approach was devised, where seeds were distributed in the vessel, obeying the cross-sectional or longitudinal geometry. Radial motion and correlation of the seeds were calculated on interpolated envelope data corresponding to the expected radial direction. Under the assumption that radial displacement should be more or less uniform over the circumference or in longitudinal directions, seeds with outlying displacement values were penalized. Next, the displacements within the segmented vessel wall were estimated using the GS algorithm.

For proof of concept, all algorithms were applied to simulated phased array data (Field II) of a homogeneous linear elastic phantom that was compressed (0 – 5.0%). Next, the algorithms were applied to cross-sectional 2D images of a porcine aorta in vitro ( $p = 0 - 130 \text{ mmHg}$ ) and an abdominal aortic aneurysm (AAA) in vivo ( $p = 80 - 125 \text{ mmHg}$ ). The elastographic SNR (SNRe) was calculated for different regions of interest and, in case of vascular data, different shells as a function of radius.

#### Results/Discussion

In the simulations, similar SNRe's were found for strains up to 2% (ML: 26 - 32 dB; GS: 27 - 30 dB; CGS: 27 - 30 dB), and an improvement of 15 dB for GS and CGS for 5%. In vitro experiments yielded similar strains for the three methods (luminal: -10 – -8.8 %; mid: -12.8 – -8.8 %; outer: -11.7 – -6.7 %). The SNRe's were higher for the (C)GS methods (ML: 3 – 8 dB; GS: 7 – 10 dB; CGS: 7 – 10 dB). These SNRe's are much lower, since the accumulated, end-systolic strains are analyzed. In vivo longitudinal AAA data revealed higher SNRe for GS and CGS in the upper wall. (SNRe: ML: -10 dB; GS: -3.5 dB CGS: -2 dB) In the lower wall, the ML and CGS performed similarly (ML: -6 dB; CGS: -7 dB), whereas GS failed. However, ML and GS resulted in non-physiological tensile radial strains during systole (ML: 2% – 7%; GS: 15% – 30%), whereas CGS did not (-5%). The adjusted guided search algorithm shows high potential for in vivo vascular elastography. In cardiac elastography, more challenges including limited field of view, high strain rates and large motion will be encountered.

## P1C5-6

### Evaluating the Intensity Level of Acoustic Radiation Force Impulse (ARFI) Imaging for Intravascular Ultrasound (IVUS): the Preliminary In Vitro Results

Cho-Chiang Shih<sup>1</sup>, Chih-Chung Huang<sup>1</sup>; <sup>1</sup>Department of Biomedical Engineering, National Cheng Kung University, Taiwan

#### Background, Motivation and Objective

Measurement of the elastic properties of plaque and vessel has a great significance in clinical diagnosis. The conventional intravascular ultrasound (IVUS) can only visualize the anatomical structure of epicardial vessels and plaque without providing the viscoelastic information. In our previous study, a novel concept of combining the IVUS and high frequency acoustic radiation force impulse (ARFI) imaging has been proposed. This method exhibited a potential for realizing a high resolution elastography to distinguish the difference between plaques and vessels. However, the intensity level of acoustic radiation force should be calibrated as a standard for further clinical diagnosis. The purpose of this study is to determine that how much acoustic force intensity is needed for creating enough tissue displacement and providing the best excitation parameters for IVUS-ARFI applications.



### Statement of Contribution/Methods

A confocal transducer with two elements was used in the study. The outer element with 11 MHz frequency was used to generate acoustic radiation force to induce the localized tissue displacements, and the displacements can be detected by 48-MHz inner element using correlation algorithm, as shown in Fig 1(a). Experiments were carried out by scanning the porcine pulmonary artery with plaque. In order to determine the suitable excitation parameters, sinusoidal tone bursts with different durations from 0.1 to 1 ms at various peak-to-peak amplitudes from 52 to 84 V were applied to drive the outer element. The spatial peak-temporal average intensity ( $I_{SPTA}$ ) of the outer element was measured by a hydrophone.

### Results/Discussion

The induced maximum displacements of artery were from 0.2 to 0.8  $\mu\text{m}$  and the maximum displacements of plaque were from 0.3 to 1.4  $\mu\text{m}$  corresponding to the measured acoustic intensity ( $I_{SPTA}$ ) from 9 to 89  $\text{mW}/\text{cm}^2$ , respectively, as shown in Fig 1(b). The artery and the plaque can be clearly distinguished after the acoustic intensity increased up to 26  $\text{mW}/\text{cm}^2$ . Figure 1(c) shows the B-mode image and its corresponding ARFI image under the acoustic intensity of 89  $\text{mW}/\text{cm}^2$ . The stiffness distributions of plaque were observed obviously using ARFI. All the experimental results demonstrated the feasibility of using high resolution ARFI for IVUS. The minimum level of acoustic intensity was provided for recognizing the artery and plaque in present study.

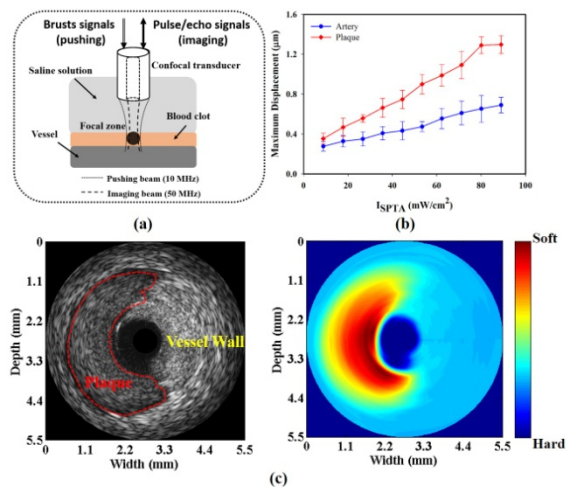


Fig 1

P1C5-7

### Using Ultrasound to Evaluate an Abdominal Aortic Fluid-Structure Interaction Model

Marie Sand Traberg<sup>1</sup>, Jørgen Arendt Jensen<sup>1</sup>; <sup>1</sup>Dept. of Elec. Eng., Technical University of Denmark, Lyngby, Denmark

### Background, Motivation and Objective

The objective of this work is to use ultrasound to validate the biomechanics of the abdominal aorta (AA) predicted by a fluid-structure interaction (FSI) model. FSI simulation models describe the complete arterial physiology by quantifying the mechanical response in the vessel wall caused by the percolating pulsating blood. But the predictability of FSI models needs validation for these to be usable for diagnostic purposes.

Ultrasound imaging is suitable for such an evaluation as the wall displacement can be measured *in vivo* and compared to the wall displacement simulated by the FSI model.

### Statement of Contribution/Methods

The ultrasound application was twofold. Blood flow data obtained by spectral Doppler was used to construct inlet profiles for the FSI model. Simultaneously, wall movement was tracked and used for comparison to FSI model results.

Ultrasound data were acquired using a convex array transducer connected to a 2202 ProFocus scanner (BK Medical, Herlev, Denmark) equipped with a UA2227 research interface. Post-processing was performed in Matlab. Inlet profiles were obtained by harmonic decomposition of the average flow velocity and using the Womersley-Evans principle to reconstruct the profiles. The wall displacement was estimated by integrating wall velocity over 1 heart cycle.

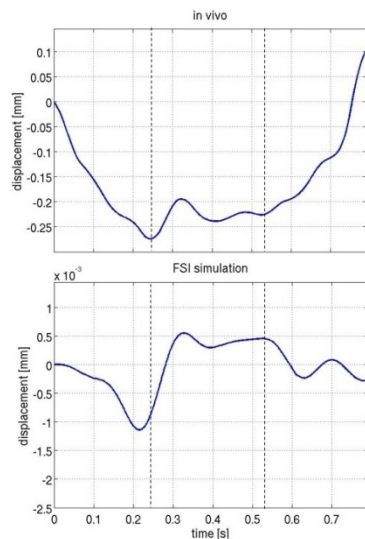
The FSI model was constructed in COMSOL Multiphysics. A 2D axis-symmetric circular cylindrical pipe (length: 100 mm, diameter: 15 mm, wall thickness: 1.5 mm) was modelled.

The AA wall material was hyperelastic nonlinear and anisotropic with age-matched material parameters. The outlet condition was a pressure of 80 mmHg. The outer wall was subjected to a 6.5 mmHg pressure to mimic intra-abdominal pressure.

Wall displacement estimated by the FSI model was compared to *in vivo* wall displacement over one heart cycle.

### Results/Discussion

The figure compares radial wall displacement, *in vivo* displacement ( $u_{iv}$ ) on top and simulated displacement ( $u_{FSI}$ ) below. Both  $u_{iv}$  and  $u_{FSI}$  drop in the first section indicated by the first dashed line, and rise in a similar way in the second section between 0.25 s and 0.53 s, so simulated motion is comparable to *in vivo*. But  $u_{FSI}$  is much smaller compared to  $u_{iv}$ , so the FSI model predicts a much stiffer AA wall compared to reality. This can be due to limitations of the FSI model as no axial pre-stress is included, and the reference position ( $t=0$ ) is assumed stress-free.



P1C5-8

### In Vivo ARFI Surveillance of Subcutaneous Hemorrhage (ASSH) For Monitoring rcFVIII Dose Response in Hemophilia A Dogs

Rebecca Geist<sup>1</sup>, Timothy Nichols<sup>2,3</sup>, Elizabeth Merricks<sup>1</sup>, Melissa Caughey<sup>2</sup>, Caterina Gallipoli<sup>4</sup>; <sup>1</sup>Department of Biomedical Engineering, University of North Carolina, Chapel Hill, NC, USA, <sup>2</sup>Department of Medicine, University of North Carolina, USA, <sup>3</sup>Department of Pathology and Laboratory Medicine, University of North Carolina, USA, <sup>4</sup>Department of Biomedical Engineering, University of North Carolina, USA

#### Background, Motivation and Objective

Bleeding is a frequent and deadly complication of hematologic and cardiovascular disorders. To control bleeding in inherited bleeding disorders, innovative therapeutic proteins, e.g., recombinant factor VIII (rFVIII), are available for replacement therapy for hemophilia A. However, translating such treatments from clinical trials to optimal dosing regimens for clinical use is challenged by insufficient assays for *in vivo* dose response. A new *in vivo* hemostasis assay, ARFI Surveillance of Subcutaneous Hemorrhage (ASSH), has previously been demonstrated to distinguish bleeding phenotype between normal and naïve hemophilia A dogs. The purpose of this investigation is to evaluate ASSH for monitoring dose response. We hypothesize that ASSH will differentiate bleeding phenotype in hemophilia A dogs treated with different levels of rFVIII.

#### Statement of Contribution/Methods

ASSH was performed in association with a standardized, B-Mode-guided puncture of a ~2 mm diameter hind leg vein in 13 dogs (N = 6 hemostatically normal, 7 hemophilia A). Hemophilia A dogs were examined in the naïve state and with three prophylactic treatment doses: infusion of rFVIII to approximately 3%, 10% and 100% of normal FVIII level. The ASSH observation period was 60 min following puncture, with serial ARFI data acquisitions every 1 to 5 min. Acquired raw RF data were processed with one-dimensional cross-correlation to measure axial displacement, and displacement variance in response to ARFI excitation discriminated hemorrhagic pixels. Then, from the hemorrhagic area temporal dynamics, ASSH bleeding rate (BR) and time to hemostasis (TTH) were estimated. ASSH was performed in each dog at each dose level with 2 repeated measures at least 2 weeks apart.

#### Results/Discussion

Fig 1A shows ASSH TTH dichotomized to normal (10-30 min) and abnormal (>30 min) outcomes in all dog cohorts. The percent within each cohort with abnormal TTH (red) progressively decreased with increasing rFVIII dose. Fig 1B depicts box plots describing ASSH BR per cohort. The median BR decreased with increasing dose, although only the naïve hemophilia A and 100% rFVIII treatment levels exhibited statistically different BRs ( $p < 0.05$ ).

These data suggests that ASSH is relevant for monitoring *in vivo* dose response to rFVIII in hemophilia A, which could support translation of this and other novel bleeding treatments to clinical usage.

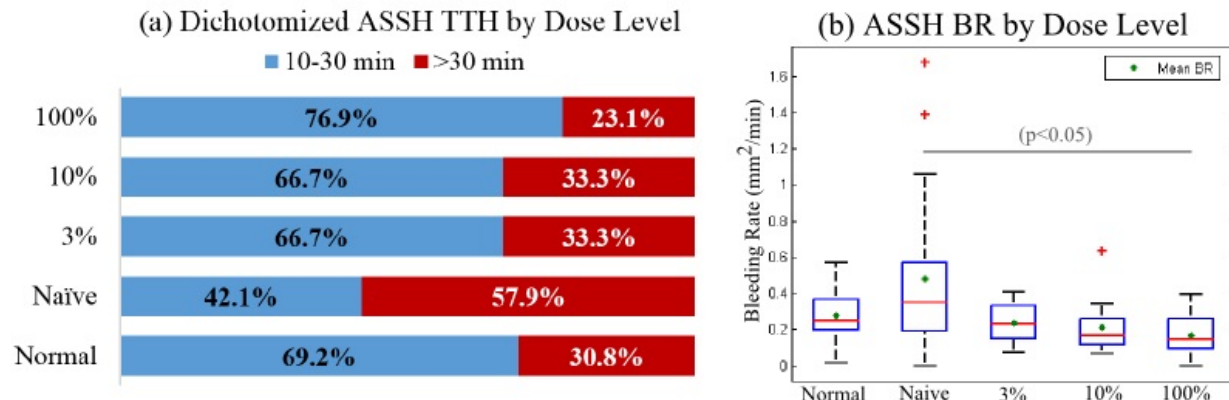


Figure 1: ASSH TTH and BR by Dose Level: (a) percent of abnormal (>30 min) TTH decreased with increasing rFVIII dose. (b) median BR decreased with increasing rFVIII dose, with statistically different ( $p < 0.05$ ) BR between naïve and 100% treatment levels.

## P1C5-9

**Wall Stress Analysis of Abdominal Aortic Aneurysms using 3D Ultrasound**

Annette M. Kok<sup>1</sup>, V. Lai Nguyen<sup>2</sup>, Lambert Speelman<sup>3</sup>, Geert-Willem H. Schurink<sup>2</sup>, Frans N. van de Vosse<sup>1</sup>, **Richard G.P. Lopata<sup>1</sup>**; <sup>1</sup>Biomedical Engineering, Eindhoven University of Technology, Netherlands, <sup>2</sup>Vascular Surgery, Maastricht University Medical Center, Netherlands, <sup>3</sup>Thorax Centre, Erasmus MC, Netherlands

**Background, Motivation and Objective**

An abdominal aortic aneurysm (AAA) is a local dilation of the aorta that will eventually rupture. Monitoring is already performed by assessing the maximum diameter with 2D ultrasound. Currently, the decision of intervention is based on the maximum diameter ( $> 5.5$  cm). However, the need for a more reliable criterion is often sought for in the mechanics of the aneurysmal wall. Multiple studies on Computed tomography (CT) and Magnetic Resonance Imaging based wall stress analysis are found in literature. The rise of 3D ultrasound (US) enables US-based wall stress analysis, but will suffer from limited contrast, field-of-view (FOV) and penetration depth. However, if feasible, the use of US will enable monitoring, studies on growth and without the use of ionizing radiation or contrast agent. In this study, the feasibility of 3D US-based wall stress analysis is examined.

**Statement of Contribution/Methods**

A total of 11 patients in the age of 55 – 83, with a AAA of 55 – 90 mm in diameter, were imaged 1 to 12 weeks prior to elective surgery. A MyLab 70 (Esaote, NL), equipped with a mechanical 3D array (BC431,  $f_c = 3.5$  MHz) and an RF-interface was used to image the AAA. One to three 3D volumes were acquired, depending on the length of the aneurysm. The sweep direction was orthogonal to the vessel axis. Computed tomography angiography (CTA) was performed for intervention planning using a Somatom CT system (Samsung, KR) with a pixel size of 0.7 - 0.8 mm.

All US data were manually segmented and different volumes were registered. Next, a radial smoothing was performed to reduce irregularities in the mesh. The CT-data were segmented using Mimics (Materialize, BE). The 3D volumes were compared in Matlab (Mathworks, USA) and the similarity index (SI) and Hausdorff distance (HD) were calculated. Next, for 6 patients the 3D US volumes were converted into volume meshes (wall thickness of 2 mm), consisting of 10 node quadratic tetrahedral elements. Wall stresses were simulated in ABAQUS (Dassault Systems, FR) using the two-parameter constitutive material model proposed by Raghavan & Vorp. The initial stresses at mean arterial pressure were reconstructed using a backward incremental method, after which the AAA was inflated to 140 mmHg.

**Results/Discussion**

The SI between 3D US and CT varied between 0.43 and 0.85 (median = 0.65) with Hausdorff distances between 4.7 to 25 mm (median 18 mm). In several datasets, a large mismatch was found in the iliac bifurcations due to the low US contrast, which is the largest limitation of US compared to CT. The 3D wall stress patterns in the resulting meshes (100,000 elements) were in accordance with previous studies, as well as the peak stresses (0.8 – 2.0 MPa). Irregularities due to the manual segmentation resulted in local high stress regions and require further improvement. This first US wall stress analysis to date revealed that the proposed technique is feasible. However, automatic segmentation and registration, and a comparison with CT-based wall stress, is required.

## PIC5-10

**Design of a fatty plaque phantom for validation of strain imaging**

Renate W. Boekhoven<sup>1</sup>, Marcel C.M. Rutten<sup>1</sup>, Frans N. van de Vosse<sup>1</sup>, Richard G.P. Lopata<sup>1</sup>; <sup>1</sup>Eindhoven University of Technology, Netherlands

**Background, Motivation and Objective**

Prior to clinical application of novel techniques such as vascular elastography and photo acoustic imaging, validation studies are of great importance. Gelatin, agar and polyvinyl-alcohol (PVA) phantoms are commonly used, however, more realistic phantoms are needed with complex geometry and different constituents with known properties. For this purpose, a fatty plaque phantom (fPP) was designed.

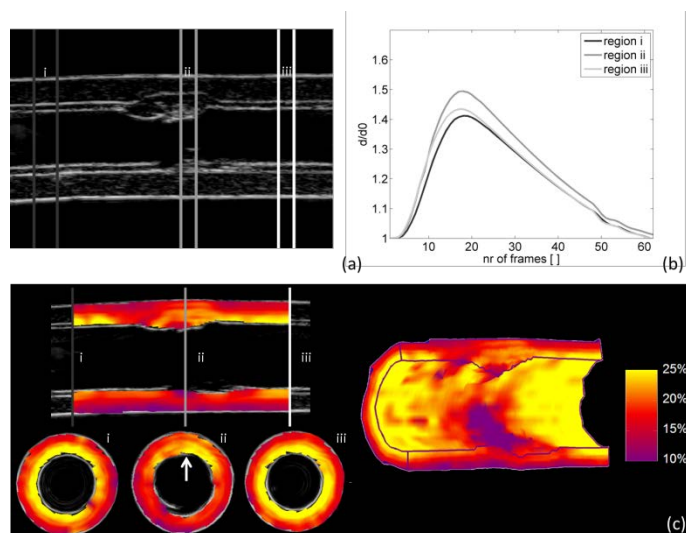
**Statement of Contribution/Methods**

A 15 weight percent (wt%) PVA solution was made, and 1 wt% of silica scatters were added (3 – 8 nm). The solution was poured into a custom-designed fPP mold. The outer wall (2.5 mm) was freeze thawed in two cycles of 16/8 hrs at  $-4^{\circ}\text{C}$  /  $24^{\circ}\text{C}$ , respectively. After 2 freeze / thaw cycles, porcine lard was injected. The structure was kept in the fridge for 30 minutes for the lard to set. Next, PVA was added and the luminal mold was inserted, to create a second layer of 0.5 mm, resulting in a total wall thickness of 3 mm, and a cap covering the lipid pool. The wall thickness of the fatty plaque was 3.5 mm. B-mode were acquired using a MyLab70 (Esaote, NL), while being pressurized from 0-80 mmHg. The phantom was imaged using a 3D echo-CT strain imaging method (Boekhoven et al. 2013a-c), to determine 3D geometry, distension and radial strains.

**Results/Discussion**

B-mode data revealed the different layers and fat inclusion in the phantom (Fig. 1a) and good natural echogenicity of the lard. Distension of the different regions, shown in Figure 1b, indicates that the distension of the healthy part, region i and iii, are similar. Distension of the fatty region is significantly larger, due to the soft lipid inclusion. Radial strains are shown (at end-systole) in longitudinal and transverse (reconstructed) cross-sections, and in 3D (Fig. 1c). Radial strains revealed the typical  $1/r^2$  relation. In accordance with the distension data, higher radial strains were found at the lipid inclusion location. The relatively low strain at the tip of the lipid inclusion is due to the high speckle density, causing strain underestimation.

In future work, strain data will be compared to numerical models that match the phantoms and experimental conditions to validate the strains measured. Additional stiffening of the PVA using a coagulation bath will be explored and, by doing so, increasing the allowed systolic pressure. Furthermore, fiber-enforced materials are currently investigated.



## P1C6 - MEL: Shear Wave Imaging Methods 2

Salon C

Saturday, September 6, 2014, 8:00 am - 5:00 pm

Chair: **David Melodelima**  
LabTAU - INSERM U1032

P1C6-1

### Comparison of Simulation Methods for Ultrasound Shear Wave Elastography: FEM vs. Green's Functions

Shiwei Zhou<sup>1</sup>, Sheng-Wen Huang<sup>1</sup>, Hua Xie<sup>1</sup>, Jean-Luc Robert<sup>1</sup>, Vijay Shamdasan<sup>2</sup>; <sup>1</sup>Philips Research North America, USA, <sup>2</sup>Philips Healthcare, USA

#### Background, Motivation and Objective

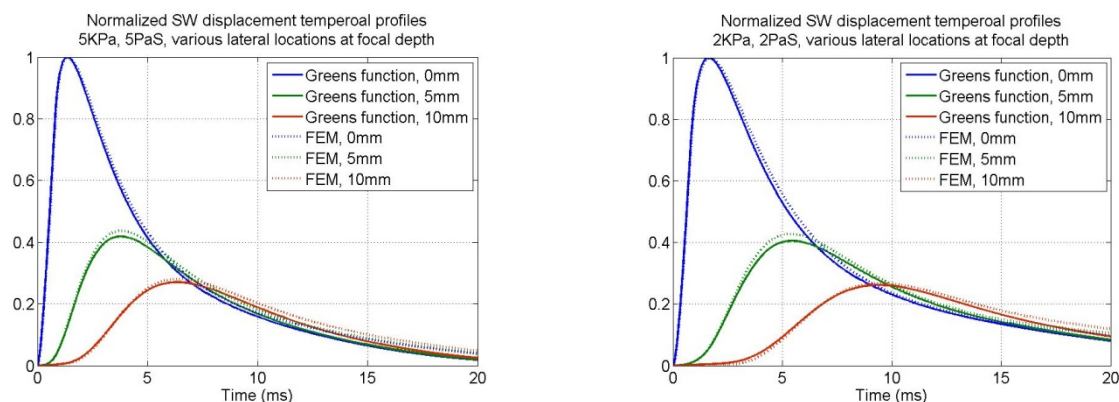
Ultrasound shear wave elastography (SWE) uses acoustic radiation force (ARF) to create shear waves in soft tissue. It is a non-invasive way for extracting quantitative tissue viscoelasticity information, as the tissue shear modulus and viscosity can be estimated by tracking the shear wave propagation speed. Soft tissues are in general viscoelastic, so it is important to develop simulation tools that can predict and analyze the viscoelastic tissue response to the applied ARF.

#### Statement of Contribution/Methods

We have created a 3D finite element model using PZFlex (WAI) for simulating from the acoustic field of the transducer to the shear wave propagation in homogenous or heterogeneous media. In parallel, we have also derived two exact Green's functions of the Voigt-model-based Navier's equation that can handle high viscosity, one in the position and temporal frequency  $x-\omega$  domain and the other in the spatial frequency and time  $k-t$  domain. The media of interest are infinite, homogenous, isotropic, and viscoelastic solids described by the Voigt model. Green's functions of position and time can be obtained from these exact solutions via inverse Fourier transform.

#### Results/Discussion

We compared the two simulation methods on one common SWE setting built upon curve-linear transducer C5-1 and homogenous media with various shear modulus and viscosity. Our results showed that the two simulation methods have very good agreement on shear wave displacement temporal profiles ( $R^2 \geq 0.988$ ). Both simulation tools are useful for developing and validating SWE methods and tissue viscoelasticity estimation algorithms.



P1C6-2

### Improving the Accuracy of Shear Wave Speed Reconstructions using 4D Directional Filters in the Presence of Reflection Artifacts.

Samantha Lipman<sup>1</sup>, Ned Rouze<sup>1</sup>, Michael Wang<sup>1</sup>, Mark Palmeri<sup>1</sup>, Kathryn Nightingale<sup>1</sup>; <sup>1</sup>Biomedical Engineering, Duke University, Durham, North Carolina, USA

#### Background, Motivation and Objective

Reflected waves from stiffness boundaries can lead to artifacts in shear wave speed (SWS) reconstructions. 2D directional filters are commonly used with planar imaging systems to reduce in-plane reflected waves; however SWS artifacts arise from both in and out-of imaging plane reflected waves. Herein, we quantify the reduction in image artifacts afforded by the use of volumetric SWS monitoring and 4D directional filters.

#### Statement of Contribution/Methods

A Gaussian acoustic radiation force impulse was simulated in a phantom with a Young's modulus (E) of 3 kPa with a 5 mm spherical lesion with E = 12 or 18.75 kPa, located 5 mm off-axis from the excitation. 2D and 4D directional filters were applied to the displacement profiles to reduce in and out-of-plane reflected wave artifacts. SWS images were reconstructed using time to peak slope methods to estimate wave arrival with a 1.5 mm regression kernel. Since the exact SWS is known, RMS error was calculated inside the lesion to quantify accuracy of each reconstruction.

#### Results/Discussion

Figure 1 shows SWS images of the E = 12 kPa lesion using 2D and 4D directional filters. Qualitatively, the reflection artifact at the right border of the lesion is removed by the 4D filter. This corresponds to a 20.4% decrease in RMS error. Figure 2 shows a SWS image of the E = 18.75 kPa lesion using 2D and 4D directional filters. Qualitatively, the reflection artifact at the right border of the lesion is reduced by the 4D filter and the corresponding RMS error decreased by 8.1%. This work shows that 4D directional filters reduce the impact of reflection artifacts in SWEI images, allowing for more accurate shear elasticity images to be generated in soft tissues.



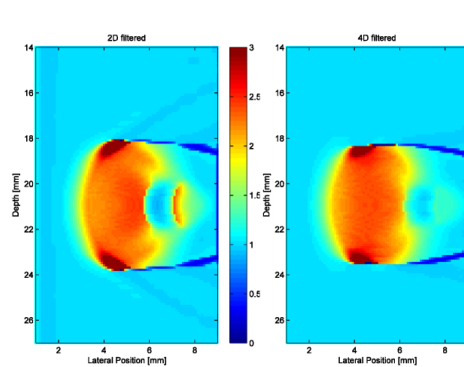


Figure 2. Elastic phantom with  $E = 3\text{ kPa}$  background and spherical lesion  $E = 18.75\text{ kPa}$ . 2D directional filtering has been applied to the image on the left, 4D directional filtering to the image on the right.

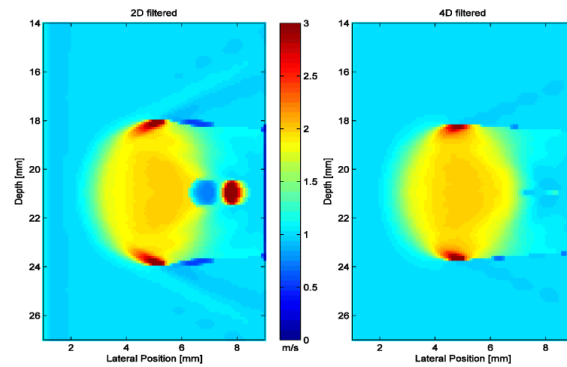


Figure 1. SWS image of an elastic phantom,  $E = 3\text{ kPa}$  background and spherical lesion  $E = 12\text{ kPa}$ . 2D directional filtering has been applied to the image on the left, 4D directional filtering to the image on the right.

P1C6-3

### Effects of Phase Aberration on Acoustic Radiation Force-Based Shear Wave Generation

Carolina Amador<sup>1</sup>, Sara Aristizabal<sup>1</sup>, James F. Greenleaf<sup>1</sup>, Matthew Urban<sup>1</sup>; <sup>1</sup>Department of Physiology and Biomedical Engineering, Mayo Clinic College of Medicine, Rochester, Minnesota, USA

#### Background, Motivation and Objective

Tissue elasticity is measured by shear wave elasticity imaging methods using acoustic radiation force to create shear waves. Reliable tissue elasticity measurements are achieved with strong shear waves. Phase aberration and tissue attenuation can hamper the generation of shear waves for *in vivo* applications. In this study we explored how phase aberration affects ultrasound focusing for creating shear waves and evaluate the resulting shear wave amplitude and the estimated shear wave velocity.

#### Statement of Contribution/Methods

A Verasonics ultrasound system (Verasonics, Inc., Redmond, WA) equipped with a linear array transducer (L7-4, Philips Healthcare, Andover, MA) was used. In the experiments, an excised piece of swine belly tissue was studied at 30°C saline bath. In the first set of experiments the tissue was placed on top of an agar phantom and two transducers were used to generate shear waves through tissue layer, one transducer on top of the phantom was used to push through the layer and a second transducer was placed on the bottom of the phantom to detect the shear wave propagation without phase aberration and attenuation. In the second set of experiments measurements of the time delay or phase screen of ultrasound pulses passing through the tissue layers were performed as described by Krammer (IEEE IUS, 1997). Then transmit geometrical delays calculated by Verasonics systems were modified by adding the measured phase screen. The ultrasound push was focused at 40 mm depth and its frequency was varied; 2.50, 3.00, 3.46, 4.09 and 4.50 MHz. The shear wave amplitude and shear wave speed measured were evaluated.

#### Results/Discussion

The shear wave particle velocity at  $t = 0.3\text{ ms}$  after the push for the tissue layer and its measured phase screen with 3.00 MHz and 4.09 MHz push are shown in Figure 1. The particle velocity decreased with the introduction of the layer and its measured phase screen; however the former affected more the shear wave generation. Shear waves generated through the tissue layer were affected by both phase aberration and attenuation whereas shear waves generated through the measured tissue phase screen were affected only by phase aberration.

In conclusion, decreasing the ultrasound frequency was important for maintaining a focused beam for creation of shear waves. [This study was supported in part by NIH grant DK092255]

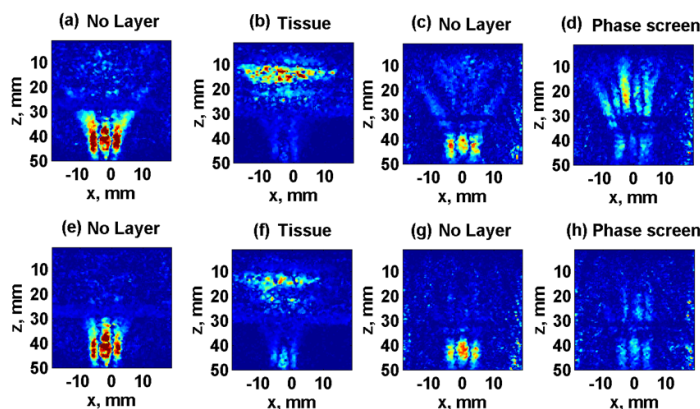


Figure 1. Particle velocity at  $t = 0.3\text{ ms}$  for (a) No Tissue, (b) Tissue, (c) No Tissue, (d) Phase screen. (a)-(d) are from 4.09 MHz push and (e)-(h) are from 3.00 MHz push. (a)-(b) and (e)-(f) have color scale from 0 to 20 mm/s, (c)-(d) and (g)-(h) have color scale from 0 to 50 mm/s.

## P1C6-4

**Loading ramp effects in uniaxial compression creep device**

Carolina Amador<sup>1</sup>, Alireza Nabavizadeh<sup>2</sup>, Randall Kinnick<sup>1</sup>, Mostafa Fatemi<sup>1</sup>; <sup>1</sup>Department of Physiology and Biomedical Engineering, Mayo Clinic College of Medicine, Rochester, Minnesota, USA, <sup>2</sup>Biomedical Informatics and Computational Biology, University of Minnesota, USA

**Background, Motivation and Objective**

Tissue viscoelastic properties measured by uniaxial compression creep ultrasound method have shown correlation with tissue state. Creep is usually induced by a uniaxial compression of tissue with an ultrasound transducer which, is also used to capture the local creep response of the tissue by ultrasound imaging and motion calculation techniques. The majority of the creep studies assume step-loading conditions, which are analytically convenient but experimentally impossible to implement. The goals of this study are to validate the global measurements of a prototype creep device with a conventional mechanical testing machine, and also to study the effects of loading rate on creep response.

**Statement of Contribution/Methods**

A uniaxial compression creep device was designed with an actuator. The creep device holds and slides the ultrasound probe forward to approximate a step function. The displacement of the probe is driven by a servo motor and a force sensor provides feedback to maintain a constant force. A 10% gelatin phantom (58x58x47 mm<sup>3</sup>) was tested by the creep device and by a uniaxial testing commercial machine (ELF 3200, Electroforce, Eden Prairie, MN) with 3 N force for 30 seconds and loading rates of 3 N/s and 20 N/s. Additionally, a Dynamic Mechanical Analysis (DMA) test was used to study the phantom viscoelastic properties. The global creep strains were used to calculate the  $\tan(\delta)$  using a conversion formula as described by Evans (2009).

**Results/Discussion**

Fig. 1 shows the force, strain and  $\tan(\delta)$  measurements. The applied force by the creep device and commercial machine were similar; however the strain measurement were fairly different. The difference in strain between creep device and commercial machine could be due to variations in contact area and location of load cell. The  $\tan(\delta)$  varied as a function of the loading rate but it was similar for creep device and commercial machine. The  $\tan(\delta)$  from creep converges to DMA results as the loading rate is increased, which agrees with the fact that at faster loading rate the force approximates a step-loading condition. In conclusion, this study shows the validation of the prototype creep device with a commercial mechanical testing machine and illustrates how the measured  $\tan(\delta)$  varies as a function of loading rate. Future work includes analysis of the local creep measurements. This study is supported by NIH grant CA168575.

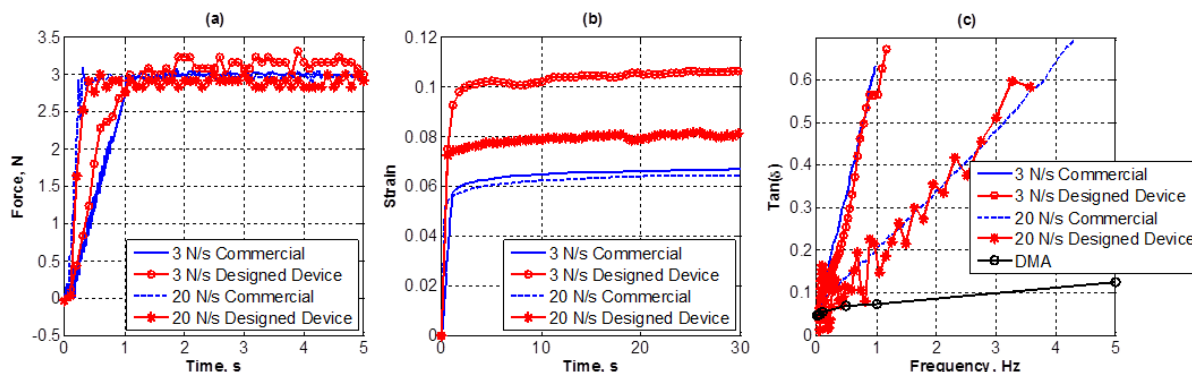


Fig. 1. (a) Applied force, (b) Measured strain, (c) Measured  $\tan(\delta)$

## P1C6-5

**A two-dimensional finite difference model of shear wave propagation in anisotropic soft tissue**

Yiqun Yang<sup>1</sup>, Matthew W. Urban<sup>2</sup>, Robert J. McGough<sup>1</sup>; <sup>1</sup>Electrical and Computer Engineering, Michigan State University, East Lansing, Michigan, USA, <sup>2</sup>Department of Physiology and Biomedical Engineering, Mayo Clinic College of Medicine, Rochester, MN, USA

**Background, Motivation and Objective**

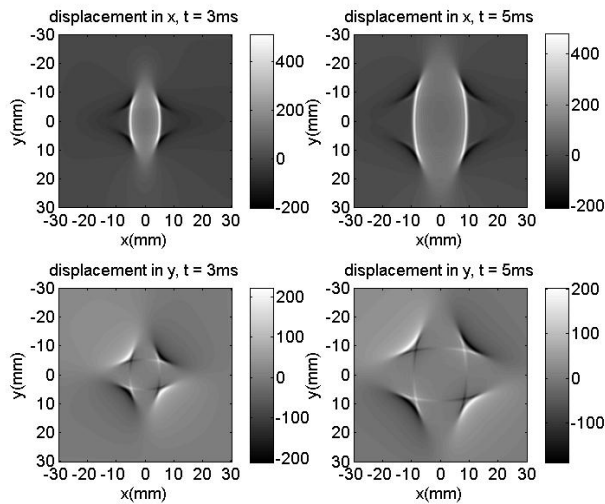
Shear waves generated by an applied acoustic radiation force propagate at different speeds in different directions within tissues such as kidney, skeletal muscle, and myocardium depending on the polarization of the shear waves with respect to the organ structural architecture. As new methods to characterize shear wave anisotropy are developed, better simulation tools are needed, which motivates the development of finite difference approaches to simulate the anisotropy of shear waves propagating in soft tissue.

**Statement of Contribution/Methods**

The elastodynamic equation of motion for a transversely isotropic medium is modeled with a two-dimensional finite difference scheme. These simulations employ an explicit time-stepping approach and a staggered spatial grid. The Courant-Fischer-Levy condition is enforced to ensure stability, and an absorbing boundary condition reduces reflections at the edge of the grid. Simulations are evaluated in an anisotropic, homogeneous, nearly incompressible elastic medium with a compressional wave speed of 1500 m/s, a shear wave speed of 2 m/s in the x-direction, and a shear wave speed of 6 m/s in the y-direction.

**Results/Discussion**

The results of these simulations are computed at 80000 time points on a 401 by 401 point spatial grid. The temporal sampling frequency is 16 MHz, and the spatial sample spacing is 0.15 mm. The applied body force is modeled by a 600  $\mu$ s positive half cycle of a sine wave induced by a point body force in the x direction at the center of the computational grid. The simulation, which is written in C, is completed in 10 minutes. The resulting displacements in the x and y directions at  $t = 3$  ms and  $t = 5$  ms are shown in the figure below. These simulations demonstrate the effects of shear wave anisotropy in two dimensions. Plans to extend these simulations to three dimensions and to combine these simulations with FOCUS, the "Fast Object-Oriented C++ Ultrasound Simulator" will also be discussed. [This work was supported in part by NIH Grants R01 EB012079 and R01 DK092255].



P1C6-6

### Shear Wave Speed Estimation from Crawling Wave Sonoelastography: A comparison between AM-FM Dominant Component Analysis and Phase Derivation Methods

Juvenal Ormachea<sup>1</sup>, Renan Rojas<sup>1</sup>, Paul Rodriguez<sup>1</sup>, Roberto Lavarello<sup>1</sup>, Kevin Parker<sup>2</sup>, Benjamin Castaneda<sup>1</sup>; <sup>1</sup>Departamento de Ingeniería, Pontificia Universidad Católica del Perú, Lima, Peru, <sup>2</sup>Department of Electrical & Computer Engineering, University of Rochester, Rochester, New York, USA

#### Background, Motivation and Objective

Crawling Wave Sonoelastography (CWS) offers quantitative estimation of shear wave speed (SWS) in soft tissues. Recently, two different methods to estimate the SWS from the crawling wave patterns have been proposed. The first method is based on the spatial phase derivation from the slow-time signal (CWS-PD) using the knowledge of the difference in vibration frequency (DVF). The second method is based on the AM-FM Dominant Component Analysis (DCA) model, which allows estimating the spatial frequency without a priori information of the DVF and without any noise model assumptions. In this work, a comparison of the performance of CWS-PD and AM-FM-DCA for the estimation of SWS is presented.

#### Statement of Contribution/Methods

Three gelatin-based phantoms of different gelatin concentrations (10%, 13% and 16%) were produced. Two mechanical sources were placed opposite to each other to generate a vibration field with frequencies between 180 and 360 Hz. A GE-Logiq 9 ultrasound system was used to perform CWS imaging. All the experiments were performed at room temperature (20C-21C). Two-dimensional SWS maps were obtained using both the CWS-PD and AM-FM-DCA methods. Average and standard deviation of SWS measurements from a central region of interest were calculated for each vibration frequency. The estimated SWS values were compared to the ones obtained from mechanical measurements (MMs), which were performed using stress relaxation tests and fitting the relaxation curve to the Kelvin-Voigt Fractional Derivative model.

#### Results/Discussion

Both CWS-PD and AM-FM-DCA provided similar SWS estimates with generally good agreement with the values obtained from MMs. Figure 1 shows the SWS as a function of the vibration frequency obtained with all methods for each phantom. The highest errors for CWS-PD and AM-FM-DCA were 5.8% and 4.7%, 5.8% and 5.6%, and 12.2% and 22.2% for the 10%, 13% and 16% concentration phantoms, respectively. Both methods presented higher errors for the 16% gel-phantom and frequencies below 200 Hz, which may be due to the increased difficulty in tracking shear waves with longer wavelengths. These results suggest that further research may be needed for a more accurate evaluation of stiffer materials.

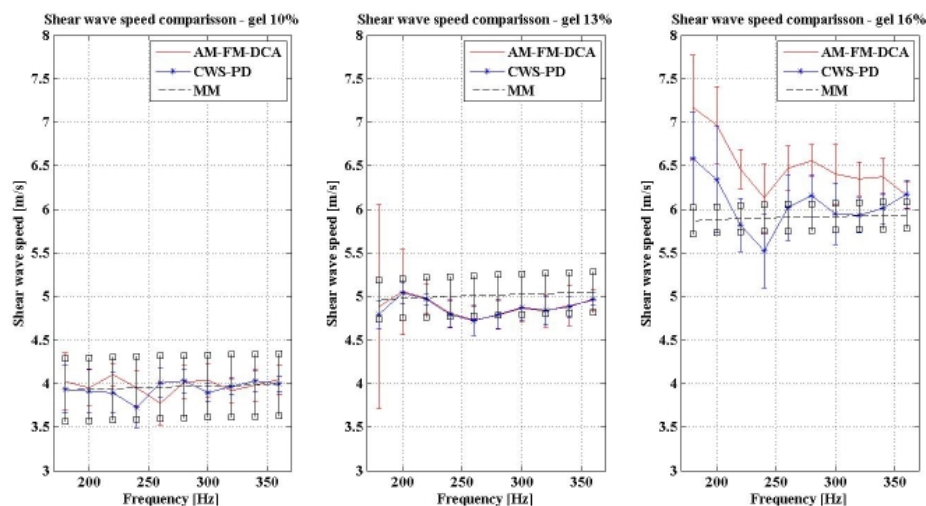


Figure 1

## P1C6-7

**Assessing tissue motions induced by orthogonal-frequency pulses and binary pulses using a laser vibrometer**

Yi Zheng<sup>1</sup>, Haoming Ling<sup>2</sup>, Xin Chen<sup>2</sup>, Panpag Liu<sup>2</sup>, Tianfu Wang<sup>2</sup>, Siping Chen<sup>2</sup>; <sup>1</sup>Electrical and Computer Engineering, St. Cloud State University, St. Cloud, MN, USA, <sup>2</sup>School of Medicine, Shenzhen University, Shenzhen, China, People's Republic of

**Background, Motivation and Objective**

Tissue motions can be induced by using pulsed ultrasound radiation force. The phase velocities of the induced shear wave at several harmonics can be measured for estimating the viscoelasticity of the tissue using an ultrasound vibrometry. Our study finds that the accurate estimation of viscosity requires high frequency components. However, it is challenging to induce and detect tissue motions that are higher than 400 Hz using binary pulses. Orthogonal frequency pulses were previously reported to increase the intensities of high harmonics of the induced shear wave. The objective of this study is to quantitatively assess the capability of binary pulses and orthogonal-frequency pulses by using a laser vibrometer to complete our early study. The relationship between the characteristics of motion and the characteristics of excitation pulses are also studied.

**Statement of Contribution/Methods**

The swine liver was embedded in gelatin phantom and placed in the water tank. The custom-made excitation transducer (IMASONIC, France) transmits the excitation pulses modulated at 2.5MHz, which was generated by an arbitrary signal generator (AFG3000, Tektronix) and amplified by a power amplifier (A150; Electronics & Innovation Ltd., Rochester, NY). Binary pulses and orthogonal frequency pulses having and six chips per period were transmitted to induce shear waves, respectively. Both pulse sequences have the same total energy. A laser vibrometer (VibroMet Model 500V; MetroLaser, Inc.) was used to detect the induced tissue motions. Detection locations were from 1 mm to 10 mm away from the center of the radiation force was applied, with 1 mm increment. The output of laser vibrometer was recorded by an oscilloscope (DPO 4104, Tektronix) with a sample frequency of 10 kHz for off-line processing.

**Results/Discussion**

The amplitudes of tissue motion induced by the orthogonal frequency pulses are higher than that of binary pulses from 12 dB to more than 20 dB from 600 Hz to 900 Hz, as the amplitude of the orthogonal pulses is only 41% of that of the binary pulses. The study also finds that the peak displacement of the motion is proportional to the excitation energy and the spectrum of the motion velocity is strongly correlated to the spectrum of the excitation pulses. These results describe how the tissue responds to the external force and raise the issues of tissue modeling. If the displacement is used in the detection and a prescribed spectrum of the displacement is preferred, the spectrum of orthogonal frequency excitation pulses should be modified by multiplying the prescribed spectrum with frequencies, and the pulse design should be guided by the modified spectrum.

## P1C6-8

**Elastic modulus contrast enhancement in shear wave imaging using mechanical nonlinearity: In vitro tissue mimicking phantom study**

Dae Woo Park<sup>1</sup>, Kang Kim<sup>1,2</sup>; <sup>1</sup>Center for Ultrasound Molecular Imaging and Therapeutics & Heart and Vascular Institute, University of Pittsburgh Medical Center, Pittsburgh, Pennsylvania, USA, <sup>2</sup>Bioengineering, University of Pittsburgh, Pittsburgh, Pennsylvania, USA

**Background, Motivation and Objective**

Shear wave elasticity imaging (SWEI) has been widely used to determine the elasticity of tissues. However, the shear modulus (G) estimated in SWEI is often less sensitive in some cases, especially to a subtle change of the elasticity that produces small mechanical contrast to the background tissues. This small mechanical contrast can be enhanced if the tissues are compressed, exhibiting nonlinearity. In this study, we propose a new nonlinear SWEI and evaluate its feasibility through experiments using a tissue mimicking phantom.

**Statement of Contribution/Methods**

SWEI was performed while a tissue mimicking phantom was continually deformed over a relatively large dynamic range of strains. A 9% gelatin inclusion of a long cylinder (Diameter: 8 mm, hard) embedded in 6% gelatin phantom block (soft) was fabricated. The phantom was continually compressed up to 30% height change using an ultrasound (US) probe (L7-4, ATL 5 MHz central frequency) fixed to a motorized translational stage, while SWEI was applied at each increment of 10% strains. The localized US push pulses, indicated by white dots in the figure, were generated and then subsequently radiofrequency (RF) frames were acquired using a commercial US scanner (V-1, Verasonics Inc.) while the created shear wave was propagating through the phantom. Axial displacements of the shear wave were estimated using the Loupas' algorithm and were averaged over 10 frames to improve the signal-to-noise ratio. Finally, the G was determined from the axial displacements field using an inversion of the Helmholtz equation. The G was spatially averaged and compared for both inclusion and surrounding phantom block over the applied overall strain ranges of 30%.

**Results/Discussion**

The average G of the inclusion exhibited relatively strong nonlinearity after 20% applied strain and sharply increased to 1.9 kPa at 30% applied strain. On the other hand, the average G of the surrounding phantom block increased linearly from 0.7 to 1.2 kPa over the same applied strain range. The elastic modulus contrast ( $(G(\text{inclusion}) - G(\text{phantom block})) / G(\text{phantom block})$ ) of the inclusion to the surrounding phantom block was increased from 0.3 at 0% applied strain to 0.5 at 30% applied strain, which displays detecting the inclusion better.

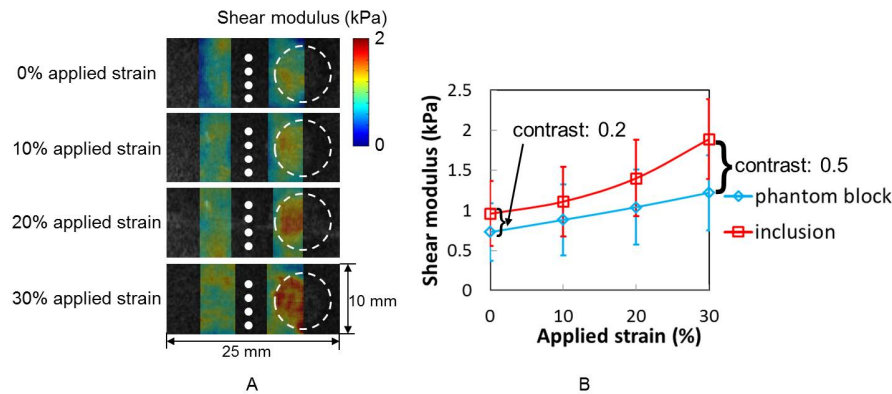


Figure: Shear wave elasticity imaging (SWEI) on a tissue mimicking phantom. (A) Reconstructed shear modulus map with 0%, 10%, 20%, and 30% applied strains. The white dots at the center indicate ultrasound pushing pulses and the white dashed circle denotes the hard inclusion. (B) Average shear modulus of the inclusion and surrounding phantom block vs. applied strain.

P1C6-9

### Shear waves in anisotropic media mimicking skeletal muscle

Armen Sarvazyan<sup>1</sup>, Oleg Rudenko<sup>2</sup>, Salavat Aglyamov<sup>3</sup>; <sup>1</sup>ARTANN Laboratories, Lambertville, New Jersey, USA, <sup>2</sup>Department of Physics, Moscow State University, Moscow, Russian Federation, <sup>3</sup>Department of Biomedical Engineering, University of Texas at Austin, Austin, Texas, USA

#### Background, Motivation and Objective

Major functions of the skeletal muscle are mechanical: generation of force and motion, posture support and protecting the skeletal system from external impacts by redistributing the energy of mechanical shock in time and space and unloading skeletal joints. Assessment of mechanical properties of muscle: its shear elasticity and dynamic viscosity, may be important for diagnosis and monitoring of treatment of various muscle disorders. However, conventional means for measurement in vivo mechanical properties of passive and contracting muscle are highly limited. Emergence of novel technique of ultrasonic elastography opens new possibilities for real-time quantitative assessment of elasticity and viscosity of skeletal muscle. In contrast to other soft tissue, skeletal muscle is highly anisotropic and shear wave propagation parameters depend on orientation of muscle fibers relative to the polarization of shear wave. The goal of this study is to develop a theory for propagation of shear waves in anisotropic medium, such as muscle, necessary for interpretation of the results of measurement of muscle mechanical properties.

#### Statement of Contribution/Methods

In the present work, the theory on propagation of acoustic waves in skeletal muscle that we developed earlier [Rudenko Sarvazyan, 2006] is adapted for analyzing available experimental data [Aristizabal et al 2013, Royer et al. 2011]. According to the specific architecture of skeletal muscle, its elastic tensor has five independent components, however, it is shown that for shear waves in soft solids there are only two independent elastic moduli. Viscosity tensor also has two components. Propagation velocity of shear waves in the muscle has two values depending on three vectors: the direction of propagation, the polarization of shear wave and orientation of the muscle fibers.

#### Results/Discussion

It follows from our theory, that propagation of shear wave in muscle is analogous to that for propagation of light in a uniaxial optical crystal: two wave modes are possible, which in optics are called "ordinary" and "extraordinary" waves. They differ in the direction of the wave vector relative to the direction of the muscle fibers ("optical axis"), as well as the direction of the polarization vector. One wave mode is polarized orthogonally to the plane of incidence containing the axis of the fiber and the wave vector, the second has a polarization in the plane of incidence. The speed of each wave depends on three vectors: the direction of propagation, the polarization and orientation of the muscle fibers. Equations for the speed and attenuation of each wave mode are derived. Theoretical predictions are in agreement with the literature and our own experimental data obtained in anisotropic phantoms modeling relaxed and contracted muscle.

The work was supported by grant NIH/NIAMSD R21AR065024.

P1C6-10

### Effect of frequency adaptation based on the attenuation coefficient to optimize shear wave displacement magnitudes

Abderrahmane Ouared<sup>1</sup>, Emmanuel Montagnon<sup>1</sup>, Guy Cloutier<sup>1</sup>; <sup>1</sup>University of Montreal Hospital, Canada

#### Background, Motivation and Objective

Over the last two decades, the acoustic radiation force (ARF) has been increasingly used in remote dynamic elastography for tissue characterization. However, one problem of this technique is the strong attenuation of generated displacements and the low signal-to-noise ratio (SNR), both factors affecting the estimation of mechanical parameters. In order to reduce the impact of such limitations, we propose a new method to optimize the displacement amplitude by adapting the frequency used for the generation of the radiation force with respect to attenuation and focus depth. The aim is to apply the adaptive radiation force to increase displacement amplitudes and improve the SNR for better assessment of viscoelastic parameters.

#### Statement of Contribution/Methods

An analytical model was developed for the prediction of the optimal frequency for the generation of ARF. Four agar-gelatin phantoms with different attenuation coefficients were made for experimental validation. Once the attenuation of each phantom was experimentally determined, the optimal frequency (Fo) for the generation of shear waves was predicted by the model. For each phantom, ARF was generated at the central frequency (Fc) of the transducer, and at Fo using an ATL L7-4 probe (Philips, USA) controlled by a Verasonics V-1 system (Verasonics Inc., USA). The performance was determined by comparing shear wave magnitudes as a function of depth between ARF generated at Fo and Fc.



### Results/Discussion

Fig. 1 shows the amplitude of displacements generated by the adaptive method at  $F_0$  (blue) and at the central frequency  $F_c$  (red). Displacements at  $F_0$  were larger than at  $F_c$ ; improvements were between 20% and 158 % depending on the focus depth and attenuation of the phantom. The SNR was improved from 7 to 16 dB with the proposed method.

We conclude that frequency adaptation is of interest to optimize the displacement amplitude. From a priori estimation of the attenuation coefficient, its implementation is quite straightforward. Performance revealed to be optimum for narrow band transducers operating between 1 MHz and 4 MHz, for tested phantom conditions.

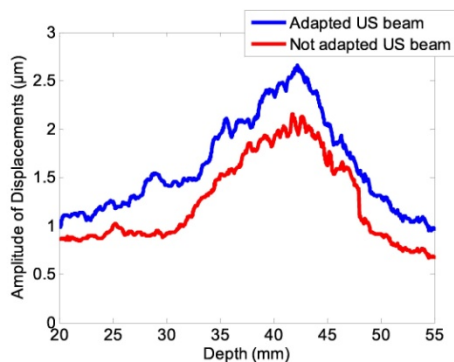


Fig. 1: Axial profile of the amplitude of displacement near to the focus in an agar (6 %) - gelatin (5 %) phantom with an attenuation coefficient of 0.7 db/cm/MHz. The source of generation of ARF is at 0 mm and the focus at 40 mm. The blue curve represents the amplitude of displacements generated by the adapted beam sequence and red curve amplitude of displacements generated by not adapted beam.

## P1C7 - MIM: Image Processing and Classification

Salon C

Saturday, September 6, 2014, 8:00 am - 5:00 pm

Chair: **Olivier Basset**  
CREATIS, Lyon

P1C7-1

### Estimation of respiratory breathing signal from 2D US sequences and 4DCT of the liver

Dominik Spinczyk<sup>1</sup>, David Melodelima<sup>2,3</sup>, Rémi Blanc<sup>1</sup>, Simon Rit<sup>1</sup>, David Sarrut<sup>1</sup>; <sup>1</sup>CREATIS, Université de Lyon, Lyon, France, <sup>2</sup>Inserm, U1032, LabTau, Université de Lyon, Lyon, France, <sup>3</sup>Centre Léon Bérard, Lyon, France

#### Background, Motivation and Objective

One challenge of High Intensity Focused Ultrasound (HIFU) when treating primary liver tumors is the management of the breathing motion during treatment. An extracorporeal HIFU transducer with an integrated ultrasound (US) imaging probe has been specifically designed for treating the liver. The US probe produces 2D images and the tumor itself may not always be visible in US images. A pre-operative 4D-Computed Tomography (CT) image is acquired to infer the tumor location. Here, we propose to retrieve spatio-temporal correspondence between the 4DCT and 2D+t US sequences to guide extracorporeal HIFU treatments.

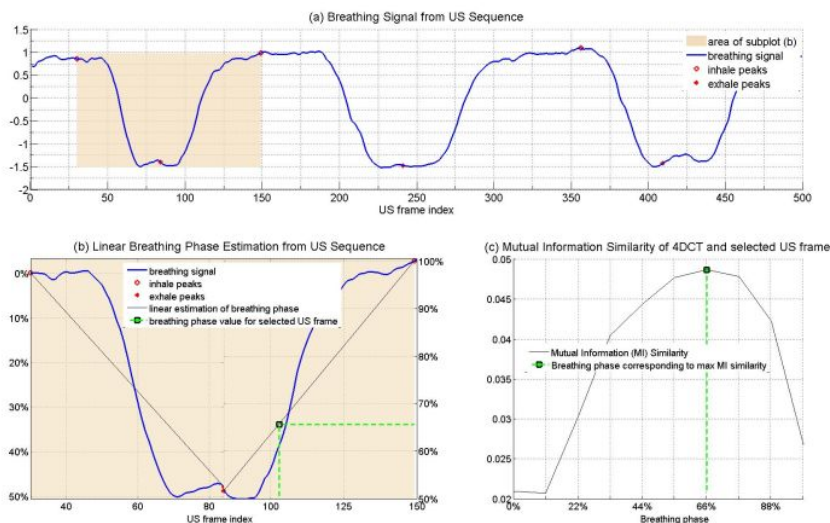
#### Statement of Contribution/Methods

To study the feasibility of US guidance according to the pre-operative planning CT image, US sequences were acquired in 10 patients after informed consent. Trials were conducted on patients undergoing radiotherapy treatment with a planned 4DCT injected image (Philips Brilliance). Several 2D+t US sequences of about 30 s, targeting structures in the liver, have been acquired after CT acquisition. A breathing signal has been extracted from each US sequence using temporal Principal Component Analysis (PCA), keeping the first main component of the PCA model. Respiratory phases were estimated by peak detection using the Hilbert transform. For each US frame of the sequence, the corresponding CT plane was extracted according to the detected phase and the slice orientation given by an optical device locating the probe position and orientation according to the patient. As preliminary validation, we compared the similarity between the extracted CT planes with CT planes at other time phases. Our assumption is that similarity values should be maximal for the corresponding retrieved phase and lower for the other phases if the breathing signal extraction and the phase retrieval are correct.

#### Results/Discussion

Figure 1(c) depicts the Mutual Information measure between 10 planes extracted from the 4DCT that correspond to the US probe orientation at a given frame. We can observe that the maximum value correspond to the one extracted by the proposed method. Preliminary results show that breathing signal could be extracted from 2D US sequences, suggesting that HIFU liver treatment guidance by a combination of 4DCT+2D US should be feasible. Further validations are still required. In the future work US image content will be used to guide the HIFU treatment.

Fig. 1. Extracted breathing signal as a function of US frames (a). Linear breathing phase estimation from US sequence (b). Mutual Information as a function of CT phases (c).



P1C7-2

### An Automated System To Assess Axillary Lymph Node Malignancy From Sonographic Images

Aneta Chmielewski<sup>1</sup>, Paul Dufort<sup>1</sup>, Ryan Ramos<sup>1</sup>, Anabel Scaranelo<sup>1</sup>; <sup>1</sup>Joint Department of Medical Imaging, University Health Network, Toronto, Ontario, Canada

#### Background, Motivation and Objective

PURPOSE: Ultrasonography is frequently used as part of diagnosis and guidance during lymph node biopsy. Axillary lymph node dissection (ALND) and sentinel lymph node biopsy (SLNB) are widely used surgical staging procedures. However, ALND alone has not been shown to improve survival of breast cancer patients and is associated with more complications than SLNB, while SLNB has false negative rates ranging from 5.6 to 29.6 % for lymph node metastasis staging, and has been associated with a significant risk of lymphoedema (14%). Establishing an accurate, non-invasive method of lymph node metastasis staging would increase the accuracy of diagnosis with ultrasound alone, decreasing

the number of unnecessary surgical staging procedures, and lowering healthcare costs. A project was therefore undertaken to automate axillary lymph node malignancy classification in two phases: (1) contouring of the lymph node and hilum; and (2) classification of node malignancy. In this first stage, the contouring for phase 1 was performed manually, and effort was focused on developing the classifier for phase 2 using the image intensities and contours as input.

#### Statement of Contribution/Methods

**METHODS:** After REB approval 110 ultrasound images of lymph nodes were selected from a database of women undergoing surgical treatment of confirmed breast cancer. Selected nodes were classified based on fine needle aspiration, ALND or SLNB. All lymph nodes and associated hila (81 benign and 29 malignant) were manually contoured. Feature triplets (intensity, distance from lymph node boundary, distance from hilum boundary) were collected for each pixel inside a region including the node plus pixels at a distance of 2.56 cm or less from the lymph node contour. The collection of triplets was then used to populate a 3D histogram, whose bin counts served as the predictor inputs to a support vector machine (SVM) learning algorithm in conjunction with a Cauchy kernel. Classification of the 110 lymph nodes was tested under a 10-fold cross-validation regime to estimate generalization performance and to produce receiver operating characteristic (ROC) curves.

#### Results/Discussion

**RESULTS:** Ten thousand random draws of 80 training and 25 test images yielded a mean test error rate of 0.07. The final classifier algorithm had an ROC area under the curve (AUC) of 0.96, yielding a sensitivity/ specificity of 0.9/0.9 along the ROC diagonal, or 0.986/0.5 in the more realistic case where false negatives are vastly more problematic than false positives. Ten thousand randomly permuted label assignments were computed and used in 80/25 train/test splits to generate a random sampling distribution of test error rates. Only 158 had accuracies less than or equal to the actual error rate of 0.07, resulting in a statistical significance of  $p = 0.0158$ . **CONCLUSION:** The classifier could be used to identify metastases with a 1.4% miss rate, while eliminating the need for 50% of patients to undergo needless invasive procedures.

#### P1C7-3

##### A fully automated method for carotid plaques segmentation in ultrasound images based on motion estimation and level-set

Francesca Galluzzo<sup>1</sup>, Luca De Marchi<sup>1</sup>, Nicola Testoni<sup>1</sup>, Mahdi Tabassian<sup>1</sup>, Nicolò Speciale<sup>1</sup>, Guido Masetti<sup>1</sup>; <sup>1</sup>DEI-Department of Electrical, Electronic and Information Engineering "Guglielmo Marconi", University of Bologna, Bologna, Italy

#### Background, Motivation and Objective

In carotid atherosclerosis diagnosis, ultrasound (US) methods are extensively used to evaluate the stenosis degree due to plaques presence and to study their composition. A fast and accurate carotid plaques segmentation (CPs-S) is essential to enable these evaluations. However, low SNR, high operator dependency and highly variable CPs appearance, make this task difficult, time consuming and poorly reproducible.

Several studies highlighted alterations in carotid walls (CWs) motion in presence of stenosis and cardiovascular disease (Golemati, TBME'13).

In this work we present a fully automated CPs-S method based on level-set (LS) with an innovative initialization procedure that, exploiting CWs motion analysis, makes the approach completely user-independent.

#### Statement of Contribution/Methods

The proposed method comprises 1) preprocessing, 2) initialization and 3) segmentation stages. Preprocessing 1) consists in envelope detection and contrast enhancement of the US acquisition IQ data. The fully automated initialization procedure is based on the analysis of relative motion between CPs, CWs and blood in the US sequence. Thus, a block matching procedure 2) is launched across multiple frames to distinguish image blocks that can be associated to CPs, from ones corresponding to the CWs or blood, basing on the estimated displacement vectors. The outputs of such procedure, combined with information related to the echogenicity, are used to produce the binary mask which constitutes the initialization of a segmentation algorithm 3) based on localized region-based active contours in LS framework.

Ten US image sequences (2960 frames) from different patients were acquired using the ULA-OP research scanner (Tortoli, TUFFC'09). Manual segmentation of selected frames (preceded by step 1)) performed by an expert sonographer was taken as reference for method validation. Sensitivity (SE), Specificity (SP) and Kappa Index (KI) were used as comparison metrics.

#### Results/Discussion

Figure 1 shows examples of manual (dotted line) and automated (full line) CPs-S at near (a) and far (b) wall. Achieved average SE (75%) and SP (80%) indicate good agreement between manual and automated segmentation which is also confirmed by KI=70%.

The proposed segmentation method allows accurate CPs-S without requiring any user interaction thus reducing task subjectivity and time consumption.

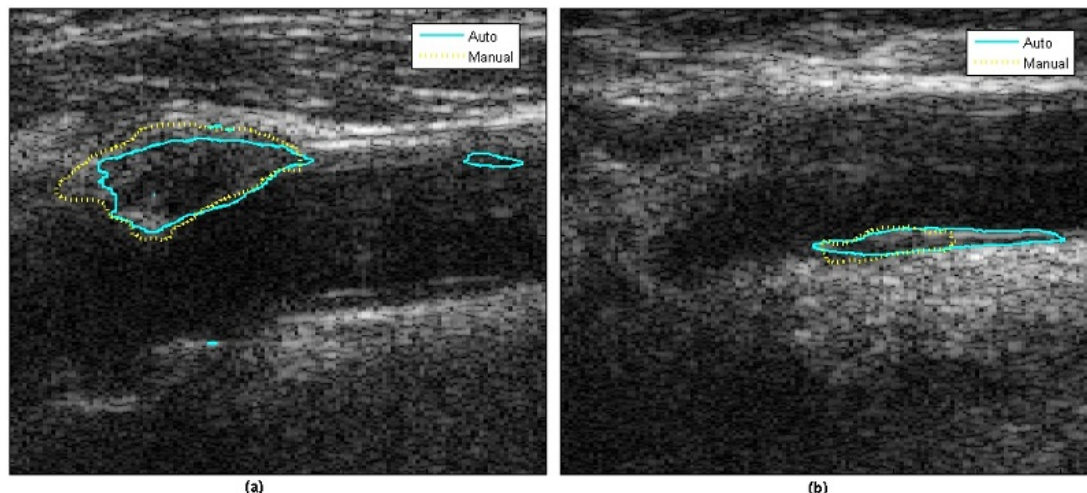


Figure 1: Manual (dotted line) and automated (full line) segmentation results for two different patients with CPs respectively at near (a) and far (b) wall.

# TPS-RPM based segmentation of three-dimensional high frequency ultrasound SAFT images for CAD/CAM based tooth digitization

Fabrice Chuembou Pekam<sup>1</sup>, Daniel Habor<sup>1</sup>, Thorsten Vollborn<sup>1</sup>, Klaus Radermacher<sup>1</sup>, Stefan Heger<sup>1,2</sup>; <sup>1</sup>Chair of Medical Engineering, RWTH Aachen University, Germany, <sup>2</sup>Institute for Biomedical Engineering, Mannheim University of Applied Science, Germany

## Background, Motivation and Objective

In a previous work, a concept for high-frequency ultrasound (HFUS) assisted micro-scanning in the context of CAD/CAM based intra-oral tooth surface digitization has been introduced. The system is based on a two degree of freedom (DOF) highly dynamic serial kinematic carrying a HFUS focused single element transducer. The limited depth of field and the low sensitivity against angular aligned specular reflectors, which might result in missing surface data, are major challenges of the system. The aim of this study was to investigate the combination of 2-DOF HFUS tooth micro-scanning and 3D synthetic aperture focusing based on a virtual point source (VSAFT) followed by thin plate spline robust point matching (TPS-RPM) based image segmentation in order to enlarge the depth of field and to close data gaps.

## Statement of Contribution/Methods

A human molar prepared for crown insertion was scanned in a water tank using a laboratory version of the 2-DOF HFUS micro-scanner (75 MHz, 78% bandwidth,  $F\# = 2$ ). RF-data was collected, filtered and processed with 3D VSAFT. After demodulation to base-band and linear gray-value coding, threshold-based maxima detection was applied in order to separate tooth surface echoes (TSE). Then, missing surface data, e.g. parts of the lateral walls of the teeth, were estimated using a TPS-RPM based 2D segmentation approach whereas the initial deformable model was generated based on the TSE data itself. The so reconstructed surface model was compared to a reference model of the same tooth which was automatically scanned by an extra-oral laser-scanning system.

## Results/Discussion

The negative / positive mean deviation between the HFUS reconstructed surface model and reference scan was  $-58 \mu\text{m} / +25 \mu\text{m}$ , respectively. The standard deviation was  $56 \mu\text{m}$ . Although the accuracy is worse if compared to earlier presented results from compounded HFUS volume scans, 3D VSAFT together with TPS-RPM based image segmentation reduces system complexity, costs and scanning time. For simplification the presented reconstruction was based on a 2D segmentation approach. Hence, not all available information might be taken into account. A 3D-implementation as well as studying the accuracy of subgingival scans based on this technique is part of our ongoing work.

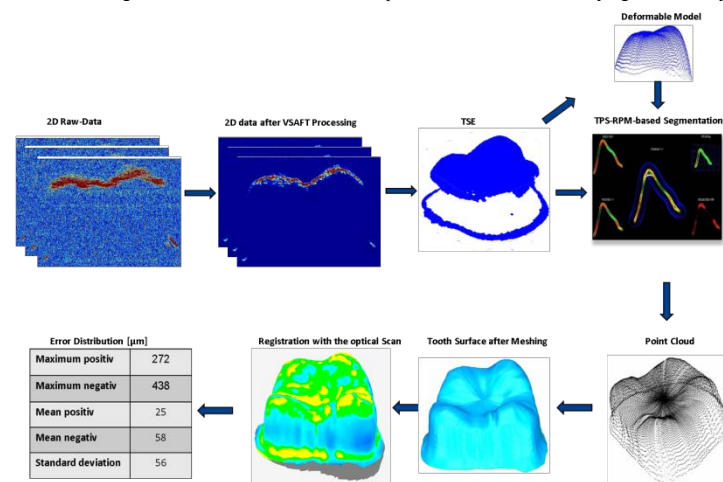


Fig. 1: HFUS-Based Tooth Surface Reconstruction Process

# Fixed Point Motion Estimation for Frame Rate Up Conversion in Cardiac Ultrasound

Hani Nozari Mirakolaei<sup>1</sup>, Sten Roar Snare<sup>1</sup>, Lars Hoføys Breivik<sup>1</sup>, Erik Normann Steen<sup>2</sup>, Anne H Schistad Solberg<sup>1</sup>; <sup>1</sup>Department of Informatics, University of Oslo, Oslo, Norway, <sup>2</sup>GE Vingmed Ultrasound, Oslo, Norway

## Background, Motivation and Objective

Frame rate up conversion in a low frame rate cardiac ultrasound scan makes the images run smoother and potentially increases the diagnostic value of the scan. Linear interpolation is one way of increasing frame rate; however, ghosting and blurring are the main drawbacks of this type of interpolation. In low frame rate cardiac ultrasound imaging, motion estimation and motion compensation techniques commonly used in optical imaging are not suitable, because of speckle noise as well as large movement of the cardiac valves compared to other anatomical features.

## Statement of Contribution/Methods

We proposed novel method termed Fixed Point Motion Estimation (FPME) to handle these problems. FPME is a bidirectional tracker which extracts search regions from the previous and next frames in a pyramidal manner. The bottom of the pyramids uses a large search area around the moving object. At the higher levels in the pyramid, the search region is narrowed down to capture the moving object. The motion vector at each level of the pyramid is used as an offset for the next level and the overall displacement will be the vector summation of motion vector at each level of the pyramid. This method works well if we don't have any out of plane movement. To have more reliable motion vectors at each level a vector median filter is applied on the vector field. The result is used as an initialization for an optical flow regularization to capture sub pixel movement.

## Results/Discussion

We demonstrate the performance of FPME on four standard cardiac ultrasound recordings. Our experiments show that, in ultrasound images, FPME works well compare to current motion estimation techniques in optical imaging. It removes ghosting and blurring artifacts. Fig. 1 shows a ground truth image as well as linear and FPME interpolated frames. FPME frame rate up conversion reduces the average sum of square error in the valve region by 5.6% relative to linear interpolation and increases the average peak signal-to-noise ratio by 2 dB.

Fig. 1. (Left) Ground truth image, (Middle) Linear interpolation, (Right) FPME interpolation



## P1C7-6

## A visualization tool for improved assessment and follow-up with ultrasound

Gabriel Kiss<sup>1</sup>, Daniel Høyer Iversen<sup>1</sup>, Øyvind Krøvel-Velle Standal<sup>1</sup>, Jochen Matthias Rau<sup>1</sup>, Hans Torp<sup>1</sup>, Lasse Lovstakken<sup>1</sup>, Svein-Erik Måsøy<sup>1</sup>; <sup>1</sup>MI Lab and Department of Circulation and Medical Imaging, ISB, NTNU, Trondheim, Norway

## Background, Motivation and Objective

Ultrasound has been shown to be a powerful imaging tool for the evaluation of musculoskeletal disease (e.g. rheumatoid arthritis or carpal tunnel syndrome). Power Doppler imaging in particular plays an important role in treatment monitoring. However it is also known that ultrasound is operator dependent and has low intra- and inter-observer repeatability. The aim of this work was to reduce the uncertainty of the follow-up process of a typical musculoskeletal exam by ensuring that the same anatomy is visualized at baseline and follow-up.

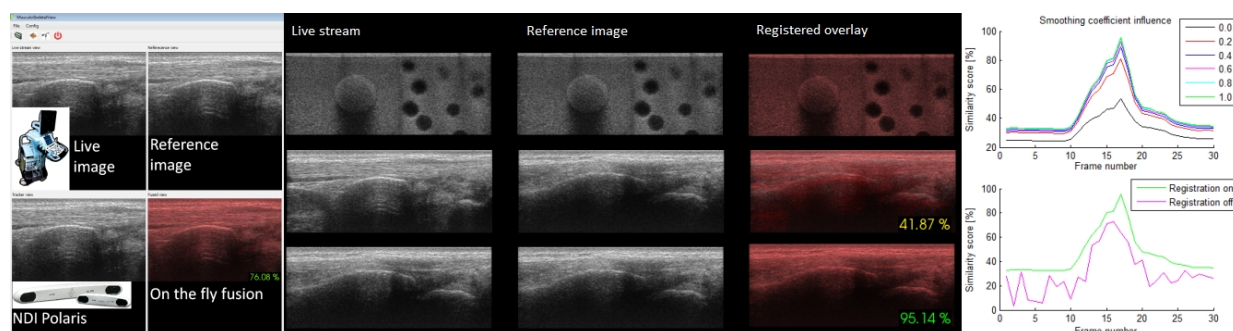
## Statement of Contribution/Methods

A visualization tool, which receives a continuous stream of ultrasound data, has been implemented in Qt. The streamed images are compared on the fly against a pre-loaded baseline image. To compensate for in plane translation and rotation differences, 2D rigid registration is performed. Normalized mutual information was used as a similarity metric and is color coded from red (0%) to green (100%) to show the amount of similarity among the current images. Several display alternatives (e.g. semi-transparent overlay, color coded overlay) have been implemented and tested. Optional anisotropic filtering can be applied to both images before registration to reduce the impact of the speckle noise on the final result.

## Results/Discussion

Two healthy volunteers and a phantom have been used for validation purposes. Both the reference and follow-up ultrasound data have been acquired with a Vivid E9 scanner, with an ML6-15 probe (GE Vingmed Ultrasound). At the same time the position of the probe with regards to a reference frame was tracked with an accurate optical position sensor (Polaris, NDI). It was shown that the highest similarity scores corresponded to the lowest translation offsets and angle differences. The average offset and angle errors for the patient data were:  $[0.68 \pm 0.97, 0.47 \pm 0.79, -2.28 \pm 1.38]$  mm,  $[2.92 \pm 2.35, -0.17 \pm 1.2, 1.24 \pm 2.38]^\circ$ . Figure 1 shows sample overlay images and the similarity metric with and without image registration and different smoothing values for a sweep around the finger.

A novel method for real-time fusion of ultrasound images aimed at musculoskeletal disease monitoring has been presented. Being provided with instant feedback, the user is more confident during the acquisition process. Furthermore the scan plane can be adjusted until a good similarity score is obtained.





### Supervised classification of long-axis echocardiograms

Hanan Khamis<sup>1</sup>, Grigoriy Zurakhov<sup>1</sup>, Zvi Friedman<sup>2</sup>, Dan Adam<sup>1</sup>; <sup>1</sup>Department of Biomedical Engineering, Technion-Israel Institute of Technology, Haifa, Israel, <sup>2</sup>GE Ultrasound, Tirat Carmel, Israel

#### Background, Motivation and Objective

2D echocardiographic exam provides B-mode sequences of different orientations of cardiac anatomy: longitudinal, short and parasternal axis. Classifying these clips is required as a pre-processing stage for functional assessment. The similarity among longitudinal clips (4 chambers (4CH), 2 chambers (2CH) and Aplx views) and their high noise levels make the classification a challenge. A new approach is proposed, based on supervised learning of dictionaries that force different sparse representations of each class. Then a linear classifier is applied for view recognition.

#### Statement of Contribution/Methods

It is hypothesized that long-axis sequences can be classified utilizing 3 dictionaries: a representative dictionary allowing sparsely representation of the sequence, a discriminative dictionary that leverages the supervised information of the training set to represent each sequence ideally from a single class, and a classifying dictionary that uses the sparse representation as a feature for classification. The algorithm learns jointly the 3 dictionaries while minimizing the 3 reconstructive, discriminative and classification sparse-code errors, respectively, utilizing the KSVD algorithm. Learning the dictionaries yields similar sparse codes to represent sequences from the same class and vice versa. Here, instead of using the sequences themselves, the polar gradient of each sequence is column-stacked and projected onto feature space using Random Gaussian matrix. The resulted columns are, then, used for training the 3 dictionaries.

#### Results/Discussion

341 clinical clips (107 for 2CH, 114 for 4CH and 120 for Aplx), were acquired by GE vivid 7, each of ~70 frames/second. 50 clips of each view were used as training set and the rest as testing set. Only 10 sequential frames were included for each view, starting from 250ms post start frame. The clips were labeled by 2 experts. A threshold of 60% of frames (i.e. 6 of 10) classified to the same class, determined to which class the clip belongs. The confusion matrix in Figure 1 depicts the recognition accuracies: 87%, 79% and 87% of 4CH, 2CH and Aplx views, respectively, were correctly recognized. This study demonstrates high potential for automatic classification, allowing automatic clip processing.

	2 CH	4 CH	APLAX	Undetermined
2 CH	0.79	0.05	0.09	0.07
4 CH	0.05	0.87	0.03	0.05
APLAX	0.06	0.02	0.87	0.04

Figure 1. Confusion Matrix for three-way view classification. Numbers are the fraction of clips classified.

### Computer-Aided-Theragnosis Using Quantitative Ultrasound Spectroscopy and Maximum Mean Discrepancy in Locally Advanced Breast Cancer

Mehrdad Gangeh<sup>1,2</sup>, Hadi Tadayyon<sup>1,2</sup>, Lakshmanan Sannachi<sup>1,2</sup>, Ali Sadeghi-Naini<sup>1,2</sup>, William Tran<sup>1,2</sup>, Gregory Czarnota<sup>1,2</sup>; <sup>1</sup>Departments of Medical Biophysics and Radiation Oncology, University of Toronto, Toronto, Ontario, Canada, <sup>2</sup>Department of Radiation Oncology and Physical Sciences, Sunnybrook Health Sciences Centre, and Sunnybrook Research Institute, Toronto, Ontario, Canada

#### Background, Motivation and Objective

Among imaging modalities, quantitative ultrasound (QUS) spectroscopy methods provide a promising framework that can non-invasively, inexpensively, and quickly assess tumour response to cancer treatment using standard clinical equipment. While previous work in the field of QUS analysis has mainly focused on feature plots and the use of a t-test to demonstrate the statistical significance of the proposed system, in this work, steps are taken towards the development of a computer-aided-theragnosis (CAT) system and advanced machine learning algorithms to discriminate between treatment responding and non-responding patients.

#### Statement of Contribution/Methods

Sixty patients with locally advanced breast cancer (LABC) who received neoadjuvant chemotherapy treatments were imaged using a Sonix RP ultrasound machine before and at 4 times during treatment, i.e., weeks 1, 4, 8 and months later pre-operatively. Mid-band fit and 0-MHz intercept parametric maps were computed by deploying quantitative ultrasound spectroscopy techniques. Patients were divided into good and poorly responding based on their ultimate clinical and pathological response to treatment. In the experiments, after computation of the intensity histogram of the parametric maps, the distance between pre- and post-treatment images of each patient was computed using maximum mean discrepancy (MMD), which is a recently proposed kernel-based metric. By using a kernel function to nonlinearly transform input vectors into a higher-dimensional feature space, enhanced group separability is obtained. The classification was subsequently performed using a nearest mean classifier and 5-fold cross-validation at subject level.

#### Results/Discussion

Performance of the proposed CAT system was quantified by several measures as shown in following table for the first 10 patients (good (6) and poor (4) responders). In this study, for the first time, an advanced machine learning technique based on MMD and supervised learning was incorporated into a complete CAT system using QUS for the classification

of patients with LABC. The CAT system achieved a high accuracy and sensitivity 8 weeks after treatment initiation in a limited number of patients. This potentially permits clinicians to receive feedback and switch to alternate treatments far earlier, which can save the costs of drugs and hospital care.

Week	Error $\pm$ STD	AUC	Type I Error	Type II Error
4	40 $\pm$ 0.00	50.83	25.00	50.00
8	23.33 $\pm$ 3.51	80.00	3.33	33.33

#### P1C7-9

##### Improved Microcalcification Detection in Breast Ultrasound: Phantom Studies

Sara Bahramian<sup>1</sup>, Michael Insana<sup>2</sup>; <sup>1</sup>University of Illinois at Urbana Champaign, Urbana, Illinois, USA, <sup>2</sup>University of Illinois at Urbana Champaign, USA

##### Background, Motivation and Objective

Breast microcalcifications (MC) are important indicators of malignancy in breast cancer. Ultrasound B-scans illustrate MC clusters as bright high contrast spots with the resolution limited by the size of speckle cells. Thus, distinguishing them from speckle noise using ultrasound B-scans is challenging. This work addresses the performance of ultrasound B-scans in detecting MC. The performance is first theoretically predicted by measuring the amount of diagnosis information available in the RF data and B-mode image. Based on these predictions, a post processing method is proposed to improve the transmission of information at the final display stage which will increase the detectability of the MC. This method is applied to lab-generated phantoms to illustrate the improvement in detectability.

##### Statement of Contribution/Methods

We previously proposed a framework to track the binary task information in difference stages of imaging process by calculating Kullback-Leibler divergence. Using this analysis, we identified the spectrum that describes the ability of an imaging system to transfer information from the object to the RF data at each spatial frequency. This spectrum shows that the RF data captures the task information available at two spectral lobes (i.e. low-frequency and high-frequency). It is further shown that the B-mode images only capture and display the low-frequency components of the task and the high-frequency information is lost.

To study the effect of the loss of information in the task of MC detection, we analyzed the spatial frequency components of this task. This reveals that at least 50% of the acquired task information is not displayed in the B-mode images which will negatively affect the performance. To address this problem, a signal processing method is proposed to retrieve the missing information and display it in a complement image. The complement image is designed to contain high-frequency task information. It is then combined with the B-mode image by color-casting it over the gray-scale B-mode image. Computer simulations are performed to illustrate the method.

Our method is also applied to RF data generated from gelatin phantoms with pre-located micro-meter calcium inclusions to mimic the microcalcified breast lesion. Human observer studies are performed on the generated images to quantify the improvement resulted by this method.

##### Results/Discussion

Our information analysis measures less than 30% efficiency in capturing the MC diagnosis information from the object to the RF data of a typical imaging system. We also measured the efficiency of transferring acquired information from the RF data to the B-mode image. For a trained human observer of the B-mode images the true positive rate is measured to be less than 10%. This rate increases significantly to up to 50% by providing the observer with improved images proposed in this work. This promising result established the effectiveness of our method in improving MC detection.

# P1C8 - MTC: Noncancer Applications of Tissue Characterization

Salon C

Saturday, September 6, 2014, 8:00 am - 5:00 pm

Chair: **Mami Matsukawa**  
*Doshisha University, Kyoto, Japan*

P1C8-1

## Early Detection of Fatty Liver Disease in Mice via Quantitative Ultrasound

Aiguo Han<sup>1</sup>, John W. Erdman, Jr.<sup>2</sup>, Douglas G. Simpson<sup>3</sup>, Michael P. Andre<sup>4</sup>, William D. O'Brien, Jr.<sup>1</sup>; <sup>1</sup>Electrical and Computer Engineering, University of Illinois at Urbana-Champaign, Urbana, IL, USA, <sup>2</sup>Food Science and Human Nutrition, University of Illinois at Urbana-Champaign, Urbana, IL, USA, <sup>3</sup>Statistics, University of Illinois at Urbana-Champaign, Champaign, IL, USA, <sup>4</sup>Radiology, University of California-San Diego, La Jolla, CA, USA

### Background, Motivation and Objective

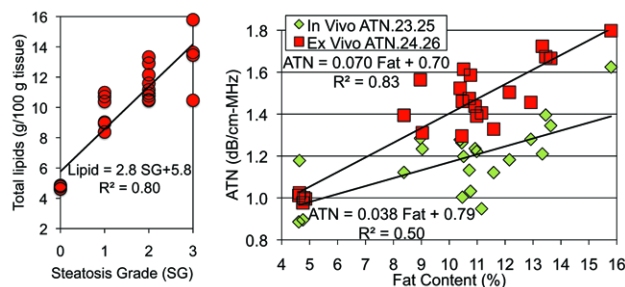
Nonalcoholic fatty liver disease (NAFLD) is estimated to have a 25-30% incidence among obese individuals and can lead to inflammation (nonalcoholic steatohepatitis, NASH) and fibrosis. While conventional ultrasound and other imaging techniques can diagnose advanced stages of fatty liver and hepatic cirrhosis (one NASH outcome), existing techniques are unable to detect early stages of NAFLD. Objective: Development methods for early detection of NAFLD in humans by examining the quantitative ultrasound (QUS) parameters of livers in diet-controlled mice.

### Statement of Contribution/Methods

Two studies were conducted, each with 25 male C57BL/6J mice; 20 fed an atherogenic (Ath) diet and 5 fed a control diet. In Study 1 (a non-QUS study), 10 mice each were fed the Ath diet for 4 and 8 wks; there was significant liver steatosis and inflammation of the Ath-diet-fed mice. Thus, Study 2 was conducted with reduced feeding times to moderate the Ath diet's liver effect; 10 mice each were on the Ath diet for 2 and 4 wks. The outcomes in Study 2 included in vivo (Vevo 2100) and in vitro QUS liver assessments (backscattered coefficient [BSC] and attenuation coefficient [ATN]), liver lipids, and pathologist's steatosis and lobular inflammation grades. For BSC and ATN outcomes, 3 in vivo (between 15 & 25 MHz) and 4 ex vivo frequency ranges (between 24 & 47 MHz) were evaluated.

### Results/Discussion

For Study 2, liver lipids compared favorably to pathologist steatosis grades. ATN (Fig) and BSC (not shown) were related to liver lipids. Although ATN for ex vivo liver was higher across the range of fat content, it shows a comparable trend to in vivo. The full six-variable (3 freq ranges) in vivo regression model for predicting number of wks on Ath diet based on the ATN and BSC measurement vector was highly statistically significant ( $R^2 = 0.57$ ,  $F = 4.03$  on 6 & 18 degrees of freedom,  $p = 0.0098$ ). The analysis produced two linear discriminant functions with 98.16% of the total variation explained by the first linear discriminant. While there was some difficulty in distinguishing 0 vs. 2 wks on Ath diet, and in distinguishing 2 vs. 4 wks on Ath diet, there were no misclassifications of control as 4 wks or vice versa. Conclusion: Preliminary findings suggest that early detection of NAFLD is feasible with QUS.



P1C8-2

## Accurate Diagnosis of Non-Alcoholic Fatty Liver Disease in Humans via Quantitative Ultrasound

Michael P. Andre<sup>1</sup>, Elhamy Heba<sup>2</sup>, Jonathan Hooker<sup>2</sup>, Rohit Loomba<sup>3</sup>, Claude B. Sirlin<sup>2</sup>, John W. Erdman, Jr.<sup>4</sup>, William O'Brien, Jr.<sup>5</sup>; <sup>1</sup>Radiology, University of California-San Diego, La Jolla, CA, USA, <sup>2</sup>Radiology, University of California-San Diego, San Diego, CA, USA, <sup>3</sup>Medicine, University of California-San Diego, San Diego, CA, USA, <sup>4</sup>Food Science and Human Nutrition, University of Illinois at Urbana-Champaign, Urbana, IL, USA, <sup>5</sup>Bioacoustics Research Laboratory, University of Illinois, Urbana, IL, USA

### Background, Motivation and Objective

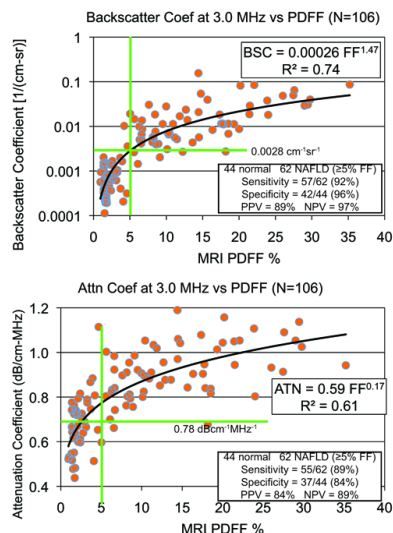
Nonalcoholic fatty liver disease (NAFLD) is the most common cause of chronic liver disease in the United States, affects 30% of adult Americans, may progress to nonalcoholic steatohepatitis (NASH) and end-stage liver disease. The diagnosis, grading, and staging of NAFLD currently is based on liver biopsy with histologic analysis. Noninvasive image-based methods to evaluate the liver in adults with NAFLD are urgently needed. Currently, the most accurate and precise noninvasive imaging method for diagnosis and quantification of hepatic steatosis is MRI, which estimates the proton-density fat fraction (PDFF) as a measure of fractional fat content. Although conventional ultrasound (US) with qualitative interpretation by radiologists is widely used for hepatic steatosis assessment, it is inaccurate. Objective: Using MRI-PDFF as reference, assess the accuracy for steatosis detection of two quantitative US (QUS) parameters - backscatter coefficient (BSC) and attenuation coefficient (ATN).

### Statement of Contribution/Methods

We developed a novel QUS method that in animal studies shows promise for detection and quantification of liver fat content. The current study's contribution is to extend the work to human subjects by assessing the accuracy of BSC and ATN for detection of hepatic steatosis in a cohort of adult patients with NAFLD (MRI PDFF  $\geq 5\%$ ) and negative controls. Liver MRI and US exams were performed on the same day using routine clinical scanners, from which MRI-PDFF and both QUS parameters (BSC and ATN) were estimated, respectively. Receiver operating characteristics analyses were performed for detection of MRI-PDFF  $\geq 5\%$ . Sensitivity and specificity at optimal BSC and ATN thresholds were calculated.

### Results/Discussion

106 adult subjects with known or suspected NAFLD were prospectively recruited, of which 62 had NAFLD (MRI PDFF  $\geq 5\%$ ) and 44 were negative controls (see fig). For detection of MRI-PDFF  $\geq 5\%$ , an ATN threshold of 0.78 dB/cm-MHz provided a raw sensitivity of 89% and specificity of 84%. A BSC threshold of 0.0028/cm-sr provided a raw sensitivity of 92% and specificity of 96%. Conclusion: QUS parameters measured using routine clinical US scanners show promise for detecting and perhaps grading NAFLD.



### P1C8-3

#### Comparison of acoustic properties in various rat organs using high frequency ultrasound

So Irie<sup>1</sup>, Kenji Yoshida<sup>2</sup>, Kazuto Kobayashi<sup>3</sup>, Jonathan Mamou<sup>4</sup>, Hitoshi Maruyama<sup>5</sup>, Tadashi Yamaguchi<sup>2</sup>; <sup>1</sup>Graduate School of Engineering, Chiba University, Chiba, Japan, <sup>2</sup>Center for Frontier Medical Engineering, Chiba University, Japan, <sup>3</sup>Honda Electronics Co., Japan, <sup>4</sup>Reverside Research, USA, <sup>5</sup>Graduate School of Medicine, Chiba University, Japan

#### Background, Motivation and Objective

Acoustic property of tissue such as speed of sound (SOS), attenuation and acoustic impedance provide beneficial information for the pathological diagnosis. High frequency ultrasound ( $f > 100$  MHz), corresponding to fine spatial resolution smaller than 15 micrometers, enables to measure properties of individual cells in tissue. This study aims to summarize the acoustic properties of various rat organs and discuss the difference of them.

#### Statement of Contribution/Methods

The SOS and attenuation of liver, kidney, heart, lung and spleen in case of normal rat were measured. A bioacoustic microscope (modified AMS-50SI; Honda Electronics Co.) incorporating 250-MHz center frequency transducer with ZnO membrane was employed for the measurement. This transducer has 4- $\mu$ m lateral resolution. Formalin-fixed paraffin-embedded specimen of each organs with thickness of 10  $\mu$ m was preliminarily prepared. In the measurement, the specimen on glass was exposed to ultrasound pulse wave via water. The SOS and attenuation were calculated by analyzing the echo data in frequency domain. The 2D image of acoustic property could be obtained by scanning the transducer in 2- $\mu$ m steps. We acquired the histological image of the same sample (HE staining) for comparing with 2D image of acoustic property.

#### Results/Discussion

Figure 1 shows the 2D image of SOS distribution of each organ. We could obtain morphological characteristics, e.g. renal tubular structure in kidney and bronchus structure in lung. Furthermore, the contrast of SOS between organs could be attributed to the difference of biological composition (e.g. type of cell), not only morphological structure. For example, we could distinguish two sections in spleen, red pulp and white pulp. The mean and standard deviation of SOSs of liver, kidney, heart, lung, spleen (red pulp), and spleen (white pulp) were 1748  $\pm$  41 m/s, 1600  $\pm$  56 m/s, 1722  $\pm$  96 m/s, 1639  $\pm$  96 m/s, 1759  $\pm$  65 m/s, 1708  $\pm$  28 m/s. Welch's t test indicated that SOS of kidney are significantly lower than those of liver and heart. This result seems the quantitative difference in SOS resulting from the difference of biological composition.

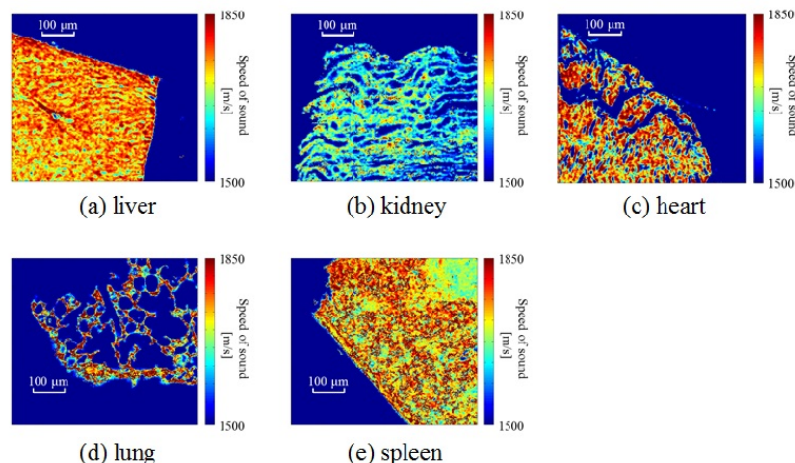


Fig. 1 Two-dimensional SOS map

P1C8-4

### Measurement of acoustic impedance for normal, fibrosis and NASH liver by using bio-acoustic microscopy

Kazuyo Ito<sup>1</sup>, Kenta Inoue<sup>1</sup>, Hitoshi Maruyama<sup>2</sup>, Kazuto Kobayashi<sup>3</sup>, Kenji Yoshida<sup>4</sup>, Tadashi Yamaguchi<sup>4</sup>; <sup>1</sup>Graduate School of Engineering, Chiba University, Japan, <sup>2</sup>Graduate School of Medicine, Chiba University, Japan, <sup>3</sup>Honda-Electronics Co., Ltd, Japan, <sup>4</sup>Research Center for Frontier Medical Engineering, Chiba University, Japan

#### Background, Motivation and Objective

Early diagnosis for non-alcoholic steatohepatitis (NASH) is desired because it may progress to cirrhosis or finally liver cancer in the severe case. To propose the possible noninvasive diagnosis using ultrasound, we aim to summarize the change of tissue property e.g. acoustic property with the progression of NASH. This basic study investigates the acoustic impedances of normal, fibrotic and NASH model based on the measurement of rat liver using bio-acoustic impedance.

#### Statement of Contribution/Methods

We prepared livers of 5 rats (normal model: 2, fibrosis model: 2, NASH model: 1, weight: 250 - 400 g, age: 18 weeks). A bio-acoustic microscopy system (modified AMS-50SI, Honda Electronics Co., Ltd, Japan) was used to measure the acoustic impedance. A tissue block extracted from a rat liver was located on the polystyrene plate. The ultrasonic pulse wave with center frequency of 80 MHz was radiated from below the polystyrene plate across water. The acoustic impedance was calculated based on the analysis of the echo amplitude. The 2D image of acoustic impedance could be obtained by scanning the transducer in 16- $\mu$ m steps. The size of 2D image was 300 \* 300 pixels (4.8 \* 4.8 mm<sup>2</sup>) and the spatial resolution of microscopy was 20  $\mu$ m. In addition, HE staining (normal liver) and Azan staining (fibrosis or NASH liver) of tissue sections were performed to pathologically evaluate the tissue structure.

#### Results/Discussion

The 2D image demonstrates that the tissue structure is homogeneous in normal liver [Fig. 1(a-1)]. In contrast, the pattern of random net texture like fibrous structure is found in NASH liver [Fig. 1(b-1)]. Focusing on the histogram of acoustic impedance in case of normal liver [Fig. 1(a-2)], it is noticed that the histogram seems to be approximately the normal distribution. The histogram of NASH liver [Fig. 1(b-2)] is significantly different from normal distribution. This trend possibly results from various biological composition of the NASH liver e.g. lipid droplet, hepatic cell, fibrosis. Therefore, these results suggest a possible statistical model of distribution of acoustic impedance in normal and NASH liver.

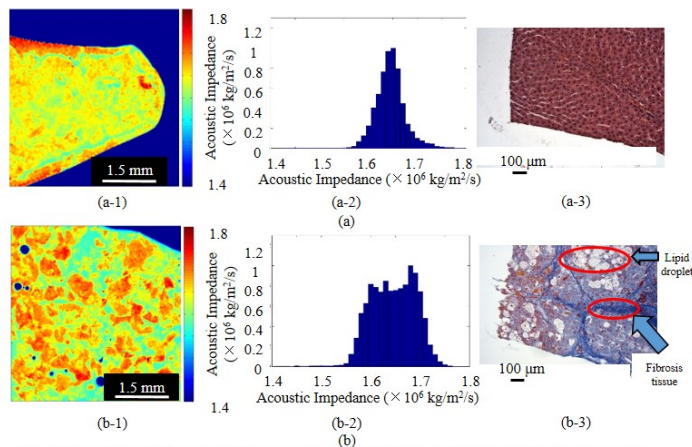


Fig. 1 Results of (a) normal liver and (b) NASH liver. (a-1) and (b-1): Acoustic impedance, (a-2) and (b-2): Histogram of Acoustic impedance, (a-3) and (b-3): Histological image.

P1C8-5

### Carotid Plaque Characterization with Histology and Quantitative Ultrasound

Xiao Wang<sup>1</sup>, Shahriar Salamat<sup>2</sup>, Tomy Varghese<sup>1</sup>, Robert Dempsey<sup>3</sup>; <sup>1</sup>Department of Medical Physics, University of Wisconsin-Madison, Madison, WI, USA, <sup>2</sup>Department of Pathology and Laboratory Medicine, University of Wisconsin-Madison, Madison, WI, USA, <sup>3</sup>Department of Neurological Surgery, University of Wisconsin-Madison, Madison, WI, USA

#### Background, Motivation and Objective

Carotid plaque is primarily composed of cholesterol, calcium, and fibrous tissue. Differences in acoustic properties, which can be assessed by quantitative ultrasound (QUS), may reflect difference in tissue composition. Heterogeneous plaques are difficult to characterize precisely. We propose a novel approach to characterize localized plaque regions with different tissue types. We will compare and correlate calcified, fibrous and lipid regions within heterogeneous plaque using a one-to-one registration with histology and ultrasound quantitative imaging.

#### Statement of Contribution/Methods

Atherosclerotic plaque excised during a carotid endarterectomy procedure was imaged ex vivo using a VisualSonics Vevo 770 ultrasound system. Attenuation coefficient images were obtained from three-dimensional radiofrequency data collected and rendered into a 3D volume. Fixed plaque tissue was then longitudinally sectioned with thickness of 5  $\mu$ m, and sections separated by 100  $\mu$ m were obtained. Two-dimensional histopathology images were digitized using a PathScan Enabler IV, registered and reconstructed into a 3D volume using Matlab. Different regions such as the lumen, calcified, lipid and fibrous regions were segmented by a pathologist and digitally color-coded into the 3D histology data. Similar tissue types from the 3D histology volume were then compared to the estimated 3D attenuation coefficient obtained using quantitative ultrasound methods.

#### Results/Discussion

Results indicate that calcified, lipid and fibrous regions in the two volumes showed a good correlation. Calcified regions delineated on the histology volume correspond to the high attenuation coefficient region (2.45 dB/cm/MHz) in the 3D attenuation coefficient volume, while lipid regions tend to have lower attenuation coefficient values (1.50 dB/cm/MHz). Fibrous regions in histology, correlate to the lowest attenuation coefficient value (0.83 dB/cm/MHz). Most plaques are heterogeneous, therefore making it difficult to classify them in the clinic as calcified or lipidic plaques. Our work demonstrates a direct correlation between histology and ultrasound quantitative imaging characterization of plaque. With the 3D volume different compositions within the plaque can be better identified and characterized.



## P1C8-6

**Toward recognising the vulnerable asymptomatic atheromatous plaque from B-mode ultrasound: the importance of the morphology of the plaque shoulder**

Spyretta Golemati<sup>1</sup>, Symeon Lehareas<sup>1</sup>, Nikolaos Tsiaparas<sup>2</sup>, Aimilia Gastounioti<sup>2</sup>, Achilles Chatziioannou<sup>1</sup>, Konstantina Nikita<sup>2</sup>, Despina Perrea<sup>1</sup>; <sup>1</sup>National Kapodistrian University of Athens, Greece, <sup>2</sup>National Technical University of Athens, Greece

**Background, Motivation and Objective**

Efficient management of the asymptomatic carotid disease remains a crucial challenge in clinical practice, because the ultrasonographically estimated degree of stenosis, which is currently used to determine treatment decisions, has been shown to be inadequate. In this study, texture (morphological) characteristics were investigated in a sample of asymptomatic male subjects, at the atheromatous plaque, the adjacent arterial wall and the plaque shoulder, i.e. the boundary between plaque and adjacent wall.

**Statement of Contribution/Methods**

A total of 25 arteries were interrogated, 11 with low (50-69%) and 14 with high (70-100%) degree of stenosis. The two groups had similar ages. Texture characteristics were estimated from B-mode ultrasound images, and included four second-order statistical parameters (contrast, correlation, energy and homogeneity), each calculated at four different image directions (0°, 45°, 90°, 135°), yielding a total of 16 characteristics.

**Results/Discussion**

Between high and low stenosis groups, 8 out of 16 characteristics were statistically different at the plaque shoulder at systole and 6 at diastole (Table). No differences were observed between the two groups for any of the texture characteristics at the plaque nor at the adjacent wall. Differences in morphology along the arterial wall (wall - shoulder - plaque) were more pronounced in cases of high stenosis.

The findings indicated that (a) the plaque shoulder is a particular area, requiring additional investigation so as to better understand the pathophysiology of atherosclerosis, (b) the phase of the cardiac cycle (systole or diastole) is important in texture analysis, and (c) the variability of morphology along the arterial wall, which is indicative of areas of tissue discontinuities, and therefore more vulnerable to rupture, can be characterised quantitatively with texture indices, toward an improved assessment of cardiovascular risk.

It can be concluded that ultrasound-based texture indices may reveal novel markers for early detection and monitoring of subjects at high risk of cerebrovascular events, in the context of individualised, noninvasive and affordable diagnosis.

**Table.** Average±standard deviation values of texture features for high (HS) and low (LS) stenosis cases at plaque shoulder for diastole and systole. Boldface indicates statistically significant differences (Wilcoxon ranksum test, p-value<0.05) compared to HS.

Texture feature	Diastole		Systole	
	HS	LS	HS	LS
1 Contrast (0°)	384.04±303.30	<b>829.72±658.73</b>	399.96±289.64	<b>994.63±841.84</b>
2 Contrast (45°)	986.46±520.94	<b>1975.38±1416.30</b>	1023.69±525.71	<b>2309.90±2226.81</b>
3 Contrast (90°)	930.08±474.16	<b>1659.06±1131.06</b>	934.73±443.30	<b>1910.03±1587.77</b>
4 Contrast (135°)	1171.31±646.58	<b>1980.88±1258.11</b>	1166.20±580.99	<b>2267.309±1708.22</b>
5 Correlation (0°)	0.950±0.032	<b>0.905±0.053</b>	0.950±0.031	<b>0.885±0.051</b>
6 Correlation (45°)	0.863±0.069	<b>0.771±0.123</b>	0.868±0.060	<b>0.740±0.119</b>
7 Correlation (90°)	0.867±0.070	<b>0.807±0.099</b>	0.877±0.056	<b>0.783±0.091</b>
8 Correlation (135°)	0.836±0.086	<b>0.764±0.115</b>	0.848±0.069	<b>0.736±0.103</b>
9 Energy (0°)	0.136±0.060	<b>0.169±0.058</b>	0.148±0.077	<b>0.187±0.054</b>
10 Energy (45°)	0.114±0.064	<b>0.132±0.052</b>	0.124±0.078	<b>0.149±0.056</b>
11 Energy (90°)	0.120±0.062	<b>0.149±0.060</b>	0.132±0.076	<b>0.167±0.056</b>
12 Energy (135°)	0.113±0.060	<b>0.138±0.055</b>	0.123±0.075	<b>0.155±0.057</b>
13 Homogeneity (0°)	0.541±0.058	<b>0.554±0.061</b>	0.547±0.067	<b>0.575±0.052</b>
14 Homogeneity (45°)	0.423±0.081	<b>0.428±0.086</b>	0.430±0.096	<b>0.456±0.075</b>
15 Homogeneity (90°)	0.436±0.076	<b>0.454±0.086</b>	0.445±0.088	<b>0.488±0.073</b>
16 Homogeneity (135°)	0.418±0.075	<b>0.435±0.090</b>	0.426±0.090	<b>0.465±0.073</b>

## P1C8-7

**Quantification of the scatterer distributions for liver fibrosis using modified Q-Q probability plot**

Mikito Ito<sup>1</sup>, Kenji Yoshida<sup>2</sup>, Jonathan Mamou<sup>3</sup>, Tadashi Yamaguchi<sup>2</sup>; <sup>1</sup>Chiba University, Chiba-shi, Chiba, Japan, <sup>2</sup>Center for Frontier Medical Engineering, Chiba University, Japan, <sup>3</sup>Lizzi Centr for Biomedical Engineering, Riverside Research, USA

**Background, Motivation and Objective**

For ultrasound tissue characterization, the probability density function (PDF) of echo envelopes is often used. However, because several types of scatterers are intermingled in liver fibrosis, its echo-signal envelopes cannot be modeled by a commonly-used PDF. In this study, PDF models of inhomogeneous media were created by mixing two with homogeneous media having different scatterer distributions in computer simulation. Simulation findings were then confirmed using clinical data sets.

**Statement of Contribution/Methods**

Our group have proposed modified Q-Q probability plot for detecting and classifying liver fibrosis. Modified Q-Q probability plot was segmented using two different approximation straight lines, assuming that the tissue composed of only two types of homogeneous media with low- and high-scatterer density. In this study, slope values of the lines were used as the evaluation parameters to estimate the ratio of scatterer density between two media (i.e., fiber tissue/normal liver tissue) and the mixing rate of high-scatterer component (i.e., fiber tissue). These parameters were varied in the simulation model of the PDF so that we could preliminarily relate them to the slopes in modified Q-Q probability plot. The proposed method was employed for analyzing *in-vivo* clinical data set obtained from patients with different fibrosis stage, where the stage was determined in accordance with the new-Inuyama classification based on the result of biopsy.

**Results/Discussion**

Region of interest (ROI) with 10 mm × 10 mm is randomly selected in each clinical data. Figure 1 shows the results in three clinical data with different fibrosis stage (F0: normal, F1: early stage and F3: advanced stage). The plots in case of F0 is located at the slope values of 2, which means that the media is homogenous. In case of F1, the scatterer density of fiber tissue was estimated as 3.5 times larger than normal liver tissue, and the amount of fiber tissue was 20 % in ROI. Also, in case of F3, the scatterer density was estimated as

5.5 times, and the amount of fiber tissue was 25 % in ROI. These results suggests that scatterer distributions can be estimated by plotting echo-signal envelope statistical parameters, and the proposed method of envelope analysis potentially can provide invaluable information for non-invasive detection and characterization of liver fibrosis.

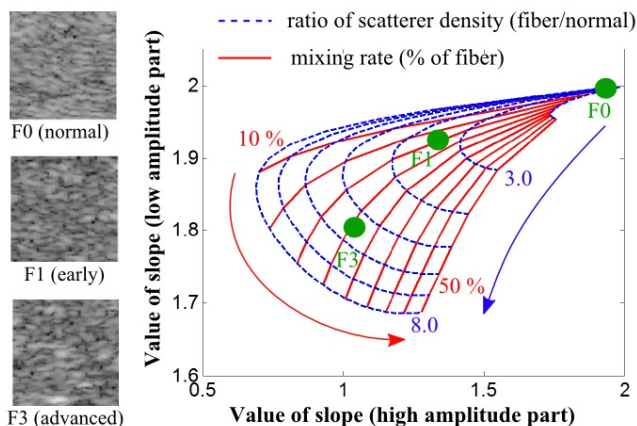


Fig.1 The result of estimation of scatterer distributions in clinical echo data with progress of the fibrosis stage, F0 (normal), F1 (early) and F3 (advanced).

P1C8-8

#### Estimation method using modified Q-Q probability plot in high-frequency ultrasound

Kazuki Tamura<sup>1</sup>, Kenji Yoshida<sup>2</sup>, Jonathan Mamou<sup>3</sup>, Tadashi Yamaguchi<sup>2</sup>; <sup>1</sup>Graduate School of Engineering, Chiba University, Japan, <sup>2</sup>Center for Frontier Medical Engineering, Chiba University, Japan, <sup>3</sup>Lizzi Center for Biomedical Engineering, Riverside Research Institute, USA

#### Background, Motivation and Objective

Previously, we proposed the diagnostic method for in vivo liver based on Q-Q probability plot which is the statistical analysis of echo envelope amplitude. Although ultrasound with the frequency range of 1-10 MHz has been used for diagnosis, more high frequency ultrasound with fine resolution possibly enables to detect smaller structure e.g. hepatic lobule and small fiber structure in early stage of disease. To investigate whether our analysis method could be applied in high-frequency range ( $f > 10$  MHz), this study conducted the measurement of rat liver by using a self-made scan system incorporating 15 MHz center frequency transducer.

#### Statement of Contribution/Methods

A 15 MHz single element concave transducer (diameter: 9.5 mm, focus length: 19 mm) was employed for the measurement. Axial and lateral resolutions are 100  $\mu$ m and 200  $\mu$ m, respectively. The transducer could be scanned in 2D plane so that series of B-mode image of the liver could be obtained. Fresh rat liver were prepared as measurement objects. In this measurement, the scanning interval was 30  $\mu$ m step. We statistically analyzed the echo amplitude in the region of interest (ROI) with three times of resolution (300  $\mu$ m in depth and 600  $\mu$ m in lateral) and evaluated the tissue structure by using our method. In our method, echo signal is separated to two different components by modified Q-Q probability plot, and the inhomogeneity of tissue is estimated as slopes of plotted line of each component ( $S_h$  and  $S_l$ ).

#### Results/Discussion

The proposed analysis method was applied to the whole area of liver by scanning the position of ROI with 200  $\mu$ m  $\times$  600  $\mu$ m. Compared the result with B mode image, we found the portion with speckle pattern where both values of slopes were approximately equal to 2 ( $S_h = S_l = 2$ ). The portion with same slopes lower than 2 ( $S_h = S_l < 2$ ) corresponded to hypoechoic area such as hepatic parenchyma and inner vascular.

The portion with different values of slopes ( $S_h \neq S_l$ ) indicated the hyperechoic area of fibrous structure and vessel wall. Those trends were consistent with that in the analysis of clinical echo data and in computer simulation. This result suggests that our proposed method enable to estimate the inhomogeneity of tissue with high accuracy by using frequency higher than clinically-used one. We will aim to associate our result with physical quantity e.g. scatterer density.

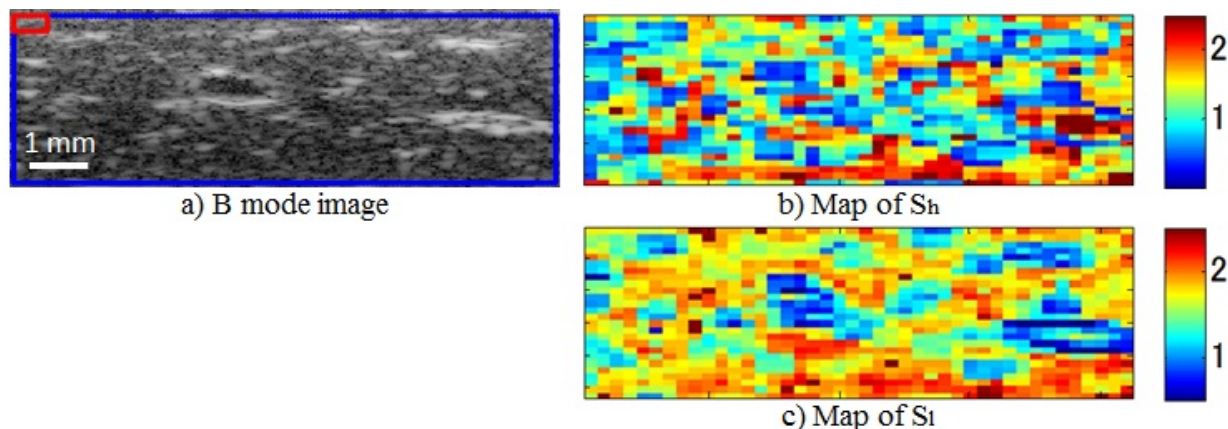


Fig.1 Analysis results of Normal liver

## P1C8-9

**New approach for objective cataract classification based on ultrasound techniques using multiclass SVM classifiers**

Miguel Caixinha<sup>1</sup>, Elena Velte<sup>2</sup>, Mário Santos<sup>1</sup>, Jaime Santos<sup>1</sup>; <sup>1</sup>Department of Electrical and Computers Engineering, University of Coimbra, Portugal, <sup>2</sup>Department of Physics, University of Coimbra, Portugal

**Background, Motivation and Objective**

Cataract severity is currently classified by human graders based on slit-lamp and retroillumination lens images. The standard classification system LOCSIII, is highly human dependent, and therefore prone to high inter-grader variability. This study aims to show that ultrasound properties can be used to objectively classify the different cataract degrees using machine learning techniques.

**Statement of Contribution/Methods**

A 25 MHz ultrasonic transducer was used to obtain the acoustical parameters velocity, attenuation, and backscattering signals in 210 porcine lenses. B-Scan and Nakagami parametric images were constructed from the backscattering signals. Different cataract degrees were induced ex-vivo by lens immersion in an ethanol:2-propanol:formalin solution. Cataract was induced in 135 lenses, 64 lenses with incipient cataract and 71 lenses with advanced cataract. Seventy-five lenses were used as control. Ninety-seven parameters were extracted from the acoustical, statistical, spectral and textural properties. For the acoustical properties the mean and variance of the velocity and attenuation were considered. For the statistical properties of the backscattering signals  $m$  and  $\Omega$  parameters of the Nakagami distribution were computed. The spectral properties of the A-Scan signals were also considered. Seven features from the Power Spectral Density and 7 features from the Hilbert spectrum were extracted. For the textural analysis of the B-Scan and Nakagami images 77 features were extracted. Besides first order statistic features from the image histogram, e.g., mean, variance, skewness and kurtosis, features from gray level co-occurrence matrix and gray level run-length matrix were also extracted. Fractal analysis and spectral analysis by 2D Fourier Transform were also performed. The different parameters were subjected to a principal component analysis (PCA) and thereafter used for cataract classification using a multi-class Support Vector Machine (SVM).

**Results/Discussion**

Fifteen components were used for the SVM. Very good sensitivity and specificity were obtained for the classification of the 3 different degrees of cataract. The overall sensibility and specificity was 85.7% and 93.7%, respectively. For healthy lenses the sensitivity was 86.0% and the specificity 96.0%. For incipient cataracts the sensitivity was 89.0% and the specificity 94.0%. Finally, for advanced cataracts the sensitivity was 79.0% and the specificity 89.0%.

Our results showed that SVM could be used as a computer-aided diagnosis system for the cataract classification based on the ultrasound analysis. The velocity and attenuation combined with the backscattering signals analysis in terms of B-Scan and Nakagami imaging allow for a good discrimination of the different cataract degrees and appear as a good alternative to the actual subjective classification system.

## P1C8-10

**Characterization of the Heart Muscle Anisotropy Using Ultrasound Nakagami Imaging**

Xue Yu<sup>1</sup>, Wei-Ning Lee<sup>1</sup>; <sup>1</sup>University of Hong Kong, Hong Kong

**Background, Motivation and Objective**

The left ventricular wall is mainly a layered myocardial fiber structure [1]. This structural anisotropy is associated with cardiac mechanical function, and therefore its assessment provides valuable information for the understanding of the heart function. Nakagami distribution can describe the statistics of backscattered ultrasound signals from tissue, and the  $m$ -parameter is found capable of differentiating various scattering conditions [2]. Backscattered signals have been demonstrated to be angle dependent in the heart muscle in the literature [3]. Our study thus aims to assess the feasibility of Nakagami imaging in characterizing heart muscles imaged in different views to assess myocardial anisotropy.

**Statement of Contribution/Methods**

An excised porcine left ventricle (LV) was dissected into anterior and posterior segments embedded in a gelatin phantom. A programmable ultrasound system (Verasonics, USA) with a linear array operating at 5.2 MHz was employed to acquire beamformed RF signals at a sampling rate of 20.8 MHz. Images were taken in the multi-focus (13.3, 20.7 and 38.5 mm) scenario in a total depth of 55.4 mm. Nakagami  $m$ -parameters were computed from signal envelopes using a sliding window of  $2.4 \times 2.4 \text{ mm}^2$ , which was determined by a pilot study on a commercial ultrasound calibration phantom to optimize the trade-off between spatial resolution and estimation stability. Histograms of the Nakagami  $m$ -parameter were then normalized by the total number of samples in each Nakagami image.

**Results/Discussion**

Fig. 1a and 1b show that the  $m$ -parameter histogram of the anterior wall was more dispersive than that of the posterior wall in both the long- and short-axis views. This finding was further manifested in Fig. 1c and 1d, showing larger variations of the  $m$ -parameter distribution in the anterior wall than in the posterior wall. More ex vivo heart samples are being collected for a more comprehensive statistical analysis to corroborate layer-specificity of anisotropic tissues. Our preliminary results show that Nakagami imaging might have a potential in myocardial anisotropy characterization.

[1] Streeter et al. vol. 24, 1969.

[2] Shankar. vol. 47, 2000.

[3] Mottley and Miller. vol. 83, 1988.

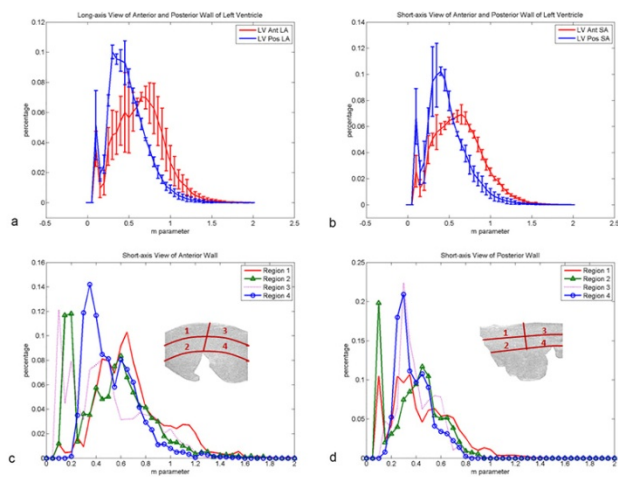


Fig. 1 Histograms of Nakagami m-parameter in the anterior and posterior LV walls in (a) long- and (b) short-axis views for repeated measurements ( $n = 3$ ), and of manually segmented regions of anterior (c) and posterior (d) walls in the short-axis view.

P1C8-11

### Experimental study on the pressure propagation in viscoelastic tube mimicking blood vessels.

Shohei NISHI<sup>1</sup>, Masashi SAITO<sup>2</sup>, Takashi ASADA<sup>2</sup>, Mami MATSUKAWA<sup>1</sup>; <sup>1</sup>Doshisha University, Kyotanabe, Japan, <sup>2</sup>Murata Manufacturing Co., Ltd., Nagaokakyo, Japan

#### Background, Motivation and Objective

The pulse wave is a displacement of surface skin and has similar characteristics with the intravascular pressure wave. We have proposed an evaluation method of arterial stiffness from the pulse wave at left carotid artery [1]. However, the properties of carotid vessel are different due to the location. For example, the property of the mother vessel at the carotid artery is different from the daughters. In this study, we studied experimentally the pressure propagation in viscoelastic tubes, which have different the properties, using blood vessel mimicking tubes.

#### Statement of Contribution/Methods

Water was discharged into a polyurethane tube by a pump (TOMITA Engineering) which mimicked the heart. The flow patterns were a half or one period of sine wave. The tube end mimicked the vascular bed. The Young modulus of the tube was 200 kPa or 80 kPa. The flow period was 0.3 s and the total flow volume was 4.5 cm<sup>3</sup>. The pressure in the tube was observed by a pressure sensor (Keyence AP-10S) at 25 cm from the pump.

#### Results/Discussion

First, we estimated the Young

The second wave is overlapping wave of the reflected wave from the tube end and the re-reflected wave at the pump. From the comparison between the 1D model [1] and the data, we estimated the Young modulus of the tube. The pressure change of case 1 is shown in Fig. 1 (b). Because stiffness of distal vessels is harder than that near the heart, case 1 corresponds of the flow from peripheral vessel to the heart and the case 2 is from the heart to peripheral vessel. The pressure at marked area in Fig. 1 (b) is negative, due to impedance matching of tubes. These results indicate the effects of properties of arteries on the pulse wave.

[1] M. Saito et al., Jpn. J. Appl. Phys. 48 (2009) 07GJ09.

[2] W. W. Nichols et al, McDonald

of Blood Flow in Arteries, 5th ed., London, UK: Hodder Arnold, 2005.

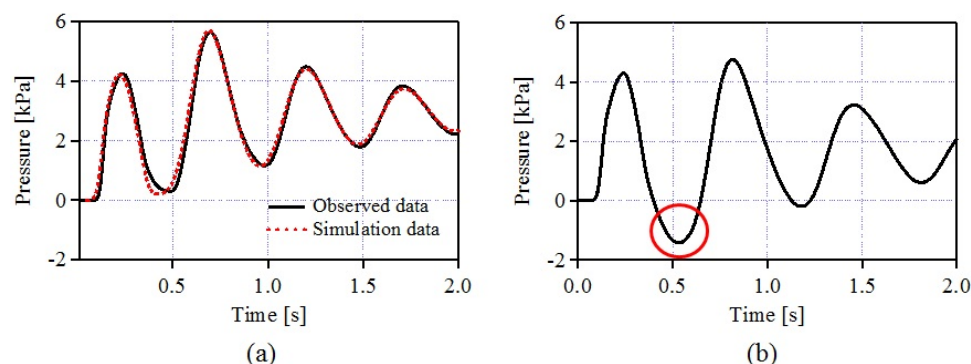


Fig. 1 Pressure waves in viscoelastic tubes  
(a) experimental and theoretical pressure waves of tube A  
(b) experimental pressure wave of case (1)



## P1C9 - MTC: Tissue Characterization Methodology

Salon C

Saturday, September 6, 2014, 8:00 am - 5:00 pm

Chair: **Michael Oelze**  
Univ. of Illinois, Urbana-Champaign

P1C9-1

### Iterative reconstruction of the ultrasound attenuation coefficient from the backscattered radio-frequency signal

Natalia Ilyina<sup>1,2</sup>, Jeroen Hermans<sup>3</sup>, Erik Verboven<sup>4</sup>, Koen Van Den Abeele<sup>4</sup>, Emiliano D'Agostino<sup>3</sup>, Jan D'hooge<sup>1</sup>; <sup>1</sup>Dept. of Cardiovascular Sciences, KU Leuven, Leuven, Belgium, <sup>2</sup>SCK.CEN, Mol, Belgium, <sup>3</sup>DoseVue NV, Hasselt, Belgium, <sup>4</sup>Dept. Of Physics, KU Leuven KULAK, Kortrijk, Belgium

#### Background, Motivation and Objective

Accurate estimation of the local acoustic attenuation based on the backscatter signal has several applications, e.g. for ultrasound tissue characterization. The aim of this study was to estimate the local attenuation coefficient based on iteratively solving the forward wave propagation problem. The proposed methodology was experimentally validated using phantoms with different attenuation characteristics.

#### Statement of Contribution/Methods

Wave propagation was modeled using the plane wave approximation taking into account the effects of attenuation, nonlinear distortion, reflection and scattering. Attenuation was modeled using a power-law in the frequency domain; nonlinearity using a time-domain operator and reflection using the standard acoustical expressions based on impedance mismatches. Backscatter was modeled by propagating the pulse received at the scattering site linearly back to the transducer assuming a given scattering cross section. This way, RF signals for a medium with given attenuation and non-linear characteristics can be simulated. These model parameters can then be iteratively changed to approximate experimentally observed RF signals, in order to determine the acoustic properties of the medium.

To test the above approach, tissue-mimicking cylindrical phantoms (4-5 cm in length; 3.5 cm in diameter) were made by mixing gelatin and agar with different concentrations of graphite. The attenuation coefficient, speed of sound and nonlinear coefficient for each phantom were determined using an insertion-substitution method. In addition, pulse-echo measurements were performed. For each phantom 10 signals were acquired, slightly moving the transducer in the plane parallel to the surface of the phantom after each acquisition. The average spectrum of these signals was compared with the simulations. All measurements were done with flat unfocused single-element transducers.

Measured and simulated backscatter signals were compared using a 2 cm-long sliding window approach using a 75% window overlap. For each set of acoustic parameters, the difference between the spectrum of the measured and the simulated signal was calculated. The attenuation coefficient corresponding to the best match was used as an estimate of the attenuation coefficient.

#### Results/Discussion

Through-transmission measurements showed the phantoms to have attenuation coefficients of 0.61, 0.75 and 0.85 dB/cm/MHz. Using the iterative forward solver, the estimated attenuation coefficients for these phantoms were  $0.65 \pm 0.08$ ,  $0.76 \pm 0.09$  and  $0.86 \pm 0.05$  dB/cm/MHz. The estimated values were thus close to the reference values (error did not exceed 1.8%). Ongoing work involves the validation in multilayered phantoms in which the boundary position is part of the optimization process. Moreover, future work will involve the experimental validation of estimation of the non-linearity parameter using this iterative approach.

P1C9-2

### Experimental validation of plane wave imaging for spectral tissue characterization of isotropic scatterers

Julian Garcia-Duitama<sup>1</sup>, Michael L. Oelze<sup>2</sup>, Aiguo Han<sup>2</sup>, Boris Chayer<sup>1</sup>, Damien Garcia<sup>1</sup>, Guy Cloutier<sup>1</sup>; <sup>1</sup>University of Montreal Hospital, Canada, <sup>2</sup>University of Illinois at Urbana-Champaign, USA

#### Background, Motivation and Objective

The central concept of spectral tissue characterization is the backscatter coefficient (BSC), defined as an instrumentation independent estimate of the tissue capacity to return acoustic energy to the probe. The accuracy of BSC estimation is of critical importance to get relevant and quantitative clinical data. Due to the statistical characteristic of BSC, it is often necessary to average multiple frames to obtain a coherent estimate. On the other hand, plane wave imaging (PWI) is currently of interest because of its capacity to generate thousands of frames per second with a sustained image quality at any depth in the field of view. In PWI, the tissue is insonified by planar waves that can be steered at several angles. To improve the image quality, the beamformed images can be coherently compounded using these different angles. Its superior image quality and the availability of a high number of frames to average, make PWI a good alternative to spectrally characterize tissues. However, the compounding process including information from different angles may result in a biased estimation of the BSC. Nevertheless, we hypothesized that in isotropic tissues, PWI compounding should not affect the BSC estimation when using the reference phantom technique [YAO, 1990]. We experimentally validated this hypothesis and compared the BSC estimation quality of PWI with that of conventional focusing.

#### Statement of Contribution/Methods

The BSC from two tissue-mimicking phantoms with isotropic scatterers were initially estimated using two single-element transducers (bandwidth 5-30 MHz). Instrument effects were compensated using the planar reflector technique [Chen, 1997]. Then, phantoms were scanned with a SonixTouch scanner (Ultrasonix, Vancouver, Canada) and a 5-14 MHz linear array using the PWI and conventional focusing protocols. RF signals were recorded using the SonixDAQ platform (Ultrasonix). Images for PWI were beamformed using the f-k migration method [Garcia, 2013]. The BSC of each phantom was estimated after compensating for instrumentation effects using the remaining phantom as a reference [Yao, 1990]. A comparison between BSCs estimated by PWI and conventional focusing was done using the BSC estimated from the single-element transducers as the gold standard.

#### Results/Discussion

Results indicate that compounded PWI can produce accurate estimates of the BSC in isotropic conditions with percentage errors below 10% over the bandwidth for one single frame but with considerable variance. Because of the high number of frames available in PWI (frame rate in the kHz range), the variability could be reduced by averaging over several frames. The conventional focusing technique gave comparable results for BSC estimation. To conclude, these results suggest that the reference phantom technique compensates accurately the effects of the compounding process in PWI for isotropic tissues.



## The Effect of Low Scatterer Number Density on Ultrasound Attenuation Estimation

Nicholas Rubert<sup>1</sup>, Tomy Varghese<sup>1,2</sup>; <sup>1</sup>Medical Physics, University of Wisconsin-Madison, Madison, WI, USA, <sup>2</sup>Department of Electrical and Computer Engineering, University of Wisconsin-Madison, Madison, WI, USA

### Background, Motivation and Objective

Ultrasound attenuation estimation has the potential to be a useful diagnostic tool for many applications including distinguishing between benign and malignant breast cancer, detecting bone density loss, and delineating the extent of thermal coagulation following thermal ablation therapy. A large research effort has been devoted to improving and utilizing reference phantom based methods for attenuation estimation. A common assumption made in the development of reference phantom based attenuation estimation algorithms is that the tissue being imaged contains a large number of uniformly, randomly distributed scatterers per unit volume. However, the assumption of high scatterer number density does not always hold in tissue. Additionally, this assumption is simple to verify by measuring envelope SNR. Specifically, an envelope significantly lower than 1.91 indicates low number density scattering.

### Statement of Contribution/Methods

We examined the performance of reference phantom attenuation estimation in computer simulations and in ex vivo bovine liver tissue prior to and following thermal coagulation. A linear array transducer was simulated at two different center frequencies using a program previously developed in our laboratory. Tissue containing point-like scatterers was simulated with a variable number density between 0.1 scatterers/mm<sup>3</sup> and 128 scatterers/mm<sup>3</sup>. Ultrasound RF data was recorded from ex vivo tissue using a Siemens S2000 ultrasound scanner with a 9L4 linear array transducer. Bovine liver was acquired from a commercial meat production facility, degassed under a low pressure vacuum, and imaged within 12 hours of animal sacrifice. RF data was recorded from the livers of five separate animals. Approximately 300 independent planes of RF data were recorded from the liver of each animal. Additionally, five more livers were obtained and immersed in a saline bath at a temperature of 80° C for 45 minutes prior to acquisition of RF data.

### Results/Discussion

In the simulations, it was found that the bias in the attenuation estimates did not have a strong dependence on the scatterer number density. On the contrary, the standard deviation in the attenuation estimates was a strong function of the envelope SNR and the kernel size. Ex vivo, a low average envelope SNR of 1.10 was found in the unheated, normal bovine liver. An average envelope SNR of 1.28 was found in the thermally coagulated bovine liver. It was found that this low envelope SNR led to a correspondingly large variance in the attenuation estimate, which depended strongly on the spatial resolution of the estimate. Specifically, as the axial extent of the attenuation estimation kernel varied from 6 to 15 mm, we found a mean estimate between 0.43 and 0.51 dB/cm MHz across all unheated livers. Meanwhile, the standard deviation of all the estimates in the unheated liver decreased from 1.8 to 0.5 dB/cm MHz.

Work supported by NIH-NCI grants R01CA112192-S103, R01CA112192-05, and T32 CA09206-32.

## Simulation of Absolute Backscattering Coefficient in Field II

Bernard Shieh<sup>1</sup>, Karim Sabra<sup>1</sup>, F. Levent Degertekin<sup>1</sup>; <sup>1</sup>G. W. Woodruff School of Mechanical Engineering, Georgia Institute of Technology, USA

### Background, Motivation and Objective

Field II and the linear systems model have been used extensively for the simulation of ultrasound propagation from phased-array transducers, with applications such as calculation of radiated field pressures and simulation of pulse-echo images, amongst many others<sup>1</sup>. In its current implementation, tissue and blood are simulated in Field II as backscatter from a collection of discrete point targets, with each target characterized by an arbitrary scalar-valued scattering strength which has unknown units and no clear physical interpretation. Consequently, pulse-echo images simulated in Field II are based solely on relative contrast and not in terms of absolute scattering strengths. In addition, the frequency-dependent characteristics of backscatter are not represented. This presents a limitation for researchers interested in using Field II in cases where an accurate value for the backscattered intensity from tissue is desired.

### Statement of Contribution/Methods

Here we outline a method to incorporate quantitative backscattering coefficient (BSC) in Field II with minimal overhead to the current implementation. An additional convolution step is introduced which acts as a filter corresponding to the spectral response of a single scatterer. By taking into account scaling and other adjustments to ground Field II's linear model physically, and also the density and spatial distribution of scatterers, the filter can be designed to match an arbitrary BSC spectrum via the Rayleigh and Rician speckle models<sup>2</sup>. The result is a modified simulation where the stochastic nature of speckle and the spectral effects of backscatter are quantitatively captured.

### Results/Discussion

To validate the proposed method, a simulation of a standard time-gated BSC measurement was performed with the desired BSC spectrum matched to empirical data for blood with 8% hematocrit. Pulse-echo data from a geometrically-focused transducer was simulated for scatterers randomly distributed in a hemispherical volume. The simulated measurement shows agreement with the desired spectrum with a mean fractional error of 5.7% and maximum fractional error of 18%. Furthermore, we demonstrate the utility of this method by reconstructing images from simulated phantoms with BSC spectra matched to empirical data for various tissues and blood (Fig. 1).

<sup>1</sup> J. Jensen. (1992). IEEE T-UFFC.

<sup>2</sup> R. Wagner (1987). JOSA A.

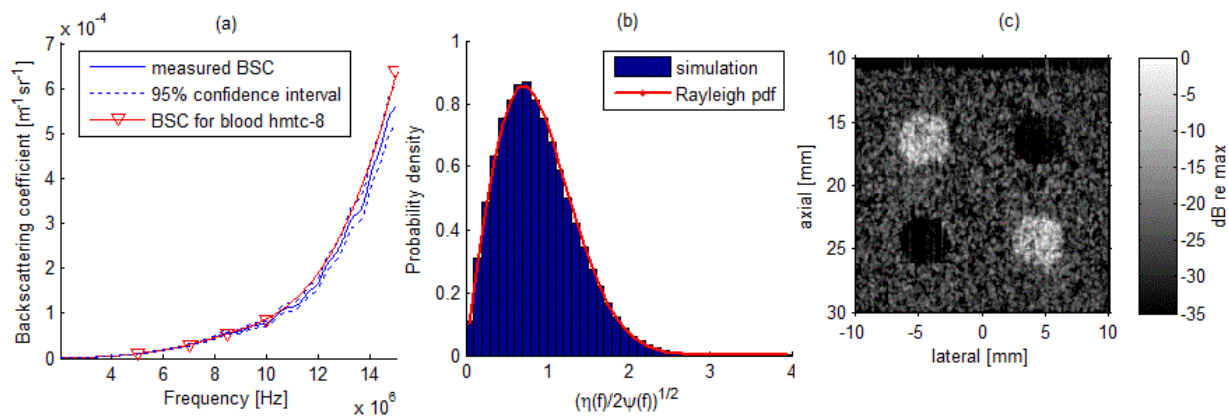


Figure 1. (a) simulation of a BSC measurement experiment with desired BSC spectrum taken from empirical data for blood with 8% hematocrit, (b) probability distribution of the square root normalized BSC from simulation showing that the generated speckle follows Rayleigh statistics, (c) reconstructed image of a simulated phantom featuring two types of inclusions: hyperechoic (+15 dB), hypoechoic (-15 dB) relative to the BSC of the background material.

P1C9-5

### Improving the quality of attenuation imaging using full angular spatial compounding

Omar Zenteno<sup>1</sup>, Adam Luchies<sup>2</sup>, Michael Oelze<sup>2</sup>, Roberto Lavarello<sup>1</sup>; <sup>1</sup>Departamento de Ingeniería, Pontificia Universidad Católica del Perú, Lima, Lima, Peru, <sup>2</sup>Department of Electrical and Computer Engineering, University of Illinois at Urbana-Champaign, Urbana, Illinois, USA

#### Background, Motivation and Objective

The quantitative imaging of attenuation coefficients slope (ACS) has the potential to improve medical diagnostics. However, attempts to characterize ACS using pulse-echo data have been limited by the large statistical variations in the estimates. Currently, ACS images have to be constructed using large data blocks in order to reduce the variance of the resulting attenuation maps. Previous studies demonstrated that it is possible to extend the trade-off between variance and spatial resolution of quantitative ultrasound, spectral-based parameters by the use of full angular (i.e., 360°) spatial compounding (FASC). In the present work, the use of FASC has been extended to the estimation of ACS and its performance has been experimentally evaluated using physical phantoms.

#### Statement of Contribution/Methods

ACS images were obtained from two agar-based phantoms with each phantom formed in the shape of a cylinder consisting of a 76.2 mm diameter background region with an eccentric 25.4 mm diameter inclusion. Powdered graphite was mixed with agar to modify the attenuation coefficient in the background and inclusion regions. The ACSs of the background and inclusion regions were estimated using insertion loss measurements to be 0.41 and 0.75 dB/cm/MHz for Phantom #1, and 0.54 and 1.04 dB/cm/MHz for Phantom #2, respectively. Pulse-echo data were collected using a 7.5 MHz,  $f/4$  transducer at 30 angles of view uniformly distributed between 0 and 360°. Single view ACS maps were generated using a spectral log difference method with 0.6 by 0.6 mm data blocks. The FASC images were constructed by assigning to a pixel the median of its corresponding estimates from all 30 angles of view.

#### Results/Discussion

An example of a single view and FASC ACS maps of Phantom #1 and Phantom #2 are shown in Figs. 1a and 1b, respectively. The reduction in the variance of the FASC estimates compared to the variance of estimates from a single view (i.e., variance averaged from the 30 single views) in the inclusion and background regions were 89.18% and 88.71% for Phantom #1 and 92.33% and 86.98% for Phantom #2. Moreover, in all the cases the estimation bias in the inclusion and background regions using FASC was lower than 9.0%. These results suggest that the variance of attenuation coefficient slope estimation can be reduced without sacrificing spatial resolution by the use of full angular spatial compounding.

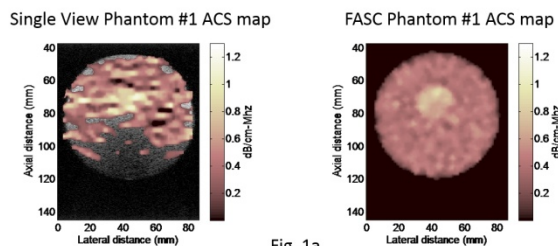


Fig. 1a

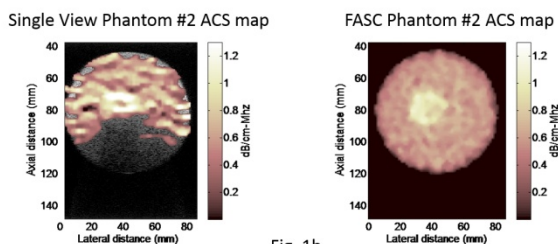


Fig. 1b

# Development of a FPGA-based quantitative ultrasound system for assessing stress- strain properties of Achilles tendon

Guan-Chun Chen<sup>1</sup>, Jian-Xing Wu<sup>1</sup>, Yi-Chun Du<sup>2</sup>, Tainong Chen<sup>1</sup>; <sup>1</sup>Department of Biomedical Engineering, National Cheng Kung University, Taiwan, <sup>2</sup>Department of Electrical Engineering, Southern Taiwan University of Science and Technology, Taiwan

## Background, Motivation and Objective

Achilles tendon (AT) is the most fragile and vulnerable part in human body. Stress-strain properties and shape changing such as cross-sectional area variations of this tendon are important biomechanical properties used clinically for assessing and monitoring surgical repair or postoperative healing progress. However, so far, there are few methods for non-invasively, precisely and quantitatively assessing in vivo AT mechanism. In this study, we develop a quantitative ultrasound system (QUS) based on FPGA aiming at estimating stress-strain properties of AT via evaluating the broadband ultrasound attenuation (BUA) parameter upon different levels of applied stress on the AT.

## Statement of Contribution/Methods

Figure A represents the fabricated ultrasound measuring system coupled with a stress device. Twenty fresh ATs of hind porcine trotters were procured from a local abattoir, and were preloaded for 30 cycles with a cyclic loading ranging from 0 to 300 N. The loading force pulled along the tendon fibers, and the changes of AT cross-sectional area were acquired by ultrasound transducer implemented in the palmar-dorsal direction which was perpendicular to the tendon fibers (Fig. B). BUA has been widely used to estimate the broadband ultrasound attenuation (dB/ MHz-l) by calculating the slope of a linear regression fit to the attenuation against frequency plot within a frequency range. The tendons were then strained from 1 to 400 N with single steps of 50 N, and the measurements were repeated for ten times following calculating the average slope of BUA to reduce the interference of noise.

## Results/Discussion

Results showed that as the tendon tissue was stretched orthogonally to the beam axis, BUA coefficient decreased linearly with increasing stress (R-squared =0.89) (Figure. C). The tendon thickness measured with the ultrasound method was significantly correlated with tendon cross-sectional area (Pearson coefficient = 0.82). This indicated that the BUA coefficient is a potentially useful parameter for quantitative characterization of ATs. The FPGA system proposed for measuring tendon thickness using QUS technique is an easy and objective method to precisely evaluate the tissue thickness, providing a new way for AT to implement high-speed online diagnosis.

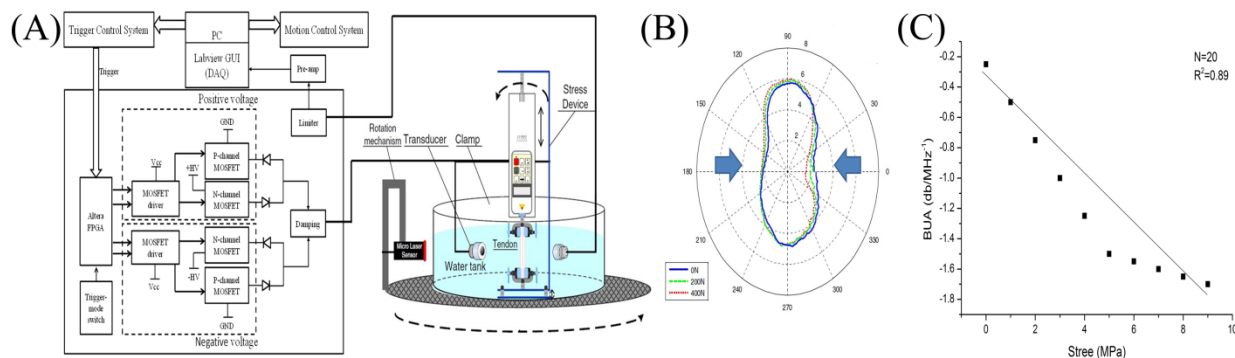


Figure (A)The schematic diagram of the tendon testing system (B)Illustration of change of cross-sectional area (C)The BUA coefficient versus stress

# Detection of subresolution sources of coherent scattering for parametric image formation: Model-free vs model-based parameters

Ivan Rosado-Mendez<sup>1</sup>, Timothy Hall<sup>1</sup>, James Zagzebski<sup>1</sup>; <sup>1</sup>Department of Medical Physics, University of Wisconsin-Madison, Madison, Wisconsin, USA

## Background, Motivation and Objective

We are developing a decision strategy for the simultaneous generation of parametric images based on coherent and incoherent scattering parameters for quantitative ultrasound applications. We describe here the optimization stage of the algorithm for the detection of coherent scattering when the echo signals are stationary which limits the use of spectral correlation techniques. This optimization involves the selection of a parameter from first-order statistics of the echo signals with the highest sensitivity to the presence of coherent scattering from periodic scatterers. The robustness of this sensitivity is studied under conditions that reduce the coherence in the signals and under data constraints (e.g., to improve image spatial resolution).

## Statement of Contribution/Methods

Simulations and phantom experiments were performed with periodically organized scatterers in a cloud of random scatterers. Simulations were performed by convolving an acoustic pulse with 1D arrays of random and periodic scatterers. The phantom consisted of a homogeneous background with Rayleigh scatterers with an array of periodically spaced nylon fibers. The acoustic pulse (both simulated and experimentally obtained with a linear array transducer and the Siemens S2000 system) had a center frequency of 6MHz and a 70% - 6dB bandwidth. Two groups of parameters of the echo signal envelope were investigated: model-free parameters (point-wise amplitude and intensity SNR), and model-based parameters (Nakagami shape parameter  $m$  and a Nakagami-based Generalized Likelihood Ratio test statistic  $T$ ). The sensitivity of the parameters to coherent scattering was quantified by the contrast (difference in values under coherent scattering vs. diffuse scattering) and the contrast-to-noise ratio (CNR, contrast divided by the quadrature summed variance). Dependence of the contrast and CNR on variables such as scattering cross section, spacing and spacing consistency of the periodic scatterers, as well as on the amount of data available for the estimation, was investigated.

## Results/Discussion

The echo amplitude SNR consistently had largest sensitivity (CNR values) among simulated and experimental conditions. CNR was significantly different from zero when the spacing was between  $0.3\lambda$  to  $1.3\lambda$  (where  $\lambda$  is the wavelength of the acoustic pulse), the coherent power per periodic scatterer was as large as the incoherent power, and the standard deviation of the scatterer spacing was smaller than 10% of the mean scatterer spacing. The Nakagami  $T$  statistic offered the highest contrast, but its sensitivity was limited by its large variance. We are investigating the performance of these parameters when the scatterer density is low for inclusion in the decision algorithm.

## Acknowledgements

This work was supported, in part, by NIH (grants R21HD061896, R21HD063031, and R01HD072077) and the Consejo Nacional de Ciencia y Tecnología of Mexico (Reg. 206414).

## P1C9-8

### Accuracy of backscatter coefficient estimation in aberrating media using different phase aberration correction strategies – A simulation study

Eduardo González<sup>1</sup>, Niraj Sheth<sup>2</sup>, Benjamin Castañeda<sup>1</sup>, Jeremy Dahl<sup>3</sup>, Roberto Lavarello<sup>1</sup>, <sup>1</sup>Pontificia Universidad Católica del Perú, Peru, <sup>2</sup>Duke University, USA, <sup>3</sup>Duke University, Peru

#### Background, Motivation and Objective

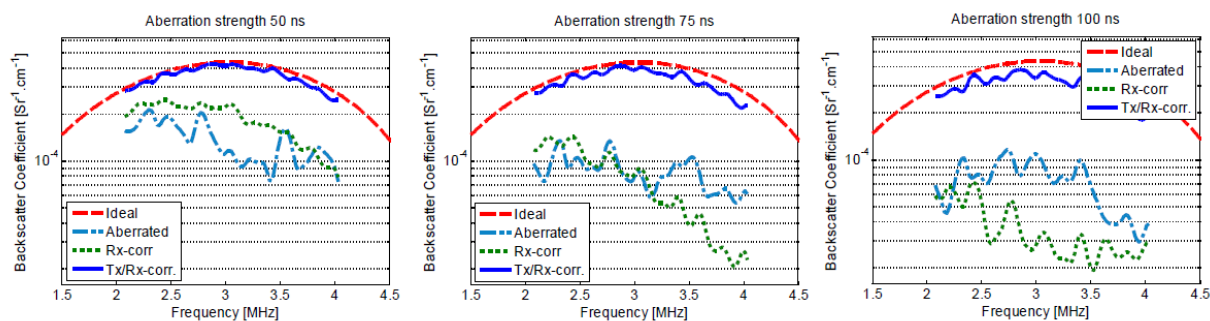
Phase aberration is the distortion of the diffraction pattern when a wave propagates in a medium with an inhomogeneous sound speed. The effects of phase aberration on the quality of B-mode imaging have been extensively documented. However, to this date only a few reports are available on the effects of phase aberration on quantitative ultrasound methods. In this study, the accuracy of the estimation of backscatter coefficients (BSCs) in the presence of near-field phase aberrations was studied through simulations. Further, the accuracy was also evaluated when using two different phase aberration correction strategies prior to BSC estimation.

#### Statement of Contribution/Methods

Simulations were performed using a 2D full-wave nonlinear acoustic wave propagation method. The simulation utilized a 128 element, 3.5 MHz linear array with 70% bandwidth. The imaging medium consisted of randomly positioned circular scatterers having a diameter of 176 microns. Near field phase aberrators were applied to the transmit and receive signals of the simulation having 50, 75, and 100 ns RMS strength and a 4 mm correlation length. Phase aberrations were estimated using a multi-lag least squares estimation technique. BSCs were estimated using the reference phantom method and radiofrequency data segments with a length of 14 wavelengths and centered around the transducer transmit focus. BSC estimation accuracy was quantified using the average difference in dB between the theoretical and estimated curves within the -10 dB bandwidth of the transducer.

#### Results/Discussion

Estimated BSCs are shown in Fig. 1 with and without the use of aberration correction. The mean BSC estimation errors were -4.6, -6.6 and -7.5 dB in the presence of the 50, 75 and 100 ns aberrators, respectively. The use of aberration correction on receive improved the BSC accuracy only for the 50 ns aberrator (-3.2 dB estimation error) and resulted in errors of -7.6 and -10.5 dB for the 75 and 100 ns aberrators, respectively. In contrast, the use of aberration correction on transmit-receive allowed an accurate BSC estimation, with estimation errors lower than 1.1 dB for all cases. These results suggest that phase aberration effects may adversely affect the performance of BSC estimation, and that a robust BSC-based tissue characterization may require compensating for the effects of aberration on both the transmit and receive beams.



## P1C9-9

### Pulse-echo sound speed estimation based on a Nakagami model of the echo amplitude

Ivan Rosado-Mendez<sup>1</sup>, Timothy Hall<sup>1</sup>, James Zagzebski<sup>1</sup>, <sup>1</sup>Department of Medical Physics, University of Wisconsin-Madison, Madison, Wisconsin, USA

#### Background, Motivation and Objective

The longitudinal propagation sound speed  $c_L$  can be used for tissue characterization and beamforming. Regardless of the  $c_L$  in tissue, beamformers in commercial ultrasound systems generally assume  $c_{bf}=1540\text{m/s}$ . When  $c_{bf}$  differs from  $c_L$  the resolution cell volume increases due to phase distortion and causes loss of image sharpness. This work explores the use of the Nakagami shape parameter " $m$ " as an indirect measure of the size of the resolution cell, and to use  $m$  in  $c_L$  estimations by tracking the size of the resolution cell as  $c_{bf}$  is varied. The estimation performance of  $m$  is compared to a direct measure of image sharpness.

#### Statement of Contribution/Methods

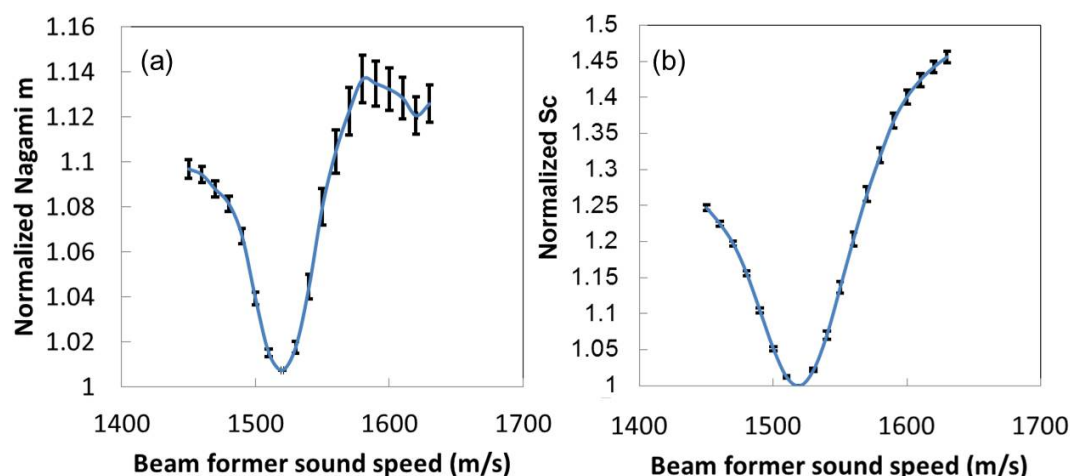
The proposed method is tested on a tissue mimicking phantom consisting of a homogeneous mixture of water-based agarose-milk mixture. Glass beads were added to mimic subresolution scattering. Gold standard values of the phantom sound speed  $c_L$  ( $1544\pm 1\text{ m/s}$ ) were obtained using a narrowband substitution technique applied to test samples. The phantom was scanned with a linear array transducer on a Siemens Acuson S2000. Keeping the transducer fixed on the scanning window of the phantom, 21 radiofrequency data frames of the same phantom plane were acquired with  $c_{bf}$  ranging from 1440m/s to 1640m/s, in steps of 10m/s. This process was repeated at 5 1cm-spaced planes. Two image sharpness metrics were explored: a direct metric (correlation cell size  $S_c$  from the 2D autocovariance matrix) and an indirect metric (Maximum Likelihood Estimator of the Nakagami shape parameter  $m$ ). Each variable was tracked as  $c_{bf}$  was varied. The  $c_{bf}$  values at which each parameter was minimized were chosen as  $c_L$  estimates. The  $c_L$  estimate error was computed as an inter-plane average of the percentage difference from laboratory measurements.

#### Results/Discussion

In Figure 1 (a)  $m$  and (b)  $S_c$  are minimized when  $c_{bf}=1520\pm 6\text{m/s}$  and  $1519\pm 3\text{m/s}$ , respectively, representing a bias of 1.6% from the expected value of 1544m/s. The Nakagami parameter was linearly correlated with  $S_c$  up to a value of  $m=1$ , where it plateaus regardless of further increase in  $S_c$  since the Rayleigh scattering limit has been reached. The Nakagami parameter is attractive due to its estimation simplicity.

#### Acknowledgements

This work was supported, in part, by NIH (grants R21HD061896, R21HD063031, and R01HD072077) and the Consejo Nacional de Ciencia y Tecnología of Mexico (Reg. 206414).



P1C9-10

# Optical and acoustic characterization of freeze-thawed poly-vinyl alcohol gels

Mustafa Umit Arabul<sup>1</sup>, Marcel Rutten<sup>1</sup>, Frans van de Vosse<sup>1</sup>, Richard Lopata<sup>1</sup>; <sup>1</sup>Biomedical Engineering, Eindhoven University of Technology, Eindhoven, Netherlands

## Background, Motivation and Objective

Vulnerability assessment plays a crucial role in the diagnosis of carotid arterial atherosclerosis. The composition of a plaque is the major precursor of its rupture. Photoacoustic imaging, when combined with ultrasound imaging, grants the functional and morphological information in addition to the mechanical and structural properties. Pre-clinical validation of non-invasive photoacoustic imaging in carotids emerges the demand for vessel phantoms that imitate optical, acoustic and mechanical properties of vascular tissue.

## Statement of Contribution/Methods

In this study, we provided a comprehensive optical and acoustic characterization of poly-vinyl alcohol (PVA) phantom material. We investigated the relation between acoustic scatterers and optical absorbers to quantify opto-acoustic properties of the phantoms.

Four different concentrations of orgasol acoustic scatterers (0 wt% – 4 wt%), and varying concentration (0.01 ml – 2.5 ml) of pen ink, Indian ink and molecular dye absorbers (Epolight 2735, Epolin, Newark, USA) were added to a 15 wt% PVA solution. Samples were subjected to 1 to 5 freeze-thaw cycles and were examined after each cycle to quantify the effect on the optical properties. Optical attenuation, the combined effect of absorption and scattering, was measured between 400 nm – 990 nm using a plate reader (SynergyHT, Biotek, Winooski, USA).

## Results/Discussion

The results show that the changing the concentration of orgasol between 0.5 wt% and 4 wt% increased the mean optical attenuation of PVA by 35% after the first freeze thaw cycle due to its contribution to optical scattering. Likewise, each freeze-thaw cycle increased the optical attenuation due to scattering of light by the microstructure of PVA. The absorbance of pure PVA increased 40% between the first and second cycle and 3% between the fourth and fifth cycle.

The absorbance measurements of PVA phantoms containing Indian ink and molecular dye revealed that the amount of chromophores added to the PVA gel mimics the optical absorption of human tissue for discrete wavelengths. In contrast, mimicking the continuous spectral properties of real tissue requires a complex mixture of various narrow-band absorbers. Preliminary results of acoustic measurements show a trend in speed of sound measurements after 2 freeze-thaw cycles, but requires further examination.

PVA phantoms that are widely used as ultrasound phantoms due to its elastic properties are also promising for photoacoustics. This study contributes to this field by quantifying the optical properties of background material, PVA gel, and aims at the characterization of realistic phantoms for future studies.



## P1C10 - MTH: Cancer Treatment and Monitoring

Salon C

Saturday, September 6, 2014, 8:00 am - 5:00 pm

Chair: **Chih-Kuang Yeh**  
National Tsing Hua University

### P1C10-1

#### Release, uptake and cytotoxicity of doxorubicin loaded lipopolyplexes exposed to low intensity ultrasound

Francois Yu<sup>1</sup>, Xucai Chen<sup>1</sup>, Jianjun Wang<sup>1</sup>, Bin Qin<sup>1</sup>, Regeant Panday<sup>1</sup>, Flordeliza Villanueva<sup>1</sup>; <sup>1</sup>Heart and Vascular Institute, University of Pittsburgh, USA

#### Background, Motivation and Objective

Cardiotoxicity is the major dose-limiting factor in the chemotherapeutic use of doxorubicin (Dox). Delivery strategies combining liposomal encapsulated Dox (LDox), microbubbles (MB) and ultrasound (US) have been shown to improve LDox toxicity but much remains to be known about the mechanisms and the US conditions that maximize cytotoxicity using this approach. In this study, we compared different US pulses in terms of drug release, acute toxicity, uptake and proliferation rates in squamous carcinoma cells (SCC) exposed to LDox conjugated to, or co-injected with, polymer MB. The aims of this study were: (1) to compare the effects of low and high pressure US on Dox release kinetics; (2) to evaluate whether conjugating LDox to MB is an important factor for drug release and cytotoxicity; (3) to determine which US parameters cause the largest decrease in cell proliferation and whether this decrease is mediated by drug release or the MB/US interaction with cells.

#### Statement of Contribution/Methods

LDox were attached to polymer encapsulated MB via biotin-streptavidin conjugation to form Dox-lipopolyplexes (DoxLPX). SCC cells ( $1 \times 10^5$  cell/mL) were suspended in media with DoxLPX (300 MB/cell) carrying 4  $\mu$ g/mL of Dox. A 1 MHz unfocussed transducer was used to deliver a variety of US pulses for 3 minutes. A 10 MHz transducer was focally aligned for passive cavitation detection. Drug release during exposure to the different pulses was assessed by fluorometry and compared to chemical release using 0.25% Triton-X100. Cell viability after US exposure was quantified using a trypan blue exclusion assay. Cells were then plated, washed with fresh media after 4h and incubated for 48h before assaying survival rate (MTT). Drug uptake at 4h was measured using flow cytometry. All experiments were repeated 3 times.

#### Results/Discussion

Low pressure US (170 kPa) at high duty cycle (50%), causing sustained non-inertial cavitation, released up to ~70% of the encapsulated Dox from the DoxLPX with low acute cytotoxicity (<5%). Release was corroborated by improved cellular uptake, increasing from  $19.5 \pm 7.5$  relative fluorescent units (RFU) without US to  $72.1 \pm 12.4$  RFU with US ( $p < 0.05$ ). For US conditions causing inertial cavitation and when LDox was co-injected with the MB (not attached to the MB surface), release was below 20%. DoxLPX+US resulted in a cell proliferation of  $49 \pm 16\%$  at 48h, which was lower than DoxLPX-US ( $84 \pm 7\%$ ,  $p < 0.05$ ) but similar to Dox ( $39 \pm 3\%$ ). Our results support that LDox, when conjugated to, MB, can be triggered to release the Dox payload more efficiently using non-inertial compared to inertial cavitation. Following release, Dox became bioavailable to the cells and induced significantly higher cytotoxicity compared to unreleased liposome encapsulated drug. Our findings raise promise for targeted drug delivery using this theranostic delivery platform at low US intensities.

### P1C10-2

#### Image-guided ultrasound and microbubble-assisted targeted delivery of 120 nm therapeutic nanocarrier into tumors in vivo

Tzu-Yin Wang<sup>1</sup>, Jung Woo Choe<sup>1</sup>, Kanyi Pu<sup>1</sup>, Steven Machtaler<sup>1</sup>, Rammohan Devulapally<sup>1</sup>, Butrus Khuri-Yakub<sup>1</sup>, Jianghong Rao<sup>1</sup>, Ramasamy Paulmurugan<sup>1</sup>, Jürgen Willmann<sup>1</sup>; <sup>1</sup>Stanford University, USA

#### Background, Motivation and Objective

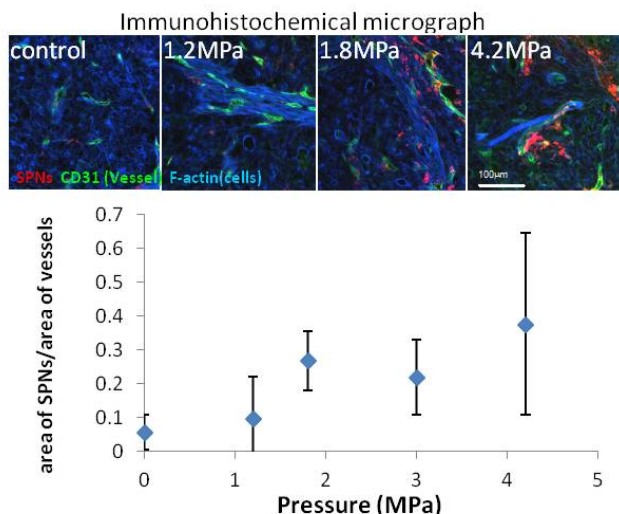
Targeted delivery of large (>100nm) therapeutic nanocarriers into tumors has significant clinical value in cancer therapy as it allows for the loaded drugs to be stably released to the diseased sites at high concentration. This may be achieved using cavitation induced by ultrasound (US) and microbubbles (MBs). This study investigates the feasibility of delivering a 120 nm therapeutic agent into tumors in vivo using an image-guided US drug delivery system, and to evaluate the effects of acoustic pressure on the delivery outcomes.

#### Statement of Contribution/Methods

Experiments were performed on 16 subcutaneous tumors established on mice. A 120-nm PEG-lipid coated semiconducting polymer nanoparticle (SPN) was used as a model drug system. A total of 150  $\mu$ L of 5.6nM SPNs were co-injected with 350  $\mu$ L ( $3.5 \times 10^8$ ) lipid shelled, perfluorocarbon encapsulated MBs via tail vein at 100  $\mu$ L/min for 1 minute. After the infusion, the tumor was exposed to 5-cycle 1.8-MHz US pulses at pulsing rate of 100Hz for 1 minute. The injection-exposure process was repeated 5 times, resulting in a total treatment time of 10 minutes. The entire process was guided and monitored using ultrasound imaging with a 25-MHz imaging probe. To study the effects of pressures on cavitation and treatment outcomes, 5 discrete pressures from 0 to 4.2 MPa were used. The drug delivery outcomes and tissue damage were evaluated ex vivo using immunohistochemical and histological staining. Quantitative analysis on the amount of SPNs delivered to the tumor was performed by calculating the area with presence of SPNs normalized to that with presence of blood vessels on fluorescence micrographs.

#### Results/Discussion

Guided by US imaging, MB cavitation was induced at the target site when the pressure exceeded 1.8MPa. Compared to the control, US and MBs caused enhanced delivery of SPNs into tumors when the pressure exceeded 1.8 MPa ( $p < 0.05$ , T-test, N=3 each). Moreover, the amount of SPNs increased with increasing pressure. Between 1.8 to 3 MPa, a 4-fold increase in the SPN delivery was achieved without significant tissue damage. At 4.2 MPa, the amount of SPNs delivery was further improved by 6.7 fold; however, noticeable hemorrhage was seen in the peritumoral tissues. These results indicate that US induced MB cavitation may be a safe and useful tool for delivering 120-nm therapeutic nanocarriers into tumors using proper acoustic parameters.



#### P1C10-3

##### Investigating Tumour Response Mechanisms in Ultrasound-Stimulated Microbubble Treatments Combined With Radiation And The Anti-Angiogenic Sunitinib.

Ahmed El Kaffas<sup>1,2</sup>, Azza Al-Mahrouki<sup>1</sup>, Anoja Giles<sup>1</sup>, Gregory Czarnota<sup>1,2</sup>; <sup>1</sup>Departments of Radiation Oncology and Physical Sciences, Sunnybrook Health Sciences Centre, Canada, <sup>2</sup>Departments of Medical Biophysics and Radiation Oncology, University of Toronto, Canada

##### Background, Motivation and Objective

We have recently demonstrated that ultrasound-stimulated microbubbles (USMB) can be used to radiosensitize endothelial cells, resulting in rapid vascular shutdown and consequently cell death upon irradiation. Studies have also demonstrated that the clinically approved anti-angiogenic Sunitinib can radiosensitize endothelial cells, induce endothelial cell death in proliferating cells, and block vascular rebounds. In this study, we investigate combined therapeutic strategies using USMB, radiation and the anti-angiogenic Sunitinib. Specifically, we aim to study if Sunitinib can increase the anti-vascular effects of USMB alone, or with radiation.

##### Statement of Contribution/Methods

Nude mice were injected with one of three tumour cell lines: LS174T, MDA-MB-231 or PC3. Each tumour line exhibits different rates of angiogenesis. Tumour xenografts were treated with single doses of 0-8 Gy ionizing radiation alone, or in conjunction with USMB and/or Sunitinib. USMB treatments consisted of a 16-cycle tone burst at 500 kHz center frequency and 570 kPa with a 2.86 cm element diameter ultrasound transducer. The total tumour insonification time was 750 ms over 5 minutes for an overall duty cycle of 0.25%. Approximately 1.08 x 10<sup>9</sup> of Definity microbubbles in 90 µL of saline was injected via tail-vein immediately before insonification. Treatment response was assessed with high frequency volumetric Doppler ultrasound acquired before, and at two time points after treatment using a VEVO2100 system coupled with a LAZR photo-acoustic system. The vascularity index (VI) was used to quantify power Doppler data, photo-acoustic parameters were used to assess tumour oxygenation, and quantitative ultrasound spectroscopy (QUS) parameters were used to monitor tumour response and tissue structural changes. Staining using ISEL, CA9 and CD31 of tumour sections was used to measure cell death, oxygenation and vascular response, respectively.

##### Results/Discussion

Preliminary results suggest that vascular rebounds are blocked when Sunitinib is administered after USMB and radiation with prolonged diminishment of the VI of up to 60% as detected by Doppler and CD31 staining. We demonstrate that blocking vascular rebounds greatly enhances the effects of USMB and radiation in highly angiogenic cell lines (i.e. LS174T). Evidence also suggests that microbubble perturbation may alter the state of endothelial cells, resulting in rapid endothelial apoptosis following treatment with Sunitinib. Overall, we provide evidence that the clinically approved anti-angiogenic agent Sunitinib may be well suited to be combined with USMB-based treatments in vascular targeting strategies. Additionally, we demonstrate the potency of using various ultrasound-based methods to assess complex treatment regimens.

#### P1C10-4

##### VEGFR-Targeted Microbubble Radiosensitization of Vascular Endothelial Cells Results in Enhanced Tumour Response to Radiation Therapy

Ahmad El-Falou<sup>1,2</sup>, Azza Al-Mahrouki<sup>1</sup>, Ahmed El Kaffas<sup>1,2</sup>, Emily Wong<sup>1</sup>, Amr Hashim<sup>1</sup>, Anoja Giles<sup>1</sup>, Gregory Czarnota<sup>1,2</sup>; <sup>1</sup>Imaging Research and Radiation Oncology, Sunnybrook Health Sciences Center, Toronto, Ontario, Canada, <sup>2</sup>Medical Biophysics and Radiation Oncology, University of Toronto, Toronto, Ontario, Canada

##### Background, Motivation and Objective

Solid tumours are highly angiogenic, in turn overexpressing VEGF (Vascular Endothelial Growth Factor) and its receptors (VEGFR-1 and VEGFR-2). Targeting VEGF-based pathways has been the basis of several anti-angiogenic agents developed in recent years. Ultrasound-based molecular imaging can also take advantage of VEGF overexpression, where microbubble contrast agents are pharmacologically adapted to target specific molecules. We have recently demonstrated that ultrasound-stimulated microbubbles (USMB) can be used to radiosensitize endothelial cells, resulting in rapid vascular shutdown and extensive tumour cell death following single doses of radiation. In this work, we investigate the use of VEGFR-2 antibody-labelled microbubbles as radiosensitizers. We posit that using targeted bubbles will increase direct endothelial effects, thus resulting in enhanced tumour response.

##### Statement of Contribution/Methods

Experiments were carried out in prostate tumour (PC3) xenografts grown in the hind leg of immunodeficient mice. Animals were treated with non-targeted or targeted (VEGFR-2 antibody-labelled) MicroMarker microbubbles (Visualsonics Inc.; Toronto, Canada). Bubbles were injected intravenously immediately before insonification at a dose of 1% of the animal blood volume. Ultrasound exposure consisted of 16-cycles tone burst at 500 kHz for 5 minutes and a 0.25% duty cycle, with a 2.86 cm element diameter ultrasound transducer. Tumours were then immediately exposed to a single radiation dose of 0, 2, 4, 8 or 16 Gy. Treatment response was evaluated using three-dimensional high-frequency power Doppler ultrasound 24 hour after treatment administration. A relative vascularity index (VI) was computed to determine relative changes in Doppler based blood measurements. Immunohistochemical ISEL and CD31 staining were used to assess overall tumour response.

**Results/Discussion**

Results demonstrate the potency of using targeted microbubbles over using regular microbubbles. In tumour treated with 2 Gy radiation only, we found an increase of 25% in relative VI. In contrast, animals treated with 2 Gy and non-targeted or targeted bubbles had a decrease of 8.6% and 56% in the VI, respectively. Overall, the use of targeted bubbles decreased the VI by a factor of 2.4 in comparison to non-targeted bubbles. ISEL-based cell death quantifications for the same conditions confirmed these results; tumours treated with non-targeted bubbles exhibited a 52% increase in cell death while those treated with targeted bubbles increased by up to 100% in cell death. These results indicate that modifying microbubbles to target VEGFR-2 is potentially more effective than using non-targeted microbubbles for endothelial radiosensitization. Our study is also the first to use MicroMarkers as radiosensitizing agents. The efficacy of these bubbles will be discussed in comparison to previously established Definity microbubbles.

**P1C10-5****Detection and Treatment Monitoring of Post-surgical Human Breast Tumors Using Harmonic Motion Imaging**

Yang Han<sup>1</sup>, Shutao Wang<sup>1</sup>, Elisa Konofagou<sup>1,2</sup>; <sup>1</sup>Biomedical Engineering, Columbia University, New York, New York, USA, <sup>2</sup>Radiology, Columbia University, New York, New York, USA

**Background, Motivation and Objective**

Breast cancer is the most common cancer and the second leading cause of cancer death among women. High-Intensity Focused Ultrasound (HIFU) techniques are slowly emerging as less invasive, but equally effective, in the treatment of early-stage breast cancer and benign tumor. To facilitate its translation to the clinic, there is a need for a simple, cost-efficient technique that can reliably monitor HIFU treatment. To this end, we employ the radiation-force-based technique of Harmonic Motion Imaging (HMI) that can be used seamlessly in conjunction with HIFU for tumor ablation monitoring, namely HMI for Focused Ultrasound (HMIFU).

**Statement of Contribution/Methods**

Specimen collection and handling of post-surgical breast tissues were approved by the Institutional Review Board (IRB) board of Columbia University and informed consent was obtained from all enrolled patients. HMIFU was performed in six normal, one benign (fibroadenoma) and four malignant (invasive ductal carcinoma (IDC)) tumors. The specimens were encased in a tissue-mimicking agar phantom and immersed in degassed PBS to better mimic *in vivo* environment. The HMIFU system consists of a 93-element, PZT-4 (focal depth = 7 cm) ceramic HIFU transducer confocally aligned with a 64-element phased array transducer to transmit and receive through a 4-board VDAS system. All HIFU channels were synchronously driven by a 25 Hz amplitude-modulated 4.5 MHz. signal. A 2D HMI raster scan was performed before and after thermal ablation using 1 s duration and an intensity of 2800 W/cm<sup>2</sup> *in situ*. For thermal ablation, the same intensity was applied with the duration increased to 120 s to generate the intended lesion.

**Results/Discussion**

After 2D raster scan, the 3D HMI displacement maps were reconstructed representing the relative stiffness of the breast tissue. The average peak-to-peak displacement in the ROI of the normal, fibroadenoma and IDC specimens were found to be 22.61±8.28 μm, 8.81±2.01 μm and 2.42±0.92 μm, respectively. Following ablation, the displacement was decreased by 57%, 35% and 28% in normal, fibroadenoma and IDC, respectively. The significant displacement differences between before and after thermal ablation in both normal and tumor specimens allowed for 3D HMI of the tumors during treatment in real-time as well as differentiation between the tumors and thermal lesions. HMI was experimentally shown to be capable of mapping and differentiating normal from pathological breast tissues as well as accurately quantifying the tumor or thermal lesion diameter when compared against pathology findings.

**P1C10-6****Harmonic Motion Imaging (HMI) and monitoring of HIFU treatment in real-time using diverging and plane wave**

Julien Grondin<sup>1</sup>, Shutao Wang<sup>1</sup>, Elisa E. Konofagou<sup>1,2</sup>; <sup>1</sup>Department of Biomedical Engineering, Columbia University, New York, NY, USA, <sup>2</sup>Department of Radiology, Columbia University, New York, NY, USA

**Background, Motivation and Objective**

Harmonic Motion Imaging for Focused Ultrasound (HMIFU) has recently been developed to perform and monitor ablation. An Amplitude-Modulated (fAM = 25 Hz) high-intensity focused ultrasound (HIFU) beam is used to induce a localized oscillatory motion at the focus which is simultaneously imaged by HMI. The feasibility of HMIFU in real-time using a 2-D system has recently been shown using a diverging wave to image the oscillatory motion. The objective of this study is to compare the performance of HMI displacement estimation using a diverging wave to that using plane wave imaging in order to achieve real-time capability with a 2D system when ablating canine livers *in vitro*.

**Statement of Contribution/Methods**

A 93-element HIFU transducer (fcenter = 4.5MHz) was used to induce a focal displacement while a coaxially-aligned 64-element phased array (fcenter = 2.5MHz) was operated using a Verasonics ultrasound system for radio-frequency (RF) channel data acquisition. A continuous 120-s HIFU excitation was performed on two canine liver specimens *in vitro* at 11 different locations total. An unfocused transmit sequence using a diverging wave (5 locations) or a plane wave (6 locations) was used to image the liver at 1000 frames/second. The beamforming was performed using a delay-and-sum algorithm by multiplying a reconstruction sparse matrix by the RF channel data matrix. The data were reconstructed at 80 MHz sampling frequency axially over a 90° angle field of view for the diverging wave and 20 mm width for the plane wave. In order to achieve real-time frame rates, the data reconstruction was performed on a Graphical Processing Unit (GPU). Axial HMI displacements were estimated from the reconstructed RF signals using 1-D normalized cross-correlation and streamed to a graphic user interface at a 1Hz display frame rate.

**Results/Discussion**

A localized oscillatory motion was observed at the focusing depth of 70 mm. For all ablation locations in the canine liver *in vitro*, an HMI peak-to-peak displacement decrease was observed between the beginning and the end of the ablation. The average peak-to-peak displacement decrease was (64.9±8.8%). The signal-to-noise ratio in the displacement map (SNRd) in the region of the focus at approximately 120 s was 22.3±13.3 for the diverging wave and 31.7±12.8 for the plane wave. These results show that HMIFU can provide real-time (1Hz) streaming of displacements simultaneously with HIFU treatment using a diverging wave or a plane wave. The SNRd was found to be 1.4 times higher using a plane wave than a diverging wave suggesting that plane wave is more applicable for HMIFU. Current ongoing studies include the translation of HMIFU in a clinical setting.

This study was supported by the National Institutes of Health (R01EB014496).

**P1C10-7****Low intensity continuous ultrasound to enhance the delivery of bisphosphonates in tumor cells.**

Sophie Tardoski<sup>1,2</sup>, Jacqueline Ngo<sup>1</sup>, Evelyn Gineys<sup>2</sup>, Philippe Cl  zardin<sup>2</sup>, David Melodelima<sup>1</sup>; <sup>1</sup>INSERM UMR1032, France, <sup>2</sup>INSERM UMR1033, France

**Background, Motivation and Objective**

Bisphosphonates are inhibitors of osteoclast-mediated bone resorption and stop the progression of established bone metastases. Bisphosphonates bind avidly to bone mineral, which limits their bioavailability and therefore their antitumor potential when used clinically. Low intensity ultrasound delivered in continuous mode can induce mild hyperthermia

as well as mechanical effects such as acoustic radiation force which are known to help the penetration of drugs into cells. Using a mouse model, we examined the feasibility of delivering bisphosphonates in bone metastases by low intensity continuous ultrasound. We present in vivo evidence that bisphosphonate is delivered in tumor cells by low intensity continuous ultrasound producing direct antitumoral effect.

### Statement of Contribution/Methods

A plane transducer working at a frequency of 2.9 MHz was used. Sonication was delivered in continuous mode for 30 minutes. In order to produce and maintain hyperthermia (between 42-43°C), the acoustic power was adjusted between 8 to 13 watts as a function of temperature. US treatments were performed each day for fifteen days. Bone metastases were created by injecting tumor cells into the tail artery of 54 mice. One clinical dose (0.1 mg/kg) of the bisphosphonate (zoledronic acid: ZOL) was administrated 18 days after tumor cell injection. Animals were randomly assigned to 4 groups (vehicle, ZOL, US, ZOL+US). Bone destruction, tumor volume, tumor angiogenesis and tumor proliferation were used as markers of the efficacy of the treatment. A marker of the penetration of ZOL into tumor cells (unprenylated Rap1A) was measured.

### Results/Discussion

With the acoustic parameters used, no detection of wideband emission and harmonics of the fundamental frequency considered as signatures of inertial and non-inertial cavitation were found. The temperature in tumors was  $42.0 \pm 2.8^\circ\text{C}$  during US treatment. No lesion was observed in surrounding tissues. US alone did not have any effect on bone metastasis and tumor outgrowth, compared with vehicle-treated animals. In sharp contrast, ZOL+US statistically significantly decreased bone destruction compared with ZOL alone. This difference was accompanied with a statistically significant reduction in the tumor volume compared with ZOL-treated mice, as determined by histomorphometry. Tumor angiogenesis and tumor cell proliferation were substantially reduced in ZOL+US groups. Analysis of bone marrow flush showed an increase of unprenylated Rap1A demonstrating a penetration of ZOL into the tumors due to US.

A single clinically relevant dose of ZOL produced meaningful antitumor effects in an animal model of bone metastasis, only when tumor-bearing mice were co-treated with low-intensity continuous ultrasound. Low intensity continuous ultrasound, without creating cavitation, facilitates the uptake of ZOL by tumor cells, thereby promoting its antitumor effects in vivo.

## P1C10-8

### Micro/Nanobubble-based Contrast-enhanced Ultrasound for Evaluating and Enhancing the Efficacy of Chemotherapeutics

Chung-Hsin Wang<sup>1,2</sup>, Hong-Jen Chiou<sup>3</sup>, Chih-Kuang Yeh<sup>1</sup>; <sup>1</sup>Department of Biomedical Engineering and Environmental Sciences, National Tsing Hua University, Taiwan, <sup>2</sup>Trust Bio-sonics, Inc., Taiwan, <sup>3</sup>Department of Radiology, Taipei-Veterans General Hospital, Taiwan

### Background, Motivation and Objective

During the past decade, microbubble-based ultrasound imaging technique has evolved from an investigational tool to a standard diagnostic procedure. Microbubbles show their capabilities in visualizing bloodstream which provides physicians to evaluate the blood perfusion of organs. However, there are seldom studies focusing on the evaluation of microcirculation of tumors because of the lack of a reliable bubble agent capable to defuse to higher interstitial fluid pressure areas. In this study, a micro/nanobubble agent was used to overcome the plight and investigate the usefulness of CEUS in osteosarcoma treatment.

### Statement of Contribution/Methods

The micro/nanobubble agent was obtained by cooperating with Trust Biosonics, Inc. (Hsinchu, Taiwan). The fabricated micro/nanobubbles have a mean size of 500 nm and the concentration of  $3 \times 10^{10}$  bubbles/mL. The drug-loaded micro/nanobubble was further prepared by mixing doxorubicin (DOX) with a specific lipid formulation in a concentration of 2 mg/mL under 60°C for 30 min before being activated to bubble solution. Cultured MG63 human osteosarcoma cells implanted into Nude mice in tibia site were used as the tumor model. The 3-MHz ultrasound insonations combined with DOX-loaded micro/nanobubble (DOX-MB) administration was delivered to locally release the drugs and facilitate the drug permeability of tumor. The tumor perfusion before and after the treatment was evaluated by three-dimensional power Doppler and contrast harmonic imaging techniques (CHI) (Aplio500, Toshiba, Japan) using a live 4D transducer (14-MHz). The color flow, contrast flow and volume of tumor were analyzed. Three experimental groups including control, DOX-MB without, and with ultrasound-triggered release were comprised for the comparisons.

### Results/Discussion

Firstly, we demonstrated that the bubble agent is capable to enhance the Doppler power of tumor vessels. The administration of micro/nanobubbles clearly performed the trend of tumor angiogenesis and perfusion. However, microcirculation or small vessels were hard to be detected under Doppler mode due to the effect of bubble destruction ( $MI=0.4$ ). Through the use of ultra-low MI CHI mode ( $MI=0.07$ ), the perfusion information could be further evaluated. With the administration of DOX-MB, ultrasound insonations enhanced the DOX molecules release. The tumor volume suppression was 2.82-fold increase compared with the group without ultrasound insonations. The introduction of DOX-MB and ultrasound insonations led to the substantial necrosis of osteosarcoma tumor in day 5 after treatment. The mean contrast flow dropped to 24.6% compared with the flow before the treatment. The results revealed that the micro/nanobubbles can be applied as a multi-functional agent for cancer diagnosis and therapy, and the use of 4D CHI technique provided a convenient tool to evaluate the tumor therapeutic outcome and might help for tumor treatment planning and new drug discovering.

## P1C10-9

### Spatial and temporal control of hyperthermia using real time thermal strain imaging with motion compensation

Josquin Foiret<sup>1</sup>, Dustin E. Kruse<sup>1</sup>, Katherine W. Ferrara<sup>1</sup>; <sup>1</sup>Department of Biomedical Engineering, University of California, Davis, CA, USA

### Background, Motivation and Objective

In previous work by our group, control of mild hyperthermia was achieved using a proportional-integral-derivative (PID) loop with thermocouple measurements used for temperature feedback [1]. Despite good temporal control, this method was limited by the fact that temperature was measured only at the thermocouple position. In this work, real time thermal strain imaging with motion compensation was implemented to control and maintain temperature elevation in a phantom. This enhanced method provides useful spatial information for controlling mild hyperthermia, particularly for temperature-sensitive drug delivery studies.

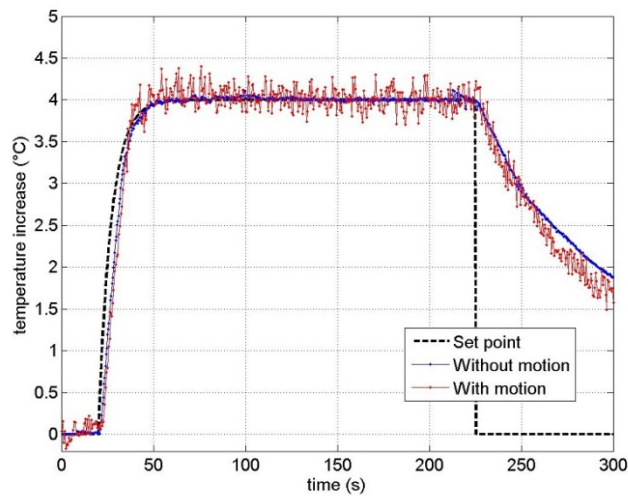
### Statement of Contribution/Methods

A single element transducer (IL0508HP, Valpey-Fischer, MA) was used to generate and maintain a 4°C increase in an agarose-based tissue mimicking phantom. RF data were acquired with a Verasonics V1 system with a 5 MHz 128-element transducer (L7-4, Philips ATL, WA). The imaging probe was placed above the focal spot at 90° from the heating transducer axis and mounted on a 2D linear stage to simulate a periodic motion in the imaging plane. Thermal strain was calculated in real time using 2D speckle tracking routines. The algorithm compares the last recorded frame to a buffer of reference frames acquired during motion before heating, as proposed in [2]. Control of the thermal dose was achieved with a PID loop using an algorithm and parameters that are similar to [1] while a 1 mm<sup>2</sup> region of interest centered on the focal spot was used to assess temperature.

### Results/Discussion

After optimization of the PID gains, temperature elevation without probe motion was maintained within  $\pm 0.1^\circ\text{C}$  of the set temperature at a frame rate of 4 Hz. With diagonal motion of the imaging probe (3 mm lateral and 1 mm axial displacement) with a 0.5 Hz periodicity, control of hyperthermia was achieved within  $\pm 0.3^\circ\text{C}$  of the set temperature. Motion introduced noise with a temperature standard deviation of  $\sim 0.1^\circ\text{C}$ . Thus, this method provides an accurate spatial and temporal estimation of the temperature in presence of motion and allows efficient control of the thermal dose. Studies of performance in the presence of complex motion and extensions to a multi-frequency array are underway.

- [1] D. E. Kruse *et al.*, IEEE TBE, 57(1), 2010.  
 [2] Simon *et al.*, Proc. SPIE 3249, 1998.



P1C10-10

### Real-time Localized Motion Imaging for Coagulation Monitoring using Acoustic Radiation Force

Ryusuke Sugiyama<sup>1</sup>, Takashi Azuma<sup>1</sup>, Ryosuke Aoyagi<sup>1</sup>, Keisuke Fujiwara<sup>2</sup>, Hideki Takeuchi<sup>1</sup>, Hiroki Shimidzu<sup>1</sup>, Kazunori Itani<sup>2</sup>, Kiyoshi Yoshinaka<sup>3</sup>, Akira Sasaki<sup>1</sup>, Shu Takagi<sup>1</sup>, Yoichiro Matsumoto<sup>1</sup>; <sup>1</sup>The University of Tokyo, Tokyo, Japan, <sup>2</sup>Hitachi Aloka, Japan, <sup>3</sup>Advanced Industrial Science and Technology, Japan

#### Background, Motivation and Objective

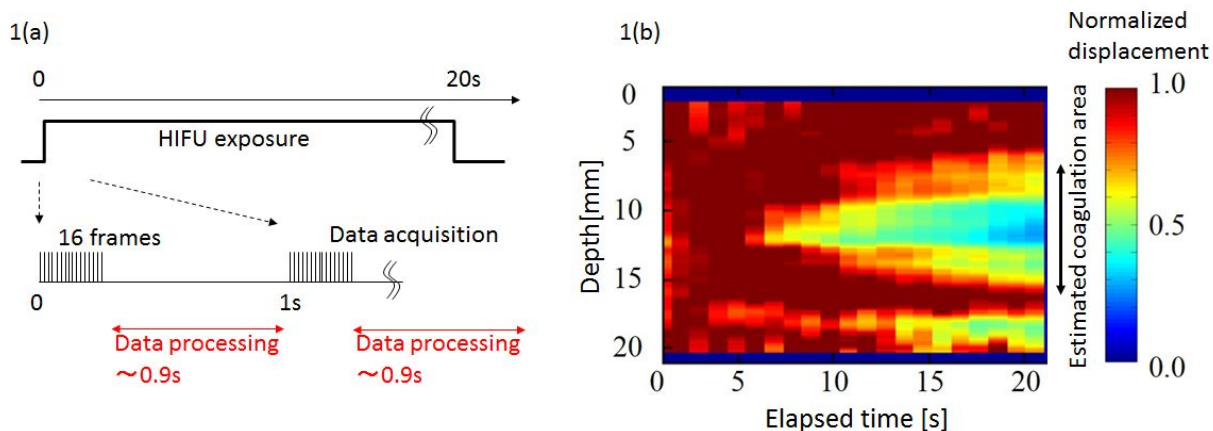
Localized Motion Imaging (LMI) to detect stiffness change caused by High Intensity Focused Ultrasound (HIFU) is described. In LMI, we used an amplitude-modulated (AM) HIFU to generate localized tissue oscillation caused by acoustic radiation force at the focal point. By measuring the amplitude ratio of tissue oscillation before and after coagulation, we can detect the thermal coagulation area. In our previous study, the sufficient sensitivity and resolution of LMI using the optimal AM frequency matching with its coagulation size was clearly demonstrated. In this study, we constructed on-line LMI system to realize a real-time monitoring.

#### Statement of Contribution/Methods

In the calculation process of LMI, a computation of cross correlation to detect the focal tissue motion is the most time-consuming process. Whereas a frame sampling speed to observe the tissue motion should be higher than AM frequency, the expansion speed of coagulated area during HIFU treatment is in the order of second. We construct a monitoring sequence as shown in Fig. 1a in view of above mentioned. 16-frames RF data obtained by an Ultrasound scanner are acquired within 0.05 s in every 1 s. A ring buffer memory is constructed in our prototype system to access a part of RF data during RF data storing process. In this condition, available the computation time for cross correlation is about 0.9 s. We used porcine liver samples as tissue samples. HIFU and AM frequencies were 2.2 MHz and 168 Hz, respectively. The HIFU intensity for heating was 1.2 kW/cm<sup>2</sup> with exposure time of 20 s.

#### Results/Discussion

Average and the maximum computation time for LMI were 0.6 and 0.85 s, respectively. The coagulated area in LMI obtained by this real-time prototype system is clearly imaged as shown in Fig. 1b. The expansion of coagulated area in the time axis during HIFU ablation is also observed in this figure. This temporal resolution is expected to be sufficient to realize a feedback control for coagulation size control. Such system is being constructed and its result will be reported in the conference.





## The role of cavitation in the ultrasonic atomization of liquids and tissues

Juliana Simon<sup>1</sup>, Oleg Sapozhnikov<sup>1,2</sup>, Vera Khokhlova<sup>1,2</sup>, Yak-Nam Wang<sup>1</sup>, Lawrence Crum<sup>1</sup>, Michael Bailey<sup>1</sup>; <sup>1</sup>Center for Industrial and Medical Ultrasound, Applied Physics Laboratory, University of Washington, Seattle, Washington, USA, <sup>2</sup>Department of Acoustics, Physics Faculty, Moscow State University, Moscow, Russian Federation

### Background, Motivation and Objective

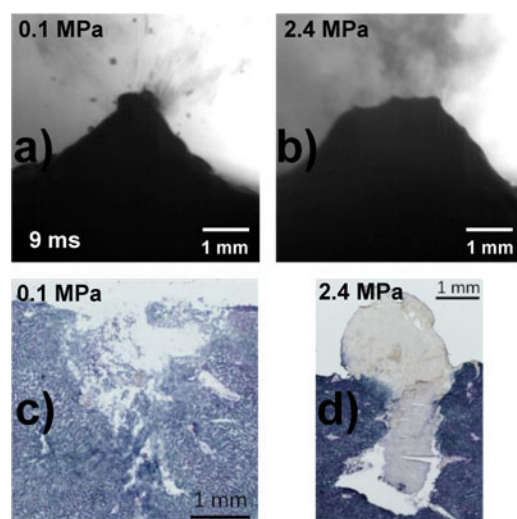
Ultrasonic atomization, or the emission of a fine spray of droplets, is currently used commercially in air humidifiers, medical nebulizers, and was recently proposed to explain tissue fractionation in boiling histotripsy. Yet even though ultrasonic atomization of liquids has been well-known since 1927, there is still some debate as to the exact mechanism, particularly the contribution of bubbles to atomization. Our objective is to test the role of cavitation in the atomization of liquids and tissues by suppressing bubble activity with overpressure.

### Statement of Contribution/Methods

An overpressure chamber that used compressed air to reach pressures up to 6.9 MPa was used. A 2-MHz aluminum-lensed focused transducer operating at linear *in situ* intensities up to 22 kW/cm<sup>2</sup> ( $p_+ = 67.4$  MPa,  $p_- = 16.4$  MPa) was built into the bottom of the chamber and focused at the water-air or *ex vivo* bovine liver-air interface. Atomization was filmed with a high speed camera (resolution  $\approx 20$   $\mu$ m). At the end of 60, 10-ms exposures repeated at 1 Hz, liver samples were collected for histology.

### Results/Discussion

In water, at a linear intensity of 850 W/cm<sup>2</sup> ( $p_+ = 5.5$  MPa,  $p_- = 4.5$  MPa), atomization arose from a fountain at atmospheric pressure and was very dramatic, with droplets ranging in size from 20-370  $\mu$ m emitted at 2-8 m/s. As the pressure increased to 3.4 MPa, the fountain became a drop-chain and fewer droplets of 100-200  $\mu$ m were emitted at 2-3 m/s. At 6.9 MPa, a drop-chain fountain formed, but no droplets were emitted. In bovine liver, at atmospheric pressure a mound formed and droplets were ejected ranging in size from 20-180  $\mu$ m at 5-7 m/s leaving a hole in the tissue surface (fig. 1a,c). However, at 1.4 MPa, atomization was qualitatively different; uniformly fine droplets ( $\approx 20$   $\mu$ m in size) were emitted at 2-3 m/s (fig. 1b). Histologically, we found that overpressure caused tissue just below the surface and in the mound to be thermally necrosed (fig. 1d). For pressures up to 3.4 MPa, the tissue in the mound was fractionated before thermal necrosis and a hole was observed beneath the tissue surface; the hole disappeared at 6.9 MPa. Evidence from both water and bovine liver indicate that cavitation is necessary in atomization; however, in *ex vivo* tissue, suppression of cavitation transforms tissue fractionation to thermal necrosis at these settings [Work supported by NIH (EB007643, DK043881) and NSBRI through NCC 9-58].



## P1C11 - MTH: Treatment Monitoring and Novel Applications

Salon C

Saturday, September 6, 2014, 8:00 am - 5:00 pm

Chair: **Ralf Seip**  
*Philips Research, Briarcliff Manor*

P1C11-1

### Imaging the microvascular response to ultrasound-stimulated therapy in a preclinical animal model of breast cancer

Anna Sorace<sup>1</sup>, Kenneth Hoyt<sup>2</sup>; <sup>1</sup>University of Alabama at Birmingham, Birmingham, USA, <sup>2</sup>University of Alabama at Birmingham, Birmingham, Alabama, USA

#### Background, Motivation and Objective

Ultrasound (US)-stimulated therapy has been shown beneficial for improving drug delivery in solid tumors; however there are potential bioeffects that can compromise efficacy. The purpose of this study was to evaluate the temporal response of tumor microvasculature to US-stimulated therapy using multimodal imaging methods.

#### Statement of Contribution/Methods

Tumor bearing mice (N = 32) underwent US-stimulated therapy using a custom system by exposing systemically circulating microbubbles (MBs, Definity) to acoustic pressures of 0 MPa (control), 0.75 MPa (low) or 3.75 MPa (high) during US treatment (frequency of 2.25 MHz, pulse repetition period of 15 sec, 5% duty cycle, 5 min duration). Mice were imaged at baseline, 20 min, and 24 h after application of US-stimulated therapy with multimodal imaging methods to evaluate the tumor and microvascular response to US-stimulated therapy exposure. The use of contrast-enhanced T1-weighted MR imaging allowed the evaluation of vascular permeability whereas dynamic contrast-enhanced US imaging was used to detect changes in tumor perfusion. Immunohistologic assays at 24 h evaluated intratumoral microvessel density (MVD), vascular hemorrhage, inflammation, apoptosis, and stress levels.

#### Results/Discussion

At 20 min following exposure to high pressure US-stimulated therapy, tumor perfusion changed by -13.1% (p = 0.71) compared to baseline measures whereas use of low acoustic pressures during US therapy increased tumor perfusion by 137.6% (p = 0.04). Changes in tumor perfusion at 24 h following US-stimulated therapy using high and low acoustic pressures were -60.5% (p = 0.06) and 12.4% (p = 0.72), respectively. MR imaging at 20 min and 24 h after applying high pressure US-stimulated therapy revealed a -71.3% and -64.9% change in vascular permeability, respectively, at the tumor site (p < 0.01). For tumors exposed to low pressure US therapy, vascular permeability changed by 132.0% and 43.6% at the 20 min and 24 h measurement times, respectively (p > 0.37). No significant changes in either tumor perfusion or vascular permeability due to sham US therapy were observed (p > 0.53). Review of H&E tissue sections revealed 2-fold (p = 0.43) and 5-fold (p = 0.09) increases in vascular hemorrhage in tumors exposed to low and high pressure US-stimulated therapy compared to control tumors, respectively. Further analyses demonstrated no differences in tissue inflammation, stress, or apoptosis levels for tumors exposed to US or sham therapy (p > 0.77). MVD levels were lower in tumor exposed to high pressure US-stimulated therapy compared to control tumor measures (p = 0.14) whereas tumors exposed to low pressure US therapy produced a slight increase in MVD levels (p = 0.35). This study helps further validate the use of low-pressure US-stimulated therapy for the effective and safe delivery of systemic drugs as well as confirming the limitations of this technology when using higher US pressures for the same therapeutic goal.

P1C11-2

### A Mechanism of Ultrasound Balloon Rupture for Fetal Surgery

Tomoo Sato<sup>1</sup>, Shunsuke Osawa<sup>2</sup>, Hiromasa Yamashita<sup>1</sup>, Hiroshi Ohtake<sup>3</sup>, Jun Yonai<sup>3</sup>, Hiroyasu Sasaki<sup>4</sup>, Takashi Mochizuki<sup>5</sup>, Toshio Chiba<sup>1</sup>; <sup>1</sup>Division of Medical Device, National Center for Child Health and Development, Japan, <sup>2</sup>Division of Pediatric Surgery, Showa University, Japan, <sup>3</sup>Japan Broadcasting Corporation, Japan, <sup>4</sup>nac Image Technology Inc., Japan, <sup>5</sup>Medical Ultrasound Laboratory, Japan

#### Background, Motivation and Objective

Fetal Endoscopic Tracheal Occlusion (FETO) with a balloon is a standard treatment for the fetus with defected diaphragm which is called Congenital Diaphragmatic Hernia (CDH). Because, without removal of the balloon, newborn is suffocated and cannot survive, the second operation must be done to remove the balloon just before birth. Our motivation is to replace the operation procedure for balloon removal with the ultrasound balloon rupture. We have demonstrated the feasibility of the ultrasound balloon rupture in the animal experiment. The objective of our study is to investigate the mechanism of the ultrasound balloon rupture for the establishment of a safe and reliable procedure.

#### Statement of Contribution/Methods

The silicon tube (φCON® SH No.7, Fuji Systems, Japan) was used as a model for the trachea. The internal diameter of the tube is 7mm. The balloon (GOLDBAL2, BALT Extrusion, France) and the tube were immersed in degassed water (<3mg/L). The balloon was filled up with 0.5mL-nanodroplets (PCND-US-100LG, HITACHI, Japan). The nanodroplets are gasified by high intensity ultrasound. The size of inflated balloon was Ø7 x 20mm. The HIFU irradiation was performed by specially designed ring transducer. The transducer generated 1MHz HIFU. The beam diameter at the focus is 2mm, and I<sub>SATA</sub> is 3 kW/cm<sup>2</sup>. The focus of HIFU was set on the bottom of the balloon. Using high speed camera (HX-3, nac Imaging Technology Inc., Japan), 40,000 fps images were captured for 2 seconds.

#### Results/Discussion

The results are shown in Fig. 1. HIFU irradiation was done twice. In second irradiation, the balloon was ruptured. The rupture began from the point away from the focus. In first irradiation, the balloon was not ruptured, however, the following changes were observed.

- (1) The balloon length was increased by the irradiation.
- (2) The color of the solution inside the balloon became muddy white.
- (3) Just after the irradiation, a lot of small bubbles were recognized at upper surface of the balloon.

We speculate the balloon rupture mechanism as follows.

- (1) The nanodroplets inside the balloon were gasified and boiled by HIFU irradiation.
- (2) The internal pressure of the balloon increased.
- (3) Finally, the balloon was ruptured at the point where was different from the focus.

Our results demonstrated the feasibility of novel HIFU treatment, which does not use thermal or cavitation effect.

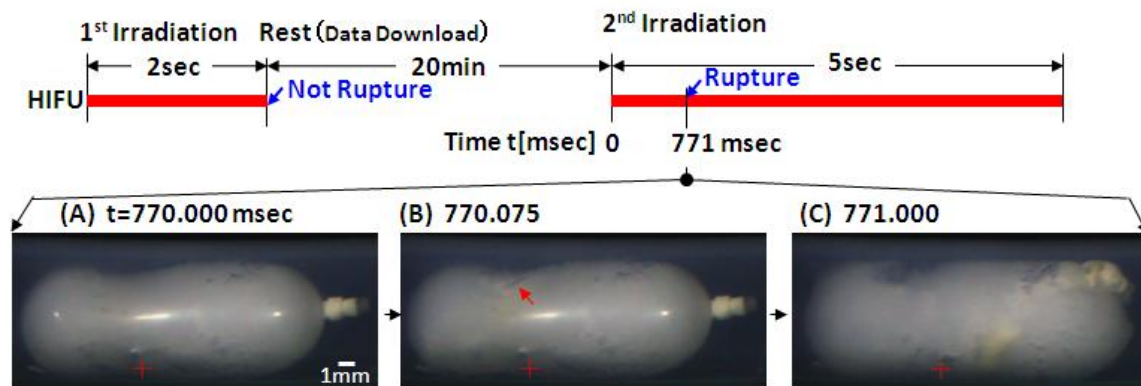


Fig. 1 High Speed Camera Pictures

+ : Focus of HIFU. The focus was set on the bottom of the balloon.  
 ↗ : Front line of rupture

P1C11-3

### Application of High Intensity Focused Ultrasound to Tissue Engineering for Local Modulation of Properties

Adam Nover<sup>1</sup>, Yang Han<sup>1</sup>, Shutao Wang<sup>1</sup>, Gerard Ateshian<sup>1,2</sup>, Clark Hung<sup>1</sup>, Elisa Konofagou<sup>1,3</sup>; <sup>1</sup>Biomedical Engineering, Columbia University, New York, New York, USA, <sup>2</sup>Mechanical Engineering, Columbia University, New York, NY, USA, <sup>3</sup>Radiology, Columbia University, New York, New York, USA

#### Background, Motivation and Objective

High Intensity Focused Ultrasound (HIFU) is a non-invasive, non-contact, low cost modality for inducing thermal elevations deep within tissues. It is FDA approved for uterine fibroid ablation, and research is currently underway to apply it to tumor ablations. While these applications concern relatively large, dense in vivo tissues, here HIFU is investigated as a potential tool for precise alteration of spatial properties within tissue engineered constructs while growing in vitro [1]. Such an instrument could greatly impact the engineering of many different tissues; here, the objective of this abstract is to demonstrate feasibility through the framework of engineering articular cartilage grafts, a potential osteoarthritis treatment alternative to allografts. Specifically, in vitro introduction of a biomimetic subchondral plate, the virtually impermeable bone-cartilage interface responsible for interstitial fluid pressurization and thus load-bearing and lubrication, could result in a more robust construct without blocking nutrient transport during critical growth periods.

#### Statement of Contribution/Methods

Consistent with past studies, 2% w/v agarose gels, (acellular or containing 30 million chondrocytes/mL) were cast either as a slab then punched into disks or atop porous metal bases (osteocondral, OC constructs) [2]. Albumin was incorporated into gels as in HIFU phantoms; its denaturation provides visualization and stiffening. Transport effects were investigated by treating acellular gels with HIFU (using system described in [3]), soaking them in 0.5 mg/mL 70 kDa fluorescein-conjugated dextran, and then imaging. Cellular OC constructs were HIFU-treated in a custom sterile apparatus, then monitored in culture.

#### Results/Discussion

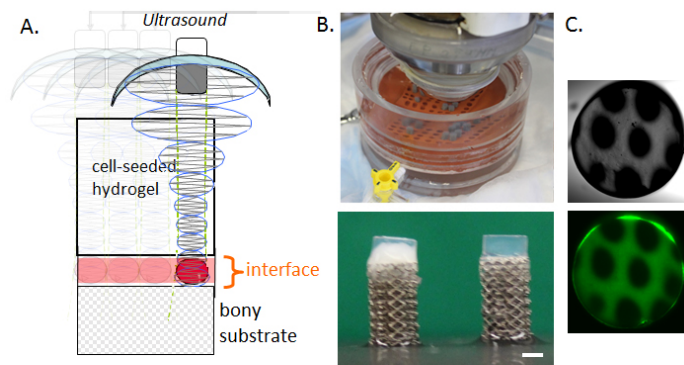
Thermally affected areas occluded dextran, indicating decreased transport. HIFU-treated OC constructs continued to grow to similar to controls without compromised sterility. These studies bolster previous work, promoting feasibility of HIFU for altering local properties in engineered constructs under aseptic conditions. Future studies will focus on HIFU's effects on the OC interface and monitoring of tissue growth via Harmonic Motion Imaging.

1 Nover+ Tissue Eng 2014 (Submitted)

2 Lima+ Biomaterials 2008

3 Maleke+Konofagou Phys Med Biol 2008

Support: NIAMS AR046568-12, AR060361-04, NIH R21 EB014382-01A1.



A. Schematic of HIFU treatment on osteochondral interface. B. Sterile holding chamber (top) and osteochondral constructs with (bottom left) internal denatured albumin (bottom right). C. Transmitted light (top) and fluorescence (bottom) images of constructs with corresponding HIFU-treated zones (darkness).

P1C11-4

#### Extracorporeal Acute Cardiac Pacing by High Intensity Focused Ultrasound

Amit Livneh<sup>1</sup>, Eitan Kimmel<sup>1</sup>, Dan Adam<sup>1</sup>; <sup>1</sup>Biomedical Engineering, Technion - Israel Institute of Technology, Haifa, Israel

##### Background, Motivation and Objective

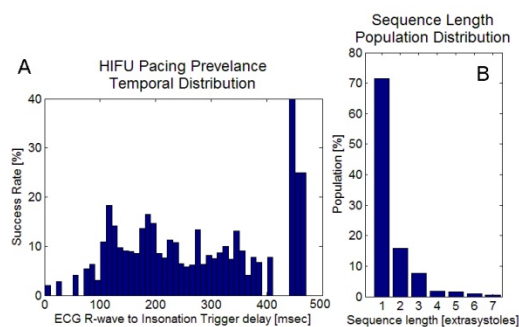
An experimental system for ultrasonic (US) pacing is presented. Two clinical applications in which noninvasive acute cardiac US pacing may be valuable are: (1) preoperative patient screening in cardiac resynchronization therapy surgery; (2) Emergency life support, following an event of sudden cardiac arrest. Yet, the compounded motion due to the cardiac and respiratory cycles requires adequate spatiotemporal control so that insonation is applied when the myocardium is at the acoustic focus.

##### Statement of Contribution/Methods

Autonomously breathing anesthetized whole rats were paced by bi-stage US insonation patterns. First, accentuated rarefaction was applied to induce cavitation; immediately later accentuated condensation was applied to enhance tissue deflection. Pacing was synchronized to ECG and respiration, using real-time vital-signs monitoring and US imaging. Respiration gating was applied to enable pacing at expiration, to mitigate breath related motion. Online US imaging was used for guidance, and its recordings were used for result analysis. This allowed to study the success rate of premature ventricular contractions (PVCs) generation at different timing post ECG R-wave, during the expiration period.

##### Results/Discussion

US PVC induction was maintained for durations longer than 50 minutes in autonomous breathing rats; while no arrhythmias were observed. Spatially focusing the beam at different locations allowed cumulative coverage of the whole left ventricle. Triggering insonation at different delays from the preceding ECG R-wave demonstrated successful US pacing induction from mid ECG T-wave till the next ECG complex's PR interval. The weighted average success rate of US pacing attempts triggered at delays 100-400msec after ECG R-wave (Panel A), was  $11.62 \pm 3.5\%$ ; significantly higher than 4.5%, which is the highest mean US PVC induction rate previously reported in rats. The observed PVC sequences distribution (Panel B) is suggested to resemble a negative binomial distribution, summing up successes PVCs until the first failure ( $r=1$ ). The prevalence of the 2-7 consecutive paced beats sequences suggests a mechano-electric capture rate of approximately 50%. Analysis of the acoustic wave patterns and temporal characteristics of paced PVCs is suggested to provide new insight into the mechanisms of US cardiac pacing.



P1C11-5

#### Real-time Feedback of Histotripsy Thrombolysis using Bubble-induced Color Doppler

Xi Zhang<sup>1</sup>, Ryan M. Miller<sup>1</sup>, Adam D. Maxwell<sup>1</sup>, Charles A. Cain<sup>1</sup>, Zhen Xu<sup>1</sup>; <sup>1</sup>Department of Biomedical Engineering, University of Michigan, Ann Arbor, MI, USA

##### Background, Motivation and Objective

Histotripsy thrombolysis is a noninvasive, drug-free and image-guided technology that fractionates blood clots using well-controlled acoustic cavitation alone. Real-time quantitative feedback is highly desired during histotripsy thrombolysis treatment to monitor the progress of clot fractionation, improve efficacy and reduce hemolysis. Bubble-induced color Doppler (BCD) monitors coherent motions following each histotripsy pulse. This bubble-induced motion has been shown in gel and ex vivo liver tissue to be correlated with histotripsy fractionation. In this paper we investigate the potential of BCD to monitor histotripsy thrombolysis in real-time.

# Statement of Contribution/Methods

First, the correlation between the degree of histotripsy thrombolysis and BCD feedback was investigated using a three-layer fibrin clot, with two layers of transparent fibrin clot and a thin central layer mixed with red blood cells (RBC). The clot fractionation was monitored by high-speed optical imaging, as the central RBC layer turned from opaque to translucent when fractionated. BCD feedback data were collected simultaneously during treatment, from which two metrics were extracted: time of peak rebound velocity (tPRV) and focal mean velocity at a fixed delay (V<sub>f, delay</sub>). Second, to validate the BCD feedback in ex vivo clots, debris volume from histotripsy thrombolysis were obtained at different therapy doses and compared with V<sub>f, delay</sub>. Finally, the ability of real-time BCD monitoring was tested in the three-layer fibrin clots.

# Results/Discussion

First, a strong correlation existed between the degree of histotripsy clot fractionation and tPRV (Fig 1a) and V<sub>f, delay</sub> (Fig 1b). The saturation point of clot fractionation (i.e., treatment completion) matched well with the saturation points detected using tPRV (mean difference: 28 pulses) and V<sub>f, delay</sub> (mean difference: 43 pulses). The mean Pearson correlation coefficients between the progressions of clot fractionation and the two BCD metrics were 93.1% and 92.6%. Second, the trends of debris growth and V<sub>f, delay</sub> from BCD also match well (Fig 1c). Finally, we were able to use V<sub>f, delay</sub> from BCD to accurately monitor clot fractionation at 30Hz frame rate, which is sufficient for histotripsy treatment. This work demonstrated the potential of BCD to real-time monitoring histotripsy thrombolysis treatment.

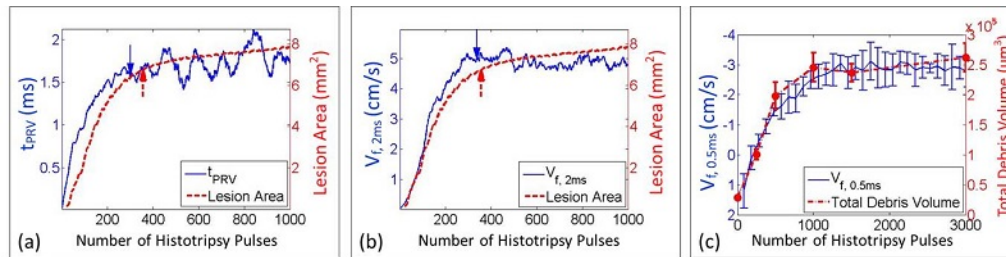


**Fig1:** (a) Representative progressions of lesion formation and the corresponding t<sub>PRV</sub> of BCD feedback (b) The same progression of lesion formation and the corresponding V<sub>f, delay</sub> of BCD feedback. The arrows show the saturation doses of the curves. (c) The growth of debris volume and the averaged trend of V<sub>f, delay</sub> over all ex vivo clot treatments.

P1C11-6

# Sonoreperfusion Efficacy is Greater With Venous Thrombi Compared to Arterial Thrombi in an In Vitro Model of Arteriolar Microvascular Obstruction

John Black<sup>1</sup>, Rick Schnatz<sup>2</sup>, Francois Yu<sup>2</sup>, Xucai Chen<sup>2</sup>, Flordeliza Villanueva<sup>2</sup>, John Pacella<sup>2</sup>; <sup>1</sup>University of Pittsburgh School of Medicine, Pittsburgh, Pennsylvania, USA, <sup>2</sup>Heart and Vascular Institute, University of Pittsburgh Medical Institute, Pittsburgh, Pittsburgh, USA

# Background, Motivation and Objective

Distal embolization of microthrombi during stenting for myocardial infarction (MI) causes microvascular obstruction (MVO). We showed that microbubble (MB)-mediated ultrasonic (US) therapy (sonoreperfusion [SRP]) resolves MVO from venous microthrombi in vitro. However, arterial thrombi that embolize during stenting are mechanically distinct from venous clot and may require different US parameters for SRP. In an in vitro model of MVO, we tested the hypothesis that compared to venous microthrombi, arterial microthrombi require higher energy US for SRP.

# Statement of Contribution/Methods

Lipid MB in plasma with blood viscosity were passed through 4mm tubing (1.5 mL/min) with a 40 μm pore mesh to simulate a microvascular cross-section; upstream pressure reflected thrombus burden. Arterial microthrombi were formed under high shear with a Chandler loop. Venous microthrombi were made statically. We occluded the mesh with microthrombi until upstream pressure reached 40 ± 5 mmHg to simulate MVO. US (1 MHz, 5000 cycles, 0.33 Hz PRF, 0.6-1.5MPa peak negative pressure (P<sub>-</sub>) was delivered with a focused single element transducer (-3 dB beam width 2.5 mm focus) for 20 min. Pressure vs time slope for initial 3 min was defined as the lytic rate. MB activity was recorded with a passive cavitation detector (PCD) (center F= 3.5 MHz). Total energy between 3.2-3.8 MHz was defined as inertial cavitation (IC) dose.

# Results/Discussion

Arterial thrombi had fewer RBC, more platelets, and denser fibrin vs venous thrombi. PCD showed a combination of stable cavitation (SC) and IC, with subharmonic and ultraharmonic peaks and broadband emission. IC dose increased with increasing P<sub>-</sub> (10 mV2 ms for 0.6 MPa, 33 mV2 ms for 1.5 MPa). Residual upstream pressure after 20 min at P<sub>-</sub> of 0.6 MPa was greater (13 ± 1 venous vs 32 ± 2 mmHg arterial, p<0.01, Fig 1), and lytic rate was less with arterial microthrombi (7 ± 1 venous vs 3 ± 2 mmHg/min arterial, p<0.01). With P<sub>-</sub> of 1.5 MPa, residual upstream pressure decreased but was greater with arterial microthrombi (1 ± 0 venous vs 3 ± 1 mmHg arterial, p<0.01) and lytic rate increased, but was lower with arterial (12 ± 1 venous vs 8 ± 2 mmHg/min arterial, p=0.02). Thus, for a given P<sub>-</sub>, greater SRP was achieved with venous microthrombi, suggesting that higher US energy is needed for treatment of arterial MVO. These data have implications for optimization of SRP to treat MVO in the setting of MI.



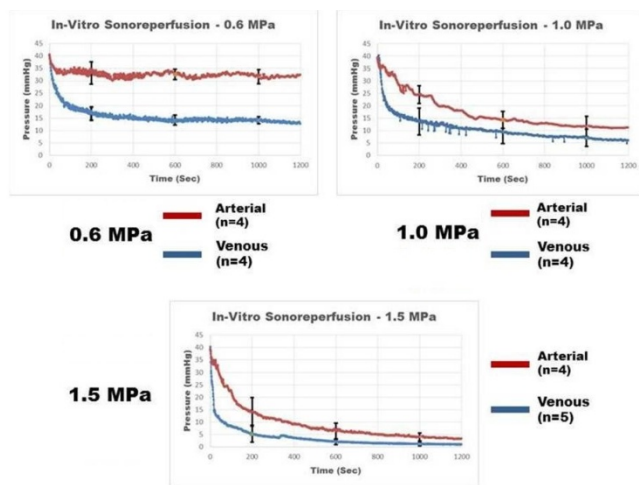


Figure 1. Pressure upstream of mesh obstructed with arterial and venous microthrombi during 20 minutes of therapy with microbubbles and ultrasound at different acoustic pressures.

P1C11-7

### Enhancement of Direct Brain Infusion with Focused Ultrasound and Microbubbles

Shutao Wang<sup>1</sup>, Tao Sun<sup>1</sup>, Oluwemi Olumolade<sup>1</sup>, Gesthimani Samiotaki<sup>1</sup>, Elisa Konofagou<sup>1,2</sup>, <sup>1</sup>Biomedical Engineering, Columbia University, USA, <sup>2</sup>Radiology, Columbia University, USA

#### Background, Motivation and Objective

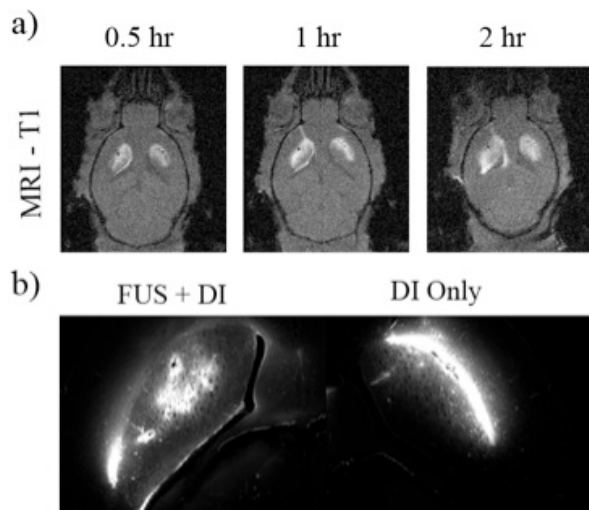
Direct infusion (DI) to the brain is widely used in pre-clinical and clinical settings for the treatment of Central Nervous System (CNS) diseases. Therapeutic agents are infused to the targeted locations via a fine needle or cannula through a small opening on the skull. Although this technique can circumvent the blood-brain barrier (BBB), efficient agent diffusion is often limited by the relatively high interstitial fluid pressure. Focused ultrasound (FUS) in combination with microbubbles has been shown to be capable of non-invasively disrupting the BBB. The goal of this study is to investigate if FUS pre-treatments can be used to enhance diffusion efficiency of DI to the brain in vivo.

#### Statement of Contribution/Methods

Each animal received four sonications (1 mm apart) using a single element FUS transducer (center frequency 1.5 MHz) at the targeted region (caudate-putamen). The acoustic parameters used for sonications are: peak rarefactional pressure 0.45 MPa, pulse length 6.7 ms, pulse repetition frequency 5 Hz, and a duration of 60 s. In-house made polydisperse microbubbles ( $\sim 2.5 \times 10^7$  #/animal) were injected immediately prior to sonications via the tail vein. Upon completion of the sonication, two holes were drilled on each side of the skull and 0.75  $\mu$ l gadolinium-labeled albumin (74 kDa) was infused via a 34G Hamilton needle. The infusion coordinates (in reference to bregma) are: AP +0.5 mm; ML  $\pm$  2.3 mm; DV +3 mm. A 9.4 T magnetic resonance imaging system was used to image the distribution of the MRI contrast agent at 0.5, 1, and 2 hr points. Animals were sacrificed at 2.5 h and brains were sectioned at 60  $\mu$ m for fluorescent imaging.

#### Results/Discussion

As shown in the T1-weighted MR images (Fig a), both FUS pre-treated side (left) and the direct infusion only side (right) showed increased diffusion over time. Nonetheless, the BBB-opened region exhibited approximately 1.5 times larger diffusion area compared to the contralateral side. This is also demonstrated in the fluorescence images (Fig b), where the fluorescently labeled MR contrast agent diffused away from the injection site, to cover most of the caudate-putamen. Preliminary findings from this study have shown the capability of FUS-induced BBB opening to assist established but limited drug delivery techniques such as direct infusion and convection-enhanced delivery to the brain for more effective drug delivery.



## Frequency-controlled fragmentation of renal calculi by burst wave lithotripsy

Adam Maxwell<sup>1</sup>, Oleg Sapozhnikov<sup>2</sup>, Bryan Cunitz<sup>2</sup>, Ryan Hsi<sup>1</sup>, Jonathan Harper<sup>1</sup>, Mathew Sorensen<sup>1</sup>, Michael Bailey<sup>2</sup>, Wayne Kreider<sup>2</sup>; <sup>1</sup>Urology, University of Washington School of Medicine, Seattle, WA, USA, <sup>2</sup>Center for Industrial and Medical Ultrasound, Applied Physics Laboratory, University of Washington, Seattle, WA, USA

### Background, Motivation and Objective

Shock wave lithotripsy is the most common procedure for treatment of renal calculi despite increasing adoption of alternative endoscopic techniques. Shock wave lithotripsy can result in incomplete treatment of stones, leaving large fragments that are not easily passed from the kidney collecting system. We are developing a new noninvasive method of stone fracture that applies sinusoidal focused ultrasound bursts – i.e., burst wave lithotripsy (BWL). This study presents theoretical and experimental investigations of the ability to control the size of fragments produced with BWL.

### Statement of Contribution/Methods

Cylindrical artificial stones (6 mm diameter x 10-12 mm length) and four types of natural kidney stones (5-15 mm largest dimension) were exposed to BWL. Focused ultrasound transducers with operating frequencies of 170, 285, and 800 kHz were used, driven by a high-voltage radiofrequency amplifier. Stones were exposed in a fixed position in a degassed water bath to 10-cycle bursts delivered at a rate of 200 per second with peak focal pressure 6.5 MPa. After exposure, fragments were passed through a series of sieves to determine their size distribution for each exposure. To complement experiments, a linear-elastic finite-difference model was used to simulate the interaction of an ultrasound burst with a stone. The transient and peak stress vs. position in the cylindrical stones was obtained for different frequencies of exposure and stone materials.

### Results/Discussion

BWL exposure caused fractures along the stone surface and fragments that separated from the main stone body until the entire stone was broken down. At 170 kHz, the largest fragments were between 2-3 mm for struvite and cystine stones, and 3-4 mm for calcium oxalate monohydrate, uric acid, and artificial stones. Artificial stones treated at 285 kHz and 800 kHz produced only fragments <2 mm and <1 mm, respectively. Simulations indicate that ultrasound bursts produce strong surface waves in the stones and evenly-spaced stresses with a spatial period proportional to the wavelength in the stone. Observations of fractures along the surface of artificial stones at each frequency confirmed this spatial pattern. These experimental and theoretical results indicate that the size of fragments generated by BWL is dependent on stone composition and ultrasound frequency. Moreover, these results provide guidance to develop a BWL system that will produce only small, easily passable fragments for all stones types. Work supported by NIH 2T32 DK007779-11A1, R01 EB007643, P01 DK043881, R01 DK092197, and NSBRI through NASA NCC 9-58.

## Thrombolysis enhanced by dual-frequency high-intensity focused ultrasound

Sijia Guo<sup>1</sup>, Dingjie Suo<sup>1</sup>, Jonathan Frank<sup>2</sup>, Weili Lin<sup>2,3</sup>, Yun Jing<sup>1</sup>, Xiaoning Jiang<sup>1</sup>; <sup>1</sup>Mechanical and Aerospace Engineering, North Carolina State University, Raleigh, NC, USA, <sup>2</sup>School of Medicine, University of North Carolina at Chapel Hill, Chapel Hill, NC, USA, <sup>3</sup>Biomedical Engineering, University of North Carolina at Chapel Hill, Chapel Hill, NC, USA

### Background, Motivation and Objective

A number of diseases with the formation of blood clots can be treated through thrombolysis. It has been demonstrated that high-intensity focused ultrasound (HIFU) can be an efficient method to induce thrombolysis. The thermal effect on neighboring tissue during HIFU thrombolysis, however, has been a concern. The goal of this work is to test the efficacy of dual-frequency HIFU-induced thrombolysis. We hypothesize that cavitation enhanced by the dual-frequency ultrasound can lead to the thrombolysis with reduced acoustic power, but with the similar thrombolysis rate (mass loss/time) of single-frequency HIFU, and hence, the negative thermal effect on neighboring tissue can be suppressed.

### Statement of Contribution/Methods

In vitro clots of mouse blood were prepared and placed at the focus of dual-frequency piezoelectric con-focal HIFU transducers (center frequencies are 1 MHz and 1.5 MHz). 0.65 W ultrasound waves with 10% duty cycle were employed in both single- and dual-frequency ultrasound exposures (in dual-frequency cases, 0.325 W was employed for each transducer). The pulse repetition rate was 1000 Hz. The mass losses of the clots were recorded after 15 seconds, 30 seconds and 60 seconds of ultrasound exposures, respectively to estimate the lysis rate. Cavitation detection tests and bubble cavitation model were conducted for both single- and dual-frequency ultrasound to explain the experimental findings, since acoustic cavitation has been generally accepted as the main mechanism of HIFU-induced thrombolysis.

### Results/Discussion

In thrombolysis tests, it was found that dual-frequency HIFU induced significant enhancement (about 30%) on lysis rate over single-frequency cases. Through cavitation detection tests and bubble cavitation model, greater radiated pressure from cavitation bubble was demonstrated in dual-frequency sonication. Therefore, the enhanced thrombolysis by dual-frequency HIFU is likely due to the greater induced cavitation effect. The results from these studies are promising to indicate the potential application of dual-frequency HIFU as a more efficient approach for thrombolysis.

## Ultrasonic Cavitation Monitoring in High-Intensity Focused Ultrasound Treatment by Pulse Inversion Harmonic Imaging with Plane Wave Transmission Pulses

Shin Yoshizawa<sup>1</sup>, Ryo Takagi<sup>1</sup>, Hiroshi Sasaki<sup>1</sup>, Kota Goto<sup>1</sup>, Takuya Miyashita<sup>1</sup>, Shin-ichiro Umemura<sup>1</sup>; <sup>1</sup>Tohoku University, Japan

### Background, Motivation and Objective

It is known that acoustic cavitation bubbles can accelerate therapeutic effect in HIFU treatments. Since the characteristics of cavitation such as cavitation generation threshold and cavitation life time depend on a target tissue, the cavitation monitoring methods is important to be developed. The objective of this study is to investigate the effectiveness of pulse inversion harmonic imaging with plane wave transmission pulses for the acoustic cavitation imaging. As the typical life time of free air microbubbles is order of ms, high-speed ultrasound imaging using plane wave pulses would have an advantage in the monitoring of small cavitation bubbles in a large region.

### Statement of Contribution/Methods

Figure 1 shows the schematic of experimental setup. A 128-array transducer was placed in a water tank. The ultrasound was focused onto a chicken breast tissue. High-intensity pulses at a maximum intensity of 35 kW/cm<sup>2</sup> were sequentially focused to six positions at hexagonal apexes in the plane perpendicular to the ultrasound propagation direction to generate cavitation in a large region. The diagonal length of the hexagon was 6 mm. Immediately after that, lower-intensity ultrasound at a maximum intensity of 1.7 kW/cm<sup>2</sup> was exposed. The sequence was repeated for 11 s at a frequency of 7.3 Hz with an interval time of 4 ms for the cavitation imaging.

### Results/Discussion

The coagulation volume in the chicken with cavitation bubbles was approximately twice of that without bubbles. Figure 2 shows ultrasound images when cavitation bubbles were induced in a chicken breast tissue. Bubbles were visualized in two orthogonal planes in real time. The imaging method would be effective for the adjustment of the ultrasound parameters to generate appropriate amount of cavitation bubbles also in-vivo study.

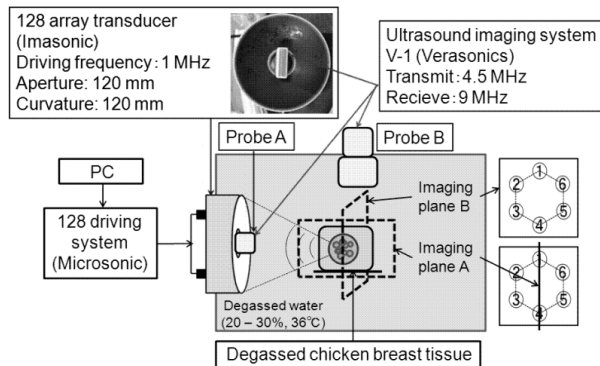


Figure 1 Experimental setup

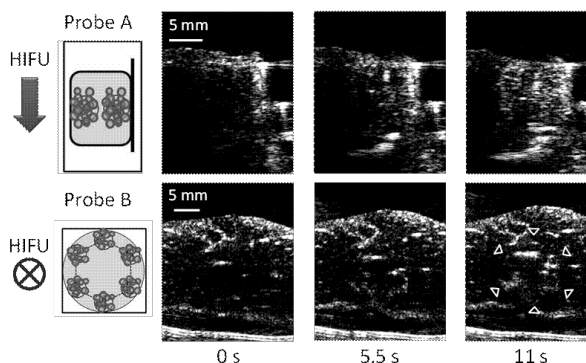


Figure 2 Pulse inversion imaging of acoustic cavitation bubbles in chicken breast tissue

P1C11-11

### A model based approach to in vivo ultrasound temperature estimation

Mahdi Bayat<sup>1</sup>, John R. Ballard<sup>2</sup>, Alyona Haritonova<sup>3</sup>, Elias Wilken-Resman<sup>4</sup>, Emad S. Ebbini<sup>1</sup>; <sup>1</sup>Electrical and Computer Engineering, University of Minnesota, Minneapolis, Minnesota, USA, <sup>2</sup>Medical Devices Center, University of Minnesota, Minneapolis, Minnesota, USA, <sup>3</sup>Biomedical Engineering, University of Minnesota, Minneapolis, MN, USA, <sup>4</sup>Electrical and Computer Engineering, University of Illinois, Urbana, IL, USA

### Background, Motivation and Objective

We have recently shown the results of *in vivo* temperature estimation using an adaptive filter technique to reduce the artifacts caused by natural motions and deformations. The key in successful implementation of such algorithm was global availability of the deformation foci outside the target region. In some cases, however, such training points might not be available or their temporal statistics might change over time (e.g. due to out of plane motion, in-plane disorientation, time-varying specular reflection) which can adversely affect the performance of the motion compensation algorithm. We present an adaptive temperature tracking method based on the discretization of the bioheat equation. A Kalman filter formulation of the problem is presented which is capable of detecting and skipping erroneous frames via innovation process thresholding and predicting the temperature over those frames using the enforced model.

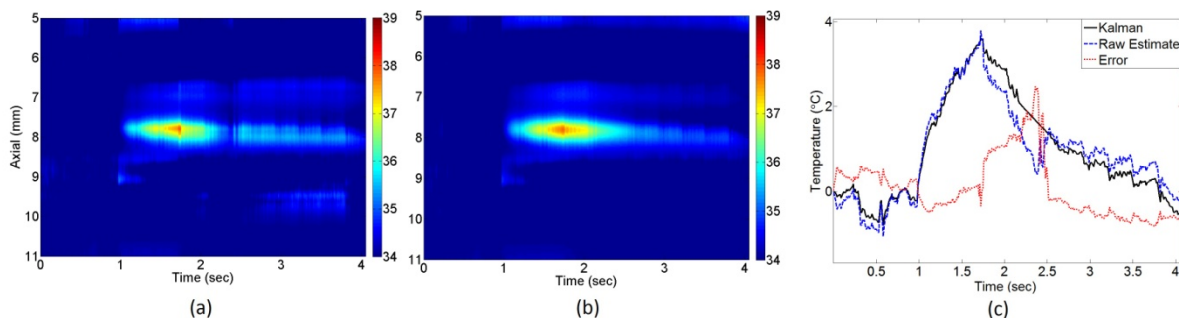
### Statement of Contribution/Methods

RF data was collected during sub-therapeutic HIFU shots in the hind limb of Copenhagen rats *in vivo* to calculate the temperature estimate. A second order approximation of the Laplacian operator of the Pennes bioheat equation in the axial direction over a 400-point grid was used to derive a dynamic model. The raw temperature estimate was then used at different grid points as the measurement inputs while the state prediction and update were performed using a classic linear Kalman filter. Natural motions due to gasping created artifacts in the raw temperature estimates. Using the innovation process, the erroneous frames were rejected and the dynamic model allowed for successful prediction of the temperature during the missing frames.

### Results/Discussion

The results of applying proposed method on the *in vivo* data are shown below. Figure (a) and (b) show the spatio-temporal distribution of the estimated temperature before and after applying the Kalman filter respectively. A gasp occurred at around 2.5 sec. As it can be seen the reconstruction model based on the Kalman filter shows more consistent profile with noticeable enhancement during gasp segment. Figure (c) shows the temporal profile of a point close to the peak temperature where the new method has been able to reduce an error of more than 1 °C in about 4 °C temperature change.

The model based temperature estimation method presented here provides a powerful tool for continues tracking of the temperature based on ultrasound echo shifts when used for *in vivo* thermography undergoing tissue deformations due to natural motions. This model can be extended to simultaneously track tissue properties and temperature via extended Kalman filter. The results show the suitability of model based *in vivo* ultrasound temperature estimation where tracking of the subtle temperature changes is challenging during large scale tissue motions and deformations.



### Quantitative imaging of temperature elevations in tissues due to thermal therapies

Jeremy Kemmerer<sup>1</sup>, Goutam Ghoshal<sup>2</sup>, Nicholas Rubert<sup>3</sup>, Kayvan Samimi<sup>3</sup>, Michael Oelze<sup>1</sup>; <sup>1</sup>Department of Electrical and Computer Engineering, University of Illinois at Urbana-Champaign, USA, <sup>2</sup>Acoustic MedSystems Inc., USA, <sup>3</sup>Department of Medical Physics, University of Wisconsin in Madison, USA

#### Background, Motivation and Objective

Thermal ablation and hyperthermia remain as potent treatment options for cancer. However, the inability to closely monitor temperature elevations from thermal therapies in real time continues to limit clinical applicability. Therefore, the development of new imaging techniques capable of providing feedback and temperature monitoring is highly medically significant. In this study, quantitative ultrasound imaging techniques based on spectral estimates were examined for their ability to monitor and map temperature elevations induced in tissues using either microwave ablation or high intensity focused ultrasound (HIFU).

#### Statement of Contribution/Methods

Ex vivo liver samples were treated with microwave ablation while ultrasound image frames were recorded using a SonixTouch system and linear array (14L5). In vivo tumors in rats (MAT) were treated using a custom-built HIFU system while concurrently imaged using a SonixRP scanner and linear array (14L5). The ultrasound scanners provided raw radio frequency (RF) data. From the RF data, the backscatter coefficient was calculated using the reference phantom technique. The backscatter coefficient was parameterized by estimating an effective scatterer diameter (ESD) and effective acoustic concentration (EAC) assuming a spherical Gaussian model. Maps of the ESD and EAC were created for each acquired frame. Temperature was measured by placing a needle thermocouple in the samples during treatment and temperature changes were correlated with changes in the scattering parameters.

#### Results/Discussion

In the ex vivo liver samples, the ESD was observed to increase with temperature elevation while the EAC was observed to decrease with temperature elevation. Specifically, the mean ESD increased by 7  $\mu\text{m}$  and EAC decreased by 1.5 dB as the temperature increased from 18 to 42  $^{\circ}\text{C}$ . Conversely, in the in vivo tumor samples treated with HIFU, the EAC was observed to increase with increasing temperature, i.e., the EAC increased by 20 to 30% as the temperature increased from 37  $^{\circ}\text{C}$  to a range of 50 to 60  $^{\circ}\text{C}$ . When the HIFU was turned off, the EAC continued to track the decrease in temperature of the tumor. In the in vivo studies, the tumors were grown on the chest wall of the rats and, therefore, large out of plane tissue motion occurred due to the breathing of the animal. In spite of this, the EAC parameter was capable of tracking temperature in the presence of large tissue motion. This work was supported by a grant from the NIH R01 EB008992.

### HIFU Beam Visualization using Beam Profile Extraction from Tissue Speckle Pattern

Kazuhiro Matsui<sup>1</sup>, Takashi Azuma<sup>1</sup>, Keisuke Fujiwara<sup>2</sup>, Hideki Takeuchi<sup>1</sup>, Kazunori Itani<sup>2</sup>, Akira Sasaki<sup>1</sup>, Shu Takagi<sup>1</sup>, Kiyoshi Yoshinaka<sup>3</sup>, Takehiro Ando<sup>1</sup>, Etsuko Kobayashi<sup>1</sup>, Junchen Wang<sup>1</sup>, Ichiro Sakuma<sup>1</sup>; <sup>1</sup>The University of Tokyo, Japan, <sup>2</sup>Hitachi Aloka Medical, Ltd., Japan, <sup>3</sup>National Institute of Advanced Industrial Science and Technology, Japan

#### Background, Motivation and Objective

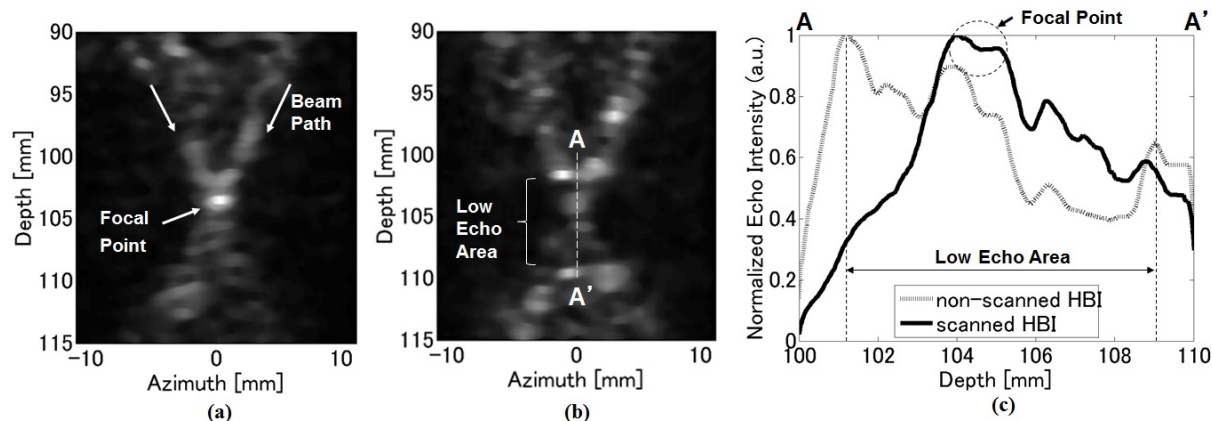
HIFU Beam Imaging (HBI) to visualize focal point and beam path of High Intensity Focused Ultrasound (HIFU) is described. For an accurate detection and control of HIFU beam, a method detecting tissue deformation caused by acoustic radiation force (ARF) of HIFU was one of promising methods for beam visualization. To realize sufficient tissue deformation at focal area, a long burst wave in the order of millisecond was transmitted. In this condition, a risk of bio-effect caused by cavitation should be investigated. We proposed novel HBI method to minimize the risk of bio-effect during the beam visualization process. In this method, a HIFU transducer irradiates microsecond pulsed HIFU beam and an imaging probe detects scattered HIFU beam signal. After scanning of receiving beam, an intensity profile of HIFU beam is visualized. Echo intensity of HBI at the sampling point reflects both beam intensity and backward-scattering coefficient at the point. In this study, an extraction method of HIFU beam profile from the background tissue pattern is proposed and estimated in experiments.

#### Statement of Contribution/Methods

HIFU beam is scanned electronically to discriminate a moving HIFU beam pattern from a fixed inhomogeneous scatter pattern at focal area. At each observing point in the beam profile, echo signals were obtained two times. The focal points were set at the original HIFU focus and set at the observing point, respectively. Each obtained signal in the former was normalized by the detected signal in the latter to suppress the intensity fluctuation reflecting the scatter profile. We used agar phantom mixed with powdery graphite as tissue samples. In experiment, HIFU frequency was 2MHz, pulse duration was 2 cycles, and HIFU acoustic intensity was 2kW/cm<sup>2</sup>.

#### Results/Discussion

Fig. 1a and 1b show the HBI image when powdery graphite was distributed homogeneously and distributed with low density scattering area, respectively. Fig. 1c showed non-scanned and scanned HBI echo intensity normalized in display range. In the beam profile with non-scanned case, a prominent artifact was observed at depth of 101mm. On the other hand, several artifacts in the profile were successfully suppressed and the beam profile was easily recognized. This result clearly demonstrates that proposed method can be used for high accuracy HBI method.





## P1C11-14

**Motion-Corrected Echo Decorrelation Imaging of *In Vivo* Focused and Bulk Ultrasound Ablation in a Rabbit Liver Cancer Model**

Tyler R. Fosnight<sup>1</sup>, Fong Ming Hooi<sup>1</sup>, Ryan D. Keil<sup>1</sup>, Swetha Subramanian<sup>1</sup>, Peter G. Barthe<sup>2</sup>, Michael H. Slayton<sup>2</sup>, Yang Wang<sup>3</sup>, Xiaoping Ren<sup>3</sup>, Syed Ahmad<sup>4</sup>, T. Douglas Mast<sup>1</sup>; <sup>1</sup>Biomedical Engineering, University of Cincinnati, Cincinnati, OH, USA, <sup>2</sup>Guided Therapy Systems/Ardent Sound, Mesa, AZ, USA, <sup>3</sup>Internal Medicine, University of Cincinnati, Cincinnati, OH, USA, <sup>4</sup>Surgery, University of Cincinnati, Cincinnati, OH, USA

**Background, Motivation and Objective**

Thermal ablation of liver cancer, including radiofrequency ablation and high-intensity focused ultrasound (HIFU), is an important treatment option for nonresectable tumors. However, performance of these modalities would be improved by a suitable real-time, ultrasound-based monitoring method. Echo decorrelation imaging is a pulse-echo method that maps heat-induced changes in ultrasound echoes over millisecond time scales. In this study, the ability of echo decorrelation imaging to map and predict heat-induced cell death was tested *in vivo* using image-ablate ultrasound arrays to perform bulk thermal ablation, HIFU ablation, and pulse-echo imaging of VX2 carcinoma in rabbit liver.

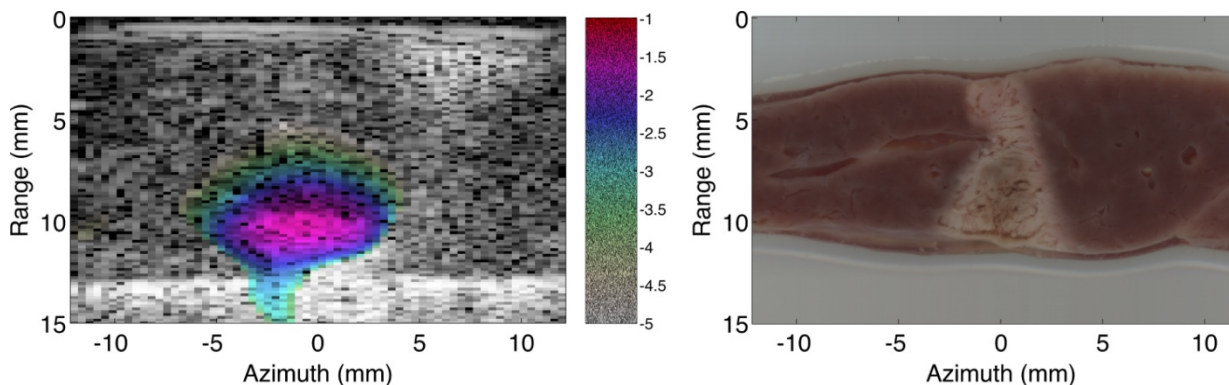
**Statement of Contribution/Methods**

VX2 tumor fragments were implanted in each of the three main rabbit liver lobes and allowed to grow for two weeks. In open surgical procedures, tumors were imaged and treated by 64-element linear image-ablate arrays. Tumors and normal liver regions were sonicated at 5.0 MHz by unfocused 64-element apertures for bulk ablation (six 7.5 s pulses, 40-90 W/cm<sup>2</sup> *in situ*  $I_{SPT}$ ) or 64-element electronically focused apertures for HIFU ablation (six 1 s pulses, 550-820 W/cm<sup>2</sup>). Echo decorrelation images were formed from pulse-echo signals recorded at 118 fps during 3-5 s rest periods following each pulse and corrected for tissue motion using decorrelation from corresponding sham trials. Corresponding integrated backscatter images were formed for comparison. Treated tissue was sectioned, vitally stained with TTC, optically scanned, and segmented based on local TTC uptake. Prediction of cell death by echo decorrelation and integrated backscatter imaging was assessed using receiver operating characteristic (ROC) curves.

**Results/Discussion**

Areas under the ROC curve (AUROC) were statistically significant for prediction of non-viable tissue regions. Echo decorrelation was significantly greater in non-viable regions than in viable regions. These results suggest that echo decorrelation imaging is promising for real-time monitoring of thermal ablation, including clinical HIFU and RFA treatments.

Figure: hybrid echo decorrelation/B-scan image (left) and TTC-stained tissue section (right) for rabbit liver treated *in vivo* by ultrasound focused at 10 mm range (six 1 s, 5.0 MHz pulses, 689 W/cm<sup>2</sup> *in situ*  $I_{SPT}$ ).



## P1C11-15

**Elimination of HIFU Noise in Monitoring of High Intensity Focused Ultrasound Lesion Formation**

Ryo Takagi<sup>1</sup>, Shin Yoshizawa<sup>2</sup>, Shin-ichiro Umemura<sup>1</sup>; <sup>1</sup>Biomedical Engineering, Tohoku University, Sendai, Japan, <sup>2</sup>Communications Engineering, Tohoku University, Sendai, Japan

**Background, Motivation and Objective**

Ultrasonic detection of focal tissue coagulation thermally induced by high intensity focused ultrasound (HIFU) has been difficult without the involvement of microbubbles. A significant length of interval between HIFU shots is set for monitoring target tissue to avoid interference between HIFU noise and RF echo signals in conventional ultrasound monitoring of HIFU treatment. This way, it is difficult to detect tissue changes in the order of milliseconds, which is required for dynamically controlling the HIFU exposure. In this study, a new filtering method to handle RF signals before beam forming is proposed, which will enable truly real-time detection of tissue coagulation during HIFU exposure.

**Statement of Contribution/Methods**

Even though the RF noise due to HIFU exposure is at specific frequencies, it is difficult to eliminate from the RF image signals after conventional dynamic focusing, because the HIFU frequencies are shifted and broadened through the dynamic focusing process. The RF signals before beam forming were processed as follows. The RF signals from the water bolus were subtracted from those from the tissue, and then dynamic focusing was applied to them to form B-mode images. Using these B-mode images, the motion-compensated detection of tissue coagulation using correlation between subimages at different frames was performed as suggested in our previous study. An excised porcine liver was perfused with degassed saline and exposed to HIFU with an F-number of 1 at 1.13MHz in degassed water at 35 degree.

**Results/Discussion**

Figure.1 shows the comparison between B-mode images (a) before and (b) after using the proposed method. As shown in Fig.1, HIFU noise was eliminated completely by the proposed method while the tissue image remained intact. Figure.2 shows the comparison between the correlation coefficient maps between B-mode images (a) with and (b) without the proposed method. As shown in Fig. 2, the proposed method enabled to detect the focal decorrelation induced by focal coagulation literally during HIFU exposure. These results imply that the proposed filtering method is useful for truly real-time detection of tissue coagulation in HIFU treatment.



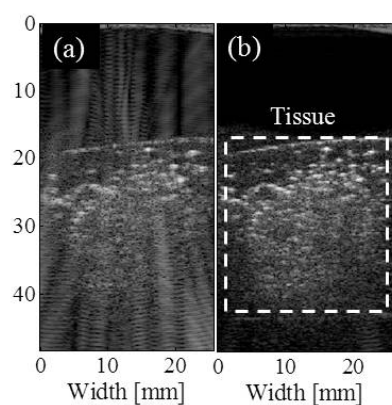


Fig.1 Comparison between B-mode images (a) before and (b) after using the proposed method

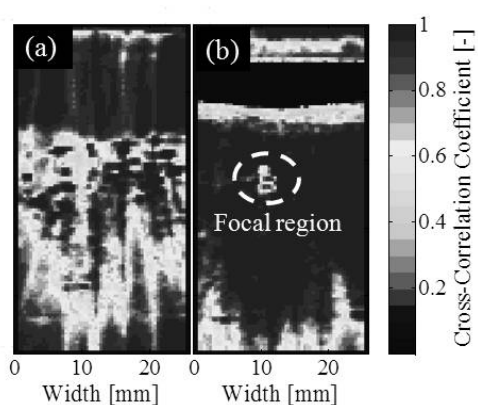


Fig.2 Comparison between the correlation coefficient maps between B-mode images (a) with and (b) without the proposed method

## P2C1 - Sensing

Salon C

Saturday, September 6, 2014, 8:00 am - 5:00 pm

Chair: **Song Gangbing**  
University of Houston

P2C1-1

### Ultrasonic piezoelectric tube resonator for physical liquid property sensing

Hannes Antlinger<sup>1</sup>, Roman Beigelbeck<sup>2,3</sup>, Thomas Voglhuber-Brunnmaier<sup>1,2</sup>, Stefan Clara<sup>1</sup>, Samir Cerimovic<sup>2,3</sup>, Franz Keplinger<sup>3</sup>, Bernhard Jakoby<sup>1</sup>; <sup>1</sup>Institute for Microelectronics and Microsensors, Johannes Kepler University, Linz, Austria, <sup>2</sup>Center for Integrated Sensor Systems, Danube University Krems, Austria, <sup>3</sup>Institute of Sensor and Actuator Systems, Vienna University of Technology, Austria

#### Background, Motivation and Objective

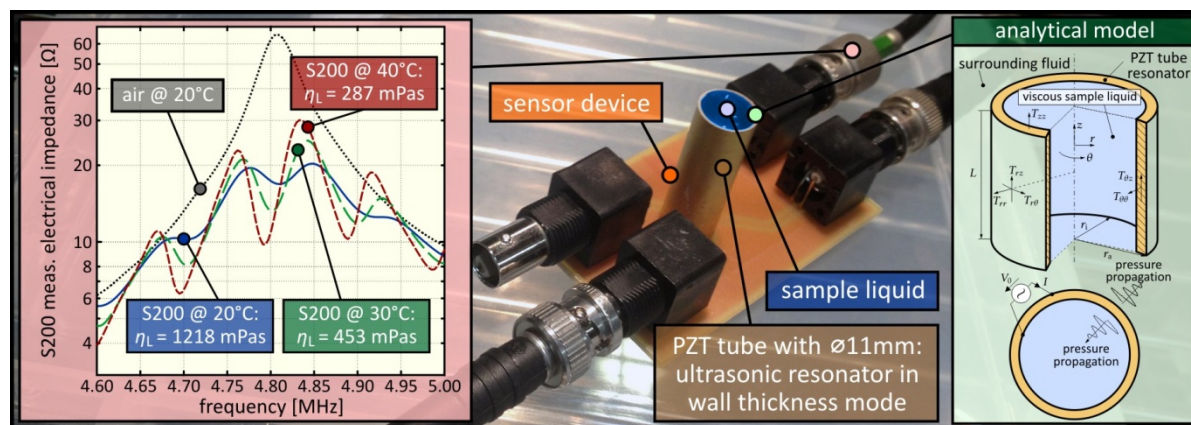
Modern online process control shows an increasing demand for low cost and robust sensors to monitor physical liquid parameters. Recently, we have evaluated the viscous attenuation of pressure waves as a promising characteristic for such liquid monitoring tools (R. Beigelbeck et al, doi:10.1088/0957-0233/24/12/125101). The crucial parameter in this context is the longitudinal viscosity  $\eta_L$ , a combination of the shear and dilatational viscosity coefficients. In contrast to many ultrasonic shear viscometers (e.g. AT-cut quartz resonators), this method benefits from the large penetration depth of pressure waves in liquids which facilitates probing the bulk of the liquid rather than a thin surface layer. However, by nature, this sensing principle requires accurate acquisition of low damping values as well as suppression (or computational correction) of spurious energy losses (e.g. diffraction effects, spurious modes) to ensure reliable results. The latter is a profound task which limits the applicability of the previously introduced parallel plate resonator (R. Beigelbeck et al, doi:10.1088/0957-0233/24/12/125101) to high-viscosity liquids. In this contribution, we present a tubular liquid resonator that overcomes this drawback and extends the attainable viscosity range to multiple orders in magnitude.

#### Statement of Contribution/Methods

The devised sensor device relies on a custom designed PZT tube filled with the sample liquid, which operates in wall thickness mode exciting microacoustic radial modes in the liquid. The electrical characteristic measured at the PZT electrodes reflects through the inverse piezoelectric effect the liquid loading and thus the physical properties of the liquid. Consequently, this method enables simultaneous determination of  $\eta_L$  and speed of sound  $c_L$  in the liquid from the attenuation and spacing of the resonance peaks, respectively, by fitting a rigorous analytical model. The validity of this model is verified by 3D finite element simulations of the liquid resonator setup.

#### Results/Discussion

We demonstrate the performance of two different PZT prototypes by measuring  $\eta_L$  of deionised water, S200 viscosity standard and various aqueous glycerol solutions in a climatic chamber between 20–40°C. The measurement range of  $\eta_L$  comprises remarkable 1–4000 mPas with good agreement of measured and reference data.



P2C1-2

### Enhanced sensitivity of a surface acoustic wave based accelerometer

Wen Wang<sup>1</sup>, Xinlu Liu<sup>1</sup>, Yangqing Huang<sup>1</sup>, **Shitang He<sup>1</sup>**; <sup>1</sup>Institute of Acoustics, Chinese Academy of Sciences, Beijing, China, People's Republic of

#### Background, Motivation and Objective

Surface acoustic wave (SAW) based accelerometer have many unique properties as small size, low cost, excellent linearity, satisfactory sensitivity, and wirelessly measurement. The developed SAW accelerometer in this paper consists of two two-ports resonators on a quartz cantilever beam acting as the feedback of the oscillator. High sensitivity, low detection limit and good linearity were observed in the acceleration experiment.

#### Statement of Contribution/Methods

The present SAW accelerometer utilizes a difference structure of dual-resonator-oscillator. Two SAW resonators were fabricated on a same quartz cantilever beam. One is used as the sensor locating at the junction of the free end and the fixed end, the other is located at the fix end and acts as the reference. The differential oscillation frequency was used to evaluate the acceleration. The applied vibration induces the bending of the cantilever beam, leading to changes of the SAW propagation length and velocity. Theoretical analysis on the sensor performance prediction and optimal design parameters determination was performed by using the equivalent isotropic model.

### Results/Discussion

Two 300MHz SAW resonators on a same ST-X quartz cantilever beam were fabricated by using a standard lithographic technique, and acts as the feedback element of the oscillator. The geometry size of the cantilever beam is set to 3mm×35mm×0.45mm. The developed SAW accelerometer was shown in Fig. 1. Excellent frequency stability of  $\pm 30\text{Hz/h}$  were observed from the fabricated sensor. The performance of the SAW accelerometer was evaluated by using the vibration table at various vibration frequency. Fig. 2 shows a typical measured sensor response. High sensitivity (6.9KHz/g), low detection limit ( $\sim 0.05\text{g}$ ), and good linearity were obtained experimentally.

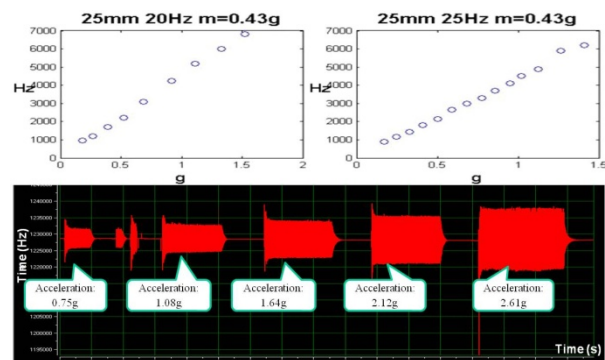


Figure 2 Performance evaluation of the developed SAW accelerometer



Figure 1 the developed SAW accelerometer and measurement setup

### P2C1-3

#### Novel method for accurate, inline sizing of nano particles

Paul van Neer<sup>1</sup>, Arno Volker<sup>1</sup>, Guillaume Pierre<sup>2</sup>, Francois Bouvet<sup>2</sup>, Sophie Crozat<sup>2</sup>; <sup>1</sup>Process and Instrumentation Development, TNO, Delft, Netherlands; <sup>2</sup>Sonaxis, Besancon, France

#### Background, Motivation and Objective

Nanoparticles are increasingly used in a number of applications, e.g. coatings or paints. To optimize nanoparticle production in-line quantitative measurements of their size distribution and concentration are needed. Ultrasound-based methods are especially suited for in-line particle sizing. Also, these methods can be used for opaque dispersions and at high concentrations. However, using ultrasound to measure nanoparticles is very challenging: despite the use of very high frequencies the scattering is in the Rayleigh regime ( $ka < 0.1$ ) and the information contained in the measurements is limited. In this work the performance of a novel ultrasonic method is evaluated using SiO<sub>2</sub> nanoparticles.

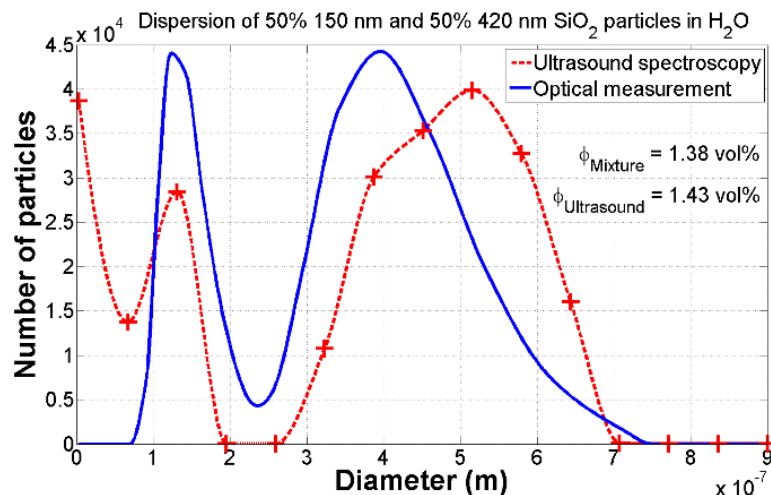
#### Statement of Contribution/Methods

The measurement method is based on ultrasound transmission spectroscopy. The effect of the nanoparticles on ultrasound propagation is measured over a bandwidth of 50 – 250 MHz. These wave propagation effects are then interpreted using the inversion of a physics model. The investigated dispersions consisted of SiO<sub>2</sub> nanoparticles (1.38 vol%) dispersed in water. Three batches, provided by Nano-H S.A.S., had monomodal size distributions with mean sizes 150, 302 and 422 nm. Also two bimodal size distributions were investigated: 1) a mix of 50% 302 nm and 50% 422 nm particles, and 2) a mix of 50% 150 nm and 50% 422 nm particles. As a reference the size distributions were measured using an optics based Malvern Zetasizer.

#### Results/Discussion

The obtained concentrations were 1.18, 1.43, 1.54, 1.43 and 1.58 vol% for the 150 nm, 302 nm, 422 nm, 50% - 50% 302 + 422 nm and 50% - 50% 150 + 422 nm dispersions respectively. The mean sizes differed from the reference by 109%, 18%, 19%, 4.5% and 7.7% for the 150 nm, 302 nm, 422 nm, 50% - 50% 302 + 422 nm and 50% - 50% 150 + 422 nm dispersions respectively (size distribution of latter case displayed in the image). The size difference for the 150 nm particles was due to the fact that a bimodal distribution was measured (150 nm and 600 nm), but the optical measurements showed a monomodal distribution. Analysis of the raw ultrasound data showed that a bimodal distribution was likely.

The concentrations and the shape of the particle size distributions obtained by the ultrasonic instrument were similar to that of the reference. Also, the ultrasound instrument was able to produce correct results for both mono- and bimodal size distributions.



## P2C1-4

**An Active Acoustic Back Cover Based on Piezoelectric Elements**Nicola Lamberti<sup>1</sup>, Giosue' Caliano<sup>2</sup>, Alessandro Savoia<sup>2</sup>; <sup>1</sup>DIIn, University of Salerno, Fisciano, Italy, <sup>2</sup>University of Roma Tre, Italy**Background, Motivation and Objective**

In recent years, the advent of portable personal digital assistants (PDAs), smartphones, and tablet PCs, has made necessary to use multi-touch or stylus-based input devices that are perceived as being more useful for mobile applications. In the past 30 years, several solutions based on different types of optical and acoustical interactions have been shown in literature; our objective is to use the back cover of tablet or smartphones as active input devices capable of detecting the presence and position of a finger on their external surface.

**Statement of Contribution/Methods**

The device is composed by the back cover of the smart device, for example the back cover of a smartphone, on which one or more small, thin piezoelectric plates are glued. The presence and position of a finger on the cover external surface is revealed by the variation of the electrical input impedance, measured by electrically connecting one or more piezoelectric plates in parallel. The device was analyzed by FEM in order to understand how many piezoelectric plates are needed and where they must be placed along the cover surface and the device resolution varying the finger position.

**Results/Discussion**

In figure 1 is shown the FEM (ANSYS ®) model of the structure that we analyzed: the back cover is a thin rectangular plate ( $L = 12$  cm,  $W = 7$  cm,  $t = 1.5$  mm); on the cover inner surfaced we inserted 4 thin piezoelectric plates ( $L = W = 1$  cm,  $t = 1$  mm); finally the finger contact is simulated by the thick parallelepiped ( $L = W = 1$  cm,  $t = 10$  cm) on the center of the outer face. In figure 2 is shown the comparison between the electrical input impedance computed connecting in parallel the 4 piezoceramics, with and without the finger. As it can be seen, the finger presence strongly modify the impedance amplitude ( $|Z_i|$ ) around 10 kHz. In the paper we will show that  $|Z_i|$  varies moving the finger along the cover surface and therefore this measurement can be used to reveal its position. We also show that the position measurement resolution can be improved evaluating  $|Z_i|$  connecting in parallel 1, 2 or 3 piezoceramics.

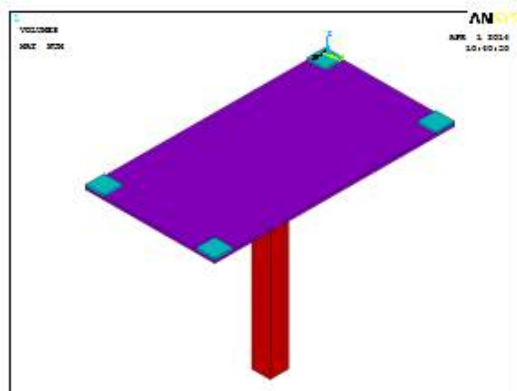


Figure 1

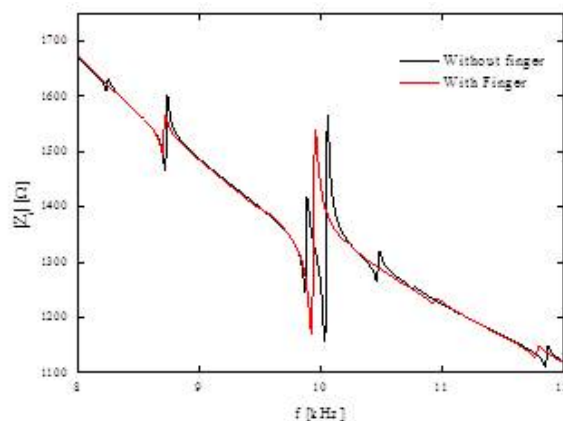


Figure 2

## P2C1-5

**Remote Excitation of a Bulk Acoustic Wave Sensing Platform**Nicole Curtis-Bray<sup>1</sup>, Rahim Stennett<sup>1</sup>, Nuri Emanetoglu<sup>2</sup>, John Vetelino<sup>1,3</sup>; <sup>1</sup>Electrical and Computer Engineering, University of Maine, USA, <sup>2</sup>Electrical and Computer Engineering, University of Maine, Orono, ME, USA, <sup>3</sup>Laboratory of Surface Science and Technology, University of Maine, USA**Background, Motivation and Objective**

The common bulk acoustic wave (BAW) sensing platform for gas and liquid media sensing applications is the quartz crystal microbalance (QCM), which has electrodes on both crystal surfaces. In the QCM, the transverse shear mode (TSM) is excited in AT-cut quartz by the electrodes and acts as the sensing probe. However, the presence of an electrode on the sensing surface precludes the measurement of electrical property changes in the target medium or from an analyte selective film deposited on the surface. An alternative, the lateral field excited (LFE) sensing platform, has both electrodes on one surface enabling it to sense both mechanical and electrical property changes. Although the LFE has advantages over the QCM, an electrode-less sensing platform would eliminate the deleterious effect introduced by electrodes. Remote excitation of acoustic waves in materials has been explored for many years by using electromagnetic acoustic transduction. Recently, antenna structures ranging from simple line antennas to spiral coil antennas have been examined for remote TSM excitation. However, little or no concern was given in these works to critical factors such as the antenna type and orientation, the orientation of the crystals relative to the electric field emanating from the antenna and the geometry of the quartz sample, all of which are critical to efficient TSM excitation.

**Statement of Contribution/Methods**

In the present work, a study of the remote excitation of the TSM in AT-cut quartz as a function of antenna type and geometry, crystal distance from the exciting antenna, crystal rotation with respect to the antenna, and crystal curvature is performed. The AT-cut quartz crystals used in this research had parallel surfaces or one surface with increasing convexity (1 to 3 diopters). Two 10 cm long end-fed short dipole and two circular antenna configurations were examined. The admittance parameters of the antennas were measured with and without the crystals using an Agilent E5071C network analyzer. The crystals were separated from the antennas using plastic spacers ranging from 250  $\mu$ m to 2 mm in thickness. The effect of crystal rotation with respect to the antenna geometry was studied.

**Results/Discussion**

Resonant TSM modes ranging from 6 to 7 MHz were remotely excited in the crystals. As expected, the quartz admittance response decreased in magnitude and phase with increasing distance from the antenna. Crystal rotation with respect to the dipole antenna was found to be significant. The strongest response was observed for the 1-diopter crystal. The circular antenna configuration was found to give the stronger response when compared to the end-fed dipole antenna. Three crystals with different resonance frequencies were simultaneously and efficiently excited to show the feasibility of an electrode-less sensor array to detect multiple target analytes. Current studies are focused on crystal arrays in liquids and the efficient excitation of higher order harmonics.

P2C1-6

# Biomarker Quantification in Bodily Fluids at Clinically Relevant Concentrations using Metal Enhanced Fluorescence Combined with Surface Acoustic Waves

Samuel Morrill<sup>1</sup>, Venkat Bhethanabotla<sup>1</sup>, Mandek Richardson<sup>2</sup>; <sup>1</sup>University of South Florida, USA, <sup>2</sup>University of South Florida, United Kingdom

## Background, Motivation and Objective

Immunofluorescence assays are capable of both detecting the amount of a protein and the location of the protein within a cell or tissue section. Unfortunately, the traditional technique is not capable of detecting concentrations on the nanoscale. Also, the technique suffers from non-specific attachment, which can cause false-positives, as well as photobleaching when detecting lower concentrations is attempted. There is also a time constraint problem since the technique can take from many hours to a few days in some cases.

To lower the cost and time of simultaneous detection of concentration and location of antigens and biomarkers, improvement of the immunofluorescence assay is essential.

## Statement of Contribution/Methods

In this contribution, we show that combining the phenomenon of metal-enhanced fluorescence (MEF) with surface acoustic waves (SAWs) allows for the development of an immunofluoresensor capable of detecting ng/ml concentrations of a biomarker in a bodily fluid, where proteins which interfere with the signal are present. Moreover, this combined MEF-SAW sensor is capable of lowering analysis time considerably.

## Results/Discussion

In this work, MEF from Ag nanocubes of approximately 50 nm edge-length is shown to reduce the detection limit to 1 ng/ml and reduce photobleaching. Combining MEF with a SAW device fabricated in ST-quartz of about 120 MHz wavelength, non-specifically bound proteins (NSBPs) are shown to be removed, improving accuracy of biomarker quantification. The micro-mixing afforded by the Rayleigh SAWs allowed for speeding up of the process considerably.

In this research, it was found that silver nanocubes can lower the detection limit to below 1 ng/mL. Quartz SAW devices are shown to remove NSBPs at a power of 10 mW applied for five minutes. Micro-mixing is shown to be improved by a factor of six at 10 mW of power for 10 minutes by saturating the antibody used in this research, which takes 1 hour without micro-mixing. A simple sensing protocol is developed to demonstrate the quantification of normal rabbit IgG at a concentration level of 50 ng/ml within minutes. Efficacy of the individual components of the device (MEL, micro-mixing and NSBP-removal) are demonstrated with specifically targeted experiments.

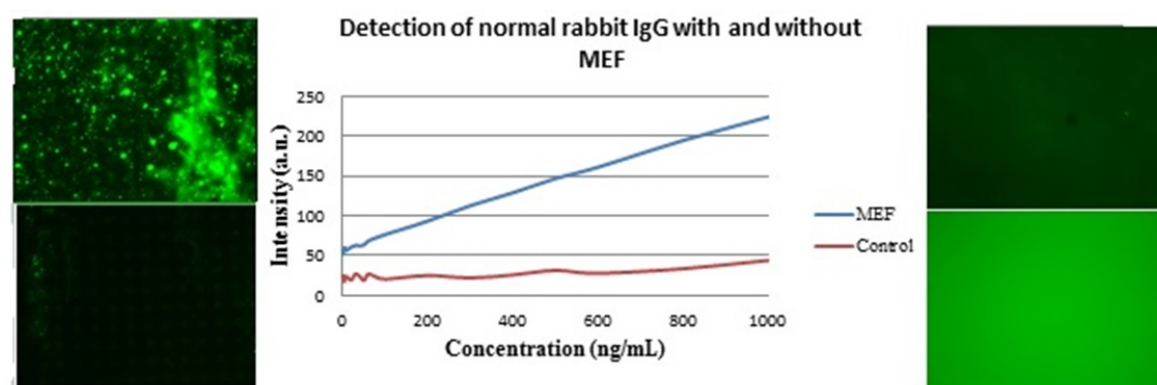


Figure 1. On the left, non-specific binding of proteins can be seen before (top) and after (bottom) removal with SAW. In the middle, detection with and without MEF can be seen. On the right, standard attachment (top) and micro-mixing (bottom) for ten minutes can be seen.



## P2C2 - Ultrasonics and Fluids

Salon C

Saturday, September 6, 2014, 8:00 am - 5:00 pm

Chair: **Roman Maev**  
University of Windsor

P2C2-1

### Ultrasonic Precise Distance Measurement and Movement Detection Installed in Sensor Network

Takeo Sato<sup>1</sup>, Mitsutaka Hikita<sup>1</sup>; <sup>1</sup>Faculty of GE, Kogakuin Univ., Tokyo, Japan

#### Background, Motivation and Objective

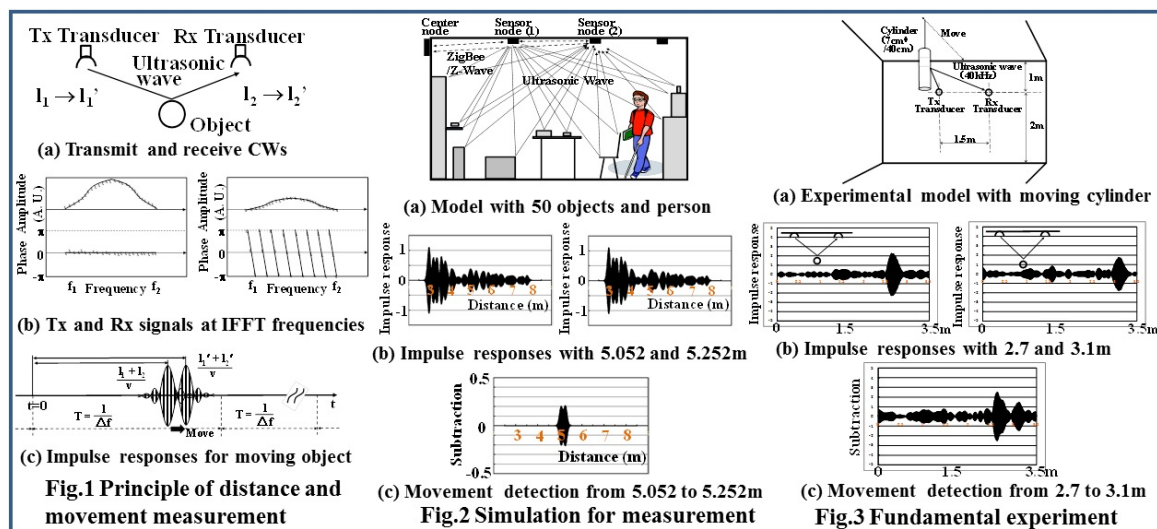
Sensor network will be a very promising system not only for achieving comfortable and energy-saving living conditions but also realizing good care environment. Especially in the latter case, checking the behaviors of elderly and sick people without an invasion of privacy is strongly required. We have proposed a novel movement-detection method based on an ultrasonic precise distance measurement combined with sensor network. In order to achieve extreme low-power consumption for ZigBee or W-wave sensor nodes, ultrasonic CWs with small amplitude are transmitted and received between them. The data are gathered in the center node, where all distance information is obtained by IFFT procedure.

#### Statement of Contribution/Methods

As shown in Fig. 1(a) and (b), Tx transmits CWs at IFFT frequencies and Rx receives them via moving reflection object. Data of relative amplitudes and phases are sent to the center node, where impulse responses are calculated by applying IFFT procedure as shown in Fig. 1(c) (Ref. 1). Subtraction between the impulse responses at different times provides movement information of the object. In the simulation model, 50 reflection objects and a walking person are assumed (Fig. 2(a)). The CWs are around 40 kHz and have Gaussian-type distribution due to transducer bandwidth. Impulse responses with the person at 5.052 and 5.252 m distances are shown in Fig. 2(b). Movement from 5.052 to 5.252 m is clearly detected and inactive objects are canceled out mutually by subtraction between two impulse responses at different times (Fig. 2(c)).

#### Results/Discussion

Results of fundamental experiment for the model illustrated in Fig. 3(a) using a moving cylinder with 7 cm diameter and 40 cm length are shown in Fig. 3(b) and (c). As shown in Fig. (b), impulse responses have clear reflection pulses at 2.7 and 3.1 m respectively. From the subtraction between two impulse responses, we can recognize movement of the cylinder (Fig. (c)). Therefore, when the proposed devices are mounted into sensor nodes, it is possible to collect all information only about moving objects in center node. This method does not require conventional code-division signals and pulse-compression procedures for sensor nodes, which achieve low-power consumption for the nodes. We will monitor elderly and sick people in near future. 1. M. Hikita, Japanese Patent, Tokugan2008-125735.



P2C2-2

### Direction Control of a Parametric Speaker

Hajime Akahori<sup>1</sup>, Hideo Furuhashi<sup>1</sup>, Masatoshi Shimizu<sup>2</sup>; <sup>1</sup>Electrical and Electronics Engineering, Aichi Institute of Technology, Toyota, Aichi, Japan, <sup>2</sup>Power Engineering R&D Center, Kansai Electric Power Co. Inc., Amagasaki, Hyogo, Japan

#### Background, Motivation and Objective

A parametric speaker has sharp directivity, and it has attracted much attention in the sound industry. However, the direction of the sound wave is fixed, and can only be changed by mechanical control. In this paper, we develop a parametric speaker in which the direction of the sound wave can be electrically controlled.

#### Statement of Contribution/Methods

Parametric speakers consist of an ultrasonic transducer array. In this experiment, 144 ultrasonic transducer elements are arranged in a 12 x 12 cm square with a distance of 10 mm between each element. The oscillation frequency is 40 kHz. For each signal of element, the applied signal is controlled by FPGA boards. Figure 1 shows a block diagram of the system. The audible sound signal is modulated by ultrasonic frequency using AM modulation.

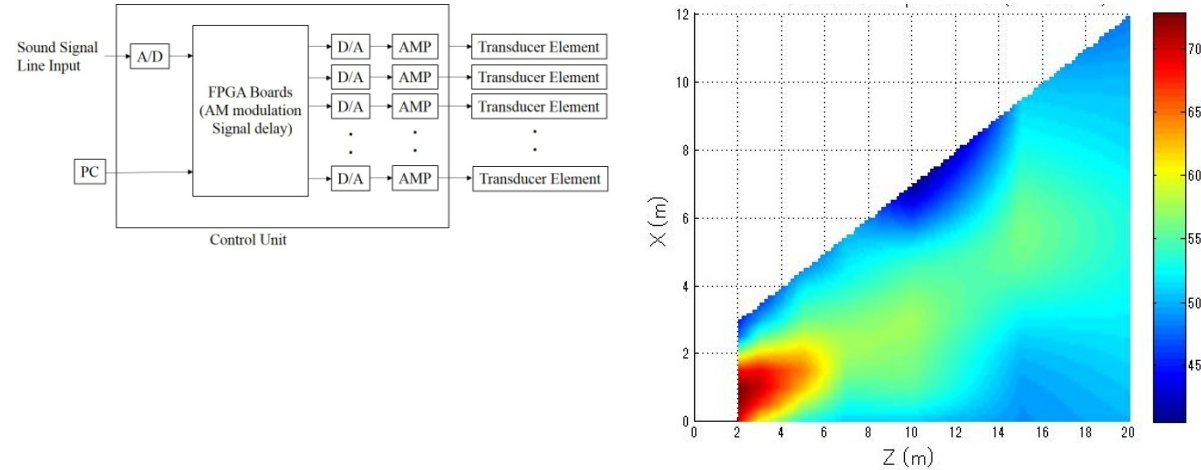
Direction control is performed by shifting the phase of the modulated signal applied to each transducer element. The required time delay is

$$\Delta t_i = (x_i \sin \theta \cos \varphi + y_i \sin \varphi) / v$$

Here,  $(\theta, \varphi)$  is the direction indicated by the spherical coordinates,  $(x_i, y_i)$  is the coordinate of the each element, and  $v$  is the sonic speed.

### Results/Discussion

The sound wave is measured with a UC-54 (Rion Co. Ltd.) microphone at a depth  $z$  of 2, 3, 5, 7, 10, 15, and 20 m and a horizontal length of 0-24 m at intervals of 0.5 m inside the direction angle of  $50^\circ$ . Figure 2 shows the two-dimensional distribution of the sound pressure (dB) directed to  $\theta = 20^\circ$  and  $\varphi = 0^\circ$ . The sound signal frequency is 1 kHz. The data are interpolated, and the data inside the direction angle of  $30^\circ$  are plotted. This confirms that the direction of the sound wave is successfully controlled by this system.



P2C2-3

### Nanosecond time-resolved thermo-acoustics in refractory metals undergoing laser pulse-induced phase transition: finite difference modelling

Istvan Veres<sup>1</sup>, Zhandos N. Utgulov<sup>2</sup>, Arthur G. Every<sup>3</sup>; <sup>1</sup>Recendt, Linz, Austria, <sup>2</sup>Department of Physics, School of Science and Technology, Nazarbayev University, Astana, Kazakhstan, <sup>3</sup>School of Physics, University of the Witwatersrand, Johannesburg, South Africa

### Background, Motivation and Objective

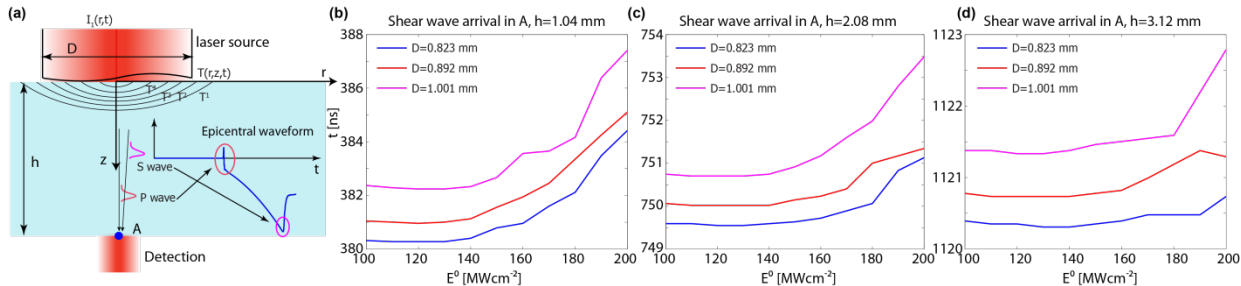
Metal-to-liquid phase transition in refractory metals can be generated by short laser pulses and detected interferometrically via laser-generated ultrasound. In such experiments metallic surfaces are irradiated by laser pulses which can lead to surface heating, melting and evaporation depending on the incident laser peak intensity. During laser-induced melting, the generation of shear waves is reduced due to loss of rigidity within dynamically evolving molten mass, while the generation of longitudinal waves remains less influenced. This leads to a delay of the shear wave arrival along the epicentral axis, providing information about the laser-induced phase transition.

### Statement of Contribution/Methods

The work presented here investigates numerically a pulsed laser-induced metal-to-liquid phase transition. The spatial-temporal temperature distributions and the propagation of the resulting ultrasonic waves are calculated from the governing coupled equations of heat conduction and ultrasonic wave propagation using finite differences. The applied nonlinear model takes into account the temperature-dependent thermo-physical properties, such as thermal conductivity, specific heat and latent heat of the laser irradiated metal during phase transition. The elastic constants employed are also temperature-dependent, whereby the shear modulus of the heated region drops to zero during melting. This leads to a non-thermoelastic source within the molten region and to a thermoelastic source outside of the molten region.

### Results/Discussion

The laser pulse-induced generation and propagation of the elastic waves are investigated numerically and experimentally in tungsten plates. The incident laser pulse with FWHM=4 ns is modeled as a spatio-temporal Gaussian pulse with beam diameters ranging from 0.8 to 1 mm and with incident peak power densities between 100 and 200 MWcm<sup>-2</sup>. The numerical results confirm the experimental observation that the arrival of the shear wave remains unaltered below the melting threshold (~140 MWcm<sup>-2</sup>) and show a growing delay with increasing peak power densities [Fig.]. Numerical simulations with different plate thicknesses also reveal a strong dependence of this effect on the plate thicknesses  $h$  and incident laser beam diameters.



P2C2-4

**Three-dimensional-positioning measurements based on echolocation using linear-period-modulated ultrasonic signal**Natee Thong-un<sup>1</sup>, Shinnosuke Hirata<sup>1</sup>, Yuishiro Orino<sup>1</sup>, Minoru K. Kurosawa<sup>1</sup>; <sup>1</sup>Tokyo Institute of Technology, Japan**Background, Motivation and Objective**

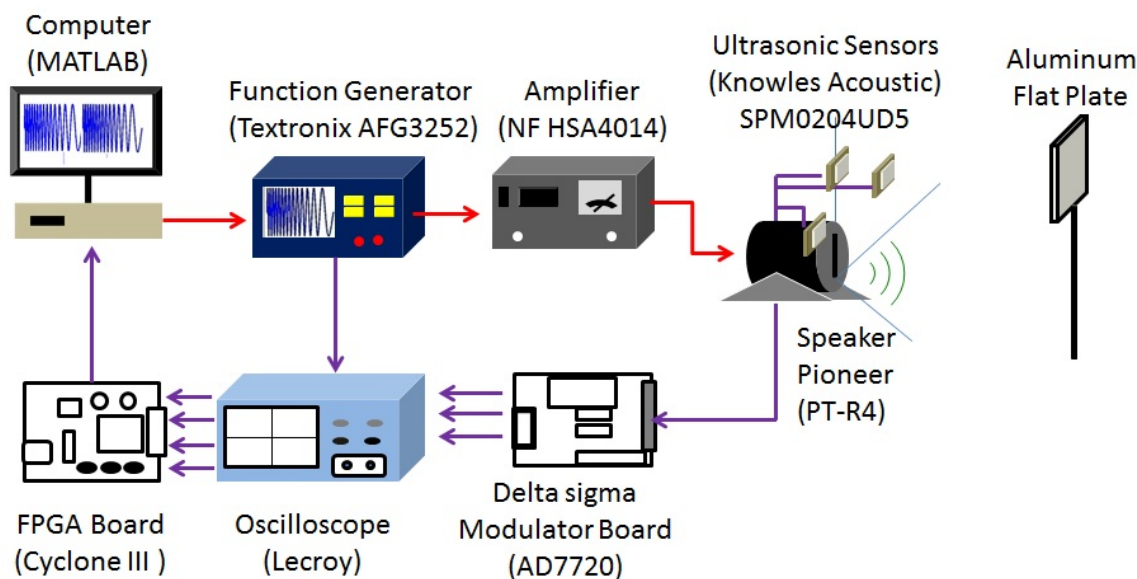
An echolocation method, which is the natural way in the navigation of bat and dolphin, is one of the simple ideas for object positioning. It can be employed in the variety applications, radar, sonar, and ultrasonic, for example. Especially in ultrasonic, it is necessary for most autonomous robots to locate the distance between their own position and obstacles because of easy reflection from structures. The benefits of ultrasonic systems, which are compared with others, are small size and simple hardware. Accordingly, it is the most up-to-date and reliable. Time-of-flight (TOF) is a key idea in computation of the location. TOF can easily be computed by the cross-correlation function, which is strong to low signal-to-noise ratio (SNR). However, this is the high-computational-time cost. To satisfy this problem, this paper selects to use one-bit cross-correlation method. It is relatively the low-computational-time cost when compared with multi-bits cross-correlation method. Moreover, this paper is the development of the object-positioning measurements from one and two into three dimensions. A three-dimensional-positioning algorithm is relied on the simple idea of Newton-Raphson estimation. The effectiveness of expanding this ability is inevitable to exploit more ultrasonic receivers. The more the number of ultrasonic sensors, the higher the price. Therefore, this paper proposes using a small commercial acoustic microphone for low-cost support.

**Statement of Contribution/Methods**

1. The small commercial acoustic microphones are given to support the low-cost and small size issue.
2. Echoes, which are obtained from microphones, are converted into one-bit signal for the low-computational-time cross correlation.
3. TOFs between an object, sound source and microphones are utilized to compute the object position by Newton-Raphson estimation.
4. To satisfy real-time application, FPGA plays the vital role of computation.

**Results/Discussion**

Experiment on three-dimensional spaces is shown in Fig.1. Three acoustic microphones were given in this system. The object was assumed as an Aluminum flat plate. The distance between the object and sound source was approximately 1 m. To evaluate the efficiency of measurements, one hundred experiments were repeated continuously and compared with the simulation results.



P2C2-5

**Development of a 1 Mbps Low Power Acoustic Modem for Underwater Communications**Nelson Pinto<sup>1</sup>, José Cabral<sup>1</sup>, Gerardo Rocha<sup>1</sup>, Marcos Martins<sup>1,2</sup>; <sup>1</sup>Algoritmi Center, Minho University, Guimarães, Portugal, <sup>2</sup>Escola Superior de Tecnologias, Instituto Politécnico do Cávado e do Ave, Barcelos, Braga, Portugal**Background, Motivation and Objective**

The need for reliable and efficient underwater wireless communication technologies is increasing due to the demand on systems for ocean exploration, research and economic. There are 3 main forms to communicate underwater: acoustic, radio frequency and optical based communications. Radio frequency is limited by the high level of absorption in water. Optical systems suffer from the same limitation as well as the disadvantages associated to the high levels of ambient light close to the water's surface and scattering due to suspended particles. As a result, acoustic communication systems are the preferential form of wireless underwater communications, since they show low sound attenuation in water. Acoustic communications have been used for long distance communications, up to 20 km, and in deep waters with stable thermal conditions. But, despite underwater wireless communications having shown strong advances in recent years, there are still many limitations concerning data rates and robustness for real-time applications.

**Statement of Contribution/Methods**

Communication Systems using high frequencies also raise strong problems related to attenuation, being directly related to the frequency, the acoustic absorption at 1 MHz can reach 280 dB/km. Consequently, the maximum transmission range decreases dramatically to a few hundred meters or less with the increasing of frequency. On the other hand, real time acoustic communications are not supported for long distances since an acoustic wave propagates at around 1500 m/s, resulting in high propagation delays and disabling, therefore, any real time connection. Summarizing, a high data rate and real time acoustic communications only can be applied at medium range, meeting therefore the needs of applications such as coastal sensor networks, underwater unmanned vehicle control, equipment monitoring, among others.

### Results/Discussion

In this work an underwater acoustic modem that allows communications over several meters, achieving a maximum data rate of 1 Mbps, using 1.4  $\mu$ W of power consumption per bit with a 1 MHz carrier is presented. This solution allows the reprogramming of the digital signal processing block and the implementation of different types of digital modulations in order to improve modem's performance. The system is based on a poly(vinylidene fluoride) PVDF ultrasonic emitter transducer which is capable of sending high quality signals but less powerful, when compared with piezoceramic transducers, needed for digital modulations with high symbol rates per carrier period.

The BER was also measured for the baud rates of 1 Mbps, 512 kbps and 256 kbps. These measurements were performed using two RS232 ports, allowing for sending and receiving a file on the same computer for comparison. The size of the file was 2 MByte and no type of error detection or correction mechanisms were implemented. The achieved results for BER were:  $3 \times 10^{-3}$  with 1 Mbps,  $2.3 \times 10^{-5}$  with 512 kbps and  $1 \times 10^{-8}$  with 256 kbps.

## P2C3 - Industrial Applications and Energy Harvesting

Salon C

Saturday, September 6, 2014, 8:00 am - 5:00 pm

Chair: **Jiromaru Tsujino**  
*Kanagawa University*

P2C3-1

### Numerical and Experimental Study on the Frequency Tuning Characteristics of a Rotating Piezoelectric Energy Harvester

Dominik Gedeon<sup>1</sup>, Stefan Johann Rupitsch<sup>1</sup>, Reinhard Lerch<sup>1</sup>; <sup>1</sup>Chair of Sensor Technology, University Erlangen-Nuremberg, Erlangen, Germany

#### Background, Motivation and Objective

Energy harvesting from vibrating structures has received much attention in recent years. Vibration energy, that would else remain unused, can be converted to the electrical domain by a mechanical oscillator, incorporating piezoelectric material. Conversion is achieved most efficiently when the structure is in resonance. When applied to a rotating structure, such as the shaft of an engine, centrifugal forces induce a shift in resonance frequency. Vibrations induced by imbalance can be harvested directly on the shaft. Here, we investigate a piezoelectric cantilever with tip mass under the influence of a continuous rotation. A PI DuraAct patch serves as piezoelectric sheet that is glued onto an aluminum substrate. We used the Finite Element Method with linear piezoelectric coupling to model the harvesting device.

#### Statement of Contribution/Methods

Our simulation approach involves a two-step Finite Element Procedure. (i) Nodal forces are calculated from the radial acceleration field. Displacements and mechanical stresses are derived from a static simulation step. (ii) The change in structural stiffness is calculated and considered in a dynamic analysis. From the dynamic simulation step, transfer functions (Fig. 1) and eigenfrequencies (Fig. 2) are computed.

In addition, we designed an experimental setup that prescribes closed-loop controlled accelerations in radial and axial direction (see Fig. 2). The rotation with frequency  $F_{rot}$  generates the radial accelerations. The harvester was excited in axial direction at a number of frequencies  $f_{ax}$  in the vicinity of the first bending resonance frequency. Fig. 1 shows the generated voltage amplitude normalized to the axial acceleration amplitude as transfer function  $H(f_{ax})$ . Therewith, the resonance frequency of the harvester at the distinct rotational frequency can be retrieved.

#### Results/Discussion

The comparison of measurements and simulations for  $H(f_{ax})$  shows good agreement, both regarding the shift of the first bending-mode resonance, as well as the voltage magnitude generated by the piezoelectric effect. The tuning characteristics of the harvester can be influenced by certain parameters, such as root offset from the center of rotation, free length  $l_{free}$  or the weight of the tip mass  $m$  (Fig. 2). The Finite-Element approach enables us to study the effect of design changes on the harvester's frequency characteristics.

Fig. 1: Transfer functions of cantilever with tip mass at different rotation frequencies  $F_{rot}$ .

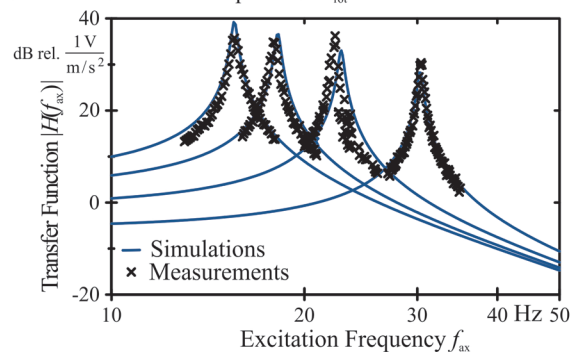
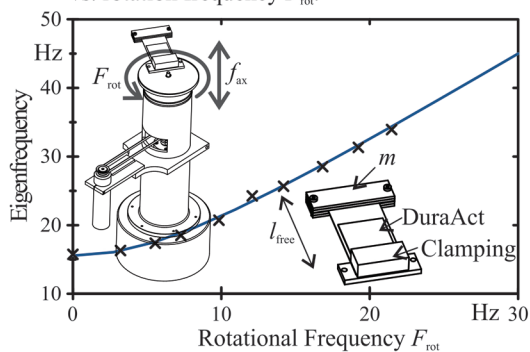


Fig. 2: First bending-mode resonance frequency vs. rotation frequency  $F_{rot}$ .



P2C3-2

### Ultrasonically induced effects in Schottky barrier structure depending on a $\gamma$ -irradiation

Oleg Olikh<sup>1</sup>; <sup>1</sup>Faculty of Physics, Taras Shevchenko Kyiv National University, Kyiv, Ukraine

#### Background, Motivation and Objective

Ultrasonic (US) was established to affect various properties of semiconductors. So, US treatment caused the change of the energy spectrum of silicon surface states, the change of the paramagnetic properties of the silicon nanocluster in  $\text{SiO}_2$ , the modification of the light emitting and other optical properties of the semiconductor structures. The goal of this study is experimental investigation of dynamic variations in electrical characteristics of  $\gamma$ -irradiated Mo/ $n$ - $n^+$ -Si structures under conditions of US loading (USL).

#### Statement of Contribution/Methods

The samples used in our experiments were 0.2  $\mu\text{m}$  thick  $n$ -Si:P epitaxial layer on  $n^+$ -Si:Sb. The thickness of the substrate was 250  $\mu\text{m}$  and the free carrier concentration was  $4.2 \times 10^{22} \text{ m}^{-3}$ . A molybdenum Schottky contact was fabricated on the epi-layer surface. The structures were exposed to  $^{60}\text{Co}$   $\gamma$ -ray radiation with the cumulative doses  $D$ , 0, 10, and 100 kGy. The current-voltage (I-V) characteristics were measured for the samples under US loading (longitudinal waves, frequency 9.6 MHz, and intensity  $W_{US}$  up to 1.3  $\text{W/cm}^2$ ).

#### Results/Discussion

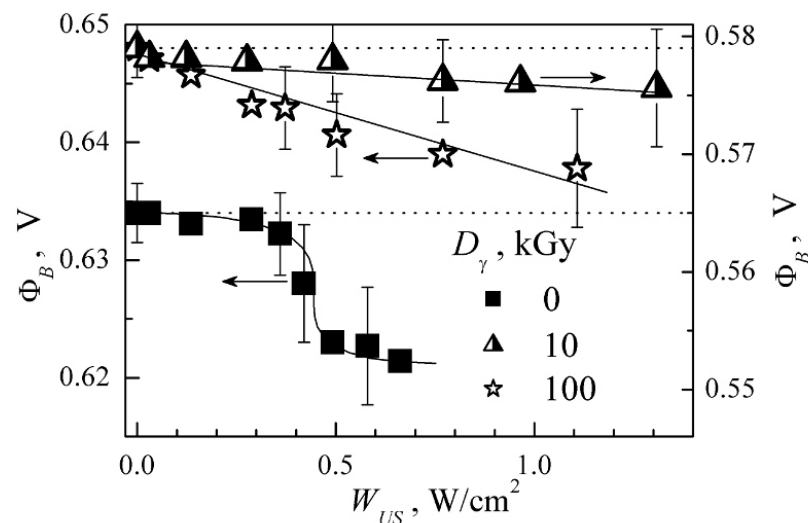
It was established that main current-transport mechanisms in the structures were thermionic emission (TE) over an inhomogeneous barrier for forward current and a TE, direct tunneling and phonon-assisted tunneling for reverse current. US affected the TE only and USL leads to the Schottky barrier height (SBH) decrease. It was found, that after  $\gamma$ -



irradiation (i) the US influence efficiency fell off; (ii) the dependence of ultrasonically induced current variation on US intensity changed. The increase in a dose led to the increase in SBH variation under USL condition.

In our opinion, the mechanism of US effect on Schottky diode's parameters changed after irradiation. Namely, the observed effects can be accounted for by the ionization of defects located at the interface due to ultrasonic dislocations and ultrasonic-point defects interaction in the non-irradiated and irradiated structures respectively. The A-centers or divacancies can be a acousto-active defect in the irradiated structures respectively.

Fig. Dependencies of the SBH on the USL intensity. Horizontal dashed lines represent the SBH values under USL absence condition.



P2C3-3

### Development of Robot Finger using Ultrasonic Motors Driven by Superimposed Signal Input

Shosho Oh<sup>1</sup>, Kenjiro Takemura<sup>1</sup>, <sup>1</sup>Keio University, Japan

#### Background, Motivation and Objective

Multi-fingered robot hands have attracted attentions in many fields. One of the promising actuator for robot hand is an ultrasonic motor (USM) because of direct drive capability etc. However, when developing a robot hand with USM, a complicated wiring problem may become one of the essential problems.

In order to solve this problem, we introduce a novel driving method for serially connected multiple USMs with a superimposed signal which contains multiple driving signals corresponding to each USM. As a preliminary stage in the development of robot hand, we develop a robot finger with embedded USMs, and characterizes the robot finger with a superimposed signal input.

#### Statement of Contribution/Methods

We designed a robot finger which is driven by USMs. Although the finger has DIP, PIP and MP joints, the DIP joint depends from PIP joint, which means, the finger totally has three DOFs of motion. Each joint is driven by a linear USM embedded in the finger via wire-pulley mechanism. As mentioned in Objective, since the USMs are connected in series and driven by a superimposed signal, the driving frequency of each USM must be different each other. Therefore, we designed three USMs with different driving frequencies using finite element analysis. Note that, the USMs we developed are single-phase standing wave linear USMs using the second/third bending vibration modes of plate-shaped vibrator for bidirectional movement of a slider. In addition, each USM has two vibrators sandwiching the slider to increase the output force.

As experiments, first we confirmed the characteristics of the USMs we developed, i.e., we confirmed the vibration characteristics of the vibrators and the driving characteristics (speed and force) of the USMs. In addition, we also experimentally confirmed if each USM could be independently driven by a superimposed signal input. Finally, we fabricated the robot fingers with the USMs developed, and characterized the finger with superimposed signal input.

#### Results/Discussion

First, we measured the natural frequencies of second/third bending vibration modes of each vibrator, and confirmed that they are different enough for independently excited with superimposed signal input. In addition, the maximum speed and force produced with the developed USMs are 150 mm/s and 1.88 N, respectively.

Next, we conducted a driving test of the fabricated robot finger and confirmed that each joint could be independently driven by inputting a superimposed signal which has driving signal for each USM. This means, the USMs could be connected in series with a single input wire, resulting in possibly solving the complicated wiring problem of USM driven robot hand.

However, the maximum rotation angles of the DIP and PIP joints are 30

joint could not be driven. This might be due to the large friction occurred at each joint. We will be introducing ball bearings in the future prototype.

DO and the DIP, that for MP joint

P2C3-4

### Tunable acoustic energy harvester using Helmholtz resonator and dual piezoelectric cantilever beams

Ping Li<sup>1</sup>, Aichao Yang<sup>2</sup>, Yumei Wen<sup>2</sup>, <sup>1</sup>College of Optoelectronic Engineering, Chongqing University, Chongqing City, Chongqing, China, People's Republic of, <sup>2</sup>Chongqing University, China, People's Republic of

#### Background, Motivation and Objective

One of the major stumbling blocks to the acoustic energy harvesting systems is the lack of practical tunable frequency band which is useful for efficiently harvesting broadband and variable-frequency ambient acoustic energy. A tunable acoustic energy harvester with dual Helmholtz resonators has been developed [1]. However, the obvious tuning is achieved only by changing the resonator volume greatly, which leads to the low volume power density.

[1] X. Peng, Y. M. Wen, P. Li, A. C. Yang, and X. L. Bai, Appl. Phys. Lett. 103, 164106 (2013).

### Statement of Contribution/Methods

In this paper, we present a tunable acoustic energy harvester consisting of dual piezoelectric cantilever beams and a Helmholtz resonator with the perforated backplate. The tunability of the operation frequency band can be achieved via simply adjusting the size of the aperture because the resonance frequencies of the Helmholtz resonator strongly depend on the acoustic impedance affected by the aperture size.

### Results/Discussion

Experimental results illustrate that the output voltage of the proposed harvester has two peaks at 125-250 Hz. The resonance frequencies (corresponding to these two peaks) and the operation frequency band are all dependent on the radius ( $r$ ) of the aperture. As compared with the lower resonant frequency, the higher resonant frequency increases more quickly with  $r$ . It can be explained by the greater effect of  $r$  on the cavity resonance mode. Additionally, the tunable frequency band of output voltage can be achieved via varying the aperture radius  $r$ . As  $r$  increases from 0 to 1.0 cm, the frequency band is broadened and varies from 179.5-193.5 Hz to 179-212 Hz.

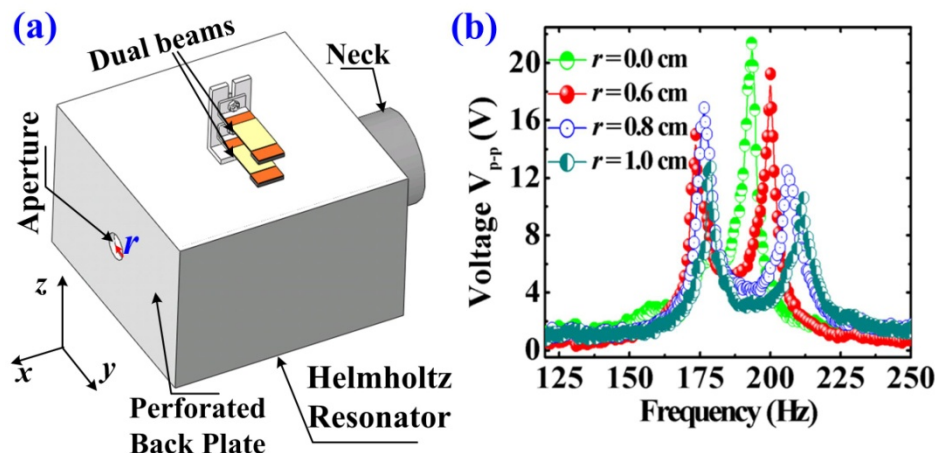


Fig. 1. Performance of the proposed acoustic energy harvester: (a) structure diagram; and (b) output voltage vs. frequency under different  $r$  ( $r=0, 0.6, 0.8, 1.0$  cm).

P2C3-5

### Enabling Composite Casting by Ultrasonic Cavitation

Kai-Alexander Saalbach<sup>1</sup>, Christian Demming<sup>2</sup>, Patrik Freytag<sup>2</sup>, Jens Twiefel<sup>1</sup>; <sup>1</sup>Institut für Dynamik und Schwingungen, Leibniz Universität Hannover, Hannover, Germany, <sup>2</sup>Institut für Werkstoffkunde, Leibniz Universität Hannover, Garbsen, Germany

### Background, Motivation and Objective

Modern electronics are getting increasingly powerful. Therefore heatsinks providing high thermal conduction are needed in order to transfer heat away from electronics components. Common heatsinks consist of a copper base plate connected to aluminum cooling fins. The two parts are usually joined by soldering or pressing in combination with a heat conductive paste. These joining processes produce an insufficient thermal conduction. The optimum thermal conduction between the copper and aluminum part would be provided by a cohesive bond. Therefore the authors aim is to create a cohesive bond during master forming. Casting experiments with solid copper parts and aluminum melt showed weak but promising connection between the two materials. To facilitate connection the authors approach is to create a cohesive bond during master forming by superimposing ultrasound to composite casting. Preliminary investigations in which copper plates were bolted to the horn of an ultrasonic transducer, submerged and excited in aluminum melt showed improvement in the desired connection.

### Statement of Contribution/Methods

To improve connection between solid copper parts and aluminum melt ultrasonic excitation is applied in order to create cavitation at the copper's surface. Cavitation then cleans the surface of impurities and oxide layers which prevent wetting by aluminum melt.

In this contribution investigations on sonicating aluminum melt to create cavitation in order to influence the surface of copper parts placed in the melt are reported. Intensity of the ultrasonic excitation and distance between horn and copper parts are varied in this investigation.

Sonication of the melt means an indirect excitation of the copper parts. Therefore ultrasonic power has to be higher than in direct excitation of the copper parts.

To analyze the influence of ultrasonic power and distance between horn and copper surface, size and location of the connection sites on the copper's surface are compared. To evaluate the connections produced, polished micrographs sections are prepared.

Further FE-simulations of the pressure distribution inside the crucible are carried out to verify that the location of pressure antinodes coincides with the occurrence of spots on the copper's surface where connections between the two metals appear.

### Results/Discussion

The investigation of copper parts, influenced by indirect cavitation generation, shows improvement in connection between aluminum melt and copper. Increasing ultrasonic power increases the size of the area of connection. Varying the distance between ultrasonic horn and copper surface also influences the size of the area of connection. Wherein there are indications of a dependence on the wavelength in the melt.

Based on simulation of the pressure distribution inside the crucible this dependence on the wavelength is validated.

## Matching Layers Design for a Plate Waveguide Ultrasonic Transducer for Flow Measurement in Hostile Environments

Michael Laws<sup>1</sup>, Sivaram Nishal Ramadas<sup>2</sup>, Steve Dixon<sup>1</sup>; <sup>1</sup>Department of Physics, University of Warwick, Coventry, United Kingdom, <sup>2</sup>Elster NV/SA, Essen, Belgium

### Background, Motivation and Objective

Ultrasonic flow measurement provides a range of benefits compared to other flow measurement techniques. As previously reported, we have developed a waveguide transducer, designed for flow measurement in hostile environments, including extreme temperatures. This design consists of a conventional piezoelectric element mounted at the end of a series of parallel, rectangular cross-section, stainless steel plates, which act as a buffer between the piezoelectric ceramic and the test fluid, allowing operation in hostile environments. One issue with such a design is the large impedance mismatch between the waveguide and the test fluid. This makes it difficult to effectively transfer energy between the transducer and the test fluid. This mismatch can be reduced by the addition of one or more matching layers, with acoustic impedance that is an intermediate of the waveguide material and the test fluid. However, our application requires extra consideration as many of the materials typically used for matching layers would not be suitable for operating in extreme temperatures. Consequently, the thermal stability of the material must also be taken into consideration along with the acoustic properties of the material, while designing the waveguide transducers.

### Statement of Contribution/Methods

We have studied the acoustic properties of several materials that are commonly used for their thermal stability in order to assess their suitability for an acoustic matching layer. Such materials include loaded epoxies, which is suitable for use at both cryogenic and extremely high temperatures. The acoustic properties of these materials were obtained via material characterisation and extensive finite element modelling (FEM) was carried out, in order to assess the suitability for matching layers for fluid coupled ultrasonic applications. In an effort to obtain matching layers suitable for use in gasses, we have also investigated the effect of loading these materials with glass microspheres, at a range of densities, allowing a further reduction in the acoustic impedance of the matching layer. Several prototype plate waveguide transducers, with integrated matching layers, have also been constructed and experimentally validated in the lab. The experimental validation includes: measuring the pressure field emitted from this plate using a wide band microphone, static pulse echo experiments in a tank and laser interferometry to study the dilation behaviour of the device.

### Results/Discussion

It has been shown that a matching layer, suitable for extreme temperatures, can be made for an ultrasonic flow meter transducer with a plate waveguide buffer. The addition of this matching layer gives an, approximately threefold, improvement in the transmission of ultrasonic waves from the waveguide into a test fluid. Allowing the flow meter to function more efficiently in harsh environments and consequently make it applicable to many practical applications.

## AlN-Si ultrasonic MEMs energy harvester for medical sensors

Victor Klymko<sup>1</sup>, Ruth Houlihan<sup>2</sup>, Brendan O'Flynn<sup>2</sup>, Javier Torres<sup>2</sup>, John Buckley<sup>2</sup>, Elena Lomonova<sup>1</sup>; <sup>1</sup>Eindhoven University of Technology, Eindhoven, Netherlands, <sup>2</sup>Tyndall National Institute, Cork, Ireland

### Background, Motivation and Objective

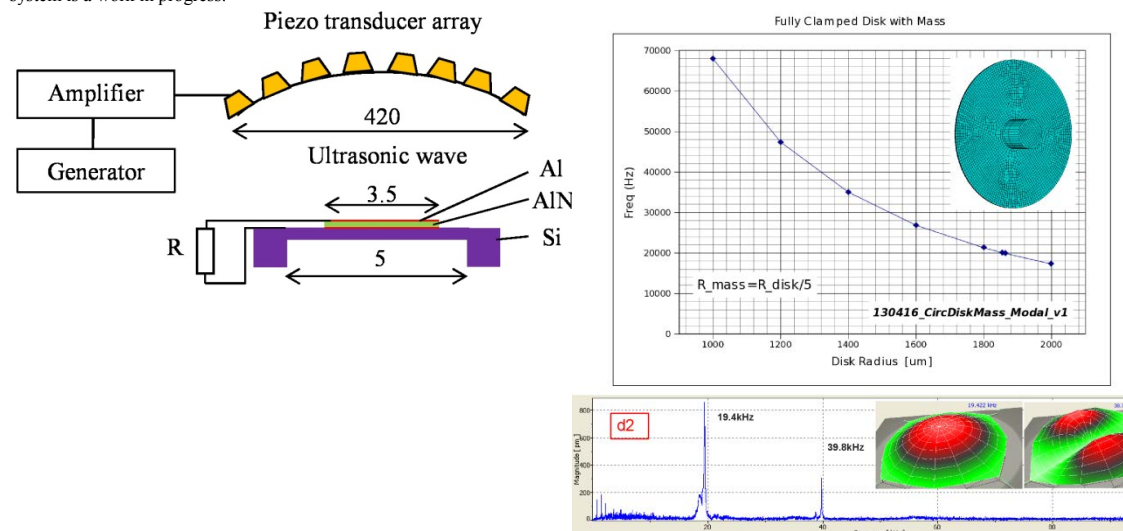
An energy scavenging system based on the use of an ultrasonic pressure field excitation is described for powering motion sensors that are located on a patient inside an MRI machine. The harvester is proposed as a wireless power source for the motion sensors that compensate for the motion of the patient during the MRI scan to reduce artifacts and noisy data. The system requires an ultrasonic wave source, which does not impact adversely on the magnetic fields. The ultrasonic source is a piezoelectric transducer array placed on the inner surface of the MRI bore. The harvester is placed at the point of maximum ultrasonic pressure on the patient's chest.

### Statement of Contribution/Methods

The piezoelectric harvesters were fabricated in a CMOS compatible process using SOI wafers and Aluminium Nitride (AlN) as the active layer. The membranes comprise a 25µm thick device silicon layer in addition to thin film passivation, AlN and metal layers. The bulk silicon beneath the membrane is removed in a dry etch process. Simple circular membranes with a 5mm diameter as well as 3.7mm diameter membranes with a centrally located mass were designed for resonance at 20kHz. The measured resonance of the membranes is within 10% of the simulated frequency.

### Results/Discussion

In the experiment described, pressure measurements up to 12 Pa are generated using the piezoelectric transducer array at the resonant frequency of the harvester. The harvester is placed at the point of maximum pressure, loaded with a set of resistors, and the output voltage and power is measured with an oscilloscope. The harvester generates 1.4 mV output with 3 kΩ load, which corresponds to a harvested power level of 0.65 nW. Integration of an array of the AlN harvesters with a low input voltage AC/DC converter and a storage system is a work in progress.



## P3C1 - Ultrasonic Motors

Salon C

Saturday, September 6, 2014, 8:00 am - 5:00 pm

Chair: **Minoru Kurosawa**  
Tokyo Institute of Technology

P3C1-1

### Rotary Motion Generated by Synthesized Circular / Elliptic Drive with Straight-Move Ultrasonic Motors

Yusuke Nagira<sup>1</sup>, Mitsutaka Hikita<sup>1</sup>; <sup>1</sup>Faculty of GE, Kogakuin Uni., Tokyo, Japan

#### Background, Motivation and Objective

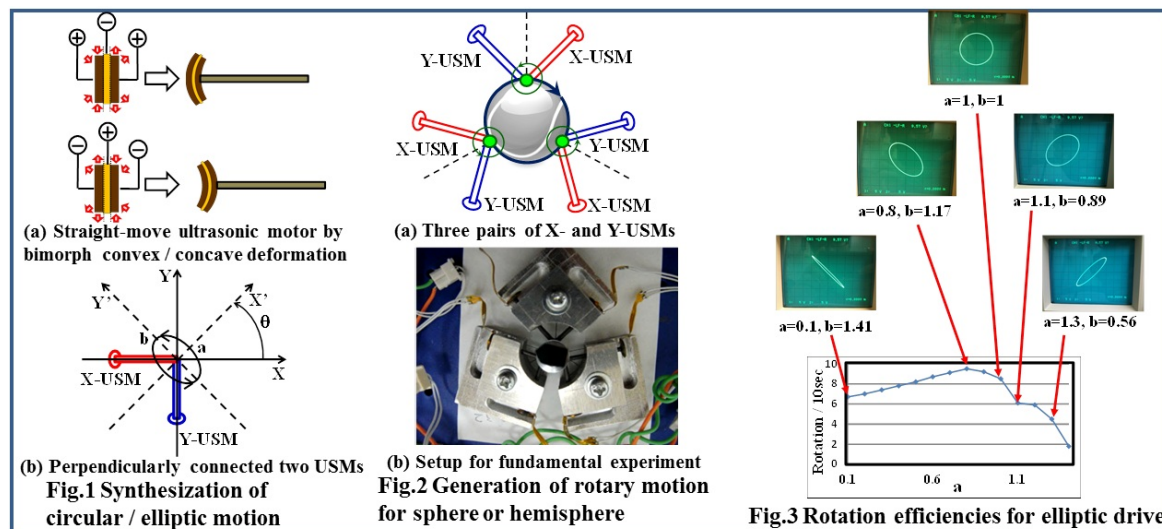
Ultrasonic motors have been widely used in consumer and industrial products. However recent high-performance machines such as robot hands, stage of direct-drawing machines, etc. require much complicated movements (Ref. 1). The target of our study is realization of simultaneous rotation and movement in any directions to meet above requirements. In this paper, we achieve rotation of a sphere or a rod with hemisphere end by newly synthesized circular / elliptic motion using perpendicularly connected two straight-move ultrasonic motors (USMs) as a basic unit. This structure can be one of the most fundamental structures to achieve more complicated movements in the future.

#### Statement of Contribution/Methods

A back-and-forth piston-type movement is achieved by a shaft attached to bimorph (Fig. 1(a)). Therefore, circular / elliptic motion with arbitrary axes of X prime and Y prime can be synthesized by controlling amplitudes and phases of perpendicularly connected X- and Y-USMs on original X and Y coordinate (Fig. 1(b)). Three pairs of basic units with the X- and Y-USMs are arranged at apexes of an equilateral triangle with 120 degrees one another (Fig. 2(a)). This system can generate rotary motion for a sphere or a rod with end of hemisphere contacted to the system. Fundamental experiments were conducted using the setup shown in Fig. 2(b). Driving voltages for X- and Y-USMs can be controlled independently. Amplitudes and phases for the motions of X- and Y-USMs were determined by those of the driving voltages.

#### Results/Discussion

Experimental results using about 70 kHz USMs are shown in Fig. 3. In the experiment, total power supplied to X- and Y-USMs is kept constant, i.e.  $a^2 + b^2 = C$ . The condition with  $a = b = 1$  corresponds to circular drive. Elliptic drive with  $a = 0.8$  and  $b = 1.17$  has the most effective rotation efficiency. From the experiment, the validity of our proposal based on synthesis of independent X and Y straight motions was confirmed. The wrist of robot hands requires not only rotation but also bending motion. A basic unit with perpendicularly connected three USMs is necessary in this case. To achieve such three-dimensional movement next, we will develop the system where four pairs of the units are arranged at apexes of regular tetrahedron. 1. Y. Nagira and M. Hikita, in Proc. of USE2013.



P3C1-2

### A Simple Mathematical Model for Piezoelectric Motor Based on Elastic Beams

Maoying Zhou<sup>1</sup>, Weiting Liu<sup>1</sup>, Xin Fu<sup>1</sup>; <sup>1</sup>The State Key Lab of Fluid Power Transmission and Control, Hangzhou, Zhejiang Province, China, People's Republic of

#### Background, Motivation and Objective

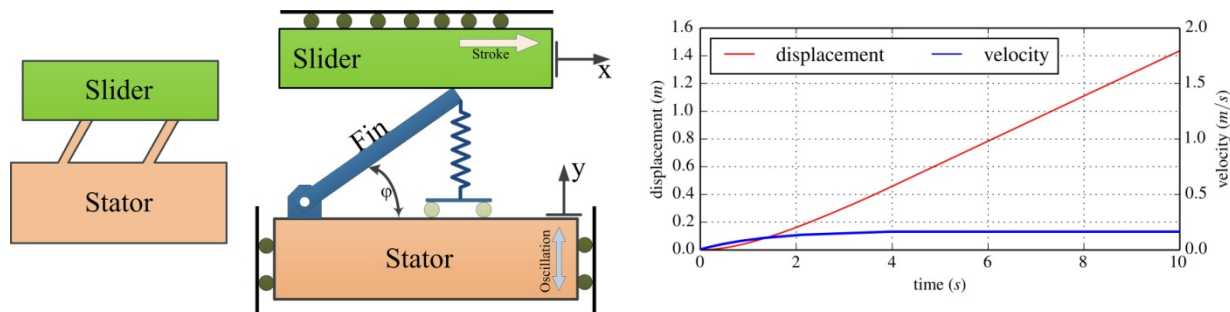
During past decades, standing wave piezoelectric motors have been widely studied for different applications. Their structure is usually simple with a structure attached to the stator and pressed onto the rotor or slider. During operation, excitation of the stator by piezoelectric elements induces the beam structure to vibrate and drives the rotor or slider to move. Despite their simple structure, reliable model of these motors is quite difficult because of the complex friction contacts between the stator and the rotor or slider, and the nonlinear response of the beam. Existing theoretical models tends to base the analysis on the quasi-static simplification of the beam model and the decomposition of longitudinal and transverse vibration of the beam tips. In this study, we report a simple mathematical model to investigate the transient and stable motion of elastic fin piezoelectric motors.

# Statement of Contribution/Methods

In the model, the elastic beam is equivalently described as a rigid link together with a linear spring. Piezoelectric actuation to the stator is treated as the periodically displacement base excitation of the stator itself. A Coulumb friction model is adopted to describe the stick, slip and separation contact status of the motor. Fig. 1 shows the equivalently modeling process of the motor.

# Results/Discussion

The transient response of the motor is calculated using computational method. Results show that after a short period of startup operation, velocity of the slider turns into stable operation and varies periodically around a mean value. Fig. 2 shows the simulated displacement of the slider, the transient velocity of the slider and the horizontal component of the velocity of the beam tip, respectively.



P3C1-3

# Evaluation of Thermal Stress of Transducers for Cryogenic Ultrasonic Motors

Yuya Noguchi<sup>1</sup>, Daisuke Yamaguchi<sup>1</sup>, Takefumi Kanda<sup>1</sup>, Koichi Suzumori<sup>1</sup>; <sup>1</sup>Graduate School of Natural Science and Technology, Okayama University, Okayama, Okayama, Japan

# Background, Motivation and Objective

In our previous study, an ultrasonic motor for cryogenic temperature was mainly made of stainless steel [1]. However, the motor had large thermal stress when the driving temperature decreased to a cryogenic temperature. The performance of the motor was degraded by the thermal stress. Additionally, the pre-load of transducer needed adjustment at the each temperature. In order to solve the problem, we have designed new transducer to reduce the thermal stress.

# Statement of Contribution/Methods

Figure 1 shows a schema of transducer. In order to estimate the thermal stress, transducers mainly made of Ti or Invar were designed. These materials have small thermal expansion coefficients compared with stainless steel. As a result of finite element method analysis, the thermal stress at the transducer made of Ti was the smallest. Transducers made of Ti or Invar were fabricated and evaluated. To measure the thermal stress from room temperature to 4.5 K, admittance of the transducers has been compared.

# Results/Discussion

Figure 2 shows the relationship between temperature and optimum clamping torque. The transducer made of Ti had the smallest shift of optimum clamping torques at temperature fewer than 270 K. A motor using the transducer made of Ti was fabricated and evaluated. When the temperature was 4.5K, and applied voltage was 100 Vp-p, the rotation speed and starting torque of the motor were 1102 rpm and 80.6uNm. The efficiency of the motor using transducer made of Ti was 5 times larger than that of stainless steel at 4.5 K.

[1] D.Yamaguchi, T.Kanda, K.Suzumori, "Evaluation of Piezoelectric Materials for Cryogenic Ultrasonic Motor", 2013 IEEE Ultrasonics Symposium, pp. 205-207

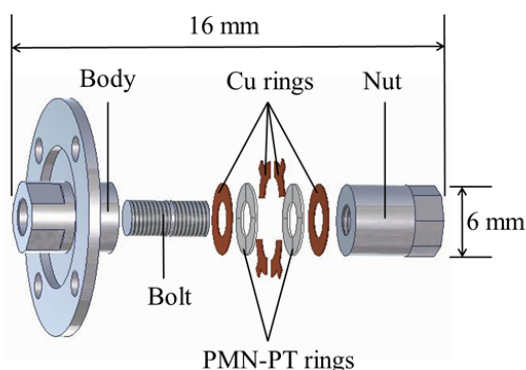


Fig. 1 Structure of bolt-camped Langevin-type transducer for cryogenic temperature

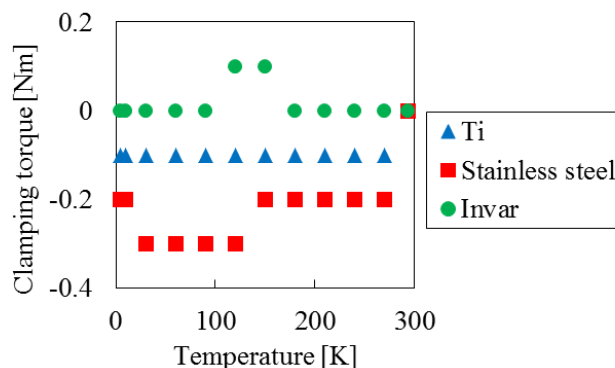


Fig. 2 Relationship between temperature and shift of optimum clamping torque of transducers



## P3C1-4

**Enlargement of floator size in ultrasonic suspension by arranging the shape of vibrating surface**Kota Uchiage<sup>1</sup>, Yuji Ishino<sup>1</sup>, Masaya Takasaki<sup>1</sup>, Takeshi Mizuno<sup>1</sup>; <sup>1</sup>Mechanical Engineering, Saitama University, Saitama-shi, Japan**Background, Motivation and Objective**

Recently, a vacuum gripper equipped on a robotic arm is used for handling small object like electric components. Today, demand of miniaturization of the components is growing with miniaturization of various products. As a result, conventional handling techniques have some problems, such as lacking of positioning accuracy, electrostatic adhesive force preventing release of objects, and so on. They have also risks of components damage because of contact between gripper and dust due to the contact. It is a serious problem for semiconductor substrates or silicon wafers. It is preferable to handle these components by non-contact handling technique. Previously, we proposed non-contact handling using ultrasonic vibration. This phenomenon is called ultrasonic suspension. A planar object can be suspended vertically downward with a gap of tens micrometers from vibrating surface. This handling technique has some advantages such as non-contact, independent from material, low cost, easy to release and restoring force acting in horizontal direction.

**Statement of Contribution/Methods**

In previous research, the attractive force acting on the object has been measured during the ultrasonic suspension. According to measurement results, it was found that by enlarging the size of facing area of vibrating surface and floator, the attractive force does not become bigger but only the repulsive force is generated. The attractive force can be generated while the ultrasonic suspension is occurred because air flows in and out from the gap between vibration surface and object. Attractive force seems to be generated in the vicinity of boundary. For this reason, it is expected that an attractive force can be strengthened by increasing the boundaries. In this research, grooves are formed on the vibrating surface which is larger than that of conventional transducer. Therefore, the method for increasing the total force by generating attractive force along each part of boundary is proposed. We expect to solve the problem of the enlargement of the floator using the new suspension method.

**Results/Discussion**

An ultrasonic transducer with large vibrating surface was fabricated. Patterned grooves were machined on the surface. Using the transducer, experiment of suspending a glass plate was conducted and suspension of the plate was confirmed. Maximum attractive force was estimated from the mass of glass plate. It was found that maximum attractive force was eight times larger than that of conventional suspension in the case of the same vibration amplitude. On the other hand, normalized maximum attractive force was half. Therefore, in order to increase attractive force in same area, optimization of the shape of vibrating surface and groove patterns will be required.

## P3C1-5

**Ultrasonic Motors Using Polymer Vibrator**Jiang Wu<sup>1</sup>, Yosuke Mizuno<sup>1</sup>, Kentaro Nakamura<sup>1</sup>, Shigeki Kambara<sup>2</sup>, Naoto Okuyama<sup>2</sup>, Kiyoshi Shimizu<sup>2</sup>; <sup>1</sup>Precision and Intelligence Laboratory, Tokyo Institute of Technology, Japan, <sup>2</sup>DAICEL Corporation, Japan**Background, Motivation and Objective**

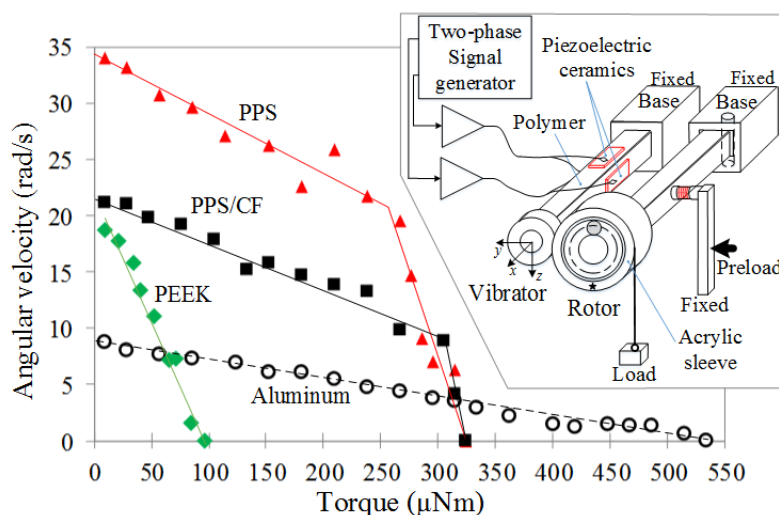
With the mature of low density and elastic modulus, polymers are promising materials for making light weight and large output ultrasonic motor (USM) if the mechanical loss is low enough at ultrasonic frequency. Exploring the possibility of polymers as vibrator for USM, in this paper, we investigated the characteristics of USM using polymer vibrator experimentally and found several polymers suitable for high amplitude vibration in USM operation. To our knowledge, this shall be the first report of polymer-based USM since its original invention.

**Statement of Contribution/Methods**

We tested polyetheretherketone (PEEK), polyphenylenesulfide (PPS) and polyphenylenesulfide filled with carbon fiber (PPS/CF) to make a bimorph to form a rotary USM, and compared its mechanical performances to the aluminum USM with the same structure and dimensions. Two pairs of piezoelectric ceramic plates are bonded on the side surface of a rectangular bar made of polymers. Two orthogonal bending vibrations are excited with the 90-phase difference using a two-phase electrical source. A rotor pressed to the end side of the vibrator, is driven by the elliptical motion of the vibrator end.

**Results/Discussion**

The polymer-based USM successfully worked as in the same way of conventional metal-based USM. Rotation speed was measured with changing the load. (1), USMs made by polymers have higher angular velocity and lower torque than the aluminum USM at the same driving voltage. (2), PPS-based USM has the largest output power among all the tested polymer prototypes, which indicates that PPS is prospective for lightweight and high speed USM.



### Actual Measurement of Surface Acoustic Wave Motor Thrust

Minoru Kurosawa<sup>1</sup>, Takehiro Yokoyama<sup>2</sup>; <sup>1</sup>Tokyo Institute of Technology, Yokohama, Japan, <sup>2</sup>Tokyo Institute of Technology, Japan

#### Background, Motivation and Objective

A surface acoustic wave (SAW) motor is small and low in profile with high speed and large thrust in linear motion. Hence the performance has been evaluated from transient response even though the reliability is rather low. We tried to measure the thrust directly using loading mass.

#### Statement of Contribution/Methods

Difficulty of thrust evaluation by loading mass is tiny size of the slider in mm dimensions and huge thrust in several N. Moreover, the moving distance of the SAW motor is short in a few cm as shown in Fig. 1. Hence the SAW motor has to be stopped before the mechanical system for the measurement becoming in static condition. The loading mass of water filled white tank in Fig.1 was connected with steel wires even though the wires were elastic. But we cannot use bulky material for mass connection due to small size as shown in Fig.1. With this measurement system, by evaluating the stretch of the steel wire, the speed vs. load was successfully measured.

#### Results/Discussion

Estimated SAW motor load performances are shown in Fig.2. A blue line was calculated from a transient response by curve fitting. Red open circles were estimated values of the mechanical loading force from actual loaded operation of the SAW motor; the loading force was estimated from the wire elasticity and the stretching value from the measurement using two sets of laser Doppler velocimeter (LDV). We successfully proved that the actual SAW motor thrust is 60 % larger than that of the estimated value from transient response; 4.0 N against 2.5 N for example.

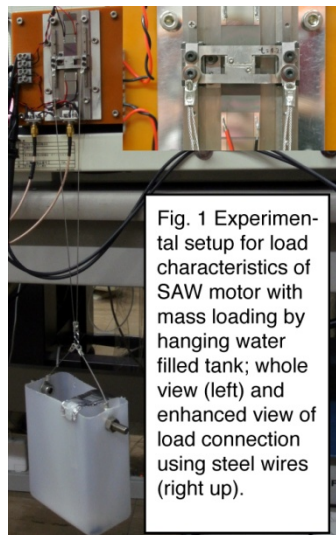


Fig. 1 Experimental setup for load characteristics of SAW motor with mass loading by hanging water filled tank; whole view (left) and enhanced view of load connection using steel wires (right up).

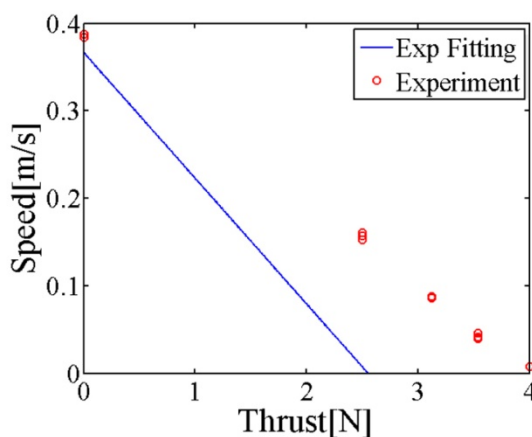


Fig.2 Load characteristics of SAW motor; calculated from transient response (blue line), and estimated by actual mass loaded with elastic wire including wire elastic force compensation (red circles).

### Measurements of sliding friction forces under ultrasonic oscillations: out-of-plane oscillations

Soohyun Kim<sup>1</sup>, Youngjae Min<sup>1,2</sup>, Young H. Kim<sup>1</sup>; <sup>1</sup>Applied Acoustics Lab, Korea Science Academy of KAIST, Busan, Korea, Republic of, <sup>2</sup>Korea Advance Institute of Science and Technology, Daejeon, Korea, Republic of

#### Background, Motivation and Objective

In-plane oscillation has been mainly considered for the reduction of friction forces. Littmann and Stork explained the reduction of friction forces of in-plane oscillation with the theoretical model based on Coulomb's friction model [1, 2]. The reduction of friction forces due to out-of-plane oscillation were not considered in the previous works. However, out-of-plane oscillations are expected to be sufficiently effective to reduce friction forces according to cold-welding theory.

In the present work, a new method to measure sliding friction force was implemented. The friction forces were measured for varying amplitude of ultrasound oscillation.

#### Statement of Contribution/Methods

Photograph and schematic diagram of system developed in the present work are shown in Figure 1. A massive disk rotates by the torque produced by a weight, and out-of-plane oscillation were applied by BLT ultrasonic transducer. The rotational motions were detected by photo-sensor which is reading the strips on the side of the rotating disk. Angle versus time graph can be constructed from photo-sensor signal as shown in Figure 2, and angular accelerations were obtained from curve fitting of angle versus time graph.

When a friction force is exerted on the rotating disk, angular acceleration is changed. Therefore measuring angular acceleration enables to determine friction force.

#### Results/Discussion

Figure 3 shows measured friction force as a function of amplitude of ultrasonic oscillation. As increasing amplitude of ultrasonic oscillation, friction force was decreased. It implies that out-of-plane oscillation can also reduce friction force.

[1] W. Littmann, H. Stork and J. Wallaschek: Arch. Appl. Mech. **71** (2001) 549-554.

[2] H. Stork, W. Littmann, J. Wallaschek and M. Mracek: Ultrasonics **40** (2002) 379-383.

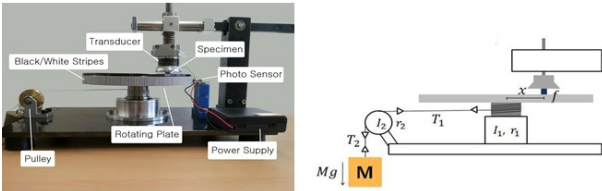


Figure 1

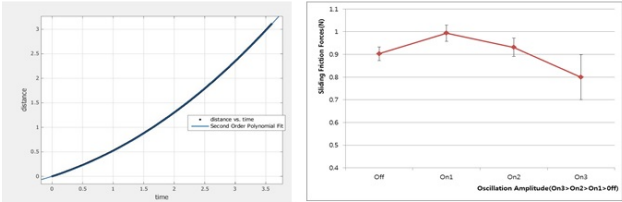


Figure 2

Figure 3

## P3C2 - Thin-Films 2

Salon C

Saturday, September 6, 2014, 8:00 am - 5:00 pm

Chair: **Alexandre Reinhardt**  
CEA-Leti, Minatec Campus

P3C2-1

### Enhancement of piezoelectric properties in Pb(Zr,Ti)O<sub>3</sub> thin films by electric field induced phase transition

Veronika Kovacova<sup>1</sup>, Nicolas Vaxelaire<sup>2</sup>, Patrice Gergaud<sup>2</sup>, Gwenaél Le Rhun<sup>2</sup>, Emmanuel Defay<sup>2</sup>; <sup>1</sup>CEA, Grenoble, France, Metropolitan, <sup>2</sup>CEA, France, Metropolitan

#### Background, Motivation and Objective

Although efficient lead-free piezoelectric thin films have been recently proposed in the literature, lead-based films as Pb(Zr,Ti)O<sub>3</sub> (PZT) or Pb(Mg,Nb)O<sub>3</sub>-PbTiO<sub>3</sub> always exhibit the best piezoelectric properties, namely at the so-called morphotropic phase boundary (MPB). For PZT, the MPB corresponds to the Zr/Ti atomic ratio close to 52/48. Three phases coexist at this composition, namely tetragonal, rhombohedral and monoclinic. In 2011, Hinterstein et al. showed by in situ observations that bulk ceramic MPB PZT experiences a tetragonal-to-monoclinic phase transition while electric field is applied [1]. An open question is therefore whether there is a correlation between piezoelectric effect and this field-induced phase transition versus tetragonal domain switching in thin films. Here, we show in situ structural modifications in MPB PZT films versus electric field in correlation with their piezoelectric properties.

#### Statement of Contribution/Methods

In order to evidence the link between piezoelectric effect and the microstructure modification, we studied by in situ X-ray diffraction two capacitors made of MPB PZT thin films with different chemical and electrical characteristics, namely Zr/Ti gradient within the thin layer and effective transverse piezoelectric coefficient  $e_{31,eff}$ . The diffraction profiles collected under different voltages were analyzed by MAUD program and microstructure modification has been quantified.

#### Results/Discussion

The in situ XRD analysis shows tetragonal-to-rhombohedral phase transition induced by electric field within both Gradient (G) and Gradient Free (GF) PZT films as shown in the figure 1. Moreover, the larger the amount of phase transition from tetragonal to rhombohedral is, the larger the  $e_{31,eff}$  coefficient is measured. Note that  $e_{31,eff}$  are 14,6 C/m<sup>2</sup> and 16,6 C/m<sup>2</sup> respectively for G and GF PZT. Improvement of the field-induced phase transition was obtained by decreasing the microscopic chemical gradient throughout the PZT films, which increased the amount of MPB composition within the PZT film. Further enhancements of PZT piezoelectric properties can be predicted. For example, optimized sputtered PZT films, without built-in gradient, should exhibit even better  $e_{31,eff}$ .

Reference:

[1] M. Hinterstein, J. Rouquette, J. Haines, Ph. Papet, M. Knapp, J. Glaum and H. Fuess, Phys. Rev. Lett. 107, 077602 (2011)

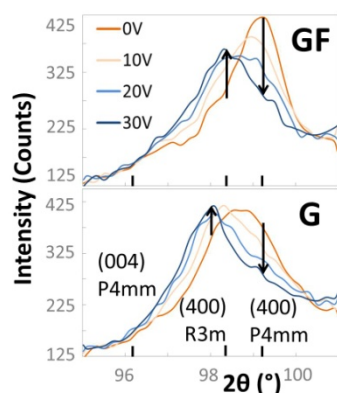


Figure 1:  $\theta$  -  $2\theta$  profile evolution of G and GF PZT films vs different voltages. {400} peak positions of P4mm and R3m phases are also indicated.

P3C2-2

### Effect of sputtering target temperature on crystalline orientations of ZnO piezoelectric films in RF magnetron sputtering

Chihiro Takata<sup>1</sup>, Shinji Takayanagi<sup>1</sup>, Takahiko Yanagitani<sup>2</sup>, Mami Matsukawa<sup>1</sup>; <sup>1</sup>Faculty of Science and Engineering, Doshisha University, Kyotanabe, Japan, <sup>2</sup>Graduate School of Engineering, Nagoya Institute of Technology, Nagoya, Japan

#### Background, Motivation and Objective

ZnO film tends to orient the most close-packed (0001) plane. However, if energetic ions bombard the substrate during an RF magnetron sputtering, the (0001) grain growth is suppressed, and c-axis parallel (11-20) and (10-10) films can be grown. These films are suitable for shear horizontal type SAW device [1]. In previous studies, we have reported that c-axis parallel oriented films can be obtained by O<sup>+</sup> bombardment from ZnO target as shown in Fig. 1(a) [2]. The ion bombardment and the final crystalline orientations of the films depended on the sputtering conditions. In this study, we focused on the target temperature during the sputtering, taking the energy distribution of ions which enter the substrate into consideration. The effect of sputtering target temperature on crystalline orientation was investigated.

### Statement of Contribution/Methods

We measured flux and energy of the ion which enter the substrate during the RF magnetron sputtering. In order to change the target temperature, the targets were bonded or not bonded to the cooled cathode. Sputtering conditions for c-axis parallel oriented film were used in previous study [2] except for target temperature. In the same sputtering conditions, ZnO films were grown on silica glass substrates and the crystalline orientation were measured by XRD analysis.

### Results/Discussion

Fig. 1(b) shows the energy distribution of  $O^-$  ions during the sputtering.  $O^-$  flux in 150-380 eV increased by changing target temperature from 380 to 540°C. On the other hand, the positive ion distribution did not change significantly with the increase of the target temperature. Fig. 1(c) shows XRD patterns of the samples. An intense (10-10) peak was observed in the sample at the target temperature of 540°C, and the full width at half maximum (FWHM) of the (10-10) plane rocking curve was 12.8°. On the other hand, an intense (11-20) peak was observed in the sample at the target temperature of 390°C, and the FWHM of the (11-20) plane rocking curve was 3.4°. The ion bombardment decreased with the decrease of target temperature, in consequence, the preferred orientation of ZnO changed from (10-10) to (11-20) plane and the crystalline orientation was improved.

[1] A. Tanaka, et al., IEEE TUFFC, **55**, 2709-2713 (2008).

[2] S. Takayanagi et al., Appl. Phys. Lett., **101**, 232902 (2012).

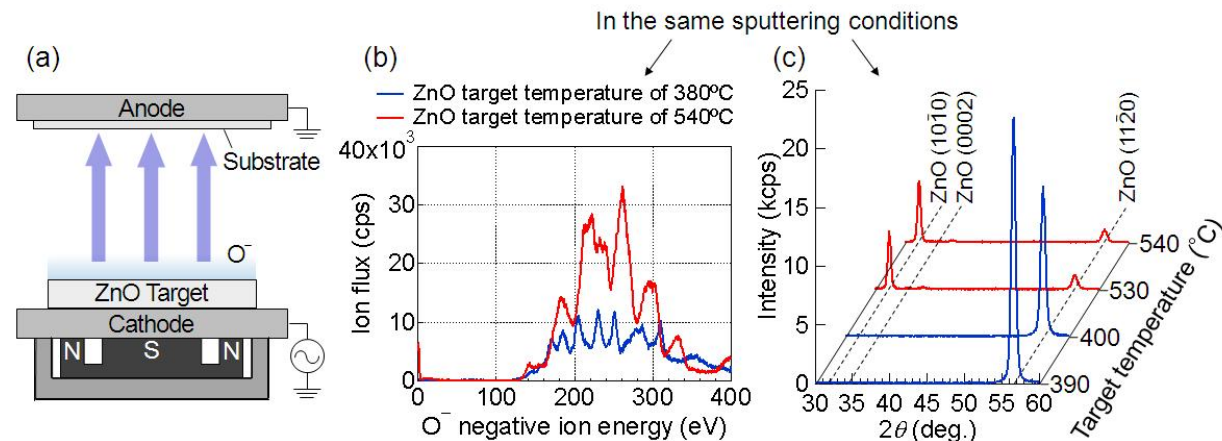


Fig. 1 (a)  $O^-$  ion is generated from ZnO target during the sputtering. (b) Energy distributions of  $O^-$  which enter the substrate and (c) XRD patterns of the ZnO film samples.

### P3C2-3

#### Silicon Poisson ratio influence on thin film piezoelectric coefficient extraction

Veronika Kovacova<sup>1</sup>, Julie Abergel<sup>1</sup>, Gwenaél Le Rhun<sup>1</sup>, Schmitz-Kempen Thorsten<sup>2</sup>, Emmanuel Defay<sup>1</sup>; <sup>1</sup>CEA LETI, France, <sup>2</sup>Aixacct, Germany

#### Background, Motivation and Objective

In the field of piezoelectric microsystems, the piezoelectric coefficient  $e_{31,eff}$  is often considered as the most important one. Indeed, it is involved in structures as membranes and cantilevers. Therefore, it is fundamental to determine  $e_{31,eff}$  accurately. To do so, the standard method is based on four-point bending set up. The idea is to collect the charges induced by the controlled bending of a beam on which the piezoelectric film has been deposited. Nowadays, Aixacct 4PB tool is considered as the reference to extract  $e_{31,eff}$  [1]. According to [1],  $e_{31,eff}$  is proportional to  $1/(1-\nu_{Si})$  with  $\nu_{Si}$  Silicon Poisson ratio, as observed in equation 1.

$$e_{31,eff} = QI^2 / (4Ah(1-\nu_{Si}))$$

Equation 1

with  $Q$  the collected charge,  $I$  the bending distance,  $A$  the electrode area,  $h$  the cantilever thickness and  $u$  the cantilever imposed displacement (cf [1] for set up details). In this paper, we propose to exemplify the fundamental role played by  $\nu_{Si}$  in extracting  $e_{31,eff}$  through the characterization of AlN thin films deposited on Si substrate and cut along different crystallographic orientations.

#### Statement of Contribution/Methods

It is well known that single crystal silicon exhibits different mechanical behaviour according to its crystallographic orientation [2]. In particular, for (100) oriented substrates, Poisson ratio varies from 0.06 to 0.28 respectively along direction [110] and [100]. Therefore, a wrong utilisation of Si orientation induces an error that can be as high as 30% in  $e_{31,eff}$  according to equation 1. Here, we deposited 0.8µm-thick AlN films by dc-pulsed sputtering on (100) Si 200mm substrates (see [3] for details). AlN has been chosen because its isotropic properties are very stable and reproducible as it was initially developed for Bulk Acoustic Wave resonators [4]. 100nm-thick Mo acts as bottom electrode whereas the top electrode is made of 80nm-thick Pt with 2 x 10 mm<sup>2</sup> rectangular shape, according to [1]. The film  $e_{31,eff}$  has been characterized with 4PB Aixacct apparatus [1], which requires preparing 25 x 3 mm<sup>2</sup> testing dies. Two types of AlN dies, cut respectively along <100> and <110> Si direction, were prepared and tested.

#### Results/Discussion

Thanks to the reproducible nature of AlN films, both samples exhibited exactly the same  $e_{31,eff} = -1.0$  C/m<sup>2</sup>, but at the very condition that one uses the correct Poisson ratio in equation 1 for each orientation. It is worth noting that using wrong  $\nu_{Si} = 0.28$  for [110] oriented beam – the natural cleavage direction of (100)Si – yields  $e_{31,eff} = 1.30$  C/m<sup>2</sup>, which is 30% larger than the correct value.

#### References

- [1] K. Prume et al., J Electroceram (2007) 19:407-411
- [2] J. J. Wortman and R. A. Evans, Journal of Applied Physics 36, 153 (1965)
- [3] P. Ivaldi et al., Journal Of Micromechanics And Microengineering 21 (8), 085023 (2011)
- [4] D. Petit et al., 2009 IEEE International Ultrasonics Symposium - Rome, 2016 (2009)



P3C2-4

# PZT Films Piezoelectric Properties From Ambient To 340°C

Julie Abergel<sup>1</sup>, Gwenael Le Rhun<sup>1</sup>, Alexandre Reinhardt<sup>1</sup>, Denis Blachier<sup>1</sup>, Aurelien Suhm<sup>1</sup>, Emmanuel Defay<sup>1</sup>, <sup>1</sup>CEA LETI, France

## Background, Motivation and Objective

Thanks to the reversible nature of piezoelectricity, PZT films can be used as sensors or actuators. Contrary to sensor applications, poling is no more an issue for thin films actuators as the applied voltage acts as the poling voltage as well. In the literature, PZT films have been characterized versus temperature, but only on the sensor mode where  $e_{31,eff}$ , the transverse piezoelectric coefficient, starts decreasing at 50°C [1]. Here, we propose to measure  $e_{31,eff}$  of PZT thin films with a permanent bias voltage versus temperature from 20°C to 340°C on a membrane device.

## Statement of Contribution/Methods

We prepared 1.6μm-morphotropic PZT films by sol gel atop platinized 200mm Silicon On Insulator wafers ([2]). Bulk Si was etched using Deep Reactive Ion Etching, in order to obtain SiO<sub>2</sub>/5μm-SOI/SiO<sub>2</sub>/TiO<sub>2</sub>/Pt/PZT/Ru rectangular membranes (300 x 1000 μm<sup>2</sup>). Finite Element Model simulation has been performed to identify the first bending mode taking place at 375 kHz. The membranes resonances were observed by monitoring their impedance versus frequency at constant bias voltage, namely 10V. The effective electromechanical coupling  $k_{eff}^2$  was obtained by extracting the resonance and anti-resonance frequencies [3].  $k_{eff}^2$  is proportional to  $e_{31,eff}^2$  in membranes and inversely proportional to the dielectric constant and the effective stiffness of the membrane. Therefore, the membrane frequencies together with PZT dielectric constant have been measured from ambient to 340°C. Eventually,  $e_{31,eff}(T)$  has been extracted.

## Results/Discussion

The described method gives the opportunity to follow the ratio  $e_{31,eff}(T)/e_{31,eff}(T=20°C)$ , as shown in figure 1. It shows that PZT films exhibit a strong piezoelectric activity until at least 340°C. More specifically, at 340°C,  $e_{31,eff}$  is still 95% the value at room temperature, which is typically -20 C/m<sup>2</sup> [2]. Therefore, this study proves that PZT films can be efficiently used as actuators at least until 340°C without losing their piezoelectric properties, as long as bias voltage is applied, contrary to what has been observed on the same films in sensor mode, that is to say without bias voltage [1].

## References

- [1] C. Rossel et al., Journal of Applied Physics 115, 034105 (2014)
- [2] J. Abergel et al., IEEE International Ultrasonics Symposium (2012), pp. 972-974.
- [3] IEEE Standard on Piezoelectricity, ANSI/IEEE Std 176-1987

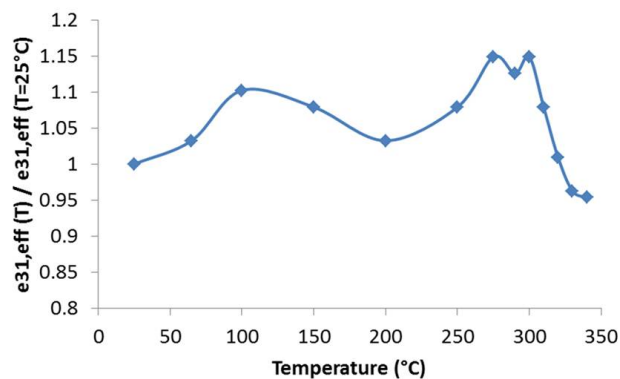


Figure 1:  $e_{31,eff}(T)/e_{31,eff}(T=20°C)$  of 52/48 PZT thin films versus temperature with 10V-bias voltage

P3C2-5

# Effect of Sc concentration on shear wave velocities in ScAlN films measured by micro-Brillouin scattering technique

Hayato Ichihashi<sup>1</sup>, Takahiko Yanagitani<sup>2</sup>, Shinji Takayanagi<sup>1</sup>, Mami Matsukawa<sup>1</sup>, <sup>1</sup>Doshisha University, Japan, <sup>2</sup>Nagoya Institute of Technology, Japan

## Background, Motivation and Objective

ScAlN film is attractive for the BAW and SAW resonators. However, although the elastic properties are necessary for BAW and SAW modeling, the shear elastic properties in the ScAlN have not been investigated yet. In this study, we investigated the shear wave velocities in ScAlN films with various Sc concentrations using a micro-Brillouin scattering technique ( $\mu$ -BR).

## Statement of Contribution/Methods

The horizontal shear wave propagating at in-plane ( $v^2 = c_{66}^E/\rho$ ) in (0001) ScAlN films with various Sc concentrations were measured using  $\mu$ -BR. The c-axis normal ScAlN films with Sc concentrations of 0 %, 21 %, and 33 % were fabricated using an RF magnetron sputtering system. All films (thickness: around 5 μm) were deposited on the Al or Ti films/silica glass substrate. The  $\mu$ -BR system is composed of a Tandem Fabry-Perot interferometer (JRS), a solid state laser (wavelength: 532 nm, Spectra Physics), and the reflection induced  $\Theta$ A scattering geometry [1]. The diameter of the measurement area was less than 10 μm.

## Results/Discussion

Figure 1(a) shows an observed Brillouin spectrum of the ScAlN film with Sc concentration of 33 %. There were several Brillouin peaks in the data. By checking the polarization of the scattered light, Brillouin scattering peaks around 13 GHz (peak A) were identified as the shear wave. The precise frequency shift was determined by fitting a Voigt function to

the peak and the shear wave velocity was from this frequency shift. Figure 1(b) shows shear wave velocities in ScAlN films as a function of Sc concentration. As can be seen, the velocities of shear waves decreased with the increase of Sc concentration. This tendency does not conflict with our previous studies on the longitudinal wave velocity in ScAlN films [2]. In the films with Sc concentration less than 33%, both longitudinal and shear wave velocities decreased with the increase of concentration.

[1] J. K. Krüger, et, al: J. Phys. D: Appl. Phys. 31 1913 (1998)

[2] T. Yanagitani et al., presented in IUS 2012, 6H-2.

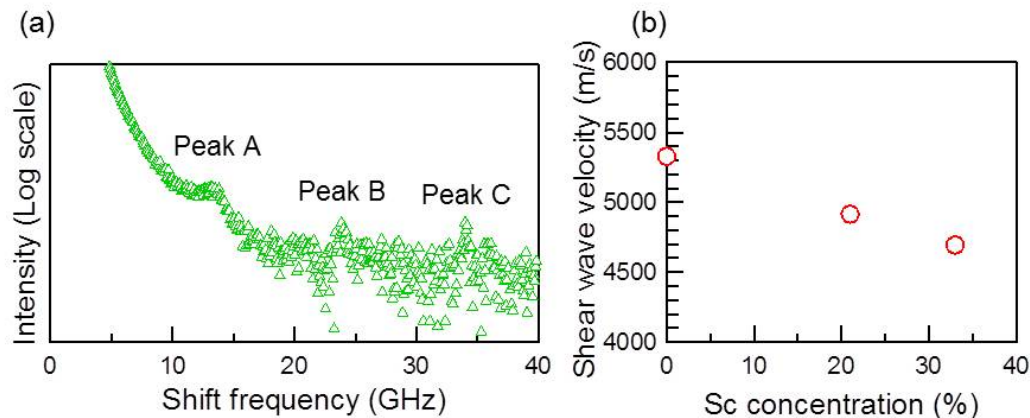


Fig. 1 (a) Observed Brillouin spectrum of a ScAlN film with Sc concentration of 33 %.  
(b) Shear wave velocities in ScAlN films as a function of Sc concentration.

## P3C3 - Phononics 2

Salon C

Saturday, September 6, 2014, 8:00 am - 5:00 pm

Chair: **Anne-Christine Hladky**  
IEMN

P3C3-1

### Extractions of reflection and velocity parameters for surface acoustic wave in two-dimensional piezoelectric phononic crystals

Yahui Tian<sup>1</sup>, **Honglang Li**<sup>1</sup>, Yabing Ke<sup>1</sup>, Wei Luo<sup>2</sup>, Shitang He<sup>1</sup>; <sup>1</sup>Institute of Acoustics, Chinese Academy of Sciences, Beijing, China, People's Republic of; <sup>2</sup>School of optical and electronic information, Huazhong university science and technology, Wuhan, China, People's Republic of

#### Background, Motivation and Objective

Interdigital transducers (IDTs), as one-dimensional (1D) phononic crystals (PCs), have obtained much attention for many years in applications of resonators, filters and sensors. Much effort has done to calculate the parameters such as reflection and velocity for designing Surface Acoustic Wave (SAW) devices [1]. Recently, two-dimensional (2D) piezoelectric PCs obtain more attention as they have richer properties of band gaps than 1D PCs. Most of the literatures focus on deriving the transmission [2] and electromechanical coupling coefficients of 2D piezoelectric PCs [3], while important parameters of reflection and velocity were not achieved for 2D PCs.

This paper proposed a model to calculate the reflection and velocity of 2D piezoelectric PCs with finite element method (FEM).

[1] Clemens C.W. Ruppel, et al, IEEE Ultrason. Symp. (1994)313-324

[2] T. T. Wu, et al, Freq. Control Symp. (2010) 515-520

[3] Marc Solal, et al, Freq. Control Symp. (2009) 226-231

#### Statement of Contribution/Methods

Three-dimensional (3D) models are composed of several pairs input IDTs and output IDTs with and without Nickel (Ni)/ 128°-YXLiNbO<sub>3</sub> PCs respectively. The distance between IDTs' edges is 130μm, the lattice constant of PCs is 10μm, the radius and height of Ni stubs is respectively 4μm and 2.2μm.

A FEM commercial software, COMSOL, was employed to analyze this model. Perfect matching layer (PML) was used in boundary of X and Z direction. A period boundary condition was used in Y direction to reduce time and memory cost of the model.

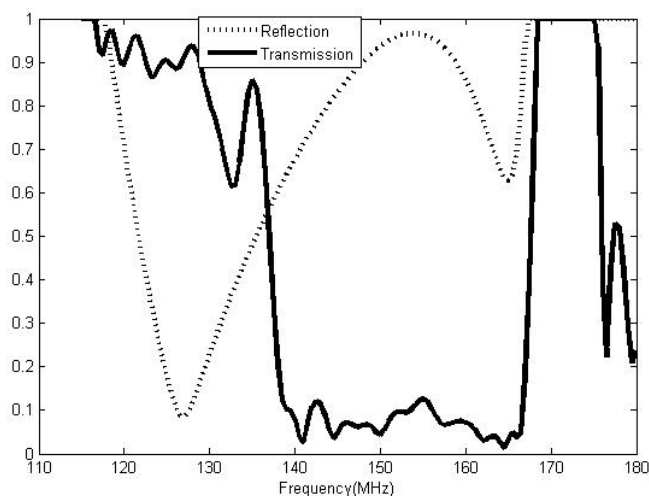
Received signal in frequency domain was firstly calculated with piezoelectric PCs. Group delay can be obtained in time domain by inverse Fourier transform (ifft). Then group velocity was achieved.

By adding suitable window function in time domain to remove the reflection of triple-transition, value of reflection and transmission can be extracted by comparing achieved signals of delay line models with and without PCs.

#### Results/Discussion

The group velocity 2889m/s was calculated by the group delay 45ns. The reflection and transmission of the PCs, as Fig.1, was not similar with that of IDTs, which changed rapidly in the band gap.

The extracted parameters of 2D PCs can be promising for future designing of SAW devices with PCs.



## P3C3-2

**Time delay estimation and correlation analysis of acoustic signals in granular media using wavelet decomposition**Jia Yang<sup>1</sup>, Omololu Akanji<sup>1</sup>, David Hutchins<sup>1</sup>, Peter Thomas<sup>1</sup>; <sup>1</sup>*School of Engineering, University of Warwick, United Kingdom***Background, Motivation and Objective**

The generation of high amplitude, short duration signals has the potential to be substantial interest to workers in both biomedical ultrasound and non-destructive evaluation (NDE). The use of non-linearity within a chain of particles allows this possibility to be realised. The transmission of pulsed ultrasonic signals along a chain of spheres has thus been studied experimentally, with a view to determining the exact nature of propagation along such chains at ultrasonic frequencies.

**Statement of Contribution/Methods**

The transmitted signals were measured using a laser vibrometer, and the resultant waves were analysed by using wavelet decomposition. This is so as to be able to identify the first arrival time and the arrival of the maximum intensity of the wave. The frequency bands of meaningful signals were also ascertained and the corresponding wavelet coefficients were extracted. The time delay was estimated based on the wavelet decomposition and threshold-crossing. Time-frequency analysis then allows the velocity dispersion to be analysed, so that the mode of propagation can be more easily identified.

**Results/Discussion**

The wave speed is much smaller than the bulk sound speed of the sphere material. Correlations are sensitive to contact law between adjacent spheres in the chain, as well as the size and material properties of each sphere. For larger spheres (e.g. 10 mm diameter), the results are complicated by linear wave propagation within each sphere, resulting in resonances. These tend to reduce at lower frequencies and smaller sphere diameters, where non-linear behaviour is expected to be more dominant. The results give an insight into the behaviour of wave propagation along such chains of spheres and suggest how to exploit the characteristics in the context of ultrasonic imaging.

## P3C3-3

**Generation of phonons in a photonic crystal slab cavity by electrostriction and the moving-interface effect**Vincent Laude<sup>1</sup>, Jean-Charles Beugnot<sup>1</sup>, Sarah Benchabane<sup>1</sup>, Rémy Braive<sup>2</sup>, Viktor Tsvirkun<sup>2</sup>, Sylvain Barbay<sup>2</sup>, Isabelle Robert-Philipp<sup>2</sup>; <sup>1</sup>*FEMTO-ST / CNRS, Besancon, France*, <sup>2</sup>*Laboratoire de photonique et de Nanostructures / CNRS, Marcoussis, France***Background, Motivation and Objective**

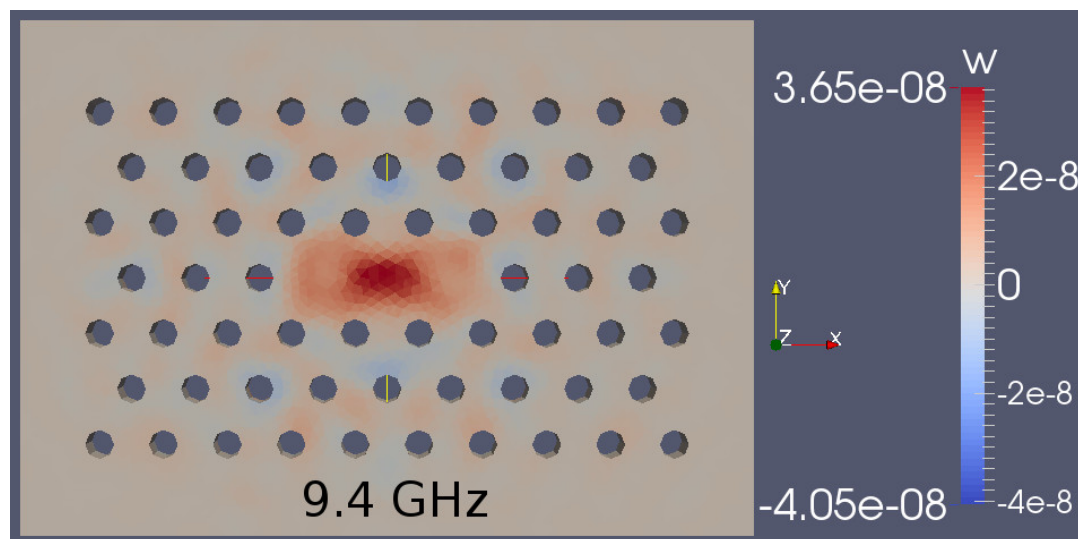
A cavity formed in a photonic crystal slab possesses modes such that the electromagnetic field at optical frequencies is confined to a very small volume, of the order of the cube of the optical wavelength. The confined field exerts mechanical forces of optical origin on the material composing the cavity. Electrostriction first results in a volume force governed by the photoelastic tensor. Coupling of the electromagnetic field with the mechanical motion of the cavity further results in an effective surface force. The objective of this study is to evaluate the generation efficiency of phonons from the photons stored in the cavity.

**Statement of Contribution/Methods**

Recent progress in optomechanics has revealed that opto-acoustic interaction in nanoscale cavities benefits from the combined photoelastic and moving-interface effects. While the photoelastic effect is at play in bulk acousto-optics, the moving-interface effect is specifically driven by the vibrations of surfaces. Assuming a photonic mode and a phononic mode are known beforehand with given amplitudes, the diffraction efficiency for the creation of new photons can be estimated by overlap integrals. We consider here the reciprocal situation where phonons are generated from the interference of photons in the cavity. We specifically solve the elastodynamic equation subject to volume and surface optical forces.

**Results/Discussion**

We consider a L3 photonic cavity created by removing a row of 3 holes from a photonic crystal in an InP membrane. The membrane is 260 nm thick, and the circular holes with a radius of 90 nm form a hexagonal array with a period of 420 nm. Such a L3 cavity is known to support a mode at an optical wavelength of 1550 nm. From the elastic and photoelastic properties of InP, and from the optical modal shape, we compute the generation efficiency of phonons with a finite element method. The model includes perfectly matched layers to terminate the elastic membrane. It is found that thickness resonances of the membrane can theoretically be excited by the optical forces, with frequencies around 10 GHz. The figure shows the vertical displacement at the surface of the slab at 9.4 GHz. Electrostriction is found to dominate over the moving-interface effect in the case considered. We hope this study will motivate the further exploration of acoustic phonon generation in optomechanical structures.



# Analysis of Rayleigh surface acoustic waves propagation on piezoelectric phononic crystal with 3-D finite element model

Yahui Tian<sup>1</sup>, Honglang Li<sup>1</sup>, Yabing Ke<sup>1</sup>, Wei Luo<sup>2</sup>, Shitang He<sup>1</sup>; <sup>1</sup>Institute of Acoustics, Chinese Academy of Sciences, Beijing, China, People's Republic of; <sup>2</sup>School of optical and electronic information, Huazhong university science and technology, Wuhan, China, People's Republic of

## Background, Motivation and Objective

Phononic crystals (PCs) composed of periodic elastic materials have a property of band gaps which has potential applications such as acoustic filter and resonator. However, most of the prior studies of PCs limited to band gaps below 1MHz. For applying PCs to micro-electro-mechanical systems, band gaps of micro air/silicon PCs at hundreds of MHz for surface acoustic wave (SAW) were theoretically and experimentally demonstrated by T. T. Wu [1]. It shows potential to SAW devices such as high-Q resonant cavity [2]. Then novel type of micro aluminum(Al)/ 128°-YXLiNbO<sub>3</sub> piezoelectric PCs were studied using 2-dimensional finite difference time domain(2D FDTD) model[3]. However, results show large deviation because of taking hypothetic line exciting source and not considering the mechanical loading effect of finite-thickness stubs.

To analyze accurately the propagation of SAW in the Al/128°-YXLiNbO<sub>3</sub> PCs, this paper proposed a 3-dimensional (3D) model using finite element method (FEM).

[1] T. T. Wu et al, Freq. Control Symp. (2010)515-520

[2] Jia-Hong Sun et al, IEEE Ultrason. Symp. (2011)996-999

[3] Zhao et al, 2012 SPAWDA Symp. ISPEC No.13327121

## Statement of Contribution/Methods

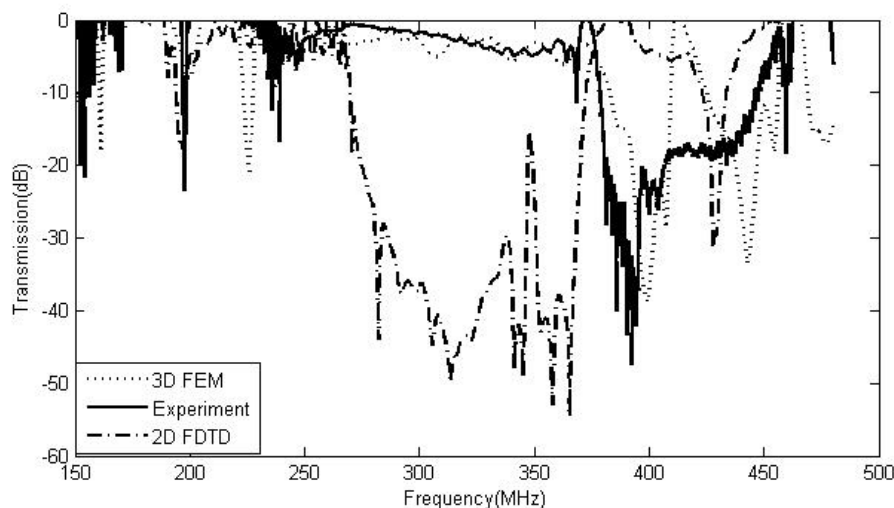
Using commercial software COMSOL, two 3D SAW delay line models were built respectively with and without PCs. Interdigital transducers were used to excite Rayleigh SAW (RSAW) exactly, while hypothetic line exciting source was used in 2D FDTD model. Perfect matching layer was used to absorb the reflective waves in wave propagation direction. To reduce time and memory cost of 3D model, period boundary condition was used in direction perpendicular to the wave propagation.

With comparing their received signal, transmission of PCs can be obtained. Experiments were designed to demonstrate this 3D FEM model by measuring the band gaps of PCs with network analyzer.

## Results/Discussion

Calculated displacement field distribution shows exactly the RSAW as displacements are mainly of  $U_x$  and  $U_z$  focusing on the surface, which demonstrates the reliability of the model used to analyze RSAW. Transmission of 2D FDTD, 3D FEM and experiments (Fig.1) denotes 3D FEM model is more accuracy than 2D FDTD in the pass band due to considering the finite-thickness stubs.

This model has proved to be accuracy to analyze the propagation of RSAW in the piezoelectric PCs and can be extended to analyze more properties of SAW devices based on PCs.



# Silicon Pillars as Resonators for an Acoustical Metamaterial

Bernard Bonello<sup>1</sup>, Rémi Marchal<sup>1</sup>, Rayisa Moiseyenko<sup>2</sup>, Yan Pennec<sup>2</sup>, Bahram Djafari-Rouhani<sup>2</sup>, Jinfeng Zhao<sup>1</sup>, Olga Boyko<sup>1</sup>; <sup>1</sup>INSP, University Pierre et Marie Curie, Paris, France, <sup>2</sup>JEMN-UMR CNRS 8520, University Lille 1, Villeneuve d'Ascq cedex, France

## Background, Motivation and Objective

Locally resonant materials are artificially structured composites designed to exhibit negative effective mass density and/or elastic constants in some frequency ranges. These two parameters become negative when the motion of the centers of mass of the resonators are 180° out-of-phase with respect to the propagating waves. In most of the composites that have been investigated to date, these unique properties were achievable only because the speed of sound in the resonators was of a few tens of m.s<sup>-1</sup>, lower by orders of magnitude than the speed of sound in the background. Very few materials exhibit such low elastic parameters and seeking for resonators made of a material commonly used in nano or micro-fabrication, whose lateral dimensions are much smaller than the wavelength, and that allow controlling the propagation of elastic waves in solids, is therefore of primary importance for designing new acoustical metamaterials.

## Statement of Contribution/Methods

In this work, we have considered the resonant frequencies of pillars deposited on a thin plate. Both are made of silicon. This last structure exhibits both monopolar and dipolar resonances that may cause respectively negative modulus and negative mass density. Moreover, since the compressional resonant frequency (monopolar) and the bending resonant frequency (dipolar) are mainly sensitive to the height and to the diameter of the pillar respectively, they can be tuned almost independently from each other. This allows in turn to easily probe the conditions for either the mass density negativity or the modulus negativity to appear.

We used a finite element method to calculate the resonant frequencies and polarizations of an isolated pillar on a slab. We then have measured the scattering of an incident Lamb waves on the pillar or on a line of pillars. The experimental technique we used is based on laser generation and detection of acoustic pulses within a broad spectrum. The technique allows measuring displacements with an amplitude as small as a few pm, in the MHz range.



**Results/Discussion**

We have measured the normal component of the displacements at  $5.5 \pm 0.5$  MHz, i.e. the frequency of a compressional mode. It is found that the pillar and the plate are  $90^\circ$  out-of-phase. When the frequency is tuned to 7 MHz, i.e. close to the frequency of the compressional mode but not exactly centered on it, a phase shift of  $180^\circ$  between the movements of the pillar and of the plate is observed. Moreover, a circular wave is emitted by the pillar, in phase with its motion, and propagating at the velocity of the  $A_0$  Lamb mode at 5.5 MHz.

We made the same analysis at the frequency of the bending mode at 1.1 MHz. The resonance of the pillar goes along with the emission of surface waves that propagate at the velocity of  $A_0$  Lamb mode on both sides of the pillar. Furthermore, we observed a  $180^\circ$  phase shift between the amplitudes measured symmetrically on either side of the pillar.

This work is supported by ANR and DGA under grant ANR-11-ASTR-015.

**P3C3-6****Focusing of Flexural Lamb Waves with "Trampoline-Based" Phononic Crystals**

Jinfeng Zhao<sup>1</sup>, Bernard Bonello<sup>1</sup>, Olga Boyko<sup>1</sup>, Yan Pennec<sup>2</sup>, Bahram Djafari-Rouhani<sup>2</sup>, Rémi Marchal<sup>1</sup>; <sup>1</sup>INSP (box 840), University Pierre et Marie Curie, Paris, France, <sup>2</sup>IEMN-UMR CNRS 8520, University Lille 1, Villeneuve d'Ascq cedex, France

**Background, Motivation and Objective**

Gradient-index (GRIN) phononic crystals (PCs) are 2D heterostructures aiming at focusing or collimating elastic waves. In contrast with conventional PCs whose focusing properties rely on the folding of some dispersion curves, they are designed to be efficient at low frequencies, where the elastic wavelength is much larger than the period of the PC. To date, most of the work dealing with these systems are considering the focusing inside the lens itself and heterostructures consisting of holes in a silicon plate, with a diameter varying along the transverse direction of the lens. We propose here a new design of GRIN lens with the two-fold purpose of focusing outside the lens and to significantly improving the spatial resolution at the focus.

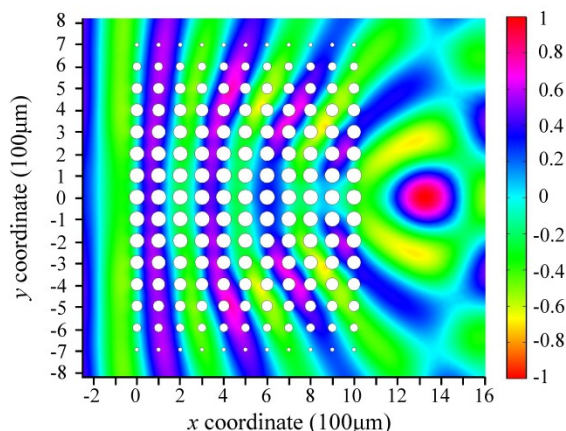
**Statement of Contribution/Methods**

The GRIN PCs we consider in this work, are designed to focus Lamb waves on the plate, in the near field of the lens. They feature a "trampoline" design which consists in inserting silicon pillars in between the holes of an otherwise conventional PC. The GRIN PCs are formed by piercing air holes in a square lattice, throughout a silicon plate. Identical pillars are standing on one side of the heterostructure, in between air holes, along  $\Gamma M$  direction. The refractive index is settled by modulating the diameter of the air holes along the transverse direction. The focusing properties are computed using FEM method; the numerical data are compared to experimental results, obtained using a laser ultrasonic technique, and coupled to an interferometric bench.

**Results/Discussion**

We show in Fig. 1 a snapshot of the anti-plane displacement  $u_z$  both inside and outside the trampoline GRIN PCs, computed on the surface free of pillars. The maximum amplitude is found to appear in the near field ( $\lambda=4.32a$ ), at  $x=13.4a$  and is about twice as large as the amplitude of the incident wave. Besides, the focus spot extends over  $0.7\lambda$  along  $y$ -axis against  $0.8\lambda$  along  $x$ -axis. This can be understood by analyzing the wave number: at the interface across the GRIN PC, the tangential component  $k_y$  can be larger than the wave number in the plate for some incident beams. As a consequence evanescent waves appear and may contribute to the resolution at the focus.

**Fig. 1.** Snapshot of the displacement  $u_z$  both inside and outside the GRIN PC, at 7MHz. The maximum amplitude is observed at  $x=13.4a$  and is twice as large as the one of the incident wave.

**P3C3-7****Topology Optimization of Two-Dimensional Holey Phononic Crystals with Large Band Gaps**

Hao-Wen Dong<sup>1</sup>, Yue-Sheng Wang<sup>2</sup>, Xiao-Xing Su<sup>1</sup>; <sup>1</sup>Beijing Jiaotong University, China, People's Republic of, <sup>2</sup>Institute of Engineering Mechanics, Beijing Jiaotong University, Beijing, China, People's Republic of

**Background, Motivation and Objective**

Phononic crystals (PnCs) are a kind of composite materials with periodic structures. One of the distinguishing features of PnCs is the existence of band gaps - the frequency intervals within which waves cannot propagate through the structures. PnCs have potential applications in many fields such as the sound shielding, vibration isolation, wave guiding, etc. They are perfect candidates of functional materials for design of acoustic devices, e.g. sensors, acoustic diodes, acoustic lens, etc. For practical applications, it is of significance to design a PnC with expected acoustic properties. The topology optimization technique provides us an effective tool for searching the optimal design.

**Statement of Contribution/Methods**

In his paper, the genetic algorithm together with the finite element method is employed to optimize a two-dimensional holey phononic crystal which exhibits a maximal bandgap. The unitcell of the structure may be of square-symmetry or the rational-symmetry. Both the anti-plane and in-plane wave modes, as well as the combined modes, are considered. Besides the maximum relative band gap width (BGW) which is defined as the band-gap-width to mid-gap ratio, the maximum porosity is also an objective. Therefore the multi-objective optimization is performed. A "coarse to fine" two-stage strategy is used in order to obtain the optimized structures with smooth edges and save computational time. To

overcome the mesh-dependency problem in the topology optimization of the holey PnCs, we introduce a geometrical constraint that the geometrical width of each connection must be bigger than a critical value so that the optimized structure is easy for fabrication.

### Results/Discussion

The optimization results for the two-dimensional square-latticed holey PnCs with silicon are presented. The multi-objective optimization shows its effectiveness for the bandgap engineering. It can yield the Pareto-optimal solution set and achieve a balance between the maximum relative BGW and a maximum porosity. The optimized structures have solid lumps with narrow connections, leading to a result of local resonance. The rational-symmetry structure exhibits a larger band gap than the square-symmetry structure with the same porosity.

### P3C3-8

#### Surface acoustic waves in finite-depth air/silicon phononic crystals

Jia-Hong Sun<sup>1</sup>, Jyun-Hua Jhou<sup>1</sup>; <sup>1</sup>Department of Mechanical Engineering, Chang Gung University, Tao-Yuan, Taiwan

### Background, Motivation and Objective

Phononic crystal (PnC) is an artificial composite made of periodic material or geometric shapes to modulate acoustic wave propagation. Important properties of PnCs such as band gaps and anisotropic propagation were studied and available for surface acoustic waves (SAW) [1]. Based on the band gaps, PnCs were proposed to be reflective gratings of SAW devices [2, 3]. Traditional PnCs for SAW were made of cylindrical inclusions arranged in the substrate and the infinite-length cylinders extended from the surface toward half-space. However, real PnCs fabricated by MEMS process usually have only finite-depth cylinders. Thus in this paper, we analyze acoustic waves in the finite-depth PnCs and discuss the effects on the band gaps and reflective gratings.

### Statement of Contribution/Methods

Square lattice PnCs formed by periodic finite-depth cylindrical holes in a silicon substrate were studied. Finite element method was used to analyze the acoustic waves in the PnCs. First, a unit cell was defined. For developing SAWs in the PnC, a traction free boundary was set on the top of the unit cell. In the bottom was the fixed boundary because the displacement of SAWs decays rapidly along the depth. A periodic boundary condition (PBC) based on Bloch theorem was set around the unit cell. In the PBC, wave vector toward  $\Gamma X$  direction varied gradually to present waves with different wavelengths. Then eigenmodes inside the unit cell were calculated to form dispersion curves. In the model, the fixed bottom reflected waves and resulted in redundant modes that do not exist in the real half-space. A post-processing of computing the depth of energy was used to select the modes whose displacement is non-zero only in the vicinity of the top surface.

Polarization of eigenmodes was observed to define the bands of SAW. In addition to Rayleigh waves, shear-horizontal modes and high-order general SAWs also exist in the finite-depth PnC, like waves in a layer on a half-space. The PnC with lattice constant  $a=10\ \mu\text{m}$ , cylinder radius  $r=0.3\ a$ , and cylinder depth  $h=1.5\ a$  performs a partial band gap for Rayleigh wave at 200.2 - 226.9 MHz. The gap range changed with the variation of radius ( $r=0.12\ a - 0.3\ a$ ) or depth ( $h=0.5\ a - 3.5\ a$ ) but did not vanish. The SAW at the range of band gaps decayed in the PnC and the attenuation was related to the size of finite-depth holes.

### Results/Discussion

In this paper, PnCs consisting of finite-depth holes in silicon substrate were studied. Periodic uniform holes on the substrate become a layer media and allow more modes of SAWs. The finite-depth PnC have similar but different gap range to the one in the infinite-depth PnC. The finite-depth PnC still can be used as gratings for SAWs.

### References:

- [1] T.-T. Wu, L.-C. Wu, and Z.-G. Huang, J. Appl. Phys., vol. 97, no. 094916, 2005.
- [2] T.-T. Wu, W.-S. Wang, J.-H. Sun, J.-C. Hsu, and Y.-Y. Chen, Appl. Phys. Lett., vol. 94, no. 101913, 2009.
- [3] J.-H. Sun and T.-T. Wu, 2012 IEEE Ultrason. Symp., Dresden, Germany

### P3C3-9

#### Sub-wavelength acoustic shielding of Lamb waves through a periodic plate with rectangular holes

Rayisa Moiseyenko<sup>1</sup>, Yan Pennec<sup>1</sup>, Rémi Marchal<sup>2</sup>, Bernard Bonello<sup>2</sup>, Bahram Djafari-Rouhani<sup>1</sup>; <sup>1</sup>IEMN, villeneuve d'ascq, France, <sup>2</sup>INSP, Paris, France

### Background, Motivation and Objective

The transmission of acoustic waves through a periodic array of sub-wavelength slits or holes have been studied in several recent works in relation with physical phenomena such as resonant (extraordinary) transmission, broadband sound shielding or acoustic induced transparency [1]- [3]. In this work, we present for the first time the study of analogous phenomena for Lamb waves propagating in a thin plate. The resonances and anti-resonances on series of parallel rows of periodically arranged rectangular junctions separated by holes are investigated as a function of the geometrical parameters, especially in the sub-wavelength regime. We show that this structure cover the important domains of the acoustic metamaterials topic and can find many applications in the field of low frequency band gap.

### Statement of Contribution/Methods

The phononic plate is constituted by one or two layers of rectangular air holes drilled in a silicon plate. We calculate the transmission of incident S0 Lamb waves with a polarization along the direction of propagation, z. All transmission computations have been performed using a finite difference time-domain method (FDTD).

### Results/Discussion

At high frequency, for one or two rows of holes, we found the existence of specific peaks and a dip which correspond to the coupling of the incident wave with both Fabry-Perot oscillations inside the vertical junctions and induced interface waves between the homogeneous media and the layer of holes. When adding a second row of holes, we show the occurrence of low frequency modes which have been associated to eigenmodes localized inside the 'H' element connecting the two homogeneous parts of the plate. With an appropriate choice of the distance between the two holes, we show that the structured plate behaves like an acoustic metamaterial displaying a wide subwavelength band gap with an attenuation of the transmission coefficient up to 99%.

### References

- [1] Christensen, J., Martin-Moreno, L. and Garcia-Vidal, F. J., "Theory of resonant acoustic transmission through subwavelength apertures", Phys. Rev. Lett. 101 014301 (2008).
- [2] Estrada, H., Garcia de Abajo, F. J., Candelas, P., Uris, A., Belmar, F. and Meseguer, F., "Angle-dependent ultrasonic transmission through plates with subwavelength hole arrays", Phys. Rev. Lett. 102 144301 (2009).
- [3] He, Z., Peng, S., Hao, R., Qiu, C., Ke, M., Mei, J. and Liu, Z., "Extraordinary acoustic reflection enhancement by acoustically transparent thin plates", Applied Physics Letters 100, 091904 (pages 4) (2012).

P3C3-10

**Frequency band gap observation of 2D phononic crystal based on Ni Pillars using slanted IDTs.**

Yu Du<sup>1</sup>, Sergey Yankin<sup>1,2</sup>, Abdelkrim Talbi<sup>1</sup>, Jean Claude Gerbedoen<sup>1</sup>, Vladimir Preobrazhensky<sup>1</sup>, Philippe Pernod<sup>1</sup>, Olivier Bou Matar<sup>1</sup>; <sup>1</sup>International Associated Laboratory LICS/LEMAC: IEMN, UMR CNRS 8520, PRES Lille Nord de France, EC L, France, <sup>2</sup>Saratov State University, Astrakhanskaya str. 83, 410012, Saratov, Russia, Russian Federation

**Background, Motivation and Objective**

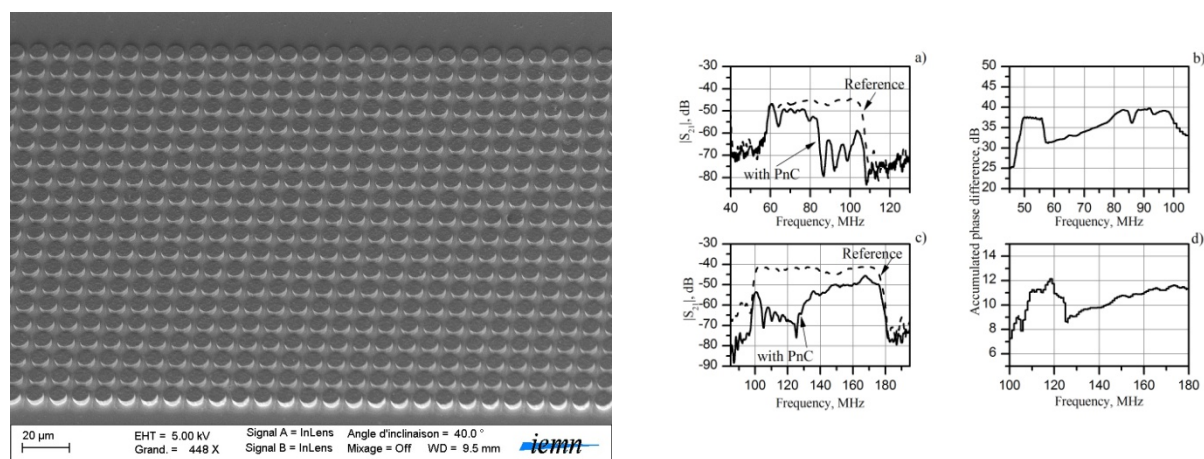
During the past decade, surface Phononic crystal (PnC) have attracted significant attention because of compatibility with standard micro-machining process and because of the ability to provide complex elastic waves processing. This will enable to open new perspectives in designing high performance acoustoelectronic devices, e.g. resonators, pass-band and low-band filters. The purpose of this study is to measure the frequency band-gap in 2D PnC based on Ni Pillars with square and hexagonal lattice symmetry using Wideband slanted IDTs instead of widely used dispersive delay line.

**Statement of Contribution/Methods**

For the experimental investigation several samples with delay lines and PnC were fabricated on a 500 $\mu$ m thick Ycut lithium niobate wafer. We uses both dispersive and slanted designs of IDTs for 60-105MHz and 100-170MHz that enable an easy observation of band-gaps for the designed PnC. Nickel thin film with thickness of 4  $\mu$ m, diameter of 8  $\mu$ m was electroplated inside a photoresist mould to obtain the desired lattice configurations of pillars (hexagonal and square lattices). The PnCs are then characterized by measuring S21 parameters (magnitude and phase) and obtained data was compared with reference characteristics without PnC.

**Results/Discussion**

Figure 1 shows an example of transmission magnitude and accumulated phase difference measured for the device composed of pillar's square lattice. From amplitude characteristics we can notice clearly the existence of band gap that correspond to local resonance of the individual pillars around 87MHz, and also we observe clearly the Bragg gap in the frequency range 105MHz-140MHz.



## P4C1 - Acoustic Sensors 2

Salon C

Saturday, September 6, 2014, 8:00 am - 5:00 pm

Chair: **Ilia Katardjiev**  
Uppsala University

P4C1-1

### Trace moisture measurement of 10 nmol/mol using a 3mm diameter silica coated ball SAW sensor

Kazushi Yamanaka<sup>1</sup>, Satoshi Hagihara<sup>1</sup>, Toshihiro Tsuji<sup>1</sup>, Toru Oizumi<sup>1</sup>, Nobuo Takeda<sup>1</sup>, Shingo Akao<sup>1,2</sup>, Tsuneo Ohgi<sup>2</sup>, Kosuke Takayanagi<sup>2</sup>, Takayuki Yanagisawa<sup>2</sup>, Noritaka Nakaso<sup>2</sup>, Yusuke Tsukahara<sup>2</sup>; <sup>1</sup>Department of Materials Processing, Tohoku University, Sendai, Japan, <sup>2</sup>TOPPAN PRINTING CO. LTD., Sugito, Japan

#### Background, Motivation and Objective

To maintain the quality of dry gasses for semiconductor devices, fast and sensitive sensors are needed to control trace moisture of less than 1 fÊmol/mol. Quartz ball surface acoustic wave (SAW) sensor [1] is a candidate since it can measure 1 fÊmol/mol with the response time of 15 s and the detection limit of 10 nmol/mol [2]. But the damaged layer introduced by the lapping causing the sensitivity is not easy to reproduce. So, in this study, we develop a reproducible trace moisture ball SAW sensor with a SiOx film replacing the damaged layer.

#### Statement of Contribution/Methods

As a first step, we coated 10 nm thick SiOx film synthesized by the sol-gel method on a harmonic quartz device, and developed a sensor cell using an ultrahigh vacuum (UHV) SMA connector and metal O-rings to suppress the leak. Then, we measured trace moisture from 17 to 790 nmol/mol calibrated using the cavity ring down spectroscopy (CRDS) as a reference sensor (Fig. 1), which is the most sensitive moisture sensor but is too large for on-line use. Temperature effect was compensated by subtracting the delay time response of 80 MHz from that of 240 MHz.

#### Results/Discussion

Measurement of trace moisture from 4 to 790 nmol/mol was achieved. The response time from 390 to 790 nmol/mol was one tenth of that of CRDS, and the detection limit evaluated from intersection of extrapolated line of responses and three times of noise was 0.2 nmol/mol (Fig.2). It is 1/50 of that of the damaged-layer sensor [2]. From these results, it was verified that a trace moisture sensor as sensitive as CRDS and faster and more compact than it could be developed using SiOx coated ball SAW sensor.

[1] Yamanaka et al: IEEE Trans. Ultrason. Ferroelectr. Freq. Control. 53 (2006) 793

[2] N. Takeda and M. Motozawa: Int. J. Thermophys. 33 (2012) 1642

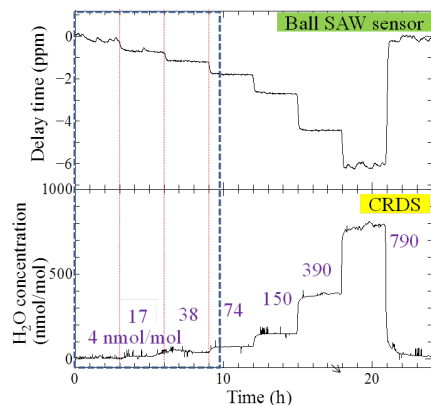


Fig.1 Ball SAW sensor and optical sensor CRDS

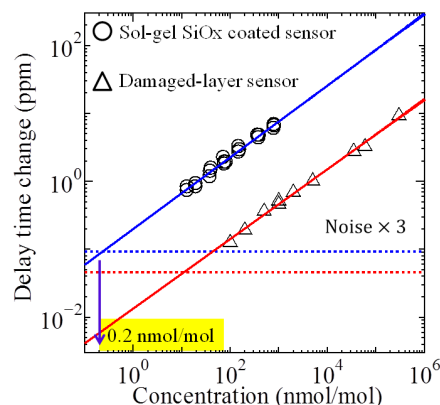


Fig.2 Sensitivity and detection limit of ball SAW sensors

P4C1-2

### Application of SAW RFID in the Inspection Management of Aerodrome Lights

Ruchuan Shi<sup>1</sup>, Chenrui Zhang<sup>1</sup>, Tao Han<sup>1</sup>, Jing Chen<sup>1</sup>; <sup>1</sup>Shanghai Jiaotong University, Shanghai, China, People's Republic of

#### Background, Motivation and Objective

It is increasingly urgent to improve the intelligent level of the equipment management for modern international airports. According to the General Administration of Civil Aviation of China (CAAC), the case that three neighboring aerodrome lights worked abnormally is identified as a serious accident; and thus the status of every light has to be inspected and recorded manually every day. The amount of manual work will be greatly reduced if radio frequency identification (RFID) technology is used in the inspection management of the aerodrome lights.

The RFID tags must be placed inside the aerodrome lights, otherwise the separated tags will become exotic objects invading the airports and threaten the safety of aircrafts. However, it is difficult for IC tags to withstand heat up to 300°C inside the light and for the reflected signals to penetrate the thick metal case. Fortunately, SAW based RFID can overcome the above shortcomings.

#### Statement of Contribution/Methods

The application of SAW RFID in aerodrome lights is firstly reported. SAW RFID with temperature sensing function and anti-metal patch antennas are designed. The positions of the tag fixed in different kinds of lights such as the runway light and the taxiway light are demonstrated. The possibility of failure diagnosis of the aerodrome lights using the

temperature information is also discussed. Meanwhile, two kinds of SAW RFID reader have been developed: a vehicle-mounted long distance reader for inspection management, and a miniaturized handheld reader for inventory management.

#### Results/Discussion

SAW tags in aerodrome lights can be steadily read at temperature as high as 300°C. The range of handheld reader is more than 30cm, and the range of vehicle-mounted reader is more than 3m. The experimental results show that SAW RFID has been successfully applied to the inspection management of aerodrome light.

#### P4C1-3

##### Surface Acoustic Wave Mass Sensor Based On 128° Y-cut Lithium Niobate For Thermogravimetric Analysis

Hongfei Zu<sup>1</sup>, Yizhong Wang<sup>1</sup>, Jiemin Xie<sup>1,2</sup>, Huiyan Wu<sup>1</sup>, Qing-Ming Wang<sup>1</sup>; <sup>1</sup>Mechanical Engineering and Materials Science, University of Pittsburgh, USA, <sup>2</sup>Department of Mechanics, Huazhong University of Science and Technology, Wuhan, Hubei, China, People's Republic of

#### Background, Motivation and Objective

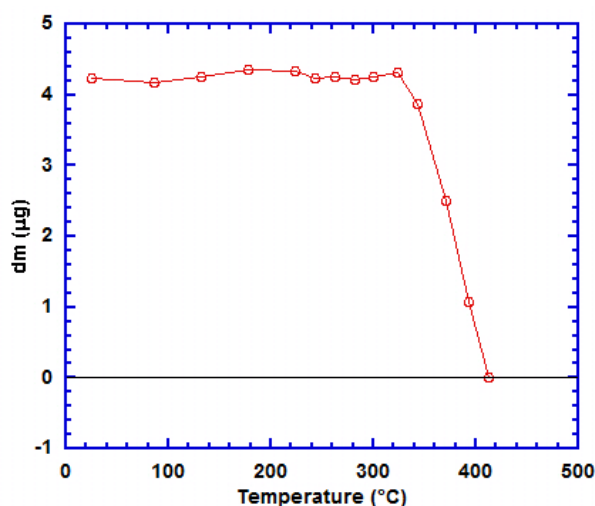
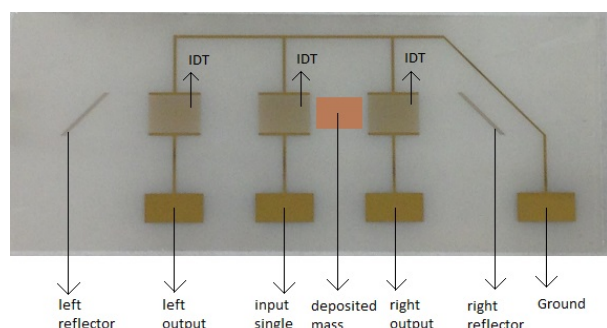
Surface acoustic wave (SAW) sensor is highly sensitive in detecting the changes of the thin film mass loading deposited on the surface of the device. Lithium niobate crystals exhibit excellent piezoelectric properties and very low acoustic wave losses, while possessing high Curie temperature (1140°C). It is expected that lithium niobate SAW mass sensor can be applied for thermogravimetric analysis in elevated temperatures. In this work, a special SAW sensor is designed, fabricated and tested for thermogravimetric analysis of polymer coating layers from room temperature to 500°C with a goal to study the feasibility and sensitivity as a thermogravimetric sensing device.

#### Statement of Contribution/Methods

SAW mass sensors with a special structure shown in Figure 1 were designed and fabricated, where the two outputs are symmetrical about the input. Therefore, the variations of the resonant frequencies between the two outputs reflect the changes of the deposited mass loading. PMMA and PPC polymer films were coated and tested as the mass loadings at elevated temperatures up to 450°C and 350°C, respectively.

#### Results/Discussion

Figure 2 presents the result of the thermogravimetric analysis of PMMA film using the SAW sensor. As can be seen, from ambient temperature to about 320°C the mass loading remains unchanged (4.2 $\mu$ g) and it quickly drops to 0 from 320°C to about 420°C. A high sensitivity of the Lithium Niobate SAW sensors is obtained in this study, indicating it can be used for high sensitive thermogravimetric analysis.



#### P4C1-4

##### Love Mode Surface Acoustic Wave Sensors for Cellular Toxicity Sensing

Fang Li<sup>1</sup>, Lifeng Qin<sup>2</sup>, Huiyan Wu<sup>3</sup>, Qing-Ming Wang<sup>3</sup>; <sup>1</sup>Mechanical Engineering, New York Institute of Technology, USA, <sup>2</sup>Xiamen University, China, People's Republic of, <sup>3</sup>University of Pittsburgh, USA

#### Background, Motivation and Objective

Cell-based biosensors have the capacity to respond to a wide range of analytes in a physiologically relevant manner and have numerous applications in pharmacology, cell biology, toxicology, environmental monitoring, and so on. Acoustic wave devices are considered as powerful candidates as cell-based biosensors. Among various types of acoustic devices, the Love mode sensor has many advantages over other acoustic wave devices, such as capability of using in liquid and high mass sensitivity. However, only few studies have been performed to probe cell behaviors using Love mode devices so far. The objective of this study is to demonstrate the use of Love mode acoustic wave sensors for cellular toxicity sensing.

#### Statement of Contribution/Methods

In this study, we performed the theoretical analysis and experimental studies for Love mode devices as cell-based sensors. A multilayer model was constructed and transfer matrix method was then used to describe the Love mode sensors with the multilayer loading. The device was fabricated with 360YX-LiTaO<sub>3</sub> substrate. The IDTs were patterned on the substrate using the photolithography and lift-off procedures. The devices deposited with different guiding layer thicknesses were tested and compared with the simulation results. The optimized devices were applied to monitor cell adhesion and toxicity sensing. It is demonstrated that the Love mode sensors can be used to monitor the dynamic processing of cell attachment and spreading. It is also shown that the changes in cell adhesion induced by toxicants can be detected by the sensors.



Results/Discussion

The simulation results show that the mass sensitivity reached the maximum value when the phase shift in the guiding layer was around  $\pi/2$ . The maximum mass sensitivity was large for the devices with a large phase velocity for the substrate and a small velocity for the guiding layer. The phase velocity and loss is determined by cell viscoelasticity as well as thickness of interfacial layer between cells and sensor surface. The normalized loss and phase change in sensors after the cell media and the EDTA solution were added onto the sensor surface were recorded. The normalization was accomplished by subtracting the loss or phase change by the cell-free media from that by cell-containing media to exclude the effect of the media and the environment. It was found that the cell attachment induced around 1dB insertion loss and 10 degrees phase shift (maximum) while the addition of EDTA caused the decrease of around 0.2 dB in loss and 3 degrees in phase shift due to the cell detachment.

P4C1-5

Passive and wireless SAW-based carbon dioxide sensor using a grapheme sheet

Chen Fu<sup>1</sup>, Keekeun Lee<sup>1</sup>, SangSik Yang<sup>1</sup>; <sup>1</sup>Department of Electrical and Computer Eng., Ajou University, Suwon, Korea, Republic of

Background, Motivation and Objective

Nowadays, there is great demand to develop low-cost, highly sensitive, repeatable sensors that can be used to monitor the CO<sub>2</sub> concentration in situ. Graphene even shows better performance than carbon nanotubes (CNTs) due to its planar nanostructure. Therefore, the aim of this work is to develop a suitable graphene film and then use it to fabricate a high sensitive CO<sub>2</sub> sensor with SAW wireless delay line technology.

Statement of Contribution/Methods

We have demonstrated CVD method and transfer process to deposit the graphene fabrication sensitivity film. A wireless and passive SAW sensor with ID-tag function was also optimally designed by FEM/BEM modeling. The flow rates of CO<sub>2</sub> and air were controlled by mass flow controllers (MFCs). To characterize the performance of the fabricated CO<sub>2</sub> sensor, the reflection peak amplitude was measured by a network analyzer upon exposure to CO<sub>2</sub> gas at different concentrations, which was connected with the graphene sheet impedance-loaded element.

Results/Discussion

The morphology of graphene sheet was observed in Fig.1 using atomic force microscopy (AFM). The graphene sheet thickness was measured about 0.55nm. The SAW sensor S11 response is shown in Fig 2(a). The large increase ( $\sim 0.35k\Omega$ ) in conductance of the film after being exposed to CO<sub>2</sub> showed that CO<sub>2</sub> can be adsorbed on the graphene sheet very effectively. The CO<sub>2</sub> gas adsorption on the graphene sheet was the dominantly physical mechanism. The response and recovery time of CO<sub>2</sub> gas detection was about 6 s and 9 s. The reflection peak amplitude change to various concentrations of CO<sub>2</sub> is shown in Fig.2(b). The estimated CO<sub>2</sub> sensitivity was of the sensor was  $1.29 \times 10^{-2} \text{dB/ppm}$ . The error was observed less than 1% in our repeating experiments.

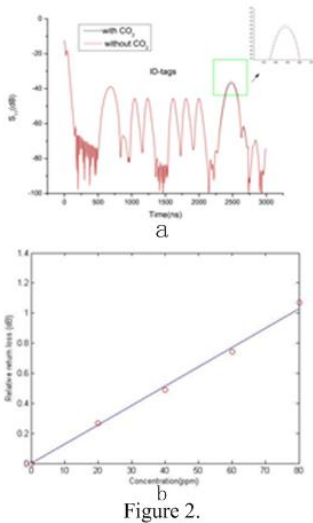


Figure 2.

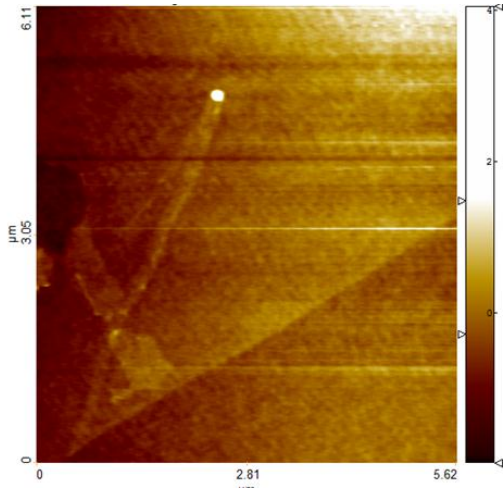


Figure 1.

## P4C2 - Innovations for Resonators and Sensors 2

Salon C

Saturday, September 6, 2014, 8:00 am - 5:00 pm

Chair: **Natalya Naumenko**  
National University of Science and Technology "MISIS"

P4C2-1

### Suppression of transverse-mode spurious responses for S0 Lamb wave resonators by bandgap engineering

Ventsislav Yantchev<sup>1</sup>, Teona Mirea<sup>2</sup>; <sup>1</sup>Uppsala University, Uppsala, Sweden, <sup>2</sup>Dpto. Tecnología Electrónica, Universidad Politécnica de Madrid, Madrid, Spain

#### Background, Motivation and Objective

Thin AlN film S0 Lamb wave resonators (LWR) have been under extensive investigation during the last decade [1]. They have demonstrated robust temperature compensation, moderate electromechanical coupling as well as low noise performance when implemented in oscillators. Further the S0 mode thin film LWRs have demonstrated superior sensitivity to mass loading and pressure as compared to their SAW and FBAR counterparts at comparable noise levels.

The practical implementation of these resonators in filters, oscillators and sensors requires suppression of spurious responses in the passband. These modes originate by the finite membrane dimensions in transverse direction which in turn determines its waveguiding properties. One peculiarity of the LWR is its operation at the upper frequency stopband edge, thus being the fastest mode in the structure. The latter promotes wave diffraction thus forming transversal spurious modes.

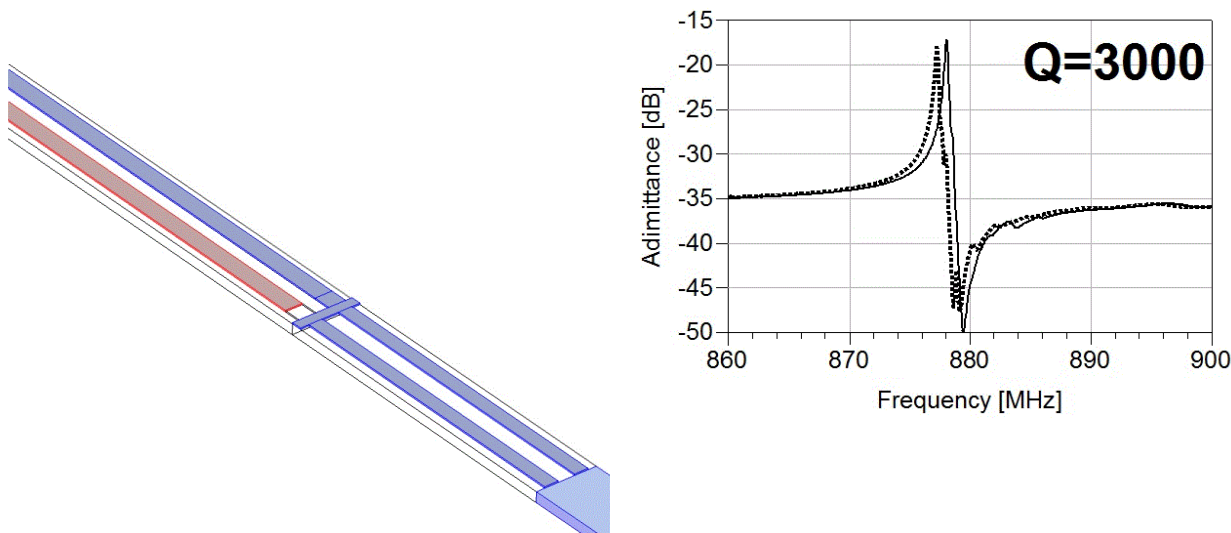
#### Statement of Contribution/Methods

Here we demonstrate a practical way for suppression of the spurious modes by redesigning the device busbars (see Figure 1). The modified busbars consist of a periodic strip grating having the same pitch as of the IDT but with narrower strips. A matching Al layer is introduced between the device strips and the modified busbar. Under these conditions the S0 wave resonance lies inside the stopband of the busbar while propagating with slightly lower velocity.

#### Results/Discussion

As a result spurious responses in the passband are significantly reduced. The latter will be experimentally demonstrated on one- and two- port S0 LWRs operating at 880MHz with  $Q=3000$  (See Figure 2).

[1] V. Yantchev et.al., "Thin film Lamb wave resonators in frequency control and sensing applications: a review", J. Micromech. Microeng., Vol. 23 (4) 2013.



P4C2-2

### Novel Submicron Process Development Tool For SAW Device Fabrication

James Jacobs<sup>1</sup>, Pierre Duflie<sup>1</sup>; <sup>1</sup>Phonon Corporation, Simsbury, CT, USA

#### Background, Motivation and Objective

SAW resonator performance is highly dependent on linewidth and metal edge quality. Small changes in each can have a strong effect on device performance. Detecting these changes is often challenging as the limited field of view at higher magnifications can make accurate navigation between and within test patterns difficult. Our objective in this work is to present a novel test pattern that will enable efficient and accurate navigation of sub micron test structures during high magnification scanning electron microscopy (SEM).

#### Statement of Contribution/Methods

A test structure having linewidth groups from 0.175 $\mu$ m to 0.7 $\mu$ m was designed with a binary encoded strip running lengthwise alongside each group. These encoded strips allow simultaneous location recognition and linewidth/edge quality inspection in the same field of view during top-down SEM analysis.

Also included with the linewidth groups are one port resonator structures which can be used for electrical verification of optical measurements and observations. The resonators are designed to resonate at the same frequency but with differing linewidths spanning from 0.25 $\mu\text{m}$  to 0.5 $\mu\text{m}$ .

### Results/Discussion

Using the presented binary encoded strips we are able to efficiently locate and distinguish between test structures with linewidth differences down to 0.025 $\mu\text{m}$ .

### P4C2-3

#### Temperature Compensated Gallium Nitride Surface Acoustic Wave Resonators for Space Applications

Ashwin Shankar<sup>1</sup>, Chih-Ming Lin<sup>2</sup>, Debbie Senesky<sup>3</sup>; <sup>1</sup>Electrical Engineering, Stanford University, Stanford, California, USA, <sup>2</sup>Silicon Laboratories, Sunnyvale, California, USA, <sup>3</sup>Aeronautics and Astronautics, Stanford University, Stanford, California, USA

### Background, Motivation and Objective

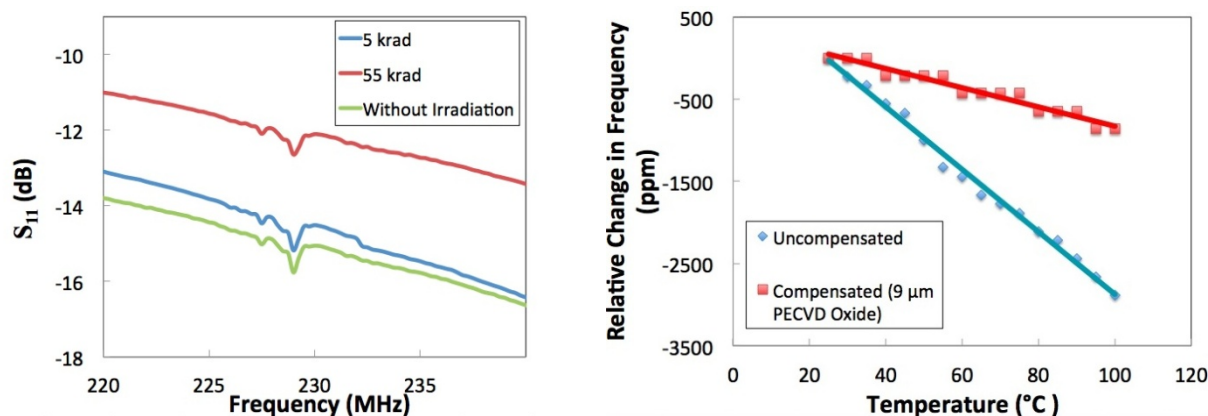
Space environments contain harsh conditions such as extreme variations in temperature and radiation exposure. Conventional electronic components, like on-board timing references are prone to degradation in performance when subjected to such harsh environments, so that complex packaging and shielding is usually required. This paper presents the characterization of wide bandgap GaN-on-Sapphire surface acoustic resonators (SAW) resonators in high-temperature and radiation environments. Ultimately, the combination of these devices with AlGaIn/GaN High Electron Mobility Transistor (HEMT) structures can provide a radiation-hard and monolithic timing solution for space environments.

### Statement of Contribution/Methods

In this work, chrome and gold (Cr/Au) interdigitated transducers are microfabricated on a GaN-on-sapphire substrate via a lift-off process to form one-port SAW resonators. In order to overcome any undesirable frequency shifts with temperature, a layer of PECVD silicon dioxide (SiO<sub>2</sub>) was deposited and patterned on the top surface of the resonator to provide temperature compensation. In addition, to observe the impact of radiation on the device response, the SAW resonators were irradiated with a Cs-137 source (up to 55kRad).

### Results/Discussion

Characterization of the devices at elevated temperatures show that the PECVD SiO<sub>2</sub> layer successfully improved the first-order TCF from -38.005 ppm/ $^{\circ}\text{C}$  to -11.689 ppm/ $^{\circ}\text{C}$ . This device will be further investigated to reduce the temperature-induced frequency drift. In addition, S11 parameters extracted after irradiation show the resonant peak intensity decreases with increasing dosage of radiation without any frequency drift. These compelling results support the use of GaN-based resonators for use in space applications.



### P4C2-4

#### Realization of a SH-SAW phononic device using high density filled microcavities for ultra-low power sensing applications

Mandek Richardson<sup>1</sup>, Subramanian Sankaranarayanan<sup>2</sup>, Venkat Bhethanabotla<sup>3</sup>; <sup>1</sup>Chemical Engineering, University of South Florida, USA, <sup>2</sup>Argonne National Laboratory, USA, <sup>3</sup>University of South Florida, USA

### Background, Motivation and Objective

SAW biosensors based on a shear horizontal wave have been developed to detect breast cancer markers, E. Coli bacteria, and in DNA hybridization studies. A current trend in these biosensing systems is to move away from clinical laboratories where expensive bulky equipment and highly skilled personnel are needed and move to point-of-care-testing (POCT). A major challenge to the incorporation of wireless sensors for biosensing/medical applications is power consumption. Here, we perform an integrated experimental-theoretical study to realize a phononic SH-SAW sensor based on ST 90 $^{\circ}$ -X Quartz. Our study reveals a dramatic reduction in power consumption for these phononic devices.

### Statement of Contribution/Methods

#### Computational details

A 3-D structural finite-element model of a SAW device based on ST 90 $^{\circ}$ -X Quartz containing filled microcavities in the delay path is used to study the frequency response and acoustic wave propagation. The array of microcavities contained individual cavities of square cross-sectional area having dimensions 40 x 40 square micron was modeled. Each cavity was filled with a high-density material (tantalum or tungsten).

#### Fabrication details

SAW devices with tantalum filled microcavities were fabricated using standard photolithography techniques, e-beam deposition, metal lift-off and deep reactive ion etching (DRIE) on an ST 90 $^{\circ}$ -X Quartz wafer 0.5 mm thick and 100 mm diameter.

### Results/Discussion

The phononic sensor is realized by artificially structuring the delay path to form an acoustic meta-material comprised of periodic microcavity array incorporating high-density materials such as tantalum or tungsten. Constructive interference of the scattered and secondary reflected waves at every microcavity interface leads to acoustic energy

confinement in the high-density regions translating into reduced power loss (Fig. 1(a)-(b)). Tantalum filled cavities show the best performance while tungsten inclusions create a phononic bandgap. Based on our simulation results, SAW devices with tantalum filled microcavities were fabricated (Fig 1(c)) and shown to significantly decrease insertion loss (IL) as seen in Fig 1(d). Our findings offer encouraging prospects for designing low power highly sensitive portable biosensors.

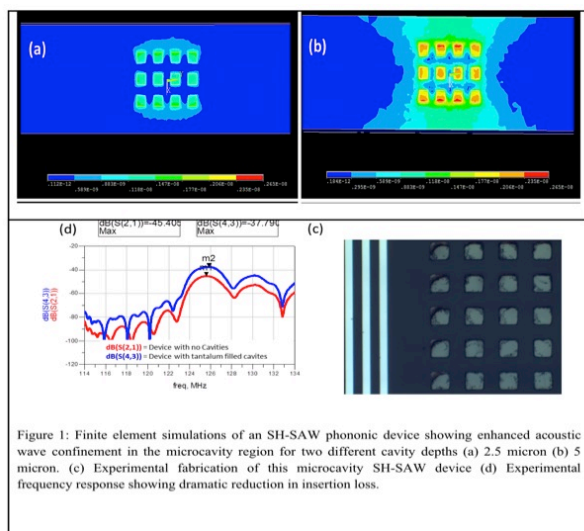


Figure 1: Finite element simulations of an SH-SAW phononic device showing enhanced acoustic wave confinement in the microcavity region for two different cavity depths (a) 2.5 micron (b) 5 micron. (c) Experimental fabrication of this microcavity SH-SAW device (d) Experimental frequency response showing dramatic reduction in insertion loss.

## P5C1 - Micromachined Ultrasonic Transducers

Salon C

Saturday, September 6, 2014, 8:00 am - 5:00 pm

Chair: **Takashi Buma**  
Union College

P5C1-1

### Designing Efficient CMUT Cells for Airborne Applications

Asli Unlugedik<sup>1</sup>, A. Sinan Tasdelen<sup>1</sup>, Abdullah Atalar<sup>1</sup>, Hayrettin Koymen<sup>1</sup>; <sup>1</sup>Bilkent University, Ankara, Turkey

#### Background, Motivation and Objective

CMUTs with thin plates are typically manufactured with perforated structure to prevent permanent collapse due to atmospheric pressure. As a result, wider bandwidth is achieved at a cost of reduced transduction efficiency. In this work, we propose a design procedure for low loss CMUT cells to achieve high transmission efficiency using silicon plates while a reasonably wide bandwidth is maintained.

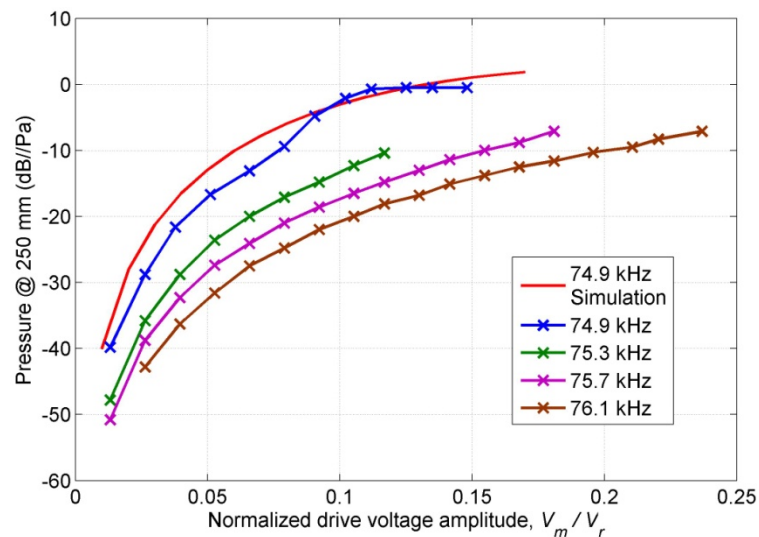
#### Statement of Contribution/Methods

CMUT cells with thin radiating plates experience increased atmospheric pressure and therefore a large plate deflection. This causes nonlinearity in compliance and the plate becomes stiffer. This effect causes an increase in the resonance frequency of the CMUT cell. The resonance frequency is also affected by the nonlinearity in the transduction force, which has an opposite effect. We propose a mode of operation where these two effects are counter balanced to provide a very large swing amplitude at resonance.

#### Results/Discussion

A very accurate circuit model-based characterization [1] with nonlinear compliance is given in this work. We introduce a new operation mode, Minimum Voltage Drive Mode (MVDM) that has the maximum swing while fully utilize existing gap height at the lowest possible drive level in unbiased operation. The performance of the fabricated CMUT cells are tested and compared with the circuit model results. Figure illustrates the comparison results for the fabricated CMUT cell at different frequencies. CMUT cell in Figure have a radius of 2mm, radius to thickness ratio of 25.6 and 6.63 $\mu$ m effective gap height. This cell has  $V_r$  (collapse voltage in vacuum) of 596V, and when under 1 atm static pressure (normalized depression of 0.554) collapse voltage becomes 252V.

[1]H. Koymen, et.al., IEEE Trans. UFFC, 59, p.1791-1799, 2012.



P5C1-2

### Design and Fabrication of cMUT using SOI Wafer for Focused Ultrasound Beam

In-Hyounk Song<sup>1</sup>, Min Gyu Cho<sup>2</sup>, Inn-Yeal Oh<sup>3</sup>, Chul Soon Park<sup>2</sup>; <sup>1</sup>Texas State University, USA, <sup>2</sup>Korea Advanced Institute of Science and Technology, Korea, Republic of

#### Background, Motivation and Objective

Non-invasive treatment or stimulation using focused ultrasound has advantages over current surgical process or acupuncture treatment. Spherical concaved or single element ultrasonic transducers enable acoustic energy to be delivered to specific areas on biological tissues with a few millimeters in diameter. The acoustic energy is accumulated on the targeted tissue, applicable for cranial nerve disease, acupuncture, etc. However, the limitation of the transducers is the fixed focal length and position required additional impedance matching layer to stimulate targeted points. This paper presents the design and fabrication of capacitive micromachined ultrasonic transducer (cMUT) using silicon on insulator (SOI) wafer for focused ultrasound beam to deliver the ultrasound energy to targeted area, which can electrically adjust the focal point and intensity.



### Statement of Contribution/Methods

The cMUT is designed to fabricate 4096-elements annular array separated by 8 ground controls as shown in Fig. 1(a). Each of the cMUTs has a side length of 100  $\mu\text{m}$ , a thickness of 2.5  $\mu\text{m}$ , and an air gap of 500 nm. Cross section of a circular diaphragm cMUT built with a circular diaphragm separated by air gap is shown in Fig. 1(b). The membrane motion will cause an oscillating pressure and hence, emit an ultrasonic wave. The first resonance frequency of designed cMUT is 1.48 MHz. The SEM picture in Fig. 1 (b) shows the fabricated cMUT using SOI wafer, which provides electrical isolation from other elements and low mechanical stress. The details of the fabrication are discussed in paper.

### Results/Discussion

The temporal peak intensity in the XZ-plane is simulated using MATLAB based ultrasound field simulation code called FOCUS. The intensity and the focus position are presented in Fig. 1(c). Ascorbyl Free Radical (AFR) intensity average of -3dB region plot and the focal dimension are 14.61 W/cm<sup>2</sup> and 0.8 mm  $\times$  4.1 mm, respectively. The structures fabricated using MEMS technology and their resonant frequencies are characterized in the paper. The focused ultrasound beam provides the high acoustic power to the target area without high pressure on the surface of the transducer. This paper presents the relationship between the size and the position of focus, the parameters of the cMUT array, and the design and evaluation of phased ultrasound transducer with MEMS array for stimulating local area.

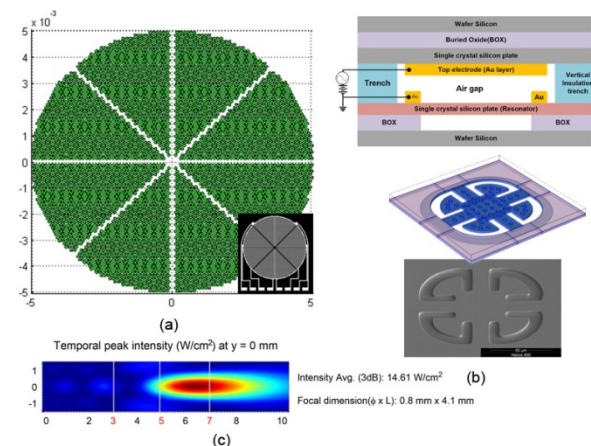


Figure 1. (a) coding structure of cMUT array, (b) cross-section view of cMUT cell structure, design and fabricated cMUT using SOI wafer, and (c) beam profile of designed annual array.

### P5C1-3

#### Surface micromachined CMUTs for liquid phase sensing

Evaldas Sapeliauskas<sup>1</sup>, Dovydas Barauskas<sup>1</sup>, Gailius Vanagas<sup>1</sup>, Darius Virzonis<sup>1</sup>; <sup>1</sup>Panevezys Faculty of Technology and Business, Kaunas University of Technology, Lithuania

### Background, Motivation and Objective

Capacitive micromachined ultrasound transducers (CMUT) are known for their excellent sensitivity to the mass loading of the transducer structure, which is successfully applied for the gas phase sensors. From the other side, flexural mode of the CMUT membranes vibration is heavily damped in the liquids, which limits the use of CMUTs for the liquid-phase sensing. Recently interdigital CMUTs were demonstrated to be effective in excitation and reception of the Scholte type of the waves traveling at the liquid and solid interface with the good potential of sensing the liquid properties (McLean, Degertekin and others).

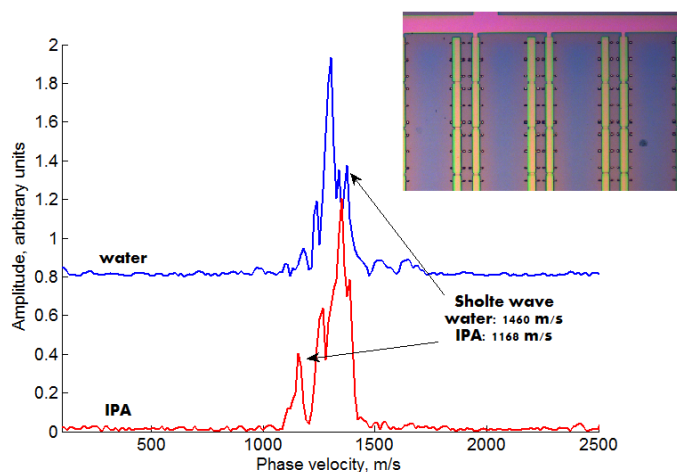
During our research we designed, fabricated and tested surface micromachined interdigital CMUTs. The aim of this work is to explore how the changing physical parameters of the surface(s) involved to the transverse waves transmission can be sensed.

### Statement of Contribution/Methods

Interdigital CMUTs were designed to have 20 MHz air resonance and 10 MHz resonance when immersed in water. Devices were fabricated in transmit/receive pairs. Each transmitter or receiver has 20 finger pairs with 146 micrometer periodicity and 3 millimeter aperture. The wave transmission distance between the receiver and transmitter is 9 millimeters. Devices were fabricated on the highly doped silicon wafers by the surface micromachining technology using silicon nitride as the structural material and chromium as the sacrificial material. The frequency response in air and immersion was measured by the network analyzer. 100 V bias with 10 V pp 10 MHz 20 period harmonic burst excitation was used to excite the transmitting part of the sensor. The silicon surface involved in the transverse waves transmission was modified by adding the self-depositing organic species to the liquid-filled microchannel.

### Results/Discussion

Fabricated devices were found to have 20 +/- 1 MHz resonance if biased at 100 V with corresponding 8.3 +/- 1.3 MHz resonance when immersed in water. The proof of the Scholte wave transmit/receive was made in deionized water and isopropanol. The measurement of the pulse travel time allowed to measure the approximate Scholte wave phase velocity, which was 1460 m/s for DI water and 1168 m/s for isopropanol. These values were confirmed by calculating the phase velocities from experimentally obtained spectra of the transmitted waves (see the figure attached).



Spectra of received pulses transmitted through the solid/liquid interface. Excitation frequency: 9 MHz; inset: fragment of the interdigital CMUT structure.

P5C1-4

#### Investigation of PDMS as coating on CMUTs for imaging

Mette Funding la Cour<sup>1,2</sup>, Matthias Bo Stuart<sup>1</sup>, Mads Bjerregaard Laursen<sup>2</sup>, Erik Vilain Thomsen<sup>2</sup>, Jørgen Arendt Jensen<sup>1</sup>; <sup>1</sup>Center for Fast Ultrasound Imaging, Department of Electrical Engineering, Technical University of Denmark, Kgs. Lyngby, Denmark, <sup>2</sup>Department of Micro and Nanotechnology, Technical University of Denmark, Kgs. Lyngby, Denmark

#### Background, Motivation and Objective

Coating of Capacitive Micromachined Ultrasonic Transducers (CMUTs) is important for insulation between the surface of the elements and the patient when applying the high voltages required for operating CMUTs. Polydimethylsiloxane (PDMS), Sylgard 170, is chosen as coating material in this work as its acoustical properties match well with water and tissue (acoustical impedance 1.5 MRayls for water, 1.63 MRayls for tissue and 1.37 MRayls for Sylgard 170) and it is biocompatible. Other coating materials, coating thickness and coating models have been investigated by others. The objective for this work is to investigate how this PDMS coating affects the CMUT performance through comparison of the transmit pressure and receive sensitivity for devices with and without coating.

#### Statement of Contribution/Methods

To test whether the PDMS is a suitable coating material for CMUTs, 128 element 1D arrays are fabricated with the fusion bonding method. Two identical devices from the same wafer are mounted on printed circuit boards (PCBs) and wirebonded. The wirebonds are covered by a protective glob top (CHIPCOAT G8345D), which is also used as a dam when applying the PDMS coating. The dam is filled with liquid PDMS and then cured in vacuum. Electronics for transmitting and receiving with the CMUTs are produced, and the measurements are performed with the experimental ultrasound system SARUS. Measurements on the non-coated device is performed in oil, while the coated device is in water. A hydrophone placed 5 mm from the transducer surface is used to measure the transmit pressure. Each measurement is repeated 10 times on every element in transmit. To measure receive sensitivity a plane reflector placed at a distance of 5 mm is used. The measurements for the transmit pressure and receive sensitivity are performed with a 12 cycle sinusoid excitation at 5 MHz. A DC bias of 50 V and an AC voltage of 25 V was used for all measurements. Compensation for the attenuation in oil was included.

#### Results/Discussion

By considering only elements within a 25% threshold of the median, inactive elements are eliminated and the RMS values for each element are considered for both transmit and receive. For the transmitted pressure, the array with coating has an output signal of 22% less than the array without coating. This is comparable to what is expected for this thickness of the PDMS. For receive, a decrease of 57% is observed for the coated device compared to the uncoated. This is higher than expected from applying the coating. When measuring repeatedly over a day a decrease in transmit signal was observed for the coated array. The receive measurements were performed after the transmit measurements which might contribute to the decreased sensitivity together with the coating. To conclude, the initial measurements performed on the two devices show that the Sylgard 170 PDMS coating does have an effect on the performance of the CMUT array, however, part of the impact might be related to the water exposure of polymer.

P5C1-5

#### Capacitive Micromachined Ultrasound Transducers (CMUT) for Resonant Gravimetric Immunosensing

Dovydas Barauskas<sup>1</sup>, Gailius Vanagas<sup>1</sup>, Asta Makaraviciute<sup>2</sup>, Almira Ramanaviciene<sup>2</sup>, Darius Virzonis<sup>1</sup>; <sup>1</sup>Panevezys Faculty of Technology and Business, Kaunas University of Technology, Lithuania, <sup>2</sup>Faculty of Chemistry, Vilnius University, Lithuania

#### Background, Motivation and Objective

Development of the rapid, reliable and label-free biosensing techniques is driven by the health, food and environment monitoring needs. Several competing MEMS approaches are known to work to satisfy these needs. CMUTs are advantageous in terms of the sensitivity, but also the advantage of CMUT approach over FBARs and SAW devices is electrostatic actuation, which eliminates the use of piezoelectric materials and enables the potential to fabricate the devices with standard CMOS technology. CMUTs can also be fabricated in large one-dimensional and two-dimensional arrays of individually wired elements, enabling a number of parallel measurement channels while still maintaining the compact dimensions of entire device. This results in high degree of parallelism, which is great advantage in biosensing, when a high number of different probes is required in a small sensor area.

As demonstrated earlier, in addition to well known resonance frequency measurement we determined significant informative content in the real part of the measured CMUT impedance. This work shows the results of experimental detection of the immune complex formation.

#### Statement of Contribution/Methods

The array of the CMUT sensors was fabricated by the direct bonding of the silicon membranes provided as a device layer of the SOI wafer with the oxidized and pre-patterned highly doped silicon wafer. The active surface of the sensors was coated with thin gold film.

We demonstrate the detection of the formed immune complex over the CMUT surface modified by the bovine leukemia virus antigen BLV gp51. The modified CMUT surface was allowed to interact with the specific antibody anti-gp51 labeled by the horseradish peroxidase. Antibody labels were activated after the interaction by wetting the sensor surface with tetramethylbenzidine to provide the reference quantification of the formation of the immune complex.

CMUT sensor readings (resonance frequency and the resonance value of the impedance real part, "resistance") were obtained by the network analyzer before and after modification by the BLV gp51 and after the interaction with anti-gp51. The readings were interpreted and fitted by the finite element analysis.

#### Results/Discussion

It was determined that 33 microgram/ml concentration of the antigen cause formation of the protein film over the gold-coated sensor surface. This increases the elasticity modulus and stress of the sensor structure with corresponding increase of the resonance frequency and some decrease of the resonance quality (resistance value). Lowering the concentration of the antigen during sensor modification would eliminate this artifact. After the immune complex is established, we observe decrease of the resonance frequency by 3% on average from the initial value. Finite element analysis model fitted to the experimental results show the sensitivity of the sensor to be not worse than 4.0 fg/(Hz\*CMUTcell).

#### P5C1-6

##### A Low Frequency Broadband Flexural Mode Ultrasonic Transducer for Immersion Applications

Alessandro Stuart Savoia<sup>1</sup>, Barbara Mauti<sup>1</sup>, Nicola Lamberti<sup>2</sup>, Giosuè Caliano<sup>1</sup>; <sup>1</sup>Dipartimento di Ingegneria, Università degli Studi Roma Tre, Roma, Italy; <sup>2</sup>Dipartimento di Ingegneria Industriale, Università degli Studi di Salerno, Fisciano, Italy

#### Background, Motivation and Objective

Ultrasonic transducers for broadband water-coupled operation in the low ultrasonic 30-100 kHz frequency range find their application in different industrial and biomedical areas, such as non-destructive testing and therapy. Thickness-mode piezoelectric transducers for broadband operation in this frequency range must be designed following the dimensional constraints given by the backing and matching layer requirements, leading to bulky and heavy transducer configurations, whose use may result impractical in those contexts where easy handling is critical.

In this paper we propose the design and the fabrication process of a multi-cell, piezoelectrically-actuated, flexural-mode transducer structure, characterized by a low mechanical impedance leading to wideband and high sensitivity immersion operation and by a high flexibility in the definition of the active area shape.

#### Statement of Contribution/Methods

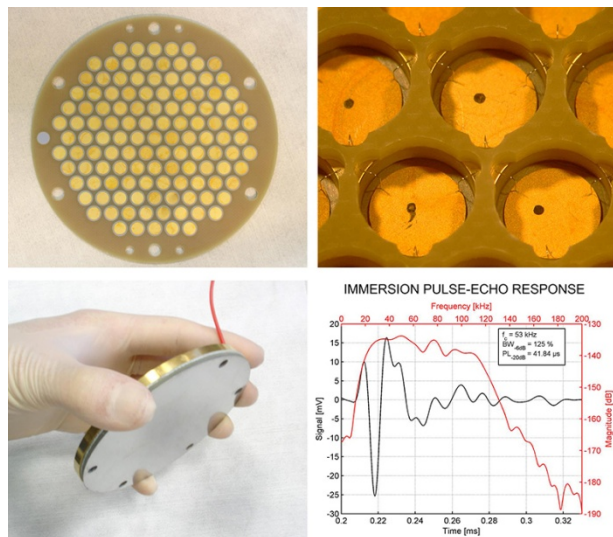
We investigate, using Finite Element Modeling (FEM), the use of different piezoelectric and structural materials for the flexural plate, for the plate support and for the backing and we define their optimum dimensions. PZT-5H ceramic disks and calibrated thickness stainless steel plate are chosen for the vibrating structure, and FR4 and brass respectively for the rails and the backing. In this way, most of the transducer parts may be fabricated using standard technologies with adequate precision and yield.

We report on the design of a fabrication process flow for the precise assembly of the transducer, based respectively on epoxy resin and wire-bonding for mechanical and electrical interconnection of the individual parts.

A transducer prototype, featuring 121 circular cells placed in a hexagonal tiling arrangement covering a quasi-circular area of 80-mm diameter, is designed and fabricated, as shown in the figure. Electrical impedance and transmission and pulse-echo characterization of the first prototype is reported.

#### Results/Discussion

A broadband low-frequency ultrasonic transducer characterized by reduced thickness (<10 mm) and weight (350 g) is successfully fabricated and characterized. A transmission sensitivity of 5 kPa/V at 100 kHz resulted from hydrophone measurements performed at 150 mm while the pulse-echo response from a planar surface placed at the same distance showed a 125% -6dB fractional bandwidth centered at 53 kHz.



#### P5C1-7

##### Dimensional Scaling for Optimized CMUT Operations

Anders Lei<sup>1</sup>, Thomas Lehmann Christiansen<sup>1</sup>, Søren Elmin Diederichsen<sup>1</sup>, Mette Funding la Cour<sup>2</sup>, Jørgen Arendt Jensen<sup>2</sup>, Erik Vilain Thomsen<sup>1</sup>; <sup>1</sup>Department of Micro- and Nanotechnology, Technical University of Denmark, Kgs. Lyngby, Denmark; <sup>2</sup>Department of Electrical Engineering, Technical University of Denmark, Kgs. Lyngby, Denmark

#### Background, Motivation and Objective

The potential benefits of utilizing CMUT arrays in ultrasonic transducers are extensively discussed in literature: large bandwidth, ease of fabrication, compatibility with CMOS, design flexibility, etc. All of these properties are nevertheless of secondary concern for imaging purposes; if the array is not capable of providing the necessary maximum output

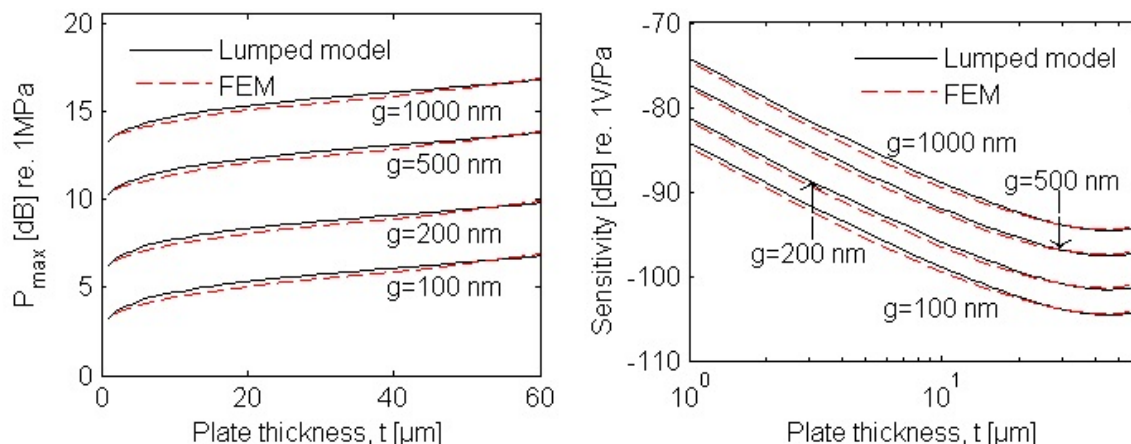
pressure and relative sensitivity, CMUT's will not be a viable alternative to piezoelectric arrays. The objective of this work is to show how these critical properties scale with the dimensional parameters for a fixed resonant frequency in immersion.

#### Statement of Contribution/Methods

In the most basic configuration, there are three adjustable dimensional parameters for a CMUT cell: gap height  $g$ , plate thickness  $t$  and plate radius  $a$  (circular cell). The resonant frequency of the CMUT is determined by the imaging purpose. This leaves two degrees of freedom (DOF) in the CMUT design: one DOF on the plate dimension (either plate thickness or radius, since the two are coupled through the resonant frequency) and one DOF on the gap height. In this study, the influence of these parameters on the maximum output pressure and relative sensitivity for both voltage and current readout is investigated through a lumped element model and a full finite element model (FEM). In the investigations, the CMUT is biased and operated at fixed fractions of the pull-in voltage.

#### Results/Discussion

In the figures, the maximum output pressure ( $P_{\max}$ ) and relative sensitivity for voltage readout ( $dV/dP$ ) are plotted as a function of thickness for four different gap heights. The plate radius is adjusted to keep a constant resonant frequency in immersion of 5 MHz. Fine agreement is observed between FEM and the lumped model and it is seen that  $P_{\max}$  in immersion scales proportionally with  $t$  and  $g$ . For receive operation, the relative sensitivity  $dV/dP$  under a voltage readout scales proportionally with  $g$  and inversely proportionally with  $t$ . For current readout (not shown here), the sensitivity  $dI/dP$  scales proportionally with  $t$  and inversely proportionally with  $g$ . It is concluded that while both  $P_{\max}$  and sensitivity can be maximised by optimising one of the adjustable parameters (gap height for voltage readout and thickness for current readout), the remaining parameter will inevitably lead to a non-ideal either  $P_{\max}$  or sensitivity, regardless of the readout method.



P5C1-8

#### Electroacoustic Response of cMUT-based Linear Arrays: Role of Inactive Elements

Audren Boulmé<sup>1</sup>, Dominique Gross<sup>1</sup>, Mathieu Legros<sup>2</sup>, Dominique Certon<sup>1</sup>; <sup>1</sup>Université François-Rabelais de Tours, GREMAN, UMR-CNRS 7347, Tours, France, <sup>2</sup>Vernon S.A., Tours, France

#### Background, Motivation and Objective

When designing an ultrasound array, current optimization criteria are based on the electroacoustic response of a single element. Although previous experimental studies showed that the elementary response is modified by inactive adjacent elements, their contribution is rarely introduced in the simulation because high computer capabilities and long computation time are required. Interactions between active and non-active elements arise from elastic guided waves of the substrate and mainly from a longitudinal wave traveling at the fluid/substrate interface. The present work focuses on this interface wave and investigates its impact on the electroacoustic response of an array element, using both theoretical and experimental results.

#### Statement of Contribution/Methods

The approach presented in previous paper [1] was reused and extended to the modeling of a full linear array, including active as well as passive elements. The electrical boundary conditions (short circuit, open circuit or Z load) applied to the passive elements were implemented through a very simple way. The output data of the model are standard electroacoustic characteristics including the electrical signal transmitted between two neighboring elements. cMUT-based sensors could also be designed using the same model. Two devices were used for experimental investigations, both fabricated with a surface micromachining process. The first was a linear array made with 64 elements working at 10 MHz. The others were a set of  $N$  ( $N = 3, 5, 7, 16$  and  $25$ ) columns of cMUTs that were electronically addressed separately, with their own connection pad.

#### Results/Discussion

The electrical impedance was firstly investigated for different numbers of inactive adjacent cMUTs. An impact on the central frequency was observed with a significant step on the considered devices: from 2.2 MHz (for a single column) to 3 MHz (for a column surrounded by 24 columns). However the amplitude of the real part was poorly affected. For all the situations, model predictions and experiments were in good agreement.

Measurements of electrical crosstalk from column to column and from element to element were also carried out. Several phenomena were observed and verified with simulations:

- the cMUT/fluid interface wave is scattered by passive cMUTs resulting in a dispersive behavior like described in [2],
- when the interface wave encounters a group of cMUT, interactions with localized acoustic modes occur, modifying hence the shape of the dispersion curve,
- the main damping sources of the fluid/cMUT interface wave are the own mechanical losses of cMUT.

Finally, the mechanical displacement produced by the traveling interface wave was also investigated showing that a reemission of an acoustic pressure is produced with a modification of the near field.

[1] A. Boulmé *et al.*, IEEE UFFC Symposium, 1873-1876, San Diego (2010)

[2] S. Lani *et al.*, APL, **104**, 051914 (2014)

P5C1-9

**Modeling of CMUTs with Multiple Anisotropic Layers and Incorporated Stress**Mathias Engholm<sup>1</sup>, Erik Vilain Thomsen<sup>1</sup>; <sup>1</sup>Department of Micro and Nanotechnology, Technical University of Denmark, Kgs. Lyngby, Denmark**Background, Motivation and Objective**

Modeling of capacitive micromachined ultrasonic transducers (CMUTs) is of great importance during the design process. Usually the analytical approach uses the single layer plate equation to obtain the deflection and does not take anisotropy and residual stress into account. Surface micromachined CMUTs are usually fabricated from a stack of different materials, such as silicon oxide and silicon nitride, which both have residual stress when grown on silicon. A highly accurate model is developed for analytical characterization of CMUTs taking an arbitrary number of layers and residual stress into account.

**Statement of Contribution/Methods**

Based on the stress-strain relation of each layer and balancing stress resultants and moments, a *general multilayered anisotropic plate equation* is developed for plates with an arbitrary number of layers. The exact deflection is calculated for circular clamped plates of anisotropic materials with incorporated bi-axial stress. From the deflection shape the critical stress for buckling is calculated and by using the Rayleigh-Ritz method the resonance frequency is estimated.

**Results/Discussion**

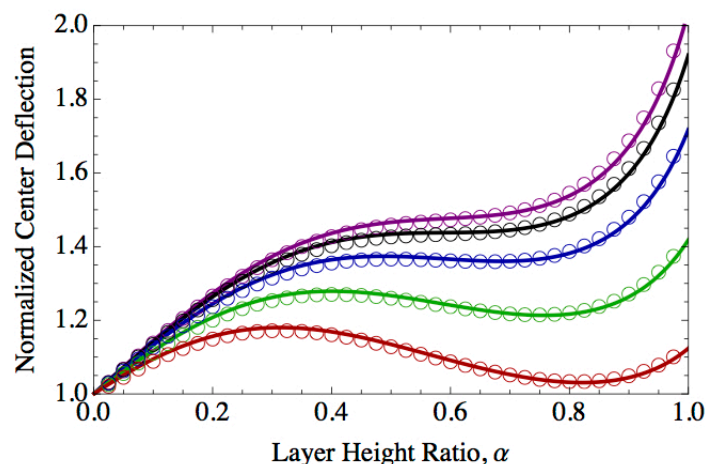
The analytical model is compared to finite element method (FEM) calculation performed in COMSOL with the full stiffness tensor for a circular plate of (100) silicon with aluminum on top. The aluminum is modeled with an incorporated bi-axial stress varying from -25 to 300 MPa. The layer height ratio,  $\alpha$ , is defined as the aluminum height relative to the total height. The figure shows the comparison of the two calculations where the circles represent the FEM calculation. An excellent agreement between the analytical and FEM calculation is seen for incorporated stress varying from -25 to 300 MPa, with a relative difference of less than 1%.

To avoid buckling of the plate the critical stress is calculated. This is compared to FEM calculation where the critical stress is computed from an eigenvalue problem. The relative difference between the two calculations is less than 2%.

The resonance frequency is estimated using the Rayleigh-Ritz and is compared to FEM calculation. A good agreement between the two calculations is seen, with a relative difference of less than 1%.

This developed model gives the possibility of analytical characterization of CMUTs with multiple layers and incorporated stress, which will make the design process more effective and precise.

— -25 MPa — 0 MPa — 50 MPa — 150 MPa — 300 MPa



P5C1-10

**An Ultra-Low-Power Fully Integrated Ultrasound Imaging CMUT Transceiver Featuring a High-Voltage Unipolar Pulser and a Low-Noise Charge Amplifier**Alessandro Stuart Savoia<sup>1</sup>, Giosuè Caliano<sup>1</sup>, Marco Sautto<sup>2</sup>, Andrea Mazzanti<sup>2</sup>, Antonio Davide Leone<sup>3</sup>, Davide Ugo Ghisu<sup>3</sup>, Fabio Quaglia<sup>3</sup>; <sup>1</sup>Dipartimento di Ingegneria, Università degli Studi Roma Tre, Roma, Italy; <sup>2</sup>Dipartimento di Ingegneria Industriale e dell'Informazione, Università degli Studi di Pavia, Pavia, Italy; <sup>3</sup>STMicroelectronics, Cornaredo, Italy**Background, Motivation and Objective**

An emerging class of portable and handheld ultrasound imaging devices is rapidly expanding and is expected to have a broad market potential. High costs and low performance, caused by the reduced availability of suitable electronics and by the transducer technology, are the current limiting factors. In this context, the well-known technical characteristics of CMUTs, such as large operation bandwidth and high electrical impedance, together with the cost reduction arising from the adoption of MEMS technology may be leveraged in the development of such kind of devices. In this paper, we report on the development of a fully-integrated, low-power analog front-end circuit, consisting in a high-voltage unipolar pulser and a low-power transimpedance low-noise amplifier (LNA), specifically designed for 1D CMUT arrays operating in the 1-15 MHz range.

**Statement of Contribution/Methods**

The circuit proposed in this paper comprises a high voltage unipolar pulser, a T/R switch, and a low-noise charge amplifier, which were carefully co-designed in order to minimize the overall parasitic capacitance and power consumption. The high voltage pulser allows generating up to 100 V unipolar pulses. The T/R switch is designed to achieve sufficient isolation of the LNA during transmission and at the same time a low parasitic resistance in on state. The LNA is based on a capacitive feedback topology providing sufficient bandwidth and better noise-power performance than commonly adopted trans-resistance topologies. The chip prototypes were fabricated using a BCD-SOI technology available at STMicroelectronics. To perform electrical characterization and acoustic measurements in conjunction with a 10 MHz linear array CMUT probe head, the chip prototype has been wire-bonded onto a test board that allows providing the chip with the power supplies and the logic control signals, as well as the CMUT with the bias voltage.



## Results/Discussion

Electrical characterization as well as transmission and pulse-echo measurements with the front-end connected to the CMUT are shown. The LNA frequency response measurement reports a 500 kHz – 40 MHz -3 dB band and an 84 dB $\Omega$  transimpedance gain at 10 MHz, with a power consumption of 1 mW. Hydrophone measurements prove successful driving of the CMUT at the maximum pulse amplitude of 100 V with single- and multi-cycle pulse patterns at various frequencies over the entire transducer band. Transmission and pulse-echo impulse responses are used to extract the transfer function of the whole reception path that is characterized by a sensitivity of 70 mV/kPa at 10 MHz. Finally, by measuring the electrical noise at the output of the LNA, the input referred noise was estimated to be 0.57 mPa/ $\sqrt{\text{Hz}}$ .

## P5C1-11

### Modulation Encoding in Top Orthogonal to Bottom Electrode (TOBE) 2D CMUT Arrays

Ryan Chee<sup>1</sup>, Roger Zemp<sup>1</sup>; <sup>1</sup>University of Alberta, Canada

## Background, Motivation and Objective

We recently introduced top orthogonal to bottom electrode (TOBE) capacitive micromachined ultrasound transducer (CMUT) 2D arrays and showed how dominant single element control could be achieved by biasing a column and transmitting or receiving across a row. A TOBE CMUT can acquire an entire column of data simultaneously. Thus it requires only N transmit/receive channels and N bias channels rather than N<sup>2</sup> channels for a NxN array. Previously proposed imaging schemes, however, required multiplexing to form images. In principle, if all elements of a 2D array could route signals simultaneously, 3D imaging could be greatly accelerated. Unfortunately, fully-wired 2D arrays are difficult and cost-prohibitive especially for large arrays, smaller elements, or catheter applications. We present a highly novel scheme for equivalently extracting signals from each element of a TOBE CMUT 2D array with only N receive channels.

## Statement of Contribution/Methods

The method involves modulating columns using frequencies above the resonant-frequency bands of the CMUTs. Each column is modulated at a distinct frequency. Receive signals inducing non-linear capacitive oscillations in CMUT cells result in sidebands about the modulation bands. Signals are received across rows and digitized at GHz sampling frequencies. Signals from each element are recovered by beating the row signals against respective modulation frequencies and low-pass filtering. We demonstrate the feasibility of this approach by acquiring several frequency modulated data points from a single row simultaneously. We vary carrier amplitude, bias voltage, and applied signal amplitude and observe signal amplitude.

## Results/Discussion

We detail the theoretical background behind modulation encoding. Experiments verify the linear increase in signal in response to carrier amplitude, bias voltage, and applied signal amplitude. Signal amplitude vs. cross section data is also presented. Crosstalk is observed, but electronics are proposed to mitigate this crosstalk. Feasibility for modulation encoding TOBE CMUTs is established. We are able to obtain a modulated signal that is 30dB above the noise floor. Through this feasibility study, we demonstrate a promising new approach for greatly increasing the speed of 3D imaging, and for complete and parallel addressing of dense 2D arrays without requiring complete wiring. It is expected that with GHz receiver bandwidths, two orders of magnitude improved data throughput may be achieved compared to previous diagnostic-frequency arrays with equivalent channel count.

## P5C1-12

### First measurements on a novel type of Optical Micro-machined Ultrasound Transducer

Suzanne Leinders<sup>1</sup>, Wouter Westerveld<sup>2,3</sup>, Jose Pozo<sup>3</sup>, Paul van Neer<sup>3</sup>, Koen van Dongen<sup>1</sup>, Paul Urbach<sup>2</sup>, Nico de Jong<sup>1</sup>, Martin Verweij<sup>1</sup>; <sup>1</sup>Lab. of Acoustical Wavefield Imaging, Delft University of Technology, Netherlands, <sup>2</sup>Optics Research Group, Delft University of Technology, Netherlands, <sup>3</sup>Technical Sciences TNO, Delft, Netherlands

## Background, Motivation and Objective

The wide use of ultrasonography for medical imaging has resulted in development of different types of ultrasound sensors. Conventional piezo-electric sensors are efficient but face challenges for small array elements (below 100  $\mu\text{m}$  x 100  $\mu\text{m}$ ). Capacitive and piezo-electric micro-machined ultrasound transducers (CMUTs and pMUTs) are an alternative to the conventional transducers. However, these have less sensitivity (CMUT) or bandwidth (pMUT) to fully compete with traditional sensors. As an alternative, we investigated the possibilities of an optical micro-machined ultrasound transducer (OMUT).

## Statement of Contribution/Methods

We designed a novel type of OMUT that consists of a straight waveguide and a micro-ring resonator on a membrane. If we transmit light through the waveguide, a part of the spectrum is coupled into the resonator. This results in a dip in the transmission spectrum at the resonance wavelength of the resonator. When we place the OMUT in water and transmit acoustic pressure waves towards the sensor, the membrane, and hence the optical resonator, will deform. This deformation of the resonator causes a measurable shift in the optical resonances.

We fabricated the OMUT with standard wafer-scale CMOS processes. The photonic circuitry was fabricated with silicon-on-insulator technology and consisted of 220 nm thick silicon waveguides embedded in silicon-dioxide to isolate it from the substrate and water. The silicon substrate underneath this layer was 250  $\mu\text{m}$  thick. The membrane was created with a DRIE etching process in which all the silicon of the substrate is removed (diameter of 124  $\mu\text{m}$ , thickness of 2.7  $\mu\text{m}$ ).

To give a proof of concept, we built a measurement set-up consisting of a wavelength tuneable laser connected via an optical fiber to the OMUT. The read-out system contained a photo-diode connected to the computer. By sweeping the laser wavelength, we measured the transmission and determined the most sensitive wavelength, located at the steepest decline point in the spectral dip. We used an external ultrasound source to transmit the ultrasound pressure waves and a calibrated needle hydrophone to measure the absolute pressure as reference.

## Results/Discussion

The measurements show that the OMUT has an acoustical resonance frequency of 755 kHz. We measured the response of the OMUT for decreasing transmitted acoustical pressures. With a linear fit through the measurement points we were able to determine the sensitivity of the OMUT at 2.0 mV/Pa. We measured a noise equivalent pressure of 0.5 Pa. By estimating the slope of the dip, we computed a noise equivalent wavelength shift of 32 fm. The OMUTs -6 dB bandwidth was 20%. These promising measurement results lead to the conclusion that this novel type of OMUT may be a good alternative as non-electrical ultrasound receiver.

P5C1-13

### High Frequency Ultrasound Array in Biopsy Needle for Breast Cancer Imaging

Thomas Cummins<sup>1</sup>, Hojong Choi<sup>1</sup>, Payam Eliahoo<sup>1</sup>, Hyung Kim<sup>1</sup>, Mary Yamashita<sup>2</sup>, Linda Larsen<sup>2</sup>, Julie Lang<sup>3</sup>, Stephen Sener<sup>3</sup>, John Vallone<sup>4</sup>, Sue Martin<sup>4</sup>, Kirk Shung<sup>1</sup>; <sup>1</sup>Biomedical Engineering, University of Southern California, Los Angeles, California, USA, <sup>2</sup>Radiology, Keck School of Medicine, Los Angeles, California, USA, <sup>3</sup>Surgery, Keck School of Medicine, Los Angeles, California, USA, <sup>4</sup>Pathology, Keck School of Medicine, Los Angeles, California, USA

#### Background, Motivation and Objective

This paper describes a novel miniaturized 64-element high frequency linear ultrasound array integrated within a biopsy needle as well as preliminary clinical results of high frequency ultrasound imaging of ex-vivo breast biopsy tissue. This array design was motivated by the need for much higher resolution imaging of suspicious lesions in the breast, especially for the visualization of microcalcifications, which are important indicators of breast cancer that are difficult to visualize with existing imaging systems because of their small size (<100 $\mu$ m). This integrated array will produce a higher resolution image that the radiologist can use to precisely target their tissue biopsies for diagnosis.

#### Statement of Contribution/Methods

To date we have fabricated the ultrasound array as well as collected preliminary images of ex-vivo breast biopsy tissue with our single-element 80MHz ultrasound system. We used a deep reactive ion etching (DRIE) process to etch the kerfs in PMN-PT single crystal bulk material to fabricate the 2-2 composite array with element width of 14 $\mu$ m, kerf width of 6 $\mu$ m, element thickness of 22 $\mu$ m and element length of 1mm. Initial array testing included capturing electrical impedance plots as well as pulse-echo waveform and FFT plots while imaging in a water tank with a pulser/receiver.

#### Results/Discussion

Initial testing has confirmed that our micromachining technique to fabricate high frequency, miniaturized arrays is feasible. We are currently building a thinner composite array with improved electrical and acoustic matching and expect to successfully test an array with 80MHz center frequency. Additionally, we have preliminary confirmation that microcalcifications in the breast less than 100 $\mu$ m in size can be clearly visualized with 80MHz ultrasound imaging.

#### 80MHz Ultrasound Imaging of Microcalcifications

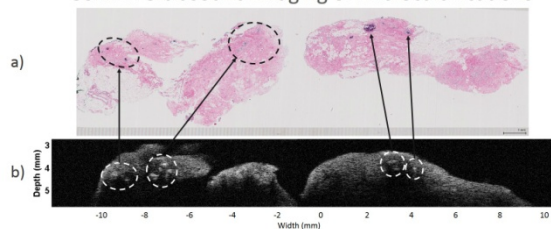


Figure 2: Comparison between co-registered (a) histological and (b) ultrasound imaging of an ex-vivo breast core biopsy tissue sample. Dashed circles in (b) highlight microcalcifications visualized with 80MHz single element ultrasound imaging system and the dashed circles and arrows in (a) show the matching features visualized with digital histology images. Microcalcifications appear as bright reflectors under 80MHz ultrasound imaging while they appear dark purple with H&E staining in histological imaging.

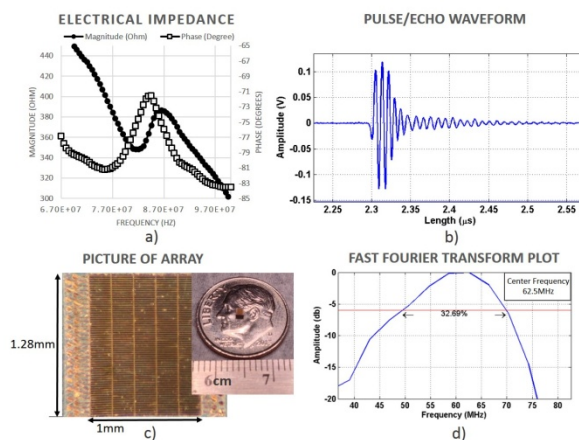


Figure 1: (a) Electrical impedance magnitude and phase plot of a single element of the 64-element linear array and (b) pulse/echo waveform and (c) FFT plot of 5 elements shorted together in a water tank with a quartz reflector target 1.75 mm from array. (d) Photograph of array with inset picture of the array placed on a dime.

P5C1-14

### Ultrasonic Beam Formation by pMUTs array using Epitaxial PZT Thin Films on $\gamma$ -Al<sub>2</sub>O<sub>3</sub>/Si Substrates

Daisuke Akai<sup>1,2</sup>, Masato Nishimura<sup>2</sup>, Nagaya Okada<sup>3</sup>, Makoto Ishida<sup>1,2</sup>; <sup>1</sup>Electronics-Inspired Interdisciplinary Research Institute (EIIRIS), Toyohashi Tech., Japan, <sup>2</sup>Dept. Electrical and Electronic Information Engineering, Toyohashi Tech., Japan, <sup>3</sup>Honda Electronics Co. Ltd., Japan

#### Background, Motivation and Objective

3-D ultrasonic imaging using miniature 2-D pMUTs arrays has been increased demanded on medical diagnosis system such as intravascular ultrasound (IVUS) and non-destructive inspection system. We have proposed  $\gamma$ -Al<sub>2</sub>O<sub>3</sub> thin films as an epitaxial buffer layer on Si substrates for obtaining epitaxial PZT thin films and reported a 2-D ultrasonic image sensor and measurement and analysis of ultrasonic transmission using pMUTs on  $\gamma$ -Al<sub>2</sub>O<sub>3</sub>/Si substrates. 3-D beam forming using a 2-D pMUTs array is also required to use for medical system. In this paper, we demonstrate analysis and characteristics of transmitting ultrasonic beam forming by 2-D pMUTs array using epitaxial PZT thin films on Si substrates.

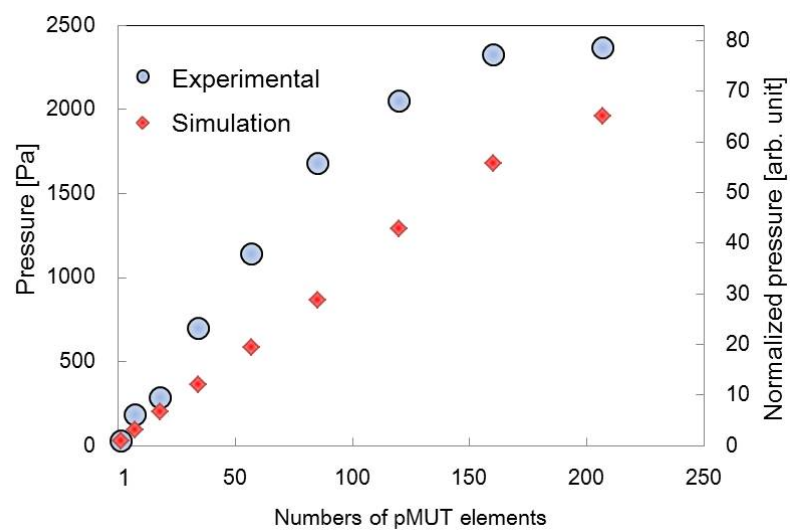
#### Statement of Contribution/Methods

A 9-ch miniature annular array was designed. First, an ultrasonic beam formation and sound pressure of ultrasonic distributions were calculated by finite element analysis in changing numbers of pMUT elements in array. A diameter of pMUTs was 100  $\mu$ m for resonant frequency of few MHz which was typical value for medical diagnosis system. Numbers of pMUT elements were 1 to 207 which a pitch of each element was 120  $\mu$ m. Each element was connected in the array to radiate ultrasonic at once. Then, pMUTs arrays with 0.5  $\mu$ m PZT thin films were fabricated to compare the distribution of sound pressure and the shape of ultrasonic beam with analysis results. A spatial distribution was measured by calibrated hydrophone in water tank with a function generator, amplifiers and an oscilloscope. PMUT arrays were driven by applying voltage of 30 V.

#### Results/Discussion

A -6 dB beamwidth and sound pressure at 5 mm from surface of the pMUT array were measured. A sound pressure was enhanced for increasing numbers of pMUT elements in an array. A pressure of ultrasonic by 34 elements pMUT array was about 10 times larger than single element as shown Fig. The beamwidth was sharpening in larger array. A 3-mm-beamwidth ultrasonic beam was obtained by driving more than 120-elements pMUTs array at once without delay operation. These experimental results good agree with analysis results.

In conclusion, we demonstrate ultrasonic beam formation and enhancing ultrasonic pressure using pMUTs array on epitaxial PZT thin films on  $\gamma$ -Al<sub>2</sub>O<sub>3</sub>/Si substrates. It will be expected miniature 2-D pMUTs array ultrasonic probe.



## P5C2 - Therapy Transducers

Salon C

Saturday, September 6, 2014, 8:00 am - 5:00 pm

Chair: **Takashi Buma**  
Union College

P5C2-1

### Cell Stimulation System using Low-Intensity Ultrasound by Piezoelectric Micromachined Ultrasonic Transducer Arrays

Wonjun Lee<sup>1,2</sup>, Joontaek Jung<sup>1,2</sup>, Mijung Bae<sup>3</sup>, Hyungsoo Han<sup>3</sup>, Hongsoo Choi<sup>1,2</sup>; <sup>1</sup>Department of Robotics Engineering, DGIST, Daegu, Korea, Republic of, <sup>2</sup>DGIST-ETH Microrobot Research Center, DGIST, Daegu, Korea, Republic of, <sup>3</sup>Department of Physiology, Kyungpook National University School of Medicine, Daegu, Korea, Republic of

#### Background, Motivation and Objective

Ultrasonic transducers are widely used in the medical community for ultrasonic imaging, treatment of disease, tissue stimulation, etc. Recently, it was reported that ultrasound can be used to stimulate cells to enhance cell differentiation and dendrite growth. Enhancing the neuronal cell differentiation is expected to expedite the recovery of damaged neurons. Many research groups reported cell stimulation using conventional ultrasonic transducers. However, those cell stimulation systems are bulky and it is not easy to characterize ultrasonic intensity with the bulky stimulation system. Those systems also have limitations to study multiple cell stimulation parameters in a confined cell culture environment in real time. To overcome these limitations, piezoelectric micromachined ultrasonic transducer (pMUT) array is adopted to develop a novel ultrasonic cell stimulation system.

#### Statement of Contribution/Methods

Two-dimensional ultrasonic transducer array based on pMUT element requires small number of wires to activate individual pMUTs, so that groups of pMUTs in the array can be selectively operated to generate ultrasound with different parameters. Figure 1 shows a cell stimulation system using pMUT arrays that can be placed in an incubator to guarantee the same experimental environment during cell culture. Ten pMUT arrays were mounted on a printed circuit board (PCB) to stimulate cells with different stimulation parameters: stimulation time, duty cycle and frequency.

#### Results/Discussion

The stimulation system was coated with 2.55  $\mu\text{m}$  parylene for waterproofing and biocompatibility. The measured resonance frequency of pMUT was measured at 1.6 MHz in air. Ten pMUT arrays were used to stimulate cells with different stimulation parameter under 10-wells and 2-wells don't have pMUT array for control group. Acoustic intensity will be measured in water shortly and cell stimulation results will be presented at the conference with optimal stimulation parameters. The proposed system can be used to investigate the effect of the ultrasound on cell stimulation with different stimulation parameters. The stimulation system has additional advantages in reducing the experimental cost and time consumption.

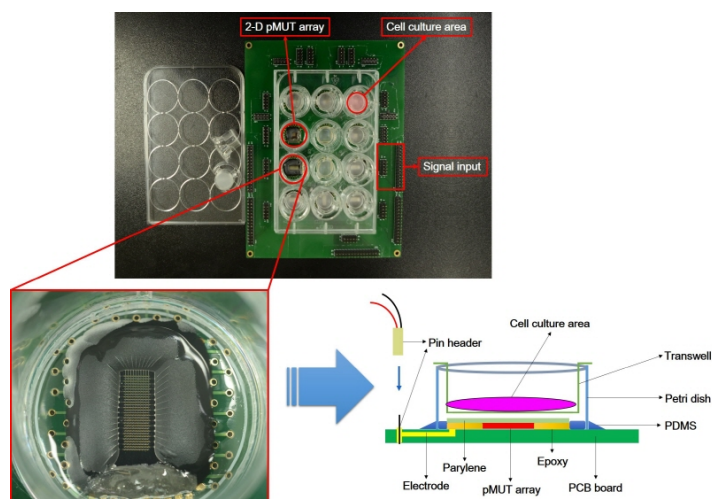


Fig. 1. Cell stimulation system using the 2-D pMUT arrays and 12-well transwell.

P5C2-2

### The study of chain-like materials for use in biomedical ultrasound

David Hutchins<sup>1</sup>, Jia Yang<sup>1</sup>, Omololu Akanji<sup>1</sup>, Peter Thomas<sup>1</sup>, **Steven Freear<sup>2</sup>**, Sevan Harput<sup>3</sup>, Nader Saffari<sup>4</sup>, Pierre Gelat<sup>5</sup>; <sup>1</sup>School of Engineering, University of Warwick, Coventry, United Kingdom, <sup>2</sup>School of Electronic and Electrical Engineering, University of Leeds, Leeds, United Kingdom, <sup>3</sup>School of Electronic and Electrical Engineering, University of Leeds, Leeds, United Kingdom, <sup>4</sup>Department of Mechanical Engineering, University College London, London, United Kingdom, <sup>5</sup>Department of Mechanical Engineering, University College London, London, United Kingdom

#### Background, Motivation and Objective

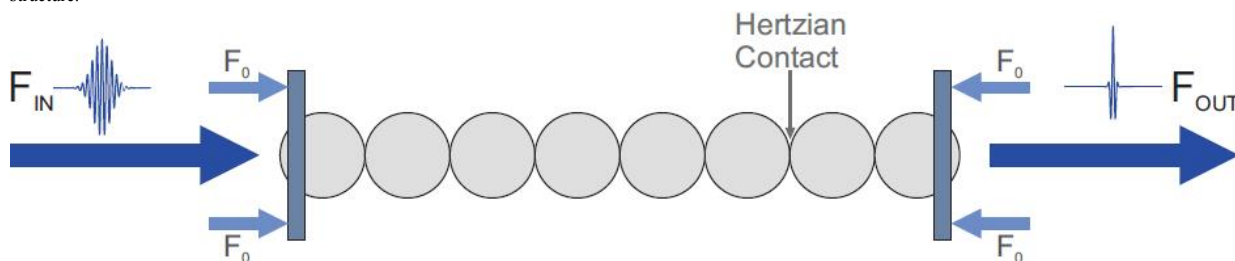
The transmission of acoustic signals along chains of spheres has been used to produce waveforms whose properties are of interest in biomedical ultrasound applications. The effects arise as a result of nonlinear Hertzian contact between adjacent spheres, which will change the nature of the signal as it propagates down the chain as shown in the Figure. The possibility thus exists of generating signals with bandwidths that are broader than that of the signal input into one end of the chain.

# Statement of Contribution/Methods

The theory of wave propagation in chain-like materials has been studied only at low frequencies. This study aims to generate these waves at frequencies relevant to biomedical ultrasound applications (>500 kHz). Therefore, chains of spheres with diameters of 1mm or less have been studied for a variety of high amplitude input waveforms from resonant transducers. Propagation along the chains then results in modifications to these waveforms due to nonlinearity and dispersion. Especially, when the static compression force ( $F_0$ ) is negligible compared to the dynamic input force ( $F_{IN}$ ), the propagation along the chain of spheres results in a highly nonlinear output. The resulting output waveforms have been compared to theoretical predictions, so that the behaviour of the chain-like waveguide can be determined. This allows the role of non-linearity in the propagation to be determined, so that output waveforms can be tailored to suit particular biomedical applications.

# Results/Discussion

The ways in which such signals could potentially be used in biomedical ultrasound will be described. These include higher-order harmonic imaging, targeted drug delivery and high intensity focussed ultrasound (HIFU). To illustrate this, scans of emitted signals in water will be presented, and the results related back to the waveforms emitted by the chain structure.



P5C2-3

## Micromachined Self-focusing Piezoelectric Composite Ultrasonic Transducer

XIAOHUA JIAN<sup>1</sup>, ZHILE HAN<sup>1</sup>, YONGJIA XIANG<sup>1</sup>, ZHANGJIAN LI<sup>1</sup>, YAOYAO CUI<sup>1</sup>; <sup>1</sup>Suzhou Institute of Biomedical Engineering and Technology, Suzhou, Jiangsu, China, People's Republic of

# Background, Motivation and Objective

Focused strong ultrasonic pulses are commonly used in many medical applications like lithotripsy, HIFU surgery, shock wave therapy in orthopedics and et al. Common transducers have large dimensions or acoustical lens in order to generate sufficiently high-pressure pulses. It is usually hard to make the focusing transducer with micro size, short focal length or high frequency. For solving these problems a micromachined self-focusing piezoelectric composite ultrasound transducer (MSPCUT) is proposed in this paper. Comparing others patterned the top and bottom electrodes into Fresnel annular rings, our method can achieve higher electromechanical coupling coefficient, piezoelectric coefficient, frequency, shorter focal length, low acoustic impedance and micro size. These advantages make it has great potential in medical interventional ultrasound imaging and treatment.

# Statement of Contribution/Methods

Based on the concept of constructive interference of acoustic waves, a MSPCUT was developed just as Fig. 1 showed. The MSPCUT consists of a piezoelectric composite thin film and Au electrodes on top and bottom faces of the composite. The piezoelectric composite were fabricated by etching a piezoelectric single crystal PMN-PT into annular rings, and then filling with the epoxy. These etched PMN-PT annular rings was similar to Fresnel half-wave pattern on the top view. Therefore, the acoustic waves generated by these adjacent annular sources arrive at the focal with a multiple of wavelength  $\lambda$  delay due to the difference in path length between the sources and the focal point. Then the acoustic waves arrive at the focal point in-phase, constructively interfering with each other, which mean that the acoustic waves generated by MSPCUT will focus at the focal plane as designed.

# Results/Discussion

To verify MSPCUT method, a particular MSPCUT with 50 MHz center frequency and 10 mm focal length was designed. When the transducer is excited with a burst of RF signal, the acoustic field was distributed as Fig. 2 showed. It is clear that the generated acoustic waves converged to the focal point, and then diffused after the focal point. The energy of the focal area is obviously stronger than else area. Fig. 3 is the acoustic intensity distribution on the focal plane, it is easy to find that the focal point is extremely small, and its intensity is much stronger than others.

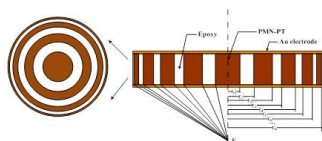


Fig. 1 Schematic of Micromachined Self-focusing Piezoelectric Composite Ultrasonic Transducer

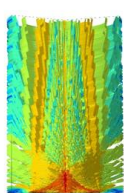


Fig. 2 Simulation result of the acoustic field distribution

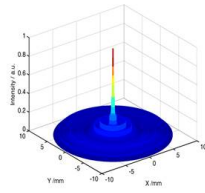


Fig. 3 Acoustic intensity distribution on the focal plane



### Analysis and Design of A Novel Shape of Piezoelectric Coupled with Tube to Increase the Radial Displacement

Yung Ting<sup>1</sup>, Yen Lung Lee<sup>1</sup>, Yun Jui Yang<sup>1</sup>; <sup>1</sup>Mechanical Engineering, Chung Yuan Christian University, Chung Li, Taiwan

#### Background, Motivation and Objective

piezoelectric actuators that constructed with a ring or several equal sectional type of piezoelectric ceramics attached to a thin tube are designed. The generated amplitude in the radial vibration of tube and other characteristics is investigated. Finite element method is used to analyze the mode shape, resonance frequency and amplitude.

#### Statement of Contribution/Methods

Piezoelectric actuator is mounted on the tube as illustrated in Fig 1. Two types of piezoelectric actuators, ring and sectional, are depicted in Fig 2. A ring type piezoelectric actuator encircled the tube with no clearance is shown in Fig 2(a), named TYPE I. Two cases, with arc 120deg and 60deg of each section of piezoelectric actuator with equivalent clearance in between the actuators for the sectional type are illustrated in Fig 2(b) and 2(c), named TYPE II and TYPE III respectively. All the ring and sectional types of piezoelectric actuators are made of PZT-5A higher piezoelectric coefficient d31 and d33 in comparison with PZT-4 at room temperature. The tube is made of stainless steel because of high tensile strength as well as elastic limit that is suitable for high power ultrasound design.

#### Results/Discussion

Using ANSYS, an example of appropriate mode shape is found and deformation with applied voltage of 50V is shown in Fig 3. As expected, resonance frequency decreases when the length of the tube increases. Also, resonance frequency is inversely proportional to the length of the tube. The first mode of simple axisymmetric deformation generating half wave is chosen to determine the resonance frequency by the modal analysis. Harmonic analysis is used to examine the vibration amplitude at the chosen resonance frequency. Fig 4 shows harmonic simulation and experiment results employed with, for example 50V and 150V. The simulation results show that amplitude of radial vibration of the tube is very small for the ring type (TYPE I) but quite large for the sectional type. Compared to the amplitude of TYPE I, TYPE II is about one thousand times, and TYPE III is about twenty thousand times. As seen, amplitude of TYPE I presents with very small difference as tube length is changed, and amplitude of TYPE II is varying, and amplitude of TYPE III is increased for longer tube but there is a maximum value for the length of 47.5 mm. The sectional-type with arc 60deg and with equal clearance between the neighboring actuators performs the best.

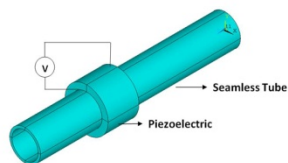


Fig. 1. Tube encircled with piezoelectric actuator

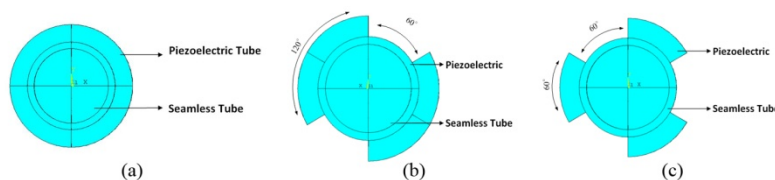


Fig. 2. Type and structure implementation of piezoelectric actuator: (a) Ring-type piezoelectric actuator encircles the tube, (b) Sectional-type (120°) piezoelectric actuator, (c) Sectional-type (60°) piezoelectric actuator

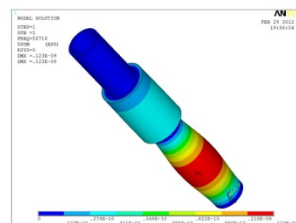


Fig. 3. Amplitude for the length of tube 50 mm

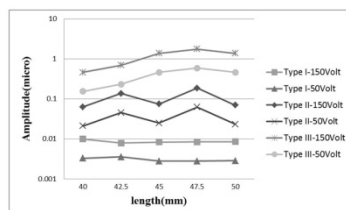


Fig. 4. Amplitude vs length for ring and sectional type

### A Sparse-element Phased Array System based on Sequentially Multiple Focusing for the Treatment of Large Tumors

Munbo Shim<sup>1</sup>, Sungjin Kim<sup>1,2</sup>; <sup>1</sup>Samsung Advanced Institute of Technology, Samsung Electronics, Korea, Republic of, <sup>2</sup>Samsung Electronics, Korea, Republic of

#### Background, Motivation and Objective

High Intensity Focused Ultrasound (HIFU) is a class of clinical therapies that necrose or remove tumors noninvasively from outside of body. Recently commercialized HIFU systems have shown successful clinical outcomes in fibroid tumor treatments. However they still have limitations on treatment time. Treatment with reduced time and costs needs fundamental innovations on HIFU technologies like transducer architecture to enable fast ablation of large tumors. The purpose of this study is the evaluation of the feasibility of cost- and time-effective HIFU treatment of tumors as well as the optimal design on HIFU transducer architecture with sparse-element to reduce the number of RF driving channels required for practical implementation.

#### Statement of Contribution/Methods

For rapid treatment of large-sized tumor while protecting healthy tissues, volumetric ablation by multi-focus is one of the promising solutions, which does not require mechanical or electrical beam steering to move focus within a focal area. In the previous study, a numerical optimization with a 1017-element spherical-section ultrasound phased array transducer operating at a frequency of 1.0MHz with 16 cm radius of curvature was performed for the generation of multiple foci (6, 6, 5, 4, 2, 2 foci in 5 by 5 foci). The ultimate design of the current study is the sparse array so as to reduce the number of driving channels and cut down the cost. It is necessary this design with less number of elements and driving channels shows similar sonication effect with the full array (total 1017 elements). The distribution of the reduced number of elements in the sparse array can be optimized by the incorporation of genetic algorithms to achieve acceptable properties for the radiation pattern.

#### Results/Discussion

The simulation results of the optimized sparse array showed that the suggested distributional pattern of phased array achieved a well-defined focal zone with multiple foci at the aimed area, and the grating lobe level kept below -10 dB in the 3D space. The results from the optimized sparse array showed equivalent performance to full array in terms of necrosis volume with thermal dose simulations. In conclusion, a sparse array can benefit from the reduction of the number of driving channels (about 1/2 of the full number of channel) to achieve similar sonication effect with the full array. Meanwhile, the necrosis volume produced by adopting the proposed transducer architecture with multi-focus was 9.6 times bigger than that by computer simulation with single focus scanning along predetermined trajectory under the same duration.

## Design and Characterization of High-Efficiency Optoacoustic Conversion Lens for Laser-Generated Focused Ultrasound

Hyoungh Won Baac<sup>1</sup>, Taehwa Lee<sup>2</sup>, L. Jay Guo<sup>2</sup>; <sup>1</sup>Sungkyunkwan University, Korea, Republic of, <sup>2</sup>University of Michigan, Ann Arbor, USA

### Background, Motivation and Objective

Laser-generated focused ultrasound (LGFU) is an emerging modality that can produce a single bipolar optoacoustic pulse (peak positive >50 MPa and negative >20 MPa) leading to strong shock and acoustic cavitation on a focal dimension of <100  $\mu\text{m}$ . Such tight spot is achieved by high-frequency operation (>15 MHz) under pulsed laser irradiation onto an optoacoustic conversion lens. In LGFU, a focal pressure is determined by an efficiency of optoacoustic conversion lens and a pulse laser energy that is delivered to a lens surface as an input; the maximum-available pressure is then limited by the laser damage threshold of a transmission layer (e.g. carbon nanotube (CNT)-polymer composite) coated on the lens. The optoacoustic lens with high focal gain, high conversion efficiency, and high damage threshold is required to reduce a pulse laser energy for acoustic cavitation and make LGFU-induced disruption effects available over a long focal length. We present our lens design and fabrication approach to improve a focal pressure.

### Statement of Contribution/Methods

In this work, a deeply curved optoacoustic lens with an f-number < 0.6 was fabricated by forming a CNT-polymer composite layer on a concave lens surface. This was greatly improved as compared with previous designs that had an f-number of >0.9 [Baac et al., Sci. Rep. 2, 989 (2012)]. As a heat transfer medium, we used an elastomeric polymer (i.e. PDMS) that is coated on CNTs directly grown on the lens substrate.

### Results/Discussion

First, we characterized a focal pressure generated by the new optoacoustic lens. We confirmed that a laser energy for acoustic cavitation on a glass boundary was greatly reduced to several mJ/pulse (previously, >10 mJ/pulse). The focal characteristics were investigated in terms of pressure waveform and amplitude, spatial profile, frequency spectrum, and conversion efficiency of the lens. Then, we performed cavitation experiments with and without a supporting boundary in water. Finally, we discuss the laser damage threshold of the CNT-PDMS layer, estimating a maximum-available energy fluence. Our design and characterization approaches presented in this work would provide a useful guideline to develop optoacoustic lenses with high focal gain and pressure for therapeutic applications.

## Session Chairs

Aigner, Robert .....	P4A1	Khuri-Yakub, Pierre.....	4E	Ren, Wei .....	7I
Bamber, Jeffrey.....	P1A7	Kolios, Michael.....	3A, P1B9	Reynolds, Paul .....	P5B1, P5B2
Bernassau, Anne .....	P3A1	Konofagou, Elisa .....	2J	Ruppel, Clemens .....	6A
Bhave, Sunil.....	6F	Kupnik, Mario.....	4K	Schafer, Mark.....	7H
Blackshire, James .....	4D	Kurosawa, Minoru .....	P3C1	Schmitz, Georg .....	1A, P1A3
Bouakaz, Ayache .....	1I	Kuypers, Jan.....	6H	Seip, Ralf.....	P1C11
Bridal, Lori .....	P1C4	Larson, John.....	5C	Shung, K. Kirk .....	5E
Buma, Takashi .....	P5C1, P5C2	Laude, Vincent.....	5K	Sinha, Bikash .....	P3B1
Byram, Brett .....	P1C5	Laugier, Pascal.....	3J	Smith, Scott.....	7G
Cloutier, Guy .....	P1A2	Lavarello, Roberto .....	P1C1	Solal, Marc.....	P4B1
Cochran, Sandy.....	7D	Li, Pai.....	3B, P1B1	Swillens, Abigail.....	P1C3
Courtney, Charles .....	5D	Liebgott, Hervé .....	3F, P1B10	Tanter, Mickael .....	2C
Cowell, David .....	P5A1, P5A2	Lopata, Richard.....	P1B6	Thomenius, Kai.....	P1C2
Dahl, Jeremy .....	P1B8	Lovstakken, Lasse.....	P1A8	Tittman, Bernhard .....	4H
Dayton, Paul .....	1B, 3D	Lu, Jian-yu .....	P1A5	Torp, Hans.....	2D
de Korte, Chris.....	2F	Maev, Roman.....	P2C2	Tortoli, Piero .....	P1B7
Degertekin, Levent .....	7B	Malocha, Don.....	6D	Tsujino, Jiromaru .....	P2C3
Deng, Cheri.....	2A	Matsukawa, Mami .....	P1C8	Ueda, Masanori .....	6I
D'hooge, Jan.....	2B	Matula, Tom.....	P1A10	Umemura, Shin-ichiro.....	P1B11
Elmazria, Omar.....	P4A3	Mayer, Andreas.....	5B	van der Steen, Ton .....	1J
Emelianov, Stanislav .....	2I	Melodelima, David .....	P1C6	Van Dongen, Koen.....	5A
Fattinger, Gernot.....	6E	Miller, James.....	1C, 1G	Vetelino, John .....	4G
Feld, David .....	P3A2	Mischi, Massimo.....	P1C7	Wagner, Karl.....	6C
Freear, Steven .....	2K, P1A6	Nakamura, Kentaro .....	4I	Wallaschek, Jörg.....	5I
Friend, James .....	4J	Naumenko, Natalya.....	P4C2	Wear, Keith.....	P1A9
Gallippi, Caterina.....	2H	Nightingale, Kathy.....	3G	Wilcox, Paul.....	4B
Gangbing, Song .....	P2C1	Nikolov, Svetoslav.....	3E, P1A11	Wilkening, Wilko.....	P1B4
Garcia, Damien.....	P1B3	Nowicki, Andrzej.....	1D	Willmann, Juergen .....	1E
Greenleaf, James.....	P1A1	O'Brien, William.....	3C	Xu, Zhen .....	1F
Greve, David.....	4A, P2A1, P2A2	Oelze, Michael .....	P1C9	Yeh, Chih-Kuang .....	P1B5, P1C10
Hall, Timothy.....	2G	O'Leary, Richard.....	7F	Yong, Yook-Kong.....	5H
Hladky, Anne-Christine .....	P3C3	Oralkan, Omer .....	7C	Yu, Alfred .....	3H, 3K
Hossack, John .....	1H, P1B2	Oruklu, Erdal .....	4F, P2B1	Yuan, Jian .....	7J
Hynynen, Kullervo .....	3I	Patel, Mihir .....	P3B2	Yuhas, Donald.....	P2A3, P2B3
Jensen, Jørgen .....	2E, P1A4	Pennec, Yan .....	5J	Zheng, Hairong .....	1K
Jiang, Xiaoning.....	7E	Pereira da Cunha, Mauricio .....	6B	Zhgoon, Sergei.....	P4C1
Kaitila, Jyrki .....	P4B2	Pitschi, Maximilian.....	P4A2	Zhou, Qifa .....	7A
Kessler, Lawrence.....	4C, P2B2	Reinhardt, Alexandre .....	P3C2		

## Author Index

## A

Abbey, Craig ..... P1C2-7, P1C3-6  
 Abdelmalek, Manal ..... 2H-5, P1A1-5  
 Abe, Hiroshi ..... P1A7-12  
 Abergel, Julie ..... P3C2-3, P3C2-4  
 Abraham, Theodore ..... P5B2-7  
 Abraham, Yamil ..... P3B2-9  
 Achenbach, Jan ..... 5B-1  
 Acker, Jason P ..... P1B1-4  
 Acosta, Camilo ..... 3K-2  
 Adachi, Masatoshi ..... 6C-4  
 Adam, Dan ..... P1B4-3, P1C11-4, P1C7-7  
 Adamowski, Julio ..... P2A3-3, P3A1-1  
 Adamson, Rob ..... 7A-3  
 Adamson, Robert ..... P5B1-9  
 Addennour, Meriem ..... P1A2-1  
 Addouche, Mahmoud ..... 5J-5  
 Adibi, Yasaman ..... P1B6-4  
 Aglyamov, Salavat ..... P1C6-9  
 Ahmad, Syed ..... P1C11-14  
 Ahn, Hongmin ..... 7J-2  
 Aigner, Robert ..... 6A-2, P4A2-3  
 Ait Aïssa, Keltouma ..... 6B-2, 6D-3  
 Akahori, Hajime ..... P2C2-2  
 Akai, Daisuke ..... P5C1-14  
 Akanji, Omololu ..... P3C3-2, P5C2-2  
 Akao, Shingo ..... 6B-5, P4C1-1  
 Akhbari, Sina ..... 7C-3  
 Akiyama, Iwaki ..... P1A11-7, P1A4-3  
 Akkus, Zeynnett ..... 1J-4  
 Albala, Lorenzo ..... P1C4-2  
 Albers, Josefine ..... P1B11-11  
 Alessandrini, Martino ..... 1G-3, P1C5-1  
 Alexander, Marci ..... P1A2-2  
 Alizad, Azra ..... 2C-5, P1A2-6  
 Alland, David ..... 7E-4  
 Allen, Jason ..... 2B-5  
 Allen, Thomas ..... 5K-5  
 Alles, Erwin ..... 3A-6, P1A7-3  
 Al-Mahrouki, Azza ..... 3K-3, P1A10-9, P1A3-7, P1B9-4, P1B9-5, P1C10-3, P1C10-4  
 Almeida, Nuno ..... 1G-4  
 Almeida, Thiago ..... P1A1-3  
 Alomari, Zainab ..... P1A5-1, P1B7-6  
 Alvar, Sushma ..... 7F-1  
 Amador, Carolina ..... 3C-6, P1C6-3, P1C6-4  
 Amaro, Joao ..... P1A6-4  
 Ambrosi, Thomas ..... P1B11-11  
 Amini, Mohammad Hossein ..... 7J-4  
 Amraoui, Sana ..... 3K-5  
 Anand, Ajay ..... P1B11-8  
 Anderson, Tom ..... P1B2-9  
 Andersson, Roger ..... 3G-1  
 Ando, Takehiro ..... P1C11-13  
 Andrade, Marco ..... P3A1-1  
 Andre, Michael P ..... P1C8-1, P1C8-2  
 Anthony, Brian ..... 3H-3  
 Antlinger, Hannes ..... P2C1-1  
 Antsev, Ivan ..... P4A3-1  
 Aoyagi, Ryouyuke ..... P1C10-10  
 Apostolakis, Iason ..... P1B6-9  
 Apostolakis, Iason Zacharias ..... 2F-2  
 Apte, Nikhil ..... 7B-1  
 Arabul, Mostafa Umit ..... P1C9-10  
 Arakawa, Mototaka ..... 3H-1, 6C-4, P2A2-8  
 Arango Ossa, Juan-Esteban ..... 1G-2, 2B-1, 2D-3, 3C-2  
 Ardanuç, Serhan ..... 6E-3, 6E-4, PA-16  
 Arena, Christopher ..... P1B5-3  
 Arendt Jensen, Jørgen ..... 7F-5, P1C5-7

Arif, Muhammad ..... P1B8-2  
 Aristizabal, Sara ..... 3C-6, P1C6-3  
 Ariyurek, Cemre ..... 7D-5  
 Arnal, Bastien ..... 2I-5, 2J-2, 3D-5, 3G-4, P1B7-3  
 Arseniyadis, Stellios ..... 4E-2  
 Arthuis, Chloe ..... P1A3-10, P1A7-4  
 Arthur, Craig ..... P1C1-7  
 Aryal, Muna ..... 3I-2  
 Asada, Akira ..... P2A2-6  
 Asada, Takaaki ..... P1B6-7  
 Asada, Takashi ..... P1C8-11  
 Asami, Rei ..... P1A10-11  
 Åsen, Jon Petter ..... P1B2-6  
 Ashida, Reiko ..... P1A10-11  
 Ashkenazi, Shai ..... 7J-3  
 Assef, Amauri ..... P1B10-3  
 Assouar, Badreddine ..... 5B-4, 5J-6  
 Atalar, Abdullah ..... 7C-2, 7C-5, P5C1-1  
 Ateshian, Gerard ..... P1C11-3  
 Atile, Esayas ..... 3G-1  
 Aubert, Isabelle ..... 3I-1  
 Aubert, Thierry ..... 6D-3  
 Audièrre, Stéphane ..... P1B7-12  
 Austeng, Andreas ..... P1B2-6  
 Avdal, Jørgen ..... P1B3-4  
 Ayazi, Farokh ..... 6F-3  
 Aydogdu, Elif ..... 7C-5  
 Azizian Kalkhoran, Mohammad ..... P1A7-7  
 Azuma, Takashi ..... 2K-6, 5E-4, P1C10-10, P1C11-13

## B

Baac, Hyoungh Won ..... 5I-6, 5K-6, P5C2-6  
 Babakhanian, Meghedi ..... P1A9-8  
 Bachawal, Sunitha ..... 1B-1, 1B-3, 3D-4  
 Bachmann Nielsen, Michael ..... P1A8-5, P1B3-1  
 Bader, Bernhard ..... PA-15  
 Bae, Mijung ..... P5C2-1  
 Bae, Minkun ..... P2B2-1  
 Bae, Mooho Bae ..... P1C1-4  
 Bae, Sua ..... P1A1-7  
 Baffa, Oswaldo ..... P1B8-1  
 Baghai-Wadji, Alireza ..... P4A2-1, P4B1-8  
 Bahramian, Sara ..... P1C7-9  
 Bai, Xiaosong ..... 2I-4  
 Bai, Yang ..... 7I-2  
 Bailey, Michael ..... 1F-4, 1F-5, 3E-4, 3K-4, 5E-2, P1B11-4, P1C10-11, P1C11-8  
 Balcerzak, Andrzej ..... P3B2-3, P3B2-4  
 Baldini, Capucine ..... P1A3-1  
 Ballard, John R ..... P1C11-11  
 Balogun, Oluwaseyi ..... 5B-1  
 Bamber, Jeffrey C ..... 3A-6, P1A7-3  
 Bandaru, Raja Sekhar ..... P1C2-1  
 Banys, Juras ..... P3B2-1  
 Bar Zion, Avinoam ..... P1B4-3  
 Baradarani, Aryaz ..... 3E-2, 4F-5  
 Barauskas, Dovydas ..... P5C1-3, P5C1-5  
 Barbay, Sylvain ..... P3C3-3  
 Barbosa, Daniel ..... 1G-4  
 Bardhan Roy, Rupak ..... P5A1-2  
 Bardong, Jochen ..... 6C-5, P4A3-3, P4B2-1  
 Barkmann, Reinhard ..... P1A9-4  
 Barrois, Guillaume ..... P1A3-1, P1B4-6, P1B4-7  
 Barry, Christopher ..... 1K-3  
 Barth, Stephan ..... 5H-2  
 Barthe, Peter G ..... P1C11-14  
 Barton, Jennifer Kehlet ..... P1B11-9  
 Bartsch, Hagen ..... 5H-2  
 Basarab, Adrian ..... P1A11-2, P1A11-3

Bassam, Abdallah ..... P4B2-2  
 Bassi, Luca ..... P1A6-12, P1A6-5, P1B10-10  
 Bastard, Cécile ..... P1B7-10, P1B7-12  
 Bause, Fabian ..... P2A1-3  
 Bayat, Mahdi ..... P1B11-3, P1C11-11  
 Bayatpur, Farhad ..... 5C-5  
 Baylor, Martha-Elizabeth ..... 7J-3  
 Beachy, Philip ..... P1A3-2  
 Beckmann, Martin F ..... 3A-4, P1A7-5  
 Bedossa, Pierre ..... P1A2-1  
 Been, Kyoungun ..... 7J-2  
 Beers, Christopher ..... 2K-2  
 Begar, Anna V ..... P3B2-8  
 Behler, Russell ..... P1A1-4  
 Beigelbeck, Roman ..... P2C1-1, P5B2-11  
 Belan, Reagan ..... P5B1-3  
 Belovickis, Jaroslavas ..... P3B2-1  
 Beltram, Fabio ..... 4E-4, 4E-5, PA-8  
 Benaissa, Lamine ..... 5H-3  
 Benchabane, Sarah ..... 5K-4, P3C3-3  
 Benech, Nicolas ..... P3B2-9  
 Benmore, Chris J ..... 5E-5  
 Benoit A La Guillaume, Emilie ..... P1A7-11  
 Bera, Deep ..... P5B2-10  
 Bercoff, Jeremy ..... 1C-4, 3G-6  
 Berer, Thomas ..... P2A1-6, P2A2-4  
 Bernal, Miguel ..... 3G-6, P1A1-2, P1B7-7  
 Bernard, Olivier ..... 1G-3, 1G-4, 3B-6, P1A5-4  
 Bernard, Simon ..... 3J-1, P1A9-4  
 Berndt, Elizabeth ..... 2G-1, 2G-5, P1B1-4, P1B9-8  
 Bertuzzo, Jose E ..... P1A6-9  
 Bettinger, Thierry ..... 1B-3, P1A3-9  
 Beugnot, Jean-Charles ..... P3C3-3  
 Beurskens, Robert ..... P1B5-7  
 Beyssen, Denis ..... P2B2-3, P4A3-4  
 Bezagu, Marine ..... 4E-2  
 Bezanson, Andre ..... 7A-3, 7G-2  
 Bhethanabotla, Venkat ..... P2C1-6, P4C2-4  
 Bi, Frank ..... 6A-4, 6A-5, 6A-6  
 Bigarré, Janick ..... P2A3-1  
 Bin Alias, Norashaz ..... 6A-5  
 Binder, Alfred ..... P4A3-3  
 Biryukov, Sergey ..... 6I-1  
 Bjällmark, Anna ..... P1B6-6  
 Blaak, Sandra ..... P5B2-10  
 Blachier, Denis ..... P3C2-4  
 Black, John ..... P1C11-6  
 Blackshire, James ..... 4C-6, 4H-4, P2A3-6  
 Blakemore, Robert ..... 7E-4  
 Blanc, Laurianne ..... P2A3-1  
 Blanc, Rémi ..... P1C7-1  
 Blank, Vladimir ..... P4A1-6  
 Blankschtein, Daniel ..... 3H-3  
 Blatter, Martijn F.J ..... P1B6-2  
 Bleyl, Ingo ..... 6C-2, 6H-2  
 Boctor, Emad ..... 3A-5  
 Boechler, Nicholas ..... 5J-4  
 Boekhoven, Renate W ..... P1B6-2, P1B6-3, P1C5-10  
 Boes, Andreas ..... 5J-1, 6E-5  
 Bogoslovsky, Sergei ..... P4A3-1  
 Böhmer, Marcel ..... P1B1-6, PA-4  
 Bok, Tae-Hoon ..... P1A7-6  
 Bokov, Alexei ..... 7I-4  
 Bonello, Bernard ..... 5J-2, P3C3-5, P3C3-6, P3C3-9  
 Boni, Enrico ..... P1A6-12, P1A6-5, P1B10-10, P1B2-3  
 Boning, Duane ..... 3H-3  
 Boppert, Stephen ..... 1J-1

Borden, Mark ..... 1E-4, P1B11-10, P1B1-5,  
P1C4-9  
Bormashov, Vitaliy ..... P4A1-6  
Borna, Amir ..... 7F-1  
Bornmann, Peter ..... 4G-4  
Borodina, Irina ..... P3B1-3, P3B1-5  
Bosch, Johan ..... 1H-2, 1J-4, 2H-2, P1B5-1,  
P5B2-10  
Boss, G. .... 3H-5  
Bossy, Emmanuel ..... P1A9-6  
Bou Matar, Olivier ..... 5B-5, P3C3-10  
Bouakaz, Ayache ..... 1D-4, 3I-6, P1A10-1,  
P1A3-10, P1A4-4, P1A7-4, P1B4-5,  
P1C4-6, P1C4-8  
Bouchard, Richard ..... P1A7-9  
Bouhouch, Nabil ..... P1A3-3  
Bouillot, Jean-Luc ..... P1A2-1  
Boulet, Clementine ..... P2B1-5  
Boulet, Pacal ..... 6D-3  
Boulmé, Audren ..... P5B2-2, P5C1-8  
Boumatar, Olivier ..... 5I-4, 6B-6  
Bour, Pierre ..... 3K-5  
Bourdeau, Ray ..... P1C4-10  
Bourgnon, Adeline ..... 2G-6  
Boutet, Jérôme ..... P1A7-7  
Boutouyrie, Pierre ..... P1B6-3  
Bouvet, François ..... P2C1-3  
Bouvot, Laurent ..... 5I-4  
Bowles, Douglas K. .... 2A-3  
Boyko, Olga ..... 5J-2, P3C3-5, P3C3-6  
Bozkurt, Ayhan ..... 7D-5, P5A1-1, P5A1-2  
Braga, Arthur ..... P2A3 -3  
Braive, Rémy ..... P3C3-3  
Branch, Darren ..... 6F-2, 7E-4, P3B1-9  
Brandt, Andreas ..... 2D-2  
Brandt, Andreas Hjelm ..... P1A5-6  
Breivik, Lars Hoføsy ..... P1A8-8, P1C7-5  
Brenner, M. .... 3H-5  
Brentnall, Teresa ..... P1A3-2  
Bridal, Lori ..... 2E-1, P1A3-1, P1B4-6, P1B4-7,  
PA-1  
Brown, Daniel ..... 1C-3  
Brown, Jeremy ..... 7A-3, 7G-2, P1C1-7, P5B1-9  
Brown, Michael ..... 5K-5  
Brown, Stephen ..... 5C-2  
Browning, Richard J ..... 1I-1  
Bruce, Matthew ..... 1C-4, P1B4-1  
Bruckner, Gudrun ..... 6C-5, P4A3-3, P4B2-1  
Brum, Javier ..... 5C-3, P1A1-2  
Brysev, Andrei ..... 5A-2  
Buch, Amanda ..... 3I-4  
Buchanan, Douglas ..... 7B-3  
Buck, Andrew ..... 2C-4  
Buckland, Daniel ..... 3E-3  
Buckley, John ..... P2C3-7  
Buckwalter, Joseph A. .... P1A4-15  
Bucovsky, Mariana ..... P1A9-5  
Buiocchi, Flávio ..... P5B1-2  
Buma, Takashi ..... 3A-2, 4D-4, 7J-1  
Bunting, Ethan ..... 1A-3, 1H-4, P1C5-3  
Burgess, Alison ..... 3I-1  
Burgholzer, Peter ..... P2A1-6, P2A2-4  
Burkov, Sergei ..... P3B1-8  
Burkov, Sergey ..... P4A1-6  
Burnett, Timothy ..... P2A1-7  
Burns, Dan ..... 5C-2  
Burns, Peter ..... P1B4-1  
Burrascano, Pietro ..... P2B1-7  
Button, Tim ..... 7G-6, 7I-2  
Button, Vera ..... P1B10-3  
Buzanov, Oleg ..... 6D-1, 6I-1  
Byra, Michal ..... 2H-3  
Byram, Brett ..... 3F-3, P1B7-2

## C

C. Kolios, Michael ..... P3A2-4  
Cabral, José ..... P2C2-5  
Cabrera-Munoz, Nestor ..... 7A-1, 7A-4  
Cachard, Christian ..... P1C1-5, P1C2-3, P5B2-8  
Cai, Ping ..... P1A4-7  
Caidahl, Kenneth ..... 2F-6, P1B6-6  
Cain, Charles ..... 1F-1, 1F-2, 1F-3, 7D-6, P1B11-1,  
P1C11-5  
Caixinha, Miguel ..... P1C8-9  
Caleap, Mihai ..... 5E-6  
Caliano, Giosuè ..... P1B2-3, P2C1-4, P5C1-10,  
P5C1-6  
Callaghan, Lori ..... 6A-4, 6A-5, 6A-6  
Callstrom, Matthew ..... P1A1-4  
Callstrom, Matthew R. .... 1K-1  
Calmon, Pierre ..... P1A4-4  
Caloone, Jonathan ..... P1B11-7  
Cao, Wenqing ..... 1K-3  
Capelle, Laurent ..... 2C-1  
Carlson, Johan E. .... 4B-4, 4J-3, P2A2-3  
Carlson, Lindsey ..... 2C-3, 3C-4  
Carneiro, Antonio ..... P1B8-1  
Carneiro, Antonio Adilton ..... P1A1-3  
Carrasco, Diego ..... P3B2-9  
Carson, Andrew R. .... 2A-2  
Carson, Paul ..... P1A7-2, P1B11-6  
Cartellier, Florian ..... 3G-5  
Carvalho, Diego D.B. .... 1J-4  
Casey, Graeme ..... 7G-6  
Casset, Fabrice ..... 5H-4  
Castañeda, Benjamín ..... P1B9-9, P1C6-6, P1C9-8  
Castaño Arranz, Miguel ..... P2A2-3  
Castellucci, John ..... P1A5-5  
Catheline, Stefan ..... 2J-6, 3C-3, 3G-5  
Caughey, Melissa ..... P1B6-1, P1C5-8  
Cazorla, Pierre-Henri ..... 7E-1, PA-20  
Cecchini, Marco ..... 4E-4, 4E-5, PA-8  
Cellai, Andrea ..... P1B10-10  
Cerimovic, Samir ..... P2C1-1  
Certon, Dominique ..... 1D-4, 7B-5, P5B2-2,  
P5C1-8  
Chabraborty, Aritra ..... 2G-6  
Chakrabarti, Chaitali ..... P1A6-7  
Chakraborty, Aritra ..... P1B11-11  
Chakraborty, Soumya ..... 4F-1  
Chalek, Carl ..... P1A3-5  
Chaline, Jennifer ..... P1C4-8  
Chambers, Ann F. .... 2E-5, P1C3-5  
Chamming'S, Foucauld ..... 3G-6  
Chan, Chao-Kuo ..... P2A3 -9  
Chang, Chun-Hsiang ..... P1A11-6  
Chang, En-Ling ..... P1A10-3  
Chang, Hing-Chiu ..... 2B-5  
Chang, Jin Ho ..... 2A-5, 3D-1, P1A1-7, P1B10-6,  
P5A2-3  
Chang, Tsung-Lun ..... 2A-4  
Chao, Min-Chiang ..... P3B1-6  
Chao, Pei-Yu ..... P1B7-5  
Chapelon, Jean-Yves ..... 2J-1, 3C-3, 3G-5,  
P1B11-7  
Chappard, Christine ..... 3J-5  
Chartier, Caroline ..... P1B7-10, P1B7-12  
Chassaing, Jean-Camille ..... 4J-2  
Chatelin, Simon ..... 1K-2, 2B-3, P1B7-7  
Chatzioannou, Achilleas ..... P1C8-6  
Chauvet, Dorian ..... 2C-1  
Chawla, Shawn ..... P1A10-10  
Chayer, Boris ..... P1B6-10, P1C3-9, P1C9-2  
Chaziachmetovas, Andrius ..... P3A2-5  
Chee, Adrian J. Y. .... 1D-5, P1C3-1  
Chee, Ryan ..... P5C1-11  
Chehami, Lynda ..... 4B-3

Chen, Albert ..... 7B-6, P1B10-2  
Chen, Bo-Rong ..... P1A2-8  
Chen, Chao ..... P5B2-10  
Chen, Choon Chowe ..... 6A-6  
Chen, Di ..... 5D-4  
Chen, Guan-Chun ..... P1C9-6  
Chen, Hao ..... 4D-2  
Chen, Hong ..... 2J-5  
Chen, Hui ..... P3B1-6  
Chen, Jeng-Wen ..... P1A11-6  
Chen, Jian Feng ..... 5C-1  
Chen, Jin ..... P5A2-15  
Chen, Jing ..... P4C1-2  
Chen, Jing-Shi ..... P2B3-1  
Chen, Kailiang ..... 1D-1  
Chen, Nan-Kuei ..... 2B-5  
Chen, San-Yuan ..... 3E-5, PA-3  
Chen, Shigao ..... 1K-1, 1K-5, 2B-2, 2C-5, 3G-3,  
P1A1-4, P1A1-6, P1A2-6  
Chen, Shuming ..... P5A2-5  
Chen, Siping ..... P1C6-7, P5A2-11  
Chen, Tainsong ..... P1C9-6  
Chen, Xian ..... 3K-1  
Chen, Xiaoye ..... 4D-6  
Chen, Xin ..... P1C6-7  
Chen, Xucai ..... 1E-1, 2A-2, P1C10-1, P1C11-6  
Chen, Yan ..... 7A-2  
Chen, Yao ..... 2J-1, 2J-6  
Chen, Yu ..... 3F-6  
Chen, Yuling ..... 2K-3  
Chen, Yun-Sheng ..... P1B1-3  
Chen, Zhongping ..... 1J-2  
Cheng, Alexis ..... 3A-5  
Cheng, Gang ..... 1K-3  
Cheng, Yi ..... P1B7-4  
Cherin, Emmanuel ..... P1C4-10  
Chi, Liyang ..... P1B10-7  
Chiba, Toshio ..... P1C11-2  
Chilipka, Tom ..... P1B10-8  
Chilla, Eduard ..... P4B1-1  
Chiou, Hong-Jen ..... P1C10-8  
Chitnis, Parag V. .... 3D-2  
Chiu, Chi Tat ..... 2F-3, P5B2-7  
Chiu, Chien-Hao ..... P1A7-13  
Chlon, Ceciel ..... P1B1-6, PA-4  
Chmielewski, Aneta ..... P1C7-2  
Cho, Min Gyu ..... P1A6-6, P5C1-2  
Cho, Sooh ..... P1B2-2  
Choe, Jung Woo ..... P1C10-2  
Choi, Gobong ..... P4A1-4  
Choi, Hajin ..... 4K-1, PA-7  
Choi, Hojong ..... 3H-2, P1B10-9, P5C1-13  
Choi, Hongsoo ..... P5C2-1  
Choi, James J. .... P1B5-4  
Chow, Robert ..... 2G-2  
Chowe Chen, Choon ..... 6A-5  
Christensen-Jeffries, Kirsten ..... 1I-1  
Christiansen, Thomas Lehmann ..... P5C1-7  
Chu, Harry ..... 4B-5  
Chu, Mincheol ..... P2B2-1  
Chu, Tang-Ting ..... P1B7-8  
Chuang, Kuang-Hsiang ..... 1K-3  
Chuembou Pekam, Fabrice ..... P1C7-4  
Chuembou, Fabrice ..... 3H-6  
Chukwunonye, Chukwunonye ..... 4C-4  
Cinthio, Magnus ..... 2E-4, 3G-1  
Clara, Stefan ..... P2C1-1  
Clement, Gregory ..... 3H-4  
Clément, Karine ..... P1A2-1  
Clement, Marta ..... P4A1-1, P4A1-3, P4A1-5,  
P4A3-6  
Clet, Michel ..... P1A2-1  
Clézardin, Philippe ..... 3K-6, P1C10-7



Cloutier, Guy	2B-6, 2F-4, 3B-5, 3C-3, P1B6-10, P1C3-9, P1C6-10, P1C9-2
Coburn, Michael	1F-4
Cochet, Martine	7E-1, PA-20
Cochran, Sandy	5D-3, 5E-1, 7A-3, 7G-5, 7G-6, 7H-2, 7H-3, 7H-4, 7H-5, 7H-6, P3A1-3, P5B1-8, PA-12
Colello Bruno, Alexandre	P1B8-1
Collado, Carlos	P4A2-3
Compas, Colin	1A-2
Cong, Bing	P2A2-2
Connors, Bret	1F-5
Contescu, Cristian I.	4C-1
Cornier, George	7H-5
Coron, Alain	P1B4-6, P1B4-7
Correa, Adrian	1J-2
Correas, Jean-Michel	1C-4
Correia, Mafalda	1K-2, 2B-3
Cossy, Janine	4E-2
Costa, David	P5B1-2
Costa, Eduardo	P1B10-3
Costa-Felix, Rodrigo	P2B3-2
Costet, Alexandre	P1C5-3
Couade, Mathieu	3G-6
Courtney, Charles	4B-5, 5E-1
Coutier, Caroline	1D-4, 7B-5
Couture, Olivier	1C-4, 1I-3, 4E-2, P1B4-8
Cowell, David	3E-1, 7H-1, P1A10-7, P1B1-1, P1C4-7
Cox, Ben	5B-2, 5K-5, P3B2-5
Cox, Benjamin	7G-5
Coyle, Thomas	7J-4
Criton, Aline	1C-4
Crozat, Sophie	P2C1-3
Crum, Lawrence	P1C10-11
Cuffe, John	5K-1
Cui, Jing	P3B1-1
Cui, Weiwei	P4A3-5
Cui, Yaoyao	P2A1-1, P5C2-3
Cular, Stefan	P3B1-9
Culjat, Martin	7D-2, P1A9-8
Cummins, Thomas	P5C1-13
Cunitz, Bryan	1F-4, 1F-5, 3E-4, P1C11-8
Curtis-Bray, Nicole	P2C1-5
Cuschieri, Alfred	5D-3, PA-12
Cygan, Szymon	1G-3
Czarnota, Gregory	2A-1, 2C-2, 3C-5, 3K-3, P1A10-9, P1A3-7, P1A4-6, P1B9-11, P1B9-3, P1B9-4, P1B9-5, P1B9-7, P1C10-3, P1C10-4, P1C7-8
Czarnota, Gregory J	P1B9-1, P1C4-5
Czernuszewicz, Tomasz	P1A1-1, P1B6-1, P1C5-4

## D

D'Agostino, Emiliano	P1C9-1
D'Armiento, Jeanine	2F-1
D'Hooge, Jan	2F-6
Daichin, Varya	P1B5-1
D'Agostino, Emiliano	P1C4-3
Dahibawkar, Manasi	P1A3-6
Dahl, Jeremy	2B-5, 2E-3, 3F-4, P1C9-8
Dahl, Torbjørn	1J-3
Dai, Jiyuan	7A-2
Dai, Yuyu	4I-4
Dalen, Håvard	P1A11-1
Dana, Nicholas	P1A7-9
Daneault, Claude	4J-5
Dangra, Nida	2F-1
Darinskii, Alexander	P4B2-4
Daugschies, Melanie	P1A9-4
Dauson, Erin	P2B2-2
Dave, Jaydev	P1A3-6

David, Jean-Baptiste	5H-3
Davis, Lee	P2A1-2, P2B1-7
Davis, Zachary	6D-5
Dayton, Paul	1E-3, 2J-3, 3A-1, 3H-2, 7G-3, P1A3-4, P1A4-9, P1B4-5, P1B5-2, P1B5-3, P1C4-6, P5B2-3, PA-17
De Craene, Mathieu	1G-3
De Jaeger, Jean Claude	P4B2-2
de Jong, Nico	1E-1, 1E-2, 1I-5, 1J-4, 2H-2, 2I-3, P1B1-6, P1B4-4, P1B5-1, P1B5-7, P1B5-9, P5B2-10, P5C1-12, PA-4
de Korte, Chris L.	2F-5, P1B3-6, P1B6-5
de la Rosette, Jean	1G-5, P1A3-3
De Marchi, Luca	P1C7-3
de Rosny, Julien	4B-3
de Vries, Rens M.J.M.	P1B6-2
DeAngelis, Dominick	P5B1-7
Decharat, Adit	P5A2-9, P5B1-1
Defay, Emmanuel	5H-3, 5H-4, 7E-1, P3C2-1, P3C2-3, P3C2-4, PA-20
Deffieux, Thomas	2B-1
Degen, Katharina	3H-6
Degertekin, F. Levent	7C-6, 7F-2, P1A8-4, P1C9-4, P5A1-3, PA-19
Dei, Kazuyuki	3F-3
Dekker, James	6D-4
Delingette, Hervé	1G-3
Demené, Charlie	2C-1, 2D-3, 2E-1, PA-1
Demi, Libertario	1G-5, P1A3-3, P1A5-8, P3A2-7
Demiguel-Ramos, Mario	P4A1-1, P4A1-3, P4A1-5, P4A3-6
Demirli, Ramazan	P2B1-1, P2B1-3
Demminger, Christian	P2C3-5
Démoré, Christine	5E-1, 7G-5, 7G-6, P3A1-3
Dempsey, Robert	P1C8-5
Den Hartog, Patric	5E-5
Dencks, Stefanie	P1B8-4
Deng, Cheri	5D-4
Deng, Mingxi	4D-1
Deng, Yiming	4D-6
Deng, Yufeng	2H-5, P1A1-5
Denis, Max	2C-5, P1A2-6
Derkach, Mikhail	P4A3-1
Desailly, Yann	1I-3
Desmulliez, Marc	7G-6
Destrempe, François	3C-3
Devos, Arnaud	5H-4
Devulapally, Rammohan	P1C10-2
Deymier, Pierre	5B-5
Dezotti, Tiago C.	P1A6-9
Dhanaliwala, Ali	1I-6, 2A-3
D'hooge, Jan	1A-1, 1G-3, 1G-4, 3B-4, P1A4-5, P1A5-2, P1A5-3, P1A5-9, P1C2-1, P1C4-3, P1C5-1, P1C9-1
Diamantis, Konstantinos	P1B2-9
Diarr, Bakary	P1C1-5, P5B2-8
Diederichsen, Søren Elmin	P5C1-7
Dieppedale, Christel	5H-4
Dimcevski, Georg	3I-5
Ding, Xuan	1D-3, P1B2-4
Divani, Afshin	P1B6-4
Dixon, Adam	1I-6
Dixon, Steve	4K-3, P2C3-6
Dizeux, Alexandre	2E-1, P1A3-1, PA-1
Djafari-Rouhani, Bahram	5K-2, P3C3-5, P3C3-6, P3C3-9, PA-10
Do, Minh	P1C2-2
Doberstein, Sergei	P4B1-5
Doherty, Joshua	2B-5
Doinikov, Alexander	P1A4-4, P1C4-6
Doležal, Ladislav	P1A6-10
Dong, Hao-Wen	P3C3-7
Dos Santos, Serge	P1C4-8

Dove, Jacob	P1B1-5
Downs, Matthew	3I-3, 3I-4, PA-5
Doyley, Marvin	3B-2
Dreier, Johan Morten	3E-6
Drinkwater, Bruce	4A-6, 5D-2, 5E-1, 5E-6, PA-13
Du, Jianke	P3B1-1, P3B1-6
Du, Juan	P1B4-2
Du, Lianfang	P1A4-7
Du, Yi-Chun	P1C9-6
Du, Yu	P3C3-10
Dubey, Sonam	3I-1
Dubois, Rémi	2A-6, 3K-5
Dubus, Bertrand	5B-6, 5J-3
Dudley, Andrew C.	P1A3-4
Dufait, Rémi	2A-6
Dufilié, Pierre	P4A2-2, P4B1-2, P4C2-2
Dufort, Paul	P1C7-2
Dulin, Kelly	P1A3-5, P1A3-6
Dumont, Douglas	3F-3, P1B7-2
Duncan, James	1A-2
Dunleavey, James M.	P1A3-4
Dunmire, Barbrina	1F-4, 3E-4, 3K-4
Dunsby, Christopher	1I-1
Dupre, Aurelien	2J-1

## E

Ebbini, Emad	P1A11-4, P1B11-2, P1B11-3, P1B4-2, P1B6-4, P1C11-11
Ebihara, Tadashi	P2A3-7
Eckersley, Robert J.	1I-1, P1B3-10, P1B5-4, P1B7-4
Ege, Oguzhan	P1A7-9
Eik-Nes, Sturla	3E-6
Eisenbrey, John	1C-2, 1C-3, P1A10-2, P1A3-5, P1C4-2
Ekroll, Ingvald	P1B3-4, P1B3-7
Ekroll, Ingvald Kinn	2D-4
El Ayouch, Aliyasin	5J-5
El Husseini, Nada	2B-5
El Kaffas, Ahmed	2A-1, P1A4-6, P1C10-3, P1C10-4
El Kateb, Mélouka	P1B7-12
El Naqa, Issam	3A-3
El-Falou, Ahmad	P1A10-9, P1C10-4
Elfarnawany, Mai	2E-5
El-Hakiki, Mohamed	6A-2
Elhosni, Meriem	5I-4
Eliahoo, Payam	P5C1-13
Eliason, Jeffrey K.	5J-4, 5K-1
El-Jallal, Said	5K-2, PA-10
Eljamel, Sam	7G-6
Elkateb, Mélouka	P1B7-10
Elmazria, Omar	5I-4, 6B-2, 6B-6, 6D-3, P2B2-3, P4A3-4
Elson, Daniel S.	P1B7-4
Emadi, Tahereh Arezoo	7B-3
Emanetoglu, Nuri	P2C1-5
Emelianov, Stanislav	1I-2, 2I-2, 3D-3, P1A7-9, P1B10-1, P1B1-3, P1B5-5
Emery, Patrick	5H-4
Endo, Naoyuki	P5A2-7
Engholm, Mathias	P5C1-9
Erdman, Jr., John W.	P1C8-1, P1C8-2
Ergun, Arif	7D-5, P5A1-2
Ergun, Arif Sanli	P5A1-1
Eriksson, Tobias Johan Robert	4K-3
Erkamp, Ramon	P1C1-6
Ermert, Helmut	4A-5
Errico, Claudia	P1B4-8
Esashi, Masayoshi	6C-1, 6H-4, 6H-6
Escoffre, Jean-Michel	3I-6, P1A10-1, P1A3-10
Esconjauregui, Santiago	P4A1-3

Espinosa, Francisco..... P5B1-2  
 Evan, Andrew..... 1F-5  
 Evertsson, Maria..... 3G-1  
 Every, Arthur G..... P2C2-3  
 Ewertsen, Caroline..... P1B3-1  
 Eyerly, Stephanie..... P1B7-2

## F

F.W. Van Der Steen, Antonius..... P1B5-7  
 Fabiilli, Mario..... P1B11-6, P1B5-10  
 Fadhel, Muhannad..... P1B9-8  
 Fadnes, Solveig..... 2D-4, P1B3-4  
 Fain, Bruno..... P1A9-6  
 Falcao, Gabriel..... P1A6-4  
 Fan, Alexander..... P1B11-10  
 Fang, Nicholas..... 5J-4  
 Fanget, Stéphane..... 5H-4, 7E-1, PA-20  
 Farber, Mark..... P1B6-1  
 Farhanieh, Omid..... P5A1-2  
 Fatemi, Mostafa..... 2C-5, P1A2-3, P1A2-6, P1C6-4  
 Fazzio, Robert..... P1A2-6  
 Fehler, Michael..... 5C-2  
 Feinstein, Steven..... 1C-1  
 Fekkes, Stein..... 2F-5, P1B3-6  
 Feld, David..... 5C-5  
 Felmetzger, Valeriy..... P5A2-6  
 Felt, Stephen..... P1A3-9  
 Feltoovich, Helen..... 2C-3, 3C-4  
 Feng, Yi..... P1A4-14, P3B2-6  
 Fenta Wakeni, Mebratu..... P4A2-1  
 Fernandes, Ramon C..... P1A6-9  
 Ferrara, Katherine W..... P1C10-9, P1C4-1  
 Ferrara, Vincent..... 3I-4  
 Feuillard, Guy..... P2A3 -1  
 Fink, Mathias..... 3C-2, 5C-3  
 Firouzi, Kamyar..... 4H-2, P2A1-5  
 Fischer Rasmussen, Morten..... 7F-5  
 Fitzgerald, Keith..... P1A10-2  
 Flewitt, Andrew J..... P4A1-1, P4A1-5  
 Flores Contreras, Sergio..... 4I-3, P2B1-6  
 Foiret, Josquin..... P1C10-9, P1C4-1  
 Ford, Peter..... P1B6-1  
 Forero-Torres, Andres..... 1C-5  
 Forsberg, Anya..... P1A3-6  
 Forsberg, Flemming..... 1C-2, 1C-3, P1A10-2, P1A3-5, P1A3-6, P1C3-10, P1C4-2  
 Forsberg, Mark..... P1A3-6  
 Fortineau, Jérôme..... P2A3 -1  
 Fortineau, Julien..... P2A3 -1  
 Fosnight, Tyler R..... P1C11-14  
 Foster, Stuart..... 7A-5, P1A3-4, P1B4-3, P1C4-10  
 Fouillet, Yves..... 7E-1, PA-20  
 Fouladi, Siamak..... 5C-5  
 Fouquet, Julie..... 6A-4  
 Fowlkes, Brian..... P1A6-7, P1B11-6  
 Fox, Glen..... 6F-5  
 Fox, Traci..... 1C-3, P1A3-6  
 Frach, Peter..... 5H-2  
 Franceschini, Emilie..... 2G-4  
 Frank, Jonathan..... P1C11-9  
 Frappart, Thomas..... 1C-4  
 Fredriksson, Sarah..... 3G-1  
 Freear, Steven..... 3E-1, 7H-1, P1A10-7, P1A5-1, P1B1-1, P1B7-6, P1C4-7, P5C2-2  
 Freitas, Miguel..... 4I-2  
 French, Brent..... 1B-4  
 Frenz, Martin..... 2K-1, 3F-2  
 Freytag, Patrik..... P2C3-5  
 Friboulet, Denis..... 1G-4, 3B-6, P1A5-4  
 Friedman, Zvi..... P1C7-7  
 Friend, James..... 4E-3, 5A-1, 5J-1, 6E-5, P1A10-8  
 Fu, Chen..... P4C1-5

Fu, Jianping..... 5D-4  
 Fu, Xin..... 4J-1, P3C1-2  
 Fuchs, Olivier..... 7E-1, PA-20  
 Fujimoto, Katsumi..... P5A2-7  
 Fujita, Fuminori..... P1A9-3  
 Fujiwara, Keisuke..... P1C10-10, P1C11-13  
 Fulton, Joseph..... P1B6-1  
 Furfaro, Luca..... 5K-4  
 Furuhashi, Hideo..... P2C2-2

## G

Gachagan, Anthony..... P2A1-7  
 Gallagher, Mark..... 6D-6  
 Gallego, Nidia C..... 4C-1  
 Gallippi, Caterina..... P1A1-1, P1A1-8, P1B6-1, P1C5-4, P1C5-8  
 Gallot, Thomas..... 5C-2  
 Galluzzo, Francesca..... P1C7-3  
 Gambhir, Alok..... 1A-3, P1C5-3  
 Gammell, Paul..... P1A4-2  
 Gan, Tian..... 5J-4  
 Gangeh, Mehrdad..... P1B9-7, P1C7-8  
 Gao, Xiaohu..... 3D-5  
 Garcia, Damien..... 1J-5, 2F-4, 3B-5, P1B3-8, P1B6-10, P1C3-9, P1C9-2, PA-6  
 Garcia-Duitama, Julian..... P1C9-2  
 Garcia-Gancedo, Luis..... P4A1-1  
 Garland, Philip..... P5B1-9  
 Gastounioti, Aimilia..... P1C8-6  
 Gavelli, Frances..... P1B8-5  
 Gedeon, Dominik..... P2C3-1  
 Geist, Craig..... P1A10-10  
 Geist, Rebecca..... P1C5-8  
 Gelat, Pierre..... P5C2-2  
 Gelderblom, Erik..... P1B1-6, PA-4  
 Gemmeke, Hartmut..... 2K-5  
 Geng, Xuecang..... P5B2-4  
 Gennisson, Jean-Luc..... 1G-2, 1K-2, 2B-1, 2C-1, 2D-3, 2E-1, 3C-2, 3G-6, 5C-3, P1A1-2, P1A3-1, P1A7-11, P1B7-7, PA-1  
 Gens, Fabrice..... 1D-4  
 Gerbedoen, Jean Claude..... 6B-6, P3C3-10  
 Gergaud, Patrice..... P3C2-1  
 Gerold, Bjoern..... 5A-3, 5D-3, PA-12  
 Gessner, Ryan..... 2J-3  
 Ghisu, Davide Ugo..... P5C1-10  
 Ghoshal, Goutam..... P1C11-12  
 Ghovanloo, Maysam..... P5A1-3  
 Giannini, Gabriele..... P1A5-8  
 Gilbert, Stephen..... 6A-4, 6A-5  
 Giles, Anoja..... 2A-1, P1A10-9, P1A3-7, P1A4-6, P1C10-3, P1C10-4  
 Gilja, Odd Helge..... 3I-5, P1A4-8, P5B1-8  
 Gilliland, Spenser..... P2B1-5  
 Gineyts, Evelynne..... 3K-6, P1C10-7  
 Girault, Jean-Marc..... P1A11-2  
 Gjertsen, Bjørn Tore..... 3I-5, P1A4-8  
 Glass, Tyler..... 2C-4  
 Gloess, Daniel..... 5H-2  
 Glier, Claus-Christian..... P1A9-4  
 Goldklang, Monica..... 2F-1  
 Golemati, Spyretta..... P1C8-6  
 Golkowski, Mark..... 4D-6  
 Gomes, Marco..... P1A6-4  
 Gomis-Bresco, Jordi..... 5K-2, PA-10  
 Gong, Peng..... 4D-3  
 Gong, Ping..... 2K-4, P1A6-1  
 Gong, Songbin..... 6F-1  
 Gong, Xiaojing..... 2I-4  
 Gong, Yuping..... 2J-4  
 Gonnot, Thomas..... P2B1-5  
 González, Eduardo..... P1C9-8  
 Gordeev, Georgy..... P4A1-6, P4B2-5

Gorjizadeh, Alborz..... P1B9-5, P1C4-5  
 Goto, Kota..... P1C11-10  
 Goto, Mikihiro..... P4B2-3  
 Goto, Yuji..... P1A4-13  
 Govindan, Pramod..... 4F-6, P2B1-2, PA-9  
 Grabar, Alexander..... P1A7-11  
 Grandis, Jennifer R..... 2A-2  
 Grasland-Mongrain, Pol..... 3C-3, 3G-5  
 Gravenkamp, Hauke..... P2A1-3  
 Gray, Joshua..... P1A7-9  
 Greenaway, Alan..... P1B2-9  
 Greenleaf, James..... 1K-1, 1K-5, 2B-2, 2H-6, 3C-6, 3G-3, P1A1-2, P1A1-4, P1A1-6, P1A2-3, P1B7-11, P1C6-3  
 Grégoire, Jean-Marc..... 1D-4, 3F-1, P1B4-5  
 Gregory, Kelvin..... P2B2-2  
 Greve, David..... 4D-3, P2B2-2  
 Griep, Stephanie..... P1B1-8  
 Grimal, Quentin..... 3J-1, P1A9-4  
 Grimsley, Thomas..... 4I-2  
 Grondin, Julien..... 1A-3, P1C10-6, P1C5-3  
 Gross, Dominique..... 1D-4, 7B-5, P5C1-8  
 Grue, Jahn Frederik..... P1A11-1  
 Grundfest, Warren..... 7D-2, P1A9-8  
 Grünsteidl, Clemens..... P2A1-6  
 Gudur, Madhu..... 5D-4  
 Guenette, Gilles..... P1C3-10  
 Guerder, Pierre-Yves..... 5B-5  
 Guerrero, Quinton..... 3C-4  
 Gui, Lin..... 7H-3  
 Guidi, Francesco..... P1B4-4  
 Guillermin, Régine..... 2G-4  
 Guo, Anthony..... 4H-5  
 Guo, Feifei..... 7A-2  
 Guo, Feng..... P2B2-5  
 Guo, L. Jay..... 5I-6, 5K-6, P5C2-6  
 Guo, Sijia..... P1C11-9  
 Guo, Xiaoyu..... 3A-5  
 Guo, Yuexin..... P1A8-6  
 Gupta, Aditi..... P1A3-6  
 Gupta, Shreyank..... P1A11-8  
 Guracar, Ismayil..... P1A3-9  
 Gurm, Hitinder..... 1F-3  
 Gutiérrez Fernández, César..... P1B10-4  
 Gutierrez, Lillian..... 7I-1  
 Gutierrez-Hartmann, Arthur..... P1B11-10  
 Gutkin, Michael..... P4A1-2

## H

H. Hasani, Mojtaba..... P3A2-4  
 Ha, Frank..... 6A-6  
 Ha, Kanglyeol..... P2B2-1  
 Haak, Alexander..... 1H-2  
 Habeshaw, Roderick..... 7H-2  
 Habor, Daniel..... 3H-6, P1C7-4  
 Hachiken, Takuma..... P1A9-3  
 Hachiya, Hiroyuki..... P2A2-9  
 Hadj Henni, Anis..... P1B7-10  
 Haeggström, Edward..... P1A9-2  
 Hagelauer, Amelie..... PA-15  
 Hagihara, Satoshi..... P4C1-1  
 Hague, M. Nicole..... 2E-5, P1C3-5  
 Hah, Zaegyoo..... 1K-3  
 Haiat, Guillaume..... P1A8-3  
 Hairong, Zheng..... P1C3-4  
 Hall, Neal..... 7B-2, 7F-4  
 Hall, Timothy..... 1F-2, 2C-3, 3C-4, 7D-6, P1B11-1, P1C9-7, P1C9-9  
 Halldorsdottir, Valgerdur..... P1A3-6  
 Ham, Suyun..... 4K-2  
 Han, Aiguo..... P1C8-1, P1C9-2  
 Han, Gang..... P5A2-5

Han, Hyungsoo	P5C2-1	Hirata, Shinnosuke	P2A2-9, P2C2-4
Han, Karen	4C-1	Hiyama, Shoko	5H-1, PA-11
Han, Pengdi	7G-1, 7I-5	Hjelm Brandt, Andreas	P1A8-5
Han, Tao	P4C1-2	Hjelmquist, Jordan	1E-3
Han, Yang	2J-5, P1C10-5, P1C11-3	Hladky, Anne-Christine	5B-6
Han, Zhile	P2A1-1, P5C2-3	Hladky-Hennion, Anne-Christine	5J-3
Hanke, Ulrik	6E-6, PA-14	Ho, C. K.	P1C3-1
Hannah, Alexander	1I-2, P1B5-5	Ho, Jee-Hou	4H-5
Hansen, Hendrik H.G.	2F-5, P1B3-6, P1B6-5	Ho, Yihsin	P1A11-7
Hansen, Jens Munk	2K-2	Hodnett, Mark	4G-4
Hansen, Peter Møller	P1A8-5, P1B3-3	Hoff, Lars	4K-5, 7J-5
Hanzawa, Hiroaki	7I-3	Hofmann, Felix	5K-1
Haput, Sevan	3E-1	Holbek, Simon	P1B3-1
Hara, Motoaki	P4B1-4	Holfort Voxen, Iben	P1B2-9
Haritaipan, Lalita	P2A2-9	Hollender, Peter	2H-1
Haritonova, Alyona	P1B11-2, P1B11-3, P1C11-11	Holm, Sverre	P1B2-6
Harley, Joel	4B-2, 4D-3	Homeister, Jonathon	P1B6-1
Harper, Jonathan	1F-4, 1F-5, 3E-4, 3K-4, P1C11-8	Hongo, Hiromichi	P3A2-1
Harput, Sevan	7H-1, P1A10-7, P1A5-1, P1B1-1, P1B7-6, P1C4-7, P5C2-2	Hooi, Fong Ming	P1C11-14
Harrington, Brandon	6D-4	Hooker, Jonathan	P1C8-2
Harris, Gerald	P1A4-2	Hoople, Jason	6E-3, 6E-4, PA-16
Harvey, Gerald	7B-4	Hopp, Torsten	2K-5
Hasegawa, Hideyuki	2D-5, 3F-5	Horiuchi, Hideya	P5A2-7
Hashiba, Kunio	P1B7-14	Hosaka, Naoto	P1A10-6, P1B5-6
Hashim, Amr	P1A10-9, P1A4-6, P1C10-4	Hoshiba, Kotaro	P2A2-9
Hashimoto, Ken-Ya	6H-3, 6H-4, 6H-6, 6I-3, 6I-4	Hosoda, Kyohei	P5B2-9
Hasjim, Bima	2A-2	Hosokawa, Atsushi	P1A9-1
Hata, Toshiho	P1A9-3	Hossack, John	1B-4, 1I-4, 1I-6, 2A-3, PA-2
Haugen, Bjørn Olav	1H-3, P1A11-1	Hossain Khan, Naiad	3E-6
Haugse, Ragnhild	P1A4-8	Houlihan, Ruth	P2C3-7
Hayward, Gordon	4A-2	Howell, Mark	3H-4
Hazard, Christopher	1K-3	Høyer Iversen, Daniel	P1C7-6
He, Hongbin	4I-4	Hoyt, Kenneth	1C-5, P1A3-8, P1C11-1
He, Shitang	P2C1-2, P3C3-1, P3C3-4	Hristov, Dimitre	1B-2
He, Xiao	4D-2	Hsi, Ryan	1F-5, 3E-4, 3K-4, P1C11-8
He, Yingjuan	P1B9-6	Hsiao, Yising	5D-4
Heath, Karl	7G-3, PA-17	Hsu, Shih-Ming	P2B3-1
Heba, Elhamy	P1C8-2	Hu, Liang	4J-1
Hecht, Frédéric	P4A2-2	Hu, Shixiao	3J-2
Heger, Max	P1B8-6	Hu, Yaxin	P1A4-10, P1A4-11, P1A4-12, P1A4-7
Heger, Stefan	3H-6, P1C7-4	Huang, Andy	P1A10-4
Hehn, Michel	5I-4	Huang, Chengwu	P1A5-9, P1B6-8
Hejazi, Mehdi	7D-4	Huang, Chih-Chung	P1A11-6, P1C5-6
Helminen, Emily	P1B7-13	Huang, Jun	P2B2-5
Hemmsen, Martin Christian	P1A8-5, P1C1-2, P1C1-3	Huang, Lingyun	1A-4
Hemsel, Tobias	4G-4	Huang, Manwei	1A-4
Henning, Bernd	4F-2, P2A1-3	Huang, Rongzhong	2J-4
Herbots, Lieven	1A-1	Huang, Sheng-Wen	P1C1-6, P1C6-1
Hermans, Jeroen	P1C9-1	Huang, Yangqing	P2C1-2
Hernanz, Elena	3J-4	Huang, Zhihong	2C-6, 7H-3, 7H-5, 7H-6
Herzberger, Jaemi	4C-5	Hueltes, Alberto	P4A2-3
Herzog, Thomas	5H-2	Hughes, David	P1A7-10, P1B8-7
Hess, Peter	5K-3	Hughes, Hana	7I-2
Hesse, Markus	3B-3	Hui, Yu	6H-5
Heuer, Henning	5H-2	Huissoud, Cyril	P1B11-7
Heusinkveld, Maarten H.G.	2B-6	Hull, David	P1B1-8
Heyde, Brecht	1G-3, 1G-4, P1C5-1	Humeida, Yousif	4A-6
Hickling, Susannah	3A-3	Hummel, Gwendolyn	6H-5
Hickock, Noreen	P1A10-2	Humphries, James	6D-6
Higashi, Yasuhiro	P2A3-2	Hung, Clark	P1C11-3
Higgins, John	1B-3	Huntzicker, Steven	3B-2
Hikichi, Kousuke	6H-6	Husmann, Douglas	P1A2-3
Hikita, Mitsutaka	P2C2-1, P3C1-1	Hutchins, David	P2A1-2, P2B1-7, P3C3-2, P5C2-2
Hine, Gabriel	P2A2-7	Hutson, David	P1B8-7
Hinshaw, James Louis	P1A2-2	Hwang, Dae Kun	P2B2-4
Hirano, Hideki	6H-4, 6H-6	Hwang, Jae Youn	2G-2, 5D-5, P1A7-8, P3A1-5
Hirao, Masahiko	6B-3, 6I-2, P1A4-13, P3A2-1	Hyder, Safeer	P1A5-1, P1B7-6
Hiraoka, Takuya	P1A11-7	Hynynen, Kullervo	3I-1, P1B2-10, P1B4-10

# I

Iborra, Enrique	4G-2, P4A1-1, P4A1-3, P4A1-5, P4A3-6
Ichihashi, Hayato	P3C2-5
Ichianagi, Mitsuhisa	5E-4
Idzenga, Tim	P1B8-2
Igasaki, Tomohiko	P5B1-6
Ikari, Takahiro	P5B1-6
Ikeda, Teiichiro	P1B2-1
Ikenna E., Ireka	P4A2-1
Ikeuchi, Shinsuke	P5A2-7
Ilyina, Natalia	P1C9-1
Imbault, Marion	1G-2, 2B-1, 2C-1, 2D-3, 3C-2
Imoto, Haruka	2K-6
Imoto, Yuki	3J-6
Inaba, Mao	6H-4
Inaba, Masahiro	6H-6
Ingle, Atul	P1A2-2, P1B7-1
Ingram, Pier	1H-5, 4K-6
Inoue, Kazuhito	5E-4
Inoue, Kenta	P1C8-4
Insana, Michael	P1C2-7, P1C3-6, P1C7-9
Irie, So	P1C8-3
Ishi, Yutaka	P3A2-1
Ishida, Makoto	P5C1-14
Ishiguro, Yasunao	P1A4-3
Ishii, Takaaki	P5A2-14
Ishino, Yuji	P3C1-4
Itani, Kazunori	P1C10-10, P1C11-13
Ito, Kazuyo	P1C8-4
Ito, Mikito	P1C8-7
Iula, Antonio	P2A2-7
Iversen, Daniel H.	1J-3
Iwai, Ikuya	P4B1-7
Iwaki, Masafumi	6A-1
Iwanaga, Hiroki	7E-3
Iwata, Kazuki	7J-6
Iwazaki, Yoshiki	6C-3

# J

J. Feleppa, Ernest	2G-3
Jacobs, James	P4C2-2
Jacobs, Ryan	4D-6
Jacobsohn, Kenneth	P1B1-8
Jaeger, Michael	2K-1, 3A-6, 3F-2
Jaffe, Samantha	P1A3-5, P1A3-6
Jäger, Philipp	6C-2
Jakoby, Bernhard	P2C1-1, P5B2-11
Jakovljevic, Marko	P1B2-7
Jambawalikar, Sachin	3I-3, PA-5
James, Sheronica	3H-4, P1A6-13
Jang, Kee W.	P1A4-15
Jansen, Krista	2I-1
Jansson, Tomas	3G-1
Janzen, William	P1A4-9
Jaros, Jiri	5B-2
Jensen, Henrik	2K-2
Jensen, Jonas	P1B3-3
Jensen, Jorgen Arendt	2D-2, P1A4-1, P1A5-6, P1A8-5, P1B2-9, P1B3-1, P1B3-3, P1B3-5, P1B6-5, P1C1-2, P1C1-3, P1C2-6, P1C3-7, P5C1-4, P5C1-7
Jensen, Kristin	1B-1
Jeong, Jong Seob	P5A2-12
Jeremic, Aleksandar	P1A10-5
Jern, Esben	P1C1-3
Jesus, Elias	P2C2-5
Jhou, Jyun-Hua	P3C3-8
Jia, Liu	P1C3-4
Jia, Xiaoping	5C-3
Jia, Yunlu	4F-4
Jian, Xiaohua	P5C2-3
Jiang, Jingfeng	P1B7-13

Jiang, Wentao.....	4K-4	Keil, Ryan D.....	P1C11-14	Kocot, Anthony.....	2J-1, 2J-6, 3K-6, P1B11-7
Jiang, Xiaoning.....	3H-2, 7G-1, 7G-3, 7G-4, P1C11-9, P1C5-4, P5B2-3, P5B2-4, PA-17	Keilman, George.....	7D-1	Koda, Ren.....	P1A10-6, P1B5-6
Jiang, Yun.....	7G-6, 7I-2	Kekoa, Lexie.....	6A-5	Kohl, Johannah.....	3B-2
Jideani, Josiah.....	4A-3	Kelley, Richard.....	6D-2	Kok, Annette M.....	P1C5-9
Jiménez Martín, Ana.....	P1B10-4	Kemmerer, Jeremy.....	P1C11-12	Kok, Maarten.....	P1B5-9
Jiménez, Noé.....	P1C4-8	Kepler, Chris.....	P1A10-2	Kokhuis, Tom.....	1I-5, P1B5-7
Jin, Chang-Zhu.....	P1B8-9	Keplinger, Franz.....	P2C1-1, P5B2-11	Kokkonen, Kimmo.....	6B-1
Jin, Lifang.....	P1A4-7	Ketterling, Jeffrey.....	P2B3-5	Kokshaiki, Aleksey.....	P3A2-8
Jing, Bowen.....	P1B4-9	Khamis, Hanan.....	P1C7-7	Kolios, Michael.....	2G-1, 2G-5, 2J-4, 2K-4, 3D-6, P1A6-1, P1A7-6, P1B1-2, P1B1-4, P1B9-11, P1B9-8, P2B2-4
Jing, Yun.....	5B-3, P1C11-9	Khelif, Abdelkrim.....	5J-5	Kondo, Kengo.....	P1A1-9, P2A2-2
Johannessen, Agne.....	6E-6, PA-14	Khokhlova, Vera.....	1F-5, P1B11-4, P1C10-11	Kondoh, Jun.....	P4A3-2, P4B2-3
Johansen, Kristoffer.....	P3A1-2	Khuri-Yakub, Butrus.....	1D-1, 4H-2, 6B-4, 7B-1, 7F-3, P1C10-2, P2A1-5	Kondratiev, Serguei.....	6D-1
Johansen, Tonni F.....	7J-5	Kielczynski, Piotr.....	P3B2-3, P3B2-4	Kong, Deqing.....	5I-1
Johnson, Bruce.....	7I-1	Kihara, Takashi.....	6H-1	Konno, Akira.....	6C-1
Johnson, Darius.....	P2A3-6	Kilappa, Vantte.....	P1A9-2	Konofagou, Elisa.....	1A-3, 1H-4, 2F-1, 2F-2, 2J-5, 3I-3, 3I-4, 3K-2, P1B6-9, P1C10-5, P1C10-6, P1C11-3, P1C11-7, P1C5-3, PA-5
Johnson, John.....	6H-2	Kilroy, Joseph P.....	2A-3	Koochakzadeh, Sina.....	P4C2-4
Johnson, Ward.....	4C-5	Kim, Christina.....	P1B9-1, P1B9-5	Kooiman, Klazina.....	1E-1, 1E-2, P1B5-1
Johnston, Keith.....	5A-3, 5D-3, PA-12	Kim, Daeseung.....	P1B11-5	Kopechek, Jonathan A.....	2A-2
Jones, Ryan.....	P1B2-10	Kim, Donghwan.....	7F-4	Koppinen, Panu.....	4G-1
Joyce, Andrew.....	P5B2-6	Kim, Gi-Duck.....	P1B10-5, P1C1-1	Korobov, Alexandr.....	P3A2-3, P3A2-8
Ju, Yang.....	2B-6	Kim, Heamin.....	2A-5	Kotopoulos, Spiros.....	3I-5, P1A4-8, P3A1-2, P5B1-8
Juffermans, Lynda.....	1I-5	Kim, Hyohee.....	P1B3-9	Kouamé, Denis.....	P1A11-2, P1A11-3
Jung, Hayong.....	P3B2-10	Kim, Hyung.....	P5C1-13	Kovacova, Veronika.....	P3C2-1, P3C2-3
Jung, Joontaek.....	P5C2-1	Kim, Hyung Ham.....	7A-1, 7A-4, P1A7-8, P3A1-4, P5B2-7	Koyama, Daisuke.....	5A-4, 5E-3
Jung, Youngsoo.....	3D-1	Kim, Hyunjung Christina.....	P1A10-9	Koymen, Hayrettin.....	7C-2, 7C-5, P5C1-1
Junker, Warren.....	4D-3	Kim, Hyunki.....	P2B3-4	Kranz, Peter.....	2B-5
<b>K</b>		Kim, Jeehoo.....	P1A6-11	Krauß, Herbert.....	P1A11-8
K. Kurosawa, Minoru.....	P2C2-4, P5A2-10	Kim, Jeesu.....	P1A8-2	Kreider, Wayne.....	1F-5, 5E-2, P1B11-4, P1C11-8
Kaczkowski, Peter.....	7D-1	Kim, Jinwook.....	7G-4	Kretzek, Ernst.....	P1B8-8
Kaddoura, Tarek.....	P1A5-7	Kim, Jinson.....	P2B2-1	Kripfgans, Oliver.....	7F-1, P1A6-7, P1B11-6, P1B5-10
Kadota, Michio.....	6C-1, 6H-4, 6H-6, P4B1-6	Kim, Kang.....	1D-3, 3D-1, P1B2-4, P1C6-8	Kruger, Robert.....	3A-1
Kadow-Romacker, Anke.....	P1B11-11	Kim, Min Gon.....	7A-1	Kruizinga, Pieter.....	2H-2, 2I-3
Kaivola, Matti.....	6B-1	Kim, Minkyong.....	P1A6-6	Kruse, Dustin E.....	P1C10-9
Kakakhel, Zubair.....	P1B1-1	Kim, Minwoo.....	P1C3-6	Kuang, Yang.....	7H-3, 7H-5
Kalashian, Aubrey.....	2F-1	Kim, Moojoon.....	P2B2-1	Kubena, Randall.....	5C-1
Kalim, Danish.....	6A-2	Kim, Myungdeok.....	P1B11-5	Kubrusly, Alan.....	P2A3-3
Kaltenbacher, Manfred.....	P4A2-4	Kim, Nam Ouk.....	P1C1-4	Kucewicz, John.....	3E-4
Kambara, Shigeki.....	P3C1-5	Kim, Pilsu.....	P1C1-1	Kuenen, Maarten.....	P1A3-3
Kamp, Otto.....	1I-5	Kim, Soohyun.....	P3C1-7	Kumamoto, Shogo.....	P5B2-9
Kanai, Hiroshi.....	2D-5, 3F-5	Kim, Sudook.....	4C-5	Kumar, Anshuman.....	5J-4
Kanda, Takefumi.....	5I-3, P3C1-3	Kim, Sung Min.....	P5A2-12	Kumar, Mohit.....	PA-18
Kaneko, Osamu.....	1B-2	Kim, Sungjin.....	P5C2-5	Kumbhat, Nitesh.....	6A-6
Kaneko, Tsukasa.....	7J-6	Kim, Tae-Young.....	6A-2	Kuntzman, Michael.....	7B-2, 7F-4
Kang, Bong Jin.....	7A-1, 7A-4, P1A7-8, P5B2-7	Kim, Ung.....	P1A8-2	Kuo, Justin.....	6E-3, 6E-4, PA-16
Kang, Bongjin.....	P3A1-4	Kim, Yohan.....	1F-3, 7D-6	Kuo, Po-Ling.....	P1A2-4, P1B7-8, P1B7-9
Kang, Hyun-Jae.....	3A-5	Kim, Young H.....	P3C1-7	Kuratani, Yasuhiro.....	P4B1-6
Kang, Jeeun.....	3D-1, P1B10-5, P1B2-2, P1C1-1	Kimmel, Eitan.....	P1C11-4	Kuribayashi Kurosawa, Minoru.....	5I-1
Kang, Jinbum.....	P1A8-7	Kimura, Tetsuya.....	6H-4, 6H-6, P4B1-6	Kurosawa, Minoru.....	P3C1-6
Kang, Kookjin.....	P1B11-5	Kinn Ekroll, Ingvald.....	P1B3-2	Kurose, Shugo.....	P5B1-6
Kang, Shih-Tsung.....	2A-4, P1B5-8, P1C4-4	Kinnick, Randall.....	1K-1, 2H-6, P1B7-11, P1C6-4	Kuroyama, Takanobu.....	P3A2-2
Kang, Yi-Da.....	3E-5, PA-3	Kiplagat, Annette.....	2B-4	Kurtz, Steven.....	P1A10-2
Kao, Wei-Pu.....	P1B5-8	Kirby, Deborah.....	5C-1	Kusanagi, Yuki.....	P3A2-1
Karakatsani, Maria Eleni.....	3I-3, PA-5	Kirk, Katherine.....	P1A7-10, P1B8-7	Kushibiki, Jun-Ichi.....	6C-1, 6C-4, 6I-4, P2A2-8
Karaki, Tomoaki.....	7E-3	Kirkendall, Christopher.....	P3A2-6	Kuwano, Hiroki.....	P4B1-4
Kärkkäinen, Anu.....	4G-1	Kishimoto, Yutaka.....	6H-4, P5A2-7	Kuznetsov, Mikhail.....	P4A1-6
Karolewski, Dominik.....	PA-15	Kiss, Gabriel.....	1H-3, 3E-6, P1C7-6	Kuznetsova, Iren.....	P3B1-3, P3B1-5
Karpiouk, Andrei.....	2I-2, P1B10-1	Kisslo, Joseph.....	P1A5-5	Kvashnin, Gennadiy.....	P4A1-6, P4B2-5
Karshafian, Raffi.....	P1B9-5	Kitazaki, Tomoaki.....	P1A1-9	Kwan, Chi-Hang.....	4F-3
Karwat, Piotr.....	P1B2-8	Kiwitt, Juergen.....	6H-2	Kwiecinski, Wojciech.....	2A-6
Kashima, Ryota.....	5E-3	Kjeldsen, Thomas.....	P1C1-2, P1C1-3	Kwon, Jae.....	P3A2-6
Kasoji, Sandeep.....	P1A4-9	Klein, Stefan.....	1J-4	Kwon, Sung-Jae.....	P1C1-4
Katada, Katsuyoshi.....	5H-5	Klemm, Markus.....	7C-1	Kybartas, Darius.....	4C-2, P3A2-5
Katardjiev, Ilia.....	P4A3-6	Klibanov, Alexander.....	1B-4, 1E-1, 1I-4, 1I-6, 2A-3, PA-2	Kyoya, Haruki.....	6H-1
Kato, Fumihito.....	6B-3	Klymko, Victor.....	P2C3-7	<b>L</b>	
Kato, Hideyuki.....	6H-4	Knapp, Matthias.....	6C-2	L. De Korte, Chris.....	P1B8-2
Kato, Yoshiya.....	5H-1, PA-11	Knieling, Ferdinand.....	1B-1, 1B-3		
Kaufman, Jonathan.....	P1A9-5	Kobayashi, Etsuko.....	P1C11-13		
Kawabata, Ken-Ichi.....	P1A10-11, P1B7-14	Kobayashi, Hideaki.....	6H-4		
Kawaguchi, Kuniko.....	P2A2-8	Kobayashi, Kazuto.....	3H-1, P1A2-7, P1C8-3, P1C8-4		
Kazys, Rymantas.....	4G-5	Kobayashi, Makiko.....	4I-5, 7J-6, P5B1-6		
Ke, Yabing.....	P3C3-1, P3C3-4				

L. Raymond, Jason	P1B5-7	Lee, Yen Lung	P5C2-4	Lindsey, Brooks	P1B5-2
La Cour, Mette Funding	P5C1-4, P5C1-7	Lee, Yeongnam	P1B10-5	Lines, Dave	7H-2
Lacefield, James C.	2E-5, P1C3-5	Lee, Yeonhwa	P1A6-11	Ling, Haoming	P1C6-7
Lad, Robert	6D-2	Leger, Pierre	3A-3	Lingeman, James	1F-4
Lafon, Cyril	3C-3, 3G-5	Legros, Mathieu	1D-4, 2A-6, 7B-5, P1B4-5, P5B2-2, P5C1-8	Link, Andreas	6A-2
Lai, Chun-Yen	P1C4-1	Lehareas, Symeon	P1C8-6	Lipiäinen, Lauri	6B-1
Lai, Priscilla	P1A3-7	Lehrmann Christiansen, Thomas	7F-5	Lipman, Samantha	P1C6-2
Lai, Simon	1J-5, P1C3-1, PA-6	Lei, Anders	P5C1-7	Lisheng, Xu	P1C3-4
Lajoinie, Guillaume	P1B1-6, P1B5-7, PA-4	Leinders, Suzanne	P5C1-12	Litman, Robert	4F-1
Lal, Amit	6E-3, 6E-4, P5A2-1, PA-16	Lelouarn, Arnaud	5H-4	Litniewski, Jerzy	2H-3, P1B9-2
Lallas, Costas	1C-3	Lemaire, Edward	P5B2-5	Liu, Chang	4D-3
Lam, Kwok Ho	P3B2-10	Lemmerhirt, David	7F-1, P1B2-5	Liu, Cheng	7A-2
Lam, Richard	3A-1	Lenge, Matteo	2D-6	Liu, Dalong	P1B11-2, P1B11-3, P1B4-2
Lamberti, Nicola	P2C1-4, P5C1-6	Lenkei, Zsolt	P1B4-8	Liu, Ji PIA10-10	
Lambrakos, Litsa	1H-4	Leone, Antonio Davide	P5C1-10	Liu, Ji-Bin	1C-3, P1A3-6
Lamothe, Marc	6D-5	Leow, Chee Hau	P1B3-10	Liu, Panpag	P1C6-7
Lanceros-Méndez, Senentxu	P2C2-5	Leow, Ruen Shan	3K-1	Liu, Ruibin	P5B2-4
Landrier, Jean-François	2G-4	Lepape, Alain	P1A7-4	Liu, Ruimin	2I-4
Lang, Julie	P5C1-13	Leuch, Reinhard	P2C3-1	Liu, Shu-Wei	P1B1-7
Lang, Roberto	1G-1	Lerondel, Stephanie	P1A7-4	Liu, Weiting	P3C1-2
Langdon, Jonathan	1K-6, 3G-2	Lewandowski, Marcin	P1A6-8	Liu, Xiaojun	P1A7-2
Lange, Theis	P1A8-5	Li, Chunhui	P1A2-9	Liu, Xinlu	P2C1-2
Langener, Sascha	4A-5	Li, Chun-Ting	P1B7-9	Liu, Yuejun	P1A2-1
Langer, Robert	3H-3	Li, Fang	P4C1-4	Liu, Yunbo	P1A4-2
Lanning, Justin	P1A1-4	Li, Guofeng	P1B10-7, P1B9-6	Liu, Ziyue	3K-4
Laptev, Pavel	P5A2-6	Li, Honglang	P3C3-1, P3C3-4	Livneh, Amit	P1C11-4
Larsen, Linda	P5C1-13	Li, Jiawen	1J-2	Lloyd, Harriet	3D-2
Larsson, David	P1B6-6	Li, Jun Bo	P1B11-8	Lo, Pei-Yuan	4H-3
Larsson, Matilda	2F-6, P1B6-6	Li, Junwei	3D-5	Lockhart, Mark	1C-5
Lasaygues, Philippe	5J-5	Li, Meng-Lin	3E-5, P1A7-13, PA-3	Lockwood, Geoff	P5B2-6
Lassen, Lee	P1C1-2, P1C1-3	Li, Mingdong	6A-2	Lok, U-Wai	P1C1-10
Latham, Katherine	P1C1-7	Li, Minghui	4A-2	Lombardo, Michael	2J-2
Latourrette, Jeff	6A-6	Li, Pai-Chi	P1A2-4, P1A2-8, P1A7-1, P1B1-7, P1B7-5, P1B7-8, P1B7-9, P1C1-10	Lomonosov, Alexey M.	5K-3
Laude, Vincent	5K-4, P3C3-3	Li, Peiyang	P2A1-1	Lomonova, Elena	P2C2-7
Laudereau, Jean-Baptiste	P1A7-11	Li, Ping	P2A3-4, P2C3-4	Lomperski, Stephen	5E-5
Laugier, Pascal	3J-1, 3J-2, 3J-5, 4D-1, P1A9-4, P1A9-6, P5B2-2	Li, Qian	1H-5	Longbottom, Christopher	P1A7-10, P1B8-7
Laureti, Stefano	P2A1-2, P2B1-7	Li, Qiaochu	5I-6	Loomba, Rohit	P1C8-2
Laursen, Mads Bjerregaard	P5C1-4	Li, Ronny	P1B6-9	Lopata, Richard	1A-5, 2B-6, P1B6-2, P1B6-3, P1C5-10, P1C5-5, P1C5-9, P1C9-10
Lautenschlager, Eric	6D-4	Li, Shuaiyong	P2A3-4	Loranger, Eric	4J-5
Lavarello, Roberto	P1B9-9, P1C6-6, P1C9-5, P1C9-8	Li, Shyh-Dar	3D-6	Lou, Edmond	P1A9-7
Laws, Michael	4K-3, P2C3-6	Li, Sibo	7G-1, 7G-4, P5B2-4	Loupas, Thanasis	1C-4
Lay, Holly	7G-5	Li, Sinan	P1B5-4, P1B7-4	Løvstakken, Lasse	1J-3, 2D-4, P1B3-2, P1B3-4, P1B3-7, P1C7-6
Le Guillou-Buffello, Delphine	P1A3-1	Li, Wencho	P1A7-2	Lowerison, Matthew R.	2E-5, P1C3-5
Le Naour, Gilles	P1A2-1	Li, Wenqi	P2A1-7	Lu, Jian-Yu	3B-1
Le Rhun, Gwenael	5H-4, 7E-1, P3C2-1, P3C2-3, P3C2-4, PA-20	Li, Yang	3H-2, 7G-3, P5A2-4, PA-17	Lu, Yi-Shiuan	P1A11-6
Le, Lawrence H.	P1A9-7	Li, Ying	P5A2-4	Lu, Yufeng	P2B1-3, P2B1-4
Léauté, Gaël Y. V.	P1C4-7	Li, You	2E-3	Luan, Ying	P1B5-7
Lediju Bell, Muyinatu	3A-5	Li, Zhangjian	P5C2-3	Lubner, Meghan	P1A2-2
Leduc, Paul	2J-6	Liang, Ji	P4A3-5, P4B1-3	Luca, Adrian	4J-2
Lee Jr., Fred T.	P1A2-2	Liang, Rongjie	P5A2-13	Lucas, Margaret	7H-4
Lee, Byung Chul	1D-1, 7F-3	Liao, Xiaochun	7H-5, 7H-6	Luchies, Adam	P1C9-5
Lee, Changyang	P1A7-8, P3A1-4, P3B2-10	Liaukonis, Dobilas	4C-2, P3A2-5	Ludvigsen, Hanne	6B-1
Lee, Daehyeon	P1A8-2	Liebgott, Hervé	1J-5, 2D-6, 3B-6, P1A5-4, P1C1-5, P1C2-3, P5B2-8, PA-6	Luke, Geoffrey	1I-2, 3D-3, P1B5-5
Lee, Franklin	1F-4, 1F-5, 3E-4, 3K-4	Lili, Niu	P1C3-4	Luo, Gangming	P1A9-5
Lee, Hae-Seung	1D-1	Lim, Hae Gyun	5D-5	Luo, Jianwen	1A-4, P1A4-5, P1A5-9, P1B6-8
Lee, Jaejin	P1B10-5, P1C1-1	Lim, Youngsub	P2B3-3	Luo, Wei	P3C3-1, P3C3-4
Lee, Jin S.	P1A8-2	Lin, Ben	1A-2	Luong, Richard	1B-3, P1A3-9
Lee, John	3H-3, P1A3-2	Lin, Chih Hao	P5A2-2	Lutz, Amelie	1B-1
Lee, Judy	4J-4	Lin, Chih-Ming	P4C2-3	Lyshchik, Andrej	1C-3, P1C3-10
Lee, Jun Su	P5A2-3	Lin, Dan	1B-4, 1I-6	Lysyuk, Igor	P3B1-4
Lee, Jung-Kun	3D-1	Lin, Hao Ping	P5A2-2		
Lee, Jungwoo	5D-5, P3A1-5	Lin, Jian-Liang	P1C4-4		
Lee, Keekeun	P4C1-5	Lin, Kuang-Wei	1F-2, 7D-6, P1B11-1		
Lee, Mike	P1A3-4	Lin, Liwei	7C-3, 7C-4		
Lee, Ming-Yen	4H-6	Lin, S. K.	3H-5		
Lee, Nan Sook	2G-2	Lin, Shengtao	P1B5-4		
Lee, Sang Goo	3D-1	Lin, Weijun	P3B1-2		
Lee, Taehwa	5I-6, 5K-6, P5C2-6	Lin, Weili	P1C11-9		
Lee, Wei-Ning	P1A8-6, P1C8-10	Lin, Yi-Hsun	3C-1		
Lee, Wonjun	P5C2-1	Linas, Svilainis	4C-2		
Lee, Yanghun	P1A6-6				

## M

Ma, Chenxiang	P3B2-6
Ma, Jianguo	3H-2, 7G-3, P1C5-4, P5B2-3, PA-17
Ma, Teng	1J-2, 2F-3
Ma, Tingfeng	P3B1-6
Ma, Xiaochuan	P1B8-8
Maccabi, Ashkan	7D-2
Macdonald, Michael	P1A1-4
Machado, João	P2B3-2



Machado, Priscilla.....	1C-2, 1C-3, P1A3-5, P1A3-6, P1C3-10	Matera, Riccardo.....	P1C3-3	Mirarkolaei, Hani Nozari.....	P1A8-8, P1C7-5
Machado, Tiago M.....	P1A6-9	Mateu, Jordi.....	P4A2-3	Mirea, Teona.....	4G-2, P4A1-1, P4A1-3, P4A1-5, P4A3-6, P4C2-1
Machi, Junji.....	2G-3	Mathieson, Andrew.....	7H-4, P5B1-7	Mischi, Massimo.....	1G-5, P1A3-3, P1A5-8
Machtaler, Steven.....	1B-3, P1A3-2, P1A3-9, P1C10-2	Matousek, Ales.....	7I-2	Mishin, Sergey.....	P4A1-2
Macutkevici, Jan.....	P3B2-1	Matrone, Giulia.....	P1B2-3	Mitcham, Trevor.....	P1A7-9
Mada, Razvan Olimpiu.....	1G-4	Matsuda, Satoru.....	6I-2, 6I-4	Mitchell, Arnan.....	5J-1, 6E-5
Madden, John.....	2C-4	Matsui, Kazuhiro.....	P1C11-13	Mitri, Farid G.....	P3B2-2
Madoka, Makajia.....	7E-2	Matsukawa, Mami.....	3J-3, 3J-4, 3J-6, 5A-4, 5E-3, 5H-1, 6I-5, P1A11-5, P1A9-3, P1B6-7, P1C8-11, P3C2-2, P3C2-5, PA-11	Miyashita, Takuya.....	P1C11-10
Maev, Roman.....	3E-2, P1B10-11, 4F-5	Matsuki, Yoshitaka.....	P5A2-7	Miyazawa, Shinya.....	P1A10-6, P1B5-6
Maeva, Elena.....	P2A3 -8	Matsumoto, Yoichiro.....	2K-6, 5E-4, P1C10-10	Mizuno, Katsunori.....	3J-3, 3J-4, P1A11-5, P2A2-6
Magenes, Giovanni.....	P1B2-3	Matsumura, Takeshi.....	6H-4, 6H-6	Mizuno, Takeshi.....	P3C1-4
Mahakian, Lisa.....	P1C4-1	Matsumura, Terry O.....	P1B5-4	Mizuno, Yosuke.....	P3C1-5
Mahboob, Syed.....	7G-6	Matsuura, Yuka.....	P1A9-3	Mizutani, Koichi.....	P2A3 -7, P3A2-2
Mahesh, Sankaranarayana.....	P1A10-10	Mattrey, Robert.....	1C-2, P1A3-5	Moallemi, Nasim.....	4A-4
Mahon, S.....	3H-5	Matula, Thomas J.....	2J-2	Mochizuki, Seiya.....	P5A2-14
Mahoney, Marshall.....	P1A3-8	Maubert, Sandrine.....	7E-1, PA-20	Mochizuki, Takashi.....	P1A10-6, P1B5-6, P1C11-2
Maia, Joaquim.....	P1B10-3, P2A3 -5	Mauldin Jr, F William.....	1I-4, PA-2	Mofid, Yassine.....	3F-1, P1B7-12
Maia, Ozana Maria De Andrade.....	P2A3 -5	Mauti, Barbara.....	P5C1-6	Moghim, Arash.....	2K-4
Maier, Florian.....	P1A7-9	Maxwell, Adam.....	1F-5, 5E-2, 7D-6, P1B11-4, P1C11-5, P1C11-8	Mohar, Dilbahar.....	1J-2
Makaraviciute, Asta.....	P5C1-5	May, Jonathan P.....	3D-6	Moilanen, Petro.....	P1A9-2
Makhoute, Abdelkader.....	5K-2, PA-10	Mayer, Andreas.....	5K-3, 6H-2	Moiseyenko, Rayisa.....	P3C3-5, P3C3-9
Maksuti, Elira.....	P1B6-6	Mayer, Elena.....	6H-2	Moncion, Alexander.....	P1B11-6
Malcolm, Alison.....	5C-2	Mayer, Markus.....	6H-2	Montagnon, Emmanuel.....	P1C6-10
Malocha, Donald.....	6D-6	Mazeika, Liudas.....	4G-5	Montero, Maria Luisa.....	P1B9-9
Malyarenko, Eugene.....	P1B10-11	Maznev, Alexei.....	5J-4, 5K-1, P3B1-7	Monti, Fabrice.....	4E-2
Mamou, Jonathan.....	2G-3, P1C8-3, P1C8-7, P1C8-8, P2B3-5	Mazura, Jiri.....	P1A6-10	Moon, Byeong-Ui.....	P2B2-4
Manduca, Armando.....	1K-1, 2B-2, P1A1-4, P1A1-6	Mazzanti, Andrea.....	P5C1-10	Moon, Wonkyu.....	7J-2
Manh, Tung.....	7J-5	Mcaleavey, Stephen.....	1K-6, 3G-2	Mooney, Robert.....	1K-3
Mano, Isao.....	3J-4, P1A9-3	Mccann, Donald.....	6D-2	Moore, Cooper.....	P1A5-5
Manohar, Srirang.....	P1B1-6, PA-4	Mccarthy, Eric.....	6D-2	Morgan, Paige.....	1K-5
Manor, Ofer.....	4E-3	McCormack, Emmet.....	3I-5, P1A4-8	Morrill, Samuel.....	P2C1-6
Mansoura, Sid Ali.....	5J-3	McDannold, Nathan.....	3I-2	Morrison, Kyle.....	7D-1
Mao, R. W.....	3H-5	McGough, Robert J.....	1F-2, P1C1-8, P1C2-5, P1C6-5	Mortet, Vincent.....	P4B2-2
Maraghechi, Borna.....	P3A2-4	McHenry, Dean.....	2K-2	Morvan, Bruno.....	5J-3
Maraes, Louise.....	P1B6-3	McKinsey, James.....	P1B6-9	Mosegaard, Jesper.....	P1C1-2, P1C1-3
Marchal, Rémi.....	5J-2, P3C3-5, P3C3-6, P3C3-9	McLaughlan, James.....	3E-1, 7H-1, P1A10-7, P1B1-1, P1C4-7	Mossad, Mathieu.....	2C-1
Marchiano, Régis.....	4J-2	McPhillips, Rachael.....	7G-6	Motoki, Kazuya.....	P5A1-4
Maréchal, Pierre.....	5J-3	McSweeney, Ian.....	P1B8-3	Moulin, Emmanuel.....	4B-3
Maresca, David.....	2E-2	McTiernan, Charles F.....	2A-2	Mountford, Paul.....	1E-4
Mari, Jean-Martial.....	3C-3	Meacci, Valentino.....	P1A6-5	Moura, José M.F.....	4B-2
Mariani, Pascale.....	P1A7-11	Medeiros Jr., Johannes D.....	P1A6-9	Moutaoukiel, Mohamed.....	6B-6
Marotti, Juliana.....	3H-6	Medvedev, Andrey.....	6D-1	Mozhaev, Vladimir G.....	P3B2-8
Marquet, Fabrice.....	3K-5	Meggs, Carl.....	7G-6, 7I-2	Mu, Peitian.....	P1B10-7
Marshall, Andrew.....	P1A3-6	Mehrmohammadi, Mohammad.....	2C-5, 2H-6, P1A2-3, P1A2-6	Mujic, Maja.....	P1A4-8
Marston, William.....	P1B6-1	Meixner, Duane.....	1K-1, P1A2-6	Mulder, Harriet.....	1H-2
Martin, Guenter.....	P4B1-1	Melandso, Frank.....	P5A2-9, P5B1-1	Mulgaonkar, Amit.....	7D-2, P1A9-8
Martin, Heath.....	P1B5-2	Melega, William.....	7D-2, P1A9-8	Munoz Del Rio, Alejandro.....	2C-3
Martin, James A.....	P1A4-15	Mellema, Daniel C.....	P1A1-6	Murphy, Brian.....	P1B8-3
Martin, K. Heath.....	2J-3, 3A-1	Melodelima, David.....	2J-1, 2J-6, 3K-6, P1B11-7, P1C10-7, P1C7-1	Murray, Todd.....	P1B1-5
Martin, Karl.....	3H-2, P5B2-3	Meltaus, Johanna.....	6D-4	Musch, Thomas.....	4A-5
Martin, Sue.....	P5C1-13	Memoli, Gianluca.....	4G-4	Myllylä, Risto.....	P1A9-2
Martin, Tom.....	P4B1-2	Meng, Jianxin.....	P2A2-5	Mynderse, Lance.....	P1A2-3
Martin-Arguedas, Carlos Julián.....	P1B10-4	Merlen, Alain.....	6B-6		
Martínez, Alejandro.....	5K-2, PA-10	Merrick, Elizabeth.....	P1C5-8	Na, Shuai.....	7B-6
Martínez-Graullera, Oscar.....	P1B10-4	Merton, Daniel.....	1C-3, P1A3-5	Naaijken, Benno.....	1I-5
Martins, Marcos.....	P2C2-5	Michaels, Jennifer.....	4B-1	Nabavizadeh, Alireza.....	3G-3, P1C6-4
Maruani, Anabel.....	P1B7-12	Miette, Véronique.....	P1A2-1, P1B7-10, P1B7-12	Nabili, Marjan.....	P1A10-10
Maruoka, Takashi.....	P1A10-11	Mikhov, Mikhail.....	P5A2-6	Nagakubo, Akira.....	6I-2
Maruvada, Subha.....	P1A4-2	Miller, Ryan M.....	P1C11-5	Nagaoka, Ryo.....	3H-1, P1A2-7
Maruyama, Hitoshi.....	P1C8-3, P1C8-4	Miller, Zachary.....	2C-4	Nagatani, Yoshiki.....	3J-3, P1A11-5, P1A9-3
Marvasti, Mohammad Hassan.....	4I-1	Milot, Guillaume.....	4J-5	Nagira, Yusuke.....	P3C1-1
Masetti, Guido.....	P1C7-3	Milot, Laurent.....	P1B4-1	Nakagawa, Ryo.....	6H-1
Mashimo, Tomoaki.....	5I-2	Min, Youngjae.....	P3C1-7	Nakajima, Kichitaro.....	P1A4-13
Masoudi, Aidin.....	3E-3	Minami, Hiroaki.....	6F-5	Nakamura, Hirofumi.....	2K-6
Måsøy, Svein-Erik.....	P1C7-6	Ming, Qian.....	P1C3-4	Nakamura, Kentaro.....	5A-4, P3C1-5
Mast, T. Douglas.....	P1C11-14	Minonzio, Jean-Gabriel.....	3J-2, 3J-5, P1A9-4, P1A9-6, P5B2-2	Nakanishi, Hidekazu.....	6I-3
Mastik, Frits.....	1E-1, 2H-2			Nakaso, Noritaka.....	6B-5, P4C1-1
Masuda, Kohji.....	P1A10-6, P1B5-6			Nam, Kweon-Ho.....	P1B8-9
Masuzawa, Hiroshi.....	P1B2-1			Nandlall, Sacha.....	2F-1
Matéo, Tony.....	3F-1				

## N

Nandlall, Sacha D. ....	2F-2	Ohtake, Hiroshi ....	P1C11-2	Park, Jongin. ....	P1A8-2
Narayanan, Prathyush ....	P1B6-9	Ohtani, Toshihiro ....	P3A2-1	Park, Jong-Seon. ....	P1A8-2
Nariyoshi, Pedro ....	P1C1-8	Oizumi, Toru ....	6B-5, P4C1-1	Park, Kwan Kyu ....	6B-4, 7B-1, 7F-3
Naumenko, Natalya. ....	6E-1, P4B2-6	Ojeda-Fournier, Haydee. ....	1C-2, P1A3-5	Park, Sung-Bae. ....	P1C1-4
Navarro-Urrios, Daniel ....	5K-2, PA-10	Ok, Jong G. ....	5I-6, 5K-6	Parker, Kevin. ....	1K-3, P1A2-5, P1C6-6
Nayak, Rohit ....	3B-2	Okada, Nagaya ....	P5A2-10, P5C1-14	Parker, Reed ....	6A-4, 6A-5, 6A-6
Nedospasov, Ilya A. ....	P3B2-8	Okada, Takashi. ....	P1C3-8	Parks, David ....	7E-5
Negreira, Carlos ....	P3B2-9	Okamura, Yoko. ....	P1C3-10	Partin, Alexander. ....	1K-3
Nelson, Keith A. ....	5J-4, 5K-1	O'Kane, Patrick ....	P1C4-2	Pascal, Nicolay ....	P4B2-1
Nenadic, Ivan ....	1K-5, 2B-2, 3C-6, P1A1-2, P1A2-3	Okasinski, Stanley. ....	1A-3, P1C5-3	Patch, Sarah. ....	P1B1-8
Ngo, Jacqueline. ....	P1C10-7	Okubo, Kan ....	P1A11-7	Patel, Mihir. ....	5A-6
Nguyen, Man ....	1D-3, P1B2-4	Okuyama, Naoto ....	P3C1-5	Patel, Nishant ....	P3B1-9
Nguyen, Nghia ....	P1C2-7	Olasov, Lauren R. ....	4C-1	Patel, Pranav M. ....	1J-2
Nguyen, Ngoc ....	6E-6, PA-14	O'Leary, Richard ....	7B-4, P2A1-7	Paterson, Alisa ....	P5B1-4
Nguyen, Thu-Mai. ....	2C-6, 2I-5, 3G-4, P1B7-3	Oleksandr, Polishko ....	4H-1	Pattenden, Sam ....	P1A4-9
Nguyen, Trong ....	P1C2-2	Olesen, Jacob Bjerring ....	P1B3-3, P1C3-7	Patton, Mark ....	4D-3
Nguyen, V. Lai ....	1A-5, P1C5-9	Olikh, Oleg ....	P2C3-2, P3B1-4	Paulmurugan, Ramasamy ....	P1C10-2
Nguyen-Dinh, An. ....	2A-6	Olikh, Yaroslav ....	P3B1-4	Paun, Marla ....	1F-4, 3E-4, 3K-4
Nichols, Timothy ....	P1B6-1, P1C5-8	Olivares, Jimena. ....	P4A1-1, P4A1-3, P4A1-5, P4A3-6	Pavan, Theo. ....	P1A1-3
Nicolay, Pascal. ....	6C-5, P4A2-4	Olive, Kenneth ....	2J-5	Payen, Thomas ....	2E-1, P1A3-1, PA-1
Nielsen, Michael Bachmann. ....	2D-2, P1A5-6, P1B3-3	Oliveira, Everande. ....	P2B3-2	Pedersen, Peder C. ....	2H-4
Niessen, Wiro J. ....	1J-4	Oliveira, Timoteo Francisco. ....	P2A3 -3	Pelivanov, Ivan. ....	2I-5, 2J-2, 4D-4
Nightingale, Kathryn. ....	1K-4, 2C-4, P1C6-2	Olsson, Roy H. ....	6F-2	Peng, Jue ....	P5A2-11
Nightingale, Kathy ....	2H-1, 2H-5, P1A1-5	Olumolade, Oluyemi ....	P1C11-7	Peng, Jun-Kai ....	P1A8-1
Niimi, Nobuo ....	P2A2-9	Omori, Tatsuya ....	6I-4	Peng, Xiaojian ....	P5A2-11
Nikita, Konstantina ....	P1C8-6	Onda, Yosuke ....	6C-3	Pennec, Yan. ....	5J-1, 5K-2, P3C3-5, P3C3-6, P3C3-9, PA-10
Nikolov, Svetoslav ....	2K-2	Ong, Gerald ....	6A-5	Penninck, Dominique ....	P1B2-5
Nikolov, Svetoslav Ivanov ....	P1A5-6	Ong, Khang Hoe Gerald. ....	6A-6	Pensala, Tuomas. ....	6D-4
Nikoozadeh, Amin ....	4H-2, 7B-1, 7F-3, P2A1-5	Onisto, Haroldo J. ....	P1A6-9	Penteado, Susete do Rocio Chiarello. ....	P2A3 -5
Nillesen, Maartje M. ....	2F-5, P1B3-6	Ono, Yuu. ....	P1A10-4, P5B2-5	Pereira da Cunha, Mauricio ....	6D-2
Ning, Xi ....	P5A2-5	Onogi, Shinya. ....	P1B5-6	Perez, Camilo ....	2J-2
Nishi, Shohei ....	P1C8-11	Onur, Tugba Özge. ....	4B-4	Perez, Nicolas. ....	P2A3 -3
Nishihara, Tokihiro ....	6C-3	Oppenheim, Irving ....	4D-3, P2B2-2	Pernod, Philippe. ....	5A-2, 5I-4, 6B-6, P3C3-10, P4B2-2
Nishimura, Masato ....	P5C1-14	Oralkan, Omer. ....	7F-6, PA-18	Pernot, Mathieu ....	1G-2, 1K-2, 2A-6, 2B-1, 2B-3, 2D-3, 2E-2, 3C-2, P1A1-2, P1B7-7
Nitta, Naotaka ....	P1A4-3	O'Reilly, Meaghan. ....	P1B2-10, P1B4-10	Perrea, Despina. ....	P1C8-6
Niu, Lili. ....	2E-6	Orino, Yuishiro ....	P2C2-4	Perroteau, Marie ....	7B-5
Noguchi, Yuya ....	P3C1-3	Ormachea, Juvenal ....	P1C6-6	Perrotin, Franck. ....	P1A3-10, P1A7-4
Noi, Kentaro ....	P1A4-13	Ortega, Alejandra ....	P1A5-2, P1A5-3	Persson, Hans W. ....	3G-1
Norli, Petter. ....	4K-5	Ortiz, Steve. ....	6A-4, 6A-5, 6A-6	Pertijs, Michiel ....	P5B2-10
Norose, Yoko. ....	P2A3 -7	Osaki, Taichi ....	5E-4	Petculescu, Gabriela ....	4C-4
Novell, Anthony. ....	1D-4, P1A10-1, P1A3-10, P1A4-4, P1A7-4, P1B4-5, P1B5-3	Osapoetra, Laurentius. ....	3G-2	Peters, Terry ....	1H-1
Nover, Adam. ....	P1C11-3	Osawa, Shunsuke ....	P1C11-2	Petit-Watelot, Sébastien. ....	5I-4
Novotny, Steffen. ....	6B-1	Osmanski, Bruno-Felix ....	P1B4-8	Petterson, Niels J. ....	P1C5-5
Nowicki, Andrzej. ....	2H-3, P1B9-2	Ossant, Frédéric. ....	3F-1, P1B7-10, P1B7-12	Pezet, Sophie. ....	P1B4-8
Nowroozi, Bryan. ....	P1A9-8	Otsu, Kenji ....	7D-3	Pfeiffer, Helge ....	P1C4-3
Nozawa, Takuya ....	P4A3-2	Otto, Paul ....	P1B8-5	Phamthi, Mai ....	5B-6
Ntziachristos, Vasilis. ....	P2A2-4	Ouared, Abderrahmane ....	P1C6-10	Phillips, Linsey. ....	2J-3, P1B5-3
Nui, Chengcheng. ....	2J-4	Ouidich, Mourad ....	5B-4, 5J-6, 5K-2, PA-10	Piazza, Gianluca. ....	6F-1, 6F-4
Nurmela, Arto ....	6D-4	Ozgurluk, Alper. ....	7C-5	Pierce, Allan ....	5A-5
Nyankima, Gloria. ....	1E-3			Pierre, Guillaume. ....	P2C1-3
Nyrmes, Siri Ann ....	2D-4			Pierre, Juliette. ....	1I-3
<b>O</b>				Pihl, Michael Johannes. ....	P1B3-1, P1C3-7
O'Donnell, Matthew ....	2I-5, 3D-5	Pacella, John. ....	P1C11-6	Piotrkowska-Wroblewska, Hanna. ....	P1B9-2
O'Brien, Jr., William ....	P1C8-1, P1C8-2	Paeng, Dong-Gu. ....	P1B8-9	Piratla, Sarvani. ....	P5A2-1
Odagawa, Hiroyuki ....	P4B1-7	Pagliazzi, Marco. ....	4E-5, PA-8	Pisano, Albert P. ....	6A-3
Odahara, Takuya ....	P1B6-7	Palermo, Carmine. ....	2J-5	Pislaru, Cristina. ....	2B-2
O'Donnell, Matthew ....	1A-2, 2C-6, 2J-2, 3G-4, 4D-4, P1B7-3	Palmeri, Mark. ....	1K-4, 2C-3, 2C-4, 2H-5, P1A1-5, P1B7-2, P1C6-2	Pislaru, Sorin V. ....	2B-2
Oelze, Michael. ....	P1B9-9, P1C11-12, P1C2-2, P1C9-5	Pålsson, Bertil ....	4J-3	Pitschi, Maximilian ....	PA-15
Oelze, Michael L. ....	P1C9-2	Panday, Regeant. ....	P1C10-1	Plessky, Victor ....	6D-5
O'Flynn, Brendan. ....	P2C3-7	Pandey, Aditya ....	1F-3	Pluim, Josien ....	1H-2
Ogi, Hirosugu. ....	4G-3, 6B-3, 6I-2, P1A4-13	Pang, Wei. ....	P4A3-5, P4B1-3	Polak, Joseph. ....	P1B2-5
Oh, Inn-Yeal ....	P1A6-6, P5C1-2	Pantea, Mircea. ....	P1B10-11	Polascik, Thomas. ....	2C-4
Oh, Shosho. ....	P2C3-3	Pao, Shi-Yung. ....	P3B1-6	Pollard, Thomas. ....	6D-2
Ohashi, Yuji. ....	6C-1, 6C-4, P2A2-8	Papadacci, Clément. ....	1G-2, 2B-1, 2B-3, 2D-3, 3C-2, P1B7-7	Ponge, Marie-Fraise. ....	5B-6
Ohayon, Jacques ....	2F-4, P1B6-10	Papaevangelou, Efthymia. ....	P1A7-3	Poon, Alexander K. K. ....	P1C3-1
Ohbuchi, Takeshi ....	P3A2-2	Park, Chul Soon ....	P1A6-6, P5C1-2	Popovics, John S. ....	4K-1, 4K-2, PA-7
Ohgi, Tsuneo. ....	6B-5, P4C1-1	Park, Dae Woo ....	1D-3, P1C6-8	Porée, Jonathan. ....	2F-4, P1B6-10
		Park, Hong-June. ....	P1A8-2	Porré, Julien. ....	4J-2
		Park, Jinhyoung. ....	P1A7-8	Posada, Daniel. ....	3B-5, P1C3-9
		Park, Jinman. ....	5D-5	Postema, Arnoud. ....	P1A3-3
		Park, Jongho. ....	P1B10-6		

Postema, Michiel.....3I-5, P1A4-8, P3A1-2,  
P5B1-8  
Poza, Jose.....P5C1-12  
Pozzo, Lilo D.....2J-2  
Prada, Claire.....4B-3  
Prata, Peter.....6D-2  
Prentice, Paul.....5A-3, 5D-3, PA-12  
Preobrazhensky, Vladimir.....5A-2, 5I-4, P3C3-10  
Provost, Jean.....1G-2, 2A-6, 2B-1, 2B-3, 2D-3,  
3C-2  
Pu, Kanyi.....P1C10-2  
Puett, Connor.....1E-3, P1A4-9, P1B5-3  
Pupyrev, Pavel D.....5K-3  
Puts, Regina.....P1B11-11  
Pysz, Marybeth.....P1A3-2

## Q

Qian, Ming.....2E-6, P1B10-7  
Qian, Xuejun.....2F-3  
Qiang, Bo.....3C-6  
Qianli, Qin.....P1C3-4  
Qin, Bin.....1E-1, P1C10-1  
Qin, Bo.....P1B8-8  
Qin, Dui.....P3B2-6  
Qin, Lifeng.....P4C1-4  
Qin, Longhui.....4J-1  
Qin, Peng.....P1A4-7  
Qin, Tao.....4K-6  
Qin, Yexian.....1H-5, 4K-6  
Qin, Zhao.....2B-6  
Qiu, Weibao.....P1A6-2, P1B10-7, P1B9-6  
Qiu, Yongqiang.....P3A1-3  
Qiu, Zhen.....7G-6, 7H-2  
Quaglia, Fabio.....P5C1-10  
Quesson, Bruno.....3K-5  
Quinsac, Céline.....P1A11-2

## R

Radermacher, Klaus.....3H-6, P1C7-4  
Radulescu, Emil.....P1C1-6  
Raes, Florian.....P1A7-4  
Raghunathan, Shreyas.....P5B2-10  
Ramadas, Sivaram Nishal.....4K-3, P2C3-6  
Ramalli, Alessandro.....2E-4, 3B-4, P1A4-5,  
P1A5-8, P1A5-9, P1A6-12, P1B2-3,  
P5B2-1  
Ramanaviciene, Almira.....P5C1-5  
Ramaz, Francois.....P1A7-11  
Ramos, Ryan.....P1C7-2  
Ramos, Tiago.....P3A1-1  
Ran, Haitao.....2J-4  
Rantakari, Pekka.....6D-4  
Rantatalo, Matti.....P2A2-3  
Rao, Jianghong.....P1C10-2  
Rapp, Cynthia.....P1C3-10  
Rashid, M Wasequr.....P5A1-3  
Rasmussen, Morten Fischer.....P1A4-1  
Rau, Jochen.....P1B3-7  
Rau, Jochen Matthias.....P1C7-6  
Raum, Kay.....2G-6, 3J-1, P1A9-4, P1B11-11  
Rautenberg, Jens.....P2A1-3  
Reindl, Leonhard M.....6C-2  
Reinhardt, Alexandre.....5H-3, P3C2-4  
Reinhardt, Brian.....P2B2-5  
Rekuvienė, Regina.....4G-5  
Ren, Ben.....1H-2  
Ren, Tianling.....P1B6-8  
Ren, Wei.....7I-4, P5B1-5  
Ren, Xiaoping.....P1C11-14  
Renaud, Guillaume.....P1B5-7  
Rezk, Amgad.....4E-3, 5A-1, 6E-5  
Ricci, Marco.....P2A1-2, P2B1-7

Ricci, Stefano.....2D-6, 2E-4, P1A6-5, P1C3-2,  
P1C3-3  
Rich, Collin.....7F-1  
Richardson, Mandek.....P2C1-6, P4C2-4  
Riekkinen, Tommi.....6D-4  
Righi, Daniele.....2D-6  
Rinaldi, Matteo.....6H-5  
Rindal, Ole Marius Hoel.....P1B2-6  
Risberg, Robert.....P2A2-3  
Rit, Simon.....P1C7-1  
Rivoire, Michel.....2J-1  
Robbin, Michelle.....1C-5  
Robert, Jean-Luc.....P1C1-6, P1C6-1  
Robert-Philipp, Isabelle.....P3C3-3  
Robertson, James.....P3B2-5  
Robertus, Jan Lukas.....2I-3  
Robini, Marc.....P1C1-5, P5B2-8  
Rocas, Eduard.....P4A2-3  
Rodriguez Sanmartin, Daniel.....7G-6  
Rodriguez, Alberto.....4C-2, 4D-5  
Rodriguez, Paul.....P1C6-6  
Roh, Yongrae.....P2B3-3, P2B3-4  
Rohde, Kerstin.....2G-6  
Rohrbach, Daniel.....2G-3, 5B-2  
Rojas, Juan.....P1B5-2  
Rojas, Juan D.....1E-3  
Rojas, Renan.....P1C6-6  
Romero-Laorden, David.....P1B10-4  
Rosado-Mendez, Ivan.....P1C9-7, P1C9-9  
Rosenberg, Jarrett.....P1A3-2  
Rosenthal, Amir.....P2A2-4  
Rosenzweig, Stephen.....2C-4, 2H-1, 2H-5  
Rosette, Fernando.....P1A9-5  
Roshchupkin, Dmitry.....6D-1  
Rosnitskiy, Pavel.....P1B11-4  
Ross, Susan.....1F-4  
Rostocki, Aleksander.....P3B2-4  
Rouhani, Bahram.....5J-1  
Roux Marchand, Thibault.....6B-6  
Roux, Emmanuel.....P1C1-5, P5B2-8  
Rouxel, Didier.....6B-2  
Roux-Marchand, Thibaut.....P2B2-3, P4A3-4  
Rouze, Ned.....1K-4, 2H-5, P1A1-5, P1C6-2  
Roy Cardinal, Marie-Hélène.....2B-6, 2F-4  
Rubens, Deborah.....1K-3  
Rubert, Nicholas.....P1A2-2, P1B9-10, P1C11-12,  
P1C9-3  
Ruby, Rich.....6A-4, 6A-5  
Rudenko, Oleg.....P1C6-9  
Rughoobur, Girish.....P4A1-1, P4A1-5  
Ruile, Werner.....6C-2, 6H-2  
Ruiter, Nicole.....2K-5, P1A11-8, P1B8-8  
Rupitsch, Stefan Johann.....P2C3-1  
Rush, Collin.....P1B5-10  
Rutten, Marcel.....P1B3-6, P1B6-3, P1C5-10,  
P1C9-10

## S

Saalbach, Kai-Alexander.....P2C3-5  
Saarilahti, Jaakko.....4G-1  
Sabra, Karim.....P1C9-4  
Sacchi, Mauricio D.....P1A9-7  
Sacher, Frédéric.....2A-6  
Saddik, George.....7D-2  
Sadeghi-Naini, Ali.....2C-2, 3C-5, P1B9-11,  
P1B9-3, P1B9-5, P1B9-7, P1C7-8  
Sadiq, Muhammad.....7H-4, 7H-6  
Sadler, Jeffrey.....3E-2  
Sadler, Sabrina.....5H-4  
Saegusa-Beecroft, Emi.....2G-3  
Safari, Ahmad.....7D-4  
Saffari, Nader.....P5C2-2  
Safont, Gonzalo.....4D-5

Saijo, Yoshifumi.....3H-1, P1A2-7  
Saito, Masashi.....P1B6-7, P1C8-11  
Sakamoto, Kensuke.....6I-4  
Sakharov, Sergey.....6D-1, 6I-1  
Sakuma, Ichiro.....P1C11-13  
Salamat, Shahriar.....P1C8-5  
Salazar, Addisson.....4C-2, 4D-5  
Salehi, Leili.....P1C2-4  
Salles, Sebastien.....1J-5, PA-6  
Salmi, Ari.....P1A9-2  
Samad, Zainab.....P1A5-5  
Samimi, Kayvan.....P1C11-12  
Samiotaki, Gesthimani.....3I-3, 3I-4, P1C11-7,  
PA-5  
Sammoura, Firas.....7C-3, 7C-4  
Samoto, Tetsuo.....6H-6  
Sampaio, Diego.....P1A1-3  
Sampaleanu, Alexander.....P5C1-11  
Sampathkumar, Ashwin.....2I-6, P1A7-10, P2B3-5  
Sampson, Richard.....P1A6-7  
Samset, Eigil.....1G-4, P1A5-3, P1C2-1  
Samulionis, Vytautas.....P3B2-1  
San Jose, Romeo Jr.....6H-2  
Sanchez, William.....1K-1, 1K-5  
Sanchez-Morcillo, Victor.....P1C4-8  
Sand Traberg, Marie.....P1C5-7  
Sand, Anders.....4J-3  
Sangrador, Jesús.....P4A1-3  
Saniie, Jafar.....4F-6, P2B1-1, P2B1-2, P2B1-3,  
P2B1-4, P2B1-5, PA-9  
Sankaranarayanan, Subramanian.....P4C2-4  
Sannachi, Lakshmanan.....P1B9-3, P1B9-4,  
P1B9-7, P1C7-8  
Santillan, Arturo.....P3B2-7  
Santos, Jaime.....P1C8-9  
Santos, Mário.....P1C8-9  
Santos, Pedro.....P1A5-2, P1A5-3  
Sapeliauskas, Evaldas.....P5C1-3  
Sapozhnikov, Gennadiy.....P4A3-1  
Sapozhnikov, Oleg.....1F-5, 3E-4, 5E-2,  
P1B11-4, P1C10-11, P1C11-8  
Saris, Anne E.C.M.....2F-5, P1B3-6  
Sarrut, David.....P1C7-1  
Sarry, Frédéric.....6B-6, P2B2-3, P4A3-4  
Sarvazyan, Armen.....P1C6-9  
Sasajima, Yuichi.....6C-3  
Sasaki, Akira.....2K-6, P1C10-10, P1C11-13  
Sasaki, Hiroshi.....P1C11-10  
Sasaki, Hiroyasu.....P1C11-2  
Sasanuma, Hideki.....P1A4-3  
Sasso, Magali.....P1A2-1  
Satir, Sarp.....7C-6  
Sato, Takeo.....P2C2-1  
Sato, Tomoo.....P1C11-2  
Sato, Toru.....P1A11-5, P1A8-3  
Satoh, Yoshio.....6A-1  
Saulnier, Gary.....4F-1  
Sautto, Marco.....P5C1-10  
Savoia, Alessandro.....P2C1-4  
Savoia, Alessandro Stuart.....P1B2-3, P5C1-10,  
P5C1-6  
Sawaguchi, Toi.....P1B5-6  
Sboros, Vassilis.....P1B2-9  
Scaranelo, Anabel.....P1C7-2  
Scaringella, Monica.....P1A6-12  
Scarton, Henry.....4F-1  
Schafer, Mark.....1D-2  
Schalk, Stefan.....1G-5  
Schamiloglu, Edl.....P3B1-9  
Schechner, Zvi.....P1A9-5  
Schiavone, Giuseppe.....7G-6  
Schiffner, Martin.....P1C1-9  
Schinkel, Arend F.L.....1J-4  
Schmid, Ulrich.....P5B2-11

Schmidt, Hagen.....	6I-1, P4B1-1, P4B2-4	Shin, Junseob.....	3F-6	Springeling, Geert.....	2I-3
Schmitt, Cédric.....	P1B7-10	Shirgina, Natalia.....	P3A2-3, P3A2-8	Sridaran, Suresh.....	6A-4
Schmitz, Georg.....	3A-4, 3B-3, P1A7-5, P1B8-4, P1C1-9, P1C2-4	Shirkovskiy, Pavel.....	5A-2	Sridharan, Anush.....	1C-2, P1A3-5
Schnatz, Rick.....	P1C11-6	Shoji, Masanari.....	P2A3 -2	Stafford, Jason.....	P1A7-9
Schneider, Fabio Kurt.....	P2A3 -5	Shung, K. Kirk.....	1J-2, 2E-6, 2F-3, 2G-2, 3H-2, 5D-1, 5D-5, 7A-1, 7A-4, 7G-3, P1A7-8, P1B10-9, P3A1-4, P3B2-10, P5B1-5, P5B2-7, P5C1-13, PA-17	Standal, Øyvind.....	P1B3-7, P1C7-6
Schneider, Johannes.....	3J-1, P1A9-4	Shung, Koping.....	P5A2-4	Stavdahl, Øyvind.....	P1B8-6
Schneider, Michael.....	P5B2-11	Shvetsov, Alexander.....	6D-1, P4A3-1	Stedman, Quintin.....	6B-4
Schoellhammer, Carl.....	3H-3	Siegotzyski, Ryszard.....	P3B2-4	Steen, Erik Normann.....	P1A8-8, P1C7-5
Scholz, Marc-S.....	5D-2, PA-13	Sierra Sanchez, Carlos.....	3I-4	Steenbergen, Wiendelt.....	P1B1-6, PA-4
Schröder, Andreas.....	4F-2, P2A1-3	Siffert, Robert.....	P1A9-5	Stein, Emily.....	P1A9-5
Schumann, Bert.....	6A-2	Sikdar, Siddhartha.....	P1B8-5	Stemper, Brian.....	3E-3
Schurink, Geert-Willem H.....	1A-5, P1C5-9	Sillanpää, Teuvo.....	4G-1	Stener, Jan.....	4J-3
Schwab, Hans-Martin.....	3A-4, P1A7-5	Silpe, Justin.....	P1B5-10	Stennett, Rahim.....	P2C1-5
See, William.....	P1B1-8	Silverman, Ronald.....	2I-6, 3D-2	Stewart, Steven.....	P1B8-7
Seeley, Scott.....	P1A3-2	Simon, Julianna.....	P1C10-11	Stifter, Michael.....	P5B2-11
Seetohul, Vipin.....	7G-5	Simpson, Douglas G.....	P1C8-1	Storve, Sigurd.....	1H-3, 1J-3, P1A11-1
Segal, Sharon.....	P1C3-10	Simsek, Ergun.....	5C-4	Stranford, Gerald.....	7I-1
Segers, Patrick.....	2E-4, 2F-5, P1B3-2	Sinclair, Anthony.....	7J-4	Strohm, Eric.....	2J-4, P1B1-2, P1B1-4, P1B9-8, P2B2-4
Segers, Tim.....	P1B5-7, P1B5-9	Sinclair, Anthony N.....	4F-3, 4I-1	Stuart, Matthias B.....	P1A4-1, P1A5-6, P1B3-5, P1B6-5, P5C1-4
Segura, Luis.....	P5B1-2	Singh, Rahul.....	7D-2	Su, Fong-Chin.....	3C-1
Selzo, Mallory R.....	P1A1-1, P1A1-8	Sinha, Bikash.....	5A-6, 5C-4	Su, Xiao-Xing.....	P3C3-7
Sen, Malabika.....	2A-2	Sinusas, Albert.....	1A-2	Suarez, Ivan.....	P1A10-5
Sener, Stephen.....	P5C1-13	Sirlire, Claude B.....	P1C8-2	Subramanian, Swetha.....	P1C11-14
Senesky, Debbie.....	P4C2-3	Sirsi, Shashank.....	1E-4	Suchkov, Sergey.....	6D-5
Serppä, Heikki.....	4G-1	Sitzer, Annette.....	2G-6	Sugimoto, Eiichi.....	4J-6
Sermesant, Maxime.....	1G-3	Skachkov, Ilya.....	1I-5, P1B5-1	Sugiura, Hiroki.....	7E-3
Servois, Vincent.....	P1A7-11	Skliar, Mikhail.....	4F-4	Sugiyama, Ryusuke.....	P1C10-10
Sethuraman, Shriram.....	P1B11-8	Slayton, Michael H.....	P1B11-9, P1C11-14	Sugondo, Amelia.....	7E-2
Severin, Fedar.....	4F-5	Sliteris, Reimondas.....	4G-5	Suhm, Aurelien.....	P3C2-4
Seviaryn, Fedar.....	P1B10-11	Smaldone, G.....	3H-5	Sukovich, Jonathan.....	1F-3
Seviaryna, Inna.....	P2A3 -8	Small, Martha.....	6A-4, 6A-5	Sulen, Andre.....	P1A4-8
Sevit, Alex.....	P1A10-2	Smeenge, Martijn.....	1G-5	Sun, Jia-Hong.....	P3C3-8
Sevrukov, Alexander.....	1C-2	Smirmov, Eugene.....	4H-1	Sun, Lei.....	7A-2, P1B10-7
Sextro, Walter.....	4G-4	Smith, Gennifer T.....	7E-4	Sun, Ming-Jian.....	P1A7-1
Shagawa, Tomohiro.....	6B-3	Smith, Peter.....	7H-1	Sun, Tao.....	3K-2, P1C11-7
Shahbazpanahi, Shahram.....	4A-4	Smith, Robert A.....	4C-3	Sun, Yang.....	2J-4, P1B1-2
Shamdasani, Vijay.....	1B-2, P1C6-1	Smith, Sten Roar.....	P1A8-8, P1C7-5	Sun, Yubing.....	5D-4
Shane, Elizabeth.....	P1A9-5	Snyder, Brian.....	3E-3	Sung, Min.....	7J-2
Shankar, Ashwin.....	P4C2-3	Socié, Ludovic.....	5K-4	Suo, Dingjie.....	P1C11-9
Shao, Weiwei.....	P2A1-1	Sodini, Charles G.....	1D-1	Suthar, Kamlesh.....	5E-5
Shapiro, Mikhail.....	1E-5, P1C4-10	Solodov, Igor.....	P2A2-1	Suzuki, Masashi.....	5H-5, 5I-5
Shaposhnikov, Kirill.....	P4A2-4	Soltani, Ali.....	P4B2-2	Suzuki, Satoshi.....	6I-4
Sharma, Srikanth.....	7A-3	Son, Jaeyoung.....	P1B10-6	Suzumori, Koichi.....	5I-3, P3C1-3
Shavrin, Igor.....	6B-1	Son, Keonho.....	P1B11-5	Svanström, Erika.....	4B-4
Shaw, Colette.....	1C-3	Song, Hi Yuen.....	P1A6-6	Svensson, Ingrid.....	3G-1
Shcherbakova, Darya.....	P1B3-2	Song, Hyunjae.....	P1B10-6	Svilainis, Linas.....	P3A2-5
Sheeran, Paul.....	1E-3, P1B5-3, P1C4-6	Song, In-Hyounk.....	P5C1-2	Swillens, Abigail.....	2E-4, P1B3-2
Shelton, Sarah.....	P1A3-4, P1B5-2	Song, Kang-Ho.....	P1B11-10	Swillens, Abigail E.S.....	2F-5
Shen, Che-Chou.....	P1A8-1	Song, Liang.....	2I-4	Szabo, Thomas.....	3E-3, 5C-2
Shen, Julian.....	P3B1-6	Song, Penfei.....	P1A2-6	Szalewski, Marek.....	P3B2-3, P3B2-4
Shen, Tueng T.....	2C-6	Song, Pengfei.....	1K-1, 2B-2, 2C-5, 3G-3, P1A1-4, P1A1-6	Szasz, Teodora.....	P1A11-3
Shenderova, Olga.....	P3B2-1	Song, Shaozhen.....	2C-6, 3G-4	Szymanska, Elzbieta.....	P1B9-2
Shengtao, Lin.....	7H-6	Song, Tai-Kyong.....	P1A1-7, P1B10-5, P1B10-6, P1C1-1		
Shenoy, Aditi.....	P1A10-10	Song, Wei.....	2I-4		
Sheth, Nirali.....	P1C9-8	Soo Im, Hyun.....	P1B8-5		
Shi, Lei.....	2C-6	Sorace, Anna.....	P1A3-8, P1C11-1		
Shi, Lisha.....	6F-4	Sorensen, Mathew.....	1F-4, 1F-5, 3E-4, 3K-4, P1C11-8		
Shi, Ruchuan.....	P4C1-2	Sornes, Anders.....	P1C2-1		
Shieh, Bernard.....	P1C9-4	Sorokin, Boris.....	P4A1-6, P4B2-5		
Shih, Cho-Chiang.....	P1A11-6, P1C5-6	Sotnikov, Andrey.....	6I-1		
Shiiba, Michihisa.....	P5A2-10, P5A2-4	Sotomayor, Clivia.....	5K-2, PA-10		
Shiina, Tsuyoshi.....	P1A1-9, P1A7-12, P1A8-3, P2A2-2	Souchon, Rémi.....	2J-6, 3C-3, 3G-5		
Shikama, Joe.....	3H-1	Soulez, Gilles.....	2B-6, P1B6-10		
Shikhabudinov, Alexander.....	P3B1-5	Speciale, Nicolò.....	P1C7-3		
Shilton, Richie.....	4E-4, 4E-5, PA-8	Speelman, Lambert.....	P1C5-9		
Shim, Dong.....	5C-5	Spicer, James B.....	4C-1		
Shim, Munbo.....	P5C2-5	Spinczyk, Dominik.....	P1C7-1		
Shimidzu, Hiroki.....	P1C10-10				
Shimizu, Hiroshi.....	6H-1				
Shimizu, Kiyoshi.....	P3C1-5				
Shimizu, Masatoshi.....	P2C2-2				
Shimizu, Tsuyoshi.....	P5A2-14				

## T

T. Nguyen, Kim-Cuong.....	P1A9-7
Ta, Dean.....	3J-2, 4D-1
Tabassian, Mahdi.....	P1C7-3
Tabeling, Patrick.....	4E-2
Tabuchi, Masaaki.....	P3A2-1
Tadayon, Mohammad Amin.....	7J-3
Tadayyon, Hadi.....	3C-5, P1B9-3, P1B9-7, P1C7-8
Tag, Andreas.....	PA-15
Tagawa, Norio.....	P1A11-7
Taghaddos, Elaheh.....	7D-4
Tailor, Hamel.....	P5B1-3
Takagi, Ryo.....	P1C11-10, P1C11-15
Takagi, Shu.....	2K-6, 5E-4, P1C10-10, P1C11-13
Takahashi, Hiroki.....	2D-5
Takano, Shinta.....	P1B2-1
Takasaki, Masaya.....	P3C1-4

Takata, Chihiro	P3C2-2	Tong, Ling	3B-4, P1A4-5, P1A5-2, P1A5-3, P1A5-9, P1C5-1	Vallet, Quentin	3J-5
Takayama, Ryoichi	6I-3	Tordjman, Joan	P1A2-1	Vallone, John	P5C1-13
Takayanagi, Kosuke	P4C1-1	Torp, Hans	1H-3, 1J-3, 2D-4, 3E-6, P1A11-1, P1B3-4, P1B3-7, P1B8-6, P1C7-6	van Burken, Gerard	1H-2
Takayanagi, Shinji	3J-4, 5H-1, 6I-5, P3C2-2, P3C2-5, PA-11	Torres, Javier	P2C3-7	van de Vosse, Frans	1A-5, P1B6-2, P1B6-3, P1C5-10, P1C5-5, P1C5-9, P1C9-10
Takeda, Dai	5I-3	Tortoli, Piero	2D-6, 2E-4, 3B-4, P1A4-5, P1A5-8, P1A5-9, P1A6-12, P1A6-5, P1B2-3, P1B4-4, P1C1-5, P1C3-3, P5B2-1, P5B2-8	Van Den Abeele, Koen	P1C4-3, P1C9-1
Takeda, Nobuo	6B-5, P2A2-8, P4C1-1	Tournaire, Franck	2G-4	van den Oord, Stijn C.H.	1J-4
Takemoto, Tsuyoshi	6F-5	Traberg, Marie Sand	P1C3-7	van der Lugt, Aad	2I-3
Takemura, Kenjiro	P2C3-3, P5B2-9	Trabulsi, Edouard	1C-3	van der Steen, Antonius F.W.	1E-2, 1H-2, 1I-5, 1J-4, 2H-2, 2I-1, 2I-3, P1B5-1
Takeshima, Yutaka	P5A2-7	Tracey, Brian	P1B2-5	van Dongen, Koen	P5C1-12
Takeuchi, Hideki	P1C10-10, P1C11-13	Trachet, Bram	P1B3-2	van Mastrigt, Ron	P1B8-2
Takeuchi, Shinichi	P5A2-10, P5A2-4	Trahey, Gregg	2B-4, 2B-5, 2H-1, 3F-4, P1B2-7	van Neer, Paul	P2C1-3, P5C1-12
Taki, Hirofumi	P1A11-5, P1A8-3	Tran, Tho N.H.T.	P1A9-7	van Rooij, Tom	1E-1, 1E-2
Talbi, Abdelkrim	5I-4, 6B-6, P3C3-10, P4B2-2	Tran, William	P1A3-7, P1B9-7, P1C7-8	van Soest, Gijs	2H-2, 2I-1, 2I-3
Talmant, Maryline	3J-5, P1A9-6	Tran, William Tyler	P1B9-1, P1C4-5	van Stralen, Marijn	1H-2
Tam, Sarah	P1C4-1	Tranquart, Francois	P1A3-2	van Walsum, Theo	1H-2
Tamagno, Iliezer	P1A6-9	Trask, Richard S.	5D-2, PA-13	Vanagas, Gailius	P5C1-3, P5C1-5
Tamalonis, Anthony	5E-5	Travagliati, Marco	4E-4, 4E-5, PA-8	Vander Meulen, François	P2A3-1
Tamano, Satoshi	2K-6	Traverso, Giovanni	3H-3	Vanderlaan, Don	2I-2, P1B10-1
Tamura, Kazuki	P1C8-8	Treeby, Bradley	5B-2, 5K-5, P3A2-7, P3B2-5	Varga, Peter	2G-6, 3J-1
Tan, Jackie	6A-5	Tremblay-Darveau, Charles	P1B4-1, P1B4-3	Varghese, Tomy	P1A2-2, P1B7-1, P1B9-10, P1C8-5, P1C9-3
Tan, Jin Jack	4H-5	Trindade, Bruno	P5B2-5	Varray, François	3B-6, P1A5-4, P1A7-7, P1C2-3
Tanaka, Shuji	6C-1, 6H-4, 6H-6, 7I-3, P4B1-6	Trokhimets, Konstantin	P4A3-1	Vasseur, Jérôme	5B-5, 5B-6
Tanaka, Tomohiko	P1C3-8	Trudeau, Tammy	P1B11-10	Vasudevan, Vidya	P2B1-2
Tang, Hu	P5A2-11	Tsai, Chen	3H-5	Vaxelaire, Nicolas	P3C2-1
Tang, Meng-Xing	1I-1, P1B3-10, P1B5-4, P1B7-4	Tsai, Chin-Hsiung	P1B7-9	Vegas-Sanchez-Ferrero, Gonzalo	1H-2
Tang, Sai Chun	P1B10-8	Tsai, S. C.	3H-5	Vejdani-Jahromi, Maryam	2B-4
Tang, Zhuoyuan	4J-1	Tsai, Scott	P2B2-4	Velte, Elena	P1C8-9
Taniguchi, Nobuyuki	P1A4-3	Tsai, Wei-Che	P2B3-1	Vencill, Thomas	7I-1
Taniguchi, Satoki	5A-4	Tsiaparas, Nikolaos	P1C8-6	Ventura, Pascal	P4A2-2
Tanter, Mickael	1C-4, 1G-2, 1I-3, 1K-2, 2B-1, 2B-3, 2C-1, 2D-3, 3C-2, 3G-6, 4E-2, 5C-3, P1A1-2, P1A3-1, P1A7-11, P1B4-8, P1B7-7	Tsuji, Toshihiro	6B-5, P4C1-1	Verboven, Erik	P1C4-3, P1C9-1
Tanter, Mickael	2A-6, 2E-1, 2E-2, PA-1	Tsujino, Jiromaru	4J-6	Verdú, Jordi	P4A2-3
Tardoski, Sophie	3K-6, P1C10-7	Tsukahara, Yusuke	P4C1-1	Veres, Istvan	4C-3, P2A1-6, P2A2-4, P2C2-3
Tasdelen, A. Sinan	P5C1-1	Tsuneda, Hiroko	3J-4	Vergara, Luis	4C-2, 4D-5
Tauveron, Valérie	P1B7-12	Tsuruta, Jim	P1A4-9	Verma, Prashant	3B-2
Tavakkoli, Jahan	P3A2-4	Tsutsumi, Jun	6A-1	Versluis, Michel	1I-5, 4E-1, P1B1-6, P1B5-7, P1B5-9, PA-4
Tavakoli, Behnoosh	3A-5	Tsvirkun, Viktor	P3C3-3	Verweij, Martin	P3A2-7, P5B2-10, P5C1-12
Taylor, Jason	3E-2, 4F-5	Tubota, Ryo	3J-6	Vetelino, John	P2C1-5
Tegnander, Eva	3E-6	Tung, Yao-Sheng	2F-3	Viard, Romain	6B-6
Tekes, Coskun	7F-2, P1A8-4, P5A1-3, PA-19	Turchin, Pavel	P3B1-8	Vignon, Francois	P1C1-6
Telichko, Arseniy	P4A1-6, P4B2-5	Twiefel, Jens	P2C3-5	Vilain Thomsen, Erik	7F-5, P5C1-9
Teplykh, Andrey	P3B1-3, P3B1-5	U		Vilkomerson, David	P1B10-8, P1C3-3
Testoni, Nicola	P1C7-3	Uchiage, Kota	P3C1-4	Villagomez Hoyos, Carlos A.	P1B3-5, P1B6-5
Thepault, Rose-Anne	P1A10-1	Uchida, Takeyoshi	P5A2-10	Villanueva, Flordeliza	1E-1, 2A-2, P1C10-1, P1C11-6
Thiran, Jean-Philippe	3B-6	Ueda, Masanori	6A-1, 6C-3	Villemain, Olivier	1G-2, 2B-3, 2D-3
Thomas, Majorca	P1B1-8	Uemura, Shin-Ichiro	2K-6, 7D-3, P1A2-7, P1C11-10, P1C11-15	Vince, Philippe	1D-4, P5B2-2
Thomas, Peter	P3C3-2, P5C2-2	Umphrey, Heidi	1C-5	Vincenot, Jeremy	2J-1
Thomenius, Kai	1D-1, 3H-3, P1A3-5	Unamuno, Anartz	7C-1	Vincenot, Jérémy	2J-6, P1B11-7
Thomsen, Erik Vilain	P5C1-4, P5C1-7	Undzys, Eljusz	3D-6	Vincent, Brice	6B-2
Thongchai, Tanikan	7I-2	Unkrich, Mark	6A-6	Virzonis, Darius	P5C1-3, P5C1-5
Thong-Un, Natee	P2C2-4	Unluggedik, Asli	P5C1-1	Viti, Jacopo	P1A5-8, P1B4-4
Thorsten, Schmitz-Kempen	P3C2-3	Urbach, Paul	P5C1-12	Vladisauskas, Alfonsas	4G-5
Tian, Jian	7G-1, 7I-5	Urban, Alexander	P2B1-6	Voglhuber-Brunnmaier, Thomas	P2C1-1, P5B2-11
Tian, Lu	1B-1, 1B-2, 1B-3, 3D-4	Urban, Matthew	1K-1, 1K-5, 2B-2, 2H-6, 3C-6, 3G-3, P1A1-2, P1A1-4, P1A1-6, P1A2-3, P1B6-6, P1B7-11, P1C6-3, P1C6-5	Vogt, Michael	4A-5
Tian, Yahui	P3C3-1, P3C3-4	Utegulov, Zhandos N.	P2C2-3	Volker, Arno	P2C1-3
Tian, Yikui	1B-4	V		Volkov, Alexander	P4A1-6
Tiercelin, Nicolas	5I-4	Vachutka, Jaromir	P1A6-10	Vollborn, Thorsten	3H-6, P1C7-4
Timonen, Jussi	P1A9-2	Vaillant, Fanny	3K-5	Von Der Weid, Jean Pierre	4I-2, P2A3-3
Ting, Chien-Yu	P1A10-3	Valerio, Clement	P4B1-2	Von Ramm, Olaf	P1A5-5
Ting, Pei-Hsien	3E-5, PA-3	Vallabhaneni, Raghuveer	P1B6-1	Vonk, Tim M.	1A-5
Ting, Yung	7E-2, P5A2-2, P5C2-4	Vallet, Maëva	P1A7-7	Voormolen, Marco	P1B3-7
Tittmann, Bernhard	7E-5, P2B2-5			Vos, Hendrik J.	P1B4-4
Tjalkens, Tjalling	P1A3-3			Vossiek, Martin	4I-3, P2B1-6
Tjong, Jimi	P2A3-8			Vray, Didier	1J-5, P1A7-7, P1C2-3, PA-6
Tobias, Richard	1D-2			Vreeland, Erika C.	7E-4
Toda, Minoru	P5A2-8				
Todd, Michael D.	4A-6				
Tofel, Pavel	7I-2				
Tomov, Borislav G.	P1A4-1, P1C1-2, P1C1-3				
Tonazzini, Ilaria	4E-5, PA-8				



Waag, Grundle.....	4K-5	Wilcox, Paul.....	4A-1, 4A-6, 5E-1	Yang, Hsiao-Bai.....	3C-1
Wagle, Sanat.....	P5A2-9, P5B1-1	Wilken-Resman, Elias.....	P1C11-11	Yang, Jia.....	P3C3-2, P5C2-2
Wagner, Karl.....	6H-2	Wilkes, Annina.....	1C-2	Yang, Jin.....	P2A3-4
Wakatsuki, Naoto.....	P2A3-7, P3A2-2	Wilkinson, Andrew.....	4A-3	Yang, Ming.....	P1A6-7
Walczak, Mateusz.....	P1A6-8	Williams, David.....	7I-1	Yang, Sangsik.....	P4C1-5
Wallace, Kirk.....	P1A3-5	Williams, Jay.....	7A-1, 7A-4, P5B2-7	Yang, Tai-Hua.....	3C-1
Walter, Susan.....	5H-2	Williams, Ross.....	P1B4-1	Yang, Wenjun.....	P1A2-2
Wamhoff, Brian R.....	2A-3	Willmann, Jürgen.....	1B-1, 1B-2, 1B-3, 1B-5, 3D-4, P1A3-2, P1A3-9, P1C10-2	Yang, Xuan.....	P1B4-9
Wan, Jennifer M. F.....	3K-1, P1A4-10, P1A4-11, P1A4-12	Wilson, Katheryne.....	1B-1, 3D-4	Yang, Yaoheng.....	7A-2
Wan, Jinjin.....	P1B4-9	Wilt, Kyle.....	4F-1	Yang, Yiqun.....	P1C6-5
Wan, Mingxi.....	P1A4-14, P1B4-9, P3B2-6	Wirtzfeld, Lauren.....	2G-1, 2G-5, 3D-6	Yang, Yun Jui.....	P5C2-4
Wang, Bixia.....	7I-4	Wissmeyer, Georg.....	P2A2-4	Yankin, Sergey.....	P3C3-10
Wang, Chung-Hsin.....	P1C10-8, P1C4-4	Witte, Russell.....	1H-5, 4K-6	Yantchev, Ventsislav.....	4G-2, 6E-2, P4A3-1
Wang, Congzhi.....	P1A6-2, P1B10-7, P1B9-6	Wójcik, Janusz.....	2H-3	Yatsuda, Hiromi.....	P4B2-3
Wang, Diya.....	P1B4-9	Wolf, Patrick.....	2B-4, P1B7-2	Yddal, Torstein.....	P5B1-8
Wang, Dong.....	2J-4	Wolfart, Stefan.....	3H-6	Ye, Zongying.....	P1B10-7
Wang, Han.....	P3A1-3	Wong, Emily.....	1A-2, 3G-4, 3K-3, P1C10-4	Ye, Zuo-Guang.....	7E-3, 7I-4, P5B1-3, P5B1-4
Wang, Huaijun.....	1B-2, 1B-3, P1A3-9	Wong, Hoi Ting.....	P5B1-4	Yeager, Doug.....	2I-2, P1B10-1
Wang, James H-C.....	P4A3-7	Wong, Lawrence.....	7B-6, P1B10-2	Yeh, Chia-Lun.....	P1A2-4, P1A2-8, P1B7-8
Wang, Ji.....	P3B1-1, P3B1-6	Wright, William.....	4K-4, P1B8-3	Yeh, Chih-Kuang.....	2A-4, P1A10-3, P1B5-8, P1C10-8, P1C4-4
Wang, Jianjun.....	P1C10-1	Wu, Chi.....	P1A8-1	Yen, Jesse.....	2K-3, 3F-6
Wang, Junchen.....	P1C11-13	Wu, Hongxiao.....	5E-1	Yeo, Leslie.....	4E-3, 5A-1, 5J-1, 6E-5, P1A10-8
Wang, Kejian.....	1C-4	Wu, Huiyan.....	P4A3-7, P4C1-3, P4C1-4	Yeo, Sunmi.....	P1B10-5, P1B3-9
Wang, Michael.....	P1A1-4, P1C6-2	Wu, Jiang.....	P3C1-5	Yeow, John.....	7B-6, P1B10-2
Wang, Qi.....	3H-4	Wu, Jian-Xing.....	P1C9-6	Yetik, Hasan.....	7D-5, P5A1-1
Wang, Qing-Ming.....	P4A3-7, P4C1-3, P4C1-4, P5A2-13	Wu, Min.....	2I-1	Yin, Ching-Chung.....	P2B3-1
Wang, Ruikang K.....	2C-6, 3G-4	Wu, Shih-Ying.....	3I-3, 3I-4, PA-5	Yin, Melissa.....	P1B4-3, P1C4-10
Wang, Shiyang.....	1I-4, PA-2	Wu, Shiwei.....	P2A2-5	Yiu, Billy Y. S.....	1D-5, 2D-1, P1A6-3, P1A6-4, P1C3-1
Wang, Shutao.....	3K-2, P1C10-5, P1C10-6, P1C11-3, P1C11-7	Wu, Xun.....	PA-18	Ylilammi, Markku.....	6D-4
Wang, Shyh-Hau.....	3C-1	Wu, Ziqi.....	5D-4	Yoganandan, Narayan.....	3E-3
Wang, Tianfu.....	P1C6-7, P5A2-11			Yokoyama, Takehiro.....	P3C1-6
Wang, Tzu-Yin.....	P1C10-2			Yokoyama, Tsuyoshi.....	6C-3
Wang, Weiqi.....	3J-2, 4D-1			Yonai, Jun.....	P1C11-2
Wang, Wen.....	P2C1-2			Yoneda, Toshimaro.....	P5A2-7
Wang, Xiao.....	P1C8-5			Yong, Yook-Kong.....	5C-1, P4A1-4
Wang, Xin.....	4H-5			Yoo, Sungjoo.....	P1A8-2
Wang, Xiong.....	4K-6			Yoo, Yangmo.....	P1A6-11, P1A8-7, P1B10-5, P1B10-6, P1B2-2, P1B3-9, P1C1-1
Wang, Xiuming.....	4D-2, 4I-4, P3B1-2			Yoon, Changhan.....	7A-1, 7A-4, P3A1-4, P3B2-10
Wang, Xueding.....	P1A7-2			Yoon, Chi Woo.....	5D-5
Wang, Yak-Nam.....	1F-5, P1C10-11			Yoon, Sangpil.....	7A-1, 7A-4
Wang, Yan.....	2J-4, P1B1-2			Yoon, Soon Joon.....	P1B1-3
Wang, Yang.....	P1C11-14			Yoon, Yeokyong.....	P1B3-9
Wang, Yizhong.....	P4C1-3			Yoshida, Kenji.....	P1C8-3, P1C8-4, P1C8-7, P1C8-8
Wang, Yu.....	P1B7-13			Yoshida, Koki.....	3H-1
Wang, Yue-Sheng.....	P3C3-7			Yoshida, Shinya.....	7I-3
Wang, Zhengbo.....	4I-4			Yoshikawa, Hideki.....	P1B7-14
Wang, Zhigang.....	2J-4, P1B1-2			Yoshinaka, Kiyoshi.....	2K-6, P1C10-10, P1C11-13
Wang, Zhuochen.....	P1C5-4, P5B2-3, P5B2-4			Yoshioka, Masahiro.....	P5A2-10
Wasa, Kiyotaka.....	5H-5, 7I-3			Yoshizawa, Shin.....	7D-3, P1A2-7, P1C11-10, P1C11-15
Watanabe, Toru.....	P5A1-4			Youn, Hong Seok.....	5K-6
Wear, Keith.....	3J-3, P1A4-2			Yu, Alfred.....	1D-5, 1J-5, 2D-1, 3K-1, P1A4-10, P1A4-11, P1A4-12, P1A4-7, P1A6-3, P1A6-4, P1C3-1, PA-6
Weber, Richard.....	5E-5			Yu, Francois.....	1D-3, P1B2-4, P1C10-1, P1C11-6
Wegener, Michael.....	P5A2-9			Yu, Jaesok.....	1D-3, 3D-1
Wei, Chen-Wei.....	2I-5, 2J-2, 3D-5			Yu, Xue.....	P1C8-10
Wei, Siyuan.....	P1A6-7			Yuan, Jie.....	P1A7-2
Weigel, Robert.....	PA-15			Yuan, Lili.....	2H-4
Weihnacht, Manfred.....	6I-1, P4B2-4			Yudistira, Didit.....	5J-1, 6E-5
Weitz, Andrew.....	2G-2			Yuldashev, Petr.....	P1B11-4
Wen, Jing.....	P2A3-4			Yurchenko, Alexander.....	4H-1
Wen, Yumei.....	P2A3-4, P2C3-4			Yurii, Pilgun.....	4H-1
Wendlandt, Robert.....	2G-6, 3J-1				
Wenisch, Thomas.....	P1A6-7				
Wessells, Hunter.....	1F-4				
Westerveld, Wouter.....	P5C1-12				
Weston, Miles.....	P2A2-3				
Wheatley, Margaret.....	P1C4-2				
White, Grady.....	4C-5				
Widman, Erik.....	2F-6, P1B6-6				
Widynski, Nicolas.....	2F-4, P1B3-8				
Wieja, Krzysztof.....	P3B2-3, P3B2-4				
Wijkstra, Hessel.....	1G-5, P1A3-3				
		Xia, Jinjun.....	2I-5, 2J-2, 4D-4		
		Xiang, Yongjia.....	P2A1-1, P5C2-3		
		Xiao, Bo.....	P2A1-7		
		Xiao, Yang.....	P1A6-2, P1B10-7, P1B9-6		
		Xie, Hua.....	P1C6-1		
		Xie, Jiemin.....	P4C1-3		
		Xie, Xiaojia.....	7H-3		
		Xie, Yujun.....	7I-4		
		Xin, Hao.....	4K-6		
		Xin, Penglai.....	4I-4		
		Xu, Kailiang.....	3J-2, 4D-1		
		Xu, Toby.....	7F-2, P1A8-4, PA-19		
		Xu, Yuan.....	2K-4, P1A6-1		
		Xu, Zhen.....	1F-2, 1F-3, 7D-6, P1B11-1, P1C11-5		
		Yagi, Hisashi.....	P1A4-13		
		Yamaguchi, Daisuke.....	5I-3, P3C1-3		
		Yamaguchi, Tadashi.....	P1C8-3, P1C8-4, P1C8-7, P1C8-8		
		Yamakawa, Makoto.....	P1A1-9, P1A8-3, P2A2-2		
		Yamamoto, Kansho.....	P5A2-7		
		Yamamoto, Yasuo.....	6C-1		
		Yamanaka, Kazushi.....	6B-5, P4C1-1		
		Yamaner, F. Yalcin.....	7F-6		
		Yamanouchi, Kazuhiko.....	P4B1-7		
		Yamashita, Hiromasa.....	P1C11-2		
		Yamashita, Mary.....	P5C1-13		
		Yamashita, Yohachi (John).....	7E-3		
		Yan, Fei.....	P1B9-6		
		Yan, Xinwei.....	P5B1-5		
		Yanagihara, Eugene.....	2G-3		
		Yanagisawa, Takayuki.....	6B-5, P4C1-1		
		Yanagitani, Takahiko.....	3J-4, 5H-1, 5H-5, 5I-5, 6I-5, P3C2-2, P3C2-5, PA-11		
		Yang, Aichao.....	P2C3-4		
		Yang, Bin.....	7A-2		
		Yang, Che-Hua.....	4H-3, 4H-6, P2A3-9		

Zang, Hua.....	P1C4-1
Zapf, Michael.....	2K-5, P1A11-8, P1B8-8
Zderic, Vesna.....	P1A10-10, P1A10-5
Zeghimi, Aya.....	3I-6, P1A10-1
Zemp, Roger.....	P1A5-7, P5C1-11
Zeng, Bo.....	P1A6-2
Zeng, Fan W.....	4C-1
Zenteno, Omar.....	P1B9-9, P1C9-5
Zeqiri, Bajram.....	4G-4
Zhang, Chao.....	P5A2-15
Zhang, Cheng.....	5I-6
Zhang, Chenrui.....	P4C1-2
Zhang, Daihua.....	P4A3-5, P4B1-3
Zhang, Han.....	P2A1-4
Zhang, Hao.....	P4A3-5, P4B1-3
Zhang, Hongxiang.....	P4B1-3
Zhang, Jinying.....	P5A2-5
Zhang, Menglun.....	P4A3-5
Zhang, Miaomiao.....	3B-6, P1A5-4
Zhang, Nan.....	7I-4
Zhang, Xi.....	P1C11-5
Zhang, Xiao.....	7F-6
Zhang, Xiaoming.....	P1B7-11
Zhang, Xiumei.....	P3B1-2
Zhang, Yaoyao.....	P5B1-9
Zhang, Yong-Zhi.....	3I-2
Zhang, Zhitian.....	P5A2-15
Zhao, Guangyi.....	P4A3-7
Zhao, Heng.....	1K-1, 1K-5, 2B-2, P1A1-4, P1A1-6
Zhao, Jinfeng.....	5J-2, P3C3-5, P3C3-6
Zhao, Jinyan.....	P5B1-5
Zhao, Lu.....	P1A4-14
Zhao, Xiaofeng.....	P1C2-5
Zhao, Xihai.....	1A-4
Zhao, Zuomin.....	P1A9-2
Zhelnavkov, Serge.....	4F-5
Zheng, Fei.....	P1A11-4
Zheng, Hairong.....	2E-6, P1A6-2, P1B10-7, P1B9-6
Zheng, Mingbin.....	P1B9-6
Zheng, Mingxin.....	3E-3
Zheng, Yi.....	P1C6-7
Zheng, Yuanyi.....	2J-4, P1B1-2
Zhgon, Sergei.....	6D-1, P4A3-1
Zhong, Wenjing.....	P1A4-10, P1A4-7
Zhou, Di.....	2J-4
Zhou, Maoying.....	P3C1-2
Zhou, Qifa.....	1J-2, 2E-6, 2F-3, 3H-2, 7G-3, P1A7-8, P5A2-15, P5A2-4, P5B1-5, PA-17
Zhou, Qunfang.....	P1B9-6
Zhou, Shiwei.....	P1C6-1
Zhou, Xiaoming.....	5B-4, 5J-6
Zhu, Benpeng.....	P5A2-4
Ziemlewicz, Timothy.....	P1A2-2
Zolek, Norbert.....	P1A6-8
Zolotova, Olga.....	P3B1-8
Zong, Yujin.....	P3B2-6
Zorgani, Ali.....	2J-6, 3G-5
Zou, Jie.....	6A-3
Zoueshtiagh, Farzam.....	5A-2
Zu, Hongfei.....	P4A3-7, P4C1-3
Zukauskas, Egidijus.....	4G-5
Zurakhov, Grigoriy.....	P1C7-7
Zywitzki, Olaf.....	5H-2



**2014 IEEE INTERNATIONAL ULTRASONICS SYMPOSIUM**

**CHICAGO, ILLINOIS, USA**

**SEPTEMBER 3-6, 2014**



**CHICAGO**



**IEEE ULTRASONICS, FERROELECTRICS,  
AND FREQUENCY CONTROL SOCIETY**



**Verasonics<sup>®</sup>**